Digitized by the Internet Archive
in 2024

https://archive.org/details/physical-society-of-japan-journal_january-december-1956_11_1-12

QC
1
P47

# JOURNAL
# OF THE
# PHYSICAL SOCIETY
# OF JAPAN

Volume 11
1956

Published by the
PHYSICAL SOCIETY OF JAPAN

JOURNAL OF THE PHYSICAL SOCIETY OF JAPAN Vol. 11, No. 1, JANUARY, 1956

# On the Neutrons from the $N^{14}(d, n)O^{15}$ Reaction

By Itaru NONAKA, Susumu MORITA, Nawoyuki KAWAI,
Toshiyuki ISHIMATSU, Shigeru SUEMATSU*,
Kenji TAKESHITA, Yutaka NAKAJIMA
and Yoshihisa WAKUDA

*Department of Physics, Faculty of Science, Kyushu University,*
*Fukuoka, Japan*

(Received August 29, 1955)

The energy spectrum and the angular distribution of the neutrons from the $N^{14}(d,n)O^{15}$ reaction were investigated by the photographic plate method. The energy of the bombarding deuterons was 1.85 MeV, and the $Q$-value corresponding to the ground state of $O^{15}$ nucleus was obtained to be $(5.21 \pm 0.07)$ MeV. The low energy neutron group corresponding to the first excited state of $O^{15}$ nucleus was also observed, but it overlapped with the contaminated $C^{12}(d,n)N^{13}$ neutrons and the accurate $Q$-value could not be determined. The estimated rough value was about $-0.1$ MeV.

The angular distribution of the high energy neutron group has a maximum at about 20 degrees (c.m.s.) and decreases considerably beyond this maximum, indicating the stripping process corresponding to $l_p=1$.

This reaction may be a good source of neutrons of about 7 MeV at the bombarding energies of deuterons below 2 MeV.

## § 1. Introduction

The neutrons from the $N^{14}(d, n)O^{15}$ reaction were investigated quantitatively first by Stephens et al.[1]. They bombarded a $NaNO_2$ thick target by an unanalysed deuteron beam of 0.93 MeV and found two groups of neutrons corresponding to the $Q$-value of $Q_0=(5.1 \pm 0.2)$ and $Q_1=(1.1 \pm 0.2)$ MeV respectively. Afterwards, Gibson and Livesey[2] also investigated this reaction at the same bombarding energy and found that there existed only one group of neutrons of which $Q$-value was $Q_0=(5.15 \pm 0.10)$ MeV, and the angular distribution of this group was almost isotropic in the centre-of-mass system.

Hudspeth and Swann[3] observed initially two groups of neutrons at the bombarding energy of 1.2 MeV of deuterons, but it was reported afterwards[4] that the observed low energy group was that from the alminium contained in the target material. Rose et al.[4] observed two groups of neutrons at the bombarding energy of 1.7 MeV of deuterons, and their $Q$-values were $Q_0=5.1$ and $Q_1=0.2$ MeV respectively.

At the bombarding energy of 7.69 MeV of deuterons, Evans et al[5]. observed seven groups of neutrons, and they measured the angular distributions of each group and estimated the $l_p$-values according to Butler's stripping theory.

Considering the above mentioned results obtained hitherto, the neutrons from this reaction are thought to consist of single group at the bombarding energies of deuterons below 1 MeV, and the low energy group corresponding to the first excited state of $O^{15}$ nucleus may begin to appear at a bombarding energy between 1 and 2 MeV, but the intensity of this group is expected to be not so strong. At these bombarding energies the energy of this group is estimated to have a value between 1 and 1.5 MeV from the $Q$-value of $Q_1=(-0.14 \pm 0.11)$ MeV obtained by Evans et al.[4] and is far below than that of the high energy group (about 7 MeV). So this reaction may be a good source of neutrons of about 7 MeV.[6]

On the other hand, the stripping process of deuterons of energy between 1 and 2 MeV contains many problems, i.e., competition with the compound process, the effect of Coulomb barrier, and the interaction between the emitted particle (neutron) and the residual nucleus.

---

* Now at Rigakudenki Ltd., Kichijōji, Tokyo.

On the above standpoint we investigated the energy spectrum and the angular distribution of the neutrons emitted by this reaction at the bombarding energy of 1.85 MeV of deuterons.

## § 2. Experimental Arrangements and Procedures

The deuteron bombardment was performed with the Van de Graaff accelerator at the Kyushu University and its voltage used in this experiment was 2.20 MV. The accelerating voltage was simply stabilized by controlling the spray voltage automatically with the corona current from the high voltage electrode to a corona point, and the voltage fluctuation of the electrode was less than one per cent..

Nitrogen gas was used as the target material. The target chamber, as shown in Fig. 1, consists of two coaxial cylinders, their bottoms being placed 4 cm apart, of which the outer one is of brass 3.5 cm in inside diameter and 0.15 cm in thickness, and the inner one is of steel 3.3 cm in outside diameter and 0.1 cm in thickness. The entrance to the target chamber is an aperture of 1.0 cm in diameter drilled in the bottom of the inner cylinder and sealed with a silver foil of 2.4 mg/cm$^2$ thick, prepared by the vacuum evaporation method. Any portion of the target assembly exposed to the deuteron beam is covered with silver plates as perfectly as possible in order to reduce the neutron background. The nitrogen gas used is commercial one and gas pressure of the chamber is 20 cm Hg.

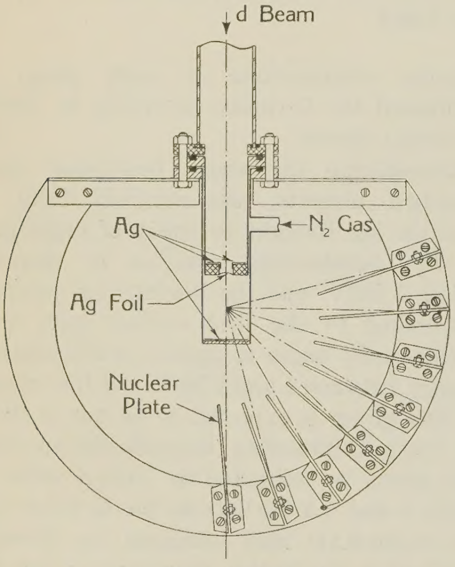

Fig. 1. Arrangements of the target chamber and photographic plates.

Nuclear photo-emulsion were used to detect the neutrons. Each nuclear plate was wraped completely in a thin black paper, after being covered with an alminium foil of about 0.1 cm in thickness to absorb protons produced in the black paper. These plates were placed on an alminium frame, surrounding the centre of the target chamber circularly at eight angles of 0.8, 14.2, 29.2, 44.2, 59.2, 74.2, 89.2 and 104.2 degrees* respectively with respect to the incident deuteron beam. The glancing angle of each plate was chosen to be 5 degrees.

The effective energy of the bombarding deuteron was taken as 1.85 MeV, considering the thickness of the silver foil window of the target chamber, 210 keV, and that of the nitrogen gas, 280 keV, respectively.

Since the target assembly itself was insulated from the ground, it was able to be used conveniently as a collector cup for the deuteron beam and was connected to both a current integrator7) and micro-ammeter in series. The analysed ion beam employed was $0.3\,\mu A$ in average during the bombardment time. The ion beam which entered into the target assembly was found to be utilized almost completely, but the available quantity of the deuterons was somewhat uncertain, since some molecular hydrogen ions were contained in the ion beam and their content was not known accurately.

The bombardment was performed in the two cases; one was the case in which the nitrogen gas was present in the target chamber and the other no gas present. Both runs were carried out similarly for about two hours in such a way that the total integrated ion currents used in both runs were equal.

The plates used were 150 micron Sakura NR-Ml nuclear plates. After the exposure the plates were processed by the two-bath development method according to the procedure recommended by the manufacturer. The original plate size was $8.2\times10.7\,\mathrm{cm}^2$, and each plate was divided into six parts for the exposure. To measure the emulsion thickness, a small piece was again cut off from the each divided plate, and the thickness of the glass backing plus emulsion and that of the glass backing alone were measured with a screw micrometer. The emulsion thickness was obtained as the difference of these two values. The thickness of the processed emulsion was measured with the fine-focus screw of a microscope, and the ratio of the thickness of the unprocessed emulsion to that of the processed one gave the shrinkage factor, the mean value of which was 2.2±0.1.

---

* The values of these angles are referred to the centres of the scanned area of each plate.

The scanning was performed throughout with Tiyoda L.C.M. binocular microscopes with ×7 eye pieces and ×135 oil immersion objectives. In each plate the region was scanned which had rectangular shape, 2 cm long and 0.6 cm wide, centred about the line connecting the centres of the target and the plate. The centre of the scanning region was about 3 cm distant from the inner edge of the plate, and 9.5 cm from the centre of the target chamber. Those recoil proton tracks were recorded which had horizontal angles of less than or equal to 15 degrees with the central line and dip angles of less than or equal to 15 degrees in the unprocessed emulsion, and originated and ended in the emulsion.

In the present experiment, for the sake of simplicity, we merely measured the projected length to the emulsion surface of the available tracks selected with the above criteria. From this measured quantity alone, the corresponding energy of the neutron is obtained with the following procedures.

The projected length $R_p$ of a recoil proton track is related to the absolute range $L_p$ of the proton in the unprocessed emulsion by the formula[8],

$$L_p = R_p/\overline{\cos\psi}\ , \qquad (1)$$

where $\overline{\cos\psi}$ is the average value of the cosine of the angle $\psi$ between $R_p$ and $L_p$, as shown in Fig. 2. With the slightly approximate calculations, it is easily found that $\overline{\cos\psi}$ is the function of the angles $\theta_{\max}$ and $\phi_{\max}$, which are the maximum values of the half angles $\theta$ and $\phi$ respectively of the rectangular pyramid formed by the recoil proton track. In the present case both $\theta_{\max}$ and $\phi_{\max}$ are 15 degrees.

The energy of the recoil proton, the absolute range of which is calculated by the above formula, is obtained directly from the range-energy relation. But the range-energy relation in the emulsion used was not known, so the relation calculated by Webb's method[9] taking into account the air humidity was used. It has been reported[9)10)11] that the relations calculated by this method of the several emulsions generally used were in good agreement with the experimental results. For the proton energies higher than 1 MeV, our calculated curve agreed well with the experimental proton range-energy curve for NTA emulsion in the air[10], as shown in Fig. 3. It was also found that the mean range of the alpha-particles in our emulsion obtained by contacting the Po-alpha source to the emulsion surface in the air was (21.5±0.5) microns, which fell within the error on the experimental curves

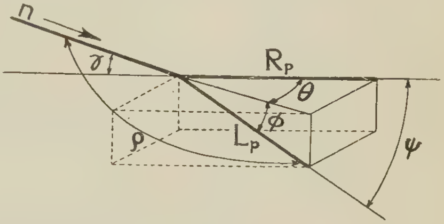

Fig. 2. Relation between the incident neutron and the recoil proton. $L_p$ is the absolute range of the proton in the unprocessed emulsion and $R_p$ is the projected length to the emulsion surface of the recoil proton track.

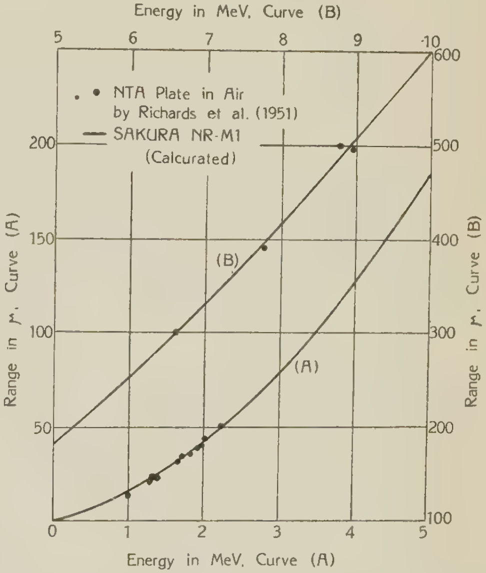

Fig. 3. Proton range-energy curve for Sakura NR-M1 emulsion, calculated by Webb's method. The circles are the experimental points by Richards et al. for NTA emulsion.

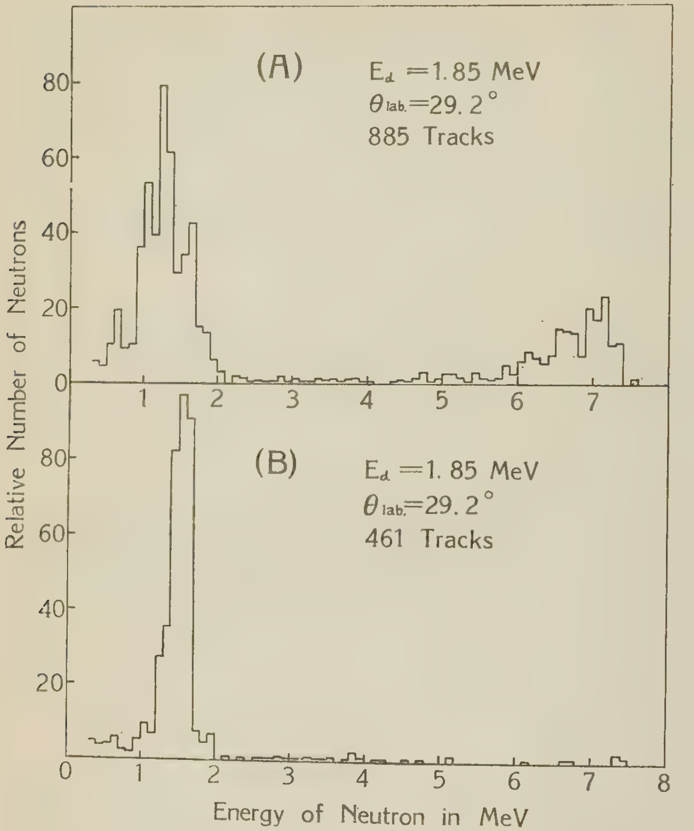

Fig. 4. Energy spectra of neutrons from $(d, n)$ reactions on $N^{14}$ at a laboratory angle of 29.2 degrees. The histogram (A) was obtained with the target chamber filled with nitrogen gas and (B), obtained with the evacuated target chamber, shows the background.

for Ilford B1[12)] and C2[13)] emulsions whose range-energy relations are supposed to differ not appreciably from NTA emulsion.

Next, the neutron energy $E_n$, corresponding to the recoil proton energy $E_p$, is given by the following relation[8)],

$$E_n = E_p / \overline{\cos^2 \rho} \qquad (2)$$

where $\overline{\cos^2 \rho}$ is the average value of the cosine squared of the angle $\rho$ between the incident neutron and the recoil proton directions and is also given as the function of $\theta_{max}$, $\phi_{max}$ and $\gamma_{max}$. $\gamma_{max}$ is the maximum value of the angle $\gamma$ that the incident neutron makes with the axis along which the projected lengths of tracks are measured.

The above described approximations lead to errors of less than one per cent. in the neutron energy $E_n$ for $\theta_{max}$, $\phi_{max}$ and $\gamma_{max} \leqq 15$ degrees[8)], which is just the present case.

Finally, in order to transform the proton energy distribution obtained by the above procedures into the neutron energy distribution, it must be still taken into account the variation of the neutron-proton scattering cross section and the escape probabilities of recoil protons from the emulsion surface. For the neutron-proton scattering cross sections, we have used the recent experimental results of several authors[14-17)]. As for the escape correction of recoil protons, it is sufficient to divide the results obtained above by the following factor $P$, so long as the tracks are rectilinear,

$$P = 1 - (L_p \sin\phi_{max} / 2t) \, , \qquad (3)$$

where $t$ is the thickness of the unprocessed emulsion[8)].

Following the above mentioned procedures, the neutron energy distributions per 0.1 MeV energy interval were obtained for each angle respectively, after being normalized with the scanned volumes.

In our experimental arrangement, the nitrogen gas target is 4 cm in length and so is considerably long. Hence, some part of neutrons emerging from the target into directions of more than 30 degrees will enter the emulsion from the backside of the photographic plates. These neutrons naturally penetrate the glasses of the plates and some of them, therefore, are taken off from the neutron beam by scattering. The correction for the presence of such neutrons was carried out rather simply for the angular distribution of the high energy group. It was found graphically that the average distances which were passed by the above described neutrons in the glass varied from 2 to 3 cm for each plate respectively. The proportions of these lost neutrons were calculated easily considering the total cross section of neutrons for the elements constituting the glass. The correction to be added to the results was found to have a maximum value of 6.2 per cent. for the plate placed at 104.2 degrees. The above mentioned correction, however, is supposed to be over-correction, because all the scattered neutrons are assumed to be lost entirely, but this is not the case as the forward scattering is predominant in general. But, as the correction itself is a small one compared with the statistical error, it is thought to have scarcely any meaning to consider the correction more accurately.

## § 3. Results and Discussions

The typical histograms of the energy spectra of neutrons are shown in Fig. 4, which were observed at an angle of 29.2 degrees in the laboratory system. The histogram (A) in Fig. 4 was obtained with the target chamber filled with nitrogen gas, while the histogram (B) of the background neutrons was obtained with the evacuated target chamber.

From these energy spectra, one can easily find the high energy group of neutrons from nitrogen with the peak at about 7 MeV.

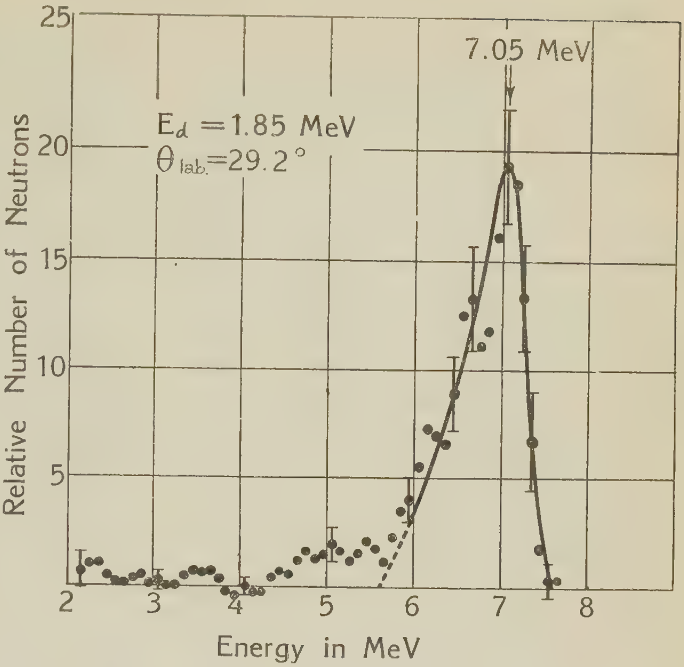

Fig. 5. Energy spectrum of neutrons of greater than 2 MeV from $(d, n)$ reactions on $N^{14}$ at a laboratory angle of 29.2 degrees, obtained by eliminating the background and smoothing up the histogram shown in Fig. 4 (A).

The interpretation of the lower energy region, below 2 MeV, of these spectra is much more complex. It is expected that the background neutrons in this region will be due to the carbon contaminant deposited on the silver foil and plate of the target chamber, because the Ag $(d, n)$ reaction has not been observed. The $Q$-value of $(-0.281 \pm 0.003)$ MeV has been reported for the $C^{12}(d, n)$ reaction by Bonner et al.[18] We have three carbon layers deposited on i) the forward surface of the silver foil of the target chamber, ii) the backward surface of this foil, and iii) the bottom surface of the target chamber. When the energy of the deuteron beam from the accelerating tube is 2.20 MeV, these three carbon layers are bombarded with the deuterons of 2.20, 1.99 and 1.71 MeV, respectively. Accordingly, the energy of neutrons observed at an angle of 29.2 degrees in the laboratory system must be 1.81, 1.61 and 1.34 MeV, respectively. The last one of these three groups will coincide in energy with the second one in case of the evacuated target chamber. And the relative intensities of these three neutron groups will depend on the thickness of the carbon layers, which are quite unknown and, moreover, may change with the bombarding time. Owing to these ambiguities, it was abandoned to treat this low energy region accurately, but some evidence of the existence of the low energy group was seen in the histograms at angles greater than 44.2 degrees. The $Q$-value was estimated roughly to be about $-0.1$ MeV which is consistent with the value obtained by Evans et al.[5]

In order to determine the energy of neutrons of high energy group, the histograms, after the background being subtracted, were smoothed up by plotting the sum of the neutron intensity in each energy interval and the halves of the neutron intensities in the both neighbouring intervals. In this way, we obtained the curve shown in Fig. 5 as an example. From these curves corresponding to each angles, we obtained the energies of neutrons at the peaks and calculated the $Q$-value for this reaction as shown in Table I, and obtained the mean value of $(5.21 \pm 0.04)$ MeV. But the absolute value of the energy of the bombarding deuterons may have an error of about 3 per cent., so the absolute value of $Q$-

Table I. $Q$-value of the high energy neutron group

| Plate number | $\theta$ in lab. system in degree | Neutron energy in MeV | $Q$ in MeV |
|---|---|---|---|
| $l$-1 | 0.8 | 7.00 | 5.19 |
| $l$-2 | 14.2 | 6.88 | 5.08 |
| $l$-3 | 29.2 | 7.05 | 5.32 |
| $l$-4 | 44.2 | 6.80 | 5.17 |
| $l$-5 | 59.2 | 6.85 | 5.36 |
| $l$-6 | 74.2 | 6.50 | 5.16 |
| $l$-7 | 89.2 | 6.50 | 5.33 |
| $l$-8 | 104.2 | 6.10 | 5.06 |
| mean value (5.21±0.04) MeV | | | |

Table II. Comparison of the $Q$-values by several investigators.

| $Q$ in MeV | Method | Investigator |
|---|---|---|
| 5.1 ±0.2 | cloud chamber | Stephens et al. (1937) [1] |
| 5.15±0.10 | nuclear plate | Gibson and Livesey (1948) [2] |
| 5.11±0.04 | nuclear plate | Mandeville et al. (1952) [19] |
| 5.1 | nuclear plate | Rose et al. (1952) [4] |
| 5.15±0.16 | nuclear plate | Evans et al. (1953) [5] |
| 5.21±0.07 | nuclear plate | Present authors |

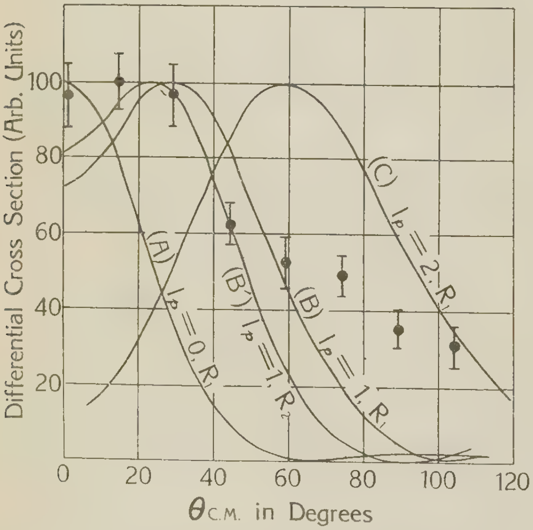

Fig. 6. Angular distribution of neutrons associated with the ground state of $O^{15}$ in the reaction $N^{14}(d, n)O^{15}$ for a deuteron energy of 1.85 MeV. Solid and broken curves were calculated from Butler's theory with $R=R_1=4.6\times10^{-13}$ cm for curves (A), (B) and (C) and $R=R_2=5.5\times10^{-13}$ cm for curve (B′), respectively. The curves (A) and (C) correspond to $l_p=0$ and 2 and the curves (B) and (B′) to $l_p=1$, respectively.

value is estimated to be (5.21±0.07) MeV, which is compared in Table II with the results previously obtained by other investigators. The agreement between the present result and the others is quite satisfactory.

In order to estimate the intensity of the high energy group of neutrons, we extrapolated the slope of lower energy side of the peak, as shown in Fig. 5 for example, and obtained the energy value of the intercept with the abscissa as 5.65 MeV, which was twenty per cent. lower than the value at the peak. As it was found that the value of twenty per cent. was almost common for all the other energy spectra obtained at other angles, we considered the neutrons of energy higher than this intercept as the ones associated with the reaction leading to the ground state of $O^{15}$ and thus we obtained the angular distribution in the centre-of-mass system, which is shown in Fig. 6. The errors indicated are statistical ones based on the number of tracks observed. The curves shown in Fig. 6 are theoretical angular distributions calculated from Butler's theory with $R=4.6\times10^{-13}$ cm for curves (A), (B) and (C) and $R=5.5\times10^{-13}$ cm for curve (B′), respectively. The curves (A) and (C) correspond to $l_p=0$ and 2 and the curves (B) and (B′) correspond to $l_p=1$, respectively. The experimental points agree with the theoretical curves for $l_p=1$ in reaching the maximum at about 20 degrees and decreasing considerably beyond this maximum, and this result agrees with that of Evans et al.[5] at 7.69 MeV of deuteron energy. As the ground state of $N^{14}$ has been measured to have the spin of unity and even parity, the result shows that the ground state of $O^{15}$ has the spin of 5/2, 3/2 or 1/2 and odd parity. According to the shell model of nuclei, the ground state of $O^{15}$ must be $P_{1/2}$ and is consistent with our present result. The experimental points lie considerably above the theoretical curves at angles greater than 60 degrees. These deviations would possibly be caused by i) the compound nucleus process, ii) the effect of the Coulomb barrier, and iii) the interaction between the emitted neutron and the residual nucleus. But it is impossible to analyse these discrepancies in the present state.

As a conclusion, we would like to make some mention on the availability of the $N^{14}$

$(d, n)O^{15}$ reaction as a neutron source. Although the low energy group of neutrons, not greater than 2 MeV, can be seen with some intensity, it is considerably apart from the high energy group. So it will not be impossible to use the high energy group as a neutron source of about 7 MeV, with some improvement on the measuring devices, but large yield will not be expected. In our present experiment, only a trace of neuterons from *d-d* reaction by deuterium contamination could be found.

The authors wish to express their cordial thanks to Mr. Y. Wakabayashi of the Chemical Research Laboratory of Konishi-Roku Photographic Industry for his kind preparation of nuclear plates. This work has been supported by the Scientific Research Expenditure of the Ministry of Education.

### References

1) W. S. Stephens, K. Djanab and T. W. Bonner: Phys. Rev. **52** (1937) 1079.
2) W. M. Gibson and D. L. Livesey: Proc. Phys. Soc. London **60** (1948) 523.
3) E. L. Hudspeth and C. P. Swann: Phys. Rev. **76** (1949) 464 (A).
4) W. B. Rose, E. L. Hudspeth and N. P. Heydenburg: Phys. Rev. **87** (1952) 382 (L).
5) W. H. Evans, T. S. Green and R. Middleton: Proc. Phys. Soc. London, **A66** (1953) 108.
6) A. O. Hanson, R. F. Taschek and J. H. Williams: Revs. Mod. Phys. **21** (1949) 635.
7) H. T. Gittings Jr.: Rev. Sci. Inst. **20** (1949) 325.
8) L. Rosen: Nucleonics, **11** (1953) 38.
9) J. H. Webb: Phys. Rev. **74** (1948) 511.
10) H. T. Richards, V. R. Johnson, F. Ajzenberg and M. J. W. Laubenstein: Phys. Rev. **83** (1951) 994.
11) C. F. Lees, G. C. Morrison and W. G. V. Rosser: Proc. Phys. Soc. London **A66** (1953) 13.
12) C. M. G. Lattes, P. H. Fowler and P. Cüer: Proc. Phys. Soc. London, **59** (1947) 883.
13) J. Rotblat: Nature, **167** (1951) 550.
14) C. L. Bailey, W. E. Benett, T. Bergstrahl, R. G. Nucholls, H. T. Richards and J. H. Williams: Phys. Rev. **70** (1946) 583.
15) D. H. Frisch: Phys. Rev. **70** (1946) 589.
16) M. Ageno, E. Amaldi, D. Bocciarelli and G. C. Trabacchi: Phys. Rev. **71** (1947) 20.
17) E. E. Lampi, G. D. Freier and J. H. Williams: Phys. Rev. **80** (1950) 853.
18) T. W. Bonner, J. E. Evans, J. C. Harris and G. C. Phillips: Phys. Rev. **75** (1949) 1401.
19) C. E. Mandeville, C. P. Swann, S. D. Chatterjee and D. M. VanPatter: Phys. Rev. **85** (1952) 193.

---

JOURNAL OF THE PHYSICAL SOCIETY OF JAPAN Vol. 11, No. 1, JANUARY, 1956

# A Lattice Theory of Quantum Fluids

By Shoichiro KOIDE

*Institute of Physics, College of General Education,*
*University of Tokyo*

(Received August 29, 1955)

Using the procedure of 'lattice space quantization', the cell method for liquids is developed quantum mechanically so as to include the inter-cellular motion of the molecules. It is shown that the statistics plays its essential roles in this inter-cellular motion just as in the case of ideal gases. The ground state of the Bose liquid and the lambda-transition of liquid helium are discussed on this stand point.

## §1. Introduction

The cell method or free volume theory is one of the most promising methods for the description of the liquid states[1]. The relation of this intuitive method to the rigorous one is discussed by Kirkwook[2], and, so far as the classical liquids are concerned, its approximation is now of established character.

However, the cell method is rather like the theory of solids than of liquids, if we take the number of cells equal to that of the molecules and neglect the probability of multiple occupations. In this respect improvements are made by the hole theory[3], and, more recently, by the cell-cluster models proposed by de Boer[4].

In most of these theories, starting point is the classical partition function $Z_c$, and the kinetic energy is included only in the factor $(2\pi mkT/\hbar)^{3N/2}$ multiplied to the 'configurational integral' $Q_N$: $Z_c=(2\pi mkT/\hbar)^{3N/2}Q_N$. In the case of quantum liquids, however, the partition function cannot be factorized in this way. Since the zero point motion of a light particle increases when confined in a small cage because of the uncertainty principle, the kinetic energy is not a small correction to the lattice potential energy even at extremely low temperatures. The above mentioned $Z_c$ cannot describe this situation.

In the calculation of the zero-point energy of helium, Pekeris[5] estimated this kinetic energy by solving the Schrödinger equation of a molecule confined in a cage of the potential by its neighbor molecules. It is, however, impossible for this kind of calculation to consider another important quantum effect, i.e. the effect of statistics. Prigogine and Philippot considered the multiply occupied cells and tried to take account of the effect of statistics[6]. They treated the molecules as rigid spheres moving freely in each cell, because the detailed shape of the cage potential is not so important. According to their theory, all molecules in a multiply occupied cell can occupy the lowest energy level if they obey the Bose statistics, but it is not the case for Fermi paticles. Their treatment still seems to be insufficient if we think about the essential role of the statistics in the case of ideal gases.

In gases, the molecules move about the whole vessels, and, if we imaginarily divide the entire volume of the vessel into cells, they migrate from cell to cell and exchange their positions with each other all the time. The statistics displays its feature in this 'inter-cellular' motion.

As is well known, liquid helium has a small density and in some respects behaves like gases. Many of its properties can be explained by the gas models, and Bose statistics is essential for the interpretation of its peculiarity. It is, therefore, highly desirable to construct a cell model, in which the inter-cellular migration of the molecules are considered quantum mechanically. This model must also be able to be connected with the usual quantum mechanical treatment of the gases, i.e. it must tend to the ideal gas in the limit of vanishing interaction and of infinitely small cell size.

According to the above considerations, most of the contribution to the inter-cellular motion should be attributed to the kinetic part of the Hamiltonian, though the potential part may affect to some extent. This inter-cellular motion is represented by the non-diagonal elements of the Hamiltonian in the cofiguration representation. Any configuration obtained by arranging the molecules among cells cannot be by itself an eigenstate of the Hamiltonian. It has an undeservedly high energy, because every molecule is locked in a small cell in an artificial way. This increase of the kinetic energy is relieved by taking linear combination of the configurations. In other words, the molecules wander about in order to relax the excessive kinetic energy. Therefore, it is essential to take account of the non-diagonal elements of the Hamiltonian, especially of its kinetic part, which are completely disregarded in previous works on the lattice theory of fluids.

If we think about the analogy between the lambda-transition of liquid helium and the Bose-Einstein condensation of the ideal gas, it may be probable that the lambda-transition arises from the inter-cellular motion of the helium atoms rather than from their intra-cellular motion, which plays an essential role in Prigogine and Philippot's theory[6].

## § 2. Lattice Hamiltonian

In this section, applying a procedure 'lattice space quantization' introduced by Wentzel and Schiff[7], we will translate the Hamiltonian of the fluid into an approximate one which is convenient to be connected with the cell method.

Using the formalism of the second quantization, the Hamiltonian of an assembly of $N$ interacting particles can be expressed as

$$H=\int dv\frac{\hbar^2}{2m}(\nabla\psi^*,\nabla\psi)+\tfrac{1}{2}\iint dvdv'\psi^*(\boldsymbol{r})\psi^*(\boldsymbol{r}')U(\boldsymbol{r},\boldsymbol{r}')\psi(\boldsymbol{r}')\psi(\boldsymbol{r}), \tag{1}$$

where $m$ represents the mass of a particle and $U(\boldsymbol{r}, \boldsymbol{r}')$ the potential of the interaction. $\psi(\boldsymbol{r})$ is the so-called quantized wave function and satisfies the following commutation relations.

$$\begin{aligned}&\psi(\boldsymbol{r})\psi^*(\boldsymbol{r}')\pm\psi^*(\boldsymbol{r}')\psi(\boldsymbol{r})=\delta(\boldsymbol{r}-\boldsymbol{r}')\\ &\psi(\boldsymbol{r})\psi(\boldsymbol{r}')\pm\psi(\boldsymbol{r}')\psi(\boldsymbol{r})=0 \qquad (2)\\ &\psi^*(\boldsymbol{r})\psi^*(\boldsymbol{r}')\pm\psi^*(\boldsymbol{r}')\psi^*(\boldsymbol{r})=0\,.\end{aligned}$$

Here and in the following, the upper and the lower sign correspond to the case of Fermi- and Bose statistics respectively.

Let us now subdivide the geometrical volume of the fluid $V=L^3$ into $N_l$ cubic cells of volume $l^3$, and suppose that $\psi(\boldsymbol{r})$ is defined only at the centers of these cells where it is characterized by a quantum mechanical operator $\psi_s$. (For the sake of simplicity, these lattice points are taken to be of simple cubic form.)

Using the averaging function introduced by Schiff,

$$f(\boldsymbol{r}-\boldsymbol{r}_s)=L^{-3}\sum_k \exp\left[i\boldsymbol{k}(\boldsymbol{r}-\boldsymbol{r}_s)\right]\,, \qquad (3)$$

we can define the operator $\psi_s$ associated with the lattice point $\boldsymbol{r}_s$ as

$$\begin{aligned}\psi_s&=l^{3/2}\int f(\boldsymbol{r}-\boldsymbol{r}_s)\psi(\boldsymbol{r})\,dv\\ \psi_s^*&=l^{3/2}\int f(\boldsymbol{r}-\boldsymbol{r}_s)\psi^*(\boldsymbol{r})dv\,. \qquad (4)\end{aligned}$$

The summation variable $\boldsymbol{k}$ in Eq. (3) is restricted to the reciprocal lattice points; each component of $\boldsymbol{k}$ ranges from $-\pi/l$ to $\pi/l$ in steps of $2\pi/L$. Since $f$ is such a function that has unit integral over $L^3$ and has its sharp maximum (height $1/l^3$, linear dimensions of order $l$) at the $s$-th lattice point, $\psi_s$ is an average of the continuous $\psi(\boldsymbol{r})$ over a distance of order $l$ about $\boldsymbol{r}_s$, multiplied by $l^{3/2}$.

Using the relation

$$\begin{aligned}&\sum_k \exp\left[i\boldsymbol{k}(\boldsymbol{r}_s-\boldsymbol{r}_t)\right]=N\delta_{st}\\ &\sum_k \exp\left[i(\boldsymbol{k}-\boldsymbol{k}')\boldsymbol{r}_s\right]=N\delta_{kk'}\,, \qquad (5)\end{aligned}$$

the commutation relations (2) can be transcribed into the following ones:

$$\begin{aligned}&\psi_s\psi_t^*\pm\psi_t^*\psi_s=\delta_{st}\\ &\psi_s\psi_t\pm\psi_t\psi_s=\psi_s^*\psi_t^*\pm\psi_t^*\psi_s^*=0\,. \qquad (6)\end{aligned}$$

There are several ways in which the Hamiltonian can be represented in the lattice space. Following Wentzel and Schiff, we may replace the kinetic energy term $(\hbar^2/2m)\int(\nabla\psi^*, \nabla\psi)\,dv$ by

$$\sum_{s,t} K_{st}\psi_s^*\psi_t\,,$$

where

$$K_{st}=(\hbar^2/2mN_l)\sum_k \boldsymbol{k}^2 \exp\left[i\boldsymbol{k}(\boldsymbol{r}_s-\boldsymbol{r}_t)\right]. \qquad (7)$$

Properly speaking, the interaction term of Eq. (1) should be replaced by the term such as $\sum U_{rs,\,tu}\psi_r^*\psi_s^*\psi_u\psi_t$. In the following, however, we may tentatively use the approximate expression

$$\tfrac{1}{2}\sum_s\sum_t U_{st}\psi_s^*\psi_t^*\psi_t\psi_s\,, \qquad (8)$$

because this has the proper limit as $l\to 0$ and we may be unable to expect any important role of the neglected small term for our purposes.

Thus the lattice Hamiltonian can now be written:

$$\mathscr{H}=\sum_s\sum_t K_{st}\psi_s^*\psi_t+\tfrac{1}{2}\sum_s\sum_t U_{st}\psi_s^*\psi_t^*\psi_t\psi_s\,. \qquad (9)$$

## § 3. Cell Model and Lattice Hamiltonian

The commutation relations (6) show that the eigenvalues of the operator $\psi_s^*\psi_s$ are restricted to 0 and 1 for the Fermion assembly and to 0,1,2,$\cdots$for the Boson assembly. We may assert that this operator $\psi_s^*\psi_s=n_s$ expresses the number of molecules localized in the $s$-th cell. It may then be reasonable to put approximately

$$U_{st}\simeq U(\boldsymbol{r}_s, \boldsymbol{r}_t)=U(r_{st})\,. \qquad (\text{for } s\neq t) \qquad (10)$$

This approximation cannot be allowed for $U_{ss}$. In the following, however, we may tentatively put $U_{ss}=+\infty$ and exclude the possibility of multiple occupations. Namely, we consider that each lattice point is either vacant or occupied by a molecule. This assumption is resonable if we take $l$ to be equal order of magnitude to the diamerter of the hard core, and, by this procedure, we can account for the effect of the repulsion between molecules. For spinless Fermions, this condition is automatically fulfilled by the exclusion principle.

Let us now consider the kinetic part of the lattice Hamiltonian. The coefficient of the diagonal term

$$K_{ss}=\frac{\hbar^2\pi^2}{2ml^2}=\frac{3\hbar^2}{2m}\left(\frac{\pi}{\sqrt{3}\,l}\right)^2, \qquad (11)$$

being equal to the zero point energy of a mass point confined in a cube of edge length $\sqrt{3}\,l$, can be interpreted as the zero-point kinetic energy of a molecule localized about the $s$-th lattice point. This becomes large if we take small value for $l$. However, as is emphasized in § 1, this zero point energy is relieved by the inter-cellular motion caused by the non-diagonal terms. The non-vanishing element of $K_{st}$ is restricted to the case in which $\boldsymbol{r}_s-\boldsymbol{r}_t$ is parallel to one of the edges of the cube $L^3$, and is given by

$$K_{st}=\frac{\hbar^2}{ml^2}\frac{(-1)^j}{j^2}\,, \tag{12}$$

where

$$j=|\boldsymbol{r}_s-\boldsymbol{r}_t|/l\,. \tag{12a}$$

Due to the existence of these non-diagonal terms, any fixed configuration of the $N$ molecules among $N_l$ lattice points cannot by itself be an eigenstate of our lattice Hamiltonian. The eigenstates are given by the proper linear combination of these configurations, and the coefficients of these combinations correspond to the usual configurational eigenfunction of the continuum Hamiltonian (1).

## § 4. Ideal Gases

To clarify the relation between the usual theory of gases and our model, we treat here the ideal gas by using our lattice gas model. The lattice Hamiltonian of an ideal gas

$$\mathscr{H}_0=\sum_s\sum_t K_{st}\psi_s{}^*\psi_t \tag{13}$$

can be easily diagonalized by the transformation

$$\psi_k=\frac{1}{\sqrt{N_l}}\sum_s\exp[i\boldsymbol{k}\boldsymbol{r}_s]\psi_s\,,$$

$$\psi_k{}^*=\frac{1}{\sqrt{N_l}}\sum_s\exp[-i\boldsymbol{k}\boldsymbol{r}_s]\psi_s{}^* \tag{14}$$

as

$$\mathscr{H}_0=\frac{\hbar^2}{2m}\sum_k k^2\psi_k{}^*\psi_k\,. \tag{15}$$

The commutation relation for the operators $\psi_k$ and $\psi_k{}^*$ is just like Eq. (6) if we replace the indices by the wave numbers. The Hamiltonian (15) is nothing but the usual one of the plane wave representation except that each component of the wave number $\boldsymbol{k}$ is restricted between $-\pi/l$ and $\pi/l$.

Let us now consider the ideal Fermi gas. Supposing the number of cells is large enough so that the Fermi sphere does not swell out from the cube of edge length $2\pi/l$. Then, in the ground state, all the molecules fill up the Fermi sphere of radius $k_0=(6\pi^2N/V)^{1/3}$, and the total kinetic energy is given by

$$K_{\mathrm{F0}}=\frac{N\hbar^2}{2m}\frac{3}{5}k_0{}^2: \tag{16}$$

Since the exclusion principle prevents the multiple occupations in the case of spinless Fermions, repulsion between molecules is effectively included in the calculation of ideal gas. The ground state of ideal Fermi gas, therefore, may be used as a good approximation of real Fermi gas when the attraction between molecules is small enough. In this state the expectation value of $n_s$ is easily calculated as

$$\langle n_s\rangle_{F0}=N/N_l\,, \tag{17}$$

indicating the uniform distribution of the molecules. Using the approximation of replacing the summation with respect to $\boldsymbol{k}$ by the integration over the Fermi sphere, we obtain the expectation value of the potential energy in this approximation as

$$\langle U\rangle_{\mathrm{F0}}=\frac{1}{2}\sum\sum_{s\neq r}\left\{\frac{N^2}{N_l{}^2}\right.$$
$$\left.-\frac{(\sin k_0r_{st}-k_0r_{st}\cos k_0r_{st})^2}{4\pi^4(r_{st}/l)^6}\right\}U_{st}\,. \tag{18}$$

Nearest neighbor interaction

$$\begin{aligned}U_{st}&=-\varepsilon\quad\text{(if $s$ and $t$ are nearest neighbors)}\\&=0\qquad\text{(otherwise)}\end{aligned} \tag{19}$$

may be a good approximation for (18), giving

$$\langle U\rangle_{\mathrm{F0}}=-\tfrac{1}{2}Nz\varepsilon\,\frac{N}{N_l}\left\{1\right.$$
$$\left.-\frac{9(\sin k_0l-k_0l\cos k_0l)^2}{(k_0l)^6}\right\}, \tag{20}$$

where $z$ denotes the number of nearest neighbors of a lattice point and is equal to 6 in our case. The second term in the curly brackets of (18) or (20) represents the effects of exchange repulsion due to the exclusion principle, and is familiar in the electron theory of metals.

## § 5. Ground State of Bose Liquids

In usual terms (i.e. expressed as a function of the coodinates of the constituent molecules), the ground state eigenfunction of a Boson assembly has no node, and drops to zero if two atoms overlap in any part of the fluid. In our language, this situation may be stated as follows: the ground state is expressed as a linear combination of such configurations in which each lattice point is either vacant or occupied by only one molecule, and all the coefficients of the combination have the same sign.

Of course it is quite difficult to obtain these coefficients exactly. So let us first consider the combination in which all the coefficients are equal. The number of configurations mentioned above is $N_l!/N!\,(N_l-N)!$. Let us denote them by $\phi_j$. Then our trial ground state function is expressed as

$$\varPhi=(N_l!/N!(N_l-N)!)^{-1/2}\sum_j\phi_j. \tag{21}$$

If we adopt the approximation of nearest neighbor interaction (19), then the expectation value of the lattice Hamiltonian with respect to $\varPhi$ can be easily calculated in the approximation of neglecting $1/N_l$ and $1/N$ to 1 as

$$\begin{aligned}E_{B0}&=N\frac{N}{N_l}\left\{\frac{\hbar^2\pi^2}{2m^2}-\frac{z}{2}\varepsilon\right\}\\&=\frac{N}{v}\left\{\frac{h^2\pi^2}{2m}l-\frac{z}{2}\varepsilon l^3\right\},\end{aligned} \tag{22}$$

where $v=V/N$ is the specific volume per molecule. Here we can see the relaxation of the kinetic energy into $(N/N_l)$ times of the original value $NK_{ss}=N\hbar^2\pi^2/2ml^2$.

The second term of the Eq. (22), being the mean value of the potential energy, shows that each lattice point is occupied by $N/N_l$ molecules on an average.

In the case of very small density, Lenz[8] calculated the lowest energy value of the gas of hard molecules ($\varepsilon=0$) as

$$K_0=\frac{N}{v}\frac{\hbar^2\pi^2}{2m}\frac{4d}{\pi}, \tag{23}$$

where $d$ is the diameter of the molecule. This agrees with the first term of our expression (22) if we let the size of our cell $l$ be equal to $4d/\pi$. In the limit of $d\to 0$ ($l\to 0$), this zero-point kinetic energy tends to zero: the ground state eigenvalue of ideal Bose gas. So $\varPhi$ may be considered to correspond to the ground state of Bose gas in the case of small density.

For high density, London[9] considered that each molecule is roughly like a mass point locked in the interior of a hollow sphere of radius $r-d$, where $r$ is the distance between the centers of nearest neighbors; and he gives the lowest energy value as

$$K_0=\frac{N}{2m}\frac{\hbar^2\pi^2}{(r-d)^2} \tag{24}$$

Based on an analogy to the one-dimensional case, Prigogine[10] puts the lowest energy as

$$K_0=\frac{3N\hbar^2\pi^2}{2m\gamma(r-d)^2}, \tag{25}$$

and determined the parameter $\gamma$ so as to get a good agreement with experiments. In the case of liquid $^4$He, he takes $\gamma=4.5$ and gets reasonable results. Our expression corresponding to these is

$$K_0=\frac{N\hbar^2\pi^2}{2m}\frac{N}{N_l l}=\frac{N\hbar^2\pi^2}{2m}\frac{l}{R^3}, \tag{26}$$

where

$$R=(V/N)^{1/3}.$$

Since $r=1.122R$ for a close packed structure, and $d<l<2d$, our expression (26) gives much smaller value than those of (24) and (25) for high density ($r-d\ll d$). This underestimation of the lowest energy arises from the imperfect consideration for the repulsive potential. So the validity of (26) may be doubtful for extremely dense liquid.

Considering $\varepsilon$ as a function of $l$, we can determine the value of $l$ so that it minimizes the energy $E_{B0}$ of (22). The value of $l$ determined in this way is independent of the volume $V$. The lowest energy $E_{B0}$, therefore, depends on the volume $V$ only through the factor $N/v$. So we cannot determine the stable volume of the liquid at $0^0K$ by our crude model.

## § 6. Possibility of Lambda Transition

The effects of statistics is most clearly exhibited if we consider the thermodynamic properties of our lattice fluid. For the sake of brevity, here we adopt the Bragg-Williams approximation for the effect of the intermolecular attraction, i.e. we replace it by its mean value

$$\bar{U}=-\frac{z}{2}\frac{N^2}{N_l}\varepsilon, \tag{27}$$

and take account of the repulsion only through the exclusion of the configurations with multiply occupied cells.

Let us divide the kinetic energy as

$$\sum_s\sum_t K_{st}\psi_s{}^*\psi_t=k_0+k_1, \tag{28}$$

where

$$k_0=\sum_s K_{ss}n_s=NK_{ss} \tag{28a}$$

and

$$k_1=\sum\sum_{s\neq t} K_{st}\psi_s{}^*\psi_t\ . \tag{28b}$$

Then we can write the partition function of our system as

$$Z=\mathrm{Tr}'\exp-\beta(k_0+k_1+\bar{U})$$
$$=\exp[-\beta(k_0+\bar{U})]\mathrm{Tr}'(1-\beta k_1+\tfrac{1}{2}\beta^2k_1{}^2-\cdots)\ , \tag{29}$$

because $k_1$ commutes with $N=\sum_s n_s$. The prime on the Tr sign means that the trace should be taken only with respect to the configurations without multiply occupied cell. Since the number of such configurations is

$$W(N_l,N)=\frac{N_l!}{N!(N_l-N)!}\ ,$$

we can immediately obtain

$$\mathrm{Tr}'1=W(N_l,N)\ . \tag{30}$$

The first order term vanishes because of its non-diagonality:

$$\mathrm{Tr}'(-\beta k_1)=0\ . \tag{31}$$

The second order term is calculated as follows:

$$\mathrm{Tr}'(\tfrac{1}{2}\beta^2k_1{}^2)=(\beta^2/2)\sum\sum_{s\neq t}\mathrm{Tr}'K_{st}{}^2\psi_s{}^*\psi_t\psi_t{}^*\psi_s$$
$$=(\beta^2/2)\sum\sum_{s\neq t}K_{st}{}^2\mathrm{Tr}'n_s(1\mp n_t)$$
$$=(\beta^2/2)N_l(\sum_{t=2}^{\infty}K_{1t}{}^2)\{W(N_l-1,N-1)$$
$$\mp W(N_l-2,N-2)\}$$
$$=(1/30)(\beta\kappa)^2NW(N_l,N)(1\mp\gamma+O(1/N)), \tag{32}$$

where

$$\gamma=N/N_l\quad\text{and}\quad\kappa=\hbar^2\pi^2/ml^2\ . \tag{33}$$

Similarly,

$$\mathrm{Tr}'(-(1/3!)\beta^3k_1{}^3)$$
$$=-(1/945)(\beta\kappa)^3NW(N_l,N)(1\mp3\gamma+2\gamma^2)\ . \tag{34}$$

The contribution to the fourth order term comes from the terms of types

$$K_{st}{}^2K_{ur}{}^2\psi_s{}^*\psi_t\psi_t{}^*\psi_s\psi_u{}^*\psi_r\psi_r{}^*\psi_u$$
$$K_{st}{}^2K_{ur}{}^2\psi_s{}^*\psi_t\psi_u{}^*\psi_r\psi_t{}^*\psi_s\psi_r{}^*\psi_u \tag{35}$$
$$K_{st}{}^2K_{ur}{}^2\psi_s{}^*\psi_t\psi_u{}^*\psi_r\psi_r{}^*\psi_u\psi_t{}^*\psi_s\ ,$$

which give

$$\frac{1}{2}\frac{(\beta\kappa)^4}{900}W(N_l,N)N^2\{(1\mp\gamma)^2+O(1/N)\}\ . \tag{36}$$

The main term of Eq. (36) comes from the terms of (35) in which $s$, $t$, $u$ and $r$ are different from each other. Similarly we obtain

$$\frac{1}{n!}\frac{(\beta\kappa)^{2n}}{30^n}W(N_l,N)N^n(1\mp\gamma)^n \tag{37}$$

as the most predominant contribution from the $2n$-th order terms. It is, however, quite difficult to get a simple expression for the remaining terms, which may give overwhelming contribution at low temperatures. So the validity of our expansion is restricted to the case of small $\beta$.

Let us now put

$$Z=W(N_l,N)\exp\{-\beta\bar{U}$$
$$-N(a\beta\kappa+b\beta^2\kappa^2+c\beta^3\kappa^3+\cdots)\}\ . \tag{38}$$

Comparing with Eqs. (30), (31), (32), (34) and (36), we get

$$a=1/2\ ,\qquad b=(-1/30)(1\mp\gamma)\ ,$$
$$c=(1/945)(1\mp3\gamma+2\gamma^2)\ ,\cdots\ . \tag{39}$$

As is well known, when the Bose-Einstein condensation takes place, an appreciable fraction of molecules occupies the state of zero momentum or of a macroscopic de Broglie wave length. Such a situation cannot be expressed by the expansion like Eq. (38). However, it may not be so unreasonable to guess that the transition corresponding to the Bose-Einstein condensation, if it exists, occurs for our system at the temperature where the series (38) diverges, because the contribution from the motions associated with long wave lengths are considered to come from the terms of the high order powers of the operator $\psi_s{}^*\psi_t$. Then the transition temperature $T_\lambda$ may be given by $\beta_\lambda$ which satisfies

$$|a\beta_\lambda\kappa|\simeq|b\beta_\lambda{}^2\kappa^2|\simeq|c\beta_\lambda{}^3\kappa^3|\simeq\cdots$$

or

$$\beta_\lambda\kappa\simeq\frac{15}{1+\gamma}\simeq\frac{31}{1+3\gamma+2\gamma^2}\simeq10\ .$$

If we put $m=m'M_p$ and $l=l'\times10^{-8}$ cm, where $M_p$ is the proton mass, then the transition temperature $T_\lambda$ is given by

$$T_\lambda\simeq50/m'l'^2\ . \tag{40}$$

For the liquid helium ($m'=4$, $l'=2\sim2.5$), we obtain $T_\lambda=2\sim3$°K, a correct order of magnitude.

Since we do not know the exact form of the partition function, we cannot explain why such transition does not occur in the case of Fermi statistics. As is seen in (39), the magnitudes of the coefficients $b, c,\cdots$ are much smaller in this case than in the case of Bose fluid. The convergence of the series (38), therefore, would be much better and be kept even at 0°K in the case of Fermi fluid.

The Helmholtz free energy $F$ is derived from $Z$ by the formula $F=-kT\log Z$. Using the relation $V=Nl^3/\gamma$, the pressure $p$ is calculated as

$$p=-(\partial F/\partial V)_T=(\gamma/V)(\partial F/\partial\gamma)_T\ .$$

This gives the eqution of state as

$$p=\frac{1}{l^3}\left\{-\frac{z\mathcal{E}V_0^2}{2V^2}+kT\log\frac{V}{V-V_0}\right.$$
$$\left.\mp\frac{V_0^2}{30kTV^2}\kappa^2+\frac{(\mp 3+4V_0/V)V_0^2}{945k^2T^2V^2}\kappa^3+\cdots\right\}, \tag{41}$$

where

$$V_0=Nl^3\ . \tag{42}$$

If we put $\kappa=0$, Eq. (41) becomes the equation of state for the simplest classical lattice gas. It is known that the isothermal $p$-$V$ curve of this classical lattice gas has a maximum and a minimum for the temperatures lower than $T_c=\mathcal{E}z/4k$. So $T_c$ is considered to express the critical point. For helium, if we use the minimum value of the intermolecular potential $-10^{-15}$ ergs for $-\mathcal{E}$, we obtain $T_c=11$°K (experimentally 5.2°K) which is higher than $T_\lambda$. For other substances, the attraction is much stronger and the mass is heavier than helium in general. So we can always expect that $T_\lambda$ is lower than the critical point $T_c$.

The terms of (41) containing $\kappa$ express the quantum correction to this classical lattice fluid. It may, however, be unpractical to discuss such a correction in detail on the basis of our rough model. Anyway, our Bose fluid seems to have two types of transitions; one is the ordinary transition between gas and liquid and the other the quantum mechanical one which presumably corresponds to the lambda-transition of liquid helium.

## § 7. Concluding Remarks

The main purpose of the present paper is to emphasize the important roles of the inter-cellular motion in the explanation of the quantum effects by the cell model. So we have attached importance to the kinetic energy part at the sacrifice of the rigorous treatment of the interaction potentials.

Our procedure adopted in § 2 is equivalent to the number representation of the Hamiltonian with the use of basic function $\varphi_s=(N_l L^3)^{-1/2}\times\sum_k\exp[i\boldsymbol{k}(\boldsymbol{r}-\boldsymbol{r}_s)]$. Apart from the imcompleteness of this function system, it may be somewhat unreasonable to assume that $\varphi_s$ describes the state of molecule confined in the $s$-th cell, because it has fairly large amplitude in the neighboring cells. It may, therefore, be worthwhile considering another choices of the basic functions more appropriate for the description of localized molecules.

In spite of the simplifications for the potential part, the lattice Hamiltonian (9) is still unmanageable. As to the eigensolution of the lattice Hamiltonian, therefore, we have had to restrict our discussion to the ground state of the Bose fluid (§ 5). It is much more difficult to investigate the Fermi fluid in the same way because of its antisymmetric property. Concerning the lower excited states of the Bose fluid, our crude theory has nothing to add to the Feynman's excellent work about the liquid helium11), though the similar treatment is possible by our model.

The statistical mechanical treatment has been also limited to the case of high temperatures, and yet quite unsatisfactory (§ 6). It is, however, natural if we think about the difficulty which lies even in solving much more simplified problems such as the Ising model for the ferromagnetics which is proved to be equivalent to the classical lattice gas with nearest neighbor interactions12).

In conclusion, the author wishes to express his sincere thanks to Professors S. Ono and T. Usui for their valuable suggestions and discussions.

## References

1) L. E. Lennard-Jones and A. F. Devonshire: Proc. Roy. Soc. London **A163** (1936) 63, **165** (1938) 1.
2) J. G. Kirkwood: Jour. Chem. Phys. **18** (1950) 380.
3) For instance, Hirschfelder, Curtiss and Bird: "*Molecular Theory of Gases and Liquids*", J. Wiley, N.Y. (1954) Chap. 4.
4) J. de Boer: Physica **20** (1954) 655.
E. G. D. Cohen, J. de Boer and Z. W. Salsburg: Physica **21** (1955) 1937.
5) C. L. Pekeris: Phys. Rev. **79** (1950) 884.
Similar calculations are performed by R. Nozawa and by S. Ueda in Japan (unpublished).
6) I. Prigogine et J. Philippot: Physica **18** (1952) 227, 235.

7) G. Wentzel: Helv. Phys. Acta. **13** (1940) 269.
L. I. Schiff: Phys. Rev. **92** (1953) 766.
8) W. Lenz: Zeits. f. Phys. **56** (1929) 778.
9) F. London: "*Superfluids* Vol. II", J. Wiley, N.Y. (1954) p. 30.
10) I. Prigogine: Advances in Phys. **3** (1954) 131.
11) R. P. Feynman: Phys. Rev. **94** (1954) 262.
12) T. D. Lee and C. N. Yang: Phys. Rev. **87** (1952) 410.

---

JOURNAL OF THE PHYSICAL SOCIETY OF JAPAN Vol. 11, No. 1, JANUARY, 1956

# Quantum Effects in the Theory of Surface Energy

By Akira HARASIMA and Yoshihisa SHIMURA

*Tokyo Institute of Technology, Oh-Okayama, Tokyo, Japan*

(Received September 9, 1955)

Applying Prigogine's method of calculating the cohesive energy and the volume of liquid helium at 0°K and also Prigogine's method of calculating the surface tension, we have discussed the quantum effects in the theory of surface energies of several substances at 0°K. Assuming that the intermolecular potential is of the form

$$\phi(R)=4\varepsilon\{(\sigma/R)^{12}-(\sigma/R)^{6}\}\ ,$$

we can express the reduced surface energy at 0°K, $U_0{}^*=U_0\sigma^2/\varepsilon$, as a function of the quantum mechanical parameter

$$\Lambda^*=\frac{h}{\sigma\sqrt{m\varepsilon}}\ , \quad m\text{: mass of a molecule}$$

It is shown that $U_0{}^*$ decreases with increasing $\Lambda^*$ in agreement with observed tendency.

## § 1. Introduction

The surface tension is the free energy associated with a unit area of the surface of a liquid. We consider a system composed of liquid and vapour phases with an interface whose area is $A$. The Helmholtz free energy of a system of $N$ monatomic molecules occupying a volume $V$ is given, in classical theory, by

$$F=-kT\log\frac{1}{N!}\left(\frac{2\pi mkT}{h^2}\right)^{3/2N}\times\int\cdots\int\exp\left(-\sum\phi_{ij}/kT\right)dr_1dr_2\cdots dr_N\ . \tag{1}$$

To obtain the expression of the surface tension in terms of molecular quantities, we deform the system so as to give the interface a change in area and calculate the increase in the free energy. Beside the liquid-vapour interface we must, generally, take into consideration the interfaces between the liquid and the wall of the vessel and those between the vapour and the walls of the container. But we can give a deformation by which only the area of the liquid-vapour interface is changed, areas of other interfaces remaining unchanged.[1] Namely, we assume the vessel to be a cube with edge length $a$ and the system to be composed of the liquid phase in the form of a macroscopically thin but microscopically thick membrane which is parallel to a pair of walls and the vapour phase in equilibrium with the liquid. Then we displace one of the walls which are perpendicular to the membrane an infinitesimal amount $\eta a$ outward while at the same time displace a wall which is parallel to the membrane the same amount inward. By such displacements only the area of the vapour-liquid interface is increased, other interfaces remaining unchanged as far as small quantities of higher orders are neglected. By these procedures one can obtain the expression of surface tension $\gamma$ in terms of the intermolecular force and the molecular distribution function:

$$\gamma=\frac{1}{2}\iiiint\frac{d\phi_{12}}{dR_{12}}\frac{x_{12}{}^2-z_{12}{}^2}{R_{12}}\rho^{(2)}(z_1,\boldsymbol{R}_{12})dz_1d\boldsymbol{R}_{12}\,, \tag{2}$$

where z-axis is perpendicular to the vapour-liquid interface and $\rho^{(2)}$ is the pair distribution function.

To consider the surface tension from the standpoint of corresponding states, it is not necessary to follow details of the derivation of the formula (2). We can derive the principle directly from the expression (1) of the free energy. If the area of the interface between the liquid and the vapour is $A$, we have

$$\gamma=\frac{\partial F}{\partial A}=-kT\frac{\partial}{\partial A}\log\int\cdots\int\exp\left(-\sum\phi_{ij}/kT\right)d\boldsymbol{r}_1d\boldsymbol{r}_2\cdots d\boldsymbol{r}_N\,. \tag{3}$$

We assume, further, that the form of the intermolecular potential is of the Lennard-Jones type, that is,

$$\phi(R)=4\varepsilon\left\{\left(\frac{\sigma}{R}\right)^{12}-\left(\frac{\sigma}{R}\right)^{6}\right\}. \tag{4}$$

If we use the reduced values

$$\left.\begin{aligned}&T^*=\frac{kT}{\varepsilon}\,,\quad A^*=\frac{A}{\sigma^2}\,,\quad R^*=\frac{R}{\sigma}\,,\quad \boldsymbol{r}^*=\frac{\boldsymbol{r}}{\sigma}\,,\\ &\text{and}\\ &\gamma^*=\gamma\frac{\sigma^2}{\varepsilon}\,,\end{aligned}\right\} \tag{5}$$

we have

$$\gamma^*=-T^*\frac{\partial}{\partial A^*}\log\int\cdots\int\exp\left[-\sum\frac{4}{T^*}\left\{\left(\frac{1}{R_{ij}{}^*}\right)^{12}-\left(\frac{1}{R_{ij}{}^*}\right)^{6}\right\}\right]d\boldsymbol{r}_1{}^*\cdots d\boldsymbol{r}_N{}^*\,,$$

so that we have

$$\gamma^*=f(T^*)\,, \tag{6}$$

that is, treated by classical theory, the reduced surface tension can be written as a universal function of the reduced temperature so long as the form of the intermolecular potential is given by the formula (4).

The surface energy is given, as is well known, by

$$U=\gamma-T\frac{\partial\gamma}{\partial T}\,, \tag{7}$$

in terms of the reduced variables, it can be written as

$$U^*=\gamma^*-T^*\frac{\partial\gamma^*}{\partial T^*}\,, \tag{8}$$

where

$$U^*=U\frac{\sigma^2}{\varepsilon}\,. \tag{9}$$

De Boer and Lunbeck[2)] showed that the reduced surface tension can be expressed as a function of the reduced temperature and the quantum mechanical parameter

$$\Lambda^*=\frac{h}{\sigma\sqrt{m\varepsilon}}\,, \tag{10}$$

and predicted the temperature dependence of surface tension of liquid $^3$He. The theoretical predictions which they made can be compared with the observations by Lovejoy[3)]. The agreement is seen to be exceptionally good.

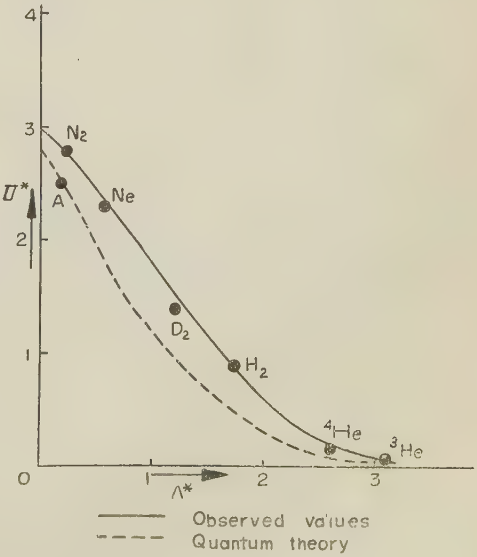

Fig. 1.

Table I.

| Substance | $U$ | Temperature Range (°K) | $\varepsilon(10^{-16}$ ergs) | $\sigma$(A.U.) | $U^*$ | $\Lambda^*$ |
|---|---|---|---|---|---|---|
| $^3$He | 0.16 | 1.5- 3.4 | 14.03 | 2.56 | 0.075 | 3.05 |
| $^4$He | 0.36 | 1.6- 4.3 | 14.03 | 2.56 | 0.168 | 2.64 |
| $H_2$ | 5.4 | 15.1-20.1 | 50.75 | 2.92 | 0.904 | 1.73 |
| $D_2$ | 8.2 | 18.7-21.1 | 50.75 | 2.92 | 1.38 | 1.22 |
| Ne | 15 | 24.8-28.3 | 48.82 | 2.74 | 2.31 | 0.591 |
| $N_2$ | 26 | 77.2-90.1 | 132.4 | 3.72 | 2.72 | 0.225 |
| A | 35 | 85.1-90.1 | 165.0 | 3.41 | 2.47 | 0.187 |

In this paper we shall show that surface energies also obey a similar law and further that we can derive a parametrical dependence of $U^*$ on $\Lambda^*$, at least qualitatively, if we resort to some approximate considerations.

Experimental data of surface energies as well as the force constants of several substances with which we are going to deal in this paper are shown in Table I.

Experimental values of $U^*$ are plotted as a function of $\Lambda^*$ in Fig. 1. The values of $U^*$ except for those of $^4$He and $^3$He are not those at 0°K, but those in the liquid region shown in Table I. Since $^4$He and $^3$He can be in the liquid state at 0°K, we have extrapolated the values at 0°K from the measurements by Allen and Misener for $^4$He[4] and by Lovejoy for $^3$He[3]. They are shown in the figure. The broken curve in the figure shows the results of computations by the theory shown in § 4.

## § 2. Prigogine's Method for Computing the Cohesive Energy

Before discussing the problem of surface energy, we shall first consider quantum effects on the volume of the condensed phase in bulk. We shall use the same method as adopted by Prigogine[5] in calculating the energies of liquid $^4$He and $^3$He at 0°K.

De Boer and Blaisse[6] showed that by quantum mechanical cell theory one can derive a relation between the reduced volume $V^*$ and the reduced energy $E^*$ which are given by

$$V_0^* = \frac{V_0}{N\sigma^3}, \quad E_0^* = \frac{E_0}{N\varepsilon}. \tag{11}$$

Their derivation consisted in expanding the pressure in a power series of the parameter $\Lambda^*$ and was valid only for small values of $\Lambda^*$. The procedure which we shall adopt in this paper is not so refined as de Boer and Blaisse's theory, but it will not be required that $\Lambda^*$ is small. Though Prigogine applied his method to liquid $^4$He and $^3$He, we shall extend the method to substances other than liquid helium. These substances are, of course, solid at 0°K except for helium. But we shall assume that we can apply the same method to these substances in the following treatment, considering the comparative crudeness of our theory which does not discriminate between liquid and solid states.

In Prigogine's theory which was applied to liquid helium, the structure of the liquid is considered to be of a lattice-like form and the energy at 0°K is assumed to be the sum of the potential energy $\Phi$ corresponding to the configuration that all the molecules are at the lattice points of a face-centred cubic lattice and the zero-point energy $E_r$ for the motion of molecules.

It is very easy to show that $\Phi$ is given by[7]

$$\Phi = 24.26N\varepsilon\left[\left(\frac{\sigma}{a}\right)^{12} - 1.191\left(\frac{\sigma}{a}\right)^{6}\right], \tag{12}$$

where $a$ is the distance between two neighbouring cell centres and it is given by

$$V = \frac{Na^3}{\sqrt{2}}.$$

Using the reduced values

$$\Phi^* = \frac{\Phi}{N\varepsilon}, \quad V^* = \frac{V}{N\sigma^3}, \tag{13}$$

we have, from (12),

$$\Phi^* = 6.065\left(\frac{1}{V^{*4}} - \frac{2.382}{V^{*2}}\right). \tag{14}$$

It is very difficult to calculate the zero-point energy. Since the substances we are treating are solid at 0°K except for $^4$He and $^3$He, it may seem most adequate to treat the problem on the line of Debye's theory of solid bodies. On the other hand, Hobbs⁸⁾ calculated the energies of solid $H_2$, HD and $D_2$ by a similar procedure as that adopted in this paper. Though it would be best to treat argon and neon by Debye's method, we shall treat them by the same method as for helium and hydrogen, since the errors would not be great considering that the quantum effect itself is rather small for these substances. In the quantum mechanical cell theory, we solve Schrödinger's equation for a molecule which is under the resulting potential field from other molecules surrounding the molecule under consideration. It is often assumed that each molecule is a hard sphere moving inside the cell in which it is locked when the density of the phase is high.

Then the zero-point energy is given by

$$E_r = \frac{Nh^2}{8m(a-\sigma)^2}\,, \tag{15}$$

where $a$ is the distance between two neighbouring cell centres and $\sigma$ is the diameter of a molecule.

If the density is small, the molecules will not be locked in cells but roam from cell to cell and the zero-point energy of a molecule will be given by the formula due to Heitler and Lenz⁹⁾:

$$E_r = \frac{Nh^2\sigma}{2\pi m R^3}\,, \qquad R^3 = \frac{V}{N}\,. \tag{16}$$

A simple interpolation formula between these two is given by the expression:

$$E_r = \frac{Nh^2\sigma}{2\pi m(R-0.891\sigma)^2(R+0.713\sigma)}\,, \tag{17}$$

which can be used for densities ranging from very small to very large values. We shall here use similar but somewhat different formula which was used by Prigogine in his theory of liquid helium, and which is written as

$$E_r = \frac{3Nh^2}{8\delta m(a-\sigma)^2}\,. \tag{18}$$

If we put $\delta=1$ in (18), $E_r$ becomes equal to the zero-point energy of a molecule in a cubic cell. We assume that by using the parameter $\delta$ we can take into consideration the type of the lattice and other modes of motion than the one in which a molecule moves in the cell it is locked, e.g. the mode in which the molecules roam from cell to cell. This idea was proposed by Prigogine and we follow him by putting

$$\delta = 4.5 \tag{19}$$

for any substance we treat in this paper, though Prigogine limited his treatment to the cases of liquid $^4$He and $^3$He.

The zero-point energy expressed in reduced variable is

$$E_r^* = \frac{E_r}{N\varepsilon} = \frac{3h^2}{8\varepsilon m\delta(a-\sigma)^2} = \frac{3}{8}\,\frac{\Lambda^{*2}}{\delta(2^{1/6}V^{*1/3}-1)^2}\,, \tag{20}$$

and adding this energy to that given by (14), we have the expression for the total energy in terms of reduced variables:

$$E^* = 6.07\left(\frac{1}{V^{*4}} - \frac{2.382}{V^{*2}}\right) + \frac{1}{12}\,\frac{\Lambda^{*2}}{(2^{1/6}V^{*1/3}-1)^2}\,. \tag{21}$$

Fig. 2 shows $\Phi^*$, $E_r^*$ and $E^*$ as functions of $V^*$ for $\Lambda^*=1$. The values of the volume $V_0^*$ and the energy $E_0^*$ for the equilibrium state are determined by the condition of minimum energy:

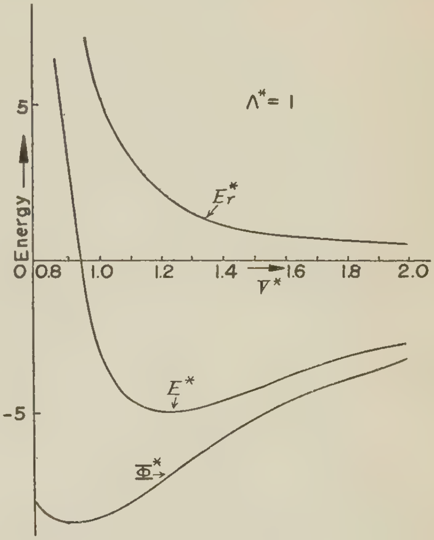

Fig. 2.

$$\left(\frac{\partial E^*}{\partial V^*}\right)_{V_0^*} = 0\,, \tag{22}$$

for each value of $\Lambda^*$. This is given by Fig. 3 together with experimental value. In Fig. 4 the values of the energy $E_0^*$ at 0°K are shown as a function of $\Lambda^*$. By these figures we may conclude that Prigogine's treatment applied to substances not limited to liquid $^4$He and $^3$He gives quantum effects in fairly good agreement with experimental values. The relation between $V_0^*$ and $\Lambda^*$ which we have obtained will be used in our theory of surface energy in § 4.

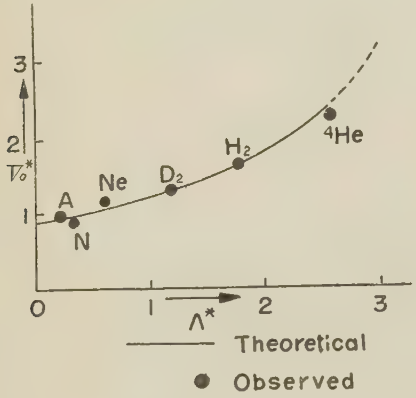

Fig. 3.

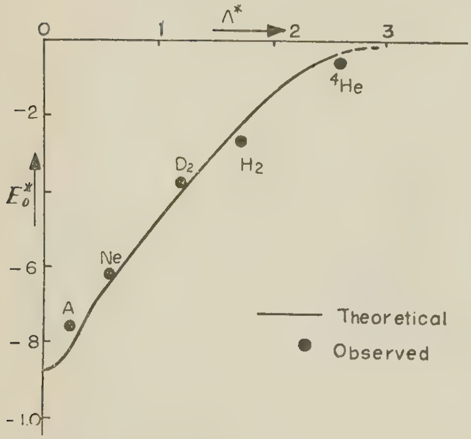

Fig. 4.

## § 3. Calculation of Surface Energy (Classical theory)

Surface energy is defined as the increase in energy per unit surface area in an isothermal change. According to the classical theory the mean value of the kinetic energy of a molecule is constant whether it is in the interior or on the surface of the liquid, so we have only to calculate the increase in the total potential energy of the system which results from an increase of the area of the surface.

The structure of the liquid near the surface is obviously different from that of the liquid in bulk. But we shall neglect this difference and assume that the molecular arrangement is kept unchanged up to the surface of the liquid.

We now divide the potential energy of the liquid into two parts, that is, the potential energy when the molecules are at the cell centres and the mean potential energy for the molecular motion around the cell centres. If the motion of a molecule is simple harmonic, the average potential energy of the molecule corresponding to motion in any direction is given by $1/2\,kT$ irrespective of the frequencies, so it is constant whether the molecule is in the interior or on the surface of the liquid. Any difference in the frequency of vibration of molecules will give rise to surface entropy, so that the difference in the frequency cannot be neglected in calculating the surface free energy, that is, the surface tension. In calculating the surface free energy one can thus neglect the difference in potential energy due to deviations of molecules from cell centres, so long as the motion of each molecule is simple harmonic. The force acting on a molecule when it deviates from the cell centre is more complicated than in the case of a harmonic oscillator and the mean potential energy due to the molecular motion when the molecule is on the surface is different from that when it is in the interior of the liquid, but it may be said that a large part of the mean potential energy will be cancelled by taking differences and the part which remains will be small compared with that which arises from the lattice energy.

By making such simplifying assumptions, we can obtain classical surface energy in the form of the increase in potential energy per unit surface area when we divide an infinite face-centred cubic lattice into two semi-infinite parts. The result depends to some extent upon the crystal plane which is to be exposed and according to the calculations by one of the writers (A.H.), the following results were obtained[10).

Exposed face: (100)-plane

$$U=\frac{8}{a^2}\varepsilon\left\{1.4\left(\frac{\sigma}{a}\right)^6-\left(\frac{\sigma}{a}\right)^{12}\right\}. \tag{23}$$

Exposed face: (110)-plane

$$U=\frac{8.8}{a^2}\varepsilon\left\{1.35\left(\frac{\sigma}{a}\right)^6-\left(\frac{\sigma}{a}\right)^{12}\right\}. \tag{24}$$

Exposed face: (111)-plane

$$U=\frac{7.2}{a^2}\varepsilon\left\{1.35\left(\frac{\sigma}{a}\right)^6-\left(\frac{\sigma}{a}\right)^{12}\right\}. \quad (25)$$

We can obtain a similar result by a somewhat different procedure due to Fowler. He obtained an expression for surface energy by assuming the molecular density to change discontinuously from the density of the bulk liquid to that of the saturated vapour. The surface energy is expressed in terms of the radial distribution function as follows:

$$U=-\frac{1}{8}\rho^{(1)}\int_0^\infty R\phi(R)\rho^{(1)}g(R)\cdot 4\pi R^2dR \quad (26)$$

where $\rho^{(1)}$ is the molecular number density and $g(R)$ is the radial distribution function. In this formula $\rho^{(1)}\cdot g(R)\cdot 4\pi R^2dR$ is the average number of molecules which are in the distance between $R$ and $R+dR$ from any specified molecule. Denoting this number by $n(R)dR$, we have

$$U=-\frac{1}{8}\rho^{(1)}\int_0^\infty Rn(R)\phi(R)dR\,.$$

This formula can be rewritten as

$$U=-\frac{1}{8}\rho^{(1)}\sum n_iR_i\phi(R_i)\,, \quad (27)$$

where $n_i$ is the number of molecules at the distance $r_i$ from a specified molecule. Assuming face-centred cubic structure, we have

$$U=\frac{8}{a^2}\phi_0\left\{1.5\left(\frac{\sigma}{a}\right)^6-1.08\left(\frac{\sigma}{a}\right)^{12}\right\}. \quad (28)$$

Since the formulas (23), (24), (25) and (28) are derived by approximate treatment it would be insignificant to discuss which one is the most accurate, but we shall use the formula (25) as it gives the smallest value for the surface energy. By writing it in the reduced form, we have

$$U^*=\frac{1.43}{V^{*2/3}}\left(\frac{2.70}{V^{*2}}-\frac{1}{V^{*4}}\right). \quad (29)$$

We see by this formula that $U^*$ can be expressed as a function of $V^*$ which is a function of the reduced temperature $T^*$ if the pressure is zero. Hence in classical theory the reduced values of the surface energy is the same for all substances if the intermolecular potential is given by the expression (4).

## § 4. Calculation of Surface Energy (Quantum theory)

We shall now consider the surface energy at 0°K taking into consideration the zero-point energy. Among substances we are to deal with, $^4$He and $^3$He are only subustances whose experimental values of surface energy can be obtained by extrapolation. But since the model which we adopt does not, strictly speaking, discriminate between solid and liquid states, we shall call them generally as condensed phases and deal with the surface tension at 0°K. In comparing theoretical values with experimental ones, we shall use the values of the latter at temperatures in the liquid region, so the comparison will be merely qualitative.

Let a molecule in the condensed phase execute simple harmonic motion under molecular forces resulting from surrounding molecules with the frequency $\nu$ when the molecule is in the interior of the phase and with the frequency $\nu_s$ when it is in the surface layer. The difference in the zero-point energies is

$$\frac{1}{2}h(\nu-\nu_s)$$

per one degree of freedom. The difference in frequencies means difference in the free volume in the cell theory of liquid. But the concept of small vibrations is not valid in some cases, so we shall not restrict ourselves to the case where molecules execute simple harmonic motion, and treat the problem in a more general though somewhat simplified way.

Prigogine[11)] treated the problem of surface tension in the following way. His treatment was limited to classical theory and it was assumed that in the surface layer the motion of any molecule parallel to the surface of the liquid is the same as it is in the interior of the liquid, while in the direction perpendicular to the surface the motion of the molecule in the surface layer is such that we obtain the expression for free volume by replacing $a-\sigma$ in the expression for a molecule in the interior of the liquid by $a-\sigma/2$. Here $a$ is the distance between nearest neighbours and $\sigma$ is the diameter of a molecule. Though this idea was proposed by Prigogine in the classical theory of surface tension, we shall adopt the same idea in discussing the zero-point energy concerning the surface energy of a liquid. Then the decrease in the zero-point energy of a molecule when it emerges from the interior to the surface of a liquid is

$$\frac{h^2}{8\delta m}\left\{\frac{1}{(a-\sigma)^2}-\frac{1}{(a-\sigma/2)^2}\right\}.$$

If we assume that the surface is the (111)-plane of the lattice the area per molecule is $(\sqrt{3}/2)a^2$ and the decrease in the zero-point energy per unit area is

$$\varDelta E_{\mathrm{r}}=\frac{h^2}{4\sqrt{3}\,\delta m a^2}\left\{\frac{1}{(a-\sigma)^2}-\frac{1}{(a-\sigma/2)^2}\right\},$$

which can be written in the reduced values

$$\begin{aligned}\varDelta E_{\mathrm{r}}^*&=\frac{\sigma^2}{\varepsilon}\varDelta E_{\mathrm{r}}\\&=\frac{\varLambda^{*2}}{4\sqrt{3}\cdot 2^{1/3}\delta\cdot V^{*2/3}}\left\{\frac{1}{(2^{1/6}V^{*1/3}-1)^2}\right.\\&\qquad\left.-\frac{1}{(2^{1/6}V^{*1/3}-1/2)^2}\right\}. \qquad (30)\end{aligned}$$

Subtracting this value from that given by (29), we obtain the surface energy of the condensed phase at 0°K, and putting $V^*=V_0^*$, we have

$$\begin{aligned}U_0^*&=\frac{1.43}{V_0^{*2/3}}\left(\frac{2.70}{V_0^{*2}}-\frac{1}{V_0^{*4}}\right)\\&\quad-\frac{\varLambda^{*2}}{39.3V_0^{*2/3}}\left\{\frac{1}{(2^{1/6}V_0^{*1/3}-1)^2}\right.\\&\quad\left.-\frac{1}{(2^{1/6}V_0^{*1/3}-1/2)^2}\right\}. \qquad (31)\end{aligned}$$

Since the values of $V_0^*$ as a function of $\varLambda^*$ are given by the equation (22) expressing equilibrium at 0°K, we can calculate the surface energy $U_0^*$ as a function of $\varLambda^*$, that is

$$U_0^*=U_0^*(\varLambda^*)\,. \qquad (32)$$

The dotted curve in Fig. 1 shows the calculated relation between $U_0^*$ and $\varLambda^*$. Since the experimental values are those obtained from experimental data of surface tension in the liquid region, the comparison between the theory and experiments is rather qualitative than quantitative. But we see from the figure, quantum effects concerning surface energy can be deduced from free volume theory at least in a qualitative way, considering that we cannot expect on the basis of such a crude simplified theory as ours to obtain satisfactory numerical values.

## § 5. More Precise Calculation for Liquid $^4$He

Keesom and Taconis[12)] made an x-ray analysis of liquid helium. It is not easy to draw a definite conclusion from their analysis, but they showed that the structure of liquid helium is such as we will obtain if we remove from a face-centred cubic lattice half of the atoms so that each atom is surrounded by six atoms and six empty sites. F. London[13)] estimated the cohesion energy of liquid helium assuming the structure to be as proposed by Keesom and Taconis.

We now show the estimation of surface energy calculated by the same method as shown in § 3. We adopt two types of inter-atomic potential, the one is the Lennard-Jones type potential given by (4) with the constants $\varepsilon=14.03\times10^{-16}$ ergs, $\sigma=2.56$ Å and the other that given by Yntema and Schneider

$$\begin{aligned}\phi(R)=[&1200\exp(-R/0.212)\\&-1.24/R^6-1.89/R^8]\cdot10^{-12}\,\text{erg}. \qquad (33)\end{aligned}$$

The results are:

| | |
|---|---|
| Exposed face: (100)-plane | |
| Using L.-J. potential | 0.69 ergs/cm$^2$ |
| Using Y. and S. potential | 1.06 ergs/cm$^2$ |
| Exposed face: (110)-plane | |
| Using L.-J. potential | 0.72 ergs/cm$^2$ |
| Using Y. and S. potential | 1.10 ergs/cm$^2$ |
| Exposed face: (111)-plane | |
| Using L.-J. potential | 0.55 ergs/cm$^2$ |
| Using Y. and S. potential | 0.74 ergs/cm$^2$ |

If we resort to the method which we used in deriving the formula (28) which is valid in the case of face-centred cubic structure, we can calculate the increase in the potential energy when the liquid is divided into two semi-infinite halves. The result is:

| | |
|---|---|
| Using L.-J. potential | 0.41 ergs/cm$^2$ |
| Using Y. and S. potential | 0.71 ergs/cm$^2$ |

These values are near those for the case where the exposed face is the (111)-plane.

As shown above there are some differences in the values according to the face to be exposed. The smallest values are those for the exposed face (111). So it would be reasonable to assume the values 0.5∼0.7 ergs/cm$^2$ to be the increase in the potential energy due to the formation of the surface. This corresponds to the reduced value of about 0.3 ergs/cm$^2$. The term due to the zero-point energy has, from the second term of (31), the value 0.27 ergs/cm$^2$, so that if we subtract this from 0.3 ergs/cm$^2$ the result will be very close to zero. The experimental value is $U_0^*=0.17$ (see Table I). Though this might seem to show the discrepancy between theory and experiment we may be satisfied with the result that our calculations show that the surface energy of liquid helium is very small, considering that we have calculated the surface energy by taking the difference between two comparatively large quantities of the same order each of which was estimated independently.

### References

1) A. Harasima: J. Phys. Soc. Japan **8** (1953) 343.
2) Hirschfelder, Curtiss and Bird: *Molecular Theory of Gases and Liquids* (John Wiley and Sons) (1954) 430.
3) D. R. Lovejoy: Canadian J. of Phys. **33** (1955) 49.
4) J. F. Allen and A. D. Misener: Proc. Cambridge Phil. Soc. **34** (1928) 299.
5) I. Prigogine et J. Philippot: Physica **18** (1952) 729; Phil. Mag. Supplement **3** (1954) 131.
6) J. de Boer and B. S. Blaisse: Physica **14** (1948) 149.
7) Lennard-Jones and Devonshire: Proc. Roy. Soc. **163** (1937) 53; **165** (1938) 1.
I. Prigogine et G. Garikian: J. Chim. Physique **45** (1948) 273.
P. H. Wentorf Jr., R. J. Buehlar, J. O. Hirschfelder and C. F. Curtiss: J. Chem. Phys. **18** (1950) 1484.
8) M. Hobbs: J. Chem. Phys. **7** (1939) 318.
9) W. Heitler: Zeits. f. Physik **44** (1927) 161.
W. Lenz: Zeits. f. Phys. **56** (1929) 778; Ann. d. Physik **33** (1938) 630.
10) A. Harasima: Proc. Phys.-Math. Soc. Japan **22** (1940) 825; *Recent Problems in Physics* (Iwanami, in Japanese) (1948) 27.
11) I. Prigogine et L. Saraga: J. de Chimie Physique **49** (1952) 399.
12) W. H. Keesom and K. W. Taconis: Physica **4** (1937) 256; **5** (1938) 270.
J. Reekie: Proc. Cambridge Phil. Soc. **36** (1940) 236.
13) F. London: *Superfluids Vol. II* (John Wiley and Sons 1954) pp. 27-33.

---

JOURNAL OF THE PHYSICAL SOCIETY OF JAPAN Vol. 11, No. 1, JANUARY, 1956

# Magnetic Properties of Nickel Telluride

By Enji UCHIDA and Hisamoto KONDOH
*Department of Physics, Naniwa University, Osaka*

(Received September 7, 1955)

Experimental results are reported of the magnetic properties of $NiTe_x$, where $x$ is the molal content of tellurium. When $0.1 \leq x \leq 0.65$, this substance is found to be ferromagnetic; the variations with composition of the saturation magnetization and of the Curie temperature show evidences of a transition at $x=0.33$ (27 atomic percent Te) from a heterogeneous phase begining at pure metallic nickel to a certain ferromagnetic homogeneous phase. A paramagnetic phase appears above $x=0.7$ (41 atomic percent Te), although its paramagnetic behaviour is not truely paramagnetic in the Curie-Weiss sense, especially at high temperatures, namely, a considerable temperature dependence of the susceptibility is observed at low temperatures and a temperature-independent susceptibility of a small value less than 0.5 emu/g at high temperatures. These behaviours of the susceptibility are apparently similar to those of Cu-rich Cu-Ni alloys studied by Kaufmann and Starr, though a marked dissimilarity is also found between their characters. Namely, an antiferromagnetic character is present in $NiTe_x$ at the paramagnetic compositions.

## § 1. Introduction

The magnetic properties of NiAs-type compounds in which one component is a transition metal and the other is a metalloid element, e.g. FeS¹⁾, MnAs²⁾, etc., are, as far as they have been studied, very peculiar and particular in each case. The antiferromagnetic properties of some of these NiAs type compounds seem to be determined on the one hand by the degree of the metallic character which is generally present in such compounds and, on the other hand, by the superexchange effect via the intermediary of the metalloid ions in the lattice. The present work has been done as one of the series of experimental investigations on tellurides in order to clarify these points. Investigations on other tellurides, FeTe[3], CoTe[4], MnTe[5] and CrTe[6], have been already reported.

There exist no through measurements of the magnetic properties of NiTe$_x$. The only data, which are due to Gal'perin and Perkallina[7], are concerned with the stoichiometric composition and the temperature range from liquid air temperature to room temperature. The present work extends the temperature range to 1150°C and the composition range to $0.10 \leq x \leq 2.00$.

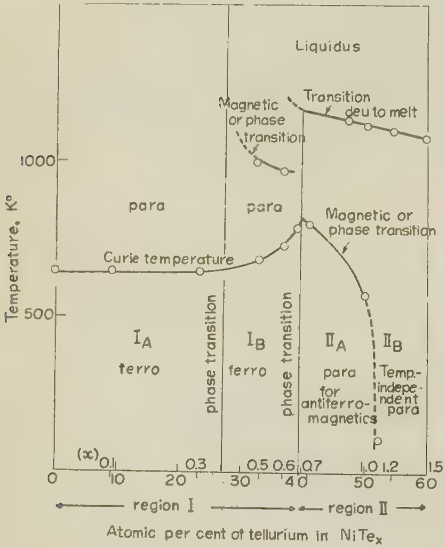

Fig. 1. The magnetic phase diagram of NiTe$_x$.
Region I: ferromagnetic composition region.
Region II: paramagnetic composition region.

## § 2. Experimental

The procedure of the preparation of the specimens is as follows: mixed powder of nickel and tellurium, both 99.9 percent pure, with a desired proportion was sealed in an evacuated silica tube ($10^{-6}$ mmHg), and this was heated in a furnace at 1200°C for 10 hours. The product was a solid material with a silvery appearance. The X-ray Debye-Scherrer diffraction pattern was compatible with the NiAs structure with lattice spacings $a_0=3.96$ A and $c_0=5.35$ A, which are in good agreement with the published data.

The same technique and the same magnetic balance as those described in previous papers[3],[4] were used for the magnetization measurements. In the present experiment, we had sometimes to observe very small values of the magnetization at paramagnetic compositions, and in such cases a relatively large quantity of the mass of the specimen, i.e. a few grams, was required for the measurements, in order to obtain sufficient deflections of the magnetic balance. However, increase in mass and thus increase in volume of the specimen introduced errors in keeping a constant field gradient over the working volume of the specimen. In such cases, the accuracy of determinig the absolute value of the magnetization was estimated to be three times less than that of the usual cases, but the errors remained within 10 percent. The accuracy of the relative values was as good as usual, since great cares were taken regarding the position of the specimen and also the blank condition of the apparatus.

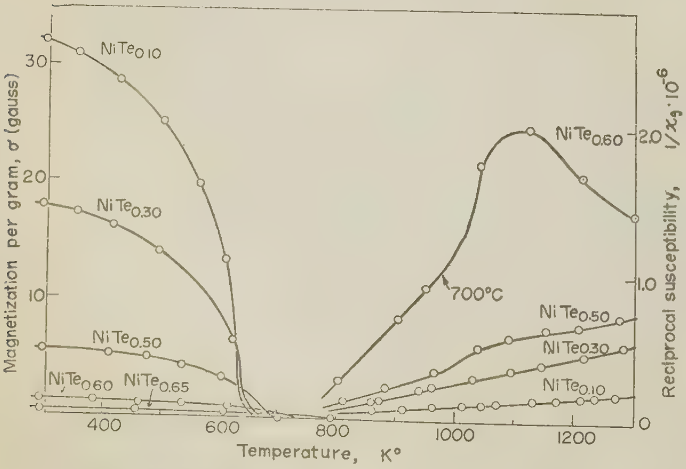

Fig. 2. Temperature dependences of the magnetization and the reciprocal susceptibility of NiTe$_x$ of ferromagnetic composition.

## § 3. Results

First some obtained data of the magnetic character of NiTe$_x$ are summarized in Fig. 1. It is found that NiTe$_x$ is definitely ferromagnetic in the range $0 < x \leq 0.65$, but paramagnetic, though not in the Curie-Weiss sense, in the range $0.7 \leq x \leq 2.00$. The ferromagnetic region, denoted as region I in Fig. 1, is divided into two sub-regions $I_A$ and $I_B$, and the paramagnetic composition region, denoted as region II, into sub-regions $II_A$ and $II_B$. These divisions have the following meanings.

a) *Ferromagnetic composition range* (*region I*)

Curves in Fig. 2 represent the magnetization and reciprocal susceptibility of $NiTe_x$ in range I as functions of temperature. Fig. 3 shows the magnetization as a function of applied field intensity at room temperature. As seen in these figures, every curve shows essentially the ferromagnetic behaviour. The molal saturation magnetization is a linear function of the atomic percentage of tellurium in region $I_A$ and another linear function in region $I_B$, as shown in Fig. 4. On the other hand, we see, in the same figure, that the Curie temperture shows little variation with composition in region $I_A$, while it rises strikingly in region $I_B$. Such a rapid rise of the Curie point with increasing composition is known in few other cases. According to Marian[9], the Curie point of Ni–Mn alloy rises rapidly and the saturation moment drops linearly with increasing Mn content in the range of composition over 17 atomic percent of Mn. In $NiTe_x$, we have found this strange type of dependence of Curie point on composition, and for this dependence no convincing explanation can be given at present.

The values of the reciprocal susceptibility above the Curie temperature are plotted against temperature in Fig. 2. They lie on a straight line for specimens in region $I_A$. For sprcimens in region $I_B$ they lie on a straight line only below 700°C and an anomalous behaviour is observed above 700°C. From these straight lines, the effective Bohr magneton numbers for a Ni atom are estimated for several compositions and given, together with the corresponding values of the Curie temperature, in Table I.

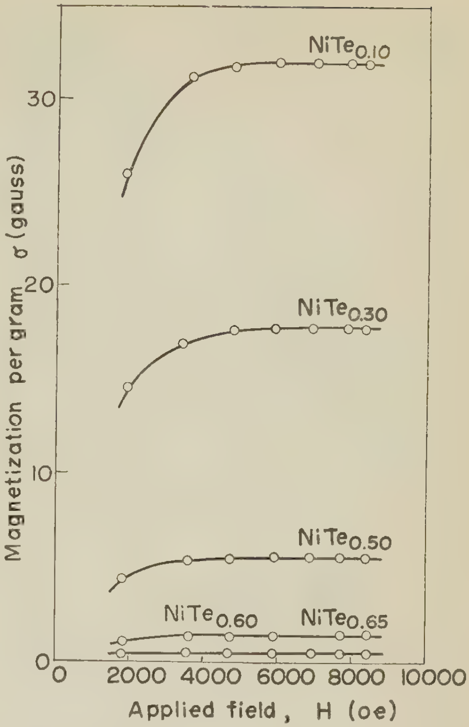

Fig. 3. Dependence on applied field of the magnetization of $NiTe_x$ of ferromagnetic composition.

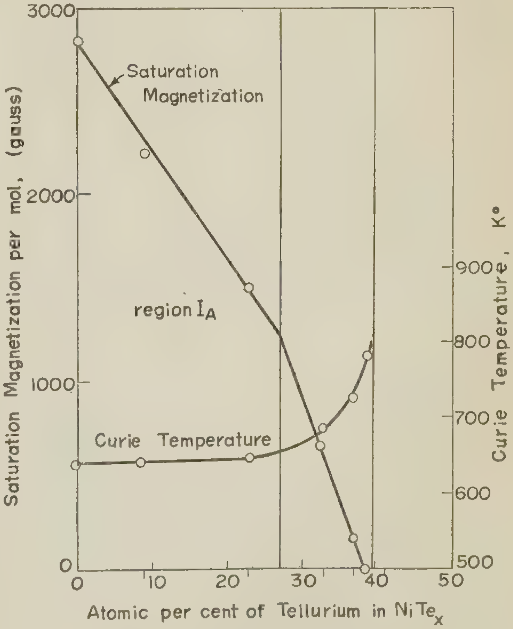

Fig. 4. Variation with composition of the molal saturation magnetization and the Curie point of $NiTe_x$ of ferromagnetic composition.

The Debye-Scherrer patterns obtained for specimens of compositions in region $I_A$, show lines due to metallic nickel beside several lines which are difficult to analyse, while the patterns for region $I_B$ are different both from those of region $I_A$ and the NiAs type pattern of NiTe in region II. Thus a heterogeneous phase whose one componet is metallic nickel is probably realized in region $I_A$. In fact,

Table I. Curie temperatures and the effective Bohr magneton numbers for a Ni atom in NiTe as a function of the molal content of tellurium.

| $x$ | $\theta_{\text{ferro}}$(K°) | $\theta_{\text{para}}$(K°) | $p_{\text{ferro}}(\mu_B)$ | $p_{\text{para}}(\mu_B)$ |
|---|---|---|---|---|
| 0.10 | 645 | 660 | 0.47 | 2.28 |
| 0.30 | 650 | 673 | 0.32 | 1.49 |
| 0.50 | 685 | 705 | 0.14 | 1.29 |
| 0.60 | 730 | 740 | 0.04 | 0.71 |
| 0.65 | 785 | | | |

$\theta_{\text{ferro}}$: ferromagnetic Curie point.
$\theta_{\text{para}}$: paramagnetic Curie point.
$p_{\text{ferro}}$: effective Bohr magneton numbers in ferromagnetic region.
$p_{\text{para}}$: effective Bohr magneton numbers in paramagnetic region.

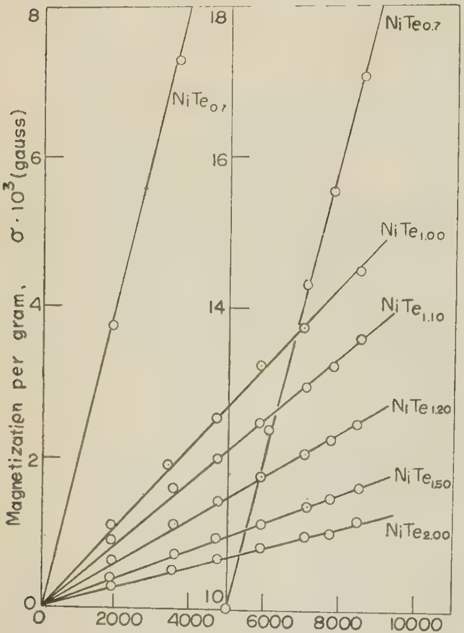

Fig. 5. Dependence on applied field of the magnetization NiTe$_x$ of paramagnetic composition.

the Curie temperature in region I$_A$ remains, as shown in Fig. 4, almost constant, and is close to the Curie point of the pure nickel, i.e., 640°K. The discontinuous change of slope of the saturation magnetization curve and the change in the Curie temperature curve in Fig. 4 for $x>0.33$ indicate a phase change at $x=0.33$. That an anomalous behaviour of $1/x-T$ curve in Fig. 2 is not observed in sub-region I$_A$ but is observed in I$_B$ is also suggestive of the phase transition.

b) *Paramagnetic composition range (region II)*

It is shown in Fig. 5 that the magnetization

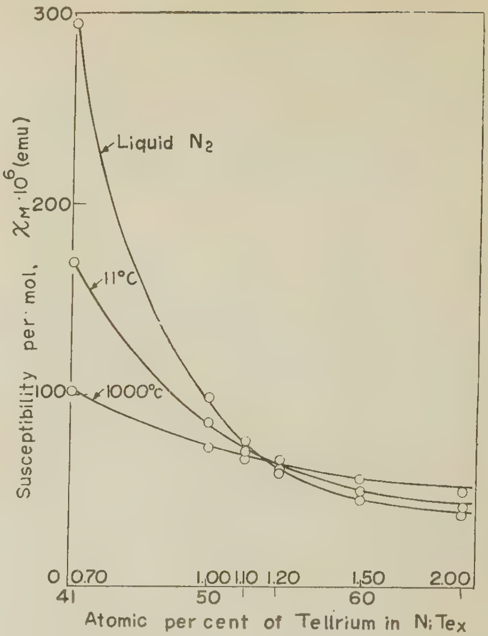

Fig. 6. Variation with composition of the susceptibility of NiTe$_x$ of paramagnetic composition.

in the region $0.7 \leq x \leq 2.00$ varies linearly with field up to about 9000 oe. This composition range is thus paramagnetic. The values of the susceptibility which are determined by taking the slopes of these straight lines are plotted against temperature in Fig. 8 and also against tellurium content in Fig. 6. In the latter curves, we see that the points fall on a smooth curve for each temperature and that the curves rise as the ferromagnetic compositions are approached.

The reciprocals of the susceptibility at various compositions in region II are plotted against absolute temperature in Fig. 7. As can be seen in this figure, plots of the reciprocal susceptibility for stoichiometric composition lie, below 300°C, on a straight line, the extrapolation of this straight line crossing the temperature axis at −1110°K. The absolute value of the temperature of this cross point appears to decrease as Te content decreases. The fact that the paramagnetic Curie point of NiTe is found in the negative region of temperature indicates an antiferromagnetic character of this compound. But this is not conclusive because the observed values of the susceptibility are too small compared with those of ordinary antiferromagnetic substances and also no Néel

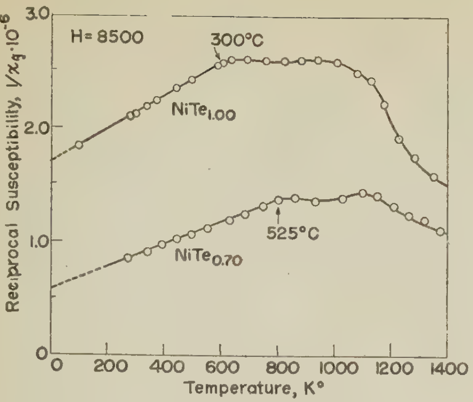

Fig. 7. Temperature dependence of the reciprocal susceptibility of $NiTe_x$ of paramagnetic composition.

point was yet found in the temperature range of the present experiment. It is to be noted, that similar phenomena have been found in other intermetallic compounds. A manganese nitride $Mn_5N_2$ recently studied by Yousef[10)] and others shows no evidence of the Néel point and yet shows an antiferromagnetic character in its $1/\chi - T$ relation. The data in the case of FeTe obtained by the present authors are another similar example in this respect. The molal susceptibility $\chi_M$ corresponding to the linear part in Fig. 7 can be represented by the formula $\chi_M = C/(T+\theta)$, with values of the Curie constant $C$, the characteristic temperature $\theta$ and the effective Bohr magneton numbers $p$ per nikel atom given by

$C=0.122$, $\theta=1110°\mathrm{K}$, $p=0.99\,\mu^B$
and for $x=1.00$,

$C=0.155$, $\theta=630°\mathrm{K}$, $p=1.12\,\mu_B$
for $x=0.70$.

The reciprocal susceptibility in the temperature region above 300°C for stoichiometric compound is independent of temperature up to 1000°K and then drops. This behaviour will be discussed later. The dissimilarity in behaviour in two temperature regions separated by 300°C might indicate a magnetic transition or a change in crystal structure at 300°C. It is to be noted that the similar break of the reciprocal susceptibility curve in FeTe was correlated with a specific heat anomaly. The same circumstance can be expected for NiTe.

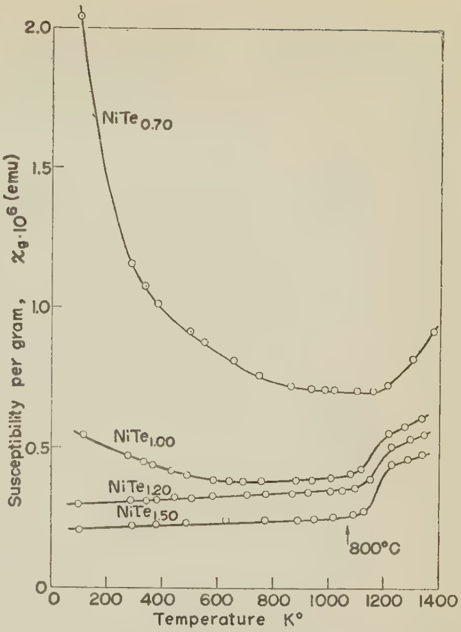

Fig. 8. Temperature dependence of the susceptibility of $NiTe_x$ of paramagnetic composition.

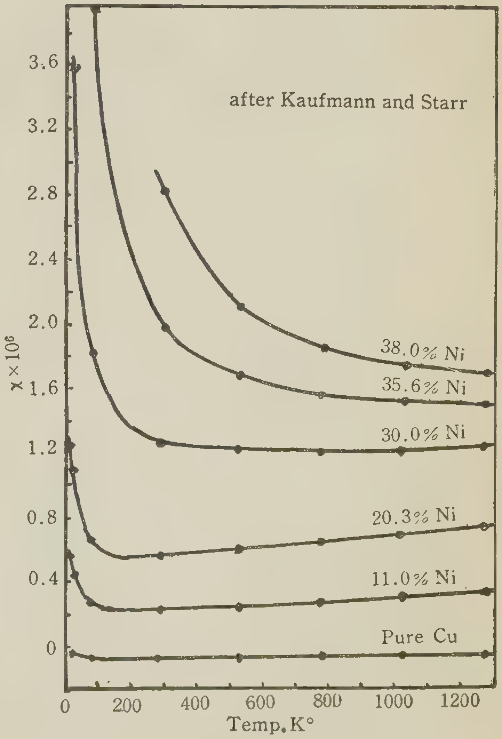

Fig. 9. Temperature dependence of the susceptibility of nickel-copper alloys of various composition (after Kaufmann and Starr).

We now mention the temperature dependence of the magnetic susceptibility shown in Fig. 8. This temperature dependence of the paramagnetic susceptibility has a close similarity in its appearance to that found by

Kaufmann and Starr[11] for Cu-rich Cu-Ni alloys. Their measurements are reproduced in Fig. 9 for the purpose of comparison. Discussions concerning this resemblance will be given later.

With regard to Fig. 8 we can point out the following characteristics of the curves. A large temperature dependence of the susceptibility exists at lower temperatures, which disappears gradually as the tellurium content is increased. At higher temperatures the susceptibility is almost temperature-independent and takes small values. Similar behaviours were found in FeTe and CoTe and were discussed previously[3]. This almost temperature-independent susceptibility exhibits, however, a slight increase with increasing temperature for Te-rich compounds. A further feature of the curves is a sudden rise of the susceptibility in the region between 800°C and 900°C, which is followed by a gradual increase with increasing temperature. This anomaly must be due to the melting of the specimens, because the specimens show different appearences at temperatures higher and lower than this temperature region. A similar anomalous behaviour due to melting has been found in FeTe and in pure Te.

We note finally that all the data obtained in the present experiment are generally reproducible and also reversible with temperature.

## §4. Discussions of the Results

Comparing the results for the paramagnetic nickel telluride obtained in the present experiment with those of the paramagnetic Cu-Ni alloys studied by Karfmann and Starr, we find similar features between them. But there are also distinctly different features.

Those found in common in both cases are the followings: a characteristic variation of the susceptibility with composition (see Fig. 6), the temperature-independent susceptibility of small values, and a tendncy to increase with increasing temperature of this susceptibility (see Fig. 8 and Fig. 9). It may be reasonable to consider that in nickel telluride these magnetic properties arise from an alloyic character present in this compound, since the similar magnetic properties pertain to paramagnetic Cu-Ni alloys. In fact, it has been shown by Schönberg[12] that tellurides of transition metals are more metallic than sulphides or selenides of the same metals.

On the other head, the low temperature susceptibility behaviours of nickel telluride (Fig. 8) are distinctly different from the corresponding behaviours of paramagnetic Cu-Ni, in spite of their apparent similarity (Fig. 8 and Fig. 9). An antiferromagnetic character of the reciprocal susceptibility pertains to the low temperature behaviours of nickel telluride, whereas the low temperature susceptibility of paramagnetic Cu-Ni shows nothing like that. It is natural to expect such a difference to exist between them since a superexchange effect via the intermediary of each negative ion must exist in the case of telluride. This consideration is supported by the fact that MnTe and FeTe are antiferromagnetic substances possessing NiAs lattice just like NiTe.

### Conclusion

It is found that NiTe is a substance of an antiferromagnetic character, although the present measurements down to liquid nitrogen temperature show no evidence of the Néel point, which might be at a lower temperature. The detection of the Néel point would deserve a further investigation.

It is also to be noted that a temperature-independent paramagnetism is commonly found in tellurides of Fe, Co and Ni, especially for Te-rich compositions in each case.

The authors wish to thank Professor T. Nagamiya of Osaka University for kind discussions, Professor Y. Mashiyama of Naniwa University for his warm encouragement and Professor Y. Shimomura for kind permission to work with his X-ray equipments. The authors would also like to thank Mr. Fukuoka for his helpful assistance in measurements. This work has been supported in part by the research expenditure of the group 'Research of Ferromagnetic Oxides' organized by Professor Kaya.

### References

1) H. Haraldsen: Z. Anorg. u. Allge. Chem. **231** (1937) 27, **246** (1941) 169.
L. Néel: Rev. Mod. Phys. **25** (1953) 59.
2) C. Guillaud: *Colloque de Ferromagnetisme et D'antiferromagnetisme, Grenoble* (1951) 77.

3) E. Uchida and H. Kondoh: Jour. Phys. Soc. Japan **10** (1955) 357.
4) E. Uchida: Jour. Phys. Soc. Japan **10** (1955) 517.
5) E. Uchida and H. Kondoh: to be published.
6) H. Kondoh and E. Uchida: The annual meeting of Phys. Soc. of Japan at Nagoya University (April 1955).
7) F. M. Gal'perin and T. M. Perkalina: Doklady Akad. Nauk. S.S.S.R. **69** (1949) 19. (Chem. Abst. **41** (1950) 1251.)
8) S. Tengner: Z. Anorg. u. Allge. Chem. **239** (1938) 126.
R. W. G. Wycoff: *Crystal Structure* (1948) Chap. III.
9) V. Marian: Phys. Rev. **51** (1937) 136.
10) Y. L. Yousef, R. K. Girgis and H. Mikhail: Jour. Chem. Phys. **23** (1955) 959.
11) A. R. Kaufmann and C. Starr: Phys. Rev. **63** (1943) 445.
12) N. Schönberg: Acta Metal. **2** (1954) 427.

---

JOURNAL OF THE PHYSICAL SOCIETY OF JAPAN Vol. 11, No. 1, JANUARY, 1956

# Magnetic and Electrical Properties of Manganese Telluride

By Enji UCHIDA, Hisamoto KONDOH and Nobuo FUKUOKA

*Department of Physics, Naniwa University, Osaka*

(Received September 7, 1955)

The temperature dependence of the susceptibility of the antiferromagnetic compound MnTe was measured over a range of temperature between liquid nitrogen temperature and 720°C. An abrupt change in slope and a maximum of the susceptibility curve were found at 37°C and at 55°C respectively. These results are compared with the observed Néel temperatures previously reported by Squire and by Serre. A thermal hysteresis was also found above the Néel temperature, relating to the heat history of the specimen. It is shown that the susceptibility of $MnTe_{1+x}$ ($0 \leq x \leq 1$), where $x$ is the excess content of tellurium, is explicable in terms of two phases, MnTe and $MnTe_2$ which possess different susceptibilities. The electrical properties, i.e., the resistivity, the thermo-emf and the Hall emf, were measured as functions of temperature. Evidence was found of anomalous behaviours at the Néel temperature for them. A large thermal hysteresis of the resistivity is also found above the Néel temperature, which suggests a change of the crystal structure at about 130°C.

## §1. Introduction

According to the previously published data[1], the crystal structure of the compound MnTe is the NiAs type with lattice spacings $a_0=4.12$ A and $c_0=6.70$A. The magnetic susceptibility has been investigated by Squire[2] and by Serre[3]. They found that the susceptibility showed the behaviour of an antiferromagnetic compound, the Néel temperature being reported as 37°C by Squire or 55.6°C by Serre. The heat capacity measurements of Kelley[4] have shown that MnTe exhibits a hump of the heat capacity with its maximum at 34°C (307° K). Antiferromagnetic resonance absorption measurements for MnTe have been made by Maxwell and McGuire[5], who reported the $g$ values to be 2.00. Squire[6] has also studied the electrical resistivity of this compound and found that it shows an anomalous behaviour with a maximum at about the Néel temperature (30°C).

As mentioned above, the Néel temperature reported by Squire differs so much from that by Serre that the difference seems to be too large as an error of measurements. The present experiment is concerned with the confirmation of the Néel temperature. From the fact that the resistivity dependence on temperature shows a maximum at about the Néel temperature, it is expected that the

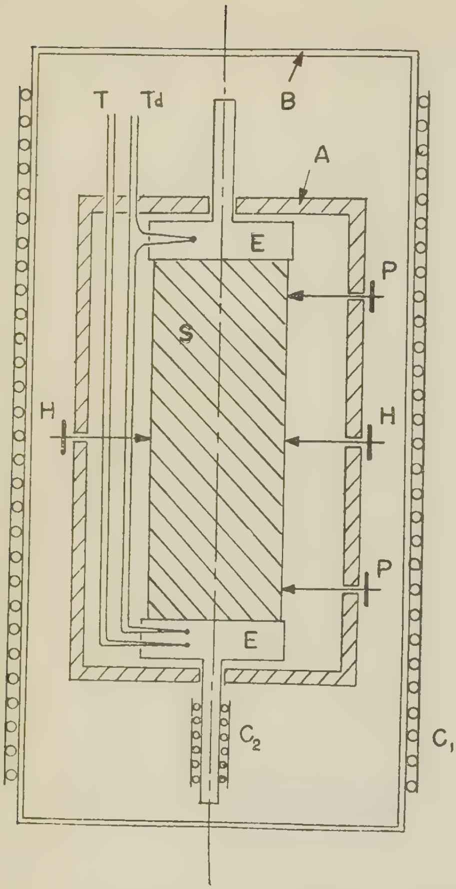

Fig. 1. Schematic representation of sample holder for electrical measurements.
A: micalex case; S: sample; E: current electrodes; P: probes for measuring potential; H: probes for measuring Hall emf; T: thermocouple (Cu-constantan); $T_d$: differential thermocouple; $C_1$: heating coil; $C_2$: heating coil for measurements of thermo-emf; B: brass case.

other electrical properties, i.e., the thermo-emf and the Hall emf, behave anomalously at the same temperature. The present experiment is also concerned with the investigations of the electrical properties in order to seek for possible evidence of the correlation of the electrical properties with the magnetic properties of this compound.

## § 2. Experimental

The procedure of the preparation of the compound MnTe$_{1+x}$ is as follows: Mixed powder of manganese (99.4 percent pure) and tellurium (99.9 percent pure) with a desired proportion was sealed in an evacuated silica tube ($10^{-6}$ mm Hg), and this was heated in a furnace at 725°C for 20 hours and slowly cooled after that. The product was a solid material with a grayish appearance. The X-ray Debye-Scherrer diffraction pattern of a sample of stoichiometric composition was compatible with the NiAs structure.

The susceptibility was measured with the same technique and the same magnetic balance as those described in previous papers7),8).

The electrical properties i.e., the resistivity, the thermo-emf and the Hall emf were measured by the usual methods. The specimens used for the present electrical measurements were prepared by moulding the powder sample to a shape of 7 mm in length, 4 mm in diameter (for the resistivity and the thermo-emf measurements) or a shape of 5 mm × 7 mm × 2 mm (for the Hall effect measurements) in a press tool, and by subsequent heat treatment of the material at 725°C to convert it to the crystalline modification. The sample holder is shown in Fig. 1. After it had been held in a brass case which was serviceable to homogenize the temperature of the sample, the measurements were carried out in vacuum ($10^{-2}$ mm Hg).

## § 3. Results

### a) *Magnetic measurements*

Fig. 2 shows the molal susceptibility of MnTe$_{1+x}$ as a function of temperature. All curves in this figure are obtained in heating runs for various compositions except the one which represents the cooling curve for the stoichiometric composition. In all cases the heating curve is found reversible up to about 100°C but it ceases to be so beyond that temperature. The cooling curve, from a higher temperature than 100°C, appears to be influenced in some way by the previous temperature history of the sample. The side curves in Fig. 2 represent a typical set of the details of the heating and cooling curves in the vicinity of the Néel point. Similar curves are obtained with different specimens, when measurements are made with special regard to the question of the Néel temperature. The heating curve indicates an abrupt change in slope at 37°C (310°K) and a maximum value of the susceptibility is obtained at 55°C (328°K), while a little lower values of the susceptibility occur with a broadening of the maximum in the cooling run. We can see, in the data of reciprocal susceptibility against temperature obtained by Serre for MnTe, a point which might possibly correspond to the abrupt change in slope in question; an observed point at about 37°C in Serre's case, in fact, deviates slightly from the curve, although the deviation is found so small that it cannot be noticed without special attention to this point.

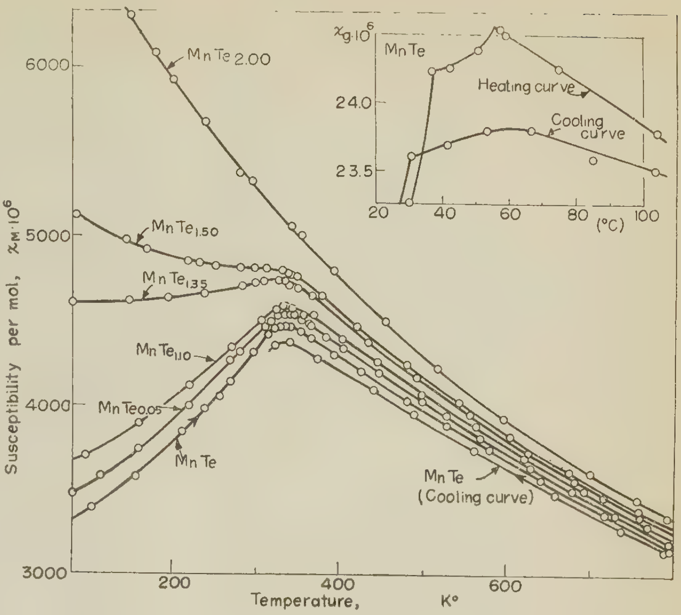

Fig. 2. Graph of molal susceptibility vs temperature for $MnTe_{1+x}$.

It is to be noted here that all the susceptibility curves of $MnTe_{1+x}$ in Fig. 2 can be understood as representing the sum of the molal susceptibilities of MnTe and $MnTe_2$, with the ratio of $(1-x)$: $x$, at corresponding temperature. Accordingly, the molal susceptibility of $MnTe_{1+x}$ is found to be a linear function of $x$ as shown in Fig. 3. This certainly indicates that $MnTe_{1+x}$ is constituted of two phases, MnTe and $MnTe_2$.

The reciprocals of the susceptibility for MnTe and $MnTe_2$ are plotted against absolute temperature in Fig. 4. As can be seen in this figure, plots for MnTe lie along a smooth curve, showing an upward concavity, which is in agreement to that previously observed by Serre. However, in the present case, the plots lie, above about 200°C, almost on a straight line, the extrapolation of this straight line crossing the temperature axis at −650°K. The molal susceptibility in the temperature range of this straight line can be written

$$\chi_M = C/(T+\theta)$$

with values of the Curie constant C, the characteristic temperature $\theta$ and the effective Bohr magneton numbers $p$ for a manganese atom given by

$$C=3.24, \quad \theta=650°\text{K}, \quad p=5.10\mu_B$$

These values of $C$, $\theta$ and $p$ are found to be a little smaller than those obtained by Serre.

From the linear relation of the reciprocal susceptibility against temperature of $MnTe_2$ (Fig. 4), the values of C, $\theta$ and $p$ for $MnTe_2$ are also estimated as follows:

$$C=4.00, \quad \theta=430°\text{K}, \quad p=5.68\,\mu_B$$

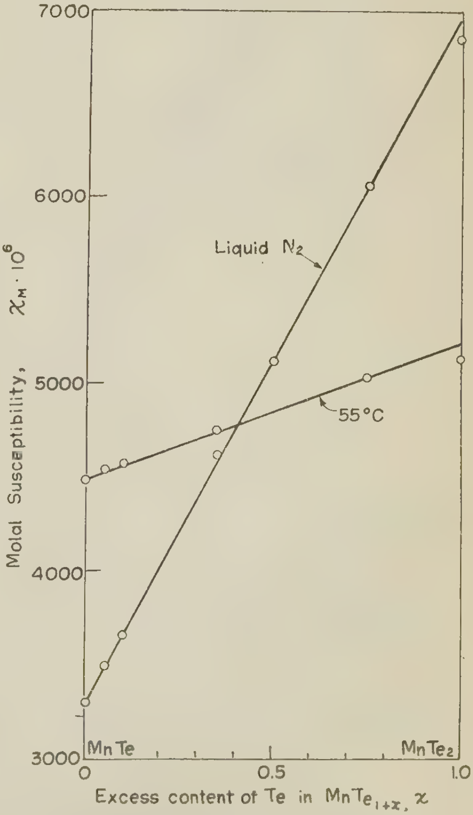

Fig. 3. Graph of molal susceptibility vs excess content of tellurium for $MnTe_{1+x}$.

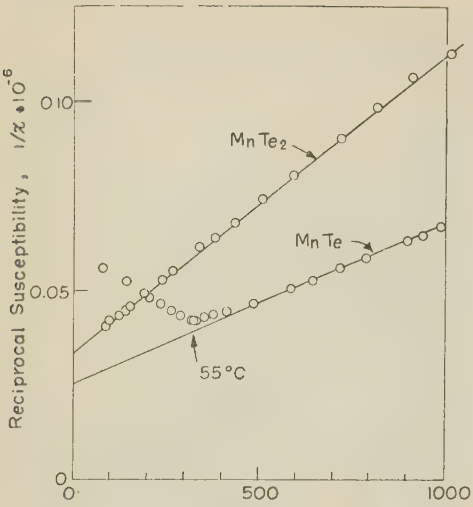

Fig. 4. Graph of reciprocal susceptibility vs temperature for MnTe and $MnTe_2$.

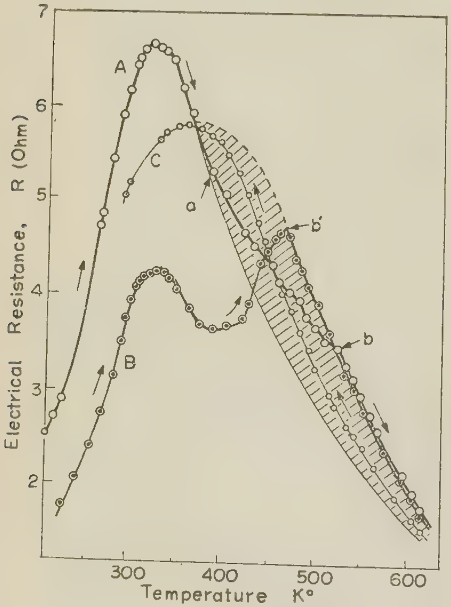

Fig. 5. Graph of electrical resistance vs temperature for MnTe.

Curve A: after 725°C heat treatment and subsequent slow cooling.

Curve B: after 725°C heat treatment and subsequent rapid cooling.

Curve C: after the runs for Curve A and for Curve B.

The fact that the paramagnetic Curie point of $MnTe_2$ is found in the negative region of temperature indicates an antiferromagnetic character of this compound, although no Néel point was yet found in the temperature range of the present experiment. It is to be noted that similar phenomena can be found in other intermetallic compounds, such as $Mn_5N_2$, FeTe or NiTe; each of them shows no evidence of the Néel point in the temperature range down to about 80°K and yet shows an antiferromagnetic character in its $1/\chi - T$ relation.

b) *Electrical properties*

The electrical properties of MnTe i.e., the resistivity, the thermo-emf and the Hall constant, are determined from liquid nitrogen temperature up to 400°C in order to see the correlation between the electrical and the magnetic properties of this compound.

The graph in Fig. 5 represents a set of typical runs in the measurements of resistivity. The data plotted on Curve A in this figure were obtained with the sample which has previously been subjected to a heat treatment at 725°C and to a subsequent slow cooling, by first cooling it to the liquid nitrogen temperature and then allowing it to warm up to the highest temperature of the measurements, usually at a rate of 2°/min. Up to the point 'a' on the curve at some ten degrees above the Néel point, Curve A shows a noticeable resemblance to the magnetic susceptibility behaviour, with a maximum at about 50°C (323°K). But, beyond this temperature, the observation generally shows a long relaxation time for the resistivity to approach its final value which is shown by the broken curve in this figure. However, after it has once reached the broken curve at the point 'b,' in the case of Curve A, this relaxation is experienced no more in the successive heating run. Curve C represents the subsequent cooling run to Curve A with a cooling rate of 2°/min. In all cases the cooling curve is a function of the interval of time during which the sample is held at the highest temperature of the run, the highest temperature itself and also the cooling rate. The hatched area in Fig. 5 represents the region in which all the cooling curves subject to different cooling conditions fall.

For the data plotted on Curve B, the heating run was started with the sample used for Curve A, which this time has previously been subjected to a heat treatment at 725°C for 20 hours and then to a rapid cooling from that temperature. The heating rate in this run is 2°/min, same as in the case of Curve

A. Compared with the case of Curve A, the lower values of the resistivity occurred up to about 100°C (373°K) and the relaxation time for the resistivity to approach to the broken line appeared to be shorter; consequently the point 'b′' on this curve, which corresponds to 'b' on Curve A, was found at a lower temperature than the latter. It is to be noted that in either cases of the run for Curve A and that for Curve B, the curve is found to be reversible up to about 100°C and it ceases to be reversible beyond, a similar phenomenon being also found in the magnetic susceptibility measurements. The hysteresis effect of the temperature dependence of resistivity above the Néel point is a good evidence of a certain change of the crystal structure at about 130°C.

The specific resistivity value of MnTe at room temperature is usually found to be of the order of 1 ohm cm. This is a very high conductivity compared with those of other antiferromagnetic manganese compounds such as MnSe, MnS or MnO.

Fig. 6 gives a typical result of the temperature dependence of the thermo-emf developed by the present specimens. For this data, a constant temperature difference of 40° is held across the specimen at every temperature of the measurements. It is found that the thermo-electric power lies between the values 0.3~0.6 mV/deg and shows a tendency to increase slowly with increasing temperature. The thermo-electric potential is always positive at the lower temperature side of the specimen, which indicates a predominanting hole conduction in MnTe.

Every plot in Fig. 7 represents the mean value of the data of ten repeated observations of the Hall voltage with a carrying current of 30 mA. The values of the Hall constant obtained by taking the slopes of the curves in this figure are plotted against temperature in Fig. 8. The sign of the Hall emf is found to be positive at all temperatures, which is consistent to the results of the thermo-emf measurements.

It is to be noted that both the thermo-emf and the Hall voltage behave anomalously at a temperature close to the Néel point (50°C), as in the resistivity; a maximum for the thermo-emf curve (Fig. 6) and a point of inflection for the Hall constant curve (Fig. 8) are found.

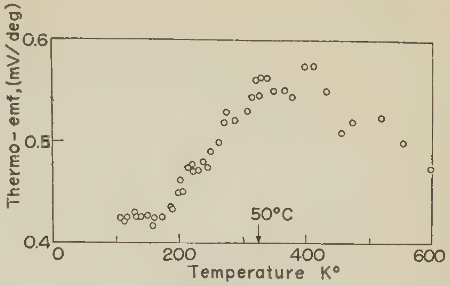

Fig. 6. Graph of thermo-electric power vs temperature for MnTe.

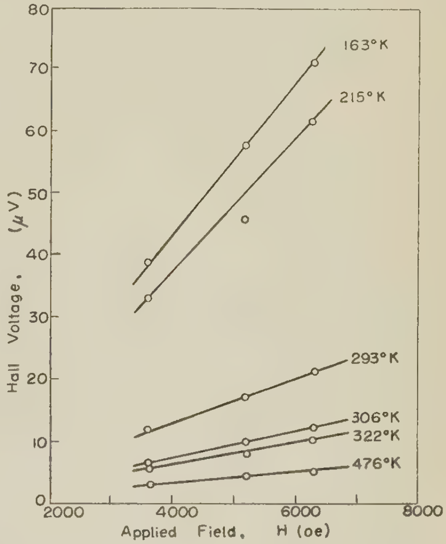

Fig. 7. Graph of Hall voltage vs applied field for MnTe.

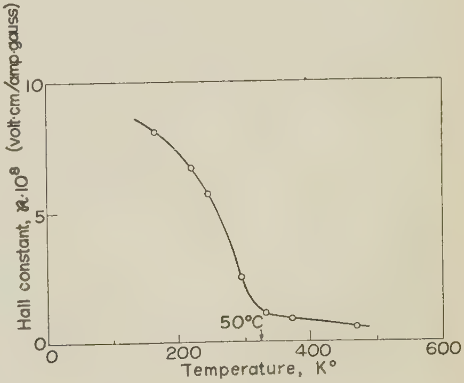

Fig. 8. Graph of Hall constants vs temperature for MnTe.

## § 4. Discussions

The results of the magnetic measurements showed the details of the behaviour of the susceptibility of MnTe in the vicinity of the

Néel point, i.e., we found a characteristic deviation from a simple $\lambda$-shape antiferromagnetic transition. Although this deviation is very small, we believe that the abrupt change in slope of the susceptibility curve at 37°C (310°K) correspond to the Néel temperature reported by Squire, and the maximum point at 55°C (328°K) to that reported by Serre. As mentioned in the preceeding section, the maximum at 55°C in fact broadens according to a heat history of the specimen. This broadening might have happened in the case of Squire. The anomalies in the resistivity and other electrical properties found at about 50°C (323°K) may be correlated with the maximum of the susceptibility curve at 55°C rather than to the abrupt change at 37°C. However, further experimental evidences (in particular of the specific heat or of the crystalline structure around the Néel point) may be necessary for the decision of the Néel point.

It should be mentioned that the temperature dependence of the electrical resistivity is very similar to that of the magnetic susceptibility, especially in the lower temperature region below 100°C. This is similar to the results reported by Squire. As shown in Fig. 5, conduction in MnTe changes its character in passing the Néel point from high to lower temperature, from a semi-conductor like conduction to a metallic one. We consider that this is an evidence of the influence of the magnetic properties of this compound on the conduction process at the Néel temperature. The decrease in conductivity with increasing temperature below the Néel point and the corresponding increases in thermo-emf and in Hall constant are qualitatively interpretable by supposing that the conduction in MnTe is contributed predominantly by holes above Néel temperature, while below the Néel temperature the part played by electrons increases with decreasing temperature.

## § 5. Conclusion

Results which are partly consistent to those of the previous works of Squire[2)] and Serre[3)] were obtained for MnTe in this experiment. It was also established that $MnTe_{1+x}$ is constituted of two phases involving MnTe and $MnTe_2$ in the range $0<x<1$.

The authors wish to thank Professor T. Nagamiya of Osaka University for kind discussions, Professor T. Hirone of Tohoku University and Professor Y. Mashiyama of Naniwa University for their warm encouragements.

### References

1) R. W. G. Wycoff: Crystal Structure (1948) Chap. III p. 28.
2) C. F. Squire: Phys. Rev. **56** (1939) 922.
3) A. Serre: Jour. de Phys. Rad. **8** (1947) 146.
4) K. K. Kelley: Jour. Am. Chem. Soc. **61** (1931) 203.
5) L. R. Maxwell and T. R. McGuire: Rev. Mod. Phys. **25** (1953) 279.
6) C. F. Squire: Phys. Rev. **56** (1939) 961.
7) E. Uchida and H. Kondoh: Jour. Phys. Soc. Japan **10** (1955) 357.
8) E. Uchida: Jour. Phys. Soc. Japan **10** (1955) 517.

JOURNAL OF THE PHYSICAL SOCIETY OF JAPAN Vol. 11, No. 1, JANUARY, 1956

# The Effects of Covalency on the Nuclear Magnetic Resonance in Ionic Crystals

By Kei YOSIDA and Tôru MORIYA

*Department of Physics, Osaka University*

(Received August 29, 1955)

Effects of covalency on the nuclear magnetic resonance in ionic crystals are discussed on the basis of perturbation calculations. Formulas for the chemical shift, the $I$-$I$ coupling and the quadrupolar relaxation time are derived. Using the degree of covalency deduced from the experimental values of the chemical shift, the coefficient of the $I$-$I$ coupling and the quadrupolar relaxation time are estimated for some ionic crystals. It is shown that, when the degree of covalency is several percent, the quadrupolar relaxation time becomes much shorter than in pure ionic case. For instance, the relaxation time of Br in KBr, assuming the degree of covalency of 1 percent, is estimated to be 1 sec, which is only several times larger than the experimental value.

## § 1. Introduction

According to experimental studies of the nuclear magnetic resonance absorption in ionic crystals, there exist the following three important problems associated with the covalency participating in the interionic binding: one is the problem of the chemical shift of the resonance field, the second is the anomalous width of the resonance line and the third is the problem concerned with the relaxation time.

Gutowsky and MacGarvey[1)] measured the chemical shift of Rb and Cs in their halides and remarked that it might arise from covalency. Kanda[2)] measured the chemical shift of halogen ions in several metal halides and deduced numerically the degree of covalency in each halide. Since the halogen ion has a closed shell structure in its pure ionic state, there is no second order paramagnetic effect, but in its excited state, where one electron of halogen ion is transferred to one of the neighbouring metal ions, the second order paramagnetic effect appears on account of the $p$-character of the halogen electronic wave function. Therefore, if the ionic state of a halide is not pure but is mixed to a certain extent with the state of covalent bonding, we can expect a paramagnetic chemical shift which is proportional to the degree of covalency.

Watkins and Pound[3)] and Watkins[4)] have performed precise experiments of the halogen nuclear magnetic resonance absorption in ionic crystals. Especially, Watkins found relaxation times of the order of $10^{-1}\sim 10^{-2}$ sec in the single crystals of KBr and KI. Although in these samples the dominant mechanism of the relaxation can be considered to be quadrupolar, the theoretical value of the relaxation time calculated under the assumption that the electric field gradient acting on each nucleus arises mainly from the surrounding ionic charges is larger than the experimental value by a factor of $10^5$. Watkins discussed possible sources of this discrepancy and pointed out as the most dominant effect the deformation of the electron shell surronding the nucleus by the thermal vibrations of the ions. It can be considered that there are two types of deformation sufferred by the ions, one is the deformation due to the mixing of higher electronic states of the ion and the other is that due to the transfer of an electron of that ion to a nearest neighbour ion, that is, the covalent bonding. Watkins considered the first type in some detail and showed that this is considerably effective to shorten the theoretical relaxation time. On the other hand Townes and Dailey[5)] pointed out that in covalent bonding state there exists a large electric field gradient at the position of the nucleus. Kanda found that the reciprocal of the relaxation time is proportional to the degree of covalency in LiBr, AgBr and TlBr. Thus, also in nuclear quadrupole relaxation, the role of covalency cannot be overlooked. In fact, the $p$-character of the electronic wave function of the halogen ion in its covalent state can produce a considerably large field gradient.

Another effect of the covalency is the formation of an indirect coupling between nuclear spins. Ruderman and Kittel[6] developed the theory of the *I–I* coupling between nuclear spins in metals, and a little later Bloembergen and Rowland[7] showed that this *I–I* coupling is the main source of the anomalously broad line width in metallic thallium and thallic oxides, and they extended Ruderman-Kittel's theory to the case of semiconductors or ionic crystals on the basis of Wilson's semiconductor model. Very recently, also Kanda[8] found very broad resonance lines in Tl-halides which can not be interpreted in terms of the ordinary dipole-dipole interactions between nuclear moments and concluded that this width arises from the *I–I* coupling. This *I–I* coupling in ionic crystals can be understood only when the covalent states are taken into account as excited states.

The purpose of this paper is to develop the theory of the chemical shift, the *I–I* coupling and the quadrupolar relaxation time arising from the excited covalent states with the use of a simple perturbational treatment and of the Heitler-London model. For the chemical shift and the *I–I* coupling, formulas presented here are not essentially different from those obtained already by Ramsey[9], Saika and Slichter[10], Ramsey and Purcell[11] and Gutowsky, McCall and Slichter[12], but they are extensions to the case of ionic crystals, and these will be given in § 2 and 3. In § 4 and 5, the contributions from the covalency to the quadrupole relaxation time is calculated along the same line as in § 2 and 3.

## § 2. Chemical Shift

Gutowsky and McGarvey and Kanda found considerably large paramagnetic chemical shifts in nuclear resonance lines for halides of heavy metals such as Rb, Cs and Tl. It may be considered that this shift originates in the covalent bonding state which mixes to some extent with the pure ionic state. In this section, we shall calculate the coefficient of the chemical shift $\sigma$ on the basis of the perturbational treatment, taking as the zero-th approximation the purely ionic state.

First let us consider the shift of a halogen nucleus whose nuclear moment $\mu$ is assumed, for convenience, to point in the direction of the external magnetic field. Then the necessary perturbing Hamiltonian for the chemical shift is expressed as

$$V=V_t+\sum_i\left(\boldsymbol{H}+\frac{2\boldsymbol{\mu}}{r_i^3}\right)\cdot\mu_B\boldsymbol{l}_i\,. \tag{2.1}$$

Here $V_t$ means the Hamiltonian which makes an electron of the halogen ion jump into a neighbouring metal ion and is of an electric nature, and the second term expresssed by a summation over electrons belonging to the halogen ion represents the interaction energy of the electrons with the external field $\boldsymbol{H}$ and with the field arising from the nuclear magnetic moment. $r_i$ and $\boldsymbol{l}_i$ mean respectively the radial distance of the $i$-th electron from the halogen nucleus and its orbital angular momentum in units of $\hbar$, and $\mu_B$ is the Bohr magneton.

According to the perturbation scheme, the fourth order perturbed energy can be written in the following form:

$$\Delta E_4=-\sum_{n,n',n''}\frac{(g|V|n)(n|V|n')(n'|V|n'')(n''|V|g)}{(E_n-E_g)(E_{n'}-E_g)(E_{n''}-E_g)}\,, \tag{2.2}$$

where $E_g$ and $E_n$ denote the unperturbed energies of the ground and excited states. The most important terms in the summation of Eq. (2.2) are those in which the first and the third excited states, i.e. $n$ and $n''$, are the same covalent state in which one electron of the halogen ion, with such a $p$-wave function that extends towards a neighbouring metal ion, has been transferred to that metal ion. Such a transition of one electron is produced by the electric part of Eq. (2.1) $V_t$. Then, Eq. (2.2) can be simplified as

$$\Delta E_4=-\sum_{n}\frac{|(g|V_t|n)|^2}{(E_n-E_g)^2}\sum_{n'}\frac{(n|V_H|n')(n'|V_H|n)}{E_{n'}-E_g}\,. \tag{2.3}$$

Here the first summation is taken over all the nearest neighbouring metal ions of the halogen ion and $V_H$ denoted the magnetic part of the Hamiltonian (2.1). In order to obtain the chemical shift from the perturbed energy $\Delta E_4$, we must take out the field-dependent term from (2.3). Each excited state $n'$, which is connected by the field-dependent term of (2.1) with the state $n$ in which one $p$-electron is missing from the halogen ion, is the state produced by the transition of one electron on another $p$-orbital to the hole of the state $n$. Since four electrons are participating in this transition and the transition from the ground state to the $n$-state, $g$, $n$, and $n'$-states are represented by the following wave functions

either

$$\psi_g = \frac{1}{\sqrt{2^2 \cdot 4!}} \Sigma_p\, \delta_p P \varphi_0(1)\varphi_0(2)\varphi_{+1}(3)\varphi_{+1}(4)\{1\cdot 2\}\{3\cdot 4\}\,, \tag{2.4}$$

$$\psi_n = \frac{1}{\sqrt{2 \cdot 4!}} \Sigma_p\, \delta_p P \varphi_M(1)\varphi_0(2)\varphi_{+1}(3)\varphi_{+1}(4)\{1\cdot 2\}\{3\cdot 4\}\,, \tag{2.5}$$

$$\psi_{n'} = \frac{1}{\sqrt{2 \cdot 4!}} \Sigma_p\, \delta_p P \varphi_M(1)\varphi_0(2)\varphi_0(3)\varphi_{+1}(4)\{1\cdot 4\}\{2\cdot 3\}\,, \tag{2.6}$$

or

$$\psi_g = \frac{1}{\sqrt{2^2 \cdot 4!}} \Sigma_p\, \delta_p P \varphi_0(1)\varphi_0(2)\varphi_{-1}(3)\varphi_{-1}(4)\{1\cdot 2\}\{3\cdot 4\}\,, \tag{2.7}$$

$$\psi_n = \frac{1}{\sqrt{2 \cdot 4!}} \Sigma_p\, \delta_p P \varphi_M(1)\varphi_0(2)\varphi_{-1}(3)\varphi_{-1}(4)\{1\cdot 2\}\{3\cdot 4\}\,, \tag{2.8}$$

$$\psi_{n'} = \frac{1}{\sqrt{2 \cdot 4!}} \Sigma_p\, \delta_p P \varphi_M(1)\varphi_0(2)\varphi_0(3)\varphi_{-1}(4)\{1\cdot 4\}\{2\cdot 3\}\,. \tag{2.9}$$

Here $\varphi_M$ means the wave function of the electron transferred to the metal ion and is in general a hybridized orbital of $s$- and $p$-functions of the metal ion, $\varphi_0$, $\varphi_{\pm 1}$ denote the wave functions of the $p$-state in the halogen ion, suffixes 0, ±1 representing the $z$-component of the angular momentum $\boldsymbol{l}$. The $z$-axis is taken in the direction joining the halogen ion to the metal ion. In this case, $\varphi_0$ is the wave function which extends towards the $z$-axis. $\{12\}$ represents the antisymmetrized spin function, that is, the abbreviation of

$$\frac{1}{\sqrt{2}}\{\alpha(1)\beta(2)-\alpha(2)\beta(1)\}\,,$$

where $\alpha$ and $\beta$ respectively mean the spin functions of plus and minus spins. Further, it must be noted that the singlet states should be taken as the excited states $\psi_n$ and $\psi_{n'}$, as well as the ground state, since the perturbing Hamiltonian (2.1) does not contain any spin variable. $\psi_{n'}$ represented by (2.6) is the state in which one electron with the wave function of $\varphi_{+1}$ has been transferred to $\varphi_0$ state, while $\psi_{n'}$ represented by (2.9) is that in which one electron with $\varphi_{-1}$ has been transferred to $\varphi_0$ state. Therefore, in calculating the matrix element of $(n|V|n')$, $\varphi_n$ given by (2.5) must be used in combination with $\psi_{n'}$ given by (2.6), and $\varphi_n$ given by (2.8) with $\psi_{n'}$ given by (2.9). The summation with respect to $n'$ in (2.3) is taken over these two states of $n'$.

Now we denote the direction cosines of the external field $\boldsymbol{H}$ by $\alpha_n$, $\beta_n$ and $\gamma_n$, referring to the coordinate system in which the $z$-axis is the direction joining the halogen ion to the metal ion under consideration. After simple calculations we obtain

$$(n|V_H|n') = -\frac{1}{\sqrt{2}}\mu_B\left(H+2\mu\left\langle\frac{1}{r^3}\right\rangle_H\right)(\alpha_n \mp i\beta_n)\,, \tag{2.10}$$

$$\Sigma_{n'}\frac{(n|V_H|n')(n'|V_H|n)}{E_{n'}-E_g} = \frac{1}{\varDelta E'}\mu_B{}^2\left(H+2\mu\left\langle\frac{1}{r^3}\right\rangle_H\right)^2(\alpha_n{}^2+\beta_n{}^2)\,, \tag{2.11}$$

where $V_H$ represents the second term of (2.1), $E_{n'}-E_g$ is denoted by $\varDelta E'$ and $\left\langle\frac{1}{r^3}\right\rangle_H$ means the average value with respect to the radial part of the $p$-wave functions of the halogen ions. Summing up $(\alpha_n{}^2+\beta_n{}^2)$ over all the neighbouring metal ions we obtain

$$\Sigma_n(\alpha_n{}^2+\beta_n{}^2)=4\,, \qquad \text{for NaCl type}$$

$$=\frac{16}{3}\,. \qquad \text{for CsCl type}\,.$$

Thus if we denote $E_n-E_g$ by $\varDelta E$ and $|(g|V_t|n)|^2$ by $b^2$, $\varDelta E_4$ becomes

$$\Delta E_4 = -\frac{2}{3} z \frac{b^2}{\Delta E^2} \frac{1}{\Delta E'} \mu_B^2 \left(H + 2\mu \left\langle \frac{1}{r^3} \right\rangle_H \right)^2 , \tag{2.12}$$

where $z$ means the coordination number. The coefficient of the chemical shift $\sigma$ is given by the coefficient of the linear term with respect to $H\mu$ in (2.12), as Ramsey pointed out. Therefore we obtain for $\sigma$ of the halogen nucleus,

$$\sigma_H = -\frac{8}{3} z \frac{b^2}{\Delta E^2} \frac{1}{\Delta E'} \mu_B^2 \left\langle \frac{1}{r^3} \right\rangle_H . \tag{2.13}$$

Here it should be noted that $\Delta E$ is the energy of the state with covalent bonding, whereas $\Delta E'$ is that of the state without bonding. Therefore the former value is generally smaller than the latter. Moreover, $zb^2/(\Delta E)^2$ represents the degree of covalency and if we write this quantity as $\lambda$, although in this paper we shall use $\lambda$ for $b^2/(\Delta E)^2$, Eq. (2.13) becomes identical with the expression derived by Saika and Slichter in the case of molecules and that derived by Kanda in the case of ionic crystals.

Next we shall turn to the consideration of the chemical shift of the metal nucleus. In this case we must pay our attention to the electron transferred to the metal ion from the halogen ion, and take as the excited states $\psi_{n'}$ the states in which the transferred electron has changed its wave function from the $s$-$p$ hybridized orbital, favourable to the covalent bonding, to another $p$-orbital, namely

$$\begin{aligned} \psi_n &: \varphi_M = a_s \varphi_s^M + a_p \varphi_0^M , \\ \psi_n' &: \varphi_{\pm 1}^M , \end{aligned} \tag{2.14}$$

where $\varphi_s^M$, $\varphi_{0,\pm 1}^M$ mean the $s$-function and the three $p$-functions of the metal ions, 0, $\pm 1$ denoting the component of the angular momentum referred to the $z$-axis which is chosen in the direction connecting the metal ion with one halogen ion. If $\varphi_M$ is one of the usual tetrahedral orbitals, $a_s = \frac{1}{2}$ and $a_p = \frac{\sqrt{3}}{2}$. The perturbing Hamiltonian is of the type of (2.1), where $r_i$ is now to be interpreted as the distance from the metal nucleus. The calculation in this case becomes very simple because we need treat only one electron. Using similar notation to the case of halogen nucleus, we obtain the following result:

$$\Delta E_4 = -\sum_n \frac{b^2}{\Delta E^2} \frac{1}{\Delta E'} a_p^2 \mu_B^2 \times \left(H + 2\mu \left\langle \frac{1}{r^3} \right\rangle_M \right)^2 (\alpha_n^2 + \beta_n^2) , \tag{2.15}$$

where $\left\langle \frac{1}{r^3} \right\rangle_M$ means the average of $1/r^3$ over the radial part of the $p$-wave functions of the metal ion and the summation runs over the neighbouring halogen ions. From (2.15) the coefficient of the chemical shift for the metal nucleus, $\sigma_M$, is given by

$$\sigma_M = -\frac{8}{3} a_p^2 z \frac{b^2}{\Delta E^2} \frac{1}{\Delta E'} \mu_B^2 \left\langle \frac{1}{r^3} \right\rangle_M , \tag{2.16}$$

where $b$, $\Delta E$ are exactly the same as those appearing in (2.13) and $\Delta E'$ would be nearly equal to that of (2.13).

Up to now we have picked up only the fourth order perturbation. The second order perturbation must include such matrix elements as $(n|V_H|g)$, which can be explicity written down, as seen from (2.1), as

$$(n|H\mu_B \textstyle\sum_i l_i|g) + \left(n\middle| \sum_i \frac{2\mu}{r_i^3} \mu_B l_i \middle| g\right) .$$

Here the first term including the external field appearently vanishes because the ground state $g$ has a closed shell structure. Therefore, the second order perturbation contributes nothing to the chemical shift. Most of the third order terms vanish on account of the same reason, and the remaining parts would give only negligibly small contributions compared to the fourth order term. Thus we can regard the results of Eqs. (2.13) and (2.16) as the lowest order contributions in the perturbation approximation. In calculating $\sigma_M$ of the metal nucleus we confined our considerations to the case that the hybridized orbital consists of only $p$ and $s$-orbitals. For Rb and Cs, however, also d-orbitals may contribute to their chemical shifts. Therefore (2.16) should be modified to some extent in these cases.

The chemical shifts of the halogen nucleus in metal halides have been measured by Kanda. We shall estimate here the factor $\lambda = b^2/(\Delta E)^2$ in (2.13), a measure of the degree of covalency in these halides, assuming appropriate values for $\Delta E'$ and $\langle 1/r^3 \rangle$, as Kanda did in his paper. From the ionic picture on which we are standing, however, the value of $\Delta E'$ could be well appoximated by the following equation:

$$\Delta E' = \frac{(2\alpha - 1)e^2}{a} + E - I , \tag{2.17}$$

Table I.

| | cryst. structure | $a\times10^8$ | $E_{ev}$ | $I_{ev}$ | $\Delta E'_{ev}$ | $\left\langle\frac{1}{r^3}\right\rangle_H a_0^3$ | $-\sigma_{\exp}\times10^4$ | $\lambda=(b/\Delta E)^2$ |
|---|---|---|---|---|---|---|---|---|
| TlCl | CsCl | 3.31 | 3.75 | 6.07 | 8.63 | 7.16 | 2.51 | 0.039 |
| TlBr | CsCl | 3.44 | 3.52 | 6.07 | 7.99 | 13.55 | 6.2 | 0.047 |
| AgBr | NaCl | 2.88 | 3.52 | 6.54 | 8.45 | 13.55 | 1.89 | 0.020 |
| LiBr | NaCl | 2.745 | 3.48 | 5.37 | 11.2 | 13.55 | 0.896 | 0.013 |
| KI | NaCl | 3.53 | 3.13 | 4.32 | 9.00 | 18.0 | 1.48 | 0.013 |

where $a$ represents the interionic distance, $\alpha$ the Madelung constant, $I$ the ionization potential of the metal atom and $E$ the affinity of the halogen atom. For a more precise estimation, it might be necessary to take into account the effect of polarization, but since it is neither easy to estimate nor very serious, we omit it in our rather rough evaluation.

Actually, the excited states are such that the electron transferred from a halogen ion moves over all the surrounding metal ions, and thus they are split into several levels with different symmetries, while the excited states used in our perturbation calculations have been assumed to be degenerate. The real states, however, can be expressed as linear combinations of our degenerate functions, so that our $\varDelta E'$ represents approximately the centre of gravity of the split levels. The value of $\varDelta E'$ given by Eq. (2.17) corresponds to this centre of gavity of the levels.

Making use of the average values of $\langle 1/r^3\rangle$ estimated semi-empirically for several ions by Barnes and Smith[13] we obtain the values of $\lambda$ shown in Table I. These values multiplied by coordination number $z$ are nearly equal to the values of the degree of covalency obtained by Kanda.

## § 3. Indirect Interaction Between Nuclear Spins

In this section we shall turn our attention to the problem concerning the indirect spin coupling between nuclei. This problem can be treated with the use of the same method as that used in the preceding section. Namely, we shall start from the purely ionic state where all the interactions of the electrons with nuclear spins would disappear in the average because of the closed shell structures of the ions. The existence of the indirect couplings between nuclear shins becomes possible only when excited configurations are taken into account.

The perturbing Hamiltonian in this case consists of the interactions between electrons and nuclear spins. Namely,

$$V=V_t+V_L+V_D+V_F\ , \tag{3.1}$$

$$V_L=2\mu_B\hbar\left\{\gamma_H\sum_i\frac{(l_i\cdot I_H)}{r_{Hi}{}^3}+\gamma_M\sum_i\frac{(l_i\cdot I_M)}{r_{Mi}{}^3}\right\}\ , \tag{3.2}$$

$$\begin{aligned}V_D=2\mu_B\hbar[\gamma_H\textstyle\sum_i r_{Hi}^{-3}\{&-(s_i\cdot I_H)\\ &+3r_{Hi}^{-2}(s_i\cdot r_{Hi})(I_H\cdot r_{Hi})\}\\ &+\gamma_M\textstyle\sum_i r_{Mi}^{-3}\{-(s_i\cdot I_M)\\ &+3r_{Mi}^{-3}(s_i\cdot r_{Mi})(I_M\cdot r_{Mi})\}]\ ,\end{aligned} \tag{3.3}$$

$$\begin{aligned}V_F=\frac{16}{3}\pi\mu_B\hbar\{&\gamma_H\textstyle\sum_i\delta(r_i-r_H)(s_i\cdot I_H)\\ &+\gamma_M\textstyle\sum_i\delta(r_i-r_M)(s_i\cdot I_M)\}\ ,\end{aligned} \tag{3.4}$$

where $V_t$ represents, as in the preceding section, the electrostatic perturbation, which makes an electron transfer from a halogen ion to one of its nearest neighbouring metal ions, $V_L$ the interactions between the orbital moment $l_i$ of electron $i$ and the nuclear spins $I_H$ and $I_M$, $V_D$ those between electron spins $S_i$ and the nuclear spins and $V_F$ the Fermi interactions. $\gamma_H$ and $\gamma_M$ mean the gyromagnetic ratio of the nuclei and suffixes $H$ and $M$ represent the halogen and metal ions, respectively. Now we shall consider the indirect couplings between nuclear spins of nearest pairs of metal and halogen ions. Also in this case, the most important effective Hamiltonian giving rise to the interaction between nuclear spins would be given by Eq. (2.2), where the excited states $n$ and $n''$ are the covalent states in which one metal ion has an excess electron transferred from the neighbouring halogen ion. The wave function of the extra electron in the metal ion is, as before, expressed by (2.14) and that of the hole left in the halogen by the same $\varphi_{H0}$ as in the previous section, both of which extending in the direction connecting the metal ion with the halogen ion and having zero $z$-component of the angular momentum $l$. Then, we have a similar expression to Eq. (2.3), except that $V_H$ is replaced by $V_L$, $V_D$ and $V_F$. In this expression, however, we must take different excited states from those taken in § 2.

Since the perturbation $V_L$ does not contain any electron spin variable, $V_L$ has non-vanishing matrix element $(n|V_L|n')$ only for singlet states $n'$ because the ground state is singlet and so the covalent state is singlet, whereas the other $V_D$ and $V_F$ have vanishing elements for singlet $n'$ because they are linear with respect to the electron spin. Therefore we can divide the matrix elements of $V_L+V_D+V_F$ into parts and consider them separately. Since $V_L$ is linear with respect to the orbital moment of an electron, its matrix elements do not vanish only for such $\psi_{n'}$ for which the vacant $\varphi_{H0}$ state of the halogen ion has become occupied by another $p$-electron or for which a $p$-orbital of the metal ion has become occupied instead of the $\varphi_M$ orbital. For such $\psi_{n'}$, however, either of the matrix elements of $V_{LH}$ and $V_{LM}$ vanishes, so that any coupling between $I_H$ and $I_M$ does not occur from $V_L$.

As for $V_D$ and $V_F$, they are linear with respect to spin variables as mentioned above so that they have non-vanishing matrix elements only for triplet states $n'$. We shall now take two electrons out of six, one of which occupies the $\varphi_M$-orbital and the other the $\varphi_{H0}$-orbital. Then the orbital part of $\psi_n$ and $\psi_{n'}$ can be written as

$$\psi_n=\frac{1}{\sqrt{2}}\{\varphi_M(1)\varphi_{H0}(2)+\varphi_M(2)\varphi_{H0}(1)\}\,, \tag{3.5}$$

$$\psi_{n'}=\frac{1}{\sqrt{2}}\{\varphi_M(1)\varphi_{H0}(2)-\varphi_M(2)\varphi_{H0}(1)\}\,. \tag{3.6}$$

The other electrons may be put out of considerations for the present calculation. Let us first calculate the transition matrix element of $V_D$ between the states (3.5) and (3.6) reserving the spin variables as operators. Using (3.5), (3.6) and (3.3), we obtain the following expression:

$$\begin{aligned}(n|V_D|n')=-\mu_B\hbar\sum_{i=1,2}(-1)^i\Big[\gamma_M\int\varphi_M(i)r_{Mi}^{-3}\{-(s_i\cdot I_M)+3r_{Mi}^{-2}(s_i\cdot r_{Mi})(I_M\cdot r_{Mi})\}\varphi_M(i)d\tau_i\\ -\gamma_H\int\varphi_{H0}(i)r_{Hi}^{-3}\{-(s_i\cdot I_H)+3r_{Hi}^{-2}(s_i\cdot r_{Hi})\,(I_H\cdot r_{Hi})\}\,\varphi_{H0}(i)\,d\tau_i\Big]\,,\end{aligned} \tag{3.7}$$

where insignificant contributions arising from the non-diagonal elements between $\varphi_M$ and $\varphi_{H0}$ are omitted. The integrals included in the above expression can easily be calculated as

$$\begin{aligned}&\int\varphi_M(r)\frac{xy}{r^5}\varphi_M(r)d\tau=\int\varphi_{H0}(r)\frac{xy}{r^5}\varphi_{H0}(r)d\tau=0,\cdots\\ &\int\varphi_M(r)\frac{x^2}{r^5}\varphi_M(r)d\tau=\int\varphi_M(r)\frac{y^2}{r^5}\varphi_M(r)d\tau=a_s{}^2\frac{1}{3}\left\langle\frac{1}{r^3}\right\rangle_{MS}+a_p{}^2\frac{1}{5}\left\langle\frac{1}{r^3}\right\rangle_{MP}\,,\\ &\int\varphi_{H0}(r)\frac{x^2}{r^5}\varphi_{H0}(r)d\tau=\int\varphi_{H0}(r)\frac{y^2}{r^5}\varphi_{H0}(r)d\tau=\frac{1}{5}\left\langle\frac{1}{r^3}\right\rangle_H\,,\\ &\int\varphi_M(r)\frac{z^2}{r^5}\varphi_M(r)d\tau=a_s{}^2\frac{1}{3}\left\langle\frac{1}{r^3}\right\rangle_{MS}+a_p{}^2\frac{3}{5}\left\langle\frac{1}{r^3}\right\rangle_{MP}\,,\\ &\int\varphi_{H0}(r)\frac{z^2}{r^5}\varphi_{H0}(r)d\tau=\frac{3}{5}\left\langle\frac{1}{r^3}\right\rangle_H\,.\end{aligned}$$

Using these results, (3.7) becomes

$$\begin{aligned}(n|V_D|n')=\frac{2}{5}\mu_B\hbar\Big[\gamma_H\left\langle\frac{1}{r^3}\right\rangle_H\{(s_1-s_2)_x\cdot I_{Hx}+(s_1-s_2)_y\cdot I_{Hy}-2(s_1-s_2)_zI_{Hz}\}\\ -a_p{}^2\gamma_M\left\langle\frac{1}{r^3}\right\rangle_{MP}\{(s_1-s_2)_x\cdot I_{Mx}+(s_1-s_2)_y\cdot I_{My}-2(s_1-s_2)_z\cdot I_{Mz}\}\Big]\,.\end{aligned} \tag{3.8}$$

For $V_F$ a similar calculation yields

$$(n|V_F|n')=\frac{16}{3}\pi a_s{}^2\,\frac{1}{2}\mu_B\hbar\gamma_M|\varphi_{MS}(0)|^2(s_1-s_2)\cdot I_M\,, \tag{3.9}$$

where the contribution from $\varphi_{H0}$ does not appear because we are assuming $\varphi_{H0}$ as a pure $p$-function. Inserting (3.8) and (3.9) into (2.3) and nothing that the summation over $n$ is unnecessary in this case and that the summation over $n'$ can be replaced by the average of the products of spins included in (3.8) and (3.9) with respect to the singlet state, we obtain the following couplings between the two nuclear spins:

$$\frac{16}{25} a_p^2 \gamma_M \gamma_H \hbar^2 \lambda \frac{1}{\Delta E'} \mu_B^2 \left\langle \frac{1}{r^3} \right\rangle_H \left\langle \frac{1}{r^3} \right\rangle_{MP} (I_H \cdot I_M)\,, \tag{3.10a}$$

$$-\left\{ \frac{8}{25} a_p^2 \gamma_H \gamma_M \hbar^2 \lambda \frac{1}{\Delta E'} \mu_B^2 \left\langle \frac{1}{r^3} \right\rangle_H \left\langle \frac{1}{r^3} \right\rangle_{MP} + \frac{32}{15} a_s^2 \gamma_H \gamma_M \hbar^2 \pi \lambda \frac{1}{\Delta E'} \mu_B^2 |\varphi_{MS}(0)|^2 \left\langle \frac{1}{r^3} \right\rangle_H \right\} \times \{ I_{Hx} \cdot I_{Mx} + I_{Hy} \cdot I_{My} - I_{Mz} \cdot I_{Mz} \}\,. \tag{3.10b}$$

This result shows that exchange and pseudodipolar couplings are acting between $I_M$ and $I_H$. Expressions analogous to (3.10a) and (3.10b) have already been obtained by Gutowsky, MacCall and Slichter for the case of molecules and, independently of the present writers, by Kanda and Saito for the case of ionic crystals.

The ratios of the coefficients of the indirect couplings derived above to that of the oridinary dipole-dipole interaction $\hbar^2 \gamma_M \gamma_H / a^3$ are given by

$$\alpha_E = \frac{16}{25} a_p^2 \frac{\lambda}{\Delta E'} \mu_B^2 \left\langle \frac{1}{r^3} \right\rangle_H \left\langle \frac{1}{r^3} \right\rangle_{MP} a^3\,, \tag{3.11a}$$

$$\alpha_D = -\frac{\lambda}{\Delta E'} \left\langle \frac{1}{r^3} \right\rangle_M a^3 \mu_B^2 \left\{ \frac{8}{25} a_p^2 \left\langle \frac{1}{r^3} \right\rangle_{MP} + \frac{32}{15} \pi a_s^2 |\varphi_{MS}(0)|^2 \right\}\,. \tag{3.11b}$$

Kanda found a broad halogen resonance line in thallium halides, especially for TlCl, TlBr and TlI. If it could be assumed that such a broadening occurs due to indirect couplings between nuclear spins of neighbouring metal and halogen ions, such indirect couplings should be about three times for TlCl and about seven times for TlBr as effective as the ordinary dipole-dipole interactions. The estimated values from Eqs. (3.11a) and (3.11b) with the use of values of $\lambda$ in Table I, which have been deduced from experimental data of the chemical shift, are less than those due to dipole-dipole interactions by a factor of about ten for the bromide and 20 for the chloride if we put $a_p=1$ and $a_s=0$. The value of $|\varphi_{Ms}(0)|^2$ for the 7$s$-orbital of Tl estimated from experimental hyperfine separation is about $3\times10^{25}\,\mathrm{cm}^{-3}$ which is one half of $\left\langle \frac{1}{r^3} \right\rangle_{\mathrm{Tl}6p}$. Accordingly, even if we put $a_p=0$ and $a_s=1$ and use this value of $|\varphi_{Ms}(0)|^2$, they are multiplied by a factor of 5 on account of the large coefficient of the Fermi interaction but still too small by a factor of 20∼10 in order to explain the experimental width for both chloride and bromide. To take into consideration a mixing of the 6$s$-orbital of Tl in $\varphi_M$ will not improve the present situation. The second and third order contributions are of course very small compared to those of the fourth order.

It could not also be expected that the effect of the inner $s$-orbital of the halogen ion might improve this situation. The calculated value of $|\varphi_{3s}(0)|^2$ for Cl$^-$ by Hartree and Hartree[14)] is $6.8\times10^{25}\,\mathrm{cm}^{-3}$ for the 3$s$-orbital which is 1.5 times as large as $\langle 1/r^3 \rangle_{\mathrm{Cl}3p}$. Even though we take account of the large numerical factor for the Fermi interaction and assume a mixing of 50 percent 3$s$-orbital in $\varphi_{H0}$, we can only get a too small value by a factor of 5∼10 to account for the experimental results.

Furthermore, according to the analysis of the experimental data by Kanda for TlCl and TlBr, there exist exchange and pseudo-dipolar couplings between thallium nuclear spins which are of magnitude about three to ten times as large as the dipolar interactions. The existence of such large indirect couplings between thallium nuclear spins seems to suggest a considerably large overlapping of the wave function of the excited electron in a thallium ion with the neighbouring thallium ion. However, we shall leave this problem for a future discussion and turn to the problem of the relaxation time.

## § 4. Quadrupolar Relaxation I: Transition Probability

The importance of the quadrupole interaction in the spin-lattice relaxation of ionic crystals was first pointed out by Pound[15]. Subsequently Watkins[4] gave a more detailed discussion on this subject, especially for metal halides, and concluded that in KBr and KI the quadrupole interaction is the dominating relaxation mechanism. Recently Kanda[2] has also confirmed the same fact in LiBr, AgBr and TlBr. Theoretical studies of this mechanism have been done by Bloembergen[16], Watkins and recently by Kranendonk[17]. They showed that the simple point charge model of ionic crystals gives too long a relaxation time to explain the experimental results, that is, the experimental values are $10^{-2}$ sec or so while Kranendonk's precise calculation gives $3\times10^{3}\sim1\times10^{6}$ sec at room temperature. As the origin of this discrepancy Watkins considered the effect of the deformation of the ions and Kranendonk discussed the importance of the shielding, anti-shielding and covalent effects. In this section we shall consider the effect of the covalency on the quadrupolar relaxation of the halogen nuclear spin, basing our calculation on the perturbation scheme developed in the preceding two sections.

In the covalent state one $p$-electron is missing from the closed shell of a halogen ion. The asymmetry of the electron distribution produced by this hole generates a strong field gradient proportional to $\left\langle \frac{1}{r^3} \right\rangle_{av.}$ at the position of the halogen nucleus. On the other hand, the field gradient due to a point charge at a neighbouring lattice position is proportional to $1/a^3$, $a$ being interionic distance. If we assume the degree of covalency to be 3 percent, the relaxation time due to covalency would be shorter than in the pure ionic case by a factor of

$$\left(3\times10^{-2}\times\left\langle\frac{1}{r^3}\right\rangle_{av.}a^3\right)^{-2}\sim(3\times10^{-2}\times5\times10^{25}\times3\times10^{-23})^{-2}\sim10^{-3}\,.$$

Moreover, in Raman processes, a factor proportional to a linear combination of the first and second derivatives of the field gradient with respect to the interionic distance appears in the expression for the transition probabilities. In the case of the covalent state, these quantities correspond to the derivatives of the degree of covalency with respect to the interionic distance, which would be large compared to the derivatives of $1/r^3$ with respect to $r$ at $r=a$ i.e. the correspondings in the pure ionic case. As this may give rise to a factor of about $10^{-1}$, the relaxation time due to the covalency will be shorter by a factor of $10^{-4}$ than in pure ionic case.

From the above considerations we neglect the quadrupole interaction of the halogen nucleus with the surrounding ionic charges and take into account only the interaction with the electrons belonging to this nucleus. Then the interaction Hamiltonian of a halogen nucleus can be expressed as folllows:

$$V_Q=\sum_{\mu}Q_{\mu}W_{\mu} \tag{4.1}$$

$$\left\{\begin{aligned} Q_0 &=3I_z^2-I(I+1)\\ Q_{\pm1}&=\frac{1}{2}[I_z(I_x\pm iI_y)+(I_x\pm iI_y)I_z]\\ Q_{\pm2}&=(I_x\pm iI_y)^2\end{aligned}\right. \tag{4.2}$$

$$\left\{\begin{aligned} W_0 &=-\frac{A}{2}\sum_j(e/r_j^5)(3z_j^2-r_j^2)\\ W_{\pm1}&=-3A\sum_j(e/r_j^5)z_j(x_j\mp iy_j)\\ W_{\pm2}&=-\frac{3}{4}A\sum_j(e/r_j^5)(x_j\mp iy_j)^2\end{aligned}\right. \tag{4.3}$$

$$A=eQ/2I(2I-1)$$

where $r_j(x_j, y_j, z_j)$ is the position vector of the $j$-th electron belonging to that nucleus. In the present case of the halogen nucleus it may be sufficient to take $3p$-electrons into consideration. Although the above expression contains only electron coordinates, the lattice vibrations provide time-dependent deformations of the electron distribution, and accordingly the lattice coordinates can be considered as implicitly included in (4.1). In other words, the expectation value of $W_\mu$ with respect to the electronic state, which itself depends on lattice coordinates, must be regarded as a function of the lattice coordinates. This situation can be called the adiabatic approximation, because the motion of the lattice is assumed to be sufficiently slow compared to the electron motion. We shall now, as before, proceed with pertubational treatment. When we take the pure ionic state as the grounds state, $W_\mu$ vanishes identically. But the actual state includes partially the excited covalent states so that $W_\mu$ takes non-zero value when the lattice deforms from cubic symmetry as it vibrates. This can be shown by the third order perturbation calculation. Namely, we have

$$\Delta E_3=\sum_{nn'}\frac{(g|V_t|n)(n|V_Q|n')(n'|V_t|g)}{(E_n-E_g)(E_{n'}-E_g)} \tag{4.4}$$

as the third order energy expression. Here $g$ means the ground state and $n, n'$ mean the excited covalent states in which one $p$-electron of the halogen ion is transferred to the neighbouring $n$ or $n'$-th metal ion. The vacant $p$-orbital is naturally the one which has the maximum stretching in the direction to the metal 'atom' which has been generated by the transfer. In (4.4) $(n|V_Q|n')$ should be very small unless $n=n'$. Therefore, we can omit such terms and get

$$\begin{aligned}\Delta E_3&=\sum_n \lambda_n(n|V_Q|n)\\ &=\sum_\mu Q_\mu \sum_n \lambda_n(n|W_\mu|n)\,,\end{aligned} \tag{4.5}$$

where $\lambda_n=\dfrac{|(g|V_t|n)|^2}{(E_n-E_g)^2}=\left(\dfrac{b_n}{\Delta E_n}\right)^2$ is a measure of a degree of covalency, which may be regarded as a function of the distance only between the halogen nucleus and the $n$-th metal nucleus. We shall denote the coordinates of the $n$-th metal nucleus by $\boldsymbol{R}_n(X_n, Y_n, Z_n)$, taking the halogen nucleus as the origin. The direction cosines of $\boldsymbol{R}_n$ will be denoted by $l_n, m_n, n_n$. Further we introduce new coordinate system $\xi$, $\eta$ and $\zeta$ whose direction cosines are $(l_\xi, m_\xi, n_\xi)$, $(l_\eta, m_\eta, n_\eta)$, and $(l_n, m_n, n_n)$, respectively, and express $W_\mu$ in terms of $\xi$, $\eta$ and $\zeta$. For instance we have

$$\frac{1}{r^5}(3z^2-r^2)=\frac{1}{r^5}[3(n_\xi{}^2\xi^2+n_\eta{}^2\eta^2+n_n{}^2\zeta^2+2n_\xi n_\eta\xi_\eta+2n_\xi n_n\xi\zeta+2n_\eta n_n\eta\zeta)-r^2]\,.$$

The electronic distribution in the excited state $n$ is axially symmetric with respect to $\boldsymbol{R}_n$ or $\zeta$ so that the expectation values of the cross products $\xi\eta$, $\eta\zeta$ and $\zeta\xi$ vanish and those of $\xi^2$ and $\eta^2$ are equal to each other and can be put equal to that of $\frac{1}{2}(r^2-\zeta^2)$. Therefore we get

$$\left(n\left|\frac{1}{r_j{}^5}(3z_j{}^2-r_j{}^2)\right|n\right)=\frac{1}{2}\left(n\left|\frac{3\zeta_j{}^2-r_j{}^2}{r_j{}^5}\right|n\right)(3n_n{}^2-1)\,.$$

Summing up this expression over the five $p$-electrons, the following relation is obtained:

$$\left(n\left|\sum_j\frac{1}{r_j{}^5}(3z_j{}^2-r_j{}^2)\right|n\right)=-\frac{1}{2}\left\langle\frac{3\zeta^2-r^2}{r^5}\right\rangle_{p0}(3n_n{}^2-1)\,.$$

Similarly

$$\begin{aligned}\left(n\left|\sum_j\frac{1}{r_j{}^5}z_j(x_j\pm iy_j)\right|n\right)&=-\frac{1}{2}\left\langle\frac{3\zeta^2-r^2}{r^5}\right\rangle_{p0}n_n(l_n\pm im_n)\,,\\ \left(n\left|\sum_j\frac{1}{r_j{}^5}(x_j\pm iy_j)^2\right|n\right)&=-\frac{1}{2}\left\langle\frac{3\zeta^2-r^2}{r^5}\right\rangle_{p0}(l_n\pm im_n)^2\,.\end{aligned} \tag{4.6}$$

Here $\langle\ \rangle_{p0}$ means the expectation value with respect to the $p$-state corresponding to $l_\zeta=0$.

By means of Eq. (4.6) the second summation in (4.5), which will henceforth be abbreviated as $W_\mu$, can be expressed in the following simple form:

$$\begin{aligned}W_0&=A'\sum_n\lambda_n\left(n_n{}^2-\frac{1}{3}\right)\\ W_{\pm1}&=2A'\sum_n\lambda_n n_n(l_n\mp im_n)\\ W_{\pm2}&=\frac{1}{2}A'\sum_n\lambda_n(l_n\mp im_n)^2\,,\end{aligned} \tag{4.7}$$

where

$$A'=\frac{3}{4}eA\left\langle\frac{3\zeta^2-r^2}{r^5}\right\rangle_{p0}=\frac{3}{5}eA\left\langle\frac{1}{r^3}\right\rangle_H\,, \tag{4.8}$$

$\langle\ \rangle_H$ means the expectation value with respect to the valence $p$-electron of the halogen ion. Now we shall expand these expressions in powers of the small deviations from equilibrium positions. Let $\boldsymbol{R}_{n0}$ and $\alpha_n$, $\beta_n$, $\gamma_n$ be the distance and the direction cosines of the equilibrium position of the $n$-th metal ion measured from the halogen nucleus and $\delta\boldsymbol{R}_n(\delta X_n, \delta Y_n, \delta Z_n)$ the displacement vector. Then we have the following expressions:

$$\lambda(R_n)=\lambda+a\lambda'\left(\boldsymbol{n}\cdot\frac{\delta\boldsymbol{R}_n}{a}\right)+\frac{1}{2}a\lambda'\left\{\left(\frac{\delta\boldsymbol{R}_n}{a}\right)^2-\left(\boldsymbol{n}\cdot\frac{\delta\boldsymbol{R}_n}{a}\right)^2\right\}+\frac{1}{2}a^2\lambda''\left(\boldsymbol{n}\cdot\frac{\delta\boldsymbol{R}_n}{a}\right)^2, \tag{4.9}$$

$$\begin{aligned}
l_n^2&=\alpha_n^2-2\alpha_n^2\left(\boldsymbol{n}\cdot\frac{\delta\boldsymbol{R}_n}{a}\right)+2\alpha_n\frac{\delta X_n}{a}-\alpha_n^2\left(\frac{\delta\boldsymbol{R}_n}{a}\right)^2+4\alpha_n^2\left(\boldsymbol{n}\cdot\frac{\delta\boldsymbol{R}_n}{a}\right)^2\\
&\qquad-4\alpha_n\left(\boldsymbol{n}\cdot\frac{\delta\boldsymbol{R}_n}{a}\right)\frac{\delta X_n}{a}+\left(\frac{\delta X_n}{a}\right)^2,\\
m_n^2&=\beta_n^2-2\beta_n^2\left(\boldsymbol{n}\cdot\frac{\delta\boldsymbol{R}_n}{a}\right)+2\beta_n\frac{\delta Y_n}{a}-\beta_n^2\left(\frac{\delta\boldsymbol{R}_n}{a}\right)^2+4\beta_n^2\left(\boldsymbol{n}\cdot\frac{\delta\boldsymbol{R}_n}{a}\right)^2\\
&\qquad-4\beta_n\left(\boldsymbol{n}\cdot\frac{\delta\boldsymbol{R}_n}{a}\right)\frac{\delta Y_n}{a}+\left(\frac{\delta Y_n}{a}\right)^2,\\
n_n^2&=\gamma_n^2-2\gamma_n^2\left(\boldsymbol{n}\cdot\frac{\delta\boldsymbol{R}_n}{a}\right)+2\gamma_n\frac{\delta Z_n}{a}-\gamma_n^2\left(\frac{\delta R_n}{a}\right)^2+4\gamma_n^2\left(\boldsymbol{n}\cdot\frac{\delta\boldsymbol{R}_n}{a}\right)^2\\
&\qquad-4\gamma_n\left(\boldsymbol{n}\cdot\frac{\delta\boldsymbol{R}_n}{a}\right)\frac{\delta Z_n}{a}+\left(\frac{\delta Z_n}{a}\right)^2,
\end{aligned}\tag{4.10}$$

$$\begin{aligned}
l_nm_n&=\alpha_n\beta_n-2\alpha_n\beta_n\left(\boldsymbol{n}\cdot\frac{\delta\boldsymbol{R}_n}{a}\right)+\alpha_n\frac{\delta Y_n}{a}+\beta_n\frac{\delta X_n}{a}-\alpha_n\beta_n\left(\frac{\delta\boldsymbol{R}_n}{a}\right)^2+4\alpha_n\beta_n\left(\boldsymbol{n}\cdot\frac{\delta\boldsymbol{R}_n}{a}\right)^2\\
&\qquad-2\alpha_n\frac{\delta Y_n}{a}\left(\boldsymbol{n}\cdot\frac{\delta\boldsymbol{R}_n}{a}\right)-2\beta_n\frac{\delta X_n}{a}\left(\boldsymbol{n}\cdot\frac{\delta\boldsymbol{R}_n}{a}\right)+\frac{\delta X_n\delta Y_n}{a^2},\\
m_nn_n&=\beta_n\gamma_n-2\beta_n\gamma_n\left(\boldsymbol{n}\cdot\frac{\delta\boldsymbol{R}_n}{a}\right)+\beta_n\frac{\delta Z_n}{a}+\gamma_n\frac{\delta Y_n}{a}-\beta_n\gamma_n\left(\frac{\delta\boldsymbol{R}_n}{a}\right)^2+4\beta_n\gamma_n\left(\boldsymbol{n}\cdot\frac{\delta\boldsymbol{R}_n}{a}\right)^2\\
&\qquad-2\beta_n\frac{\delta Z_n}{a}\left(\boldsymbol{n}\cdot\frac{\delta\boldsymbol{R}_n}{a}\right)-2\gamma_n\frac{\delta Y_n}{a}\left(\boldsymbol{n}\cdot\frac{\delta\boldsymbol{R}_n}{a}\right)+\frac{\delta Y_n\delta Z_n}{a^2},\\
n_nl_n&=\gamma_n\alpha_n-2\gamma_n\alpha_n\left(\boldsymbol{n}\cdot\frac{\delta\boldsymbol{R}_n}{a}\right)+\gamma_n\frac{\delta X_n}{a}+\alpha_n\frac{\delta Z_n}{a}-\gamma_n\alpha_n\left(\frac{\delta\boldsymbol{R}_n}{a}\right)^2+4\gamma_n\alpha_n\left(\boldsymbol{n}\cdot\frac{\delta\boldsymbol{R}_n}{a}\right)^2\\
&\qquad-2\gamma_n\frac{\delta X_n}{a}\left(\boldsymbol{n}\cdot\frac{\delta\boldsymbol{R}_n}{a}\right)-2\alpha_n\frac{\delta Z_n}{a}\left(\boldsymbol{n}\cdot\frac{\delta\boldsymbol{R}_n}{a}\right)+\frac{\delta Z_n\delta X_n}{a^2},
\end{aligned}$$

where $a=|\boldsymbol{R}_{n0}|$, the nearest neighbour distance in the equilibrium, and $\boldsymbol{n}$ is the unit vector whose components are $\alpha_n$, $\beta_n$, $\gamma_n$.

We shall neglect the small effect of direct processes on the relaxation and confine our calculation to the contribution from Raman processes which can be considered to be the main part of the relaxation mechanism at least at room temperature. Thus picking up in Eq. (4.6) the second order terms with respect to displacements, we have

$$\begin{aligned}
W_{\pm1}&=\frac{2A'}{a^2}\sum_n[u\{n^{\mp}\gamma_n(\delta\boldsymbol{R}_n)^2+2(\boldsymbol{n}\cdot\delta\boldsymbol{R}_n)(\gamma_n\delta R_n^{\mp}+n^{\mp}\delta Z_n)\}\\
&\qquad+vn^{\mp}\gamma_n(\boldsymbol{n}\cdot\delta\boldsymbol{R}_n)^2+\lambda\delta Z_n\delta R_n^{\mp}],\\
W_{\pm2}&=\frac{A'}{2a^2}\sum_n[u\{(n^{\mp})^2(\delta\boldsymbol{R}_n)^2+4n^{\mp}\delta R_n^{\mp}(\boldsymbol{n}\cdot\delta\boldsymbol{R}_n)\}\\
&\qquad+v(n^{\mp})^2(\boldsymbol{n}\cdot\delta\boldsymbol{R}_n)^2+\lambda(n^{\mp})^2(\delta R_n^{\mp})^2],
\end{aligned}\tag{4.11}$$

$$u=\frac{1}{2}a\lambda'-\lambda,\qquad v=4\lambda-\frac{5}{2}a\lambda'+\frac{1}{2}a^2\lambda'', \tag{4.11$'$}$$

where $\delta X_n\pm i\delta Y_n$ and $\alpha_n\pm i\beta_n$ have been replaced by $\delta R_n^{\pm}$ and $n^{\pm}$ respectively.

Next we shall express the displacements in terms of the normal coordinates of the lattice vibrations. We shall adopt a simplifying assumption employed by Kranendonk that all the ions in the crystal are equivalent as far as the lattice vibrations are concerned. Furthermore, the frequency distribution will be approximated by the Debye model. Then the displacement $s_n$ of the $n$-th metal ion from its equilibrium position $\boldsymbol{R}_{no}$ can be expressed in terms of the lattice normal modes as

$$\boldsymbol{s}_n = \sum_{k,p} a_{kp} \boldsymbol{e}_{kp} \exp(i\boldsymbol{k}\cdot\boldsymbol{R}_{no}) \,, \tag{4.12}$$

where $\boldsymbol{k}$ represents a wave vector, $p$ signifies one of the three directions of polarization, which are here assumed to be orthogonal to each other. Then the displacement relative to the halogen ion $\delta\boldsymbol{R}_n$ becomes, using the same notation as that of Kranendonk,

$$\delta\boldsymbol{R}_n = \sum_\sigma{}' q_\sigma B_n(\sigma) \boldsymbol{e}_\sigma \,, \tag{4.13}$$

where the prime means the summation over half the $k$-space and

$$q_\sigma = \delta(s,1)(a_{kp}+a_{-kp}) + i\delta(s,2)(a_{kp}-a_{-kp}) \,, \tag{4.14}$$

$$B_n(\sigma) = \delta(s,1)(\cos a\boldsymbol{k}\cdot\boldsymbol{n}-1) + \delta(s,2)\sin a\boldsymbol{k}\cdot\boldsymbol{n} \,, \tag{4.15}$$

and $\sigma$ stands for a set of $k, p$ and $s$, $s$ taking values 1 and 2. The normal coordinate $q_\sigma$ has the following non-vanishing matrix elements:

$$(n_\sigma+1\,|\,q_\sigma|\,n_\sigma) = (n_\sigma\,|\,q_\sigma\,|\,n_\sigma+1) = (\hbar/M\omega_k)^{1/2}\,(n_\sigma+1)^{1/2} \,, \tag{4.16}$$

where $M$ is the mass of the crystal and $\omega_k$ the angular frequency which is assumed to be independent of $p$ and of the direction of $\boldsymbol{k}$. We assume further that the phonon system is in equilibrium, that is, the average number of the phonons is given by

$$n_\sigma = \left[\exp\left(\frac{\hbar\omega_k}{\kappa T}\right) - 1\right]^{-1}, \tag{4.17}$$

$\kappa$ being the Boltzmann constant.

The transition probability $P(m, m+\mu)$ for Raman processes, in which a nuclear spin changes its direction from $I_z = m$ to $m+\mu$ and simultaneously absorption of one phonon and emission of one phonon, with adequate energies, occur, is given by

$$P(m, m+\mu) = \frac{2\pi}{\hbar}\left(\frac{V}{8\pi^3}\right)^2 \iint \sum_{\substack{p,s\\p',s'}} |V_Q(\sigma\sigma')_\mu|^2 \delta(\hbar\omega_k - \hbar\omega_{k'}) d^3\boldsymbol{k} d^3\boldsymbol{k}' , \tag{4.18}$$

where $V_Q(\sigma\sigma')_\mu$ means the matrix element of $V_Q$ between the initial and final states of a Raman process. The Zeeman energy of the nucleus can be neglected as compared with the phonon energy. If we take the directional average in the $k$-space, and use the relation $kv = \omega_k$, $v$ being the sound velocity, (4.18) becomes

$$P(m, m+\mu) = \frac{V^2}{8\pi^3 v^2 \hbar^2} \int_0^{\omega_m} k^4 \sum_{p,s} \{|\,V_Q(\sigma\sigma')_\mu\,|^2\} d\omega_k \,, \tag{4.19}$$

where $\{\ \ \}$ means the directional average and $\omega_m$ is the cut off frequency in the usual Debye model.

On the other hand, from (4.1) and (4.7), making use of (4.11) and (4.13), we obtain the following expression for $V_Q$:

$$V_Q = \frac{A'}{a^2} \sum_{\mu=-2}^{2} Q_\mu \sum_{\sigma\sigma'} q_\sigma q_{\sigma'} \sum_n B_{n\sigma} B_{n\sigma'} w_{\mu n}(\sigma\sigma') \,, \tag{4.20}$$

where

$$\begin{aligned} w_{\pm1,n}(\sigma\sigma') = 2[&u\{n^\mp \gamma_n(\boldsymbol{e}_\sigma\cdot\boldsymbol{e}_{\sigma'}) + (\boldsymbol{n}\cdot\boldsymbol{e}_{\sigma'})(\gamma_n e_\sigma{}^\mp + n^\mp e_{\sigma z}) \\ &+ (\boldsymbol{n}\cdot\boldsymbol{e}_\sigma)(\gamma_n e_{\sigma'}{}^\mp + n^\mp e_{\sigma' z})\} + v n^\mp \gamma_n (\boldsymbol{n}\cdot\boldsymbol{e}_\sigma)(\boldsymbol{n}\cdot\boldsymbol{e}_{\sigma'}) \\ &+ \tfrac{1}{2}\lambda(e_{\sigma z} e_{\sigma'}{}^\mp + e_{\sigma' z} e_\sigma{}^\mp)] \,, \end{aligned} \tag{4.21}$$

$$\begin{aligned} w_{\pm2,n}(\sigma\sigma') = \tfrac{1}{2}[&u\{(n^\mp)^2(\boldsymbol{e}_\sigma\cdot\boldsymbol{e}_{\sigma'}) + 2n^\mp e_\sigma{}^\mp(\boldsymbol{n}\cdot\boldsymbol{e}_{\sigma'}) + 2n^\mp e_{\sigma'}{}^\mp(\boldsymbol{n}\boldsymbol{e}_\sigma)\} \\ &+ v(n^\mp)^2(\boldsymbol{n}\cdot\boldsymbol{e}_\sigma)(\boldsymbol{n}\cdot\boldsymbol{e}_{\sigma'}) + \lambda(n^\mp)^2 e_\sigma{}^\mp e_{\sigma'}{}^\mp] \,, \end{aligned} \tag{4.22}$$

$e_\sigma^\pm$ standing for $e_{\sigma x} \pm i e_{\sigma y}$.

Accordingly, from (4.20) and (4.16), the transition matrix element becomes

$$V_Q(\sigma\sigma')_\mu = \frac{2A'\hbar Q_{\mu m}}{a^2 M \omega_k}\{(n_\sigma+1)n_{\sigma'}\}^{1/2} \sum_n B_{n\sigma} B_{n\sigma'} w_{\mu n}(\sigma\sigma') \,, \tag{4.23}$$

where

$$Q_{\mu m} = (m+\mu \,|\, Q_\mu \,|\, m) \,. \tag{4.24}$$

Using (4.17) the transition probability (4.19) becomes

$$P(m, m+\mu) = \frac{A'^2 |Q_{\mu m}|^2}{2\pi^3 a^4 d^2 v^2} \int_0^{\omega_m} \frac{k^4}{\omega^2} \frac{e^x}{(e^x-1)^2} M_\mu(ka) d\omega \,, \tag{4.25}$$

where $d$ is the density $M/V$, $x = \hbar\omega/\kappa T$ and

$$M_\mu(ka) = \sum_{\substack{p,s \\ p',s'}} \{ | \sum_n B_{n\sigma} B_{n\sigma'} w_{\mu n}(\sigma\sigma') |^2 \} \,. \tag{4.26}$$

In this summation terms with $s \neq s'$ vanish, so that

$$M_\mu(ka) = \sum_{nn'} \sum_s \{B_{n\sigma} B_{n\sigma'} B_{n'\sigma} B_{n'\sigma'}\} \sum_{pp'} w_{\mu n}{}^*(\sigma\sigma') w_{\mu n'}(\sigma\sigma') \,. \tag{2.26'}$$

Here we made use of the fact that $B_{n\sigma}$ does not depend on $p$ but depends on $k$ and $s$, while $w_{\mu n}(\sigma\sigma')$ depends on $p$ and $p'$ but neither on $s, s'$ nor on $k, k'$.

In the case of NaCl or CsCl structure, there are only four independent expressions of $\{B_{n\sigma} B_{n\sigma'} B_{n'\sigma} B_{n'\sigma'}\}$. Adopting the same notation as Kranendonk, they are:

For $n = \pm n'$

$$L_1(ka) = \{S_1{}^2\}^2 = \left\{\frac{1}{2} - \frac{1}{2} f(2ka)\right\}^2 \qquad \text{both for NaCl- and CsCl-types,}$$

$$L_2(ka) = \{C_1{}^2\}^2 = \left\{\frac{3}{2} - 2f(ka) + \frac{1}{2} f(2ka)\right\}^2 \qquad \text{both for NaCl- and CsCl-types.}$$

For $n \neq \pm n'$

$$L_3(ka) = \{S_1 S_2\}^2 = \begin{cases} 0 & \text{for NaCl-type,} \\ \left\{\frac{1}{2} f\left(\frac{2}{\sqrt{3}} ka\right) - \frac{1}{2} f\left(\frac{2\sqrt{2}}{\sqrt{3}} ka\right)\right\}^2 & \text{for CsCl-type,} \end{cases} \tag{4.27}$$

$$L_4(ka) = \{C_1 C_2\}^2 = \begin{cases} \{1 - 2f(ka) + f(\sqrt{2}\, ka)\}^2 & \text{for NaCl-type,} \\ \left\{1 - 2f(ka) + \frac{1}{2} f\left(\frac{2}{\sqrt{3}} ka\right) + \frac{1}{2} f\left(\frac{2\sqrt{2}}{\sqrt{3}} ka\right)\right\}^2 & \text{for CsCl-type,} \end{cases}$$

where

$$f(y) = \frac{\sin y}{y} \,, \qquad S_n = \sin a\boldsymbol{K}\cdot\boldsymbol{n} \,, \qquad C_n = \cos(a\boldsymbol{K}\cdot\boldsymbol{n}) - 1 \,.$$

Next we define, for convenience, the quantities

$$N_{\mu 1} = N_{\mu 2} = \sum_{\substack{nn' \\ (n=\pm n')}} \sum_{pp'} w_{\mu n}{}^*(\sigma\sigma') w_{\mu n'}(\sigma\sigma') \,,$$

$$N_{\mu 3} = N_{\mu 4} = \sum_{\substack{n,n' \\ (n\neq\pm n')}} \sum_{pp'} w_{\mu n}{}^*(\sigma\sigma') w_{\mu n'}(\sigma\sigma') \,. \tag{4.28}$$

Then Eq. (4.26) can be abbreviated as

$$M_\mu(ka) = \sum_{\nu=1}^{4} N_{\mu\nu} L_\nu(ka) \,. \tag{4.29}$$

This simplifies the expression for the transition probability (4.25). A further simplification is made by using the relation between the maximum Debye frequency or wave number and the Debye temperature:

$$\hbar\omega_m=\hbar v k_m=\kappa\Theta\ , \tag{4.30}$$

and introducing the reduced temperature $T^*$ defined by

$$T^*=T/\Theta\ .$$

Then we get the final expression for the transition probability:

$$P(m,\, m+\mu)=\frac{A'^2C^3|Q_{\mu m}|^2}{2\pi^3a^7d^2v^3}T^{*2}\sum_{\nu=1}^{4}N_{\mu\nu}D_\nu(T^*)\ , \tag{4.31}$$

$$D_\nu(T^*)=T^*\int_0^{1/T^*}\frac{x^2e^x}{(e^x-1)^2}L_\nu(cT^*x)dx\ , \tag{4.32}$$

where $c=k_ma$ is equal to $(6\pi^2)^{1/3}$ for NaCl-type and $(9\sqrt{3}\,\pi^2/2)^{1/3}$ for CsCl-type. At high temperatures, including room temperature, $D(T^*)$ can be expanded in descending powers of $T^*$, as Kranendonk did. Numerical expressions for $D_\nu$'s are then as follows:

for NaCl or simple cubic crystals (after Kranendonk)

$$\begin{aligned} &D_1(T^*)=0.20-0.0071/T^{*2}+\cdots && D_3(T^*)=0.50-0.031/T^{*2}+\cdots \\ &D_2(T^*)=0.92-0.055\ /T^{*2}+\cdots && D_4(T^*)=0.28-0.017/T^{*2}+\cdots \end{aligned} \tag{4.33}$$

for CsCl-type crystals

$$\begin{aligned} &D_1(T^*)=0.20-0.0067/T^{*2}+\cdots && D_3(T^*)=0.013-0.00036/T^{*2}+\cdots \\ &D_2(T^*)=1.17-0.066\ /T^{*2}+\cdots && D_4(T^*)=0.55-0.026/T^{*2}+\cdots \end{aligned} \tag{4.34}$$

Now it is left to calculate $N_{\mu\nu}$'s. The quantity $\sum_{pp'}w_{\mu n}^*(\sigma\sigma')w_{\mu n'}(\sigma\sigma')$ can be calculated straight-forwardly from Eq. (4.21) and (4.22). After somewhat lengthy calculations we obtain the following results:

$$\begin{aligned} \sum_{pp'}w_{1n}^*(\sigma\sigma')w_{1n'}(\sigma\sigma')=4[&u^2\{15(\alpha_n\alpha_{n'}+\beta_n\beta_{n'})\gamma_n\gamma_{n'}+2(\alpha_n\alpha_{n'}+\beta_n\beta_{n'})(\boldsymbol{n}\cdot\boldsymbol{n}') \\ &+4(\alpha_n^2+\beta_n^2)\gamma_{n'}^2+4\gamma_n\gamma_{n'}(\boldsymbol{n}\cdot\boldsymbol{n}')\}+v^2\{(\alpha_n\alpha_n'+\beta_n\beta_{n'})\gamma_n\gamma_{n'}(\boldsymbol{n}\cdot\boldsymbol{n}')^2\} \\ &+\lambda^2+uv\{2(\alpha_n\alpha_{n'}+\beta_n\beta_n')\gamma_n\gamma_{n'}+4(\alpha_n\alpha_{n'}+\beta_n\beta_{n'})\gamma_n^2(\boldsymbol{n}\cdot\boldsymbol{n}') \\ &+4(\alpha_n^2+\beta_n^2)\gamma_n\gamma_{n'}(\boldsymbol{n}\cdot\boldsymbol{n}')\}+\lambda u\{2(\alpha_n^2+\beta_n^2)+4\gamma_n^2\} \\ &+2\lambda v(\alpha_n^2+\beta_n^2)\gamma_n^2]\ , \end{aligned} \tag{4.35}$$

$$\begin{aligned} \sum_{pp'}w_{2n}^*(\sigma\sigma')w_{2n'}(\sigma\sigma')=u^2\Big[&\frac{11}{4}\{-(\alpha_n^2+\beta_n^2)(\alpha_{n'}^2+\beta_{n'}^2)+2(a_n\alpha_{n'}+\beta_n\beta_{n'})^2\} \\ &+4(\alpha_n\alpha_{n'}+\beta_n\beta_n')(\boldsymbol{n}\cdot\boldsymbol{n}')+2(\alpha_n^2+\beta_n^2)(\alpha_{n'}^2+\beta_{n'}^2)\Big] \\ &+\frac{1}{4}v^2\{-(\alpha_n^2+\beta_n^2)(\alpha_{n'}^2+\beta_{n'}^2)+2(\alpha_n\alpha_{n'}+\beta_n\beta_{n'})^2\}(\boldsymbol{n}\cdot\boldsymbol{n}')^2 \\ &+\lambda^2+uv\left\{\frac{1}{2}(\alpha_n-i\beta_n)^2(\alpha_{n'}+i\beta_{n'})^2+2(\alpha_n\alpha_{n'}+\beta_n\beta_{n'})(\alpha_n^2+\beta_n^2)(\boldsymbol{n}\cdot\boldsymbol{n}')\right\} \\ &+4\lambda u(\alpha_n^2+\beta_n^2)+\frac{1}{2}\lambda v(\alpha_n^2+\beta_n^2)^2\ . \end{aligned} \tag{4.36}$$

In the case of NaCl-type crystals, $(\boldsymbol{n}\cdot\boldsymbol{n}')=0$ for $n\neq\pm n'$ and $(\boldsymbol{n}\cdot\boldsymbol{n}')=\pm1$ for $n=\pm n'$. All the other terms are expressible in terms of $\gamma_n$ and $\gamma_{n'}$, for example,

$$\begin{aligned} (\alpha_n\alpha_{n'}+\beta_n\beta_{n'})\gamma_n\gamma_{n'}&=-\gamma_n^2\gamma_{n'}^2 && \text{for } n\neq n'\ , \\ &=(1-\gamma_n^2)\gamma_n^2 && \text{for } n=\pm n'. \end{aligned}$$

If we denote the direction cosines of the $z$-axis, i.e. the direction of the external field with respect to the crystal axes, by $\alpha_H$, $\beta_H$ and $\gamma_H$, $\gamma_n$ is equal to $\pm\alpha_H$ or $\pm\beta_H$ or $\pm\gamma_H$ according as the direction cosines of $n$ referred to the crystal axes are equal to $(\pm1, 0, 0)$ or $(0, \pm1, 0)$ or $(0, 0, \pm1)$. Therefore we can express $N_{\mu\nu}$'s as functions of $\alpha_H$, $\beta_H$, and $\gamma_H$, which appear only in a combined form $(\alpha_H^2\beta_H^2+\beta_H^2\gamma_H^2+\gamma_H^2\alpha_H^2)$ because of the cubic symmetry of the crystal. Thus we get the following results for NaCl-type crystals:

$$N_{11}=N_{12}=16(8u^2+3\lambda^2+8u\lambda)+\alpha\cdot16(38u^2+2v^2+20uv+4v\lambda)\,,$$

$$N_{14}=8(16u^2+12\lambda^2+32u\lambda)-\alpha\cdot8(61u^2+8uv-16v\lambda)\,,$$

$$\begin{aligned}N_{21}=N_{22}=&(70u^2+2v^2+12\lambda^2+20uv+32u\lambda+4v\lambda)\\&-\alpha(38u^2+2v^2+20uv+4v\lambda)\,,\end{aligned}$$

$$\begin{aligned}N_{24}=&(-6u^2+24\lambda^2-4uv+64u\lambda+8v\lambda)\\&+\alpha(38u^2+4uv-8v\lambda)\,.\end{aligned}$$

Using (4.11′) we can express these quantities as functions of $\lambda$, $\lambda'$, and $\lambda''$:

$$N_{11}=N_{12}=48\lambda^2\left[\left\{1-\frac{4}{3}\left(\frac{a\lambda'}{\lambda}\right)+\frac{2}{3}\left(\frac{a\lambda'}{\lambda}\right)^2\right\}+2\alpha\left\{1+\frac{1}{3}\left(\frac{a\lambda'}{\lambda}\right)-\frac{1}{2}\left(\frac{a\lambda'}{\lambda}\right)^2+\frac{1}{12}\left(\frac{a^2\lambda''}{\lambda}\right)^2\right\}\right],$$

$$N_{14}=32\lambda^2\left[\left\{-1+\left(\frac{a\lambda'}{\lambda}\right)^2\right\}+5\alpha\left\{1-\frac{9}{20}\left(\frac{a\lambda'}{\lambda}\right)^2+\frac{3}{5}\left(\frac{a^2\lambda''}{\lambda}\right)-\frac{1}{10}\left(\frac{a^2\lambda''}{\lambda}\right)\left(\frac{a\lambda'}{\lambda}\right)\right\}\right],$$

$$\begin{aligned}N_{21}=N_{22}=18\lambda^2\Bigg[&\left\{1-\frac{7}{9}\left(\frac{a\lambda'}{\lambda}\right)+\frac{5}{18}\left(\frac{a\lambda'}{\lambda}\right)^2+\frac{1}{30}\left(\frac{a^2\lambda''}{\lambda}\right)^2\right\}\\&-\frac{1}{3}\,\alpha\left\{1+\frac{1}{3}\left(\frac{a\lambda'}{\lambda}\right)-\frac{1}{2}\left(\frac{a\lambda'}{\lambda}\right)^2+\frac{1}{12}\left(\frac{a^2\lambda''}{\lambda}\right)^2\right\}\Bigg],\end{aligned}$$

$$\begin{aligned}N_{24}=2\lambda^2\Bigg[&\left\{1+\frac{7}{4}\left(\frac{a\lambda'}{\lambda}\right)^2+3\left(\frac{a^2\lambda''}{\lambda}\right)-\frac{1}{2}\left(\frac{a^2\lambda''}{\lambda}\right)\left(\frac{a\lambda'}{\lambda}\right)\right\}\\&-5\alpha\left\{1-\frac{9}{20}\left(\frac{a\lambda'}{\lambda}\right)^2+\frac{3}{5}\left(\frac{a^2\lambda''}{\lambda}\right)-\frac{1}{10}\left(\frac{a^2\lambda''}{\lambda}\right)\left(\frac{a\lambda'}{\lambda}\right)\right\}\Bigg].\end{aligned}\tag{4.37}$$

Also for the CsCl-type the calculation can be carried out in quite a similar way. The results are

$$\begin{aligned}N_{11}=N_{12}=\frac{320}{3}\lambda^2\Bigg[&\left\{1-\frac{2}{3}\left(\frac{a\lambda'}{\lambda}\right)+\frac{1}{5}\left(\frac{a\lambda'}{\lambda}\right)^2+\frac{1}{30}\left(\frac{a^2\lambda''}{\lambda}\right)^2\right\}\\&+\frac{4}{5}\,\alpha\left\{-1-\frac{1}{3}\left(\frac{a\lambda'}{\lambda}\right)+\frac{1}{2}\left(\frac{a\lambda'}{\lambda}\right)^2-\frac{1}{12}\left(\frac{a^2\lambda''}{\lambda}\right)^2\right\}\Bigg],\end{aligned}$$

$$\begin{aligned}N_{13}=N_{14}=\frac{64\times35}{81}\,\lambda^2\Bigg[&\left\{-1+\frac{26}{7}\left(\frac{a\lambda'}{\lambda}\right)+\frac{8}{7}\left(\frac{a^2\lambda''}{\lambda}\right)+\frac{8}{35}\left(\frac{a^2\lambda''}{\lambda}\right)\left(\frac{a\lambda'}{\lambda}\right)-\frac{33}{35}\left(\frac{a\lambda'}{\lambda}\right)^2-\frac{1}{70}\left(\frac{a^2\lambda''}{\lambda}\right)^2\right\}\\&+\frac{4}{7}\,\alpha\left\{-1-\frac{83}{5}\left(\frac{a\lambda'}{\lambda}\right)+\frac{113}{10}\left(\frac{a\lambda'}{\lambda}\right)^2-4\left(\frac{a^2\lambda''}{\lambda}\right)-\frac{4}{5}\left(\frac{a^2\lambda''}{\lambda}\right)\left(\frac{a\lambda'}{\lambda}\right)+\frac{1}{20}\left(\frac{a^2\lambda''}{\lambda}\right)^2\right\}\Bigg],\end{aligned}$$

$$\begin{aligned}N_{21}=N_{22}=\frac{64}{3}\lambda^2\Bigg[&\left\{1-\frac{11}{12}\left(\frac{a\lambda'}{\lambda}\right)+\frac{3}{8}\left(\frac{a\lambda'}{\lambda}\right)^2+\frac{1}{48}\left(\frac{a^2\lambda''}{\lambda}\right)^2\right\}\\&+\frac{1}{4}\,\alpha\left\{1+\frac{1}{3}\left(\frac{a\lambda'}{\lambda}\right)-\frac{1}{2}\left(\frac{a\lambda'}{\lambda}\right)^2+\frac{1}{12}\left(\frac{a^2\lambda''}{\lambda}\right)^2\right\}\Bigg],\end{aligned}$$

$$\begin{aligned}N_{23}=N_{24}=\frac{640}{81}\,\lambda^2\Bigg[&\left\{-1+\frac{47}{40}\left(\frac{a\lambda'}{\lambda}\right)+\frac{67}{80}\left(\frac{a\lambda'}{\lambda}\right)^2+\frac{1}{2}\left(\frac{a^2\lambda''}{\lambda}\right)+\frac{1}{10}\left(\frac{a^2\lambda''}{\lambda}\right)\left(\frac{a\lambda'}{\lambda}\right)-\frac{1}{160}\left(\frac{a^2\lambda''}{\lambda}\right)^2\right\}\\&+\frac{1}{8}\,\alpha\left\{1+\frac{83}{5}\left(\frac{a\lambda'}{\lambda}\right)-\frac{113}{10}\left(\frac{a\lambda'}{\lambda}\right)^2+4\left(\frac{a^2\lambda''}{\lambda}\right)+\frac{4}{5}\left(\frac{a^2\lambda''}{\lambda}\right)\left(\frac{a\lambda'}{\lambda}\right)-\frac{1}{20}\left(\frac{a^2\lambda''}{\lambda}\right)^2\right\}\Bigg].\end{aligned}$$

## § 5. Quadrupolar Relaxation II: Relaxation Time and Comparison with Experimental Data

In the previous section we have calculated the thermal transition probabilities between Zeeman levels by quadrupoler interaction. We shall now give theoretical expression for $T_1$ and compare it with experimental values determined by saturation method[18][14]. When the quadrupole interaction exists, the relaxation process cannot in general be described in terms of a unique characteristic time. However, when we observe an absorption line due to transition between specified two levels, a usual saturation curve will give a measure for the relaxation rate between these two levels. Watkins and Pound [3][4] found that, in resonance experiments for halogen nuclei in KBr and KI, only the central line corresponding to the transition between $m=\pm\frac{1}{2}$ levels was observable while the satellite lines were almost smeared out by the qnadrupole interaction with field gradients distributed at random in the crystals owing to irregular internal strains. This situation seems to be realized in any available alkali halide samples except when the nuclei have a very small or no quardrupole moment. Therefore we may safely assume that, also in Kanda's measurements of the Br resonance in metal bromides, only the central line was observed

As is well known, the saturation intensity of the resonance absorption obeys a simple $1/(1+x^2)$ law. In the case of spin $\frac{1}{2}$, $x^2$ is connected with the spin-lattice relaxation time $T_1$, the spin-spin relaxation time $T_2$ and the intensity of the r.f. field $H_1$ by

$$x^2=\gamma^2 H_1^2 T_1 T_2\,, \tag{5.1}$$

where $H_1$ is the amplitude of circularly polarized r.f. field, so that the amplitude of linearly polarized r.f. field must be taken as $2H_1$. In our case of $I>\frac{1}{2}$, we may still define $T_1$, for convenience, by Eq. (5.1). Of course $T_1$ thus defined has no usual significance, but anyhow it can be regarded as a sort of characteristic time of the relaxation process.

Theoretically the saturation factor can be calculated by considering surplus stationary population in $-\frac{1}{2}$ state over $\frac{1}{2}$ state in a given resonating r.f. field. The transition probability due to a r.f. field is

$$P_{m\rightleftarrows m-1}=\frac{1}{4}\gamma^2 H_1^2 g(\nu)(I+m)(I-m+1)\,, \tag{5.2}$$

where $g(\nu)$ is the normalized line shape function. The transition probabilities by the quadrupole interaction are

$$\begin{aligned} P(m,m+1)&=\frac{(2m+1)^2(I-m)(I+m+1)}{2I(2I-1)^2}W_1\,,\\ P(m,m+2)&\\ &=\frac{(I-m-1)(I+m+2)(I-m)(I+m+1)}{2I(2I-1)^2}W_2\,,\\ P(m+1,m)&=P(m,m+1)(1+\varDelta)\,,\\ P(m+2,m)&=P(m,m+2)(1+2\varDelta)\,, \end{aligned} \tag{5.3}$$

where $\varDelta=\hbar\omega_0/\kappa T$, $\omega_0$ being the Larmor frequency, and $W_1$ and $W_2$ are, as we saw in the previous section, functions of the orientation of the external magnetic field and are independent of $m$. By using these formulas we can write down the differential equations of the time variation of populations in Zeeman levels. From the stationary solution of these equations the surplus population, and consequently $T_1$, can be obtained. It is interesting to note that there is no quadrupolar transition between $+\frac{1}{2}$ and $-\frac{1}{2}$ states so that the relaxation between these two states takes place indirectly via the other states. The surplus population, which will be denoted by $n=n_{-1/2}-n_{1/2}$, and the relaxation time $T_1$ thus calculated are as follows:

for $I=3/2$,

$$\begin{aligned} n&=\frac{N}{4}\varDelta\frac{1}{1+\gamma^2 H_1^2 T_1 T_2}\,,\\ T_1&=\frac{1}{W_1}+\frac{1}{W_2}=\frac{1}{P\left(\frac{1}{2},\frac{3}{2}\right)}+\frac{1}{P\left(\frac{3}{2},-\frac{1}{2}\right)}\,, \end{aligned} \tag{5.4}$$

for $I=5/2$,

$$\begin{aligned} n&=\frac{N}{6}\varDelta\frac{1}{1+\gamma^2 H_1^2 T_1 T_2}\,,\\ T_1&=\frac{9}{4}\left\{\frac{1}{\frac{9}{10}W_2}+\frac{1}{\frac{W_1\cdot\frac{1}{2}W_2}{W_1+\frac{1}{2}W_2}+\frac{2}{5}W_1}\right\}\,,\\ &=\frac{9}{4}\left\{\frac{1}{P\left(\frac{1}{2},\frac{3}{2}\right)+\left(\frac{1}{P\left(\frac{1}{2},\frac{5}{2}\right)}+\frac{1}{P\left(\frac{5}{2},\frac{3}{2}\right)}\right)^{-1}}\right.\\ &\qquad\left.+\frac{1}{P\left(\frac{3}{2},\frac{1}{2}\right)}\right\}\,. \end{aligned} \tag{5.5}$$

Here the value of $\frac{1}{2}g(\nu)$ at the resonance frequency was replaced by $T_2$.

Table II. Numerical values of $N_{\mu\nu}$ calculated on the assumption: $\lambda \propto e^{-R/0.345}$.

| | $N_{11}\times 10^{-3}$ | $N_{14}\times 10^{-3}$ | $N_{21}\times 10^{-3}$ | $N_{24}\times 10^{-3}$ |
|---|---|---|---|---|
| LiBr | $2.6+29\alpha$ | $2.0+9.7\alpha$ | $2.45-1.8\alpha$ | $1.1-0.61\alpha$ |
| AgBr | $2.8+35.5\alpha$ | $2.2+11\alpha$ | $2.9-2.2\alpha$ | $1.25-0.70\alpha$ |
| TlBr | $38+66\alpha$ | $-9.9+34\alpha$ | $5.4+4.1\alpha$ | $-0.32-2.15\alpha$ |
| KBr | $3.6+62\alpha$ | $2.9+16\alpha$ | $4.8-3.9\alpha$ | $1.7-1.0\alpha$ |
| KI | $4.05+82\alpha$ | $3.3+20\alpha$ | $6.1-5.1\alpha$ | $2.1-1.2\alpha$ |

Table III. The experimental and calculated values of $T_1$.

| | experimental (sec.) | calculated (sec.) | |
|---|---|---|---|
| $Br^{79}$ in LiBr | 0.028 | $0.089(10^{-6}\Theta^3)/T^{*2}$ | $0.20(\Theta=180)$ |
| $Br^{79}$ in AgBr | 0.016 | 0.13 | |
| $Br^{79}$ in TlBr | 0.0060 | $0.057(10^{-6}\Theta^3)/T^{*2}$ | $0.025(\Theta=130)$ |
| $Br^{79}$ in KBr | 0.26 | $1.3(10^2\lambda)^{-2}$ | $0.77(\lambda=0.013)$ |
| $I^{127}$ in KI | 0.039 | 0.11 | |

In the case of powder samples the apparent saturation factor should be the average over all orientations of the above expressions. The apparent relaxation time $T_1{}^p$, in this case, may be defined by

$$\frac{1}{1+\gamma^2H_1{}^2T_1{}^pT_2}=\left\langle\frac{1}{1+\gamma^2H_1{}^2T_1T_2}\right\rangle_{\text{av. over directions}} \tag{5.6}$$

with the assumption that $T_2$ is isotropic.

Now we shall turn to the comparison with experiments. Watkins measured $T_1$ for the single crystals of KBr and KI with external field applied in the [100] direction, and Kanda measured $T_1$ for the powder specimens of LiBr, AgBr and TlBr. All these substances, except TlBr, have NaCl-type structure while TlBr has CsCl-type structure. Numerical values of the parameters in expression (4.31), which gives the thermal transition probability, can be obtained, are available for the majority of the substances under consideration, with the exception of $\lambda$, $\lambda'$ and $\lambda''$, which can be estimated as follows.

For the degree of covalency $\lambda$ we can take its values deduced from chemical shift data. To estimate $\lambda'$ and $\lambda''$, we must know the dependence of $\lambda$ on interionic distance. Since $\lambda$ is proportional to the square of the overlap integral, it is approximately proportional to the repulsive potential between ions, which itself is proportional to $\exp-(R/0.345)$ according to Born and Mayer's wellknown theory of ionic crystals, $R$ being the interionic distance in A unit.* So we may assume

$$\lambda \propto e^{-R/0.345} \tag{5.7}$$

From this we have $\lambda'/\lambda=-1/0.345$, and $\lambda''/\lambda=(1/0.345)^2$, respectively. There is another approximate method of the estimation. Honig, Mandel, Stitch and Townes[19] measured the microwave spectra of alkali halide molecules and deduced the degree of convalency for some of them, for example for LiBr and KI, which have been studied by Kanda for the case of solid. If we assume the functional form of the degree of covalency to be $c.\exp(-R/\rho)$ and utilize experimental values for two values of $R$, one for molecule and the other for solid, we can determine $\rho$. The values of $\rho$ so determined are 0.33 for LiBr and 0.42 for KI. These results support the assumption (5.7).

The values of $N_{\mu\nu}$'s calculated under the assumption (5.7) are given in Table II.

We summarize the calculated and experimental values of the relaxation time $T_1$ at room temperature in Table III. For powder samples we did not actually use Eq. (5.6), but approximated it, for simplicity, by (5.4), $W_1$ and $W_2$ being substituted by their directional averages. For the numerical values of the Debye temperature we employed those determined from specific heat data for AgBr and

---

* Strictly, the overlap integral questioned now is that between the wave function of the state of $Cl^-$ and that of the excited state of a metal ion. Therefore, the value of 0.345 may not be so reliable.

LiBr, and that determined from elastic data for KI. For LiBr and TlBr there are no available data, as far as we know, so that we left $\Theta$ and $T^*$ undetermined in this Table.

The calculated values of the relaxation time are, on the whole, about 3～10 times as long as the experimental values, whereas their ratios are resonable. As the possible origin of this discrepancy we can point out first that our treatment of the lattice vibrations is too much simplified. We took the simple Debye model and neglected the particular character of the optical modes which will be effective in the relaxation mechanism, though the number of normal modes was taken correctly so that the optical modes have been effectively taken into account as the high frequency part of the frequency spectrum. Nevertheless the treatment of the lattice vibrations is at any rate far from being satisfactory, and its crudeness might be an origin of the factor 3～10.

Ambiguities in determining the Debye temperature $\Theta$ or the sound velocity $v$ must also be pointed out. Further refinements of the treatment appear, however, to be very difficult and laborious at the present stage of the theory.

We remark here also that we have neglected the shielding and anti-shielding effects. It may be expected that when covalent electrons penetrate into the ion core, their interaction with the quadrupole moment will not be markedly affected by the shielding and anti-shielding effects. By any means, this point is left for further discussions.

In conclusion, the authors would like to express their cordial thanks to Dr. Kanda for informing us of his experimental results prior to publication. They are also much indebted to Professor T. Nagamiya and Professor J. Itoh for their illuminating discussions and valuable comments.

## References

1) H. S. Gutowsky and B. R. MacGarvey: J. Chem. Phys. **21** (1953) 1423.
2) T. Kanda: J. Phys. Soc. Japan **10** (1955) 85.
3) G. D. Watkins and R. V. Pound: Phys. Rev. **89** (1953) 658.
4) G. D. Watkins: Thesis, Harvard (1952).
5) C. H. Townes and B. P. Dailey: J. Chem. Phys. **17** (1949) 782, **20** (1952) 35.
6) M. A. Ruderman and C. Kittel: Phys. Rev. **96** (1954) 99.
7) N. Bloembergen and T. J. Rowland: Phys. Rev. **97** (1955) 1679.
8) T. Kanda: unpublished.
9) N. F. Ramsey: Phys. Rev. **78** (1950) 699, **86** (1952) 243.
10) A. Saika and C. P. Slichter: J. Chem. Phys. **22** (1954) 26.
11) N. F. Ramsey and E. M. Purcell: Phys. Rev. **85** (1952) 143.
12) Gutowsky, McCall and Slichter: J. Chem. Phys. **21** (1953) 279.
13) R. G. Barnes and W. V. Smith: Phys. Rev. **93** (1954) 95.
14) D. R. Hartree and W. Hartree: Proc. Roy. Soc. A **156** (1936) 45.
15) R. V. Pound: Phys. Rev. **79** (1950) 685.
16) N. Bloembergen: Thesis, Leiden (1948).
17) J. Van. Kranendonk: Physica **20** (1954) 781.
18) Bloembergen, Purcell and Pound: Phys. Rev. **73** (1948) 679.
19) Honig, Mandel, Stitch and Townes: Phys. Rev. **96** (1954) 629.

JOURNAL OF THE PHYSICAL SOCIETY OF JAPAN Vol. 11, No. 1, JANUARY, 1956

# Dipolar Broadening of the Central Line of a Magnetic Resonance for Half-integral Spin

By Kenjiro KAMBE
*College of Electro-Communications, Tokyo*
and John F. OLLOM
*West Virginia University, Morgantown, West Virginia*

(Received September 26, 1955)

The second moment of the central line of a magnetic resonance for half-integral spins, for which quadrupole coupling (nuclear spin case) or crystalline field effect (electronic spin case) is present, is calculated by the Van Vleck procedure. The interactions between like spins, unlike spins and semi-like spins are considered separately. The results are compared with the Van Vleck results for which no quadrupole coupling or crystalline effect is assumed.

The broadening of the magnetic resonance line due to the magnetic interaction between atoms has been discussed theoretically in several cases[1-7]. However, the line width in the following case has not been calculated, as far as we know. Namely, that is, the width of the central line of nuclear magnetic resonance in the system of half-integral spins, where the electric quadrupole coupling is present. The equivalent case in the paramagnetic resonance phenomena arises when the half-integral electronic spins are placed under the influence of the crystalline electric field. The electric quadrupole coupling or the crystalline field effect should be so large that the central line is well resolved from the satellite lines. For instance, for spin 3/2 case, the central line corresponds to the transition $m=1/2 \longleftrightarrow m=-1/2$, and it should be resolved from the satellite line which arises from the transition $m=(3/2) \longleftrightarrow m=(1/2)$ or $m=-(3/2) \longleftrightarrow m=-(1/2)$, where $m$ is the magnetic quantum number for individual spin.

In this paper, we will calculate the second moment of the central line by means of the well-known formula given by Van Vleck[1]:

$$\langle \Delta\nu^2\rangle_{\mathrm{Av}} = \langle \nu^2\rangle_{\mathrm{Av}} - \nu_0{}^2 = -h^{-2} T_r[\mathscr{H}_1 S_x - S_x \mathscr{H}_1]^2 / T_r S_x{}^2, \tag{1}$$

where $\nu_0$ is the frequency of the center of the central line, $\mathscr{H}_1$ the Hamiltonian of the interaction, $S_x$ the component of the total spin vector operator along the direction of the high frequency field.

The interaction Hamiltonian $\mathscr{H}_1$ takes different forms depending upon the type of the interaction. In the present paper, three types of interaction will be considered: (a) Interaction between resonant spins, (b) interaction between unlike spins, (c) interaction between semi-like spins. Here, resonant spins are the same species of spins with the same quadrupole coupling (nuclear spin case) or with the same crystalline field splittings (electronic spin case). Semi-like spins are the identical spins located at the different lattice sites, where the values of the quadrupole coupling constant or those of crystalline field are different. For semi-like spins the central line of the resonance coincides, since the central line is not affected by the crystalline field. Satellite lines do not coincide however. We will discuss the three cases separately in the following.

### (a) *Interaction Between Resonant Spins*

The interaction Hamiltonian in the usual notation is

$$\mathscr{H}_1 = \Sigma_{j>k} \mathscr{H}_{jk} = \Sigma_{j>k}\{\tilde{A}_{jk} \boldsymbol{S}_j \cdot \boldsymbol{S}_k + g^2\beta^2 r_{jk}{}^{-3}[\boldsymbol{S}_j \cdot \boldsymbol{S}_k - 3r_{jk}{}^{-3}(\boldsymbol{S}_j \boldsymbol{r}_{jk})(\boldsymbol{S}_k \cdot \boldsymbol{r}_{jk})]\} \tag{2}$$

We should not use, however, the whole matrix elements given by (2). Those matrix elements which contribute only to the satellite lines have to be omitted in applying (1). The same precaution should be taken with respect to $S_x$.

Since $\mathscr{H}_1$ is a sum of the two-body type operators, it is sufficient to consider the system of two spins $j$ and $k$. The unperturbed energies are

$$W(m_j, m_k)=g\beta H(m_j+m_k)+\delta(m_j^2+m_k^2)$$
$$-(2/3)\delta S(S+1) \qquad (3)$$

Here, the eigenstates are specified by the eigenvalues $m_j$ and $m_k$ of $S_{jz}$ and $S_{kz}$.

The matrix elements of $\mathscr{H}_{jk}$ connect the unperturbed states, which satisfy the selection rule

$$\Delta m_j\,,\ \Delta m_k=\pm 1 \text{ or } 0\,. \qquad (4)$$

Those matrix elements which connect the unperturbed states with different energies should be discarded, because these elements contribute only to the satellite lines. Besides the diagonal elements of $\mathscr{H}_{jk}$, the matrix elements connecting the states $(m, m')$ with the state $(m', m)$ should be retained, since $W(m, m')=W(m', m)$ by (3). Decomposing the expression of $\mathscr{H}_{jk}$ given by (2) into the form given by Equation (2) of Abragam and Kambe[7], and inspecting the matrix elements term by term, we find that the matrix elements which should be retained in the present problem are

$$(m, m'|\mathscr{H}_{jk}|m, m')$$
$$=[\tilde{A}_{jk}+g^2\beta^2 r_{jk}^{-3}(1-3\gamma_{jk}^2)]mm' \qquad (5)$$
$$(m, m-1|\mathscr{H}_{jk}|m-1, m)$$
$$=(m-1, m|\mathscr{H}_{jk}|m, m-1)$$
$$=\left[\frac{1}{2}\tilde{A}_{jk}-\frac{1}{4}g^2\beta^2 r_{jk}^{-3}(1-3\gamma_{jk}^2)\right]$$
$$\times(S+m)(S-m+1)\,. \qquad (6)$$

It is easily shown that the non-vanishing matrix elements of $S_x$ after discarding the irrelevant elements are

$$\left(m, \pm\frac{1}{2}\middle| S_{xj}+S_{xk}\middle| m, \mp\frac{1}{2}\right)$$
$$=\left(\pm\frac{1}{2}, m\middle| S_{xj}+S_{xk}\middle| \mp\frac{1}{2}, m\right)=\frac{1}{4}(2S+1)\,. \qquad (7)$$

The calculation of the traces involved in (1) is elementary and the result is

$$h^2\langle\Delta\nu^2\rangle_{\text{Av}}$$
$$=\left[\frac{S(S+1)}{3}+\frac{2S^2(S+1)^2-3S(S+1)+(1/8)}{2(2S+1)}\right]\Sigma_k{}'\tilde{A}_{jk}^2$$
$$+\left[-\frac{4}{3}S(S+1)+\frac{4S^2(S+1)^2+(7/4)}{2(2S+1)}\right]\Sigma_k{}'\tilde{A}_{jk}\frac{g^2\beta^2}{r_{jk}^3}\left(\frac{3}{2}\gamma_{jk}^2-\frac{1}{2}\right)$$
$$+\left[\frac{4}{3}S(S+1)+\frac{2S^2(S+1)^2+3S(S+1)+(13/8)}{2(2S+1)}\right]\Sigma_k{}'\frac{g^4\beta^4}{r_{jk}^6}\left(\frac{3}{2}\gamma_{jk}^2-\frac{1}{2}\right)^2. \qquad (8)$$

If there is no exchange, as in the nuclear resonance, $\tilde{A}_{jk}=0$. The resulting expression of the second moment is to be compared with the expression

$$h^2\langle\Delta\nu^2\rangle_{\text{Av}}$$
$$=3S(S+1)\Sigma_k{}'g^4\beta^4 r_{jk}^{-6}\left(\frac{3}{2}\gamma_{jk}^2-\frac{1}{2}\right)^2, \qquad (9)$$

which holds when there is no electric quadrupole coupling (nuclear spin case) or crystalline field splitting (electronic spin case). The expression (9) has been derived by Van Vleck.

The comparison has been done in Table I.

Table I. The ratio of the second moment $\langle\Delta\nu^2\rangle_{\text{Av}}$ for cases (a) and (c) to that of the straight resonance line given by (9). The exchange interactions are assumed to vanish.

| Spin | Case (a) | Case (c) |
|---|---|---|
| 1/2 | 1 | 1 |
| 3/2 | 9/10 | 4/5 |
| 5/2 | 107/105 | 257/315 |
| 7/2 | 881/756 | 164/189 |

(b) *Interaction Between Unlike Spins*

Now, we shall consider the contributions from the unlike neighbors to the broadening of the central line. Here we shall assume that the unlike neighbors have arbitrary spin $S'$. Then the effective interaction hamiltonian is

$$\mathscr{H}_1=\Sigma_{jk}{}'\,C_{jk}{}'\,S_{zj}\,S_{zk}{}' \qquad (10)$$

with

$$C_{jk}{}'=\tilde{A}_{jk}{}'+(1-3\gamma_{jk}{}')^2 gg'\beta^2 r_{jk}^{-3}. \qquad (11)$$

All other matrix elements of the interaction should be discarded because they contribute only to the satellite lines.

The $x$ component of moment $S_x$ to be used in (1) involves only the summation $\Sigma_j S_{xj}$ over the unprimed spins, and the matrix elements of $S_{xj}$ to be used are

$$\left(\pm\frac{1}{2}\middle| S_{xj}\middle|\mp\frac{1}{2}\right)=\frac{1}{4}(2S+1)\,.$$

After some elementary calculation, we get

$$h^2\langle\Delta\nu^2\rangle_{\mathrm{Av}}=\frac{1}{3}S'(S'+1)\Sigma_k' C_{jk}'^2\,, \qquad (12)$$

as the contribution from unlike neighbors to the second moment of the central line. This is exactly the same expression which Van Vleck has given as the contribution from the unlike neighbors with spin $S'$ to the broadening of the resonance line from spin $S$ without taking into account the effect of the crystalline field.

### (c) *Interaction Between Semi-Like Spins*

Although they are located at the different lattice sites, semi-like spins are the same species of spins. Therefore, the interaction hamiltonian is given by (2) as in the case of (a). However, the matrix elements of $\mathscr{H}_1$ to be retained in calculating (1) are different from those used in the case (a).

The unperturbed energies of two semi-like spins are given by

$$W(m, m')=g\beta H(m+m')+\delta m^2+\delta' m'^2 \qquad (13)$$

Here one should note that the quadrupole coupling constants are different for semi-like spins. The energy of state $(m, m')$ is not equal to that of the state $(m,' m)$ except when $m=\pm\frac{1}{2}$ and $m'=\pm\frac{1}{2}$. The diagonal elements of $\mathscr{H}_1$ should be retained as in the case (a), but only the elements given by (6) with $m=\frac{1}{2}$ should be retained among the off-diagonal elements. The matrix elements of $S_x$ to be retained are same as in the Case (a).

The second moment of the central line arising from the interaction with the semi-like neighbors is

$$\begin{aligned}
&h^2\langle\Delta\nu^2\rangle_{\mathrm{Av}}\\
&=\left[\frac{1}{3}S(S+1)-\frac{1}{4}(2S+1)+\frac{(2S+1)^3}{32}\right]\Sigma_k'\tilde{A}_{jk}^2\\
&\quad+\left[-\frac{4}{3}S(S+1)+\frac{1}{4}(2S+1)+\frac{(2S+1)^3}{16}\right]\Sigma_k'\tilde{A}_{jk}\frac{g^2\beta^2}{r_{jk}^3}\left(\frac{3}{2}\gamma_{jk}^2-\frac{1}{2}\right)\\
&\quad+\left[\frac{4}{3}S(S+1)+\frac{1}{2}(2S+1)+\frac{(2S+1)^3}{32}\right]\Sigma_k'\frac{g^4\beta^4}{r_{jk}^6}\left(\frac{3}{2}\gamma_{jk}^2-\frac{1}{2}\right)^2. \qquad (14)
\end{aligned}$$

The second moment without exchange is compared with the Van Vleck formula (9) in Table I.

We wish to thank Professor Van Vleck and Professor Bloembergen for discussion. One of us (K.K.) would like to thank Prof. Bloembergen for suggesting this problem. He also indebted to the Office of Naval Research for the financial support which enabled him to do this work during his stay at Harvard University from 1953 to 1954.

### References

1) J. H. Van Vleck: Phys. Rev. **74** (1948) 1168.

2) M. H. L. Pryce and K. W. H. Stevens: Proc. Phys. Soc. (London) **A 63** (1950) 36.

3) J. H. Van Vleck and J. F. Ollom: Physica **17** (1951) 205.
J. F. Ollom: thesis, Harvard University, 1952 (unpublished).

4) Ishiguro, Kambe and Usui: Physica **17** (1951) 310.

5) K. W. H. Stevens: Proc. Roy. Soc. (London) **A 214** (1952) 237.

6) R. Bersohn: J. Chem. Phys. **20** (1952) 1505.

7) A. Abragam and K. Kambe: Phys. Rev. **91** (1953) 894.

8) For nuclear spin case, see R. V. Pound, Phys. Rev. **79** (1950) 685. For electronic spin case, see, for instance, A. Abragam and M. H. L. Pryce: Proc. Roy. Soc. **A 205** (1951) 135. For both cases, we assume an axial symmetry for crystalline field.

JOURNAL OF THE PHYSICAL SOCIETY OF JAPAN Vol. 11, No. 1, JANUARY, 1956

# On the Plastic Deformation of $\alpha$-brass Single Crystals by Compression

By Hiroshi KIMURA

*Institute of Industrial Science, University of Tokyo, Chiba City*

(Received April 25, 1955)

The relationship between the crystallographic orientation of specimens and the easy glide was examined with $\alpha$-brass single crystals deformed by compression. Micrographic observations were performed and discussed together.

Besides these main studies, it was found that the hardening in copper alloys due to low temperature annealing after cold working, which was observed in polycrystalline specimen, was not observed in single crystals.

## §1. Introduction

There are many studies with aluminum single crystals in the field of plastic deformation, and it has been found that the shape of shear stress-strain curve depends on the crystallographic orientation of specimen, and that the appearance of slip bands also depends on the orientation of the specimen.

As for the other metals except aluminum, few studies have been reported. It is dangerous to think that the plastic properties of aluminum are typical for the face-centered cubic crystals. To avoid this danger it is necessary that more siudies are carried on with many face-centered cubic metals and alloys other than aluminum.

Mathewson and his co-workers[1], in their studies of the plasticity of $\alpha$-brass, reported that the slip bands were clustered, that there were no deformation bands (kink bands) and that the asterism of Lauespots was not observed. It was also found that the shear stress-strain curves had a long range of easy glide. But the relationship between these phenomena and the crystallographic orientations of specimens cannot be discussed, because the number of specimens used is not enough.

Hardening of copper alloys due to low temperature annealing after cold working is one of the current problems[2][3], but there are few studies with single crystals.

The author, therefore, studied the following two problems using $\alpha$-brass single crystals:

1. How the shear stress-strain curves and the appearance of slip bands depend on the crystallographic orientations of specimens.
2. The change of yield point due to low temperature annealing after cold working.

## §2. Experimental Method

Single crystals were made by melting and solidifying the alloy which was casted in our laboratory from electrolytic copper and pure zinc. They were 11 mm in diameter and 120–130 mm in length.

Their crystallographic orientations were determined by optical method. After the determination of orientation, two flat faces were made on the side surfaces of these single crystal rods and they were polished mechanically. One of the faces was parallel and the other normal to the plane containing the axis of rod and the slip direction. These two faces were named *A*-plane and *B*-plane respectively. And then, these rods were cut into pieces of 10 mm in length, which were used as specimens.

The end surfaces of the specimens were made parallel, and the specimens were annealed for 2 hours at 200°C in an oil-bath and electropolished. The two flat faces were examined by means of X-ray and found to be free from the stress due to mechanical polishing. The specimens were compressed a little over the yield point and observed by light microscope. Then, they were deformed about 30% in shear strain and the shear stress-strain curves were obtained.

Some of the specimens were used for the low temperature annealing experiment. They were deformed about 30% in shear strain and annealed for 2 hours at 175°C and their yield points were measured by deforming them again. The second deformation was about 40% in shear, then they were annealed again for 2 hours at 125°C and the yield points were measured again.

The samples for chemical analysis were taken from the bottom and the middle part of each rod. The chemical compositions and the crystallographic orientations of single crystal rods were shown in Table I and Fig. 1.

Table I. The Chemical Composition of Single Crystal Rods.

| No. of Crystals | Cu | Zn | Fe |
|---|---|---|---|
| 1 | 80.5% | 18.3% | 1.2% |
| 2 | 79.6 | 20.0 | 0.4 |
| 3 | 78.7 | 21.0 | 0.3 |
| 4 | 82.2 | 17.2 | 0.6 |
| 5 | 86.4 | 13.1 | 0.5 |
| 6 | 72.4 | 27.1 | 0.5 |

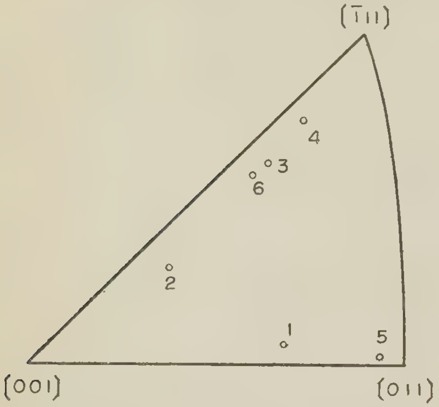

Fig. 1. Orientation of crystals.

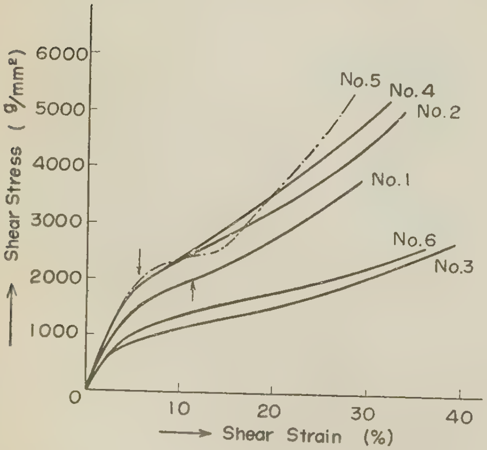

Fig. 2. Shear stress-strain curves of α-brass single crystals deformed by compression.

## § 3. Experimental Results and Discussions

### (1) *The Relationship between the Shape of Shear Stress-Strain Curves and the Crystallographic Orientation of Specimens.*

Fig. 2 shows the shear stress-strain curves for the crystals, of which axial orientations are shown in Fig. 1. According to the classical calculation of Taylor and Elam, crystals No. 1 and 5 are deformed by single slip system until the strains pointed by the arrows are reached, and after these points double slips occur; the other crystals are deformed by single slip system through the whole range shown in Fig. 2.

It is found from these figures that the crystals, of which axial orientations are near the middle of [100]-[111] side, show a long range of easy glide. It may be concluded that such crystals that satisfy the following two conditions have a long range of easy glide:

1) The axial orientation of the crystal is far from the three apexes of stereographic triangle.
2) The crystal has a long distance of slip process in which only one slip system is active.

This can be interpreted as follows: The classical geometrical plane and direction of the maximum shear stress may not have very important meaning, when the axial orientation of the crystal is near to one of the apexes of stereographic triangle. The axis may change slightly its direction favourablly for other slip systems, and then those new slip systems will easily become active. If more than two slip systems are active, the rate of hardening becomes larger because of the interaction hardening. In the case of ordinary double slip, the interaction hardening does, of course, operate.

Microscopic observation seems to support the above discussion. Generally speaking, the longer range of easy glide a crystal has, the simpler is the appearance of slip bands. And in the crystals, which harden rapidly, two or three slip systems are active and the appearance of slip bands is complicated. In Photo. 1, which shows a part of $A$-plane of specimens No. 2, we can see that three slip systems are active.

### (2) *Some Microscopic Observations*

#### (a) *Primary Slip*

Slip bands were clustered in all specimens and never uniformly distributed. Deformation bands (kink bands) were not observed. We can also see the interactions between slip bands and etch pits produced by electropolishing. These are shown in Photo. 2 and 3, which show the *A*-plane and *B*-plane of specimen No. 2 respectively. In *A*-plane slip bands are hardly disturbed by etch pits (black figures), but they are almost straight and pass through the pits. However, in *B*-plane slip bands are markedly disturbed by etch pits. Near the compression ends of *B*-plane the slip bands

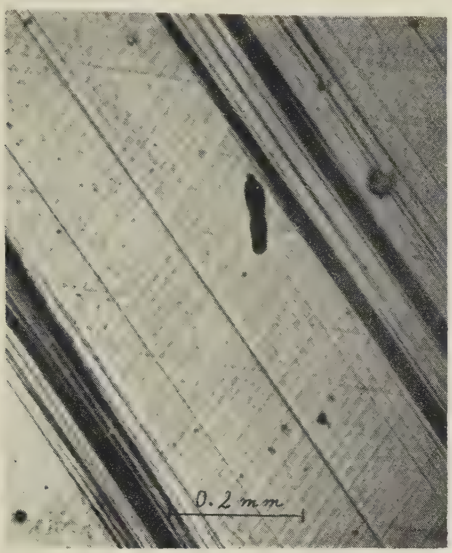

Photo. 1. Slip bands in *A*-plane of crystal No. 2. (Shear Strain 4%). Three systems are active.

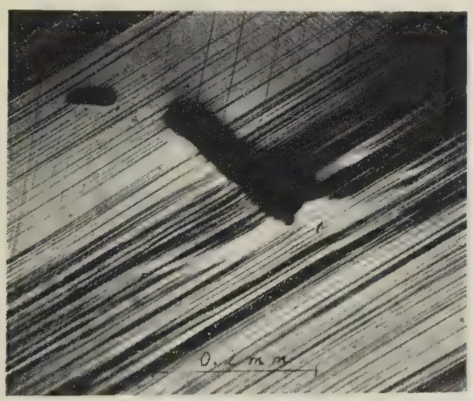

Photo. 2. The interaction between slip bands and etch pit in *A*-plane of crystal No. 2. (Shear strain 12%).

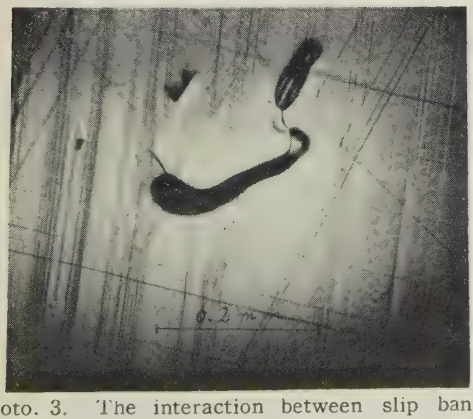

Photo. 3. The interaction between slip bands and etch pit in *B*-plane of crystal No. 2. (Shear strain 12%).

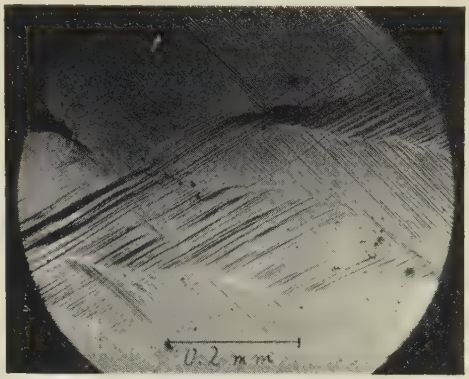

Photo. 4. Special appearance of bands of secondary slip in *A*-plane of crystal No. 2. (Shear strain 12%).

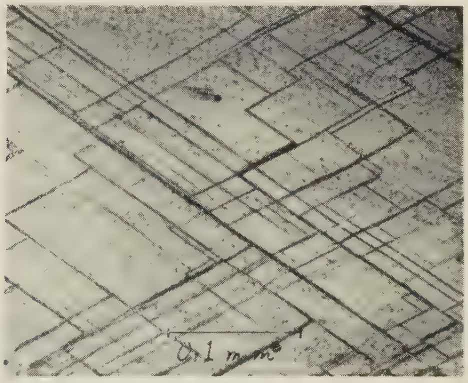

Photo. 5. Cross-slip in *A*-plane of crystal No. 3. (Shear strain 20%).

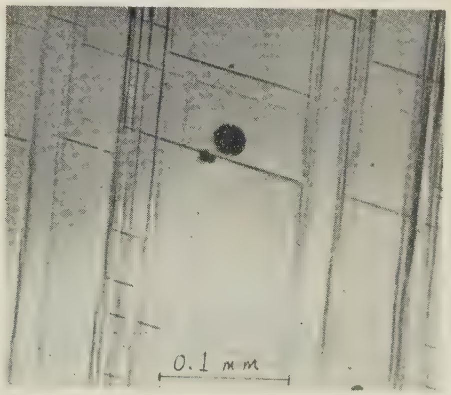

Photo. 6. Cross-slip in *B*-plane of crystal No. 2. (Shear strain 4%).

are not clustered so markedly as in the middle part of the specimen.

(b) *Bands of Secondary Slip and Cross-Slip*

*A*-plane: The appearance of slip bands in the middle part of the specimen differs from that in the part near both ends, and at the boundary between the middle part and the end parts slip bands sometimes show special appearances (Photo. 4). They show bands of secondary slip. Sometimes cross-slip appears instead of the bands of secondary slip (Photo. 5). The slip systems that are active are $(111)$–$[\bar{1}01]$ system, which is predicted system, and $(\bar{1}\bar{1}1)$–$[011]$ system. These slip patterns described above would be interpreted in terms of grip effect.

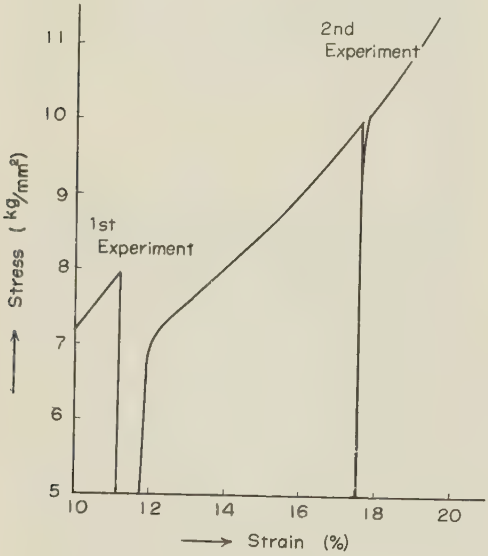

Fig. 4. The effect of annealing on the yield point of α-brass. (Crystal No. 6).

*B*-plane: *B*-planes are not so complicated as *A*-planes. Usually the predicted system is predominant. Sometimes typical cross-slip is observed, as shown in Photo. 6.

(3) *The Change of the Yield Point by Low Temperature Annealing after Cold Working*

It is well known that cold worked specimen of copper alloys, especially the $\alpha$-phase alloy, becomes harder when they are subjected to suitable low temperature annealing[2][3]. But there are few studies with single crystals.

In this work the annealing conditions were decided by Mishima's studies[4]. He studied the tensile strength of polycrystalline $\alpha$-brass and found that the tensile strength of specimens which were subjected to more than 8% elongation was increased by 175°C×2 hours annealing. The specimens used in the present experiment were subjected to compression of more than 9% and less than 17%, most of them 10%. By 175°C×2 hours annealing their yield points recovered for several per cent and no hardening was observed. Then, they were compressed again and annealed. The degree of second compression were between 17% and 28%, most of them were 23%. The annealing was performed for 2 hours at 125°C. Again, no hardening was observed and this time no recovery was observed, either. One of the results is shown in Fig. 4.

It should be noticed that hardening phenomenon is observed in polycrystalline specimen, but not in single crystal.

## §4. Conclusions

From above experimental results and discussions, the following conclusions are drawn for $\alpha$-brass single crystals deformed by compression.

(1) Such crystals that satisfy the following two conditions have a long range of easy glide:
1. The axial orientation of the crystal is far from the three apexes of stereographic triangle.
2. The crystal has a long distance of slip process in which only one slip system is active,

(2) Slip systems other than the predicted one become active even in single slip range, and they are the main causes that makes the rate hardening large.

(3) Kink bands are not observed, but cross-slip and bands of secondary slip are usually seen. They may be the results of grip effect.

(4) The low temperature annealing hardening in copper alloys, which is observed in polycrystalline specimen, are not observed in single crystals.

### Acknowledgement

This study is one of my works in the graduate course under Professor Isshiki, and I want to express my hearty gratitude to him for his kind direction and encouragement throughout the work. I must also express my hearty thanks to Professor Hasiguti and Dr. Kanzaki who has given many useful suggestions and discussions as well as the kind

directions. To Mrs. Inaba who has earnestly helped me in my experiments, I am also greateful.

Three photographs in this work were taken when I studied the possibility of short range order in $\alpha$-brass under Professor Tani, to whom also my great thanks must be given.

### References

1) R. Maddin, C. H. Mathewson and W. R. Hibbard: Trans. A.I.M.M.E. **175** (1948) 86; *ibid.* **185** (1949) 528.
2) M. Kawasaki and Y. Mishima: Journ. of Japan Inst. of Metals (Review) **16** (1952) **A**–61.
3) R. R. Hasiguti: Journ. of Japan Inst. of Metals **19** (1955) 103.
4) M. Kawasaki and Y. Mishima: Journ. of Japan Inst. of Metals (Review) **16** (1952) **A**–209.

---

Journal of the Physical Society of Japan Vol. 11, No. 1, January, 1956

# On the Floating Probe Method for the Measurement of Ionized Gas

By Kenzo YAMAMOTO and Takayoshi OKUDA
*Faculty of Engineering, Nagoya University*

(Received August 29, 1955)

Several problems connected with the floating probe method are discussed and solved. Analysing the variation of ion current due to sheath expansion, the authors obtain the criterion for applicability of the usual double probe method and also the general expression available for the estimation of electron temperature.

From the relation between probe characteristic and electron energy distribution, a floating triple method is newly proposed. This method is useful for the measuring of energy distribution in electrodeless or h.f. discharges.

By special use of the floating double or triple probe, the measurement of potential distribution in such a quasi-plasma as ion sheath and the transition region between plasma and ion sheath can be attained. As one example, the floating potential becomes measurable.

The floating, or insulating, potential is discussed in detail and expression is given showing good agreement with measured values.

## §1. Introduction

To the experimental method proposed by Reifman and Dow[1] for double probe measurements in gaseous discharges, using two probe electrodes having no connections with electrodes of discharges, fundamental treatments were simultaneousely advanced by Johnson and Malter[2] and by Kojima and Takayama[3] based upon their own interpretations. The method of this floating double probe has the following two merits in a comparison with the single probe method developed by Langmuir and Mott-Smith[4]. (1) The probe electrodes are in a floating state having no relation to the electrodes of discharge; (2) The amount of current flowing into the probe is so small that the probe measurement does not have any effect on the plasma because it does not exceed the saturation value of the positive ion current.

Under conditions where it can be used, the practical value of the double probe method should be recognized especially in its application to changing plasma, viz. after-glow, electrodeless and high frequency discharges, in none of which the standard potential can be given under any circumstances, suggesting an application of the double probe method as the only one enabling us to measure such plasma.

In this paper we give the correct application of the double probe theory and discuss

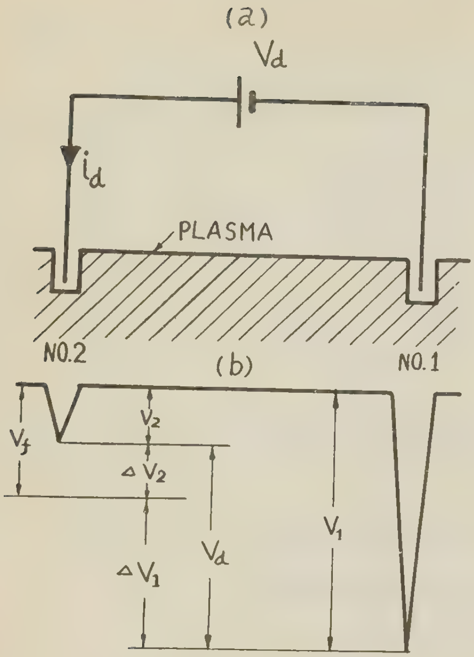

Fig. 1. Basic circuit and potential diagram for the double probe method.

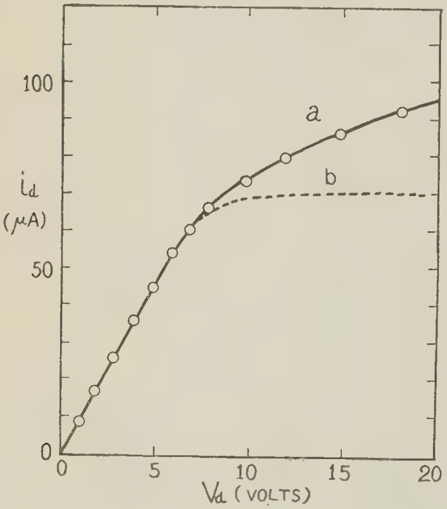

Fig. 2. Typical voltage-current characteristic of the dooble probe method.
Curve *a*, experimentally obtained characteristic, with a slope, low voltage arc of argon, pressure 2 mm Hg, voltage 60.5 voltage current 15 mA.
Curve *b*, idealized characteristic, with no slope.

some problems in connection with this method, extending it into a new method—the triple floating method.

## § 2. Correct Application of Double Probe Theory

When the voltage applied to probes is increased, an increase of positive ion current caused by expansion of the sheath area can be observed even in the saturated part of the flowing current in double probe circuit. When plasma density is of the ordinary value, we do not usually expect the existence of a slope in the saturated part of a probe characteristic curve because the expansion is small, but in many cases a slight or even a remarkable slope may appear, which leads to an error in the estimation of plasma quantities. Here, we make some corrections in the process of estimation.

Making use of the analysis of ideal case by Johnson and Malter[2] in which the probe characteristic has a symmetrical form with no slope in its saturated part, the following expressions of probe current in terms of associated voltage are naturally derived.

Notation of these terms are shown in Fig. 1.

$$i_{p1}+i_{p2}=I_p=i_{e1}+i_{e2} \tag{1}$$

$$\left.\begin{aligned} i_{e1}&=F_1 j_{01}\exp(-\phi V_1)\,,\\ i_{e2}&=F_2 j_{02}\exp(-\phi V_2)\end{aligned}\right\} \tag{2}$$

$$V_1=V_2+V_d \tag{3}$$

$$i_d=i_{p1}-i_{e1}=i_{e2}-i_{p2} \tag{4}$$

where $i_{p1}$, $i_{p2}$=positive ion current to probe
$i_{e1}$, $i_{e2}$=electron currrent to probe
$i_d$=probe current
$I_p$=sum of both ion current
$F_1$, $F_2$=surface area of probe
$V_1$, $V_2$=voltage applied across the space charge sheath serrounding probe
$V_d$=voltage applied between two probes, No. 1 and No. 2
$T_e$=electron temperature
$\phi=e/kT_e=11{,}600/T_e$ °K

The subscripts 1 and 2 refer to Probes No. 1 and No. 2, respectively. For simplicity if

$$F_1=F_2=F\,,\quad j_{01}=j_{02}=j_0$$

and

$$\left.\begin{aligned} & \\ & i_{p1}=i_{p2}=i_p=(1/2)I_p\end{aligned}\right\} \tag{5}$$

then the theoretical expressions of double probe characteristic with no slope in the saturated part can be expressed as follows:

$$\left.\begin{aligned} \ln[(I_p/i_{e2})-1]&=-\phi V_d\\ \ln[(I_p/i_{e1})-1]&=\phi V_d\end{aligned}\right\} \tag{6}$$

$$i_d=(I_p/2)\tanh(\phi V_d/2) \tag{7}$$

These are the results derived by Johnson and Malter[2].

Now in cases where the saturated part of probe characteristic has a slope (see Fig. 2), e.g. where $I_p$ is a function of $V_d$ rather than a constant, in order to obtain the exact values of electron temperature, electron concentration and electron energy distribution, we should separate the electron current from the positive ion current of this function.

(i) *Variation of Positive Ion Current and Probe Current with Probe Voltage when the Saturated Part has a Slope*

First we have the following derivative of equation (1) with respect to $V_d$:

$$\frac{dI_p}{dV_d}=\frac{di_{p1}}{dV_1}\frac{dV_1}{dV_d}+\frac{di_{p2}}{dV_2}\frac{dV_2}{dV_d} \qquad (8)$$

For simplicity we may here assume the symmetry of probe characteristic. Inserting $i_{e1}$ and $i_{e2}$ of equations (2) into equations (6), we immediately have

$$\left.\begin{aligned} V_1&=-(1/\phi)\ln I_p\\ &\quad+(1/\phi)\ln F_0 j_0\{\exp(\phi V_d)+1\}\\ V_2&=-(1/\phi)\ln I_p\\ &\quad+(1/\phi)\ln F_0 j_0\{\exp(-\phi V_d)+1\} \end{aligned}\right\} \qquad (9)$$

or their derivatives:

$$\left.\begin{aligned} dV_1/dV_d&=-(1/\phi I_p)(dI_p/dV_d)\\ &\quad+\exp(\phi V_d)/\{\exp(\phi V_d)+1\}\\ dV_2/dV_d&=-(1/\phi I_p)(dI_p/dV_d)\\ &\quad-\{\exp(\phi V_d)+1\}^{-1}, \quad V_d>0 \end{aligned}\right\} \qquad (10)$$

Here we define $S$ as the ratio between the increase of positive ion current and that of potential across sheath due to sheath expansion, i.e.

$$di_{p1}/dV_1=di_{p2}/dV_2=S \qquad (11)$$

In a rough approximation, we can assume that $S$ is constant throughout the whole range of voltage in this problem. Then, combining equations (8), (10) and (11) we have the following general relation between $I_p$ and $V_d$,

$$dI_p/dV_d=[S\phi I_p/(2S+\phi I_p)]\tanh(\phi V_d/2) \qquad (12)$$

The solution of this equation is

$$I_p\exp(\phi I_p/2S)=2A\exp(\phi A/S)\cdot\cosh(\phi V_d/2) \qquad (13)$$

where

$$2A=[I_p]_{V_d=0} \quad \text{or} \quad [i_{p1}]_{V_d=0}=[i_{p2}]_{V_d=0}=A \qquad (14)$$

Typical plots of equation (13) are shown in Fig. 3.

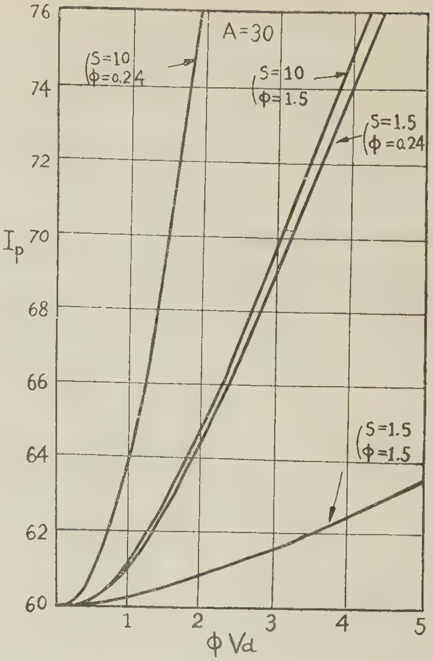

Fig. 3. Variation of total ion current ($I_p=i_{p1}+i_{p2}$) with $\phi V_d$, taking $S$ and $\phi$ as parameters, $A=30$.

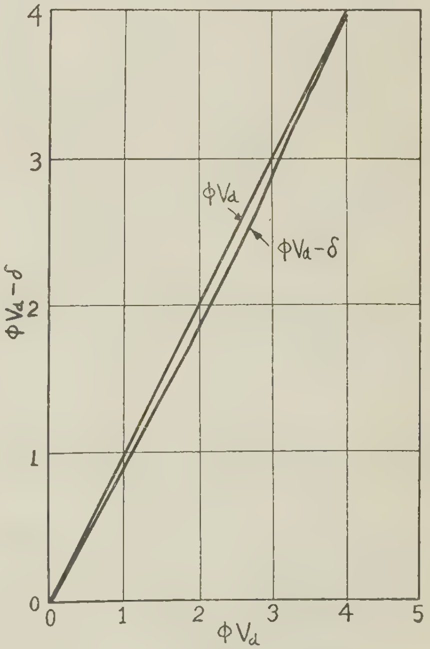

Fig. 4. Plot of $\phi V_d$ vs. $\phi V_d-\delta$.

Next step is to obtain the expressions for $i_{p1}$, $i_{p2}$ and $i_d$ as functions of $V_d$. Using the relation $di_{p1,2}/dV_d=(di_{p1,2}/dV_{1,2})(dV_{1,2}/dV_d)$ with (10), (11) and (14) at once we can get

$$\left.\begin{aligned} i_{p1}&=(S/\phi)\ln[A\{1+\exp(\phi V_d)\}/I_p\}+A\\ i_{p2}&=(S/\phi)\ln[A\{1+\exp(-\phi V_d)\}/I_p\}+A \end{aligned}\right\} \qquad (15)$$

From equation (15) and the relation

$$\ln[(i_{p1}-i_d)/(i_{p2}+i_d)]=-\phi V_d \qquad (16)$$

$i_a$ can be expressed by

$$i_a = A+(S/\phi)\ln(A/I_p)\}\tanh(\phi V_a/2) + V_aS-(S/\phi)\delta \qquad (17)$$

where

$$\phi V_a-\delta=\{1+\exp(-\phi V_a)\}^{-1}[\ln(\exp\phi V_a+1) -\exp(-\phi V_a)\ln\{1+\exp(-\phi V_a)\}] \qquad (18)$$

The probe characteristic with slope in the saturated part is not expressed by equation (7) but by equations (17) and (18), in which $\delta$ becomes smaller when $\phi V_a$ is either considerably greater or much smaller than unity, as shown in Fig. 4.

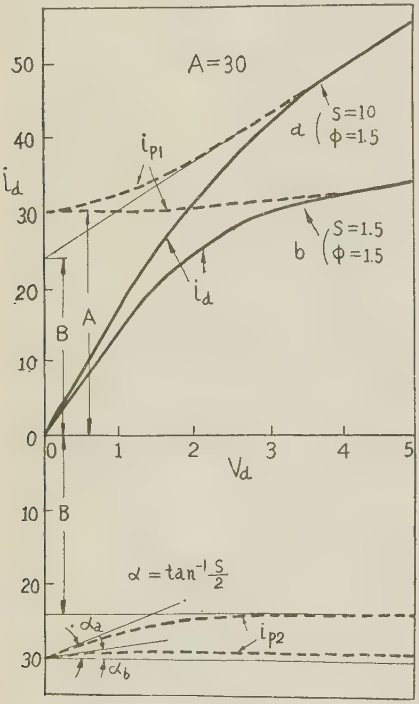

Fig. 5. Analytical double probe characteristic and each ion current for two cases, assuming $S=10$, $\phi=1.5$, A=30 and $S=1.5$, $\phi=1.5$, A=30.
Curve $a$, $S=10$, $\phi=1.5$.
Curve $b$, $S=1.5$, $\phi=1.5$.

(ii) *Expressions for Positive Ion Current*

Instead of equation (15) we can have the following expressions for $i_{p1}$ and $i_{p2}$ which we get by inserting equation (13) into (15)

$$\left.\begin{aligned} i_{p1} &= I_p/2+(S/2)V_a \\ i_{p2} &= I_p/2-(S/2)V_a\,, \quad V_a>0 \end{aligned}\right\} \qquad (19)$$

showing that both $i_{p1}$ and $i_{p2}$ in the region of $V_a>0$ near to $V_a$=zero have the same slope:

$$(di_{p1}/dV_a)_{Va=0}=(di_{p2}/dV_a)_{Va=0}=S/2 \qquad (20)$$

or, one-half of the degree of slope of the saturated part. When $V_a$ increases, the slope of $i_{p1}$ increases up to $S$, while that of $i_{p2}$ decreases down to zero at large $|V_a|$.

We show below how the ultimate values at $V_a=0$ of $i_{p1}$ and $i_{p2}$ can be derived. As in Fig. 5, if we denote $B$ for the value at which a straight line extending from the large value of $V_a$ along probe characteristic cuts the axis of $V_a=0$, then for large values of $V_a$ the characteristic curve can be expressed by

$$I_p=2B+SV_a \qquad (21)$$

and

$$\left.\begin{aligned} i_{p1} &= B+SV_a \\ i_{p2} &= B\,, \quad V_a>0 \end{aligned}\right\} \qquad (22)$$

instead of (19).

Under the above considerations we shall present a criterion for the applicability of the double proble method. From equation (17), we have

$$(di_a/dV_a)_{Va=0}=\{A-(S/\phi)\ln 2\}\phi/2+S \qquad (23)$$

If the slope $(di_a/dV_a)_{Va=0}$ is much greater than $S$ (the slope at large $V_a$)*, then the probe characteristic has in effect a saturated part. Therefore, the conditions of

$$(di_a/dV_a)_{Va=0} \gg S \qquad (24)$$

or

$$A \gg 0.693(S/\phi) \qquad (25)$$

are necessary for the application of the usual double probe method. In most cases $S$ is so small that equation (25) is satisfied.

(iii) *Determination of Electron Temperature*

The use of the log-plot method for determining electron temperature, one of the methods proposed by Johnson and Malter2), is not appropriate unless the exact form of

---

* In the double probe characteristic $i_p$ near $V_a=0$ has a complicated form while at large $V_a$, it is clear from equations (17) and (19) that

$$(di_a/dV_a)_{Va\to\infty}=S$$
$$(di_{p1}/dV_a)=S/2+(1/2\phi)(dI_p/d\phi V_a)$$
$$(di_{p2}/dV_a)=-S/2+(1/2\phi)(dI_p/d\phi V_a)\,.$$

Inasmuch as the second terms of these last two equations become $S/2$ when $V_a$ tends to an infinite (see Fig. 3), we have at large $V_a$

$$di_{p1}/dV_a=S\,, \qquad di_{p2}/dV_a=0$$

proving that the slope at large $V_a$ in the double probe method is equal to that in the single probe method. For example, in our experiment

single probe method: $S=1.2\,\mu A/V$, $(i_p)_{Vf}=67\,\mu A$
double probe method: $S=1.2\,\mu A/V$, $(i_p)_{Va\to\infty}=69\,\mu A$
($V_f$ means the floating potential)

positive ion current can be obtained. Fortunately when $S$ is small, electron currrent can be obtained with almost no error by subtracting an approximately evaluated ion current from probe current, so that the electron temperature can be determined. However if $S$ is large, this approximation can not be permitted because $i_p$ becomes a complicated function of $V_d$.

Here we shall find the formula of electron temperature, including the effect of $S$, by making a correction in the equivalent resistance method[2)] in which the electron temperature is calculated by both $di_d/dV_d$ and $i_p$ at $V_d=0$. From equation (6)

$$i_{e2}=I_p/\{1+\exp(-\phi V_d)\} \tag{26}$$

Differentiating this equation with respect to $V_d$ and setting $V_d=0$, we can write

$$(di_{e2}/dV_d)_{Vd=0}=A\phi/2 \tag{27}$$

Since $\quad di_{e2}/dV_d=di_d/dV_d+di_{p2}/dV_d$ ,

equation (27) leads to

$$(di_{e2}/dV_d)_{Vd=0}=(1/R_0)-(S/2) \tag{28}$$

where $R_0$ is termed "equivalent resistance".

Combining equations (27) and (28) we have the following expression for the electron temperature $T_e$;

$$A\phi/2=1/R_0-S/2$$

or

$$T_e=(e/2k)A(1/R_0-S/2)$$

$$=5,800A(1/R_0-S/2) \quad °\mathrm{K}\,. \tag{29}$$

This formula holds generally in all cases either with or without a slope in the saturated part, including Johnson-Malter's expression as a special case of $S=0$.

The value of $A$, i.e. the value of $i_p$ at $V_d=0$ can be estimated by the same procedure as used by Johnson-Malter. When $V_d$ vs. $i_d$ characteristic has a sufficient symmetry, it is reasonable for practical purposes to choose as the value of $A$ the value of $i_d$ at $V_d=0.15V_s$ on the extraporated line of $i_p$ along the saturated curve, where $V_s$ is a certain value of $V_d$ at which the saturation begins. According to the calculations aided by equations (13) and (19), we have also recognized that the estimated $A$ becomes the value of $i_d$ at $V_d=(0.14\sim0.18)V_s$.

From equation (29) it can be clearly seen that with a large $R_0$, by neglecting $S$ there is a considerable error which results in the under-estimation of the electron temperature.

### (iv) *Electron energy Distribution*

Previous considerations based upon the Maxwell-Boltzmann distribution of electron velocities are not justifiable with such special plasmas as in the negative glow.

In the double probe method, the probes automatically settle near the so-called floating potential, forming positive ion sheaths around themselves, and permitting electrons of such high energy to flow into the probes as to overcome the retarding fields of the sheaths. The floating potential is always much greater than the potential corresponding to the most probable velocity, so that the electrons collected by probes come from portion of higher velocities in the distribution. For example, in $T_e=1000°\mathrm{K}$ in argon[2)] the ratio of collected electrons to total electrons amounts to merely 0.21%, where $V_f$ is 0.5 volt, while the potential corresponding to the most probable velocity is 0.08 volt.

It has been extensively reported that some deviations from the Maxwell-Boltzmann distribution often arise in the portion of higher velocities, depending upon the kind of gas and $E/p$, where $E$ is electric field and $p$ pressure. In such cases in the double probe method, considerable errors may be introduced in the estimation of plasma quantities.

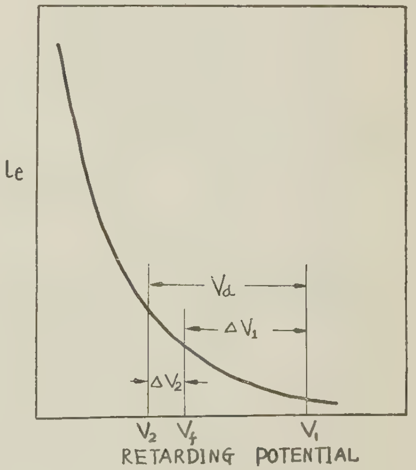

Fig. 6. Electron current as a function of retarding potential, illustrating correspondency with double probe characteristic.

Now we shall illustrate the way in which the higher portion in the velocity distribution curve contributes to the probe characteristic. If the analysis could succeed, we would

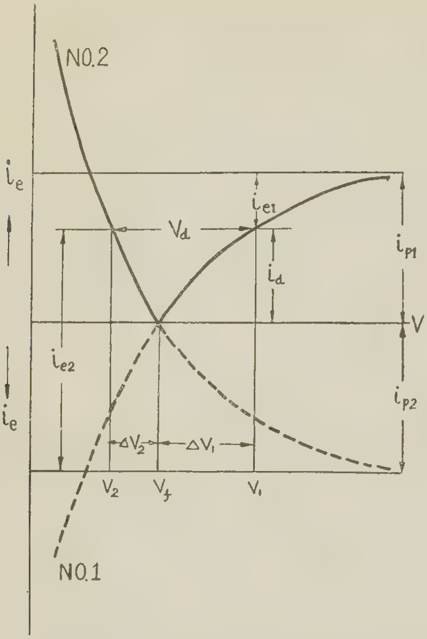

Fig. 7. Relation between electron current as a function of retarding potential and probe current as a function of probe voltage, without slope.

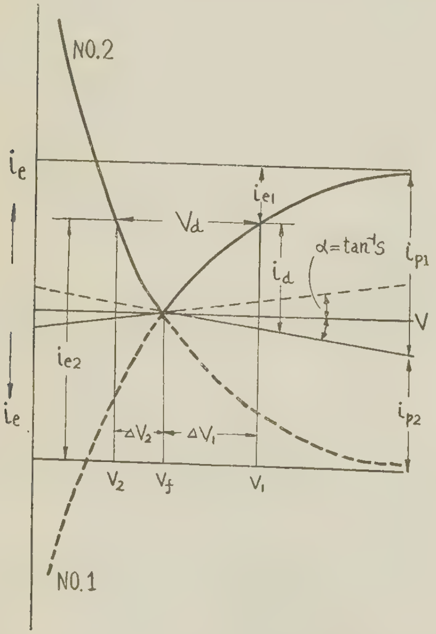

Fig. 8. Relation between electron current as a function of retarding potential and probe current as a function of probe voltage, with slope.

acquire quantitative knowledge on the collected current in non-Maxwellian cases.

Fig. 1 shows schematically a rough outline of the potential distributed to the two probes

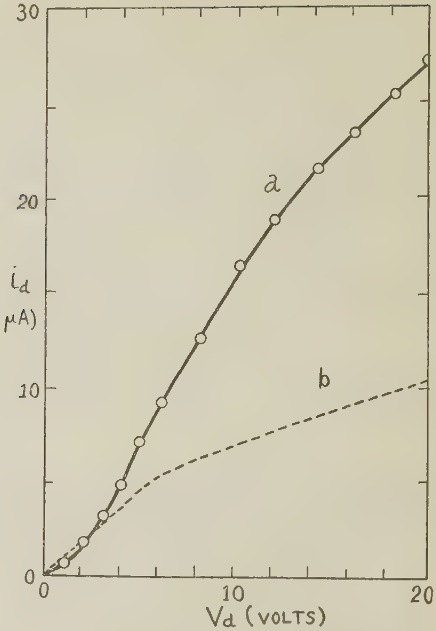

Fig. 9. A distorted probe characteristic.
Curve *a*, negative glow of d.c. glow discharge of air, pressure 0.17 mm Hg, voltage 520 V, current 12 mA.
Curve *b*, non-distorted characteristic, positive column of the same discharge as curve *a*.

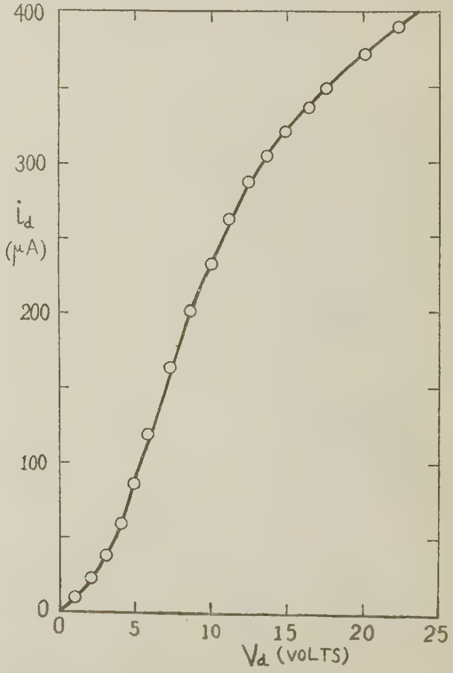

Fig. 10. A distorted probe characteristic. The glow surrounding hot cathode in low voltage arc of argon, pressure 2 mm Hg, voltage 40 V, current 80 mA.

between which a voltage $V_d$ is applied. If $V_d=0$, both probes have the equal floating potential $V_f$. If $V_d>0$, the potential of No. 1 probe is decreased by $\Delta V_1$ and that of No. 2 increased by $\Delta V_2$. We can divide $V_d$ into $\Delta V_1$ and $\Delta V_2$ along the curve of collected electron current vs. negative potential shown in Fig. 6, the relation being always $\Delta V_1>\Delta V_2$.

First, considering such an ideal case as $S=0$, the operation of double probes can be schematically illustrated as in Fig. 7. By lapping inversely the curves of No. 2 at the point of $V=V_f$, the figure shows the relations between the probe potential, the saturated positive ion current and the electron current collected by the two probes. The solid lines refer to the operation for $V_d>0$ and the dotted lined the operation for $V_d<0$.

From Fig. 7, it is evident that

$$V_d=\Delta V_1+\Delta V_2=V_1-V_2 \qquad (30)$$

Taking the voltage difference $V_d$ between the two branches of solid lines vs. $i_d$, we can obtain the simple relation $i_d=i_p\tanh(\phi V_d/2)$ if we assume Maxwell-Boltzmann distribution.

Next, taking slope into consideration, the only thing to do is to rotate the abscissa around the point $V=V_f$ by an angle $\theta=\tan^{-1}S$ (see Fig. 8).

These illustrations are useful for the analysis of non-Maxwellian distribution in which $i_{e1}$ and $i_{e2}$ can not be expressed by such a simple exponential form with respect to $V$ as equation (7).

Figs. 9 and 10 show typical non-Maxwellian examples obtained in the negative glow of d.c. glow discharge in air and in the glow surrounding hot cathode in low voltage argon arc, respectively.

## § 3. Triple Probe Method

Hitherto the only method capable of determining the electron energy distribution was the single probe method developed by Langmuir and Mott-Smith. However, this is not applicable to electrodeless or high frequency discharge because it gives no fixed potential for the base of probe.

Here we propose a "triple probe method", adding to the double probe method the third probe, which is always held at the floating potential in order to make the floating probe able to measure the electron energy distribution.

Fig. 11 shows a connection diagram of the triple probe method. If we adjust a potential divider so that the current $i_{d3}$ flowing into No. 3 probe is zero, then the potential of No. 3 probe becomes equal to the floating potential $V_f$ and No. 1 and 2 remain the usual double probe for the measurement. The potential difference between No. 1 and No. 3 then becomes equal to $\Delta V_1$ and that between No. 2 and No. 3 to $\Delta V_2$. At the same time we can get the relations between both $\Delta V_1$ and $i_{e1}$, and $\Delta V_2$ and $i_{e2}$ from the double probe characteristic. Thus the curve of electron current vs. voltage near $V_f$ can be drawn, from which the electron energy dis-

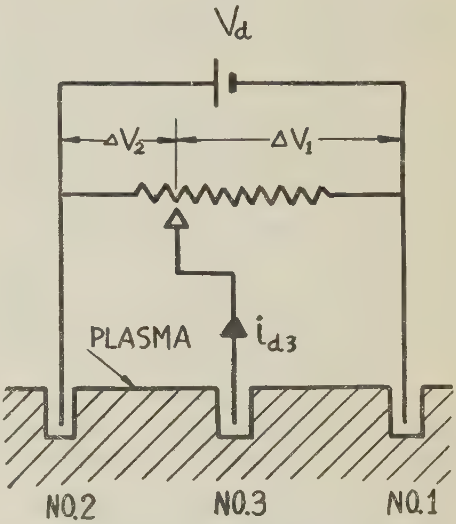

Fig. 11. Basic circuit for the triple probe method.

Table I. A measurement by triple probe method. H. f. discharge of air, pressure $1\times10^{-2}$mm Hg, voltage 215 V.

| $V_d$(V) | $\Delta V_1$ (V) | $i_{e1}$ ($\mu$A) | $\Delta V_2$ (V) | $i_{e2}$ ($\mu A$) |
|---|---|---|---|---|
| 1 | 0.4 | 103 | 0.6 | 92 |
| 2 | 0.8 | 107 | 1.2 | 88 |
| 3 | 1.2 | 110 | 1.8 | 83 |
| 4 | 1.6 | 116 | 2.4 | 79 |
| 5 | 2.0 | 120 | 3.0 | 76 |
| 7 | 2.8 | 128 | 4.2 | 68 |
| 9 | 3.4 | 135 | 5.6 | 62 |
| 11 | 3.9 | 142 | 7.1 | 55 |
| 12.5 | 4.3 | 151 | 8.2 | 48 |
| 15 | 5.0 | 160 | 10.0 | 40 |
| 20 | 6.4 | 180 | 13.6 | 25 |
| 25 | 7.4 | 194 | 17.6 | 14 |
| 30 | 7.9 | 207 | 22.1 | 6 |
| 35 | 8.5 | 215 | 26.5 | 4 |
| 40 | 9.0 | 223 | 31.0 | 1 |
| 45 | 9.3 | 230 | 35.7 | 0 |

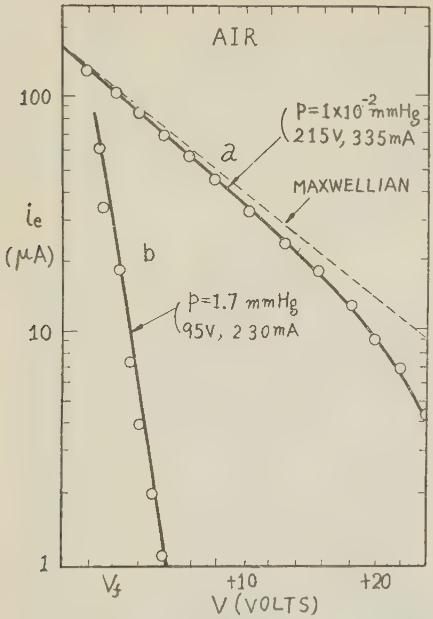

Fig. 12. Plot of electron current vs. retarding potential obtained in high frequency (77 Mc) discharge.
Curve *a*, pressure $1\times10^{-2}$ mm Hg, setting h.f. electrodes outside the discharge tube.
Curve *b*, pressure 1.7 mm Hg, setting h. f. electrodes in the discharge tube.

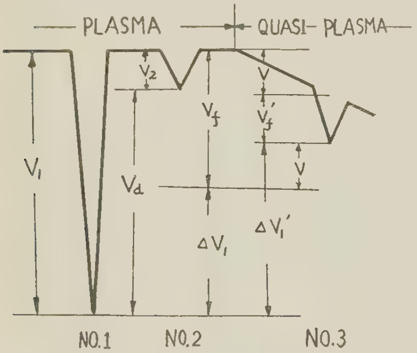

Fig. 13. Potential diagram for the triple probe method applied to quasi-plasma.
$\Delta V_1$=potential difference between No. 1 and No. 1 and No. 3, placing No. 3 in a plasma.
$\Delta V_1'$=potential difference between No. 1 and No. 3, placing No. 3 in a quasi-plasma.
$V_f$=floating potential in a plasma.
$V_f'$=floating potential in a quasi-plasma.

tribution can be decided by Druyvesteyn's method[5]. For the separation of $i_e$ from $i_d$, the procedure given in paragragh II, (i) must be applied.

We describe here the experimental results obtained by using this method for high frequency electrodeless discharge. Three probes equally separated are placed on an equipotential plane in a discharge tube with air of $1.7\sim10^{-3}$ mm Hg, frequency of 77 M.c. Table I shows a result of the experiment, pressure $1\times10^{-2}$ mm Hg, applied high frequency voltage 215 V.

From many measurements of energy distribution in the h.f. discharge the following conclusions are deduced;

(1) Mean energy decreases with increasing pressure.

(2) Electron energy distribution tends toward the Maxwellian when the pressure rises.

(3) Generally, there appears a deficiency in the higher energy portion, as shown in Fig. 12.

These experimental results are consistent with Margenau's theoretical analysis[6].

Although the triple probe method is not available for determining the whole range of energy distribution, it is useful in cases where the single probe method cannot be applied.

## § 4. Applications of Floating Triple and Double Probe Methods for the Ion Sheath and the Transition Region between Plasma and Sheath

In this section we describe another application of triple probe method as well as special use of double probe method for determining potential distribution in positive ion sheath and in the transition region between plasma and ion sheath.

When two of three probes or one of a double probe are inserted into a plasma and the remaining one probe into "quasi-plasma" such as the ion sheath or the transition region between plasma and sheath, the probe characteristic must be changed.

(i) *Triple Probe Method*

As shown in Fig. 13, when No. 1 and No. 2 probes are set at the points of equal potential in a plasma for the purpose of usual double probe measurement and movable No. 3 probe, adjusted to be no current, is settled at a point in a quasi-plasma under measurement, then the deviation *V* of the potential at the point in the quasi-plasma from the plasma potential can be obtained by comparing the potential of No. 3 of this state with that in the plasma. By transfering No. 3 probe from the plasma into the transition region along the equipotential plane, we can observe the potential change throughout the whole region of transition.

This statement is based upon the following experimental fact. When a plane electrode floats in a plasma producing a positive ion sheath around itself, and when No. 3 probe approaches infinitely near the plane electrode, then $\varDelta V_1 - \varDelta V_1'$ becomes experimentally equal to the floating potential $V_{fp}$ where $\varDelta V_1$ is the potential difference between No. 1 and No. 3, placing the latter in a plasma and $\varDelta V_1'$ is the potential difference between No. 1 and No. 3, placing No. 3 in the transition region or in the ion sheath, and where $V_{fp}$ is the floating potential of the plane electrode.

As an example, in the glow discharge of a discharge current 30 mA in air of 2.5 mmHg, using an insulating plane electrode of 0.5 cm × 0.5 cm and a thin wire probe of 0.0035 cm diameter, we obtained 24.5 V for the value of $\varDelta V_1 - \varDelta V_1'$, while the floating potential of the plane electrode $V_{fp}$ was 25.2 V measured by the single probe method. Therefore we may assume that the following relation is held at any point in the transition region or the ion sheath.

$$\varDelta V_1' - \varDelta V_1 = V \qquad (31)$$

This fact shows that by trasfering No. 3 probe from the plasma to a point where the potential is lower by $V$ than the potential of the plasma, the potential of No. 3 probe rises by $V$. Fig. 14 indicates a potential curve near an insulating plane electrode, obtained by this method.

Now we shall give consideration to the above measurment. When two probes of geometrically equal dimensions are placed in equal plasma states, the double probe characteristic shows symmetrical curve. No. 3 probe does not influence the double probe characteristic because No. 3 probe is always used in floating state or without current.

The electron density $n_e$ at a point where the potential is lower by $V$ with respect to the plasma, is expressed by Boltzmann's relation

$$n_e = n_0 \exp(-eV/kT_e) \qquad (32)$$

where $n_0$ is the electron density of the plasma. Asssuming the quasi-neutrality, we have $n_e \approx n_p$, where $n_p$ is the positive ion density.

For simplicity, assuming that $E/p$ of plasma is small enough so that the positive ion current flowing into No. 3 is

$$\begin{aligned} i_{pf} &= (n_0 e \bar{v}_p/4)(2\pi r_c') \exp(-eV/kT_e) \\ &= 1.87 \times 10^{-8} (n_0 e/4)(T_p/M)^{1/2} (2\pi r_c') \\ &\quad \times \exp(-eV/kT_e) \qquad (33) \end{aligned}$$

where $\bar{v}_p$ is mean thermal velocity of positive ion, $M$ is mass of ion, $T_p$ is positive ion temperature and $r_c'$ is radius of positive ion sheath in the quasi-plasma.

The electron currrent of No. 3 probe is

$$\begin{aligned} i_{ef} &= j_{e0} \exp(-eV/kT_e) \cdot \exp(-eV_f'/kT_e) \cdot (2\pi r_a) \\ &= 1.87 \times 10^{-8} (n_0 e/4)(T_e/m)^{1/2} (2\pi r_a) \\ &\quad \times \exp\{-e(V+V_f')/kT_e\} \qquad (34) \end{aligned}$$

where $j_{e0}$ is random electron current density in plasma, $V_f'$ is floating potential in the quasi-plasma, $r_a$ is radius of the probe and $m$ is electron mass. From the condition of no current, we have

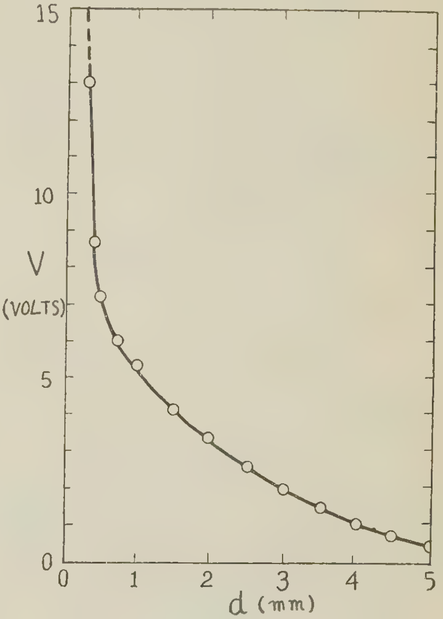

Fig. 14. Measured potential distribution near the floating plane electrode, air of pressure 2.5 mm Hg, current 40 mA, probe voltage $V_d = 40$ V. Potential $V$ is measured with respect to plasma potential. Distances $d$ is measured from the floating plane electrode.

$$i_{pf} = i_{ef} \qquad (35)$$

or $\quad V_f' = (kT_e/e) \ln[(r_a/r_c')(T_e M/T_p m)^{1/2}]$ . (36)

On the other hand, when No. 3 probe is placed in the plasma, its floating potential $V_f$ is given by

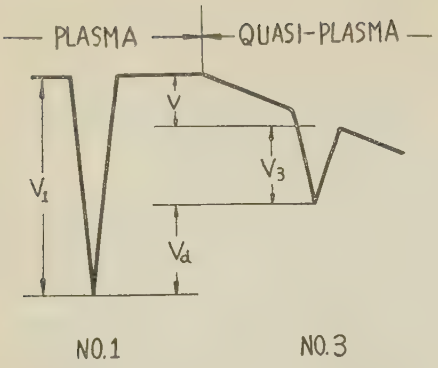

Fig. 15. Potential diagram for the double probe method applied to quasi-plasma.

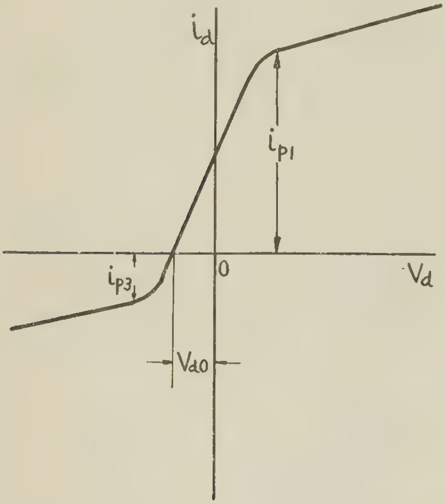

Fig. 16. Double probe characteristic for quasi-plasma.

$$V_f=(kT_e/e)\ln[(r_a/r_c)(T_eM/T_pm)^{1/2}] \qquad (37)$$

where $r_c$ is the radius of ion sheath produced around No. 3 probe when No. 3 probe is placed in the plasma.

From (36) and (37) we get at once

$$V_f-V_f'=(kT_e/e)\ln(r_c'/r_c) \qquad (38)$$

and from (31) and (38) we get

$$(kT_e/e)\ln(r_c'/r_c)=2V\,. \qquad (39)$$

This indicates the relation between the expansion of ion sheath and the potential deviation from plasma.

From (38) and (39) we get

$$V_f'=V_f-2V \qquad (40)$$

viz., at the point where the potential is lower by $V$ than the potential of a plasma, the floating potential is lower by $2V$ than the floating potential of the plasma.

According to the above consideration, we can find the potential distribution in the transition region and eventually can know floating potential of a floating probe by means of extrapolation of potential distribution to the floating probe.

(ii) *Double Probe Method*

In the double probe measurement, omitting No. 2 probe in the triple probe method (Fig. 15), the probe characteristic is not symmetrical but rather asymmetrical as indicated in Fig. 16. In cases where each probe is not of equal potential, we can describe the relations following Johnson and Malter.

Denoting electron current densities $j_{01}$, $j_{03}$, positive ion currents $i_{p1}$, $i_{p3}$ for each probe, in place of (3), we have

$$V_1-V_d=V_3+V \qquad (41)$$

From equation (1), (2) and (41)

$$(I_p/i_{e3})-1=i_{e1}/i_{e3}=(j_{01}/j_{03})\exp\{-\phi(V_1-V_3)\}$$
$$=(j_{01}/j_{03})\exp\{-\phi(V+V_d)\} \qquad (42)$$

at a point on the probe characteristic curve where the probe currrent becomes zero we have

$$i_{e1}=i_{p1} \quad \text{and} \quad i_{e3}=i_{p3} \qquad (43)$$

Denoting $V_{d0}$ for the value of $V_d$ which satisfies the above condition, from (42) and (43) we have

$$i_{p1}/i_{p3}=j_{01}/j_{03}\exp\{-\phi(V+V_{d0})\} \qquad (44)$$

or

$$V=-V_{d0}-(1/\phi)\ln(i_{p1}j_{03}/i_{p3}j_{01})\,. \qquad (45)$$

This relation is useful for a simple measurement of potential gradient in a positive column in which, as the second term can be omitted, we have

$$V=|V_{d0}|\,. \qquad (46)$$

When one probe No. 3 is placed in the transition region, relation are as follows:

$$j_{03}=j_{01}\exp(-\phi V)\,. \qquad (47)$$

From (44) and (47),

$$i_{p1}/i_{p3}=\exp(\phi|V_d|)\,. \qquad (48)$$

Inserting (47) into (42),

$$i_{e1}/i_{e3}=\exp(-\phi V_d)\,. \qquad (49)$$

By using equation (4) or $i_{e1}/i_{e3}=(i_{p1}-i_d)/(i_{p3}+i_d)$, we have

$$i_d=\frac{i_{p1}-(i_{e1}/i_{e3})i_{p3}}{1+(i_{e1}/i_{e3})}\,. \qquad (50)$$

Inserting (48) and (49) into (50),

$$i_d = \frac{i_{p1}}{1+\exp(-\phi V_d)}[1-\exp\{-\phi(V_d-V_{d0})\}] \tag{51}$$

and

$$[i_d]_{Vd=0} = \{1-\exp(\phi V_{d0})\}(i_{p1}/2)\ . \tag{52}$$

Assuming the positive ion energy to be constant, we have

$$j_{p3} = j_{p1}\exp(-\phi V)$$

or

$$i_{p1}/i_{p3} = (r_{c1}/r_{c3})\exp(\phi V) \tag{53}$$

where $j_p$ is the positive ion current density. From (39) and (48), we get

$$V = |V_{d0}|\ . \tag{54}$$

Thus by means of double probe we can also obtain the potential distribution. Table II indicates some results giving the measured values of $V$ by the triple probe method (column 2) which agree fairly well with those measured by double probe method (column 3), outside the boundary ($d=2$ mm). In the sheath ($d<2$ mm) the potentials measured by triple probe method do not coincide with that by double probe method. The error seems to arise from the disturbance caused by the inserting of probe in the sheath, absorbing the current.

Table II. Observed potential deviations from plasma potential at several points near the floating plane electrode. D. c. glow discharge of air, pressure 2.5 mm Hg, current 30 mA, plane electrode of 0.5 cm × 0.5 cm, wire probe of diameter 0.0035 cm.

| $d$ (mm) | $V$ (V) | | $i_{p3}$ ($\mu$A) |
|---|---|---|---|
| | triple | double | |
| 6 | 0.2 | 0.3 | 22.7 |
| 4 | 1.0 | 1.2 | 22.4 |
| 3 | 2.0 | 2.2 | 22.2 |
| 2 | 3.5 | 4.1 | 21.4 |
| 1 | 5.3 | 8.4 | 16.6 |
| 0.5 | 10.0 | 16.5 | 9.7 |
| 0.2 | 18.0 | 27.0 | 5.2 |

$d$: distance from the floating plane electrode (mm).
$V$: potential deviation from plasma potential (V).
$i_{p3}$: saturated probe current of No. 3 probe ($\mu$A).

## § 5. On the Floating Potential

The only defect of the double probe method lies in that it gives no information on the space and floating, or insulating, potentials. Particularly, it is necessary to know the floating potential because that is the standard of potential or energy in the measurement of energy distribution.

As has already been pointed out by Tonks and Langmuir⁷⁾, the ratio between saturation values of electron and positive ion current is not given by $(T_eM/T_pm)^{1/2}$. Consequently, the expression (37) for $V_f$ is not justifiably held. It is confirmed by the experiment that the calculation using equation (37) could agree with the observation only when the ion temperature would be as high as, or sometimes higher than, the electron temperature. We cannot explain the measured value of $V_f$, even when permitting the use of the high ion temperatures lately reported by several investigators, for instance $T_p \approx (1/3 \sim 1/10)T_e$ by Boyd⁸⁾

In ordinary plasma, the collection of positive ion by probe must be caused by some mechanism other than thermal motion of positive ion.

Bohm⁹⁾ stated that the boundary between sheath and plasma in low pressure should be found where the following relation is satisfied.

$$eV_0 = kT_e/2 \tag{55}$$

where $eV_0$ is the mean energy of positive ion at the boundary, i.e.

$$eV_0 = eV + kT_p/3 \tag{56}$$

The mean velocity of positive ion at the boundary is

$$v_p = \sqrt{\frac{2}{M}}\sqrt{eV_0} = \sqrt{\frac{2}{M}}\sqrt{eV+\frac{kT_p}{3}}$$
$$= \sqrt{\frac{2}{M}}\sqrt{\frac{kT_e}{2}} \tag{57}$$

We may here assume

$$n_p \approx n_e = n_0\exp(-eV/kT_e)\ . \tag{58}$$

Therefore the positive ion current density $j_p$ which flows into the boundary is

$$j_p = \sqrt{\frac{2}{M}}\sqrt{\frac{kT_e}{2}}\,n_0\exp(-eV/kT_e) \tag{59}$$

or, neglecting $T_p$,

$$j_p = n_0\sqrt{\frac{2}{M}}\sqrt{\frac{kT_e}{2}}\,e^{-1/2} = 0.4288n_0\sqrt{\frac{2kT_e}{M}}^{**} \tag{60}$$

---

** Equation (60) resembles Langmuir's equations of wall current dependent on electron temperature.

Notations P, C and S signify plane, cylindrical and spherical forms of plasma, respectively; L the long mean free path; $\lambda$ ions produced proportionally to electron density; J constant ion production.

$$j_p = Kn_0(2kT_e/M)^{1/2}$$

| | PL $\lambda$ | CL $\lambda$ | PLJ | CLJ | SLJ |
|---|---|---|---|---|---|
| K | 0.3444 | 0.2703 | 0.3443 | 0.2914 | 0.2569 |

Table III. Floating potential of a plane probe. Low voltage arc of argon, plane probe of 2.0 mm diameter.

| pressure (mm Hg) | current (mA) | electron temperature (°K) | ion * temperature (°K) | $V_f$ (V) observed | $V_f$ (V) calculated by (56) | $V_f$ (V) calculated by (37-II) ** |
|---|---|---|---|---|---|---|
| 0.45 | 20 | 34,800 | 1,400 | 10.0 | 12.4 | 21.5 |
| | 40 | 31,300 | 1,100 | 8.8 | 11.2 | 19.5 |
| | 100 | 27,800 | 850 | 8.0 | 9.9 | 17.6 |
| 0.02 | 30 | 43,000 | 8,200 | 15.5 | 15.5 | 24.9 |
| | 50 | 40,000 | 7,100 | 14.0 | 14.5 | 22.3 |
| | 60 | 39.000 | 6,500 | 14.0 | 14.2 | 21.8 |

* Ion temperature in the Table of $V_f$ are calculated by the following equation:

$$T_p=T_g/2+1/2\{T_g{}^2+1.66(eE\lambda_{0p}/kp)^2\}^{1/2}$$

where $T_g$ = gas temperature (°K). $k$ = Boltzmanns constant.
$e$ = electronic charge. $\lambda_{0p}$ = ionic mean free path at 1 mmHg (cm).
$p$ = pressure (mmHg). $E$ = electric field (V/cm).

** For plane probe, we must use following equation instead of (37).

$$V_f=(kTe/e)\ln(TeM/T_pm)^{1/2}\,. \qquad (37\text{-II})$$

From Bohm's equation and the relation

$$j_p=j_e\exp(-eV_f/kT_e)\,,$$

we get an expression for $V_f$ of plane probe

$$V_f=\frac{kT_e}{e}\ln\left[\frac{(n_0/4)(8kT_e/\pi m)^{1/2}}{0.4288(2kTe/M)^{1/2}}\right]$$

$$=\frac{kT_e}{e}\ln\left(0.6578\sqrt{\frac{M}{m}}\right) \qquad (61)$$

and numerically

for $N_2$ $V_f=5{,}004\,T_e/11{,}600$ °K
Ar $V_f=5{,}599\,T_e/11{,}600$ °K
Hg $V_f=6{,}405\,T_e/11{,}600$ °K

If we use the expression (61) for $V_f$ of plane probe, the calculated values agree fairly well with the observed values, as shown in Table III.

We can note in Table III that the observed value is always smaller than the calculated value, a difference which increases with increased pressure, and which seems to be caused by a disturbance resulting from insertion of probe in a plasma of small density.

## Conclusion

The authors herein discuss all the problems which arise in practical uses of floating probe method, and shows ways to overcome the difficulties encountered in measurement.

There remain no serious problems connected with idealized plasma. There are various kinds of plasma which have not yet been exactly measured owing to the limitations of probe method. The triple probe method and some corrections in the double probe method may be conveniently used to make such measurements.

## References

1) A. Reifman and W. G. Dow: Phys. Rev. **76** (1949) 987.
2) E. O. Johnson and L. Malter: Phys. Rev. **76** (1949) 1411, **80** (1950) 58.
3) S. Kojima and K. Takayama: J. Phys. Soc. Japan **4** (1949) 346, **5** (1950) 357.
4) I. Langmuir and H. Mott-Smith: Gen. Elec. Rev. **27** (1924) 449, 538, 616, 762, 810.
5) M. J. Druyvesteyn: Z. Physik **64** (1930) 790.
6) H. Margenau: Phys. Rev. **69** (1946) 508.
7) L. Tonks and I. Langmuir: Phys. Rev. **34** (1929) 876.
8) R. L. F. Boyd: Proc. Roy. Soc. **A 201** (1950) 329.
9) D. Bohm, E. H. S. Burhop and H. S. W. Massey: *Characteristics of Electrical Discharge in Magnetic Field*, McGraw-Hill Book Co, Chapter 2 and 3 (1949).

JOURNAL OF THE PHYSICAL SOCIETY OF JAPAN Vol. 11, No. 1, JANUARY, 1956

# On the Sheen Gloss

By Hirosi HASUNUMA and Jiro NARA

*Department of Applied Physics, Faculty of Engineering,*
*University of Tokyo*

(Received September 10, 1955)

Experiments of sheen gloss of metals and theoretical explanation of them are given. Sheen gloss is related with the specularly reflected light which appears by a incident angle above a critical angle $\theta_c$. $\theta_c$ is connected with the r.m.s. roughness $h$ as:

$$2h\cos\theta_c=\lambda/k \qquad k=2\sim3$$

This formula is explained by a theory similar to the Kirchhoff's diffraction theory, treating the roughness as a stationary random function given by Ornstein-Uhlenbeck process. Scattered light is separated to $R$- and $D$-comp. the former corresponds to sheen and its brightness is given as a function of incident angle $\psi$ by

$$\exp\left(-\frac{16\pi^2h^2}{\lambda^2}\cos^2\psi\right) .$$

$D$- comp. is the part that represents scattered light.

## § 1. Introduction

The light incident upon a rough surface is scattered to every direction. The intensity of light reflected at the specular angle is a measure of gloss of the surface and is called specular gloss. When the angle of incidence is glazing, intensity at the specular angle is distinctly increased. This is a different kind of gloss and is called sheen gloss¹⁾.

Barkas²⁾ had given a theory of diffuse reflection of papers based on geometrical optics and separated each scattered light beam to specular and diffuse component. The specular component is the one which is reflected by mirror facets distributed on the surface of the paper and follows the Fresnel's formula. The diffuse component is the one which is scattered by particls in the interior of the paper and obeys the Lambert's low. Kurita, Yano and the authers³⁾ have pointed out that although the Barkas' theory is formally applicable to matt papers²⁾⁴⁾, it can not be applied to glossy papers because the diffuse component calculated by his theory takes even a negative value. The analysis indicates that at least for grazing incidence, so called specular components do not follow the Fresnel's formula. We⁵⁾ also pointed out in the case of coated papers that the intensity at the specular angle considerably increases as the angle of incidence increased, the rate of increase being larger than that expected from the Fresnel's formula. These results are related with sheen. Accordingly sheen should be explained by wave optics.

Jentzsch⁶⁾ pointed out that some rough surfaces behave like smooth surfaces when the angle of incidence is larger than the critical angle and derived the following relation from the viewpoint of the Rayleigh's limit:

$$2h'\cos\theta_c=\lambda/4 .$$

Here $\theta_c$ is the critical angle, $h'$ the roughness height of the surface and $\lambda$ the wave length of light. There are a few papers in which the discussion concerning sheen gloss and the critical angle are given.

We have investigated experimentally, for metals, relations between the critical angles and the roughness of surfaces and the intensity of scattered light near the critical angle, then explained them by the wave optical theory similar to that given by Davies⁷⁾.

## § 2. The Measurement of Critical Angles⁸⁾

The method is the same as that of Jentzsch. Fig. 1 is the essentials of the apparatus used. The test pattern is a set of narrow slit drawn on a silvered glass plate by the intervals of 0.1 mm. The test pieces are situated between microscope objective and eye-piece. The angle of incidence can be freely changed, keeping the angle of view the same as the angle of incidence. When the angle of the centre line of the eye-piece coincide with the critical angle, images of slits in the left half of the field of view are sharp because the angle of reflection exceeds the critical angle, and images in the right half are diffuse in contrast with them. By such a way the critical angle can be determined.

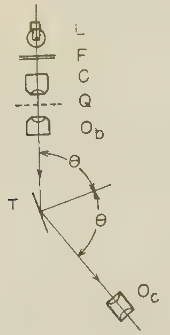

Fig. 1. Apparatus for the measurement of the critical angle.
L: Light source. F: Filter (Corning glass λ550 mμ). C: Condenser lens. Q: Test pattern. T: Sample. Ob: Microscope Objective (10×). Oc: Ocular (5×).

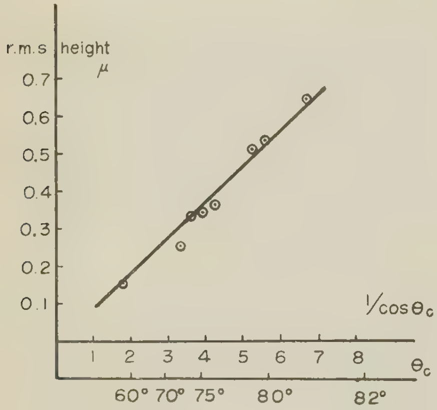

Fig. 2. Relation between r.m.s. height and critical angle.

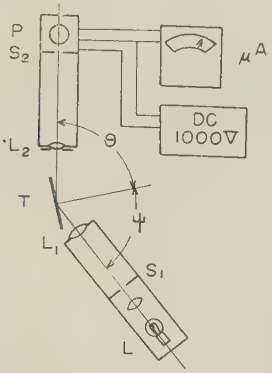

Fig. 3. Goniophotometer.
P: Photomultiplier 931. $S_2$: Slit 1.5 mm width. T: Sample. $L_2$: Lens with aperture stop φ10 mm *f*, 14.5 cm. $L_1$: Lens φ60 mm *f* 18 cm. $S_1$: Slit 1.5 mm width. L: Light source.

Test pieces used are steel plates lapped by $Al_2O_3$ powder of different grain size. The r.m.s. roughness $h$ of plates are measured by an Abott's profilometer.

The relation between $\theta_c$ and $h$ obtained is given in Fig. 2, the abscissa being written in scale of $1/\cos\theta_c$. From the inclination of the line, the following formula is obtained:

$$2h\cos\theta_c=\lambda/k \qquad (1)$$

Here $k$ is a constant and for steel $k=3$.

The similar experiment by the other test pieces show that the constant $k$ is not always the same but changes from metal to metal and also by the lapping process of the samples, for example for steel polished with sand paper $k=2.2$ and for chrome plated brass $k=2$.

It should be noted here that the effective light beam for observation is not absolutely parallel one but has the angle subtended by the pupil to the point in the range of clear vision, i.e., about 30′∼1°.

## § 3. The Measurement by a Goniophotometer[9)]

Fig. 3 gives the goniophotometer used. The light source is a small lamp having a linearly wounded filament and the receiver is a 931 photomultiplier tube fed by a stabilized source. The out put current is read by microammeter directly. The flux reaching the receiver is limited to an angle of 40′ by a slit of 1.5 mm width at $S_2$ and the incident flux has an angle of 30′ depending on the size of the slit $S_1$. The dimention of the optical system is carefully selected so that the brightness is directly read.

By this apparatus, the intensity of the light at the specular direction vs. the incident angle (named the curve of sheen) and the intensity of scattered light near the critical angle vs. the angle of incidence (named the goniophtometer curve) is measured. The test pieces are the same as that used in the preceding measurement.

Fig. 4 shows the curves of sheen taken with lapped steel surfaces, the intensity being written by log-scale with arbitrary unit. Each curve consists of two straight lines, crossed just at the critical angle of each test pieces.

The same charactor of curves are seen by the other test pieces, such as ones made of chrome plated brass or of ground glass.

The goniophotometer curves are taken fixing the receiver angle at $\theta_c$, $\theta_c+5°$ and $\theta_c-5°$, and changing the angle of incidence from the specular direction toward a smaller angle. Some examples of the curves taken are given in Fig. 5, abscissa $\varphi$ indicating the differences between the angle of the receiver and the angle of incidence. The intensities are also given by log-scale. When the angle of specular reflection exceeds the critical angle, the curves $(\theta_c+5°)$ consist of two part. The one, named *R*-comp., appearing only in the vicinity of the specular reflection, has a strong intensity. The half width of them may be very small, but the accurate value can not be known due to the insufficient resolving power of our apparatus. The other component, named *D*-comp., extends over a wider angular range. The log. intensity of it decreases linearly with $\varphi$. The intensity of the *R*-comp. decreases as the angle of receiver approaches to the critical angle and nearly vanish as the former reaches the later. The curves $\theta_c-5°$ consists of *D*-comp. only. In general the inclination of *D*-comp. differs by $h$ as well as by the methods by which they are prepared.

## § 4. Theoritical Consideration

If we limit the problem to the case of metals and approximate them as perfect conductors, the approximation of the Kirchhoff's diffraction theory is applicable. This means that the polarization of reflected light and the variation of intensity with incident angle is neglected. Davies had given a theory for the reflection of wave by this approximation. We have used his theory making a little modification on the statistical property of the surface, and limiting to the case that the receiver is in the plane of incidence.

Metal surfaces prepared by the methods such as lapping, grinding and paper polish have irregular profile and the height $z$ of any point $(x, y)$ should be given statistically. A necessary and most simple model of such a surface is to take $z$ as a random variable obeying the stationary linear Markov process. That is, a surface is considered to be given by the probability density $P(z)$ and the correlation coefficient $\langle zz' \rangle = h^2\rho(r)$, $r$ being the distance of two point $(x, y)$ and $(x', y')$.

It will further be assumed that the distribution of height $z$ is Gaussian:

$$P(z)=\frac{1}{h\sqrt{2\pi}}\exp\left(-\frac{z^2}{2h^2}\right) \qquad (2)$$

$h$ is the r.m.s. value of the roughness of the surface. There is no experimental data for the correlation function $\rho(r)$. In the following calculation it is assumed for the sake of simplicity that the correlation exists only in the direction of $x$. It is also assumed that the process is that of the stationary Markov's. Then the distribution is that of the Ornstein-Uhlenbeck process* and the correlation coefficient is given by:

$$\rho(r)=\exp\{-\beta|x'-x|\}\,. \qquad (3)$$

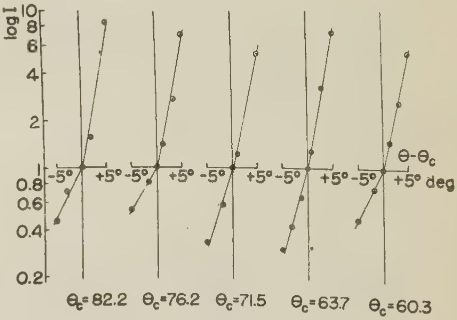

Fig. 4. Curves of sheen.

Then the conditional probability density $P(z, z', r)$, the probability of finding $z'$ at $(x', y')$ when $z$ at $(x, y)$ is given, can be written by the general theory of probability as follows:

$$P(z, z', r)=\frac{1}{\sqrt{2\pi}\,h(1-\rho^2)^{1/2}}\times\exp\left\{-\frac{(z'-z\rho)^2}{2h^2(1-\rho^2)}\right\}. \qquad (4)$$

Thus the surface is represented by two constants $h$ and $\beta$. The former is the r.m.s. height and is easily measureable, but the later is completely unknown. The further consideration shows that $h\beta$ indicates the mean inclination of the profile of the surface. It is known from the roughness curves that the order of magnitude of the inclination of metal surface is generally 0.1 radian or less. In general the length $1/\beta$ is much shorter than the aperture diameter of the optical system.

---

* This assumption is different from that of Davies'.

Consider a plane wave obliquely incident on a rough rectangular reflector of dimensions $2L$ and $2M$, the plane of incidence being parallel to the side $2L$. If we take $\psi$ as the angle of incidence, $\theta$ as the angle of scattering, $C$ as the amplitude of incident wave and $x, y$ as the rectangular coordinate taken on the mean surface, $x$ being parallel to the side $2L$. Then as in the usual diffraction problem, the field $E$ at a distance $R$ is: putting

$$\left.\begin{aligned} q&=\frac{2\pi}{\lambda}(\sin\theta-\sin\psi)\\ p&=\frac{2\pi}{\lambda}(\cos\theta+\cos\psi)\end{aligned}\right\} \tag{5}$$

$$f=-\frac{iC}{4\pi R}\left(q\frac{dz}{dx}+p\right)\cdot\exp i(qx+pz) \tag{6}$$

$$E=\int_{-M}^{M}dy\int_{-L}^{L}dx\, f(x, y, z)\,. \tag{9}$$

The intensity of the light is given by

$$I=|E|^2/8\pi\,.$$

We are interested to the statistical mean valus $\langle E\rangle$ and $\langle I\rangle$, as $z$ is the random function. The average is taken over an ensemble of such reflectors, all having the same statistical properties. It will be assumed that this ensemble average is the same as the time average:

$$\begin{aligned}\langle E\rangle&=\left\langle\iint f(x, y, z)dxdy\right\rangle\\ &=\iint\langle f(x, y, z)\rangle dxdy\end{aligned} \tag{8}$$

It is evident that

$$\langle|E|^2\rangle=\langle E\rangle^2+\langle|E-\langle E\rangle|^2\rangle \tag{9}$$

The statistical mean of $dz/dx$ is zero. If the correlation of $dz/dx$ be assumed zero, the calculation can be furnished by a similar method to that of Davies':

$$\begin{aligned}\langle E\rangle&=-\frac{iCMp}{2\pi R}\int_{-L}^{L}\exp(iqx)\,dx\\ &\quad\times\int_{-\infty}^{\infty}P(z)\exp(ipz)dz \qquad (10)\\ &=E_0\exp\left(-\frac{p^2h^2}{2}\right) \qquad (11)\end{aligned}$$

The exponential factor is the Fourier's transform of $P(z)$. $E_0$ is given by putting $z=0$ in the above equation (10) and is the amplitude of diffraction pattern by the slit of the width $2L$.

$$E_0=\frac{iCMp}{\pi R}\,\frac{\sin qL}{q} \tag{12}$$

As $2L$ is sufficiently large, the fringe has a very narrow width in the vicinity of specular direction, i.e, $q=0$. $\langle E\rangle$ has the pattern of $E_0$ modified by the factor $\exp(-p^2h^2/2)$ which practically does not influence the width of the pattern. Thus the component of the intensity corresponding to $\langle E\rangle$ appears, speaking in a sense of geometrical optics, only in the direction of specular reflection and may be called the $R$-comp. as it corresponds to that of the experiment.

Furthermore, taking into account:

$$\int P(z, z', r)\exp(-ipz')dz'=\exp\left\{-\frac{p^2h^2}{2}(1-\rho^2)-ip\rho z\right\} \tag{13}$$

$$\begin{aligned}\langle|E-\langle E\rangle|^2\rangle&=\frac{c^2M^2p^2}{4\pi^2R^2}\int_{-L}^{L}\int_{-L}^{L}dxdx'\exp\{-q(x'-x)\}\\ &\quad\times\iint dzdz'P(z)P(z, z', r)\{\exp(ipz)-\exp(-p^2h^2/2)\}\{\exp(-ipz')-\exp(-p^2h^2/2)\}\\ &=\frac{c^2M^2p^2}{4\pi^2R^2}\int_{-L}^{L}\int_{-L}^{L}dxdx'\exp\{-q(x'-x)\}\exp(-p^2h^2)\{\exp(p^2h^2\rho)-1\}\,.\end{aligned} \tag{14}$$

We can expand the exponential term as follows:

$$\exp(p^2h^2\rho)=\sum_{n=0}^{\infty}\frac{(p^2h^2)^n}{n!}\exp\{-n\beta|x'-x|\} \tag{15}$$

Hence

$$\begin{aligned}\langle|E-\langle E\rangle|^2=\frac{c^2M^2p^2}{4\pi^2R^2}\exp(-p^2h^2)\sum_{n=1}^{\infty}\frac{(p^2h^2)^n}{n!}\Bigg[&\frac{4n\beta L}{n^2\beta^2+q^2}-\frac{2(n^2\beta^2-q^2)}{(n^2\beta^2+q^2)^2}\\ &+2\exp(2n\beta L)\frac{(n^2\beta^2-q^2)\cos 2qL-2n\beta q\sin 2qL}{(n^2\beta^2+q^2)^2}\Bigg]\,.\end{aligned} \tag{16}$$

We can neglect the 2nd and 3rd terms as $L \gg 1/\beta$.

$$\langle|E-\langle E\rangle|^2\rangle = \frac{c^2M^2L}{\pi^2R^2}\frac{1}{\beta}\exp(-p^2h^2)\sum_{n=1}^{\infty}\frac{(p^2h^2)^n}{n\cdot n!}\frac{1}{1+q^2/n^2\beta^2} \tag{17}$$

The intensity corresponding to $\langle|E-\langle E\rangle|^2\rangle$ has a maximum at $q=0$ and distribute to a wide range of $q$, and may be called the $D$-comp.. The total intensity distribution of the light scattered from a fixed area are given by taking a proper constant $I_0$:

$$\langle I\rangle = \langle I\rangle_1 + \langle I\rangle_2 = \frac{\lambda^2}{16\pi^2}I_0 p^2\exp(-p^2h^2)\left[\frac{\sin^2 qL}{q^2L^2} + \frac{1}{L\beta}\sum_{n=1}^{\infty}\frac{(p^2h^2)^n}{n\cdot n!}\frac{1}{1+q^2/n^2\beta^2}\right] \tag{18}$$

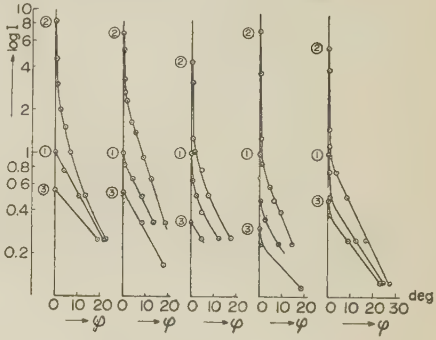

① $\theta_c$, ② $\theta_c+5°$, ③ $\theta_c-5°$

Fig. 5. Goniophotometer curves.

The intensity given by (18) is that of the total flux of scattered light from a given area, and consequently the brightness $B$ is given dividing it by $\cos\theta$.

$$B = \langle I\rangle/\cos\theta\,. \tag{19}$$

If the eye or the photocell receives a reflected light beam covering an angular range from $\theta_1$ to $\theta_2$, the intensity measured is given by

$$\bar{I} = \int_{\theta_1}^{\theta_2}\langle I\rangle d\theta \tag{20}$$

or

$$\bar{B} = \int_{\theta_1}^{\theta_2}\frac{\langle I\rangle}{\cos\theta}d\theta\,. \tag{21}$$

## § 5. Comparison with Experiment

For the comparison of the experiment with the theory, we have to estimate the angular aperture of the light beam received. If the slit at the focal plane of the receiver lens has a width $d$, the light beam received has angular aperture $2\varepsilon$:

$$2\varepsilon = d/f \tag{22}$$

$f$ is the focal length of the lens.

Then the intensity measured at the specular direction is:

$$\bar{I} = 2\int_{\psi}^{\psi+\varepsilon}(\langle I\rangle_1 + \langle I\rangle_2)d\theta \tag{23}$$

$\varepsilon$ being considered small.

Since the width of the $R$-comp. is much smaller than $\varepsilon$, the 1st term of (23) can be approximated as follows:

$$dq = \frac{2\pi}{\lambda}\cos\psi\, d\theta$$

$$\frac{\lambda^2 I_0}{16\pi^2}\int_{\psi-\varepsilon}^{\psi+\varepsilon}p^2\exp(-p^2h^2)\left(\frac{\sin qL}{qL}\right)^2 d\theta$$

$$= \frac{\lambda^2}{16\pi^2}\frac{\lambda I_0}{\pi L\cos\psi}p_0^2\exp(-p_0^2h^2)$$

$$\times\int_0^{\infty}\left(\frac{\sin qL}{qL}\right)^2 d(qL)$$

$$= \frac{\lambda}{2L}\frac{I_0}{\cos\psi}\cos^2\psi\exp(-p_0^2h^2) \tag{24}$$

here $\qquad p_0 = 4\pi\cos\psi/\lambda\,.$ (25)

The 2nd term of $\langle I\rangle$, although has a maximum at $q=0$, is not so sharp as the 1st term and may be put constant in the range $\varepsilon$ as 1st approximation. We obtain the intensity corresponding to the $D$-comp., substituting the 2nd term of integral (23) by the value of $(\langle I\rangle)_{q=0}$ multipled by $2\varepsilon$ as 1st approximation.

i.e. $\quad \dfrac{\lambda^2}{16\pi^2}2\varepsilon I_0 p_0^2\exp(-p_0^2h^2)\dfrac{1}{L\beta}\displaystyle\sum_{n=1}^{\infty}\frac{(p_0h)^n}{n\cdot n!}\,.$

(26)

The total brightness $\bar{B}$ is:

$$\bar{B} = \frac{L_0\lambda}{2L}\left\{B_1 + \frac{4\varepsilon}{\beta\lambda}B_2\right\} \tag{27}$$

$$B_1 = \exp(-p_0^2h^2) \tag{28}$$

$$B_2 = \cos\psi\exp(-p_0^2h^2)\sum_{n=1}^{\infty}\frac{(p_0^2h^2)^n}{n\cdot n!} \tag{29}$$

$B_2$ can be expressed by the exponential integral $\overline{E_i}(\xi)$:

$$\overline{E}_i(\xi)=\sum_{n=1}^{\infty}\frac{\xi^n}{n\cdot n!}+C\xi\ . \qquad (30)$$

For small values of the argument, $\overline{E}_i(\xi)$ is given by tables* and for large values of the argument, it is given by an assymptotic series:

$$\overline{E}_i(\xi)=\frac{\exp(\xi)}{\xi}\left\{1+\frac{1}{\xi}+\frac{2!}{\xi^2}+\cdots\right\} \qquad (31)$$

$C$ is the Euler's constant and is 0.577.

If we take $2\varepsilon=40'$, i.e., 1/170 radian, and assume that $1/\beta=5\mu=10\lambda$ as a allowable value, we get the factor

$$\frac{4\varepsilon}{\lambda\beta}\doteq\frac{1}{4} \qquad (32)$$

Curves $B_1+\frac{1}{4}B_2$ are plotted for $h=\lambda/2$ and $\lambda/3.14$ in Fig. 6. It is seen that the curve is represented by bent straight lines, similar to that given by the experiment. The upper line corresponding to $B_1$ decreases rapidly with $\psi$ and the lower line corresponding to $B_2$ changes slowly in the region 1~0.1. Roughly speaking, it can be said that the bending point of these straight lines are the points where $B_1$ takes a negligible value or $\exp(-p_0^2h^2)$ takes value of the order 0.01, i.e.,

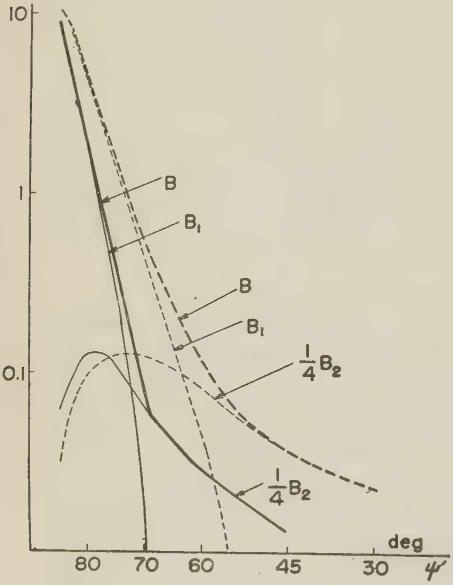

Fig. 6. Calculated curves of sheen.
full lines $h=\lambda/2$, dotted lines $h=\lambda/3.14$

$$p_0^2h^2=\left(\frac{4\pi h}{\lambda}\cos\psi\right)^2=4$$

or

$$\frac{2h}{\lambda}\cos\psi\doteq1/3\ . \qquad (33)$$

The relation (33) coinside with (1), which we have gotten experimentally for lapped steel samples. Such a perfect coinsidence may be accidental because we have made many assumption in the course of calculation.

The goniophotometer curves are given by plotting (18) as a function of $\theta$ of $\psi$ fixing $\psi$ or $\theta$. The $R$-comp. given by the 1st term exists in a very narrow region at the direction of $\theta=\psi$ only. When $\psi$ is smaller than the critical angle, the magnitude of the 1st term is smaller than the 2nd term as discussed by the preceding calculation. This is the case of our experiment.

The $D$-comp. of the experiment (Fig. 5) are given by the 2nd term of (18). The slope of lines takes any values as desired by the proper choice of the unknown constant $\beta$, so it will be meaningless to calculate the slope of each individual curve. If we assume a value 5~10 $\mu$ for $1/\beta$, the 2nd term reprents a curve close to that of the experiment. Thus qualitatively it may be said that the above theory agrees with the experiment.

## §. 6. Discussion

The $R$-comp. concern only with $P(z)$ and not with $\rho(r)$. The amplitude of the reflected light may be obtained as the Fourier transform of the probability density. If we assume some distribution $P'(z)$, differing a little to that of the Gaussian, and suppose the Fourier transform of it as $Q(p^2h^2)$, then we have to put $Q(p^2h^2)$ instead of the exponential term in the equation (11) for the $R$-comp.. While the charactor that the $R$-comp. decreases rapidly by the increase of $ph$ is reserved. This is the case of the most of the metal surfaces.

$D$-comp. are obtained taking into account the correlation of the distribution of the height of each point on the surface. The $1/\beta$ in (3) is a measure of the range where the correlation extend. The coefficient of $D$-comp. is smaller than that of $R$-comp. by the ratio $1/\beta:L$ as indicated by the result (18). If we assume the other correlation than (3), the expression of $B_2$ may change and it will be characterized by a constant other than $\beta$. If we indicate the range of the correlation in this case as $1/\beta'$, which is of the order of $1/\beta$ the coefficient of $B_2$ may be the order of $1/\beta L$ as expected from the physical meaning of the term.

---

* e.g. Jahnke and Emde, Tab. of Functions, p. 82 (1933).

Thus the appearence of sheen gloss (or *R*-comp) and the sharp bend of goniophotometer curve may be similar to that we have calculated. The critical angle is defined by the bending point. The numerical value in the equation (33) corresponding to the constant $k$ in the equation (1) may differ by the nature of the roughness or the nature of the surface.

Our calculation includes other basic assumption. We have assumed that no shadow effect is present, e.g. that the incident ray reach to every point of the surface being undisturbed by the neighbouring peaks and that the reflected ray does not strike the neighbouring surface. This may be the most common case of the scattering by metal surface as the roughness slopes of them are generally small. But for the case of grazing angle some error are expected from this factor. We have assumed also one directional correlation (3) for the surface. This may influence the numerical values given in the § 5.

## § 7. Conclusions

Experiments related with sheen gloss and a theoretical interpretation of them are given by the following results:

1) The reflected light from a rough metal surface consists of two parts, that is, the one named *R*-comp. which obeys the law of regular reflection and the other named *D*-comp. which constitutes the scattered light.

2) The intensity of the *R*-comp. is given by the probability density of the roughness only. If we assume that the distribution is Gaussian, the brightness of the *R*-comp. is given by

$$\exp\left\{-\frac{16\pi^2 h^2}{\lambda^2}\cos^2\psi\right\}.$$

The variation of intensity by the angle of incidence $\psi$ is much larger than that of Fresnel's coefficient.

3) The *R*-comp. appears only when the incident angle is larger than the critical angle $\theta_c$, and it is too weak to be observed when the incident angle is smaller than $\theta_c$. The relation between $\theta_c$ and the r.m.s. value of roughness $h$ is given by

$$2h\cos\theta_c=\lambda/k$$

where $k=2\sim3$ differing by the difference of material and by the method of machining of surfaces.

4) The appearence of the *R*-comp. is the cause of sheen gloss.

5) The *D*-comp. is due to the existance of the correlation of the height of two points on the surface. The intensity of *D*-comp. is given by the 2nd term of (18), assuming the statistics of the surface as given by the Ornstein-Uhlenbeck process.

### References

1) R. S. Hunter: J. Res. N.B.S. **51** (1937) 19.
2) W. W. Barkas: Proc. Phys. Soc. **51** (1939) 274.
3) T. Kurita, H. Yano, J. Nara and H. Hasunuma: Ōyobuturi (J. App. Phys. Japan) **24** (1955) 318. (in Japanese)
4) V. G. W. Harrison: Brit. J. App. Phys. **1** (1950) 46.
5) H. Hasunuma and J. Nara: Ōyobuturi **24** (1955) 74 (in Japanese)
6) F. Jentzsch: Zeits. tech. Phys. **7** (1926) 310.
7) H. Davies: Proc. Inst. Elect. Eng. **101** (1954) 209.
8) Details were given in Japanese: Ōyobuturi **22** (1953) 389.
9) Details were given in Japanese: Ōyobuturi **24** (1955) 457.

JOURNAL OF THE PHYSICAL SOCIETY OF JAPAN Vol. 11, No. 1, JANUARY, 1956

# A Cloud Chamber Study of the Cosmic-Ray Hard Showers

By Saburo MIYAKE, Kensaku HINOTANI,
*Institute of Polytechnics, Osaka City University*
and Kan-ichi NUNOGAKI
*Faculty of Science, Osaka University*

(Received March 2, 1955)

Cosmic ray hard showers produced in iron and in lead have been studied by using the multiplate cloud chamber at 2740 m above sea level.

Primary energies of the meson producing showers were estimated from the angular and the momentum distributions of the secondaries by various methods and the results were compared with each other. The observed hard showers were classified according to their median angles.

About half of the showers which belong to the smaller median angle group may be interpreted as that they have been produced at the periphery of the Pb nuclei. They amount to about 20% of total hard showers.

The mean free path for the production of hard showers was obtained as $250\pm50$ gr/cm$^2$ in lead, and the mean free path of the charge exchange scattering of pions was $1.0\pm0.3$ Kg/cm$^2$ in lead for energies greater than 1 Bev.

## § 1. Introduction

The hard showers which are produced by nucleon-nucleus collision have been analysed assuming that the hard showers produced by nucleon-nucleus collision may not be much different from those produced by nucleon-nucleon collision[1]. This treatment, however, may not be appropriate for the energy of the interaction by which only a few mesons are produced, and it is expected that the difference of the character of the hard shower produced by the nucleon-nucleon collision and the nucleon-nucleus collision becomes bigger for the heavier nucleus.

In this paper, some evidences, which show that the above treatment is too simple to understand the hard shower, will be reported. Some of the experimental results will be discussed mentioning that some of the hard showers are plausibly interpreted as to be produced by elementary nucleon-nucleon collisions though they are produced in complex nuclei.

This experiment was performed in the cosmic ray observatory of the Osaka City University at Mt. Norikura (2740 meter elevation) from July to October in 1953.

## § 2. Experimental Arrangement

As shown in Fig. 1, a multiplate cloud chamber arranged beneath a high pressure cloud chamber[2] was used to observe the hard showers.

The hard shower, originated in the iron wall (8 cm thick) of the latter chamber or the iron ceiling (1 cm thick) of the former chamber, was named "Fe shower", and the one originated in five lead plates (1 cm thick) within the former chamber was named "Pb shower".

The cloud chamber was filled with 1.5 atm. argon, the illuminated region of the chamber was 30 cm × 50 cm × 20 cm, and the photographs were taken stereoscopically at an angle of 23° by two cameras.

The cloud chamber was triggered by a coincidence of G. M. counters which are described in the following;

| tray | diameter | length | numbers |
|---|---|---|---|
| **A** | 4 cm | 50 cm | 10 |
| **B** | 2 cm | 25 cm | 17 |
| **C** | 4 cm | 30 cm | 15 |
| **D** | 4 cm | 50 cm | 15 |

The coincidence of at least two G. M. counters in **B**, **C** and **D** and the anticoincidence of **A** was required for the triggering of the cloud chamber. The anticoincidence was to exclude air showers. The coincidence rate of this counter system was about 15/hr.

Each counter tray **B**, **C** and **D** was connected to hodoscope circuits and the hodoscope figures were used in order to check whether the tracks in the chamber were coincident tracks or not.

## § 3. Fe Shower

The Fe showers was defined as those showers which shows more than three tracks of penetrating particles. If a cascade shower originated from same point was seen clearly, it was counted as a penetrating particle.

380 of Fe showers were obtained and examined for the production of Pb showers by the shower particles of Fe shower. 97 of them were analysed in detail to present the following information on Fe showers.

### (A) Multiplicity and angular distribution

Fig. 2 shows the integral multiplicity distribution and the zenith angle distribution of charged secondary particles. The average multiplicity was 2.1±0.2 and the mean angle is 20 degrees. These values have to be corrected for the geometrical condition, as described in § 3 (D).

### (B) Properties of the secondary particles

The shower particles of 97 Fe showers which produce 44 nuclear interactions in lead plates are listed.

| | |
|---|---|
| charged | 30 |
| neutral | 11 |
| questionable | 3 |

This gives some information on the meson components of the secondaries. If the number of protons is equal to that of neutrons and events with neutral primaries are due to neutrons, and the nuclear interaction mean free path of nucleon and mesons are equal³⁾, the fraction of the charged meson component in the charged secondaries is given as follows,

$$\frac{\pi^{\pm}}{\text{charged secondaries}}=\frac{30-11}{30}=0.63\pm0.20.$$

It is possible to estimate that the number of neutral pions was 57 from the number of cascade showers. By combining this with the number of charged mesons estimated as 126 from the above fraction, we obtained;

$$\pi^0/\pi^{\pm}=0.45\pm0.15\ .$$

These results show that about 60% of charged secondaries were pions and the rest were protons⁴⁾, and that number of neutral pions was about half of charged ones.

The mean free path of these charged shower particles for nuclear interaction was estimated as 250±50 g/cm² in lead, by using the length of traversing lead plates and the number of the events. This value does not include nuclear scattering or small energy events which are not observed, and it will be seen that the cross section of the total nuclear interaction of the shower particle is not so different from the geometrical one.

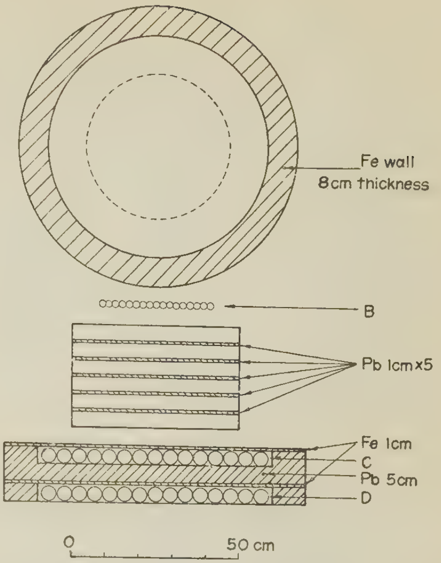

Fig. 1. Experimental arrangement for investigation of hard showers observed in normal pressure cloud chamber.

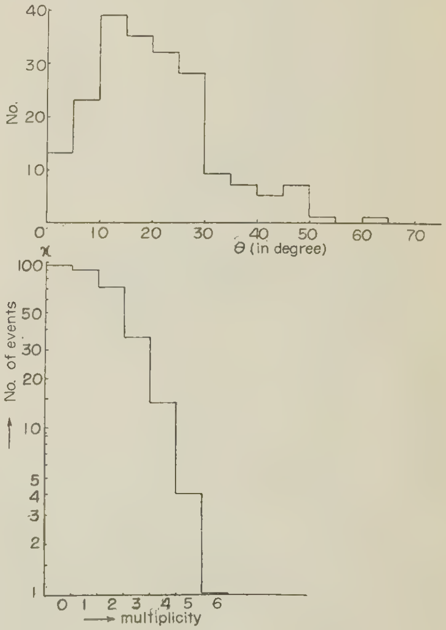

Fig. 2. Angular distribution of secondaries and integral multiplicity distribution of Fe showers.

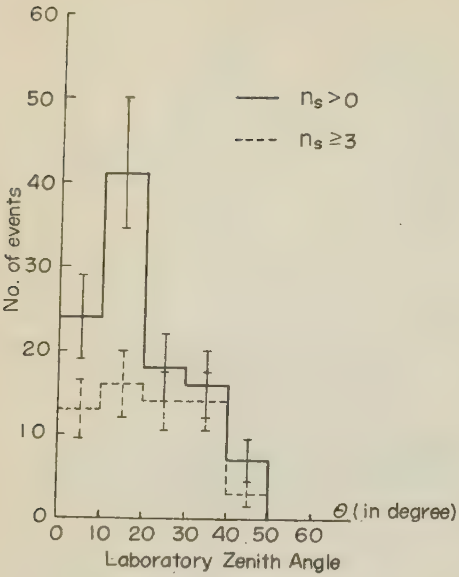

Fig. 3. Zenith angle distribution of the primary particles of Pb showers.

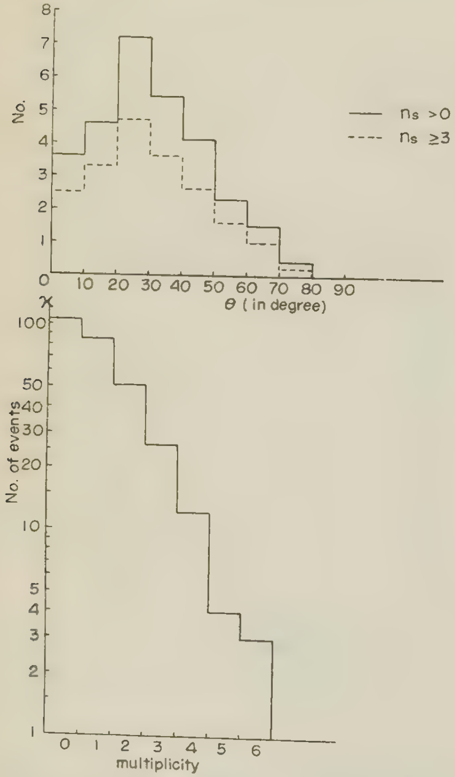

Fig. 4. Angular distribution of secondaries and integral multiplicity distribution of Pb showers.

(C) Energy distribution of the shower particles

Energy distribution was obtained by measuring the scattering in lead plates[5]. The result is shown in the following table. The shower particles were divided into two groups according to the mean zenith angle of the shower.

| group | | momentum range<br>below<br>500 Mev/c | <br>500 to<br>1000 Mev/c | <br>above<br>1 Bev/c |
|---|---|---|---|---|
| I | 0° to 20° | 20% | 30% | 50% |
| II | 20° to 30° | 33% | 44% | 23% |

(D) Estimation of the primary energy of Fe shower from the angular distribution

By the well known relation of nucleon nucleon collision[1]

$$\tan(\theta_{1/2})=1/\gamma$$

the primary energy was estimated by the median angle of the secondaries.

For group I, including showers with a median angle of below 20°, $\gamma_c$ was estimated as 5. But, it must be corrected for the particles which were missed. Assuming that the angular distribution of the shower secondaries is proportional to $\cos^n\theta$, the correction has been done and the corrected value of $\gamma_c$ was 4.3. Thus, it was estimated that the apparent average energy was 35 Bev for the primary energies of Fe showers.

## §4. Pb Shower

167 of Pb showers were produced by shower particles of 380 Fe showers. Definition of Pb shower is similar to one of Fe shower.

(A) Properties of the Pb shower primaries

The primaries of the Pb showers are consist of 120 charged and 47 neutral particles. The fraction of the meson component of the charged primaries was estimated as 0.60±0.07 from similar consideration described in § 3 B.

The zenith angle distribution of these primaries was shown in Fig. 3. These angles were real zenith angles using the stereoscopical measurement. In the case of neutral primary of Pb shower, the direction which connects the both origins of the Fe and Pb shower was used as the trace of the neutral shower particle if it was consistent with the axis of the secondary flux of Pb showers.

The events, in which the direction of the primaries was ambiguous, and the one which occurred in the border of the illuminated region or in the last Pb plate, were excluded and 107 events were used for the discussion which will be mentioned in later sections.

Table I.

| | Group | | | |
|---|---|---|---|---|
| | **I** | **II** | **III** | **IV** |
| Median angle | 0°~20° | 20°~30° | 30°~40° | >40° |
| No. of events | 17 | 37 | 33 | 20 |
| Average multipicity | 2.4<br>3.8 | 2.8<br>3.8 | 2.8<br>3.9 | 2.7 (total)<br>4.0 ($n_s \geqq 3$) |
| $\frac{\text{No. of } \pi^0}{\text{No. of p.p.}}$ | 0.20 | 0.16 | 0.15 | 0.14 |
| $\gamma_c$ estimated by $F$-plot | 5 | 2.3 | 1.5 | — |
| $\cos^n\theta$ | 3.3 | 2.1 | 1.3 | — |
| §4. (**D**). (1) | 2.2 | 1.5 | 1.1 | — |
| §4. (**D**). (2) | 2.8 | 2.0 | 1.5 | — |

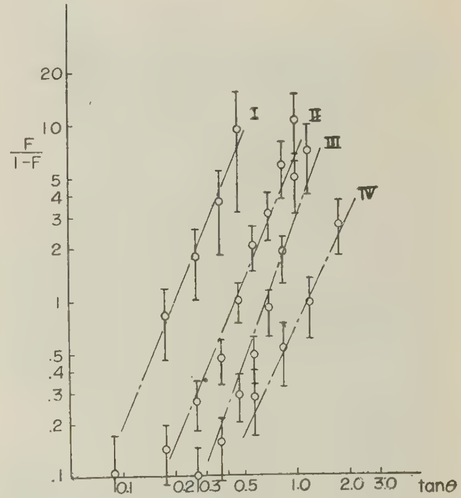

Fig. 5. F-plots for showers originating in Pb for each group.

(**B**) Multiplicity and angular distribution

The integral multiplicity distribution and the distribution of the angles between the incident particles and the charged secondaries are shown in Fig. 4. The angle was derived from each zenith and azimuthal angles by the formula of the spherical trigonometry.

The average multiplicity and the mean angle of the charged secondaries were 2.7±0.3 and 30.5°±1.5° respectively. The average projected angle between the incident and the secondaries was 20.5°±1.0°. From the comparison of the mean angle and the mean projected angle it is concluded that the observed charged secondaries were emitted uniformly in azimuthal angle.

The events, which have at least 3 secondaries, were classified in four groups by the median angle, namely, 0° to 20°, 20° to 30°, 30° to 40° and more than 40° respectively. The average primary energy of each group has been estimated in the following.

(**C**) Energy estimation of the showers from the angular distribution[1)]

Assuming the shower particles are emitted isotropically in c.m.s. and $\beta_c/\beta_\pi=1$, (where $\beta_c$ =velocity of c.m.s. and $\beta_\pi$=velocity of the secondary particle in c.m.s.) the following equation was obtained,

$$\tan^2\theta=\frac{F(\theta)}{\gamma_c^2(1-F(\theta))}\ . \qquad (1)$$

In this equation, $F(\theta)$ is the fraction of the particles emitted within the angle $\phi$ in c.m.s. and is given by $F=\sin^2(\phi/2)$ and $\gamma_c=1/(1-\beta_c^2)^{1/2}$. $\theta$ is the angle of emission in l.s. related to the angle $\phi$ by the following formula

$$\tan\theta=\tan(\phi/2)/\gamma_c\ . \qquad (2)$$

$F(\theta)$ for each group are plotted in Fig. 5. When the shower is not isotropic but is symmetry for the forward and the backward direction in the c.m.s., $\gamma_c$ is determined from $F=1/2$. The average apparent energies of the showers for each of these groups are estimated and listed in Table I. Geometrical correction has been done on the basis of assumption that the angular distribution is $\cos^n\theta$.

(**D**) Energy estimation of the shower by scattering measurement

Momenta of the secondary particles were measured using the multiple scattering by lead plates (11.3 g/cm² per one sheet) in the chamber, and those of each group were classified into several subgroups by their real

Table II. The $p\beta$ distribution of the shower particles from scattering measurement. (in Mev/c)

| Group | Emitted angle 0°~10° | 10°~20° | 20°~30° | 30°~40° | 40°~60° | >60° |
|---|---|---|---|---|---|---|
| I | 807 | 403 | 278 | | — | — |
| II | 550 | | 530 | 320 | 330 | |
| III | 755 | | 581 | 515 | 490 | 432 |

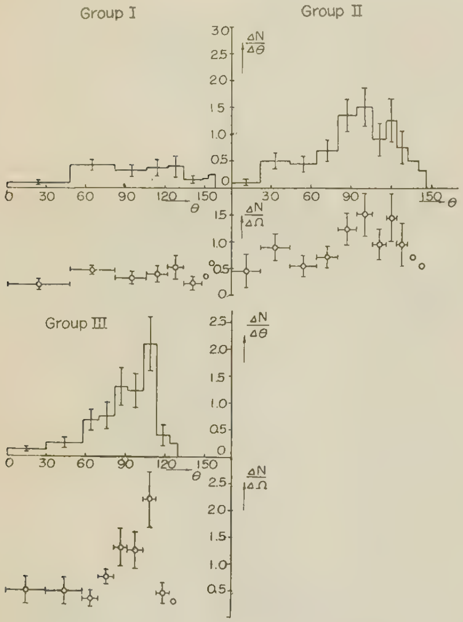

Fig. 6. Differential angular distribution of the secondary particles in the center of mass system for lead showers.

angles to the primary. In order to obtain the average $p\beta$ of each subgroup, the mean scattering angles of all tracks which belong to each subgroup were used, except the cases of wider scattering angles than 3 times of the mean value.

Assuming that the all secondaries are pions, the relation between momenta and angles gives the estimates of shower energies by two methods[6], 1) the shower particles are emitted with the uniform energy in c.m.s. and 2) the summation of the momenta of the charged secondary particles on the incident direction is equal to zero in c.m.s.

The results of the energy estimation in both cases are summarized in Table I, and the $p\beta$ distributions of the shower secondaries for each subgroups are given in Table II.

This analysis was carried out assuming nucleon-nucleon collision, but this is not appropriate because there are some indications of nucleon-nucleous collision accordingly the following inconsistencies arose.

**a**) a group of larger median angle has rather higher multiplicity, in spite of the estimated energy being lower,

**b**) as seen from the observed momenta of the secondaries, a group of larger median angle has not necessarily lower average energy,

**c**) when the energy is estimated from the median angle, the group **I** has much higher energy than that obtained by other estimations. (though one of the reason may be statistical fluctuation for grouping)

**d**) in $F$ plot, the slope of the curve for larger median angle group is not consistent with Eq. (1) which shows that the slope must be 2.

(**E**) Properties of Pb showers

1) Angular distribution of the secondaries in c.m.s.

Since the angular distribution of the secondaries in c.m.s. is not clear from $F$-plot, $\Delta N/\Delta\theta$ and $\Delta N/\Delta\Omega$, computed by equation (2), are plotted in Fig. 6.

From these figures, the following features are seen,

**a**) the distribution of the secondaries is not isotropic, but shows somewhat large value in perpendicular direction in c.m.s. to the incident. This tendency is clearly seen in the larger angle group.

**b**) in the smaller median angle group, the distribution seems to have two maxima.

As these features may be due to the successive collisions in the nucleus, the ratio of the frequency of the showers with slow particles to that without them has been figured out. The slow particles are observed as black tracks probably in same bias for each group. According to this result, the smaller median angle group has the larger ratio of the showers containing no slow particle, namely, 50% for group **I**, 25% for group **II**, 30% for group **III** and nearly zero for group **IV**.

2) Number of neutral pions

Measuring the ratio of high energy $\gamma$ rays to penetrating particles the relative number of $\pi^0$ and charged secondaries was estimated[4]. The results are given in Table I, but these ratio may be somewhat smaller by missing low energy $\gamma$ ray and one emitted in wide angle.

It can be seen that the proportion of $\pi^0$ decreases as the median angle increases. This would be also explained by considering that the protons due to successive collisions in lead nucleus may be contained[7].

## § 5. The Charge Exchange Scattering of Pions in Lead

Recently, several results of the experiments[3,8-12] for the charge exchange scattering at various energies were reported. High energy photons arising from the interaction of energetic pion with nuclei are mostly attributed to the charge exchange scattering of charged pions namely, $\pi^+ + N \rightarrow \pi^0 + P$ and $\pi^- + P \rightarrow \pi^0 + N$.

Fermi et al.[8,9] have shown that cross sections for the above processes are nearly equal at energy range 100–200 Mev, and the cross section for the only possible competing processes $\pi^- + P \rightarrow N + \gamma$, $\pi^+ + N \rightarrow P + \gamma$, has a magnitude of only 2% of the charge exchange. Therefore, the possibility that the photon arises from other mechanism was neglected in this case.

The charge exchange scattering events were picked up by the following conditions,

1) The shower particle of Fe shower has to penetrate at least two lead plates without multiplication and, then, start cascade showers.
2) the events must contain neither heavy track nor penetrating particle.

Some of the event, $\pi^+ + N \rightarrow P + \pi^0$ may be missed by the condition 2), but this condition is necessary to exclude the hard shower which may have this appearance.

The events selected by this procedure are also ascertained by studying the other 230 electron showers originated from lead plates in the chamber. The frequency of the electron showers of $\gamma$ ray or electron primary decreases strongly after passing through one sheet of the lead plate to about 15%, and

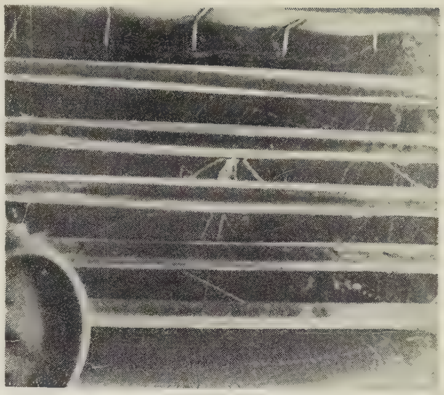

Fig. 7. An example of low energy Pb shower produced by neutron.

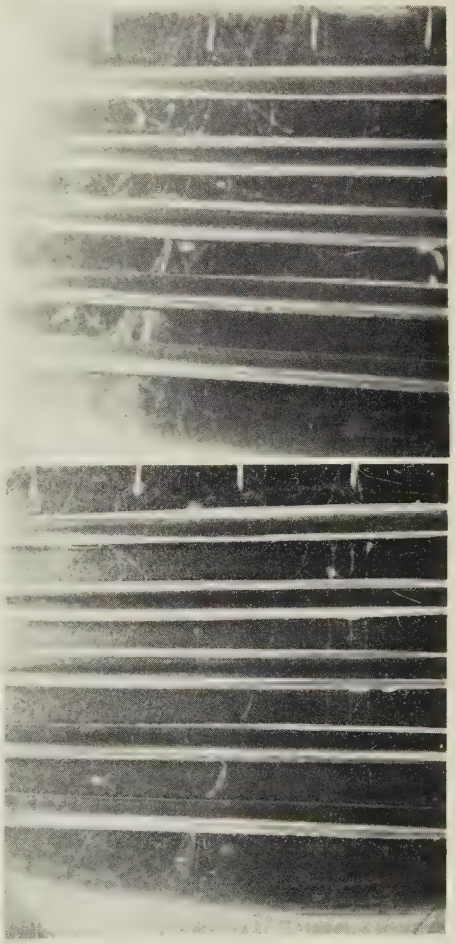

Fig. 8. Two examples of charge exchange scattering.

most of them are not accompanied by Fe shower of the same origin. Then it is possible to estimate the frequency of the charge exchange scattering of pions without contribution of electron initiated showers.

As the results, 10 probable events were observed. The energies of these events were estimated from the size of the cascade showers[13] and the angle of the two cores of the cascade showers, and all events have energies greater than 1 Bev.

As described in § 3, (**B**) and (**C**), pion component in charged secondaries is about 60 %, and about 50% of them have momentum greater than 1 Bev/c. It is concluded that the mean free path of pions of this energy range for the event is 1.0±0.3 Kg/cm².

Lock and Yekutiele[10] have given a large charge exchange cross section (30% geometric) for 160 Mev mesons in nuclear emulsion, and G. Salvini has estimated the cross section for complex nucleus as follows

$$0.16\sigma_{\text{total}} \leqslant \sigma_{\text{ch.ex.}} \leqslant (0.31\pm0.1)\sigma_{\text{total}}$$

for energies 200–1000 Mev. The ratio 0.25 of this event to nuclear interaction, obtained in this experiment, is somewhat lower as compared with these results, although it is contained in this region. It may be explained by considering that the contribution of the hard shower is not so small in this energy region (>1 Bev).

## § 6. Discussion

Since the hard showers, observed in this experiment, were treated as meson producing interaction by the single collision, it is unavoidable that some inconsistencies have resulted. As described in § 4 (**D**), it is not plausible that the high energy hard showers have low multiplicity, even if the energy dependency of the multiplicity is not so strong[14].

It may be plausible to suppose that about half of the events which belong to the groups of smaller median angle were produced by collisions at the periphery of the nucleus. This supposition can be ascertained by the angular distribution of the secondaries and the ratio of the neutral pions to the charged one, described in § 4, (**E**), Most of the showers which belong to the larger angle group are supposed to be nearly head-on collision between the incident particle and the target nucleus. By the successive collisions in the nucleus, it would be expected that the several angular distributions are superposed and the resultant distribution has somewhat large value in perpendicular direction to the incident and the contribution of the recoil protons is also large.

This interpretation shows that the classification of the hard showers in heavy nucleus by apparent median angle is not good enough to classify the energies of the showers in this energy region, but rather proves the aspects of the collisions, without the problem of the fluctuations of the secondary particles.

On the mean free path of the charge exchange scattering, it should be considered that the high energy pion collides with the almost free nucleon at the periphery of lead nucleus, because if such high energy pion collides nearly head-on to the lead nucleus, it will be observed as hard shower.

Under these consideration, it may be concluded that the cross section of the charge exchange scattering in the case of $\pi$-nucleon interaction at this energy region is nearly comparable to that of hard showers, and the probability for single collision is about 20% of the total events in lead.

## § 7. Acknowledgement

The authors are indebted to Professor Y. Watase for his valuable advice and encouragement and express their thanks to Mr. T. Shiota lor his financial support for this work. Thanks are also due to Mr. T. Matano for his invaluable aid during the observation.

## References

1) for an example N. M. Duller and W. D. Walker Phy. Rev. **93** (1954) 215.
2) S. Miyake: to be published.
3) G. Salvini: Nuovo Cimento **10** (1953) 1018.
4) G. Salvini and Y. B. Kim: Phys. Rev. **88** (1952) 40.
5) Rossi and Greisen: Rev. Mod. Phys. **13** (1941) 263.
6) Marshak: "*Meson Physics*" (1952).
7) Carlson, Hooper and King: Phil. Mag. **41** (1950) 701.
8) H. L. Anderson, E. Fermi, D. E. Nagle and G. B. Yodh: Phys. Rev. **86** (1952) 413.
9) H. L, Anderson, E. Fermi, D. E. Nagle and G. B. Yodh: Phys. Rev. **86** (1952) 793.

10) W. O. Lock and G. Yekutiele: Phil. Mag. **43** (1952) 231.
11) J. O. Kessler and Ledermann: Phys. Rev. **94** (1954) 689.
12) Fowler, Fowler, Shutt, Thorndike and Whittmore: Phys. Rev. **91** (1953) 135.
13) R. R. Wilson: Phys. Rev. **86** (1952) 261.
14) E. Fermi: Prog. Theor. Phys. **5** (1950) 570.

# Short Notes

J. PHYS. SOC. JAPAN **11** (1956) 83~84

## On the Impurity Conduction in Germanium

By Yasuo KANAI and Riro NII

*The Electrical Communication Laboratory,*
*Nippon Telegraph and Telephone Public*
*Corporation, Tokyo, Japan*

(Received September 26, 1955)

Recently Hung and Gliessmann1) observed an anomalous behaviour of the Hall coefficient in the course of the investigation of the electrical properties of germanium at very low temperatures. They found that, when the temperature was lowered, the Hall coefficient did not increase infinitely but once reached a maximum value and then began to decrease. Further investigations by them2) and Fritzsche and Lark-Horovitz3) showed that the anomaly of the Hall coefficient was well explained by assuming the existence of the impurity conduction at very low temperatures. In their experiments the impurity is the ordinary donor or acceptor, and the energy difference of the donor or acceptor level from the conduction or valence band is so small that the impurity conduction is observed only at very low (i.e. liquid helium) temperatures. If the other impurity, the level of which lies apart from the bottom of the conduction band or the top of the valence band, is added to germanium, it may be expected that the impurity conduction will occur at higher temperatures.

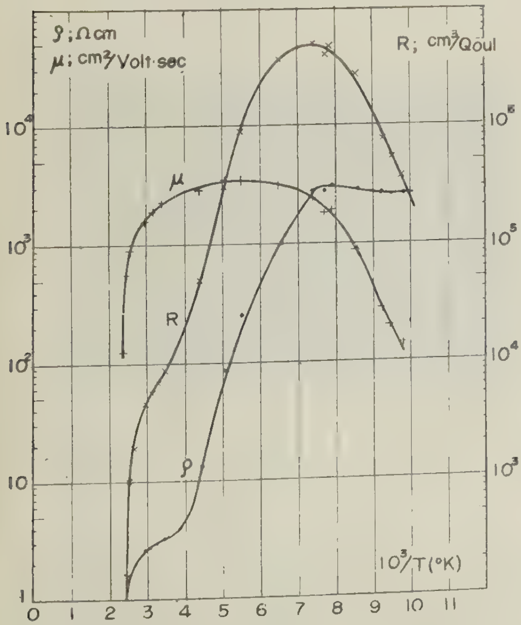

Fig. 1. The resistivity ($\rho$), Hall coefficient ($R$), and Hall mobility ($\mu=R/\rho$) as a function of the inverse absolute temperature. The sample is a nickel-doped $p$-type germanium.

Germanium samples in which nickel4) was added as such impurity have been prepared, and their electrical properties were measured from room temperature to liquid air temperature. The uniformity5) of the samples was checked and the effects of carrier multiplication by the photon or avalanche breakdown were carefully avoided. A typical example of the experimental results on $p$-type sample is shown in Fig. 1, and it shows that the decrease of the Hall coefficient at low temperature occurs. Although the mechanism of the so-called impurity conduction is not clear at present, we shall analyse our data by the conventional method. If we assume that the carrier in the impurity band is hole in this sample, then the conductivity $\sigma$ and the Hall coefficient $R$ are given by the next fourmula;

$$\sigma=e(n_v\mu_v+n_i\mu_i)$$

$$R=e(r_vn_v\mu_v^2+r_in_i\mu_i^2)/(n_vu_v+n_i\mu_i)^2$$

where

$e$; the absolute value of the electronic charge.
$n_i$, $\mu_i$; the density and mobility of the hole in the impurity band.
$n_v$, $\mu_v$; the density and mobility of the hole in the valence band.
$r$; numerical factor which depends upon the statistics and the scattering mechanism of the carrier.

In our experiment, holes in the valence band are scattered mainly by the impurity ions, so $r_v$ is approximately 1.9. But information about $r_i$ is quite insufficient, hence we assume, for simplicity, that $r_v=r_i=1$. Furthermore, if we consider the fact that $n_v+n_i=N$ ($N$; the hole density in the impurity band at 0°K.), then, after simple calculations, the maximum value of $R$ occurs at the condition $n_i\mu_i = n_v\mu_v$, and at this temperature the following simple relations are hold;

$$2R_m\sigma_m = \mu_i + \mu_v \doteqdot \mu_v$$
$$R_mR_S\sigma_m^2 = \mu_i\mu_v$$
$$3.1\times10^{18}\cdot\sigma_m/\mu_i = n_i$$
$$n_i\mu_i/\mu_v = n_v$$

where

$\sigma_m$; the value of the conductivity at which the Hall coefficient has the maximum value $R_m$.

$R_S$; the saturation value of the Hall coefficient at high temperature.

and the units of $\sigma$, $R$, $\mu$ and $n$ are mho/cm., cm³/coulomb, cm²/volt.sec. and no./c.c. respectively.

For example, if we analyse our experimental data by the above formula, the following results are obtained.

$\mu_v \doteqdot 3\times10^3$ cm²/volt.sec.
$\mu_i \doteqdot 1$ cm²/volt.sec.
$n_i \doteqdot 1\times10^{15}$/c.c. at −140°C.
$n_v \doteqdot 3\times10^{11}$/c.c.

Further systematic investigations are now in progress.

## References

1) C. S. Hung and J. R. Gliessmann: Phys. Rev. **79** (1950) 726.
2) C. S. Hung and J. R. Gliessmann: Phys. Rev. **96** (1954) 1226.
3) H. Fritzsche and K. Lark-Horovitz: Physica **20** (1954) 834.
4) J. A. Burton, G. W. Hull, F. J. Morin and J. C. Severiens: J. Phys. Chem. **57** (1953) 853.
5) W. W. Tyler, R. Newman and H. H. Woodbury: Phys. Rev. **98** (1955) 461.

---

J. Phys. Soc. Japan **11** (1956) 84~85

# Pure Quadrupole Spectra of Phosphonitrile Chloride Polymers

By Kazuo Torizuka

*Tokyo Gakugei University, Koganei, Tokyo, Japan*

(Received September 30, 1955)

Nuclear quadrupole resonances of two phosphonitrile chloride polymers, $(PNCl_2)_3$ and $(PNCl_2)_4$, have been measured by the method of frequency modulated super-regenerative detector at room temperature. Crystals of about 2 gram were used as samples. The measured resonance frequencies of $Cl^{35}$ are listed in table I. Among them the resonances of $(PNCl_2)_3$ are doublets. The seperations are about 80 kc/sec for the resonance of 27.87 mc/sec and about 75 kc/sec for the resonance of 27.58 mc/sec. The resonance absorptions of $Cl^{37}$ were also observed at the frequencies expected from the known ratio of the quadrupole moments.1)

Table I. Resonance frequencies of $Cl^{35}$ at 294°K.

| Compound | Frequency |
|---|---|
| 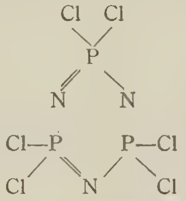 | mc/sec<br>27.80<br>27.58 |
| 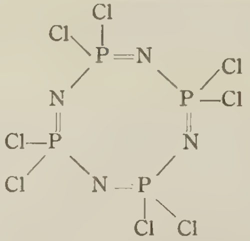 | mc/sec<br>28.14<br>28.02 |

The crystal structure of $(PNCl_2)_4$ has been investigated by Ketelaar and de Vries.2) Their results show that this compound has octagonal type ring structure and for P-Cl distances the two different values of 1.975 A and 2.015 A are given. The above obtained two quadrupole resonance frequencies of this compound will correspond to the two P-Cl distances.

The molecular structure of $(PNCl_2)_3$ has been studied by Brockway and Bright.3) Their results show that this compound has planer benzene-like ring structure and all P–Cl distances have equal value of 1.97 A. However, the quadrupole resonance of this compound has two frequencies and their seperations is larger than in $(PNCl_2)_4$. This suggests that there are two different P–Cl distances in this crystal.

The average value of the two resonance frequencies of $(PNCl_2)_4$ is near the average frequency of $OPCl_3$ quadrupole resonances4) considering the temperature dependence of resonance frequency and P–Cl distances of 1.99 A in $OPCl_3$ is almost equal to the average of the two P–Cl distances in $(PNCl_2)_4$. Also the bond angle Cl–P–Cl is 103.6° in $OPCl_3$5) and 105°30′ in $(PNCl_2)_4$.

Comparing the two average values of the resonance frequencies of $(PNCl_2)_3$ and $(PNCl_2)_4$, the lower value of former compound corresponds the shorter P–Cl distances in the former, and the difference between them is perhaps due to the difference of their ring structures.

The auther expresses his sincere thanks for preparing the sample crystals to Mr. S. Fujii at Tokyo Institute of Technology and to Mr. H. Hamano for his helpfull discussions.

### References

1) Wang, Townes, Schawlow and Holden: Phys. Rev. **86** (1952) 809.
2) Ketelaar and de Vries: Rec. Trav. Chim. **58** (1939) 1081.
3) Brockway and Bright: J. Am. Chem. Soc. **65** (1943) 1551.
4) Livingston: Phys. Rev. **82** (1951) 289.
5) Williams, Sheridan and Gordy: J. Chem. Phys. **20** (1952) 164.

---

J. PHYS. SOC. JAPAN **11** (1956) 85

## Sub-microwave Absorptions in Potassium Bromate

By Yasaburo YOKOZAWA and Itaru TATSUZAKI

*Research Institute of Applied Electricity, Hokkaido University, Sapporo*

(Received October 18, 1955)

We have found many absorption lines in potassium bromate powder by the use of a super-regenerative detector with a transmission line tuned circuit in the frequency range of 120 Mc/s to 270 Mc/s.

The absorption appears weakly at the dry ice temperature and very strongly at the liquid nitrogen temperature. At room temperature such absorptions do not appear. For precise frequency measurement, the autodyne detector is used to exclude the beat frequencies acompanied inherently with the super-regenerative detector. The spectra consist of a great number of lines, the intervals of which vary from about 30 Kc/s to 40 Kc/s at the liquid nitrogen temperature, and the widths of these lines are very sharp as seen in Fig. 1. By lowering temperature these lines shift toward the higher frequency side.

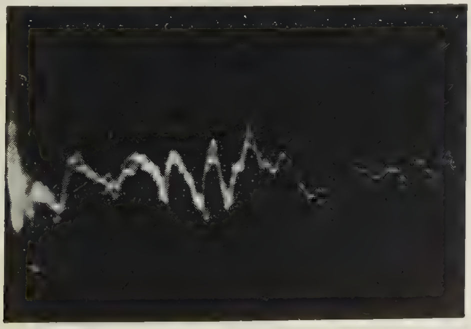

Fig. 1. Pattern for the absorption lines of potassium bromate powder using the autodyne detector. The frequency was swept from the left to the right between 180.21 Mc/s and 179.78 Mc/s.

The potassium bromate is a piezoelectric substance. The similar results were obtained for silver iodine, rochelle salt, zinc sulphide and quartz by S. Kojima and co-researchers1)2) and for levo-chloramphenical by J. Duchesne and A. Monfils3).

The origin of these spectra was considered due to the lattice imperfection by S. Kojima. On the other hand J. Duchesnse and A. Monfils attributed its origin to the lattice vibration in the crystal. However, as pointed above, we could not detect any absorption at room temperature. Furthermore, in spite of quenching at the room temperature after the sample had been heated to 170°C, it showed no absorption at room temperature.

Although there are some new features in potassium bromate different from that of the substances studied by other researchers, the absorption lines seem to be caused by the lattice imperfection as well as the lattice vibration.

In order to clarify the origin of the absorption, further experiments are now planned in broader frequency range.

### References

1) S. Kojima, K. Tsukada, S. Ogawa and A. Shimauchi: Phys. Rev. **92** (1953) 1571.
2) S. Kojima, K. Tsukada, S. Ogawa, A. Shimauchi and N. Matsumura: J. Phys. Soc. Japan **10** (1955) 265.
3) J. Duchesne and A. Monfils: J. Chem. Phys. **23** (1955) 762.

---

J. PHYS. SOC. JAPAN **11** (1956) 85~87

## An Analysis of Two τ-Meson Decays

By Kuni IMAEDA and Mitsuko KAZUNO

*Department of Physics, Faculty of Liberal Arts and Education, Yamanashi University*

(Received August 15, 1955. Revised October 12, 1955)

In the course of the general scanning of Ilford G5 emulsion 600 microns thick exposed at the altitude of 70,000 ft about four hours in England 1954, we have observed two τ-mesons decaying in the emulsion.

τ–1 had the track length of 33.7 mm in 32 emulsion sheets and decayed into three particles. One of the three secondaries showed a typical π-μ-e decay after a total track length of 8.6 mm in 5 emulsion sheets. The track was produced by a positive π-meson. Another secondary left the emulsion stack, after the track length of 9.0 mm

Table I. For $\tau$-1, the energies of the $\pi$-2 and the $\pi$-3 are obtained by the calculation using the observed values of the energy of the $\pi$-1 meson, the angles between $\pi$-1, $\pi$-2 and $\pi$-3 and the momentum balance assuming that $\pi$-2 and $\pi$-3 tracks are produced by $\pi$-mesons.

$R_0$: Observed range in the emulsion.
$R_p$: Range corresponding to the path length in paper.
$N$: Number of the emulsion sheets.

* $\theta$, $\phi$ is the spherical polar coordinates of the direction of emission of the $\tau$-meson from the parent star or the incident direction of the $\tau$-meson onto the emulsion stack, where in the polar coordinate system $x$ and $y$ axis are taken the direction of emission of the negative $\pi$-meson and the direction of the normal to the $3\pi$-decay plane, respectively.

| | Sign | $R_0$ (mm) | $R_0+R_p$ $\times 1.04$ (mm) | $N$ | Energy (Mev) | | Mean Energy (Mev) |
|---|---|---|---|---|---|---|---|
| | | | | | $E$-2 | $E$-3 | |
| $\pi$-1 | + | 8.60 | 9.00 | 5 | 21.53<br>(21.44)* | 22.45<br>(22.35)* | 21.99<br>(21.90)* |
| $\pi$-2 | ? | 3.3 | — | >5 | — | — | 27.90<br>(27.78)* |
| $\pi$-3 | ? | 9.0 | — | 9 | — | — | 24.61<br>(24.51)* |

| Angle | $Q$ (Mev) | $\theta$ | $\phi$ | Note |
|---|---|---|---|---|
| ($\pi$-2, $\pi$-3) = 126° 4′ ± 15′ | 74.4 ± 1.0 | 28° | 95° | if the $\pi$-3 is negative |
| ($\pi$-3, $\pi$-1) = 113° 11′ ± 15′ | | | | |
| ($\pi$-1, $\pi$-2) = 120° 47′ ± 15′ | (74.2 ± 1.0)* | | 69° | if the $\pi$-2 is negative |

Table II. Results obtained for $\tau$-2.

| | Sign | $R_0$ (mm) | $R_0+R_p$ $\times 1.04$ (mm) | $N$ | Energy (Mev) | | | Mean Energy (Mev) |
|---|---|---|---|---|---|---|---|---|
| | | | | | $E$-1 | $E$-2 | $E$-3 | |
| $\pi$-1 | + | 3.51 | 3.65 | 1 | 12.79 | | 13.20 | 13.00 |
| $\pi$-2 | − | 5.97 | 6.26 | 5 | 17.37<br>(17.29)* | | 18.13<br>(18.08)* | 17.75<br>(17.67)* |
| $\pi$-3 | + | 27.0 | 28.34 | 20 | | 43.74<br>(43.61)* | 44.11<br>(43.89)* | 43.93<br>(43.75)* |

| Angle | $p/\sin(\pi, \pi)$ (Mev/c) | $Q$ (Mev) | $\theta$ | $\phi$ |
|---|---|---|---|---|
| ($\pi$-2, $\pi$-3) = 59° 20′ ± 15′ | $p$-1/sin ($\pi$-2, $\pi$-3) = 135.8 | 74.7 ± 0.5 | 83° | 106° |
| ($\pi$-3, $\pi$-1) = 153° 00′ ± 25′ | $p$-2/sin ($\pi$-3, $\pi$-1) = 134.5 | | | |
| ($\pi$-1, $\pi$-2) = 147° 40′ ± 25′ | $p$-3/sin ($\pi$-1, $\pi$-2) = 138.5 | (74.4 ± 0.5)* | | |

in 9 emulsion sheets. The length was enough to decide from the grain density and the scattering that the track was produced by a L-meson.

The third secondary could be followed 3.3 mm in 5 emulsion sheets, but the track was missed at the entrance of the adjoint emulsion sheet.

$\tau$-2 was in a better geometrical configuration than $\tau$-1. (See Fig. I.) It came from the star of type $5+1n$ and had the track length of 40.0 mm in 8 emulsion sheets. All the decay products were stopped in the emulsion stack and it was assured that $\tau$-2 was a positive $\tau$-meson. One of the three secondaries showed a typical $\pi$-$\mu$-e decay after a total track length of 3.51 mm in the same emulsion sheet in which the $\tau$-decay occurred. Another secondary produced a two pronged $\sigma$-star after a total track length of 5.97 mm in 5 emulsion sheets. It was decided that the secondary was a negative $\pi$-meson. One of the two prongs of the star was produced by an $\alpha$-particle of the energy of 17 Mev, and the other of the prongs was produced by a slow electron. It is concluded that the star was the disintegration produced by the absorption of a negative $\pi$-meson by a nucleus in the emulsion. The third secondary showed a typical $\pi$-$\mu$-e decay after a total track length of 27.0 mm in 20 emulsion sheets. All track length measurements in the emulsion plane were made using the Olympus' Ramsden ocular micrometer which was able to measure a length of 1/100 mm in the field of the microscope.

The shrinkage factor was checked by the measurement of the length of the tracks of the $\mu$-mesons of $\pi$–$\mu$–e decay which were nearly vertical to the emulsion plane. The stopping power of the emulsion at the time of the exposure was obtained from the mean track length $\bar{R}_\mu$ of nine flat $\mu$-meson tracks of $\pi$–$\mu$–e decays. The calibration of the range-energy relation was made as follows: we calculated the range of the $\mu$-meson of the energy of 4.12 Mev, by the following range-energy relation,

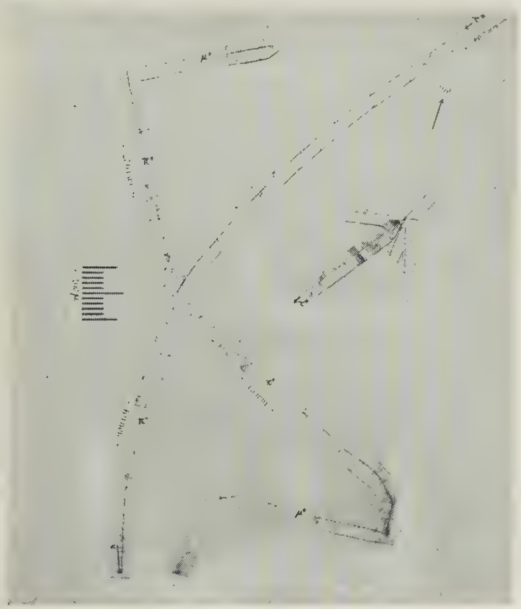

Fig. 1. Microphotograph of the $\tau$–2.

$$4.12\,\mathrm{Mev}=0.276(M_\mu/M_n)^{0\cdot432}(R)^{0\cdot568}\ ,$$

where $M_\mu/M_n=207/1837$ is the ratio of the mass of $\mu$-meson to that of nucleon, and then we have decide the numerical factor $f$ from the mean length $\bar{R}_\mu=590\pm10$ microns of the nine flat $\mu$-meson tracks by the following relation:

$$\bar{R}=fR_\mu\ .$$

The energy of the $\pi$-mesons were calculated using the following range-energy relations according to their length of the $\pi$-meson tracks:

(1) for $fR=0\sim6(M_\pi/M_n)$ mm,
$$E\text{–}1=0.276(M_\pi/M_n)^{0\cdot432}(fR)^{0\cdot568},$$
(2) for $fR=50\sim250(M_\pi/M_n)$ mm,
$$E\text{–}2=0.1605(M_\pi/M_n)^{0\cdot382}(fR)^{0\cdot618},$$
(3) for $fR=6\sim250(M_\pi/M_n)$ mm,
$$E\text{–}3=0.2303(M_\pi/M_n)^{0\cdot411}(fR)^{0\cdot589},$$

where $R$ is the observed length of the $\pi$-meson track, and took the mean of $E$–1 and $E$–3 or $E$–2 and $E$–3.

The results obtained are shown in the following tables:

In the Tables I and II, ( )* are the values obtained from without taking into consideration of the stopping power of the thin sheets of tissue paper between the emulsion sheets[2].

The $Q$-values obtained for $\tau$–1 and $\tau$–2 show rather a good agreement with the values obtained in the other laboratories[1]. The values of $p/\sin(\pi,\pi)$ in the Table II are not in good agreement, but agree within the experimental errors of the energies and the angles.

The authors are grateful to Professor C. F. Powell, Dr. Y. Fujimoto and Professor S. Nakagawa for the supply of the emulsion plates. They are also thanks to the emulsion group of Rikkyō University, who gave us the facility for the measurements, and Mr. T. Ogata, the assistance for the microphotograph and Assistant Professor H. Mōri the constant interest in this work.

This experiment was supported by the Scientific Research Expenditure of Ministry of Education.

## References

1) E. Amaldi et al.: Nuovo Cimento, Suppl. **11** (1954) 419.
2) K. Gottstein: Nuovo Cimento. **1** (1955) 284.

---

J. Phys. Soc. Japan **11** (1956) 87~88

# On the Image of Phase Microscope in Metastable Region

By Shigenori Nawata

*Research Institute for Scientific Measurements, Tōhoku University, Sendai*

(Received November 18, 1955)

Intensity distribution of the image of the phase microscope was calculated. Let $\chi=\beta\exp(-i\varphi)$ for $-a<x_0<0$ and $\chi=\alpha\exp(i\varphi)$ for $0<x_0<a$ as the object and $h\exp(i\delta)$ for the coated function of phase strip, complex amplitude in the neighbourhood $x_0=0$ (metastable region) is given by

$$F=\frac{(\alpha+\beta)}{2}h\cos\delta\cos\varphi-\frac{(\alpha-\beta)}{2}h\sin\delta\sin\varphi$$
$$-\frac{Si(\theta_2)}{\pi}\Big[(\alpha-\beta)\cos\varphi-h\{\alpha\cos(\varphi+\delta)$$
$$-\beta\cos(\varphi-\delta)\}\Big]\pm\frac{(\alpha-\beta)}{2}\cos\varphi$$
$$+i\Big[\Big[\frac{(\alpha-\beta)}{2}h\cos\delta\sin\varphi+\frac{(\alpha+\beta)}{2}h\sin\delta\cos\varphi$$

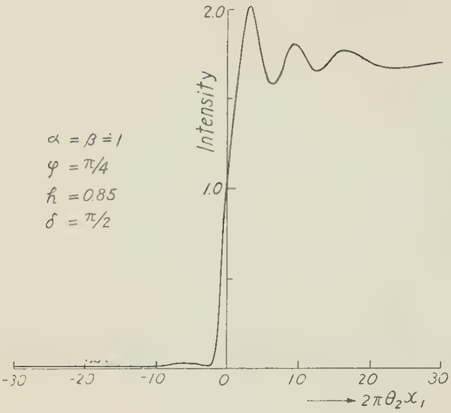

Fig. 1.

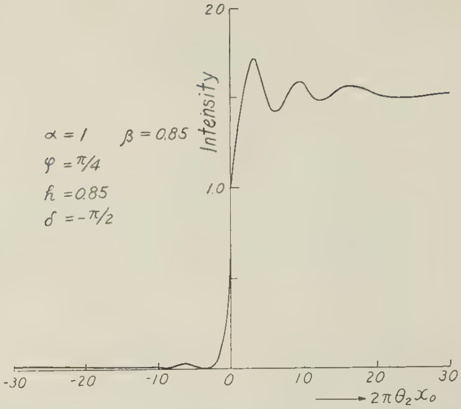

Fig. 2.

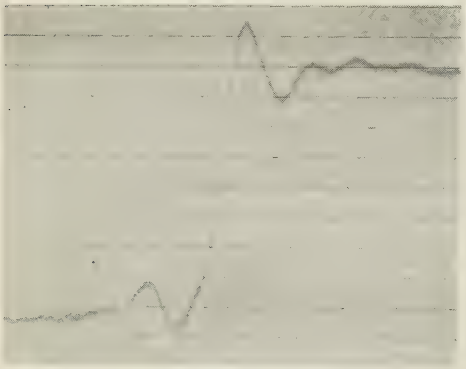

Photo. 1.

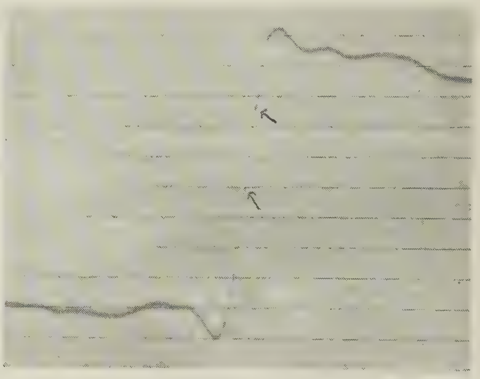

Photo. 2.

$$-\frac{Si(\theta_2)}{\pi}\Big[(\alpha+\beta)\sin\varphi-h\{\alpha\sin(\varphi+\delta)$$

$$+\beta\sin(\varphi-\delta)\}\Big]\pm\frac{(\alpha+\beta)}{2}\sin\varphi\Big]\Big],$$

where $$Si(\theta_2)\equiv\int_0^{2\pi\theta 2x_0}\sin\mu/\mu d\mu\ .$$

In this calculation, the geometrical image of the point of the light source under consideration (hereafter, refered as pinpoint) is formed on the line of center of the phase strip and the diffraction patten about this point crosses the edges of the phase strip at $\pm\theta_2$ (the direction cosines of the diffracted wave normal at the edges of the phase strip). Intensity distribution is given by $FF^*$. When $\alpha=\beta=1$ the results are the same as that of the phase annulus[1].

The author is especially interested in the continuity of the intensity at $x_0=0$, which were concluded from above equation as follows:

i) when $h=0$, the curve is continuous independent of the absorption of the object $\alpha$, $\beta$ and also $\varphi$,

ii) when $\varphi=\pm\pi/2$, the curve is continuous independent of $\alpha, \beta$ and also independent of the $h$, $\delta$ of the phase strip,

iii) when $h\doteqdot 0$, $\varphi=\pm\pi/2$, and moreover

   (1) if $\alpha=\beta$, the curve is continuous only in the case of $\delta=\pm\pi$,

   (2) if $\alpha\doteqdot\beta$, the curve is usually discontinuous.

Now if, point corresponds to the pinpoint in the phase strip is not coated, that is $h=1$, it causes the change of the brightness of back ground of the image. In this case, the first and second terms of real and imaginary parts of the equation change their form, which give the conclusion as follows:

i) when $\alpha=\beta$, the curve is usually continuous at $x_0=0$ independent of $\varphi, h$ and $\delta$ of phase strip except pinpoint,

ii) when $\alpha\doteqdot\beta$, the curve is always discontinuous independent of $\varphi$, $h$, $\delta$.

Some examples calculated are shown in Fig. 1, and 2 together with the results of experiments shown in Photo. 1 and 2. In Photo. 2, the discontinuities which were not observed in Photo. 1 can be seen as are indicated by arrows. Details will be given in the paper which will be published soon in Sci. Rep. Res. Insts. Tōhoku Univ. A. Vol. 8, No. 1, 1956.

## Reference

1) L. I. Epstein: J. Opt. Soc. Am. **40** (1950) 291.

J. Phys. Soc. Japan **11** (1956) 89

# The Measurement of the Galvanomagnetic Tensors of Bismuth

By Toshihiro Okada

*Department of Physics, Faculty of Science, Kyushu University, Fukuoka*

(Received October 10, 1955)

According to the phenomenological theory, the galvanomagnetic effect of a single crystal could be expressed by the following tensor-equation¹⁾:

$$E_i=\rho_{ij}I_j+\rho_{ij,mn}I_jH_mH_n+\cdots$$
$$+\varepsilon_{ijk}I_j(R_{k,m}H_m+R_{k,mno}H_mH_nH_o+\cdots)\ ,$$

where $E_i$ $(i=1,2,3)$ are the components of the electric field which is applied to the crystal, $I_j$ $(j=1,2,3)$ the components of the electric current flowing through the crystal, $H_m$, $H_n$, $H_o$ $(m,n,o=1,2,3)$ the components of the applied magnetic field, and $\varepsilon_{ijk}$ is a tensor of the third rank which is equal to zero when $i=j$ or $k$, or $j=k$, but equal to 1 when $ijk=123$, 231 or 312, and equal to $-1$ when $ijk=213$, 321 or 132.

For bismuth crystal, which has the symmetry $D_{3d}{}^5=R\bar{3}m$, the non-zero components of the resistivity tensor are

$$\rho_{11}\quad\text{and}\quad\rho_{33}\ ,$$

if the binary axis is taken as the first axis and the principal axis as the third axis, and also the non-zero components of the magneto-resistance tensor are²⁾,³⁾,⁴⁾

$$\rho_{11,11}=\rho_{22,22},\ \ \rho_{11,22}=\rho_{22,11},\ \ \rho_{11,33}=\rho_{22,33},$$
$$\rho_{33,11}=\rho_{33,22},\ \ \rho_{33,33},$$
$$\rho_{11,23}=\rho_{12,13}=-\rho_{22,23},\ \ \rho_{23,11}=\rho_{13,12}=-\rho_{23,22},$$
$$\rho_{23,23}=\rho_{13,13},\ \text{and}\ \rho_{12,12}=\tfrac{1}{2}(\rho_{11,11}-\rho_{11,22})\ ,$$

and those of the Hall teosor are²⁾,³⁾

$$R_{1,1}\quad\text{and}\quad R_{3,3}\ ,$$

and those of the higher order Hall tensor (the third order galvanomagnetic effect) are⁴⁾

$$R_{1,111}=R_{2,222}=3R_{1,122}=3R_{2,112},$$
$$R=_{1,123}=R_{2,113}=-R_{2,223},$$
$$R_{1,133}=R_{2,233},\ \ R_{3,112}=-R_{3,222},\ \ R_{3,113}=R_{3,223},$$
$$\text{and}\ R_{3,333}.$$

As for a single crystal of pure bismuth, the writer carried out the measurement of the above given tensor components for the temperature range $-160°\sim+45°$C by the method described in the previous paper⁴⁾. Results are shown in the following table.

The detail of this research will be published in near future.

Table I.

| Tensor | +45°C | 0°C | −70°C | −160°C |
|---|---|---|---|---|
| $\rho_{11}$ | 1.26 ±0.01 $\times 10^{-4}$ | 1.055±0.01 $\times 10^{-4}$ | 0.76 ±0.02 $\times 10^{-4}$ | 0.445±0.02 $\times 10^{-4}$ |
| $\rho_{33}$ | 1.595±0.01 | 1.35 ±0.01 | 0.995±0.02 | 0.52 ±0.02 |
| $R_{1,1}$ | 1.21 ±0.02 $\times 10^{-8}$ | 1.69 ±0.02 $\times 10^{-8}$ | 2.74 ±0.04 $\times 10^{-8}$ | 5.9 ±0.2 $\times 10^{-8}$ |
| $R_{3,3}$ | −0.06 ±0.01 | −0.06 ±0.02 | −0.09 ±0.02 | −0.17 ±0.02 |
| $\rho_{11,11}$ | 0.665±0.04 $\times 10^{-12}$ | 1.64 ±0.10 $\times 10^{-12}$ | 5.65±0.3 $\times 10^{-12}$ | 42.0 ±2.5 $\times 10^{-12}$ |
| $\rho_{11,33}$ | 0.448±0.03 | 0.95 ±0.06 | 3.5 ±0.2 | 20.4 ±1.5 |
| $\rho_{33,11}$ | 1.79 ±0.04 | 3.81 ±0.06 | 15.25±0.2 | 78.2 ±2.5 |
| $\rho_{33,33}$ | 0.24 ±0.04 | 0.53 ±0.06 | 2.35±0.2 | 11.2 ±2.5 |
| $\rho_{11,22}$ | 1.02 ±0.03 | 2.28 ±0.06 | 8.74±0.2 | 59.2 ±1.5 |
| $\rho_{11,23}$ | 0.175±0.03 | 0.425±0.07 | 1.47±0.3 | 13.2 ±3 : |
| $\rho_{23,11}$ | 0.055±0.03: | 0.12 ±0.06: | 0.90±0.2 | 6.4 ±2 |
| $\rho_{23,23}$ | −0.122±0.02 | −0.25 ±0.05 | −0.80±0.2 | −5.1 ±2 |
| $R_{1,111}$ | $-2._8$ * $\times 10^{-16}$ | | −28 $\times 10^{-16}$ | −105 :** $\times 10^{-16}$ |
| $3R_{1,123}$ | $-3._1$ * | | $-23._5$ | −137 :** |
| $R_{1,133}$ | −0.5:* | | −13 | − 90 :** |
| $R_{3,112}$ | $-0.1_5$* | | $-1._0$ | − 13 :** |
| $3R_{3,113}$ | $-0.6_3$* | | $-7._9$ | − 46 :** |
| $R_{3,333}$ | $-0.2_9$* | | $-2._9$ | $-5._0$:** |

The unit: $\rho_{ij}$ in ohm.cm, $R_{k,m}$ in ohm.cm/gauss; $\rho_{ij,mn}$ in ohm.cm/gauss², $R_{k,mno}$ in ohm.cm/gauss³.

* at $+27._5$°C ** at −167°C : less accurate values

## References

1) W. P. Mason, W. H. Hewitt and R. F. Wick: J. Appl. Phys. **24** (1953) 166.
2) M. Kohler: Ann. d. Phys. **20** (1934) 878 and 891.
3) D. Shoenberg: Proc. Camb. Phil. Soc. **31** (1935) 265 and 271.
4) T. Okada: Memoirs Faculty Sci. Kyushu Univ. Ser. B. Vol. 1, No. 5 (1955).

J. PHYS. SOC. JAPAN **11** (1956) 90~91

# Change of Photocurrent of CdS Single Crystal in a Magnetic Field

By Shōji TANAKA, Taizō MASUMI
and Sigeru IIJIMA

*Department of Applied Physics,*
*University of Tokyo, Tokyo, Japan*

(Received November 19, 1955)

The photoelectromagnetic effects in semiconductors have been investigated recently.[1)-5)]. These effects are closely related to the surface properties of semiconductors.

The experiments reported here concern the changes of photocurrents of CdS single crystals in magnetic fields, and the obtained results seem to be different from the other effects which may be expected in the ordinary galvanomagnetic effects.

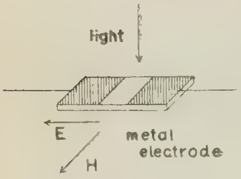

Fig. 1 (a).

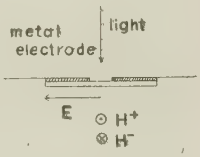

Fig. 1 (b).

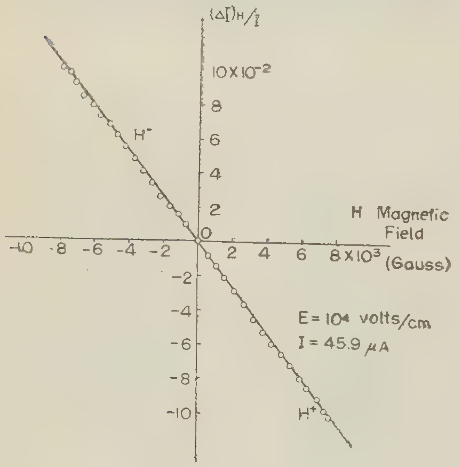

Fig. 2.

With application of magnetic field, the photocurrents of CdS single crystals increase or decrease according to the directions of the field. The experimental arrangement is shown in Fig. 1 schematically.

The specimens are thin flakes of CdS single crystals which were prepared by the Frerichs' method.[6)] The samples are illuminated on one face by the light. The applied electric and magnetic fields are parallel to this face and perpendicular to each other. The low potential end of the sample is connected to ground through a low impedance resistor, the voltage across which was measured with the differential amplifier. The distance of the metal electrodes is 0.2 mm and the applied voltage between them is 200 volts at most. For illumination, the monochromatic blue light (436 m$\mu$ in wavelength) and green light (548 m$\mu$ in wavelength) are used, the former lies in the strong absorption region and the latter in the long wavelength tail of the absorption edge.

The changes of the photocurrents induced by the illumination of the blue light with magnetic fields increase or decrease proportional to the strength of the magnetic field $H$ as shown in Fig. 2.

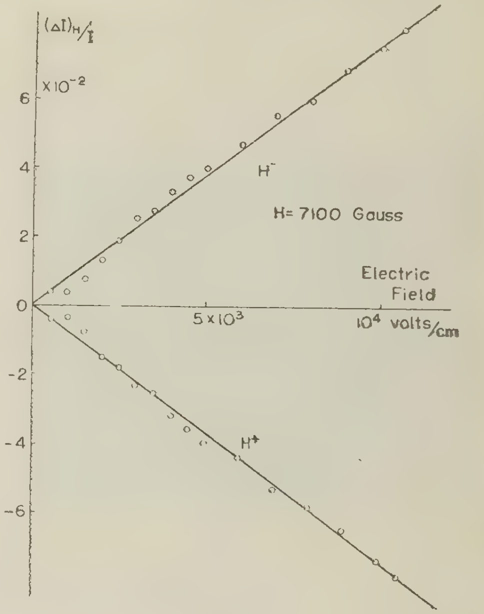

Fig. 3.

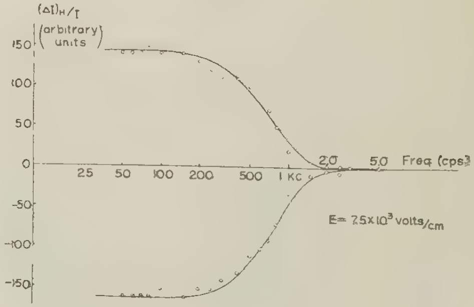

under the illumination of the blue light
Fig. 4.

In this figure, $I$ is the photocurrent in the absence of the magnetic field, while $(\Delta I)_H$ is its change due to the application of the magnetic field, and the positive direction of the magnetic field $H$ is such that the flowing current carriers in the crystal are deflected towards the illuminated surface.

Under a constant magnetic field, the absolute value of the ratio $(\Delta I)_H/I$ increases linearly with the applied electric field $E$ in both directions of the magnetic field (Fig. 3), and when the direction of the electric field is reversed, the reversal sign of $(\Delta I)_H/I$ is also observed. That is, for our observations the following expression may be probable,

$$(\Delta I)_H/I=\pm C\cdot EH \qquad (1)$$

where $C$ is a constant, independent of the intensity of illumination in the range of the present experiments in which the photocurrent is at most 70 $\mu$A with the electric field of about 8000 volts/cm.

These effects, however, have considerable fluctuations from sample to sample, and these fluctuations might be caused by some sensitive properties which are included in the constant $C$ in the Eq. (1).

When the sample is illuminated by the green light, general features of the results are similiar to the case of the blue light, while the value $(\Delta I)_H/I$ is smaller by a factor of ten although the photocurrent is the same order in both cases.

The experiments above mentioned are the static case. The further experiments in which the alternating electric field and the static magnetic field are used indicate that the relaxation effects are observed under relatively low frequencies. In the present experiments the alternating electric fields are sinusoidal and their amplitudes are kept at a constant value over the frequency range from 25 cps to 5 kc/s.

The measurements of the changes of the alternating photocurrents are made by reading the change of the positive peak voltage across the connecting resistor.

A typical example of the experimental results illustrated in Fig. 4 indicates that the relaxation effects appear even below 300 cps and in the frequency range above 2 kc/s the effects of the static magnetic fields are not observed, while the photocurrent is nearly independent of the frequency of the electric fields.

It might be considered that the behaviour of the excited current carriers near the illuminated surface of CdS single crystals contributes to these phenomena as the internal behaviours of the carriers, i.e. the surface recombination of excited carriers discussed by R. H. Bube[7] in CdS or the decrease of the effective carrier mobility in the space charge layer discussed by J. R. Schrieffer[8] in Germanium.

## References

1) P. Aigrain and H. Bulliard: Compt. Rend. **236** (1953) 95.
2) Moss, Pincherle and Woodward: Proc. Phys. Soc. London **B 66** (1953) 743.
3) T. S. Moss: Proc. Phys. Soc. London **B 66** 993.
4) H. Bulliard: Phys. Rev. **94** (1954) 1564.
5) Kurnick, Strauss and Zitter: Phys. Rev. **94** (1954) 1791.
6) R. Frerichs: Phys. Rev. **72** (1947) 594.
7) R. H. Bube: Jour. Chem. Phys. **21** (1953) 1409.
8) J. R. Schrieffer: Phys. Rev. **97** (1955) 641.

---

J. PHYS. SOC. JAPAN **11** (1956) 91~92

# On the Transition Temperatures of Superlatties $Au_3Cu$ and $AuCu_3$

By M. SHIMOJI

*Dept. of Chemistry, Faculty of Science, Hokkaido University, Sapporo, Japan*

(Received October 7, 1955)

It is interesting that solid alloys $Au_3Cu$ and $AuCu_3$ have different transition temperatures of order-disorder[1], while the usual theory predicts the same transition temperatures for them. This discrepancy is evidently related to the simplicity of the theoretical model for the system, just as described in Guggenheim's text book. In the usual statistical theory of order-disorder the atomic structure of the system is quite ignored in the view of taking into account only combinatory factor and the concentration-independent interaction energy between a pair of the binary components, i.e., ($W_s$ = const.) Accordingly, theory must be improved by the reexamination of the model. Of course, the difference of electronic structure of the alloys should give the asymmetric behaviour.

However, another improvement is presented here. This is based upon the fact that the atoms of Au and Cu have different atomic sizes respectively. The molar volume of the gold-copper alloys is given by

$$V_m=x_{Cu}v_{Cu}+x_{Au}v_{Au}\,, \qquad (1)$$

where $x_{Cu}$ and $x_{Au}$ are the mole fractions of Cu and Au, $v_{Cu}$ and $v_{Au}$ are the molar volumes of pure components respectively. On the other hand, the energies between each pair are functions of the volume of the assembly. The "interchange energy" $W_s$ is determined by the "volume". The general relation between $W_s$ and volume is complicated. However, we take a simple assignment, putting

$$W_s=W_c/V_m\,, \qquad (2)$$

where $W_c$ is a constant independent of the concentration. This choice coincides with the Hildebrand-Scatchard relation[2] in regular solution. The statistical thermodynamics of the mixtures of atoms with slightly different sizes[3] shows that the equation (1) is approximately the reasonable expression in the lattice model of liquid alloy. The evaluation of the partition function for the order-disorder of the whole assembly is unaffected by any absolute magnitude of the interchange energy.

As $W_s$ is given by (2), we have the relations

$$W_s(\mathrm{Au_3Cu}) = 0.10\, W_c\,, \tag{3}$$

and

$$W_s(\mathrm{AuCu_3}) = 0.12\, W_c\,. \tag{4}$$

The theoretical transition temperature of these alloys is

$$T_t = \frac{W_s}{14.593\,k} \tag{5}$$

in the first approximation of quadruplets[1]. Thus we see that

$$\frac{T_t(\mathrm{Au_3Cu})}{T_t(\mathrm{AuCu_3})} = \frac{0.10}{0.12} \approx 0.83 \quad \text{(calc.)} \tag{6}$$

from equation (3), (4) and (5). The present theoretical ratio agrees with the experimental results, i.e.,

$$\frac{T_t(\mathrm{Au_3Cu})}{T_t(\mathrm{AuCu_3})} = \frac{516^\circ}{664^\circ} \approx 0.78 \quad \text{(obs.)}. \tag{7}$$

Taking into account the degree of the approximation, the similar tendancy between (6) and (7) is quite to be surprised. The transition temperature of AuCu is outside of the present theoretical application, because the change in spacing which accompanies the disorder-order transition is ignored in the usual statistical theory.

The author is grateful to Prof. E. A. Guggenheim for making communications about this problem.

## References

1) E. A. Guggenheim: "*Mixtures*" (1952).
2) Hildsbrand and Scott: "*Solubility of Non-electrolyte*" (1950).
3) M. Shimoji: unpublished.

---

## Erratum

### On the Nature of Silent Electric Discharge

By Kanji HONDA and Yoshihide NAITO

J. Phys. Soc. Japan Vol. **10** (1955) 1007-1011.

pp. 1010 line 11 (left side) 186 should be read 493

Journal of the Physical Society of Japan Vol. 11, No. 2, February 1956

# Theory of the Ortho-Para Conversion in Solid Hydrogen

By Kazuko Motizuki and Takeo Nagamiya
*Department of Physics, Osaka University*

(Received September 14, 1955)

The rate of ortho-para conversion in solid hydrogen ($H_2$) is calculated taking two kinds of interactions between ortho-molecules into consideration: interaction between the nuclear spins of one molecule and those of the other molecule and interaction between the rotational magnetic moment of one molecule and the nuclear spins of the other molecule. When an ortho-molecule converts into a para molecule, the rotational energy of the former is emitted as lattice phonons; we take the Debye model for the lattice vibrations and find that the dominant process is the emission of two phonons. The result for the rate of conversion (including a small effect arising from the emission of three phonons) is 1.94 percent per hour, which is comparable with the observed value of 1.75 percent per hour due to Cremer and of 0.9 percent per hour obtained recently by Hill. Further, the effect of a small amount of oxygen dissolved in solid hydrogen is treated and curves for the increase in average concentration as functions of time are plotted for various values of the oxygen concentration and of the initial ortho concentration. They are compared with preliminary measurements made in Tōhoku University.

## § 1. Introduction

The problem of ortho-para conversion of hydrogen molecule dates from old days: the conversion rate in gaseous hydrogen was calculated by Bonhoeffer and Harteck (1929)[1] for the case where the gas is pure and by Wigner (1933)[2] for the case where gas contains a catalytic substance. The rate of conversion is enhanced by introducing paramagnetic ions or molecules, since the inhomogeneous magnetic field produced at an ortho-hydrogen molecule by these paramagnetic ions or molecules decouples the parallel spins of the two protons of that molecule. Kalckar and Teller (1935)[3] calculated the ratio of the conversion rates in $H_2$ and $D_2$ when oxygen molecules were used as catalysers and pointed out that the interaction between the inhomogenous electric field and the quadrupole moment of the nuclei is important in the case of $D_2$. Farkas and Sandler (1939)[4] confirmed this point experimentally. Further, Casimir (1940)[5] discussed in detail the interaction between such inhomogeneous electric field and the quadrupole moment of heavy hydrogen and explained successfully the experimental results. An ingeneous point in Casimir's treatment is that he avoided the complicacy of the motion of hydrogen molecules by taking the ratio between the effect of the magnetic field and that of the electric field.

The rate of conversion from ortho to para in solid hydrogen presents another interesting problem. No theoretical treatment of it appears to have been made so far. It is known that hydrogen molecules in solid hydrogen are rotating freely (to a good approximation) as in gaseous hydrogen, so long as the temperature is not lower than about 2°K, which a lambda transition is observed for the crystal of high enough ortho concentration[6]. When an ortho-molecule converts into a para-molecule, the rotational state of this molecule changes from $J=1$ to $J=0$, and the difference of the energies of these states must be taken up by the lattice vibrations. Measurements of the natural ortho-para conversion in solid $H_2$ (also liquid $H_2$) have been made by Cremer and Polanyi (1932, 1933)[7] and by Cremer (1935, 1938)[8] who found that the rate is proportional to the square of ortho-concentration, independent of temperature from 4°K to 14°K, and has a value of about 2% per hour for virtually 100% ortho hydrogen. More recently, Hill and Ricketson (1954)[6], in their precise measurements of the thermal properties of solid hydrogen of various ortho-concentrations down to 1.15°K, resumed the measurements of the conversion rate, and they used the heat liberated by conversion to warm up the specimens; they confirmed that the rate is independent of temperature between 1.8°K and 4.5°K and assumed this constant value for lower temperatures. The value was, however, about one half of that given by Cremer. Kanda, Sugawara and Kobayashi[9] at Tohoku University are doing similar experiments and are obtaining similar results. They are also investigating the effect of a trace of oxygen molecules mixed in hydrogen.

We report in this paper our calculation of the rate of conversion in solid hydrogen ($H_2$) with the use of the Debye approximation for the lattice vibrations. We treat the natural ortho-para conversion as well as the effect of dissolved small amount of oxygen molecules. It can be expected that the Debye approximation is poor since large zero-point motion of the molecules must exist in solid hydrogen. However, it can be conceived that, for long waves, phonons are superimposed on this zero-point motion and that, by taking the average of the matrix elements of the transition over this zero-point motion, one would obtain a reasonable result for the conversion rate. In our actual calculation, we did not carry out this averaging procedure. More serious errors might arise from the circumstance that for short waves, which are actually important for our calculation, the assumption of the separability of phonons from the zero-point motion would be a poor approximation, and, even if an appropriate approximate separation could be made in a reasonable way, the phonon spectrum would be much different from that given by Debye's continuum model. At present, however, we have no rigorous treatment of the lattice vibrations in solid hydrogen, so that we have no other ways than to resort to the Debye approximation. That the result obtained (2% per hour) is in reasonable agreement with experiment seems, however, to support the validity of this approximation.

The programme of our calculation is as follows. We first write down the interaction between two ortho-hydrogen molecules which gives rise to the conversion; this consists of magnetic interactions between the nuclear spins of one molecule and those of the other molecule and the magnetic interactions between the magnetic moment of one molecule produced by its rotation and the nuclear spins of the other molecule. Taking these interactions as perturbations, we calculate the matrix elements which connect the ortho-state to para-state of one of the two molecules. The matrix elements are given as functions of the mutual distance between the two molecules. They are expanded in powers of the mutual displacement measured from the mean distance of the neighbouring molecules in the actual crystal. This displacement is expressed in terms of the normal modes of vibrations of the lattice. Finally, the probability of the ortho-para transition with the simultaneous emission of phonons to balance the energy change due to change in the rotational state is calculated. Emission of only one phonon is impossible because of the conservation of energy. Emission of two phonons turns out to be most effective for the conversion. The probability of the emission of three phonons is also calculated, but this probability is small. In the final section, the effect of oxygen molecules dissolved in solid hydrogen is discussed for the case where no diffusion of hydrogen molecules is taking place.

## § 2. Wave Functions and Interactions

The ortho-hydrogen molecule has a resultant nuclear spin of magnitude one and its rotational state has an odd quantum number; the para-hydrogen molecule has zero resultant nuclear spin and its rotational quantum number is even. Since the difference of the rotational energies of $J=1$ and $J=0$ amounts to 172°K in temperature scale, the ortho and para molecules in solid hydrogen, whose melting point is 14°K, are practically in the rotational state of $J=1$ and that of $J=0$, respectively. Thus the spin and rotational wave functions of the ortho-molecule are given by

$$\left.\begin{aligned} \varphi_{1,1}&=\alpha(1)\alpha(2)\,, \\ \varphi_{1,0}&=(1/\sqrt{2})[\alpha(1)\beta(2)+\alpha(2)\beta(1)]\,, \\ \varphi_{1,-1}&=\beta(1)\beta(2); \end{aligned}\right\} \tag{2.1}$$

$$\left.\begin{aligned} \psi_{1,1}&=-(1/2)(3/2\pi)^{1/2}\sin\theta\, e^{i\varphi}\,, \\ \psi_{1,0}&=(3/4\pi)^{1/2}\cos\theta\,, \\ \psi_{1,-1}&=(1/2)(3/2\pi)^{1/2}\sin\theta e^{-i\varphi} \end{aligned}\right\} \tag{2.2}$$

and those of the para-molecule by

$$\varphi_0=(1/\sqrt{2})[\alpha(1)\beta(2)-\alpha(2)\beta(1)]\,, \tag{2.3}$$

$$\psi_0=1/(2\sqrt{\pi})\,, \tag{2.4}$$

where $\alpha$, $\beta$ are Pauli's spin functions, 1, 2 represent two protons in the molecule, and $\theta$, $\varphi$ denote the polar and azimuthal angles of the molecular axis. The polar axis can be taken arbitrarily in the space.

The interaction between two molecules which causes the ortho-para conversion consists of two parts: 1. interaction between the proton spin moments of one molecule and those of the other molecule, 2. interaction between the proton spin moments of one molecule and the magnetic moment due to rotation of the other molecule. We shall denote these two interactions by $H_{ss}$ and $H_{rs}$, respectively. We shall further denote by $a$ and $b$ the two molecules and by $a1$, $a2$, etc. the first and second protons of the molecule $a$, etc. of one of the two molecules is para, the matrix elements of $H_{ss}$ and $H_{rs}$ connecting the ortho and para states of the other molecule vanish when averaged over the rotational motion of the para molecule, so that we have only to consider pairs of ortho-molecules. The $rs$-interaction between two ortho-molecules $a$ and $b$, which converts the molecule $b$ into para, can be written

$$H_{rs}=H_{rs}(a,b1)+H_{rs}(a,b2) \tag{2.5}$$

where

$$\begin{aligned} H_{rs}(a,b1)=(\mu_r\mu_p/R^5_{a,b1}|\boldsymbol{i}|)(A+B+C&\\ +D+E+F)\,,& \end{aligned}$$

$$\left.\begin{aligned}
A&=\boldsymbol{J}_{aZ}\boldsymbol{i}_{b1,Z}(R^2_{a,b1}-3Z^2_{a,b1})\,,\\
B&=-\frac{1}{4}[(\boldsymbol{J}_{aX}-i\boldsymbol{J}_{aY})(\boldsymbol{i}_{b1,X}+i\boldsymbol{i}_{b1,Y})\\
&\qquad+(\boldsymbol{J}_{aX}+i\boldsymbol{J}_{aY})(\boldsymbol{i}_{b1,X}-i\boldsymbol{i}_{b1,Y})]\\
&\qquad\times(R^2_{a,b1}-3Z^2_{a,b1})\,,\\
C&=-\frac{3}{2}[(\boldsymbol{J}_{aX}+i\boldsymbol{J}_{aY})\boldsymbol{i}_{b1,Z}+\boldsymbol{J}_{aZ}(\boldsymbol{i}_{b1,X}+i\boldsymbol{i}_{b1,Y})]\\
&\qquad\times Z_{a,b1}(X_{a,b1}-iY_{a,b1})\,,\\
D&=-\frac{3}{2}[(\boldsymbol{J}_{aX}-i\boldsymbol{J}_{aY})\boldsymbol{i}_{b1,Z}+\boldsymbol{J}_{aZ}(\boldsymbol{i}_{b1,X}-i\boldsymbol{i}_{b1,Y})]\\
&\qquad\times Z_{a,b1}(X_{a,b1}+iY_{a,b1})\\
E&=-\frac{3}{4}(\boldsymbol{J}_{aX}+i\boldsymbol{J}_{aY})(\boldsymbol{i}_{b1,X}+i\boldsymbol{i}_{b1,Y})\\
&\qquad\times(X_{a,b1}-iY_{a,b1})^2\,,\\
F&=-\frac{3}{4}(\boldsymbol{J}_{aX}-i\boldsymbol{J}_{aY})(\boldsymbol{i}_{b1,X}-i\boldsymbol{i}_{b1,Y})\\
&\qquad\times(X_{a,b1}+iY_{a,b1})^2\,.
\end{aligned}\right\} \tag{2.6}$$

Here $\mu_r$ and $\mu_p$ are the rotational and proton magnetic moments, $\boldsymbol{J}$ and $\boldsymbol{i}$ the rotational and proton angular momenta in units of $(|\boldsymbol{i}|=1/2)$ ($i$ appearing in brackets being $\sqrt{1}$), $R_{a,b1}$ the magnitude of the vector joining the centre of gravity of molecule $a$ to the first proton of molecule $b$ and $X_{a,b1}$, $Y_{a,b1}$, $Z_{a,b1}$ its components. The $ss$-interaction which converts the molecule $b$ into para can be written

$$\begin{aligned} H_{ss}=H_{ss}(a1,b1)+H_{ss}(a1,b2)&\\ +H_{ss}(a2,b1)+H_{ss}(a2,b2)& \end{aligned} \tag{2.7}$$

where for instance $H_{ss}(a1,b1)$ represents the interaction between proton $a1$ and proton $b1$ and can be written in a similar form as (2.6), the first factor in the right-hand side of (2.6) being replaced by $(\mu_p{}^2/R^5_{a1,b1}|\boldsymbol{i}|^2)$ and $\boldsymbol{J}_{az}$, $R_{a,b1}$, $Z_{a,b1}$, etc. in $A, B,\cdots, F$ by $\boldsymbol{i}_{a1,z}$, $R_{a1,b1}$, $Z_{a1,b1}$, etc.

We look for the matrix elements of $H_{ss}+H_{rs}$ between the state $a$=ortho and $b$=ortho and the state $a$=ortho but $b$=para. These matrix elements can be grouped into two: one is of such a property that the initial and final states of molecule $a$ are the same, both with respect to its rotational state and spin state, and the other is such that either the rotational state or the spin state, or both, of molecule $a$ change. When only the latter group is concerned, we are allowed to calculate the transition probability due to the interaction $H_{ss}+H_{rs}$ between $a$ and $b$ and then sum up this probability over the molecules $a$ which surround the molecule $b$. However, when the former group is concerned, we must, in principle, first sum $H_{ss}+H_{rs}$ over the molecules $a$ surrounding the molecule $b$ and then calculate the transition probability; this introduces a great complicacy of calculation since the state of each ortho-molecule is ninefold degenerate. We therefore treat the first group in the same way as the second group, hoping that the interference effect among the interactions coming from different $a$ molecules is negligible. Thus we calculate the transition probability from the interaction Hamiltonian between neighbouring two ortho-molecules and then multiply it by the average number of ortho-molecules surrounding each ortho-molecule. This simplification introduces a further simplification of the calculation when we adopt the Debye approximation of lattice vibration: namely, we can take the axis of quantization ($z$-axis) to be the line joining the equilibrium positions of the molecules $a$ and $b$, since in the Debye approximation the lattice is treated as isotropic, though actually the lattice of molecular hydrogen is hexagonal close-packed.

All the mathematical details of the calculation of the transition probability will be given in Appendices $A$ and $B$, and we shall proceed directly to the result.

## § 3. Numerical Result and Comparison with Experiment

The crystal of hydrogen molecules is hexagonal close-packed with $R_0=3.75$ Å[12) for the intermolecular distance of any of the neighbouring pair. The corresponding density is $\rho=0.0897$ gr/cm$^3$. Other necessary data for our calculation are as follows:

Difference in rotational energy between $J=1$ and $J=0$ (in temperature scale): $E_r=172°$K

Debye temperature: $\Theta_D=91°$K

Sound velocity: $v=\left(\frac{4\pi}{3}\right)^{1/3}\frac{V}{N}\frac{k\Theta_D}{h}$
$=1.021\times10^5$ cm/sec

Internuclear distance[12): $2r=0.74$ Å

Proton magnetic moment:
$\mu_p=1.403\times10^{-23}$ erg/gauss

Rotational magnetic moment[13):
$\mu_r=0.316\times\mu_p$

The integrations of (B. 11) and (B. 12), which give the probability of ortho-para transition with the emission of two and three phonons, respectively, were carried out graphically. The results are:

$$\left.\begin{aligned}12W(2)&=1.74\times10^{-2}\text{ per hour,}\\12W(3)&=0.20\times10^{-2}\text{ per hour,}\end{aligned}\right\}$$

total: $1.94\times10^{-2}$ per hour.

Thus, the three-phonon process yields a probabiltiy about one tenth as large as the two-phonon process and the total calculated probability is 1.94% or roughly 2% per hour.

Polanyi and Cremer[7),8) found that the ortho-concentration $c$ changes with time according to the equation

$$\frac{dc}{dt}=-kc^2 \tag{3.1}$$

with

$$k=1.75\times10^{-2}\text{ per hour,} \tag{3.2}$$

which they found to be independent of temperature between 4°K and 14°K. This value of $k$ should be compared with our result given above. The agreement is apparently perfect, but it must be somewhat fortuitous for the following reasons.

From the theoretical point of view, we cannot expect more than the correct order of magnitude of $k$, since we assumed small vibrations of the lattice, which should be inadequate for such a light molecule as hydrogen, and moreover the Debye approximation for the high frequency part of the vibration spectrum, which is efficient for the two-phonon process, is most poor (possibly it gives too large level densities there). Further we assumed that each interacting pairs of ortho-molecules contributes independently to the conversion rate; actually, as each ortho-molecule is surrounded by a number of ortho-molecules, we must in principle first take the sum of all the interactions between the former and the latter, calculate the matrix elements of the sum and then square it, whereas we first calculated the square of the matrix elements or each interaction and then took their sum (actually multiplied by $12c$). One may hope, however, that the errors caused by such a procedure are cancelled out after taking the average of the total conversion rate over all the possible initial states of the surrounding molecules and, when the ortho-concentration is not 100%, over all the possible distributions of the surrounding ortho-molecules. Should this conjecture be incorrect, we have no more the bi-molecular law (3.1).

One more point overlooked by the present calculation, which, however, seems to be unimportant when the time of measurements is not too long and the ortho-concentration is not too low, is this: when an ortho-molecule becomes isolated because all the surrounding ortho-molecules happened to change to para, it can no more change to para. This effect was investigated theoretically and experimentally by Cremer[8), who found that the effect is noticeable only after 60 hours, starting with the normal concentration of ortho. If diffusion of hydrogen molecules is taking place rapidly enough, we should have no effect of this isolation, but actually the diffusion seems to be practically negligible according to Cremer, though his estimation of the effect of isolation is crude and consequently his value of the diffusion constant deduced by comparing his theory with his experiment cannot be claimed to be accurate*.

Also from the experimental point of view, it seems that Polanyi-Cremer's value of $k$ is not the ultimate one. Recent measurements by Hill[14)] (also by Kanda, Sugawara and Kobayashi[9)]) give a value of $k$ of 0.9% per hour. Further, oxygen molecules contaminated in solid hydrogen will greatly enhance the conversion rate, as we shall see in the next section.

## § 4. Effect of Oxygen Molecules Contained in Solid Hydrogen

Oxygen molecule in its ground state has a spin of magnitude one, the corresponding magnetic moment being two Bohr magnetons, so that even a small amount of oxygen contained in the crystal of hydrogen can influence the rate of conversion to a great extent. Ortho-molecules in the neighbourhood of an oxygen molecule will change to para in a short time, so that the initial increase of para-concentration will be great. Since the rate of conversion due to an oxygen molecule is proportional to the inverse twelvth power of the distance between the oxygen molecule and the hydrogen molecule, as we shall see below, a small sphere of complete para-molecules is formed instantaneously around the oxygen molecule and this sphere subsequently expands slowly.

We shall assume that the effect of diffusion of hydrogen molecules is entirely negligible, as suggested by Cremer's[8)] experiment. If diffusion takes place, ortho-hydrogen molecules at distances from the oxygen molecules will migrate into the action spheres of the oxygen molecules, change to para, and then leave the spheres. Therefore, the rate of conversion is increased. (Measurements of this increase might provide a mean of determining the self-diffusion constant if the latter depends significantly on temperature.)

The spin of each oxygen molecule changes its orientation with time. The relaxation time associated with this change of orientation may depend on the oxygen concentration as well as the thermal agitation of the surrounding hydrogen atoms; the former governs the spin-spin relaxation and the latter the spin-lattice relaxation. At high concentrations of oxygen, say 0.1 atomic percent, thes pin-spin relaxation might predominate but the relaxation time might still be as long as $10^{-6}$ or $10^{-7}$ sec, which is very long compared with $\hbar/E_r \approx 10^{-13}$ sec, where $E_r$ is, as before, the difference in rotational energy of the ortho and para molecules. We can therefore safely assume that oxygen spins are at rest when considering the ortho-para conversion.

We first calculate the rate of conversion into para of an ortho-molecule at a distance $R$ from an oxygen molecule which has substituted a hydrogen molecule in the lattice of solid hydrogen ($R$ measures the distance between the centres of these molecules). The possible distortion of the lattice and the change of the lattice vibrations due to this substitution will be neglected. The oxygen molecule is assumed to be at rest (so that certain modes of lattice vibrations are eliminated and a smaller conversion rate should result). The oxygen molecule produces an inhomogeneous static magnetic field around itself and the nuclear spins of the hydrogen molecule couple with it. The interaction Hamiltonian is the same as (2.6) except that the rotational magnetic moment of molecule $a$ is now replaced by the magnetic moment of the oxygen molecule. The calculation of the transition probability proceeds in quite a similar manner as before, so that we shall motion only its essential points:

First, the matrix elements connecting the ortho state to para stste are calculated, taking account of only the spin and rotational states of the hydrogen molecule. Then, they are expanded in powers of the displacement of the hydrogen molecule, measured from its equilibrium position, as in § 4. The displacement of the oxygen molecule is taken to be zero. Terms corresponding to the emission of two phonons are considered, others neglected. All the final matrix elements are squared and summed up, then divided by 9, the number of the initial states. The result is the same as (B. 6) with $W_i(2)$ given by (B. 11(, except that we now have different values to the coefficients $C_i$ and that the factor 81 in the denominator of (B. 11) is replaced by 9; the present $C_i$'s are as follows:

---

* Recent measurements by Rollin and Watson (B. V. Rollin and E. Watson, Conference de Physique des Basses Températures, Paris, Sept. 1955) by the method of proton magnetic resonance show also that the diffusion rate is very small below about 8°K.

$$\left.\begin{aligned} C_0 \qquad &= 12\mu_p{}^2\mu^{p}{}_2{}^2 \\ C_1+C_2 &= 24\mu_p{}^2\mu_{o2}{}^2 \\ C_3+C_4 &= 15\mu_p{}^2\mu_{o2}{}^2 \\ C_5 \qquad &= 36\mu_p{}^2\mu_{o2}{}^2 \end{aligned}\right\} \tag{4.1}$$

Further, we average the result with respect to isotropic orientation of the oxygen spin.

In this way we finally obtain the rate of conversion of the hydrogen molecule at distance $R$ as:

$$k_{oxy.} \equiv W_{owy.}(2) = 250(R_0/R)^{12} \text{ per hour} \tag{4.2}$$

where $R_0 = 3.75\text{A}$ is the interatomic distance in hydrogen crystal. Comparing this result with $k$ given by (3.2), we find that the distance at which $k_{oxy.}$ equals $k$ is $R = 2.7R_0$.

Fig. 1 respresents the number of para molecules produced around an oxygen molecule as a function of time; curve $A$ is obtained by calculating the same

$$n_{para}(t) = \sum_i [1-\exp(-k_{oxy.})\boldsymbol{R}_i)t_0 \tag{4.3}$$

over all the surrounding hydrogen atoms $i$, and curve $B$ by replacing this sum by an integral. assuminig that the hydrogen atoms are distributed continuously and uniformly around the oxygen molecule with the density of the actual solid hydrogen, and subracting 1 from it because the oxygen molecule has replaced one hydrogen molecule. That is, (4.3) is replaced by

$$n_{para}(t) = n_{H2}\int_0^\infty [1-\exp(-k_{oxy.}(r)t)]4\pi r^2 dr - 1 \ , \tag{4.4}$$

where $n_{H2}$ is the number of hydrogen molecule per unit volume. Both correspond to the case of 100% ortho. We see that the difference between these two curves is smell, particularly after a long time. So we proceed below with this continuum model. (Curves $C$ will be explained later.)

We seek the number of para-molecules produced in time $t$ by the action of the oxygen molecules and simultaneously by the action of ortho-ortho interactions. Let the concentration of ortho-molecules at distance $r$ from an oxygen molecule at time $t$ be $c(r, t)$. The time rate of change of this quantity can be obtained from the equation

$$\frac{dc(r,t)}{dt} = -k_{oxy.}(r)c(r,t) - h_{hybr.}c(r,t)\bar{c}(r,t) \ , \tag{4.5}$$

where $k_{hydr.}$ is the previous $k$ and $\bar{c}(r, t)$ means the average of the concentration over the sphere of radius $R_0$ which encircles the point under consideration; to a good approximation, this average concentration may be put equal to $c(r, t)$, because $\bar{c}$ differ significantly from $c$ only near the boundary of the small region within which all the ortho-molecules have converted to para molecules by the action of the oxygen molecule and which expands with time mainly due to this action, while the dominant effect of the last term in (6.6) if found in the larger outer region. So, putting $\bar{c} = c$, and integrating, we have

$$c(r,t) = \frac{c_0 k_{oxy.}(r)}{[k_{oxy.}(r) + c_0 k_{hydr.}]\exp[k_{oxy.}(r)t] - c_0 k_{hydr.}} \tag{4.6}$$

which reduces to the solution of (3.1)

$$c(t) = \frac{c_0}{1 + c_0 k_{hydr.} t} \tag{4.7}$$

when $k_{oxy.}$ is neglected. Here $c_0$ is the initial concentration.

The excess number of para-molecules, $\Delta n_p$, produced in time $t$ when one oxygen molecule is present is calculated by integrating the difference between (4.6) and (4,7) over the whole volume, multiplying the result by $n_{H_2}$, the number of $H_2$ molecules per unit volume, and subtracting $c_0$ (the probability that the oxygen molecule replaces an ortho-molecule):

$$\Delta n_{para}(t) = n_{H_2}\int_0^\infty \left[\frac{c_0}{1 + c_0 k_{hydr.} t} - c(r,t)\right] 4\pi r^2 dr - c_0 \ . \tag{4.8}$$

This is not the number of para-molecules produced by the action of the oxygen molecule when there is simultaneously the action of the interactions among ortho-molecules; it is given by

$$n_{H_2}\int_0^\infty k_{oxy.}(r)\int_0^t c(r,t)dt 4\pi r^2 dr \ , \tag{4.9}$$

which, when calculated, comes close to the curve B of Fig. 1. To avoid confusion, however, we have given only curves of (4.8) in Fig. 1 (denoted as C). The increase of the average concentration of para-molecules at an arbitrary molar concentration of oxygen $\alpha$, is

$$\Delta c_{para}=\frac{c_0^2 k_{hydr.} t}{1+c_0 k_{hydr.} t}+\alpha \Delta n_{para}(t)\,. \qquad (4.1)$$

Full curves in Fig. 2 have been calculated with the use of (4.10) and broken curves with the use of the approximate formula

$$\Delta c_{para}=\frac{c_0^2 k_{hydr.} t}{1+c_0 k_{hydr.} t}+\alpha n_{para}(t)\,, \qquad (4.11)$$

$n_{para}(t)$ being given by (4.4). The value of $k_{hydr.}$ used in these curves is the calculated one.

In the above derivation, we have tacitly assumed that each oxygen molecule contributes to the conversion independently of one another. If oxygen concentration is so high that action spheres of the oxygen molecules come close together, this assumption is no longer valid. In such a case, we may take the following approximation. Oxygen molecules are first supposed to form, for convenience, a simple cubic lattice with a unit cell volume equal to the total volume divided by the number of the oxygen molecules. Then, forming a sphere around each oxygen molecule whose radius is equal to the lattice constant, and distributing six oxygen molecules on each such spherical surface, with a uniform probability, and putting an oxygen molecule at its centre, we calculate the central-symmetric field of conversion with the use of (4.2). Finally, a smaller sphere with the same centre and with a volume equal to the volume per oxygen molecule is described and equation (4.5) is applied within this sphere. Possibly, $\bar{c}$ cannot be approximated by $c$ in this case, but then we encounter a great mathematical difficulty, so we put $\bar{c}=c$. The solution obtained in this way for the case of 75% initial ortho and 0.5 molar percent of oxygen is shown by a dotted curve in Fig. 2. It does not differ much from the corresponding curve obtained with the use of (4.10). Comparison with preliminary measurements made in Tōhoku University reveals that the specimen used might have contained about 0.2 molar percent of oxygen. Measurements with intentively mixed oxygen are desirable for a further verification of the present theory.

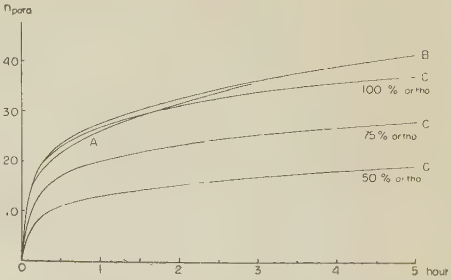

Fig. 1. Number of para-molecules produced around an oxygen molecule, as a function of time; Curve A is obtained with the use of Eq. (4.4), Curve C Eq. (4.9).

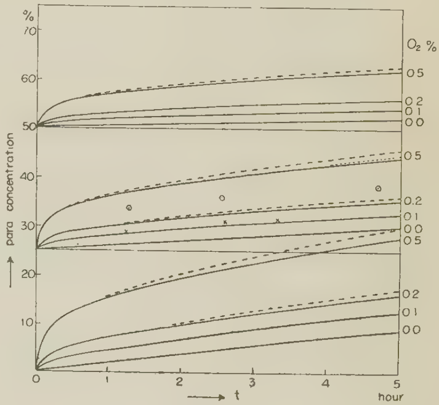

Fig. 2. Increase of the average concentration of para-molecules as a function of time for various values of the molar oxygen concentration and of the initial ortho-concentration. Full curves ware calculated with the use of Eq. (4.10) and broken curves with the use of Eq. (5.11). A dotted curve for 0.5 molar percent of oxygen and 75% initial ortho-concentration was calculated taking account of the simultaneous effect of neighbouring oxygen molecules.
⊙ and × represent experimental values obtained at Tōhoku University.

We are indebted to Professor E. Kanda, Dr. C. Sugawara and Miss H. Kobayashi of Tōhoku University for kind communications of their results and to Dr. Yoshida and other members of our laboratory for helpful discussions.

## Appendix A. The matrix elements of $H_{rs}$ and $H_{ss}$ with respect to the spin and rotational states.

This and the next appendices fill the gap between § 2 and § 3.

(a) The matrix elements of $H_{rs}$. $H_{rs}$ does not contain the spin operators of molecule $a$, so that we have only diagonal elements of it with respect to the spin states of $a$. The non-vanishing matrix elements of the spin operators of molecule $b$ with respect to the spin states of molecule $b$ are as follows:

$$\left.\begin{array}{ll}
\langle\varphi_{1,0}(b)|i_{b1,z}|\varphi_0(b)\rangle=\dfrac{1}{2} & \langle\varphi_{1,0}(b)|i_{b2,z}|\varphi_0(b)\rangle=-\dfrac{1}{2} \\
\langle\varphi_{1,1}(b)|i_{b1,x}+ii_{b1,y}|\varphi_0(b)\rangle=-\dfrac{1}{\sqrt{2}} & \langle\varphi_{1,1}(b)|i_{b2,x}+ii_{b2,y}|\varphi(b)\rangle=\dfrac{1}{\sqrt{2}} \\
\langle\varphi_{1,-1}(b)|i_{b1,x}-ii_{b1,y}|\varphi_0(b)\rangle=\dfrac{1}{\sqrt{2}} & \langle\varphi_{1,1}(b)|i_{b2,x}-ii_{b2,y}|\varphi_0(b)\rangle=-\dfrac{1}{\sqrt{2}}
\end{array}\right\} \tag{A. 1}$$

The non-vanishing matrix elements of the angular momentum operator of molecule $a$ are:

$$\left.\begin{array}{l}
\langle\psi_{1,1}(a)|J_{az}|\psi_{1,1}(a)\rangle=1 \\
\langle\psi_{1,-1}(a)|J_{az}|\psi_{1,-1}(a)\rangle=-1 \\
\langle\psi_{1,0}(a)|J_{ax}+iJ_{ay}|\psi_{1,-1}(a)\rangle=\langle\psi_{1,1}(a)|J_{ax}+iJ_{ay}|\psi_{1,0}(a)\rangle=\sqrt{2} \\
\langle\psi_{1,0}(a)|J_{ax}-iJ_{ay}|\psi_{1,1}(a)\rangle=\langle\psi_{1,-1}(a)|J_{ax}-iJ_{ay}|\psi_{1,0}(a)\rangle=\sqrt{2}\,.
\end{array}\right\} \tag{A. 2}$$

In taking the matix elements of $H_{rs}$ with respect to the rotational states of molecule $b$, we have to calculate those of $(R^2_{a,b1}-3Z^2_{a,b1})/R^5_{a,b1}$, etc. We expand the latter quantities in powers of $r/R$, where $r$ is half the internuclear distance of each molecule and $R$ the distance between the centres of the two molecules; $r/R \fallingdotseq 1/10 \ll 1$ if we take for $R$ the mean distance in the actual crystal. Since $H_{rs}$ is the sum of $H_{rs}(a, b1)$ and $H_{rs}(a, b2)$, and is invariant against the inversion of molecule $b$ with respect to its centre, and since the matrix elements of $i_{b1}$ have opposite sign to those of $i_{b2}$, as seen from (A. 1), we have only to retain those terms of the expansion which change sign under the inversion of molecule $b$. The first terms of the expansion are discarded by this reason, the second terms adopted, and the higher order terms neglected. Then we have the following results:

$$\left.\begin{array}{ll}
\text{$A$ and $B$ terms:} & \left\langle\psi_{1,1}(b)\left|\dfrac{R^2_{a,b1}-3Z^2_{a,b1}}{R^5_{a,b1}}\right|\psi_0(b)\right\rangle=\sqrt{\dfrac{3}{2}}\,f_1 \\
 & \left\langle\psi_{1,0}(b)\left|\dfrac{R^2_{a,b1}-3Z^2_{a,b1}}{R^5_{a,b1}}\right|\psi_0(b)\right\rangle=-\sqrt{3}\,f_0 \\
 & \left\langle\psi_{1,-1}(b)\left|\dfrac{R^2_{a,b1}-3Z^2_{a,b1}}{R^5_{a,b1}}\right|\psi_0(b)\right\rangle=-\sqrt{\dfrac{3}{2}}\,f_2 \\
\text{$C$ term} & \left\langle\psi_{1,1}(b)\left|\dfrac{Z_{a,b1}(X_{a,b1}-iY_{a,b1})}{R^5_{a,b1}}\right|\psi_0(b)\right\rangle=\dfrac{5}{\sqrt{6}}f_3 \\
 & \left\langle\psi_{1,0}(b)\left|\dfrac{Z_{a,b1}(X_{a,b1}-iY_{a,b1})}{R^5_{a,b1}}\right|\psi_0(b)\right\rangle=\dfrac{1}{\sqrt{3}}f_1 \\
 & \left\langle\psi_{1,-1}(b)\left|\dfrac{Z_{a,b1}(X_{a,b1}-iY_{a,b1})}{R^5_{a,b1}}\right|\psi_0(b)\right\rangle=f_5 \\
\text{$D$ term:} & \left\langle\psi_{1,1}(b)\left|\dfrac{Z_{a,b1}(X_{a,b1}+iY_{a,b1})}{R^5_{a,b1}}\right|\psi_0(b)\right\rangle=-f_5 \\
 & \left\langle\psi_{1,0}(b)\left|\dfrac{Z_{a,b1}(X_{a,b1}+iY_{a,b1})}{R^5_{a,b1}}\right|\psi_0(b)\right\rangle=\dfrac{1}{\sqrt{3}}f_2 \\
 & \left\langle\psi_{1,-1}(b)\left|\dfrac{Z_{a,b1}(X_{a,b1}+iY_{a,b1})}{R^5_{a,b1}}\right|\psi_0(b)\right\rangle=-\dfrac{5}{\sqrt{6}}f_4 \\
\text{$E$ term:} & \left\langle\psi_{1,1}(b)\left|\dfrac{(X_{a,b1}-iY_{a,b1})^2}{R^5_{a,b1}}\right|\psi_0(b)\right\rangle=\dfrac{5}{\sqrt{6}}f_6 \\
 & \left\langle\psi_{1,0}(b)\left|\dfrac{(Y_{a,b1}-iY_{a,b1})^2}{R^5_{a,b1}}\right|\psi_0(b)\right\rangle=-\dfrac{5}{\sqrt{3}}f_3
\end{array}\right\} \tag{A. 3}$$

$$\left\langle \psi_{1,-1}(b)\left|\frac{(X_{a,b1}-iY_{a,b1})^2}{R^5_{a,b1}}\right|\psi_0(b)\right\rangle=2f_8$$

F term:

$$\left\langle \psi_{1,1}(b)\left|\frac{(X_{a,b1}+iY_{a,b1})^2}{R^5_{a,b1}}\right|\psi_0(b)\right\rangle=-2f_9$$

$$\left\langle \psi_{1,0}(b)\left|\frac{(X_{a,b1}+iY_{a,b1})^2}{R^5_{a,b1}}\right|\psi_0(b)\right\rangle=-\frac{5}{\sqrt{3}}f_4$$

$$\left\langle \psi_{1,-1}(b)\left|\frac{(X_{a,b1}+iY_{a,b1})^2}{R^5_{a,b1}}\right|\psi_0(b)\right\rangle=-\frac{5}{\sqrt{6}}f_7$$

where $f_0, f_1, \cdots, f_9$ are functions of the relative coordinates $X, Y, Z\,(X^2+Y^2+Z^2=R^2)$ of the centres of molecules $a$ and $b$ and are given as follows:

$$f_0=Z\{3(X^2+Y^2)-2Z^2\}\frac{r}{R^7}$$

$$f_1=(R^2-5Z^2)(X-iY)\frac{r}{R^7}$$

$$f_2=(R^2-5Z^2)(X+iY)\frac{r}{R^7}$$

$$f_3=Z(X-iY)^2\frac{r}{R^7}$$

$$f_4=Z(X+iY)^2\frac{r}{R^7}$$

$$f_5=\frac{1}{\sqrt{6}}Z\{2R^2-5(X^2+Y^2)\}\frac{r}{R^7}$$

$$f_6=\{(X^3-3XY^2)-i(3X^2Y-Y^3)\}\frac{r}{R^7}$$

$$f_7=\{(X^3-3XY^2)+i(3X^2Y-Y^3)\}\frac{r}{R^7}$$

$$f_8=\frac{1}{2\sqrt{6}}\{4R^2-5(X^2+Y^2)\}(X-iY)\frac{r}{R^7}$$

$$f_9=\frac{1}{2\sqrt{6}}\{4R^2-5(X^2+Y^2)\}(X+iY)\frac{r}{R^7} \tag{A. 4}$$

The same formulas apply when $b1$ is replaced by $b2$. Combining all the above formulas, we can calculate the required matrix elements of $H_{rs}$.

(b) The matrix elements of $H_{ss}$. In calculating the matrix elements of e.g. the product of $i_{a1,z}$ and $i_{b1,z}$, we can apply the formulas (A. 1) separately for molecules $a$ and $b$; the results may not need be reproduced here. In calculating the matrix elements with respect to the rotational states of $a$ and $b$, we again expand $H_{ss}$ in powers of $r/R$. A little consideration will show that we have only to calculate those terms of $H_{ss}(a1, b1)$ which are invariant againt the inversion of molecule $a$ and change sign against the inversion of molecule $b$, and then to multiply the result by 4 in order to take account of $H_{ss}(a1, b2)$, $H_{ss}(a2, b1)$ and $H_{ss}(a2, b2)$. The leading terms of the expansion of $H_{ss}(a1, b1)$ which satisfy these conditions are the same as those which we considered above in (a) in the expansion of $H_{rs}(a,b1)$, so that we can utilize the results (A. 3) and (A. 4) for each of the three rotational states of molecule $a$.

Now we can proceed further. We have initially an ortho-molecule $a$ and an ortho-molecule $b$ and finally an ortho-molecule $a$ and a para-molecule $b$. Each ortho-state is nine-fold degenerate, so that the initial state is 81-fold degenerate. The final state is 9-fold degenerate. As we are interested in the probability of transition from one of the 81 initial states to any one of the 9 final states, we sum up the probabilities of all the possible transitions between these sets of states and then divide the sum by 81.

The change in energy of the rotational state of molecule $b$, which has converted into para, must be balanced by an emission of phonons. We shall denote by $\psi_T$ and $\psi_{T'}$ the wave functions of the initial and final vibrational states of the lattice. Then the ortho-para transition probability is proportional to

$$\frac{1}{81}\sum\left|\langle\psi^a_{1m_a}\varphi^a_{1n_a}\psi^b_{1m_b}\varphi^b_{1n_b}\psi_T|H_{rs}+H_{ss}|\psi^a_{1m_a'}\varphi^a_{1n_a'}\psi_0^b\varphi_0^b\psi_{T'}\rangle\right|^2 \tag{A. 5}$$

where $m, m'$ and $n, n'$ with suffixes $a$ or $b$ are magnetic quantum numbers of rotational and spin angular momenta of molecules $a$ or $b$, and suffixes 1 and 0 refer, as before, to ortho and para states. The summation in (A. 5) runs over the initial 81 and final 9 states. The matrix elements of the Hamiltonian with respect to rotational and spin states have been calculated as sketched above, and the result was expressed in terms of $f_i$ ($i=0, 1, 2, \cdots 9$), (A. 4), which are functions of the relative coordinates of molecules $a$ and $b$. So, (A. 5) can be expressed as

$$\frac{1}{81}\sum_{i=0}^{9} C_i\,|\langle\psi_T|f_i|\psi_{T'}\rangle|^2 \tag{A. 6}$$

where $C_i$ are

$$\left.\begin{aligned} C_0 &= 108\mu_p{}^4[4+(\mu_R/\mu_p)^2] \\ C_1+C_2 &= 252\mu_p{}^4[4+(\mu_R/\mu_p)^2] \\ C_3+C_4 &= 2700\mu_p{}^4[4+(\mu_R/\mu_p)^2] \\ C_5 &= 432\mu_p{}^4[4+(\mu_R/\mu_p)^2] \\ C_6+C_7 &= 450\mu_p{}^4[4+(\mu_R/\mu_p)^2] \\ C_8+C_9 &= 432\mu_p{}^4[4+(\mu_R/\mu_p)^2] \end{aligned}\right\} \tag{A. 7}$$

In Appendix $B$, we express $f_i$ in terms of the lattice vibrations.

## Appendix B. Emission of phonons

We shall adopt the Debye approximation for the lattice vibrations, as mentioned in § 1. The Debye temperature $\Theta_D$ is 91°K[10], while the difference of the rotational energy of ortho-molecule and that of para-molecule is 172°K[11], so that at least two phonons must be emitted.

We now denote the two molecules $a$ and $b$ by $k$ and $l$, these numbers running over the lattice points, and write small displacements of the centres of these molecules from their respective equilibrium positions as $x_k$, $y_k$, $z_k$ and $x_l$, $y_l$, $z_l$. We expand the functions $f_i$ in powers of the relative displacement

$$x=x_k-x_l\,,\quad y=y_k-y_l\,,\quad z=z_k-z_l \tag{B. 1}$$

as

$$f=f_0+\sum_x\left(\frac{\partial f}{\partial x}\right)_0 x+\frac{1}{2!}\sum_{x,y}\left(\frac{\partial^2 f}{\partial x\partial y}\right)_0 xy+\frac{1}{3!}\sum_{x,y,z}\left(\frac{\partial^3 f}{\partial x\partial y\partial z}\right)_0 xyz+\cdots\,, \tag{B. 2}$$

where the suffix 0 means the equilibrium position. In calculating the process of emission of two phonons, the second order terms of the above expansion are to be considered, for the emission of three phonons the third order terms, and so on. The displacement of molecule $k$ and that of molecule $l$ can be written in the Debye approximation as

$$x_k=\sum_\sigma\sum_{j=1}^{3}(a_{\sigma j}\cos\boldsymbol{\sigma}\cdot\boldsymbol{k}+b_{\sigma j}\sin\boldsymbol{\sigma}\cdot\boldsymbol{k})x_{\sigma j}\,,\quad\text{etc.}, \tag{B. 3}$$

$$x_l=\sum_\sigma\sum_{j=1}^{3}(a_{\sigma j}\cos\boldsymbol{\sigma}\cdot\boldsymbol{l}+b_{\sigma j}\sin\boldsymbol{\sigma}\cdot\boldsymbol{l})x_{\sigma j}\,,\qquad\text{etc.} \tag{B. 4}$$

where $\boldsymbol{\sigma}$ is $a$ wave vector, $\boldsymbol{k}$ and $\boldsymbol{l}$ vectors representing the lattice points $k$ and $l$, $j$ the three components of polarization, and $x_{\sigma j}$, $y_{\sigma j}$, $z_{\sigma j}$ the Cartesian components of the unit vector which represents polarization $j$ of wave $\sigma$. The amplitude operators $a_{\sigma j}$ and $b_{\sigma j}$ are independent of each other and have matrix elements between those states in which the number of phonons differs by one:

$$\left.\begin{aligned} \langle m_{\sigma j}|a_{\sigma j}|m_{\sigma j}+1\rangle &= (\hbar/2M)^{1/2}(m_{\sigma j}+1)^{1/2}\omega_{\sigma j}{}^{-1/2}\,, \\ \langle n_{\sigma j}|a_{\sigma j}|n_{\sigma j}+1\rangle &= (\hbar/2M)^{1/2}(n_{\sigma j}+1)^{1/2}\omega_{\sigma j}{}^{-1/2}\,. \end{aligned}\right\} \tag{B. 5}$$

$M$ is the total mass of the crystal. We assume, for the sake of simplicity, that $\omega_{\sigma j}$ does not depend on $j$, and denote it simply as $\omega_\sigma$. Further we assume the relation $|\sigma|=\omega_\sigma/v$, where $v$ is the sound velocity.

For the process of emission of two phonons, we are interested in the transition probability:

$$W(2)=\sum_i W_i(2)\,, \tag{B. 6}$$

$$\begin{aligned} W_i(2)=\frac{1}{81}\frac{2\pi}{\hbar}C_i\int\sum_{j,j'}\Bigg[&\left|\left\langle m_{\sigma j}, m_{\sigma' j'}\right|\frac{1}{2}\sum_{x,y,z}\left(\frac{\partial^2 f_i}{\partial x\partial y}\right)_0 xy\left|m_{\sigma j}+1,\ m_{\sigma' j'}+1\right\rangle\right|^2 \\ &+\left|\left\langle m_{\sigma j}, n_{\sigma' j'}\right|\frac{1}{2}\sum_{x,y,z}\left(\frac{\partial^2 f_i}{\partial x\partial y}\right)_0 xy\left|m_{\sigma j}+1,\ n_{\sigma' j'}+1\right\rangle\right|^2 \\ &+\left|\left\langle n_{\sigma j}, m_{\sigma' j'}\right|\frac{1}{2}\sum_{x,y,z}\left(\frac{\partial^2 f_i}{\partial x\partial y}\right)_0 xy\left|n_{\sigma j}+1,\ m_{\sigma' j'}+1\right\rangle\right|^2 \\ &+\left|\left\langle n_{\sigma j}, n_{\sigma' j'}\right|\frac{1}{2}\sum_{x,y,z}\left(\frac{\partial^2 f_i}{\partial x\partial y}\right)_0 xy\left|n_{\sigma j}+1,\ n_{\sigma' j'}+1\right\rangle\right|^2\Bigg] \\ &\times\delta(\hbar\omega_{\sigma'}+\hbar\omega_\sigma-E_r), \end{aligned} \tag{B. 7}$$

where the integration is carried out with respect to the states of the phonons and $E_r$ is the difference in rotational energy for states $J=1$ and $J=0$. The numbers of phonons appearing in the above expression are replaced by their thermal average values;

$$m_{\sigma j}=n_{\sigma j}=\frac{1}{e^{\hbar\omega_\sigma/kT}-1}, \qquad m_{\sigma j'}=n_{\sigma j'}=\frac{1}{e^{\hbar\omega_\sigma/kT}-1}. \tag{B. 8}$$

The number of states of phonons within frequency range $(\omega_\sigma, \omega_\sigma+d\omega_\sigma)$ and within solid angle $d\Omega_\sigma$ is

$$\frac{V}{(2\pi)^3}\sigma^2 d\sigma d\Omega_\sigma=\frac{V}{(2\pi)^3}\frac{\omega_\sigma^2}{v^3}d\omega_\sigma d\Omega_\sigma\,, \tag{B. 9}$$

where $V$ is the volume of the crystal; $V$ and $M$ appear in a combined form $\rho=M/V$, which is the density. So $W_i$ can be written

$$W_i(2)=\frac{1}{81(2\pi)^5V^6\rho^2}C_i\left[\sum_{x,y,z}\left|\left(\frac{\partial^2 f_2}{\partial x\partial y}\right)_0\right|^2\right]\iiint d\omega d\Omega d\Omega'\frac{e^{\hbar\omega/kT}}{e^{\hbar\omega/kT}-1}\frac{e^{\hbar(E_r/\hbar-\omega)/kT}}{e^{\hbar(E_r/\hbar-\omega)kT}-1}$$
$$\times\,\omega(E_r/\hbar-\omega)\sin^2\left(\frac{\boldsymbol{k}-\boldsymbol{l}}{2}\cdot\sigma\right)\sin^2\left(\frac{\boldsymbol{k}-\boldsymbol{l}}{2}\cdot\sigma'\right). \tag{B. 10}$$

We may put the first two factors of the integrand equal to one, since, we are interested in the temperature region much lower than the Debye temperature and since the frequencies of phonons under consideration cannot be much lower than the maximum Debye characteristic frequency by virtue of the energy conservation. This approximation leads to a temperature independent conversion rate. Integrations with respect to solid angles can be carried out easily and the result is

$$\mathrm{W}_i(2)=\frac{1}{81(2\pi)^3v^6\rho^2}C_i\left[\sum_{x,y,z}\left|\left(\frac{\partial^2 f_i}{\partial x\partial y}\right)_0\right|^2\right]\int_{\omega_r-\omega_D}^{\omega_D}\left[\frac{\sin(R_0\omega/v)}{R_0\omega/v}\right]\cdot\left[1-\frac{\sin\{R_0(\omega_r-\omega)/v\}}{R_0(\omega_r-\omega)/v}\right]$$
$$\times\,\omega(\omega_r-\omega)d\omega\,, \tag{B. 11}$$

where $\omega_r=E_r/\hbar$, $\omega_D=k\Theta_D/\hbar$ and $R_0$ is the equilibrium distance between neighbouring molecules. The above integration can be carried out numerically or graphically.

Since there are twelve neighbours for each molecule, we must multiply $W(2)$ by 12 for 100% ortho hydrogen and $12c^2$ for hydrogen with ortho concentration $c$.

Similar calculation can be performed for the probability of emission of three phonons. In order to avoid unnecessary complicacies of the calculation, we assume for $h\omega_r/k$ a value higher by 10 degrees than its actual value, thus making $\omega_r=2\omega_D$; the result for the probability should be somewhat greater than the actual one. The probability is given by

$$W(3)=\frac{2\hbar}{81\times9\times(2\pi)^5v^9\rho^3}\sum_i C_i\left[\sum_{x,y,z}\left|\left(\frac{\partial^3 f_i}{\partial x\partial y\partial z}\right)_0\right|^2\right]\int_0^{\omega_D}d\omega'\int_{\omega_r-\omega_D-\omega'}^{\omega_D}\omega\omega'(\omega_r-\omega-\omega')$$
$$\times\left[1-\frac{\sin(R_0\omega/v)}{(R_0\omega/v)}\right]\cdot\left[1-\frac{\sin(R_0\omega'/v)}{(R_0\omega'/v)}\right]\cdot\left[1-\frac{\sin\{R_0(\omega_r-\omega-\omega')/v\}}{R_0(\omega_r-\omega-\omega')/v}\right]d\omega\,. \tag{B. 12}$$

We must again multiply this by $12c^2$ in order to obtain the ortho-para conversion probability per molecule.

It is shown that the three-phonon process is much less important than the two-phonon process. In the above calculation of the three-phonon process we made the same assumption as that in the two-phonon process, i.e. we assumed that the number of phonons in thermal equilibrium is zero; actually, phonons in the neighbourhood of zero frequency play some role in the three-phonon process, and for these phonons the assumption is not valid. But the correction due to this circumstance will not appreciably change the magnitude of $W(3)$ and, since $W(3)$ is much less $W(2)$, this correction is not important.

There are many other processes: absorption of one phonon and emission of two phonons, emission of four phonons, absorption of one or two phonons and emission of three or two phonons, etc. All these processes are expected to give much less contributions to the ortho-para conversion rate than the two-phonon emission process.

### References

1) K. F. Bonhoeffer und P. Harteck: Z. f. Phys. Chem. **B 4** (1929) 113; 127.
2) E. Wigner: Z. f. phys. Chem. **B 23** (1933) 28.
3) F. Kalckar and E. Teller: Proc. Roy. Soc. **A 150** (1935) 520.
4) L. Farkas and L. Sandler: Trans. Far. Soc. **35** (1939) 337.
5) H. B. G. Casimir: Physica **7** (1940) 169.
6) R. W. Hill and B. W. A. Ricketson: Phil. Mag. **45** (1954) 277.
7) E. Cremer and M. Polanyi: Trans. Far. Soc. **28** (1932) 435; Z. f. phys. Chem. **B 21** (1933) 459.
8) E. Cremer: Z. f. phys. Chem. **B 28** (1935) 199; *ibid.* **39** (1938) 445.
9) E. Kanda, T. Sugawara and H. Kobayashi: Private communication. (To appear in J. Phys. Soc. Japan).
10) K. Mendelssohn, M. Ruhemann und F. Simon: Z. f. phys. Chem. **B 15** (1932) 121.
11) F. Reif and E. M. Purcell: Phys. Rev . **91** (1953) 631.
12) P. W. G. Wyckoff: *The Structure of Crystals* (1931) 205.
13) J. M. B. Kellogg, I. I. Rabi, N. F. Ramsey and J. R. Zacharias: Phys. Rev. **56** (1939) 728.
14) R. W. Hill: Private communication to Dr. Sugawara, Tōhoku University.

---

JOURNAL OF THE PHYSICAL SOCIETY OF JAPAN Vol. 11, No. 2, FEBRUARY, 1956

# On Ferroelectric Barkhausen Pulses of Rochelle Salt

By Ryuji ABE

*Faculty of Science, Nagoya, University, Nagoya, Japan*

(Received July 19, 1955)

Ferroelectric Barkhausen pulses were observed when an electric field was applied on a rochelle salt crystal. The volume corresponding to a pulse and the dependence of the number of the pulse on temperature, humidity and strength of applied electric field were studied. It is found in the present experiment that the volume is the order of $10^{-9}$ cm$^3$ which is in accordance with Kojima and Kato's result. It is also found that the critical field at which pulses begin to take place is proportional to the $n$'th power of spontaneous polarization. The value of $n$ determined from the experiment is $2.7 \pm 0.5$. This result can be explained satisfactorily assuming that walls are stabilized at hollows in a crystal before a field is applied on the crystal.

## § 1. Introduction

Recently the domain structure and the movement of domain walls of rochelle salt were observed through the crossed nicols¹⁾. The direction of the spontaneous polarization is normal to $a$-plane and two neighboring domains have polarization of opposite sense, resulting in 180° boundary walls parallel to $b$- or $c$-planes. When an electric field is applied normal to $a$-plane, the walls parallel to $c$- and $b$-plane move in the directions of $b$- and $c$-axis, respectively. The movement of wall may cause a phenomenon similar to Barkhausen effect in ferromagnetic substances.

In 1933 M. Kluge and von H. Schönfeld²⁾ reported that they observed pulses similar to the ferromagnetic Barkhausen pulse when an electric field was applied on rochelle salt crystal. In 1935, however, Schönfeld assured³⁾ that these pulses were not Barkhausen pulse but they were caused by electric discharges through the gap between the crystal surface and the electrode. According to him the discharge began to take place at a certain voltage independent of the thickness of the crystal. The voltage estimated from his figure[2)]′ is about 100 volts for rochelle salt.

The true ferroelectric Barkhausen effect was reported by Newton, Ahearn and Mckey[4)] for barium titanate, and by Takahashi, Hara and Nakamura[5)] and Kojima and Kato[6)] for rochelle salt. They observed pulses quite different from Schönfeld noise. According to Kojima and Kato the volume corresponding to a pulse, i. e. the volume in which the polarization is reversed to produce a Barkhausen pulse, is the order of $10^{-8}$ cm$^3$. This volume is much smaller than the volume of a domain observed through the crossed nicols.

The present investigation was undertaken to clarify the cause of the ferroelectric Barkhausen pulse. The volume corresponding to a pulse and the dependence of the number of the pulse on temperature, humidity and strength of applied electric field were studied. From the analysis of the experimental results it is concluded that a pulse is not produced by an uniform motion of a boundary wall but it is produced by a jerky motion which occurs when a wall passes across a hollow in a crystal.

## § 2. Experimental

*Specimen* Crystals used in the present experiment are thin slabs normal to *a*-axis. Their thickness is 1 mm and their area is 1.2 × 1.2 cm$^2$. Silver electrodes were made by evaporation in vacuum on both sides of the slab. The thickness of the electrodes was about 500 Å and the area was about 1 × 1 cm$^2$. Since there is no gap between the electrodes and the slab, the evaporated electrodes are advantageous to avoid Schönfeld noise.

*Specimen chamber* To keep the temperature and the humidity constant during an experiment a crystal was set in a closed chamber in a thermostat (Fig. 1 (b)). The constancy of temperature was about ±0.1°C. The humidity in the chamber was controlled by changing concentration of sulfuric acid. Although humidity was not measured, fluctuation was inferred from the experimental results to be about 2%. To obtain more constant temperatures the other specimen chamber (Fig. 1(a)) was used although it could be used only at room temperatures.

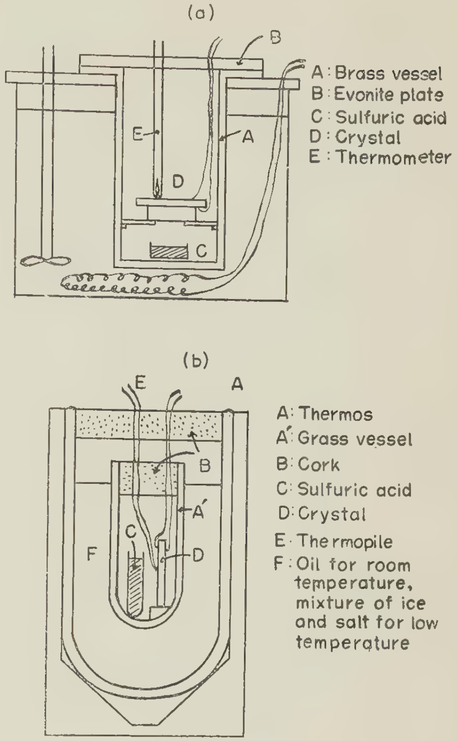

Fig. 1.

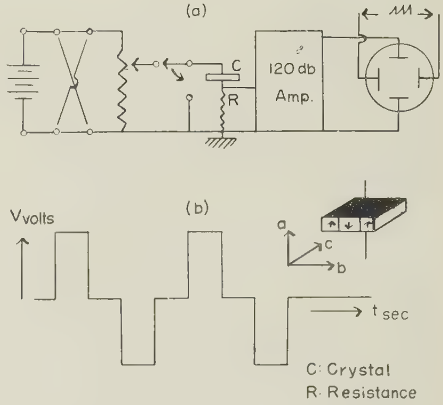

Fig. 2.

*Circuit* Since the pulse is very small, 120 db voltage amplifier was used. To remove the noises of external origins all instruments were shielded perfectly. The block diagram of the circuit is shown in Fig. 2 (a). The pulses produced in the crystal were introduced into the amplifier through the resistance *R* and the amplified pulses were applied to the longitudinal axis of C. R. O.. The horizontal axis was scanned by 1000 c. p. s. sawed pulses. To eliminate the fluctuation of line voltage the power was supplied into C. R. O. and the amplifier through a voltage stabilizer.

*Observation of pulses* The electric field applied to the crystal was raised step by step, for example 5 volts/cm for each step. The pulses begin to take place when the field is raised to about 30 volts/cm. The pulses take place also when the electrodes are shortcircuited after the application of a field. These pulses are smooth and generally separated one by one (Fig. 3), although sometimes a little more complicated pulses were observed (Fig. 3(d)). The figures 3(a) and 3(c) show the pulses observed when an electric field is applied, and 3(b) shows the pulses when the electrodes are shortcircuited. A pulse in 3(c) has a tail below the holizontal line. This tail was frequently observed when the pulse was high.

The pulses were not observed in paraelectric regions even when a considerably high field (about 100 volts/cm) was applied.

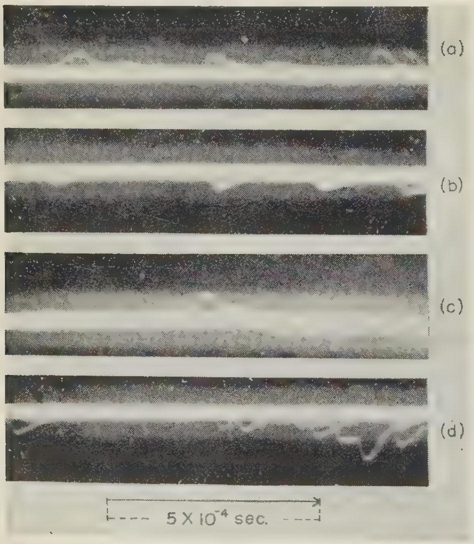

Fig. 3.

*Counting method* The number of pulses was counted by the naked eye. In the present experiment the number of pulses observed during 2 minutes was used as an indication of the total number of pulses under a certain field, since the frequency of the pulses decreases so rapidly after the application of the field that only a few pulses are observed after 2 or 3 minutes. To avoid irreversible results the alternative field as shown in Fig. 2(b) was applied. The mean value of the total number of pulses for both directions of a field was used as the final value, since the numbers of pulses appearing in these directions were not exactly equal.

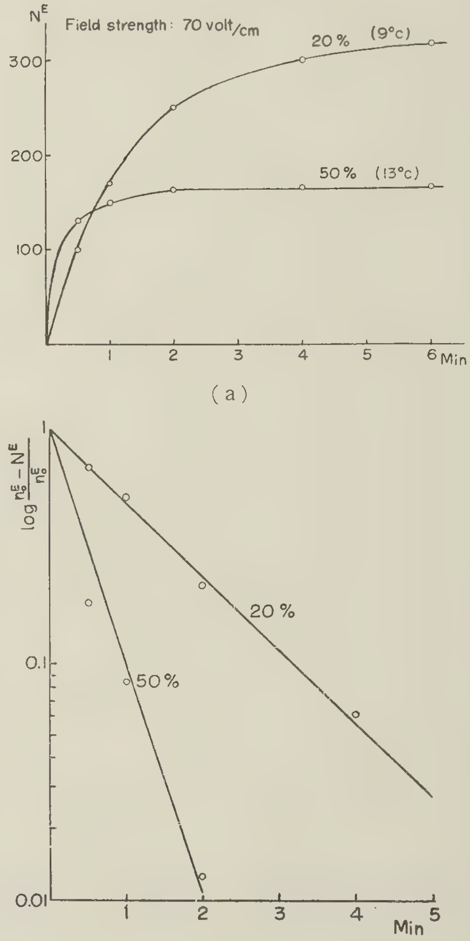

(a)

(b)

Fig. 4.

## § 3. Behaviors of Pulses

*Total number of pulses* The total number of the pulses saturates exponentially with the lapse of time under a constant field (Fig. 4 (a)). This relation may be explained as follows:

Let us assume sources that produce pulses in a crystal and let the total number of the sources under a certain field $E$ be $n_0^E$. If we assume that a source disappears when a pulse is produced, then we get the relation

$$dn=nPdt$$

where $n$ is the number of the sources at the time $t$ and $P$ is the probability that a pulse appears in unit time under the field. If $P$ is independent of $n$, we get

$$n = n_0^E \exp(-Pt)\ .$$

Then the total number of pulses appearing during a period of time $t$ is

$$N_0^E = n_0^E(1-\exp(-Pt))\ .$$

This relation indicates that the total number saturates exponentially with time.

The experimental results in Fig. 4(a) are replotted in Fig. 4(b), the ordinate being log $(n_0^E - N^E)/n_0^E$ and the abscissa $t$. From the inclination of the lines the value of $P$ is determined. This value is about 3 $\sec^{-1}$ for 20% relative humidity and about 1 $\sec^{-1}$ for 50% relative humidity. Thus almost all the pulses appear within 2 minutes after the application of the field.

*Volume corresponding to a pulse* From the area of a pulse observed in C. R. O., the volume in which the polarization is revesed can be calculated as follows:[*]

The order of magnitude of the charge $q$ corresponding to a pulse is given as

$$q \sim (V/RA)\tau$$

where $V$ is the maximum voltage of a pulse in the C. R. O., $\tau$ the duration of the pulse, $A$ the amplification factor and $R$ the grid resistance of the first stage. If the thickness of the crystal is denoted by $L$ and the surface area by $S$, then the volume corresponding to a pulse is given by

$$v = q/q' \times L \times S$$

where $q' = S \times 2P_0$ and $P_0$ is the spontaneous polarization. Using the experimental values, $V \doteqdot 10$ volts, $A \doteqdot 10^6$, $R = 2.5 \times 10^5 \Omega$, $t \doteqdot 1/1000 \times 1/10$ sec, $L \doteqdot 0.1$ cm and $P_0 = 2.5 \times 10^{-7}$ coulomb /cm$^2$, the volume turns out

$$8 \times 10^{-10}\ \text{cm}^3 \sim 1 \times 10^{-9}\ \text{cm}^3\ .$$

This is much smaller than the volume of a domain which is the order of $10^{-5}$ cm$^3$.

*Relation between total number and applied field* Pulses are not observed at very low fields. They begin to take place at a certain field, e. g. about 30 volts/cm. The total number of pulses $n_0^E$ increases with the increase of the field and it begins to saturate at about 70 volts/cm (Fig. 5). Since the relation between $n_0^E$ and the field is almost linear at lower fields, the intersection of the line with the holizontal axis is called in this paper the critical field for the pulse.

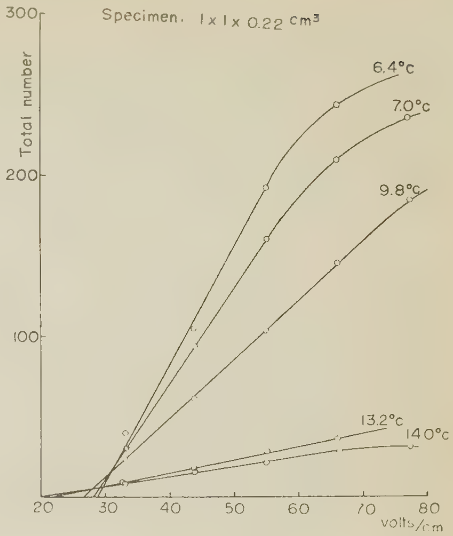

Fig. 5.

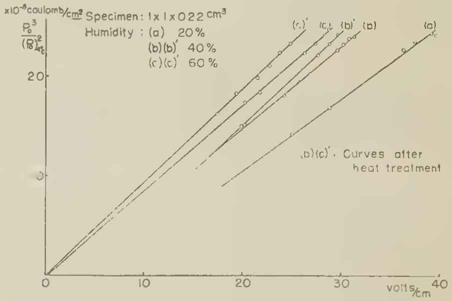

Fig. 6.

*Influence of humidity on the critical field* The dielectric constant and the piezo-electric modulus of rochelle salt change with humidity as reported by Kawai7). The critical field for the pulse also changes with humidity. It becomes lower with the increase of humidity under a constant temperature (Fig. 6).

*Influence of temperature on total number* It is recognized in Fig. 5 that the total number of pulses at higher fields decreases with the rise of temperature. This relation is reversed at temperatures lower than 0°C (Fig. 7). This behavior suggests that the total

---

[*] In the present experiment the time constant of the circuit containing the crystal is about $4 \times 10^{-5} \sim 8 \times 10^{-5}$ sec, if the dielectric constant of the crystal is assumed as 200～400. This is the same order as the period of time in which the pulse rises and falls (Fig. 3). This indicates that the time constant is really the same order as the duration in which the polarization is reversed abruptly.

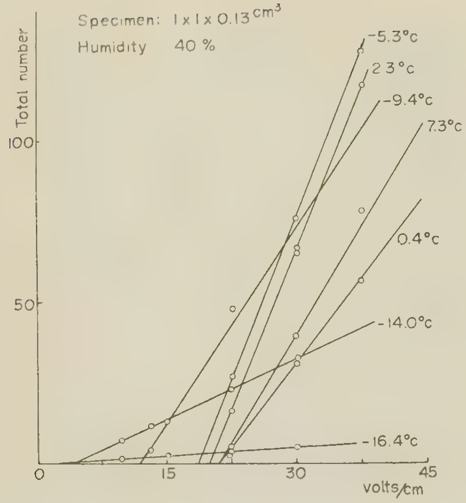

Fig. 7.

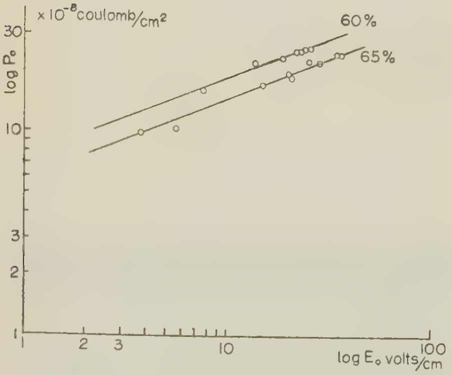

Fig. 8.

Table I.

| Experimental arrangement | Humidity | $n$ |
|---|---|---|
| Fig. 1 (a) | 60% | 2.7 |
| Fig. 1 (b) | 60% | 2.6 |
| | 65% | 2.5 |

number of pulses under a certain field is dependent upon the spontaneous polarization.

*Influence of temperature on the critical field* The critical field of the pulse $E_0$ is dependent upon temperature under a constant humidity (Fig. 6). If $\log E_0$ is plotted against $\log P_0$, a linear relation is found between them provided the humidity is higher than 60% (Fig. 8). This mean that there holds a relation $E_0=\text{constant}\times P_0^n$. The value of $n$ can be determined from the inclination of the line. A few examples of the value are given in Table I. The mean value of Table I is $\bar{n}=2.6$.

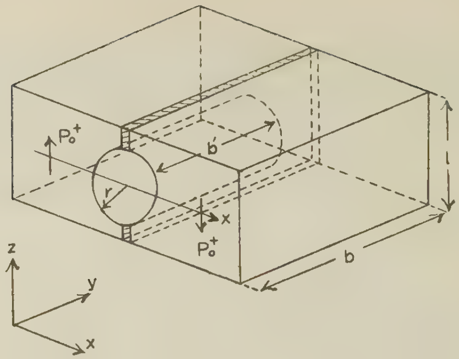

Fig. 9.

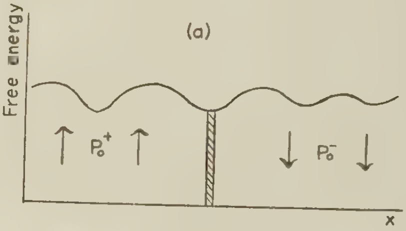

Before the application of a field

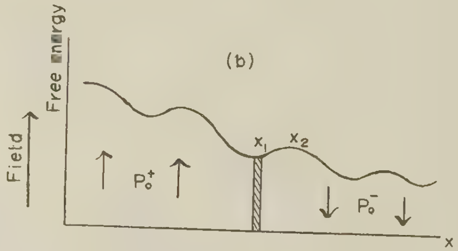

After the application of a field

Fig. 10.

It was observed that the critical field becomes lower soon after the crystal is heat-treated (see curve (b)′ and (c)′ in Fig. 6).

## § 4. Explanation of the Experimental Results

I) It is well known that there are many hollows in a rochelle salt crystal[8]. The hollow is generally cylindrical, having the radius of $10^{-4}\sim10^{-5}$ cm and the length of 1 mm$\sim10^{-4}$ cm and it is mostly extending to the direction of $c$-axis. If a boundary wall parallel to $c$-plane moves across a hollow by the application of a field, a pulse is caused with its movement because the potential energy of the wall is changed abruptly by the hollow. The volume corresponding to such a pulse can be roughly estimated by both the radius of a hollow and the surface area of a wall which moves cooperatively. If the value for the surface area obtained by the calculation in the next section is used, the volume turns out $10^{-8}\sim10^{-9}$ cm$^3$, which is the same order with the volume obtained from the experimental result. Thus the experimental result for the volume corresponding to a pulse can be explained favourably on the assumption that a pulse is caused when a wall passes across a hollow by the application of a field.

II) As known by the observation through the crossed nicols, there are many boundary walls in a crystal before the application of a field. These walls are generally arranged parallel to *c*-plane or *b*-plane with a little different intervals. If one of the walls passes through a hollow, it is stabilized at this hollow (Fig. 9) because the hollow cuts off a certain volume of the wall and therefore it decreases the potential energy of the wall (Fig. 10(a)). When a field is applied on the crystal, the potential energy changes and the wall moves as shown in Fig. 10(b). If the field becomes a certain strength, the wall can just leave the hollow and moves freely getting over other hollows. This motion of the wall results in pulses as explained before. Therefore the critical field for the pulse is identified with such a field that a wall can just leave a hollow first of all if it is assumed that all the walls are stabilized at hollows before the application of the field. Taking this assumption into consideration the relation between the critical field and the spontaneous polarization can be explained as given in the next section.

III) If a wall stays at a hollow before the application of a field, there are two causes which prevent the wall from its movement to leave the hollow by the application of the field. One of the causes is the increase of the wall energy and the other is the increase of the depolarizing field due to the charge produced on the hollow surface. The former is not influenced by humidity, but the latter is influenced severely because the higher humidity is, the faster the surface charge is neutralized by floating charges. Thus the increase of humidity facilitates the movement of a wall to leave a hollow by the application of a field. This tendency is in accordance with the one obtained from the experimental result. Therefore the experimental result can be explained qualitatively on a further assumption that the conductivity of the hollow surface is increased with the increase of humidity as well as the one of the crystal surface. In the calculation of the next section it is assumed that the critical field is not influenced by the surface charge. This assumption seems to be satisfied from the experimental result if humidity is higher than 60%.

Now let us summarize the assumptions necessary to explain all the experimental results.

1) All the walls in a crystal are stabilized at hollows before the application of a field.

2) A pulse is caused by the jerky motion of a wall passing across a hollow.

3) The critical field for the pulse is such a field that a wall can just leave a hollow first of all.

4) The conductivity of a hollow surface is increased with the increase of humidity as well as one of the crystal surface.

## § 5. Theoretical Treatment of the Relation between the Critical Field and the Spontaneous Polarization

For convenience of calculation let us assume only one wall and only one hollow in a crystal. The wall passes through the center of the hollow (Fig. 9) before the application of a field. Then the change of the free energy for a movement of the wall by a distance $x$ under a field $E$ is given by

$$F=2\sigma b'\left[\int_{-\Delta/2}^{\Delta/2}\sqrt{r^2-(x-r)^2}\,dx-\int_{x-\Delta/2}^{X}\sqrt{r^2-(x-r)^2}\,dx\right]-2EP_0\left(blx-2b'\int_{-\Delta/2}^{x-\Delta/2}\sqrt{r^2-(x-r)^2}\,dx\right) \tag{1}$$

where $r$ and $b'$ are the radius and the length of the hollow respectively; $b$, $l$ and $\Delta$ are the length, the thickness and the breadth of the wall respectively; $\sigma$ is the wall energy per volume. The value $X$ is $x+\Delta/2$ for $2r-\Delta/2\geq x>r$ and $r$ for $2r+\Delta/2\geq x>2r-\Delta/2$. The first bracketed term gives the increase of the wall energy and the second bracketed term the derease of the interaction energy between the polarization and the field. Since the relation $l\gg r$ ($\sim10^{-5}$ cm) is generally satisfied, the last term of the equation can be neglected. This equation has a minimum at $x_1$ for

$2r-(\varDelta/2)\geqq x>r$ and has a maximum at $x_2$ for $2r+(\varDelta/2)\geqq x>2r-\varDelta/2$ provided $E$ is constant. Thus the difference between the free energies at $x_1$ and $x_2$, $\varDelta F$, is the potential barrier for the wall. The value of $x_1^0$ and $x_2^0$ can be obtained by the following equations:

$$\sqrt{r^2-(x_1^0-r-\varDelta/2)^2}-\sqrt{r^2-(x_1^0-r+\varDelta/2)^2}=(E_0P_0bl)/(\sigma b') \quad (2)$$

$$\sqrt{r^2-(x_2^0-r-\varDelta/2)^2}=(E_0P_0bl)/(\sigma b') \quad (3)$$

where $x_1^0$ and $x_2^0$ is the values of $x_1$ and $x_2$ when $E$ is equal to the critical field $E_0$. If $\varDelta F$ becomes the same order of $kT$, the wall can get over the barrier in a few minutes. By putting $\varDelta F=kT$, we can get the critical field $E_0$:

$$kT=-2E_0P_0bl(x_2^0-x_1^0)+2\sigma b'\left[\int_{x_1^0-\Delta/2}^{x_1^0+\Delta/2}\sqrt{r^2-(x-r)^2}\,dx-\int_{x_2^0-\Delta/2}^{r}\sqrt{r^2-(x-r)^2}\,dx\right]. \quad (4)$$

It may be inferred that the $x_1^0$ and $x_2^0$ have the values nearly equal to $r$ because $kT$ is much smaller than the other terms in eq. (4).

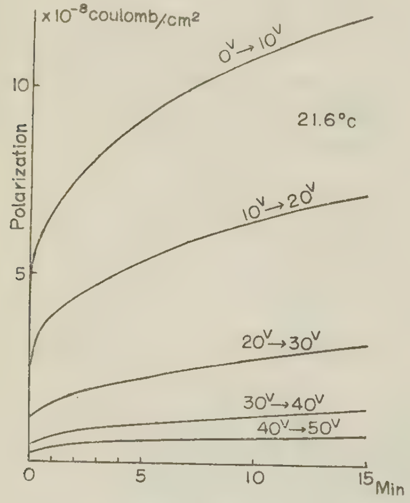

Fig. 11.

Putting $x_1^0=2r-\xi$, $x_2^0=2r-\eta$ and assuming $r\gg\xi$, $\eta$ and $\varDelta$, from eqs. (2), (3) and (4) we get

$$\xi=\varDelta/2+kT/(E_0P_0bl) \quad (5)$$

$$\eta=[(E_0P_0bl)/(\sigma b')-r\varDelta]/2r \quad (6)$$

and

$$[(E_0P_0bl)^2/((\sigma b')^2/2r)-\varDelta]^2-(2kTE_0P_0bl)/(r(\sigma b')^2)=0\,. \quad (7)$$

Since $\varDelta\geqq\left(\frac{E_0P_0bl}{\sigma b'}\right)^2\Big/2r$ from eq. (6), the second term in eq. (7) is smaller than $3\times10^{-22}/bl$ using the values $\varDelta=2\times10^{-7}$ cm, $r=10^{-5}$cm, $V\fallingdotseq1/10$ e. s. u., $P_0=760$ e. s. u. about at 4°C and $kT\sim10^{-13}$ e. s. u.. This value is much smaller than the value $\varDelta^2$ because $bl$ is much larger than $10^{-8}\,\text{cm}^2$ as proved later. Thus from eq. (7) we get approximate relation

$$\varDelta=\left(\frac{E_0P_0bl}{\sigma b'}\right)^2\Big/2r \quad (8)$$

Substituting the relation $r=\frac{8}{3}P_0^3\sqrt{cd}$ and $\varDelta=\frac{2}{P_0}\sqrt{\frac{c}{d}}$ obtained by Mitui and Furuichi[9)] into (8), the wall energy per volume comes out

$$\sigma=\gamma/\varDelta=4/3\,d\,P_0^4$$

where $c$ and $d$ are certain constants. Using this $\sigma$ and $\varDelta$, eq. (8) becomes

$$E_0bl=\frac{4}{3}\,dP_0^3b'\sqrt{2r\varDelta}=\frac{8}{3}\sqrt{r}\,d^{3/4}c^{1/4}b'P_0^{2\cdot5}\,.$$

Assuming that $c$, $d$ and $b'$ are independent of temperature, $E_0$ changes proportional to $p_0^{2\cdot5}$. This agrees with the experimental result within the error. Using $d\fallingdotseq6\times10^{-7}$ and the previous values, we get

$$bl\fallingdotseq6\times10^{-3}b'\,.$$

If we assume that $b'=0.1$ cm and $b=0.5$ cm, then $l\fallingdotseq10^{-3}$ cm which satisfies the condition $l\gg r$. The area $bl$ may be considered as the area which moves cooperatively under a constant field.

## § 6. Discussion

1) As calculated in § 3, a volume corresponding to a pulse is the order of $10^{-9}\,\text{cm}^3$. This is much smaller than the volume of a domain which is the order of $10^{-5}\,\text{cm}^3$. Kojima and Kato reported that a volume corresponding to a largest pulse is the order of $10^{-8}\,\text{cm}^3$. This value is in good accordance with the value obtained in this experiment.

2) According to the assumption described in § 4, a close relation is expected between the polarization charge and the number of pulses because both the charge and the pulses are caused by the movement of walls. Although the polarization charge is not studied in the present experiment, its variation with time was already studied by Takahashi and Hara[10)] (Fig.

11). This curve agrees qualitatively with the curve of the total number of pulses which is shown in Fig. 4(a). This indicates that our assumption is correct.

## § 7. Summary

1) When a field is applied on a crystal of rochelle salt, the pulses different from Schönfeld noise are observed.

2) The volume corresponding to such a pulse is the order of $10^{-9}$ cm$^3$.

3) With the increase of the applied field the total number of pulses increases but begins to saturate at about 70 volts/cm. This indicates that the source of the pulse is finite. The maximum number observed on C. R. O. is about 400 for the crystal the volume of which is about $1\times1\times0.1$ cm$^3$.

4) The critical field for the pulse decreases with the increase of humidity. This effect can be explained taking account of the influence of humidity on the conductivity of the hollow surface.

5) The relation between the critical field $E_0$ and the spontaneous polarization $P_0$ is given by $E_0=\alpha P_0{}^n$ where $\alpha$ is a constant and $n=2.7\pm0.5$. This result can be explained on the assumption that all the walls are stabilized at the hollows before the application of a field.

6) A pulse observed in the present experiment may take place by the jerky motion of a wall when it passes across a hollow.

7) The critical field changes a little by the heat-treatment for the same crystal, for example a few volts/cm at 4°C.

Finally the author wishes to express his appreciation to Professor Ryozi Uyeda for his encouragement and to Mr. H. Yoshioka for his helpful discussions. This work was supported partly by the Scientific Research Fund of the Ministry of Education.

## References

1) T. Mitui and J. Furuichi: Buseiron Kenkyu **39** (1951) 96, in Japanese.
T. Mitui and J. Furuichi: Phys. Rev. **90** (1953) 193.
2) M. Kluge u. H. Schönfeld: Naturw. **20** (1933) 194.
2)′ von H. Schönfeld: Ann. d. Phys. **19** (1934) 754, Fig. 19.
3) von H. Schönfeld: Ann. d. Phys. **22** (1935) 53.
4) P. R. Newton, A. J. Ahearn and K. G. Mckey: Phys. Rev. **75** (1949) 103.
5) H. Takahashi, S. Hara and T. Nakamura: read at the 4th Annual Meeting of the Phys. Soc. Japan (1949).
6) S. Kojima and K. Kato: J. Phys. Soc. Japan **4** (1949) 362.
S. Kojima and K. Kato: J. Phys. Soc. Japan **5** (1950) 379.
7) H. Kawai: J. Phys. Soc. Japan **3** (1948) 105, 111.
8) S. Miyake: *Rochelle Salt* p. 10 (1948), in Japanese.
9) T. Mitui and J. Furuichi: Buseiron Kenkyu **45** (1951) 69.
10) H. Takahashi and S. Hara: J. Phys. Soc. Japan **4** (1949) 257.

JOURNAL OF THE PHYSICAL SOCIETY OF JAPAN Vol. 11, No. 2, FEBRUARY, 1956

# Experimental Evidence for the Collective Nature of the Characteristic Energy Loss of Electrons in Solids

## —Studies on the Dispersion Relation of Plasma Frequency—

By Hiroshi WATANABE

*Hitachi Central Research Laboratory, Kokubunji, Tokyo, Japan*

(Received September 17, 1955)

The energy loss of 25 kv. electrons was studied by a modified velocity analyzer of Möllenstedt type. By means of the analyzer we obtained the diagram which shows the variation of energy loss with the scattering angle. The specimens studied were Be, Mg, Al, Ge and C (graphite).

In the diagram we classified six types of patterns in which two are of the fundamental importance: (1) The first type is the sharp energy loss lines such as first discovered for Al and Be by Ruthemann. In the present experiment it was found that the value of energy loss of these lines increases with the scattering angle. To represent this relation an emprical formula was established. On the other hand, a theoretical formula was derived from the dispersion relation in Bohm-Pines' plasma oscillation theory. These two formulas are in good agreement for the lines of Be (19 ev), Mg (10.3 ev) and Al (14.8 ev). This agreement proves most decisively that the sharp lines are caused by the excitation of the collective plasma oscillation. For Ge (16.4 ev) and C (7.3 ev) the agreement is less perfect. (2) The lines of second type are observed at 23 ev for Al and 25 ev for C. They are rather diffuse and their energy losses do not vary with the scattering angle. The author attributes them to the excitation of individual electrons in energy bands. The value 23 ev for Al is in agreement with the energy difference between the large peaks in the fine structure of L-absorption edge.

According to the theory the curving and the position of the patterns in the first type are insensitive to the temperature of the specimen, being in agreement with the experiment.

## § 1. Introduction

Experiments on the energy analysis of electrons which have passed through thin foils were originally carried out by Ruthemann[1] and Lang[2]. They observed several equally spaced sharp lines in the energy spectrum from Be and Al, which lines indicate that incident electrons lose their energy in integral multiples of a sharply defined basic unit. Comparing the observed energy losses with the fine structures of $K$-absorption edge, Cauchois[3] suggested that such losses might be caused by the excitation of metal electrons from the occupied band to unoccupied ones. Although her suggestion seemed to be reasonable at first, the sharpness of the lines can hardly be explained because the unoccupied bands in metals are much broader than the observed breadth (3 or 4 ev) of lines. On the other hand Bohm and Pines[4][5] proposed that such an energy loss is caused by the excitation of a collective plasma oscillation of electron gas in metals, the angular frequency of which is $\omega_p$. They noted that the calculated values of the fundamental quantum of energy loss ($\hbar\omega_p$) are in remarkably good agreement with the observed values. Following this interpretation we can easily understand the sharpness of the lines which is difficult to be explained by Cauchois' suggestion.

Utilizing the high chromatic aberration of an electrostatic lens Möllenstedt[6] devised a new velocity analyzer of extremely high resolution. Using the analyzer of his type energy losses in numerous substances have been studied in detail by several authors[7][8][9]. Based upon these studies the substances can be classified into two groups. In the first group loss values are in good agreement with $\hbar\omega_p$ which is given by Bohm-Pines' theory, and in the second they are in no agreement. Elements Be, Mg, Al, Ta and Mo belong to

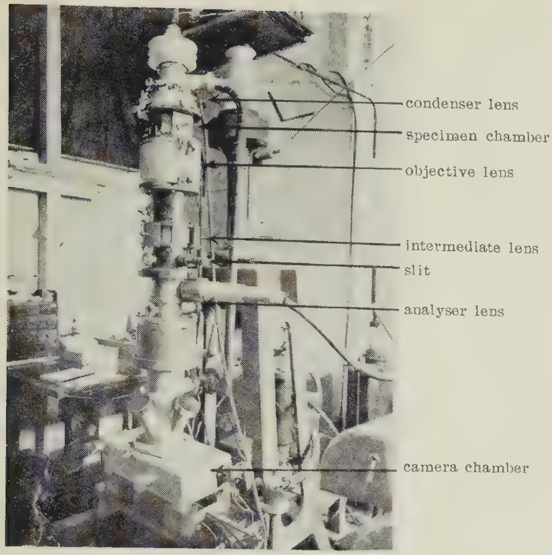

Fig. 1 a. A photograph of the velocity analyzer used in this experiment.

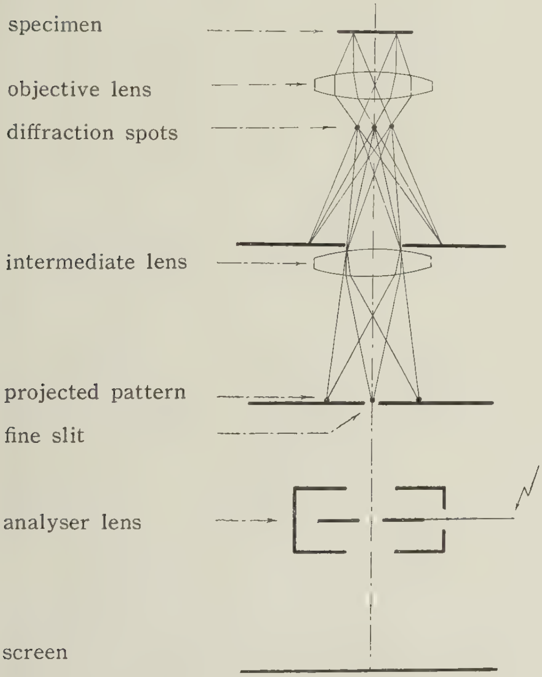

Fig. 1 b. A schematic diagram of the electron optical system.

the first, and noble metals and transition metals to the second. In this classification $\hbar\omega_p$ is calculated under the assumption that the valence electrons are all free. Since this assmption is not always adequate, it cannot be decided whether the plasma oscillation is actually the caused of the energy loss or not.

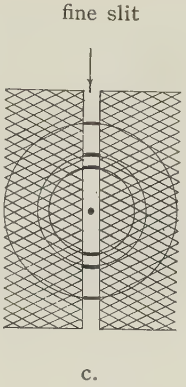

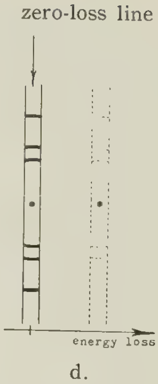

Fig. 1 c. A diffraction pattern on the fine slit plane.

Fig. 1 d. The energy loss spectrum. Rings drawn by dotted lines are due to the inelastically scattered electrons losing a certain discrete energy.

In the experiments mentioned above, the energy loss was measured for electrons which are scattered in a small angle of ca. $10^{-2}$ rad. Recently Leonhard[10] and the present author[11] studied the angular dependence of the energy loss up to $10^{-1}$ rad., using a modified velocity analyzer of Möllenstedt type. The author found that the energy loss increases with the scattering angle for the sharp lines which were originally found by Ruthemann and Lang. Kanazawa[12] has pointed out to the author that such dependence can be interpreted by the dispersion relation in Bohm-Pines' theory (see eq. (67) in reference (5),).

In this paper the author describes in detail the angular dependence of energy loss of the sharp lines, and comparing the experimental results with Bohm-Pines' theory he concludes that the sharp lines are caused by the excitation of plasma oscillation.

## § 2. Experimental Procedure

Figure 1a shows a photograph of the velocity analyzer used in this experiment and Fig. 1b a schematic diagram of its electron optical system. A diffraction pattern on the back focal plane of the objective lens is imaged by an intermediate lens on a plane with a fine slit. The electrons forming the pattern have various energy values owing to the inelastic collisons in the specimen. The velocity of the electrons which have passed through the slit is analyzed by an analyzer lens. The analyzer lens is a cylidrical unipotential electrostatic lens with rectangular electrode apertures, the same as that original-

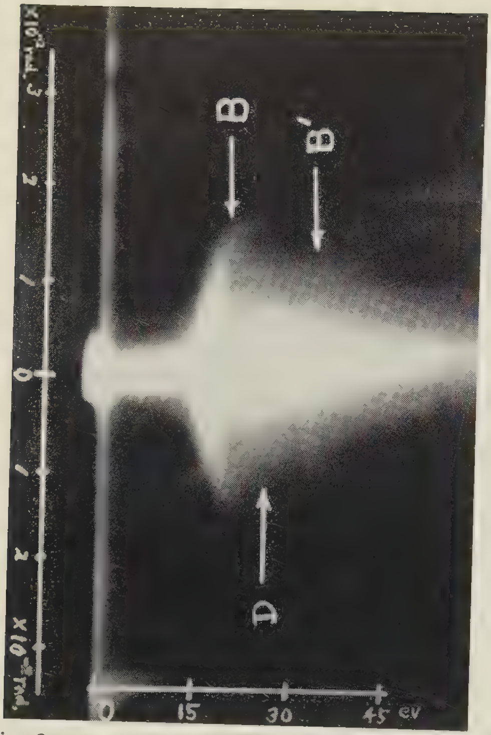

Fig. 2 a. An energy loss spectrum from Al corresponding to Fig. 1 d.

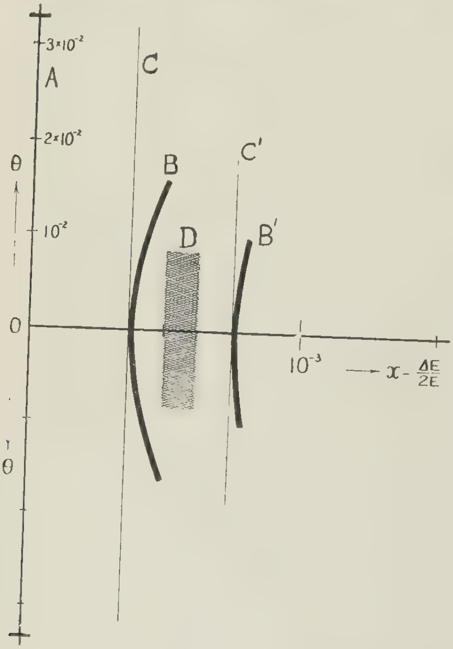

Fig. 2 b. The loss-angle diagram constructed from Fig. 2 a.

ly devised by Möllenstedt.

Figure 2a shows an example of energy spectra obtained in the energy analysis. From this photograph we make a diagram the abscissa of which is $x = \Delta E/2E$ and the ordinate the scattering angle $\theta$, where $\Delta E$ is energy loss and $E$ the accelerating voltage. In this paper we call this diagram a "loss-angle diagram". The energy loss is calibrated by a known accelerating voltage difference. The scattering angle is obtained from the radii of diffraction rings. The accelerating voltage used in this experiment was 25 kv, and the least detectable energy difference was ca. lev.

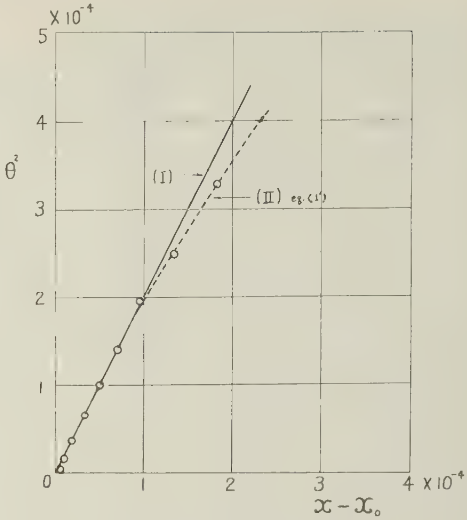

Fig. 2 c. Relation between $\theta^2$ and $(x - x_0)$. ○: experimental point.

Specimen examined were prepared by evaporation in vacuum higher than $10^{-4}$ mm Hg, as determined by an ionization gauge. The evaporated metal was condensed on a slide glass coated with collodion. To eliminate the effects of the collodion the slide was then immersed in 50% ether-alcohol to free the evaporated film from its backing. The unbacked metal foils were mounted on sheet meshes of copper. Thicknesses of the foils ranged from 150Å to 250Å. In the case of Mg we used very thick foils (ca. 500 Å) to avoid the influence of oxides covering the film. We examined each foil by the electron diffraction method and used only those foils which give few rings of the oxides.

Sometimes the electron optical system was changed as shown in Fig. 3 so that the specimens can be heated. In this system the diffraction pattern was reduced by the intermediate lens so that the electron beam enters into the analyzer with an angular

Table I. Comparison of the experimental values of $x_0$, $a$, $b$ with the theoretical values of $x_0$, $\alpha$ and $1/8x_0$.

| | B Type | | | | | | B′ Type | | | |
|---|---|---|---|---|---|---|---|---|---|---|
| | $x_0$ * (exp.) | $x_0$ (theo.) | $a$ (exp.) | $\alpha$ (theo.) | $x_0$ (exp.) | $1/8x_0$ (theo.) | $x_0$ (exp.) | $x_0$ (theo.) | $a$ (exp.) | $\alpha$ (theo.) |
| | $\times 10^{-4}$ | $\times 10^{-4}$ | | | $\times 10^{2}$ | $\times 10^{2}$ | $\times 10^{-4}$ | $\times 10^{-4}$ | | |
| Be | 3.8 | 3.8 | 0.42 ±0.04 | 0.45 | — | 3.3 | — | 7.6 | — | 0.22 |
| Mg | 2.1 | 2.2 | 0.62 ±0.04 | 0.44 | 4±1 | 5.7 | 4.2 | 4.4 | 0.40±0.05 | 0.22 |
| A | 3.0 | 3.2 | 0.50 ±0.05 | 0.45 | 3±1 | 3.9 | 6.0 | 6.4 | 0.32±0.04 | 0.22 |
| Ge | 3.3 | 3.1 | 0.83 ±0.15 | 0.45 | — | 4.0 | — | 6.2 | — | 0.22 |
| C (graphite) | 1.5 | 4.9 | 1.0 ±0.3 | 0.50 | — | 2.6 | — | 9.8 | — | 0.25 |

* To obtain the energy loss values in electron volts multiply $x_0$ by $5\times10^4$.

Table II. Experimental values of $a$ and $x_0$ for Al at various temperatures.

| Temperature (°K) | $a$ | $x_0$ |
|---|---|---|
| | | $\times 10^{-4}$ |
| 300 | 0.52±0.08 | 2.9±0.1 |
| 690 | 0.52±0.08 | 2.9±0.1 |
| 830 | 0.52±0.08 | 2.9±0.1 |
| 890 | 0.50±0.1 | 3.0±0.1 |

divergence as small as possible. The temperature of the specimen is measured by a Cu-Pt thermocouple attached to the copper mesh. The thermocouple was calibrated by the melting points of Sn and Pb which were placed at the position of the specimen.

## § 3. Experimental Results

Figure 2a is an example of photographs obtained from Al foil. Figure 2b is the loss-angle diagram obtained from Fig. 2a. In this diagram there are contained all of the typical patterns as denoted by A, B, B′, C, C′ and D.

The patterns B and B′ are of the fundamental importance in the following interpretation of the patterns. They indicate that the energy loss increases with the scattering angle. The discrete energy loss obtained in all the previous experiments is the energy loss of electrons averaged over the scattering angle of ca. $10^{-2}$ rad. The pattern $B'$ is a discrete energy loss which is about twice of loss of B, and the curvature at its vertex is smaller than that of B.

In order to treat quantitatively the relation between the energy loss and the scattering angle, we assume the empirical formula

$$(x-x_0)=a\cdot\theta^2+b\theta^4+\cdots\cdots \qquad (1)$$

where $x_0$ represents $x$-coordinate of the vertex of the pattern. To determine the coefficients $a$ and $b$, $\theta^2$-values are plotted against $(x-x_0)$-values. An example is shown in Fig. 2c which corresponds to the pattern B in Fig. 2b. A linear relation between $\theta^2$ and $(x-x_0)$ holds in the range of $(x-x_0)$ $<1.0\times10^{-4}$ (line (I) in Fig. 2c), the tangent of this line giving the value of $a$. The coefficient of $\theta^4$ term is determined by the magnitude of the deviation of the experimental points from the line (I). The curve (II) in Fig. 2c represents

$$(x-3.0\times10^{-4})=0.5\cdot\theta^2+3\times10^2\cdot\theta^4. \qquad (1')$$

The experimental points lie on curve (II) in the range of $(x-x_0)<2.0\times10^{-4}$. The pattern B fades out into the background at about $\theta$ $=1.5\sim1.8\times10^{-2}$ rad. Table I gives the value of $a$ and $b$ as well as $x_0$ for the patterns $B$ and $B'$ of Be, Mg, Al, Ge and C (graphite).

Table II gives the values of $a$ and $x_0$ for Al under various temperatures. It is easily concluded from this table that $a$ and $x_0$ do not depend on the temperature of the specimen.

The pattern D is an energy loss line which is distinguished from $B$ or $B'$ by its straightness and diffusedness. This straightness indicates the energy loss concerned is independent upon the scattering angle. For Al the energy loss of this type is 23 ev. Patterns of this type are observed also for collodion (21.2 ev), MgO (11.4 ev), MoS$_2$ (8.7, 22.8 ev), Ag(25 ev) and Au(25 ev).

## § 4. Interpretation of the Patterns

### *4·1* Pattern B

### *4·1·1* Theory

Let us assume that an incident electron of

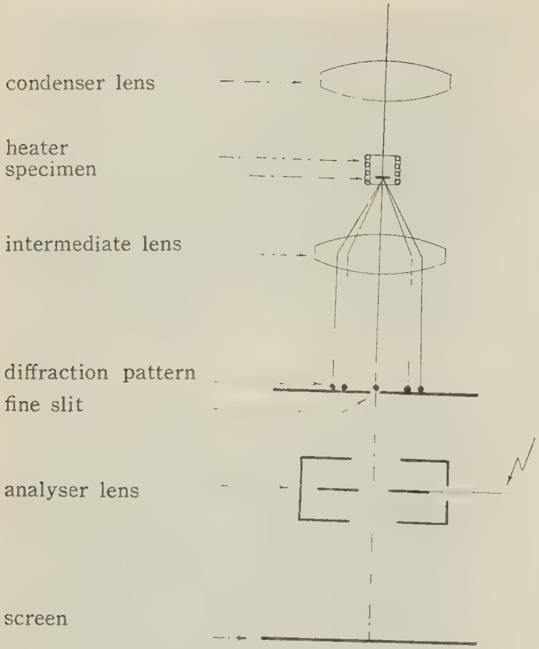

Fig. 3. A schematic diagram of the electron optical system in the arrangement for specimen heating. An electron diffraction specimen holder with a heater is inserted between the condenser and intermediate lenses.

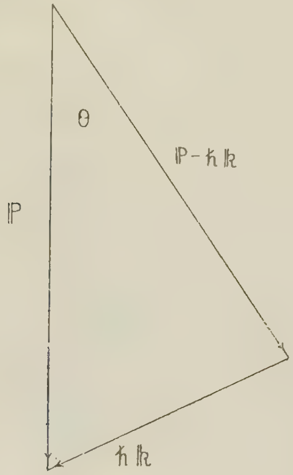

Fig. 4. Illustration of the momentum relation of the electron before and after the collision.

energy $E$ excites a plasma oscillation of frequency $\omega$ in the electron gas, thus it loses energy quantum of $\hbar\omega$ and is scattered into a direction $\theta$ from the incident direction. We will derive a relation between the scattering angle $\theta$ and the energy loss $\hbar\omega$ from the law of momentum conservation. When the momentum of the incident electron $p$ is large compared with $\hbar k$ we have the relation

$$p\theta=\hbar k \tag{2}$$

where $k$ is the wave number of the excited plasma wave. The dispersion relation of the plasma frequency is given by Bohm and Pines (see eq. (67) in reference (5)) as follows,

$$\omega=\omega_p+\frac{k^2}{m\omega_p}\cdot\frac{1}{n}\sum_i\frac{P_i^2}{2m}+\frac{\hbar^2k^4}{8m^2\omega_p} \tag{3}$$

where

$$\omega_p=\sqrt{4\pi ne^2/m}$$

$n$: density of free electrons
$P_i$: momentum of $i$-th electron
$e, m$: charge and mass of the free electron.

Substituting $k$ from eq. (2) into (3) we have

$$\hbar\omega=\hbar\omega_p+\alpha\frac{p^2}{m}\theta^2+\frac{p^4\theta^4}{8m^2\hbar\omega_p} \tag{4}$$

where

$$\alpha=\frac{1}{n}\sum_i\frac{P_i^2}{2m}\Big/\hbar\omega_p\,. \tag{5}$$

Introducing a dimensionless variable

$$x=\frac{m\hbar\omega}{p^2}=\frac{\hbar\omega}{2E}\quad\left(E=\frac{p^2}{2m}\right) \tag{6}$$

and a dimensionless constant

$$x_0=\frac{m\hbar\omega_p}{p^2}=\frac{\hbar\omega_p}{2E} \tag{7}$$

we have

$$x-x_0=\alpha\theta^2+\frac{\theta^4}{8x_0}\,. \tag{8}$$

Adopting the free electron model of metal, we can easily calculate the numerator of the expression of $\alpha$[13],

$$\frac{1}{n}\sum_i\frac{P_i^2}{2m}=\frac{3}{5}\varepsilon_0'\left[1+\frac{5}{12}\pi^2\left(\frac{kT}{\varepsilon_0'}\right)^2\right], \tag{9}$$

where

$$\varepsilon_0'=\frac{1}{2}\frac{\hbar^2}{m}\left(\frac{3n}{8\pi}\right)^{2/3}. \tag{9'}$$

### *4·1·2* Comparison with experiment

Equation (8) has the same form as the empirical formula (1). In Table I the theoretical values of $\alpha$, $1/8x_0$ and $x_0$ are compared with the experimental values of $a, b$ and $x_0$, respectively. Agreements between these values are good enough for Be, Mg and Al to conclude that the pattern B is caused by the excitation of a plasma oscillation.

For Ge and C (graphite) the agreement is less perfect, especially the experimental value of $x_0$ for graphite is much smaller than theoretical value. This may be attributed to the inadequacy of the free electron model adopted.

### *4·1·3* Temperature dependence

As given in Table II the position and shape of the pattern $B$ in Fig. 2 are independent of the temperature of specimen. This temperature independence is easily understood when we refer to eqs. (5), (7), (8) and (9). Equation (7) and (3′) show that the position of the pattern depends upon the temperature only through $\sqrt{n}$, which decreases with increasing temperature,

$$\sqrt{n}=\sqrt{n_0}\cdot\left(1-\frac{3}{2}\alpha_l T\right) \qquad (10)$$

where $n_0$ means the electron density at 0°K and $\alpha_l$ the linear expansion coefficient. For Al ($\alpha_l=2.3\times10^{-5}$ deg.$^{-1}$) we have

$$\frac{3}{2}\alpha_l T=3\times10^{-2} \qquad (11)$$

at 1000°K. This is too small to be detected in our analysis.

The shape of the pattern is determined by the dispersion coefficient $\alpha$ which contains explicitly the temperature T (cf. eq. (9)). The temperature dependent term $\frac{5}{12}\pi^2\left(\frac{kT}{\mathcal{E}_0'}\right)^2$, however, is extremely small even at 1000°K for most metals. For example, with $\mathcal{E}_0'=11.7$ ev for Al, we have at 1000°K

$$\frac{5}{12}\pi^2\cdot\left(\frac{kT}{\mathcal{E}_0'}\right)^2=5\times10^{-4}\,. \qquad (12)$$

This is also beyond the resolution of our analyzer. Thus the temperature dependence of the position and the shape of the pattern are indetectable by means of our instrument, being in agreement with the experiment.

### *4·1·4* Maximum scattering angle

Ferrell[14] has pointed out that such a loss-angle diagram as Fig. 2a provides us with an information as to the critical wave number $k_c$ for collective plasma oscillation. Here, $k_c$ is defined as $2\pi/\lambda_c$, and the critical wave length $\lambda_c$ is nearly equal to Debye length $\lambda_D$. A plasma oscillation with the shorter wave length than $\lambda_c$ can not be excited in solids. Based upon eq. (2) we expect that the maximum scattering angle $\theta_c$ is

$$\theta_c=\frac{\hbar k_c}{p}\,. \qquad (13)$$

The maximum wave number $k_c$ is given by Bohm and Pines[15] as follows,

$$k_c=0.353\ (r_0/a_0)\cdot k_0 \qquad (14)$$

where $k_0$ is the wave number of an electron at the top of the Fermi distribution, $r_0$ is the interelectronic spacing defined by

$$n=(4\pi r_0^3/3)^{-1}, \qquad (15)$$

and $a_0$ is Bohr radius. For Al we calculate $\theta=1.1\times10^{-2}$rad. for 25 kv electrons. This is to be compared with the maximum angle at which the pattern $B$ fades away into background. As given in the preceeding section, the maximum scattering angle measured in Fig. 2a is 1.5∼1.8×10$^{-2}$ rad. which is somewhat larger than the theoretical value.

### *4·2* Pattern B′

It is evident that in passing through a solid an incident electron undergoes more than one collision unless the solid is very thin. As an electron scattered inelastically in a direction $\theta$ with an energy loss of $\hbar\omega$ proceeds through the specimen, the second chance of the electron surffering the similar process of inelastic scattering occurs. As illustrated in Fig. 5 the dependence of the energy loss upon the scattering angle in such double scattering process is represented approximately by a parabola similar to B, the vertex of which is situated on a parabola ($B''$ in Fig. 5)

$$(x-2x_0)=\alpha\theta^2\,. \qquad (16)$$

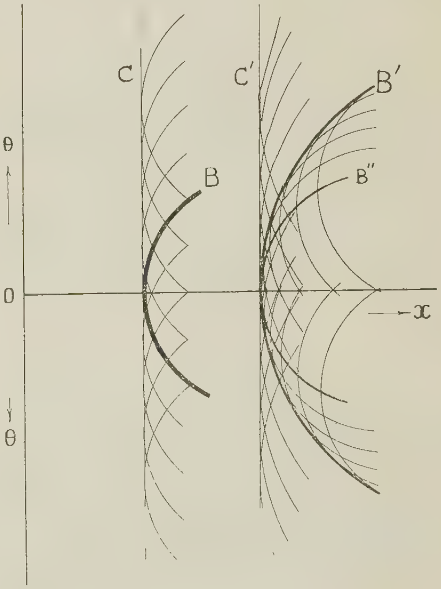

Fig. 5. Illustration of the arc $B'$ and lines $C$, $C'$.

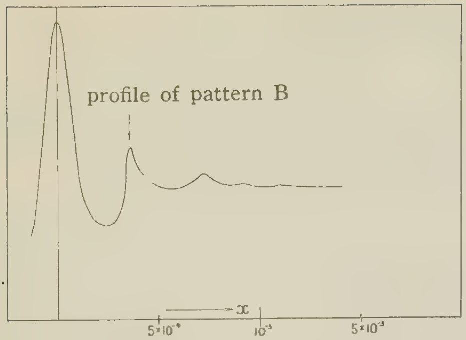

Fig. 6 a. An intensity distribution curve obtained along the $x$-axis in Fig. 2 a. The arrow indicates the position of arc $B$.

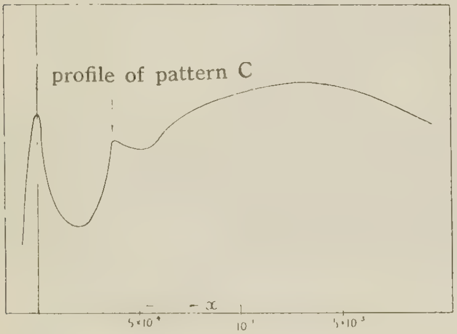

Fig. 6 b. An intensity distribution curve obtained along a straight line of $\theta=2\times10^{-2}$ rad. The arrow indicates the position of line $C$.

(We will neglect the small $\theta^4$ term in the following discussions.) If the envelop of a group of such parabolas is observed as the arc of $B'$ type, the equation representing the envelop becomes

$$(x-2x_0)=\frac{\alpha}{2}\theta^2 . \qquad (17)$$

Thus the coefficient $a$ for B patterns is twice that of $B'$. Since. however, the brightness of each parabola is largest at the vertex, we may observe an intermediate curve which lies between two parabolas of eqs. (16) and (17). In Table I we see that the ratio of the coefficients of $B$ and $B'$ is 1.6 for Al as well as for Mg.

### *4·3* Pattern *D*

The loss line of $D$ type is characterized by its straightness and diffusedness. This can be interpreted as due to the excitation of the conduction electrons to the allowed unoccupied levels. The fact that in the fine structure of the $L$-absorption edge of $X$-ray in Al there is a relatively large absorption peak at an energy distance of 23 ev[16) from the edge may support this explanation.

For Ag and Au we observed diffuse and straight patterns similar to D. It is, however, premature to conclude that they are caused by interband transitions because the plasma oscillation should be excited in these metals. The diffusedness may be due to some unknown factors and the curving is not observed because of the diffusedness.

### *4·4* Other Patterns

The line $A$ represents the angular distribution of scattered electrons the energy loss of which is less than 1 ev. The bright parts on this line give the positions of diffraction rings, by which we can determine the scattering angle.

For the interpretation of the parallel lines $C$ and $C'$ in Fig. 2b we have to take into account the double or triple scattering of the incident electrons. Electrons scattered onto a point $(0, \theta_1)$ on the line A in Fig. 2b undergo the secondary inelastic collision losing an energy quantum of $\hbar\omega$. Since the secondary inelastic collision process gives the similar angular distribution of scattered electrons as in the case of direct excitation of the plasma oscillation, the resulting angular dependence of the double scattering is obtained from eq. (8) to give

$$(x-x_0)=\alpha(\theta-\theta_1)^2 . \qquad (18)$$

As is illustrated in Fig. 5, the line $C$ is thought to be the envelop of a group of these parabolas

$$(x-x_0)=0 . \qquad (19)$$

The pattern $C'$ can be interpreted by the similar consideration. In this case, of course, one more inelastic collision process must be taken into account.

Although in the above consideration we took only elastic-inelastic process, the reverse inelastic-elastic process is also possible.

An experimental evidence in support of the above consideration is given by a comparison of relative intensity curves obtained along the $x$-axis with that along a straight line of $\theta=2\times10^{-2}$ rad. in Fig. 2a. The curves are reproduced in Fig. 6. The peak indicated by an arrow in Fig. 6a represents a profile of a section of pattern $B$ cut along $x$-axis and slopes to the larger $x$ side by a steeper des-cent in comparison with the case of the peak corresponding to *C* in Fig. 6b. Such a difference in the slopes of the two intensity curves can be easily explained by adopting the above interpretation for line *C*. (see Fig. 5).

## § 5. Discussions

As stated in the introduction two ways of explanation are proposed concerning the origin of energy losses of electrons. The one is that the losses are caused by the interband transitions and the other is that by the excitation of collective plasma oscillation. It was not yet decided which theory is adequate for the interpretation of a loss line.

Only by the coincidence of the observed values of the loss with the calculated values it is difficult to conclude that the energy loss is due to the plasma oscillation, because the assumption under which the calculation is carried out is not always adequate. And we can not derive a decisive conclusion from the breadth of the lines because of the lack of the knowledge about it. Wolff(17) has suggested that the breadth of plasma lines should increase from element to element as the 3d shell is filled in the transition metals Sc–Ni. This suggestion, however, was not supported by experiment(7)(13), and we failed to decide whether the lines are due to the plasma oscillation or not, by this suggestion.

In the present experiment the curving of the patterns *B* and *B'* is observed. Based upon the plasma oscillation theory we explained curving as described in § 4. It is difficult to see how an angular distribution like this can be reconciled with interband transitions, since it has its origin in the $k^2$ term in the dispersion relation, (3). Thus the sharp lines observed in Mg, Be, Al and etc. are without doubt caused by the excitation of plasma oscillation.

We observed also the diffuse and straight lines in the loss-angle diagrams. These lines are conceivable as due to the interband transitions, being in agreement with the observation of the fine structure of *L*-absorption edge.

## § 6. Acknowledgement

The author is indepted to Prof. H. Kanazawa of Tokyo University who kindly suggested the interpretation of the pattern *B* to the present author, and also to Dr. N. Kato of Kobayashi Institute of Physical Research and Prof. R. Uyeda of Nagoya University for the helpful discussions. It is a preasure of the author to express his appreciation to Drs. D. Pines and R. A. Ferrell for their kind criticism and encouragement. The author is grateful to Dr. B. Tadano and Mr. N. Morito for their encouragement throughout this study.

### References

1) G. Ruthemann: Ann. d. Phys. **2** (1948) 113.
2) W. Lang: Optik **3** (1948) 233.
3) Y. Cauchois: Acta. Cryst. **5** (1952) 351.
4) D. Pines: Phys. Rev. **85** (1952) 338.
5) D. Bohm and D. Pines: Phys. Rev. **92** (1953) 609.
6) G. Möllenstedt: Optik **5** (1949) 499.
7) L. Marton and L. B. Leder: Phys. Rev. **94** (1954) 203.
8) W. Kleinn: Optik **11** (1954) 226.
9) H. Watanabe: Journ. Phys. Soc. Japan **9** (1954) 920.
H. Watanabe: Journ. Phys. Soc. Japan **9** (1954) 1035.
10) F. Leonhard: Zeits. f. Naturforsch. **9a** (1954) 727, 1019.
11) H. Watanabe: Journ. Phys. Soc. Japan **9** (1955) 321.
12) H. Kanazawa: Private communication.
13) F. Seitz: The modern theory of solids (McGraw-Hill Book Company, Inc., New York, 1940) p. 149.
14) R. A. Ferrell: Private communication.
15) D. Pines: Phys. Rev. **92** (1953) 626.
16) J. E. Johnston: Proc. Camb. Phil. Soc. **35** (1939) 108.
17) P. A. Wolff: Phys. Rev. **92** (1953) 18.
18) H. Watanabe: to be published in this Journal.

JOURNAL OF THE PHYSICAL SOCIETY OF JAPAN Vol. 11, No. 2, FEBRUARY, 1956

# Observation of Dislocations in Silver Halides
## Part I. Annealed Crystals

By Hiroshi KANZAKI

*Institute of Industrial Science, University of Tokyo, Chiba, Japan*

(Received August 5, 1955)

It has been concluded that the distribution of both the printed-out silver particles and the chemical etching pits reveals that of dislocations in annealed crystals of silver chloride. In the crystals with (110) surfaces, however, the existing dislocations do not contribute to the formation of silver particles and in those with (100) surfaces the existing dislocations do not produce etch pits. The necessary condition for the formation of silver has been concluded to be the existence of extra effective charge on the surface of the crystal.

## § 1. Introduction

Hedges and Mitchell[1] have found that the printed-out silver particles precipitate at the dislocations in polygonized crystals of AgBr and thus have succeeded in observing the distribution of dislocations inside the crystals for the first time.

On the other hand, several experimental results[2] have shown that the dislocations can produce "chemical etching pits" at the surface.

In this part of the article, the observation of both the printed-out silver particles and the etch pits is adopted for the direct examination of dislocation patterns in annealed crystals of AgCl. Special attention will be paid to the following problems:

(1) What is the mechanism which enables us to see the dislocations?

(2) What is the origin of existing dislocations?

## § 2. Experimental Procedures

### 2-1. Specimens

Powders of AgCl were specially prepared by Dr. Koseki of the Research Laboratory, Fuji Photo Film Co., Ltd..

The specimens were prepared by the gradual solidification from the melt. The procedures in making crystals are schematically shown in Fig. 1. and carried out in the following ways.

(1) Powders of AgCl have been melted in the crucible of Pyrex glass as shown in Fig. 1 (a).

(2) By reducing the temperature, the solid crystals are grown under considerable temperature gradient in 20 to 30 minutes (shown in Fig. 1(b) and (c)).

(3) Liquid AgCl is removed out from the crucible and solid crystals remain as attached to the wall of the crucible as shown in Fig. 1(d).

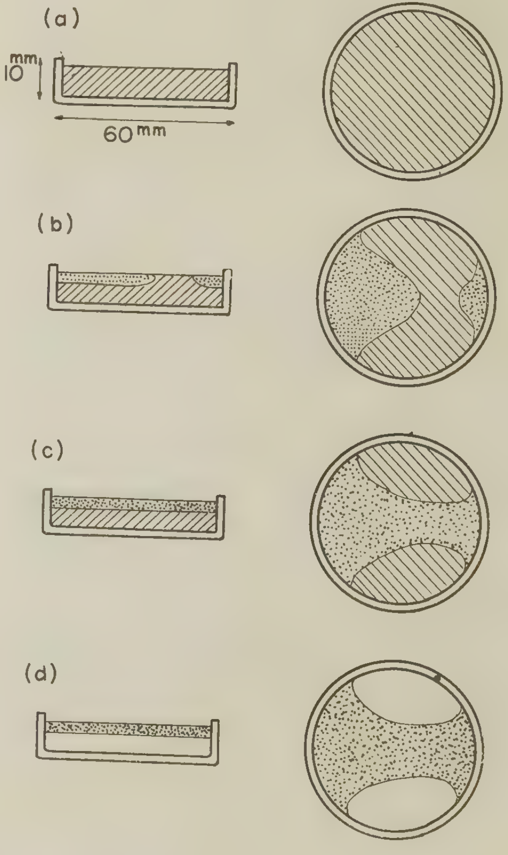

Fig. 1. Procedures of preparing the "usual crystals" of AgCl from the melt. Hatched areas; molten AgCl, dotted areas; solid AgCl.

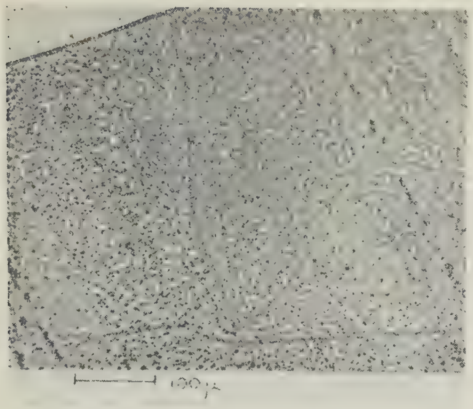

Photo. 1. Printing-out pattern of the "usual crystal" with (100) surface. Left-upper corner is the crystal with (110) surface.

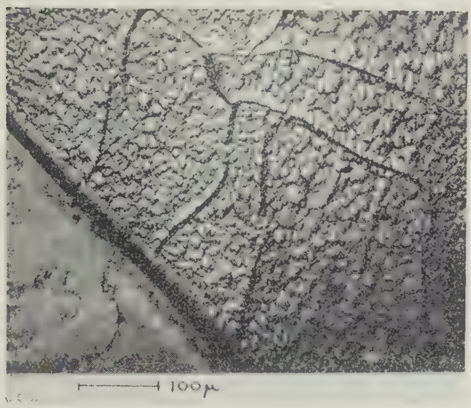

Photo. 2. Etching pattern of the "usual crystal" with (110) surface. Left-lower corner is the crystal with (100) surface.

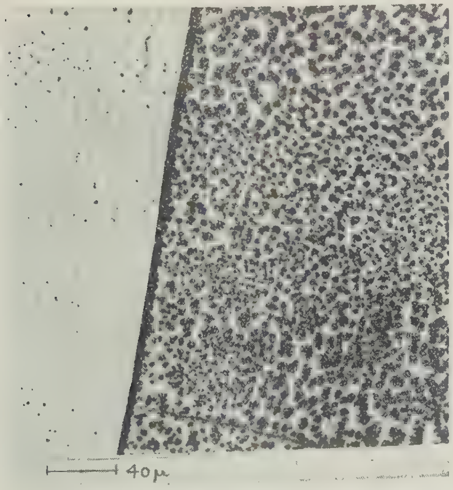

Photo. 3. Printing-out pattern near the grain boundary of the "usual crystal". The right-hand grain has (100) surface and the left-hand one has (110) surface.

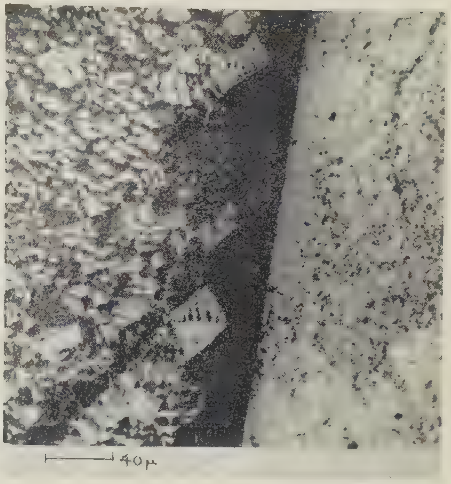

Photo. 4. Etching pattern of the same area with Photo. 3.

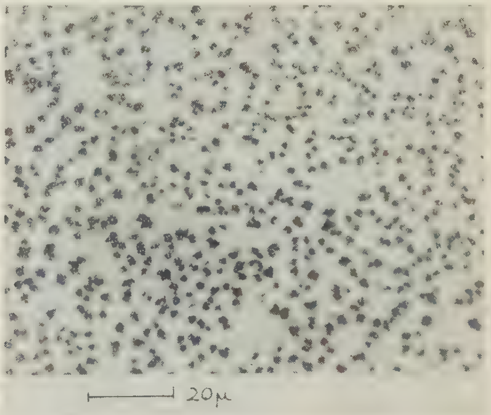

Photo. 5. Printing-out pattern of "perfectly annealed" crystal with (100) surface.

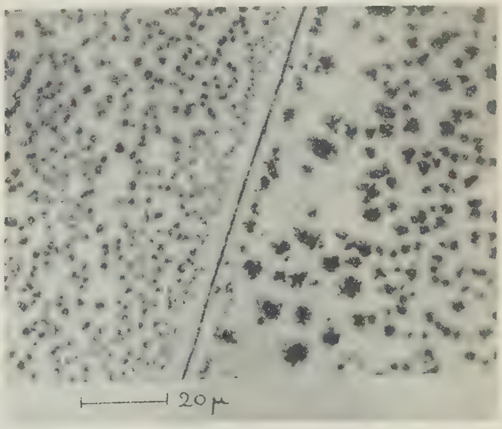

Photo. 6. Printing-out pattern of "perfectly annealed" crystals near the grain boundary.

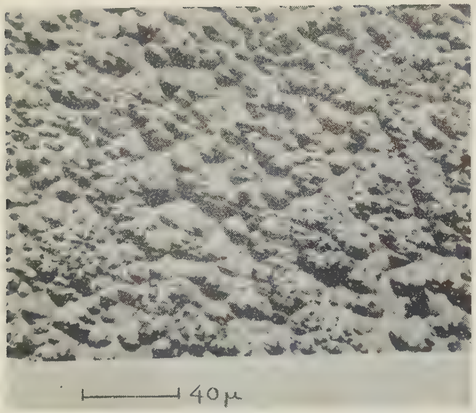

Photo. 7. Etching pattern of "perfectly annealed" crystal with (110) surface.

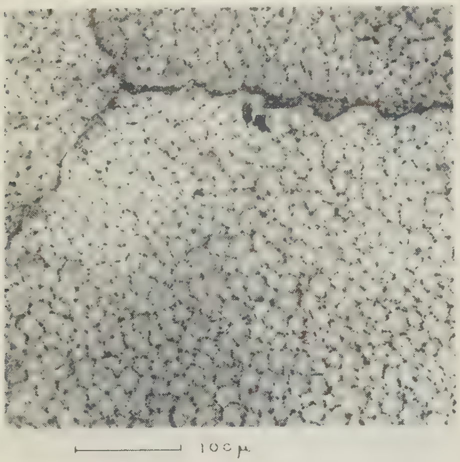

Photo. 8. General view of the printing-out pattern of the "special crystal No. 1".

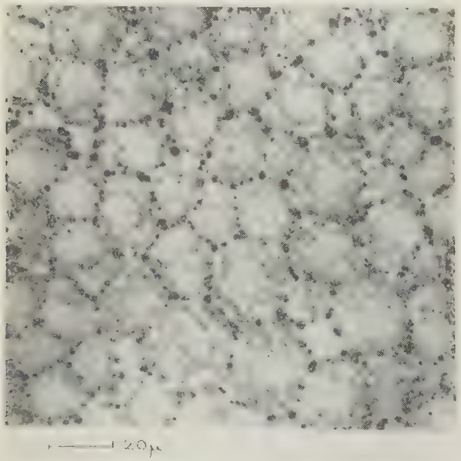

Photo. 9. Printing-out pattern at the surface of the "special crystal No. 1".

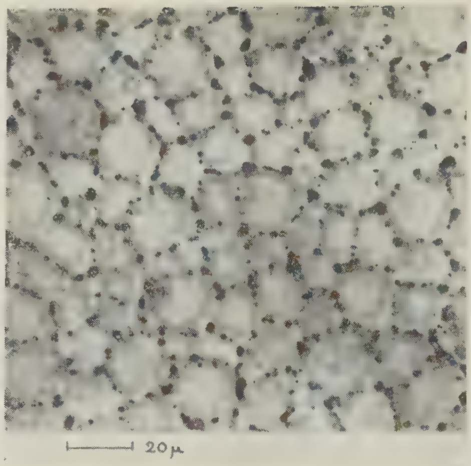

Photo. 10. Printing-out pattern in the interior of the "special crystal No. 1".

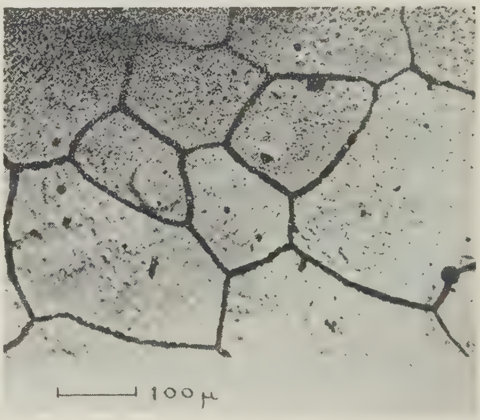

Photo. 11. General view of the surface of the "special crystal No. 2". Each of the "islands" of crystal is separated by the "valleys".

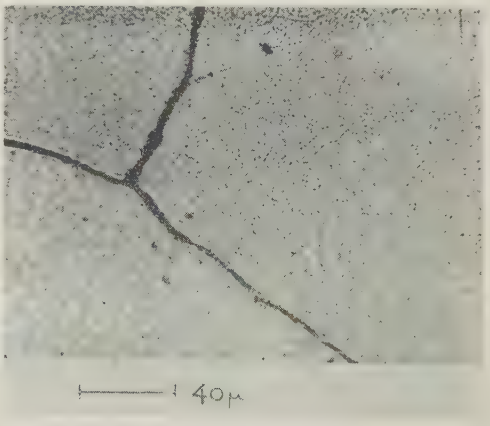

Photo. 12. Printing-out pattern of the "special crystal No. 2".

(4) The solid AgCl is annealed at 420 to 430°C for 2 hours and then slowly cooled to the room temperature in about 20 hours.

The specimens thus produced were made of several single crystals with dimensions of 5 to 10 mm. The central part of them may be reasonably identified as the strain-free crystals grown from the melt and was used in the main of the following experiments. They may be designated as the "usual crystals" in the following. Their surfaces were nearly parallel to either (100) or (110) face.

The special type of crystals used in some of the experiments were prepared in the following way.

One of them were thin crystals grown on the surface of the "usual crystals." They were produced by decanting the molten AgCl on the crystals which had been kept at the temperature slightly below the melting point. They may be designated as the "special crystals No. 1" in the following. Their surfaces were usually nearly parallel to (111) face.

The other special crystals were thin crystals grown on the surface of Pyrex glass plates, by decanting the melt in the simillar manner with the "special crystals No. 1". They may be designated as the "special crystals No. 2." The rate of solidification of these special crystals No. 1 and 2 was somewhat more rapid than that of the usual ones.

### 2-2. Printing-out

The crystals were exposed to the filtered radiation of 405 m$\mu$ (just in the long wavelength edge of the fundamental absorption band of AgCl) from the high pressure mercury lamp. After exposure of several hours under the photon intensities of $10^{14}$ quanta per sec. cm$^2$, the printed-out silver became visible under the microscope.

### 2-3. Chemical Etching

Etching was carried out by using the commercial photographic fixer* for a few minutes.

This etching procedure was also useful for the determination of crystal orientation. The crystals with (100) surface orientation showed hardly any pits and became glossy. Crystals with (110) and (111) surfaces showed etch pits on the entire surface and the pits took square and triangle form, respectively, according to the crystallographic symmetry.

## § 3 Results Obtained

### 3-1. Crystals with (100) or (110) Surface ("Usual Crystals")

In annealed crystals of AgCl, both the printing-out and the chemical etching revealed the grain boundaries and the sub-boundaries (boudaries with low angle of misfit inside the single crystals) at the surface of the specimens, as shown in Photos. 1 and 2. It may reasonably be concluded that the silver particles and the etch pits correspond to the existing dislocations. The results on strained crystals also support this conclusion and will be described in Part II.

The important experimental results are as follows:

(1) The silver particles appear in the crystals with (100) surface but do not appear in those with (110) surface, as seen in Photo. 1.

(2) The etch pits appear in the crystals with (110) surface but do not in those with (100) surface, as seen in Photo. 2.

Photos. 3 and 4 show the both types of patterns along the same grain boundary. They clearly show that the dislocations in (110) grains do not contribute to the printing-out and those in (100) ones do not to the formation of etch pits.

The sub-boundaries such as seen in Photos. 1 and 2 can be removed by the most careful annealing of specimens. Photos. 5,6 and 7 show the printing-out and etching patterns of these "perfectly annealed crystals".

The densities of dislocations are estimated as $5\times10^6$ per cm$^2$ from printing-out and $3\times10^6$ per cm$^2$ from etching.

### 3-2. Crystals with (111) Surface ("Special Crystals No. 1")

The printing-out of this type of crystals revealed the silver particles which outlined the somewhat regular hexagonal pattern both at the surface and in the interior of specimens. The general view of distribution of silver is shown in Photo. 8.

At the surface, the two groups of silver particles are observed as shown in Photo. 9. They are: (1) the larger particles which outline the hexagonal pattern and (2) the smaller particles which are distributed around the hexagonal pattern.

---

* FFH photographic fixer (Fuji-fix; Fuji Photo Film Co., Ltd. Kanagawa, Japan) was used in our experiments.

In the interior of the specimen, as shown in Photo. 10, the particles are distributed *discontinuously* upon the hexagonal cylindrical surfaces which were outlined by the particles of the group (1) at the surface as described above.

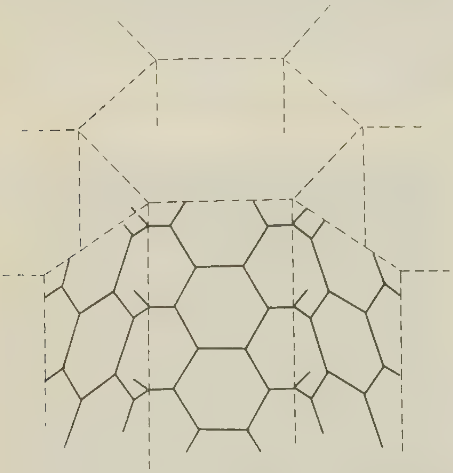

Fig. 2. The hexagonal columnar distribution of plane networks of dislocations in the "special crystal No. 1".

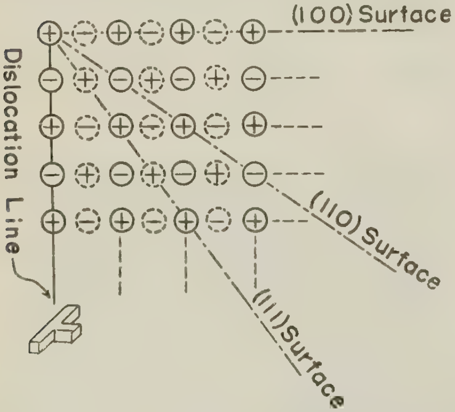

Fig. 3. Intersection of "extra-half-plane of edge dislocation" by the surfaces with various orientations. The plane of the full circles and the plane of the dotted circles are separated by on atomic spacing.

These results can be interpreted in the following manner. In this type of crystals, the silver particles are preferentially produced,

(a) at the emergence points of dislocations at the surface........the group (1) of Photo. 9.

(b) at the kink sites at the surface, that is to say, the defect sites at the surface ........the group (2) of Photo. 9.

(c) at the nodes in the dislocation networks inside the crystals........Photo. 10.

These interpretations will be further discussed later in § 4-1. When we assume their validity, the distribution of dislocations in these crystals may be supposed to be such as those shown schematically in Fig. 2. They may be described that the plane network of dislocations is extended upon the hexagonal cylindrical surfaces which are approximately perpendicular to the (111) plane.

The linear dimensions of plane-networks upon cylindrical surfaces could be estimated to be of the order of 10 microns from the vertical displacement of the objective lens of microscope.

The density of dislocations is found to be about $4\times10^6$ per $cm^2$ in these crystals.

### 3-3. Crystals Grown on the Glass Surface ("Special Crystals No. 2")

The general view of the surface of these crystals are quite similar to that of metal crystals prepared by the similar procedures³⁾, and is shown in Photo. 11. Each of the "islands" of crystals is separated by the "valleys" or "cracks".

Printing-out on the "free" surface of them revealed the existence of plentiful sub-boundaries inside the islands as shown in Photo. 12. The printing-out patterns of each island are quite similar to those of strained crystals to be discussed in Part II. The existence of internal strains in these islands is naturally expected from the existence of constraints at the contract surface of AgCl with glass.

The density of silver particles is found to be about $3\times10^7$ per $cm^2$ in these crystals.

## § 4. Discussions

### 4-1. Formation of Silver Particles

Several experimental evidences⁴⁾ are now available for trapping of photo-electrons along dislocations in AgCl. Seitz⁴⁾ proposed that the traps are incipient vacancies with an effective charge of $+e/2$ and his prediction has received further support in the work of Hedges and Mitchell¹⁾.

The writer⁵⁾ intends to propose that the following trapping centres in addition to the incipient vacancies must be effective in the case of annealed crystals;

(a) the kink sites at the surface,
(b) the emergence points of edge dislocations at the surface, and
(c) the nodes in the dislocation networks inside the crystal.

This proposal stands mainly on the observation described in § 3–2 and the mechanism of these preferential production of silver particles may be explained by the trapping of electrons due to the extra effective charge existing there.

In the case of trapping at the (b) sites, the extra half plane of (110) type accompanied with the edge dislocations may produce extra charge by intersecting the surface plane of (111) and (100), but may not at the surface plane of (110) as schematically shown in Fig. 3. This type of orientation dependence has been confirmed by the experimental results described in § 3–1, which show that the edge dislocations in the (110) grains (revealed by the etch pits) do not contribute to the formation of silver particles*.

The size of silver particles differs sometimes from grain to grain under the same amount of exposure (for example as seen in Photo. 6). It is naturally expected that their size is determined by the crystallographic orientation of their surface or, in other words, the orientation dependence of the effective range of the extra electric charge due to the intersection of edge dislocations with the surface.

This conclusion on the existence of extra charge on the surface due to dislocations may support the possibility of the extra charge at the nodes in the dislocation networks. This problem, however, merits further consideration.

### 4–2. Formation of Etch Pits

The etching experiments on annealed and strained crystals have been concluded not to contradict the generally accepted viewpoints that the impurity atmosphere around dislocations make dislocations visible to us by producing etch pits.

The most remarkable fact is the difficulty of revealing etch pits on the (100) surface**. The etched pattern of the crystal with (100) surface is usually very flat and the rate of chemical etching takes the minimum value in the crystal with (100) surface as seen in the photographs. It may be explained by the well-confirmed viewpoint that the value of the surface energy takes the minimum at (100) plane.

### 4–3. Origin of Dislocations

Seitz[7)] and Frank[8)] suggested the origin of dislocations by the condensation of thermal vacancies in the course of cooling from the melting point. The predominant defects of AgCl in equilibrium are, however, those of Frenkel type (Ag interstitials and Ag vacancies). It is not possible for them to produce the extra-half planes by their condensation.

On the other hand, the predominant defects in NaCl are those of Schottky type (Na and Cl vacancies) and thus have an ability to produce edge dislocations by their condensation.

The unpublished results by the present writer on the thermal etching patterns of NaCl single crystals revealed etch pits of the order of $10^5$ per cm$^2$ on their (100) surfaces†.

Comparing this value with that of AgCl of $10^6$ to $10^7$ per cm$^2$, we must conclude that some other origin of dislocations, in addition to the vacancy condensation, is important in these crystals.†† This another factor is supposed to be the misorientation of micro-crystals grown from different nuclei of solidification from the melt.

Next, the discussions will return to our crystals of AgCl prepared under various conditions of crystal growth.

How will become the dislocations which were produced during solidification process and are supposed to form the boundaries between neibouring micro-crystals?

In the case of the "usual crystals", there are little restrictions to their movement and they may move rather freely and thus become randomly distributed inside the crystals as seen in Photos. 5, 6 and 7.

---

* These results also show that the atmosphere of impurity atoms around dislocations, cannot, by itself, act as the nuclei for the precipitation of silver.

** Imura and Suzuki[6)] have experienced the similar kind of difficulty in the etching of Aluminium. The degree of anisotropy of the difficulty was, however, far less than our case, as expected reasonably.

† See also, W. Dekeyser: Proc. Defects in Solid, 134 (1955).

†† Of course, we cannot neglect the presence of small number of Schottky defects in AgCl. Their density at the malting point, however, can be estimated to be the order of $10^{-5}$. On the other hand, the density of Schottky defects in NaCl at the Melting point is $1 \times 10^{-4}$.

In the case of the "special crystals No. 2", the resistance to their movement is the largest and some of the grain boundaries change themselves into "valleys" or "cracks" as seen in Photo. 11.

In the case of the "special crystals No. 1", the restriction is the medium and the boundaries of micro-grains may remain in the form of hexagonal columnar patterns of dislocation networks as seen in Photos. 8, 9 and 10. The hexagonal patterns of this type of crystals are quite similar to those expected from the theory of T. Suzuki and H. Suzuki[9], but the mechanism of the appearance of such special arrangements seems to be not the same with that proposed by Suzuki and Suzuki; because, in our experiments as described above, they did appear only under special condition of crystal growth, rather than in the crystals annealed under ideal free and unrestricted circumstances.

### Acknowledgements

The writer wishes to express his gratitude to Professor Y. Tani for his kind guidance and also to the cordial hospitality by the Research Groups in the Research Laboratory, Fuji Photo Film Co., Ltd., especially to Dr. S. Fujisawa, Dr. Y. Koseki and E. Mizuki in the course of this work.

### References

1) J. M. Hedges and J. W. Mitchell: Phil. Mag. **44** (1953) 223, 357.
2) A. J. Forty: Advances in Phys. **3** (1954) 1.
3) J. W. Rutter and B. Chalmers: Can. J. Phys. **31** (1953) 15.
U. M. Martius: Progress in Metal Phys. vol. **5** (1954) 279.
4) F. Seitz: Rev. Mod. Phys. **23** (1951) 328; Proc. of Hakone Symposium on Photographic Sensitivity held Sept. 1953 (in the press). See also ref. (1) and (5).
5) H. Kanzaki: Phys. Rev. (to appear).
6) T. Imura and T. Suzuki: J. of Japan Inst. of Metals **19** (1955) 15 (in Japanese).
7) F. Seitz: Phys. Rev. **79** (1950) 890.
8) F. C. Frank: Symposium on Plastic Deformation (1950; Pittsburgh, Mellon Institute).
9) T. Suzuki and H. Suzuki: Sci. Rep. RITU **A 6** (1954) 573. Proc. International Conference of Theoretical Physics (1953) 570.

---

JOURNAL OF THE PHYSICAL SOCIETY OF JAPAN Vol. 11, No. 2, FEBRUARY, 1956

# Observation of Dislocations in Silver Halides
## Part II. Strained Crystals

By Hiroshi KANZAKI
*Institute of Industrial Science, University of Tokyo, Chiba, Japan*

(Received August 5, 1955)

The appearance of sub-boundaries are revealed in the crystals of AgCl and AgBr deformed at room temperature, by the technique of printing-out and etching. The origin of sub-boundaries can be explained by the progress of polygonization during the deformation.

### § 1. Introduction

The main object of this Part of the article is to obtain the knowledge on the distribution of dislocations in deformed crystals by using the techniques described in the Part I.

### § 2. Experimental Procedures

Experiments were made on the crystals of AgBr and AgCl grown from the melt.

Specimens of AgBr were prepared by the method exactly the same with that adopted by Hedges and Mitchell[1]. Their original size was about 20 mm × 20 mm and 0.3 mm in thickness. Their surface was usually nearly parallel to (100). After being separated from Quartz plates, they were cut to the size of 5

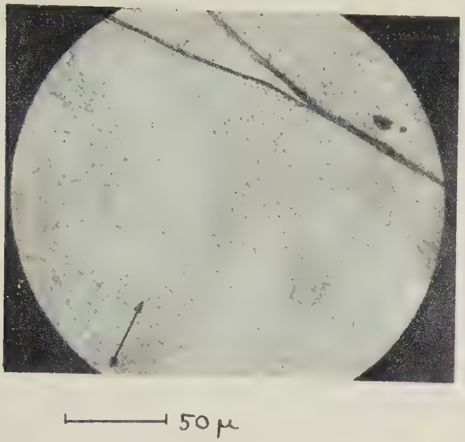

Photo. 1. Printing-out pattern of deformed crystal of AgBr. The arrow shows the direction of faint slip bands observed in the same area.

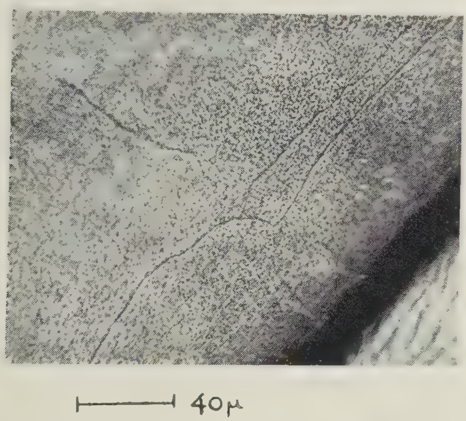

Photo. 2. Printing-out pattern of deformed crystal of AgCl with (100) surface. The grain of the right-lower corner has the (110) surface and its pattern is shown in Photo. 3.

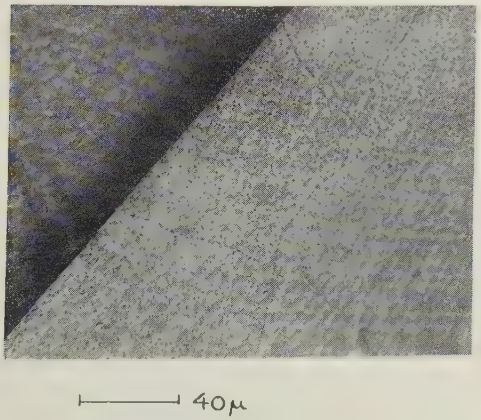

Photo. 3. Printing-out pattern of deformed crystal of AgCl with (110) surface (faint slip bands may also be seen). The left-hand grain is that shown in Photo. 2 and the slip bands in that area may be seen in this photograph.

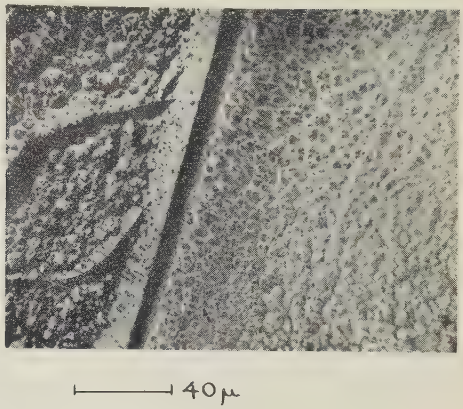

Photo. 4. Etching pattern of deformed crystal of AgCl near grain boundary.

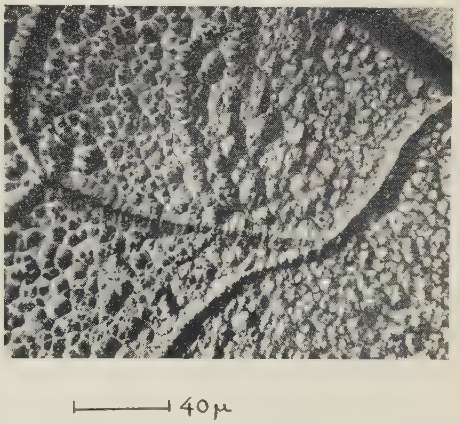

Photo. 5. Etching pattern of deformed crystal of AgCl. The polygon boundaries as well as grain boundaries have been revealed in Photos. 4 and 5.

mm × 20 mm and then annealed at 400 to 410°C. Deformation was given by plastic bending at room temperature. Exposure to light was given by the filtered radiation from the tungsten lamp with wavelengths at the long wave edge of the absorption band of AgBr.

Specimens of AgCl were prepared in the same manner as described in Part I. Deformation was given at room temperature by indentation on their free surfaces with the fine head (0.3 mm in diameter) of the Pyrex glass rods. The exposure and the etching were carried out in the same manner as in Part I.

## § 3. Results Obtained

### 3-1. AgBr

Printing-out of annealed crystals of AgBr revealed the random distribution of silver particles at the surface with the density of about $10^6$ per $cm^2$.

Printing-out of the deformed crystals revealed the existence of the sub-boundaries made of rows of silver particles in the interior of the crystals (about 10 micron below the surface) as shown in Photo. 1. These boundaries became clearly visible when the value of the surface strain exceeded over 0.5 percent.

These boundaries which appear in the strained crystals of both AgBr and AgCl are developed especially well near the grain boundaries and also at the places where the slip bands on the surface become "faint", and are approximately perpendicular to the slip bands.

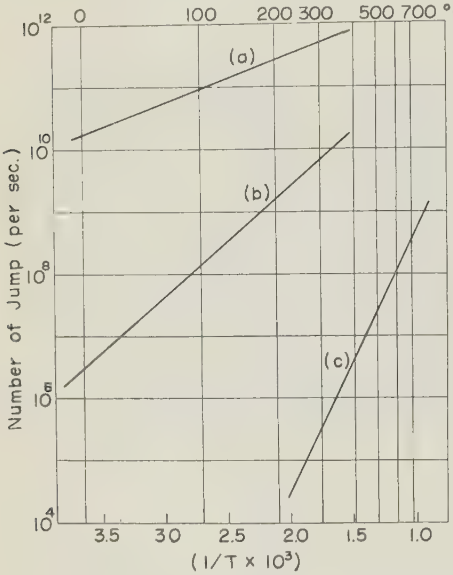

Fig. 1. Temperature dependence of the mobility of defects calculated from the conductivity data3)4).
(a) Ag interstitial ions in AgBr,
(b) Ag vacancies in AgBr,
(c) Na vacancies in NaCl.

From the experimental results on the relation between these boundaries and the slip bands, it has been concluded that the origin of these sub-boundaries is the polygonization accompanied by the deformation at room temperature and these boundaries are made of rows of dislocations with strong edge components.

### 3-2. AgCl

As stated above, the "polygon" boundaries were also observed in the interior of the deformed AgCl as well as in the case of AgBr.

Photos. 2 and 3 show some of the printed-out patterns of deformed AgCl in the interior of the crystal. It is also remarkable that the size of the silver particles has been decreased and the density of them has been increased by the deformation. The measured density is about $6\times10^7$ per $cm^2$ in the deformed crystals with (100) surface orientation (as seen in Photo. 2) and 1 to $2\times10^7$ per $cm^2$ in those with (110) surface (Photo. 3). Such orientation dependence of the particle densities may be explained in the same manner with that of annealed crystals shown in § 3-1 of Part. I. The degree of such anisotropy is, however, far less in deformed crystals than in annealed ones of § 3-1 of Part I. Actually, we could confirm one-to-one correspondence between silver particles and etch pits along the same polygonization boundaries in the crystals with (110) surface. In the case of annealed crystals, it was quite impossible to make this kind of experimental confirmation because of strong anisotropy in producing both silver particles and etching pits.

Chemical etching also revealed the polygonization boundaries in deformed crystals as shown in Photos. 4 and 5. The density of etch pits is calculated to be 1 to $2\times10^7$ per $cm^2$.

## § 4. Discussions

### 4-1. Formation of Silver Particles

The printed-out silver particles in deformed crystals of AgBr and AgCl appeared always below the surface of crystals. This fact is to be contrasted with the appearance of particles on the surface of annealed crystals. These results are consistent with those by Hedges and Mitchell1). In the case of strained crystals, a lot of jogs are expected along dislocation lines and they contribute effective traps for photo-electrons. Under these circumstances, the location of silver particles is determined by the density of jogs along dislocations as has been fully discussed by Hedges and Mitchell1).

### 4-2. Formation of Etch Pits

Experimental results have shown that the dislocations produced by deformation contribute fairly well to the formation of etch pits. We must then conclude that the impurity atmospheres are well formed around these dislocations. This conclusion may be reasonably accepted by considering the rather high values of defects mobilities in silver halides which are to be discussed in the next paragrahps.

### 4-3. Plastic Deformation of Silver Halides

It seems generally accepted[2] that the temperature dependence of plastic properties of solids is determined by the mobility of the atomic defects in the solids.

Fig. 1 shows the temperature dependence of the mobility of defects (number of jumps per unit time) calculated from the conductivity experiments of AgBr[3] and NaCl[4]. It may also be supposed[5] that the mobility of the neutral pair of vacancies is nearly the same with that of positive ion vacancies.

Assuming the value of $10^7$ to $10^8$ per sec for the jumping frequency of vacancy pair in AgBr, it may be well conceivable that the polygonization proceeds considerably during the course of deformation at room temperature.

From the results of Fig. 1, it is supposed that the deformation of AgBr at room temperature corresponds to that of NaCl at 500°C. The temperature dependence of the plastic properties of NaCl may be the most interesting from this point of view.

### Acknowledgements

The writer wishes to express his gratitude to Professor Y. Tani for his continual guidance and also to the cordial hospitality by the Research Groups headed by Dr. S. Fujisawa in the Research Laboratory, Fuji Photo Film Co., Ltd., in the course of this work.

### References

1) J. M. Hedges and J. W. Mitchell: Phil. Mag. **44** (1953) 223, 357.
2) N. F. Mott: Phil. Mag. **43** (1952) 1151, **44** (1953) 742.
3) J. Teltow: Ann. Physik **5** (1950) 63, 71.
S. W. Kurnick: J. Chem. Phys. **20** (1952) 218.
See also, H. Kanzaki: Proc. of Hakone Symposium on Photographic Sensitivity held in 1953 (in the press).
4) H. W. Etzel and R. J. Maurer: J. Chem. Phys. **18** (1950) 1003. See also ref. (5).
5) F. Seitz: Rev. Mod. Phys. **26** (1954) 7.

---

JOURNAL OF THE PHYSICAL SOCIETY OF JAPAN Vol. 11, No. 2, FEBRUARY, 1956

# Electron Diffraction and Microscope Study of the Surface Structure of Copper Single Crystals

By Susumu YOSHIDA

*The Government Mechanical Laboratory, Suginami-ku, Tokyo, Japan*

(Received March 31, 1955, and in revised form September 27, 1955)

The submicroscopic structure of electrolytically polished and etched surfaces of copper single crystals was studied by means of electron diffraction and electron microscope, supplemented by the method of light figures. Our results indicate that the etched surfaces are composed of submicroscopic facets which belong to [100] zone and the electropolished surfaces are smooth and undulating. Assuming a simple model for the undulation, the mean inner potential of copper crystal was determined. The mean value of the mean inner potential turned out to be 11 volts.

## §1. Introduction

Many authors studied the submicroscopic surface structure of metal single crystals by the method of electron diffraction. For example, Raether *et al*[1-3]. found that the electropolished surfaces of copper crystals were smooth and undulating. Pashley[4] studied the electrolytically etched and polished surfaces of silver crystals and found that fine structure effects, in the form of split spots or streaks, gave information concerning the surface structure of the various surfaces of the crystals. However, the origin of split spots and streaks in the electron diffraction pattern has not yet been fully elucidated. So it is often difficult to study in detail the submicroscopic surface topography of crystals only by electron diffraction and the observation by means of electron microscope is required.

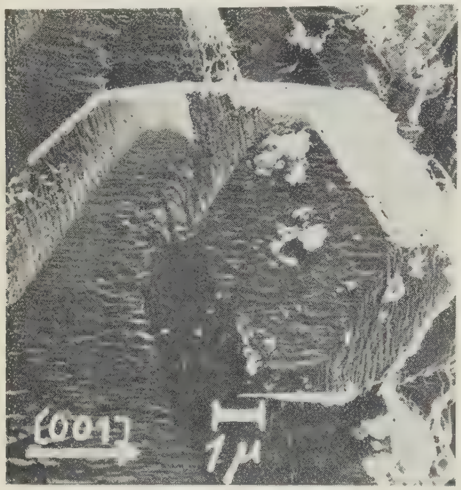

Fig. 1. {110} surface electrolytically etched for 15 minutes.

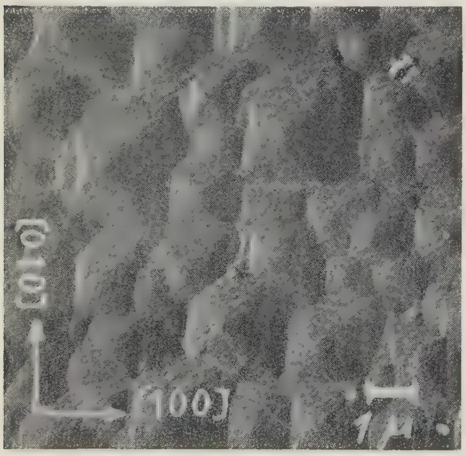

Fig. 2. {001} surface electrolytically etched for 15 minutes.

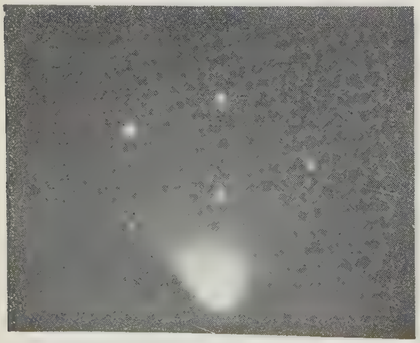

Fig. 3. {111} surface electrolytically etched for 15 minutes. [$\bar{1}$10] azimuth.

In the present work the electrolytically etched and polished copper single crystals were studied by electron diffraction and electron microscope, supplemented by the observation by the method of light figure. Our results indicate that the etched surfaces are composed of minute facets which belong to [100] zone, and the electropolished surfaces are smooth and undulating. Assuming a simple model for the undulation, we determined the mean inner potential of copper crystal and the mean angle of the undulation.

## § 2. Experimental

The copper single crystals used in this experiment were made from melted electrolytic copper by slow cooling. Surfaces of the crystals were polished mechanically and then etched. After determining the orientation of the crystal axes by electron diffraction, flat surfaces parallel to {100}, {110} and {111} planes were prepared by grinding and mechanical polishing. The surface layer distorted by mechanical working was removed by electropolishing.

The electrolytic solution used for polishing was a mixture containing 40 cc of water and 50 cc of orthophosphoric acid (90%). Electropolishing and etching were carried out at 15 ∼20°C with the specimen as the anode. The electrode potential applied was 0.4∼0.6 volt for electrolytic etching and 1.6∼1.8 volts for electropolishing. The oxide layer which was often formed on the surface in the process of electropolishing was removed by light etching in dilute solution of sulphuric acid. The lustre of the polished surface showed no change after this process. Specimens thus prepared were rinsed in distilled water, dried quickly in air flow and then examined by electron microscope and diffraction. For the electron microscope specimens the methyl-methacrylate aluminium replicas shadowed with germanium were used. The electrolytically etched surfaces were also studied by light figures, i.e., the figures produced by reflecting a narrow beam of light on the surface of a crystal.

Fig. 4. The light figure from {100} surface electrolytically etched for 15 minutes.

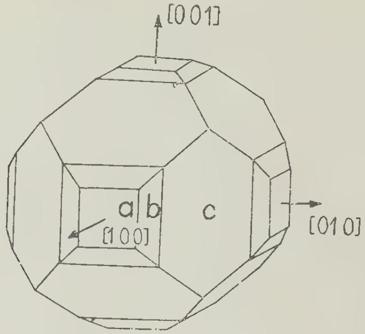

Fig. 6.
a: {100}
b: {210}
c: {110}

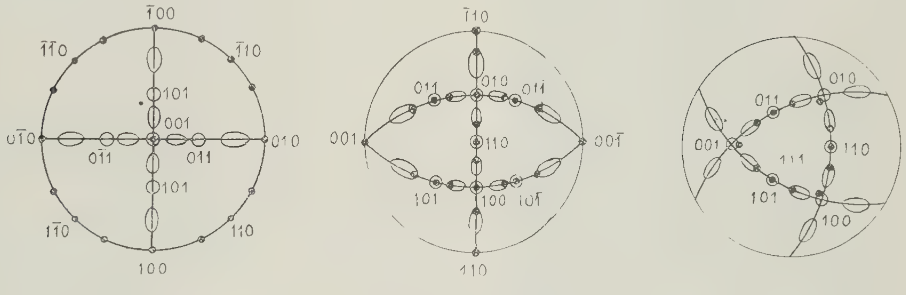

{001} surface {110} surface {111} surface

Fig. 5. Stereographic projections of minute facets.
○ Facet observed by light figure, ● Facet observed by electron diffraction.

## § 3. Results on the Surface Structure

### (a) Electrolytically etched surfaces

*Strongly etched surfaces.* When the electrolytic etching is continued for more than 10 minutes, the surface of the crystal becomes mat and reflects light strongly in certain definite directions. The electron micrograph shows that the surface is covered with etch pits which are 1 to several microns in size. They are of characteristic shapes which depend on the indices of the surfaces (Figs. 1 and 2). From the shape of the facets which compose the etch pits it can be concluded that they belong to [100] zone. Generally the facets are not smooth, but covered with submicroscopic projections. Only on a few specimens smooth facets are observed.

The electron diffraction spots are streaked from the centres into a few directions (Fig. 3). According to several authors[4)–6)] the streaks are caused by the refraction effect of electrons on submicroscopic facets and the indices of those facets can be determined by the direction of streaks*. In the present experiment the streaks indicate that the indices of submicroscopic facets are {100}, {110}, {210} and {310}, irrespective of the indices of the microscopic surfaces, although a few streaks cannot be attributed to any faces of simple indices.

When the electron micrograph of a surface shows many etch pits which have smooth facets, the streaks observed by electron diffraction is replaced by a subsidiary spot separated from the normal diffraction spot. In such a case the mean inner potential of copper crystal can be measured approximately. Using {110} surface a mean inner potential of 13~14 volts was obtained from (400) spot. This is con-

---

* Pashley[4)] observed for electrolytically etched silver surfaces several evidences which suggest that the observed streaks are not solely due to the refraction effect. We also observed the similar evidences.

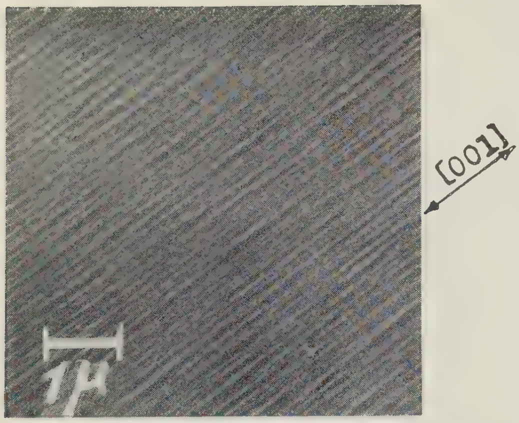

Fig. 7. {110} surface electropolished for 5 minutes and lightly etched for 30 seconds.

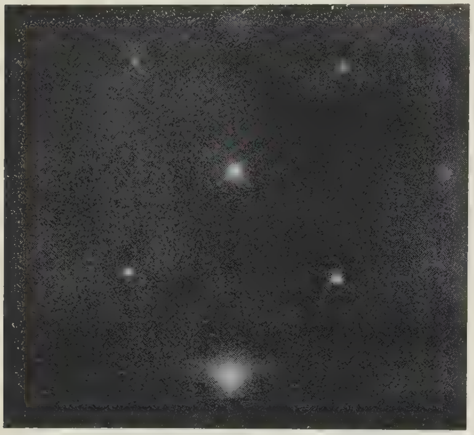

Fig. 8. {110} surface electropolished for 5 minutes and lightly etched for 30 seconds. [001] azimuth.

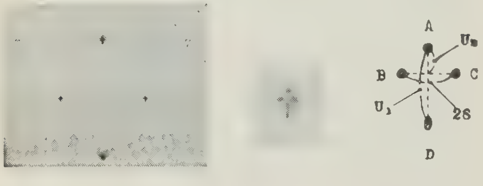

(a) (b) (c)

Fig. 9. (a) {110} surface electropolished for 5 minutes and lightly etched for 30 seconds. [$\bar{1}$10] azimuth.
(b) Enlargement of the (222) spot.
(c) Illustration os the distances given in Table 1.

sistent with the value (13.7 volts) calculated by Tull[7].

The indices of the microscopic facets of the etch pits are determined by analysing light figures. Although the recorded figures are diffuse and elongated, the direction of strong intensity correspond to {100}, {110} faces and a face intermediate between {210} and {310} (Fig. 4).

The indices observed by both methods, electron diffraction and light figure, are summarized in Fig. 5. Although the facets observed by different methods are not perfectly in accordance, all the observed facets belong to [100] zone. This is consistent with the observation by the electron microscope. No {111} facets were found in accordance with Pashley's result[4] for silver crystals. Fig. 6 represents a polyhedron which is bounded by the observed facets. The etch pits shown in the electron micrographs resemble some parts of this polyhedron.

*Lightly etched {110} surface.* When a {110} surface is electropolished and then electrolytically etched for a short time (30 sec.~1 minute), the electron micrograph of this surface shows stripes running along [001] direction (Fig. 7). The width of the stripes is from 500 to 2000 Å.

The electron diffraction pattern at [001] azimuth shows long, sharp streaks along [100] and [101] directions (Fig. 8). At [$\bar{1}$10] azimuth split spots are observed (Fig. 9). The split spots cannot be explained by the simple refraction effect. But the spot D is explained by assuming spikes in reciprocal lattice space

Table I. Comparison between observed and calculated positions of the split spots.
(The definitions of $U_1$, $U_2$ and $S$ are given in Fig. 9.)

| Split spot | $U_1$(mm) | | $U_2$(mm) | | $S$(mm) | |
|---|---|---|---|---|---|---|
| | Obs. | Calc. | Obs. | Calc. | Obs. | Calc. |
| (220) D | 0.7 | 0.78 | | | | |
| 〃 B, C | | | 0.3 | 0.33 | 0.2 | 0.21 |
| (440) D | 2.2 | 2.06 | | | | |
| 〃 B, C | | | 0.8 | 0.73 | 0.5 | 0.45 |
| (222) D | 1.9 | 1.70 | | | | |
| 〃 B, C | | | 0.4 | 0.35 | 0.3 | 0.25 |
| (311) D | 0.7 | 0.67 | | | | |
| 〃 B, C | | | 0.3 | 0.30 | 0.2 | 0.19 |
| (331) D | 1.4* | 1.4* | | | | |
| 〃 B, C | | | 0.6** | 0.6** | 0.38** | 0.38** |
| (442) D | 2.3 | 2.22 | | | | |

* The angle of incidence of the electron beam with the {110} crystal plane is calculated from Pashley's formulae[4] (1) and (2), assuming the split spot D for the (311) diffraction spot to be due to the [010] spike.

** The direction cosines for the spikes which cause split spots B, C are calculated from their positions for the (311) diffraction spot,

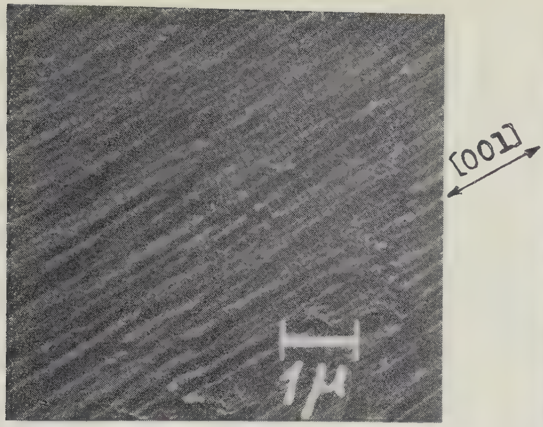

Fig. 10. {110} surfaces electrolytically etched for 5 minutes.

as considered by Pashley[4]. The result of analysis indicates that the spot D is due to a spike along [010] or [100] direction (Table 1). Therefore, the stripes observed by the electron microscope is concluded to be due to a furrow-like structure which is bounded by oblique {100} and {010} facets.

When the etching is continued further, the period of the furrow-like structure becomes larger (Fig. 10) and sometimes a step-like structure develops (Fig. 11). Finally etching pits of the type such as described in the previous section (Fig. 1) appear and gradually cover the surface. The characteristic furrow-like structure still remains as a fine structure on the facets of the pits even in this stage of etching.

(**b**) **Electropolished surfaces**

The surface of the specimen becomes lustrous by 3∼5 minutes' electropolishing. At this stage of polishing, the electron micrograph from {100} surface shows a very smooth surface structure (Fig. 12). {110} surface is also smooth, but generally faint streaks are observed along [001] direction (Fig. 13). When the electropolishing is continued for a longer time, the streaks gradually become distinct and the appearance of the surface becomes somewhat similar to that from the lightly etched {110} surface (Fig. 7).

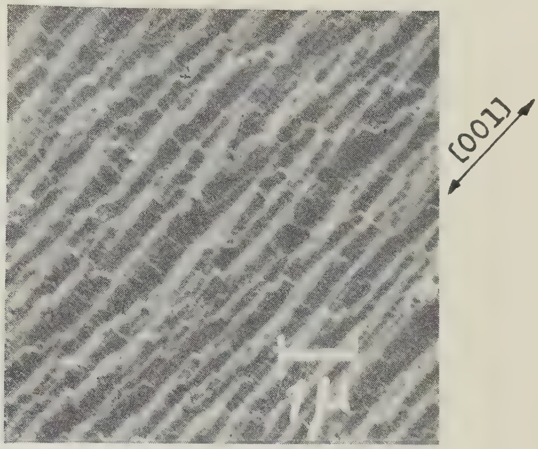

Fig. 11. {110} surface electrolytically etched for 10 minutes.

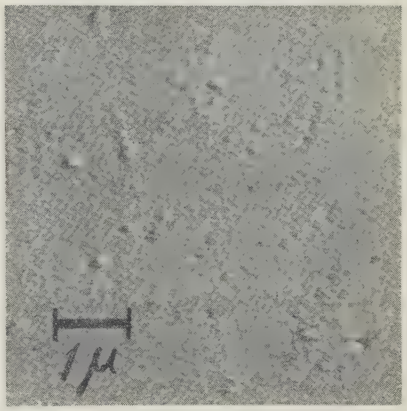

Fig. 12. {100} surface electropolished for 5 minutes.

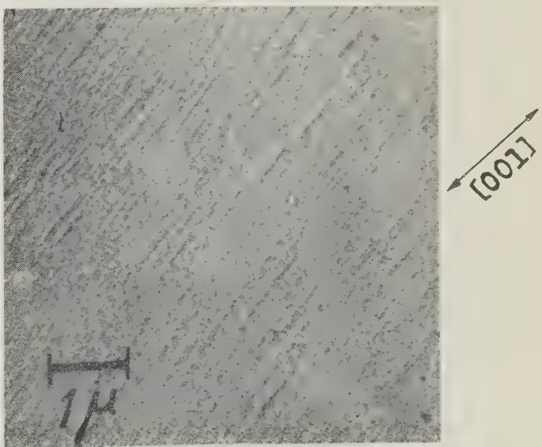

Fig. 13. {110} surface electropolished for 5 minutes.

Though slight changes in the condition of polishing result in variations in details of electron diffraction patterns, the general features of the patterns well correspond to the electron microscopic observation as given below. For {100} surface the diffraction spots elongate towards the shadow edge. The elongated streaks are sharp and show no difference when the azimuth of the incident beam is changed. This fact indicates that

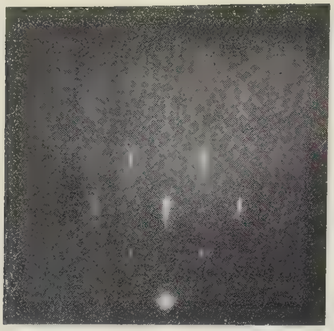

Fig. 14. {110} surface electropolished for 5 minutes. [$\bar{1}$10] azimuth.

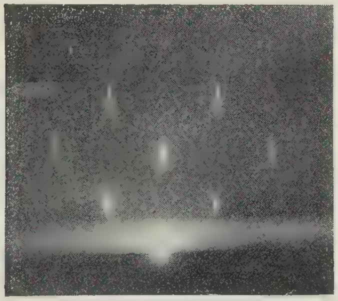

Fig. 15. {110} surface electropolished for 5 minutes. [001] azimuth.

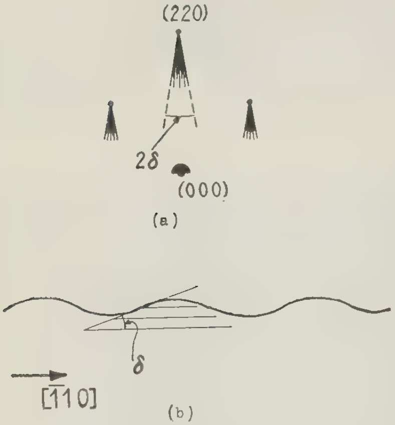

Fig. 16. (a) Illustration of the electron diffraction pattern from electropolished {110} surface at [001] azimuth (Fig. 15).
(b) Illustration of the submicroscopic profile of the surface corresponding to the pattern (a).

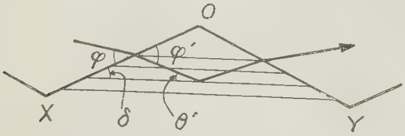

Fig. 17.

the surface is slightly undulated, though it appears very smooth in the electron micrograph, and that the undulation is not along any definite crystallographic direction. For {110} surface the diffraction spots also elongate towards the shadow edge at [$\bar{1}$10] azimuth, but they look like comets at [001] azimuth (Figs. 14 and 15). These patterns indicate that the streaks observed in the electron micrograph of {110} surface correspond to slight undulation along [$\bar{1}$10] direction. The mean angle of inclination of the undulation is given by half the angle ($\delta$) of the spread of the trail of the comet-like spot (Fig. 16). It comes out 3∼5° for a well polished surface*.

When the electropolishing of {110} surface is continued for a longer time, the appearance of the diffraction spots changes as follows. At [$\bar{1}$10] azimuth the elongated part of a diffraction spot splits from the normal spot and the normal spot tends to protrude on both sides parallel to the shadow edge. At [001] azimth the trail of the comet-like spot becomes smaller and the angle $\delta$ increases, often amounting to 60∼70°. Therefore the diffraction pattern becomes somewhat similar to that from the lightly etched surface (Fig. 8 and 9). This fact corresponds well to the change observed in the electron micrograph.

## § 4. Measurement of the Mean Inner Potential and Angle $\delta$[8)]

It was already found that an electropolished surface of a metal crystal is slightly undulated and the undulation forms a small angle with the macroscopic surface. By the electron diffraction method, Kranert, Leise and Raether[1)] formerly estimated the angle to be 1∼2° for a copper crystal. However, they had to assume the value of the mean inner potential. If we assume the undulating surface as represented in Fig. 17, we can determine both the mean inner potential and the angle $\delta$ by the following method. When an incident electron beam falls upon the facet OX, it is refracted on the facet and then reflected by the net plane when the Bragg condition is fulfilled. Since the Bragg angle $\theta'$ for the refracted beam is approximately equal to $\theta$ for the unrefracted beam the deviation of the beam due to refraction effect is calculated by Snell's law[9]:

---

* The mean angle $\delta$ of the inclination can be measured also by the method described in the later section (§ 4.). The measured value (Table II) is consistent with the value given here.

$$\phi'-\phi=\frac{\mu^2-1}{\phi'+\phi}\doteq\frac{\mu^2-1}{2\phi'}\doteq\frac{\mu^2-1}{2(\delta+\theta)}\,, \qquad (1)$$

where $\mu$ is the refractive index for electrons and $\phi$ and $\phi'$ are the angles shown in Fig. 17. The reflected beam departs from the crystal through another facet OY and the total deviation due to the effect of refraction is $2(\phi'-\phi)$. Using the familiar relation $\mu^2-1=V/E$ where $V$ is the mean inner potential and $E$ the accelerating voltage, we get the following equation:

$$\varDelta_n\equiv2(\phi_n'-\phi_n)=\frac{V}{E}\,\frac{1}{\delta+\theta_n}\,, \qquad (2)$$

where the suffix $n$ indicates the order of reflexion. This formula can be rewritten as

$$B_n=-\delta A_n+V\,, \qquad (3)$$

where $A_n=\varDelta_n E$ and $B_n=\varDelta_n\theta_n E$. Equation (3) is a linear relation between $A_n$ and $B_n$, both of which can be obtained by measuring $\varDelta_n$ and $\theta_n$ on a rotation photograph. Plotting $A_n$ and $B_n$ on a diagram for a series of reflexions, we can determine $V$ and $\delta$.

Electron diffraction rotation photographs were taken of electropolished {110} surface of copper crystals. Specimens were set in an azimuth where the incident electron beam was approximately parallel to [$\bar{1}$10] but the effect of simultaneous reflextion was avoided as far as possible[10]. The surface of real crystals always deviates from the ideal model (Fig. 17) and the angle $\delta$ is not unique but is distributed in a certain range. This results in diffraction spots elongated toward the shadow edge. We measured the point of maximum intensity of the elongated spot and applied equation (3). Thus we obtained the average value of $\delta$. A few examples are given in Fig. 18. Sometimes the plots don't lie on an exact straight line. This may be due in part to the fact that the effective angle $\delta$ depends upon $\theta_n$ and in part to the variation of apparent mean inner potential in low order reflexions[11]. The same method was applied also to {100} surface. In this case, however, physical meaning of $\delta$ is not so clear as for {110} surface, for the {100} surface is not undulated along a definite crystallographic direction (§ 3. (b)). The results are given in Table II. Our data agree inorder of magnitude with the value 13.7 volts which was theoretically calculated by Tull[7].

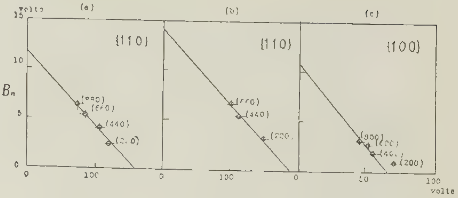

Fig. 18. Diagrams for calculating V and $\delta$.

Table II. The mean inner potential V and facet angle $\delta$ of copper crystal.

| Crystal face | Specimen No. | V(volts) | $\delta$(°) |
|---|---|---|---|
| (110) | 1 | 12±3 | 4.5±3 |
| 〃 | 2 | 13±3 | 5±3 |
| 〃 | 3 | 9±3 | 3.5±3 |
| 〃 | 4 | 8±4 | 3±3 |
| 〃 | 5 | 14±3 | 4.5±3 |
| (100) | | 11±4 | 10±4 |

## § 5. Discussions

We observed a furrow-like structure on the lightly etched {110} surface. Even when the etching was continued for a longer time, this characteristic structure was found accompanying the etching pits. Moreover, its traces still remained as undulation on an electropolished surface. Thus, it may be concluded that the furrow-like structure represents an elementary process in the electrolytic etching and polishing. The facets of the furrows ({100} planes) seem to be the most stable surface formed in the electrolytic dissolution of copper crystal.

A similar furrow-like structure was formerly observed on electropolished aluminium surfaces by Brown[12)13)] and Bucknell and Geach[14]. Brown called it the " micro-etch " structure. Although both are alike, the one for aluminium is different from that for copper in the following points: 1) The period of the former structure (400 A) is a little smaller than that of the latter. 2) The facets of the former are not {100} planes as for copper, but {111}. It is not yet clear whether both structures have the same origin or not.

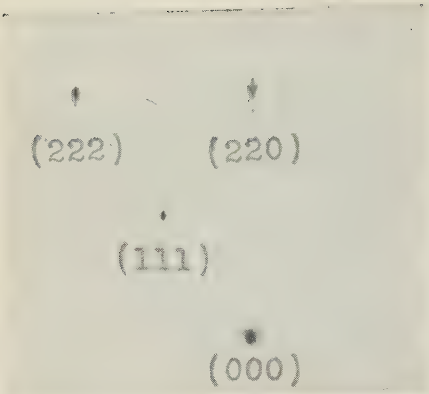

Fig. 19. {110} surface electropolished for 5 minutes and lightly etched for 30 seconds. Azimuth rotated 4° from $[\bar{1}10]$.

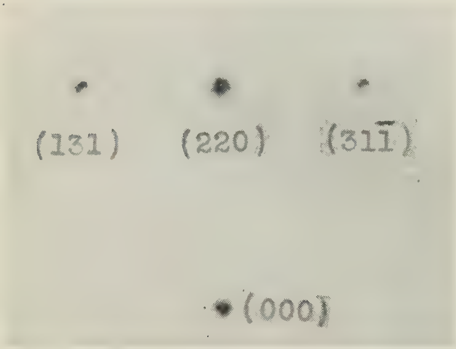

Fig. 20. {110} surface electropolished for 5 minutes and lightly etched for 30 seconds. $[\bar{1}11]$ azimuth.

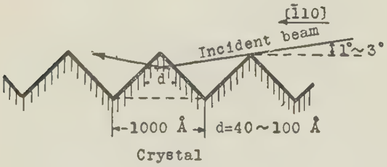

Fig. 21.

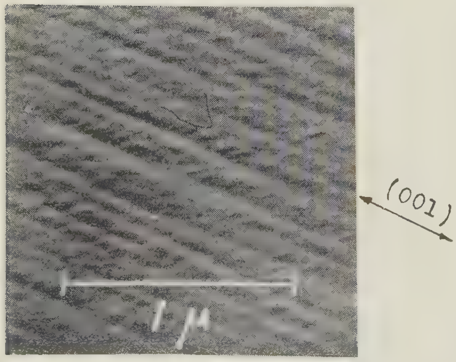

Fig. 22. {110} surface electropolished for 5 minutes and lightly etched for 30 seconds.

Electron diffraction patterns from a surface with the furrow-like structure, if closely examined, show complex appearance. They cannot be explained in several points by the simple refraction effect or reciprocal lattice spikes based on the kinematical theory. The points are as follows. (1) Among the splits spots observed with the incident beam parallel to $[\bar{1}10]$ (Fig. 9), the spot D was already explained. If the spots B and C were similarly caused by reciprocal lattice spikes, the direction cosines of the spikes would be 0.90:0.23:±0.37 (Table I). If the spot A were also caused by a spike, it would be $[\bar{1}10]$ spike parallel to the incident beam. Actually, however, the spikes corresponding to the spots A, B and C are not observed at other azimuths, while streaks corresponding to [201], [102] and [101] spikes are observed. (2) When the azimuth is a little rotated from $[\bar{1}10]$, the split spots take more complex appearance (Fig. 19). (3) Streaks which belong to one diffraction spot sometimes don't cross on the same point (Fig. 20).

As already shown, the mean period of the furrows is about 1000 Å. The size of crystals which diffract electrons are, therefore, about 50 Å for $[\bar{1}10]$ azimuth (Fig. 21). This size is of the order of magnitude where the application of the dynamical theory becomes gradually more adequate than that of the kinematical theory[15]. This seems to be the cause that makes the diffraction patterns complex and difficult to be explained. Moreover, we often observed in the electron micrograph of the furrow-like structure fine traces of lines lying obliquely to the ridge of the furrows (Fig. 22). The direction of the traces show that they are caused by {101} or {201} plane. Such a subsidiary structure of the furrows may also complicate the diffraction patterns.

In conclusion the author wishes to express his sincere thanks to Professor Ryozi Uyeda for his kind advices and criticisms. He is also indebted to Dr. T. Kawada of this laboratory for his continual encouragement during the course of this work.

## References

1) W. Kranert, K. H. Leise and H. Raether: Z f. Phys. **122** (1944) 248.
2) H. Raether: Optik **1** (1946) 69.

3) H. Raether: Mētaux et Corrosion **22** (1947) 2.
4) D. W. Pashley: Proc. Phys. Soc. **B 64** (1951) 1113.
5) T. Yamaguti: Proc. Phys. Math. Soc. Japan. **17** (1935) 443.
6) R. Uyeda, S. Takagi and H. Hagihara: Proc. Phys. Math. Soc. Japan **23** (1941) 1049.
7) V. F. G. Tull: Proc. Roy. Soc. **A 206** (1951) 232.
8) S. Yoshida: Acta Cryst. **7** (1954) 592.
9) G. P. Thomson and W. Cochrane: *Theory and Practice of Electron Diffraction* (1939) 110. (London, MacMillan).
10) R. Uyeda: Proc. Phys. Math. Soc. Japan **20** (1936) 280.
11) T. Yamaguti: Proc. Phys. Math, Soc. Japan **16** (1934) 95.
12) A. F. Brown: *Symposium on Metallurgical Applications of the Electron Microscope*, (1949) 103. (Monograph and Report Series No. 8, Inst. Metals, London)
13) A. F. Brown: Adv. in Physics **1** (1952) 427.
14) G. L. Bucknell and G. A. Geach: Nature **164** (1949) 231.
15) N. Kato: J. Phys. Soc. Japan **7** (1952) 406.

---

JOURNAL OF THE PHYSICAL SOCIETY OF JAPAN Vol. 11, No. 2, FEBRUARY, 1956

# Paramagnetic Resonance Absorption in Copper Formate

By J. SHIMADA, H. ABE and K. ÔNO

*Institute of Science and Technology, University of Tokyo, Tokyo, Japan*

(Received September 17, 1955)

Paramagnetic resonance in single crystals of copper formate tetrahydrate and its dihydrate was investigated at room temperature with microwaves of $\lambda=11\sim5$ mm. Either crystal has only one absorption peak at any direction of static magnetic field. The line width of the tetrahydrate is 400 oer. in order and that of dihydrate is 200 oer. The shape of these lines is Lorentzian.

## § 1. Introduction

Paramagnetic resonance absorption in single crystals of copper formate tetrahydrate $Cu(HCOO)_2 \cdot 4H_2O$ and its dihydrate $Cu(HCOO)_2 \cdot 2H_2O$ have been investigated at room temperature and with 3 wave-lengths (11∼5.4 mm). Experiments on the same crystals have been performed by Itoh et al at Ôsaka University with a longer wave-length (3 cm)[1]. The anomaly in paramagnetic resonance absorption as in copper acetate $Cu(CH_3COO)_2 \cdot H_2O$[2,3] and copper propionate $Cu(CH_3CH_2COO)_2 \cdot H_2O$[4] is not observed in these crystals but a single peak is observed in any direction of static magnetic field.

The X-ray analysis of these salts was performed in Kiriyama's laboratory at Ôsaka University[5]. Both crystals are monoclinic and short data are listed in Table I, $z$ being the number of inequivalent copper ions in unit cell.

Table I. Short results of X-ray analysis[5].

| | $z$ | $\beta$ | $a$ | $b$ | $c$ |
|---|---|---|---|---|---|
| $Cu(HCOO)_2 \cdot 4H_2O$ | 2 | 101°5′ | 8.18Å | 8.15Å | 6.35Å |
| $Cu(HCOO)_2 \cdot 2H_2O$ | 4 | 96°38′ | 9.54Å | 7.16Å | 8.59Å |

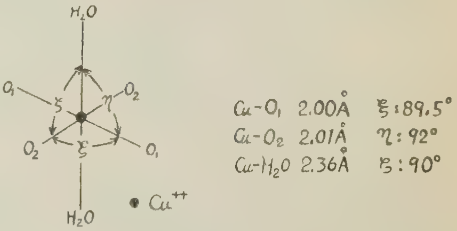

Fig. 1. Atomic configuration surrounding a $Cu^{++}$ ion in $Cu(HCOO)_2 \cdot 4H_2O$.

## § 2. Results from Resonance Absorption

### i) *Copper Formate Tetrahydrate* *$Cu(HCOO)_2 \cdot 4H_2O$*

The configuration of atoms surrounding a $Cu^{++}$ ion in this crystal is shown in Fig. 1. Since we have no exact information about the crystalline field at $Cu^{++}$ ion, we assume that

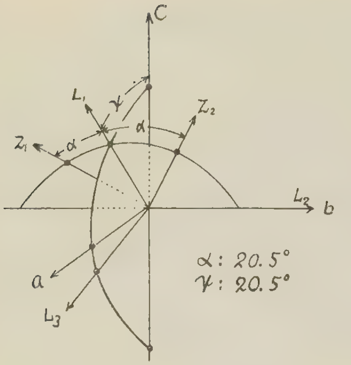

Fig. 2. Direction of $Z$-axes in $Cu(HCOO)_2\cdot 4H_2O$.

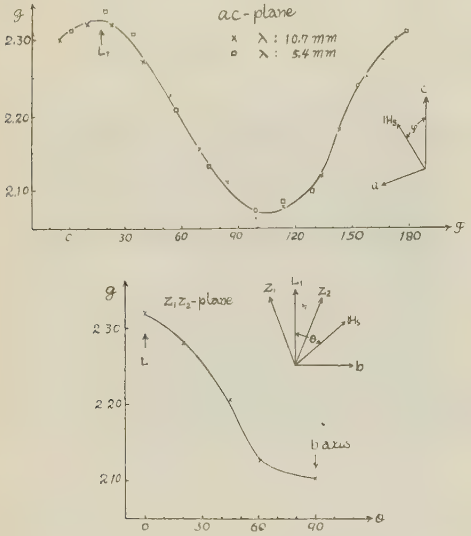

Fig. 3. Variation of $g$-value with orientation for static magnetic field in $Cu(HCOO)_2\cdot 4H_2O$.

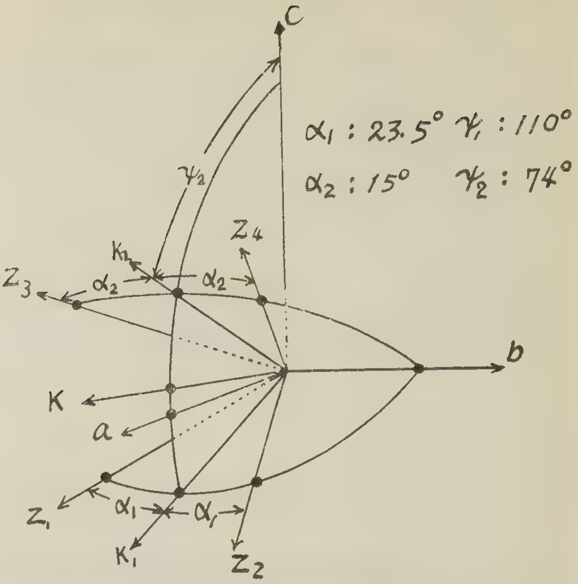

Fig. 4. Directions of $Z$-axes in $Cu(HCOO)_2\cdot 2H_2O$.

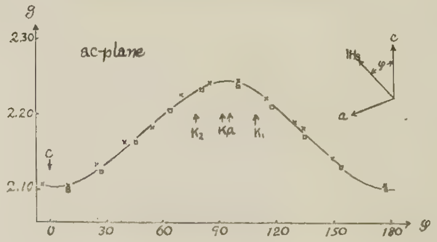

Fig. 5. Variation of $g$-value with orientation for $H_s$ in $Cu(HCOO)_2\cdot 2H_2O$.

Table II. Line width of $Cu(HCOO)_2\cdot 4H_2O$ at $\lambda=11$ mm in oer.

| | $H//a$ axis | $H//b$ axis | $H//c$ axis |
|---|---|---|---|
| Observed line width $\Delta H$ | 360 | 420 | 460 |
| Calculated dipolar width | 310 | 390 | 570 |

Table III. Line width of $Cu(HCOO)_2\cdot 2H_2O$ at $\lambda=11$ mm in oer.

| | $H//a$ axis | $H//b$ axis | $H//c$ axis |
|---|---|---|---|
| Observed line width | 230 | 240 | 140 |
| Calculated dipolar width | 590 | 400 | 480 |

the $H_2O$–$H_2O$ direction is the symmetry axis of crystalline field and we call this the $Z$-axis. There are two inequivalent $Cu^{++}$ ions in unit cell, so axes $Z_1$ and $Z_2$ which means the $Z$ axes of these ions orientate themselves differently as shown in Fig. 2. $L_1$ and $L_2$ in Fig. 2 are the bisector of the acute and obtuse angle between $Z_1$ and $Z_2$, and $L_3$ is the normal to the plane of $Z_1$ and $Z_2$. In $Z_1Z_2$ plane, only one peak is observed in every direction which may be ascribed to the exchange interaction, so we assume the observed peak shows the mean of $g$ values of two $Cu^{++}$ ions in unit cell. The observed $g$ values are shown in Fig. 3 as a function of direction. Assuming that the crystalline field arround each $Cu^{++}$ ion has tetragonal symmetry, the $g$ value may be estimated from these data as $g_{//}=2.35$ and $g_{\perp}=2.06$. The full line widths $\Delta H$ of absorption at $\lambda=11$ mm are listed in Table II, and the experimental error of $\Delta H$ is less than 20 oer. The calculated dipolar width is also listed in this table[6,7]. Though the exchange narrowing for these directions with the identical $g$ values may be expected[8,9], the observed widths are approximately the same as the calculated dipolar ones. All the line shapes are of Lorentzian type.

ii) *Copper Formate Dihydrate*
*$Cu(HCOO)_2 \cdot 2H_2O$*

This crystal has four $Cu^{++}$ ions in an unit cell, which make a face centered lattice of coppers. Directions of four $Z$-axes in this crystal are shown in Fig. 4. Each $Cu^{++}$ ion is surrounded by four oxygens and two water molecules as in its tetrahydrate. Only one peak is observed in any direction as the case of its tetrahydrate. When the sample is rotated in the $ac$-plane, the observed $g$-value reaches to its maximum value in $K$-direction as shown in Fig. 5. The observed half value widths at $\lambda = 11$ mm and calculated dipolar widths are shown in Table III. Now a considerable narrowing of width occurs.

Our thanks are due to Prof. Hiroo Kumagai for his continuous guidance and encouragement and to Miss H. Ibamoto at Ôsaka University for her preparation of the single crystals used in our measurements.

### References

1) Itoh et al: Private communication. We wish to thank them.
2) H. Kumagai, H. Abe and J. Shimada: Phys. Rev. **87** (1952) 385.
3) B. Bleaney and K. D. Bowers: Proc. Roy. Soc. (London) **214** (1952) 451.
4) H. Abe: Phys. Rev. **92** (1953) 1572.
5) R. Kiriyama, H. Ibamoto and K. Matsuo: Acta Cryst. **7** (1954) 482.
6) J. H. Van Vleck: Phys. Rev. **74** (1948) 1168.
7) H. Kumagai et al: Journ. Phys. Soc. Japan **9** (1954) 369.
H. Kumagai et al: Phys. Rev. **83** (1951) 1077.
8) P. W. Anderson and P. R. Weiss: Rev. Mod. Phys. **25** (1953) 269.
9) H. Abe et al: Journ. Phys. Soc. Japan **9** (1954) 814.

---

JOURNAL OF THE PHYSICAL SOCIETY OF JAPAN Vol. 11, No. 2, FEBRUARY, 1956

# Apparent Molecular Weight of Polytrifluorochloroethylene

By Atsuo NISHIOKA and Ryuzo KOYAMA
*Electrical Communication Laboratory, Musashino, Tokyo*

(Read June 3rd, 1955 and received September 20, 1955)

To clarify the accuracy and physical basis of the two methods, NST and ZST, giving the apparent molecular weight of Polytrifluorochloroethylene, some experiments were made by statistical means and their variances were analysed. We have derived theoretical relations between these apparent molecular weights and true average molecular weight by a simple model. The observed tendency of our experimental results between NST and ZST are qualitatively in accordance with our theoretical relations.

## § 1. Introduction

Fluorocarbon polymers are known by their excellent heat resistant, moisture proof and chemically resistant properties, but on the other hand, their insolubility at ordinary temperatures makes the measurement of their molecular weight difficult. Polytrifluorochloroethylene, $(-CF_2CFCl-)_n$, one of the fluorocarbon polymers, dissolves in certain chlorofluorocarbons at elevated temperature, but the operation of the measurement of molecular weight in dilute solution at high temperature is not easy, and these solvents are not easily available, and so the solution viscosity method is not suitable for the control of polymer and fabricating process. Therefore, several methods of determining apparent molecular weight related with melt viscosity were developed. Among these methods, there are parallel plate melt viscosity method, flow index method, no-strength-temperature test, and zero-strength-time test. Owing to the simple

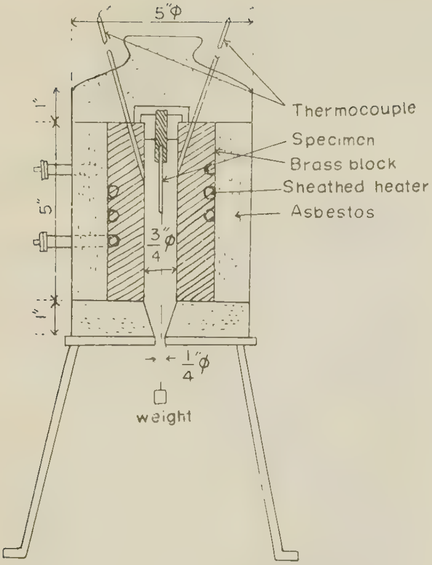

Fig. 1. NST testing apparatus.

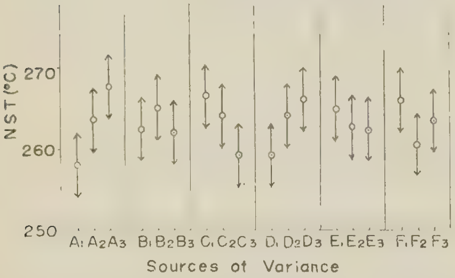

Fig. 2. Changes of sources of variances with each level at the confidence level of 95%.

operation, the last two methods are more practical than the others. No Strength Temperature test (NST) determines the temperature at which a standard notched and loaded sample breaks at constant heating rate, and Zero Strength Time test (ZST) determines the time at which the similar specimen breaks at constant temperature. Both the NST and the logarithm of ZST were already observed in a linear relation approximately with molecular weight. ZST test was developed recently as an improved method of NST test, but the accuracy of NST test and the physical basis of their dependence upon molecular weight has not been studied in detail.

We have performed some experiments on these two tests by a statistical method. In the following we discuss their accuracies and derive the relation between the apparent molecular weights and true average molecular weight by a simple model.

Table I. Design of Experiment.

| source of variation \ level | | 1 | 2 | 3 |
|---|---|---|---|---|
| width of notch | (A) | 1.0 mm | 1.2 mm | 1.4 mm |
| thickness | (B) | small | medium | large |
| weight | (C) | 0.4 gr. | 0.5 gr. | 0.6 gr. |
| heating rate | (D) | 80°C/hr. | 90°C/hr. | 100°C/hr. |
| starting temperature | (E) | 200°C | 210°C | 220°C |
| waiting time | (F) | 1 min. | 5 min. | 10 min |

Table II. Analysis of Variance.

| source of variation | degrees of freedom | sum of squares | mean square | F test |
|---|---|---|---|---|
| A linear | 1 | 271 | 271 | 17.6** |
| residue | 1 | 3 | 3 | 0.3 |
| B | 2 | 31.5 | 15.8 | 1.0 |
| C linear | 1 | 149 | 149 | 9.7* |
| residue | 1 | 7.8 | 7.8 | 0.5 |
| D linear | 1 | 140 | 140 | 9.1* |
| residue | 1 | 11.5 | 11.5 | 0.8 |
| E linear | 1 | 20 | 20 | 1.3 |
| residue | 1 | 2.7 | 2.7 | 0.2 |
| F | 2 | 82.3 | 41.2 | 2.7 |
| Error | 5 | 77.1 | 15.4 | |
| Total | 17 | 795 | | |

**: significant at the risk of 1%.
*: significant at the risk of 5%.

## § 2. No Strength Temperature Test

No Strength Temperature is the point at which a standard notched and loaded sample breaks under a standard rate of temperature rising¹⁾. To perform the test, a sample of the polymer is pressed into a 1/16 in. thick disc. A strip $1\frac{5}{8}$ in. long by 1/8 in. wide, which was cut from this disc, has a double notch end 3/64 in. wide, 1 in. from the end. A weight is then attached to the one end to give a total weight, 0.5 gram, of the sample and added weight from the notch down. This sample is then suspended in a heated oven held at 210°C, and the temperature is raised 1.5°C per min. until the sample breaks at the notch. The temperature of the oven is then read as the No Strength Temperature.

a) *Design of Experiment*

The sources of variation of NST are mainly composed of six factors, that is, the width of the notch, the thickness of the sample, the weight, the heating rate, starting temperature, and the waiting time from the insertion of the specimen to the beginning of heating. We designed our experiment by the statistical procedure with Latin Square of 18 specimens shown in Table I. The tested sample was Daiflon-resin of NST 270 manufactured by Osaka Kinzoku Kogyo K. K.

### b) *Experimental Results*

The testing apparatus used for this test was similar to that originally designed by Giannotta[2], but the NST was read by chromel-almel thermocouple (Fig. 1). Since the accuracy of the width of the notch seems to give predominant influence on NST value, we cut the double notch by means of special cutter and zig, not by a punch. The heating rate was adjusted by a geared temperature controller. The NST of the samples specified by the Table I were measured in randomized order. The numerical analysis of variance of the observed NST values is listed in the following Table II, and the tendencies of each factor were shown in Fig. 2.

As seen from Table II, NST is significantly affected by the notch width, weight and heating rate, but negligibly by the thickness, starting temperature and waiting time. The fact that the effect of thickness is very small, seems to be curious, but could be explained as follows. The weight of the specimen under the notch is comparable to the added weight, so the change of tensile stress due to the change of thickness is almost cancelled with the change of total weight due to that of the weight of the specimen. The mean value of NST under the specified condition is 267±6°C at the confidence level of 95%. The relative error of this value is small, but the variance of ±6°C seems to be large compared with the temperature range usually observed from 240°C to 310°C.

Another factor seemed to affect the NST value. It is the anisotropy effect which means the difference of tensile strength between the parallel and perpendicular to the radial direction, but this effect is not significant at the confidence level of 95%. So we have neglected this anisotropy effect.

### c) *Theory*

As seen from the above description, the result of this test seemed to be mainly determined by the notch width of the specimen, and NST increased proportionally with notch width and heating rate, and decreased with the added weight. Also the molecular weights of polytrifluorochloroethylene by high temperature osmometry[3] shows the approximately linear relationship to NST. However, the physical interpretation of this dependence of NST has not been ever studied. Difficulties of this study seem to lie in the special form of double notch, but we considered that the essential point of this test is the section of the notch and so we simplified this part in the following model.

We assume a rod-like specimen with the sectional area $A$ and the length $l$, attached a weight $W$ at the end. When the temperature of the specimen is raised at a constant rate, the elongation rate will be proportional to the tensile stress and the length, and reciprocally to melt viscosity at the temperature, So we have the next equation,

$$\frac{dl}{dt}=C\frac{Wl}{A\eta} \tag{1}$$

where $t$ is time, $C$ is the proportionality constant and $\eta$ is melt viscosity. And in relatively short range of temperature, the melt viscosity is related with absolute temperature $T$ by the formula,

$$\eta=\eta_0\exp(E/RT)\ , \tag{2}$$

where $\eta_0$ is a constant dependent upon molecular weight, $E$ is the activation energy for melt viscosity, and $R$ is the gas constant. Also the heating rate $k$ is constant, so we have

$$T=T_0+kt\ , \tag{3}$$

where $T_0$ is the starting temperature. Combining these equations, we have

$$\frac{dl}{dt}=\frac{CWl}{A\eta_0}\exp[-E/RT]. \tag{4}$$

Assuming that the volume of the specimen is constant, and NST is defined when $l$ becomes infinite at a temperature $T_c$, we have

$$\int_{T_0}^{T_c}\exp(-E/RT)dT=A_0k\eta_0/CW, \tag{5}$$

where $A_0$ is the initial area of cross section and $T_c$ is the No Strength Temperature. The exponential term of the left hand side of Eq. (5) can be expanded in series form around the starting temperature $T_0$. Then we have

$$\exp(-E/RT)=\exp\left\{(-E/RT_0\left[1-\left(\frac{T-T_0}{T_0}\right)+\left(\frac{T-T_0}{T_0}\right)^2-\left(\frac{T-T_0}{T_0}\right)^3+\cdots\right]\right\}. \tag{6}$$

Since $T_0$ is 210°C, and No Strength Temperature is usually found between 240°C and 310°C, $(T-T_0)/T_0$ is smaller than unity (1/16∼1/5). So, if we neglect the higher order term of $(T-T_0)/T_0$ in Eq. (6), then we have

$$\int_{T_0}^{T_c}\exp(-E/RT)dT=\int_{T_0}^{T_c}\exp\left\{(-E/RT_0)\left(1-\frac{T-T_0}{T_0}\right)\right\}dT$$
$$=\exp\left(-\frac{E}{RT_0}\right)\left(\frac{RT_0^2}{E}\right)\left\{\exp\left(\frac{E}{RT_0^2}(T_c-T_0)\right)-1\right\}. \tag{7}$$

From Eq. (5), we have

$$\exp\left(\frac{E}{RT_0^2}(T_c-T_0)\right)\left\{1-\exp\left(-\frac{E}{RT_0^2}(T_c-T_0)\right)\right\}=\frac{A_0k\eta_0}{CWT_0}\frac{E}{RT_0}\exp\left(\frac{E}{RT_0}\right) \tag{8}$$

$$\therefore\quad \frac{E}{RT_0^2}(T_c-T_0)+\log\left\{1-\exp\left(-\frac{E}{R^2T_0}(T_c-T_0)\right)\right\}=\log\eta_0+\log\frac{A_0kE}{CWRT_0^2}+\frac{E}{RT_0}. \tag{9}$$

If we assume that the molecular weight $M$ is approximately proportional to logarithm of melt viscosity in our temperature range, we can write

$$\log\eta_0=\alpha+\beta M. \tag{10}$$

So, Eq. (9) becomes

$$\frac{E}{RT_0^2}(T_c-T_0)+\log\left\{1-\exp\left(-\frac{E}{RT_0^2}(T_c-T_0)\right)\right\}=\beta M+\log\frac{A_0kE}{CWRT_0^2}+\alpha+\frac{E}{RT_0}. \tag{11}$$

Here the activation energy $E$ had already been found to be 15 Kcal/mol by Dexter[4], but recently Furuya[5] has obtained some higher values. So, if we assume it to be 20 Kcal/mol and take the range of $T_c$ between 240°C and 310°C, the first term of the left hand side of Eq. (11) varies from 1.207 to 4.025, whereas the second term varies from −0.357 to −0.018 and its contribution may be negligible above 250°C within the error of 5°C as seen from Fig. 3. In this figure $f_1$ and $f_2$ show the first and second terms of the left hand side of Eq. (11) respectively. The correction term $f_2$ cannot be neglected in the lower temperature range near 240°C, so the left hand side of Eq. (11) is not rigorously proportional to $T_c$ from 240°C to 310°C, but may be approximately considered to be linear above 250°C within the error of 5°C, and this error is decreased rapidly in higher temperature. Therefore this equation would be considered to show the approximate linear relation between NST and molecular weight in usually available temperature range of NST. Further, the second term of the right hand side of Eq. (11) show the dependence of NST upon cross section of the specimen $A_0$, heating rate $k$, added weight $W$, which is qualitatively in well accordance with the observed tendencies[6] (Fig. 2).

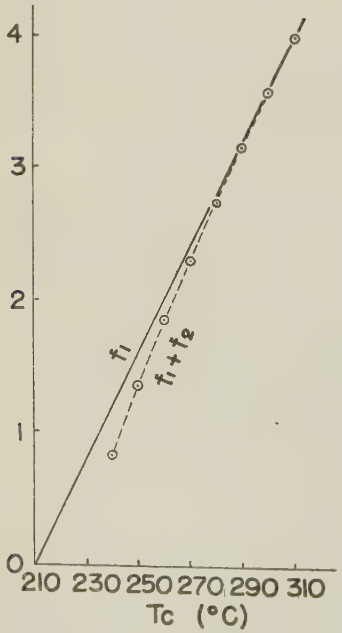

Fig. 3. Linearity of the left hand side of Eq. (12) with NST.

## § 3. Zero Strength Time Test

This test, developed recently by Kaufman et al[7], determines the time at which the standard sample like the NST test, breaks under the standard weight of 7.5 gram at constant temperature of 250°C. The specimen is almost the same as that of NST except the width of the notch (3/16 in.). We have performed this test using the same specimen of NST test. The weight was about 8.3 gram. The merit of this test is in its simple linear relation between the logarithm of ZST and solution viscosity.

a) *Experimental Results*

The tested specimens were three grades of Daiflon-resin, which have the NST of 242, 268 and 306, and another three grades of Fluorothene, namely FYTD, FYTH and FYTS, which have the NST of 281, 287 and 296 respectively. These values of NST were the average values measured on five specimens of each grade. The experiment was performed on two groups of 3×3 Latin Square specified by NST, furnace temperature and thickness of the sample. The observed ZST values were plotted against to NST as shown in Fig. 4. This result shows the linear relation between the NST and the logarithm of ZST in the temperature range from 240°C to 310°C. Although Kaufman[7] has reported the non-linear relation between the two values above 300°C and attributed this to the thermal degradation of this polymer, we observed fairly good linearity between NST and log ZST in this range and the effect of thermal degradation seems to be relatively small and practically negligible.

b) *Theory*

The feature of this test is in the linearity between log ZST and molecular weight. We shall now try to derive this relation by the similar model to that of NST test previously described. The fundamental equation is also the same in this case. Now in ZST test, as the temperature is constant, the melt viscosity is also constant. Assuming the constant volume of the notched part, we can obtain the following equation from Eq. (1).

$$t_c = A_0\eta/CW\,, \tag{12}$$

where $t_c$ is the Zero Strength Time and another symbols are the same as in NST case. This relation means that the Zero Strength Time is proportional to the melt viscosity. Then, from (12), we have

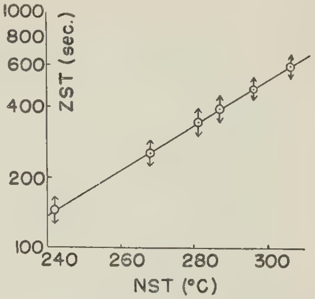

Fig. 4. Zero Strength Time versus No Strength Temperature.

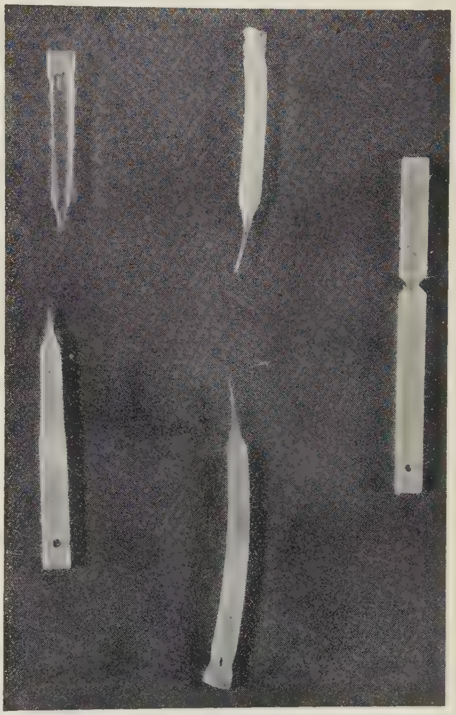

Fig. 5. Broken specimens of ZST (left) and NST (central). Original specimen is at the right.

$$\log t_c = \text{const.} + \log\eta + \log A_0/W\,, \tag{13}$$

Since $\log\eta$ is proportional to molecular weight $M$ as in the previous section, logarithm of the Zero Strength Time is proportional to molecular weight. Therefore we have

$$\log t_c = \beta M + \log A_0/W + \text{const.} \tag{14}$$

Comparing the equation (11) with (14), we can easily derive the linear relationship between NST and log ZST, which was observed experimentally. Since the variation term, $A_0/W$, is included in the same logarithmic form in Eqs. (11) and (14), the variance of NST and log ZST are comparable about these terms. This means that the accuracy of NST is higher than ZST, but comparable to log ZST.

In our simplified theory, the mechanism of the breaking of the specimen is assumed to be same in both cases, but the observation of the broken sample shown in Fig. 5 suggests different mechanisms for these two tests. The fact that the broken part of the notch is considerably elongated in NST test would be probably in favour of our model based on the melt viscosity, but the broken specimen of the ZST test is less elongated and has a finite sectional area at the tip, different from the negligible area of NST sample. Further, the surface of the tip is not uniform, suggesting the mechanism of breaking at weak points, pointed out by Yamada[8]. Therefore the mechanism of the breaking in both cases may be slightly different.

Another point to be mentioned is the assumption of constant volume. In our model, the narrow part of the notch is replaced by a rod-like specimen, but the possibility of the polymer flowing into the notched part from the other part cannot be neglected and so the above assumption may not be applied rigorously in our case.

Therefore, we must study in further detail about these points to interprete the mechanism of the breaking of the specimen more elaborately.

## § 4. Conclusion

From the observed results in our experiments and the theoretical discussion, we have the following conclusions.

(1) NST depends largely upon the notch width, but not upon the thickness of the specimen in its small variance.

(2) NST increases with the heating rate and the reciprocal of the added weight.

(3) NST does not depends significantly upon the small variance of starting temperature, the waiting time and anisotropy.

(4) NST is approximately proportional to molecular weight and logarithm of ZST from 240°C to 310°C.

(5) The accuracy of NST is higher than ZST, but comparable to log ZST.

(6) The thermal degradation effects in NST test is not significant up to 310°C.

These conclusions would not suggest the superiority of ZST test to NST test, differing from the suggestion of Kaufman[7].

### Acknowledgement

The authors express their sincere thanks to Mr. Ichimiya and Mr. Miyazaki for their encouragement on this work, and to Mr. Furuya for the use of his unpublished data, and Mr. Yamada for his helpful discussions. We are indebted to the courtesy of Osaka Kinzoku Kogyo K. K. for the performance of this experiment.

### References

1) C. R. Giannotta: Plastics, May, (1953) 166.
2) C. R. Giannotta: J. Soc. Plastic Eng., Feb., (1953) 50.
3) H. S. Kaufman and M. S. Muthana: J. Polymer Sci. **6** (1951) 251.
4) F. D. Dexter: Mod. Plastics, April, (1953) 125.
5) S. Furuya: unpublished data.
6) A. Nishioka and R. Koyama: Rheology Symposium, June, 1955, Tokyo.
7) H. S. Kaufman et al: Mod. Plastics, Oct., (1954) 146.
8) N. Yamada: Rheology Symposium, June, 1955, Tokyo.

JOURNAL OF THE PHYSICAL SOCIETY OF JAPAN Vol. 11, No. 2, FEBRUARY, 1956

# A Study of the Compressilbe Flow past a Cherry Profile

By Hideo TAKAMI

*Department of Physics, Faculty of Science, University of Tokyo*

(Received September 14, 1955)

In this paper the compressible gas flow past a Cherry profile is studied by means of Kármán-Tsien's method, the $M^2$-expansion method and Meksyn-Imai's method. The velocity distributions over the surface of the profile are calculated for various free stream Mach numbers and compared with Cherry's exact one as well as with one another. Imai's $\Phi\Psi$-procedure in the $M^2$-expansion method is shown to be the most efficient for the study of the flow up to comparatively high (subsonic) Mach number. It is found that there exists a qualitative difference between the velocity distribution of Cherry's exact solution and those calculated by means of the approximate methods, and some discussions are given about Cherry's solution.

## § 1. Introduction

A number of methods of approach have been devised by many investigators to deal with the two-dimensional compressible flow of the inviscid gas past an obstacle; namely, the hodograph method, the thin-wing-expansion method and the $M^2$-expansion method. Among these the hodograph method alone enables us to treat the problem exactly even in the case of the transonic flow, because only in the hodograph variables we can have linear equations governing the compressible flow. Thus exact solutions of continuous transonic flow past a cylindrical obstacle were obtained by Lighthill [12] and Cherry [2] (for the adiabatic gas), and by Tomotika and Tamada [16] (for a certain hypothetical gas) by using the hodograph method.

In its exact form, however, the hodograph method has a disadvantage that it can hardly be applied to the study of the flow past an obstacle of *given* shape. For this purpose we must have recourse to some simple approximations in the hodograph plane itself or to successive approximations in the physical plane.

As for the former we may mention Kármán-Tsien's method [17] and Imai's WKB method [9], both of which essentially reduce the compressible flow problem to that of the incompressible one and have been applied to many cases on account of the simplicity of calculation.

On the other hand, the $M^2$-expansion method has been developed and applied by many investigators to the treatment of the flow past bodies of arbitrary shapes at moderate (subsonic) Mach number, while the thin-wing-expansion method has also been successfully applied to the study of the flows past thin obstacles under the condition that the disturbance velocities from the uniform flow are small.

Recently Meksyn [13] proposed an approximate method for the treatment of the flow at comparatively high Mach number, of which Imai [11] soon after pointed out the intimate relationship with the usual $M^2$-expansion method.

In this paper we shall apply the Kármán-Tsien method, the $M^2$-expansion method and the Meksyn-Imai method to the study of the compressible flow past a Cherry profile, and calculate the velocity distributions over its surface for various free stream Mach numbers. The calculated velocity distributions will be compared with Cherry's exact one as well as with one another to investigate the limitations of the validity of these approximate methods, and some conjectural discussions on Cherry's solution will be given.

## § 2. Cherry's Exact Solution

As is well known, Cherry [2] constructed a family of exact solutions for two-dimensional potential flow of a compressible fluid past a cylindrical obstacle by means of the hodograph method, and performed numerical calculations for particular values of parameters [3] [4]. One of his numerical solutions gives a continuous

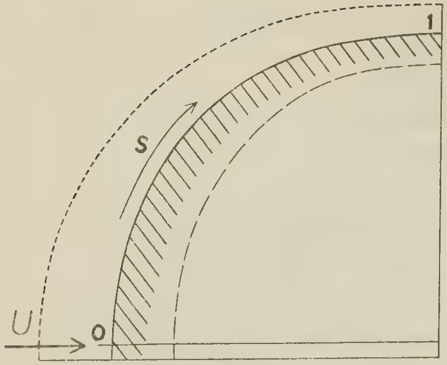

Fig. 1. The shapes of the profiles (one quadrant).
- Cherry's profile,
the profile into which Cherry's profile is deformed for $M=0.5098$ in Kármán-Tsien's method (§ 4),
------ the profile which is deformed into Cherry's profile for $M=0.5098$ in Kármán-Tsien's method (§ 4).

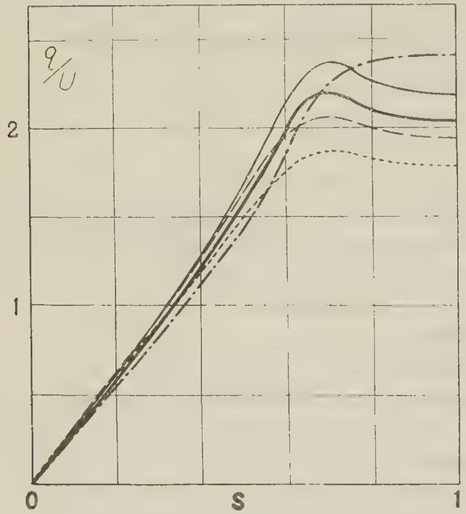

Fig. 2. The velocity distributions over the surface.
- Cherry's exact solution ($M=0.5098$),
- incompressible flow,
—— Kármán-Tsien's method (simplified. $M=0.350$),
Kármán-Tsien's method (simplified, $M=0.5098$),
———— Kármán-Tsien's method ($M=0.5098$).

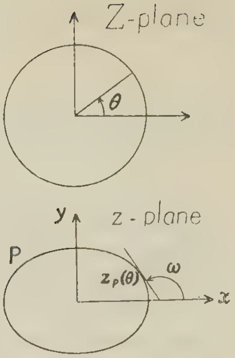

Fig. 3. The correspondence between the $Z$-plane and the $z$-plane.

transonic flow with free stream Mach number 0.5098 past a cylinder whose section is a doubly symmetrical oval with thickness ratio 0.931, the incident stream being parallel to the major axis of symmetry (Fig. 1). The flow field contains two supersonic regions adjacent to the body and the velocity distribution over the quadrant of its surface is shown in Fig. 2.

## § 3. The Mapping Function for the Cherry Profile and the Incompressible Velocity Distribution

For the present study of the flow past a Cherry profile, it is necessary to obtain the analytic function which maps the profile into the unit circle. This is conveniently done by means of the successive procedure developed by Imai [5] [10], of which the outline will be given in the following.

It is well known that the region outside an arbitrary profile $P$ in the $z(=x+iy)$-plane can be mapped conformally onto the region outside the unit circle $Z=e^{i\theta}$ in the $Z$-plane by an analytic function of the form:

$$z=c_{-1}Z+c_0+\frac{c_1}{Z}+\frac{c_2}{Z^2}+\cdots . \tag{3·1}$$

If the profile itself is expressed as $z_P=x_P(\theta)+iy_P(\theta)$ (cf. Fig. 3), the following relation holds between $x_P$ and $y_P$:

$$x_P(\theta)=\left\{1-\frac{1}{2}\,y_P{}^*(0)+\frac{1}{2}y_P{}^*(\pi)\right\}\cos\theta+y_P{}^*(\theta)$$
$$-\frac{1}{2}y_P{}^*(0)-\frac{1}{2}y_P{}^*(\pi)\ , \tag{3.2}$$

where $y^*(\theta)$ denotes the conjugate Fourier series associated with $y(\theta)$, i.e., if

$$y(\theta)=a_0+\sum_{n=1}^{\infty}(a_n\cos n\theta+b_n\sin n\theta)\ ,$$

then

$$y^*(\theta)=\sum_{n=1}^{\infty}(a_n\sin n\theta-b_n\cos n\theta)$$
$$=-\frac{1}{2\pi}\int_0^{2\pi}\{y(\varphi+\theta)-y(\theta)\}\cot\frac{\varphi}{2}d\varphi\ , \tag{3.3}$$

and it is assumed that the profile is symmetric with respect to the $x$-axis and cuts it at the points (1, 0) and (−1, 0).

Eq. (3.2) is the basic relation for the successive procedure. Let us calculate the values of $x_P$ and $y_P$ for $\theta=\theta_k=2\pi k/40$ $(k=0, 1, 2, \cdots, 39)$[*] as follows:

(1) Take $x^{(0)}(\theta_k)=\cos\theta_k$ as the 0th approximation and read the ordinates $y^{(1)}(\theta_k)$ on the profile corresponding to the abscissae $x^{(0)}(\theta_k)$.

(2) Calculate $y^{(1)\prime}(\theta_k)$ by the use of the Stirling interpolation formula.

(3) Replacing the integration in Eq. (3.3) by the summation, calculate

$$y^{(1)*}(\theta_k)=-\frac{1}{20}y^{(1)\prime}(\theta_k)+\sum_{s=1}^{19}\{y^{(1)}(\theta_{k+s})-y^{(1)}(\theta_{k-s})\}\frac{1}{40}\cot\frac{s\pi}{40}\,.$$

(4) By the use of Eq. (3.2) calculate

$$x^{(1)}(\theta_k)\equiv\left\{1-\frac{1}{2}y^{(1)*}(0)+\frac{1}{2}y^{(1)*}(\pi)\right\}\cos\theta_k+y^{(1)*}(\theta_k)-\frac{1}{2}y^{(1)*}(0)-\frac{1}{2}y^{(1)*}(\pi)\,,$$

thus completing the first approximation.

But, in general, the points $(x^{(1)}(\theta_k), y^{(1)}(\theta_k))$ do not lie on the original profile, so the above process must be repeated with $x^{(1)}(\theta_k)$ instead of $x^{(0)}(\theta_k)$, etc., until the process converges.

For the Cherry profile 7 steps are necessary in order to obtain the final values of $x_P$ and $y_P$.

Once we get $x_P$ and $y_P$, the velocity $q_{\text{inc}}$ on the surface for the incompressible flow with its undisturbed stream direction parallel to the $x$-axis is easily calculated as

$$\frac{q_{\text{inc}}}{U_{\text{inc}}}=\frac{1-\frac{1}{2}y_P{}^*(0)+\frac{1}{2}y_P{}^*(\pi)}{\sqrt{\left(\frac{dx_P}{d\theta}\right)^2+\left(\frac{dy_P}{d\theta}\right)^2}}\sin\theta\,, \qquad (3.4)$$

where $U_{\text{inc}}$ is the velocity of the undisturbed flow.

In Fig. 2 the values of $q_{\text{inc}}/U_{\text{inc}}$ are plotted against the arc length measured from the stagnation point. It may be noted that there exists a qualitative difference from the velocity distribution of Cherry's solution for the compressible flow.

## § 4. The Kármán-Tsien Method

Now we shall study the flow past the Cherry profile by means of Kármán-Tsien's method [17].

According to this, the velocity $q$ for the compressible flow with free stream Mach number $M$ is approximately given in terms of $q_{\text{inc}}$ and $M$ simply as follows:

$$\frac{q}{U}=\frac{q_{\text{inc}}}{U_{\text{inc}}}\,\frac{1-\lambda}{1-\lambda(q_{\text{inc}}/U_{\text{inc}})^2} \qquad (4.1)$$

where $U$ is the free stream velocity and

$$\lambda=\frac{1-\sqrt{1-M^2}}{1+\sqrt{1-M^2}}\,.$$

In Fig. 2, the values of $q/U$ calculated by Eq. (4.1) are shown for $M=0.350$ and 0.5098. (For comparison with the results obtained by the other methods, the values of $q/c_*$ are also shown for $M=0.420$ and 0.5098 in Figs. 5(b) and (d), $c_*$ being the critical sound velocity.)

As is well known, however, the velocity distribution thus obtained does not correspond to the original profile $P$, but to a different one, say $P'$, which is given as

$$\zeta_{P'}=z_P-\lambda\int_0^\theta(q_{\text{inc}}/U_{\text{inc}})^2(dz_P/d\theta)d\theta\,,$$

or

$$\left\{\begin{aligned}\xi_{P'}&=\int_0^\theta\{1-\lambda(q_{\text{inc}}/U_{\text{inc}})^2\}(dx_P/d\theta)d\theta\,,\\ \eta_{P'}&=\int_0^\theta\{1-\lambda(q_{\text{inc}}/U_{\text{inc}})^2\}(dy_P/d\theta)d\theta\,.\end{aligned}\right. \qquad (4.2)$$

The deformed contour for $M=0.5098$ is shown in Fig. 1 in comparison with the original Cherry profile.

So we must start with the incompressible flow past certain other profile which is to be deformed into the original one after the above-mentioned transformation. For this purpose, the following iterative procedure may be employed for the Mach number in question (cf. Fig. 4):

(1) For given $P$, calculate $q_{\text{inc}}/U_{\text{inc}}$ and the deformed profile $(\xi_0, \eta_0)$ according to (3.4) and (4.2).

(2) The profile $(\xi_0, \eta_0)$ is similarly enlarged into $(\xi_{0N}, \eta_{0N})$ so that $\xi_{0N}(0)=-\xi_{0N}(\pi)=1$.

(3) For $\xi_{0N}(\theta_k)$ read the ordinates $\bar{\eta}_{0N}(\theta_k)$ on $P$.

(4) Calculate $\bar{\eta}_0(\theta_k)\equiv\bar{\eta}_{0N}(\theta_k)\cdot\xi_0(0)$ and $\bar{\eta}_0{}'(\theta_k)$.

---

[*] Later we shall calculate the velocity only for these points, and this may be sufficient for the purpose of this paper.

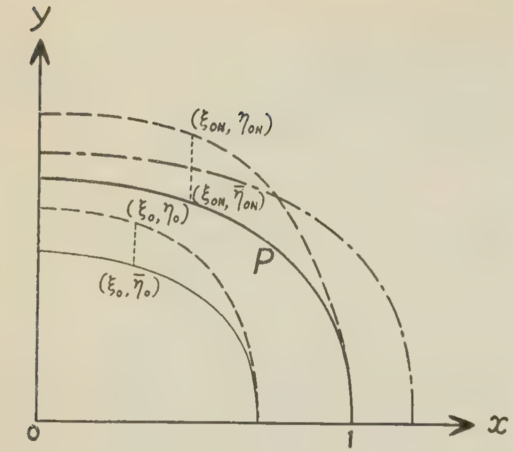

Fig. 4. The shapes of the profiles (one quadrant).
━━━ The original profile $P$,
——— the original profile (reduced),
– – – the deformed profile,
━ ━ ━ the deformed profile (enlarged),
━ - ━ - $(x_1, y_1)$.

(5) Calculate $y_1'(\theta_k) \equiv \bar{\eta}_0'(\theta_k)/\{1-\lambda(q_{\text{inc}}/U_{\text{inc}})^2\}$ (cf. (4.2)), $y_1''(\theta_k)$ and $y_1'^*(\theta_k)$.

(6) Calculate.

$$x_1'(\theta_k) \equiv -\left\{1-\frac{1}{2}y_1^*(0)+\frac{1}{2}y_1^*(\pi)\right\}\sin\theta_k + y_1'^*(\theta_k)\,, \qquad \text{(cf. (3.2))}$$

and

$$Q_1(\theta_k) \equiv \frac{1-\frac{1}{2}y_1^*(0)+\frac{1}{2}y_1^*(\pi)}{\sqrt{\left(\frac{dx_1}{d\theta}\right)^2+\left(\frac{dy_1}{d\theta}\right)^2}}\sin\theta_k\,. \qquad \text{(cf. (3.4))}$$

(7) Calculate

$$\begin{cases} \xi_1(\theta_k) \equiv \int_0^{\theta_k}(1-\lambda Q_1^2)x_1'\,d\theta\,, \\ \eta_1(\theta_k) \equiv \int_0^{\theta_k}(1-\lambda Q_1^2)y_1'\,d\theta\,. \end{cases}$$

If the shape of this profile $(\xi_1, \eta_1)$ is not similar to that of $P$, the above procedure is repeated for $(\xi_1, \eta_1)$ instead of $(\xi_0, \eta_0)$, etc., until the iteration converges and a profile, say $(\xi_n, \eta_n)$, similar to $P$ is finally obtained.

For the points $(\xi_n(\theta_k), \eta_n(\theta_k))$ on $P$ the velocities are calculated from (3.4) and (4.1) with $x_n$ and $y_n$ instead of $x_P$ and $y_P$.

In our case for $M=0.5098$, 11 steps of iteration are necessary to find the profile which is deformed into the Cherry profile. The profile is shown in Fig. 1 and the velocity distribution $q/U$ in Fig. 2. (Also $q/c_*$ is shown in Fig. 5(d).)

## § 5. The $M^2$-Expansion Method

We now apply the $M^2$-expansion method in the form developed by Imai [6], of which also a brief account will be given.

Suppose that a symmetrical obstacle* is placed in a uniform flow of Mach number $M$ whose direction is parallel to the axis of symmetry which we shall take as the $x$-axis (Fig. 3).

Now let us assume that the velocity potential $\Phi$ can be expanded in a power series in $M^2$:

$$\Phi(z)=\Phi_0(z)+M^2\Phi_1(z)+M^4\Phi_2(z)+\cdots, \qquad (5.1)$$

then the values of $\Phi_0, \Phi_1, \Phi_2, \cdots$ on the profile are calculated as

$$\begin{cases} \Phi_0(\theta)=2A\cos\theta\,, \\ \Phi_1(\theta)=P_1(\theta)-Q_1^*(\theta)\,, \\ \Phi_2(\theta)=\Phi_{20}(\theta)+(\gamma+1)\Phi_{21}(\theta) \\ \qquad =\{P_{20}(\theta)-Q_{20}^*(\theta)\}+(\gamma+1)\left\{P_{22}(\theta)-Q_{22}^*(\theta)-\frac{1}{2}\Phi_1(\theta)\right\}\,, \\ \cdots\cdots\cdots\cdots\cdots\cdots \end{cases}$$

Here $\theta$ has the same meaning as in Eq. (3.2), and

$$A=1-\frac{1}{2}y_P^*(0)+\frac{1}{2}y_P^*(\pi)\,,$$

$$\begin{cases} P_1(\theta)=-\frac{1}{2}q_0\sin\omega\int_0^s q_0^2\sin\omega\,ds\,, \\ Q_1(\theta)=-\frac{1}{2}q_0\cos\omega\int_0^s q_0^2\sin\omega\,ds\,. \end{cases}$$

---

* To avoid unnecessary complication the formulae will be given for a profile which is symmetrical with respect to the direction of the uniform flow.

$\omega$ is the angle between the $x$-axis and the tangent to the profile, so that

$$\sin\omega=\frac{y_P'}{\sqrt{x_P'^2+y_P'^2}}\,,\qquad \cos\omega=\frac{x_P'}{\sqrt{x_P'^2+y_P'^2}}\,,$$

$s$ is the arc length measured from the downstream stagnation point; and $q_0=-d\Phi_0/ds$ is equal to $q_{\rm inc}/U_{\rm inc}$ in Eq. (3.4). Further

$$\left\{\begin{aligned}
P_{20}(\theta)&=-\frac{1}{16}(q_0^2+1)A-\frac{1}{8}\,CF+\frac{1}{8}\left(\frac{dB}{d\theta}\cos\omega-\frac{dB^*}{d\theta}\sin\omega\right)E\\
&\qquad+\frac{1}{4}\,q_0\sin\omega\cdot G-\frac{A}{4}\cos\theta\,,\\
Q_{20}(\theta)&=-\frac{1}{16}(q_0^2-1)A-\frac{1}{8}\,DF-\frac{1}{8}\left(\frac{dB}{d\theta}\sin\omega+\frac{dB^*}{d\theta}\cos\omega\right)E\\
&\qquad+\frac{1}{4}\,q_0\cos\omega\cdot G\,,
\end{aligned}\right.$$

where

$$\left\{\begin{aligned}
A&=q_0\cos\omega\int_0^s q_0^2\cos\omega\,ds+q_0\sin\omega\int_0^s q_0^2\sin\omega\,ds\,,\\
B&=q_0\sin\omega\int_0^s q_0^2\cos\omega\,ds-q_0\cos\omega\int_0^s q_0^2\sin\omega\,ds\,,\\
C&=\sin\omega\,\frac{d}{d\theta}(q_0\cos\omega)+\cos\omega\,\frac{d}{d\theta}(q_0\sin\omega)\,,\\
D&=\cos\omega\,\frac{d}{d\theta}(q_0\cos\omega)-\sin\omega\,\frac{d}{d\theta}(q_0\sin\omega)\,,\\
E&=\left\{\left(\frac{dx_P}{d\theta}\right)^2+\left(\frac{dy_P}{d\theta}\right)^2\right\}^{-1/2}\int_0^s q_0^2\sin\omega\,ds\,,\\
F&=E\int_0^s q_0^2\cos\omega\,ds\,,\\
G&=\int_0^\theta\left(\frac{dB}{d\theta}\cos\omega-\frac{dB^*}{d\theta}\sin\omega\right)q_0\,d\theta\,,
\end{aligned}\right.$$

and

$$\left\{\begin{aligned}
P_{22}(\theta)&=-\frac{1}{8}\,q_0^2\sin 2\omega\int_0^s q_0^3\sin 2\omega\,ds\,,\\
Q_{22}(\theta)&=-\frac{1}{8}\,q_0^2\cos 2\omega\int_0^s q_0^3\sin 2\omega\,ds\,.
\end{aligned}\right.$$

$\gamma$ is the ratio of the specific heats, which we shall take to be 1.40 in the calculation.

If we also expand the velocity $q(\theta)$ as

$$q(\theta)=q_0(\theta)+M^2q_1(\theta)+M^4q_2(\theta)+\cdots,\tag{5.2}$$

then

$$q_n(\theta)=-\frac{d\Phi_n}{ds}=-\frac{d\Phi_n}{d\theta}\frac{d\theta}{ds}=-\frac{d\Phi_n/d\theta}{\sqrt{x_P'^2+y_P'^2}}\qquad (n=0,1,2,\cdots)^*.$$

Imai [7] further developed the theory as follows:

(1) The $\Psi$-procedure. From the mathematical point of view, the velocity potential $\Phi$ and the stream function $\Psi$ are equivalent quantities since the flow field is completely determined by giving either of them; in fact, we could have obtained the velocity from the steam function $\Psi$ according to the equation

---

* Here and later we take the velocity of the undisturbed flow as the unit of velocity.

$$\frac{\partial\Psi}{\partial n}=\frac{\rho q}{\rho_\infty}=q\left\{1+\frac{\gamma-1}{2}M^2(1-q^2)\right\}^{1/(\gamma-1)},$$

where $dn$ is the line element normal to the streamline, $\rho$ is the density and suffix $\infty$ means the value in the uniform flow. This procedure for calculating the velocity may be called "$\Psi$-procedure" as the counterpart of the usual "$\Phi$-procedure".

In general, the velocities calculated according to the $\Psi$-procedure is not identical with those from the $\Phi$-procedure, but the difference between them is, of course, within the order of the approximation employed and may give a measure of the errors involved in this approximation.

Practically $\partial\Psi/\partial n$ can easily be calculated if we know $q_0, q_1, q_2, \cdots$ in the $\Phi$-procedure.

Let the stream function $\Psi$ and the density $\rho$ be expanded as

$$\begin{cases}\Psi=\Psi_0+M^2\Psi_1+M^4\Psi_2+\cdots,\\ 1-\dfrac{\rho}{\rho_\infty}=M^2\rho_1+M^4\rho_2+\cdots,\end{cases}$$

where

$$\rho_1=\frac{1}{2}(q_0^2-1),\quad \rho_2=q_0q_1-\frac{2-\gamma}{8}(q_0^2-1)^2,\ \cdots,$$

then inserting these expansions and (5.1) into the relation

$$\frac{\partial\Psi}{\partial n}=-\frac{\rho}{\rho_\infty}\frac{\partial\Phi}{\partial s},$$

and comparing the terms of the same powers of $M^2$, we get

$$\begin{cases}\dfrac{\partial\Psi_0}{\partial n}=-\dfrac{\partial\Phi_0}{\partial s}=q_0,\\ \dfrac{\partial\Psi_1}{\partial n}=-\dfrac{\partial\Phi_1}{\partial s}+\rho_1\dfrac{\partial\Phi_0}{\partial s}=q_1-\rho_1q_0,\\ \dfrac{\partial\Psi_2}{\partial n}=-\dfrac{\partial\Phi_2}{\partial s}+\rho_1\dfrac{\partial\Phi_1}{\partial s}+\rho_2\dfrac{\partial\Phi_0}{\partial s}\\ \qquad=q_2-\rho_1q_1-\rho_2q_0,\\ \cdots\cdots\cdots\cdots\cdots\cdots\,.\end{cases}$$

In order to obtain $q$ from $\rho q/\rho_\infty$, it is convenient to use the numerical table (e.g. [8]).

(2) The $\Phi\Psi$-procedure. Also by means of the relation

$$\frac{\rho}{\rho_\infty}=\left\{1+\frac{\gamma-1}{2}M^2(1-q^2)\right\}^{1/(\gamma-1)},$$

in which the value from the $\Phi$-procedure is substituted for $q$, the velocity can be obtained as

$$q=\frac{\rho_\infty}{\rho}\frac{\partial\Psi}{\partial n},$$

which is the "$\Phi\Psi$-procedure" For the evaluation of $\rho/\rho_\infty$ also the use of the numerical table is convenient in practice.

Applying these procedures to the cases of a circular cylinder and a circular-arc aerofoil, Imai found some properties about them which may be summarized as follows:

(1) In the $\Psi$-procedure, as the iteration proceeds the approximated velocity in the high (low) speed region decreases (increases) contrary to the familiar character observed in the $\Phi$-procedure. It is therefore expected that by their combination we may be able to estimate the error involved less ambiguously than by using the $\Phi$-procedure alone, and so the $\Phi\Psi$-procedure may give the most plausible result within the order of the approximation employed since the latter is considered to give a mean (in some sense) of the results obtained by the $\Phi$- and the $\Psi$-procedures.

(2) In the $\Phi\Psi$-procedure the convergency is remarkably good even for such a high (subsonic) velocity that the convergency in the $\Phi$-procedure is too poor to presume the final value from the first few steps.

Now for the Cherry profile, numerical calculations are performed up to the second approximation, i.e. to the order of $M^4$, for $M$=0.350, 0.420, 0.483 and 0.5098 in order to confirm the above-mentioned properties and to study the limitations of the validity of these methods. The velocity distributions are shown in Figs. 5(a), (b), (c) and (d).

## § 6. The Meksyn-Imai Method

Meksyn [13] derived an approximate formula for calculating the velocity in a high subsonic flow and applied it to a few cases with success. He assumed that the streamlines change their shapes very little if the Mach number of the incident stream is increased from zero. Under this assumption, which he justifies from the numerical results by Woods, he shows that the velocity at any point in the flow can be obtained by solving an algebraic equation; namely, if $\alpha$ and $\beta$ are the velocity potential and the stream function for the incompressible flow and $\Phi$ the velocity potential for the compressible flow with free stream Mach number $M$, then the approximate integration of the fundamental equation gives

$$\frac{\partial\Phi}{\partial\alpha}=1+\frac{M^2}{8}\left(\frac{\partial\Phi}{\partial\alpha}\right)^3\left(1-\frac{\gamma-1}{2}M^2\right)P(\alpha,\beta)+\frac{M^4}{32}\left(\frac{\partial\Phi}{\partial\alpha}\right)^5S(\alpha,\beta)\,, \tag{6.1}$$

where $P(\alpha,\beta)$ and $S(\alpha,\beta)$ are certain functions of $\alpha$ and $\beta$ which are determined by the shape and the configuration of the obstacle in the flow*; and an appropriate root of this equation for $\partial\Phi/\partial\alpha$ gives us the desired velocity $q$ as

$$q=q_0\frac{\partial\Phi}{\partial\alpha}\,,$$

where $q_0$ is the velocity for the incompressible flow.

This formula enables us to calculate not only the velocity at each point in the flow, with $M$ as a parameter, but also a kind of critical Mach number above which no reasonable value for the velocity is obtained.**

Now Imai [11] points out that the functions $P$ and $S$ in Eq. (6.1) can easily be obtained if we know the results of the successive approximation by the $M^2$-expansion method; and that Meksyn's method is equivalent to the usual $M^2$-expansion method; namely, if we expand the velocity $q$ as in (5.2) and put $x=Mq/q_0$, then Eq. (6.1) leads to the following quintic equation for $x$:

$$x(1-ax^2-bx^4)=M\,, \tag{6.2}$$

where

$$\begin{cases} a=\left(1-\dfrac{\gamma-1}{2}M^2\right)\dfrac{q_1}{q_0}\,,\\[2ex] b=\dfrac{q_2}{q_0}+\dfrac{\gamma-1}{2}\dfrac{q_1}{q_0}-3\left(\dfrac{q_1}{q_0}\right)^2, \end{cases}$$

and an appropriate root of Eq. (6.2) again gives the velocity required.

By this procedure Imai has calculated the velocity on the surfaces of circular and elliptic cylinders, showing that this method gives quite satisfactory results even when the sonic velocity is approached on the surface.

The critical Mach number $M_c$, beyond which no physical solutions are possible in this method, is obtained as follows.

For $M=M_c$, Eq. (6.2) for $x$ must have double roots at the point of the greatest velocity; in other words, equations

$$bx^5+ax^3-x+M=0 \tag{6.2'}$$

and

$$5bx^4+3ax^2-1=0 \tag{6.3}$$

must have at least one root in common; so $M_c$ is determined as an appropriate root of the equation

$$\begin{vmatrix} b & 0 & a & 0 & -1 & M & 0 & 0 & 0\\ 0 & b & 0 & a & 0 & -1 & M & 0 & 0\\ 0 & 0 & b & 0 & a & 0 & -1 & M & 0\\ 0 & 0 & 0 & b & 0 & a & 0 & -1 & M\\ 5b & 0 & 3a & 0 & -1 & 0 & 0 & 0 & 0\\ 0 & 5b & 0 & 3a & 0 & -1 & 0 & 0 & 0\\ 0 & 0 & 5b & 0 & 3a & 0 & -1 & 0 & 0\\ 0 & 0 & 0 & 5b & 0 & 3a & 0 & -1 & 0\\ 0 & 0 & 0 & 0 & 5b & 0 & 3a & 0 & -1 \end{vmatrix}=0\,,$$

which is reduced to a sextic equation for $y=M^2$:

$$y^6+a_1y^5+a_2y^4+a_3y^3+a_4y^2+a_5y+a_6=0\,,$$

where

$$\begin{cases} a_1=-\dfrac{10}{\gamma-1}\,,\\[2ex] a_2=\dfrac{4}{27(\gamma-1)^2}\left\{270+2(\gamma-1)\dfrac{q_0}{q_1}+225b\left(\dfrac{q_0}{q_1}\right)^2\right\},\\[2ex] a_3=-\dfrac{8}{27(\gamma-1)^3}\left\{270+8(\gamma-1)\dfrac{q_0}{q_1}+675b\left(\dfrac{q_0}{q_1}\right)^2\right\},\\[2ex] a_4=\dfrac{8}{27(\gamma-1)^4}\left\{270+24(\gamma-1)\dfrac{q_0}{q_1}+1350b\left(\dfrac{q_0}{q_1}\right)^2\right.\\[2ex] \qquad\qquad\left.+32(\gamma-1)b\left(\dfrac{q_0}{q_1}\right)^3+1000b^2\left(\dfrac{q_0}{q_1}\right)^4-3125b^3\left(\dfrac{q_0}{q_1}\right)^5\right\},\\[2ex] a_5=-\dfrac{16}{27(\gamma-1)^5}\dfrac{q_0}{q_1}\left\{8(\gamma-1)+225b\dfrac{q_0}{q_1}+32(\gamma-1)b\left(\dfrac{q_0}{q_1}\right)^2+500b^2\left(\dfrac{q_0}{q_1}\right)^3\right\},\\[2ex] a_6=\dfrac{128}{27(\gamma-1)^5}\dfrac{q_0}{q_1}\left\{1+4b\left(\dfrac{q_0}{q_1}\right)^2\right\}^2. \end{cases}$$

---

* $S$ contains also $\gamma$ as a parameter.

** In this respect the $\Psi$-procedure also enables us to calculate another critical Mach number at which the method fails. It is clear that this Mach number corresponds to the first appearance of the sonic speed in the flow.

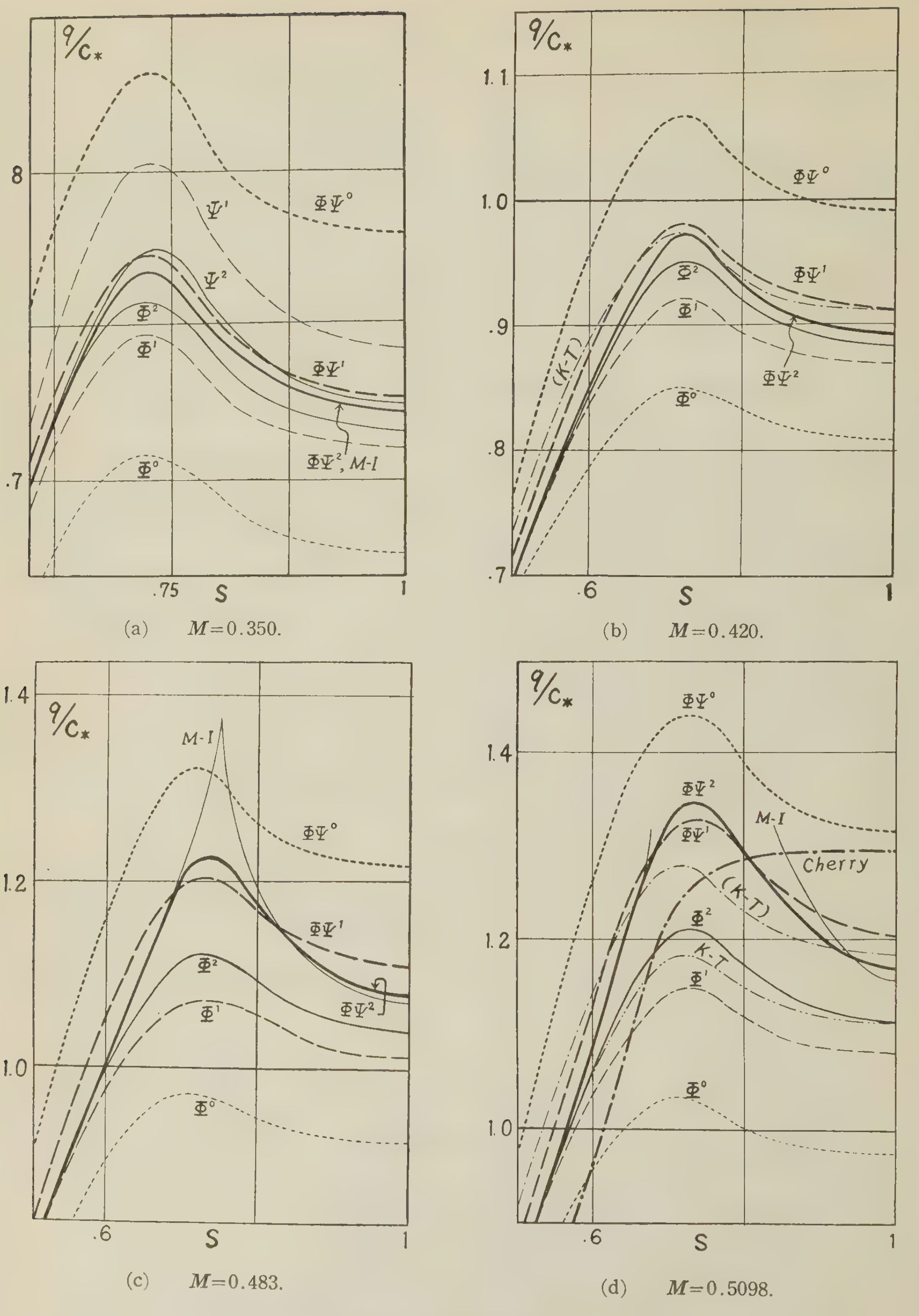

(a) $M=0.350$. (b) $M=0.420$.

(c) $M=0.483$. (d) $M=0.5098$.

Fig. 5 (a–d). The velocity distributions over the surface.

Cherry's exact solution,

0th, 1st, 2nd: approximations of the $\Phi$- and the $\Psi$-procedures,

0th, 1st, 2nd: approximation of the $\Phi\Psi$-procedure,

Kármán-Tsien's method (simplified),

Kármán-Tsien's method,

Meksyn-Imai's method.

For the Cherry profile the value 0.483 for $M_c$ is obtained. The velocity distributions calculated by this method are shown in Figs. 5(a), (c) and (d).

## § 7. Numerical Discussions and Some Conjectures on Cherry's Hodograph Solution

(1) $M=0.350$ (Fig. 5(a)). It is almost certain that the $M^2$-expansion method will converge at this Mach number.

(2) $M=0.420$ (Fig. 5(b)). The sonic velocity begins to appear on the profile near this Mach number.

(3) $M=0.483$ (Fig. 5(c)). This is the critical Mach number according to Meksyn-Imai's method. Judging from the singular behaviour of the second approximation by the $\Phi\Psi$-procedure, the iteration will probably diverge in the high speed region.

(4) $M=0.5098$ (Fig. 5(d)). The velocity distributions calculated by all the methods are shown with that of Cherry's solution. The divergency of the $M^2$-expansion method in the high speed region is almost evident.

To sum up:

(1) The $\Phi\Psi$-procedure proves to have the following advantages over the $\Phi$- or the $\Psi$-procedure:

(i) The convergency is better as in the examples treated by Imai.

(ii) The singular behaviour of the velocity distribution calculated by this procedure suggests the divergency of the iteration (e. g. the second approximation for $M=0.483$), while it is more difficult to discriminate whether it converges or not by the $\Phi$-procedure.

(2) Meksyn-Imai's method gives almost the same velocity distribution as the $\Phi\Psi$-procedure though the latter excels the former a little in the labour for calculation. It is to be noted that the Meksyn-Imai method enables us to calculate a kind of critical Mach number and describes the probable flow pattern near this Mach number (Fig. 5(c)), but its numerical value seems to be somewhat larger than that at which the actual breakdown of the potential flow occurs, as was also the case with the examples treated by Meksyn.

(3) If the deformation of the profile is properly taken into account, Kármán-Tsien's method exactly solves the flow problem of a gas with $\gamma=-1$ and is expected to give a result lying between the first and the second approximations in the $\Phi$-procedure; in fact this is seen in the present calculation with $M=0.5098$ (Fig. 5(d)). Since the deformation takes place towards the increase of the thickness ratio, its disregard may result in an over-estimation of the effect of the compressibility so as to compensate the deficiency of the velocity which results from taking $\gamma$ to be $-1$. For example, this is seen from Tamada's result about a circular cylinder [14]. But in the case of the Cherry profile the disregard of the deformation gives the velocities somewhat larger than those calculated by the $M^2$-expansion method in the high speed region.

In the region where $q/c_* \lesssim 0.5$ the simplified procedure which neglects the deformation is also satisfactory as well as all other methods.

Now as our numerical results show, the velocity distributions calculated by various approximate methods are all different not only quantitatively but also qualitatively from that of Cherry's exact solution. The approximated velocity distribution has two maxima along each boundary streamline while in Cherry's solution it has only one maximum at the point of the maximum thickness. This discrepancy may be interpreted as follows.

Consider the compressible flow past the Cherry profile and suppose that we increase the Mach number $M$ of the main flow continuously from zero and that we investigate the flow by means of the $M^2$-expansion method.

In view of the fact that the Cherry profile has maxima of curvature in the neighbourhood of the points where the tangent to the profile makes the angle of 30° to the direction of the uniform flow, it is quite natural that the velocity distribution should have two maxima for $M=0$ and that these maxima should become more and more conspicuous with increasing $M$ as the calculation shows, until certain Mach number is reached at which a continuous potential flow breaks down.

Now, in general, the existence and uniqueness of the compressible potential flow past an obstacle of arbitrary shape have been mathematically proved [1] provided that the whole flow field is subsonic, so it is certain that the Mach number $M_{cr}$ at which the potential flow ceases to exist is not smaller than the Mach number $M_s$ which corresponds to the first appearance of the sonic speed in the flow.

As regards the convergency of the $M^2$-expansion method such a theorem does not seem to have been established, but it might be expected that the $M^2$-expansion method also does not fail till the appearance of the sonic speed if we examine the proof of the general existence theorem and remember the results of the famous electrical experiments by Taylor and Sharman [15], which also lead to the expectation that the $M^2$-expansion method may fail just at $M_s$.

For the Cherry profile the value of $M_s$ seems to be about 0.42 and the covergency of the $M^2$-expansion method is uncertain near this Mach number, but judging from the obvious divergency at $M=0.5098$ it is certain that Cherry's solution cannot be approximated by any of the methods employed in this paper.

On the other hand, it is also yet to be known whether the potential flow, in general, continues to exist or not beyond $M_s$, but it may be conjectured from the present calculation that the flow pattern represented by Cherry's hodograph solution does not belong to the family of potential flows which appear by increasing the Mach number of the main flow from zero, the shape of the profile being fixed.

## Acknowledgements

The writer would like to express his sincere and profound gratitude to Professor Isao Imai for his suggestion of this problem, and his continual guidance and encouragement and much valuable advice throughout this study.

The writer's thanks are also due to Professor Saburô Asaka, Dr. Mitutosi Kawaguti and Dr. Hidenori Hasimoto for their advice and discussions in the course of the calculation, and their kind inspection of the manuscript.

## References

1) L. Bers: Comm. Pure Appl. Math. **7** (1954) 441.
2) T. M. Cherry: Proc. Roy. Soc. **A 192** (1947) 45.
3) T. M. Cherry: Rep. Coun. Sci. Indust. Res. Div. Aeron. A 48, Melbourne (1948).
4) T. M. Cherry: Proc. Roy. Soc. **A 196** (1949) 32.
5) I. Imai: J. Soc. Aeron. Sci. Japan **9** (1942) 865 (in Japanese).
6) I. Imai: Rep. Aeron. Res. Inst., Tokyo Imp. Univ. No. 275 (1943) (in Japanese).
7) I. Imai: read at the monthly meeting of the Phys.-Math. Soc. Japan, Tokyo (May 1944).
8) I. Imai: J. Phys. Soc. Japan **3** (1948) 342.
9) I. Imai: J. Math. Phys. **28** (1949) 173.
10) I. Imai, I. Kaji and K. Umeda: J. Fac. Sci. Hokkaidô Univ. Japan, Ser. II, Vol. 3, No. 8 (1950).
11) I. Imai: read at the 4th Japan Nat. Congr. Appl. Mech., Tokyo (Sept. 1954).
12) M. J. Lighthill: Proc. Roy. Soc. **A 191** (1947) 352.
13) D. Meksyn: Proc. Roy. Soc. **A 220** (1953) 239.
14) K. Tamada: Proc. Phys.-Math. Soc. Japan **22** (1940) 208.
15) G. I. Taylor and C. F. Sharman: Brit. A. R. C., R. & M., No. 1195 (1928).
16) S. Tomotika and K. Tamada: Quart. Appl. Math. **9** (1951) 129.
17) H. S. Tsien: J. Aeron. Sci. **6** (1939) 399.

JOURNAL OF THE PHYSICAL SOCIETY OF JAPAN Vol. 11, No. 2, FEBRUARY, 1956

# Supersonic Jet with the Ambient Pressure corresponding to its Constant Pressure Point

By Hakuro OGUCHI

*Institute of Science and Technology, University of Tokyo, Tokyo, Japan*

(Received September 27, 1955)

In the present paper, a plane jet issuing from a parallel supersonic nozzle into the chamber where the pressure corresponds to the constant pressure point on the shock polar related to the uniform velocity at the exit of the nozzle is investigated by the hodograph method under the transonic approximation. The analytical expression for the stream function $\psi$ is obtained in the form containing appropriate constants which are determined from the condition on the shock polar. Actually, $\psi$ is calculated so that the shock condition is satisfied at three points on the shock polar. Using this value of $\psi$, the shock pattern and the velocity distribution along the axis of the jet are obtained. It is seen from these results that large variations of the flow variables occur in a comparatively narrow region downstream of the exit of the nozzle.

## §1. Introduction

Let us consider a jet issuing from a parallel supersonic nozzle. As is well known, a Mach shock configuration appears at the exit of the nozzle when the ambient pressure is moderately higher than the jet pressure. Guderley¹⁾ has given a clear physical interpretation to this phenomenon by applying a representation in the hodograph plane. If the ambient pressure is increased and the velocity on the free streamlines of the jet reaches just the local speed of sound, then Mach shock configuration is no more possible. The hodograph representation shows that, in case the ambient pressure lies between this critical one and the pressure corresponding to a normal shock, a single-shock pattern will appear at the exit in place of a Mach shock configuration. Flow patterns of this kind will be considered here (Fig. 1).

For simplicity, we make the assumption that the jet velocity inside the nozzle is so slightly greater than the local speed of sound that the transonic approximation is applicable without losing any essential features of the flow. It is, however, not easy to treat the problem analytically even under this approximation because of the existence of singularities at the ends of the nozzle walls similar to that appearing at the nose of a finite wedge in the case when a subsonic flow occurs behind the attached shock.

Especially, as will be seen in the subsequent section, if the ambient pressure takes the value corresponding to the constant pressure point on the shock polar, then the above singularities disappear. This particular value corresponds to the Crocco state for a finite wedge which has recently been analyzed by Tamada and Shibaoka²⁾. Since no singularities appear at the ends of the nozzle walls, the problem is considerably simplified in this particular case. In the following sections, this case will be analyzed by the hodograph method.

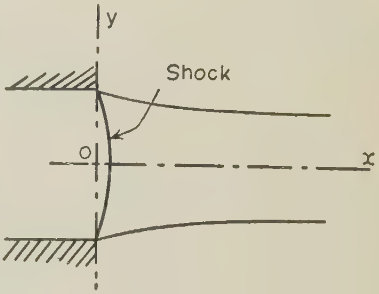

Fig. 1.

## §2. Mathematical Formulation

Let $V$ and $\tilde{\theta}$ be the magnitude of the velocity vector and its angle of inclination to the direction of the uniform flow ahead of the shock, respectively. A quantity $\tilde{u}$ is introduced according to the following relation:

$$\tilde{u}=(\gamma+1)^{1/3}\frac{V-a^*}{a^*}=(\gamma+1)^{-2/3}(M^2-1)\,, \qquad (1)$$

where $\gamma$ is the adiabatic exponent, $a^*$ the critical speed and $M$ the Mach number related to the velocity $V$. If $\tilde{u}$ and $\tilde{\theta}$ are assumed to be sufficiently small so that only their lowest power terms need be retained in the analysis, the equation for the upper half of the shock polar in the simplified hodograph has the form

$$\tilde{\theta}=(\tilde{u}_0-u)\sqrt{(\tilde{u}_0+\tilde{u})/2}\ ,$$

where $u_0$ is the value of $\tilde{u}$ corresponding to the jet velocity $V_0$ ahead of the shock. From the above relation, $-\tilde{u}_0$ corresponds to the velocity behind the normal shock. Let us consider the case when the modified velocity $\tilde{u}_A$ corresponding to the pressure on the free streamlines lies between 0 and $-\tilde{u}_0$. In Fig. 2 the states of flow immediately behind the shock emanuating at the end of the lower nozzle wall and on the lower free streamline of the jet map into the point A and the line AB, respectively. Then single-shock patterns are possible at the exit of the nozzle so that the image of its lower half in the hodograph is AC, the part of the upper half of the shock polar. Since, in this case, the axis of the jet maps into the line BC, the lower half of the jet hehind the shock at the exit of the nozzle corresponds to the imbedded domain ABC in the hodograph.

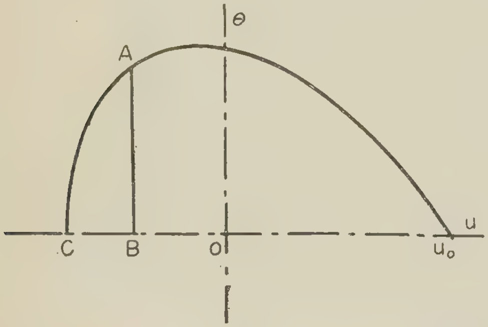

Fig. 2.

In the transonic approximation, as has been shown by Guderley[1)], the fundamental equation for the stream function $\psi$ reduces to the form

$$\psi_{\tilde{u}\tilde{u}}-\tilde{u}\psi_{\tilde{\theta}\tilde{\theta}}=0\ . \qquad (2)$$

On the upper half of the shock polar, the boundary condition requires that the lines of constant $\psi$ must have the slope

$$\frac{d\tilde{\theta}}{d\tilde{u}}=-\frac{\tilde{u}_0+7\tilde{u}}{3\tilde{u}_0+5\tilde{u}}\sqrt{\frac{\tilde{u}_0+\tilde{u}}{2}}\ .$$

On a line of constant $\psi$, $d\tilde{\theta}/d\tilde{u}$ can be replaced by $-\psi_{\tilde{u}}/\psi_{\tilde{\theta}}$ and therefore condition can also be written as

$$\psi_{\tilde{u}}-\frac{\tilde{u}_0+7u}{3\tilde{u}_0+5\tilde{u}}\sqrt{\frac{\tilde{u}_0+\tilde{u}}{2}}\psi_{\tilde{\theta}}=0\ . \qquad (3)$$

Since AB is the image of a free stream line, the condition $\psi$=const. is imposed on it and hence

$$\psi_{\tilde{\theta}}=0 \quad \text{on} \quad \text{AB}\ . \qquad (4)$$

At the point A, these two conditions cannot be, in general, simultaneously satisfied by regular functions, and as a due result, the flow is singular. In a particular case when $\tilde{u}_A=-3/5\ \tilde{u}_0$, however, the former condition reduces to the latter one at this point. Hence, no singularity appears at the point A. This point on the shock polar is called the constant pressure point[3)].

Let us investigate the behavior of the singularity from the local solution near the neighborhood of the point A. According to Guderley[1)], the following transformations are introduced as

$$\xi=\sqrt{|\tilde{u}_A|}(\tilde{u}+|\tilde{u}_A|)$$

and

$$\eta=\tilde{\theta}-\tilde{\theta}_A\ ,$$

where $\tilde{\theta}_A$ is the value of $\theta$ at the point A. Applying these transformations the differential equation (2) is rewritten in the form

$$\psi_{\xi\xi}+(1-\xi/\sqrt{|\tilde{u}_A|^3})\psi_{\eta\eta}=0\ .$$

For small values of $\xi$, this equation reduces to

$$\psi_{\xi\xi}+\psi_{\eta\eta}=0\ . \qquad (5)$$

Let us apply the boundary conditions (3) and (4) to the neighborhood of the point A, then these take the approximate forms as

$$\frac{d\eta}{d\xi}=-\frac{\psi_\xi}{\psi_\eta}=-\sqrt{\frac{\tilde{u}_0-|\tilde{u}_A|}{2|\tilde{u}_A|}}\frac{\tilde{u}_0+7|\tilde{u}_A|}{3\tilde{u}_0-5|\tilde{u}_A|}$$

$$=\tan\left(\frac{\pi}{2}-\gamma_2\right)$$

for $\quad \eta/\xi=\tan\left(\dfrac{\pi}{2}-\gamma_1\right)$

$$\psi=0 \qquad \text{for} \qquad \xi=0\ ,$$

when $\gamma_1$ is the angle of the tangent of the shock polar in the coordinates system with the $\eta$-axis and $\gamma_2$ the angle of the tangent of the streamline with the $\eta$-axis at the point A, and these signs are positive when measured clockwise (Fig. 3). From the definition, $\gamma_2$ is positive or negative according as the point A lies between the constant pressure point and the critical speed or the normal shock point, and $\gamma_1$ is always positive between the critical speed and the normal shock point. The solution of Eq. (5) satisfying the above two conditions is obtained in the form

$$\psi=\mathrm{Im}(i\zeta)^m\ ,$$

where

$$\zeta=\xi+i\eta$$

and

$$m=1-\gamma_2/\gamma_1\ .$$

At the constant pressure point, $\gamma_2=0$ or $m=1$. Since, according to Guderley[1], the curvature of the shock is proportional to $|\zeta|^{1-m}/m$, it tends to zero for the region between the critical speed and the constant pressure point as the point A is approached along the shock polar, while it tends to infinity in the region between the constant pressure point and the normal shock point. Hence it is seen that the constant pressure point in the case of a free jet plays the same role as the Crocco point in the case of a finite wedge. It is the subject of the present analysis to determine the full solution of this particular case.

Now it is convenient to introduce the following transformations[4]:

$$u=\tilde{u}/\tilde{u}_0\ ,\quad \theta=\sqrt{2}\,\tilde{\theta}/\tilde{u}_0{}^{3/2}\ . \tag{6}$$

Then, we obtain the normalized form of the boundary value problem. By substitution of Eq. (6), the fundamental equation (2) becomes

$$\psi_{uu}-2u\psi_{\theta\theta}=0\ . \tag{7}$$

The boundary conditions can now be summarized as follows:

1) On the image of the free stream line, AB,

$$\psi=-K \qquad \text{for} \qquad u=u_A=-3/5.$$

Here $K$ is a half of the total flow discharge and is given by

$$K=\rho^*a^*l\ ,$$

where $l$ is the semi-height of the nozzle and $\rho^*$ the density related to the critical velocity $a^*$.

2) On the image of the axis of the jet, CB,

$$\psi=0 \qquad \text{for} \qquad \theta=0\ .$$

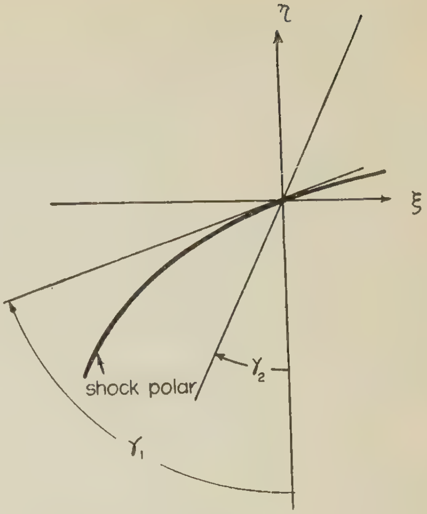

Fig. 3.

3) On the part of the shock polar, AC,

$$\psi_u-\frac{1+7u}{3+5u}\sqrt{1+u}\,\psi_\theta=0$$

for

$$\theta=(1-u)\sqrt{1+u}\ . \tag{8}$$

## § 3. Computation of $\psi$

As follows from the boundary conditions 1) and 2), there occurs a sink-type singularity at the point B corresponding to the flow infinitely downstream from the exit. Its behavior is the same as that in the subsonic free jet[5]. It can be shown that the singular solution, $\psi_s$, of the differential equation (4), subject to the boundary conditions 1) and 2), is written in the form

$$\psi_s=-\frac{2K}{\pi}\left(\frac{\theta}{2}\right.$$
$$\left.+\sum_{m=1}^{\infty}\left(\frac{u}{u_A}\right)^{1/2}\frac{K_{1/3}[m(-2u)^{3/2}/3]}{K_{1/3}[m(-2u_A)^{3/2}/3]}\sin m\theta\right)\ , \tag{9}$$

where $K_{1/3}$ is the modified Bessel function of the second kind of order 1/3. It follows by separation of variables that $\psi_s$ is a solution of Eq. (4). Also Eq. (6) becomes for $u=u_A$

$$\psi=-\frac{2K}{\pi}\left(\frac{\theta}{2}+\sum_{m=1}^{\infty}\frac{1}{m}\sin m\theta\right)$$
$$=\begin{cases}-K & \text{for} \quad 0<\theta<\pi \\ 0 & \text{for} \quad \theta=0\ .\end{cases}$$

Hence, $\psi_s$ of Eq. (6) satisfies the boundary conditions 1) and 2). If $m$ is sufficiently large, by the use of the asymptotic representation of $K_{1/3}$

$$\left(\frac{u}{u_A}\right)^{1/2}\frac{K_{1/3}[m(-2u)^{3/2}/3]}{K_{1/3}[m(-2u_A)^{3/2}/3]}$$
$$\simeq\left(\frac{u_A}{u}\right)^{1/4}\exp.\,[-m\{(-2u)^{3/2}-(-2u_A)^{3/2}\}/3]\ .$$

Since, in the region under consideration, $|u|\geq|u_A|$, then

$$\left(\frac{u}{u_A}\right)^{1/2}\frac{K_{1/3}[m(-2u)^{3/2}/3]}{K_{1/3}[m(-2u_A)^{3/2}/3]}\cdot 1\ .$$

Hence, in view of the convergence of the series $\sum\frac{1}{m}\sin m\theta$, the series in Eq. (9) is always convergent in the region ABC.

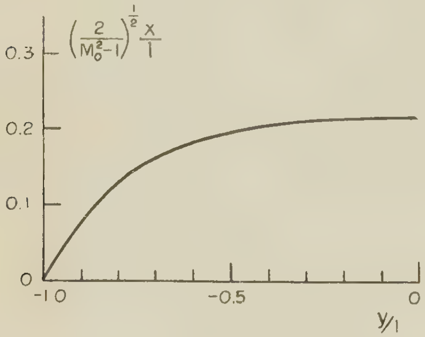

Fig. 4.

The regular solution satisfying the conditions $\psi=0$ on both AB and BC may be arbitrally added to $\psi_s$. In general, such regular solution, $\psi_r$, is written in the form

$$\psi_r=\sum_{m=1}^{\infty}KA_m\sqrt{-u}J_{1/3}[\lambda_m(-2u)^{3/2}/3]\sinh\lambda_m\theta\ , \tag{10}$$

where $A_m$s are appropriate constants and $\lambda_m$s are related to $j_m$s, the positive zeroes of Bessel function $J_{1/3}$, as

$$\lambda_m=3j_m(-2u_A)^{-3/2}\ .$$

Hence, the general solution of the differential equation (7) satisfying the condition 1) and 2) is given by

$$\begin{aligned}\psi&=\psi_s+\psi_r\\&=-\frac{2K}{\pi}\left(\frac{\theta}{2}+\sum_{m=1}^{\infty}\frac{1}{m}\left(\frac{u}{u_A}\right)^{1/2}\right.\\&\qquad\left.\times\frac{K_{1/3}[m(-2u)^{3/2}/3]}{K_{1/3}[m(-2u_A)^{3/2}/3]}\sin m\theta\right)\\&\quad+\sum_{m=1}^{\infty}KA_m\sqrt{-u}J_{1/3}[\lambda_m(-2u)^{3/2}/3]\sinh\lambda_m\theta\ .\end{aligned} \tag{11}$$

Finally the shock condition 3) determines the $A_m$s. In the actual calculation the aproximation has been adopted so that the shock condition 3) is satisfied at three points on the shock polar except the points A and C where it is apparent that this condition is fulfilled. Thus the first three terms in second series in Eq. (11) are used.

## § 4. Shock Patterns and Velocity Distributions along the Axis

The transformation from the hodograph to the physical one is, as is well known, governed by the following equation:

$$\left.\begin{aligned}&d(x/l)=(\gamma+1)^{1/3}(\tilde{u}_0/2)(2\tilde{u}\varphi_{\tilde{\theta}}d\tilde{u}+\varphi_{\tilde{u}}d\tilde{\theta}),\\&d(y/l)=d\varphi\ ,\end{aligned}\right\} \tag{12}$$

where

$$\varphi=\psi/K\ .$$

In the transonic approximation the slope of the shock is given by

$$dy/dx=(V_1-V_2)/a^*\tilde{\theta}\ , \tag{13}$$

where $V_1$ and $V_2$ are the velocities ahead of and behind the shock, respectively. By the use of Eqs. (1) and (6), Eq. (13) can be expressed in terms of $u$ and $\theta$ as

$$\frac{dy}{dx}=\sqrt{\frac{2}{\tilde{u}_0}}(\gamma+1)^{-1/3}\frac{1-u}{\theta}=\sqrt{\frac{2}{M_0{}^2-1}}\frac{1-u}{\theta}\ . \tag{14}$$

Substituting $\theta$ from Eq. (8) into the above equation, we get

$$\frac{dy}{dx}=\sqrt{\frac{2}{(M_0{}^2-)(1+u)}}\ .$$

Hence, if the origin of the Cartesian coordinates $(x, y)$ is chosen at the center of the nozzle exit, the shape of the shock is given by

$$\left.\begin{aligned}&\frac{x}{l}=\sqrt{\frac{M_0{}^2-1}{2}}\int_{-1}^{\varphi}\sqrt{1+u}\,d\varphi\ ,\\&\frac{y}{l}=\varphi\ .\end{aligned}\right\} \tag{15}$$

By the use of the above equations the shock pattern is calculated and its shape is shown in Fig. (4).

Let $x_N$ be the $x$ coordinate of the point of intersection of the shock with the exit of the jet. Then, it yields a maximum deviation of the shock from the exit and its value is obtaind as

$$x_N=\sqrt{\frac{M_0{}^2-1}{2}}\,l\int_{-1}^{0}\sqrt{1+u}\,d\varphi$$
$$\simeq 0.22[(M_0{}^2-1)/2]^{1/2}l\ .$$

Finally, the velocity distribution along the axis of the jet behind the shock is obtained by the integration of the first of Eqs. (12) and plotted in Fig. (5). The velocity on the axis is only slightly lower than that at the free streamline in the downstream part of the jet where

$$x > x_N + 2\sqrt{(M_0^2-1)/2}\cdot l$$
$$\cong 2.22\sqrt{(M_0^2-1)/2}\cdot l\ .$$

Hence, as the Mach number $M_0$ is close to unity in the present problem, it follows that large variations of the flow variables occur in a comparatively narrow region immediately behind the shock.

In the preceeding analysis only the particular case when the point A lies just at the constant pressure point has been treated. In general cases, however, the representation of the singularity at the point A should be added to the solution (11) so that the boundary conditions are fulfilled. In view of the local solution obtained before, it is suggested that, if the point A lies near the neighborhood of the constant pressure point, the existence of the singularity at the point A will have only little influence on the region except for its neighborhood. Hence, in these cases, the solution (11) may be considered to be the main part of the full solution.

The author wishes to express his sincere thanks to Professor Ryuma Kawamura for his helpful advice and kind inspection of the manuscript.

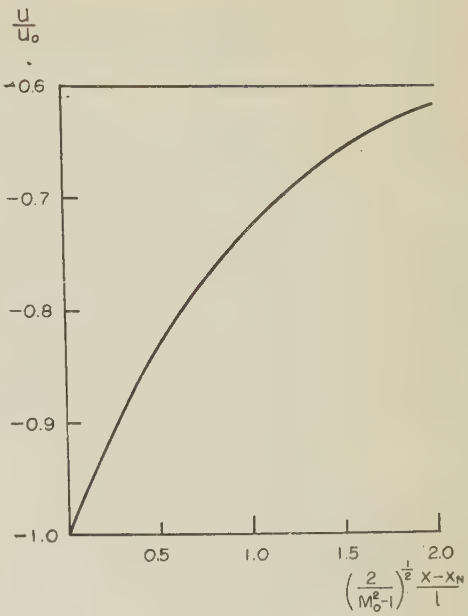

Fig. 5.

## References

1) G. Guderley: Wright Field Report F-TR-2168-ND (1947).
2) K. Tamada and Y. Shibaoka: J. Aero. Sci. **22** (1955) 261.
3) A. Busemann: NACA TN (1949) 1858.
4) W. G. Vincenti and C. B. Wagoner: NACA TR (1952) 1095.
5) S. A. Chaplygin: NACA TM (1944) 1063.

JOURNAL OF THE PHYSICAL SOCIETY OF JAPAN Vol. 11, No. 2, FEBRUARY, 1956

# On the Error of the Finite Difference Method in 1-dimensional Boundary Value Problems

By Hiroshi FUJITA

*Department of Physics, Faculty of Science, University of Tokyo*

(Received September 28, 1955)

The present paper is concerned with the error estimation of the finite difference method. Bounds of the error, which is committed in approximating the boundary value problem

$$-y''+qy=f,\quad y(0)=y(1)=0\,,\quad (q\geqq 0)\,.$$

by the corresponding difference equation, are given in some forms not involving the solution $y$ and, hence, calculable without solving the original problem. Our treatments are based on a theorem concerning an operator of the type $T^*T$ in a Hilbert space. The degree of convergence of the difference equation solution to the differential equation solution, as the difference interval approaches zero, is also studied.

## §1. Introduction and Survey of the Method

As for the numerical solution of boundary value problems associated with ordinary differential equations there are a number of methods[1)3)4)]. Among them the most familiar one in practice is the finite difference method, i.e., to approximate the differential equation by its *difference analogue* with a suitable difference interval (mesh length), though the use of the finite difference method seems more suitable for partial differential equations. Nevertheless, even if discussions are confined to cases of ordinary differential equations, little appears to be known about the accuracy of this method.

The object of the present paper is to estimate error bounds of this method, in the case of the boundary value problem associated with the ordinary differential equation $-y''+qy=f$ of the Schrödinger type and also to study the degree of convergence of the difference equation solution, as the difference interval approaches zero, under various continuity hypotheses on the coefficients $q(x), f(x)$ of the original equation. In this sort of error estimation it is a matter of question in what quantities the error bounds are expressed. Usual bounds explained in text-books do not seem satisfactory, at least, from the theoretical point of view, since they involve bounds of certain higher derivatives of the solution of the original problem, which may not exist and are, in general, very hard to estimate unless the original problem is solved. We intend to derive some error bounds expressible in terms of the "known" quantities in the sense that they are explicitly composed only of the values of $q(x)$, $f(x)$, and the quantities which are available once the difference equation is solved. We also give some error bounds involving neither the solution of the original problem nor the solution of the corresponding difference equation. The absence of the unknown quantities in error bounds permits us to study somewhat more easily the degree of convergence mentioned above.

Now we formulate our problem in precise terms and give a survey of the course we shall pursue.

By Problem (I) (abbr. P. (I)) we mean the following boundary value problem in the interval $I=(0,1)$:

$$\text{P. (I)}\begin{cases}-\dfrac{d^2y}{dx^2}+qy=f\,,\quad (0<x<1)\,, & (1.1)\\[4pt] y(0)=y(1)=0\,, & (1.2)\end{cases}$$

where $q(x)$ is a piecewise continuous* *non-negative* function and $f(x)$ is a piecewise continuous function.

Dividing the interval by equidistant $n+1$ "nodes" $\{x_k\}$, we denote the values of $q(x)$, $f(x)$ at $x_k$ by $q_k$, $f_k$ respectively, i.e.,

$$x_k=k/n,\qquad q_k=q(x_k),\qquad f_k=f(x_k),\qquad (k=0,1,\cdots,n). \tag*{(1.3)**}$$

---

* A function $u(x)$ is said to be piecewise continuous in $I$ if it is continuous everywhere in $I$ except a finite number of points $\xi_k$ and also $u(+0)$, $u(1-0)$, $u(\xi_k-0)$, $u(\xi_k+0)$ exist. Hence a piecewise continuous function is bounded in $I$.

** For example, if $q(x_k)$ does not exist, $(q(x_k-0)+q(x_k+0))/2$ is used for it.

Then the difference analogue of P. (I) corresponding to the difference interval $h=1/n$ turns out to be the following problem (P. (II)) for a $(n+1)$-component vector $u=\{u_k\}=\{u_0, u_1, \cdots, u_n\}$:

$$\text{P. (II)}\begin{cases} -\dfrac{1}{h^2}(u_{k+1}+u_{k-1}-2u_k)+q_k u_k=f_k\ , \\ \qquad\qquad (k=1, \cdots, n-1), & (1.4) \\ u_0=u_n=0\ . & (1.5) \end{cases}$$

Before going into the estimation of

$$R=\max_r |y(x_r)-u_r|\ ,$$

which is our main object, we note that even if $q(x)$ and $f(x)$ are modified in such a manner that their values at $\{x_k\}$ are not altered, the difference analogue of P. (I) still remains the same. In view of this fact, the estimation of $R$ is carried out in two steps as below. First, introducing $\bar{q}(x)$ and $\bar{f}(x)$ specified by the conditions that the graph of $\bar{q}(x)$ is the polygonal line composed of the segments connecting $(x_k, q_k)$ and $(x_{k+1}, q_{k+1})$ and $\bar{f}(x)$ is related with $\{f_k\}$ in the same manner, we set the following auxiliary problem, P. (I′),

$$\text{P. (I}'\text{)}\begin{cases} -\dfrac{d^2\bar{y}}{dx^2}+\bar{q}\bar{y}=\bar{f}\ , \quad (0<x<1)\ , & (1.6) \\ \bar{y}(0)=\bar{y}(1)=0\ . & (1.7) \end{cases}$$

In place of dealing with $R$ directly we appraise separately two quantities $R_1, R_2$ defined by

$$R_1=\max_{0\leqq\xi\leqq1} |y(\xi)-\bar{y}(\xi)|\ ,$$

$$R_2=\max_{0\leqq r\leqq n} |\bar{y}(x_r)-u_r|\ , \qquad (1.8)$$

the bounds of which can be combined to yield the desired estimate of $R$ by means of the obvious relation $R\leqq R_1+R_2$. The estimation of $R_1$ as well as that of $R_2$ is based on the following theorem[2)6)] given by Kato, which reads:

**Theorem 1.** *Let $T$ be a linear operator[5)] with its domain in a Hilbert space $\mathfrak{H}$ and its range in a second Hilbert space $\mathfrak{H}'$. Let $y$ be an element satisfying the equation*

$$T^*Ty=f\ , \qquad (1.9)$$

*where $T^*$ is the adjoint of $T$. For an element $d$ in the range of $T^*$ we set $\eta=(y, d)$. Let $u, v, \phi, \psi$ be any elements subjected to the conditions that $u, \phi$ belong to the domain of $T$ and $v, \psi$ belong to the domain of $T^*$ and, furthermore,*

$$T^*v=f\ , \qquad T^*\psi=d\ . \qquad (1.10)$$

*Then we have*

$$|\eta-A|\leqq\frac{1}{2}\varepsilon_1\varepsilon_2\ , \qquad (1.11)$$

*where*

$$\left.\begin{aligned} A&=\frac{1}{2}[(u, d)+(f, \phi)+(v, \psi)-(Tu, T\phi)]\ , \\ \varepsilon_1&=\|Tu-v\|\ , \qquad \varepsilon_2=\|T\phi-\psi\|\ . \end{aligned}\right\} \qquad (1.12)$$

To make this theorem applicable to our problem we reduce P. (I′) to the form of (1.9), choosing $T$ and $T^*$ as follows. As $\mathfrak{H}$ we take the real Hilbert space composed of functions in $L^2(0, 1)$ with the norm defined by

$$\|u\|^2=\int_0^1 u^2dx \qquad (1.13)$$

and as $\mathfrak{H}'$ we take the real Hilbert space composed of 2-component vector functions $v=\{v_1, v_2\}$ in $L^2(0, 1)\times L^2(0, 1)$ with the norm defined by

$$\|v\|^2=\|\{v_1, v_2\}\|^2=\int_0^1 v_1{}^2dx+\int_0^1 \bar{q}v_2{}^2dx\ . \qquad (1.14)$$

When we choose the operator $T$ so that any continuous and piecewise smooth*** function vanishing at $x=0, 1$ belongs to the domain of $T$ and

$$Tu=\left\{\frac{du}{dx}, u\right\}\ , \qquad (11.5)$$

then $T^*$ is determined so that

$$T^*v=T^*\{v_1, v_2\}=-\frac{dv_1}{dx}+\bar{q}v_2 \qquad (11.6)$$

and any $v=\{v_1, v_2\}$ with continuous and piecewise smooth $v_1$ belongs to the domain of $T^*$. It is easily verified that the equation

$$T^*T\bar{y}=\bar{f} \qquad (1.17)$$

implies P. (I′)****. In dealing with $R_1$, $d$ is taken to be Dirac's delta function $\delta(x-\xi)$ with its singularity at $\xi$ so that $\eta$ reduces to $\bar{y}(\xi)$, although this use of the delta function requires a later justification, which can be carried out by a customary procedure but is omitted here. The other elements $u, v, \phi, \psi$ are constructed in a certain connection with the solution $y(x)$ of P. (I) and the Green

---

*** A function $u(x)$ is said to be piecewise smooth if $u'(x)$ is piecewise continuous.

**** Strictly speaking, all operators appearing here must be closed. Hence, the differential operators in above should be interpreted as their closed extensions.

function of P. (I). Details and results of this procedure are shown in § 2.

For the estimation of $R_2$ worked out in § 3, $d$ is again Dirac's delta function $\delta(x-x_r)$ with its singularity at $x_r$ and $u, v$ are constructed in a certain manner making use of the solution $\{u_k\}$ of P. (II), while the constitution of $\phi, \psi$ is related with the following difference equation, P. (III), which may be regarded as the difference analogue of the formal equation $T^*TG=\delta(x-x_r)$ characterizing the Green function of P. (I′):

$$\text{P. (III)}\begin{cases} -\dfrac{1}{h^2}(g_{k+1}+g_{k-1}-2g_k)+q_k g_k=d_k\,, \\ \qquad\qquad (k=1,\cdots,n-1)\,, & (1.18) \\ g_0=g_n=0\,, & (1.19)\end{cases}$$

where $d_k=0$ or $1/h$, according as $k\neq r$ or $k=r$. We can derive from (1.11) a bound of $R_2$ in terms of $\{q_k\}$, $\{f_k\}$, $\{u_k\}$ and $h$, which are to be regarded as quantities given originally or known after solving P. (II). Furthermore, it is also possible to give another bound of $R_2$ in a form not containing $\{u_k\}$ but $\{q_k\}$, $\{f_k\}$ only, and hence, calculable without solving P. (II).

Having obtained the bounds of $R$ in the way stated above, we shall pass to the study of the order of $R$ as $h\to 0$ under various continuity hypotheses on $q(x)$ and $f(x)$ in § 4.

## § 2. Estimation of $R_1$

In this section we are concerned first with the deduction of some preliminary inequalities and thereafter with the estimation of $R_1$ referred to in the preceding section. While all notations which already appeared keep the same meanings, by $T_0$ and $T_0^*$ we denote those operators defined in the same way as $T$ and $T^*$ except that use is made of $q(x)$ in place of $\bar{q}(x)$. Then P. (I) can be written as

$$T_0^*T_0y=f\,. \tag{2.1}$$

In this section ′ is used only in order to represent the differentiation with respect to $x$. Now we establish the following lemma.

**Lemma 1.** *Let $y(x)$ be the solution of* P. (I). *Then we have*

$$\max_x|y(x)|\leqq\frac{\|f\|}{2a}\,, \tag{2.2}$$

*where $a=(\pi^2+Q_m)^{1/2}$ and $Q_m$ is the minimum (or g.l.b.) of $q(x)$.*

Proof. For any $\xi(0<\xi<1)$ let $K_\xi(x)$ be a function of $x$ equal to $(1-\xi)x$ or $\xi(1-x)$, according as $0\leqq x\leqq\xi$ or $\xi\leqq x\leqq 1$, i.e., the Green function associated with the differential operator $-d^2/dx^2$ and the boundary condition (1.2). It is known that for any continuous and piecewise smooth function $u(x)$ vanishing at $x=0$, 1, the relation

$$|u(\xi)|=|(u', K_\xi')|\leqq\|u'\|\cdot\|K_\xi'\|$$

holds, which can be combined with the relation

$$\|K_\xi'\|^2=\xi(1-\xi)\leqq 1/4 \quad \text{to yield}$$

$$\max_x|u(x)|\leqq\|u'\|/2\,. \tag{2.3}$$

On the other hand, the inequalities

$$\|T_0y\|\geqq\lambda_0\|y\|\geqq(\pi^2+Q_m)^{1/2}\|y\|=a\|y\|\,, \tag{2.4}$$

where $\lambda_0^2(\lambda_0>0)$ is the least eigenvalue of the operator $T_0^*T_0$, follow immediately from Rayleigh's principle and the fact that $\pi^2+Q_m$ is a positive lower bound of $\lambda_0^2$.

In view of (2.1) and (2.4), we have

$$\|T_0y\|^2=(f,y)\leqq\|f\|\cdot\|y\|\leqq\|f\|\cdot\|T_0y\|/a\,,$$

and consequently

$$\|y'\|\leqq\|T_0y\|\leqq\|f\|/a\,, \tag{2.5}$$

whence follows the desired inequality by virtue of (2.3).

**Lemma 2.** *Let $G_\xi=G_\xi(x)$ be the Green function of* P. (I), *with the discontinuity of its derivative at $x=\xi$, considered as a function of $x$. Then we have*

$$0\leqq G_\xi(x)\leqq 1/4\,,\quad (0\leqq x\leqq 1, 0<\xi<1)\,. \tag{2.6}$$

Proof. Since the left inequality is well-known, we need only to prove the right inequality. From the relation

$$\|G_\xi'\|^2+(qG_\xi, G_\xi)=G_\xi(\xi)$$

we obtain at once $\|G_\xi'\|^2\leqq G_\xi(\xi)$, which can be combined with (2.3) to yield

$$\|G_\xi'\|^2\leqq G_\xi(\xi)\leqq\|G_\xi'\|/2\,.$$

In consequence we have

$$\|G_\xi'\|\leqq 1/2\,. \tag{2.7}$$

Again taking account of (2.3) we observe that the desired inequality follows from (2.7).

Making use of these lemmas, from Theorem 1 we can deduce the following theorem which gives bounds of $R_1$.

**Theorem 2.** *Let $\hat{q}$ and $\hat{f}$ be any upper bounds of $\int_0^1|\Delta q|dx$ and $\int_0^1|\Delta f|dx$ respective-*

*ly, where* $\Delta q=q(x)-\bar{q}(x)$ *and* $\Delta f=f(x)-\bar{f}(x)$. *Then for* $R_1$ *in* (1.8) *we have the following estimate*:

$$R_1\leqq(1+\hat{q})\left(\frac{\hat{q}}{8a}\|f\|+\frac{\hat{f}}{4}\right), \tag{2.8}$$

*where* $a$ *is the same as in Lemma 1.*

Proof. Let $T$ and $T^*$ be those defined in §1. $\delta(x-\xi)$ is taken as the element $d$ in Theorem 1 as stated there. On the other hand, we choose $u$, $v$, $\phi$, $\psi$ such that

$u=y(x)$, the solution of P. (I),

$\phi=G_\xi(x)$, the Green function of P. (I) with its singularity at $\xi$,

$v=\{v_1, v_2\}$, where $v_2$ is $y(x)$ and $v_1$ is defined as

$$v_1=y'(0)+\int_0^x(\bar{q}y-\bar{f})dx ,$$

$\psi=\{\psi_1, \psi_2\}$, where $\psi_2$ is $G_\xi(x)$ and $\psi_1$ is defined as

$$\psi_1=G_\xi'(0)+\int_0^x(\bar{q}G_\xi-\delta(x-\xi))dx .$$

It can be easily verified that these elements satisfy the conditions required in Theorem 1.

$v_1$ can be reduced to another form more convenient for calculations:

$$\begin{aligned}v_1&=y'(0)+\int_0^x(qy-f)dx+\int_0^x(\Delta f-\Delta qy)dx\\&=y'(0)+\int_0^x y''dx+\int_0^x(\Delta f-\Delta qy)dx\\&=y'(x)+\int_0^x(\Delta f-\Delta qy)dx ,\end{aligned}$$

that is, putting

$$r_1(x)=\int_0^x(\Delta f-\Delta qy)dx ,$$

we can write as

$$v_1=y'(x)+r_1(x) .$$

Similarly, we can derive

$$\psi_1=G_\xi'(x)+r_2(x) ,$$

where $$r_2(x)=-\int_0^x\Delta qG_\xi dx .$$

With these elements we calculate $A$, $\varepsilon_1$ and $\varepsilon_2$ in (1.12). First, we have

$$\begin{aligned}&(u, d)=y(\xi) ,\\&(\bar{f}, \phi)=(f-\Delta f, G_\xi)=(f, G_\xi)-(\Delta f, G_\xi)\\&\qquad=y(\xi)-(\Delta f, G_\xi)\end{aligned}$$

and, moreover,

$$\begin{aligned}(v, \psi)-(Tu, T\phi)&=(v_1, \psi_1)-(y', G_\xi')\\&=(y'+r_1, G_\xi'+r_2)-(y', G_\xi')\\&=(r_1, G_\xi')+(y', r_2)+(r_1, r_2) .\end{aligned}$$

On the other hand, noting

$$r_1'=\Delta f-\Delta qy , \quad r_2'=-\Delta qG_\xi ,$$

we obtain

$$\begin{aligned}(r_1, G_\xi')&=-(r_1', G_\xi)=-(\Delta f-\Delta qy, G_\xi)\\&=-(\Delta f, G_\xi)+(\Delta qy, G_\xi) ,\\(y', r_2)&=-(y, r_2')=(y, \Delta qG_\xi)=(\Delta qy, G_\xi) .\end{aligned}$$

Thus we find

$$A=y(\xi)+(\Delta qy, G_\xi)-(\Delta f, G_\xi)+\frac{1}{2}(r_1, r_2) ,$$

while it is obvious that

$$\begin{aligned}\varepsilon_1&=\|Tu-v\|=\|y'-v_1\|=\|r_1\| ,\\\varepsilon_2&=\|T\phi-\psi\|=\|G_\xi'-\psi_1\|=\|r_2\| .\end{aligned}$$

From these results, in view of (1.11), we arrive at

$$\begin{aligned}|y(\xi)-\bar{y}(\xi)|\leqq&|(\Delta qy, G_\xi)|\\&+|(\Delta f, G_\xi)|+\|r_1\|\cdot\|r_2\| .\end{aligned} \tag{2.9}$$

By referring to Lemma 1 and Lemma 2 we can appraise the terms on the right side of (2.9) as

$$\begin{aligned}|(\Delta qy, G_\xi)|&\leqq\frac{1}{4}(\max|y(x)|)\int_0^1|\Delta q|dx\\&\leqq\frac{1}{8a}\|f\|\cdot\hat{q} ,\\|(\Delta f, G_\xi)|&\leqq\frac{1}{4}\int_0^1|\Delta f|dx\leqq\frac{1}{4}\hat{f} ,\\\|r_1(x)\|\leqq\max|r_1(x)|&\leqq\int_0^1|\Delta f|dx\\&+\int_0^1|\Delta qy|dx\leqq\hat{f}+\frac{1}{2a}\|f\|\cdot\hat{q} ,\\\|r_2(x)\|\leqq\max|r_2(x)|&\leqq\int_0^1|\Delta q|G_\xi dx\leqq\frac{1}{4}\hat{q} ,\end{aligned}$$

which lead (2.9) to the form

$$|y(\xi)-\bar{y}(\xi)|\leqq(1+\hat{q})\left(\frac{\hat{q}}{8a}\|f\|+\frac{\hat{f}}{4}\right). \tag{2.10}$$

Since the right side of (2.10) is independent of $\xi$, we have established the validity of (2.8).

**Corollary.** *As* $h$ *tends to zero, we have*

$$R_1=O\left(\int_0^1|\Delta q|dx\right)+O\left(\int_0^1|\Delta f|dx\right).$$

*Remark* 1. Occasionally in practice

$$\int_0^1|\Delta q|dx , \quad \int_0^1|\Delta f|dx$$

may be appraised graphically. Moreover, $\max|\Delta q|$ and $\max|\Delta f|$ are admissible as $\hat{q}$ and

$\hat{f}$ respectively.

*Remark* 2. Without applying Theorem 1 we can derive another bound of $R_1$ as follows. Putting $r(x)=y(x)-\bar{y}(x)$, we note that $-r''+\bar{q}r=-\Delta qy+\Delta f$, i.e., $T^*Tr=-\Delta qy+\Delta f$, which yields

$$\|Tr\|^2\leq(\|\Delta qy\|+\|\Delta f\|)\cdot\|r\| .$$

Hence, we have, in view of (2.3) and the relation $\|Tr\|\geq a\|r\|$,

$$|r(x)|\leq\frac{1}{2}\|r'\|\leq\frac{1}{2}\|Tr\|\leq\frac{1}{2a}(\|\Delta qy\|+\|\Delta f\|)$$

which can be led by means of Lemma 1 to the following inequality:

$$R_1\leq\frac{1}{4a^2}\|\Delta q\|\cdot\|f\|+\frac{1}{2a}\|\Delta f\| . \qquad (2.11)$$

In some cases (2.11) is possibly sharper than (2.8). However, (2.8) is seen more convenient for our subsequent study of the degree of convergence.

## § 3. Estimation of $R_2$

This section is devoted to the deduction of bounds of $R_2$ along the line indicated in § 1. It seems convenient to introduce some notions and formulae concerning finite differences beforehand. All notations already defined hold their meanings here, unless otherwise stated. We denote the interval $(x_k, x_{k-1})$ by $I_k$ $(k=0, 1, \cdots, n-1)$.

**1.** First of all, we introduce three real unitary spaces $E_{n+1}, E_n$ and $E_{n-1}$ such that

$E_{n+1}$ is $(n+1)$-dimensional and provided with the norm

$$\|u\|^2=\|\{u_k\}\|^2=h\sum_{k=0}^{n}u_k^2$$

$E_n$ is $n$-dimensional and provided with the norm

$$\|u\|^2=\|\{u_k\}\|^2=h\sum_{k=0}^{n-1}u_k^2 ,$$

$E_{n-1}$ is $(n-1)$-dimensional and provided with the norm

$$\|u\|^2=\|\{u_k\}\|^2=h\sum_{k=1}^{n-1}u_k^2 .$$

Besides usual inequalities valid for the norm in a unitary space, e.g., Schwarz' inequality, it holds in $E_n$ that

$$h\sum_{k=0}^{n-1}|u_k|\leq\|u\|\leq\max_k|u_k| . \qquad (3.1)$$

The vectors $\{q_i, q_{i+1}, \cdots, q_j\}$ and $\{f_i, f_{i+1}, \cdots, f_j\}$, where $q_k$ and $f_k$ are those in (1.3), may be regarded as elements of $E_{n+1}$, $E_n$ or $E_{n-1}$, according as $(i=0,\ j=n)$, $(i=0,\ j=n-1)$ or $(i=1, j=n-1)$. Whichever space may $\{q_k\}$ belong to, we shall use always the same letter $q$ to denote it, since any confusions in the sequel possibly caused by this convention seem avoidable with a little care. This is the same for $\{f_k\}$. For any vector $u=\{u_k\}$ in one of these spaces $qu$ means the vector $\{q_k u_k\}$. Evidently we have

$$\|qu\|=\|\{q_k u_k\}\|\leq\max_k|u_k|\cdot\|q\| . \qquad (3.2)$$

We turn to the definition of some finite difference operators. To any vector $u=\{u_k\}$ in $E_{n+1}$ we make correspond a vector $Du$ in $E_n$ specified by

$$(Du)_k\equiv Du_k=(u_{k+1}-u_k)/h ,$$
$$(k=0, 1, \cdots, n-1) ,$$

where $h$ is $1/n$ as before.

It is worthwhile to remark that if $y_k$ is the value of a function $y(x)$ at $x=x_k$ $(k=0, 1, \cdots, n)$, $Dy_k$ turns out to be the divided finite difference (the finite difference quotient) of $y(x)$ at $x_k$ in accordance with the customary definition. Moreover, if $y(x)$ is a function such that its graph is the polygonal line joining $(x_k, y_k)$ in order, which is the case for $\bar{q}(x)$ and $\bar{f}(x)$, $y(x)$ can be expressed as

$$y(x)=y_k+(x-x_k)Dy_k \quad \text{in} \quad I_k ,$$
$$(k=0, 1, \cdots, n-1) ,$$

and also we find

$$\|dy/dx\|=\|Dy\| ,$$

where the left side represents the norm of $dy/dx$ in the sense of (1.13) and the right side the norm of the vector $Dy$ in $E_n$. The following formulae concerning the operator $D$ are almost evident by definition:

$$h\sum_{k=i}^{j}Du_k=u_{j+1}-u_i , \qquad (3.3)$$

$$h\|Du\|\leq2\|u\| , \qquad (3.4)$$

$$D(qu)_k\equiv Dq_k u_k=u_k Dq_k$$
$$+q_k Du_k+hDu_k Dq_k , \qquad (3.5)$$

$$\|D(qu)\|\leq\max_k|q_k|\cdot\|Du\|$$
$$+\max_k|u_k|\cdot\|Dq\| . \qquad (3.6)$$

Furthermore, we introduce the operator $D^{(2)}$ from $E_{n+1}$ to $E_{n-1}$ defined by the conditions

$$(D^{(2)}u)_k\equiv D^{(2)}u_k=(u_{k+1}+u_{k-1}-2u_k)/h^2 ,$$
$$(k=1, \cdots, n-1) .$$

By definition it is evident that

$$D^{(2)}u_k=(Du_k-Du_{k-1})/h , \qquad (3.7)$$

$$h\sum_{k=i}^{j}D^{(2)}u_k=Du_j-Du_{i-1} . \qquad (3.8)$$

If we identify any $u, v$ in $E_{n+1}$, such that

$u_0=u_n=v_0=v_n=0$, with $\{u_1, u_2, \cdots, u_{n-1}\}$ and $\{v_1, v_2, \cdots, v_{n-1}\}$ in $E_{n-1}$ respectively, we have

$$(Du, Dv)=-(D^{(2)}u, v)=-(u, D^{(2)}v)\,, \qquad (3.9)$$

and we note that P. (II) and P. (III) can be written respectively as

$$-D^{(2)}u+qu=f\,, \quad u_0=u_n=0\,, \qquad (3.10)$$

$$-D^{(2)}g+qg=d\,, \quad g_0=g_n=0\,, \qquad (3.11)$$

and also that the relation

$$(f, g)=(-D^{(2)}u+qu, g)=(u, -D^{(2)}g+qg)$$
$$=(u, d)=u_r \qquad (3.12)$$

holds, which shows that $g=\{g_k\}$ displays a role similar to that of the Green function.

Some inequalities, which is useful later, concerning the solution $u=\{u_k\}$ of P. (II) are written out in the following lemma.

**Lemma 3.** *Let* $u=\{u_k\}$ *be the solution of* P. (II) *and let* $\bar{Q}_m$ *be* $\min_k q_k$. *Then we have*

$$\max_k |u_k| \leq \frac{\|f\|}{2a}\,, \qquad (3.13)$$

$$\|Du\| \leq \frac{\|f\|}{a}\,, \qquad (3.14)$$

$$\|D^{(2)}u\| \leq \|f\|+\frac{\|f\|\cdot\|q\|}{2a}\,, \qquad (3.15)$$

*where* $a$ *is the positive square root of* $(2(1-\cos \pi h)/h^2)+\bar{Q}_m$ *and* $\|q\|$, $\|f\|$ *are those in* $E_{n-1}$.

Proof. First we note that for any vector $u$ in $E_{n+1}$ such that $u_0=u_n=0$, the inequality

$$\max_k |u_k| \leq \|Du\|/2 \qquad (3.16)$$

can be established in a manner similar to that used for (2.3). Then noting that the least eigenvalue of the eigenvalue problem

$$-D^{(2)}v=\lambda v\,, \qquad v_0=v_n=0\,,$$

is known to be $2(1-\cos \pi h)/h^2$, we can deduce (3.13) and (3.14) similarly to (2.2) and (2.5). Finally (3.15) follows immediately from (3.10) by virtue of (3.2) and (3.13).

*Remark* 1. In our later treatments it is convenient to put

$$D^{(2)}u_0=-f_0 \quad \text{and} \quad D^{(2)}u_n=-f_n$$

for the solution of P. (II) so that we can write

$$-D^{(2)}u_k+q_k u_k=f_k\,, \quad (k=0, 1, \cdots, n)$$

and $DD^{(2)}u$ is well-defined. Even if we interpret $\|D^{(2)}u\|^2$ as $h\sum_{k=0}^{n}(D^{(2)}u_k)^2$ in accordance with this convention, (3.15) still remains valid, provided that $\|f\|$, the first term of the right side of it, is interpreted as that in $E_{n+1}$.

Concerning the solution $g=\{g_k\}$ of P. (III) we can deduce the following lemma analogous to Lemma 2.

**Lemma 4.** *Let* $g=\{g_k\}$ *be the solution of* P. (III). *Then we have*

$$0 \leq g_k \leq 1/4\,, \quad (k=0, 1, \cdots, n) \qquad (3.17)$$

$$\|Dg\| \leq 1/2\,. \qquad (3.18)$$

2. We have now reached a point to derive the bounds of $R_2$ by use of Theorem 1. We agree with the convention that any functions or constants not exceeding 1 in their absolute values may be denoted always by the same letter $\theta$. Here in applying Theorem 1 we let $d$ be $\delta(x-x_r)$ and $T$, $T^*$ be those defined in § 1. The elements $u, v, \phi, \psi$ in Theorem 1 are constructed from $u=\{u_k\}$, $g=\{g_k\}$, the solutions of P. (II) and P. (III) as below.

$u$ and $\phi$ are defined respectively by the conditions that

$$u=\bar{u}(x)=u_k+(x-x_k)Du_k\,,$$
$$\phi=\bar{g}(x)=g_k+(x-x_k)Dg_k$$

in $I_k$, $(k=0, 1, \cdots, n-1)$.

In other words, the graph of $\bar{u}(x)$, $\bar{g}(x)$ are the polygonal line joining $(x_k, u_k)$ in order and the polygonal line joining $(x_k, g_k)$ in order respectively. Hereby we remark that $\bar{q}(x)$, $\bar{f}(x)$ in P. (I′) can be expressed as

$$\bar{q}(x)=q_k+(x-x_k)Dq_k\,,$$
$$\bar{f}(x)=f_k+(x-x_k)Df_k$$

in $I_k$, $(k=0, 1, \cdots, n-1)$.

In accordance with the conditions $T^*v=\bar{f}$, $T^*\psi=\delta(x-x_r)$, we take $v=\{v_1, v_2\}$ and $\psi=\{\psi_1, \psi_2\}$ such that

$$v_1=\int_0^x (\bar{q}\bar{u}-\bar{f})dx+Du_0+\frac{h}{2}f_0\,, \qquad (3.19)$$

$v_2$ is identical with $\bar{u}(x)$,

$$\psi_1=\int_0^x (\bar{q}\bar{g}-\delta(x-x_r))dx+Dg_0\,, \qquad (3.20)$$

$\psi_2$ is identical with $\bar{g}(x)$.

We note that $v_1$ can be reduced to a form more convenient for our calculations. In fact, the contribution of $I_l$ to the integral in (3.19) is calculated as

$$h(q_l u_l-f_l)+\frac{h^2}{2}(u_l Dq_l+q_l Du_l-Df_l)$$
$$+\frac{h^3}{3}Du_l Dq_l$$

$$=hD^{(2)}u_i+\frac{h^2}{2}DD^{(2)}u_i-\frac{h^3}{6}Du_iDq_i$$

by means of (3.5) and (3.10).

By referring to (3.3), (3.7), (3.8) and Remark 1 we note that

$$h\sum_{i=0}^{k-1}D^{(2)}u_i=hD^{(2)}u_0+(Du_{k-1}-Du_0)$$
$$=Du_k-hD^{(2)}u_k-Du_0-hf_0\ ,$$
$$h\sum_{i=0}^{k-1}DD^{(2)}u_i=D^{(2)}u_k-D^{(2)}u_0=D^{(2)}u_k+f_0\ ,$$

and hence,

$$\int_0^{x_k}(\bar{q}\bar{u}-\bar{f})dx+Du_0+\frac{h}{2}f_0$$
$$=Du_k-\frac{h}{2}D^{(2)}u_k-\frac{h^3}{6}\sum_{i=0}^{k-1}Du_iDq_i\ .$$

On the other hand, putting $t=x-x_k$, we find

$$\int_{x_k}^{x}(\bar{q}\bar{u}-\bar{f})dx=tD^{(2)}u_\kappa+\frac{t^2}{2}DD^{(2)}u_k$$
$$-\left(\frac{ht^2}{2}-\frac{t^3}{3}\right)Dq_\kappa Du_k\ .$$

From these results and the inequality

$$\left|\frac{ht^2}{2}-\frac{t^3}{3}\right|\leqq\frac{h^3}{6}\ ,\quad(0\leqq t\leqq h)\ ,$$

we obtain

$$v_1=Du_k+r_1(x)\quad\text{in}\quad I_k\ ,$$

where

$$r_1(x)=\left(t-\frac{h}{2}\right)D^{(2)}u_k+\frac{t^2}{2}DD^{(2)}u_k$$
$$+\theta\frac{h^2}{6}\|Dq\|\cdot\|Du\|\quad\text{in}\quad I_k\ .$$

In a similar manner, noting that for $x$ contained in $I_k$, the relation

$$\int_0^x\delta(x-x_r)dx=h\sum_{i=0}^{k}d_i$$

holds, $\{d_i\}$ being those defined in P. (III), we can take $\psi_1$ into the form

$$\psi_1=Dg_k+r_2(x)\quad\text{in}\quad I_k\ ,$$

where

$$r_2(x)=\left(t-\frac{h}{2}\right)(qg)_k+\frac{t^2}{2}D(qg)_k$$
$$+\frac{h^2}{6}\theta\|Dq\|\cdot\|Dg\|\quad\text{in}\quad I_k\ .$$

Making use of these elements, we calculate $A$, $\mathcal{E}_1$ and $\mathcal{E}_2$ in (1.12). First, it is easily seen that

$$\mathcal{E}_1=\|Tu-v\|=\|r_1\|\ ,$$
$$\mathcal{E}_2=\|T\phi-\psi\|=\|r_2\|\ . \qquad (3.21)$$

By definition we have

$$\eta=\bar{y}(x_r)\ ,\quad(u,d)=(\bar{u}(x),\delta(x-x_r))=u_r\ ,$$

and moreover, be means of (3.12) we can verify

$$(\bar{f},\phi)=(\bar{f}(x),\bar{g}(x))=(f,g)-\frac{h^2}{6}(Df,Dg)$$
$$=u_r-\frac{h^2}{6}(Df,Dg)\ .$$

Also we note that

$$(v,\psi)-(Tu,T\phi)$$
$$=\sum_{k=0}^{n-1}\left(Du_k\int_{I_k}r_2dx+Dg_k\int_{I_k}r_1dx\right)+(r_1,r_2)\ ,$$

while by a little calculation we obtain

$$\sum_{k=0}^{n-1}Du_k\int_{I_k}r_2dx=\frac{h^2}{6}(Du,Dqg)$$
$$+\theta\frac{h^2}{6}\|Dq\|\cdot\|Du\|\cdot\|Dg\|\ ,$$
$$\sum_{k=0}^{n-1}Dg_k\int_{I_k}r_1dx=\frac{h^2}{6}(Dg,DD^{(2)}u)$$
$$+\theta\frac{h^2}{6}\|Dq\|\cdot\|Du\|\cdot\|Dg\|\ .$$

Consequently, $A$ can be written by use of (3.10) and (3.18) as

$$A=u_r-\frac{h^2}{12}[(Df,Dg)-(DD^{(2)}u,Dg)-(Du,Dqg)]$$
$$+\theta\frac{h^2}{6}\|Dq\|\cdot\|Du\|\cdot\|Dg\|+\frac{1}{2}(r_1,r_2)$$
$$=u_r-\frac{h^2}{12}[2(Df,Dg)-(Dqu,Dg)-(Du,Dqg)]$$
$$+\theta\frac{h^2}{12}\|Dq\|\cdot\|Du\|+\theta\frac{1}{2}\|r_1\|\cdot\|r_2\|\ .$$

Thus by virtue of (3.21) and the above results, (1.11) implies

$$|\bar{y}(x_r)-u_r|\leqq\frac{h^2}{12}|2(Df,Dg)-(Dqu,Dg)$$
$$-(Du,Dqg)|+\frac{h^2}{12}\|Dq\|\cdot\|Du\|+\|r_1\|\cdot\|r_2\|\ .$$

Since by referring to (3.1) and Lemma 4 we have

$$|(Df,Dg)|\leqq\|Df\|/2\ ,$$
$$|(Dqu,Dg)|\leqq\|D(qu)\|/2,$$
$$|(Du,Dqg)|=|(D^{(2)}u,qg)|\leqq\|(D^{(2)}u\|\cdot\|qg\|$$
$$\leqq\|D^{(2)}u\|\cdot\|q\|/4\ ,$$

only $\|r_1\|$ and $\|r_2\|$ still remain to be calculated. By elementary calculations we find

$$\|r_1\|^2\leqq\frac{h^2}{12}\|D^{(2)}u\|^2+\frac{h^3}{12}\|D^{(2)}u\|\cdot\|DD^{(2)}u\|$$

$$+\frac{h^3}{12}\|D^{(2)}u\|\cdot\|Dq\|\cdot\|Du\|+\frac{h^4}{20}\|DD^{(2)}u\|^2$$
$$+\frac{h^4}{18}\|DD^{(2)}u\|\cdot\|Dq\|\cdot\|Du\|+\frac{h^4}{36}\|Dq\|^2\cdot\|Du\|^2, \tag{3.22}$$

and, consequently, by use of (3.4) we deduce

$$\|r_1\|^2\leq\frac{h^2}{12}\|D^{(2)}u\|^2+\frac{h^2}{6}\|D^{(2)}u\|^2$$
$$+\frac{h^2}{6}\|Du\|\cdot\|D^{(2)}u\|\cdot\|Dq\|$$
$$+\frac{h^2}{5}\|D^{(2)}u\|^2+\frac{2h^2}{9}\|D^{(2)}u\|\cdot\|q\|\cdot\|Du\|$$
$$+\frac{h^2}{9}\|q\|^2\cdot\|Du\|^2$$
$$=h^2\Big[\frac{9}{20}\|D^{(2)}u\|^2+\frac{7}{18}\|D^{(2)}u\|\cdot\|Du\|\cdot\|q\|$$
$$+\frac{1}{9}\|q\|^2\cdot\|Du\|^2\Big]. \tag{3.23}$$

The estimate of $\|r_1\|$ given by (3.23) can be reduced to the following one less sharp but more concise than (3.23), i.e.,

$$\|r_1\|\leq h\Big[\frac{3}{\sqrt{20}}\|D^{(2)}u\|+\frac{1}{3}\|q\|\cdot\|Du\|\Big].$$

Similarly, we obtain

$$\|r_1\|^2\leq\frac{h^2}{12}\|qg\|^2+\frac{h^3}{12}\|qg\|\cdot\|Dqg\|$$
$$+\frac{h^3}{12}\|qg\|\cdot\|Dq\|\cdot\|Dg\|+\frac{h^4}{20}\|Dqg\|^2$$
$$+\frac{h^4}{18}\|Dqg\|\cdot\|Dq\|\cdot\|Dg\|+\frac{h^4}{36}\|Dq\|^2\cdot\|Dg\|^2, \tag{3.24}$$

whence in consideration of (3.1), (3.4), (3.17) and (3.18) we arrive, after modifying the numerical coefficient without breaking the validity, at

$$\|r_2\|\leq\frac{h}{3}\|q\|.$$

Summing up all results so far obtained and again modifying the numerical coefficient of $\|D^{(2)}u\|\cdot\|q\|$ appropriately, we observe that the inequality

$$|y(x_r)-u_r|\leq h^2\Big[\frac{1}{12}\|Df\|+\frac{1}{24}\|Dqu\|$$
$$+\frac{1}{12}\|Dq\|\cdot\|Du\|+\frac{1}{4}\|D^{(2)}u\|\cdot\|q\|$$
$$+\frac{1}{9}\|q\|^2\cdot\|Du\|\Big]$$

holds. Furthermore, since the right side of this inequality is independent of $r$, we have established the following theorem concerning $R_2$.

**Theorem 3.** *Let notations be above. We have the following estimate of $R_2$.*

$$R_2\leq h^2\Big[\frac{1}{12}\|Df\|+\frac{1}{24}\|Dqu\|+\frac{1}{12}\|Dq\|\cdot\|Du\|$$
$$+\frac{1}{4}\|D^{(2)}u\|\cdot\|q\|+\frac{1}{9}\|q\|^2\cdot\|Du\|\Big]. \tag{3.25}$$

*Remark* 2. As for the norms appearing in (3.25), it is remarked that $\|D^{(2)}u\|$ should be interpreted as that in $E_{n+1}$ in the sense of Remark 1 of this section, while on the other hand $\|q\|$ may be taken as that in $E_{n-1}$.

*Remark* 3. When we are interested particularly in the asymptotic bounds of $R_2$ ($h\to0$) under more stringent conditions of regularity for $q(x)$ and $f(x)$, we can derive one different from (3.25) in its form, although (3.25) gives a bound of $R_2$ for any $h$ and for any $q(x)$, $f(x)$ provided with the properties stated in P. (I). That is, we assume that each of $q(x)$ and $f(x)$ satisfies the Lipschitz condition of order 1, which implies that $Dq_k$ and $Df_k$ as well as $\|Dq\|$ and $\|Df\|$ are bounded as $h$ tends to zero. Under this assumption, noting (3.6), Lemma 3 and the inequality

$$\|DD^{(2)}u\|\leq\|Df\|+\|D(qu)\|,$$

we observe that all norms appearing in (3.22) are bounded, and hence,

$$\|r\|^2{}_1\leq\frac{h^2}{12}\|D^{(2)}u\|^2+o(h^2), \quad (h\to0).$$

Similarly from (3.24) follows the inequality

$$\|r_2\|^2\leq\frac{h^2}{12}\|qg\|^2+o(h^2), \qquad (h\to0).$$

Thus we find, taking account of (3.17),

$$\|r_1\|\cdot\|r_2\|\leq\frac{h^2}{48}\|D^{(2)}u\|\cdot\|q\|+o(h^2), \quad (h\to0) \tag{3.26}$$

Making use of (3.26) we can deduce

$$R_2\leq h^2\Big[\frac{1}{12}\|Df\|+\frac{1}{12}\|Dq\|\cdot\|Du\|+\frac{1}{24}\|Dqu\|$$
$$+\frac{1}{24}\|D^{(2)}u\|\cdot\|q\|\Big]+o(h^2), \quad (h\to0), \tag{3.27}$$

by a reasoning similar to that used for (3.25).

Furthermore, from Theorem 3 we can derive a bound of $R_2$ not involving $u=\{u_k\}$, i.e., by referring to (3.6) and Lemma 3 we immediately obtain the following theorem.

**Theorem 4.** *Let $a$ be the same as in Lemma 3 and let $Q_M$ be $\max\limits_k q_k$. Then we have*

$$R_2 \leq h^2 \left[ \frac{1}{12} \|Df\| + \frac{5}{48} \frac{\|f\| \cdot \|Dq\|}{a} + \frac{1}{24} \frac{Q_M \|f\|}{a} + \frac{1}{4} \|q\| \cdot \|f\| + \frac{1}{4} \frac{\|q\|^2 \cdot \|f\|}{a} \right]. \tag{3.28}$$

**Corollary.** *As $h$ tends to zero, we have*

$$R_2 = O(h^2) + O(h^2 \|Dq\|) + O(h^2 \|Df\|) .$$

*Remark* 4. In (3.28) $\|f\|$ should be interpreted as that in $E_{n+1}$ and $\|q\|$, on the contrary, may be taken as that in $E_{n-1}$.

*Remark* 5. Under the same conditions as for (3.27), we have the following asymptotic bound of $R_2$:

$$R_2 \leq h^2 \left[ \frac{1}{12} \| Df \| + \frac{5}{48} \frac{\|f\| \cdot \|Dq\|}{a} + \frac{1}{24} \frac{Q_M \cdot \|f\|}{a} + \frac{1}{24} \|q\| \cdot \|f\| + \frac{1}{48} \frac{\|q\|^2 \cdot \|f\|}{a} \right] + o(h^2) , \quad (h \to 0) . \tag{3.29}$$

## § 4. Degree of Convergence

In this section we study the degree of convergence of $u = \{u_k\}$, the solution of P. (II), to $y(x)$, the solution of P. (I), under various continuity hypotheses on $q(x)$ and $f(x)$, which are originally assumed to be picewise continuous (See the foot note in § 1.), as the difference interval $h$ approaches zero. Rewriting $u = \{u_k\}$ by $u(h) = \{u_k(h)\}$, we define $u(x, h)$ for any $x$ contained in $I$ by the condition

$$u(x, h) = u_r(h), \quad \text{where} \quad r = x/h .$$

It is intended to ascertain the degree of convergence of

$$E(x, h) = y(x) - u(x, h)$$

uniform with respect to $x$, provided that $h$ tends to zero in such a manner that the sequence $\{E(x, h)\}$ is infinite. For this purpose, noting that the bounds of $R = R(h)$, which we have succeeded in obtaining, can be regarded as uniform bounds of $E(x, h)$, we need, by virtue of Corollaries in § 2 and § 3, only to investigate the orders with respect to $h$ of the following quantities:

$$Q_1 = \int_0^1 |\Delta q| dx , \qquad F_1 = \int_0^1 |\Delta f| dx ,$$

$$Q_2 = h^2 \|Dq\| , \qquad F_2 = h^2 \|Df\| .$$

In estimating these quantities, it may be worthwhile to note that the relations

$$Q_1 \leq \max_x |\Delta q(x)| , \qquad Q_2 \leq h^2 \max_k |Dq_k| ,$$

$$Q_2 \leq 2h \|\{q_k\}\| ,$$

$$F_1 \leq \max_x |\Delta f(x)| , \qquad F_2 \leq h^2 \max_k |Df_k| ,$$

$$F_2 < 2h \|\{f_k\}\| ,$$

hold and, moreover, for example, if $\Delta q = O(h^\alpha)$ in $I_k$, the contribution of $I_k$ to $Q_1$ turns out to be $O(h^{\alpha+1})$. Although in view of these facts we can rather easily study the degree of convergence under various situations, we do not give the results in full but only illustrate some of them in the following propositions. Concerning these propositions we remark that the relation $R = O(h^\alpha)$ implies that $E(x, h)$ converges to zero, as $h$ tends to zero, uniformly with the degree of convergence equal to or higher than that of $h^\alpha$. Furthermore, we assume without loss of generality that $f(x)$ is provided with its regularity same as or better than that of $q(x)$, since $F_1$ and $F_2$ depend on $f(x)$ respectively in the same manner as $Q_1$ and $Q_2$ depend on $q(x)$ and also the order of $R$ is specified as the lowest one among the orders of $Q_1, Q_2, F_1, F_2$.

($a$) Let $q''(x)$ exist and be bounded in $I$. Then

$$R = O(h^2) , \qquad (h \to 0) .$$

($b$) Let $q(x)$ satisfy the *Lipschitz condition* of order 1, i.e., let a constant $M$ exist such that the inequality

$$|q(x_1) - q(x_2)| \leq M |x_1 - x_2|$$

holds for any $x_1$ and $x_2$ contained in $I$. Then

$$R = O(h) , \qquad (h \to 0) .$$

This is the case, in particular, if $q'(x)$ exists and is bounded in $I$.

($c$) Let $q(x)$ satisfy the Lipschitz condition of order 1 and let $q''(x)$ be piecewise continuous. Then

$$R = O(h^2) , \qquad (h \to 0) .$$

This is the case, in particular, if the graph of $q(x)$ is a polygonal line.

($d$) Let $q'(x)$ be piecewise continuous. Then

$$R = O(h) , \qquad (h \to 0) .$$

This is the case, in particular, if $q(x)$ is a step function which has jumps at a finite number of points.

In conclusion the author wishes to express his sincere thanks to Prof. T. Kato for his valuable suggestions and kind advices.

### References

1) L. V. Kantorovich and V. I. Krylov: Approximate methods of higher analysis (Russian) (1952).
2) T. Kato: Math. Ann. **126** (1953) 235.
3) W. E. Milne: Numerical solution of differential equations (1953).
4) E. J. Nyström: Acta Math. **76** (1945) 158.
5) M. H. Stone: Linear transformations in Hilbert space (1932).
6) H. Fujita: J. Phy. Soc. Japan **10** (1955) 1.

---

JOURNAL OF THE PHYSICAL SOCIETY OF JAPAN Vol. 11, No. 2, FEBRUARY, 1956

# The Time Lag and other Undesirable Phenomena observed in Vacuum Photo-tubes at Weak Illumination I

By Masao SUGAWARA

*Hitachi Central Research Lab. Kokubunji-machi, Kitatamagun, Tokyo*

(Received August 29, 1955)

It has been known that in the case of accurate photoelectric photometry of weak light intensity, even the vacuum photo-tube shows the abnormal and undesirable effects such as non-linearity of photoelectric current to the flux of illumination, the variation of photoelectric current with the lapse of time, etc. But, it has not yet been clarified on what factors they depend.

The present writer has experimentally studied these abnormal effects by varying the applied voltage, the wave length, and the flux of illuminating light.

The results show that photoelectric materials, such as caesium, adhering to the undesired portion of the tube wall in poor contact with the photocathode are presumed to be the main cause of these abnormalities.

## §1. Introduction

The photo-tube is often used for measuring the flux of weak illumination, but some abnormal effects are observed in some tubes and the effects introduce the error in measurements.

The classical papers by Ives, Dushman and Karrer$^{1)}$, Preston and McDermott$^{2)}$ described these abnormal effects. For the photo-tubes and photo-multipliers, generally used now, researches have been made by Kortum and Maier$^{3)}$. They have pointed out that in many cases the photoelectric current or the secondary emission current is not accurately proportional to the flux of illumination, and this is due to residual gasses in the tube, the fatigue of the photo-cathode, space charges, photoelectric materials adhering to the undesired portion of the tube wall and temperature variation of the tube. Kuwabara$^{4)}$ has investigated the fatigue of silver-caesium oxide photo-tube from the view of photometry. Discontinuous change in current-voltage characteristics of the photo-tubes which affects the validity of the measurement was reported by Taylor$^{5)}$ and Mori$^{6)}$. They attributed this phenomenon to the electric charges on the inner wall of the tube and photo-electrons as well as secondary electrons from the photoelectric materials on the undesired portion of the tube wall. As described above, various abnormalities have been observed and various factors to be considered as their causes were suggested. But unfortunately, the relations between these factors and abnormalities have not yet been fully clarified. It was found experimentally that there were a few tubes which did not show abnormalities at all. In what follows, the results obtained in the experi-

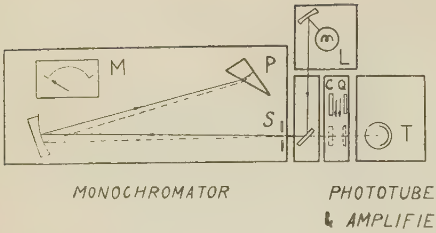

Fig. 1. Schematic Diagram of the Optical System.
L: Light Source P: Prism S: Slit
M: Micro ammeter T: Photo-tube
C: Filter Q: Shutter

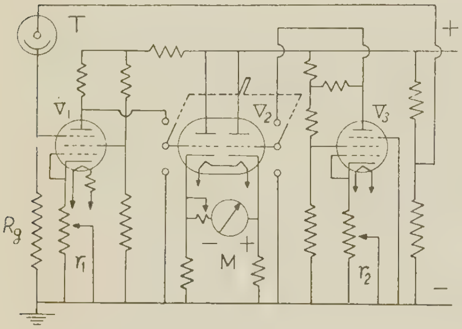

Fig. 2. Amplifier Circuit.
T: Photo-tube $V_2$: 6SN7
$V_1$, $V_3$: Specially designed Vacuum Tube
Rg: 800 MΩ M: Microammeter

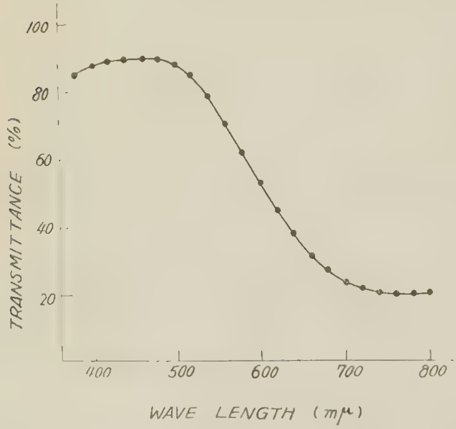

Fig. 3. Standard Spectral Transmitteance of the Filter used.

ments and some considerations regarding to the abnormalities will be described.

## § 2. Experimental Arrangement of Apparatus used and Procedures

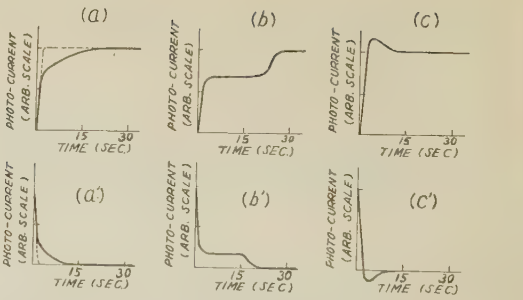

Fig. 4. Typical Time-Photocurrent Curves for Time Lag.
(a), (b), (c) : Light on
(a′), (b′), (c′) : Light off
Dotted line : Normal Case

In fig. 1, the optical system used in this experiment is shown schematically. A light source *L* is a 2800°K tungsten incandescent lamp, and the monochromatic beam enters into the photo-tube *T* through a slit *S* and a shutter *Q*. Between *S* and *Q*, a filter *C* can be inserted. The measurement was carried out under a sufficiently dry condition to avoid the leakage through the outside of the tube. The photoelectric current is amplified and measured with an ammeter *M*.

The amplifier used in this experiment was shown in Fig. 2. Its linearity was previously examined by applying various voltages to the input side and was proved to be quite reliable over a wide range of the voltage. The time constant of the amplifier, including the ammeter responsibility 1.4∼1.8 seconds, was less than 1 second. Resistance *Rg* was 800 megohms. One scale reading on the ammeter corresponded to $1.8\times10^{-12}$ amp. of the phototube current. The time interval was measured with a stopwatch of the scale division one second reading.

At first, after the shutter was opened, the time elapsed till the photo-electric current attained an ultimate value was measured. At the same time, the variation of the current during this interval was also observed. Similar measurements were also carried out immediately after closing the shutter.

Secondly, the spectral transmittance of a filter was measured and compared with the standard value which was determined by using a standard photo-tube*. The standard spectral transmittance of the filter used is shown in Fig. 3.

---

* Recently, the spectral transmittance of the standard filter has been measured accurately with photo tubes at Electrotechnical Laboratory, Japan. Some silver-caesiumoxide phototubes made in this laboratory were checked with the transmittance of the same filter. From these were selected the ones which revealed an error within 0∼+0.3% in the range from 380 mμ to 800 mμ compared with that measured at E. T. L., and these were used as standard photo-tubes.

## § 3. Experimental Results

### (1) *Abnormal Effects*

### (a) *Time lag*

The time lag of the photo-tube current can be classified into three types as "A", "B" and "C".

In "A" type time lag (Fig. 4 a, a′), the photo-tube current immediately reaches a certain value lower than the ultimate value and gradually approaches the ultimate one. In "B" type (Fig. 4 b, b′), the tube current immediately reaches a certain value, and after remaining there for a time, increases to an ultimate value. And in "C" type (Fig. 4 c, c′), the tube current, after overpassing an ultimate value, comes to the ultimate one.

In many cases, one of the above mentioned types appears individually, but sometimes more complex phenomena, such as successive appearance of "A" and "C" type are observed. In the cases of "A" and "C" types, the duration before coming to the ultimate value is comparatively short (within 30 secs.), while in the case of "B" type it often requires a few minutes.

Time lag phenomenon must be distinguished from the so-called fatigue of the photo-tube and it will be considered as one of the abnormal effects of the photo-tube. Photo-tubes whose time lag is greater than 1.4∼1.8 seconds, which correspond to the responsibility of the microammeter used, are regarded as abnormal.

### (b) *Fluctuations in the measured transmittance of a filter.*

In the cases of using different photo-tubes, the results of transmittance measurements of a filter are generally different from the standard value of that filter, and this difference will be designated by a term "discordance". This discordance may be mainly due to the lack of flux-current proportionality. Photo-tubes which show a discordance of more than 0.5% are regarded as those with an abnormality.

### (2) *Relation between abnormalities and Wave Length*

Abnormal effects are affected by the illuminating wave length, but it seems that there are no fixed relations between abnormal effects and wave lengths. Somewhat common facts are as follows;

(i) Abnormal effects are generally conspicuous at a shorter wave length

(ii) "A" type and "C" type time lags occur in a rather wide range of wave length, while "B"-type is limited to a narrow range.

(iii) In many cases, photo-tubes with "B" type time lag at the beginning of illumination show "A" type time lag at the interception of light and reveal a large discordance.

Table I represents the results on the abnormal effects of the caesiumoxide vacuum photo-tube whose shape is shown in Fig. 5.

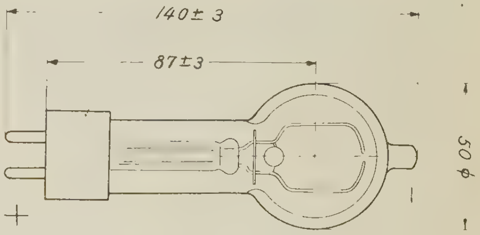

Fig. 5. Front View of the Photo-tube used for Measurement.

Table I. Abnormal Effects of Phototube.
(for Silver-Caesiumoxide Phototube)

| Wave length in mμ | Discordance in % | Time lag | | | |
|---|---|---|---|---|---|
| | | Light off | | Light on | |
| | | Type | Seconds | Type | Seconds |
| 380 | 1.5 | A-Type | 35 | B-Type | 200 |
| 440 | 0.7 | 〃 | 50 | 〃 | 100 |
| 500 | −0.6 | C-Type | 20 | C-Type | 20 |
| 540 | −0.6 | 〃 | 30 | 〃 | 〃 |
| 600 | −0.4 | 〃 | 〃 | 〃 | 1.4 |
| 700 | −0.9 | 〃 | 〃 | 〃 | 〃 |
| 800 | −0.5 | 〃 | 〃 | 〃 | 〃 |

Remarks: Photocurrent: $1.8 \times 10^{-10}$A
Anode voltage: 30 volts
Discordance: (measured)
-(standard)

### (3) *Effects of Applied Voltage and Illuminating Flux*

The abnormal effects varies according to the applied voltage as well as the flux of illumination. The oscillograms of the time-current characteristics at various illuminating fluxes are reproduced in Fig. 6. From (a) in

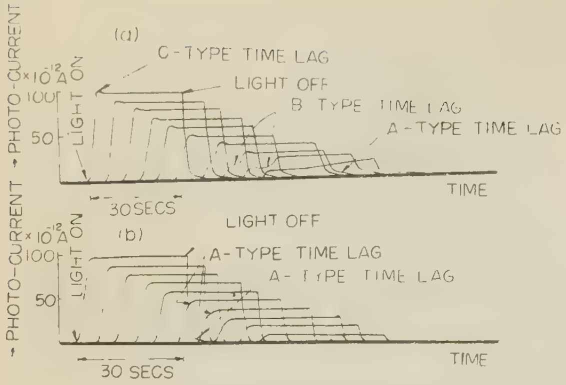

Fig. 6. Variations of Time Lag by the Flux of incident Light.
(a) Antimony-Caesium Photo-tube, Anode Voltage: 70 Volts, Wave length: 480 m$\mu$.
(b) Silver-Caesiumpxide Photo-tubes, Anode Voltage: 90 Volts, Wave length: 780 m$\mu$.

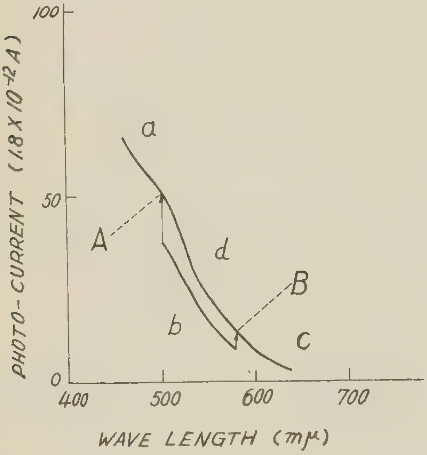

Fig. 7. Typical Example of Dual Characteristics observed in Spectral Response (for Antimony-Caesium Photo-tubes).

the figure for antimony-caesium tubes, it can be seen that the time lag at the beginning of illumination changes from "C" to "B" type and finaly to "A" type as the illuminating intensity is decreased. While, from (b) for silver-caesiumoxide tubes, only "A" type can be seen in a certain range of illuminating flux. Similar phenomena can be observed when the applied voltage is changed.

The discordance does not show any fixed relation with the applied voltage and the flux of illuminating light. Examples of the discordance measured are shown in Table II. The discordance is not always large even at the point where the current-voltage characteristic is not saturated, at such a voltage as 5V and 10V.

(4) *"B" type time lag*

Among the abnormal effects, the most noticeable is "B" type time lag. Furthermore, it is interesting to note that photo-tubes with "B" type time lag often show duality in spectral sensitivity which will be described in detail hereafter.

In Fig. 7, the most typical example is shown. A discontinuous response curve a-b-c is obtained when the illuminating flux is cut off in the intervals of the current measurements at different wave lengths, while in the case of continuous illumination a continuous curve a-d-c is obtained. "B" type time lag is often observed at points near *A* and *B* in Fig. 7. Namely, the duality of the response occurs generally accompanying the "B" type time lag. The current-voltage curves of the photo-tubes, in the case of the wave length at which "B" type time lag appears, generally show discontinuous changes at certain voltages, the duality being observed as well. Similar abnormality is observed in the current-flux characteristics. According to these facts three abnormalities are seemed to be brought about by the same cause.

As previously mentioned, in the case that, "B" type, time lag occurs at the beginning of illumination, "A" type time lag often appears when light is cut off. No abnormal effects, however, are observed if the illumination is resumed before the photo-current fully returns to zero. In the cases of other types of time lags, similar phenomena are also observed. The time lag decreases as the interval of interruption of light is shortened.

(5) *Effects of Heating*

Heating the whole tube above the room temperature affects the appearance of the abnormal effects and often changes normal photo-tubes to abnormal ones. "C" type time lag is usually observed after heating is repeated. (refer to Table III)

Local heatings of a portion of the neck or the window at 100°∼200°C for 20∼30 minutes also cause considerable changes in the abnormal effects. Contrary to the case of whole tube heating, a portional heating often changes abnormal tubes into normal ones. But after a few days, these phototubes show again, similar abnormal effects as before. (Fig. 8)

Table II. Discordance of Phototubes at Various Voltages.
(for Silver-Caesiumoxide Phototubes)

| | Wave length used | Voltage (V) / Relative light intensities | 150 | 110 | 50 | 20 | 10 | 5 |
|---|---|---|---|---|---|---|---|---|
| Ordinary Photo-tube | (mμ) 500 | 200 | 0.3 | 0.1 | 0.1 | -0.5 | -0.1 | -0.2 |
| | | 100 | 0.2 | 0.1 | 0 | -0.8 | -0.2 | -0.2 |
| Photo-tube Containing film | (mμ) 500 | 200 | 0 | 0 | 0 | 0 | -0.1 | 0.2 |
| | | 100 | 0 | 0 | 0 | 0 | -0.2 | 0 |

Photo-tubes kept in a dark place at room temperature often show a variation of abnormal effects with the lapse of time. This is also believed to be due to a similar cause.

## § 4. Effects of Transparent Conducting Film at the Window

Solution of $SnCl_2$ in conc. HCl, for example, sprayed onto the inner surface of glass bulb heating at 400°C forms a transparent conducting film. Silver-caesiumoxide photo-tubes with the bulb treated in this manner were trially made to remove the surface charge on the inner wall, which often had been described by many experimenters. It was found that time lags of these tubes were always within 1.8 sec. in the wave length range of 380~800 mμ. Discordance was also measured. They were quite satisfactory compared with the results obtained with the ordinary phototubes (Table II). The current-voltage characteristics showed no stepwise changes.

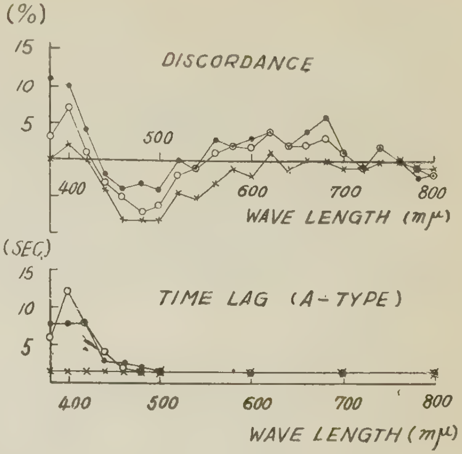

Fig. 8. Example of the Changes of Abnormal Effects caused by Heating the Photo-tube Neck and Window.
— — before heating
—×— after heating (30 min. 200°C)
—○— left at room temp. for 24 hours after heating.

Furthermore, even after a continuous heating

Table III. Changes of the abnormal Effects due to the Heating 50°C.
(Silver-caesiumoxide Tubes)

| | Wave length in mμ | Before heating: Discordance | Before heating: Time lag | After 1000 hours heating: Discordance | Time lag, Light off: Type | Time lag, Light off: Seconds | Time lag, Light on: Type | Time lag, Light on: Seconds |
|---|---|---|---|---|---|---|---|---|
| Phototube Containing Conducting film | 380 | 0.2 | less than 1.6 seconds regardless the light putting on or off | 0.2 | less than 1.6 seconds | | less than 1.6 seconds | |
| | 440 | 0.1 | | 0 | | | | |
| | 500 | -0.4 | | 0 | | | | |
| | 560 | 0.2 | | 0.1 | | | | |
| | 620 | 0 | | 0.3 | | | | |
| | 680 | 0 | | 0 | | | | |
| | 740 | 0 | | 0 | | | | |
| | 800 | 0 | | 0 | | | | |
| Ordinary Phototube | 380 | -0.8 | less than 1.6 seconds regardless the light putting on or off | -0.3 | A | 10 | C | 8 |
| | 440 | -0.6 | | 0.4 | 〃 | 40 | 〃 | 10 |
| | 500 | -0.1 | | 0.4 | 〃 | 40 | 〃 | 10 |
| | 560 | 0 | | 1.0 | 〃 | 30 | 〃 | 5 |
| | 620 | 0 | | 0.1 | 〃 | 5 | 〃 | 3 |
| | 680 | -0.1 | | 0 | | 1.6 | | 1.6 |
| | 740 | 0 | | 0 | | 1.6 | | 1.6 |
| | 800 | -0.1 | | -0.3 | | 1.6 | | 1.6 |

of the tube at 50°C for 1,000 hours, the time lag was within 1.6 sec. for the monochromatic light in the wave length range from 380 m$\mu$ to 800 m$\mu$. Discordance was also within 0.5% at the anode voltage 30 V and photoelectric current $1.8 \cdot 10^{-10}$ amp.

In Table III, examples of the results for these tubes measured before and after heating in comparison with ordinary tubes, are shown.

## § 5. Discussion

As shown Figs. 4 and 6, there are three types of time lag and the type of time lag of photo-tube varies from one to another when the applied voltages, the flux of illuminating beam and the wave length are changed. Therefore, it is presumed that the main cause of time lag is irrespective of type.

Furthermore, from the fact that the appearances of time lag as well as discordance are changed by heating only a limited portion of the neck or the window of the tube at 100°∼200°C for 20∼30 minutes as shown in Fig. 8, it is considered that above two kinds of abnormalities are due to common causes.

It has been known that the photoelectric current decreases with the lapse of time and this phenomenon has been called the fatigue of the photo-cathode. According to de Boer's hypothesis[7], which is still generally accepted though it is not perfect, caesium ions produced by photo-ionization on the photoelectric surface are not all neutralized because of the poor supply of the electron through the layer of photo-cathode and consequently the fatigue phenomenon takes place. But neither the occurrence of various types of time lag, nor their dependence on the flux of illumination, the anode voltage and the wave length used, can be explained by Boer's hypothesis.

Asmus[8] carried out the experiment on the alkali-halide photo-tubes with similar effects and some interpretations have been attempted[9]. But unfortunately, these seem to be still insufficient to explain such complex abnormal effects as observed in our experiments.

Residual gas and the temperature change of the tube surface cannot be considered as the main factor and the slight discordance, as shown in Table II, even in the unsaturated region of the current-voltage curve suggests that the space charge effect is not important.

The interpretation of the abnormalities might be conceived as follows: Small quantities of caesium or the like adhere on the inner surface of the photo-tube in poor contact with the main cathode. By incident of light their potential will change with the photo-emission, and these cause the abnormalities. The change of abnormalities by local heating of the tube would be due to the fact that caesium on the portion heated would evaporate and remove to other portions and consequently the distribution of caesium be changed. As this is an enforced state, naturally a thin film of caesium would be gradually built up again on the former position, and the more or less similar state as before be formed with the lapse of time.

The fact that the photo-tubes provided with a conducting film on the wall as stated in the section 4 hardly show any abnormality, endorses the above reasoning.

The observed results in detail relating to the process of how the photoelectric materials adhering to the tube wall will produce these abnormalities will be described in the next paper.

## § 5. Conclusion

The writer has carried out the experiments about the abnormal effects and found out that photo-tubes without abnormalities are scarce. The abnormal effects differ according to the tubes and are affected by the applied anode voltage, the flux of illuminating light, the wave length and lapse of time. Results are summarized as follows:

(a) Fatigue phenomenon should be separated from the abnormal effect.

(b) Space charge and residual gas cannot be considered as the main cause of abnormalities.

(c) Photoelectric materials, such as caesium, adhering to the undesired portion of the tube wall in poor contact with the main photocathode are regarded as the governing factor.

## Acknowledgment

The writer wishes to express his gratitude to Dr. Hamada, Dr. Tadano, Mr. Kiuchi and Mr. Makino for their kind guidance throughout this work and he also wishes to thank

Messrs. Takei and Morito for their helpful discussions.

### References

1) H. E. Ives, S. Dushman and E. Karrer: Astroph. J. **43** (1916) 9.
2) J. S. Preston and L. H. McDermott: Proc. Phys. Soc. (A) **46** (1934) 256.
3) G. Kortüm and H. Maier: Z. Naturverforsch. **8a** (1953) 253.
4) G. Kuwabara: J. Phys. Soc. Japan **8** (1953) 229.
5) A. H. Taylor: G. E. Review **52** (1949) 43.
6) K. Mori: read at the 11th meeting of the Society of Applied Physics, Japan at Osaka University, October 1953.
7) de Boer and M. C. Teves: Zeit. f. Phys. **74** (1932) 604.
8) E. Asmus: Ann. d. Physik **26** (1936) 723.
9) G. Maurer and Stuttgart Zeit. f. Physik **118** (1941) 104.

# Short Notes

J. Phys. Soc. Japan **11** (1956) 175～176

## Energy Band Structure of the Carborundum SiC Crystal

By Syôiti Kobayasi

*Department of Physics, Faculty of Science Hiroshima University, Hiroshima, Japan*

(Received October 29, 1955)

Here we report a preliminary result (namely, the result computed by Bloch's tight-binding approximation) of the energy band structure of SiC crystal.

There exist some modifications in the crystal structure of SiC, the typical one of which is of zinc blende (diamond) type. The band structures of the zinc blende type of monatomic crystals such as diamond, silicon, and germanium have been already studied by many workers[1] by various methods.

The assumptions in our computation by Bloch's tight-binding method are as follows: the electronic configurations of C and Si atoms in their free state are assumed to be

$$[(1s)^2](2s)^1(2p)^3 \text{ and } [(1s)^2(2s)^2(2p)^6](3s)^1(3p)^3,$$

respectively. As for AO's of core electrons of both atoms, we have used the SCF solutions of each atom.[2,3] As for AO's of valence electrons of both atoms, the Hartree solution[2] is adopted for $2s$ orbital of C atom, the Hartree solution[3] of $\mathrm{Si}^{+2}$ for $3s$ orbital of Si atom, and Slater's function with atomic shielding constants[4] for both $2p$ orbitals of C atom and $3p$ of Si atom. Concerning the atomic energy levels, the computed values[2] based on the Hartree approximation are used for the levels of $2s$ and $2p$ electrons of C atom, while the empirical ones derived from the analysis of atomic spectra[5] are used for $3s$ $(-0.52008e^2/a_0)$ and $3p$ $(-0.29955e^2/a_0$; $a_0$ is the Bohr radius) of Si atom. In practical computation, we have only taken into account the overlapping of a chosen Si–AO with the nearest neighboring AO's of four C atoms ($\sqrt{3}a/4$ apart from it) and the next nearest AO's of twelve Si atoms ($a/\sqrt{2}$ apart from it; $a$ is the edge length of the cube which contains four unit cells). Similar approximation is taken for a chosen C–AO. Further, the three center integrals are neglected approximately throughout our calculation.

In accordance with the mentioned approximations, we calculated the band structure by essentially the same method as what Morita[1] applied to diamond. The results obtained are shown in Fig. 1.

In Fig. 1 the minimum separation between valence and conduction bands seems to occur at $\vec{k}=(0,0,0)$, being about 6 ev in comparison with the experimental value[6] of about 3 ev by ultraviolet absorption. According to our computation, the valence bands at $\vec{k}=(1/a, 0, 0)$ are separated, by 10 ev, into branches; this result may be taken to show the characteristic difference between monatomic and diatomic crystals, since two $X_1$-points in Fig. 1 have been found[1] to coincide with each other in the monatomic crystals. Further, it should be

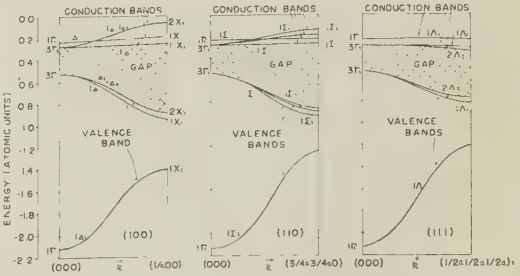

Fig. 1. Behavior of energy bands of the carborundum SiC crystal along 100, 110, and 111 directions, respectively. $a$ is the edge length of the cube which contains four unit cells.

noted that the result shown in Fig. 1 is a little modified, by allowing for Parmenter's consideration[7] on the symmetry properties of the energy bands of the zinc blende structure.

Our next program is to perform a quantitative computation by using the OPW method,[8] which is now in progress.

The author wishes to express his sincere gratitude to Professor T. Muto of Tokyo University for suggesting this work as well as for constant guidance. He is grateful to Dr. J. Yamashita of Tokyo University for his kind advices. Thanks are also due to Mr. E. Yamaka, Dr. A. Morita, Professors T. Matsubara, E. Hirahara, and H. Tazaki for their valuable suggestions.

## References

1) F. Herman: Phys. Rev. **88** (1952) 1210; **93** (1954) 1214.
F. Herman and J. Callaway: Phys. Rev. **89** (1953) 518.
G. E. Kimball: J. Chem. Phys. **3** (1935) 560.
J. F. Mullaney: Phys. Rev. **66** (1944) 326.
A. Morita: Science Repts. Tôhoku Imp. Univ. **33** (1949) 92.
T. Sugita and E. Yamaka: Repts. of ECL, NTT (Tokyo) **2** (1954) 24.
2) C. C. Torrance: Phys. Rev. **46** (1934) 388.
3) H. L. Donley: Phys. Rev. **50** (1936) 1012.
4) J. C. Slater: Phys. Rev. **36** (1930) 57.
5) National Bureau of Standards, *Atomic Energy Levels* Vol. **1** (1949) 144.
6) O. Weigel: Nachr. Ges. Wiss. Göttingen (1915) p. 264.
7) R. H. Parmenter: unpublished paper to which my attention has been directed by Professor T. Muto.
8) C. Herring: Phys. Rev. **57** (1940) 1169.
C. Herring and A. G. Hill: Phys. Rev. **58** (1940) 132.

---

J. PHYS. SOC. JAPAN **11** (1956) 176~177

# Photo-induced Hall Effect of V-center in KI

By E. YAMAKA and K. SAWAMOTO
*The Electrical Communication Laboratory*
T. ISHIDA
*Tokyo College of Science*

(Received November 24, 1955)

Although some investigations for optical absorption of V-centers in alkali-halide crystals have been done in the past[1], measurements of photoconductivity and Hall effect have not yet been carried out, the mechanisms of electronic transitions associated with optical absorptions being left unclarified. Especially determination of signs of charge carriers released by lights from composite V centers, such as $V_2$ of $V_3$, will be interested in interpretation of bleaching. This article describes a preliminary report of photo-induced Hall effect in KI.

Large single crystals of KI were made from melt and additive colorations were performed with iodine at about 530°C. Absorption curves without and with coloration are shown in Fig. 1. Light sources for various absorption bands were obtained by combinations of a high pressure mercury dicharge tube with various filters, their transparent curves being shown in Fig. 2. The apparatus used has the high input impedance preamplifier developed by MacDonald[2].

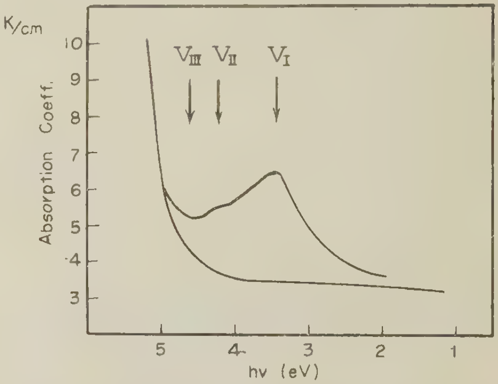

Fig. 1. Absorption curves of KI without and with iodine-coloration. The notation of bands is followed to that of reference 3.

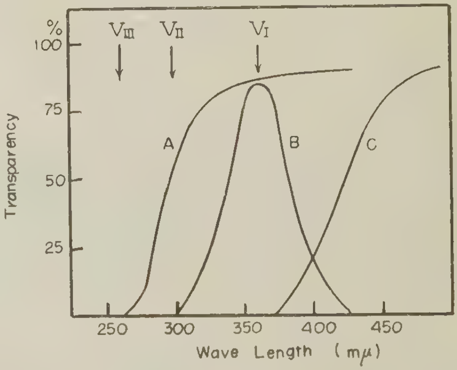

Fig. 2. Transparent curves of various filters used to obtain light of $V_I$, $V_{II}$, $V_{III}$ bands.

Samples were sealed in vacuum in order to avoid humidity.

Photoresponce was observed only with filter A, which in turn indicates that only $V_{II}$ band is responsible for photocurrent and Hall effects showed that associated charge carriers are holes. On the other hand Uchida and Nakai[3] concluded from their optical measurements that $V_I$ and $V_{II}$ bands correspond transitions from the ground state of $V_2$ center (composed from two positive ion vacancies and two holes) to two excited states. From this model our results lead to the conclusions that a electron tranfers from the valence band or excited state, which lies near the top of that band, to the ground state of V-center, leaving a mobile positive hole in the valence band.

Hall mobility of holes lies in the range of 2 to 6 cm²/volt sec at 30 CPS (the lowest frequency available in our apparatus). The measurements at higher frequencies were impossible due to a parastic capacity, so that we could not decide the true mobility free from space charge. Distribution of observed values may be due to various states of space charge in each specimen.

## References

1) F. Seitz: Rev. Mod. Phys. **26** (1954) 7.
2) MacDonald: Rev. Sci. Inst. **25** (1954) 144.
3) Uchida and Nakai: J. Phys. Soc. Jap. **9** (1954) 928.

---

J. PHYS. SOC. JAPAN **11** (1956) 177~178

# Disturbance by Probe in Plasma

By Takayoshi OKUDA and Kenzo YAMAMOTO

*Faculty of Engineering, Nagoya University, Nagoya*

(Received November 18, 1955)

The recently published articles[1,2,3] on the probe study concern with the situation of the probe with negative potential with respect to the space potential and the mechanism of positive ion collection through the transition (or extra-sheath) region between plasma and positive ion sheath, particularly at the low pressure.

Now we deal with some problems which concerns with the disturbance by probe, including both cases of negative and positive probes. To see how the disturbance is responsible for the deformation of the probe characteristic in plasma at higher pressure, we carry out following experiments.

A thin probe (diameter 0.1~0.2 mm) is movably inserted into a disturbed region formed around a thick probe (diameter 0.5~1.5 mm) fixed in a plasma. As the disturbance made by the thin probe is negligibly small compard with that made by the thick probe, we can observe the disturbance made by the thick probe by using the thin probe to measure the ion current and the potential distribution in the disturbed region. The discharge tube used has a diameter of 3.5 cm, and is filled with argon of the pressure 10~$10^{-4}$ mm Hg, mounted by an oxide cathode, a nickel anode, and molybdenum probes.

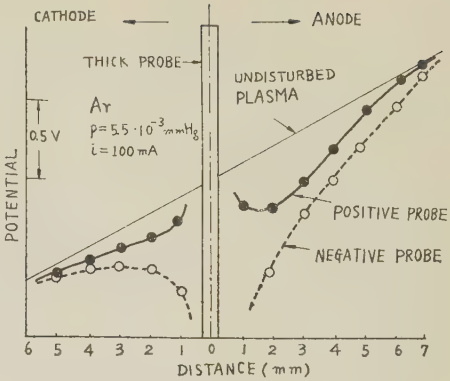

Fig. 1. Potential distribution near a cylindrical thick probe. The solid line: the thick probe is at 5 V positive against plasma potential, electron current is 4 mA. The dotted line: the thick probe is at 77 V negative against plasma potential, positive ion current is 150 μA. Argon, pressure $1\times10^{-2}$ mm Hg, discharge current 100 mA. The thick probe: diameter 0.5 mm, length 4 mm. The thin probe: diameter 0.1 mm, length 4 mm.

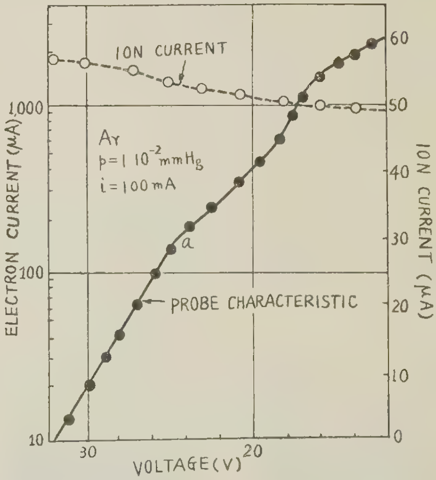

Fig. 2. Probe characteristic of a cylindrical thick probe and saturated ion current of a cylindrical thin probe. The solid line: probe characteristic of the thick probe, voltage is measured with reference to the anode. The dotted line: saturated ion current of the thin probe 1 mm away from thick probe. Argon, pressure $5.5\times10^{-3}$ mm Hg, discharge current 100 mA. The thick probe: diameter 1.5 mm, length 4 mm. The thin probe: diameter 0.1 mm, length 4 mm.

The solid line in Fig. 1 represents the measured potential distribution when the pressure is $1.10^{-2}$ mm Hg, the discharge current 100 mA and the thick probe has a positive potential with reference to its space potential; the dotted line shows the potential distribution of a negative probe. In all pressure we can observe such a potential distribution accompanying a potential sinking formed near the probe even in a case of positive probe. In this case the potential sinking occurs in the same place as the transition region which exists for the negative probe. Here, it must be expected that the potential sinking has a considerable effect on the electron current collected by the probe. The saturated positive ion current of the thin probe in the region of the potential sinking is weaker than that in the undisturbed plasma which is several mm away from the thick probe. That extent to which the probe disturbs the plasma increases with increasing pressure.

The solid line in Fig. 2 indicates a Langmuir's probe characteristic[4] of the thick probe when the argon pressure is $5.5\times10^{-3}$ mm Hg and the discharge current 100 mA, the dotted line indicates the saturated ion current of the thin probe put in the anodic side 1 mm away from the thick probe, showing that when the potential of the thick probe approaches the space potetial, the plasma density near the probe decreases. Therefore, the departure from the linearity at point $a$ on the characteristic curve is not due to the deviation from the Maxwellian distribution of electron energy but the decrease of the plasma density near the probe. This is new interpretation for the nonlinearity of the semi-log plot of the probe characteristic. Further, we find that the linearity in the semi-log plot of the probe characteristic at higher retarding voltage is fairly well held (see Fig. 2), but the reciprocal of the slope of the semi-log plot or the value of the electron temperature evaluated directly from the slope appreciablly decreases as the probe diameter increases and this effect is more appreciable as the pressure increases. The electron temperatures evaluated from the slope of the semi-log plot are tabulated in Table I, for several probes with different diameters. At lower pressure less than $10^{-4}$ mm Hg, no appreciable variation of electron temperature with probe diameter is observed.

Table I. Electron temperature evaluated from the slope of the semi-log plot of probe characteristic for several cylindrical probes with different diameters. Low voltage arc of argon, discharge current 100 mA, probe length 5 mm.

| pressure (mm Hg) | diameter (mm) | | | |
|---|---|---|---|---|
| | 0.2 | 0.5 | 0.8 | 1.5 |
| 1 | 24,600 | 22,000 | 19,300 | 13,900 |
| 0.1 | 31,300 | 23,000 | 22,000 | 20,300 |
| 0.005 | 34,800 | 34,800 | 34,000 | 33,500 |

(unit: °K)

Accordingly, from the experimental results above mentioned, it is cofirmed that the disturbance occuring in a plasma near a probe results in a non-linearity of semi-log plot of the probe characteristic or erratic evaluation of the variables of the plasma such as the electron temperature and the plasma density.

The probe measurement in plasma at higher pressure is valid only if this disturbance is taken into consideration.

## References

1) R. L. F. Boyd: Proc. Roy. Soc. **201 A** (1950) 329.
2) A. Guthrie and R. K. Wakerling: *The Characteristics of Electrical Discharges in Magnetic Fields,* (McGraw-Hill, New York, 1949), first edition, pp. 31, 77.
3) F. Wenzel: Zeits. f. ang. Physik. **2** (1950) 59.
4) I. Langmuir and H. Mott-Smith: G. E. Rev. **26** (1923) 731; **27** (1924) 449, 538, 616, 762, 810; Phys. Rev. **28** (1926) 729.

---

J. Phys. Soc. Japan **11** (1956) 178~180

# Experimental Studies of the Interaction of a Plane Shock Wave with a Circular Cylinder

By Kim, Chul-Soo
*Department of Physics, Faculty of Science,*
*University of Tokyo*
and Kôichi Ôshima
*Institute of Industrial Science,*
*University of Tokyo*

(Received November 18, 1955)

When a plane shock wave of arbitrary strength advances into a still air and encounters a body of arbitrary shape, an unsteady flow takes place within the region bounded by the reflected shock and the surface of the body. Although considerable attention has been paid to "pseudo-stationary interaction" (1), (2), no work on "pure unsteady problem" seems to have been undertaken, so far as the authors are aware.

Here, an attempt is made to give a brief survey of unsteady shock interaction with a circular cylinder as a typical body which has an intrinsic length. Numerous observations at different times are necessary even for the case of given shock strength and given dimension of the cylinder, since the flow patterns in the reflected region are not similar to each other. Experiments were carried out at the Institute of Industrial Science using the shock tube

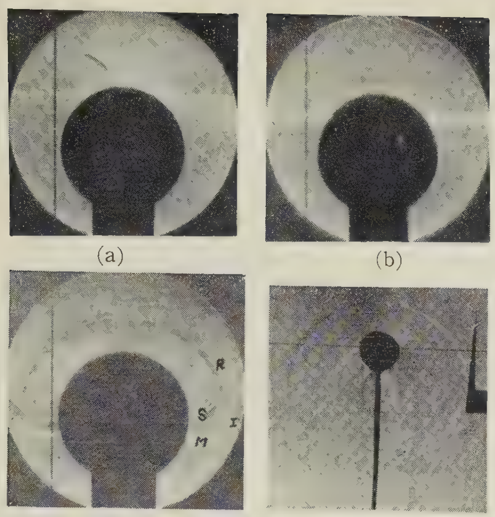

(a) (b)
(c) (d)

Fig. 1. Locations of shock reflection.
(a, b, c: $\xi=0.33$, $d=40$ mm; d: $\xi=0.24$, $d=20$ mm)

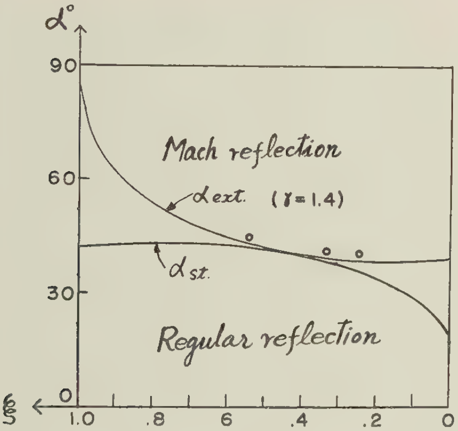

Fig. 2. Transition angles from regular to Mach reflection.

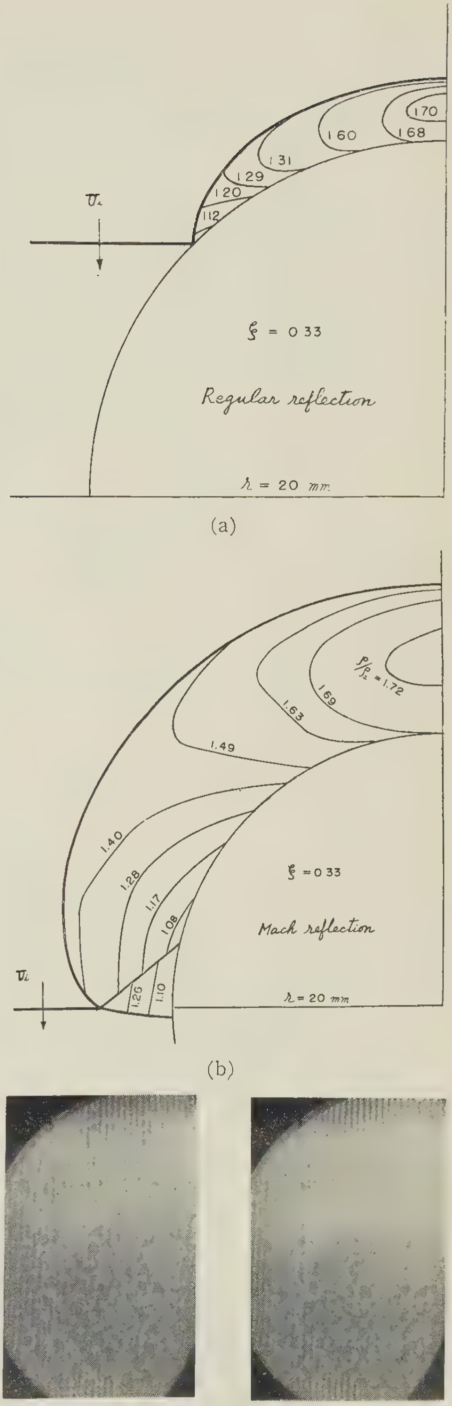

(a)

(b)

(a) (b)

Fig. 3. Isopicnics in reflected regions and their corresponding interferograms.
(a) regular reflection, (b) Mach reflection.

(3) with a uniform cross section of $6\times15$ cm$^2$. As the first series of our studies, circular cylinders with diameters of $d=2$ and 4 cm, and shock intensities of $\xi=P_1/P_2=0.24$, 0.33 and 0.54 were used, where $P$ is the pressure and the subscripts 1, 2 refer to the states just in front of and behind the incident shock respectively. Reflection and diffraction of the plane shock were observed by schlieren photographs using the delay circuit (3) with which $1\sim2\,\mu$ sec time control was possible. The locations of reflected shocks for $\xi=0.33$ and $d=4$ cm are shown in Fig. 1, where $I$, $R$ and $M$ represent the incident, the reflected and the Mach shocks respectively, and $S$ the slip stream. The angles of transition from regular to Mach reflection for fixed $\xi$ are given in Fig. 2. Here it is interesting that the regular reflection continues to exist slightly above the theoretical extreme value for the range of $\xi$ in our experiments, and this phenomenon has the same tendency as in the pseudo-stationary case of a wedge (4), (5). The isopycnics $\rho/\rho_2=$const in

the region behind the reflected front are shown in Fig. 3 as well as their corresponding interferograms. In every case of our experiments, the density in the vicinity of the cylinder nose was at most 7~12% smaller than the theoretical value for the shock reflection at rigid plane wall. This fairly large discrepancy may be due to the convexity of the surface of the circular cylinder.

Further experiments with widely varying cylinder diameters and shock strengths seem to be necessary for the full understanding of these phenomena.

We wish to express our gratitude to Professor F. Tamaki for suggesting this study as well as for continual encouragement. We also wish to thank Dr. M. Kawaguti for his helpful discussions during this work.

### References

1) K. Munakata: Journ. Aero. Sci. **21** (1954) 501.
2) H. F. Ludloff and M. B. Friedman: Journ. Aero. Sci. **22** (1955) 27.
3) F. Tamaki and K. Ôshima: Seisan-kenkyu **5** (1953) 87 (in Japanese).
4) W. Bleakney and A. H. Taub: Rev. Mod. Phys. **21** (1949) 584.
5) R. Kawamura, H. Oguchi and H. Saito: to be published.

---

J. PHYS. SOC. JAPAN **11** (1956) 180~181

## Effect of $Fe_2O_3$ on the Properties of Barium Titanate Single Crystals

By Atsuo NISHIOKA, Kyozo SEKIKAWA
and Masakazu OWAKI

*Electrical Communication Laboratory,*
*Musashino, Tokyo*

(Read at October 10, 1955,
Received November 13, 1955)

Recently Remeika[1] has reported a method of growing large single crystals of barium titanate from the melts of barium titanate powder and potassium fluoride with a small amount of added impurity of ferric oxide, and briefly described the change of Curie point and d.c. conductivity with the atomic percentage of iron. D.c. conductivity of barium titanate ceramics had already been measured by Swanson[2], Ogawa[3], Nomura[4], and Weise[5], but the data on single crystals have not yet been published in detail.

We have prepared the single crystals of barium titanate by the method of Remeika, varying the atomic percentage of iron, and have measured the optical and dielectric Curie point, lattice constants and d.c. conductivity. The content of iron included in the melts except the added ferric oxide was less than 0.057 atomic percentage, whereas the range of the content of added iron lay between 0.2 and 10 atomic percentage.

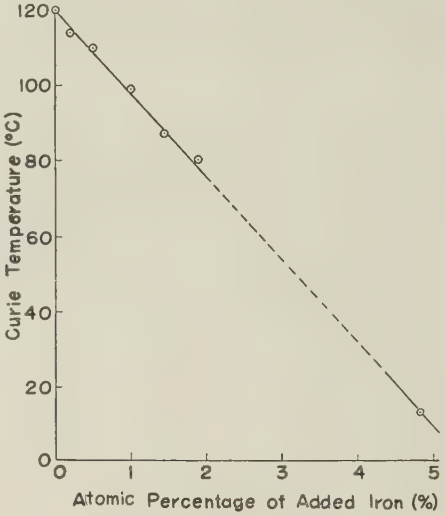

Fig. 1.

The change of Curie point with the content of iron is shown in Fig. 1, determined by the observation using polarizing microscope and the measurement of dielectric constant at 1 kc/s. From 0.2 to 5 atomic percentage the Curie point drops linearly and the value at 25°C was estimated about 4.5 atomic percentage. This value is different from the data of Remeika (2.5%). Above 2.0 atomic percentage the colours of the crystals become dark green to blackish. This would be considered to correspond the change of the gap of the energy band.

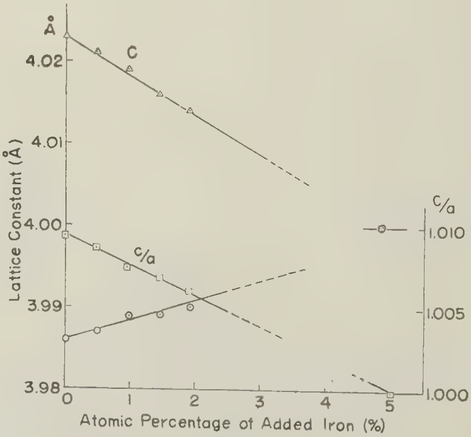

Fig. 2. Lattice Constants and Axial Ratio.

The X-ray analysis shows the gradual change of lattice constants a and c, and axial ratio of this tetragonal crystal as seen from Fig. 2. The crystal of 5.0 atomic percentage of iron has cubic symmetry at room temperature. The observed changes of the crystal structure was seemed to be in well accordance with the tendencies of optical and dielectric Curie points. The lattice volume does not change appreciablly in the range of added iron in our experiment.

Fig. 3 shows d.c. conductivity measured from room temperature to about 150°C. Single crystals did not show appreciable absorption current, which had been suggested by Nomura and Sawada[4]. So the contribution to the conductivity should be entirely due to electrons. The activation energy of d.c. conductivity $\Delta E$, defined by the following formula

$$\sigma=\sigma_0 \exp(-\Delta E/2kT),$$

is the energy between impurity level and conduction or full band. The values of $\Delta E$ estimated from Fig. 3 are shown in Table I. They have some fluctuations in small content of added iron, but would have a tendency of gradual decrease in larger content about 5.0 atomic percentage. Its value of no added iron would be corresponding to the energy gap between donour level of $Ti^{3+}$ ion and conduction band as in the case of titanium dioxide semiconductor[6], and in the larger content of added iron would be the gap between the acceptor level of $Fe^{3+}$ ion and full band as suggested by Remeika[1]. The maximum resistivity at room temperature was found near 0.2 atomic percentage, which is well accorded with the data of Remeika[1], but the tendency of the change in this case is very complicated, different from other cases. Therefore the definite value of $\Delta E$ cannot be estimated. These interesting character would be perhaps due to the coexistence of nearly equall numbers of electrons and holes. Further experimental results and detailed discussions will be published lately.

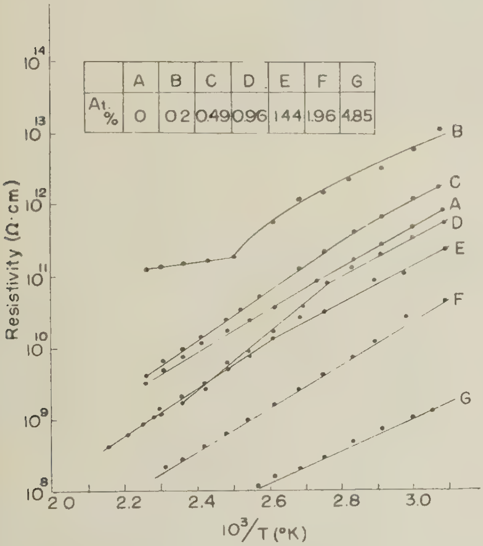

Fig. 3. Temperature Dependence of the Resistivity.

Table I. Activation energy of d.c. conductivity $\Delta E$.

| Atomic percentage of added iron (%) | 0 | 0.49 | 0.96 | 1.44 | 1.91 | 4.95 |
|---|---|---|---|---|---|---|
| $\Delta E$ (eV) | 0.68 | 0.76 | 0.86 | 0.78 | 0.70 | 0.50 |

## References

1) J. P. Remeika: J. Am. Chem. Soc. **76** (1954) 940.
2) D. C. Swanson: Phys. Rev. **69** (1946) 546.
3) T. Ogawa: Busseiron Kenkyu, No. 6 (1947) 1.
4) S. Nomura and S. Sawada: J. Phys. Soc. Japan **5** (1950) 227.
5) E. K. Weise and I. A. Lesk: J. Chem. Phys. **21** (1953) 801.
6) R. G. Breckenbridge and W. R. Hosler: Phys. Rev. **91** (1953) 793.

# Errata

## Hyperfine Structure of the Spectrum of Ruthenium. Part III

By Kiyoshi MURAKAWA

J. Phys. Soc. Japan **10** (1955) 919~926

In Table V of the Appendix, the signs of the following elements must be reversed.

$J=4 \quad ({}_{4}{}^{3}H,\ {}_{4,2}{}^{1}G)\,; \qquad J=2 \quad ({}_{4,2}{}^{3}F,\ {}_{4,2}{}^{1}D)\,.$

I appreciate the kindness of Dr. Trees for directing my attention to these corrections.

JOURNAL OF THE PHYSICAL SOCIETY OF JAPAN Vol. 11, No. 3, MARCH, 1956

# Focusing Properties of a large Mass Spectrograph newly constructed at Osaka University

By Hisashi MATSUDA

*Department of Physics, Faculty of Science, Osaka University*

(Received November 4, 1955)

A large double focusing type mass spectrograph was newly constructed at Osaka University in order to increase the accuracy of atomic mass measurement by about one order of magnitude. In this apparatus are adopted $\sqrt{2}\pi/3$ cylindrical electric field and $\pi/3$ uniform magnetic field. The focusing properties of this apparatus are discussed from both theoretical and experimental aspects. The direction and velocity focal planes are calculated, and their deviations due to various conditions such as the change of the position of source, the fringing field effect, the deviation of the geometry, etc. are discussed. These results are compared with the experimental procedure of the focal adjustment. A maximum resolving power of 500,000 was obtained experimentally at the present condition, and the mass dispersion is about 9 cm for 1% mass difference in this case.

## § 1. Introduction

The accuracy of the atomic mass determination in the field of mass spectroscopy has been increased greatly since several years ago. This increase of the accuracy was caused mainly by the improvement of the focusing conditions, that is, the improvement of the collimation of the ion beam, the adoption of the device to make the width and length of the main slit as small as possible, the fine adjustment of the geometry of the apparatus, etc.$\cdots$. A resolving power of several ten thousands was obtained with the apparatus of the same size as before, which was several times larger than before[1][2][3]. At Osaka University, the improvement of the Bainbridge-Jordan type mass spectrogaph, which had been constructed by Asada, Okuda, Ogata, et al. in 1939[4], was achieved during 1949~1950 and a maximum resolving power of about 60,000 was obtained, while the experimental resolving power of this apparatus had been estimated to be 7,000~8,000 before the improvement.

These results show that the focusing property of cylindrical electric field and uniform magnetic field is empirically very good when these fields are combined in tandem and that the ion optical analysis calculated by Herzog[5] is very useful for the construction of mass spectrograph.

After the successful improvement of the Bainbridge-Jordan type mass spectrograph, the construction of a new large mass spectrograph, was planned at Osaka University in order to raise the resolving power and increase the accuracy by about one order of magnitude. This plan was accomplished upon the foundation of the Herzog's analysis, and the double focusing mass spectrograph with a cylindrical electric field and a uniform magnetic field was adopted from the reason described above. In order to have large mass dispersion, which is necessary to measure the line distance on the photographic plate accurately, the distance from the exit of the magnetic field to the photographic plate must be made as long as possible, while the total length of the ion path must be made as small as possible to reduce the loss of ion intensity and to decrease the scattering effect. As the dimension of the apparatus was restricted by the floor space of the laboratory and by the economical reason, the resolving power of the apparatus was deviced to be as large as possible for a given size of the apparatus. In these considerations, the angle of the electric field was chosen to be $\sqrt{2}\pi/3$, and that of the magnetic field $\pi/3$. The schematic view of the apparatus is shown in Fig. 1.

The construction of the new large mass spectrograph was started in 1952 and a resolving power of 500,000 was experimentally obtained with this apparatus near the end of 1954. It proved that the accuracy of the

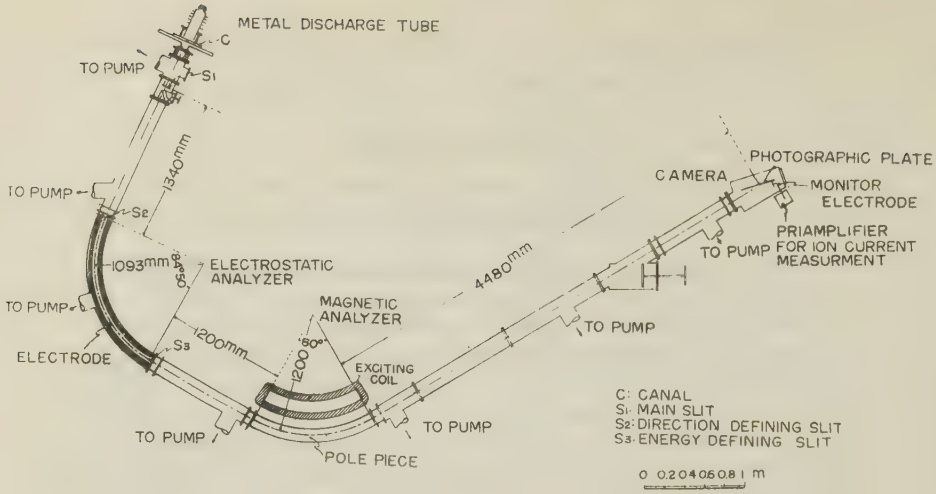

Fig. 1. Schematic diagram of the apparatus.

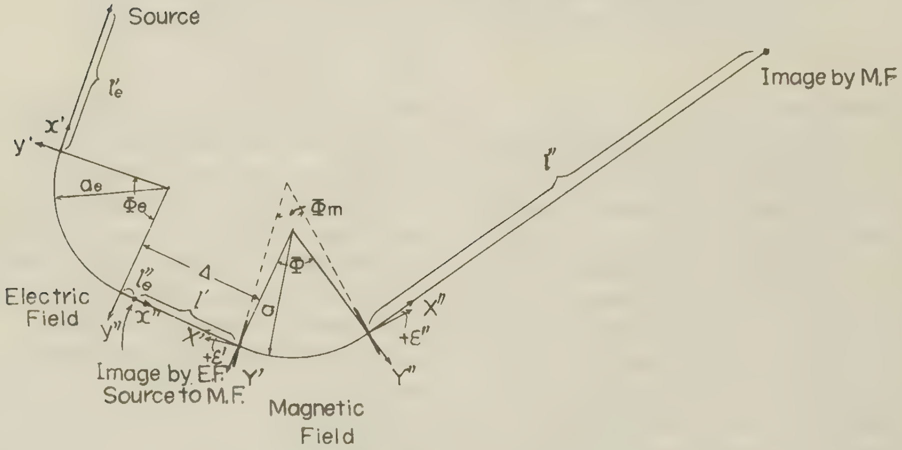

Fig. 2. Coordinate system.

measurement of doublet mass difference may be estimated to be several times larger than that by modified Bainbridge-Jordan type mass spectrograph.

The detail of the basic consideration and the general description of this apparatus have been published already[6]. In this paper, the focusing properties of this apparatus are described from both theoretical and experimental aspects.

## § 2. Focusing Properties in the Ideal Case

In the coordinate system shown in Fig. 2, the quantities which describe the focusing characteristics are given in the following way:

$\Phi_e$: angle of the cylindrical electric field,

$\Phi_m$: angle of the uniform magnetic field,

$\Phi$: deflection angle of the ion beam in the magnetic field,

$a_e$: radius of the central beam in the electric field,

$a_m$: distance from the entrance point of the ion beam to the apex of the pole boundary of the magnetic field,

$a$: radius of the ion beam in the magnetic field,

$\Delta$: distance from the exit of the electric field to the entrance of the magnetic field,

$l_e'$ and $l_e''$: distance respectively from the source and from the image to the edge of the electric field,

$l'$ and $l''$: distance respectively from the source and from the image to the edge of the magnetic field,

$\varepsilon'$ and $\varepsilon''$: angle respectively between the incident-, and deflected-, ion beam and the normal to the pole edge of the magnet.

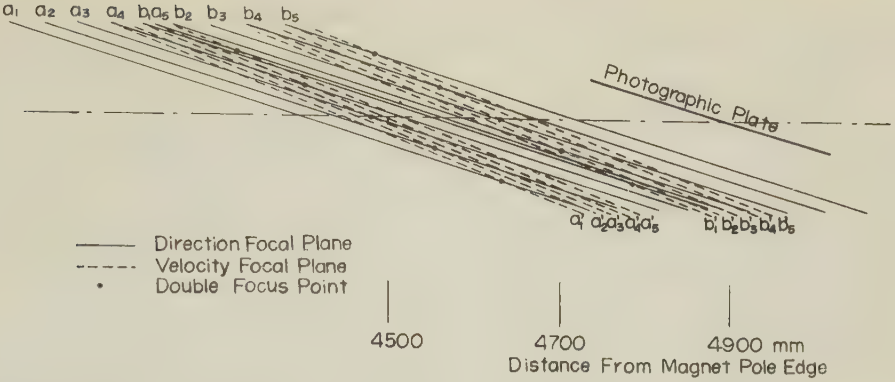

Fig. 3. Deviation of focal planes by the change of the position of source.

$a$ : direction-

$a'$: velocity- focal planes in ideal case.

$b$ : direction-

$b'$ : velocity- focal planes in consideration of the effect due to fringing field $d=5$ mm).

suffix $1{:}\eta=-0.008$, $2{:}\eta=-0.004$, $3{:}\eta=0$, $4{:}\eta=+0.004$, $5{:}\eta=+0.008$.

When designing a double focusing mass spectrograph, some of these quantities can be chosen arbitrarily. The following values were chosen from the standpoint to obtain high resolving power and large mass dispersion in comparison with the size of the apparatus:

$$\Phi_e=\frac{\sqrt{2}\,\pi}{3}\,,\qquad \Phi_m=\frac{\pi}{3}\,,$$

$$a_m=\Delta=1200\text{ mm}\,,$$

$$\varepsilon'=0\,,\qquad l_e''=0\,.$$

The quantities $a$, $\Phi$, $\Phi_m$, $\varepsilon''$ have the following relations to each other;

$$\Phi=\Phi_m+\varepsilon'+\varepsilon''=\frac{\pi}{3}+\varepsilon''$$

$$a=\frac{a_m\sin\Phi_m}{\sin\varepsilon''+\sin(\Phi_m+\varepsilon')}=\frac{a_m}{1+\frac{2}{\sqrt{3}}\sin\varepsilon''}\,.$$

The relation between the source and the image in the direction focusing is as follows: cylindrical electric field

$$(l_e'-g_e)(l_e''-g_e)=f_e^2 \qquad (1)$$

$$f_e=\frac{a_e}{\sqrt{2}\sin\sqrt{2}\,\Phi_e}=\frac{2}{\sqrt{6}}a_e \qquad (1\text{ a})$$

$$g_e=\frac{a_e\cot\sqrt{2}\,\Phi_e}{\sqrt{2}}=-\frac{a_e}{\sqrt{6}}\,, \qquad (1\text{ b})$$

uniform magnetic field

$$(l'-g')(l''-g'')=f^2 \qquad (2)$$

$$g'=a\frac{\cos\varepsilon'\cos(\Phi-\varepsilon'')}{\sin(\Phi-\varepsilon'-\varepsilon'')}=\frac{a}{\sqrt{3}} \qquad (2\text{ a})$$

$$g''=a\frac{\cos\varepsilon''\cos(\Phi-\varepsilon')}{\sin(\Phi-\varepsilon'-\varepsilon'')}$$

$$=\frac{2}{\sqrt{3}}a\cos\varepsilon''\cos\left(\frac{\pi}{3}+\varepsilon''\right) \qquad (2\text{ b})$$

$$f=a\frac{\cos\varepsilon'\cos\varepsilon''}{\sin(\Phi-\varepsilon'-\varepsilon'')}=\frac{2}{\sqrt{3}}a\cos\varepsilon''. \qquad (2\text{ c})$$

In the case when the arrangement of the both fields is in tandem as shown in Fig. 2, the image by the electric field is also the source of the magnetic field in itself, that is,

$$l'=\Delta-l_e''=\Delta=1200\text{ mm}\,.$$

The ion beam having a small velocity difference can be focused by the combination of the electric and magnetic fields, and the distance between the pole edge of the magnetic field and the velocity focusing point, $X''$, is given by the following relation:

$$X''=g''+\frac{f^2}{X'-g'} \qquad (3)$$

$$X'=\frac{-B+a(1-\cos\Phi)}{C-\sin\Phi-\tan\varepsilon'(1-\cos\Phi)}$$

$$=\frac{-B+a(1-\cos\Phi)}{C-\sin\Phi} \qquad (3\text{ a})$$

$$B=\Delta\sqrt{2}\sin\sqrt{2}\,\Phi_e+a_e(1-\cos\sqrt{2}\,\Phi_e)$$

$$=\frac{\sqrt{6}}{2}\Delta+\frac{3}{2}a_e \qquad (3\text{ b})$$

$$C=-\sqrt{2}\sin\sqrt{2}\,\Phi_e=-\frac{\sqrt{6}}{2} \qquad (3\text{ c})$$

The double focusing condition, which makes the velocity focus and the direction focus coincide at one point, is given by

$$a_e\left(1+\frac{l_e''-g_e}{f_e}\right)=a(1-\cos\Phi)$$
$$-l'[\sin\Phi+\tan\varepsilon'(1-\cos\Phi)]\,. \quad (4)$$

In order to hold the double focusing condition in the case of $a=a_m$, the radius of the electric field, $a_e$, must be 1093 mm, and $l_e'$ is determined to be $1.225\,a_e=1340$ mm from eq (1), and the distance between the magnet pole edge and the double focusing point is calculated to be 4480 mm.

In the case of mass spectrograph, mass spectra must be taken on the photographic plate and it is desirable to set the photographic plate along the focal plane. From the relations described above, both directional and velocity focal planes may be calculated by changing radius $a$ in the magnetic field and are shown in Fig. 3. The angle between the ion beam and the directional, and velocity, focal plane is proved to be $\theta_d=17°$ and $\theta_v=21°$ respectively. Each plane lies along almost straight line in the region of several ten centimeters at both sides the double focusing point and they intersect with an angle of about 4°.

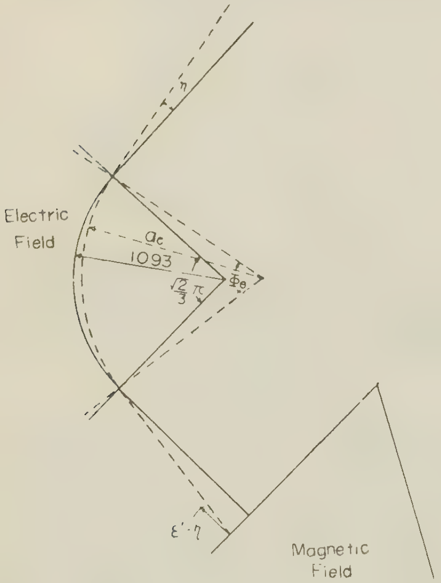

Fig. 4. Relation between $\eta$, $a_e$ and $\Phi_e$.

The resolving power $R$ is given by the relation:

$$R=\frac{a_e}{2s}\left(1+\frac{l_e'-g_e}{f_e}\right)=\frac{3}{2}\frac{a_e}{s}\,,$$

where $s$ is the width of the source slit. A resolving power of 550,000 is expected in the case of $s=0.003$ mm. The width of the final image, $2b''$, is calculated to be

$$2b''=\left|\frac{f}{g'-l'}\cdot\frac{f_e}{l_e'-g_e}\cdot s\right|=1.37\,s$$

and when the photographic plate is located along the directional focal plane, the image width on the plate is expected to be $1.37\,s$ cosec $17°=4.66\,s$, that is about 4.5 times as large as the initial slit width. The mass dispersion for 1% mass difference may prove to be 76 mm in this case.

The convergent angle $\alpha''$ after the beam leaves the magnet is calulated to be

$$\tan\alpha''=0.732\,\alpha+0.866\,\beta$$

where $\alpha$ is the divergent angle at the source and $\beta$ is defined by the relation $v=v_0(1+\beta)$ where $v$ is the velocity of the ion. In the case of $\alpha=1/2000$, which corresponds to the slit width of 1.37 mm at the entrance of the electric field, the increase of the image width on the photographic plate may be estimated to be 0.034 mm by 1 cm deviation from the direction focusing point, and in the case $\beta=1/2000$, corresponding to the slit width of 2.2 mm at the exit of the electric field, the increase is about 0.04 mm. In order to keep the breadth of the image not to exceed 0.01 mm in the region about 20 cm long on the photographic plate which is located through double focusing point, $\beta$ must be chosen to be smaller than 1/8000 if the plate is just on the directional focal plane, and the deviation of the plate from the direction focal plane has to be smaller than 3 mm along the beam direction if $\alpha=1/2000$. These conditions are rather rigorous in the actual adjustment but not impossible.

## § 3. The Shift of the Double Focusing Point due to the Change of the Position of Source

Let us consider the deviation of the focal plane when the position of the source is changed while the positions of the electric and magnetic fields are unchanged. Consider a beam entering into the electric field with the incident angle $\eta$ but at the same position and going out from the same point of the exit as shown in Fig. 2. These relations are shown in Fig. 4. Assume that this beam goes through the electric field along a circular orbit and that the electrostatic force acting on the ion is towards the center of the circle. These assumptions may be considered to be reliable if the angle $\eta$ is not so large. In this case the deflection angle in the electric field, $\Phi_e$, and the radius $a_e$ is given as follows:

$$\Phi_e=\frac{\sqrt{2}}{3}\pi-2\eta\ ,$$

$$a_e=\frac{1093\sin(\pi/3\sqrt{2})}{\sin((\pi/3\sqrt{2})-\eta)}\ \mathrm{mm}\ .$$

This beam enters into the magnetic field with the angle $\varepsilon'=\eta$ at the position $1200(1+\tan\eta)$ mm apart from the apex, so that the following values are given concerning the magnetic field:

$$a_m=1200(1+\tan\eta)\,\mathrm{mm}\ ,$$

$$\Delta=\frac{1200}{\cos\varepsilon'}\ \mathrm{mm}\ ,$$

$$\varepsilon'=\eta\ ,$$

$$l'=\frac{1200}{\cos\varepsilon'}\ \mathrm{mm}-l_e''\ .$$

$l_e''$ is no longer zero though $l_e'$ maintains the same value of 1340 mm as before. The values $l''$ and $X''$ can now be calculated by the eqs. (2), (3). Fig. 3 shows the focal planes with various values of $\eta$, keeping the distance $l_e'$ constant (1340 mm). It must be noted that the position of the double focusing point can be adjusted by changing $\eta$, that is, by adjusting the position of source along the direction perpendicular to the berm direction. The deviation of $l_e'$ causes a change in the direction focusing ponit, but no change in the velocity focal plane. The change of 5 mm in $l_e'$ causes about 10 mm change in $l''$. The adjustment of the double focusing point can also be achieved by changing $l_e'$.

## § 4. The Effect due to the Fringing Field and the Deviation of the Dimensions

In the discussions described above, the calculations are all based on the assumption that the field is sharply cut off at the boundary of the field region. On the other hand, in the actual case, there exists a fringing field near the boundary which changes gradually from the maximum constant value to zero. To discuss the focusing properties, this effect must be considered.

In the cylindrical electric field, the effect by the fringing field causes a change in the deflection angle $\Phi_e$ and other lens constants, the magnitude of which depends on the shape and size of the earth plate placed near the edge of the condenser electrodes⁷⁾, so that the effect can be adjusted by changing its shape. In our case, the structure of the electrodes near the edge of the cylindrical electric field is as shown in Fig. 5. According to Herzog's calculation, the effective boundary of the electric field may be changed from $\xi=0$ to $\xi=-3$ mm, $\xi$ being the distance from the edge of the condenser electrode to the effective boundary, by changing the slit-width $2b$ from $b=10$ mm to $b=3$ mm.

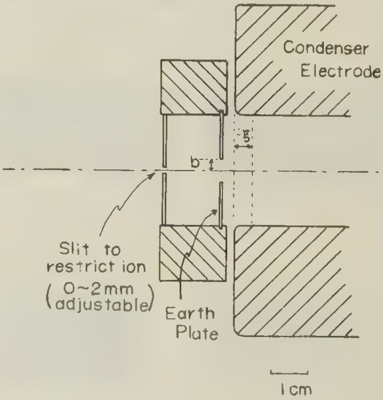

Fig. 5. Structure of the electrodes near the edge of the electric field.

In the uniform magnetic field, the effect due to the fringing field is considered as follows. Consider a beam entering into the uniform field region through the fringing field. The focusing action due to the magnetic field which has two parallel boundaries may be considered to be zero on the median plane independently of the field strength, because $\Phi-\varepsilon'-\varepsilon''=\Phi_m$ in eq (2) is zero. Therefore there is no focusing action in the fringing field so long as the strength of it is uniform along the direction parallel to the magnet edge. The fringing field causes only the deflection of ion beam and the displacement of the entrance point into the uniform field region. The deflection in the fringing field causes a change in the incident angle, $\varepsilon'$, to the uniform field region. This gives also a change in the lens constants $g'$, $g''$, $f$ in eq (2). The change in $\varepsilon'$, denoted by $\delta\varepsilon'$, is calculated to be⁸⁾⁹⁾¹⁰⁾

$$\tan\delta\varepsilon'=\frac{d}{(a^2-d^2)^{1/2}}\ ,$$

Table I. The deviation of image position due to the change of $\varepsilon'$ and $\varepsilon''$.
($a=1200$ mm, $\Phi=\pi/3$)

a) Direction focus; the deviation of $l''$.

| $\varepsilon'$ \ $\varepsilon''$ | −0.03 | −0.02 | −0.01 | 0 | +0.01 | +0.02 | +0.03 |
|---|---|---|---|---|---|---|---|
| −0.03 | −661 | −536 | −401 | −258 | −104 | + 61 | +241 mm |
| −0.02 | −593 | −462 | −323 | −174 | − 14 | +158 | +348 mm |
| −0.01 | −523 | −388 | −243 | − 88 | + 78 | +250 | +454 mm |
| 0 | −451 | −311 | −161 | 0 | +175 | +361 | +566 mm |
| +0.01 | −378 | −233 | − 77 | + 92 | +272 | +467 | +682 mm |
| +0.02 | −303 | −152 | + 11 | +184 | +373 | +557 | +801 mm |
| +0.03 | −226 | − 69 | + 99 | +280 | +477 | +690 | +925 mm |

b) Velocity focus; the deviation of $X''$.

| | | | | | | | |
|---|---|---|---|---|---|---|---|
| −0.03 | −709 | −587 | −456 | −318 | −177 | − 7 | +167 mm |
| −0.02 | −625 | −498 | −361 | −215 | − 58 | +111 | +297 mm |
| −0.01 | −539 | −406 | −262 | −109 | + 56 | +236 | +428 mm |
| 0 | −451 | −311 | −161 | 0 | +175 | +361 | +566 mm |
| +0.01 | −361 | −214 | − 57 | +106 | +294 | +492 | +709 mm |
| +0.02 | −267 | −114 | + 53 | +229 | +421 | +630 | +858 mm |
| +0.03 | −170 | − 8 | +163 | +350 | +552 | +773 | +1015 mm |

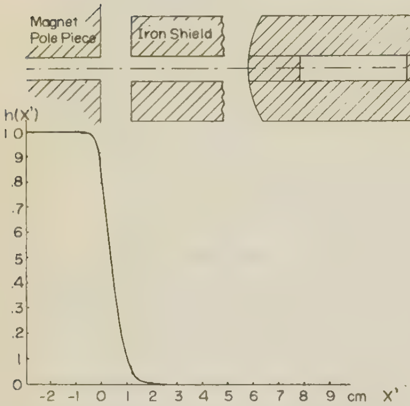

Fig. 6. Dimension of the magnetic shield and value of $h(X')$.

$$d=\int_{X'=l'}^{X'=-1} h(X')dX'-1\ ,$$

$$\int h(X')dX'=\int \frac{\mathrm{H}(X')}{\mathrm{H}_0}dX'\ .$$

where $\mathrm{H}_0$ is the field stregth of the uniform field region and $\mathrm{H}(X')$ the field strength of the fringing field at the position $X'$, and $X$ is measured by the gap width of the magnet in this formula. The distance from the apex of the magnetic field to the entrance point at $X'=0$ is given by $a_m'$ and is

$$a_m'=a_m\int_{l'}^{0}\frac{\int_{l'}^{X'} h(X')dX'}{\left[a^2-\left\{\int_{l'}^{X'} h(X')dX'\right\}^2\right]^{1/2}}dX'\ .$$

The same effect may exist at the exit from the magnetic field too. The value of $h(X')$ may be determined experimentally by measuring the fringing field distribution, and $\int h(X')dX'$ by using a planimeter from the curve of $h(X')$.

The fringing field effect can be decreased by a considerable amount if a suitable magnetic shield is placed near the edge of the megnetic field. The dimension of the magnetic shield placed near the both edges of the magnet of the large mass spectrograph is shown in Fig. 6 with the measured value of $h(X')$. In this case the shift in $a_m$ is almost negligible so that it may be allowable to put $a_m'=a_m$. The value of $d$ is estimated to be about 5 mm from the curve, and the gap width is 9 mm in this case. The focal plane can now be calculated in consideration of the effect due to the fringing field. For simplicity the deflection angle $\Phi_e$ in the electric field is considered to be unchanged by the adjustment of $b$ in Fig. 5. The focal planes thus obtained are shown in Fig. 3 with various positions of source as before.

In the actual case of the large mass spectrograph, the focal plane determined experimentally differs very much from this. The distance from the magnet pole edge to the focal point obtained experimentally is about

30 cm longer than that calculated. This fact may be considered to be due to the effect that the effective edge of the magnetic field due to the fringing field has a curvature. This causes a change in $\mathcal{E}'$ and $\mathcal{E}''$ so that the focal point is shifted by a considerable amount. The deviations of $l''$ and $X''$ from the ideal case, $a=1200$ mm, $\varPhi=\pi/3$, are shown in Table I referring to the various values of $\mathcal{E}'$ and $\mathcal{E}''$. From this, if the effective edge has a curvature of radius ~1 m and the direction of entering ion beam has a distance of ~1 cm from the center of curvature, the shift of focal point may be estimated to be about 30 cm. This effect is more serious to the velocity focus. The fact that the effective edge of the magnetic field has a curvature is likely to happen because of the finite size of the pole piece. The effect due to the change of the position of source described in § 3 becomes much larger in this case.

The effect due to the deviation of $\varDelta$ and $\varPhi_e$, keeping other values to be constant, are shown in Table II and Table III respectively. These results show that if $\varDelta$ or $\varPhi_e$ is made to be large, the focusing point has a tendency to approach to the magnet.

Table II. The deviation of image position due to the change of $\triangle$.
($a=1200$ mm, $\varepsilon'=\varepsilon''=0$)

| $\triangle$ | 1190 | 1200 | 1210 | 1220 | 1230 mm |
|---|---|---|---|---|---|
| deviation of $X''$ | +41 | 0 | −43 | −85 | −127 mm |
| deviation of $l''$ | +76 | 0 | −73 | −134 | −211 mm |

Table III. The deviation of image position due to the change of $\varPhi_e$.
($a_e=1093$ mm, $a=1200$ mm, $\varepsilon'=\varepsilon''=0$)

| $\varPhi_e$ | 1.47296 | 1.47696 | 1.48096 ($\sqrt{2}\pi/3$) | 1.48496 |
|---|---|---|---|---|
| $\xi$ | −4.3 | −2.2 | 0 | +2.2 mm |
| deviation of $X''$ | +20 | +10 | 0 | −10 mm |
| deviation of $l''$ | +26 | +12 | 0 | −12 mm |

## § 5. The Comparison with the Experiment

In the actual case, many quantities such as $a$, $\varPhi$, $\mathcal{E}'$, etc. are not able to be known precisely and can only be estimated. However, the tendency of the shift of focal plane by the change of various conditions is expected from the theoretical calculation and nearly coincide with the experiment.

The effect due to the fringing field is most important. This gives the influence not only to the change in the focusing point but also to the shape of the image. When the fringing field of the magnet has field components other than $z$-component perpendicular to the ion beam, the image on the photographic plate may be curved. In Fig. 7, some of these examples are shown: (a) is the image when ion beam is passed through near the center of the magnetic shield, (b) is the image when it is passed through near the side wall, and (c) is the image without the magnetic shield. The image is not curved in (a), but curved in (b) and (c). In the case of (c) the fringing field may be disturbed by the iron pipe placed near the magnet to obtain vacuum. The effect shown in Fig. 7 (b) is not appreciable if the ion beam passes through the region apart from the side wall by more than gap width of the magnetic shield.

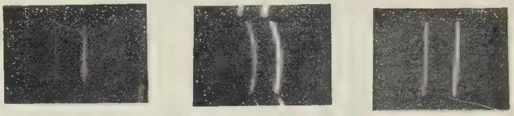
(a) (b) (c)

Fig. 7. Examples of the effect of the fringing field to the shape of the image.

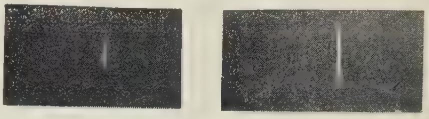
(a) diameter: 0.7 mm (b) diameter: 1 mm

Fig. 8. Examples of the image distorted when the entrance slit of the electric field is a hole.

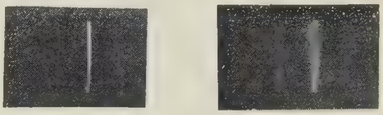
(a) slit position is good (b) not good

Fig. 9. Example of distorted image.

The local electric field near the slit placed at the entrance or the exit of the electric field gives a influence to the image. Fig. 8 shows the image in the case that the entrance slit of the electric field is a hole in a metal plate; the image is distorted in both up and down sides. Fig. 9 shows the distortion of image when a long slit (long along the direction perpendicular to the electric force line) is shifted to the radial direction. So the slit which restricts the breadth of ion beam is placed in the field free region and another wide slit is placed near the electrodes to cut off the electric field as shown in Fig. 5.

The effect due to the change of the position of source is rather larger than that the calculation described in § 3 predicts. This fact may be considered to be caused by the curved effective edge of the magnetic field. The radius of curvature is estimated to be 50~100 cm from the experimental procedure. For the beam passed near the side wall of the magnetic shield, the experimental focal plane was seriously curved and this suggest that the curvature is large near the side of the shield and this is plausible. This region can not be used too by the effect to the shape of image as described above. The adjustment of the position of source is also useful for the purpose to hold the ion beam in the desirable region of the magnetic shield.

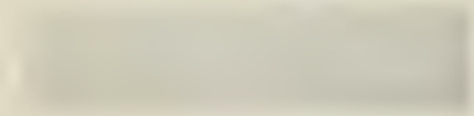

Fig. 10. $N_2^{14}-C^{12}O$ doublet.

Doublets were shifted by changing the potential between the energy selectrodes. The base potential (doublet 1) was 1350.40 volts and each shift (doublet 2-7) was made by successive addition of 2.03670 volts. During the whole exposure the magnetic and electric fields were kept constant within a change of less than $10^{-6}$. From this, a value of $112.441 \pm 0.019$ ($10^{-4}$ amu) was obtained as the doublet mass difference.

In our case, the length $l''$ and $X''$ obtained experimentally was much longer than that expected. This fact may be considered to be due to large $a$ and $\varepsilon'$. However, a large $l''$ (or $X''$) is desirable to have a large mass dispersion, so that the distance was made as long as possible. On the other hand, the distance from the exit of the magnetic field to the photographic plate is restricted by the floor space of the laboratory, that is, $X''$ can not be made too large. Therefore, the distance $\Delta$ was elongated in order to maintain $X''$ within a desirable length, and the adjustment to obtain double focusing point on the photographic plate was made by changing the position of source. In the final geometry by which the sharpest image was obtained, the values of $l_e'$, $\Delta$, and $l''(X'')$ were 132 cm, 124 cm, and 490 cm respectively. In this case other values of the focal quantities are estimated to be as follows:

$$a \sim 1220 \text{ mm} ,$$

$$\Phi \sim \frac{\pi}{3} ,$$

$$\varepsilon' \sim 0.02 ,$$

$$\eta \sim 0.01 .$$

The angle between the direction of ion beam and the photographic plate was about 16° and the plate was located nearly along the direction focal plane.

The image width of about 0.02 mm was obtained by photographing the $N_2^{14}-C^{12}O^{16}$ doublet, and this corresponds to a resolving power of about 500,000. In this case the width of the slit placed near the entrance and exit of the electric field was both 0.4 mm, and this corresponds to $\alpha = 1/6600$, and $\beta = 1/11000$ respectively. For this value of $\alpha$ and $\beta$, the second order aberration is almost negligible. The main slit width $s$ was about 0.002 mm and the image width on the photographic plate that is expected theoretically is calculated to be $5.6s = 0.011$ mm. The broadening of the image may be due to the instability of the magnetic field and the scattering effect of ions by the residual gas in the vacuum chamber. The mass dispersion was estimated to be about 9 cm for 1% mass difference and almost coincide to the value obtained graphically. The photograph of the $N_2^{14}-C^{12}O^{16}$ doublet is shown in Fig. 10.

## § 6. Conclusion

The final dimension of the large mass spectrograph differed from the initial design by a considerable amount but it was not too large, It proved that the large mass spectrograph has a experimental resolving power and mass dispersion nearly expected.

The calculation of the fundamental characteristics of the apparatus and of the focal planes based upon the Herzog's analysis is very useful for the initial design and for experimental procedure of the adjustment. The calculation gives the knowledge about the tendency of the shift of the focusing point due to the change of various focusing conditions.

At any rate, the focusing points exists if the fields and focusing conditions are good. In order to place the double focusing point to a desirable place, there may be many possibilities of methods by changing some of the focal quantities. Especially the adjustment by the change of the position of source is useful for this purpose. The calculation of the focal plane in the case of these variations gives a knowledge about focusing properties and suggest how to proceed the experiment. The fringing fields give serious effects to the focusing properties, so that the treatment must be prudent.

### References

1) H. Ewald: Mass Spectroscopy in Phisics Research (1953) 37.
2) J. Mattauch and R. Bieri: ibid. (1953) 71.
3) K. Ogata and H. Matsuda: ibid. (1953) 59; Phys. Rev. **89** (1953) 27.
4) Asada, Okuda, Ogata and Yoshimoto: Nature **143** (1939) 797; Proc. Phys.-Math. Soc. Japan **22** (1940) 41.
5) R. Herzog: Z. Physik **89** (1934) 447.
R. Herzog and V. Hauk: Z. Physik **108** (1938) 609.
6) K. Ogata and H. Matsuda: Z. Naturforsch. **10 a** (1955) 843.
7) R. Herzog: Z. Physik **97** (1935) 596; Phys. Z. **41** (1940) 18.
8) N. D. Coggeshall and M. Muskat: Phys. Rev. **66** (1944) 187.
9) N. D. Coggeshall: J. App. Phys. **18** (1947) 855.
10) K. T. Bainbridge: Experimental Nuclear Physics (1953) 559.

---

JOURNAL OF THE PHYSICAL SOCIETY OF JAPAN Vol. 11, No. 3, MARCH, 1956

# On the Analysis of the Slow Particles Emitted from Cosmic-Ray Stars (I)

By Shigeo NAKAGAWA, Eiji TAMAI, Humiaki HUZITA
and Kiyoaki OKUDAIRA

*Department of Physics, Rikkyo (St. Paul's) University,*
*Ikebukuro, Tokyo, Japan*

An analysis of the nature of tracks of the stars ending in the G5 emulsion was made by measuring their width (diameter). Six groups of tracks having different width were observed. We identified two of these groups as that of $\alpha$ particles and Li nuclei by comparing their width with those of $\alpha$ particles emitted from radiothorium stars and with those of hammer tracks. As for the more thicker tracks, the charge determination on the tracks of each group was made by measuring their thin-down lengths. These measurements seem to indicate that the width of track was approximately proportional to $\sqrt{Z}$ ($Z$: atomic number).

The energy and the angular distribution of each group were also examined. The curves of the energy distribution of protons and $\alpha$ particles approximately agreed with those deduced from the evaporation model, assuming the appropriate nuclear temperature and Coulomb barrier height. The angular distributions of these were nearly isotropic. It was noted that the number of slower $\alpha$ particles measured seems to be considerably larger than that deduced from theory.

## § 1. Introduction

Charges of particles stopped in the nuclear emulsion usually have been identified by the following methods of measuring[1]:

(i) $\delta$ ray frequency
(ii) $\delta$ ray cut off length
(iii) gap density
(iv) thin-down length

As methods (i), (ii), and (iii) need comparatively long tracks, they do not seem to be suitable

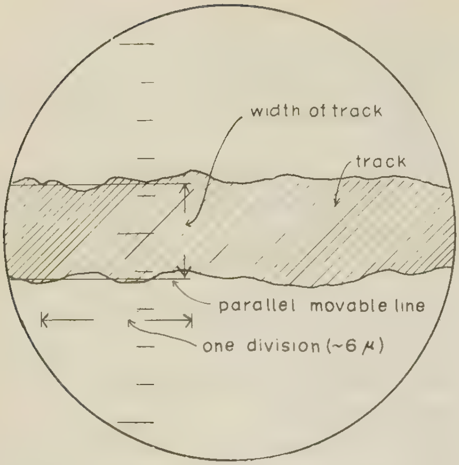

Fig. 1. Eyepiece with screw micrometer.

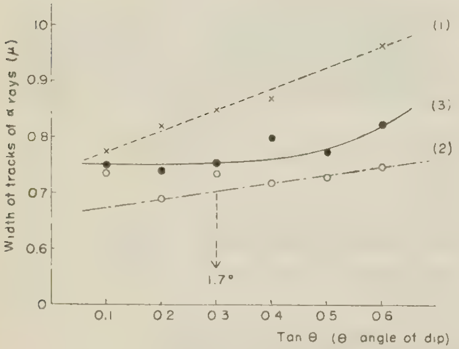

Fig. 2. Width of tracks of α rays from radiothorium stars (Number of curve indicates the region of location of the tracks;
(1) 0→20 μ from the surface
(2) 0→20 μ above the bottom
(3) between (1) and (2).)

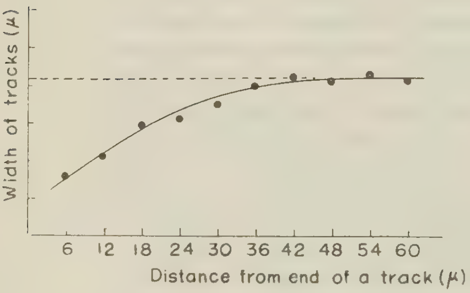

Fig. 3. Width of each division along a track.

for analysing short tracks. The fourth method also is not suitable to analyse tracks of comparatively low charged particles.

It is well known that as the velocity of the charged particles decreases passing through the emulsion, energies of δ rays emitted by it decrease also, while their density increases. When the velocity of the particle decreases to some extent and the density of δ rays becomes very large, their individual tracks can not be separated. For this reason, the width of the track increases, and this width varies with energies of δ rays.

Lonchamp[2)] examined the relationship between slow δ rays and the width of the tracks. In the present analysis we have examined also the width of tracks of stars to determine the nature of the particles which are emitted by disintegration of Ag or Br nuclei contained in the emulsion by cosmic rays.

The G5 emulsions 400 μ and 600 μ thick were exposed to cosmic rays at high altitude (25,000∼30,000 *m*) and the tracks in the emulsion were measured by the microscope with eyepiece micrometer. It was found that these tracks can be classified into six groups according to their width, and that the width of track was approximately proportional to $\sqrt{Z}$ ($Z$: atomic number).

## § 2. Experimental Procedure

The width of track is generally not uniform on account of clogging, so the mean width over 6 μ lengths was measured step by step along the track from its end point using an eyepiece with screw micrometer as shown in Fig. 1. In order to test whether the width may vary in the difierent layers of the same emulsion, the track widths of α particles from radiothorium stars located in all parts of the emulsion were measured. The results are shown in Fig. 2. It is shown in Fig. 2 that α ray tracks located between 20 μ and 380 μ (400 μ thick emulsion) or 580 μ (600 μ thick emulsion) from the surface of the emulsion have nearly the same width, provided that their angles of dip are less than 17°.

According to above results, the prongs which were selected to analyse were from among those which terminated in the emulsion, which were located more than 20 μ appart from the surface and from the bottom of the emulsion, and which lay within 17° of the angle of dip before processing. Moreover, since it was the intension to analyse stars from heavy nuclei (Ag or Br) contained in the emulsion, stars which had more than 9 prongs (grey tracks + black tracks) were selected.

An example of the measured width along a track is showed in Fig. 3. The curve shows a flat portion, the ordinate of which was designated as the width of the track. The ordinate of each track was measured, and the tracks were then classified. That is, the tracks which had nearly the same value of ordinate were considered as belonging to one group. The width of the tracks belonging to any one group definitely differed from that of the tracks belonging to any other group. The curves in Fig. 4 show the mean width of the tracks which belong to each group, at each 6 $\mu$ division along the tracks.

## § 3. Identification of Prongs

It is shown in Fig. 4 that all prongs are classified into six groups. The mean width of tracks which belong to the second and third groups amounts to 0.77 $\mu$ and 0.94 $\mu$ respectively. The former value agrees fairly well with 0.75 $\mu$ obtained from the width of forty-five $\alpha$ particle tracks from radiothorium stars contained in the emulsion, and the latter with 0.94 $\mu$ obtained from seven $Li^8$ tracks, known as hammer tracks. It seems to be possible to conclude that particles which belong to the second group have charge two, and those which belong to the third group have charge three. Hence, the particles of the first group may have charge one.

As for the particles of another groups, there was no direct method to identify them; but from the measurement of their thindown lengths, it seems to be probable that they have charge four, five, and six, respectively. Fig. 5 shows the relation between the thin-down lengths and the charges of the particles. Some more thicker tracks were observed. However, they showed steeper dip angles than 17°, therefore we have not made any further analysis. In Table I, the ratios of the width of each group to the width of the first group were compared with the ratios of $\sqrt{Z}$ ($Z$: atomic number). This comparison indicates that the width of tracks are approximately proportional to $\sqrt{Z}$. In Fig. 5, the thin-down track lengths are also shown to be approximately proportional to $Z$. Thus, the results of our experiment show same tendency with those of Hoang Tchang-Fong[3]. In addition, especially the longer tracks of lower charged particles were roughly examined by counting gap number, and the results of both measurements (width and gap) agreed well.

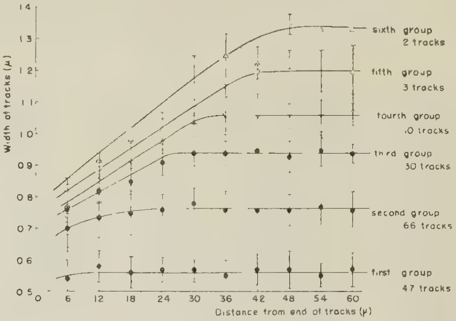

Fig. 4. Curves showing mean width of tracks belonging to each group, at each division along tracks.

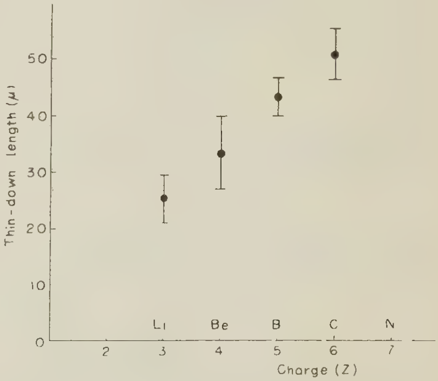

Fig. 5. Thin-down length versus charge of particle.

## § 4. Energy Distribution and Angular Distribution

The energies of tracks above analysed were obtained by measuring their ranges, and their energy distribution was examined. The energy distribution of a singly-charged group (proton group) is shown in Fig. 6. In this figure, the distribution in the higher energy region is not certain in as much as only tracks which stopped in the emulsion were selected. The full curve shows the calculated evaporation distribution, assuming that the mean temperature is 3 MeV and the mean Coulomb potential is 5 MeV. Fig. 7 shows the energy distribution histogram of particles of charge $Z=2$ with the curve calculated from the evaporation theory. The statistics are not adequate for describing the energy distribution of particles of charge $Z \geqq 3$.

To obtain the angular distributions of particles of each group, stars were selected in which the direction of incident particles was accurately observed. The results are presented

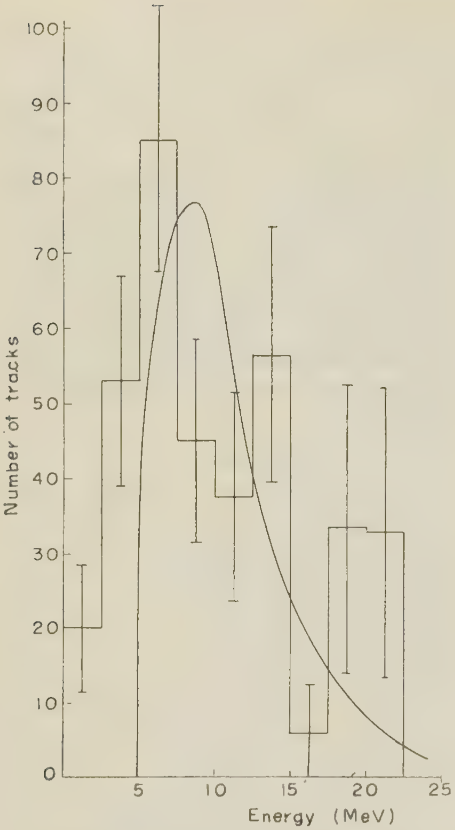

Fig. 6. Energy distribution of protons.
(Full curve was obtained from evaporation formula by assuming Coulomb barrier height 5 MeV and mean nuclear temperature 3 MeV.)

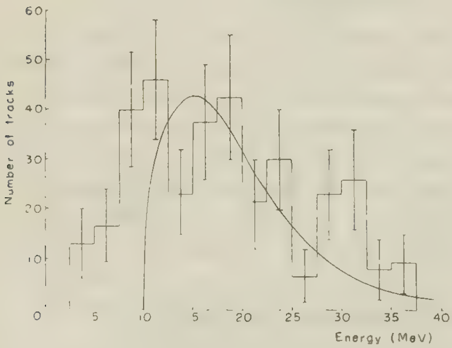

Fig. 7. Energy distribution of $\alpha$ particles.
(Curve: Coulomb barrier height—10 MeV, mean nuclear temperature—5 MeV).

in Figs. 8 and 9. In Figs. 8 and 9 are shown the angular distribution of protons and of $\alpha$ particles respectively. They show approximately isotropic distribution. As the measured number of the particles of charge $Z \geqq 3$ is comparatively small, we are now accumulating more data.

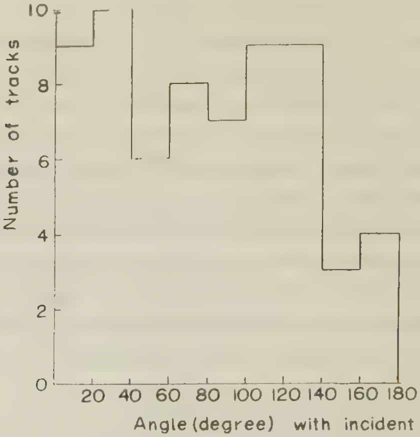

Fig. 8. Angular distribution of protons.

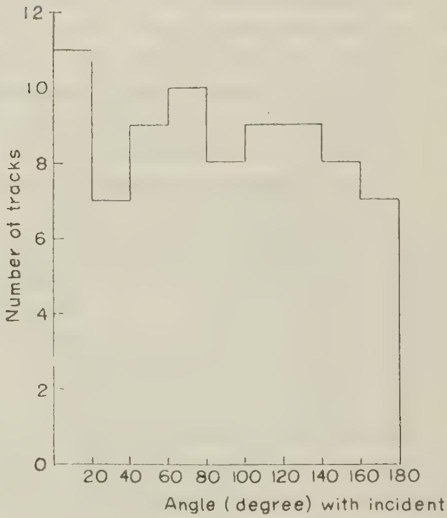

Fig. 9. Angular distribution of $\alpha$ particles.

Table 1.

| | group | width ($\mu$) | ratio of width | ratio of $\sqrt{Z}$ |
|---|---|---|---|---|
| 1 | first group | 0.55 | 1 | 1 |
| 2 | second group | 0.77 | 1.40 | 1.41 |
| 3 | third group | 0.94 | 1.72 | 1.73 |
| 4 | fourth group | 1.06 | 1.93 | 2 |
| 5 | fifth group | 1.2 | 2.18 | 2.23 |
| 6 | sixth group | 1.34 | 2.44 | 2.45 |

The measured energy spectra of protons and $\alpha$ particles nearly agree with those calculated, assuming the mean Coulomb barrier height V and the mean nuclear temperature T; although, on account of poor statistics, the excitation energies and potential barrier could not be analysed more precisely by classifying the star size.

In addition to the spectra, the angular distributions of these particles are nearly isotropic as mentioned above, so the mechanism of emission of particles may be mainly due to the evaporation process. In Fig. 7, however, it is shown that the number of slow $\alpha$ particles from heavy nuclei is considerably larger than expected by the evaporation process, as was reported by Harding, Lattimore and Perkins[4]. Therefore, the authors are now accumulating more data on these and also on heavy particles.

**Acknowledgement**

This work has been partly supported by the Scientific Research Expenditure from the Ministry of Education.

### References

1) D. H. Perkins: Proc. Roy. Soc. **A 203** (1950) 399.
2) J. P. Lonchamp: Jour. Phys. Radium **14** (1953) 433.
3) Hoang Tchang-Fong: Jour. Phys. Radium **12** (1951) 739.
4) J. B. Harding, S. Lattimore and D. H. Perkins: Proc. Roy. Soc. **A 196** (1949) 325.

---

JOURNAL OF THE PHYSICAL SOCIETY OF JAPAN Vol. 11, No. 3, MARCH, 1956

# A High Pressure Cloud Chamber for Cosmic Ray Observation

By Saburo MIYAKE

*Institute of Polytechnics, Osaka City University*

(Received July 29, 1955)

A high pressure cloud chamber (50 cm in dia, 20 cm deep and used at 150 atm.) was built in the summer of 1952. The cloud chamber can be operated automatically by counter control with a recycling time of about 20 minutes. It was filled with 5.6 kg of nitrogen or 8 kg of argon gas in its illuminated space of about 30 litres, and it became much easier to observe some cosmic ray phenomena especially those events occuring in the gas nuclei in comparison with observations using the smaller type chamber (25 cm in dia, 7 cm deep and used at 100 atm.) which has been used previously.

## §1. Introduction

Observations using a high pressure cloud chamber are similar to those with photographic emulsions in a sense, although the density of the matter of the former case is about 1/15 of that in the latter. The chamber has the following advantages; there is a relatively larger mass of sensitive matter, the matter is simple, and the instrument may be controlled with the counters in the same manner of normal pressure cloud chamber.

To date, several high pressure cloud chambers have been constructed[1], and some of them have been used for cosmic ray observation recently. In an earlier paper (hereafter cited as "A") the smaller high pressure cloud chamber (25 cm in dia and 7 cm deep and used at 100 atm.) was reported in detail, and some experiments[2] were done with this equipment. It seemed too small, however, for investigating some important cosmic ray phenomena, especially hard showers produced in the gas. The large size chamber was therefore planned, expecting the following advantages;

(1) A long sensitive time (about 2–3 sec) and a mass of inner gas of about 5.6 kg for nitrogen and 8 kg for argon. These properties mean, for random expansions, that the efficiency is about 20 times as large as that for the small chamber.

(2) An increased number of events, occuring in the gas space, is favourable for the study of rare events.

(3) An increase in the stopping power, the multiple scattering angles and the number of knock-on electrons permit better estimation of the energy, mass etc.

On the otherh and, there are some disadvantages.

(1) A long recovering time is required for thermal equilibrium and uniform vapour distribution. It is about 20 minutes in this case.

(2) The thick metal wall of the chamber acts as the producer or the absorber of cosmic ray phenomena.

(3) The technical difficulties and the heavy weight of the equipment are not convenient.

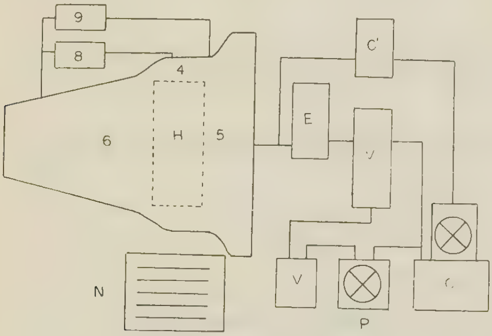

Fig. 1. Block diagram.

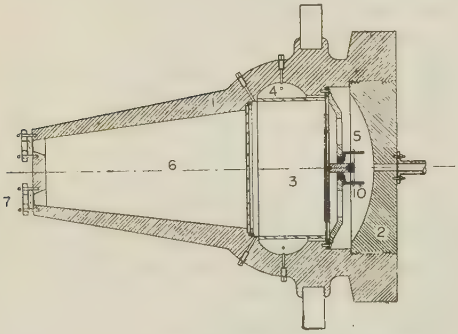

Fig. 2. Crosse Section (harizontal).

## §2. The Main Body of the Chamber

In the design of the chamber, the following conditions were considered;

(1) The weight of each separate piece of the chamber must not be more than about 2 tons for the purpose of transport to the mountain site.

(2) The volume of the chamber should be as large as possible, subject, of course, to limitations of the weight and the cost.

(3) The construction and handling should be simple.

(4) The illumination in the chamber must be kept uniform. The method of illumination is the same as that used in the former chamber, but more light is necessary. It was also desired to increase the transparency of the liquids through which light must pass.

Fig. 1 shows the block diagram of the main parts, H is the main body of the chamber, E is the expansion valve, V is the expansion vessel, P is the vacuum pump to pump the oil from the expansion vessel, C is the high pressure oil compressor and N is the multiplate cloud chamber to study the secondary particles from the upper chamber (sometimes a counter hodoscope is used for this purpose.)

Fig. 2 shows the cross section of main body of the cloud chamber. 1 is an iron case (pressure tight). It was made from cast steel of $17\ \mathrm{kg/mm^2}$ ultimate strength. 2 is a back plate, which was made from the same material and was set in the case 1 by a 1.4 cm pitch triangular saw-shaped screw. 3 is the cloud chamber space 50 cm in dia and 25 cm in deep. It is surrounded by the front glass, a glass cylinder and the back piston. The back piston is a rubber sheet sandwiched by aluminum plates, and held by its shaft as it moves in the axial direction. 10 is a slide rheostat which forms one arm of a bridge circuit so that the position of the piston can be shown from the out side. 5 is an oil space which is filled by ordinary spindle oil. At the expansion a part of this oil is allowed to flow into the expansion vessel. 6 is a water space, it is filled with transparent water of about 80 liters. Its inside surface is all painted with black vinyl paint to prevent corossion and rust. 5 to 10 g of NaOH was added to the water to clear it and to protect further colourization by iron rust. 7 is a glass window to permit photography. The diameter of this window is 4 cm and tempered glass of 2 cm thickness was put with steel fringe by bolts and nuts from the outside. The rubber gasket is used to protect the glass plate and made a leakproof seal.

8 and 9 are pressure balancers which balance the pressures between the water space 6, the

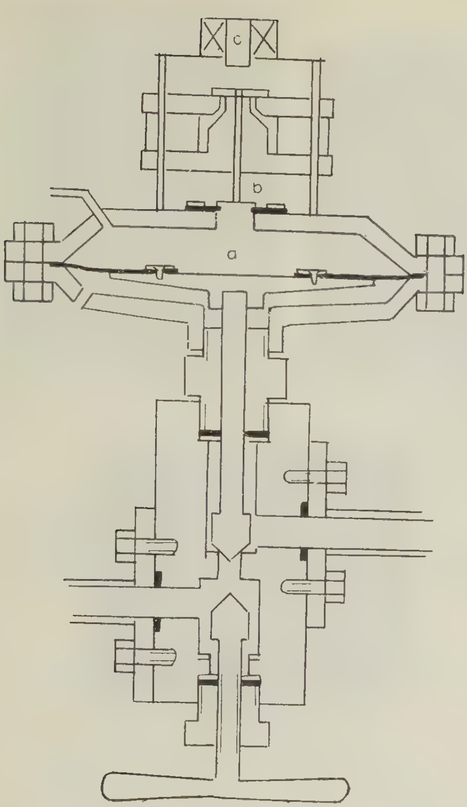

Fig. 3. Expansion valve.

light space 4 and the oil space 5 respectively. These are the vessels in which the boundaries between the water, the transparent oil and the oil of back space are separated by soft vinyl bags, and even at the fast expansion, pressures of spaces are reduced equally.

4 is the space for the light source, surrounding the cloud chamber. The iron wall is a nickel-plated parabolic mirror of 4 cm focal length. The circular flash lamp was set at the circular focal line, and the flash lamp surface facing the chamber was silvered to prevent direct illumination.

## § 3. Auxiliary Equipments

Fig. 3 shows an expansion valve. “a” is a compressed air space (about 2 atm.). The oil valve is closed by a force of about 400 kg. b is an air valve to reduce the pressure in “a” operated by a permanent magnet and demagnetizing coils as is usually done with chamber valves. The electro-magnet, c, keeps the valve open for about 2 sec. The hand valve, d, also adjusts the expansion velocities.

Fig. 4 shows the expansion vessel, the total volume of which is about 12 litres. The effective volume is varied by moving the center pipe, which has a check valve, at the top.

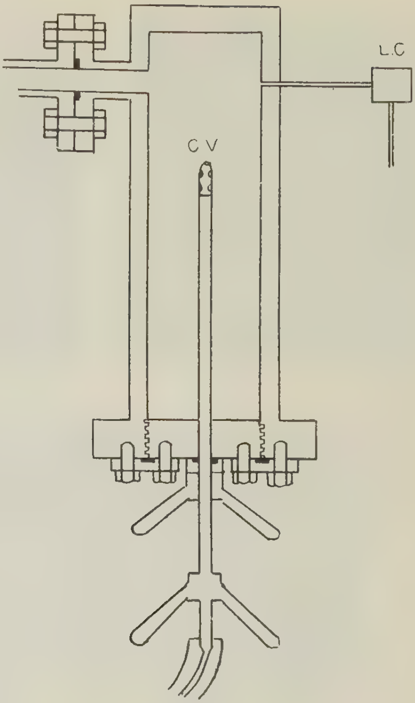

Fig. 4 Expansion vessel.

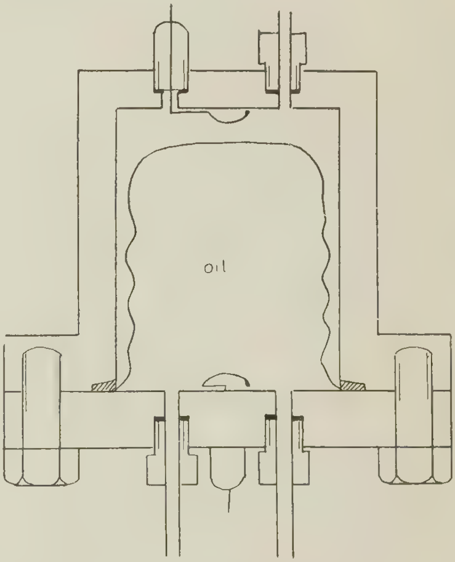

Fig. 5. High pressure oil tank.

The operation is as follows: fist, the entire space of the expansion vessel is filled with oil by an expansion of the cloud chamber and the check valve is, then, closed. After closing the expansion valve, the leak cock is opened and the pressure is reduced. Then the check valve is opened and oil is pumped out toward a vacuum pump until the oil level has gone down to the position of the check valve. The oil flows into the oil reservoir, b, and is pumped out slowly through a capillary tube. Most of the dust in the oil is deposited in the reservoir.

The oil compressor is driven by a 2 H.P. motor. The compressor has a capacity of 2 L/min. at 150 atm., the maximum available pressuae being about 300 atm. When the chamber is expanded, about 6–7 litres of the oil flow out. The time for pushing the chamber piston to the normal position is about 3 minutes. In order to shorten this time, the apparatus shown in Fig. 5 is used. Oil is stored in the vinyl bag at a pressure higher than that in the chamber the top relay being closed. The oil is pushed into the chamber by opening the valve (a valve similar to that of expansion valve). A gas tank of about 50 litres was used as the high pressure air reservoir to push the oil towards the chamber.

Two semicircular flash lamps are set along the focal line of the circular parabolic mirror. These are made by glass pipes of 4 mm inner diameter and 2 mm thickness. The aperture of the parabolic mirror is 18 cm of which about 15 cm is uniformly illuminated. Frequently the chamber is used without the glass cylinder. A circular solar silt is then used to avoid illumining the back plate. The electrical source for each lamp is 100 mf. condensors charged to 3000 volts. One of the electric leads is described in A, and the other leads are spark plugs of the common type for the gasonline engine. After a pressure test at 300 atm. they are painted to make them leak proof.

The gas cocks and oil cocks are not of special type, but the parts, connected to the chamber directly, are designed to have small gas spaces.

Sometimes, counters are set in the chamber for the purpose of triggering the chamber in favor of the showers which start in the gas. Glass tube counters of 2 cm diameter are used for this purpose. The end of the counter is carefully made in a spherical shape and these are used after the test up to 200 atm.

The main body is supported by its side shaft on a wooden rack and the entire assembly can be rotated by a chain block. The assembly of the chamber is done in a vertical position. Finally the back plate, held by a chain block, is screwed into the main body, and the whole assembly is rotated to a horizontal position. This work is done easily by two men. After that the spaces or water and oil are filled up and the vapour source and gas are pushed into the chamber up to 150 atm. driving the residual air off.

The time sequence circuits, the potentiometer circuits which shows the position of the piston and the thyratron relay circuits are described in " A ". The operating cycle is as follows

pulse in gate close —at once— cut the sweeping field
open the camera shutter
open the expansion valve

—0.5 sec.—light flash—0.5 sec

—apply the field
close the shutter—20 min.—gate open
close the valve

## § 4. The Operation and the Character of the Chamber

The uniformity of the illumination in the chamber are estimated by stereoscopic analysis of the photographs. Fig. 6 shows some examples of the photographs. The effective volume is about 50 cm in diameter and 15 cm in depth. The stopping power and the total weight for various gases in this effective volume are as follows;

| the sort of gas | stopping power per 50 cm | total weight |
|---|---|---|
| hydrogen (150 atm.) | 0.67 g/cm² | 400 g |
| nitrogen ″ | 9.4 | 5.6 k |
| argon ″ | 13.4 | 8.0 |

The purity of the inner gases were good, but a small amount of alcohol vapor and air were contained as impurities. The maximum content of such impurities was about 0.5%.

The following points have to be considered in selection of the vapour source. The pressure should not be high (to keep the gas impurity small), the resistance in liquid state should be high (to avoid the leakage of the electricity at the plugs when the vapor condences) and the required expansion ratio should be small and so on. In the case of one to 3 ethyl alcohol-propyl alcohol mixture,

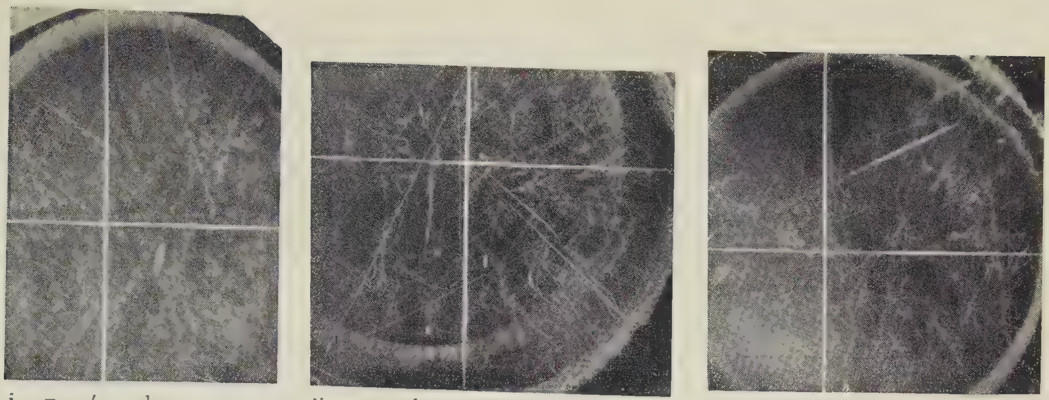

i. $\pi-\mu'-e$ decay.

ii. $\mu-e$ decay and pair production by decay electron.

iii. decay of charged heavy meson.

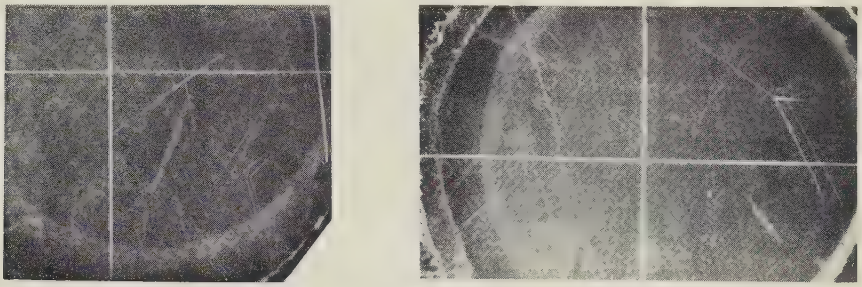

iv. Production and decay of neutral heavy particle.

v. Neutron-proton and proton-proton collision.

Fig. 6. Examples of events in 92 atm. Hydrogen (these are observed by K. Hinotani, T. Matano, K. Nunogaki and Author).

the expansion ratios were 1.06 for argon, 1.13 for nitrogen and 1.14 for hydrogen (at 100 atm.)

The expansion time is adjustable from 0.5 sec to 0.2 sec by a hand valve. The expansion ratio depends somewhat upon the expansion time. A slower expansion requires larger expansion ratio.

The expansion time determines the width of the tracks. Although the expansion is rather slow, the diffusion of ions in high pressure gas is also slow. The chamber can be adjusted to have about 1 mm track width. The best condition is determined by looking at random cosmic ray tracks illuminated by a small lamp set in the chamber.

The sensitive time is longer than that in a low pressure cloud chamber because the sensitive time varies as the square root of the pressure. It is estimated to be about 2–3 sec. and varies with the kind of inner gas and expansion time. The track width, for the same expansion delay, varies inversely as the square root of the pressure.

When the photograph is taken about 0.5–1 sec. after the start of the expansion, about 50 tracks are seen in one expansion. These are random tracks of electrons and mu mesons. The age of these tracks are estimated from the sweeping separation and the track width. In the case of nitrogen the separation of plus and minus ions is about 4 cm/sec at the sweeping field of about 150 V/cm and the track width is proportional to $\sqrt{t}$, where $t$ is a time before expansion.

Two photographs are taken with the stereoscopic angle of about 20 degrees. The pictures are analysed after the correction was done for the deformation of images by the deflection of light path in the water. This deformation is not so large at the center of the chamber, but the image moves forward for about 2 cm at the edge and this has to be corrected in all cases.

The tracks are classified as thin, gray and black in a similar way as in emulsion works. But this classification is not so clear in this case, because the drops are so dense that they can not be counted. The tracks are seen as continuous lines. Therefore, they are

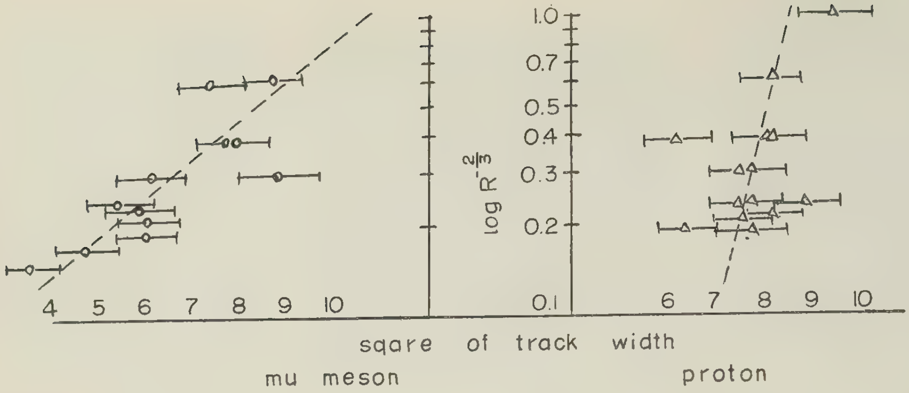

Fig. i.

discriminated by their width and knock-on electrons. Thin tracks are characterized by minimum ionization or by their production of knockon electrons. Black tracks are heavily ionizing tracks whose width is about twice the width of a thin track of the same age, and gray tracks comes between the above two. (see Appendix I) Momenta are easily measured by multiple scattering angle, for light particles especially for electrons. Momenta lower than 50 Mev/c for argon, 30 Mev/c for nitrogen and 4 Mev/c for hydrogen can be measured in this way. In these cases the average deflection angles are larger than about 2 deg./cm. This measurement can not be applied to high energy particles because of the distortion in the chamber and inaccuracy arising from track width. (see Appendix II)

The stopping powers of the inner gases are as follows:

| | energy for the range of 5 cm | | |
|---|---|---|---|
| | electron | mu meson | proton |
| argon | 2.7 Mev | 14 Mev | 36 Mev |
| nitrogen | 2.0 | 10 | 26 |
| hydrogen | 0.5 | 3.8 | 11 |

The masurements in the well known events, for instance the range of the mu meson in pi-mu-e decay etc. were used for checking these figures.

A range of 5 cm in nitrogen corresponds to about 3000 microns in emulsion. Such tracks, which correspond to about 60 microns in emulsion, as in the case of prongs from evaporation stars, are missed, because they are shorter than 1 mm in the nitrogen gas of 150 atm. Low energy stars from neutrons appear as only points of a few mm diameter.

Sometimes the lead plate of 1–2 cm thickness is placed in the chamber to distinguish the soft component.

It is very important to make the dead times in cycling operation as short as possible. For this purpose several methods have been tried., 1) Vapour sources were placed at many places in the chamber, 2) Vapour source were circulated by the variation of the pressure at the expansion and at the compression of the chamber, through the pipe which connect the top and the bottom of the chamber, 3) Slow expansions were repeated, 4) The inner gas was circulated by mechanical and thermal methods. All these procedures were effective in shortening the dead time, but the procedure (4) gave some disturbance, to the following cycle of observation.

## Acknowledgment

The authors are indebted to Professor Y. Watase for his valuable advice and encouragement and express their thanks to Mr. Nakamura for his aids in construction of the equipment.

## Appendix I

*Estimation of the mass from the ionization and the range*

The ionization density $I(x)$ at a distance $x$ from the track centre, after ions have diffused during $t$ sec, is given by

$$I(x)=(4Dt)^{-1/2}N_0 \exp(-x^2/4Dt)$$

and the track width is proportional to $(Dt)^{1/2}$. Where $D$ is a diffusion constant and $N_0$ is the number of ions per unit length and is proportional to the inverse square of the velocity of a particle. On the other hand, the range of a track is proportional to the cube of the velocity in low energy region. Thus log (range)$^{-2/3}$ is proportional to square of track width.

Fig. i shows this relation for mesons and protons and each curve is normarized at the end of the tracks.

The mass of each particle will be determined from the gradient of the curve in this figure.

## Appendix II

### *Scattering measurement*

Preliminary scrttering measurement was done for low energy electrons (about 2 Mev) in nitrogen, excepting the tracks inclined more than 30° to vertical plane.

There is a well known relation

$$\eta=\varphi R^{\alpha}$$

where $\varphi$ is the projected scattering angle, $R$, the residual range and $\alpha$ is a constant which is about 0.66 in this energy region.

Fig. ii A shows the distribution of $\eta$ and it is consistent with the expected value

$$g(\eta)=\frac{1}{\sqrt{2\pi}\rho}\exp\left(-\frac{\eta^2}{2\rho^2}\right)$$

with $\rho$ defined by

$$\rho=(4\pi r_e NZ^2A^{-1}tG)^{1/2}(m_e c^2 A)^{\alpha}(m_e/m)^{1-\alpha}$$

where $t$ is the cell length (0.5 cm in this case), $G$ is 4.22, $A_z$ is 1.32 cm/Mev and other notations are those usually used.

From the root mean square of $\eta$ or the average of the absolute value of $\eta$, the mass of the particles was given as $0.97^{+0.08}_{-0.06}$ electron mass.

Distribution of $\eta$ for each track is also shown together with computed distribution in Fig. ii B, but the accuracy of the result is not enough to decide whether there are other particles whose mass is different from that of electrons or not.

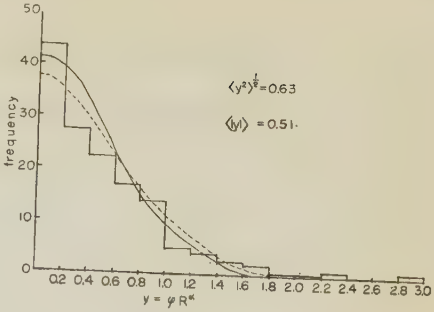

Fig. ii. A

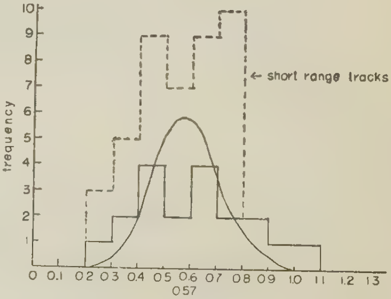

$$\xi=\left(\frac{1}{n-1}\sum_{i=1}^{n}\eta_i^2\right)^{1/2}$$

Fig. ii. B

## References

1, T. H. Johnson, S. DeBenedetti and R. P. Shutt: R. S. I. **14** (1943) 265.

G. E. Valley and J. A. Vitale: R. S. I. **20** (1949) 411.

"A" S. Miyake, K. Suga and O. Kusumoto: Journal of the Institute of Polytechnics, Osaka City University **B 2** (1951) 1.

E. H. S. Burhop: Nuovo Cimento 11 Suppl. (1954) 343.

2) "A" or Y. Watase, S. Miyake, K. Suga and O. Kusumoto: Journ. Phys. Soc. Japan **6** (1951) 204 (L).

O. Kusumoto, S. Miyake, K. Suga and Y. Watase: Phys. Rev. **90** (1953) 998 (L).

JOURNAL OF THE PHYSICAL SOCIETY OF JAPAN Vol. 11, No. 3, MARCH, 1956

# Statistical Theory of Phase Transition III

## Application to Vapor-Liquid-Solid Equilibrium

By Ikuro SHIMOSE

*Faculty of Literature and Science, Yamaguchi University*

(Received August 12, 1955)

Generalizing the idea of molecular-clusters introduced for a lattice gas with no sublattice in our paper, we calculate the equation of state for a lattice gas with many interstitial sublattices. Thus it is shown that the stable liquid phase, together with the vapor and solid phases, can exist in the above system. Furthermore, we make clear the relation between the two phase transitions, that is the vapor-liquid and the liquid-solid transitions, from the point of view of molecular-clusters.

### § 1. Introduction

In our previous paper[1]*, by extending the idea of order-disorder in the alloy theory to the case having many ordered parameters, we calculated the equation of state for a lattice gas with many interstitial sublattices in the degree of Bragg-Williams' approximation[2]. Thus we showed that the stable liquid phase, together with the vapor and solid phases, can exist in the above system, and we were able to make fairly clear the relation between the vapor-liquid and the liquid-solid transitions.

In this paper, by extending the idea of molecular-clusters introduced for a lattice gas with no sublattice in Parts I and II of this paper[3]** to the system with many sublattices, we deal with the same problem as in the previous paper[1]. Thus we wish to show that the stable liquid phase can exist in the above system, and to make still clearer the relation between the two phase transitions.

### § 2. Partition Function

We assume the potential energy $\varphi(r)$ between any two molecules to be of the following form;

$$\left.\begin{array}{ll}\text{(i)} & \varphi(r)=+\infty \quad \text{for} \quad 0\leqq r<a\,, \\ \text{(ii)} & \varphi(r)=-2\mathcal{E}\ (\mathcal{E}>0) \ \text{for}\ a\leqq r<\sqrt{2}\,a\,, \\ \text{(iii)} & \varphi(r)=0 \quad \text{for} \quad r\geqq\sqrt{2}\,a\,,\end{array}\right\} \qquad (1)$$

where $r$ is the distance between two molecules. Then we consider a square lattice composed of $sL$ lattice points, in which the distance between nearest neighbors is $a/s^{1/2}$, where $s$ is a integer. We can divide the above $sL$ lattice points into $s$ square lattices, in each of which the distance between nearest neighbors is $a$. We define each of the above $s$ lattices as "sublattice." A square lattice for $s=9$ is shown in Fig. 1.

The partition function $\Omega(T, L, s, N)$ of the system composed of $N$ molecules at the absolute temperature $T$ is given by

$$\Omega(T, L, s, N)=(2\pi mkT/h^2)^N(1/x)^{4N}s^N \times Q(T, L, s, N)\,, \qquad (2)$$

$$Q(T, L, s, N)=(1/s)^N\sum x^{N'}\,, \qquad (3)$$

$$x=\exp(-\mathcal{E}/kT)\,, \qquad (4)$$

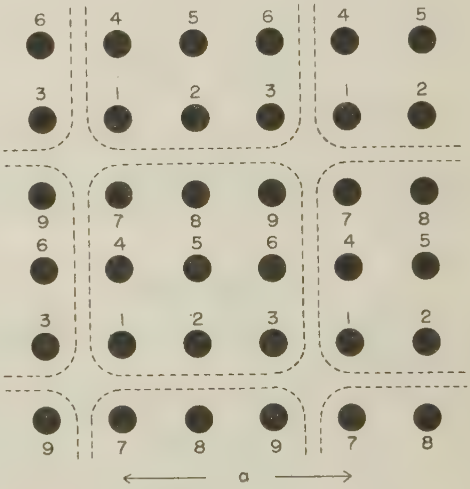

Fig. 1. Square lattice with 9 interstitial sublattices. The figure affixed to each lattice point shows the number of sublattice to which that lattice point belongs. The closed curves (dotted) show the l. p. groups (as will be stated in § 3).

---

* The paper "Equation of State for Vapor-Liquid-Solid system."

** The paper "Statistical Theory of Phase Transition" is denoted by "STPT" for short in the later articles.

where $\sum$ in Eq. (3) means the summation of $x^{N'}$ over all the possible cases, in which $N$ molecules are distributed among the $sL$ lattice points. $(4N-N')/2$ is the total number of $(r_1)$ pairs of any two molecules in one of the molecular configurations mentioned above, where "$(r_1)$ pair" of two molecules denotes the pair of two molecules existing at a distance $r_1(a\leqq r_1<\sqrt{2}\,a)$. $m$ is the mass of a molecule, $k$ Boltzmann's constant, $h$ Planck's constant.

## § 3. Molecular Configuration

As in STPT(1.3)***, we define a "molecular cluster" as the group of molecules in which every molecule either directly or indirectly is connected with each other at a distance $r_1$ $(a\leqq r_1<\sqrt{2}\,a)$. Then we divide all the lattice points into $L$ groups so that each group may contain $s$ lattice points, each of which belongs to each of $s$ sublattices respectively (such groups for $s=9$ are shown in Fig. 1). We denote such a group by "l.p. group", and a l.p. group with no molecule by "hole". Furthermore, we define a hole cluster as in STPT(1.3). Now we consider the following configuration types (viz. $A'$-, $B'$- and $C'$-types)[†] and the types including two or all of them (viz. $A'B'$-, $B'C'$-, $A'C'$- and $A'B'C'$-types).

($A'$) The configuration consisting of micro-molecular and macro-hole clusters,

($B'$) the configuration consisting of micro-hole and macro-molecular clusters,

($C'$)[††] the configuration consisting of micro-molecular and micro-hole clusters,

where micro- and macro- clusters (molecular and hole) are defined as in STPT(1.3). Then we can easily ascertain that the configuration consisting of macro-molecular and macro-hole clusters may give little contribution to the partition function. Furthermore, there may also exist intermediate (molecular and hole) clusters. However, we can deduce by the same consideration as in STPT(1.3) that intermediate clusters may be omitted in calculation, causing no alternation of the statistical properties.

## § 4. Calculation of Partition Function

Generalizing the method of STPT(I), we can calculate the contributions of the $A'$-, $B'$-, $C'$-, $A'C'$-, $B'C'$- and other type configurations to $Q_1(T, L, s, \rho)(=Q(T, L, s, N))$, where $\rho$ is molecular density and is given by $\rho=N/L$. We numerically calculate those contributions for $s=9$ and $x=0.3$. In low density region ($\rho\approx0$), the $A'$-type configuration gives a maximum contribution to $Q_1(T, L, s, \rho)$. This contribution is given by the curve $OAA'$ with a maximum in Figs. 2 and 3. In high density region ($\rho\approx1$), the $B'$-type configuration gives

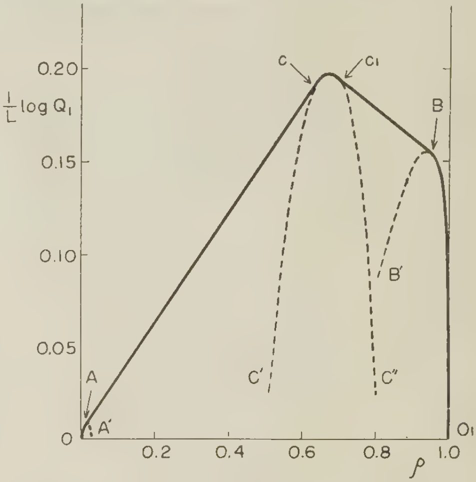

Fig. 2. $1/L\cdot\log Q_1-\rho$ curve for $s=9$ and $x=0.3$.

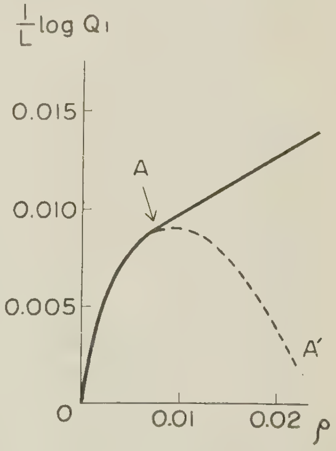

Fig. 3. $1/L\cdot\log Q_1-\rho$ curve for $s=9$ and $x=0.3$.

---

*** STPT (I.3) denotes § 3 of Part I in the paper "STPT".

[†] $A$- and $B$- types in STPT (I) and (II) correspond respectively to $A'B'$- and $A'$-types in this paper.

[††] In STPT (I) and (II), we considered without notice the configuration corresponding to the above $C'$-type one as the special case of $A$- and $B$-type configurations.

a maximum contribution to $Q_1(T, L, s, \rho)$ This contribution is given by the curve $O_1BB'$ with a maximum in Fig. 2.

The calculation of $C'$-type contribution is very difficult. We assume in order to simplify this estimation that each l. p. group with molecule at least has one adjacent hole. This assumption may hold in the molecular configuration for the small value of $m$, but it may not accurately hold in the configuration for the great value of $m$. Here $m$ denotes the greatest value of the number of holes constituting a hole cluster effective for the partition function. For the system with sublattices, owing to the great number of molecular configurations in a l.p. group and the form of potential in Eq. (1), the contribution per molecule to $Q_1(T, L, s, \rho)$ is several times as great as that for the system with no sublattice. Therefore, for the system with sublattices the $C'$-type contribution is effective for $Q_1(T, L, s, \rho)$ in temperature region ($x \gtrsim 0.3$) higher than a definite temperature. On the contrary, for the system with no sublattice the $C'$-type contribution is not effective for $Q_1(T, L, s, \rho)$ in the whole temperature region. This contribution for $s=9$ and $x=0.3$ is given by the curve $C'CC_1C''$ in Fig. 2. In this estimation, only the hole clusters consisting of single hole are taken into consideration to simplify the calculation. Then the l.p. groups having molecule but with no adjacent hole exist in the $B'$-type configuration. However, according to the above assumption every l.p. group with molecule has one adjacent hole at least in the $C'$-type configuration. Therefore, the contribution per molecule to $Q_1(T, L, s, \rho)$ for the $C'$-type case can be greater than that for the $B'$-type case.

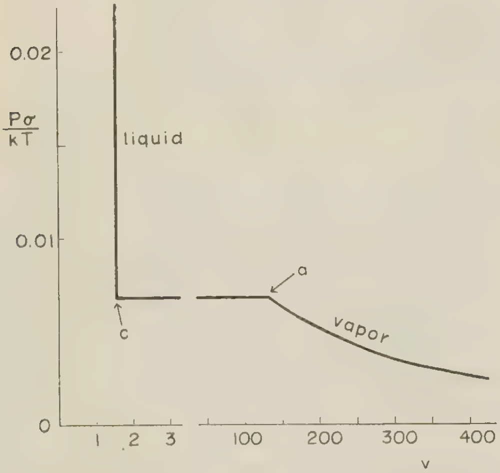

Fig. 4. $P\sigma/kT-v$ curve for $s=9$ and $x=0.3$.

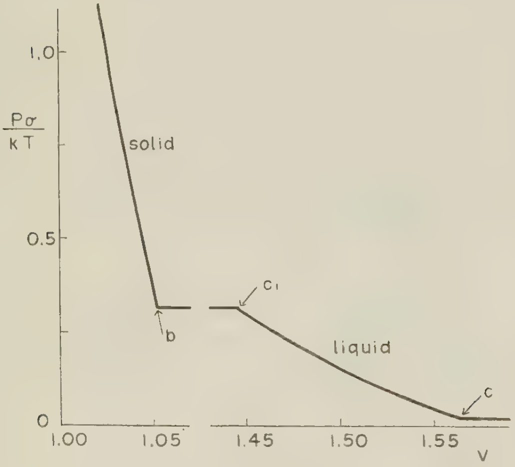

Fig. 5. $P\sigma/kT-v$ curve for $s=9$ and $x=0.3$.

In the comparatively low temperature region (for example $x=0.3$), by generalizing the theory of STPT(1·3·5) we can prove the following for the $A'C'$-type configuration in the intermediate region of the two densities, in the vicinity of which the $A'$- and $C'$-type contributions respectively become maximum. In this density region, (i) the $A'C'$-type contribution (for $x=0.3$) is exactly given by the common tangent $AC$ (in Figs. 2 and 3) to the $OAA'$ and $C'CC_1C''$ curves, which correspond respectively to $A'$- and $C'$-type contributions, (ii) the $A'C'$-type contribution is greater than any other type contributions. Furthermore, the same relation holds also for the $B'C'$-type configuration. The $B'C'$-type contribution (for $x=0.3$) is given by the common tangent $BC$ (in Fig. 2) to the $O_1BB'$ and $C''C_1CC'$ curves, which correspond respectively to $B'$- and $C'$-type contributions.

By the same consideration as in STPT(1·3·4), we shall see that the value of $1/L\cdot\log Q_1(T, L, s, \rho)$ is given by the greatest value of the contributions to $1/L\cdot\log Q_1(T, L, s, \rho)$ of all the possible type configurations. $1/L\cdot\log Q_1-\rho$ curve for $s=9$ and $x=0.3$ is shown in Figs. 2 and 3.

## §5. Equation of State

From the $1/L\cdot\log Q_1-\rho$ curve for $s=9$ and $x=0.3$ (Figs. 2 and 3), we can calculate the equation of state by using the theory of STPT

(1·4). The $P\sigma/kT-v$ curve (the isotherm) obtained is shown in Figs. 4 and 5, where $P$ is the pressure, $v$ the specific volume (two-dimensional) per molecule, and $\sigma$ the total volume (two dimensional) divided by $L$.
Particularly the two straight parts $AC$ and $BC_1$ in $1/L\cdot\log Q_1-\rho$ curve (in Fig. 2) correspond respectively to portions $ac$ (in Fig. 4) and $bc_1$ (in Fig. 5) parallel to $v$-axis ($P$=constant) on $P\sigma/kT-v$ curve. And these two portions represent respectively the two phase transitions that is the vapor-liquid and the liquid-solid transitions.

## § 6. Conclusion

For the lattice gas with many interstitial sublattices, we were able to calculate the equation of state from the point of view of moleculnr clusters, and theoretically show as in the previous paper[1] that the stable liquid phape, together with the vapor and solid phases, can exist in the above system. Though the degree of approximation for the method used was not so definite, we were able to obtain the reasonable result that the regions of two phase transitions (that is the vapor-liquid and the liquid-solid transitions) correspond respectively to the two portions parallel to the $v$-axis on the $P\sigma/kT-v$ curve (the isotherm) in the comparatively low temperature region.

The author wishes to express his sincere thanks to professor A. Harashima, Tokyo Institute of Technology, for his valuable discussions.

### References

1) I. Shimose: J. Phys. Soc. Japan **10** (1955) 860.
2) W. L. Bragg and E. J. Williams: Proc. Roy. Soc. **A 145** (1934) 399.
3) I. Shimose: J. Phys. Soc. Japan **9** (1954) 451, 457.

JOURNAL OF THE PHYSICAL SOCIETY OF JAPAN Vol. 11, No. 3, MARCH, 1956

# Oriented Overgrowth of Evaporated Crystallites

## Fluoride Crystallites on Cleavage Surfaces of Single Crystals

By Jiro SHIGETA

*Department of Physics, Okayama University, Okayama, Japan*

(Received October 17, 1955)

The orientation of crystallites in fluoride films (LiF, NaF, $CaF_2$, $MgF_2$, $AlF_3$ and $Na_3AlF_6$) evaporated in vacuum onto the cleavage surfaces of several kinds of single crystals (galena, rocksalt, molybdenite and zincblende) were investigated by means of electron diffraction. The oriented overgrowth occurs even when the misfit is larger than 20%; for LiF and NaF on galena misfits are −33% and −23% respectively, for LiF on rocksalt misfit is −29% and for $CaF_2$ on molybdenite +23%. On the other hand, for $CaF_2$ on rocksalt the random orientation occurs though the misfit is only −3%. Therefore, the occurrence of orientation can not be predicted solely by the value of misfit. It is worth mentioning that in the present experiment no twin was observed provided the evaporated layer is thin, as previously stated by Uyeda [Proc. Phys.-Math. Soc. Jap. **26** (1942) 809]. This excludes the mechanism of oriented overgrowth which was proposed by Menzer [Naturw. **26** (1938) 385; Z. Krist. **A 99** (1938) 410] and later adopted by Frank and Merwe [Proc. Roy. Soc. **A 198** (1949) 205].

## § 1. Introduction

The oriented overgrowth of crystals has been studied extensively by many investigators. It is generally accepted that the fitting of lattices on the boundary surface is an important factor for the occurrence of oriented overgrowth. However, there are many examples[1] in which oriented overgrowth takes place even when the misfit is larger than 20%. For example, silver ($a_0$=4.08 Å) shows a definite orientaion on rocksalt ($a_0$=5.63 Å), where the misfit is −27%. This fact is not in accordance with the idea that the fitting of lattices is the only cause of the oriented overgrowth. To get rid of this difficulty Menzer[3][4] suggested the formation of a twinned structure in the initial layers of deposit. His suggestion, however, was denied by Uyeda's[2] experiment. Later, Frank and Merwe[5] proposed a mono-layer hypothesis which leads to the conclusion that the fitting is the only factor to cause the oriented overgrowth. Smollett and Blackman[6] criticized this theory and pointed out the disagreement of Frank-Merwe's theory with experimental facts. Recently, Schultz[7] and Raether[8] reported that Menzer's twin was not found in the initial deposit of alkali halides on substrates of alkali halides. More recently, Lüdemann[9] and Ogawa[10] also denied Menzer's twin by their experiments. In the present experiment the oriented overgrowth of crystallites in various fluoride films evaporated onto various substrates is studied with special attention to Menzer's twin.

## § 2. Experimental

Thin films of fluorides were prepared by evaporation on substrates in a vacuum furnace. Fluorides used in this experiment were LiF, NaF, $CaF_2$, $MgF_2$, $AlF_3$ and $Na_3AlF_6$ (cryolite); the substrates were cleavage surfaces of galena (PbS), rocksalt (NaCl), molybdenite ($MoS_2$) and zincblende (ZnS). Orientations were studied for all the combinations of the fluorides and the substrates.

The fluorides to be evaporated were preheated in a tungsten spiral long enough to exclude occuluded gas. When the vaporization started, the pressure in the bell jar was $1\sim2\times10^{-4}$ mm Hg. A few minutes later, it became $3\sim5\times10^{-5}$mm Hg. A shutter between the spiral and the substrate was then opened to make deposit. The evaporation of the sample in the spiral was generally completed in a few minutes. The temperature of the substrates during evaporation was kept at 15, 200, 300 and 400°C. For galena and rocksalt substrates the highest temperature was 400°C,

Table I. Orientations of fluorides crystallites on various crystalline substrates.

| Fluorides / Substrates | LiF | NaF | $Na_3AlF_6$ | $CaF_2$ | $MgF_2$ | $AlF_3$ |
|---|---|---|---|---|---|---|
| | $a_0=4.01$ | $a_0=4.62$ | $a_0=5.46$<br>$b_0=5.61$<br>$c_0=7.80$<br>$\beta=90°11'$ | $a_0=5.46$ | $a_0=4.66$<br>$c_0=3.08$ | $a_0=4.92$<br>$c_0=6.25$ |
| PbS(100)<br>$a_0=5.97$ | 15°C (2)>(3)≫(1)<br>200°C (2)>(1)≫(3)<br>300°C (2), (1)<br>400°C (1) | 27°C (1)<br>100°C (1), (2)<br>200°C (1), (4)<br>300°C (1) | 200°C ×<br>270°C (15) | 300°C ×<br>400°C × | 300°C<br>400°C } × | 270°C × |
| NaCl(100)<br>$a_0=5.628$ | 15°C<br>200°C } (1)<br>300°C (1), (3)<br>400°C (1), (3)≫(2) | 27°C<br>≀<br>300°C } (1)<br>400°C trace | 200°C ×<br>300°C (16) | 400°C × | 400°C × | 270°C ×<br>400°C × |
| $MoS_2$(0001)<br>$a_0=3.15$<br>$c_0=12.30$ | 15°C (6)<br>200°C<br>≀<br>400°C } (5), (6) | 27°C<br>100°C<br>200°C<br>300°C } (6) | 200°C<br>300°C<br>400°C } (17) | 300°C<br>400°C } (7) with D. R. | 400°C × | 400°C × |
| ZnS(110)<br>$a_0=5.43$ | 15°C (18)<br>200~300°C (20)<br>400°C (19)<br>450°C complicated | 27°C (21),(22)<br>100°C<br>200°C<br>300°C } (21) | 200°C ×<br>300°C<br>≀<br>450°C } (8)~(14) | 300°C (23)?<br>400°C (23) | 400°C × | 400°C × |

*Note.* The number in brackets indicates the orientation illustrated in Fig. 1. The mark × indicates no definite orientation. The mark ? is used when the pattern is not sharp enough to be analized although some definite orientations exist. The notation (2)>(3), for example, means that the orientation (2) prevails over (3).

while for molybdenite and zincblende substrates it was 500°C; above these temperatures the thermal etching became remarkable. For NaF deposit the highest temperature was 300°C for all the substrates because NaF re-evaporated above this temperature. The mean thickness of fluoride films was generally of the order of 60 Å. However, for LiF on galena at 200°C the mean thickness was varied from 6 Å to 740 Å to examine in detail the relation between orientation and thickness.

After the furnace was cooled, the samples thus prepared were taken out from the vacuum and was set in an electron diffraction camera as quickly as possible. Then they were examined by reflection method.

## § 3. Experimental Results

The main result of the present experiment is summarized in Table I and in Fig. 1. $MgF_2$ and $AlF_3$ shows no definite orientation, while all the other deposits show definite orientations above certain temperatures.

The result of LiF on galena is explained in detail below. The diffraction patterns for various temperatures are reproduced in Fig. 2, and those for various thicknesses in Fig. 3. On galena substrate LiF shows three types of orientations (1), (2) and (3) (Fig. 1).

Table II. The orientations of LiF deposit of various thickness on galena substrates at 200°C.

| Thickness of deposit | Orientation | Twin |
|---|---|---|
| 6 Å | (2), (1) both faint | no |
| 12 Å | (2)>(1), (3) | no |
| 52 Å | (2)>(1) both sharp | no |
| 100 Å | (2)>(1) | {111}, {012} |
| 300 Å | (2)≫(1), sharp, rather faint D. R. | {111}, {012} remarkable |
| 500 Å | (2), D. R. developed | {111}, {012} conspicuous |
| 740 Å | D. R. only | |

Remarks. (1), (2) and (3): Cf. Fig. 1.

At 15°C the type (2) is most predominant, the type (3) rather weak and the type (1) faint (Fig. 2a). No twin spots appear provided films are thinner than several tens Å (Fig. 2a). For films thicker than 100 Å {012} twin spots appear along circular arcs, but {111} twin spots do not appear.

At 200°C the type (3) becomes faint and the type (1) becomes so strong that it is comparable to the type (2) (Fig. 2b). At this temperature the variation of orientations with the thickness was examined in detail, the result being summarized in Table II. Both

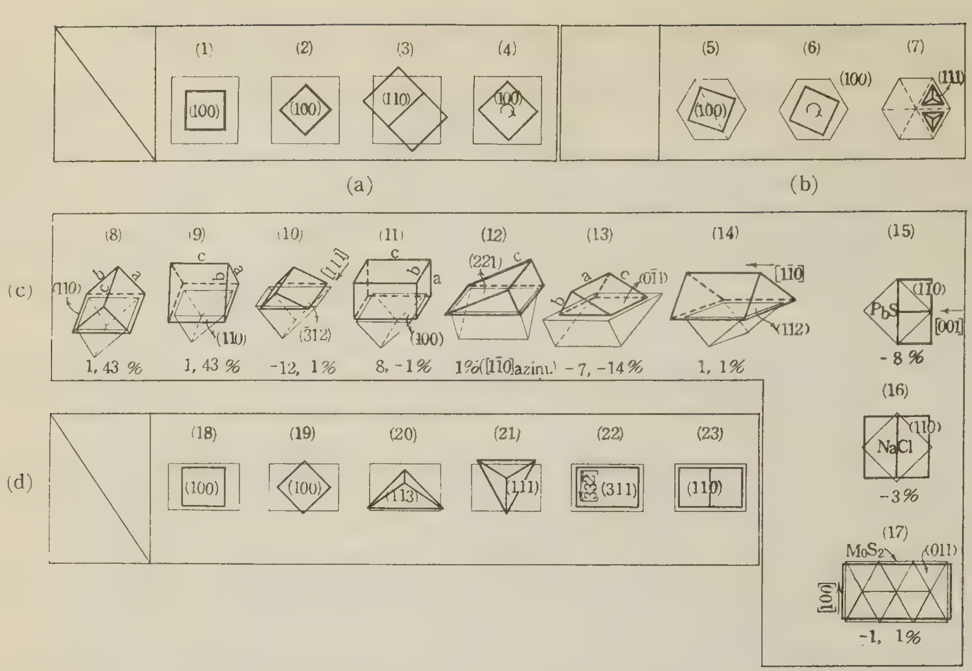

(a) Cubic Crystals on Cubic Face (1～4).

| Types of orientation / Base-deposit | (1) | (2) | (3) | (4) |
|---|---|---|---|---|
| PbS–LiF | * −33% | −5% | −33, − 5% | no |
| PbS–NaF | * −23% | 9% | ( 9, −23%) | yes |
| PbS–CaF$_2$ | (− 9%) | (29%) | ( 29, − 9%) | no |
| NaCl–LiF | * −29% | 1% | −29, 1% | no |
| NaCl–NaF | * −19% | (16%) | (−19, 9%) | no |
| NaCl–CaF$_2$ | (− 3%) | (37%) | (− 3, 37%) | no |

(b) Cubic Crystals on Hexagonal Face (5～7).

| Types of orientation / Base-deposit | (5) | (6) | (7) |
|---|---|---|---|
| MoS$_2$–LiF | −9, 4% | yes | (34%) |
| MoS$_2$–NaF | ( 4%) | yes | ( 4%) |
| MoS$_2$–CaF$_2$ | (22%) | no | * 23% |

(c) Orientation of Cryolite (8～14: on Zincblende, 15～17: on The Other Substrates).

(d) Cubic Crystals on Zincblende (18～23).

| Types of orientation / Base-deposit | (18) | (19) | (20) | (21) | (22) | (23) |
|---|---|---|---|---|---|---|
| ZnS–LiF | 4, −26% | −27, 4% | 11, −13% | (−26, −10%) | (−26, −13%) | (−26, −26%) |
| ZnS–NaF | ( 20, −15%) | (−14, 20%) | (27, 0%) | −15, 4% | −15, − 1% | (−15, −15%) |
| ZnS–CaF$_2$ | (−28, 0%) | ( 0, 40%) | (51, 18%) | ( 0, 23%) | ( 0, 18%) | 0% |

Fig. 1. Orientations of fluoride crystallites on various crystalline substrates. Miller's indices of the contact plane of fluoride crystallites are indicated in the figures. The mark ↻ indicates fiber structure. The numerals under the figures are the misfit values, the brackets for misfit values correspond to orientations which do not actually take place and the mark * indicates misfits larger than 15%. In all the figures thick lines represent the crystallite of the deposit and thin lines that of the substrate.

{111} and {012} twins do not appear in films thinner than several tens Å (Fig. 3a). They appear remarkably in the range 100～500 Å (Fig. 2b). As the thickness increases the type (2) prevails over (1) and at about 500 Å the type (1) disappears (Fig. 3b). When the thickness increases over 300 Å, weak Debye rings indicating random orientation are superposed on spot patterns (Fig. 3b), then the rings become gradually strong and finally at about 700 Å they mask the spot patterns.

At 300°C the types (1) and (2) are com-

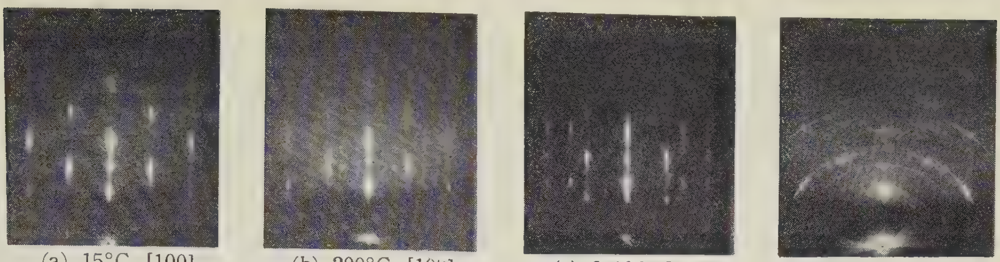
(a) 15°C, [100] (b) 200°C, [100] (c) 300°C, [100] (d) 400°C. [110]

Fig. 2. Lithium fluoride on galena, temperatures and directions of the incident beam are indicated. The thickness for (b) is 150 Å and that for the others is 70 Å.

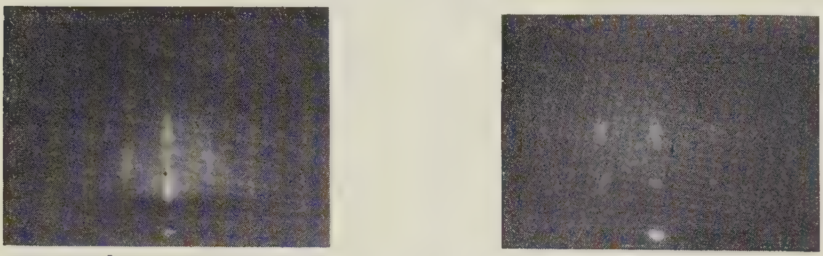
(a) 12 Å, beam//$[100]_{PbS}$ (b) 500 Å, beam//$[110]_{PbS}$

Fig. 3. Lithium fluoride of various thickness evaporated on galena at 200°C, thickness is indicated above. Cf. Fig. 2 b also.

(a) (b) (c)

Fig. 4. Calcium fluoride on various substrates at 400°C: (a) rocksalt, (b) galena and (c) molybdenite ($[120]_{azim.}$).

parably strong and the type (3) disappears (Fig. 2c). At 400°C the type (1) in which the diffraction spots spread along circular arcs becomes strong and the type (2) which was most predominant at lower temperatures disappears (Fig. 2d). The both types of twin spots do not appear at temperatures 300∼400°C.

For LiF on rocksalt the three types (1), (2) and (3) appear similarly as for LiF on galena. However, the change of orientations with substrate temperature is different for these two substrates. On rocksalt all the three types appear at 400°C and only the type (1) appears at 15∼200°C, while on galena all the three types appear at 15∼200°C and only the type (1) appears at 400°C.

On galena substrate NaF shows usually the type (1), and this is often accompanied by the type (2) or the type (4). On rocksalt substrate NaF shows only the type (1). On molybdenite substrate NaF and LiF show usually the type (6) and for LiF deposit the type (5) is superimposed as the temperature rises. On zincblende substrate NaF and LiF show different orientations as given in Table I.

The orientations of cryolite crystals appear only above about 300°C for all of the substrates. The orientation of cryolite on zincblende is very complicated. Besides seven types of orientations shown in Fig. 1c complicated diffraction patterns were often observed, separately or superimposed. Their appearance took place by chance and was uncontrollable.

On zincblende and molybdenite $CaF_2$ shows definite orientations, while on galena and rocksalt $CaF_2$ shows random orientation through the temperature range 15~400°C (Fig. 4a, b).

In all the experiments above mentioned, Menzer's twin never appears in the initial layers of deposits.

## § 4. Discussions

The misfit (or mismatch) $M$ between the deposit and the substrate on the contact plane is defined as $M=(b-a)/a$, where $a$ denotes the spacing of the substrate, $b$ that of the deposit. The oriented overgrowth occured very often even for misfit larger than 15% (Fig. 1). In Fig. 1a there are four examples indicated by stars * in which the misfit exceeds 15%. According to the theory of Frank and Merwe⁵⁾, the critical misfit value for stable orientations is ±9% and that for metastable orientations ±14%. The misfit of 15% mentioned above exceeds both of the critical values. For LiF on galena the misfit of the type (1) is −33%. It is noteworthy that for cubic crystals on cubic faces (Fig. 1a) the type (1) occurs generally in the temperature range 15~400°C, even though the misfit is the largest of the three possible orientations. This tendency is also observed for LiF on (100) faces of NaCl and KBr crystals, where the misfits are as large as −29% and −39% respectively. On the other hand, random orientation is observed through the whole temperature range 15~400°C for $CaF_2$ on rocksalt, where the misfit is only −3%.

As described in § 3 Menzer's twin was never observed in the present experiment provided films are thinner than several tens Å. This coincides with the experimental results by Uyeda²⁾, Schultz⁷⁾, Raether⁸⁾, Lüdemann⁹⁾ and Ogawa et al¹⁰⁾. Thus all the experiments are against Menzer's hypothesis and the values of misfit mentioned so far are regarded as the actual values of misfit. Therefore, Frank-Merwe's theory cannot explain definite orientations which take place with the misfit exceeding their critical values. In such a case the cause of the definite orientation may be found in the nucleus theory such as proposed by Uyeda²⁾ and Schultz¹¹⁾.

### Acknowledgement

The author wishes to express his sincere thanks to Prof. Ryozi Uyeda for suggesting the problem, his pertinent guidance and encouragement. He also thanks Miss F. Yamamoto and Mr. M. Hiramatsu for their helpful assistance. The expense for this research has been partly defrayed by the Ministry of Education Scientific Research Grant.

### References

1) O. G. Engel: J. R. N. B. S. **50** (1953) 249.
2) R. Uyeda: Proc. Phys.-Math. Soc. Japan **26** (1942) 809.
3) G. Menzer: Naturw. **26** (1938) 385.
4) G. Menzer: Z. Krist. **A 99** (1938) 410.
5) F. C. Frank and J. H. Merwe van der: Proc Roy. Soc. **A 198** (1949) 205.
6) M. Smollett and M. Blackman: Proc. Phys. Soc. **A 63** (1951) 683.
7) L. G. Schultz: Acta Cryst. **5** (1952) 130.
8) H. Raether: Erg. d. exakt. Naturw. **24** (1951) 121.
9) Von H. Lüdemann: Z. f. Naturf. **9 a** (1954) 252.
10) S. Ogawa, D. Watanabe and F. E. Fujita: J. Phys. Soc. Japan **10** (1955) 429.
11) L. G. Schultz: Acta Cryst. **4** (1951) 483.

JOURNAL OF THE PHYSICAL SOCIETY OF JAPAN Vol. 11, No. 3, MARCH, 1956

# On the Magnetic Anisotropy of $FeF_2$ and $CoF_2$

By Tôru MORIYA, Kazuko MOTIZUKI, Junjiro KANAMORI
and Takeo NAGAMIYA

*Department of Physics, Osaka University*

(Received September 26, 1955)

The magnetic anisotropies of $FeF_2$ and $CoF_2$ are studied in detail by calculating the crystalline field acting on their magnetic ions and considering the effect of the spin-orbit coupling. The electronic energy level splittings of the ions $Fe^{++}$ and $Co^{++}$ in the crystalline field are calculated assuming first that all the surrounding ions are point charges and then taking account of the overlapping of their $3d$ electrons with the electron clouds of the surrounding fluorine ions. The spin-orbit coupling is then introduced and the $g$-values are calculated. Further, introducing the exchange coupling in the approximation of molecular field, the parallel and perpendicular susceptibilities of $FeF_2$ are calculated and a reasonable agreement with experiment is found. For $CoF_2$, however, the calculated level splitting is not successful in explaining the observed susceptibilities. Discussions are given on the possible sources of this disagreement and the nature of the approximations made in this study.

## § 1. Introduction

Iron-group fluorides, $MnF_2$, $FeF_2$, $CoF_2$, etc., crystallize in the rutile type structure and their magnetic properties show tetragonal symmetry. Their magnetic anisotropies were studied experimentally by Stout, Griffel¹⁾ and Stout, Matarrese²⁾ over the temperature range 10°～340°K. They showed that the difference of the two principal values of the susceptibility, $\chi_{\parallel}-\chi_{\perp}$, is positive for $MnF_2$ and $FeF_2$ in their paramagnetic temperature range, except very near the Curie temperature, while for $CoF_2$, whose Curie point is 37.7°K, $\chi_{\parallel}-\chi_{\perp}$ changes sign at 140°K from positive to negative as temperature is decreased. The magnitude of $\chi_{\parallel}-\chi_{\perp}$ for $FeF_2$ and $CoF_2$ is about 100 times as large as that for $MnF_2$. Their low temperature measurements show that all these substances are antiferromagnetic and the spins prefer the c-axis as the easy direction of ordering. Measurements of the specific heat were carried out by Stout, Adams³⁾ and Stout, Catalano⁴⁾; they observed a sharp peak at the Curie temperature.

We confine our considerations to the magnetic anisotropy of these substances. For $MnF_2$, in which the $Mn^{++}$ ions are in the $^6S$ state and therefore the spin-orbit coupling is negligible, Keffer⁵⁾ has shown that the magnetic dipole-dipole interaction is the predominant origin of the anisotropy. For $FeF_2$ and $CoF_2$, however, their 100 times larger anisotropy should be attributed to other origin, namely, the spin-orbit coupling of the electrons in the $3d$ orbitals modified by the influence of the crystalline electric field. Theoretical investigations of this subject were undertaken by Niira and Oguchi⁶⁾ for $FeF_2$, and by Nakamura and Taketa⁷⁾ for $CoF_2$. They could give an explanation of the experimental results by adjusting several parameters contained in the crystalline field potential or in Pryce's effective spin Hamiltonian. These parameter theories could correlate various facts to each other, but it is desirable to look into the detail by studying directly the crystalline field itself and the resulting magnetic anisotropy. In this paper we attempt to make such a study, by making in part use of the crystaline field potential calculated in our previous paper⁸⁾. We make the following approximation. The crystal is assumed to be perfectly ionic. We consider the electronic structure of the cations to be that of an isolated cation we then take account of the effect of their environment. The latter is considered to be a static crystalline electric field. Exchange coupling between spins is approximated by a molecular field. One-body approximation is made for the electronic wave function of the cations, and other electronic states than those which result from the $3d$

electrons are neglected.

In § 2 we shall first give expressions for the energy level splittings of $Fe^{++}$ and $Co^{++}$ in an ortho-rhombic crystalline field, and then calculate their numerical values, making use of our previous results[8)] for the crystalline field obtained with the point charge model. The results, however, cannot explain the experimental fact. In § 3 we shall consider the effect of the overlapping of the $3d$ electron cloud with the surrounding fluorine electron clouds. This effect proves to be large and improves the results. In § 4 and § 5 are given calculations and discussions of the energy level splittings and paramagnetic susceptibilities of $FeF_2$ and $CoF_2$. For $FeF_2$ we find a reasonable result, but for $CoF_2$ we do not. Finally, in § 6, we discuss the nature of our approximation and possible sources of the discrepancy found for $CoF_2$.

## § 2. The Energy Level Splitting in the Crystalline Electric Field

Ions of the iron group elements have electrons residing in their incomplete $3d$-shells. The Hund rule tells us that the lowest lying electronic state has the maximum spin multiplicity and also the maximum orbital angular momentum consistent with this multiplicity; the ground states of $Fe^{++}$ and $Co^{++}$ are thus $^5D$ and $^4F$, respectively. These states are degenerate in their orbital states as well as in their spin states. When these ions are found in cystals, they are acted upon by the crystalline electric fiield and the degeneracy of their orbital states are lifted partly or perfectly according to the degree of symmetry of the field. The spin-orbit coupling, however, recovers a part of the orbital moment, which is carried by the spin so that the $g$-value becomes different from the spin only value 2. The $g$-value thus modified is generally anisotropic, namely it is a tensor. This is because the spin-orbit coupling, together with the action of the crystalline electric field on the $3d$ electrons, relates the spin to the crystalline axes. Therefore, the spin-orbit coupling lifts the spin degeneracy except for the Kramers doublets. These are the facts which underlie the anisotropic paramagnetic properties of the crystals.

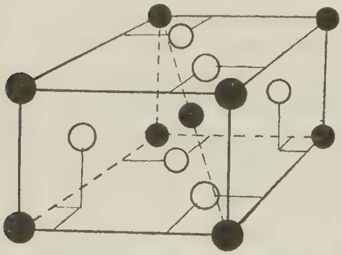

Fig. 1. The rutile type crystal structure of $FeF_2$ and $CoF_2$. Solid circles are cations, open circles anions.

There might be cases where some orbital levels lie closely above the non-degenerate ground level of the ion so that they obtain statistical populations which vary sensitively with temperature. In such cases the paramagnetic susceptibility of the substance will show unusual behaviours.

In this section, we shall first treat the general theoretical problem of the level splittings of $Fe^{++}$ and $Co^{++}$ ions in the orthorhombic crystalline electric field of their fluorides and then calculate the numerical values of the energy level splittings, basing our calculations on the 'point charge model' of the crystals which we studied earlier[8)]. We shall see, however, that this model does not give satisfactory results; we will modify the model in the next section.

Fig. 1 shows the rutile type crystal structure of $FeF_2$ and $CoF_2$, in which the cations form a body-centred tetragonal lattice and the anions surround each of the cations with an arrangement of orthorhombic symmetry. There are two kinds of sites for the cations, i.e. the corner and body-centre sites. Two of the principal axes of the crystalline field, perpendicular to the $c$-axis, are interchanged for these two kinds of sites. We shall take the [110], [$\bar{1}$10] and [001] directions as $x$, $y$ and $z$ axes for the body-centre sites and interchange the $x$ and $y$ axes for the corner sites. The electrostatic potential $V(\boldsymbol{r})$ around each cation can be developed in spherical harmonics as below, but we do not need terms beyond the fourth order, since we are dealing with $d$-electrons and the matrix elements of the higher order terms with respect to $d$-orbitals vanish. We have

$$\begin{aligned} V(\boldsymbol{r})=&A(r)\cdot(x^2-y^2)/r^2+B(r)\cdot(3z^2-r^2)/r^2\\ &+D(r)\cdot[(x^4+y^4+z^4)-3r^4/5]/r^4\\ &+F(r)\cdot[z^4-6(x^2+y^2)z^2+3r^4/5]/r^4\\ &+G(r)\cdot[-x^4+y^4+6(x^2-y^2)z^2]/r^4\,, \end{aligned} \tag{2.1}$$

where the third term has cubic symmetry, the second and fourth terms have tetragonal symmetry and the first and last terms orthorhombic symmetry.

The energy level splitting can be calculated in the first order perturbation, taking the free ion as the unperturbed system and the crystalline field potential as the perturbing Hamiltonian. We shall carry out this calculation separately for $FeF_2$ and $CoF_2$.

(i) The case of $FeF_2$

A free $Fe^{++}$ ion has the configuration $(3d)^6$ and the ground state, $^5D$, is the only quintet which results from this configuration. In this state, five electrons with parallel spinsform a closed shell and the remaining one with the reverse spin is in one of the five orbitals. The first five electrons can be neglected when we are concerned with the relative separations of the energy levels, because the crystalline potential is the sum of one-electron potentials, and a closed shell makes a constant contribution to the energy.

If the angular parts of the five orbital functions are taken to be proportional to

$$x^2-y^2,\ 3z^2-r^2,\ xy,\ zx,\ yz, \tag{2.2}$$

the first two of these mix in the crystalline field of the orthorhombic symetry but the remaining three are already the eigenfunctions. The matrix of $V(\boldsymbol{r})$ given by Eq. (2.1) with respect to the wave functions of the first two of (2.2) is calculated to be

$$\begin{pmatrix} \frac{4}{7}\langle B\rangle+\frac{4}{35}\langle D\rangle+\frac{16}{35}\langle F\rangle & -\frac{4\sqrt{3}}{21}(\langle A\rangle-\langle G\rangle) \\ -\frac{4\sqrt{3}}{21}(\langle A\rangle-\langle G\rangle) & -\frac{4}{7}\langle B\rangle+\frac{4}{35}\langle D\rangle+\frac{8}{105}\langle F\rangle \end{pmatrix} \tag{2.3}$$

where $\langle A\rangle$, etc. are defined by

$$\langle A\rangle=-e\int_0^\infty A(r)|\psi(r)|^2r^2dr\,,\quad \text{etc.,}\qquad (e>0) \tag{2.4}$$

$\psi(r)$ being the normalized $3d$ radial wave function. The eigenvalues of (2.3) are

$$\left.\begin{matrix}E_g\\E_h\end{matrix}\right\}=\frac{4}{35}\langle D\rangle+\frac{4}{15}\langle F\rangle\mp\frac{4}{7}\sqrt{\left(\langle B\rangle+\frac{1}{3}\langle F\rangle\right)^2+\frac{1}{3}\left(\langle A\rangle-\langle G\rangle\right)^2}\,. \tag{2.5}$$

The corresponding wave functions can be found in the usual way. The energy eigenvalues corresponding to the last three of (2.2) are calculated to be

$$\begin{aligned} E_{\mathrm{I}} &=-\frac{4}{7}\langle B\rangle-\frac{8}{105}(\langle D\rangle-\langle F\rangle)\,,\\ E_{\mathrm{II}} &=\frac{2}{7}(\langle A\rangle+\langle B\rangle)-\frac{8}{105}\langle D\rangle-\frac{32}{105}\langle F\rangle+\frac{8}{21}\langle G\rangle\,,\\ E_{\mathrm{III}} &=\frac{2}{7}(-\langle \mathrm{A}\rangle+\langle B\rangle)-\frac{8}{105}\langle D\rangle-\frac{32}{105}\langle F\rangle-\frac{8}{21}\langle G\rangle\,. \end{aligned} \tag{2.6}$$

(ii) The case of $CoF_2$

A free $Co^{++}$ ion has the configuration $(3d)^7$ from which quartet states $^4F$ and $^4P$ result. We may confine ourselves to these two multiplets. In this case, too, the orthorhombic crystalline field lifts the orbital degeneracy perfectly. We can confine ourselves to two $3d$ electrons of the cobalt ion outside the half-filled $3d$-shell. The wave functions of the $^4F$ and $^4P$ can be obtained by antisymmetrizing the following product of the one-electron spin-free functions since we are dealing with the state of the highest multiplicity:

$^4F$:

$$M=\pm3\qquad \phi_{\pm2}(1)\phi_{\pm1}(2)$$
$$M=\pm2\qquad \phi_{\pm2}(1)\phi_0(2)$$

$$\begin{array}{ll} M=\pm 1 & \sqrt{\frac{3}{5}}\,\phi_{\pm 2}(1)\phi_{\mp 1}(2)+\sqrt{\frac{2}{5}}\,\phi_{\pm 1}(1)\phi_0(2) \\ M=0 & \frac{1}{\sqrt{5}}\,\phi_2(1)\phi_{-2}(2)+\frac{2}{\sqrt{5}}\,\phi_1(1)\phi_{-1}(2)\;; \end{array} \tag{2.7}$$

$^4$P:

$$\begin{array}{ll} M=\pm 1 & \sqrt{\frac{2}{5}}\,\phi_{\pm 2}(1)\phi_{\mp 1}(2)-\sqrt{\frac{3}{5}}\,\phi_{\pm 1}(1)\phi_0(2) \\ M=0 & \frac{2}{\sqrt{5}}\,\phi_2(1)\phi_{-2}(2)-\frac{1}{\sqrt{5}}\,\phi_1(1)\phi_{-1}(2)\;. \end{array} \tag{2.8}$$

Here the suffixes of $\phi$ are the magnetic quantum numbers of the individual electrons. The antisymmetrized wave functions may be denoted as $\psi_{3M}$ ($M=\pm 3, \pm 2, \pm 1, 0$) and $\psi_{1M}$ ($M=\pm 1, 0$); they transform under rotation, as known well, in the same way as the surface harmonics of the third and first degrees. We combine them into such forms that are eigenfunctions for the field of orthorhombic symmetry (i.e. the bases of the irreducible representations of the group $V_h$). The third column of the following are such combinations:

$$\begin{array}{lll} A_1 & xyz & \frac{1}{\sqrt{2}\,i}(\psi_{32}-\psi_{3-2}) \\ B_1 1 & z\left(z^2-\frac{3}{5}r^2\right) & \psi_{30} \\ B_2 1 & y\left(y^2-\frac{3}{5}r^2\right) & \frac{1}{4}\{\sqrt{5}\,(\psi_{33}-\psi_{3-3})-\sqrt{3}\,(\psi_{31}-\psi_{3-1})\} \\ B_3 1 & x\left(x^2-\frac{3}{5}r^2\right) & \frac{1}{4i}\{\sqrt{5}\,(\psi_{33}+\psi_{3-3})+\sqrt{3}\,(\psi_{31}+\psi_{3-1})\} \\ B_1 2 & z(x^2-y^2) & \frac{1}{\sqrt{2}}(\psi_{32}+\psi_{3-2}) \\ B_2 2 & y(z^2-x^2) & \frac{1}{4}\{\sqrt{3}\,(\psi_{33}-\psi_{3-3})+\sqrt{5}\,(\psi_{31}-\psi_{3-1})\} \\ B_3 2 & x(y^2-z^2) & \frac{1}{4i}\{-\sqrt{3}\,(\psi_{33}+\psi_{3-3})+\sqrt{5}\,(\psi_{31}+\psi_{3-1})\} \\ B_1 3 & z & \psi_{10} \\ B_2 3 & x & \frac{1}{\sqrt{2}}(\psi_{11}-\psi_{1-1}) \\ B_3 3 & y & \frac{1}{\sqrt{2}\,i}(\psi_{11}+\psi_{1-1})\;. \end{array} \tag{2.9}$$

The second column gives in cartesian coordinates the functions which transform in the same way as the corresponding wave functions and the first column specifies the kinds of the irreducible representations; $A_1$, $B_1$, $B_2$, $B_3$ are all different irreducible representations, but since we have three wave functions for each of $B_1$, $B_2$, $B_3$, we number them as $B_1^1$, $B_1^2$, $B_1^3$, etc. For the perturbing potential $V(\boldsymbol{r})$ given by (2.1), each set of these three yields a three-dimentional energy matrix from which the energy eigenvalues and the corresponding wave functions can be obtained. These matrices were calculated, and the results are as follows. We write, in order to save the space, simply $A, B, \cdots$ for $\langle A\rangle$, $\langle B\rangle, \cdots$ and $(i, j)_k$ for the matrix element of $V(\boldsymbol{r})$ with respect to the wave functions of $B_k i$ and $B_k j$; then the matrix elements are:

$$(A_1|V(\boldsymbol{r})|A_1)=8D/35+8F/15; \tag{2.10}$$

$$(1,1)_1=4(2B-D-4F)/35\;,$$

Table I. (atomic units)

| | $FeF_2$ | | $CoF_2$ | |
|---|---|---|---|---|
| | TKS | Pauling | TKS | Pauling |
| $A/r^2$ | 0.004,430 | 0.004,045 | 0.001,141 | −0.000,282 |
| $B/r^2$ | −0.003,245 | −0.003,615 | −0.004,074 | −0.005,482 |
| $D/r^4$ | −0.004,970 | −0.004,858 | −0.004,870 | −0.004,489 |
| $F/r^4$ | 0.001,464 | 0.001,441 | 0.001,722 | 0.001,647 |
| $G/r^4$ | −0.002,338 | −0.002,341 | −0.002,539 | −0.002,568 |

$$\begin{aligned}
&(1,2)_1=4(-A+G)/7\sqrt{15}\ ,\\
&(2,2)_1=4D/105+8F/15\ ,\\
&(1,3)_1=8(-9B+D+4F)/105\ ,\\
&(2,3)_1=8(-A+G)/7\sqrt{15}\ ,\\
&(3,3)_1=-4B/5+(^4\mathrm{P})-(^4\mathrm{F});
\end{aligned}\qquad(2.11)$$

$$\begin{aligned}
&(1,1)_2=2(2A-2B-2D-3F+5G)/35\ ,\\
&(1,2)_2=2(-A-3B-F+G)/7\sqrt{15}\ ,\\
&(2,2)_2=4D/105-2F/15-2G/3\ ,\\
&(1,3)_2=4(-3A+3B+F)/35\\
&\qquad\qquad +8D/105-4G/21\ ,\\
&(2,3)_2=4(-A-3B-F+G)/7\sqrt{15}\ ,\\
&(3,3)_2=2(-A+B)/5+(^4\mathrm{P})-(^4\mathrm{F});
\end{aligned}\qquad(2.12)$$

$$\begin{aligned}
&(1,1)_3=-2(2A+2B+2D+3F+5G)/35\ ,\\
&(1,2)^3=2(-A+3B+F+G)/7\sqrt{15}\ ,\\
&(2,2)_3=4D/105-2F/15+2G/3\ ,\\
&(1,3)_3=-4(3A+3B+F)/35\\
&\qquad\qquad -8D/105-4G/21\ ,\\
&(2,3)_3=4(A-3B-F-G)/7\sqrt{15}\ ,\\
&(3,3)_3=2(A+B)/5+(^4\mathrm{P})-(^4\mathrm{F})\ .
\end{aligned}\qquad(2.13)$$

In the above expressions for $(3,3)_k$, $(^4\mathrm{P})-(^4\mathrm{F})$ means the energy difference between the $^4$P and $^4$F levels of the free cobalt ion; its value is 14000 cm$^{-1}$.

We assume in this section the 'point charge model' of the crystals, for which the authors have reported numerical results for the crystalline electric potential[8]. In this model, the ions are replaced by point charges and the dipole-moments induced on the fluorine ions by point dipoles. The magnitude of these dipole moments has been determined by a self-consistent method using the value of the polarizability of the fluorine ion given either by Pauling[9] or Tessman, Kahn and Shockley[10]. We reproduce the result for the coefficients in (2.1) in Table I, in atomic units (abbreviated as A. U. in the following).

Table II. (in cm$^{-1}$)

| | $FeF_2$ | | $CoF_2$ | |
|---|---|---|---|---|
| | TKS | Pauling | TKS | Pauling |
| $\langle A\rangle$ | − 3137 | − 2864 | − 663 | + 164 |
| $\langle B\rangle$ | + 2297 | + 2560 | + 2367 | + 3185 |
| $\langle D\rangle$ | +18240 | +17829 | +12032 | +11089 |
| $\langle F\rangle$ | − 5373 | − 5288 | − 4253 | − 4069 |
| $\langle G\rangle$ | + 8579 | + 8590 | + 6272 | + 6344 |

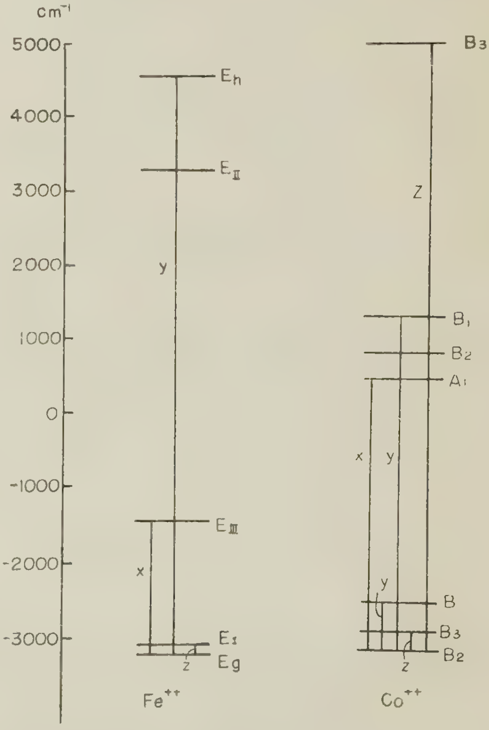

Fig. 2. Energy level splitting of Fe$^{++}$ ion in Fe$_2$F and Co$^{++}$ in CoF$_2$ calculated with the use of the point charge model. $x$, $y$ and $z$ represent the components of orbital angular momentum connecting the orbital ground and excited states.

Values of $\langle A\rangle$, $\langle B\rangle$, etc. defined by (2.4) can be obtained from the average values of $r^2$ and $r^4$ with respect to the 3$d$ radial function. We adopt Slater's[11] semi-empirical functions for the radial wave functions of Fe$^{++}$

and $Co^{++}$. They are hydrogen-like with effective nuclear charges $Z=6.25$ and 6.9 A. U., respectively for $Fe^{++}$ and $Co^{++}$. With these functions we obtain $\langle r^2\rangle=126Z^{-2}$ A.U. and $\langle r^4\rangle=25515\ Z^{-4}$ A.U., namely, we have

$$\langle r^2\rangle_{\mathrm{Fe}}=3.226\ \mathrm{A.U.} \qquad \langle r^2\rangle_{\mathrm{Co}}=2.647\ \mathrm{A.U.}$$

$$\langle r^4\rangle_{\mathrm{Fe}}=16.72\ \mathrm{A.U.} \qquad \langle r^4\rangle_{\mathrm{Co}}=11.26\ \mathrm{A.U.}$$

The values of $\langle A\rangle$, etc. thus calculated are enlisted in Table II, and the energy level splittings obtained with these values are shown in Fig. 2.

We see that both in $FeF_2$ and $CoF_2$ the first excited level liesly close to the ground level, the separation between them being of the order of 100 cm$^{-1}$, i.e. comparable with the magnitude of the spin-orbit coupling. Therefore, we are lead to conclude that the ground state posesses a considerable amount of orbital moment and so principal values of $g$ much different from 2. Also, the first excited state produces the $z$-component of the orbital angular momentum in both cases, so that $g_{\parallel}$ must be much greater than $g_{\perp}$ and consequently $\chi_{\parallel}$ much greater than $\chi_{\perp}$. The measurements of Stout and Mattarrese show, however, that although $\chi_{\parallel}$ exceeds $\chi_{\perp}$ above $T_c$ (except when close to $T_c$) in $FeF_2$, the values of $g$ in this substances are not much different from 2. Therefore the level separation must actually be much greater than that calculated here, i.e. 1000 cm$^{-1}$ or greater. Also, in the case of $CoF_2$, the measured $g$ values are not much different from 2. These facts show clearly the inadequacy of our point charge model. We shall therefore take account of the spatial extension of the electron clouds of the fluorine ions in the next section.

## § 3. Effect of Overlap Between Electron Clouds

We now wish to calculate the potential around a cation, taking account of the effect of the extension of the surrounding six fluorine electron clouds which inevitably overlap the cation $3d$ electron cloud. If this potential is expressed in the form (2.1), the coefficients $A(r)$, etc. are no longer proportional to $r^l$ ($l=2$ or 4). They must be determined by solving Poisson's equation. We shall denote the charge density of the $j$-th of the six fluorine ions at point $\boldsymbol{r}$ by $\sigma(x_j)$, where $x_j=|\boldsymbol{x}_j|=|\boldsymbol{r}-\boldsymbol{P}_j|$ ($j=1, 2\cdots, 6$), $\boldsymbol{P}_j$ being the position vector of the $j$-th fluorine ion, and for this we shall make use of the Hartree charge distribution modified by Benson and Wylie[12]).

Then the following potential must be added to the potential calculted with the point charge model:

$$\Phi_0(\boldsymbol{r})=\sum_{j=1}^{6}\phi(x_j) \tag{3.1}$$

where

$$\begin{aligned}\phi(x_j)&=-\frac{1}{x_j}\int_0^{x_j}\sigma(x)4\pi x^2dx\\&\quad-\int_{x_j}^{\infty}\frac{\sigma(x)}{x}4\pi x^2dx+\frac{ne}{x_j} \qquad (3.2)\\&=\frac{1}{x_j}\int_{x_j}^{\infty}\sigma(x)4\pi x^2dx-\int_{x_j}^{\infty}\sigma(x)4\pi x\,dx\ ,\end{aligned}$$

$n$ being the number of electrons in the fluorine ion so that $n=\int\sigma(x)4\pi x^2dx$. We shall consider in the following only six $2p$ electrons of the fluorine ion and neglect the two $2s$ electrons ($n=6$). This is because the $2s$ electron were neglected by Benson and Wyllie when they modified the Hartree charge cloud of fluorine ion so as to explain the observed diamagnetic susceptibility (they changed the linear scale of the Hartree $2p$ radial function in a suitable way) and this modification appears to take account to some extent of the effect of the $2s$ electron cloud. Moreover, we shall later arbitrarily change the overlap potential $\Phi_0(\boldsymbol{r})$ by multiplying it by a suitable factor not much different from unity so that the effect of the $2s$ electron will there again approximately be taken into consideration.

Expanding (3.1) in (normalized) spherical harmonics, we have

$$\begin{aligned}\Phi_0(\boldsymbol{r})&=\sum_m\varphi_{2m}(r)Y_{2m}(\theta,\varphi)\\&\quad+\sum_m\varphi_{4m}(r)Y_{4m}(\theta,\varphi)\ .\end{aligned} \tag{3.3}$$

$\varphi_{2m}(r)$'s and $\varphi_{4m}(r)$'s are related in a certain way to the overlap part $A_0(r)$, $B_0(r)$, etc. of $A(r)$, $B(r)$, etc. In calculating each contribution from $\phi(x_j)$ to $\varphi_{2m}(r)$ and $\varphi_{4m}(r)$, it is convenient to transform the coordinate axes in such a way that the new polar axis points to the $j$-th fluorine ion; then, since $\phi(x_j)$ has axial symmetry, we have only axially symmetric surface harmonics in the new system. This calculation is given in Appendix.

Lattice parameters for $FeF_2$ and $CoF_2$ are

$FeF_2$: $a=4.670$ Å $c=3.297$ Å $u=0.31$

$CoF_2$: $a=c=4.69$ $c=3.19$ $u=0.31$

and the values $P_1, P_2$ and $\theta$ in Fig. 3 are as follows:

| | $P_1$ | $P_2$ | $\theta$ |
|---|---|---|---|
| $FeF_2$ | 3.869,2 Å | 3.915,3 Å | 0.795,70 |
| $CoF_2$ | 3.885,7 | 3.841,6 | 0.619,95 |

The Hartree radial density distribution of the $2p$-electrons in a free fluorine ion can be fitted by an analytical expression of the form

$$R(r)=r\{A_1 \exp(-\alpha_1 r)+A_2 \exp(-\alpha_2 r)\},$$

and, as mentioned before, Benson and Wyllie changed the linear scale of this radial distribution so as to make the calculated diamagnetic susceptibility of the fluorine ion with $2p$ electrons only fit the observed value. The results were

$$A_1=16.445,9 \qquad \alpha_1=3.29$$
$$A_2=0.703,87 \qquad \alpha_2=1.18 \quad \text{(atomic units)}$$

We use these values and, after numerical calculations, obtain for the potential $\phi(x)$

$$\phi(x)=\sum_{i=1}^{3} D_i e^{-\delta_i x}\left[\frac{24}{\delta_i x}+18+6\delta_i x+\delta_i^2 x^2\right],$$

with

$$D_1=0.865,69 \quad D_2=0.347,94 \quad D_3=0.095,827$$
$$\delta_1=6.58 \quad \delta_2=4.47 \quad \delta_3=2.36\,. \quad \text{(atomic units)}$$

This potential is substituted in eq. (A. 3) of the Appendix, and the integrations were carried out graphically. In Table III we give the result for $\varphi_l(r; j)$ for $j=1$ in the case of $FeF_2$, where

$$\varphi_l(r;j)=\int \phi(x_j) Y_{l0}(\theta_j, \varphi_j) d\Omega\,. \qquad (3.4)$$

For $j=2$ of the case of $FeF_2$, we arrived at the following results:

$$\varphi_2(r;2)=0.90\varphi_2(r;1), \quad \varphi_4(r;2)=0.89\varphi_4(r;1).$$

For $CoF_2$, we assumed a relation $\varphi(r;j)_{Co}=k_j^{(l)}\varphi(r;j)_{Fe}$ and determined the ratio $k_j^{(l)}$ by calculating $\varphi_l(r;j)_{Co}$ at $r=2$ (A.U.) and comparing it with $\varphi_l(r;j)_{Fe}$ at $r=2$. The results were

$$k_1^{(2)}=0.97, \qquad k_2^{(2)}=1.06,$$
$$k_1^{(4)}=0.97, \qquad k_2^{(4)}=1.04.$$

Table III. (atomic units)

| $r$ | $\varphi_2(r;1)_{Fe}$ | $\varphi_4(r;1)_{Fe}$ |
|---|---|---|
| 0.6 | 0.001,509 | 0.000,126,3 |
| 1.0 | 0.004,756 | 0.000,730,3 |
| 1.6 | 0.015,655 | 0.005,092 |
| 2.0 | 0.030,52 | 0.014,74 |
| 2.6 | 0.081,25 | 0.058,67 |
| 3.0 | 0.163,1 | 0.145,2 |
| 3.6 | 0.503,5 | 0.568,8 |
| 4.0 | 0.615,6 | 0.721,9 |

Table IV.

| | $FeF_2$ | $CoF_2$ |
|---|---|---|
| $\langle A_0\rangle$ | + 2461 cm⁻¹ | + 784 cm⁻¹ |
| $\langle B_0\rangle$ | − 1494 | − 1374 |
| $\langle D_0\rangle$ | −24953 | −15522 |
| $\langle F_0\rangle$ | + 6622 | + 4610 |
| $\langle G_0\rangle$ | − 9373 | − 6282 |

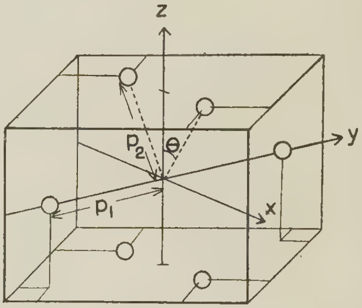

Fig. 3. Definition of coordinate axes, angle $\theta$ and lengths $P_1$ and $P_2$.

For the $3d$ wave function of the cation we tried a few possible ones, including that which is obtainable by modifying in a suitable way the Mn $3d$ function determined by neutron diffraction, but finally decided to adopt Slater's wave function[11]. After graphical integrations, we obtained the following result for the average of $\varphi_l(r;j)$ over the $3d$ electron cloud:

For $FeF_2$ $\langle\varphi_2(r;1)\rangle=0.034,89$

$\langle\varphi_4(r;1)\rangle=0.024,72$

For $CoF_2$ $\langle\varphi_2(r;1)\rangle=0.024,11$

$\langle\varphi_4(r;1)\rangle=0.014,95$

With all these results, we calculate the average values $A_0(r)$, $B_0(r)$, etc., the results of which are summarized in Table IV.

Finally, we might mention about another correction to the point-charge model. In this model, we tacitly assumed that the coefficients of the spherical harmonics of the second and fourth degrees of the potential are proportional to $r^2$ and $r^4$. This is valid only when $r$ is less than the radius of the sphere on whose surface lies one of the six neighbouring fluorine point charges; when $r$ exceed this radius these coefficient will no longer be proportional to $r^2$ and $r^4$. The actual $3d$ electron does not extend so far away and the correction due to this change is very small. Nevertheless, we took this small correction into account in the present calculation.

## § 4. Paramagnetic Susceptibility of FeF$_2$

The energy level splitting of the Fe$^{++}$ ion in FeF$_2$ obtained by the calculations described in the preceding sections is shown in Fig. 4. We adopted TKS's value of the polarizability $\alpha$ of the F$^-$ ion (the same for CoF$_2$, next paragraph). According to this result, the lowest excited level lies at about 1000 cm$^{-1}$ above the ground level, so that the ground state is predominantly populated at and below room temperature. In this temperature range, we are therefore allowed to confine ourselves to the ground state in calculating the paramagnetic susceptibility. Each of the split levels has five-fold degeneracy which, however, is lifted by introducing the spin-orbit coupling. The magnitude of the spin-orbit coupling constant is about $-100$ cm$^{-1}$, which is small compared to the energy level separations, so we can use Pryce's[13)] effective spin Hamiltonian for the ground quintet.

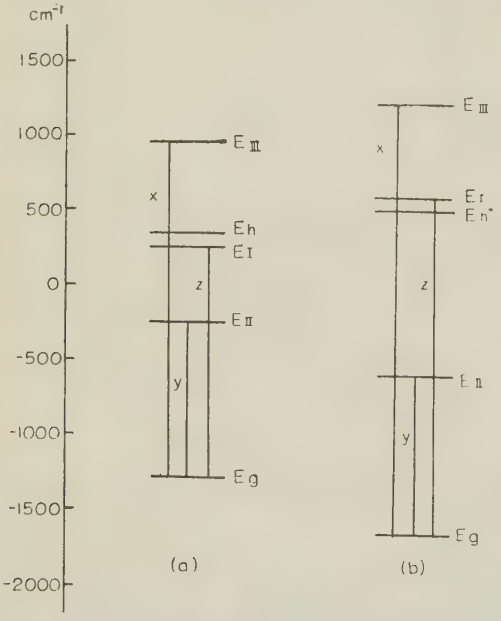

Fig. 4. Energy level splitting of Fe$^{++}$ ion in FeF$_2$. (a) is obtained taking account of the overlap effect calculated in § 3 and (b) increasing this effect by 10%. $x$, $y$ and $z$ represent the components of orbital angular momentum connecting the orbital ground and excited states.

We denote the spins on the body-centre sites by $\boldsymbol{S}^{(1)}$ and those on the corner sites by $\boldsymbol{S}^{(2)}$, and use the molecular field approximation to describe the exchange coupling among them. The effective spin Hamiltonian for the spins, say on the body-centre sites, is then written

$$\begin{aligned}\mathscr{H}^{(1)}=&-\lambda^2(\Lambda_x S_x^{(1)2}+\Lambda_y S_y^{(1)2}+\Lambda_z S_z^{(1)2})\\ &-\beta^2(\Lambda_x H_x^2+\Lambda_y^2 H_y+\Lambda_z H_z^2)\\ &+\beta(g_x H_x S_x^{(1)}+g_y H_y S_y^{(1)}+g_z H_z S_z^{(1)})\\ &-2J_1 z_1 \boldsymbol{S}^{(1)}\cdot\langle \boldsymbol{S}^{(2)}\rangle-2J_2 z_2 \boldsymbol{S}^{(1)}\cdot\langle \boldsymbol{S}^{(1)}\rangle\,, \quad (4.1)\end{aligned}$$

where $\lambda$ is the spin-orbit coupling constant ($\lambda=-100$ cm$^{-1}$ for the free Fe$^{++}$ ion[14)]), $\beta$ the Bohr magneton, $\boldsymbol{H}$ the external magnetic field, $J_1$, $J_2$ the exchange integrals between nearest neighbours and between second neighbours, $z_1(=6)$, $z_2(=2)$ the numbers of the nearest and second neighbours, and $\Lambda_x$, etc. are defined by

$$\Lambda_x=\sum_i \frac{(g|L_x|i)(i|L_x|g)}{E_i-E_g}\,,\ \text{etc.,} \quad (4.2)$$

where $\boldsymbol{L}$ stands for the orbital angular momentum and $g$, $i$, refer to the ground and excited orbital states; $g_x$, $g_y$, $g_z$ are the principal values of the $g$-tensor, the principal axes of which being the $x$-, $y$-, $z$-axes, and are related to $\Lambda_x$, etc. by

$$g_x=2(1-\lambda\Lambda_x)\,,\ \text{etc.} \quad (4.3)$$

The Hamiltonian for the ions on the corner sites is obtained by interchanging $\Lambda_x$, $g_x$ with $\Lambda_y$, $g_y$. The second term of the Hamiltonian (4.1), which is spin-independent and quadratic in $H$, corresponds to the second order interaction between the orbital magnetic moment and the external field, and gives a temperature-independent paramagnetic susceptibility. For a moment we drop this constant term from the Hamiltonian but will add it later. The third and fourth terms are to be regarded as small perturbations to the first term when we discuss the field-independent paramagnetic susceptibility above the Curie point, because then $H$ and $\langle S\rangle$ are small. So we write the Hamiltonian as

$$\mathscr{H}=\mathscr{H}_0+\mathscr{H}'\,,$$

where $\mathscr{H}'$ is the perturbing term. The matrices of $\mathscr{H}_0$ and $\mathscr{H}'$ in the representation diagonalizing $S_z^{(1)}$ can be obtained easily, and $\mathscr{H}_0$ can be diagonalized after transforming the spin functions of $S_z^{(1)}=1, -1$ by

$$\frac{1}{\sqrt{2}}\begin{pmatrix}1 & 1\\ 1 & -1\end{pmatrix}, \tag{4.4}$$

and the spin functions of $S_z^{(1)}=2, 0, -2$ by

$$\frac{1}{\sqrt{2}}\begin{pmatrix}\cos\theta & \sqrt{2}\sin\theta & \cos\theta\\ \sin\theta & -\sqrt{2}\cos\theta & \sin\theta\\ 1 & 0 & -1\end{pmatrix} \tag{4.5}$$

where

$$\tan 2\theta=\frac{\sqrt{3}\Lambda_-}{3\Lambda_z-\Lambda_+} \quad (\Lambda_\pm=\Lambda_x\pm i\Lambda_y)\,. \tag{4.6}$$

The diagonal elements of $\mathscr{H}_0/\lambda^2$ are then

$$\begin{aligned}
&1.\quad -\left(\Lambda_z+\frac{5}{2}\Lambda_++\frac{3}{2}\Lambda_-\right),\\
&2.\quad -\left(\Lambda_z+\frac{5}{2}\Lambda_+-\frac{3}{2}\Lambda_-\right),\\
&3.\quad -2(\Lambda_z+\Lambda_+)+\sqrt{4\Lambda_z^2+\Lambda_+^2+3\Lambda_-^2-4\Lambda_z\Lambda_+}\,,\\
&4.\quad -2(\Lambda_z+\Lambda_+)-\sqrt{4\Lambda_z^2+\Lambda_+^2+3\Lambda_-^2-4\Lambda_z\Lambda_+}\,,\\
&5.\quad -4\Lambda_z-\Lambda_+\,.
\end{aligned} \tag{4.7}$$

In this representation, the matrix of $\mathscr{H}'$ becomes as follows (the off-diagonal elements below the diagonal are omitted):

$$\mathscr{H}'=\begin{pmatrix}
0 & F_z^{(1)} & F_x^{(1)}(\cos\theta+\sqrt{3}\sin\theta) & F_x^{(1)}(\sin\theta-\sqrt{3}\cos\theta) & iF_y^{(1)}\\
 & 0 & iF_y^{(1)}(\cos\theta-\sqrt{3}\sin\theta) & iF_y(\sin\theta+\sqrt{3}\cos\theta) & F_x^{(1)}\\
 & & 0 & 0 & 2F_z^{(1)}\cos\theta\\
 & & & 0 & 2F_z^{(1)}\sin\theta\\
 & & & & 0
\end{pmatrix} \tag{4.8}$$

where

$$F_z^{(1)}=\beta g_zH_z-2J_1z_1\langle S_z^{(2)}\rangle-2J_2z_2\langle S_z^{(1)}\rangle\,, \quad \text{etc.}, \tag{4.9}$$

The paramagnetic susceptibility is given by the formula

$$\chi=\frac{1}{H}\frac{1}{Z_0}\sum_{nn'}\frac{\exp(-E_n/kT)-\exp(-E_{n'}/kT)}{E_{n'}-E_n}\frac{\partial}{\partial H}|(\mathscr{H}')_{nn'}|^2\,, \tag{4.10}$$

where $n$, $n'$ $(=1, 2, 3, 4, 5)$ refer to the eigen-state of $\mathscr{H}_0$ and $Z_0=\sum_n\exp(-E_n/kT)$. Taking the differentiation in (4,10) along the $z$-axis, $\chi_{\|}$ is obtained as

$$\chi_{\|}=\frac{\delta_1}{kT}\frac{1}{2H_z}\frac{\partial}{\partial H_z}F_z^2=\frac{\delta_1}{kT}\{g_z^2\beta^2+(2J_1z_1+2J_2z_2)\chi_{\|}\}\,,$$

where $\delta_1$ is given below by (4.14). The relation $g_z\beta\langle S_z\rangle=\chi_{\|}H_z$ was here used. It follows thus

$$\chi_{\|}=\frac{\delta_1\beta^2g_z^2}{kT-(2J_1z_1+2J_2z_2)\delta_1}\,.$$

The perpendicular susceptibility is obtained as the average of $\chi_x^{(1)}$ and $\chi_x^{(2)}$ $(=\chi_y^{(1)})$, which can be calculated in the same way as $\chi_{\|}$. With abbreviations

$$-(2J_1z_1-2J_2z_2)/k=\alpha\,, \qquad -(2J_1z_1+2J_2z_2)k=\gamma\,, \tag{4.11}$$

expressions for $\chi_{\|}$ and $\chi_{\perp}$, after adding the temperature-independent susceptibility, are obtained as

$$\chi_{\|}=N_0\beta^2\left[\frac{1}{k}\frac{\delta_1g_z^2}{T+\gamma\delta_1}+2\Lambda_z\right] \tag{4.12}$$

$$\chi_{\perp}=N_0\beta^2\left[\frac{\delta_2g_x^2+\delta_3g_y^2+\delta_2\delta_3\{(g_x-g_y)^2\gamma-(g_x+g_y)^2\alpha\}/2T}{k\{2T+(\delta_2+\delta_3)(\gamma-\alpha)-2\delta_2\delta_3\alpha\gamma/T\}}+\Lambda_x+\Lambda_y\right], \tag{4.13}$$

where

$$\delta_1=\frac{2kT}{Z_0}\left[\frac{\exp(-E_1/kT)-\exp(-E_2/kT)}{E_2-E_1}+\frac{\exp(-E_3/kT)-\exp(-E_5/kT)}{E_5-E_3}4\cos^2\theta\right.$$
$$\left.+\frac{\exp(-E_4/kT)-\exp(-E_5/kT)}{E_5-E_4}4\sin^2\theta\right]$$

$$\delta_2=\frac{2kT}{Z_0}\Big[\frac{\exp(-E_1/kT)-\exp(-E_3/kT)}{E_3-E_1}(\cos\theta+\sqrt{3}\sin\theta)^2 \tag{4.14}$$

$$+\frac{\exp(-E_1/kT)-\exp(-E_4/kT)}{E_4-E_1}(\sin\theta-\sqrt{3}\cos\theta)^2+\frac{\exp(-E_2/kT)-\exp(-E_5/kT)}{E_5-E_2}$$

$$\delta_3=\frac{2kT}{Z_0}\Big[\frac{\exp(-E_1/kT)-\exp(-E_5/kT)}{E_5-E_1}+\frac{\exp(-E_2/kT)-\exp(-E_3/kT)}{E_3-E_2}(\cos\theta-\sqrt{3}\sin\theta)^2$$

$$+\frac{\exp(-E_2/kT)-\exp(-E_4/kT)}{E_4-E_2}(\sin\theta+\sqrt{3}\cos\theta)^2\Big].$$

Next we turn to numerical evaluations. $\alpha$ can be estimated from the experimental value of the Curie temperature with the use of the relation $T_c=\alpha\delta_1$, which is given by the molecular field theory. $\gamma$ may be so chosen as to make the calculated susceptibilities fit their experimental values. For convenience, however, we estimate it from the powder susceptibility data[15] using the relation between $\Theta$ (paramagnetic Curie temperature) and $T_c$ given by the molecular field theory; then we obtain $\gamma=1.48\,\alpha$. $T_c$ is 78.3°K from the specific heat measurements.

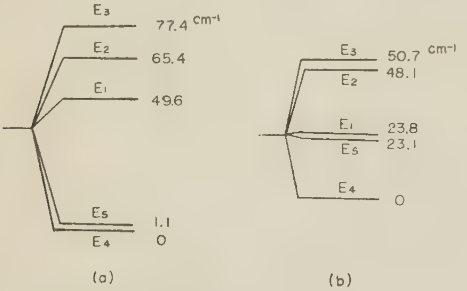

Fig. 5. Quintet separation of orbital ground state of Fe⁺⁺ ion.
(a) is obtained taking account of the overlap effect calculated in § 3 and (b) increasing this effect by 10%.

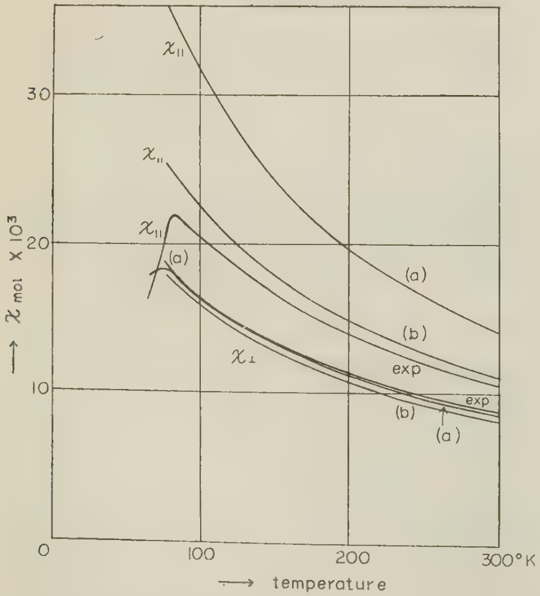

Fig. 6. Paramagnetic parallel and perpendicular susceptibilities of $FeF_2$.
(a) are obtained taking account of the overlap effect calculated in § 3 and (b) increasing this effect by 10%.

The results of the numerical computations are as follows. The $g$-tensor and $\alpha$ and $\gamma$ are

$$g_x=2.168,\quad g_y=2.063,\quad g_z=2.492;$$
$$\alpha=26.8,\quad \gamma=39.7.$$

The quintet separations are as shown in Fig. 5 (a), where we used for $\lambda$ the value of the free iron ion.

The obtained paramangetic susceptibility is shown by curve (a) in Fig 6; we see that, though its general feature and the order of magnitude of $\chi_{\parallel}-\chi_{\perp}$ are right, the quantitative agreement is poor.

In order to improve the agreement, we changed the overlap potential calculated in § 3 by multiplying it by a suitable constant factor. In § 3 we took account of the extension of the $2p$-electron cloud of the F⁻ ion but neglected those of the $1s$ and $2s$ cloud. There may be other effects such as a change in the radial distribution of the electron density of the fluorine ions when they are brought into the crystal and also exchange effect between fluorine ions and the iron ions. With a hope to take all these effects, we simply multiply the overlap potential factor by a constant numerical factor. When this is taken to be 1.10, we get the following values:

$$g_x=2.175,\quad g_y=2.013.\quad g_z=2.306;$$
$$\alpha=32.9,\quad \gamma=48.6.$$

The quintet separations become as shown in Fig. 5 (b) and the calculated paramagnetic susceptibility as shown in Fig. 6, curve (b). The agreement has now become much improved;

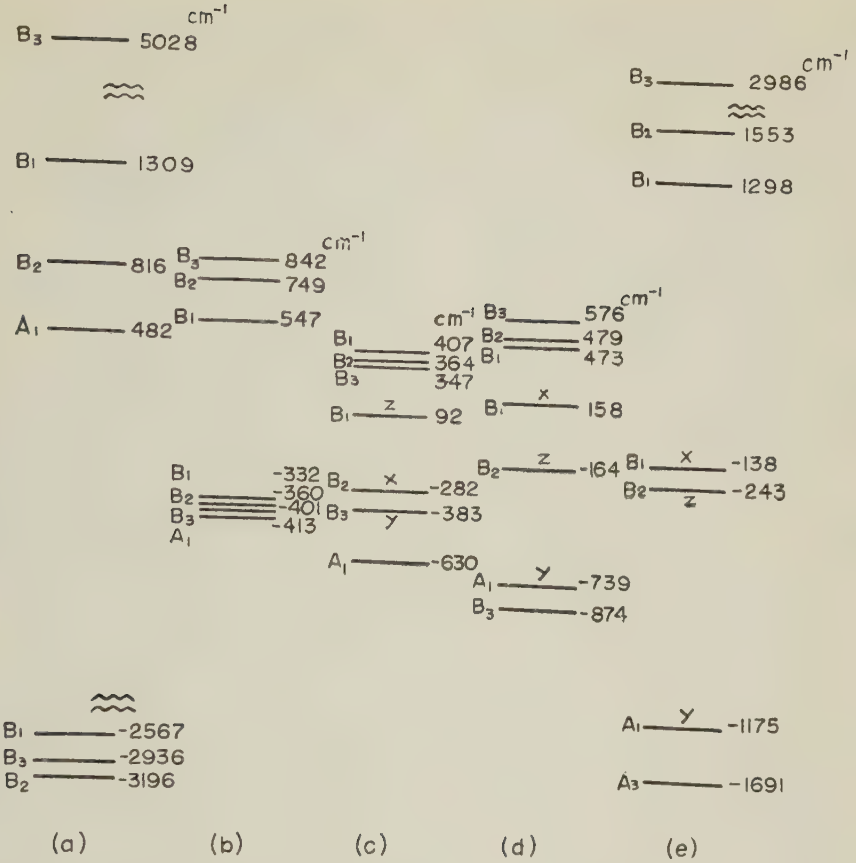

Fig. 7. Separation of orbital levels of $Co^{++}$ ion in $CoF_2$.
(a) is obtained with the use of the point charge model, (c) taking account of the overlap effect calculated in § 3, (d) and (e) increasing this effect by 10% and 50%, respectively, and (b) decreasing it by 20%. $x$, $y$ and $z$ represent the components of orbital angular momentum connecting the orbital ground state and the excited states indicated by them.

no better agreement could be obtained by taking other multiplicative factor.

## § 5. Calculation for $CoF_2$

The magnetic anisotropy of $CoF_2$ has been measured by Stout and Matarrese[2]. By combining their data with the powder susceptibility measurd by de Haas and Schultz[16], they have calculated the principal susceptibilities $\chi_\perp$ and $\chi_\parallel$. They found that the magnetic behaviours of $CoF_2$ differ much from those of $FeF_2$. According to the specific heat measurements by Stout and Catalano[4], $CoF_2$ has a Curie temperature of 37.7°K which is low compared with the Curie temperatures of other iron group fluorides. The magnetic anisotropy $\chi_\parallel - \chi_\perp$ of $CoF_2$ changes its sign at a temperature much higher than the Curie temperature, whereas in the case of $FeF_2$ this takes place just below the Curie temperature. The susceptibility perpendicular to the $c$-axis increases rapidly with decreasing temperature in the range between 100°K and 10°K; the susceptibility parallel to the $c$-axis does not tend to zero at 0°K. Though these anomalous behaviours of the principal susceptibilities are not yet confirmed by measurement with single crystal specimens, they make the study of $CoF_2$ very interesting.

We calculated the separation of the orbital levels of $Co^{++}$ using the potential calculated in § 2 and § 3. The results are shown in Fig. 7 (a)~(e). In these diagrams are indicated the components of the orbital angular momentum which connect the ground level to the corresponding upper levels. The magnitude of the matrix elements between these levels are nearly equal to 2 measured in units of $\hbar$. If we adopt the potential obtained by increasing the overlap effect by 10%, as we did in the case of $FeF_2$, the total energy separation of $^4F$ state of $Co^{++}$ is about 1450 $cm^{-1}$ and the separation between the ground level and the next level is only 140 $cm^{-1}$ as shown in Fig.7(d). Taking the spin-orbit coupling into account, each orbital state is split into two Kramers' doublets. When the energy separation between any two orbital levels is smaller than the spin-orbit coupling energy between them, the separations of doublets coming from these orbital levels are determined mainly by the spin-orbit coupling energy and there is a considerable mixing of the orbital wave functions of the doublets. If one of these doublets is the ground level and another of them lies closely to it, the orbital angular momentum will have a large effect on the magnetic behaviour of the substance. The absolute value of the coefficient $\lambda$ of the spin-orbit coupling energy is $-180$ $cm^{-1}$ for Co[14], which is larger than the separation between the ground orbital level and the next one shown in Fig. 7 (d), and the calculation with the spin-orbit interaction yields a separation as large as 300 $cm^{-1}$ between the lowest two doublets. We then have a large anisotropy of the $g$-factor, and the average $g$-value will exceed 3. Also the susceptibility will show an anomalous temperature dependence. However, the measurements of the powder susceptibility show that the average $\chi$ follows approximately the Curie-Weiss law and the $g$-value is about 2.4, and according to the measurements of the magnetic anisotropy at temperatures above 100°K, the anisotropy amounting only to 10% or less of the principal susceptibilities. Therefore we are led to conclude that the orbital angular momentum does not contribute so much to the magnetic property of $CoF_2$ as is expected from our potential. Moreover, with our potential, the population in the lowest doublet will always predominate below room temperature, so that it will be difficult to expect the change in sign of the anisotropy at a temperature considerably lower than room temperature. In § 4 we have obtained appropriate orbital levels for $FeF_2$ by increasing arbitrarily the overlap effect by 10%. So we expected to get a reasonable result also for $CoF_2$ by increasing or decreasing the overlap effect by a suitable percentage. This proved to be unsuccessful, however. In Fig. 7 (c) we show the levels when we adopt for the overlap effect the original value obtained in § 3. Other diagrams refer to cases where we assumed various percentage increases of the overlap effect. When we reduce the overlap effect, we cannot obtain a separation larger than 300 $cm^{-1}$ at any percentage between the ground orbital level and the next one. When we increase the overlap effect, we can obtain a larger separation, but in this case we see from the level separations and the value of the matrix elements that $\chi_\perp$ is always greater than $\chi_\parallel$. If we compare the cubic term, tetragonal term and orthorhombic term of the overlap potential calculated in § 3 with the corresponding ones of the potential calculated in § 2, we find that they are approximately equal in magnitude but have opposite signs to each other. So these two potentials have the same angular dependence. We therefore must conclude that this angular dependence cannot give a satisfactory explanation of the magnetic properties of $CoF_2$. There must be some other effects missing in our calculation which would give a different angular dependence of the potential energy of the cobalt $3d$ electrons. This point will be discussed further in the next section.

A consistent explanation of the magnetic properties of $CoF_2$ seems to have been given by Nakamura and Taketa. Their theory is based on the assumption that the energy differences between the ground orbital level and other levels are sufficiently large so that one can use safely the Hamiltonian derived by Pryce. Estimating phonomenologically the parameters included in the Hamiltonian, they showed that the orthorhombicity of the crystalline field is essential to the problem. The change in sign of the magnetic anisotropy with varying temperature was explained by the change in populations in two doublets into which the ground level is split by spin-orbit coupling. Qualitatively satisfactory explanations have been given of other properties. Though we cannot deny the possibility that these properties may come from a more complicated situation than those we considered in the present treatment, it is not yet clear where to find it.

## § 6. Discussions

The result of our calculation proved to be reasonable for $FeF_2$ but not for $CoF_2$. Though we cannot see clearly at present wherein the discrepancy for the latter originates, we can imagine other possibilities than those taken into account in the present paper which might (or might not) improve the result for $CoF_2$ but preserve the good agreement obtained for $FeF_2$. We shall give below a brief discussion on this and the nature of the approximations made in our treatment.

We assumed at first that the crystal is purely ionic. We took into account only $(3d)^6$ and $(3d)^7$ configurations for $Fe^{++}$ and $Co^{++}$, respectively, and neglected all other higher configurations. From the standpoint of the perturbational treatment this means that we have calculated the first order correction to the free ion state. Therefore, if the actual crystal contains a considerable degree of covalency, our approximation will be poor. Even if the ionic model were correct, contraction and higher order deformations of the cation electron cloud due to a mixing of higher ionic configurations would have existed, but it seems that these deformations are less important than the covalent bonding because the energies of the ionic excited states are higher. As regards covalency, each of the $d$ orbitals split in the orthorhombic field will have different degree of covalency because each has different spatial distribution. Thus the split levels of $^4F$ of $CoF_2$ in crystalline field will have different degrees of covalency since they consists of different combinations of the split $d$ orbitals. Consequently one may expect that the relative separations of the energy levels suffer a considerable change when covalency is taken into account. Although we cannot see without calculation how large this effect is, a possible improvement might be found in it.

There are evidences of the existence of covalent bonding in ionic crystals. Kanda[17] found by means of nuclear magnetic resonance that some alkali halide crystals possess several percent of covalency. More recently, Owen[18] showed that the optical and magnetic data of hydrated iron group salts can consistently be explained by considering a partial covalency between the metallic $3d$ orbitals and the surrounding oxygen $2s$ and $2p$ orbitals. Assuming a partial covalency, he explained an apparent reduction of the spin-orbit coupling constant $\lambda$ and of the term separation observed in these crystals.

We can naturally consider the existence of a partial covalency also in iron group fluorides. However, the state of affairs to be considered is much more complicated in this case than in the hydrated salts because we have to seek wave functions appropriate to a less symmetrical arrangement of ions and moreover to consider them simultaneously for all the ions in the crystal. It is not clear, however, that the effect of covalency is important only for $CoF_2$.

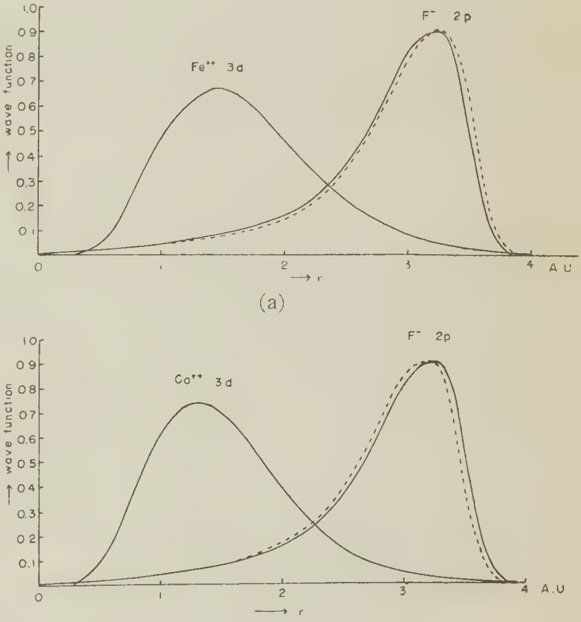

(a)

(b)

Fig. 8. (a) Electron cloud density of a $3d$-electron of $Fe^{++}$ and that of a $2p$-electron of $F^-$ in $FeF_2$. $r$ measures (in atomic units) the distance from the nuclei of the $Fe^{++}$. Solid curve for $F^-$ represents the electron cloud of one of the two fluorine ions which contact with the iron in along the [110] direction and broken curve that of these which contact at above and below. (b) The same for $CoF_2$.

In our calculation of the overlap correction we neglected the exchange interaction between the $3d$ electrons of the metal ions and the closed shells of the surrounding $F^-$ ions. It appears, however, that, as the exchange integral is large when overlapping is large, a considerable part of this effect has been effectively included in the correction factor to overlapping which we rather arbitrarily introduced in § 4 and § 5. Thus the exchange interaction would probably not improve our result.

Effect of the polarization of $F^-$ ions (the displacement of their electron cloud) on the overlap potential was also neglected, but the estimation of its order of magnitude shows that it is negligible.

A possible error might have arisen in our calculations also from the use of the Slater function for the *d* orbital. We tried other functions as we mentioned in § 3. We did this for $FeF_2$ but found it rather unsatisfactory. Possibly, a more suitable wave function than Slater's will improve the result for $CoF_2$, but we do not know what is the better wave function. We show in Fig. 8 the radial charge distribution of a $3d$ electron of $Fe^{++}$ and $Co^{++}$ ion as well as that of a $2p$ electron of $F^-$ ion, of which we made use in this study.

In concluding, we would like to stress again on our conclusion that for iron group fluorides the simple point charge model is not enough for the crystalline field but the overlapping of the electron clouds is likewise important. Although we could not get a reasonable result for $CoF_2$ (since the effects of these two cancelled each other to a great extent), one cannot by any means deny that these two are of primary importance in considering the magnetic anisotropy of this salt and of other salt; there must be some minute effects in $CoF_2$ which we could not find in the present calculation.

The authors wish to thank Dr. K. Yosida for many valuable discussions. The present work has been supported in part by a Grant in Aid from the Ministry of Education.

## Appendix

### Calculation of the coefficients of the crystalline field due to the space charge of fluorine ions.

We donote by $(\beta_j, \alpha_j)$ the polar and azimuthal angles of $\boldsymbol{P}_j$ (vector drawn from the magnetic ion to the $j$-th neighbouring fluorine ion) referred to the $x$, $y$, $z$-axes defined in § 2 and by $(r, \theta_j, \varphi_j)$ the polar coordinates of point $\boldsymbol{r}$ taking $\boldsymbol{P}_j$ as the polar axis, then we have the relation[19)]

$$Y_{lm}(\theta, \varphi)=\sum_{m'} \mathfrak{D}^{(l)}(\{\alpha_j, \beta_j, 0\})_{mm'}{}^* Y_{lm'}(\theta_j, \varphi_j)\ , \tag{A.1}$$

where $\mathfrak{D}^{(l)}(\{\alpha, \beta, \gamma\})$ is the matrix of the $l$-th irreducible representation of the rotation group and $\alpha$, $\beta$, $\gamma$ are the Euler angles of the coordinate transformation from the $x$, $y$, $z$-system to a new system which, in the present case, is such that the new $z$-axis is along $\boldsymbol{P}_j$ and $\gamma$ is taken to be zero for convenience.

From eqs. (3.2), (3.3) and (A.1). we obtain

$$\begin{aligned}\varphi_{lm}(r)&=\int Y_{lm}{}^*(\theta, \varphi) \sum_{j=1}^{6} \phi(x_j) d\Omega \\ &=\sum_{j=1}^{6} \sum_{m'} \mathfrak{D}^{(l)}(\{\alpha_j, \beta_j, 0\})_{mm'} \int \phi(x_j) Y_{lm'}{}^*(\theta_j, \varphi_j) d\Omega_j\ .\end{aligned}$$

where $d\Omega$ and $d\Omega_j$ are the solid angle elements. Since $\phi(x_j)$ has an axial symmetry around the direction of $\boldsymbol{P}_j$, the integral in the above expression vanishes except for $m'=0$, so that

$$\varphi_{lm}(r)=\sum_{j=1}^{6} \mathfrak{D}^{l}(\{\alpha_j, \beta_j, 0\})_{m0} \varphi_0(r;\ j)\ , \tag{A.2}$$

where

$$\begin{aligned}\varphi_l(r;\ j)&=\int \phi(x_j) Y_{l0}(\theta_j, \varphi_j) d\Omega \\ &=\sqrt{2\pi} \int_{-1}^{1} \phi(\sqrt{r^2+P_j{}^2-2P_j r z})\, \Theta_{l0}(z) dz\ ,\end{aligned} \tag{A.3}$$

with

$$\Theta_{20}(z)=\sqrt{\frac{5}{8}}\,(3z^2-1)\,,$$
$$\Theta_{40}(z)=\frac{9}{8\sqrt{2}}\left(\frac{35}{3}z^4-10z^2+1\right). \tag{A.4}$$

Referring to Fig. 3, we have the following matrix elements appearing in (A. 2):

| | for $j=1, 2$ | $j=3, 4, 5, 6$ |
|---|---|---|
| $\mathfrak{D}_{\pm 20}{}^{(2)}=$ | $-\frac{\sqrt{6}}{4}$ | $\frac{\sqrt{6}}{4}\sin^2\theta$ |
| $\mathfrak{D}_{00}{}^{(2)}=$ | $-\frac{1}{2}$ | $\frac{1}{2}(3\cos^2\theta-1)$ |
| $\mathfrak{D}_{\pm 40}{}^{(4)}=$ | $\frac{\sqrt{70}}{16}$ | $\frac{\sqrt{70}}{16}\sin^4\theta$ |
| $\mathfrak{D}_{\pm 20}{}^{(4)}=$ | $\frac{\sqrt{10}}{8}$ | $\frac{\sqrt{10}}{8}(7\cos^2\theta-1)$ |
| $\mathfrak{D}_{00}{}^{(4)}=$ | $\frac{3}{8}$ | $\cos^4\theta-3\sin^2\theta\cos^2\theta+\frac{3}{8}\sin^4\theta$ . |

From these results we obtain the overlap part $A_0(r)$, $B_0(r)$, $\cdots G_0(r)$ of $A(r)$, $B(r)$, $\cdots G(r)$ follows:

$$A_0(r)=\frac{3\sqrt{5}}{4\sqrt{\pi}}[-\varphi_2(r;1)+2\sin^2\theta\varphi_2(r;2)]$$
$$B_0(r)=\frac{\sqrt{5}}{4\sqrt{\pi}}[-\varphi_2(r;1)+2(3\cos^2\theta-1)\varphi_2(r;2)]$$
$$D_0(r)=\frac{105}{16\sqrt{\pi}}[\varphi_4(r;1)+2\sin^4\theta\,\varphi_4(r;2)]$$
$$F_0(r)=\frac{15}{16\sqrt{\pi}}\left[\left(\frac{3}{4}-70\right)\varphi_4(r;1)+\left\{4\cos^2\theta-12\sin^2\theta\cos^2\theta-\left(2\sqrt{70}-\frac{3}{2}\right)\sin^4\theta\right\}\varphi_4(r;2)\right]$$
$$G_0(r)=\frac{15}{16\sqrt{\pi}}[\varphi_4(r;1)+2\sin^2\theta(7\cos^2\theta-1)\varphi_4(r;2)]\,. \tag{A.5}$$

## References

1) J. W. Stout and M. Griffel: Phys. Rev. **76** (1949) 144.
2) J. W. Stout and L. M. Matarrese: Revs. Mod. Phys. **25** (1953) 338.
3) J. W. Stout and H. E. Adams: J. Amer. Chem. Soc. **64** (1942) 1535.
4) J. W. Stout and E. Catalano: Phys. Rev. **92** (1953) 1575; also, E. Catalano and J.W. Stout: J.C.P. **23** (1955) 1803, 2013.
5) F. Keffer: Phys. Rev. **87** (1952) 608.
6) K. Niira and T. Oguchi: Prog. Theor. Phys. **11** (1954) 425.
7) T. Nakamura and H. Taketa: Prog. Theor. Phys. **13** (1955) 129.
8) J. Kanamori, T. Moriya, K. Motizuki and T. Nagamiya: J. Phys. Soc. Japan **10** (1955) 93.
9) L. Pauling: Proc. Roy. Soc. A **114** (1927) 191.
10) J. R. Tessman, A. H. Kahn and W. Shockley: Phys. Rev. **92** (1953) 890.
11) J. C. Slater: Phys. Rev. **36** (1930) 57.
12) G. C. Benson and G. Wyllie: Proc· Phys. Soc. A **64** (1951) 276.
13) M. H. L. Pryce: Proc. Phys. Soc. **63** (1950) 25.
14) E. U. Condon and G. H. Shortly: The Theory of Atomic Spectra (Cambridge 1935) Chap. 6.
15) H. Bizette and B. Tsai: Comptes Rendus **212** (1941) 119.
16) W. J. De Haas and B. H. Schultz: Physica **6** (1939) 48.
17) T. Kanda: J. Phys. Soc. Japan **10** (1955) 85.
18) J. Owen: Proc. Roy. Soc. A **227** (1955) 183.
19) E. Wigner: Gruppentheorie und ihre Anwendungung auf die Quantenmechanik der Atomspektren (Vieweg & Sohn 1931) Chap. 15.

JOURNAL OF THE PHYSICAL SOCIETY OF JAPAN Vol. 11, No. 3, MARCH, 1956

# On the Superstructure of the Ordered Alloy $Cu_3Pd$ *
# I. Electron Diffraction Study

By Denjiro WATANABE and Shiro OGAWA

*The Research Institute for Iron, Steel and Other Metals,*
*Tohoku University, Sendai*

(Received October 24, 1955)

Ordered structures of copper-palladium alloys, chiefly of $\alpha''$ phase (18 ~28 atomic per cent Pd) were investigated by electron diffraction, using orientated, evaporated films. The elucidated structure of $\alpha''$ phase can be thought of as formed from the elementary face-centred tetragonal lattice, in which the atoms arrange themselves as in the ordered lattice of $Cu_3Au$ but the two kinds of step-shift occur at every definite distance along two directions parallel to the crystallographical axes, respectively. Thus, a two-dimensional anti-phase domain structure takes place, which is considered to have a large orthorhombic unit cell. The present model seems to be connected, not with that proposed by Geisler and Newkirk, but closely with that proposed by Schubert *et al.*

## § 1. Introduction

It has been known that two types of ordered alloy, CuPd and $Cu_3Pd$, are present in the copper-palladium alloy system[1]. The former has the CsCl type and is styled $\beta$ phase, as shown in Fig. 1, and the phase to which the latter belongs is subdivided into $\alpha'$ and $\alpha''$ phases. According to Jones and Sykes[2], $\alpha'$ phase has the $Cu_3Au$ type, while $\alpha''$ phase seemed to have a more complicated structure and it was only known that the lattice of $\alpha''$ phase is built up from face-centred tetragonal cells in terms of original disordered face-centred cubic cells, the lattice constants being $a=3.707$ Å, $c/a=0.986$ at 25 per cent Pd* after a slow cooling from 500 to 250°C in four months. The distributing manner of copper and palladium atoms in the lattice, however, could not definitely be determined by them. Recently, some experimental works on this ordered phase have been done. Jones and Owen[3] estimated by X-rays the temperature dependence of the long-range order of $\alpha''$ phase from values of $c/a$ measured in a polycrystalline alloy containing 25 per cent Pd, but reported none on the atomic arrangement of this phase. On the other hand, Geisler and Newkirk[4] analyzed by X-rays the ordered structure of the polycrystalline alloy, $Cu_4Pd$, which had been annealed at 450°C for three months, and concluded that the ordered phase is stable below 478°C and has a tetragonal unit cell of the modified $Ni_4Mo$ type, $a$ and $c$ being 5.826 Å and 7.328 Å respectively, and that a lattice of the $Cu_3Au$ type is produced by suitable introduction of some errors to this lattice.

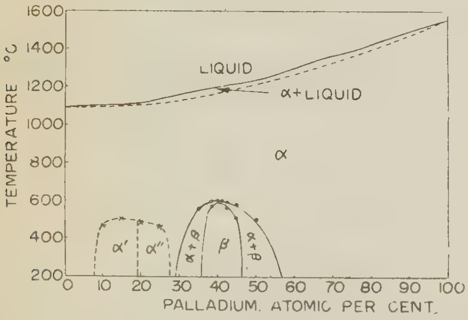

Fig. 1. Cu–Pd phase diagram.

The present work was undertaken to elucidate by electron diffraction the ordered structure of $\alpha''$ phase and also to examine the structure of the other ordered alloys, i.e., of $\alpha'$ and $\beta$ phases. Electron diffraction patterns of single-crystallike evaporated films of alloys give much informations to the problems of ordering, as proved in our previous work on the structure of CuAu II[5], because such a diffraction pattern nearly reproduces the intensity distribution on principal planes in reciprocal space, and hence informations concerning a crystal lattice can often intuitively be obtained. This method of observation was also adopted in the present work and the nature of the ordered phase $\alpha''$ has fully been elucidated, as shown in § 3 and 4. The results obtained are entirely different from those obtained by Geisler and Newkirk and show that this phase has a complicated two-dimensional anti-phase domain structure which contains a new type of out-of-step, besides a known type of out-of-step already found in $Cu_3Au$ and CuAu II. The change of sizes of these anti-phase domains with composition leads to the structural connection between $\alpha''$ and $\alpha'$ phase.

---

* A short note concerning this work has been published in Acta Cryst. **8** (1955) 510.

* Hereafter, a mere "per cent" will be used in place of "atomic per cent", since all compositions are expressed by atomic per cent of palladium in the present paper.

## § 2. Experimental Method

Single-crystallike films of copper-palladium alloys were formed in a usual way: copper and palladium were drawn to wires of 0.2mm in diameter, laid together in a tungsten filament and evaporated *in vacuo* on to cleavage surface of rocksalt heated at 300~350°C. The suitable thickness of films was 400~550 Å. Films mounted on a supporter of nickel were heated *in vacuo* in a silica tube and quenched by pouring water to the tube. This procedure of quenching seems to be nearly sufficient for copper-palladium alloys except $\beta$ phase, because the relaxation time for ordering is very large, especially, for $\alpha''$ phase, but the method may be considered to be insufficient, e.g., for drawing some conclusions from diffuse scatterings observed at superlattice reflection positions in patterns of films quenched from temperatures above the critical point. Such an investigation should be carried out by a high-temperature diffraction camera, the use of which is scheduled in a sequel of the present work. All results in the present work were obtained only from quenched films. After being homogenized at 600~800°C and quenched from the disordered state, films were annealed at various temperatures below the critical point for various durations. The composition of films was determined from the lattice parameter at the disordered state, using the X-ray data6) combining composition and lattice parameter. The used diffraction camera7) was of ED-C type made by Hitachi Co. and the applied voltage was about 50 KV. The majority of diffraction photographs was taken at normal incidence, i.e., the beam direction was parallel to a cube edge of disordered single crystal.

## § 3. Experimental Results

Alloy films of $\alpha'$ and $\alpha''$ phases were prepared, their palladium contents being 10, 13, 16, 18, 21, 25 (two specimens), 28 and 30 per cent, respectively, within the experimental error of ±1 per cent. Specimens whose compositions were planned to correspond to $\beta$ phase were also prepared, but their palladium contents were not determined, because the quenching of the disordered state was not successful owing to very quick formations of the ordered $\beta$ phase. In this section, experimental results obtained from specimens of $\beta$ phase will first be given and next those obtained from specimens of $\alpha'$ and $\alpha''$ phases will fully be described.

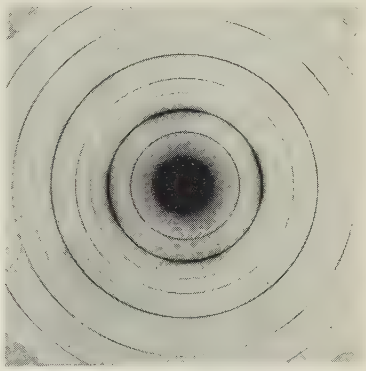

Fig. 2. $\beta$-phase, CsCl type.

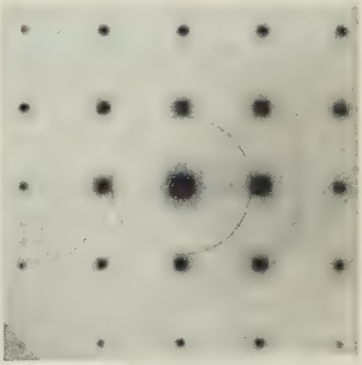

Fig. 3. Secondary diffraction from films containing Pd more than 25 per cent before homogenization.

### (1) *Specimens of $\beta$ phase*

From specimens whose compositions were planned to correspond to $\beta$ phase, both sharp body-centred cubic rings arising from a lattice of the CsCl type and weak face-centred cubic spots showing the orientation which follows that of the substrate were obtained before homogenization of films. The rings remained almost unchanged in their aspect even after being annealed at about 400°C for 10 hours, while the spots completely vanished, as shown in Fig. 2. Lattice spacings obtained from the rings nearly coincided with the X-ray data[6][8] for the ordered phase CuPd. But these X-ray data are somewhat different with different investigators and do not seem to permit the determination of compositions. It is noted that single-crystallike films of β phase were not formed by the present method.

(2) *Specimens of* α′ and α″ *phases*

Films containing palladium less than 25 per cent showed only face-centred cubic spots with weak superlattice reflections before homogenization, but those containing palladium more than 25 per cent exhibited, besides face-centred cubic spots with weak superlattice reflections, sharp body-centred cubic rings due to β phase. These rings often appeared also around intense normal spots, owing to the secondary diffraction as shown in Fig. 3. The body-centred rings, probably arising from places of high concentration of palladium before homogenization, became very faint after annealing above 350°C, and at the same time diffuse crosses and streaks appeared at superlattice reflection positions of the face-centred cubic pattern, just as in CuAu II. In such patterns (Fig. 4) faint spots were occasionally observed close to the direct spot and along two ⟨110⟩ directions passing through it. A discussion on this fact will be given in § 4. The body-centred rings completely vanished at 500°C, leaving the face-centred cubic spots with diffuse crosses and streaks. These crosses and streaks also appeared in patterns of films containing palladium less than 25 per cent and decreased their sizes with decreasing palladium content, finally transforming to spots at palladium content less than 18 per cent. The superlattice reflections remained, becoming faint and diffuse, even after quenching from any temperature between 500 and 800°C.

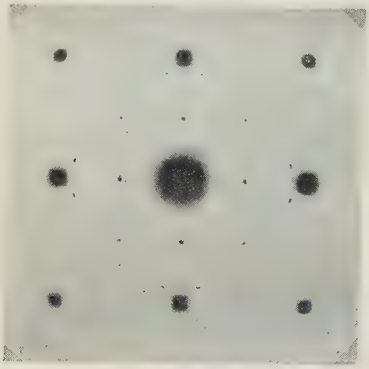

Fig. 4. Satellites flanking the direct spot due to secondary diffraction.

Detailed observations on patterns of alloys subject to various heat-treatments were carried out. After quenching from the disordered state seven samples were annealed *in vacuo* in such a manner as shown in Table I. These treatments seemed to be sufficient to develop a highly ordered structure, because the ordering process probably proceeds more rapidly in thin films, owing to the small grain size as well as the presence of a large number of dislocations and vacancies, than in bulk specimens. Specimens were quenched at the end of duration at each maintained temperature and, after observation of diffraction patterns, again subjected to a next heat-treatment. The results of observation are divided into the following two articles, the latter of which concerns α″ phase and is a main product in the present work.

Table I. Heat-treatments of samples of α′ and α″ phases.

| Sample. / Annealing Temp. (°C) | 25, 28, 30% Pd. | 18, 21% Pd. | 13% Pd. |
|---|---|---|---|
| 450 | 5～8 (hours) | 3 (hours) | 2 (hours) |
| 440 | 8 | ↓ | |
| 400 | 40 | 15 | ↓ |
| 380 | ↓ | ↓ | 10 |
| 350 | 41 | 30 | |
| 300 | 80 | 80 | |
| 250 | 97 | 97 | |
| 230 | 100 | 100 | |
| 320 | 19 | 19 | |
| 360 | 20 | 20 | |
| 390 | 16 | 16 | ↓ |
| 420 | 10 | 10 | 10 |
| 450 | 10 | 10 | 10 |
| 470 | 6 | 6 | 6 |
| 490 | 6 | 6 | 6 |
| 510 | 4 | 4 | 4 |
| 530 | | 5 | 5 |

*a*) *Specimen of* α′ *phase* (13 *per cent Pd*)

The superlattice reflections became sharp

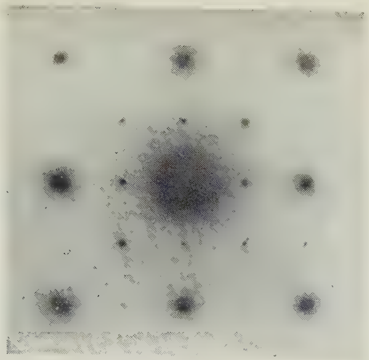

Fig. 5. Sharp superlattice reflections from $\alpha'$-film containing 13 per cent Pd.

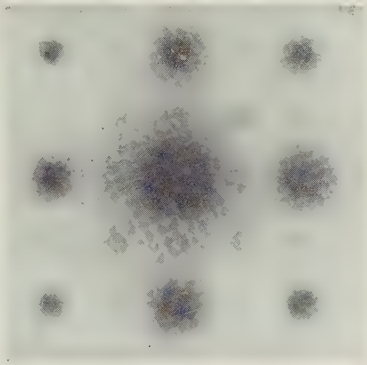

Fig. 6. Residual diffuse superlattice reflections from $\alpha''$-film containing 25 per cent Pd, quenched from the disordered state.

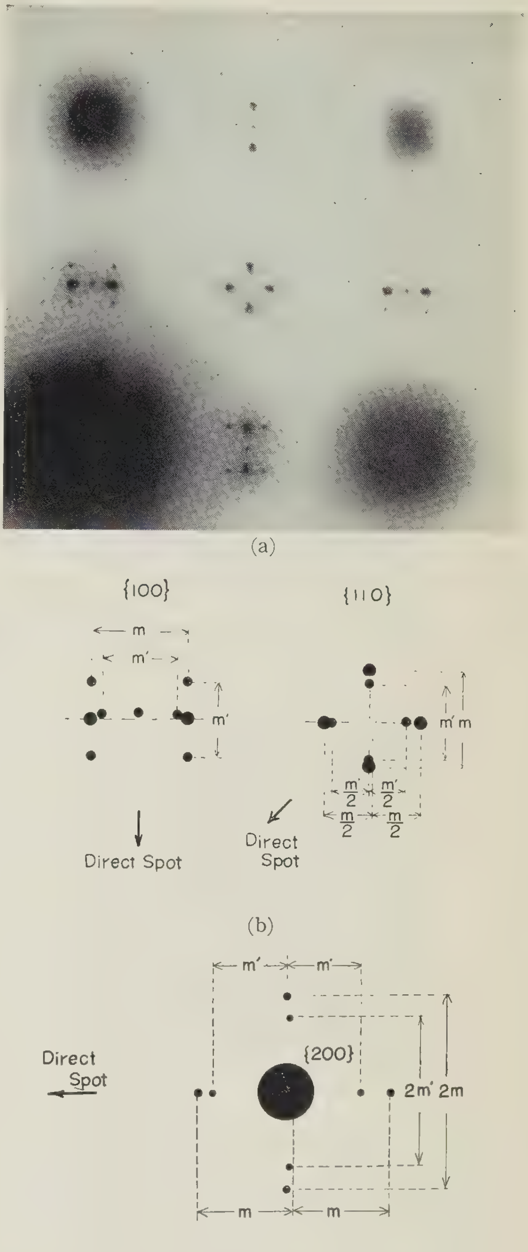

Fig. 7. (a) Diffraction pattern from $\alpha''$-film containing 25 per cent Pd, annealed at 440°C.
(b) Illustrations of splittings in {100} and {110} in (a).
(c) Illustration of satellites flanking {200} spot.

and intense after annealing at 450°C for 2 hours, and the pattern did not change its aspect through the successive treatments at lower temperatures, except the further intensification of the superlattice reflections (Fig. 5). From the resemblance of the patterns the ordered structure of the present alloy is considered to be analogous to that of $Cu_3Au$. This result agrees with previous works[2)9)10)]. When the alloy film was again heated at higher temperatures, the pattern scarcely changed until 490°C, though the superlattice reflections were somewhat weakened. These reflections became faint and slightly diffuse at 510°C and still fainter above 530°C but did not advance in their diffuseness. The simple form of the superlattice reflections seems to reveal that anti-phase domains, such as observed in incompletely ordered $Cu_3Au$[11)], are absent in this composition below and above the critical temperature. Alloys of 10 and 16 per cent Pd were treated in a simpler way than the case of the alloy 13 per cent, and diffraction patterns similar to those of 13 per cent were observed.

### b) *Specimens of $\alpha''$ phase (palladium content more than* 18 *per cent)*

The ordered alloys of this phase were shown to have a face-centred tetragonal lattice in

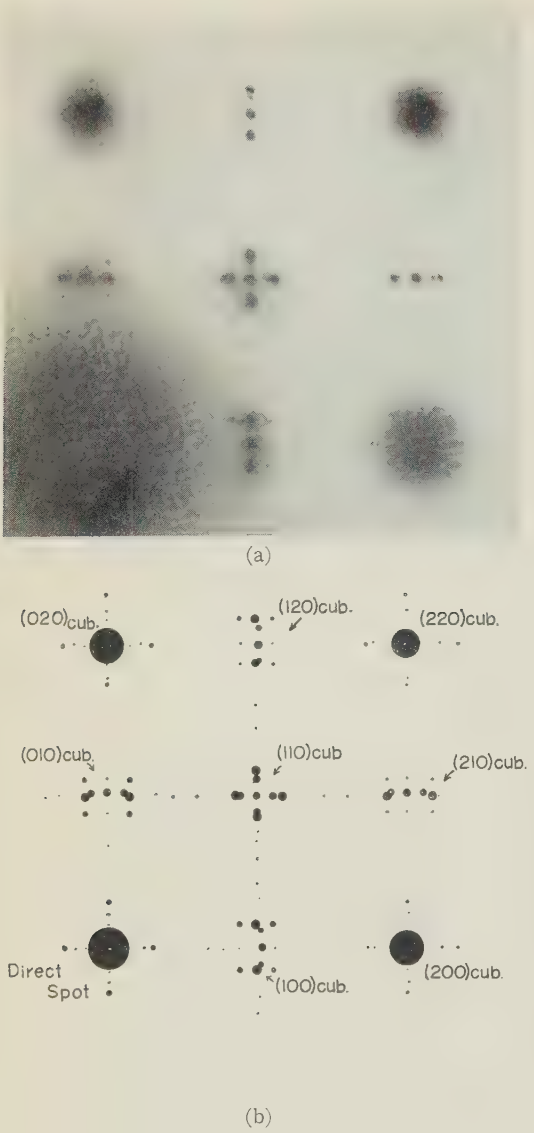

(a)

(b)

Fig. 8. (a) Diffraction pattern from $\alpha''$-film containing 25 per cent Pd, annealed at 230°C.
(b) Illustration of splittings in superlattice reflections and of satellites flanking intense normal spots. A new kind of satellites around the direct and {200} spots is illustrated.

terms of the disordered face-centred cell, as reported by Jones and Sykes[2], though a true unit cell is considered to be a large orthorhombic one, as will be described in § 4. The axial ratio of the tetragonal lattice decreased down to 0.993 at 25 per sent Pd and seemed to have a minimum in the neighbourhood of this content, increasing to unity with deviation of palladium content from 25 per cent. With the progress of ordering the superlattice reflections exhibited complex splits and satellites appeared around the normal spots including the direct spot. Details of these aspects are described about the sample of 25 per cent Pd as follows: After quenching from 500~750°C the alloy film showed diffuse crosses and doublets in its diffraction pattern, as seen in Fig. 6. These residual superlattice reflections looked far more distinct than those obtained from CuAu quenched from temperatures above the critical point[5]. They became very sharp and distinct after annealing at 440~450°C for some hours, as shown in Fig. 7a. Two splitting manners are seen in {100}* in this pattern. One of them occurs along a direction perpendicular to a line connecting the centre of the said reflection with the direct spot and is similar to that obtained from CuAuII or partially ordered $Cu_3Au$. The other splitting more faintly occurs along a direction parallel to the line connecting the centre of the said reflection with the direct spot and has not so far been observed. There are two values of separation, "$m$" and "$m'$", in these splittings, which are observed also in {110}, as illustrated in Fig. 7b. On further annealings at 440~450°C the complex splits in superlattice reflections became still sharper and more intense, and at the same time two kinds of satellites appeared around the normal spots including the direct spot, as illustrated in Fig. 7c, their separations being twice as large as those of corresponding splits of superlattice reflections respectively. At about 400°C splits of the normal spots of higher indices due to the tetragonality were clearly seen, and faint reflections appeared at positions along lines connecting {100} with neighbouring {110}. After such a long period of annealing at lower temperatures that it took full fifteen days before finishing of the treatment at 230°C, the superlattice reflections and the satellites flanking the normal spots fairly increased their intensities, so that details in their aspect were made clear. For example, two kinds of separation became clearer in {100} and {110} and a new kind of satellites appeared around the normal spots, its separation being half as large as that of the one kind of the satellites mentioned above. The axial ratio decreased to 0.993 at this stage. This value do not agree with the X-ray data, 0.986[2)3)12)]. The estimated error in the present experiment is not so large. The origin of this discrepancy is not clear. The aspect of the pattern mentioned above is well reproduced in Fig. 8a and illustrated in Fig. 8b.

---

* Miller's indices relevant to the ordered lattice are used in terms of the original disordered face-centred cubic lattice throughout the present paper.

When the film was again heated up, the pattern changed almost reversibly. At 450°C the superlattice reflections somewhat weakened and the satellites flanking the normal spots became extremely faint. The tetragonality seemed still to remain, but the axial ratio very closely approached to unity. At 470°C the pattern completely changed. The diffuse superlattice reflections in this pattern means the collapse of long range order, but their shapes similar to those in lower temperatures may mean that anti-phase domains of a definite size still persist. The critical temperature seems to lie between 450 and 470°C for 25 per cent Pd, if the quenching is satisfactory.

The aspects of patterns corresponding to compositions other than 25 per cent Pd are described as follows. For 28 and 30 per cent Pd the patterns were much similar to those of 25 per cent, as shown in Fig. 9, except that the separations of the splits of the superlattice reflections became larger and the critical temperature decreased to a value between 390 and 420°C. The satellites flanking the normal spots were observed for 28 per cent, but not for 30 per cent. For 21 per cent Pd the separations of the splits became smaller than those for 25 per cent. The superlattice reflections somewhat weakened but increased in sharpness at 470°C (Fig. 10) before they diffused at 510°C. The critical temperature seems to lie between 490 and 510°C for this composition. For 18 per cent the behaviour of the superlattice reflections was just like for 21 per cent and the critical temperature seems to lie very close to that for 21 per cent. The satellites were absent for 21 and 18 per cent.

## § 4. Interpretations and Discussions for the Results

The determination of the structure of $\alpha''$ phase is a chief subject in the present work, and discussions will be concentrated on this topic. Prior to this, however, some photographs will be called to account. In Fig. 4 faint satellites are observed at a small scattering angle. Satellites close to the direct spot were observed also in the patterns of CuAu II[5)] or of the ordered $\alpha''$ alloys in the present work (e.g., Fig. 8), but the positions of satellites are entirely different in Fig. 4. After some considerations they could be interpreted as due to the secondary diffraction, intense {200} spots acting as secondary incident spots and twin spots situated inside {200} spots being reproduced around the primary incident spot. Intensities in reciprocal space due to {111} twin formation lie along the body-diagonals of the reciprocal lattice, and hence twin spots cannot appear at the [001] incidence, if the crystal is perfect. In thin films considerable rotations of crystallites occur after removal of films from rocksalt substrates[7)13)], therefore twin spots are observed even at the [001] incidence.

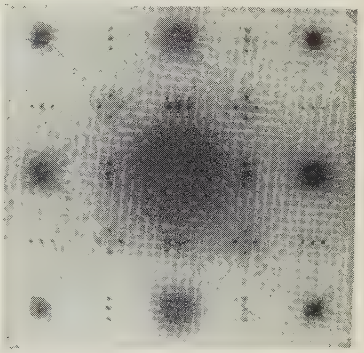

Fig. 9. Diffraction pattern from $\alpha''$-film containing 28 per cent Pd.

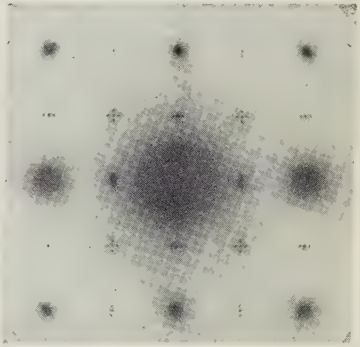

Fig. 10. Diffraction pattern from $\alpha''$-film containing 21 per cent Pd.

When the alloys of $\alpha''$ phases were quenched from temperatures above the critical points, weak diffuse crosses and doublets (or streaks) remained at superlattice reflection positions, as shown, e.g., in Fig. 6. It is suspected that these reflections are caused by the incomplete quenching. But, as the relaxation time for ordering is considerably large in the present alloys[2)], the aspect of superlattice reflections may probably reveal the actual state of the alloys above the critical point, that is, anti-phase domains of a nearly definite size may be present there. At any rate, this problem should be examined by direct observations at high temperatures.

Now, we shall closely examine the diffraction patterns of $\alpha''$ phase: The patterns shown in Fig. 7 and 8 resemble pretty well those obtained from CuAu II[5)], but the difference can be found in some respects, as already described in § 3. The main features in the present patterns are the splitting manner of {100} as well as {110} and the presence of two distinct values of separation. These features are difficult to discern just after quenching from temperatures above the critical point, but they distinguish themselves after a prolonged annealing. The tetragonality mentioned in § 3 is seen, in Fig. 8, not only in the fine splits of normal reflections of higher indices but also in the splits of superlattice reflections such as {100} and {110}. In such diffraction patterns it should be considered that a pattern corresponds to a superposition of orientations such that the tetragonal axis distributes into three directions of the original cubic axes. After a careful examination it is shown that the fundamental intensity distribution in reciprocal space can be induced from Fig. 8 and is depicted in Fig. 11, where separation "$m$" lies along the tetragonal direction and separation "$m'$" lies along another direction. The actual diffraction pattern corresponds to a sixfold superposition of this fundamental distribution, separation "$m$" taking three orientations and separation "$m'$" taking either orientation for a fixed orientation of separation "$m$". This superposition will later be discussed once more. Satellites around the main lattice points will also later be referred.

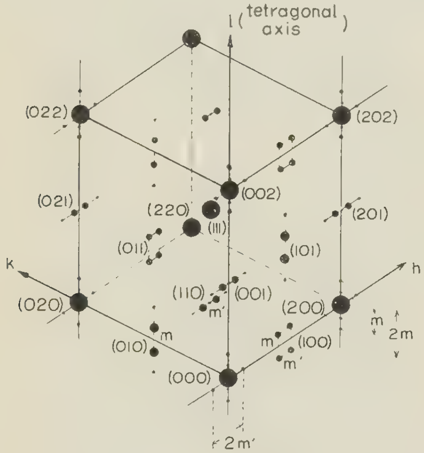

Fig. 11. Fundamental intensity distribution in reciprocal space induced from Fig. 8. Two symbols, •------• and •——•, are given to the two separations in superlattice reflections, $m$ and $m'$, respectively.

In Fig. 11 all the superlattice reflections with separation "$m$" or "$m'$" are thought of as formed by splitting of the reciprocal lattice points with mixed integers, $h_1, h_2$ and $h_3$. Hence the fundamental lattice of $\alpha''$ phase must be built up from face-centred cells with the atomic arrangement similar to that in $Cu_3Au$, and some kinds of out-of-steps must be introduced to this lattice. On the analogy of anti-phase domains in CuAu II or incompletely ordered $Cu_3Au$, the splits of the superlattice reflections of mixed $h_1$ and $h_2$ along $[00\,h_3]$ direction suggest that there is in a crystal a line-up of anti-phase domains with step shift $\pm(\boldsymbol{a}_1\pm\boldsymbol{a}_2)/2$ at every $M_3$-th atom along the $z$ direction[5)11)14)]. $\boldsymbol{a}_1, \boldsymbol{a}_2$ and $\boldsymbol{a}_3$ are the fundamental lattice vectors along $x, y$ and $z$ axes in terms of the fundamental cells. We shall call this type of out-of-step "the first kind of out-of-step". In reciprocal space the separation of the said split measured from its centre should be $(n_3/2M_3)a_3^*$, where $a_3^*$ is a reciprocal lattice constant corresponding to $\boldsymbol{a}_3$ and $n_3$ is an odd integer. On the other hand, the splits along $[h_1\,00]$ direction occur for mixed $h_3$ and $h_1$, with$_3$ a definite separation. This fact means a presence of anti-phase domains having a new kind of out-of-step with step shift $\pm(\boldsymbol{a}_3\pm\boldsymbol{a}_1)/2$ at every $M_1$-th atom along the $x$ direction. We shall call this "the second kind of out-of-step". In the above-mentioned consideration the number of anti-phase domains is assumed to be sufficiently large in every case. If the two kinds of out-of-step mentioned above occur in a crystal independently of each other, (100) in Fig. 11, e.g., should be split up from its centre along two directions, $[00\,h_3]$ and $[h_1\,00]$, forming a cross-like platelet as in CuAu II. Such a splitting manner is actually observed, faintly in Fig. 8, but in this figure as well as in Fig. 7 the oblique splits are distinctly visible. That is, the intensity distribution of (100) or (011) in Fig. 11 is mainly formed by double splits, which can be considered as follows: first, the original reciprocal lattice point is split up by either kind of out-of-step, and secondly, these splitted intensities are further split up by the other kind of out-of-step. The double splits mean both kinds of out-of-step not to be independent of but intimately connected with each other. These considerations lead to formation of a two-dimensional anti-phase domain structure, and a model of such a structure is proposed, as shown in Fig. 12(a), where $M_1$ and $M_3$ are assumed to be 5 and 4 respectively. If both $M$'s were definite throughout the crystal, an orthorhombic unit cell would be considered, as shown by the broad black lines.

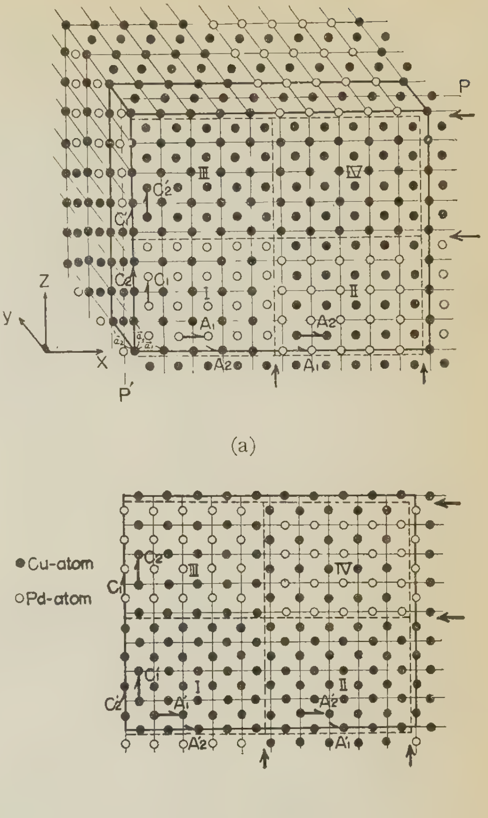

Fig. 12. Two-dimensional anti-phase domain structure. $M_1=5$ and $M_3=4$ are chosen in this model. Out-of-steps occur at places indicated by arrows.

(a) Orthorhombic unit cell is shown by the broad black lines.

(b) Distribution of atoms in the plane **PP′** situated immediately behind the front plane in (a).

Some explanations seem to be required about this model. Atom rows along the $z$ direction behave as follows: Any row of palladium atoms in the domain I, e. g. $\boldsymbol{C}_1$ row, has shifts, $(-\boldsymbol{a}_1+\boldsymbol{a}_2)/2$ and $(+\boldsymbol{a}_1-\boldsymbol{a}_2)/2$, alternately at every $M_3$-th atom, and any row of copper atoms in the domain I, e. g. $\boldsymbol{C}_2$ row, has shifts, $(+\boldsymbol{a}_1+\boldsymbol{a}_2)/2$ and $(-\boldsymbol{a}_1-\boldsymbol{a}_2)/2$, alternately at every $M_3$-th atom. Rows of copper atoms, $\boldsymbol{C}'_1$ and $\boldsymbol{C}'_2$ in Fig. 12(b), can be thought to have shifts $\pm(-\boldsymbol{a}_1-\boldsymbol{a}_2)/2$ and $\pm(\boldsymbol{a}_1-\boldsymbol{a}_2)/2$ respectively. Atom rows along the $x$ direction behave as follows: Any row of palladium atoms in the domain I in Fig. 12(a), e.g. $\boldsymbol{A}_1$ row, has shifts, $(-\boldsymbol{a}_3-\boldsymbol{a}_1)/2$ and $(+\boldsymbol{a}_3+\boldsymbol{a}_1)/2$, alternately at every $M_1$-th atom, and any row of copper atoms in the domain I, e.g. $\boldsymbol{A}_2$ row, has shifts, $(+\boldsymbol{a}_3+\boldsymbol{a}_1)/2$ and $(-\boldsymbol{a}_3-\boldsymbol{a}_1)/2$, alternately at every $M_1$-th atom. Rows of copper atoms, $\boldsymbol{A}_1'$ and $\boldsymbol{A}_2'$, can be thought to have shifts $\pm(-\boldsymbol{a}_3+\boldsymbol{a}_1)/2$ and $\pm(\boldsymbol{a}_3-\boldsymbol{a}_1)/2$ respectively. Thus, it will be seen that each of four basic atoms in the fundamental face-centred tetragonal cell has some of shifts, $\pm(\boldsymbol{a}_1\pm\boldsymbol{a}_2)/2$, at every $M_3$-th atom along the $z$ direction and also some of shifts, $\pm(\boldsymbol{a}_3\pm\boldsymbol{a}_1)/2$, at every $M_1$-th atom along the $x$ direction. These circumstances can be described in the following way: When the large orthorhombic unit cell is divided into four domains, as shown by the broken lines, sites of palladium atoms in these four domains correspond to four basic sites in the fundamental face-centred tetragonal lattice, respectively.

The structure amplitude for the lattice shown in Fig. 12, $|\boldsymbol{S}|$, is given by the following equation.

$$|S|=\left|\frac{\sin\pi N_1(2M_1)A_1}{\sin\pi(2M_1)A_1}\right|\cdot\left|\frac{\sin\pi M_1A_1}{\sin\pi A_1}\right|\cdot\left|\frac{\sin\pi N_2A_2}{\sin\pi A_2}\right|\cdot\left|\frac{\sin\pi N_3(2M_3)A_3}{\sin\pi(2M_3)A_3}\right|\cdot\left|\frac{\sin\pi M_3A_3}{\sin\pi A_3}\right|\cdot|\Phi|, \tag{1}$$

$$\begin{aligned}|\Phi|=|&[E_{Cu}\{1+\exp\pi i(A_1+A_2)+\exp\pi i(A_2+A_3)\}+E_{Pd}\exp\pi i(A_3+A_1)]\\&+[E_{Cu}\{1+\exp\pi i(A_1+A_2)+\exp\pi i(A_3+A_1)\}+E_{Pd}\exp\pi i(A_2+A_3)]\exp 2\pi iM_3A_3\\&+[E_{Cu}\{\exp\pi i(A_1+A_2)+\exp\pi i(A_2+A_3)+\exp\pi i(A_3+A_1)\}+E_{Pd}]\exp 2\pi iM_1A_1\\&+[E_{Cu}\{1+\exp\pi i(A_2+A_3)+\exp\pi i(A_3+A_1)\}+E_{Pd}\exp\pi i(A_1+A_2)]\exp 2\pi i(M_3A_3+M_1A_1)|,\end{aligned}$$

Table II. Calculation of $|\Psi|^2/|\Psi|^2_{(200)}$ for various splittings of superlattice reflections.
$M_1$ and $M_3$ are assmmed to be 5 and 4 respectively.
Splittings having $|\Psi|^2/|\Psi|^2_{(200)}$ less than $1.5\times10^{-4}$ and those corresponding to higher indices are omitted.

| $h_2, h_3$: unmixed (100), (011), (102), | | | | |
|---|---|---|---|---|
| $A_1$, | $A_2$, | $A_3$, | | $\|\Psi\|^2/\|\Psi\|^2_{(200)}\times100$ |
| $1+(1/2M_1)$, | 0, | $\pm1/2M_3$ | (100) | 0.206 |
| $1-(1/2M_1)$, | 0, | $\pm1/2M_3$ | | 0.232 |
| $1+(3/2M_1)$, | 0, | $\pm1/2M_3$ | | 0.022 |
| $1-(3/2M_1)$, | 0, | $\pm1/2M_3$ | | 0.036 |
| $1+(1/2M_1)$, | 0, | $\pm3/2M_3$ | | 0.025 |
| $1-(1/2M_1)$, | 0, | $\pm3/2M_3$ | | 0.027 |
| $\pm1/2M_1$, | 1, | $1-(1/2M_3)$ | (011) | 0.183 |
| $\pm1/2M_1$, | 1, | $1+(1/2M_3)$ | | 0.162 |
| $\pm3/2M_1$, | 1, | $1-(1/2M_3)$ | | 0.021 |
| $\pm3/2M_1$, | 1, | $1+(1/2M_3)$ | | 0.019 |
| $\pm1/2M_1$, | 1, | $1-(3/2M_3)$ | | 0.026 |
| $\pm1/2M_1$, | 1, | $1+(3/2M_3)$ | | 0.017 |
| $1-(1/2M_1)$, | 0, | $2-(1/2M_3)$ | (102) | 0.105 |
| $1-(1/2M_1)$, | 0, | $2+(1/2M_3)$ | | 0.093 |
| $1+(1/2M_1)$, | 0, | $2-(1/2M_3)$ | | 0.099 |
| $1+(1/2M_1)$, | 0, | $2+(1/2M_3)$ | | 0.087 |

| $h_1, h_3$: unmixed (010), (101), (012), | | | | |
|---|---|---|---|---|
| $A_1$, | $A_2$, | $A_3$, | | $\|\Psi\|^2/\|\Psi\|^2_{(200)}\times100$ |
| 0, | 1, | $\pm1/2M_3$ | (010) | 0.553 |
| 0, | 1, | $\pm3/2M_3$ | | 0.064 |
| 0, | 1, | $\pm5/2M_3$ | | 0.027 |
| 0, | 1, | $\pm7/2M_3$ | | 0.018 |
| 1, | 0, | $1-(1/2M_3)$ | (101) | 0.446 |
| 1, | 0, | $1+(1/2M_3)$ | | 0.400 |
| 1, | 0, | $1-(3/2M_3)$ | | 0.060 |
| 1, | 0, | $1+(3/2M_3)$ | | 0.042 |
| 1, | 0, | $1-(5/2M_3)$ | | 0.029 |
| 1, | 0, | $1+(5/2M_3)$ | | 0.016 |
| 1, | 0, | $1-(7/2M_3)$ | | 0.022 |
| 0, | 1, | $2-(1/2M_3)$ | (012) | 0.251 |
| 0, | 1, | $2+(1/2M_3)$ | | 0.218 |
| 0, | 1, | $2-(3/2M_3)$ | | 0.036 |
| 0, | 1, | $2+(3/2M_3)$ | | 0.023 |
| 0, | 1, | $2-(5/2M_3)$ | | 0.019 |
| 0, | 1, | $2-(7/2M_3)$ | | 0.016 |

| $h_1, h_2$: unmixed (001), (110), (021), (201), (112) | | | | |
|---|---|---|---|---|
| $A_1$, | $A_2$, | $A_3$, | | $\|\Psi\|^2/\|\Psi\|^2_{(200)}\times100$ |
| $\pm1/2M_1$, | 0, | 1 | (001) | 0.549 |
| $\pm3/2M_1$, | 0, | 1 | | 0.062 |
| $\pm5/2M_1$, | 0, | 1 | | 0.025 |
| $\pm7/2M_1$, | 0, | 1 | | 0.015 |
| $\pm1/2M_1$, | 2, | 1 | (021) | 0.234 |
| $\pm3/2M_1$, | 2, | 1 | | 0.027 |
| $1-(1/2M_1)$, | 1, | 0 | (110) | 0.443 |
| $1+(1/2M_1)$, | 1, | 0 | | 0.403 |
| $1-(3/2M_1)$, | 1, | 0 | | 0.057 |
| $1+(3/2M_1)$, | 1, | 0 | | 0.044 |
| $1-(5/2M_1)$, | 1, | 0 | | 0.025 |
| $1+(5/2M_1)$, | 1, | 0 | | 0.015 |
| $1-(7/2M_1)$, | 1, | 0 | | 0.016 |
| $2-(1/2M_1)$, | 0, | 1 | (201) | 0.240 |
| $2+(1/2M_1)$, | 0, | 1 | | 0.220 |
| $2-(3/2M_1)$, | 0, | 1 | | 0.033 |
| $2+(3/2M_1)$, | 0, | 1 | | 0.023 |
| $2-(5/2M_1)$, | 0, | 1 | | 0.015 |
| $1-(1/2M_1)$, | 1, | 2 | (112) | 0.204 |
| $1+(1/2M_1)$, | 1, | 2 | | 0.197 |
| $1-(3/2M_1)$, | 1, | 2 | | 0.026 |
| $1+(3/2M_1)$, | 1, | 2 | | 0.021 |

In this table, $|\Psi|^2/|\Psi|^2_{(200)}$ has been calculated under the following condition in order to simplify the calculation: $a=3.688$ Å, $c/a=1$.

where $A_1$, $A_2$ and $A_3$ are continuous variables in the reciprocal lattice, provided that the reciprocal lattice constants, $a_1^*$, $a_2^*$ and $a_3^*$, are considered in terms of the fundamental tetragonal cell, $N_1$ and $N_3$ are halves the numbers of anti-phase domains, i. e. the numbers themselves of orthorhombic unit cells, along the $x$ and $z$ directions respectively and assumed to be far larger than $M_1$ and $M_3$ respectively, $N_2$ is the number of unit cells, either tetragonal or orthorhombic, along the $y$ direction, and $E_{Cu}$ and $E_{Pd}$ are the atomic scattering factors for electron of copper and palladium respectively. $|\Phi|$ consists of sixteen terms corresponding to sixteen basic atoms in four fundamental face-centred cells, which represent the four domains in Fig. 12 respectively. There are such chances in equation (1) that $|S|$ has maxima at $A_1=h_1 \pm(n_1/2M_1)$, $A_2=h_2$, $A_3=h_3\pm(n_3/2M_3)$, where $h_1$, $h_2$ and $h_3$ are integers and $n_1$ and $n_3$ are 0 or odd integers. We shall calculate $|\sin\pi M_1A_1/\sin\pi A_1|\cdot|\sin\pi M_3A_3/\sin\pi A_3|\cdot|\Phi|\equiv|\Psi|$ to evaluate these maxima. At the said values of $A_1$, $A_2$ and $A_3$,

---

$$
\begin{aligned}
|\Psi| = & \left|\frac{\sin\dfrac{n_1\pi}{2}}{\sin\dfrac{n_1\pi}{2M_1}}\right| \cdot \left|\frac{\sin\dfrac{n_3\pi}{2}}{\sin\dfrac{n_3\pi}{2M_3}}\right| \cdot \\
\times & \Bigg|\left[E_{Cu}\left\{1+\exp\pi i\left(h_1+h_2\pm\frac{n_1}{2M_1}\right)+\exp\pi i\left(h_2+h_3\pm\frac{n_3}{2M_3}\right)\right\}+E_{Pd}\exp\pi i\left(h_3+h_1\pm\frac{n_3}{2M_3}\pm\frac{n_1}{2M_1}\right)\right] \\
+ & \left[E_{Cu}\left\{1+\exp\pi i\left(h_1+h_2\pm\frac{n_1}{2M_1}\right)+\exp\pi i\left(h_3+h_1\pm\frac{n_3}{2M_3}\pm\frac{n_1}{2M_1}\right)\right\}+E_{Pd}\exp\pi i\left(h_2+h_3\pm\frac{n_3}{2M_3}\right)\right] \\
& \times\exp(\pm\pi i n_3) \\
+ & \left[E_{Cu}\left\{\exp\pi i\left(h_1+h_2\pm\frac{n_1}{2M_1}\right)+\exp\pi i\left(h_2+h_3\pm\frac{n_3}{2M_3}\right)+\exp\pi i\left(h_3+h_1\pm\frac{n_3}{2M_3}\pm\frac{n_1}{2M_1}\right)\right\}+E_{Pd}\right] \\
& \times\exp(\pm\pi i n_1) \\
+ & \left[E_{Cu}\left\{1+\exp\pi i\left(h_2+h_3\pm\frac{n_3}{2M_3}\right)+\exp\pi i\left(h_3+h_1\pm\frac{n_3}{2M_3}\pm\frac{n_1}{2M_1}\right)\right\}\right. \\
& \left.+E_{Pd}\exp\pi i\left(h_1+h_2\pm\frac{n_1}{2M_1}\right)\right]\cdot\exp\pi i(\pm n_3\pm n_1)\Bigg|. \qquad (2).
\end{aligned}
$$

---

$|\Psi|^2/|\Psi|^2_{(200)}$ is tabulated in Table II, $M_1$ and $M_3$ being assumed to be 5 and 4 respectively. On the basis of these estimated intensities the splitting manner of the superlattice reflections is depicted in Fig. 13a. The coincidence of this figure with Fig. 11 is fairly good, concerning the splits of the superlattice reflections. Since Fig. 13a or Fig. 11 represents the intensity distribution in reciprocal space corresponding to one orientation of the lattice, the intensity distribution in reciprocal space corresponding to an actual ordered alloy must be a sixfold superposition of the intensity distribution in Fig. 13a and is illustrated in Fig. 13b. The observed diffraction pattern is tolerably reproduced in the intensity distribution in the $hk$ plane in Fig. 13b. This tolerable reproducibility enables us to understand the propriety of the present model except some respects. There are some differences between the model and the observed facts as follows:

(1) The intensities cannot be expected at centres of the split superlattice reflections from the present model, while they were, in general, actually observed at some of centres, as in Fig. 11. In Fig. 8 the appearance of the centre spots of {100} groups may be explained from the model by assuming rotations of crystallites about the crystallographical axes, as often observed in thin films, but this manner of explanation does not apply to the centres of {110} groups. In Fig. 7, which corresponds to a state near the critical temperature, the centres of {100} groups are clearly visible, while the centres of {110} groups are very faint. This fact will be explained by assuming rotations of crystallities. In this

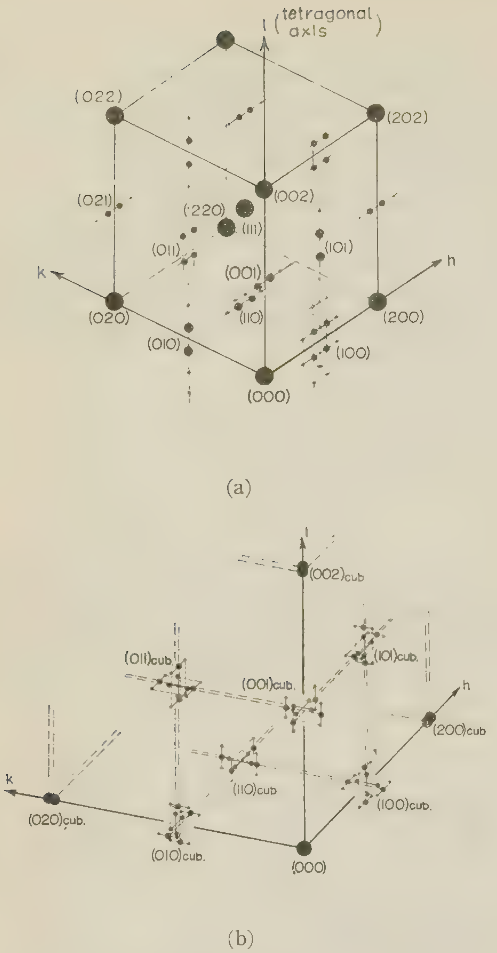

(a)

(b)

Fig. 13. (a) Fundamental intensity distribution in reciprocal space derived from the proposed model. Intensities corresponding to $|\Psi|^2/|\Psi|^2_{(200)}$ less than $2\times10^{-4}$ are omitted. The symbols, •------• and •——•, are used in the meaning similar to those in Fig. 11.
(b) Sixfold superposition of the intensity distribution in (a). This figure corresponds to the actual state of the ordered alloy.

sense, the model seems to have a better fitness to Fig. 7 than to Fig. 8. The appearance of the centre spots of {100} and {110} groups in the latter photograph suggests the increase of regions without the second kind of anti-phase domains at lower temperatures*. (In photographs from incompletely ordered $Cu_3Au$ intensities remain at centres of split maxima after formation of anti-phase domains.) The tendency that the centre spots of {110} become faint immediately below the critical temperature and become strong at lower temperatures was also observed in the specimens other than 25 per cent Pd. Higher order splits ($n_1, n_3=3$) which should be expected from the model are seen at some of the superlattice reflections in Fig. 11. They appear distinctly between {100} and {110} groups at lower temperatures (Fig. 8), but are not observed above about 400°C (Fig. 7). As the appearance of these reflections proves a high degree of development of the present anti-phase domain structure, the model seems to have a better fitness to Fig. 8 than to Fig. 7 in this sense. Thus, an ambiguity seems to be present, strictly speaking, about the propriety of the model, judging from the splitting manner of the superlattice reflections.

(2) Satellites flanking the intense normal spots cannot be derived from the present model. Three kinds of satellites are perceived in Fig. 11, and their separations from the relevant main reflections are $(a_1^*/M_1)$, $(a_3^*/M_3)$ and $(a_3^*/2M_3)$ in reciprocal space respectively. Satellites of a separation of the last value just appear after a long period of annealing, with a fainter intensity than the satellites of the other kinds. $|\Psi|$ has a finite value at $A_1=h_1\pm(n_1/2M_1)$, $A_2=h_2$, $A_3=h_3\pm(n_3/2M_3)$, where $h_1$, $h_2$ and $h_3$ are unmixed and $n_1$ and $n_3$ are odd integers. Some of these positions are only ones which can be expected in the neighbourhood of the main spots from the model, but they are entirely different from positions actually observed, and moreover, should belong, not to the normal reflections, but to the superlattice reflections, due to the term, $|E_{Cu}-E_{Pd}|$. Thus, the present model are not connected with the formation of the satellites.

Some discussions will be given of the origin of the satellites as follows. Two kinds of imperfection in a crystal lattice are considered as their causes, i.e., a periodic change of the scattering factor or a periodic change of the lattice constant[15]. For example, if the composition at each boundary between anti-phase domains would become different for some reason from that inside each domain in the course of the development of ordering, satellites should arise from the first cause. However, the observed satellites became strong and clear with the annealing time, i.e., proba-

---

* The presence of regions without both kinds of anti-phase domains cannot be considered, because only some of centres of split superlattice reflections have intensities in Fig. 11.

Table III. Values of $c/a$, $M_1$ and $M_3$ measured from specimens in $\alpha''$ phase quenched from various temperatures.

| Sample / Temperature (°C) | 18% Pd | | | 21% Pd | | | 25% Pd (a) | | | 25% Pd (b) | | | 28% Pd | | | 30% Pd | | |
|---|---|---|---|---|---|---|---|---|---|---|---|---|---|---|---|---|---|---|
| | $c/a$ | $M_1$ | $M_3$ | $c/a$ | $M_1$ | $M_3$ | $c/a$ | $M_1$ | $M_3$ | $c/a$ | $M_1$ | $M_3$ | $c/a$ | $M_1$ | $M_2$ | $c/a$ | $M_1$ | $M_3$ |
| 450 | 1 | 10.5 | | ~1 | 6.4 | | | | | ~1 | 4.2 | 3.8 | | | | | | |
| 400 | | | | | | | 0.995 | 5.4 | 3.7 | 0.996 | 4.7 | 3.6 | ~1 | 3.6 | 3.2 | 1 | 3.3 | 3.1 |
| 300 | | | | | | | | | | 0.995 | 4.7 | 3.6 | | | | | | |
| 250 | | | | <1 | 7.6 | 5.7 | 0.994 | 5.4 | 3.7 | 0.995 | 4.8 | 3.6 | <1 | 3.5 | 3.2 | 1 | 3.3 | 3.1 |
| 230 | | | | | | | 0.993 | 5.5 | 3.7 | 0.994 | 4.8 | 3.6 | | | | | | |
| 360 | | | | | | | | | | | | | ~1 | 3.6 | 3.1 | | | |
| 390 | | | | | | | 0.994 | 5.4 | 3.7 | 0.996 | 4.7 | 3.6 | ~1 | 3.5 | 3.2 | 1 | 3.2 | 3.1 |
| 450 | | | | | | | 0.997 | 5.3 | 3.8 | <1 | 4.7 | 3.7 | | | | | | |
| 470 | 1 | 10.5 | | <1 | 6.8 | 5.6 | 1 | 3.9<br>2.9* | | 1 | 3.8<br>2.8* | | 1 | 3.1<br>2.3* | | 1 | 3.0<br>2.2* | |
| 490 | 1 | 9.9 | | 1 | 6.8 | | | | | | | | | | | | | |
| 530 | | | | 1 | 6.8<br>5.0* | | | | | | | | | | | | | |

* These values are estimated, assuming $N$ to be smaller than $M$.

bly with the development of the two-dimensional anti-phase domain structure, and it is difficult at the present stage to consider that this structure should ultimately have a periodic change of composition. A remark should be made here. If the anti-phase domains characterized by the second kind of out-of-step are developed, as shown in Fig. 12, like atoms gather at each boundary between domains, the kind of atoms alternating. If the first kind of out-of-step would not occur, a periodic change of composition should be present and the scattering amplitude of the lattice should be modulated at a definite period, $2M_1a_1$, along the $x$ direction, the normal reflections being flanked with satellites of a separation $(a_1^*/2M_1)$. The existence of the first kind of out-of-step, however, compensates this periodic change of composition, and hence the normal reflections must be free from the effects of anti-phase domains. Next, if a periodic elongation or contraction of the lattice would occur at each boundary between anti-phase domains[5], satellites should arise from the second cause. In Fig. 12, an excess force cannot be considered to act at boundaries between domains along the $z$ direction characterized by the first kind of out-of-step, the circumstance being entirely different from that in CuAu II. On the other hand, a repulsive force might arise at boundaries between domains along the $x$ direction characterized by the second kind of out-of-step because of the gathering of like atoms. Thus, the origin of the satellites having a separation, $(a_1^*/M_1)$, might be found out here. An apparent expansion of the lattice along the $x$ direction should result from such a periodic error, but has not actually been detected. This condition, together with the complete lack of information about the origin of the stronger satellites having a separation, $(a_3^*/M_3)$, and of the faint satellites having a separation, $(a_3^*/2M_3)$, makes us give up a further research on this topic at the present stage. Satellites due to a periodic error of the scattering factor should be distinguished in the following point from those due to a periodic error of the lattice constant: The ratio of the intensity of satellites to that of the main reflection is independent of the order of reflection in the former case, while it increases with the order of reflection in the latter case. In thin films, however, the secondary diffraction often takes place and makes this criterion useless. In the previous work[5] the secondary diffraction effect increased the intensities of satellites flanking the normal spots other than the direct spot. Also in the present case the effect is probably present, though no distinct evidence for it has been given. The intensity of the satellites flanking the direct spot should be noticed, but its estimation is very difficult in Fig. 7 as well as in Fig. 8 owing to the intense background.

Although some corrections and replenishments to the present model may be necessary to explain completely not only the splitting manner of the superlattice reflections but also the origin of the saltellites flanking the normal spots, it will probably be safe to say that the two-dimensional anti-phase domain structure represents the actual state without serious error. In Fig. 12 the $y$ direction is equivalent to the $x$ direction with respect to the tetragonal axis, therefore, anti-phase domains characterized by the second kind of out-of-step might simultaneously be lined up also along the $y$ direction, that is, a three-dimensional anti-phase domain structure might be formed. The structure amplitude for such a lattice is easily calculated. The intensity distribution in reciprocal space derived from this structure amplitude, however, does not coincide with the observed results at all. Therefore, such a three-dimensional anti-phase domain structure is not thought to form actually.

The periods of occurrence of out-of-steps in the present structure, $M_1$ and $M_3$, were measured from separations of splits of the superlattice reflections as well as from separations of satellites flanking the normal spots and are given in Table III, together with the axial ratio of the fundamental tetragonal cell, for 18∼30 per cent Pd. The $M$ values are not integers in every concentration even after a long period of annealing. This fractional property is beyond experimental errors* and seems to suggest that some periodic fluctuation of the domain size is present within a coherent lattice, that is, that the structure shown in Fig. 12 is, strictly speaking, approximate and, in point of fact, a larger orthorhombic unit cell containing more than two domains of different size along the $x$ or $z$ direction may be considered. It is not certain whether the $M$ values settle in integers or remain fractional after a very long period of annealing.

According to the conception involved in the present work, there seems to be no discrete phase boundary between $\alpha'$ and $\alpha''$ phases. At 18 per cent Pd the separations in the splits of the superlattice reflections are so small that $M_3$ has a very large value, 10.5, and the axial ratio cannot be distinguished from unity. Thus, both the anti-phase domain structure and the tetragonality of the fundamental face-centred lattice, characteristic of $\alpha''$ phase, gradually fade away in the neighbourhood of 18 per cent Pd, and the structure is continuously changed to $\alpha'$ phase of the $Cu_3Au$ type with the decrease of palladium content. The present work has been carried out on the crystallographical standpoint, and the reason why the complicated anti-phase domain structure takes place in $Cu_3Pd$ should be explained from the standpoint of the electron theory of alloys.

## § 5. Conclusion

The present electron diffraction work on the ordered structure of $Cu_3Pd$ in thin orientated films has elucidated a complicated anti-phase domain structure present in $\alpha''$ phase. This structure can be thought of as formed from the elementary face-centred tetragonal lattice, in which the atoms arrange themselves as in the ordered structure of $Cu_3Au$ but the two kinds of step-shift, $\pm(\boldsymbol{a}_1\pm\boldsymbol{a}_2)/2$ and $\pm(\boldsymbol{a}_3\pm\boldsymbol{a}_1)/2$, occur at every $M_3$-th atom and $M_1$-th atom along the $z$ and $x$ directions respectively. Thus, the two-dimensional anti-phase domain structure is formed, which is considered to have a large orthorhombic unit cell, if $M_1$ and $M_3$ are sufficiently definite throughout the lattice. $M_1$ and $M_3$ are, however, not integers actually, even after a long period of annealing. The $M$ values monotonously decrease with the increase of palladium content. It is still better if the present model proposed on the basis of the experimental facts in thin films is confirmed in bulk specimens. This confirmation has recently succeeded in our laboratory, by taking X-ray stationary-crystal and oscillation photographs of ordered $\alpha''$ alloys of single-crystal. The detailed results will be reported in the second part of the present work.

The model of $\alpha''$ phase proposed by Geisler and Newkirk[4)] is entirely different from the present model. On the other hand, the structure reported by Schubert *et al*[16)], seems to be included in the present model. According to them ordered alloys of 18.5 to 25 atomic per cent Pd possess a one-dimensional anti-phase domain structure characterized by the first kind of out-of-step and ordered alloys of 25 to 29 atomic per cent Pd show a more complicated structure. It seems to the present authors that the last structure may be a two-dimensional anti-phase domain structure.

In conclusion, the present authors wish to express their sincere thanks to Mr. M. Hirabayashi for his kind discussions.

The present investigation has been supported

---

* The estimated error of the $M$ value is within ±3 per cent.

partly by the fund of the Ministry of Education in Aid of Scientific Researches.

### References

1) Gmelins Handbuch der Anorganischen Chemie 8. Aufl. (1949) Teil **68**, Platin A5, "Legierungen des Rutheniums, Rhodiums, Palladiums." 624/652.
2) F. W. Jones and C. Sykes: J. Inst. Metals **65** (1939) 419.
3) D. M. Jones and E. A. Owen: Proc. Phys. Soc. **B 57** (1954) 297.
4) A. H. Geisler and J. B. Newkirk: Trans. AIME **198** (1954) 1076, J. Metals (September 1954).
5) S. Ogawa and D. Watanabe: Acta Cryst. **7** (1954) 377, J. Phys. Soc. Japan **9** (1954) 475.
6) J. O. Linde: Ann. Phys. [5] **15** (1932) 249.
7) S. Ogawa, D. Watanabe and F. E. Fujita: J. Phys. Soc. Japan **10** (1955) 429.
8) L. Graf: Phys. Zeit. **36** (1935) 489.
9) C. H. Johansson und J. O. Linde: Ann. Phys. [4] **82** (1927) 449.
10) G. Borelius, C. H. Johansson und J. O. Linde: Ann. Phys. [4] **86** (1928) 299.
11) H. Raether: Z. f. angew. Phys. **4** (1952) 53.
12) M. Hirabayashi and S. Ogawa: to be published.
13) O. Goche and H. Wilman: Proc. Phys. Soc. **51** (1939) 625.
14) A. Guinier et R. Griffoul: Rev. Métallurg. **14** (1948) 387.
15) V. Daniel and H. Lipson: Proc. Roy. Soc. **A 181** (1943) 368, **A 182** (1944) 378.
M. E. Hargreaves: Acta Cryst. **4** (1951) 301.
16) K. Schubert, B. Kiefer und M. Wilkens: Z. f. Naturforsch. **9 a** (1954) 987.

---

JOURNAL OF THE PHYSICAL SOCIETY OF JAPAN Vol. 11, No. 3, MARCH, 1956

# Nuclear Magnetic Resonance Experiment on the Single Crystal of Lithium Sulfate Monohydrate, $Li_2SO_4H_2O$

By Eiji HIRAHARA and Miyuki MURAKAMI

*Department of Applied Physics, Faculty of Engineering,*
*Hiroshima University, Hiroshima*

(Received November 5, 1955)

Proton magnetic resonance absorption of water molecules in the single crystal of $Li_2SO_4 \cdot H_2O$ was observed, and the length and directions of the proton—proton line (p—p) of the water of crystallization were determined. The results obtained are as follows: there are two kinds of orientations of the p—p line in the unit cell, which contains two molecules of $Li_2SO_4 \cdot H_2O$, and they are symmetrically disposed with respect to the *ac*-plane, the plane of mirror, making the angles ±51° to that plane.

The angle between the projection of each p—p line on the *ac*-plane and the positive direction of *a*-axis is 94°, and the length of p—p line is 1.59 Å.

From the results obtained and the crystal structure by X-ray analysis, the bond angle of H—O—H is expected to lie between 106°50′ and 112°40′, and presumably some value nearer to 112°40′ may be taken to be favorable from the consideration of the bonding character.

The single crystals were prepared by a slow evaporation method from an aqueous solution in a water bath at 80°C.

## §1. Introduction

Nuclear magnetic resonance experiments on $Li_2SO_4 \cdot H_2O$ have been made by several workers[1]. Concerning the orientation of *the line joining the two protons of a water molecule* (say briefly p–p) in the crystal, however, their results are not consistent with the results of X-ray diffraction study by Ziegler[2]. Recently, Larson and Helmholz[3] have made a redetermination of the crystal structure by

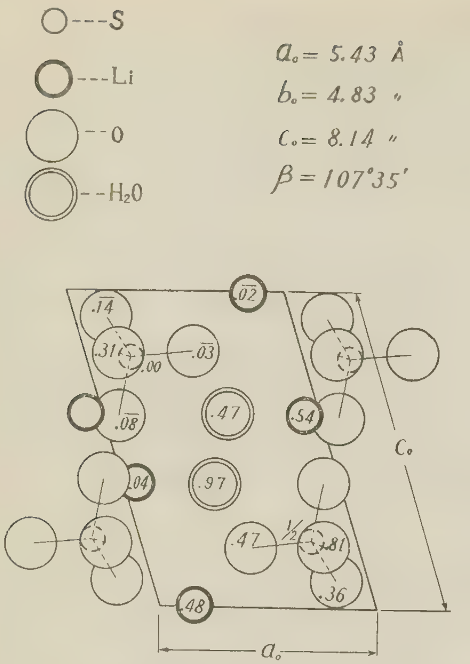

Fig. 1. Crystal structure of $Li_2SO_4 \cdot H_2O$. The projection of unit cell on the $b$-plane.

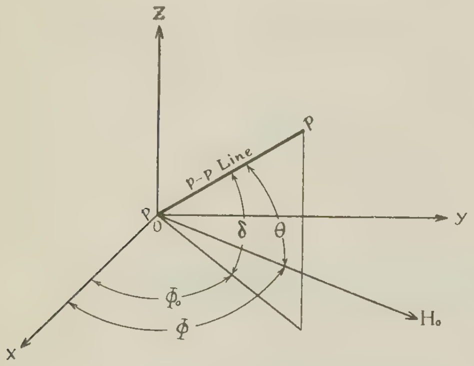

Fig. 2. Diagram defining various angles $\delta$, $\theta$, $\Phi$ and $\Phi_0$.

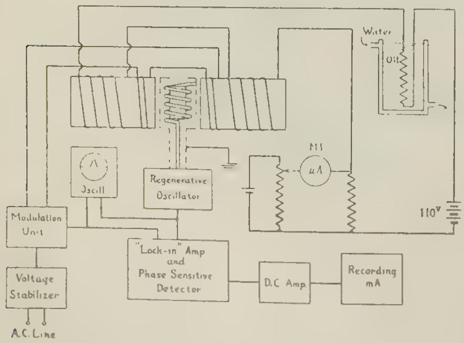

Fig. 3. Block diagram of apparatus and circuit system.

X-ray diffraction in order to check the work of Ziegler, and showed that their results are favorable for the orientation of the p–p line suggested by Pake[1]. In view of the situation, we have attempted to determine the orientation of the p–p line by means of nuclear magnetic resonance method and obtained the results somewhat different from Pake's in detailed respects.

According to Ziegler's results the crystal structure of $Li_2SO_4 \cdot H_2O$ is monoclinic and its space group is $C_2^2 - P2_1$. The dimensions of the unit cell are of $a_0 = 5.43$ Å, $b_0 = 4.83$ Å, $c_0 = 8.14$ Å, the angle between the $a$- and $c$-axes being 107°35′ $(=\beta)$, and the unit cell containing two molecules. Fig. 1 shows the projection of the unit cell on the $ac$-plane, and one of the two lithium ions in one molecule is seen to be situated nearer to a water molecule than the other.

According to the pioneer work by Pake[4] the shifts of the absorption lines of two-proton system from that of a free proton are represented as a function of the angle between the external field and the p–p line, by

$$\left.\begin{aligned} \Delta H &= \pm \alpha (3\cos^2\theta - 1) \\ \alpha &= \frac{3}{2}\mu r^{-3}, \end{aligned}\right\} \qquad (1)$$

under the assumption of rigid lattice. In these formulas $\mu$ is the magnetic moment of proton, $r$ the distance between two protons, $\theta$ the angle between the p–p line and the external field $H_0$, and $\delta$ the angle between the p–p line and its projection on the $xy$-plane (a plane perpendicular to the axis of rotation). A disposition of the p–p line with respect to the external field $H_0$ is shown in Fig. 2, from which the vector $\vec{H}_0$ is always on the $xy$-plane on rotating the crystal around $z$.

$\Phi$ is the angle between the external field $H_0$ and the reference line (say $x$-axis), and $\Phi_0$ the angle between the projection of the p–p line on the $xy$-plane and the reference line, of which a following relation holds

$$\cos\theta = \cos\delta \cdot \cos(\Phi - \Phi_0)\,. \qquad (2)$$

The orientation of the p–p line will be determined from the relations (1) and (2) observed at various values of $\Phi$.

## § 2. Preparation of Single Crystals and Experimental Arrangement

A single crystal of the hydrate was prepared from a solution of $Li_2SO_4$ by a slow evaporation method at constant temperature 80°C, through which the crystal grew up to the dimension of about $30 \times 15 \times 15\ \mathrm{mm}^3$ in a week. Then a sample was cut in a suitable shape, and the directions of the symmetry axes of crystal were examined with the aid of X-ray diffraction.

A block diagram of apparatus and circuit system is shown in Fig. 3. The oscillator used is an autodyne type detector, and the sample inserted in an oscillator coil is rotatable around the axis of the coil. A signal picked up from the oscillator coil is introduced to a narrow-band amplifier and detected by a phase-sensitive detector, from which the output is recorded by a recording milliammater through a d.c. amplifier. The electromagnet, with the pole face of 14 cm in diameter and the pole gap of 35 mm in length, yields the field strength of about 3800 gauss when it is excited by a d.c. current of about 4 ampere from a set of storage batteries.

A field modulation with a small amplitude at 60-c.p.s. is supplied from the commercial a.c. line through a voltage stabilizer and a modulation controller. A sweep of resonance line is attained by a slow changing of the magnet-coil current, which is realized as the result of Joule's heat generated in the magnet-coil. The current through the magnet-coil is measured by a potentiometric device as shown in Fig. 3, and the values of the magneticfield strength corresponding to the current are marked on the recording-milliammeter chart.

## § 3. Measurements and Results

The sample first measured (its dimension, $20 \times 10 \times 6\ \mathrm{mm}^3$) is shown in Fig. 4, in which (a) is its perspective diagram and (b) is its horizontal section cut perpendicularly to the *b*-axis. On rotating the sample around the *b*-axis in an external field the derivative curves of absorption obtained were shown in Fig. 5. The corresponding values of the angle between the external field $H_0$ and the line $x$ shown in Fig. 4 (b) are indicated beside each curve. The modulation width is indicated by the horizontal line at the upper left-side corner in the figure. The corresponding integral curves are shown in Fig. 6.

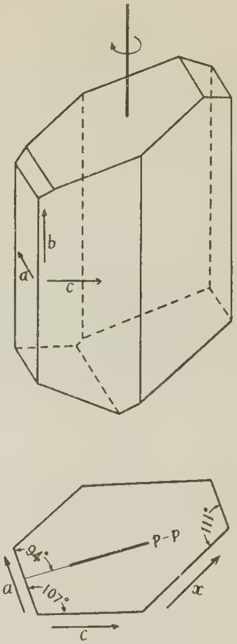

Fig. 4. Perspective diagram of the single crystal sample, and its horizontal section. The axis of rotation is *b*-axis.

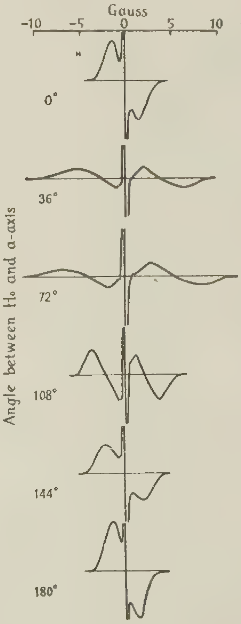

Fig. 5.

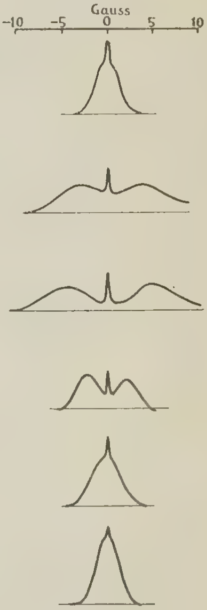

Fig. 6.

Fig. 5. Derivative curves of resonance lines at various angle positions. In this case the axis of rotation is *b*-axis. The width of modulation is indicated by a horizontal line at the upper left side of the figure.

Fig. 6. Integral curves of resonance derivative curves at the angles corresponding in Fig. 5. In Figs. 5 and 6, the sharp peak appearing in the center of resonance curve is the resonance line for free water molecules.

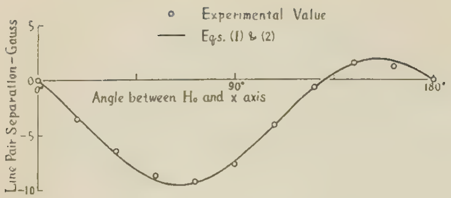

Fig. 7. $2\Delta H$, the twice of a separation of absorption lines from their center of gravity as a function of rotation angle $\Phi$. In this case, the rotation axis was $b$-axis, and angles of rotation were measured from $x$-line in Fig. 4. The solid line is the calculated line by use of Eqs. (1) and (2) with $\delta=51°$.

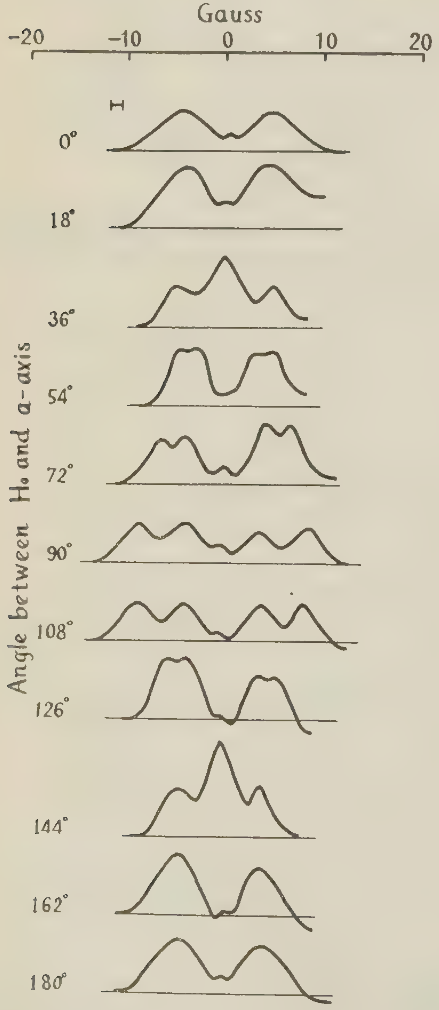

Fig. 8. Integral curves of resonance lines. The axis of rotation was the line nearly parallel to the one of two permitted p—p lines, and the angles of rotation were the angles between $H_0$ and $a$-axis. The width of modulation is indicated by a horizontal line at the upper left side of the figure.

The sharp peak in the center of each curve in Fig. 5 and 6 is attributed to the resonance line due to free water molecules contained in the cracks of the sample; and this attribution is justified by the facts that the sharp peak is as same as one from a little of water in an ampoule, and disappears after the sample is desiccated in a desiccator.

The observed separations of two component lines ($=2\Delta H$) in Fig. 5 or 6 are shown in Fig. 7 (open circles) as a function of the rotating angle $\Phi$ together the theoretical curve calculated by Eqs. (1) and (2). The value of $\cos\delta$ in Eq. (2) was determined by fitting the calculated one to the measured points in Fig. 7, which leads to $\delta=50°47'$ for the angle of inclination of a p–p line to the $xy$-plane ($ac$-plane). The curve in Fig. 7 has a minimum at 65° and a maximum at 155°, corresponding to $\Phi-\Phi_0=90°$ and 0° in Eqs. (1) and (2), respectively. From these data the angle between the projection of the p–p line and the positive direction of $a$-axis will be $94°\pm1°$ as shown in Fig. 4 (b).

The observed data can not uniquely determine the orientation of p–p line, as indicated by Eq. (1), but actually the permitted orientations of p–p lines in a unit cell containning two water molecules will have either only one group or two groups in accord with the observation mentioned above, in the latter case of which the $ac$-plane will bisect the angle of a pair of p–p lines belonging to each group, in other words, one permitted p–p line will be the mirror image of another permitted p–p line with respect to the $ac$-plane.

In order to settle the above alternative in p–p orientation, therefore, the following measurement was carried out. The sample was rotated around an axis parallel to the mentioned p–p line, and the external field $H_0$ was applied perpendicularly to it. When two permitted directions of p–p line exist, the values of $\Delta H$ from each permitted p–p should be different in such measurement, that is, $\Delta H$ from the p–p disposed parallel to the rotating axis will be constant at all angles $\Phi$, while, for another group of permitted p–p, $\Delta H$ will change with $\Phi$ as indicated by Eqs. (1) and (2).

The integral curves of the observed absorption are shown in Fig. 8. The angles between $a$-axis and the external field $H_0$ are indicated[3] beside each curve in the figure. The small peaks appeared at the center of several curves are the resonance lines from free water molecules contained in the crystal as seen in Figs. 5 and 6. The modulation width is indicated by the horizontal line at the upper left side corner in the figure.

In Fig. 9 are shown $2\Delta H$, the separation of the pair of lines for each group, as a function of the angle $\Phi$ between the external field $H_0$ and the $a$-axis. In the figure open circles show the measured values of $2\Delta H$, and the curves (1) and (2) are calculated by the use of Eqs. (1) and (2) with $\delta=90°$ and $\delta=-12°$, respectively. In the actual measurement, the rotating axis was deviated by 5° from the p–p line according to the circumstance of the crystal-cutting. Therefore, the minute deviations of the observed points from the curves (1) and (2) will be mainly ascribed to the exprimental conditions mentioned above, together with the effect of the interaction of the proton system with the other neighboring atoms such as Li- and H-ions.

From the observed value of $\alpha$ in Eq. (1), we have $r=1.59$ Å as the proton-proton distance, and assuming 0.99 Å for the bond length of O–H as in the case of ice, the bond angle of H–O–H is found to become of 106°50′.

## § 4. Discussion and Conclusion

In summing up our observed results mentioned above, it may be concluded that there exist two groups of permitted directions for the p–p lines of the water molecules in a unit cell, which directions are mutually related through mirror image with respect to the $ac$-plane and their inclinations with the $ac$-plane are about ±51°; The projection of a pair of p–p line on the $ac$-plane makes an angle of 94° with the positive direction of $a$-axis. The distance between two protons in each water molecule is 1.59 Å.

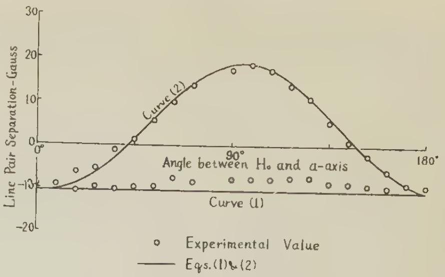

Fig. 9. $2\Delta H$, the twice of a separation of absorption lines from their center of gravity as a function of rotationg angles. The solid curves (1) and (2) are the calculated curves by the use of Eqs. (1) and (2) with $\delta=90°$ and $-12°$, respectively.

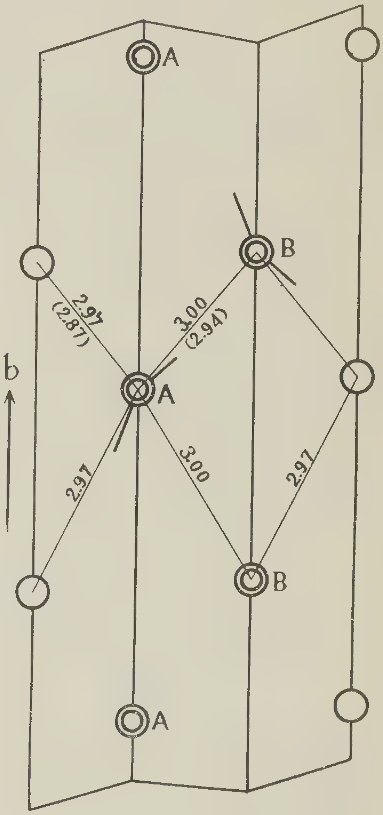

Fig. 10. The arrangement of the atoms in the neighborhood of the water molecules in the crystal lattice. The short heavy bars stretched from the double circle oxygen indicate the orientation of O—H.

The result of X-ray analysis by Larson and Helmholz[3] is in agreement with the one by Ziegler[2] in most essentials, from which the arrangement of the atoms in the neighborhood of the water molecules in the crystal lattice will be obtained as described in Fig. 10. The figure shows a projection of the crystal lattice on a plane perpendicular to the $a$-axis, in which double and single circles indicate the oxygen ions of water molecules and of the sulfate groups, respectively. Lithium ions are situated on the back of A-oxygen atoms and also in front of B-oxygen atoms. The distances (in Ångstrom) between the ions calculated from the data given by Ziegler are shown in the figure. The values in bracket denote the ones given by Larson and Helmholz[3)] in their X-ray measurement*.

As seen in ice, it may be suggested that a hydrogen atom stretches a covalent bond to the oxygen atom to which it belongs and simultaneonsly makes a hydrogen bonding with another neighboring oxygen atom. Since the shortest distance between the water molecule and the neighboring oxygen atom of sulfate group is 2.87 Å, using the X-ray data by Larson and Helmholz, the length of O–H···O in the substance is a little longer than in ice (2.76 Å). Therefore, the hydrogen bonding in this substance will be weaker than of ice, which, in turn, will have the hydrogen atom coordinate, by the covalent bonding, nearly on the line jointing the water molecule and a neighboring oxygen atom.

From the above considerations, it may be said that the water molecule will have a certain orientation of hydrogen bond under a slight restriction by the surrounding oxygen, consisting with the direction of p–p line determined in the analysis.

Next we shall go on to discuss the bond angle H–O–H of water molecule. As seen in the above discussion, the hydrogen bonding of H-ion in the crystal under consideration is taken to be weak and, its covalent bounding to be rather strong compared with those of ice. Thus, the length of O–H in the crystal will be expected to lie between 0.99 Å for ice and 0.955 Å for free gas molecule of water. Using the obtained value of 1.59 Å for the p–p distance and, further, the limiting values of O–H bond length mentioned above, the bond angle of H–O–H may be considered to take a certain value in between 106°50′ (corresponding to 0.99 Å) and 112°40′ (corresponding to 0.955 Å). In view of the rather small interaction of proton system with surrounding oxygens at large distance from the water molecule, the O–H length of water molecule in the crystal will presumably have more similar behaviour to that of a free gas in comparison with that of ice, the bond angle H–O–H being nearer to 112°40′.

So far we have confined ourselves to the discussion of the peak values of the proton resonance absorptions in $Li_2SO_4 \cdot H_2O$ in comparison with the calculated results based upon the rigid two-proton picture, as in the work of Pake. Although the observed data have been shown to be well understood theoretically, the analysis of the line width will be hardly carried through without taking into consideration the more distant interactions of the mentioned proton-system with the other protons and the neighboring Li-ions; the discussion of this problem shall be reserved till the more detailed measurements will be made.

Finally the authors wish to express their sincere thanks to Prof. T. Muto, University of Tokyo for his kind discussions. This work has been in part supported by the financial aid of the Educational Ministry.

### References

1) G. E. Pake: Thesis, Harvard University (1947).
R. V. Pound: Phys. Rev. **76** (1950) 685.
M. Soutif, Y. Ayant and B. Dreyfus: J. Chim. Phys. **50** (1953) C 107.
G. E. Pake: J. Chim. Phys. **50** (1953) C 104.
2) G. E. Ziegler: Z. Krist. **89** (1934) 456.
3) A. C. Larson and L. Helmholz: J. Chem. Phys. **22** (1954) 2049.
4) G. E. Pake: J. Chem. Phys. **16** (1948) 327.
5) N. J. Hopkins: Rev. Sci. Instr. **20** (1949) 401.

---

* Our calculation of the corresponding quantities by the use of the data in Table II of the reference (3) seems to show a slight different value compared with those in the figure. The discrepancies might be ascribed to some misprints of data in the Table II.

JOURNAL OF THE PHYSICAL SOCIETY OF JAPAN Vol. 11, No. 3, MARCH, 1956

# Determination of the End-to-End Distance of High Polymer Molecule in Solution

By Hiroshi MIZUTANI

*Department of Physics, Faculty of Science, Hokkaido University, Sapporo, Japan*

(Received May 27, 1955)

Two convenient methods have been developed for calculating the end-to-end distance of the high polymer molecule in solution from the intrinsic viscosity and the angular distribution of the intensity of the scattered light, in which the volume-exclusion effect of the chain elements of the molecule and the effect of the interaction between chain elements and solvent molecules are taken into consideration. By making use of one of these methods, the determinations of the end-to-end distances of several kinds of polystyrenes in their solutions have been made.

## § 1. Introduction

In the present paper it is intended to consider the problem of determining the extension of high polymer molecules in solution. Inasmuch as the direct determination of this quantity is impossible, it must be derived through calculation from some measurable quantities such as the intrinsic viscosity $[\eta]$ or the angular distribution of the scattered light intensity $I(\theta)$[1][2]. Such calculation involves the assumption of the distribution function for the chain elements of the molecule. In the methods hitherto used it has been assumed that the chain elements are geometrical segments having no volume and there is no interaction between the elements and solvent molecules and further that their distribution is Gaussian, that is, the formula for the mean square end-to-end distance of the chain is given by

$$\langle r^2\rangle = b^2N\,, \tag{1}$$

where $N$ is the degree of polymerization and $b$ the effective bond length.

For the real high polymer molecule in solution, to which the above assumption does not actually correspond, the distribution function of the chain elements must be sought for by taking account of the volume-exclusion effect of the elements and the effect of the interaction between the elements and the solvent molecules. As yet, however, there has been obtained no correct distribution function that might be used for deriving molecular constants from experimental data. We therefore assume that, since all the theoretical formulas for $\langle r^2\rangle$ of high polymer molecules in vacuum can be rewritten, within a narrow range of $N$, approximately in the form

$$(\langle r^2\rangle)^{1/2} = CN^{\gamma} \quad \left(\gamma \geqq \frac{1}{2}\right), \tag{2}$$

the distribution function for the real high polymer in solution is of Gaussian type which gives Eq. (2) for $\langle r^2\rangle$. Thus, by making use of it, we can determine from the measurement of $[\eta]$ or $I(\theta)$ the constants $C$ and $\gamma$ which were primarily regarded as parameters, and consequently the mean square end-to-end distance $\langle r^2\rangle$. The detailed account of the method will be given below.

## § 2. Methods

### I. Method of Determining $\langle r^2\rangle$ from $[\eta]$

Eq. (2) can be rewritten as

$$(\langle r^2\rangle)^{1/2} = \alpha b N^{1/2}\,, \tag{3}$$

where $b$ is the effective bond length and $\alpha$ the factor meaning the expansion ratio of the real chain molecule as compared with the idealized one consisting of geometrical segments. It is to be noted that $\alpha$ is a function of $N$. Thus $\langle r^2\rangle$ can be determined, provided $\alpha$ and $b$ can be obtained in one way or another.

The method of obtaining $\alpha$ is as follows. It is required from thermodynamics that $\alpha$ is related to the molecular weight $M$ by

$$\alpha^5 - \alpha^3 = C'M^{1/2}\,, \tag{4}$$

where $C'$ is a constant. For $[\eta]$, on the other hand, we assume that the relation worked out by Debye and Bueche[1)]

$$[\eta]=\frac{4\pi}{3}\frac{R_s^3}{M}\phi(\sigma) \tag{5}$$

holds approximately. Here, $\phi(\sigma)$ is a certain function of the shielding ratio $\sigma$, and $R_s$ is the equivalent radius. If now we take it for granted that $R_s$ is related to $(\langle r^2\rangle)^{1/2}$ in the same way as calculated in the random-flight problem, namely

$$R_s=\sqrt{\frac{1}{6}}(\langle r^2\rangle)^{1/2}\,, \tag{6}$$

we obtain from Eqs. (3), (5) and (6)

$$[\eta]=K_0\phi M^{1/2}\alpha^3\,, \tag{7}$$

with

$$K_0=\frac{4\pi}{3}\left(\frac{1}{6m}\right)^{3/2}b^3\,, \tag{8}$$

in which $m$ is the mass of a monomer of the molecule. Eliminating $\alpha$ from Eqs. (4) and (7), we get

$$\frac{[\eta]^{5/3}}{(K_0\phi)^{5/3}M^{4/3}}-\frac{[\eta]}{K_0\phi M}=C'\,. \tag{9}$$

In so far as $K_0\phi$ and $C'$ vary only slowly with $M$, they may be regarded as constant in a narrow range of $M$, so that

$$\frac{d}{d([\eta]/M)}\left\{\frac{[\eta]^{5/3}}{M^{4/3}}\right\}=(K_0\phi)^{2/3}\,. \tag{10}$$

Thus, with the aid of Eqs. (7) and (10) we can obtain $\alpha$ for the given molecular weight $M$ of high polymer from its intrinsic viscosity $[\eta]$.

To obtain $b$ we employed the following procedure: For the intrinsic viscosity $[\eta]$, we have from Eqs. (2), (5) and (6) the relation

$$[\eta]=K_1N^{3\gamma-1}\phi\,, \tag{11}$$

in which $K_1$ is the quantity independent of $N$ and $\sigma$, and further we have for the same quantity an empirical relation

$$[\eta]=AN^{\varepsilon}\,. \tag{12}$$

$\sigma$ is, on the other hand, by definition and with the help of Eqs. (2) and (6), given by

$$\sigma=\left(\frac{27}{8}\right)^{1/4}\left(\frac{f}{\pi C\eta_0}\right)^{1/2}N^{(1/2)-(\gamma/2)}\,, \tag{13}$$

where $f$ is the frictional constant of the chain elements and $\eta_0$ the viscosity of the solvent. Thus, from Eqs. (11), (12) and (13), we get

$$\varepsilon=(3\gamma-1)+\left(\frac{1}{2}-\frac{\gamma}{2}\right)\frac{\sigma}{\phi}\frac{d\phi}{d\sigma}\,. \tag{4)^*$$

By the use of this equation and the relation for $\gamma$ given by

$$\gamma=\frac{1}{2}+\frac{dl_n\alpha}{dl_nN}\,, \tag{15}$$

we can determine $\phi$ with known values of $\alpha$ and $\varepsilon$, and hence $K_0$ from $K_0\phi$ given by Eq. (10). The final relation to be used for determining $b$, and consequently $\langle r^2\rangle$, is Eq. (8) rewritten as

$$b=\left(\frac{243}{2}\right)^{1/6}\pi^{-(1/3)}m^{1/2}K_0^{1/3}\,. \tag{16}$$

## II. Method of Determining $\langle r^2\rangle$ from $I(\theta)$

When the volume-exclusion effect of the chain elements and the effect of interaction between chain elements and solvent molecules are taken into account, and we can still assume the Gaussian distribution of the elements, the distribution function for the end-to-end distance of high polymer molecules with $Z$ chain elements, of which the mean square end-to-end distance takes the form

$$\langle r^2\rangle=C^2Z^{2\gamma}\,, \tag{17}$$

comes out to be

$$W(r)dr=\left(\frac{3}{2\pi C^2Z^{2\gamma}}\right)^{3/2}\exp\left(-\frac{3r^2}{2C^2Z^{2\gamma}}\right)4\pi r^2dr\,. \tag{18}$$

Consider that a parallel beam of light be incident upon a dilute solution of high polymer molecules, were $\nu$ molecules each consisting of $N$ elements are contained in volume $V$ of the solution. We define a distribution function $\rho(r)$ such that the probability of finding the center of some chain element within the volume element $d\tau$ at a distance $r$ from some other arbitrarily chosen element is $N\nu\rho(r)d\tau/V$. Let the wave-length of the light be $\lambda$, the unit vectors in the directions of incident and scattered light be $\boldsymbol{s}_1$ and $\boldsymbol{s}_2$ respectively, their difference be $\boldsymbol{s}=\boldsymbol{s}_1-\boldsymbol{s}_2$, and the angle between these directions be $\theta$, then we have for the intensity of the scattered light

$$I(\theta)=\frac{kN^2\nu^2}{V^2}\int\rho(r)\exp\left(\frac{2\pi i\boldsymbol{s}\cdot\boldsymbol{r}}{\lambda}\right)d\tau\,, \tag{19}$$

where $k$ is a constant factor. If we further define a probability function $W_{ij}(r)$ so that $W_{ij}(r)d\tau$ may give the probability of finding the $j$ th element in the volume element

---

* When $\gamma=1/2$ this relation reduces to that obtained by Debye and Bueche.[1)]

$d\tau$ at a distance $r$ from the $i$ th element, Eq. (19) turns out, according to Zimm[2], to be

$$I(\theta)=K(MP(\theta)c-2A_2M^2P^2(\theta)c^2) \tag{20}$$

with

$$\left.\begin{aligned} c&=\nu M/V\,,\\ K&=kN^2/M^2\,,\\ A_2&=-N_0N^2X/2M^2\,,\\ X&=\int\chi(r_{\kappa\lambda})d\tau\,. \end{aligned}\right\} \tag{21}$$

Here $\chi(r_{\kappa\lambda})$ is a function of the potential energy between the $\kappa$ th and $\lambda$ th element, and

$$P(\theta)=\frac{1}{N^2}\sum_i\sum_j\int W_{ij}(r)\exp\left(\frac{2\pi i\boldsymbol{s}\cdot\boldsymbol{r}}{\lambda}\right)d\tau\,. \tag{22}$$

In place of $W_{ij}(r)$ in this equation we may use Eq. (18) just by putting $Z=j-i$. Substituting Eq. (18) in Eq. (22) and replacing summation by integration, we obtain the formula

$$P(\theta)=\frac{2}{N^2}\int_0^N(N-Z)\exp(-uC^2Z^{2\gamma})dZ\,, \tag{23}$$

where

$$u=\frac{8\pi^2}{3\lambda^2}\sin^2\frac{\theta}{2}\,. \tag{24}$$

Thus from Eqs. (23) and (20) $I(\theta)$ becomes in the limiting case of infinitely dilute concentration:

$$\lim_{c\to 0}\frac{I(\theta)}{c}=\frac{2KM}{N^2}\int_0^N(N-Z)\exp(-uC^2Z^{2\gamma})dZ\,. \tag{25}$$

This is the formula for the intensity of the scattered light when the volume-exclusion effect and the effect of interaction between chain elements and solvent molecules are taken into account. By means of this formula, we can determine $C$ and $\gamma$ from the measurement of $I(\theta)$, and hence the end-to-end distance from Eq. (17).

## § 3. Experimental Results; Determination of $\langle r^2\rangle$ of High Polymer Molecule in Solution by the Method I

We prepared the benzene solutions of polystyrenes with three different molecular weights and measured their $[\eta]$ by the use of a capillary viscometer, of which the capillary had a length of 17 cm and inside diameter of 0.02 cm. The results are given in Table I. The values of $\mathcal{E}$ were determined from the values of $[\eta]$ given in Table I, by refering to the $\mathcal{E}$-values measured by R.A. Gregg and F. R. Mayo[3] at 30°C. Tables II～IV show the values of $\mathcal{E}$, $K_0\phi$, $\gamma$, $\phi$, $K_0$, $b$, $\alpha$ and $(\langle r^2\rangle)^{1/2}$, and Table V gives the expansion coefficients as calculated from Table IV.

Table I.

| M.W. | $[\eta]$ g$^{-1}$cm$^3$ | |
|---|---|---|
| | 20°C | 30°C |
| 388.000 | 183.8 | 181.0 |
| 355.000 | 163.1 | 161.2 |
| 195.000 | 110.8 | 110.2 |

Table II.

| Temp. | 20°C | 30°C |
|---|---|---|
| $\varepsilon$ | 0.728 | 0.720 |
| $K_0\phi$ | $0.664\times10^{11}$ | $0.738\times10^{11}$ |
| $\gamma$ | 0.572 | 0.564 |
| $\phi$ | 2.30 | 2.22 |
| $K_0$ | $0.29\times10^{11}$ | $0.33\times10^{11}$ |
| $b_0$ | $6.16\times10^{-8}$ | $6.42\times10^{-8}$ |

Table III.

| M.W. | $\alpha$ | |
|---|---|---|
| | 20°C | 30°C |
| 388.000 | 1.512 | 1.45 |
| 355.000 | 1.49 | 1.428 |
| 195.000 | 1.432 | 1.378 |

Table IV.

| M.W. | $(\langle r^2\rangle)^{1/2}=\alpha bN^{1/2}$ | |
|---|---|---|
| | 20°C | 30°C |
| 388,000 | $569\times10^{-8}$ | $566\times10^{-8}$ |
| 355,000 | 523 〃 | 521 〃 |
| 195,000 | 383 〃 | 382 〃 |

Table V.

| M.W. | Expansion coefficient |
|---|---|
| 388,000 | −0.0054 |
| 355,000 | −0.0039 |
| 195,000 | −0.0026 |

The measurement of $\langle r^2\rangle$ by the method II is now being carried on and will be reported in a subsequent paper.

## § 4. Remark

For comparison's sake, let us inquire into

Table VI.

| Temp. | 20°C | 30°C |
|---|---|---|
| $\varepsilon$ | 0.728 | 0.72 |
| $K_0\phi$ | $2.14 \times 10^{11}$ | $2.12 \times 10^{11}$ |
| $\phi$ | 1.225 | 1.26 |
| $K_0$ | $1.75 \times 10^{11}$ | $1.68 \times 10^{11}$ |
| $b_0$ | $11.18 \times 10^{-8}$ | $11.04 \times 10^{-8}$ |

Table VII.

| M.W. | $(\langle r^2\rangle)^{1/2}=b_0N^{1/2}$ | |
|---|---|---|
| | 20°C | 30°C |
| 388,000 | $694 \times 10^{-8}$ | $688 \times 10^{-8}$ |
| 355,000 | 636 〃 | 630 〃 |
| 195,000 | 468 〃 | 463 〃 |

the end-to-end distance of the chain corresponding to the simple formula $(\langle r^2\rangle)^{1/2}=b_0N^{1/2}$, in which $b_0$ is the effective bond length. For that purpose we first determine $\phi$ by means of Debye-Buche's method[1], and then determine $K_0$ from the formula for $[\eta]$, $[\eta]=K_0M^{1/2}\phi$. The value of $b_0$ can be obtained by the help of the relation

$$b_0=\left(\frac{243}{2}\right)^{1/6}\pi^{-1/3}m^{1/2}K_0^{1/3} .$$

The results are given in Tables VI and VII.

From comparison between Table IV and Table VII we see that the $\langle r^2\rangle$-value comes out different according as the assumed distribution function of the chain elements is different; in other words, in determining the value of $\langle r^2\rangle$, it is necessary to adopt the correct distribution function, taking into account the volume-exclusion effect and the effect of the interaction between chain element and solvent molecules.

## Acknowledgments

The author wishes to express his hearty thanks to Prof. T. Hori of the Institute of Low Temperature Science, Hokkaido University, Prof. J. Huruichi and other members belonging to the High Polymer Research Section of Hokkaido University, and Dr. S. Oka of Kobayashi Institute of Physical Research, Tokyo, for their kind discussions on the present subject.

## References

1) J. G. Kirkwood and J. Riseman: J. Chem. Phys. **16** (1948) 565.
P. Debye and A. M. Bueche: J. Chem. Phys. **16** (1948) 573.

2) B. H. Zimm: J. Chem. Phys. **16** (1948) 1093.

3) R. A. Gregg and F. R. Mayo: J. Am. Chem. Soc. **70** (1948) 2373.

JOURNAL OF THE PHYSICAL SOCIETY OF JAPAN Vol. 11, No. 3, MARCH, 1956

# A Theoretical Analysis of the Magnetic Hyperfine Structure of the Microwave Spectrum of $C_{2v}$ Molecules

By Akira OKAYA

*Department of Physics, Faculty of Science, University of Kyoto*

(Received July 11, 1955)

A theoretical analysis of magnetic hyperfine structure due to the magnetic interaction between the spins of off or on axis nuclei and the molecular rotational magnetic field is developed for asymmetric $C_{2v}$ molecules in ${}^1A$ electronic and vibrational ground state.

This analysis is for the special case where two equivalent nuclei of spin 1/2 are off the molecular axis, one nucleus of spin zero and one nucleus of arbitrary spin are on the molecular axis.

This analysis predicts that a triplet will be observed for prolate rotational transitions for which $\Delta J=0$, $\Delta K_{+1}=-1$, and both initial and final $K_{-1}$ values are odd.

## §1. Introduction

The author has observed that the main line of the rotational spectrum of formaldehyde, $H_2CO$[1], is split into two lines. This doublet character is due to the magnetic interaction between the spin of two protons and the magnetic field caused by molecular rotation just as in the case of the ammonia molecule[2][3][4][5].

Theoretical calculations show that a triplet composed of three $\Delta F=0$ transitions can explain the observed doublet appearance as shown in a subsequent experimental report[1].

The above interaction is treated for asymmetric $C_{2v}$ molecules in a ${}^1A$ electronic and vibrational ground state, which includes formaldehyde as a typical example. We treat the case in which two equivalent nuclei of spin 1/2 are off the molecular axis, while one nucleus, $K_0$, of any optional spin value and another nucleus, $K_0'$, of spin zero are on the molecular axis.

This treatment can also be applied to such molecules as $H_2O$, $H_2S$, $CH_2O$, $CF_2O$, etc.

## §2. The Hamiltonian

The Hamiltonian[5][6] of a free prolate molecule in a ${}^1A$ electronic state is based on the Pauli approximation:

$$H=C(J_x-L_x)^2+B(J_y-L_y)^2+A(J_z-L_z)^2 \tag{1.0}$$

$$+(e\mu_0/c)\sum_{K,i} r_{Ki}^{-3}(\boldsymbol{r}_i-\boldsymbol{r}_K)\times\{\boldsymbol{V}_i-[1+Z_KM_P/(g_KM_K)]\boldsymbol{V}_K\}\cdot g_K\boldsymbol{I}_K \tag{1.1}$$

$$-(e\mu_0/c)\sum_{\substack{K,L\\(K\neq L)}} Z_Lr_{KL}^{-3}(\boldsymbol{r}_K-\boldsymbol{r}_L)\times\{[1+Z_KM_P/(g_KM_K)]\boldsymbol{V}_K-\boldsymbol{V}_L\}\cdot g_K\boldsymbol{I}_K \tag{1.2}$$

$$+g_e\mu_0\mu_e\sum_{j,k} r_{jK}^{-5}[g_K\boldsymbol{I}_K\cdot\boldsymbol{S}_jr_{jK}^2-3g_K\boldsymbol{I}_k\cdot(\boldsymbol{r}_K-\boldsymbol{r}_j)\boldsymbol{S}_j\cdot(\boldsymbol{r}_K-\boldsymbol{r}_j)] \tag{1.3}$$

$$+\mu_0^2\sum_{\substack{K,L\\(K>L)}} r_{KL}^{-5}[g_K\boldsymbol{I}_K\cdot g_L\boldsymbol{I}_Lr_{KL}^2-3g_K\boldsymbol{I}_K\cdot(\boldsymbol{r}_K-\boldsymbol{r}_L)g_L\boldsymbol{I}_L\cdot(\boldsymbol{r}_K-\boldsymbol{r}_L)] \tag{1.4}$$

$$+H_Q \tag{1.5}$$

$$+(16/3)\pi\mu_0\mu_e\sum_{K,j} g_K\delta(\boldsymbol{r}_K-\boldsymbol{r}_j)\boldsymbol{S}_j\cdot\boldsymbol{I}_K \tag{1.6}$$

In (1.0) to (1.6), capital-letter subscripts refer to nuclei and small-letter subscripts to electrons. These particles have, respectively, position vectors $\boldsymbol{r}_k$, $\boldsymbol{r}_j$ and velocities $\boldsymbol{V}_k$, $\boldsymbol{V}_j$ relative to the molecular centre of mass which is assumed to coincide with the centre of mass of the nuclei only. The nuclei and electrons have charges $Z_ke$, $e$; spins $\boldsymbol{I}_k$, $\boldsymbol{S}_j$; and $g$-factors $g_k$, $g_e$, respectively. $\mu_0$ and $\mu_e$ are the nuclear and Bohr magnetons respectively, while $M_P$

is the proton mass and $M_K$ the mass of the $K$th nucleus. $C$, $B$ and $A$ are the transverse and axial rotational constants of the prolate $C_{2v}$ symmetry molecule exclusive of the electrons. $J_x, J_y, J_z$ are the components of the total molecular angular momentum exclusive of nuclear spin, and $L_x, L_y, L_z$ are the total electronic orbital angular momentum components.

## § 3. The Molecular Wave Function

Molecular rotational wave functions are classified by the irreducible representations of the rotation group $C_2$. The correspondence of the irreducible representations to the, $K_{-1}$, $K_{+1}$, rotational states are shown in Table I. The symmetries of nuclear spin functions are classified by the permutation group, $P_2$, and their irreducible representations are also shown in Table I. The total molecular wave function is represented by

$$\psi=\psi_{RA}(J, \tau, M, \gamma)\psi_0(\sigma_0)\psi(\sigma_1)\psi_2(\sigma_2) . \qquad (2)$$

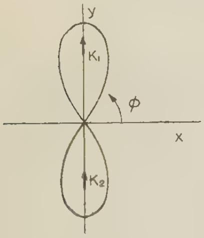

Fig. 1 (a).

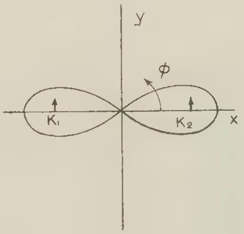

Fig. 1 (b).

The details of the rotational wave function, $\psi_{RA}$, for an asymmetric molecule are shown in Appendix I. $\psi_0$ is the spin function for nuclei on the molecular axis, while $\psi_1$ and $\psi_2$ are the spin functions for the two equivalent nuclei which are off the symmetry axis.

The permutation group, $P_2$, is homomorphic to the $C_{2v}$ rotation reflection group and forms a molecular rotational group by itself.

The total wave function belongs to the irreducible representation, $A$, or $B$[7], of the $P_2$ group according as the off axial nuclear spins are 0 or 1/2.

For the calculations of this paper, it is necessary to define the coupling scheme for angular momenta in the molecule. We can assume that the quadrupole coupling of the on-axis nucleus to the molecular rotation is stronger than the intra-molecular magnetic interaction. Then

$$\boldsymbol{I}_0+\boldsymbol{J}=\boldsymbol{F}_1 ,$$

and the spins of the equivalent nuclei are coupled to become $\boldsymbol{I}_1+\boldsymbol{I}_2=\boldsymbol{I}$. $\boldsymbol{I}$ is coupled further to $\boldsymbol{F}_1$ as

$$\boldsymbol{I}+\boldsymbol{F}_1=\boldsymbol{F} .$$

In this coupling scheme the total wave functions are

$$\begin{aligned}\psi_{E=W_0}&=|K, J, M, F_1, I_0, I=0>+(-1)^{\gamma}|-K, J, M, F_1, I_0, I=0>\\&=|\tau, J, M, F_1, I_0, I=0> ,\\ \psi_{E=W_0+W_1+f}=\psi_{E=W+f}&=|K, J, M, F_1, I_0, I=1>+(-1)^{\gamma}|-K, J, M, F_1, I_0, I=1>\\&=|\tau, J, M, F_1, I_0, I=1> ,\end{aligned}$$

where $W=W_0+W_1$ .

From the permutation $P_{12}$ of two equivalent nuclei, we can obtained the following relations:

$$P_{12}=P_{12}^{(z)}P_{12}^{(\sigma)}=P_{12}^{(z)}\{1/2+2(\boldsymbol{I}_1\cdot\boldsymbol{I}_2)\} ,$$

$$P_{12}^{(\sigma)}|F_1, I=1>=|F_1, I=1> ,$$

and

$$P_{12}^{(\sigma)}|F_1, I=0>=-|F_1, I=0> .$$

For the $P_{12}^{(z)}$ operation we can use the results of Mulliken[13] together with the fact that $P_{12}$ is homomorphic to the $C_{2v}$ group. Then we have

$$C_2^{(z)}\psi_{RA}=P_{12}^{(z)}\psi_{RA}=(-1)^{K_{-1}}\psi_{RA} \qquad \text{(prolate case)},$$

$$C_2^{(y)}\psi_{RA} \qquad =(-1)^{J+\gamma}\psi_{RA} \qquad \text{(oblate case)}.$$

The wave function symmetries are shown in Table I (a) for the prolate case ($I_1=I_2=1/2$ and $I_1=I_2=0$) and in Table I (b) for the oblate case ($I_1=I_2=1/2$ and $I_1=I_2=0$).

It may be helpful to give a simple physical argument for the magnetic interactions. The rotational wave function of a prolate asymmetric rotor* may be rewritten as:

---

* See Appendix I and Table II.

Table I a. Symmetry properties of the molecular wave function.

| Rotational levels | | $\psi(\tau, J, M, \gamma, I_0, M_{I0})$ Wave functions without off axial nuclear spins | | $\psi(I, I_1, M_I)$ Off-axial nuclear spin functions | | | | $\psi(\tau, J.M, \gamma, I_0, M_{I0}, I, I_1, M_I)$ Total wave functions | | | Signs of energy levels $f$ | |
|---|---|---|---|---|---|---|---|---|---|---|---|---|
| $K_{-1}$ | $K_{+1}$ | Number of functions | Irre. rep. | Values of $I$ | $M_I$ | Number of functions | Irre. rep. | Values of $F$ | Number of functions | Irre. rep. | $J:e$ | $J:o$ |
| ($I_1=I_2=1/2$ prolate case) | | | | | | | | | | | | |
| $e$ | $e$ | $2F_1+1$ | $A$ | | | | | | | $A$<br>$\underline{B}$* | + | − |
| | $o$ | $2F_1+1$ | $A$ | 1 | $\pm1$<br>$0$ | 3 | $A$ | $F_1\pm1$<br>$F_1$ | $3(2F_1+1)$ | $A$<br>$\underline{B}$ | − | + |
| $o$ | $e$ | $2F_1+1$ | $B$ | 0 | 0 | 1 | $B$ | $F_1$ | $2F_1+1$ | $\underline{B}$<br>$A$ | − | + |
| | $o$ | $2F_1+1$ | $B$ | | | | | | | $\underline{B}$<br>$A$ | + | − |
| ($I_1=I_2=0$ prolate case) | | | | | | | | | | | | |
| $e$ | $e$ | $2F_1+1$ | $A$ | | | | | | | $\underline{A}$ | | |
| | $o$ | $2F_1+1$ | $A$ | 0 | 0 | 1 | $A$ | $F_1$ | $2F_1+1$ | $\underline{A}$ | | |
| $o$ | $e$ | $2F_1+1$ | $B$ | | | | | | | $B$ | | |
| | $o$ | $2F_1+1$ | $B$ | | | | | | | $B$ | | |
| ($I_1=I_2=1/2$ oblate) | | | | | | | | | | | | |
| $e$ | $e$ | $2F_1+1$ | $A$ | | | | | | | $A$<br>$\underline{B}$ | + | − |
| | $o$ | $2F_1+1$ | $B$ | 1 | $\pm1$<br>$0$ | 3 | $A$ | $F_1+1$<br>$F_1$ | $3(2F_1+1)$ | $\underline{B}$<br>$A$ | − | + |
| $o$ | $e$ | $2F_1+1$ | $B$ | 0 | 0 | 1 | $B$ | $F_1$ | $2F_1+1$ | $\underline{B}$<br>$A$ | − | + |
| | $o$ | $2F_1+1$ | $A$ | | | | | | | $A$<br>$\underline{B}$ | + | − |
| ($I_1=I_2=0$ oblate) | | | | | | | | | | | | |
| $e$ | $e$ | $2F_1+1$ | $A$ | | | | | | | $\underline{A}$ | | |
| | $o$ | $2F_1+1$ | $B$ | 0 | 0 | 1 | $A$ | $F_1$ | $2F_1+1$ | $B$ | | |
| $o$ | $e$ | $2F_1+1$ | $B$ | | | | | | | $B$ | | |
| | $o$ | $2F_1+1$ | $A$ | | | | | | | $\underline{A}$ | | |

* Underline shows the wave functions which are allowed.

$$\psi_{RA}=\psi_{MJ}(e^{iK_{-1}\phi}+(-1)^{\gamma}e^{-iK_{-1}\phi}) ,$$

where $\phi$ is the azimuthal angle about the molecular symmetry axis, and $\gamma$ is the parity which is uniquely determined by the rotational quantum numbers of each rotational level. According as the case $\gamma=1$ or $0$ applies, the the above wave function becomes:

$$\propto\psi_{MJ}\sin K_{-1}\phi \qquad (\text{for } \gamma=1),$$
$$\propto\psi_{MJ}\cos K_{-1}\phi \qquad (\text{for } \gamma=0).$$

A plot of the probability of a given value of $\phi$ is given in Fig. 1(a) and 1(b).

We can see that the interactions between nuclear spin wave functions and rotational wave functions are reasonably different for the two cases, $\gamma=0$ or 1, so clearly the interaction energies for these cases are different.

Then if we consider the cases of transitions between $\gamma=0$ and $\gamma=1$ levels[1], the triplet splitting of these lines are expected.

## § 4. Perturbation

Van Vleck's second order perturbation

method[5)6)] has been used.

(a) *Calculation of the first order effective Hamiltonian* ($G_1$).

The terms which are diagonal relative to ground electronic quantum number $l_0$ in Eq. (1) are shown below.

$$
\begin{aligned}
H_1 = {} & CJ_x^2 + BJ_y^2 + AJ_z^2 && (3.0)\\
& + (e\mu_0/c)\sum_{i,K} r_{iK}^{-3}(\boldsymbol{r}_i - \boldsymbol{r}_K)\times[1+Z_K M_P/(g_K M_K)]\boldsymbol{V}_K \cdot g_K \boldsymbol{I}_K && (3.1)\\
& - (e\mu_0/c)\sum_{K,L} Z_L r_{KL}^{-3}(\boldsymbol{r}_K - \boldsymbol{r}_L)\times\{[1+Z_K M_P/(g_K M_K)]\boldsymbol{V}_K - \boldsymbol{V}_L\}\cdot g_K \boldsymbol{I}_K && (3.2)\\
& + \mu_0^2 \sum_{\substack{K,L\\(K>L)}} r_{KL}^{-5}[g_K \boldsymbol{I}_K \cdot g_L \boldsymbol{I}_L r_{KL}^2 - 3 g_K \boldsymbol{I}_K \cdot (\boldsymbol{r}_K - \boldsymbol{r}_L) g_L \boldsymbol{I}_L \cdot (\boldsymbol{r}_K - \boldsymbol{r}_L)] && (3.3)\\
& + H_Q && (3.4)
\end{aligned}
$$

The term (3.0) can be calculated very accurately by the KHC method[8)]. The approximation formula of Bragg and Golden[9)10)] is applicable to (3.4). The coupling schemes in molecular and laboratory frames are shown in Figs. 2 and 3 respectively, in which we adopted the inverted spin quantum number[6)] $\bar{I}_0 = -I_0$, $\bar{I}_1 = -I_1$, and $\bar{I}_2 = -I_2$, in order to be able to use the same relations for angular quantum numbers in a laboratory frame and to use the matrix elements tabulated by Condon and Shortley[11)]. The notation for geometry of molecule in shown in Fig. 4.

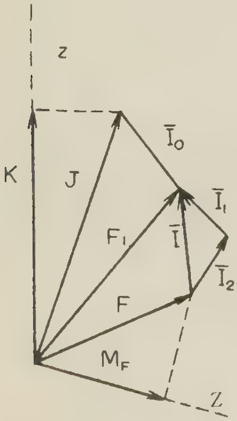

Fig. 2.

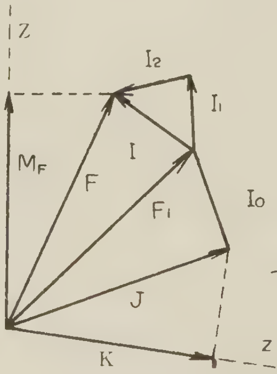

Fig. 3.

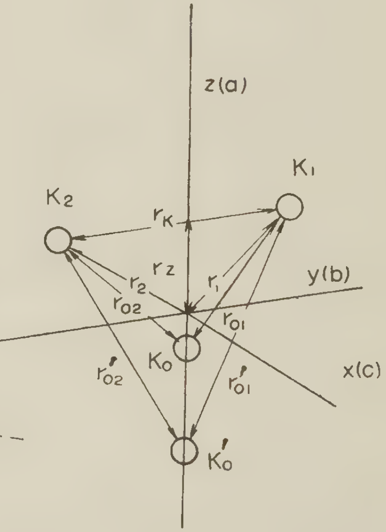

Fig. 4.

A part of (3.1) which is concerned with off-axial nuclei $K_1, K_2$ is reduced, after some calculations, to the following form:

$$-(\gamma_1 J_x \bar{I}_{1x} + \beta_1 J_y \bar{I}_{1y} + \alpha_1 J_z \bar{I}_{1z}) \,, \tag{4}$$

where

$$
\begin{aligned}
\gamma_1 = {} & -2(e\mu_0/c\hbar)C[1+Z_1 M_P/(g_1 K_1)]g_1\{r_z \langle l_0 | \sum_{i,K=1,2} r_{iK}^{-3}(\boldsymbol{r}_i - \boldsymbol{r}_K)_z | l_0 \rangle \\
& + r_y \langle l_0 | \sum_{i,K=1,2} r_{iK}^{-3}(\boldsymbol{r}_i - \boldsymbol{r}_K)_y | l_0 \rangle \} \,,\\
\beta_1 = {} & -2(e\mu_0/c\hbar)Br_z[1+Z_1 M_P/(g_1 M_1)]g_1 \langle l_0 | \sum_{i,K=1,2} r_{iK}^{-3}(\boldsymbol{r}_i - \boldsymbol{r}_K)_z | l_0 \rangle \,,
\end{aligned}
$$

and

$$\alpha_1 = -2(e\mu_0/c\hbar)Ar_y[1+Z_1M_P/(g_1M_1)]g_1\langle l_0|\sum_{l,K=1,2} r_{iK}^{-3}(\boldsymbol{r}_i-\boldsymbol{r}_K)_y|l_0\rangle \,.$$

A part concerning nucleus $K_0$ in (3.1) is reduced to

$$-(c_1J_x\bar{I}_{0x}+b_1J_y\bar{I}_{0y}+a_1J_z\bar{I}_{0z}) \,, \tag{5}$$

where

$$c_1 = -2(e\mu_0/c\hbar)Cr_{0z}[1+Z_0M_P/(g_0M_0)]g_0\langle l_0|\sum_i r_{0i}^{-3}(\boldsymbol{r}_i-\boldsymbol{r}_0)_z|l_0\rangle \,,$$

and

$$b_1 = -2(e\mu_0/c\hbar)Br_{0z}[1+Z_0M_P/(g_0M_0)]g_0\langle l_0|\sum_i r_{i0}^{-3}(\boldsymbol{r}_i-\boldsymbol{r}_0)_z|l_0\rangle$$

$$a_1 = 0 \,.$$

A part which is concerned with $K_1, K_2$ in (3.2) becomes

$$-(\gamma_2J_x\bar{I}_{1x}+\beta_2J_y\bar{I}_{1y}+\alpha_2J_z\bar{I}_{1z}) \,, \tag{6}$$

where

$$\gamma_2 = -\frac{e\mu_0}{c\hbar}g_1C\left\{Z_1\left(2+\frac{Z_1M_P}{g_1M_1}\right)\frac{1}{r_{01}\sin\beta}+4\sum_{0,0'}\frac{Z_0}{r_{01}}\left[1+\frac{Z_1M_P}{g_1M_1}\left(\sin^2\beta+\frac{r_z}{r_{01}}\cos\beta\right)\right]\right\} \,,$$

$$\beta_2 = -\frac{4e\mu_0}{c\hbar}g_1B\sum_{0,0'}\frac{Z_0}{r_{01}}\left(\cos^2\beta+\frac{Z_1M_P}{g_1M_1}\frac{r_z}{r_{01}}\cos\beta\right) \,,$$

and

$$\alpha_2 = -\frac{e\mu_0}{c\hbar}g_1A\left\{Z_1\left(2+\frac{Z_1M_P}{g_1M_1}\right)\frac{1}{r_{01}\sin\beta}+4\sum_{0,0'}\frac{Z_0}{r_{01}}\left[\sin^2\beta+\frac{Z_1M_P}{g_1M_1}\left(\sin^2\beta+\frac{r_z}{r_{01}}\cos\beta\right)\right]\right\} \,.$$

A part concerning $K_0$ in the term (3.2) is reduced to

$$-(c_2J_x\bar{I}_{0x}+b_2J_y\bar{I}_{0z}+a_2J_y\bar{I}_{0z}) \,, \tag{7}$$

where

$$c_2 = -\frac{4e\mu_0}{c\hbar}Z_1g_0C\frac{1}{r_{01}}\left(1+\frac{Z_0M_P}{g_0M_0}\frac{r_z}{r_{01}}\cos\beta\right) \,,$$

$$b_2 = -\frac{4e\mu_0}{c\hbar}Z_1g_0B\frac{1}{r_{01}}\left(\cos^2\beta+\frac{Z_0M_P}{g_0M_0}\frac{r_z}{r_{01}}\cos\beta\right) \,,$$

and

$$a_2 = -\frac{4e\mu_0}{c\hbar}Z_1g_0A\frac{1}{r_{01}}\sin^2\beta \,.$$

The term in (3.3) which is concerned with the mutual interaction between equivalent off-axial nuclei does not vanish in the case when $I_1=I_2=1/2$, but has not been calculated in this paper, since it seems to be of small value. Those terms in (3.3) which involve interactions of $K_0$, with $K_1$ or $K_2$ are

$$\mu_0^2g_1g_0\sum_{0,0'}r_{01}^{-3}[(\bar{I}_0\,\bar{I})-3(\bar{I}_0\bar{I}_z\cos^2\beta+\bar{I}_{0y}\bar{I}_y\sin^2\beta)] \,. \tag{8}$$

This equation is rewritten as follows:

$$c_3\bar{I}_{0x}\bar{I}_x+b_3\bar{I}_{0y}\bar{I}_y+a_3\bar{I}_{0z}\bar{I}_z \,,$$

where

$$c_3 = \mu_0^2g_0g_1r_{01}^{-3} \,,$$
$$b_3 = \mu_0^2g_0g_1r_{01}^{-3}(1-3\sin^2\beta) \,,$$
$$a_3 = \mu_0^2g_0g_1r_{01}^{-3}(1-3\cos^2\beta) \,.$$

By using the general relation which was derived by Condon and Shortley11), the matrix elements in (8) are rewritten as:

$$\overline{I}_{0\nu}\overline{I}_{\nu}=\frac{(\boldsymbol{F}_1\cdot\boldsymbol{I})}{F_1(F_1+1)}\left(\frac{(\boldsymbol{I}_0\cdot\boldsymbol{J})}{J(J+1)}J_{\nu}^2+\overline{I}_{0\nu}^2\right), \tag{9}$$

where

$$\nu=x,\, y,\, z\,.$$

Furthermore, these are transformed by the following relations[5]

$$\langle\overline{I}_0,\, F_1,\, J,\, \tau\,|\,\overline{I}_{0\nu}^2\,|\,\overline{I}_0,\, F_1,\, J,\, \tau'\rangle=4\frac{(2I_0-1)}{J(J+1)}\frac{2JY}{2J+3}\langle J,\tau\,|\,J_{\nu}^2\,|\,J,\tau'\rangle\,,$$

where

$$Y=\frac{3(\boldsymbol{J}\cdot\boldsymbol{I}_0)^2+(3/2)(\boldsymbol{J}\cdot\boldsymbol{I}_0)-\boldsymbol{J}^2\boldsymbol{I}_0^2}{2J(2J-1)2I_0(2I_0-1)}\,.$$

By making use of (9) together with the above relations, the expression (8) is rewritten as:

$$\frac{(\boldsymbol{F}_1\cdot\boldsymbol{I})}{F_1(F_1+1)J(J+1)}\left\{(\boldsymbol{I}_0\cdot\boldsymbol{J})+\frac{8YI_0(2I_0-1)J}{2J+3}\right\}(c_3J_x^2+b_3J_y^2+a_3J_z^2)\,.$$

Moreover, $\overline{I}_{1\nu}$ and $\overline{I}_{0\nu}$ in the above expressions (4), (5), (6), (7) and (8) are rewritten by using the following relations:[11]

$$\overline{I}_{1\nu}=-\frac{(\overline{\boldsymbol{I}}\cdot\overline{\boldsymbol{I}}_1)(\boldsymbol{F}_1\cdot\boldsymbol{I})(\boldsymbol{F}_1\cdot\boldsymbol{J})}{I(I+1)F_1(F_1+1)J(J+1)}J_{\nu},\quad \overline{I}_{0\nu}=\frac{-(\boldsymbol{J}\cdot\boldsymbol{I}_0)}{J(J+1)}J_{\nu}\,.$$

If we use all of the above results (from (4) to the last relation), the expression for the effective Hamiltonian $G_1$ becomes

$$G_1=CJ_x^2+BJ_y^2+AJ_z^2 \tag{10.0}$$

$$+\frac{(\overline{\boldsymbol{I}}\cdot\overline{\boldsymbol{I}}_1)(\boldsymbol{F}_1\cdot\boldsymbol{I})(\boldsymbol{F}_1\cdot\boldsymbol{J})}{I(I+1)F_1(F_1+1)J(J+1)}(\gamma'J_x^2+\beta'J_y^2+\alpha'J_z^2) \tag{10.1}$$

$$+\frac{(\boldsymbol{J}\cdot\boldsymbol{I}_0)}{J(J+1)}(c'J_x^2+b'J_y^2+a'J_z^2) \tag{10.2}$$

$$+\frac{(\boldsymbol{F}_1\cdot\boldsymbol{I})}{F_1(F_1+1)J(J+1)}\left\{(\boldsymbol{I}_0\cdot\boldsymbol{J})+\frac{8YI_0(2I_0-1)J}{2J+3}\right\}(c_3J_x^2+b_3J_y^2+a_3J_z^2) \tag{10.3}$$

$$+2eQ\left\langle\frac{\partial^2V}{\partial z^2}\right\rangle_{\mathrm{AV}}Y\,, \tag{10.4}$$

where

$$\alpha'=\alpha_1+\alpha_2\,,\qquad \beta'=\beta_1+\beta_2\,,\qquad \gamma'=\gamma_1+\gamma_2\,,$$
$$a'=a_2\,,\qquad b'=b_1+b_2\,,\qquad c'=c_1+c_2\,.$$

### (b) *Calculation of the second order effective Hamiltonian* ($G_2$)

The terms which contribute to the second order effective Hamiltonian, $G_2$, are included in the following:

$$H_2=(CL_x^2+BL_y^2+AL_z^2)-2(CJ_xL_x+BJ_yL_y+AJ_zL_z) \tag*{(1.0)$'$}$$

$$+(e\mu_0/c)\sum_{K,i}[r_{iK}^{-3}(\boldsymbol{r}_i-\boldsymbol{r}_K)\times V_i]\cdot g_K\boldsymbol{I}_K \tag*{(1.1)$'$}$$

$$+(1.3)+(1.6)\,.$$

The terms (1.0)′ and (1.1)′ are off-diagonal relative to electronic orbital quantum numbers. Likewise the terms (1.3) and (1.6) are off-diagonal relative to electronic spin quantum numbers.

Now we are only concerned with the case where all spins are paired off so that the total spin is 0, and the terms (1.3) and (1.6) can be neglected. We can also neglect the cross terms between (1.3), (1.6) and (1.0)′ compared to cross terms between (1.0)′ and (1.1)′.

The relative magnitudes of these terms can be evaluated by referring to the results of Ref. 5. We can expect that only two terms contribute to $G_2$: namely, (1)$(G_2)_2$, the interaction between $I_0$ and the molecular rotational magnetic field and (2)$(G_2)_1$, interaction between $I$ and the molecular rotational magnetic field. Therefore, $G_2$ becomes

$$G_2=(G_2)_1+(G_2)_2=\frac{(\bar{\boldsymbol{I}}\cdot\bar{\boldsymbol{I}}_1)(\boldsymbol{F}_1\cdot\boldsymbol{I})(\boldsymbol{F}_1\cdot\boldsymbol{J})}{I(I+1)F_1(F_1+1)J(J+1)}(\gamma_3 J_x{}^2+\beta_3 J_y{}^2+\alpha_3 J_z{}^2) \tag{11.1}$$

$$+\frac{(\boldsymbol{J}\cdot\boldsymbol{I}_0)}{J(J+1)}(c_4 J_x{}^2+b_4 J_y{}^2+a_4 J_z{}^2)\,. \tag{11.2}$$

The coefficients of $(G_2)_1$ and $(G_2)_2$ in our case correspond to those of $(G_2)_4$ and $(G_2)_5$ respectively in Ref. 4. $a_4, b_4, c_4$ and $\alpha_3, \beta_3, \gamma_3$ are nearly the same with $a_3, b_3$ and $\alpha_3, \beta_3$ in Ref. 4, except that $c_4 \neq b_4$ and $\gamma_3 \neq \beta_3$. These terms are the contributions from excited electronic states.

## § 5. Secular Equation

For the convenience of the calculation the matrix $G$ shall be considered in the molecular frame

$$|M_F, F, \bar{I}, F_1, \bar{I}_0, J, \tau>\,.$$

In this frame the degeneracies of $I_0$ and $I$ are removed and therefore it is sufficient to consider only the elements which are concerned with $I_0$ and $I$.

The expression (3.0) becomes[8)]

$$CJ_x{}^2+BJ_y{}^2+AJ_z{}^2=\frac{A-C}{2}E(\kappa)+\frac{A+C}{2}J(J+1)\,,$$

where

$$\kappa=(2B-A-C)/(A-C) \qquad \text{(Ray's asymmetry parameter)}$$

and

$$A>B>C\,.$$

The terms $\gamma J_x{}^2+\beta J_y{}^2+\alpha J_z{}^2$ and $cJ_x{}^2+bJ_y{}^2+aJ_z{}^2$ which appear in the sum of Eq. (10) and Eq. (11) are calculated by the same method as that of Bragg and Golden[9)] which has been applied to the calculation of $\langle\partial^2 V/\partial Z^2\rangle_{\mathrm{AV}}$ for the asymmetric rotor.
Then we obtain, from Ref. 9, the following relation:

$$\gamma J_x{}^2+\beta J_y{}^2+\alpha J_z{}^2=\frac{1}{2}(\alpha+\gamma)J(J+1)+\frac{1}{2}(\alpha-\gamma)E(\kappa)$$
$$-\frac{1}{2}\{(\kappa+1)\alpha-2\beta-(\kappa-1)\gamma\}\frac{\partial E(\kappa)}{\partial\kappa}\,,$$

where $\alpha=\alpha'+\alpha_3,\ \beta=\beta'+\beta_3,\ \gamma=\gamma'+\gamma_3.$

The matrix elements which appear in this equation can be written as follows. The matrix elements of $(\bar{\boldsymbol{I}}\cdot\bar{\boldsymbol{I}}_1)$ which are labeled by $I=1,\ 0$ are

$$(\bar{\boldsymbol{I}}\cdot\bar{\boldsymbol{I}}_1)=\begin{pmatrix}1 & 0\\ 0 & 0\end{pmatrix}.$$

The matrix elements of $(\boldsymbol{I}.\boldsymbol{F}_1)$ for the case $I=1$ which are labeled by $F=F_1+1$. $F_1, F_1-1$ are

$$(\boldsymbol{I}\cdot\boldsymbol{F}_1)=\begin{pmatrix}F_1 & 0 & 0\\ 0 & -1 & 0\\ 0 & 0 & -F_1-1\end{pmatrix}.$$

The matrix elements of $(\boldsymbol{F}_1\cdot\boldsymbol{J})$ which are labeled by $F_1=J+I_0, J+I_0-1,\cdots, J,\cdots, J-I_0+1, J-I_0$ are

$$-(\boldsymbol{F}_1\cdot\boldsymbol{J})=\begin{pmatrix} J(J+1)+JI_0 & \cdots & 0 \\ \vdots & \ddots & \vdots \\ \vdots & J(J+1) & \vdots \\ \vdots & \ddots & \vdots \\ 0 & \cdots & J(J+1)-JI_0-I_0 \end{pmatrix}.$$

The matrix elements of $(\boldsymbol{J}\cdot\boldsymbol{I}_0)$ which are labeled by $F_1=J+I_0,\cdots, J-I_0$ are

$$(\boldsymbol{J}\cdot\boldsymbol{I}_0)=\begin{pmatrix} JI_0 & \cdots & 0 \\ \vdots & \ddots & \vdots \\ \vdots & 0 & \vdots \\ \vdots & \ddots & \vdots \\ 0 & \cdots & -JI_0-I_0 \end{pmatrix}.$$

Then as we can see from the angular momentum coupling scheme and the expressions for $G_1$ and $G_2$, the degeneracy relative to $F_1$ is removed first and that relative to $F$ second.

The off-diagonal eigenvalue of the Hamiltonian which are produced by wave functions $\psi(+K)$ and $\psi(-K)$ are to be found only in the element $\partial E(\kappa)/\partial\kappa$ and take different signs in the levels which have different parities, $\gamma$.

Now we can solve the secular equation completely. We take the energy levels as:

$$E=W_0+W_1+f,$$

where $W_0$ is the term which appears when only the $(\boldsymbol{I}_0\cdot\boldsymbol{J})$ coupling is considered, namely:

$$\begin{aligned} W_0= & \frac{A-C}{2}E(\kappa)+\frac{A+C}{2}J(J+1) \\ & +\frac{(\boldsymbol{J}\cdot\boldsymbol{I}_0)}{2J(J+1)}[(a+c)J(J+1)+(a-c)E(\kappa)] \\ & +eQ[(A'+C')J(J+1)+(A'-C')E(\kappa)]Y\,, \end{aligned}$$

where

$$a=a'+a_4,\quad b=b'+b_4,\quad c=c'+c_4\,.$$

$W_1$ represents the term when only the $(\boldsymbol{F}_1\cdot\boldsymbol{I})$ coupling is considered and is given by

$$\begin{aligned} W_1= & \frac{(\bar{\boldsymbol{I}}\cdot\bar{\boldsymbol{I}}_1)(\boldsymbol{F}_1\cdot\boldsymbol{I})(\boldsymbol{F}_1\cdot\boldsymbol{J})}{2I(I+1)F_1(F_1+1)J(J+1)}[(\alpha+\gamma)J(J+1)+(\alpha-\gamma)E(\kappa)] \\ & +\frac{(\boldsymbol{F}_1\cdot\boldsymbol{I})}{2F_1(F_1+1)J(J+1)}\left\{(\boldsymbol{I}_0\cdot\boldsymbol{J})+\frac{8YI_0J(2I_0-1)}{2J+3}\right\}[(a_3+c_3)J(J+1) \\ & +(a_3-c_3)E(\kappa)]\,, \end{aligned}$$

where

$$C'=\frac{2}{(J+1)(2J+3)}\frac{\partial^2V}{\partial x^2}\,,\qquad B'=\frac{2}{(J+1)(2J+3)}\frac{\partial^2V}{\partial y^2}\,,\qquad A'=\frac{2}{(J+1)(2J+3)}\frac{\partial^2V}{\partial z^2}$$

and $f$, which corresponds to the off diagonal $-K$, $+K$ states, has a value which is negative or positive depending on whether the parity, $\gamma$, is even or odd.

$f$ is

$$\begin{aligned} f=\Bigg[ & \frac{-(\boldsymbol{F}_1\cdot\boldsymbol{I})}{2F_1(F_1+1)J(J+1)}\left\{\frac{(\bar{\boldsymbol{I}}\cdot\bar{\boldsymbol{I}}_1)(\boldsymbol{F}_1\cdot\boldsymbol{J})}{I(I+1)}[(\kappa+1)\alpha-2\beta-(\kappa-1)\gamma]\right. \\ & \left.+\left[(\boldsymbol{I}_0\cdot\boldsymbol{J})+\frac{8YI_0J(2I_0-1)}{2J+3}\right][(\kappa+1)a_3-2b_3-(\kappa-1)c_3]\right\} \\ & -\frac{(\boldsymbol{J}\cdot\boldsymbol{I}_0)}{J(J+1)}[(\kappa+1)a-2b-(\kappa-1)c]-eQ[(\kappa+1)A'-2B'-(\kappa-1)C']Y\Bigg]\frac{\partial E(\kappa)}{\partial\kappa}\,. \end{aligned}$$

Then from the above results, we can see that

$$E=W+(-1)^{\gamma}|f| \, .$$

The signs before $|f|$ are shown in last column of Table I.

We can see from Table I and Ref. I that a triplet will occur in the case of $\Delta J=0$, $\Delta K_{+1}=-1$ transition between two levels of a prolate top for both of which $K_{-1}$ is odd.

Until now we only used the notations for prolate molecules, but for oblate molecules we must take care for the different notation for rotational constants between prolate and oblate molecules as shown in Appendix II.

The results of the above calculations are all valid even for the case of an oblate molecule and the change of notation from $A$, $B$, and $C$ to $C$, $B$, and $A$, are only to make the notation in this paper agree with that of Ref. 7, 8, 12.

### Acknowledgement

The author wishes to thank Professor I. Takahashi for his encouragement and helpful advice. The author's thanks are also due to Mr. H. Narumi for his kind advice in calculations and to Dr. Robert Poynter for his helpful comments and suggestions.

### Appendix I

#### *The asymmetric top wave function and its properties**

The asymmetric wave function $\psi_{\mathrm{RA}}(J, \tau, M, \gamma)$ is expressed as a linear combination of Wang functions:

$$\psi_{\mathrm{RA}}(J, \tau, M, \gamma)=\sum_{k} t_{K\tau} S(J, K, M, \gamma) \, . \quad \text{(A1)}$$

The summation over $K$ concerns only those $K$'s which occur as squares in main diagonals of the submatrixes. The values of $\gamma$ is fixed for each submatrix.

Since any $\psi_{\mathrm{RA}}$ belongs to one of the four species of $V$ group, only $S(J, K, M, \gamma)$'s of such particular species have non-vanishing $t_{K\tau}$'s in Eq. (A1). In general (i. e., for $J$ not very small), there exist several different $\psi_{\mathrm{RA}}$'s of the same species, characterized by different sets of $t_{K\tau}$'s: hence, the subscript $\tau$.

If two moments of inertia of an asymmetric top become nearly equal and if $S(J, K, M)$'s for the case of a nearly symmetric top are used in (A1), then one of the $t_{K\tau}$'s approaches unity and the remaining ones approach zero. Thus, for each $\psi_{\mathrm{RA}}(J, \tau, M, \gamma)$ of a slightly asymmetric top there is one particular $S(J, K, M, \gamma)$ to which it closely approximates, namely:

$$S(J, K, M, \gamma)=2^{1/2}[\psi^{*}(J, K, M) +(-1)^{\gamma}\psi(J, -K, M)] \, , \quad \text{(A2)}$$

where, $\gamma$, the parity, is odd or even, say 1 or 0. The parities corresponding to $J, K_{-1}, K_{+1}$ states are shown in Table 2.

Table II. Parities of Rotational Wave Function.

| $K_{-1}$ | $K_{+1}$ | $J+\gamma$ | $\gamma$ | |
|---|---|---|---|---|
| | | | $J$:*even* | $J$:*odd* |
| *e* | *e* | *e* | *e* | *o* |
| *e* | *o* | *o* | *o* | *e* |
| *o* | *e* | *o* | *o* | *e* |
| *o* | *o* | *e* | *e* | *o* |

This table has been taken from Ref. 8.

For $K=0$, only the case $\gamma=0$ exists and

$$S(J, O, M, O)=\psi^{*}(J, O, M) \, . \quad \text{(A3)}$$

Following the definition of Van Vleck**

$$\psi^{*}(J, K, M)=(-1)^{\beta}\psi_{J,K,M} \, , \quad \text{(A4)}$$

where $\beta$ denotes the larger of the two quantities $K$ and $M$, and $\psi_{J,K,M}$ is a symmetric top wave function*** which is given by

$$\psi_{J,K,M}(\theta, \phi, \chi)=\Theta_{J,K,M}(\theta)e^{iK\phi}e^{iM\chi}, \quad \text{(A5)}$$

with

$$\Theta_{J,K,M}(\theta)=N_{J,K,M}\chi^{1/2|K-M|}(1-\chi)^{1/2|K+M|} \times \sum_{0}^{n} a_{\nu}\chi^{\nu} \, .$$

### Appendix II

Following the notations of Ref. 7, 8, 12 the rotational constants $A$, $B$, and $C$, which are inversely proportional to the moments of inertia along the $a$, $b$, and $c$ axes are defined in any case as

$$A>B>C \, .$$

The axis of geometric symmetry is assigned as the $z$ axis at any time. Then the $a$, $b$, and $c$ axes coincide with the $z$, $y$, and $x$ axes for a prolate top molecule in which

---

* R. S. Mulliken: Phys. Rev. **59** (1941) 873.

** S. C. Wang: Phys. Rev. **34** (1929) 243.

*** C. H. Townes and A. L. Schawlow: Microwave Spectroscopy (McGraw-Hill Book Co. Inc., New York, 1955).

$$A>B\geqslant C \qquad \kappa=\frac{2B-A-C}{A-C}\geqslant -1\ .$$

On the other hand, the $a, b$, and $c$ axes coincide with the $x, y$, and $z$ axes for an oblate top molecule in which

$$A\geqslant B>C\ .$$

So the Hamiltonian of molecular rotation for each base becomes:

$$CJ_x^2+BJ_y^2+AJ_z^2 \qquad \text{prolate,}$$
$$AJ_x^2+BJ_y^2+CJ_z^2 \qquad \text{oblate}$$

### References

1) A. Okaya: Microwave Hyperfine Spectrum of Formaldehyde Molecule, J. Phys. Soc. Japan **11** (1956) 258.
2) W. E. Good, D. K. Coles, G. R. Gunther-Mohr, A. L. Schawlow and C. H. Townes: Phys. Rev. **83** (1951) 880A.
3) J. H. Van Vleck: Phys. Rev. **83** (1951) 880A.
4) G. R. Gunther-Mohr, R. L. White and A. L. Schawlow: Phys. Rev. **94** (1954) 1184.
5) G. R. Gunther-Mohr, C. H. Townes and J. H. Van Vleck: Phys. Rev. **94** (1954) 1191.
6) J. H. Van Vleck: Rev. Mod. Phys. **23** (1951) 213.
7) G. Herzberg: Molecular Spectra and Molecular Structure II Infrared and Raman Spectra of Polyatomic Molecules (D. Van Nostrand Co., Inc., New York, 1945).
8) G. W. King, R. M. Hainer and P. C. Cross: J. Chem. Phys. **11** (1943) 27.
9) J. K. Bragg and S. Golden: Phys. Rev. **75** (1949) 735.
10) J. K. Bragg: Phys. Rev. **74** (1948) 533.
11) E. U. Condon and G. H. Shortley: Theory of Atomic Spectra (Cambridge University Press, Cambridge, 1951).
12) Report on Notation for the Spectra of Polyatomic Molecules, J. Chem. Phys. **23** (1955) 1997.
13) R. S. Mulliken: Thys. Rev. **59** (1941) 873.

---

JOURNAL OF THE PHYSICAL SOCIETY OF JAPAN Vol. 11, No. 3, MARCH, 1956

# The Microwave Hyperfine Spectrum of Formaldehyde

By Akira OKAYA

*Department of Physics, Faculty of Science, University of Kyoto*

(Received July 11, 1955)

A hyperfine structure of the $4_{1,4}\rightarrow 4_{1,3}$ transition in the microwave spectrum of formaldehyde has been observed. The observed hyperfine features are mainly explained in terms of the interaction of the magnetic moments of the protons with the moleculer rotational magnetic field.

The main absorption lines were composed of three strong lines with total quantum numbers $F=3$, 4 and 5 respectively. The determined splitting frequency between the $F=5$ and the $F=3$ lines was $188\pm15$ kc. For a detailed explanation of this value, further information on electronic and magnetic properties of this molecule is required.

## §1. Introduction

The magnetic hyperfine structure of the microwave spectrum of the $NH_3$ molecule which is due to the interaction between proton spins and the molecular rotational magnetic field has been well investigated experimentally[1)3)] and theoretically[2)4)].

The author has observed and analyzed such magnetic hyperfine spectra in the formaldehyde molecule which is one of the typical molecules having $C_{2v}$ symmetry. A theoretical discussion of the general case of $C_{2v}$ asymmetric molecules has been described in a preceding paper[5)] by the author.

In the present paper, experimental results and their analysis will be described. Fortunately, the mirowave spectrum of this molecule has been well studied[6)7)8)] and this knowledge is of great use in interpreting the observed hyperfine structure in the spectrum.

The main rotational line in the $4_{1,4}\rightarrow 4_{1,3}$ transition has been resolved into a doublet.

The origin of this doublet is theoretically interpreted[5)] as the magnetic interaction between the two proton spins and the molecular rotational magnetic field. The results of detailed calculation show that the main line of $\Delta J=0$, $\Delta K_{+1}=-1$, $\Delta I=0$ transitions between $K_{-1}=1$ levels is composed of three strong $\Delta F=0$ lines and four weak $\Delta F=\pm1$ lines. Since the frequency splitting between $F=J-1$ and $F=J$ lines is smaller than the splitting between $F=J$ and $F=J+1$ lines, the triplet was not completely resolved but observed as a doublet.

Good agreement has been obtained between the experimental line shape and a theoretical line shape which can be obtained by assuming a definite splitting frequency relative to individual line breadths in the triplet. Then the absolute splitting frequency, $f_{SP}=188\pm15$ ks., between $F=5$ and $F=3$ lines of the $4_{1,4}\to4_{1,3}$ transition is obtained semi-empirically.

## § 2. Experimental Method and Results

The author has used a millimeter wave spectrograph consisting of a crystal frequency multiplier, *K*-band low loss Stark cell of 5 feet length and high sensitivity lock-in detector, all of which use new techniques[9)]. The millimeter wave radiation was obtained from a demountable crystal multiplier driven by a 2K33A klystron. A L. P. C. R. O. 5FP7 was used to display the absorption line at frequencies of 1/2 *c/s* to 1 *c/s*. Maximum resolution has not been achieved by mechanical recorder technique. The maximum sensitivity of this spectrograph was estimated to be about $5\times10^{-8}\text{cm}^{-1}$.

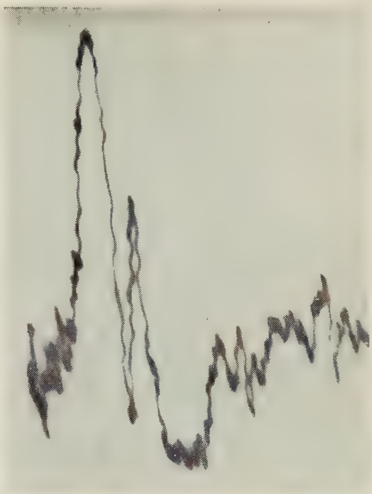

Fig. 1. The doublet spectrum of the $J_{K_{-1},K_{+1}}4_{1,4}\to4_{1,3}$ line. (Source modulation was used.)

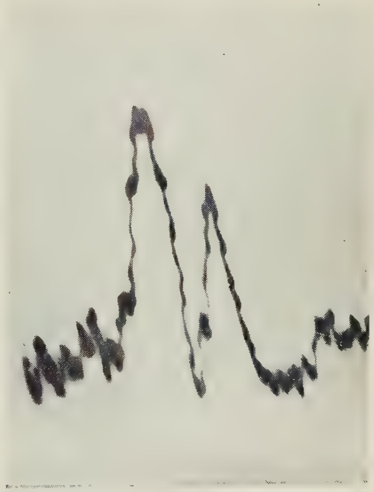

Fig. 2. The doublet spectrum of the $J_{K_{-1},K_{+1}}4_{1,4}\to4_{1,3}$ line. (Source modulation was used.)

Photographs of the observed $4_{1,4}\to4_{1,3}$ line doublet are shown in Figs. 1 and 2 for sample pressures of about $5\times10^{-4}$ mmHg. The doublet lines have been observed clearly both by 5 kc Stark and 5 kc source modulation spectrographs. Line shape distortion, which affects the accuracy of frequency measurements, has been minimized, but unfortunately, the distortion of the lower parts of the lines appearing in Figs. 1 and 2 was not completely eliminated due to the cut-off character of the amplifier tubes. In Fig. 2 the frequency scale is enlarged a little more than in Fig. 1.

## § 3. Comparison between Experimental and Theoretical Results

Theoretical calculations[5)] for $C_{2v}$ molecules, such as formaldehyde, yield for the total energy levels $W=W_0+W_1\pm|f|$, the following equations to first order

$$W_0=\frac{A-C}{2}E(\kappa)+\frac{A+C}{2}J(J+1)\,,$$

$$W_1=\begin{cases}\dfrac{-1}{4J}\{(\alpha+\gamma)J(J+1)+(\alpha-\gamma)E(\kappa)\} & M_{\mathrm{I}}=-1\,,\\[2mm] \dfrac{-1}{4J(J+1)}\{(\alpha+\gamma)J(J+1)+(\alpha-\gamma)E(\kappa)\} \qquad \text{for} & M_{\mathrm{I}}=0\,,\\[2mm] \dfrac{1}{4J(J+1)}\{(\alpha+\gamma)J(J+1)+(\alpha-\gamma)E(\kappa)\} & M_{\mathrm{I}}=+1\,,\end{cases}$$

and (1)

$$f=\begin{cases}\dfrac{1}{4J}\{(\kappa+1)\alpha-2\beta-(\kappa-1)\gamma\}\dfrac{\partial E(\kappa)}{\partial\kappa} & M_{\mathrm{I}}=-1\,,\\[2mm] \dfrac{1}{4J(J+1)}\{(\kappa+1)\alpha-2\beta-(\kappa-1)\gamma\}\dfrac{\partial E(\kappa)}{\partial\kappa} \qquad \text{for} & M_{\mathrm{I}}=0\,,\\[2mm] \dfrac{-1}{4(J+1)}\{(\kappa+1)\alpha-2\beta-(\kappa-1)\gamma\}\dfrac{\partial E(\kappa)}{\partial\kappa} & M_{\mathrm{I}}=+1\,,\end{cases}$$

where $I=1$.

Where $W_0$ is the rotational energy of molecule, $W_1$ is the diagonal term due to $(\boldsymbol{I}\cdot\boldsymbol{J})$ coupling, and $f$ is the off-diagonal term of the $(\boldsymbol{I}\cdot\boldsymbol{J})$ coupling.

The coefficients in the above equations (1) are

$$\alpha=\alpha_1+\alpha_2+\alpha_3\,,$$
$$\beta=\beta_1+\beta_2+\beta_3\,,$$
$$\gamma=\gamma_1+\gamma_2+\gamma_3\,,$$

where $\alpha_1$, $\beta_1$, $\gamma_1$ are to be determined from electronic orbital motions, $\alpha_2$, $\beta_2$, $\gamma_2$ are to be determined by nuclear orbital motions, and $\alpha_3$, $\beta_3$, $\gamma_3$ are to be determined by excited electronic states. The calculated results for the terms of the coefficients are shown below, except for $\alpha_3$, $\beta_3$, $\gamma_3$:

$$\alpha_1=-2\left(\frac{e\mu_0}{c\hbar}\right)g_1(1+1/g_1)Ar_y\langle l_0|\sum_{i,K=1,2}r_{iK}{}^{-3}(\boldsymbol{r}_i-\boldsymbol{r}_K)_y|l_0\rangle\,,$$

$$\beta_1=-2(e\mu_0/c\hbar)g_1(1+1/g_1)Br_z\langle l_0|\sum_{i,K=1,2}r_{iK}{}^{-3}(\boldsymbol{r}_i-\boldsymbol{r}_K)_z|l_0\rangle\,,$$

$$\gamma_1=-2(e\mu_0/c\hbar)g_1(1+1/g_1)C\{r_z\langle l_0|\sum_{i,K=1,2}r_{iK}{}^{-3}(\boldsymbol{r}_i-\boldsymbol{r}_K)_z|l_0\rangle\,,$$
$$+r_y\langle l_0|\sum_{i,K=1,2}r_{iK}{}^{-3}(\boldsymbol{r}_i-\boldsymbol{r}_K)|l_0\rangle\}\,,$$

and

$$\alpha_2=-\frac{e\mu_0}{c\hbar}g_1A\left\{\left(2+\frac{1}{g_1}\right)\frac{1}{r_{01}\sin\beta}+4Z_0\sum_{0,0'}r_{01}{}^{-1}\left[\sin^2\beta+\frac{1}{g_1}\left(\sin^2\beta+\frac{r_z}{r_{01}}\cos\beta\right)\right]\right\}\,,$$

$$\beta_2=-\frac{4e\mu_0}{c\hbar}g_1BZ_0\sum_{0,0'}r_{01}{}^{-1}\left(\cos^2\beta+\frac{1}{g_1}\frac{r_z}{r_{01}}\cos\beta\right)\,,$$

$$\gamma_2=-\frac{e\mu_0}{c\hbar}g_1C\left\{\left(2+\frac{1}{g_1}\right)\frac{1}{r_{01}\sin\beta}+4Z_0\sum_{0,0'}r_{01}{}^{-1}\left[1+\frac{1}{g_1}\left(\sin^2\beta+\frac{r_z}{r_{01}}\cos\beta\right)\right]\right\}\,,$$

where $A$, $B$, and $C$ are given by

$$A=\hbar^2/(2I_a),\qquad B=\hbar^2/(2I_b),\qquad C=\hbar^2/(2I_c),$$
$$A>B>C\,.$$

Table I.

| Assignment of line | *F* values | | Relative intensity | Relative frequency splitting |
|---|---|---|---|---|
| $J_{K_{-1},K_{+1}} \rightarrow J_{K'_{-1},K'_{+1}}$ | $F \rightarrow F'$ | | $I_1$, $I_2$ or $I_3$ | $X_1$ or $X_2$ |
| $1_{1,1} \rightarrow 1_{1,0}$ | 2 | 2 | 100 | |
| | 1 | 1 | 20 | |
| | 2 | 1 | 33 | |
| | 1 | 2 | 33 | |
| | 1 | 0 | 27 | |
| | 0 | 1 | 27 | |
| $2_{1,2} \rightarrow 2_{1,1}$ | 3 | 3 | 100 | 3 |
| | 2 | 2 | 56 | 2 |
| | 1 | 1 | 36 | |
| | 3 | 2 | ~12 | |
| | 2 | 1 | | |
| $3_{1,3} \rightarrow 3_{1,2}$ | 4 | 4 | 100 | 4 |
| | 3 | 3 | 70 | 3 |
| | 2 | 2 | 53 | |
| | 4 | 3 | ~7 | |
| | 3 | 2 | | |
| $4_{1,4} \rightarrow 4_{1,3}$ | 5 | 5 | 100 | 5 |
| | 4 | 4 | 77 | 4 |
| | 3 | 3 | 62 | |
| | 5 | 4 | ~4 | |
| | 4 | 3 | | |
| $5_{1,5} \rightarrow 5_{1,4}$ | 6 | 6 | 100 | 6 |
| | 5 | 5 | 81 | 5 |
| | 4 | 4 | 68 | |
| | 6 | 5 | ~3 | |
| | 5 | 4 | | |

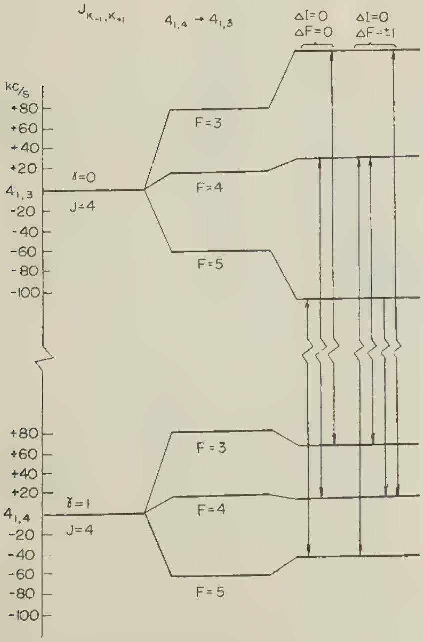

Fig. 3.

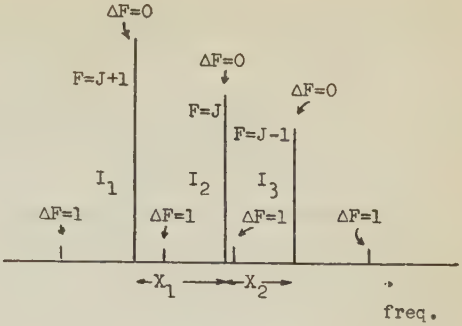

Fig. 4. The spectrum of $\Delta K_{+1}=-1$ transitions between $K_{-1}=1$ levels, where $X_1$. $X_2$ are relative splitting frequencies of the lines.

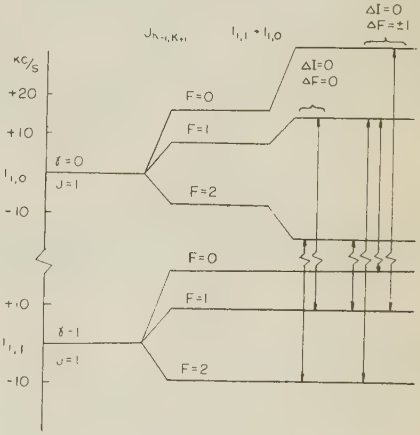

Fig. 5.

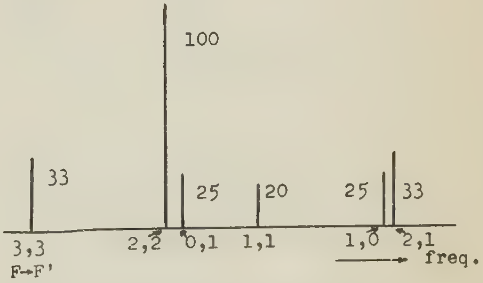

Fig. 6. The spectrum of $1_{1,1} \rightarrow 1_{1,0}$ line of which splitting frequency is calculated from the results of $4_{14} \rightarrow 4_{13}$ line.

$E(\kappa)$[10)] is the reduced energy for an asymmetric rotor and $\kappa$ is Ray's parameter defining its asymmetry.

The spectrum of $\Delta K_{+1}=-1$ transitions between $K_{-1}=-1$ levels, which is applicable to the cases of $2_{1,2} \rightarrow 2_{1,1}$, $3_{1,3} \rightarrow 3_{1,2}$, $4_{1,4} \rightarrow 4_{1,3}$, $5_{1,5} \rightarrow 5_{1,4}$, $\cdots$ transitions, is shown in Figs. 3 and 4 and Table 1. The weak $\Delta F = \pm 1$ lines are masked by strong $\Delta F=0$ lines within their line breadths, so they are not observed. On the other hand, the $1_{1,1}\rightarrow 1_{1,0}$ line is different from the lines of higher $J$, because the intensity of $F=0$, $\Delta F=0$ line is zero and the $\Delta F=\pm 1$ lines are of intensities comparable with that of $\Delta F=0$ lines as shown in Figs. 5 and 6 and Table 1. The values of $W_1$ in the upper and lower levels of the transition are almost equal within a few kc., because $J(J+1)$ is larger than $E(\kappa)$ and yet the values of $E(\kappa)$ in both levels are nearly equal when $\kappa=-0.9611$.

Then, from equation (1) above, we can obtain an approximate formula for frequency splitting between $F=J-1$ and $F=J+1$ levels for the triplet line of $K_{-1}=1$, $\Delta K_{+1}=-1$ transitions in general, namely:

$$f_{\mathrm{SP}}=|f|_{\mathrm{Up}}+|f|_{\mathrm{Low}}$$
$$=\frac{2J+1}{4J(J+1)}\left(\frac{\partial E(\kappa)_{\mathrm{Up}}}{\partial\kappa}+\frac{\partial E(\kappa)_{\mathrm{Low}}}{\partial\kappa}\right)$$
$$\times\{(\kappa+1)\alpha-2\beta-(\kappa-1)\gamma\} \qquad (2)$$

Here, the values of $E(\kappa)$ and $\partial E(\kappa)/\partial\kappa$ can be easily calculated by the interpolation from the table given in Appendix I of the paper[10] by King, Hainer, and Cross for the range of $J\leqslant 12$, and the values thus calculated are shown in Table 2.

Table II.

| Line assignment $J, K_{-1}, K_{+1}$ | $E(\kappa)$ | $\frac{\partial E(\kappa)}{\kappa}$ |
|---|---|---|
| $5_{1,5}$ | $-27.738$ | 6.74 |
| $5_{1,4}$ | $-27.177$ | 21.172 |
| $4_{1,4}$ | $-17.827$ | 4.305 |
| $4_{1,3}$ | $-17.438$ | 14.28 |
| $3_{1,3}$ | $-9.904$ | 2.453 |
| $3_{1,2}$ | $-9.671$ | 8.45 |
| $2_{1,2}$ | $-3.96$ | 1 |
| $2_{1,1}$ | $-3.84$ | 4 |
| $1_{1,1}$ | 0 | 0 |
| $1_{1,0}$ | 0.04 | 1 |

For the splitting measurement the author has adopted, instead of using standard frequency markers, the line breadth frequency as a frequency standard. Its reliability has been demonstrated in Ref. 3 and 11. First the theoretical line shape is plotted assuming a definite splitting frequency relative to the individual line breadths of the triplet and Gaussian line shape, and then drawing the first derivative as shown in Fig. 7. A comparison between the latter theoretical curve and the experimental curve of the $4_{1,4}\rightarrow 4_{1,3}$ line shows agreement as seen in Fig. 8.

The line broadenings by the Doppler effect and collisions[11] is calculated for the case of a $K$-band Stark cell at the temperature 290°K as shown below:

$$2\Delta\nu_D=107\ \mathrm{KC},$$

and

$$2\Delta\nu_W=28\ \mathrm{KC},$$

whence the total line breadth becomes

$$2\Delta\nu=2\sqrt{(\Delta\nu_D)^2+(\Delta\nu_W)^2}=110\ \mathrm{KC},$$

neglecting the modulation line broadining[11][12][13] due to source modulation since it is about 0.2% compared to the above total. $f_{\mathrm{sp}}$ is determined as

$$f_{\mathrm{sp}}=188\pm 15\ \mathrm{KC}.$$

We can obtain the value of $(\kappa+1)\gamma-2\beta-(\kappa-1)\alpha$ semi-émpirically from Eq. (2) and the result is

$$(\kappa+1)\gamma-2\beta-(\kappa-1)\alpha=-45.8\pm 4\ \mathrm{KC}.$$

On the other hand, we want to calculate the values of $\alpha$, $\beta$, $\gamma$ theoretically for comparison but we can only calculate the values of $\alpha_2$ $\beta_2$, $\gamma_2$ but not $\alpha_1$, $\beta_1$ $\gamma_1$ and $\alpha_3$, $\beta_3$, $\gamma_3$, because of the difficulty of establishing an electronic model, for which further theoretical and experimental considerations are needed. The calculated values of $\alpha_2$, $\beta_2$, $\gamma_2$ are

$$\gamma_2=-3.29-6.38\,Z_0-3.23\,Z_0' \qquad \mathrm{Kc},$$
$$\beta_2=-2.15\,Z_0-2.85\,Z_0' \qquad \mathrm{Kc},$$

and

$$\alpha_2=-27.3-41.5\,Z_0-8.48\,Z_0' \qquad \mathrm{Kc},$$

where $Z_0$ and $Z_0'$ are the effective charges of carbon and oxygen respectively. For the calculation of $\alpha_2$, $\beta_2$, $\gamma_2$ in Ref. 5, the following values for various constants have been used:

$\kappa=-1+2\delta=-0.96107$,
$r_{01}=(C-H)=1.12\pm 0.01\ A$,
$r_{01}'=(O-H)=2.02\ A$,
$I_C=14.864$ amu $A^2$,
$I_B=13.015$ amu $A^2$,
$I_A=1.792$ amu $A^2$,
$\beta=59°$, $\beta'=29°$,
$g_H=2\times 2.79255$,
$\mu_0=e\hbar/(2M_pc)=5.049\times 10^{-24}$ erg/gauss,
$c=3\times 10^{10}$ cm/s,
$e=1.602\times 10^{-19}$ coulomb.

## § 4. Discussion

As we can see in Fig. 7, the reason the theoretical triplet appears as a doublet is well understood, but the differences between ex-

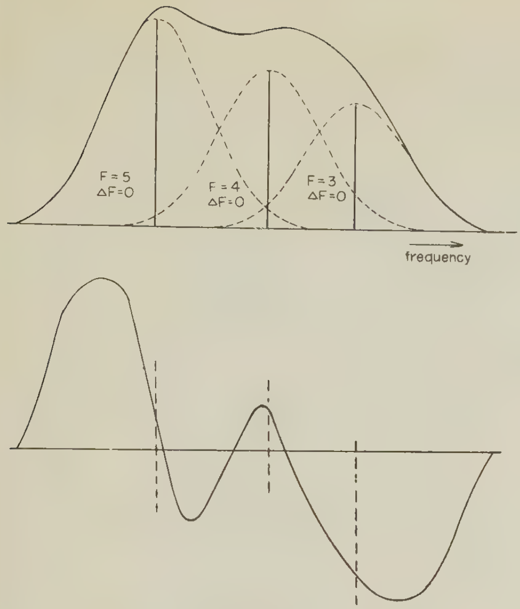

Fig. 7.

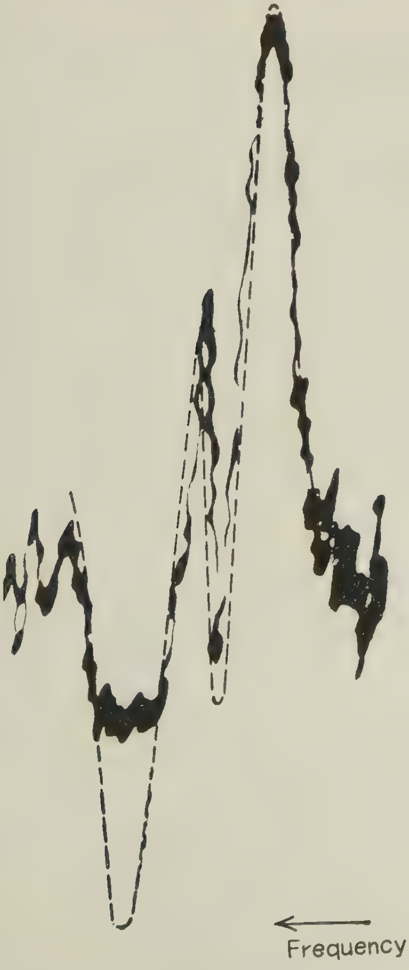

Fig. 8.

perimental and theoretical values are somewhat large and more detailed experiments are needed for the better understanding of this problem.

The author is now preparing experiments on other absorption lines in which the observation of multiplets can be expected.

The interpretation of the experimental values of $\alpha$, $\beta$, $\gamma$ depends on the model of the electronic orbits for which ionic characters, slipping effects, etc., should be taken into account. But it is very difficult to calculate these values definitely.

On the other hand, we can expect reasonable contributions from excited electronic states and spin spin interaction, and for the latter the calculations will be done elsewhere. The latter contribute to make the splitting frequency ratio $X_1/X_2$ and splitting frequency larger.

## Acknowledgement

The author wishes to thank Professor I. Takahashi for his encouragement and helpful advice.

## References

1) W. E. Good, D. K. Coles, G. R. Gunther-Mohr, A. L. Schawlow, and C. H. Townes: Phys. Rev. **83** (1951) 880 A.
2) J. H. Van Vleck: Phys. Rev. **83** (1951) 880 A.
3) G. R. Gunther-Mohr, R. L. White and A L. Schawlow: Phys. Rev. **94** (1954) 1184.
4) G. R. Gunther-Mohr, C. H. Townes and J. H. Van Vleck: Phys. Rev. **94** (1954) 1191.
5) A. Okaya: A Theoretical Analysis of the Magnetic Hyperfine Structure of the Microwave Spectrum of $C_{2v}$ Molecule. J. Phys. Soc. Japan **11** (1956) 249.
6) J. K. Bragg and A. H. Sharbaugh: Phys. Rev. **75** (1949) 1774.
7) R. B. Lawrence and M. W. P. Strandberg: Phys. Rev. **83** (1951) 363.
8) A. Okaya: J. Phys. Soc. Japan **9** (1954) 135.
9) A. Okaya: Rev. Sci. Instr. **26** (1955) 1024.
10) G. W. King, R. M. Hainer and P. C. Cross: J. Chem. Phys. **11** (1943) 27.
11) M. Danos and S. Geschwind: Phys. Rev. **91** (1953) 1159.
12) C. H. Townes and F. R. Merritt: Phys. Rev. **72** (1947) 1266.
13) R. Karplus: Phys. Rev. **73** (1948) 1027.
14) K. Shimoda: J. Phys. Soc. Japan **9** (1954) 567.

JOURNAL OF THE PHYSICAL SOCIETY OF JAPAN Vol. 11, No. 3, MARCH, 1956

# Molecular Structure of Methylamine*

By Takashi ITOH

*Department of Physics, Faculty of Science, University of Tokyo, Tokyo*

(Received September 29, 1955)

The matrix elements of the Hamiltonian of a semiasymmetric internal rotor which have been given by Hecht and Dennison are rederived in a different way and in a form which is also applicable to more general semiasymmetric internal rotors. This theory together with a semi-empirical formula for the inversion splitting is applied to the analysis of the microwave spectrum of methylamine.

The barrier height of internal rotation is determined to be 691.1 cm$^{-1}$. The moments and product of inertia are obtained as $A=37.085$, $B=38.662$, $C=8.136$, $C_1=2.805$, $C_2=5.331$, $D=-0.120$ all times $10^{-40}$ g cm$^2$. The hypothetical inversion splitting in the absence of the coupling between inversion and internal rotation is determined to be 28604 Mc/sec for $n=0$ and 29358 Mc/sec for $n=1$. The molecular dimensions are obtained from the inertial constants as follows: $d_{CH}=1.093$ A (assumed), $d_{NH}=1.014$ A (assumed), $d_{CN}=1.474$ A, ∠HCH=109°30′, ∠HNH=105°50′, ∠CNH=112°10′, and the methyl axis passes through the $NH_2$ triangle making an angle of 3°30′ with the CN direction.

## § 1. Introduction

In the previous paper[1] a rather qualitative analysis of the microwave spectrum of methylamine has been given, and an approximate value of 680 cm$^{-1}$ for the barrier height of internal rotation was obtained from the starting points of $p_1$ and $p_2$ series.

On the other hand Lide[2] has assigned three inversion pairs of lines showing second-order Stark effects, which are pertinent to be used in the determination of inertial constants.

In this paper we will determine the precise values for the barrier height and molecular dimensions of methylamine by the combined use of the above experimental data.

## § 2. Theory of Semiasymmetric Internal Rotor

Theory of hindered internal rotation in $CH_3$-OH type molecule has been developed by Burkhard, Hecht and Dennison[3),4], and their theory is also applicabrele to $CH_3NH_2$. Here their formulas will be rederived in a different way and in a form which is also applicable to more general semiasymmetric internal rotors.

A semiasymmetric internal rotor is defined as a molecule with two mutually rotating groups, of which one is a symmetric rotor and the other is not[5]. Let the asymmetric and symmetric groups of a semiasymmetric internal rotor be called 1 and 2 respectively. Each of the two mutually rotating groups are assumed to be rigid, and the angle between the symmetry axis of group 2 and the principal axes of group 1 are assumed to remain constant during internal rotation. Then, the principal axes of the entire molecule are embedded in group 1, and the inertia tensor of the molecule, when referred to a coordinate system fixed in group 1, is constant during internal rotation. We denote by $x$ the angle of rotation of group 1 with respect to group 2. Then, the orientation of the molecule can be fixed by the Eulerian angles of group 1, which are also equal to the Eulerian angles of the entire molecule, and by the torsional angle $x$. The rotational motion of the molecule can be described by the angular velocity $\boldsymbol{\omega}=(\omega_\xi, \omega_\eta, \omega_\zeta)$ of group 1, which is also equal to the angular velocity of the ellipsoid of inertia of the entire molecule, and by the time derivative $\dot{x}$ of the torsional angle. The $\xi, \eta, \zeta$ axes are for the present arbitrary rectangular axes fixed in group 1.

The kinetic energy of the system may be derived as follows. Consider the $i$th constituent particle whose mass is $m_i$ and whose position vector is $\mathbf{r}_i$. We divide the velocity of this particle into three parts $\mathbf{u}_i$, $\mathbf{v}_i$, and $\mathbf{w}_i$

---

* A brief report has been given in J. Chem. Phys. **23** (1955) 1735.

as follows. $\mathbf{u}_i$ is the velocity when group 1 of the molecule stays at rest while group 2 rotates about its own symmetry axis with an angular velocity $\dot{x}$. $\mathbf{v}_i$ is the velocity when the entire molecule rotates rigidly as a whole with an angular velocity $\boldsymbol{\omega}_1$, such that $\mathbf{u}_i+\mathbf{v}_i$ gives zero resultant angular momentum of the entire molecule, i.e.

$$\sum_i m_i\mathbf{r}_i\times(\mathbf{u}_i+\mathbf{v}_i)=0 .$$

$\mathbf{w}_i$ is the velocity when the molecule rotates as a whole with an angular velocity $\boldsymbol{\omega}_2\equiv\boldsymbol{\omega}-\boldsymbol{\omega}_1$. The kinetic energy of the molecule is written

$$T=\tfrac{1}{2}\sum_i m_i(\mathbf{u}_i+\mathbf{v}_i+\mathbf{w}_i)^2=\tfrac{1}{2}\sum_i m_i\mathbf{u}_i^2$$
$$-\tfrac{1}{2}\sum_i m_i\mathbf{v}_i^2+\tfrac{1}{2}\sum_i m_i\mathbf{w}_i^2+\sum_i m_i(\mathbf{u}_i+\mathbf{v}_i)(\mathbf{v}_i+\mathbf{w}_i). \tag{1}$$

By using the relation

$$\mathbf{v}_i+\mathbf{w}_i=(\boldsymbol{\omega}_1\times\mathbf{r}_i)+(\boldsymbol{\omega}_2\times\mathbf{r}_i)=\boldsymbol{\omega}\times\mathbf{r}_i ,$$

the last term in (1) can be transformed as

$$\sum_i m_i(\mathbf{u}_i+\mathbf{v}_i)\cdot(\mathbf{v}_i+\mathbf{w}_i)=\boldsymbol{\omega}\cdot\sum_i m_i\mathbf{r}_i\times(\mathbf{u}_i+\mathbf{v}_i) .$$

Now, since $\mathbf{u}_i+\mathbf{v}_i$ represents an 'angular momentum less' motion, the right hand side of the above equation vanishes. So, the kinetic energy (1) becomes

$$T=\tfrac{1}{2}\sum_i m_i\mathbf{u}_i^2-\tfrac{1}{2}\sum_i m_i\mathbf{v}_i^2+\sum_i m_i\mathbf{w}_i^2 . \tag{2}$$

If we denote by $\mathbf{c}\dot{x}=(c_\xi\dot{x}, c_\eta\dot{x}, c_\zeta\dot{x})$ the three components of angular momentum produced by the motion $\mathbf{u}_i$ (i.e. $\sum_i m_i\mathbf{r}_i\times\mathbf{u}_i=\mathbf{c}\dot{x}$), then the following condition must be satisfied in order for $\mathbf{u}_i+\mathbf{v}_i$ to be an 'angular momentum less' motion:

$$\mathbf{c}\dot{x}+\mathbf{I}\cdot\boldsymbol{\omega}_i=0 ,$$

where $\mathbf{I}$ is the tensor of moment of inertia of the entire molecule. From the above condition, $\boldsymbol{\omega}_1$ is determined as

$$\boldsymbol{\omega}_1=\boldsymbol{\lambda}\dot{x},\ \boldsymbol{\lambda}=-\mathbf{I}^{-1}\cdot\mathbf{c}. \tag{3}$$

Therefore, the second term in (2) becomes

$$\tfrac{1}{2}\sum_i m_i\mathbf{v}_i^2=\tfrac{1}{2}\boldsymbol{\omega}_1\cdot\mathbf{I}\cdot\boldsymbol{\omega}_1=\tfrac{1}{2}\boldsymbol{\lambda}\cdot\mathbf{I}\cdot\boldsymbol{\lambda}\dot{x}^2 . \tag{4}$$

The first term in (2) is written

$$\tfrac{1}{2}\sum_i m_i\mathbf{u}_i^2=\tfrac{1}{2}C_2\dot{x}^2 , \tag{5}$$

where $C_2$ is the moment of inertia of group 2 about its own symmetry axis. The third term in (2) is written

$$\tfrac{1}{2}\sum_i m_i\mathbf{w}_i^2=\tfrac{1}{2}\boldsymbol{\omega}_2\cdot\mathbf{I}\cdot\boldsymbol{\omega}_2=\tfrac{1}{2}(\boldsymbol{\omega}-\boldsymbol{\omega}_1)\cdot\mathbf{I}\cdot(\boldsymbol{\omega}-\boldsymbol{\omega}_1)$$
$$=\tfrac{1}{2}(\boldsymbol{\omega}-\boldsymbol{\lambda}\dot{x})\cdot\mathbf{I}\cdot(\boldsymbol{\omega}-\boldsymbol{\lambda}\dot{x}) . \tag{6}$$

Putting (4), (5) and (6) into (2), we obtain the expression for the kinetic energy

$$T=\tfrac{1}{2}U\dot{x}^2+\tfrac{1}{2}\sum_{j,k} I_{jk}(\omega_j-\lambda_j\dot{x})(\omega_k-\lambda_k\dot{x}) , \tag{7}$$

where

$$U=C_2-\sum_{j,k} I_{jk}\lambda_j\lambda_k . \tag{8}$$

The components of the total angular momentum $P_\xi, P_\eta, P_\zeta$ conjugate to $\omega_\xi, \omega_\eta, \omega_\zeta$ are

$$P_j=\frac{\partial T}{\partial\omega_j}=\sum_k I_{jk}(\omega_k-\lambda_k\dot{x}) , \tag{9}$$

and the internal rotational angular momentum $P$ which is conjugate to $\dot{x}$ is

$$P=\frac{\partial T}{\partial\dot{x}}=U\dot{x}-\sum_{j,k}\lambda_j I_{jk}(\omega_k-\lambda_k\dot{x})$$
$$=U\dot{x}-\sum_j\lambda_j P_j . \tag{10}$$

Putting (9) and (10) into (7) we have

$$T=\tfrac{1}{2}U^{-1}\left(P+\sum_j\lambda_j P_j\right)^2+\tfrac{1}{2}\sum_{j,k} I^{-1}_{j,k}P_jP_k ,$$

where $I^{-1}_{jk}$'s are elements of the inverse inertia tensor. Adding the potential energy $V(x)$ to the above expression, we obtain the rotational Hamiltonian

$$\mathbf{H}_r=\tfrac{1}{2}U^{-1}\left(P+\sum_j\lambda_j P_j\right)^2+\tfrac{1}{2}\sum_{j,k} I^{-1}_{jk}P_jP_k+V(x) . \tag{11}$$

The potential $V(x)$ may, as usual, be assumed to be of the sinusoidal form

$$V(x)=\tfrac{1}{2}H(1-\cos 3x) . \tag{12}$$

Thus far, the coordinate axes $\xi, \eta, \zeta$ have been chosen arbitrarily. Now we take a new system of coordinate axes in the following way: we take the $\bar{\zeta}$ axis in the direction of the vector $\boldsymbol{\lambda}$, while take $\bar{\xi}$ and $\bar{\eta}$ axes arbitrarily under the restriction that they are perpendicular to the $\bar{\zeta}$ axis and to each other. The Hamiltonian then have the form

$$\mathbf{H}_r=\tfrac{1}{2}U^{-1}(P+\lambda P_{\bar{\zeta}})^2+\tfrac{1}{2}\sum_{\bar{j}\bar{k}}\bar{I}^{-1}_{\bar{j}\bar{k}}P_{\bar{j}}P_{\bar{k}}+V(x) , \tag{13}$$

where $\lambda=|\boldsymbol{\lambda}|$, and $\bar{\mathbf{I}}$ denotes the inertia tensor referred to the new coordinate axes.

In quantum mechanics, we replace $P^{-}$, $P_{\bar{\eta}}$ and $P_{\bar{\zeta}}$ by matrices whose elements are

$$\begin{cases}(P_{\bar{\eta}}\mp iP_{\bar{\xi}})^{JK}_{JK\pm1}=\hbar\sqrt{(J\mp K)(J\pm K+1)} , \\ (P_{\bar{\zeta}})^{JK}_{JK}=\hbar K ,\end{cases} \tag{14}$$

and replace $P$ by $\frac{\hbar}{i}\frac{\partial}{\partial x}$.

The merit of using $\bar{\xi}, \bar{\eta}, \bar{\zeta}$ axes lies in that, if we adopt the basic wave functions which diagonalize $P_{\bar{\zeta}}(=\hbar K)$ and

$$\frac{\hbar^2}{2}U^{-1}\left(\frac{1}{i}\frac{d}{dx}+\lambda K\right)^2+V(x), \tag{15}$$

then the off-diagonal elements of the Hamiltonian (13) do not contain any terms involving $P$ or $P^2$. Since the magnitudes of terms involving $P$ and $P^2$ are of the orders of $\sqrt{h\nu_r\cdot h\nu_t}$ and $h\nu_t$, where $h\nu_r$ and $h\nu_t$ are rotational and torsional energies respectively, and since in most cases $h\nu_t$ is much larger than $h\nu_r$, the elimination of the terms involving $P$ and $P^2$ from the off-diagonal elements of the Hamiltonian usually facilitates the calculation of energy levels. This will be an improvement on the method of Burkhard and Dennison.

The eigenfunction of the internal rotational Hamiltonian (15) can be expanded in the Fourier series

$$Q(x)=\sum_m a_m e^{imx}, \tag{16}$$

where $m$ takes every third integral values. We may introduce an internal rotational quantum number $\mu(=0, 1, -1)$ by the definition $\mu=m\,(\mathrm{mod.}\ 3)$. Then the eigenstates of the Hamiltonian (15) are designated by $\mu$ and the torsional quantum number $n$. It can be shown that $\mu$ is related to $\tau$ of Burkhard and Dennison⁴⁾ by the equation

$$K+\tau+\mu=1\ (\mathrm{mod.}\ 3)\,. \tag{17}$$

The use of $\mu$ will be more convenient than $\tau$, because the energy matrix factors into three submatrices belonging to $\mu=0$, $\mu=1$ and $\mu=-1$, and also the selection rule for the spectral transition becomes simply $\Delta\mu=0$ instead of $\Delta(K+\tau)=0$.

By the way, it can be easily shown that the eigenvalue $E^{K\mu n}$ of the internal rotational Hamiltonian (15) is a periodic function of $\gamma=\frac{2\pi}{3}(\lambda K+\mu)$:

$$E^{K\mu n}=\alpha_n-\beta_n\cos\gamma-\beta_n'\cos 2\gamma-\cdots. \tag{18}$$

The method of numerical evaluation of $E^{K\mu n}$ has been devised by Koehler and Dennison⁶⁾.

## § 3. CH$_3$NH$_2$ Type Molecules

The theory of the preceding section applies to all the semiasymmetric internal rotors. In the present section, we consider a somewhat specialized type of semiasymmetric rotor, i.e. a semiasymmetric rotor with a plane of symmetry. CH$_3$NH$_2$ and CH$_3$OH are sush molecules.

In this type of molecules, if we take the $\xi$ axis to be the normal to the plane of symmetry, two products of inetia $-I_{\xi\eta}$ and $-I_{\xi\zeta}$ vanishes, and only $-I_{\eta\zeta}$ remains non-vanishing. So the inertia tensor is written

$$\mathbf{I}=\begin{pmatrix} A & 0 & 0 \\ 0 & B & -D \\ 0 & -D & C \end{pmatrix}, \tag{19}$$

where $A, B, C$ are moments of inertia about $\xi, \eta, \zeta$ axes and $D$ is the product of inertia with respect to $\eta$, and $\zeta$ axes ($I_{\eta\zeta}=-D$). We may take $\zeta$ axis to be parallel to the symmetry axis of group 2 (symmetric group). Then the above $A, B, C, D$ are just those defined in I.

The vectors $\boldsymbol{\lambda}$ and $\mathbf{c}$ defined in §2 are written explicitly

$$\mathbf{c}=-\begin{pmatrix} 0 \\ 0 \\ C_2 \end{pmatrix}, \tag{20}$$

$$\boldsymbol{\lambda}=-\mathbf{I}^{-1}\cdot\mathbf{c}=\begin{pmatrix} 0 \\ \dfrac{DC_2}{BC-D^2} \\ \dfrac{BC_2}{BC-D^2} \end{pmatrix}, \tag{21}$$

from which we obtain

$$\lambda=|\boldsymbol{\lambda}|=\frac{C_2\sqrt{B^2+D^2}}{BC-D^2}, \tag{22}$$

and

$$U=C_2-\boldsymbol{\lambda}\cdot\mathbf{I}\cdot\boldsymbol{\lambda}=C_2\frac{BC_1-D^2}{BC-D^2}, \tag{23}$$

where $C_1=C-C_2$.

The coordinate transformation $\xi, \eta, \zeta\to\bar{\xi}, \bar{\eta}, \bar{\zeta}$ can be achieved by a rotation about $\xi(=\bar{\xi})$ axis by an angle

$$\theta=-\tan^{-1}\frac{D}{B}. \tag{24}$$

The inertia tensor referred to the new coordinate axes is

$$\bar{\mathbf{I}}=\mathbf{S}\mathbf{I}\tilde{\mathbf{S}}, \tag{25}$$

where

$$\mathbf{S}=\begin{pmatrix} 1 & 0 & 0 \\ 0 & \cos\theta & \sin\theta \\ 0 & -\sin\theta & \cos\theta \end{pmatrix}, \qquad (26)$$

and $\tilde{\mathbf{S}}$ is the transposed matrix of $\mathbf{S}$. From (19), (24), (25) and (26), the inverse inertia tensor referred to the new coordinate axes is obtained as

$$\bar{\mathbf{I}}^{-1}=\mathbf{S}\mathbf{I}^{-1}\tilde{\mathbf{S}}=\begin{pmatrix} \frac{1}{A} & 0 & 0 \\ 0 & \frac{B}{B^2+D^2} & \frac{D}{B^2+D^2} \\ 0 & \frac{D}{B^2+D^2} & \frac{B+C}{BC-D^2}-\frac{B}{B^2+D^2} \end{pmatrix}. \qquad (27)$$

The matrix elements of the Hamiltonian (13) is obtained as

$$\left\{\begin{aligned} (\mathbf{H}_r)^{JK\mu n\pm}_{JK\mu n\pm}&=\frac{\hbar^2}{4}\left(\frac{1}{A}+\frac{B}{B^2+D^2}\right)[J(J+1)-K^2]+\frac{\hbar^2}{2}\left(\frac{B+C}{BC-D^2}-\frac{B}{B^2+D^2}\right)K^2+E^{K\mu n}\,, \\ (\mathbf{H}_r)^{JK\quad\mu n\pm}_{JK+1\mu n'\pm}&=\frac{\hbar^2}{2}\frac{D}{B^2+D^2}(K+\tfrac{1}{2})\sqrt{(J-K)(J+K+1)}\,I^{K\quad\mu n}_{K+1\mu n'}\,, \\ (\mathbf{H}_r)^{JK\quad\mu n\pm}_{JK+2\mu n'\pm}&=-\frac{\hbar^2}{8}\left(\frac{1}{A}-\frac{B}{B^2+D^2}\right)\sqrt{(J-K)(J-K-1)(J+K+1)(J+K+2)}\,I^{K\quad\mu n}_{K+2\mu n'}\,, \end{aligned}\right. \qquad (28)$$

where

$$I^{K\mu n}_{K'\mu n'}=\int_0^{2\pi} Q^{K\mu n}(x)^*Q^{K'\mu n'}(x)dx\,. \qquad (29)$$

We have included in the above expressions a superfluous index ± which designates the sublevels of inversion doubling described in the following section. It is to be mentioned that the formulas of (28) have also been derived by Hecht and Dennison[4] in a different way independently.

## § 4. Inversion Doubling

In $CH_3NH_2$, inversion takes place in addition to the internal rotation, and there occurs a very complicated interaction between inversion and internal rotation. To avoid the difficulty involved in the rigorous treatment of this two dimensional internal motion, we have proposed in I a simple semiempirical formula for the inversion splitting, and it will be also used in this paper. The summary of I will be given in the following with some complementary remarks.

When the $NH_2$ group turns over from one side to the opposite side of the $CH_3$ group, the minima and maxima of the torsional potential are reversed. Therefore, the internal rotational state undergoes a transition $Q(x)\to Q(x-\pi)$ accompanying the inversion. The inversion splitting is considered to be proportional to

$$\int_0^{2\pi} (x)^*Q(x-\pi)dx\,,$$

and the constant of proportionality may be regarded as an empirical parameter.

One of the component levels of the inversion doublet is symmetric and the other is antisymmetric with respect to the exchange of the positions of two protons in the $NH_2$ group. The nuclear statistical weights of these levels are 1 and 3 respectively. Which of these levels is the lower or the higher can be found as follows. Let the positions of two protons be exchanged by ( i ) the turning over of the $NH_2$ group from one side to the opposite of the $CH_3$ group followed by (ii) a 180° rotation of the $NH_2$ group about the $CH_3$ figure axis. Operation (i) is represented by a transformation $V_a\to V_b$, where $V_a$ and $V_b$ denote the wave functions for the vibrational states of the $NH_2$ group in each side of the $CH_3$ group. (We assume as the first approximation that the molecule is a symmetric top and that its principal axes are not moved by operation (i)). Operation (ii) is represented by a simultaneous transformation of internal and overall rotational wave functions $Q(x)\to Q(x-\pi)$, $\Theta_{JKM}(\theta,\phi,\psi)\to\Theta_{JKM}(\theta,\phi,\psi+\pi)=(-1)^K\times\Theta_{JKM}(\theta,\phi,\psi)$, where $\Theta_{JKM}$ denotes the wave function of the symmetric rotor and $\theta,\phi,\psi$ are the Eulerian angles of the $NH_2$ group. The overall transformation, therefore, is

$$\begin{aligned} V_a\Theta_{JKM}(\theta,\phi,\psi)Q(x)\to&(-1)^K \\ \times& V_b\Theta_{JKM}(\theta,\phi,\psi)Q(x-\pi). \end{aligned} \qquad (30)$$

Now the symmetric and antisymmetric states correspond to the sum and difference of the two sides of (30), form which we know that the energy of inversion splitting measured from the singlet (symmetric) to the triplet (antisymmetric) level is given by

$$\varDelta=(-1)^K\varDelta_0\int_0^{2\pi}Q(x)Q(x-\pi)dx \tag{31}$$

inclusive of sign, where $\varDelta_0$ is a positive constant to be determined empirically.

We may now formally introduce the Hamiltonian of inversion $\mathbf{H}_i$ which is defined by its matrix elements

$$(\mathbf{H}_i)^{JK\mu n\pm}_{JK\mu n\pm}=\pm\tfrac{1}{2}(-1)^K\varDelta_0 \times\int_0^{2\pi}Q^{K\mu n}(x)^*Q^{K\mu n}(x-\pi)dx\,. \tag{32}$$

By adding $\mathbf{H}_i$ to the rotational Hamiltonian $\mathbf{H}_r$ of (13) we obtain the total Hamiltonian

$$\mathbf{H}=\mathbf{H}_r+\mathbf{H}_i\,. \tag{33}$$

The matrix elements of $\mathbf{H}$ can be obtained by adding (28) and (32). The calculations of the following sections will be based on this Hamiltonian $\mathbf{H}$.

By the way, it can be shown from the form of the internal rotational Hamiltonian (15) that the integral $\int_0^{2\pi}Q(x)^*Q(x-\pi)dx$ is a periodic function of $\gamma'=\frac{\pi}{3}(\lambda K+\mu)+\pi\mu$:

$$\int_0^{2\pi}Q(x)^*Q(x-\pi)dx=\sigma_n\cos\gamma'+\sigma_n{}'\cos3\gamma'+\cdots, \tag{34}$$

where $\sigma_n, \sigma_n{}', \cdots$ are constants for each torsional state $n$. It is to be noted that only odd multiples of $\gamma'$ appear in (34).

## § 5. Determination of Molecular Constants

Apparent rotational constants of methylamine were determined by Lide[2] from the three lines of 23341 Mc ($J_{K_{-1},\,K_{+1}}=5_{1,4}\to4_{2,2}$), 36452 Mc ($5_{1,5}\to4_{2,3}$) and 23450 Mc ($5_{2,3}\to6_{1,5}$), neglecting the effects of internal rotation and inversion. Later, however, the inversion partners of these lines have been found at 17476 Mc, 30566 Mc and 29312 Mc[2], and it is necessary to take the mean values of the two sets of frequencies to eliminate the effect of inversion doubling. The mean frequencies are expressed as

$$-13\frac{h}{16\pi^2}\left(\frac{1}{A}+\frac{B}{B^2+D^2}\right)+3\frac{h}{8\pi^2}\left(\frac{B+C}{BC-D^2}-\frac{B}{B^2+D^2}\right)-15\frac{h}{16\pi^2}\left(\frac{1}{A}-\frac{B}{B^2+D^2}\right)I^{-100}_{100} +\frac{E^{200}}{h}-\frac{E^{100}}{h}+\frac{\mathcal{E}_1}{h}=20408\text{ Mc}\,, \tag{35a}$$

$$-13\frac{h}{16\pi^2}\left(\frac{1}{A}+\frac{B}{B^2+D^2}\right)+3\frac{h}{8\pi^2}\left(\frac{B+C}{BC-D^2}-\frac{B}{B^2+D^2}\right)+15\frac{h}{16\pi^2}\left(\frac{1}{A}-\frac{B}{B^2+D^2}\right)I^{-100}_{100} +\frac{E^{200}}{h}-\frac{E^{100}}{h}+\frac{\mathcal{E}_2}{h}=33509\text{ Mc}\,, \tag{35b}$$

$$15\frac{h}{16\pi^2}\left(\frac{1}{A}+\frac{B}{B^2+D^2}\right)-3\frac{h}{8\pi^2}\left(\frac{B+C}{BC-D^2}-\frac{B}{B^2+D^2}\right)+21\frac{h}{16\pi^2}\left(\frac{1}{A}-\frac{B}{B^2+D^2}\right)I^{-100}_{100} -\frac{E^{200}}{h}+\frac{E^{100}}{h}+\frac{\mathcal{E}_s}{h}=26381\text{ Mc}\,, \tag{35c}$$

where the last terms in the left hand sides are the contributions from the off-diagonal elements of the Hamiltonian.

In addition to the above frequencies, the origins of the $p_1$ and $p_2$ series[1] may be used in the determination of the molecular constants. These series correspond to the transitions $J\to J$, $K=0\to1$, $\mu=1$, $n=1$, and the mean frequency of the origins of the $p_1$ and $p_2$ series is expressed as

$$-\frac{h}{16\pi^2}\left(\frac{1}{A}+\frac{B}{B^2+D^2}\right) +\frac{h}{8\pi^2}\left(\frac{B+C}{BC-D^2}-\frac{B}{B^2+D^2}\right) +\frac{E^{111}}{h}-\frac{E^{011}}{h}+\frac{\mathcal{E}_4}{h}=30187\text{ Mc}. \tag{36}$$

The frequencies of the lines of (35) and (36) are all quite insensitive to $D$. On the other hand, the Stark coefficients of the lines of the $p_1$ and $p_2$ series are sensitive to $D$, so that they are pertinent to be used in the determination of the value of D.

One more condition is necessary to fix all the molecular constants $A, B, C_1, C_2, C(=C_1+C_2), D$ and $H$ (barrier height). However, it is known that the value of $C_2$ is almost equal to the moment of inertia of methane in many molecules such as methylalcohol and methyl halides. Therefore, as a first step, we tentatively assume that the value of $C_2$ is equal to the moment of inertia of methane.

The determination of molecular constants is a problem of successive approximation, and after several cycles of calculations a fairly good set of trial values has been obtained. Using these trial values, the Stark coefficients of the lines of the $p_1$ series are expressed by the following equation:

$$\left[\frac{\mu_{\|}}{J^2+J}+\mu_{\pm}\frac{h}{4\pi^2c}\frac{D}{(B^2+D^2)}\left(\frac{0.116}{J^2+J}+0.439\right)\right]\frac{M}{\hbar}$$

The value of $\mu_{\|}$ and $\alpha_{\pm}$ have been obtained by Lide[2)] as $\mu_{\|}=0.304$ D and $\mu_{\pm}=1.232$ D from the Stark coefficients of the lines of (35) with a sufficient accuracy to be put into the above expression. The experimental value of Stark coefficients were measured on the third line ($J=3$) of $p_1$ series to be $0.0228\times10^{-24}$ $M/h$ $Mc$/sec[1)]. Thus we obtain

$$\frac{h}{4\pi^2c}\frac{D}{B^2+D^2}=-0.0045\ \text{cm}^{-1}\ . \qquad (37)$$

The pertubation terms in (35) and (36) have been calculated from the trial values of molecular constants as

$\varepsilon_1/h=149$ Mc, $\varepsilon_2/h=44$ Mc, $\varepsilon_3/h=-330$ Mc and $\varepsilon_4/h=0$, and these values have been put into (35) and (36). Then, from (35), (36) and (37) and by repeated cycles of calculations we have obtained the values of the molecular constants are listed in Table I. In Table I, the values of inversion splitting constant $\varDelta_0$ for the ground and first excited torsional states are also given. The value of $\varDelta_0$ for $n=0$ has been obtained from the frequency difference of the pair of lines of 23341 Mc and 17476 Mc, while the values of $\varDelta_0$ for $n=1$ has been obtained from the origins of the $p_1$ and $p_2$ series.

From the constants in Table I the moments and products of inertia of the molecule and the barrier height of internal rotation can be determined. The results are given in Table II.

Table I. Molecular Constants.

$$\frac{h}{16\pi^2}\left(\frac{1}{A}+\frac{B}{B^2+D^2}\right)=22164.6\ \text{Mc}$$

$$\frac{h}{8\pi^2}\left(\frac{B+C}{BC-D^2}-\frac{B}{B^2+D^2}\right)=103144.8\ \text{Mc}$$

$$\frac{h}{16\pi^2}\left(\frac{1}{A}-\frac{B}{B^2+D^2}\right)=461.46\ \text{Mc}$$

$$\frac{h}{4\pi^2}\frac{D}{B^2+D^2}=-135\ \text{Mc}$$

$$\frac{h}{8\pi^2}\frac{1}{U}\left(=\frac{h}{8\pi^2}\frac{1}{C_2}\frac{BC-D^2}{BC_1-D^2}\right)=456609\ \text{Mc}$$

$$\lambda\left(=\frac{C_2\sqrt{B^2+D^2}}{BC-D^2}\right)=0.655276$$

$$\alpha\left(=\frac{UH}{2\hbar^2}\right)=11.3444$$

$$\Delta_0=\begin{cases}28604\ \text{Mc (for } n=0)\\ 29358\ \text{Mc (for } n=1)\end{cases}$$

Table II. Inertial constants and barrier height.

$A = 37.085\times10^{-40}$ gcm²
$B = 38.662$ 〃
$C = 8.136$ 〃
$C_1 = 2.805$ 〃
$C_2 = 5.331$ 〃
$D = -0.120$ 〃
$H = 691.1$ cm⁻¹

The values in Tables I and II are dependent on the assumption on the value of $C_2$. However, calculations of the frequencies of the other lines have shown a good agreement with the experimental results[1),2)] within errors of an order of 100 to 200 Mc*, and additional adjustment of the molecular constants proved to give no appreciable improvement on the agreement between observed and calculated frequencies. Therefore, the values in Tables I and II may be accepted as final values within an uncertainty of a few tenth of a percent which correspond to the discrepancies of 100 to 200 Mc mentioned above. These discrepancies will be due to the neglect of various higher-order effects, and are of an allowable order of manitude. Further checks on our results have been obtained by the comparison of observed and calculated values for the Stark coefficients and hyperfine splittings of the assigned lines and the expansion coefficients of $p_1$ and $p_2$ series*.

The percentage error in the value of $D$, however, is expected to be rather large, since the Stark pattern of the line was contaminated by the quardrupole effect and since the Stark coefficients of the line of the $p_1$ series were used instead of the mean values of the coefficients of the lines of the $p_1$ and $p_2$ series. The maximum possible error in $D$ will be about $0.05\times10^{-40}$ g cm$^2$, which however, results only in an error of 10′ in the angle between the CN axis and the methyl axis.

---

* T. Nishikawa: to be published.

## § 6. Molecular Structure and Barrier Height

There are seven structural parameters of the molecule while only five inertial constants are available, so that it is necessary to make two assumptions to fix the molecular structure. The most acceptable assumption will be to set the CH distance equal to the methane value 1.093 A. This assumption is also equivalent to set the HCH angle equal to the tetrahedral angle 109°28′, on account of the assumption made in the preceding section on the value of $C_2$. The next assumption we make on the locations of the hydrogen atoms in the amino group, since hydrogen atoms are light and have minor effects on the inertial constants. Among the three structural parameters involving these hydrogen atoms ($d_{NH}$, $\angle$HNH and $\angle$CNH), we take $d_{NH}$ equal to that in ammonia, 1.014 A, since in general bond lengths are less affected by the surroundings than bond angles, i.e. bond stretching force constants are usually larger than bond bending force constants.

With the above assumptions the molecular structure of methylamine is determined as shown in Table III. The possible errors for these values are also indicated in Table III. These possible errors take account of the above assumptions and of the discrepancies between observed and calculated frequencies mentioned in the preceding section.

Table III. Structural Parameters.

| | |
|---|---|
| $d_{CH}$ = 1.093 A (assumed) | $\angle$HCH = 109°30′ ± 1° |
| $d_{NH}$ = 1.014 A (assumed) | $\angle$HNH = 105°50′ ± 1° |
| $d_{CN}$ = 1.474 A ± 0.005 A | $\angle$CNH = 112°10′ ± 1° |

The angle between CN and the methyl axis = 3°30′ ± 20′. (The methyl axis passes through the $NH_2$ triangle.)

The CN distance of 1.474 A is in good agreement with the electron diffraction value 1.47 A[7], while both are somewhat shorter than the sum of covalent radii 1.50 A. The HNH angle of 105°50′ is slightly smaller than that in ammonia 106°47′ but the difference is almost within the probable error. The CNH angle of 112°10′ is considerably larger than the HNH angle in ammonia. The CN direction is not on the symmetry axis of the methyl group, being deviated by an angle of 3°30′. These deviations are probably due to the repulsion between the amino group and the methyl group.

The height of potential barrier to internal rotation is obtained from $U^{-1}$ and $\alpha$ as 691.1 ±1.0 cm$^{-1}$. This value is about twice as large as that in methylalcohol[8] (374.8 cm$^{-1}$), apparently corresponding to the presence of two hydrogen atoms in the amino group as compared to one hydrogen atom in the hydroxyl group. However, this apparent relation may be merely an accidental one, since three are various types of complicated interactions between the two mutually rotating groups of these molecules to be taken into account.

The values of the inversion splitting constant $\Delta_0$, 28604 Mc for $n=0$ and 29358 Mc for $n=1$, are rather large as compared with the inversion splittings in ammonia (0.7935 cm$^{-1}$) and deuterated ammonias $NH_2D$ (0.406 cm$^{-1}$), $NHD_2$ (0.1705 cm$^{-1}$) and $ND_3$ (0.068 cm$^{-1}$)[9]. The large $\Delta_0$ of methylamine may be related to the large CNH angle, i.e. the small distance between the two minima of the potential to inversion, which facilitates the inversion motion. Except for this point, the potential curves for these molecules will be similar.

## § 7. Discussion

The internal motion of methylamine is a very complicated problem, so that a number of simplifying assumptions has been made in its treatment. The main assumptions made are as follows. (1) In treating internal and overall rotations it was assumed that the molecule is rigid except for the internal rotation. (2) The potential to internal rotation was approximated by a sinusoidal function. (3) The inversion doubling was treated semi-empirically. In spite of these assumptions, however, satisfactory agreement between theory and experiment has been obtained within allowable errors. The remaining discrepancies between observed and calculated frequencies are considered to be due to various higher-order effects. In particular, the rigorous treatment of the wave equation of the internal motion on a two dimensional potential surface will be necessary to obtain a complete agreement with experiment.

### § 8. Acknowledgement

The author wishes to express his hearty thanks to Prof. M. Kotani for his encouragement during the course of this investigation. He also wishes to express his appreciation to Prof. K. Shimoda for helpful advice, and to Dr. T. Nishikawa for valuable discussion and for the help in some of the numerical calculations. He is indebted to Dr. D. R. Lide, Jr. for the communication of his results.

### References

1) K. Shimoda, T. Nishikawa and T. Itoh: J. Phys. Soc. Japan **9** (1954) 974; J. Chem. Phys. **22** (1954) 1456. These are referred to as I in the text.
2) D. R. Lide, Jr.: J. Chem. Phys. **20** (1952) 1812; **21** (1953) 571; **22** (1954) 1613.
3) D. G. Burkhard and D. M. Dennison: Phys. Rev. **84** (1951) 408.
4) K. T. Hecht and D. M. Cennison: cited in C. H. Townes and A. L. Schawlow: Microwave Spectroscopy of Gases, McGraw-Hill (1955) p. 324.
5) D. Kivelson: to be published.
6) J. S. Koehler and D. M. Dennison: Phys. Rev. **57** (1940) 1006.
7) P. W. Allen and L. E. Sutton: Acta Crys. **3** (1950) 46.
8) E. V. Ivash and D. M. Dennison: J. Chem. Phys. **21** (1953) 1804.
9) M. T. Weiss and M. W. P. Strandberg: Phys. Rev. **83** (1951) 567.

---

JOURNAL OF THE PHYSICAL SOCIETY OF JAPAN Vol. 11, No. 3, MARCH, 1956

# The Time Lag and other undesirable Phenomena observed in Vacuum Photo-tubes at Weak Illumination II

By Masao SUGAWARA

*Hitachi Central Research Lab. Kokubunji-machi, Kitatamagun, Tokyo*

(Received October 4, 1955)

Using the tubes with two photocathodes the abnormalities of photocurrents were studied. The abnormalities of the tubes were conspicuous when one of the cathodes was isolated. These abnormal effects could be well explained from the results obtained when the potential of the isolated cathode was varied and current characteristics of the tubes were measured at various wave length of light. The effects were considered to be due to the voltage changes of the isolated cathode resulting from its own photoemission and secondary emission caused by the incidence of light. Photoelectric materials of usual photo-tubes adhering to the undesired portion of the inner surfaces can be analogously considered to the isolated cathodes of the tubes.

### § 1. Introduction

In the previous paper¹⁾ the writer has described that the photoelectric materials adhered to the undesired portion of the inner surface of the photo-tube are main cause of the non-proportionality of the photocurrent to the illuminating flux and also of the time lag of photocurrent, Preston and McDermott²⁾ have carried out calculations in simple cases and explained the current-flux non-proportionality observed in their experiment. It seems, however, that the relations between these phenomena and the behavior of photoelectric materials on the tube wall have not yet been sufficiently clarified.

As it is very hard to study the behavior of the adhered photoelectric materials with ordinarily prepared photo-tubes, we have

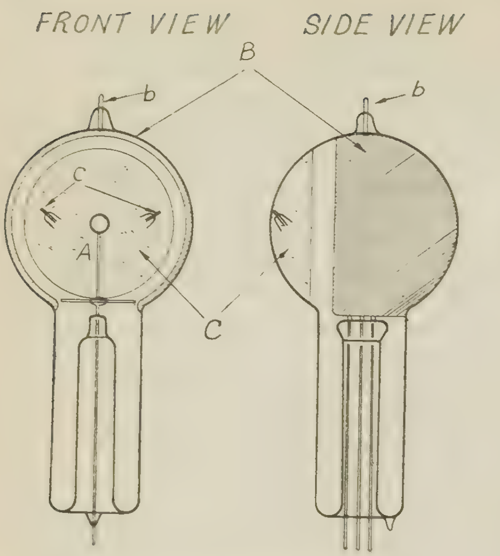

Fig. 1. Photo-tube used for Experiment.
*A*: anode *B*: 1st cathode *C*: 2nd cathode
*b*: 1st cathode lead *c*: 2nd cathode lead.

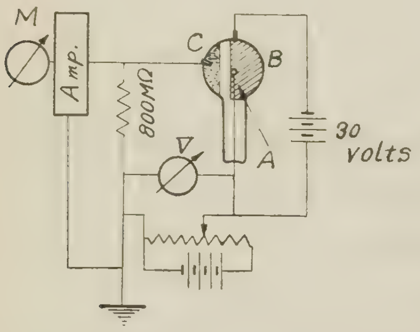

Fig. 2. Circuit Diagram for measuring the 2nd Cathode Current.
*M*: micro-ammeter *V*: voltmeter *A*: anode
*B*: 1st cathode *C*: 2nd cathode.

made the tubes comprising two photo-cathods, and further experiments were carried out with them.

## § 2. Experimental Procedures

In Fig. 1, the tube used in this experiment is shown, where A is an anode, B an ordinary photo-cathode and C an additive photocathode which is semi-transparent and adhered on the inner surface of the window. Hereafter, B and C will be called the first and the second cathodes, respectively. Too cathodes are separated, so that one can apply different voltages on them individually. To the 2nd cathode, two leads are attached. The resistance between them was about $10^4\,\Omega$ and which is small compared with those between any two electrodes of the tube.

Silver-caesium oxide photo-surface and antimony-caesium photo-surface where used for cathodes and following four kinds of tubes were made.

(a) 1st cathode : silver-caesium oxide
  2nd cathode : antimony-caesium
(b) 1st cathode : antimony-caesium
  2nd cathode : silver-caesium oxide
(c) Both 1st and 2nd cathodes : silver-caesium oxide
(d) Both 1st and 2nd cathodes : antimony-caesium.

The monochrometer and the current amplifier were the same as described in the previous paper¹⁾. The tube was so placed that the monochromatic beam illuminated the 1st cathode, after shining on and passing through the 2nd cathode. At first, maintaining the 1st cathode at a constant voltage, the voltage of the 2nd cathode was varied and the photoelectric current and dark current, i.e. the current flowing in the un-illuminated case, to the anode and to the 1st and the 2nd cathodes were measured respectively. The circuit used for the measurement of the current to the 2nd cathode is shown in Fig. 2. Secondly, isolating the 2nd cathode and maintaining the 1st cathode at the same constant voltage as above the abnormal effects as well as the spectral sensitivity were measured. At last, the two cathodes were connected, and similar measurements were carried out. The method was the same as reported in the previous paper except that the current was measured on the anode side.

## § 3. Experimental Results

Experiments were carried out with four kinds of tubes above mentioned, the results obtained in every case were similar in many respects and were summarized as:

(a) In the case that the 1st and 2nd cathodes are connected, abnormal effects are hardly observable.
(b) In the case that the 2nd cathode is isolated, abnormal effects markedly appear.
(c) The wave length range, where the abnormal effects appear, depends on the photoelectric material of the 2nd

Table I. Abnormal Effects of Tube I.

1st cathode : −30V
2nd cathode : isolated

| Wave length (mμ) | Discordace (%) | Time lag | | | |
|---|---|---|---|---|---|
| | | light off | | light on | |
| | | Type | Secs. | Type | Secs. |
| 380 | 2.9 | A | 50 | C | 20 |
| 400 | 2.2 | 〃 | 30 | 〃 | 〃 |
| 420 | 2.1 | 〃 | 〃 | 〃 | 〃 |
| 440 | 2.0 | 〃 | 〃 | 〃 | 〃 |
| 460 | 1.9 | 〃 | 〃 | 〃 | 〃 |
| 480 | 1.9 | 〃 | 〃 | 〃 | 〃 |
| 500 | 2.0 | 〃 | 〃 | 〃 | 〃 |
| 520 | 2.5 | 〃 | 〃 | 〃 | 〃 |
| 540 | 3.3 | 〃 | 〃 | 〃 | 〃 |
| 560 | 4.6 | 〃 | 〃 | 〃 | 〃 |
| 580 | 6.1 | 〃 | 〃 | 〃 | 〃 |
| 600 | 6.8 | 〃 | 〃 | 〃 | 〃 |
| 620 | 4.6 | 〃 | 〃 | 〃 | 〃 |
| 640 | −0.1 | normal | | normal | |
| 660 | −0.4 | | | | |
| 680 | −0.2 | | | | |
| 700 | −0.3 | | | | |
| 720 | −0.5 | | | | |
| 740 | −0.4 | | | | |
| 760 | −0 | | | | |

Remarks: Photocurrent: $1.8 \times 10^{-10}$ A
Discordance : (measured)−(standard).

Table II. Abnormal Effects of Tube I.

both 1st and 2nd cathode: −30 V

| Wave length (mμ) | Discordace (%) | Time lag | | | |
|---|---|---|---|---|---|
| | | light off | | light on | |
| | | Type | Secs. | Type | Secs. |
| 380 | 0.1 | normal | normal | normal | normal |
| 400 | 0 | | | | |
| 420 | 0 | | | | |
| 440 | 0 | | | | |
| 460 | −0.1 | | | | |
| 480 | −0.1 | | | | |
| 500 | −0.2 | | | | |
| 520 | −0.1 | | | | |
| 540 | −0.2 | | | | |
| 560 | 0 | | | | |
| 580 | 0.2 | | | | |
| 600 | 0.1 | | | | |
| 620 | 0 | | | | |
| 640 | −0.1 | | | | |
| 660 | −0.2 | | | | |
| 680 | −0.1 | | | | |
| 700 | 0 | | | | |
| 720 | −0.2 | | | | |
| 740 | −0.1 | | | | |
| 760 | 0.8 | | | | |

Remark: Photocurrent: $1.8 \times 10^{-10}$ A
Discordance : (measured)−(standard).

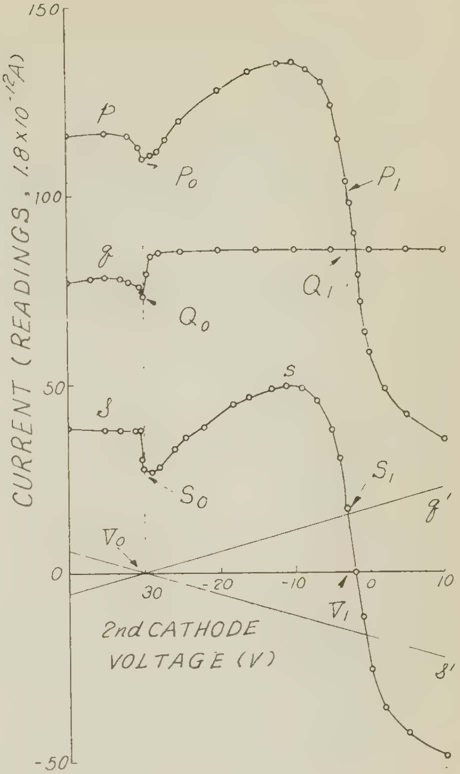

Fig. 3. Current—2nd Cathode Voltage Characteristics of Tube I.
1st cathode voltage: −30 V wave length: 600mμ
$p$: anode photocurrent $q$: 1st cathode photocnrrent $s$: 2nd cathode photocurrent $q'$: 1st cathode dark current $s'$: 2nd cathode dark current.

cathode, irrespective of that of the 1st.

(d) In some tubes of which the dark current to the 1st cathode is large, the dual characteristics are observed.

Therefore, in following paragraphs, only the results for Tube I and Tube II will be described. Both tubes have the silver ceasium-oxide as the 1st cathode and antimony-ceasium as the 2nd, and the dark current of Tube I is small, while that of Tube II is large.

(1) *Tube I*

In Fig. 3 are shown the photocurrent and dark current readings in the anode lead and two cathode leads in the case of the 1st cathode being held at −30 V and a variable potential being supplied to the 2nd. Tables I and II represent the abnormalities of the tube in the cases that the 2nd cathode is isolated and is connected to the 1st cathode respectively, the 1st cathode voltage being −30 V

Table III. Abnormal Effects of Tube I.
1st cathode : isolated
2nd cathode : −30 V

| Wave length (mμ) | Discordace (%) | Time lag light off Type | Secs. | light on Type | Secs. |
|---|---|---|---|---|---|
| 380 | 0 | | | | |
| 400 | 0 | ↑ | | ↑ | |
| 420 | 0 | | | | |
| 440 | 0 | | | | |
| 460 | 0 | normal | | normal | |
| 480 | 0 | | | | |
| 500 | 0 | | | | |
| 520 | 0 | ↓ | | ↓ | |
| 540 | −0.2 | | | | |
| 560 | 0.9 | A | 13 | C | 20 |
| 580 | 4.5 | 〃 | 15 | 〃 | 〃 |
| 600 | 7.2 | 〃 | 〃 | 〃 | 〃 |
| 620 | 9.0 | 〃 | 〃 | 〃 | 〃 |
| 640 | 10.9 | 〃 | 〃 | 〃 | 〃 |
| 660 | 13.6 | 〃 | 〃 | 〃 | 〃 |
| 680 | 18.7 | 〃 | 〃 | 〃 | 〃 |
| 700 | Photocurrent <1.8×10⁻¹⁰A, at maximum slit width of the monochrometer used | | | | |
| 720 | | | | | |
| 740 | | | | | |
| 760 | | | | | |

Remarks: Photocurrent: $1.8\times10^{-10}$A
Discordance : (measured)—(standard)

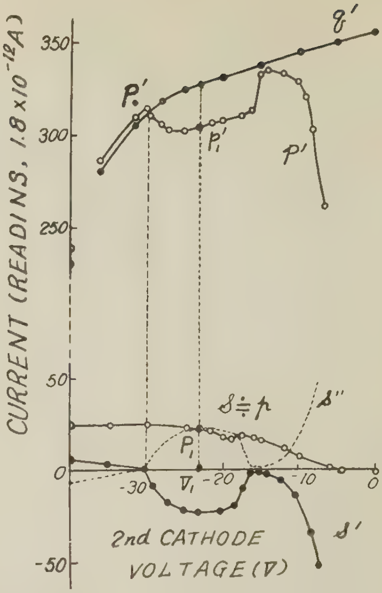

Fig. 5. Current—2nd Cathode Voltage Characteristics of Tube II.
1st cathode: −30 V, wave length: 500 mμ
$s$: 2nd cathode photocurrent $p'$: anode dark current $q'$: 1st cathode dark current $s'$: 2nd cathode dark current $s''$: Symmatrical curve to $s'$.

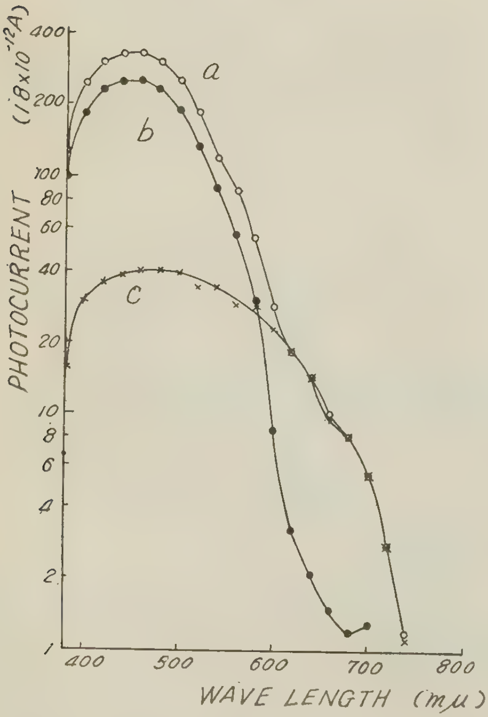

Fig. 4. Spectral Response of Tube I.
$a$: 1st and 2nd cathode: −30 V
$b$: 1st cathode: isolated, 2nd cathode: −30 V
$c$: 1st cathod: −30 V. 2nd cathode: isolated.

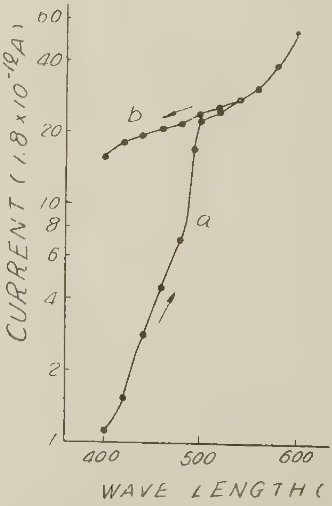

Fig. 6. Dual Characteristic observed with Tube II.
$a$: measured from λ 400 mμ to longer wave length $b$: measured from λ 600 mμ to shorter wave length with continuous illumination.

in both cases. In Table III are given the abnormalities when the 1st cathode is isolated and the 2nd cathode is maintained at −30 V. In Fig. 4 are shown the spectral sensitivity curves of the tube.

(2) *Tube II*

The results in the case of Tube II illuminated with the light of 500 m$\mu$ are plotted in Fig. 5. As the photocurrent to the 1st cathode is very small, the curve corresponding to it is omitted. This small photocurrent seemed to be due to the absorption of illuminating light at the 2nd cathode. Photocurrent to the anode was almost equal to that to the 2nd cathode.

In Fig. 6, is shown the photocurrent variation due to the change of wave length of incident light at constant slit width, 0.05 mm, measured when the 2nd cathode is isolated. Curve *a* was obtained in which the wave length was increased from 400 m$\mu$ towards red side, while curve *b* was obtained when the wave length was decreased from 600 m$\mu$ to violet side without interrupting the light. When the light was interrupted, however, the measured values after the interruption come to curve *a*. No duality was observed in the range of wave length longer than 520 m$\mu$.

## § 4. Discussions

(1) *Tube I*

In Fig. 3, the photocurrent curves $p, q$ and $s$ are rather complicated, these are probably due to the fact that some photoelectrons emitted from the 1st cathode arrive at the 2nd cathode, and from there the secondary electrons may be emitted. The dark current to the anode is very small and omitted in this figure. This fact represent that the thermal emission of the cathodes is negligibly small in this tube and that the dark current is mainly due to the leakage between the two cathodes. Further the relations $P \doteqdot Q+S$ and $Q'+S'=0$ are obtained, where $P, Q, S, Q'$, and $S'$ are the values corresponding to the 2nd cathode voltage on the curves $p, q, s, q'$ and $s'$ respectively.

From Fig. 3, it is conceived that when the 2nd cathode is connected to the 1st, by the illumination of the light of 600 m$\mu$, the photocurrent readings in the anode, the 1st and the 2nd cathode leads would be $P_0$, $Q_0$ and $S_0$, but when the 2nd cathode is isolated, $P_1$, $Q_1$ and $S_1$ respectively. In the latter case, the voltage of the isolated 2nd cathode varies from $V_0$ to $V_1$, because at the lower voltages than $V_1$, the supply of electrons by the leakage current is not large enough to compensate the photoelectrons emitted from the 2nd cathode.

Owing to the capacitance between the 2nd cathode and the soroundings, some durations will be required before the potential of the 2nd cathode becomes to $V_1$, and therefore, the time lag of the anode photocurrent appears. In the case shown in Fig. 3, the anode photocurrent increases to a maximum from $P_0$ then decreases and becomes $P_1$. It is expected to be the *C*-type time lag as classified in the previous paper.

An ultimate current $S_1$ of the 2nd cathode depends rather on the resistance between cathodes and does not change in proportion to the illumination when a standard filter is inserted. This is perhaps the reason why the discordance appears and it would be larger in the light more sensitive to the isolated cathode as shown in Tables I and III.

The decrease of the sensitivity of the response curves *b* and *c* in Fig. 4 in the wave length range 620∼720 m$\mu$ and 380∼640 m$\mu$ respectively can be understood from the result in Fig. 3 that $P_1$ is smaller than $P_0$. As seen from Table II, when the 2nd cathode is connected to the 1st, little abnormalities are observed, since in this case there are no isolated parts.

As stated in the previous paper, one can keep off the abnormalities by providing the tube wall with a conductive film. This fact will be explained similarly.

Now, the ascertainment of the above considerations will be made more quantitatively. Let us consider the case, for ex., of isolating the 2nd cathode. The abnormalites when illuminated by the light of 600 m$\mu$ are summarized in Table IV including those shown in Table I. The transient abnormality or the time lag may be considered analogously to the transient phenomena at the charge of the condensers in the equivalent circuit as shown in Fig. 7, where $R_1$, $R_2$ are the resistances between the two cathodes, and between the 2nd cathode and the anode, $C_1$, $C_2$ and $C_3$ are the capacitances of het 2nd cathode with

Table IV. Abnormal Effect of Tube I at 600 m$\mu$ observed when the 2nd cathode was isolated. (see Table I.)

| Wave width (m$\mu$) | Standard value at 600 m$\mu$ (J) | Measured value (j) | Discordance (J–j) | light off | | light on | |
|---|---|---|---|---|---|---|---|
| | | | | Type | Secs. | Type | Secs. |
| 1 | 52.9 | 59.7 | +6.8 | A | 30 | C | 20 |

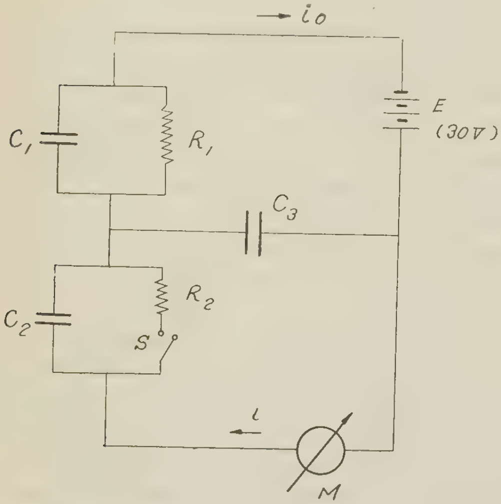

Fig. 7. Equivalent Circuit Diagram of the Phototube used when the 2nd cathode is isolated.

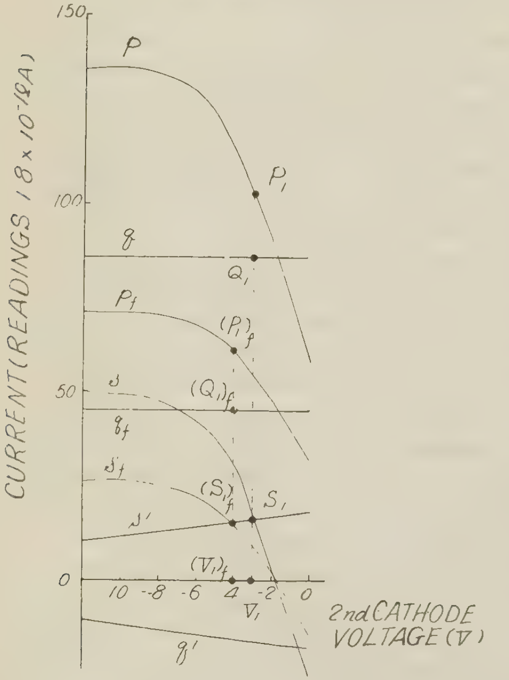

Fig. 8. Current—2nd Cathode Voltage Characteristics of Tube I.

$p$: anode photocurrent $q$: 1st cathode photocurrent $q$: 2nd cathode photocurrent $q'$: 1st cathode dark current $s'$: 2nd cathode dark current suffix $_f$: when filter was inserted.

respect to the 1st cathode, the anode and the container of the tube, respectively.

Following equations are obtained when the switch is off;

$$\begin{aligned} i_0 &= (1/R_1+pC_1)V_1=p(C_2+C_3)V_2\,, \\ i &= pC_2V_2\,, \qquad\qquad (1) \\ V_1+V_2 &= E\,, \end{aligned}$$

where $i$ is the current measurable in a meter, $i_0$ is the total current, $V_1$ and $V_2$ are the voltages of $C_1$ and $C_2$, respectively and $p$ is an operator representing $d/dt$. Considering the initial condition,

$$V_2=R_2E/(R_1+R_2) \quad \text{at} \quad t=0\,,$$

The current $i$ is given by

$$i=\frac{C_2E}{(R_1+R_2)(C_1+C_2+C_3)}\exp\left(-\frac{t}{R_1(C_1+C_2+C_3)}\right) \tag{2}$$

Similarly when the switch is on, the current $i$ is given by

$$i=\frac{E}{R_1+R_2}+\frac{E}{R_2}\left(\frac{R_1}{R_1+R_2}-\frac{C_2}{C_1+C_2+C_3}\right)\times\exp\left(-\frac{(R_1+R_2)t}{R_1R_2(C_1+C_2+C_3)}\right) \tag{3}$$

It can be seen from Eq. (2) that the A-type time lag appears when the light is cut off. On the other hand, from Eq. (3) A-type or C-type is expected at the beginning of the illumination.

The numerical values of $C_1$, $C_2$ and $C_3$ of the tube are measurable. Since the curve $s'$ is almost straight line, $R_1$ can be easily obtained from its inclination in Fig. 3. For $R_2$, as the first approximation, the value obtained from the inclination of the curve $s$ at the point $S_1$ will be used. The numerical values of these quantities are as follows;

$$R_1=1\times10^{12}\,\Omega\,,$$
$$R_2=4\times10^{10}\,\Omega\,,$$
$$C_1=C_2=1\ \mu\mu\text{F}\,,$$
$$C_3=10\ \mu\mu\text{F}\,.$$

Substituting above values and $E=30$ V into Eqs. 2 and 4, the equations lead to

Table V. Values concernning the Discordance calculated from Fig. 8.

| Condition of measurements | 2nd cathode voltage (V) | Anode Photo-current $(1.8\times10^{-12}A)$ | 1st cathode photocurrents $(1.8\times10^{-12}A)$ | 2nd cathode photocurrents $(1.8\times10^{-12}A)$ | $P'/P$ ×100 | $Q'/Q$ ×100 | $S'/S$ ×100 |
|---|---|---|---|---|---|---|---|
| no filter | $V_1=-3$ | $P_1=103$ | $Q_1=86.8$ | $S_1=16$ | 59.2 | 52.5 | 93.9 |
| inserting filter | $V_f=-4$ | $(P_1)_f=61$ | $(Q_1)_f=45$ | $(S_1)_f=15$ | | | |

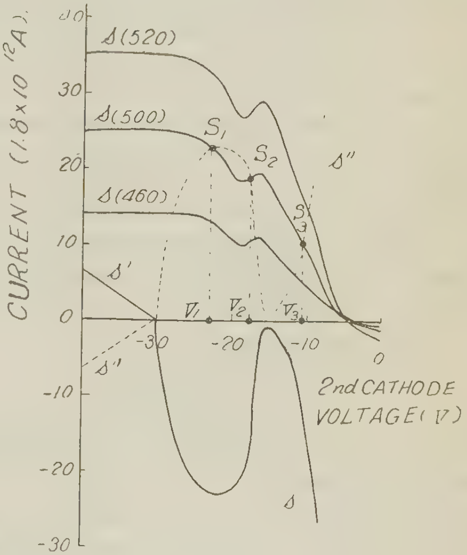

Fig. 9. Current—2nd Cathode Voltage Characteristics of Tube II.
1st cathode: $-30$ V.
$s$ (460): 2nd cathode photocurrent for 460 m$\mu$
$s$ (500): for 500 m$\mu$ $s$ (520): for 520 m$\mu$
$s'$: 2nd cathode dark current $s''$: symmetrical curve to $s'$.

$$i=2.4\times10^{-12}e^{-0.08t}\,, \qquad (2')$$

and

$$i=2.9\times10^{-11}+6.6\times10^{-10}e^{-2.2t}\,, \qquad (3')$$

respectively. Equation (3′) represents the time lag corresponding to the C-type, and above results well coincide with the experimental results shown in Table IV. If the time intervals needed before the current reaches to the ultimate value is assumed to be the time elapsed before the photocurrent comes as near as $1.8\times10^{-13}$ A to the ultimate one, the value 33 secs. and 4 secs. are obtained from Eqs. (2′) and (3′) respectively. The former coincides with the experimental value in Table IV, whereas the latter somewhat but tolerably differs from the experimental result, this may be due to the rough approximation for $R_2$.

To consider the discordance, the photocurrent readings when the filter is inserted are necessary in addition to the result shown in Fig. 3. The results are shown in Fig. 8, where the readings in the filter inserted case are designated with sufix $f$. To compare with the measured values shown in Table IV, expected values from Fig. 8 are summarizely described in Table V, in which $(P_1)_f/P_1\times100$ should be the value measured as the transmittance of the filter. The transmittance of the filter is 59,7% in Table IV and 59.2% in Table V, two values being in good agreement. The ratio for the 1st cathode photocurrent (52.5%) well coincides with the standard transmittance (52.9%), whereas that for the 2nd cathode (93.9%) quite disagrees. The discordance is apparently due to the fact that the 2nd cathode photocurrent is not proportional to the illumination.

### (2) *Tube II*

The curves corresponding to the dark currents in Fig. 5 are rather complicated. It is presumed that some thermally emitted electrons from the 1st cathode arrive at the 2nd cathode and, in a certain circumstances, emit secondary electrons. Accurate measurements were difficult in this case, as the thermal emission was very sensitive to temperature. However, the relation $P'\doteqdot Q'+S'$, also exists in this case.

The duality as shown in Fig. 6 can be similarly interpreted as in the case of Tube I. In Fig. 9, the curve $s''$ is the one drawn in symmetry to the dark current curve $s'$ with regards to the horizontal axis, Curves $s_{(460)}$, $s_{(500)}$, $s_{(520)}$ correspond to the cases of the incident light of 460 m$\mu$, 500 m$\mu$ and 520 m$\mu$, respectively. Curve $s''$ intersects the curve $s_{(500)}$ at three different point $S_1$, $S_2$ and $S_3$, and from these three potentials $V_1$, $V_2$ and $V_3$ are obtained, but the potential $V_2$ is unstable and may not be held. On the other hand, at longer wave length for which the photocurrent is larger, curve $s$ intersects curve $s''$ at only one point like as curve $s_{(520)}$ in Fig. 9. The anode current, of course, takes different values according to whether $V_1$ or $V_2$ is the potential of the 2nd cathode.

Then it is conceived that there are the cases where $S_1$ is adjacent to $S_2$. In these cases, the photocurrents may take the value $S_1$ at first, but it may change beyond $S_2$, due to any accidental causes such as temperature change, and terminates to $S_3$ instead of $S_1$. This is expected to be the B-type time lag, and would accompany with the duality as stated in the previous paper.

In this case numerical treatment is not so simple as in the case of Tube I, because the dark current varies with the 2nd cathode voltage.

Taking the variation of the dark current in calculation, the photocurrent reading in the anode by the light of 500 mμ, when the 2nd cathode is isolated is given by

$$\begin{aligned} i_p &= P_1-(P_0'-P_1') \\ &= 23-(313-304)=14 \text{ (scales)} \end{aligned}$$

from Fig. 5. In the same way, the anode current to be measured for another stable 2nd cathode potential $V_3$, is calculated to be 28 scales. For various wave lengths, these values are plotted in Fig. 10, which qualitatively agree with Fig. 6. The disagreements in absolute values seem to be attributed to the change in temperature. If the measurements are started from shorter wave length, the 2nd cathode would have a potential $V_1$ and the curve *a* in Fig. 6 or Fig. 10 would be obtained. When the wave length is longer than 500 mμ, the 2nd cathode can take the potential $V_3$ only and the duality should disappear. In the measurements started from longer wave length towards the violet side, the 2nd cathode would have a potential $V_3$, thereby curve *b* will be obtained. If the illumination is once cut off, the 2nd cathode potential would become −30 V and, therefore, the 2nd cathode would take a potential $V_1$ instead of $V_3$ when re-illuminated.

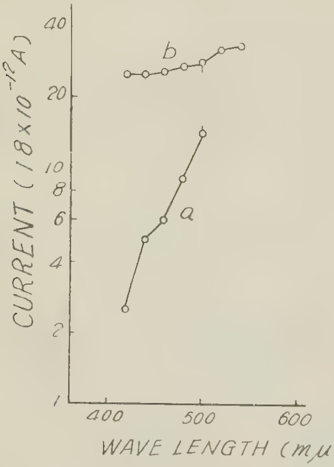

Fig. 10. Dual Character of Tube II obtained by calculation.
*a*: at lower voltage *b*: at higher voltage.

## § 5. Conclusion

The photo-tubes having two cathodes were prepared and the abnormal effects of them were measured in the case when one of the cathodes was isolated. It has been proved that the abnormalities are explained by considering the following factors; photoemission and secondary emission from the isolated cathode, the leakage resistances between the isolated cathode and other electrode, and the thermal emission from the ordinary cathode. It has been found that the abnormal effects can be explained quantitatively by presuming the isolated cathode potential and taking its capacitance into consideration. The abnormalities observed in usual photo-tubes are believed to be caused by the similar factors, that is the photoelectric materials adhering on the undesired portion of the inner surfaces of the tube.

## Acknowledgment

The writer wishes to express his gratitude to Dr. H. Hamada and Dr. B. Tadano for their kind guidance throughout this study and to Mr. S. Kobayashi, Mr. M. Matsuki, Miss A. Saito and Miss F. Kumasaka for their helpful assistance in the production of the experimental tubes. He also wishes to thank Mr. S. Takei and Mr. N. Morito for their valuable advises on preparing this paper.

## References

1) M. Sugawara: J. Phys. Soc. Japan. **11** (1956) 169.
2) J. S. Preston and L. H. McDermott: Proc. Phys. Soc. (A) **46** (1934) 256.

JOURNAL OF THE PHYSICAL SOCIETY OF JAPAN Vol. 11, No. 3, MARCH, 1956

# Diffraction of Elastic Waves by a Spherical Surface

By Masahumi NAGASE

*Department of Physics, Faculty of Liberal Arts,*
*University of Saga, Saga, Japan*

(Received February 8, 1955)

To clarify the effect of the curvature of a surface on the propagation of elastic waves generated at a point source, as alluded to by Lamb in the case of a plane surface, we investigate the properties of waves in an infinite elastic medium enclosing a spherical cavity. Waves of any kind are shown to be represented as linear combinations of $\Phi$, $A_\varphi$, $d_\varphi$, the scalar potential, the $\varphi$-component of the vector potential and the $\varphi$-component of the displacement, if the phenomena are independent of $\varphi$, the longitudinal angle in spherical polar coordinates with the polar axis joining the source and the center of the cavity. Taking as the initial waves $\Phi$, $A_\varphi$, $d_\varphi$ with monochromatic dipole character respectively, we obtain, in the ordinary way of mathematical physics, the solutions satisfying the boundary conditions in series forms, which are transformed into more rapidly convergent ones. In the first two cases we find the waves representing $\Phi$, $A_\varphi$ in three separated groups, correponding to three types in the case of a plane surface respectively, and in the third we find only group of solutions representing $d_\varphi$. The angular and distance dependence of their amplitudes and phases are investigated in detail.

## I. INTRODUCTION

**§1.** When the propagation of such elastic waves over a plane surface of a semiinfinite homogeneous isotropic elastic solid as are produced by a disturbance concentrated at a point on the surface was studied By H. Lamb[1], he pointed out that it remains to inquire how far the theory is to be modified by the situation of an internal source, by the heterogeneity of the earth and by the curvature of the surface. While the problem of an internal source has been discussed by H. Nakano[2], K. Sezawa[3], T. Sakai[4] and others, especially in details by Sakai, the one of a curved surface was treated by Y. Nomura[5] only with reference to the propagation of elastic waves in a spherical body. The aim of the present work is to discuss thoroughly the case of an internal source under a curved surface from another point of view having a closer relationship to the Lamb's.

As our main interest is in the effect of the curvature of the surface, we may take a spherical surface as the simplest curved one. Imagining a large spherical cavity of radius $r_0$ in an infinite elastic medium and a wave source at distance $r_s$ $(>r_0)$ from its center, we consider how the behavior of the incident simple harmonic waves of frequency $\omega$ emitted from this source will be modified by the presence of the spherical surface. The results, therefore, may be indeed less interesting from the practical point of view, except in its application to the propagation of seismic waves in seabeds or large valleys, but will show some features noteworthy from the standpoint of mathematical physics, especially in contrast with geometrical optics.

If we assume, for the sake of simplicity, the symmetry about the axis joining the center of the sphere and the source and introduce such a spherical polar coordinate system $(r, \theta, \varphi)$ as has this axis as the polar axis, the fundamental equantions of elastic vibrations are reduced to three separated wave equations, concerning the scalar potential $\Phi$ of the displacement field $\mathbf{d}$, the $\varphi$-component of the vector potential $\mathbf{A}$ and the $\varphi$-component of the displacement itself respectively.

Now, since all possible states of incident waves emitted by the source can be represented as the superposition of those derived from these three fundamental quantities, we may classify any incident waves into three characteristic types corresponding to these quantities, respectively, one being of dilatational and two of distortional character, and shall pick up for each type a wave of dipole-character as the representative one.

Then for each given incident wave we assume, as the secondary waves corresponding to the fundamental quantities, the series of which each term is such a particular solution, multiplied by an unknown coefficient, of the above-mentioned wave equations as has the character of outward radiations at a large distance from the center and we shall formally determine the coefficients so that the superposed waves satisfy the condition of a free surface for $r=r_0$. The series thus formally obtained will not be shown so useful, though convergent, to compute any physical quantities from them on account of their slow convergence.

In order to transform these series into more rapidly convergent ones, we shall employ such a method as was adopted by G. N. Watson[6] and others when treating the diffraction of electromagnetic waves by the earth. The essential point is that we can transform

$$\Sigma_{n=0}^{\infty}(2n+1)P_n(\cos\theta)f(n)/g(n)$$

into

$$\Sigma_i[2\nu\pi P_{\nu-1/2}(\cos(\pi-\theta))f(\nu-1/2) \times\{\cos\nu\pi\partial g(\nu-1/2)/\partial\nu\}^{-1}]_{\nu=\nu_i}$$

noticing that $-(2n+1)P_n(\cos\theta)f(n)/g(n)$ is the residue at $\nu=n+1/2$ of

$$2\nu\pi P_{\nu-1/2}(\cos(\pi-\theta))f(\nu-\tfrac{1}{2})/\{g(\nu-1/2)\cos\nu\pi\},$$

where $f(n)$, $g(n)$ denote any functions satisfying some conditions and $\nu_1, \nu_2, \cdots$ the zero of $g(\nu-1/2)$ qua function of $\nu$. In our problem the function corresponding to $g(\nu-\frac{1}{2})$ is shown to be such a complicated transcendental function that one cannot find out the zeros intuitively. On the location of these zeros, however, the present author has already discussed in detail[8]. By employing this result we shall find that the series thus derived converge very rapidly unless $\theta$ is very small, and are suited for our purpose. For small $\theta$, instead of summing up the terms of the series, we shall evaluate them directly from the integrals along the contours enclosing these zeros by utilizing the method of steepest descents.

Lastly, we discuss all the properties of the vibrations given by these series minutely in the respective cases, especially in contrast with the diffractions of electromagnetic waves.

## II. GENERAL FORMULATIONS

### § 2. Fundamental Equations and Particular Solutions

When **d** is expressed as $\mathbf{d}=\text{grad}\,\Phi+\text{curl}\,\mathbf{A}$ (div $\mathbf{A}=0$), then $\Phi$, $\mathbf{A}$ are the respective solutions of the wave equations with the velocities of propagation $v_l, v_t$, i.e. those of dilatational and distortional waves respectively. If we, introducing spherical polar coordinates, consider axially symmetrical cases only and take further only such harmonically oscillating waves as contain $\exp(i\omega t)$ as the time factor, the wave equations will be reduced to

$$\{\partial^2/\partial r^2+(2/r)\partial/\partial r+(1/r^2\sin\theta)\partial/\partial\theta(\sin\theta\partial/\partial\theta)\} \times(\Phi, A_\varphi^*, d_\varphi^*)+(h^2\Phi, k^2A_\varphi^*, k^2d_\varphi^*)=0, \quad (2.1)$$

where $A_\varphi=\partial A_\varphi^*/\partial\theta$, $d_\varphi=\partial d_\varphi^*/\partial\theta$, $h=\omega/v_l$, $k=\omega/v_t$.

Their particular solutions without any singularity at $\theta=0$ and $\pi$ are only those which take the forms $r^{-1/2}C_{n+1/2}(hr)P_n(\cos\theta)$, $r^{-1/2}C_{n+1/2}(kr)P_n(\cos\theta)$, respectively, where $C_{n+1/2}$ is a cylinder function of order $n+1/2$ and $P_n$ is Legendre function of order $n$, $n$ being a positive integer.

### § 3. Incident Waves

Whatever kinds of waves are emitted by the source, they are naturally represented as the superposition of those derived from $\Phi$, $A_\varphi^*$, $d_\varphi^*$, so it suffices for our purposes to consider the waves of such types respectively. Since among the waves that have infinities at the site of the source the simplest one is obviously that of dipole-character and the waves emitted by multipoles are obtained from it by differentiation with respect to the coordinates of the source and hence the corresponding results may be inferred from the dipole case, we take as the representative one the wave of dipolecharacter without losing the generality of our consideration, though in some actual cases, for example, that of earthquakes, waves of quadrupole character are thought to be prevalent. Let us consider their respective features more closely.

1. Dilatational incident wave. We assume as the dilatational incident wave such one as corresponds to

$$\Phi^p=\exp(-ihR)/R\,,\quad A_\varphi^{*p}=0\,,\quad d_\varphi^{*p}=0\,, \quad (3.1)$$

where $R=(r^2+r_s^2-2rr_s\cos\theta)^{1/2}$; this function obviously satisfies the wave equation and has the character of outward radiations in view of the time factor. Among the non-vanishing displacement components comming from it, $d_r$, $d_\theta$ tend to $-ih\exp(-ihR)/R+0(R^{-2})$ and $0(R^{-2})$ respectively as $r\to\infty$: it shows that the elementary portion at any field point at a large distance from the surface vibrates longitudinally.

2. Distortional incident wave of the first kind. We take such a wave as corresponding to

$$\Phi^p=0\ ,\quad A_\varphi{}^{*p}=\exp(-ikR)/R\ ,\quad d_\varphi{}^{*p}=0\ . \qquad (3.2)$$

This also satisfies the wave equation obviously and has the character of outward radiations. $d_r$, $d_\theta$, then, tend to

$$0(R^{-2})\ ,\quad k^2 r_s\sin\theta\exp(-ikR)/R+0(R^{-2})$$

respectively; it shows that at a large distance the vibration is transverse and in the incident plane.

3. Distortional incident wave of the second kind. We take such a wave as corresponds to

$$\Phi^p=0\ ,\quad A_\varphi{}^{*p}=0\ ,\quad d_\varphi{}^{*p}=\exp(-ikR)/R\ . \qquad (3.3)$$

Then $d_r$, $d_\theta$ vanish and

$$d_\varphi\to-ikr_s\sin\theta\exp(-ikR)/R+0(R^{-2})\ ,$$

as $R\to\infty$; it shows that the vibration is transverse and perpendicular to the incident plane: all the points of the spherical surface of radius $R$ oscillate together rotationally about the polar axis, as if the whole sphere were a rigid one.

## § 4. Boundary Conditions

Since secondary waves to be looked for must represent at a large distance from the surface some outward radiating waves, they comprise as cylinder functions $C_{n+1/2}$ only the second of the two Hankel functions, $H^{(2)}_{n+1/2}$, taking account of their asymptotic behavior for large $r$ together with the time factor.

Secondly they must, superposed on the primary one, satisfy the condition of a free surface at $r=r_0$ or any stress components must vanish there.

## III. DILATATIONAL SOURCE

## § 5. Primary and Secondary Waves

The dilatational primary wave $\exp(-ihR)/R$, defined in the last section, can be expanded by the addition theorem as follows:

$$\Phi^p=-(i/hrr_s)\Sigma_{n=0}^{\infty}(2n+1)[\zeta_n(hr_s)\psi_n(hr),\ \text{or}\ \psi_n(hr_s)\zeta_n(hr)]P_n(\cos\theta)\ , \qquad (5.1)$$

according as $r<r_s$ or $r>r_s$, where

$$\begin{aligned}\zeta_n(x)&=(\pi x/2)^{1/2}H^{(2)}_{n+1/2}(x)\ ,\\ \psi_n(x)&=(\pi x/2)^{1/2}J_{n+1/2}(x)\ .\end{aligned} \qquad (5.2)$$

In view of this expression we assume as the secondary waves the following ones:

$$\Phi^s=-(i/hrr_s)\Sigma_{n=0}^{\infty}(2n+1)a_n\zeta_n(hr)P_n(\cos\theta)\ , \qquad (5.3.1)$$

$$A_\varphi{}^s=-(i/krr_s)\Sigma_{n=0}^{\infty}(2n+1)b_n\zeta_n(kr)\times dP_n(\cos\theta)/d\theta\ , \qquad (5.3.2)$$

$$d_\varphi{}^s=0\ , \qquad (5.3.3)$$

where $a_n$, $b_n$ are unknown coefficients.

Assuming further the convergence of these series and the uniform convergence of those obtained by differentiating these series term by term, we can find out the values of $a_n$, $b_n$ from the boundary condition for $r=r_0$. Thus we have as the resultants

$$\Phi=-(i/hrr_s)\Sigma_{n=0}^{\infty}(2n+1)\{[\zeta_n(hr_s)\psi_n(hr)\ ,\ \text{or}\ \zeta_n(hr)\psi_n(hr_s)] -\zeta_n(hr_s)\zeta_n(hr)D_1(n)/D(n)\}P_n(\cos\theta)\ , \qquad (5.4.1)$$

$$A_\varphi=-(2/hrr_sma)\Sigma_{n=0}^{\infty}(2n+1)(a^2-2n(n+1)+4)\times\zeta_n(hr_s)\zeta_n(kr)dP_n(\cos\theta)/d\theta\cdot 1/D(n)\ , \qquad (5.4.2)$$

according as $r<r_s$ or $r>r_s$, where

$$\begin{aligned}D(n)=&4\{2-n(n+1)\}\zeta_n'(ma)\zeta_n'(a)\\ &+4a\zeta_n'(ma)\zeta_n(a)+(2/ma)\\ &\times\{a^2+2n(n+1)-4\}\zeta_n(ma)\zeta_n'(a)\\ &+(1/ma^2)\{(a^2-2n(n+1))^2-4a^2\\ &-8n(n+1)\}\zeta_n(ma)\zeta_n(a)\ ,\end{aligned}$$

and $D_1(n)$ is $D(n)$ with $\zeta_n(ma)$ replaced by $\psi_n(ma)$ and $a=kr$, $m=h/k$.

## § 6. Convergence of the Series

To ascertain whether the series obtained formally in the preceding section have their proper sense or not, we will investigate their convergence. Since the dominant term of $\zeta_n(a)$ for large $n$ is $(-1)^n i\pi^{1/2}(a/2)^{-n}/\Gamma(\frac{1}{2}-n)$, we find after some calculations that the $n$-th term of the series representing $\Phi$ is, for large $n$,

$$-(1/2r)(2n+1)[(r/r_s)^{n+1},\ \text{or}\ (r_s/r)^{n+1}]\times P_n(\cos\theta)\{1+0(1/n)\}$$

and so this series is convergent in virtue of $|P_n(\cos\theta)|\leqq 1$.

As to the series representing $A_\varphi$, since the $n$-th term of the series is, if $n$ is large, equal to $4n^2m/(1-m^2)1/r_0(r_0{}^2/r_sr)^{n+1}dP_n(\cos\theta)/d\theta$ within the error of $0(n^{-1})$, as we can show in the same way, we find that this series also converges, in view of $|P_n'(\cos\theta)|\leqq n^2$.

Since the series expected to represent $d_r$, $d_\vartheta$, which are obtained by differentiating the series representing $\varPhi$, $A_\varphi$ term by term with respect to $r$, $\theta$ and then by combining them linearly, are convergent uniformly for $r\leqq r_s-\delta$, $r\geqq r_s+\delta(\delta>0)$, $0\leqq\theta\leqq\pi$, as easily shown in an analogous way, these series also have their meaning as $d_r$, $d_\vartheta$.

Thus the series have been shown to be convergent indeed but their convergency is so slow that we cannot estimate them by using the first several terms only, unless $r\gg r_s$, $r\gg r_0$, and therefore we want to have other expressions, more convenient for computation.

## § 7. Transformation of the Series

If we notice that $-(2n+1)P_n(\cos\theta)f(n)$ is the residue at $\nu=n+\frac{1}{2}$ of

$$2\nu\pi P_{\nu-1/2}(-\cos\theta)f(\nu-\tfrac{1}{2})/\cos\nu\pi\ ,$$

we are led to the study of the integrals:

$$\frac{i}{hrr_s}\int\frac{\nu P_{\nu-1/2}(-\cos\theta)}{\cos\nu\pi}\times\left\{\begin{bmatrix}\zeta_{\nu-1/2}(hr_s)\psi_{\nu-1/2}(hr)\\ \text{or}\ \ \zeta_{\nu-1/2}(hr)\psi_{\nu-1/2}(hr_s)\end{bmatrix}-\zeta_{\nu-1/2}(hr_s)\times\zeta_{\nu-1/2}(hr)\frac{D_1(\nu-1/2)}{D(\nu-1/2)}\right\}d\nu\ ,$$

$$\frac{2}{krr_sma}\int\frac{\nu}{\cos\nu\pi}\frac{dP_{\nu-1/2}(-\cos\theta)}{d\theta}\times\frac{a^2-2(\nu^2-1/4)+4}{D(\nu-1/2)}\zeta_{\nu-1/2}(hr_s)\zeta_{\nu-1/2}(kr)d\nu\ ,$$

taken round a suitable contour.

Since

$$P_{\nu-1/2}(-\cos\theta)=F(\tfrac{1}{2}-\nu,\ \tfrac{1}{2}+\nu;\ 1;\ \tfrac{1}{2}+\tfrac{1}{2}\cos\theta),$$

it is obvious that $P_{\nu-1/2}(-\cos\theta)$ is an even integral function of $\nu$ when $\cos\theta$ has any assigned value such that $-1\leqq\cos\theta<1$. Thus, in view of the relations,

$$\left.\begin{aligned}H_{-\nu}^{(1)}(x)&=\exp(\nu\pi i)H_\nu^{(1)}(x)\ ,\\ H_{-\nu}^{(2)}(x)&=\exp(-\nu\pi i)H_\nu^{(2)}(x)\ ,\end{aligned}\right\}\qquad(7.1)$$

we find that the integrands of the above integrals are odd functions of $\nu$, whose only poles are at the zeros of the function

$$\cos\nu\pi D(\nu-\tfrac{1}{2})\ ,$$

since $H_\nu^{(2)}(x)$ is an integral function of $\nu$ when $\mathrm{Re}\,x$ is positive.

We assume for the moment that $D(\nu-\frac{1}{2})$, qua function of $\nu$, has no zeros on the positive half of the real axis or on the imaginary axis, and then we take the contour of integration to be formed by a semicircle of large radius $R$, whose center is at origin, which lies on the right of the imaginary axis, together with the part of the imaginary axis which joins the points $\pm Ri$. It will be supposed that $R\rightarrow\infty$ through such values that no poles of the integrands ever lie on the contour. Since the integrands are odd functions of $\nu$, the integrals along the part of the imaginary axis vanish.

Next consider the integrals along the semicircle; so long as $\theta\not\approx 0,\ \pi$, we may use Laplace's approximations,

$$P_{\nu-1/2}(-\cos\theta)\sim\cos\{\nu(\pi-\theta)-\pi/4\}\times\{(\pi/2)\nu\sin\theta\}^{-1/2}\ ,$$

which is valid when $|\nu|$ is large and $\mathrm{Re}(\nu-\frac{1}{2})\geqq 0$; also the dominant terms of $H_\nu^{(2)}(x)$ are

$$i(\sin\nu\pi)^{-1}\{(x/2)^{-\nu}/\Gamma(1-\nu)-\exp(\nu\pi i)(x/2)^\nu/\Gamma(1+\nu)\}\ ,$$

of which the latter part is negligible except near the ends of the semicircle; it follows that, since the path of integration avoids the infinities of the integrands, the values of the integrands, except the factors $P_{\nu-1/2}(-\cos\theta)$, $dP_{\nu-1/2}(-\cos\theta)/d\theta$, have their moduli on the coutour, comparable respectively with those of $(\nu/2r)[(r/r_s)^{\nu+1/2}$, or $(r_s/r)^{\nu+1/2}](\cos\nu\pi)^{-1}$, $(4/r_0)m/(1-m^2)\nu^2(r_0^2/rr_s)^{\nu+1/2}(\cos\nu\pi)^{-1}$ and so, by an application of Jordan's Lemma, the integrals round the semicircle tend to zero as the radius to infinity. Hence the sums of the residues of the respective integrands at their poles on the right of the imaginary axis are zero. If we assume the zeros of $D(\nu-\frac{1}{2})$ all simple and call them $\nu_1,\nu_2,\cdots$, then, transforming $\zeta$ into Hankel function, we have

$$\varPhi=\frac{4\pi}{a}\frac{1}{(rr_s)^{1/2}}\sum_j\left[\frac{\nu P_{\nu-1/2}(-\cos\theta)}{\cos\nu\pi}\times\frac{H_\nu^{(2)}(hr_s)H_\nu^{(2)}(hr)}{H_\nu^{(2)}(ma)}\left\{\frac{2}{a^2}\left(\nu^2-\frac{9}{4}\right)H_\nu^{(2)\prime}(a)+\frac{1}{a}\left(\frac{\nu^2-9/4}{a^2}-2\right)H_\nu^{(2)}(a)\right\}\Big/\frac{\partial\varDelta(\nu)}{\partial\nu}\right]_{\nu=\nu_j},\qquad(7.2.1)$$

$$A_\varphi=-\frac{4\pi}{a^2}\frac{1}{(rr_s)^{1/2}}\sum_j\left[\frac{\nu}{\cos\nu\pi}\frac{dP_{\nu-1/2}(-\cos\theta)}{d\theta}\times\left\{1-\frac{2(\nu^2-9/4)}{a^2}\right\}\times H_\nu^{(2)}(hr_s)H_\nu^{(2)}(kr)\Big/\frac{\partial\varDelta(\nu)}{\partial\nu}\right]_{\nu=\nu_j},\qquad(7.2.2)$$

where

$$\Delta(\nu)=-4m\frac{\nu^2-9/4}{a^2}H_\nu^{(2)\prime}(a)H_\nu^{(2)\prime}(ma)$$
$$+\frac{2}{a}\left(1+\frac{\nu^2-9/4}{a^2}\right)H_\nu^{(2)\prime}(a)H_\nu^{(2)}(ma)$$
$$+\frac{2m}{a}\left(2-\frac{\nu^2-9/4}{a^2}\right)H_\nu^{(2)}(a)H_\nu^{(2)\prime}(ma)$$
$$+\left\{1-\frac{4\nu^2}{a^2}+\frac{4\nu^2}{a^4}\left(\nu^2-\frac{9}{4}\right)\right\}$$
$$\times H_\nu^{(2)}(a)H_\nu^{(2)}(ma)\,. \tag{7.3}$$

It is to be noted that the distinction between the cases $r>r_s$, $r<r_s$, treated hitherto separately, and therefore the singularity at $r=r_s$ have disappeared.

## § 8. Zeros of $\Delta(\nu)$

In order to evaluate the newly-obtained series, it is necessary to know the zeros of $\Delta(\nu)$. Here we recapitulate the result of 8) briefly.

There exist such three groups of zeros of the first order, as enumerated below, in the fourth quadrant of the $\nu$-plane and no zeros lie on the real and imaginary axes; the zeros in the second quadrant are irrelevant to our problem. To avoid the analytical difficulties we assume henceforth $a$ to be fairly large, which does not limit the applicability of our result, since we are always interested in the waves whose wave-length is far shorter than the radius of curvature of the surface.

1. There is a zero $\nu_0$ near the real axis, whose real part is given asymptotically by the following formula:

$$\mathrm{Re}\,\nu_0\sim a\zeta^{1/2}-p_1(\zeta-1)^{1/2}$$
$$+(1/2p_1{}^2\zeta^{1/2}-p_2(\zeta-1)^{1/2})a^{-1}+\cdots, \tag{8.1}$$

where $\zeta$ is the unique real root of the cubic equation,

$$(1-m^2)\zeta^3-(3/2-m^2)\zeta^2+1/2\zeta-1/6=0\,,$$

and as to $p_1$, $p_2$ 8) is to be refered to. We are informed from the well-known discussion on Rayleigh wave that $\zeta$ is greater than unity. Really, from the definition

$$m=h/k=\{1/2(1-2\sigma)/(1-\sigma)\}^{1/2}\,,$$

where $\sigma$ denotes Poisson's ratio, we know $m<1/\sqrt{2}$, in view of $0<\sigma<\frac{1}{2}$ and, therefore, if we assign $\frac{1}{2}$ the commonest value to $m$, or 1/3 to $\sigma$, then we have $\zeta=1.149947966\cdots$, and further

$$\mathrm{Re}\,\nu_0\sim a(1.072\cdots+11.32\cdots a^{-1}$$
$$+263.2\cdots a^{-2}+\cdots\cdot)\,. \tag{8.2}$$

Its imaginary part is given by

$$\mathrm{Im}\,\nu_0\sim -a\zeta^{-1/2}[\exp\{-2a(\zeta^{1/2}\cosh^{-1}\zeta^{1/2}$$
$$-(\zeta-1)^{1/2})\}+\exp\{-2a$$
$$\times(\zeta^{1/2}\cosh^{-1}(\zeta^{1/2}/m)-(\zeta-m^2)^{1/2})\}]\,, \tag{8.3}$$

which becomes, for $m=\frac{1}{2}$,

$$-0.277\cdot\cdot a(\exp(-0.037\cdot\cdot a)+\exp(-1.10\cdot\cdot a)\}.$$

If we put $a=100$, 200, 500 to show its smallness, $\mathrm{Im}\,\nu_0$ takes $-0.69\cdot\cdot$, $-0.03\cdot\cdot$, $-0.000001\cdots$, respectively.

2. The second group of zeros $\nu_{1j}$ $(j=1, 2, \cdots)$ are placed nearly along the curve

$$\mathrm{Re}\,(\gamma\cosh\gamma-\sinh\gamma)=0 \quad (\nu=a\cosh\gamma),$$

which starts from $\nu=a$ making an angle $-\pi/3$ with the positive axis and passes off to $-\infty i$. The first several zeros, the most interesting ones, are given by

$$\nu_{1j}\sim a[1+1/2q_j{}^2-(4i/3\rho_j)(1-m^2)^{1/2}q_j{}^3+1/120q_j{}^4$$
$$-\{-17/6+1/2(1-m^2)^{-1}+16/3(1-m^2)\}$$
$$\times(4i/3\rho_j)(1-m^2)^{1/2}q_j{}^5+\cdots]\,,$$
$$j=1, 2, 3, \cdots, \tag{8.4}$$

where $q_j=(3\rho_j/a)^{1/3}\exp(5/6\cdot\pi i)$, $\rho_j$ being one of the roots of $H^{(2)}_{-1/3}(\rho e^{\pi i})=0$, i.e. $2.383466\cdots$, $5.5101956\cdots$, $8.6473577\cdots$, $11.7868429\cdots$, $14.9272068\cdots$, $\cdots$.

3. The third group lies nearly along the curve

$$\mathrm{Re}\,(\gamma^*\cosh\gamma^*-\sinh\gamma^*)=0 \quad (\nu=ma\cosh\gamma^*).$$

This curve starts from the point $\nu=ma$, making an angle $-\pi/3$ with the positive real axis, and goes off to $-\infty i$. The first several zeros are given by

$$\nu_{2j}\sim ma[1+1/2q_j{}^{*2}-(4m^3/3\rho_j)(1-m^2)^{1/2}$$
$$\times(2m^2-1)^{-2}q_j{}^{*3}+1/120q_j{}^{*4}$$
$$-\{1/6-(2m^2+1)/(2m^2-1)$$
$$-1/2m^2/(1-m^2)-16/3m^6(1-m^2)$$
$$\times(2m^2-1)^{-4}\}(4m^3/3\rho_j)(1-m^2)^{1/2}$$
$$\times(2m^2-1)^{-2}q_j{}^{*5}+\cdots]\,,$$
$$j=1, 2, 3, \cdots\,, \tag{8.5}$$

where $q_j{}^*=(3\rho_j/ma)^{1/3}e^{5/6\pi i}$.

The zeros of large moduli are approximately given by $-(n+\frac{1}{2})\pi i/\log(1/m)$, where $n$ denotes a large positive integer. Though these zeros seem to lie on the imaginary axis, it is due to the imperfection of the approximations. They never cross the axis, as shown in 8) § 3.2.

## § 9. Convergence of the New Series

In order to investigate the convergence of the series newly obtained we estimate the order of magnitude of the higher terms of the series, corresponding to the zeros of large moduli.

For such zeros we find that $\partial\Delta(\nu)/\partial\nu$ becomes $32/\pi\cdot(-1)^n \log m\nu^{-1}\cosh^4\gamma\{1+0(a^{-1})\}$, and so a higher term of the series representing $\Phi$ is

$$4(rr_s)^{-1/2}(2/\sin\theta)^{1/2}(\log(1/m))^{-1/2}(n+\tfrac{1}{2})^{-1/2}$$
$$\times\exp[-\{(n+\tfrac{1}{2})\pi/\log(1/m)\}\theta]O(1).$$

Thus it is obvious that the series representing $\Phi$ is convergent, rapidly especially for not small $\theta$.

Secondly a higher term of the series representing $A_\varphi$ is shown to be

$$2(rr_s)^{-1/2}(2/\sin\theta)^{1/2}(\log(1/m))^{-1/2}(n+\tfrac{1}{2})^{-1/2}$$
$$\times\exp[-\{(n+\tfrac{1}{2})/\log(1/m)\}\theta)O(1).$$

Thus the convergence of this series also has been shown.

It is easily seen that their convergence is uniform with respect to $r_s$, $r$ when $r_s\geqq r_0$, $r\geqq r_0$; and so, by Abel's theorem, we may write $r_0$ for $r_s$, $r$ in the series when we wish to find the effect due to an oscillator placed on the surface and the state on the surface respectively. And the series obtained by differentiating term by term the above-mentioned series with respect to $r$ and $\theta$ are uniformly convergent, as easily shown in an analogous way, so it is permissible to obtain the displacement components from these series in such a way.

Since the above-mentioned series are rapidly convergent except when $\theta$ is quite small, we can estimate them correctly by taking up the first several terms in such a case. We shall discuss them in detail and investigate of vibration in the following sections.

## § 10. Terms Corresponding to $\nu_0$

We are to evaluate the first terms, corresponding to $\nu_0$, of the series representing $\Phi$ and $A_\varphi$, respectively.

Let us evaluate $\Phi_0$, the term of the right-handed side of (7.2.1) corresponding to $\nu_0$. Among the factors of this expression

$$\nu P_{\nu-1/2}(\cos(\pi-\theta))/\cos\nu\pi$$

is equal to

$$-i(2\nu/\pi\sin\theta)^{1/2}[\exp\{\nu(\pi-\theta)i+\pi/4i\}$$
$$-\exp\{-\nu(\pi-\theta)i-\pi/4i\}]$$
$$\times\{\exp(\nu\pi i)+\exp(-\nu\pi i)\}^{-1}\{1+O(\nu^{-1})\}$$

in view of Laplace's approximation formula; if we expand the denominator in series considering that $\mathrm{Im}\,\nu_0<0$, we have

$$\nu P_{\nu-1/2}(\cos(\pi-\theta))/\cos\nu\pi$$
$$=(2\nu/\pi\sin\theta)^{1/2}[\Sigma_{s=0}^{\infty}(-1)^s$$
$$\times\exp\{-\nu(\theta+2s\pi)i-\pi/4i\}+\Sigma_{s=0}^{\infty}(-1)^s$$
$$\times\exp\{-\nu(2(s+1)\pi-\theta)i+\pi/4i\}]$$
$$\times\{1+O(\nu^{-1})\}\,. \tag{10.1}$$

In this expression the first sum means the superposition of waves each of which propagates on the surface in the direction of positive $\theta$ after having passed $s$ times $2\pi$ and the second the one of waves propagating backward, as it is obvious when we consider the time factor and the fact, $\nu_0\sim\zeta^{1/2}kr_0$. Though $\mathrm{Im}\,\nu_0$ is so small in this case that the damping factors depending on $\theta$, $\exp\{-\mathrm{Im}\,\nu_0(\theta+2s\pi)\}$, $\exp\{-\mathrm{Im}\,\nu_0(2s\pi+2\pi-\theta)\}$ is not so effective and the second and further terms are not negligible compared with the first, it suffices for our purpose to consider only the first term, i.e. that with the factor $\exp(-\nu\theta i-(1/4\pi i)$, since the other terms behave in quite the same way.

By employing the asymptotic expansions of Hankel functions for such values of $\nu$ (9) §8.6); we have

$$\Phi_0=8k\zeta(\zeta-1)^{1/2}[8(\zeta-1)^{1/2}(\zeta-m^2)^{1/2}-8(2\zeta-1)$$
$$+2\zeta\{(\zeta-m^2)^{1/2}(\zeta-1)^{-1/2}$$
$$+(\zeta-1)^{1/2}(\zeta-m^2)^{-1/2}\}+1/2(2\zeta-1)^2$$
$$\times\{(\zeta-m^2)^{-1}+(\zeta-1)^{-1}\}]^{-1}$$
$$\times(2\pi/\zeta^{1/2}kr_0\sin\theta)^{1/2}\exp[-(\zeta-m^2)^{1/2}$$
$$\times k(r_s-r_0+r-r_0)-i\zeta^{1/2}kr_0\theta\{1-p_1(\zeta-1)^{1/2}$$
$$\times\zeta^{-1/2}(kr_0)^{-1}\}-\pi/4i]\{1+O(1/kr_0)\}$$
$$\times\{1+O((r_s-r_0)/r_0)\}\{1+O((r-r_0)/r_0)\}\,. \tag{10.2}$$

We enumerate its properties as follows:

1. $\Phi_0$ is of finite amplitude, only if the source is near the surface, i.e. $r_s-r_0\ll r_0$.
2. $\Phi_0$ is of finite magnitude only in the vicinity of the surface, i.e. $r-r_0\ll r_0$; in other words it is of character of a surface wave.
3. $\Phi_0$ is inversely proportional to $(r_0\sin\theta)^{1/2}$, i.e. to the square root of the length of the perpendicular from the field point to the polar axis, as it must be so if we consider the energy flow concentrated in the neighborhood of the surface.

4. Its phase, combined with the time factor, is given by $\exp[i\omega\{t - v_R^{-1}(1 - p(\zeta-1)^{1/2}\zeta^{-1/2} \times (kr_0)^{-1} + \cdots)s\}]$, where $v_R = \zeta^{-1/2}v_t$, the velocity of Rayleigh wave, and $s = r_0\,\theta$ the circumferential distance between the source and the field point concerned. It shows that the wave propagates on the surface with the velocity $v_R\{1 + p_1(\zeta-1)^{1/2}(v_R/\omega r_0) + \cdots\}$, which is, for $m=1/2$, $0.9325\cdots v_t\{1 - 10.56\cdots(v_t/\omega r_0) + \cdots\}$. Since the velocity of propagation depends on the frequency $\omega$, this wave is of dispersive chracter, the group velocity of which is $v_R\{1 + O((kr_0)^{-2})\}$, or is equal to the well-known propagation velocity of Rayleigh wave.

5. Since $\mathrm{Im}\,\nu_0$ is small, the damping with $\theta$ is negligible and the wave propagating in both directions and reappearing after several round trips are to be considered at the same time.

6. The displacement components derived from it are

$$d_r \sim -k(\zeta - m^2)^{1/2}\Phi_0\,, \quad d_\theta \sim -ik\zeta^{1/2}\Phi_0\,.$$

thus

$$d_r/d_\theta \sim \exp(-\pi/2i)(\zeta - m^2)^{1/2}\zeta^{-1/2}\,,$$

and it shows that there is a phase difference $\frac{1}{2}\pi$ between the two components. The point moves along an elliptic orbit whose major and minor axes are in the directions of $d_\theta$ and $d_r$ respectively and the sense of motion is from the direction of positive $d_\theta$ to that of positive $d_r$. The ratio of two principal axes is, for $m=\frac{1}{2}$, $1:0.885\cdots$.

We will then evaluate $A_{\varphi 0}$, the term of the right-handed side of (7.2.2) corresponding to $\nu_0$. The procedure is quite the same as in the preceding case. The result of the calculation is

$$\begin{aligned} A_{\varphi 0} = 4k\zeta^{1/2}&(2\zeta-1)[8(\zeta-m^2)^{1/2}(\zeta-1)^{1/2} \\ &-8(2\zeta-1) + 2\zeta\{(\zeta-m^2)^{1/2}(\zeta-1)^{-1/2} \\ &+(\zeta-1)^{1/2}(\zeta-m^2)^{-1/2}\} + 1/2(2\zeta-1)^2 \\ &\times\{(\zeta-m^2)^{-1} + (\zeta-1)^{-1}\}]^{-1} \\ &\times(2\pi/\zeta^{1/2}kr_0 \sin\theta)^{1/2} \\ &\times\exp[-(\zeta-m^2)^{1/2}k(r_s-r_0) - (\zeta-1)^{1/2} \\ &\times k(r-r_0) - i\zeta^{1/2}kr_0\theta\{1-(\zeta-1)^{1/2} \\ &\times\zeta^{-1/2}p_1(kr_0)^{-1}\} + \pi/4i]\{1+O(a^{-1})\} \\ &\times\{1+O((r_s-r_0)/r_0)\}\{1+O(r-r_0)/r_0)\}\,. \end{aligned} \tag{10·3}$$

Its properties are as follows:

1. $A_{\varphi 0}$ is of finite magnitude only in the vicinity of the surface, though its rate of damping with $r$ is smaller than that of $\Phi_0$ as shown by the factor $\exp\{-(\zeta-1)^{1/2}k(r-r_0)\}$, compared with $\exp\{-(\zeta-m^2)^{1/2}k(r-r_0)\}$, $\zeta$ being fairly close to unity.

2. It has the same properties as 1, 3, 4, 5 shown by $\Phi_0$.

3. The displacement components are

$$d_r \sim -ik\zeta^{1/2}A_{\varphi 0}\,, \quad d_\theta \sim k(\zeta-1)^{1/2}A_{\varphi 0}\,,$$

then

$$d_r/d_\theta \sim \exp(-\pi/2i)\zeta^{1/2}(\zeta-1)^{-1/2}\,.$$

It shows an elliptically polarized oscillation with the major and minor axes coinciding with the directions of $d_r$ and $d_\theta$ respectively, $d_\theta$ being $\frac{1}{2}\pi$ in advance to $d_r$. Their ratio for $m=1/2$ is $2.77\cdots:1$.

Though $\Phi_0$ and $A_{\varphi 0}$ behave differently for arbitrary $r$, they behave in a similar way for $r=r_0$ and can be superposed to one state; the displacement components coming from the superposed one are, in view of the equation for $\zeta$ to satisfy,

$$\begin{aligned} d_r = 2k^2(2\zeta-1)&[8(\zeta-1)^{1/2}(\zeta-m^2)^{1/2} - 8(2\zeta-1) \\ &+2\zeta\{(\zeta-m^2)^{1/2}(\zeta-1)^{-1/2} \\ &+(\zeta-1)^{1/2}(\zeta-m^2)^{-1/2}\} + 1/2(2\zeta-1)^2 \\ &\times\{(\zeta-m^2)^{-1} + (\zeta-1)^{-1}\}]^{-1} \\ &\times(2\pi/\zeta^{1/2}kr_0\sin\theta)^{1/2}\exp[-(\zeta-m^2)^{1/2} \\ &\times k(r_s-r_0) - i\zeta^{1/2}kr_0\theta\{1-p_1(\zeta-1)^{1/2} \\ &\times\zeta^{-1/2}(kr_0)^{-1}\} - \pi/4i]\{1+O(1/kr_0)\} \\ &\{1+O((r_s-r_0)/r_0)\}\,, \end{aligned} \tag{10.4.1}$$

$$\begin{aligned} d_\theta = -4ik^2\zeta^{1/2}&(\zeta-1)^{1/2}[8(\zeta-1)^{1/2}(\zeta-m^2)^{1/2} \\ &-8(2\zeta-1) + \cdots\,, \end{aligned} \tag{10.4.2}$$

where the dots mean the same expression as in the first equation. Then

$$d_r/d_\theta \sim (\zeta - 1/2)\zeta^{-1/2}(\zeta-1)^{-1/2}i\,.$$

The point oscillates along the elliptic orbit, whose major and minor axes are in the direction of $d_r$ and $d_\theta$, in the sense from the direction of positive $d_r$ to that of positive $d_\theta$. The ratio of the axes is

$$(v_t^2 - 1/2v_R^2)v_t^{-1}(v_t^2 - v_R^2)^{-1/2}\,,$$

whose numerical value for $m=1/2$ is $1.565\cdots$. These results are entirely compatible with those of Sakai's study on the propagation of Rayleigh wave on a plane surface (4) § 16).

At the end of the section we notice that the expansion representing this zero is useful so far as $a$ is several scores as shown in (8.2). Now the method of separating this zero from the second group of zeros $\nu_{1j}$ is valid only when $a^{-1/3} \ll \cosh^{-1}(\nu_0/a)$, since $\cosh^{-1}(\nu_{1j}/a) = O(a^{-1/3})$ (see (8.4)) and so $\nu_0$ can be separated so far as $a \gg 1000/64 \sim 1000/27$, as we see from § 8, $\cosh^{-1}(\nu_0/a)$ being 0.3∼0.4; hence $a$ must be larger than several scores. Thus we know that $r_0$ must be larger than several scores times of the wave-length in order that such a surface wave propagates with negligible damping.

## § 11. Terms Corresponding to $\nu_{1j}$

Let us investigate such terms of the series representing $\Phi$ and $A_\varphi$ as corresponding to $\nu_{1j}$, given by (8.4). At first we evaluate $\Phi_{1j}$, the term in the right-handed side of (7.2.1) corresponding to $\nu_{1j}$.

As to the factor $\nu P_{\nu-1/2}(\cos(\pi-\theta))/\cos\nu\pi$, we scrutinize the formula (10.1), corresponding to $\nu_{1j}$; since now

$$\mathrm{Im}\,\nu_{1j}=-(3\rho_j)^{2/3}\sqrt{3}/4a^{1/3}\{1+O(a^{-2/3})\}\ ,$$

the second and further terms are negligible to the first and we have

$$\begin{aligned}\nu P_{\nu-1/2}(\cos(\pi-\theta))/\cos\nu\pi=&(2a/\pi\sin\theta)^{1/2}(1+1/4q_j^2)\\&\times\exp[-ia\theta\{1+1/2q_j^2-(4i/3\rho_j)(1-m^2)^{1/2}q_j^3+1/120q_j^4-(-17/6+1/2(1-m^2)^{-1}\\&+16/3(1-m^2))(4i/3\rho_j)(1-m^2)^{1/2}q_j^5\}]\{1+O(a^{-1})\}\ .\end{aligned}\tag{11.1}$$

Then we have, employing for $H_\nu^{(2)}(ma)$ the ordinary asymptotic expansion of large order and for $H_\nu^{(2)}(a)$ the asymptotic formula in the transitional region 10),

$$\begin{aligned}\Phi_{1j}=&-(8/r_0)\{1+(-31/12+16(1-m^2))q_j^2\}(2\pi/kr_0\sin\theta)^{1/2}\\&\times\exp[-(1-m^2)^{1/2}k(r_s-r_0+r-r_0)-ikr_0\theta\{1+\tfrac{1}{2}q_j^2-(4i/3\rho_j)(1-m^2)^{1/2}q_j^3\\&+1/120q_j^4-(-17/6+1/2(1-m^2)^{-1}+16/3(1-m^2))(4i/3\rho_j)(1-m^2)^{1/2}q_j^5\}-\pi/4i]\\&\times\{1+O(1/kr_0)\}\{1+O((r_s-r_0)/r_0)\}\{1+O((r-r_0)/r_0)\}\ .\end{aligned}\tag{11.2}$$

Its properties are as follows;

1. $\Phi_{1j}$ is of finite magnitude only if $r_s-r_0\ll r_0$.
2. $\Phi_{1j}$ is of finite magnitude only in the vicinity of the surface on account of the factor $\exp[-(1-m^2)^{1/2}k(r-r_0)]$, or it has a character of a surface wave and has such a factor as $(r_0\sin\theta)^{1/2}$ as it must be so.
3. It propagates on the surface with the propagation velocity $v_t\{1-1/4(3\rho_i v_t/\omega r_0)^{2/3}\}\{1+O(v_t/\omega r_0)\}$, fairly close to $v_t$; the waves corresponding to different values of $\rho_i$ thus propagate with different velocities and the wave corresponding to the lowest $\rho_i$ is the fastest. They have also their own character of dispersion.
4. It attenuates with $\theta$, the rate of which is given by $\exp[-\sqrt{3}/4(3\rho_j)^{2/3}(\omega r_0/v_t)^{1/3}\theta]$, if we retain the first term only to estimate its order of magnitude. Its values for $a(=\omega r_0/v_t)=100$ are tabulated, for several values of $\rho$ and $\theta$, as follows:

| | $\theta=0.1$ | 0.2 | 0.5 | 1 |
|---|---|---|---|---|
| $\rho_1$ | 0.4743.. | 0.2249.. | 0.02399.. | 0.00058.. |
| $\rho_2$ | 0.2714.. | 0.0736.. | 0.00134.. | 0.000002.. |
| $\rho_3$ | 0.1718.. | 0.0295.. | 0.00015.. | |
| $\rho_4$ | 0.1152.. | 0.0132.. | | |
| $\rho_5$ | 0.079.. | 0.006.. | | |
| $\rho_6$ | 0.056.. | 0.003.. | | |
| $\rho_7$ | 0.041.. | | | |

It becomes obvious that in order to estimate within the error of 1 per cent we must take 6 $\rho$'s for $\theta=0.2$, 2 $\rho$'s for $\theta=0.5$ and for $\theta=1$ have only to take the first one. For $\theta\sim0.1$ this method is not effective obviously.

5. The displacement components derived from it are

$$d_r\sim-(1-m^2)^{1/2}k\Phi_{1j}\ ,\qquad d_\theta\sim-i\Phi_{1j}\ ;$$

thus

$$d_r/d_\theta\sim e^{-\pi/2i}(1-m^2)^{1/2}\ .$$

The point oscillates along an elliptic orbit, whose major and minor axes are in the direction of $d_\theta$ and that of $d_r$ respectively. Its sense is from the direction of positive $d_\theta$ to that of positive $d_r$. The ratio of two axes is $1:(1-m^2)^{1/2}$, or $2:\sqrt{3}$, for $m=1/2$ on the surface.

We further evaluate $A_{\varphi ij}$, the term of the right-handed side of (7.2.2) corresponding to $\nu_{1j}$, After the consideration analogous to the previous one, we reach the following result for $r$ not close to $r_0$:

$$\begin{aligned} A_{\varphi 1j}=&(12ik/q_j^2)(J_{2/3}(\rho_j)-J_{-2/3}(\rho_j))^{-1}(1/kr_0kR_{AP})(\sin\theta_1/\sin\theta)^{1/2}\{1+(-23/20+8(1-m^2)\\ &+1/4\cot^2\theta_1)q_j^2\}\exp[-(1-m^2)^{1/2}k(r_s-r_0)-ikr_0(\theta-\theta_1)\{1+1/2q_j^2\\ &-(4i/3\rho_j)(1-m^2)^{1/2}q_j^3+1/120q_j^4-(-17/6+1/2(1-m^2)^{-1}\\ &+16/3(1-m^2))(4i/3\rho_j)(1-m^2)^{1/2}q_j^5\}-ikR_{AP}-ikr_0\cot\theta_1(1/8q_j^4\\ &-(2i/3\rho_j)(1-m^2)^{1/2}q_j^5)]\{1+0(1/kr_0)\}\{1+0((r_s-r_0)/r_0)\}\,, \end{aligned} \tag{11.3}$$

if we denote by $\theta_1$, $R_{AP}$ the angle $AOP$ and the distance from $A$ to $P$, the field point, where $A$ is the contact point of the tangent line through $P$ to the meridian in the meridian plane through $P$ (see Fig. 1); the values of $J_{2/3}(\rho_j)-J_{-2/3}(\rho_j)$ for the above-mentioned values of $\rho_j$ are computed to be 0.899715, −0.589375, 0.470172, −0.402633, 0.357749,⋯⋯

For such $r$ that $kr-kr_0=0(a^{1/3})$ we obtain

$$\begin{aligned} A_{\varphi 1j}=&(4k/q_j^2)3^{1/2}e^{-\pi/4i}(J_{2/3}(\rho_j)-J_{-2/3}(\rho_j))^{-1}(1/kr_0)(2\pi/kr_0\sin\theta)^{1/2}(q_j^2\\ &-\tan^2\theta_1)^{1/2}[H_{-1/3}^{(2)}(ia/3(q_j^2-\tan^2\theta_1)^{3/2})-4i(1-m^2)^{1/2}(q_j^2\\ &-\tan^2\theta_1)^{1/2}H_{2/3}^{(2)}(ia/3(q_j^2-\tan^2\theta_1)^{3/2})+\{-7/20\tan^2\theta_1-73/60q_j^2+16(1\\ &-m^2)q_j^2-(16/9\rho_j^2)(1-m^2)q_j^6(q_j^2-\tan^2\theta_1)^{-2})-8(1-m^2)\tan^2\theta_1\}H_{-1/3}^{(2)}(ia/3(q_j^2\\ &-\tan^2\theta_1)^{3/2})+ia/3(q_j^2-\tan^2\theta_1)^{3/2}\{-(16/3\rho_j^2)(1-m^2)q_j^6(q_j^2-\tan^2\theta_1)^{-2}\\ &+1/5\tan^2\theta_1(q_j^2-3\tan^2\theta_1)(q_j^2-\tan^2\theta_1)^{-1}\}H_{2/3}^{(2)}(ia/3(q_j^2-\tan^2\theta_1)^{3/2})]\\ &\times\exp[-(1-m^2)^{1/2}k(r_s-r_0)-ikr_0\theta\{1+1/2q_j^2-(4i/3\rho_j)(1-m^2)^{1/2}q_j^3\\ &+1/120q_j^4-(-17/6+1/2(1-m^2)^{-1}+16/3(1-m^2))(4i/3\rho_j)(1-m^2)^{1/2}q_j^5\}]\{1\\ &+0(1/kr_0)\}\{1+0((r_s-r_0)/r_0)\}\,, \end{aligned} \tag{11.4}$$

and for $r$ close to $r_0$,

$$\begin{aligned} A_{\varphi 1j}=&16(1-m^2)^{1/2}e^{\pi/4i}/r_0(2\pi/kr_0\sin\theta)^{1/2}\{1+(-49/12+1/2(1-m^2)^{-1}\\ &+16(1-m^2))q_j^2\}\{1-1/4(1-m^2)^{-1/2}(1+(3-1/2(1-m^2)^{-1})q_j^2)k(r-r_0)\}\\ &\times\exp[-(1-m^2)^{1/2}k(r_s-r_0)-ikr_0\theta\{1+1/2q_j^2-(4i/3\rho_j)(1-m^2)^{1/2}q_j^3\\ &+(1/120)q_j^4-(-17/6+1/2(1-m^2)^{-1}+16/3(1-m^2))(4i/3\rho_j)(1-m^2)^{1/2}q_j^5\}]\{1\\ &+0(1/kr_0)\}\{1+0(k^2(r-r_0)^2/(kr_0)^{2/3})\}\{1+0((r_s-r_0)/r_0)\}\,. \end{aligned} \tag{11.5}$$

It has the following properties:

1. $A_{\varphi 1j}$ is of finite order as far as the source is near the surface on account of the factor $\exp\{-(1-m^2)^{1/2}k(r_s-r_0)\}$.

2. Its amplitude is proportional to $(1/kR_{AP})$ $(\sin\theta_1/\sin\theta)^{1/2}$ unless the field point is close to the surface.

3. When $\theta>\theta_1$, as we see from its phase, it behaves as if, starting from $Q_1$, the projection of the source on the surface, it propagated to $A$ on the surface with a velocity of propagation fairly close to $v_t$ and depending on $\rho$ and $\omega$, then traveled on a straight line to $P$ with the velocity $v_t$. Its behavior when propagating on the surface is quite analogus to that of $\Phi_{1j}$. When $\theta<\theta_1$, though the geometrical interpretation is not so simple, the phase is given in the first approximation by $-ik\{R_{AP}-r_0(\theta_1-\theta)\}$, which closes to $-ikR_{Q_1P}$ for $R_{AP}\gg r_0(\theta_1-\theta)$. This difference comes from the fact that, while in the latter case the field point is exposed to the direct radiation, in the former case the state of affairs there is determined in the main by the wavelet at $A$ in Huygens' meaning.

4. It attenuates on its way on the surface, if $\theta>\theta_1$, or $P$ is in the shade; its rate is given by $\exp\{-\sqrt{3}/4(3\rho_j)^{2/3}(\omega r_0/v_t)^{1/3}(\theta-\theta_1)\}$, if we retain its first terms only; its numerical values

corresponding to various values of $\rho$ are the same as those of $\Phi_{1j}$ with $\theta$ replaced by $\theta-\theta_1$. If $\theta<\theta_1$, it means on the contrary, the increase of the amplitude, corresponding to the case $P$ being exposed to the direct radiation. In this case its numerical value increases with increasing $\rho$, though it does not mean the divergence of the series since such a form holds in the first several terms only, and, therefore, this procedure is not suited here for quantative treatment, but useful for qualitative discussion only.

5. The displacement components at a field point not near the surface are

$$d_r \sim -ik(r_0/r)A_{\varphi 1j}\,, \qquad d_\theta \sim ik\{1-(r_0/r)^2\}^{1/2}A_{\varphi 1j}\,,$$

and so

$$d_r/d_\theta \sim -r_0/(r^2-r_0^2)^{1/2} \doteqdot -\cot\theta_1;$$

the particle thus oscillates on a line perpendicular to $AP$, or transversely, while on the surfac elliptically polarized ones with $d_r$ as the major axis prevail since $d_r/d_\theta \sim -4i(1-m^2)^{1/2}$.

6. It is noticeable that $A_{\varphi 1j}$ radiates out into the exterior medium, while $\Phi_{1j}$ is finite only in the vicinity of the surface.

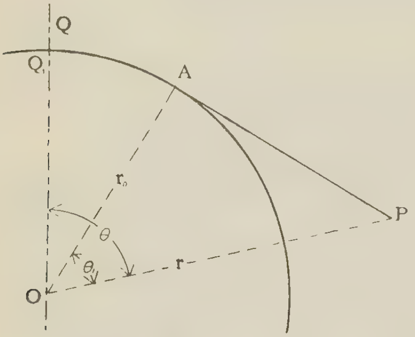

Fig. 1.

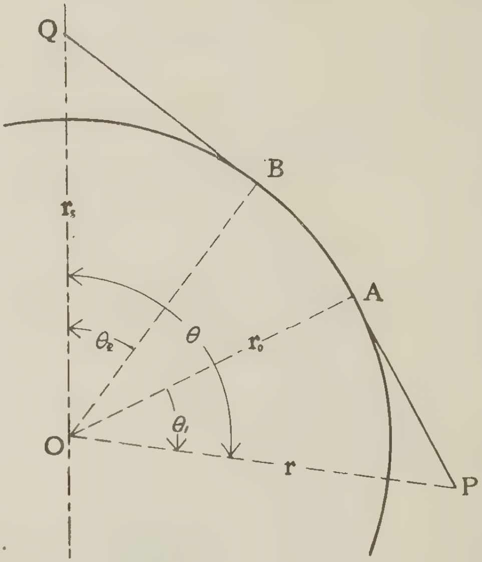

Fig. 2.

## § 12. Terms Corresponding to $\nu_{2j}$

Let us investigate such terms of the series representing $\Phi$ and $A_\varphi$ as correspond to $\nu_{2j}$, given by (8.5).

For such values of $\nu$ we obtain

$$\begin{aligned}\Phi_{2j} = {} & (9h/q_j^{*4})^i e^{\pi/4i}(J_{2/3}(\rho_j)-J_{-2/3}(\rho_j))^{-2}(hR_{QB}hR_{AP})^{-1}(2/\pi hr_0)^{1/2}(\sin\theta_1 \sin\theta_2/\sin\theta)^{1/2}\{1 \\ & +(17/60+1/4\cot^2\theta_1+1/4\cot^2\theta_2+32m^6(1-m^2)(2m^2-1)^{-4})q_j^{*2}\} \\ & \times\exp[-ihr_0(\theta-\theta_1-\theta_2)\{1+1/2q_i^{*2}-(4m^3/3\rho_j)(1-m^2)^{1/2}(2m^2-1)^{-2}q_j^{*3} \\ & +1/120q_j^{*4}-(1/6-(2m^2+1)/(2m^2-1)-16/3m^6(1-m^2)(2m^2-1)^{-4})(4m^3/3\rho_j) \\ & \times(1-m^2)^{1/2}(2m^2-1)^{-2}q_j^{*5}\}-ihR_{QB}-ihR_{AP}+ihr_0(\cot\theta_1+\cot\theta_2)(-1/8q_j^{*4} \\ & +(2m^3/3\rho_j)(1-m^2)^{1/2}(2m^2-1)^{-2}q_j^{*5})]\{1+0(1/hr_0)\}\,,\end{aligned}$$

for $r$, $r_s$ not close to $r_0$, if we denote, beside the notations employed in § 11, by $\theta_2$ and $R_{QB}$ the angle $QOB$ and the distance from $Q$ to $B$, $B$ being the contact point of the tangent line through $Q$ on the meridian in the meridian plane throuth $P$ (see Fig. 2); for $r$, $r_s$ close to $r_0$, or $hr_s-h_0<0(a^{1/3})$, $hr-hr_0<0(a^{1/3})$, we have further

$$\begin{aligned}\Phi_{2j} = {} & -16he^{-\pi/4i}m^6(1-m^2)(2m^2-1)^{-4}(1/hr_0)(2\pi/hr_0\sin\theta)^{1/2}\{1+(5/12-2(2m^2 \\ & +1)/(2m^2-1)-m^2/(1-m^2)+16m^6(1-m^2)(2m^2-1)^{-4})q_j^{*2}\}[1-i/4(2m^2-1)^2m^{-3}\end{aligned}$$

$$\times(1-m^2)^{-1/2}\{1+((2m^2+1)/(2m^2-1)+1/2m^2/(1-m^2))q_j^{*2}\}h(r-r_0+r_s-r_0)]$$
$$\times\exp[-ihr_0\theta\{1+1/2q_j^{*2}-(4m^3/3\rho_j)(1-m^2)^{1/2}(2m^2-1)^{-2}q_j^{*3}$$
$$+1/120q_j^{*4}-(1/6-(2m^2+1)/(2m^2-1)-1/2m^2/(1-m^2)-16/3m^6(1-m^2)$$
$$\times(2m^2-1)^{-4})(4m^3/3\rho_j)(1-m^2)^{1/2}(2m^2-1)^{-2}q_j^{*5}\}]\{1+0(1/hr_0)\}\{1$$
$$+0((hr-hr_0)^2/(hr_0)^{2/3})\}\{1+0((hr_s-hr_0)^2/(hr_0)^{2/3})\}\,. \tag{12.2}$$

Though for such value of $r$, $r_s$ that $hr-hr_0=0\ ((hr_0)^{1/3})$, $hr_s-hr_0=0\ ((hr_0)^{1/3})$ we have found an expression somewhat analogous to (11.4), we refrain from reproducing it here on account of its complexness and sterility.

Its properties are as follows:

1. Its magnitude is proportional to $R_{QB}^{-1}R_{AP}^{-1}$ $(\sin\theta_1\sin\theta_2/\sin\theta)^{1/2}$, unless the source and the field point are very close to the surface.

2. If $\theta>\theta_1+\theta_2$, we find from the exponential function that the dilatational wave propagates straight from $Q$ to $B$ with the velocity $v_l$, and then decomposes into many waves, each of them travels on the spherical surface to the point $A$ with a velocity near to $v_l$ and from here again straight to $P$ with the propagation velocity $v_l$. If $\theta<\theta_1+\theta_2$, the phase is approximately equal to $-ih(R_{QB}-\text{arc}\,AB+R_{AP})$ or $-ih(R_{QB}-\text{arc}\,Q_1B+R_{AP}-\text{arc}\,Q_1A)$ according as $\theta>\theta_1$ or $\theta<\theta_1$, as shown in Fig. 3; these become $-ih(R_{QA}+R_{AP})$ and $-ih(R_{QQ_1}+R_{Q_1P})$ respectively, as $R_{QB}$, $R_{AP\to\infty}$.

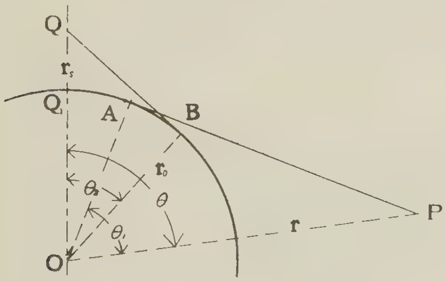

Fig. 3. (a) $\theta>\theta_1$.

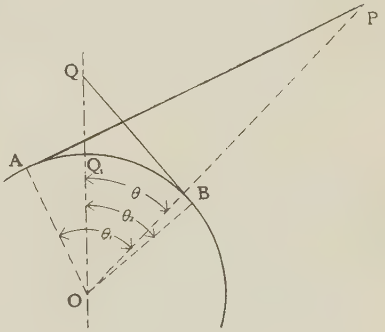

Fig. 3. (b) $\theta<\theta_1$.

3. The propagation velocity on the surface is $v_l\{1-1/4(3\rho_jv_l/\omega r_0)^{2/3}\}$; the waves are dispersive and the one corresponding to the lowest $\rho$ is the fastest.

4. While propagating on the surface it attenuates so far as $\theta>\theta_1+\theta_2$; the rate of damping is given by $\exp\{-\sqrt{3}/4(3\rho_j)^{2/3}(\omega r_0/v_l)^{1/3}(\theta-\theta_1-\theta_2)\}$, if we retain the first term only; it means that the field point $P$ is in the shade. Its values for $a=100$, $m=1/2$ are tabulated, for several values of $\rho_j$ and $\theta-\theta_1-\theta_2$ as follows:

| | $\theta-\theta_1-\theta_2=0.2$ | 0.5 | 1 |
|---|---|---|---|
| $\rho_1$ | 0.3060 | 0.0518 | 0.0027 |
| $\rho_2$ | 0.1249 | 0.0057 | 0.00004 |
| $\rho_3$ | 0.0611 | 0.0009 | |
| $\rho_4$ | 0.0322 | 0.0001 | |
| $\rho_5$ | 0.0179 | | |
| $\rho_6$ | 0.0104 | | |
| $\rho_7$ | 0.0029 | | |

If $\theta<\theta_1+\theta_2$, it increases its intensity with the rate given by

$$\exp\{\sqrt{3}/4(3\rho_j)^{2/3}(\omega r_0/v_l)^{1/3}(\theta_1+\theta_2-\theta)\}\,,$$

which corresponds to the case of the direct exposure to the radiation. In this case such a discussion as that stated in § 11 still holds.

5. The displacement components at a field point not near the surface are given by

$$d_r \sim -ih(r^2-r_0^2)^{1/2}/r_0\Phi_{2j}\,, \qquad d_\theta \sim -ihr_0/r\Phi_{2j}\,.$$

Thus

$$d_r/d_\theta \sim (r^2-r_0^2)^{1/2}/r_0 = \tan\theta_1\,.$$

The particle oscillates in the line $AP$, or longitudinally, while on the surface such linearly polarized oscillations prevail that $d_r/d_\theta \sim 1/4(2m^2-1)m^{-3}(1-m^2)^{-1/2}$, which is $1/\sqrt{3}$ for $m=0.5$.

Secondly we evaluate $A_{\varphi 2j}$. This leads to

$$\begin{aligned} A_{\varphi 2j} = & -12imh(2m^2-1)^{-1}q_j^{*-2}(J_{2/3}(\rho_j)-J_{-2/3}(\rho_j))^{-1}(hR_{QB}kR_{A^*P})^{-1} \\ & \times(\sin\theta_1^*\sin\theta_2\sin\theta_3/\sin\theta)^{1/2}\{1+(17/20-1/4(\cot^2\theta_3-\cot^2\theta_1^*-\cot^2\theta_2) \\ & +24\mathrm{m}^6(1-m^2)(2m^2-1)^{-4}-2m^2/(2m^2-1))q_j^{*2}\}\exp[-ihR_{QB}-ihr_0(\theta-\theta_1^* \\ & -\theta_2+\theta_3)\{1+1/2q_j^{*2}-(4m^3/3\rho_j)(1-m^2)^{1/2}(2m^2-1)^{-2}q_j^{*3}+1/120q_j^{*4} \\ & -(1/6-(2m^2+1)/(2m^2-1)-1/2m^2/(1-m^2)-16/3m^6(1-m^2)(2m^2-1)^{-4}) \\ & \times(4m^3/3\rho_j)(1-m^2)^{1/2}(2m^2-1)^{-2}q_j^{*5}\}-ikR_{DP}+ihr_0(\cot\theta_1^*+\cot\theta_2 \\ & -\cot\theta_3)(-1/8q_j^{*4}+(2m^3/3\rho_j)(1-m^2)^{1/2}(2m^2-1)^{-2}q_j^{*5})]\{1+0(1/kr_0)\}\,, \end{aligned} \tag{12.3}$$

for $r_s$ not close to $r_0$, if we denote by $A^*$ the contact point of the tangent line through $P$ on the circle which is formed by the intersection of the meridian plane through $P$ and the sphere of radius $mr_0$, by $D$ the point of intersection of $PA^*$ and the original sphere by $\theta_1^*$, $\theta_3$ the angle $POA^*$, $DOA^*$ (see Fig. 4), and by $R_{DP}$ the distances between $D$ and $P$.

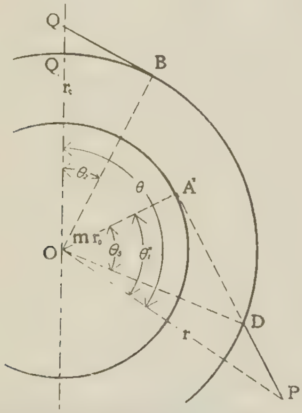

Fig. 4.

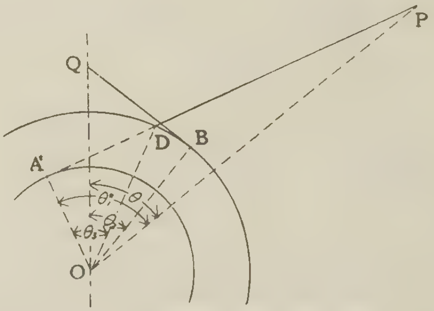

Fig. 5.

For $r_s$ close to $r_0$, or $hr_s-hr_0<0(a^{1/3})$,

$$\begin{aligned} A_{\varphi 2j} = & -16he^{-\pi/4i}m^4(1-m^2)^{1/2}(2m^2-1)^{-3}(1/kR_{A^*P})(2\pi\sin\theta_1^*\sin\theta_3/hr_0\sin\theta)^{1/2}\{1 \\ & +(-13/12-3/(2m^2-1)+16m^6(1-m^2)(2m^2-1)^{-4}-3/4\cot^2\theta_3 \\ & +1/4\cot^2\theta_1^*)q_j^{*2}\}\{1-i/4(2m^2-1)^2m^{-3}(1-m^2)^{-1/2}(1+(2m^2+1)/(2m^2-1) \\ & +1/2m^2(1-m^2)^{-1})q_j^{*2})h(r_s-r_0)\}\exp[-ihr_0(\theta-\theta_1^*+\theta_3)\{1+1/2q_j^{*2} \\ & -(4m^3/3\rho_j)(1-m^2)^{1/2}(2m^2-1)^{-2}q_j^{*3}+1/120q_j^{*4}-(1/6-(2m^2+1)/(2m^2-1) \\ & -1/2m^2(1-m^2)^{-1}-16/3m^6(1-m^2)(2m^2-1))^{-4})(4m^3/3\rho_j)(1-m^2)^{1/2}(2m^2 \\ & -1)^{-2}q_j^{*5}\}-ikR_{DP}+ihr_0(\cot\theta_1^*-\cot\theta_3)(-1/8q_j^{*4}+(2m^3/3\rho_j)(1 \\ & -m^2)^{1/2}(2m^2-1)^{-2}q_j^{*5})]\{1+0(1/kr_0)\}\{1+0((hr_s-hr_0)^2/(hr_0)^{2/3})\,. \end{aligned} \tag{12.4}$$

The formula corresponding to the case that $h(r-r_0)=0\ ((hr_0)^{1/3})$, $h(r_s-r_0)=0\ ((hr_0)^{1/3})$ is omitted here because we do not need it so much.

Its properties are as follows;

1. The magnitude is proportional to $(R_{A^*P}R_{QB})^{-1}(\sin\theta)^{-1/2}(\sin\theta_1^*\sin\theta_2\sin\theta_3)^{1/2}$; the last factor is to be interpreted to be $(\sin\theta_3)^{-1/2}\sin\theta_3$, whose latter factor appears to represent the

component in the direction of the line $DP$ of the vector, tangential to the surface at the point $D$, as it should be so if we consider the transversality and the longitudinality of the wave to be discussed below.

2. From its phase it appears that, if $\theta > \theta_1^* + \theta_2 - \theta_3$, the initial wave travels out straight from $Q$ to $B$ with the velocity $v_l$ and then many waves corresponding to various $\rho_j$ propagate on the surface with velocities close to $v_l$, respectively, attaining $D$ and from here they straight to $P$ with the velocity $v_t$. If $\theta < \theta_1^* + \theta_2 - \theta_3$ the phase is approximately equal to $-ih(R_{QB} - \text{arc}\, DB) - ikR_{DP}$ as shown in Fig. 5, which closes to $-ihR_{QD} - lk_{DP}$ with increasing $R_{QB}$, $R_{DP}$; this shows the path in the sense of geometrical optics.

3. The propagation velocity on the surface is $v_l\{1 - 1/4(3\rho_j v_l/\omega r_0)^{2/2}\}$; the waves are dispersive and the one corresponding to the smallest $\rho$ is the fastest.

4. If $\theta > \theta_1^* + \theta_2 - \theta_3$, it attenuates in the propagation on the sphere, whose rate of damping is given by $\exp\{-\sqrt{3}/4(3\rho_j)^{2/3}(\omega r_0/v_l)^{1/3}(\theta - \theta_1^* - \theta_2 + \theta_3)\}$ in the first approximation, the state corresponding to the shade in geometrical optics, while, for $\theta < \theta_1^* + \theta_2 - \theta_3$, it increases its intensity, as given by the same formula; this represents the case where the source is visible from the field point.

5. The displacement components resulting from it are

$$d_r \sim -ih(r_0/r)A_{\varphi 2j}\,, \qquad d_\theta \sim ik/r(r^2 - m^2 r_0^2)^{1/2} A_{\varphi 2j}\,,$$

and so

$$d_r/d_\theta \sim -mr_0/(r^2 - m^2 r_0^2)^{1/2} = -\cot\theta_1^*\,.$$

The elementary portion at $P$ oscillates in the line perpendicular to $A^*P$, or transversely; this state still holds, when $P$ is on the surface.

## § 13. Case of Small $\theta$

It was shown in § 9 that, while the series representing $\Phi$ and $A_\varphi$ are so rapidly convergent for not small $\theta$ that it suffices for our purpose to sum up, beside the one corresponding to Rayleigh wave, first several terms corresponding to the residues at the two rows of zeros near the real axis, this method fails for small $\theta$ and we need some other procedures. We can now attain our end by evaluating $\Phi$ and $A_\varphi$ in their original integral forms along the contours $C_1$, $C_2$ enclosing these two rows of zeros respectively. The case of small $\theta$, however, does not arouse any more interest but its importance lies only in the point that it shows behaviors transitional to the case of reflection by a plane surface, treated by Sakai. To compare with his result, we limit ourselves to treat the components of the displacement on the surface without treating $\Phi$, $A_\varphi$ in their general forms throughly, and further assume $r - r_0 \ll r_0$, $r_s - r_0 \ll r_0$.

Let us evaluate following integrals derived from the discussion in § 7:

$$\begin{aligned} d_r = -\frac{i}{r_0(r_0 r_r)^{1/2}} \int_{C_1+C_2} &\frac{\nu P_{\nu-1/2}(\cos(\pi-\theta))}{\cos\nu\pi} \frac{H_\nu^{(2)}(hr_s)}{H_\nu^{(2)}(ma)} \left[\frac{2}{a}F(\nu, a) + 1 - \frac{2\nu^2}{a^2}\left(1 - \frac{3}{4\nu^2}\right)\right] \\ &\times \left[1 - \frac{4\nu^2}{a^2} + \frac{4\nu^2}{a^4}\left(\nu^2 - \frac{9}{4}\right) + \frac{2}{a}\left(1 + \frac{\nu^2 - 9/4}{a^2}\right)F(\nu, a) + \frac{2m}{a}\left(2 - \frac{\nu^2 - 9/4}{a^2}\right)F(\nu, ma) \right. \\ &\left. - 4m\frac{\nu^2 - 9/4}{a^2}F(\nu, ma)F(\nu, a)\right]^{-1} d\nu\,, \end{aligned} \tag{13.1.1}$$

$$\begin{aligned} d_\theta = -\frac{2i}{ar_0(r_0 r_s)^{1/2}} \int_{C_1+C_2} &\nu \frac{dP_{\nu-1/2}(\cos(\pi-\theta))}{d\theta} \frac{1}{\cos\nu\pi} \frac{H_\nu^{(2)}(hr_s)}{H_\nu^{(2)}(ma)} \left(F(\nu, a) - \frac{3}{2a}\right) \\ &\left[1 - \frac{4\nu^2}{a^2} + \frac{4\nu^2}{a^4}\left(\nu^2 - \frac{9}{4}\right) + \frac{2}{a}\left(1 + \frac{\nu^2 - 9/4}{a^2}\right)F(\nu, a) + \frac{2m}{a}\left(2 - \frac{\nu^2 - 9/4}{a^2}\right)F(\nu, ma) \right. \\ &\left. - 4m\frac{\nu^2 - 9/4}{a^2}F(\nu, a)F(\nu, ma)\right]^{-1} d\nu\,, \end{aligned} \tag{13.1.2}$$

where

$$F(\nu, a) = H_\nu^{(2)\prime}(a)/H_\nu^{(2)}(a)\,, \qquad F(\nu, ma) = H_\nu^{(2)\prime}(ma)/H_\nu^{(2)}(ma)\,, \tag{13.2}$$

the contours $C_1$, $C_2$ being such as shown in Fig. 6.

By investigating the analytical behavious of the constituents of the integrands on the contours in detail, we can reduce these integrals to

$$\begin{aligned} d_r = & -(ik/r_0)(2a/\pi \sin\theta)^{1/2} e^{-\pi/4i} \int_{C_1'} \exp\{-a\theta\, i \cosh w - (\cosh^2 w - m^2)^{1/2} k(r_s \\ & - r_0)\} \cosh^{1/2} w (1 - 2\cosh^2 w - 2/a \sinh w\{(1 - 2\cosh^2 w)^2 - 4\cosh^2 w \\ & \times \sinh w (\cosh^2 w - m^2)^{1/2}\}^{-1} \sinh w dw\{1 + 0((a\theta)^{-1})\} \\ & - ih/r_0 (2ma/\pi \sin\theta)^{1/2} e^{-\pi/4i} \int_{C_2'} \exp\{-ma\theta i \cosh w - \sinh w h(r_s - r_0)\} \\ & \times \cosh^{1/2} w\{1 - 2m^2 \cosh^2 w - 2/a(m^2 \cosh^2 w - 1)^{1/2}\}\{1 - 2m^2 \cosh^2 w)^2 \\ & - 4m^3 \cosh^2 w (m^2 \cosh^2 w - 1)^{1/2} \sinh w\}^{-1} \sinh w dw\{1 + 0((ma\theta)^{-1})\}\,, \end{aligned} \tag{13.3.1}$$

$$\begin{aligned} d_\theta = & -(2i/r_0^2)(2a^3/\pi \sin\theta)^{1/2} e^{\pi/4i} \int_{C_1'} \exp\{-a\theta i \cosh w - (\cosh^2 w - m^2)^{1/2} k(r_s \\ & - r_0)\} \cosh^{3/2} w\{\sinh w + (3/2a)\}\{(1 - 2\cosh^2 w)^2 - 4\cosh^2 w \sinh w \\ & \times (\cosh^2 w - m^2)^{1/2}\}^{-1} \sinh w dw\{1 + 0((a\theta)^{-1})\} \\ & - 2ihm/r_0 (2ma/\pi \sin\theta)^{1/2} e^{\pi/4i} \int_{C_2'} \exp\{-ma\theta i \cosh w - \sinh w h(r_s - r_0)\} \\ & \times \cosh^{3/2} w\{(m^2 \cosh^2 w - 1)^{1/2} + 3/(2a)\}\{(1 - 2m^2 \cosh^2 w)^2 \\ & - 4m^3 \cosh^2 w (m^2 \cosh^2 w - 1)^{1/2} \sinh w\}^{-1} \sinh w dw\{1 + 0((ma\theta)^{-1})\}\,, \end{aligned} \tag{13.3.2}$$

where $C_1'$, $C_2'$ are such as shown in Figs. 7, 8.

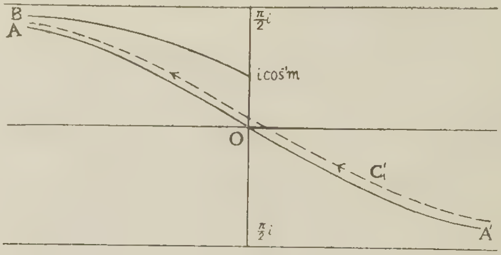

Fig. 7.

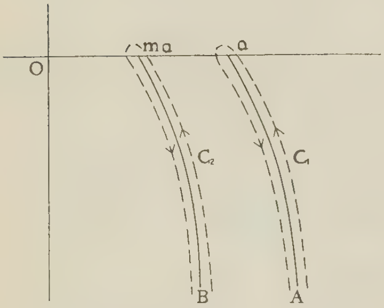

Fig. 6.

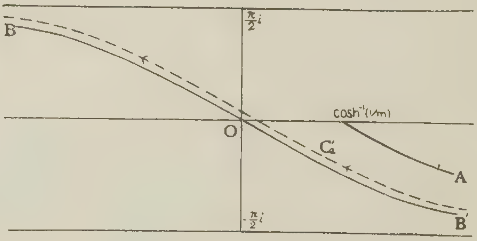

Fig. 8.

By integration along the contours of steepest descents through $w=0$, $i(\pi/2-\psi)$ they become

$$\begin{aligned} d_r = & [-8e^{\pi/4i}(1-m^2)^{5/4}(\sin\psi)^{-1/2}\{(1-m^2)^{1/2} i \sin\psi + \cos\psi\}^{-3/2} R^{-2} \exp\{-ikR \sin\psi \\ & - (1-m^2)^{1/2} kR \cos\psi\} + 2ih(1 - 2m^2 \sin^2\psi) \cos\psi\{(1 - 2m^2 \sin^2\psi)^2 \\ & + 4m^3 \sin^2\psi (1 - m^2 \sin^2\psi)^{1/2} \cos\psi\}^{-1} \exp(-ihR)/R]\{1 + 0(1/kR)\}\,, \end{aligned} \tag{13.4.1}$$

$$\begin{aligned} d_\theta = & [4e^{-\pi/4i}(1-m^2)^{3/4}(\sin\psi)^{-1/2}\{(1-m^2)^{1/2} i \sin\psi + \cos\psi\}^{-3/2} R^{-2} \exp\{-ikR \sin\psi \\ & - (1-m^2)^{1/2} kR \cos\psi\} - 4\, ihm \sin\psi \cos\psi (1 - m^2 \sin^2\psi)^{1/2}\{(1 - 2m^2 \sin^2\psi)^2 \\ & + 4m^3 \sin^2\psi (1 - m^2 \sin^2\psi)^{1/2} \cos\psi\}^{-1} \exp(-ihR)/R]\{1 + 0(1/kR)\}\,, \end{aligned} \tag{13.4.2}$$

where $\psi$ denotes the incident angle. These results are completely equivalent to those of

Sakai's research on the behavior of distortional and dilatational waves on a plane surface (4) p. 35) and so we refrain from proceeding further.

## IV. DISTORTIONAL SOURCE OF THE FIRST KIND

### § 14. General Form of the Solutions

The treatment of the case of a distortional source follows much the same course as in the preceding case, so that we shall not enter into particulars except some new points.

The distortional primary wave, expressed by (3.3), can be expanded as follows:

$$A_\varphi{}^p=-(i/krr_s)\sum_{n=0}^{\infty}(2n+1)[\zeta_n(kr_s)\psi_n(kr),\ \text{or}\ \psi_n(kr_s)\zeta_n(kr)]dP_n(\cos\theta)/d\theta\ , \tag{14.1}$$

according as $r<r_s$ or $r>r_s$.

Assuming, in view of this expression, as the secondary waves the expression (5.3), we determine the coefficients from the boundary condition. After the same transformation as in § 7, we have as the resultants

$$\varPhi=-\frac{4\pi}{(rr_s)^{1/2}}\sum_j\left[\nu\frac{P_{\nu-1/2}(-\cos\theta)}{\cos\nu\pi}\frac{\nu^2-1/4}{a^2}\left\{1-2\frac{(\nu^2-9/4)}{a^2}\right\}\frac{H_\nu{}^{(2)}(kr_s)H_\nu{}^{(2)}(hr)}{\partial\varDelta(\nu)/\partial\nu}\right]_{\nu=\nu_j}, \tag{14.2.1}$$

$$A_\varphi=\frac{2\pi}{(rr_s)^{1/2}a}\sum_j\left[\nu\frac{dP_{\nu-1/2}(-\cos\theta)}{d\theta}\frac{1}{\cos\nu\pi}\frac{H_\nu{}^{(2)}(kr_s)H_\nu{}^{(2)}(kr)}{H_\nu{}^{(2)}(a)\partial\varDelta(\nu)/\partial\nu}\left\{4m\frac{\nu^2-9/4}{a^2}H_\nu{}^{(2)\prime}(ma)\right.\right.$$
$$\left.\left.-\frac{2}{a}\left(1+\frac{\nu^2-9/4}{a^2}\right)H_\nu{}^{(2)}(ma)\right\}\right]_{\nu=\nu_j}. \tag{14.2.2}$$

for all values of $r$.

### § 15. Terms Corresponding to $\nu_0$

The result of the calculation is

$$\varPhi_0=-4k^2r_0\zeta(2\zeta-1)[8(\zeta-1)^{1/2}(\zeta-m^2)^{1/2}-8(2\zeta-1)+2\zeta\{(\zeta-m^2)^{1/2}(\zeta-1)^{-1/2}$$
$$+(\zeta-1)^{1/2}(\zeta-m^2)^{-1/2}\}+(1-2\zeta)^2\tfrac{1}{2}\{1/(\zeta-m^2)+1/(\zeta-1)\}]^{-1}e^{-\pi/4i}(2\pi/\zeta^{1/2}kr_0\sin\theta)^{1/2}$$
$$\times\exp[-(\zeta-m)^{1/2}k(r-r_0)-(\zeta-1)^{1/2}k(r_s-r_0)-i\zeta^{1/2}kr_0\theta\{1-\zeta^{-1/2}(\zeta-1)^{1/2}$$
$$\times(p_1/kr_0)\}]\{1+0(1/kr_0)\}\{1+0((r_s-r_0)/r_0)\}\{1+0((r-r_0)/r_0)\}\ .$$

Its behaviors are quite the same as those of $\varPhi_0$ in § 10, except for its rate of damping with respect to $r$.

Then we have

$$A_{\varphi0}=-8k^2r_0\zeta^{3/2}(\zeta-m^2)^{1/2}[8(\zeta-1)^{1/2}(\zeta-m^2)^{1/2}-8(2\zeta-1)+2\zeta\{(\zeta-m^2)^{1/2}(\zeta-1)^{-1/2}$$
$$+(\zeta-1)^{1/2}(\zeta-m^2)^{-1/2}\}+(1-2\zeta)^2\tfrac{1}{2}\{1/(\zeta-m^2)+1/(\zeta-1)\}]^{-1}e^{\pi/4i}(2\pi/\zeta^{1/2}kr_0\sin\theta)^{1/2}$$
$$\times\exp[-(\zeta-1)^{1/2}k(r_s-r_0+r-r_0)-i\zeta^{1/2}kr_0\theta\{1--(\zeta-1)^{1/2}\zeta^{-1/2}(p_1/kr_0)\}]\{1$$
$$+0(1/kr_0)\}\{1+0((r_s-r_0)/r_0)\}\{1+0((r-r_0)/r_0)\}\ . \tag{15.2}$$

Its behaviors are quite the same as those of $A_{\varphi0}$ in § 10, except for its rate of damping with respect to $r$.

The components of the resultant displacement on the surface are

$$d_r=-4e^{-\pi/4i}\zeta(\zeta-m^2)^{1/2}k^3r_0(2\pi/\zeta^{1/2}kr_0\sin\theta)^{1/2}[8(\zeta-1)^{1/2}(\zeta-m^2)^{1/2}-8(2\zeta-1)$$
$$+2\zeta\{(\zeta-m^2)^{1/2}(\zeta--1)^{-1/2}+(\zeta-1)^{1/2}(\zeta-m^2)^{-1/2}\}+(1-2\zeta)^2\tfrac{1}{2}\{1/(\zeta-m^2)$$
$$+1/(\zeta-1)\}]^{-1}\exp[-(\zeta-1)^{1/2}k(r_s-r_0)-i\zeta^{1/2}kr_0\theta\{1-(\zeta-1)^{1/2}\zeta^{-1/2}(p_1/kr_0)\}]$$
$$\times\{1+0(1/kr_0)\}\{1+0((r_s-r_0)/r_0)\}\{1+0((r-r_0)/r_0)\}\ , \tag{15.3.1}$$

$$d_\theta=2e^{\pi/4i}k^3r_0\zeta^{1/2}(2\zeta-1)(2\pi/\zeta^{1/2}kr_0\sin\theta)^{1/2}[8(\zeta-1)^{1/2}(\zeta-m^2)^{1/2}-\cdots\cdots\ , \tag{15.3.2}$$

therefore

$$d_r/d_\theta\sim\zeta^{1/2}(\zeta-m^2)^{1/2}/(\zeta-\tfrac{1}{2})i\ ;$$

It shows that the volume element on the surface oscillates in an elliptic orbit, whose major and minor axes are in the directions of $d_r$, $d_\theta$ respectively, in the sense from the positive direction of $d_r$ to that of $d_\theta$. The ratio of the axes is $v_t^2/(v_t^2-\frac{1}{2}v_R^2)(v_t^2-v_R^2)^{1/2}/v_t$, and its numerical values for $m=\frac{1}{2}$ is 1.56520…. This result is compatible with that of Sakai's study on the propagation of Rayleigh wave on a plane surface 4) p. 58).

### 16. Terms Corresponding to $\nu_{1j}$

We obtain

$$\begin{aligned}\Phi_{1j}=&12q_j^{-2}(J_{2/3}(\rho_j)-J_{-2/3}(\rho_j))^{-1}(1/kR_{QB})(\sin\theta_2/\sin\theta)^{1/2}\{1+(1/4\cos^2\theta_2\\&-13/20+8(1-m^2))q_j^2\}\exp[-(1-m^2)^{1/2}k(r-r_0)-ikR_{QB}-ikr_0(\theta-\theta_2)\\&\times\{1+1/2q_j^2-(4i/3\rho_j)(1-m^2)^{1/2}q_j^3+1/120q_j^4-(-17/6+1/2(1-m^2)^{-1}\\&+16/3(1-m^2))(4i/3\rho_j)(1-m^2)^{1/2}q_j^5\}-ikr_0\cot\theta_2\{1/8q_j^4-(2i/3\rho_j)\\&\times(1-m^2)^{1/2}q_j^5\}]\{1+0(1/kr_0)\}\{1+0((r_s-r_0)/r_0)\}\{1+0((r-r_0)/r_0\},\end{aligned}\tag{16.1}$$

for $k(r_s-r_0)>0((kr_0)^{1/3})$.

For $k(r_s-r_0)<0((kr_0)^{1/3})$, we have

$$\begin{aligned}\Phi_{1j}=&16ke^{-\pi/4i}(1-m^2)^{1/2}\{1+(-43/12+1/2(1-m^2)^{-1}+16(1-m^2))q_j^2\}(2\pi/kr_0\\&\times\sin\theta)^{1/2}[1-1/4(1-m^2)^{1/2}\{1+(3-1/2(1-m^2)^{-1})q_j^2\}k(r_s-r_0)]\exp[-(1\\&-m^2)^{1/2}k(r-r_0)-ikr_0\theta\{1+1/2q_j^2-(4i/3\rho_j)(1-m^2)^{1/2}q_j^3+1/120q_j^4\\&-(-17/6+1/2(1-m^2)^{-1}+16/3(1-m^2))(4i/3\rho_j)(1-m^2)^{1/2}q_j^4\}[\\&\times\{1+0(1/kr_0)\}\{1+0((r-r_0)/r_0)\}\{1+0((kr_s-kr_0)^2/(kr_0)^{2/3})\}.\end{aligned}\tag{16.2}$$

Its properties are as follows:

1. $\Phi_{1j}$ is of finite magnitude only if $r-r_0\ll r_0$, or has the character of a surface wave.
2. $\Phi_{1j}$ is proportional to $1/(kR_{QB})(\sin\theta_2/\sin\theta)^{1/2}$.
3. From the phase it seems that, if $\theta>\theta_2$, a distortional wave travels from the source to $B$ and then many waves corresponding to various values of $\rho_j$ propagate on the surface to the field point with propagation velocities fairly close to $v_t$, whose values are given approximately by $v_t\{1-1/4(3\rho_j v_t/\omega r_0)^{2/3}\}$; the wave corresponding to the lowest $\rho$ is the fastest. They are all dispersive. Although we have not such a conspicuous geometrical interpretation for $\theta<\theta_2$, the phase approximately given by $-ik((R_{QB}-r_0(\theta_2-\theta))$ is close to $-ikR_{QP}$ so far as $\theta$ is not small; this means the wave propagates from $Q$ to $P$ directly with $v_t$.
4. If $\theta>\theta_2$, it attenuates with $\theta-\theta_2$, the rate of which is given by $\exp\{-\sqrt{/}3/4(3\rho_j)^{2/3}(\omega r_0/v_t)^{1/3}(\theta-\theta_2)\}$ if we retain only the first term in the exponent; this is the same as in § 11, if we replace $\theta$ by $\theta-\theta_2$, so we need not consider further. If $\theta<\theta_2$, it increases with $\theta_2-\theta$ exponentially, which means that the field point is exposed to the direct radiation. It was already discussed in the last part of § 11 that this procedure is not so suited to the computation in the latter case.
5. The displacement components resulting from it are as follows:

$$d_r\sim-(1-m^2)^{1/2}k\Phi_{1j},\qquad d_\theta\sim-ik\Phi_{1j}.$$

Then

$$dr/d_\theta\sim-i(1-m^2)^{1/2},$$

which means that the elementary portion at the field point oscillates along an elliptic orbit whose major and minor axes are in the directions of $d_\theta$, $d_r$, respectively; the sense is from the positive direction of $d_\theta$ to that of $d_r$. The numerical value of the ratio of these axes is, for $m=(1/2)$, 1: 0.866.

Next we consider $A_{\varphi 1j}$. As the result of the calculation we obtain for $k(r--r_0)>0\ ((kr_0)^{1/3})$, $k(r_s-r_0)>0((kr_0)^{1/3})$

$$\begin{aligned}A_{\varphi 1j}=&9ke^{3/4\pi i}q_j^{-4}(J_{2/3}(\rho_i)-J_{-2/3}(\rho_j))^{-2}(1/kR_{QB}kR_{AP})(2kr_0\sin\theta_1\sin\theta_2/\pi\sin\theta)^{1/2}\\&\times\{1+(47/60-1/2\cot^2\theta_1-1/2\cot^2\theta_2)q_j^2\}\exp[-ikR_{QB}-ikR_{AP}\\&-ikr_0(\theta-\theta_1-\theta_2)\{1+1/2q_j^2-(4i/3\rho_j)(1-m^2)^{1/2}q_j^3+1/120q_j^4-(-17/6\end{aligned}$$

$$\begin{aligned}&+1/2(1-m^2)^{-1}+16/3(1-m^2))(4i/3\rho_j)(1-m^2)^{1/2}q_j^5\}-ikr_0(\cot\theta_1+\cot\theta_2)\\&\{1/8q_j^4-(2i/3\rho_j)(1-m^2)^{1/2}q_j^5\}]\{1+0(a^{-1})\}\ ,\end{aligned}\tag{16.3}$$

if we use such notations as in § 12, and for the case corresponding to $r, r_s$ close to $r_0$

$$\begin{aligned}A_{\varphi 1j}=&(32/r_0)e^{\pi/4i}(\pi/kr_0\sin\theta)^{1/2}(1-m^2)\{1+(-61/12+(1-m^2)^{-1}+16(1-m^2))q_j^2\}\\&\times[1-1/4(1-m^2)^{1/2}\{1+(3-1/2(1-m^2)^{-1})q_j^2\}k(r-r_0+r_s-r_0)]\exp[-ikr_0\theta\\&\times\{1+1/2q_j^2-(4i/3\rho_j)(1-m^2)^{1/2}q_j^3+1/120q_j^4-(-17/6+1/2(1-m^2)^{-1}\\&+16/3(1-m^2))(4i/3\rho_j)(1-m^2)^{1/2}q_j^5\}]\{1+0(1/kr_0)\}\{1+0((kr-kr_0)^2/\\&(kr_0)^{2/3})\}\{1+0((kr_s-kr_0)^2/(kr_0)^{2/3})\}\ .\end{aligned}\tag{16.4}$$

Its properties are as follows:

1. $A_{\varphi 1j}$ is proportional to $1/(kR_{QB}kR_{AP})(\sin\theta_1\sin\theta_2/\sin\theta)^{1/2}$ unless $\theta_1$, $\theta_2$ are quite small.
2. From the phase it seems that if $\theta>\theta_1+\theta_2$ the distortional wave travels from $Q$ to $B$, then many waves, corresponding to various values of $\rho$ respectively, propagate on the surface with the same velocities as those of $\Phi_{1j}$ and then from $A$ to $P$ in a straight line with $v_t$. If $\theta<\theta_1+\theta_2$, on the contrary, the geometrical interpretation is not so simple; the phase $-ikR_{QB}+ikr_0(\theta_1+\theta_2-\theta)-ikR_{AP}$ is approximately equal to $-ikR_{QA}-ikR_{AP}$ or $-ikR_{QQ_1}-ikR_{Q_1P}$, according as $\theta>\theta_1$, or $\theta<\theta_1$, if $P, Q$ are far from the surface. These phases correspond to the case where the field is out of the geometrical shade.
3. As to the damping with $\theta$, the same discussion as in the case of $\Phi_{1j}$ is possible, if we replace $\theta-\theta_2$ by $\theta-\theta_1-\theta_2$.
4. The displacement components are

$$d_r\sim -ik\cos\theta_1A_{\varphi 1j}\ ,\qquad d_\theta\sim ik\sin\theta_1A_{\varphi 1j}\ ,$$

and we find

$$d_r/d_\theta\sim -\cot\theta_1;$$

that is, the elementary portion at $P$ vibrates in the line perpendicular to $AP$ in the meridian plane through $P$, as it should be if we consider the waves at $P$ transverse.

## § 17. Terms Corresponding to $\nu_{2j}$

We have

$$\begin{aligned}\Phi_{2j}=&12\pi kr_0m^3k(2m^2-1)^{-1}(J_{2/3}(\rho_j)-J_{-2/3}(\rho_j))^{-2}q_j^{*-2}(1/hR_{AP}kR_{QB}^*)\\&\times(\sin\theta_3\sin\theta_1\sin\theta_2^*/\sin\theta)^{1/2}[1+\{27/20+1/4(\cot^2\theta_2^*-\cot^2\theta_3+\cot^2\theta_1)-2m^2\\&\times(2m^2-1)^{-1}+24m^6(1-m^2)(2m^2-1)^{-2}\}q_j^{*2}]\exp[-ikR_{QB}-ihR_{AP}-ihr_0\\&\times(\theta-\theta_1-\theta_2^*+\theta_3)\{1+1/2q_j^{*2}-(4m^3/3\rho_j)(1-m^2)^{1/2}(2m^2-1)^{-2}q_j^{*3}+1/120q_j^{*4}\\&-(1/6-(2m^2+1)/(2m^2-1)-1/2m^2(1-m^2)^{-1}-(16m^6/3)(1-m^2)(2m^2-1)^{-4})\\&\times(4m^3/3\rho_j)(1-m^2)^{1/2}(2m^2-1)^{-2}q_j^{*5}\}-ihr_0(\cot\theta_1-\cot\theta_3+\cot\theta_2^*)\{1/8q_j^{*4}\\&-(2m^3/3\rho_j)(1-m^2)^{1/2}(2m^2-1)^{-2}q_j^{*5}\}]\{1+0(1/kr_0)\}\ ,\end{aligned}\tag{17.1}$$

for $h(r-r_0)>0((hr_0)^{1/3})$ if we employ such notations as shown in Fig. 9, and for $h(r-r_0)<0((hr_0)^{1/3})$ we have

$$\begin{aligned}\Phi_{2j}=&-16hr_0m^5k(1-m^2)^{1/2}(2m^2-1)^{-3}e^{\pi/4i}(2\pi\sin\theta_3\sin\theta_2^*/hr_0\sin\theta)^{1/2}(1/kR_{QB}^*)\\&\times[1+\{-7/12-3/4\cot^2\theta_3+1/4\cot^2\theta_2^*-3/(2m^2-1)+16m^6(1-m^2)\\&\times(2m^2-1)^{-4}\}q_j^{*2}]\exp[-ikR_{QB}-ihr_0(\theta-\theta_2^*+\theta_3)\{1+1/2q_j^{*2}-(4m^3/3\rho_j)(1-m^2)^{1/2}\\&\times(2m^2-1)^{-2}q_j^{*3}+1/120q_j^{*4}-(1/6-(2m^2+1)/(2m^2-1)-1/2\,m^2(1-m^2)^{-1}-(16m^6/3)\\&\times(1-m^2)(2m^2-1)^{-4}((4m^3/3\rho_j)(1-m^2)^{1/2}(2m^2-1)^{-2}q_j^{*5}\}-ihr_0(\cot\theta_2^*-\cot\theta_3)\\&\times\{1/8\,q_j^{*4}-(2m^3/3\rho_j)(1-m^2)^{1/2}(2m^2-1)^{-2}q_j^{*5}\}]\{1+0(1/kr_0)\}\\&\times\{1+0((hr-hr_0)^2/(hr_0)^{2/3})\}\ .\end{aligned}\tag{17.2}$$

We omit here the case $h(r-r_0)=0((hr_0)^{1/3})$ for the same reason as before.

The properties are as follows:

1. It is proportional to $1/(kR_{QB*}hR_{AP})(\sin\theta_1 \sin\theta_3 \sin\theta_2^*/\sin\theta)^{1/2}$ unless $r$ is close $r_0$, or if we consider the component tangential to the circle at $E$ of the vector perpendicular to $QE$, it may be more reasonable to write $(\sin\theta_3/kR_{QB*}hR_{AP})(\sin\theta_1 \sin\theta_2^*/\sin\theta \sin\theta_3)^{1/2}$.

2. If $\theta-\theta_1-\theta_2^*+\theta_3>0$. it seems from the phase that the distortional wave propagates from $Q$ to $E$ straight and then many waves of the dilatational character corresponding to various values of $\rho$ travel on the surface to $A$ with the velocities $v_l\{1-1/4(3\rho_j v_l/\omega r_0)^{2/3}\}$, propagating lastly to $P$ straight with $v_l$. If $\theta-\theta_1-\theta_2^*+\theta_3<0$, though the geometrical interpretation is not so obvious, the phase is approximately given by $-ikR_{QE}-ihR_{EP}$, showing that the distortional wave resumed by the dilatational wave at $E$.

3. If $\theta-\theta_1-\theta_2^*+\theta_3>0$, they attenuate with increasing $\theta$, the rate of damping being given by $\exp\{-\sqrt{3}/4(3\rho_j)^{2/3}(\omega r_0/v_l)^{1/3})(\theta-\theta_1-\theta_2^*+\theta_3)\}$, where only the first term in the exponent is retained. Refer to § 12. For $\theta-\theta_1-\theta_2^*+\theta_3<0$, the amplitude increases exponentially and as to the accompanying trouble we have already discussed.

4. The displacements are

$$d_r \sim -ih \sin\theta_1 \Phi_{2j} \qquad d_\theta \sim -ih \cos\theta_1 \Phi_{2j};$$

then

$$d_r/d_\theta \sim \tan\theta_1 ,$$

which shows that the element at $P$ vibrates in parallel with $AP$ and in the meridian through $P$, or longitudinally.

Next we obtain

$$\begin{aligned}A_{\varphi 2j}=&8m^5ka^2e^{\pi/4i}(2\pi/hr_0 \sin\theta)^{1/2} \sin^2\theta_3(1/kR_{QB}{}^*kR_{A^*P})(\sin\theta_1^*/\sin\theta_3)^{1/2}\\ &(\sin\theta_2^*/\sin\theta_3)^{1/2}[1+\{1/4\cot^2\theta_2^*+1/4\cot^2\theta_1^*-1/2\cot^2\theta_3\\ &+23/12-4m^2(2m^2-1)^{-1}+16m^6(1-m^2)(2m^2-1)^{-4}\}q_j^{*2}]\exp[-ik(R_{QE}\\ &+R_{DP})-ih(\theta-\theta_1^*-\theta_2^*-2\theta_3)\{1+1/2q_j^{*2}-(4m^3/3\rho_j)(1-m^2)^{1/2}(2m^2-1)^{-2}q_j^{*3}\\ &+1/120q_j^{*4}-(1/6-(2m^2+1)/(2m^2-1)-1/2m^2(1-m^2)^{-1}-16/3m^6(1-m^2)\\ &\times(2m^2-1)^{-4})(4m^3/3\rho_j)(1-m^2)^{1/2}(2m^2-1)^{-2}q_j^{*5}\}-ihr_0(\cot\theta_1^*+\cot\theta_2^*-2\cot\theta_3)\\ &\times(1/8q_j^{*4}-(2m^3/3\rho_j)(1-m^2)^{1/2}(2m^2-1)^{-2}q_j^{*5})]\{1+0(1/kr_0)\} ,\end{aligned}$$

the notations being illustrated in Fig. 10.

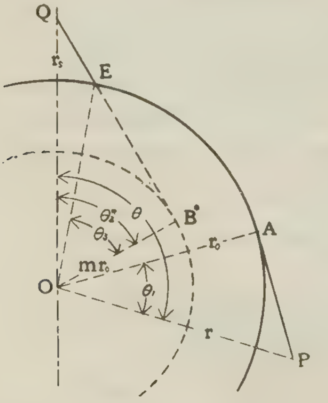

Fig. 9.

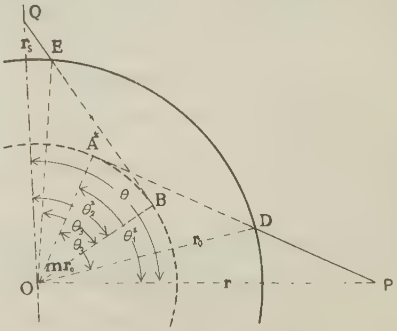

Fig. 10.

Its properties are as follows:

1. It is proportional to $(\sin^2\theta_3/kR_{QB}{}^*kR_{A^*P})(\sin\theta_1^* \sin\theta_2^*/\sin\theta_3 \sin\theta_3)^{1/2}$; the factor $\sin^2\theta_3$ means that we take the component, tangential at $E$, of the vector perpendicular to $QE$ and the component, perpendicular to $DP$, of the vector tangential at $D$.

2. If $\theta-\theta_1^*-\theta_2^*-2\theta_3>0$, it represents that the distortional wave propagates straight to $E$, then splits up into many dilatational waves, corresponding to various values of $\rho_j$ and travelling on the surface to $D$ and there each of them becomes distortional wave propagating straight to $P$. Their behavior on the surface is the same as that of $\Phi_{2j}$.

3. As to the damping with the angle $\theta-\theta_1^*-\theta_2^*-2\theta_3$, it is quite the same as in the case of $\Phi_{2j}$, if we replace $\theta-\theta_1-\theta_2^*+\theta_3$ by $\theta-\theta_1^*-\theta_2^*+2\theta_3$.

4. The displacement components are

$$d_r\sim-ih(r_0/r)A_{\varphi 2j} \qquad d_\theta\sim-ik(r^2-m^2r_0^2)^{1/2}/rA_{\varphi 2j};$$

then

$$d_r/d_\theta\sim-\cot\theta_1^*\,,$$

which means the vibration at $P$ is transverse in the meridian plane through $P$.

## § 18. Case of Small $\theta$

For the same reason as in § 13, we obtain for the series representing $d_r$, $d_\theta$ on the surface, except for the terms corresponding to $\nu_0$,

$$d_r=\frac{2ih}{(r_0r_s)^{1/2}}\int_{c_1+c_2}\frac{\nu P_{\nu-1/2}(-\cos\theta)}{\cos\nu\pi}\,\frac{H_\nu^{(2)}(kr_s)}{H_\nu^{(2)}(a)}\,\frac{\nu^2-1/4}{a^2}\left(F(\nu,ma)-\frac{3}{2ma}\right)\left[\left(1-\frac{2\nu^2}{a^2}\right)^2\right.$$
$$-\frac{9\nu^2}{a^2}+\frac{2}{a}\left(1+\frac{\nu^2-9/4}{a^2}\right)F(\nu,a)+\frac{2m}{a}\left(2-\frac{\nu^2-9/4}{a^2}\right)F(\nu,ma)-4m\frac{\nu^2-9/4}{a^2}F(\nu,ma)$$
$$\left.\times F(\nu,a)\right]^{-1}d\nu\,, \tag{18.1.1}$$

$$d_\theta=\frac{i}{(r_0r_s)^{1/2}r_0}\int_{c_1+c_2}\frac{\nu dP_{\nu-1/2}(-\cos\theta)/d\theta}{\cos\nu\pi}\,\frac{H_\nu^{(2)}(kr_s)}{H_\nu^{(2)}(a)}\left\{1-\frac{2(\nu^2+3/4)}{a^2}+\frac{4m}{a}F(\nu,ma)\right\}$$
$$\left[\left(1-\frac{2\nu^2}{a^2}\right)^2-\cdots\right]^{-1}d\nu\,, \tag{18.1.2}$$

where the integral contours $C_1$, $C_2$ are shown in Fig. 6.

The integrals along $C_1$ can be evaluated by the method employed in § 13 and we have

$$d_r=-4k^3r_0\sin^2\psi(m^2-\sin^2\psi)^{1/2}\cos\psi\{(1-2\sin^2\psi)^2+4\sin^2\psi\cos\psi(m^2-\sin^2\psi)^{1/2}\}^{-1}$$
$$\times(kR)^{-1}\exp(-ikR)\{1+0(1/kR)\}\,, \tag{18.2.1}$$

$$d_\theta=-2k^3r_0\sin\psi\cos\psi(1-2\sin^2\psi)\{(1-2\sin^2\psi)^2+4\sin^2\psi\cos\psi(m^2-\sin^2\psi)^{1/2}\}^{-1}$$
$$\times(kR)^{-1}\exp(-ikR)\{1+0(1/kR)\}\,, \tag{18.2.2}$$

by calculating the integrals along $C_1'$ through $i(\pi/2-\psi)$.

Next we investigate the integral along $C_2$; we put here

$$\nu=ma\cosh w$$

and investigate the contour $C_2'$ in $w$-plane. By studing the curve of steepests descents we find that for $\sin\psi<m$ these integrals are reduced to the previous ones and only for $\sin\psi>m$ we have new ones; they are shown to be

$$d_r=-4ikm^3a(1-2m^2)^{-2}\sin^{-1/2}\psi\cos^{3/2}\psi\sin^{-3/2}(\psi-\psi_1)(kR)^{-2}\exp\{-ikR\cos(\psi-\psi_1)\}$$
$$\{1+0(1/kR)\}\,, \tag{18.3.1}$$

$$d_\theta=8ik^2m^4a(1-2m^2)^{-3}\cos^{5/2}\psi\sin^{-1/2}\psi\sin^{-3/2}(\psi-\psi_1)(kR)^{-2}\exp\{-ikR\cos(\psi-\psi_1)\}$$
$$\{1+0(1/kR)\}\,, \tag{18.3.2}$$

where $\psi_1$ denotes the critical angle.

The displacement represented by (18.2.1), (18.2.2) is of the distortional wave and the one by (18.3.1), (18.3.2) is of the dilatational wave. These results are completely equivalent to those of Sakai's research (4) § 27~28).

## V. DISTORTIONAL SOURCE OF THE SECOND KIND

### § 19. General Form of the Solution

Since in this case the primary wave is given by (3.3), we assume as the secondary wave

$$d_\varphi{}^s=-(i/krr_s)\sum_{n=0}^{\infty}(2n+1)c_n\zeta_n(kr)dP_n(\cos\theta)/d\theta\ , \tag{19.1.1}$$

$$\Phi^s=A_\varphi{}^s=0\ , \tag{19.1.2}$$

where $c_n$ is an undetermined coefficient. Then the resultant is

$$\begin{aligned} d_\varphi=-(ikrr_s)\sum_{n=0}^{\infty}(2n+1)\{c_n\zeta_n(kr)+[\zeta_n(kr_s)\psi_n(kr),\ \text{or}\ \psi_n(kr_s)\zeta_n(kr)]\}& \\ \times dP_n(\cos\theta)/d\theta\ ,& \end{aligned} \tag{19.2}$$

according as $r<r_s$ or $r>r_s$.

After the same procedure as before we have

$$d_\varphi=-\frac{2\pi}{(rr_s)^{1/2}a}\sum_j\left[\nu\frac{dP_{\nu-1/2}(-\cos\theta)}{d\theta}\frac{1}{\cos\nu\pi}\frac{H_\nu{}^{(2)}(kr_s)H_\nu{}^{(2)}(kr)}{H_\nu{}^{(2)}(a)\partial\{H_\nu{}^{(2)\prime}(a)-(3/2a)H_\nu{}^{(2)}(a)\}/\partial\nu}\right]_{\nu=\nu_j}\ , \tag{19.3}$$

where $\nu_j$ means a zero of $H_\nu{}^{(2)\prime}(a)-(3/2a)H_\nu{}^{(2)}(a)$ qua function of $\nu$. According to 7) the zeros lie near the curve in the $\nu$-plane, which starts from $\nu=a$, making an angle $-\pi/3$ with the positive real axis, and goes off to $-\infty i$; the ones close to the real axis are given by

$$\nu_j\sim a\{1+(1/2)p_j{}^2+(1/120+(17/90\sigma_j{}^2))p_j{}^4+\cdots\}\qquad j=1,2,3,\cdots \tag{19.4}$$

where $p_j=(3\sigma_j/a)^{1/3}e^{5/6\pi i}$ and $\sigma$'s denote the roots of

$$H_{2/3}{}^{(2)}(\sigma e^{\pi i})=0\ ,$$

the first several ones being $0.6853843\cdots$, $3.9027676\cdots$, $7.0549300\cdots$, $10.2006884\cdots$, $13.3445027\cdots$; the zeros of extremely large moduli are of order of $-(m+1/4)\pi i/\log m$ with a large positive integer $m$.

To ascertain the convergence of this series, we estimate the order of magnitude of the terms corresponding to the large zeros, and find such terms are comparable with

$$-\nu^{3/2}e^{-i\nu\theta}a/\{\log\nu(\nu^2-a^2)^{1/2}\}$$

except when $\theta$ is small, and, therefore, the convergence is secured. Considering its rapid convergence for not small $\theta$, we evaluate the first several terms to estimate $d_\varphi$ in this case.

### § 20. Evaluation of the First Several Terms

Let us evaluate the term of the right-handed side of (19.3) corresponding to $\nu_j$, given by (19.4). As the result of calculation we find

$$\begin{aligned} d_{\varphi j}=-9kp_j{}^{-4}e^{-\pi/4i}&(J_{1/3}(\sigma_j)-J_{-1/3}(\sigma_j))^{-2}(1/kR_{QB}kR_{AP})(2kr_0\sin\theta_1\sin\theta_2/\pi \\ &\times\sin\theta)^{1/2}[1+\{59/60+1/4\cot^2\theta+1/4\cot^2\theta_2-(2/45\sigma_j{}^2)\}p_j{}^2] \\ &\times\exp[-ikR_{QB}-ikR_{AP}-ikr_0(\theta-\theta_1+\theta_2)\{1+1/2p_j{}^2+(1/120+17/90\sigma_j{}^{-2})p_j{}^4\} \\ &-i/8kr_0(\cot\theta_1+\cot\theta_2)p_j{}^4]\{1+0(1/kr_0)\} \end{aligned} \tag{19.5}$$

for $k(r-r_0)>0((kr_0)^{1/3})$, $k(r_s-r_0)>0((kr_0)^{1/3})$, if we use such notations as in Fig. 2, and

$$\begin{aligned} d_{\varphi j}=2kp_j{}^{-2}e^{-\pi/4i}&(2\pi/kr_0\sin\theta)^{1/2}[1+\{51/60-(2/45\sigma_j{}^2)-1/2k^2(r-r_0)^2-1/2k^2 \\ &\times(r_s-r_0)^2\}p_j{}^2]\exp[-ikr_0\theta\{1+1/2p_j{}^2+(1/120+17/90\sigma_j{}^{-2})p_j{}^4\}] \\ &\times\{1+0(1/kr_0)\}\{1+0((r-r_0)^3/r_0{}^3)\}\{1+0((r_s-r_0)^3/r_0{}^3)\} \end{aligned} \tag{19.6}$$

for $k(r-r_0)<0((kr_0)^{1/3})$, $k(r_s-r_0)<0((kr_0)^{1/3})$; the numerical values of $J_{1/3}(\sigma_j)-J_{-1/3}(\sigma_j)$ are $1.592206\cdots$, $-0.697477\cdots$, $0.519806\cdots$, $-0.432500\cdots$, $-0.378209\cdots$, $\cdots$ .

The properties are as follows:

1. The magnitude is proportional to $(kR_{QB}kR_{AP})^{-1}(\sin\theta_1\sin\theta_2/\sin\theta)^{1/2}$.

2. From the phase it is found that, if $\theta-\theta_1-\theta_2>0$, the distortional wave travels straight to $B$, then many waves corresponding to various $\sigma_j$ propagate on the surface to $A$ with the respective propagation velocity fairly close to $v_t$, that is, $v_t\{1-1/4(3\sigma_j v_t/\omega r_0)^{2/3}\}$, and then straight to $P$ with $v_t$. If $\theta-\theta_1-\theta_2<0$, the phase, approximately equal to $-ik\{R_{QB}-r_0|\theta-\theta_1-\theta_2|+R_{AP}\}$, means that the wave is reflected directly by the part of the surface between $A$ and $B$, as in the case of $\Phi_{2j}$ in § 12.

3. If $\theta-\theta_1-\theta_2>0$, it attenuates with increasing $\theta$, the rate being approximately given by $\exp\{-\sqrt{3}/4(3\sigma_j)^{2/3}(\omega r_0/v_t)^{1/3}(\theta-\theta_1-\theta_2)\}$. We tabulate below the numerical values of the rate corresponding to various values of $\sigma_j, \theta$ to give some idea about the order of each term, where $a$ is taken to be 100:

| | $\theta-\theta_1-\theta_2=0.1$ | 0.2 | 0.5 | 1.0 |
|---|---|---|---|---|
| $\sigma_1$ | 0.7225 | 0.5220 | 0.2725 | 0.03877 |
| $\sigma_2$ | 0.3548 | 0.1258 | 0.0158 | 0.00003 |
| $\sigma_3$ | 0.2149 | 0.0461 | 0.0021 | |
| $\sigma_4$ | 0.1400 | 0.0196 | | |
| $\sigma_5$ | 0.0952 | 0.0091 | | |

We see from it that for $\theta-\theta_1-\theta_2=0.2$ it suffices for us to take five terms to keep the error under one per cent, if we take only this point into consideration. For $\theta-\theta_1-\theta_2<0$ it increases exponentially with $\theta-\theta_1-\theta_2$, but this is to be interpreted as representing the qualitative behavior of the partial wave and we must sum up fairly many terms to estimate $d_\varphi$, since the terms increase their magnitude at first with increasing $\sigma_j$ and then begin to decrease when the relation $\nu_j-a=0(a^{1/3})$ becomes invalid.

4. The vibration at $P$ is apparently transverse and perpendicular to the meridian plane through $P$.

## § 21. Case of Small $\theta$

When $\theta\ll 1$, we can express $d_\varphi$ on the surface as

$$d_\varphi=\frac{i}{(r_0r_s)^{1/2}a}\int_{C_1}\frac{\nu dP_{\nu-1/2}(-\cos\theta)}{d\theta}\,\frac{1}{\cos\nu\pi}\,\frac{H_\nu^{(2)}(kr_s)}{H_\nu^{(2)\prime}(a)-(3/2a)H_\nu^{(2)}(a)}\,d\nu \tag{21.1}$$

referring to § 13. This becomes

$$d_\varphi=ika^{1/2}e^{\pi/4i}(2/\pi\sin\theta)^{1/2}\int_{C_1'}\cosh^{3/2}w\sinh w\exp\{-kR\sin\psi\cosh wi-kR\cos\psi\sinh w\}\{\sinh w+(3/2a)\}^{-1}dw\{1+0(1/kR)\}\,. \tag{21.2}$$

By integrating it along the curve of steepest descents through $i(\pi/2-\psi)$ we obtain

$$d_\varphi=-i2ka\sin\psi\exp(-ikR/(kR)\{1+0(1/kR)\}\,, \tag{21.3}$$

which is compatible with Sakai's result in the case of a plane surface 4) § 38).

## VI. CONCLUSION

### § 22.

By summarising the above results we have come to the following conclusion.

1. When a monochromatic elastic wave of dilatational character or distortional character of the first kind generated at the source reaches the surface, many secondary waves are produced, which, combined with the initial one, will be separated into three groups corresponding to three types of elastic waves on a plane surface, i.e. to the dilatational, distortional and Rayleigh waves. While the third group, $\Phi_0$, $A_{\varphi 0}$, consists of waves having such phase differences as correspond to the path differences of integral multiples of the whole circumference among themselves, the first two, $\Phi_1$ $A_{\varphi 1}$, $\Phi_2$, $A_{\varphi 2}$ are the groups of an infinite number of waves, corresponding to the two rows of the zeros of the function represented by the right side of (7.3) in the $\nu$-plane. When a distortional wave of the second kind has reached the surface, only the group of the same kind consisting of an infinite number of components occurs, corresponding to the zeros of the function $d/da\log H_\nu^{(2)}(a)-(3/2a)$.

2. If the field point is in such a position as exposed to the direct radiation from the source, the situation is not different essentially from that in the case of the reflection by a plane surface, already dealt with by, say, Sakai and our method is shown not to be so effective but to give us only some qualitative informations. The range we stated here to be exposed to the direct radiation does not always mean the region of points, which we can join with the source by a straight line without being intercepted by the surface as in geometrical optics, but the extent where the angle $\theta-\theta_1, \theta-\theta_1-\theta_2$, etc. are negative respectivly. This range, consequently, varies according as which wave are we concerned with and sometimes, as in the case of $A_\varphi$ in § 17, the field point fairly closed to the source may be still out of this range with respect to a certain kind of waves.

Out of this range, that is, in the shade, our method has shown its effectiveness and we have obtained the results that exhibit some significant features we shall state below.

3. In the shade, except for $\Phi_0, A_0$ in § 10, § 15, corresponding to Rayleigh wave in the case of a plance surface, the amplitudes of the waves attenuate exponentially with $\theta, \theta-\theta_1$, etc., the angles measuring their respective shades, which shows the continual dissipation on the surface on account of the continual change of the direction of propagation. The damping of $\Phi_0$. $A_{\varphi 0}$ in this respect is negligible so far as the radius of curvature of the surface is considerably large compared with their wave-length.

When travelling on the surface, all kinds of waves are of dispersive character, their propagation velocities depending on the frequency, although they are close to some of $v_l, v_t, v_R$, the veloctíes of dilatational, distortional and Rayleigh waves. Among the waves of the same kind the first-numbered, corresponding to the smallest $|\mathrm{Im}\nu|$ is the fast.

4. The case of a dilatational source. If the source is placed fairly far from the surface, only two sorts of waves belonging to the first group, $\Phi_2, A_{\varphi 2}$, are observable at any distance from the surface. These two sorts of waves propagate on the surface with the propagation velocities, though different for each member, considerably close to $v_l$ and then travel straight to the field point with $v_l$ and $v_t$ respectively, their respective vibrations being longitudinal and transverse in the meridian plane through the field point. While the so-called path of the former is tangential to the surface, that of the latter is oblique. Their amplitude is, except for the angluar dependence, inversely proportionaly to $R_{QB}R_{AP}$ and $R_{QB}R_{BA^*P}$, which are the product of the length of the straight path starting from the source and that of the straight path terminating at the field point and the product of the similar ones, respectively; this is essentially compatible with Huygens' principle. The extent of the shade is considerably larger for the latter than for the former, the shade of the former coinciding with that of geometrical optics.

When the source approaches to the surface, another kind of waves $A_{\varphi 1}$ becomes observable at any distance from the surface; the waves of this kind propagate round on the surface with the velocities close to $v_t$ and then travel to the field point along the straight path, tangential to the surface, with the velocity $v_t$, the vibration being transverse in the meridian plane. Their extent of the shade coincides with that in geometrical optics. The amplitude is, except for angular dependence, inversely proportional to $R_{AP}$. Still more, in the vicinity of the surface, waves of other three kinds $\Phi_0, A_{\varphi 0}, \Phi_1$ are observable. The first two propagate on the surface with the velocity, of which the group velocity is equal to $v_R$, and the last with the velocities equal to those of $A_{\varphi 1}$. The oscillations resulting from them are elliptically polarized ones with their own peculiarities.

5. The case of a distortional source of the first kind. If the source is considerably far from the surface, three sorts of waves, $\Phi_2$, $A_{\varphi 2}, A_{\varphi 1}$, belonging to the first and the second groups, are observable at any distance from the surface. The waves of the first two sorts propagate on the surface with the velocity, though differents from one another, close to $v_l$ and then straight to the field point with $v_l$, $v_t$, respectively. The path to the field point is tangential to the surface for $\Phi_2$, while for $A_{\varphi 2}$ it is oblique. The waves $A_{\varphi 1}$ travel on the surface with the velocity close to $v_t$ and propagate to the field point with $v_t$ along the path tangential to the surface. The extent of their shade increases in the order of $A_{\varphi 1}, \Phi_2$,

$A_{\varphi 2}$, the shade of $A_{\varphi 1}$ being coincident with that in geometric optics. Their amplitudes, omitting their angle-dependence, are inversely proportional to $R_{AP}R_{QB}$, $R_{QB^*}R_{AP}$, $R_{QB^*}R_{A^*P}$ respectively, the product of the lengths of the two straight paths or that of the analogous ones. The vibrations are transverse or longitudinal according as it results from $A_{\varphi}$ or $\Phi$. In the vicinity of the surface, waves of another short $\Phi_1$ also observable, which propagate with velocities close to $v_t$ and whose amplitudes are proportional to $R_{QB}$, the length of the straight path from the source. Their shade is coincident with that in geometrical optics. The vibrations resulting from them are elliptically polarized ones.

When the source approches the surface we can observe in the vicinity of the surface the surface waves $\Phi_0$, $A_{\varphi 0}$ which are quite analogout to those in the preceding case.

6. The case of a distortional source of the second kind. The waves of $d_{\varphi}$, corresponding to numerous zeros, propagate on the surface with velocities close to $v_t$ and travel straight to the field point with $v_t$. The extent of the shade is equal to that in geometrical optics. They, of cource, represent transverse vibration perpendicular to the meridian plane.

## Acknowledgment

I which to acknowledge my indebtness to to several persons for their help of my work. My gratitude is first due to late Professor Takuzo Sakai who indicated this problem and kindly guided me to establish the general plan. To Professor Isao Imai, I am indebted as well for much valuable advice during the work as for much encouragement during my depressive years due to my personal condition. I also wish to thank Professor Tosio Kato for many useful suggestions in informal talks. Further I wish to express my thanks to Dr. Hisamitu Nisi, President of University of Saga, for his kindness to administer to my convenience for research. I also wish to thank Dr. Tatudiro Sasaki, Chief of the Numerical Computation Bureau, Tokyo, for his generous permission to use the facilities of the institute and all the staffs of the Bureau, above all Mr. Masanori Masiko, for their sincere collaboration.

## References

1) H. Lamb: Phil. Trans. Roy. Soc. London, A **203** (1904) 1.
2) H. Nakano: Japan. Journ. Astron. Geophys. **2** No. 5 (1925).
3) K. Sezawa: Bull. Earthq. Res. Inst. **6** (1929) 1.
4) T. Sakai: Geophys. Mag. **8** (1934) 1.
5) Y. Nomura and K. Takaku: Journ. Phys. Soc. Japan. **7** (1952) 204.
6) G. N. Watson: Proc. Roy. Soc. A **95** (1919) 83.
7) M. Nagase: Journ. Phys. Soc. Japan **9** (1954) 826.
8) M. Nagase: Journ. Phys. Soc. Japan **9** (1954) 842.
9) G. N. Watson: The Theory of Bessel Functions (Combridge, 1922).
10) M. Nagase: Journ. Phys. Soc. Japan **9** (1954) 296.

JOURNAL OF THE PHYSICAL SOCIETY OF JAPAN Vol. 11, No. 3, MARCH, 1956

# Experimental Investigation of the Wakes behind Cylinders and Plates at Low Reynolds Numbers

By Sadatoshi TANEDA

*The Kobe University of Mercantile Marine*

(Received October 27, 1955)

Wakes behind cylinders and plates were photographically investigated at Reynolds numbers from 0.1 to 2,000. Main results are as follows.

In the case of a circular cylinder, the rear twin-vortices begin to form at $R=5$ ($R$ is $Ud/\nu$), then become more and more enlarged as $R$ increases, and finally become asymmetrical at about $R=45$. The laminar wake, on the other hand, begins to oscillate sinusoidally some distance downstream at $R=30$.

In the case of a flat plate parallel to the flow, the wake begins to oscillate sinusoidally some distance downstream at about $R=700$ ($R$ is $Ul/\nu$, where $l$ is the length of the plate).

Lastly, some detailed knowledges about the structure and the nature of the Kármán vortex street are obtained by a new method.

## § 1. Purpose and Outline of the Experiments

As for the flow of a fluid at low Reynolds numbers, some experimental and theoretical investigations have been made up to the present, but not a few problems are left still unsolved. It is well known that the calculations are successfully made with the approximations of Stokes or Oseen for very small Reynolds numbers, but as Reynolds number is increased, Oseen's as well as Stokes's approximations become more and more remote from the exact solution of the Navier-Stokes equations. On the other hand, the experiments which serve as a verification or guidance of the theories seem to be in great lack. The present author planned to investigate minutely the wakes behind circular cylinders and flat plates at Reynolds numbers from 0.1 to 2,000.

First, it was tried to determine the critical Reynolds number at which twin-vortices make their appearance in the rear of a circular cylinder. Concerning this problem there are several theoretical calculations[1][2][3]. It is from this aspect that the author is interested in the subject. Though some photographs of the flow around cylinders at low Reynolds numbers have already been taken by several experimenters[4][5], they are not fit for searching the critical Reynolds number, because the stream-lines in the immediate neighborhood of the rear stagnation point are not clear. Theauthor has succeeded in getting the clear stream-lines by giving long duration of the exposure.

Secondly, the experiments were made concerning the oscillation of the wake behind a circular cylinder. It is extremely difficult to detect the oscillation which appear in the wake for the first time, as it is very faint. In the present experiment, however, the ocillation was sensibly detected by utilizing the reflection of light from the aluminium dust suspended in the water. And it was found that the wake begins to oscillate at about $R=30$ and that the twin-vortices are independent, at least directly, of the oscillation of the wake.

Thirdly, the experiments were made using a model coated with condensed milk. This method enables us to see clearly the positions of separation point and the structure of twin-vortices. This series of experiments showed that the solutions of Navier-Stokes equations are in good agreement with the experimental data even in the case of $R=40$.

Fourthly, the wake behind a flat plates parallel to the direction of motion was investigated. In the case of a flat plate the separation does not occur, in other words twin-vortices do not appear, for this reason it is very interesting to investigate the relationship between the wake of a circular cylinder and that of a flat plate.

Lastly, the experiments by a new method clarifying the structure and the nature of the Kármán vortex street were carried out and some detailed knowledges concerned were obtained.

## § 2. Apparatus and Experimental Method

The experiments were carried out in the glass water tank of 100 cm in length, 20 cm in breadth and 30 cm in depth. The carriage, to which the model was attached, was moved on straight rails above the tank by means of a nut engaging on the lead screw which was turned by a 200 watt a.c. motor through a great box. The velocity of the carriage was varied in 10 steps by exchanging the gears. According to circumstances, d.c. motor could also be used. To obtain a uniform velocity, every part of the apparatus was carefully adjusted for a long period. Fig. 1 shows the general arrangement of the apparatus.

Table I.

| Circular Cylinder | | |
|---|---|---|
| $d$(mm) | $L$(mm) | $d/D$ |
| 6.00 | 300 | 1/33 |
| 3.93 | 250 | 1/51 |
| 2.95 | 250 | 1/68 |
| 1.99 | 200 | 1/100 |
| 1.54 | 200 | 1/130 |
| 1.02 | 180 | 1/196 |
| **Flat Plate** | | |
| $l$(mm) | $b$(mm) | $L$(mm) |
| 37.00 | 0.24 | 280 |
| 20.05 | 0.24 | 250 |

$d$: Diameter of the cylinder
$L$: Span of the model
$D$: Tank width
$l$: Length of the flat plate
$b$: Thickness of the flat plate

In order to visualize the motion of water below the free surface, aluminium dust was suspended uniformly in the water. And illuminating it by a sheet of intense light through a narrow slit, we could clearly observe the motion of water in the illuminated layer from the direction normal to the light. A 500 watt incandescent lamp with a line filament was used as the source of light.

The camera used was a Nikon F 1.4, and when necessary a Mirax (an enlarging equipment) was put on.

The sizes of the models are given in the Table I.

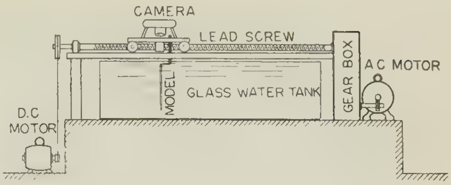

Fig. 1. Schematic diagram of the apparatus.

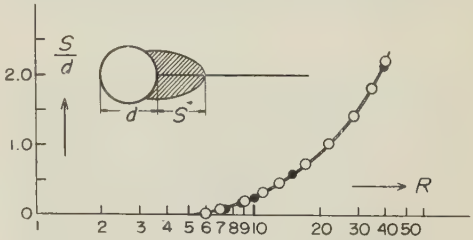

Fig. 2. Plot of $s/d$ against $R$.

## § 3. The Reynolds Number at which Twin-Vortices begin to Form in the Rear of a Cylinder

Concerning the critical Reynolds number at which twin-vortices begin to form in the rear of a circular cylinder, there has been no investigation except that by H. Nisi and A. Porter$^{6)}$, and little is known of the accurate value of the critical Reynolds number. This seems to be chiefly due to the extreme difficulties of the experimental technique.

In the present experiments the method of moving a model through still water was adopted. For such a low Reynolds number, even a very small residual motion of water cannot be neglected, therefore great care was taken to allow the water to come to rest before beginning an experiment.

A careful photographic technique was also required to get a sufficiently clear and sharp picture. A Mirax enlarging equipment was put on and the duration of the exposure was made sufficiently long.

It can be noticed from the photographs obtained that the twin-vortices are seen at $R=7$, though they are very small, but they are not seen at $R=6$. ($R$ is $Ud/\nu$, where $d$ is the diameter of the cylinder, $U$ is the model speed and $\nu$ is kinematic viscosity.) In the neighborhood of the critical Reynolds number, it is very difficult to detect the twin-vortices accurately for two reasons (i) the dimension of twin-vortices is still very small, (ii) the position they appear is situated in the immediate neighborhood of the rear stagnation

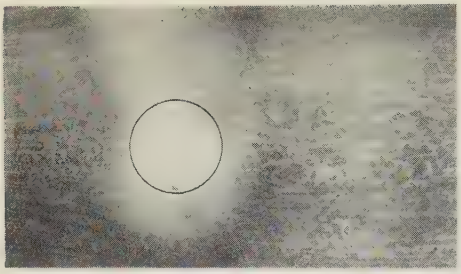

Photo 1. (a) $R=57.7$.

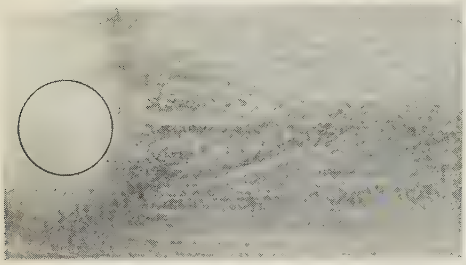

Photo 1. (b) $R=42.0$.

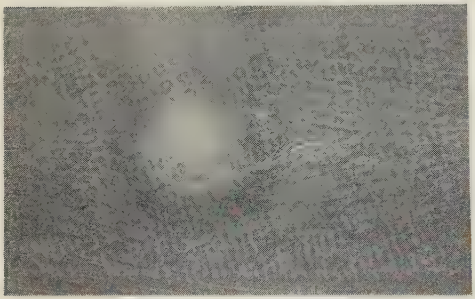

Photo 1. (c) $R=13.05$.

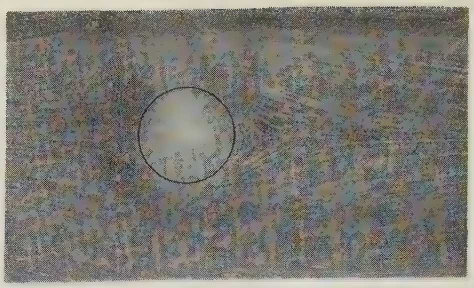

Photo 1. (d) $R=9.10$.

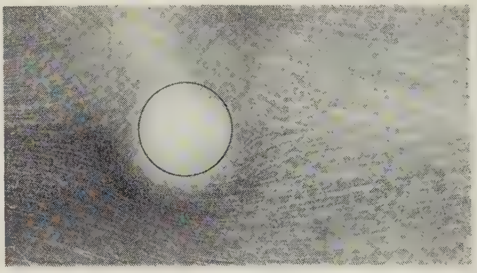

Photo 1. (e) $R=6.10$.

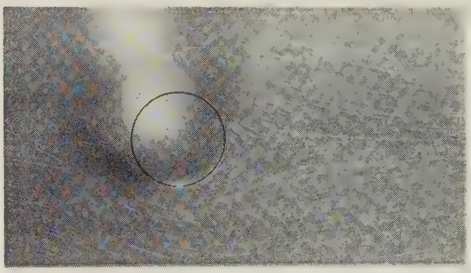

Photo 1. (f) $R=3.64$.

point where the velocity of the flow is extremely small. The size of twin-vortices, however, can be accurately measured at Reynolds numbers exceeding 7.

In Fig. 2 the size of twin-vortices is plotted against the Reynolds numbers, and from this curve the critical Reynolds number can be deduced. It may be concluded that the critical Reynolds number at which the twin-vortices begin to form in the rear of circular cylinder is 5.

Plate 1 shows the examples of the photographs obtained.

Further, the experiments indicate that the wall effect of the tank can be neglected when $d/D<1/50$ (where $d$ is the diameter of the cylinder and $D$ is the tank width).

## § 4. Twin-Vortices

The twin-vortices appear in the rear of a cylinder at $R=5$, and as the Reynolds number is increased these two eddies grow and become more and more elongated in the flow direction. But they adhere stably on the cylinder until the Reynolds number is reached of about 45.

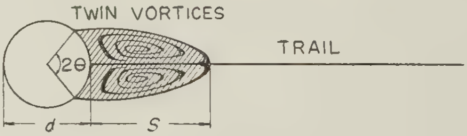

Fig. 3.

Thus, the wake behind a circular cylinder consists of two parts, twin-vortices and trail, at Reynolds numbers between 5 and 45. (see Fig. 3).

When a cylinder coated with condensed milk is set in motion in water, the milk melts in the wake little by little and draws clearly the boundary-line of the twin-vortices. Plate 2 are the examples of the photographs obtained by this method.

At $R>35$ a remarkable phenomenon is

observed. Tiny irregular gathers appear in the boundary of the twin-vortices, move downstream along the boundary-line till they reach the rear end of the twin-vortices, tremble for a short time and are died away. This small irregular motion, however, does not produce any effect on the flow behind the twin-vortices untill the Reynòlds number is reached of about 45.

The trail, on the other hand, begins to oscillate sinusoidally some distance downstream at $R=30$, and its amplitude becomes larger as the Reynolds number is increased. When the Reynolds number is reached of 45, the oscillation of the trail begins to exert an influence upon the twin-vortices. At Reynolds numbers above 45, the gathers of the twin-vortices are elongated along the trail, shed alternately from each of the twin-vortices and pass downstream, where they arrange themselves in a configuration corresponding to that of a Kármán vortex street. But a large portion of the twin-vortices is still stably attached on the cylinder. The size of the gather which travel downstream increases with the Reynolds number, and for Reynolds numbers above 150 a large portion of the twin-vortices are shed.

In 1953 Kawaguchi[7) carried out calculations about the flow arround a circular cylinder for the case $R=40$, integrating numerically the exact Navier-Stockes equations. Comparison between the calculations and the experimental data is shown in Table II. It may be concluded from Table II that the solutions of Navier-Stokes equations are in good agreement with the experimental data in the neighborhood of a circular cylinder even for $R=40$.

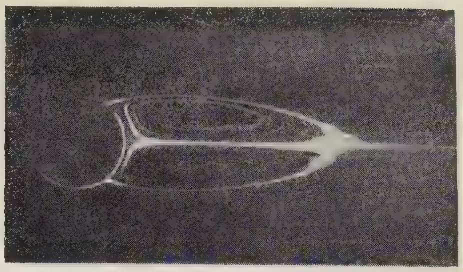

Photo 2. (a) $R=41.0$.

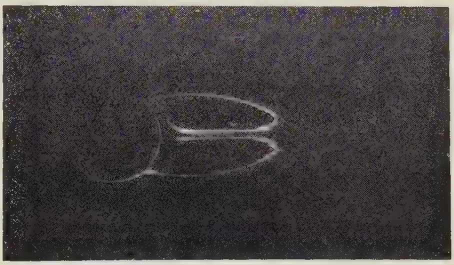

Photo 2. (b) $R=28.4$.

Table II.

| | | Calculated | Measured |
|---|---|---|---|
| Position of separation | $\theta$ | 52.2° | 53° |
| Size of twin-vortices | $s/d$ | 1.9 | 2.1 |

## § 5. Oscillation of the Wake behind a Circular Cylinder

The experiments about the oscillation of the wake behind a circular cylinder were carried out in the past by Thom (1933)[8) and Kovasznay (1949)[9), but comparatively little is known about the process of its development. The author planned to investigate this problem minutely.

As the oscillation which appears for the first time in the trail is very faint, its detection is extremely difficult. In the present study, however, the oscillation was sharply detected by means of the aluminium dust method. When the light comes into the water with suspended aluminium dust, we see innumerable tiny particles continually twinkling in the illuminated layer, and of course the brightness distributes homogeneously over the illuminated section so far as no motion of water exists. However, as soon as the wake begins to oscillate, there appears periodically striped pattern of brightness. As was clarified in the previous paper[10), this pattern relates to the direction of the local flow. Thus the wave-length of the wake was determined by examining the photographs. The relation between the wave-length $\lambda$ and the frequency $N$ is given by

$$\frac{d}{\lambda}=\frac{Nd}{U}\,\frac{U}{U-v}$$

where $U$ is the velocity of the cylinder and $v$ the velocity of the vortex filament. The wave length shows a tendency to increase downstream, so all the measurements were made at 20 diameters downstream from the cylinder.

The results are illustrated graphically in Fig. 4, and an example of the photographs is shown in Plate 3. The present experiment

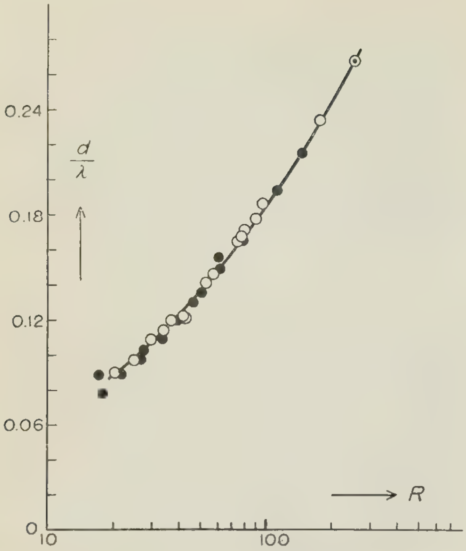

Fig. 4. Plot of $d/\lambda$ against $R$.

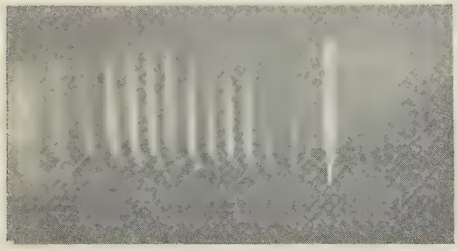

$R=42.0$.

Photo 3. Oscillation of the wake behind a circular cylinder.

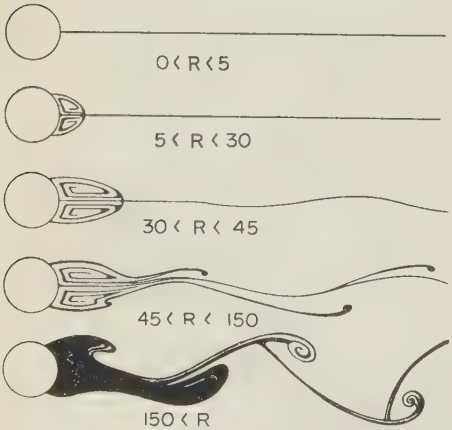

Fig. 5. Process of the development of the wake behind a circular cylinder.

indicates that the critical Reynolds number at which the wake begins to oscillate is 30.

Of course if the cylinder is given a slight shock, the oscillation of the wake appears even at Reynolds numbers below 30. It should be noticed that the $d/\lambda-R$ curve is continuous at Reynolds numbers above 20, and does not show any sign of discontinuity at $R=30$ and at $R=45$.

As oscillation of the wake is affected strongly by the wall of the water tank, the present experiment was carried out at $d/D < 1/100$.

The process of the development of the wake behind a circular cylinder is summarized in Fig. 5.

## § 6. Oscillation of the Wake behind a Flat Plate

In the case of the cylinder the phenomenon is complicated as the wake is constituted from two parts, the twin-vortices and the trail. On the other hand, in the case of the flat plate parallel to the direction of motion, the phenomenon is simple because it consists of only one part, i.e. the trail.

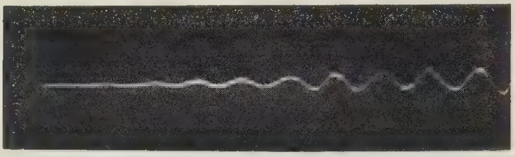

(a) Neighborhood of plate. ($R=1815$)

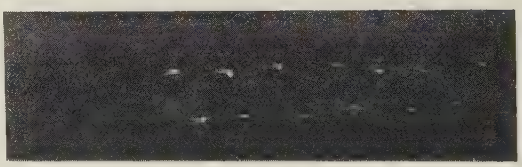

(b) Downstream development of oscillation. ($R=1815$)

Photo 4. Oscillation of the wake behind a flat plate.

The plates used were made of steel and carefully tapered smoothly to sharp edges. The dimensions are shown in Table 1.

The results of the experiment indicated that the wake begins to oscillate at about $R=700$ ($R$ is $Ul/\nu$, where $l$ is the length of the plate) some distance downstream from the plate.

Some examples of the photographs obtained are shown in Plate 4.

As is seen from the photographs, the wake is laminar for a short distance behind a flat plate whilst further downstream it becomes sinusoidal and vortices appear in its loops. The appearance of the Karman vortex street is similar to the case of a circular cylinder. However, there is a little difference between the two cases of a plate and a cylinder; in the case of a flat plate the vortex filaments are produced from the general flow, while in the case of a circular cylinder they are shed from the twin-vortices. For this reason the shape of the wake behind the flat plate is a little different from that of the wake behind the circular cylinder.

## § 7. Structure of the Kármán Vortex Street

In order to observe the fine structure of the Kármán vortex street, experiments were carried out by two methods at the same time; one the aluminium dust method and the other, the condensed milk method. The aluminium dust enables us to see the velocity field, and the milk clearly shows the boundary between the flow which passed the right hand side of the cylinder and that passed the left.

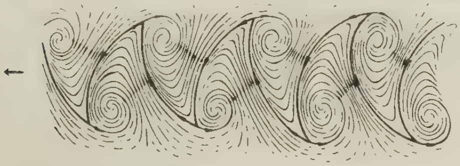

Fig. 6. Sketch of the Kármán vortex street. This is the picture seen from the view point which rests relatively to the vortex street.

Thus, when two methods are applied at the same time, we can acquire the detailed knowledges about the structure and the nature of the vortex street. The sketch of the Kármán vortex street is shown in Fig. 6.

The Kármán vortex street is deformed as time goes on and finally it is destroyed into pieces. But after an interval these scattered vortices are united and there appears again a new Kármán vortex street, the dimension of which is much larger than that of the primary one. This does, however, not always take place. It was often observed that the primary Kármán vortex street became directly turbulent flow.

In conclusion, the author wishes to express his thanks to Professor Hikoji Yamada of Research Institute for Applied Mechanics, for suggesting this investigation as well as for constant guidance in the course of this work.

## References

1) S. Tomotika and T. Aoi: Quart. Journ. Mech. App. Math. **3** (1950) 140.
2) I. Imai: Unpublished (1954).
3) H. Yamada: Rep. Res. Inst. App. Mech. **3** (1954) 11.
4) F. Homann: Forschung auf dem Gebiete des Ingenieurwesens **7** (1936) 1.
5) L. Prandtl and O. Tietjens: *Hydro-und Aeromechanik* **2** (Springer, Berlin).
6) H. Nisi and A. W. Porter: Phil. Mag. (6) **46** (1923) 754.
7) M. Kawaguchi: J. Phys. Soc. Japan **8** (1953) 747.
8) A. Thom: Proc. Roy. Soc. **A 141** (1933) 651.
9) L. S. G. Kovasznay: Proc. Roy. Soc. **A 198** (1949) 174.
10) S. Taneda: Rep. Res. Inst. App. Mech. **1** (1952) 131.

JOURNAL OF THE PHYSICAL SOCIETY OF JAPAN Vol. 11, No. 3, MARCH, 1956

# Apparatus for the Study of Spectral Response of Photoelectric Surface

By Hiroji MITSUHASHI and Tadahisa NAKAYAMA

*Technical Research Laboratory, Japan Broadcasting Corporation*
*Kinuta-machi, Setagaya-ku, Tokyo, Japan*

(Received September 19, 1955)

An optical instrument was designed which measures the photoelectricity for the visible wavelength region rapidly and accurately. *The output from a monochromator is kept constant for a long time.* The monochromatic beam emerging from it is split into two beams, one of which is brought to focus on a thermocouple alternately with the other white beams coming from a reference light source of well-stabilized brightness. Difference in intensity between these monochromatic and white beams generates ac signal which drives the optical attenuator in front of the entrance slit of the monochromator until their intensities are brought into balance. The other monochromatic beam is fallen upon a photoelectric surface, spectral response of which is recorded automatically.

## § 1. Introduction

It has become necessary to know the spectral response of the photoelectric surface, not only for study of their properties but also for their applications to spectrophotometry and television. If $E_\lambda$ is the intensity of the incident monochromatic beam and $I_\lambda$ the photocurrent from the surface then the spectral response $S_\lambda$ is given by

$$S_\lambda = k\frac{I_\lambda}{E_\lambda}\,. \tag{1}$$

It is clear from (1) that if we can keep $E_\lambda$ constant irrespective of wavelength by some means, then $I_\lambda$ is directly proportional to the spectral response. This is the principle of the instrument described here. Although there are many other ways of measurement of the photoelectric response,[1)2)3)4)] the authors believe that this is one of the most reliable methods.

To keep $E_\lambda$ constant, the intensity of the beam is controlled by the double beam principle: that is the radiation from the monochromator and reference white light are fed alternately to a thermocouple to induce the alternating thermoelectric voltage, which after being amplified operates a comb attenuator in front of the entrance slit of the monochromator so as to compensate the difference in intensity between them. Thus the intensity of monochromatic beam becomes automatically constant.

## § 2. General Arrangements of the Instrument

The arrangements of the instrument are shown schematically in Fig. 1. $S$ is a tungsten lamp and its color temperature is about 2800°K, whose intensity distribution is corrected by a blue filter. The monochromator consists of a single Littrow prism $P$ and collimating mirror $M_1$, operating about 7° off axis. Width of the entrance and exit slits $SL_1$ and $SL_2$ is fixed at 0.3 mm for all wavelengths. The intensity of the monochromator is stronger at 7000 Å than at 4000 Å by a factor of about 400. (ca $10^{-6}$ watt at 4000 Å.) W is an optical attenuator of comb form. The attenuation factor of about 3 percent of the maximum transmission is attainable.

The beam from the monochromator is brought to focus on the surface of a rotating semi-circular mirror $M_6$, which splits the beam into two. The reflected beam is introduced to the photosurface under investigation. The other beam is focused on a thermocouple connected with a servo-system to control the intensity of the beam. $S_0$ is a small standard lamp, whose wattage is very small (less than 1 watt), so the brightness is kept exactly constant for a long time. L is a lens, $M_9$ a plane mirror, and B a semi-annular shutter which rotates coaxially with $M_6$. The shutter is open while the beam from the monochromator is reflected toward the photosurface, and *vice versa*. The thermocouple generates an ac signal, as long as the intensities of the monochromatic and white beams are unbalanced. The phase of the signal is dependent on which of the beams is the stronger. This signal after amplification and subsequent phase-sensitive demodulation drives the balancing motor $MO_3$. The comb attenuator W is driven by this motor.

## § 3. Radiation Detector and Amplifiers

In order to keep the neutrality of pulsating monochromatic beam well, the radiation detector must have a rapid and non-selective response. Thermocouple of Bi–Sb and Bi–Cd alloy with gold-black receiver is best fitted for the purpose. The one here used has the following characteristics:

Radiation receiving area $=0.3\,\text{mm}\times2.3\,\text{mm}$
Electrical resistance $=5$ ohms
Sensitivity to stationary radiation $=1\,\mu\text{V}/1\,\mu\text{W}$
Time constant $=0.03$ second

If we assume the exponential build-up and decay of the thermocouple temperature in response to the pulsating radiation, the following relation for the ratio of the fundamental frequency component $E_\nu$ of the resulting thermoelectric voltage to that caused by stationary radiation $E_0$ is obtained;

$$E_\nu/E_0=2/(\pi\sqrt{1+4\pi^2\nu^2\tau^2})\ , \qquad (2)$$

where $\tau$ is the time constant of the thermocouple and $\nu$ is the frequency of the incident radiation. It is found advisable from (2) that $\nu\tau$ is not larger than 0.2. We chose $\nu=5$ c.p.s., as it cannot be made so small due to frequency susceptible of amplification. As the incident energy to the thermocouple by the violet radiation generates a signal of about $10^{-6}$ volt, the least effective radiation in putting the comb in motion corresponds to the signal as low as $10^{-8}$ volt. If the band width of amplification is made less than 0.5 c.p.s., Johnson noise of our thermocouple becomes $2\times10^{-10}$ volt. Although there are many literatures of the amplifier for very feeble signal,[5)6)] the one we constructed is of four stages, sharply tuned to 5 c.p.s. (Fig. 2.) The signal of the thermocouple is fed to a input transformer. The electron tube used for preamplification is a pentode 6SJ7 whose input noise level is about $5\times10^{-8}$ volt, partition noise being decreased by adopting triode connection. It is necessary for the noise transformed at the secondary winding to surpass that of the preamplifier tube. Therefore, the least turn ratio required for the transformer is 250, whereas it is 280 in our case. A twin-T filter is used to reduce the band width of the amplifier, with the result that $\Delta\nu=0.6$ c.p.s. The amplified 5 c.p.s. signal is fed to rotating phase-sensitive detector. The overall voltage gain of the ac amplifier preceding the servo amounts to about 145 db. By photographing the noise pattern using oscilloscope, it was made clear that Johnson noise of the thermocouple limits the minimum perceptible signal.

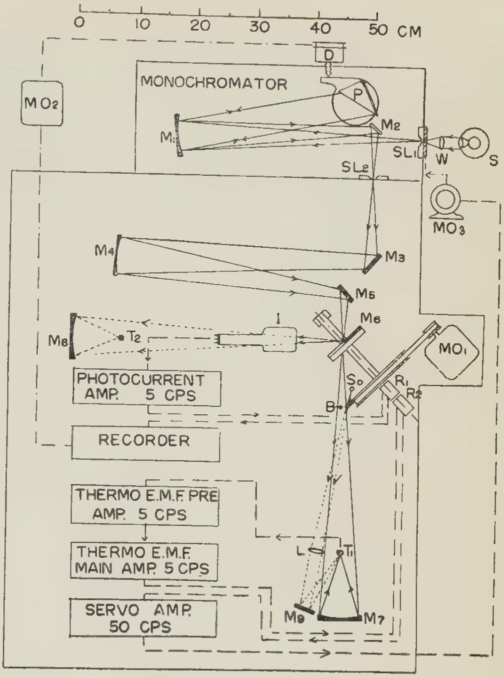

Fig. 1. General arrangements of the apparatus. S: Light source, W: Optical attenuator, $SL_1$, $SL_2$: Slits of the monochromator, P: Prism, D: Wavelength drum, $M_1$, $M_4$, $M_7$, $M_8$: Concave mirrors, $M_2$, $M_3$, $M_5$, $M_9$: Plane mirrors, $M_6$: Rotating semi-circular mirror, $S_0$: Standard lamp, L: Lens, B: Rotatng semi-annular shutter for $S_0$, $T_1$: Thermocouple for energy control, $T_2$: Photoconductor studied, I: Phototube studied, $R_1$, $R_2$: Phase-sensitive detectors, $MO_1$: semi-circular mirror drive motor, $MO_2$: Wavelength motor, $MO_3$: Attenuator drive motor.

The photocurrent is amplified through another feed-back amplifier reported by Sturtevant.[7)] Two such amplifier units are connected in tandem to give overall voltage

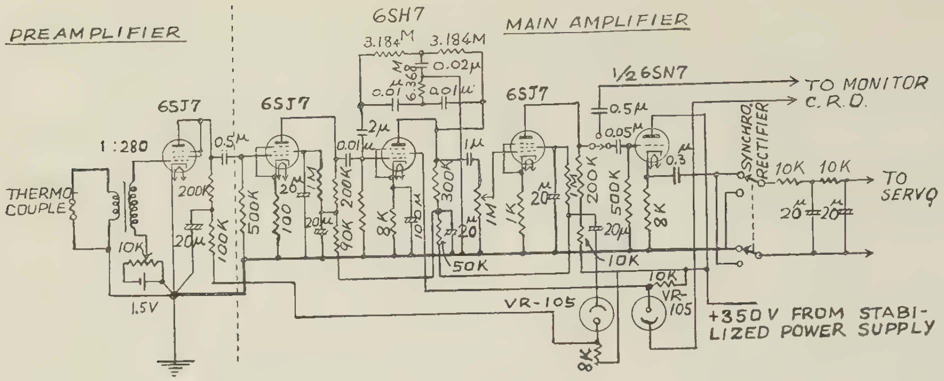

Fig. 2. Electrical circuit of the thermocouple amplifier.

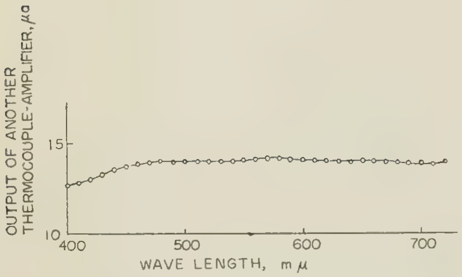

Fig. 3. Effectiveness of the controlling thermocouple.

amplification of 90 db. Ordinarily the band width of 0.3 c.p.s. is admitted. Excellent linearity as well as stability was obtained by heavy application of negative feed-back.

## § 4. Accuracy and Results of Measurements

The accuracy of our instrument mainly depends on the following characteristics.

i) Neutrality of the thermocouple receiver.
ii) Constancy of the beam energy from the monochromator.
iii) Spectral purity of the output radiation from the monochromator.

To test the neutrality of the thermocouple, diffuse spectral reflectance and transmittance of gold-black evaporated on a glass substratum were measured with a spectrophotometer of Beckman type. Deviation from perfect neutrality is less than ±2 percent.[8] The constancy of the output from the monochromator was studied with another thermocouple $T_2$, placed at the position optically symmetrical to the controlling thermocouple $T_1$. The signal from the controlled beam at $T_2$ is amplified through another amplifier, the microammeter record of which after demodulation is shown in Fig. 3. The control is satisfactory within ±1 percent. As to the spectral purity, resolving power of the monochromator is about 20 Å at 4000 Å and about 160 Å at 7000 Å.

Time required for the measurement of the spectral response of one surface is about 20 minutes. The final error can be reduced to

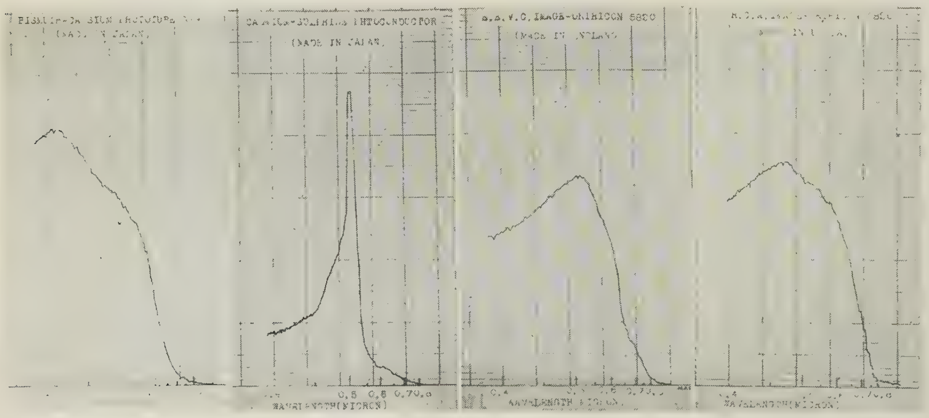

(a) (b) (c) (d)

Fig. 4. Measured spectral responses of some photosurfaces.

about one percent if we calibrate the errors arising from thermocouple with black body. Various experimental data are shown in Fig. 4.

## § 5. Conclusion

The instrument here described has been used in our laboratory for more than one year giving good results.

In conclusion, the authors are greatly indebted to Mr. T. Matsunami of Tokyo Optical Company for the efforts he made in mounting the double-beam arrangements, and to Mr. M. Nakamura and Mr. K. Kudo of Tokyo University of Education, for the preparation of gold-black and thermocouples. In addition, the authors wish to express their appreciation to the members of the Technical Research Laboratory, Japan Broadcasting Corporation, particularly to Dr. A. Yamashita, Mr. H. Kobayashi, Dr. K. Matsuyama and Mr. M. Yamada for their encouragements they have given throughout the work.

### References

1) J. T. Tykociner and L. R. Bloom: J. Opt. Soc. Am. **31** (1941) 689.
2) H. B. DeVore and J. W. Dewdney: Phys. Rev. **83** (1951) 805.
3) D. G. Avery and P. H. Hammond: J. Sci. Instr. **30** (1953) 400.
4) H. S. Moran: J. Opt. Soc. Am. **45** (1955) 12.
5) L. C. Roess: Rev. Sci. Instr. **16** (1945) 172.
6) Baird et al: J. Opt. Soc. Am. **37** (1947) 211.
7) J. M. Sturtevant: Rev. Sci. Instr. **18** (1947) 124.
8) H. Mitsuhashi: Science of Light **4** (1955) 61.

---

JOURNAL OF THE PHYSICAL SOCIETY OF JAPAN Vol. 11, No. 3, MARCH, 1956

# New Determination of the Temperature of Gold and Silver Points on the Thermodynamic Temperature Scale

By Jiro OISHI, Mitsuru AWANO and Takeshi MOCHIZUKI*

*Physics Department, Tokyo Institute of Technology,*
*Oh-Okayama, Meguro-ku, Tokyo*

(Received September 29, 1955)

The freezing points of gold and silver are determined by a constant volume nitrogen gas-thermometer with a gas bulb made of silica glass.

The temperature of the gold point which is adopted as 1063.0°C on the International Temperature Scale is determined as

$$T_{\mathrm{Au}}=1336.84\pm0.05$$

on the Kelvin Scale and

$$t_{\mathrm{Au}}=1063.69\pm0.05$$

on the Celsius Scale.

The temperature of the silver point which is 960.8°C on the International Temperature Scale is

$$T_{\mathrm{Ag}}=1234.43\pm0.05 \quad \text{and} \quad t_{\mathrm{Ag}}=961.28\pm0.05$$

on the Kelvin and Celsius Scales respectively.

## § 1. Introduction

The freezing point of gold is the only fundamental fixed point in radiation region of the International Temperature Scale. The temperature on the Kelvin Scale is to be determined by gas-thermometric measurement with the triple point of water or the ice point as reference point which is 273.16 or 273.15°K respectively. From the measurements by Holborn and Day[1] in 1901 and Day and Sosman[2] in 1910, the "gold point" was estimated as 1063°C which was subsequently adopted on the International Temperature Scale. Based on this temperature of the gold point, a number of pyrometric measurement had been made on the radiation constant $C_2$ in the past and 1.432 cm·deg was obtained as the mean value which was also adopted for the International Temperature Scale in 1927.

---

* Now at the Central Inspection Institute of Weights and Measures, Ginza-Higashi, Chuo-ku, Tokyo.

On the other hand, recently revised values of the atomic constants, from which the most reliable value of $C_2$ was obtained, necessitated a change in the value to 1.43868 cm·deg[3)] and 1.438 cm·deg was adopted for the International Temperature Scale in 1948. As it is presumed that this discrepancy in the value of $C_2$ might have been caused by inexactness of the past temperature or radiation measurements, carrying out of accurate measurement is advisable to determine anew the thermodynamic temperature of the gold point with present day technique not only to do away with the confusion but also because of the gold point being the only fundamental fixed point on which all the other temperatures in radiation region depend. Reproducibility in measurement of high temperature fixed points is now 0.1 deg and so the value of the gold point is given to the decimal place as 1063.0°C on the International Temperature Scale in 1948, whereas, the accuracy of measurement in those days of Holborn, Day and Sosman was about 1 deg.

The present work was undertaken with the objects of determining the thermodynamic temperature of some high temperature fixed points by a gas thermometer and, at the same time, of examining the propriety of the old measurements at the gold and silver points.

## § 2. Theoretical

### (a) Reduction of the gas thermometer temperature by constant volume gas thermometer to the Kelvin temperature

For a definite mass of gas enclosed in a constant volume gas thermometer, the following relation holds between two temperatures $T$ and $T_0$, the ice point, on the Kelvin Scale:

$$p_0\left(\frac{V_{0p_0}}{T_{vo}}+\sum_{n=1}^{n}\frac{v_n}{T_{vn}}\right)=p_t\left(\frac{V_{tp_t}}{T_v}+\sum_{n'=1}^{n'}\frac{v_{n'}}{T'_{vn'}}\right), \qquad (1)$$

where $p_0$ and $p_t$ are the observed pressures when the gas bulb is kept at the ice point and $t$°C, $V_{0p_0}$ and $V_{tp_t}$ the volumes of the gas bulb at the ice point and $t$°C, $T_{v0}$ and $T_v$ the absolute temperatures of the ice point and $t$°C on the constant volume gas thermometer scale respectively. $T_{vn}$ is the absolute temperature of the part $n$ of the dead space $v$ at the time of measuring the ice point, and $T'_{vn'}$ is that of $v_{n'}$ at $t$°C.

The volumes of the gas bulb at 0°C and $t$°C are expressed by

$$V_{0p_0}=[V_{0p}]_{p=0.76}\,[1+\mu(p_0-0.76)] \qquad (2)$$

and

$$V_{tp_t}=[V_{0p}]_{p=0.76}(1+\lambda t) \qquad (3)$$

respectively, for the outside pressure 1 atm and the inside pressure $p_t$ which is also nearly equal to 1 atm.

Expressing the slopes of $pv$-$p$ isotherms of a gas at the ice point and $t$°C by $B_0$ and $B_t$ respectively, we have the following relation which gives the correction due to gas imperfection:

$$\frac{T_v}{T_{v0}}=\frac{T}{T_0}\frac{1}{F_t}, \qquad (4)$$

where

$$F_t=\frac{1+p_0B_0}{1+p_0B_t}. \qquad (5)$$

Hence, we have from the above equations

$$T=T_0\frac{p_t}{p_0}\cdot\frac{1+\lambda t+T_v/[V_{0p}]_{p=0.76}\sum_{n'=1}^{n'}v_{n'}/T'_{vn'}}{1+\mu(p_0-0.76)+T_{v0}/[V_{0p}]_{p=0.76}\sum_{n=1}^{n}v_n/T_{vn}}\cdot F_t\,, \qquad (6)$$

where the latter fractional expression of the right side is to correct the entire gas occupying the same volume to be at 0°C and $t$°C respectively. Thus we obtain the value of $T$ from the observations of the related quantities, using $T_0=273.15$, the value adopted at the Tenth General Conference of Weights and Measures in 1954, and $B_0$- and $B_t$-values of the thermometric gas.

For nitrogen gas which was used in the

present work, $B_t$- values have not been measured at high temperatures above 400°C, but by extrapolating Keyes'[4)] formula, we find $B_{t_{\mathrm{Au}}}=179.6\times10^{-5}$ 1/mHg and $B_{t_{\mathrm{Ag}}}=177.2\times10^{-5}$ 1/mHg for the gold and silver points respectively. Taking these $B_t$-values and $B_0=-58.7\times10^{-5}$ 1/mHg, we have as the correction factors of the gas scale for the Kelvin scale at these two fixed points:

$$F_{t_{\mathrm{Au}}}=1-0.00238\,p_0 \tag{7}$$

and

$$F_{t_{\mathrm{Ag}}}=1-0.00236\,p_0\,, \tag{8}$$

and these relations also hold at temperatures near the gold and silver point respectively.

### (b) The determination of the thermodynamic temperatures of the gold and silver points

Difference of temperatures in the neighbourhood of the gold or silver point is determined by a standard thermocouple, for which the temperature-emf relation is expressed by the equation

$$e=a+bt+ct^2\,,$$

where the constants $a, b$ and $c$ are determined by the calibrations at antimony, silver and gold points.

Expressing the emf's at the gold point $t_{\mathrm{Au}}$, the silver point $t_{\mathrm{Ag}}$ and a temperature $t$ near $t_{\mathrm{Au}}$ or $t_{\mathrm{Ag}}$ by $e_{\mathrm{Au}}, e_{\mathrm{Ag}}$ and $e_t$ respectively, we have

$$t_{\mathrm{Au}}=t+(e_{\mathrm{Au}}-e_t)\Big/\left(\frac{de}{dt}\right)_{t_{\mathrm{Au}}} \tag{9}$$

or

$$t_{\mathrm{Ag}}=t+(e_{\mathrm{Ag}}-e_t)\Big/\left(\frac{de}{dt}\right)_{t_{\mathrm{Ag}}}, \tag{10}$$

where

$$\left(\frac{de}{dt}\right)_{t_{\mathrm{Au}}}=k+2c\,\frac{t_{\mathrm{Au}}-t_{\mathrm{Ag}}}{2}\,,$$

$$\left(\frac{de}{dt}\right)_{t_{\mathrm{Ag}}}=k-2c\,\frac{t_{\mathrm{Au}}-t_{\mathrm{Ag}}}{2}$$

and

$$k\equiv\frac{e_{\mathrm{Au}}-e_{\mathrm{Ag}}}{t_{\mathrm{Au}}-t_{\mathrm{Ag}}}=\left(\frac{de}{dt}\right)_{(t_{\mathrm{Au}}+t_{\mathrm{Ag}})/2}\,.$$

We obtain $k=11.57\,\mu\mathrm{V\cdot deg^{-1}}$ and $c=1.558\times10^{-3}\,\mu\mathrm{V\cdot deg^{-2}}$, from the characteristics of one of the standard thermocouples given in Table II shown later on. Hence, we have

$$T_{\mathrm{Au}}-T=t_{\mathrm{Au}}-t=(e_{\mathrm{Au}}-e_t)\times0.0853 \tag{11}$$

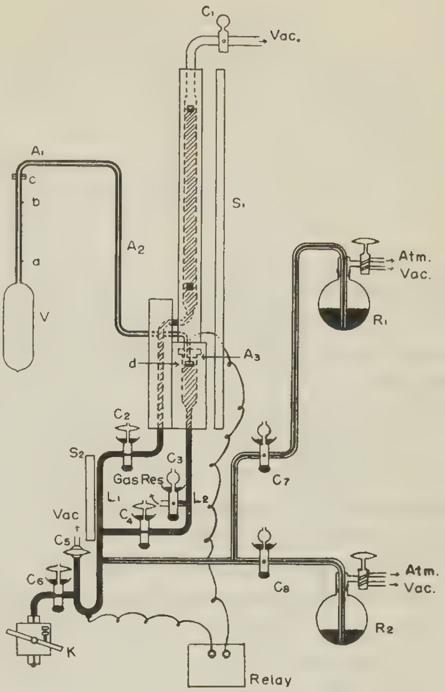

Fig. 1. The constant volume gas thermometer.

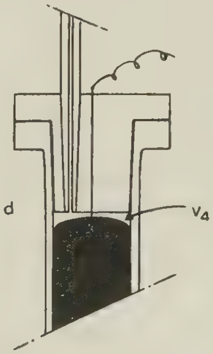

Fig. 2. Top portion of the lower tube of the manometer.

or

$$T_{\mathrm{Ag}}-T=t_{\mathrm{Ag}}-t=(e_{\mathrm{Ag}}-e_t)\times0.0876 \tag{12}$$

for a temperature near the gold or silver point respectively. Therefore, we can determine the values of the gold and silver points on the thermodynamic temperature scale from the gas-thermometric measurements at temperatures near the gold and silver points respectively.

## § 3. Experimental

### (a) The gas thermometer

The gas thermometer of the constant volume type, with the gas bulb made of silica glass,

Table I. Effect of cooling velocity on the change in volume of silica bulb.

| Method of cooling | Cooling rate (deg/hour) | $p_h$ (atm) | $p_0$ (atm) | $V_0$ (cc) | $V_0'$ (cc) | $\Delta = V_0' - V_0$ (cc) | $\lvert\Delta\rvert$ (%) |
|---|---|---|---|---|---|---|---|
| Natural cooling | 350 | 1 | 1 | 230.250 | 230.309 | +0.059 | 0.026 |
| Slow cooling | 45 | 1 | 1 | 230.113 | 230.114 | +0.001 | <0.001 |
| 〃 | 〃 | 2 | 2/5 | 230.113 | 230.161 | +0.048 | 0.021 |
| 〃 | 〃 | 1 | 1/5 | 151.540 | 151.539 | −0.001 | <0.001 |

is shown diagramatically in Fig. 1. At the mark c, a ground flange joint of 2 cm in diameter, which is pressed hard between two metal plates and the perimeters of which are cemented by Glyptal lacquer, is used to connect the capillary stem of the gas bulb to a soda glass capillary of about 0.3 mm in inner diameter which is connected to the lower tube of the mercury manometer. The whole system was assuredly made leak-proof to retain the mass of gas absolutely constant. In fact the 0°-pressure of the gas in the thermometer remained unchanged for days before the gas bulb was heated at high temperatures.

*The manometer* Top portion of the lower tube of the manometer is shown in Fig. 2. A glass lid with a ground cone joint is used at the top of the manometer. The lid and the manometer are set with flanges, carefully ground and vacuum greased, and perimeters sealed by Glyptal lacquer. The glass capillary is connected to the lid by a ground cone joint and cemented by Glyptal lacquer. Setting of the level of the mercury meniscus was made by electric contact of a platinum needle of 0.3 mm in diameter and 1 mm in length fixed to the lid which was covered with carbon black to make the observation of the meniscus easy. Fine adjustment of the contact was secured by a sensitive relay5).

The manometer tube of about 2 cm in diameter was the one previously used by one of the authors5) and the whole was encased with a series of aluminium tubes of 10 mm in wall thickness with which the temperature difference between the top and the bottom of the mercury column of about 76 cm in the manometer was reduced to about 0.5 deg under the laboratory condition in measuring high temperatures, that being about one half of what a naked column would give. Mean value of readings of mercury thermometers attached to the aluminium casing was taken as the mean temperature of the mercury column. Every thermometer was inserted in a hole drilled in an aluminium knob welded to the casing to read the temperature of the latter. An error of 0.2 deg in the mean temperature of mercury for the pressure determination at about 1 atm pressure will cause an error of 0.05 deg in the temperature of the gold point.

The gas pressure of 1 atm at the gold point was about 155 mmHg at 0°C. The aluminium casing had three holes through which each of the menisci of mercury at 1 atm, 155 mmHg and at the lower level of the manometer could be observed by comparator telescopes. The level of meniscus was observed with an accuracy of 0.005 mm. This error of 0.005 mm in the pressure determination at 0°C would give an error of 0.04 deg in the temperature of the gold point.

*The gas bulb* After heating at high temperatures, the bulb, even carefully annealed in advance, did not always come back to its original volume at 0°C. As it seemed depending on the cooling velocity, this effect was studied on two pure silica glass bulbs to learn what rate of cooling will cause the change in volume of less than 0.001% at 0°C. The result is shown in Table I, where $p_h$ and $p_0$ are the inner pressures of the bulb at about 1060°C and 0°C respectively, and $V_0$ and $V_0'$ are the volumes of the bulb at 0°C before and after heating, measured by weighing mercury filled in vacuum. With the bulb opened to the outer atmosphere, the volume increase was 0.026% by natural cooling in extinct furnace with a cooling rate of about 350 deg per hour, taking 3 hours to cool down to the room temperature. On the other hand, the volume change was negligibly small by slow cooling with a cooling rate of about 45 deg per hour, taking 24 hours to cool down to the room temperature. But with the closed bulb, permanent volume changes were observed even by slow cooling because of the temperature reaching near the softening point of silica glass and the pressure rising higher inside. However, when the gas pressure was made to become about 1 atm at high temperatures, no volume change was observed when cooled down to 0°C at which the inner pressure became about 1/5 atm.

So it was decided to use a silica glass bulb for the gas thermometer with the gas pressure to become about 1 atm at aimed-at temperatures, thus saving the trouble of going into the effect of inner pressure on the volume of the bulb and the evaluation of the pressure coefficient $\mu$ at high temperatures.

In Fig. 1, the gas bulb V made of silica glass with 4.4 cm in outer diameter and 18 cm in length is maintained at 0°C or $t$°C up to the mark a on a capillary stem of 1.0 mm in inner diameter. Its volume $V_{0p}$ at 0°C was

$$V_{0p}=205.725(1+3.7\times10^{-5}p)\text{cc}$$

for the inside pressure of $p$mHg and the outside pressure of 1 atm, with the pressure coefficient $3.7\times10^{-5}$ 1/mHg$=\mu$.

The volume $V_{tp}$ at the temperature $t$°C was

$$V_{tp}=205.725(1+3.7\times10^{-5}\times0.76)$$
$$\times(1+1.68\times10^{-6}t)\text{ cc}$$

for the pressure $p$ in the bulb which is nearly equal to 1 atm and the outside pressure of 1 atm, with the expansion coefficient $1.68\times10^{-6}$ 1/deg$=\lambda$. The expansion coefficient was taken as three times the mean linear expansion coefficient $\beta$ between 0°C and 1000°C, measured by the comparator method for a silica stem of the same quality as the gas bulb, having about 12 cm in length. The measurement was made with a horizontal electric furnace jacketed with water. The result obtained is

$$\beta=(0.56\pm0.02)\times10^{-6}\text{ 1/deg .}$$

This $\beta$-value is in agreement with the value 0.54 by Randall⁶⁾ within experimental error.

*The dead space* The volume of the dead space was divided into four parts in consideration of the temperature distribution at the time of measuring high temperatures:

$v_1$: the volume of the part of the capillary stem of the gas bulb immersed in the furnace (a-b in Fig. 1)

$v_2$: the volume of the rest of the capillary stem of the gas bulb, outside the furnace (b-c in Fig. 1)

$v_3$: the volume of the connecting glass capillary (c-d in Fig. 1)

$v_4$: the volume above the lower meniscus of mercury in the manometer (d in Fig. 1).

$v_1$, $v_2$ and $v_3$ were 0.164 cc, 0.082 cc and 0.459 cc* respectively, measured by mercury substitution.

$v_4$ was determined by the following procedure:
In Fig. 1, after the whole system was evacuated, the stop cocks $C_2, C_3, C_5$ and $C_7$ were closed, and then mercury was introduced into the lower tube of the manometer through the cock $C_8$ from the reservoir $R_2$. After closing the cock $C_8$ and by delicate manipulation of the compressor handle K, which exerts pressure on a piece of rubber tube, the mercury meniscus was adjusted to maintain its maximum height and just to touch the platinum point. Then the cock $C_6$ was closed, and mercury was introduced into $v_4$ and further into the capillary through the cock $C_7$ from the reservoir $R_1$. Thus the volume $v_4$ was obtained from the difference in the mass of mercury in the reservoir $R_1$ before and after this treatment, subtracted by the mass of mercury that occupied the part of the capillary, as

$$v_4=0.421\pm0.002\text{ cc .}$$

If there exists an error of 0.002 cc in determining the volume occupied by the gas, it would cause an error of 0.05 deg in determining the temperature of the gold point.

Let $T_1$, $T_2$, $T_3$ and $T_4$ be the mean temperatures of the gases in $v_1, v_2, v_3$ and $v_4$ at the time of measuring $p_0$, and $T_1', T_2', T_3'$ and $T_4'$ those at $p_t$ respectively. $T_1, T_2, T_3$ and $T_4$ were always equal within 0.5 deg. The temperature $T_1'$ at the part of $v_1$ was determined from the temperature distribution measured by a thermocouple as shown in Fig. 5 (an example at the silver point) as

$$T_1'{}_{\text{Au}}=273+720$$

and

$$T_1'{}_{\text{Ag}}=273+667$$

for the gold and silver points respectively. $T_2'$ was taken as the mean of the temperatures 85°C at the point of 1 cm above the upper surface of the lid of the furnace and 35°C at the point of the mark c, that is,

$$T_2'=273+60.$$

$T_3'$ was determined from the mean of the three temperatures measured by mercury thermometers placed at the points $A_1, A_2$ and

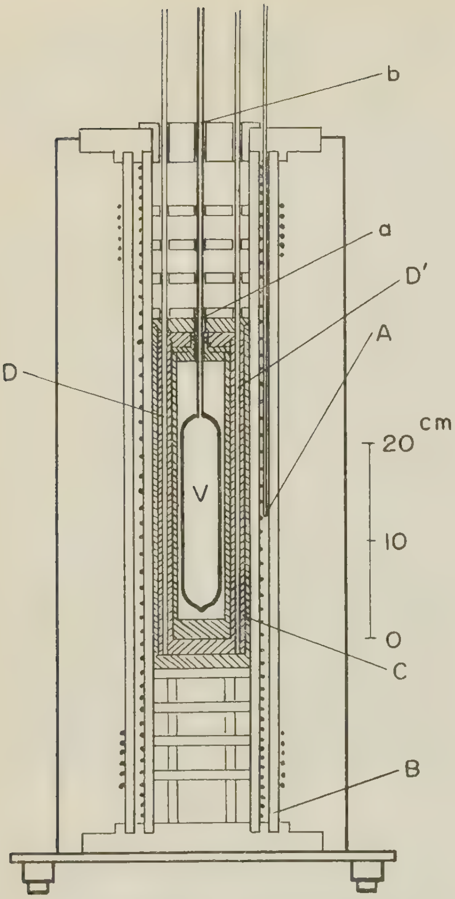

Fig. 3. The high temperature thermostat.

$A_3$ in Fig. 1, the last of which gave $T_4'$.

It would cause only an error less than 0.01 deg in the determination of the gold point, even if the mean temperature $T_m$ of $T_1$, $T_2$, $T_3$ and $T_4$ were used for the respective temperatures, ignoring the difference which was less than 0.5 deg if any.

On the other hand, an error of 30 deg in $T_1'$, 10 deg in $T_2'$ and 1 deg in $T_3'$ would cause an error of 0.04 deg, 0.06 deg and 0.04 deg respectively in the determination of the gold point.

*The gas* As the thermometer gas, nitrogen was used, which was obtained by heating a mixture of saturated solution of $NaNO_2$ and saturated solution of $NH_4Cl$ and purified by the usual method[5)].

The part $L_1L_2$ in Fig. 1 was used as a U-tube manometer to introduce nitrogen gas into the thermometer at pressures of about 155 mmHg and 168 mmHg at 0°C in the measurements of the gold and silver points respectively.

### (b) **The thermostats**

The thermostat for the ice point was the same as used previously by one of the authors[5)].

The thermostat for high temperatures, designed so as to have a constant and uniform temperature space of 5.5 cm in diameter and 25 cm in length, in which the gas bulb was maintained at a temperature near the gold or silver point, was an electric furnace of Nichrome resistance wire of vertical mounting and is shown in Fig. 3. As the main heating coil, Nichrome wire of 2.5 mm in diameter was wound on a refractory porcelain tube of 10 cm in inner diameter, 1 cm in wall thickness and 70 cm in height, the winding being made more closely toward both ends of the tube than at the center to compensate the cooling effect at the ends. The pitch of the coil was determined so that the heating energy generated at a height $x$ measured from the lower end of the porcelain tube was expressed as the function:

$$H=a+b\left(\frac{2x-L}{L}\right)^2,$$

where $L$ is the length of this tube, and constants $a$ and $b$ are to be determined empirically, by means of trial and error. Around the main coil, another porcelain tube B was mounted coaxially, each end part of which was wound with Nichrome wire of 2.0 mm in diameter used as an independent subsidiary heater.

To secure temperature uniformity in the thermostat space, a pure copper cylinder C of the inner diameter 6.2 cm, the wall thickness 1.3 cm and the height 32 cm with closed bottom and a lid, protected from oxidation with graphite cylinders of 5 mm thickness on both surfaces inside and outside and with graphite plates of 15 mm thickness at the top and the bottom, was set in contact with the inner wall of the porcelain tube of the furnace. Two thermocouple holes D and D' of 8 mm in diameter were bored through the wall of the copper cylinder parallel to its axis for insertion of thermocouple protection tubes made of silica glass. The spaces between the protection tubes and the holes were filled with graphite powder.

After several rewindings of the main heating coil and adjusting the currents flowing through the two independent subsidiary heating coils, the temperature uniformity along the wall of the copper cylinder, observed in the thermocouple holes, was ±0.3 deg as shown in Fig. 4, which was almost the same at both temperatures of the gold and silver points.

To examine the temperature distribution along the axis of the gas bulb, a silica bulb similar to the gas bulb, with a tube of 6 mm in outer diameter instead of the capillary, was set where the gas bulb would be placed. Measurements by a thermocouple inserted into the bulb through the tube showed that the uniformity along the axis was within ±0.1 deg and that the mean temperature in the bulb coincided with that in the thermocouple holes of the wall of the copper cylinder within 0.1 deg. The temperature distribution was also traced (Fig. 5) by moving the thermocouple along the 6 mm tube of the bulb up to the upper surface of the lid of the furnace, and it was used for determining the mean temperature of the part of the dead space $v_1$ between the marks a and b in Fig. 1, assuming that the temperature distribution along the capillary stem of the gas bulb was the same as that along the 6 mm tube. An error of 30 deg in determining the mean temperature at the part would cause an error of 0.04 deg in determining the gold point.

The electric power to the furnace was supplied through an induction transformer of 5 kVA, the output voltage of which was regulated automatically at 100±0.2 volts.

Using a standard thermocouple A, as a temperature indicator, inserted in the furnace between the main heating coil and the outer porcelain tube B, and by means of a simple temperature control device as shown in Fig. 6, the temperature of the thermostat was maintained constant within ±0.1 deg with the "on-off ripple" of about ±0.02 deg for a long duration of time.

The temperature of the thermostat was determined by taking a slight correction in the measurements by two standard thermocouples in silica protection tubes of 6 mm diameter, inserted in the thermometer holes of the wall of the copper cylinder.

### (c) The standard thermocouples

Before and after each set of gas-thermometric measurements, the standard thermocouples, made of platinum to 90 platinum-10 rhodium, were calibrated at the gold or silver point. For the calibration, standard metals, 1600 g gold of 99.998% and 900 g silver of 99.994% in purity, were used, which were melted in crucibles of 3 cm in inner diameter, 1 cm in wall thickness and 15 cm in depth, made of pure artificial graphite.

The standard thermocouples had a reproducibility of 0.5 microvolts in emf, determined from their cooling curves at the calibration points. The emf was measured by a Diesselhorst compensator, combined with a galvanometer of a sensitivity of $5\times10^{-8}$ volts/mm. Accuracy of the calibration was the same even when the quantity of gold was reduced to about 1000 g in the same crucible. A result

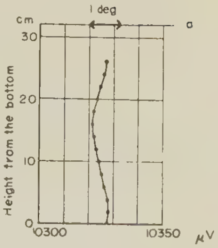

Fig. 4. Temperature distribution in the thermocouple hole of the copper cylinder along the axis.

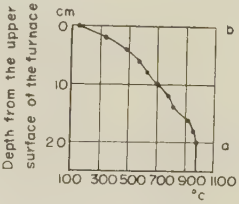

Fig. 5. Temperature distribution at the upper part of the furnace along the axis. The levels a and b show the respective positions on the capillary stem of the gas bulb in Fig. 1.

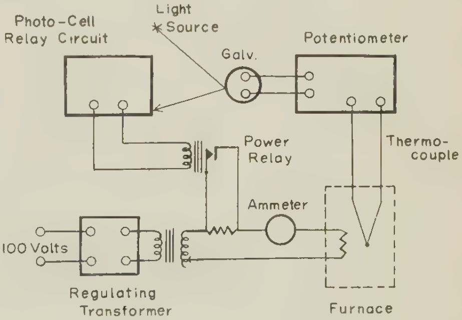

Fig. 6. Temperature control device.

Table II. Characteristics of one of the standard thermocouples.

| Constants in temperature-emf relation | | | Resistance ratio, indicating purity of platinum element | Emf at the fixed point in units of $\mu$V | | |
|---|---|---|---|---|---|---|
| $a$ ($\mu$V) | $b$ ($\mu$V·deg$^{-1}$) | $c$ ($\mu$V·deg$^{-2}$) | $R_{100}/R_0$ | gold | silver | antimony |
| −385.2 | 8.413 | $1.558\times10^{-3}$ | 1.39242 | 10318.3 | 9136.2 | 5538.4 |

Table III. The result of measurements at the silver point.

| Date | Pressure | | Thermocouple data | | | Thermodynamic temperature | | |
|---|---|---|---|---|---|---|---|---|
| | 0°C | $t$°C | No. | Thermostat | Silver point | Thermostat | Silver point | |
| | $p_0$ (mmHg) | $p_t$ (mmHg) | | $e_t$ ($\mu$V) | $e_{Ag}$($\mu$V) | $T$ (°K) | $T_{Ag}$ (°K) | $t_{Ag}$ (°C) |
| 18, Jan. 1954 | 167.045 | | | | | | | |
| 22, | | 742.563 | 1001 | 9118.6 | 9122.9 | 1234.18 | 1234.56 | |
| 25, | 167.056 | | | | | | | |
| 27, | | 742.575 | 〃 | 9120.0 | 9122.9 | 1234.08 | 1234.33 | |
| 29, | 167.107 | | | | | | | |
| 7, Feb. | 167.220 | | | | | | | |
| 11, | | 743.022 | 〃 | 9111.0 | 9121.0 | 1233.51 | 1234.39 | |
| 15, | 167.249 | | | | | | | |
| 12, March | 167.469 | | | | | | | |
| 15, | | 744.523 | 〃 | 9118.5 | 9120.0 | 1234.32 | 1234.45 | |
| 17, | 167.479 | | | | | | | |
| 19, | | 745.312 | 〃 | 9127.5 | 9119.2 | 1235.14 | 1234.42 | |
| 21, | 167.516 | | | | | | | |
| | | | | | Mean | | 1234.430 | 961.280 |
| | | | | | Standard deviation | | 0.085 | |
| | | | | | Standard deviation of mean | | 0.038 | |

Table IV. The result of measurements at the gold point.

| Date | Pressure | | Thermocouple data | | | Thermodynamic temperature | | |
|---|---|---|---|---|---|---|---|---|
| | 0°C | $t$°C | No. | Thermostat | Gold point | Thermostat | Gold point | |
| | $p_0$ (mmHg) | $p_t$ (mmHg) | | $e_t$ ($\mu$V) | $e_{Au}$ ($\mu$V) | $T$ (°K) | $T_{Au}$ (°K) | $t_{Au}$ (°C) |
| 26, Oct. 1954 | 158.346 | | | | | | | |
| 27, | | 760.987 | 1008 | 10310.0 | 10315.8 | 1336.31 | 1336.80 | |
| 29, | 158.414 | | | | | | | |
| 28, Apr. 1955 | 154.114 | | | | | | | |
| 30, | | 741.994 | 1007 | 10341.5 | 10317.8 | 1338.87 | 1336.85 | |
| 2, May | 154.150 | | | | | | | |
| 6, | | 742.521 | 1010 | 10344.5 | 10314.2 | 1339.40 | 1336.81 | |
| 9, | 154.182 | | | | | | | |
| 17, | 154.439 | | | | | | | |
| 18, | | 741.140 | 〃 | 10282.1 | 10313.8 | 1334.12 | 1336.83 | |
| 20, | 154.473 | | | | | | | |
| 21, | | 741.612 | 〃 | 10291.0 | 10313.6 | 1334.96 | 1336.89 | |
| 23, | 154.485 | | | | | | | |
| | | | | | Mean | | 1336.836 | 1063.686 |
| | | | | | Standard deviation | | 0.036 | |
| | | | | | Standard deviation of mean | | 0.016 | |

Table V. Random errors.

| Item involving error | | Amount of error | Error amounted to at the gold point (in deg) |
|---|---|---|---|
| Pressure at 0°C | | <0.005 mmHg | <0.04 |
| Pressure at the gold point | | <0.025 〃 | <0.05 |
| Mean temperature $T_m$ of the dead space at the time of measuring the ice point | | <0.2 deg | <0.005 |
| Mean temperature of the dead space at the time of measuring the gold point: | $T_3'$ | <1 〃 | <0.04 |
| | $T_4'$ | <0.1 〃 | <0.004 |
| 0°C thermostat | | <0.001 〃 | <0.005 |
| High temperature thermostat | | <0.1 〃 | <0.1 |
| Standard thermocouple | | <0.05 〃 | <0.05 |

Table VI. Systematic errors.

| Item involving error | | Amount of error | Error amounted to at the gold point (in deg) |
|---|---|---|---|
| Pressure coefficient $\mu$ of the gas bulb | | $<0.4\times10^{-5}$ 1/mHg | <0.003 |
| Expansion coefficient $\lambda$ of the gas bulb | | $<0.06\times10^{-6}$ 1/deg | <0.09 |
| Volume of the dead space: | $v_1$ | <0.001 cc | <0.003 |
| | $v_2$ | <0.001 〃 | <0.02 |
| | $v_3$ | <0.001 〃 | <0.02 |
| | $v_4$ | <0.002 〃 | <0.05 |
| Mean temperature of the dead space at the time of measuring the gold point: | $T_1'$ | <30 deg | <0.04 |
| | $T_2'$ | <10 〃 | <0.06 |
| $B_t$-value for nitrogen at high temperatures | | <20 % | <0.07 |

of calibration, conforming to the definition of the International Temperature Scale in 1948, within the limits admitted for the standard thermocouple, is shown in Table II.

## § 4. The Result of Measurements

The measurements were made in the following order: that is, first the ice point, then the gold or silver point and lastly the ice point again.

The results obtained for the silver and gold points are given in Tables III and IV respectively, in which the value for the silver point, reported preliminary to the Session in 1954 of the Comité Consultatif de Thermométrie under the Comité International des Poids et Mesures[7], was corrected for a part of the dead space.

By the constant volume nitrogen gas-thermometer at $p_0=167$ mmHg, the Kelvin temperature of the thermostat at a temperature near the silver point was obtained by Equation (6), taking $T_0=273.150$, $T_{v0}=272.99$, and $F_t=0.999606$ by Equation (8). Finally, the thermodynamic temperature of the silver point was obtained by Equation (12).

In the measurements at the gold point, $F_t=0.999624$ and $0.999633$, obtained by Equation (7), were used for $p_0=158$ and 154 mmHg respectively.

If the gas did not at all diffuse through the walls of the gas bulb at any temperature, there would be no difference between 0°-pressures $p_{0i}$ and $p_{0f}$ taken before and after the measurements at high temperatures. It is known that nitrogen gas diffuses through silica wall at high temperatures when there exists a difference in partial pressure of the gas at both sides of the wall. It was, however, found that the diffusivity became smaller after the gas bulb was maintained at high temperatures for many hours and increased gradually after the lapse of time at a room temperature.

The result of experiments showed that $\Delta p$

$=p_{0f}-p_{0i}$, which was 0.2 mmHg with previous heating of the bulb at a high temperature for one day, was reduced to about 0.03 mmHg when the heating was continued for two or three days. So, the measurements were taken after heating the bulb for a few days and $p_0=\frac{1}{2}(p_{0i}+p_{0f})$ was used as 0°-pressure in calculation.

## § 5. Discussion of the Result

Errors estimated in the value of the gold point, which might have been affected by the random error involved in every related experimental quantity, are listed in Table V.

In a single set of measurements, the value of the gold point would have been affected by 0.1 deg or less by the random errors in the measurements as shown in Table V.

In addition to the above random errors, the items which would have involved systematic errors in the value of the gold point should be considered. They are shown in Table VI. But, in general, it is difficult to estimate reasonably their amounts of error.

An important subject to be discussed is that the gas becomes impure by diffusion through the walls of the bulb from the outer atmosphere when the bulb is kept at high temperatures. As the bulb was surrounded by graphite, it is likely that the outer atmospheres of the bulb were mainly nitrogen and carbon dioxide. Hence, the pressure increase 0.4 mmHg in the 0°-pressure of 154 mmHg in the whole course of the experiments would have been mostly contributed by carbon dioxide. Error in the correction for the gas imperfection caused by intermixing of a small quantity of a different gas can be estimated by Equation (5).

For carbon dioxide, $B_0$ was measured previously by one of the authors[8], giving $B_0=-0.00921$ 1/mHg. $B_r$-values were measured at high temperatures up to 600°C and expressed analytically as a function of temperature by MacCormack and Schneider[9]. We find $B_{t_{\text{Au}}}=0.00121$ 1/mHg for the gold point by extrapolating the formula.

In the measurements in which impure nitrogen was used as the thermometric gas, the temperature obtained might not be true when $B_0$- and $B_t$-values for pure nitrogen are taken in the correction factor for the gas imperfection. Now if the impure gas consists of pure nitrogen of 0°-pressure $p_0$ and carbon dioxide of $p_0'$ as the impurity, $B_t$-value for impure nitrogen may be taken approximately as

$$(B_t)_{\text{impure N}_2}=\frac{1}{p_0+p_0'}\,[p_0(B_t)_{\text{N}_2}+p_0'(B_t)_{\text{CO}_2}]$$

for the temperature $t$. Supposing that the pressure increase of 0.4 mmHg were all by carbon dioxide and substituting $B_0$- and $B_{t_{\text{Au}}}$-values mentioned above for nitrogen and carbon dioxide in the above equation, we have

$$(B_0)_{\text{impure N}_2}=-60.9\times10^{-5}\ 1/\text{mHg}$$

and

$$(B_{t_{\text{Au}}})_{\text{impure N}_2}=179.5\times10^{-5}\ 1/\text{mHg}\ ,$$

$B_0$ being affected by 3.7% and $B_{t_{\text{Au}}}$ little affected by the impurity, the former affecting the value of the gold point by 0.004 deg. So, the gas impurity produced by the diffusion of gas through the walls of the gas bulb will result no appreciable error in the value of the gold point in the present experiment.

The next subject to be discussed is on the inequality of the gas quantity in the measurements at the ice point and the gold or silver point. In raising and lowering the temperature to and from the gold or silver point respectively, if nearly equal hours are taken at the temperature region at which gases would diffuse through the walls of the gas bulb, such being the case with the present experiment, it may be considered that the quantity of the gas was the same at the ice and gold or silver points in case $p_0=\frac{1}{2}(p_{0i}+p_{0f})$ was taken as the 0°-pressure in calculation. But the value of the gold point would be affected by about 0.13 deg, if $p_{0i}$ or $p_{0f}$ was used singly in place of $p_0$ in calculation.

Although the mean values of the gold and silver points on the thermodynamic temperature scale were obtained with the standard deviation of 0.016 and 0.038 deg respectively, by taking into consideration that some independent systematic errors might have been involved in the measurements as discussed above, we take the temperatures of the gold and silver points, which were adopted as 1063.0°C and 960.8°C respectively on the International Temperature Scale in 1948, as

$$T_{\text{Au}}=1336.84\pm0.05\,^\circ\text{K},\quad t_{\text{Au}}=1063.69\pm0.05\,^\circ\text{C}$$

and

$$T_{\text{Ag}}=1234.43\pm0.05\,^\circ\text{K},\quad t_{\text{Ag}}=961.28\pm0.05\,^\circ\text{C}$$

respectively.

Several investigations on the gold and silver points had been made in the early period of development of the gas thermometry. The most precise ones are those by Holborn and Day in 1901⁽¹⁾ and Day and Sosman in 1910⁽²⁾, the results of which are listed in Table VII with the present authors'.

Table VII. The gold and silver points by the authoritative workers and the present authors.

| Author | Year | $t_{Au}$ | $t_{Ag}$ |
|---|---|---|---|
| Holborn and Day | 1901 | 1063.5 | 961.5 |
| Day and Sosman | 1910 | 1062.4 | 960.0 |
| The present authors | 1955 | 1063.69 | 961.28 |

Accuracy was ±0.8 deg in the measurements by Day and Sosman, and also perhaps the same in those by Holborn and Day, while it is ±0.03 deg in the present measurements.

For the high temperature gas-thermometric work, higher accuracy would have been obtainable by using a double walled gas bulb so that the pressure between the walls could be made always equal to that in the bulb by the same gas, provided that the determination of the temperature of the high temperature thermostat, the measurements and corrections were able to be made with higher accuracies in the present work.

## Acknowledgments

Special financial support by the Institute enabled the present work to be completed, for which the authors express their appreciation to President Dr. S. Uchida. A part of the expence was borne by the Grant in Aid for Fundamental Scientific Research from the Ministry of Education. The authors wish to express their hearty thanks to Mr. T. Nemoto, Director of the Japan Electric Association, and Dr. M. Kinoshita who gave them their favourable supports for the completion of this work. They also appreciate to Dr. K. Okada of the Electro-Technical Laboratory in Osaka for his encouragement and valuable suggestions. The authors are indebted to Mr. K. Okabe, President of the Nippon Mining Co. Ltd., and Dr. H. Ishizuka, Director and Chief of the Metallurgy Section, for taking trouble in refining gold and silver, and producing the elements of the standard thermocouple. Crucibles and other graphite articles were all made at and contributed by the Nippon Carbon Co. Ltd., for which the authors express their appreciation to Mr. A. Kikkawa, Vice-President. The authors are also indebted to Dr. T. Aoki of the Electro-Technical Laboratory for his kind cooperation in calibrating the Diesselhorst compensator.

## References

1) L. Holborn u. A. Day: Ann. Phys. **4** (1901) 99.
2) A. Day and R. B. Sosman: Am. J. Sci. **29** (1910) 93.
3) J. W. M. Dumond and E. R. Cohen: Phys. Rev. **82** (1951) 555.
4) Temperature, Its Measurement and Control in Science and Industry (1941) 55 (by F. G. Keyes).
5) M. Kinoshita and J. Oishi: Phil. Mag. **24** (1937) 52.
6) H. M. Randall: Phys. Rev. **30** (1910) 216.
7) J. Oishi, M. Awano and T. Mochizuki: Procès-Verbaux des Séances du Comité International des Poids et Mesures **24** (1954) T 148.
8) J. Oishi: J. Sci. Res. Inst. **43** (1949) 220.
9) K. E. MacCormack and W. G. Schneider: J. Chem. Phys. **18** (1950) 1269.

---

* 0.456 cc after a breakdown of this part in March, 1955.

JOURNAL OF THE PHYSICAL SOCIETY OF JAPAN Vol. 11, No. 3, MARCH, 1956

# Statistical Study of Electron Avalanches in Gaseous Discharge

By Shoji KOJIMA and Kiyoe KATO

*Faculty of Science, Tokyo University of Education, Otsuka, Tokyo*

(Received October 28, 1955)

Size distributions of electron avalanches were observed at a potential several percent below the breakdown value. The distributions at low pressure discharge agreed well with Wijsman's formula which was derived from the Townsend theory in the absence of space charge effect. The distributions at atmospheric pressure, however, are different from this formula in that the pulses had a tendency to become uniform in size. This tendency was accounted by the space charge effect. In connection with these mesurement the pulses of corona discharges were also measured.

## § 1. Introduction

As a method to study the breakdown process the measurements of the formative time lag have been performed by many authors[1][2][3]. A study of electron avalanches which are observed at a potential several percent below the breakdown value is also valuable as another method to attack the problem.

In the view of the Townsend mechanism the distribution of pulses in gaseous discharge, each of which was due to an electron avalanche, was studied theoretically by Wijsman[4]. The probability that an electron started from the cathode has grown to an avalanche of $n$ electrons was expressed by

$$p(n)=(1/\bar{n})\exp(-n/\bar{n}) , \qquad (1)$$

in which

$$\bar{n}=\exp\int_0^d \alpha dx , \qquad (2)$$

where $d$ was the gap length and $\alpha$ was Townsend's first ionization coefficient. Recently Legler obtained the same formula using another method[5]. Lacking suitable experimental data he compared the theory with the measurement which was carried out on a proportional counter by Curran, Cockroft and Angus[6]. We intended to give a more detailed measurement for pulse distribution in low pressure discharges where the Townsend mechanism seemed to be valid, and to extend the measurement to atmospheric pressure where the discharge might rather support the streamer mechanism than the Townsend one. Furthermore, experiments on corona discharge were carried out.

## § 2. Method of Measurement

The pluse caused by an electron avalanche was amplified by an audio-frequency amplifier of four stages whose gain was about 100 db. The output of the amplifier was put into a discriminator of a counting device. The shape of the pulse was simultaneously observed by an oscilloscope. The diagrams of the input circuits are shown in Fig. 1. The connection $a$, by which the voltage pulse was taken up, was used mainly at low applied voltage. On the other hand the connection $b$, by which the current pulse was picked up, was used mainly at high applied voltage. Either of the connections, however, gave the same result for the same applied voltage.

Measurements were carried out in the following way. At first the applied voltage was gradualy increased until a breakdown occurred, and then the voltage was fixed at a potential several percent below the breakdown value. At this condition sufficient number of pulses were not observed except the cases of atmospheric

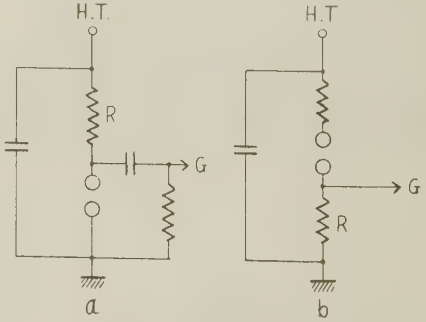

Fig. 1. Input circuits. ($a$) $R$=20 MΩ ($b$) $R$=50 KΩ $G$: Grid of the first tube.

pressure. Therefore the cathode was irradiated by visible rays or ultraviolet rays.

Since the pulse was detected by the discriminator, the height of the pulse alone was observed. From the observed pulse height, $V$, the number of electron in the avalanche was estimated by the formula.

$$n=\frac{1}{R}\frac{V}{G}\frac{\tau}{e} \qquad (3)$$

where $R$ was the series resistance shown in Fig. 1, $G$ the gain of amplifier, $e$ the electronic charge and $\tau$ the obsreved duration of the pulse. Although the formative time of avalanche should be very small, the observed duration of the pulse was about $10^{-4}$ sec., which was mainly due to the time constant of the input circuit and to the band width of the amplifier. The numbers of electrons calculated from Eq. (3) had an error which came from the rough estimation of $\tau$. This error, however, did not affect upon the study of distribution where the relative values were important.

The reading of the counting device gives integrated number of avalanches which are larger than a cirtain value. From Eq. (1), the integrated value of avalanches larger than $n$ electrons, $\nu(n)$, is expressed by

$$\nu(n)=\nu_0 \exp(-n/\bar{n}) , \qquad (4)$$

where $\nu_0$ is the number of electrons emitted from the cathode in unit time. Eq. (4) indicates that the semi-logarithmic plots of $\nu(n)$ give linear form. Therefore the measured results were plotted in a semi-logarithmic diagram.

In order to extend the experiment to atmospheric pressure a power source of several thousands volts with high stability was required. The stabilization was achieved with the discharge tubes made by Gosho*, by which the fluctuation of the voltage could be reduced below 2 volts.

## § 3. Experimental Results

### (*a*) *Uniform field at low pressure* ($pd$=6 mmHgmm)

Two discharge tubes, of which electrodes were made of aluminum disk of diameter of 3 cm, were used. One of the tubes, $A$, had a gap length of 5 mm and was filled with air at 1.2 mmHg. The other tube, $B$, had a gap length of 20 mm and was filled with air at 0.3 mmHg. So that $pd$'s of both tubes were 6 mmHgmm. One of the results of the experiment with the tube $A$ was shown in Fig. 2. The distributions of avalanches were always linear. This result agrees well with Wijsman's formula (4). The intersecting points between the lines and the ordinate axis give $\nu_0$'s, which are almost independent of the applied voltage. The average sizes of the avalanches, $\bar{n}$, which were determined from the increment of the lines are shown in Fig. 3.

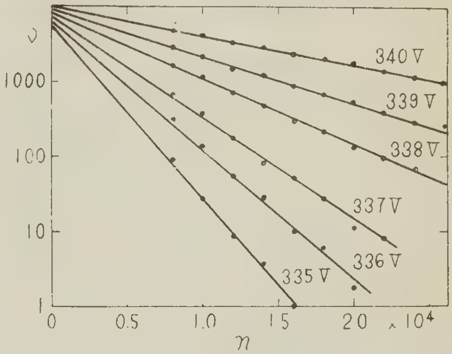

Fig. 2. Pulse size distribution at low pressure. ($p$=1.2 mm Hg air, $d$=5 mm, breakdown potential=311 V.) $n$ is the number of electrons in the avalanche, ν is the number of occurrence per minute of avalanches, which contain more than $n$ electrons, Figures on the line are the applied voltages.

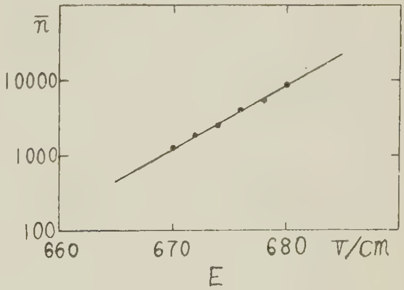

Fig. 3. Average sizes of the avalanches, $\bar{n}$, *vs* applied field $E$.

Townsend's ionization coefficient, $\alpha$, which was calculated by the aid of Eq. (2), was 15 at $p$=1.2 mmHg and $E$=670 V/cm or 4.3 at $p$=0.3 mmHg and $E$=219.75 V/cm. These values seem to be in reasonable order. More precise discussion, however, is not adequate because of rough determination of the pressure and the time of duration.

---

* Gosho: Abstract of the general meeting of the Institute of Electrical Engineers of Japan, Tokyo (1950).

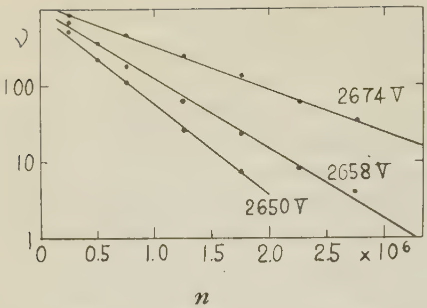

Fig. 4. Pulse size distribution ($p$=300 mmHg $Cl_2$, $d$=1 mm).

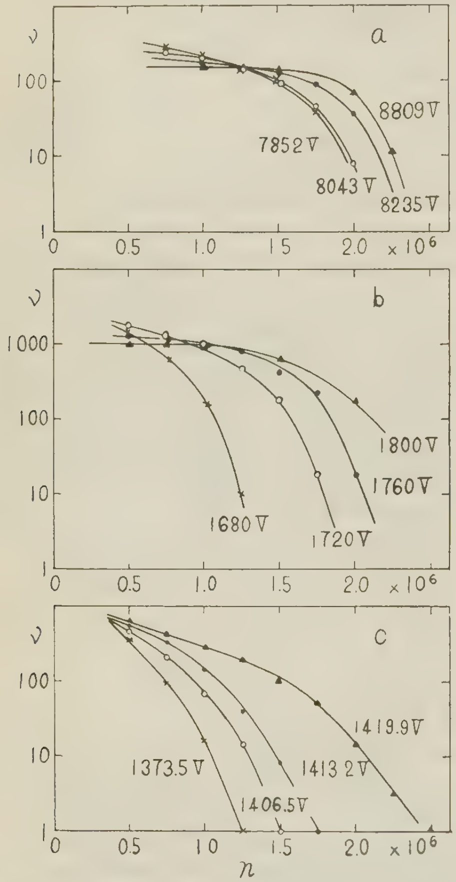

Fig. 5. Pulse size distributions at atmospheric pressure. ($a$) Gap length=2.2 mm, breakdown potential=9000 V. ($b$) Gap length=0.3 mm, breakdown potential=1840 V. ($c$) Gap length=0.2 mm, breakdown potential=1427 V.

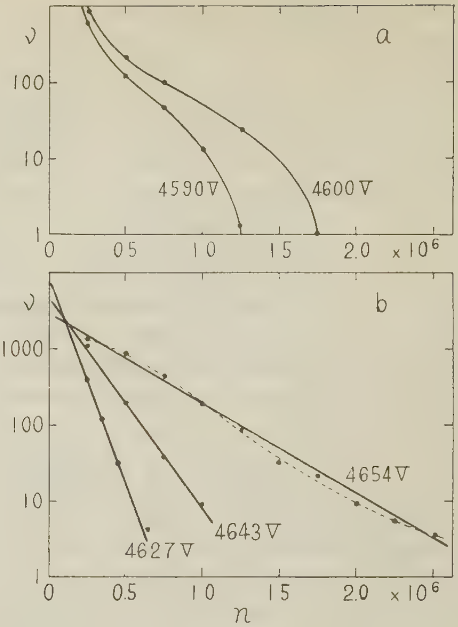

Fig. 6. Pulse size distributions ($p$=760 mmHg air, $d$=1 mm).

### ($b$) *Uniform field at* 300 mmHg

Two discharge tubes of same size were prepared, having the disk electrodes of 3 cm diameter and the 1 mm gap length. The electrodes of both tubes were made of graphite. One of the tubes was filled with air at 300 mmHg and the other with chlorine at the same pressure. The semi-logarithmic plots of the observed points were linear for both tubes. The result for the tube filled with chlorine is shown in Fig. 4.

### ($c$) *Uniform field at atmospheric pressure*

With sphere to plane gaps, pulse distributions were studied at various gap lengthes. The anode was a sphere of diameter of 4 cm, the cathode was a disk of 6 cm and the gap length was varied between 2.5 mm and 0.2 mm. The observed typical distributions are shown in Fig. 5. These distributions were plainly different from the cases of low pressure in such a way that larger pulses occurred less frequently.

With the same graphite electrodes which were used in the experiment at 300 mmHg, pulse distributions were also studied at atmospheric pressure. One of the observations yielded a curved distribution as shown in Fig. 6 $a$. Another observation, which was carried out several days later, yielded almost linear character as shown in Fig. 6 $b$, although this distribution slightly deviated from a line and a few pulses of very large sizes were observed, as the case of the positive corona which will be mentioned below. (*cf.* Fig. 8 $b$) Consequently, there were two types of distributions: the curved distribution and the nearly linear distribution. When the curved distributions were seen, the voltage region

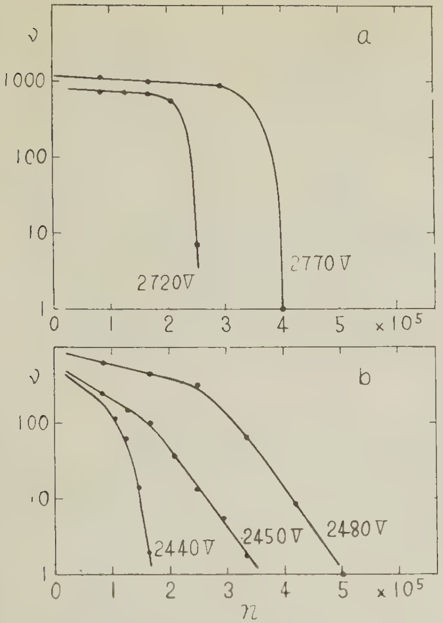

Fig. 7. Pulse size distribution with needle to plane gap (negative needle). (*a*) Gap length=5 mm, breakdown potential=3000 V. (*b*) Gap length=2.5 mm, breakdown potential=2500 V.

between the pulse on-set potential* and the breakdown potential was larger than when the nearly linear distributions were observed.

What condition did yield these different distributions? We tested surface condition with metal sphere electrodes. When the surface of the anode was rough and the surface of cathode was smooth, the nearly linear distributions were more often observed. On the contrary, the opposite condition gave more frequently the curved distributions.

(*d*) *Non-uniform field*

Size distributions of pulses at pre-breakdown were studied with needle to plane gaps. When the needle was negative, the distribution was curved as shown in Fig. 7. The fact that this distribution was like as the distribution in uniform field at atmospheric pressure might give an interpretation that the observed pulses in sphere gaps were due to corona pulses. But the differences in the breakdown potentials and in the size of avalanches seem to make this interpretation unlikely.

When the needle was positive, the distributions are shown in Fig. 8. The curve shown in Fig. 8*a* seemed to consist of two parts. One was represented by a inclined line which gave a continuous distribution and the other

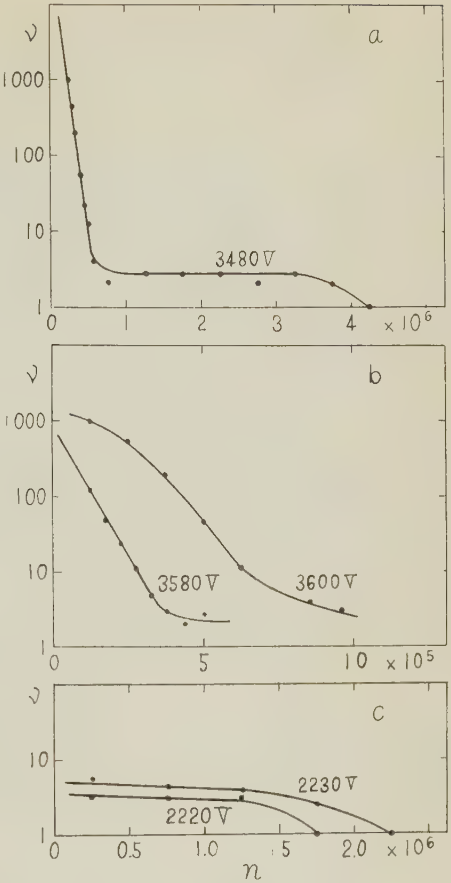

Fig. 8. Pulse size distribution with needle to plane gap (positive needle). (*a*) Gap length=5 mm, breakdown potential=3700 V. (*b*) Same as *a*, but this shows a part of small size pulses as analysed at higher amplifier gain. (*c*) Gap length=1 mm, breakdown potential=2250 V.

was represented by a horizontal line which gave a line spectrum. The curves shown in Fig. 8*c* lacked the continuous part. It seemed to be due to the smallness of pulses.

## § 4. Discussion and Conclusion

At the low pressure discharges where the Townsend mechanism is valid the measured distributions were linear and agreed well with Wijsman's formula. At atmospheric pressure the measured distributions showed a saturation character such that the number of large pulses were depressed. It suggests that the pulses at large *pd* have a tendency to become more uniform in size.

---

* The pulse on-set potential means the potential, above which the pulses are observed with the present amplifire. This potential depends on the apparatus and is not so definite as the breakdown potential.

The decrease of the large pulses might be explained by the attachment of the electron on a neutral atom, by which the ionization power of the electron is lost. The experiment of the avalanches in chlorine gas, however, makes this mechanism implausible.

To electron avalanches at atmospheric pressure the space charge effect has been introduced by many authors[1)7)8)]. In the theory of time lags of spark breakdown Fletcher estimated the number of electrons at which the space charge first became important, and gave it the value of the order of $10^4$ electrons from the observed time lags. The sizes of avalanches observed in the present experiment are greater than this order. It is plausible that the space charge effect accounts for the saturation character and the tendency to make uniform pulses. This mechanism is supported by a strong saturation character of the pulses of the negative corona, where the space charge effect is predominant because of its geometry.

The largest sizes of the avalanches at atmospheric pressure were about $2.5 \times 10^6$ electrons for sphere gap of 2.2 mm, and $5 \times 10^5$ electrons for negative needle-plane gap of 2.5 mm.

In the above discussion on the space charge effect we have assumed that the observed pulses were due to a single avalanche. This assumption seems to be reasonable under the condition that the applied potential is considerably below the breakdown potential*. Indeed, it is known that the negative corona gives rise to a self-quenching Geiger discharge where the single pulse contains successive avalanches[9)11)]. The mechanism of self-quenching due to space charge[10)11)] probably gives a uniform distribution in size. In our experiment, when the applied potential was increased, such pulses were observed, although these pulses were much larger than the pulses treated in this paper. The plane gaps at atmospheric pressure exhibit another type of distribution, as shown in Fig. 6 *b*. This was nearly linear distribution accompanying a small number of the large pulses, and this was observed mainly when the surface of the anode was rough. It is interesting to compare this distribution with that of the positive needle to plane gaps. The latter distribution indicated that it consisted of a line spectrum and a continuous spectrum expressed in a nearly linear curve. This result alone might be insufficient to give a definite interpretation on the mechanism. However, by several reasons it seems to be plausible that the large uniform pulses of the line spectrum are due to the streamer mechanism and that the pulses belonging to the continuous spectrum is caused by the avalanches started from intermediate space between the electrodes. In view of the interpretation of this distribution the nearly linear distribution in the case of uniform field are also attributed to the avalanches started from the intermediate space in addition to the avalanches from the cathode. When the all avalanches started from the cathode, the curved distribution as shown in Fig. 6 *a* will be seen. A few pulses of the large sizes which were observed on the side of the nearly linear distribution seem to be due to the streamer mechanism.

The authors wish to thank Prof. Honda of Tokyo University for valuable discussions. Also, the authors are indebted to Mr. Kono who prepared the discharge tubes. This work was partially supported by the Scientific Research Expenditure of the Ministry of Education.

### References

1) R. C. Fletcher: Phys. Rev. **76** (1949) 1501.
2) L. H. Fisher and B. Bederson: Phys. Rev. **81** (1950) 109.
3) H. W. Bandel: Phys. Rev. **95** (1954) 1117.
4) R. Wijsman: Phys. Rev. **75** (1949) 833.
5) W. Legler: Z. Physik **140** (1955) 221.
6) S. C. Curran, A. L. Cockroft and J. Angus: Phil. Mag. Ser. 7, **40** (1949) 929.
7) Varney, White, Loeb and Posin: Phys. Rev. **48** (1935) 818.
8) R. W. Crowe, J. K. Bragg and V. G. Thomas: Phys. Rev. **96** (1954) 10.
9) G. W. Trichel: Phys. Rev. **54** (1938) 1078.
10) L. B. Loeb: Phys. Rev. **86** (1952) 256.
11) M. R. Amin: J. Appl. Phys. **25** (1954) 210, 358 and 627.

---

* Near the breakdown potenial, however, multiple avalanches are not necessarily exclued.

# Short Notes

This section is intended to secure prompt publication of important discoveries in physics. The reports should not exceed 800 words in length. A figure of size 7 cm×7 cm will be counted as 150 words.

J. PHYS. SOC. JAPAN **11** (1956) 327

## Ferromagnetic Resonance Absorption in a Pyrrhotite Single Crystal

By Tadao FUJIMURA and Yosiharu TORIZUKA
*Research Institute for Scientific Measurements, Tohoku University, Sendai, Japan*

(Received Sept. 17, 1955)

Pyrrhotite is an iron sulfide in which the sulfur content is slightly greater than in the stoichiometric compound FeS, and its chemical formula is written as $FeS_{1+x}$. The spontaneous magnetization of Pyrrhotite was first explained by K. Yosida1) on the basis of ferrimagnetism which is composed of magnetic ions $Fe^{2+}$ and $Fe^{3+}$.

The Pyrrhotite single crystal used in this experiment is the same as that studied by Kaya and Miyahara2). We performed a resonance experiment on a disk-formed specimen at a frequency of 47,000 Mc/sec at room temperature.

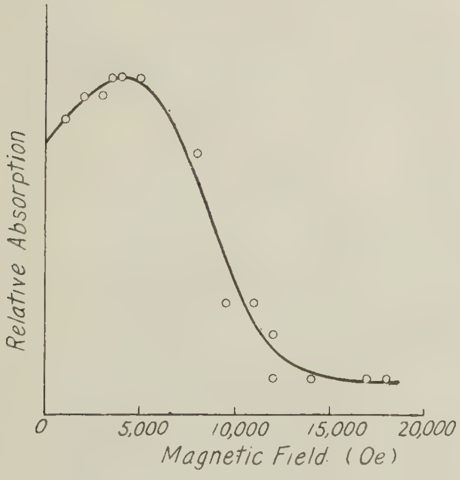

Fig. 1. Absorption curve of Pyrrhotite at 47,000 Mc/sec in the direction of easy magnetization.

The crystal was cut at a plane containing the hexagonal axis (the direction of difficult magnetization) into a diskformed specimen, which was mounted on the bottom of the resonant cavity so as to make the above plane consistent with the direction of both the *rf* magnetic field and the static magnetic field. When the crystal is rotated in the direction of easy magnetization (perpendicular to the hexagonal axis) parallel to the static magnetic field, we can observe the resonance absorption as shown in Fig. 1.

The absorption line width is about 10,000 Oe, and this width is extremely large as that obtained using single crystals in other ferromagnetic resonance absorption experiments.

When the crystal is rotated by more than 10 degrees from the above direction, the resonance absorption disappears in the presently available range of magnetic field, $0\sim2\times10^4$ Oe, and this disappearing may be due to a large magnetic anisotropy energy in Pyrrhotite.

The extremely broad absorption line cannot be explained by magnetic interaction in the ferroing magnetic. Néel suggested, referring to R. Pauthonet's experimental results, that Pyrrhotite might be composed of microcrystals, causing the broadening of absorption line3).

In the experiment using disk specimen containing the plane of easy magnetization showed the similar absorption as shown in Fig. 1, but we could not detect the variation of resonance field in the easy plane.

Neglecting any ordinary demagnetizing effects, because of the low saturation value for Pyrrhotite, and anisotropyenergy within the basal plane, then the Kittel's resonance formula4)5) for directions in the basal plane of hexagonal crystals is given by

$$(\omega/\gamma)^2 = H_{app}(H_{app}+H_A), \qquad (1)$$

were $\gamma = ge/2mc$
$H_{app}$ = applied magnetic field
$H_A$ = anisotropic field

Pyrrhotite has come to be known through the study of the gyromagnetic ratio by Coeterier3) yielding the extraordinary value $g=0.67$. But it is difficult to recognize this value from the composed magnetic ions and total magnetic moments in Pyrrhotite. The deviation of $g$-factor from 2 which corresponds to spin only would be small, so we may assume $g=2$ in Pyrrhotite.

When we taken $H=4\times10^3$ Oe, equation (1) gives the value of anisotropy energy as $H_A=6.6\times10^4$ Oe.

### References

1) K. Yosida: Prog. Theoret. Phys. **6** (1951) 356.
2) S. Kaya and S. Miyahara: Sci. Rep. Tohoku **27** (1939) 450.
3) L. Néel: Private communication at Sendai after International Union of Pure and Applied Physics Science Council of Japan 1953.
4) C. Kittel: Phys. Rev. **73** (1948) 155.
5) P. W. Anderson, F. R. Merritt, J. P. Remeika and W. A. Yager: Phys. Rev. **93** (1954) 717.

J. Phys. Soc. Japan **11** (1956) 328~329

# Variation of the Young's Modulus of the Alloy $Mg_3Cd$ with the Order-Disorder Transition

By Kayako TANAKA, Hidetaro ABE
*Department of Physics, Faculty of Science Ochanomizu University, Tokyo*
and Hideyo MANIWA
*Department of Physics Tokyo Institute of Technology, Tokyo*

(Received Sept. 20, 1955)

The order-dependent changes of Young's modulus of the alloy $Mg_3Cd$ with temperature and with time at various annealing temperatures below the transition point are obtained by measuring the change of resonant frequency of forced longitudinal vibration applied to the polycrystalline rod of dimensions, 1.12 cm in diameter and 13.25 cm in length.

The curve, ***ABC***, in Fig. 1 is obtained upon heating the specimen in the perfect ordered state at the rate of 1°C/min. Point ***D*** showing the equal as-quenched value from both 200°C and 400°C, falls on the extrapolation of the line ***CB***. Then, it is clearly observed that the value of Young's modulus, $E$, decreases continuously from room temperature to 160°C as a consequence of the gradual evanescence of equilibrium long-range order. The $dE/dT$ curve, also shown in Fig. 1, is very similar to the specific heat and the expansion coefficient versus temperature curves1)-3). Moreover, it seems that in conformance with other measurements the order-disorder transition in this alloy is of the second-order, since a discontinuous change cannot be detected at the transition point, $T_c$,1)-3) which corresponds to 160°C.4)

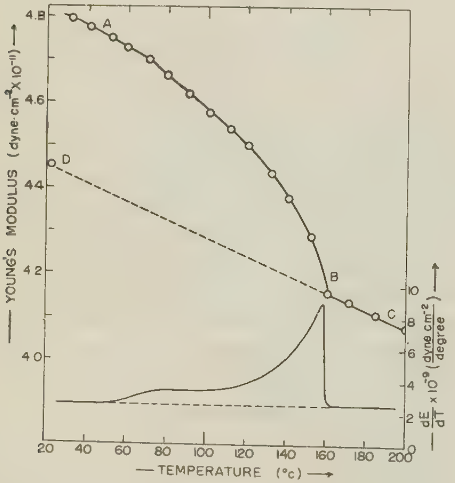

Fig. 1. The Temperature Variation of Young's Modulus.

The isothermal variation of $E$ with time, accompanied by the ordering process, is shown in Fig. 2 and indicates that the equilibrium order is achieved in monotonous way of increase. The variation is obtained as follows: After quenching from 200°C into water, the specimen is annealed at the various temperatures below $T_c$ and the measurements are made at room temperature by re-quenching into water from those annealing temperatures. Let $\tau_h$ denote the time required, at an absolute temperature $T$ °K, for attaining the half value of the equilibrium state. Then, the linear relationship between $\log_e \tau_h$ and $1/T$ is observed in Fig. 3. The upward deviation at above 100°C may be attributed partly to the too much shortness of $\tau_h$ to be measured with proper accuracy. The activation energy for the ordering process determined from the linear relationship is 19.5 Kcal/mol.

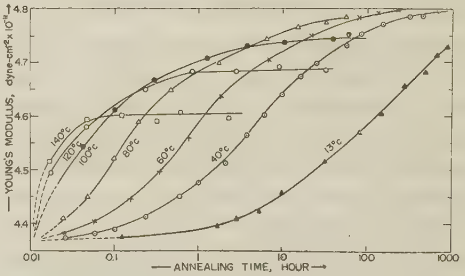

Fig. 2. The Isothermal Variation of Young's Modulus with Time at Various Temperatures.

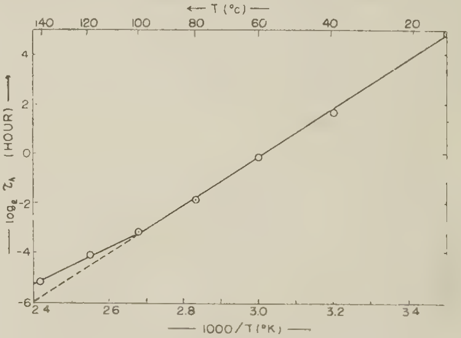

Fig. 3. The Temperature Variation of the Rate of Ordering, $\tau_h$.

On the temperature dependence of the internal friction, determined from the half value width of the resonant frequency curve, a distinct change depending on the order-disorder transition is not detected.

Together with results on MgCd, pure Mg and pure Cd, full report will be published later in the Nat. Sci. Rept. of the Ochanomizu University.

## References

1) S. Nagasaki, M. Hirabayashi and H. Nagasu:

J. Japan Inst. Metals, **13** (1949) No. 6, 1.
2) M. Hirabayashi, S. Nagasaki, H. Maniwa and H. Nagasu: J. Japan Inst. Metals **13** (1949) No. 6, 6.
3) B. Welber, R. Webeler and F. Trumbore: Acta Met. **1** (1953) 374.
4) H. Steeple and H. Lipson: Nature, **167** (1951) 110.

---

J. PHYS. SOC. JAPAN **11** (1956) 329~330

## Graphical Solution of Linear Heat Flow with Radiation

By Mashige NAGAI

*Matsuda Research Laboratory,*
*Tokyo Sibaura Electric Co. Kawasaki, Japan*

(Received December 13, 1955)

It is well known that differential equation of the linear heat flow with surface radiation which determines the temperature distribution on a uniform wire or plate is

$$\frac{d^2\theta}{dx^2}=-\frac{A\varepsilon\sigma}{J\kappa S}\left(\frac{q}{A\varepsilon\sigma}+\theta_0{}^4\right)-\frac{A\varepsilon\sigma}{J\kappa S}\theta^4\,, \qquad (1)$$

where

$\theta$: the absolute temperature of the wire (deg.)
$x$: the distance along the wire (cm.)
$A$: the surface area of the wire per unit length (cm)
$\varepsilon$: the emissivity of the wire
$\sigma$: the Stefan-Boltzmann constant (Joule./cm$^2$, sec, deg$^4$)
$J$: the mechanical equivalent of heat (Jonle/cal.)
$\kappa$: the conductivity of the wire (cal./cm, sec, deg.)
$S$: the sectional area of the wire (cm$^2$)
$q$: the heat yield per unit length (Joule/cm, sec.)
$\theta$: the ambient temperature (deg.)

It has been considered that tedious calculations are inevitable to obtain a numerical solution of this equation whose analytical solution probably can not be expressed in terms of elementary functions.[1] But in the following way, the general solutions of this equation are given by an array of curves in a graph and one can immediately obtain temperature distributions corresponding to various conditions.

For simplicity we assume that only variables are $\theta$ and $x$, others being constant. Furthermore we put the constant terms as follows

$$q/A\varepsilon\sigma+\theta_0{}^4=t^4 \qquad (2)$$

$$A\varepsilon\sigma/J\kappa S=a \qquad (3)$$

then Eq. (1) becomes

$$d^2\theta/dx^2=-at^4+a\theta^4. \qquad (4)$$

This can be further normalized using new dimensionless variables:

$$\eta=\theta/t \qquad (5)$$

$$\xi=x/\sqrt{5/2at^3} \qquad (6)$$

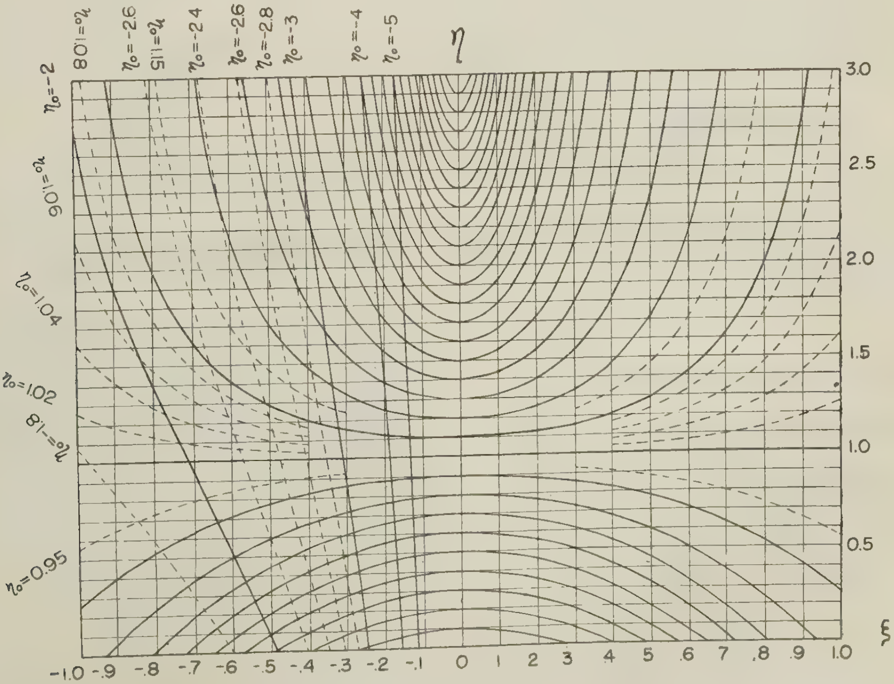

Fig. 1.

which reduce Eq. (4) to

$$d^2\eta/d\xi^2=5/2(\eta^4-1) \tag{7}$$

Integration of Eq. (7) gives

$$(d\eta/d\xi)^2=\eta^5-5\eta-C\,, \tag{8}$$

where $C$ is an integration constant.

The result obtained by direct integration of Eq. (8) includes two integration constants, requiring two paramaters in the graphical representation of the solution. Fortunately the origin of $\xi$, however, can be chosen arbitrarily.

In order to reduce the number of the parameter, let us choose this origin at the extreme value of $\eta$ or the point of

$$d\eta/d\xi=0 \qquad (\xi=0) \tag{9}$$

This requires that the solution of Eq. (8) should always have an extreme value or

$$\eta^5-5\eta-C=0 \tag{10}$$

should have a real root.

This is always true, if we allow $\eta$ to have negative value. From the physical point of view $\eta$ must be positive, but the derivation of the above equations are free from such a limitation. So we can carry out the integration without considering the sign of $\eta$, if only the positive region of $\eta$ is adopted as the final result.

Then let $\eta_0$ be a real root of Eq. (10) so that

$$d\eta/d\xi=0 \quad \text{at} \quad \xi=0 \quad \text{and} \quad \eta=\eta_0\,.$$

From above conditions the solution of Eq. (8) becomes

$$\xi=\pm\int_{\eta_0}^{\eta}\frac{d\eta}{\sqrt{\eta^5-5\eta-(\eta_0^5-5\eta_0)}}\,. \tag{11}$$

The graph shows this integral in the practical range of $\xi$ and $\eta$ with $\eta_0$ taken as a parameter.

## References

1) Carslaw Jeager: Conduction of Heat in Solid p. 136.
2) H. Hatano: Denpa Nippon **45** (1948).
3) S. Nakamura: Advance copy of the disc-seal tube conference (1950).

---

J. Phys Soc. Japan **11** (1956) 330~331

# Hydration of Ions and Coordinate Bond

By Isao Oshida and Ohi Horiguchi

*Kobayasi Institute of Physical Research, Kokubunzi, Tokyo*

(Received December 16, 1955)

It has been generally accepted that the energy of hydration of ions is of electrostatic nature, since Born's expression[1] for the decrease $Q$ of electrostatic energy when a sphere with the ionic charge $Ze$ and the ionic radius $r$ enter a medium with dielectric constant $\varepsilon$ from vaccuum

$$Q=\frac{Z^2e}{2r}\left(1-\frac{1}{\varepsilon}\right) \tag{1}$$

serves as the rough measure of the energy of hydration of monatomic ions. Latimer *et al*[2] showed that a better quantitative agreement with experimental values is obtained if we use for $r$ in (1) the effective radius, somewhat larger than the true ionic radius.

We have determined the experimental heats of hydration for about seventy ions from the recent thermochemical data such as heat of formation, heat of solution, heat of sublimation, ionization potential, electron affinity and energy of dissociation of diatomic molecule[3]. The plot of $Q$ against ionic radius do show the general downward trend with the increasing radius (Fig. 1).

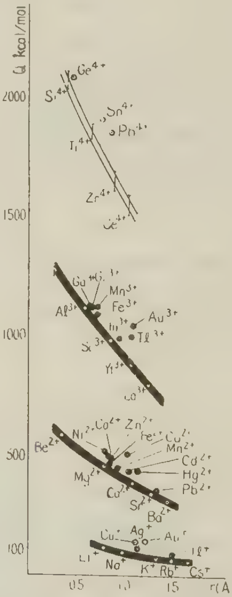

Fig. 1. Hydration-heat *versus* ionic radius (Goldschmidt's crystal radius).

It can be seen from Fig. 1, however, the rare-gas type ions have always smaller energy than the ions with incomplete electronic shell, if we compare the ions of same charge and same radius.

For example, the ions with eighteen-electron shell of each valency lie on the curves about 50 kilocalories higher than the corresponding curves for the rare-gas type ions. This suggests that the hydration results from the *electronic* interaction, rather than the *electric* interaction, between the central ion and the surrounding water molecules.

The study of the ionic hydration of the transition metals can draw a clearer picture in this connection. The heats of hydration of the divalent cation of transition metals plotted against the ionic

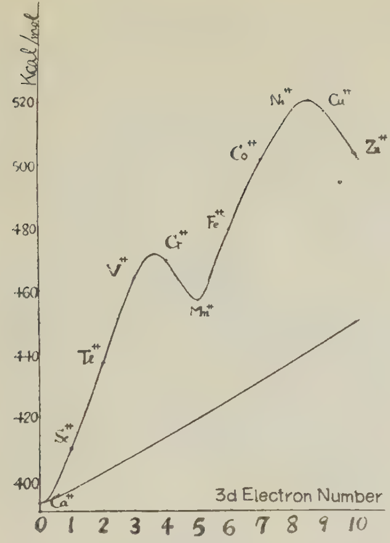

Fig. 2. Hydration-heat of transition metal ion (II). *versus* 3d electron number.

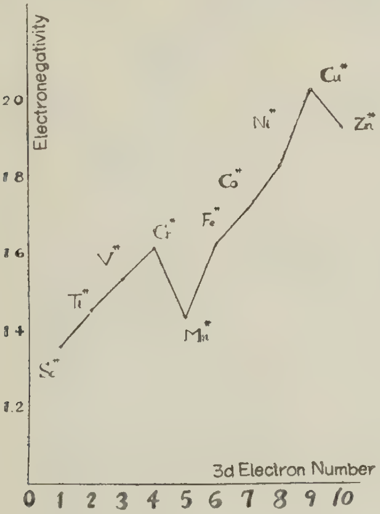

Fig. 3. Electronegativity of transition metal ion (II). *versus* 3d electron number.

radius or the number of 3d electron show two maxima (Fig. 2). On the other hand, the electronegativities of these ions have been known in recent by Haïssinsky[4], and by Ito and Kuroda[5]. Though the latter values are obtained by calculation, they are in very good agreement with Haïssinsky's values empirically induced. The plot of Ito and Kuroda's electronegativity has striking resemblance to Fig. 2, showing that the hydration is proportional to the electronegativity of the central ion (Fig. 3). As for the trivalent ions, though the lack of the data prevents us from deriving a definite conclusion, there seems to exist similar parallelism. Thus we can conclude that in the phenomena of hydration, the formation of coordinate bonds between the central ion and the water molecules plays an important role.

The details will be published elsewhere.

### References

1) M. Born: Zeit. F. Physik **1** (1920) 45.
2) W. M. Latimer: J. Am. Chem. Soc. **48** (1926) 1234.
W. M. Latimer, K. S. Pitzer and C. M. Slansky: J. Chem. Phys. **7** (1939) 108.
3) I. Oshida and O. Horiguchi: Bulletin of the Kobayasi Institute of Physical Research **5** (1955) 61 (in Japanese).
4) M. Haïssinsky: J. Phys. Radium **7** (1946) 7.
5) Y. Kuroda, K. Ito: Journ. Chem. Soc. Japan **76** (1955) 762 (in Japanese).

---

J. PHYS. SOC. JAPAN **11** (1956) 331~332

## A Note on the Theory of Dislocation in Germanium

By Takuzo SHINDO

*The Electrical Communication Laboratory*
*Musashinoshi, Tokyo, Japan*

(Received December 19, 1955)

Recently Read[1] has proposed a theory of dislocation in germanium and pointed out that the number of trapped electrons in the dangling bonds is determined by a different statistics from that of Fermi. We have studied the same problem employing the principle of detailed balance and found more general expression for $f$, the fraction of sites that are full in the dangling sites.

To begin with, we shall derive the Nijboer formula from the principle of detailed balance. Let there be $N$ impurity levels and $N_e$ electrons per cm³, of which, at temperature $T$, $n$ are excited. Let $\Delta E$ be the energy required to remove an electron from an impurity level into the conduction band. In thermal equilibrium, the principle of detailed balance requires

$$\left(1-\frac{N_e-n}{N}\right)P_r(E)F(E)\mathfrak{N}(E)dE$$
$$=\frac{N_e-n}{N}P_i(E)\mathfrak{N}(E)dE\,, \qquad (1)$$

where $P_r(E)$ is the recombination probability of the conduction electron of energy $E$ and $P_i(E)$ is the ionization probability of the trapped electron and $\mathfrak{N}(E)$ is the number of energy levels in the conduction band, given by

$$\mathfrak{N}(E)=4\pi(2m^*)^{3/2}h^{-3}V\overline{E}\,,$$

and $F(E)$ is the probability of finding an electron of energy $E$ in the conduction band. Usually the probabilities $P_i(E)$ and $P_r(E)$ are complicated functions depending upon the number of phonons associated with the transitions[2)3)]. But their ratio, $P_i(E)/P_r(E)$, has rather simple form and we have, according to Shockley and Read[4)],

$$P_i(E)/P_r(E)=\exp[-(E+\Delta E)/kT]\,. \qquad (2)$$

On the other hand, in a steady state we may put

$$F(E)=A\cdot\exp(-E/kT),$$

where $A$ is a constant to be determined by the condition:

$$\int_0^\infty F(E)\mathfrak{N}(E)dE=n\,.$$

Thus we obtain

$$A=n/N_c\,,\quad N_c=2(2\pi m^*kT/h^2)^{3/2}\,. \qquad (3)$$

From the Eqs. (1), (2) and (3), we have

$$\frac{n(N-N_c+n)}{N_c-n}=2\left(\frac{2\pi m^*kT}{h^2}\right)^{3/2}\exp(-\Delta E/kT).$$

This is the well known Nijboer's formula.

In the case of dangling bonds in nonpolar crystals $\Delta E$ depends on $f$, as was pointed out by Read, and was shown to be

$$\Delta E=E_2-\varepsilon^*(f)\,,$$

in which $E_2$ is an energy required to remove an electron from a dangling site, when $f=0$, into the conduction band and $\varepsilon^*(f)$ is the work done in forming the space charge cylinder with the line of evenly spaced electrons along its axis. Read has calculated $\varepsilon^*(f)$ in the form

$$\varepsilon^*(f)=\varepsilon_0 f\left(ln\frac{f}{f_0}-0.232\right)\,.$$

Let $N_s$ be the total number of dangling sites per unit volume, of which, at temperature $T$, $n_t$ are filled with electrons, and $n_i$ be the concentration of donor centers, then we have, in place of Eq. (1),

$$\left(1-\frac{n_t}{N_s}\right)P_r(E)F(E)\mathfrak{N}(E)dE=\frac{n_t}{N_s}P_i(E)\mathfrak{N}(E)dE\,. \qquad (4)$$

The Eq. (4) holds in the saturation range, where the donors are completely ionized. In the same way as before we have

$$\frac{f}{(1-f)(1-N_sf/n_i)}=\frac{n_i}{2}\left(\frac{2\pi m^*kT}{h^2}\right)^{-3/2}\exp\{[E_2-\varepsilon^*(f)]/kT\}\,, \qquad (5)$$

where $n_t=N_sf$.

In the low temperature range, where no electrons are excited into the conduction band, we have

$$\frac{f^2}{(1-f)(1-N_sf/n_i)}=\frac{n_i}{N_s}\exp\{[E_2'-\varepsilon^*(f)]/kT\}\,, \qquad (6)$$

where $E_2'$ is an energy difference between the donor level and the dangling level at $f=0$. When the trapped electrons in the dangling sites, $n_t$, are small compared with $n_i$, the Eq. (5) reduces to

$$\frac{f}{1-f}\sim\frac{n_i}{2}\left(\frac{2\pi m^*kT}{h^2}\right)^{-3/2}\exp\{[E_2-\varepsilon^*(f)]/kT\}\,. \qquad (7)$$

The Eq. (7) is identical with Eq. (9.1) of Read.

The author thanks Mr. Y. Uemura for his valuable discussions.

## References

1) W. T. Read: Phil. Mag. **45** (1954) 775.
2) H. Gummel and M. Lax: Phys. Rev. **97** (1955) 1469.
3) R. Kubo and Y. Toyozawa: Prog. Theor. Phys. **13** (1955) 160.
4) W. Shockley and W. T. Read: Phys. Rev. **87** (1952) 835.

---

J. Phys. Soc. Japan **11** (1956) 332~333

# Electrostatic Deflection of a Cyclotron Ion Beam

By Jun Kokame and Sukeaki Yamashita
*Institute for Chemical Research,*
*University of Kyoto*

(Received December 28, 1955)

Ions accelerated by a cyclotron to the maximum energy are usually extracted by an electrostatic deflector. In this case, it is necessary to know the ion trajectory for designing the deflector, dees and the vacuum chamber, and the design is usually performed by drawing ion paths step-by-step, corresponding to an instantaneous radius of rotation of the ion in the field of the cyclotron magnet and deflecting channel. If the ion trajectory could be represented in the form of an analytical function of $R, \theta$, the tedious procedures of drawing the path could be avoided. Although the remarkable contributions have been made by Coggeshall[1)] about the mathematical analysis of the motion of charged particles in non-uniform crossed electric and magnetic field, and Courant-Bethe[2)] also investigated theoretically an electrostatic deflection of a betatron or synchrotron beam, their works are not immediately available in our case.

The differential equation describing the ion path was investigated and solved using the measured fringing field of the magnet of the Kyoto University cyclotron (pole diameter 42″, beam energy ~16 Mev of deuteron). The following relation was obtained.

$$\frac{d^2R}{d\theta^2}=R-\frac{R^2}{r}\,, \qquad (1)$$

with

$$r=\frac{2E}{e(H\beta-V)}.$$

$R$ and $\theta$ are the radial and azimuthal coordinates of the deflected ion in the median plane of the magnetic field respectively, $r$ the radius of rotation, $E$ the energy of deflected ion in erg, $-e$ the electron charge in e.s.u., $H$ the magnetic field strength in gauss, $V$ the electric field strength in the deflecting channel in e.s.u., $\beta=v/c$ and $v$ is the velocity of the deflected ion. The origin of the coordinate system being fixed at the pole centre of the magnet, the $R-\theta$ relation indicates the deflected ion path. Eq. (1) is more accurate than the equation deduced by Courant and Bethe[2].

Integrating Eq. (1) we obtain

$$\left(\frac{dR}{d\theta}\right)^2\Big|_{R_1}^{R}=(R^2-R_1^2)-2\int_{R_1}^{R}\frac{R^2}{r}dR, \qquad (2)$$

in which

$$\int_{R_1}^{R}\frac{R^2}{r}dR=\frac{e\beta}{2E}\int_{R_1}^{R}HR^2dR-\frac{e}{2E}\int_{R_1}^{R}VR^2dR, \qquad (3)$$

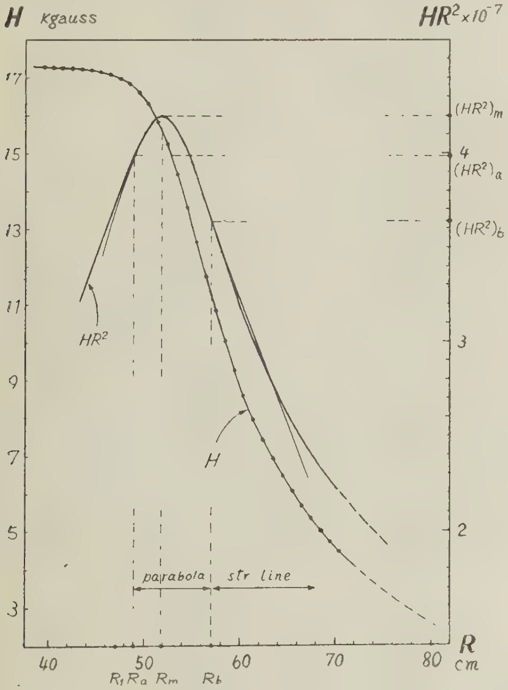

Fig. 1. The magnetic field profile and the curve of $HR^2$.

where $R_1$ is the radius at which the ion enters the deflecting channel. If we assume that $V/H$ is equal to a constant over the whole range in the deflector (this assumption is not so far from the actual condition, of which the minute discussion will be given elsewhere), the second term of the right-hand side of Eq. (3) becomes

$$\frac{e}{2E}\frac{V}{H}\int_{R_1}^{R}HR^2dR. \qquad (4)$$

Then Eq. (2) becomes

$$\left(\frac{dR}{d\theta}\right)^2=\left(\frac{dR}{d\theta}\right)^2_{R_1}+(R^2-R_1^2)-\frac{e}{E}\left(\beta-\frac{V}{H}\right)\int_{R_1}^{R}HR^2dR. \qquad (5)$$

On the other hand, from the measured values of $H$ along the radial direction from the centre, $HR^2$ can be calculated (cf. Fig. 1). The curve of $HR^2$ has a rather simple shape. It is expressed by a parabola in a considerably wide range of $R$ and by a straight line in other part with good accuracy. In the range $R_a(49\text{ cm})\leqq R<R_b(57\text{ cm})$, $HR^2$ is expressed by the formula $HR^2=(HR^2)_m-\alpha(R_m-R)^2$, where $(HR^2)_m$ is the maximum value of $HR^2$ at $R=R_m$, where the $n$-value of the magnetic field is equal to 2 (see Fig. 1); and in the range $R_b\leqq R$, $HR^2=(HR^2)_b-\gamma(R-R_b)$. At large $R$ some deviation from real $HR^2$ occurs, but $H$ is sufficiently small in this range so that there is no practical trouble. In the case when a more accurate path in this range is wanted, it is better to use another curve of the second degree for $HR^2$. If the deflector entrance might be set at so small radius that the deviation of $HR^2$ from the parabola $[(HR^2)_m-\alpha(R_m-R)^2]$ would become a considerable amount, the value of $HR^2$ in the range $R_a>R$ should be represented by another straight line, for in this range the magnetic field is so strong that even a little difference of $HR^2$ exerts an influence on the ion path.

Thus, Eq. (5) can be written in the following form:

$(dR/d\theta)^2=f(R^3, R^2, R)$ in the parabola range (6)

or

$(dR/d\theta)^2=\varphi(R^2, R)$ in the straight line range (7)

Eqs. (6) and (7) can be solved by usual procedure, and $R-\theta$ relation is expressed by elliptic functions and logarithmic functions respectively.

Ion trajectories through the fringing field of the cyclotron obtained from above calculation were compared with those obtained from step-by-step drawing. Good agreements between them were obtained. It seems to be useful to apply the above-mentioned method for designing deflector instead of using tedious drawing process.

The authors wish to express sincere thanks to Prof. K. Kimura for his kind discussion and criticism, and to Assistant Prof. R. Ishiwari for his kind advice and encouragement. We are also indebted to the staff of our laboratory for the data of magnetic field.

## References

1) N. D. Coggeshall: Phys. Rev. **70** (1946) 270.
2) E. D. Courant and H. A. Bethe: Rev. Sci. Inst. **19** (1948) 632.

J. Phys. Soc. Japan **11** (1956) 334~335

## Microwave Spectra of Formaldehyde and Methylamine in the SHF Region

By Hiromasa HIRAKAWA, Akira MIYAHARA and Koichi SHIMODA

*Department of Physics, Faculty of Science, University of Tokyo*

(Received January 14, 1956)

Microwave spectra of formaldehyde and methylamine have been observed in the frequency range from 2700 to 8100 Mc/sec using Stark modulation of 110 Kc/sec. The absorption cell was constructed of 4 meters length of 29×58 mm copper waveguide, with copper Stark septum and polystyrene supports. Klystron oscillators, 2K25, 2K26, 2K22, 2K56, 726A and 726C were used as the microwave source, while silicon diodes 1N23B and 1N21C were used as detectors. The spectrum was displayed on a CRO screen. The accuracy of the frequency measurement is ±0.01 Mc/sec for strong lines, while for very weak lines errors incurred in determining the centre of lines are as much as ±0.5 Mc/sec, being the minimum detectable absorption coefficient around $1\times10^{-8}$ cm$^{-1}$.

Six lines of $C^{12}H_2O^{16}$, three of $C^{13}H_2O^{16}$, and one of $C^{12}H_2O^{18}$ have been measured and they are tabulated in Table I. For $C^{12}H_2O^{16}$, Lawrance and Strandberg[1] analysed the centrifugal distortion effect of this molecule, and determined the molecular constants together with the centrifugal coefficients. Frequencies calculated from their constants agree well to our observations.

Table I. Observed Frequencies of Formaldehyde Spectrum.

| Transition $J_{K_{-1},K_{+1}}$ $\rightarrow J_{K_{-1},K'_{+1}}$ | Observed Frequency (Mc/sec) | Calculated Frequency (Mc/sec) | Intensity |
|---|---|---|---|
| (1) $C^{12}H_2O^{16}$ | | | |
| $1_{1,1}\rightarrow 1_{1,0}$ | 4829.73 | 4829.6 | S |
| $6_{2,5}\rightarrow 6_{2,4}$ | 4954.76 | 4954.62 | S |
| $12_{3,10}\rightarrow 12_{3,9}$ | 3225.58 | 3224.11 | MS |
| $13_{3,11}\rightarrow 13_{3,10}$ | 5136.58 | 5136.12 | S |
| $20_{4,17}\rightarrow 20_{4,16}$ | 3518.85 | 3518.65 | MW |
| $21_{4,18}\rightarrow 21_{4,17}$ | 5138.57 | 5138.50 | W |
| (2) $C^{13}H_2O^{16}$ | | | |
| $1_{1,1}\rightarrow 1_{1,0}$ | 4593.26 | | W |
| $7_{2,6}\rightarrow 7_{2,5}$ | 8012.56 | | W |
| $14_{3,12}\rightarrow 14_{3,11}$ | 6752.31 | | W |
| (3) $C^{12}H_2O^{18}$ | | | |
| $1_{1,1}\rightarrow 1_{1,0}$ | 4388.85 | | WW |

Fourty-four observed lines of methylamine molecule and their Stark patterns are listed in Table II. The classiffcations of the Starkeffects are as follows:

1( i ) or 1( O ): the first order effects with inner or outer components stronger than outer or inner ones.

2(+) or 2(−): the second order effects, with positive or negative Stark shifts.

1→2: Superposition of first and second order effects which are comparable at the field strength of $E\sim50$ V/cm.

Most of these lines could be assigned according to the interpretation already described by Nishikawa et al[2].

Table II. Observed Frequencies of Methylamine Spectrum.

| Observed Frequency (Mc/sec) | Stark Effect | Intensity |
|---|---|---|
| 7515.56 | 1→2 | M |
| 7383.78 | 2(+) | MS |
| 7382.93 | 2(+) | MS |
| 6867.17 | 1( i ) | MW |
| 6837.58 | 2(+) | W |
| 6748.80 | 2(+) | M |
| 6655.04 | 2(+) | S |
| 6500.42 | 1( i ) | W |
| 6487.99 | 1( i )? | WW |
| 6469.43 | 2(+) | WW |
| 6450.42 | 1( i ) | MW |
| 6350.09 | 2(+) | MW |
| 6349.51 | 2(+) | MW |
| 6269.81 | 1( i ) | MW |
| 6246.42 | 1( i ) | W |
| 6172.20 | 1→2 | M |
| 6153.64 | 1→2 | M |
| 5876.61 | 1( i )? | WW |
| 5766.68 | 2(−) | MW |
| 5680.84 | 2(+) | MW |
| 5679.92 | 2(+) | MW |
| 5602.57 | 2(+) | M |
| 5546.75 | 1→2 | M |
| 5284.82 | 2(+) | S |
| 5006.82 | 1→2 | MW |
| 4963.00 | 1→2 | M |
| 4859.88 | 1( i ) | W |
| 4857.86 | 1( i ) | W |
| 4660.42 | 1( i ) | W |
| 4543.00 | 1→2 | W |
| 4480.55 | 2(+) | M |
| 4142.15 | 1→2 | W |
| 4129.84 | 2(+) | W |
| 4129.01 | 2(+) | W |
| 4076.65 | 2(+) | MS |
| 3921.96 | 1→2 | MW |
| 3797.95 | 1→2 | W |
| 3505.76 | 1→2 | W |
| 3483.67 | 2(+) | W |
| 3389.74 | 2(+) | MW |
| 3019.90 | 1→2 | MW |
| 3015.17 | 2(+) | M |
| 2782.62 | 2(+) | W |
| 2781.95 | 2(+) | W |

### References

1) R. B. Lawrance and M. W. P. Strandberg: Phys. Rev. **83** (1951) 363.
2) K. Shimoda, T. Nishikawa and T. Itoh: J. Phys. Soc. Japan **9** (1954) 974.
T. Nishikawa, T. Itoh, and K. Shimoda: J. Chem. Phys. **23** (1955) 1735.

---

J. PHYS. SOC. JAPAN **11** (1956) 335

## *l*-Type Doubling Spectra of HCN and DCN in the SHF Region

By Akira MIYAHARA, Hiromasa HIRAKAWA and Koichi SHIMODA

*Department of Physics, Faculty of Science, University of Tokyo*

(Received January 14, 1956)

Bending vibration of a linear triatomic molecule such as HCN is peculiarly coupled to rotation of the molecule, and it introduces a splitting of each rotational level known as *l*-type doublets. We have observed three lines of HCN and three lines of DCN, corresponding to the direct transitions between *l*-type doublets, in the frequency ranges between 2600 and 7900 Mc/sec. The same Stark modulation spectrometer of 4 meters long was used as that described in the preceeding note. The observed frequencies of HCN and DCN are given in Table I. These values have been obtained by extrapolating the observed frequencies at various Stark fields to those at zero field, considering that the Stark effects are of the second order. According to Nielsen's theory[1], the *l*-type doubling constant $q(=\nu/J(J+1))$ can be written as

$$q=q_0-\varepsilon J(J+1)\ .$$

Plotting of $\nu/J(J+1)$ from observed values against $J(J+1)$ shows a good linear relation. Using above results together with the observed frequencies of HCN for $J$ from 6 to 12, given by Westerkamp[2], we obtain the *l*-type doubling constant as $q=224.478-0.002667\,J(J+1)$ Mc/sec for HCN. As to the constant for DCN, $q=186.193-0.002197\,J(J+1)$ Mc/sec is obtained from the six observed frequencies, given by Weatherly and Williams[3] and by us.

Table I.

(1) HCN observed frequencies.

| $J$ | $\nu$(Mc/sec) | $q(=\nu/J(J+1))$ | $q=224.478$ $-0.002667\,J(J+1)$ |
|---|---|---|---|
| 3 | 2693.35±0.02 | 224.446 | 224.446 |
| 4 | 4488.50±0.01 | 224.425 | 224.425 |
| 5 | 6731.95±0·01 | 224.398 | 224.398 |

(2) DCN observed frequencies.

| $J$ | $\nu$(Mc/sec) | $q(=\nu/J(J+1))$ | $q=186.193$ $-0.002197\,J(J+1)$ |
|---|---|---|---|
| 4 | 3722.98±0.02 | 186.149 | 186.149 |
| 5 | 5583.85±0.02 | 186.128 | 186.127 |
| 6 | 7816.20±0.02 | 186.100 | 186.101 |

The absorption coefficient $\alpha$, computed from the following values, $\mu=2.96$D, $\nu_2=712\ \text{cm}^{-1}$, $T=290°$K, $\Delta\nu/P=25$ Mc/sec/mmHg, for the $J=3$ line of HCN, is $2\times10^{-7}\text{cm}^{-1}$, which differs from Collier's[4] calculation by about a factor of 7. Our observed intensity of the $J=3$ line seems rather consistent with our calculation. It is also confirmed by the observed ratio of intensity of this line to the lines of formaldehyde molecule.

### References

1) H. H. Nielsen: Phys. Rev. **75** (1950) 1961, **78** (1950) 296.
2) J. F. Westerkamp: Phys. Rev. **93** (1954) 716.
3) T. L. Weatherly and D. Williams: Phys. Rev. **87** (1952) 517.
4) R. J. Collier: Phys. Rev. **95** (1954) 1201.

# PROGRESS OF THEORETICAL PHYSICS

*(Founded by H. Yukawa in 1946)*

Published for the

**Research Institute for Fundamental Physics**

**The Physical Society of Japan**

---

Progress of Theoretical Physics Vol. 14, No. [illegible] [illegible]ember 1955

The Formal Theory of Scattering................................Sigeno[illegible] [illegible]KAWA..175

Phenomenological Analysis of Elastic $\pi^-$-p Scattering at 1.4 Bev..........Daisuke ITÔ and Shigeo MINAMI..198

Solutions of a Bethe-Salpeter Equation for Scattering States....Kazuhiko NISHIJIMA..203

The Energy-Levels and Transition Probabilities for a Bounded Lin[illegible] [illegible]rmonic Oscillator ..................................J. S. BAL[illegible] and K. K. SINGH..214

On the Jauch Field..........................Susumu KAMEFU[illegible] and Shô TANAKA..225

Connection of the Strong Coupling Theory with the Weak Coupling Theory in the Bound Meson Problem.........Sumio TANI and Wataro WATARI..243

Letters to the Editor:

Some Remarks on the Applicability of the [illegible] [illegible]ory from the Standpoint of the Distribution Analysis. [illegible] ........H. WAKITA..260

The Character of the Roton State in Liquid Hel[illegible] ........................................R[illegible] [illegible]IAN and M. COHEN..261

The Cloudy Crystal Ball Model for 14 Mev N[illegible] [illegible]actions...........................................M. KA[illegible] NAGASAKI and H. UI..263

Errata ............................................................265

---

Progress of Theoretical Physics Vol. 14, No. 4, October 1955

Relativistic Wave Equations with Maximum S[illegible] ........................Toshihiko TSUNETO[illegible] [illegible]ROSIGE and Izuru FUJIWARA..267

The Vector Representation of Spinning Partic[illegible] [illegible]antum Theory, I ................................Takehiko TAKABAYASI..283

On the Recoil Correction to Adiabatic N[illegible] ...........................Iw[illegible] [illegible]BASHI and Shinji SATO..303

$\beta$-Ray Spectrum of RaE....Hisao TAKE[illegible] S[illegible] and Mitsuo TAKETANI..317

On the Bose-Einstein Liquid Model for Liquid He[illegible] ——*A Revised Model*——. ...........Ziro MIKURA..337

A New Approach to Quantum-Statist[illegible] Mechanics...[illegible]eo MATSUBARA..351

On the Extension of the Casimir Tri[illegible]....——*On the Definition of Density Matrix and its* [illegible]—.......................Tsuneyuki KOTANI..379

Letters to the Editor:

Note on the Non-P[illegible] [illegible]roach to Quantum Field Theory.............................T. GOTO and T. IMAMURA..396

A Note on the Static Appro[illegible]ation of the Nuclear Anomalous Magnetic Moment.........................................A. KANAZAWA..397

Stripping Reactions and Nuclear Shell Model..........S. OKAI and M. SANO..399

On Quantum-Mechanical Nuclear Dipole Vibrations................J. FUJITA..400

On the Nuclear Photo-Reaction, I ..................S. FUJII and S. TAKAGI..402

On the Nuclear Photo-Reaction, II ..................S. FUJII and S. TAKAGI..405

An Exactly Soluble Example in Quantum Field Theory..........S. MACHIDA..407

On the Heisenberg's Non-Linear Meson Equation................T. TANIUTI..408

---

Price $ 1.25 per copy

$ 15.00 per year (postage inclusive)

Annual dues for foreign members (individual subscribers)

$ 12.00 (postage inclusive)

" for foreign members of the Physical Society of Japan

$ 10.00 (postage inclusive)

Application for members, subscriptions and orders for back mumbers should be sent, directly or through book-dealers, to

The Publication Office

in

**Yukawa Hall, Kyoto University, Kyoto, Japan**

JOURNAL OF THE PHYSICAL SOCIETY OF JAPAN Vol. 11, No. 4, APRIL, 1956

# On the Ionization-energy Relation for Alpha-particles in Air

By Ryutaro ISHIWARI, Sukeaki YAMASHITA, Kazunori YUASA[*],
*Institute for Chemical Research, University of Kyoto, Kyoto*
and Kozo MIYAKE
*Department of Physics, Faculty of Science, University of Kyoto, Kyoto*

(Received November 25, 1955)

To investigate the effect of columnar recombination on the ionization measurement in air, the ratio of the specific ionizations at two fixed residual ranges for polonium alpha-particles was measured with a shallow ionization chamber under various field strengths and angles between the field and the alpha-track. It was found that the observed ratio varies appreciably with varying field strength and angle. It was shown that the observed variation of the ratio can be explained by the effect of columnar recombination and agrees qualitatively with Jaffé's theory. The value of the parameter $b$ in Jaffé's formula, which gives the best agreement with the experiments, was newly determined as $9.5\times10^{-4}$ for alpha-particles in atmospheric air.

The observed specific ionization curve was corrected for recombination by Jaffé's theory. Then, the corrected curve was integrated and the true ionization-range relation free from recombination was determined. By comparing this relation with the fixed points of the range-energy relation obtained from nuclear reaction data, an empirical formula for the average energy loss per ion pair for alpha-particles in air relative to polonium alpha-particles, $w$, was obtained as;

$$w=0.948+\frac{0.119}{\sqrt{E}}\ ,$$

where $E$ is the initial alpha-energy in Mev. This formula is valid at least for the alpha-energy down to 1 Mev.

## §1. Introduction

For many years, it has been well known that the average energy expended by a heavy charged particle to produce one ion pair in gases is nearly constant and almost independent of the particle energy. The method to determine the particle energy by measuring the total ionization produced by the particle and assuming the proportionality between the total ionization and the energy of the particle, has, therefore, been universally adopted. However, recent progress in accuracy of the experiments in nuclear physics has come to require more precise information on the relationship between $W$, the average energy to produce one ion pair, and the particle energy for different gases and for different types of particles.

Gray[1] has summarized the experimental data up to 1942, and concluded that $W$ for alpha-particle in air depends appreciably upon the particle energy at low energies. More recently Jesse et al.[2][3] performed a series of experiments on the ionization-energy relation for alpha-particles in argon and in air. According to their result, $W$ in argon is constant independently of the particle energy, whereas $W$ in air increases considerably with the decreasing energy. On the basis of this result, Jesse et al.[3] and Bethe[4] have revised the range-energy curve for alpha-particles in air given by Holloway and Livingston[5], which was derived from an experimental range-ionization curve in the energy region below 5 Mev under the assumption of the strict proportionality between the ionization and the particle energy in air. The revised range-energy curve is in satisfactory agreement with the data[6] obtained from some nuclear reactions in which accurate values for energies and ranges of emitted particles have been determined independently from each other.

Recently, nevertheless, some evidences conflicting with the result of Jesse et al. on the ionization-energy relation have been reported by several authors. Cranshaw and Harvey⁷⁾ have measured the total ionizations produced by natural alpha-particles in argon, and obtained such a result that $W$ in argon depends on the energy of alpha-particles. They gave an empirical formula for the relation between $W$ and the particle energy in argon. In succession to this, Hanna⁸⁾, Bichsel, Hälg, Huber and Stebler⁹⁾, and Rhodes, Franzen and Stephens¹⁰⁾ have measured the total ionization of the $B^{10}(n, \alpha)Li^7$ reaction in argon and its separate ionizations respectively. Their results all in concert conflict with the constancy of $W$, but agree with the result of Cranshaw and Harvey. Tunnicliffe and Ward¹¹⁾ have also reported similar result that indicates the variation of $W$ with the particle energy in argon mixed with a small amount of helium and methane.

---

[*] Present address: Department of Physics, Konan University, Kobe.

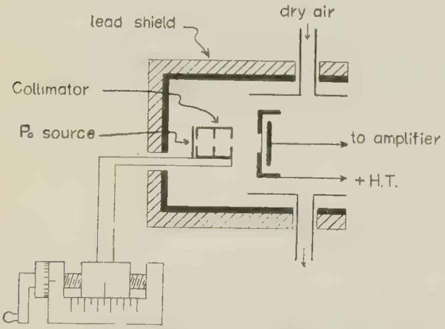

Fig. 1. The schematic diagram of the ionization chamber.

In a previous paper¹²⁾, on the other hand, we have pointed out that the effect of columnar recombination should be carefully treated in the discussion of the ionization-energy relation in air. If the field strength is not sufficient to prevent columnar recombination, the degree of saturation will decrease with the decrease of the particle energy because of the increasing ion density. This results in an apparent decrease of the observed ionization, i.e. an increase of $W$, in the low energy region. Experimental evidence has also been presented about the fact that the result of Holloway and Livingston is not free from the effect of columnar recombination and $W$ in air may be more nearly constant than reported by Jesse et al..

Thus, it can be concluded that there are still many doubtful points about the behaviour of $W$ in argon as well as in air, on which the revision of the range-energy relation made by Jesse et al. and Bethe is based, although their revised range-energy relation is useful from the practical point of view.

In the present paper, we have studied the effect of columnar recombination on the ionization measurement in air more quantitatively than the previous work, and determined the true range-ionization relation free from the recombination effect for alpha-particles in air. Further, comparing this relation with the fixed points on the range-energy relation obtained from the nuclear reaction data, we have attempted to establish an empirical formula for the energy dependency of $W$ in air.

## § 2. Apparatus

We have measured the specific ionization for polonium alpha-particles with a shallow ionization chamber. The arrangement of the equipments is similar to that of Holloway and Livingston⁵⁾ as shown in Fig. 1. The depth of the chamber is 1 mm, and the diameter of the collecting electrode is 15 mm. The front window is 8 mm in diameter, and is covered with aluminium foil of $0.41_2$ mg/cm² thick instead of metal gauze to prevent the inequality of the field and the possible occurrence of corona discharge when a high voltage is applied. Pure polonium newly deposited on a silver foil was used as the alpha-particle source. The source was mounted on a screw micrometer stage with a divided drum of 0.5 mm pitch, and moved perpendicular to the front face of the chamber. Alpha-particles were collimated by three thin ebonite sheets with small holes placed in front of the source at intervals of 5 mm. Three sets of collimeters with different hole diameters were prepared as described later. The time constant of the amplifier was chosen as $2\times10^{-3}$ sec which was adequately larger than the collecting time of ions even when the lowest voltage was applied. The gain and the linearity of the amplifier were frequently checked with a pulse generator during the measurement. The output of the amplifier was connected to a register with a thyratron discriminator and an oscilloscope in parallel.

At the operation of this apparatus, the shallowness of the chamber and the use of aluminium foil at the window have required special precautions to avoid the microphonic noise. The outside of the chamber was covered with lead shield of 3 mm thick and wrapped with thick felt sheet. Further, the source stage and the chamber together with the preamplifier were mounted in a sound arresting box tamped with rock wool. These precautions made it possible to work with sufficiently low noise level. The signal to peak noise ratio in the measurement at the peak of the specific ionization for alpha-particles was 12 to 14, that is, the peak value of the noise corresponds to about 20 Kev. Air admitted into the chamber was desicated by $CaCl_2$, but the elimination of $CO_2$ was not made.

## § 3. Experimental Procedure

According to Jaffé's theory(13) of columnar recombination, the saturation of the observed ionization depends upon the field strength and the angle between the field and the track of the particle as well as the ion density. So we have investigated the effect of columnar recombination by means of changing the field strength and its relative angle respectively.

### A. *Effect of Variation of Field Strength*

In order to investigate straightforwardly the effect of columnar recombination, we have measured the ratio of the pulse heights at two fixed points on the specific ionization curve under the various field strengths. As the fixed points, we have chosen the peak of the specific ionization curve (the residual range at this point is 4.5 mm; henceforth referred to as point P) and the point 18 mm off the peak (the residual range at this point is 22.5 mm; henceforth referred to as point F). The specific ionization at the point F is about half that at the point P.

The degree of columnar recombination at each point, if its effect is present, is different in accordance with the difference of the ion density under the same experimental conditions of the field and its relative angle. That is, the pulse height observed at the point P suffers the greater effect of columnar recombination than that at the point F because of the greater ion density, and so the ratio of the pulse heights at P and F is smaller than the ratio of the true ionizations produced primarily. Since the degree of recombination decreases with the increase of the field strength, the observed ratio of the pulse heights increases with the increasing applied voltage and comes to be equal to the ratio of the true ionizations as the perfect saturation is attained.

The applied voltages were chosen as 50 volts and 135 volts that have hitherto been considered as appropriate for a chamber of 1 mm depth, and also 1,140 volts was chosen as an extraordinary high voltage. That is, the field strength in each case is 500 volts/cm, 1,350 volts/cm and 11,400 volts/cm respectively. The diameter of the hole of the collimator used was 1.5 mm.

The pulse height was measured with the thyratron discriminator by determining the half-maximum point of the number-bias curve. More than one thousand pulses were always counted for each bias setting.

The positions of the source corresponding to the point P and the point F were determined by taking account of the correction for the pressure and the temperature of air and the change of the stopping power of the aluminium foil with the alpha-energy. The position of the source for the point P was determined by the following procedure. First the specific ionization curve near the peak was measured carefully with the field strength of 500 volts/cm, and the shape of the observed curve was compared with the curve(14) of Holloway and Livingston. The point was sought on the scale of the measured relative distance in such a way that the two curves give the best fit, and thus the position of the point P and the absolute scale of the distance measurement were determined*. The change of the stopping power of the foil was also determined experimentally. An additional foil cut from the same sheet as used at the window was inserted at proper distances from the source corresponding to the point P and the point F, and then the number-distance curve was measured. The air equivalent values for the stopping power of the foil for the alpha-energies at the point P and the point F can be obtained from the change of the half-maximum point of the number-distance curve measured with and without the additional foil, and they are 2.09 ±0.06 mm N.T.P. (15°C, 760 mm Hg) air at the point P and 2.48±0.06 mm N.T.P. air at the point F respectively. So, if the source is moved by 18.39 mm in N.T.P. air from the position corresponding to the point P, it in effect corresponds to the position 18.39−(2.48−2.09)=18.00±0.09 mm off the point P, i.e. the position of the point F.

---

* As discussed in detail by Holloway and Livingston, the present experimental arrangement is not suited for the precise determination of the absolute range corresponding to the measurement with zero bias. The method adopted here is fairly sensitive, and the absolute scale related to the precise determination of Holloway and Livingston can be easily determined within 0.2 mm.

It has several advantages to measure the ratio of the pulse heights at these two points, as follows.

I) The change of the ratio of the amplifier time constant to the collecting time caused by the change of the chamber voltage, does not prevent to study purely the effect of the field strength*.

II) The effect of gas multiplication, even if it occurs under the highest field strength (11,400 volts/cm), is eliminated and does not affect the result.

III) The change of the effective chamber depth due to different atmospheric pressures in different runs is also eliminated automatically.

IV) The result is easily compared with that of previous works, especially of Holloway and Livingston, on the effect of columnar recombination.

### B. *Effect of Variation of Angle*

When the incident beam of alpha-particles is approximately parallel with the field as in this experiment, the effective angle between the alpha-track and the field depends upon the collimating condition. Because the method used for determining the pulse height is to measure the half-maximum of the number-bias curve, the effective angle $\tilde{\theta}$ should be defined in such a way that the number of alpha-particles with angles greater than $\tilde{\theta}$ is equal to that with smaller angles. Now, let $b$ denote the length of the collimator and $2a$ denote the diameter of the collimating hole, the effective angle $\tilde{\theta}$ as defined above is given by

$$\tilde{\theta}=0.891\,a/b \quad \text{in radian,}$$

provided that the polonium source is uniform and alpha-particles are emitted spherically symmetrically. The following three collimators were used.

$2a=1.0$ mm: $\tilde{\theta}=2.55°$

$2a=1.5$ mm: $\tilde{\theta}=3.83°$

$2a=2.0$ mm: $\tilde{\theta}=5.11°$

Of each one the length $b$ was 10 mm. Using these collimators, the ratios of the pulse heights at the point P and the point F were determined by the same procedure as described above with applied voltages of 50 volts and 135 volts. Since Jaffé's theory indicates that the degree of recombination decreases as the angle increases, it is expected that if any effect of recombination is present the ratio of the pulse heights increases with the angle $\tilde{\theta}$. The error, introduced into the determination of the source position by the oblique incidence as a result of the change of $\tilde{\theta}$, is less than 0.1% and no correction was made for this.

### C. *Measurement of Whole Specific Ionizations*

Further, we have measured the whole specific ionizations of residual range below 22 mm applying the voltages of 50 volts and 1,140 volts. In this case, the pulse heights were measured directly on the screen of the oscilloscope. The accuracy of this method is somewhat lower than the preceding measurements using thyratron discriminator. That is, when the pulse height corresponding to the maximum specific ionization was about 30 mm on the screen, the standard deviation of several determinations of the pulse height amounted to 0.3 mm to 0.5 mm. The collimator of $2a=1.5$ mm, $\tilde{\theta}=3.83°$ was used. All distance measurements were corrected to N.T.P. as before.

## § 4. Experimental Results

### A. *Effect of Variation of Field Strength*

The observed values of the ratio of the pulse heights at the two points P and F for

---

* In many of previous works, the voltage saturation of the pulse height was often measured under a certain geometry with the purpose of preventing columnar recombination. But, such a method is not adequate for this purpose because of the fact that the change of the pulse height with the applied voltage is affected in complicated ways by the change of the ratio between the amplifier time constant and the collecting time. Moreover, when the chamber is fairly deep, the observed saturation is responsible only for the average ion density over the total length of the track, so it is difficult to certify the saturation at the most dense part of the track.

Table I. The ratio of the pulse heights at the points P and F observed for different voltages with $\tilde{\theta}=3.83°$.

| No. of run | Applied voltage | | |
|---|---|---|---|
| | 50 volts | 135 volts | 1,140 volts |
| 1 | $1.83_3$ | $1.94_7$ | $1.96_0$ |
| 2 | $1.89_0$ | $1.94_5$ | $1.97_2$ |
| 3 | $1.85_8$ | $1.95_5$ | $2.02_5$ |
| 4 | $1.82_3$ | $1.91_9$ | $1.99_4$ |
| 5 | $1.88_2$ | $1.93_4$ | |
| Average | $1.85_7$ <br> $\pm 0.013$ | $1.94_0$ <br> $\pm 0.006$ | $1.98_3$ <br> $\pm 0.014$ |

Table II. The ratio of the pulse heights at the points P and F observed for different effective angles with the applied voltage of 50 volts.

| No. of run | Effective angle $\tilde{\theta}$ | | |
|---|---|---|---|
| | 2.55° | 3.83° | 5.11° |
| 1 | $1.83_0$ | $1.86_8$ | $1.86_6$ |
| 2 | $1.83_0$ | $1.87_2$ | $1.87_0$ |
| 3 | $1.84_2$ | $1.86_8$ | $1.91_6$ |
| 4 | $1.84_1$ | $1.86_2$ | $1.87_7$ |
| Average | $1.83_6$ <br> $\pm 0.003$ | $1.86^8$ <br> $\pm 0.002$ | $1.88_2$ <br> $\pm 0.012$ |

Table III. The ratio of the pulse heights at the points P and F observed for different effective angles with the applied voltage of 135 volts.

| No. of run | Effective angle $\tilde{\theta}$ | | |
|---|---|---|---|
| | 2.55° | 3.83° | 5.11° |
| 1 | $1.90_4$ | $1.95_2$ | $1.95_4$ |
| 2 | $1.92_1$ | $1.92_0$ | $1.93_0$ |
| 3 | $1.90_2$ | $1.92_5$ | $1.95_2$ |
| 4 | $1.90_9$ | $1.91_2$ | $1.92_2$ |
| Average | $1.90_9$ <br> $\pm 0.004$ | $1.92_7$ <br> $\pm 0.009$ | $1.94_0$ <br> $\pm 0.008$ |

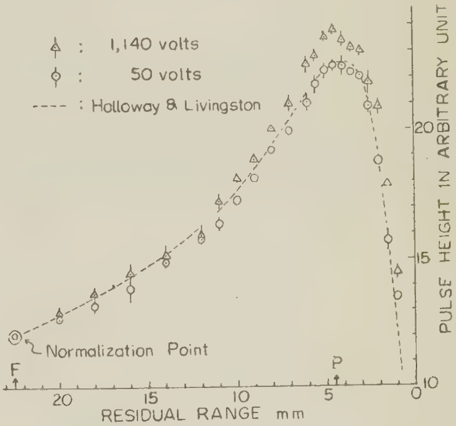

Fig. 2. The specific ionizations for polonium alpha-particles under the field strengths 500 volts/cm and 11,400 volts/cm.

different voltages are shown in Table I* and Fig. 3.

The error given to the average value is the standard deviation of the observed values. In each run the error of the ratio caused by the uncertainties in the pulse height measurement is of the order of ±0.011 to ±0.015, and well accords with the standard deviations given above.

As obviously seen from Table I, the observed ratio increases with the rise of the applied voltage. And this is consistent with the expected effect of columnar recombination.

B. *Effect of Variation of Angle.*

The ratios of the pulse heights observed for different effective angles $\tilde{\theta}$ with the two fixed voltages (50 volts and 135 volts) are shown in Tables II and III, and also in Fig. 4.

The error is also the standard deviation. It is clearly seen that the value of the ratio increases with the effective angle, and this is explained by the effect of columnar recombination. Moreover, the fact that the increase of the ratio with $\tilde{\theta}$ is prominent in the case of 50 volts than 135 volts, and that for each value of $\tilde{\theta}$ the ratio is greater in the case of 135 volts than 50 volts, is characteristic of columnar recombination.

C. *Measurement of Whole Specific Ionizations*

In Fig. 2 are shown the whole specific ionization curves observed with 50 volts and 1,140 volts applied. As the absolute value of the pulse height is changed for different voltages by the time constant to collecting time ratio even when an adequately large time constant is adopted, the curves in the figure are normalized at the point F. In the figure, the curve of Holloway and Livingston is also

---

* The values given in Table I are the same data as reported in the previous paper, but corrected for the fact that in dynamic operation the flashing bias voltage of the thyratron used is shifted by about 1.5 volts from the value determined statically. As a consequence, in the previous paper the values for the ratio were too high by about 2 percent.

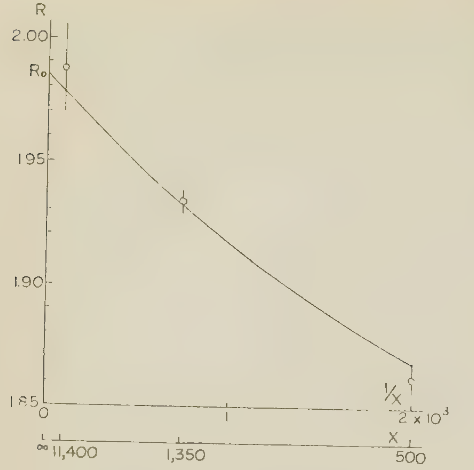

Fig. 3. The ratios of the pulse heights at the two points P and F for different field strengths with $\tilde{\theta}=3.83°$. The solid curve represents the values calculated by Jaffe's theory. The points at $X=$ 500 and 1,350 volts/cm are the averages of the values given in Tables I, II and III.

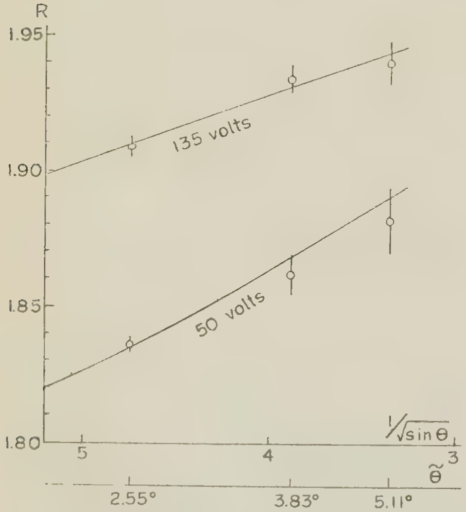

Fig. 4. The ratios of the pulse heights at the two points P and F for different effective angles with the voltages 50 volts and 135 volts. The solid curves represent the theoretical values. The points at $\tilde{\theta}=3.83°$ are the averages of the values given in Tables I, II and III.

shown by a dotted curve. The curve observed with 1,140 volts shows larger ionization around the peak than that with 50 volts in accord with the results of Table I. The latter curve nearly agrees with the curve of Holloway and Livingston.

## § 5. Comparison with Jaffé's Theory

We have tried to compare our result with Jaffé's theory[13] of columnar recombination, and examined to what extent the observed phenomena are quantitatively explained by the effect of columnar recombination.

According to Jaffé's theory, the fraction of the ions escaping from recombination, $Y$, is given by*

$$Y=1\Big/\left\{1+\frac{\alpha N_0}{8\pi D}\sqrt{\frac{\pi}{z}}S(z)\right\},$$

$$z=\frac{b^2k^2X^2\sin^2\theta}{2D^2},$$

where $N_0$ denotes the linear inonization density produced primarily, $\alpha$ the volume recombination coefficient, $D$ the diffusion coefficient, $k$ the ionic mobility, $X$ the field strength, $\theta$ the angle between the alpha-track and the field, and $b$ is the parameter representing the radius of the ion column. And $S(z)$ is expressed by using Hankel function[15] as

$$\sqrt{\frac{\pi}{z}}S(z)=\frac{\pi}{2}e^{z/2}\cdot iH_0^{(1)}(iz/2)\,.$$

Now, if we denote the ion densities at the points P and F by $N_P$ and $N_F$, and the values for $Y$ by $Y_P$ and $Y_F$ respectively, the observed ratio of the pulse heights, $R$, is expressed by

$$R=\frac{N_PY_P}{N_FY_F}=R_0\frac{Y_P}{Y_F},$$

with

$$R_0\equiv\frac{N_P}{N_F}\,.$$

Here, $R_0$ represents the ratio of the true ionizations primarily produced. For the numerical calculation, the following values were used for the constants:

$$\alpha=1.66\times10^{-6}\ \mathrm{cm^3/sec}\,,$$

$$D=0.055\ \mathrm{cm/sec/cm^2}\,,$$

$$k=2.22\ \mathrm{cm/sec/volt/cm}.$$

$b$ is undetermined from the theory and must be adjusted to fit the experimental result.

First, assuming the energy loss at the point P to be 2.4 Mev/cm and the value of $W$ to be 35.6 ev/ion, we can put

$$N_P=2.4\times10^6/35.6=6.74\times10^4\,.$$

Since $R_0$ is known to be nearly equal to 2, we took for the first approximation

$$N_F=N_P/2=3.37\times10^4\,.$$

---

* This formula is not valid for very small angles. Though the angles are considerably small in the present experiment, the condition for the theory to be valid is well satisfied.

Table IV. The values of $Y_P$, $Y_F$ and the ratio $R=1.985\ Y_P/Y_F$ calculated for different field strengths with $\tilde{\theta}=3.83°$.

| Field strength (volts/cm) | 500 | 1,350 | 11,400 | ∞ |
|---|---|---|---|---|
| $Y_P$ | 0.8816 | 0.9460 | 0.9931 | 1 |
| $Y_F$ | 0.9367 | 0.9720 | 0.9965 | 1 |
| $R$ | $1.868_3$ | $1.931_9$ | $1.978_2$ | $1.98_5$ |

Table V. The values of $Y_P$, $Y_F$ and the ratio $R=1.985\ Y_P/Y_F$ calculated for different angles with the field strength 500 volts/cm.

| Effective angle $\tilde{\theta}$ | 2.55° | 3.83° | 5.11° |
|---|---|---|---|
| $Y_P$ | 0.8474 | 0.8816 | 0.9040 |
| $Y_F$ | 0.9168 | 0.9367 | 0.9492 |
| $R$ | $1.834_7$ | $1.868_3$ | $1.890_4$ |

Table VI. The values of $Y_P$, $Y_F$ and the ratio $R=1.985\ Y_P/Y_F$ calculated for different angles with the field strength 1,350 volts/cm.

| Effective angle $\tilde{\theta}$ | 2.55° | 3.83° | 5.11° |
|---|---|---|---|
| $Y_P$ | 0.9239 | 0.9460 | 0.9586 |
| $Y_F$ | 0.9602 | 0.9720 | 0.9787 |
| $R$ | $1.910_0$ | $1.931_9$ | $1.944_2$ |

Using these value for $N_P$ and $N_F$, $Y_P$ and $Y_F$ were calculated for different values of $b$. Substituting the latter values into the equation $R=R_0Y_P/Y_F$ and adjusting the value of $R_0$, the calculated values for $R$ were compared with the experiment. The best fit was obtained for the following values:

$$R_0=1.98_5\ ,$$

and

$$b=9.5\times10^{-4}\ .$$

The final values for $R$ were calculated again by using the above values for $R_0$ and $b$ and $N_F=N_P/1.98_5$. The results of the calculation are shown by solid curves in Figs. 3 and 4 together with the observed values.

The calculated curves are in good agreement with the observed points within the experimental error in each case that either the voltage or the angle was changed. Thus, the observed change of the ratio with the field strength and the angle is considered to be entirely explained by the effect of columnar recombination. Especially, this conclusion is supported by the fact that remarkable variations of the ratio are observed for the moderate field strengths, i.e. 500 volts/cm and 1,350 volts/cm, and that the ratio is affected definitely by the collimating conditions.

The calculated values of $Y_P$ and $Y_F$ for the present experimental conditoins are tabulated in Tables IV, V and VI.

## § 6. Discussion on Experimental Results

The highest field strength 11,400 volts/cm applied in this experiment is much higher than the fields hitherto usually used. But there is no fear that gas multiplication or other secondary effects may disturb the measurement. The procedure of taking the ratio of the pulse heights removes such effects, so far as the number of secondary ions is proportional to the initial ionization. Furthermore, it is not likely that gas multiplication should occur in this experiment. The first Townsend coefficient $\alpha$ for atmospheric air has been accurately measured by Sanders[16]. According to Sanders, the lowest observable value is $\alpha/p=3.4\times10^{-5}$ at $X/p=20$, and he gave an empirical formula for $\alpha/p$ in the range of $X/p$ from 20 to 36. For the field strength 11,400 volts/cm in this experiment, $X/p$ is equal to 15 and this is fairly smaller than the lowest of Sanders's experiment. If we extend the empirical formula of Sanders down to $X/p=15$, the multiplication factor for this experiment is calculated as 1.00045. Such disturbance, even if it exists, is smaller than the experimental uncertainty involved in the pulse height determination. The second Townsend coefficient is much smaller than the first coefficient and is, of course, out of the question. Thus, according to the conclusion of § 5, the ratio of the true specfic ionizations at the points P and F can be estimated as $1.98_5$ by the help of Jaffé's theory.

The corresponding ratio obtained from the specific ionization curve of Holloway and Livingston is 1.87. This indicates definitely that the experiment of Holloway and Livingston was considerably subjected to the effect of columnar recombination. Taking $R_0=1{,}98_5$, the values for $Y_P$ and $Y_F$ giving the observed value of $R=1.87$ are estimated as $Y_F=0.8830$ and $Y_F=0.9373$ respectively.

For the sake of comparison, the corresponding ratios were also obtained from the results of other authors. The curve of

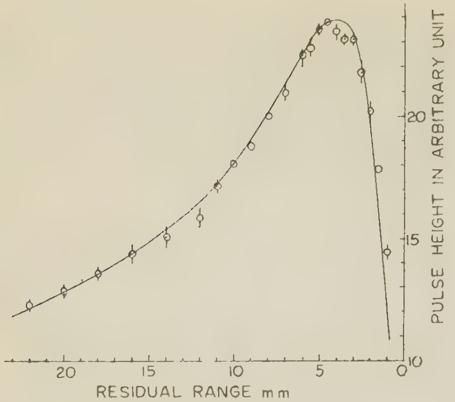

Fig. 5. The specific ionizations for the field strength 11,400 volts/cm. The solid curve is Holloway and Livingston's curve corrected by Jaffé's theory and normalized at the residual range 22.5 mm.

Stetter and Jentschke[17)] gives $R=1.95$. Their experiment was performed with $\theta=90°$ and $X=240$ volts/cm. Since in Jaffé's formula the role of the field is the same as the angle, this condition is equivalent to ours when $\tilde{\theta}=3.83°$ and $X=3,600$ volts/cm is applied. From our calculation, $R=1.964$ is expected for this condition. The earlier work of Curie and Behounek[18)] gives $R=1.85$ for both polonium and RaC′ alpha-particles. The results of Henderson[19)] give $R=1.93$ for RaC′ and 1.79 for ThC′.

The straggling of the polonium source used was determined from the number-distance curve. The straggling parameter, defined by Holloway and Livingston, was about 0.2 cm, this being somewhat larger than the value 0.084 cm quoted by Holloway and Livingston for newly prepared source. It is not clear whether this is due to the thickness of the source or to the straggling effect in the aluminium foil. In any case, the straggling phenomenon has the tendency to lower the observed ratio to some extent. However, this effect may be thought to be not large, since our specific ionization curved observed with 500 volts/cm well accords with that of Holloway and Livingston.

The value for $b$ used in this paper is considerably smaller than the value $1.79\times10^{-3}$ originally used by Jaffé to explain Moulin's experiment[20)]. This discrepancy is caused by the difference in the estimation of the ion density $N_0$, because $b$ is very sensitive to the estimate of $N_0$. If we use the recent data to estimate the value of $N_0$, Moulin's experiment is explained as well by the present values for the constants.

The value of $W$ 35.6 ev/ion assumed in our calculation is the one given by Gray[1)] as an average value of $W$ for polonium alpha-particles. If $W$ depends upon the initial energy of the particle, the instantaneous values of $W$ corresponding to the points P and F would be different from 35.6 ev/ion. But no further calculation was carried out, although in principle it is possible to proceed with the successive approximation by using the relation between $W$ and the particle energy described later.

## § 7. Establishment of Ionization-energy Relation for Alpha-particles in Air

Now, we can correct the specific ionization curve observed under a certain experimental condition by the help of Jaffé's theory, and obtain the true ionization-range relation which is not subjected to the effect of columnar recombination. The solid curve shown in Fig. 5 is the curve obtained by correcting the original curve of Holloway and Livingston. In Fig. 5 also are shown the observed points measured with the field strength 11,400 volts/cm in this experiment. The pulse heights are normalized at the residual range of 22.5 mm. These points are in good agreement with the solid curve, since the saturation of the ionizations at the points P and F are 0.9931 and 0.9965 as shown in Table IV.

Taking into account the fact that in the experiment of Holloway and Livingston the determination of the absolute distance seems to be more accurate than the present experiment and that the correction for the finite depth of the chamber was also carried out in their experiment, we have adopted the corrected Holloway and Livingston curve given above as the true specific ionization curve free from recombination, and the following arguments are based on this curve.

The true total ionization versus range relation may be obtained by integrating the true specific ionization curve determined above. If the integrated relation is normalized to the polonium energy 5.2984 Mev at the polonium range, we get a provisional range-energy relation for alpha-particles in air which is based on the assumption of the constancy of $W$ in the same manner as the original range-energy relation of Holloway and Livingston. If this relation deviates from the true range-energy relation, it can be concluded that $W$ in air depends upon the particle energy.

Now, let $E$ be the alpha-energy for a given range $R$, and $E'$ be the energy value obtained from the provisional range-energy relation (i.e. essentially the total ionization) for the same range, the ratio of $E$ to $E'$, $w$ say, may represent the average energy loss per ion pair in air for an alpha-particle of energy $E$ relative to that for the polonium alpha-particle (5.2984 Mev),

$$w \equiv E/E' = W(E)/W_{\mathrm{Po}} \, .$$

To perform the integration of the true specific ionization curve from zero to the polonium range (3.842 cm), the $dE/dR$ curve obtained from the original Holloway and Livingston range-energy curve was utilized in the region 2.8 to 3.842 cm, and was made to connect smoothly with the corrected specific ionization curve shown in Fig. 5 at the point of 2.8 cm. Since the variation of the ion density along the track is relatively small in the range 2.8 to 3.8 cm, the error introduced by this substitution is expected to be negligibly small. The integration was performed graphically and normalized to the polonium energy at the polonium range*.

The results are tabulated in the third column of Table VII. In the second column of this table are given the energy values from Jesse's revised relation, while in the fourth column the ratios of Jesse's value to the provisional energy value given in the third column. Since it is known that Jesse's revised relation nearly agrees with the fixed points obtained from some nuclear reactions, the ratio given in the fourth column stands for the approximate value of $w$ above defined. It is obvious from the table that the value of $w$ depends upon the alpha-energy.

Table VII. The provisional energy values derived in this experiment and the comparison with Jesse's values.

| Range (mm) | Energy values of Jesse (Mev) | Provisional energy values derived in this exp. (Mev) | Ratio of Jesse's values to provisional values |
|---|---|---|---|
| 1 | | 0.075 | |
| 2 | 0.271 | 0.235 | 1.152 |
| 3 | 0.508 | 0.451 | 1.127 |
| 4 | 0.761 | 0.685 | 1.111 |
| 5 | 0.994 | 0.919 | 1.081 |
| 6 | 1.214 | 1.146 | 1.059 |
| 7 | 1.422 | 1.362 | 1.044 |
| 8 | 1.624 | 1.565 | 1.038 |
| 9 | 1.816 | 1.757 | 1.034 |
| 10 | 1.995 | 1.940 | 1.029 |
| 11 | 2.162 | 2.113 | 1.023 |
| 12 | 2.321 | 2.279 | 1.018 |
| 14 | 2.620 | 2.592 | 1.011 |
| 16 | 2.907 | 2.885 | 1.008 |
| 18 | 3.174 | 3.160 | 1.004 |
| 20 | 3.425 | 3.420 | 1.002 |
| 22 | 3.668 | 3.665 | 1.001 |
| 24 | 3.896 | 3.898 | 1.000 |
| 26 | 4.103 | 4.118 | 0.997 |
| 28 | 4.300 | 4.326 | 0.994 |
| 30 | 4.502 | 4.526 | 0.995 |
| 33 | 4.798 | 4.812 | 0.997 |
| 35 | 4.987 | 4.996 | 0.998 |
| 38.42 | 5.298 | 5.2984 | 1.000 |

Table VIII. The comparison of the provisional range-energy relation with the fixed points obtained from the nuclear reactions.

| Reaction | Observed range (cm) | Observed energy $E$ (Mev) | Provisional energy $E'$ (Mev) | Ratio of $E$ to $E'$, $w$ |
|---|---|---|---|---|
| $B^{10}(n, \alpha)Li^{7*}$ | 0.720 | 1.474 | 1.403 | $1.050_3$ |
| $Li^6(p, \alpha)He^3$ | 0.85 | 1.726 | 1.662 | $1.038_5$ |
| $B^{10}(n, \alpha)Li^7$ | 0.868 | 1.779 | 1.697 | $1.048_3$ |
| $Li^6(n, \alpha)H^3$ | 1.04 | 2.060 | 2.010 | $1.024_9$ |
| Sm-$\alpha$ | 1.12 | 2.18 | 2.147 | $1.015_4$ |

Further, in Table VIII the provisional range-energy relation is compared with the fixed points[6)] obtained from the nuclear reactions for which the ranges and energies of the emitted alpha-particles have been independently determined. In the fifth column are given the ratios of the observed energy value $E$ to the value $E'$ from the provisional curve corresponding to its range. These ratios can be considered as the observed values of $w$.

---

* For the sake of contrast, the original specific ionization curve of Holloway and Livingston was integrated and normalized by the same procedure. And it was ascertained that the result agrees with the original range-energy curve given by Holloway and Livingston within about 2 Kev.

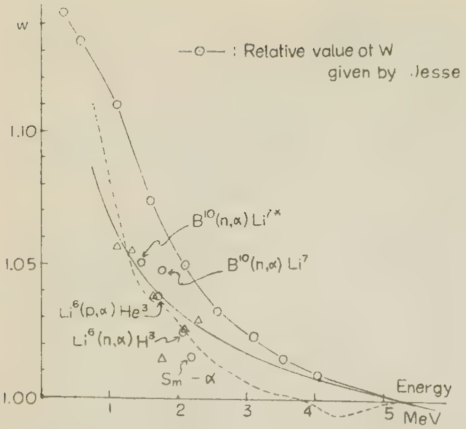

Fig. 6. The values of $w$, the average energy loss per ion pair in air for an alpha-particle of the energy $E$ relative to that for the polonium alpha-particle (5.2984 Mev). The solid curve shows the values obtained from the present experiment. The dotted curve shows the ratios of Jesse's values to the provisional energy values given in the fourth column of Table VII.

Cranshaw and Harvey[7] reported that $W$ for alpha-particles in argon can be represented by a formula of the type:

$$W=A+B/\sqrt{E}\ .$$

After this, we have assumed a formula of the same type for $w$ in air, as follows:

$$w=a+b/\sqrt{E}\ .$$

The values of the constants $a$ and $b$ were determined by the method of least squares to agree with the five observed values for $w$ as shown in Table VIII, obtaining

$$a=0.948 \quad \text{and} \quad b=0.119\ .$$

Hence,

$$w=0.948+0.119/\sqrt{E}\ ,$$

where $w$ is the relative value of $W$ for alpha-particles in air to that for the polonium alpha-particles, and $E$ is the initial alpha-energy in Mev. The result is shown by the solid curve in Fig. 6. The dotted curve in the figure represents the ratio of Jesse's value to the provisional energy value at the corresponding range given in the fourth column of Table VII. The latter curve becomes less than unity for energies above 4 Mev. This is probably due to the fact that Jesse has actually revised the curve only up to the range of 2.8 cm (4.3 Mev) and joined this to the original range-energy curve of Holloway and Livingston at the range of 2.8 cm as stated in his paper. In the figure is also shown the variation of $W$ in air reported by Jesse. The five observed values for $w$ given in Table VIII are represented by the small circles.

Freeman and Burcham[21] have made a relative measurement of the ranges for alpha-groups emitted from several $(p, \alpha)$ reactions, $F^{19}(p, \alpha)O^{16*}$, $B^{10}(p, \alpha)Be^7$, and $Be^9(p, \alpha)Li^6$, for which the energies are accurately known from the $Q$-values. They found that, if the range for the alpha-group of energy $2.272\pm 0.010$ Mev emitted from the $F^{19}(p, \alpha_1)$ reaction is assumed to be 1.157 cm from the revised curve of Bethe, all the other observed ranges agree with the revised curve down to 1.113 Mev except for small discrepancy of about 10 Kev. We have compared the result deduced by them with our provisional range-energy relation, and calculated the ratio $w=E/E'$ in the same manner as above. These values for $w$ are shown in Fig. 6 by the small triangles, and well accord with the empirical formula for $w$ obtained in this experiment. Consequently, this formula is considered to be valid at least for the alpha-energy down to 1 Mev.

## § 8. Conclusion

The effect of columnar recombination on the ionization measurement in air was examined by measuring the ratio of the specific ionizations for alpha-particles at two fixed points under various field strengths and various angles between the field and the alpha-track. It was found that the observed change of the ratio with the field and the angle can be completely explained by Jaffé's theory of columnar recombination. The value of the parameter $b$ which appears in Jaffé's theory was determined anew so as to give the best agreement with the experiments. By the help of this theory, the observed specific ionization curve of Holloway and Livingston was corrected for columnar recombination and the true ionization-range relation for alpha-particle in air was obtained. Comparing this relation with the fixed points of the range-energy relation obtained from nuclear reaction data, an empirical formula representing the energy dependency of the average energy loss per ion pair for alpha-particles in air relative to polonium alpha-particle, $w$, was deduced.

The energy dependency of *w* deduced in the present experiment is considerably smaller than the conclusion of Jesse et al..

It was also made clear that the experiment of Holloway and Livingston, on which the revision of the range-energy relation made by Jesse et al. or Bethe was based, was certainly subjected to the effect of columnar recombination. Therefore, we should consider that the success of the revised range-energy relation may be attributed to the incidental compensation of several factors.

The fact that in air the effect of columnar recombination is severe, is of cource an indefensible defect of air for the filling gas of ionization chambers. However, De Juren and Rosenwasser[22] have recently pointed out that even in argon the effect of columnar recombination is also serious and cannot be ignored. The results of the present study have made it possible to correct the observed ionization in air for columnar recombination by the help of Jaffé's theory. In addition, in some cases it is also an useful method[23] to plot the reciprocals of the pulse heights measured with various field strengths against the reciprocal of the field strength and to extrapolate the plot to infinite field strength. In consequence, the empirical formula for *w* obtained in the present study can be applied effectively to the corrected results of the ionization measurements which are free from recombination, and may be of use in the accurate determination of the energy of alpha-particles.

In conclusion, the authors wish to express their sincere thanks to Prof. K. Kimura for his valuable suggestions and continual encouragements throughout the work, and to Mr. S. Kimura for his help in the measurements. Thanks are also due to Prof. H. Yamaguchi of Osaka University who kindly presented us with radon tubes for the preparation of the polonium source. Finally, this work was financially supported by a grant-in-aid for Fundamental Scientific Research of the Ministry of Education.

## References

1) L. H. Gray: Proc. Camb. Phil. Soc. **40** (1944) 72.
2) W. P. Jesse, H. Forstat and J. Sadauskis: Phys. Rev. **77** (1950) 782.
3) W. P. Jesse and J. Sadauskis: Phys. Rev. **78** (1950) 1.
4) H. A. Bethe: Rev. Mod. Phys. **22** (1950) 213.
5) M. G. Holloway and M. S. Livingston: Phys. Rev. **54** (1938) 18.
6) These are summarised in Ref. 3).
7) T. E. Cranshaw and J. A. Harvey: Can. Jour. Res. **A 26** (1948) 243.
8) G. C. Hanna: Phys. Rev. **80** (1950) 530.
9) H. Bichsel, W. Hälg, P. Huber and A. Stebler: Helv. Phys. Acta **25** (1952) 119.
10) J. Rhodes, W. Franzen and W. E. Stephens: Phys. Rev. **87** (1952) 141.
11) P. R. Tunnicliffe and A. C. Ward: Proc. Phys. Soc. **A 65** (1952) 233.
12) K. Kimura, R. Ishiwari, K. Yuasa, S. Yamashita, K. Miyake and S. Kimura: J. Phys. Soc. Japan **7** (1952) 111.
13) G. Jaffé: Ann. Physik **42** (1913) 303.
14) Fig. 9 in Holloway and Livingston's paper.
15) E. Jahnke and F. E. Emde: Funktionentafeln, Teubner (1933).
16) F. H. Sanders: Phys. Rev. **41** (1932) 667; Phys. Rev. **44** (1933) 1020.
17) G. Stetter and W. Jentschke: Phys. Zeits. **36** (1935) 441.
    W. Jentschke: Wien. Ber. **144** (1935) 151.
18) I. Curie and F. Behounek: Jour. de Phys. et Rad. **7** (1926) 125.
19) G. H. Henderson: Phil. Mag. **42** (1921) 538.
20) see Ref. 13).
21) J. M. Freeman and W. E. Burcham: Phil. Mag. **42** (1951) 434.
22) J. A. De Juren and H. Rosenwasser: Phys. Rev. **93** (1954) 831.
23) W. Haeberli, P. Huber and E. Baldinger: Helv. Phys. Acta **26** (1953) 145.

Journal of the Physical Society of Japan Vol. 11, No. 4, April, 1956

# The Multiple Scattering of Fast Electrons

By Seizaburo Kageyama

*Physical Institute, Tokyo University of Education*

(Received December 17, 1955)

The angular distribution, caused by the multiple scattering, of the fast electron with an energy of 1.66 MeV passing through thin foils of Al, Cu and Pb has been investigated.

The experimental results obtained were in good agreement with Moliere's theory modified by Hanson et al. on the basis of their experimental data. The theoretical $1/e$ width values given by Shinohara were also in good agreement with those observed in light elements, but they seem to be slightly larger in heavy elements.

## § 1. Introduction

The experimental investigation of the scattering of electrons by multiple collisions in passing through various materials has been carried out by Kulchitsky and Latyshev[1] with 2.25 MeV electrons and by Sheppard and Fowler[2] with 6.2 MeV electrons. Their results were in good agreement with the theories of Williams[3] and Goudsmit and Saunderson[4] for the light elements if the electron-electron scatterings were accounted by replacing Z with $(Z^2+Z)^{1/2}$. For heavy elements, however, the 1/e width of the angular distribution curves obtained by them were from 10 to 15% narrower than the theoretical predictions.

Thereafter, Moliere[5] has been able to solve the scattering problem, making the only assumption that all scattering angles are small. He has given the scattering into the angular interval $d\theta$ at $\theta$ in a power series of $1/B$:

$$f(\vartheta)d\vartheta = \vartheta d\vartheta[f^{(0)}(\vartheta)+B^{-1}f^{(1)}(\vartheta)+B^{-2}f^{(2)}(\vartheta)+\cdots] \tag{1}$$

where

$$\vartheta=\theta/\chi_c B^{1/2},\quad \chi_c{}^2=4\pi e^4 Z(Z+1)Nt/(pv)^2,$$

$$f^{(n)}(\vartheta) = n!\int_0^\infty ydyJ_0(\vartheta y)\exp\left(-\frac{1}{4}y^2\right)\left[\frac{y^2}{4}ln\left(\frac{y^2}{4}\right)\right]^n$$

and the parameter $B$ is defined as follows by the characteristic screening angle $\chi_a$ and $\chi_c$.

$$B-lnB=ln\left(\frac{\chi_c{}^2}{1.167\,\chi_a{}^2}\right)$$

The first term $f^{(0)}$ in the above expression is the well-known Caussian. The angle at which the intensity drops to 1/e of the maximum is

$$\theta_w=\chi_c=B^{1/2} \tag{2}$$

while the second term goes over into the single scattering formula at large angle and the third is a correction. The evaluations of each term have been done by him and Bethe[6] as a function of variable $\vartheta$.

For small angles, $\vartheta<2$, the dominant term is the Gaussian $f^{0)}$. In this region Hanson et al[7]. have pointed out that a better agreement with the experimental results could be obtained by assuming a Gaussian distribution of which 1/e width is given by

$$\theta_w=\chi_c(B-1.2)^{1/2} \tag{3}$$

rather than by Eq. (2).

The same problem has been treated by Shinohara[8], by the same method as Williams, on the assumption that the electrons are diffracted by minute crystals forming the foil. The distribution given by him shows a slightly smaller scattering than those of Williams and Goudsmit and Saunderson, and is in better agreement with most of the experiments, especially for heavy elements. But in the case of Al, his theory is not in good agreement with the experimental result obtained by Kulchitsky and Latyshev, which was already in fairly good agreement with Williams' theory.

In the present work, we have observed the angular distribution of electrons scattered by multiple collisions in passing through thin Al, Cu and Pb foils and compared both with Moliere's formula modified empirically by Hanson et al. and with Shinohara's theory.

## § 2. Experimental Arrangement

The experimental arrangement used was similar to the one employed by Kulchitsky and Latyshev. A homogeneous and almost paral-

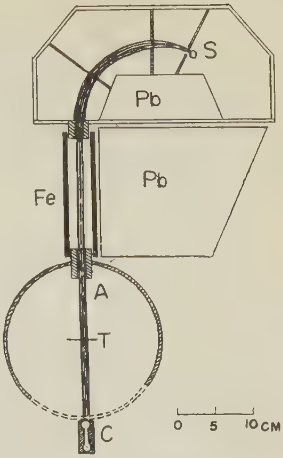

Fig. 1. Experimental arrangement for the measurement of angular distribution. S, the source, Fe, iron pipe, A, the last slit, T, the target and C, the G–M counters. The dotted line in front of C shows that the scattering chamber has a window in this part.

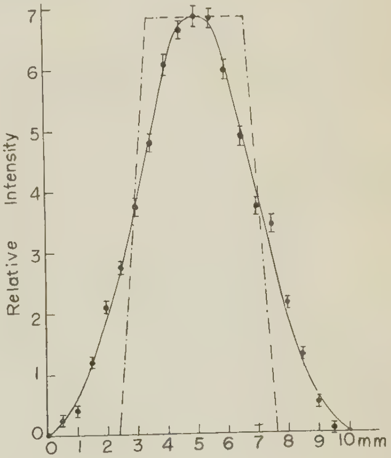

Fig. 2. Horizontal angular distribution of incident beam observed at C with the coincidence counter. The dash-point curve gives the distribution of incident beam calculated.

lel beam of fast electrons was obtained by placing a thin-walled glass tube of about 4 mg/cm², containing Rn of about 50 MC, at “S” (Fig. 1) in the magnetic field. The electrons described an arc of about 116° on the radius of about 10 cm in the magnetic field.

As can be seen from Fig. 1, electrons after passing a series of slits were focused on the scattering foil (T) placed at the center of a brass scattering chamber 8 cm high and 20 cm in diameter. The scattered electrons were detected by two G-M counters placed just behind a thin mica window of scattering chamber and working in coincidence. The thickness of mica of the scattering chamber and the counter was about 4.5 mg/cm². The hole in the last slit A was 3.0 mm in diameter.

The energy of the electron beam used was estimated from the energies and spread of internal conversion lines of RaC and RaC′ observed at the center of the scattering chamber. The precise estimation of the energy and spectral constitution of the beam employed was done by replacing the scattering chamber with the second $\beta$-ray spectrometer described in the previous paper[9]. Applying the correction of the most probable energy loss for conversion electrons, we have obtained the value of 1.66±0.04 MeV for our electron beam.

In order to estimate the divergence of the incident beam, the angular distribution of electrons in the horizontal and vertical plane were measured in front of the last slit (A), at the center of the scattering chamber (T), and at the position C with a single G-M tube. As an example, the horizontal distribution of incident beam measured at the position C with the coincidence G-M tubes used in the main experiment was shown in Fig. 2.

The dash-point curve in the figure shows the angular distribution of incident electron beams from which the theoretical angular distributions of transmitted beam have been calculated. From these distributions, we have found that the diameter of the beam is about 4 mm at *T* and that the angular divergence of electrons from the central beam does not exceed 1/3°.

The scattering materials examined were Al, Cu and Pb foils of following thicknesses;

| | | | | | |
|---|---|---|---|---|---|
| Al: | 3.43 | 6.86 | 10.3 | 13.7 | mg/cm² |
| Cu: | | 6.3 | 12.6 | | mg/cm² |
| Pb: | | 6.2 | | | mg/cm². |

## § 3. Experimental Results and Comparison with Theories

The observed angular distributions of scattered electrons are shown in Figs. 3 and 4. The theoretical distributions calculated from the original theory of Moliere are shown by broken line in Fig. 3. The solid lines in both figures represent the corrected distribution, in

Table I. 1/*e* width of the angular distribution curve.

| Material | Thickness of foil (mg/cm²) | Theoretical | | | | Observed |
|---|---|---|---|---|---|---|
| | | Williams | G–S | Shinohara | Moliere (Eq. 5) | |
| Al | 3.5 | 3.5 | 3.6 | 3.4 | 3.4 | 3.4±0.1 |
| | 7.0 | 5.7 | 5.6 | 5.5 | 5.4 | 5.4±0.2 |
| | 10.5 | 7.4 | 7.2 | 7.3 | 7.3 | 7.3±0.3 |
| | 14.0 | 8.8 | 8.6 | 8.7 | 8.4 | 8.4±0.3 |
| Cu | 6.3 | 7.9 | 7.9 | 7.9 | 8.2 | 8.0±0.3 |
| | 12.6 | 12.2 | 11.8 | 12.2 | 12.6 | 12.2±0.4 |
| Pb | 6.2 | 12.6 | 12.6 | 13.5 | 11.5 | 11.2±0.4 |

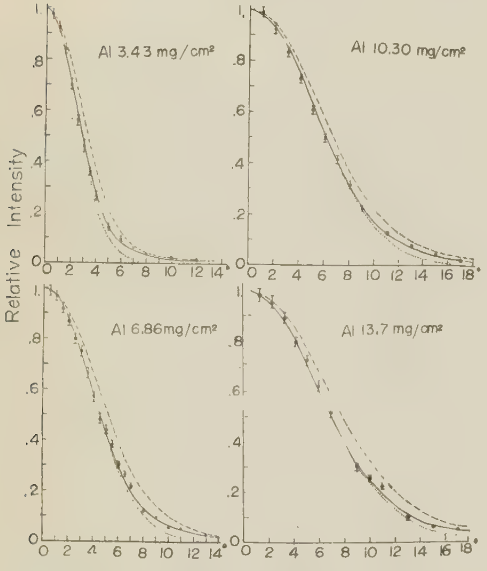

Fig. 3. Comparison between theoretical and experimental angular distributions of multiple scattering by Al foils. The broken lines are calculated according to the original Moliere's theory. The solid lines are modified empirically by Hanson et al. The dotted lines are a Gaussian distribution drawn through the observed point at the 1/*e* intensity.

which Eq. (3) was adopted instead of Eq. (2) for the 1/e width of $f^{(0)}$ in Eq. (1). The experimental results were in good agreement with the solid lines over all the region examined within the experimental errors. The Gaussian distribution drawn through the observed point at the 1/e intensity are shown by the dotted curves. In very small angle ($\vartheta < 1$), this distribution coincides completely with the solid lines.

The 1/e widths of the distribution curves obtained are tabulated in Table I, together with the theoretical values calculated from the formulae of Williams, Goudsmit and Saunderson, Shinohara and Moliere. All the theoretical values were corrected for the finite dimension and the divergence of electron beam.

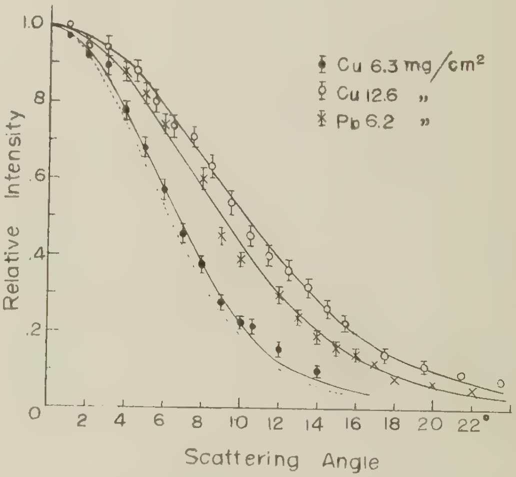

Fig. 4. Comparison between the modified Moliere's theory of multiple scattering of electrons and the experimental angular distribution for Cu and Pb. The broken line was calculated with $Z_{eff}=Z$. The solid curves were all calculated with $Z_{eff}=Z(Z+1)$.

According to Shinohara's theory, the 1/e width of the Gaussian distribution of projection angle is given by

$$\theta_w = 2\overline{\alpha}^2$$

$$\overline{\alpha}^2 = \nu\overline{\theta}^2$$

$$\nu = N_1 \sigma t$$

where $\nu$ is the average number of collisions of electron in passing through the foil, $N_1$ the number of minute crystals per unit volume $\delta$V, $t$ the thickness of the foil, and $\sigma$ the cross section of the minute crystal and

$$\overline{\theta^2} = \frac{1}{\sigma}\Big(\pi\sum\cdot\chi_i{}^3\int_0^{\chi_c} f_{1i}(\chi)d\chi + \pi\int_0^{\chi_c}\chi^3 f_2(\chi)d\chi + \frac{D}{3}\delta V\Big)$$

$$D=\frac{16e^4Z^2}{m^2v^4v_a}$$

where $v_a$ is the volume of the unit cell. The first term in the right-hand side of the upper expression represents the contribution of the beam reflected from a net plane of crystals, the second the temperature diffuse scattering and the third the contribution of the single greater than $\chi_c$. The effect of the inelastic scattering is not included in the above expression.

Under the assumption that the minute crystal are kept at the room temperature (290°K), the calculation has been numerically for the first term and graphically for the second$^{10)}$. The 1/e width calculated for the electrons of total energy 2.16 MeV (wave length $\lambda=7.42$ $10^{-11}$cm) are given in the fifth column of the Table 1.

In light elements, the experimental results for the 1/e width of angular distribution are in good agreement with all the theoretical predictions within the experimental errors. However, in heavy elements, the differences between theoretical and experimental values are outside of the experimental errors except for Moliere's theory. The observed value is about 10 and 20% lower than those given by the theories of Williams, Goudsmit and Saunderson, and Shinohara. As Shinohara has pointed out, it may be responsible for this discrepancy that the thickness of Pb foil examined was too thin to examine his theory.

Inelastic collisions with atomic electrons also contribute to multiple scattering, especially in light element, but are disregarded in the theories of Moliere and Shinohara. Thereafter, Bethe, Fano$^{11)}$ and Spencer and Blunchard$^{12)}$ have shown that the electron-electron collisions brought corrections to the elastic scattering of the order of 2% in Au, and that the effect of inelastic collision should be accounted for approximately by increasing the cross section by the factor $(Z+1)/Z$. This procedure has already been suggested experimentally by Kulchitsky and Latyshev and is in complete agreement with the present results, as shown in Fig. 4.

Moreover, Fano has shown that the Moliere's B must be increased by

$$(Z+1)^{-1}\{ln[0.160\,Z^{-2/3}(1+3.33\,Ze^2/\hbar v)]-U_{in}\}$$

where $-U_{in}$ is defined as an integral over the incoherent scattering function whose value is about 5.

This contribution, however, is too small to be tested with our results.

In conclusion, the author expresses his cordial thanks to Prefessor Mitsuo Miwa for the helpful suggestions and valuable discussions. The author wishes to express his thanks to the Japanese Foundation for Cancer Research for the supply of Rn through Dr. K. Tsukamoto and Mr. Y. Onai. Thanks are also due to Mr. K. Nishimura for his cooperation in this work. This study was supported by the Scientific Research Expenditure of the Ministry of Education.

## References

1) L. A. Kulchitsky and G. D. Latyshev: Phys. Rev. **61** (1942) 254.

2) C. W. Sheppard and W. A. Fowler: Phys. Rev. **57** (1940) 273.
C. W. Sheppard: Phys. Rev. **62** (1942) 313.

3) E. J. williams: Proc. Roy. Soc. **169** (1939) 531; Phys. Rev. **58** (1940) 292.

4) S. Goudsmit and J. L. Saunderson: Phys. Rev. **57** (1940) 24, **58** (1940) 36.

5) G. Moliere: Natureforschung **2a** (1947) 133, **3a** (1948) 78.

6) H. A. Bethe: Phys. Rev. **89** (1952) 1256.

7) A. O. Hanson, L. H. Lanzl, E. M. Lyman and M. B. Scott: Phys. Rev. **84** (1951) 634.

8) K. Shinohara: J. Phys. Soc. Japan **4** (1948) 144.
K. Shinohara, K. Inoue and N. Hirohata: J. Phys. Soc. Japan **4** (1948) 227.

9) S. Kageyama: J. Phys. Soc. Japan **8** (1953) 689.

10) Authors wish to thank Dr. K. Shinohara for his advices in the calculation of these terms.

11) U. Fano: Phys. Rev. **93** (1954) 117.

12) L. V. Spencer and C. H. Blanchard: Phys. Rev. **93** (1954) 114.

Journal of the Physical Society of Japan Vol. 11, No. 4, April, 1956

# Theory of the Lattice Vibration of Graphite

By Akio Yoshimori and Yoshiharu Kitano

*Department of Physics, University of Osaka Prefecture,*
*Mozu-Higashi, Sakai*

(Received November 9, 1955)

A theory of the lattice vibration and specific heat of graphite, which has a typical lamellar structure, is worked out using the Born-von Kármân method. Four types of restoring forces are assumed; the first and second ones are associated with changes in the bond lengths and bond angles of the honey-comb net planes, respectively, the third with change in distance between neighoring atoms on adjacent net planes, and the fourth with the bending of the net planes. We have obtained modes whose polarizations are parallel and perpendicular to the planes. The former are essentially two-dimensional, but the latter are of more complex characters and play a particular role in the temperature range 45° to 100°K. As our main interest is in this and higher temperature ranges, we neglect the shearing forces between neighboring net planes which are effective at much lower temperatures. For small wave numbers, our theory naturally reduces to the semi-continuum theory developed by Komatsu and Nagamiya (1951) and Komatsu (1955). The calculated specific heat curve is in good agreement with the one observed by DeSorbo (1954) in the temperature range 45° to 300°K. We have concluded that the discrepancy found by Komatsu at temperatures higher than 60°K between his theoretical values of the specific heat and the observed ones is due to the failure of his semi-continuum treatment.

## § 1. Introduction

Graphite is a typical substance with lamellar structure and is well known, since old days, to show at low temperatures a specific heat which is remarkably different from that of ordinary substances of less anisotropic character. Recently, with renewed interest in the specific heat of substances with anisotropic lattices, there appeared a number of investigations, both experimental and theoretical[1)-10)], on the low temperature specific heat of graphite. The measurements of specific heat by DeSorbo and Tyler[2)] and more recently by DeSorbo[8)] in the temperature range from 13° to 300°K gave results that it follows apparently the $T^2$-law from 13° to 54°K. Another series of measurements by Bergenlid, Hill, Webb and Wilks[6)] in a lower temperature range from 1.5° to 90°K showed that the specific heat deviates from the apparent $T^2$-law below 15°K and varies with temperature as $T^{2.4}$ below about 10°K.

Komatsu[7)] explained satisfactorily such behaviors of the specific heat of graphite below 60°K down to 1.5°K, improving the semi-continuum treatment of this problem made by Komatsu and Nagamiya[1)]. In his work, the graphite crystal is considered as an assembly of elastic plates equally spaced and with compressional and shearing couplings between adjacent plates. The elastic constants of each plate, except for the bending modulus, were estimated from the force constants of benzen molecule with a modification of taking account of the different bond strengths in benzene and graphite; the compressional coupling constant was determined from the observed compressibility and the shearing modulus theoretically (actually, three times the theoretical value was needed to attain a perfect agreement). The remaining undetermined modulus, i. e. the bending modulus of each plate, was so determined as to obtain the best fit of the calculated specific heat curve to the experimental one in the temperature range where the shearing modulus could be neglected. This theory, however, could not satisfactorily account for the observed specific heat curve above 60°K. The discrepancy must be due to his oversimplification of replacing the atomic honeycomb net planes by continuous elastic plates. Evidently, such a continuum treatment describes correct aspects of the lattice vibrations for low frequencies and small wave numbers but is not valid for high frequencies or large wave numbers, so that even if the model employed by Komatsu is adequate at low temperatures, we cannot expect it to explain the experimental specific heat over the whole temperature range. A more rigorous theory must be based upon the Born-von Kármán approach.

The aim of our paper is to develop such a theory of the lattice vibration of graphite. We shall assume four types of restoring forces among atoms. The first and second are the restoring forces of the valence force type, the first being associated with changes in the bond lengths and the second with changes in the bond angles of the honey-comb net planes. The third is of the central force type and is related to changes in the distance between those atoms which are on adjacent planes and are neighbors along the $c$-direction. The fourth is the bending force constant of each honey-comb net plane; this is of the non-central force type and may conveniently be defined as the force for the displacement of each atom relative to the average of the normal displacements of the three neighboring atoms in the same net plane.

There may be other central forces than the third force mentioned above, namely, forces among other pairs of atoms in adjacent (or more distant) net planes. They will give rise to additional compressional, as well as shearing, forces among different net planes. However, as was shown by Komatsu7), the shearing forces are so weak that they become effective only at extremely low temperatures where the specific heat shows a deviation from the $T^2$-law, whereas in the present paper we confine our arguments to higher temperatures. Furthermore, these compressional forces could be absorbed, to a good approximation, into the single force constant of the third type mentioned above, for the net planes of graphite are so stiff that the relative displacements of atoms of each net plane would be small compared with the relative displacements of adjacent planes and, consequently, the net planes would behave as if they were locally rigid when they interact with one another.

## § 2. Analysis of the Normal Modes

The definition of the four force constants introduced in the previous section is illustrated in Fig. 2, in which we give also expressions for the corresponding increases in potential energy. We denote these force constants by

$\kappa$: for the change in each bond length of the honey-comb net plane,

$\mu$: for the change in each bond angle of the honey-comb net plane,

$\kappa'$: for the change in distance between two atoms which are on adjacent net planes and are neighbors in the $c$-direction,

$\mu'$: for the bending of the honey-comb net plane.

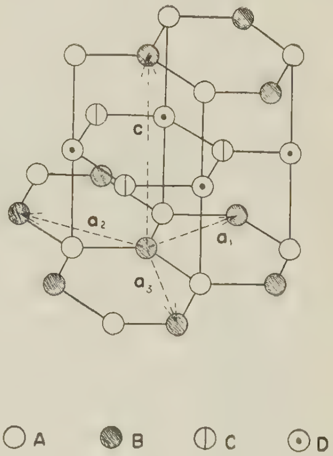

Fig. 1. The crystal structure of graphite.
$|\boldsymbol{a}_i|=a=2.46$ Å, $|\boldsymbol{c}|=c=6.70$ Å.

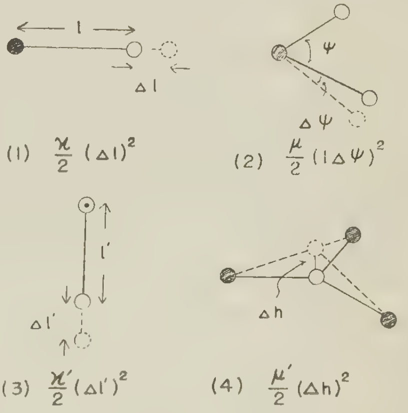
l
Δl
ψ
Δψ
(1) $\frac{\kappa}{2}(\Delta l)^2$
(2) $\frac{\mu}{2}(l\Delta\psi)^2$
l'
Δl'
Δh
(3) $\frac{\kappa'}{2}(\Delta l')^2$
(4) $\frac{\mu'}{2}(\Delta h)^2$

Fig. 2.

Using these constants, the total harmonic potential energy is given as a quadratic form of displacement $\boldsymbol{u}(X, r_i)$ of atom $X$ in unit cell $i$ whose translation vector is $r_i$:

$$V=(1/2)\sum_{i,j}\sum_{X,Y}\boldsymbol{u}(X,\boldsymbol{r}_i)\cdot\boldsymbol{V}(X,Y;\boldsymbol{r}_i-\boldsymbol{r}_j)\cdot\boldsymbol{u}(Y,\boldsymbol{r}_j)\,, \tag{1}$$

where $X$ or $Y$ runs over $A, B, C$ and $D$ atoms in the unit cell (see Fig. 1), and $\boldsymbol{V}(X, Y;\ \boldsymbol{r}_i-\boldsymbol{r}_j)$ are given as follows:

$$\begin{aligned}
&\boldsymbol{V}(A,A;\ 0)=\boldsymbol{V}(D,D;\ 0)\\
&=\{(3/2)\kappa+(15/2)\mu\}(\boldsymbol{i}_1\boldsymbol{i}_1+\boldsymbol{j}_1\boldsymbol{j}_1)\\
&\quad+\{\kappa'+(4/3)\mu'\}\boldsymbol{kk}\,,\\
&\boldsymbol{V}(B,B;\ 0)=\boldsymbol{V}(C,C;\ 0)\\
&=\{(3/2)\kappa+(15/2)\mu\}(\boldsymbol{i}_1\boldsymbol{i}_1+\boldsymbol{j}_1\boldsymbol{j}_1)+(4/3)\mu'\boldsymbol{kk}\,,\\
&\boldsymbol{V}(A,B;\ (\boldsymbol{a}_3-\boldsymbol{a}_2)/3=\boldsymbol{V}(B,A;\ (\boldsymbol{a}_2-\boldsymbol{a}_3)/3)\\
&=\boldsymbol{V}(C,D;(\boldsymbol{a}_3-\boldsymbol{a}_2)/3)=\boldsymbol{V}(D,C;\ (\boldsymbol{a}_2-\boldsymbol{a}_3)/3)\\
&=-(\kappa/2)\boldsymbol{i}_1\boldsymbol{i}_1-3\mu\boldsymbol{j}_1\boldsymbol{j}_1-(\mu'/3)\boldsymbol{kk}\,,\\
&\boldsymbol{V}(A,A;\boldsymbol{a}_1)=\boldsymbol{V}(B,B;-\boldsymbol{a}_1)\\
&=\boldsymbol{V}(C,C;a_1)=\boldsymbol{V}(D,D;-\boldsymbol{a}_1)\\
&=-\mu\boldsymbol{j}_2\boldsymbol{j}_3+(\mu'/9)\boldsymbol{kk}\,,\\
&\boldsymbol{V}(A,A;-\boldsymbol{a}_1)=\boldsymbol{V}(B,B;\ \boldsymbol{a}_1)\\
&=\boldsymbol{V}(C,C;-\boldsymbol{a}_1)=\boldsymbol{V}(D,D;\ \boldsymbol{a}_1)\\
&=-\mu\boldsymbol{j}_3\boldsymbol{j}_2+(\mu'/9)\boldsymbol{kk}\,,\\
&\boldsymbol{V}(A,D;\boldsymbol{c}/2)=\boldsymbol{V}(A,D;-\boldsymbol{c}/2)\\
&=\boldsymbol{V}(D,A;\boldsymbol{c}/2)=\boldsymbol{V}(D,A;-\boldsymbol{c}/2)\\
&=-\kappa'\boldsymbol{kk}\,,
\end{aligned} \tag{2}$$

The above $\boldsymbol{V}$'s and those which one obtains from them by permuting cyclically the suffices (1, 2, 3) are the only nonvanishing $\boldsymbol{V}$'s. $\boldsymbol{j}_i (i=1, 2, 3)$ and $\boldsymbol{k}$ are unit vectors along the primitive translation vectors $\boldsymbol{a}_i$ and $\boldsymbol{c}$, respectively, and $\boldsymbol{i}_i$ is the unit vector perpendicular to $\boldsymbol{a}_i$ and $\boldsymbol{c}$ (see Fig. 2). Thus

$$\boldsymbol{j}_i=\boldsymbol{a}_i/|\boldsymbol{a}_i|,\quad \boldsymbol{k}=\boldsymbol{c}/|\boldsymbol{c}|,\quad \boldsymbol{i}_i=\boldsymbol{j}_i\times\boldsymbol{k}\,.$$

Equation of motion for this vibrating system is

$$M\ddot{\boldsymbol{u}}(x,\boldsymbol{r}_j)=-\mathrm{grad}_u V\,, \tag{3}$$

which has a solution of the form

$$\boldsymbol{u}(X,\boldsymbol{r}_j)=\boldsymbol{e}(X,\boldsymbol{q})\exp\{i(\boldsymbol{q}\cdot\boldsymbol{r}_j-\omega t)\}\,, \tag{4}$$

where $\boldsymbol{q}$ is the wave vector, $\omega$ the angular frequency and $\boldsymbol{e}(X, \boldsymbol{q})$ the polarization vector. $\omega$ and $\boldsymbol{e}(X, \boldsymbol{q})$ are determined by the equation

$$M\omega^2\boldsymbol{e}(X,\boldsymbol{q})=\sum_{Y,\boldsymbol{r}_l}\exp(i\boldsymbol{q}\cdot\boldsymbol{r}_l)\boldsymbol{V}(X,Y;\ \boldsymbol{r}_l)\cdot\boldsymbol{e}(X,\boldsymbol{q})\,.$$

Owing to the properties of $\boldsymbol{V}(X, Y; \boldsymbol{r})$, expressed by (2), the secular determinant of these equation separates into two parts: one gives modes whose polarization vectors are in the honey-comb net plane (which we shall designate as vibrations in the plane) and the other those whose polarization vectors are perpendicular to the net plane (which we shall designate as vibrations perpendicular to the plane).

(*A*) *Vibrations in the plane*

The equation determining $\omega$ and $\boldsymbol{e}$ is

$$\begin{bmatrix}\boldsymbol{U}-\lambda\cdot\boldsymbol{S}_0 & -\boldsymbol{W}\\ -\boldsymbol{W}^* & -\boldsymbol{U}-\lambda\cdot\boldsymbol{S}_0\end{bmatrix}\cdot\begin{bmatrix}\boldsymbol{e}(A,\boldsymbol{q})\\ \boldsymbol{e}(B,\boldsymbol{q})\end{bmatrix}=0\,, \tag{5}$$

where

$$\begin{aligned}
&\boldsymbol{k}\cdot\boldsymbol{e}(X,\boldsymbol{q})=0\,,\\
&\lambda=M\omega^2-(3/2)\kappa-(15/2)\mu\\
&\qquad-(\mu/2)X(\boldsymbol{q})-\mu\boldsymbol{X}(\boldsymbol{q})\,,\\
&\boldsymbol{U}=(\sqrt{3}/2)\mu Y(\boldsymbol{q})\boldsymbol{S}_2\,,\\
&\boldsymbol{W}=\{\kappa+6\mu)/2\}\{X(\bar{\boldsymbol{q}}/\sqrt{3})+iY(\bar{\boldsymbol{q}}/\sqrt{3})\}\boldsymbol{S}_0\\
&\qquad+\{(\kappa-6\mu)/2\}\{\boldsymbol{X}(\bar{\boldsymbol{q}}/\sqrt{3})+i\boldsymbol{Y}(\bar{\boldsymbol{q}}/\sqrt{3})\}\,,
\end{aligned} \tag{6}$$

and

$$\begin{aligned}
&X(\boldsymbol{q})=\sum_{j=1,2,3}\cos(\boldsymbol{a}_j\cdot\boldsymbol{q})\,,\\
&Y(\boldsymbol{q})=\sum_j\sin(\boldsymbol{a}_j\cdot\boldsymbol{q})\,,\\
&\boldsymbol{X}(\boldsymbol{q})=\sum_j\boldsymbol{S}_1^{(j)}\cos(\boldsymbol{a}_j\cdot\boldsymbol{q})\,,\\
&\boldsymbol{Y}(\boldsymbol{q})=\sum_j\boldsymbol{S}_1^{(j)}\sin(\boldsymbol{a}_j\cdot\boldsymbol{q})\,,
\end{aligned} \tag{7}$$

$$\begin{aligned}
&\boldsymbol{S}_0=\boldsymbol{i}_j\boldsymbol{i}_j+\boldsymbol{j}_j\boldsymbol{j}_j\,,\\
&\boldsymbol{S}_1^{(j)}=\boldsymbol{i}_j\boldsymbol{i}_j-\boldsymbol{j}_j\boldsymbol{j}_j\,,\\
&\boldsymbol{S}_2=(1/i)(\boldsymbol{i}_j\boldsymbol{j}_j-\boldsymbol{j}_j\boldsymbol{i}_j)\,.
\end{aligned} \tag{8}$$

$\boldsymbol{S}_0$ and $\boldsymbol{S}_2$ are independent of $j$, and $\bar{\boldsymbol{q}}$ is a vector into which $\boldsymbol{q}$ is transformed by a rotation through $\pi/2$ about the $\boldsymbol{k}$-axis, i. e.,

$$\bar{\boldsymbol{q}}=\boldsymbol{q}\cdot i\boldsymbol{S}_2=(\boldsymbol{q}\cdot\boldsymbol{i})\boldsymbol{j}-(\boldsymbol{q}\cdot\boldsymbol{j})\boldsymbol{i}\,.$$

Equation for $\begin{pmatrix}\boldsymbol{e}(C,\boldsymbol{q})\\ \boldsymbol{e}(D,\boldsymbol{q})\end{pmatrix}$ has the same form as (5), that is, two adjacent honey-comb net planes, which are crystallographically different each other, have the same vibrations in the plane in our treatment. $\boldsymbol{e}(A, \boldsymbol{q})$ and $\boldsymbol{e}(B, \boldsymbol{q})$ are two-dimensional vectors so that the above secular equation is four-dimensional. It is laborious to solve this equation for general $\boldsymbol{q}$, but quite easy for certain special values of $\boldsymbol{q}$. Solutions for two special cases $\boldsymbol{q}=q\boldsymbol{i}_j$ and $\boldsymbol{q}=q\boldsymbol{j}_j$ (Fig. 3) are obtained as given below. Further, the frequencies of the vibrations in the plane are independent of the $\boldsymbol{k}$-component of $\boldsymbol{q}$, as we can see from expressions (5), (6) and (7). Hence, the contours of constant frequency in the $\boldsymbol{q}$-space are cylindrical with axes parallel to $\boldsymbol{k}$.

($A1$) The case of $\boldsymbol{q}=q\boldsymbol{i}_j$

The secular equation simplifies also in this case and its roots are found to be

$$\omega^2=M^{-1}\{(3/2)\kappa+9\mu-\sqrt{\alpha_1^2+\beta_1^2}\}\,, \quad (9)$$

$$\omega^2=M^{-1}\{(3/2)\kappa+9\mu+\sqrt{\alpha_1^2+\beta_1^2}\}\,, \quad (10)$$

$$\omega^2=M^{-1}\{(3/2)\kappa+7\mu+2\mu\cos(\sqrt{3}\,aq/2)-\sqrt{\alpha_2^2+\beta_2^2}\}\,, \quad (11)$$

$$\omega^2=M^{-1}\{(3/2)\kappa+7\mu+2\mu\cos(\sqrt{3}\,aq/2)+\sqrt{\alpha_2^2+\beta_2^2}\}\,, \quad (12)$$

where

$$\alpha_1=\kappa\cos(\sqrt{3}\,aq/3)+\{(\kappa/2)+9\mu\}\cos(\sqrt{3}\,aq/6),$$

$$\beta_1=\kappa\sin(\sqrt{3}\,aq/3)-\{(\kappa/2)+9\mu\}\sin(\sqrt{3}\,aq/6)\,,$$

$$\alpha_2=6\mu\cos(\sqrt{3}\,aq/3)+\{(3/2)\kappa+3\mu\}\times\cos(\sqrt{3}\,aq/6)\,,$$

$$\beta_2=-6\mu\sin(\sqrt{3}\,aq/3)+\{(3/2)\kappa+3\mu\}\times\sin(\sqrt{3}\,aq/6)\,.$$

These four solutions correspond, in the given order, to acoustical and optical longitudinal waves and acoustical and optical transverse waves.

($A2$) The case of $\boldsymbol{q}=q\boldsymbol{j}_j$

We find the following roots of the simplified secular equation;

$$\omega^2=M^{-1}\{2\kappa+(9/2)\mu+(\mu/2)\cos aq-(\kappa/2)-4\mu)\cos(aq/2)-\sqrt{\alpha_3^2+\beta_3^2}\} \quad (13)$$

$$\omega^2=M^{-1}\{\kappa+(21/2)\mu+(\mu/2)\cos aq+((\kappa/2)-2\mu)\cos(aq/2)+\sqrt{\alpha_4^2+\beta_4^2}\}\,, \quad (14)$$

$$\omega^2=M^{-1}\{\kappa+(21/2)\mu+(\mu/2)\cos aq+((\kappa/2)-2\mu)\cos(aq/2)-\sqrt{\alpha_4^2+\beta_4^2}\}\,, \quad (15)$$

$$\omega^2=M^{-1}\{2\kappa+(9/2)\mu+(\mu/2)\cos aq-((\kappa/2)-4\mu)\cos(aq/2)+\sqrt{\alpha_3^2+\beta_3^2}\}\,, \quad (16)$$

where

$$\alpha_3=((\kappa+6\mu)/2)+\mu\cos aq+(\kappa+5\mu)\cos(aq/2)\,,$$

$$\beta_3=-(\sqrt{3}/2)\mu\sin aq+(\sqrt{3}/2)(\kappa-4\mu)\sin(aq/2)\,,$$

$$\alpha_4=((\kappa+6\mu)/2)-\mu\cos aq+(\kappa+7\mu)\cos(aq/2)\,,$$

$$\beta_4=(\sqrt{3}/2)\mu\sin aq+(\sqrt{3}/2)(\kappa-8\mu)\sin(aq/2)\,.$$

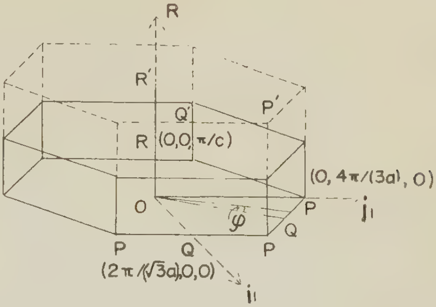

Fig. 3. The upper half of the Brillouin zone.

These also correspond, in the given order, to the acoustical and optical longitudinal waves and acoustical and optical transverse waves, though they are not linearly polarized but elliptically polarized in general cases. When, however, $q$ is small, they reduce exactly to longitudinal or transverse waves. (Waves in the direction of $\boldsymbol{q}=q\boldsymbol{i}_j$, that is, those dealt with in ($A1$) are always linearly polarized.) Another remarkable fact in the present case is that for longitudinal waves the acoustical mode and the optical mode degenerate at the corners of the Brillouin zone, $\boldsymbol{q}=\pm(4\pi/(3a))\boldsymbol{j}_j$ (i.e. $P$ in Fig. 3). This degeneracy is due to the symmetry of the crystal.

There are other cases that the above two where the equation (5) is soluble, for example, $\boldsymbol{q}\approx0$ and $\boldsymbol{q}\approx\pm(4\pi/(3a))\boldsymbol{j}_j$.

When $\boldsymbol{q}$ is small, we find, with the help of the perturbation theory, that the frequencies of the longitudinal and transverse acoustical modes are given by

$$\omega=(\kappa a^2/M)^{1/2}\{(\kappa+18\mu)/(8(\kappa+6\mu))\}^{1/2}|\boldsymbol{q}|\,, \quad (17)$$

$$\omega=(\kappa a^2/M)^{1/2}\{3\mu/(2(\kappa+6\mu))\}^{1/2}|\boldsymbol{q}|\,. \quad (18)$$

Sound velocities determined by these equation agree completely with those calculated on the basis of the semi-continuum theory by Komatsu and Nagamiya[1]. The values of $\kappa$ and $\mu$ estimated by them from the observed force constants of planar vibrations of benzen molecule are

$$\kappa=6.71\times10^5\ \text{dyne/cm}$$

$$\mu=0.48\times10^5\ \text{dyne/cm}\,.$$

($B$) *Vibration perpendicular to the plane*

The normal modes of vibrations perpendicular to the plane are determined from the remaining one of the two separated secular equations;

$$\begin{bmatrix} 2\kappa'-\lambda & -W' & 0 & -2\kappa'\cos(\boldsymbol{c}\cdot\boldsymbol{q}/2) \\ -W'^{*} & -\lambda & 0 & 0 \\ 0 & 0 & -\lambda & -W' \\ -2\kappa'\cos(\boldsymbol{c}\cdot\boldsymbol{q}/2) & 0 & -W'^{*} & 2\kappa'-\lambda \end{bmatrix} \cdot \begin{bmatrix} e(A,\boldsymbol{q}) \\ e(B,\boldsymbol{q}) \\ e(C,\boldsymbol{q}) \\ e(D,\boldsymbol{q}) \end{bmatrix} = 0 . \tag{19}$$

where

$$e(X,\boldsymbol{q})=e(X,\boldsymbol{q})\boldsymbol{k} ,$$
$$\lambda=M\omega^2-(4/3)\mu'-(2/9)\mu'X(\boldsymbol{q}) ,$$
$$W'=(2/3)\mu'\{X(\bar{\boldsymbol{q}}/\sqrt{3})+iY(\bar{\boldsymbol{q}}/\sqrt{3})\} , \tag{20}$$

It is easy to solve this secular equation. The roots are found to be

$$\omega^2=M^{-1}\{(4/3)\mu'+(2/9)\mu'X(\boldsymbol{q}) + \alpha_1'-\sqrt{\alpha_1'^2+|\beta'|^2}\} , \tag{21}$$
$$\omega^2=M^{-1}\{(4/3)\mu'+(2/9)\mu'X(\boldsymbol{q}) + \alpha_1'+\sqrt{\alpha_1'^2+|\beta'|^2}\} , \tag{22}$$
$$\omega^2=M^{-1}\{(4/3)\mu'+(2/9)\mu'X(\boldsymbol{q}) + \alpha_2'-\sqrt{\alpha_2'^2+|\beta'|^2}\} , \tag{23}$$
$$\omega^2=M^{-1}\{(4/3)\mu'+(2/9)\mu'X(\boldsymbol{q}) + \alpha_2'+\sqrt{\alpha_2'^2+|\beta'|^2}\} , \tag{24}$$

where

$$\alpha_1'=\kappa'\{1-\cos(\boldsymbol{c}\cdot\boldsymbol{q}/2)\} ,$$
$$\alpha_2'=\kappa'\{1+\cos(\boldsymbol{c}\cdot\boldsymbol{q}/2)\} ,$$
$$\beta'=(2/3)\mu'\{X(\bar{\boldsymbol{q}}/\sqrt{3})+iY(\bar{\boldsymbol{q}}/\sqrt{3})\} .$$

when the projection of $\boldsymbol{q}$ on the net plane, $\boldsymbol{q}\cdot\boldsymbol{S}_0$, is small, the formulas (21) and (23) reduce to

$$\omega^2=\{\mu' a^4/(144\,M)\}|\boldsymbol{q}\cdot\boldsymbol{S}_0|^4 + (2\kappa'/M)\begin{cases}\sin^2(\boldsymbol{c}\cdot\boldsymbol{q}/4) \\ \cos^2(\boldsymbol{c}\cdot\boldsymbol{q}/4) .\end{cases} \tag{25}$$

when we neglect higher order terms of $\kappa'/\mu'$ than the first order. This formula has the same form as that derived of the basis of semi-continuum model[1]. Komatsu[7] estimated the numerical value of $\{\kappa'/(2M)\}^{1/2}$ from the observed compressibility and determined the value of $(1/(2\pi)^2)\{\mu' a^4/(144\,M)\}^{1/2}$ by making the calculated specific heat curve fit the experimental one in the temperature range from 15° to 60°K. Using his results, the values of $\kappa'$ and $\mu'$ are determined to be

$$\kappa'=5.57\times10^3\ \text{dyne/cm}$$
$$\mu'=2.92\times10^5\ \text{dyne/cm} .$$

We employ these values for $\kappa'$ and $\mu'$. The ratio of $\kappa'$ to $\mu'$ is of order $10^{-2}$, so we are allowed to neglect the higher order terms of $\kappa'/\mu'$.

A remarkable fact in the vibrations perpendicular to the plane is that when $\boldsymbol{c}\cdot\boldsymbol{q}=0$ the lower frequencies (25) are proportional to $|\boldsymbol{q}|^2$.

## § 3. Frequency Distribution

### (*A*) *Vibrations in the plane*

For these branches we employ the method developed by Houston[11] for cubic lattice. First, we define $f(\nu,\varphi)$ as frequency distribution function along a line of azimuthal angle $\varphi$ in the basal hexagon of the Brillouin zone (see Fig. 3). Since the contours of constant frequency in the $\boldsymbol{q}$-space are cylindrical with axes parallel to $\boldsymbol{k}$, as was mentioned in section 2 (A), we can confine ourselves to the basal plane. From the symmetry about the $\boldsymbol{k}$-axis in the Brillouin zone we can expand $f(\nu,\varphi)$ in a Fourier series of $\cos 6n\varphi (n=0,1,2,\cdots)$ as

$$f(\nu,\varphi)=f_0(\nu)+f_1(\nu)\cos6\varphi+\cdots , \tag{26}$$

We have solved the secular equation along two different directions $\boldsymbol{q}=q\boldsymbol{i}_j$ and $\boldsymbol{q}=q\boldsymbol{j}_j$. Hence two distribution functions, $f(\nu,0)$ and $f(\nu,\pi/6)$, along these particular directions have become available. We take the first two terms of (26) and neglect the higher terms. To this approximation $f_0(\nu)$ can be determined by the simultaneous equations:

$$f(\nu,0)=f_0(\nu)+f_1(\nu) ,$$
$$f(\nu,\pi/6)=f_0(\nu)-f_1(r) .$$

With a further simplification of replacing the basal hexagon by a circle of the same area, the total distribution function becomes

$$f(\nu)=(2\pi/c)\int_0^{2\pi} f(\nu,\varphi)d\varphi=\{(2\pi)^2/c\}f_0(\nu)$$
$$=\{(2\pi^2)/(2c)\}\{f(\nu,0)+f(\nu,\pi/6)\} . \tag{27}$$

Curves for the total frequency distribution functions corresponding to the four branches ear shown in Fig. 4 to Fig. 7.

### (*B*) *Vibrations perpendicular to the plane*

Though we have rigorous solutions (21)–(24) for these vibrations, it is very laborious to calculate the frequency distribution functions from them. We shall replace the contours of

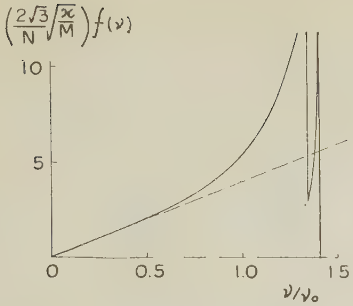

Fig. 4. The frequency distribution function for the longitudinal acoustical modes of the vibrations in the plane. The dashed line is that due to the semi-continuum theory.
$\nu_0=(2\pi)^{-1}(\kappa/M)^{1/2}=2.92\cdot10^{13}\,\sec^{-1}$
($\Theta_0=h\nu_0/k\sim1400°$K)

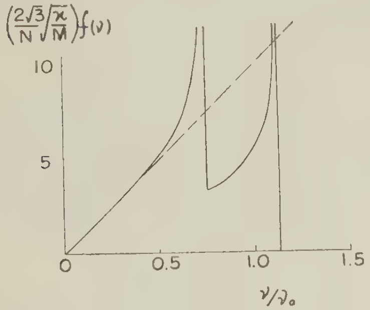

Fig. 5. The frequency distribution function for the transverse acoustical modes of the vibrations in the plane.

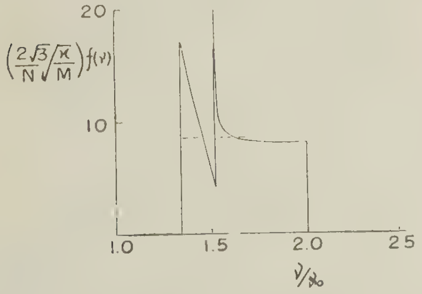

Fig. 6. The frequency distribution function for the longitudinal optical modes of the vibrations in the plane.

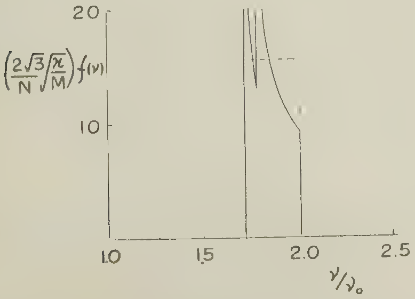

Fig. 7. The frequency distribution function for the transverse optical modes of the vibrations in the plane.

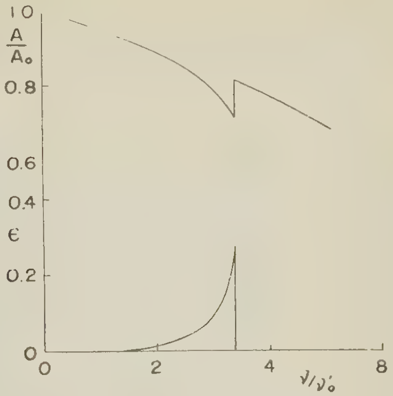

Fig. 8. The curves of $A/A_0$ and $\varepsilon$.
$A_0=\{\mu' a^4/(4\pi^2/44M)\}^{1/2}$

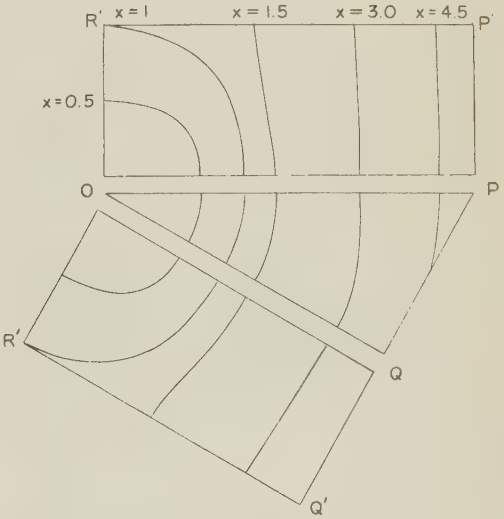

Fig. 9. The approximate contours of constant frequency for the lower frequency modes in the enlarged Brillouin zone. $x=\nu/\nu_0'$.

constant frequency in the Brillouin zone by approximate ones from which we can easily obtain the frequency distribution functions in simple closed forms.

First, let us consider the lower frequency branches (21) and (23). Instead of considering these two, we extend the Brillouin zone to a size twice as large in the direction of $\boldsymbol{k}$ as the original one and consider the branch (21) only; this is allowed since $\alpha_2'$ of (23) in the original zone is replaced by $\alpha_1'$ of (21) in the extended part of the zone. Then, for (21), we employ the approximate frequency formula of the form

$$\nu^2=A^2(1+\mathcal{E}\cos 6\varphi)|\boldsymbol{q}\cdot\boldsymbol{S}_0|^4+B^2\sin^2(\boldsymbol{c}\cdot\boldsymbol{q}/4)\,, \tag{28}$$

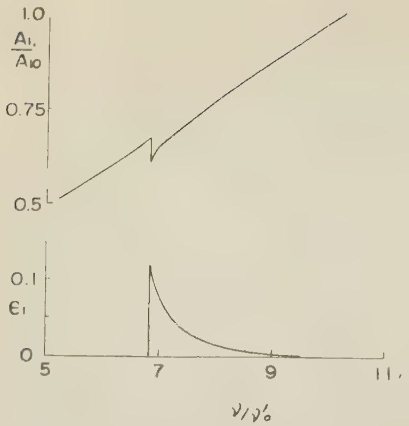

Fig. 10. The curves of $A_1/A_{10}$ and $\varepsilon_1$. $A_{10}=\mu' a^2/(12\pi^2 M)$

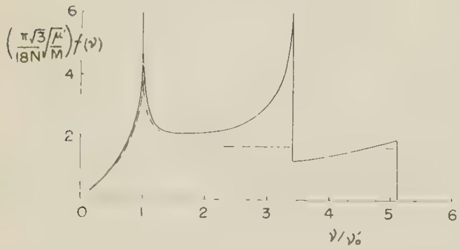

Fig. 11. The frequency distribution function for the lower frequency modes of the vibrations perpendicular to the plane. The dashed line is that due to the semi-continuum theory.
$\nu_0'=(2\pi)^{-1}(2\kappa'/M)^{1/2}=3.76\cdot 10^{12}\ \mathrm{sec}^{-1}$
$(\Theta_0'=h\nu_0'/k=180°\mathrm{K})$

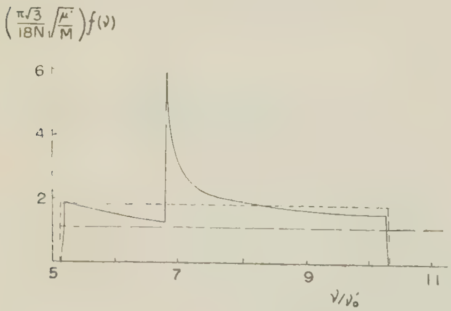

Fig. 12. The frequency distribution function for the higher frequency modes of the vibrations perpendicular to the plane.

which is a modification of (25). For each given $\nu$-value $A$, $\mathcal{E}$ and $B$ are so determined that the approximate contour given by (30) passes the points where the true contour cuts the lines OP, OQ and OR′ in Fig. 3. In this way we get $A$, $\mathcal{E}$ and $B$ as functions of $\nu$. In particular, $B(\nu)$ turns out to be nearly constant and equal to $(2\pi)^{-1}(\kappa'/M)^{1/2}$. The curves of $A(\nu)$ and $\mathcal{E}(\nu)$ are shown in Fig. 8 and the contours of constant frequency in the enlarged Brillouin zone are shown in Fig. 9.

With a further simplification of replacing the Brillouin zone by a circular cylinder, the number of modes, $N(\nu)$, with frequencies less than $\nu$ becomes

$$N(\nu)=\{V/(2\pi)^3\}\int_0^{2\pi}\int_{-q_{z,m}}^{q_{z,m}} q\cdot S_0|^2 dq_z d\varphi \tag{29}$$

where $V$ is the volume of crystal and $q_{z,m}$ is

$$q_{z,m}=\begin{cases}(4/c)\sin^{-1}(\nu/\nu_0') & (\nu/\nu_0')\leq 1\\ 2\pi/c & (\nu/\nu_0')\geq 1\ ,\end{cases}$$

$\nu_0$ is $B$, i.e. $(2\pi)^{-1}(2\kappa'/M)^{1/2}$. The frequency distribution function is given by differentiating $N(\nu)$ with respect to $\nu$:

$$f(\nu)=dN(\nu)/d\nu\ ,$$

From (30) and (31) $f(\nu)$ is calculated to be

$$\begin{aligned}f(\nu)=&\{2V/(4\pi^2)\}(C(\nu)/A(\nu))\\&\times[(\nu/\nu_0')K(\nu/\nu_0')-\nu_0\{(A'(\nu)/A(\nu))\\&-(C'(\nu)/C(\nu))\}\\&\times\{(1-(\nu/\nu_0')^2K(\nu/\nu_0')-E(\nu/\nu_0')\}]\\&\quad\text{for } (\nu/\nu_0')\leq 1\ ,\\f(\nu)=&\{2V/(4\pi^2)\}(C(\nu)/A(\nu))\\&\times[K(\nu_0'/\nu)+\nu\{(A'(\nu)/A(\nu))\\&-(C'(\nu)/C(\nu))\}\\&\times E(\nu_0'/\nu)]\\&\quad\text{for } (\nu/\nu_0')\geq 1\ ,\end{aligned}\tag{30}$$

where $C(\nu)$ is

$$C(\nu)=(2/\pi)(1+\mathcal{E}(\nu))^{-1/2}\times K(\{2\mathcal{E}(\nu)/(1+\mathcal{E}(\nu))\}^{1/2})\ ,$$

$K(x)$ and $E(x)$ are eliptic integrals of the first and second kinds, and $A'(\nu)$ and $C'(\nu)$ are the derivatives of $A(\nu)$ and $C(\nu)$ with respect to $\nu$.

For the higher frequency branches, (22) and (24), we employ in the enlarged Brillouin zone a single approximate contour expressed by

$$\nu^2=\nu^2_m-A_1(1+\mathcal{E}_1\cos 6\varphi)|\boldsymbol{q}\cdot S_0|^2+B^2\sin^2(\boldsymbol{c}\cdot\boldsymbol{q}/4)\ , \tag{31}$$

$\nu_m$ being the maximum frequency of these modes. In the same manner as above, we get $f(\nu)$ for the higher frequency modes, after simpler calculations. The curves of $A_1(\nu)$ and $\mathcal{E}_1(\nu)$ are shown in Fig. 10. The courves of $f(\nu)$ are shown in Fig. 11 and Fig. 12.

Table I.

| $T$ | $C_1$ | $C_2$ | $C_v$ calculated | $C_p$(i) observed | $C_p-C_v$ | $C_v$(ii) observed | $C_p$(iii) observed |
|---|---|---|---|---|---|---|---|
| °K | cal./g-atom.deg. | .. | .. | .. | .. | .. | .. |
| 45 | 0.0189 | 0.0872 | 0.1061 | 0.0990 | | 0.0990 | 0.0998 |
| 60 | 0.0335 | 0.1441 | 0.1776 | 0.1710 | | 0.1710 | 0.1665 |
| 75 | 0.0524 | 0.2045 | 0.2569 | 0.2528 | | 0.2528 | 0.2510 |
| 100 | 0.0938 | 0.3082 | 0.4020 | 0.4010 | 0.0001 | 0.4009 | 0.3963 |
| 125 | 0.1492 | 0.4121 | 0.5613 | 0.5566 | 0.0002 | 0.5564 | 0.5723 |
| 150 | 0.2172 | 0.5143 | 0.7315 | 0.7297 | 0.0005 | 0.7292 | 0.7718 |
| 175 | 0.2982 | 0.6125 | 0.9107 | 0.9123 | 0.0008 | 0.9115 | 0.9804 |
| 200 | 0.3890 | 0.7063 | 1.095 | 1.101 | 0.001 | 1.100 | 1.180 |
| 225 | 0.4852 | 0.7980 | 1.283 | 1.291 | 0.002 | 1.289 | 1.461 |
| 250 | 0.5887 | 0.8825 | 1.471 | 1.486 | 0.003 | 1.483 | 1.629 |
| 275 | 0.6979 | 0.9642 | 1.662 | 1.684 | 0.005 | 1.679 | 1.843 |
| 300 | 0.8116 | 1.0412 | 1.853 | 1.889 | 0.006 | 1.883 | 2.053 |

( i ) Observed values by DeSorbo6) (1954) ( ii ) $C_v$ values from ( i ).
(iii) Observed values by DeSorbo and Tyler5) (1953)

## § 4. Specific Heat

The specific heat at constant volume of the lattice vibrations is given by the formula

$$C_v=k\int_0^{\nu_{\max}}(h\nu/kT)^2\exp(h\nu/kT)\times\{\exp(h\nu/kT)-1\}^{-2}\}f(\nu)d\nu \quad (32)$$

where $k$ is the Boltzmann constant. Using the results of the previous section for $f(\nu)$, we get $C_1$ and $C_2$ which are contributions from the vibrations in the plane and perpendicular to the plane, respectively. However, for the optical branches we need not use the results calculated in the previous section for $f(\nu)$; it is sufficient to use its mean values given by $(\nu_2-\nu_1)^{-1}\int_{\nu_1}^{\nu_2}f(\nu)d\nu$ where $\nu_1$ and $\nu_2$ are the lower and upper limits of the optical branch; the errors produced by this procedure are negligible. The constant distribution functions with this mean value are shown by dotted lines in Fig. 6, Fig. 7 and Fig. 12.

Contributions from the electronic specific heat is negligible below 300°K as confirmed by Komatsu and Nagamiya1). The values of the $C_p-C_v$ correction are calculated by the formula

$$C_p-C_v=AC_p^2T\,,\quad A=\alpha^2V/(C_p^2K)$$

with values $\alpha=2.2\times10^{-5}\text{deg}^{-1}$, $C_p=1.88$ cal $\text{deg}^{-1}\text{mol}^{-1}$ at 300°K and $K=2.98\times10^{-12}\text{cm}^2$ dyne. The results of the calculation are shown in Fig. 13 and Table I.

## § 5. Conclusion and Discussion

The calculated specific heat values are in very good agreement with the recent measurements by DeSorbo8) with Ceylon natural graphite whose crystallite size is larger than 400Å in the direction of the ***c***-axis. The agreement is within experimental errors in the temperature range 45°K to 300°K. The measurements by DeSorbo and Tyler2) in 1953 (dotted curve in Fig. 11) were made with Acheson graphite, CS grade, whose crystallite size in the ***c***-direction was about 230 Å. Considerably large differences between these two series of measurements might be due to the effect of the crystallite size. Our culculated values can be better compared with the measurements with Ceylon natural samples.

The semi-continuum treatment made by Komatsu and Nagamiya1) explained the general behaviors of the specific heat curve over the whole temperature range and its refinement made by Komatsu7) explained in an excellent way the behaviors below 60°K down to 1.5°K. The latter calculation showed small deviations of the theoretical values from the observed ones above 60°K, which may be attributed to the failure of his semi-continuum treatment, particularly as regards the vibrations perpendicular to the planes. The present calculation eliminates such deviations up to 300°K. However, the following points must be noted in spite of the excellent agreement. First, the force constants determined by Komatsu in the manner mentioned in § 1 and used by the present calculation without alteration, cannot be claimed to be very accurate, since three of them were determined in certain approxi-

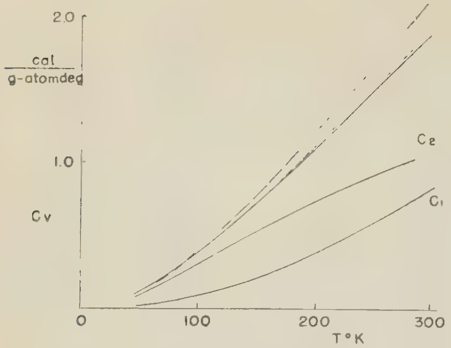

Fig. 13. —— calculated
- - - observed by DeSorbo (1954)
— observed by DeSorbo and Tyler (1953).

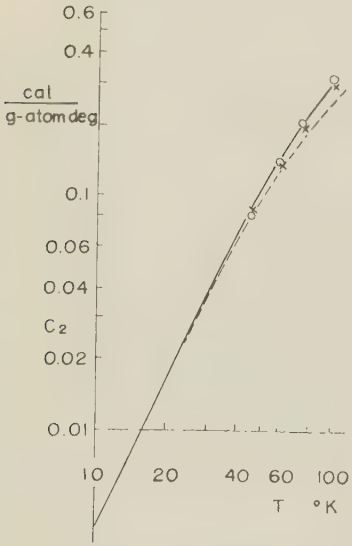

Fig. 14. The curves of $C_2$ (from the vibrations perpendicular to the plane).
—— present calculation,
- - - semi-continuum theory,
○ $C_v^{(i)}-C_1$, × $C_v^{(ii)}-C_1$,
(1°) observed values by DeSorbo (1954),
(2°) observed values by DeSorboan and Tyler (1953).

mate ways and the remaining one in such a way as to obtain the best fit with experiment; hence possible errors in the former must have been cancelled to a certain extent by that of the latter. Secondly, our $f(\nu)$'s are approximate and particularly crude near the zone boundary, though the details of the frequency distribution in this region cannot appreciably affect the specific heat curve. Anyhow, however, the success of the present theory supports the reasonableness of our assumption of the types of forces and the magnitudes of the adopted force constants.

It should, in principle, be possible to derive significant informations about the interatomic forces from the specific heat data in highly anisotropic cryatals, such as graphite, by a proper theoretical interpretation. For such substances, even the low frequency part of the spectrum consists of a number of branches whose frequency spectra are of different structures, so that the specific heat at low temperatures is a superposition of components with various temperature dependences. In graphite, the specific heat in the temperature range 15°K to about 100°K consists approximately of two components. One of them comes from the vibrations in the plane and obeys the simple two-dimensional $T^2$-law and the other from the vibrations perpendicular to the plane and has a more complex temperature dependence. The latter vibrations are not simply two-dimensional and are characteristic of the graphite-like lattice. They relate to weak restoring forces associated with changes in distances between adjacent sets of planes and to strong bending forces of the planes($\kappa' \ll \mu'$). When both $|\boldsymbol{q}\cdot\boldsymbol{S}_0|$ and $(\boldsymbol{q}\cdot\boldsymbol{k})$ are small, the frequency distribution has a linear $\nu$-depencence according to the frequency equation, $4\pi^2\nu^2=\{\mu' a^4/(144M)\}|\boldsymbol{q}\cdot\boldsymbol{S}_0|^4+\{\kappa' c^2/(8M)\}(\boldsymbol{q}\cdot\boldsymbol{k})^2$, Both terms of the right-hand side are effective and the specific heat is proportional to $T^2$. When $\nu$ is large enough so that the contour of constant $\nu$ crosses the upper and lower surfaces of the enlarged Brillouin zone (see § 3 (*B*)), one can neglect the second term in (25); then only the bending forces become effective. In the semi-continuum theory the frequency distribution function in this higher frequency range is almost independent of $\nu$, that is, it is nearly constant and the specific heat curve comes nearer to a straight line. In the Born-von Kármán treatment (see Fig. 8), this $\nu$-independent part is more obscure since equation (25) is not valid in this range of $\nu$. Furthermore, the frequency distribution function in the latter treatment tends to infinity at $\nu=\nu_0'$ and $\nu=3.4\,\nu_0'$ (see also Fig. 8). Owing to these facts the specific heat arising from the vibrations perpendicular to the plane shows a complex temperature dependence, as shown in Fig. 14. Only at very low temperatures (below about 10°K) does it strictly obey the $T^2$-law. In the range 15° to 60°K, the specific heat obeys only approximately the $T^2$-law. More specifically speaking, the difference in the range 45° to 100°K between the experimental curve and the calculated $C_1$ shows such theoretical predictions but, below 45°K, they show more complicated behaviors which could only be explained by taking account of the influence of the shearing forces.

Newell⁹⁾, in discussing the vibrations perpendicular to the plane in a qualitative way, considered the following three possible types of forces: (1) central forces between atoms on different planes, (2) non-central forces between neighboring atoms in the same plane, which are proportional to their relative perpendicular displacements, and (3) valence forces for the bending of the planes. He showed that the modes of the vibrations are mostly determined by the relative magnitudes of these three types of forces. If the forces of type (1) and type (3) prevail, one obtains the same results as ours, but if the forces of type (1) and type (2) prevail, the results are as those found by Krumhansl and Brooks²⁾. However, the origin of the forces of type (2) is yet unclear.

We might consider the following situation. Atoms other than those directly in contact simply attract each other, so that the springs between nearest neighbors in each net plane will not be in their natural state. Attractions between atoms in the same net plane will have caused them shrink. Attraction between atoms on different net planes will bring the net planes together and cause them shrink, too, but, on the other hand, repulsions between for instance, $B$ atoms and $C$, $D$ atoms in Fig. 2 will cause the hexagons formed by the latter two kinds of atoms expand. We do not know whether the springs are elongated or compressed in the equilibrium state of the whole lattice. In order to take account of this situation, one is evidently not allowed to confine himself, beside forces (1) and (3), to merely non-central forces of the type (2) proposed by Newell, though his forces (or the negative of them) might approximately care for the surface tension (or pressure) of the planes. The general conclusion to be attained when such fine details of the interaction and the shearing force introduced by Komatsu are considered is that the low-frequency part of the lattice vibrations is essentially three-dimensional and consequently that the specific heat is proportional to $T^3$ at sufficiently low temperatures. Possibly the shearing force considered by Komatsu⁷⁾ is most important in view of his success at low temperatures.

We wish to express our deep thanks to Professor T. Nagamiya of Osaka University and Doctor K. Komatsu of our University for their continual kind advices and discussions. We are indebted to Doctor Warren DeSorbo of the General Electric Company Research Laboratory for supplying his experimental data and to Doctor Gorden F. Newell of Brown University for supplying copies of his works before publication.

## References

1) K. Komatsu and T. Nagamiya: J. Phys. Soc. Japan **6** (1951) 438.
2) W. DeSorbo and W. W. Tyler: J. Chem. Phys. **21** (1953) 1660.
3) J. Krumhansl and H. Brooks: J. Chem. Phys. **21** (1953) 1663.
4) H. Rosenstock: J. Chem. Phys. **21** (1953) 2064.
5) T. Nagamiya and K. Komatsu: J. Chem. Phys. **22** (1954) 1457.
6) U. Bergenlid, R. W. Hill, E. J. Webb and J. Wilks: Phil. Mag. **45** (1954) 851.
7) K. Komatsu: J. Phys. Soc. Japan **10** (1955) 346.
8) W. DeSorbo: G. E. Tech. Rep. No. RL–**1202**.
9) G. P. Newell: J. Chem. Phys. **23** (1955) in press.
10) G. F. Newell: to appear in J. Chem. Phys.
11) W. V. Houston: Rev. Mod. Phys. **20** (1948) 161.

JOURNAL OF THE PHYSICAL SOCIETY OF JAPAN Vol. 11, No. 4, APRIL, 1956

# Virial Coefficients and Intermolecular Potential for Small Nonspherical Molecules

By Taro KIHARA, Yukio MIDZUNO and Shobu KANEKO

*Department of Physics, Faculty of Science, University of Tokyo*

(Received November 10, 1955)

It has been proved that for a special model of nonspherical intermolecular potential the nonspherical correction to the virial coefficients is equivalent to the quantum correction. The second and third virial coefficients of hydrogen has been investigated by use of this model, and the intermolecular potential has been determined, which can be compared with the result of quantum-mechanical calculations. The model has also been applied to the second virial coefficient between argon and hydrogen.

## § 1. Introduction

The equation of state of gases may be expressed in the form

$$pv=kT(1+Bv^{-1}+Cv^{-2}+\cdots)\,, \tag{1.1}$$

where $p$ is the pressure, $v$ is the volume per molecule, $k$ is the Boltzmann constant, and $T$ is the temperature. In this expression $B$, $C$, $\cdots$, which are functions of the temperature, are called second, third, $\cdots$ virial coefficients. These coefficients indicate the deviation of a real equation of state from that of the ideal gas. They have been given in terms of the interaction between molecules, or the intermolecular potential.

With regards the interaction between molecules, let us assume as usual the additivity of the intermolecular potential; we assume namely that the total potential energy be equal to the sum of the potential energies between pairs of molecules. Under this assumption the second and third virial coefficients have been calculated[1] for the Lennard-Jones potential between two molecules,

$$U(r)=\frac{U_0}{n-6}\left[6\left(\frac{r_0}{r}\right)^n-n\left(\frac{r_0}{r}\right)^6\right], \tag{1.2}$$

with two parameters $U_0$ and $r_0$, $n$ being chosen as 9 and 12. Here $r$ indicates the distance between the centers of molecules.

For this intermolecular potential the quantum-mechanical effect has also been calculated in the form of the series

$$B=B^{(0)}+\frac{\hbar^2}{4mkT}B^{(1)}+\left(\frac{\hbar^2}{4mkT}\right)^2B^{(2)}+\left(\frac{\hbar^2}{4mkT}\right)^3B^{(3)}+\cdots, \tag{1.3}$$

$$C=C^{(0)}+\frac{\hbar^2}{4mkT}C^{(1)}+\cdots \tag{1.4}$$

up to the terms explicitely given above[2]. Here $\hbar$ is Planck's constant divided by $2\pi$; $m$ is the mass of a molecule. Except the case of helium, terms proportional to the fourth or higher powers of $\hbar$ may be neglected at moderate temperatures. (We do not take account of the quantum-statistical effect, which is always negligible at temperatures where expansions (1.3) and (1.4) are practical.)

For monatomic molecules the intermolecular potential is a function of $r$ only and may be approximated by (1.2). The aim of the present paper is to treat *small* nonspherical molecules whose intermolecular potential is slightly different from the spherically symmetric potential (1.2). By means of a suitable model of molecules and by virtue of a relationship in regard to the model, the treatment is simple and perhaps instructive.

There are several investigations on the second virial coefficient of nonspherical molecules[3]; the third virial coefficient of nonspherical molecules is for the first time treated in this paper.

## § 2. A Molecular Model and a Formula

Let us assume within each molecule a distribution $\rho\geqq 0$ of potential source with normalized volume integral

$$\int\rho(\boldsymbol{s})d\boldsymbol{s}=1\,. \tag{2.1}$$

Here $\boldsymbol{s}$ is the radius vector to the source element from the molecular center defined by the "mean value" of the distribution, so that

$$\int \boldsymbol{s}\rho(\boldsymbol{s})d\boldsymbol{s}=0\ . \tag{2.2}$$

The intermolecular potential $V$ is assumed to be a superposition of a usual potential function $U$(e. g. of the type (1.2)) between source elements $\rho_1(\boldsymbol{s}_1)d\boldsymbol{s}_1$ of one molecule and those $\rho_2(\boldsymbol{s}_2)d\boldsymbol{s}_2$ of the other:

$$V=\iint \rho_1(\boldsymbol{s}_1)\rho_2(\boldsymbol{s}_2)U(|\boldsymbol{r}+\boldsymbol{s}_2-\boldsymbol{s}_1|)d\boldsymbol{s}_1d\boldsymbol{s}_2\ . \tag{2.3}$$

Here $\boldsymbol{r}$ is the radius vector from the center of molecule 1 to that of molecule 2.

We define the standard deviation $\delta$ of the distribution by

$$\delta^2=\int s^2\rho(\boldsymbol{s})d\boldsymbol{s}\ ,\quad s\equiv|\boldsymbol{s}|\ , \tag{2.4}$$

and assume that $\delta$ be sufficiently small in comparison with the molecular size.

For this model of molecule the virial coefficients of a simple gas may be expanded into double series in $\hbar$ and $\delta$. Up to the terms proportional to $\hbar^2$ and to $\delta^2$ hold

$$B=B^{(0)}+\left(\frac{\hbar^2}{4mkT}+\delta^2\right)B^{(1)}\ , \tag{2.5}$$

$$C=C^{(0)}+\left(\frac{\hbar^2}{4mkT}+\delta^2\right)C^{(1)}\ , \tag{2.6}$$

and similar relations as regards higher virial coefficients. A proof of this formula will be given in the next section. This formula shows that $\hbar^2/4mkT$ and $\delta^2$ are equivalent so far as both quantum and polyatomic effects are small.

## § 3. Proof of the Formula

With respect to (2.3) we have, up to the term of $\delta^2$,

$$|\boldsymbol{r}+\boldsymbol{s}_2-\boldsymbol{s}_1|=[r^2+s_2{}^2+s_1{}^2+2\boldsymbol{r}\cdot\boldsymbol{s}_2-2\boldsymbol{r}\cdot\boldsymbol{s}_1-2\boldsymbol{s}_2\cdot\boldsymbol{s}_1]^{1/2}$$

$$=r+\frac{1}{2r}(s_2{}^2+s_1{}^2+2\boldsymbol{r}\cdot\boldsymbol{s}_2-2\boldsymbol{r}\cdot\boldsymbol{s}_1-2\boldsymbol{s}_2\cdot\boldsymbol{s}_1)-\frac{1}{2r^3}(\boldsymbol{r}\cdot\boldsymbol{s}_2-\boldsymbol{r}\cdot\boldsymbol{s}_1)^2\ ,$$

$$U(|\boldsymbol{r}+\boldsymbol{s}_2-\boldsymbol{s}_1|)=U(r)+\frac{U'(r)}{2r}(s_2{}^2+s_1{}^2+2\boldsymbol{r}\cdot\boldsymbol{s}_2-2\boldsymbol{r}\cdot\boldsymbol{s}_1-2\boldsymbol{s}_2\cdot\boldsymbol{s}_1)$$

$$+\left(\frac{U''(r)}{2}-\frac{U'(r)}{2r}\right)\frac{(\boldsymbol{r}\cdot\boldsymbol{s}_2-\boldsymbol{r}\cdot\boldsymbol{s}_1)^2}{r^2}\ ,\ r\equiv|\boldsymbol{r}|\ .$$

Zeroth approximation to $V$ is the basic potential $U(r)$, and the first correction is, by use of (2.1), (2.2) and (2.4),

$$V-U(r)=\frac{U'(r)}{r}\delta^2$$

$$+\left(\frac{U''(r)}{2}-\frac{U'(r)}{2r}\right)\left[\int\rho_1(\boldsymbol{s}_1)\left(\frac{\boldsymbol{r}}{r}\cdot\boldsymbol{s}_1\right)^2d\boldsymbol{s}_1+\int\rho_2(\boldsymbol{s}_2)\left(\frac{\boldsymbol{r}}{r}\cdot\boldsymbol{s}_2\right)^2d\boldsymbol{s}_2\right].$$

What we need is the average with respect to all orientations of the two molecules, $r$ being kept constant:

$$\langle V-U(r)\rangle_{\mathrm{Av}}=\frac{\delta^2}{3}\left[U''(r)+2\frac{U'(r)}{r}\right].$$

Here we have used the relationships as

$$\left\langle\int\rho(\boldsymbol{s})\left(\frac{\boldsymbol{r}}{r}\cdot\boldsymbol{s}\right)^2d\boldsymbol{s}\right\rangle_{\mathrm{Av}}=\frac{1}{3}\int\rho(\boldsymbol{s})s^2d\boldsymbol{s}=\frac{1}{3}\delta^2$$

(The average with respect to orientations of a molecule for a fixed $\boldsymbol{r}$ is equal to the average with respect to the direction of $\boldsymbol{r}$ for a fixed orientation of the molecule.)

Let us denote the distance and the potential between $i$th and $j$th molecules by $r_{ij}$ and $V_{ij}$ respectively so that

$$\langle V_{ij}-U(r_{ij})\rangle_{\mathrm{Av}}=\frac{\delta^2}{3}\left[U''(r_{ij})+2\frac{U'(r_{ij})}{r_{ij}}\right].$$

Hence the classical configurational partition function for a system of $N$ identical molecules,

$$\frac{1}{N!}\int\cdots\int\left\langle\exp\left(-\frac{1}{kT}\sum_{i<j}V_{ij}\right)\right\rangle_{\mathrm{Av}}d\boldsymbol{r}_1\cdots d\boldsymbol{r}_N\ ,$$

is given, up to the term of $\delta^2$, by

$$Q^{(0)}+\delta^2Q^{(1)}$$

$$Q^{(0)}=\frac{1}{N!}\int\cdots\int\exp\left(-\frac{\Phi}{kT}\right)d\boldsymbol{r}_1\cdots d\boldsymbol{r}_N\ ,$$

$$Q^{(1)}=-\frac{1}{3kT}\frac{1}{N!}\int\cdots\int\exp\left(-\frac{\Phi}{kT}\right)$$

$$\times\sum_{i<j}\left[U''(r_{ij})+2\frac{U'(r_{ij})}{r_{ij}}\right]d\boldsymbol{r}_1\cdots d\boldsymbol{r}_N\ .$$

Here

Table I. Second and third virial coefficients of hydrogen.

| $T$°K | $B$ Å$^3$ | $C\times10^{-2}$ Å$^6$ |
|---|---|---|
| 65.1 | −30.3 | 13.9 |
| 90.0 | − 9.2 | 18.2 |
| 123 | 4.9 | 14.9 |
| 173 | 15.1 | 10.1 |
| 223 | 20.0 | 9.6 |
| 273 | 23.2 | 8.4 |
| 323 | 25.1 | |
| 373 | 25.7 | |
| 473 | 26.0 | |

L. Holborn, J. Otto; Zeits. f. Phys. **23** (1925) 1.

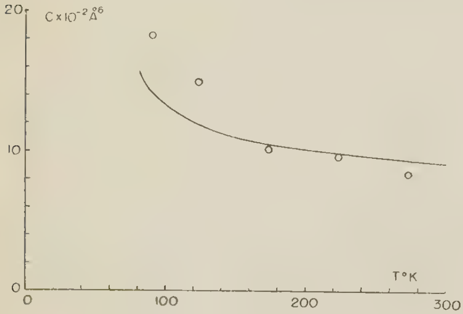

Fig. 1. The third virial coefficient of hydrogen compared with a curve for an intermolecular potential determined from the second virial coefficient.

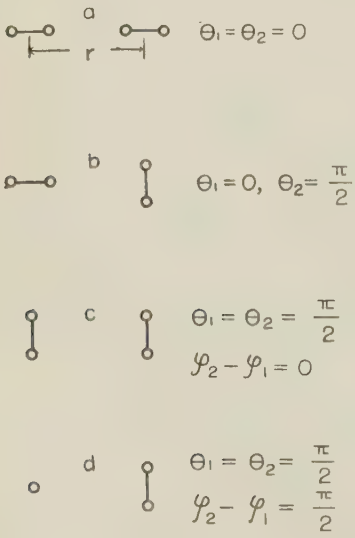

Fig. 2.

$$\Phi=\sum_{i<j}U(r_{ij})$$

is the zeroth approximation to the potential energy of the total system.

Since

$$U''(r_{ij})+\frac{2}{r_{ij}}U'(r_{ij})$$
$$=\frac{\partial}{\partial \boldsymbol{r}_i}\cdot\frac{\partial}{\partial \boldsymbol{r}_i}U(\boldsymbol{r}_{ij})$$
$$=\frac{1}{2}\left(\frac{\partial}{\partial_i}\cdot\frac{\partial}{\partial \boldsymbol{r}_i}+\frac{\partial}{\partial \boldsymbol{r}_j}\cdot\frac{\partial}{\partial \boldsymbol{r}_j}\right)U(r_{ij})$$
$$=\frac{1}{2}\sum_{k=1}^{N}\frac{\partial}{\partial \boldsymbol{r}_k}\cdot\frac{\partial}{\partial \boldsymbol{r}_k}U(r_{ij}),$$

$Q^{(1)}$ can be transformed into

$$Q^{(1)}=-\frac{1}{6kT}\frac{1}{N!}\int\cdots\int\exp\left(-\frac{\Phi}{kT}\right)\times\sum_{i=1}^{N}\frac{\partial}{\partial \boldsymbol{r}_i}\cdot\frac{\partial}{\partial \boldsymbol{r}_i}\Phi d\boldsymbol{r}_1\cdots d\boldsymbol{r}_N$$

or

$$Q^{(1)}=-\frac{1}{6(kT)^2}\frac{1}{N!}\int\cdots\int\exp\left(-\frac{\Phi}{kT}\right)\times\sum_{i=1}^{N}\left(\frac{\partial}{\partial \boldsymbol{r}_i}\Phi\right)^2 d\boldsymbol{r}_1\cdots d\boldsymbol{r}_N\,.$$

On the other hand the configurational partition function for spherical molecules with the intermolecular potential $U(r)$ is, up to the first quantum correction,

$$Q^{(0)}+\frac{\hbar^2}{4mkT}Q^{(1)}\,, \tag{3.2}$$

$Q^{(1)}$ being the same as above[4].

Combining (3.1) and (3.2) we finally obtain the partition function of the form

$$Q=Q^{(0)}+\left(\frac{\hbar^2}{4mkT}+\delta^2\right)Q^{(1)} \tag{3.3}$$

so far as terms of higher order can be neglected. The formula given in the preceding section can be derived from (3.3).

## § 4. Second and Third Virial Coefficients of Hydrogen at Moderate Temperatures

For hydrogen at moderate temperatures we may assume that both the quantum and the polyatomic effects can be treated as small perturbations.

Let the potential source of a hydrogen molecule be located at the two nuclei. Then the standard deviation $\delta$ is the one half of the internuclear distance, $\delta=0.37$Å. ($\hbar^2/4mkT=\delta^2$ at $T=44$°K). Let furthermore the basic potential function $U(r)$ in (2.3) be of the Lennard-Jones type (1.2) with $n=9$. Then $B^{(0)}$, $B^{(1)}$, $C^{(0)}$, $C^{(1)}$ in (2.5) and (2.6) are all known.

Using the formula (2.5) and the observed values of the second virial coefficient given in

Table I we can determine two parameters $U_0$ and $r_0$. The result is

$$U_0/k=39.8°\text{K}, \quad r_0=3.20\text{Å} . \tag{4.1}$$

Using these parameters and the formula (2.6) we can calculate the third virial coefficient. The calculated curve is compared in Fig. 1 with observed values given also in Table I. (The polyatomic correction is $\delta^2C^{(1)}/C^{(0)}=0.25$ at the Boyle temperature 109°K.)

We have been taking the electrostatic quadrupole of a hydrogen molecule not into account. The energy of quadrupole-quadrupole interaction is proportional to the square of the moment. When the virial coefficients are expanded into series with respect to the moment, however, the term of the square of the moment vanishes because of the orientational average. The first non-vanishing term is proportional to the 4th power of the moment and can consistently be neglected.

## § 5. Intermolecular Potential of Hydrogen

There are quantum-mechanical calculations of the intermolecular potential for hydrogen⁵⁾. The calculations are made for four mutual orientations *a*, *b*, *c*, and *d* as shown in Fig. 2. Here *r* is the distance between two centers, $(\theta_1, \varphi_1)$ and $(\theta_2, \varphi_2)$ are polar angles of both molecular axes in regard to the line connecting the centers. The potential curves are given in Fig. 3.

With these curves let us compare the result obtained in the preceding section. For this purpose we must take the quadrupole interaction into account.

Let us assume a point quadrupole at the molecular center along the axis in addition to the distribution of source of van der Waals' potential. As the moment of the quadrupole we adopt James and Coolidge's⁶⁾ value

$$q=0.124 \text{ electron charge Å}^2,$$

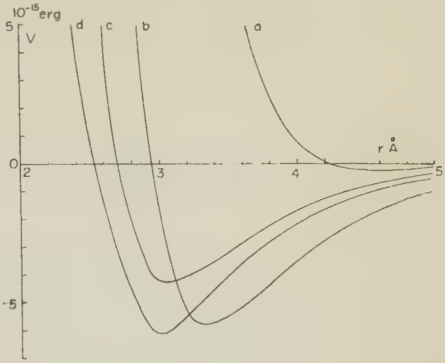

Fig. 3. Intermolecular potential of hydrogen calculated quantum-mechanically for several mutual orientations shown in Fig. 2. (From Hirschfelder, Curtiss and Bird: *Molecular Theory of Gases and Liquids* (Wiley, 1954) Fig. 14.4–1).

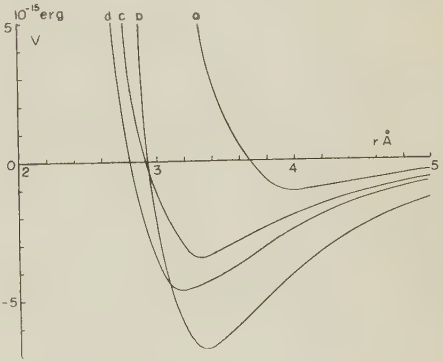

Fig. 4. Intermolecular potential of hydrogen determined from the virial coefficients. The four curves are for four orientations shown in Fig. 2. (Compare Fig. 3.)

with which the quadrupole-quadrupole interaction is given by the potential energy

$$\frac{3}{4}\frac{q^2}{r^5}[1-5\cos^2\theta_1-5\cos^2\theta_2-15\cos^2\theta_1\cos^2\theta_2$$
$$+2\{\sin\theta_1\sin\theta_2\cos(\varphi_2-\varphi_1)-4\cos\theta_1\cos\theta_2\}^2] .$$

Then the total intermolecular potential becomes

$$\frac{2}{4}U(r)+\frac{1}{4}U(r+2\delta)+\frac{1}{4}U(r-2\delta)+6\frac{q^2}{r^5} \qquad \text{for position } a,$$

$$\frac{2}{4}U(\sqrt{(r+\delta)^2+\delta^2})+\frac{2}{4}U(\sqrt{(r-\delta)^2+\delta^2})-3\frac{q^2}{r^5} \qquad \text{for position } b,$$

$$\frac{2}{4}U(r)+\frac{2}{4}U(\sqrt{r^2+(2\delta)^2})+\frac{9}{4}\frac{q^2}{r^5} \qquad \text{for position } c,$$

$$\frac{4}{4}U(\sqrt{r^2+(2\delta)^2})+\frac{3}{4}\frac{q^2}{r^5} \qquad \text{for position } d.$$

Table II. Second virial coefficient between argon and hydrogen.

| $T$°K | $B_{AB}$ Å$^3$ |
|---|---|
| 298 | 13.6 |
| 323 | 15.4 |
| 348 | 18.3 |
| 373 | 20.8 |
| 398 | 22.9 |
| 423 | 24.7 |
| 447 | 26.2 |

E. A. Guggenheim, Mixtures (University Press, Oxford, England, 1952) p. 160.

the four curves being shown in Fig. 4, which correspond to four curves in Fig. 3.

## § 6. Second Virial Coefficient between Unlike Molecules

The second virial coefficient for a binary mixture of species $A$ and $B$ is expressed by

$$B_{AA}\xi_A^2+2B_{AB}\xi_A\xi_B+B_{BB}\xi_B^2$$

Here $\xi_A$ and $\xi_B=1-\xi_A$ are mole fractions of the species $A$ and $B$, respectively; $B_{AA}$ is the virial coefficient for molecule $A$, $B_{BB}$ that for molecule $B$; $B_{AB}$ is the virial coefficient between $A$ and $B$, which we will treat in this section.

The potential $V_{AB}$ between $A$ and $B$ is assumed to be a superposition of the mutual potential function $U_{AB}$ between the source element $\rho_A$ of molecule $A$ and $\rho_B$ of molecule $B$:

$$V_{AB}=\iint\rho_A(\boldsymbol{s}_1)\rho_B(\boldsymbol{s})U_{AB}(|\boldsymbol{r}+\boldsymbol{s}_2-\boldsymbol{s}_1|)d\boldsymbol{s}_1d\boldsymbol{s}_2$$

compare (2.3)). Let the standard deviation be $\delta_A$ and $\delta_B$ respectively. Then mixed second irial coefficient is, up to the first corrections, f the form

$$B_{AB}=B_{AB}^{(0)}+\left(\frac{\hbar^2}{8m^*kT}+\frac{\delta_A^2+\delta_B^2}{2}\right)B_{AB}^{(1)}, \tag{6.1}$$

where $m^*$ is the reduced mass (compare (2.5)).

Let us treat, as an example, mixtures of rgon and hydrogen which we denote by species $A$ and $B$ respectively. We assume $\delta_A=0$, $\delta_B=0.37$Å. Using the data given in Table II and the basic potential

$$U_{AB}(r)=U_{0AB}\left[2\left(\frac{r_{0AB}}{r}\right)^9-3\left(\frac{r_{0AB}}{r}\right)^6\right],$$

we can determine the parameters $U_{0AB}$ and $r_{0AB}$. The result is

$$U_{0AB}/k=60.3°\text{K},\quad r_{0AB}=3.77\text{Å}.$$

Since the corresponding parameters for argon are[7)]

$$U_{0AA}/k=89.7°\text{K},\quad r_{0AA}=3.29\text{Å}$$

and those for hydrogen is given by (4.1), we obtain

$$\frac{2r_{0AB}}{r_{0AA}+r_{0BB}}-1=0.04$$

$$\frac{U_{0AB}}{(U_{0AA}U_{0BB})^{1/2}}-1=0.01\ .$$

Namely $r_{0AB}$ is approximately equal to the arithmetical mean of $r_{0AA}$ and $r_{0BB}$, $U_{0AB}$ to the geometrical mean of $U_{0AA}$ and $U_{0BB}$. These relations are similar to those verified by Kihara and Koba[8)] for the "core-model" of molecules.

### References

1) T. Kihara: J. Phys. Soc. Japan **3** (1948) 265; **6** (1951) 184.
Bird, Spotz and Hirschfelder: J. Chem. Phys. **18** (1950) 1395.
Epstein, Hibbert, Powers and Roe: J. Chem. Phys. **22** (1954) 464.

2) Kihara, Midzuno and Shizume: J. Phys. Soc. Japan **10** (1955) 249. See errata at the end of the present paper.

3) See Hirschfelder, Curtiss and Bird: *Molecular Theory of Gases and Liquids* (Wiley 1954) Chp. 3, Sec. 8.
T. Kihara: Revs. Modern Phys. **25** (1953) 831; **27** (1955) 412.

4) See, for example, J. de Boer and R. B. Bird: *Quantum Theory and the Equation of State* (Chap. 6 of Hirschfelder et al. loc. cit.) Sec. 1.

5) Hirchfelder et al. loc. cit. p. 1083.

6) H. M. James and A. S. Coolidge: Astrophys. J. **87** (1938) 447.

7) For example, T. Kihara: Revs. Modern Phys. **25** (1953) 831.

8) T. Kihara and S. Koba: J. Phys. Soc. Japan **9** (1954) 688.

---

## Errata

### Virial Coefficients and Intermolecular Potential of Helium

By KIHARA, MIDZUNO and SHIZUME

J. Phys. Soc. Japan **10** (1955) 249

Four lines above (5.8), change $1/V$ on the right-hand side to $\beta/V$.

Seven lines below Eq. (5.8), change "since the integral of cross terms vanishes" to "since the integral of cross terms is very small. (Exact calculation taking account of the integral of cross terms is given in Revs. Modern Phys. **27** (1955) ) 412".

Six lines below Eq. (6.3), omit $1/6n$.

Reference 2 should read Phys. Rev. **76** (1949) 18.

JOURNAL OF THE PHYSICAL SOCIETY OF JAPAN Vol. 11, No. 4, APRIL, 1956

# On the Two Schemes of Approximating the Transport Coefficients (Chapman – Cowling and Kihara)

By S. C. SAXENA

*Indian Association for the Cultivation of Science, Calcutta-32, India*

(Received January 14, 1956)

The three elementary transport coefficients and the isotopic thermal separation ratio have been evaluated over an extensive range of temperatures by utilizing the expressions derived on the approximation procedure due to Kihara, for the Lennard-Jones 12:6 model. These values have been compared with the corresponding and a still higher order approximation values calculated on an alternative approximation scheme of Chapman and Cowling. The comparison of the results obtained on the two schemes of approximation indicates that the simple expressions of Kihara are more accurate and preferable even to the corresponding higher approximation expressions of Chapman and Cowling.

## § 1. Introduction

Chapman and Cowling1) have expressed the transport coefficients as ratios of infinite determinants which they subsequently expand into an infinite series by applying the theory of determinants. The various orders of Chapman and Cowling approximation correspond to taking into account increasing number of terms of this infinite series. On the other hand Kihara2)3) noted that the off-diagonal elements of these determinants are small compared to the diagonal elements. His approximation scheme is based on expanding the infinite determinants in powers of the off-diagonal elements in which the second and higher order temperature derivatives of collision integrals and also the third and higher powers of the first derivative are neglected. Kihara's approximation scheme leads to the results which are considerably simpler than the corresponding Chapman and Cowling expressions and are easier for computational purposes as these involve fewer collision integrals. Kihara's expressions are known to be more accurate in the case of a Lorentzian gas with a simple intermolecular potential. The purpose of the present report is to critically examine the two approximation schemes for the more realistic molecular model of the Lennard-Jones 12:6 type and further to estimate the relative accuracy of Kihara's expressions over those of Chapman and Cowling which are known to a still higher degree of approximation. Mason4) has recently made such quantitative comparison of the isotopic thermal diffusion ratio for his modified Buckingham Exp-six model.

## § 2. Calculation and Discussion of Transport Coefficients

Kihara's expressions for the second approximation to the correction factors for viscosity, $f_\eta^{(2)}$, thermal conductivity, $f_\lambda^{(2)}$, and diffusion, $f_D^{(2)}$, of pure gases and the first approximation to the thermal separation ratio, $[K_T]^*_1$, for a mixture of heavy isotopes are given in the book by Hirschfelder, Curtiss and Bird5). Making use of these expressions we have computed the values of $f_\eta^{(2)}$, $f_\lambda^{(2)}$, $f_D^{(2)}$ and $[K_T]_1^*$ over an extensive range of temperatures and these are recorded in tables I and II. The symbol * means reduced quantities, compare reference 5.

On Chapman and Cowling scheme of approximation values of $f_\eta^{(3)}$ and $f_\lambda^{(3)}$ are given in reference 5, while that of $f_D^{(3)}$ have been recently reported by Saxena6), over an extensive range of temperatures and these values are almost identical with those given in table I.

Mason4) has derived the expression for the second approximation to $[K_T]^*$ according to the method of Chapman and Cowling and recently Saxena and Srivastava7) have developed expressions for the additional collision integrals occuring in $[K_T]_2^*$ for the Lennard-Jones 12:6 model. The values of these collision integrals have been reported by Saxena8) over a large temperature range and these values along with those given by

Table I. Functions for calculating the elementary transport coefficients on the approximation Scheme of Kihara.

| $T^*$ | $f_\eta^{(2)}$ | $f_\lambda^{(2)}$ | $f_D^{(2)}$ |
|---|---|---|---|
| 0.30 | 1.0012 | 1.0019 | 1.0001 |
| 0.40 | 1.0004 | 1.0007 | 1.0000 |
| 0.50 | 1.0001 | 1.0001 | 1.0000 |
| 0.75 | 1.0000 | 1.0000 | 1.0001 |
| 1.00 | 1.0000 | 1.0000 | 1.0000 |
| 1.25 | 1.0001 | 1.0001 | 1.0002 |
| 1.50 | 1.0004 | 1.0006 | 1.0006 |
| 1.75 | 1.0009 | 1.0013 | 1.0010 |
| 2.0 | 1.0014 | 1.0022 | 1.0016 |
| 2.5 | 1.0025 | 1.0040 | 1.0027 |
| 3.0 | 1.0035 | 1.0054 | 1.0038 |
| 3.5 | 1.0043 | 1.0066 | 1.0045 |
| 4.0 | 1.0049 | 1.0077 | 1.0052 |
| 5.0 | 1.0058 | 1.0090 | 1.0060 |
| 7.0 | 1.0067 | 1.0105 | 1.0071 |
| 10.0 | 1.0073 | 1.0114 | 1.0078 |
| 50 | 1.0077 | 1.0120 | 1.0082 |
| 100 | 1.0078 | 1.0121 | 1.0082 |
| 400 | 1.0078 | 1.0121 | 1.0081 |

Table II. Calculated values of the first approximation to the thermal separation ratio, $[K_T]_1^*$, on Kihara's scheme of Approximation.

| $T^*$ | $[K_T]_1^*$ | $T^*$ | $[K_T]_1^*$ | $T^*$ | $[K_T]_1^*$ |
|---|---|---|---|---|---|
| 0.80 | −0.039 | 2.0 | 0.294 | 4.4 | 0.542 |
| 0.85 | −0.025 | 2.1 | 0.313 | 4.5 | 0.546 |
| 0.90 | −0.011 | 2.2 | 0.333 | 4.6 | 0.551 |
| 0.95 | 0.0048 | 2.3 | 0.347 | 4.7 | 0.556 |
| 1.00 | 0.019 | 2.4 | 0.366 | 4.8 | 0.560 |
| 1.05 | 0.034 | 2.5 | 0.381 | 4.9 | 0.560 |
| 1.10 | 0.048 | 2.6 | 0.395 | 5 | 0.565 |
| 1.15 | 0.067 | 2.7 | 0.409 | 6 | 0.597 |
| 1.20 | 0.082 | 2.8 | 0.424 | 7 | 0.610 |
| 1.25 | 0.101 | 2.9 | 0.433 | 8 | 0.623 |
| 1.30 | 0.110 | 3.0 | 0.448 | 9 | 0.627 |
| 1.35 | 0.130 | 3.1 | 0.457 | 10 | 0.636 |
| 1.40 | 0.144 | 3.2 | 0.462 | 20 | 0.645 |
| 1.45 | 0.159 | 3.3 | 0.476 | 30 | 0.647 |
| 1.50 | 0.173 | 3.4 | 0.481 | 40 | 0.645 |
| 1.55 | 0.188 | 3.5 | 0.490 | 50 | 0.643 |
| 1.60 | 0.202 | 3.6 | 0.495 | 60 | 0.642 |
| 1.65 | 0.216 | 3.7 | 0.504 | 70 | 0.641 |
| 1.70 | 0.226 | 3.8 | 0.509 | 80 | 0.641 |
| 1.75 | 0.236 | 3.9 | 0.514 | 90 | 0.640 |
| 1.80 | 0.250 | 4.0 | 0.523 | 100 | 0.639 |
| 1.85 | 0.260 | 4.1 | 0.528 | 200 | 0.635 |
| 1.90 | 0.270 | 4.2 | 0.532 | 300 | 0.632 |
| 1.95 | 0.284 | 4.3 | 0.537 | 400 | 0.630 |

Table III. Values of the first and the second approximations of Chapman and Cowling (designated as $[cc]_1$ and $[cc]_2$ respectively) and the first approximation of Kihara (designated as $[K]_1$) for the isotopic thermal separation ratio $[K_T]^*$.

| $T^*$ | $[cc]_1$ | $[cc]_2$ | $[K]_1$ |
|---|---|---|---|
| 0.5 | −0.048 | −0.048 | −0.048 |
| 1.0 | 0.019 | 0.018 | 0.019 |
| 1.5 | 0.169 | 0.165 | 0.173 |
| 2.0 | 0.286 | 0.284 | 0.294 |
| 2.5 | 0.370 | 0.371 | 0.381 |
| 3.0 | 0.434 | 0.439 | 0.448 |
| 3.5 | 0.475 | 0.483 | 0.490 |
| 4.0 | 0.507 | 0.518 | 0.523 |
| 4.5 | 0.529 | 0.543 | 0.546 |
| 5.0 | 0.547 | 0.562 | 0.565 |
| 6.0 | 0.578 | 0.594 | 0.597 |
| 7.0 | 0.591 | 0.608 | 0.610 |
| 8.0 | 0.604 | 0.622 | 0.623 |
| 9.0 | 0.607 | 0.633 | 0.627 |
| 10 | 0.616 | 0.643 | 0.636 |
| 50 | 0.623 | 0.655 | 0.643 |
| 100 | 0.619 | 0.650 | 0.639 |
| 400 | 0.611 | 0.642 | 0.630 |

Hirschfelder, Bird and Spotz⁵⁾ have been utilized to calculated $[K_T]_2^*$. In table III are recorded the computed values of $[K_T]_2^*$ along with $[K_T]_1^*$ values on the two approximation schemes over a wide range of temperatures. It is interesting to note that first approximation expression of Kihara yields values which are in excellent agreement with those obtained from the tedious calculations of Chapman and Cowling second approximation formula. Thus the over-all accuracy of Kihara's expressions seems to be somewhat better and are definitely preferable to the complicated expressions of Chapman and Cowling. Mason⁴⁾ too has arrived at a similar conclusion for his Exp-Six model.

Similar computation have been performed for the thermal and interdiffusion coefficients of binary inert gas mixtures, and these again have established the supriority of Kihara's formulae.

## Acknowledgement

It is a great pleasure to thank Prof. B. N. Srivastava for helpful discussions and to Dr. T. Kihara of the University of Tokyo, Japan, for some useful suggestions. An award of a research scholarship from the Council of Scientific and Industrial Research, New Delhi, is also gratefully acknowledged.

## References

1) S. Chapman and T. G. Cowling: 1952, The Mathematical Theory of Non-uniform gases, Cambridge University Press, England.
2) T. Kihara: 1949, Imperfect gases, originally published in Japanese (Asakura Bookstore, Tokyo) and translated into English by the U.S. Office of Air Research, Wright Patterson Air Force Base.
3) T. Kihara: Revs. Modern Phys. **25** (1953) 831.
4) E. A. Mason: J. Chem. Phys. **22** (1954) 169.

5) J. O. Hirschfelder, C. F. Curtiss and R. B. Bird: 1954, The Molecular Theory of Gases and Liquids, John Wiley & Sons, Inc. New York.
6) S. C. Saxena: Ind. J. Phys. **29** (1955) 453.
7) S. C. Saxena and B. N. Srivastava: J. Chem. Phys. **23** (1955) 1571.
8) S. C. Saxena: J. Chem. Phys. (In course of publication).

---

JOURNAL OF THE PHYSICAL SOCIETY OF JAPAN Vol 11, No. 4, APRIL, 1956

# Adsorption and Surface Potential of Semi-conductors, Part II. Surface Vacancies and its Reaction with Oxygen on ZnS

By Akio KOBAYASHI and Shinji KAWAJI

*Research Institute for Catalysis, Hokkaido University, Sapporo*

(Received October 6, 1955)

The surface potential and its change with illumination for the (110) cleavage surface of zincblende have been measured. It was found that electron trap centers were created near the surface of the crystal, when the crystal was heat-treated in vacuum, and these traps were diminished by the reaction with oxygen. The traps are attributed to sulphur vacancies which are formed by evaporation of sulphur component by the following reasons; (1) the higher the temperature of heattreatment in vacuum, the number of traps becomes the larger and (2) after heat-treatment at 350°C for 4 hours in vacuum, the surface becomes charged positively. It is concluded that oxygen reacts with these traps making the surface to be charged negatively.

An overall change of surface potential in the range between the initial and saturated adsorption agrees fairly well with the initial heat of adsorption observed, as expected theoretically.

## § 1. Introduction

Chemisorbed molecules, which are adsorbed in an ionic form on the surface of semiconductors, induce the opposite charge in the crystal near the surface and thus a barrier layer due to space charge is formed next to the free surface. When the surface is illuminated with light to generate conduction electrons and free holes in the crystal, photo-currents induced in the barrier will produce a change of the surface potential. This is the recently developed method for studying the free surface after Brattain and Bardeen (1). They studied on silicon and germanium, Tanaka and Aoki (2) and Wlerick (3) studied on the surface of the single crystals of cadmium sulphide with this method and found that the surface of CdS was charged negatively either in air or in vacuum. The authors studied previously on ZnS phosphor with Brattain's method and observed enhanced adsorption of oxygen with illumination (4). It was found the change of the contact potential with illumination, $(\Delta\text{c.p.})_L$, increased with oxygen pressures and was always positive showing the work function of the crystal to be decreased with illumination. The results showed the surface of ZnS charged always negatively in oxygen ambient.

In the present paper the authors have studied on the cleavage surface of zincblende which might have more definit nature of the surface than that of the powder of the phosphor studied by the previous paper.

## § 2. Experiments

A natural zincblende crystal used was transparent and slightly straw-coloured. Contact potentials of the cleavage surface (110) of the crystal were measured by the Kelvin method. The geometry of the crystal was $8\times5\ \text{mm}^2$ in area and 0.7 mm thick. The back of the crystal was coated with aquadag to ensure good contact with the lead. Fig. 1 shows the absorption curve of the crystal and

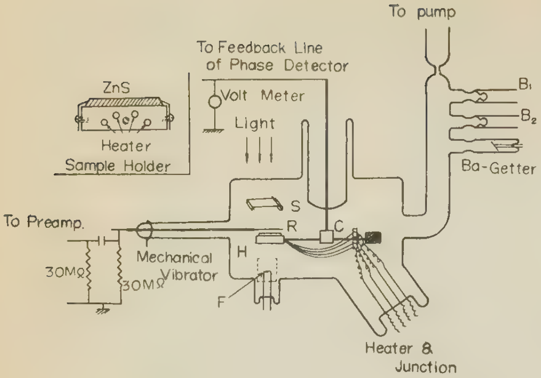

Fig. 1. A sketch of the sealed-off type bulb and an inset showing the sample holder.
$B_1$, $B_2$: Breakable joints to introduce oxygen gas; *F* filament for evaporation of gold; *H*: sample holder; *R*: reed of mesh; *S*: movable screen.

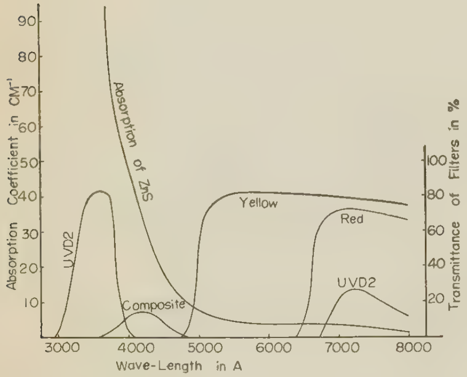

Fig. 2. The absorption curve of the sample of ZnS and spectral transmission of the filters.

the transmission curves of filters employed.

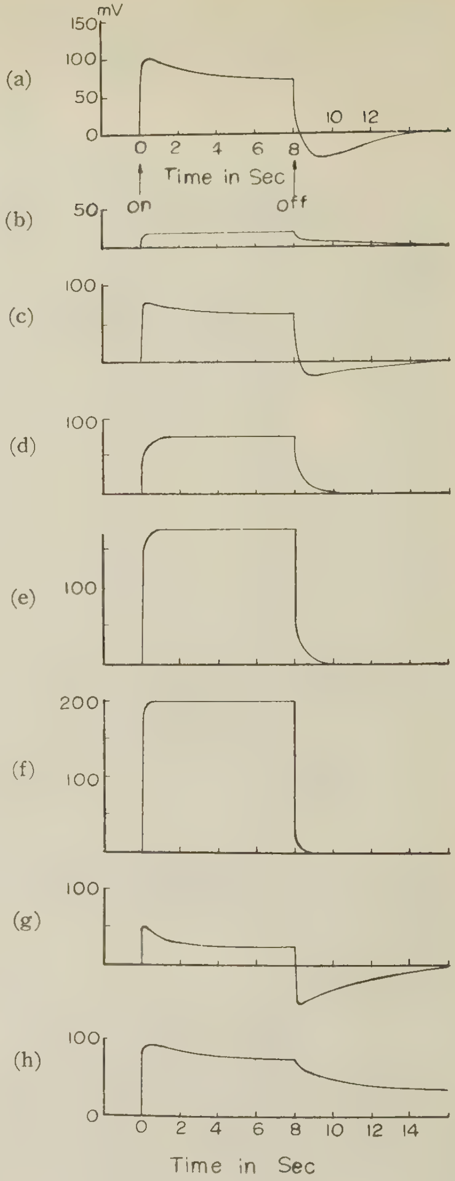

Fig. 3. Variation of rise and decay of the change of contact potential with illumination of 3650 A light for successive treatments.
(a) The fresh crystal evacuated for 2 hours at 180°C, then cooled to room temperature, (b) at 100°C, (c) then cooled to room temperature, (d) evacuated at 200°C for 2 hours, then cooled to room temperature, (e) at pressure of $9\times10^{-4}$ mmHg of oxygen, (f) at $5\times10^{-2}$ mmHg of oxygen, (g) after heattreatment in vacuum and (h) at $2.3\times10^{-3}$ mmHg of oxygen at 85°C.

The sample was first observed being mounted in a bulb of a kinetic vacuum system described in the previous paper, then mounted in a sealed-off-type bulb shown in Fig. 2. In this figure *H* is a sample holder made of a brass block having four filaments to serve for heater in it. Man can rotate the holder around a center rod *C* of 2 mm in dia. with a magnetic device. Temperatures of the holder is measured with a copper-constantan junction. The stem tube of the center rod serves for a small reservoir of liquid nitrogen. The surface is illuminated by light from an ultra high pressure mercury lamp of 500 watts in conjunction with filters through the grid of the reference electrode which is gold-plated and removes 15 per cent of the light. The distance between the reed and the sample is about 1 mm and amplitude of vibration of the reed is about 0.1 mm at resonance.

After carefully preheating and evacuating of the system, the getter is flashed, then the bulb is sealed off. Then gold is evaporated onto the reed from the filament *F*. During this procedure the window for light above the reed is covered by a screen *S* in order to prevent it from darkning. The vibrating reed is driven electromagnetically at its resonant frequency of 310 cps. A self-balancing circuit with phase detection is employed to record the changes of contact potential with ambient and with illumination on oscillograms.

The results obtained with the kinetic vacuum system are shown in Fig. 3 which represents that the time dependence of the change of contact potential with light, $(\Delta c.p.)_L$, depends remarkablly on whether the sample are heat-treated in vacuum or in oxygen atmosphere. When the crystal freshly cleaved was mounted in the bulb and evacuated for 2 hours at 180°C, then cooled to room temperature, the contact potential shown in Fig. 3 (a) overshoots on switching off the illumination of ultra-violet light having a peak of intensity at 3650 A. Fig. 3 (6) shows this overshooting vanishes at higher temperatures about 100°C. The overshooting appears again when the crystal is cooled in vacuum (Fig. 3 (c)).

After standing for six months in air, the crystal was heated in vacuum at 200°C for 2 hours and then cooled to room temperature ((d) in Fig. 3), then oxygen was introduced ((e) and (f)). After sequent heattreatment in vacuum for 2 hours, the overshooting of residual $(\Delta c.p.)_L$ again appeared at low temperature in vacuum and disappeared with introduction of oxygen at 85°C as shown in (g) and (h). It was found from the results of the above experiments that the overshooting of residual $(\Delta c.p.)_L$ disappeared with rising the temperatures of the crystal or with introduction of oxygen at somewhat higher temperatures, say 100°C, and appeared again with heattreatment in vacuum.

In succession of the above-mentioned experiments, the crystal was mounted in the bulb shown in Fig. 2 and evacuated thoroughly at 300°C for several hours, then sealed off from the pumping system. The temperature dependence of the residual $(\Delta c.p.)_L$ and the extinction effects with light with long wave-length were measured and then process of the change of contact potential and $(\Delta c.p.)_L$ resulted from abrupt introduction of oxygen has been observed. Fig. 4 shows oscillograms of $(\Delta c.p.)_L$'s for the sealed-off bulb. The lower curve in this figure shows the surface potential, which reaches an maximum abruptly with illumination of the U. V. light, decreases exponentially with time upto lower value than the initial. After the light is removed, it decreases rapidly furthermore by about 100 mV and then recovers slowly from negative residual $(\Delta c.p.)_L$ to the initial in few minutes. If the crystal be illuminated with the light

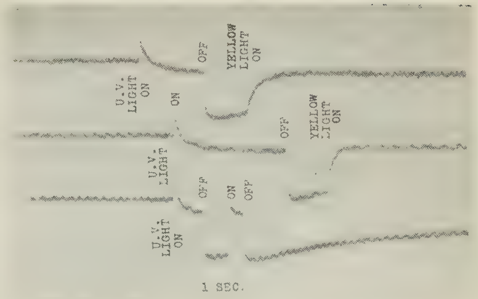

Fig. 4. Oscillograms of overshooting of residual $(\Delta c.p.)_L$ for the sealed-off bulb. The lower curve for switching on and off of the ultra-violet light, the middle curve showing extinction with the yellow light and the upper showing that with a half intensity of the yellow light.

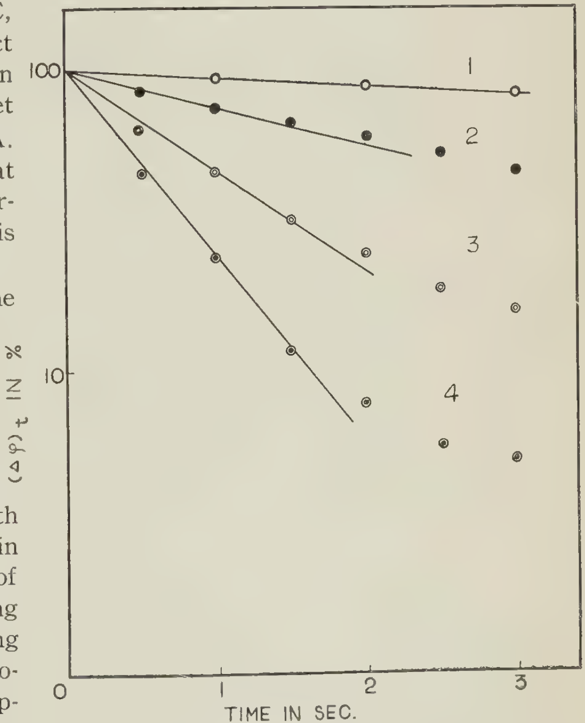

Fig. 5. The initial decays due to extinction of overshooting. Curve 1 for natural (thermal) decay, Curves 2, 3 and 4 for relative intensities of the yellow light 1/4, 1/2 and 1 respectively.

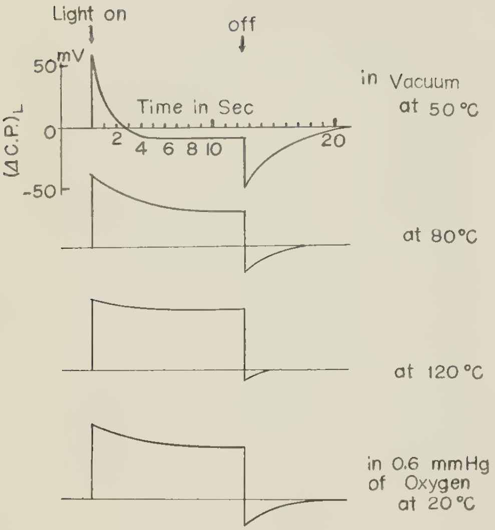

Fig. 6. Temperature dependence of overshooting.

passed through the yellow filter shown in Fig. 1 during this decay of the residual $(\Delta c.p.)_L$, extinction occurs as shown on upper curves of Fig. 4. This effect on the decay occurs also with infra-red light.

Since initial decays of extinction with the yellow light vary almost exponentially with time as shown in Fig. 5, one can obtain decay constants $\tau_L$ for illumination with the yellow light from the following equations denoting natural, i.e. thermal, decay constants as $\tau_0$ and apparent decay constants under illumination of yellow light as $\tau$,

$$(\Delta\varphi)_t=(\Delta\varphi)_0\exp(-t/\tau)$$

$$\frac{1}{\tau}=\frac{1}{\tau_0}+\frac{1}{\tau_L}$$

where $(\Delta\varphi)_0$ is the value of the residual $(\Delta$ c. p.$)_L$ at the beginning of illumination with the yellow light and $(\Delta\varphi)_t$ that after $t$ seconds.

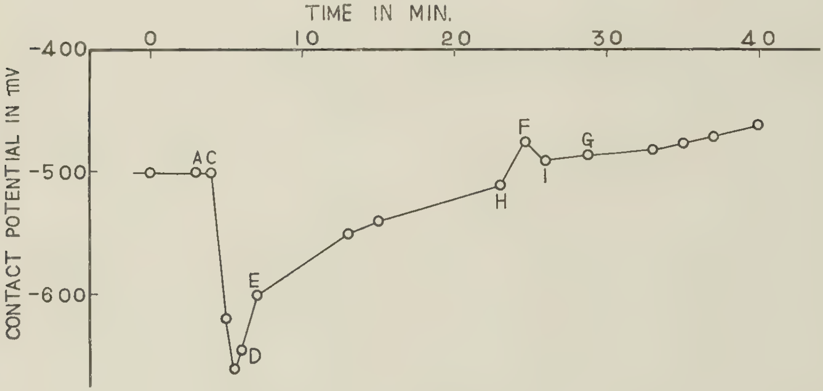

Fig. 7. The change of contact potential due to introduction of oxygen. Oxygen introduced at $C$.

Table I. Decay constants of extinction of the residual $(\Delta$ c.p.$)_L$ under illumination with the yellow light after the U.V. light is removed.

| Relative intensities of the yellow light | |
|---|---|
| 1 | 0.05 sec |
| 1/2 | 0.11 |
| 1/4 | 0.23 |

Using the value 1.1 sec. for $\tau_0$ at 18°C, one can obtain $\tau_L$'s for different intensities of the light as tabulated in Tab. I. It is found in this table $1/\tau_L$'s are propotional to intensity of light.

Since the yellow light also gives rise to the change of contact potential with illumination by an amount of 20 mV, there are some ambiguity in above values, but the rise time of this change is greater by one order of magnitude than the above-mentioned decay constants of extinction. One can, therefore, neglect $(\Delta$ c.p.$)_L$ for the yellow light at the beginning of extinction in the above-mentioned calculation. The overshooting of the residual $(\Delta$c. p.$)_L$ are diminished with rising the temperatures as shown in Fig. 6. From these results the activation of the decay are estimated at about 0.2 eV.

When oxygen was introduced in the bulb through the breakable joint and the sample was heattreated up to about 100°C, the overshooting of the residual $(\Delta$c.p.$)_L$ were vanished at room temperature as same as the above-described experiments with the bulb of the kinetic vacuum system. At the end of the experiments, the current of the heaters inserted into the sample holder was switched off after 2 hours standing at 350°C in vacuum, then oxygen was introduced. This procedure serves to prevent the contamination of the crystal surface by residual gases. The change of contact potential during introduction of the gas is shown in Fig. 7, where the heaters are switched off at the point *C* and at the same time oxygen is introduced. The surface potential decreases to *D* by an amount of 160 mV as soon as the gas is introduced and then turns upwards gradually. The $(\Delta \text{c.p.})_L$'s measured at points *A*, *D*, *E*, *F*, *G*, *H* and *I* during this process are shown in Fig. 8. The light used to measure the $(\Delta \text{c.p.})_L$'s at *A*, *D*, *E* and *F* is the violet light from the mercury lamp in conjunction with a composite filter having a peak of transmission at 4300 A wavelength and having no trace of infra-red light, and the U. V. light is used for *G*, the yellow light for *H* and the red light for *I*. The spectral transmission of these filters are shown in Fig. 1.

## § 3. Discussion of the Results

(A) The change of contact potential due to the introduction of oxygen gas.

It is a characteristic nature of ionic adsorption of gases on the surface of semi-conductors that heats of adsorption decrease rapidly with increase of covering factor, therefore, the adsorption of gases ends with small amounts of covering factor (5)*. For instance, Kwan and Kinuyama (6) have observed on the adsorption of $CO_2$ on ZnO that the differential heats of adsorption decreased from 48 to 35 kcal in the range between the covering factors $\Theta = 0$ and 0.03. The authors (7) also have found on the adsorption of oxygen on the powder of wurtzite type ZnS phosphor that heats of adsorption decrease from 7 kcal to almost zero in the range between $\Theta = 10^{-4}$ and $10^{-2}$.

The origin of such large changes of heats of adsorption can be attributed to rapid increase of electrostatic self-energy of the space charge near the surface due to increase of adsorbed ions. An illustration for this point of view is given in the electronic energy level diagram of Fig. 9, where *E* and $\zeta$ denote the electronic level of an initially adsorbed negative ion and the Fermi level respectively.

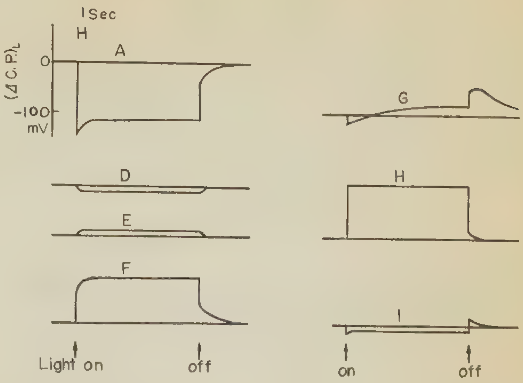

Fig. 8. The $(\Delta \text{c.p.})_L$'s measured at points *A*, *D*, *E*, *F*, *G*, *H* and *I* in Fig. 7. They change the sign after introduction of oxygen.

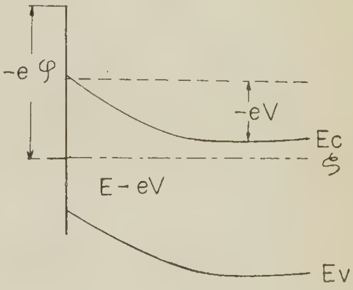

Fig. 9. The electronic energy level diagram near the surface.
$E_c$: the bottom of conduction band, $E_v$ the top of valence band, $\zeta$ the Fermi level, $-e\varphi$ the work function of the crystal, $-eV$ the barrier potential drop due to adsorbed ions and charged surface traps and *E* energy level of an initially adsorbed ion.

From this diagram one can obtain $\zeta - E$ as the initial heat of adsorption. Since with increase of coverage the work function $-e\varphi$ increases by an amount of $-eV$, which is the height of the potential barrier due to space charge and adsorbed ions, *E* becomes $E - eV$ and the heat of adsorption *q* becomes

$$q = \zeta - (E - eV)$$

One would, therefore, find that the adsorption terminates if the work function of the semi-conductor increases by an amount of $-eV = \zeta - E$ with increasing adsorptive ions. This change of the contact potential has been expected by Hauffe and Engel, Aigrain and

---

* One must multiply Airgain and Dugas's values for the maximum adsorption by $\sqrt{2}$, because they overestimate an electrostatic self-energy of surface polarization due to ionic adsorption by a factor of two.

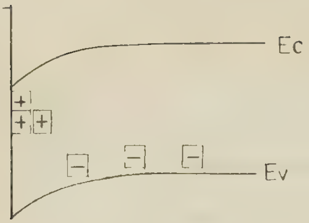

Fig. 10. The electronic energy level diagram near the surface after heavy heattreatment.
$\boxed{+}$ and $\boxed{-}$ denote electron traps of sulphur vacancies and acceptors respectively.

Dugas (5).

In Fig. 7 the change of the surface potential due to introduction of oxygen is 160 mV, i. e. 4 kcal, whereas the authors have found that the initial heat of adsorption of oxygen on the wurtzite ZnS powder is 7 kcal and the overall change of the contact potential due to adsorption is 200 mV, i. e. 5 kcal. Hence one can see qualitatively the expectation comes true. But in the case of Fig. 7 one must take into account both the chemisorption and migration of oxygen into the crystal since the surface is at high temperature at the beginning of introduction of oxygen. No explanation for the increase of c. p. from *D* to *F* can be given, but it seems to be attributed to contamination of grease.

(B) Anion vacancies and the overshooting of the residual $(\Delta \text{c.p.})_L$.

The change of contact potential with illumination, $(\Delta \text{c.p.})_L$, is composed of two photo-electromotive forces; the one part is induced at the potential barrier near the surface and the other induced in the bulk. When the barrier is illuminated with the light giving rise to the internal photo-conduction, photo-currents flow along the field at the barrier, hence a counter electromotive force, which is the former component of the $(\Delta \text{c.p.})_L$, is built up at the barrier. The other part of $(\Delta \text{c.p.})_L$ is due to a photo-voltaic effect caused by diffusion of charge carriers in the bulk. But the most part of the $(\Delta \text{c.p.})_L$ would have to be attributed to the effect at the barrier, since in the case of the present paper $(\Delta \text{c.p.})_L$'s depend remarkably upon the adsorption of oxygen as shown in Fig.'s 3, 6 and 8. One may, therefore, see that the sign of charge of the surface can be determined as positive or negative according to whether the sign of $(\Delta \text{c.p.})_L$ is negative or positive.

Overshooting of the residual $(\Delta \text{c.p.})_L$ is enhanced with heattreatment in vacuum and shows extinction by means of illumination of light with long wave-length and diminishes with rising temperatures. All the results lead us to a conclusion that the overshooting is attributed to trap-centers which are produced by the sublimation of the sulphur constituent near the surface and can trap photo-electrons. Kröger (8) has attributed the traps caused by sublimation of the sulphur constituent to sulphur vacancies. When the crystal be illuminated, electrons will begin to charge the traps of sulphur vacancies at the surface, on the cessation of illumination the photo-voltatic voltage due to photo-currents disappears, then the surface potential decreases by an amount of the contribution of the excess negative charge due to filled electron-traps. This is the reason for the overshooting of contact potential after the light is removed. Garret and Brattain (9) have ascribed the overshooting to photo-enhanced adsorption to which the authors also have done with wrong interpretation (4). But the time constants of $(\Delta \text{c.p.})_L$, both rise and decay, are of two order of magnitude smaller than that of photo-enhanced adsorption and moreover the overshootings appear even in very high vacuum. The effect must, therefore, associate with electronic process rather than ionic process.

If sulphur ions at lattice points near the surface leave the crystal for vacuum, electrons of the sulphur ions may be captured by internal impurity centers forming acceptor levels, e. g. interstitial zinc ions, and thus the surface may be charged positively by an amount of sublimated sulphur as shown in Fig. 10. This point of view is supported by the case of the heavy heattreatment of Fig. 8 where the surface is charged undoubtedly positively, since the $(\Delta \text{c.p.})_L$ in vacuum is negative. When oxygen is introduced into the bulb, the surface becomes charged negatively changing the sign of the slope of the barrier, since the $(\Delta \text{c.p.})_L$ at this time becomes positive with adsorption of oxygen.

Vanishing of overshooting means annihilation of such traps, thus one may conclude that adsorbed oxygen molecules bind with negative ion vacancies near the surface at higher temperatures charging them negatively and thus the function of trapping will be lost. Considering the convers of this conclusion as an extension of the problem, we will reach an important rule that ions should be able to be adsorbed only on the surface vacancies and defects, since only these points have enough large Madelung potential to attract and bind with them.

Usually the surface is charged negatively unless the crystal is heavily heattreated in vacuum, because oxygen in the atmosphere binds with sulphur vacancies and furthermore zinc vacancies, which is effectively negative, are also created at the surface during oxydation. This may be the reason that the $(\Delta \text{c.p.})_L$'s are always positive except the case of Fig. 8. (A), where it has been obtained at the highest heattreatment during this study.

## § 4. Conclusions

It has been studied that the contact potential and its change with illumination vary remarkably with the treatments wether the crystal is heattreated in vacuum or in oxygen. The overshootings of the surface potential on switching off the ultra-violet light and their extinctions with illumination of the yellow light lead us to a conclusion that there are electron traps of sulphur vacancies near the surface and these traps bind with oxygen. As an extension of this conclusion, we will reach an expectation that ions should be able to be adsorbed only on the surface vacancies and defects. An overall change of surface potential in the range between the initial and saturated adsorption agrees fairly well with the initial heat of adsorption as expected.

This study has been supported by the research grant from the Ministry of Education.

### References

1) W. H. Brattain: Semi-Conducting Materials, p. 37 (1951).
W. H. Brattain and J. Bardeen: Bell System Tech. Jour. **32** (1953) 1.
J. Bardeen and S. R. Morrison: Physica **20** (1954) 873.
2) S. Tanaka and M. Aoki: Japanese Jour. of Appl. Phys. **22** (1953) 311 (in Japanese).
3) G. Wlérick: Physica **20** (1954) 1099.
4) A. Kobayashi and S. Kawaji: Jour. Phys. Soc. Japan **10** (1955) 270.
5) P. Aigrain and C. Dugas: ZS. für Elektrochem. **56** (1952) 363.
H. J. Engel and K. Hauffe: ZS. für Elektrochem. **57** (1953) 762, 773.
6) T. Kwan, T. Kinuyama and Y. Fujita: J. Res. Inst. for Catalysis of the Hokkaido Univ. **3** (1953) 31.
7) To be published shortly.
8) F. A. Kröger: Luminescence, p. 58, British J. Appl. Phys. (1954) Supplement 4.
9) C. G. B. Garret and W. H. Brattain: Phys. Rev. **99** (1955) 376.

JOURNAL OF THE PHYSICAL SOCIETY OF JAPAN Vol. 11, No. 4, APRIL, 1956

# On the Application of the Thomas-Fermi-Dirac Method to the Study of the Residual Resistance of Binary Alloys containing Foreign Atoms in small Concentrations

By Hiroshi FUJIWARA

*Department of Physics, Faculty of Science, University of Tokyo*

(Received November 15, 1955)

By taking the exchange interaction among electrons which was neglected in our previous work, into account, modified screened potential around the substitutional impurities of di- or trivalent metal in monovalent metal in dilute solid solution is exactly obtained from the Thomas-Fermi-Dirac type equation by numerical integration.

As one of the applications of our obtained potential, we took the residual resistance due to the foreign atoms. We use the method of partial waves together with the Born approximation for the calculation of the scattering cross section and the residual resistance is calculated. The disagreement of theoretical values with experiment has been greatly improved by introducing the exchange effects.

## §1. Introduction

In the previous paper, to be referred as I hereafter[1], we have treated the problem about the non-periodic charge distribution around the dissolved atoms in an alloy which contains such dissolved foreign atoms in the form of dilute solid solution.

As is well known, in such an alloy, the dissolved atoms form impurity centres around which the charge distribution of electrons deviates from the periodic one which is characteristic of the pure solvent metal. Therefore, it is important to find such non-periodic charge distribution as exactly as possible for the theoretical interpretation of several physical problems concerning alloys[2].

In I, we investigated the case where the di- or trivalent metal existed as a substitutional impurity in monovalent metals, and using thus obtained modified screened Coulomb potential around an impurity atom, we computed the increase of the electrical resistance due to those dissolved foreign atoms. In part I, we took the Thomas-Fermi type equation as the starting fundamental equation. We tried to find the much accurater solution of the problem than the usual one, that is, we solved the non-linear differential equation of the T. F. exactly by numerical integration*, instead of solving the equation approximately by linearization. And we used the method of partial waves as well as the Born approximation in order to obtain the scattering cross section. However, our model was still a simple one as far as we neglected the exchange interaction among electrons as in Mott's original work on this problem[3].

As the result of this calculation, we find that our modified screened potential reduces the disagreement between theoretical and experimental values of residual resistance, when we use the Born approximation at the same time. However, if we improve the calculation of the scattering cross section by employing the method of partial waves instead of the Born approximation, the theoretical values of residual resistance becomes too large.

In this paper, we shall take the exchange interaction among electrons into account, i.e., instead of the Thomas-Fermi type equation, we take the Thomas-Fermi-Dirac type equation[4] as the starting fundamental equation. Solving this equation by numerical integration, we obtain the new screened Coulomb potential and using this potential, the subsequent calculations of the residual resistance are carried out in the same way as in I.

And we find that the disagreement which has remained in the previous work between the theory and experiment can be diminished by introducing the exchange interaction.

---

* Recently, L. C. R. Alfred & N. H. March reported about this problem (Phil. Mag. **46** (1955) 759) and their results consist with our previous work (without exchange).

## A. Modified Screened Potential

### § 2. Fundamental Equation

In the dilute solid solution which consists of two metals with different valencies, the whole charge distribution is not uniform on account of the presence of the foreign atoms.

For example, if a small quantity of divalent metal Cd is dissolved in the monovalent metal Ag, $Cd^{++}$ ion has one excess positive charge compared with the body $Ag^{+}$ ion. So, the conduction electrons are attracted to the impurity centre so as to screen the excess charge.

We regard this excess positive charge which represents the difference between the atomic valency of the dissolved and that of the solvent metal as a point charge localized near the nucleus of the impurity atom. Although the nature of rest positive charge depends on the kind of the solvent and dissolved atoms, we assume, in the first approximation, that the rest positive charge is distributed with a uniform density $\rho_+$.

For treating our problem, we take the Thomas-Fermi-Dirac type equation as our starting equation.

Then the electrostatic potential $\Phi(r)$ around the dissolved atom is now determined from the following Poisson's equation:

$$\nabla^2\Phi=-4\pi\rho_+ +4\pi e n(r)\,, \tag{1}$$

where $n(r)$ is given by the formula:

$$\left(\frac{8\pi}{3h^3}\right)\left\{\frac{2e^2m}{h}+\left[\frac{4e^4m^2}{h^2}+2em\Phi(r)\right]^{1/2}\right\}^3. \tag{2}$$

We assume the radial symmetry and introduce the new dimensionless variables $\phi$, $x$ which are related to $\Phi$, $r$ by

$$\Phi(r)+\frac{2e^3m}{h^2}=\frac{e}{r}\phi \tag{3 a}$$

$$r=ax\,, \tag{3 b}$$

where $a$ is:

$$a=\frac{1}{2}\left(\frac{3\pi}{4}\right)^{2/3}\frac{h^2}{me^2}=0.885\,a_H\,.$$

$$(a_H\text{: Bohr radius}) \tag{4}$$

With these substitutions, the equation (1) takes the following dimensionless form:

$$\frac{d^2\phi}{dx^2}=x\left[B+\left(\frac{\phi}{x}\right)^{1/2}\right]^3-xA^{3/2}\,, \tag{5}$$

where

$$A^{3/2}=\left(\frac{3\pi}{4}\right)^3\left(\frac{Z_0}{2\pi}\right)\left(\frac{a_H}{r_0}\right)^3 \tag{6 a}$$

$$B=\left(\frac{3}{32\pi^2}\right)^{1/3}. \tag{6 b}$$

Here, $A$ is a new constant which has been introduced in I, and depends only on the kind of the solvent metal, $Z_0$ and $r_0$ being atomic valency and atomic radius in Å of the solvent atom respectively. Equation (5) reduces to the Thomas-Fermi equation in the former case, if we put $B=0$.

It we denote by $Z$ the difference between the atomic valency of the dissolved and that of the solvent metal, the boundary conditions of $\phi$ are given as follows:

$$x=0,\qquad \phi=Z \tag{7 a}$$

$$x\to\infty,\qquad \phi\to k^2x, \tag{7 b}$$

where $k=A^{1/2}-B$.

### § 3. The Solution of the Equation (5)

The following computation is performed by the same method as in the previous paper, i.e.,

We shall consider the form of solution $\phi$ of (5) by dividing the whole range $0<x<\infty$ in the following two regions: (i) in the neighbourhood of $x=0$, (ii) in the region of large $x$, and finally, to simplify our subsequent analysis, we shall try to put these two solutions in one expression over the whole region of $x$.

(i) Near the origin, we cannot use the Taylor expansion[5], because $\phi''$ is infinite at the origin. Instead of that, we use the follwing expansion for small $x$, which satisfies the boundary condition (7 a):

$$\begin{aligned}\phi=&Z+c_2x+\frac{4}{3}Z\sqrt{Z}\,x^{3/2}\\&+\frac{3}{2}BZx^2+\frac{4}{15}\left[3B^2\sqrt{Z}+\frac{3}{2}\sqrt{Z}\,c_2\right]x^{5/2}\\&+\frac{1}{6}[2Z^2-A^{3/2}+B^3+3Bc_2]x^3+\cdots\,,\end{aligned} \tag{8}$$

where $c_2$ is an adjustable parameter, which gives the starting slope at the origin.

We perform the numerical integration from the origin to large $x$ for several different numerical values of $c_2$ and try to find the numerical value of $c_2$ corresponding to the correct solution of equation (5), which satisfies the boundary condition (7 b) as well as (7 a).

The behaviors of variation of $\phi$ with $c_2$ thus obtained are shown in Fig. 1.

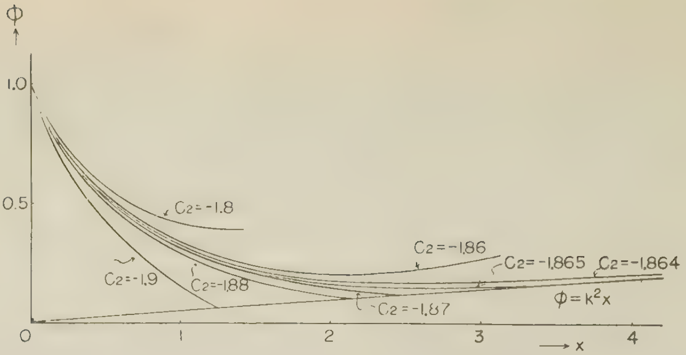

Fig. 1. The behaviors of variation $\phi$ with $c_2$. Solvent metal is Ag and $Z=1$.

(ii) When $x$ is large, $\phi$ can be written asymptotically in the form:

$$\phi=k^2x+y\,, \tag{9}$$

$y$ being small.

$y$ can be expressed with two integration constants $B_1$ and $B_2$ as:

$$y=B_1\exp(-\beta_1'x)+B_2\exp(+\beta_1'x)\,, \tag{10}$$

where $\beta_1'=\sqrt{\frac{3}{2}\frac{A}{k}}$.

As stated in I, $B_1$ and $B_2$ are determined by joining smoothly the numerical solution obtained in (8) with (9) for each assumed value of $c_2$. For the correct solution, $B_2$ must be zero. In this way, $c_2$ and $B_1$ corresponding to the correct solution can be determined. Hereafter, we denote them by $m_0$ and $\alpha_1$ respectively.

Thus $\phi$ can be expressed by the following formula:

(a) when $x$ is small:

$$\phi=Z+m_0x+\frac{4}{3}Z\sqrt{Z}\,x^{3/2}+\frac{3}{2}BZx^2+\frac{4}{15}\left[3B^2\sqrt{Z}+\frac{3}{2}\sqrt{Z}\,m_0\right]x^{5/2}+\frac{1}{6}[2Z^2-A^{3/2}+B^3+3Bm_0]x^3+\cdots\,. \tag{11}$$

(b) when $x$ is large:

$$\phi=k^2x+\alpha_1\exp(-\beta_1'x)\,. \tag{12}$$

For the convenience of our further calculations, it is desirable to express these two formulas (11) and (12) by one analytical form which is valid over the whole region of $x$.

Thus, we find the following expression of $\phi$, which represents (11) and (12) with sufficient accuracy.

$$\phi=k^2x+\alpha_1\exp(-\beta_1'x)+(Z-\alpha_1)\times\exp(-\beta_2'x)+\alpha_2'x\exp(-\beta_3'x)\,. \tag{13}$$

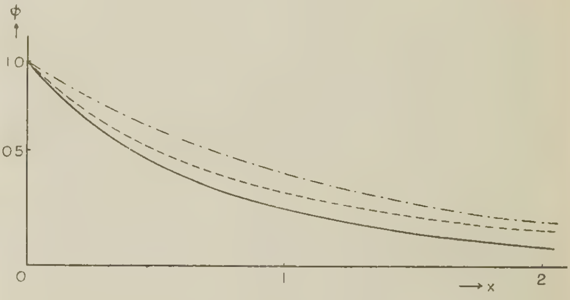

Fig. 2. Curves of $\phi$ for several cases.
(Solvent metal is Ag and $Z=1$)
—— with exchange
– – – – without exchange
–·–·– $Z\exp(-qax)$

Our modified screened Coulomb potential is therefore expressed as follows:

$$V(r)=-\frac{e^2}{r}[\alpha_1\exp(-\beta_1r)+(Z-\alpha_1)\times\exp(-\beta_2r)+\alpha_2r\exp(-\beta_3r)]\,, \tag{14}$$

where

$$\alpha_2=\frac{\alpha_2'}{a},\quad \beta_1=\frac{\beta_1'}{a},\quad \beta_2=\frac{\beta_2'}{a}\ \text{and}\ \beta_3=\frac{\beta_3'}{a}.$$

To compare our modified screened potential with that of the previous one and the usual one $\left(V(r)=-\frac{Ze^2}{r}\exp(-qr)\right)$, these three curves are shown in Fig. 2.

For convenience, we plott in the dimensionless coordinates $(\phi, x)$. We find that the curve of $\phi(x)$ obtained in I (without exchange) is further lowered by taking the exchange effect into acount.

Our obtained values of $A^{3/2}$, $m_0$, $k^2$, $\alpha_1$ etc. are tabulated in Table I and Table II. In these tables, those values obtained in I are also retabulated in parenthesis. The solvent metals are Ag and Cu and $Z=1$.

Table I. The values of $A^{3/2}$, $m_0$, $k^2$ and $\sqrt{\frac{3}{2}\frac{A}{k}}$.

| Z | Solvent | $A^{3/2}$ | $m_0$ | $k^2$ | $\sqrt{\frac{3}{2}\frac{A}{k}}$ |
|---|---|---|---|---|---|
| 1 | Ag | 0.0762 | −1.8647<br>(−1.4939) | 0.0405<br>(0.1798) | 1.1272<br>(0.7975) |
|  | Cu | 0.1093 | −1.8453<br>(−1.4615) | 0.0709<br>(0.2286) | 1.1347<br>(0.8469) |

Table II. The values of the coefficients $\alpha_l$ and $\beta_l$.

| Solvent | $\alpha_1$ | $\alpha_2$ | $\beta_1$ | $\beta_2$ | $\beta_3$ |
|---|---|---|---|---|---|
| Ag | 0.8384<br>(0.7476) | −0.427<br>(−0.491) | 2.41<br>(1.71) | 7.05<br>(4.70) | 10.7<br>( 7.9) |
| Cu | 0.8333<br>(0.7724) | −0.427<br>(−0.448) | 2.42<br>(1.81) | 7.37<br>(4.80) | 14.9<br>( 7.5) |

The values in parenthesis are those obtained in our previous work (without exchange).

## B. Residual Resistance due to the Foreign Atoms

### § 4. Scattering Cross Section by the Foreign Atoms

In the course of considering the elastic scattering of electrons by a foreign atom which is represented by our screened Coulomb potential $V(r)$, the calculation of the differential cross section $I(\theta)$ is carried out by the method of partial waves as well as the Born approximation.

The total cross section $\sigma$ which is effective for our case is:

$$\sigma=2\pi\int_0^\pi I(\theta)(1-\cos\theta)\cdot\sin\theta\,d\theta\ , \qquad (15)$$

where the differential cross section $I(\theta)$ is given as $|f(\theta)|^2$ by the scattering amplitude $f(\theta)$.

(i) The Born approximation

The scattering amplitude $f_B(\theta)$ for the Born approximation is given by:

$$f_B(\theta)=-\frac{2m}{\hbar^2}\int_0^\infty V(r)\frac{\sin Kr}{K}rdr\ , \qquad (16)$$

where $K=2k\sin\frac{1}{2}\theta$ and $k=2\pi mv/h$. Here, $V(r)$ is (14), but hereafter we shall neglect the third term in (14) for its small magnitude. For our purpose of calculation, the scattering of electrons at the Fermi surface is important, so we have $k=1.92/r_0$ after introducing the numerical values, $r_0$ being the atomic radius of the solvent metal in Å.

(ii) The method of partial waves

Since the de Broglie wavelength for electrons $\lambda=2\pi/k$ near the Fermi surface is fairly large in comparison with the force range due to impurity centre, the legitimacy of the Born approximation is doubtful, so we have calculated the cross section also by the method of partial waves.

The exact expression for the scattering amplitude is given by:

$$f(\theta)=\frac{1}{2ik}\sum_{l=0}^{\infty}(2l+1)\{\exp(2i\eta_l)-1\}P_l(\cos\theta)\ , \qquad (17)$$

where $\eta_l$ is the phase shift of the $l$ th order. The direct use of this formula would require rather tedious numerical evaluation of a fairly large number of the phase shifts $\eta_l$, but since the higher phase shifts are small, they can be replaced by the corresponding quantities given by the Born approximation. In fact, the scattering amplitude $f_B(\theta)$ in the Born approximation can be written in terms of partial amplitude of different orders as follows

$$f_B(\theta)=\frac{1}{2ik}\sum_{l=0}^{\infty}(2l+1)(2i\zeta_l)P_l(\cos\theta) \qquad (18)$$

$$\zeta_l=-\frac{\pi m}{\hbar^2}\int_0^\infty V(r)[J_{l+1/2}(kr)]^2r\cdot dr\ . \qquad (19)$$

and, for partial waves of higher order, $\exp(2i\eta_l)-1$ are closely approximated by $2i\zeta_l$. Hence $f(\theta)$ in (17) can be obtained from $f_B(\theta)$ by correcting only lower order phase shifts:

$$f(\theta)=f_B(\theta)+\frac{1}{2ik}\sum_{l=0}^{l'}(2l+1)$$
$$\times[\{\exp(2i\eta_l)-1\}-2i\zeta_l]P_l(\cos\theta)\ , \qquad (20)$$

where the series converge very rapidly. It has been found sufficient to take only two terms $l=0$ and 1.

$\zeta_l$ is obtained by the following formula by the use of the formulas about the Bessel functions:

$$\zeta_l=\frac{1}{a_H\cdot k}\left\{\alpha_1Q_l\left(1+\frac{\beta_1^2}{2k^2}\right)+(Z-\alpha_1)Q_l\left(1+\frac{\beta_2^2}{2k^2}\right)\right.$$
$$\left.+\frac{\alpha_2\beta_3}{k^2}\frac{d}{dX}Q_l(X)\right\};\quad X=1+\frac{\beta_3^2}{2k^2}\ . \qquad (21)$$

$\eta_l$ can be obtained by numerical calculation in the usual way and for full information, the readers are referred to the previous paper I.

(iii) Total cross section

The total cross section $\sigma$ can be expressed by the sum of three terms $\sigma_1$, $\sigma_2$ and $\sigma_3$ as follows;

Table III. The values of $\eta_l$ and $\zeta_l$.

| Solvent | $\zeta_0$ | $\zeta_1$ | $\zeta_2$ | $\eta_0$ | $\eta_1$ | $\eta_2$ | Fridel sum $\frac{2}{\pi}\sum(2l+1)\eta_l$ |
|---|---|---|---|---|---|---|---|
| Ag | 0.4742<br>(0.6995) | 0.0531<br>(0.1181) | 0.0075<br>(0.0250) | 0.8538<br>(1.1374) | 0.0599<br>(0.1349) | 0.0079<br>(0.0262) | 0.676<br>(1.064) |
| Cu | 0.4895<br>(0.6885) | 0.0637<br>(0.1249) | 0.0080<br>(0.0284) | 0.8232<br>(1.0705) | 0.0736<br>(0.1420) | 0.0082<br>(0.0276) | 0.691<br>(1.041) |

Table IV. The values of $\sigma_l$ and $\sigma$ ($10^{-16}\text{cm}^2$)

| Solvent | $\sigma_1$ | $\sigma_2$ | $\sigma_3$ | $\sum\sigma_l$ | $\sigma$ |
|---|---|---|---|---|---|
| Ag | 0.246<br>(0.474) | −0.021<br>(−0.521) | 0.429<br>(1.052) | 0.654<br>(1.005) | 4.11<br>(6.31) |
| Cu | 0.194<br>(0.353) | −0.030<br>(−0.332) | 0.310<br>(0.690) | 0.474<br>(0.711) | 2.98<br>(4.47) |

Table V. Tables for $\Delta\rho$ (microohm·cm)

| Used screened potential | | Calculated values: Born approximation, Solvent Ag | Born approximation, Solvent Cu | Partial waves, Solvent Ag | Partial waves, Solvent Cu |
|---|---|---|---|---|---|
| Our modified | with exchange (this time) | 0.75 | 0.67 | 2.01 | 1.67 |
| | without exchange (previons work) | 1.45 | 1.14 | 3.09 | 2.50 |
| Usual type without exchange $V(r)=-\frac{Ze^2}{r}\exp(-qr)$ | | 2.20 | 1.88 | 4.34 | 3.28 |

Experimental values
Cd in Ag 0.38 Zn in Ag 0.62
Cd in Cu 0.21 Zn in Cu 0.34

$$\sigma=2\pi\{\sigma_1+\sigma_2+\sigma_3\}, \qquad (22)$$

where $\sigma_1$ is the term due to the Born approximation and $\sigma_2$ and $\sigma_3$ are the terms which are introduced by using the formula (20). Terms $\sigma_i$ correspond to $I_i$ in the previous paper I. The full information about the calculation and the explicit expression for $\sigma_i$ are given in I.

Thus we obtained $\eta_l$, $\zeta_l$ and $\sigma_i$ in the same way as in I. Our calculated values of $\eta_l$, $\zeta_l$ and $\sigma_i$ are tabulated in Table III and IV. For the sake of comparison, we retabulated those corresponding values which were obtained in the previous work.

## § 5. Residual Resistance due to the Foreign Atoms

If we denote by $p$ the atomic ratio of dissolved metal to the solvent one, the increase $\Delta\rho$ of the electrical resistance due to the substitutional impurity is given by:

$$\Delta\rho=\left(\frac{mv}{e^2}\right)p\cdot\sigma=78\cdot p\left(\frac{\sigma}{r_0}\right)\text{microohm. cm.} \qquad (23)$$

where $\sigma$ is to be expressed in the unit of $10^{-16}$ cm². As the standard concentration, we take $p=1/100$.

Calculated values of $\Delta\rho$ are tabulated in Table V together with those values which have been obtained for other two screened potentials: the one is our previous one without exchange and the other is the one which was obtained from the linearized equation, i.e., $V(r)=-\frac{Ze^2}{r}\exp(-qr)$.

## § 6. Results and Discussions

In this paper, the exchange interaction among electrons which was neglected in the previous paper I, is taken into account, i.e., we take the Thomas-Fermi-Dirac equation as the starting equation.

Considering our results together with the previous ones, the following conclusions are obtained.

At first, a fairly remarkable improvement has been made by introducing the exchange effect in comparison with the previous case in which this effect was neglected. And we find that our results are improved step by step in accordance with the procedures for solving our problem, i.e., solving (i) analytically from the linearized equation without exchange, (ii) exactly by numerical integration, (iii) from the equation in which the exchange effect has been taken into account and in the same way as (ii).

It is true that our calculated values have been much improved both for the cases of using the Born approximation and the method of partial waves, but, as was the case in I, the values obtained by the latter method are still greater than those obtained by the former one. But, from the purely theoretical viewpoints, we can not find any reason for which the Born approximation should yield more reliable results than the method of partial waves. In fact, the validity condition $k/q \gg 1$ ($q$ is the screening constant in the potential $V(r) = -\frac{Ze^2}{r}\exp(-qr)$) is hardly satisfied in our case, so that the method of partial waves would be preferable.

As stated in the previous paper, our starting model is an approximated one for the actual case, i.e., we have neglected the details of the charge distribution due to the difference of the values $\rho_+$ due to the kind of the dissolved atoms of the same valency. Therefore, when we improve the above-mentioned shortcoming of our model in our further study, we expect that the agreement between the experimental values and theoretical values which are obtained by the method of partial waves will be much better than the one between experiment and theoretical values which are calculated by the Born approximation.

The considerations about these points are still to be taken into account in our further study on this kind of problem.

As Cd–Ag and Zn–Cu are neighbouring elements in the periodic table and the valence electrons are in 4s in Zn, Cu and in 5s in in Cd, Ag, the behaviors of ion cores of both solvent and dissolved metals will be similar in the solid solution Cd–Ag and Zn–Cu. But conversely, for the case of Cd in Cu and Zn in Ag, the behaviors of ion cores do not resemble. Taking these circumstances into account, we may be allowed to expect that the theoretical values which would be obtained in our further study will agree with the experimental ones more closely in the case of Cd in Ag and Zn in Cu than in the case of Zn in Ag and Cd in Cu.

Finally we shall discuss about the Friedel sum*. Friedel$^{6)}$ has proved that the sum $(2/\pi)\Sigma(2l+1)\eta_l$, where $\eta_l$ is the phase shift of the $l$ th order partial wave for electrons at the Fermi surface, is equal to the extra number of electrons attracted by the impurity centre, provided that the exchange interaction is negligible. Since in metals, the screening must be complete, Friedel-sum must be equal to the excess charge $Z$ of the impurity centre

$$\frac{2}{\pi}\Sigma(2l+1)\eta_l = Z$$

neglecting the exchange interaction. In the rightest column of Table III in parenthesis, we have tabulated this sum using the phase shifts obtained in our previous work (without exchange), which shows that Friedel sum is actually close to one. Small deviation from 1, of the order of a few %, may be due to the fact that we did not use the band-theoretical procedures of costructing the wave-function for individual electron, but employed the method of Thomas-Fermi to find the form of the potential function. The fact that the deviation is very small may be interpreted as indicating the self-consistency of this procedure. However, when the exchange interaction is introduced, there is no reason that the relation $Z$=Friedel-sum must be true. And our results show that the deviation from this rule is actually fairly remarkable.

## § 7. Acknowledgment

The author wishes to express his sincere thanks to Prof. M. Kotani for his continued guidance and encouragement throughout this work and also to Prof. Blatt who kindly discussed about this work and many thanks are also due to Drs. D.K.C. MacDonald and G.K. White of National Research Council, Ottawa, Canada for their kind discussions.

## References

1) H. Fujiwara: J. Phys. Soc. Japan **10** (1955) 339, 727.
2) K. Huang: Proc. Phys. Soc. **60** (1948) 161.
K. I. Arafa: Proc. Phys. Soc. **B 62** (1949) 238.
J. Friedel: Phil. Mag. **43** (1952) 153; Advances in Physics **3** (1954) 447.
Shinohara and Toya: Butsuseiron-Kenkyu in Japanese No. 55 (1952).
D. K. C. MacDonald and G. K. White:
1. Reprint of a paper to be delivered at the First International Instrument Congress and Exposition of the Instrument Society of America, September 13–23, 1954.
2. Phil. Mag. **45** (1954) 491.

---

* The author owes to Prof. Blatt (Illinois University) kind discussion about the Friedel-sum and his unpublished datas given through his private communication.

Edward I. Salkovitz and A. I. Schindler: Phys. Rev. **98** (1955) 543.

3) N. F. Mott: Proc. Camb. Phil. Soc. **32** (1936) 281.

4) J. C. Slater and H. M. Krutter: Phys. Rev. **47** (1935) 559.

5) V. Bush and S. H. Caldwell: Phys. Rev. **38** (1931) 1898.
L. C. R. Alfred and N. H. March: Phil. Mag. **46** (1955) 759.

6) J. Friedel: loc. cit.

---

JOURNAL OF THE PHYSICAL SOCIETY OF JAPAN Vol. 11, No. 4, APRIL, 1956

# Deformation of Thin Copper Crystals

By Hideji SUZUKI, Susumu IKEDA and Sakae TAKEUCHI

*The Research Institute for Iron, Steel and Other Metals,*
*Tohoku University, Sendai*

(Read October 15, 1955; Received December 2, 1955)

Stress/strain curves of many number of copper crystals having various radii from 0.06 to 1 mm were measured. The range of easy glide increases considerably when the radius of crystal decreases. In the case of suitably oriented crystal the range of easy glide reaches to 50 per cent in shear, when the radius of crystal decreases less than 0.1 mm. The extrapolation of the range of easy glide to the infinitesimal radius gives a value between 40 to 80 per cent in shear irrespectively to the initial crystal orientation. The hardening rate in the easy glide region considerably decreases with the decreasing crystal radius. Meanwhile, the critical shear stress, the stress required for the transition from the easy glide to the rapid hardening region, the hardening rate in rapid hardening region reveal only slight dependence on the crystal radii, i.e. the former two slightly increase and the last slightly decreases with the decreasing crystal radii. These results are discussed qualitatively by introducing a concept 'mean free path of dislocations' in a crystal.

## § 1. Introduction

Dislocation loops multiplied from a Frank-Read source[1] proceed in a usual crystal over finite area of the slip plane on account of the increasing resistance caused by the formation and migration of jogs[2][3]. Those multiplied dislocations exert back stress on the swept area of the slip plane, and the source ceases its action. One of the authors[4] has pointed out that the large slip as first observed by Heidenreich and Shockley[5] takes place through the co-operative action of Frank-Read sources situated in a thin zone parallel to the slip plane. This idea for the explanation of large slip has been appeared in many papers[2][6][7][8] independently, and implied that the dimension of crystal in a direction along the active slip plane must have large effects on the work-hardening of the crystal. Measurements made hitherto, however, have paid little attention to the role of specimen size, and have been carried out on crystals having certain dimension determined by the technique of the preparation of single crystals.

The experiments on single crystals of copper described in the following pages were carried out with the object throwing light on the mechanism of deformation in easy glide and rapid hardening regions, by systematic investigation of the effect of crystal radius on work-hardening.

## § 2. Preparation of Crystals

The single crystals of copper were grown from electrolytic copper about 99.98 per cent pure. Those copper wires of 1.7 mm diameter were inserted into porcelain tubes which were 2 mm in inner diameter, 10 or 30 cm in length and closed in the one end by alumina including some amount of clay. The crucible containing the copper wire was doubly protected from atmosphere by two silica tubes and made pass through an electric furnace. In order to avoid the reaction between the porcelain tube and molten copper, the porcelain tubes were previously dipped in aqueous solution of suger and were dried in air for a few days. The crucibles containing the copper wires were lowered at a rate of 3 cm $\text{min}^{-1}$. The porcelain tubes were then cracked gently by a pinchers, and were removed from the copper crystals. When sufficiently porous tubes were used, the yield of perfect crystals exceeded 80 per cent and the remainder contained small angle boundaries in the direction of growth.

The crystal orientations were determined by optical figure method extensively developed by Yamamoto and Watanabe[9]. Using their method it is not difficult to determine the orientations of several tens crystals in a day. The observed crystal orientations are plotted stereographically in Fig. 1.

The crystals were annealed in vacuum (about $10^{-4}$ mm Hg) at 1000°C for three hours after orientation determination. The crystals with radii of about 1 mm were electro-polished using 30 per cent ortho-phosphoric acid in water before deformation.

The thin crystals less than 0.5 mm in radii were produced from those annealed 1 mm crystals by etching in dilute nitric acid, after cutting the long crystal into pieces having suitable lengths by a pinchers. By means of careful etch, thin crystals with uniform cross sections as small as 0.01 $\text{mm}^2$ were obtained. The cross section of an etched crystal was usually of an elliptic shape, eccentricity of which depended on crystal orientation. Those thin crystals were then polished electrolytically using 30 per cent ortho-phosphoric acid in water, putting on a hook made of the same purity copper wire, which was connected to positive electric source. The crystals were then washed by water, dried in air and then set on the testing machine, which will be described in the next section, by 'De Khotinsky cement' the paste for high vacuum. The examined crystals, therefore, were not subjected to high temperature annealing after the etching.

The term 'radius of crystal' will be used in the following to denote the radius of a circle having the same area with the cross section of the crystal. The part of a crystal between guage markings was clipped by a nail-scissors after deformation and then measured the weight by a chemical balance. The cross section is obtained from the weight of the crystal assuming a uniform cross section over the guage length.

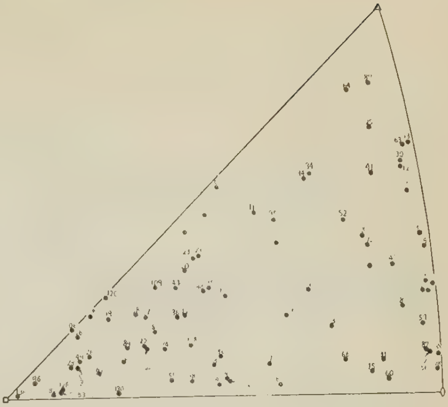

Fig. 1. Stereographic projection of crystal orientations.

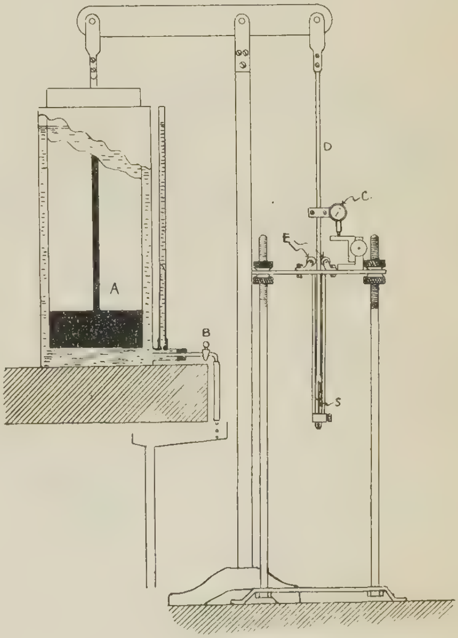

Fig. 2. Schematic representation of the tensile machine used for crystals of about 1 mm in radius.
A: Counter balance. B: Cock to control the loading rate. C: Dial-gauge. D: Pulling rod. E: Roller. S: Specimen.

## § 3. Stress/strain Measurement

Two tensile machines were used according

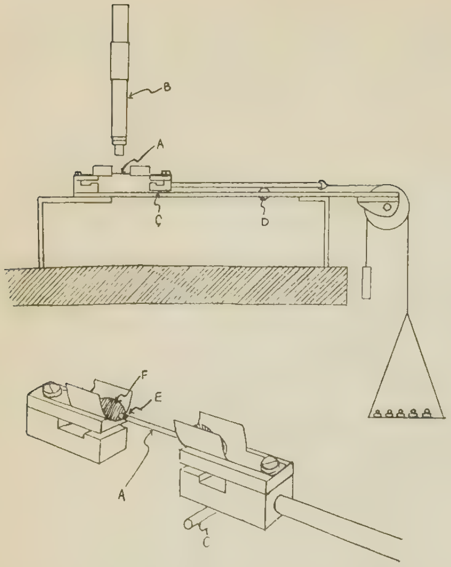

Fig. 3. Schematic representation of the tensile machine used for thin crystals less than 0.5 mm in radius.
A: Specimen. B: Travelling microscope to measure the elongation of crystal. C and D: Roller. E: Gauge marking. F: De Khotinski cement.

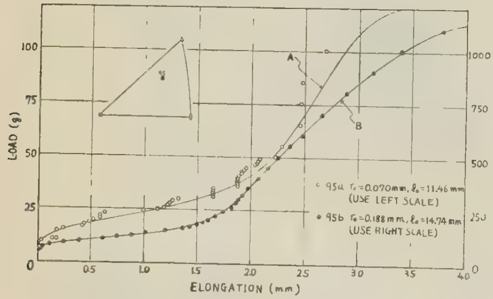

Fig. 4. Load/elongation curves obtained by the testing machine for thin crystals.

to the required stress range. The machine shown in Fig. 2 can be loaded up to 50 Kg by decreasing the buoyoncy of the counter balance A. The load is proportional to the relative displacement of the counter balance to the water level. The loading rate is propotional to the rate of flow from the water tank, which is controlled by the degree of turning the cock B. The loading is thus continuous in the machine shown in Fig. 2. The elongation was read by the dial-guage C attatched at the pulling rod D.

The machine shown in Fig. 3 was used for thin crystals less than 0.5 mm in radii. The maximum load applicable to this machine is about 10 Kg. The tension was applied on the crystal through adding wire pieces, each of which is of 1 g in weight, in the initial region of deformation. The elongation was measured on the guage length between two markings drawn by ink on the crystal A, using a travelling microscope B. The accuracy of the load was 1 g in the best condition, but in many cases there was greater error than this on account of friction by dusts attatched to the roller, ball bearing, etc. during the measurement.

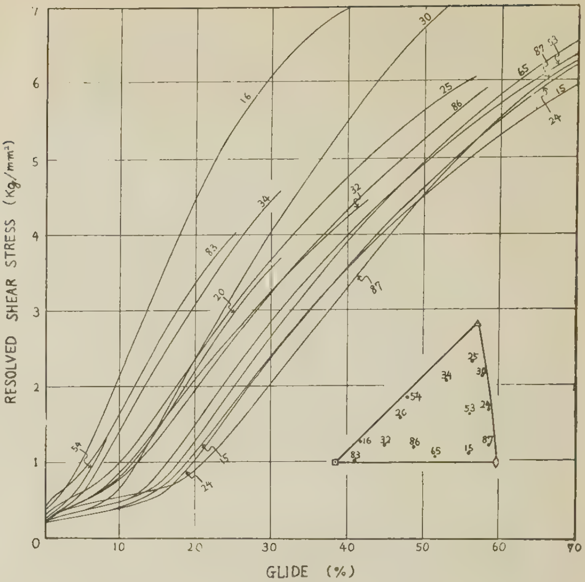

Fig. 5. Shear stress/glide relations of some crystals of about 1 mm in radii.

Fig. 4 shows a few examples of load/elongation curves, by which the accuracy of loading can be seen. If there is random solid friction in the tensile machine, the full curve *A* in the figure may be regarded as a reasonable approximation to the true load/elongation curve. Such scattering of each observed value from a smooth curve was hardly observed in a crystal greater than 0.15 mm in radius as shown by curve *B*.

The computations of the shear stress and the shear strain were performed in the usual manner[10]. It was assumed that duplex slip occurs when the specimen is in the dodecahedral plane or has rotated into the plane. It is also assumed that the tensile axis remains in the dedecahedral plane and rotates towards the [112] direction during the duplex slip.

## § 4. Deformation of Crystals of 1 mm in Radii

Some of the shear stress/glide curves of crystals of about 1 mm in radii are shown in Fig. 5. The curves reveal considerable scattering between those crystals according to the crystal orientations of the tensile axes as was observed first in aluminium by Masing and Raffelsieper[11] and investigated in detail by Lücke and Lange[12]. The orientation dependence of shear stress / glide curves is now generally established in some face-centred cubic metals[13][14][15][16].

The stress/strain curves can be approximated by two linear segment if the stress is not too large as shown in Fig. 5. The stress/strain curves may then be characterized by four quantities[14], i.e. the critical shear stress $S_1$, the shear stress for the initiation of the rapid hardening $S_2$, the hardening rate in the easy glide region $(dS/da)_1$ and the hardening rate in the rapid hardening region $(dS/da)_2$. The glide amount in the easy glide region $a$ is also very important quantity representing the feature of work-hardening, though this quantity can be derived from the above-mentioned four quantities. The definition of these five quantities will be seen in Fig. 6.

The observed values of five quantities, $S_1$, $S_2$, $(dS/da)_1$, $(dS/da)_2$ and $a$, are summarized in Table I. Here $l_0$ is the initial guage length of a sample, $r_0$ the initial radius of the crystal, $\chi_0$ the original angle between the slip plane and tensile axis, $\lambda_0$ the original angle between the tensile axis and the slip direction. The crystal orientations of these crystals were already shown in Fig. 1.

The orientation dependence of $S_1$, $S_2$, $(dS/da)_1$, $(dS/da)_2$ and $a$ for the crystals of 1 mm in radius are shown in Fig. 7a, b, c, d and e, respectively. The critical shear stress, $S_1$, which is extrapolated from easy glide region, increases in the crystals oriented near the three corners of the triangle. The amount of increase in each corner seems to be proportional to the number of slip systems on which nearly equal shear stresses are applied.

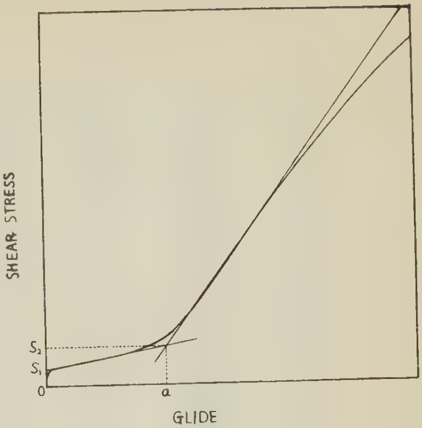

Fig. 6. Schematic representation of shear stress /glide relation.

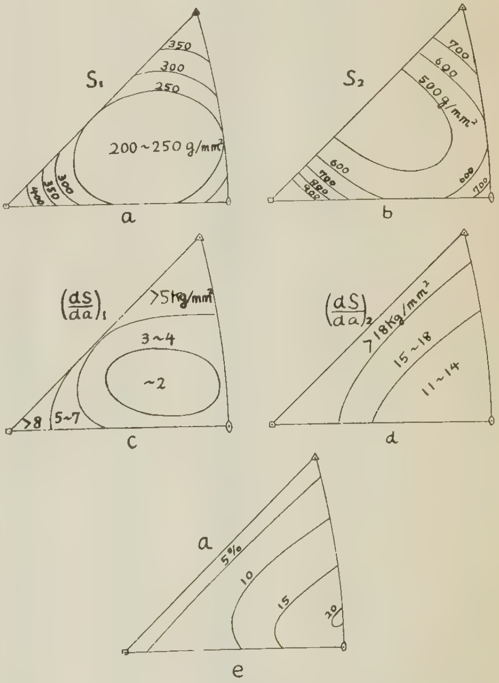

Fig. 7. Orientation dependence of $S_1$, $S_2$, $(dS/da)_1$, $(dS/da)_2$ and $a$ of crystals of about 1 mm in radii.

Following Fujita, T. Suzuki and Yamamoto[17], let us represent a slip system by the triangle in the sterographic projection of the imaginary tension axis, in which the slip system might be subjected to the maximum resolved shear stress. The real wire axis is always in the triangle $a$ in Fig. 8, then other triangles represent latent slip systems.

The orientation dependence of $S_2$ is very similar to that of $S_1$, but it seems to be not affected by the conjugate slip system, $e$.

The hardening rate $(dS/da)_1$ shows stronger dependence on the orientation than $S_1$, but the contours of equi-hardening resembles with those of $S_1$.

The hardening rate $(dS/da)_2$ seems to be

Table I. Observed values of five constants characterizing the shear stress/glide curves.

| Sample No. | $l_0$ in mm | $r_0$ in mm | $\chi_0$ in degree | $\lambda_0$ in degree | $S_1$ in Kg/mm² | $S_2$ in Kg/mm² | $a$ in mm/mm | $(dS/da)_1$ in Kg/mm² | $(dS/da)_2$ in Kg/mm² |
|---|---|---|---|---|---|---|---|---|---|
| 3 | 69.26 | 1.075 | 39 | 43 | 0.46 | 0.95 | 0.050 | 9.80 | 14.2 |
| 5 | 69.30 | 1.07 | 45 | 52 | 0.23 | 1.00 | 0.17 | 4.53 | 16 |
| 11 | 69.36 | 1.00 | 41 | 41 | 0.25 | 0.50 | 0.107 | 2.34 | 14 |
| 12 | 50.15 | 0.930 | 34 | 43 | 0.25 | 0.45 | 0.080 | 2.50 | 14.2 |
| 13 | 50.16 | 0.920 | 32 | 43 | 0.32 | 0.60 | 0.108 | 2.59 | 12.3 |
| 14 | 50.19 | 0.925 | 43 | 45 | 0.33 | 0.64 | 0.072 | 4.30 | 15.2 |
| 15 | 50.14 | 0.920 | 52 | 54 | 0.22 | 0.47 | 0.145 | 1.72 | 12.5 |
| 16 | 50.11 | 0.930 | 36 | 40 | 0.36 | 0.66 | 0.027 | 11.1 | 20.0 |
| 17 | 49.86 | 0.930 | 45 | 52 | 0.19 | 0.52 | 0.15 | 2.20 | 11 |
| 18 | 50.16 | 0.930 | 39 | 45 | 0.27 | 0.49 | 0.057 | 3.68 | 13.5 |
| 19 | 50.18 | 0.915 | 37 | 38 | 0.30 | 0.60 | 0.037 | 8.11 | 17.5 |
| 20 | 50.27 | 0.925 | 36 | 36 | 0.25 | 0.42 | 0.086 | 1.98 | 15.5 |
| 22 | 50.19 | 0.940 | 41 | 42 | 0.23 | 0.46 | 0.065 | 3.54 | 14.3 |
| 23 | 50.08 | 0.940 | 36 | 36 | 0.37 | 0.45 | 0.013 | 6.15 | 19.5 |
| 24 | 50.13 | 0.910 | 41 | 49 | 0.22 | 0.52 | 0.162 | 1.85 | 13.0 |
| 25 | 50.33 | 0.935 | 30 | 39 | 0.33 | 0.75 | 0.080 | 5.25 | 13.5 |
| 26 | 50.17 | 0.920 | 39 | 42 | 0.30 | 0.80 | 0.057 | 8.77 | 19.0 |
| 27 | 50.20 | 0.930 | 36 | 45 | 0.27 | 0.64 | 0.088 | 4.20 | 15.5 |
| 28 | 50.18 | 0.920 | 46 | 46 | 0.25 | 0.53 | 0.092 | 3.04 | 13.8 |
| 29 | 50.11 | 0.915 | 36 | 36 | 0.27 | 0.37 | 0.030 | 3.33 | 17.5 |
| 30 | 50.11 | 0.935 | 33 | 43 | 0.25 | 0.77 | 0.102 | 5.10 | 16.3 |
| 31 | 50.10 | 0.900 | 51 | 54 | 0.27 | 0.58 | 0.158 | 1.96 | 13.0 |
| 32 | 50.18 | 0.930 | 41 | 42 | 0.27 | 0.57 | 0.080 | 3.75 | 13.0 |
| 34 | 50·23 | 0.930 | 33 | 37 | 0.27 | 0.50 | 0.047 | 4.89 | 17 |
| 35 | 50.11 | 0.925 | 48 | 48 | 0.27 | 0.63 | 0.105 | 3.42 | 12.5 |
| 36 | 50.28 | 0.940 | 40 | 41 | 0.25 | 0.55 | 0.065 | 4.62 | 14 |
| 37 | 50.12 | 0.900 | 40 | 49 | 0.28 | 0.50 | 0.090 | 2.44 | 13.2 |
| 38 | 50.17 | 0.890 | 47 | 47 | 0.25 | 0.62 | 0.085 | 4.49 | 14.8 |
| 41 | 50.12 | 0.940 | 34 | 42 | 0.30 | 0.80 | 0.073 | 6.85 | 15.3 |
| 43 | 50.17 | 0.930 | 48 | 48 | 0.27 | 0.68 | 0.082 | 5.00 | 13.5 |
| 44 | 50.18 | 0.930 | 37 | 37 | 0.22 | 0.43 | 0.050 | 4.20 | 17.5 |
| 45 | 50.14 | 0.910 | 43 | 48 | 0.19 | 0.40 | 0.120 | 1.75 | 13.5 |
| 47 | 50.25 | 0.930 | 48 | 48 | 0.27 | 0.53 | 0.060 | 4.34 | 14.2 |
| 48 | 50.25 | 0.920 | 39 | 39 | 0.25 | 0.42 | 0.085 | 2.00 | 14.5 |
| 49 | 50.09 | 0.930 | 38 | 42 | 0.30 | —— | 0.000 | —— | 22.0 |
| 50 | 50.22 | 0.910 | 41 | 43 | 0.30 | 0.62 | 0.050 | 6.40 | 18.0 |
| 51 | 50.19 | 0.890 | 45 | 52 | 0.22 | 0.47 | 0.16 | 1.56 | 11 |
| 52 | 50.22 | 0.940 | 37 | 42 | 0.21 | 0.50 | 0.060 | 4.84 | 16.5 |
| 53 | 50.24 | 0.930 | 43 | 47 | 0.23 | 0.58 | 0.133 | 2.63 | 13.5 |
| 54 | 50.19 | 0.940 | 32 | 32 | 0.23 | 0.48 | 0.037 | 6.76 | 17.5 |
| 55 | 50.29 | 0.950 | 45 | 46 | 0.32 | 0.67 | 0.058 | 6.04 | 12.8 |
| 56 | 50.08 | 0.940 | 51 | 57 | 0.23 | 0.52 | 0.153 | 1.89 | 11.5 |
| 57 | 50.29 | 0.915 | 39 | 39 | 0.23 | 0.47 | 0.070 | 3.43 | 18.5 |
| 58 | 50.16 | 0.925 | 38 | 39 | 0.20 | 0.60 | 0.055 | 7.29 | 18 |
| 59 | 50.18 | 0.890 | 49 | 54 | 0.23 | 0.52 | 0.153 | 1.89 | 11.5 |
| 60 | 50.40 | 0.930 | 53 | 56 | 0.29 | 0.64 | 0.103 | 3.40 | 12.3 |
| 62a | 21.52 | 0.290 | 31 | 31 | 0.30 | 0.50 | 0.105 | 1.90 | 17.5 |
| b | 26.76 | 0.820 | 〃 | 〃 | 0.18 | 0.40 | 0.037 | 5.95 | 17.5 |
| 63a | 9.83 | 0.174 | 32 | 43 | 0.22 | 0.47 | 0.257 | 0.97 | 6.3 |
| b | 10.63 | 0.277 | 〃 | 〃 | 0.32 | 0.52 | 0.140 | 1.43 | 7.2 |
| 64 | 26.76 | 0.910 | 26 | 35 | 0.25 | 0.58 | 0.092 | 3.59 | 13 |
| 65a | 30.61 | 0.448 | 51 | 51 | 0.23 | 0.69 | 0.233 | 1.97 | 13.0 |
| b | 27.96 | 0.823 | 〃 | 〃 | 0.23 | 0.59 | 0.148 | 2.43 | 13.5 |
| 66a | 11.35 | 0.082 | 50 | 52 | 0.37 | 0.99 | 0.342 | 1.81 | 10.0 |
| b | 11.30 | 0.157 | 〃 | 〃 | 0.30 | 0.89 | 0.274 | 2.15 | 10.8 |
| c | 15.56 | 0.267 | 〃 | 〃 | 0.25 | 0.60 | 5.262 | 1.33 | 11.3 |
| 67a | 13.05 | 0.111 | 41 | 43 | 0.20 | 0.62 | 0.268 | 1.57 | 19.8 |
| b | 12.90 | 0.218 | 〃 | 〃 | 0.24 | 0.63 | 0.257 | 1.52 | 18.2 |
| 71a | 31.81 | 0.441 | 33 | 32 | 0.29 | 0.58 | 0.093 | 3.12 | 20.5 |
| b | 37.33 | 0.860 | 〃 | 〃 | 0.23 | 0.52 | 0.102 | 2.84 | 17.5 |

Table I. continued.

| Sample No. | $l_0$ in mm | $r_0$ in mm | $\chi_0$ in degree | $\lambda_0$ in degree | $S_1$ in $Kg/mm^2$ | $S_2$ in $Kg/mm^2$ | $a$ in mm/mm | $(dS/da)_1$ in $Kg/mm^2$ | $(dS/da)_2$ in $Kg/mm^2$ |
|---|---|---|---|---|---|---|---|---|---|
| 72a | 19.20 | 0.468 | 40 | 45 | 0.38 | 0.90 | 0.188 | 2.76 | 10.5 |
| b | 27.00 | 0.921 | 〃 | 〃 | 0.27 | 0.67 | 0.182 | 2.20 | 11.3 |
| 74 | 9.18 | 0.349 | 42 | 43 | 0.31 | 0.61 | 0.143 | 2.10 | 11.0 |
| 75a | 13.15 | 0.174 | 45 | 52 | 0.34 | 1.04 | 0.37 | 1.89 | 11 |
| b | 12.56 | 0.256 | 〃 | 〃 | 0.47 | 1.10 | 0.44 | 1.43 | 10.7 |
| 78a | 18.84 | 0.319 | 35 | 37 | 0.40 | 0.68 | 0.097 | 2.89 | 20.0 |
| b | 26.37 | 0.366 | 〃 | 〃 | 0.35 | 0.65 | 0.120 | 2.50 | 19.0 |
| 80a | 28.30 | 0.388 | 46 | 52 | 0.25 | 0.60 | 0.24 | 1.46 | 11.7 |
| b | 32.26 | 0.903 | 〃 | 〃 | 0.32 | 0.67 | 0.13 | 2.69 | 12 |
| 81a | 9.34 | 0.174 | 40 | 41 | 0.32 | 0.77 | 0.388 | 1.16 | 13.0 |
| b | 11.46 | 0.319 | 〃 | 〃 | 0.31 | 0.72 | 0.275 | 1.49 | 12.6 |
| 82a | 26.82 | 0.394 | 39 | 45 | 0.42 | 0.95 | 0.095 | 5.58 | 20.8 |
| b | 26.58 | 0.924 | 〃 | 〃 | 0.45 | 0.97 | 0.067 | 7.76 | 17.7 |
| 83 | 27.37 | 0.882 | 39 | 45 | 0.45 | 0.90 | 0.058 | 7.76 | 19.0 |
| 84a | 12.12 | 0.227 | 40 | 41 | 0.27 | 0.70 | 0.275 | 1.56 | 14.0 |
| b | 12.49 | 0.377 | 〃 | 〃 | 0.32 | 0.60 | 0.143 | 1.96 | 11.2 |
| 86a | 22.02 | 0.497 | 46 | 46 | 0.19 | 0.55 | 0.170 | 2.12 | 11.5 |
| b | 27.37 | 0.885 | 〃 | 〃 | 0.38 | 0.75 | 0.107 | 3.46 | 13.2 |
| 87a | 26.59 | 0.475 | 51 | 56 | 0.23 | 0.62 | 0.235 | 1.66 | 13.8 |
| b | 27.31 | 0.906 | 〃 | 〃 | 0.35 | 0.78 | 0.200 | 2.15 | 12.5 |
| 88a | 18.50 | 0.312 | 51 | 57 | 0.31 | 0.70 | 0.365 | 1.07 | 10.8 |
| b | 27.16 | 0.890 | 〃 | 〃 | 0.27 | 0.78 | 0.190 | 2.68 | 11.0 |
| 89a | 25.64 | 0.321 | 26 | 37 | 0.48 | — | 0.000 | — | 19.3 |
| b | 27.08 | 0.884 | 〃 | 〃 | 0.38 | 0.75 | 0.098 | 3.94 | 14.2 |
| 93 | 13.60 | 0.201 | 47 | 49 | 0.18 | 0.55 | 0.370 | 1.00 | 15.0 |
| 94a | 10.86 | 0.145 | 33 | 37 | 0.20 | 0.57 | 0.295 | 1.25 | 17 |
| b | 11.32 | 0.190 | 〃 | 〃 | 0.40 | 0.97 | 0.313 | 1.82 | 21.5 |
| 95a | 11.46 | 0.070 | 36 | 38 | 0.30 | 1.25 | 0.378 | 2.51 | 15.5 |
| b | 14.74 | 0.188 | 〃 | 〃 | 0.31 | 0.78 | 0.237 | 1.98 | 17.5 |
| 96a | 9.28 | 0.156 | 36 | 43 | 0.42 | 1.13 | 0.053 | 13.4 | 25.3 |
| b | 12.08 | 0.245 | 〃 | 〃 | 0.25 | 0.86 | 0.066 | 9.25 | 17.0 |
| c | 10.27 | 0.320 | 〃 | 〃 | 0.40 | 0.78 | 0.040 | 9.50 | 20.0 |
| 97 | 11.12 | 0.289 | 49 | 49 | 0.23 | 0.72 | 0.267 | 1.83 | 10.8 |
| 101a | 13.26 | 0.135 | 38 | 40 | 0.18 | 0.58 | 0.345 | 1.16 | 15.5 |
| b | 13.25 | 0.205 | 〃 | 〃 | 0.30 | 0.90 | 0.265 | 2.26 | 21.0 |
| 104 | 12.88 | 0.252 | 45 | 45 | 0.50 | 1.20 | 0.123 | 5.69 | 24.3 |
| 106a | 11.25 | 0.108 | 35 | 38 | 0.25 | 0.68 | 0.255 | 1.68 | 20.6 |
| b | 12.55 | 0.181 | 〃 | 〃 | 0.25 | 0.65 | 0.240 | 1.67 | 20.6 |
| c | 12.13 | 0.320 | 〃 | 〃 | 0.23 | 0.55 | 0.186 | 1.66 | 19.7 |
| d | 10.99 | 0.434 | 〃 | 〃 | 0.25 | 0.58 | 0.052 | 6.35 | 18.1 |
| 107a | 13.11 | 0.188 | 41 | 41 | 0.25 | 0.88 | 0.305 | 2.06 | 13.0 |
| b | 14.37 | 0.297 | 〃 | 〃 | 0.27 | 0.62 | 0.382 | 0.916 | 17.0 |
| 108 | 7.51 | 0.266 | 43 | 43 | 0.19 | 0.60 | 0.325 | 1.26 | 12.0 |
| 109a | 13.19 | 0.176 | 36 | 36 | 0.35 | 0.97 | 0.095 | 6.53 | 16.8 |
| b | 12.53 | 0.310 | 〃 | 〃 | 0.38 | 1.02 | 0.097 | 6.60 | 16.8 |
| 111a | 12.26 | 0.177 | 34 | 35 | 0.35 | 0.70 | 0.180 | 1.94 | 21.0 |
| b | 14.71 | 0.359 | 〃 | 〃 | 0.22 | 0.38 | 0.090 | 1.72 | 15.6 |
| 115a | 15.55 | 0.211 | 39 | 39 | 0.37 | 0.95 | 0.320 | 1.81 | 17.5 |
| b | 13.65 | 0.251 | 〃 | 〃 | 0.27 | 0.68 | 0.330 | 1.24 | 17.0 |
| c | 17.46 | 0.348 | 〃 | 〃 | 0.27 | 0.65 | 0.285 | 1.33 | 13.5 |
| 120a | 11.39 | 0.061 | 34 | 36 | 0.53 | 1.05 | 0.350 | 1.48 | 21.0 |
| b | 10.75 | 0.103 | 〃 | 〃 | 0.36 | 0.68 | 0.250 | 1.28 | 15.0 |
| c | 14.28 | 0.180 | 〃 | 〃 | 0.25 | 0.67 | 0.252 | 1.67 | 20.5 |
| d | 11.20 | 0.227 | 〃 | 〃 | 0.35 | 0.62 | 0.205 | 1.32 | 22.3 |
| e | 14.71 | 0.265 | 〃 | 〃 | 0.37 | 0.70 | 0.110 | 3.00 | 19.2 |
| f | 10.88 | 0.271 | 〃 | 〃 | 0.32 | 0.58 | 0.150 | 1.67 | 18.3 |
| 126a | 9.23 | 0.104 | 39 | 44 | 0.37 | 0.53 | 0.145 | 1.10 | 9.3 |
| b | 16.11 | 0.129 | 〃 | 〃 | 0.75 | 1.30 | 0.085 | 6.47 | 16.5 |
| c | 13.67 | 0.192 | 〃 | 〃 | 0.59 | 1.20 | 0.068 | 8.97 | 12.8 |
| d | 12.95 | 0.222 | 〃 | 〃 | 0.36 | 1.20 | 0.075 | 11.2 | 15.0 |

Table I. continued.

| Sample No. | $l_0$ in mm | $r_0$ in mm | $\chi_0$ in degree | $\lambda_0$ in degree | $S_1$ in Kg/mm$^2$ | $S_2$ in Kg/mm$^2$ | $a$ in mm/mm | $(dS/da)_1$ in Kg/mm$^2$ | $(dS/da)_2$ in Kg/mm$^2$ |
|---|---|---|---|---|---|---|---|---|---|
| 126e | 15.42 | 0.244 | 39 | 44 | 0.59 | 1.20 | 0.068 | 8.97 | 12.8 |
| f | 14.56 | 0.284 | 〃 | 〃 | 0.49 | 1.18 | 0.093 | 7.12 | 12.3 |
| g | 17.21 | 0.305 | 〃 | 〃 | 0.40 | 1.05 | 0.135 | 4.82 | 17.0 |
| h | 14.89 | 0.418 | 〃 | 〃 | 0.57 | 1.28 | 0.068 | 10.82 | 15.5 |
| 128a | 12.67 | 0.105 | 53 | 58 | 0.32 | 0.88 | 0.49 | 1.14 | 10.7 |
| b | 12.37 | 0.134 | 〃 | 〃 | 0.25 | 0.88 | 0.358 | 1.76 | 10.5 |
| c | 11.73 | 0.155 | 〃 | 〃 | 0.23 | 0.75 | 0.377 | 1.38 | 12.3 |
| d | 11.05 | 0.185 | 〃 | 〃 | 0.22 | 0.66 | 0.427 | 1.03 | 11.0 |
| e | 12.44 | 0.209 | 〃 | 〃 | 0.20 | 0.60 | 0.485 | 0.825 | 11.0 |
| f | 15.69 | 0.344 | 〃 | 〃 | 0.28 | 0.58 | 0.296 | 1.01 | 11.8 |
| 130a | 12.25 | 0.204 | 43 | 46 | 0.25 | 0.58 | 0.300 | 1.10 | 10 |
| b | 10.56 | 0.270 | 〃 | 〃 | 0.31 | 0.74 | 0.132 | 3.26 | 11.1 |
| c | 15.29 | 0.295 | 〃 | 〃 | 0.36 | 0.88 | 0.198 | 2.62 | 16.0 |
| 136a | 12.14 | 0.087 | 36 | 44 | 0.65 | —— | 0.00 | —— | 37.0 |
| b | 10.46 | 0.126 | 〃 | 〃 | 0.60 | —— | 0.00 | —— | 34.2 |
| c | 11.72 | 0.193 | 〃 | 〃 | 0.45 | —— | 0.00 | —— | 30.3 |

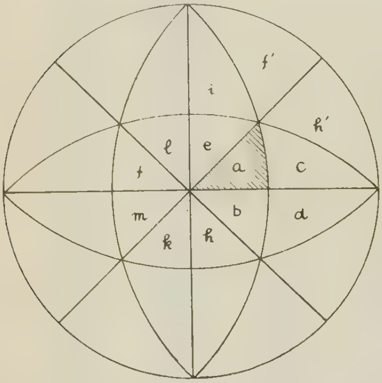

Fig. 8. Slip systems in a face-centred cubic crystal.

increased only by the influence of the conjugate slip system, $e$, as already pointed out by Rosi[14] in the case of thicker crystals than in this investigation.

The range of easy glide seems also to depend strongly on the action of the conjugate slip system, $e$, and slightly on $b$ and $d$ systems, but not on $c$-system.

## § 5. Effects of Radii of Crystal on Work-Hardening

Figs. 9, 10 and 11 show stress/strain curves of crystals with various radii. The crystal orientations of the tensile axes are in the vicinity of [011] in Fig. 9, in the vicinity of [001] in Fig. 10, and in a direction far from any of [001], [011] and [111] in Fig. 11.

In the case of the crystals oriented in the vicinity of [011] direction, the range of easy glide $a$ increases and the corresponding hardening rate in this region $(dS/da)_1$ seems to be irrespective to the radius of crystal as shown in Fig. 12. $S_1$ and $S_2$ increase slightly with the decreasing radius.

The situation is not so simple in the case of the crystals oriented near [001]. The crystals 136 and 96, which make angles of about 1 and 3 degrees with [001] respectively, reveal more rapid hardening in thinner crystals than in thicker crystals. Meanwhile, in crystals making with [001] an angle about 6 degrees the hardening rate decreases with the decreasing radius. The increase in the range of easy glide is very significant in crystals 16, 78, 106 and 120, which make with [001] angles from 10 to 16 degrees. These results indicate that there are strong orientation dependence of size effect especially in the vicinity of [001]. The effects of radii of crystals on $S_1$, $S_2$, $(dS/da)_1$ and $(dS/da)_2$ are represented in Fig. 13. There are only slight orientation dependence of $S_1$, $S_2$, $(dS/da)_2$, while $(dS/da)_1$ considerably decreases with the decreasing radius. The extrapolated value of $(dS/da)_1$ to the infinitensimal radius, however, seems to reach about 1.2 Kg/mm$^2$, which is equal to the corresponding value of the crystals oriented near [011]. The orientation dependence of $(dS/da)_1$ may be, therefore, recognized more rationally as the orientation dependence of the size effect of $(dS/da)_1$.

Fig. 11 shows the stress/strain curves of some crystals making a large angle with any

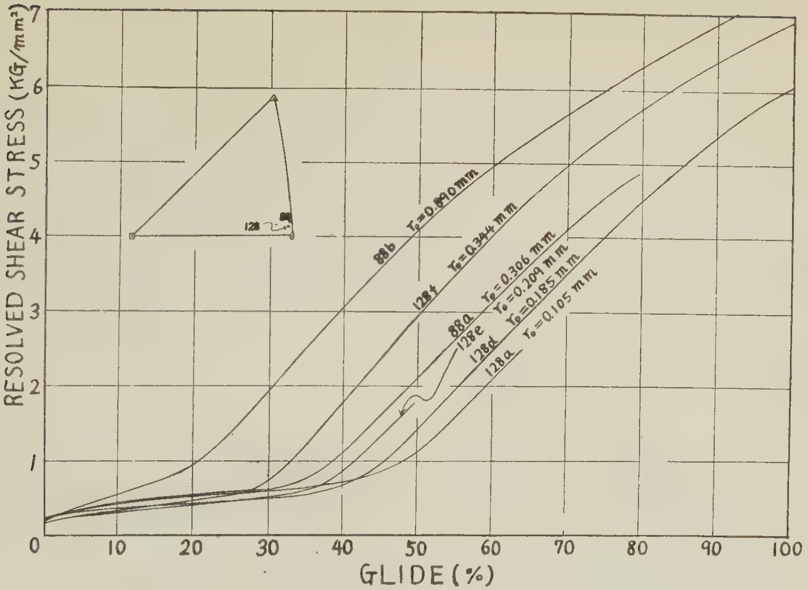

Fig. 9. Shear stress/glide curves of crystals having various radii; in the vicinity of [011].

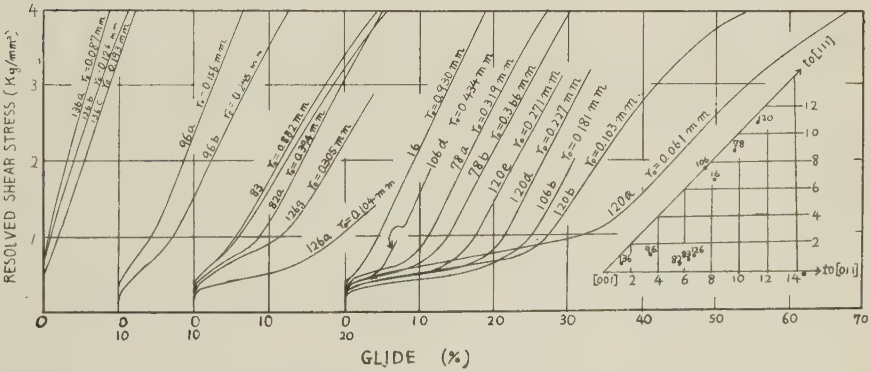

Fig. 10. Shear stress/glide curves of crystals having various radii; in the vicinity of [001].

one of [001], [011], [111]. The hardening rate is not a unique function of the crystal radius, but these irregular effects seem to be caused by difficulty in the measurements, especially, in handling of crystals before mounting it. It is, however, distinctly shown that the decrease of radius results in the increase of range of easy glide.

The range of easy glide has a relation with the radius of crystal. In Fig. 14 the range of easy glide in logarithmic scale is plotted against the radius of crystal for two groups of crystals having the orientations shown in Figs. 12b and 13a, respectively. Though the observed values reveal considerable scattering, there is a linear relation between the loga-

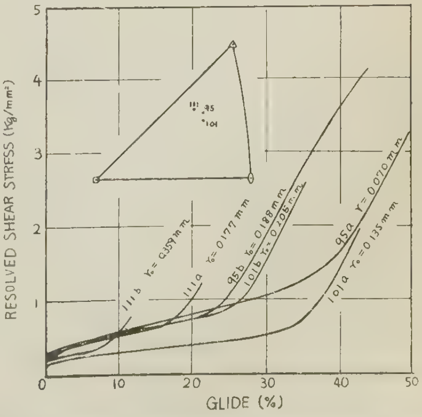

Fig. 11. Shear stress/glide curves of crystals having various radii; in the vicinity of [459].

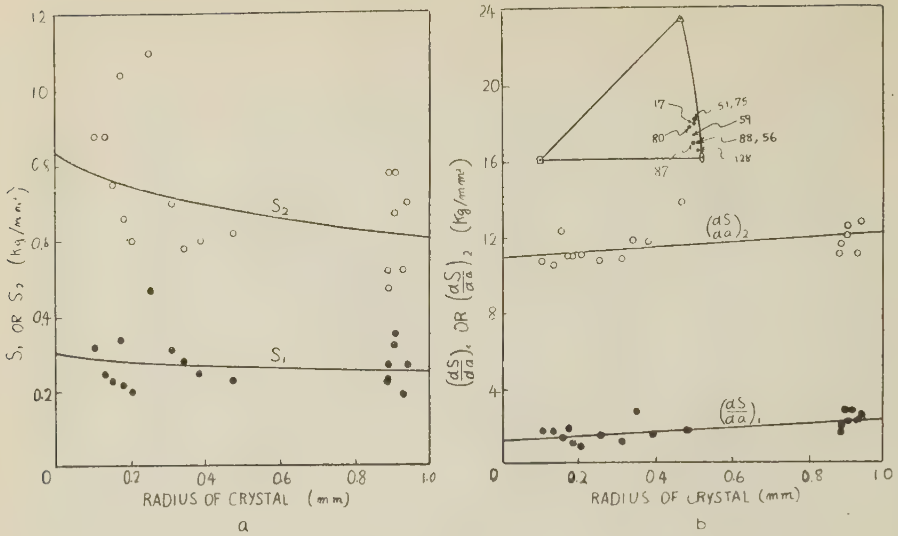

Fig. 12. Dependence of $S_1$, $S_2$, $(dS/da)_1$ and $(dS/da)_2$ on radius of crystal; in the vicinity of [011].

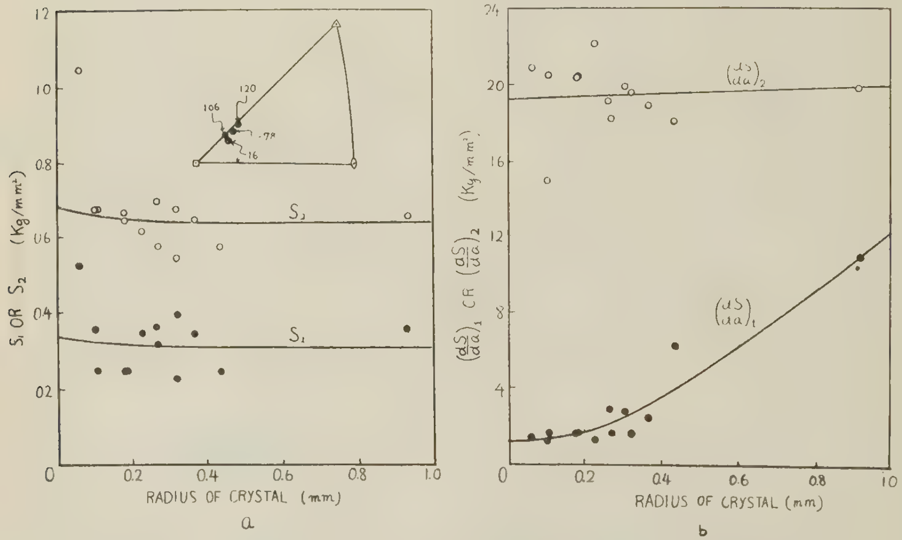

Fig. 13. Dependence of $S_1$, $S_2$, $(dS/da)_1$ and $(dS/da)_2$ on radius of crystal; in the vicinity of [001].

rithms of range of easy glide and radii of crystals at least when the radii of crystals are less than a certain value depending on the crystal orientation. There are, of course, some other empirical formulae, which fit in the observed values at the same degree of scattering with this. This relation, however, seems to be the most reasonable according to the dislocation theory of deformation.

Fig. 14 indicates very important fact, that is, the range of easy glide reaches to a value between 0.4 and 0.8 irrespectively to the crystal orientation when the radius of crystal decreases to a sufficiently small value.

## § 6. Discussion of the Results

The results described in the forgoing sections may be explained from the theory of dislocation. The precise treatment of the size effect in the deformation of crystals, however, requires extensive considerations on the deformation process of crystals, so only a preliminary consideration will be given in this section.

The relation shown in Fig. 14 may be derived as follows. The easy glide may correspond to the exhaustion hardening process of Frank-Read sources[18], which have existed in annealed state. Let us suppose that a dislocation can proceed in the crystal freely by the distance $l$ in average, namely, it meets with any obstacle $P$ times during the dislocation sweeps unit area. The shear deformation performed by dislocations, which pass through the whole cross sections of the crystal, is then given by the expression

$$S = ns \exp(-Pr) \qquad (1)$$

where $n$ is the number of operated Frank-Read sources which have existed at the annealed state, and $S$ the shear produced by the operation of a Frank-Read source. If a Frank-Read source multiplies a dislocation in every atomic plane[4][19][20], and the radius of crystal is not too large compared with the mean free path of dislocations, Frank-Read sources existed at the annealed state must consumed when $ns$ reaches to the value $b/h$. Here $b$ is the strength of a dislocation, $h$ is the spacing of the two neighbouring atomic planes parallel to the slip plane. The shear shown in (1), then may be equal to the range of easy glide. There is thus a linear relationship between the logarithm of range of easy glide and the radius of crystal. The range of easy glide extrapolated to the infinitesimal radius will be about 1.2 irrespectively to the orientation of the crystal, if Eq. (1) is valid. Meanwhile, the corresponding value in Fig. 14 is 0.4~0.8. This difference may be caused from two sources: in the first place the hardening in the vicinity of a slip zone is neglected, which will forbid the formation of another slip zone in contact with the former one. In the second place, the easy glide is apt to be disturbed by any heterogeneity in the crystal, so we have measured rather low values than in the ideal case.

The explanation described above seems to be adequate to understand the various kinds of stress/strain curves of face-centred cubic metals and alloys[21][22][23][24]. The wide range of easy glide in high alloy crystals, especially well known in $\alpha$-brass crystals, may be attributed to longer mean free path of dislocations in these alloy crystals than in pure metals. Then the situations appeared in thin metal crystals take place in rather thick alloy crystals. Actually there are slight size effect on the range of easy glide in $\alpha$–brass crystals[25].

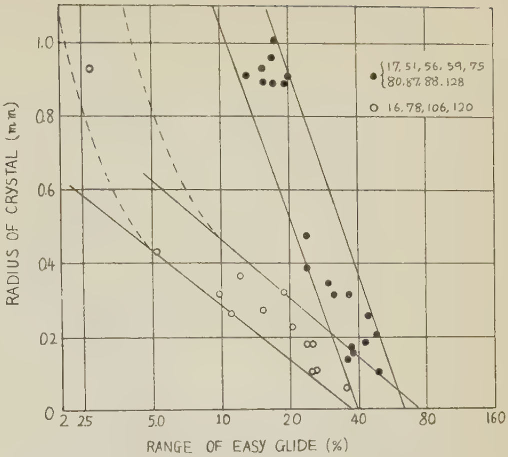

Fig. 14. The relation between the range of easy glide and radius of crystal.

The term, mean free path of dislocations, is of course a rude concept, but it may be very useful to understand the phenomena of work-hardening. The mean free path of dislocations may be determined by some factors such as the frequency of sessile reaction proposed by Lomer(26) and Cottrell(27), the density of intersecting dislocations etc. as already discussed by Mott[2], and Seeger[8]

The effect of surface film on the range of easy glide seems to be exaggerated, for example, in the investigation by Andrade and Henderson[28] on silver crystals. They ignored the orientation dependence of work-hardening as generally believed at the time of their investigation, and compared the work-hardening of two crystals, the one was annealed in argon and immediately examined in argon gas without exposing to atmosphere and the other was exposed to the air for about two hours. The range of easy glide was about 30 per cent in the former crystal, while it was about 8 per cent in the latter crystal. The difference of the range of easy glide between these two crystals was attributed to the existence of oxide layer formed by the action of the atmosphere at room temperature by Andrade and Henderson, and this interpretation was accepted in Cottrell's famous book[29]. This difference, however, can also be explained by the orientation effect on work-

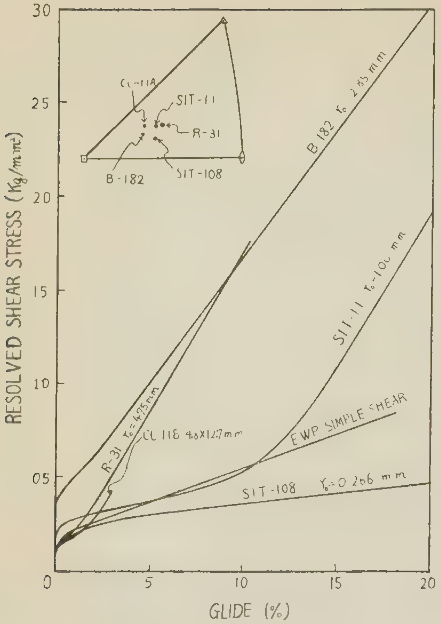

Fig. 15. Comparism of shear stress/glide curves with those by previous workers.
B: T. H. Blewitt[13]. EWP: E. H. Edwards, J. Washburn and E. R. Parker[31]. CC: C. R. Cupp and B. Chalmers[30] R: F. D. Rosi[14]. SIT: This investigation.

hardening as already shown in Fig. 5.

It is interest to compare the results obtained here with those by previous investigators. Fig. 15 represents stress / strain curves of crystals having nearly the same orientation by these investigators[13][14][30][31]. There are considerable scattering in the vicinity of small amount of deformation, but the range of easy glide changes systematically with the change of crystal radii. It must be noted, especially, the hardening rate in simple shear experiment by Edwards, Washburn and Parker is considerably greater than the hardening rate in tensile test of thin crystals. Edwards et al obtained the hardening rate of the order of 4 Kg/mm², which is about three times greater than the extrapolated hardening rate to the infinitesimal radius. The discrepancy indicates that the simple shear experiment is also governed by some complex process of dislocation reaction in face-centred cubic crystals.

## § 7. Summary

Using many number of copper crystals, the orientation dependence of work-hardening and the effects of crystal radii on the work-hardening are observed. The main results are summarized as follows.

(1) The stress / strain curves of copper crystals are usually composed of linear parts, providing the stress is not too large, corresponding to the easy glide and rapid hardening region, respectively.

(2) In the case of 1 mm radius of crystals, there are strong orientation dependence of stress/strain curves especially in the range of easy glide. The critical shear stress, work-hardening rate in the rapid hardening region reveals a weak but systematic orientation dependence.

(3) When the radius of crystal decreases, the range of easy glide increases considerably. The dependence of the range on the radius differs between crystals of different orientations, but the limitting value extrapolated to the infinitesimal radius is identically about 50 per cent in shear for any crystal orientation.

(4) Hardening rate in rapid hardening region depends weakly on the radius but the hardening rate in easy glide region depends strongly on the crystal radius, and reaches to 1.2 Kg/mm² when the radius decreased to the infininitesimal, irrespectively to the crystal orientation.

(5) The size effect of work-hardening depends strongly on the crystal orientation in the vicinity of [001], but moderately in the vicinity of [011]. The behaviour in the vicinity of [111] might be similar to [001], but the measurement was not performed on account of the difficulty to produce crystals having such an orientation.

The authors wish to express their thanks to Professor M. Yamamoto and Mr. J. Watanabe for their help in determining crystal orientation.

## References

1) F. C. Frank and W. T. Read: Phys. Rev. **79** (1950) 722.
2) N. F. Mott: Proc. Phys. Soc. **64B** (1951) 729; Phil. Mag. **43** (1952) 1151.
3) J. C. Fisher, E. W. Hart and R. H. Pry: Phys. Rev. **87** (1952) 958.
4) H. Suzuki: J. Phys. Soc. Japan **9** (1954) 531.
5) R. D. Heidenreich and W. Shockley: J. Appl. Phys. **18** (1947) 1029; *The Strength of Solids* (London, Phys. Soc. 1948) 57.
6) H. G. van Bueren: Acta Metallurgica **1** (1953)

464.
7) G. Leibfried and P. Haasen: Z. Phys. **137** (1954) 67.
8) A. Seeger: Z. Naturforschung **9a** (1954) 758.
9) M. Yamamoto: Sci. Rep. Tohoku Imp. Univ. **29** (1940) 113; **31** (1943) 121.
M. Yamamoto and J. Watanabe: Sci. Rep. RITU **A 2** (1950) 81, 270; **A 4** (1952) 127; **A 5** (1953) 124, 135; **A 7** (1955) 161, 329.
10) E. Schmid and W. Boas: *Kristallplastizität* (Berlin, Springer, (1935).
11) G. Masing and J. Raffelsieper: Z. Metallkunde **41** (1950) 65.
12) K. Lücke and H. Lange: Z. Metallkunde **43** (1952) 55.
H. Lange and K. Lücke: Z. Metallkunde **44** (1953) 183.
13) T. H. Blewitt: Phys. Rev. **91** (1953) 1115.
14) F. D. Rosi: J. Metals (1954) 1009.
15) J. Saukill and R. W. K. Honeycombe: Acta Metallurgica **2** (1954) 854.
16) B. Jaoul and P. Lacombe: Compt. Rend. **240** (1955) 2411.
17) F. E. Fujita, T. Suzuki and M. Yamamoto: To be published.
18) J. S. Koehler: Phys. Rev. **86** (1952) 52.
19) T. Suzuki: Sci. Rep. RITU **A 6** (1954) 309.
20) B. A. Bilby: *Defects in Crystalline Solids* (London Phys. Soc. 1955) 123.
21) G. Sachs and J. Weerts: Z. Phys. **62** (1930) 473.
22) F. van Göler and G. Sachs: Z. Phys. **55** (1929) 581.
23) M. Mashima and G. Sachs: Z. Phys. **50** (1928) 161.
24) E. Osswald: Z. Phys. **83** (1933) 55.
25) H. Suzuki, S. Ikeda and S. Takeuchi: To be published.
26) W. M. Lomer: Phil. Mag. **42** (1951) 1327.
27) A. H. Cottrell: Phil. Mag. **43** (1952) 645.
28) E. N. da C. Andrade and C. Henderson: Phil. Trans. Roy. Soc. London **244** (1951) 177.
29) A. H. Cottrell: *Dislocations and Plastic Flow in Crystals* (Oxford 1953) 161.
30) C. R. Cupp and B. Chalmers: Acta Metallurgica **2** (1954) 803.
31) E. H. Edwards, J. Washburn and E. R. Parker: J. Metals **5** (1953) 1525.

---

JOURNAL OF THE PHYSICAL SOCIETY OF JAPAN Vol. 11, No. 4, APRIL, 1956

# On the Metastable Transition and the Crystal Structure of Ammonium Nitrate (Tetragonal Modification)

By Yasuhiro SHINNAKA

*Faculty of Literature and Science, Yamaguchi University*

(Received November 28, 1955)

Conditions for the appearance of the metastable transition (IV)⇄(II) were studied by X-ray method and dilatometer method and it was found that when the single crystals of the phase (IV) were formed from the aqueous solution at room temperature the metastable transition was always observed and that in dry ones it often proceeded as a single crystal transformation without any noticeable change in orientation. The crystal structure of the phase (II) was determined by using a single crystal obtained by the single crystal transformation. It was found that tetragonal modification (II) has also CsCl-like structure, and a hindered rotation of the nitrate groups was proposed.

## §1. Introduction

It is known that ammonium nitrate has five stable transitions and in some cases a metastable transition occurs at ordinary pressure.[1][2][3] They are shown in the following table. (Table I, and Table II.)

Among five modifications, information about the tetragonal modification (II) was particularly incomplete: nothing has been determined concerning atomic positions along the *c* axis. The reason is that it was very difficult to obtain reliable intensity measurements since the particle size increased rapidly during powder photographing. The author studied the metastable transition (IV)⇄(II) and determined the structure of this modification (II) by using

Table I. Stable Transition

| Phase | Liquid | | (I) | | (II) | | (III) | | (IV) | | (V) |
|---|---|---|---|---|---|---|---|---|---|---|---|
| Trans. Temp. (°C) | | 169.5 | | 125.2 | | 84.2 | | 32.3 | | −18 | |
| Crystal System | | | Cub. | | Tet. | | Ortho-rhomb. | | Ortho-rhomb. | | Hex. |

Table II. Metastable Transition.

| Phase | (II) $\rightleftarrows$ (IV) |
|---|---|
| Trans. Temp. (°C) | ~50 |

a single crystal obtained by the process of this metastable transition (IV)→(II) under certain conditions.

## § 2. Metastable Transition

The conditions for the appearance of the metastable transition were studied by the method of dilatometer; they are related to the maximum temperature reached, the time of heat treatment and the water content of the specimen.

On the metastable transition (II)→(IV), conditions for the appearance of it were recently studied also by K. Tanaka and his co-worker[4] and the same results were obtained by this experiment.

On the other hand, on the metastable transition (IV)→(II), it was found that conditions for the appearance of it have the same tendency as that of the metastable transition (II)→(IV). When the phase (IV) was originally formed from the phase (III), it was required for the appearance of this metastable transition that the samples were to be left untouched more than one week at room temperature (20°C) in wet samples, but in dry ones the samples were to be left untouched for several months at the same temperature. And when the phase (IV) was originally formed directly either from the phase (II) by the process of metastable transition (II)→(IV), or from the aqueous solution at room temperature, the metastable transition was always observed.

The character of the metastable transition was investigated by the X-ray method using the single crystal of the phase (IV) prepared from the aqueous solution at room temperature. The metastable transition often proceeded in dry samples as a single crystal transformation without any noticeable change in orientation, and the single crystal was sometimes found to be broken even in dry samples by distinct recrystallization after the above transformation; also in wet samples, it was broken by the transformation to stable modification (III) after the metastable transition.

These phenomena might be explained as K. Tanaka[4] did on the metastable transition (II)→(IV): Nuclei of the phase (III) in the phase (IV), still remaining after the transformation (III)→(IV), were completely destructed by leaving untouched at room temperature in a long period, and so the phase (IV) changes directly to the phase (II) without nucleation of the phase (III) in the course of heating. The phase (II) has similar structure (CsCl-like structure) to the phase (IV) as will be described in the next paragraph. But the phase (III) has NiAs-like structure and a larger specific volume than those of the phases (IV) and (II). Wet specimens are easier to get in and out of metastable conditions than dry ones are. The action of moisture is now under investigation.

## § 3. Crystal Structure of the Phase (II)

Thus the single crystal (II) was obtained by the single crystal transfomation (IV)→(II) from the single crystal (IV), and it had mosaic structure with slight diffuse Laue spots. As the needle axis of the crystal is $a$ axis, photographs were taken with a crystal rotating about $a$ axis with CuK$\alpha$ and MoK$\alpha$ radiations at 60°C and 100°C. At both temperatures the noticeable change was not observed in the photographs. In this experiment it was observed that several reflection planes have different values of intensity from those given by S. B. Hendricks and his co-workers[2].

The data require a tetragonal unit of structure with $a = 5.74$ Å, $c = 4.95$ Å at 60°C, containing two molecules. Among possible six space groups ($P_4$, $P_{\bar{4}}$, $P_{4mm}$, $P_{4bm}$, $P_{\bar{4}2_1m}$ and $C_{\bar{4}2m}$) $P_{4bm}$ and $P_{\bar{4}2_1m}$ seem to be selected by the fact that planes of the type $(0\,k\,l)$ with odd values of $k$ and $(h\,0\,0)$ with odd values of $h$ are absent.

The intensities were calculated on the basis of the assumed $f$-curves.[5][6][7] From the reflections of $(h\,k\,0)$ it was determined that the atomic arrangement on (001) corresponds to positions $x$, $\frac{1}{2}+x$, $w$; etc., with $x = 0.12$ for space groups $P_{4bm}$, and $P_{\bar{4}2_1m}$ (see Fig. 1). But the atomic arrangements derived from these space groups lead to calculated intensities entirely out of agreement with the observed intensities of planes of type either $(0\,0\,l)$ or $(0\,k\,l)$.

Possible escape from this contradiction might be achieved by rotation of nitrate groups, as it was considered in cubic modification (I). Several modes of randomness in orientations of the nitrate groups were tried. When nitrate groups are assumed to be rotating in a plane of each nitrate group determined from the atomic arrangement on (001) mentioned above, the calculated intensities were in good agreement with the observed intensities. However, the rotation of the nitrate group in the plane is required to be not free, but is almost bound in two orientations (in opposite directions) considered from the atomic arrangement on (001).

Atomic positions are approximately as follows.

$$2NH_4 : 0, 0, 0;\ \tfrac{1}{2}, \tfrac{1}{2}, 0$$

Two orientations of nitrate group:

| $2NO_3$ | One nitrate group | | | Other nitrate group | | |
|---|---|---|---|---|---|---|
| N | $\frac{1}{2}, 0, u$ | or | $\frac{1}{2}, 0, \bar{u}$ | $0, \frac{1}{2}, u$ | or | $0, \frac{1}{2}, \bar{u}$ |
| O (1) | $\frac{1}{2}, 0, v$ | | $\frac{1}{2}, 0, \bar{v}$ | $0, \frac{1}{2}, v$ | | $0, \frac{1}{2}, \bar{v}$ |
| (2) | $\frac{1}{2}+x, x, w$ | | $\frac{1}{2}+x, x, \bar{w}$ | $\bar{x}, \frac{1}{2}+x, w$ | | $\bar{x}, \frac{1}{2}+x, \bar{w}$ |
| | $\frac{1}{2}-x, \bar{x}, w$ | | $\frac{1}{2}-x, \bar{x}, \bar{w}$ | $x, \frac{1}{2}-x, w$ | | $x, \frac{1}{2}-x, \bar{w}$ |

with $x=0.12$, $u=0.53$, $v=0.75$, and $w=0.42$.

The agreement of observed and calculated intensities from the atomic positions is shown in Table III.

The results mentioned above show that the phase (II) has also the CsCl-like structure. The unimolecular pseudocell resembling CsCl has the same value of $c$ axis as the true unit, and each of the $a'$ axes is half the face diagonal of the latter (see Fig. 2). Each nitrate ion has eight nearest ammonium ions and all the nearest $NH_4-O$ distances are approximately the same (about 3.1 Å). From this structure it is natural to consider that the nitrate groups are in hindered rotation in the phase (II) before the free rotation sets in at higher temperatures (the phase (I)).

In conclusion the author wishes to express his hearty thanks to Dr. K. Tanaka of Kyoto University for many valuable suggestions and discussions. He is also grateful to Prof. T.

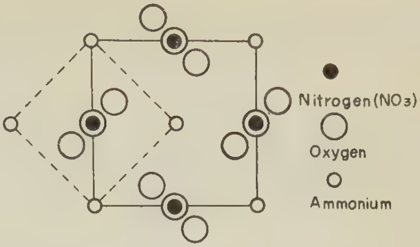

Fig. 1. Projection on (001). Full line represents the true unit and broken line the unimolecular pseudocell.

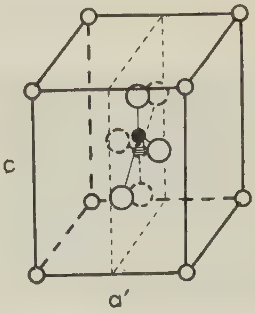

Fig. 2. The unimolecular pseudocell resembling CsCl, showing proposed rotation of nitrate group.

Table III. Calculated intensity:
$I=C\cdot|\bar{F}|^2(1+\cos^2 2\theta)/(\sin 2\theta)$

| Plane | (1) | (2) | Plane | (1) | (2) | Plane | (1) | (2) |
|---|---|---|---|---|---|---|---|---|
| (0 1 0) | *a* | 0 | (2 2 2) | *v·w* | 20 | (3 3 2) | *a* | 30 |
| (0 0 1) | *m·s* | 3900 | (1 1 3) | *m·w* | 470 | (1 1 4) | *v·w* | 20 |
| (1 1 0) | *m·s* | 5100 | (2 3 1) | *w* | 480 | (3 4 0) | | 0 |
| (0 1 1) | *a* | 0 | (0 3 2) | *a* | 0 | (0 5 0) | *a* | 0 |
| (1 1 1) | *v·s* | 14000 | (1 3 2) | *w* | 670 | (2 3 3) | *a* | 1 |
| (0 2 0) | *v·s* | 13000 | (0 4 0) | *v·w* | 30 | (2 4 2) | | 10 |
| (1 2 0) | *s* | 2600 | (0 2 3) | | 10 | (0 2 4) | *w* | 400 |
| (0 2 1) | *w* | 450 | (1 4 0) | *a* | 0 | (1 5 0) | *a* | 0 |
| (0 0 2) | *s* | 2800 | (1 2 3) | *a* | 1 | (3 4 1) | | 2 |
| (1 2 1) | *m* | 1500 | (0 4 1) | *w* | 600 | (0 5 1) | *a* | 0 |
| (0 1 2) | *a* | 0 | (3 3 0) | *w* | 500 | (1 2 4) | *a* | 20 |
| (1 1 2) | *m* | 760 | (1 4 1) | *a* | 4 | (1 5 1) | *v·w* | 20 |
| (2 2 0) | *s* | 3800 | (2 3 2) | *a* | 100 | (0 4 3) | *v·w* | 0 |
| (0 3 0) | *a* | 0 | (3 3 1) | *w* | 600 | (1 4 3) | *a* | 0 |
| (2 2 1) | *a* | 90 | (2 4 0) | *w* | 680 | (2 2 4) | | 350 |
| (0 2 2) | *v·w* | 70 | (2 2 3) | | 1 | (3 3 3) | | 140 |
| (1 3 0) | *a* | 50 | (0 3 3) | *a* | 0 | (2 5 1) | | 60 |
| (0 3 1) | *a* | 0 | (2 4 1) | *a* | 1 | (3 4 2) | | 1 |
| (1 2 2) | *v·w* | 250 | (0 0 4) | *w* | 200 | (0 3 4) | | 0 |
| (1 3 1) | *w* | 100 | (0 4 2) | | 50 | (1 5 2) | *v·w* | 100 |
| (0 0 3) | *a* | 20 | (1 3 3) | *w* | 180 | (1 3 4) | | 100 |
| (2 3 0) | *w* | 740 | (1 4 2) | *a* | 1 | (2 4 3) | | 1 |
| (0 1 3) | *a* | 0 | (0 1 4) | *a* | 0 | (0 0 5) | | 130 |

(1) I (Obs.) (2) I (Cal.)

Shimose and Prof. M. Tokuhisa for their encouragement throughout this experiment.

### References

1) N. L. Bowen: J. Phys. Chem. **30** (1926) 721.
2) S. B. Hendricks, E. Posnjak and F. C. Krack: J. Am. Chem. Soc. **54** (1932) 2766.
3) R. Tiemeyer: Z. Krist. **97** (1937) 386.
4) K. Tanaka and I. Fukuyama: J. Phys. Soc. Japan **8** (1953) 428.
5) R. W. G. Wyckoff and A. H. Armstrong: Z. Krist. **72** (1929) 319.
6) R. W. G. Wyckoff: Phys. Rev. **35** (1930) 583.
7) Internationale Tabellen zur Bestimmung von Kristallstrukturen **II**, (1935) 571.

---

JOURNAL OF THE PHYSICAL SOCIETY OF JAPAN Vol. 11, No. 4, APRIL, 1956

# Electron-Diffraction Study of the Structure of Supercooled Liquid Bismuth

By Mieko TAKAGI

*Physics Department, Tokyo Institute of Technology,*
*Oh-Okayama, Meguro, Tokyo*

(Received December 3, 1955)

Thin bismuth films were prepared on crystal surfaces by evaporation and the liquid state of the films at temperatures above and below the ordinary melting point (271°C) has been studied by means of the reflexion method of electron diffraction. The marked supercooling of the films (M. Takagi: J. Phys. Soc. Japan **9** (1954) 359) has been utilized for the study below the melting point. A method to eliminate difficulties inherent to the intensity measurement by reflexion method and a method to refine the observed intensity values were developed.

The radial distribution curves at 400°C, 271°C (the melting point), 175°C, 130°C and 110°C (a little above the solidification temperature) were computed from experimental data. The curves showed a systematic change with temperature. It was revealed that the atomic arrangement at 110°C resembles closely that of solid bismuth. Above the melting point a tendency towards close-packed structure was noted.

## § 1. Introduction

The radial distribution function is an important characteristic of liquid substances, metals and non-metals. From this function, direct information on the degree of the short range regularity present in atomic arrangement of liquids can be derived. For instance, it has been revealed by the temperature dependence of the function that the regularity increases as temperature lowers, tending to manifest a quasi-crystalline structure.

There have been reported many studies on structure of the liquid phase of metals not only by $X$-ray but recently even by neutron diffraction method. Of the studies which treated the temperature dependence of the distribution function, we can mention the work of Boyd and Wakeham1) on liquid mercury at the temperature ranging from −36°C (just above the melting point) to 250°C. That the melting point of mercury is fairly low (−38.9°C) is especially favorable to observe a characteristic change in the radial distribution function with temperature. However, it has been reported that the similar change is not appreciable for metals having higher melting point. For instance, the structures of liquid tin studied by Hendus2) by means of $X$-rays, and of liquid lead and bismuth studied by Chamberlain3) and by Scharrah and Smith4) by means of neutron diffraction showed no remarkable difference with temperature. If we can maintain the supercooled state of these metals at temperatures far below the melting point so that the variation of radial distribution curves is studied over much wider temperature range including the melting point, the temperature effect will appear more distinctly. However such a study is very difficult by *X*-ray or neutron diffraction method because in these methods a mass of metal must be used as a sample and the supercooled state is hardly maintained for a long period.

On the other hand, as has been shown by the electron diffraction studies by Sayama⁵⁾ on tin and the present author⁶⁾ on lead, bismuth and tin, thin metal films prepared in vacuum by evaporation on crystal surfaces show a quite marked nature of supercooling. For example, the observed solidification temperature of *Bi* films, *Pb* films and *Sn* films with thickness of about 50 Å were 124°C, 170°C and 40°C respectively, while the ordinary melting points of these metals are 271°C, 327°C and 232°C respectively. In my previous paper⁶⁾ the phenomenon was explained, with reference to Turnbull's⁷⁾ experiment and his theory, as that the evaporated films are made of droplets whose diameters are so small that each of them contains scarcely any accidental inclusion which acts as a nucleus of crystallization.

The fact that the supercooled liquid state is maintained during the period of observation means that the electron diffraction method is very suitable for the study of liquid states of metals over an extended temperature range. There are, however, some experimental difficulties inherent to the reflexion method of electron diffraction. In the present paper a method to analyse the liquid pattern in reflexion photographs of electron diffraction is developed, and the change of the radial distribution function of liquid bismuth is studied over the temperature range from 400°C to 110°C. Since the crystal structure of solid bismuth is not of a close-packed type, we expected the radial distribution function at lower temperatures to show some interesting behaviors.

## § 2. Experimental

Bismuth films of about 50 Å in mean thickness were prepared by evaporation in an evacuated electron diffraction camera⁸⁾. The base crystals employed were either fresh cleavage surfaces of zincblende single crystals or flat natural surfaces of silicon carbide single crystals. Oxide films formed on the surfaces of silicon carbide were removed beforehand by the following treatment: the crystals were boiled in conc. aqueous caustic soda, dipped in dilute nitric acid, washed in water, dipped in absolute alchol and then dried.

While evaporating bismuth, the base crystal was kept at about 400°C so that a bismuth film in liquid state was formed on its surface. The temperature of the crystal is measured by a thermocouple⁶⁾. After the formation of the film, the temperature of the crystal was lowered gradually. The solidification temperature of the film was easily determined by observing the diffraction pattern on a fluorescent screen because at this temperature the pattern changed abruptly from halos to Debye-Scherrer rings. The film thus solidified was reheated through the melting point up to 400°C, and then cooled again gradually. The diffraction patterns from the liquid film were taken at various temperatures during the second course of cooling. The cooling rate near the solidification temperature was kept at about 1°C per minute. As the exposure time needed was 1∼2 seconds, it was possible to observe the state at a temperature within 0.2°C of the solidification temperature.

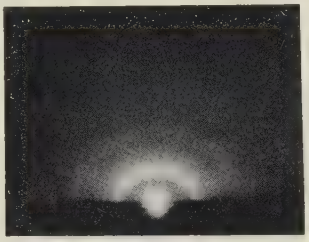
a. 400°C

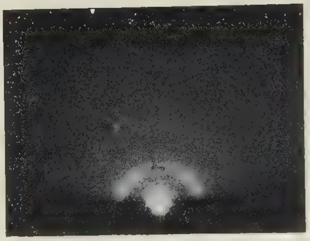
b. 110°C

Fig. 1. Diffraction photographs.

The camera length was 30 cm and the acceleration voltage of electrons was in general about 50 kV. The patterns were always

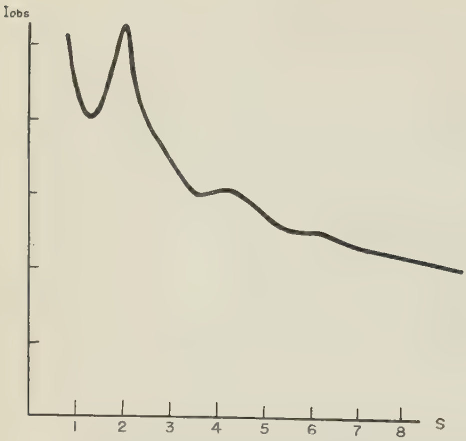

Fig. 2. Observed intensity $I_{obs}$ at 110°C in arbitrary scale. $s=4\pi\sin\theta/\lambda$, $2\theta$ is the scattering angle, $\lambda$ the wave length.

Table I. Position of maximum intensity in $s$ value.

| | 1st. max. | subsidiary | 2nd. max. | 3rd. max. |
|---|---|---|---|---|
| 400°C | 2.0 | | 4.2 | 6.4 |
| 271°C | 2.0 | | 4.1 | 6.4 |
| 175°C | 2.0 | 2.9 | 4.1 | 6.2 |
| 130°C | 2.0 | | 4.2 | 6.5 |
| 110°C | 2.0 | 2.9 | 4.0 | 6.1 |

completely free from rings due to oxides of *Bi*. The photographs obtained at 400°C and 110° (just above the solidification temperature) are shown in Fig. 1.

All the photometry of the halo patterns from liquid bismuth was performed along radius nearly perpendicular to the shadow edge. The obtained microphotometer curves were converted into the intensity curves in accordance with the method of Karle and Karle⁹⁾. In their method, a pair of diffraction photographs with different exposure time were taken at each temperature concerned. The blackness-intensity curve of the photographic film used was determined by the photometry of the pair of photographs assuming the linearity of this curve in the range of weak electron intensity.

An example of the obtained intensity curve, $I_{obs}$ is shown in Fig. 2. In this curve which corresponds to the film of liquid bismuth at 110°C, intensity maxima are observed at about 2.0 $\text{Å}^{-1}$, 4.0 $\text{Å}^{-1}$ and 6.1 $\text{Å}^{-1}$ in $s$ value, where $s=4\pi\sin\theta/\lambda$, $2\theta$ being the scattering angle and $\lambda$, the wave length. In addition a subsidiary maximum is noted at about 2.9 $\text{Å}^{-1}$. This subsidiary maximum is more conspicuous at lower temperatures than at higher temperatures. Positions of maxima in the observed liquid patterns are summarized in Table I.

The decrease of $I_{obs}$ is approximately inversely proportional to the scattering angle, and is not so rapid as expected from the law of the inverse fourth power of scattering angle. This is because the background in $I_{obs}$ includes components which depend only a little on the scattering angle. The nature of the background is discussed in more detail in the following section.

## § 3. Method of Calculation of Radial Distribution Function from Observed Intensity

Similarly to the well known procedure in X-ray diffraction¹⁰⁾, the radial distribution function $4\pi r^2\rho(r)$ for a monatomic liquid is obtained by the following formula:

$$4\pi r^2\rho(r)$$

$$=4\pi r^2\rho_0+\left(\frac{2\pi}{\pi}\right)\int_0^\infty si(s)\sin sr\,ds,$$

$$i(s)=\frac{I_{co}-NI_e|f|^2}{NI_e|f|^2},$$

$$f=Z-F,\quad s=4\pi\sin\theta/\lambda\,, \qquad (1)$$

where $\rho_0$ is the mean density of atoms in the liquid, $I_{co}$ is the intensity of coherent electron scattering from the liquid, $N$ is the total number of scattering atoms, $I_e$ is the intensity of the electron wave scattered by a point charge $+e$, $Z$ is the atomic number, $F$ is the atom form factor for X-rays and $f$ is the atom form factor for electrons.

We are required to deduce $I_{co}$ from the observed total intensity, $I_{obs}$, which is written as

$$I_{obs}=I_{co(obs)}+I_{back} \qquad (2)$$

where $I_{co(obs)}$ is the coherent single scattering from the liquid film and $I_{back}$, the general background. Since the interference pattern proper to the base crystal is mostly covered by the liquid pattern, the scattering from the base crystal contributes only to the general background. Besides, $I_{back}$ contains the stray scattering from slits and residual gases, the incoherent scattering from the liquid film, and the secondary or multiple scatterings of the coherent part from the liquid film.

It should be noted that $I_{co(obs)}$ is not the same as $I_{co}$ in (1) because the scatterings from the liquid suffer a intensity modulation due to the presence of the surface of the base crystal, the circumstance which is peculiar to the reflexion method in the present study. This modulation is due to the absorption of the scattered electrons due to the surface, and depends upon the topography of the surface, the thickness of the film, as well as the kind of substance of the base crystal and that of the evaporated metal. Let us define for each photograph the modulation function $\Phi$ as follows:

$$\Phi = \frac{I_{co(obs)}}{I_{co}} . \qquad (3)$$

From (3), (2) is rewritten as

$$I_{obs} = \Phi \cdot I_{co} + I_{back} . \qquad (4)$$

$I_{co}$ can be obtained provided the function $\Phi$ is available and the background term $I_{back}$ is separable from (4).

$\Phi$ is, of course, an angle dependent function; it depends not only on the scattering angle but also on the direction of radius along which photometry is performed. It also depends on the glancing angle of the incident electrons to the base crystal. The method employed to obtain the function $\Phi$ and the procedure of separation of the $I_{co}$ term were as follows.

### a) Experimental Determination of the Modulation Function

To determine the function $\Phi$, we assume that this function remains unchanged whether the film concerned is in liquid state or in solid state. This assumption will be reasonable provided that the submicroscopic structure of the film undergoes no marked change at the time of melting or solidification. This can be considered to be the case for evaporated metal films as thin as 50 Å, for the films are composed of almost independent colonies. Then the function $\Phi$ for a liquid film is given by the ratio of observed to theoretical values of the integrated intensities of the Debye-Scherrer rings from crystallized state. In order to apply this method, it is required that the crystalline texture of the solidefied film is free from preferred orientation.

Though the function $\Phi$ should be obtained for the same sample which was used in the study of liquid, it was impossible unfortunately for evaporated *Bi* film because of a preferred orientation of crystallites. We were therefore obliged to apply an approximate procedure in the following way.

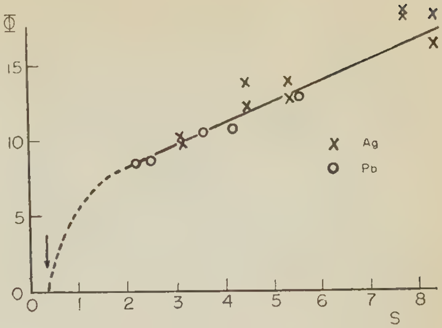

Fig. 3. Modulation function $\Phi$ obtained from two Ag films and a lead film in arbitrary scale. An arrow in the fig. indicates the position of shadow edge in diffraction patterns.

We prepared orientationless films of silver or lead metal, instead of bismuth, on base crystals of zincblende or silicon carbide, which were similar in size and in nature of the surface to the base crystals used for the study of liquid. The orientationless silver films were prepared by evaporating AgI on the base kept at about 450°C (Silver is formed as the result of decomposition of AgI.). The orientationless lead film was prepared by evaporating lead on the base crystal at room temperature. The diffraction patterns from these films were taken with glancing angles of incident beams approximately equal to the angles adopted in the study of the liquid bismuth. The modulation functions for these samples were obtained as the ratios of the observed values to the theoretical ones of the integrated intensities of the diffraction rings.

Some of the earlier experiments have shown that the intensities of the Debye-Scherrer rings from certain metal films of about 50 Å in mean thickness or in grain size can be estimated in accordance with the kinematical theory11)12), while other experiments have shown that the intensity of (111) and (200) rings from similar metal films deviates about 10%* from the kinematical value13)14). Since both the grain size estimated from the half

---

* The value 10% was estimated making allowance for different values of the mean thickness, grain size and energy of electrons in different experiments.

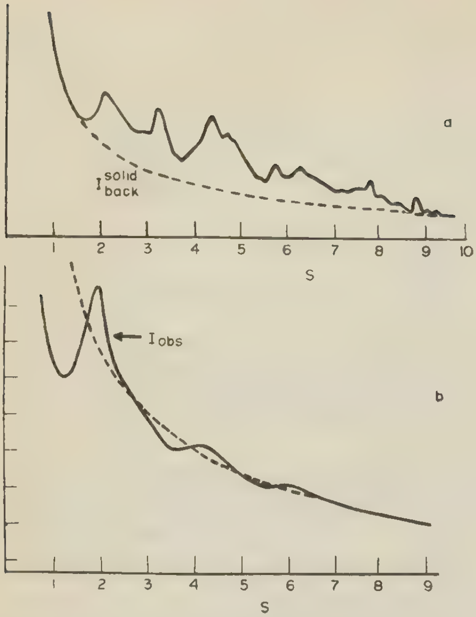

Fig. 4. The experimental procedure to deduce $I_{co}$ and $NI_e|f|^2$.

a. Full line shows the intensity curve of Debye-Scherrer ring from solid *Bi*. The broken line shows the background $I^{solid}_{back}$.

b. Full line shows the total intensity of liquid halo $I_{obs}$, and the broken line shows $b|f|^2+a\cdot I^{solid}_{back}$. $a$ and $b$ were determined so as to make the broken line agrees with the full line at large value of $s$.

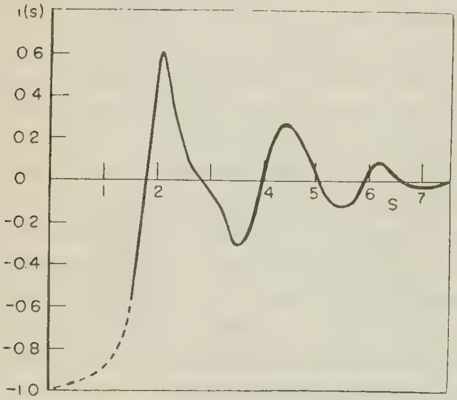

Fig. 5. $i(s)$ curve at 110°C.

breadth of the diffraction rings and the mean thickness of silver and lead films used in the present study were about 50 Å, there is a possibility that the Debye-Scherrer rings from these films contain the dynamical effect. However, for simplicity, we have neglected the dynamical effect. Also, the Debye temperature factor was neglected. The influence of the approximate estimation of ring intensities on the final result of the present study will be discussed in § 5.

Similarly to the case of the halo patterns from liquid bismuth, the photometry of the ring patterns to determine the function $\Phi$ was performed along radius nearly perpendicular to the shadow edge. Fig. 3 shows the function $\Phi$ obtained from two Ag films made on zinc-blende and a *Pb* film made on silicon carbide. We can see in Fig. 3 that the observational points in the three cases lie approximately on a commom curve irrespective of the kinds of evaporated metals and of base crystals. Considering this fact together with the fact that the size of colonies in the films of silver, lead and bismuth are similar (about 50 Å), and that the atomic numbers of lead ($Z=84$) and bismuth ($Z=83$) are near, it is most probable that the modulation function for bismuth films will not be so different from the average curve given in Fig. 3. We, therefore, adopted this curve for the modulation function for the bismuth films.

### b) Separation of $I_{co}$

Though the theoretical estimation of background $I_{back}$ in (4) is most difficult, $I_{back}$ can be separated from $I_{obs}$ when we assume:

(i) For one sample the dependence of $I_{back}$ on scattering angle is the same independent of the state of the film, liquid and solid.

(ii) $I_{co}$ is proportional to the square of the atomic scattering factor $f$ for sufficiently large value of $s$.

Let us denote the background intensity in the Debye-Scherrer ring pattern from a solidified film as $I^{solid}_{back}$. Then, from the assumption (**i**) the background in the liquid halo pattern is.

$$I_{back}=a\cdot I^{solid}_{back}\,, \tag{5}$$

where $a$ is a certain constant which depends on the ratio of the effective exposure time for the photograph from the liquid state to that for the photograph from the solid state. Then, we have

$$I_{obs}=\Phi\cdot I_{co}+a\cdot I^{solid}_{back}\,. \tag{6}$$

Next, by the assumption (**ii**) and from (6) we have

$$I_{obs}=\Phi\cdot b|f|^2+a\cdot I^{solid}_{back}\,, \tag{7}$$

in the range where $s$ is sufficiently large. $b$

is again a certain proportional constant. $NI_e|f|^2$ in (1) is given by

$$b|f|^2 = NI_e|f|^2 \,. \qquad (8)$$

The experimental procedure to deduce $I_{co}$ and $NI_e|f|^2$ in (1) is as follows. The constant $a$ and $b$ are determined so that the experimental curves $I_{obs}$ and $I_{back}^{solid}$ (Fig. 4a), both of which are given in arbitrary scale, fulfil the relation (7) in the range where $s$ is large (Fig. 4b). Then from (6) and (8), $I_{co}$ and $NI_e|f|^2$ can be determined, from which $i(s)$ in (1) is obtained. An example of $i(s)$ curve is showed in Fig. 5.

## § 4. Refinement of the Radial Distribution Curve

The errors of the radial distribution function calculated by the relation (1) may be mainly due to the error of $I_{co}$, hence of $i(s)$, and to the termination effect.

**a) Refinement of the Intensity Curve $I_{co}$.** The inaccuracy of $I_{co}$ may be mainly caused by the inaccurate determination of the curve $I_{back}$ and that of the modulation function $\Phi$. As described in the previous section, we have utilized $I_{back}^{solid}$ to deduce $I_{back}$. Actually, however, the Debye-Scherrer rings from solid *Bi* films were so broad that determination of the curve $I_{back}^{solid}$ is not free from arbitrariness. As $I_{back}$ amounts to a relatively large part in the total intensity $I_{obs}$, the error of $I_{back}$ due to the error of $I_{back}^{solid}$ influence sensitively the final values of the radial distribution function. In order to minimize the above error, the $I_{back}$ curve was corrected in the following way.

In electron diffraction studies of structure of gas molecules, the background intensity curve has been refined to conform to the criterion that there should be no negative value of the atomic density for all value of the distance $r$[15]. In the case of liquid, the same criterion is not effective to make refinement of the result because the atomic distribution density of liquid fluctuates around the mean density $4\pi r^2 \rho_0$ which possesses an appreciable positive value except for a range of small $r$. In the present study, therefore, the refinement of the curve $I_{back}$, or that of the curve $I_{co}$ was made by imposing a more severe condition as follows: *the atomic distribution function must be zero for* $r$ *which is smaller than the atomic diameter* $d$. From (1) the condition requires,

$$u(r) \equiv \int_0^\infty s i(s) \sin rs \, ds = -2\pi^2 r \rho_0 \quad \text{for} \quad r < d. \qquad (9)$$

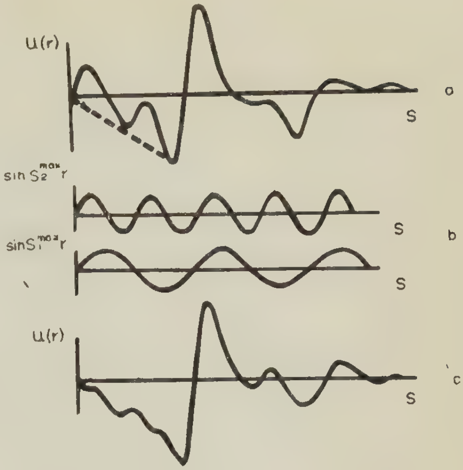

Fig. 6. Experimental method of refining the intensity curve.
a. Uncorrected $u(r)$ curve at 271°C. Broken line shows the theoretical value $-2\pi^2 r \rho_0$.
b. Value of $\sin s_2^{\max} r$ and of $\sin s_1^{\max} r$.
c. The $u(r)$ curve calculated with improved $i(s)$.

The experimental method of refining the intensity curve is explained below with an example.

Fig. 6a shows the function $u(r)$ calculated by using an uncorrected intensity curve measured on a pattern from a liquid *Bi* film at 271°C. The broken line drawn in the range of small $r$ represents the theoretical value $-2\pi^2 r \rho_0$. A ripple having two prominent peaks in this range is gohst peaks which should be extinguished by the appropriate correction of the intensity curves $I_{co}$ or $I_{back}$. The method of correction is generally trial and error guided by the following principle.

Let us denote the $s$-values at maxima and at minima of a $i(s)$ curve by $s_1^{max}, s_2^{max}, \cdots$ and $s_1^{min}, s_2^{min}, \cdots$. Since the contribution of these values amounts to a large value in the integral (9), errors of maximum and minimum values have an important influence on the results. If, for instance, one of maxima say at $s = s_i^{max}$, is too low or too high compared with the correct value of $i(s)$, a ripple with the period $2\pi/s_i^{max}$ may appear in the calculated $u(r)$ curve. This may be noticed most distinctly in the range $r < d$. The same is true of $s_i^{miu}$. Therefore, it may be said that the ripple appearing in Fig. 6a was caused by a too low estimation of the value of the second maximum at $s_2^{max}$ in the $I_{co}$ or $i(s)$ curves. This circumstance is seen clearly from the comparison of Fig. 6a with Fig. 6b showing $\sin s_2^{max}r$ and $\sin s_1^{max}r$ respectively. In order to approach the condition (9) more, the second peak of $I_{co}$ must be lowered and accordingly the background $I_{back}$ must be corrected to a little higher value in the range near $s=s_2^{max}$. By repeating this process we can obtain the $i(s)$ curve improved throughout the whole range of $s$. The $u(r)$ curve calculated with the improved $i(s)$ is showh in Fig. 6c, in which we can see that the ripple has almost disappeared.

The radial distribution function shown in Fig. 7 (§ 5) are calculated with the intensity curves refined by the above procedure.

We have no systematic method to elliminate the error which might come from inaccuracy of the modulation function, in particular when liquid bismuth is dealt with. Also the influence of the error accompanying the photometry may not be negligible. However, we can say that the above procedure of refining the intensity curve simultaneously mitigates effect of the errors due to these sources to some extent, though not satisfactorily.

**b) Termination effect**

The upper limit of the $s$-value adopted in the present study is $s=8$, as the magnitude of $i(s)$ falls to the order of experimental error for larger values of $s$. For the purpose of testing whether or not the termination of the integral in (1) at $s=8$ gives rise to spurious maxima or minima in the calculated distribution curves, we computed the integral by using $i(s)$ multiplied by a damping factor[15] exp $(-as^2)$. By means of the convolution theorem such an integral is related to $\rho(r)$ as follows:

$$\int_0^{s_{max}} si(s)\exp(-as^2)ds=[1/2(\pi a)^{1/2}]$$
$$\times\int_{-\infty}^{\infty} 2\pi^2 t[\rho(t)-\rho_0]\exp[-(r-t)^2/4a]dt. \tag{10}$$

In order to keep the half breadth[15] of $\exp[-(r-t)^2/4a]$ small enough compared with those of peaks present in the radial distribution function, the value adopted for the constant $a$ was $a=0.0145$ Å$^2$, thence $\exp(-as^2)\approx 1/2.5$ at $s=8$.

The calculations carried out on a few selected examples showed that the radial distribution curves remain almost unchanged. From this evidence we can conclude that the termination effect is small and does not give rise to any extra peaks.

That the effect of the termination is negligible can be endorsed also from the following consideration. Since the density function $\rho(r)$ for monatomic liquid distributes over a wider range of $r$ and since it contains broader peaks compared with the density function of gas molecules, the intensity function $i(s)$ of liquid (being the Fourier transform of $\rho(r)-\rho_0$) must damp with $s$ more rapidly than the intensity function of gas molecules. This explains why the termination effect is less important for monatomic liquid than for gas molecules.

## § 5. Result and Discussion

By using improved values of $i(s)$, the integral in (1) up to $s=8$ was calculated with the aid of punched cards and a Remington Band machine. For $i(s)$ in the range from $s=0$ to $s=1.3$ the extrapolated value was used. Fig. 7 shows the obtained radial distribution functions $4\pi r^2\rho(r)$ for bismuth films of about 50 Å in mean thickness at 400°C, 271°C (the ordinary melting point), 175°C, 130°C and 110°C (a little above the solidification temperature of the film).

In Fig. 8 our distribution curve at 271°C is compared with the curve at 310°C obtained by neutron diffraction by Chamberlain[3]. Though the temperatures are different, the change in atomic distribution in liquid above the melting point is negligible for such a small temperature difference. The similarity in both curves and the systematic change of the radial distribution curves with temperatures support the validity of our result in spite of difficulties accompanying the electron diffraction method as mentioned in § 3.

Moreover, we can show that the influence of systematic errors of the modulation function (§ 3a) on the final result is not so important. Let us denote the correct modulation function for the film concerned by $\Phi'$. $\Phi'$ will be related to $\Phi$ used in the present calculation as $\Phi'=m(s)\cdot\Phi$, where $m(s)$ is a monotoneus function. The difference between $\Phi$ and $\Phi'$ mainly results from the neglect of the dyna-

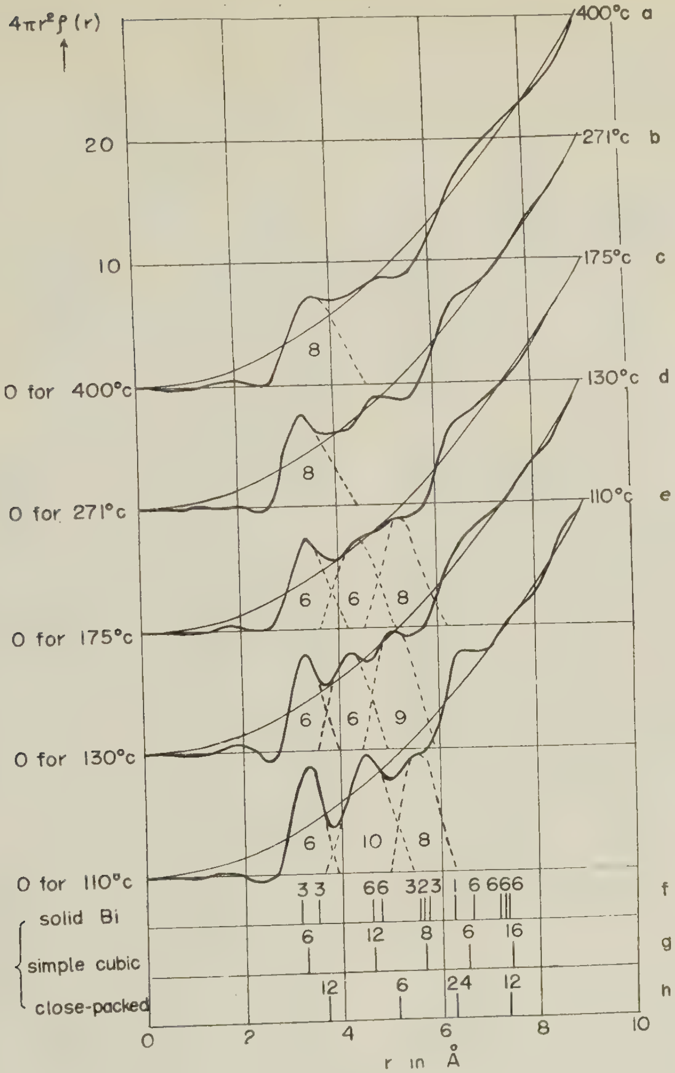

Fig. 7. a∼e. Obtained radial distribution function $4\pi r^2\rho(r)$ at 400°C, 271°C, 175°C, 130°C and 110°C.
f. Atomic shells in solid $B_i$.
g. Atomic shells in simple cubic structure.
h. Atomic shells in close-packed structure.

mical effect which is negligible at large $s$-values and is conspicuous at small $s$-values. The deviation of intensity at the position of (111) rings from films of metals such as silver or lead is at most about 10% as was described in § 3 a. Therefore $m(s)$ is approximately equal to unity but increases slightly as $s$-value decreases and may attain to a value∼1.1 at $s=2$ (the position of (111) ring). The correct value of $i(s)$ for the film, which we denote here by $i'(s)$, is related to $i(s)$ as $i'(s) \sim i(s)/m(s)$. Thus the integral in (1) for the film should be $\int si'(s)\sin rs\,ds$, while in the present calculation the integral $\int si(s)\sin rs\,ds$, or $\int si'(s)m(s)\sin rs\,ds$, has been used instead. According to the convolution theorem, this integral can be written as the convolution of the Fourier inversion of $si'(s)$ and of $m(s)$. Because of the monotonous nature of $m(s)$ as mentioned above, the Fourier inversion of $m(s)$ will have a dominant peak only at the

Table II. Position of peaks in the radial distribution curves and the number of atoms (shown in parenthesis) under each peak.

| | position of peaks and the number of atoms | | | |
|---|---|---|---|---|
| 400°C | 3.6 Å (8) | | 5.0 Å | ~7 Å |
| 271°C | 3.3 Å (8) | | 4.8 Å | 6.5 Å |
| 175°C | 3.3 Å (6) | 4.4 Å (6) | 5.2 Å (8) | 6.4 Å |
| 130°C | 3.3 Å (6) | 4.3 Å (6) | 5.2 Å (9) | 6.7 Å |
| 110°C | 3.3 Å (6) | 4.5 Å (10) | 5.6 Å (8) | 6.5 Å |

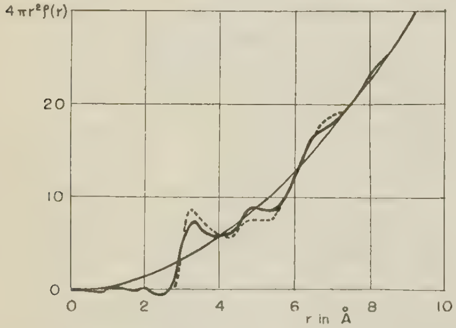

Fig. 8. Comparison of a obtained distribution function with that from other experiment. Full line shows the distribution curve at 271°C in this experiment, and broken line shows that at 310°C with neutrons by Chamberlain.

origin and no other serious ripples at larger distances[16], thus the integral $\int si'(s)m(s)\sin rs ds$ will differ not greatly from the integral $\int si'(s) \sin rs\, ds$.

The distribution curves can be divided into peaks as are shown by broken lines in Fig. 7. Numerals inscribed are the number of atoms under the peak concerned. The positions of the peaks and the number of atoms under each peak are summarised in Table II.

Solid bismuth has the rhombohedral structure with the cell dimension $a_0=4.736$ Å, $\alpha=57°14.5'$, containing two atoms in the position $uuu$; $\bar{u}\bar{u}\bar{u}$, where $u=0.237$. This structure is a sort of distorted simple cubic structure; when $\alpha=60°$ and $u=0.25$, it is a simple cubic structure. The distribution of atomic shells in solid bismuth and that in a fictitious structure which is a simple cubic arrangement of atoms with the same atomic volume as bismuth are shown in Fig. 7f and 7g, respectively. The distribution of the fictitious close-packed structure of atoms with the same atomic volume is also shown in Fig. 7h. The feature of the radial distribution curves at each temperature are described below in detail.

### Supercooled state

**i) 110°C** (0.2°C above the solidification temperature) (Fig. 7e). Four peaks are observed at 3.3 Å, 4.5 Å, 5.5 Å and 6.5 Å. The number of atoms under the first, second and third peaks are 6, 10 and 8, respectively. At this temperature, both the position and the number of atoms under each peak are almost the same as those in the structure of solid bismuth (Fig. 7f) or in the above mentioned simple cubic structure (Fig. 7g).

**ii) 130°C and 175°C** (Fig. 7d and 7c). The positions of peaks are at about 3.3 Å, 4.4 Å, 5.2 Å and 6.5 Å. The number of atoms under the first, second and third peaks are 6, 6 and 8 respectively. The second and the third peaks at 130°C and 175°C are nearer the origin than the corresponding peaks at 110°C. The three curves at 110°C, 130°C and 175°C show that the sharpness of the peaks, hence the deviation from the mean atomic distribution $4\pi r^2\rho_0$ is more conspicuous at lower temperatures.

### Above the melting point

271°C and 400°C (Fig. 7b and 7a). The position of peaks at 271°C are 3.3 Å, 4.8 Å and 6.5 Å, and those at 400°C are 3.6 Å, 5.0 Å and 7 Å. The number of atoms under the first peak at these temperatures is about 8. The second peak corresponds to the unified peak of the second and the third peaks observed at 110°C, 130°C and 175°C.

From the above result we can see that the nature of homopolar binding persists in the liquid state of bismuth. The fact that the number of atoms under the first peak is 6 in the supercooled state indicates that the shell structure in this state is almost the same as that of solid. At 110°C, not only the first but the second and the third peaks are also related to the corresponding atomic shells in the solid structure. At the melting point the number of atoms under the first peak increases from 6 to 8 and the position of the peak shifts outwards slightly. The positions of the first and the second peaks above the melting point tend to the positions for the fictitious close-packed structure (Fig. 7h), suggesting a tendency towards the close-packed structure.

For mercury, Harasima[17] showed as an application of his theory that the peak value of the first maximum is inversely proportional to $\sqrt{T}$, where $T$ is absolute temperature. The same trend is observed in the present experiment in the supercooled state. In Table III the maximum value of the first peak $4\pi r^2 \rho(r)_{max}$ and also $4\pi r^2\rho(r)_{max}\cdot\sqrt{T}$ are tabulated. We can see in it that the latter value remains almost unchanged for the supercooled state.

Table III.

| | $4\pi r^2\rho(r)_{\max}$ | $4\pi r^2\rho(r)_{\max}\cdot\sqrt{T}$ |
|---|---|---|
| 175°C | 7.4 | 16×10 |
| 130°C | 8.0 | 16×10 |
| 110°C | 8.7 | 17×10 |

The result of the present study shows that the application of the electron diffraction method is quite useful for study of the liquid state of metals. The merits exclusive to this method are the feasibility of treating the supercooled state over a wide temperature range. On the other hand, the most important weakpoint of this method is found in inevitable limit in the accuracy of the intensity measurement. The accuracy of the photometric or Geiger counter determination of the intensity of X-ray pattern is superior to the photometric determination of the intensity of electron diffraction pattern, mainly because of higher background and of larger intensity range in the electron diffraction pattern compared with those in the X-ray patterns. This defect in electron diffraction method can be lessened to some extent with the use of rotating sectors which have been applied in the study of gas molecules. It will be interesting to extend the present study to other kind of metals with such an improved method of intensity measurement.

In concluding the present article the author wished to express her sincere thanks to Prof. S. Miyake for his kind advices throughout this work and also to Prof. A. Harasima and to Mr. S. Takagi for discussing this paper with me. The author's thanks are also due to Prof. Y. Morino for allowing me to use punched cards and to Mr. K. Kuchizu and Mr. E. Hirota for their advices and for laborious work in computing integral in the formula (1) with punched cards and machines.

## References

1) R. N. Boyd and H. R. Wakeham: J. Chem. Phys. **7** (1939) 958.
2) H. Hendus: Z. Naturforschg. **2 a** (1947) 505.
3) O. Chamberlain: Phys. Rev. **77** (1950) 305.
4) P. C. Scharrah and G. P. Smith: J. Chem. Phys. **21** (1952) 228.
5) Y. Sayama: Proc. Phys.-Math. Soc. Japan **23** (1941) 869.
6) M. Takagi: J. Phys. Soc. Japan **9** (1954) 359.
7) D. Turnbull: J. App. Phys. **21** (1950) 1022.
8) M. Kubo (Takagi) and S. Miyake: J. Phys. Soc. Japan **3** (1948) 115.
9) J. Karle and I. L. Karle: J. Chem. Phys. **18** (1950) 961.
10) P. Debye and H. Menke: Ergebnisse der technischen Röntgenkunde Bd. 11 (1931) 1.
11) H. Mark and R. Wierl: Zs. f. Phys. **60** (1930) 741.
12) Z. G. Pinsker: Electron Diffraction (Translated in English) Chap. 8 London, 1953.
13) S. Lennander: Arkiv För Fysik; Bd. 8 **54** (1954) 551.
14) L. Ornstein, H. Brinkman, A. Hauer and T. Tol: Physica **V** (1938) 693.
15) I. L. Karle and J. Karle: J. Chem. Phys. **17** (1949) 1052.
16) J. Waser and V. Schomaker: Rev. Mod. Phys. **25** (1953) p. 675 Fig. 1 (b)~(j).
17) A. Harasima: Proc. Phys.-Math. Soc. Japan **25** (1943) 425.

JOURNAL OF THE PHYSICAL SOCIETY OF JAPAN Vol. 11, No. 4, APRIL, 1956

# Application de la Méthode de Décapage Ionique en Diffraction Electronique:

## Etude de la Structure de Dépôts Thermiques d'Or sur des Supports Cristallisés ou Amorphes

Par Jean Jacques TRILLAT, Nobuzo TERAO, Léa TERTIAN
et Henri GERVAIS

*Laboratoire de Rayons X du Centre National de la Recherche
Scientifique á Bellevue (S. & O.), France*

(Received December 17, 1955)

We have done a new arrangement which allows us to bomb a sample with ions and at the same time examine its structure. In these conditions we obtain a progressive scouring of the superficial coats; electron diffraction gives information about the structure so laid bare.

In this paper we first describe the experimental method and give an example referring to the study of the gold coats laid down on different props. So it's possible to study continuously the relations of epitaxy between the prop and the metal laid down in various conditions. Then we point out the limits of that method and the causes of error.

## §1. Introduction

On sait que l'impact d'un faisceau d'ions positifs sur une cible métallique peut provoquer l'arrachement de particules du métal; c'est le principe même de la pulvérisation cathodique, qui a été utilisé par divers auteurs pour l'attaque ou l'amincissement des préparations destinées à la Microscopie électronique (HEINDENREICH1), CASTAING et LABORIE2)). Récemment FERT3) a montré qu'en utilisant un "canon à ions" approprié, il était possible de bombarder un échantillon en cours d'observation en microscopie ou diffraction électronique, et d'explorer ainsi la structure de l'échantillon en fonction de la profondeur, par arrachement des couches successives de la surface.

Les observations de FERT laissent entrevoir un champ d'applications considérable pour l'étude des structures superficielles et des phénomènes d'épitaxie, sous la condition formelle que l'action du faisceau d'ions ne donne pas lieu à des phénomènes parasites (contamination, action chimique, échauffement etc.). Or, nous avons montré que ces actions pouvaient parfois être importantes et qu'il était donc nécessaire de bien préciser les limites et les possibilités de la méthode de bombardment ionique associée à la diffraction électronique (J. J. TRILLAT)4).

Le but du présent travail est précisément d'étudier en détail une application du décapage ionique dans un cas caractéristique, celui d'un dépôt métallique orienté par son support. Pour cela, nous avons choisi un métal non oxydable et chimiquement inerte, l'or, et des supports variés, cristallisés ou amorphes. De plus, nous avons cherché, à cette occasion, à perfectionner la technique et à l'appliquer non seulement aux examens par réflexion, mais aussi aux examens par transmission.

## §2. Méthode Expérimentale

Le schéma du canon à ions que nous avons utilisé est représenté sur la figure I; cet appareil, construit dans notre laboratoire par H. GERVAIS, permet de réaliser l'ionisation d'une petite quantité d'air ou de gaz raréfié (argon, azote, etc.) entre une anode pouvant être portée jusqu'à 27 Kilovolts et une cathode mise au sol et servant de diaphragme.

L'isolement électrique est assuré par un double manchon en verre Pyrex. Les parties métalliques sont en lation recouvert d'une couche de nickel; le diaphragme de sortie (cathode) est constitué d'une pastille d'aluminium ou de molybdène percée d'un trou. (Fig. 2)

L'alimentation haute tension continue est fournie par un générateur du type employé en

Télévision, mais modifié pour permettre de disposer à la sortie d'une tension variable à volonté entre 2 et 27 Kilovolts; le débit total dans le circuit est de l'ordre de 200 $\mu$A; il est fonction de la quantité de gaz admise dans le canon, qui est elle-même réglée au moyen d'une soupape du type Induni, utilisée dans le diffractographe électronique Trüb-Tauber. Dans les conditions usuelles, en employant pour le vide la pompe moléculaire Holweck qui équipe ce diffractographe, (4 à 5 litres/sec), on obtient un vide de l'ordre de $10^{-3}$ m/m Hg, qui peut être abaissé à $3.10^{-4}$ m/m Hg par l'emploi d'une pompe à débit plus élevé (120 litres/sec.).

La mise au point et les perfectionnements apportés au canon ont eu pour but essentiel d'éviter ou d'atténuer un certain nombre d'inconvénients, portant en particulier1), sur la stabilité de fonctionnement2), sur la contamination des échantillons sous l'action des ions, 3) sur la formation d'un cratère au point d'impact du faisceau ionique, 4) sur l'échauffement de la préparation.

1) *La stabilité de fonctionnement* est avant tout fonction des caractéristiques géométriques des diverses pièces constituant le canon à ions, et en particulier des dimensions du diaphragme de sortie. Ces dimensions ont dû être déterminées par des tâtonnements successifs; pour le diaphragme, les meilleurs résultats ont été obtenus avec un canal de sortie de 1 m/m de diamètre et 1 m/m, 5 de longueur. Le fonctionnement de l'appareil est très stable entre 2 et 27 Kilovolts.

2) *La contamination* des échantillons apportée par le faisceau ionique est bien connue et a été signalée par CASTAING et DESCAMPS5) à propos du microanalyseur à sonde électronique. L'un de nous a montré antérieurement qu'elle se produit également sous l'action d'un faisceau d'électrons rapides (TRILLAT et MERIGOUX)6) et qu'elle est dûe alors à un dépôt de carbone provenant de la décomposition des traces de vapeurs hydrocarbonées présentes dans le diffractographe. Dans le cas du canon à ions, nous avons été amenés à remplacer les parties en plexiglass par du verre et à supprimer les joints de caoutchouc susceptibles de s'échauffer; la contamination est ainsi fortement diminuée et devient même négligeable grâce au perfectionnement indiqué dans le paragraphe suivant.

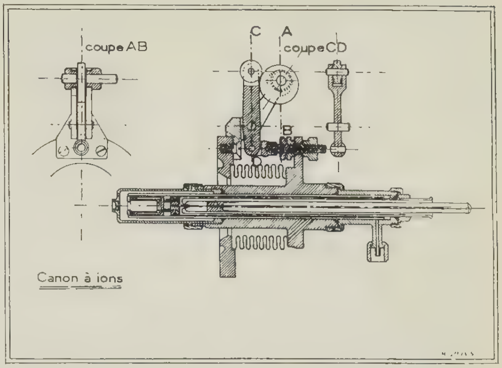

Fig. 1. Schéma du canon à ions. A, B, C, dispositif d'oscillation.

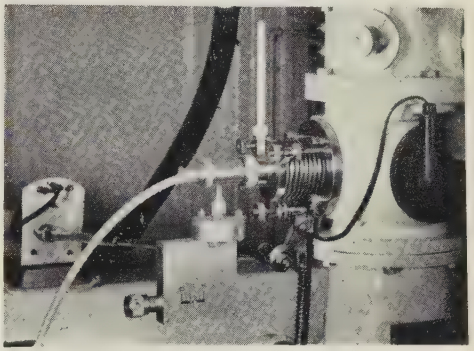

Fig. 2. Réalisation et montage du canon à ions, avec dispositif d'oscillation, sur un diffractographe électronique Trüb Tauber.

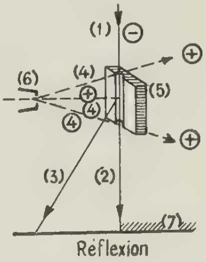

Fig. 3. Balayage ionique et diffraction électronique par réflexion.

⊖ électrons ⊕ ions positifs

1. direction du faisceau d'électrons primaire.
2. direction du faisceau d'électrons non diffracté.
3. direction d'un faisceau électronique diffracté.
4. faisceau d'ions oscillant.
5. Préparation par réflexion, avec le canal creusé par le balayage ionique.
6. Canons à ions.

3) *La formation d'un cratère* au point d'impact du faisceau d'ions sur la préparation s'observe très rapidement lorsque le faisceau ionique et l'échantillon sont immobiles. Le faisceau d'électrons qui, dans la méthode par

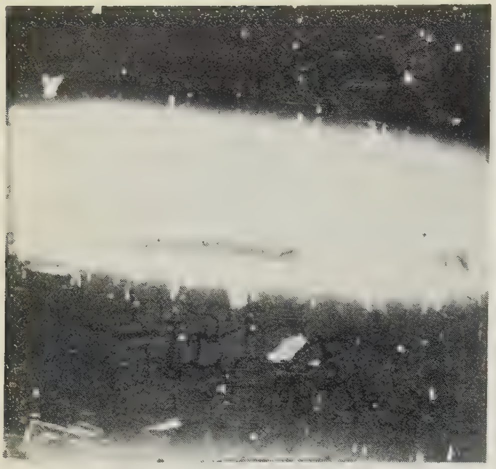

Fig. 4. Trace du faisceau d'ions sur un cristal NaCl recouvert d'une mince couche d'or. La région balayée par le faisceau apparaît en blanc sur la photographie.

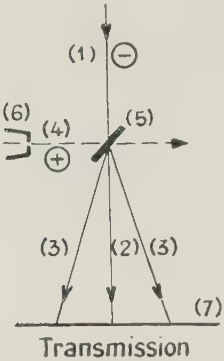

Fig. 5. Bombardement ionique et diffraction électronique par transmission.
1. faisceau électronique primaire.
2. faisceau électronique non diffracté.
3. faisceaux électroniques diffractés.
4. Direction du faisceau d'ions.
5. préparation.
6. canon à ions.
7. plaque photographique.

réflexion, est sensiblement parallèle à la surface de l'échantillon et perpendiculaire à la direction des ions, cesse donc bientôt d'y pénétrer, et toute observation par diffraction devient impossible. Si en outre il s'est formé un dépôt de contamination tout autour du cratère, la faisceau électronique rencontre ces parties contaminées et le diagramme de diffraction devient celui de l'impureté. Pour remédier à cet inconvénient, nous avons réalisé un système de balayage de la surface suivant une direction qui coïncide avec celle du faisceau (Fig. 3); ce balayage est réalisé mécaniquement, avec l'amplitude et la vitesse désirées, par l'emploi d'une came en coeur venant déformer un tube flexible étanche au vide et portant à son intérieur le dispositif de production d'ions. Le décapage ionique creuse dans ces conditions un fin canal dans lequel le faisceau d'électrons peut toujours pénétrer et se diffracter (Fig. 3). Le tube flexible est muni de vis de réglage qui permettent de pointer le canon et d'amener exactement la trajectoire des ions à rencontrer le faisceau d'électrons.

La figure 4 montre la trace du décapage ionique obtenu avec ce dispositif oscillant pour un dépôt d'or sur une lame de verre; l'échantillon est décapé sur toute sa hauteur (5 mm), sur une largeur d'environ 1 mm.

Les principaux avantages de ce systéme de balayage sont la suppression du cratère et donc la possibilité d'examiner la surface d'une préparation sur une profondeur notable (quelques microns au moins), la suppression du dépôt de contamination le long du trajet des électrons et enfin la réduction de l'échauffement superficiel.

4) *L'échauffement* de la préparation, si le faisceau ionique est immobile, est en effet notable, surtout si l'énergie des ions est grande (au-dessus de 20 KV). En recevant un faisceau d'ions de 20 KV (débit total $200\,\mu$A) sur la soudure d'un couple thermoélectrique disposé au foyer d'un paraboloïde en platine, nous avons trouvé, à l'équilibre, une température de l'ordre de 200°C. Cette température varie naturellement avec le débit des ions, la tension d'accélération, la nature et les dimensions de la cible; elle peut être localement encore plus élevée. Or, à une telle température, des métaux oxydables comme le fer, le nickel, le cobalt, etc. peuvent déjà subir une légère oxydation superficielle grâce à la présence de l'oxygène résiduel, comme nous l'avons montré antérieurement (J. J. TRILLAT)[4]. C'est d'ailleurs la raison qui nous a fait choisir l'or dans cette étude, de façon à éliminer cette cause d'erreur.

Le dispositif de balayage provoquant un changement incessant du point d'impact, permet de réduire considérablement l'effet thermique, comme on peut le vérifier au thermocouple.

*Méthode par transmission.*

Nous avons pu également adapter la technique du bombardement ionique aux examens par transmission. Pour cela, la préparation, d'une épaisseur de l'ordre de 100 à 500 Å, est disposée à 45° du faisceau d'électrons et du faisceau d'ions (Fig. 5); le faisceau d'ions la traverse au même point que le faisceau d'électrons et s'y diffracte. Les préparations résistent bien en général à l'action du faisceau ionique et, malgré la diminution progressive d'épaisseur, permettent un examen prolongé; cette technique est à rapprocher par certains côtés de celle décrite par CASTAING et LABORIE[2] pour l'examen des métaux au microscape électronique.

La méthode du bombardement ionique ainsi améliorée nous a donné des résultats intéressants dans de nombreux cas et elle peut être généralisée pour l'étude d'un grand nombre de problèmes de structures superficielles. Nous l'avons appliquée ici à l'examen de la structure des couches d'or déposées par évaporation thermique sur différents supports.

## § 3. Etude des Couches d'Or Déposées sur Différents Supports

Des couches d'or d'une épaisseur de 2.000 Å sont déposées, par évaporation thermique dans un vide de $10^{-4}$ mm Hg, soit sur des supports amorphes (lames de verre ou de plexiglass), soit sur des supports parfaitement cristallisés (plan de clivage (001) d'un cristal de NaCl).

Le dépôt est effectué de deux façons différentes suivant que les supports sont maintenus à la température de 20°C ou au contraire chauffés à une température de 400° à 450°C. Selon les cas, la méthode du décapage ionique conduit comme nous verrons, à des résultats différents. (J. J. TRILLAT, N. TERAO, L. TERTIAN et H. GERVAIS)[7].

Nous donnerons d'abord les résultats expérimentaux que nous discuterons ensuite.

*Dépots sur supports froids* (20°C).

Si l'on examine des couches d'or de 2000 Å d'épaisseur, le diagramme initial obtenu avant bombardement ionique est toujours un diagramme de Debye-Scherrer (Fig. 6), indiquant une structure microcristalline désordonnée de la surface métallique.

En bombardant le dépôt par le faisceau d'ions, avec le dispositif de balayage, on constate l'apparition rapide d'une structure fibreuse (Fig. 7) qui se précise après quelques minutes d'attaque. La disposition des arcs, dont les indices sont donnés sur la figure 8, correspond à une orientation privilégiée des microcristaux d'or autour d'un axe [110] perpendiculaire à la surface et à son support. Cette orientation est la même sur support amorphe (verre) ou unicristallin (NaCl). En continuant l'attaque ionique, le diagramme d'or fibreux s'affaiblit progressivement à mesure que l'épaisseur du métal diminue et finit par disparaître.

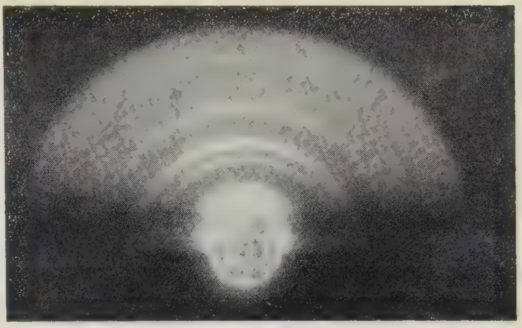
Fig. 6. Couche d'or de 2000 Å déposée sur NaCl froid, examinée par réflexion avant le bombardement ionique.

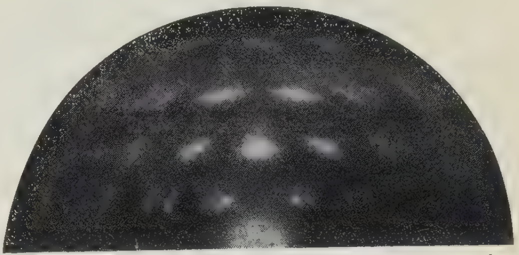
Fig. 7. Même préparation que sur figure 6, aprés quelques minutes de bombardement ionique (Au orienté).

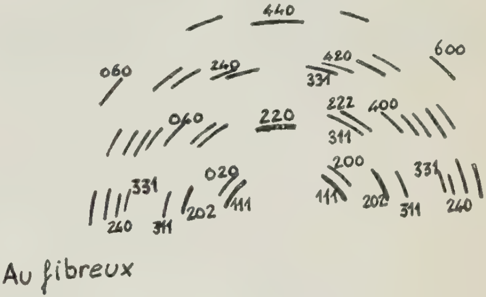

Fig. 8. Schéma correspondant à la figure 7.

Si le support est amorphe (verre), on observe alors quelques halos diffus dûs au verre. La figure 4 montre l'aspect macroscopique de la préparation, sur laquelle le faisceau d'ions a marqué sa trace après avoir arraché tout le

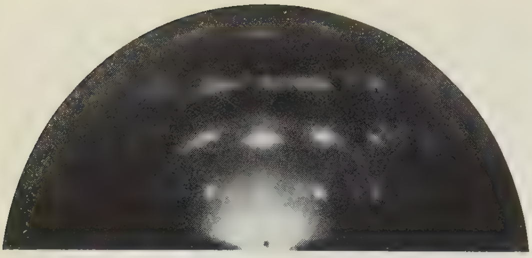

Fig. 9. Même préparation que sur figure 6, après décapage ionique plus long (Au+NaCl).

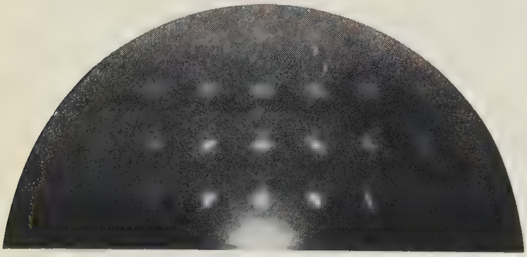

Fig. 10. Même préparation que sur figure 6, après décapage ionique prolongé (NaCl).

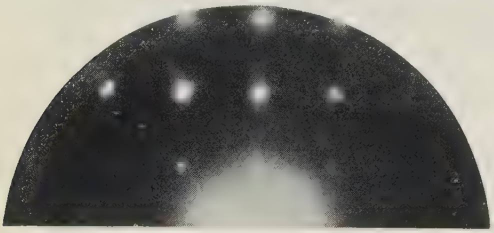

Fig. 11. Couche déposée sur NaCl chaud, après quelques minutes de bombardement ionique-structure monocristalline Au.

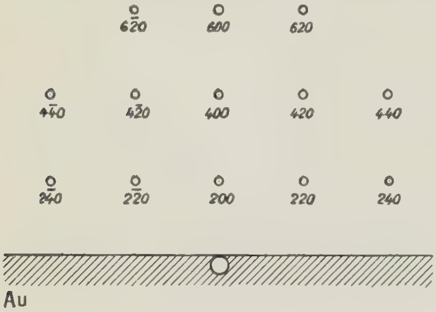

Fig. 12. Schéma correspondant à la figure 11.

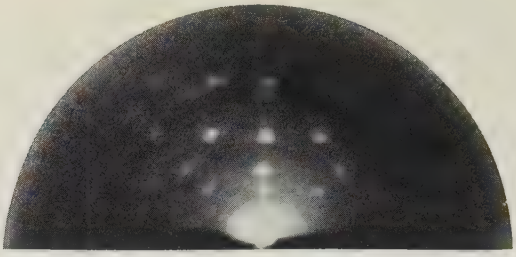

Fig. 13. Même préparation que sur figure 11, mais après bombardement ionique plus long. (Au+NaCl).

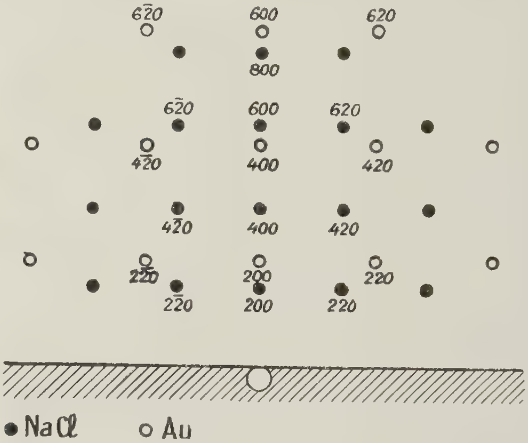

Fig. 14. Schéma correspondant à la figure 13.

métal déposé.

Si le support est unicristallin (NaCl), il arrive un moment où la couche d'or étant fortement amincie laisse pénétrer les électrons jusqu'à la surface du cristal de NaCl. Le diagramme de taches de ce dernier commence alors à apparaître et se superpose aux arcs de l'or (Fig. 9), pour bientôt subsister seul lorsque tout l'or a été enlevé par le décapage ionique (Fig. 10).

*Depots sur supports chauds* (400°C).

Dans ces expériences, le dépôt thermique est effectué sur les mêmes supports amorphes ou cristallins que précédemment, mais portés à une température de 400–450°C. L'examen de la structure de ces dépôts est faite de la meme manière en employant le décapage ionique avec balayage.

a) *Sur support verre*, les phénomènes observés sont exactement les mêmes que lorsque la condensation de la vapeur métallique a lieu à froid. D'abord apparaissent des anneaux de Debye-Scherrer dûs à l'or, puis une structure fibreuse [110] et enfin les halos du verre amorphe.

b) *Sur support constitué par un plan de clivage* (100) *de NaCl*, les résultats sont au contraire très différents. Au départ, et avant décapage ionique, la structure est encore celle de microcristaux d'or disposés au hasard (anneaux D. S.) (Fig. 6); par contre, le bombardement ionique fait apparaître très rapidement des taches de diffraction très nettes, (et non des arcs), localisées sur certains anneaux et qui bientôt subsistent seules en donnant un diagramme typique de monocristal (Fig. 11) correspondant à un plan (100) du réseau c.f.c. de l'or ($a$=4,07 Å), (voir figure 12 obtenue à partir du diagramme de la figure 11); une direction [001] est parallèle au faisceau d'électrons.

Le balayage ionique continuant, le diagramme se transforme progressivement, et de nouvelles taches de diffraction apparaissent. La figure 13 montre l'aspect observé, qui est la superposition du diagramme d'or monocristallin (figures 11 et 12) et du diagramme de NaCl monocristallin (Fig. 10), les réseaux de l'or et du sel étant disposés parallèlement. La figure 14 représente schématiquement la disposition des taches de diffraction avec leurs indices.

*Interprétation et discussion des résultats*

Les résultats expérimentaux que nous venons d'indiquer s'interprètent aisément dans le cas des dépôts d'or obtenus sur une *face de clivage de NaCl chauffé à* 400°C–450°C. Différents auteurs (BRUCK-OGAWA et WATANABE-SHIRAI) (8) (9) (10) ont en effet déja étudié l'orientation des couches métalliques vaporisées thermiquement et déposées sur une face (100) de NaCl fraîchement clivé; BRUCK (8) en particulier a montré en examinant *par transmission* des films métalliques minces, qu'au delà d'une température critique (400°C pour l'or), le support imposait au métal une orientation privilégiée, donnant lieu à la formation d'une mosaïque de petits cristaux tous orientés de la même façon, ce qui, au point de vue de la diffraction électronique, est analogue à une structure unicristalline. Cette température critique varie pour un support donné, avec la nature du métal vaporisé.

Selon BRUCK8), pour les métaux cubiques à faces centrées comme l'or, les cubes ont la même orientation que le cube support (NaCl); pour les métaux cubiques centrés (Fe $\alpha$), la face de contact est tournée de 45° par rapport au cube de NaCl. Sans préciser aussi nettement l'orientation relative de l'or et du sel, OGAWA et WATANABE9) ont signalé qu'ils obtenaient la structure pseudo-unicristalline de de l'or, quand le NaCl est chauffé à 400°C au moins. C'est la raison pour laquelle nous avons adopté la température de 400°C pour le support, dans la seconde série de nos expériences.

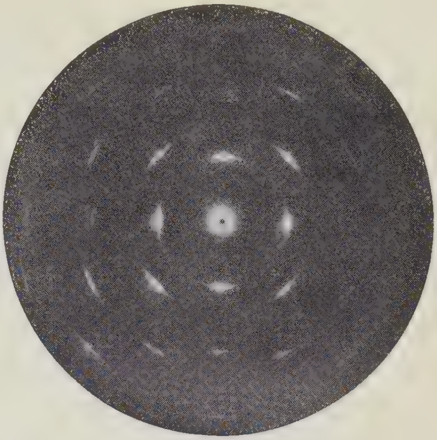

Figure 15. Couche d'or mince (~200 Å) sur NaCl chaud (par transmission).

La méthode du décapage ionique montre en outre que l'orientation imposée par le support ne se produit que jusqu'à une certaine distance de celui-ci, et qu'elle se détruit progressivement à mesure que l'épaisseur du dépôt métallique augmente, ce qui se traduit dans nos expériences (épaisseurs Au=2.000 Å) par l'apparition des anneaux D. S. de l'or *avant* l'attaque ionique. En utilisant des dépôts plus minces, nous avons en effet obtenu, dans les mêmes conditions de température du support, des couches d'or qui, par réflexion comme par transmission (après enlèvement du film d'or par dissolution de NaCl dans l'eau), présentent la structure orientée ou pseudounicristalline, imposée par le support. La figure 15 représente un diagramme par transmission d'une couche d'or de 150 Å condensée sur NaCl chauffé à 450°C; on peut y vérifier facilement que les arêtes des deux réseaux Au et NaCl sont parallèles en prenant soin de repérer la disposition de la couche d'or détachée par rapport aux directions [010] et [001] du support. Par réflexion, sur des couches d'or de 150 Å, on obtient directement et sans attaque ionique, un diagramme tel que celui de la figure 13 qui consiste en la superposition des diagrammes unicristallins de l'or et du NaCl.

Dans le cas des couches d'or déposées sur NaCl froid, il semble au contraire assez difficile de conclure à une action orientante du support; on sait en effet qu'une température suffisamment élevée est nécessaire pour permettre aux atomes du métal la mobilité

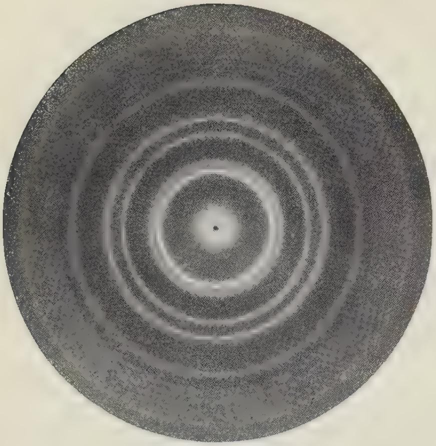

Fig. 16. Couche d'or mince (~200 Å) sur NaCl froid (par transmission).

indispensable à l'apparition de plages unicristallines.

Comment expliquer dès lors l'apparition de la structure fibreuse telle que celle de la figure 7? Tout d'abord, il faut noter qu'une telle structure n'a pu être observée dans des couches plus minces (150 Å) évaporées sur NaCl *froid* et examinées par transmission (Fig. 16); de même, elle n'apparaît pas lorsqu'on amincit par attaque chimique un dépôt épais (2000 Å) d'or. On serait donc amené à penser que cette structure fibreuse est due à un effet secondaire du bombardement ionique; l'effet thermique seul ne suffit pas, car si l'on chauffe à 400–450°C, dans le diffractographe même, des couches d'or obtenues à froid sur NaCl et qu'on les examine par réflexion, *sans bombardement ionique*, aucune orientation n'apparaît. On peut alors provisoirement faire l'hypothèse que l'orientation est produite par une action mécanique des ions, dont la direction est toujours perpendiculaire (ou presque perpendiculaire) à la surface de la couche étudiée.

Enfin, dans le cas d'un support amorphe (verre), nous avons vu que les résultats sont les mêmes si le support est chaud ou froid et qu'on obtient les mêmes diagrammes qu'avec NaCl froid. De plus, quelle que soit l'épaisseur de la couche d'or déposée, le diagramme, observé par réflexion avant attaque ionique, ne montre aucune orientation mais seulement une structure microcristalline confuse.

Là encore, ces expériences semblent montrer que l'effet d'orientation est dû à une action mécanique du faisceau d'ions, l'arrachement du métal s'accompagnant peut être d'effets mécaniques susceptibles d'orienter les cristaux sous-jacents; nous rappellerons à ce sujet les expériences faites dans notre Laboratoire par COURTEL[11] qui a montré que par abrasion dans le vide, les cristaux sont fortement orientés à chaque passage de la meule. Mais bien entendu notre hypothèse demande encore à être confirmée.

## § 4. Conclusion

Ces résultats et leur discussion indiquent qu'il est parfois nécessaire d'interpréter avec prudence les diagrammes qui apparaissent pendant le décapage ionique, et qu'il est toujours indispensable de contrôler avec soin toute action possible (chimique, thermique, mécanique) dûe aux ions. Ces causes d'erreurs étant connues, la méthode du décapage ionique combiné à la diffraction électronique est susceptible d'apporter des renseignements extrêmement intéressants pour de nombreux problèmes relatifs aux structures superficielles.

## References

1) R. D. Heidenreich: Electron Microscopy: Academic Press Inst- New York 1950.
2) R. Castaing et P. Laborie: C.R. Acad. Sc. Paris **237** (1953) 1330.
3) Ch. Fert: C.R. Acad. Sc. Paris **238** (1954) 233.
4) J. J. Trillat: Sur quelques récents progrès dans les techniques de Diffraction électronique et applications. Colloque de Microscopie électronique, Toulouse, Avril 1955.
5) R. Castaing et J. Descamps: C.R. Acad. Sc. Paris **238** (1954) 1506.
6) J. J. Trillat et R. Merigoux: J. de Phys. **5** (1939) 245.
7) J. J. Trillat, N. Terao, L. Tertian et H. Gervais: C.R. Acad. Sc. Paris **240** (1955) 1557–1559.
8) L. Brück: Ann. Phys. **26** (1936) 233.
9) S. Ogawa et D. Watanabe: J. Phys. Soc. Japan **9** n° 4, (1954) 475.
10) S. Shirai: Proc. of Phys. Math. Journ. of Japan **19** (1937) 937, **20** (1938) 855, **21** (1939) 800.
11) R. Courtel: C.R. Acad. Sc. Paris, **226** (1948) 793, Revue Métallurgie, n° 1 p. 24, 1949.

JOURNAL OF THE PHYSICAL SOCIETY OF JAPAN Vol. 11, No. 4, APRIL, 1956

# The Visco-elastic Properties of Network Structure
## I. General Formalism

By Misazo YAMAMOTO

*Department of Chemistry, Faculty of Science, University of Kyoto*

(Received October 25, 1955)

Many kinds of amorphous high polymer substances show the non-ideal rheological behaviours even in the "static" observations. In this paper, the general stress-strain-time relation and energy of dissipation of these systems are treated by adopting the modified rubber-like network model in which the junctions connecting the polymer chains break up and reform continually. The probability of the breakage of the junction, namely the breakage of the chain, per unit time is not a constant but a functions of both the number of segments which construct the chain and the end-to-end distance of the chain. It is assumed that the velocities of deformation of the system and of the change of the situation of network structure are extremely slower than those of the micro-Brownian movements of polymer segments. Therefore the statistical mechanical considerations of equilibrium states may be used to derive the stress-strain-time ($S$–$S$–$T$) relation at each "instance" of macroscopic observations. From our general expression of $S$–$S$–$T$ relation it is pointed out that, in the case of small deformation, the $S$–$S$–$T$ relation is essentially similar to that of the phenomenological generalized Maxwell model and the reciprocal of the probability of chain-breakage corresponds to the relaxation time of each Maxwell element.

### § 1. Introduction

Remarkable progress has been made in the field of the statistical mechanics of the high polymer systems, particularly in the problems of rubber-like elasticity and of dilute polymer solutions. The basic molecular model used in these investigations is the so-called "random flight chain", i.e., the chain constructed from the volumeless "statistical chain-segments" which can rotate freely around each of their bonds, and the statistical properties of which are generally characterized by the mean length and the total number of segments in the chain. In the case of the rubber-like elasticity, the chains involved in the system are permanently connected with each other at their end points, "junctions", by primary chemical bonds, such as –S–S– bonds, to form a three dimensional network structure. It is usually assumed that, besides the liquid-like isotropic interactions, these chains mutually interact only at their junction points and that the effects of the external force upon any part of the system instantaneously spread over all parts of the network through these junctions. In this respect, these systems may be considered to have an infinite value of the coupling parameter. On the other hand, in the case of dilute polymer solutions, each chain molecule seems to be almost independent of others, so the value of the coupling parameter may be zero. In the latter case, many authors have had interests in the mean extension and shape of a chain molecule, and the coefficient of the osmotic pressure, the intrinsic viscosity coefficient, etc. have been calculated in various ways.

Contrary to the above cases, fairly concentrated high polymer solutions and melts show various anomalous rheological properties which cannot be seen in the dilute solutions or bulk rubbers: for instance, visco-elasticity, structural viscosity (which depends upon the rate of deformation), spinnability (formation of liquid thread), Weissenberg effect (anomalous pressure distribution in the system), etc. From the rheological point of view, these properties are very interesting, but their molecular theoretical explanations have been seldom given because of the difficulties due to the existence of the complicated mutual interactions between the chain molecules. Here, it is necessary to consider these systems having the finite value of the coupling parameter in the above sense. They are too complicated to be attacked by any direct method. However, there seems to be two different ways of approaching this problem. One is that, starting from the dilute solution, the mutual interactions between two or more chain molecules are taken into account successively in just the same manner as those in Mayer's imperfect gas theory.

The other approach is that of Green and Tobolsky[1]. They start from the rubber-like system, and assume that in these substances the rubber-like network structure is formed not by the primary chemical bonds but by the entanglements in the physical sense or by the secondary bonds, such as the hydrogen bonds, between the chain molecules. The connection between the chains at these junctions is rather weak and supposed to break up and reform continually. Consequently, the system can deform and flow in the liquid-like manner. Green and Tobolsky derived the phenomenological Maxwell equation of visco-elasticity by considering the shearing deformation of the system and also obtained the viscosity coefficient; but, owing to the assumptions used in their theory, they failed to derive the structural viscosity. Recently, Scott and Stein[2] have examined this model, treating the breakage and reformation processes of junctions in more detail, and found that the stress relaxation phenomenon has the relaxation time, which is slightly different from that of molecular mechanism.

In this paper, we shall formulate the statistical mechanical theory of the same system in a more general form. The chains involved in our system are permitted to have the arbitrary free energy function depending on the degree of their elongations. It is assumed that the probability of the chain-breakage is the function of the tension caused by the chain itself. We shall derive the stress-deformation-time relation and the energy of dissipation in the case of the arbitrary deformation tensor. It will become clear that our model corresponds phenomenologically to the "generalized" Maxwell model.

On the basis of our results, the anomalous rheological properties of such system will be discussed in a next paper.

## § 2. Rubber-like Network Model

In this paper we shall treat the rubber-like network as the model of concentrated polymer solutions or melts. The following assumptions will be used in our calculations to be developed here:

(i) Although the processes considered here are neither stationary nor reversible, but are irreversible, we shall assume that the velocities of the change of macroscopic condition (for example, the rate of deformation) are sufficiently slower than those of the micro-Brownian movements of the segments and also of the breakage and reformation processes, so that the equilibrium statistical mechanical theory can be applied at each instant of macroscopic measurements.

(ii) The free energy of single chain-molecule in the system is a function of the total number of segments of the chain and of its end-to-end distance.

(iii) The free energy of the whole network consists of two parts; the sum of the free energies of individual chains involved and the liquid-like internal energy caused by the interactions between the segments. The latter is assumed to depend solely upon the density of the segments.

(iv) Brownian movements of the junctions are here neglected. The junctions are assumed to be always at their most probable positions. Furthermore, their distribution is assumed to obey the "requirement of proportionality". In other words, when the whole system is deformed, the displacements of the junctions are proportional to the bulk deformation of the system.

(v) The origin of the dissipative mechanism is ascribed to the breakage and reformation of the junctions. The probability of breakage of a chain at a junction is dependent on the number of segments and on its end-to-end distance, but independent of the time.

The assumption (i) is introduced as the first approximation to the problem of the present irreversible phenomena. It should be noted that the assumption (ii) does not necessarily mean the Gaussian chain-network. The requirement of proportionality in the assumption (iv) has never been proved in general cases except in the Gaussian networks. Without this requirement the calculations would become very complicated and one could not gain an insight into our problem because of the lack of the detailed informations concerning the situation of network structure as a whole. With this requirement, however, one needs no longer any knowledge other than that of the distribution of chain length.

Finally, some comments must be made about the assumption (v). In the actual network, the breakage of the chain is caused by that of the junction. For example, in Fig. 1, if the breakage of the junction P occurs, the chains AP, BP, CP and DP disappear, and the new chains AB and CD are reformed. Therefore, the probability of the breakage of a chain may be influenced by the situation of the surrounding chain. However, owing to the same reason as that in the assumption (iv), it is necessary to adopt this assumption on the average. This assumption does make difference between the Green-Tobolsky's theory and ours. They assumed the constant probability of breakage of the chains. As will be shown in the next paper, their assumption of the constant probability is the main reason why they could not succeed to derive any non-linear rheological behaviour. Our more general assumption (v) is just sufficient to explain the essential feature of anomalous rheological properties of the systems.

## § 3. Free Energy of Network, Stress Tensor

Under the assumption (ii), the free energy of a chain $\phi(|\boldsymbol{h}|, N, T)$ is a function of the end-to-end distance $\boldsymbol{h}=(\xi, \eta, \zeta)$, number of segments $N$ and the temperature $T$. If the chain is assumed to be a Gaussian chain with $N$ segments of the length $a$, this energy becomes

$$\phi(|\boldsymbol{h}|, N, T)=(3kT/2)(|\boldsymbol{h}|^2/a^2N)\ . \qquad (1)$$

Owing to the assumption (iii), the free energy of the network per unit volume can be written in the form

$$\begin{aligned}\Phi(T, v)&=\sum_{\text{chain}}\phi(|\boldsymbol{h}|, N, T)+E(\rho)\\ &=\Sigma_N\iiint\phi(|\boldsymbol{h}|, N, T)F(\boldsymbol{h}, N, t)d\boldsymbol{h}+E(\rho),\end{aligned} \qquad (2)$$

where $E(\rho)$ is the internal energy depending on the density $\rho$ of the segments in the network, and $F(\boldsymbol{h}, N, t)$ is the number of the chains per unit volume which consist of $N$ segments with end-to-end distance $\boldsymbol{h}$ and which actually construct the network at the time $t$. Hereafter we shall call $F(\boldsymbol{h}, N, t)$ "chain-distribution function".

In order to obtain the stress tensor, we consider the change of the free energy due to the (small) virtual deformation $\boldsymbol{e}'_v$ of the sample, assuming that there are no breakage and reformation of junctions although in the actual deformation some of the junctions may break and reform. Namely, differentiating the free energy, which depends on $\boldsymbol{e}'_v$ through $F(\boldsymbol{h}, N, t)$, with respect to each component of $\boldsymbol{e}'_v$ and taking the limit $\boldsymbol{e}'_v\rightarrow\mathbf{1}$, we have the stress tensor at the time $t$:

$$\boldsymbol{s}=\Sigma_N\iiint(\boldsymbol{hh})\left(\frac{1}{r}\ \frac{d\phi(r, N, T)}{dr}\right)_{r=|\boldsymbol{h}|}\times F(\boldsymbol{h}, N, t)d\boldsymbol{h}+P\mathbf{1}\ , \qquad (3)$$

where $(\boldsymbol{hh})$ is a tensor:

$$(\boldsymbol{hh})=\begin{pmatrix}\xi^2 & \xi\eta & \xi\zeta\\ \eta\xi & \eta^2 & \eta\zeta\\ \zeta\xi & \zeta\eta & \zeta^2\end{pmatrix} \qquad (4)$$

and the "inner pressure" $P$ comes from the internal energy $E(\rho)$. This inner pressure should be determined by the suitable boundary conditions as in the case of the theory of rubber-like elasticity. In our formalism, the stress tensor is always accompanied with the inner pressure, but we are interested only in the term which essentially depends upon the network structure. Therefore, in this paper, we shall consider the quantity:

$$\boldsymbol{s}_n=\boldsymbol{s}-P\mathbf{1} \qquad (5)$$

where subscript $n$ indicates the "network". As is easily seen, the factor $d\phi(r, N, T)/dr$ in the integrand of $\boldsymbol{s}_n$ is the tension of the chain in the direction from one end to another, and when multiplied by the factor $(1/r)(\boldsymbol{hh})$ it is the contribution of this tension to the total stress $\boldsymbol{s}_n$ of the network.

In order to obtain the stress-deformation-time relation in the concrete form, it is necessary to know the explicit form of chain-distribution function in terms of the (actual) deformation tensor $\boldsymbol{e}(t)$ and the time $t$.

## § 4. Chain-distribution Function

Let us consider a volume element of the sample, the shape of which at the initial time $t=0$ is the rectangular parallelepiped whose edges $\Delta x_0$, $\Delta y_0$ and $\Delta z_0$ are parallel to the external coordinate axes $x$, $y$ and $z$, respectively. In this volume element, the chain-distribution

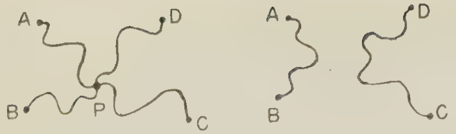

Fig. 1.

function at $t=0$ is expressed by $F_0(\boldsymbol{h}, N) \equiv F(\boldsymbol{h}, N, 0)$. This volume element changes in general not only its shape but also the volume with the time. This change is characterized by the deformation tensor $\boldsymbol{e}(t)$, which is the unit tensor at $t=0$: $\boldsymbol{e}(0)=\mathbf{1}$. The relative coordinate $d\boldsymbol{r}=(dx, dy, dz)$ of the two points in this volume element at the time $t$ is given by

$$d\boldsymbol{r}=\boldsymbol{e}(t)d\boldsymbol{r}_0 \qquad (6)$$

where $d\boldsymbol{r}_0$ is the initial relative coordinate, and the volume of this volume element is $|\boldsymbol{e}(t)|\Delta x_0 \Delta y_0 \Delta z_0$. It is to be noted that this deformation $\boldsymbol{e}(t)$ is rather large, and the classical procedure of symmetrization cannot in general be applied.

In this section we derive the equation of motion of the chain-distribution function in both the integral and differential forms. Let us begin with the expression of the former.

Suppose that a chain has $N$ segments and its end-to-end distance is $\boldsymbol{h}$ at $t$. If the junctions do not break, according to Eq. (6), one has $\boldsymbol{h}_0=\boldsymbol{e}^{-1}(t)\boldsymbol{h}$ where $\boldsymbol{h}_0=(\boldsymbol{h})_{t=0}$. More generally,

$$(\boldsymbol{h})_{t=t'} \equiv \boldsymbol{h}'=\boldsymbol{e}(t')\boldsymbol{e}^{-1}(t)\boldsymbol{h} \,. \qquad (7)$$

Actually, the chain has a chance to break during the time interval from $t'$ to $t$. If $F'(\boldsymbol{h}, N, t)$ is the number of the chains at $t$ with $\boldsymbol{h}$ and $N$ per unit volume which constructed the network at the initial time $t=0$ and which have not broken until $t$, the number of such chains in our volume element is $f'(\boldsymbol{h}, N, t) =F'(\boldsymbol{h}, N, t)|\boldsymbol{e}(t)|\Delta x_0 \Delta y_0 \Delta z_0$. The number of such chains which break in the time interval $t \sim t+\Delta t$ can be written by the assumption (V). as $\beta(\boldsymbol{h}, N)f'(\boldsymbol{h}, N, t)\Delta t$. $\beta(\boldsymbol{h}, N)$, the "chain-breakage coefficient", is the probability of chain-breakage in unit time interval and is considered as the function of $\boldsymbol{h}$ and $N$. It will become clear afterwards that $\beta(\boldsymbol{h}, N)$ has the meaning of the reciprocal of the relaxation time. Comparing the values of $f'$-function at $t'$ and $t''=t'+\Delta t'$, one has the following equation:

$$f'(\boldsymbol{h}'', N, t'')=[1-\beta(\boldsymbol{h}', N)\Delta t']f'(\boldsymbol{h}', N, t').$$
$$\boldsymbol{h}' \equiv \boldsymbol{e}(t')\boldsymbol{e}^{-1}(t)\boldsymbol{h} \,, \quad \boldsymbol{h}'' \equiv \boldsymbol{e}(t'')\boldsymbol{e}^{-1}(t)\boldsymbol{h}. \qquad (8)$$

Taking the successive products of such equations from $t'=0$ to $t''=t$, and carrying out the limit process $\Delta t' \to 0$, we obtain

$$\begin{aligned} f'(\boldsymbol{h}, N, t) &= \lim_{\Delta t' \to 0} \prod_{\substack{\Delta t' \\ (t'=0)}}^{(t''=t)} [1-\beta(\boldsymbol{e}(t')\boldsymbol{e}^{-1}(t)\boldsymbol{h}, N)\Delta t'] \\ &\qquad \times f_0(\boldsymbol{e}^{-1}(t)\boldsymbol{h}, N) \\ &= \exp\left[-\int_0^t \beta(\boldsymbol{e}(t')\boldsymbol{e}^{-1}(t)\boldsymbol{h}, N)dt'\right] \\ &\qquad \times f_0(\boldsymbol{e}^{-1}(t)\boldsymbol{h}, N) \,, \qquad (9) \end{aligned}$$

$$f_0(\boldsymbol{h}, N)=F_0(\boldsymbol{h}, N)\Delta x_0 \Delta y_0 \Delta z_0 \,.$$

This is the number of chains that construct the network with $\boldsymbol{h}$ and $N$ at $t$, which were certainly involved in the network at $t=0$.

In order to obtain the total number of the chains at $t$, we must consider the effect of the reformation of the junctions. Let

$$g(\boldsymbol{h}', N, t')\Delta t'=G(\boldsymbol{h}', N, t')|\boldsymbol{e}(t')|\Delta x_0 \Delta y_0 \Delta z_0 \Delta t'$$

be the number of chains $\boldsymbol{h}', N$ in our volume element reformed in the time interval $t' \sim t'+\Delta t'$. It contributes

$$g(\boldsymbol{e}(t')\boldsymbol{e}^{-1}(t)\boldsymbol{h}, N, t') \times \exp\left[-\int_{t'}^t \beta(\boldsymbol{e}(t'')\boldsymbol{e}^{-1}(t)\boldsymbol{h}, N)\,dt''\right]\Delta t' \qquad (10)$$

to the real distribution function $f(\boldsymbol{h}, N, t)$. Summing up these quantities from $t'=0$ to $t'=t$ and adding it to Eq. (9), we obtain the actual number of chains at $t$:

$$\begin{aligned} f(\boldsymbol{h}, N, t) &= f_0(\boldsymbol{e}^{-1}(t)\boldsymbol{h}, N) \\ &\quad \times \exp\left[-\int_0^t \beta(\boldsymbol{e}(t')\boldsymbol{e}^{-1}(t)\boldsymbol{h}, N)dt'\right] \\ &\quad + \int_0^t g(\boldsymbol{e}(t')\boldsymbol{e}^{-1}(t)\boldsymbol{h}, N, t') \\ &\quad \times \exp\left[-\int_{t'}^t \beta(\boldsymbol{e}(t'')\boldsymbol{e}^{-1}(t)\boldsymbol{h}, N)\,dt''\right]dt' \,. \qquad (11) \end{aligned}$$

Or, in terms of the chain-distribution function $F$ and the chain-reformation function $G$,

$$\begin{aligned} |\boldsymbol{e}(t)|F(\boldsymbol{h}, N, t) &= F_0(\boldsymbol{e}^{-1}(t)\boldsymbol{h}, N) \\ &\quad \times \exp\left[-\int_0^t (\boldsymbol{e}(t')\boldsymbol{e}^{-1}(t)\boldsymbol{h}, N)dt'\right] \\ &\quad + \int_0^t |\boldsymbol{e}(t')|G(\boldsymbol{e}(t')\boldsymbol{e}^{-1}(t)\boldsymbol{h}, N, t') \\ &\quad \times \exp\left[-\int_{t'}^t \beta(\boldsymbol{e}(t'')\boldsymbol{e}^{-1}(t)\boldsymbol{h}, N)\,dt''\right]dt' \,. \qquad (12) \end{aligned}$$

This is the integral form of the equation satisfied by the chain-distribution function.

In order to obtain the differential form, we may differentiate Eq. (12) with respect to $t$. After some elementary tensor calculations, we have

$$\frac{\partial F(\boldsymbol{h}, N, t)}{\partial t} = -\nabla F(\boldsymbol{h}, N, t) \frac{d\boldsymbol{e}}{dt} \boldsymbol{e}^{-1}\boldsymbol{h} - \frac{1}{|\boldsymbol{e}|}\frac{d|\boldsymbol{e}|}{dt} F(\boldsymbol{h}, N, t) + G(\boldsymbol{h}, N, t) - \beta(\boldsymbol{h}, N)F(\boldsymbol{h}, N, t) \,. \tag{13}$$

The meaning of the right-hand-side of the above equation is easily seen as follows: The first term gives the change of distribution function due to the change of the shape of the sample. The second term corresponds to the volume change. These two terms are the same as that appeared in the general theory of rubber-like elasticity. The third and fourth terms are due to the chain-reformation and the chain-breakage, respectively. They are new, and, as will become clear afterwards, it is these two terms that are responsible for the dissipative processes in our system.

## § 5. Stress-Deformation-Time Relation

Now, we have a chain-distribution function-deformation-time relation in both the differential and the integral forms. Substituting these relations into Eq. (3) or into its time derivative, we can obtain the stress-deformation-time relation in both forms.

We shall consider at first the differential form. If Eq. (12) is substituted into the time derivative of Eq. (3):

$$\frac{d\boldsymbol{s}_n}{dt} = \Sigma_N \iiint (\boldsymbol{h}\boldsymbol{h}) \left(\frac{1}{r}\frac{d\phi}{dr}\right)_{r=|\boldsymbol{h}|} \frac{\partial F(\boldsymbol{h}, N, t)}{\partial t} d\boldsymbol{h} \,, \tag{14}$$

and after some tensor calculations, we find

$$\frac{d\boldsymbol{s}_n}{dt} = \frac{d\boldsymbol{e}}{dt}\boldsymbol{e}^{-1}\boldsymbol{s}_n - \boldsymbol{s}_n\boldsymbol{e}^{+-1}\frac{d\boldsymbol{e}^+}{dt} + \Sigma_N \iiint (\boldsymbol{h}\boldsymbol{h}) \left( \boldsymbol{h} \left( \frac{d\boldsymbol{e}}{dt}\boldsymbol{e}^{-1} \right) \boldsymbol{h} \right) \times \left[ \frac{1}{r}\frac{d}{dr}\left(\frac{1}{r}\frac{d\phi}{dr}\right) \right]_{r=|\boldsymbol{h}|} F(\boldsymbol{h}, N, t) d\boldsymbol{h} + \left(\frac{d\boldsymbol{s}_n}{dt}\right)^{b,r} \tag{15}$$

$$\left(\frac{d\boldsymbol{s}_n}{dt}\right)^{b,r} = \Sigma_N \iiint (\boldsymbol{h}\boldsymbol{h}) \left(\frac{1}{r}\frac{d\phi}{dr}\right)_{r=|\boldsymbol{h}|} \times [G(\boldsymbol{h}, N, t) - \beta(\boldsymbol{h}, N)F(\boldsymbol{h}, N, t)] d\boldsymbol{h} \,. \tag{16}$$

where $\boldsymbol{e}^+$ is the transpose of $\boldsymbol{e}$. In this expression, the first three terms on the right-hand side express the change of stress due to the deformation only, and the last term $(d\boldsymbol{s}_n/dt)^{b,r}$ gives the effect due to the change of the situation of the chains in the network. If the chains are the Gaussian, $(d/dr)(d\phi/rdr)$ vanishes and the third term does not appear. In this case, the tension-stretching relation of a chain is exactly the Hookeian and this characteristic will be kept even in the network. Actually, in the first two terms on the right-hand side of Eq. (15), the factors $\boldsymbol{e}^{-1}\boldsymbol{s}_n$ or $\boldsymbol{s}_n\boldsymbol{e}^{+1}$ have the meaning of the elastic modulus. Thus these terms express the Hookeian law and the third term gives the deviation from the " linearity ". It should be noted that the effect of volume-change does not appear explicitly, but it is involved implicitly through both the chain-distribution and the reformation functions. Indeed, in the case of ideal rubber-like elasticity, in which

$$G(\boldsymbol{h}, N, t) = 0, \quad \beta(\boldsymbol{h}, N) = 0$$

and the chains are the Gaussian, the isotropic volume-change does not at all affect the stress tensor. This fact is understood as follows: On the one hand, the increase in volume decreases the number of chains per unit volume and, on the other hand, this change produces the increase of the tension of each chain, and these two tendencies balance each other.

Next, the integral form is obtained by substituting Eq. (12) into Eq. (3). After exchanging the order of integration, we have the integral stress-deformation-time relation:

$$\boldsymbol{s}_n = \boldsymbol{e}(t)\boldsymbol{S}(t)\boldsymbol{e}^+(t) \,, \tag{17}$$

$$\boldsymbol{S}(t) = \boldsymbol{S}_0(t) + \int_0^t \boldsymbol{e}^{-1}(t')\boldsymbol{T}(t, t')\boldsymbol{e}^{+-1}(t')dt' \,, \tag{18}$$

$$\boldsymbol{S}_0(t) = \Sigma_N \iiint (\boldsymbol{h}\boldsymbol{h}) \left(\frac{1}{r}\frac{d\phi}{dr}\right)_{r=|\boldsymbol{e}(t)\boldsymbol{h}|} F_0(\boldsymbol{h}, N) \times \exp\left[ -\int_0^t \beta(\boldsymbol{e}(t')\boldsymbol{h}, N) dt' \right] d\boldsymbol{h} \,, \tag{19}$$

$$\boldsymbol{T}(t, t') = \Sigma_N \iiint (\boldsymbol{h}\boldsymbol{h}) \left(\frac{1}{r}\frac{d\phi}{dr}\right)_{r=|\boldsymbol{e}(t)\boldsymbol{e}^{-1}(t')\boldsymbol{h}|} \times G(\boldsymbol{h}, N, t') \exp\left[ -\int_{t'}^t \beta(\boldsymbol{e}(t'')\boldsymbol{e}^{-1}(t')\boldsymbol{h}, N) dt' \right] d\boldsymbol{h} \,. \tag{20}$$

$\boldsymbol{S}(t)$ is nothing but the stress at $t$ when the deformation is suddenly removed at that instant. If the chain-breakage and the chain reformation had not occurred, and the chains are Gaussian, it would be proportional to the unit tensor. In the actual case, however, because of the above effect, $\boldsymbol{S}(t)$ becomes a complicated tensor, and consists of two terms: One is the contribution from the chains which constructed initially the network, and the other that from the newly formed chains during the course of the deformation. It should be noted that, unlike the case of the differential form, the deviation from the "linearity" does not appear explicitly.

## § 6. Energy of Dissipation

In a similar manner to the integral stress-deformation-time relation, it is possible to obtain the free energy of the network per unit volume as the function of the time. Substituting Eq. (12) into Eq. (2), we have

$$\Phi_n = \Phi - E(\rho) = \Psi_0(t) + \int_0^t \Psi(t, t')dt' \ . \tag{21}$$

$$\Psi_0(t) = \Sigma_N \iiint \phi(|\boldsymbol{e}(t)\boldsymbol{h}|, N, T) F_0(\boldsymbol{h}, N) \times \exp\left[-\int_0^t \beta(\boldsymbol{e}(t')\boldsymbol{h}, N)dt'\right] d\boldsymbol{h} \ , \tag{22 a}$$

$$\Psi(t, t') = \Sigma_N \iiint \phi(|\boldsymbol{e}(t)\boldsymbol{e}^{-1}(t')\boldsymbol{h}|, N, T) G(\boldsymbol{h}, N, t') \times \exp\left[-\int_{t'}^t \beta(\boldsymbol{e}(t'')\boldsymbol{e}^{-1}(t')\boldsymbol{h}, N)dt''\right] d\boldsymbol{h} \ . \tag{22 b}$$

Green-Tobolsky called $\Phi_n$ the "strain free energy". Differentiating this with respect to $t$, we obtain the rate of change of the strain free energy

$$\frac{d\Phi_n}{dt} = \frac{1}{2}\mathrm{Sp}\left[\frac{d\boldsymbol{e}(t)}{dt}\boldsymbol{S}(t)\boldsymbol{e}^+(t)\right] + \frac{1}{2}\mathrm{Sp}\left[\boldsymbol{e}(t)\boldsymbol{S}(t)\frac{d\boldsymbol{e}^+(t)}{dt}\right] - \frac{\delta W}{dt} \tag{23}$$

where

$$\frac{\delta W}{dt} = \Sigma_N \iiint \phi(|\boldsymbol{h}|, N, T) \times [\beta(\boldsymbol{h}, N)F(\boldsymbol{h}, N, t) - G(\boldsymbol{h}, N, t)]d\boldsymbol{h} \ , \tag{24}$$

Now, we may consider the physical meaning of the right-hand side of Eq. (23).

The work done by the external force is given essentially by the product of the three factors: The first is the stress $\boldsymbol{s}_n$, the next is the area $\boldsymbol{e}^{-1}$, and the last is the deformation-length $d\boldsymbol{e}/dt$. Thus, remembering Eq. (17), the first two terms on the right-hand side are the work done by the external force. As is well known, the change of the free energy in the isothermal processes is the sum of the work done by the external forces and the negative of the heat generated within the system through the dissipative mechanisms. The third term on the right-hand side of Eq. (22) is, therefore, considered to give the energy of dissipation.

Actually, Eq. (24) shows that the dissipation arises from the chain-breakage-reformation processes. This result is consistent with our basic assumption (v). The viscosity coefficient can be calculated from this energy of dissipation, as will be shown in the next paper.

## § 7. Small Deformation

As was mentioned in § 2, the deformation of our system is in general large and the procedure of the symmetrization of the deformation tensor cannot be taken into the theory. These circumstance have made the results rather complicated. However, if the deformation is sufficiently small, these difficulties will no longer occur, as will be shown in this section, and the (differential) stress-deformation-time relation is expressed in a simpler form. Furthermore, this relation is essentially equivalent to that of the phenomenological generalized Maxwell model and the chain-breakage coefficient corresponds to the reciprocal of the relaxation time of this model.

In the case of the small deformation, we can introduce "prime" quantities as follows:

$$\boldsymbol{e}(t) = \boldsymbol{1} + \varepsilon\boldsymbol{e}'(t) \ , \tag{25}$$

$$\boldsymbol{s}_n(t) = \boldsymbol{s}_{n,0} + \varepsilon\boldsymbol{s}'_n(t) = -P_0\boldsymbol{1} + \varepsilon(\boldsymbol{s}'(t) - P'(t)\boldsymbol{1}) \ , \tag{26}$$

$$G(\boldsymbol{h}, N, t) = G_0(\boldsymbol{h}, N) + \varepsilon G'(\boldsymbol{h}, N, t) \ , \tag{27}$$

$$F(\boldsymbol{h}, N, t) = F_0(\boldsymbol{h}, N) + \varepsilon F'(\boldsymbol{h}, N, t) \ , \tag{28}$$

where $\varepsilon$ is the parameter characterizing the order of magnitude of the deformation. In these expressions, the zeroth order quantities are those of the natural state, in which $\boldsymbol{e}(t) = \boldsymbol{1}$, $\boldsymbol{s} = \boldsymbol{0}$. After substituting these expressions into Eq. (13), we can equate the coefficients of equal powers of $\varepsilon$ on both sides:

$$G_0(\boldsymbol{h}, N) = \beta(\boldsymbol{h}, N)F_0(\boldsymbol{h}, N) \ , \tag{29}$$

$$\frac{\partial F'(\boldsymbol{h}, N, t)}{\partial t} + \beta(\boldsymbol{h}, N)F'(\boldsymbol{h}, N, t) = -\nabla F_0(\boldsymbol{h}, N)\frac{d\boldsymbol{e}'}{dt}\boldsymbol{h} - F_0(\boldsymbol{h}, N)\frac{d(\mathrm{Sp}\,\boldsymbol{e}')}{dt} + G'(\boldsymbol{h}, N, t) \ . \tag{30}$$

Eq. (29) is the relation between the chain-distribution function and the chain-reformation function in the natural state, as expected. Eq. (30) gives the correction of the chain-distribution function due to the small deformation $\boldsymbol{e}'(t)$, when $F_0(\boldsymbol{h}, N)$ and $G'(\boldsymbol{h}, N)$ are known. Hereafter, we assume that $G_0(\boldsymbol{h}, N)$, $\beta(\boldsymbol{h}, N)$ and then also $F_0(\boldsymbol{h}, N)$ are spherically symmetric. Because of the fact that in the natural state the system is isotropic, this assumption is quite reasonable. Substituting Eqs. (29) and (30) into Eq. (3) and carrying out the elementary calculations, we have

$$\frac{d\boldsymbol{s}'_n}{dt}=\kappa\frac{d}{dt}\left(\boldsymbol{e}'_s(t)+\frac{1}{2}v'(t)\mathbf{1}\right)+P_0\frac{dv'(t)}{dt}\mathbf{1}+\left(\frac{d\boldsymbol{s}'_n}{dt}\right)^{b,r}, \quad (31)$$

$$\left(\frac{d\boldsymbol{s}'_n}{dt}\right)^{b,r}=\Sigma_N\iiint(\boldsymbol{hh})\left(\frac{1}{r}\frac{d\phi}{dr}\right)_{r=|\boldsymbol{h}|}\times[G'(\boldsymbol{h}, N, t)-\beta(\boldsymbol{h}, N)F'(\boldsymbol{h}, N, t)]d\boldsymbol{h}\,. \quad (32)$$

$$\kappa=-\frac{8\pi}{15}\Sigma_n\int r^5\left(\frac{1}{r}\frac{d\phi}{dr}\right)\frac{dF_0(r, N)}{dr}dr\,, \quad (33)$$

$$P_0=-\frac{4}{3}\pi\Sigma_n\int r^4\left(\frac{1}{r}\frac{d\phi}{dr}\right)F_0(r, N)dr\,, \quad (34)$$

where $\boldsymbol{e}'_s(t)\equiv\frac{1}{2}(\boldsymbol{e}'(t)+\boldsymbol{e}'^{+}(t))$ is the symmetrized deformation tensor and

$$1+\varepsilon v'(t)\equiv1+\varepsilon\,\mathrm{Sp}\,\boldsymbol{e}'(t)=|\boldsymbol{e}(t)|\equiv v(t) \quad (35)$$

is the volume of the volume element which was the unit volume at $t=0$. Owing to the fact that the quantities having the subscript 0 in Eq. (29) are independent of time, the primes in Eqs. (31) and (32) can be removed. The first two terms on the right-hand side of Eq. (31) give the change in the stress due to the deformation of the network. $\frac{1}{2}\kappa(dv/dt)\mathbf{1}$ is the effect of the volume-change through the deformation of the network, and $\kappa$ has the meaning of the elastic modulus. The third term shows the effect of the volume-change in the sense of hydrodynamics and $P_0$ corresponds to the hydrostatic pressure. The last is the term due to the irreversible processes.

In order to simplify further the stress-deformation-time relation, we consider the re-construction of the network. Let us pick up from the network all the chains which constitute the network at time $t$ with a common value of $\beta(\boldsymbol{h}, N)$. (They may have various values of $N$ and $\boldsymbol{h}$.) Using these chains we re-construct a new network which extends over the same volume and shape as those of the original network. This "subnetwork" is characterized by the magnitude of $\beta$. We shall call it $\beta$-subnetwork. In a $\beta$-subnetwork, by definition, the chain-breakage coefficient $\beta$ is constant and their deformation tensor is just the same as that of the original one i.e. $\boldsymbol{e}(t)$. Although these subnetworks may not always be "networks" in the true sense of the word, it will make no difference in the following discussions. In the mathematical speaking, the chain-distribution function of the $\beta$-subnetwork is

$$\left(\frac{\delta(\beta(r, N)-\beta)}{\mathrm{grad}\,\beta(r, N)}\right)_{r=|\boldsymbol{h}|}F(\boldsymbol{h}, N, t)\,, \quad (36)$$

where $F(\boldsymbol{h}, N, t)$ is the distribution function of the original network.

If we characterize by the parameter $\beta$ the contributions from the $\beta$-subnetwork, we have the following equations instead of Eqs. (31)~(34):

$$\boldsymbol{s}_n=\int\boldsymbol{s}_n(\beta)d\beta\,, \quad (37)$$

$$\frac{d\boldsymbol{s}_n(\beta)}{dt}=\kappa(\beta)\left(\frac{d\boldsymbol{e}_s}{dt}+\frac{1}{2}\frac{dv}{dt}\mathbf{1}\right)+P_0(\beta)\frac{dv}{dt}\mathbf{1}+\frac{d\boldsymbol{s}_n^*(\beta)}{dt}-\beta\boldsymbol{s}_n(\beta)\,, \quad (38)$$

where

$$\kappa(\beta)=-\frac{8\pi}{15}\Sigma_N\int r^5\left(\frac{1}{r}\frac{d\phi}{dr}\right)\frac{dF_0}{dr}\times\frac{\delta(\beta(r, N)-\beta)}{\mathrm{grad}\,\beta(r, N)}dr\,, \quad (39)$$

$$P_0(\beta)=-\frac{4}{3}\pi\,\Sigma_N\int r^4\left(\frac{1}{r}\frac{d\phi}{dr}\right)\times F_0(r, N)\frac{\delta(\beta(r, N)-\beta)}{\mathrm{grad}\,\beta(r, N)}dr\,, \quad (40)$$

$$\frac{d\boldsymbol{s}_n^*(\beta)}{dt}=\Sigma_N\iiint(\boldsymbol{hh})\left[\frac{1}{r}\frac{d\phi}{dr}G(r, N, t)\times\frac{\delta(\beta(r, N)-\beta)}{\mathrm{grad}\,\beta(r, N)}\right]_{r=|\boldsymbol{h}|}d\boldsymbol{h}\,. \quad (41)$$

The last equation gives the change of the stress caused by the chain-reformation.

If the chain-reformation function $G(\boldsymbol{h}, N, t)$ is independent of $\boldsymbol{e}$ and $t$, Eq. (38) becomes*:

$$\frac{d\boldsymbol{e}_s}{dt}+\mu(\beta)\frac{dv}{dt}\mathbf{1}=\frac{1}{\kappa(\beta)}\frac{d\boldsymbol{s}_n(\beta)}{dt}-\frac{1}{\eta(\beta)}\boldsymbol{s}_n(\beta)\,, \quad (42)$$

where

---

*) Since $ds^*_n(\beta)/dt$ becomes a constant scalar, it can be put into the hydrostatic pressure in Eq. (5).

$$\mu(\beta)=(\kappa(\beta)+2P_0(\beta))/2\kappa(\beta)\ , \tag{43}$$

$$\eta(\beta)=\kappa(\beta)/\beta\ , \tag{44}$$

From these expression we can see that $\kappa(\beta)$, $\eta(\beta)$ and $\mu(\beta)$ have the meaning of elastic modulus, viscosity coefficient and compressibility, respectively. If there is no volume-change, i.e. $dv/dt=0$, Eq. (42) is equivalent to the equation of the so-called Maxwell model of visco-elasticity. We can conclude, therefore, that a single $\beta$-subnetwork just corresponds to the above model and that the whole network is equivalent to the "generalized" Maxwell model.

Here a remark may be added on the general and rather large deformations. As was mentioned previously, on the right-hand side of Eq. (13), $\boldsymbol{e}^{-1}\boldsymbol{s}_n$ has the meaning of modulus and the third term expresses the deviation from the linearity between the stress and the deformation by the irreversible processes. We assume as before that $G(\boldsymbol{h}, N, t)$ is spherically symmetric and separate the last term into two. The one is due to $G(\boldsymbol{h}, N, t)$ in Eq. (14) and this can be included into the $P\mathbf{1}$ term of Eq. (5). The other part is due to the chain-breakage and, if we consider a single $\beta$-subnetwork, this term becomes $-\beta\boldsymbol{s}_n(\beta)$. Now we define the "mean chain-breakage coefficient" $\boldsymbol{B}$ and the "mean elastic modulus" $\boldsymbol{K}$: $[\boldsymbol{K}\cdot(d\boldsymbol{e}/dt)]=$(the first three terms on the right-hand side of Eq. (13)), $\boldsymbol{B}\boldsymbol{s}_n=\int\beta\boldsymbol{s}_n(\beta)d\beta$. They are in general non-scalar but tensor quantities. Then Eq. (13) may be written as

$$\frac{d\boldsymbol{s}}{dt}=\left[\boldsymbol{K}\cdot\frac{d\boldsymbol{e}}{dt}\right]-\boldsymbol{B}\cdot\boldsymbol{S}_n\ , \tag{45}$$

This equation has the same form as the Maxwell model. But, $\boldsymbol{K}$ and $\boldsymbol{B}$ are non-scalar quantities and are the functions of $t$ and $\boldsymbol{e}(t)$.

## § 8. Comparison with Green-Tobolsky's Theory

Green-Tobolsky's formulae can be derived from our results subject to the following restrictions:

a) The chains are the Gaussian ones.

b) The number of the chains involved in the network is a constant:

$$\Sigma_N\iiint F(\boldsymbol{h}, N, t)d\boldsymbol{h}=M=\text{const}\ . \tag{46}$$

c) The probability of the chain-breakage is independent of the state of the chain:

$$\beta(\boldsymbol{h}, N)=\beta=\text{const}. \tag{47}$$

d) The chain-reformation function is independent of the deformation:

$$G(\boldsymbol{h}, N, t)=\beta F_0(\boldsymbol{h}, N)\ . \tag{48}$$

where $F_0(\boldsymbol{h}, N)$ is the chain-distribution function in the natural state.

For example, let us consider the differential stress-deformation-time relation. Define the scalar quantity $Q$:

$$\frac{3kT}{a^2}\Sigma_N\frac{1}{N}\iiint(\boldsymbol{h}\boldsymbol{h})F_0(\boldsymbol{h}, N)d\boldsymbol{h}=Q\mathbf{1}\ . \tag{49}$$

and Eq. (15) becomes

$$\begin{aligned}\frac{d\boldsymbol{s}}{dt}+\beta\boldsymbol{s}=&\frac{d\boldsymbol{e}}{dt}\boldsymbol{e}^{-1}\boldsymbol{s}+\boldsymbol{s}\boldsymbol{e}^{+-1}\frac{d\boldsymbol{e}^+}{dt}\\&-P\left[\frac{d\boldsymbol{e}}{dt}\boldsymbol{e}^{-1}+\boldsymbol{e}^{+-1}\frac{d\boldsymbol{e}^+}{dt}\right]\\&+\left(\frac{dP}{dt}+\beta Q+\beta P\right)\mathbf{1}\ .\end{aligned} \tag{50}$$

This equation may be compared with Green-Tobolsky's equation (B.7), namely:

$$\begin{aligned}\frac{d\boldsymbol{s}}{dt}+\beta\boldsymbol{s}=&\frac{d\boldsymbol{e}}{dt}\boldsymbol{e}^{-1}\boldsymbol{s}+\boldsymbol{s}\boldsymbol{e}^{+-1}\frac{d\boldsymbol{e}}{dt}\\&+\left(\frac{\mathrm{Sp}\,(\boldsymbol{s}^{-1}(d\boldsymbol{s}/dt))}{\mathrm{Sp}\,(\boldsymbol{s}^{-1})}-\frac{3\beta}{\mathrm{Sp}\,(\boldsymbol{s}^{-1})}\right)\mathbf{1}\ .\end{aligned} \tag{51}$$

The quantity in the round bracket of this equation can be obtained by rewriting that of Eq. (50) by means of the boundary conditions. In their Eq. (51), there is no term corresponding to the quantity in the square bracket of Eq. (50). Without this quantity, however, the well-known stress-deformation relation of the rubber-like elasticity can not be derived even if the breakage and reformation of the chains do not occur.

## § 9. Conclusion

For the purpose of the molecular theoretical explanation of the visco-elastic behaviours displayed by the amorphous high-polymeric substances, we have made the statistical-mechanical studies of the modified rubber-like networks. In this paper, the general formalisms have been given to the stress-deformation-time relation and the energy of dissipation.

The main assumptions adopted in our treatment are as follows:

a) The application of the theory of equilibrium rubber-like elasticity to the derivation of the stress in each "instant" in which the measurement is carried out,

b) The application of the requirement of proportionality to the displacements of the junctions.

As was mentioned in § 2, the first one is allowed as the first approximation to the treatment of our irreversible processes, if the rate of the deformation is small. In the case of rapid deformation, it becomes essentially important to consider the irreversible " relaxation phenomena " of the micro-Brownian movements of the molecular segments. The molecular theories of this case are statistical-mechanically formulated by Kirkwood, Rouse, and others⁴⁾. The second one may be correct in the case of the rubber-like network in which the Gaussian chains permanently connect with each other. In our case, however, this is nothing but the assumption. Although it will be very difficult, one of the prospective improvement of the theory may be carried out by the removal of this assumption.

It was shown in § 7 that our network model is phenomenologically equivalent to the generalized Maxwell model. As is well known in the phenomenological theory of visco-elasticity, there are two types of the so-called " mechanical " models, i.e. Maxwell type and Voight type. The general excitation-response-theory shows that the models of these two tppes are essentially equivalent. In the view-point of the application, however, there is a difference between these models. The model of the Voigt type is in general convenient to obtain the deformation under the knowledge of the stress. On the other hand, from the given deformation, the stress is calculated in a simple way by the model of Maxwell type. In our study of the network model, we derive the stress tensor assuming that the deformation tensor is given. This analogy seems to be the reason why our network model corresponds not to the generalized Voigt model but to the Maxwell one.

The author wishes to express his thanks to Professor T. Yamamoto and Mr. E. Teramoto for their constant instructions and encouragements. He is further obliged to the members of Research Group of High Polymer in Kyoto, especially, Professors H. Inagaki, who suggested this probelm, H. Fujita and M. Kurata for their kind discussions.

## References

1) M. S. Green and A. V. Tobolsky: J. Chem. Phys. **14** (1946) 80.
P. J. Blatz and A. V. Tobolsky: ibid. 113.
2) K. W. Scott and R. S. Stein: J. Chem. Phys. **21** (1953) 1291.
3) Similar treatment is also made by J. Furukawa: J. Polymer Sci. **15** (1955) 193.
4) J. G. Kirkwood: Rec. trav. Chim. **68** (1948) 649.
P. E. Rouse: J. Chem. Phys. **21** (1953) 1272.
P. E. Rouse and K. Sittel: J. Appl. Phys. **24** (1953) 690.
F. Bueche: J. Chem. Phys. **21** (1953) 603.
O. Nakata: J. Phys. Soc. Japan
B. H. Zimm: J. Chem. Phys. (to be published.).

JOURNAL OF THE PHYSICAL SOCIETY OF JAPAN Vol. 11, No. 4, APRIL, 1956

# The Quadrupole Moment of $V^{51}$

By Kiyoshi MURAKAWA

*Institute of Science and Technology, Komaba-machi, Meguro-ku, Tokyo*

(Received November 14, 1955)

The hyperfine structure (hfs) of the spectrum of V I was investigated. From the hfs of $\lambda$ 4851 the quadrupole coupling constant of the ground level $3d^34s^2\,{}^4F_{3/2}$ was deduced. Assuming that the screening correction for the $d$-electron of V I is 13, the quadrupole moment of $V^{51}$ was calculated to be $(0.2_8 \pm 0.15)10^{-24}\text{cm}^2$, in which the polarization correction due to Sternheimer is taken into account. The indicated probable error does not include the uncertainty of the screening correction of the $d$-electron. In addition to the hfs of $\lambda$ 4851, the hfs of $\lambda\lambda$ 4881, 4875, 4832, 4594, 4330 were measured, and the interval factors of the quartet levels $3d^34s^2\,{}^4F$ and of $3d^34s4p\,{}^4G_{11/2}$ were obtained.

## § 1. Introduction

The quadrupole moment ($Q$) of $V^{51}$ is worthy of special investigation, because the current shell model of the nucleus predicts negative $Q(V^{51})$, whereas the regularity among the actual $Q$'s of numerous nuclei leaves a slight amount of room for positive $Q(V^{51})$. In view of this interest, Kamei and the author[1] studied some years ago the hyperfine structure (hfs) of the spectrum of VI and deduced $Q(V^{51}) = (0.3 \pm 0.2) \times 10^{-24}\text{cm}^2$. The investigation of the screening correction of the $d$-electron[2] gave the author an opportunity of studying again the hfs of VI; the result of this study will be reported in the present paper.

Kopfermann and Rasmussen[3] had previously studied the hfs of the spectrum of VI, but they detected no deviation from the cosine interval rule in any level of VI. The accuracy of the interval factors given by them is not sufficient enough to allow us to investigate the regularity of the hfs contribution of the $3d$-electron. It is therefore necessary to investigate the hfs of several lines (having $d^3s^2\,{}^4F$ as the final level) in addition to that of $\lambda$4851.

In the present work the hfs was studied by means of a liquid-air cooled hollow cathode discharge tube and a Fabry-Pérot etalon. The classification of the spectrum of VI was taken from the work of Meggers and Russell[4].

## § 2. Hfs of the Spectrum of VI

As shown in the previous work[1], the hfs of $\lambda$4851 is the most suited for deducing $Q(V^{51})$. In the present work this line was again studied, and the result of measurement is given in Fig. 1; this is essentially the same as the previous work[1], with the exception that this time the splitting of the upper level was detected. Fig. 2 is a reproduction of the hfs of $\lambda$4851 taken with a 15 mm etalon. The first row of Fig. 1 shows the result of measurement on patterns in which the components $b$ and $c$ are recognized to be resolved (although not so sufficiently). The position of the component $d$ is difficult to measure and was therefore calculated. The hfs scheme deduced from the resolved structure has, however, only an accuracy sufficient for determinig the interval factor of the levels, but insufficient for determining the quadrupole coupling constant. The second row of Fig. 1 shows the result when the hfs was measured, assuming that the components $b$ and $c$ are not resolved. Denoting the interval factors of the final and the initial levels of $\lambda$4851 by $A$ and $\delta/4$ respectively and the quadrupole coupling constant of the final level by $B$, we get from the second row of Fig. 1:

$$A - \frac{1}{12}\delta = 0.02073\ \text{cm}^{-1},$$

$$B = -0.004_0 \times 10^{-3}\ \text{cm}^{-1}.$$

Since $\delta = -0.014\ \text{cm}^{-1}$, we get

$$A = 0.0195\ \text{cm}^{-1}.$$

The hfs of $\lambda$4330 is shown in Fig. 3. Denoting the interval factors and the quadrupole coupling constants of the final and the initial levels of $\lambda$4330 by $A$, $B$ and $A'$, $B'$ respectively, we get from Fig. 3:

$$A - \frac{11}{15}A' = 0.0180\ \text{cm}^{-1}, \quad A = 0.0195\ \text{cm}^{-1}$$

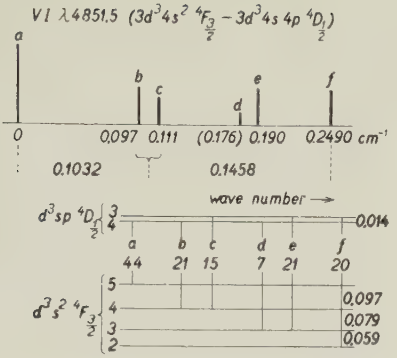

Fig. 1. Hfs of λ 4851.5.

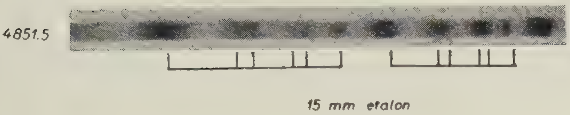

Fig. 2. Interference pattern of λ 4851.5.

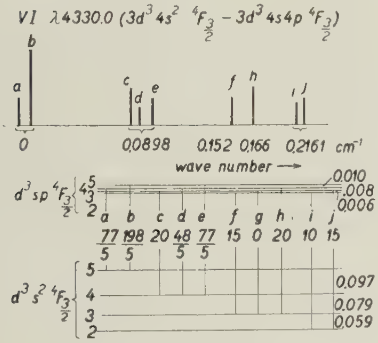

Fig. 3. Hfs of λ 4330.0.

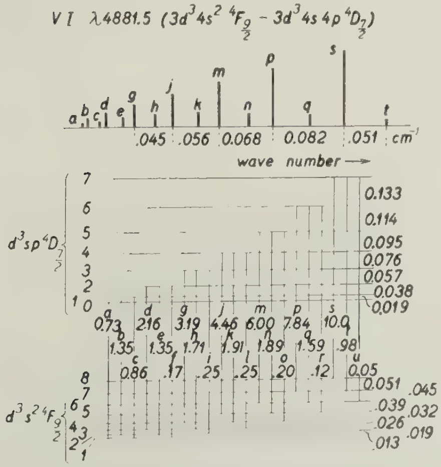

Fig. 4. Hfs of λ 4881.5.

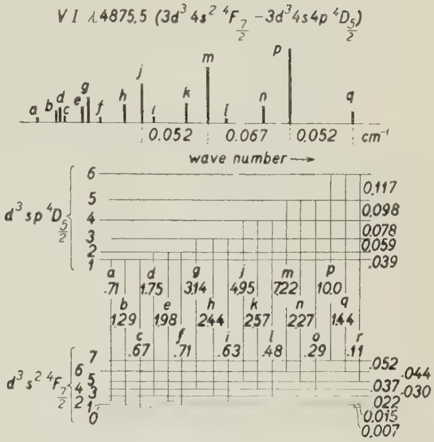

Fig. 5. Hfs of λ 4875.5.

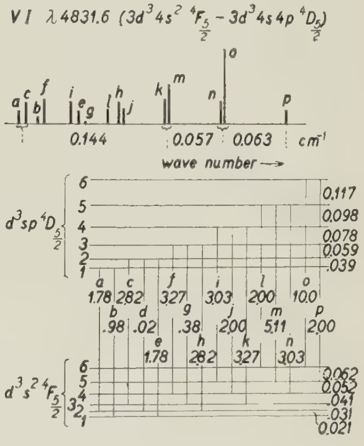

Fig. 6. Hfs of λ 4831.6.

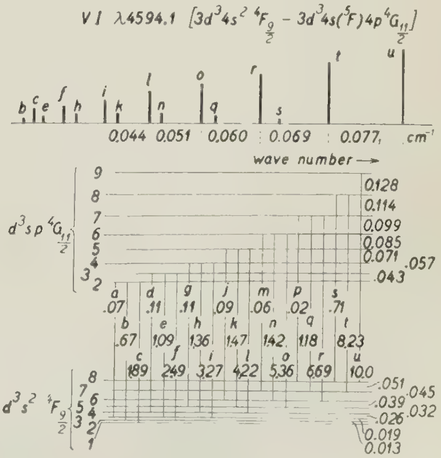

Fig. 7. Hfs of λ 4594.1.

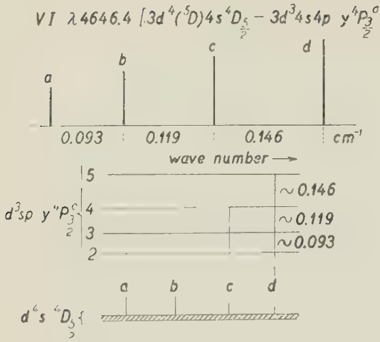

Fig. 8. Hfs of λ4646.4.

$$B-\frac{1}{5}B'=-0.002\times10^{-3}\text{cm}^{-1}\,.$$

In this case the accuracy of measurement is not so good as in the case of λ4851. Moreover the wave function of the upper level $3d^3 4s4p\,{}^4F_{3/2}$ is not pure and therefore difficult to calculate accurately. However it could be probably concluded that the measured hfs of λ4330 does not contradict with the negative value of $B$.

In order to investigate the interval factors of the term $3d^3\,4s^2\,{}^4F$, the hfs of λλ4881, 4875 and 4832 were investigated. The results of measurement are shown in Figs. 4, 5 and 6.

The interval factor of the level $3d^3\,4s\,4p\,{}^4G_{11/2}$ can be deduced from the hfs of λ4594 (Fig. 7). The experimental material for this line is not much different from that of Kopfermann and Rasmussen³⁾, but the hfs splittings of both the initial and the final levels given by them are different from those of the present author.

Finally, the hfs of λ4646 is shown qualitatively in Fig. 8. Since another line lies very close, it was difficult to measure the hfs accurately. In order to isolate λ4646, a large grating (instead of a prism spectrograph) would be needed. The interval factor of the final level must be small, and therefore the hfs of λ4646 could be used as a check for $Q(V^{51})$ if this could be measured accurately.

## § 3. Calculation of $Q(V^{51})$

Before calculating $Q(V^{51})$ from the value of $B(3d^3\,4s^2\,{}^4F_{3/2})$, it is necessary to find the value of the effective charge for the $3d$ electrons of VI. For that purpose the interval factors of the term $3d^3\,4s^2\,{}^4F$ (see Table I) could be used. Since this configuration of VI is of a typical $LS$-coupling, we can use the $LS$-coupling formulas that were derived previously²⁾:

$$A(d^3\,{}^4F_{9/2})=(8a_d'+a_d''+8a_d''')/9,$$
$$A(d^3\,{}^4F_{7/2})=(281a_d'+34a_d''+128a_d''')/315,$$
$$A(d^3\,{}^4F_{5/2})=(712a_d'+163a_d''-424a_d''')/875,$$
$$A(d^3\,{}^4F_{3/2})=(59a_d'+66a_d''-368a_d''')/125,$$
$$a_d'=a(d_{5/2}),\ a_d''=a(d_{3/2}),\ a_d'''=a(d_{5/2},\ d_{3/2}).$$

Putting $a_d'=\dfrac{3}{7}\dfrac{F_2'}{F_2''}a_d''$, $a_d'''=-\dfrac{1}{16}\dfrac{G_2}{F_2''}a_d''$ in each of the above formulas, we can calculate $a_d''$ from the observed value of $A$ of each level. The value of $a(d_{3/2})$ calculated in this way is shown in Table I.

Finally the configuration $3d^3 4s4p$ is also of good $LS$-coupling, so that the level $3d^3 4s({}^5F)\,4p\,{}^4G_{11/2}$ should obey the $LS$-coupling formula:

$$A[d^3s({}^5F)p\,{}^4G_{11/2}]$$
$$=\frac{9}{110}a(s)+\frac{1}{550}(381a_d'+54a_d''+348a_d''')$$
$$+\frac{1}{165}(13a_p'+8a_p''-32a_p''')\,.$$

Putting $F$(relativity correction factor)$=1.07$, $1-\delta$(finite volume correction factor)$=0.994$, $Z=23$, $(dn^*/dn)/n^{*3}_{4s}=0.44$, $\mu/I=1.4709$ in the modified Goudsmit-Fermi-Segre formula, we get $a(4s)=0.091\text{ cm}^{-1}$ for VI. Putting this value in the above formula, we get $a(d_{3/2})=0.015$ cm⁻¹. The actual wave function for $3d^3\,4s({}^5F)4p\,{}^4G_{11/2}'$ would contain a slight amount of $3d^3\,4s({}^3F)\ 4p\,{}^4G_{11/2}$, so the above-mentioned value of $a(d_{3/2})$ would have to be slightly corrected.

Table I. Interval factors of the levels of V I.

| Level | $A$ cm⁻¹ | $a(d_{3/2})$ cm⁻¹ |
|---|---|---|
| $3d^3 4s^2\,{}^4F_{9/2}$ | 0.0064 | 0.015 |
| ${}^4F_{7/2}$ | 0.0074 | 0.016 |
| ${}^4F_{5/2}$ | 0.0103 | 0.018 |
| ${}^4F_{3/2}$ | 0.0195 | 0.021 |
| $3d^3 4s({}^5F)4p\,{}^4G_{11/2}$ | 0.0142 | ≈0.015 |

From Table I it is apparent that the values of $a(d_{3/2})$ calculated in this way are not satisfactorily consistent. A simple calculation shows that the electrostatic interaction with $3d^4\,4s\,{}^4F$ can not be made responsible for this inconsistency. We would therefore leave this question undetermined, and assume that the screening correction for the $d$-electron of VI is 13, a value obtained by extrapolation from heavier elements.

We can now calculate $Q(V^{51})$ from the level $3d^3\,4s^2\,{}^4F_{3/2}$. For this level the following *LS*-coupling formula is valid according to Schmidt[5)] and Kamei[6)].

$$(d^3\,{}^4F_{3/2}{}^{3/2}|3\cos^2\theta-1|d^3\,{}^4F_{3/2}{}^{3/2})=\frac{8}{875}(13\,R_2'+14\,R_2''-12\,S_2).$$

Putting $Z^*_d=23-13=10$, $R_2'\approx S_2=1.00$, $R_2''=1.004$, in the above formula, and putting $\zeta_{3d}=158$, $\Delta$ (polarization correction due to Sternheimer)$=0.23$, $H_2=1.00$, $I=7/2$ and $B=-0.004\times10^{-3}\text{cm}^{-1}$ in the modified Casimir's formula

$$Q=-B\frac{Z^*H_2(1+\Delta)}{\zeta<\sum(3\cos^2\theta-1)>_{\text{Av}}}\times I(2I-1)J(2J-1)1.988,$$

we get finally

$$Q(V^{51})=(0.2_8\pm0.15)10^{-24}\text{cm}^2.$$

The indicated probable error does not include the uncertainty of the screening correction of the *d*-electron, because it is impossible to estimate the maximum error of $Z-Z_d^*$.

$V^{51}$ is the only nucleus whose $Q$ comes out with an opposite sign in the calculation of Horie and Arima[7)]. However, their calculation shows that by assigning a suitable configuration to $V^{51}$ it is possible to obtain a positive $Q$. The theory put forward by Moszkowski and Townes[8)] and Moszkowski[9)] predicts a positive $Q$ for $V^{51}$.

The investigation of the hfs of the spectrum of vanadium will be continued, and it is hoped that a more knowledge will be gained of the effective charge for the *d*-electrons.

## References

1) K. Murakawa and T. Kamei: Phys. Rev. **92** (1953) 325.
2) K. Murakawa: Phys. Rev. **98** (1955) 1285.
3) H. Kopfermann and E. Rasmussen: Zeits. f. Phys. **98** (1936) 624.
4) W. F. Meggers and H. N. Russell: Jour. Research Natl. Bur. Standards **17** (1936) 125.
5) T. Schmidt: Zeits. f. Phys. **121** (1943) 63.
6) T. Kamei: Phys. Rev. **99** (1955) 789.
7) H. Horie and A. Arima: Phys. Rev. **99** (1955) 778.
8) S. A. Moszkowski and C. H. Townes: Phys. Rev. **93** (1954) 306.
9) S. A. Moszkowski: Phys. Rev. **99** (1955) 803.

---

JOURNAL OF THE PHYSICAL SOCIETY OF JAPAN Vol. 11, No. 4, APRIL, 1956

# Phosphorescence of Sodium- and Potassium-Acetates

By Kikusaburo OSADA

*Faculty of Engineering, Nagoya University*

(Received November 18, 1955)

Sodium- and potassium-acetates emit green light for a few seconds, after excited *in vacuo* with radiation of 254 mμ. Their spectra are composed of green band with a maximum at 530 mμ and blue one at 465 mμ. The phosphorescence is quenched by oxygen adsorbed in molecular state, and the initial intensity is inversely proportional to the pressure of oxygen, but water vapour and hydrogen do not affect at all. The intensity is also changed by the treatment of the crystal. The activation energy calculated from the temperature dependence of the lifetime is 0.034 eV. Their ultraviolet absorption spectra are also measured in aqueous or acetic acid solution to 220 mμ with a quartz spectrophotometer.

From these results, it may be considered that the phosphorescence is due to imperfections of crystal.

## § 1. Introduction

The luminescent phenomena of organic compounds, *e.g.* acetic salts[1)], dyes etc.[2)], have been known by many works, but nothing is known for sodium- and potassium-acetates. However, we could observe green phosphorescence of the latters after excitation of ultraviolet radiation *in vacuo*.

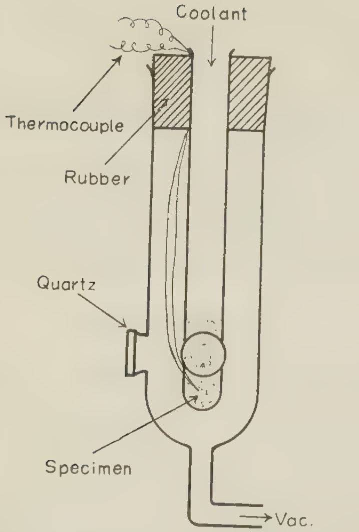

Fig. 1. Apparatus for observation of phosphorescence.

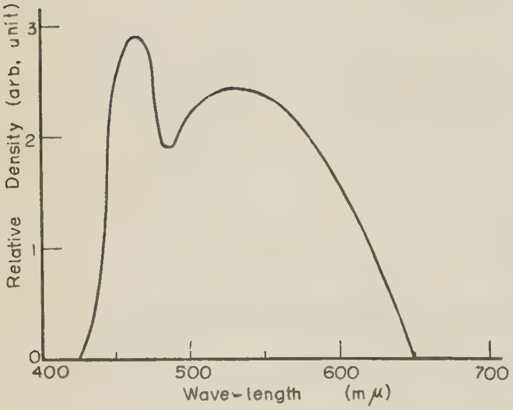

Fig. 2. Phosphorescence spectrum of acetic salt.

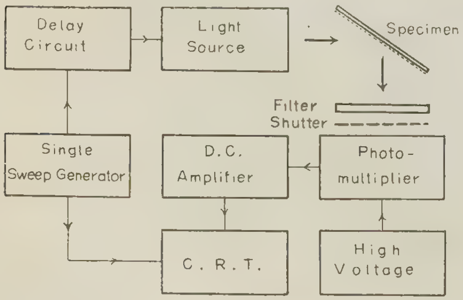

Fig. 3. Block diagram of apparatus for observation of afterglow of phosphorescence.

To investigate the mechanism of this phosphorescence, we observed with an ocilloscope how the intensity and the decay of the afterglow depended on temperature, pressure, and kinds of ambient gas. Further, their ultraviolet absorption spectra were measured to 220 mμ in aqueous or acetic acid solution, as it was difficult to measure the spectra in solid state.

From these results, the mechanism of this phosphorescence is considered.

## § 2. Phosphorescence Spectra

Specimens used were sodium- and potassium-acetates (NaOAc and KOAc), and the former was one of commercial reagents of the special grade and the latter of the first grade. They were powdered and cooled at about −50°C with the mixture of dry ice and amyl acetate in the apparatus shown in Fig. 1. Temperature was measured with a copper-constantan thermocouple inserted in the specimen. They emitted green light for a few seconds after illumination of a germicidal lamp.

The spectra of the afterglow were photographed by using panchromatic photographic film (super-*XX*), and small glass spectrograph whose dispersion is 10 mμ/mm at 400 mμ and 70 mμ/mm at 600 mμ. The density on the film was measured with microphotometer.

The spectrum of every specimen is composed of green band with a maximum at 530 mμ and blue one at 465 mμ. One of the results is shown in Fig. 2.

When they are excited with the light of the lamp passed through a plate of sodium glass, the afterglow can not be observed. So this phosphorescence should appear only by the excitation of radiation of the mercury line at 254 mμ.

## § 3. Afterglow of Phosphorescence

The decay of afterglow of the phosphorescence was measured with an apparatus as shown in Fig. 3. The light of afterglow is sent to a photomultiplier tube (RCA 931 A) supplied a stabilized high voltage[3]. The photo-current is amplified with a d.c. amplifier, and is fed to a cathod-ray tube which is sweeped with a single sweep generator. Trace on the cathod-ray tube is photographed by camera. The instrument is so adjusted as the deflection is proportional to the intensity of light. The germicidal lamp is operated with a constant d. c. voltage. To separate the green band from the blue one, two filters were used; one transmits the light whose wavelength is shorter than 500 m$\mu$ (Matsuda V–C1B), and the other longer than 490 m$\mu$ (Matsuda V–Y1A).

The features of decay of both bands are of exponential type:

$$I=I_0 \exp(-t/\tau)$$

where $\tau$ is lifetime, $I_0$ the initial intensity and $I$ the intensity at time $t$.

We have produced the monochromatic light of 254 m$\mu$ to excite the emission from the specimen by passing the filter[4], but the intensity of monochromatic light was too weak to observe any emission from both specimens. So we could not use the monochromatic light, and it was difficult to measure experimentally the initial intensity. We were able to estimate its value only by the extrapolation of the decay curve.

Effects of temperature, pressure, and kinds of ambient gas on the phosphorescence were measured.

(*a*) *Effect of Temperature*

The lifetime and the initial intensity were measured from room temperature down to about −50°C.

The intensity increases with decreasing temperature. The lifetime of NaOAc is shorter than that of KOAc, and that of the green band is longer than the blue one in both cases. The results obtained are shown in Table I and Fig. 4.

The well-known relation between the lifetime and the activation energy $E$:

$$\tau^{-1}=s \exp(-E/kT)$$

where $s$ is a constant, $T$ absolute temperature, and $k$ Boltzmann's constant, also holds in this case well.

From the slope of the lines in Fig. 4, we obtained $E$ as 0.034 eV in all cases.

Table I. Lifetime of acetic salts.

| Specimen | Temp. | Green Band | Blue Band |
|---|---|---|---|
| $Na(CH_3CO_2)$ | 14.5°C | 1.29 sec. | 1.09 sec. |
| | −38 | 1.75 | 1.46 |
| $K(CH_3CO_2)$ | 10 | 1.11 | 0.99 |
| | −38 | 1.52 | 1.35 |

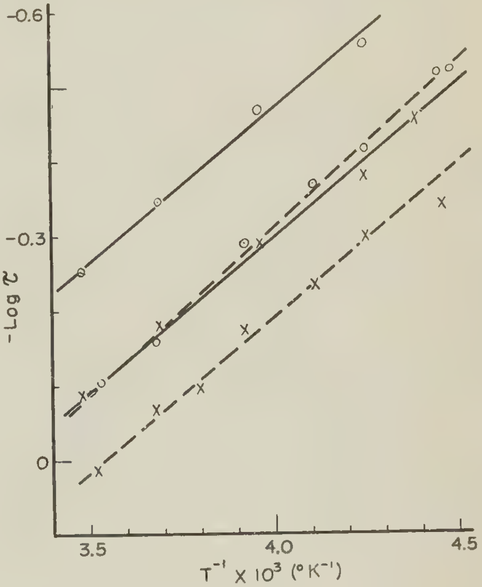

Fig. 4. Temperature dependence of lifetime of NaOAc (——) and KOAc (– – –). (⊙: green band, ×: blue band)

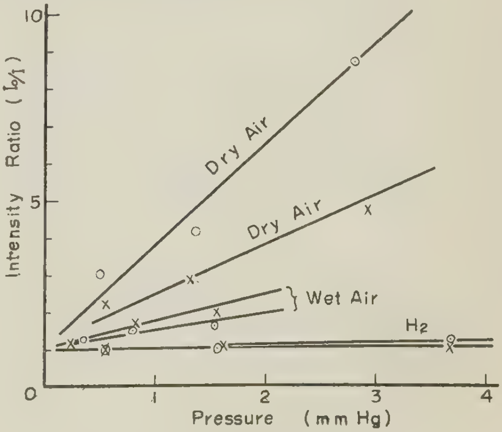

Fig. 5. Quenching by gas of phosphorescence of NaOAc. (⊙: green band, ×: blue band)

(*b*) *Effect of ambient Gas*

To observe how the quenching of phosphorescence depends on pressure and kinds of ambient gas, three kinds of gas were used: hydrogen gotten from Kipp's generator and passed through solution of potassium permanganate and potassium hydorate and traps of calcium chloride, wet air passed through water pool, and dry air passed through calcium chrolide trap. The pressure were changed from $10^{-2}$ to 4 mmHg.

The initial intensity and the lifetime decrease gradually with increasing pressure. Quenching by the dry air is remarkable, and the

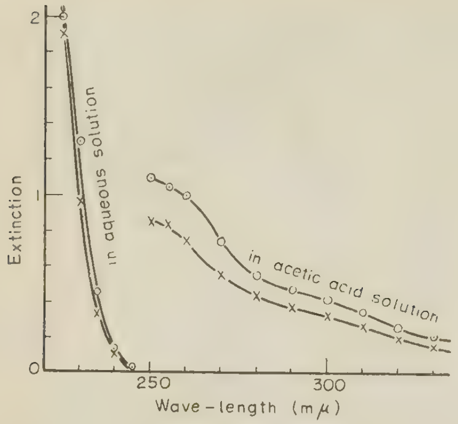

Fig. 6. Absorption spectra of NaOAc (⊙) and KOAc (×) in solution.

green band is more quenched than the blue one. This recovers at once when gas is pumped out. This phenomenon is reversible. The results for NaOAc are shown in Fig. 5, and KOAc behaves in a similar way.

Dry air contains oxygen and nitrogen, but as nitrogen is inactive, the quenching by the dry air must be due to oxygen. Quenching by wet air is smaller than dry air. Although humidity of the wet air was not measured, partial pressure of oxygen in the former is lower than in the latter. So the degree of quenching by water vapour may be very small. Quenching by hydrogen is also very small. This is due to oxygen contained in the residual air.

Here, we shall consider the relation between initial intensity and pressure of oxygen. Assuming that oxygen is adsorbed in molecular state, the following relation is known as Langmuir's isothermal adsorption formula:

$$\theta = \frac{p}{p_0 + p}$$

where $p$ is pressure, $p_0$ a constant, $\theta$ a covering factor. If we assume that the intensity is proportional to $(1-\theta)$, the following equation is derived from the previous one:

$$I = I_0(1-\theta) = I_0\left(\frac{p_0}{p_0+p}\right)$$

and

$$I_0/I = 1 + p/p_0$$

where $I_0$ is the intensity at zero pressure, and $I$ at pressure $p$.

We can see from this equation that $(I_0/I)$ changes linearly with pressure. This relation can be confirmed by the experiments as shown in Fig. 5. This is also similar to the formula for the quenching by oxygen of fluorescence of organic compounds in solution[5].

From these consideration, we can conclude that the phosphorescence is quenched by oxygen adsorbed in molecular state, but water vapour and hydrogen do not affect at all. The initial intensity is inversely proportional to the pressure.

## § 4. Ultraviolet Absorption Spectra

As it was difficult to prepare transparent films of specimens, their characteristic ultraviolet absorption spectra could not be measured in solid state. So we measured their spectra in aqueous or acetic acid solution to 220 mμ with the quartz spectrophotometer of Hitachi Co. Their solutions are contained in a cell of 1cm thickness and their concentration is 0.1 g/cc. The results obtained are shown in Fig. 6.

In the aqueous solution, absorption edge appears at 245 mμ. In the acetic acid solution, edge appears at longer wave-length than 245 mμ and absorption increases gradually as the wave-length becomes shorter. It was difficult to measure the absorption below 250 mμ as the absorption of acetic acid is very large in this region[6].

The reasons for the dependence of the absorption on solvents are as follows. In the aqueous solution the solutes dissociate almost into metallic- and acetic-ions and the interaction between them is small or nearly negligible. But in the acetic acid solution a metallic ion is surrounded with acetic ions, and as there are no other kinds of interaction, they interact mutually very strong. Therefore, in the latter case the absorption near 250 mμ becomes very large.

From these results, their absorption spectra in solid state should also be similar to ones in acetic acid solution.

## § 5. Discussion

Phosphorescence of the acetic salts appears *in vacuo* under the excitation of radiation at 254 mμ and is quenched by oxygen adsorbed in molecular state. From the absorption spectra of solution, the wave-length of this radiation should be in the region of their fundamental absorption spectra. The mechanism of their phosphorescence may be interpreted as follows.

From many results of the phosphorescence of organic compounds, it has been supposed that the emission is due to impurities, triplet state, or imperfections of crystal. The phosphorescence of dyes7) in rigid medium originates from the triplet state. Some organic crystals8), *e.g.* anthracene, naphthalene etc., phosphoresce also for a few minutes. Their emission is not due to the triplet state, but to other causes.

Biacetyl vapour9)10) phosphoresces emitting green and blue band under the excitation of ultraviolet or violet radiation. The lifetime of the green band is longer than the blue. The former band is quenched by oxygen, but the latter is not affected. Aceton vapour11)12) shows also a similar behaviour. It is not yet concluded whether a band is due to the singlet state and the other the triplet one or both are the triplet ones. But these phenomena seem due to the double bond between oxygen and carbon. NaOAc is also found to have the similar bond from its infrared spectrum13).

The following experiments were carried out to determine whether the phosphorescence of the acetic salts originates from impurities or not. In order to purify NaOAc, we make it triply recrystallized and dried hanging over calcium chloride in a desiccator. This specimen emits very weak light. After being left alone in air for some time, it is put instantly *in vacuo*. The intensity of its emission is as strong as the commercial one. On the other hand, when it is dried again in the desiccator before put *in vacuo*, its emission becomes very weak again. On account of deliquescence, the specimen adsorbs water vapour while it is exposed in air, but the water adsorbed may vaporized again when it is put *in vacuo* or desiccator. Speed of vaporization in the former case is faster than in the latter. Owing to the different speed, crystal of specimen in the former case may be more imperfect than in the latter. The commercial one which is dried in the desiccator, also emits weak light.

If the phosphorescence of the acetic salts is due to the triplet state or impurities, the intensity of the emission may not depend on the treatment of the crystal. But this assumption leads to the contradiction to our experiments. Moreover as the activation energy is small, the phosphorescence may be due to imperfections of crystal rather than the other causes.

## § 6. Conclusion

Green phosphorescence of sodium- and potassium-acetates is observed *in vacuo* for a few seconds by excitation of the radiation whose wave-length lies in the region of their fundamental absorption spectra. The emission must be due to imperfections of crystal.

## References

1) F. A. Kröger: *Some Aspects of the Luminescence of Solids*, (Elsevier Pub. Co. Inc., Amsterdam, 1948) Table III.
2) T. Förster: *Fluoreszenz Organischer Verbindungen*, (Vandenhoech & Ruprecht, Göttingen, 1951).
3) W. S. Plymale, Jr. and D. F. Hansen: Electronics **23** No. 2 (1950) 102.
4) K. Osada: J. Phys. Soc. Japan **9** (1954) 136.
5) J. A. Miller and C. A. Baumann: J. Am. Chem. Soc. **65** (1943) 1540.
6) *International Critical Tables*, **5** (1929) 376,
7) M. Kasha: Chem. Rev. **41** (1947) 401.
8) H. Kallmann, B. Kramer and E. Sucov: J. Chem. Phys. **23** (1955) 1043.
9) H. J. Groh, Jr.: J. Chem. Phys. **21** (1953) 674.
10) N. A. Coward and W. A. Noyes, Jr.: J. Chem. Phys. **22** (1954) 1207.
11) G. W. Lucky and W. A. Noyes, Jr.: J. Chem. Phys. **19** (1951) 227.
12) H. J. Groh, Jr., G. W. Lucky and W. A. Noyes, Jr.: J. Chem. Phys. **21** (1953) 115.
13) L. H. Jones and E. MacLaren: J. Chem. Phys. **22** (1954) 1796.

JOURNAL OF THE PHYSICAL SOCIETY OF JAPAN Vol. 11, No. 4, APRIL, 1956

# On the Absorption of Light by Colour-centres in the Region between *F*-band and *M*-band

By Hisao YAGI

*Department of Physics, University of Kyoto*

(Received December 20, 1955)

When the absorption coefficient of *F*-band of coloured alkali-halide crystal is about 2 cm$^{-1}$, six new bands called $R_\alpha$, $R_\beta$, $R_\gamma$, $R_\delta$, $R_\varepsilon$ and $R_\zeta$ respectively are observed in the region between *F*-band and *M*-band. On the other hand, however, Molnar's *R*-bands ($R_1$ and $R_2$) are observed when the absorption coefficient of *F*-band is about 20 cm$^{-1}$. The characteristic properties of our new bands are similar to those of Molnar's *R*-bands.

## §1. Introduction

As is well known, Molnar1) has observed M- and R-bands in coloured alkali-halide crystals in the region of longer wavelength than that of the F-band and has reported that the R-bands ($R_1$ and $R_2$) are very stable and have no photoconductivity. Based upon Molnar's report, Seitz2) has regarded the two R-centres as "$F_2$" and "$F_2{}^+$" respectively. It has been pointed out by Pringsheim3), however, that contrary to Molnar's report, the R-bands are not sufficiently stable. Also, it has been remarked by Oberly and Burstein4) that not only the R-bands but also the M- and N-bands have all photoconductivity. Thus, it may be said that the absorption of light by colour-centres in the region between the F-band and the M-band is not yet well understood.

In our laboratory, six bands called $R_\alpha$, $R_\beta$, $R_\gamma$, $R_\delta$, $R_\varepsilon$ and $R_\zeta$ respectively have been newly observed5) in the said region, and to the precise description of these bands the present paper is mainly directed.

## §2. Formation of R-bands and Measurement of their Absorption

Seitz considered that the R-centres are observed only in crystals coloured by X-rays, but Petroff6) has observed the R-bands, together with F-, M- and N-bands, in additively coloured crystals.

In our experiment, we have coloured alkali-halide crystals by following methods. In order to subject crystals to electrolysis, they were mounted in a furnace in a manner as shown in Fig. 1. (This is called "pointed-electrode method".) A crystal was supported between two iron rods which served as a part of electrical circuit supplying the current for electrolysis. The one rod (A) is pointed sharply at its end and acts as cathode. The other (B) contacts the crystal with the carbon plate covered with platinum foil and acts as anode. All parts except the furnace can be evacuated. Current is supplied by a 450 volts power supply with a 500 KΩ resistor.

After inserting a crystal in the furnace, the temperature of the furnace was first raised up to 450°C–500°C, and the current was supplied, and coloured cloud was made electrolytically in the crystal. (This coloured condition is called "F-coloured".) Then the temperature of the furnace was brought down to 350°–400°C, and the coloured cloud in the crystal was removed by reversing the polarity of the current. (This coloured condition is called "K-coloured".)

For the irradiation with X-rays, a Mazda Sealex tube, operated at a voltage of 30 KV D.C. and a current of 8 mA, was used. During the irradiation the crystal was kept in dark and at room temperature.

NaCl, KCl, KBr and LiF crystals used in our experiment were prepared in our laboratory7) by Kyropoulos's method. The crystals used were always freshly cleaved on all sides at the last possible moment before starting experiment.

The absorption spectra of the crystals were obtained with a large apertured glass-prism spectrophotometer with 1.5 meter focal length objective, and a quartz spectrophotometer of medium size. Monochromatic light from the exit slit was measured photoelectrically by Sb, Rb or Cs photocells and a Dolezaleck quadrant electometer (sensitivity: 1,500 D/V)

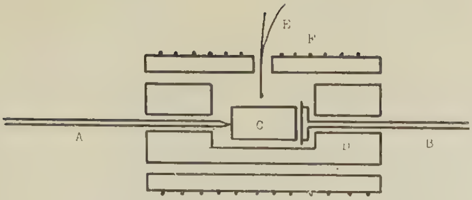

Fig. 1. Arrangement for subjecting crystals to electrolysis.
A: cathode, B: anode, C: crystal, D: holder, E: thermocouple, F: furnace.

connected as shown in Fig. 2.

For light source, a projection lamp (10 volts, 80 watts) was used for visible region, while a hydrogen discharge tube (6,000 volts, 1 Amp.) was used for ultraviolet region. RCA photomultiplier tubes 1P–28 and 1P–22 were also used in place of photocells. A Beckman Quartz Spectrophotometer Model DU was also used.

In our experiment, six bands called $R_\alpha$, $R_\beta$, $R_\gamma$, $R_\delta$, $R_\varepsilon$ and $R_\zeta$ respectively were obtained in every crystal in the region between the F-band and M-band, as shown in Fig. 3. Wavelengths of absorption maxima of these bands are given in Table I, the numerical values having been obtained at room temperature. These R-bands appear conspicuously when a crystal is coloured by X-ray irradiation, but in crystals coloured by electrolysis they are only observed when the crystal is K-coloured.

In the region between the F-band and the M-band, there are Molnar's R-bands ($R_1$ and $R_2$), which were observed in our experiment when the absorption coefficient of F-band was more than 20 cm$^{-1}$ and the temperature of crystals was about −180°C, while our R-bands were remarkable when the absorption coefficient of F-band was about 2 cm$^{-1}$ and enhanced with the increase of F-band. Since the increase of the absorption coefficient of F-band is always accompanied with enhancement of its tail, we cannot discriminate between our R-bands and the tail of F-band as regards these enhancements in the same region. But our R-bands and Molnar's R-bands show similar behaviours as described below, and so we wonder whether these bands can be attributable to the same kind of centres.

## § 3. Characteristic Properties of R-bands

### A. *Classification*

Numerical values of wavelengths of absorption maxima of these bands as shown in Table I are in agreement with those obtained from the empirical formura due to Ivey*. Empirical formulae calculated from the values of absorption bands of NaCl, KCl, KBr and LiF are shown in Table II.

Moreover, among these R-bands, a peculiar wavenumber relationship of the following form holds approximately, namely:

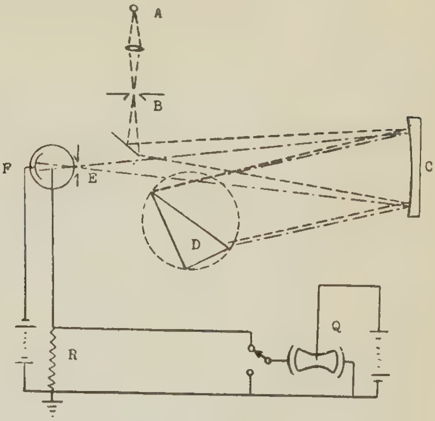

Fig. 2. Arrangement for measuring absorption. A: light source, B: 1st slit, C: collimator mirror, D: prism, E: 2nd slit, F: photocell, R: $10^{10}$ ohms, Q: quadrant electrometer.

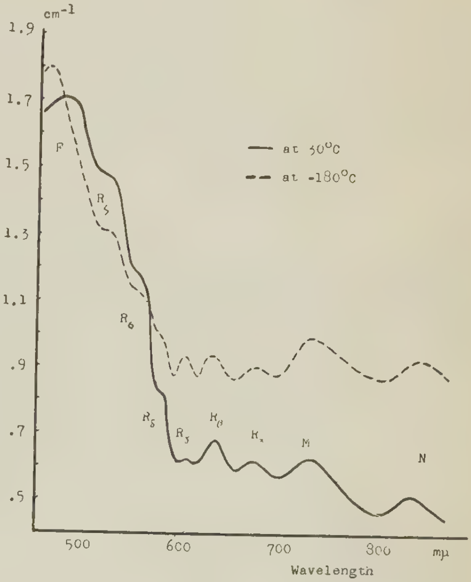

Fig. 3. Absorption of R-bands of X-ray coloured NaCl.

---

* Ivey's empirical formula is given by[8]

$$\lambda_{\max} = cd^x,$$

where $\lambda_{\max}$ is wavelength of absorption maximum of each band, $d$ is the lattice constant of each crystal, $c$ is a certain constant and $x$ is a certain exponent. The latter two vary from band to band.

Table I. *R*-bands of alkali-halide crystals.

| Absorption bands | Crystals | | | | | | | |
|---|---|---|---|---|---|---|---|---|
| | NaCl | | KCl | | KBr | | LiF | |
| | mμ | eV | mμ | eV | mμ | eV | mμ | eV |
| $R_\alpha$ | 660 | 1.87 | 782 | 1.56 | 847 | 1.46 | 408 | 3.02 |
| $R_\beta$ | 620 | 1.99 | 738 | 1.67 | 795 | 1.55 | 377 | 3.27 |
| $R_\gamma$ | 596 | 2.07 | 700 | 1.76 | 780 | 1.58 | 355 | 3.47 |
| $R_\delta$ | 572 | 2.16 | 671 | 1.84 | 741 | 1.66 | 338 | 3.65 |
| $R_\varepsilon$ | 552 | 2.23 | 635 | 1.94 | 704 | 1.75 | 315 | 3.91 |
| $R_\zeta$ | 526 | 2.34 | 608 | 2.03 | 669 | 1.84 | 297 | 4.15 |

Table II. Empirical formulae.

$R_\alpha$ : $\lambda_{\max} = 1330 \times d^{1.55}$
$R_\beta$ : $1263 \times d^{1.54}$
$R_\gamma$ : $1227 \times d^{1.53}$
$R_\delta$ : $1165 \times d^{1.54}$
$R_\varepsilon$ : $1124 \times d^{1.54}$
$R_\zeta$ : $1071 \times d^{1.54}$
$F$ : $724 \times d^{1.80}$

$$\frac{\nu_\alpha - \nu_\beta}{\nu_\gamma - \nu_\delta} = \frac{\nu_\beta - \nu_\varepsilon}{\nu_\delta - \nu_\zeta} .$$

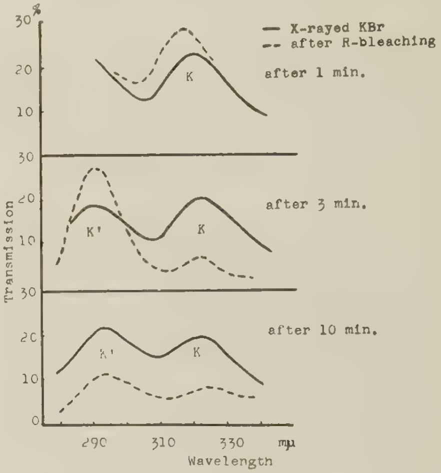

Fig. 4. Changes of K and K′ absorption bands after R-bleaching.

This means that our six bands may be classified into two groups, namely, Group A including $R_\alpha$, $R_\beta$ and $R_\varepsilon$, and Group B including $R_\gamma$, $R_\delta$ and $R_\zeta$. From the results of measurements at different temperatures, it has been found that Group A is enhanced at higher temperatures, while Group B at lower temperatures (see Fig. 3). At lower temperatures, the absorption coefficients of F-, R-, M- and N-bands increase and their wavelength maxima shift to shorter wavelength side.

B. *Phototransformation*

When the coloured crystals are irradiated by the light in any one of our R-bands, all the other R-bands are reduced at the same time with the illuminated R-band, and M-, F-, K- and K′-absorptions are enhanced suddenly for a while and then decrease, approaching final equilibrium values. Therefore, the light lying in any one of R-bands was used to irradiate crystals. Similarly, in order to observe prosperity and decay of R-bands irradiated by the light lying in any one of the

Table III. *F*-bleaching in NaCl.

| Bleaching time in minutes | Centres | | | | | | | |
|---|---|---|---|---|---|---|---|---|
| | *F* | $R_\alpha$ | $R_\beta$ | $R_\varepsilon$ | $R_\delta$ | $R_\zeta$ | *M* | *N* |
| 1 | − 1.5 | 0 | 0 | 0 | 0 | 0 | 11 | 9 |
| 3 | − 3.9 | 20 | 15 | 17 | 16 | 14 | 3 | 15 |
| 5 | − 4.8 | − 1.7 | 8 | 8 | 8 | 5.7 | 1 | 15 |
| 10 | − 7.5 | −10 | − 3.5 | 5 | 5.3 | 3.3 | − 2 | 7 |
| 20 | −10.5 | −15 | −13 | 0 | 5 | 2 | − 2.7 | 4 |
| 30 | −12.2 | | −14 | − 1 | 5 | 2 | − 3.5 | 3 |

The values in this table are $[(K-K_0)/K_0] \times 100$, where $K_0$ is initial absorption coefficient and $K$ absorption coefficient after bleaching.

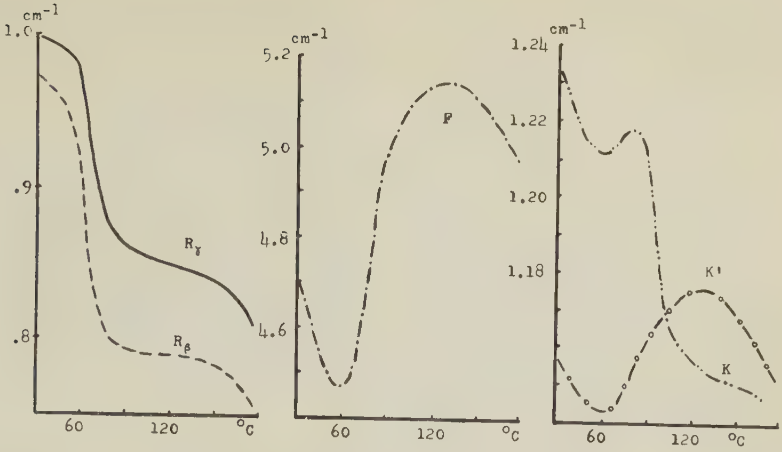

Fig. 5. Thermal transformation of the absorption bands of coloured KBr crystal.

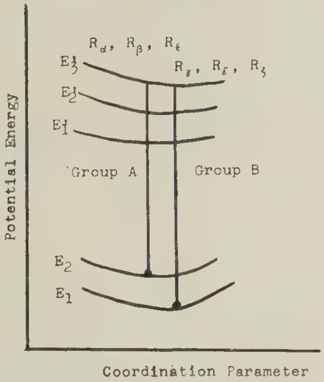

Fig. 6. Electronic levels of R-bands.

other centres, only one of the R-bands was practically measured. This also suggests strongly that all six R-bands are attributable to a single kind of centre.

When a crystal is irradiated by the light lying in the K- and M-bands respectively, the R-absorptions are enhanced. But, when irradiated by the light in the F-band, the M-band is at first enhanced and then reduced, and R-bands are enhanced (see Table III).

Hence, the F→M→R transformation may be a photothermal transformation. This is the case in the R→K→K′ transformation, that is, when a crystal is irradiated by the light lying in the R-bands, the K-absorption is at first enhanced and then the K′-absorption is enhanced after the K-absorption is reduced (see Fig. 4)

When a crystal is irradiated by the light lying in the N- and K′-bands respectively, the R-absorptions are invariable.

### C. *Thermal Transformations*

When coloured crystals are heated at 250°C in the case of NaCl, at 200°C in the case of KCl and at 130°C in the case of KBr respectively, the R-bands are reduced and the F- and K-bands are enhanced remarkably (see Fig. 5).

## § 4. Discussion

According to the experimental results described above, new six R-bands may be attributable to a single kind of centre. It is highly probable that each of the two groups (A and B) is due to the transition between each of the two lower electronic levels and common three higher electronic levels as shown in Fig. 6.

In conclusion, the writer wishes to express his cordial thanks to Professor Yôichi Uchida for his kind advices during the course of this work.

### References

1) Molnar, (Unpublished) see Ref. 2.
2) F. Seitz: Rev. Mod. Phys. **18** (1946) 384.
3) R. Casler, P. Pringsheim and P. Yuster: J. Chem. Phys. **18** (1950) 1564.
4) J. J. Oberly and E. Burstein: Am. Phys. Soc. Washington April 28, 1950.
5) S. Petroff: ZS. für Phys. **127** (1950) 443.
6) Y. Uchida and H. Yagi: J. Phys. Soc. Japan **7** (1952) 109.
7) Y. Uchida and H. Yagi: J. App. Phys. Japan **16** (1947) 65.
8) H. Ivey: Phys. Rev. **72** (1947) 341.

JOURNAL OF THE PHYSICAL SOCIETY OF JAPAN Vol. 11, No. 4, APRIL, 1956

# A Divergent Shock Tube for Obtaining Supersonic Flows

By Fumio TAMAKI

*Institute of Industrial Science, University of Tokyo*

(Received November 18, 1955)

A shock tube having a divergent low pressure chamber just downstream of a partition diaphragm is presented as a simple method for obtaining supersonic flows of fairly high Mach numbers. Flow character in the divergent channel is examined both theoretically and experimentally. Interferometric studies of the flow past a double-wedge profile are presented for Mach numbers of 4.0 and 6.0. At $M=6.0$, pressure distribution on the wedge surface deviates considerably from theory due to the thickening of the boundary layers.

## §1. Introduction

A method of generating a hypersonic flow in a shock tube having a diverging section was first presented by Hertzberg¹⁾. In his method, hypersonic flow is obtained by the expansion into the divergent channel of the hot air compressed by the primary shock. The method has the advantage over the conventional blow-down tunnel in that the air-liquefaction after the expansion can be avoided due to the high temperature of the air prior to expansion. However, in order to obtain a steady flow of sufficient duration, a long channel of constant cross-section is necessary between the diaphragm and the divergent channel.

In this paper, a shock tube having a divergent low pressure chamber just downstream of the diaphragm is presented as a simple device for obtaining a flow of Mach number near 5, in which the problem of air-liquefaction is considered not to be serious. In this shock tube, supersonic flow is obtained by the expansion of the cold air, that is, the air which effuses from high pressure chamber after the rupture of the partition diaphragm. Although low air temperature after the expansion is inevitable, the method has some convenience in that the total length of the tube can be made very short and the initial pressure difference between high and low pressure chambers can be made comparatively small.

The use of this type of shock tube may be extended to higher Mach numbers, if the air in the high pressure chamber is heated by some means, say, by a shock wave. A double-diaphragm shock tube, consisting of a high and a medium pressure chamber of equal cross-section and a low pressure chamber with narrow inlet and large area-divergence, seems to be a practical device for such a purpose. Investigation of this type of shock tube is now being carried out as a continuation of the present work.

It should be noted here that the flow of high Mach number can also be realized in the cold air in a conventional shock tube with constant cross-section, provided that sufficiently large pressure difference is applied to the diaphragm. In this case, however, the length of the low pressure chamber must be made long in order to get sufficient duration of the steady flow, and a rather delicate control of the initial pressure ratio is necessary in order to secure reproducibility of the Mach number of the flow.

As the main object of our work was to examine the possibility of the present method for comparatively high Mach numbers, experiments were mainly carried out for the cases of Mach numbers of 4.0 and 6.0. Application of the same shock tube to lower Mach numbers were subsequently made by C. S. Kim⁵⁾.

## §2. Shock Tube and Optical Equipment

After some preliminary experiments, a shock tube shown in Fig. 1 was set up at the Institute of Science and Technology, University of Tokyo. High pressure chamber has a length of about 60 cm and a cross-section of $1\times6\,\mathrm{cm}^2$. Divergent channel in the low pressure chamber are made of wooden walls inserted inside the tube of $14\times6\,\mathrm{cm}^2$ cross-section. Two kinds of straightly diverged channel were used in the experiments.

The first channel has an initial section of $1\times6\,\mathrm{cm}^2$, the same size as the high pressure channel, and a final section, situated 28.2 cm downstream from the initial section, is $11\times6\,\mathrm{cm}^2$. A cellophane diaphragm which separates high and low pressure chamber is situated 5 mm upstream of the initial section.

The second channel has a length of 28.7 cm, with initial and final section of $0.5\times6$ and $14\times6\,\mathrm{cm}^2$, respectively. In this case, there is an area constriction at the inlet of the divergent channel. A short converging duct made of steel is attached to the inlet in order to improve the condition of inflow and to protect wooden walls from the impact of high pressure air.

Compressed air at 4～6 atms. abs. was supplied to the high pressure chamber from a reservoir of $0.7\,\mathrm{m}^3$ volume. Low pressure chamber was evacuated by a 1/4 horse-power rotary pump to the pessure of 5～10 mmHg. A long steel needle with a trigger mechanism fitted to the end of the high pressure chamber was used for breaking the diaphragm.

This shock tube was set vertical in order to facilitate the use of Mach-Zehnder interferometer.

As will be shown later, Mach number of the quasi-steady flow obtained at the end of the divergent channel is related to the ratio of the area of that section to that of the inlet by the usual relation of steady isentropic flow. The first channel has the area-ratio of 11, corresponding to $M=4.03$. The value $M=4.0$ was actually obtained in the experiments. In the second channel, the area-ratio is 28, which corresponds to $M=5.1$. However, much higher Mach number was obtained in the experiments. This seems to be partly due to the viscosity effect which acts to decrease the mass flow at the throat, and partly due to the imperfect removal of the diaphragm, which in this case forms a strip of too small a width to be broken uniformly. From these reasons, Mach number of the flow depended on the initial pressure ratio across the cellophane, and it was necessary to adjust the preesure ratio to a constant value in order to get a constant Mach number. Mach number of 6.0 was obtained when the pressures in high and low pressure chamber were 6 atms. abs. and 5 mmHg, respectively.

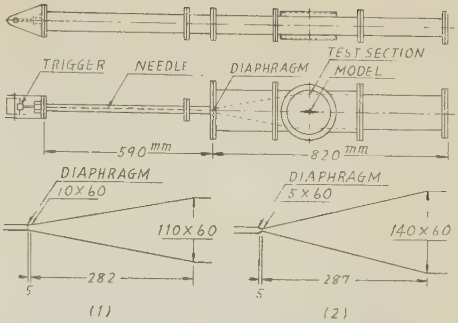

Fig. 1. Shock tube and divergent channels.

For the measurement of density in the flow, a Mach-Zehnder interferometer with glass plates of 21 cm diameters was used. Windows of the test section and the compensater plates were of 16 cm diameters. A spark discharge through magnesium electrodes of a 0.5 $\mu$F paper condenser charged at 6 kV was used as a light source, and monochromatic light of 4481 Å was obtained by using two glass filters.

A pair of spherical concave mirrors, each having 20 cm diameter and 4 m radius of curvature was used for collimating and focusing the light beams.

The same optical system was used for schlieren observations, by wholly cutting off the light rays on the compensater side.

Timing of the spark discharge was effected by the method of Hertzberg and Kantrowitz[2)]. Through a small orifice on the channel wall at the position 5 cm downstream from the inlet of the divergent part, the pressure of the primary shock was conducted into a glass tube having a metallic contact unit at its end. This unit is made of thin aluminum leaf faced with small clearance to the plane brass surface. Contact of the two metallic surfaces due to the pressure wave induces, viâ thyratron and automobile ignition coil, a high voltage pulse in the third electrode placed near the cathode of the spark unit, and initiates the main spark. Glass tubes of various lengths were used for varying the time of spark discharge.

## § 3. Theoretical Considerations

Assuming that the flow in the channel is one-dimensional, the unsteady flow after the rupture of the diaphragm can be calculated by the method of characteristics in the $x$-$t$ plane. Graphical method described by Os-

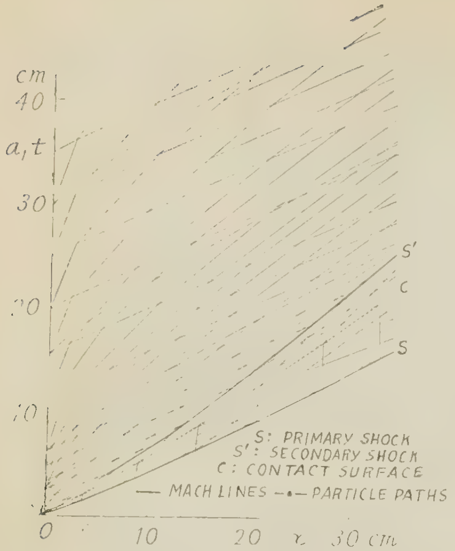

Fig. 2. Wave Diagram for the divergent channel for $M=4.0$ (parallel part at the test section neglected).

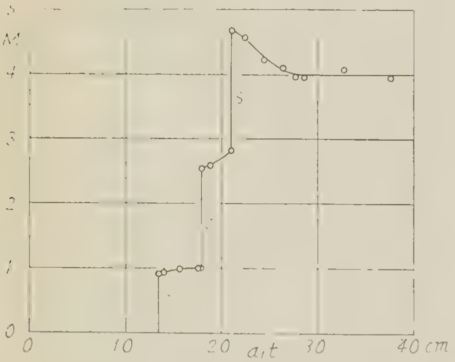

Fig. 3. Mach number at $x=28.2$ cm.

watitsch3) was used in the present calculation.

Fig. 2 shows a typical wave diagram for the divergent channel for $M=4.0$, when the flow behind the primary shock is supersonic at the inlet of the divergent part. Actual channel has a parallel part at the test section, but this was omitted for simplicity and a simpe divergent channell was considered in the calculation. Further, between the diaphragm and the inlet, a parallel part of 5 mm was assumed. Such an entrance region is necessary in theoretical calculation, in order to determine the flow state prior to expansion into the divergent channel. Experimental channel has also such an entrance region, but, owing to the deflection of the cellophane due to pressure, actual length of this region is nearly zero.

In Fig. 2, $x$ is the distance along the channel axis from the initial section, and $t$ the time measured from the instant of removal of the diaphragm. In the diagram, $t$ multiplied by $a_1$ is used, where $a_1$ is the sound velocity corresponding to the initial temperature. Pressure ratio $p_0/p_1$, where $p_0$ and $p_1$ denote the initial pressures in high and low pressure chamber respectively, is assumed to be 304, which corresponds to $p_0=4\times 760$ and $p_1=10$ mmHg. Flow Mach number just behind the shock is 1.29 at the inlet.

The diagram shows that: (1) the primary shock weakens gradually as it advances through the divergent channel, and the flow behind it becomes subsonic at a certain distance from the inlet, and (2) a secondary shock appears behind the contact surface.

In Fig. 3, flow Mach number at $x=28.2$ cm is plotted against $a_1t$. It is shown that nearly steady flow of $M=4.0$ is established for $a_1t$ larger than 25 cm. As the flow at $x=0$ is nearly sonic except for small values of $a_1t$, Mach number of the quasi-steady flow at the test section can be calculated approximately from the ratio of its area to the inlet area, by using the relation of one-dimensional isentropic steady flow and assuming $M=1$ at the inlet. This gives $M=4.03$. Values of $M$ for large $a_1t$ agree with this value within the errors in the graphical solution. In the actual channel, the diaphragm bursts nearly at the inlet, so the assumption that the flow is sonic at the inlet will be a good approximation to the real flow.

As already mentioned, the channel considered in the calculation differs from the experimental channel in that it has no parallel part at the test section. As the flow behind the shock is subsonic near the test section, the existence of this parallel part affects the states upstream and slightly modifies the velocities of contact surface and secondary shock. However, the above simplified calculation seems to be sufficient for roughly estimaing the time necessary for the establishment of the steady flow.

Next, a brief account will be made of the flow temperature in this channel.

Flow states in the high pressure chamber are given by the equation of unsteady isentropic expansion:

$$[2/(\gamma-1)]a+u=[2/(\gamma-1)]a_0\,, \quad \gamma=1.4$$

or $$5+M=5a_0/a \qquad (1)$$
where $a$, $u$ and $M$ are sound velocity, flow velocity and Mach number, $\gamma$ is the specific heat ratio and subscript 0 denotes the state of rest in the high pressure chamber. Assuming that $M=1$ at $x=0$, and using asterisks for the quantities at the sonic condition, we have $a_*/a_0=0.833$. As $a$ is proportional to the square root of absolute temperature $T$, we have $T_*/T_0=0.694$.

Relation between the temperature of the flow at $M=4.0$ and that of the sonic condition is given by the equation of steady isentropic flow:

$$(1/2)u^2+c_pT=const.=(1/2)a_*^2+c_pT_*$$

or $$1+0.2M^2=1.2T_*/T \qquad (2)$$
From this we get $T/T_*=0.286$ for $M=4.0$, whence we have $T/T_0=0.198$. This is lower than the corresponding value in the blow-down tunnel, in which the whole process is considered to follow the equation of steady flow. In this case, we have $T_*/T_0=0.833$, so that $T/T_0=0.238$. At any rate, there is no fear of air-liquefaction yet.

The channel for $M=6.0$ has a throat at the inlet, and the diaphragm is broken nearly at this position. Flow at the throat becomes sonic, provided that the initial pressure ratio is sufficiently large, and the wave diagram downstream of the throat is of the same character as explained above. However, the condition upstream of the throat is somewhat different. Acceleration from rest to sonic condition is considered to occur in two stages: unsteady expansion to a certain Mach number $M'$ and a steady expansion from $M'$ to sonic condition. $M'$ is determined by the ratio of the cross-section of the high pressure chamber to that of the throat. As the effective throat area is estimated to be 1.58 cm², the area-ratio is 6/1.58=3.8, so that $M'=0.15$. Writing $T'$ for the corresponding temperature, we have $T_*/T'=0.837$ from Eq. (2), and $T'/T_0=0.943$ from Eq. (1), so that we have $T_*/T_0=0.789$.

Temperature $T$ ofthe flow at $M=6.0$ is given by Eq. (2) as $T/T_*=0.146$, so we obtain finally $T/T_0=0.115$. This value is slightly lower than the value 0.122 for the case of the blown-down tunnel.

Assuming $T_0=295°\mathrm{K}$, we obtain $T=34°\mathrm{K}$. This is lower than the air-liquefaction temperature, which is estimtated to be nearly 45°K, when $T_0=295°\mathrm{K}$ and $p_0=6$ atms. abs. However, the effect of air-liquefaction may be considered not to be serious in the present experiments, since a ceetain degree of supersaturation may be expected to occur and the expansion of the flow to high Mach number takes place in a very short length in our channel.

## § 4. Experimental Results and Discussion

Schlieren photographs showing the flow history at the test section of the channel for $M=4.0$ are given in Fig.4. These photographs were obtained under the condition $p_0=5$ atms. abs. and $p_1=10$ mmHg. A double-wedge profile with a wedge-angle of 10° and with 4 cm chord and 6 cm span was placed in the stream. A thin supporting ring was soft-soldered to the mid-span of the airfoil. Photo. (a) shows the primary shock advancing toward the airfoil. Photo. (b) shows flow near the contact surface. Instead of a sharp contact surface, a wide zone appears in which a strong mixing of hot and cold air takes place. Photo. (c) shows the flow near the secondary shock, which too appears as a wide band of compression. This shock is accompanied with the boundary layer separation. After the passage of the secondary shock and the separated region, a quasi-steady flow of $M=4.0$ is established with a time duration of about 1 millisecond.

Similar flow character was observed in the channel for $M=6.0$, though a little higher pressure ratio $p_0/p_1=6\times760/5$ was necessary for establishing the steady flow of this Mach number.

Mach number of the steady flow was determined by two methods, i.e., by the interferogram and by the measurement of Mach angle. For the latter purpose, several strips of thin cellophane tape were sticked to the wall surfaces upstream of the test-section, so as to give weak waves in the flow. These waves can be considered safely as Mach waves, so Mach number is obtained from the measurement of the angle between wave fronts of two families. Both methods agreed in giving the values, $M=4.0$ and 6.0, for the two cases considered in the experiments.

Fig. 5 shows the interferograms of the steady flows past the double-wedge. Pressure distributions on the surface obtained from the fringe shifts from the free stream states are given in Figs. 6 and 7, where $p$ is the pressure

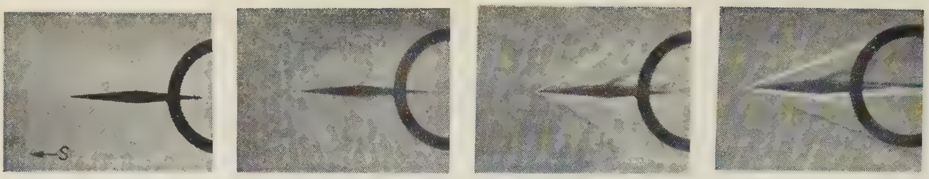

(a) Primary Shock (b) Flow near the contact surface (c) Flow near the secondary shock (d) Quasi-steady flow ($M=4.0$)

Fig. 4. Flow history at the test section.

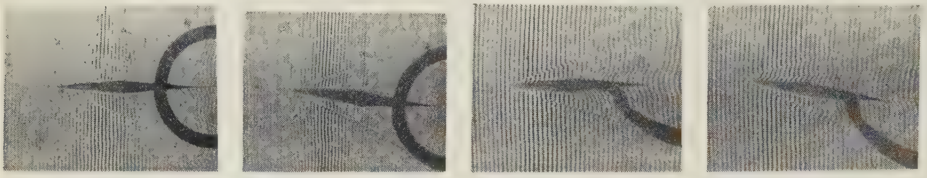

(a) $M=4.0$, $\alpha=0°$ (b) $M=4.0$, $\alpha=5°$ (c) $M=6.0$, $\alpha=0°$ (d) $M=6.0$, $\alpha=8°20'$

Fig. 5. Steady flow past 10° double-wedge.

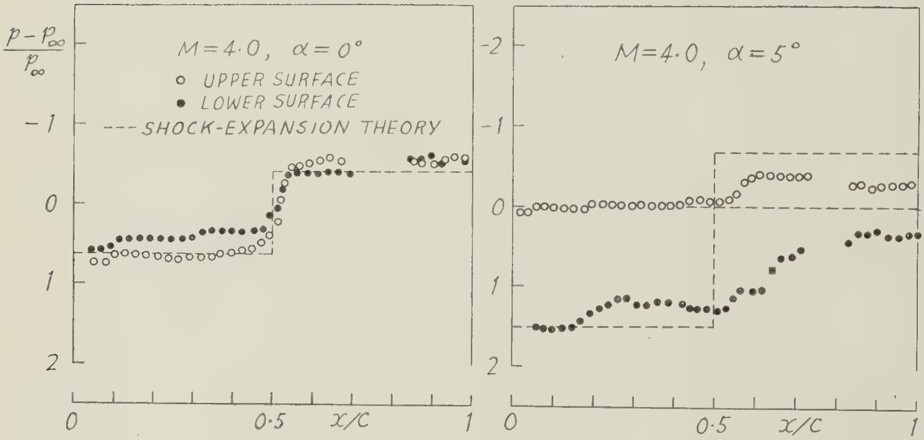

(a) (b)

Fig. 6. Pressure distribution on 10° double-wedge ($M=4.0$).

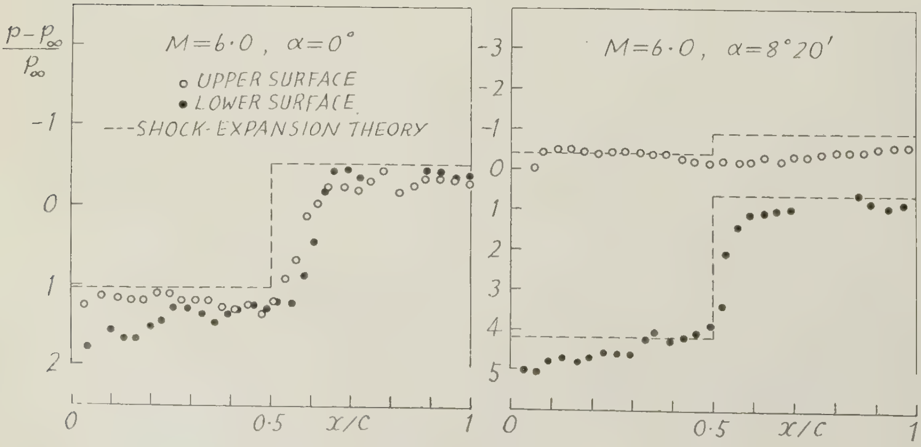

(a) (b)

Fig. 7. Pressure distribution on 10° double-wedge ($M=6.0$).

on the surface, $p_\infty$ the pressure in the free stream, $x$ the distance from the leading edge and $c$ the chord length. Theoretical values based on the shock-expansion theory are given in broken lines. Reynolds numbers based on chord length are $6.6\times10^5$ and $4.7\times10^5$ for $M=4.0$ and 6.0, respectively.

Photographs show that the thickening of the boundary layer becomes considerable at high Mach numbers. Its effect on the pressure distribution along the surface can be clearly seen in Fig. 7; pressure near the leading edge is higher than the theoretical value, and the expansion at the ridge-lines becomes incomplete. These facts agree with the results obtained by McLellan[4] using a hypersonic tunnel of a larger scale.

The author wishes to express his thanks to Mr. S. Fukui for his helpful assistance in carrying out the experiments.

The present work has been partly supported by the fund of the Ministry of Education for scientific researches.

### References

1) A. Hertzberg: J. Aero. Sci. **18** (1951) 803.
2) A. Hertzberg and A. Kantrowitz: J. Appl. Phys. **21** (1950) 874.
3) K. Oswatitsch: Gasdynamik, Springer, Wien (1952) 127.
4) C. H. McLellan: J. Aero. Sci. **18** (1951) 641.
5) C. S. Kim: J. Phys. Soc. Japan **11** (1956) 439.

---

JOURNAL OF THE PHYSICAL SOCIETY OF JAPAN Vol. 11, No. 4, APRIL, 1956

# Experimental Studies of Supersonic Flow past a Circular Cylinder

By Kim, CHUL-SOO

*Department of Physics, Faculty of Science, University of Tokyo*

(Received November 28, 1955)

Experimental studies using shock tubes are presented of the mixed type flow around a circular cylinder placed normal to the general flow of Mach number 1.35, 1.8, 2.7, 3.5, 4.0, and 6.0. With the Mach-Zehnder interferometer and schlieren method the followings were measured: a) shape of detached shock wave, b) distance $d$ of shock wave from the cylinder nose, c) pressure coefficient $C_p$ on the surface of the cylinder, d) density distribution behind the detached shock, e) streamlines in subsonic region.

## § 1. Introduction

The flow field of velocity greater than that of sound, in which a circular cylinder is mounted, is very much complicated, because a detached shock wave is originated ahead of the cylinder and behind it a rotational flow field of mixed type, that is, containing super- and subsonic regions, appears. Theoretical approach of the problem is very difficult because the governing equation of the flow field is of a mixed type and the boundary between sub- and supersonic regions is not given a priori. So all the existing calculations except Uchida's graphical solution [1] are based on the assumption of a certain shape of the detached shock. Further, in most of the earlier works [2] the flow behind the detached shock is assumed to be irrotational and incompressible. Recently more laborious calculations have been reported by Lin and Rubinov [3], Kawamura [4] and Hida [5] taking into account the vorticity behind the shock wave.

Experimentally, the distance between the detached shock and the cylinder nose has been measured by Alperin [6] in the range of Mach number 1.3 to 2.0. As to this distance, some discrepancies are found between theories

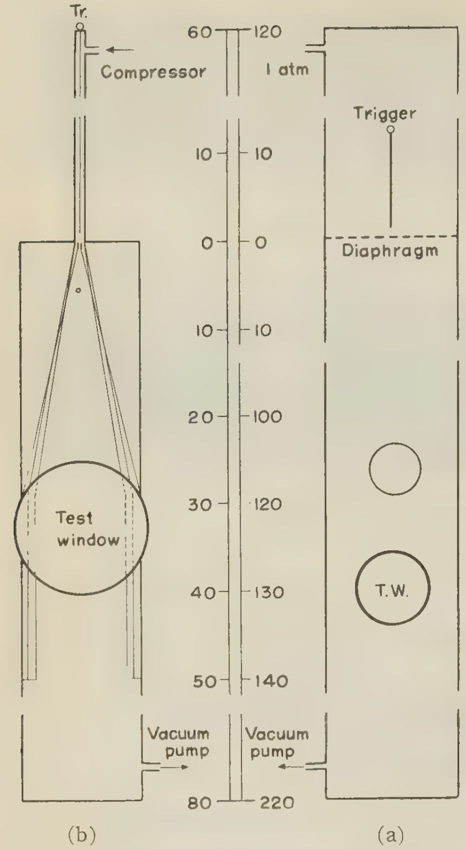

Fig. 1. a) Straight shock tube.
b) Divergent shock tube.

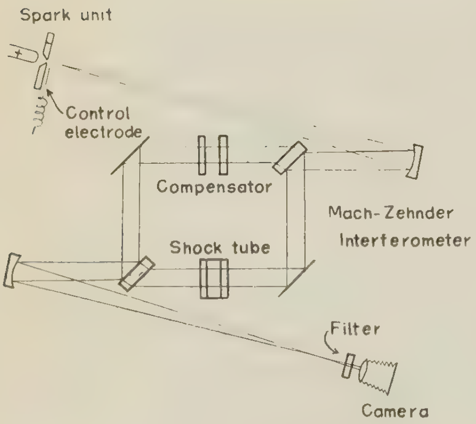

Fig. 2. Optical equipments.

and experiments; the cause for these discrepancies is as yet not clarified. Therefore it seems to the author that the detailed measurements of the whole flow field are necessary for the full understanding of the problem. Experiments at higher Mach number range may be also necessary in order to study the effects of compressibility, vorticity and heat conductivity.

In the present paper, the results of experiments are given for the Mach number from 1.35 to 6.0, and the reason for the disagreement of theories and experiments is discussed.

## § 2. Experimental Methods and Equipments

Two types of shock tubes, straight and divergent, were used for the experiments. Experiments at Mach number of 1.35 were carried out with a straight shock tube of the Institute of Industrial Science [7], having a cross-section of $6\times15\,\text{cm}^2$ (Fig. 1, a)). Cold air, that is, the flow behind the contact surface, was used for the experiments. A divergent shock tube designed by Prof. Tamaki [8] and installed in the Institute of Science and Technology was used for the experiments at higher Mach numbers. In this shock tube, a cellophane diaphragm is situated just in front of the divergent part of the channel, and high Mach number flow is obtained by the expansion of the cold air in the divergent part (Fig. 1, b)). High pressure chamber has a section of $1\times6\,\text{cm}^2$, and compressed air at 4～6 atms. abs. is supplied from the compressor. Low pressure chamber has a section of $14\times6\,\text{cm}^2$, and wooden divergent walls corresponding to each Mach number are inserted in it. The pressure in this chamber is lowered by a vacuum pump to 5～10 mm Hg. Flow history after the rupture of the diaphragm was studied in detail by Tamaki [8]. In the test section situated at the end of the diverging walls, a quasi-steady flow whose duration is of the order of 1 millisecond is obtained after the passage of the primary shock, contact surface and the secondary receding shock. Optical equipments used with the divergent shock tube are shown schematically in Fig. 2. Mach-Zehnder interferometer with glass plates of 21 cm diameter was used for the measurement of density field. Magnesium spark was used as a light source, and the timing of the spark discharge was effected by the method of Hertzberg and Kantrowitz [9]. Detailed description of the optical equipments will be omitted here, as it is found in Reference [8].

In the experiments reported here, circular cylinders made of brass with diameters of 4, 6, 8, 10 and 12 mm were used. To realize two-dimensional flow, i.e., to avoid the end effects of the cylinder and the interaction between boundary layer and shock wave, the cylinder was mounted in the test section parallel to the light path leaving clearances of 0.4～0.7 mm between both ends of the cylinder and the glass windows. In order to investigate the effects on the flow of the aspect ratio of the cylinder, cylinders of various lengths were also used for schlieren observations. As shown in Section 3, schlieren photographs taken when the axis of the cylinder is set normal to the light beam give good information as to the end effects of the cylinder.

## § 3. Results and Discussions

### *i) Distance between the detached shock and the circular cylinder*

At the first stage of the experiments, the distance $d$ of the shock wave from the cylinder nose was observed for various aspect ratios $l/D$ at constant free stream Mach number $M_1$, where $l$ is the length and $D$ is the diameter of the cylinder.

The distance $d$ was determined from the schlieren photographs taken by setting the cylinder axis perpendicular to both air stream and light path. Such photographs are given in Fig. 3, a) and b). When the aspect ratio is larger than 5.5, there exists a region in which the shock front is straight and parallel to the cylinder. In the case of small aspect ratio, shock front is curved as a whole (Fig. b)), so the shock distance in the central section was adopted for $d$. Fig. 3, c) and d) are the photographs taken by setting the cylinder axis parallel to the light beam. When the aspect ratio is large, detached shock does not appear as a distinct line (Fig. c)). However, when the aspect ratio is small, the shock appears as a sharp line as shown in Fig. d); in this case the shock distance coincides with that of the central section of Fig. b).

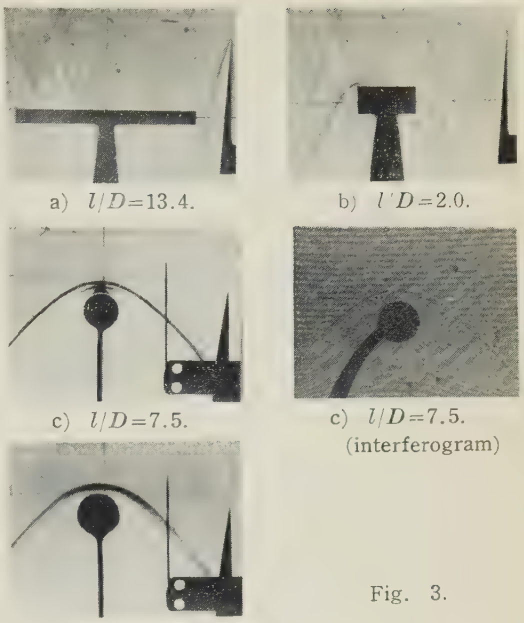
a) $l/D=13.4$.
b) $l/D=2.0$.
c) $l/D=7.5$.
c) $l/D=7.5$. (interferogram)
d) $l/D=2.0$.

Fig. 3.

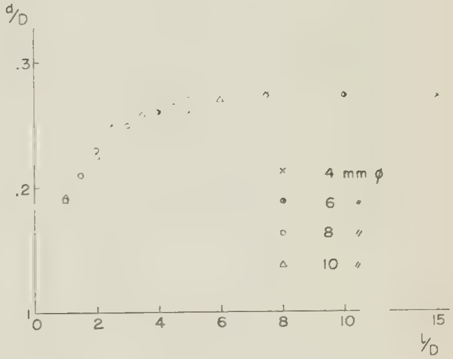

Fig. 4. $d/D$ vs. $l/D$ for $M_1=4.0$.

The relation between $d/D$ and $l/D$ is given in Fig. 4 in the case of $M_1=4.0$. The same character was obtained in the cases of $M_1=2.7$ and 6.0. The results show that two-dimensionality is obtained at the aspect ratio $l/D$ larger that 5.5 in the Mach number range of our experiments $M_1=2.7$～6.0. Sugimoto's [10] experimental data which were obtained in the case of $l/D=1$ agree well with our experiments of the same aspect ratio. But the results obtained in such a low aspect ratio do not satisfy the two-dimensionality as is shown in Fig. 4.

In order to determine the Mach number $M_1$ of the main stream in the divergent shock tube, strips of thin cellophane tape were sticked to several positions on each divergent wall; waves originating from the edges of these tapes are very weak, and its inclination to the main flow can be considered with a good approximation as the Mach angle of the flow. So the Mach number was determined by measuring the angle between the wave fronts originating from the two opposite walls.

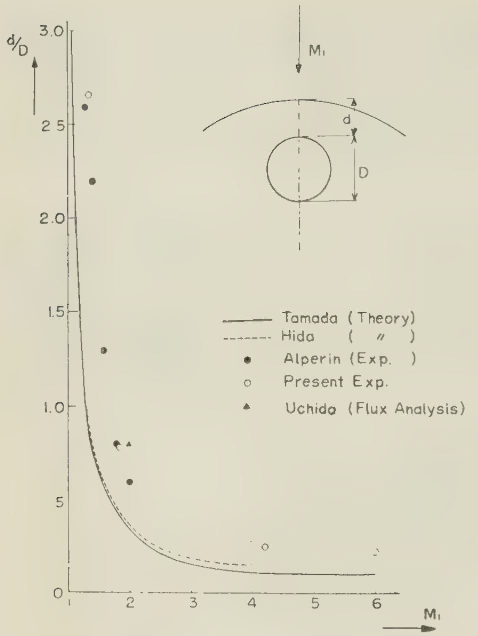

Fig. 5. $d/D$ vs. $M_1$.

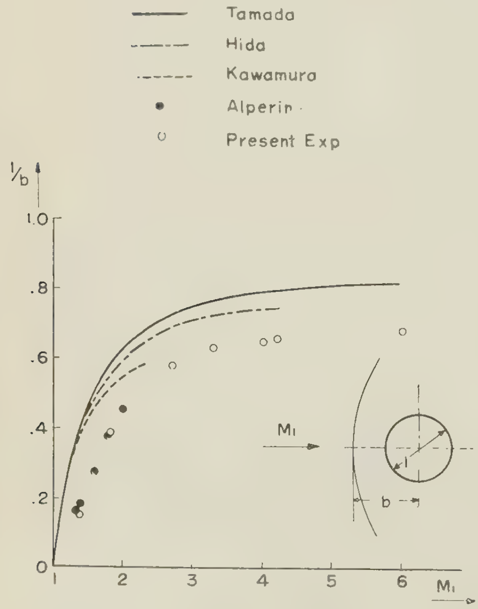

Fig. 6. $1/b$ vs. $M_1$.

Fig. 5 shows the relation between $d/D$ and $M_1$, and Fig. 6 shows the relation between $b=(D+2d)/D$ and $M_1$. In these figures, we have also included Alperin's results obtained for $M_1=1.3\sim2.0$ in a continuous running supersonic wind tunnel. The agreement between our results and Alperin's is very good. These results show some discrepancy to the theoretical values. The author considers that this is due to the facts: a) the shape of the shock wave assumed in the theory is not adequate, b) the effects of compressibility, thermal conductivity and viscosity are neglected in the theoretical analysis. It should be noted here, that Uchida's [1] graphical solution for $M_1=2.0$ by the flux analysis gives a good agreement with our experimental results.

### *ii) Isopycnics and streamlines*

In Fig. 7 the isopycnics (contours of constant density) in the whole flow field for $M_1=4.0$ are given. Streamlines in the subsonic region are also shown in the same figure. As the flow behind the shock is rotational, there is no simple way to calculate the values of pressure, temperature and velocity in this region. However, the values of the density in the whole field can be determined from the interferograms and one is able to calculate the streamlines at each point step by step by using the well-known gasdynamical relations. The simplest way is to use the equation of continuity, $A\rho u=$ const., where $A$ is the area between adjacent streamlines, $\rho$ the density and $u$ the velocity. Of course, the product $A\rho u$ has a fixed value in front of the shock. To draw the streamlines behind the shock, the shock is replaced by several straight tangential segments (in our case it is replaced by five segments between the point $A$ on the $x$-axis to the sonic point $B$ on the shock wave). Then, the entropy change and the stagnation pressure are calculated from the inclination of the segment to the main stream. In this procedure, the following relations are used:

$$\frac{\rho_1}{\rho_2}=\frac{2}{\gamma+1}\left(\frac{1}{M_1^2\cos^2\alpha}+\frac{\gamma-1}{2}\right), \qquad (1)$$

$$u_2=u_1\sin\alpha$$

$$\times\left[\frac{1}{\tan^2\alpha}\left\{\frac{\dfrac{1}{M_1^2\cos^2\alpha}+\dfrac{\gamma-1}{2}}{\frac{1}{2}(\gamma+1)}\right\}^2+1\right]^{1/2}, \qquad (2)$$

$$\beta=\tan^{-1}\left\{\frac{\frac{1}{2}(\gamma+1)\tan\alpha}{\dfrac{1}{M^2\cos^2\alpha}+\dfrac{(\gamma-1)}{2}}\right\}-\alpha, \qquad (3)$$

where suffixes 1, 2 denote the values in front of and immediately behind the shock wave respectively, $\alpha$ is the shock wave angle, and

$\beta$ is the deflection of the stream. Then the velocity at each point behind the shock wave is obtained from the measured $\rho$-values by the use of the adiabatic relation and the gasdynamic equations. Now, the continuity condition for each flow passing through the segment must also be satisfied, and this condition determines the cross sectional area $A$ of stream tubes, the boundaries of which are equivalent to streamlines.

In flows where the deflection of the stream is considerably large, as in our experiment, the approximations involved in this method become rather poor theoretically. Moreover to expect good accuracy for the determination of streamlines a large number of fringe shifts should be read (about 400 points were read by comparator in our experiment). Nevertheless, the followings may be concluded a) Streamlines in the subsonic region behind the shock are nearly straight and parallel to each other except in the vicinity of the cylinder. This suggests that, in subsonic region, the vorticity just behind the shock conserves its intensity along each streamline. b) Sonic line curves inward in the neighbourhood of the shock. It is not clear whether this is the essential feature of the phenomena, or due to the fact that shock wave has some breadth which is caused by the effect of the boundary layers on the test windows.

### *iii*) *Pressure coefficient*

As the flow on the cylinder surface comes from the normal portion of the shock wave ahead of the cylinder, the pressure coefficient $C_p$ can be obtained from the following equation:

$$C_p=\frac{2}{\gamma M_1^2}\left(\frac{p}{p_1}-1\right)=\frac{2}{\gamma M_1^2}\left\{\left(\frac{\rho}{\rho_1}\right)^{\gamma}e^{(\Delta s/c_v)}-1\right\}, \tag{4}$$

where $c_v$ is the specific heat at constant volume, $s$ is the entropy change across the normal shock.

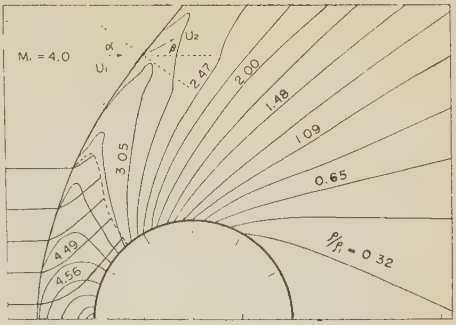

Fig. 7. Isopycnics, streamlines and sonicline for $M_1$=4.0.

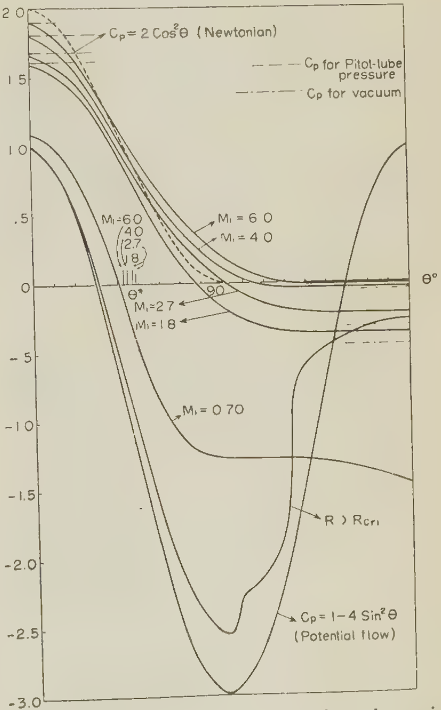

Fig. 8. Pressure coefficient and sonic point.

In Fig. 8 pressure coefficient against $\theta$ are shown in full lines for $M_1$=1.8, 2.7, 4.0, and 6.0. In the same figure the stagnation pressure coefficients calculated from the normal shock relation are given by broken lines at $\theta=0°$. Also in the same figure, the vacuum pressure coefficients, which are calculated from the Eq. (4) by putting $p=0$, are given by chain lines at $\theta=180°$. From this figure, we can see that the pressure at $\theta=0°$ agrees very well with the theoretical stagnation pressure. The pressure coefficient behind the separation point decreases as $M_1$ increases, and at $M_1$=6.0, wide region at the rear of the cylinder is nearly in the state of vacuum. The dotted line in Fig. 8 shows the Newtonian theoretical curve $C_p=2\cos^2\theta$, based on the principle of collisions of fluid elements on a body. Experiments show that in the neighbourhood of the stagnation point, the pressure coefficient approaches the Newtonian theoretical value asymptotically as $M_1$ increases. For comparison, the pressure coefficients of

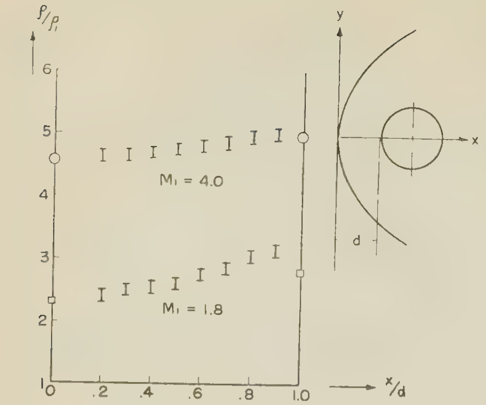

Fig. 9. Density distribution along the $x$-axis.

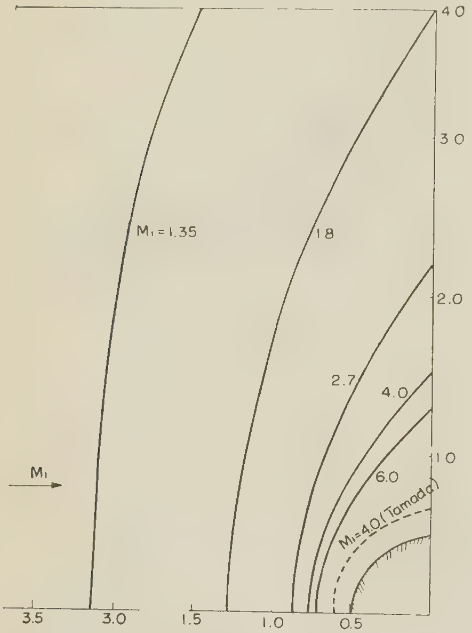

Fig. 10. The shape of the detached shock wave.

subsonic potential flow and of real subsonic flows are also shown in the same figure. In summary, there seems to be no significant change in the pressure distribution on the cylinder, moving with supersonic velocity, from that of high subsonic case.

### *iv) The density distribution along the $x$-axis*

As is pointed out in the previous section, disagreement of the experimental shock distance with the available theories is probably due partly to the fact that the effect of compressibility of the air flow is not accounted in the theory. Density distribution along the $x$-axis seems to be useful for the examination on this effect. Fig. 9 shows such distributions for $M_1=1.8$ and 4.0. In this figure, it is noteworthy that the density distribution for $M_1=1.8$ is more steeper than that for $M_1=4.0$.

### *v) Separation region and sonic point on the surface of circular cylinder*

It is difficult to determine the separation point by optical measurements. This is because of the fact that the observed separation point changes with the sensitivity of schlieren method, and that the separation phenomena themselves are likely somewhat unstable. Nevertheless, a number of data obtained ascertain that: a) the separation point moves downstream as $M_1$ increases, b) the area of separation region decreases as $M_1$ increases, and c) the minimum cross section of the wake also decreases and the location of this minimum cross section approaches the cylinder as Mach number $M_1$ increases.

The sonic point $\theta^*$ on the cylinder, where the flow speed becomes equal to the sound speed, can easily be calculated from the pressure coefficient. The values of $\theta^*$ for various Mach numbers are given in Fig. 8. This shows that $\theta^*$ decreases gradually as $M_1$ increases.

### *vi) The shape of the detached shock wave*

Fig. 10 shows the shapes of the detached shock wave in front of circular cylinder at $M_1=1.35$, 1.8, 2.7, 4.0, and 6.0. For comparison the shape of shock wave assumed by Tamada is given for $M_1=4.0$ in the same figure. Here, Tamada assumed that the most effective element for determining the shock distance is the shape of the shock wave near the $x$-axis. But the author considers that the disagreement of the assumed wave form with the real one, as in Fig. 10, is one of the causes of the discrepancy between the measured and the theoretical values of $d/D$.

### *vii) Supersonic flow around a cut circular cylinder*

Fig. 11 shows the variation of the shock distance when the cylinder is cut at $\theta=\pm\theta_i°$, parallel both to cylinder axis and to wind tunnel axis. If the angle $\theta_i$ is decreased from 90° continuously, we can expect that, the shock wave distance from the cylinder does not change until the value of $\theta_i$ reaches some critical value, say $\theta_{cri}$, and with the value $\theta_i<\theta_{cri}$, the distance will decrease. The value

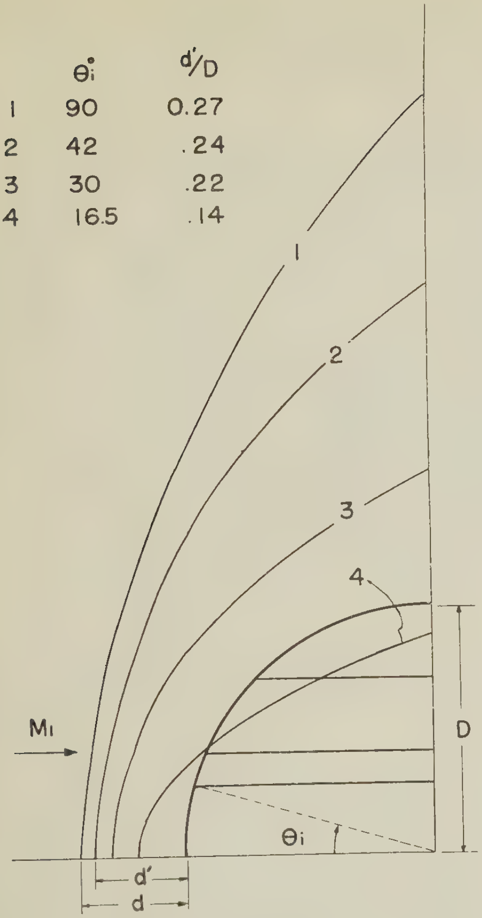

Fig. 11. Variation of detached shock wave for cut circular cylinder ($M_1=4.0$).

of $\theta_{cri}$ must coincide with the foot of the last Mach line. The cases of $\theta_i=42°$, 30°, and 16.5° were experimented for $M_1=4.0$ (the sonic point on the full cylinder is located at $\theta^*=44°$).

In Fig. 12 the relation between $d/D$ to $\theta_i$ is given, where $\theta_{cri}\doteqdot 48°$ is obtained. In this figure the value of $\theta_{cri}$ turned out to be slightly greater than the value of $\theta^*$ determined by means of either pressure coefficient in Fig. 8 or interferogram in § 3. ii), although both giving almost identical value. This fact gives a fairly quantitative justfication to our previous experiments including those of pressure coefficient, isopycnics, sonic point, $M_1$ vs. $d/D$ etc.

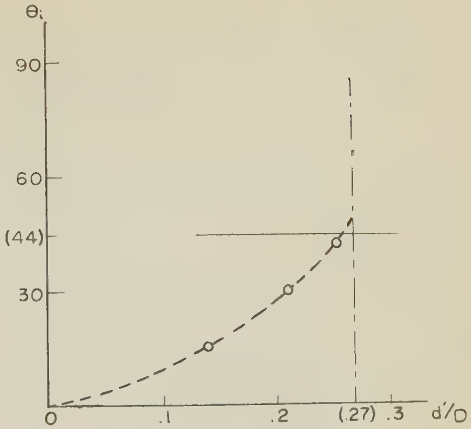

Fig. 12. $d/D$ vs. $\theta_i$ for $M_1=4.0$.

The author would like to express his sincere thanks to Prof. I. Imai for his suggestion of this problem, to Prof. F. Tamaki for his continual guidance and encouragement in the course of the investigation, and to Mr. K. Ôshima and Mr. S. Fukui for their cooperation in conducting the experiments.

## References

1) S. Uchida: Pre-print of the 4th Nat. Cong. Theo. Appl. Mech. Part **2** (1954) 26.
2) K. Tamada: Preliminary Reports of the Tomotika Lab. Fac. Sci. Univ. Kyoto, No. 2 (1950).
3) C. C. Lin and S. I. Rubinov: Journ. Math. Phys. **27** (1948) 105.
4) T. Kawamura: Journ. Phys. Soc. Japan **7** (1952) 486.
5) K. Hida: Journ. Phys. Soc. Japan **8** (1953) 740.
6) M. Alperin: Progress Rep. No. 44 Jet Propul. Lab. C.I.T. (1950).
7) F. Tamaki and K Ôshima: Seisan-Kenkyu, **5** 1953) 87, (in Japanese).
8) F. Tamaki: Journ. Phys. Soc. Japan **11** (1956) 434.
9) A. Hertzberg and A. Kantrowitz: Journ. Appl. Phys. **21** (1950) 874.
10) M. Sugimoto: Giken-Zappo, No. 355 (1944), (in Japanese).

JOURNAL OF THE PHYSICAL SOCIETY OF JAPAN Vol. 11, No. 4, APRIL, 1956

# A Study of the Compressible Flow past Tomotika-Tamada's Profiles

By Hideo TAKAMI

*Department of Physics, Faculty of Science, University of Tokyo*

(Received November 29, 1955)

In this paper a number of approximate methods are applied to study the two-dimensional high subsonic flow of the adiabatic gas past a family of profiles given by Tomotika and Tamada.

The velocity distributions over the profiles are calculated by means of Kármán-Tsien's, the WKB, the $M^2$-expansion and Meksyn-Imai's methods, and are compared with Tomotika-Tamada's exact solutions as well as with Naruse's results by the thin-wing-expansion method. The convergency and validity of the above-mentioned methods are discussed.

It is noticed that there exists certain amount of discrepancy between Tomotika-Tamada's results and those of the present calculation, which might be considered as being due to the difference between the characteristic of the hypothetical gas assumed in Tomotika-Tamada's study and that of the adiabatic gas.

## § 1. Introduction

A great many investigations have been made with various approximate methods for the study of the compressible flow past bodies such as circular and elliptic cylinders, Joukowski aerofoils sphere, ellipsoids of revolution, etc.

But, on account of the nonlinearity of the fundamental equations in the physical plane the studies of the flow past a body of prescribed shape have necessarily relied on perturbation methods or on certain approximations in the fundamental equations, so that in spite of the numerous investigations we might say that little is known about the validity of the results and the actual flow patterns near the sonic speed.

On the other hand, it is well known that the difficulty of the nonlinearity in the equations can be removed by means of the hodograph transformation if we give up the study of the flow past a profile of *prescribed* shape; in fact, certain examples of exact solutions of the transonic flow past a cylindrical body have been obtained by the hodograph method [1] [13].

These exact solutions are considered to be of great importance, not only because they have shown the existence of the continuous transonic flow past a body, but also because they may serve as the tests of various approximate methods.

The flow past a profile appearing in one of Cherry's exact solutions has already been studied by the present writer with a number of approximate methods [11]. On account of the existence of the supersonic regions in the flow this example was not quite adequate as the criterion in the above-mentioned sense, but it was found that Cherry's solution might probably correspond to a flow which cannot be obtained by increasing the free stream Mach number continuously from zero.

Also in this paper, a number of approximate methods, such as Kármán-Tsien's, the WKB, the $M^2$-expansion and Meksyn-Imai's methods, are applied to study the compressible flow past a family of profiles for each of which an exact solution of continuous transonic flow has been obtained by Tomotika and Tamada [13].

We shall first calculate the velocity distributions over the surfaces of these profiles by the above-mentioned methods, and compare them with those of Tomotika-Tamada's exact solutions as well as with Naruse's numerical results by the thin-wing-expansion method [10].

Thus we shall see, quantitatively to some extent, how these approximate methods lose their accuracy and applicability when the sonic speed is approached in the flow. Further we shall notice certain amount of discrepancy between the values of the velocity obtained by the present calculation and those in Tomotika-Tamada's solutions; which might be regarded as being due to the difference between the characteristics of the adiabatic gas and the hypothetical gas used in Tomotika-Tamada's investigation.

## § 2. Tomotika-Tamada's Exact Solutions

By means of the hodograph method Tomotika and Tamada [13] have obtained a family of exact solutions of two-dimensional continuous transonic flow past a cylindrical body for a certain hypothetical gas which approximately satisfies the adiabatic gas relation.

Further, by numerical calculation, they have given three examples of transonic flow past a thin profile. The shape of each profile, only slightly different from those of the other two, is symmetrical with respect to the direction of the oncoming flow, and has a finite angle at the leading edge and a cusp at the trailing edge. The Mach numbers of the undisturbed flow are 0.717, 0.745 and 0.752 respectively. For convenience' sake we shall designate these profiles as $P_1$, $P_2$ and $P_3$ (Figs. 1(a), (b) and (c)).

Of these three, the flow past $P_1$ seems to be most important for the purpose of the present paper, since in this flow the sonic speed appears just at the points of the maximum velocity on the surface, while in the others supersonic regions show themselves adjacent to the profiles so that it is anticipated at the outset that the approximate methods which will be employed here are invalid in these regions.

## § 3. The Mapping Functions for Tomotika-Tamada's Profiles and the Incompressible Velocity Distributions

Let $P$ be a profile in the $z(=x+iy)$-plane, and we can map the region outside $P$ conformally onto the region outside the unit circle $Z=e^{i\theta}$ in the $Z$-plane by an analytic function of the form:

$$z=c_{-1}Z+c_0+\frac{c_1}{Z}+\frac{c_2}{Z^2}+\cdots .$$

In practice the coordinates of the profile $(x_P, y_P)$ are evaluated as functions of $\theta$ conveniently by means of Imai's iterative method [2] [11].

His procedure rests on the following relation between $x_P$ and $y_P$:

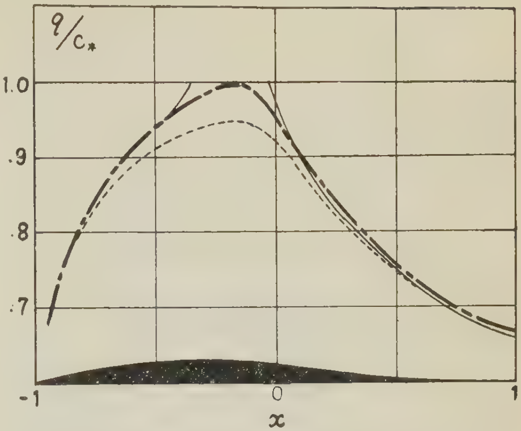

Fig. 1 (a). The profile $P_1$ and the velocity distribution over its surface ($M=0.717$).

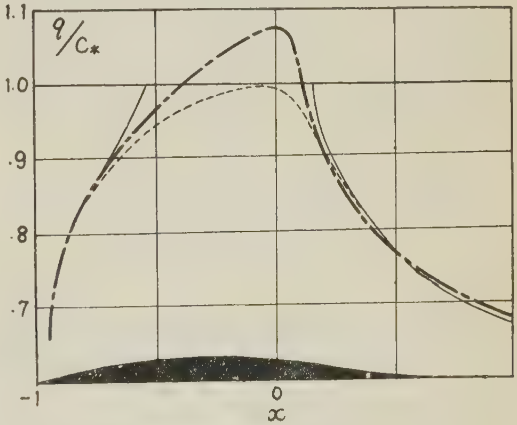

Fig. 1 (b). The profile $P_2$ and the velocity distribution over its surface ($M=0.745$).

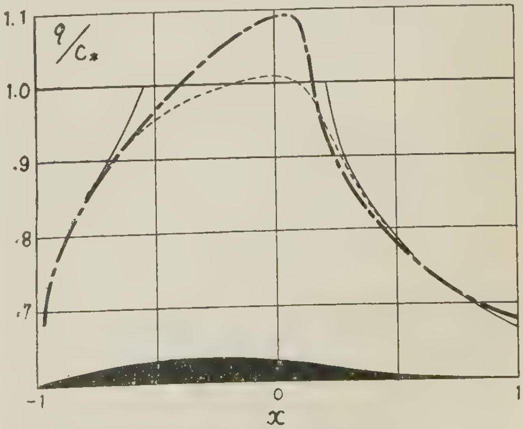

Fig. 1 (c). The profile $P_3$ and the velocity distribution over its surface ($M=0.752$).

—·—·— Tomotika-Tamada's exact solution,
Kármán-Tsien's method (simplified),
the WKB method (simplified).

$$x_P(\theta)=\left\{1-\frac{1}{2}y_P{}^*(0)+\frac{1}{2}y_P{}^*(\pi)\right\}\cos\theta+y_P{}^*(\theta)-\frac{1}{2}y_P{}^*(0)-\frac{1}{2}y_P{}^*(\pi)\,, \tag*{(3.1)*}$$

where $y_P{}^*(\theta)$ denotes the conjugate Fourier series associated with $y_P(\theta)$.

In the following we calculate the values of $(x_P, y_P)$ and also the velocities for $\theta=(2\pi/40)k$ ($k=0, 1, 2, \cdots, 39$), which may be sufficient for our purpose.

For $P_1$ the 0th approximation is taken to be $x_{P_1}{}^{(0)}(\theta)=\cos\theta$, and after three steps of iteration the final values of $x_{P_1}(\theta)$ and $y_{P_1}(\theta)$ are obtained. On the other hand, by taking $x_{P_1}(\theta)$ as the 0th approximation, it is found that only one step is sufficient for $P_2$ and $P_3$, which shows how favourably the iteration proceeds if we have already known the values of the mapping functions for approximately the same profile as the original one.

The velocity $q_{\text{inc}}$ on the surface for the incompressible flow is calculated as

$$\frac{q_{\text{inc}}}{U_{\text{inc}}}=\frac{1-\frac{1}{2}y_P{}^*(0)+\frac{1}{2}y_P{}^*(\pi)}{\sqrt{\left(\frac{dx_P}{d\theta}\right)^2+\left(\frac{dy_P}{d\theta}\right)^2}}\sin\theta\,, \tag{3.2}$$

where $U_{\text{inc}}$ is the velocity of the undisturbed flow with its direction parallel to the $x$-axis.

## § 4. The Kármán-Tsien Method

From the incompressible flow velocity we can calculate the velocity $q$ for the compressible flow approximately by means of Kármán-Tsien's formula [14]:

$$\frac{q}{U}=\frac{q_{\text{inc}}}{U_{\text{inc}}}\,\frac{1-\lambda}{1-\lambda\left(\frac{q_{\text{inc}}}{U_{\text{inc}}}\right)^2}\,, \tag{4.1}$$

where $U$ is the velocity of the undisturbed flow with Mach number $M$ and

$$\lambda=\frac{1-\sqrt{1-M^2}}{1+\sqrt{1-M^2}}\,.$$

The velocity distributions for the three profiles are shown in Figs. 1(a), (b) and (c). (In order to show the transonic character of the flow, $q/c_*$ are plotted against the chordwise length $x$, $c_*$ being the critical sound velocity corresponding to the free stream Mach number $M$.)

Strictly speaking, however, the velocity given by the formula (4.1) corresponds to the flow past a different profile from the one in question. But it can be shown that if the thickness of the original profile is small, the deformed profile is almost similar to the original one [5].

In fact, the variations in the thickness ratio are quite small for the present examples. They are shown in Table I together with other examples. In our case only very small corrections will be expected for the velocity distributions even if the effect of the deformation is properly taken into account.

## § 5. The WKB Method

According to Imai's WKB method [6] the problem of the compressible flow is reduced to that of the incompressible flow just as in Kármán-Tsien's method.

The velocity $q$ for the compressible flow is calculated from the related incompressible velocity $Q$ by the following formula:

$$Q=\frac{2}{(1+a)^{1/a}}\,\frac{q}{c_*}\left(1-a^2\frac{q^2}{c_*{}^2}\right)^{(1-a)/2a}\times(1+a\mu)^{1/a}\frac{1}{1+\mu}\,, \tag*{(5.1)**}$$

where

$$\mu=\left(\frac{1-q^2/c_*{}^2}{1-a^2q^2/c_*{}^2}\right)^{1/2},$$

and

$$a^2=\frac{\gamma-1}{\gamma+1}\,.$$

Practically, by using the numerical table [7] for Eq. (5.1) we may proceed as follows:

(i) Calculate $U/c_*$ from the free stream Mach number $M$.

(ii) Calculate $Q_\infty$ from the numerical table.

(iii) From the incompressible velocity $Q/Q_\infty$ ($=q_{\text{inc}}/U_{\text{inc}}$ in § 3) calculate $Q=(Q/Q_\infty)\times Q_\infty$.

(iv) Again by means of the table we obtain $q/c_*$ from $Q$.

The velocity distribution thus obtained does not correspond to the flow past the original profile $P$ as is also the case in Kármán-Tsien's method.

The coordinates $(\xi_{P'}, \eta_{P'})$ of the deformed

---

* It is assumed here that the profile is symmetrical with respect to the $x$-axis and cuts it at the points $(1, 0)$ and $(-1, 0)$.

** In Imai's original paper [6], $q$ is referred to the critical sound velocity so that $q/c_*$ in Eq. (5.1) corresponds to $q$ in [6].

Table I.

| | $P_1$ | $P_2$ | $P_3$ | Circular cylinder (Tamada [12]) | Cherry's profile [11] |
|---|---|---|---|---|---|
| $M$ | 0.717 | 0.745 | 0.752 | 0.40 | 0.51 |
| $t_0$ | 0.107 | 0.111 | 0.112 | 1.00 | 0.93 |
| $t$ | 0.109 | 0.113 | 0.114 | 1.07 | 1.05 |
| $(t-t_0)/t_0$ | 0.019 | 0.018 | 0.018 | 0.07 | 0.13 |

$t_0$: thickness ratio of the original profile. $t$: thickness ratio of the deformed profile.

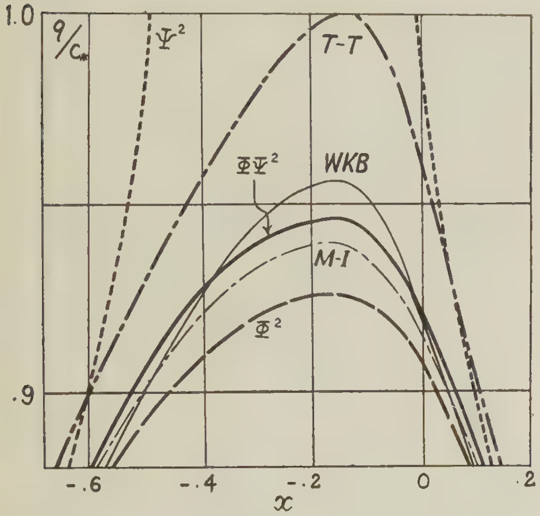

Fig. 2. The velocity distribution over the surface of the profile $P_1$ near the point of the maximum velocity ($M=0.717$).
-·-·- Tomotika-Tamada's exact solution,
— — — the $\Phi$-procedure (2nd approximation),
- - - - - the $\Psi$-procedure (2nd approximation),
——— the $\Phi\Psi$-procedure (2nd approximation),
------ Meksyn-Imai's method,
——— the WKB method.

profile $P'$ are given by

$$\begin{cases} \xi_{P'} = \displaystyle\int \frac{Q}{(q/c_*)} K^{1/4} dx_P\,, \\ \eta_{P'} = \displaystyle\int \frac{Q}{(q/c_*)} K^{1/4} dy_P\,, \end{cases}$$

where

$$K = \frac{1-\left(\dfrac{q}{c_*}\right)^2}{\left\{1-\dfrac{\gamma-1}{\gamma+1}\left(\dfrac{q}{c_*}\right)^2\right\}^{(\gamma+1)/(\gamma-1)}}\,.$$

The velocity distributions for the three profiles are shown in Figs. 1(a), (b) and (c)*. The velocity in the supersonic region cannot be calculated by this procedure since too large a value of $Q$ does not give a real $q$ as can be seen from Eq. (5.1).

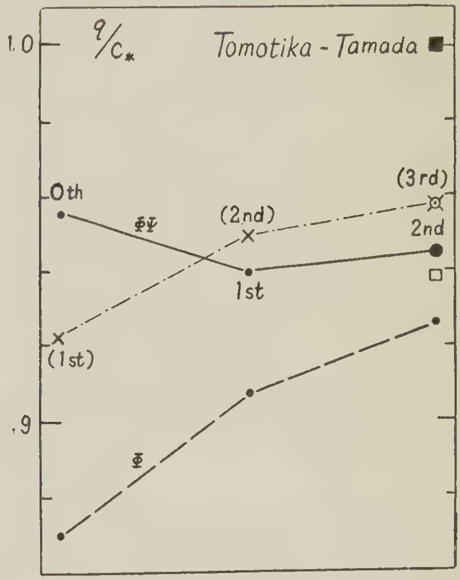

Fig. 3. The maximum velocity on the surface of the profile $P_1$ for $M=0.717$.

Especially for the profile $P_1$, for which no supersonic regions appear in the exact solution, we can calculate the velocity distribution over the whole surface by properly taking account of the deformation of the profile.

The iterative procedure for this purpose is performed in almost the same way as in the Kármán-Tsien method [11], except that this procedure is made somewhat complicated by the occurrence of the seeming supersonic speed in the course of the calculation.

The velocity distribution thus obtained is shown in Fig. 2.

## § 6. The $M^2$-Expansion Method

Now the $M^2$-expansion method is applied to the flow past the profile $P_1$. The velocity distributions are calculated for $M=0.717$ and 0.500 to the order of $M^4$ by means of Imai's $\Phi$-, $\Psi$- and $\Phi\Psi$- procedures [3] [4] [11] (Figs. 2, 3, 4 and 5).

---

* In the following calculations we shall take $\gamma$ as 1.40.

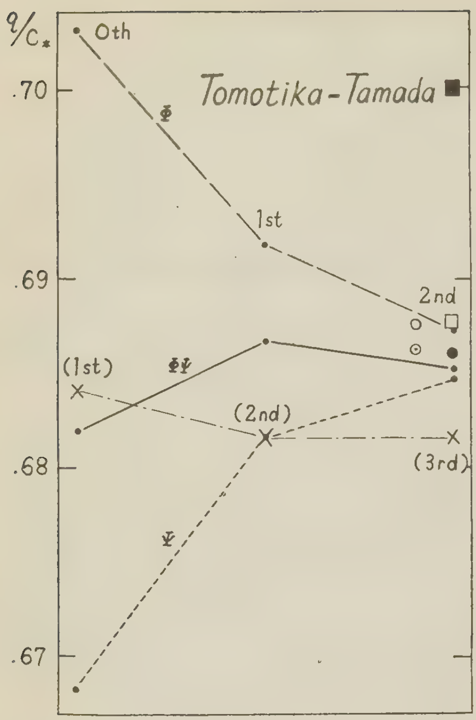

Fig. 4. The velocity at a point on the surface ($x=0.8$) near the trailing edge of the profile $P_1$ for $M=0.717$.

## § 7. The Meksyn-Imai Method

Meksyn-Imai's method [9] [8] [11], as a variant of the usual $M^2$-expansion method, has also been shown to be useful for the study of the high speed flow.

Calculation is made for $P_1$ with $M=0.717$ and 0.500 (Figs. 2, 3, 4 and 5).

The critical Mach number above which the method fails is evaluated to be 0.888.

## § 8. Numerical Results and Discussions

(1) For $P_1$:

(i) M=0.717. As is clearly seen from Figs. 2 and 3, none of the approximate methods gives a satisfactory result in the high speed region.

Numerical results by the $M^2$-expansion method suggest that the iteration will diverge in the neighbourhood of the maximum speed near this Mach number, so that the critical Mach number 0.888 calculated by the Meksyn-Imai method seems to be too large to be regarded as the Mach number below which the $M^2$-expansion method is valid.

Such an over-estimation of the critical Mach number has already been seen in the examples studied by Meksyn [9] and by the present writer [11].

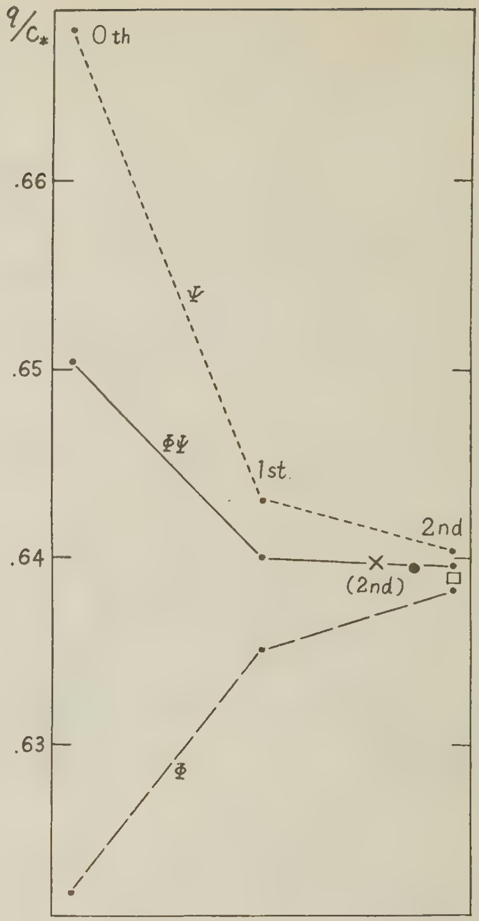

Fig. 5. The maximum velocity on the surface of the profile $P_1$ for $M=0.500$.

| | |
|---|---|
| ■ | Tomotika-Tamada's exact solution, |
| □ | Meksyn-Imai's method, |
| ● | Kármán-Tsien's method (simplified), |
| ○ | the WKB method (simplified), |
| ⊙ | the WKB method, |
| ---×--- | the thin-wing-expansion method (Naruse), |
| — · • —— | the Φ-procedure, |
| • ----- | the Ψ-procedure, |
| —— • —— | the ΦΨ-procedure. |

Considering that the convergency of the iterative method will become poorer and poorer as the critical state is approached, this bad estimation of the critical Mach number is rather a matter of course. Thus the merit of Meksyn's procedure is to be found in its qualitative description of the probable flow pattern at high Mach number.

On the other hand, the results of the approximate methods seem to be reliable in the relatively low speed region (Fig. 4). But it must be noted that there exists some discrepancy between the value of the exact solution and those obtained by the present calculation. Its magnitude, though small, cannot be considered as being within the range of the errors due to the approximate methods; rather we might regard this as a measure of the deviation of the characteristic of the gas assumed in the exact solution from that of the adiabatic gas.

(ii) $M=0.500$. Though the exact solution which may serve as the standard for comparison has not yet been obtained for this case, we may regard Naruse's result of the second approximation by the thin-wing-expansion method [10] as reliable enough in view of the small thickness of the profile and the relatively low values of the free stream Mach number.

The agreement of the present results with that of Naruse is very good; Kármán-Tsien's method and the WKB method are both satisfactory, and the advantage of the $\Phi\Psi$-procedure is clearly seen also in this example [4] [11] (Fig. 5).

(2) For $P_2$ ($M=0.745$) and $P_3$ ($M=0.752$):

The results of Kármán-Tsien's method and the WKB method agree well with each other in the low speed region. There also exist small differences from the values of the exact solutions; we may interpret them just as in the case of the profile $P_1$ (Figs. 1(b) and (c)).

### Acknowledgements

The writer would like to express his hearty thanks to Professor Isao Imai who suggested this problem and has guided and encouraged him throughout this study.

The writer's thanks are also due to Professor Saburô Asaka, Dr Mitutosi Kawaguti and Dr Hidenori Hasimoto for their advice and kind inspection of the manuscript, and also due to Mr Humio Naruse who kindly showed him the numerical data.

### References

1) T. M. Cherry: Proc. Roy. Soc. **A 192** (1947) 45.
2) I. Imai: J. Soc. Aeron. Sci. Japan **9** (1942) 865 (in Japanese).
3) I. Imai: Rep. Aeron. Res. Inst., Tokyo Imp. Univ. No. 275 (1943) (in Japanese).
4) I. Imai: read at the monthly meeting of the Phys.-Math. Soc. Japan, Tokyo (May 1944).
5) I. Imai: Rep. Aeron. Res. Inst., Tokyo Imp. Univ. No. 323 (1945) (in Japanese).
6) I. Imai: J. Math. Phys. **28** (1949) 173.
7) I. Imai and H. Hasimoto: J. Math. Phys. **28** (1950) 205.
8) I. Imai: read at the 4th Japan Nat. Congr. Appl. Mech., Tokyo (Sept. 1954).
9) D. Meksyn: Proc. Roy. Soc. **A 220** (1953) 239.
10) H. Naruse: read at the 8th annual meeting of the Phys. Soc. Japan, Tokyo (Oct. 1953).
11) H. Takami: J. Phys. Soc. Japan **11** (1956) 145.
12) K. Tamada: Proc. Phys.-Math. Soc. Japan **22** (1940) 208.
13) S. Tomotika and K. Tamada: Quart. Appl. Math. **9** (1951) 129.
14) H. S. Tsien: J. Aeron. Sci. **6** (1939) 399.

---

## Errata to [11]

| page | line | | should be read |
|---|---|---|---|
| 145 | 1 | Compressilbe | Compressible |
| 147 | 15 | $+\sum_{s=1}^{19}$ | $-\sum_{s=1}^{19}$ |
| | (4.2) | $\zeta_{P'}=\cdots$ | $\zeta_{P'}=\cdots+\text{const.}$ |
| | | $\xi_{P'}=\int_0^\theta$ | $\xi_{P'}=\int_{\pi/2}^\theta$ |
| 148 | 3 | Calculate. | Calculate |
| 149 | 3 right | steam | stream |
| 154 | 16 | covergency | convergency |

JOURNAL OF THE PHYSICAL SOCIETY OF JAPAN Vol. 11, No. 4, APRIL, 1956

# Application of Imai's Transonic Approximation Method to the Compressible Flow past a Kaplan Bump

By Yaso'o MATUNOBU

*Department of Physics, Faculty of Science, University of Tokyo*

(Received December 28, 1955)

Imai's transonic thin-wing-expansion method is applied to the compressible flow past a Kaplan bump. Calculation is carried out as far as the fourth approximation. The results are compared with those obtained by means of the usual thin-wing-expansion method which is based on the exact equation of motion, and then with those deduced from von Kármán's similarity hypothesis for the transonic flow, showing that Imai's method is more adequate than von Kármán's; the former presents satisfactory results over a wider range of the free stream Mach number.

## § 1. Introduction and Summary

Recently, as an extension of von Kármán's transonic similarity rule, Imai[1] has suggested an approximate treatment for the two-dimensional compressible flow. His idea is based on the fact that, when the free stream Mach number is considerably large in the subsonic range, the usual thin-wing-expansion method[2] is capable of being subjected to some analytical simplification. In contrast to von Kármán's similarity theory[3] which starts from the two assumptions that the perturbation velocity caused by the presence of an obstacle is sufficiently small and the free stream velocity is close to the sound velocity, Imai's method, here called transonic thin-wing-expansion method, is based only upon the assumption of small disturbance to the main flow, without any restriction about the free stream Mach number. In other words, Imai has succeeded in extending the conception of the similarity law for the transonic flow to the compressible flow at an arbitrary speed, taking exactly the second order perturbations into account.

Here, in connection with a previous paper[4], the author will investigate the transonic flow past a Kaplan bump, using the transonic thin-wing-expansion method. Attempts are made chiefly to calculations of the velocity distribution over the surface and to appreciation of the accuracy of the present method superior to that of the usual similarity theory. Comparison with the results of the usual, or complete, thin-wing-expansion method which have already been obtained exactly up to the third approximation by Kaplan[5] and the present author[4] independently, indicates that our procedure yields satisfactory results over a wider range of free stream Mach number than the ordinary similarity theory does.

Further, based upon our results including the fourth approximation, we point out Kaplan's overestimation for the critical Mach number above which the continuous potential flow ceases to exist. Whereas he guessed this value to be about 0.83 for a Kaplan bump of thickness ratio 0.1, our results show that it may be a little less than 0.8. But it is still open to question whether or not the continuous mixed flow containing both the subsonic and supersonic regions actually takes place.

## § 2. Outline of the Transonic Thin-Wing-Expansion Method

For convenience, a brief account of the transonic approximation method due to Imai will be given here.

The two-dimensional irrotational flow of a compressible fluid is governed by the equations

$$u=\frac{\partial\Phi}{\partial x}=\frac{\rho_\infty}{\rho}\frac{\partial\Psi}{\partial y}\,,\qquad v=\frac{\partial\Phi}{\partial y}=-\frac{\rho_\infty}{\rho}\frac{\partial\Psi}{\partial x}\,, \tag{2.1}$$

$$\frac{\rho}{\rho_\infty}=\left[1-\frac{\gamma-1}{2}M^2\left(\frac{q^2}{U^2}-1\right)\right]^{1/(\gamma-1)}, \tag{2.2}$$

where $(u, v)$ are the component velocities in the $x$- and $y$-directions, $q$ is the magnitude of velocity, $\rho$ the density, $\rho_\infty$ the density of the undisturbed fluid, $\Phi$ the velocity potential, $\Psi$ the stream function, $U$ and $M$ are the magnitude of velocity and the Mach number of the undisturbed flow respectively, and $\gamma$ is the ratio of specific heats. The assumption of small disturbance velocity leads to

$$\Phi = x + \varepsilon\phi\,, \quad \Psi = y + \varepsilon\psi\,, \tag{2.3}$$

where $\varepsilon$ is a certain constant of small quantity, and $U$ has been taken as unity. Further, let us introduce the following quantities:

$$\xi = x,\ \eta = \mu y; \quad \zeta = \xi + i\eta,\ \ \bar{\zeta} = \xi - i\eta, \tag{2.4}$$

$$\chi = \psi/\mu; \qquad G = \phi + i\chi,\ \ \bar{G} = \phi - i\chi, \tag{2.5}$$

where $\mu = \sqrt{1-M^2}$. Then (2.1) and (2.2) can be combined and expressed in terms of the complex variables as

$$\frac{\partial G}{\partial \bar{\zeta}} = -\frac{\varepsilon}{4} M^2 \left(\frac{df}{d\zeta}\right)^2 + \frac{\varepsilon}{4} \nu \left(\frac{\partial \phi}{\partial \xi}\right)^2 + O\left(\frac{\varepsilon^2}{\mu^2}\right), \tag{2.6}$$

which, on integrating, gives

$$G = \frac{\varepsilon}{4} M^2 \left(\frac{df}{d\zeta}\right)^2 (\zeta - \bar{\zeta}) + \frac{\varepsilon}{4} \nu \int \left(\frac{\partial \phi}{\partial \xi}\right)^2 d\bar{\zeta} + O\left(\frac{\varepsilon^2}{\mu^2}\right), \tag{2.7}$$

where $f$ is an arbitrary analytic function of $\zeta$, and

$$\nu = 4M^2 \left(1 + \frac{\gamma+1}{4} \frac{M^2}{1-M^2}\right). \tag{2.8}$$

In most cases we are interested only in the state of affairs on or near the surface of the body, where $\bar{\zeta} - \zeta = -2i\eta = O(\mu t)$, $t$ being the thickness ratio. As for the parameter $\varepsilon$, it is favourable to assume that $\varepsilon = O(t/\mu)$ in view of the similarity hypothesis. This will be clarified later in § **3**. Therefore, neglecting the terms of $O(\varepsilon^2/\mu^2)$ in (2.7), one is led to the basic equation for the present method:

$$\frac{\partial G}{\partial \bar{\zeta}} = \frac{\varepsilon}{4} \nu \left(\frac{\partial \phi}{\partial \xi}\right)^2 = \beta \left(\frac{\partial G}{\partial \zeta} + \frac{\partial G}{\partial \bar{\zeta}} + \frac{\partial \bar{G}}{\partial \zeta} + \frac{\partial \bar{G}}{\partial \bar{\zeta}}\right)^2, \tag{2.9}$$

where

$$\beta = \frac{\varepsilon}{16} \nu\,. \tag{2.10}$$

Noting that the perturbation velocity potential is the real part of $\varepsilon G$ and $G$ is of $O(1)$, we find that the error caused by the adoption of (2.9) in place of (2.1) and (2.2) is of $O(\varepsilon^3/\mu^2) = O(t^3/\mu^5)$.

Since $\beta = O(t)$ for a moderate subsonic flow, $G(\zeta, \bar{\zeta})$ may be expanded as

$$G = G_1 + \beta G_2 + \beta^2 G_3 + \beta^3 G_4 + \cdots. \tag{2.11}$$

Then substituting (2.11) into (2.9) and integrating successively, we obtain*

$$G_1 = f(\zeta)\,, \tag{2.12}$$

$$G_2 = 2f'\bar{f} + \int \bar{f}'^2 d\bar{\zeta} + g_2(\zeta)\,, \tag{2.13}$$

$$\begin{aligned} G_3 = {} & 10f'^2\bar{f} + 2g_2'\bar{f} + 4ff'\bar{f}' + 2f''\bar{f}^2 \\ & + 12f'\int \bar{f}'^2 d\bar{\zeta} + 2f'\bar{g}_2 + 2f\bar{f}'^2 + \frac{10}{3}\int \bar{f}'^3 d\bar{\zeta} \\ & + 2\int \bar{f}'\bar{g}_2' d\bar{\zeta} + g_3(\zeta)\,, \end{aligned} \tag{2.14}$$

$$\begin{aligned} G_4 = {} & \left(\frac{200}{3} f'^3 + 20f'g_2' + 2g_3'\right)\bar{f} + \left\{20ff'^2 + 24f'\int f'^2 d\zeta + 4(fg_2)'\right\}\bar{f}' + 4ff'^2\bar{f}'' \\ & + (40f'f'' + 2g_2'')\bar{f}^2 + 8(ff')'\bar{f}\bar{f}' + (130f'^2 + 12g_2')\int \bar{f}'^2 d\bar{\zeta} + (10f'^2 + 2g_2')\bar{g}_2 \\ & + \left(44ff' + 12\int f'^2 d\zeta + 2g_2\right)\bar{f}'^2 + 4ff'\bar{g}_2' + 4f^2\bar{f}'\bar{f}'' + \frac{4}{3}f'''\bar{f}^3 + 4f''\bar{f}\bar{g}_2 \\ & + 24f''\bar{f}\int \bar{f}'^2 d\bar{\zeta} + 4f'\bar{f}\bar{f}'^2 + \frac{260}{3} f'\int \bar{f}'^3 d\bar{\zeta} + 24f'\int \bar{f}'\bar{g}_2' d\bar{\zeta} + 2f'\bar{g}_3 + 20f\bar{f}'^3 \\ & + 4f\bar{f}'\bar{g}_2' + \frac{47}{3}\int \bar{f}'^4 d\bar{\zeta} + \int \bar{g}_2'^2 d\bar{\zeta} + 10\int \bar{f}'^2\bar{g}_2' d\bar{\zeta} + 2\int \bar{f}'\bar{g}_3' d\bar{\zeta} + g_4(\zeta)\,, \end{aligned} \tag{2.15}$$

where $f$, $g_2$, $g_3$, and $g_4$ are arbitrary analytic functions of $\zeta$ alone which should be determined in compliance with the boundary conditions; and the primes denote differentiation with respect to $\zeta$ or $\bar{\zeta}$ and the bars denote the complex conjugates of the designated variables. It is to be noted that in the above formulae (2.13) to (2.15) the terms multiplied by the factors $(\bar{\zeta} - \zeta)^n$ have been neglected since they become small near the surface of the aerofoil.

---

* These formulae were given in reference (1) in more refined forms. Here we have reproduced them with some modification, correcting an error in the original expression corresponding to (2.15).

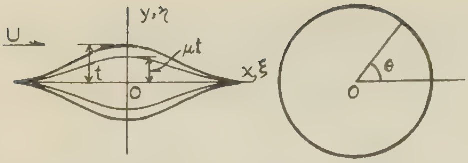

Fig. 1. Profile shapes in the $x$–$y$ and $\xi$–$\eta$ planes (left) and unit circle in the $Z$-plane (right).

## § 3. Boundary Conditions

In calculating $G$, the above-mentioned arbitrary functions $f$ and $g_n$ should be chosen according to the following conditions:

(i) $\partial G/\partial\zeta$ is one-valued and continuous in the field of flow,

(ii) $\partial G/\partial\zeta$ vanishes at infinity,

(iii) $\mathrm{Im}\,(\zeta+\varepsilon\mu^2G)=0$ at the boundary surface.

The last condition corresponds to the fact that the velocity vector at the surface is tangential to the profile contour.

Now consider a Kaplan bump of thickness ratio $t$ at zero incidence (Fig. 1). Then the analytic function which maps the flow region in the $\zeta$-plane onto the region outside the unit circle in the $Z$-plane is given by[4]

$$\zeta(Z)=\frac{1}{2}\left(Z+\frac{1}{Z}\right)+\frac{\mu t}{4}\left(1-\frac{1}{Z^2}\right)^2Z+O(\mu t^2). \tag{3.1}$$

Therefore, by virtue of the relation

$$\mathrm{Im}\,(Z+Z^{-1})=0$$

at the surface, the condition (iii) can be written in the form

$$\mathrm{Im}\left[G+\frac{t}{\varepsilon\mu}\left\{\frac{1}{4}\left(-\frac{3}{Z}+\frac{1}{Z^3}\right)+O(t)\right\}\right]=0\,. \tag{3.2}$$

Hence, if we let

$$f(\zeta)=\frac{k}{4}\left(\frac{3}{Z}-\frac{1}{Z^3}\right), \tag{3.3}$$

with

$$k=t/\varepsilon\mu\,, \tag{3.4}$$

all the conditions (i) to (iii) are satisfied to the first approximation. The foregoing assumption that $\varepsilon=O(t/\mu)$ is then deduced from the requirement that $f(\zeta)$, and hence $k$, be of $O(1)$.

In the present case the mapping function $\zeta(Z)$ can be expressed only in a series expansion; nevertheless, it is favourable to regard as if the condition (iii) would be strictly satisfied by equation (3.3), because we are interested in the results based on the similarity law. Thus, the conditions to be satisfied by the remaining $G_n$ $(n\geq 2)$ are as follows:

(i′) $\partial G_n/\partial\zeta$ is one-valued and continuous in the field of flow,

(ii′) $\partial G_n/\partial\zeta$ vanishes at infinity,

(iii′) $\mathrm{Im}\,G_n=0$ at the surface $(n=2,3,4,\cdots)$.

In other words, the above statement corresponds to applying the prescribed boundary condition to an aerofoil whose thickness is vanishingly small, as is often effectuated in the usual transonic similarity theory.

## § 4. Calculation of the Velocity Potential

If we put

$$\mathrm{Re}\,\zeta(e^{i\theta})=\zeta(\theta),\quad \mathrm{Re}\,G_n[\zeta(e^{i\theta}),\,\bar{\zeta}(e^{-i\theta})]=\phi_n(\theta),$$

then the velocity potential at the surface is expressed in a non-dimensional form

$$\begin{aligned}\Phi(\theta)=\xi(\theta)+\varepsilon\{\phi_1(\theta)+\beta\phi_2(\theta)\\ +\beta^2\phi_3(\theta)+\beta^3\phi_4(\theta)\}\,.\end{aligned} \tag{4.1}$$

Now, from (3.1), there follows

$$\xi(\theta)=\cos\theta \tag{4.2}$$

for a vanishingly thin profile. Further, taking the real part of (3.3), one obtains

$$\phi_1(\theta)=\frac{k}{4}(3\cos\theta-\cos 3\theta)\,. \tag{4.3}$$

As for the higher order terms in (4.1), calculations of $G_n$ are necessary. Thus, substitutions of (3.3) into (2.13) leads to

$$\begin{aligned}G_2=-\frac{3}{4}k^2\frac{1}{Z^2}\left(\frac{3}{\bar{Z}}-\frac{1}{\bar{Z}^3}\right)\\ -\frac{3}{8}k^2\left(\frac{1}{\bar{Z}^3}-\frac{3}{5\bar{Z}^5}\right)+g_2(\zeta)\,,\end{aligned}$$

which, by virtue of the relation $Z\bar{Z}=1$ at the surface, becomes

$$G_2=-\frac{3}{8}k^2\left(\frac{6}{Z}-2Z+Z^3-\frac{3}{5}Z^5\right)+g_2(\zeta)\,.$$

If we assume that

$$g_2(\zeta)=\frac{3}{8}k^2\left(\frac{8}{Z}-\frac{1}{Z^3}+\frac{3}{5Z^5}\right), \tag{4.4}$$

the conditions (i′) to (iii′) for $n=2$ are satisfied. Thus,

$$\phi_2(\theta)=\frac{3}{4}k^2\left(2\cos\theta-\cos 3\theta+\frac{3}{5}\cos 5\theta\right). \tag{4.5}$$

The expressions for $\phi_3(\theta)$ and $\phi_4(\theta)$ can be obtained in a similar manner. The results are as follows:

$$\phi_3(\theta)=k^3\left(12\cos\theta-\frac{36}{5}\cos 3\theta+\frac{18}{5}\cos 5\theta-\frac{18}{7}\cos 7\theta\right), \tag{4.6}$$

$$\phi_4(\theta)=k^4\left(\frac{582}{5}\cos\theta-\frac{388}{5}\cos 3\theta+\frac{1644}{25}\cos 5\theta-27\cos 7\theta+21\cos 9\theta\right). \tag{4.7}$$

(Reference (4) should be referred to concerning practical procedure.)

## § 5. Velocity Distribution

If $ds$ denotes the line element of the profile contour measured in the positive sense, the flow velocity at the upper surface is given by

$$q(\theta)=-\frac{d}{ds}\Phi(\theta)\,. \tag{5.1}$$

Now, provided that the departure of the profile shape from a straight-line segment is negligible, it follows that

$$-ds=dx=d(\cos\theta)\,. \tag{5.2}$$

Hence, from (4.1) together with (4.3), (4.5), (4.6), and (4.7), differentiation of $\Phi(\theta)$ with respect to $\cos\theta$ leads to

$$\begin{aligned}q(\theta)=1+\frac{t}{\mu}\Bigg[&-\frac{3}{2}\cos 2\theta+\frac{3}{32}\frac{\nu t}{\mu}(1+3\cos 4\theta)\\&-\frac{3}{320}\left(\frac{\nu t}{\mu}\right)^2(4+18\cos 2\theta+15\cos 6\theta)\\&+\frac{3}{10240}\left(\frac{\nu t}{\mu}\right)^3(177+160\cos 2\theta\\&+548\cos 4\theta+315\cos 8\theta)\Bigg],\end{aligned} \tag{5.3}$$

or, in terms of $x(=\cos\theta)$,

$$\begin{aligned}q=1+\frac{t}{\mu}\Bigg[&-\frac{3}{2}(2x^2-1)+\frac{3}{8}\frac{\nu t}{\mu}(6x^4-6x^2+1)\\&-\frac{3}{320}\left(\frac{\nu t}{\mu}\right)^2(480x^6-720x^4+306x^2-29)\\&+\frac{3}{640}\left(\frac{\nu t}{\mu}\right)^3(2520x^8-5040x^6+3424x^4\\&-884x^2+55)\Bigg].\end{aligned} \tag{5.4}$$

In deriving (5.3), the dummy parameter $\mathcal{E}$ thus far employed has been automatically eliminated owing to the relations $\mathcal{E}k=t/\mu$ and $\beta k=\nu t/16\mu$.

## § 6. Comparison with the Results of the Complete Thin-Wing-Expansion Method

For simplicity, we write equation (5.3) in the form

$$q=1+t\alpha_1(\theta)+t^2\alpha_2(\theta)+t^3\alpha_3(\theta)+\cdots\,. \tag{6.1}$$

On the other hand, the rigorous result including the terms of $O(t^3)$, obtained by means of the complete thin-wing-expansion method, can be written in a similar form; namely,

$$q=1+tA_1(\vartheta)+t^2A_2(\vartheta)+t^3A_3(\vartheta)\,, \tag{6.2}$$

where $\vartheta$, unlike $\theta$, is exactly equal to $\cos^{-1}x$, and the coefficients $A_n$ are known functions of the free stream Mach number as well as $\vartheta$. Then, comparison of (6.1) and (6.2) shows that $\alpha_1(\vartheta)=A_1(\vartheta)$; but that $\alpha_2(\vartheta)\not\doteq A_2(\vartheta)$, because the loose boundary condition (iii′) for $n=2$ has been applied. Therefore, in order to make a correct estimation of the validity of the transonic thin-wing-expansion method on the basis of equation (2.9), we should prefer

$$\begin{aligned}q=1+tA_1(\vartheta)&+t^2A_2(\vartheta)\\&+t^3\alpha_3(\vartheta)+t^4\alpha_4(\vartheta)+\cdots\end{aligned} \tag{6.3}$$

to (6.1). Thus, if the boundary conditions are strictly fulfilled, the error involved in the basic equation (2.9) is reduced to the difference between $t^3\alpha_3(\vartheta)$ and $t^3A_3(\vartheta)$. In fact, putting $\vartheta=\pi/2$, say, we have

$$\alpha_3(\pi/2)=\frac{87}{320}\frac{\nu^2}{\mu^3}=\frac{87}{20}\left(\frac{M^4}{\mu^3}+2\kappa\frac{M^6}{\mu^5}+\kappa^2\frac{M^8}{\mu^7}\right), \tag{6.4}$$

$$\begin{aligned}A_3(\pi/2)=\frac{15}{16}+\frac{9}{16\mu}+\frac{39}{40}\frac{M^2}{\mu}+\frac{3}{40}(13+62\kappa)\frac{M^4}{\mu^3}\\+\frac{21}{8}\left(\frac{M^2}{\mu^2}+\kappa\frac{M^4}{\mu^4}\right)+\frac{3\kappa}{40}(53+72\kappa)\frac{M^6}{\mu^5}+\frac{87}{20}\kappa^2\frac{M^8}{\mu^7},\end{aligned} \tag{6.5}$$

with $$\kappa=\frac{1}{4}(\gamma+1)\,,$$

whence the difference between $t^3\alpha_3(\pi/2)$ and $t^3A_3(\pi/2)$ is of $O(t^3/\mu^5)$, as was expected in § 2. In general it can be conjectured that both $\alpha_n$ and $A_n$ contain an equal dominant term of $O(1/\mu^{3n-2})$ for $M$ close to unity and their difference is of $O(1/\mu^{3n-4})$ for $n\geqq 2$.

Fig. 2 shows how the curves of $\alpha_3(\pi/2)$ approximate that of $A_3(\pi/2)$ with increasing $M$. In Fig. 3, the maximum velocity $q_{max}=q(\pi/2)$ is plotted against the free stream Mach number for three values of the thickness ratio. These

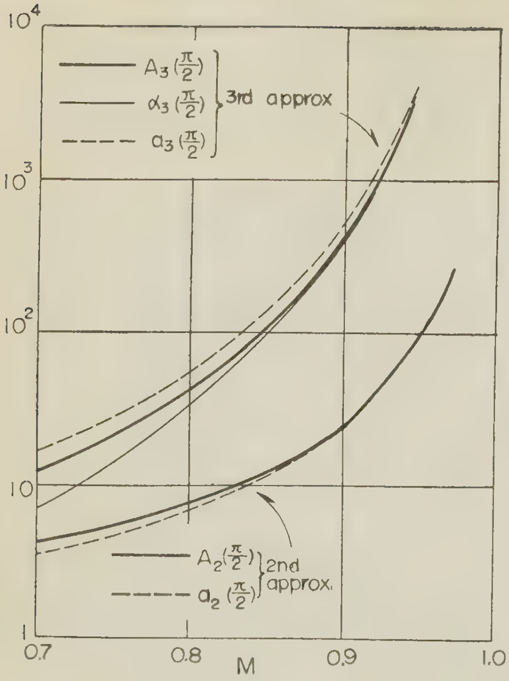

Fig. 2. Comparison of the coefficients of the maximum velocity expanded in $t$ ($\gamma=1.405$).

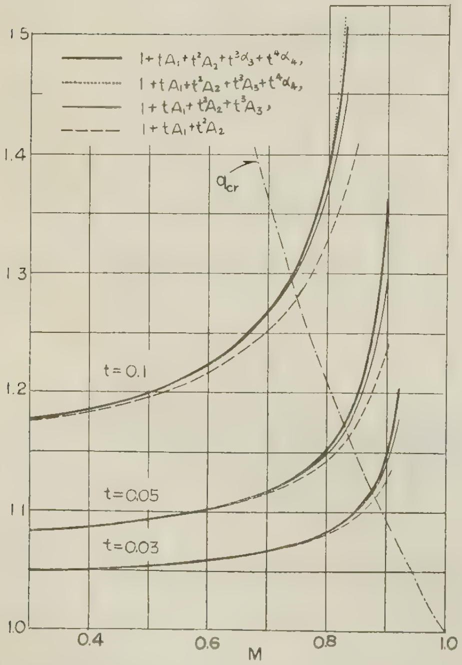

Fig. 3. Maximum velocity distribution vs. free stream Mach number, where $q_{cr}$ denotes the critical speed of sound.

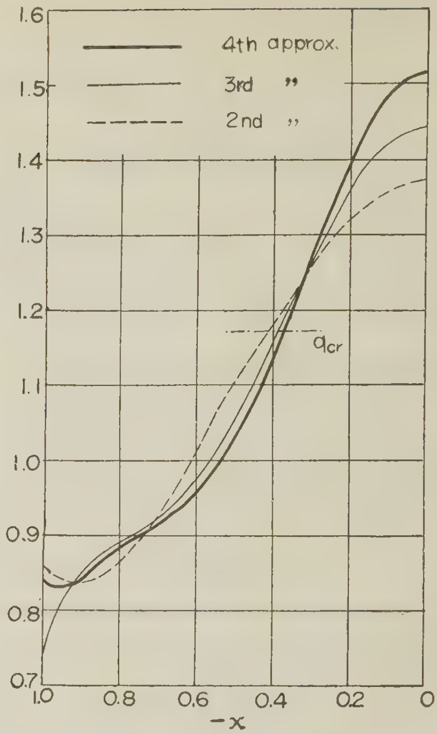

Fig. 4. Chordwise velocity distribution for Kaplan bump of thickness ratio 0.1 at $M=0.83$ ($\gamma=1.405$).

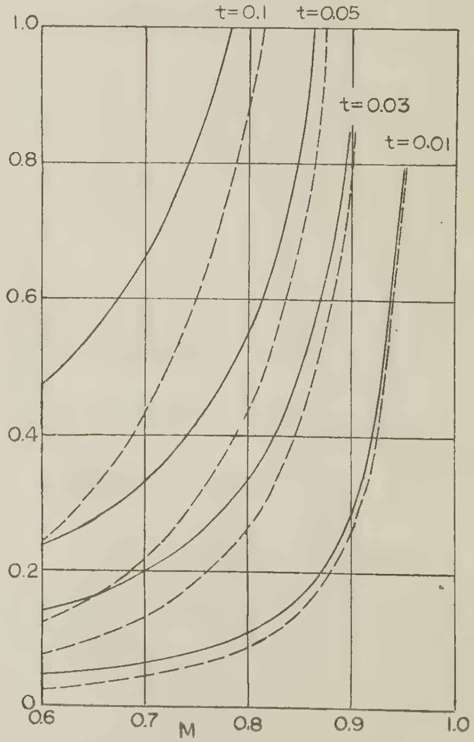

Fig. 5. Two transonic similarity parameters: Imai's (solid lines) and von Kármán's (broken lines), for $\gamma=1.4$.

curves present some information with regard to the critical value of the free stream Mach number. For instance, when $t=0.1$, this value presumably does not exceed 0.8. In this respect the value 0.83 which Kaplan conjectured from the result including $O(t^3)$ due to the complete method, seems too large. In fact, the velocity distribution curves for $M=0.83$ (Fig. 4) do not enable us to expect its convergence, at least, at the mid-chord point.

A recent study of the transonic flow past an infinite sinusoidal wall[6] has presented a plausible inference concerning the critical state of the continuous flow: "Once the local Mach number exceeds unity at the ridge of the wavy wall, the smooth symmetrical potential flow is no longer possible to exist." Our results seem to show, though not affirmatively, that the same statement is also valid with the Kaplan bump, for its shape can be regarded as an isolated single wavy wall without stagnation points.

## § 7. Relation to von Kármán's Transonic Similarity Rule

In the limiting case $M\to 1$ and $t\to 0$, the similarity parameter $\nu t/\mu$ utilized in the foregoing sections is reduced to

$$(\gamma+1)t/(1-M^2)^{3/2}\,. \tag{7.1}$$

This combination composed of free stream Mach number, thickness parameter, and adiabatic index is well known in von Kármán's transonic similarity theory. In Fig. 5 these two parameters are compared for four values of $t$.

From the consideration that the equation on which von Kármán's theory is based can be looked upon as an alternative form of the basic equation (2.9) of the present method (see Ref. 1), the results due to the latter can be converted into those due to the former merely by replacing $\nu t/\mu$ with the parameter (7.1). Thus, the velocity distribution (5.3) is transformed into

$$q=1+ta_1(\theta)+t^2a_2(\theta)+t^3a_3(\theta)+\cdots\,. \tag{7.2}$$

Again, $a_2(\pi/2)$ and $a_3(\pi/2)$ are plotted with broken lines in Fig. 2. Then it will be concluded that the present analysis due to Imai yields more excellent results in comparison with von Kármán's theory, provided that the boundary condition is satisfied correctly up to the second order in thickness ratio.

The author wishes to express his sincere thanks to Professor Isao Imai for his valuable suggestion and continual guidance throughout this work.

### References

1) I. Imai: Journ. Phys. Soc. Japan **9** (1954) 103.
2) I. Imai: Rep. Aeron. Res. Inst. Tokyo Imp. Univ. No. 294 (1944).
3) Th. von Kármán: J. Math. Phys. **26** (1947) 182.
4) Y. Matunobu: Journ. Phys. Soc. Japan **10** (1955) 814.
5) C. Kaplan: N.A.C.A. Tech. Rep. No. 768 (1943).
6) C. Kaplan: N.A.C.A. Tech. Rep. No. 1149 (1953).

JOURNAL OF THE PHYSICAL SOCIETY OF JAPAN Vol. 11, No. 4, APRIL, 1956

# A Direct Reading Counting Rate Ratio Meter

By Hirohide MIWA

*Nucleonics Sec. Kobe Kogyo Corporation, Hyogo, Japan*

(Received June 25, 1955)

A nonlogarithmic direct reading counting rate ratio meter was constructed, which proved to be more stable and precise than the logarithmic one using diode character.

A counting rate $f_1$ of channel 1 was applied to the rate meter which is very similar to the conventional meter only with an alteration in the charging circuit of the pumping condenser, which is made to give the charge modulated by a D.C. voltage proportional to $1/f_2$ ($f_2$ being the counting rate of channel 2). Thus arranged, the out-put of the rate meter became proportional to $f_1/f_2$, namely the rate ratio.

The D.C. voltage propotional to $1/f_2$ was generated by utilizing a low-pass filter and a saw-tooth generator. The height of the saw-tooth voltage was made to be proportional to the pulse interval, $1/f_2$, by controlling the start and stop of the saw-tooth voltage with a pair of adjacent pulse from channel 2.

The statistics of the $1/f_2$ D.C. voltage and the rate ratio was also described.

## § 1. Introduction

The counting rate ratio meter is a direct ratio indicating instrument of two radiation counting rates. Some approximate ratio indicating devices have been reported[1], but theoretically, precise ratio figure and wide ratio range could not be obtained.

Logarithmic indication[2] was also reported, but lability in diode character is inherent. The present ratio meter includes two parts.

(1) The voltage generator, the out put of which is proportional to the inverse of the counting rate. As the inverse of the counting rate is proportional to the mean pulse time interval, the output of a sawtooth voltage generator, whose starting and quenching time of the sawtooth voltage is controlled by the impulse from the counter, led through a low-pass filter indicates a voltage inverse to the counting rate.

(2) The ordinary counting rate meter. Its electric charge associated with each pulse is proportional to the voltage described in (1).

Statistical considerations of the inverse voltage and a practical circuit construction are also given in § 3 and § 4, respectively.

## § 2. Voltage Proportional to the Inverse of the Counting Rate

Each count (Fig. 1–a) is converted into a sharp pulse. This pulse triggers a flip-flop circuit, the out-put of which is a series of rectangular pulses with uniform amplitude and various duration. The moment of rise and fall of the rectangular pulse is determined by the incoming pulse (Fig. 1–b).

The rectangular pulses (b) control the sawtooth voltage generator. The voltage in the low level period of (b) swings the tube $V_{11}$ (Fig. 3) beyond cut-off. This actuates the sawtooth voltage generation, the out put of which is as Fig. 1–c.

A proper low pass filter smooths out the sawtooth voltages and gives a D. C. voltage proportional to the inverse of the counting rate, namely, the pulse interval.

## § 3. Statistic of the "Inverse" Voltage

A series of sawtooth voltage pulses as shown in Fig. 2 (a) is fed to a simple $RC$ integrating net-work as shown in Fig. 2 (b).

The D. C. voltage component is easily found to be

$$E_A = \frac{a t_m}{4} \qquad (1)$$

where $t_m$ is the mean pulse interval and a is a proportional constant between amplitude and pulse interval (Fig. 2). The pulse interval, however, is distributed according to Poisson's law, and consequently, the sawtooth are not uniform. Hence the D. C. voltage component varies with time.

Assumed that only the D. C. component $E_A$ can pass the $RC$ net work, we can determine the out put voltage $E_B$ as follows.

The effect of voltage pulse ($E_A$ in height, $\Delta t$ in duration) at a time $t$ in the past to the present time $t_0$ is (See, Fig. 2(c))

$$\Delta E_B = E_A \cdot \frac{\Delta t}{RC} \exp\left(-\frac{t_0 - t}{RC}\right)$$

$$E_B = \int_{-\infty}^{t_0} \Delta E_B = \int_{-\infty}^{t_0} E_A \frac{\Delta t}{RC} \exp\left(-\frac{t_0 - t}{RC}\right). \quad (2)$$

When $E_A$ is assumed to have a standard deviation $\sigma E_A$ at time $t$, the standard deviation $\sigma E_B$ at present time $t_0$ is obtained in the same manner,

$$\sigma E_B{}^2 = \int_{-\infty}^{t_0} \left\{ \sigma E_A \frac{\Delta t}{RC} \exp\left(-\frac{t_0 - t}{RC}\right) \right\}^2. \quad (3)$$

The observed pulse interval can be determined by observing the elapsed time between $n$ pulses. The probability $W_T{}^n$ with which the $n$th pulse comes between time $T$ and $T + \Delta T$, is

$$W_T{}^n = \frac{T^{n-1}}{(n-1)!\, t_m{}^n} \exp\left(-\frac{T}{t_m}\right) dT.$$

Where $t_m$ is the mean pulse interval. The mean $(\overline{T})$ of time $T$ is

$$\overline{T} = n\, t_m\ .$$

and the standard deviation $(\sigma_T)$ of $T$ is

$$\sigma_T{}^2 = \int_0^\infty T^2\, W\, dT - \overline{T}^2 = (\sqrt{n}\ t_m)^2\,.$$

Thus, the observed pulse interval $(t)$ is

$$t = \frac{\overline{T}}{n} \pm \frac{\sqrt{n}\ t_m}{n} = t_m \pm \frac{t_m}{\sqrt{n}}$$

Hence, the standard deviation of the pulse interval $(\sigma\, t_m)$ observed during $\Delta t$ is

$$\sigma t_m = \frac{t_m}{\sqrt{\dfrac{\Delta T}{t_m}}} \quad (4)$$

From equations (1), (3) and (4), we derive the standard deviation $(\sigma_{EB})$ of the out-put voltage $E_B$

$$\sigma E_B{}^2 = \frac{a^2 t_m{}^2}{32RC/t_m}$$

$$\therefore\ \sigma E_B/E_B = \sqrt{\frac{t_m}{2RC}} \quad (5)$$

Equation (5) gives the fractional standard deviation of a single observation of pulse interval.

The fractional standard deviations of $n$ observations and continuous observation can be obtained similarly and are found to coincide with the case of counting rate meter obtained by R. D. Evans and L. I. Schiff[3].

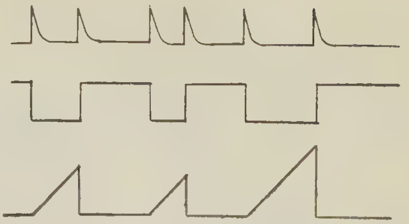

Fig. 1.

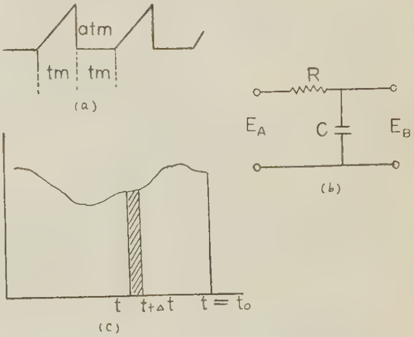

Fig. 2.

## § 4. Practical Construction and Moduration by the "Inverse Voltage"

A practical circuit diagram of the important parts are shown in Fig. 3.

A counting rate ratio $f_1/f_2$ of two channels is considered. Each counting channel of $f_1$ and $f_2$ has a system of a preamplifier and a Schmidt type voltage discriminater. Channel $f_2$ has a scale of two circuit, the out put of which is rectangular in wave form and is applied to a sawtooth generator comprised of $V_{11}$, $V_{12}$, $V_{10}$ through an impedance converter $V_{10'}$. The sawtooth voltage is fed into a low-pass filter, and the "inverse" D. C. Voltage is obtained across the resistor $R_{79}$ (between point (a) and (b)).

The out-put of the discriminater of $f_1$ system triggers a scale of two circuit, the out-put of which is rectangular in shape and is fed to pulse height limiter $V_8$ whereby the lower level of the pulse is fixed at 150 V D. C. (b) and the higher level is also caught at the voltage level of the point (a). $R_{78}$ is to compensate for the D. C. voltage produced by the leaking current through $R_{77}$ while point (c)

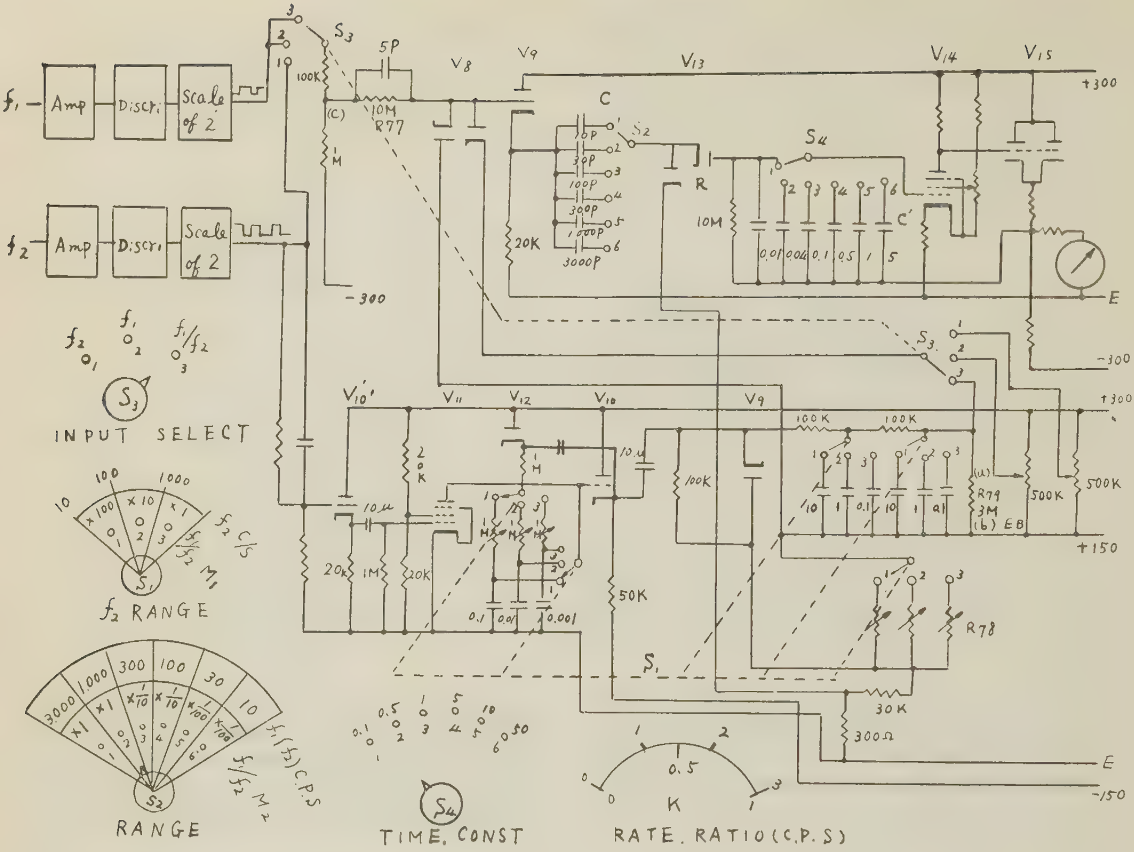

Fig. 3.

lies at a higher voltage than point (a). This effect can be minimized by altering the preceeding scale of two stage to the univibrater circuit, the out put of which being fixed at a lower level than (b) while no triggering occures. The reduction of the internal resistance between (a) and (b) is also effective.

The rectangular pulses synchronized with $f_1$ and modulated in height by the voltage $E(a\sim b)$ which is proportional to $1/f_2$ are fed to ordinary rate meter circuit.

The D. C. out-put appearing across the $RC'$ tank circuit is

$$V=E_B\,CR\cdot\frac{f_1}{2}\quad\text{where } E_B=\alpha\cdot 1/f_2$$

$$=\frac{\alpha}{2}\cdot\frac{f_1}{f_2}\cdot CR=\frac{\alpha CR}{2}\cdot\frac{f_1}{f_2}\qquad(6)$$

This voltage is read by a vacuum tube volt meter $V_{14}$ and $V_{15}$ in ratio figure.

Practically, $f_2$ or $f_1$ can also be measured by selecting the switch position of $s_3$ (See Fig. 3. INPUT SELECT, $S_3$). In this case $S_2$ acts as the range selecter (10 c/s to 3000 c/s, See Fig. 3. RANGE, $S_2$).

$S_1$ should be placed to an apropriate position according to the $f_2$ value and a multiplication facter $M_1$ should be remembered associated with the position (See Fig. 3. $f_2$ RANGE, $S_1$).

When $S_3$ is turned on to the position $f_1/f_2$, $S_2$ acts as a range selector ($M_2=1$ to 1/100). If meter reading gives the value $K$ (See Fig. 3 RATE RATIO), the ratio is obtained by maltiplying $M_1$ and $M_2$ with $K$.

$$\text{Ratio}=K.\cdot M_1\cdot M_2$$

With a proper combination of $M_1$ and $M_2$, it is possible to realize a wide range of 100 to 1/100. $S_4$ functions as a time constant selector (See Fig. 3 TIME CONST.). The time constant ranges from 0.1 to 50 sec.

Experimental data showed an accuracy of ±2%. Some error occured in too high a counting rate for a specified switch positions, because the $1/f_2$ voltage decreases in high $f_2$ value until it conceals itself under the noise level. In too low a counting rate for a specified switch positions, the linear rise of sawtoothwave form cannot hold in such a long pulse interval so that some error were introduced.

These characters were investigated in constant ratio figures of 1.0 and 0.027. In the former, the same signal from an audio frequency oscillator was applied to both channels. In the latter, two thin metal discs, each with different number of slits (the difference being 2.7%) on the periphery, were attached to a common rotating axis. This device, with the aid of light source and a photo-cell, produced an electrical signal of two frequencies that corresponded to the R. P. M. of the axis and number of slits. The beat frequency of the two signals was applied to channel 1. One of the original frequency was applied to channel 2. The R. P. M. of the D. C. motor way controlled by the rheostat. In this way we could vary the frequencies while keeping the ratio constant.

To avoid the nonlinear rise of the sawtooth voltage, proper selection of switch position was necessary, but the accuracy described above was held for specified positions in about 2 decades of frequency range.

## § 5. Statistics of the Rate Ratio

Now we consider two quantities $A$ and $B$, and assume that they have statistical fluctuations. A has the mean value of $\bar{A}$, standard deviation of $\sigma A$ and the probability of $W(A)\cdot\Delta A$ with which $A$ lies between $A$ and $A+\Delta A$. As for $B$, we can define similar expression $\bar{B}$, $\sigma B$, $W'(B)\cdot\Delta B$.

Some relationships as follows are too obvious.

$$\bar{A}=\int A\cdot W_{(A)}\cdot\Delta A.\quad \bar{B}=\int B\cdot W'_{(B)}\cdot\Delta B. \tag{7}$$

$$(\sigma A)^2=\int(A-\bar{A})^2W_{(A)}\cdot\Delta A=\int A^2W_{(A)}\cdot\Delta A-\bar{A}^2.$$

$$(\sigma B)^2=\int(B-\bar{B})^2W'_{(B)}\cdot\Delta B=\int B^2W'_{(B)}\cdot\Delta B-\bar{B}^2. \tag{8}$$

Then we consider the product of two quantities $A$ and $B$. The mean value of $AB$ can be obtained from the next eq. (9).

$$\overline{AB}=\iint ABW_{(A)}\Delta A.\,W'_{(B)}\Delta B\,. \tag{9}$$

As $A$ and $B$ are quite independent of each other, eq, (9) becomes

$$\overline{AB}=\int AW_{(A)}\Delta A.\cdot\int BW'_{(B)}\Delta B=\bar{A}\cdot\bar{B} \tag{9'}$$

Similarly, the standard deviation of $AB$ can be obtained.

$$\begin{aligned}(\sigma AB)^2&=\iint(AB-\overline{AB})^2W_{(A)}\Delta A.\quad W'_{(B)}\Delta B\\&=\iint A^2B^2W_{(A)}\Delta A.\quad W'_{(B)}\Delta B-\overline{AB}^2\\&=\int A^2W_{(A)}\Delta A.\cdot\int B^2W'_{(B)}\Delta B-\bar{A}\cdot\bar{B}^2\end{aligned}$$

From eqs. of (8) and (9′),

$$\begin{aligned}(\sigma AB)^2&=(\sigma A^2+\bar{A}^2)\cdot(\sigma B^2+\bar{B}^2)-\bar{A}^2\cdot\bar{B}^2\\&=\sigma A^2\cdot\bar{B}^2+\sigma B^2\bar{A}^2\,.\end{aligned}$$

Dividing the both side of this eq. with $\overline{AB}^2=\bar{A}^2\cdot\bar{B}^2$,

$$\left(\frac{\sigma AB}{AB}\right)^2=\left(\frac{\sigma A}{A}\right)^2+\left(\frac{\sigma B}{B}\right)^2. \tag{10}$$

Hence, from eqs. (6) and (10), we obtain the fractional standard deviation of the rate ratio output.

$$\left(\frac{\sigma V}{V}\right)^2=\left(\frac{\sigma E_B}{E_B}\right)^2+\left(\frac{\sigma CRf_1/2}{CRf_1/2}\right)^2. \tag{11}$$

As the scale of two of channel 1 cannot change the statistical nature of $f_1$, the statistics of the quantity $CRf_1/2$ of eq. (6) can be obtained from the statistics of the ordinary counting rate meter output $V^1(E_B=\text{const}$, without scale of two).

$$V^1=E_B\cdot C\cdot R\cdot f_1=\beta\frac{f_1CR}{2},\quad(\beta=\text{Const.})$$

$$\frac{\sigma f_1CR/2}{f_1CR/2}=\frac{\sigma V^1}{V^1}=\sqrt{\frac{1}{2\tau_1f_1}}\,, \tag{12}$$

Where $\tau_1$ is the time constant of the tank circuit.

As seen in § 3 eq. (5), the "inverse" voltage of the counting rate $f_2$ has the fractional standard deviation of

$$\frac{\sigma E_B}{E_B}=\sqrt{\frac{1}{2\tau_2f_2}}\,, \tag{13}$$

Where $\tau_2$ is the time constant of the filter circuit of the "inverse" voltage and $f_2=1/t_m$.

From eqs. (11), (12) and (13), we obtain the fractional standard deviation of the counting rate ratio $f_1/f_2$.

$$\frac{\sigma f_1/f_2}{f_1/f_2}=\sqrt{\frac{1}{2\tau_1f_1}+\frac{1}{2\tau_2f_2}} \tag{14}$$

This is an expression for a single observation.

For $n$ observations (at equal time interval $t$) and continuous observation (overall time, $T$), we can derive respective expressions from eq. (10), eqs of the fractional standard deviation corresponding to the ordinary counting rate meter given by R. D. Evans et. al.(3) and the eqs. of the "inverse" voltage described in § 3.

For $n$ observations, whose time interval of observation is uniform and equal to $t$ sec,

$$\frac{\sigma f_1/f_2}{f_1/f_2}=\sqrt{\frac{1+(n-1)(1-e^{-(2t/\tau_1)})}{[1+(n-1)(1-e^{-(t/\tau_1)})]^2 2\tau_1 f_1}+\frac{1+(n-1)(1-e^{-(2t/\tau_2)})}{[1+(n-1)(1-e^{-(t/\tau_2)})]^2 2\tau_2 f_2}} \qquad (15)$$

For continuous observation, whose overall time is $T$,

$$\frac{\sigma f_1/f_2}{f_1/f_2}=\sqrt{\frac{(1+2T/\tau_1)}{(1+T/\tau_1)^2 2\tau_1\cdot f_1}+\frac{(1+2T/\tau_2)}{(1+T/\tau_2)^2 2\tau_2 f_2}} \qquad (16)$$

## § 6. Conclusion

The result was satisfactory and proved to be more stable than the rate meter using logarithmic diode character and a difference amplifier.

Radioactivity measurement, however, needs background correction, and thereby some error might be introduced to the reading if the counting rate of both channels is low. However, the intensity is ordinarily much higher than the background count, so the error will be negligible. If $f_1$ is not high, but $f_2$ high, the correction can be made easily.

Statistical considerations of the rate ratio was made exactly and proved to coincide with the approximate expressions for the ratio of two quantities.

This will be useful in nuclear experiments where the ratio figure is important and the absolute value is not so important, such as in the determination of angular distribution of scattering, or in the $X$ ray analysis using Geiger tubes, which suffers intensity variations from power supply fluctuations; and in the radioisotope tracer experiments of physical and chemical researches, especially when short half life isotopes are their tools.

This rate ratio meter was initially constructed with the financial support of the fund of Aide for Engineering Development of the Ministry of Transportation for the purpose of constructing the radiation defect detector or the radiation thickness gauge of casted irons and welded steel sheets of a ship and her engines. The author wishes to express his gratitude to the persons concerned.

### References

1) T. Tomura and G. Shinoda. Aural report at the meeting of the Applied Physics, Japan, in 1953.

2) R. D. Evans and E. Meagher: R.S.I. **10** (1939) 339.

3) R. D. Evans and L. I. Schiff: R.S.I. **7** (1936) 456.

# Short Notes

This section is intended to secure prompt publication of important discoveries in physics. The reports should not exceed 800 words in length. A figure of size 7 cm × 7 cm will be counted as 150 words.

J. PHYS. SOC. JAPAN **11** (1956) 463~464

## Specimen Contamination in Electron-microscope

By Y. MIZUSHIMA, S. HIROTA
and H. NOAKE
*Electrical Communication Laboratory,*
*Nippon Telegraph and Telephone*
*Public Corporation, Tokyo, Japan*

(Received January 9, 1956)

In the course of a study of evaporated gold films by an electron-microscope, a curious effect due to electron-bombardment was observed. Pure gold black deposits were evaporated onto a substrate, which was mounted on a mesh, in an inert atmosphere of purified argon. Substrates were evaporated glass films of 100 angstrom thickness, collodion films, or evaporated thin films of germanium. The electron-microscope was evacuated by a diffusion pump using silicone oil. The specimen was subjected to the irradiation of a fine electron probe of relatively low intensity (30 mA/cm$^2$). The temperature rise due to absorbed heat caused by the electron impact at the black particles is estimated as less than 50°C.

During the observation, the specimen changes its shape as shown in series of Photographs 1~4. The contamination of the sample occurs only at the electron-bombarded area within a hole of the mesh. Other area shows no change. Several features observed in this phenomenon are as follows:

1) Contamination spreads roughly proportionally to the bombarding time, independent of the size of the smoke particles.

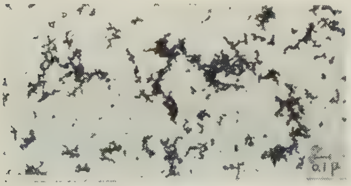

Photo 1. Before irradiation.

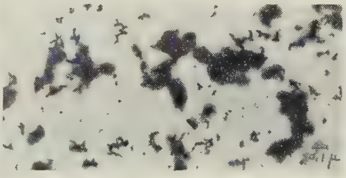

Photo 2. After 20 min. irradiation, 30 mA/cm$^2$.

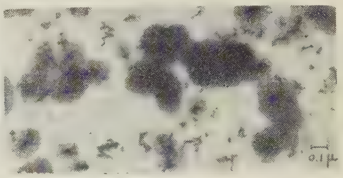

Photo 3. After 40 min. irradiation.

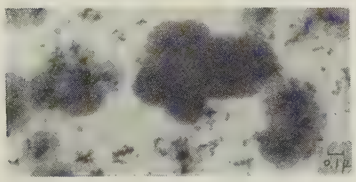

Photo 4. After 60 min. irradiation.

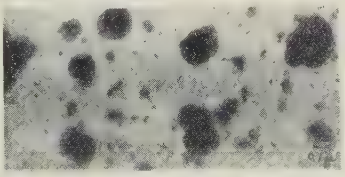

Photo 5. Shadow-cast by germanium.

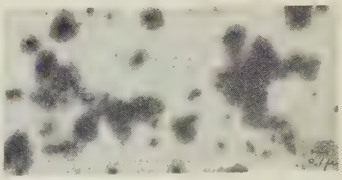

Photo 6. After the 1 hr. heat-treatment at 350°C.

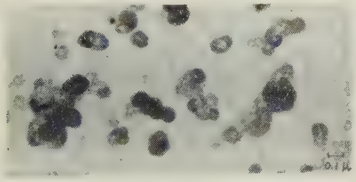

Photo 7. After the treatment with KCN solution.

2) The contamination is independent of the nature or the conductivity of the substrate.

3) Electron-diffraction of the contaminated region shows strengthened background, probably due to the formation of some organic material, while the pattern of gold is weakened as the contamination grows up.

4) The contamination occurs even by the bombardment of low-voltage (1 to 5 kV) electrons in an usual kinetic vacuum chamber of about $10^{-6}$ mmHg.

5) It has been reported that contaminations produced by a discharge method in an organic vapor such as benzene[1)] or di-butyl-phtalate are formed as continuous layers covering all over the substrate. While, shadow-cast micrograph (Photo-5) of the contaminated specimen reveals that the contamination, which is translucent for 50 kV electron, has rather sharply defined edges, and is formed only at the particles.

6) Though it has been confirmed that the black changes its shape remarkably by sintering at above 200°C[2)], the contaminated specimen persists in its original shape even at 350°C. (Photo-6)

7) Heat-treated blacks show the contamination

very little. Also, the vacuum-evaporated films do not suffer any obvious trace of contamination.

8) Electron-impact at the copper part of the mesh has a slight but positive influence on the production of the contamination.

9) When the contaminated specimen is etched in a solution of KCN, gold blacks dissolves away and there remain only shells of the contamination. (Photo-7)

Some considerations have been so far reported on the nature of the contamination[3]. The above evidences seem to indicate that the electron beam in a kinetic vacuum induces unknown interaction with residual organic gas molecules only on metal blacks, probably due to a special activity of a metal black and, or, the sucessively contaminating layer on it.

## References

1) H. König and O. Helwig: Z. Phys. **129** (1951) 491.
2) To be published elsewhere.
3) J. Hillier: J. App. Phys. **19** (1948) 226.
   J. H. L. Watson: J. App. Phys. **22** (1951) 1387.
   S. G. Ellis: J. App. Phys. **23** (1952) 728.
   A. E. Ennos: Brit. J. App. Phys. **4** (1953) 101.
   A. E. Ennos: Brit. J. App. Phys. **5** (1954) 27.

---

J. PHYS. SOC. JAPAN **11** (1956) 464~465

# On the Elastic Scattering of Electrons observed in Kikuchi Patterns

By Hatsujiro HASHIMOTO

*Kyoto Technical University, Matsugasaki, Sakyoku, Kyoto*

Eiji YODA and Hiroshi MAEDA

*Kyoto University, Kitashirakawa, Sakyoku, Kyoto*

(Received December 30, 1955)

Boersch[1] showed with the use of the electron filter the fact that the Kikuchi lines in electron diffraction are due to the inelastic scattering of electrons, in accordance with the interpretation originally given by Kikuchi[2]. The present authors[3] formerly studied Kikuchi lines from the cleavage surface of zinc-blende by using a net-type electron filter[1,4] inserted between the second specimen holder and the second projector lens in our microscope[5]. By this experiment it was revealed that the Kikuchi lines contain a certain amount of elastically scattered electrons besides the inelastically scattered part. The similar conclusion has been subsequently obtained also for Kikuchi lines in transmission patterns from molybdenite. During the progress of our study, Watanabe[5] reported an energy spectrum of Kikuchi lines which contains clearly the conponent of no energy loss. His result coincides exactly with our observation. In the present paper the results on molybdenite is reported.

We observed the transmission electron diffraction patterns from a thin film of molybdenite containing the Kikuchi pattern and the Kossel-Möllenstedt (K–M) pattern simultaneously. The K–M pattern is useful for the investigation of the elastic and inelastic scatterings, because it has been considered that the K–M pattern consists of elastic scattering of electrons, while the Kikuchi pattern consists of inelastic scattering.

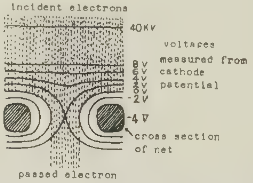

Fig. 1. Potential distribution in electron filter.

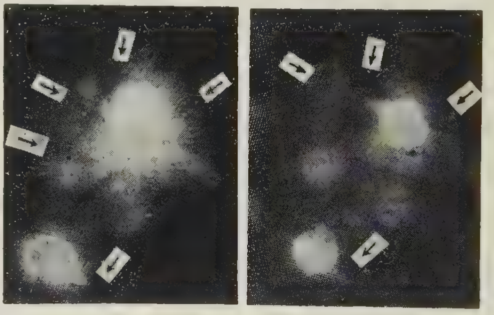

Fig. 2. Kikuchi lines (mark ↾) and K–M patterns which passed through electron filter.
(a) $\Delta v = 180$ volts.
(b) $\Delta v = 2$ volts, Kikuchi lines can be still observed.

The effective potential for filteration is not the same as the potential applied to the net as shown schematically in Fig. 1. Let us denote the voltage difference between the net and the cathode by $\Delta V$, and that between the effective potential for filteration and the cathode by $\Delta v$, then in general $\Delta v > \Delta V$. In our study nets having $50\,\mu$ spacing (with 60% transmission coefficient) and $150\,\mu$ spacing were used. It was confirmed that for these nets $\Delta v = (\Delta V + 8)$ volts and $\Delta v = (\Delta V + 17 \sim 18)$ volts, respectively.

The patterns through the electron filter varied with the variation of the potential of filter as follows:

1) By the change of $\Delta v$ from 200 volts to 20 volts, the intensity of Kikuchi patterns decreased little by little, but they were still observed clearly.

2) At values of $\Delta v$ lower than 20 volts, Kikuchi lines become very weak but were still observed. However, a part of Kikuchi lines far from a spot of K–M pattern faded away.

3) In certain specimens, in spite of Kikuchi lines having been observed for $\Delta v=10$ volts, they disappeared for $\Delta v=8$ volts.

4) In other specimens, Kikuchi lines were still observed even for $\Delta v=2$ volts, as shown in Fig. 2. At the value of $\Delta v=0$, all Kikuchi lines as well as K–M pattern disappeared completely.

From the above observations we can see that in certain specimens Kikuchi lines consist of an inelastic scattering of electrons whose energy loss is more than 20 volts or 8 volts, while in other specimens they contain, besides inelastic part, electrons whose energy loss is less than 2 volts. The existence of electrons of such a small energy loss seems to show that Kikuchi lines are partly due to the thermal scattering or the elastic scattering at imperfections in the crystal. It is probable that the parts of Kikuchi lines far from the spots of K–M pattern are solely due to the inelestic scattering, because it is supposed that when electrons change their directions greatly, they may suffer inelastic scattering at least more than once during the process of multiple scattering.

The authors wish to express their sincere thanks to Prof. K. Tanaka of Kyoto University for his kind guidance. They are also grateful to Prof. R. Uyeda of Nagoya University for his advice to take up this problem.

## References

1) H. Boersch: ZS. f. Phys. **134** (1953) 156.
2) S. Kikuchi: Japan J. Phys. **5** (1928) 83.
3) K. Tanaka and H. Hashimoto: Read at the meeting of the Physical Society of Japan, April (1954).
4) T. Ichinokawa and R. Uyeda: Proc. Jap. Acad. **30** (1954) 857.
5) K. Tanaka and H. Hashimoto: Rev. Sci. Inst. **24** (1953) 699.
6) H. Watanabe: J. Phys. Soc. Japan **10** (1955) 908.

---

J. Phys. Soc. Japan **11** (1956) 465~466

# Note on the Ferromagnetism of CoTe

By Enji Uchida

*Department of Physics*
*The University of Osaka Prefecture*
*Naniwa University*

(Received January 10, 1956)

In a previous paper[1] on the magnetic measurements of CoTe, the experimental data were so interpreted that CoTe would be a ferrimagnetic substance. At the annual meeting of the Phys. Soc. of Japan, Oct. 12th. 1955, at Tokyo, Professor T. Hirone suggested, however, that $CoTe_x$ $(1.00\leq x\leq 1.20)$ might be an eutectic mixture of metallic cobalt and a nonmagnetic compound $CoTe_{1.20}$ and that the magnetic transition observed at 1003°C could be explained on this basis. The author made

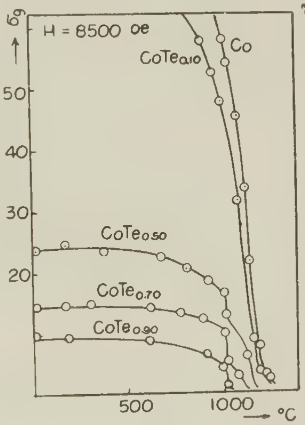

Fig. 1

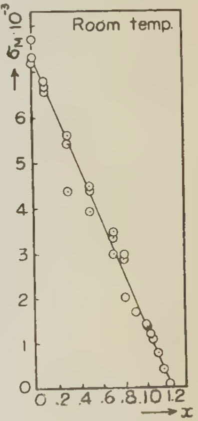

Fig. 2

Fig. 1. Dependence of the magnetization of $CoTe_x$ $(0<x<1.00)$ on temperature.

Fig. 2. The molar magnetization of $CoTe_x$ as a function of molar content of tellurium. Plots in the region $1.00\leq x\leq 1.20$ are reproduced from the data in the previous paper.

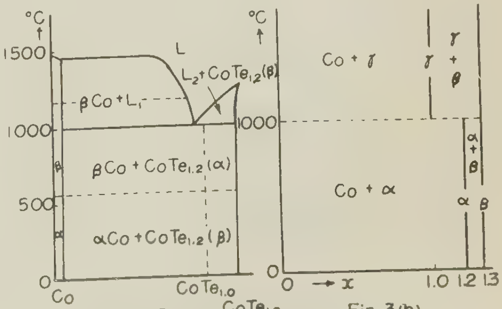

Fig. 3(a) Fig. 3(b)

Fig. 3 (a). Hypothetic phase diagram of $CoTe_x$ $(0<x\leq 1.20)$.

(b). Hypothetic phase diagram of $CoTe_x$, suggested by Dr. Lotgering.

magnetization measurements on samples $CoTe_x$ with $0<x\leq1.00$ and also detailed x-ray investigations on $CoTe_{1.00}$ and $CoTe_{1.20}$, the results of which will settle the question raised above. These results are as follows.

Samples of $CoTe_x$ $(0<x\leq1.00)$ were prepared by the same procedure as mentioned in the previous paper. The temperature of heat treatment in the present case was 1200°C. In the case of $x=0.3\sim0.7$ a precipitation of cobalt was clearly detected in the upper part of the products. In order to give a homogenous composition to the samples, they were ground into powder and were once more subjected to a heat treatment at 900°C for 10 hours in vacuum.

The temperature dependence of the magnetization of these powder samples is shown in Fig. 1. The magnetization curves for $x=0.3\sim0.9$ show a sharp drop at 1003°C and their ferromagnetic Curie point is near that of metallic cobalt. In Fig. 2, the molar saturation magnetization is plotted against $x$, i.e. the molar content of tellurium. Its values distribute along a straight line, which starts approximately from the molar saturation magnetization of Co and ends at $CoTe_{1.20}$. This seems to show the presence of two phases, Co and $CoTe_{1.20}$, in samples of $CoTe_x$ with $0.1\leq x\leq1.20$. That the present observed value of the saturation magnetization for $x=0$ is smaller than that observed by Sucksmith[2] ($\sigma_{\infty 0}=163.9$ gauss/g) would mainly be due to a large demagnetizing effect in powder samples.

Careful x-ray investigations of $CoTe_{1.00}$ and $CoTe_{1.20}$ were performed in cooperation with Prof. Shimomura of our University. The Debye-Scherrer diffraction pattern obtained with $CoTe_{1.20}$ conforms to that of the NiAs-type structure both in arrangement of lines and in intensity distribution, with lattice spacings $a=3.88$ A, and $c=5.37$ A, which are in full accord with those previously reported by Oftendal[3] for $CoTe_{1.00}$. However, the pattern for $CoTe_{1.00}$ showed the presence of three additional lines ($\theta=25.9°$, $45.5°$ and $56.9°$). These three lines were so weak that they could scarcely be detected without taking a special care. It appears that they are coincident in $\theta$ with those of metallic cobalt, the corresponding planes being (0002), $(11\bar{2}0)$ and $(11\bar{2}2)$, respectively. The writer has prepared single crystals of $CoTe_{1.20}$ and $CoTe_{1.50}$ (both about 2 mm × 2mm × 4mm), and a precise x-ray study of them is now being carried out by Prof. Shimomura.

The results obtained in the present experiment support Professor Hirone's suggestion. A hypothetic phase diagram shown in Fig. 3 (a) can interpret all the experimental data, in particular the magnetic transition at 1003°C, a small jump of $\sigma$ at this temperature, and a temperature hysteresis of the transition (Fig. 1 and Fig. 3 of the previous paper).

In the course of preparing this note, I have received a letter from Dr. F. K. Lotgering of the Philips Research Laboratory in Netherlands, who suggested a similar interpretation. He assumed a decomposition of $CoTe_{1.00}$ into metallic cobalt and $CoTe_{1.20}$, with a similar hypothetic phase diagram shown in Fig. 3 (b). He supposes the phases $\alpha$, $\beta$ and $\gamma$ to have NiAs structures, $\alpha$ having the composition $x=1.2$, $\beta$ a composition $x>1.2$ (for example $x=1.3$) and $\gamma$ the composition $x=1.0$ (or $x<1.0$).

The writer is much obliged to Professor T. Hirone for kind suggestions, to Professor T. Nagamiya and Professor Y. Mashiyama for kind discussions, to Professor Y. Shimomura for his cooperation in $x$-ray study and to Messrs. M. Kojima, S. Saito, H. Kondoh and N. Fukuoka for their eager assistance. The writer also wishes to express his thanks to Dr. Lotgering for his kind communication.

## References

1) E. Uchida: J. Phys. Soc. Japan **10** (1955) 517.
2) L. F. Bates: *Modern Magnetism*, Cambridge (1951) 317.
3) I. Oftendal: Z. Phys. Chem. 128 (1927) 135.

---

J. PHYS. SOC. JAPAN **11** (1956) 466~467

## On the Electroluminescence in ZnS phosphor

By Morihiko KIMATA and Tsutomu NOMURA

*Department of Electrical Engineering of Waseda University Tokyo*

(Received February 10, 1956)

An investigation has been made of the properties of electro-luninescence of ZnS phosphor doped with Pb and Cu[1]. The powder phosphor is imbedded in Lucite, which is sandwiched between a conductive glass and an alminium plate, before Lucite solidifies. Luminous light outputs are received by the photomultiplier, amplified and observed by a two beam oscilloscope.

At low voltage two peaks were observed per half cycle of the external field. One was almost in phase and the other appeared at the maximum of time derivative of the external field. This is the well known experimental result of many authors. But increasing the voltage, a third peak was found at the time of exact maximum of the external field (Fig. 1, a). For the sake of simplicity we named these peaks P, C and I in the order they were referred above. Simultaneous results were obtained with samples using the same phosphor not imbedded in Lucite, but sandwiched between two conductive galses (Fig. 1, b). The reason for this was to eliminate any possible blocking of the electrode caused by the use of Lucite. In this case the I-peak did not show a smooth form on the oscilloscope pattern, but exhibited a rugged form. Considering the shape and the stability of this peak, it is not reasonable to conceive that the peak is caused by discharge light.

When DC bias is superposed on the AC field, the different characteristics were induced for three peaks. (Fig. 2)

1) I-peak was strengthened at the maximum of the field and weakened at the minimum.

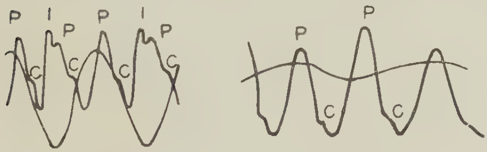

(a) (b)

Fig. 1. (a) Sinusoidal voltage (1800 V/mm) and light output. I, P and C-peaks are seen, but I-peaks do not always appear twice a cycle.
(b) Light output shape is identical with those of the above. The I-peak does not appear in this figure but was observed to have a rugged shape.

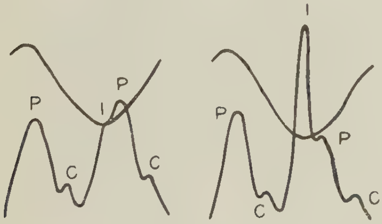

(a) (b)

Fig. 2. Bias effects. (a) No bias. (b) Bias. (AC. 1800 V/mm, DC. 400 V/mm)

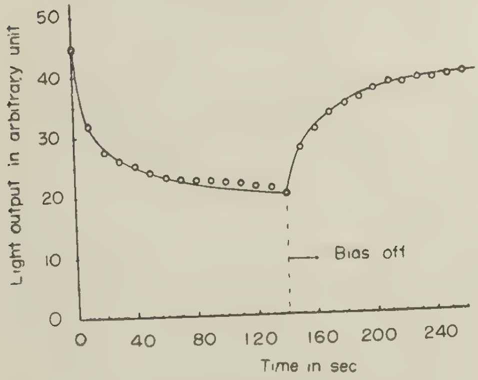

Fig. 3. DC bias was on, at $t=0$ and off at $t=140$ sec. The decreased light gradually recovered after the bias was removed. (AC. 800 V/mm, DC. 1200 V/mm)

2) The behavior of the P-peak was very interesting in contrasts with I-peak. This peak was weakened at the maximum of the field, and slightly strengthened at the minimum field.

3) Change in the C-peak is not distinct because of the effects of the others, but this is not likely to be affected by the DC bias.

From these observations we can conclude that these three peaks were induced by quite different mechanisms.

From the result 1) the I-peak can be explained by the impact model[2]. But from 2) the P-peak cannot be explained by this mechanism, because, if it is so P-peak should have to increase by the increased field. The P-peak may be closely related with the polarization of the phosphor. To explain this effect, a more elaborate experiment must be devised.

From the result 3) in which C-peak is independent of the field intensity but depends only on the field change, the C-peak cannot be explained by the recombination at 0 field[3]. We prefer to explain the C-peak as having arisen from the effect of field changes. Such mechanism may be obtained by the release of the carrier at the trap by abrupt change of the field.

The total light output is lowered by the DC bias and its time dependence is shown in Fig. 3.

The authors wish to thank Prof. H. Tsutsumi for his encouragements and invaluable comments.

## References

1) The impurity percentage is identical to the F. Waymouth's.
F. Waymouth: Phys. Rev. **95** (1954) 941.
2) D. Curie: J. Phys. radium **13** (1952) 317.
3) F. Matossi: Phys. Rev. **98** (1955) 434.

---

J. PHYS. SOC. JAPAN **11** (1956) 467~468

# On the Correlation between Screw Dialocations and Twin Structure in $WO_3$ Crystal

By Terutaro NAKAMURA

*Department of Physics, University of Tokyo*

(Received January 25, 1956)

Recently S. Tanisaki[1] observed growth spirals on the tungsten trioxide crystal, indicating that screw dislocations imerge on the surface. This substance was reported to have ferro- or antiferroelectric properties[2] and to posses twin structure[3]. The present note suggests that the screw dislocations parallel to [001] axis may affect the twin structure.

It is well known that the crystal is composed of domains (90° domains), twinned on (110) plane. Furthermore, each domain contains a number of repeated twins (180° domains), twinning plane being (100), as showh in Figs. 1 and 2[3]. Unit cell is monoclinic with lattice constants:[3] $a=7.27$ A, $b=7.50$ A, $c=3.82$ A, $\beta=90°56'$ (Fig. 2).

Some of photographs by Tanisaki indicate the existence of screw dislocation parallel to $c$-axis[1]. These dislocations must cause stress $Z_x$, whereas each (100) type domain has spontaneous strain $z_x$. Therefore, stress $Z_x$ may affect (100) type domain structure.

Suppose a screw dislocation parallel to $c$-axis in a domain characterized by positive $z_x$ strain, then in the vicinity of the dislocation a portion of negative $z_x$ strain must be existing. It is possible that this negatively polarized portion provides a nucleous of new domain which may grow when a mechanical stress is applied.

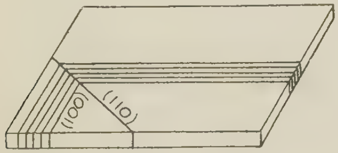

Fig. 1. Twin structure of WO$_3$ according to Ueda and Kobayashi.

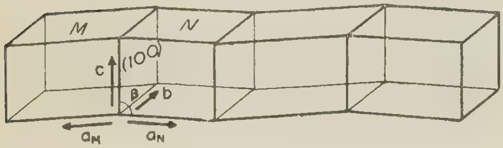

Fig. 2. 180° domain structure according to Ueda and Kobayashi.

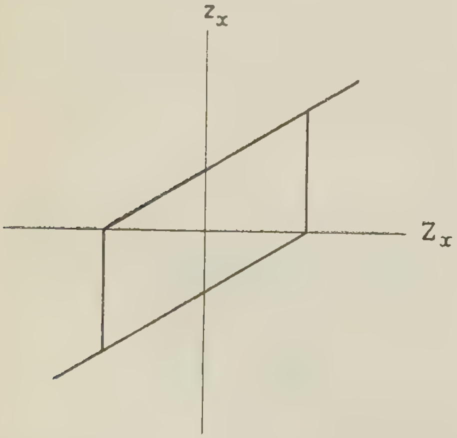

Fig. 3. The $z_x-Z_x$ characteristic curve, assumed.

The information on the size of the nucleous of the domain can be roughly estimated as follows. Strain $z_x$ due to a screw dislocation situated in a positive domain is:

$$z_x=-\frac{b}{2\pi}\frac{y}{x^2+y^2}+z_{xs} \tag{1}$$

provided for brevity that elastic constants are isotropic, and that $z_x-Z_x$ characteristic curve is as shown in Fig. 3; where $z_{xs}$ denotes spontaneous strain $\beta-(\pi/2)=1.6\times10^{-2}$, and $b$ denotes the modulus of Burgers vector. If Burgers vector is equal to the lattice constant in [001] direction, 3.82 A, the nucleous of opposite domain fixed to the dislocation can be roughly estimated from Eq. (1) as a circular cylinder of radious 50 A in the order of magnitude. The nucleous of the domain, therefore, cannot be detected by microscopic study. There is, however, a possibility that stress $Z_x$ applied by a certain treatment may produce observable domains at the screw dislocations parallel to the $c$-axis.

If the $z_x-Z_x$ characteristic shown in Fig. 3, is not the case, (1) is not correct, hence the nucleous of the domain will not be circular cylinder. The estimation of the size, however, will be roughly the case.

## References

1) S. Tanisaki: J. App. Phys., Japan **24** (1955) 253 (in Japanese); read before the Conference of Physical Society of Japan, Oct. 1955.
2) B. T. Matthias: Phys. Rev. **76** (1949) 430.
C. Kittel: Phys. Rev. **82** (1951) 729.
3) R. Ueda and J. Kobayashi: Phys. Rev. **91** (1953) 1565.
J. Kobayashi: Mem. Sch. Sci. Eng. Waseda Univ. **18** (1954) 92.

---

J. PHYS. SOC. JAPAN **11** (1956) 468~470

# The Effect of Frequency on the Fatigue of Metals

By Alan K. HEAD

*Aeronautical Research Laboratories,*
*Department of Supply*
*Melbourne, Australia*

(Received January 27, 1956)

In the theory of fatigue fracture of Yokobori[1] one of the predictions is that the number of cycles to cause fracture is proportional to the frequency of the applied stress. Recent fatigue tests in these laboratories on 24 S–T aluminium alloy and pure annealed copper have not shown this predicted frequency dependance. Fig. 1 shows the S–N curves for 24 S-T at frequencies from 21 to 12000 cycles per minute obtained by Mann[2] and Table I is a summary of the results obtained by

Mann and Finney for copper.

Some care is necessary in this type of experiment to ensure that the characteristics of the testing machine do not vary with frequency; for instance the reported variations with frequency in X-ray diffraction patterns from copper tested in push-pull fatigue3) have since been shown4) to be mainly due to the characteristics of the fatigue machine used. All the tests in Fig. 1 and Table I (a total of 250 specimens) were run in the same standard A.R.L. 12,000 c.p.m. rotating cantilever fatigue machine5). For the lower frequencies a reduction gear box and pulleys were used between the motor and the machine. Full details of the experimental procedure are given in reference2). The S–N curves in Fig. 1 have been drawn through the logarithmic means of groups of test points since it has been shown6) that the scatter of fatigue tests is approximately log-normal. When the testing frequency is increased from 21 c.p.m. to 12,000 c.p.m. the theory of Yokobori predicts that the fatigue life should be increased by a factor of 571. From Fig. 1 it will be seen that the factor is actually from 1 to 3, depending on the stress level. For the results in Table I the measured factor is from 3 to 4 while the predicted increase is by a factor of 286.

Table I.

| Stress p.s.i. | Fatigue Life at 21 c.p.m. | Fatigue Life at 6000 c.p.m. |
|---|---|---|
| 20,000 | $3.5\times10^4$ | $1.5\times10^5$ |
| 16,000 | $2.5\times10^5$ | $9\times10^5$ |
| 14,000 | $7\times10^5$ | $2\times10^6$ |

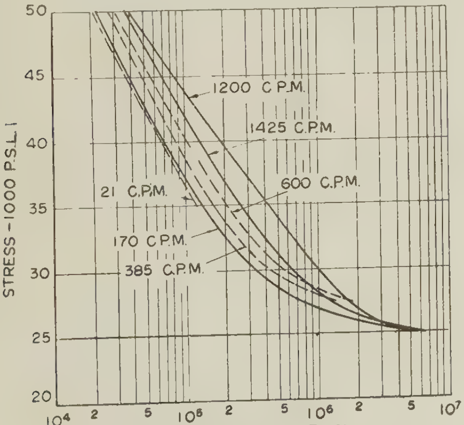

S-N CURVES AT DIFFERENT TESTING SPEEDS

Fig. 1.

This theoretical prediction that fatigue life should be proportional to frequency is actually composed of two parts. Firstly it is assumed that the initial formation of a crack is a rate process of nucleation and it is then shown that the number of cycles to nucleate a crack is proportional to frequency. It is then assumed that this nucleation takes the major part of the fatigue life and it then follows that the fatigue life will be (approximately) proportional to frequency. As the above experimental results do not show this proportionality the following alternatives exist:—

(i) If the number of cycles to initiate a fatigue crack is the major part of the fatigue life then the formation of the crack cannot be by the mechanism described by Yokobori.

or (ii) If the number of cycles to initiate a crack is only a small part of the fatigue life then Yokobori's mechanism could be correct but it is not then possible to compare the theory directly with experiment as done in reference (1).

Of the three stages of the fatigue process, the first (the initial work hardening) is very short compared with the total fatigue life. It appears7)8)9) that the crack is formed early in the fatigue life and that the growth of the crack takes the major part of the life. Although there have been no experiments on the effect of frequency on the growth of the crack, a theory of the rate of growth of fatigue cracks9)10), which is in reasonable agreement with experiment11), would predict frequency independent growth. Thus it may be permissable to analyse the fatigue life as the sum of a frequency dependent part (the nucleation of the crack) and a frequency independent part (the subsequent growth of the crack). However if this is done for the data of Fig. 1 the dependence on frequency does not appear to be linear.

## Acknowledgement

This note is published by permission of the Chief Scientist, Department of Supply. Thanks are due to J. Y. Mann and J. M. Finney for making available experimental data.

## References

1) T. Yokobori: J. Phys. Soc. Japan **10** (1955) 368.
2) J. Y. Mann: Report ARL/SM 188, Department of Supply. Commonwealth of Australia (1954).
3) W. A. Wood and A. K. Head: J. Inst. Metals **72** (1951) 97.
4) R. B. Davies: Nature **174** (1954) 980.
5) W. W. Johnstone: The Failure of Metals by Fatigue (1947) (Melbourne University Press), Paper No. 11.
6) A. K. Head: Am. Soc. Test. Mat. Bull. (1950) 51.
7) A. K. Head: J. Mech. Phys. Solids **1** (1953) 134.

8) N. J. Wadsworth and N. Thompson: Phil. Mag. **45** (1954) 223.
9) A. K. Head: Phil. Mag. **44** (1953) 925.
10) A. K. Head: J. Appl. Mech. (to be published).
11) F. A. McClintock and F. J. Ryan: J. Appl. Mech. **21** (1954) 296.

---

J. Phys. Soc. Japan **11** (1956) 470

# The Crystal Structure of Stannous Selenide SnSe

By Atsushi Okazaki

*Department of Physics, Faculty of Science,*
*Kyusyu University, Fukuoka*

and Ikuhiko Ueda

*General Education Department,*
*Kyusyu University, Fukuoka*

(Received January 30, 1956)

In connection with its semi-conducting properties¹⁾, the crystal structure of stannous selenide was determined.

Stannous selenide was prepared by heating a mixture of tin and selenium in stoichiometric proportions. Single crystals were grown from the melt by slow cooling in a crucible being covered with rock salt powder.

X-ray diffraction data were obtained mainly from oscillation photographs taken with nickel-filtered Cu $K$-radiation. The crystal belongs to the orthorhombic system and the dimensions of the unit cell containing four chemical units, SnSe, are

$$a=4.46,\ b=4.19,\ \text{and}\ c=11.57\ \text{Å}\ .$$

The observed reflections conformed to the following rules:

$hkl$ present for all,
$hk0$ present only for $h+k$ even,
$0kl$ present only for $l$ even.

These rules are satisfied only in the two space groups, $D_{2h}^{16}-Pcmn$ and $C_{2v}^{9}-Pc2_1n$. If all the $y$ parameters of the two kinds of atoms in $C_{2v}^{9}-Pc2_1n$ are equall to $\pm 1/4$, these two space groups give the same results. The results obtained by the application of Wilson's method favour $D_{2h}^{16}-Pcmn$, and after determination of $z$ parameters shown below it is found that the intensities of the $0kl$ reflections are in good agreement, within the probable experimental error, with $y=1/4$. Thus the most probable space group is found to be $D_{2h}^{16}-Pcmn$.

The intensities of the $0kl$, $h0l$ and $hk0$ reflections were estimated visually from oscillation photographs which were taken by the multiple film technique. Since the linear absorption coefficient is $1.10\times10^3$ cm$^{-1}$, it was necessary to correct for the absorption effect; the method suggested by Grdenić²⁾ was followed.

The signs of about five-sixths of all $F(h0l)$ were at once determined from the coordinates given by the Patterson peaks. By successive approximations using the two-dimensional Fourier syntheses and structure factor calculations, the following atomic coordinates for the two kinds of atoms were obtained:

| | $x$ | $z$ |
|---|---|---|
| Sn | 0.103 | 0.118 |
| Se | 0.479 | 0.855 |

The reliability index $R=\sum||F_0|-|F_c||/\sum|F_0|$ has the value 0.27 including all the non-observed reflections. If they are excluded $R$ becomes 0.24.

It is found that this structure is of a distorted NaCl type, isomorphous with GeS and SnS³⁾. The Sn–Se distances in SnSe and the Sn–S ones in SnS are as follows:

| | |
|---|---|
| Sn–Se | 2.77(1), 2.82(2), 3.35(2), 3.47(1) |
| Sn–S | 2.62(1), 2.68(2), 3.27(2), 3.39(1). |

Numbers in the brackets show the number of the Sn–Se or Sn–S bonds corresponding to the ones between the nearest neighbours in NaCl. Distances are given in Å.

The full paper will be soon published in the Memoirs of the Faculty of Science, Kyusyu University.

The authors wish to thank Dr. T. Watanabe and Dr. M. L. Huggins for their kind discussions.

## References

1) Y. Matukura, T. Yamamoto and A. Okazaki: Memoirs of the Faculty of Science, Kyusyu University, Ser. B, **1** (1953) 98.
2) D. Grdenić: Acta Cryst. **5** (1952) 283.
3) W. Hofmann: Z. Krist. **92** (1935) 161.

Journal of the Physical Society of Japan Vol. 11, No. 5, May, 1956

# Second Virial Coefficient of Helium from the Square-well Potential*

By Shobu KANEKO and Taro KIHARA

*Department of Physics, Faculty of Science, University of Tokyo*

(Received January 12, 1956)

The second virial coefficient of helium at low temperatures has been investigated by use of the square-well model of the intermolecular potential for a systematic set of potential parameters.

The notion of depth parameter introduced by Blatt and Jackson¹⁾ for nuclear potentials can also be applied to the potential $U(r)$ between helium molecules, $r$ being the intermolecular distance. Let us choose a dimensionless positive number, $s$, in such a way that the reduced potential, $s^{-1}U(r)$, gives a resonance at the zero energy and no discrete energy level. The number $s$ is called the depth parameter. If one or more discrete levels exist in the two-body system, $s$ is greater than unity; if no discrete level exists, $s$ is less than unity.

In the case of the unit depth parameter, the low temperature limit of the second virial coefficient of helium, He$^4$, is independently of the shape of the intermolecular potential,

$$B=-\frac{9}{16}\left(\frac{4\pi\hbar^2}{mkT}\right)^{3/2}, \tag{1}$$

where $\hbar$ is Planck's constant divided by $2\pi$, $m$ is the mass of a helium atom, $k$ is the Boltzmann constant, and $T$ is the temperature. The second virial coefficient at low temperatures does not sensitively depend on the shape of the intermolecular potential so far as the depth parameter is close to unity.

In fact, it has been known that the depth parameter of He$^4$ is very close to unity²⁾³⁾⁴⁾. For He$^4$, therefore, a highly idealized model of the intermolecular potential can be used, especially for the purpose of deciding whether or not the two-body system of helium has a discrete energy level.

The calculation of the second virial coefficient at low temperature is relatively simple for the intermolecular potential

$$U(r)=\begin{cases}\infty & \text{for} \quad r<\sigma \\ -\varepsilon & \text{for} \quad \sigma<r<g\sigma \\ 0 & \text{for} \quad g\sigma<r\,,\end{cases} \tag{2}$$

where $\varepsilon>0$, $\sigma>0$ and $g>1$ are three model constants. The depth parameter for this model is given by

$$s=\left(\frac{2(g-1)}{\pi\hbar}\sigma\right)^2 m\varepsilon\,. \tag{3}$$

The second virial coefficient $B$ of He$^4$, which obeys Bose-Einstein statistics and has zero spin, is expressed in the form⁵⁾

$$B=-\frac{1}{16}\left(\frac{4\pi\hbar^2}{mkT}\right)^{3/2}+2\sum_{\text{even } l}(2l+1)B_l\,, \tag{4}$$

where summation is to be taken over even quantum numbers $l=0, 2, \cdots$ of the angular momentum. The $B_l$ is given by

$$B_l=-\frac{1}{2}\left(\frac{4\pi\hbar^2}{mkT}\right)^{3/2}\left[\sum_{\text{discrete}}\exp\left(-\frac{E_{nl}}{kT}\right)+\frac{1}{\pi}\int_0^\infty \exp\left(-\frac{E}{kT}\right)\frac{d\eta_l}{dE}dE\right], \tag{5}$$

in which $\eta_l$ is the phase shift defined by the asymptotic form

$$R(r)\sim\sin(\kappa r-\tfrac{1}{2}l\pi+\eta_l) \quad \text{for} \quad r\to\infty \tag{6}$$

of the regular solution of

$$\left[\frac{d^2}{dr^2}+\kappa^2-\frac{m}{\hbar^2}U(r)-\frac{l(l+1)}{r^2}\right]R(r)=0\,, \tag{7}$$

where

$$\kappa^2=mE/\hbar^2\,, \tag{8}$$

$E_{0l}, E_{1l}, \cdots$ ($<0$) being discrete energy levels, if any.

For the square-well potential (2) the phase shifts can be expressed analytically by means of the spherical Bessel functions

$$j_l(x)=(\pi/2x)^{1/2}J_{l+1/2}(x)\,.$$

The function $R$ in (7) with the asymptotic (6) is given by

$$R=\kappa r[\cos\eta_l j_l(\kappa r)+(-1)^l\sin\eta_l j_{-l-1}(\kappa r)]$$

for $r>g\sigma$, while the solution which vanishes at $r=\sigma$ may be written as

---

* A part of this article has been published in Revs. Modern Phys. **27** (1955) 412 and, as a short note, in J. Phys. Soc. Japan **10** (1955) 314.

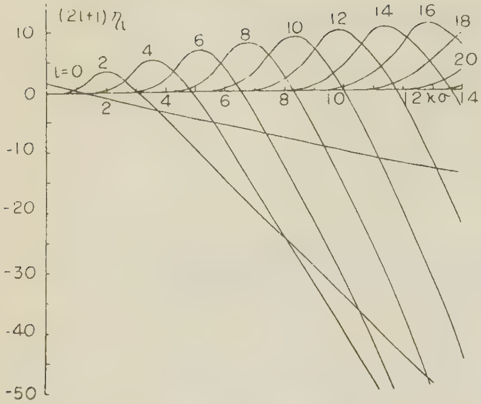

Fig. 1. Phase shift $\eta_l$ for $He^4$–$He^4$ collisions calculated from the square-well potential with $g=3/2$ and $s=1$.

$$R=\text{const}\,\kappa' r[j_{-l-1}(\kappa'\sigma)j_l(\kappa' r)-j_l(\kappa'\sigma)j_{-l-1}(\kappa' r)]$$

for $\sigma<r<g\sigma$, where

$$\kappa'^2=\kappa^2+m\mathcal{E}/\hbar^2$$

or, by use of (3)

$$(\kappa'\sigma)^2=(\kappa\sigma)^2+\pi^2 s/4(g-1)^2\ .$$

The requirement that $R$ and $dR/dr$ be continuous leads to

$$(-1)^l\tan\eta_l=\frac{Aj_{l-1}(g\kappa\sigma)-j_l(g\kappa\sigma)}{Aj_{-l}(g\kappa\sigma)-j_{-l-1}(g\kappa\sigma)}$$

$$A\equiv\frac{\kappa}{\kappa'}\,\frac{j_{-l-1}(\kappa'\sigma)j_l(g\kappa'\sigma)-j_l(\kappa'\sigma)j_{-l-1}(g\kappa'\sigma)}{j_{-l-1}(\kappa'\sigma)j_{l-1}(g\kappa'\sigma)+j_l(\kappa'\sigma)j_{-l}(g\kappa'\sigma)}$$

for $l=0, 1, 2, \cdots$. Here relations

$$\frac{d}{dx}[x^{l+1}j_l(x)]=x^{l+1}j_{l-1}(x)\ ,$$

$$\frac{d}{dx}[x^{l+1}j_{-l-1}(x)]=-x^{l+1}j_{-l}(x)$$

have been used. The phase shifts $\eta_l$ for $s=1$ and $g=3/2$ are shown in Fig. 1 as an example.

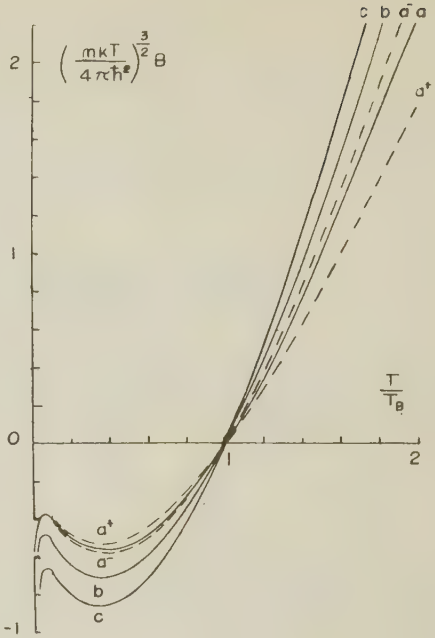

Fig. 2. Reduced second virial coefficient of helium calculated from the square-well potential *vs.* $T/T_B$, $T_B$ being the Boyle temperature. Curve $a$ is for $g=3/2$, $s=1.00$; curve $b$ is for $g=3/2$, $s=1.05$; curve $c$ is for $g=3/2$, $s=1.10$. Broken curve $a^+$ is for $g=2$, $s=1.00$; broken curve $a^-$ is for $g=4/3$, $s=1.00$.

For $s$ slightly greater than unity there exists only one discrete level, $E_{00}$, which is calculated for any $g$ to be

$$E_{00}/\mathcal{E}=-0.00145 \quad \text{for} \quad s=1.05\ ,$$

$$E_{00}/\mathcal{E}=-0.0052 \quad \text{for} \quad s=1.10\ .$$

The expression (4) with (5) for the square-

| $\tau$ | $f(\tau)$ for $g=2$ $s=1.00$ | $f(\tau)$ for $g=3/2$ $s=1.00$ | $f(\tau)$ for $g=4/3$ $s=1.00$ | $f(\tau)$ for $g=3/2$ $s=1.05$ | $f(\tau)$ for $g=3/2$ $s=1.10$ |
|---|---|---|---|---|---|
| 0 | −0.5625 | −0.5625 | −0.5625 | −∞ | −∞ |
| 0.5 | −0.384 | −0.380 | −0.377 | −0.483 | −0.667 |
| 0.75 | — | — | −0.390 | −0.495 | −0.648 |
| 1 | −0.453 | −0.422 | −0.412 | −0.525 | −0.670 |
| 2 | −0.535 | −0.522 | −0.512 | −0.646 | −0.791 |
| 4 | −0.456 | −0.551 | −0.579 | −0.711 | −0.872 |
| 6 | −0.202 | −0.423 | −0.516 | −0.597 | −0.783 |
| 8 | 0.153 | −0.174 | −0.342 | −0.373 | −0.568 |
| 10 | 0.600 | 0.152 | −0.078 | −0.055 | −0.253 |
| 12 | 1.111 | 0.559 | 0.257 | 0.350 | 0.133 |
| 14 | 1.65 | 1.059 | 0.642 | 0.821 | 0.584 |
| 16 | 2.26 | 1.59 | 1.091 | 1.34 | 1.110 |
| 18 | 2.93 | 2.16 | 1.61 | 1.96 | 1.68 |
| 20 | 3.69 | 2.78 | 2.18 | 2.56 | 2.31 |

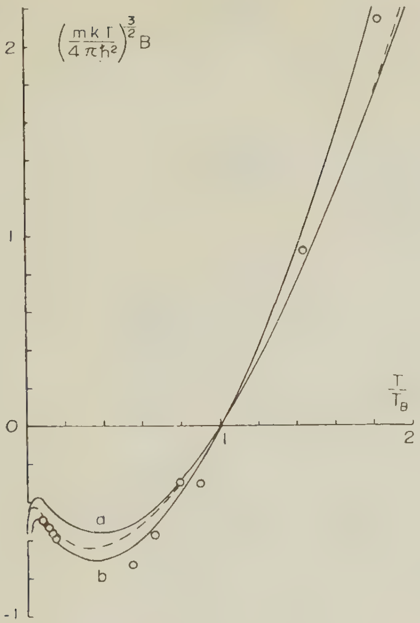

Fig. 3. Reduced second virial coefficient of helium *vs.* $T/T_B$, $T_B$ being the Boyle temperature 26.0° K. Curves *a* and *b* are for the square-well potential with $g=3/2$, $s$ being 1.00 and 1.05 respectively. The broken curve is for Lennard-Jones (61,2) potential with $s=1$. Experimental results are compared with these curves.

well potential then assumes, for each $g$ and $s$,

$$B=\left(\frac{4\pi\hbar^2}{mkT}\right)^{3/2} f(\tau) \quad \text{where} \quad \tau=\frac{\pi^2 skT}{4(g-1)^2\varepsilon}, \quad (9)$$

the function $f$ being given in the table.

Curves of $(mkT/4\pi\hbar^2)^{3/2}$ for ordinary helium, He$^4$, are shown in Fig. 2. The dependence of these curves on the depth parameter $s$ is conspicuous, while that on the "width parameter" $g$ is very slight at low temperatures. For smooth, less idealized models of the intermoleculer potential the calculation of the second virial coefficient at low temperatures is laborious; and at present there is no other result for a systematic set of potential parameters.

In Fig. 3 experimental results[6] for He$^4$ are compared with two curves for the square-well potential with $g=3/2$ and a curve for the Lennard-Jones (6,12)-potential with unit depth parameter. The latter has been drawn taking account of recent calculations by Kilpatric et al[3]. in the case $s=0.99$, slight modification being made by virtue of Fig. 2. From the comparison we know that the depth parameter for the two-body system of He$^4$–He$^4$ is very close to, probably a little greater than, unity.

## References

1) J. M. Blatt and J. D. Jackson: Phys. Rev. **76** (1949) 18. See also T. Kihara: Revs. Modern Phys. **27** (1955) 412.
2) J. de Boer and A. Michels: Physica **5** (1938) 945, **6** (1939) 409.
3) Kilpatrick, Keller, Hammel and Metropolis: Phys. Rev. **94** (1954) 1103.
4) Kilpatrick, Keller and Hammel: Phys. Rev. **97** (1955) 9.
5) G. E. Uhlenbeck and E. Beth: Physica **4** (1937) 915.
L. Gropper: Phys. Rev. **50** (1936) 963, **51** (1937) 1108.
6) W. E. Keller: Phys. Rev. **97** (1955) 1, and others.

JOURNAL OF THE PHYSICAL SOCIETY OF JAPAN Vol. 11, No. 5, MAY, 1956

# Dielectric Breakdown and Pulse Conduction of Silver Halide Crystals

By Tokuo SUITA and Noriaki ITOH

*Department of Electrical Engineering, College of Engineering, Osaka University*

(Received January 9, 1956)

Several experiments on the dielectric breakdown of silver halide crystals were made, concerning about the effect of illumination and temperature. The temperature dependency of the breakdown strength of silver halide crystals seems to be similar to that of alkali halide crystals. The photographic silver specks in the crystals, which were made by illumination and then by being kept in the dark, are found to raise the breakdown strength. The effect of illumination are dependent on the interval between illumination and breakdown and on the repetition rate. These effects seem to be explained by photoelectrons, positive holes, ions and their space charge. Electrical conductivity of pulse electric field was also measured, showing that the ionic current is predominant even in such a short pulse field.

## § 1. Introduction

We have been studying the dielectric breakdown of alkali halide crystals for several years and have found that the actual dielectric breakdown is too complex to be treated by simple theories which mainly concern about ionization by electron collision in the crystal[1)2)]. There seem to be still many other factors, besides this main mechanism, which determine actual breakdown phenomena; for example, space charge of electrons, holes and ions, conditions of the contact surfaces of electrodes, kind of the applied electric field, and mechanical stress or annealing conditions of the specimens.

To clarify some of these second effects we have used silver halide crystals which seem to show some convenient properties for the studies of contact conditions, impurity contents and mechanical stress owing to their photochemical reaction.

On the other hand, in manufacturing photo films there are some damages due to surface electric discharge when the films are rolled. To prevent these phenomena it is necessary to know about dielectric beakdown of silver halide or gelatine itself.

First we tried the dielectric breakdown of AgBr and AgCl crystals under a non-uniform electric field in order to know qualitatively about some photchemical effects on their dielectric breakdown. Next we used a uniform electric field and applied both electrical and optical pulses on the specimens with variation in time interval between the two pulses. Finally the pulse conductivity was measured at various temperatures and then the activation energies were calculated.

## § 2. Experimental Procedures

The specimens were single crystals manufactured by Kyropoulus method such as alkali halides and well annealed. Recrystalization of the parent crystals was necessary to get good specimens. The crystal blocks were cut by a metal wire with emery to roughly proper dimensions. For non-uniform field the specimens were flat plates ($10\times10\times1$ mm$^3$) and for uniform field they were recessed plates ($10\times10\times0.3$ mm$^3$). To prevent mechanical stress in the recessed specimens we used the following process. The flat crystal plates were first coated by paraffin except their center part of radius 1.5 mm on the one side of the crystal, and then dipped in sodium thiosulphate solution for several hours until the desired thickness was obtained. Finally they were washed with distilled water and then well annealed again.

The electrodes used for the non-uniform field were a platinum needle and painted aquaduck plate, and for the uniform field they were evaporated gold and painted aquaduck. All these preparatory works were done in the dark.

Owing to the high ionic conductivity of silver halides, any D. C. dielectric breakdown experiments could not be carried out, and therefore we used (1) non-uniform pulse electric field of normal wave form ($1\times40\,\mu$ sec) and continuous illumination, (2) uniform pulse electric field of rectangular wave form and pulse illumination. The breakdown voltage was measured by sphere gap meter and oscilloscope. Photochemical change of the specimens was produced by a ordinally 100 watt tungsten lamp which was placed 20 cm apart from the specimens. We use insulating oil as an ambient medium to prevent surface discharge of the specimens.

The pulse conductivity was measured by the use of the same rectangular electric field at various temperatures. The voltage across a small series resistance to the specimen was amplified by a transient amplifier[3)] and the conduction current was calculated. The specimen had a guard ring in order to eliminate the effect of leakage current.

## § 3. Experimental Results and Discussions

### (1) *Non-uniform Electric Field*

Some experimental results concerning about AgBr will be shown. In a non-uniform field there are many combinations of the electrode arrangement and the illuminated surface, which we will explain later.

Fig. 1, 2 and 3 show the results of the cases in which the specimens were illuminated for a given time and then kept in the dark for about 12 hours, and at the breakdown the pointed electrode was placed upon the illuminated surface. Even in such a case there are two different relative position, the negative and the positive needle.

Fig. 1 indicates relation between the breakdown voltage and the illuminated period. It is very interesting to see that in the case of the negative needle the effect of the illumination raises the breakdown voltage very rapidly in a first few minutes and then gradually decreases, but in the case of the positive needle the breakdown voltage rather decreases at first and gradually increases with illumination. Therefore the effect of the illumination makes much difference in the both cases.

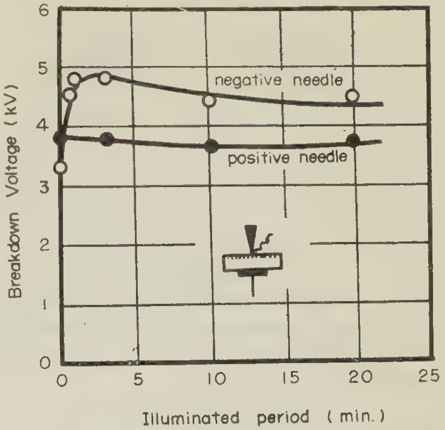

Fig. 1. The curves of the dielectric breakdown voltage of AgBr vs illuminated period at 32°C, the specimens being 1 mm thick and kept in the dark for 12 hours after illumination.

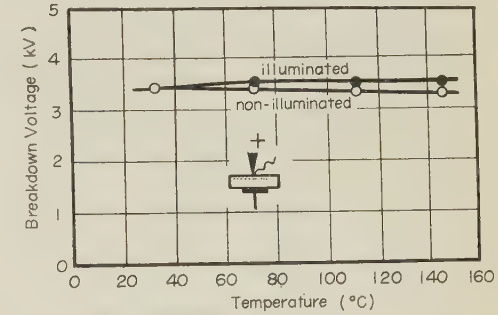

Fig. 2. The temperature dependence of the breakdown voltage of AgBr, positive needle, 1 mm thick, illuminated for 20 min. and kept in the dark for 12 hours.

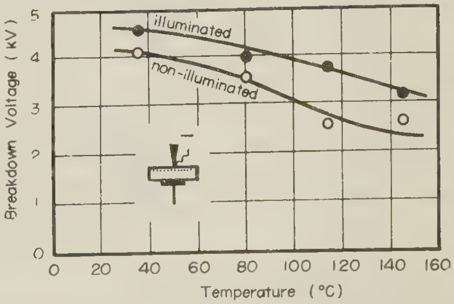

Fig. 3. The temperature dependence of the breakdown voltage of AgBr, negative needle, 1.2 mm thick, 20 min., 12 hours.

We studied the temperature dependence of the breakdown voltage of 20 minutes illuminated specimens under the same conditions. The results are indicated in Fig. 2 and 3.

In the case of the positive needle the breakdown voltages are almost independent of the temperature and the effect of the illumination is also very small, while in the case of the negative needle the breakdown voltages decrease with temperature and the effect of

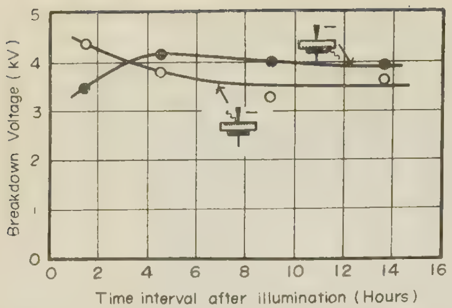

Fig. 4. Time dependence of the breakdown voltage of illuminated AgBr for 20 min., 25°C, 1 mm thick.

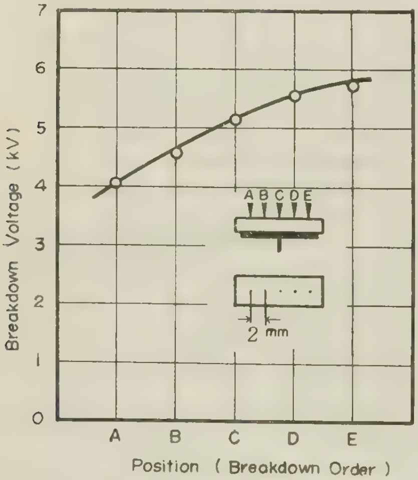

Fig. 5. Partial breakdown effect of AgBr, 32°C, 1.2 mm thick.

Table I. The effect of illumination on the breakdown voltage in non-uniform field. Specimens are illuminated for 20 min. and kept in the dark for 12 hours. Thickness 1 mm. Temperature 25°C.

| Treatment and illuminated side | Non-illuminated | illuminated | |
|---|---|---|---|
| | | Needle side | Plate side |
| Negative needle | 3.2 kV | 4.0 kV | 4.8 kV |
| Positive needle | 3.8 kV | 3.6 kV | 3.6 kV |

illumination is large and nearly constant in the whole temperature range. This dependence of breakdown voltage upon temperature seems to be similar to that of alkali halides above 150°C.

Next we examined the breakdown voltage under various combinations of the electrodes and the illuminated surface at room temperature. The results are shown in Table I. It is very easy to note that in the case of the positive needle the illumination effect is negligible in all positions, but in the case of the negative needle the effect is very large especially in the case where the illuminated surface coincides with the plate electrode, or the illuminated surface is placed under the lower field intensity side. For that reason we are much interested in the case of the negative needle from the standpoint of dielectric breakdown.

Another factor which seems to play an important role upon the breakdown is the period during which the illuminated specimens were kept in the dark, in other words, the time elapsed between the illumination and the breakdown.

The result concerning about this time effect in the case of the negative needle are shown in Fig. 4. The specimens used in this experiment were illuminated for 20 minutes and kept in the dark for different time intervals after light was cut. It is very interesting to note that this time effect is quite different in the both cases, that is, in the case where the negative needle and the illuminated surface are on the same side the breakdown voltage decreases with time, while in the other case it gradually increases and therefore after several hours the order of magnitude is inverted from the beginning. These results show that some internal changes may occur in the illuminated crystal even in the dark and the breakdown voltage depends on the nature of these created impurity centers.

In a non-uniform field something like partial breakdown may easily occur in the crystal. We tried to study the effect of light produced by the breakdown itself upon the following breakdown of the same crystal. The specimen was rectangular as shown in Fig. 5, and the breakdown took place in order of A, B, C, D, and *E* progressively, so that *E* was most influenced by the preceding breakdowns.

The curve taken at the room temperature shows clearly that the preceding breakdowns raise the following breakdown voltages by the effect of the light produced by the breakdowns themselves. From these facts we can conclude that any partial breakdown may influence the following perfect breakdown by the illumination effect of the partial breakdown.

Our results of non-uniform field can be summarized as follows.

1. Light illumination has much effect on

the dielectric breakdown of AgBr crystal.

2. Especially in the case of the negative needle the breakdown voltage increases rapidly with illuminations.

3. The illuminated AgBr crystal changes its electronic properties even in the dark.

4. The breakdown voltage is influenced by its partial breakdown.

### (2) *Uniform Electric Field*

Fig. 6 shows the temperature dependence of the dielectric breakdown strength of AgCl in the dark under rectangular pulse field. The repetition rate was 30 cycles/sec.

It is clearly seen that there exists a critical temperature at which the temperature coefficient of the breakdown strength changes even in such a pulse field. In AgCl the critical temperature was about 50°C. The pulse length has an important role in the temperature dependence of the breakdown strength especially at higher temperatures, which is very similar to that of the breakdown behavior of alkali halide at temperatures higher than about 150°C.

To clarify the effect of photochemical changes of AgCl on the dielectric breakdown we used both optical and electrical pulses with variation of the time relation between the two kinds of the pulses. In addition the breakdown strength with a single optical and a single electric pulse was also tested about the same crystal. Our results under various conditions are given in Table II. Each value corresponds to the average value of about 20 specimens.

Table II. The effect of pulse illumination on the breakdown strength of AgCl in pulse uniform field. Light pulses of 120 $\mu$ sec duration and voltage pulses of 70 $\mu$ sec duration are synchronized and the maximum point of each light pulse coincides to the start point of the corresponding voltage pulse. Temperature 25°C.

| Experimental condition | Non-illuminated | Illuminated |
|---|---|---|
| single pulse | 65 kV/cm | 60 kV/cm |
| repeated pulse, 30 cycles/sec | 90 〃 | 60 〃 |
| repeated pulse, $\frac{1}{2}$ cycles/sec | 90 〃 | 130 〃 |

From these data we can summarise as follows.

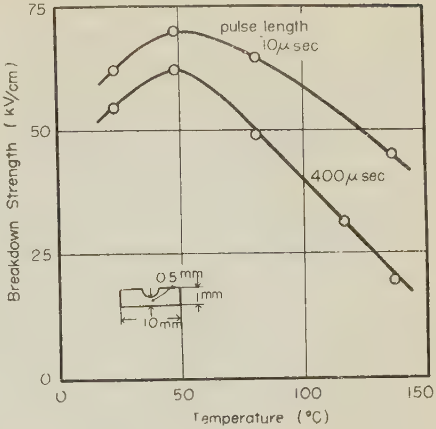

Fig. 6. The temperature dependence of breakdown strength of AgCl by rectangular pulse field repeated 30 cycles/sec.

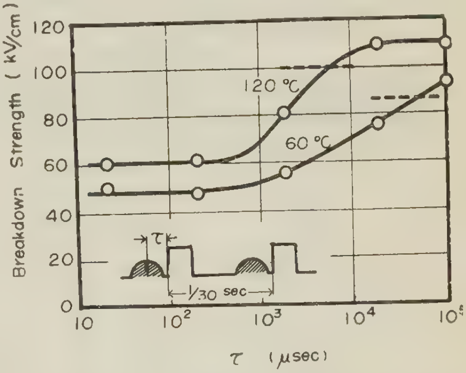

Fig. 7. The curves of the breakdown strength of AgCl vs time interval between illumination and breakdown. The repetition rate of both pulses is 30 cycles/sec except $\tau = 10^5 \mu$ sec where it is 10 cycles/sec. --- denotes the dielectric breakdown strength in the dark.

1. The pulse breakdown strength without illumination become larger when the pulse field is repeated.

2. The breakdown strength is not much affected by illumination when it occurs through a single optical and a single electrical pulse superimposed.

3. The breakdown strength is strongly affected by illumination when the both pulses are repeated.

The time elapsed between the optical pulse and the following electrical pulse seems to be important as in the case of the nonuniform field and the observed results are shown in Fig. 7; the breakdown strength is nearly constant up to the time interval of $10^3 \mu$ sec and then increased with increasing the interval. This time effect also depends on the

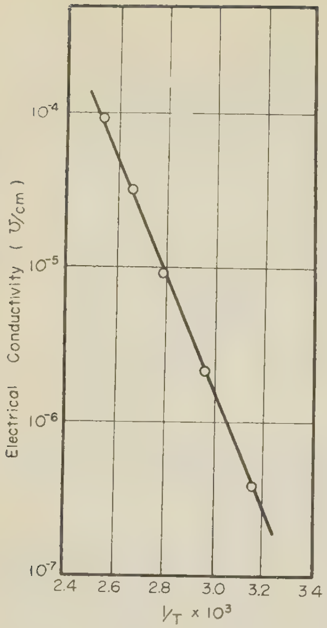

Fig. 8. Temperature dependence of pulse conductivity of AgBr.

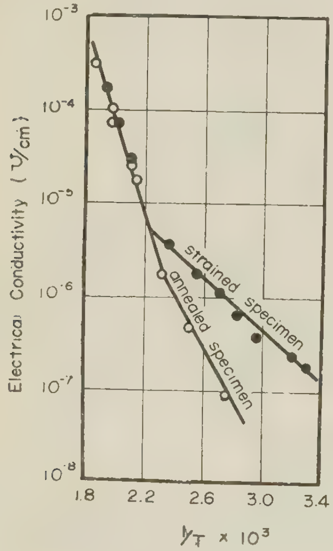

Fig. 9. Temperature dependence of pulse conductivity of AgCl. ○: annealed specimen, ●: strained specimen.

temperature as seen in Fig. 7.

### (3) *Pulse Conduction*

We measured pulse conductivities of AgBr and AgCl, using pulse of length 10 $\mu$ sec at various temperatures.

Our results are shown in Fig. 8 and 9. It is easy to see that logarithm of the conductivity of AgBr linearly increases with decreasing the reciprocal of the absolute temperature, while in AgCl the conductivity has a kink point near $1/T=2.3\times10^{-3}$, and at lower temperatures than this point it is structure sensitive and depends an the anealing process or other second conditions.

The activation energy for AgBr is 0.80ev and for the insensitive point of AgCl it is 0.81 ev. It is of interest to see that these values are almost coincident with D.C. values of Koch and Wagner[4]. Therefore we may conclude that even in such a pulse field $Ag^+$ positive ions would play an important roll in the conductivity as in D. C. field.

It is evident that our present experimental data on the electrical properties of the silver halides is not adequate to provide a complete interpretation of the mechanisms responsible for their intricate behavior.

It seems very likely that electron avalanches play an important role in the dielectric braekdown of silver halides like in that of alkali halides.

In addition, photochemical reaction and dislocation in silver halide seem to be essential factors to determine the breakdown. The illuminated silver halide crystal has many silver specks, or some neutral silver atoms due to the trapping of the photoelectrons by interstitial silver ions near crystal imperfections, on the other hand, the positive holes produced by the light may migrate to the surface by thermal diffusion[5].

Judging from the experimental data on the pulse dielectric breakdown of mixed crystals, any imperfection makes the breakdown strength higher than that of the pure crystals[1]. Moreover in the silver halides, the ionic conductivity is so large even in the pulse field that the breakdown field seems to be much modulated by silver atoms deposited near the cathode which can be seen from the data in Table. II.

From the facts that in the case of single optical pulse or high repetition rate the increase of breakdown strength due to the ionic conduction seems to be cancelled by illumination and shows the minimum value, we can therefore speculate that positive holes produced by illumination migrate toward the cathode and recombine with the neutral silver atoms resulting in the formation of silver ions, or positive holes prevent the silver ions from going toward the cathode to take electron from it by space charge effect of the holes.

It is interesting to note that at the low repetition rate the illumination effect is very large which suggests that some gradually changing factors in the dark come into the breakdown phenomena. This means that, according to the present assumption, about two seconds interval between the optical pulse of one pair and the electrical pulse of the following pair seems to be sufficient to produe neutral silver atoms or their aggregates by recombination of the silver ions and thermally released electrons which had been created by illumination and trapped in imperfections, probably near the surface.

In order to clarify the mechanisms, it would be necessary to carry out further experiments on the existence of space charges of ions, electron and holes at various conditions.

## § 4. Conclusion

Light illumination has much effect on the dielectric breakdown of silver halide crystals owing to their photographic sensitivity.

The dielectric breakdown strength of the illuminated crystals is, in general, larger than that of non-illuminated crystals, and its value depends on relative positions of the illuminated surface and the polarity of electrode, time interval between the illumination and the voltage application, repetition rate of the optical and electrical pulses, and temperature.

We are now trying to investigate the photoelectric conductivity with reference to the dielectric breakdown.

The authors wish to thank to Dr. E. Mizuki and other staffs of Fuji Photo Film Co., Ltd. for supplying silver halide materials and for their valuable discussions.

## References

1) T. Suita: Tech. Rep. Osaka Univ. **1** (1951) 51.
2) Y. Inuishi and T. Suita: Tech. Rep. Osaka Univ. **4** (1954) 203.
3) W. C. Elmore and M. Sands: *Electronics* (McGraw-Hill Book Co., New York, 1949).
4) E. Koch and C. Wagner: Zeits. f. Phys. Chem. **B 38** (1937) 295.
5) J. M. Hedges and J. W. Mitchell: Phil Mag. **44** (1953) 223.

---

JOURNAL OF THE PHYSICAL SOCIETY OF JAPAN Vol. 11, No. 5, MAY, 1956

# On the Coupled Dislocations along a Grain Boundary

By Yasutada UEMURA*

*Matsuda Research Laboratory, Tokyo-Shibaura Electric Co.*
*Kawasaki City, Japan*

(Received January 14, 1956)

By analyzing the interesting patterns of the etch-pits due to the coupled dislocations along a grain boundary in germanium crystals, the direct and quantitative verification of the law of interaction between edge dislocations is obtained.

## § 1. Introduction

In the course of a study of the dislocations in germanium crystals by means of the etching process, J. Okada in this laboratory and J. J. Oberly[1] observed interesting patterns of coupled dislocations along a grain boundary which are shown in Fig. 1 and Fig. 2.

The aims of this paper are to investigate some of the fundamental properties of the observed dislocations and to suggest that the origin of forces which determine the arrangement of these patterns is the simple elastic interaction between coupled dislocations.

## § 2. Qualitative Discussions

The crystals were grown by pulling in the ⟨100⟩ direction, and {100} surfaces perpendicular to the growth direction were etched by C.P.–4 solution. The regular array of etch-pits in Fig. 1 and Fig. 2 corresponds to

---

* The present adress: Department of Physics, University of Tokyo, Bunkyoku, Tokyo, Japan.

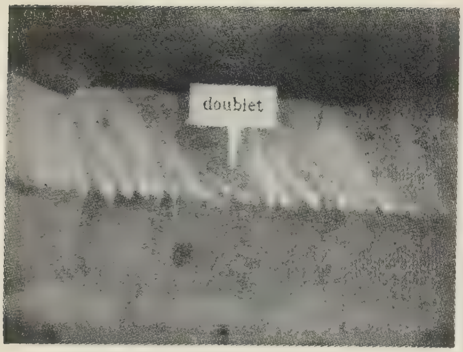

Fig. 1.

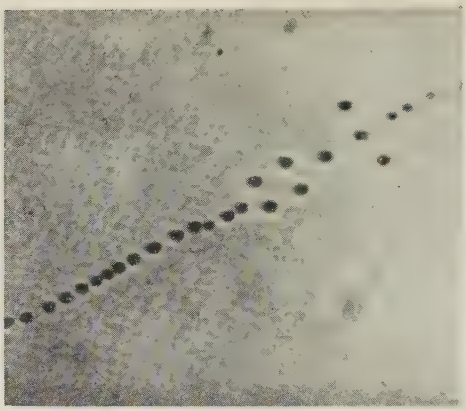

Fig. 2.
(reproduced from Oberly's paper[1])

Table I.

| | | | |
|---|---|---|---|
| D.A. | 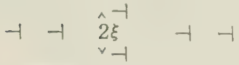 | $\frac{1}{\xi}\left[-C(\xi)-2R(2\xi)+\frac{1}{2}\right]=0$ | $2\xi=1.16$ |
| D.B. | 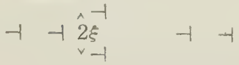 | $\frac{1}{\xi}\left[S(\xi)-R(\xi)-\frac{1}{2}\right]=0$ | $2\xi=1.14$ |
| T.A. | 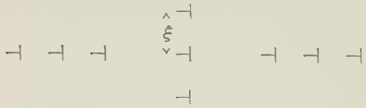 | $\frac{1}{\xi}\left[S(\xi)-2R(\xi)+\frac{1}{2}\right]=0$ | $\xi=1.48$ |
| T.B. | 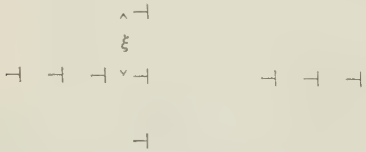 | $\frac{1}{\xi}\left[S(\xi)-R(\xi)-R\left(\frac{\xi}{2}\right)+\frac{1}{2}\right]=0$ | $\xi=2.04$ |
| Q.A. | 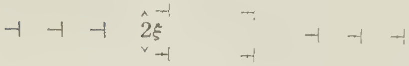 | $\frac{1}{\xi}\left[-C(\xi)-2R(2\xi)-R\left(\frac{2\xi}{3}\right)-R\left(\frac{2\xi}{5}\right)+\frac{1}{2}R\left(\frac{2\xi}{2}\right)+\frac{1}{2}\right]=0$ | $2\xi=1.52$ |
| Q.B. | 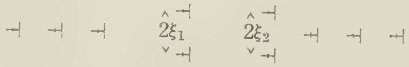 | $\begin{cases}\frac{1}{\xi_1}\left[S(\xi_1)-2R(\xi_1)-R\left(\frac{\xi_1}{2}\right)-\frac{1}{2}\right]+\frac{1}{\xi_1+\xi_2}R\left(\frac{\xi_1+\xi_2}{2}\right)+\frac{1}{\xi_1-\xi_2}R\left(\frac{\xi_1-\xi_2}{2}\right)=0\\ \frac{1}{\xi_2}\left[S(\xi_2)-R(\xi_2)-R\left(\frac{\xi_2}{2}\right)-R\left(\frac{\xi_2}{3}\right)-\frac{1}{2}\right]+\frac{1}{\xi_1+\xi_2}R\left(\frac{\xi_1+\xi_2}{2}\right)+\frac{1}{\xi_2-\xi_1}R\left(\frac{\xi_2-\xi_1}{2}\right)=0\end{cases}$ | $2\xi_1=1.34$<br>$2\xi_2=1.22$ |

the dislocations in the small-angle-of misfit grain boundary. The array runs in the ⟨110⟩ direction and has an interval of 1.7 $\mu$ in Fig. 1 or 4 $\mu$ in Fig. 2.

At first we assume that all dislocations discussed in this paper are the edge type having the same direction of lines as pulling and their Burgers vectors are perpendicular to the surface of the observed grain boundary. This assumption seems to be supported also by the observed characters of these boundaries which were reported by J. Okada[2]. We assume further that the arrangement of etch-pits along a boundary satisfies the condition that the small angle of mis-fit near the coupled dislocations is not so different from that in the regular array. In fact we can find the "vacancies" of etch-pits in the regular array which correspond to the excess pits in the form of coupled dislocations near the "vacancies".

What is the condition that detremine the separation of these coupled dislocations? This is the main problem treated in this paper, and we would like to propose the following interpretation. The condition is the equilibrium of the forces of interaction between dislocations, in the direction perpendicular to the boundary. These patterns may appear in the case in which the temperature is not so high to permit the appreciable climbing of coupled dislocations and they are quenched in their metastable positions near the grain boundary. In fact the doublet of etch-pits shown in Fig. 1 is absorbed into the regular array by heating the crystal for 10 hourse at the temperature about 850°C.

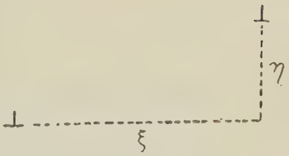

Fig. 3. (A).

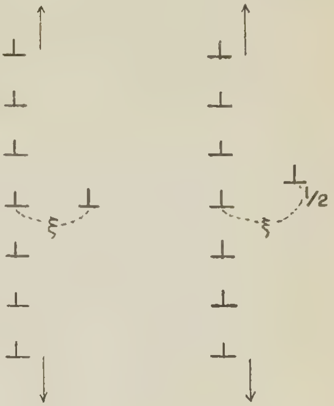

Fig. 3. (B).

## § 3. Simple Models

In order to verify the above interpretation quantitatively, we estimate the separation of coupled dislocations by using the simple models of doublets, triplets and quartets shown in Table I. The equations in Table I represent the condition to balance the forces of interaction between the dislocations along the direction of their Burgers vectors. In these equations, $\xi$ means distance of a dislocation from the boundary measured in the unit of length $w$ which is the regular interval between etch-pits along the array.

If we regard the crystal as an isotropic elastic medium, the functions $R(s)$, $S(\xi)$ and $C(\xi)$ are given by the following expressions[3].

$$R(s)=s^2(s^2-1)(s^2+1)^{-2} \tag{1}$$

$$S(\xi)=\pi^2\xi^2\sinh^{-2}(\pi\xi) \tag{2}$$

$$C(\xi)=\pi^2\xi^2\cosh^{-2}(\pi\xi) \tag{3}$$

The force $F_x$ of interaction between two edge dislocations shown in Fig. 3A is related to $R(s)$ as follows.

$$F_x=F_0\xi^{-1}R(s),\quad s=\xi\eta^{-1},\quad \xi=xw^{-1},\quad \eta=yw^{-1}. \tag{4}$$

The forces $A_x$ and $B_x$ between a dislocation and a regular boundary shown in Fig. 3B are described by the functions $S(\xi)$ and $C(\xi)$ respectively as follows.

$$\begin{aligned} &A_x=F_0\xi^{-1}S(\xi) \\ &\quad S(\xi)=\sum_{n=-\infty}^{+\infty}\xi^2(\xi^2-n^2)(\xi^2+n^2)^{-2}=\pi^2\xi^2\sinh^{-2}(\pi\xi) \end{aligned} \tag{5}$$

$$\begin{aligned} &B_x=-F_0\xi^{-1}C(\xi) \\ &\quad C(\xi)=-\sum_{n=-\infty}^{+\infty}\xi^2\left\{\xi^2-\left(n+\frac{1}{2}\right)^2\right\}\left\{\xi^2+\left(n+\frac{1}{2}\right)^2\right\}^{-2}=\pi^2\xi^2\cosh^{-2}(\pi\xi) \end{aligned} \tag{6}$$

In these expressions, $F_0$ is the unit of force per unit length of a dislocation and is given by

$$F_0=b^2G(2\pi w)^{-1}(1-\nu)^{-1} \tag{7}$$

where $b$ is the length of Burgers vector, $G$ is the rigidity and $\nu$ is the Poisson's ratio.

The total forces appearing in the models of Table I are all described by the combination of $F_x$, $A_x$ and $B_x$. In order to solve the equations in Table I, we employed the graphical method using the calculated curves of $R(s)$, $S(\xi)$ and $C(\xi)$ which are show in Fig. 4 and

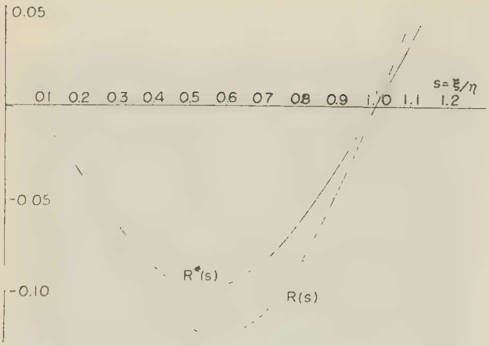

Fig. 4. (A).

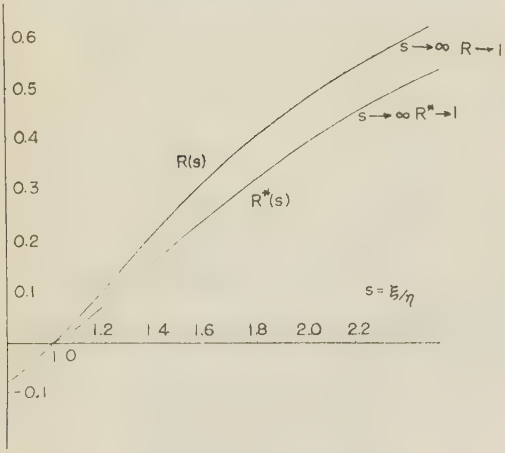

Fig. 4. (B).

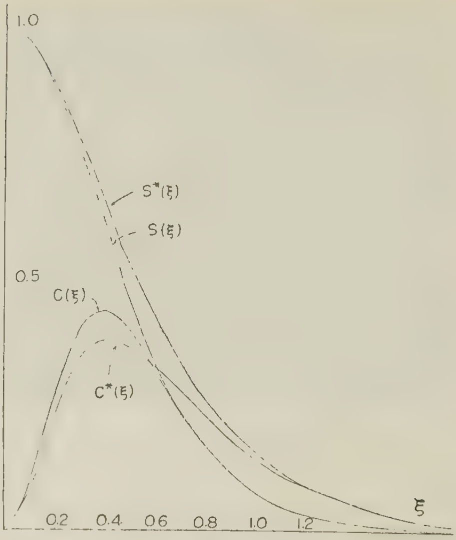

Fig. 5.

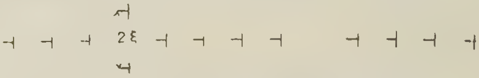

Fig. 6.

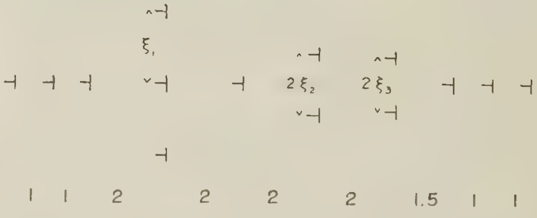

Fig. 7. The numbers indicate the ratio of intervals in the array. Those in parenthesis are the observed values corresponding to Fig. 2.

Fig. 5. In the case of the model Q.B. in Table I, we obtained the coupled equations of two variables $\xi_1$ and $\xi_2$, and solved it by the self-consistent methed.

The calculated separations are also tabulated in Table I, and, roughly speaking, the results suggest that our interpretation may hold quantitatively in the case of more complicated patterns in Fig. 1 and Fig. 2.

## § 4. Analysis of Observed Patterns

To compare the results of calculations with the observed patterns in Fig. 1 and Fig. 2 more quantitatively, we further try to estimate the separations of the models in Fig. 6 and Fig. 7 which have a better fit of arrangement along the boundary than the models in Table I.

The equation for the doublet of Fig. 6 is

$$\xi^{-1}\left[S(\xi)-R\left(\frac{\xi}{5}\right)-\frac{1}{2}\right]=0 \tag{8}$$

and the coupled equations for the coupled dislocations in Fig. 7 are

$$\begin{aligned}&\frac{1}{\xi_1}\left[\frac{1}{2}\{S(\xi_1)-C(\xi_1)\}-\sum_{n=0}^{6}R\left(\frac{2\xi_1}{2n+1}\right)-R(\xi_1)+R\left(\frac{\xi_1}{2}\right)+1\right]+\frac{1}{\xi_1+\xi_2}R\left(\frac{\xi_1+\xi_2}{4}\right)\\&\qquad+\frac{1}{\xi_1-\xi_2}R\left(\frac{\xi_1-\xi_2}{4}\right)+\frac{1}{\xi_1+\xi_3}R\left(\frac{\xi_1+\xi_3}{6}\right)+\frac{1}{\xi_1-\xi_3}R\left(\frac{\xi_1-\xi_3}{6}\right)=0\\&\frac{1}{\xi_2}\left[\frac{1}{2}\{S(\xi_2)-C(\xi_2)\}-\sum_{n=0}^{2}R\left(\frac{2\xi_2}{2n+1}\right)-\sum_{n=0}^{2}R\left(\frac{\xi_2}{2n+1}\right)\right]+\frac{1}{\xi_2+\xi_1}R\left(\frac{\xi_2+\xi_1}{4}\right)\end{aligned} \tag{9}$$

$$+\frac{1}{\xi_2-\xi_1}R\left(\frac{\xi_2-\xi_1}{4}\right)+\frac{1}{\xi_2+\xi_3}R\left(\frac{\xi_2+\xi_2}{2}\right)+\frac{1}{\xi_2-\xi_3}R\left(\frac{\xi_2-\xi_3}{2}\right)=0$$

$$\frac{1}{\xi_3}\left[\frac{1}{2}\{S(\xi_3)-C(\xi_3)\}-R(2\xi_3)-\sum_{n=0}^{2}R\left(\frac{\xi_3}{2n+1}\right)-R\left(\frac{\xi_3}{2}\right)\right]+\frac{1}{\xi_3+\xi_2}R\left(\frac{\xi_3+\xi_2}{2}\right)$$

$$+\frac{1}{\xi_3-\xi_2}R\left(\frac{\xi_3-\xi_2}{2}\right)+\frac{1}{\xi_3+\xi_1}R\left(\frac{\xi_3+\xi_1}{6}\right)+\frac{1}{\xi_3-\xi_1}R\left(\frac{\xi_3-\xi_1}{6}\right)=0$$

If we take the functions (1), (2) and (3) of isotropic case, the calculated separations are obtained as tabulated in Table II, and they are about 10% smaller than the observed separations.

What is the main origin of these discrepancies? Now we would like to show that they are removed by considering the effect of crystal anisotropy.

Table II.

| Models | | Separations | | |
|---|---|---|---|---|
| | | Calc. (iso.) | Calc. (aniso.) | obs. |
| Okada's doublet | $2\xi$ | 0.95 | 1.07 | 1.0~1.1 |
| Oberly's pattern | $\xi_1$ | 1.60 | 1.80 | 1.8~1.9 |
| | $2\xi_2$ | 1.59 | 1.72 | 1.6~1.7 |
| | $2\xi_3$ | 1.38 | 1.54 | 1.5~1.6 |

Table III.

| | |
|---|---|
| $c_{11}'$ | $12.98\times10^{11}$ dyne cm$^{-2}$ |
| $c_{12}'$ | $4.88\times10^{11}$ 〃 |
| $c_{44}'$ | $6.73\times10^{11}$ 〃 |

In the case of the symmetrical boundary in the crystals of cubic system, Eshelby, Read and Shockley[4] deduced the expression of the force $F_x{}^*$ of interaction between two dislocations. Instead of (4) for the isotropic case, it is given as follows:

$$F_x{}^*=F_0{}^*\xi^{-1}R^*(s;\,\beta),\quad R^*(s;\,\beta)=s^2(s^2-1)[(s^2+1)^2+\beta^2s^2]^{-1} \tag{10}$$

By a simple calculation we can also deduce the formula of the force due to the boundary. Corresponding to (5), (6) and (2), (3) of the isotropic case, they are

$$A_x{}^*=F_0{}^*\xi^{-1}S^*(\xi;\,\beta)$$

$$\begin{aligned}S^*(\xi;\,\beta)&=\sum_{n=-\infty}^{+\infty}\xi^2(\xi^2-n^2)[(\xi^2+n^2)^2+\beta^2\xi^2n^2]^{-1}\\&=\pi^2\xi^2\frac{\sinh(\beta\pi\xi)}{\beta\pi\xi}\left[\sinh^2\left(\pi\xi\sqrt{1+\frac{\beta^2}{4}}\right)-\sinh^2\left(\frac{\beta\pi\xi}{2}\right)\right]^{-1}\end{aligned} \tag{11}$$

$$B_x{}^*=-F_0{}^*\xi^{-1}C^*(\xi;\,\beta)$$

$$\begin{aligned}C^*(\xi;\,\beta)&=-\sum_{n=-\infty}^{+\infty}\xi^2\left[\xi^2-\left(n+\frac{1}{2}\right)^2\right]\left[\left\{\xi^2+\left(n+\frac{1}{2}\right)^2\right\}^2+\beta^2\xi^2\left(n+\frac{1}{2}\right)^2\right]^{-1}\\&=\pi^2\xi^2\frac{\sinh(\beta\pi\xi)}{\beta\pi\xi}\left[\cosh^2\left(\pi\xi\sqrt{1+\frac{\beta^2}{4}}\right)+\sinh^2\left(\frac{\beta\pi\xi}{2}\right)\right]^{-1}\end{aligned} \tag{12}$$

In these expressions $F_0{}^*$ is not the same as $F_0$ in (7), but to determine the separations it is not necessary to know the absolute values of $F_0$ and $F_0{}^*$. The effect of anisotropy is taken into account through the single parameter $\beta^2$ which is given as follows:

$$\beta^2=-2\frac{(c_{11}+c_{12})}{c_{11}}\left(1-\frac{c_{44}'}{c_{44}}\right) \tag{13}$$

where $c_{11}$, $c_{12}$, $c_{44}$ and $c_{11}'$, $c_{12}'$, $c_{44}'$ are the elastic constants which are referred to the systems of the caystal axis ⟨100⟩, ⟨011⟩, ⟨0$\bar{1}$1⟩ and ⟨100⟩, ⟨010⟩, ⟨001⟩ respectively, because the Burgers vectors of observed dislocations have ⟨011⟩ directions. Using the known values of $c_{11}'$, $c_{12}'$, $c_{44}'$ tabulated in Table III[5] and the following relations,

$$2c_{44}'=c_{11}-c_{12},\qquad 2c_{11}'=c_{11}+c_{12}+2c_{44},$$
$$c_{11}'+c_{12}'=c_{11}+c_{12} \tag{14}$$

we can estimate $\beta^2=1.506$ in germanium crystals.

The calculated curves of $R^*(s)$, $S^*(\xi)$ and $C^*(\xi)$ are also shown in Fig. 4 and Fig. 5. The separations are calculated by solving the equations (8) and (9) where we replaced $R(s)$, $S(\xi)$ and $C(\xi)$ by $R^*(s)$, $S^*(\xi)$ and $C^*(\xi)$. The results are also tabulated in Table II, and the agreement with observed data is fairly good when we taken into account the effect of crystal anisotropy.

## § 5. Conclusions

Above discussions lead us to the following conclusions.

(A) The observed dislocations have the edge type and their Burgers vectors have ⟨110⟩ directions.

(B) The arrangement of the etch-pits along a boundary satisfies the condition that the small-angle-of misfit near the coupled dislocations is not so different from that in the regular array.

(C) The condition to determine the arrangement of the etch-pits along the direction perpendicular to a boundary, i.e. to determine the separations of the coupled dislocations is the balancing of the forces of interaction between edge dislocations.

Thus we believe that the quantitative analysis of the patterns in Fig. 1 and Fig. 2 is the first attempt to verify the law of interaction between edge dislocations directly.

## § 6. Acknowledgement

The author thanks Drs. H. Inuzuka and H. Miyazawa for their kind encouragement throughout this work. The thanks are also expressed to Messrs. J. Okada, M. Takabayashi, T. Kobayashi and K. Maeda for their valuable information on this problem.

## References

1) J. J. Oberly: J. of Metals **6** (1954) 1026.
2) J. Okada: J. of Phys. Soc. Japan **10** (1955) 1018.
3) A. H. Cottrel: Dislocations and Plastic flow in Crystals, Oxford (1954).
4) J. D. Eshelby, W. T. Read and W. Shockley: Acta Metallurgica **1** (1953) 251.
5) W. L. Bond, W. P. Mason, H. J. McSkimin, K. M. Olsen and G. K. Teal: Phys. Rev. **78** (1950) 176.

JOURNAL OF THE PHYSICAL SOCIETY OF JAPAN Vol. 11, No. 5, MAY, 1956

# An Electron Diffraction Study on the Plastic Deformation of Aluminium Single Crystals

By Kazuo KIMOTO

*Physical Institute, Nagoya University, Nagoya, Japan*

(Received February 18, 1956)

Plastic deformation of aluminium single crystals was studied through Kikuchi lines of electron diffraction by the introduction of a new technique: large angle convergent beam method. By this method the irradiated area on the specimen surface can be reduced to 5×20 sq. microns and therefore laminar regions and deformation bands can be studied seperately. For 99.99% aluminium it was found that in laminar regions the distortion is so small that Kikuchi lines are produced even at 10% elongation and that in deformation bands it is large enough to extinguish Kikuchi lines. For 99.55% aluminium, at any place in the crystal the distortion is so large that Kikuchi lines become diffuse at about 3% elongation and are extinguished at about 7% elongation. It was confirmed in all cases that no rotation occurs in the slip plane. The interior of elongated crystals was studied after removal of the surface layer by electro-polishing. Irrespective of the purity of crystals, no recognizable difference was found in the surface layer and in the interior. The order of dislocation density was estimated through Kikuchi line experiment. The results obtained for 99.99% aluminium are $10^6$ lines/sq. cm., $10^7$ lines/sq. cm., and $10^8$ lines/sq. cm. for well annealed crystals, for laminar regions of 10% elongated crystals, and for deformation bands of 10% elongated crystals, respectively.

## § 1. Introduction

Heidenreich and Shockley[1)] first applied the electron diffraction method to the study of slip in aluminium single crystals. According to their results, Kikuchi lines from high purity aluminium single crystals (99.99% French aluminium) disappear when they are elongated more than several percent. However, Heidenreich and Shockley used the ordinary reflection method in which the electron beam falls upon the specimen surface at a grazing incidence. Thus the irradiated area of the specimen is rather large; it was about 0.1×6 sq. mm. in their experiment. The diffraction patterns obtained by them represent the state of crystals in the large irradiated area. Moreover, if the specimen surface is not flat, their diffraction patterns would be influenced by the surface topography.

Recently Fujita, Watanabe, Yamamoto and Ogawa[2)] carried out a similar experiment using the same experimental technique. They studied further the interior of elongated crystals and found that Kikuchi lines which were extinguished by elongation appeared again when the surface layer was removed by electro-polishing.

It is generally accepted that the plastic state of deformed metal single crystals is not homogeneous. Therefore it seems almost certain to the present author that the results of Heidenreich and Shockley, and Fujita et al. are confused because of a large irradiated area. In discussing Kikuchi lines from strained aluminium crystals, careful consideration must be given to the dimension of the irradiated area and to the surface undulation which influences diffraction patterns.

For that reason we performed an experiment similar to that of Heidenreich and Shockley but using the large angle convergent electron beam method by which the irradiated area can be reduced as small as 5×20 sq. microns. Thus laminar regions and deformation bands can be studied seperately. For high purity aluminium (99.99%) we found that laminar regions produce Kikuchi lines even at 10% elongation, and that deformation bands do not produce Kikuchi lines. For low purity aluminium (99.55%), Kikuchi lines are extinguished at about 7% elongation. We also studied the interior of crystals. Contrary to the

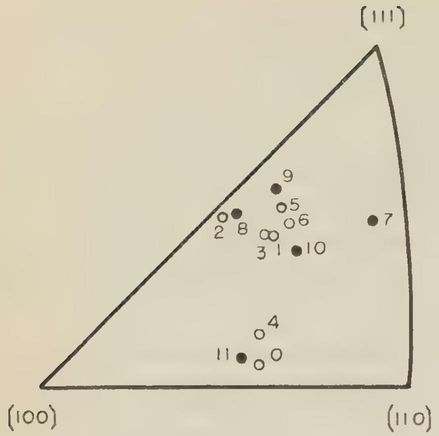

Fig. 1. Stereographic projections of the axes of crystals used in the present experiment. Open circles denote specimens of 99.99% purity. Closed circles denote specimens of 99.55% purity.

Table I.

| No. | Purity Percent | Elongation Percent | Thickness* Microns |
|---|---|---|---|
| 1 | 99.99% | 1% | 120μ |
| 2 | 〃 | 4 | 30 |
| 3 | 〃 | 6 | 100 |
| 4 | 〃 | 9 | 70 |
| 5 | 〃 | 10 | 40 |
| 6 | 〃 | 10 | 90 |
| 0 | 〃 | 5 | 80 |
| 7 | 99.55 | 3 | 50 |
| 8 | 〃 | 3 | 100 |
| 9 | 〃 | 3 | 100 |
| 10 | 〃 | 7 | |
| 11 | 〃 | 7 | 90 |

* See text, page 186.

result of Fujita et al. we found no recognizable difference between the surface and the interior of elongated specimens. The purpose of the present paper is to describe our experiment and to give an interpretation of the results.

## § 2. Experimental

### (*a*) *Specimen*

In the present experiment two kinds of aluminium materials were used, one of 99.99% and one of 99.55%. Thin plates of these materials 0.5–1.2 mm. thick, 100 mm. long and 5 mm. wide, were converted into single crystals by the strain-annealing method, first introduced by Fujiwara[3]. Orientation of the crystals was determined by transmission Laue photographs. Fig. 1 shows the stereographic projection of the axes of crystals used in this experiment. These single crystals were carefully cut into two parts; the shorter about 4 cm. long and the longer about 6 cm.

Both were polished electrolytically by using Jaquet electrolyte (mixture of perchloric acid 34.5 c.c. and acetate anhydride 63.5 c.c.) at about 5°C until their surfaces became mirror smooth. Immediately after the electro-polishing, the crystals were rinsed in distilled water, then in methanol and finally in acetone-methanol solution. After being dried in the air, they were ready for use. To avoid the surface effects pointed out by Brown and Honeycombe[4], mechanical polishing was not applied to the surface. The shorter pieces were examined to obtain diffraction patterns for non-elongated state. The longer pieces were gripped at one end by a fixed vice and at the other end by a movable vice. By turning a screw on the movable vice manually, the pieces were elongated at room temperature. After elongation, about 15 mm. at both ends of the specimen were carefully cut off with knippers. Then the middle part of the specimen was examined by electron diffraction. The degree of elongation for each specimen is given in Table I. To study the interior of elongated crystals, the specimens were reexamined after removal of their surface layer by electro-polishing. The thickness of the removed layer is given in the last column of Table I.

Specimen No. 0 was furnished through the kindness of Dr. F. E. Fujita of The Research Institute for Iron, Steel and Other Metals, Tōhoku University. It was prepared by Bridgeman's method. The cross section and the length were 3×3 sq. mm. and 100 mm. respectively. Following the procedure indicated by Dr. Fujita, this specimen was mechanically polished with care to remove the coarse surface layer, 0000 and 00000 emery papers being used; then electro-polished to remove the surface layer of more than 100 microns in thickness and finally annealed in vacuum at 630°C for 5 hours. Before the examination the specimen was again electropolished lightly.

(*b*) *Electron diffraction technique*

In the ordinary reflection method, the electron beam is focused on the photographic plate and the electron beam falls upon the specimen surface at a grazing incidence (Fig. 2a). If the specimen surface is undulating[5] the electron beam irradiates only the higher curves of the undulation (Fig. 3). Consequently through diffraction patterns, information is obtained from elevations only and none from lower bends. Even when the specimen surface is perfectly flat, the length of the irradiated area is considerable, usually about 3 mm. in the direction of the incident beam. Since the spacing of deformation bands is usually less than 3 mm, it is impossible to study deformation bands and laminar regions separately.

To reduce the irradiated area, we focused the electron beam on the specimen surface (small angle convergent beam method, Fig. 2b) and the length of the irradiated area was reduced to about 0.7 mm. which is still larger than the spacing of small deformation bands. For further reduction of the irradiated area we deflected the electron beam by a small electric magnet so that the beam falls upon the specimen surface at a large glancing angle (large angle convergent beam method, Fig. 2c). Although larger glancing angles are more suitable for reduction of the irradiated area, Kikuchi lines become weaker as the glancing angle increases, and are finally invisible on the fluorescent screen[6]. Thus in the present experiment we used a glancing angle of 15–20°. The irradiated area under this condition was approximately 5 microns in width and 20 microns in length. It is worth mentioning here that the geometrical arrangement of Kikuchi patterns remains fixed in relation to the crystal, independent of the method of irradiation.

Throughout the experiment, the specimen-to-plate distance was 40 cm. and the accelerating voltage was about 65 kV.

## § 3. Experimental results

(*a*) 99.99% *aluminium*

Unstrained crystals produce good Kikuchi patterns irrespective of the method of irradiation (Photos. 1a, b, c). On the other hand, elongated crystals produce Kikuchi patterns of varying sharpness according to the method of irradiation. When the ordinary reflection method (Fig. 2a) is used, crystals which have been elongated several percent do not produce Kikuchi patterns, as observed by Heidenreich and Shockley. When the small angle convergent beam method is used, elongated crystals produce split Kikuchi lines, running parallel (Photo. 2b).

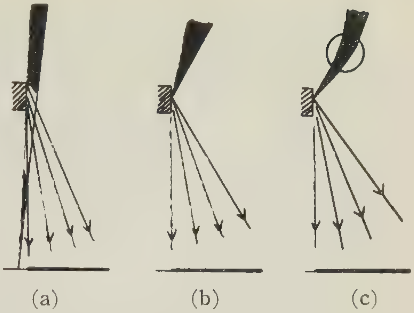
Fig. 2. Schematic illustrations of three methods of irradiation.
(a) Ordinary reflection method.
(b) Small angle convergent beam method.
(c) Large angle convergent beam method.

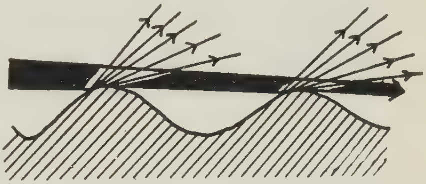
Fig. 3. Schematic illustrations of effective portions of undulated specimen surface when irradiated by the ordinary reflection method.

The split lines can be interpreted as Kikuchi lines produced by crystal blocks having slightly different orientation*. It is certain that slightly disoriented blocks exist in the irradiated area. The angle of disorientation is 20–40′ for neighbouring lines. By the small angle method, it can not be made clear whether split lines are due to crystal blocks connected by boundary walls or to separate blocks (Fig. 3). To eliminate this ambiguity, the large angle convergent beam method was adopted in which it was found that elongated crystals produce good Kikuchi patterns

---

* Heidenreich and Shockley also observed a similar splitting (Fig. 14 of their paper[1]) suggesting that it might be interpreted by using the dynamical theory of diffraction. Uyeda, Fukano and Ichinokawa[7], however, disagreed with Heidenreich and Shockley's interpretation because according to Kainuma[8] no subsidiary maxima are expected in reflection Kikuchi patterns. Uyeda et al. advanced the above interpretation.

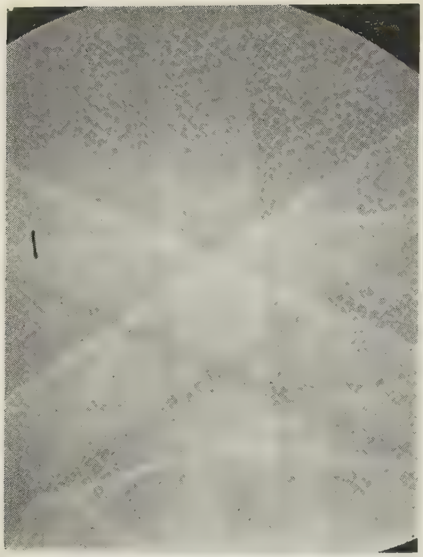
(a)

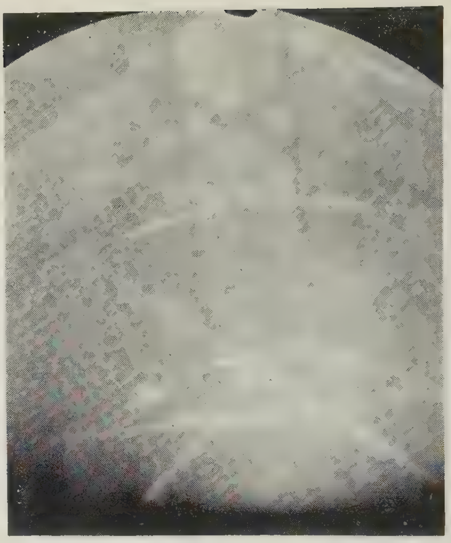
(b)

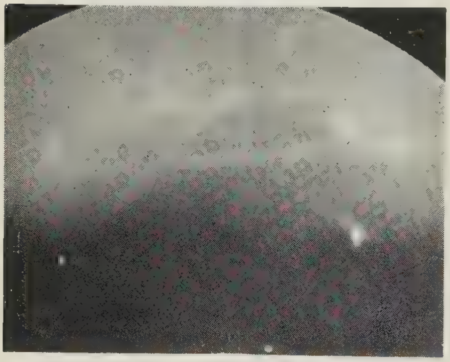
(c)

Photos. 1. Kikuchi patterns from unstrained aluminium crystal (99.99% purity. No. 2*).
(a) Large angle convergent beam method.
(b) Small angle convergent beam method.
(c) Ordinary reflection method.
All these photographs are taken at the same azimuthal setting. Photo. (c) is one of the most diffuse patterns from unstrained crystals. Most of other unstrained crystals gives sharper patterns even by the ordinary reflection method.
* See Table I and Fig. 1.

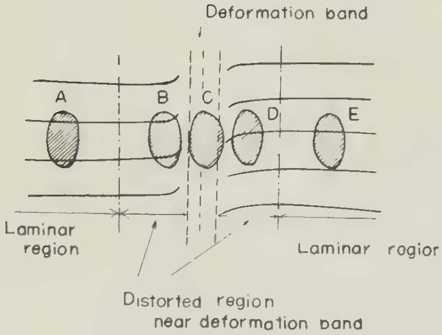

Fig. 4. Schematic drawing of irradiated areas.

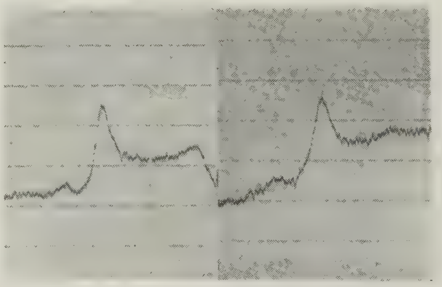
(a) (b)

Fig. 5. Microphotometer curves along line segments indicated in Photos. 1 a and 2 a.
(a) corresponds to Photo. 1 a.
(b) corresponds to Photo. 2 a.

(Photos. 2a, 3a) or diffuse Kikuchi bands (Photo. 3b) depending upon the irradiated position. By this we infer that laminar regions produce good Kikuchi patterns and deformation bands produce only diffuse Kikuchi bands.

To prove our inference correct, a specimen which had been elongated about 10% was examined under a light microscope. The surface of the specimen was covered by slip bands spaced 3–5 microns apart and also by fine deformation bands spaced about 300 microns apart. This specimen was set in the diffraction camera so that the electron beam was approximately parallel to the deformation bands. Then it was examined by the large

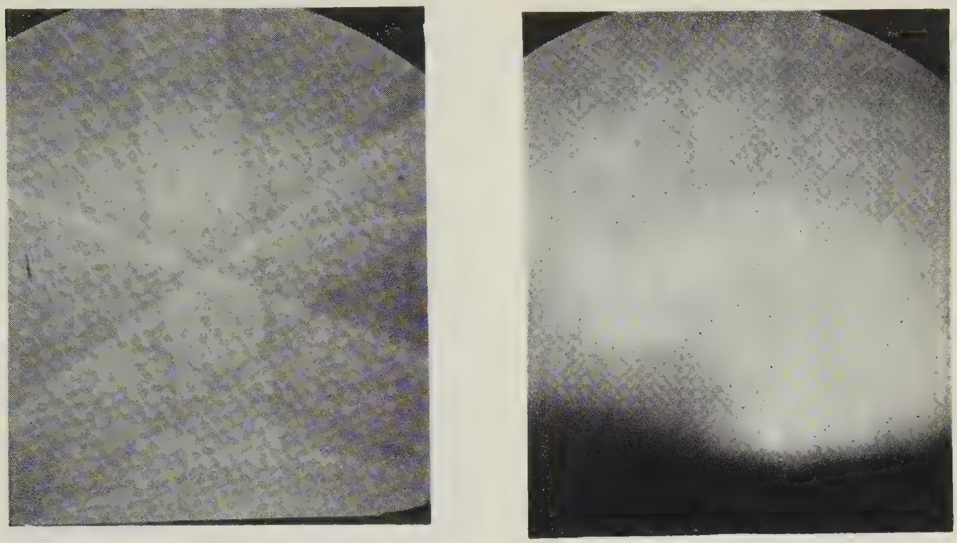

(a) (b)

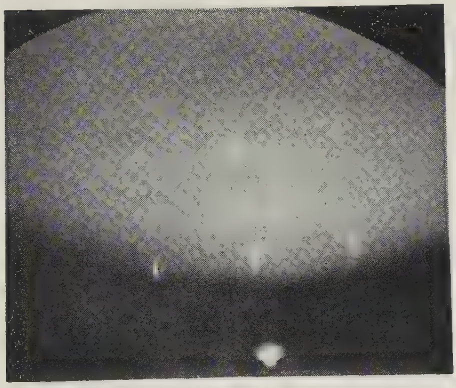

(c)

Photos. 2. Diffraction patterns from a 4% elongated crystal (99.99% purity. No. 2).
(a) Large angle convergent beam method.
(b) Small angle convergent beam method.
(c) Ordinary reflection method.
All these photographs are taken at the same azimuthal setting as in Photos. 1.

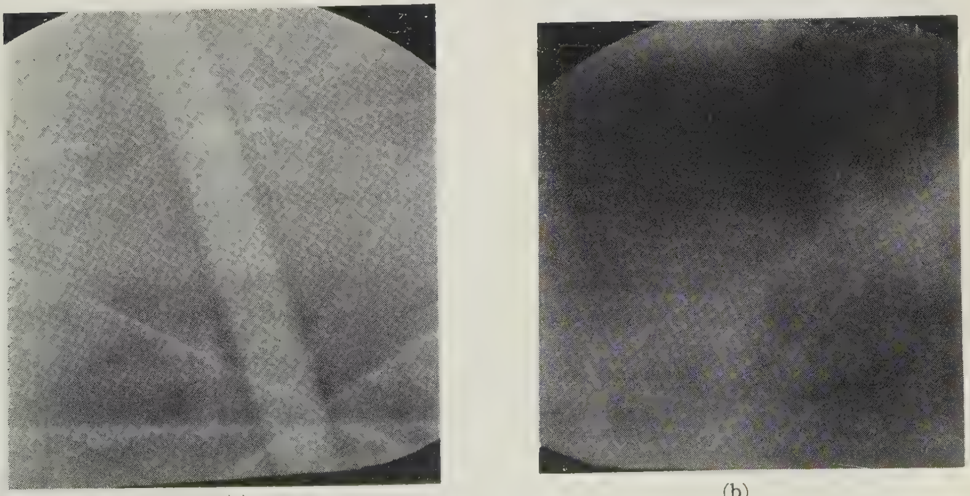

(a) (b)

Photos. 3. Diffraction patterns from a 10% elongated crystal (99.99% purity. No. 6).
(a) Laminar region. Kikuchi lines and bands are visible.
(b) Deformation band. Only edges of bands are scarcely visible.

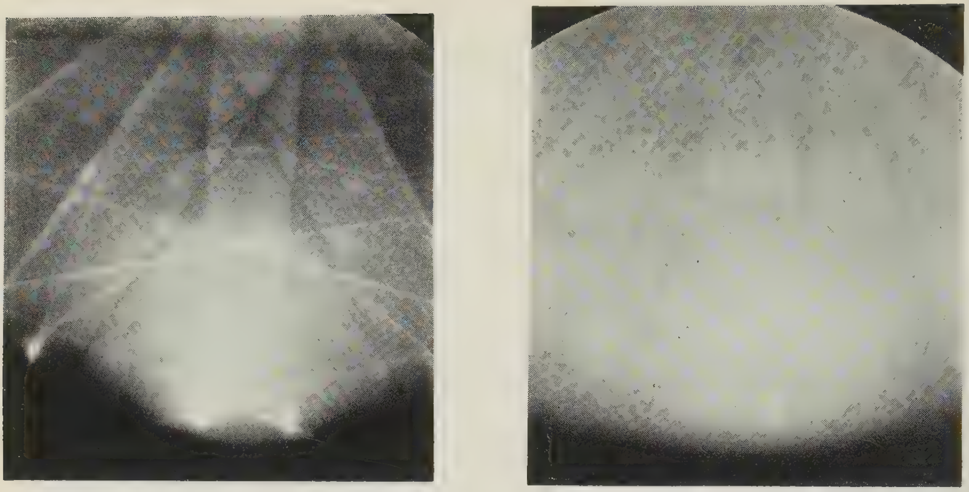

(a) (b)

Photos. 4. Diffraction patterns from 99.55% aluminium (No. 7).
(a) Unstrained crystal. (b) 3% elongated crystal.

angle convergent beam method. During the examination, the specimen was moved slowly in the direction normal to the deformation bands, the deformation bands and the laminar regions being alternately irradiated. On the fluorescent screen diffuse Kikuchi bands and good Kikuchi patterns appeared alternately. Displacement of the specimen for the successive appearance of diffuse Kikuchi bands was about 300 microns in agreement with the spacing of deformation bands observed under a microscope. Thus the inference was proved.

Laminar regions produce good Kikuchi patterns even though they are covered by slip bands, independent of the direction of the incident beam as related to the direction of slip bands. The microphotometer curves along the line segments indicated in Photos. 1a and 2a are reproduced in Figs. 5a and 5b. Even when specimens are elongated by 10%, the maximum rate of elongation in this experiment, Kikuchi lines are always produced although the background is somewhat dark. When the electron beam is slightly defocused on the specimen surface, Kikuchi lines are immediately extinguished leaving only diffuse Kikuchi bands, especially when the deformation is large.

When the electron beam irradiates laminar region A (Fig. 4), good Kikuchi lines appear and they do not move on the fluorescent screen even when the irradiated area is moved. When it irradiates B (Fig. 4), which is in the immediate neighbourhood of a deformation band, they fade away leaving only a diffuse Kikuchi band. When the electron beam moves from B to C, the corresponding Kikuchi band jumps to a parallel position and when the electron beam moves from C to D, the Kikuchi band jumps back again to nearly its original position. Sometimes two Kikuchi bands appear indicating that both sides of an extremely fine deformation band are irradiated. From the distance between two bands the bending across a fine deformation band is estimated to be about 1°.

Sometimes, even in laminar regions, Kikuchi lines split in two (Photo. 6). Since this is observed in large angle convergent beam method, this means that both sides of a boundary wall are irradiated. The disorientation across the wall is estimated to be 10–30′. The sharpness of the split lines indicates that neither side is much distorted.

(*b*) 99.55% *aluminium*

Unstrained single crystals of 99.55% aluminium produce as good Kikuchi patterns (Photo. 4a) as 99.99% aluminium. When, however, a crystal is elongated about 3% Kikuchi patterns become diffuse on the entire surface of the crystal (Photo. 4b) even by the large angle convergent beam method. At about 7% elongation no Kikuchi lines are produced and only diffuse Kikuchi bands remain. Under a light microscope no distinct deformation bands are observed. By electron diffraction no alternation of good Kikuchi patterns and diffuse Kikuchi bands are observed. This fact

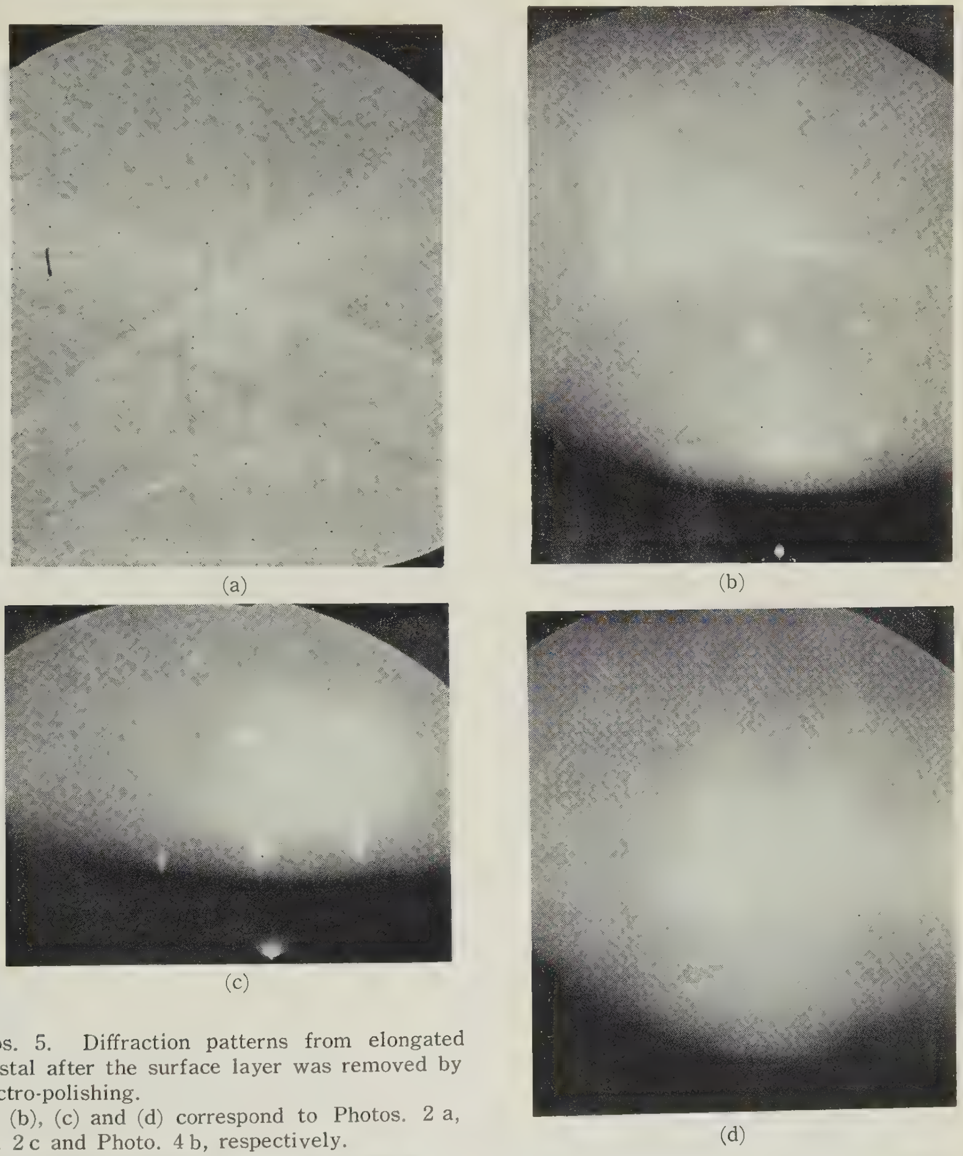

(a) (b) (c) (d)

Photos. 5. Diffraction patterns from elongated crystal after the surface layer was removed by electro-polishing.
(a), (b), (c) and (d) correspond to Photos. 2 a, 2 b, 2 c and Photo. 4 b, respectively.

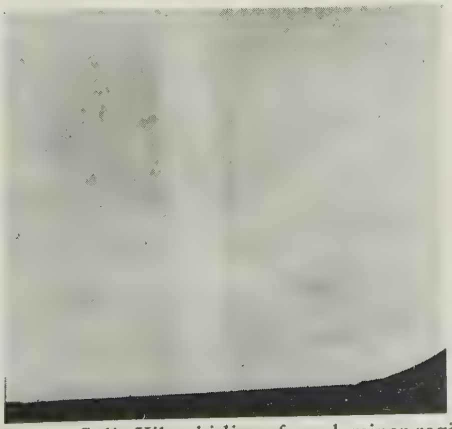

Photo. 6. Split Kikuchi lines from laminar regions of 10% elongated crystal (99.99% purity. No. 6).

is essentially different from that observed in 99.99% aluminium.

### (*c*) *Study of the interior of crystals*

When the surface layer is removed by electro-polishing, no definite change was found in diffraction patterns for either 99.99% or 99.55% aluminium* (Photos. 5a, 5b, 5c, and 5d). We could recognize no change in sharpness of Kikuchi lines or in the relative intensity of the background. The microphoto-

---

* For 99.55% aluminium we had one exception in four specimens (No. 8) where no pattern was observed before removal of surface layer, but diffuse Kikuchi patterns were produced after removal. This is probably due to failure in electro-polishing before the first examination.

meter curves along the line segments indicated in Photos. 2a and 5a are reproduced in Fig. 6. No remarkable change is found in the width of Kikuchi lines. For 99.99% aluminium the alternation of sharp Kikuchi lines and diffuse Kikuchi bands was also observed. Strictly speaking, however, we observed slight changes but they did not take definite form; in some cases patterns were improved and in other cases they deteriorated. Such changes are inevitable because the grade of Kikuchi patterns depends not only on the irradiated position but also on the surface topography and the glancing angle. Therefore it is dangerous to draw conclusions by observing slight changes which are generally of trivial importance.

Experimental results may be set forth as:

(1) For high purity crystals, (a) laminar regions produce Kikuchi lines even at 10% elongation, but (b) deformation bands do not produce Kikuchi lines;

(2) For low purity crystals, Kikuchi lines become diffuse at 3% elongation over the whole crystal surface. They are extinguished at about 7% elongation;

(3) Irrespective of the purity of crystals, no recognizable change occurs when a surface layer of about 100 microns is removed.

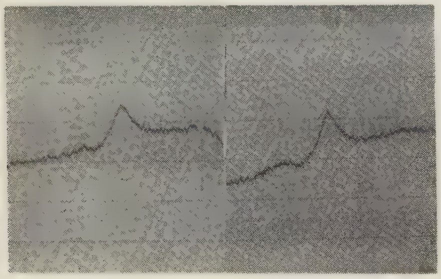

(a) (b)

Fig. 6. Microphotometer curve along line segments indicated in Photos. 2 a and 5 a.
(a) corresponds to Photo. 2 a.
(b) corresponds to Photo. 5 a.

## § 4. Discussion

### (*a*) *Comparison with the result of Heidenreich and Shockley*

According to Heidenreich and Shockley, when aluminium single crystals are elongated several percent, they have two results: (1) Kikuchi lines are extinguished and (2) Laue spots become multiple. Although their result (1) apparently contradicts our result (1a, § 3c), there is no physical contradiction between them. The apparent contradiction is caused by the difference in the size of the irradiated area. Even in our experiment, Kikuchi lines are extinguished if the irradiated area is increased by defocusing. Heidenreich and Shockley's result (1) is reasonable because the length of the irradiated area was more than 1 mm. Moreover, in their experiment the irradiated area might include deformation bands which extinguish Kikuchi lines.

Based upon their result (2) Heidenreich and Shockley suggested that " the slip band is not a region where only translation has occurred but that rotation about the normal to the slip plane occurs also ". From the splitting of Laue spots in their photographs the angle of rotation is estimated to be the order of $10^{-2}$ radians. Although their suggestion has been cited as an experimental evidence of rotational slip in authoritative literatures[9)10)], our result (1) contradicts their suggestion. In our experiment with large angle convergent beam method, a few slip bands are irradiated simultaneously because the irradiated area is about $5\times20$ sq. microns. Therefore, if there was rotation of the order of $10^{-2}$ radians about the normal to the slip plane, Kikuchi lines would have split into several lines. Since we have never observed such a splitting, we conclude that no such rotation exists. Even if the rotation did exist, it would have to be less than $10^{-3}$ radians which is the resolving power of the present experiment.

It is more likely that the splitting of Laue spots observed by Heidenreich and Shockley is due to deformation bands. The rotation of about $10^{-2}$ radians is the same order of rotation due to deformation bands. The splitting of Laue spots can be caused by random sampling of surface undulations (Fig. 3) although the bending due to deformation band is continuous. Moreover, the splitting is better interpreted by rotation about $[12\bar{1}]$-axis which lies in the active slip plane than by rotation about $[\bar{1}11]$-axis which is normal to the slip plane. This fact will be described in (c).

### (*b*) *Slip in pure and impure crystals*

Blewitt and Koehler,[11)] interpreted result (1) of Heidenreich and Shockley to be that " the material between successive slip bands contains enough internal strain to cause disappearances of Kikuchi lines". We think that their interpretation is not complete because they did not take into account the size of the irradiated area which is most important in the Kikuchi line experiment. Their interpretation may be correct for low purity crystals* because for these crystals the strain is large enough to extinguish Kikuchi lines even in the large angle convergent beam method. For high purity crystals, however, their interpretation can not be accepted because according to our result (1a) laminar regions produce Kikuchi lines in the large angle convergent beam method.

(*c*) *Deformation bands*

It has been made clear that asterism in *X*-ray Laue photographs is due to a large strain of deformation band[12][13][14]. The strain of deformation bands extinguishes Kikuchi lines and a large disorientation across a deformation band causes a jump of Kikuchi band.

We can study the rotation or bending of the crystal produced by deformation bands by the movement of Kikuchi patterns which is described in the next to the last paragraph of § 3a. This is best shown by a photographic plate on which two Kikuchi bands are recorded where under such a condition only the (111)-band appeared and by analysis it was found that the (111)-plane which produced the band is parallel to the active slip plane. From the distance between the two bands, the angle of disorientation is calculated to be the order of $10^{-2}$ radians. The fact that the two bands are separated from each other indicates that the active slip planes are rotated about the axis which lies in the slip plane. If the slip planes are rotated about the normal to themselves, such a separation can not be expected. This is in accordance with the *X*-ray results obtained by Chen and Mathewson[12] and Nishimura and Takamura[14] which indicate that the rotation axis in elongated aluminium single crystals is $[12\bar{1}]$ in the slip plane and is at right angles to the direction of slip, and that this rotation about the $[12\bar{1}]$ is produced by deformation bands. Thus it is most likely that Heidenreich and Shockley's split spots were given by random sampling of surface undulations and that the rotation corresponding to the split spots was caused by deformation bands.

It is noteworthy that we found splitting of Kikuchi lines coming from laminar regions as described in the last paragraph of § 3a. From the sharpness of Kikuchi lines we infer that the two domain which are disoriented to each other about $3\times10^{-3}$ radians are unstrained in the neighbourhood of the boundary. Therefore, the boundary can be considered to be a polygon-wall. Because dislocations are movable in high purity crystals, dislocations on fine slips may arrange themselves in such polygon-walls. This may be the polygonization without climb suggested by Mott[15].

Heidenreich and Shockley reported that Kikuchi lines were extinguished when an aluminium crystal was loaded near its yield point and simultaneously tapped or brought into vibration although no slip bands were visible. Kuhlmann-Wilsdorf, van der Merwe and Wilsdorf[16] explained this phenomenon as fine slips (not observed by Heidenreich and Shockley) extinguishing Kikuchi lines. However, we believe fine slips do not extinguish Kikuchi lines as we describe in the next subsection. The extinguishing cause of Kikuchi lines in Heidenreich and Shockley's experiment may be weak deformation bands. This is supported by observations of Takamura[17] that in aluminium single crystals weak deformation bands appear even for deformation so small that no slip bands are visible under a light microscope.

(*d*) *Interior of crystals*

Heidenreich and Shockley observed that a lightly tapped surface of aluminium crystals after removal of a surface layer of 200–400 microns in thickness again produced Kikuchi lines. Kuhlmann-Wilsdorf at al[16] ascribed this phenomenon to the location of fine slips in the surface layer. Mott[15], in explaining the appearance of fine slips observed by Wilsdorf et al.[18], suggested that fine slips occur in the surface layer approximately 0.1–1.0 mm. thick and below which only coarse slips occur. Suzuki[19] suggested another explanation for this phenomenon.

According to the experiment of Fujita et al.[2] Kikuchi lines were extinguished by several percent elongation and appeared again after the surface layer had been eliminated by electro-polishing. They reported that the re-appearance of Kikuchi lines took place on a rather definite boundary which lies 10–20 microns below the crystal surface. This result contradicts our result (3), and the cause of contradiction is not clear. However, we should be most careful in drawing any conclusion from an experiment of Kikuchi pattern because the quantitative study of Kikuchi patterns is almost impossible, as described in § 3c.

---

* See our result (2).

Fujita et al. suggested that extinguishing is due to fine slips. They considered that the re-appearance of Kikuchi lines is a proof of the fact that fine slips are confined to the surface layer. However, we believe that fine slips do not extinguish Kikuchi lines. If the fine slips extinguish Kikuchi lines, Kikuchi lines would have been extinguished in the initial stage of elongation. We conclude that neither fine slips nor coarse slips extinguish Kikuchi lines so far as they are laminar. Therefore by this experiment it is impossible to test whether or not fine slips are confined to the surface layer.

(*e*) *Estimation of dislocation density*

From our experimental results we can estimate the density of dislocations by the method described by Cottrell²⁰⁾. Let $\Theta$ denote the total angular spread observed in an irradiated area of diameter L. Let 1 be the mean diameter of a block in the crystal and $\theta$ be the mean angle between neighbouring blocks. For simplicity we assume that one dislocation defines one crystal block, then the dislocation density $\rho$ is given by

$$\rho=1/1^2 \tag{1}$$

If we assume that $\theta$ is randomly positive and negative, we have

$$\Theta=\theta(L/1)^{1/2} \tag{2}$$

Eliminating 1 from (1) by the use of (2) and the relation $\theta=b/1$, we obtain

$$\rho=(\Theta/b\times L^{1/2})^{4/3} \tag{3}$$

where $b$ is the Burgers vector. Using (110)-spacing of aluminium for $b$, $b=3\times10^{-8}$ cm. By the equation (3) $\rho$ is estimated if $\Theta$ and $L$ can be measured.

The measurement of $\Theta$ and $L$ in the experiment of Kikuchi lines is not easy. However, it may be adequate to assume that sharp Kikuchi lines disappear when the angular spread $\Theta$ in the irradiated area is about $1\times10^{-3}$ radians. Therefore, if we measure the value of $L_0$, at which sharp Kikuchi lines disappear, dislocation density $\rho$ can be estimated. In our experiment the size of the irradiated area can be easily changed by focusing. Although we did not carry out exact measurements in the present experiment, the order of magnitude of dislocation density was estimated as follows.

*Unstrained crystals of* 99.99% *and* 99.55% *aluminium.* Our specimens of unstrained crystals produce very sharp Kikuchi lines which do not disappear even when the area of irradiation is increased to $L=7\times10^{-2}$cm. Thus we obtain

$$\rho\simeq6\times10^6 \text{ lines/sq. cm.}$$

This result is much smaller than the usually accepted value $10^8$–$10^{10}$ lines/sq. cm. but is in agreement with the more recent value $10^6$ lines/sq. cm. obtained by Noggle and Koehler²¹⁾ for well annealed aluminium single crystals.

*Laminar regions of* 99.99% *aluminium.* In the laminar regions of 10% elongated crystals, Kikuchi lines disappear when the convergent electron beam is slightly defocused. Although the value of $L_0$ was not measured exactly, it was estimated to be the order of 50 microns. Thus we obtain

$$\rho\simeq4\times10^7 \text{ lines/sq. cm.}$$

This indicates that the dislocation density at 10% elongation increases about ten times.

*Deformation band of* 99.99% *aluminium.* In the region indicated by *B*, *C*, and *D* in Fig. 4, only diffuse Kikuchi bands remain even for the irradiated area of 5×20 sq. microns. From the width of Kikuchi band we may assume that $\Theta$ is about $5\times10^{-3}$ radians. Taking $L_0=20$ microns, we obtain

$$\rho\simeq6\times10^8 \text{ lines/sq. cm.}$$

This density is far less than that usually accepted value $10^{12}$ lines/sq. cm. for heavily worked metals even when it is taken into account that deformation is not very heavy in the present experiment. In the above value the dislocations on boundary walls are not considered. If they were estimated and included, the density would be increased.

*Elongated* 99.55% *aluminium.* At 3% elongation, sharp Kikuchi lines disappear for $L_0$ of 20 microns. Thus we obtain

$$\rho\simeq2\times10^8 \text{ lines/sq. cm.}$$

At 7% elongation, only diffuse Kikuchi bands remain as in deformation bands of 99.99% aluminium crystals. Thus the density is increased to

$$\rho \simeq 6\times10^{8}\ \text{lines/sq. cm.}$$

Although the above is a rough estimation of dislocation density, we can recognize the fact that the density in laminar regions of high purity aluminium is very much smaller than that in low purity aluminium. This may be due to the good mobility of dislocations in high purity aluminium.

### Acknowledgement

The author wishes to express his sincere thanks to Prof. Ryozi Uyeda for his kind guidance and encouragement throughout the entire course of this experiment. He also wishes to thank Dr. F. E. Fujita for his stimulating discussions and for his kindness in furnishing an aluminium single crystal. Thanks are also given to Mr. Y. Fukano and Mr. T. Fukatsu for their assistance in the early stage of this experiment.

This study has been supported in part by a Grant in Aid for Scientific Research from the Ministry of Education.

### References

1) R. D. Heidenreich and W. Shockley: Report on Conference on Strength of Solids. The Physical Society, London, (1948), p. 57.
2) F. E. Fujita, D. Watanabe and S. Ogawa:
   (a) Read before the Spring Meeting of the Physical Society of Japan, Tokyo, April, 1954.
   (b) Circular of the Research Association of Crystal Plasticity **3** (1954) 10 (in Japanese).
   (c) F. E. Fujita, D. Watanabe, M. Yamamoto and S. Ogawa: To be published.
3) T. Fujiwara and K. Yamasaki: Jour. Sci. Hiroshima Univ. **11** (1941) 89.
4) A. F. Brown and R. W. K. Honeycombe: Phil. Mag. **42** (1951) 1146.
5) W. Kranert, K. H. Leise and H. Raether: Zeits. f. Phys. **122** (1944) 248.
   Z. G. Pinsker: Electron Diffraction. (Translated by J. A. Spink and E. Feigl. Butterworth's Scientific Publications., 1953, p. 373.)
6) M. N. Alam, M. Blackman and D. W. Pashley: Proc. Roy. Soc. **A 221** (1954) 224.
7) R. Uyeda, Y. Fukano and T. Ichinokawa: Acta Cryst. **7** (1954) 217.
8) Y. Kainuma: Acta Cryst. **8** (1955) 247.
9) A. H. Cottrell: Dislocations and Plastic Flow in Crystals. (Oxford University Press, London, 1952, p. 91.)
10) P. Gay, P. B. Hirsch and A. Kelly: Acta Cryst. **7** (1954) 41.
11) T. H. Blewitt and J. S. Koehler: Report on Pittsburgh Conference on the Plastic Drformation of Crystalline Solids, (1950), p. 77.
12) N. K. Chen and C. H. Mathewson: Trans. A. I. M. E., J. Metals, **3** (1951) 653.
13) P. Gay and R. W. K. Honeycombe: Proc. Phys. Soc. **A 64** (1951) 844.
14) H. Nishimura and J. Takamura: Tech. Rep. Eng. Res. Inst., Kyoto University **2** (1952) 139.
15) N. F. Mott: Phil. Mag. **44** (1953) 742.
16) D. Kuhlmann-Wilsdorf, J. H. van der Merwe and H. Wilsdorf: Phil. Mag. **43** (1952) 632.
17) J. Takamura: Private Communication.
18) H. Wilsdorf and D. Kuhlmann-Wilsdorf: Zeits. f. Angew. Phys. **4** (1952) 409, 418.
19) H. Suzuki: Jour. Phys. Soc. Japan **9** (1954) 531.
20) A. H. Cottrell: Dislocations and Plastic Flow in Crystals. (Oxford University Press, London, 1952, p. 102.
21) T. S. Noggle and J. S. Koehler: Acta Met. **3** (1955) 260.

JOURNAL OF THE PHYSICAL SOCIETY OF JAPAN Vol. 11, No. 5, MAY, 1956

# The Study on Substances having the Ilmenite Structure I. Physical Properties of Synthesized $FeTiO_3$ and $NiTiO_3$ Ceramics

By Yoshikazu ISHIKAWA and Shozo SAWADA

*Institute of Science and Technology, University of Tokyo*

(Received December 2, 1955)

$FeTiO_3$ and $NiTiO_3$ ceramics were synthesized, their thermal, electrical and magnetic properties were investigated and the results obtained were discussed in connection with the crystal structure. Although $NiTiO_3$ is stable up to high temperatures even in air, $FeTiO_3$ is partially oxidized even when it is cooled, being kept in vacuum ($10^{-5}$ mmHg), to room temperature from the maturing temperature (1350°C). Electrical and magnetic properties of annealed $FeTiO_3$, therefore, differ greatly from those of $NiTiO_3$, but properties of quenched $FeTiO_3$, tend to those of $NiTiO_3$. From these facts, it is concluded that the properties of $NiTiO_3$ are characteristics of the ilmenite structure.

In discussion attention was paid especially to the relation between the ilmenite structure and its magnetic properties and to the mechanism of electrical conduction, and it was speculated, from these considerations, what kind of roles $Ti^{4+}$ ions would play in this structure.

## §1. Introduction

Ilmenite ($FeTiO_3$), which is a common constituent of the igneous rocks has recently come to attract special attention of physicists in the field of rock ferromagnetism. Its crystal structure is nearly equal to that of $\alpha$-Hematite1) and natural Ilmenite has weak spontaneous magnetization having the Curie point at about 100°C2), the origin of which is thought to be the same as that of parasitic ferromagnetism in $\alpha$-Hematite. So judging from these results some authors have suggested Ilmenite might be also antiferromagnetic3)4).

On the other hand, $LiTaO_3$ and $LiNbO_3$ which have the ilmenite structure have been reported to be ferroelectric5). It is not easy, however, to imagine that the spontaneous polarization induced by shifting of Ta or Nb ions within distorted oxygen octahedrons follows the reversal of external electric field in such a low symmetrical structure contrary to the perovskite structure which has the higher symmetry. Hence Megaw has proposed an idea that $LiTaO_3$ and $LiNbO_3$ do not belong to the ilmenite structure strictly6). But no detailed investigation of the ferroelectricity of the ilmenite structure has been done until now.

These facts indicate that this structure is interesting from both magnetic and dielectric points of view, and furthermore, considering the fact that this substance contains ferrous ions which have a partially filled $d$-shell, the mechanism of conduction is also thought to be worth investigating.

There have been, however, only a few reports on the measurement of physiclal properties of synthesized Ilmenite. Naylor and Cook, and Shomate measured the heat capacity in a temperature range between 52°K and 1800°K7)8) and Chevallier measured the magnetic susceptibility below room temperature9). The former reported only a marked hump on the heat capacity vs. temperature curve at 52°K which, according to the authors' opinion, is not uncommon in the ferrous ions componds, and the latter reported the paramagnetic property of Ilmenite. In both cases, however, the results obtained were not fully discussed in connection with the crystal structure.

We, then, intended to synthesize Ilmenite as purely as possible, investigate its many physical properties and discuss them in connection with the crystal structure. At the same time, properties of synthesized $NiTiO_3$ which has the same crystal structure as Ilmenite were investigated so that we may clarify the obscurity in Ilmenite which comes from the unstableness of ferrouss ions and may understand the intrinsic character of the ilmenite strucuture.

## § 2. Preparation of Samples

$FeTiO_3$ (sample I) was prepared by stoichiometrically mixing $Fe_2O_3$, $TiO_2$ and Fe powders following the equation

$$Fe_2O_3+3TiO_2+Fe=3FeTiO_3\ ;$$

milling, pressing and sintering the mixture in a vacuum furnace ($10^{-5}$ mmHg) at 1350°C for six hours, then cooling it down to room temperature in an hour in this furnace. Quenched sample of $FeTiO_3$ (sample II) was prepared by sealing sample I into a silica tube in vacuum ($10^{-5}$ mmHg), heating it again up to 1250°C and then quenching it. $NiTiO_3$ was prepared by heating a mixture of NiO and $TiO_2$ powders in stoichiometric proportion at 1350°C in air for three hours.

$Fe_2O_3$, $TiO_2$ and NiO powders used were purified at our laboratory and it was confirmed that they contained no detectable impurities. Fe powder was carbonyl iron (99.99% purity). Chemical analysis for both iron and titanium in $FeTiO_3$ prepared indicated the ratio of iron and titanium was 0.9945:1, where the lack of iron was due to the existence of unreacting $Fe_3O_4$ which was washed out with dil. $HNO_3$ before this analysis. No other impurities were detected.

The crystal structure of these samples was checked by Debye-Sherrer X-ray photographs. The lattice constants obtained are given in Table I.

Table I. Lattice constants of synthesized $FeTiO_3$ and $NiTiO_3$.

| Samples | $a$ (Å) | $\alpha$ |
|---|---|---|
| $FeTiO_3$ (sample I) | 5.55 (5.52) | 54°23′ (54°49′) |
| $NiTiO_3$ | 5.44 (5.45) | 54°49′ (55°08′) |

Values in the brackets are due to Wyckoff.

## § 3. Thermal Expansion

Thermal expansion was measured in air using a simple dilatometer in order to detect any anomalies present in these samples over a range of temperatures between liquid air and 1000°C. No anomalies could be found for $NiTiO_3$, but $FeTiO_3$ (sample I) showed an anomalous expansion from about 420°C ceasing at about 800°C, when heated at the rate of 2°C/sec. (Fig. 1). On cooling, the contraction followed along a broken line illustrated in the figure, which fact indicates this phenomenon is irreversible and seems to be due to the oxidation of the sample.

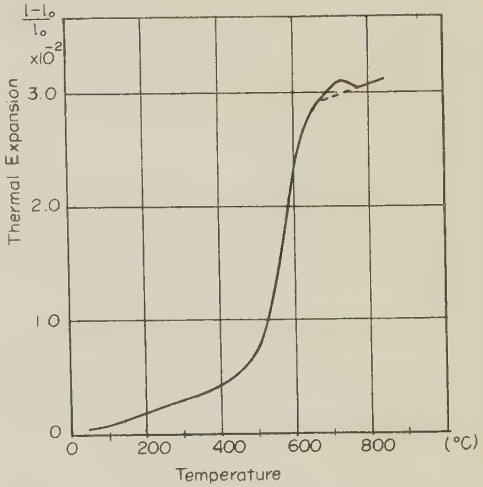

Fig. 1. Thermal expansion of $FeTiO_3$ (sample I) measured in air. The heating rate was 2°C/sec.

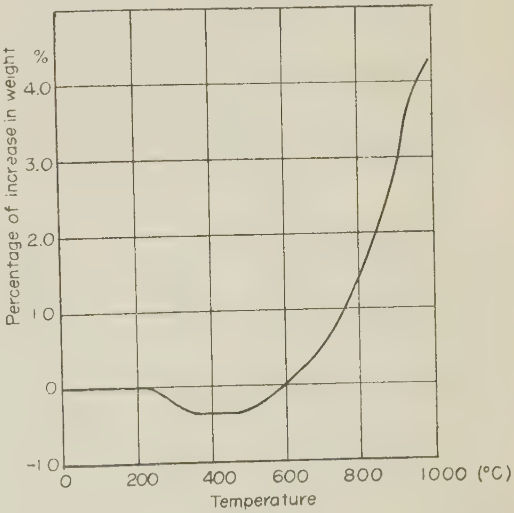

Fig. 2. Percentage of increase in weight of $FeTiO_3$ (sample I) during heaing it at the rate of about 4°C/sec in air.

## § 4. Weighing with a Thermal Balance

In order to confirm the anomaly detected in the above observation to be due to the oxidation, the increase of weight during heating was measured using a thermal balance. The heating rate was about 4°C/sec and a powder sample of 1 g weight was used. The result is shown in Fig. 2, where a decrease of weight from 200°C to 500°C may be an apparent one resulting from ejecting out gases which were

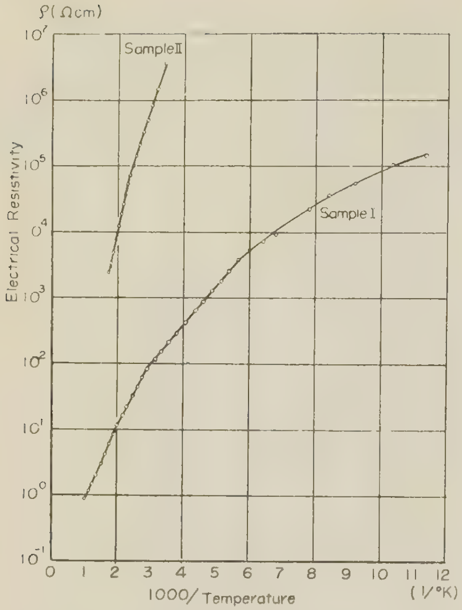

Fig. 3. Direct current resistivity of $FeTiO_3$ measured in vacuum.

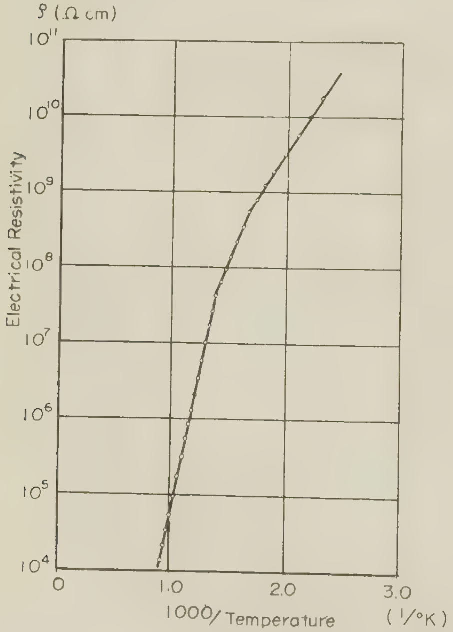

Fig. 4. Direct current resistivity of $NiTiO_3$ measured in air.

present in the powder. The increase of weight at 1000°C was 4.62% and when keeping it at this temperature for a long time it increased up to about 5%, but it is still less than the theoretical value 5.27% calculated assuming all $Fe^{2+}$ in $FeTiO_3$ changed into $Fe^{3+}$.

We find from these results that $FeTiO_3$ is stable even in air up to about 500°C, so measurements can be made in air reproducibly in this temperature region.

Table II. The values of $\rho_0$ and $E$.

| Samples | Temperature ranges | $\rho_0$($\Omega$ cm) | $E$(ev) |
|---|---|---|---|
| $FeTiO_3$ (samples I) | −61.7°C~ 80.3°C | $1.45\times10^{-1}$ | 0.249 |
| | 80.3°C~ 186.0°C | $1.35\times10^{-2}$ | 0.389 |
| | 186.0°C~ 800°C | $8.00\times10^{-3}$ | 0.426 |
| $FeTiO_3$ (sample II) | ~ 180.3°C | 7.00 | 0.662 |
| | 180.3°C~ 300°C | $2.10\times10^{-2}$ | 0.934 |
| $NiTiO_3$ | ~ 310°C | $1.00\times10^{5}$ | 0.901 |
| | 310°C ~ 440°C | $1.60\times10^{2}$ | 1.52 |
| | 440°C ~1000°C | $8.20\times10^{-3}$ | 2.83 |

## § 5. Electrical Conductivity

Direct current resistance was measured by using a potential probe method on low resistance samples, or by reading the current through a sample using a galvanometer on high resistance ones. The dimension of samples used in both cases were approximately 4 mm × 3 mm × 20 mm.

$FeTiO_3$ (sample I) was measured both in vacuum (between liquid air temperature and 800°C) and in air (from 0°C to 400°C), and both results showed no difference. Quenched $FeTiO_3$(sample II) was measured only in vacuum (from 0°C to 300°C) and it was found we could safely repeat the measurement reversibly in this temperature range. These results are given in Fig. 3, which shows the resistivity obeys the formula $\rho=\rho_0 \exp(+E/2kT)$ above room temperature and values of $\rho_0$ and $E$ are given in Table II. Fig. 4 shows the resistivity of $NiTiO_3$ measured in air. The values of $\rho_0$ and $E$ are also given in Table II.

## § 6. Seebeck Effect

Seebeck effect was measured in order to understand the mechanism of conduction. Measurements were made in air by putting Pt–PtRh thermo-junctions on both sides of a sample, and thermo-electric power was measured with respect to a PtRh wire. A temperature gradient was established by putting the sample in an eccentric position of a furnace or heating one side of the sample by an auxiliary heater, and temperature difference between both ends was usually about 5°C at low temperatures and 10°C at high temperatures. The results obtained are shown in Figs.

5 and 6. It was found that the sign of thermoelectric power is positive in both cases.

## § 7. Dielectric Constant and Loss

A sample of 130 mm² area and 1.2 mm thickness with fired-on Ag films on both sides was used in the case of $NiTiO_3$. A resonance method was adopted and the result was shown in Fig. 7. The value of dielectric constant at room temperature is about 13, which is very small for a substance containing $Ti^{4+}$ ions surrounded by oxygen octahedrons and this fact supports the supposition that it would be difficult for $Ti^{4+}$ ions to move following the external electric field in this structure, as expected previously. Increase in permittivity above 200°C is an apparent one which is on account of increase in conductivity. Although we may thus expect this structure has little possibility for ferroelectricity, $D\sim E$ hysteresis loop which is considered to be the most typical characteristic of ferroelectrics can not be observed for such a unipolar substance as this, if existed, unless we use a single crystal, so we can not say any more about ferroelectricity of this crystal structure.

Though dielectric constant of $FeTiO_3$ (sample I) can not be measured with the present method owing to its high conductivity and low permittivity, we may expect the same situation.

Table III. The values of $C$, $\Theta$ and $\mu_{eff}$.

| Samples | $C$/gr | $\Theta$ | $\mu_{eff}$ |
|---|---|---|---|
| $FeTiO_3$ (sample I) | 0.0206 | 65°C | 5.02 |
| $FeTiO_3$ (sample II) quenched from 1250°C | 0.0221 | 30°C | 5.20 |
| $FeTiO_3$ quenched from 1350°C | 0.0260 | 17°C | 5.62 |
| $NiTiO_3$ | 0.0096 | 0°C | 3.47 |

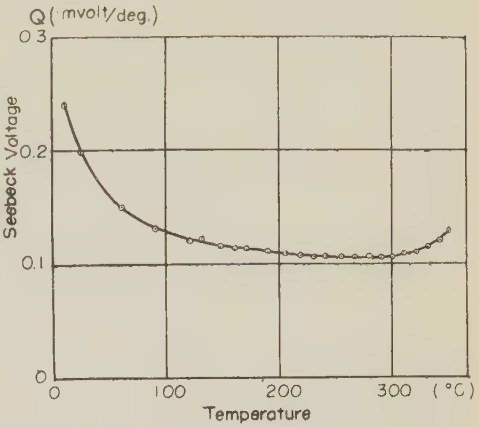

Fig. 5. Seebeck voltage of $FeTIO_3$ (sample I) measured in air.

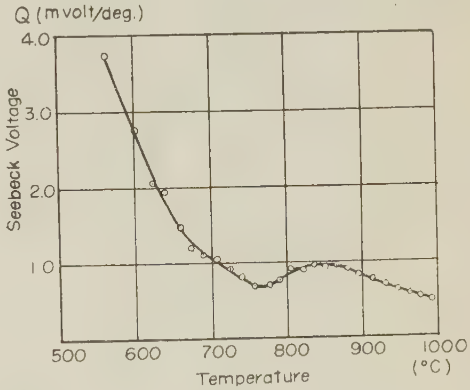

Fig. 6. Seebeck voltage of $NiTiO_3$ measured in air.

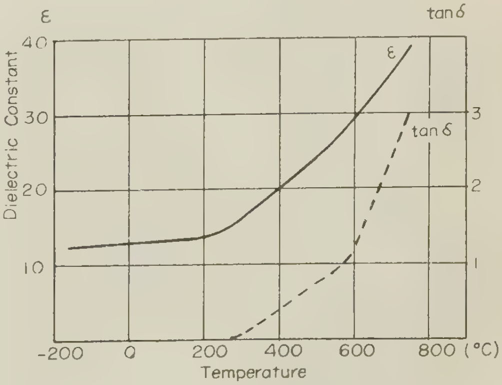

Fig. 7. Dielectric constant and tan $\delta$ of $NiTiO_3$ measured in air.

## § 8. Magnetic Susceptibility

Magnetic susceptibility of these samples above room temperature was measured using a magnetic balance which can detect one percent of a milligram. It was found all samples obey the Curie-Weiss law $\chi=C/T-\Theta$ in this temperature region and the values of $C$, $\Theta$ and the effective Bohr magneton number calculated from the Curie constant are given in Table III. In Table III, we can find the more perfect quenching is the smaller $\Theta$ and the greater $\mu_{eff}$ become, and this can be explained if we consider $FeTiO_3$ may be oxidized even in the vacuum furnace ($10^{-5}$ mmHg) during cooling it, that is, metal vacancies produced by addition of excess oxygens de-

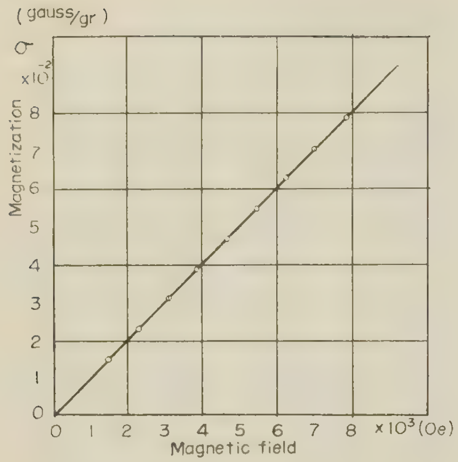

Fig. 8. Field dependence of magnetization of $FeTiO_3$ (sample I) at room temperature.

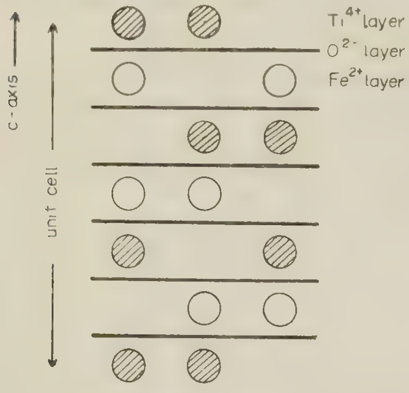

Fig. 9. Schematical representation of the arrangement of ions in Ilmenite.

crease the apparent value of effective Bohr magneton number and some distortion of crystalline field due to the presence of excess oxygens or metal vacancies increases the value of $\Theta$ as was suggested by Van Vleck.[10] This explanation is supported by the fact that quenching and annealing did not affect the behavior of magnetic susceptibility in the case of $NiTiO_3$. The values of the sample quenched from 1350°C agree well with those of Chevallier's sample which was sintered in the hydrogen atmosphere.

Fig. 8 shows the field dependence of magnetization in $FeTiO_3$ (sample I) at room temperature, which indicates clearly there is no spontaneous magnetization in the synthesized Ilmenite, and together with the Chevallier's results and that for $NiTiO_3$, we can conclude spins in the ilmenite structure are left free in the whole temperature region.

## § 9. Discussion

### 1. *Ilmenite structure and its magnetic properties*

According to the X-ray analysis of natural Ilmenite, the arrangement of ions in Ilmenite can be written schematically as shown in Fig. 9. In this configuration, $Fe^{2+}$ ions' and $Ti^{4+}$ ions' layers which are perpendicular to the c-axis are arranged alternately and each is seperated by an oxygen layer. Consequently the superexchange interaction which operates between spins of $Fe^{3+}$ ions through this oxygen layer in $\alpha$-Hematite where $Fe^{2+}$ and $Ti^{4+}$ ions in Ilmenite are all replaced by $Fe^{3+}$ ions can not operate in Ilmenite because of $Ti^{4+}$ ions having zero spin. It is, therefore, rather plausible that spins of $Fe^{2+}$ ions are left free as our experimental results showed and the fact that $NiTiO_3$ and $FeTiO_3$ (unoxidized) have very little $\Theta$ values indicates the dilution of $Ni^{2+}$ and $Fe^{2+}$ ions by $Ti^{4+}$ ions in this structure is nearly perfect.

There are, however, two interesting points relating to this structure. Firstly, if the ordering of $Fe^{2+}$ and $Ti^{4+}$ ions were disturbed, magnetic properties of $FeTiO_3$ would be greatly changed because of the local formation of $Fe^{2+}-O^{2-}-Fe^{2+}$ configuration in it. But the fact that the behavior of magnetic susceptibility of the sample quenched even from above the melting point (1450°C) tends only to be perfect paramagnetic shows, together with the fact that the heat capacity of Ilmenite has no anomaly up to 1800°K in the high temperature region, the disturbance of the order seems not to occur up to this temperature.

Next, when $Ti^{4+}$ ions are partially replaced by other ions having no vanishing spins, it is expected the superexchange which operates between these ions and $Fe^{2+}$ or $Ni^{2+}$ ions through oxygen ions might arrange their spins antiperallel, then an uncompensating component would appear as a spontaneous magnetization and this is realized in the case of solid solutions of $NiTiO_3$ or $FeTiO_3$ and $\alpha-Fe_2O_3$,* details of which will be reported soon.

### 2. *Mechaism of electrical conduction*

The great difference in conductivity between the sample I and sample II of $FeTiO_3$ indicates the conduction in these substances is due to *d*-electrons, that is, as stated in the above paragraph, metal vacancies produced by addition of excecss oxygen contribute to the conduction by changing surrounding $Fe^{2+}$ ions into $Fe^{3+}$ ions and increasing the number of $Fe^{2+}$ ions adjacent to $Fe^{3+}$ ions, which is believed to be the cause of increase of the conductivity of *d*-electrons by many investigators. Carriers in this case are necessarily holes trapped by these metal vacancies.

---

* As to solid solutions of $FeTiO_3-Fe_2O_3$ which were produced naturally, see the reference (2).

Then assuming only holes are carriers, we have the following relations between Seebeck voltage $Q$, concentration of carriers $n_p$ conductivity $\sigma_p$ and mobility $\mu_p$,

$$eQT=E\,, \qquad (1)$$

$$\sigma_p=n_p\mu_p e\,, \qquad (2)$$

$$n_p=N\exp(-E/KT)\,, \qquad (3)$$

where $E$ denotes the Fermi level measured from the filled *d*-electron level and $N$ is $1.89\times10^{22}$ Fe atoms/cm³ in this case, and the kinetic energy term in Seebeck voltage was neglected in the equation (1) following Morin's suggestion¹²⁾.

Hole concentration computed from the value at 20°C given in §§5 and 6, is found to be $1.85\times10^{21}$ atoms/cm³ which is not inconsistent with the increase of weight at high temperatures and observed results of magnetic susceptibility, and mobility calculated using these results is $2{,}14\times15^{-5}$ cm²/volt sec which is very low even comparing with that of carriers in $\alpha$-Hematite having the lowest concentration of carriers. This suggests that $Ti^{4+}$ ions which may not contribute to conduction in this substance prevent *d*-electrons of $Fe^{2+}$ ions from overlapping and reduce their mobilitiy greatly.

On the other hand, in the case of $NiTiO_3$ we can expect both holes and electrons are contributing to conduction as is usually the case with intrinsic semiconductors. Then an analysis is not easy but a rough estimation shows concentration of carriers is very low and mobility is relatively high, so conduction is not expected to be that of *d* levels. We may assume, then, in this case holes which were left in the *sp*. bands of oxygen by jumps of their electrons into unoccupied $Ni^{2+}$ levels (that is, to $Ni^{3+}$ ions) contribute to conduction, which results in high mobility. Though the mechanism seems to be complex because $Ti^{3+}$ ions may contribute to conduction in this case, we may safely say conduction in only *d* levels as in $FeTiO_3$ is hidden because of low concentration of carriers and low mobility.

In conclusion, we should like to say $Ti^{4+}$ ions act always as to dilute the interaction between *d*-electrons of divalent metal ions in the ilmenite structure, so properties $NiTiO_3$ where this dilution seems to be perfect are characteristic of the ilmenite structure and are to be contrasted with those of $\alpha$-Hematite where there is no dilution of this sort.

## Acknowledgement

The authors wish to express their thanks to Prof. A. Minami for the spectroscopical and chemical analysis of $FeTiO_3$ and to Mr. S. Nomura for his various discussions.

## References

1) F. W. Barth and E. Posnjak: Zeit. für Krist. **88** (1934) 265.
2) S. Akimoto: Japanese Journ. Geophys. **1** (1955) No. 2, 1.
3) G. D. Nicholls: Advance in Phys. **4** (1955) 129.
4) L. Néel: ibid. **4** (1955) 203.
5) B. T. Mathias and J. P. Remaika: Phys. Rev. **76** (1949) 1886.
6) H. D. Megaw: Act. Cryst. **7** (1954) 187.
7) B. F. Naylor and O. A. Cook: J. Am. Chem. Soc. **68** (1946) 1003.
8) C. Howard Shomate: ibid. **68** (1946) 964.
9) R. Chevallier: Bull. Soc. Chim. France **20** (1953) 973.
10) J. H. Van Vleck: The Theory of Electric and Magnetic Susceptibilities, p. 303.
11) E. J. Verwey: Semiconducting Material (1951) p. 151.
12) F. J. Morin: Phys. Rev. **93** (1954) 1195.

JOURNAL OF THE PHYSICAL SOCIETY OF JAPAN Vol. 11, No. 5, MAY, 1956

# Study of Plastic Deformation in Aluminium Crystals by Electron Diffraction and Electron Microscopy

By F. E. FUJITA, D. WATANABE, M. YAMAMOTO
and S. OGAWA

*The Research Institute for Iron, Steel and Other Metals,
Tohoku University, Sendai, Japan*

(Received January 11, 1956)

Single crystals of highly pure aluminium (99.99%) were plastically deformed and examined by means of electron microscopy and electron diffraction. Surfaces of the deformed crystals produce innumerable slip lines of various slip amounts and deformation bands. The latter greatly affect the diffraction pattern; Laue spots are split, Kikuchi lines are extinguished, and a very high background results. So that, the diffraction pattern from the crystal part containing deformation bands becomes obscured after only a few per cent elongation. While, the effect of crystal imperfections associated with slip lines on the electron diffraction patterns appears to be considerably small, Kikuchi patterns being obtained from laminar-slip regions in a crystal even after 20% elongation. The local distortions expected from the diffraction patterns cannot be explained in terms of the rotations about the $[\bar{1}11]$ axis or in the active slip planes, but rather consist with the local bendings about the [211] axis due to deformation bands. Difference between the state of plastic deformation in the vicinity of the surface and that in the interior of the crystal is conjectured from the difference between the corresponding diffraction patterns. Some considerations on this point are also made.

## §1. Introduction

Since the first application of electron microscopy and electron diffraction by Heidenreich and Shockley1) to the study of the slip bands on aluminium crystals, quite many electron microscopical investigations on the surface structures of plastically deformed metal crystals have been carried out, and much information on the nature of the plastic deformation of metal crystals by slip mechanism was provided as shown in the follwing.

1. Heidenreich and Shockley1) have shown that in aluminium crystals the slip band was a laminar region resulting from a stepwise slip process. The thickness of the laminae was about 200 Å and the amount of slip on each step surface was about 2000 Å. From the multiple Laue spots in the electron diffraction pattern they have suggested that a relative rotation of adjacent laminae about an axis normal to the slip plane should occur as well as the simple translation. Kikuchi lines were quite sensitive to the state of plastic deformation in their experiment; at about 5% elongation the lines disappeared leaving only the spots unless the electron beam was parallel to the slip traces. It was also found that even the intermittent stress application by slight tapping or vibrating could extinguish the Kikuchi lines.

2. Recent works by Kimoto *et al.*2) have, however, indicated that when the convergent electron micro-beam was focused on the specimen, laminar slip regions of plastically deformed alminium single crystals produced good Kikuchi lines, while deformation bands produced only diffuse Kikuchi bands. The study was begun in a somewhat different way and is still in progress. We deeply owe our undertaking of the present investigation to their early results.

3. Brown3) has confirmed the regular fine structure of the slip bands revealed by Heidenreich and Shockley, but, soon later, he and Honeycombe4) have pointed out that this kind of slip bands was typical of aluminium crystal with the surfaces subjected to a certain kind of cold-working, and that crystals with the purely electropolished surfaces usualy exhibited the irregular slip

band structures including innumerable fine slips when they were stretched.

4. Wilsdorf and Kuhlmannn-Wilsdorf[5] have reported irregular structures of slip bands on polycrystals of aluminium, copper and silver: The slip distances varied continuously from a few Å to 1200 Å or more but always less than 2000 Å. Especially, a very fine surface structure which they called the elementary structure was found covering the whole surface even at the early stages of deformation.

5. The effect of the surface oxide film on the slip band structure was studied by Takamura[6] and the effect of the surface abrasion together with some other effects by Fujita, Suzuki and Yamamoto[7] for aluminium single crystals.

It may be argued from the above-stated that some essential points are necessary to be further investigated: For instance, it should be noted that the experimental results so far obained do not necessarily lead to the same conclusion for the state of plastic deformation of metal crystals, as the results of electron microscopy and electron diffraction are various and, in some cases, inconsistent with one another. It should be also pointed out that such investigations as mentioned above were confined to the observation of merely the surface structure of deformed crystal, the state of affairs in the interior of the crystal being quite unknown. To examine the interior of the deformed crystal, the electron diffraction method will be very powerful if carefully used.

The first aim of the present study was to elucidate the features of plastic deformation on the surfaces of metal crystals by using ordinary microscopy, electron microscopy and electron diffraction simultaneously. The second aim was to search into the deformation structures in the interior of the crystals by means of electron diffraction and to offer some information to the question, whether or not the deformation texture of the interior of the crystals is appreciably different from that of the surface, for which some theoretical predictions have been made.

## § 2. Preparation of Specimens

The specimens employed were single crystals of high purity (99.99%) aluminium grown from the melt in graphite moulds *in vacuo* by Bridgeman's method. The crystallographic orientations of their rod axes and of the surfaces examined are shown in Fig. 1. The original size of the specimens, about 200 mm in length and 3 mm square in cross-section, was reduced in length to 40 mm. by cutting and in cross-section to about 2.5 mm. × 2mm. by abrasion on a series of emery papers from 0 to 05. The distorted surface layer of about 100 $\mu$ in depth was removed by electropolishing in the Jaquet electrolyte (perchloric acid (S.G = 1.55) 220 cc. and acetic anhydride 780 cc.) or in the De Sy Haemers electrolyte (Perchloric acid 200cc., ethylalchol 790cc. and ether 10cc.). The specimens were then annealed at 630~640°C for about 5 hours *in vacuo*. After annealing they were again electropolished very carefully in the Jaquet electrolyte which contained more than 3 grams of aluminium ions in 1000 cc., quickly washed with distilled water and dried. The surfaces prepared in this manner were sufficiently clean and free from sensible oxide film, so they could be examined by the electron microscope and electron diffraction without any disturbance; for instance, sharp Kikuchi lines and Kikuchi bands were easily obtained from these surfaces even after several hours exposure to the atmospheric air.

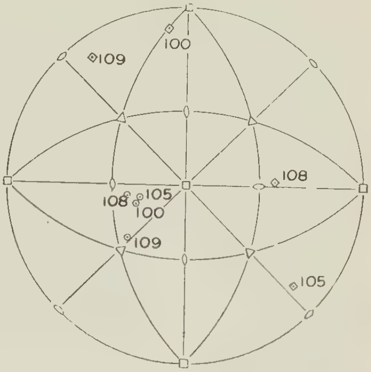

Fig. 1. Crystallographic orientations of specimens.
⊙ rod axis.
◇ surface normal.

## § 3. Experimental

### (a) *Tensile Test and Optical and Electron Microscopy*

Seven specimens with the rod axes of four crystallographic directions illustrated in Fig. 1

Table I.

| Specimen | Elongation (Shear strain) | Surface structure |
|---|---|---|
| 100 B | 1% (2.3%) | Laminar slip lines. |
| 100 A | 5% (11%) | Laminar slip lines. Deformation bands with 0.1∼0.5 mm spacings. |
| 108 A | 7% | Laminar slip lines. Deformation bands. |
| 105 | 10% | Laminar slip lines. Deformation bands with 0.3∼1 mm spacings. |
| 109 | 10% | Slip clusters alternated with very broad non-slipped regions. |
| 108 B | 20% | Laminar slip lines. Many deformation bands. |
| 108 C | 55% | Numerous single slip lines. Quite many random deformation bands. |

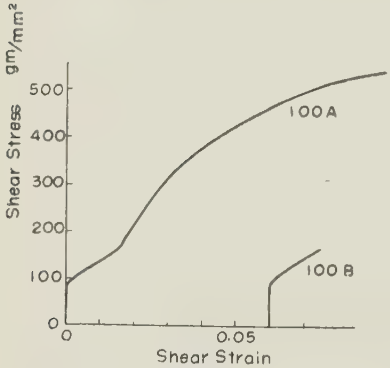

Fig. 2. Stress-strain curves of the specimens 100 A and 100 B.

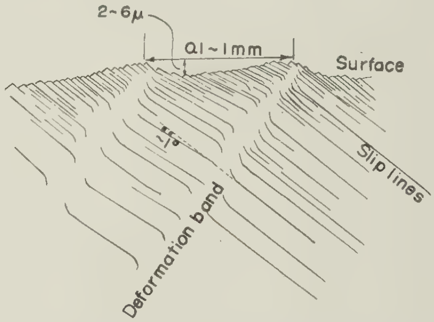

Fig. 5. Schematic representation of vertical section of a plastically deformed crystal.

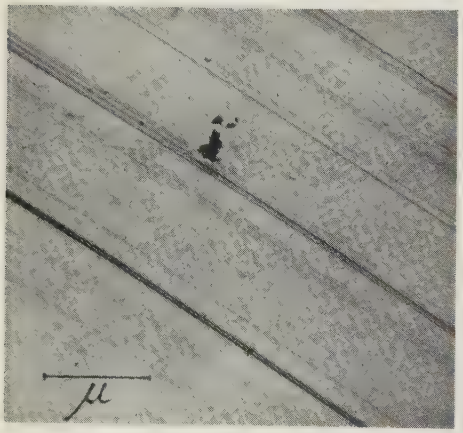

Fig. 3. Electron micrograph of the surface structure of the specimen 108 A after 7% elongation.

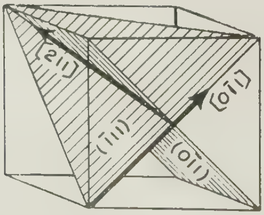

Fig. 4. Relation between some special directions and planes.

were subjected to the tensile test followed by examinations through the ordinary and interferometer microscopes, then electron diffraction photographs were taken immediately after. Some specimens were also examined by means of the electron microscope, collodion one-step chromium-shadowed replica being used. Various amounts of the ultimate tensile deformation cited in Table I were achieved in order to realize the effect of the amount of plastic deformation on the diffraction pattern. A typical stress-strain curve is presented in the left of Fig. 2, which is taken from the specimen 100 A; the critical shear stress is about 90 gms/mm², and the yielding is followed by the linear hardening range or "easy glide" which extends to a few per cent in shear strain, then the range of parabolic hardening.

All specimens except 109 produced laminar slip lines, slip amounts of which varied in a fairly wide range as can be seen in Fig 3. Well-known locally distorted regions, called the deformation bands, were also clearly observed. In general, they form a kind of walls about 0.1 mm. in breadth and nearly in the $(0\bar{1}1)$ plane that is perpendicular to the slip direction $[0\bar{1}1]$, where most of slips are arrested and the crystal is highly distorted and especially bent to an angle of the order of 10° about the [211] axis which is perpendicular to the slip direction [01̄1] and lies in both the slip plane (1̄11) and the deformation band plane (01̄1). The relation between these orientations is illustrated in Fig. 4. Consequently, the original flat surfaces of the specimens had a deformed structure in two topological seneses, after stretched, as shown in Fig. 5, i.e. first the stepwise structure due to the slip lines, in which step heights varied from less than 30 Å to about 1000 Å and their separation distances were a few hundred Å, and secondly the wavy surface unevenness in a larger scale due to the deformation bands, the wave-length of which were from about 0.3 mm. to about 1 mm. and the wave-heights were found by the interferometer-microscope to be several microns. The numbers of slip lines and deformation bands and the local distortion associated with the latter increased with the increasing deformation.

The specimen 100 B, which produced laminar slip lines, exhibited no appreciable deformation bands because of a small amount of tensile deformation, i.e. about 1% elongation, which was in the linear hardening region as illustrated in the right of Fig. 2. The orientation of the specimen 109 was not suitable for single slip, so its stress-strain curve was very steep and parabolic from the beginning. The surface produced neither the regular slip lines nor the deformation bands, but instead another kind of deformation structure, " slip clusters ", in which the main slip lines are clustered into large groups forming broad bands roughly parallel to the active slip plane and they are alternated with bands of similar width in which slip is almost suppressed. These two specimens, 100 B and 109, actually presented behaviours remarkably different from those of the others in producing the electron diffraction patterns.

The mechanical properties and the surface topological structures of the present single crystals subjected to the tensile test were in good agreement with those of previous experiments carried out by other investigators. As will be mentioned below, these made an important rôle in the interpretation of electron diffraction patterns affected by cold-working.

### (b) *Electron Diffraction*

Before and after the mechanical testing, all the specimens were subjected to the electron diffraction study. A diffraction camera with a 309 mm. camera length and the electron beam about 100 $\mu$ in diameter at the specimen, accelerated by finely stabilized high voltage of 50 KV (common with the electron microscope), were employed. The glancing angle of the incident beam was 2∼3° as usual. In consequence, an elliptical domain with its major axis of about 1 mm. long and minor axis of about 0.1 mm. long was illuminated on the surface of the specimen and the crystal near the surface was traversed by the beam to a depth of several 10 Å. This is of great importance in comparing the results of electron diffraction with those of the microscopes.

Before any deformation had occured in the crystal, the reflection pattern consisted of sharp Laue spots and Kikuchi lines as are seen in Figs. 7a, 8a, 8c and 10a. The Laue spots were always small and distinct but stretched towards the shadow edge presumably due to the refraction effect. It was therefore concluded that the crystal surface was feebly undulating but otherwise perfect and flat, so the diffraction pattern was substantially of the reflection type, not arising by transmission of the electron beam through any kind of ragged protuberance. Kikuchi lines were superimposed on a background originating from incoherent scattering in the crystal and more or less in the surface oxide layer. Kikuchi envelopes and Kikuchi bands were also observed in some cases, the latter being of singnificance in this study.

In the preliminary test, two kinds of nasty disturbances were encountered at times; one was narrow splitting of Kikuchi lines showing existence of a small angle crystal boundary likely introduced during the preparation of the specimen, and the other was a high background indicating that the surface finishing by electropolishing had been failed and fairly thick oxide film (probably more than 20 Å) existed on the surface. These unfavourable cases were, of course, excluded as much as possible.

Since at first sight the results of electron diffraction on the plastically deformed crystals were various and rather unsystematic, it seems difficult to give an outline of them in the first

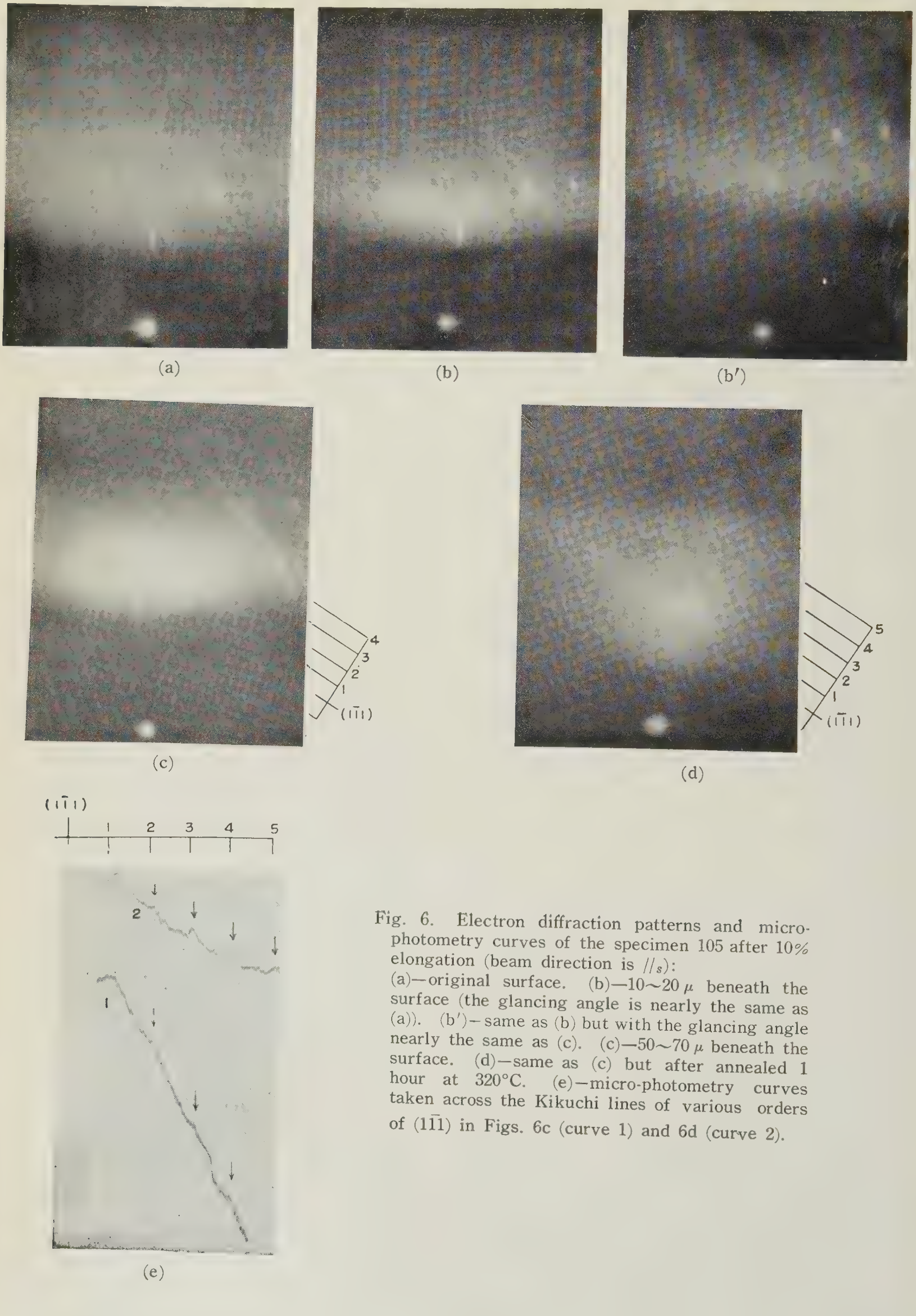

(a) (b) (b′)

(c) (d)

(e)

Fig. 6. Electron diffraction patterns and micro-photometry curves of the specimen 105 after 10% elongation (beam direction is $//_s$): (a)—original surface. (b)—10∼20 $\mu$ beneath the surface (the glancing angle is nearly the same as (a)). (b′)—same as (b) but with the glancing angle nearly the same as (c). (c)—50∼70 $\mu$ beneath the surface. (d)—same as (c) but after annealed 1 hour at 320°C. (e)—micro-photometry curves taken across the Kikuchi lines of various orders of (1$\bar{1}$1) in Figs. 6c (curve 1) and 6d (curve 2).

place. It may rather be adequate to begin by describing individually the results obtained from each specimen, then to have a general aspet therefrom.

The specimen 105 was first deformed to 10% elongation. When the incident beam was nearly parallel to the slip traces, the background considerably increased, Laue spots were generally broadened, and Kikuchi lines extremely diffused as in Fig. 6a. When the beam was normal to the slip traces, the changes of the diffraction pattern due to tensile deformation were not essentially different from the above case, although slightly clearer patterns were obtained.

From these incipient results some conjectures were made as follows: There might be many local distortions, presumably due to the deformation bands, in the crystal, which are responsible for the severe changes of the diffraction pattern, for instance, such that splitting of spots and disappearance of Kikuchi lines. If, therefore, the incident beam favourably gets in a region which does not contain the strongly distorted places, the diffraction pattern will suffer less disturbance, as actually obtained by chance. The fact that Laue spots generally split into a few and the corresponding misorientations in the crystal were of the order of 1° seemed to support these conjectures, since the area illuminated by the incident beam on the crystal surface was of such an order as to accommodate a few deformation bands in usual situations and the misorientation between two crystal portions bounded by a deformation band was likely to fit the observed value. In order to ascertain these, more systematic observations were made on the other specimens; for instance, the crystal surface was scanned with the electron beam, azimuth of the beam was taken to be parallel and normal to the traces of the deformation bands, the specimen without appreciable deformation bands was examined, etc. The results thus obtained were exactly such as what should be expected, which will be mentioned respectively in the following.

A further investigation was intended on the specimen 105 to elucidate whether the state of plastic deformation in the interior of the crystal appreciably differs from that near the surface. The surface which produced the obscure patterns as in Fig. 6a was electropolished for about 5 minutes in the Jaquet electrolyte which was kept below 10°C; this caused removal of metal $10\sim20\,\mu$ thick from the surface, the velocity of dissolution of aluminium by this method being in thickness about $3\,\mu$/min. Then, the diffraction pattern appeared to become clear slightly, irrespective of the beam direction, as in Figs. 6b and 6b′ (Fig. 6b should be compared with Fig. 6a because of nearly the same glancing angle). Further electropolishing was done to expose the interior of the crystal to the depth of $50\sim70\,\mu$, and the pattern became undoubtedly sharper than the former ones, as in Fig.6c,(which should be compared with Fig. 6b′) in which the sharp Laue spots, Kikuchi lines (especially lines of various orders of $(1\bar{1}1)$) and Kikuchi bands can be seen. It was feared that there might have been produced any annealing effect on the crystal near the dissolving surface during electropolishing. So, the crystal suffering removal of the surface to a depth of $50\sim70\mu$ was actually annealed 1 hour at 120°C *in vacuo* and then very slightly electroplished. Although this heat treatment was thought to be more effective than that conceivable in electropolishing in the prior treatment, no changes on the diffraction pattern were presented. Whereas, the stronger annealing, 1 hour at 320°C *in vacuo*, additionally imposed upon the same specimen clearly raised further restoration of Kikuchi lines, as shown in the diffraction pattern of Fig. 6d and the microphotometry curves of Fig. 6e. Consequently, the annealing effect by electropolishing seemed to be improbable, and it was supposed that the deeper the crystal part from the surface of the deformed specimen the more perfect it became and correspondingly the clearer the diffraction pattern appeared.

The specimens 100A and 100B having a common crystallographic orientation given in Fig. 1 were submitted to more precise examinations. For the former specimen, four beam directions were chosen as follows; parallel to slip traces, normal to slip traces, parallel to deformation bands and normal to deformation bands, which we shall denote by $//_s$, $\perp_s$, $//_d$ and $\perp_d$ respectively. The results of the diffraction tests in these four cases are given in the following:

(1) $//_s$. Owing to the unsuitable orienta-

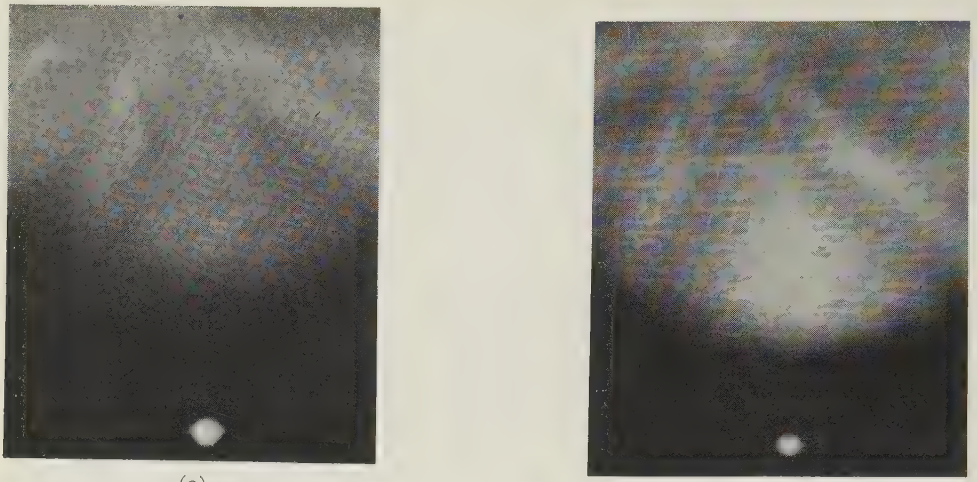

(a) (b)

Fig. 7. Electron diffraction patterns of the specimen 100 B before ((a), left) and after ((b), right) 1% elongation. Beam direction is $//_s$.

tion, Laue spots were not observed whether before or after the tensile deformation. After the deformation Kikuchi lines from those crystal planes which were nearly perpendicular to slip planes were barely observable, while those of the other kinds were absent.

(2) $\perp_s$. Most of the spots split, showing discrete relative rotations of various parts of the crystal. Very weak Kikuchi lines were also observable.

(3) $//_a$. The spots were multiple, but some regions produced single spots during scanning of the surface with the electron beam. This fact, together with the result obtained from the specimen 105, suggested that multiplication of Laue spots would not be caused by the relative rotations in activated slip planes but produced by another kind of rotations in a larger scale, probably due to deformation bands as illustrated in Fig. 5. The angle of the rotation was again of about 1°. The Kikuchi lines were diffuse even when accompanied with the single Laue spots, but they were not weak.

(4) $\perp_a$. The spots generally broadened and split as well. The spots from the crystal planes with certain indices, however, did not exhibit appreciable splitting, so that the corresponding rotations should be confined to a certain kind, say, the rotation about some definite axis. According to the concept that these splittings are due to the relative rotations or bendings between the crystal parts sectioned by the roughly parallel deformation bands, the axis of rotation most conceivable is [211] which is in the slip plane $(\bar{1}11)$ and the plane of deformation band $(0\bar{1}1)$ and consequently perpendicular to the slip direction $[0\bar{1}1]$ as shown in Fig. 4. No Kikuchi lines were visible presumably due to the screening effect of surface undulation provoked by the deformation bands; as presented in Fig. 5, slipped but otherwise perfect regions between deformation bands are generally screened from the incident beam by the wavecrests where the deformation bands exist, so that the greater part of the beam will illuminate the highly distorted parts of the crystal and produce the exceedingly diffuse Kikuchi lines difficult to observe unless the incident beam is more or less parallel to the deformation bands. This screening effect of the deformation band was found to be a general tendency, so it should possibly be rejected if the effect of crystal imperfections produced by the simple slip mechanism on Kikuchi lines is to be investigated.

From this point of view, the specimen 100 B which was stretched to only 1% elongation was examined to elucidate to what extent the Kikuchi lines will be affected by the pure laminar plastic flow. As already stated, the specimen in reality had laminar slip lines and no remarkable undulation, i.e. no appreciable deformation bands. Laue spots after the deformation did not exhibit any detectable change as expected. Hence, the concept that

Table II.

| Specimen 105 (10% elong.) | | Specimen 100 A (5% elong.) | |
|---|---|---|---|
| Depth | General aspect of diffraction pattern | Depth | General aspect of diffraction pattern |
| 0 $\mu$ (surface) | Obscured pattern with a high background, Kikuchi lines extremely diffuse and Laue spots diffuse. | 0 $\mu$ | Obscured pattern. |
| | | 1 $\mu$ | Much the same obscured pattern. |
| 10–20 $\mu$ | Slight recovery of Kikuchi lines and Kikuchi bands and decrease of background. | 11 $\mu$ | Very slight recovery of some Kikuchi lines. Fairly clear Kikuchi bands. |
| 50–70 $\mu$ | Clearer change of Kikuchi lines and Kikuchi bands. Sharp Laue spots. | 25 $\mu$ | Recovery of many Kikuchi lines.<br>Clear Kikuchi bands.<br>A weak background. |
| | | 42 $\mu$ | Considerable sharpening of Kikuchi lines. Clear Kikuchi bands.<br>Sharp spots. |
| | | 62 $\mu$ | A slight further recovery. |
| | | 99 $\mu$ | No more appreciable improvement. |

the splitting of Laue spots is due to deformation bands seemed more rigidly confirmed. On the other hand, a close inspection revealed slight broadening and weakening of Kikuchi lines as well as slight increase of the background. Both diffraction patterns before and after the deformation are to be compared in Figs. 7a and 7b. It may, therefore, be stated that in general the diffraction pattern is partly affected by macroscopic local distortions such as deformation bands and partly by somewhat uniformly distributed crystal imperfections associated with the formation of laminar slip lines, the effect of the former being some times so preponderant as to thoroughly cover that of the latter. We shall call the latter effect the intrinsic effect of slip lines on the diffraction pattern, and this is one of the subjects of the greatest significance in the present study.

The state of plastic deformation in the interior of the crystal was investigated on the specimen 100 A by means of electron diffraction like the specimen 105 but more precisely: Careful electropolishings were repeatedly imposed upon the specimen to expose crystal parts at various depths from the surface, each depth being measured with a micrometer with the error of the order of a few microns. The result was much similar to that of the specimen 105; i.e., when the depth of about 20 $\mu$ was reached, the diffraction pattern visibly recovered irrespective of the direction of the incident beam, and the deeper the crystal, the sharper the diffraction pattern until the depth of about 50 $\mu$ was reached. However, the patterns obtained at the depths of 62 $\mu$ and 99 $\mu$ were not appreciably different from each other; it might follow from this that the situation of deformation does no longer undergo a sensible change below the depth of about 50 $\mu$ in contrast with the considerable change taking place at 10$\sim$20 $\mu$. The results of both specimens are summarized in Table II.

The specimens 108 A, 108 B and 108 C which were extended respectively to 7%, 20% and 55% elongations as cited in Table I were examined in the next place, particular attentions being concentrated upon the intrinsic effect of slip on the electron diffraction pattern in respect to the amount of tensile deformation. The surface structure, resembling foregoing ones, consisted of single slip lines as in Fig. 3 and almost parallel deformation bands intersecting them. On the specimen 108 C, however, deformation bands were no longer parallel but randomly intersecting one another as a result of the rotation of their own in various degrees which had taken place during the large deformation. The results of electron diffraction obtained from these crystals were analogous to those already given in this paragraph, and such effects as above-mentioned were confirmed. In the following is their brief explanation:

In general, the Laue spots from the crystal planes related nearly to the (211) plane, which, was perpendicular to the active slip plane $(\bar{1}11)$ and containing the slip direction $[01\bar{1}]$, were less multiple, and the Kikuchi lines from these planes correspondingly remained com-

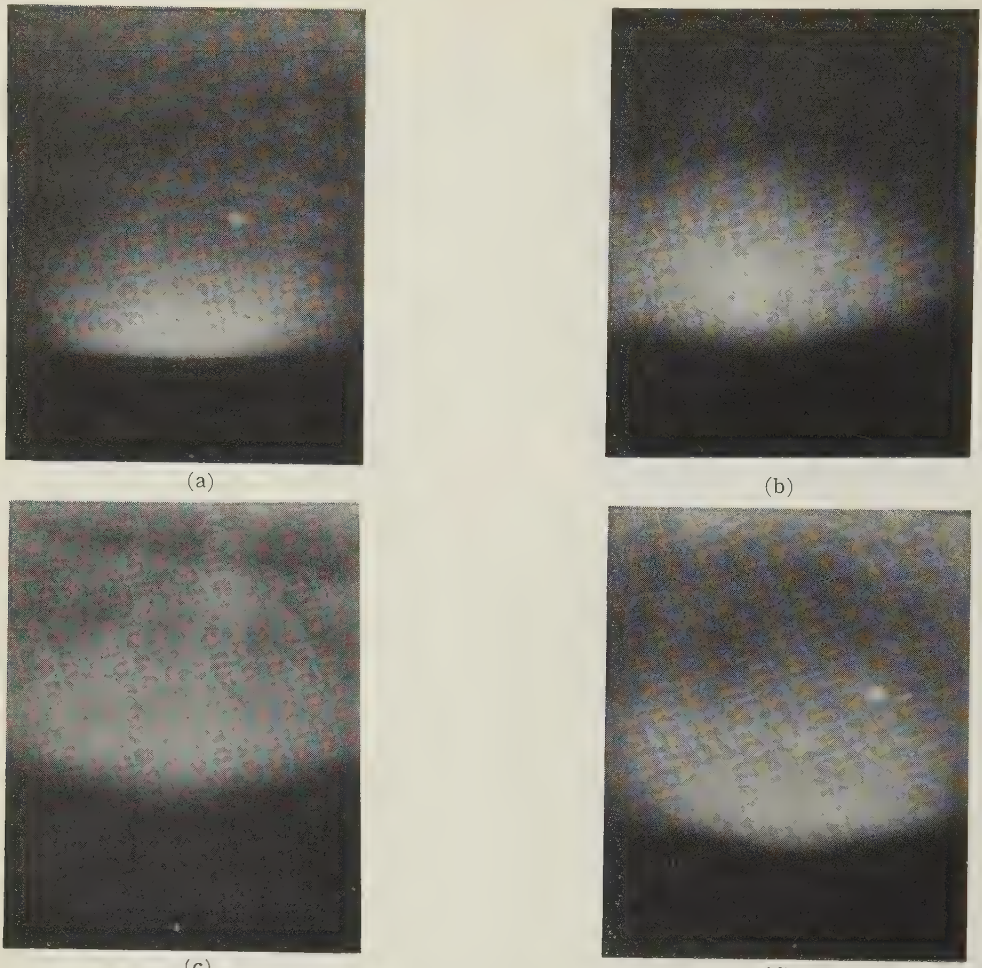
(a) (b)
(c) (d)

Fig. 8. Electron diffraction patterns of the specimen 108 A: (a)—$\perp_s$, before deformation. (b)—$\perp_s$, after 7% elongation. (c)—$//_a$, before deformation. (d)—$//_a$, after 7% elongation.

paratively sharp. So that, the relative rotations of various parts most probable in the crystal are those produced by deformation bands which are the rotations about the [211] axis. On the other hand, there existed no signs in the diffraction pattern attributable to the rotations in the active slip planes or about the [$\bar{1}$11] axis.

When the direction of incident beam was chosen as $//_a$ and less distorted crystal parts between the deformation bands were illuminated, the screening effect due to the deformation band could be avoided to a great extent; for instance, Laue spots barely split, Kikuchi lines and Kikuchi bands were fairly sharp even if they were from the crystal planes necessarily bent by the [211] rotations. Such appearances will be recognizable from comparison between diffraction photographs of Fig. 8 taken before and after deformation for two beam directions, where the pattern for $//_a$ remains considerably sharp after 7% elongation. Presumably for such reason, the specimen 108 B could produce broadened single spots and some faint Kikuchi lines in spite of the large amount of tensile deformation, provided that the condition of the incident beam was just as desired. For the specimen 108 C, there seemed no preferential beam direction in producing the diffraction pattern with tolerable distinctness. The diffraction pattern was composed of the blurred Laue spots and very high background as shown in Fig. 9. It should be noted, however, that the beam direction of $//_s$ appeared to give the pattern with a slightly better contrast than other directions, and even a certain contrast which might be referred to Kikuchi lines or Kikuchi bands was observed in this case. It follows from this that if the screening effect of deformation bands were sufficiently excluded in higher stages of deformation in the present method of investigation, fairly sharp Kikuchi bands and Kikuchi lines would be obtained and the intrinsic effect of slip lines on the diffraction pattern would be estimated to some extent.

By removing metal of various thicknesses from the surfaces of these specimens, electron diffraction tests to clarify the state of deformation in the interiors were repeated; the results obtained from the specimens 108 A and 108 B were much similar to those from the specimens 105 and 100 A, but from the specimen 108 C no conclusive result was obtained.

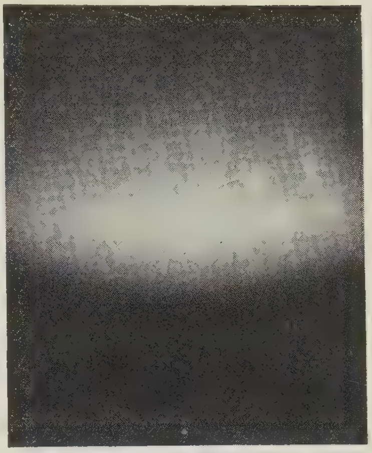
Fig. 9. Electron diffraction pattern of the specimen 108 C after 55% elongation. Beam direction is //s.

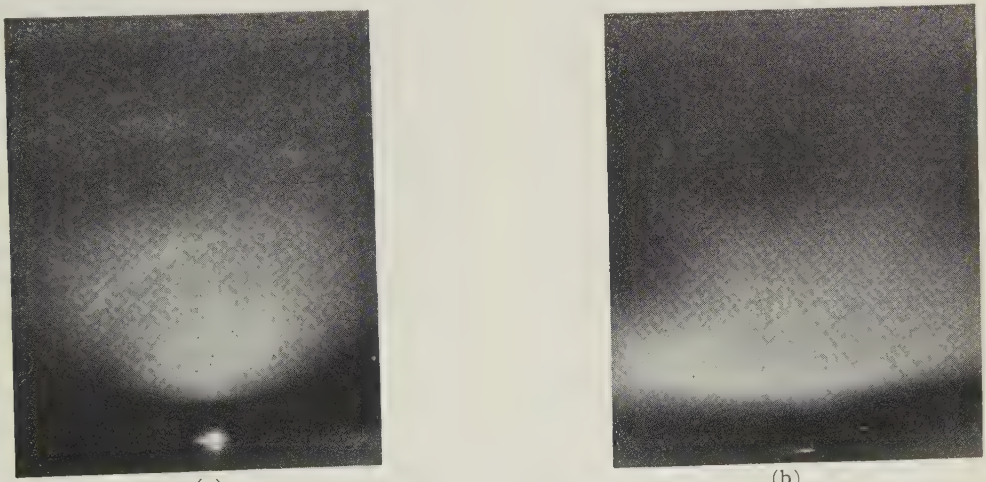
(a) (b)

Fig. 10. Electron diffraction patterns of the specimen 109 before ((a), left) and after ((b), right) 10% elongation. Beam direction is //s.

The specimen 109 was examined in the last place to elucidate the effect of plastic deformation in case of operation of many slip systems in complicated manner, as its structure of deformation was the slip-clusters as mentioned in the preceding paragraph. The incident beam was made to hit a seemingly nonslipped region, in which slip was almost suppressed even after 10% elongation and very small undulation was observed by using the phase-contrast microscope. By means of electron microscope, however, it was realized that in this region more than one slip system were actually activated and mutually interacted, from place to place, producing extremely fine slip lines in various directions. The electron diffraction patterns before and after deformation are presented in Figs. 10a and 10b, there being broadened weak spots, a high background and no Kikuchi lines in the latter. It may be concluded from this result that when many slip systems strongly interact with one another, the effect of plastic deformation on the diffraction is strong. It is worth noticing that the diffraction pattern did not yield any noticeable change even after removal of a layer of 90 $\mu$ thick from the surface of the specimen, in other words, the states of plastic deformation near the surface and in the interior of this crystal were barely different from each other in contrast with the considerable difference between both states in the other crystals as far as electron diffraction could perceive.

A general aspect of the effects of plastic deformation on the diffraction patterns which was established by the above experiments is summarized below:

1. With increasing plastic deformation Laue spots generally become broad and weak, showing increase of imperfections of the crystal presumably such as relative rotations and bendings of various parts of the crystal which occur in a minute scale. This is only remarkable at fairly high deformation, say, several per cent elongation. The other type of change of Laue spots associated with deformation, that is splitting or multiplication, is very frequently observed as well. However, it can be regarded as due to deformation bands, where slip is almost arrested and sharp bending of crystal occurs, not due to slip lines themselves, from the following facts; single spots can be obtained when the incident beam favourably illuminates a region between deformation bands, the crystals without appreciable deformation bands do never produce multiple Laue spots, and the splitting manner actually observed is not such that produced by $[\bar{1}11]$ rotations most likely occurring in active slip planes but such that expected from [211] rotations or bendings taking place at deformation bands.

2. In appearence, Kikuchi lines are very sensitive to plastic deformation; for instance, only a few per cent tensile deformation can sometimes extinguish whole Kikuchi lines. However, this phenomenon undoubtedly results from the screening effect of deformation bands and cannot be referred to the intrinsic effect of slip lines. In reality, Kikuchi lines are visible even after 20% tensile deformation when the electron beam is directed so as to avoid possibly the disturbance produced by deformation bands. Of course, Kikuchi lines become increasingly diffuse and weak with increasing deformation even though accompanied with single Laue spots, and we named this the intrinsic effect of slip lines on the Kikuchi lines.

3. Kikuchi bands behave in parallel with Kikuchi lines but somewhat less markedly in regard to the sensitivity to plastic deformation. The background always increases with increasing deformation, so that Kikuchi lines, Kikuchi bands and weak spots generally dissolve into it at higher stage of deformation.

4. It is, therefore, concluded that the electron diffraction pattern is fairly distinct when obtained from a crystal part deformed with a single slip system but otherwise perfect, and is very obscure when obtained from a highly distorted crystal part such as in the vicinity of deformation bands or deformed with many slip systems mutually interacting.

5. Except highly distorted crystals, clearer patterns are obtained by removing metal progressively from the surface as much as about $100\,\mu$; this indicates that the deeper the crystal part the more perfect it becomes. In particular a noticeable change appears to take place at the depth between 10 and $20\,\mu$, and there is no longer appreciable change below $60\,\mu$.

## § 4. Discussion

The observation carried out by Heidenreich and Shockley[1] that the slip bands spaced a few microns apart can be resolved into clusters of finer lines with the slip distances of about 2000 Å and separated by distances of about 200 Å seems nowadays difficult to consider as a general representation of the structure of slip bands on the surfaces of pure metals not affected by any kind of surface cold-working. All recent studies seem to advance that the surface structures of deformed pure metals are somewhat finer and more irregular than the above as shown in Fig. 3. It should be noted that the local distortions caused by the deformation bands were inevitable for such crystals and played a very important rôle in producing various electron diffraction patterns; this fact had perhaps been overlooked by Heidenreich and Shockley. Their opinions on the effect of plastic deformation on the diffraction patterns such that, Kikuchi lines are so sensitive to slip that they can be extinguished by only a few per cent tensile deformation, and such that rotational components of slips possibly produced in active slip planes are responsible for multiple Laue spots, have so far been admitted. Nevertheless, according to the present study, these effects are thoroughly attributable to the deformation bands as stated in the preceding paragraph. It is quite interesting that Kimoto[2] *et al*. have recently found that when a convergent electron micro-beam was used, considerably different diffraction patterns were obtained from aluminium single crystals plastically deformed. That is, the patterns from the laminar slip regions were so sharp as to be indistinguishable from those produced by the undeformed crystal, they suddenly become blurred when the incident beam entered a highly distorted region where a deformation band most likely existed, and a discrete jump of the pattern occurred when such a region was traversed by the beam, indicating a relative rotation of two crystal parts bounded by this region. Their result appears to correspond with the demonstration of Gay and Honeycombe[8] using an X-ray micro-beam that asterisms were not obtained unless the beam straddled a deformation band. Such results, we consider, substantially accord with that of the present study. Reconsideration should be needed at this point for the widely acknowledged opinion of Heidenreich and Shockley. The effect of deformation bands is remarkable in our experimental results, and its intuitive but convincing explanation may be given in terms of the dislocation model in which only the edge dislocations are of significance. On the other hand, the effect of slip lines or the intrinsic effect is less evident both in the experimental results and in their interpretation with dislocation model. In general, slip lines are considered to be not only mere traces but actually containing dislocations piling up and anchored against obstacles or without obstacles to cause hardening of the crystal. If such dislocations are almost of the edge type, subsequent crystal distortions around them will be bendings more or less similar to the case of deformation bands. Hence, the axis of rotations or bendings should be [211]. On the contrary, if screw dislocations are very predominant, the distortions will be represented by the rotations in active slip planes, the axis of which should be $[\bar{1}11]$. At the present stage of study of plastic flow, it seems difficult to decide which state is more essential, although this is a very important and urgent problem. In principle, the electron diffraction study should be able to reveal this as Heidenreich and Shockley[1] suggested. That is, apart from the effect of deformation bands, if Kikuchi lines from those crystal planes which orient near to $(\bar{1}11)$ were sharper than those from otherwise orienting planes (this means comparative sharpness of the diffraction pattern of $//_s$), comparative perfectness of the $(\bar{1}11)$ planes would be indicated and, therefore, $[\bar{1}11]$ rotations in active slip planes or piling up of only screw dislocations would be verified. While, if only Kikuchi lines from crystal planes of (211) and near kinds remained sharp, bendings of active slip planes around [211] and, in consequence, piling up of edge dislocations would be demonstrated. In actual observations, however, it is scarcely possible to determine which of the two representations is more correct as far as the present method of investigation is employed, because the screening effect of deformation bands is very intense as already stated. Our experimental results could only give some evidence for the existence of the intrinsic effect of slip lines but no further information. It will be noticed that Heidenreich and Shockley[1] have emphasized in their report that the diffraction pattern of $//_s$ was clearer than that of $\perp_s$, by which $[\bar{1}11]$ rotations were indicated as well as by the multiple Laue spots. In view of the consideration of the present investigation, however, we believe that the result obtained by them was rather accidental and seems inadequate to regard as indicating a general feature of diffraction patterns affected by cold-working. It is of particular importance that Kimoto[2] showed that the intrinsic effect was very little in the case of convergent-beam electron diffraction. In order to give a clear-cut explanation for these outwardly contradicted results, it would be necessary to have such kind of experiments further repeated under various circumstances. Although we have above-described the change of diffraction patterns associated with plastic deformation in terms of local rotations of certain kinds introduced in the crystal, there might be still other possible imperfections capable of accounting for the diffusing of electron diffraction patterns than the rotations or bends; for instance, such that the metal is broken up into small crystallites $10^{-6}\sim10^{-7}$ cm in diameters and such that the lattice parameter changes from place to place in the crystal. These other types of imperfections may be sometimes expected to play a principal part at higher stages of deformation, but it seems very unlikely that either of them is of any importance as far as the simply stretched single crystals are concerned.

Another important problem, i.e., whether or not the state of plastic deformation in the interior of the crystal sensibly differs from that in the vicinity of the original surface, appears to be somewhat clear in the present experimental results as already mentioned. Nevertheless, a little further consideration seems to be necessary for the conclusive discussion, because there can be some other causes to produce the increase of sharpness of the diffraction patterns with the increasing depth:

(1) One of the possible causes is annealing associated with the stepwise electro-polishing to remove metal from the surface, which has however been found to be ineffective as stated in the preceding paragraph. The other annealing effect due to the incident beam is also unprofitable to induce recovery of metal, as known from the fact that the diffraction patterns from the deformed crystals were not alterd even after fairly long exposure of the specimens to the incident beam.

(2) Difference between the surface topological structures of the deformed crystal just prior to and after electro-polishing might cause the difference in sharpness of the diffraction patterns, the surface after electro-polishing being lacking in the stepwise structure due to the slip lines. However this is very unlikely as well from the fact that after a slight electro-polishing of the first stage removing only about 1 $\mu$ of metal from the original surface but sufficient to extinguish the stepwise structure, the diffraction pattern exhibited no appreciable change as shown in Table II.

(3) It does not seem unreasonable to expect that the surface unevenness brought about by the deformation bands is smoothed to some extent by electropolishing, and, if so, the diminished screening effect of deformation bands will permit the clearer pattern to appear after a proper electro-polishing. The interferometer-microscope, however, revealed that such unevenness could not be reduced so strikingly as to decrease the screening effect even after an electro-polishing removing metal of as much as 100 $\mu$. Moreover, even when the beam direction was taken to be parallel to the deformation bands in order to avoid highly distorted regions, the general tendency above-mentioned was not altered. So that, it is clear that change of surface unevenness can not be considered as the cause of the phenomenon in question.

Consequences of the above considerations thus give support to the conclusion stated in the preceding paragraph that the observed increasing sharpness of the diffraction patterns with increasing depth is originated from no other than the variation of internal structures produced by plastic deformation.

In regard to this point, there have been some notable predictions mainly from theoretical point of view as follows: Hollomon[9]) has pointed out that the dislocation lines terminating at the free surface can behave just like the Frank-Read sources twice the length of themselves when they are subjected to the applied stress, so it may be expected that much more slips can be initiated at the surface of the crystal than the interior. H. Suzuki[10]) has postulated that the dislocation lines forming fairly regular plane networks in the crystal should be unknitted in the vicinity of the free surface to sustain the mechanical balance between the dislocation segments themselves and thus long dislocation lines terminating at the free surface should already exist in the unstretched crystal, and they will give many slips near the surface. Kuhlmann-Wilsdorf[5]) has also considered a certain type of sources of slip situated at the free surface and she has attributed the elementary structure to these surface sources. The present experimental results appear to be verifying these predictions that the distribution of slip lines should be much finer in the vicinity of the free surface than in the interior of the crystal, but the question how such difference of deformation structures results in the observed difference of sharpness in the diffraction patterns still remains open.

Another apparently possible explanation for this phenomenon is that an oxide thin film presumably formed during electropolishing prior to deformation might prevent a part of the dislocations produced in the body of the crystal from comming up to the surface and therefore might cause the excess piling up of the dislocations near the surface; this will have an intense effect on the electron diffraction pattern, if actually happens. However, it is scarcely conceivable at least in the present experiment, for the oxide film in this case is considered as too thin (probably less than 30 Å) to arrest sufficiently the dislocations. In order to elucidate this point, a crystal with a suitable orientation was subjected to anodic oxidation to form a surface oxide film a few hundred Å thick and was stretched to several per cent, but the diffraction study was unsuccessful because of miscarriage of subsequent electropolishings to remove metal together with the oxide film from the surface.

## § 5. Summary

The suitably oriented single crystals of aluminium subjected to the tensile deformation of various amounts were investigated by electron diffraction together with the ordinary microscope, interferometer microscope and electron microscope. The outstanding results are as follows:

1. Slip distances vary continuosly from less than 30 Å to more than 1000 Å, and spacings of the slip lines are several hundred Å. Hence, the stepwise structure of such sizes is produced on the crystal surface. Further, the deformation bands cause the local high distortions and the surface undulation with spacings of 0.1∼1 mm.

2. The deformation bands strongly affect the diffraction patterns by themselves and by screening the laminar slip regions; for instance, Kikuchi lines are extremely diffused and extinguished, a high background is produced and Laue spots are split as a result of existence of the deformation bands.

3. From the splitting manner of the Laue sports and variations of diffusing of the Kikuchi lines it is concluded that the discontinuous bending about the [211] axis to the angle of the order of 1° should occur at each deformation band.

4. The intrinsic effect of slip lines other than deformation bands on the diffraction pattern is also indisputable from diffusing of patterns in the absence of deformation bands. Especially this effect is remarkable in the case of the simultaneous operations of more than one slip system. However, rotations of crystal parts about the $[\bar{1}11]$ axis or in the active slip planes can not be distinguished.

5. From the increasing sharpness of the diffraction patterns with increasing depth of the crystal parts examined it is strongly suggested that the state of plastic deformation in the vicinity of the crystal surface may be quite different from that in the interior, a plausible interpretation being possible based on some theoretical predictions.

The authors wish to express their hearty thanks to Prof. R. Uyeda of Nagoya University for his valuable discussions and advices.

### References

1) R. D. Heidenreich and W. Shockley: Report of a Conference on the Strength of Solids, Bristol 1947 (London: The Physical Soc.)
2) K. Kimoto and Y. Fukano: Read at the 9th annual meeting of Phys. Soc. Japan (1954). K. Kimoto: Read at the Symposium of Plasticity in April 1955 held at Nagoya. K. Kimoto: J. Phys. Soc. Japan **11** (1956) 485.
3) A. F. Brown: J. Inst. Metals **80** (1951–2) 115.
4) A. F. Brown and R. W. K. Honeycombe: Phil. Mag. **42** (1951) 1146.
5) D. Kuhlmann-Wilsdorf and H. Wilsdorf: Acta. Met. **1** (1953) 394.
6) J. Takamura: Report of the Symposium on Crystal Plasticity and Dislocation, Nikko, 1954.
7) F. E. Fujita, T. Suzuki and M. Yamamoto: to be Published.
8) P. Gay and R. W. K. Honeycombe: Proc. Phys. Soc. **64 A** (1951) 844.
9) J. H. Hollomon: Report of 9th Solvay Conference, 1952, 576.
10) H. Suzuki: J. Phys. Soc. Japan **9** (1954) 531.

Journal of the Physical Society of Japan Vol. 11, No. 5, May, 1956

# Intersections of {301}, {101} Twin Bands in Tin

By Saiyu MARUYAMA
*Department of Physics, Osaka Women's University*
and Hiroshi KIHO
*Department of Physics, Kyoyo-bu, Kyoto University*

(Received September 14, 1955)

In the course of impact tests on single crystals of β-Sn, we found twin bands of the type {301} and its reciprocal {101}, intersecting each other. The intersections were investigated with reflecting microscope, and it was observed that crossing twins were accompanied by at least one of the three types of additional twinning process, namely, secondary twin, bouncing twni, and the broadening or narrowing of crossed twin. Here are given our interpretation for the mechanisms of these additional twinning processes obtained from the results of shear strain measurements around intersections. Several photographs are added with explanations in detail.

## § 1. Introduction

The mechanical twin plane {301} in β-Sn is well-known[1]. The twin plane {101}, other than the well-known twin plane {301}, was recently found by several investigators[2][3]. The twin plane, and the second undistorted plane are usually denoted by $K_1$ and $K_2$. The direction of the twinning shear, and the intersect of $K_2$ on the shear plane are denoted by $\eta_1$ and $\eta_2$ respectively. When $K_1$ and $\eta_2$ of a twin are found to have the same indices as $K_2$ and $\eta_1$ of the other twin, the twins are said to be "reciprocal"[4]. In the case of β-Sn, $\eta_1, \eta_2$ and $K_2$ of (301) twin are $[\bar{1}03]$, [101] and $(\bar{1}01)$, while those of $(\bar{1}01)$ twin are [101], $[\bar{1}03]$ and (301). Therefore, $(\bar{1}01)$ twin is the reciprocal twin of (301) twin, although the reciprocal twin is rarely found in metals. The atom movements are similar in both {301} and {101} twins. The magnitude of the twinning shear strain is 0.119 in either case.

The {101} twin bands are hardly produced by the usual impact tests, while {301} twins are easily produced. But when {301} twins were prevented from further broadening by external constraint, {101} twin can be produced usually in a form of narrow band.

In our work, normal impact stress was applied on a single crystal of tin constrained in a glass tube, in order to produce {101} twins as many as possible. The numerous {301} and {101} twin bands thus produced were scarcely broader than 0.1 mm and they intersected each other. At these intersections various additional twins were produced. These intersections attracted our attention, and we tried to interpret their mechanisms.

For Bi and As, Gough and Cox[5][6] demonstrated photographs of the intersections of twin bands and the secondary twins; and for Neumann bands in Fe, Smith, Dee, and Young did the same[7].

Recently, R. W. Cahn[4], in his excellent paper on "Plastic Deformation of α-Uranium", mentioned the two necessary conditions for secondary twin formations, as follows:

1. The traces of $A$ and $C$ in the $K_1$ plane of $B$ must be parallel to each other.
2. The direction, magnitude and sense of shear must be identical in $A$ and $C$.

Note: $A$, $B$ and $C$ show, respectively, crossing, crossed and secondary twins.

In our work on β-Sn, as might be easily seen crystallographically, none of the secondary twins in β-Sn has the shear direction indentical with that of the incident one. Therefore, Cahn's first condition holds good, but the second does not. Our methods of treating all the additional twinning processes at twin intersection are given in the following.

After Cahn's work, P. L. Pratt examined the twin intersections in single crystals of zinc[8], and found that there were secondary twins which did not satisfy even Cahn's first condition.

## § 2. Experimental Methods

Rod single crystals of tin, about 4~5 mm in diameter, were prepared in glass tubes following a method similar to Czochralski's. A seed single crystal, X-rayed in advance and covered in a glass tube, was put in the melt. The lower end of the crystal was immersed in it, while the upper end was cooled by water continuously. Then the system was raised slowly from the melt, producing rod single crystal with the same orientation of the seed. As the glass tube was constricted, the narrowest diameter being about 1 mm, and bent at some angle, the crystal below the constricted part took the orientation different from that of the seed. By this means, we prepared specimens with any desired orientations suitable for our experiment. Fig. 1 shows these orientations determined by light figure or X-ray methods, which varied within about 5° from specimen to specimen.

Leaving each specimen in the glass tube, impact shocks were applied. The glass tube was dissolved in hydrofluoric acid and the specimen was etched chemically. Then it was observed that {301} twins had been prevented from broadening, {101} had been stimulated and intersections of these twins had been produced. The twin lamellae were so narrow that the conventional X-ray method failed in verifying twin relations. But, by measuring the angles of twin traces on the specimen surface with respect to a system of coordinates of specimen, the indices of twin planes were determined without confusion, because there are wide differences in orientations (at least 30°) between any types of twin planes.

The intersections of these twin traces were photographed by reflecting microscope with oblique illumination. The photographs are magnified about 70 times.

## § 3. Results of Observation and Discussion

In these photographs, we observe various additional twins generated from the intersections. These are classified into the following three types.

*Type* I). *Secondary Twin*: In the crossed twin band, the secondary twin succeeds the crossing one (as shown in Plates 5, 6 and 8).

*Type* II). *Bouncing Twin*: Starting from the intersection, the bouncing twin is reflected in the matrix region (as shown in Plates 1, 2, 3 and 5).

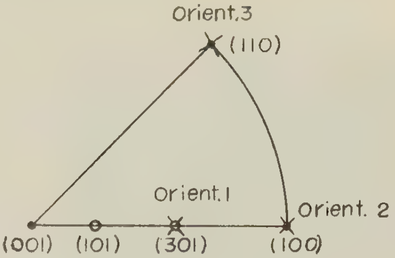

Fig. 1. Orientations of specimen axes.
○ pole of twin plane
× direction of specimen axis.

*Type* III). *Narrowing or Broadening of the Crossed Twin*: Narrowing or broadening of the crossed twin is promoted on either side of the intersection, as a result of for- or backward boundary movement (as shown in every Plate).

As is seen in every plate, the intersection of twin bands is not composed of only two bands, as in the case of slip bands, but of several more twin bands which start from there. Sometimes each twin band has sides keeping parallel up to the intersection (as shown in Plates 1, 4 and 5, and under part of Plate 2), while sometimes it takes the lenticular or tapering shape in the vicinity of the intersection (as shown in upper part of Plate 2, and Plates 3, 6, 7 and 8). These complicated figures of the intersections may be interpreted as follows. A crossing twin band impinges upon a crossed twin. Here, the former carries the macroscopic twinning shear strain into the intersection, and promotes the various deformations by which the strain may be accomodated, e. g. generation of new twin bands, broadening or narrowing of the crossed twin, (we may call them additional twinning processes), slipping, kinking, cracking, etc. When crossing twin band tapers in front of crossed twin, the strain carried by the former is not accomodated perfectly at the intersection, but has been accomodated gradually before crossing, accompanying presumably slipping, or kinking. We attended to the case in which each twin band has sides keeping parallel up to the intersection, and tried to estimate the degree of accomodation which is made only by additional twinning processes.

The net twinning shear displacement around

Table I. The Observed Values of $d$ (in micron).

| No. | (301) | | $(\bar{3}01)$ | | (101) | | $(\bar{1}01)$ | | $\sum S_i d_i / S$ | *Residual* ($\mu$) |
|---|---|---|---|---|---|---|---|---|---|---|
| 1 | 18 | — | 38 | 28 | 23 | 8 | — | — | 1 | 0.1 |
| 2 | — | — | 98 | 100 | 28 | 20 | — | — | 8 | 0.9 |
| 3 | 22 | 10 | 8 | 2 | 9 | — | — | — | 1 | 0.1 |
| 4 | 14 | — | 22 | 15 | 32 | 22 | — | — | 2 | 0.2 |
| 5 | 27 | — | 96 | 75 | 21 | — | — | — | 3 | 0.4 |
| 6 | 17 | 6 | 25 | — | — | — | 22 | — | 1 | 0.2 |
| 7 | 52 | — | 33 | — | 45 | — | — | — | 7 | 0.8 |

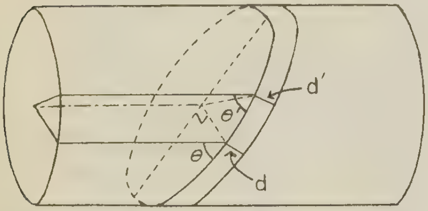

Fig. 2. Method of calculation of the true thickness $d$ from the apparent one $d'$.

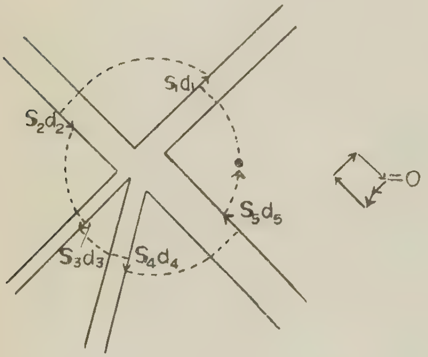

Fig. 3. Twinning shear vectors around intersection referring to Eq. (1).

the intersection is represented by vector sum

$$\sum_i S_i d_i \ ,$$

where $S_i$ denotes the shear displacement per unit thickness of $i$-th twin band. Its sense is the one which appears when we encircle the intersection in one sense, as illustrated in Fig. 3, and the magnitude $S$ in {301} and {101} twins is 0.119 in either case. Next, $d_i$ denotes the thickness of the $i$-th band. In the case where the twin plane is not perpendicular to the specimen surface (e. g. Plate 4, 5, 6 and 7), we calculate the true thickness $d_i$ from the apparent one $d_i'$ on the specimen surface by the following relationship:

$$d_i = d_i' \frac{\sin\theta}{\sin\theta'} \ ,$$

where $\theta$ represents the angle between the specimen axis and the twin plane, and $\theta'$ between the specimen axis and the twin trace on the plate (as shown in Fig. 2).

The values of $\sum S_i d_i$ are listed in Table I. Subcolumns in each twin plane show the values of $d_i$ in both parts of the intersections. *Residual* means the magnitude of $\sum S_i d_i$ around the intersection, which is very small considering that the shear displacement carried into the intersection is of macroscopic scale. It may be worth noting that the residual always increased when we tried to neglect any one of the additional twins.

As a result, when the sides of each twin band were parallel, we found that the shear strains carried by the twins were nearly perfectly accomodated around the intersections, only by additional twins without accompanying any other deformations.

The net shear displacement takes the form, different from the above mentioned, including the Burgers vectors of twin dislocations[9),

$$\sum_i S_i d_i = \sum_i n_i b_i \ ,$$

where $n_i$ denotes the total number of twin dislocations carried in the $i$-th band. Following the above result, the residual twin dislocations in the intersection are rare, or even if they remain, the total vector sum of the Burgers vectors piled up in the intersection is very small.

From the above result, we may proceed to interpret the mechanism of additional twinning processes. A twin band is crossed by another. For the reduction of $S_i d_i$ brought about by the latter around the intersection, one of additional twins which implies shear strain $S$ holding the relation

$$(S_i S) < 0 \ ,$$

may be expected to generate. Here again the

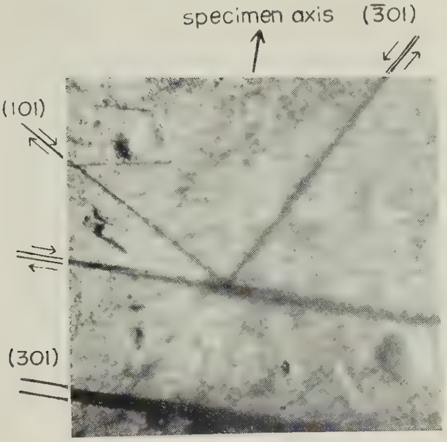

Plate 1.

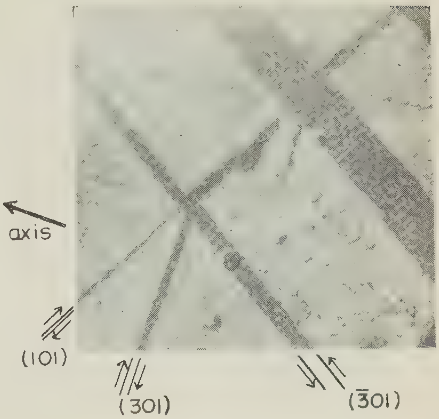

Plate 2.

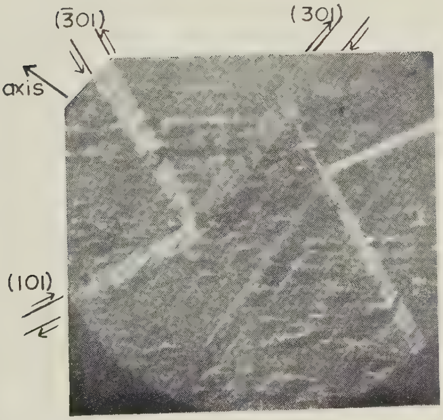

Plate 3.

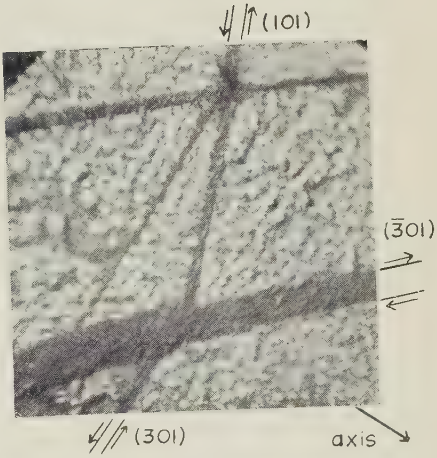

Plate 4.

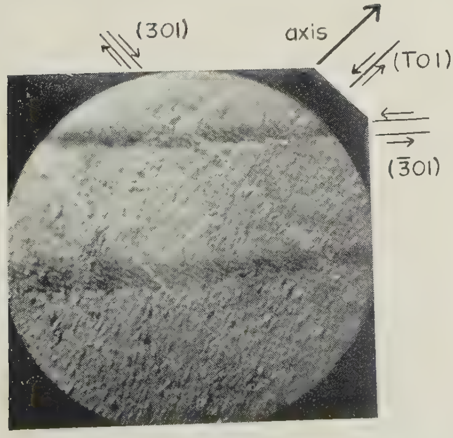

Plate 5.

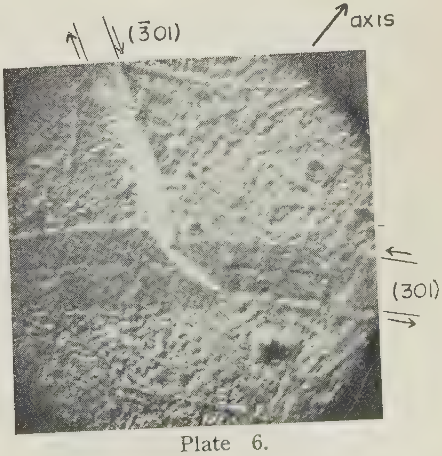

Plate 6.

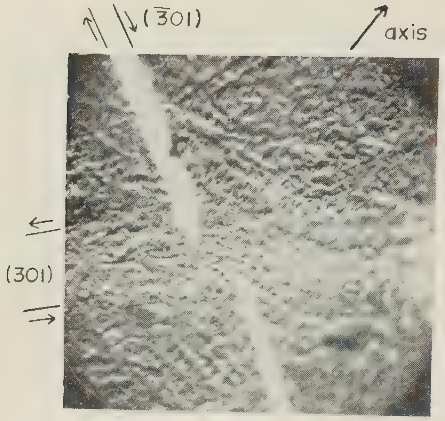

Plate 7.

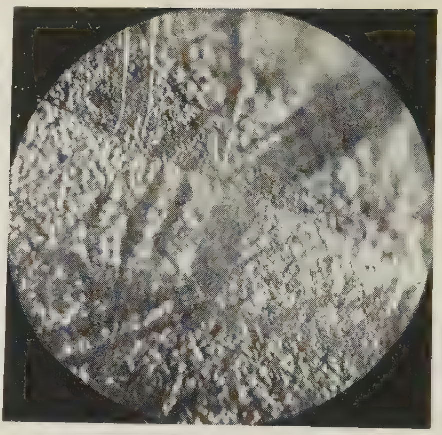

Plate 8.

Table II. List of additional twin planes selected by the aid of our two conditions, in the specimen axes 1 and 2 in Fig. 1.

| No. | Crossed twin | Crossing twin | Secondary twin | Bouncing twin | Observation |
|---|---|---|---|---|---|
| 1 | (301) | $(\bar{3}01)$ | $(101)_t$* | (101)* | Plate 1<br>Plate 5 |
| 2 | (301) | (101) | $(\bar{3}01)_t$*<br>$(101)_t$<br>$(\bar{1}01)_t$** | $(\bar{3}01)$<br>$(\bar{1}01)$ | Plate 1<br>Plate 4<br>Plate 5 |
| 3 | (301) | $(\bar{1}01)$ | $(101)_t$** | (101) | Plate 4 |
| 4 | (101) | $(\bar{3}01)$ | $(301)_t$** | (301)* | Plate 2<br>Plate 3 |
| 5 | (101) | (301) | $(\bar{3}01)_t$**<br>$(301)_t$**<br>$(\bar{1}01)_t$ | $(\bar{3}01)$<br>$(\bar{1}01)$ | Plate 2<br>Plate 3 |
| 6 | (101) | $(\bar{1}01)$ | $(301)_t$ | (301) | |

* Additional twin plane clearly seen in plate.

** Additional twin plane indirectly seen from the offset of crossing twin.

sense of the shear strains is assigned as before. This relation corresponds to Cahn's second condition which does not hold in our case.

The shear strain carried by the crossing twin would not be accomodated only by the above single additional twin, without any other ones. These other additional twins should accomodate not only the strain carried by the crossing twin, but also the strain carried by the additional twin already generated. Therefore, some additional twins might be generated which satisfy the relation $(\boldsymbol{S}_i\boldsymbol{S})=0$ in the limiting case.

## § 4. Interpretation of Photographs

Taking the two conditions described above into account, the additional twin planes in the specimens of orientation 1 or 2 in Fig. 1 are selected and are listed in Table II. Of course, only simultaneous inversions of signs of indices in each row from $\{h0l\}$ to $\{\bar{h}0l\}$ are admitted. By the way, (031), $(0\bar{3}1)$, (011) and $(0\bar{1}1)$ twin bands are not found in these specimens, because (1) the normal impact stress has not the component in the twinning shear directions on these twin planes, and (2) any twin planes having these indices do not satisfy the first condition in the cases listed in Table II, and cannot be produced by additional twinning processes. All additional twinning processes shown in Plates 1 to 5 having the specimen axes of orientation 1 are consistently interpreted using Table II.

In Plate 1, ($\bar{3}$01) twin crosses (301) twin, reflecting (101) twin in mother crystal, generating $(101)_t$ secondary twin in crossed twin (here subscript $t$ means that the indices should be taken with respect to the crossed twin orientation), and causing forward movement of the left part of (301) twin boundary. Further, $(101)_t$ twin in crossed twin generate again ($\bar{3}$01) secondary twin in mother crystal (which is twin region with respect to (301) twin band), and cause backward movement of the left part of (301) twin boundary. As a result, the left part of (301) twin band gets narrowing relative to the right.

In Plate 3, two ($\bar{3}$01) twins impinge upon the opposite sides of (101) twin, reflecting (301) twins and promoting (101) boundary movements. Consequently, the section of (101) between both intersections becomes narrower and narrower and gets finally out of sight. (We observed the quite similar configuration to Plate 3, except that the section of (101) twin was just disappearing.)

Secondary twins in Column 4 of Table II are often indistinct, but we can find some of them by slightly changing the direction of the illumination, and confirm without fail their existence by the offset of one twin just before and after crossing over another. It should be noted that this offset is due to the secondary twin formation in crossed twin, and is not due to the stress concentration "without any true secondary twin" as cited in the book by E. O. Hall⁽¹⁰⁾. Here, for reference, we show Plate 5 (orientation 1 in Fig. 1), 6 (orientation 3) and 8 (orientation missed), in which secondary twins are clearly seen in the crossed twins.

It is unsuccessful to find that the crossing twin dislocations are resolved into or composed by new additional twin dislocations produced at the intersection. It seems better to consider that new twin dislocations independent of transported ones are produced at the intersections by the aid of shear stress of crossing twin.

We express our cordial thanks to Prof. Kenzo Tanaka, Kyôto University, for his constant interest in and encouragement to our work, and to A. Aitani, Y. Mitsunari, T. Takahashi and E. Zen, students of Osaka Women's Univ., for their helpful assistances in the present experiment. This work was performed by a grant-in-aid of the Ministry of Education.

## References

1) B. Chalmers: Proc. Phys. Soc. **47** (1935) 733.
2) K. Tanaka, K. Ishii and H. Kihô: "X-ray" (in Japanese) **6** No. 2 (1950) (A).
3) T. Hirokawa: Read at the Annual Meeting of the Physical Society of Japan, Tôkyô, (1953).
4) R. W. Cahn: Acta Metallurgica **1** (1953) 49.
5) H. J. Gough and H. T. Cox: J. Inst. Metals **38** (1932) 227.
6) H. J. Gough and H. T. Cox: Proc. Roy. Soc. **A 127** (1930) 431.
7) S. W. J. Smith, A. A. Dee and J. Young: Proc. Roy. Soc. **A 121** (1928) 477.
8) P. L. Pratt: Acta Metallurgica **1** (1953) 692.
9) F. C. Frank: Phil. Mag. **42** (1951) 809.
10) E. O. Hall: "Twinning and Diffusionless Transformations in Metals", (1954) 92.

JOURNAL OF THE PHYSICAL SOCIETY OF JAPAN Vol. 11, No. 5, MAY, 1956

# Electron Microscopic Study on the Structure of Mosaic Boundaries in Ni–Mn Single Crystal

By Tadami TAOKA and Shoichiro AOYAGI

*Institute of Science and Technology, University of Tokyo*

(Received February 6, 1956)

For the purpose of studing the structure of mosaic boundaries in an alloy, observation of etching pits on the (110) plane of a Ni–Mn single crystal has been made by an electron microscope. The results obtained are summarized as follows: i) Mosaic boundary is composed of a set of parallel edge dislocations which are regularly spaced on a crystal lattice plane, as shown by Burgers, model. ii) These edge dislocations are along <112> crystallographic direction with Burgers vector $a/2\langle 110\rangle$, or along <100> direction with Burgers vector $\boldsymbol{a}\,\langle 100\rangle$ as suggested by Frank. iii) The dislocations are regularly spaced on {110} or {100} plane respectively which are perpendicular to its Burgers vector.

## § 1. Introduction

The structure of real single crystals, either metals or minerals, is very different from the ideal one in which the lattice planes have the same orientation in all parts of the crystal. The microscopic studies as well as the examinations by *X*-ray diffraction method have shown that real crystals are composed of small blocks with slightly different orientations. This structure is called the "mosaic structure", and the boundaries between the small blocks are called the "mosaic boundary" or "low angle boundary". Up to the present, the structure of the mosaic boundaries have been represented by the transition layers between two neighbouring crystal blocks inclined at small angles to each other, which may be possible by considering a suitable array of dislocations which is dealt with in this paper.

Models of grain boundaries in terms of dislocations were first proposed by Burgers¹⁾ and Bragg²⁾. Read and Schockley³⁾ have later developed the model in detail and derived the expression for the relationships between the boundary energy and the angle between the axes of two crystals. The experimental results of Aust and Chalmers for lead⁴⁾ and tin⁵⁾ are found to be in good agreement with their theory not only at low angles, but also at large angles where the theory is less reliable.

According to the model, the boundary consists of a sheet of parallel edge dislocations of the same sign, parallel to the $z$ axis and are spaced at intervals $h=b/\theta$ along the $y$ axis as shown in Fig. 1, where $b$ is the appropriate lattice transition vector and $\theta$ is the angle between the two crystals. In advance, this was demonstrated in the two-dimensional crystals of bubbles by Bragg and Nye⁶⁾. Some evidence for supporting this model has been offered, chiefly in the observations on the etching pits formed on a surface of single crystals⁷⁾⁸⁾. Recently, Vogel and his collaborators⁹⁾ succeeded to show directly the clear-cut correlation between $h$ and $\theta$, on the basis of microscopic and *X*-ray studies carried out on germanium single crystals.

The present work aims to study the structure of the mosaic boundaries, especially to find the crystallographic directions of the dislocation arrays within the transition layers by the electron microscopic observations on the etching pits formed on the surface of Ni-Mn single crystal.

## § 2. Specimen and Experimental Procedure

Single crystals of Ni-Mn alloy were prepared by solidifying slowly the melt of electrolytic nickel and metallic manganese in vacuum. The sample was then annealed at 1200°C for 20 hours. A specimen was cut to obtain a surface approximately parallel to (100) plane with an area of about 2 cm². After deep etching, this was annealed at 900°C for 3 hours, and then slowly cooled to room temperature, especially very slowly in the temperature range from 700°C to 300°C for 12 days within pure hydrogen atmosphere. After this heat treatment the alloy was chemically analysed and was found to contain 22.0 atomic percent Mn. Low specific electrical resistance of this specimen was considered to be an evidence that Ni and Mn atoms were in ordered state. The diffuseness of Laue spots, taken by back reflection, showed that the specimen was composed of mosaic blocks with the maximum deviation of their orientations 2∼3 degrees.

The procedure finally adopted as a standard preparation for the electron micrography of this alloy is as follows:

1. Carefull polish using conventional metallographic technique.
2. Electropolish with a current of 2.0 amp. /cm² at 40°C for 2 minutes in an electrolyte containing 100-cc phosphoric acid and 100-cc ethylalcohol. The cathode is a copper plate of large area.
3. Wash specimen in distilled water, rinse in ethylalcohol and dry rapidly. The surface of the specimen which is nearly parallel to (110) plane, is then ready for the preparation of a replica after the method developed by Fukami[10].
4. Formation of the collodion replica film using a solution of 0.5% collodion in amylacetate.
5. Formation of the reinfore film using a solution of 2% Ethocel in trichlorethylene.
6. Striping the replica film in hot water at 60°C.
7. Shadow casting by paradium.
8. Dissolving of backed Ethocel film in trichlorethylene.
9. After volatilization of the solvent the collodion reprlica films, ahered to a mesh, are ready for examination.

Observations have been made on the whole area of the specimen using one replica film. Some examples of the electron micrographs thus obtained, as well as the interpretation of their patterns will be given in the next section.

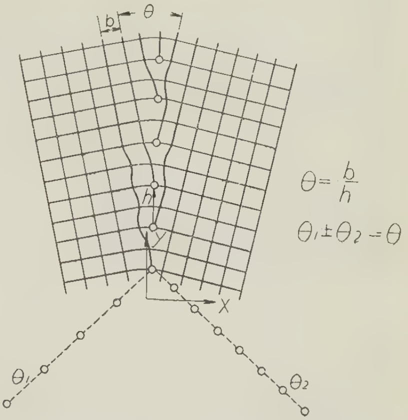

Fig. 1. A simple set of three low angle boundaries passed through one point which is composed of parallel edge dislocations.

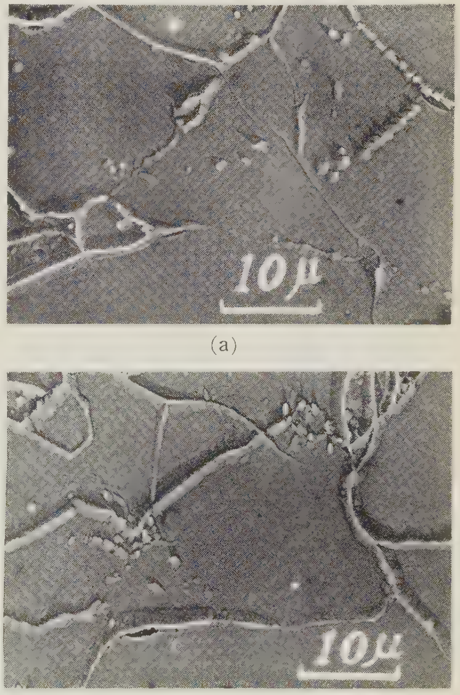

(a)

(b)

Fig. 2. Examples of electron micrographs of mosaic boundaries at low magnification.

## § 3. Observation and Discussion

Some examples of the electron micrographs of low magnification are shown in Fig. 2 (a), (b) which show that the single crystal is composed of small blocks with dimensions of the order of 1∼50 $\mu$. The boundaries between blocks consist of straight arrays of pits or ridges with fine structure, which can clearly be seen in the micrographs of high magnification as shown in Fig. 3 (a), (b) and (c). The individual pits which compose the boundaries are of sharp conical form, as shown in Fig. 3 (a), (b), and they are regularly spaced along straight lines. The ridge is seen to be composed of closely overlapping conical pits, as shown in Fig. 3 (c). In view of the tendency that etching pits will be formed around crystal defects such as dislocations, these observations

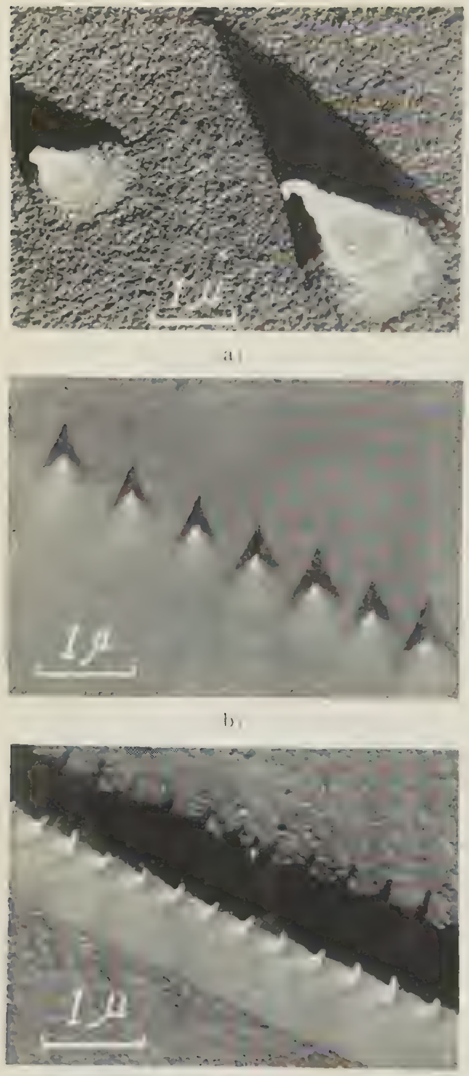

(a)

(b)

(c)

Fig. 3. Examples of electron micrographs of mosic boundaries at high magnification.

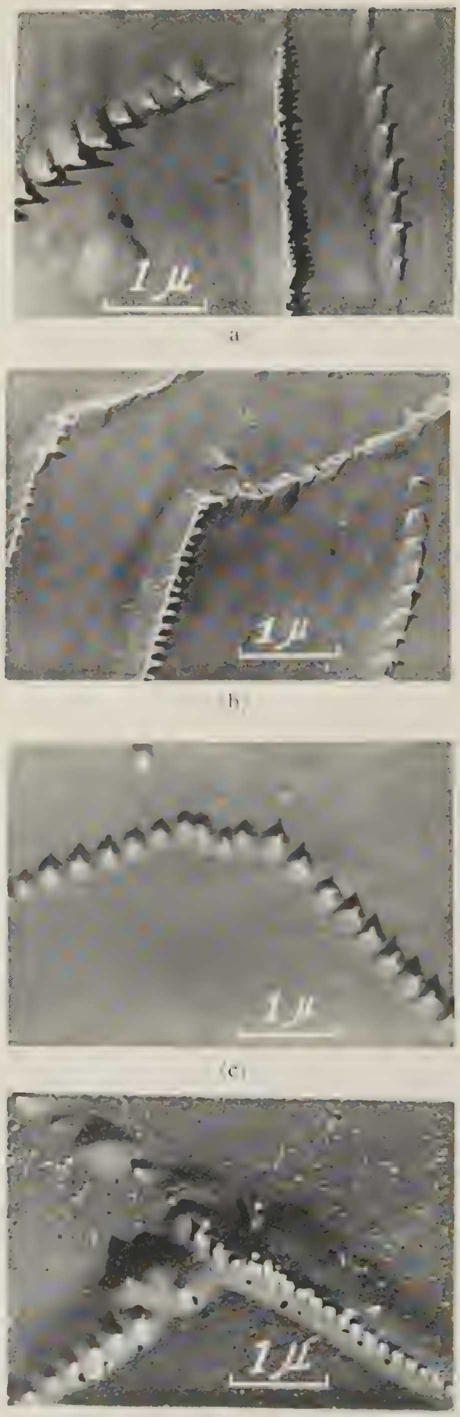

(a)

(b)

(c)

(d)

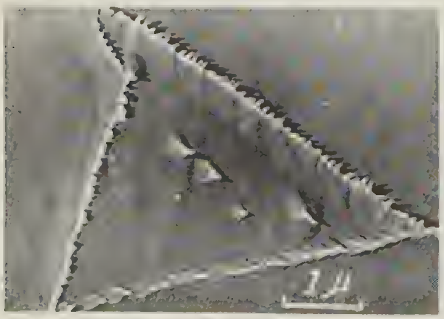

(e)

Fig. 4. Examples of electron micrographs of mosaic boundaries.

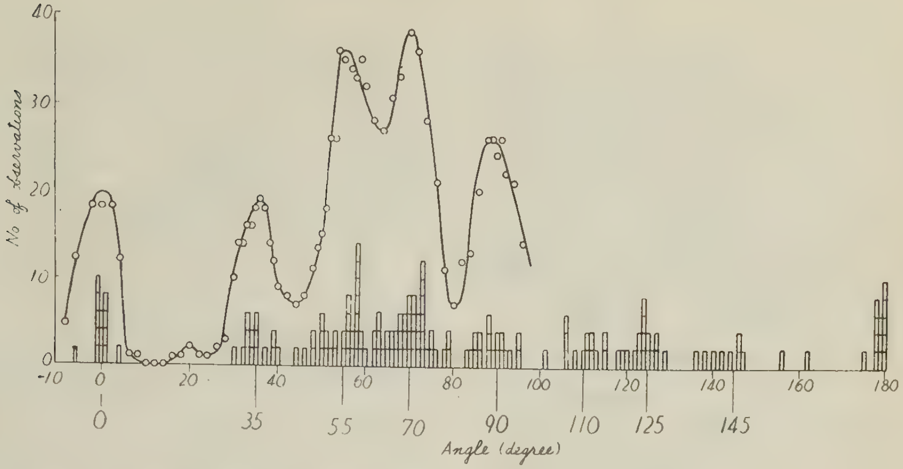

Fig. 5. Distribution of observed values of angles subtended between mosaic boundaries on (110) plane.

suggest that the mosaic boundaries are arrays of parallel edge dislocations which may be regularly spaced on some crystallographic plane. This possibility will be confirmed from the experimental fact that the maximum orientation diference between neighbouring crystal-blocks calculated from *X*-ray measurement (about 2∼3 degrees) is in good agreement with the estimation from the separation of pits, as already described in § 2.

Next, we will concentrate our attention on the values of angles subtended between mosaic boundary lines which meet at one point on the observed plane.

Some examples of electron micrographs are represented in Fig. 4 (a), (b), (c), (d) and (e). In Fig. 4 (a), two boundaries at the right side are almost parallel, while the angle between the two left boundaries is 57 degrees. Fig. 4 (b) shows three parallel boundaries and two of them change their directions with same angle 57 degrees. Fig. 4 (c) shows the micrograph near the intersecting point of two boundaries. The angle between these boundaries is 114 degrees and the transition from one to the other is not smooth but zigzag. Fig. 4 (d) shows three mosaïc boundaries intersecting at one point with angles of 68, 113 and 179 degrees. Fig. 4 (e) shows a triangle composed of three boundaries which intersect with angles of 73, 57 and 50 degrees respectively.

The angles subtended between two linear boundaries have been observed in 170 cases, and the result is plotted in Fig. 5 where a small rectangle represents one observation which corresponds to the angle represented by the abscissa. It seems that the observed values are not distributed at random, but make groups around several particular values. For the purpose of making the situation more clear, the angles from 90 to 180 degrees are replaced by their supplementary angles. Each small circle shown in the figure represents the number of observations, in which angles are contained within the range of ±5 degrees of the value specified by the absissa. The graph shows five peaks at 0, 35, 55, 70 and 90 degrees.

Interpretation of these five peaks would be given as follows: We may consider that dislocations are in the most stable state after prolonged annealing, especially after the annealing for the formation of superlattice. Frank[11] has given a simple criterion for the possibility of a dislocation-formation on the basis of the assumption that the energy of a dislocation is proportional to the square of its Burgers vector. The shortest lattice vector in a face-centered cubic lattice is $a/2\ \langle 110\rangle$ where $\boldsymbol{a}$ is lattice constant. The next shortest vector, $\boldsymbol{a}\ \langle 100\rangle$, can be decomposed into two shortest vector, $\boldsymbol{a}/2\ \langle 110\rangle$, but there is no gain of energy when this occurs. Then the Burgers vector of a stable perfect edge dislocation may be a lattice vector $a/2\ \langle 110\rangle$ or $\boldsymbol{a}\ \langle 100\rangle$.

Let us assume, as shown in Fig. 6 (a), that the dislocations along the direction $\langle 112\rangle$ with Burgers vector $a/2\ [\bar{1}10]$ on (111) plane are

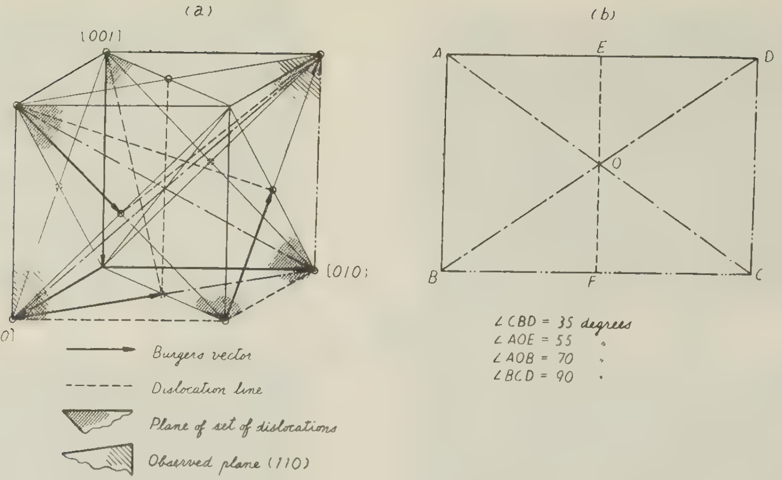

Fig. 6. Stable dislocations and boundaries composed of parallel edge dislocations (a), and patterns of boundaries on (110) plane (b) in face-centered cubic crystal.

stable and are regularly spaced on $(\bar{1}10)$ plane which is perpendicular to Burgers vector $a/2$ $[\bar{1}10]$ and (111) plane. The pits of a set of parallel dislocations on the observed plane (110) should be represented on the intersection of $(\bar{1}10)$ and (110) plane. i. e., EF as shown in Fig. 6 (b). In the same way, the pits of sets of parallel dislocations along $\langle 121\rangle$ with Burgers vector $a/2$ $[\bar{1}01]$ and $\langle 211\rangle$ with Burgers vector $a/2$ $[01\bar{1}]$ appear along AC and DB respectively on the observed plane. Moreover, if we assume that the dislocations along [100] or [010] with Burgers vector $\boldsymbol{a}$ $[00\bar{1}]$ are regularly spaced on the (001) plane, the pits of these parallel dislocations on the observed plane are represented along BC which is the intersection of (001) and (110) plane. In the same way, the pits of set of parallel dislocations along $\langle 100\rangle$ with Burgers vector $\boldsymbol{a}$ [010] appear along DC on the observed plane. Thus the mosaic boundaries composed of stable parallel dislocations may be observed along only EF (DC), AC, DB and BC on the (110) plane, as shown in Fig. 6 (b). Thus the angles subtended between any two among four kinds of boundaries are 0, 35, 55, 70, 90 degrees and their supplementary angles which really correspond to five peaks as shown in Fig. 5.

The plausibility of this interpretation can be confirmed by checking the relation among the three orientation differences of crystals on both sides of the three boundaries, passed through one point as shown in Fig. 1. The dislocations shown by the pits along DB and AC intersect the observed plane (110) with the same angle 35 degrees and have the same appropriate transition vector. Then the relation $\theta_1\pm\theta_2=\theta$ should be satisfied among three orientation differences of crystals on both sides of three boundaries along DB and AC, as seen in Fig. 4 (d). The relation has been checked by measuring the pits spacings on the boundaries. The result is in agreement with this expectation within a experimental error, as listed in Table I.

Table I. Relation among orientation differences of crystals on both sides of three boundaries passed through one point on (110) plane.

| Photograph No. | $\theta_1$ degrees | $\theta_2$ degrees | $\theta_1\pm\theta_2$ degrees | $\theta$ degrees |
|---|---|---|---|---|
| 65b3 | 0.028 | 0.050 | 0.078 | 0.081 |
| 98a3 | 0.11 | 0.15 | 0.26 | 0.28 |
| 101b1 | 0.13 | 0.09 | 0.22 | 0.23 |

## § 4. Conclusions and Acknowledgement

The electron microscopic studies on the mosaic boundaries in a Ni-Mn single crystal lead to the following conclusions. i) The mosaic boundary is composed of a set of parallel edge dislocations which are regularly spaced on some crystal lattice planes, as shown by Burgers, model. ii) The edge dislocations comprised in the mosaic boundary are stable in the crystal, as suggested by Frank. iii) The dislocations are regulary spaced on the plane which is perpendicular to the Burgers vector.

We wish to express our hearty thanks to Prof. S. Kaya for his kind guidance throughout this work. We also wish to thanks Messrs H. Noda, A. Fukami and S. Sakata for their suggestions and guidance in the electron microscopic technique.

## References

1) J. M. Burgers: Proc. Kon. Ned. Akad. Wet. **42** (1939) 293; Proc. Phys. Soc. London **52** (1940) 23.
2) W. L. Bragg: Proc. Phys. Soc. London **52** (1940) 54.
3) W. Shockley and W. T. Read: Phys. Rev. **75** (1949) 692; ibid. **78** (1950) 275.
4) K. T. Aust and B. Chalmers: Proc. Roy. Soc. A **201** (1950) 210.
5) K. T. Aust and B. Chalmers: Proc. Roy. Soc. A **204** (1950–1) 359.
6) W. L. Bragg and J. F. Nye: Proc. Roy. Soc. **A 190** (1947) 474.
7) P. La Combe: Report of Conference of the Strength of Solids (1948) P. 91.
8) J. J. Oberly: J. Metals **6** (1954) 1025.
9) F. L. Vogel, W. G. Pfann, H. E. Corey and E. E. Thomas: Phys. Rev. **90** (1953) 489.
F. L. Vogel: Acta Met. **7** (1955) 675.
10) A. Fukami: J. Electronmicroscopy of Japan **1** (1953) 28.
11) F. C. Frank: Physica **15** (1949) 131.
F. C. Frank and J. F. Nicholas: Phil. Mag. **44** (1953) 1213.

---

Journal of the Physical Society of Japan Vol. 11, No. 5, May, 1956

# Low Temperature Specimen Method for Electron Diffraction and Electron Microscopy

By Goro Honjo, Norihisa Kitamura, Kohji Shimaoka
*Tokyo Institute of Technology, Oh-okayama, Tokyo, Japan*
and Kazuhiro Mihama
*Japan Electron Optics Laboratory, Ltd., Kami-renjyaku Mitaka, Tokyo*

(Received February 18, 1956)

Techniques of low temperature specimen method for electron diffraction and electron microscopy were developed. Convenient low temperature specimen holders were constructed with a sufficient number of freedoms to adjust specimen settings for various observations. The temperature of specimen support could be varied within a range from liquid nitrogen temperature to +200°C. Contaminations of specimen caused by condensation of residual vapours, which usually occur considerably below −80°C, were practically eliminated by improving the vacuum of the apparatus and by the use of a special shield around specimen.

Results of preliminary studies on ice and mercury were briefly described: For ice, the contribution of hydrogen atoms to the diffraction pattern of ice was recognized; for mercury, the solid-liquid phase transition was studied by electron diffraction and the growth of hair-like mercury crystallites was observed by electron microscopy.

## § 1. Introduction

The application of electron diffraction method to specimens at low temperatures was reported by Gen et al. and other workers[1]. By this method, for example, the cubic modification of ice was discovered by König[2]. However, as yet the low temperature method of electron diffraction is not in as general use as the low temperature method of *X*-ray diffraction. Until recently no report has been

Table I.

| Mode of movement | Mechanism | Range |
|---|---|---|
| 1. Translation perpendicular to the plane of Fig. 1 | Glide of *H* on *G* | ±5 mm |
| 2. Translation along *XY*-axis | Glide of *FN* in *L* (The movement is made by turning *M* against *N*.) | ±7 mm |
| 3. Rotation around the axis perpendicular to the plane of Fig. 1 | Glide of *L* on the cylindrical surface of *H*. | ±6° |
| 4. Rotation around *XY*-axis | Rotation of cylinder *E* in *F* | ±30° |

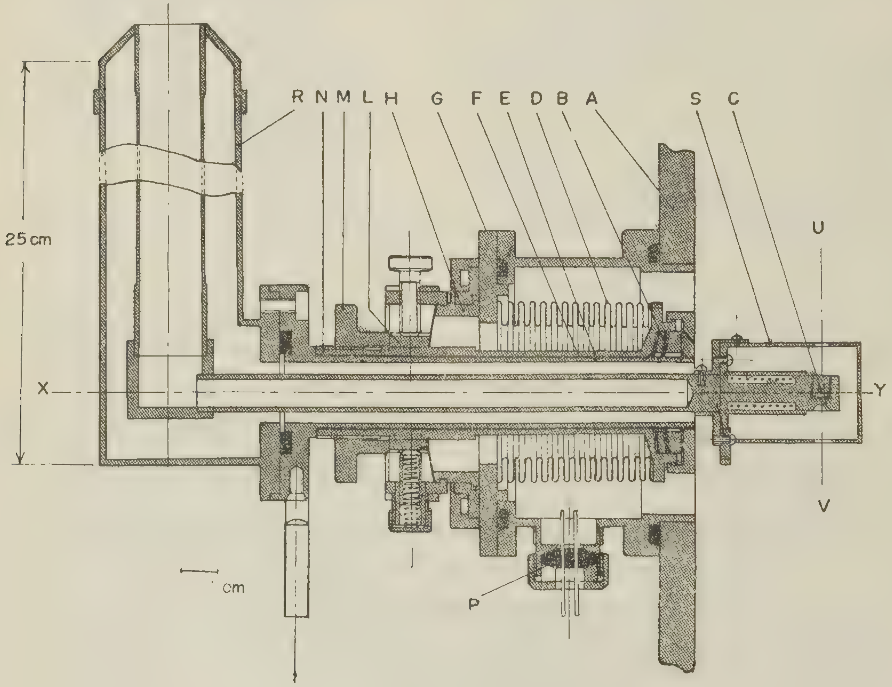

Fig. 1.

published concerning a similar method for electron microscopy.

The present authors have constructed convenient low temperature specimen holders for electron diffraction and electron microscopy and have applied the low temperature method to the studies on ice and mercury. Details of the techniques and preliminary results of these studies are reported here.

## § 2. Specimen Holder

One of the difficulties in constructing low temperature specimen holders is the requirement that the holder must carry a refrigerant reservoir of considerable size. Because of this difficulty, previous workers have designed only transmission specimen holders with restricted freedoms to adjust settings of specimen. Since the reflexion method also was required for our study, a holder was constructed which could work for both methods.

Photo. 1 shows arragement in the specimen chamber and Fig. 1 gives the detailed construction of our holder. *R* is the refrigerant reservoir to be filled with liquid nitrogen or other refrigerants. The reservoir is essencially a vessel of double walls, the space between the walls to be evacuated as well as the specimen chamber. The vertical inner and outer walls were made of brass tubes of thickness 0.5 and 1 mm, respectively, and they are as long as about 25 cm. Thus the vessel is provided with a sufficient capacity (about 60 cc.) and good thermal insulation (see, § 4). Wilson vacuum seal *B* and sylphon bellow *D* give allowance for the specimen movements as tabulated in Table I.

The range of the rotation 3 is sufficient to change the glancing angle of a reflexion specimen and the range of rotation 4 is sufficient to change the azimuthal angle of a reflexion specimen.

Detail of the part around specimen *C* are shown in Fig. 2 and Photo. 2. *S* is a cylindrical shield against radiation and contamination (Cf. § 3). Shutter *W* with throats *T* and *T′* can be rotated around shield *S* by a loosely coupled hook *K* which can be controled from the outside of the specimen chamber by nob *Q* (Photo. 1). During observation the windows of the shield are opened for the electron beam, while the windows can be closed (see, § 3) by turning the throats to positions as indicated by dotted line in Fig. 2b. Part *d* in Fig. 2a is the support of reflexion specimen and *e* is an additional shield. For transmission specimen, *d* and *e* of Fig. 2a are replaced by *d* and *e* of Fig. 2c. Heating coil *h* has a power about 20 Watts. A copper-constantan thermocouple is attached to *e*. The lead-wires for the heater and the couple are connected to terminals such as *P* in Fig. 1 through tunnels *a* and *b*.

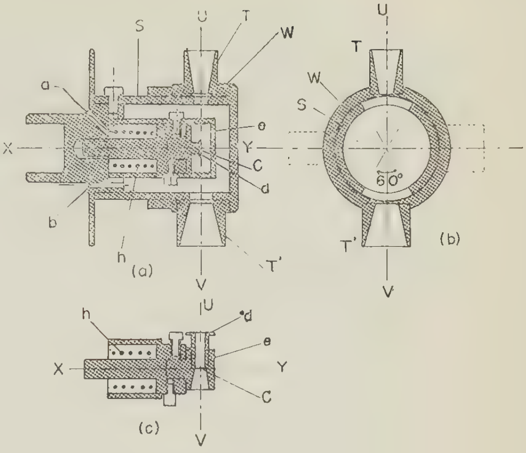

Fig. 2. Arrangement around specimen.

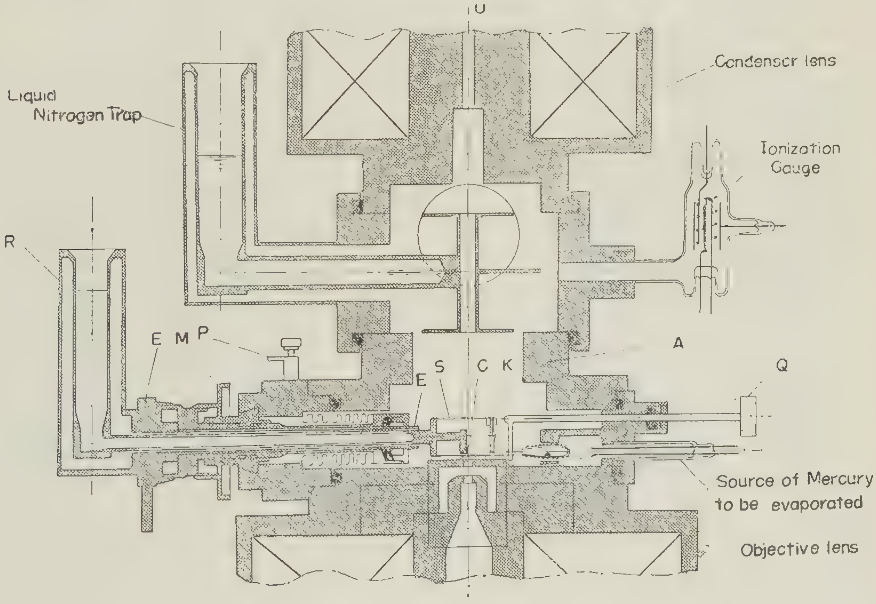

Fig. 3.

The specimen holder for electron microscopy* (Fig. 3) is similar to that for electron diffraction but much more compact since the stage *L* of Fig. 1 is omitted. Thus the rotation 3 of specimen (Table I) is not possible. Boiling of a refrigerant such as liquid nitrogen caused irregular specimen vibration of amplitude of about 1 $\mu$. To eliminate the vibration, the part connected to the specimen was clamped to *E* by a piece of cork. In this way electron micrographs of electron optical magnification

---

* This was designed for use in E. M. type 5 of Japan Electron Optics Laboratory, Ltd. in which the object plane is in a position about 4 mm above the top of objective pole piece. With slight modification, it can be also used in any electron microscope of conventional type in which a specimen is inserted into the throat of objective pole piece.

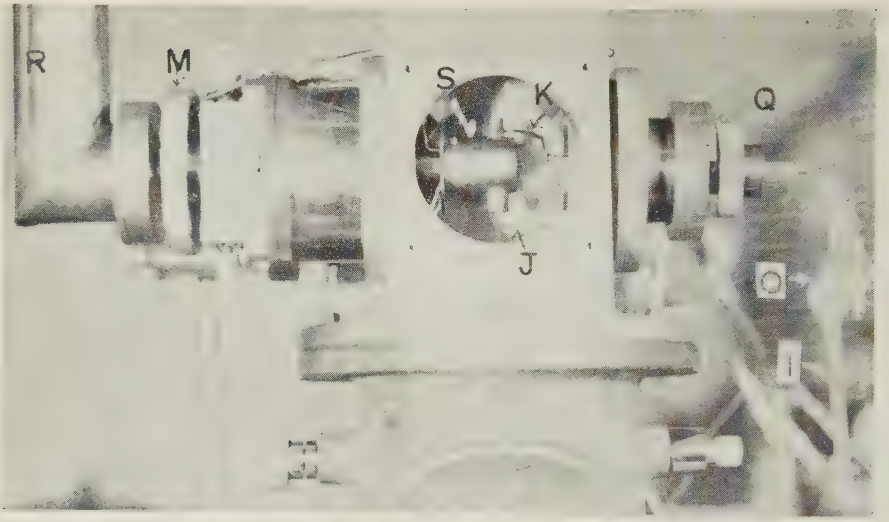

Photo. 1. Specimen chamber arrangement for low temperature method of electron diffraction.

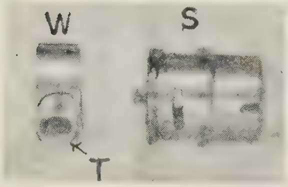

Photo. 2. Shield around specimen.

as high as 10,000 can be taken without much difficulty.

## § 3. Contamination of Specimen

One of principal difficulties of the low temperature method which must be overcome is the contamination of specimens due to materials condensing from residual vapours.

In preliminary experiments carried out under conventional vacuum of $5\times10^{-4}\sim1\times10^{-5}$mmHg of electron diffraction camera and electron microscope, we found that the condensed materials were negligible above $-80\sim-100$°C but below these temperatures we found them to be considerable to the extend that within several minutes they cover the specimen surface so thickly that the diffraction pattern due to specimen is concealed behind the pattern of the condensed material (Photo. 3).

Oily vapour has been considered the main source of contamination, but water vapour may be more likely, because the larger part of residual vapours is usually water vapour. The above mentioned findings correspond to the fact that dew points of water vapour of pressures $4\times10^{-4}$ and $1\times10^{-5}$ mmHg are at $-80\sim-100°C$. König identified the condensed material with cubic ice and we have confirmed his identification (Photo. 3b and see, § 5(a)).

By the use of the kinetic theory of gas, the number of water molecules impinging onto the specimen through the windows of shield is calculated as

$$n\approx3\times p\cdot\alpha\times10^{22}$$

molecules per cm² per minute

at room temperature, where $p$ is the pressure of the water vapour in mmHg. and $\alpha$ is given by $\alpha=\sin\Theta$, $\Theta$ being the effective semi-aperture angle of the windows. If all the molecules were condensed on the specimen at low temperatures, it would result in a deposition of ice at a rate of thickness increase given by

$$dh/dt=n\cdot m/\rho\approx1\times p\cdot\alpha \quad \text{cm per minute.}$$

(The mass $m$ of a water molecule is $3.0\times10^{-23}$ gr. and the density $\rho$ of ice at $-100$°C is 0.92 gr./cm³.) When $\alpha$ is the order of 1/10, as it was in our experiment, $dh/dt$ is 5,000∼100Å/min. for $p$ of $5\times10^{-4}\sim1\times10^{-5}$mmHg. and thus it seems natural that contamination occurs as rapidly as stated above.

Contamination of another nature occurred in our preliminary electron microscopic experiments. Although this contamination also became remarkable below $-80\sim-100$°C, it remains on the specimen even when it is rewarmed up to $+200°C$ in the apparatus (Photo. 4). It was proved that this contamination is caused by electron irradiation and that

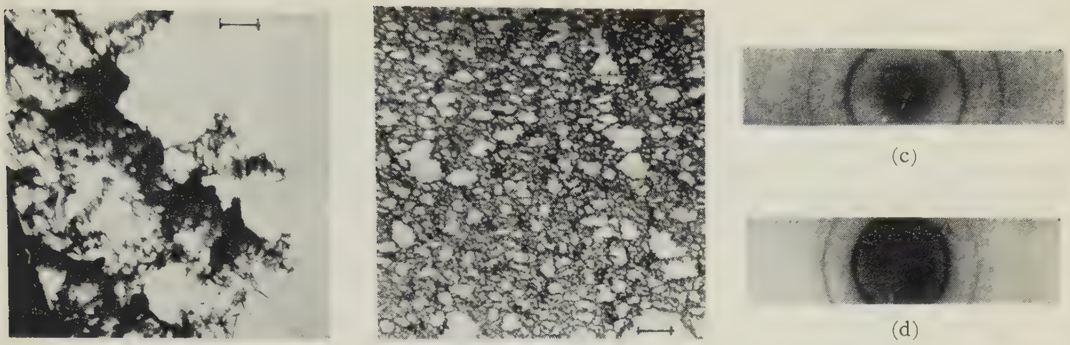

(a) (b) (c) (d)

Photo. 3. Micrographs and diffraction patterns of ice condensed from residual vapours of pressure of the order of $1\times10^{-4}$ mmHg. Micrographs were taken at electron optical magnification of ×5,000 with exposures of about 5 seconds. Diffraction patterns were taken by the method of three-stage microscope.

(a) Zinc oxide smoke covered by ice within several minutes after the charge of liquid nitrogen at −80°C.

(b) Ice condensed on collodion film at −80°C (The temperature was measured at the specimen support. Thickness and radius of the film were 400Å and 5 $\mu$, respectively).

Diffraction patterns (c) and (d) correspond to (a) and (b), respectively. All the rings can be indexed by the structure of cubic ice found by König.

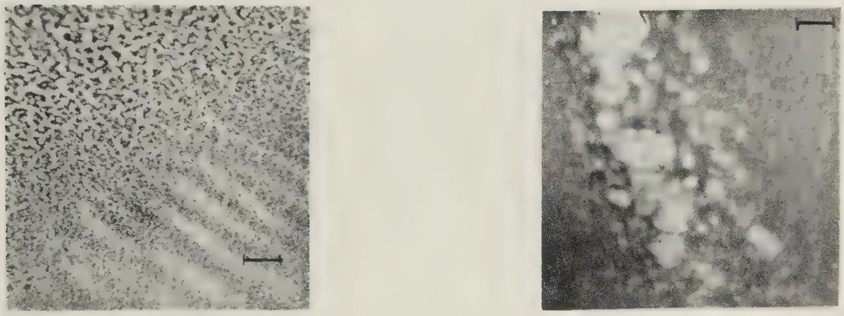

(a) (b)

Photo. 4. Contamination on collodion films produced by electron irradiation for several minutes at liquid nitrogen temperature in conventional vacuum of the order of $1\times10^{-4}$ mmHg. These micrographs were taken after the films were rewarmed upto +200°C.

the amount of deposit depends on dosage of electron irradiation. It produces an electron diffraction pattern of only two diffuse halos at $\sin\theta/\lambda=0.24$ and 0.44Å$^{-1}$. The origin and nature of this product have not yet been studied, but it is very likely that this contamination is similar to that which occurs in ordinary electron microscopy and which is considered as a product of hydrocarbon vapour decomposed by electrons$^{3)}$. The rate of deposition seems to be considerably accelerated below −80∼−100°C by the condensing water vapour.

In order to reduce contaminations, we can minimize $\alpha$ down to 1/100. Since, however, a larger aperture of the order of $\alpha\sim1/10$ is desirable in practice for the sake of wider freedom of observation, we tried to reduce the contamination by (i) shutting out the contaminating vapour from specimen by keeping the windows of shield around specimen closed except during observation, and especially during the procedure of cooling down the specimen to desired temperatures, and (ii) with special precautions, improving the working vacuum as far as possible. The actual procedure of the experiment was as follows:

First, the apparatus is evacuated up to 1∼2

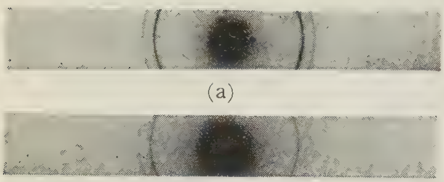
(a)

(b)

Photo. 5.

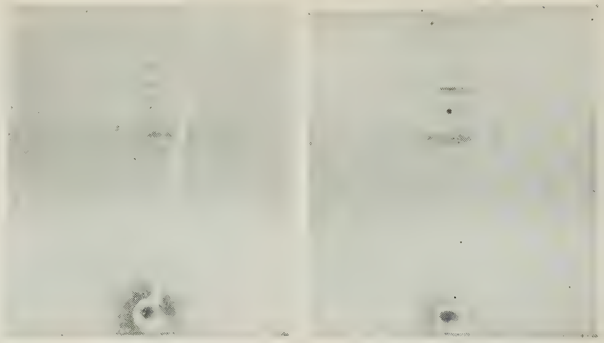
(a) (b)

Photo. 6.

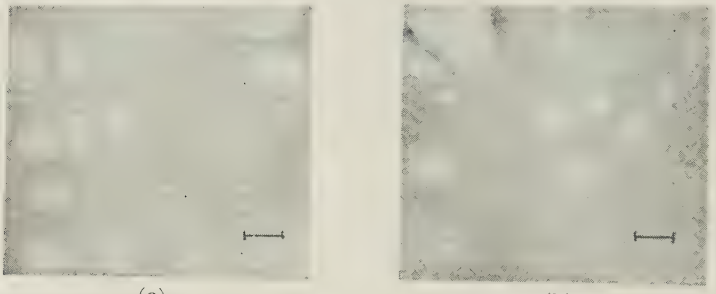
(a) (b)

Photo. 7.

Photo. 5. Electron diffraction patterns from aluminium film of about 200 Å thick.
(a) at room temperature before cooling.
(b) after 30 minute continual observation at liquid nitrogen temperature.

Photo. 6. Electron diffraction patterns from cleavage face of zincblende.
(a) at room temperature before cooling.
(b) after 10 minute continual observation at liquid nitrogen temperature.

Hhoto. 7. Electron micrographs of collodion film of about 400 Å thick.
(a) at room temperature before cooling.
(b) after 45 minute continual observation at liquid nitrogen temperature.

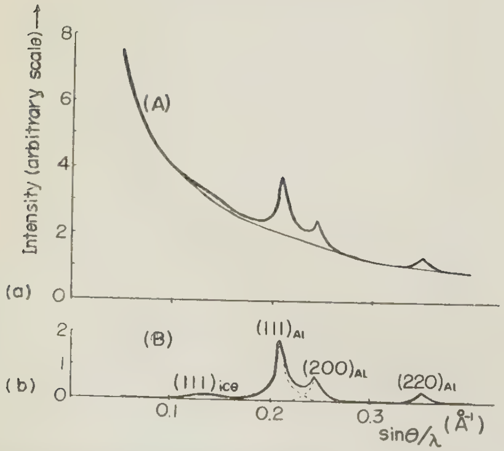

Fig. 4. Intensity plot of the diffraction pattern of Photo. 5 b.

$\times 10^{-5}$mmHg*. Next, a liquid nitrogen trap is charged. For electron diffraction camera the trap is attached to the top of the pumping system and for electron microscope (Fig. 3) it is attached just above the specimen part. Then, after the window shutters are closed, refrigerant is poured into the reservoir to cool down the specimen. At this stage the vacuum of the specimen chamber becomes about 1~2 $\times 10^{-6}$mmHg. Finally the shield is bombarded by the electron beam for several minutes and then the shutter are opened to the electron beam.

This procedure efficiently reduced contami-

---

* It was possible to attain to this vacuum within one-half hour after each recharge of photographic plates. The pumping system utilized in our experiments was a 3-inch oil diffusion pump backed by a phosphorus pentoxide trap and a 150$l$/min. oil rotary pump. Inside walls of all parts of the apparatus were throughly cleaned and baked before assembling them. Only well-dried air was let into the apparatus when the vacuum was broken. Photographic plates were well-dried beforehand in another vacuum system.

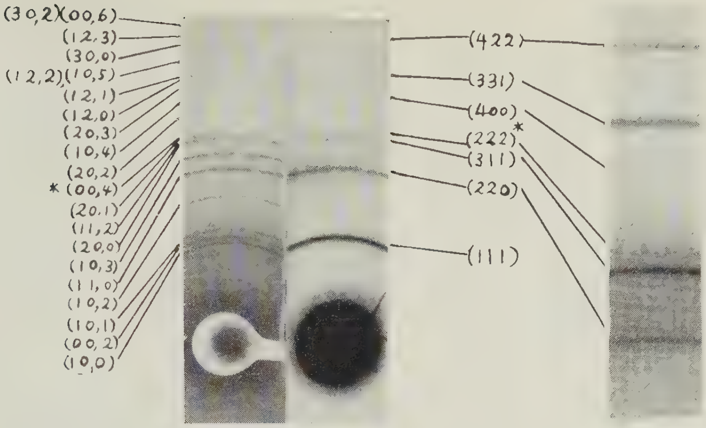

(a) (b) (c)

Photo. 8. Electron diffraction patterns from two modifications of ice.
(a) Hexagonal ice, (b) Cubic ice, (c) Magnified reproduction of (b). Pay attention to (222)-reflexion in (b) and (00,4)-reflexion in (a).

Table II.

| Index of ring | $\sin\theta/\lambda$ (in Å$^{-1}$) | | Relative intensity* | |
|---|---|---|---|---|
| | Al | Ice | Al | Ice |
| 111 | 0.214 | 0.136 | 100 | 38 |
| 200 | 0.247 | — | 37 | — |
| 220 | 0.350 | 0.222 | 15 | 18 |
| 311 | 0.410 | 0.261 | 14 | 6 |

* The intensity was calculated by the formula $I=k\cdot d/v^2\cdot q\cdot F_{hkl}/(\sin\theta/\lambda)^6$, where $k$ is a constant, $d$; the thickness of the film, $q$; the multiplicity factor and $v$; the unit cell volume. For the structure factor for cubic ice, see § 5.

nations. Photo. 5(a) and (b) reproduce electron diffraction patterns produced from an aluminium film of thickness of about 200Å; (a) was taken before cooling at room temperature and (b) at liquid nitrogen temperature after a continual observation for 30 minutes. Curve (A) of Fig. 4 gives the intensity plot obtained by photometry of the pattern Photo. 5 (b). Calculated relative intensity and values of $\sin\theta/\lambda$ of Debye rings are tabulated in Table II for aluminium and cubic ice films of the same thickness.

The intensity peaks of curve (A) in Fig. 4 can be analysed into curve (B). The intensity peak of (111)-reflexion of ice does not exceed one-half that of (200)-reflexion of aluminium. We can safely say, therefore, that deposition of ice on the aluminium film was less than 100 Å and, according to the above estimation of the rate of deposition of ice, the pressure of residual water vapour must have been as low as a fraction of $1\times10^{-6}$mmHg.

Since in practice the necessary observation time is less than 30 minutes, the contamination is quite negligible.

Photo. 6 (*a*) and (b) reproduce electron diffraction patterns from a cleavage face of zinc blende; (*a*) was taken before cooling at room temperature and (b) at liquid nitrogen temperature after a continual observation of 10 minutes. In these patterns no appreciable effect of contamination is found. It may be worth noting here that the contaminating effect on diffraction patterns should be nearly the same for reflexion specimens as for transmission specimens, because in the reflexion method the aperture of the shield is inclined towards the specimen surface and consequently the rate of deposition is reduced by the factor by which the effect of contaminations is multiplied.

Photo. 7 (a) and (b) show a pair of electron micrographs of a collodion film of about 400 Å thick; (a) taken before cooling at room temperature and (b) at liquid nitrogen temperature after a continual observation of 45 minutes. There is no appreciable change in the contrast between the film itself and the holes, proving that contaminations were completely eliminated.

## § 4. Temperature of Specimen

The temperature of the specimen support *e* (Fig. 2) can be varied within a range from

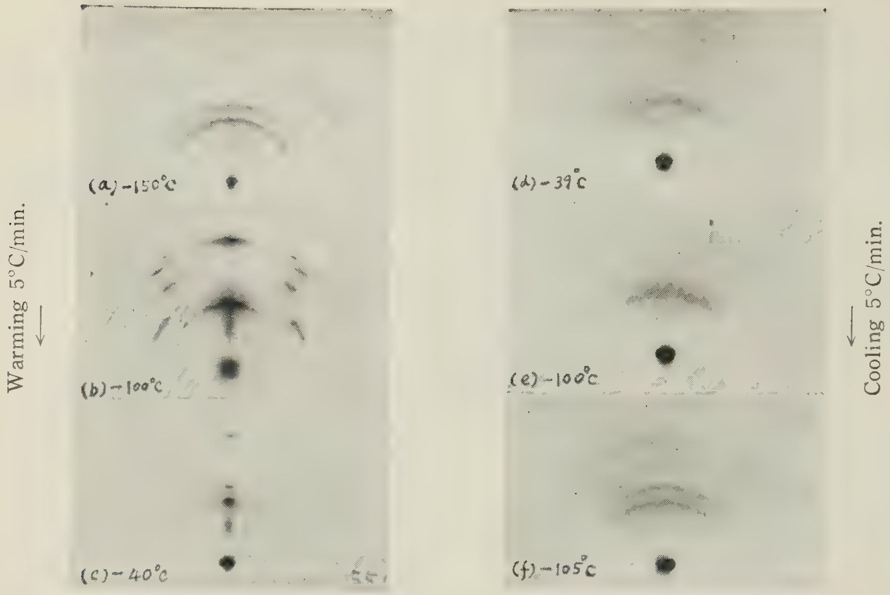

Photo. 9. Electron diffraction patterns from mercury at various temperatures.

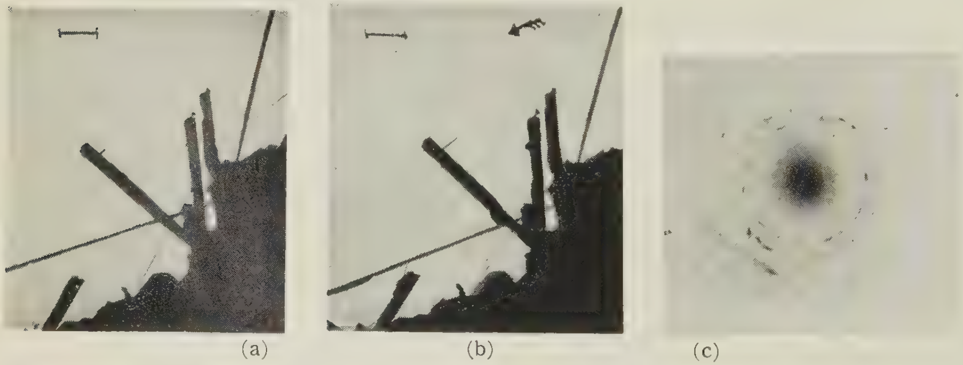

Photo. 10. Micrographs and diffraction pattern of hair-like crystals of mercury.
(a) Hair-like crystals formed by condensing mercury vapour at about −100°C.
(b) Two minutes after (a). The crystal indicated by the arrow completed its growth within a fraction of a second.
(c) Diffraction pattern corresponding to (b), taken by three-stage method.

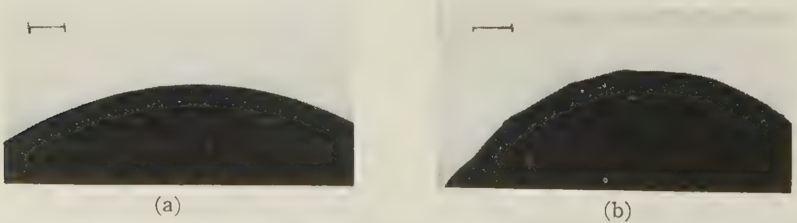

Photo. 11. Micrographs of mercury droplet.
(a) Liquid state, (b) Solid state, crystallized at about −100°C. Pay attention to polygonization in (b).

the temperature of liquid nitrogen to +200°C. The lowest temperature can be maintained for 20 minutes by one charge of liquid nitrogen without further supply. It is not difficult to maintain a desired temperature within a fluctuation less than a few degrees for an observation period of as long as an hour.

The electron irradiation, however, produces a temperature difference between specimen and the specimen support. Although an exact estimation of the temperature difference is difficult to make, the following discussion may be valuable.

As already noted, it was observed by electron microscope that water vapour condenses on a specimen surface when it is in a coarse vacuum. By this phenomenon we were able to prove that the temperature rise due to electron irradiation is not so large as that predicted by Borries and Glaser[4]. They gave a formula to calculate the temperature $t$ at the centre of a film spanning on a circular aperture of radius $r$ for a given temperature $t_0$ of the support and for a given specific specimen load (Objektbelastung) $\Delta n_0$. According to their formula, the calculated temperature $t$ turns out as high as $-40°\mathrm{C}$ for a collodion film of thickness 400 Å and $r=50\,\mu$, provided $t_0=-80°\mathrm{C}$ and and $\Delta n_0=0.05$ Watt/cm$^2$. The values of thickness and radius adopted here are those of our experiments (Photo. 3b). Although the specific load is difficult to estimate, the value 0.05 Watt/cm$^2$ adopted here is the lowest possible value for electron microscopic observations according to Borries and Glaser. If the calculated temperature is actually the real one, no ice would be deposited on our collodion film at $t_0=-80°\mathrm{C}$. However, we did observe the deposition at $t_0=-80°\mathrm{C}$ (Photo. 3b) under a moderate irradiation (Photo. 3b). This discrepancy may be due either to failure in estimation of specific load or to some change in thermal conductivity of the film because of irradiation. In any event, our observation proves that the specimen temperature must be kept very low contrary to the openion of Borries and Glaser.

In ordinary electron diffraction, the specific load is more than one hundred times less than that in electron microscopy. For example, for the former the load is $5\times10^{-4}$Watt/cm$^2$ (total current$\sim1\times10^{-10}$Amp. for specimenn area$\sim(0.1\,\mathrm{mm})^2$[5]). Thus, even according to Borries and Glaser, the temperature rise is only a fraction of a degree at $t_0=-200°\mathrm{C}$ for collodion film of the same thickness and radius as above (400Å; $r=50\,\mu$).

## § 5. Application of the Low Temperature Method

Some results of preliminary studies on ice and mercury are briefly described below.

(a) *Study on ice*

As mentioned before, König identified the material condensed from residual vapour as ice of new modification of a diamond-type structure with the lattice constant $a=6.36$ Å. This structure is closely related to the well-known hexagonal structure of ice ($a=4.50$ and $c=7.34$Å; the relation is similar to that between cristobalite and tridimite.

Since in our experiment the condensation of residual vopour was eliminated, the vapour was supplied from a prepared source to form ice. In the glass tube $I$ in Photo. 1 we enclosed small pieces of silica gel which had absorbed a suitable amount of water vapour. By opening the cock $O$ the water vapour from the gel was ejected from the jet $J$ onto collodion film at low temperatures.

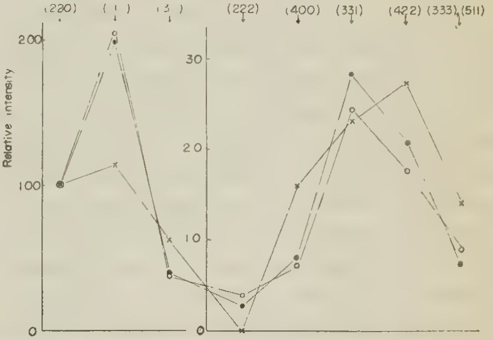

Fig. 5. Comparison of the observed and calculat- intensities of cubic ice. Plain circles, black circles and crosses represent, the observed intensity, the calculated intensity taking account of hydrogen atoms and the calculated intensity neglecting the hydrogen atoms, respectively.

Photo. 8 (a) and (b) reproduce electron diffraction diagrams produced from ice; (a) was produced from ice formed above $-80°\mathrm{C}$ and then cooled down to $-150°\mathrm{C}$ and (b) from ice formed at $-150°\mathrm{C}$. Diagrams (a) and (b) can well be indexed, respectively, by hexagonal and cubic structures of ice. The ice formed below $-160°\mathrm{C}$ was found to produce only diffuse halos, indicating that the crystal growth is poor at these temperatures. When the specimen was warmed up to $-150°\mathrm{C}$, the halos developed rapidly into sharp rings appropriate for cubic structure.

Although König could not detect (222)-reflexion from cubic ice, we were able to find the reflexion and the corresponding reflexion (00,4) for hexagonal ice. If the scattering of electron by hydrogen atoms were negligible as supposed by König, these reflexions would not appear. Actually, electrons are scattered appreciablely by hydrogen atoms⁶⁾, and the observed intensity of our diffraction diagrams deviates considerably from the value calculated by neglecting the scattering by hydrogen atoms (Fig. 5). If, however, the scattering by hydrogen atoms is taken into account, the observed intensity agrees very well with the calculated value (Fig. 5). In the calculation we assumed Pauling's positions for hydrogen atoms⁷⁾ and adopted Weinstein's scattering power⁶⁾. Further studies concerning the structure of ice is now in progress.

(b) *Study on mercury*

Liquid and solid states of mercury were studied by electron diffraction and electron microscopy. Our interest was directed to this study by the following reasons: ( i ) Previous electron diffraction studies which belong to earlier dates of the developement of electron diffraction method gave results contradicting to each other even about the types of diffraction patterns⁸⁾. (ii) The characteristic crystal growth "whiskers" has been suggested for mercury by Sears⁹⁾. (iii) It was expected that the temperature rise of specimen caused by electron irradiation could be checked by observing the liquid-solid phase transition.

Mercury evaporated onto a rigid substrate such as cleavage face of crystal produced clear electron diffraction patterns of solid and liquid phases without ambiguities as reported by previous observers.

Photo. 9 reproduces a series of diffraction patterns of mercury at various temperatures; Pattern (a) is ordinary Debye-rings of solid mercury. When the specimen warmed, the ring pattern changed to pattern (b) of fibrous orientation at about −100°C. Degrees of orientation were improved at higher temperatures as shown by pattern (c). Pattern (c) changed to halo pattern (d) exactly at the melting point −39°C. When the specimen was cooled, the halo pattern remained down to as low as −100°C (e), indicating a remarkable supercooling, and changed to ordinary Debye-rings (f) at lower temperatures. Solid patterns showed sometimes fine structures (Photo. 10c), suggesting the characteristic crystal growth.

Electron micrographs revealed a conspicuous hair-like growth of mercury crystals (Photo. 10). It was noteworthy that the growth of hair-like crystallites completed themselves within a fraction of a second as could be observed on the fluorescent screen. The thickness and length of crystallites differed considerably according to the temperature and supply rate of mercury vapour.

The two micrographs in Photo. 11 show that a droplet of liquid mercury was polygonized through crystallization at about −100°C.

Unless electron irradiation was made unnecessarily heavy, the solid state of mercury could be maintained under electron microscopy up to $t_0 \sim -40°\mathrm{C}$ without appreciable effect of the irradiation. Thus, for the reflexion specimens of above observations, the temperature rise due to electron irradiation was not significant. If mercury particles were dispersed on collodion film well-separated from each other, the temperature rise might be considerable. But we could not prepare such mercury specimen and could not check the temperature rise for this more interesting case.

In conclusion, the authors express their sincere appreciation to Professors Shizuo Miyake and Ryozi Uyeda for their interest and helpfull suggestions. Credit is due Mr. Kenzi Kazato, Dr. Kazuo Ito and technical staffs of Japan Electron Optics Laboratory, Ltd. for providing facilities used in this research.

## References

1) M. I. Gen, I. Zellmanoff and A. I. Schalnikoff: Phys. Zeit. Sowjetun. **4** (1933) 825.
G. Hass: Ann. d. Phys. **31** (1938) 245.
A. Charlesby: Proc. Phys. Soc. **57** (1945) 510.
J. Skrebowski: Proc. Phys. Soc. **61** (1947) 430.
2) H. König: Nach. Akad. Wiss. in Göttingen, Math.-Phys. Kl. (1942) Heft 1, 1. Zeit. Kristallog. (A) **105** (1943) 273.
3) H. König: Naturwiss. **35** (1948) 261.
4) B. von Borries and W. Glaser: Koll. Zeit. **106** (1944) 123.
5) L. Germer: Rev. Sci. Inst. **6** (1935) 188.
S. Lennander: Arkiv f. Fys. **8** (1954) 551.
6) B. K. Weinstein: Doklady Akad. Naouk **85** (1952) 1239. J. eksp. teoret. Fiziki **25** (1953) 157.
J. M. Cowley: Acta Cryst. **6** (1953) 516.
7) L. Pauling: J. Amer. Chem. Soc. **57** (1935) 2680.
8) Cf. G. P. Thomson and W. Cochrane: Theory and Practice of Electron Diffraction. MacMillan, London, (1939).
9) G. W. Sears: Acta Metal. **1** (1953) 457; **3** (1955) 361.

JOURNAL OF THE PHYSICAL SOCIETY OF JAPAN Vol. 11, No. 5, MAY, 1956

# Magnetic After-Effect in $Ni_3Mn$ Alloy

By Tadami TAOKA

*Institute of Science and Technology, University of Tokyo*

(Received January 10, 1956)

In nickel-manganese alloy with stoichiometric composition $Ni_3Mn$, very remarkable magnetic after-effect has been found. The after-effect (i) is large at the intermediate state of order of the alloy, (ii) is most noticeable at the steepest part of the magnetization curve, (iii) is comparatively temperature insensitive, and (iv) is not affected by mechanical deformation. The experimental formula of the phenomenon is well expressed by an analytical form derived by Street and Woolley on the basis of the concept of thermal activation process of single domain particles. It has been confirmed by electron microscopic study that the alloy with remarkable magnetic after-effect is composed of innumerable number of small particles of prolate ellipsoidal form embedded in matrix. The dimension of these particles is of such a order of magnitude that is occupied by only single magnetic domain.

## § 1. Introduction

In our previous paper[1] on $Ni_3Mn$ alloy, we have reported some preliminary observations on the anomalously large and long magnetic "after-effect" or "viscosity" which was observed in the alloy having intermediate state of order, but the mechanism of this anomalous effect has remained unsolved.

Formal theories have been developed to express the various types of the phenomena observed on many materials since Preisach[2] and Richter[3]. Recently, some investigators have proposed various hypotheses concerning the physical origin of the phenomena.

Snoek[4] has assumed that the magnetic viscosity is due to the retarded rearrangement of impurity atoms following the movement of domain walls. This theory has been recently extended by Néel[5], and further, Snoek and independently Tomono[6] have confirmed the theory by experiments carried out on low carbon steel.

There are another types of magnetic after-effect which was called "irreversible after-effect" by Néel[7]. He has proposed two kinds of mechanisms to interpret this category of after-effect. Firstly, he[8] has investigated the magnetic properties of fine powders which are small enough for each one to contain only a single elementary Weiss domain. In his theory, he takes account not only of the usual rotations of the domain orientations produced by the application of magnetic field against the different forces of anisotropy: anisotropy of form, magnetocrystalline anisotropy etc···, but the spontaneous rotations due to thermal fluctuations which provoke a kind of magnetic Brownian motion. This concept has been applied to the interpretation of the thermoremanent magnetization of lavas and clays. Secondary, Néel[9] has considered the magnetic after-effect due to the thermal activation of domain walls. On activation, the domain boundary wall sweeps through a certain volume which corresponds to a Barkhausen discontinuity. He applied this theory to the results obtained by Barbier[10] on an Alnico specimen.

Street and Woolley[11] have carried out a mathematical treatment on magnetic viscosity based on activation energy concepts, and applied the results thus obtained to the phenomenon occuring in materials in which bulk magnetization proceeds by the rotation of each single domains. Experiments have been made in detail on specimens of Alnico maintained at various temperatures and its results have been shown to be in agreement with the theoretical analysis.

In spite of these extensive investigations, there appears to be no experiment which leads to an unambiguious confirmation of the underlying physical origin except for the case in which the after-effect is caused by diffusion of impurity atoms. The observed phenomena on different materials may probably be attributed to the different mechanism.

In this paper the magnetic after-effect

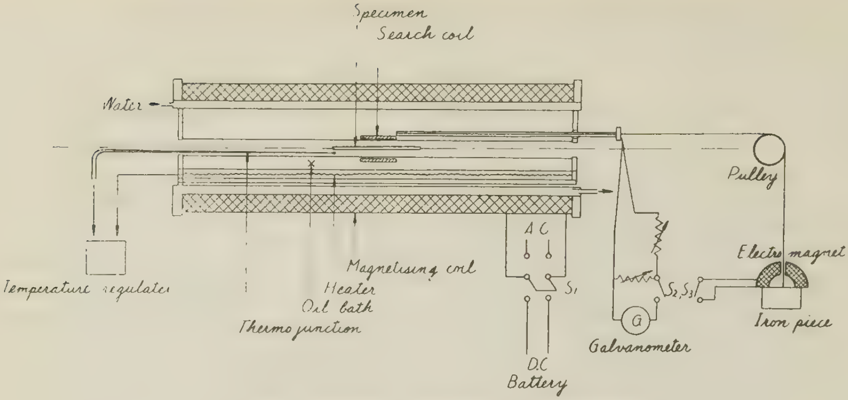

Fig. 1. Schematic diagram of apparatus.

observed on the virgin magnetization curve of $Ni_3Mn$ alloy is reported in detail. The phenomenon is affected by the strength of the applied field, the temperature and especially the degree of the material.

The present observations will be compared with the previous experiment results, as well as with the results expected from the theories described above. Finally, a physical mechanism is proposed in connection with the stages of development of ordered phase within the alloy, which have been comfirmed by the electron microscopic study.

## § 2. Specimen, Apparatus and Method

The specimen used in this study was a rod of $Ni_3Mn$ alloy of length 214 *mm*. and diameter 1.5 *mm* with the demagnetizing factor $D=0.00251$. This is the same specimen described in the previous paper.

The heat treatments necessary for the formation of the superlattice of appropriate degrees of order have been made after the suggestion described in the paper put forwarded by S. Kaya²⁾. Different states of order were obtained by quenching the specimen, in the course of slow cooling from 700°C (disorder), 530°C, 520°C, 500°C, 480°C, 420°C and room temperature (perfect order) respectively. The dependence of the saturation induction on quenching temperature has been shown in Fig. 2 of the previous paper.

The arrangement of the apparatus is shown in the schematic diagram of Fig. 1. The specimen was placed inside a search coil in an oil bath which could be maintained at any constant temperature between 10°C and 100°C within about 1°C during measurement. External magnetic field was applied by means of solenoid of length 90 *cm*, of which temperature could be maintained constant by supplying water of constant temperature. The required stability of the magnetic field (about 0.2%) could only be obtained by supplying the current to the solenoid from a 12 V battery of large capacity. The search coil of 4100 turns was connected, through a suitable variable resistance, to be ballistic galvanometer of period 10 sec. The galvanometer deflection was 1.0 *mm* when the intensity of magnetization of the specimen changed by about 2.0 gauss.

In order to keep the temperature of the specimen exactly constant during the very long course of measurements, minute precaution has been added to the procedure of the measurement. At first, a constant magnetizing current of desired strength was supplied to the solenoid for a long time until a thermal equilibrium was established between specimen and its environment. The procedure from hereon was as follows:

The battery circuit was opened and the specimen was carefully demagnetized in alternating field. Then the field of previous strength was again applied through the battery circuit. After a desired interval of time, the circuit of the electromagnet, by which a weight was suspended, was suddenly opened, immediately after the galvanometer circuit was closed. Then the search coil was consequently pulled out by the dropping weight from the specimen, and the galvanometer made a deflection, which corresponds to the induction of the specimen at this instant. This measurement of induction was repeated at

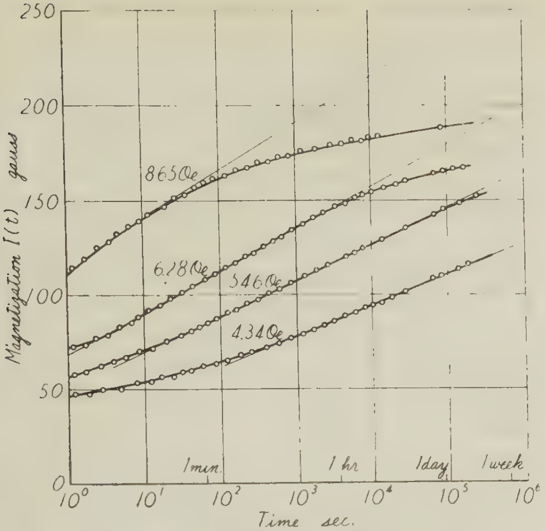

Fig. 2. Variation of magnetization as a logarithmic functions of time at 50°C for the specimen quenched from 500°C. The applied external fields are indicated on the curves.

various interval of time after the application of the magnetic field. Thus the intensity of magnetization of the specimen was observed as a function of time after application of the field, from 1 sec. up to one day or week. Special attention was paid to the construction of the apparatus and the arrangement of the circuit, in order to avoid mechanical and magnetic shock, which would be added to the specimen during the measurement.

## § 3. Experimental Results

The experimental results so far obtained are as follows:

i) Magnetic after-effect curves

A typical result from a set of measurements is shown in Fig. 2, which represents the variation of magnetization as a logarithmic function of time $t$ measured from an instant of application of external field of various strength (the "magnetic after-effect curve"). The measurement were made at 50°C for the specimen quenched from 500°C. The main parts of these curves can be represented by straight lines with different inclinations. Similar after-effect curves at 20°C for the specimen quenched from 460°C are shown in Fig. 3 (*a*) and for the specimen with perfect order in Fig. 3 (*b*). As can be seen in these figures, the length of the linear portion depends on the strength of applied field, temperature and the degree of order of the specimen.

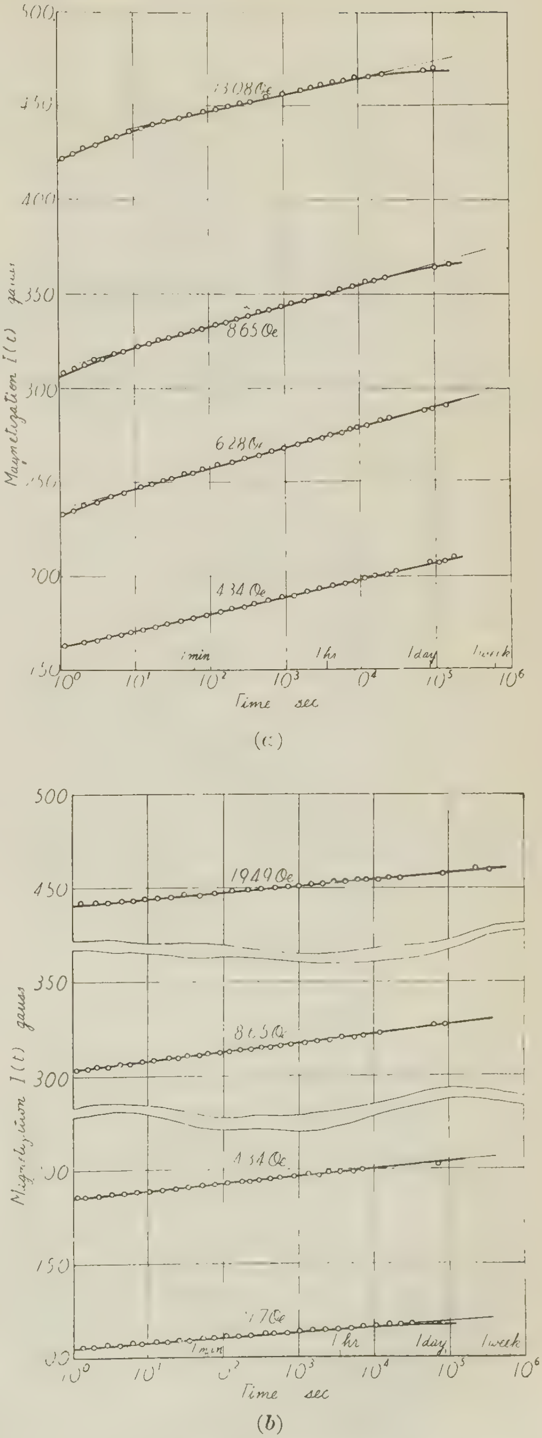

(*a*)

(*b*)

Fig. 3. Variation of magnetization as a logarithmic function of time, (*a*), for the specimen quenched from 460°C, and (*b*), for the specimen with perfect order which are measured at 20°C. The applied external fields are indicated on the curves.

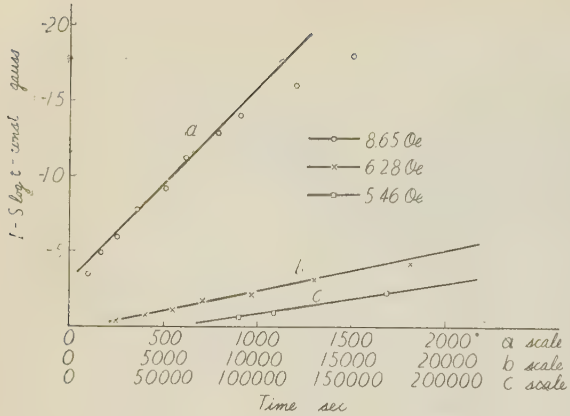

Fig. 4. Variation of $I$- $S\log t$- const. as a function of time $t$.

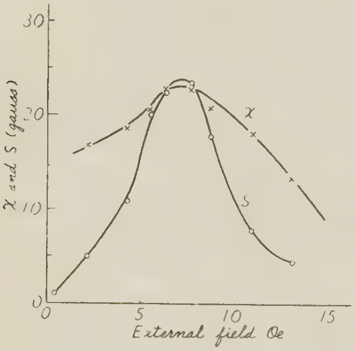

Fig. 5. Variation of $S$ and $\chi$ as a function of applied field at 50°C for the specimen quenched from 500°C.

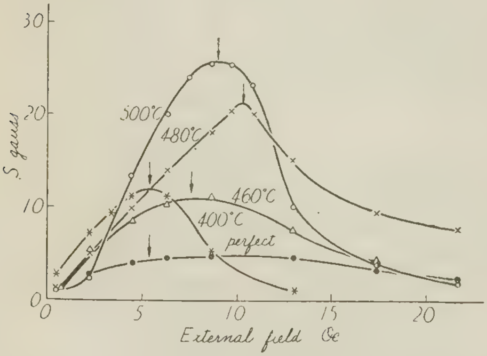

Fig. 6. Variation of $S$ as a function of applied field at 20°C for the specimen with various degrees of order. The quenching temperatures are indicated on the curves and the arrows on each curves represent the field correspond to maximum value of $\chi$.

Generally speaking, the regions of straight lines have a tendency to extend longer with a decrease of applied field, as well as with the decrease of temperature and the formation of the superlattice.

In general, these curves can be expressed fairly well by

$$I(t)=S\,log\,t-\gamma t+\text{const}\,. \qquad (1)$$

where $S$ and $\gamma$ are independent of time but depend on the intensity of applied field, temperature and the degree of order of the specimen. In order to examine the experimental formula (1), the variation of $I(t)-S\log t$ $-$const. as a function of time $t$ is show in Fig. 4, referred to the curves represented in Fig. 2. Linear relationship over a wide range of time, as shown in this figure, indicates that the observed curves are represented well by equation (1), except for short time intervals between $t=1\sim10$ sec.

Both parameters $S$ and $\gamma$ are to be considered as important characteristic factors for the after-effect studied here. Firstly we will study how $S$ is affected by the variation of experimental conditions.

### ii) Effect of applied field

The dependence of $S$ on the intensity of applied field is shown in Fig. 5 for the same specimen as in Fig. 2. The susceptiblity $\chi$ is also plotted on this same figure against the field, and it will be seen that the maximum value of $S$ occurs within the experimental error where $\chi$ has the greatest value. Similar variations of $S$ against the external field are shown in Fig. 6 which was measured at 20°C for the specimens with various degrees of order. It shows that the maxima of $S$ and $\chi$ are reached on the same field irrespective to the change of conditions in case of measurements.

### iii) Effect of temperature

The temperature dependence of $S$ will be shown quite simply by the relation between the maximum value of $S$ shown in Fig. 5 and 6 and temperature. Fig. 7($a$) is a plot of $S_{\max}$ as a function of the absolute temperature for the specimens with various degrees of order. It shows that $S_{\max}$ is represented approximately as linear function of the temperature, and also that the inclinations of the lines change its sign from negative to positive with the formation of the superlattice. In order to take into account the dependence of the saturation magnetization on temperature, as well as on degree of order, the maximum value of $S$ was replaced by $S_{\max}/I_s$ where $I_s$ is the saturation magnetization. Fig. 7($b$) shows a plot of $S_{\max}/I_s$ against the absolute

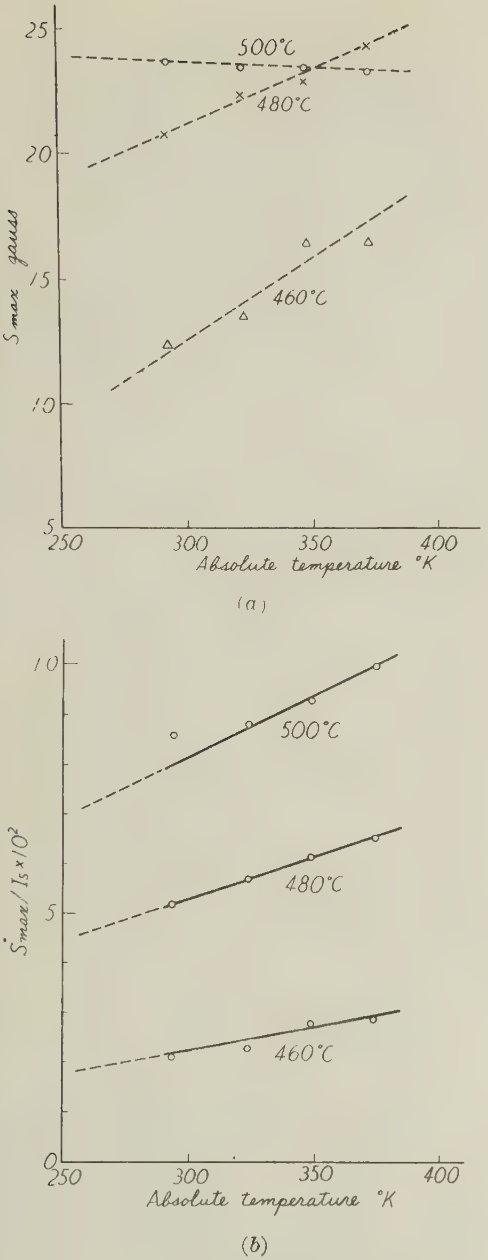

(a)

(b)

Fig. 7. Variation of (a) $S$ and (b) $S_{\max}/I_s$ as a function of absolute temperature. The quenching temperatures are indicated on the curves.

temperature for the specimens with various states of order. The fact, that the straight lines roughly pass through the origin of temperature axis, shows that $S_{\max}/I_s$ is proportional to the absolute temperature for the various states of order. The value of the inclination of the line decreases with the formation of superlattice.

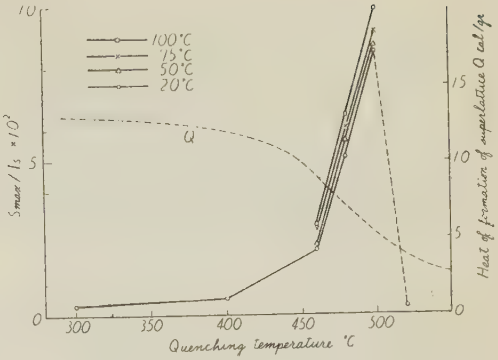

Fig. 8. Variation of $S_{\max}/I_s$ and formation heat of superlattice as a function of quenching temperatures.

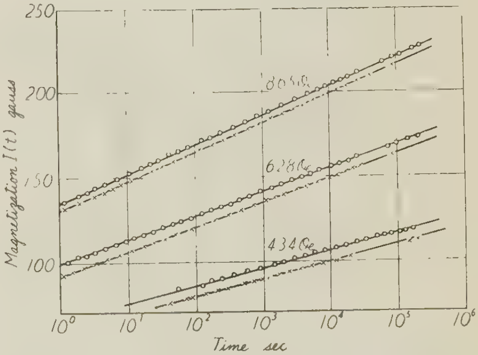

Fig. 9. Variation of magnetization as a logarithmic function of time at 20°C for the specimen quenched from 480°C. The applied external fields are indicated on the curves.
- • - • - without longitudinal tension.
- x - x - with longitudinal tension.

### iv) Effect of degree of order

The dependence of $S_{\max}/I_s$ on the quenching temperature is shown in Fig. 8, together with the change of heat of formation of the superlattice with quenching temperature measured by Kaya and Nakayama[12]. The values of $S_{\max}/I_s$ decrease rapidly with the decrease of quenching temperature. It can be seen that the after-effect is closely related to the formation of superlattice and become most remarkable at the intermeniate state of order.

### v) Effect of mechanical deformation

In order to study the dependence of the after-effect on mechanical deformation, studies have been carried out for the specimen which had been streched by a tension of the strength 2.1 $Kg/mm^2$ for 24 hours before the measurements. This strength of the tension will be considered to be on the transition point from $\alpha$ region to $\beta$ in the initial creep rate curves. The result obtained for the specimen quenched from 480°C, measured at 20°C, is shown in Fig. 9. It can be seen that the values of $S$ and the range of linearity are independent of the mechanical deformation. However, a slight parallel displacement of the curves to lower field can be acknowledged as the consequence of the deformation.

## § 4. Discussion

We can summarize here the experimental results thus obtained as follow:

i ) In general, the magnetic after-effect curves can be well expressed by the experimental formula (1).

ii ) The maximum value of $S$ occures at the magnetic field where $\chi$ has the greatest value.

iii) $S_{\max}/I_s$ is always protortional to the absolute temperature for every states of order.

iv) This phonomenon is closely related to the formation of superlattice and is most remarkable at the intermediate state of order.

v ) Mechanical deformation has no sensible influence on this phenomenon.

These five facts, especially iv), must be explained by assuming a reasonable physical model. One of the mechanisms by which a quantitative explanation has been given on the magnetic after-effect is the diffusion of the impurity atoms such as carbon or nitrogen in iron. However Richter's measurements seem to indicate that the variation of $S$ with temperature in soft iron is essentially different from that shown in the results iii). In the former case, $S$ appears to be substantially independent on temperature. Moreover, the crystal structure of $Ni_3Mn$ alloy is different from that of iron, and the magnetostriction, the existence of which is the cause of rearrangement of impurity atoms in case of change of magnetization, is very small[1] in this alloy. This mechanism, therefore, may not be applied in the case of $Ni_3Mn$ alloy. As was described in the previous section, Néel has proposed two mechanisms for the irreversible magnetic after-effect: the one is the rotation of the magnetization in isolated single domain and the other is the displacement of the domain walls, both of which are to be activated by thermal fluctuation. In these cases, the analytical forms are expressed by $S$ *log* $t$, same as the first term of the equation (1). In the former, $S$ is proportional to $T$ in the first approximation within a certain range of time, but in the latter $S$ is proportional to $\chi_i T^{1/2}$ where $\chi_i$ is the irreversible differential susceptibility at the temperature concerned. A precise comparison between Néel's theories and the present results may be difficult because of the ambiguity on the assumption in the theory as well as of the lack of data of $\chi_i$. Moreover, both mechanisms suggested by Néel can not be applied to our results, because the 2nd term $-\gamma t$, whose existence is clearly comfirmed by our experiment, could not be derived from his treatments unless some auxiliary assumption will be introduced on the distribution of activation energy of single domains or walls.

Street and Woolley have also treated the isolated single domain model and derived the analytical form similar to the experimental formula (1). They assume that fine particles, the dimention of which are smaller than the critical value for the formation of domain walls, are embedded in a less ferromagnetic matrix.

Thus, at time $t$ after the sudden application of fiield, let the number of particles assigned by activation energies lying between $E$ and $E+dE$ be $f(E)\,dE$. The time rate of change of $f(E)\,dE$ due to thermal activation at constant temperature will be given by

$$\frac{df(E)}{dt}=-Cf(E)dE\exp(-E/kT) \qquad (2)$$

assuming that successive activations do not produce additional states in the same range of $E$. If at time $t=0$, the value of $f(E)$ is a constant $p$ within the energy range from 0 to $E_0$ and is equal to zero outside this range, the required formula is given by

$$I(t)=ipkT(\log t-\lambda_0 t)+\text{const.} \qquad (3)$$

where $i$ is an average component of the magnetization of the particles in the direction of applied field, and

$$\lambda_0=C\exp(-E_0/kT) \qquad (4)$$

The equation (3) is identical with the experimental formula, if we put

$$S=ipkT \qquad (5)$$

and

$$\gamma=\lambda_0 S \qquad (6)$$

Table I.

| quenching temp. C | 500 | | | 480 | | 460 |
|---|---|---|---|---|---|---|
| external field, *Oe.* | 5.46 | 6.28 | 8.65 | 6.28 | 8.65 | 8.65 |
| $E_0$ $10^{12}$ *erg* | 1.6 | 1.6 | 1.4 | 1.25 | 1.37 | 0.58 |
| $\log_{10} C$ | 10.0 | 11.1 | 10.1 | 6.4 | 8.7 | 2. |
| $S$ gauss at 50°C | 19.9 | 22.4 | 30.0 | 17.5 | 22.3 | 11.6 |

Prior to the comparison of this theory with the experimental results, we must consider the influence of the changes of the effective magnetic field while the experiments are made using specimens with demagnetizing factor other than zero, since the effective field acting in the specimen varies continuously with time under the constant value of the external field. Street and Woolley have given, semi-experimentally, the variation of $S$ for the same material having different demagnetizing factor $D$ by

$$\frac{1}{S}=\frac{1}{S_0}+\left(\frac{g}{kT}+\frac{\chi_{\mathrm{rev}}}{S_0}\right) \qquad (7)$$

where $S_0$ is the value of $S$ in the case $D=0$, $g$ is the proportional factor, with which the domain activation energy changes proportionally with changes of field strength, and $\chi_{\mathrm{rev}}$ is the reversible susceptibility concerned. When $D$ is small, the influence of changes of effective field will be small. If the numerical values in the present measurements are substituted in the expression, the difference of $S$ and $S_0$ will be shown to be less than a few percent, and may be neglected in the following discussions without considerable error.

Thus the comparison of the experimental results with equation (3) may be summarized as follows:

1) The magnetic after-effect curves, except for short time interval immediately after the application of extarnal field, can be well expressed by equation (3), which includs the 2nd term, the existence of which was not comfirmed in case of Alnico *V*.

2) $S_{\max}/I_s$, if it is replaced by $S$, is proportional to the absolute temperature as expected from equation (5), and shown in Fig. 7 (b).

3) The relations between $\log \lambda_0$ and $1/T$ within the range of observed temperature from 20°C to 100°C measured under constant field are shown in Fig. 10 for the specimen quenched from 480°C. The slopes of these straight lines give, according to the equation (4), the maximum values $E_0$ of activation energies of the small particles.

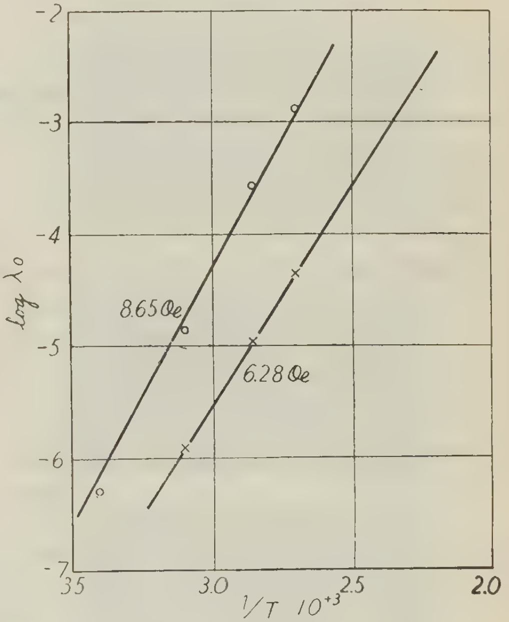

Fig. 10. Variation of $S_{\max}/I_s$ as a function of $1/T$. The applied fields are indicated on the lines.

The numerical values of $E_0$, $\log C$ and $S$ are summarized in Table I which shows slight decrease of $E_0$ and rapid decrease of $C$ with the formation of superlattice.

Thus the experimental results seem to be well explained by Street and Woolley's theory using the isolated single domain model. If we assume the existence of such particles contributing to the magnetic after-effect in Ni$_3$Mn alloy, the maximum volume of these particles can be estimated as follows. The energy required to reverse the magnetization of single domain of volume $v$ would be roughly expressed by

$$E_0=I_sH_cv \qquad (8)$$

where $H_c$ is the coercive force. Putting $I_s=270$ gauss, $H_c=12.5$ *Oe* and $E_0=1.6\times10^{-12}$ *ergs* which are the observed values of the specimen quenched from 500°C, we obtained $v=4.7\times10^{-16}cm^3$ and the linear dimension $d=1\times10^{-5}$ $cm$, assuming a spherical shape.

On the other hand, in a material with a low magnetic anisotropy, we can estimate the critical diameter $d_s$ of the single domain of uniform spontanious magnetization by the following expression derived by Néel[8)]

$$d_s^2=\frac{3Na}{2k}\left(\log\frac{ds}{a}-0.307\right) \qquad (9)$$

where $N$ is the coefficient of the molecular field (36,000 for $Ni_3Mn$) and $a$ is the distance between magnetically active neighbours. For the same specimen, we obtain $d_s=1\times10^{-5}\,cm$ in agreement with the above estimated value.

In case of Alnico *V*, it has been concluded by Heidenreich and Nesbitt[13)] from electron metallographic study that the high values of both coercive force and anisotropy are caused by very finely divided precipitation produced by the permanent heat treatment. If we take these fine precipitates into consideration, the influence of heat treatment on the magnetic viscosity in Alnico *V* investigated by Street, Woolley and Smith[14)] can easily be understood.

Now, in the $Ni_3Mn$ alloy, question will be raised as to the existence of single domain particles such as those in Alnico *V*. In this alloy, the ferromagnetic Curie point increases with the formation of superlattice, and more ordered phase has more stronger intensity of magnetization. It seems plausible that small particles of more ordered phase are embedded in a less ordered matrix. Two kinds of studies have been carried out directly to examine the above hypothesis.

One of them was the domain pattern observation on the alloy with various degrees of order using the technique developed by H. J. Williams and his collaborators[15)]. In the perfect ordered state, large, simple domains were observed, whereas the size of domains decreases with the decrease of degree of order, and in the intermediate state of order at which the magnetic after-effect was most remarkable, the fine colloid particles of magnetite were distributed at random, showing no distinct figure.

The other was the electron microscopic study, carried out on six specimens with various ordered states. The electron microscopic observation was made on the surface of the disks of the polycrystalline $Mi_3Mn$ alloy.

The procedure finally adopted is as follows:

1) Careful abrade by usual metallographic technique.

2) Electropolish for about one min. with current density 1 $amp/cm^2$ in an electrolyte containing one part of phosphoric acid and one part of ethylalcohol at about 40°C.

3) Rinsing in distilled water and ethylalcohol, and rapid drying.

4) Preparation of the negative Pd-shadowed collodion replica using the technique developed by Fukami[16)].

The replica thus obtained have been examined under electron microscope. Some examples of the electron micrographs are shown in Fig. 11. As can be seen in the photograph (*a*), no speciality exists in perfectly disordered state, while the photograph (*c*) for the specimen quenched from 500°C clearly shows that there exists the ordered phase of elliptical form, the dimension of which is less than about 750Å for the short axis and 3500 Å for the long axis, which is the same order of magnitude estimated from equation (8). In the course of superlattice formation, these ellipsoids are gradually formed, and again become undistinguishable in the perfect ordered state.

For the purpose of examining the relation between the highly preferred orientation of the ellipsoids and crystal axes, the same electron microscopic observations have been made on the (**110**) plane of a single crystal of Ni-Mn alloy. Unfortunnately, the specimen was richer in Ni content than the alloy of stoichometric composition of $Ni_3Mn$ by 3 percent. In this alloy, the ordered phases can easily be distinguished from the disordered region after chemical etching for about 5 minutes in a mixture containing 10 $gr.$ ferric chloride, 30-cc concentrated HCl and 120-cc distilled water at room temperature. This will be ascribed to the difference of composition in the ordered and disordered phases. The replicas were made after quenching the same specimen from different temperatures. The electron micrographs show in Fig. 12 illustrate the change of the structure with the formation of superlattice.

The following conclusions are drawn from these results:

1) As can be seen in Fig. 12 (*b*), the elongated ordered phases exhibited themselves at

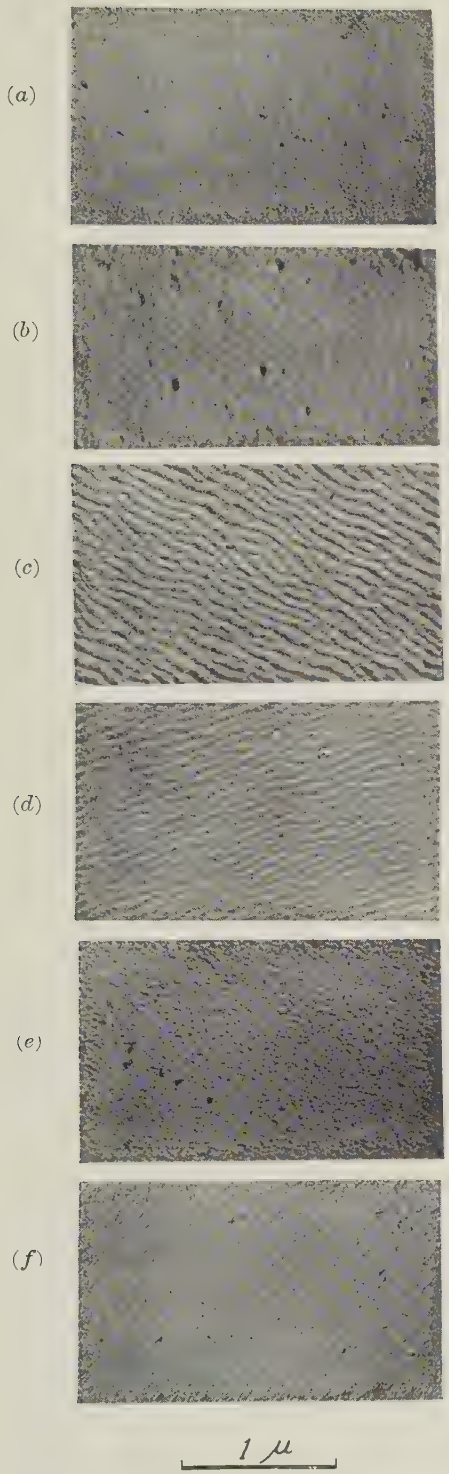

Fig. 11. Electron micrographs of Pd-shadowed collodion replica of Ni$_3$Mn alloy quenched from (*a*) 700°C, (*b*) 520°C, (*c*) 500°C, (*d*) 460°C, (*e*) 400°C and (*f*) room temperature.

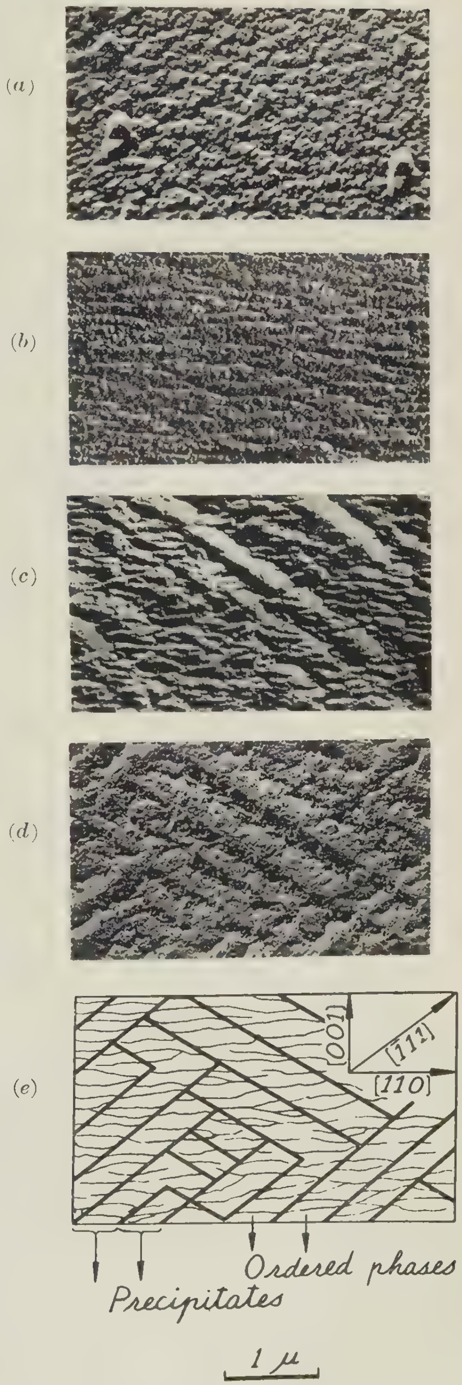

Fig. 12. Electron micrographs of Pd-shadowed replica on (**110**) plane of single crystal of Ni–Mn alloy, which contains 22 atomic percent Mn, quenched from (*a*) 700°C, (*b*) 510°C, (*c*) 360°C, (*d*) room temperature and (*e*) its interpretation.

intermediate state of order and their long axes are parallel to ⟨**110**⟩ directions as illustrated in Fig. 12(*e*).

2) The ordered phases become undistinguishable when the superlattice formation made progress, and mutually parallel valleys along two ⟨**111**⟩ directions in (**110**) plane gradually appear, as shown in Fig. 11(*c*). In the perfectly ordered state, rod-like structure, the dimension of which is about $0.55\,\mu\times 2\sim 5\mu$, can be clearly observed as shown in Fig. 11 (*d*). It seems that the precipitates are elongated to the ⟨**111**⟩ directions. Quite similar phenomena was found by Nesbitt, Williams and Bozorth[17].

Moreover the measurements of magnetic anisotropy[18] carried out by using the disk of the single crystal of the alloy have showed that the anisotropy energy has the same order of magnitude as the magnetostatic energy caused by free poles of the ordered phase within the specimen, which can be expressed by

$$E_m=(1/2)N(\Delta I_s)^2V(1-V) \qquad (10)$$

Where $N$ is the demagnetizing factor of the ordered phase, $\Delta I_s$ is the difference of the magnetization of ordered phase and matrix, and $V$ is the volume proportion of the ordered phase. If the values $I_s=300$ gauss, $V=0.9$, $N=0.75$ which is estimated from the photograph, we obtain an anisotropy energy of about $3\times 10^3\,erg/cm^3$ which is in agreement with the observed value.

## § 5. Summary and Acknowledgement

Now, it can be concluded that the after-effect observed in $Ni_3Mn$ alloy with intermediate state of order is ascribed to the thermal activation process, which causes relaxed rotation of magnetization of the ordered phase of ellipsoidal form from the direction having an obtuse angle with the applied field to one having an acute angle. The experimental results can be explained as follows:

i ) The assumptions to derive the equation (3) are that number of particles per unit energy range is a constant within some energy range and successive activations do not produce additional states in the same range. The second assumption is understood plainly on the proposed mechanism. The first one could not be accepted after the above experimental results, however, unless $f(E)$ at $t=0$ varies as steeply with $E$ as does $\exp(-\lambda T)$, the logarithmic form of $t$ at equation (3) cannot be profoundly affected where $\lambda=C\exp(-E/kT)$. The existence of maximum activation energy $E_0$ is ascribed to the critical size of the single magnetic domain.

ii ) The relation of $\chi$ and $S$ is reasonable.

iii) The value of $S_{\max}/I_skT$ which is proportional to the volume of one of domains contributing to the after-effect is not affected by the temperature.

iv) It was pointed out by the electron microscopic study, that the most distinguished magnetic viscosity is associated with the formation of small ordered region of ellipsoidal form within the matrix of disordered phase.

v ) The absence of the influence of mechanical deformation on the phenomenon is also reasonable, because the direction of magnetization in the ordered phase cannot be changed easily by longitudinal tension.

The author wishes to express his hearty thanks to Prof. S. Kaya for his kind guidance, to Mr. Y. Tomono for his kind discussion throughout the course of this research. He also wishes to thank Prof. Y. Tani and Mr. A. Fukami for their guidance, and Messrs. S. Sakata and S. Aoyagi for their assistance on the techniques of the electron microscopic study.

## References

1) T. Taoka and T. Ohtsuka: J. Phys. Soc. Japan **9** (1954) 723.
2) F. Preisach: Z. Physik **94** (1935) 277.
3) G. Richter: Ann. d. Physik **29** (1937) 605.
4) J. L. Snoek: Physica **5** (1938) 663.
J. L. Snoek: Physica **6** (1939) 161.
J. L. Snoek: New Developments in Ferromagnetic Materials (1949).
5) L. Néel: J. Phys. Rad. **13** (1952) 249.
6) Y. Tomono: Unpublished.
7) L. Néel: J. Phys. Rad. **12** (1951) 339.
8) L. Néel: Ann. Géophys. **5** (1949) 99.
L. Néel: Compt. rend. **228** (1949) 664.
L. Néel: Rev. Mod. Phys. **25** (1953) 293.
9) L. Néel: J. Phys. Rad. **11** (1950) 49.
10) J. C. Barbier: C. R. Acad. Sci., Paris **230** (1950) 1040.
J. C. Barbier: Ann. de Phys. **9** (1954) 84.
11) R. Street and J. C. Woolley: Proc. Phys. Soc. **A 62** (1949) 562; Ibid. **B 63** (1950) 509; Ibid **B 65** (1952) 679.
12) S. Kaya and M. Nakayama: Proc. Phys. Math. Soc. Japan **22** (1940) 126.

13) R. D. Heidenreich and E. A. Nesbitt: J. App. Phys. **23** (1952) 352; Ibid. **23** (1952) 366.
14) R. Street, J. C. Woolley and P. B. Smith: Proc. Phys. Soc. **B 65** (1952) 461.
15) H. J. Williams, R. M. Bozorth and W. Shockley: Phys. Rev. **75** (1949) 155.
16) A. Fukami: J. of Electronmicro. Japan **1** (1952) 28.
17) A. Nesbitt, H. J. Williams and R. M. Bozorth: J. App. Phys. **25** (1954) 1014.
18) R. Honda and T. Taoka: Unpublished.

---

JOURNAL OF THE PHYSICAL SOCIETY OF JAPAN Vol. 11, No. 5, MAY, 1956

# Note on the Paramagnetic Susceptibility and the Gyromagnetic Ratio in Metals

By Ryogo KUBO and Yukio OBATA

*Department of Physics, University of Tokyo*

(Received February 17, 1956)

Although the orbital magnetic moments of the electrons in metals are "quenched" by the crystal field, their contribution to the paramagnetic susceptibility for partly filled degenerate bands is shown to be of the same order of magnitude as the Pauli spin paramagnetism. This contribution corresponds to the so-called "temperature independent high frequency term" in the theory of the paramagnetic susceptibility of atoms. Due to this contribution, the gyromagnetic ratio is reduced by an appreciable amount.

## § 1. Introduction

In the usual treatment of the susceptibility of non-forromagnetic metals, paramagnetism has been considered to be entirely due to the unpaired spins of electrons. The contribution of the orbital magnetic moments to paramagnetism has been neglected for the reason that they are queched by the crystal field. Pauli's expression is used for theoretical estimation, and the discrepancy between theory and experiment is attributed to the exchange and correlation effects.

The purpose of the present note is to point out that, for metals with partly filled non-*s* bands, the orbital magnetic moment contributes to the paramagnetic susceptibility through the second order perturbation, the order of which is in general not negligibly small compared with the Pauli spin paramagnetism. In connection with this, it is shown that the gyromagnetic ratio, $g'$, of non-ferromagnetic metals is smaller than 2 by an appreciable amount.

The reasoning to the above conclusion is as follows: In the case of paramagnetic salts, where the magnetic electrons are well localized, the orbital contribution* through the second order perturbation is of the order of $\mu^2/\Delta$, where $\mu$ is the Bohr magneton and $\Delta$ is the mean separation of the energy levels connected by the orbital angular momentum. This is negligibly small compared with the spin contribution, which is of the order $\mu^2/kT$ at room temperatures. In the case of metals, however, the spin paramagnetism is *reduced*** by the factor $T/T_0$, where $T_0$ is the degeneracy temperature. The orbital magnetic moment is also partly quenched by an effective crystal field which comes from the itenerant character of the electrons. The orbital paramagnetism of free atoms will thus be reduced in the metal to the fraction $T/T_0$, that is, the ratio of the thermal and the hopping energy. Therefore the orbital paramagnetism in metals with degenerate bands can be an appreciable part of the total paramagnetism. This is only because the spin part is greatly reduced. As an illustration of this idea, an estimation of the effect is given in § 3 for a much simplified $p$-band model, which is followed by some discussions in § 4.

---

* Apart from the first order term $\mu^2\lambda/kT\Delta$ through the spin-orbit coupling.

** For rare earth metals, the $4f$ electrons are localized rather than itinerant, so this reduction does not take place.

## § 2. General Expressions for the Susceptibility and the Gyromagnetic Ratio

Throughout the present paper we shall use the one-electron approximation. For a single electron in a metal subject to an external magnetic field $\boldsymbol{H}$, represented by the vector potential $\boldsymbol{A}$, the Hamiltonian may be written in the form,

$$\mathscr{H}=-\frac{\hbar^2}{2m}\Delta+V(\boldsymbol{r})+\Lambda+\frac{e^2}{2mc^2}A^2 -\frac{ie\hbar}{mc}\boldsymbol{A}\cdot\boldsymbol{\nabla}+\frac{e\hbar}{mc}\boldsymbol{H}\cdot\boldsymbol{S}\,, \qquad (1)$$

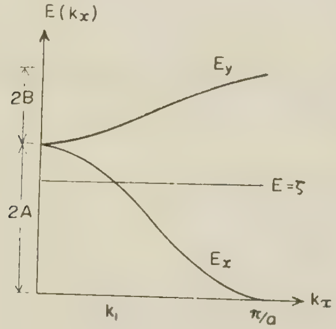

Fig. 1.

where $V$ is the electrostatic potential in the metal and $\Lambda$ is the spin-orbit coupling operator. We shall divide this Hamiltonian into two parts

$$\mathscr{H}=\mathscr{H}_0+\mathscr{H}_1\,,$$

where

$$\mathscr{H}_0=-\frac{\hbar^2}{2m}\Delta+V(\boldsymbol{r})+\Lambda+\frac{e^2}{2mc^2}A^2\,, \qquad (1\text{ a})$$

$$\mathscr{H}_1=-\frac{ie\hbar}{mc}\boldsymbol{A}\cdot\boldsymbol{\nabla}+\frac{e\hbar}{mc}\boldsymbol{H}\cdot\boldsymbol{S}$$

$$=\mu\boldsymbol{H}(\boldsymbol{L}+2\boldsymbol{S})\,, \qquad (1\text{ b})$$

in which the usual gauge $\boldsymbol{A}=(\boldsymbol{H}\times\boldsymbol{r})/2$ is used.

$\boldsymbol{A}$ is linear in electron coordinate and is not a small perturbation in the usual sense. Using Peierls' technique[1)2)], however, we can get rid of this difficulty.

The susceptibility of the metal is given by

$$\chi=-\left(\frac{\partial^2F}{\partial H^2}\right)_{\zeta=\text{const},\,H\to0}, \qquad (2)$$

$$F=N\zeta+\text{Tr}\,g(\mathscr{H})\,, \qquad (3)$$

where

$$g(\mathscr{H})=-kT\log(1+\exp(\zeta-\mathscr{H})/kT)\,. \quad (4)$$

Since $\mathscr{H}_1$ is digonal in the wave vector $\boldsymbol{k}$ in the tight binding approximation[2)], $\text{Tr}\,g(\mathscr{H})$ may be expanded in powers of $\mathscr{H}_1$ as follows;

$$\text{Tr}\,g(\mathscr{H}_0+\mathscr{H}_1)=\text{Tr}\,g(\mathscr{H}_0)+\sum_m g'(E_m)\langle m|\mathscr{H}_1|m\rangle$$

$$+\frac{1}{2}\sum_m\sum_{m'}\frac{g'(E_m)-g'(E_{m'})}{E_m-E_{m'}}|\langle m|\mathscr{H}_1|m'\rangle|^2+\cdots\,, \qquad (5)$$

where the representation in which $\mathscr{H}_0$ is diagonal is used. The first term in the right-hand side of the Eq. (5) was discussed by Peierls for a single-band case. The contribution from this term to the susceptibility* will be denoted by $\chi_d$. The second term vanishes except for ferromagnetic metals. From the third term the paramagnetic susceptibility $\chi_p$ is obtained. Since we are interested in the terms of the order of $H^2$, we can substitute for $E_m$ the value in the absence of $\boldsymbol{H}$. Thus, the susceptibility is given by

$$\chi=\chi_d+\chi_p\,,$$

with

$$\chi_p=\mu^2\sum_{nn'}\int\frac{dk}{(2\pi)^3}\frac{f(E_n(\boldsymbol{k}))-f(E_{n'}(\boldsymbol{k}))}{E_{n'}(\boldsymbol{k})-E_n(\boldsymbol{k})}\langle n\boldsymbol{k}|\boldsymbol{L}+2\boldsymbol{S}|n'\boldsymbol{k}\rangle\langle n'\boldsymbol{k}|\boldsymbol{L}+2\boldsymbol{S}|n\boldsymbol{k}\rangle\,, \qquad (6)$$

where

$$f(x)\equiv g'(x)$$

$$=\{\exp(x-\zeta)/kT+1\}^{-1}\,, \qquad (7)$$

is the Fermi distribution function.

$\chi_p$ consists of three contributions:

---

* In the presence of the spin-orbit coupling, the expression given by Peierls may be modified. In this paper, however, we shall not discuss this point in detail.

i) $$\chi_S=\mu^2\sum_{nn'}\int\frac{d\boldsymbol{k}}{(2\pi)^3}\frac{f(E_n(\boldsymbol{k}))-f(E_{n'}(\boldsymbol{k}))}{E_{n'}(\boldsymbol{k})-E_n(\boldsymbol{k})}\langle n\boldsymbol{k}|2\boldsymbol{S}|n'\boldsymbol{k}\rangle\langle n'\boldsymbol{k}|2\boldsymbol{S}|n\boldsymbol{k}\rangle\simeq 2\mu^2 n(\zeta)\,, \tag{8}$$

where $n(\zeta)$ is the state density at the Fermi surface. This is the well-known Pauli spin paramagnetism.

ii) $$\chi_{S0}=\mu^2\sum_{nn'}\int\frac{d\boldsymbol{k}}{(2\pi)^3}\frac{f(E_n(\boldsymbol{k}))-f(E_{n'}(\boldsymbol{k}))}{E_{n'}(\boldsymbol{k})-E_n(\boldsymbol{k}))}\{\langle n\boldsymbol{k}|\boldsymbol{L}|n'\boldsymbol{k}\rangle\langle n'\boldsymbol{k}|2\boldsymbol{S}|n\boldsymbol{k}\rangle + \langle n\boldsymbol{k}|2\boldsymbol{S}|n'\boldsymbol{k}\rangle\langle n'\boldsymbol{k}|\boldsymbol{L}|n\boldsymbol{k}\rangle\}\,. \tag{9}$$

This term is smaller than $\chi_S$ by the factor of $\lambda/\Delta$, where $\lambda$ is the spin-orbit energy and $\Delta$ is the mean band width. This is usually unimportant.

iii) $$\chi_0=\mu^2\sum_{nn'}\int\frac{d\boldsymbol{k}}{(2\pi)^3}\frac{f(E_n(\boldsymbol{k}))-f(E_{n'}(\boldsymbol{k}))}{E_{n'}(\boldsymbol{k})-E_n(\boldsymbol{k})}\langle n\boldsymbol{k}|\boldsymbol{L}|n'\boldsymbol{k}\rangle\langle n'\boldsymbol{k}|\boldsymbol{L}|n\boldsymbol{k}\rangle\,. \tag{10}$$

This is the term which comes from the second-order effect of the orbital angular momentum. It is a polarization effect and is always paramagnetic. The magnitude of this term is of the order $\mu^2/\Delta$.

The expression for the gyromagnetic ratio $g'$ is given by

$$\begin{aligned} g'&=\frac{\sum_{nn'}\int\frac{d\boldsymbol{k}}{(2\pi)^3}\frac{f(E_n(\boldsymbol{k}))-f(E_{n'}(\boldsymbol{k}))}{E_{n'}(\boldsymbol{k})-E_n(\boldsymbol{k})}\langle n\boldsymbol{k}|\boldsymbol{L}+2\boldsymbol{S}|n'\boldsymbol{k}\rangle\langle n'\boldsymbol{k}|\boldsymbol{L}+2\boldsymbol{S}|n\boldsymbol{k}\rangle}{\sum_{nn'}\int\frac{d\boldsymbol{k}}{(2\pi)^3}\frac{f(E_n(\boldsymbol{k}))-f(E_{n'}(\boldsymbol{k}))}{E_{n'}(\boldsymbol{k})-E_n(\boldsymbol{k})}\langle n\boldsymbol{k}|\boldsymbol{L}+2\boldsymbol{S}|n'\boldsymbol{k}\rangle\langle n'\boldsymbol{k}|\boldsymbol{L}+\boldsymbol{S}|n\boldsymbol{k}\rangle}\\ &=\frac{\chi_S+\chi_{S0}+\chi_0}{\frac{1}{2}\chi_S+\frac{3}{4}\chi_{S0}+\chi_0}\\ &=\frac{2(1+\chi_{S0}/\chi_S+\chi_0/\chi_S)}{1+3\chi_{S0}/2\chi_S+2\chi_0/\chi_S}\sim\frac{2(1+\chi_0/\chi_S)}{1+2\chi_0/\chi_S}\,. \end{aligned}\tag{11}$$

Thus it is clear from the above expression (11) that $2-g'$ can become quite appreciable in those metals which have partly filled degenerate bands.

It should be noted that orbital paramagnetism, represented by $\chi_0$, has little to do with the deviation of the spectroscopic splitting factor, $g$, from 2, since $g$ is determined by the first order Zeeman effect. Therefore, for paramagnetic metals* the following inequality is generally valid,

$$g-2<2-g'\,.$$

## § 3. Simple Model

For the numerical estimation of $\chi_0$, detailed knowledges of the band structure and wave functions are necessary. Even when these are at hand, calculation for actual metals would be laborious. So, in this section, we shall consider a much simplified model.

For a rather fictitious case of $p$ electrons in a simple cubic lattice, without spin-orbit coupling, we can give a little more explicit forms for $\chi_S$ and $\chi_0$. In this case, the matrix element of $\boldsymbol{L}$ and $\boldsymbol{S}$ are independent of $\boldsymbol{k}$, so the expression (10) is greatly simplified. If the magnetic field is applied in the $z$ direction, we have

$$\chi_S=2\mu^2 n(\zeta)\,, \tag{12}$$

and

$$\chi_0=2\mu^2\int\frac{d\boldsymbol{k}}{(2\pi)^3}\frac{f(E_x(\boldsymbol{k}))-f(E_y(\boldsymbol{k}))}{E_y(\boldsymbol{k})-E_x(\boldsymbol{k})}\,, \tag{13}$$

where $E_x(\boldsymbol{k})$, $E_y(\boldsymbol{k})$ are given in the usual text-books[3)].

Even in this case, the numerical calculation would be tedious. As seen from Eqs. (11), (12) and (13), we get the following relations

$$g'=2\frac{1+\xi}{1+2\xi}\,, \tag{14}$$

$$\xi=\chi_0/\chi_S \simeq\frac{1}{\Delta}\Big/n(\zeta)\sim 1\,. \tag{15}$$

Let us simplify the above model further, and consider one-dimensional case (which corresponds to (100) cut in the $\boldsymbol{k}$ space). The band energy will be written in the form

---

* Of course, the statement made here does not apply to the ferromagnetic substances.

$$E_x = A(1+\cos k_x a)\ ,$$
$$E_y = 2A + B(1-\cos k_x a)\ .$$

In this case, as easily calculated, the susceptibility is given by

$$\chi_S = 2\mu^2 \left| \frac{1}{\pi a A \sin k_1 a} \right| , \tag{16}$$

and

$$\chi_0 = 2\mu^2 \frac{1}{2\pi a(A+B)} \cot \frac{k_1 a}{2} , \tag{17}$$

where

$$\zeta = E_x(k_1)\ .$$

The ratio of the two contributions is given by

$$\xi = \frac{\chi_0}{\chi_S} = \frac{A}{A+B}(1+\cos k_1 a)\ .$$

Since $A$ is much greater than $B$, we have

$$\xi \simeq 1 + \cos k_1 a\ .$$

## § 4. Discussions

Although the model in the preceding section is too much simplified, it is an illustration of the importance of $\chi_0$ when the distribution of electrons is given by the Fermi distribution function. Therefore, if one wishes to calculate the absolute value of the paramagnetic susceptibility or gyromagnetic ratio for paramagnetic metals, one should, except for alkali metals where electrons are almost $s$-like take into account the orbital contribution besides the corrections due to exchange and correlation effects. The exchange and correlation effects usually almost cancel each other. Their effects on $\chi_0$ are also expected to be small.

If the experimental data of the electron spin resonance, static susceptibility, $g$ and $g'$ of a metal are at hand, we can get a measure of each of the three contributions to the paramagnetic susceptibility, $\chi_S$, $\chi_{S0}$ and $\chi_0$. Therefore, it is highly desirable that measurements on the electron spin resonance and gyromagnetic ratio are carried out for paramagnetic metals.

Often the experimental value of the paramagnetic part of the susceptibility is larger than the calculated $\chi_S$, using the state density obtained by some other kinds of experimental data. In such cases the contribution of the orbital paramagnetism may be important.

The interband contribution to the susceptibility has already been considered by A. H. Wilson[4] and N. E. Adams[5]. Wilson obtained for the susceptibility the expression (35) of his paper, beside the Peierls susceptibility. If the Fermi distribution is used instead of Boltzmann's, it may be written in the form

$$\chi = \frac{m^2\mu^2}{\hbar^2} \int \frac{d\boldsymbol{k}}{(2\pi)^3} g[E_n(\boldsymbol{k})] \int_{\text{unit cell}} \left( \frac{\partial^2 u_{\boldsymbol{k}n}{}^*}{\partial k_x{}^2} \frac{\partial^2 u_{\boldsymbol{k}n}}{\partial k_y{}^2} + \frac{\partial^2 u_{\boldsymbol{k}n}{}^*}{\partial k_y{}^2} \frac{\partial^2 u_{\boldsymbol{k}n}}{\partial k_x{}^2} - 2 \frac{\partial^2 u_{\boldsymbol{k}n}{}^*}{\partial k_x \partial k_y} \frac{\partial^2 u_{\boldsymbol{k}n}}{\partial k_x \partial k_y} \right) d\tau_0\ .$$

In the case of tight-binding this term represents the difference of gauge factor for ajacent atomic functions and becomes zero in the limit of isolated atoms. The physical meaning of this term is not clear.

Adams obtained a paramagnetic term

$$\chi_A = \frac{1}{4} \mu^2 n(\zeta) \langle (l^{xy} - l^{yx})^2 \rangle ,$$

which is connected to the presence of the orbital angular momentun. This is, however, different from the effect we considered. This is important only for the case in which orbital momentum has nonvanishing diagonal elements.

In both Wilson's and Adams' calculations, the orbital contribution is not fully taken into account.

### References

1) R. Peierls: Zeits. f. Physik **80** (1933) 763.
2) G. C. Fletcher: Proc. Phys. Soc. **A 67** (1954) 505.
3) A. H. Wilson: *Theory of Metals* (1953) p. 40.
4) A. H. Wilson: Proc. Camb. Phil. Soc. **49** (1953) 292.
5) N. E. Adams: Phys. Rev. **89** (1953) 633.

JOURNAL OF THE PHYSICAL SOCIETY OF JAPAN Vol. 11, No. 5, MAY, 1956

# Study of Magnetic Annealing on $Ni_3Fe$ Single Crystal

By Sōshin CHIKAZUMI

*Department of Physics and Chemistry, Gakushuin University,*
*Mejiro, Tokyo, Japan*

(Received at February 17, 1956)

Magnetic anisotropy induced by magnetic annealing was measured for $Ni_3Fe$ single crystal by means of a high temperature-torque magnetometer. It was found that the magnitude of anisotropy depends upon the crystallographic direction of the field which is applied during annealing. It was largest for <111>, next for <110> and smallest for <100>. It was also found that the minimum of the anisotropy energy lies not in just the same direction as that of annealing field, but in the direction nearer to the neighboring <111>. These facts could be explained qualitatively by Néel-Taniguchi-Yamamoto's formula. Quantitative discrepancy between them could be attributed to the nature of face-centred cubic lattice that some of the nearest neighbors of one atom are also in nearest neighbors of one another. Influence of ordinary order was also investigated.

## § 1. Introduction

It was first found by Kelsall[1] that the presence of a magnetic field during heat treatment of the iron-nickel alloys causes a large increase in maximum permeability. This phenomenon can be interpreted as a result of appearance of the magnetic anisotropy, which has its stable direction parallel to the annealing field. Many investigators have studied the mechanism of this anisotropy, to which reference was made in the foregoing paper[2].

The author has investigated this phenomenon on a single crystal of $Ni_3Fe$ for the purpose of studying the details of this anisotropy. A part of this result has been referred by S. Kaya[3] in his report. Recently L. Néel[4] and independently S. Taniguchi and M. Yamamoto[5] carried out the detailed calculations on this anisotropy and showed that their result is in good agreement with the observation of the present author.

In this paper the author will give a full report on the details of the experiment and will make a comparison with the theory.

## § 2. Apparatus and Specimen

Measurement of magnetic anisotropy was carried out by means of the torque magnetometer as shown in Fig. 1, which was specially constructed for the purpose of this investigation. This apparatus is characterized by a high sensitivity and high temperature uses. Specimen **O** mounted to a quartz disk **Q** is suspended freely under the elastic string **P** without any mechanical bearing for the purpose of avoiding any frictional forces. The horizontal displacement of the specimen could be avoided by using the generallized Helmholtz coil **C**, which is designed to produce an accurately uniform field. The coil constant of this coil is 107.4 Oe/amp. The current is

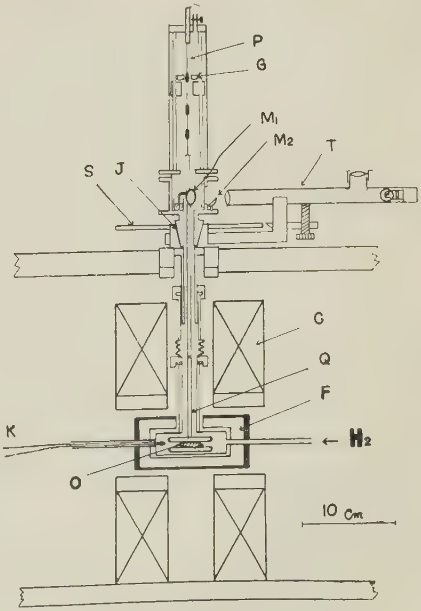

Fig. 1. Construction of high temperature torque magnetometer. **P**: elastic string, **G**: grip for fixing the top of P, $\mathbf{M}_1, \mathbf{M}_2$: mirrors, **T**: autocollimation telescope, **S**: circular scale, **J**: metal joint, **C**: large Helmholtz coil, **F**: electric furnace, **Q**: specimen holder, **O**: specimen, **K**: junction.

limited within 6 amp. By using a small electric furnace **F** set in this coil, the specimen could be heat-treated under the presence of a magnetic field. This furnace is also useful for the measurement of torque curve at elevated temperature. In order to protect the specimen from oxidation, the specimen together with the suspended system is confined in a hydrogen atmosphere.

The upper part of the apparatus, separated from the lower part at a ground metal joint **J**, is rotatable around vertical axis together with the suspended system. The orientation of the specimen can be determined by the mirror $\mathbf{M}_1$, which is attached to the suspended system. The torque exerted on the specimen can also be determined by the twisted angle of elastic string **P**, which is equal to the angle between $\mathbf{M}_1$ and $\mathbf{M}_2$, the latter being the mirror attached at a rotatable part. Both mirrors were previously adjusted to be parallel when no torque exerted on the specimen. The direction of the mirror was determined by means of the autocollimation telescope **T**, which is movable around the circular scale **S**. Accuracy of the measurement of the angle was about ±0.05°. The sensitivity of the elastic string can be altered by changing the fixing point of the string by means of the grip **G**, which is movable vertically along the elastic string by the externally controlled action of mechanism. The sensitivity for each grip was 11.3, 27.9, 91.8 and 341 dyne-cm /degree respectively.

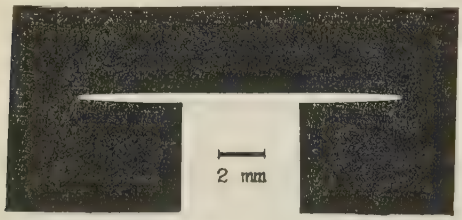

Fig. 2. The profile-projection of the specimen disk.

The specimen used was an oblate of $Ni_3Fe$ single crystal having a surface parallel to (110). On account of the low intensity of the magnetic field, a demagnetizing factor of specimen must be limited within the value smaller than 0.3. Moreover, since the anisotropy in question is as small as $10^2$erg/cc, specimen must be made in an accurate shape, otherwise a slight deviation would cause a disturbing anisotropy.

The preparation of the specimen in such a thin and accurate shape was the most difficult task in this experiment. Various methods were tried on twelve specimens. The method finally adopted was as follows: The crystal was firstly cut into an accurate circular plate, the size of which was 0.445±0.001 mm in thickness and 14.005±0.001 mm in diameter. This shaping was made by means of a small grinder lathe. This plate was then attached by magnetic means to a rotatable axis made of M. K. magnet and was electropolished with about 20 amp (40 volt) by dipping an under half of the plate into the electrolyte and by rotating it with a high speed of 2000~4000 r.p.m. Sometimes the plate was reset to an optical projector and its profile was compared with a standard elliptic form. The depth of the dipping was sometimes altered so as to fit its shape to a required one. This operation, however, need not be very delicate, because the shape of the plate tends to approach to a nearly ellipsoidal form, if it is done without careful adjustment. The rotational motion must be maintained at high speed, because it was found that a low speed polishing results in a slightly deviated shape having a cyrstallographic symmetry. When the speed was lowered down to 100~200 r.p.m., the resulting fluctuation of diameter was about 1 %, which is large enough to arise the anisotropy $0.5 \times 10^2$ erg/cc. The reason why a high speed rotation has a good effect is not clear, but it may be related to the following fact: When the speed is increased, it is found that the electrode resistance increases and the electrolytic efficiency is largely decreased. Accordingly the voltage difference between electrodes could be largely increased, while maintaining the current within relatively small value.

The final shape of the specimen was 13.698±0.005 mm in diameter and 0.452 mm in thickness at the center. The projection is shown in Fig. 2. A calculated demagnetizing factor was 0.288.

## § 3. Details of the Experimental Method

After the specimen was set in a torque meter, the heat treatments and torque measurements were repeated without removing the specimen from the apparatus.

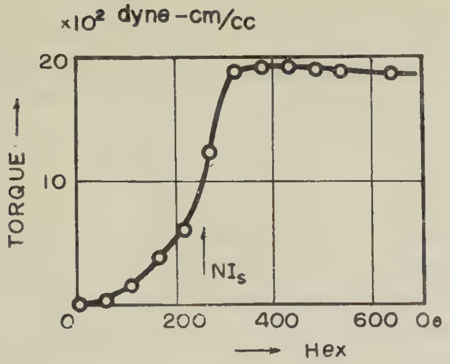

Fig. 3. Dependence of the torque upon intensity of a magnetic field.

The process of the magnetic annealing is as follows: Firstly the specimen is heated up to 650°C and annealed for 30 min., then it is cooled at a controlled rate down to room temperature in a magnetic field. The intensity of the field is 320∼430 Oe, which is large enough to magnetize the specimen parallel to the field. During this treatment the suspended system is fixed by the grip **G** and the orientation of the specimen relative to the field is accurately determined by using the mirror $\mathbf{M}_1$ and the telescope.

After cooling the torque curve is measured at room temperature. The intensity of the magnetic field in this case is 430 Oe, which is also large enough to induce the saturated intensity of the torque. The dependence of the torque upon intensity of the field is shown in Fig. 3 for the present specimen. It is seen in this figure that the torque saturates at about 300 Oe, which is nearly equal to the calculated intensity of the demagnetizing field $NIs=260$ Oe. If the specimen were in a shape of circular plate, as is usually the case, the torque would increase gradually with an increase of the field intensity. In such a case the true torque value must be determined by the extrapolation to $H_{ex}=2\pi I_s$. It was, however, unnecessary for the present specimen.

It should be added here that a very small change in the torque (positive or negative) was observed in the high field region. The magnitude and the sign of this change depend upon the crystallographic direction of the field. In the case of Fig. 3 it was negative. In other words, there is a small field-dependent anisotropy, whose curve form is different from the fundamental one. Since this anomalous anisotropy can be reduced by the

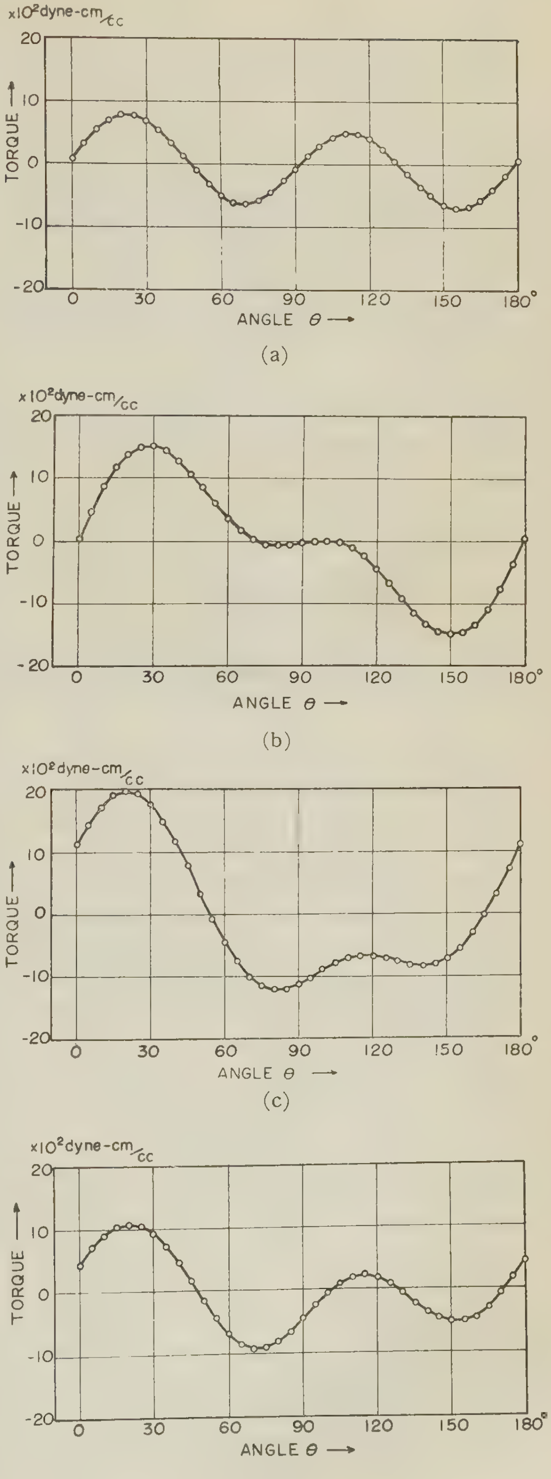

(a)

(b)

(c)

(d)

Fig. 4. The torque curves in (110) plane of $Ni_3Fe$ crystal observed after cooling in a magnetic field, the direction of which parallel to (a) $\theta=0°$ (<100>), (b) $\theta=90°$ (<110>), (c) $\theta=54.8°$ (<111>), and (d) $\theta=10°$.

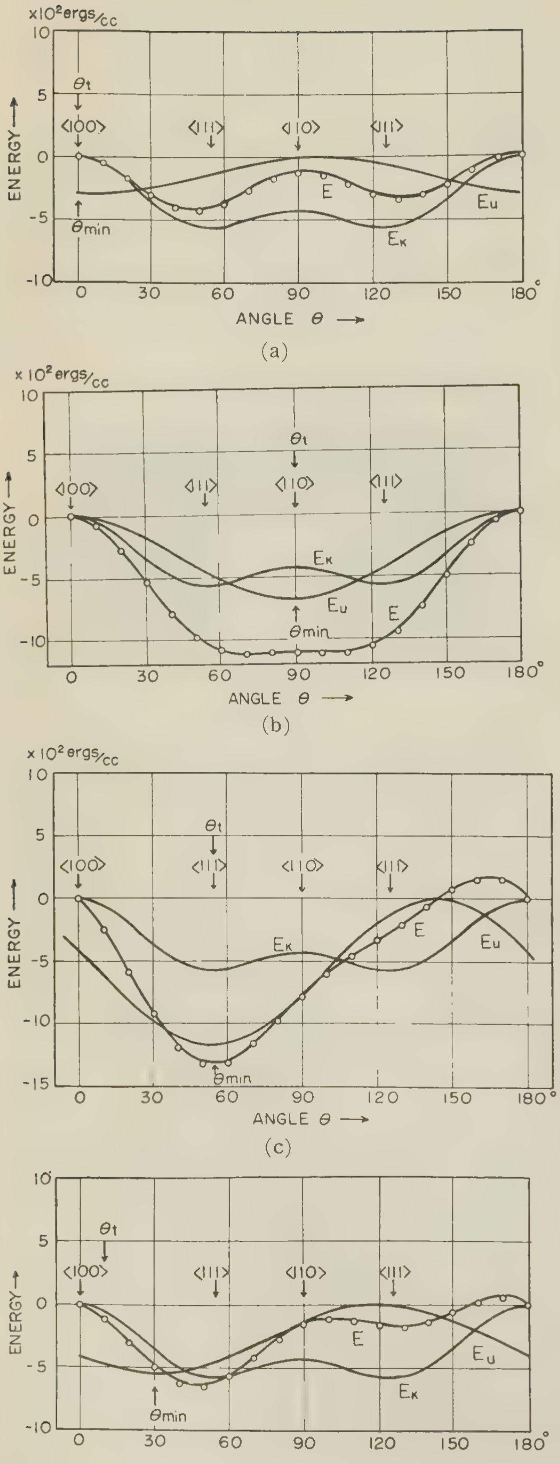

(a)

(b)

(c)

(d)

Fig. 5. The energy curves $E$ calculated from Fig. 4 by integration. (a), (b), (c) and (d) correspond to that of Fig. 4. $E$ is analyzed into crystal anisotropy $E_k$ and uniaxial anisotropy $E_u$. The circles means the sum of $E_k$ and $E_u$.

thermal treatment, it may be caused by the residual strain. After annealing it becomes smaller than 50 dyne cm/cc, which was negligibly small as compared to the fundamental one.

## § 4. Experimental Results

Some of the torque curves obtained after cooling in a magnetic field are shown in Fig. 4 for various crystallographic directions of annealing field. In order to make the interpretation easier, the torque curves were converted to energy curves as shown in Fig. 5 by integrating the torque values with respect to the angle. The integration was made by summing the torque values at each five degrees, the calculation of which introduces the error less than 0.1%.

It will be natural to consider that the anisotropy energy thus obtained consists of the usual crystal anisotropy $E_k$ and the uniaxial anisotropy $E_u$ induced by magnetic annealing. The anisotropy energy in (110) plane will then be given by

$$\begin{aligned} E &= E_k + E_u \\ &= K_1(\sin^4\theta/4+\sin^2\theta\cos^2\theta)+K_2\sin^4\theta\cos^2\theta/4 \\ &\quad -K_u\cos^2(\theta-\theta_0)\,, \qquad (1) \end{aligned}$$

where $K_1$ and $K_2$ are the usual constants of crystal anisotropy, $K_u$ is the constant of uniaxial anisotropy and $\theta$ is the direction of intrinsic magnetization as measured from ⟨100⟩ direction.

The experimental curves in Fig 5 could be analyzed into several terms in Eq. (1) by means of the Fourier analysis. This calculation was easily carried out by summing up the products of energy values and $\sin 2\theta$, $\cos 2\theta$, $\sin 4\theta$, $\cos 4\theta$, $\sin 6\theta$ or $\cos 6\theta$ at every 15 degrees in $\theta$, where the values of sin or cos at these angles are limited into one of 1.00, 0.866, 0.500 or 0.00. For the present specimen the $K_2$ term was found to be less than 1% of $K_1$ term, so $K_2$ term can be reasonably neglected. $E_k$ and $E_u$ terms thus analyzed are shown in Fig. 5, together with sum of these terms (shown by circles), which agrees well with original curves.

By comparing the $E_u$ curves, in Fig. 5 one may find that the depthes of the minimum, namely $K_u$, are considerably different with one another. It is noticed, further, that when the direction of the annealing field does not coinside with the principal crystallographic directions (Cf. Fig. 5 (d)), the minimum in $E_u$ lies not in just the same direction as that of the annealing field, but in the direction nearer to the neighboring ⟨111⟩ direction. The angle of deviation will be denoted by $\Delta\theta$ hereafter, which is given by

$$\Delta\theta=\theta_0-\theta_t\ , \qquad (2)$$

where $\theta_t$ is the direction of annealing field.

The values of $K_1, K_u$ and $\Delta\theta$ are plotted as a function $\theta_t$ in Figs. 6 and 7 for various cooling rate.

It is seen in Fig. 6 that $K_u$ depends upon the crystallographic direction of the annealing field, being largest at ⟨111⟩, second at ⟨110⟩ and smallest at ⟨100⟩, while the $K_1$ is fixed at a constant value. The value of $K_1$ increases with decrease of cooling rate as seen in the same figure. This is due to the development of ordinary order. Since the development of the ordinary order means a decrease of B–B pairs, the $K_1$ value can be interpreted as an indication of a decrease of B–B pairs. ($K_1$ is negligibly small at disordered state for the present composition Cf. Fig. 10). On the other hand, since $K_u$ can be interpreted as resulting from the unbalanced distribution of B–B pairs Cf. § 5), we can regard $K_u$ versus $K_1$ curve as indicating the variation of the unbalanced B–B pairs as a function of total number of B–B pairs. Fig. 8 shows such a variation of $K_u$ as a function of $K_1$, together with the variation of $\Delta\theta$. In this case the direction of the annealing field, $\theta_t$, was fixed at 13.5°, where $\Delta\theta$ takes the maximum value as seen in Fig. 7. It is seen that $K_u$ increases at first with order formation, but it decreases with an approach to perfect order. It is quite natural that the unbalancing of B–B pairs vanishes with vanishing of B–B pairs. The variation of $\Delta\theta$ will be interpreted in § 5.

## § 5. Interpretation of the Result

Néel[4] and independently Taniguchi and Yamamoto[5] carried out the calculation on the anisotropy induced by magnetic annealing in terms of directional order and dipole coupling between atom pairs. They showed that their result is in good agreement with the preliminary result[3] of the present author. The same mechanism has independently been considered by the present author[2] in order to interprete the variation of $K_u$ with composition of iron-nickel system.

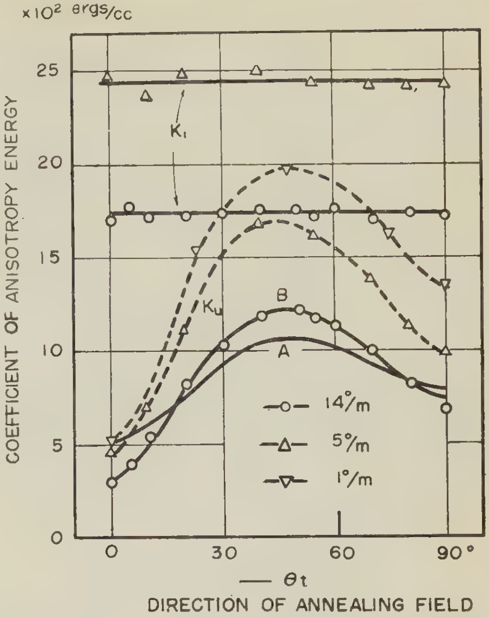

Fig. 6. $K_u$ and $K_1$ as a function of $\theta_t$ (direction of annealing field). A: Neel-Taniguchi-Yamamoto's formula, B: Experimental formula with $k_2/k_1=8.5$.

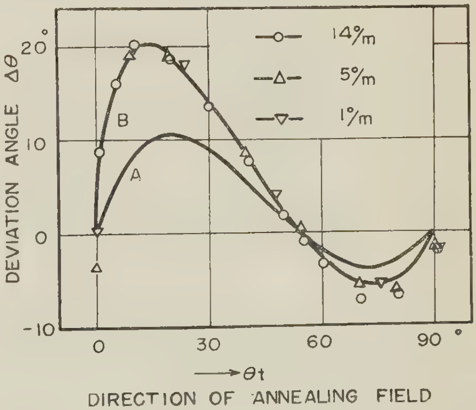

Fig. 7. $\Delta\theta$ (deviation of minimum direction $\theta_0$ from $\theta_t$) as a function of $\theta_t$. A: Néel-Taniguchi-Yamamoto's formula, B: Experimental formula with $k_2/k_1=8.5$.

Now we shall briefly follow their calculation: Firstly it is assumed that in binary alloy of A–B system the dipole-dipole interactions between neighboring atoms are different between different sorts of atom pairs A–A, B–B and A–B. Since the distribution of A–A or B–B pairs are necessarily determined by the distribution of B–B pairs, we may keep our attention exclusively on B–B pair by regarding it as having the energy

$$\omega_k=(l_{AA}+l_{BB}-2l_{AB})\cos^2\varphi_k$$
$$=l\cos^2\varphi_k\ , \qquad (3)$$

where $l_{AA}$, $l_{BB}$ and $l_{AB}$ are the coefficients of dipole-dipole interaction of A–A, B–B and A–B pairs and $\varphi_k$ is the angle between $k$-th bond direction and the intrinsic magnetization. When the alloy is annealed in a magnetic field, since the energy of B–B pair depends upon its bond direction relative to the field, the number of B–B pairs having $k$-th bond direction, $N_k$, will be proportional to the Boltzman factor $\exp(-w_k/kT)$. After the alloy is cooled down to room temperature, such an unbalanced distribution of B–B pairs (called directional order) shoud give rise to the anisotropy energy, which is given by

$$E_u=\sum_k N_k\omega_k'$$
$$=\left(\frac{N_0}{z}\right)\sum_k \exp(-\omega_k/kT)\omega_k'\ , \qquad (4)$$

where $\omega_k'$ is the energy after cooling, $N_0$ is the total number B–B pair contained in 1 cc and $z$ is the number of nearest neighbors. Putting Eq. (3) and

$$\omega_k'=l'\cos\varphi_k'\ . \qquad (5)$$

into Eq. (4), we have approximately

$$E_u=-\frac{N_0ll'}{zkT}\sum_k \cos^2\varphi_k\cos^2\varphi_k'\ . \qquad (6)$$

After summing up over all bond directions, we have

$$E_u=-\frac{N_0ll'}{kT}\left(k_1\sum_i \beta_i\gamma_i+k_2\sum_{i>j}\beta_i\beta_j\gamma_i\gamma_j\right) \qquad (7)$$

where $\beta_i$ and $\gamma_i$ are the direction cosines of intrinsic magnetization and the annealing field. The values of $k_1$ and $k_2$ are given in Tab. I for various crystal type.

Table I.

| crystal type | $k_1$ | $k_2$ |
|---|---|---|
| face-centred cubic | 1/12 | 4/12 |
| body-centred cubic | 0 | 4/9 |
| simple cubic | 1/3 | 0 |

We shall call the formula (7) together with Tab. I as Néel-Taniguchi Yamamoto's formula (N.T.Y.). When the intrinsic magnetization lies in (110) plane, Eq. (7) becomes

$$E_u=-K_u\cos^2(\theta-\theta_0)\ , \qquad (8)$$

where

$$K_u^2=K^2(p_0+p_1\cos 2\theta_t+p_2\cos^2 2\theta_t) \qquad (9)$$

with

$$p_0=\frac{1}{64}(4k_1^2+4k_1k_2+17k_2^2)$$
$$p_1=\frac{1}{32}(12\,k_1^2-4\,k_1k_2-k_2^2)$$
$$p_2=\frac{3}{64}(12\,k_1^2+4\,k_1k_2-5k_2^2)\ , \qquad (10)$$

and

$$\cot 2\theta_0'=q_1\operatorname{cosec} 2\theta_t+q_2\cot 2\theta_t \qquad (11)$$

with

$$q_1=\frac{1}{2}-\frac{k_2}{4k_1}$$
$$q_2=\frac{3}{2}+\frac{k_2}{4k_1}\ . \qquad (12)$$

By using the values of $k_1$ and $k_2$ for face-centred cubic lattice (Tab. I), we can have the theoretical relations $K_u(\theta_t)$ and $\Delta\theta(\theta_t)$ from Eqs. (9) and (11). They are graphically shown as curve A in Figs. 6 and 7. It is seen that qualitative features of the experimental curve can be well explained by these theoretical curves.

Now we shall determine the values of $k_1$ and $k_2$ so as to fit the formula (7) with experiment. By analysing the experimental curves of Figs. 6 and 7 by Fourier analysis and comparing it with Eqs. (9) and (11), we have the values

$$p_0K^2=147.6\times10^4,\qquad p_1K^2=-22.6\times10^4,$$
$$p_2K^2=-115.6\times10^4;$$
$$q_1=-0.191,\qquad q_2=0.427 \qquad (13)$$

for the case of cooling rate 14°/min. From these values we can easily have

$$k_1K=2.8_1\times10^2,\qquad k_2K=23.8\times10^2\ . \qquad (14)$$

It is seen in Figs. 6 and 7 that the formulas with the values of (14), shown graphically by the curve $B$, well represent the experimental plots. We have from Eq. (14)

$$k_2/k_1=8.5 \qquad (15)$$

as a experimental value, while we have obtained the theoretical value

$$k_2/k_1=4 \qquad (16)$$

as seen in Tab. I.

Now we shall consider the origin of this discrepancy between theory and experiment. It was found that it can be reasonably attributed to the nature of face-centred cubic lattice. In this lattice some of the nearest neighbors of one atom are also in nearest neighbor of one another. When, therefore, two B–B pairs enter into the neighboring bonds belonging to the same atom, the third B–B pair is necessarily produced, thus making the trigonal B–B–B group ($\varDelta$ B group) as shown in Fig. 9. It is easily proved that $\varDelta$B group has an energy $-(3/2)l\cos^2\varphi$, where $l$ is equal to that of Eq. (3) and $\varphi$ is the angle between magnetization and the normal of $\varDelta$B plane. Thus the $\varDelta$B group is equivalent to the atom pair having its bond direction parallel to ⟨111⟩ direction and will behave similarly to the atom pair in body-centred cubic lattice. Accordingly it may induce the magnetic anisotropy of body-centred cubic type. Then the magnetic anisotropy induced by B–B pair and $\varDelta$B group is given by

$$E_u=-\frac{ll'}{kT}\left\{\frac{N}{12}\sum_i\beta_i\gamma_i+\left(\frac{N_0}{3}+N'\right)\sum_{i>j}\beta_i\beta_j\gamma_i\gamma_j\right\} \tag{15}$$

where $N'$ is the total number of $\varDelta$B group and $N$ is that of B–B pairs which are not belonging to $\varDelta$B. Then

$$k_2/k_1=4+12\,N'/N\,. \tag{16}$$

In order to explain the experimental value 8.5, $N'=0.375\,N$, which may not be unreasonable value.

Now we shall consider the meaning of the variation of $\varDelta\theta$ in Fig. 8. For small value of $K_1$, $\varDelta\theta$ remains at a constant value which correspond to $k_2/k_1=8.5$. This means that the number of $\varDelta$ B group, $N$, decreases at first almost proportionally to the number of B–B pairs. It is seen, however, that when the alloy approaches to perfect order, $\varDelta\theta$ decreases gradually to about 10°, which is nearly equal to the value of N. T. Y curve (at 13.5°) in Fig. 7 and accordingly corresponds to $k_2/k_1=4$. This means that the number of $\varDelta$ B groups decreases more rapidly than that of B–B pairs. It will be reasonable, because the development of order would reject the presence of $\varDelta$ B group more severely than that of B–B pair, as being expected from the cooperative nature of the phenomenon. In short range ordered state, however, the cooperative effect is so weak that the rate of decrease of $\varDelta$ B group would not largely differ from that of B–B pairs.

Fig. 10 shows the variation of $K_1$ as a function of duration of the order treatment observed for the other specimen of Ni₃Fe.

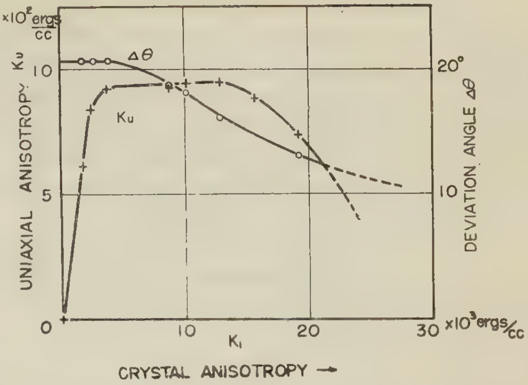

Fig. 8. $K_u$ and $\Delta\theta$ at $\theta_t=13.5°$ as a function of $K_1$. (Variation due to order formation.)

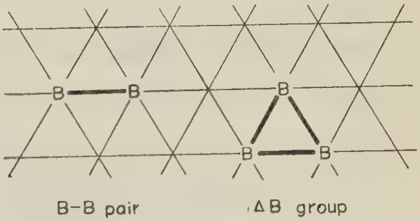

Fig. 9. Two types of the assembly of B atom in (111) plane of face-centred cubic lattice.

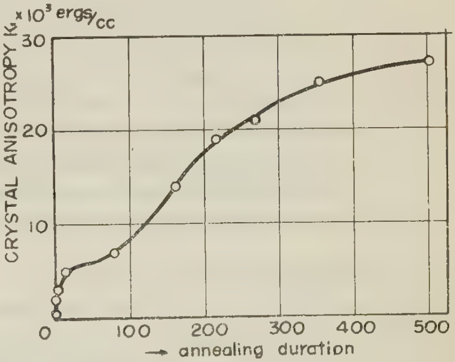

Fig. 10. Variation of $K_1$ with duration of order treatment (at from 490° to 430°C) for Ni₃Fe crystal.

It is interesting that the first increase of $K_1$ corresponds to the range where $\varDelta\theta$ remains unchanged.

It should be added that the influence of second nearest neighbor may not be important, because such pairs have the bond direction parallel to ⟨100⟩ and would induce the anisotropy of simple cubic type which increases $k_1$ instead of $k_2$ (Cf. Tab. I).

## § 6. Conclusions

It was shown that the characteristics of the magnetic anisotropy induced by magnetic annealing observed on $Ni_3Fe$ single crystal are well explained qualititavely by Néel-Taniguchi-Yamamoto's formula. Qualitative discrepancies between them can be interpreted by the nature of face-centred cubic lattice.

This research was supported by the research grant of the Ministry of Education.

### References

1) G. A. Kelsall: Physics **5** (1934) 169.
2) S. Chikazumi: J. Phys. Soc. Japan **10** (1955) 842.
3) S. Kaya: Rev. Mod. Phys. **25** (1953) 49.
4) L. Néel: Compt. Rend. **237** (1953) 1613; J. Phys. et Rad. **15** (1954) 225.
5) S. Taniguchi and M. Yamamoto: Sci. Rep. Res. Inst. Tohoku Univ. **A 6** (1954) 330.
S. Taniguchi: Sci. Rep. Res. Inst. Tohoku Univ. **A 7** (1955) 269.

---

JOURNAL OF THE PHYSICAL SOCIETY OF JAPAN Vol. 11, No. 5, MAY, 1956

# The Forces Acting on Two Equal Circular Cylinders placed in a Uniform Stream at Low Values of Reynolds Number

By Hiroomi FUJIKAWA

*Junior College of Engineering, University of Osaka Prefecture*

(Received December 8, 1955)

The steady slow motion of a viscous fluid past two parallel circular cylinders of equal radius with their axes in one plane perpendicular to a uniform flow is discussed on the basis of Oseen's linearized equations of motion.

Expansion formulae in powers of Reynolds number $R$ for the forces acting on one of the cylinders are obtained correct to the order of $R$, the lowest order terms being $O(R^{-1})$.

After detailed numerical calculations, it is shown that the drag on one cylinder decreases as the distance between the two cylinders decreases and also that each cylinder experiences a repulsive force.

## §1. Introduction and Summary

The steady flow of a viscous fluid past an obstacle at small Reynolds numbers has been discussed so far by many authors on the basis of Oseen's linearized equations of motion. From these investigations it can be seen that the disturbance due to the obstacle spreads to a great distance at small Reynolds numbers. Therefore, it is expected in the case of flow past several obstacles that the interference effect would be very conspicuous.

In the present paper, the writer treats the steady slow motion of an incompressible viscous fluid past two parallel circular cylinders of equal radius with their axes in one plane perpendicular to a uniform stream. Expansion formulae in powers of Reynolds number for the forces acting on one of the cylinders are obtained up to the second term. Making use of these formulae, detailed numerical discussion is made for several cases when the distance between the axes of the two cylinders is equal to 10, 50, 100 and 500 times their diameter, the Reynolds number of the flow varying from 0 to 1.0.

Thus, it is found that, on increasing the distance between the two cylinders, the drag on one cylinder increases and approaches the value for a single cylinder in an unlimited stream. Also, it is found that each cylinder experiences a repulsive force in the direction perpendicular to the uniform stream.

## §2. Fundamental Equation and its Solutions

We consider two infinitely long parallel circular cylinders $C_1$, $C_2$, of equal radius $a$, set in a steady uniform stream of velocity $U$

of an incompressible viscous fluid in such a manner that their axes lie in a plane perpendicular to the uniform stream.

Let O$x$, O$y$ be the rectangular co-ordinate axes in the plane of fluid motion, the axis of $x$ being taken along the direction of the uniform stream and the origin coinciding with the centre of the cylinder $C_1$. The centre of the other cylinder $C_2$ is situated on the $y$-axis, its coordinates being denoted by $(0, -2h)$ (Fig. 1).

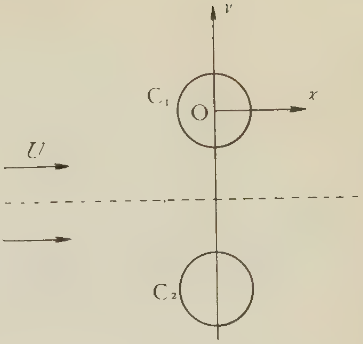

Fig. 1.

As is well known, the Navier-Stokes equations for the two-dimensional steady motion of an incompressible viscous fluid are written in a single equation as:

$$\left.\begin{aligned}\Delta\omega&=-\frac{1}{\nu}\frac{\partial(\Psi,\omega)}{\partial(x,y)}\,,\\ \omega&=-\Delta\Psi\,,\end{aligned}\right\} \tag{2.1}$$

where $\omega$ is the vorticity, $\Psi$ the stream function, $\nu$ the kinematic viscosity, and $\Delta$ stands for the operator $\partial^2/\partial x^2+\partial^2/\partial y^2$.

Now we may regard the flow under consideration as consisting of two parts, namely the uniform flow of the velocity $U$ and the perturbation due to the presence of the cylinders. Thus, denoting the perturbation stream function and the perturbation velocity components by $\psi$ and $u, v$ respectively, we may write

$$\Psi=Uy+\psi\,, \tag{2.2}$$

$$u=\partial\psi/\partial y\,,\qquad v=-\partial\psi/\partial x\,. \tag{2.3}$$

Inserting (2.2) into Eq. (2.1) and neglecting the second order terms in $\psi$, we arrive at Oseen's linearized equation of motion:

$$\Delta\left(\Delta-2k\frac{\partial}{\partial x}\right)\psi=0\,, \tag{2.4}$$

where

$$k=U/2\nu\,. \tag{2.5}$$

From (2.4), it will be seen that $\psi$ may be separated into two parts, namely harmonic and unharmonic parts:

$$\psi=\psi_h+\psi_u\,, \tag{2.6}$$

with

$$\Delta\psi_h=0\,, \tag{2.7}$$

and

$$\left(\Delta-2k\frac{\partial}{\partial x}\right)\psi_u=0\,. \tag{2.8}$$

For the case of a single circular cylinder placed in an unlimited uniform flow, the appropriate solutions of (2.7) and (2.8) which satisfy the boundary conditions at infinity have been given by Filon[1] in the forms;

$$\psi_h=\alpha_0\log r+a_0\theta+\sum_{n=1}^{\infty}r^{-n}(\alpha_n\cos n\theta+a_n\sin n\theta)\,, \tag{2.9}$$

$$\begin{aligned}k\psi_u=\beta_0e^{kx}K_0(kr)&+b_0\int_0^\theta kr\{K_1(kr)+K_0(kr)\cos\theta\}e^{kr\cos\theta}d\theta\\ &+e^{kx}\sum_{n=1}^{\infty}K_n(kr)(\beta_n\cos n\theta+b_n\sin n\theta)\,,\end{aligned} \tag{2.10}$$

where

$$x=r\cos\theta\,,\qquad y=r\sin\theta\,,$$

$a_n$, $\alpha_n$, $b_n$, $\beta_n$ are arbitrary real constants, and $K_n(kr)$ is the modified Bessel function of the second kind†. Also the condition that $\psi$ must be one-valued throughout the field of flow requires an additional condition

$$b_0/k=-a_0\,. \tag{2.11}$$

Let us here introduce the conjugate complex velocity

$$w=u-iv \tag{2.12}$$

for the perturbation flow, which is related to $\psi$ in the form:

---

† The definition of the modified Bessel function used here is identical with those in G. N. Watson's "*A Treatise on the Theory of Bessel Functions*" (Cambridge, 1922).

$$w=\psi_y+i\psi_x=2i\frac{\partial\psi}{\partial z},\qquad z=x+iy,\qquad \bar{z}=x-iy\,. \tag{2.13}$$

Then, after some calculations, it can be seen that

$$\left.\begin{aligned}
&w=w_h+w_u\,,\\
&w_h=\frac{A_0}{z}+\frac{A_1}{z^2}+\cdots\cdots\cdots\,,\\
&w_u=e^{kx}\Big\{\Big(B_0-\frac{1}{2}B_1\Big)K_0(kr)+\frac{1}{2}B_1K_1(kr)e^{i\theta}\\
&\qquad\qquad+\Big(\bar{B}_0-\frac{1}{2}\bar{B}_1\Big)K_1(kr)\,e^{-i\theta}+\frac{1}{2}\bar{B}_1K_2(kr)e^{-2i\theta}+\cdots\Big\}\,,
\end{aligned}\right\} \tag{2.14}$$

where

$$\left.\begin{aligned}
&A_0=a_0+i\alpha_0\,,\qquad A_1=a_1-i\alpha_1\,,\qquad \cdots\cdots\\
&B_0=b_0+i\beta_0\,,\qquad B_1=b_1+i\beta_1\,,\qquad \cdots\cdots\,.
\end{aligned}\right\} \tag{2.15}$$

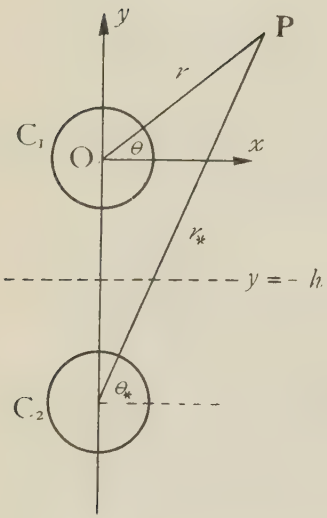

Fig. 2.

Now it may be observed from (2.9) and (2.10) that the perturbation flow due to the obstacle is composed of the harmonic and the unharmonic singularities (multiplets) situated at the origin. Therefore, in the present case in which the two circular cylinders are placed in the other-wise uniform stream, the perturbation flow may also be represented by the two systems of the fundamental singularities mentioned above, each being situated at the centre of the respective cylinder.

Thus, we may take the perturbation velocity $w$ in the form:

$$w=w_h^{(1)}+w_u^{(1)}+w_h^{(2)}+w_u^{(2)}\,, \tag{2.16}$$

with

$$\left.\begin{aligned}
&w_h^{(1)}=\frac{A_0}{z}+\frac{A_1}{z^2}+\cdots\cdots\,,\\
&w_u^{(1)}=e^{kx}\Big\{\Big(B_0-\frac{1}{2}B_1\Big)K_0(kr)+\frac{1}{2}B_1K_1(kr)e^{i\theta}\\
&\qquad\qquad+\Big(\bar{B}_0-\frac{1}{2}\bar{B}_1\Big)K_1(kr)e^{-i\theta}+\frac{1}{2}\bar{B}_1K_2(kr)e^{-2i\theta}+\cdots\cdots\Big\}\,,\\
&w_h^{(2)}=\frac{A_0{}^*}{z_*}+\frac{A_1{}^*}{z_*{}^2}+\cdots\cdots\,,\\
&w_u^{(2)}=e^{kx}\Big\{\Big(B_0{}^*-\frac{1}{2}B_1{}^*\Big)K_0(kr_*)+\frac{1}{2}B_1{}^*K_1(kr_*)e^{i\theta_*}\\
&\qquad\qquad+\Big(\bar{B}_0{}^*-\frac{1}{2}\bar{B}_1{}^*\Big)K_1(kr_*)\,e^{-i\theta_*}+\frac{1}{2}\bar{B}_1{}^*K_2(kr_*)e^{-2i\theta_*}+\cdots\cdots\Big\}\,,\\
&\text{where}\\
&\qquad\qquad z_*=r_*e^{i\theta_*}=z+2ih\,.
\end{aligned}\right\} \tag{2.17}$$

The flow field under consideration must be symmetric with respect to the straight streamline $y=-h$, i.e. $\mathfrak{I}(w)=0$ along $y=-h$. This condition yields immediately the following relations between the constants in (2.17):

$$\left.\begin{array}{lll} A_0^* = \overline{A}_0\,, & A_1^* = \overline{A}_1\,, & \cdots\cdots \\ B_0^* = \overline{B}_0\,, & B_1^* = \overline{B}_1\,, & \cdots\cdots\,. \end{array}\right\} \tag{2.18}$$

## § 3. Fulfilment of the Boundary Conditions on the Cylinders

We now proceed to consider the remaining boundary conditions, namely the conditions at the surfaces of the two cylinders. The flow is symmetric with respect to the streamline $y=-h$ and since the solution (2.16) together with (2.17) and (2.18) already satisfies this condition, it is sufficient to consider the fulfilment of the condition on one cylinder $C_1$ ($z=ae^{i\theta}$) only.

The resultant velocity $U+w$ must be zero on the surface of the cylinder, so that the required boundary condition is written as:

$$(w)_{r=a} = -U\,. \tag{3.1}$$

In order to apply this to $w$ as given by (2.16), we expand $w$ in a Fourier series in $\theta$ on the surface ($r=a$) of the cylinder $C_1$.

$w_h^{(1)}$ has already the required form:

$$(w_h^{(1)})_{r=a} = \frac{A_0}{a}\,e^{-i\theta} + \frac{A_1}{a^2}\,e^{-2i\theta} + \cdots\cdots\,. \tag{3.2}$$

Making use of the formula

$$e^{kx} = e^{kr\cos\theta} = \sum_{n=-\infty}^{\infty} I_n(kr)e^{in\theta}\,, \tag{3.3}$$

$w_u^{(1)}$ can be easily expanded in the form:

$$\begin{aligned} (w_u^{(1)})_{r-a} = {} & B_0I_0K_0 + \overline{B}_0I_1K_1 - \frac{1}{2}B_1(I_0K_0 - I_1K_1) - \frac{1}{2}\overline{B}_1(I_1K_1 - I_2K_2) \\ & + \left\{B_0I_1K_0 + \overline{B}_0I_0K_1 - \frac{1}{2}B_1(I_1K_0 - I_2K_1) - \frac{1}{2}\overline{B}_1(I_0K_1 - I_1K_2)\right\}e^{-i\theta} \\ & + \left\{B_0I_1K_0 + \overline{B}_0I_2K_1 + \frac{1}{2}B_1(I_0K_1 - I_1K_0) - \frac{1}{2}\overline{B}_1(I_2K_1 - I_3K_2)\right\}e^{i\theta} \\ & + \left\{B_0I_2K_0 + \overline{B}_0I_1K_1 - \frac{1}{2}B_1(I_2K_0 - I_3K_1) - \frac{1}{2}\overline{B}_1(I_1K_1 - I_0K_2)\right\}e^{-2i\theta} \\ & + \cdots\cdots\cdots\cdots\cdots\,, \end{aligned} \tag{3.4}$$

where the argument $ka$ of the modified Bessel functions $I_n$, $K_n$ has been omitted for simplicity.

Further, assuming that $h \gg a$, $w_h^{(2)}$ may be immediately expanded as:

$$\begin{aligned} (w_h^{(2)})_{r=a} = {} & \frac{1}{2ih}\overline{A}_0 + \frac{1}{(2ih)^2}\overline{A}_1 + \cdots\cdots - \left\{\frac{a}{(2ih)^2}\overline{A}_0 + \frac{2a}{(2ih)^3}\overline{A}_1 + \cdots\cdots\right\}e^{i\theta} \\ & + \cdots\cdots\cdots\cdots\cdots\,, \end{aligned} \tag{3.5}$$

where the condition (2.18) has been taken into account.

Finally, we proceed to obtain the expansion of $w_u^{(2)}$. Making use of the addition theorem[†] of the modified Bessel functions, we get

$$K_\sigma(kr_*)e^{i\sigma\theta_*} = \sum_{s=-\infty}^{\infty} i^{s+\sigma} I_s(kr) K_{s-\sigma}(2kh) e^{is\theta}\,. \tag{3.6}$$

Therefore, combining this with (3.3), we obtain the expansion

---

[†] See, for example, G. N. Watson, *A Treatise on the Theory of Bessel Functions* (Cambridge, 1922), § 11.3, p. 361.

$$\left.\begin{aligned} &[e^{kx}K_\sigma(kr_*)e^{i\sigma\theta_*}]_{r=a}=\sum_{n=-\infty}^{\infty}\lambda_{n,\sigma}e^{in\theta}\,,\\ &\lambda_{n,\sigma}=\sum_{s=-\infty}^{\infty}i^{s+\sigma}I_s(ka)I_{s-n}(ka)K_{s-\sigma}(2kh)\,,\\ &\sigma=0,\ \pm1,\ \pm2,\ \cdots\,. \end{aligned}\right\} \tag{3.7}$$

Obviously it follows

$$\lambda_{-n,-\sigma}=\overline{\lambda_{n,\sigma}}\,. \tag{3.8}$$

Using (3.7) together with (2.18), we finally obtain the expansion of the function $w_u^{(2)}$ in (2.17) in the following form:

$$[w_u^{(2)}]_{r=a}=\sum_{n=-\infty}^{\infty}\left\{\lambda_{n,0}\overline{B}_0+\frac{1}{2}(\lambda_{n,1}-\lambda_{n,0})\overline{B}_1+\lambda_{n,-1}B_0+\frac{1}{2}(\lambda_{n,-2}-\lambda_{n,-1})B_1+\cdots\right\}e^{in\theta}\,. \tag{3.9}$$

Substituting (3.2), (3.4), (3.5) and (3.9) into (2.16), we arrive at the Fourier expansion of the solution $w$ on the circular cylinder $r=a$.

According to the boundary condition (3.1), every coefficient of $e^{in\theta}$ ($n=0, \pm1, \pm2, \cdots$) in the expansion should vanish except for the constant term ($n=0$), which must be equal to $-U$. Thus, we obtain a doubly infinite set of linear algebraic equations for determining the constants $A_n$'s and $B_n$'s. Namely, for $n=0, -1, 1, -2, \cdots$, we have

$$\left.\begin{aligned} &(I_0K_0+\lambda_{0,-1})B_0+(I_1K_1+\lambda_{0,0})\overline{B}_0\\ &\quad+\frac{1}{2}(I_1K_1-I_0K_0+\lambda_{0,-2}-\lambda_{0,-1})B_1+\frac{1}{2}(I_2K_2-I_1K_1+\lambda_{0,1}-\lambda_{0,0})\overline{B}_1+\cdots\\ &\quad+\frac{1}{2ih}\overline{A}_0+\frac{1}{(2ih)^2}\overline{A}_1+\cdots\cdots=-U\,,\\ &(I_1K_0+\lambda_{-1,-1})B_0+(I_0K_1+\lambda_{-1,0})\overline{B}_0\\ &\quad+\frac{1}{2}(I_2K_1-I_1K_0+\lambda_{-1,-2}-\lambda_{-1,-1})B_1+\frac{1}{2}(I_1K_2-I_0K_1+\lambda_{-1,1}-\lambda_{-1,0})\overline{B}_1+\cdots\\ &\quad+\frac{A_0}{a}+\cdots\cdots=0\,,\\ &(I_1K_0+\lambda_{1,-1})B_0+(I_2K_1+\lambda_{1,0})\overline{B}_0\\ &\quad+\frac{1}{2}(I_0K_1-I_1K_0+\lambda_{1,-2}-\lambda_{1,-1})B_1+\frac{1}{2}(I_3K_2-I_2K_1+\lambda_{1,1}-\lambda_{1,0})\overline{B}_1+\cdots\\ &\quad-\frac{a}{(2ih)^2}\overline{A}_0-\frac{2a}{(2ih)^3}\overline{A}_1-\cdots\cdots=0\,,\\ &(I_2K_0+\lambda_{-2,-1})B_0+(I_1K_1+\lambda_{-2,0})\overline{B}_0\\ &\quad+\frac{1}{2}(I_3K_1-I_2K_0+\lambda_{-2,-2}-\lambda_{-2,-1})B_1+\frac{1}{2}(I_0K_2-I_1K_1+\lambda_{-2,1}-\lambda_{-2,0})\overline{B}_1+\cdots\\ &\quad+\frac{A_1}{a^2}+\cdots\cdots=0\,, \end{aligned}\right\} \tag{3.10}$$

where the argument $ka$ of the modified Bessel functions has been dropped for simplicity.

## § 4. Approximate Solution for the Case $ka \ll 1$, $(kh)^{-1}=O(1)$

The system of simultaneous equations (3.10) for determining constants $A_n$'s and $B_n$'s having been derived, we can obtain, the required solution satisfying all the boundary conditions. But, it is difficult to solve the equations (3.10) exactly. Since, however, we are mainly interested in the flow at small Reynolds numbers, i.e. the flow for which $ka$ takes small values, where the Oseen approximation is applicable, we next proceed to find out the approximate solution valid for such small values of $ka$.

Eliminating $A_n$'s from (3.10) and separating real and imaginary parts, we obtain the system of equations for determining $B_n=b_n+i\beta_n$:

$$\left.\begin{aligned}
&C_{11}b_0+C_{12}\beta_0+C_{13}(b_1/2)+C_{14}(\beta_1/2)+\cdots\cdots=-U\,,\\
&C_{i1}b_0+C_{i2}\beta_0+C_{i3}(b_1/2)+C_{i4}(\beta_1/2)+\cdots\cdots=0\\
&\qquad\qquad (i=2,\ 3,\ 4,\ \cdots)\,.
\end{aligned}\right\}\tag{4.1}$$

The coefficients $C_{ij}$ are given as follows:

$$\left.\begin{aligned}
C_{11}&=I_0K_0+I_1K_1+p_{0,\,0}+p_{0,\,-1}+(a/2h)(q_{-1,\,0}+q_{-1,\,-1})\\
&\qquad+(a/2h)^2(I_2K_0+I_1K_1+p_{-2,\,0}+p_{-2,\,-1})\,,\\
C_{12}&=-q_{0,\,-1}+(a/2h)(I_1K_0-I_0K_1-p_{-1,\,0}+p_{-1,\,-1})+(a/2h)^2(q_{-2,\,0}-q_{-2,\,-1})\,,\\
C_{13}&=I_2K_2-I_0K_0+p_{0,\,1}+p_{0,\,-2}+(a/2h)(q_{-1,\,1}+q_{-1,\,-2})\\
&\qquad+(a/2h)^2(I_3K_1-I_2K_0+I_0K_2-I_1K_1+p_{-2,\,1}+p_{-2,\,-2})\,,\\
C_{14}&=q_{0,\,1}-q_{0,\,-2}+(a/2h)(I_2K_1-I_1K_0-I_1K_2+I_0K_1-p_{-1,\,1}+p_{-1,\,-2})\\
&\qquad+(a/2h)^2(q_{-2,\,1}-q_{-2,\,-2})\,,\\
C_{21}&=q_{0,\,-1}+(1/2kh)-(a/2h)^2(q_{-2,\,0}+q_{-2,\,-1})\,,\\
C_{22}&=I_0K_0-I_1K_1-p_{0,\,0}+p_{0,\,-1}-(a/2h)^2(I_2K_0-I_1K_1-p_{-2,\,0}+p_{-2,\,-1})\,,\\
C_{23}&=q_{0,\,1}+q_{0,\,-2}-(a/2h)^2(q_{-2,\,1}+q_{-2,\,-2})\,,\\
C_{24}&=2I_1K_1-I_0K_0-I_2K_2-p_{0,\,1}+p_{0,\,-2}\\
&\qquad-(a/2h)^2(I_3K_1-I_2K_0-I_0K_2+I_1K_1-p_{-2,\,1}+p_{-2,\,-2})\,,\\
C_{31}&=I_1K_0+I_2K_1+p_{1,\,0}+p_{1,\,-1}-(1/2kh)^2ka+2(a/2h)^3(q_{-2,\,0}+q_{-2,\,-1})\,,\\
C_{32}&=q_{1,\,0}-q_{1,\,-1}+2(a/2h)^3(I_2K_0-I_1K_1-p_{-2,\,0}+p_{-2,\,-1})\,,\\
C_{33}&=I_0K_1-I_1K_0+I_3K_2-I_2K_1+p_{1,\,1}+p_{1,\,-2}+2(a/2h)^3(q_{-2,\,1}+q_{-2,\,-2})\,,\\
C_{34}&=q_{1,\,1}-q_{1,\,-2}+2(a/2h)^3(I_3K_1-I_2K_0-I_0K_2+I_1K_1-p_{-2,\,1}+p_{-2,\,-2})\,,\\
C_{41}&=q_{1,\,0}+q_{1,\,-1}+(a/2h)^2(q_{-1,\,0}+q_{-1,\,-1})+2(a/2h)^3(I_2K_0+I_1K_1+p_{-2,\,0}+p_{-2,\,-1})\,,\\
C_{42}&=I_1K_0-I_2K_1-p_{1,\,0}+p_{1,\,-1}+(a/2h)^2(I_1K_0-I_0K_1-p_{-1,\,0}+p_{-1,\,-1})\\
&\qquad+2(a/2h)^3(q_{-2,\,0}-q_{-2,\,-1})\,,\\
C_{43}&=q_{1,\,1}+q_{1,\,-2}+(a/2h)^2(q_{-1,\,1}+q_{-1,\,-2})\\
&\qquad+2(a/2h)^3(I_3K_1-I_2K_0+I_0K_2-I_1K_1+p_{-2,\,1}+p_{-2,\,-2})\,,\\
C_{44}&=I_0K_1-I_1K_0-I_3K_2+I_2K_1-p_{1,\,1}+p_{1,\,-2}\\
&\quad+(a/2h)^2(I_2K_1-I_1K_0-I_1K_2+I_0K_1-p_{-1,\,1}+p_{-1,\,-2})+2(a/2h)^3(q_{-2,\,1}-q_{-2,\,-2})\,,
\end{aligned}\right\}\tag{4.2}$$

where we have put

$$\left.\begin{aligned}
&\lambda_{n,\,0}=p_{n,\,0}+iq_{n,\,0}\,, &&\lambda_{n,\,-1}=p_{n,\,-1}+iq_{n,\,-1}\,,\\
&\lambda_{n,\,1}-\lambda_{n,\,0}=p_{n,\,1}+iq_{n,\,1}\,, &&\lambda_{n,\,-2}-\lambda_{n,\,-1}=p_{n,\,-2}+iq_{n,\,-2}\,,\ \cdots\cdots
\end{aligned}\right\}\tag{4.3}$$

$p_{n,\,\sigma}$ and $q_{n,\,\sigma}$ being all real.

In the first place, let us consider the case where $(kh)^{-1}=\mathrm{O}(1)$[†] and $ka\ll 1$. In this case the coefficients $C_{ij}$ given by (4.2) can be expanded as follows:

$$\left.\begin{aligned}
C_{11}&=H_*+\{(1/4)+2K_0+H_*+N\}(ka/2)^2+\mathrm{O}(k^4a^4)\,,\\
C_{12}&=-M-2\{M-(1/kh)(1+H)\}(ka/2)^2+\mathrm{O}(k^4a^4)\,,\\
C_{13}&=(3/4)-H_*+N-\{(1/6)+2(K_0+H_*)-(1/kh)(K_1-M)\}(ka/2)^2+\mathrm{O}(k^4a^4)\,,\\
C_{14}&=-(1/2kh)(1+4H)(ka/2)^2+\mathrm{O}(k^4a^4)\,,\\
C_{21}&=M-2K_1(ka/2)^2+\mathrm{O}(k^4a^4)\,,\\
C_{22}&=H+\{(11/4)+2K_2+3H+N\}(ka/2)^2+\mathrm{O}(k^4a^4)\,,\\
C_{23}&=2K_1+(5K_1-K_3)(ka/2)^2+\mathrm{O}(k^4a^4)\,,\\
C_{24}&=(1/4)-H+N-\{(10/3)+(1/2k^2h^2)+4(K_2+H)\}(ka/2)^2+\mathrm{O}(k^4a^4)\,,\\
C_{31}&=-\{(1/4)-H_*+N\}(ka/2)+\{(1/3)+K_2+H_*\}(ka/2)^3+\mathrm{O}(k^5a^5)\,,\\
C_{32}&=2K_1(ka/2)+(1/2)\{5K_1-K_3-(2/k^3h^3)\}(ka/2)^3+\mathrm{O}(k^5a^5)\,,
\end{aligned}\right\}\tag{4.4}$$

---

[†] $4kh=2Uh/\nu$ is a Reynolds number referred to the distance $2h$ between the two cylinders.

$$\left.\begin{aligned}
C_{33}&=(1/2)(ka/2)^{-1}+2\{(5/12)-K_2-H_*\}(ka/2)\\
&\qquad -(1/2)\{(31/24)+4K_2-K_4+5H_*\}(ka/2)^3+O(k^5a^5)\ ,\\
C_{34}&=-(2N/kh)(ka/2)+(4/kh)\{K_2+(1/4k^2h^2)\}(ka/2)^3+O(k^5a^5)\ ,\\
C_{41}&=(1/kh)\{K_2+(2/kh)M\}(ka/2)^3+O(k^5a^5)\ ,\\
C_{42}&=\{(1/4)+H-N\}(ka/2)+2\{(13/12)+2K_2+H+N+(H/k^2h^2)\}(ka/2)^3+O(k^5a^5)\ ,\\
C_{43}&=(2N/kh)(ka/2)-(4/kh)\{K_0+(1/4k^2h^2)\}(ka/2)^3+O(k^5a^5)\ ,\\
C_{44}&=(1/2)(ka/2)^{-1}-2\{(5/12)+K_2+H\}(ka/2)\\
&\qquad -(1/2)[(185/24)-(3/kh)K_3+(1/k^2h^2)+(K_2+H)\{7+(4/k^2h^2)\}](ka/2)^3+O(k^5a^5)\ ,
\end{aligned}\right|$$

$$\left.\begin{aligned}
&\text{where}\quad H=S-1-K_0\ ,\quad H_*=S+K_0\ ,\quad M=(1/2kh)-K_1\ ,\quad N=(1/2k^2h^2)-K_2\ ,\\
&\text{with}\quad S=(1/2)-\gamma-\log(ka/2)\ ,
\end{aligned}\right\}\tag{4.5}$$

$\gamma$ being the Eulerian constant, and the argument $2kh$ of the modified Bessel function $K_n$'s has been omitted for brevity.

Inserting (4.4) in (4.1) and solving for $b_0$, $\beta_0$, $b_1$, $\beta_1$ etc., we obtain, after some straightforward calculations, the result as

$$\left.\begin{aligned}
b_0/U&=-\frac{H}{\varDelta}\left\{1+\left(\frac{3}{4}+\frac{1}{2}H+N-\frac{P}{H}-\frac{T}{\varDelta}\right)(ka)^2+O(k^4a^4)\right\}\ ,\\
\beta_0/U&=\frac{M}{\varDelta}\left\{1+\left(\frac{1}{4}+H_*+N-\frac{Q}{M}-\frac{T}{\varDelta}\right)(ka)^2+O(k^4a^4)\right\}\ ,\\
b_1/U&=-\frac{H}{\varDelta}\left(\frac{1}{4}-H_*+N+\frac{2K_1M}{H}\right)(ka)^2+O(k^4a^4)\ ,\\
\beta_1/U&=-\frac{M}{\varDelta}\left(\frac{1}{4}+H-N\right)(ka)^2+O(k^4a^4)\ ,\\
&\cdots\cdots\cdots\cdots\cdots\cdots\cdots\cdots\ ,
\end{aligned}\right\}\tag{4.6}$$

$$\left.\begin{aligned}
&\text{where}\qquad \varDelta=HH_*+M^2\ ,\\
P&=-\frac{5}{8}+\frac{1}{4k^2h^2}-\frac{2}{kh}M+M^2-\frac{1}{2}\left(N-\frac{1}{4}\right)^2,\\
Q&=\frac{1}{2kh}\left\{H_*-\left(N-\frac{1}{4}\right)\right\},\\
T&=\frac{1}{2}HH_*(1+H+H_*)-H\left\{\frac{3}{32}+\frac{1}{8}(H-H_*)-\frac{1}{2}\left(N+\frac{1}{2}\right)^2\right\}\\
&\quad +H_*\left\{\frac{5}{8}-\frac{1}{4k^2h^2}+\frac{1}{2}\left(N-\frac{1}{4}\right)^2\right\}-\frac{M}{4kh}\{1+H-4(H_*+N)\}\ .
\end{aligned}\right\}\tag{4.7}$$

Further, solving the second equation of (3.10) for $A_0=a_0+i\alpha_0$ and separating the real and imaginary parts we get

$$\left.\begin{aligned}
a_0/a&=-b_0/ka\ ,\\
\alpha_0/a&=-2q_{-1,0}b_0-(I_1K_0-I_0K_1-2p_{-1,0})\beta_0\\
&\quad -q_{-1,1}b_1-\left\{\frac{1}{2}(K_1I_0-K_0I_1+K_1I_2-K_2I_1)-p_{-1,1}\right\}\beta_1+\cdots\ ,
\end{aligned}\right\}\tag{4.8}$$

where the argument $ka$ of the modified Bessel function has been again omitted. Here it is noted that the first relation in (4.8) is nothing but the condition in (2.11).

Inserting (4.6) into (4.8) and expanding as before the right-hand sides for small values of $ka$, we get

$$\left.\begin{aligned}
\frac{a_0}{Ua}&=\frac{H}{ka\varDelta}\left\{1+\left(\frac{3}{4}+\frac{1}{2}H+N-\frac{P}{H}-\frac{T}{\varDelta}\right)(ka)^2+O(k^4a^4)\right\}\ ,\\
\frac{\alpha_0}{Ua}&=\frac{M}{ka\varDelta}\left\{1+\left(-\frac{1}{4}+H_*+N-\frac{T}{\varDelta}+\frac{3-8S+4N}{8khM}\right)(ka)^2+O(k^4a^4)\right\}\ ,
\end{aligned}\right\}\tag{4.9}$$

where the functions $S, H, H_*, M, N, P, T, \varDelta$ are given by (4.7).

In a similar manner, the fourth equation in (3.10) determines the constant $A_1 = a_1 - i\alpha_1$. It is, however, unnecessary for the calculation of the forces acting on the cylinder and therefore its explicit expression is not given here.

## § 5. Calculation of the Drag and Lift

The total drag $D$ acting on the cylinder $C_1$ $(r=a)$ may be considered as composed of the pressure drag $D_p$ and the frictional drag $D_f$ in the form:

$$D = D_p + D_f\ , \qquad D_p = -a\int_0^{2\pi} p\cos\theta d\theta\ , \qquad D_f = -a\rho\nu\int_0^{2\pi}\omega\sin\theta d\theta\ , \tag{5.1}$$

where $p$, $\rho$, $\omega$ are the pressure, density and vorticity on the surface $r=a$ respectively.

Similarly, the lift $L$ may be expressed as follows:

$$L = L_p + L_f\ , \qquad L_p = -a\int_0^{2\pi} p\sin\theta d\theta\ , \qquad L_f = a\rho\nu\int_0^{2\pi}\omega\cos\theta d\theta\ . \tag{5.2}$$

Combining (5.1) and (5.2), we have

$$L - iD = a\int_0^{2\pi}(ip + \rho\nu\omega)e^{i\theta}d\theta\ . \tag{5.3}$$

In the Oseen approximation, it can be shown that

$$p = -\rho U u_h\ , \qquad \omega = -\Delta\psi_u = 2kv_u\ , \tag{5.4}$$

where $u$, $v$ denote as before the $x$, $y$ components of the perturbation velocity and suffices $h$, $u$ indicate the harmonic and unharmonic parts respectively. Since $v = v_h + v_u = 0$ on the surface of the cylinder, we may also write

$$\omega = -2kv_h\ . \tag{5.5}$$

Inserting these expressions in (5.3), we get

$$L - iD = -\rho U\oint_{|z|=a} w_h dz\ . \tag{5.6}$$

Since, by (2.17),

$$w_h = w_h^{(1)} + w_h^{(2)} = \sum_{n=0}^{\infty}\{A_n z^{-n-1} + A_n^*(z+2ih)^{-n-1}\}\ ,$$

we obtain a general formula

$$L - iD = -2\pi i\rho U A_0\ , \tag{5.7}$$

or

$$L = 2\pi\rho U\alpha_0\ , \qquad D = 2\pi\rho U a_0\ . \tag{5.8}$$

Therefore, by using (4.9), we can finally obtain expansion formulae for the drag and lift. Thus, correct as far as terms of the order of $R$, we have

$$\begin{aligned} C_D &= \frac{D}{2\rho U^2 a} \\ &= 4\pi\frac{H}{R\varDelta}\left\{1 + \frac{1}{16}\left(\frac{3}{4} + \frac{1}{2}H + N - \frac{P}{H} - \frac{T}{\varDelta}\right)R^2 + O(R^4)\right\}\ , \end{aligned} \tag{5.9}$$

$$\begin{aligned} C_L &= \frac{L}{2\rho U^2 a} \\ &= 4\pi\frac{M}{R\varDelta}\left\{1 + \frac{1}{16}\left(-\frac{1}{4} + H_* + N - \frac{T}{\varDelta} + \frac{3 - 8S + 4N}{2MR_h}\right)R^2 + O(R^4)\right\}\ , \end{aligned} \tag{5.10}$$

where as before

$$\left.\begin{aligned}
&S=\frac{1}{2}-\gamma-\log\left(\frac{R}{8}\right)\,,\\
&H=S-1-K_0(R_h/2)\,,\\
&H_*=S+K_0(R_h/2)\,,\\
&M=2/R_h-K_1(R_h/2)\,,\\
&N=8/R_h^2-K_2(R_h/2)\,,\\
&\Delta=HH_*+M^2\,,\\
&P=-\frac{5}{8}+(2/R_h)^2-8(M/R_h)+M^2-\frac{1}{2}\left(N-\frac{1}{4}\right)^2,\\
&T=\frac{1}{2}HH_*(1+H+H_*)-H\left\{\frac{3}{32}+\frac{1}{8}(H-H_*)-\frac{1}{2}\left(N+\frac{1}{2}\right)^2\right\}\\
&\qquad+H_*\left\{\frac{5}{8}-(2/R_h)^2+\frac{1}{2}\left(N-\frac{1}{4}\right)^2\right\}-(M/R_h)\{1+H-4(H_*+N)\}\,,
\end{aligned}\right\}\tag{5.11}$$

and

$$\left.\begin{aligned}
&R=4ka=\frac{2Ua}{\nu}\,, &&R_h=4kh=\frac{2Uh}{\nu}\,,\\
&R\ll 1\,, &&1/R_h=O(1)\,,
\end{aligned}\right\}\tag{5.12}$$

$R$ and $R_h$ being the Reynolds numbers referred respectively to the diameter $2a$ of the cylinder and the distance $2h$ between the two cylinders.

It may be mentioned here that when the distance $2h$ tends to infinity, i.e. $R_h\to\infty$, all the modified Bessel functions $K_n(R_h/2)$ $(n=0, 1, 2, \cdots)$ tend to zero, and the above formulae reduce to

$$\left.\begin{aligned}
&C_D{}^*=\frac{4\pi}{RS}\left\{1-\frac{1}{S}\left(S^2-\frac{1}{2}S+\frac{5}{16}\right)\frac{R^2}{32}\right\},\\
&C_L{}^*=0\,.
\end{aligned}\right\}\tag{5.13}$$

As should be expected, the former result is in perfect agreement, up to the first two terms, with the formula obtained by Tomotika and Aoi[2)] for the case of a single circular cylinder in an unbounded stream.

## § 6. Approximate Solution for the Case $ka\ll 1$, $kh\ll 1$

The preceding analysis depends upon the assumption that $(kh)^{-1}=O(1)$. However, when $kh\ll 1$ for sufficiently small $k$, the values of $(kh)^{-n}$ and $K_n(2kh)$ $(n=0, 1, 2,\cdots)$ in (4.2) become very large and therefore the analysis for small values of $k$ should be reconsidered.

Detailed examination[†] of the coefficients $C_{ij}$ in the equations (4.1) shows however that the correct expansion for this case just agrees, up to the order of $(a/h)^2$, with the one which is obtained by considering formally the case $kh\ll 1$ in the preceding results (5.9) and (5.10).

Thus, making use of the expansions:

$$\left.\begin{aligned}
&H=\kappa-(S-\kappa)(R_h/4)^2+O(R_h^4)\,,\\
&H_*=2S-\kappa-1+(S-\kappa)(R_h/4)^2+O(R_h^4)\,,\\
&M=\left(S-\kappa-\frac{1}{2}\right)(R_h/4)+\frac{1}{2}\left(S-\kappa+\frac{1}{4}\right)(R_h/4)^3+O(R_h^5)\,.\\
&N=\frac{1}{2}-\frac{1}{2}\left(S-\kappa-\frac{1}{4}\right)(R_h/4)^2+O(R_h^4)\,,\\
&\cdots\cdots\cdots\cdots\cdots\cdots\cdots\cdots\cdots\,,
\end{aligned}\right\}$$

---

[†] Detailed discussion for this fact will be given elsewhere.

we obtain the results

$$\left.\begin{aligned} C_D &= \frac{4\pi}{R(2S-\kappa-1)}\{1+O(a^4/h^4)\}\,, \\ C_L &= \frac{\pi}{2\kappa}\,\frac{h}{a}\,\frac{2S-2\kappa-1}{2S-\kappa-1}\left\{1+\frac{1}{4}\left(\frac{1}{\kappa}+\frac{5-8S}{2S-2\kappa-1}\right)\left(\frac{a}{h}\right)^2+O\left(\frac{a^4}{h^4}\right)\right\}\,, \end{aligned}\right\} \tag{6.1}$$

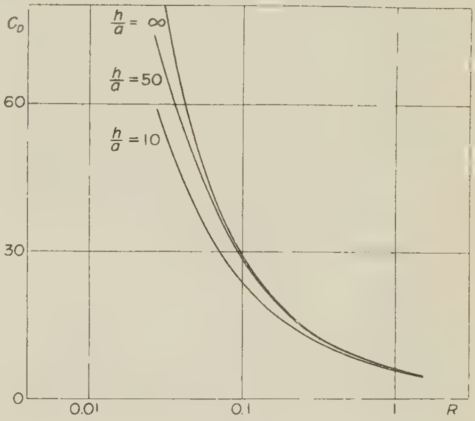

Fig. 3.

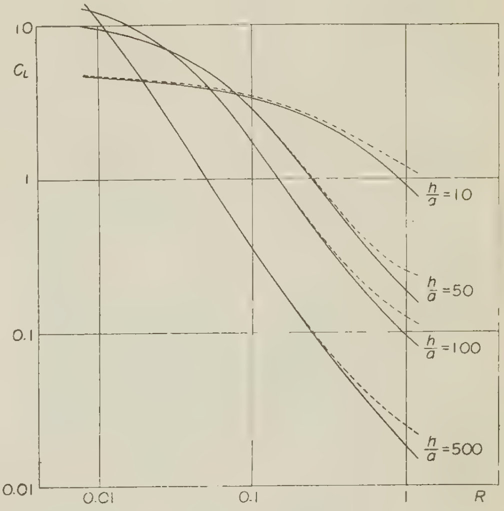

Fig. 4. - - - - first approximation,
— second approximation.

where

$$\kappa=\log\left(\frac{2h}{a}\right)-\frac{1}{2}\,. \tag{6.2}$$

It may be noted here that (5.13) gives

$$C_D{}^*\sim\frac{4\pi}{R\log R}$$

for the value of $C_D{}^*$ of a single circular cylinder in an unbounded stream at sufficiently small Reynolds number. But, from (6.1), we obtain a different value

$$\lim_{h\to\infty} C_D \longrightarrow \frac{2\pi}{R\log R}\,.$$

The limiting value of $C_D$ depends upon the order of the limiting processes $R\to 0$ and $h\to\infty$. Besides, the value of $C_L$ given by (6.1) increases as $h$ increases. This result should also be accepted under the restriction that $kh\ll 1$.

## § 7. Numerical Discussions

Making use of the formulae (5.9), (5.10) and (6.1), the writer has calculated the values of $C_D$ and $C_L$ for various values up to unity of the Reynolds number $R$ $(=4ka)$ as well as for various values ranging from 10 to 500 of the ratio $h/a$. These results are given in Tables I∼VIII and are also shown graphically in Figs. 3 and 4.

Further, the values of $C_D$ for a single circular cylinder in an unbounded stream have been calculated from (5.13) and tabulated in Table IX for the sake of reference. In these tables, values of the first and second approximations with respect to powers of $R^2$ are separately given in order to see the convergence of the successive approximations.

From these tables and figures, it will be seen that, as the Reynolds number increases, the value of $C_D$ for a given distance ratio $h/a$ decreases monotonously and the interference effect becomes imperceptible.

As for the variation of the drag coefficient $C_D$ with the ratio $h/a$ for a given Reynolds number, we see that the value of $C_D$ increases monotonously with the increase of the ratio $h/a$ and tends to the values for the case of a single circular cylinder in an unbounded stream. These results are also showngra phically in Figs. 5 and 6.

On the other hand, the variation of the lift coefficient $C_L$ with the distance ratio $h/a$ is somewhat complicated. When the Reynolds number is not so small, it decreases with the increase of the ratio $h/a$ and ultimately tends to zero. But, when the Reynolds number be-

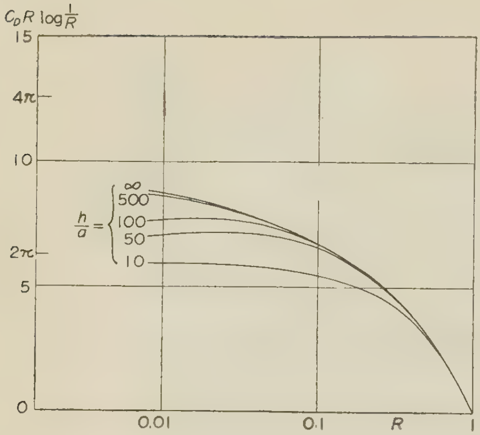

Fig. 5.

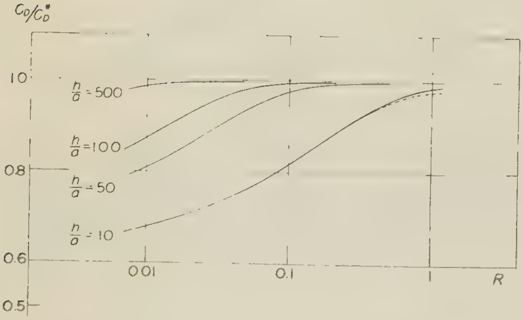

Fig. 6. ---- first approximation,
—— second approximation.

Table I. Values of $C_D$ $(h/a=10)$.

| $R$ | calculated by the expansion formula (6.1) | calculated by the formula (5.9) 1st approx. | 2nd approx. |
|---|---|---|---|
| 0.0001 | 6639 | | |
| 0.0005 | 1600 | | |
| 0.001 | 877.3 | | |
| 0.005 | 226.3 | | |
| 0.01 | 129.3 | 129.2 | 129.1 |
| 0.02 | | 75.19 | 75.18 |
| 0.04 | | 44.88 | 44.87 |
| 0.06 | | 33.64 | 33.62 |
| 0.08 | | 27.62 | 27.60 |
| 0.1 | | 23.79 | 23.76 |
| 0.2 | | 15.29 | 15.24 |
| 0.4 | | 10.11 | 10.01 |
| 0.6 | | 8.03 | 7.88 |
| 0.8 | | 6.87 | 6.66 |
| 1.0 | | 6.14 | 5.87 |

Table II. Values of $C_D$ $(h/a=50)$.

| $R$ | calculated by the expansion formula (6.1) | calculated by the formula (5.9) 1st approx. | 2nd approx. |
|---|---|---|---|
| 0.0001 | 7255 | | |
| 0.0005 | 1782 | | |
| 0.001 | 988.3 | | |
| 0.005 | 264.7 | | |
| 0.01 | 155.0 | 153.8 | 153.8 |
| 0.02 | | 91.40 | 91.39 |
| 0.04 | | 55.25 | 55.24 |
| 0.06 | | 41.27 | 41.25 |
| 0.08 | | 33.54 | 33.52 |
| 0.1 | | 28.54 | 28.51 |
| 0.2 | | 17.29 | 17.22 |
| 0.4 | | 10.73 | 10.60 |
| 0.6 | | 8.32 | 8.12 |
| 0.8 | | 7.04 | 6.78 |
| 1.0 | | 6.26 | 5.94 |

Table III. Values of $C_D$ $(h/a=100)$.

| $R$ | 1st approx. | 2nd approx. |
|---|---|---|
| 0.01 | 166.2 | 166.2 |
| 0.02 | 98.59 | 98.58 |
| 0.04 | 58.51 | 58.49 |
| 0.06 | 42.96 | 42.94 |
| 0.08 | 34.45 | 34.42 |
| 0.1 | 29.07 | 29.04 |
| 0.2 | 17.37 | 17.30 |
| 0.4 | 10.75 | 10.61 |
| 0.6 | 8.33 | 8.13 |
| 0.8 | 7.06 | 6.79 |
| 1.0 | 6·27 | 5.95 |

Table IV. Values of $C_D$ $(h/a=500)$.

| $R$ | 1st approx. | 2nd approx. |
|---|---|---|
| 0.01 | 187.8 | 187.8 |
| 0.02 | 105.9 | 105.9 |
| 0.04 | 60.11 | 60.10 |
| 0.06 | 43.47 | 43.45 |
| 0.08 | 34.67 | 34.64 |
| 0.1 | 29.17 | 29.13 |
| 0.2 | 17.38 | 17.31 |
| 0.4 | 10.76 | 10.62 |
| 0.6 | 8.33 | 8.13 |
| 0.8 | 7.06 | 6.79 |
| 1.0 | 6.28 | 5.95 |

Table V. Values of $C_L$ ($h/a=10$).

| $R$ | calculated by the expansion formula (6.1) | calculated by the formula (5.10) 1st approx. | 2nd approx. |
|---|---|---|---|
| 0 | 6.24 | | |
| 0.0001 | 5.40 | | |
| 0.0005 | 5.23 | | |
| 0.001 | 5.13 | | |
| 0.005 | 4.81 | | |
| 0.01 | 4.60 | 4.67 | 4.60 |
| 0.02 | | 4.42 | 4.34 |
| 0.04 | | 4.07 | 3.99 |
| 0.06 | | 3.82 | 3.74 |
| 0.08 | | 3.61 | 3.53 |
| 0.1 | | 3.43 | 3.34 |
| 0.2 | | 2.78 | 2.68 |
| 0.4 | | 2.02 | 1.88 |
| 0.6 | | 1.59 | 1.41 |
| 0.8 | | 1.35 | 1.10 |
| 1.0 | | 1.21 | 0.895 |

Table VI. Values of $C_L$ ($h/a=50$).

| $R$ | calculated by the expansion formula (6.1) | calculated by the formula (5.10) 1st approx. | 2nd approx. |
|---|---|---|---|
| 0 | 19.12 | | |
| 0.0001 | 14.59 | | |
| 0.0005 | 13.55 | | |
| 0.001 | 12.95 | | |
| 0.005 | 10.85 | | |
| 0.01 | 9.44 | 9.57 | 9.56 |
| 0.02 | | 7.87 | 7.86 |
| 0.04 | | 5.79 | 5.77 |
| 0.06 | | 4.46 | 4.45 |
| 0.08 | | 3.54 | 3.52 |
| 0.1 | | 2.87 | 2.85 |
| 0.2 | | 1.30 | 1.27 |
| 0.4 | | 0.560 | 0.528 |
| 0.6 | | 0.367 | 0.325 |
| 0.8 | | 0.288 | 0.235 |
| 1.0 | | 0.250 | 0.184 |

Table VII. Values of $C_L$ ($h/a=100$).

| $R$ | 1st approx. | 2nd approx. |
|---|---|---|
| 0 | 32.73 | 32.73 |
| 0.01 | 12.19 | 12.18 |
| 0.02 | 8.73 | 8.72 |
| 0.04 | 5.13 | 5.12 |
| 0.06 | 3.33 | 3.32 |
| 0.08 | 2.33 | 2.32 |
| 0.1 | 1.72 | 1.71 |
| 0.2 | 0.662 | 0.650 |
| 0.4 | 0.279 | 0.263 |
| 0.6 | 0.183 | 0.163 |
| 0.8 | 0.144 | 0.118 |
| 1.0 | 0.125 | 0.092 |

Table VIII. Values of $C_L$ ($h/a=500$).

| $R$ | 1st approx. | 2nd approx. |
|---|---|---|
| 0 | 122.6 | 122.6 |
| 0.01 | 11.04 | 11.04 |
| 0.02 | 4.23 | 4.23 |
| 0.04 | 1.42 | 1.42 |
| 0.06 | 0.757 | 0.755 |
| 0.08 | 0.490 | 0.488 |
| 0.1 | 0.353 | 0.351 |
| 0.2 | 0.133 | 0.131 |
| 0.4 | 0.056 | 0.053 |
| 0.6 | 0.037 | 0.033 |
| 0.8 | 0.029 | 0.023 |
| 1.0 | 0.025 | 0.018 |

Table IX. Values of $C_D^*$.

| $R$ | 1st approx. | 2nd approx. |
|---|---|---|
| 0.01 | 190.1 | 190.1 |
| 0.02 | 106.2 | 106.2 |
| 0.04 | 60.16 | 60.14 |
| 0.06 | 43.48 | 43.46 |
| 0.08 | 34.68 | 34.65 |
| 0.1 | 29.18 | 29.14 |
| 0.2 | 17.39 | 17.32 |
| 0.4 | 10.76 | 10.62 |
| 0.6 | 8.33 | 8.13 |
| 0.8 | 7.06 | 6.79 |
| 1.0 | 6.27 | 5.95 |

comes sufficiently small, the values of $C_L$ increases first and then decreases.

As for the sign of the lift, we see that it is always positive, i.e. the cylinder $C_1$ experiences a repulsive force from the second cylinder $C_2$. Further, for each case of the distance ratio $h/a$, the value of $C_L$ decreases monotonously as the Reynolds number increases.

## Acknowledgements

The present investigation has been carried out at the suggestion of Professor S. Tomotika. The writer wishes to express his cordial thanks to him for his suggestions and continual encouragement throughout this work and especially for his kind inspection of the manuscript. Also, the writer is much indebted to Professor K. Tamada for his invaluable advices throughout the present investigation. The writer's thanks are also due to the Ministry of Education for a grant-in-aid for fundamental scientific research.

## References

1) L. N. G. Filon: Proc. Roy. Soc. **A 113** (1926) 7.
2) S. Tomotika and T. Aoi: Quart. J. Mech. and Applied Math. **4** (1951) 401.

JOURNAL OF THE PHYSICAL SOCIETY OF JAPAN Vol. 11, No. 5, MAY, 1956

# On the Viscous Shear Flow around a Circular Cylinder
## II. Oseen's Approximation

By Mitutosi KAWAGUTI
*Institute of Science and Technology, University of Tokyo*

(Received February 3, 1956)

The shear flow of a viscous fluid around a circular cylinder has been studied to Oseen's approximation and has been compared with the author's previous results of Stokes' approximation. The formulae for the drag and the lift have been obtained neglecting the terms of orders $O(Re)$, $O(\alpha Re^{-1})$, $O(\alpha^2)$, and it has been shown that the drag is not affected by the presence of the shear and the direction of the lift is the same as that for the inviscid shear flow within the order of our approximation.

### § 1. Introduction

The shear flow of a perfect fluid around an obstacle has been rather fully investigated, and it is well known that the lift acts upon the obstacle in the direction of positive $y$-axis when the velocity $(U, V)$ of the shear flow at infinity $(x\rightarrow\pm\infty)$ is represented by $U=U_0(1+\alpha y)$ and $V=0$ where $U_0$ and $\alpha$ are positive constants. As far as the author is aware, there have been few works which treated such problem in the case of viscous fluid, and we have no knowledge concerning the lift which may act upon the obstacle submerged in a viscous shear flow.

Strictly speaking, we cannot realize such a viscous shear flow of which region extends infinitely, since the magnitude of velocity becomes infinite as $|y|$ tends to infinity. Nevertheless it may be useful as a two-dimensional model for the following problems, i.e., to study the force which acts upon a body submerged in a boundary layer, or that acts upon a body in the Poiseuille (two- or three-dimensional) flow, etc.

In a previous paper [1]*, the author studied the viscous shear flow past a circular cylinder to Stokes' approximation, and showed that the lift acts in the same direction as in the case of perfect fluid. To Stokes' approximation, however, we cannot satisfy the boundary condition at infinity, so that in [1] the condition was replaced by the requirement that viscous and perfect fluid solutions should be smoothly joined with each other on a circle $r=R$ ($R$ being large but finite). The appropriate value of $R$ cannot be given theoretically, and the author suggested two simple relations; (i) $R=A/Re$, (ii) $R=B/\sqrt{Re}$ where $Re$ is the Reynolds number and $A$ and $B$ are constants. Thus, there remained some ambiguity concerning the results of [1].

In this paper, the same problem is studied to Oseen's approximation, but it is far difficult for us to obtain the exact solution of Oseen's approximate equation in the case of shear flow. So, assuming the smallness of the rate of shear $\alpha$**, we expand the solution in power series in $\alpha$ and obtained an approximate solution neglecting the terms of order $\alpha^2$.

### § 2. Fundamental Equation and Boundary Conditions

For the two-dimensional steady motion of an incompressible viscous fluid the Navier-Stokes equation is written in the form

$$\frac{\partial(\Psi, \Delta\Psi)}{\partial(x, y)}+\frac{2}{Re}\Delta\Delta\Psi=0\,, \qquad (2.1)$$

$$\Delta=\frac{\partial^2}{\partial x^2}+\frac{\partial^2}{\partial y^2}\,,$$

where $\Psi$ is the stream function from which the components of velocity $U, V$*** in the positive $x$ and $y$ directions are given as

$$U=\frac{\partial\Psi}{\partial y}\,,\qquad V=-\frac{\partial\Psi}{\partial x}\,, \qquad (2.2)$$

and $Re$ is the Reynolds number $U_0L_0/\nu$ where

---

* This paper will be referred to as [1] in the following lines.

** In the course of this study, it became clear that $\alpha$ must be small compared with the Reynolds number $Re$.

*** In this paper, we use $U$, $V$ for the $x$-, $y$-components of velocity in rectangular coordinates, and $u$, $v$ for the $r$-, $\theta$-components in polar coordinates.

$U_0$ and $L_0$ are the characteristic magnitude of velocity and the diameter of circular cylinder, and $\nu$ is the kinematic viscosity. In our paper, the velocity at infinity on the $x$-axis and the radius of the circular cylinder are taken as the units of magnitude of velocity and length respectively.

We have boundary conditions:

$$U=V=0 \quad \text{at} \quad r=1$$

$$\text{(on the surface of the cylinder),} \tag{2.3}$$

$$\left.\begin{array}{l} U\to 1+\alpha y \\ V\to 0 \end{array}\right\} \quad \text{as } r\to\infty \tag{2.4}$$

for our problem, where $\alpha$ is a constant which shall be called the rate of shear and we may assume that $\alpha$ is positive without loss of generality.

## § 3. Stokes' Approximation

In this section, the resumé of [1] will be given for the sake of convenience.

In polar coordinates $(r, \theta)$, Eq. (2.1) can be written as

$$\varDelta_r\varDelta_r\varPsi=-\frac{Re}{2}\frac{1}{r}\frac{\partial(\varPsi, \varDelta_r\varPsi)}{\partial(r, \theta)}\,, \tag{3.1}$$

where

$$\varDelta_r=\frac{\partial^2}{\partial r^2}+\frac{1}{r}\frac{\partial}{\partial r}+\frac{1}{r^2}\frac{\partial^2}{\partial\theta^2}\,. \tag{3.2}$$

Then we expand $\varPsi$ in a power series of $Re$, i.e.,

$$\varPsi=\varPsi_1+Re\varPsi_2+\cdots \tag{3.3}$$

assuming that $Re$ is sufficiently small. Introducing (3.3) into (3.1) and equating the terms of the same power in $Re$ to zero, we have

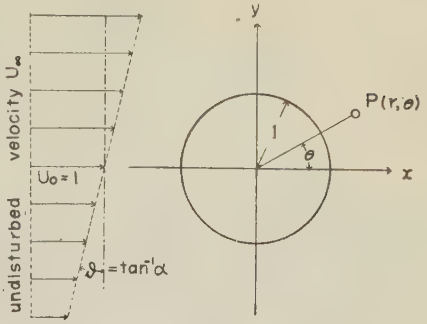

Fig. 1.

$$\varDelta_r\varDelta_r\varPsi_1=0\,, \tag{3.4}$$

$$\varDelta_r\varDelta_r\varPsi_2=-\frac{1}{2}\frac{1}{r}\frac{\partial(\varPsi_1, \varDelta_r\varPsi_1)}{\partial(r, \theta)}\,, \tag{3.5}$$

which are linear differential equations for $\varPsi_1$, $\varPsi_2, \cdots$.

Exact boundary conditions for our problem are (2.3) and (2.4), but we cannot satisfy (2.4) to Stokes' approximation as was noted in § 1, so we must find approximate conditions which replace (2.4). We choose the requirement that viscous and perfect fluid solutions should be smoothly joined with each other on a circle $r=R$ ($R$ being large but finite). Since the solution for the shear flow of perfect fluid around a circular cylinder is already known as

$$\varPsi_p=\left(r-\frac{1}{r}\right)\sin\theta+\alpha\left\{\left(\frac{1}{4}r^2+\beta\log r-\frac{1}{4}\right)\right.$$
$$\left.-\frac{1}{4}\left(r^2-\frac{1}{r^2}\right)\cos 2\theta\right\}, \tag{3.6}$$

where $\beta$ is a circulation constant, we have the condition which replaces (2.4) as

$$\left.\begin{array}{l} \varPsi=\left(R-\dfrac{1}{R}\right)\sin\theta+\alpha\left\{\left(\dfrac{1}{4}R^2+\beta\log R-\dfrac{1}{4}\right)-\dfrac{1}{4}\left(R^2-\dfrac{1}{R^2}\right)\cos 2\theta\right\} \\ \dfrac{\partial\varPsi}{\partial r}=\left(1+\dfrac{1}{R^2}\right)\sin\theta+\alpha\left\{\left(\dfrac{1}{2}R+\beta\dfrac{1}{R}\right)-\dfrac{1}{2}\left(R+\dfrac{1}{R^3}\right)\cos 2\theta\right\} \end{array}\right\} \tag{3.7}$$
$$\text{at} \quad r=R\,.$$

Solving (3.4) and (3.5) subject to boundary conditions (2.3) and (3.7), we obtained

$$\varPsi_1=g_1\sin\theta+\alpha(f_0+f_2\cos 2\theta)\,, \tag{3.8}$$

$$\varPsi_2=\alpha(F_1\cos\theta+F_3\cos 3\theta)+G_2\sin 2\theta+\alpha^2G_4\sin 4\theta\,, \tag{3.9}$$

where $g_i, f_i, G_i$, and $F_i$ are functions of $r$ which depend on the parameter $R$ but not on $\alpha$*.

Thus we can determine the moment, the drag, and the lift coefficients as follows

$$C_M=-\frac{4\pi\alpha}{Re}\,, \tag{3.10}$$

$$C_D=\frac{8\pi(1-R^{-2})}{Re[(1+R^{-2})\log R-(1-R^{-2})]}\,, \tag{3.11}$$

---

* Their full functional forms were given in [1].

$$C_L=\frac{\alpha\pi N}{48(1-R^{-2})^3[(1+R^{-2})\log R-(1-R^{-2})]^2}\,, \tag{3.12}$$

where

$$\begin{aligned}N=&24(4-17R^{-2}-63R^{-4}-23R^{-6}-R^{-8})R^{-2}(\log R)^2\\&+4(-21+37R^{-2}+298R^{-4}-241R^{-6}+45R^{-8})(1-R^{-2})\log R\\&+(6R^2+49-293R^{-2}-215R^{-4}-141R^{-6}-6R^{-8})(1-R^{-2})^2\,.\end{aligned} \tag{3.12a}$$

*Determination of R*: So far, we have treated $R$ as an arbitrary constant. It is, however, shown that the forces depend not only upon the Reynolds number but upon the parameter $R$. So we must seek for some relation between $R$ and $Re$, but we cannot find it theoretically. We can only guess its general tendency that $R$ will increase as $Re$ decreases. Therefore, two rather arbitrary, but mathematically simple relations are suggested;

(i) $R=A/Re$ ($A$ is a constant).

The drag coefficient (3.11) then becomes

$$C_D=\frac{8\pi\{1-(Re)^2/A^2\}}{Re[\{1+(Re)^2/A^2\}(\log A-\log Re)-\{1-(Re)^2/A^2\}]}\,. \tag{3.13}$$

We determined the constant $A$ as 20.13 by the condition that the drag coefficients from (3.13) and Oseen's approximation in the case of no shear [2] should coincide with eath other in the limiting case of $Re\rightarrow 0$*.

(ii) $R=B/\sqrt{Re}$ ($B$ is another constant).

The drag coefficient (3.11) then becomes

$$C_D=\frac{8\pi(1-Re/B^2)}{Re[(1+Re/B^2)(\log B-\frac{1}{2}\log Re)-(1-Re/B^2)]}\,. \tag{3.14}$$

We determined the constant $B$ as 14.92 by the condition that the drag coefficients from (3.14) and experimental study [3] should coincide with each other in the case of $Re=4$.

The drag, the lift, and the moment coefficients thus calculated are shown in Figs. 3–5, and compared with the results to Oseen's approximation.

## § 4. Fundamental Equations in Oseen's Approximation

In this and following sections, we shall seek for the solution for our problem to Oseen's approximation.

We can rewrite (2.1) as

$$U\frac{\partial\Delta\Psi}{\partial x}-V\frac{\partial\Delta\Psi}{\partial y}=\frac{1}{2k}\Delta\Delta\Psi\,, \tag{4.1}$$

where

$$k=Re/4\,. \tag{4.2}$$

According to Oseen's approximation, $U$ and $V$ in the left-hand side of (4.1) must be replaced by the undisturbed values at infinity, i.e.,

$$U_\infty=1+\alpha y\,,\quad V_\infty=0\,. \tag{4.3}$$

Thus, (4.1) becomes

$$2k(1+\alpha y)\frac{\partial\Delta\Psi}{\partial x}-\Delta\Delta\Psi=0\,, \tag{4.4}$$

which is the fundamental equation for our problem. It is, however, too difficult to seek for exact solution, so we expand $\Psi$ in a power series of $\alpha$:

$$\Psi=(y+\psi_1)+\alpha(\tfrac{1}{2}y^2+\psi_2)+O(\alpha^2)\,, \tag{4.5}$$

assuming that the rate of shear $\alpha$ is sufficiently small. Introducing (4.5) into (4.4), and equating the terms of $O(1)$ and $O(\alpha)$ to zero, we have

$$2k\frac{\partial\Delta_1\psi}{\partial x}-\Delta\Delta\psi_1=0\,, \tag{4.6}$$

and

$$2k\frac{\partial\Delta\psi_2}{\partial x}-\Delta\Delta\psi_2=-2ky\,\frac{\partial\Delta\psi_1}{\partial x}\,, \tag{4.7}$$

which are the linear differential equations for $\psi_1$ and $\psi_2$ respectively.

---

* It is easily seen from (3.11) that the drag coefficient is not affected by the presence of shear within our order of approximation.

## § 5. First Approximation

### § 5.1. Equations of Motion, Boundary Conditions

Equation (4.6) can be replaced by a system of differential equations:

$$\left(\varDelta-2k\frac{\partial}{\partial x}\right)\omega_1=0\,, \tag{5.1}$$

$$\omega_1=-\varDelta\psi_1\,, \tag{5.2}$$

where $\omega_1$ is the first approximation for the vorticity $\omega$.

Boundary conditions for the first approximation are shown as

$$U_1=V_1=0 \quad \text{at } r=1\,, \tag{5.3}$$

$$U_1\to 1\,,\quad V_1\to 0 \quad \text{as } r\to\infty \tag{5.4}$$

from (2.3) and (2.4).

It is easily seen that equations (5.1) and (5.2) with the boundary conditions (5.3) and (5.4) are identical with those in the case of no shear for which the solution was already obtained [2]. It should be noted that Imai recently gave an ingenious method for solving Oseen's equation which enables us to obtain the solution for the flow past a simply-connected obstacle of general shape [4]. Since in the treatment of the second approximation in § 6, we shall use his method, we shall here calculate the first approximation for the sake of reference in § 6, although it is the same as the solution for the case of no shear and has already been known.

### § 5.2. Integration of (5.1)

If we put

$$\omega_1=e^{kx}H_1(x,y)\,, \tag{5.5}$$

and introduce it into (5.1), we have the equation for $H_1(x,y)$:

$$(\varDelta-k^2)H_1=0\,. \tag{5.6}$$

Further putting

$$H_1(x,y)=R_1(r)\Theta_1(\theta)\,, \tag{5.7}$$

we can separate the variables;

$$\Theta_1''+m^2\Theta_1=0\,, \tag{5.8}$$

$$R_1''+\frac{1}{r}R_1'-\left(k^2+\frac{m^2}{r^2}\right)R_1=0\,, \tag{5.9}$$

where $m$ is a constant.

It is well known that general solutions of (5.8) are

$$\sin m\theta \text{ and } \cos m\theta \quad ; \text{ or } e^{im\theta}\,, \tag{5.10}$$

where $m$ must be an integer as $\omega_1$ must be single-valued in the region considered, and that general solutions of (5.9) are

$$I_m(kr) \quad \text{and} \quad K_m(kr)\,, \tag{5.11}$$

where $I_m(kr)$ and $K_m(kr)$ are the modified Bessel functions. It is shown that only $K_m(kr)$ is appropriate to our purpose considering that $I_m(kr)$ and $K_m(kr)$ behave as $e^{kr}$ and $e^{-kr}$ as $r\to\infty$.

Thus, we have

$$\omega_1=\Re\sum_{n=0}^{\infty}C_n e^{kx}K_n(kr)e^{in\theta} \tag{5.12}$$

as the solution of (5.1), where $\Re$ denotes "the real part of", and $C_m$ is a complex constant. It will be shown later (cf. (5.20)) that there must be a relation

$$\Re\sum_{n=0}^{\infty}C_n=0$$

between $C_n$'s.

### § 5.3. Integration of (5.2)

If we define the complex velocity

$$W_1=U_1-iV_1=2i\frac{\partial\Psi_1}{\partial z}\,, \tag{5.13}$$

where $z=x+iy$, $\bar{z}=x-iy$, Eq. (5.2) can be transformed as

$$\begin{aligned}\frac{\partial W_1}{\partial\bar{z}}&=-\frac{i}{2}\omega_1\\&=-\frac{i}{4}\left[\sum_{n=0}^{\infty}C_n e^{kx}K_n(kr)e^{in\theta}+\sum_{n=0}^{\infty}\bar{C}_n e^{kx}K_n(kr)e^{-in\theta}\right].\end{aligned} \tag{5.14}$$

Integrating (5.14) with respect to $\bar{z}$, we have

$$W_1=-\frac{i}{4}\int\left[\sum_{n=0}^{\infty}C_n e^{kx}K_n(kr)e^{in\theta}+\sum_{n=0}^{\infty}\bar{C}_n e^{kx}K_n(kr)e^{-in\theta}\right]d\bar{z}+\frac{df_1}{dz}\,, \tag{5.15}$$

where $f_1$ is an arbitrary function of $z$ alone. As it is easily shown that

$$\int e^{kx}K_n(kr)e^{in\theta}d\bar{z}=-\frac{2}{k}e^{kx}\sum_{m=0}^{n-1}e^{mi\theta}K_m(kr)+\int e^{kx}K_0(kr)d\bar{z}\,, \tag{5.16}$$

and

$$\int e^{kx}K_n(kr)e^{-ni\theta}d\bar{z}=\frac{2}{k}e^{kx}\sum_{m=1}^{n}e^{-mi\theta}K_m(kr)+\int e^{kx}K_0(kr)d\bar{z}\,, \tag{5.17}$$

the first term on the right-hand side of (5.15) is evaluated as

$$\frac{i}{2k}e^{kx}\left\{A_1K_0(kr)+\sum_{n=1}^{\infty}(A_{n+1}e^{ni\theta}-\bar{A}_ne^{-ni\theta})K_n(kr)\right\}-\frac{i}{4}(A_0+\bar{A}_0)\int e^{kx}K_0(kr)d\bar{z}\,, \tag{5.18}$$

where $A_n$ are the complex constants defined by

$$A_n=\sum_{m=n}^{\infty}C_m\,. \tag{5.19}$$

Since $\int e^{kx}K_0(kr)d\bar{z}$ is not single-valued, its coefficient in (5.18) must be zero, i.e.,

$$\frac{1}{2}(A_0+\bar{A}_0)\equiv\Re A_0=\Re\sum_{m=0}^{\infty}C_n=0\,, \tag{5.20}$$

which was referred to at the end of § 5.2.

Thus we have

$$W_1=\frac{i}{2k}e^{kx}\left\{A_1K_0(kr)+\sum_{n=1}^{\infty}(A_{n+1}e^{ni\theta}-\bar{A}_ne^{-ni\theta})K_n(kr)\right\}+\frac{df_1}{dz} \tag{5.21}$$

for the complex velocity.

### § 5.4. Determination of Coefficients $A_n$

The coefficients $A_n$'s must be determined from the boundary conditions (5.3) and (5.4). (5.4) is easily satisfied by putting

$$f_1(z)\to z+O(1) \qquad \text{as} \quad z\to\infty, \tag{5.22}$$

since the first term on the right-hand side of (5.21) becomes vanishingly small as $r\to\infty$, and (5.3) gives

$$W_1=0 \qquad \text{at } z\bar{z}=1\,. \tag{5.23}$$

Now if we put

$$\bar{A}_n=k^{2n-1}(a_{n1}+k^2a_{n2}+\cdots)\,,$$

$$f_1=k^{-1}(f_{10}+kf_{11}+\cdots)\,, \tag{5.24}$$*

and expand the exponential and Bessel functions in (5.21) into the power series of $k$, (5.23) gives, after equating the terms of the same power in $k$ to zero,

$$f_{10}'=\frac{i}{2}\frac{a_{11}}{z}\,, \tag{5.25}$$

$$f_{11}'=\frac{1}{2}\left(z+\frac{1}{z}\right)f_{10}'+\frac{i}{2}\left(\bar{a}_{11}s+\frac{2}{z^2}a_{21}\right), \tag{5.26}$$

$$f_{12}'=\frac{1}{2}\left(z+\frac{1}{z}\right)f_{11}'-\frac{1}{8}\left(z+\frac{1}{z}\right)^2f_{10}'$$
$$+\frac{i}{2}\left\{-z\bar{a}_{21}+\frac{1}{z}a_{12}+\frac{1}{2z}\left(s-\frac{1}{2}\right)a_{11}+\frac{8a_{31}}{z^3}\right\}, \tag{5.27}$$

---

* In the most general case, the expansion for $\bar{A}_n$ must be of the form

$$\bar{A}_n=k^{n-1}(a_{n1}+ka_{n2}+k^2a_{n3}+\cdots),$$

but in our special case of a circular cylinder, it will be clear that the expansion (5.24) is legitimate.

$$f_{13}'=\frac{1}{2}\left(z+\frac{1}{z}\right)f_{12}'-\frac{1}{8}\left(z+\frac{1}{z}\right)^2 f_{11}'+\frac{1}{48}\left(z+\frac{1}{z}\right)^3 f_{10}'$$

$$+\frac{i}{2}\left\{\frac{1}{4}(s-1)\bar{a}_{11}+s\bar{a}_{12}-2z^2\bar{a}_{31}+\frac{2}{z^2}a_{22}-\frac{1}{2z^2}a_{21}+\frac{48}{z^4}a_{41}\right\}, \tag{5.28}$$

$$\cdots\cdots\cdots\cdots\cdots\cdots,$$

where $s=\log(\frac{1}{2}k)+\gamma$, $\gamma$ being Euler's constant $(0.57721\cdots)$.

If we write (5.26) as

$$f_{11}'-\frac{1}{2}\left(z+\frac{1}{z}\right)f_{10}'-\frac{i}{2}\left(\bar{a}_{11}s+\frac{2}{z^2}a_{21}\right)=0, \tag{5.29}$$

the terms of each power in $z$ must be zero. Considering the fact that $f_{11}'=1+O(z^{-1})$, and $f_{10}'=O(z^{-1})$(cf. (5.22)) and (5.25), we can determine $a_{11}$ as

$$a_{11}=4i/(2s-1), \tag{5.30}$$

from the condition that the constant terms in $z$ in (5.29) must be zero. Introducing (5.30) into (5.25) we have

$$f_{10}'=-\frac{2}{2s-1}\frac{1}{z}. \tag{5.31}$$

In the same way, we have, from (5.27)

$$a_{21}=i\frac{4s-1}{2(2s-1)}, \tag{5.32}$$

$$f_{11}'=1-\frac{4s+1}{2(2s-1)}\frac{1}{z^2}, \tag{5.33}$$

and from (5.28)

$$a_{31}=-i\frac{3s-1}{12(2s-1)}, \qquad a_{12}=i\frac{4s+3}{4(2s-1)^2}, \tag{5.34}$$

$$f_{12}'=-\frac{16s^2-8s+5}{8(2s-1)^2}\frac{1}{z}-\frac{1}{3(2s-1)}\frac{1}{z^3}. \tag{5.35}$$

### § 5.5. Results of § 5

Thus, we have for $A_i$ and $f_1'(z)$

$$A_1=-ik\left\{\frac{4}{2s-1}+\frac{4s+3}{4(2s-1)^2}k^2\right\}+O(k^5),$$

$$A_2=-ik^3\frac{4s-1}{2(2s-1)}+O(k^5),$$

$$A_3=ik^5\frac{3s-1}{12(2s-1)}+O(k^7),$$

$$A_i=O(k^{3+i}) \qquad (i\geq 4), \tag{5.36}$$

and

$$f_1'=-\frac{1}{k}\frac{2}{2s-1}\frac{1}{z}+\left\{1-\frac{4s-1}{2(2s-1)}\frac{1}{z^3}\right\}-k\left\{\frac{16s^2-8s+5}{8(2s-1)^2}\frac{1}{z}+\frac{1}{3(2s-1)}\frac{1}{z^3}\right\}+O(k^2). \tag{5.37}$$

Introducing (5.36) into (5.12) we have for $\omega_1$;

$$\omega_1=e^{kz}\sum_{n=1}^{\infty}C_nK_n(kr)\sin n\theta, \tag{5.38}$$

where

$$C_1=k\frac{4}{(2s-1)}-k^3\frac{16s^2-16s-1}{4(2s-1)^2}+O(k^5)\,,$$

$$C_2=k^3\frac{4s-1}{2(2s-1)}+O(k^5)\,,$$

$$C_3=-k^5\frac{3s-1}{12(2s-1)}+O(k^7)\,,$$

$$C_i=O(k^{3+i})\qquad(i\geq 4). \tag{5.39}$$

Although we can easily determine the drag from these data, its determination will be postponed until § 7.

## § 6. Second Approximation

### § 6.1. Equations of Motion, Boundary Conditions

The fundamental equation for the second approximation is (4.7) which is rewritten as

$$\left(\Delta-2k\frac{\partial}{\partial x}\right)\omega_2=2ky\frac{\partial\omega_1}{\partial x}\,, \tag{6.1}$$

$$\omega_2=-\Delta\psi_2-1\,. \tag{6.2}$$

The boundary conditions are

$$\left.\begin{array}{l}\psi_2+\frac{1}{2}y^2=0\\ \partial(\psi_2+\frac{1}{2}y^2)/\partial y=0\end{array}\right\}\qquad \text{at}\quad r=1\,, \tag{6.3}$$

$$\psi_2\to 0\qquad \text{as}\quad r\to\infty\,. \tag{6.4}$$

### § 6.2. Integration of (6.1)

Using the explicit form (5.38) for $\omega_1$, the right-hand side of (6.1) can be written as

$$\begin{aligned}2ky\frac{\partial\omega_1}{\partial x}&=e^{kx}\sum_{n=1}^{\infty}C_n\Big\{-\frac{1}{2}k^2rK_{n-1}(kr)\cos(n-2)\theta+k^2rK_n(kr)\cos(n-1)\theta\\&\quad -nkK_n(kr)\cos n\theta-k^2rK_n(kr)\cos(n+1)\theta+\frac{1}{2}k^2rK_{n+1}(kr)\cos(n+2)\theta\Big\}\\&=e^{kx}\Omega_1(r,\theta)\qquad(\text{say}).\end{aligned} \tag{6.5}$$

Then putting

$$\omega_2=e^{kx}H_2(x,y)\,, \tag{6.6}$$

and introducing it into (6.1), we have

$$\frac{\partial^2H_2}{\partial r^2}+\frac{1}{r}\frac{\partial H_2}{\partial r}+\frac{1}{r^2}\frac{\partial^2H_2}{\partial\theta^2}-k^2H_2=\Omega_1\,. \tag{6.7}$$

The general solution of the homogeneous equation

$$\frac{\partial^2H_2}{\partial r^2}+\frac{1}{r}\frac{\partial H_2}{\partial r}+\frac{1}{r^2}\frac{\partial^2H_2}{\partial\theta^2}-k^2H_2=0 \tag{6.8}$$

has already been obtained in § 5.2 as

$$\Re\sum_{n=0}^{\infty}D_nK_n(kr)e^{ni\theta}\,, \tag{6.9}$$

where $D_n$'s are real constants in our case (in general they are complex). The particular solution of (6.7) can be rather easily obtained, and for the general solution of (6.7) we have

$$\omega_2 = \Re \sum_{n=0}^{\infty} D_n e^{kx} K_n(kr) e^{ni\theta} - 1 + e^{kx} \sum_{n=1}^{\infty} C_n \left\{ \frac{1}{8} kr^2 K_n(kr) \cos(n-2)\theta \right.$$
$$- \frac{1}{4} kr^2 K_{n+1}(kr) \cos(n-1)\theta + \frac{1}{2} nrK_{n-1}(kr) \cos n\theta$$
$$\left. + \frac{1}{4} kr^2 K_{n-1}(kr) \cos(n+1)\theta - \frac{1}{8} kr^2 K_n(kr) \cos(n+2)\theta \right\}, \qquad (6.10)$$

where $-1$ is added to $\omega_2$ considering (6.2) and (6.4) and the fact that a constant is a solution of the homogeneous equation derived from (6.1).

### § 6.3. Integration of (6.2)

As in § 5.3, we define a complex velocity $W_2$ as

$$W_2 = U_2 - iV_2 = 2i \frac{\partial \Psi_2}{\partial z}. \qquad (6.11)$$

Then, $W_2$ can be obtained as

$$W_2 = -\frac{i}{2} \int \omega_2 d\bar{z}. \qquad (6.12)$$

The integration on the right-hand side of (6.12) can be performed separately. The integration of the first term in (6.10) was already made in (5.18) as

$$\frac{i}{2k} e^{kx} \left\{ E_1 K_0(kr) + \sum_{n=1}^{\infty} (E_{n+1} e^{ni\theta} - E_n e^{-ni\theta}) K_n(kr) \right\} - \frac{i}{2} E_0 \int e^{kx} K_0(kr) d\bar{z} + \frac{df_2}{dz}, \qquad (6.13)$$

where $E_n = \sum_{m=n}^{\infty} D_m$ and $f_2$ is an analytic function of $z$. In the next place, the integration of $-1$ is simply $-\bar{z}$. The integration of the remaining terms of (6.10) is elementary but cumbersome, and the results are given in Appendix.

Thus, we have for $W_2$

$$W_2 = \frac{i}{2k} e^{kx} \left\{ E_1 K_0(kr) + \sum_{n=1}^{\infty} (E_{n+1} e^{ni\theta} - E_n e^{-ni\theta}) K_n(kr) \right\} - \frac{i}{2} E_0 \int e^{kx} K_0(kr) d\bar{z}$$
$$+ \frac{i}{2} \bar{z} + \frac{df_2}{dz} + \sum_{n=1}^{\infty} C_n F_n(r, \theta), \qquad (6.14)$$

where

$$F_n = \frac{iz^2}{16} e^{kx} \{ K_{n+4} e^{-i(n+4)\theta} - K_{n+3} e^{-i(n+3)\theta} - K_{n+2} e^{-i(n+2)\theta} + K_{n+1} e^{-i(n+1)\theta}$$
$$- K_{n-4} e^{i(n-4)\theta} + K_{n-3} e^{i(n-3)\theta} + K_{n-2} e^{i(n-2)\theta} - K_{n-1} e^{i(n-1)\theta} \}$$
$$+ \frac{iz}{4k} e^{kx} \{ -(n+2) K_{n+3} e^{-i(n+3)\theta} + nK_{n+2}{}^{-i(n+2)\theta} - (n-2) K_{n-3} e^{i(n-3)\theta} + nK_{n-2} e^{i(n-2)\theta} \}$$
$$+ \frac{i}{4k^2} e^{kx} \left\{ (n^2+3n+2) K_{n+2} e^{-i(n+2)\theta} - (n^2-n-2) K_{n+1} e^{-i(n+1)\theta} + (n^2+n+2) \sum_{m=1}^{n} K_m e^{-im\theta} \right.$$
$$\left. - (n-1)(n+2) \sum_{m=0}^{n-3}{}' K_m e^{im\theta} - 2n(n-1) K_{n-2} e^{i(n-2)\theta} \right\} + \frac{in(n+1)}{4k} \int e^{kx} K_0 dz, \qquad (6.15)^*$$

where the summation $\sum_{m=0}^{n-3}{}' K_m e^{im\theta}$ must be taken as 0 when $n-3<0$, i.e., $n=1$ or 2.

### § 6.4. Fulfilment of the Boundary Conditions

The boundary conditions (6.3), (6.4) can be written as

---

* The argument $kr$ of $K_n(kr)$ is omitted in (6.15) for the sake of simplicity.

(i) $$W_2=0 \quad \text{at} \quad r=1\,, \tag{6.16}$$

(ii) $$W_2\to y+O(1) \quad \text{as} \quad r\to\infty \tag{6.17}$$

in terms of $W_2$. It is also clear that

(iii) $W_2$ *must be single-valued throughout the field of flow*, for the solution to have physical meaning.

In the first place, we consider the condition (iii). On the right-hand side of (6.14), the terms which are not single-valued are the terms multiplied by $\int e^{kx}K_0(kr)d\bar{z}$. (Note that there are such terms also in $F_n(r,\theta)$.) Equating these terms to zero, we can determine $E_0$ as

$$E_0=\sum_{m=1}^{\infty}\frac{(m+1)m}{2k}C_m\,. \tag{6.18}$$

Secondly, we examine the condition (ii). It is readily shown that the first term is of $O\{(kr)^{-1/2}\}$ if we remember [5] that

$$K_n(kr)\sim\left(\frac{\pi}{2kr}\right)^{1/2}e^{-kr}\left[1+\frac{4n^2-1}{8kr}+\frac{(4n^2-1)(4n^2-9)}{2(8kr)^2}+\cdots\right] \tag{6.19}$$

as $kr\to\infty$. Since the last term $\sum\limits_{n=1}^{\infty}C_nF_n(r,\theta)$ has the form $r^m e^{kx}K_n(kr)(m\leq 2)$, only the examination of the region $\theta\sim 0$ becomes important. The terms which correspond to $m=1, 2$ in $F_n$(6.15) (excluding the last term which is already cancelled) become as $\sim O\{(1/r)^{1/2}\}$ as $r\to\infty$. From the remaining terms we have

$$\frac{df_2}{dz}=-\frac{i}{2}z+O(1)\,. \tag{6.20}$$

In the next subsection, we shall determine $E_n$ and $f_2$ by the condition (i).

### § 6.5. Determination of Coefficients $E_n$

The determination of coefficients $E_n$'s is performed in the same way as in § 5.4 but more tedious. Here we give only the results neglecting the details for want of space:

$$\begin{aligned}
&E_0=C_{11}+k^2(C_{12}+3C_{21})+O(k^4)\,,\\
&E_1=\frac{3}{2s+1}C_{11}+k^2\left\{\frac{1}{2(2s+1)}+\frac{3(16s^2-20s+7)}{16(2s+1)^2}C_{11}+\frac{4s+5}{2s+1}C_{21}+\frac{3}{2s+1}C_{12}\right\}+O(k^4)\,,\\
&E_2=k^2\left\{1-\frac{3}{8(2s+1)}C_{11}\right\}+O(k^4)\,,\\
&E_3=k^4\left\{-\frac{1}{4}-\frac{6s^2+4s-1}{48(2s+1)}C_{11}\right\}+O(k^6)\,,\\
&E_i=O(k^{2i-2}) \qquad (i\geq 4)\,,
\end{aligned} \tag{6.21}$$

and

$$\begin{aligned}
f_2'=i\Bigg[&-\frac{1}{k^2}\frac{s-1}{2s+1}\frac{1}{z}C_{11}+\frac{1}{k}\left\{1+\frac{3}{8(2s+1)}C_{11}-C_{21}\right\}\frac{1}{z^2}\\
&+\left\{-\frac{1}{2}z+\left(\frac{1}{4(2s+1)}-\frac{64s^3-80s^2+40s-15}{32(2s+1)^2}C_{11}-\frac{8s+1}{2(2s+1)}C_{21}-\frac{s-1}{2s+1}C_{12}\right)\frac{1}{z}\right.\\
&\left.-\left(\frac{1}{2}+\frac{6s^2+4s-1}{12(2s+1)}C_{11}+4C_{31}\right)\frac{1}{z^3}\right\}\Bigg]+O(k)\,,
\end{aligned} \tag{6.22}$$

where $s=\log(\frac{1}{2}k)+\gamma$, $\gamma$ being Euler's constant, and $C_{nm}$ is the coefficient of $k^{2(n+m)-3}$ in the expansion of $C_n$(5.39) in powers of $k$, i.e.,

$$C_{11}=\frac{4}{2s-1}\,, \qquad C_{12}=-\frac{16s^2-16s-1}{4(2s-1)^2}\,,$$
$$C_{31}=\frac{4s-1}{2(2s-1)}\,, \qquad C_{31}=-\frac{3s-1}{12(2s-1)}\,. \tag{6.23}$$

## § 7. Hydrodynamic Forces

### § 7.1. Oseen's Equations in Polar Coordinates

Oseen's equations in rectangular coordinates $(x, y)$;

$$(1+\alpha y)\frac{\partial U}{\partial x}=-\frac{\partial p}{\partial x}+\frac{1}{2k}\Delta U\,, \tag{7.1}$$

$$(1+\alpha y)\frac{\partial V}{\partial x}=-\frac{\partial p}{\partial y}+\frac{1}{2k}\Delta V\,, \tag{7.2}$$

where $p$ is the pressure, can be transformed as

$$(1+\alpha r\sin\theta)\left(\cos\theta\frac{\partial u}{\partial r}-\frac{\sin\theta}{r}\frac{\partial u}{\partial\theta}+\frac{\sin\theta}{r}v\right)=-\frac{\partial p}{\partial r}+\frac{1}{2k}\left(\Delta_r u-\frac{u}{r^2}-\frac{2}{r^2}\frac{\partial v}{\partial\theta}\right), \tag{7.3}$$

$$(1+\alpha r\sin\theta)\left(\cos\theta\frac{\partial v}{\partial r}-\frac{\sin\theta}{r}\frac{\partial v}{\partial\theta}-\frac{\sin\theta}{r}u\right)=-\frac{1}{r}\frac{\partial p}{\partial\theta}+\frac{1}{2k}\left(\Delta_r v-\frac{v}{r^2}+\frac{2}{r^2}\frac{\partial u}{\partial\theta}\right) \tag{7.4}$$

in polar coordintes $(r, \theta)$, where $\Delta_r$ is the operator defined by (3.2), and $(u, v)$ are the $r$-, and $\theta$-components of velocity.

Since $u=v=0$ on the surface $(r=1)$, (7.4) can be written on the surface:

$$\frac{\partial p}{\partial\theta}=\frac{1}{2k}\left(\frac{\partial^2 v}{\partial r^2}+\frac{\partial v}{\partial r}\right)-(1+\alpha\sin\theta)\cos\theta\frac{\partial v}{\partial r} \qquad \text{at } r=1. \tag{7.5}$$

Integrating it we have for the pressure over the surface:

$$p-p_0=\int_{\theta_0}^{\theta}\left[\frac{1}{2k}\left(\frac{\partial^2 v}{\partial r^2}+\frac{\partial v}{\partial r}\right)_{r=1}-(1+\alpha\sin\theta)\cos\theta\left(\frac{\partial v}{\partial r}\right)_{r=1}\right]d\theta\,, \tag{7.6}$$

where $p_0$ is the pressure at the point $(1, \theta_0)$.

### § 7.2. Expression for the Velocity near the Surface

If we introduce (5.36) and (5.37) into (5.21), and expand it in powers of $k$ considering the smallness of $kr$ near the surface $r=1$, we have

$$\begin{aligned}W_1=&-\frac{2}{2s-1}\log r-\frac{1}{2s-1}\left(1-\frac{1}{r^2}\right)e^{-2i\theta}\\&+k\left[\left\{-\frac{4s-1}{4(2s-1)}\left(r-\frac{1}{r}\right)-\frac{r\log r}{2s-1}\right\}e^{i\theta}+\frac{1}{4(2s-1)}\left\{r+\frac{4s-1}{r}-\frac{4s}{r^3}\right\}e^{-3i\theta}\right]+O(k^2)\,,\end{aligned} \tag{7.7}$$

which is zero at $r=1$ as should be expected from the boundary conditions. Since (7.7) has a form

$$W_1=\sum g_n(r)e^{ni\theta}\,,$$

we have by separating real and imaginary parts,

$$U_1=\sum g_n(r)\cos n\theta\,, \qquad V_1=-\sum g_n(r)\sin n\theta\,.$$

Thus we have for $v_1$

$$v_1=-\sum g_n(r)\sin(n+1)\theta\,,$$

which is explicitly written as

$$v_1=\left\{\frac{1}{2s-1}+\frac{2\log r}{2s-1}-\frac{1}{2s-1}\frac{1}{r^2}\right\}\sin\theta+k\left\{\frac{r\log r}{2s-1}+\frac{s}{2s-1}r-\frac{s}{2s-1}\frac{1}{r^3}\right\}\sin 2\theta+O(k^2)\,. \tag{7.8}$$

Differentiating (7.8) with respect to $r$, and putting $r=1$, we have

$$\left[\frac{\partial v_1}{\partial r}\right]_{r=1}=\frac{4}{2s-1}\sin\theta+k\frac{4s+1}{2s-1}\sin 2\theta+O(k^2)\,, \tag{7.9}$$

$$\left[\frac{\partial^2 v_1}{\partial r^2}\right]_{r=1}=-\frac{8}{2s-1}\sin\theta-k\frac{12s-1}{2s-1}\sin 2\theta+O(k^2)\,. \tag{7.10}$$

Similarly we have for $W_2$ near the surface

$$\begin{aligned}W_2/i=&\frac{1}{k}\left\{-\frac{3}{4s^2-1}\log r-\frac{3}{4s^2-1}\left(1-\frac{1}{r^2}\right)e^{-2i\theta}\right\}+\left\{-\frac{3}{4s^2-1}r\log r-\frac{8s^2-5}{4(4s^2-1)}\left(r-\frac{1}{r}\right)\right\}e^{i\theta}\\&+\left\{\frac{4(s-1)}{4s^2-1}r\log r+\frac{12s^2-8s-1}{2(4s^2-1)}\left(r-\frac{1}{r}\right)\right\}e^{-i\theta}-\frac{1}{4(4s^2-1)}\left\{3r+\frac{8s^2-5}{r}-\frac{2(4s^2-1)}{r^3}\right\}e^{-3i\theta}+O(k)\,,\end{aligned} \tag{7.11}$$

which is also zero at the surface as should be so. From (7.11) we have for $v_2$,

$$\begin{aligned}v_2=&\frac{1}{k}\left\{\frac{6}{4s^2-1}\log r+\frac{3}{4s^2-1}\left(1-\frac{1}{r^2}\right)\right\}\cos\theta-\frac{4(s-1)}{4s^2-1}r\log r-\frac{12s^2-8s-1}{2(4s^2-1)}\left(r-\frac{1}{r}\right)\\&+\left\{\frac{3}{4s^2-1}r\log r+\frac{1}{2}\left(r-\frac{1}{r^3}\right)\right\}\cos 2\theta+O(k)\,.\end{aligned} \tag{7.12}$$

Differentiating (7.12) with respect to $r$, and putting $r=1$, we have

$$\left[\frac{\partial v_2}{\partial r}\right]_{r=1}=\frac{1}{k}\frac{12}{4s^2-1}\cos\theta+\left[-\frac{6s-5}{2s-1}+\frac{8s^2-1}{4s^2-1}\cos 2\theta\right]+O(k)\,, \tag{7.13}$$

$$\left[\frac{\partial^2 v_2}{\partial r^2}\right]_{r=1}=-\frac{1}{k}\frac{24}{4s^2-1}\cos\theta+\left[\frac{3(2s-1)}{2s+1}-\frac{3(8s^2-3)}{4s^2-1}\cos 2\theta\right]+O(k)\,. \tag{7.14}$$

### § 7.3. Drag, Lift, and Moment

Introducing (7.9), (7.10), (7.13), (7.14) into (7.6), and performing the integration, we have a formula for the pressure distribution over the surface;

$$\begin{aligned}p_{r=1}-p_0=&\frac{1}{k}\frac{2}{2s-1}\cos\theta+\frac{4s+1}{2(2s-1)}\cos 2\theta+O(k)\\&-\alpha\left[\frac{1}{k^2}\frac{6}{4s^2-1}\sin\theta+\frac{1}{k}\left\{\frac{2}{2s-1}\theta+\frac{8s^2+1}{2(4s^2-1)}\sin 2\theta\right\}+O(1)\right]+O(\alpha^2)\,.\end{aligned} \tag{7.15}$$

Since there is a term which is proportional to $\theta$ in the second term of $O(\alpha)$, (7.15) is not single-valued which contradicts the physical explanation*. However, if we retain only the first term in $O(\alpha)$, (7.15) will be single-valued. In the calculation of the hydrodynamical forces, we shall retain two terms for $O(\alpha^0)$, and one for $O(\alpha)$.

When there is shear in the undisturbed flow, we have another difficulty that the pressure on the surface becomes infinite if we take the pressure at infinity $p_\infty$ as the standard of the pressure. So we take the pressure at a point ($r=1,\theta=0$) as the standard. Following these assumptions, we have calculated the pressure distribution over the surface for the cases of $Re=1$ ($k=0.25$), and $\alpha=0$, 0.1. The pressure distributions thus calculated are

---

* In regard to this difficulty, the author cannot give adequate explanation. It may be that this difficulty originates from the fact that we cannot give finite value for the pressure at infinity ($r\to\infty$) for the whole value of $\theta$ ($2\pi\geqq\theta\geqq 0$), it being the very reason that we cannot construct a viscous shear flow extending over the entire region.

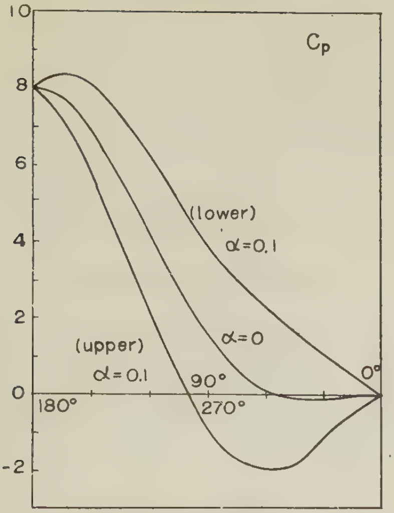

Fig. 2. Pressure distribution over the surface of circular cylinder, $Re=1$, $\alpha=0$, $0.1$.

given in Fig. 2, where $C_p$ is the coefficient of pressure defined as

$$C_p=\frac{p-p_0}{\frac{1}{2}\rho U_0^2}\,, \tag{7.16}$$

where $U_0$ is the undisturbed velocity at infinity on the $x$-axis.

The drag, the lift and the moment are given respectively as follows:

$$D=\int_0^{2\pi}\{[p_{rr}]_{r=1}\cos\theta-[p_{\theta r}]_{r=1}\sin\theta\}d\theta\,, \tag{7.17}$$

$$L=\int_0^{2\pi}\{[p_{rr}]_{r=1}\sin\theta+[p_{\theta r}]_{r=1}\cos\theta\}d\theta\,, \tag{7.18}$$

$$M=\int_0^{2\pi}[p_{\theta r}]_{r=1}d\theta, \tag{7.19}$$

where

$$[p_{rr}]=-[p]_{r=1}\,,$$

$$[p_{\theta r}]_{r=1}=\frac{1}{2k}\left[\frac{\partial v}{\partial r}\right]_{r=1}\,.$$

Thus, introducing (7.15), (7.9), (7.13) into (7.17), (7.18), we have

$$C_D=\frac{4\pi}{k(1-2s)}+O(k)+O(\alpha k^{-1})+O(\alpha^2)\,, \tag{7.20}$$

$$C_L=\alpha\frac{12\pi}{k^2(4s^2-1)}+O(\alpha k^{-1})+O(\alpha^2)\,. \tag{7.21}$$

As far as our approximation is concerned, the drag is given from the first approximation and is not affected by the presence of shear, the fact coinciding with the results of Stokes' approximation. On the other hand, the lift is given only from the second approximation, and its direction coincides with that for the inviscid shear flow. The moment cannot be given in terms of our approximation since it is of the order $\alpha k^{-1}$.

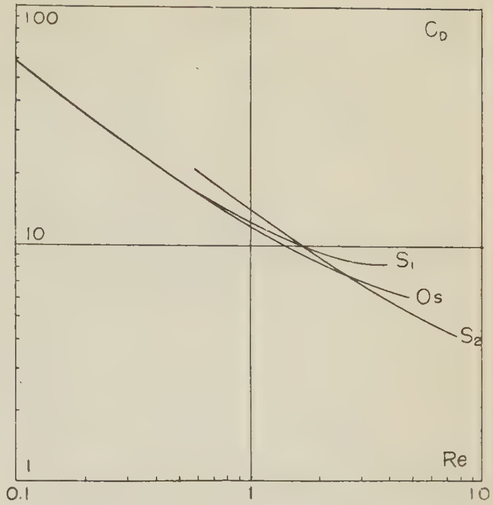

Fig. 3. Drag coefficient: $S_1$, Stokes' approximation (i), $S_2$, Stokes' approximation (ii), Os, Oseen's approximation.

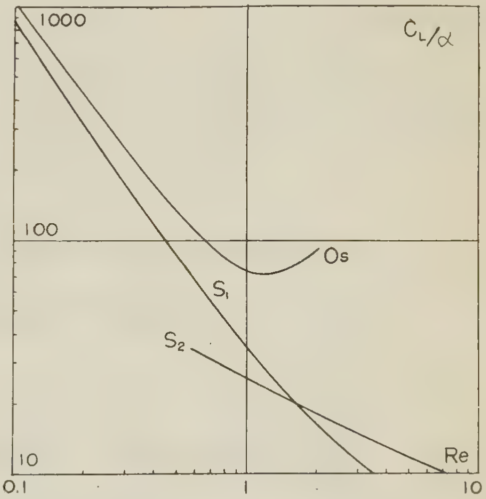

Fig. 4. Lift coefficient; $S_1$, Stokes' approximation (i), $S_2$, Stokes' approximation (ii), Os, Oseen's approximation.

The drag and the lift coefficients thus calculated are given in Figs. 3–4 where the results to Stokes' approximation are also given. It will be seen that the results of Oseen's approximation and one of Stokes' approximation (§3. (i)) coincide with each

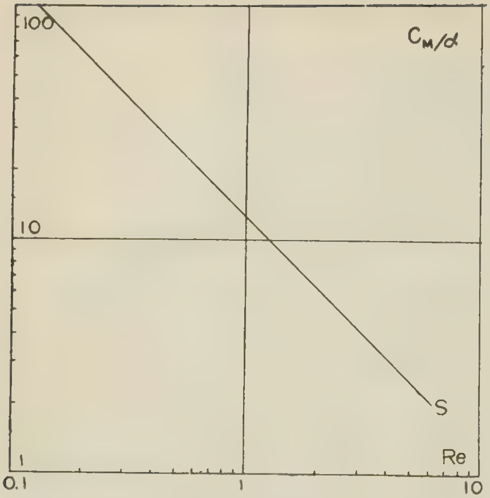

Fig. 5. Moment coefficient; S, Stokes' approximation (i), (ii).

other fairly well.

## § 8. Summary

The shear flow of a viscous fluid around a circular cylinder has been studied to Oseen's approximation and has been compared with the results of Stokes' approximation [1]. The formulae for the drag and the lift have been obtained neglecting the terms of orders $O(Re)$, $O(\alpha Re^{-1})$, $O(\alpha^2)$, and it has been shown that the drag is not affected by the presence of the shear and the direction of the lift is the same as that for the inviscid shear flow within the order of our approximation.

**Acknowledgement**

In conclusion, I wish to express my hearty gratitude to Professor Isao Imai for his kind suggestion and discussion in the course of this work, and to my colleague Dr. Hidenori Hasimoto who kindly read the manuscript.

## Appendix

The integration of the last term of (6.10) can be performed separately, by using the formula for the modified Bessel function:

$$K_{\nu-1}(z)-K_{\nu+1}(z)=-\frac{2\nu}{z}K_\nu(z) \tag{A.1}$$

and the results of § 5.3 (5.16), (5.17), as follows:

$$-\frac{i}{2}\int\frac{1}{8}kC_nr^2K_n(kr)e^{kx}\cos(n-2)\,\theta d\bar{z}$$

$$\begin{cases}
=\frac{i}{16}\Big[-z^2e^{kx}\Big\{K_1(kr)e^{-i\theta}+\sum_{m=1}^{3}K_m(kr)e^{-mi\theta}\Big\}-z^2k\int e^{kx}K_0(kr)\,d\bar{z} \\
\quad+\frac{4z}{k}e^{kx}\sum_{m=1}^{2}K_m(kr)e^{-mi\theta}+2z\int e^{kx}K_0(kr)\,d\bar{z}\Big]C_1 \qquad (n=1)\,, \\
=\frac{i}{16}\Big[-2z^2e^{kx}\sum_{m=1}^{2}K_m(kr)e^{-mi\theta}-z^2k\int e^{kx}K_0(kr)\,d\bar{z}\Big]C_2 \qquad (n=2)\,, \\
=\frac{i}{16}\Big[-z^2e^{kx}\Big\{\sum_{m=1}^{3}K_m(kr)e^{-mi\theta}+K_1(kr)e^{-i\theta}\Big\}-z^2k\int e^{kx}K_0(kr)\,d\bar{z} \\
\quad+\frac{8}{k^2}e^{kx}K_0(kr)-\frac{4}{k}\int e^{kx}K_0(kr)\,d\bar{z}-2z\int e^{kx}K_0(kr)\,d\bar{z}\Big]C_3 \qquad (n=3)\,, \\
=\frac{i}{16}\Big[-z^2e^{kx}\Big\{\sum_{m=1}^{n}K_m(kr)e^{-mi\theta}\sum_{m=0}^{n-5}K_m(kr)e^{mi\theta}\Big\}-z^2k\int e^{kx}K_0(kr)\,d\bar{z} \\
\quad+\frac{4(n-1)(n-2)}{k^2}e^{kx}\sum_{m=0}^{n-3}K_m(kr)e^{mi\theta}-\frac{2(n-1)(n-2)}{k}\int e^{kx}K_0(kr)\,d\bar{z} \\
\quad+\frac{4(n-2)}{k}e^{kx}\sum_{m=0}^{n-4}K_m(kr)e^{mi\theta}-2(n-2)z\int e^{kx}K_0(kr)\,d\bar{z}\Big]C_n \qquad (n\geq 4);
\end{cases} \tag{A.2}$$

$$-\frac{i}{2}\int -\frac{1}{4}kC_n r^2 K_{n+1}(kr)e^{kx}\cos(n-1)\theta d\bar{z}$$

$$\left\{\begin{aligned}
&=\frac{i}{8}\left[2z^2e^{kx}\left\{\sum_{m=1}^{2}K_m(kr)e^{-mi\theta}\right\}+kz^2\int e^{kx}K_0(kr)\,d\bar{z}\right]C_1 \qquad (n=1)\,,\\
&=\frac{i}{8}\left[z^2e^{kx}\left\{\sum_{m=1}^{3}K_m(kr)e^{-mi\theta}+K_1(kr)e^{-i\theta}\right\}+kz^2\int e^{kx}K_0(kr)d\bar{z}\right.\\
&\qquad\left.+2z\int e^{kx}K_0(kr)\,d\bar{z}-\frac{8}{k^2}e^{kx}K_0(kr)+\frac{4}{k}\int e^{kx}K_0(kr)d\bar{z}\right]C_2 \qquad (n=2),\\
&=\frac{i}{8}\left[z^2e^{kx}\left\{\sum_{m=1}^{n+1}K_m(kr)e^{-mi\theta}-\sum_{m=0}^{n-4}K_m(kr)e^{mi\theta}\right\}+kz^2\int e^{kx}K_0(kr)d\bar{z}\right.\\
&\qquad-\frac{4(n-1)z}{k}e^{kx}\sum_{m=0}^{n-3}K_m(kr)e^{mi\theta}+2(n-1)z\int e^{kx}K_0(kr)d\bar{z}\\
&\qquad\left.-\frac{4n(n-1)}{k^2}e^{kx}\sum_{m=0}^{n-2}K_m(kr)e^{mi\theta}+\frac{2n(n-1)}{k}\int e^{kx}K_0(kr)d\bar{z}\right]C_n \qquad (n\geq 3);
\end{aligned}\right. \tag{A.3}$$

$$-\frac{i}{2}\int\frac{1}{2}nC_m re^{kx}K_{n-1}(kr)\cos n\theta d\bar{z}$$

$$\begin{aligned}
&=\frac{i}{4}\left[\frac{nz}{k}e^{kx}\left\{\sum_{m=0}^{n-2}K_m(kr)e^{mi\theta}-\sum_{m=1}^{n+1}K_m(kr)e^{-mi\theta}\right\}-nz\int e^{kx}K_0(kr)d\bar{z}\right.\\
&\qquad\left.+\frac{2n^2}{k^2}e^{kx}\sum_{m=1}^{n}K_m(kr)e^{-mi\theta}+\frac{n^2}{k}\int e^{kx}K_0(kr)\,d\bar{z}\right]C_n\ ;
\end{aligned} \tag{A.4}$$

$$-\frac{i}{2}\int\frac{1}{4}kC_m r^2e^{kx}K_{n-1}(kr)\cos(n+1)\theta d\bar{z}$$

$$\begin{aligned}
&=\frac{i}{8}\left[z^2e^{kx}\left\{\sum_{m=0}^{n-2}K_m(kr)e^{mi\theta}-\sum_{m=0}^{n+3}K_m(kr)e^{-mi\theta}\right\}-kz^2\int e^{kx}K_0(kr)d\bar{z}\right.\\
&\qquad+\frac{4(n+1)z}{k}e^{kx}\sum_{m=1}^{n+2}K_m(kr)e^{-mi\theta}+2z(n+1)\int e^{kx}K_0(kr)d\bar{z}\\
&\qquad\left.-\frac{4n(n+1)}{k^2}e^{kx}\sum_{m=1}^{n+1}K_m(kr)e^{-mi\theta}-\frac{2n(n+1)}{k}\int e^{kx}K_0(kr)d\bar{z}\right]C_n;
\end{aligned} \tag{A.5}$$

$$-\frac{i}{2}\int\frac{i}{4}-\frac{1}{8}kC_n r^2e^{kx}K_n(kr)\cos(n+2)\theta d\bar{z}$$

$$\begin{aligned}
&=\frac{i}{16}\left[z^2e^{kx}\left\{-\sum_{m=0}^{n-1}K_m(kr)e^{mi\theta}+\sum_{m=1}^{n+4}K_m(kr)e^{-mi\theta}\right\}+kz^2\int e^{kx}K_0(kr)d\bar{z}\right.\\
&\qquad-\frac{4(n+2)}{k}ze^{kx}\sum_{m=1}^{n+3}K_m(kr)e^{-mi\theta}-2(n+2)z\int e^{kx}K_0(kr)d\bar{z}\\
&\qquad\left.+\frac{4(n+1)(n+2)}{k^2}e^{kx}\sum_{m=1}^{n+2}K_m(kr)e^{-mi\theta}+\frac{2(n+1)(n+2)}{k}\int e^{kx}K_0(kr)d\bar{z}\right]C_n;
\end{aligned} \tag{A.6}$$

where the notation $\sum_{m=a}$ indicates the summation from $m=a$ to $b$ when $a\leq b$, while it is zero when $a>b$.

## References

1) M. Kawaguti: Rep. Inst. Sci. Technol. Tokyo **6** (1952) 85 (in Japanese).
2) S. Tomotika and T. Aoi: Quart. Journ. Mech. Appl. Math. **3** (1950) 140.
3) L. Bairstow, B. M. Cave and E. D. Lang: Phil. Trans. Roy. Soc. London **223** (1923) 420.
4) I. Imai: Proc. Roy. Soc. London **A 224** (1954) 141.
5) G. N. Watson: A treatise on the theory of Bessel functions, Cambridge, 1922, p. 202.

---

JOURNAL OF THE PHYSICAL SOCIETY OF JAPAN Vol. 11, No. 5, MAY, 1956

# Reflection of Shock Waves-1 Pseudo-Stationary Case

By Ryuma KAWAMURA and Haruo SAITO

*Institute of Science and Technology, University of Tokyo*

(Received February 7, 1956)

Results of theoretical and experimental investigations on shock reflection at a fixed wall are reported in this paper. In the region of regular reflection, agreement of theory and experiment is found to be good except for the fact that experimental points extend a litter bit beyond the theoretical limit. A theoretical investigation of the flow characteristics is made on Mach reflection cases with the conclusion that a singularity would appear at the triple point, and hence, the reflected shock angle would not coincide with the theoretical one when the flow is subsonic behind the reflected shock. This theoretical prediction is fully confirmed by the results of shock angle measurement in schlieren pictures obtained by the experiment. In case of a strong incident shock, angle of the reflected shock decreases discontinuously at the transition from regular to Mach reflection as expected from the theory. In case of a weak incident shock, on the other hand, its change is continuous against the ordinary three-shock theory. It is found in the experiment that the boundary between these two cases takes place approximately at $\xi=0.42$, where $\xi$ is the pressure ratio across the incident shock. This is in good agreement with the theoretically predicted value, $\xi=0.433$, above which the Mach reflection with a singularity at the triple point would appear. It corresponds to the condition of the stationary Mach reflection. Comparisons of theory and experiment are also made in this paper on the condition at which the flow behind the incident shock is just sonic relative to the triple point and on the angle of the Mach stem. Throughout the present study experiment was made by use of a shock tube.

## § 1. Introduction

It is well known that there exist two types of reflection of shock waves at a fixed boundary. The one is called the regular reflection and the other the Mach reflection. Wave patterns in the two cases are shown schematically in Figs. 1 (a) to (d).

Let us first consider the case where an incident shock moves forward in still air and strikes a wedge at zero angle of attack (Fig. 1 (c) and (d)). If the wedge angle is sufficiently large, a regular reflection takes place at the wedge surface. In case of a small wedge angle, on the contrary, the reflection point detaches the wedge surface and another shock, called the Mach stem, is issued from the reflection point to the wedge surface. This is the Mach reflection. Hence, two shocks intersect at the reflection point in the former type of reflection, while three in the latter. The similar wave patterns appear at the exit of a supersonic jet when the ambient pressure is higher than that of the jet. The transition from two- to three-shock configuration takes place when the ambient pressure is increased up beyond a certain limit.

Theory of two- and three-shock interactions at one point has already been exploited by Taub1), Bleakney2) and other investigators.

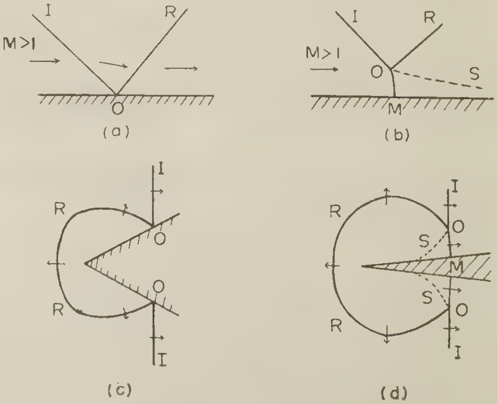

Fig. 1. (a) (b) stationary
(c) (d) non-stationary.

There is no significant difficulty in the development of the theory as far as the treatment is limited to the local problem around the reflection point since it is simply an application of the shock wave theory. Moreover, the theory can be applied in all the sawe way to the stationary case as well as to the pseudo-stationary one provided definition of velocity is changed in a proper way according to the cases.

In applying the two-shock theory to the above shock-wedge interaction problem, one finds that solution does not exist for wedge angles larger than a certain critical value which varies according to the incident shock strength. The same thing can also be said in the stationary case such as the above supersonic jet. Even beyond this critical state, possible solutions can be obtained in the three-shock theory. Hence, it is a reasonable expectation that transition from the regular to the Mach reflection would take place at the above mentioned critical state. The experimental verification of this theoretical prediction was first given by the senior author³⁾ for the stationary case. Later in 1949, detailed experiment of shock reflection was made by Bleakney and others at Princeton University²⁾,⁴⁾ by use of a shock tube and the theory was found to be correct even in the pseudo-stationary case as far as the transition was concerned

The experimenal results obtained by the Princeton group show good agreement with the theory in case of regular reflection, while in Mach reflection, substantial disagreement between theory and experiment was found to appear when strength of the incident shock was weak. In analysing their results, it seems that the inconsistency first appears at a shock strength somewhere between 0.4 and 0.5 in terms of the pressure ratio across the incident shock. Bleakney and Taub²⁾ attributed the discrepancy to the existence of a singularity such as an infinite curvature of the reflected shock at the intersection point which could not be found from the ordinary schlieren pictures.

The present study has been started with the primary intention of getting a deeper understanding of the phenomena mentioned above and also of accumulating more experimental data on shock reflection on which no reliable ones other than those obtained at Princeton have been available. Experiments of the stationary and the pseudo-stationary cases have been carried on in parallel by use of supersonic jets and a shock tube, respectively, in which only the latter is reported in this paper. The results of the stationary case and comparison of the two cases will be reported later in another paper.

## § 2. Analysis of the Existing Data and Theoretical Investigation

In order to get a rough idea about shock reflection problem, it is of convenience, especially in the steady case, to make use of shock-polar diagram in a $p$-$\theta$ plane, where $p$ is the pressure and $\theta$ the flow angle. Fig. 1 (a) shows a typical shock configuration of a regular reflection in the stationary case. The incoming supersonic flow along the wall is deflected down by the incident shock, *OI*, and again deflected up by the reflected shock, *OR*, so that flow behind the shock *OR* is parallel to the wall surface. The pressure is increased at each time when the flow passes through a shock. The shock polar diagram in the hodograph plane is popular in gas-dynamics. In this case, however, it is of more value to express the shock polar in the $p-\theta$ plane as is shown in Fig. 2. Here, the abscissa is the pressure divided by the stagnation pressure in the region ahead of the incident shock and the ordinate is the flow angle $\theta$ measured from the initial direction. The curve *ABCDA* is a shock polar corresponding to the Mach number of the flow in front of the incident shock. If once we are given any one of the characteristic quantities of the incident shock such as its strength or its inclination, we can fix a point, say *I* in Fig. 2, on the shock polar which represents $p$ and $\theta$ in the region behind

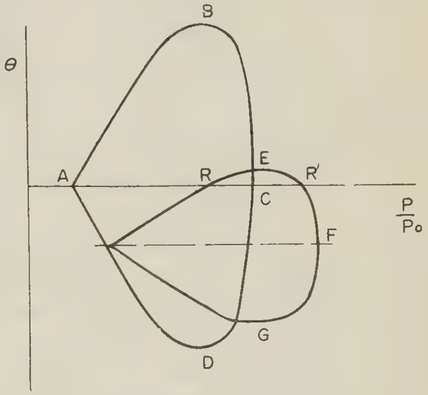

Fig. 2.

the incident shock. Now, in case the point $I$ lies on the supersonic part of the shock polar, we can draw the second shock polar $IEFGI$ starting from the point $I$. The state of flow behind the reflected shock, $OR$ in Fig. 1, has to correspond to any one point on the curve. The determination of the correct position of the point is easily made by applying the hydrodynamical condition that the flow has to be parallel to the wall surface. It means that the point must lie on the $p$-axis where $\theta=0$. In the ordinary case, there are two intersection points of the second shock polar with the $p$-axis. These are shown by the marks $R$ and $R'$ in Fig. 2. Though both of them are the correct solutions to the problem, the point, $R'$, corresponding to a higher pressure is usually discarded by analogy to the acoustic theory.

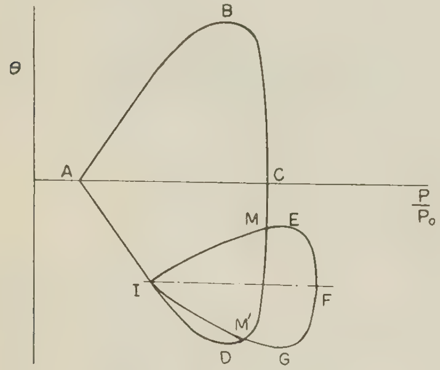

Fig. 3.

Now, let us examine what would happen if the strength of the incident shock is increased while the Mach number of the incoming flow is unaltered. The more the point $I$ gets away from the point $A$ in Fig. 2, the smaller becomes the second shock polar and finally it shrinks to a point when $I$ reaches the sonic point of the first shock polar. Hence, it is clear that the intersection points $R$ and $R'$ disappear beyond a certain critical state. This critical condition would correspond to the limitation of existence of regular reflection. Even in case of the non-stationary case the same thing can be said provided velocities are measured relatively to the reflection point. The critical point can be computed algebraically by applying the shock relations to the incident and the reflected shocks.

Experimental evidence of the theory concerning the critical condition of regular reflection was given by the senior author3) in steady case and also by Bleakney and Taub2) in pseudo-stationary case. In examining these experimetal data, one finds that the above theoretical prediction is clearly verified by the experiments within the experimental accuracy. A slight doubt seems to remain yet on whether the transition takes place either at the maximum deflection point of the second shock polar as the above theory predicts or at the sonic point. When the flow behind the reflected shock is subsonic, the flow behavior at the reflected point may be affected by downstream condition. Therefore, the state where the sonic point on the second shok polar falls on the axis of $\theta=0$ may be a possible critical one. However, since the sonic point and maximum deflection point are quite close to each other on a shock polar, it is almost impossible to make discrimination between them by experiment and the difference does not seem to be of significance in the problem.

Fig. 3 shows a schematic diagram of shock polars in case the incident shock is strong enough to cause a Mach reflection. In the physical plane, the flow behind the triple point is divided into two parts by the slip-stream. The one passes through both of the incident and the reflected shocks and the other only the Mach stem. Therefore, the former has to correspond to one point on the second shock polar and the latter to that first one. The two flows have a common stream-line, the slip-stream, behind the triple point, and because of the hydrodynamical condition, their pressures as well as flow directions have to be identical to eacho ther. It means that the flows behind the triple point are represented by the intersection point of the first shock polar with the second one in the $p$–$\theta$ plane. The points are marked by $M$ and $M'$ in Fig. 3. The number of the intersection point is either zero, one, two or three according to the cases. In case more than two intersection points exist, the one on the branch $IEF$ of the second shock polar is thought from physical consideratons to give the correct solution to the problem. Since the Mach stem, $OM$ in Fig. 1 (b), must be normal to the wall at its root $M$, the flow just behind $OM$ is represented by the segment $MC$ on the first shock polar in Fig. 3.

The same kind of treatment can be done in the pseudo-stationary case, though in this case, it is more convenient to take the strength of the incident shock as a parameter instead of the Mach number in the stationary case.

Now, Figs. 4 (a) and (b) show two typical examples of the shock polar diagram at the transition from the regular to Mach reflection. In these figures, the points *R* and *M* represent the flow behind the reflection point in the regular and the Mach reflections, respectively and the point *C* corresponds to the root of the Mach stem. The essential difference between these two diagrams is that the position of *M* is on the weak shock part of the second shock polar in Fig. 4 (a), while it is on the strong shock part in Fig. 4 (b). Neglecting the narrow subsonic part between the sonic point and the maximum deflection point, these shock polar diagrams show the fact that, at the initiation of Mach reflection, the flow behind shock is either supersonic in the case shown in Fig. 4 (a) or subsonic in Fig. 4 (b). At a certain condition, where the so-called "stationary Mach reflection" appears in the physical plane, in which the Mach stem is a straight line normal to the wall, the triangular region *CMR* in Fig. 4 degenerates into one point. The condition of the stationary Mach reflection is computed from the shock reflection theory and is given as follows: The Mach number of the flow in front of the incident shock is 3.203, the pressure ratio across the incident shock is 0.433, and hence, the angle of the incident shock measured from the wall surface is 41.5 deg.

The first type of transition shown in Fig. 4 (a) always takes place when the incoming Mach number is higher than the above mentioned critical value in case of shock reflection in a supersonic flow and also when the shock strength is higher than the above in case of reflection of a moving shock in still air. In other cases the type of transition is as shown in Fig. 4 (b). These two types of transition would be clearly discriminated by measuring the change of angle of the reflected shock at the transition if they do occur as the theory shows: in the first type of reflection, the angle between the reflected shock and the wall would decrease discontinuously at the transition, while in the second, it would show a sudden rise.

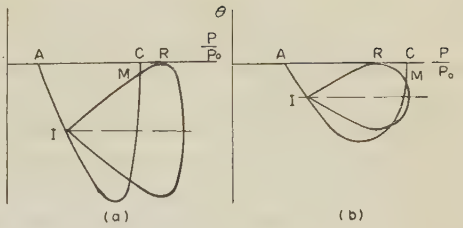

Fig. 4.

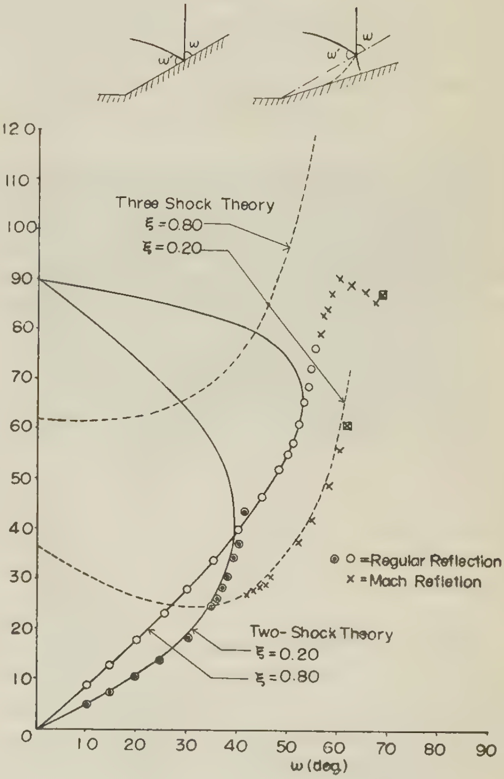

Fig. 5.

Here, let us make examination of the existing experimental data in order to check whether or not experiment agrees with theory on this point. Fig. 5 is the reproduction of the one given in the paper by Bleakney and Taub[2)] on shock reflection. Their experiment was made by use of a shock tube. The special feature seen in this figure is the fact that experimental results do not show substantial deviation from the theoretical curves in case of $\xi=0.2$, while they do in case of $\xi=0.8$, where $\xi$ is the pressure ratio across the shock. The transition from the regular to the Mach reflection seems to occur almost continuously in case of the weaker incident shock in spite of the theory indicating an appreciable jump of the angle of the reflected shock at the transition point. More detailed data of the same experiment can be obtained in the paper by Smith[4)], in which one finds that theory and experiment agree well with each other for $\xi$ smaller than 0.4, while qualitative disagreement always appers for $\xi$ larger than 0.5. Hence, there arises a doubt if the inconsistency between theory and experiment might occur in Mach reflections of the type shown in Fig. 4 (b).

Let us now make considerations about the flow behavior behind the triple point near transition. In case the flow is supersonic behind the reflected shock, it is determined totally by the local conditions without being influenced by downstream disturbances. In such a flow a possible singularity of the flow at the triple point, if it does exist, should be the one called the Prandtl–Meyer flow which gives an angular variation of flow parameters around a point. However, it was already demonstrated theoretically that the Prandtl-Meyer flow cannot exist in any angular regions around the triple point in both of the stationary and the pseudo-stationary cases[2)]. Moreover, the senior author[5)] has shown that the curvatures of the reflected shock and the Mach stem have to vanish at the triple point in case of a supersonic flow behind the reflected shock. In another word, the flow behind the triple point is locally uniform. Under these circumstances, it is reasonable to expect that agreement of experiment with theory would be realized.

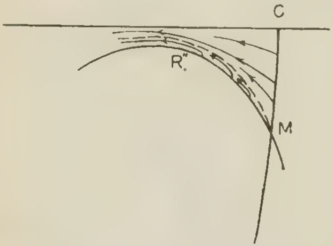

Fig. 6.

Now, what would happen when the flow behind the reflected shock is subsonic as is shown in Fig. 4 (b)? Fig. 6 is a shock polar diagram showing the state just after the transition. The segments *CM* and *MR''* correspond to the Mach stem and the reflected shock, respectively. The lines issuing from *CM* and *MR''* are stream-lines behind the shocks. The dotted line corresponds to the slip-stream. As we can see in this figure, stream lines are dense near *R''*, the maximum deflection point of the second shock polar, and they are rare in the triangular region *CMR''*. The substantially same thing can be said in the corresponding diagram on the hodograph plane. In 1949, Busemann intuitively pointed out that, in case of a subsonic flow, a region on the hodograph plane where stream-lines are crowded corresponds to a nearly uniform flow field in the physical plane, while that where stream-lines are rare in the hodograph to a narrow field of rapidly changing flow. In applying the theorem to the present case it can be said that the triangular region *CMR''* on the $p$–$\theta$ plane in Fig. 6 would shrink to a very narrow field in the physical plane. Hence, region *CMR''* would degenerate to one singular point in the actual flow field just after the transition and the quantities at the triple point measured in the experiment would be those corresponding to the point *R''*, not to the point *M*, in Fig. 6. If it is the case, a seemingly continuous transition would take place in case the flow behind the reflected shock is subsonic. The singularity mentioned above is quite similar to the one which appears at the detachment of a bow wave from a wedge tip.

The above statement is correct only when the flow field in question is subsonic. Accordingly, the boundary of the two cases, in one side of which experiment would agree with theory and in another would not because of the appearance of a singularity, would be determined by the condition where the intersection of the line $\theta=0$ with the second shock polar coincides with its sonic point in the $p-\theta$ plane. However, since the sonic point and the maximum deflection point are quite close to each other as stated before, it seems almost impossible to make clear distinction between them by experiment.

The conclusion of the above discussion concerning the transition from the regular to the Mach reflection is as follows: there would exist two types of the transition. The one would occur when the flow behind the reflected shock is supersonic. In this case the angle of the reflected shock would decrease discontinuously at the transition. The other one would take place when the flow behind the reflected shock is subsonic. In this case, a singularity would appear at the triple point and a seemingly continuous change at least of the reflected shock angle would occur at the transition. The critical point between the two cases would be near the stationary Mach reflection condition.

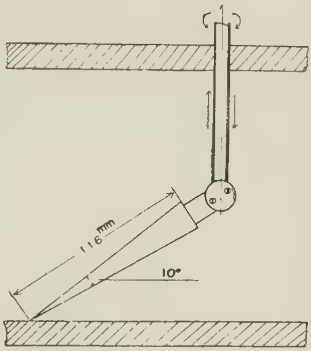

Fig. 7.

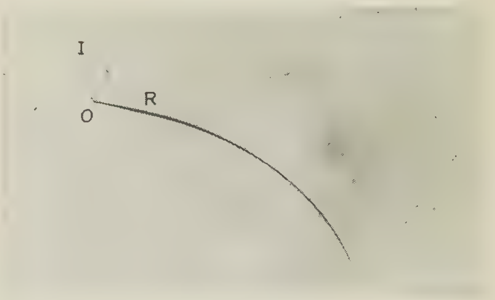

Plate 1.

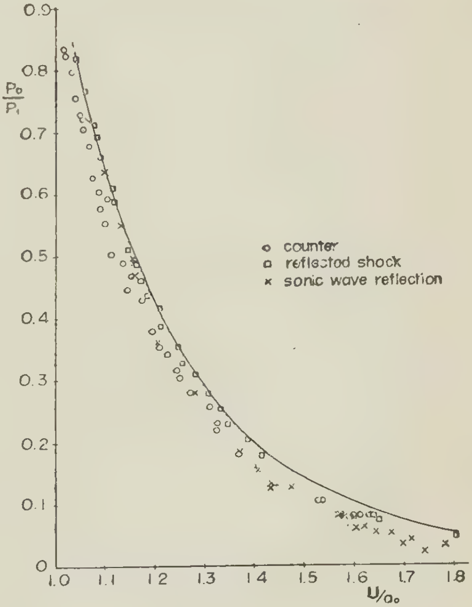

Fig. 8.

## § 3. Experiment

An experiment on shock reflection was made by use of a shock tube in order primarily to check the above theoretical investigation.

The 5×15 cm. shock tube at I.S.T. was used througout the present experiment. The details of the tube itself as well as the measuring equipments such as the spark unit and the shock velocity measuring counter are described in Ref. (7).

A wedge of 10 deg. vertex angle is set inside the testing chamber as shown in Fig. 7. The angle of attack is changed by means of the screw from out side of the shock tube. Series of tests were made by changing the wedge angle at each run with the strength of the incident shock being kept constant. Pictures such as shown in Plate 1 were taken by the instantaneous schlieren method on standard size movie films. The strength of the incident shock was computed from the shock velocity measured by the electronic time counter in the upstream part of the testingh chamber at each run. The relation between the incident shock strength, $\xi$ (pressure ratio of the gas in front of and behind the incident shock), and Mach number of the incident shock $M_0$ (the shock velocity divided by the velocity of sound in the stagnant field ahead of it), is given in the following form:

$$M_0=\sqrt{\frac{\mu+\xi}{(\mu+1)\xi}}\,, \quad \mu=\frac{\gamma+1}{\gamma-1}\,,$$

where $\gamma$ is the ratio of the specific heats of air and is assumed to be 1.40 in this paper. In one-dimensional shock-tube theory, $\xi$ is connected to the initial pressure ratio, $P_0/P_1$, of the expansion and the compression chambers. Neglecting viscosity and heat conductivity of air, the following relation is obtained.

$$\frac{P_0}{P_1}=\xi\left[1-\frac{1-\xi}{\sqrt{(\mu+1)\xi(\mu+\xi)}}\right]^{\mu+1}.$$

Hence, from the above two equations, relation of $M$ to $P_0/P_1$ is easily computed. The theretical

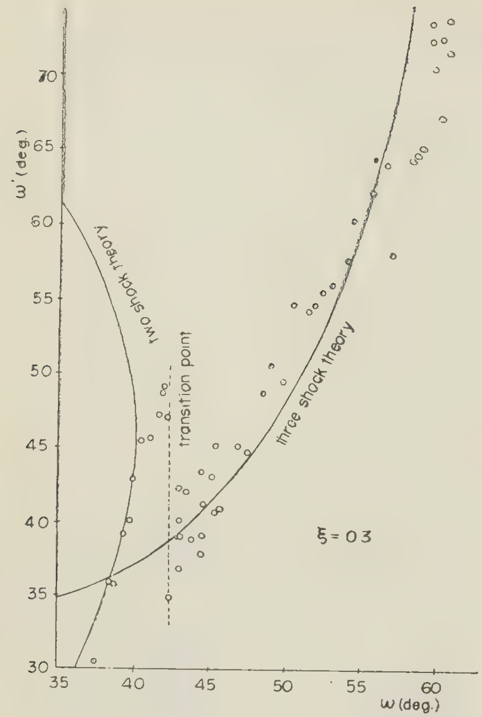

Fig. 9 (a).

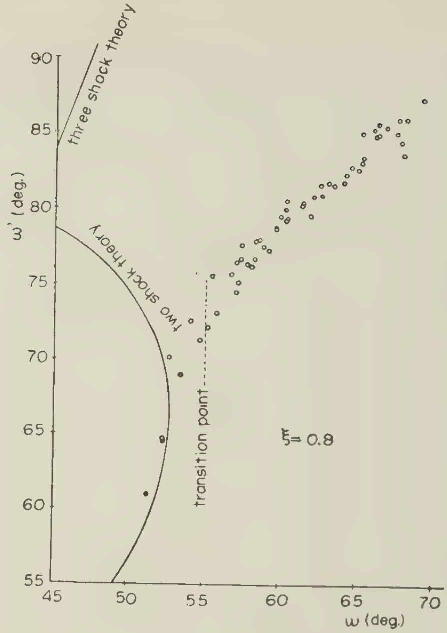

Fig. 9 (b).

result is shown in Fig. 8 by a solid line. Experimental results are also shown in the same figure. They show a systematic deviation from the calculated curve which is thought to be caused by viscosity and heat conductivity. Anyhow, we could almost regulate the shock strength by setting the initial pressures in the two chambers accurately at the predetermined values.

In the experiment $\xi$ was changed from 0.3 to 0.9 at an interval of 0.1. A series of tests was added at $\xi=0.35$. Angles of shocks were measured by the following way: the developed film was projected on a white paper and the shock fronts and wall surface were traced near the reflection point. These traced curves were approximated by 5-th order polynomials and the slopes at the triple points were computed by differentiation.

At the initiation of the transition from the regular to the Mach reflection, the length of the Mach stem is very short. Therefore, the occurrance of the transition cannot accurately be made distinct by the Mach stem. In case of a strong incident shock, the existence of the slip-stream behind the reflection point is a nice measure of making sure of the occurrance of the transition. In such cases, the slip-stream is seen clearly almost on the wall surface before the Mach stem is distinguished. In case of a weak incident shock, the slip-stream is faint on the schlieren picture and the determination of the transition becomes less accurate.

## § 4. Experimental Resulats and Comparison with the Theory

Examples of mesured shock angles are shown in Fig. 6 for cases of $\xi=0.8$ and 0.3. The definition of angles, $\omega$ and $\omega'$ is illustrated in Fig. 5. Theoretical curves of the regular and Mach reflections for the two cases are also given in solid lines. The boundary of the two types of reflection, or the critical value of $\omega$ at the transition, determined by observation of the schlieren pictures is marked by dotted lines.

In examining the figure one finds that experimental points agree farely well with the theory as far as the reflection remains regular. Even in this case, experimental points extend a little bit beyond the theoretical limit. The reason of the discrepancy is not clear for the time being. Very gradual growth of the Mach stem after the transition might make it impossible to make clear determination of the boundary by the picture observation method. This was already pointed out by White[8]. Since not only these two examples but also other experimental data show the same tendency, we can conclude that there is no essential deviations of the experimental results from the theoretical ones in the regular reflection.

Now, let us turn to the case of Mach reflection. The greatest difference between the case of $\xi=0.8$ and 0.3 seen in Fig. 9 appears at the transition. In the former, $\omega'$ changes almost continuously as $\omega$ increses through the transition point, while in the latter, it decreases discontinuosly. Moreover, deviation of the experimental results from the calculated ones are enormous in the weak shock case ($\xi=0.8$). When the incident shock is strong as is the case of $\xi=0.3$ in Fig. 9, such a substantial disagreement does not exist between theory and experiment. These results seem to give an experimental evidence of the validity of the theoretical discussion mentioned in § 2.

Fig. 10 shows the rate of growth of the Mach stem as $\omega$ is increased. The ordinate is the ratio of the distance from the triple point to the wall (roughly the same as the length of the Mach stem) to the length from the wedge tip to the triple point. The points surrounded by a circle on the $\omega$-axis are the transition points calculated by the theory. Though only two curves for $\xi=0.4$ and 0.6 are given in Fig 10, it is a general tendency that the curves obtained by the experiment seem to be tangent to the $\omega$-axis. It shows a very gradual growth of the Mach stem at the initiation of the Mach reflection. Because of this character of the Mach stem, accurate determination of occurrance of the transition by observation of the schlieren pictures is quite a difficult problem as mentioned beofore.

In case of a strong incident shock, the angle of the reflected shock, $\omega'$, takes two different values for one $\omega$-value at the transition as is seen in Fig. 9. The one corresponds to the regular reflection and the other to the Mach reflection. The former is always greater than the latter. We use the notation $\Delta\omega'$ to express difference of these two angles.

Fig. 11 shows the relation between $\Delta\omega'$ and $\xi$ obtained by the experiment. As mentioned before, the discontinuity never appeared for $\xi$ greater than 0.5. Three points in Fig. 11 which give finite values of $\Delta\omega'$ make it possible to draw approximte curve showing the variation of $\Delta\omega'$ with $\xi$. It is shown by a dotted line in Fig. 11. The curve intersects with the $\xi$-axis approximately at $\xi=0.42$. Discontinuous change of the reflected shock angle at the transition would not take place for $\xi$ greater than this critical value. It coincides very well with the one corresponding to the stationary Mach reflection case ($\xi=0.433$) already mentioned in § 2. Hence, it may be said that full experimental evidences are given to the

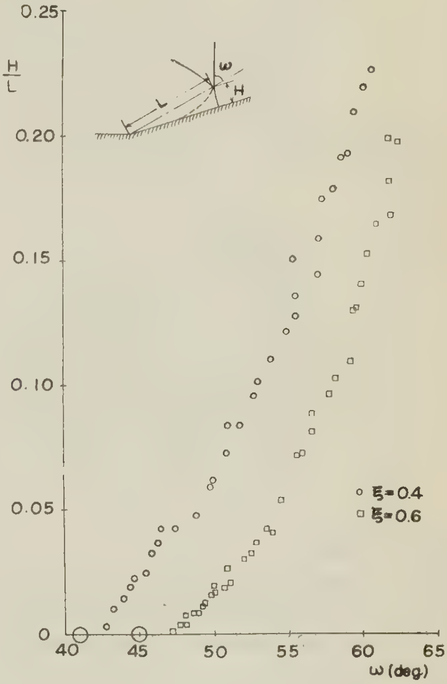

Fig. 10.

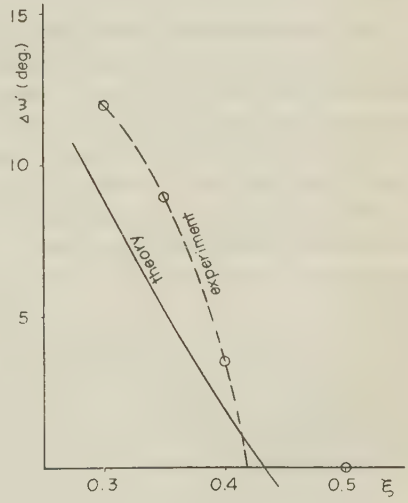

Fig. 11.

Table I.

| $\xi$ | $M_2$ | $\xi$ | $M_2$ |
|---|---|---|---|
| 0.3 | 1.0109 | 0.6 | 0.9992 |
| 0.35 | 0.9896 | 0.7 | 1.0116 |
| 0.4 | 0.9861 | 0.8 | 1.0088 |
| 0.5 | 0.9991 | 0.9 | 1.0203 |

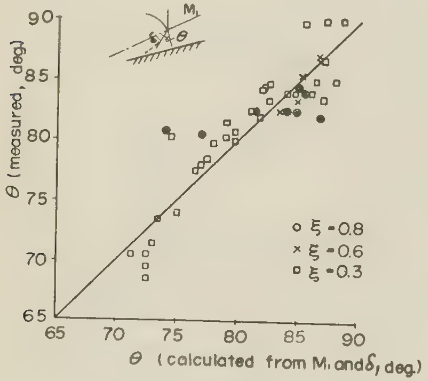

Fig. 12.

theoretical prediction stated in § 2 concerning the Mach reflection.

At the final stage of Mach refliction (large $\omega$) it happens that passage of the triple point does not change as the angle of attack of the wedge is decreased, and thus, both of $\omega$ and $\omega'$ remain unaltered. This corresponds to the state where the Mach number of the flow behind the incident shock measured relative to the triple point is just unity. This Mach number, $M_2$, is easily calculated from the strength and the angle of the incident shock obtained in the experiment. The $M_2$ values thus computed for the terminal points of $\omega-\omega'$ curves are shown in Table I. These values deviates slightly from unity. The deviation shows the accuracy of the present experiment.

Fig. 12 also shows comparison of theory and experiment on the angle of the Mach stem at the triple point. Since we can measure the Mach number of the flow in front of the incident shock relative to the triple point and also the direction of the slipstream there, we can compute the theoretical shock angle by applying the simple shock theory to the Mach stem. On the other hand, the angle can be measured in the schlieren pictures. These theoretical and experimetal shock angles are compared in Fig. 12. In case complete consistency exists between them, the experimential points must lie on a line of 45 deg. with the axes shown by a solid line in the figure. The agreement of the experiment with the theory is mostly good for $\xi$ equal to 0.3 and 0.6. Greater deviation is seen in case $\xi=0.8$ than the other two cases, which is mainly caused by inaccuracy of the angle measurement due to the faintness of the slip-stream in the schleren pictures. It must be noted, however, that such an agreement between theory and experiment does not necessarily mean non-existence of singularity at the triple point. A singularity such as an infinite curvature of the shock could not be found by these angle measurements if it does exist.

## § 5. Summary

Theoretical and experimental investigation has been made on shock reflection at a fixed wall. Theoretical analysis of shock polar diagrams on pressure-flow-direction plane has led us to a conclusion that the type of Mach reflection of weak incident shock would differ qualitatively from that of strong ones. The prediction has been fully confirmed by shock angle measurement in schlieren pictures obtained in shock tube experiment. Comparisons of theory and experiment also has been made concerning the terminal point of the Mach reflection and slope of the Mach stem.

In the end the authors' thanks are due to Prof. H. Oguchi for his stimulating discussions on the subject and also to Mr. K. Watanabe for his faithful assistance throughout the present study. Mrs. I. Noguchi helped the authors in preparing the manuscript.

### References

1) A. H. Taub: Phys. Rev. **72** (1947) 51.
2) W. Bleakney and A. H. Taub: Rev. Mod. Phys. **21** (1949) 584.
3) R. Kawamura: Rep. Aero. Res. Inst., Tokyo Imp. Univ. No. 328 (1945).
4) L. G. Smith: OSRD No. 6271 (1945).
5) R. Kawamura: J. Phys. Soc. Japan **6** (1951) 533.
6) A. Busemann: NACA TN No. 1858 (1949).
7) R. Kawamura and H. Saito: Rep. Inst. Sci. Tech., Tokyo Univ. **9** (1955) No. 4.
8) D. R. White: Proc. 2nd Midwestern Conf. Fluid Mech. (1952) 253.
9) F. B. Harrison and W. Bleakney: Rep. to ONR, Contract N6ori-105 Task II (1947).

JOURNAL OF THE PHYSICAL SOCIETY OF JAPAN Vol. 11, No. 5, MAY, 1956

# On the Coarsening of Non-Sag Tungsten Lamp Filament Wires

By Sunao OGHI

*Mitsubishi Mining and Metallurgical Laboratory, Omiya City, Saitama Pref.*

(Received April 19, 1955)

In order to make clear the non-sag nature of tungsten lamp filament its recrystallization behaviour was studied by means of microscopic scrutiny and X-ray diffraction.

Filament having sag nature begins the recrystallization in a preferred orientation related to initial fibre direction at temperature about 1000°C. This orientation is destroyed at about 1300°C, leading to an ordinary non-preferential polygon structure.

The subsequent grain growth is very slow even at considerably higher temperatures. On the contrary, with non-sag wires this oriented recrystallization is maintained up to 2000～2100°C, followed by the abrupt coarsening, in which the coarsened crystals encroach directly the remaining fibre structure. Thus, the coarsened crystals tend to occupy the whole cross-section of the wire, and the filament becomes finally to form a successive chain consisting of single crystals.

This phenomenon was interpreted as the inhibition dependent coarsening advocated by Beck and others in 1949. This inhibiting action in tungsten filament is most likely caused by the minute quantities of doped materials.

## §1. Introduction

It has well been established that the minute impurities doped into the tungsten metal for filament wire, such as $SiO_2$, $Al_2O_3$ and alkali metals, have dominant effects upon the recrystallization behaviour, which is supposed to govern the sagging property of filament wire.

Smithells[1)] brought forward many relationships between the minute doped materials and the recrystallization of tungsten filaments. He observed the recrystallization of the filaments annealed for various periods at a fixed temperature (2570°C), which had been instantaneously attained by direct application of over-voltage to the filaments. Consequently, his paper unfortunately lacks the description of intermediate stages of the recrystallization and their relation to the sagging properties of the filaments.

In Wulff's text book of powder metallurgy Wretblad[2)] discussed these problems, presuming that when additives of the proper amounts are used in conjunction exaggerated grain growth may occur in a preferred direction, because during the drawing of wire the inhibiting materials have been distributed as stringers parallel to the wire axis, thus preventing lateral diffusion. Thus at elevated temperatures diffusion and grain growth persist in the longitudinal direction, therefore grain boundary surfaces tending to favour an acute-angle orientation with respect to the wire axis. The anti-offsetting property of filament in subsequent use was supposed to be due to this geometrical configuration. Above interpretation, however, is rather illative, and has not been replaced with a more exact elucidation even in the recent text books[3)4)].

Another paper treating these problems was written by Robinson[5)], who measured quantitatively the grain growth velocities after recrystallization by the cylindrical electron emission microscope. He proposed the small grain hypothesis, according to which the mechanism of recrystallization is pictured as follows:

*Fibre⟶small grain⟶large crystals.*

Nishidoi and Kasamatsu[6)] studied the recrystallization of tungsten filaments at the stepwisely elevated temperatures. They showed that with non-sag wires the exaggerated grain growth commenced at temperature about 1400°C, and the grain growth velocity obtained by them was in qualitative agreement with Robinson's results.

In the mean time, since the beginning of this decade the studies of secondary recry-

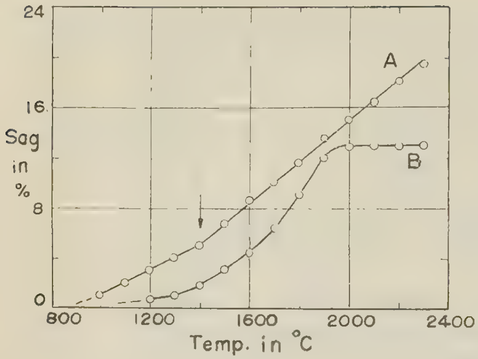

Fig. 1. Sag *versus* temperature curves. Sag was measured after 5 min keeping at each temperature. A slight concave bent in curve **A** is indicated by an arrow.

stallization or coarsening have become active, chiefly by the group of Kronberg and Wilson(7) and of Beck, Sperry and Hu(8). They proved the existence of the inhibition dependent as well as texture dependent coarcening. Since these theories are based upon the experiments on the high purity aluminium or copper crystals, where the orientation dependencies were clearly determined, we have as yet very little information as to the interpretation of recrystallization of sintered material such as tungsten filament on the line of these new theories.

The purpose of the present study is to elucidate the mechanism of recrystallization of non-sag tungsten filaments by the picture of oriented recrystallization and coarsening, adopting the microscopic scrutiny and *X*-ray diffraction analysis as experimental methods.

## § 2. Experimental

### 1) *Specimens*

Ammonium-paratungstate, refined from wolframite of Takatori mine, was reduced to oxides and then re-reduced to metal powder in hydrogen stream.

Before the final reduction, materials so-called insoluble in tugsten, $SiO_2$, $Al_2O_3$, and soluble alkali metals, potassium, sodium, in the form of silicates or chlorides, were doped into the oxides simultaneously.

To compare the recrystallization properties of filament wires of sag and non-sag nature, the specimen filaments were prepared in the following way: for non-sag ones 0.03% and for sag ones 0.11% of alumina were doped into the oxides, while the other materials were doped as usual in equal quantities for each series of specimens. These powders were pressed, sintered and worked under the same conditions to about 8 MG (about 0.05 mm in diameter) filament wires for single coiled 60 Watt hous lamp.

### 2) *Apparatus*

Heat treatments of specimen and measurements of sagging were carried out in a hard glass bulb of 10 cm in diameter, through which passed the hydrogen gas. The coiled filaments were supported in every time with the same span as in 60 Watt lamps. The sagging magnitude of each filament was measured on the optical image of the incandescent filament focused by a fixed camera. Temperatures of the filaments were roughly measured by the optical pyrometer without precise calibration, since only relative temperature difference between specimens sufficed the present purpose.

## § 3. Results

### 1) *Sag increase with temperatures*

The sag of filaments was measured at each temperature in the following way: after 5 min keeping at any desired temperature, which had been attained in about 3 sec from room temperature by the sudden application of an a c voltage. The reason for choosing 5 min as a duration of keeping at desired temperature is that the recrystallization of non-sag wires completes usually in this period. Although the recrystallization of sag wires is slow, the above 5 min keeping seems to afford a sufficient measure for comparison between the two types of filaments.

In Fig. 1 the obtained sagging magnitude, represented by percentage scale, *versus* temperature curves are shown, where curve **A**, which has a slight concave bent at 1400°C, represents the nature of sag wire. This curve shows a linear increase of sagging with temperature above 1400°C, saturating by no means in the present temperature range; this is the general feature of the sag wires.

With the non-sag wire, the sag curve, *e. g.* curve **B**, shows a quite different feature; *i.e.*, there is no bent point in the neighbourhood of 1400°C, the sag being very little in this region, then it increases until the saturation at 1900~2000°C. This situation that the

Series ***A***.

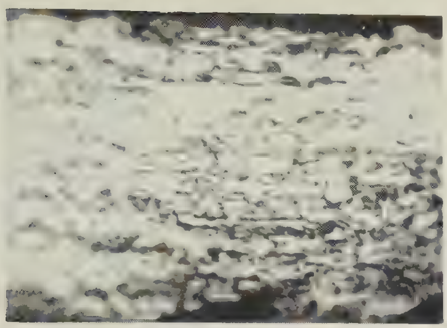
Photo. 1 **a**. 1300°C

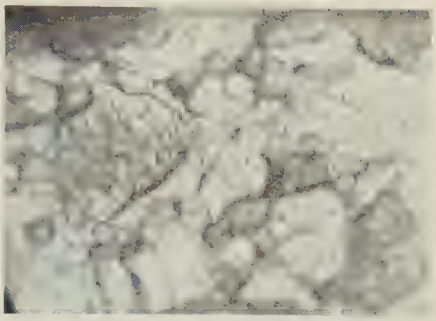
Photo. 2 **a**. 2000°C

Series ***B***.

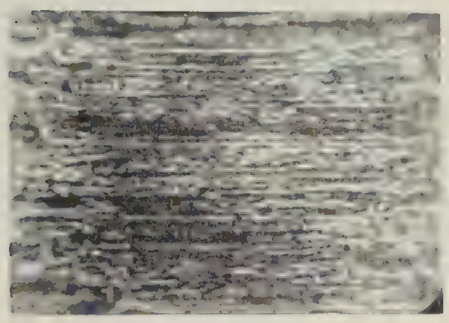
Photo. 1 **b**. 1300°C

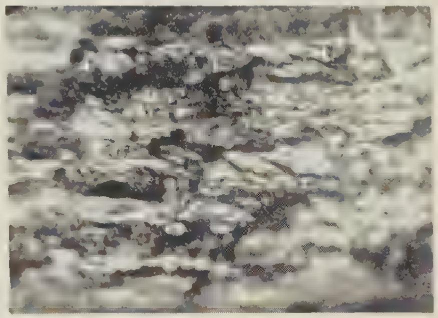
Photo. 2 **b**. 2000°C

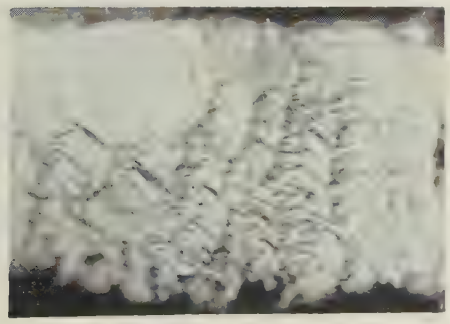
Photo. 3 **b**. 2000°C

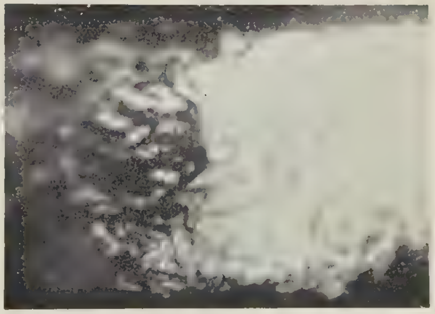
Photo. 4 **b**. 2000°C
(fibre) (single)

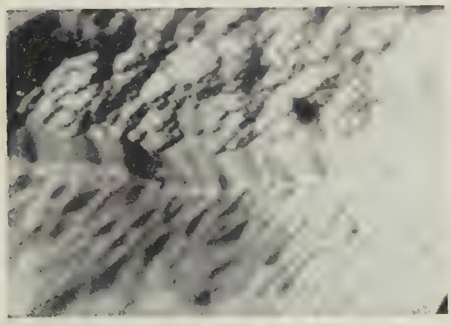
Photo. 5 **b**. 2000°C

Fig. 2. (×1000)

Recrystallization textures of coiled filaments. Series ***A*** represents the textures of sag wires, and Series ***B*** the non-sag ones. The temperatures of treatment are given at the bottom of each photographs. The thickness and the longitudinal direction of the specimen wires correspond practically with the vertical length and the traverse direction of each photographs respectively.

non-sag wire exhibits actually a certain sagging in the present condition is most likely ascribed to the probable deformation of filament due to the evapolation of tungsten into the flow of the hydrogen stream. In fact, when these filaments are heated in the gas-filled and sealed-off lamps, the sagging is almost negligible.

Be the matter as it may, the radical difference between the sagging tendencies of

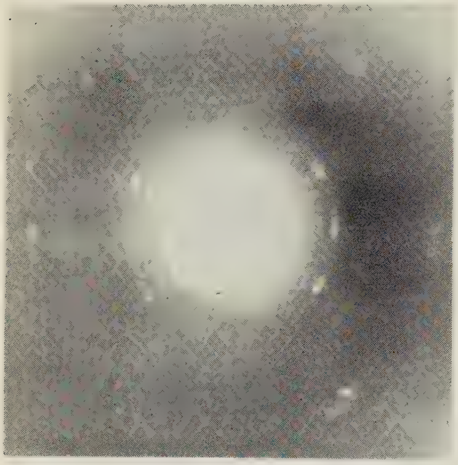

Photo. 1. 1800°C

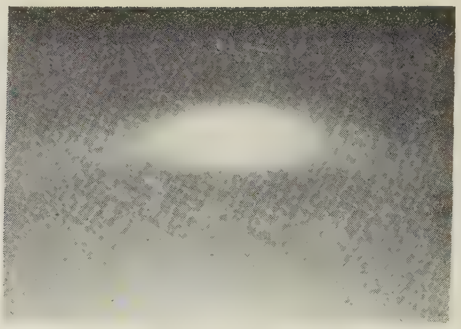

Photo. 2. "as drawn"

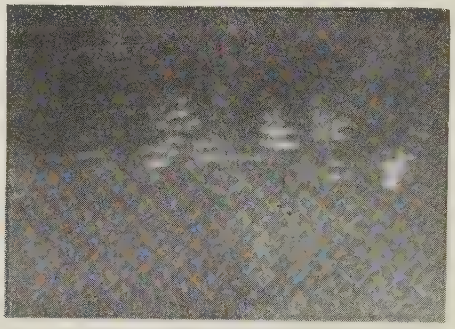

Photo. 3. 1700°C

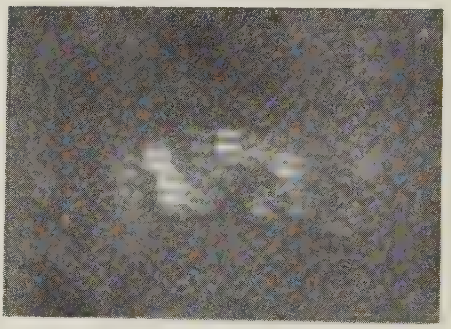

Photo. 4. 2000°C

Fig. 3.

A back reflected Debye-Scherrer pattern, and a series of a change of one of the diffuse spots on the (321) ring with temperatures, of non-sag tungsten wires. The discete small spots, representing the recrystallized fibre texture, become larger at the expnese of their decrease in number, while their distributed area remains approximately constant. This tendency is corresponding to the proceding of oriented recrystallization and to the persistency of the tolerance of fibre orientation.

two sorts of filaments has been pointed out in these experiments.

2) *Microscopic scrutiny of recrystallization textures*

In Fig. 2, two series of photographs represent two types of the recrystallization textures of coiled filaments. Series ***A*** corresponds to curve **A** in Fig. 1, of sagging nature, and series ***B*** to curve **B**, of nonsagging.

Photos. 1**a** and 1**b** show the fibre textures of specimen wires, heat treated at 1300°C for 5 min. In Photo. 1**b** slightly broadened fibre crystals of non-sag wire are seen, while in 1**a**, among the appreciably broadened fibre crystals, the newly formed crystallites are observed.

This phenomenon is regarded as the beginning of recrystallization in ordinary meaning, corresponding most likely to the concave bent point of the curve **A** in Fig. 1 of sagging wire. By further elevation of the temperature these recrystallized new cryslallites increase in number, while the fibre orientation becomes less predominant. Above 1800°C the fibre orientation completely disappears, while the slow grain growth proceeds until the non-preferential structure, such as encountered in molten metals is formed (Photo. 2**a** of heat treated at 2000°C). Even at 2300°C, the grain growth does not proceed so extensively as to occupy the whole cross-section of the wire in the present experimental procedures.

With non-sag wire, on the contrary, the fibre orientation remains completely up to

1900°C, and it does remain partly even at as high as 2000 to 2100°C (Photo. 2**b**), although the fibre texture becomes coarser with increasing temperature. This behaviour clearly corresponds to the increasing region of curve **B** in Fig. 1. Then abruptly are formed the large crystals occupying the whole cross-section of the wire (*e. g.* Photos. 3**b** and 5**b**), so that the wire becomes to form a successive chain consisting of single crystals. The crystal growth under this condition is so rapid in spite of the very gradual temperature rise that we could find no germs, which usually be generated at inter-fibre boundaries.

For this reason this phenomenon should be assumed as the so-called " coarsening ", which was observed with aluminium or copper crystals by Beck and others in 1949[8)]. If this assumption is valid, the structural change preceding the coarsening must be an inhibited recrystallization in Beck's meaning, which is illustrated as the thickening of fibres in Photos. 1**b** and 2**b**, and will be shown more clearly by *X*-ray diffraction in the next paragraph.

Now, taking into account the fact that the less the quantity of doped alumina the more increases the possibility of coarsening, while the undoped pure tungsten wires have no sign of coarsening, and that the recrystallization temperature of sag wires is lower than that of non-sag ones, the nature of coarsening is appropriately regarded as an inhibition dependent one. To realize the coarsening it seems necessary to combine several doping impurities in optimum quantities.

Then, turning to the configuration of coarsened crystals, they usually grow directly at the expense of residual fibre crystals, as shown in Photo. 4**b**, where the bright right half is a single crystal and the left side is a residual fibre structure. Therefore the boundaries, encroaching the fibre texture, are reasonably expected to proceed along the inter-fibre boundaries, which are parallel to the wire axis. Accordingly, after this coarsening process, considerable large parts of the newly formed grain boundaries are to be oriented parallel to the wire axis at the expense of the former fibre texture (Photo. 5**b**).

Thus we have put forward a new interpretation for formation of the anti-offsetting longitudinal grain boundaries in terms of inhibiting oriented recrystallization and coarsening.

### 3) *X-ray diffraction analysis of non-sag wires*

Back reflected Debye-Scherrer rings from characteristic ray of Cu $K\alpha$ recorded on flat films and a series of one of the spots on the (321) rings are reproduced in Fig. 3, where the temperatures of treatment are given under each photographs.

Photo. 1 is a tipical pattern of fibre texture, showing the appreciable oriented recrystallization promoted by the heat treatment of 1800°C. And, in order to show a detailed feature, a change of one of the spots with temperatures is shown in Photo. 2 to 4. The diffuse spots of " as drawn " wire (Photo. 2), caused by the preferred orientation of thin fibres, tend to form aggregates of discrete small spots as the temperature rises, then the small spots become larger at the expense of their decrease in number. This tendency corresponds to the proceeding of oriented recrystallization, *i. e.*, to the thickening of fibre crystals, as shown in Photos. 3 to 4, and has also been shown in the series ***B*** of Fig. 2 in the preceding papagraph, *e.g.*, Photos. 1**b** and 2**b**. The area, over which the discrete small spots are distributed, remains approximately constant irrespective of treated temperatures, showing that the tolerance of fibre orientation is not changed by this oriented recrystallization*.

At higher temperatures, *i. e.* 2000 to 2100°C, besides these discrete small spots, the spots of a new kind reflected from the coarsened large crystals appear (corresponding to those in Photo. 4**b** of Fig. 2, where the fibre texture and the coarsened large crystals are in coexsistence).

These results from *X*-ray study are in good agreement with those from microscopic scrutiny, by which alone the persistency of the tolerance of fibre orientation has not been proved.

---

* Besides this, the doublets due to the $K\alpha_1$ and $K\alpha_2$ radiations as well as the splitting of the spots of other kind are seen. These were mentioned and discussed in detail by Becker[9)]. Nevertheless the detailed description of this kind is ommited here, because it has no relation to the essential proceeding of present argument.

## § 4. Discussion and conclusion

In regard to inhibition dependent coarsening of non-sag tungsten wire, the picture offered by Robinson,

*Fibre⟶small grain⟶large crystals,*

should be replaced by new one, i. e.

$$\textit{Fibre} \longrightarrow \begin{array}{l}\textit{inhibiting}\\ \textit{oriented}\\ \textit{recrystallization}\end{array} \longrightarrow \begin{array}{l}\textit{coarsened}\\ \textit{large}\\ \textit{crystals.}\end{array}$$

Coarsening temperature of non-sag wire, formerly called "germinative" or "exaggerated grain growth" temperature by the precedent researchers, generally ranges between 1700° and 2000°C, and the higher this temperature the surer the non-sag characteristics are garanteed.

Now turning to the problem of sagging, it has been generally said, the sagging is supposed to result from a slip of inter-crystalline boundaries. If so, for preventing the sagging there is no remedy but to reduce the slipping boundary area by the breaking out of coarsening. This coarsening also contributes to the easy formation of the anti-offsetting longitudinal boundaries in the way described in preceding section, where the encroaching behaviour of coarsening crystals against the fibre texture has been elucidated.

Thus, the present paper has clarified several essential points underlying the sag and non-sag natures of tungsten filaments.

## Acknowledgement

The author is grateful to Mr. K. Asada, former director of our laboratory, for his support and permission to publish this article, and to Dr. Koto, professor of Ehime University, for his encouragement and discussion. The author is also indebted to Mr. Sawada and Dr. Hijikata, manager and chief researcher of our laboratory, respectively, for their continuous interest and reading the manuscript.

## References

1) C. J. Smithells: J. Inst. Met. **24** (1922) 194.
C. J. Smithells: Trans. Faraday Soc. **14** (1921) 485.
2) J. Wulff: "*Powder Metallurgy*", Am. Soc. Met. Cleveland, Ohio. (1942) 420.
3) P. Schwarzkopf: "*Powder Metallurgy*", MacMillan Co. (1947).
4) C. G. Goetzel: "*Pewder Metallurgy*", Interscience Pub. Incorp. (1949).
5) C. S. Jr. Robinson: J. App. Phys. **13** (1942) 647.
6) T. Nishidoi and T. Kasamatsu: Tech. Rep. of Kobe Kogyo, No. **12** (1951) 8.
7) M. L. Kronberg and F. H. Wilson: Trans. A. I. M. E. **185** (1949) 501.
8) P. A. Beck and H. Hu: J. Met. **1** (1949) 627.
P. A. Beck and P. R. Sperry: J. App. Phys. **21** (1950) 150.
P. A. Beck, P. R. Sperry and H. Hu: *ibid*, 420.
9) K. Becker: Z. Phys. **42** (1927) 226.

JOURNAL OF THE PHYSICAL SOCIETY OF JAPAN Vol. 11, No. 5, MAY, 1956

# Spark Ignition of Flowing Gases

By Itsuro KIMURA and Seiichiro KUMAGAI

*Department of Aeronautics, Faculty of Engineering,*
*University of Tokyo*

(Received January 12, 1956)

Spark ignition of flowing gases is investigated experimentally at room temperature and atmospheric pressure. Under laminar condition the inflammability of flowing gases increases with gas velocity. This is due to the tendency of initial flames to escape from the quenching effect of electrodes under the influence of gas flow. Under turbulent condition the inflammability of flowing gases decreases with increasing gas velocity. This is ascribed to the increased eddy diffusivity and is in accordance with the result of Swett's experiment under turbulent condition at reduced pressures.

## § 1. Introduction

There have been many investigations on spark ignition of gas mixture. Nevertheless, the phenomenon of spark ignition could not be understood properly till recent years owing to its complex nature connected with spark characteristics, reaction kinetics, quenching effect of electrodes, etc. In practical problems, as in internal combustion engines and jet engines, there exists additionally the relative motion between gas mixtures and spark electrodes more or less.

There have been Swett's report (1) about spark ignition of flowing gases. He performed the experiment at pressures ranging from 2 to 4 inches mercury absolute under turbulent condition and concluded that the spark energy required for ignition increased with gas velocity.

The investigation described below is performed over the wide range of gas velocity including laminar and turbulent conditions at atmospheric pressure.

## § 2. Apparatus and Procedure

City gas-air mixtures are used. In the experimental arrangement shown in Fig. 1, orifices 1 and 2 are used for measuring mixture ratio, and orifice 3, for mass flow in the ignition unit. Gas velocity can be regulated by a control valve from 0 to 80 m/s at the spark gap, where the pressure of a flowing gas is almost atmopspheric.

Two kinds of ignition units are used. In the case of the ignition unit A shown in Fig. 2, the mixture flows with a nearly uniform velocity profile in the bakelite nozzle, which supports the spark electrodes, and issues out into atmosphere. The ignition unit B is essentially a glass piping of 5 mm inner diameter as shown in Fig. 3. The spark gaps of both ignition units are made up of two iron wires of 1 mm diameter with ends rounded off into a hemisphere.

A mercury-switch with a parallel condenser of 0.4 microfarad is used to break the primary current of the ingition coil. In this paper, the ignition coil spark which is not modified is called "normal spark", and the spark, which is produced with a condenser of sufficient capacity connected across the spark gap, is called "capacity spark".

When ignition occurs in the ignition unit A, a stationary flame is established outside the nozzle in the case of gas mixtures used, and in the ignition unit B, a flame is seen to propagate in its glass part.

For the purpose of photographing initial flames by the schlieren method, the park gap is located just outside the nozzle of ignition unit A. The time interval between ignition spark and light source spark of the schlieren method depends upon the time constant RC of the cyratron circuit shown in Fig. 4.

## § 3. Results and Discussion

Figs. 5–9 show the ignition percentage versus gas velocity relations for different values of the primary break current of the ignition coil. The ignition percentage is determined by ten or more trials of sparking. In these experiments the ignition unit A is used, and

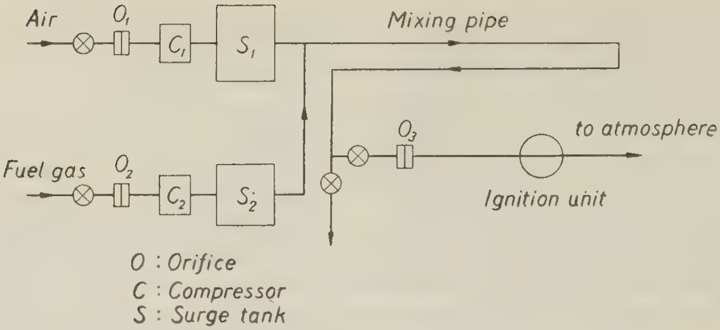

Fig. 1. Mixture control system.

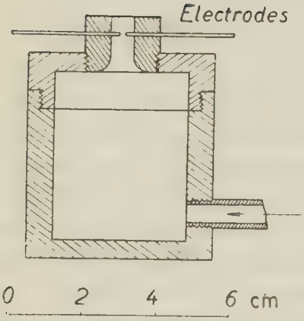

Fig. 2. Ignition unit A.

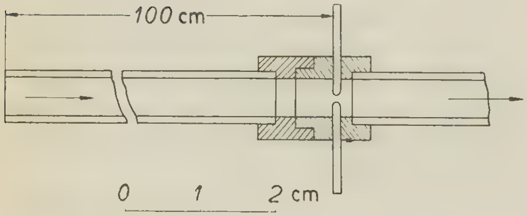

Fig. 3. Ignition unit B.

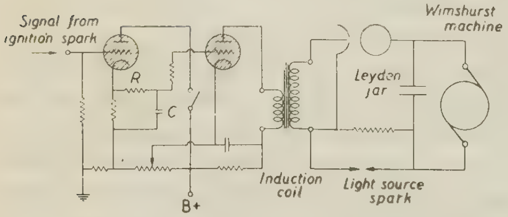

Fig. 4. Electronic system for instantaneous schlieren photography.

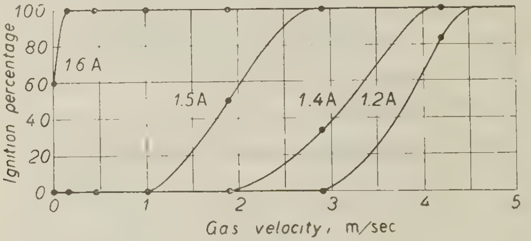

Fig. 5. Inflammability vs. gas velocity for different break current.
34% by volume city gas,
0.4 mm gap width, normal spark.

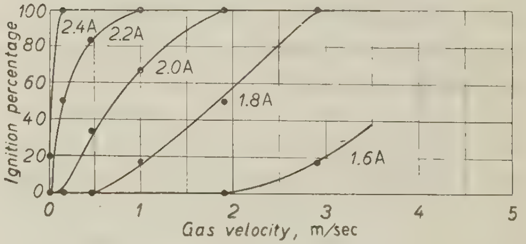

Fig. 6. Inflammability vs. gas velocity for different break current.
37%, 0.7 mm, normal.

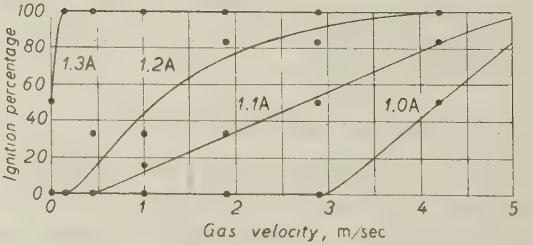

Fig. 7. Inflammability vs. gas velocity for different break current.
38%, 1.0 mm, normal.

the gas flow in the nozzle is kept laminar always. The ignition percentage for zero gas velocity is obtained from experiment with a quiescent gas mixture in a closed vessel containing the nozzle piece in it. Detailed experimental conditions are written in the notes of the figures. Figs. 8 and 9 show the case of needle electrodes and the case of capacity sparks, respectively. It is found that the inflammability is the lowest in the quiescent state and increases with gas velocity.

For the experiment ranging from laminar to turbulent condition the ignition unit B is

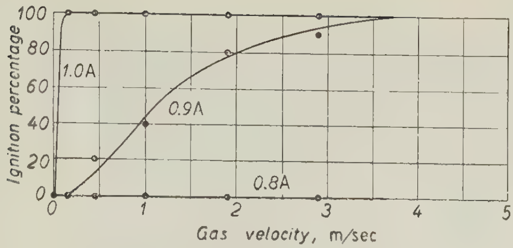

Fig. 8. Inflammability vs. gas velocity for different break current.
36%, 0.7 mm needle gap, normal.

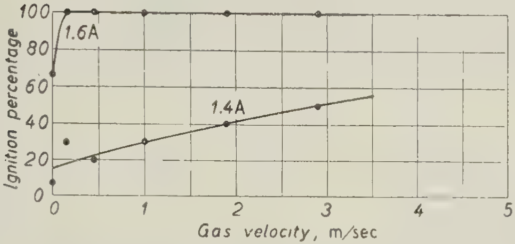

Fig. 9. Inflammability vs. gas velocity for different break current.
36%, 0.7 mm, capacity.

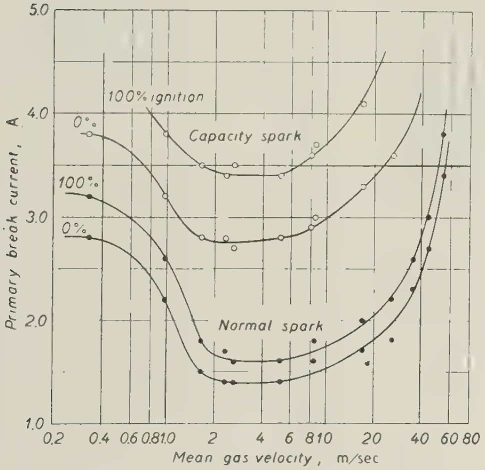

Fig. 10. Inflammability vs. gas velocity.
30% by volume city gas,
0.58 mm gap width.

used. Fig. 10 shows the influence of the gas velocity on the inflammability of flowing gases. In these experiments the relative inflammability is expressed by the critical primary break current of the ignition coil for 0 or 100 percent ignition. 30 percent by volume city gas-air mixtures are used and the spark gap is held at 0.58 mm width. It is found that the incendivity of a normal spark is greater than that of a comparable capacity spark in the same manner as in the spark ignition of quiescent gas mixtures (2).

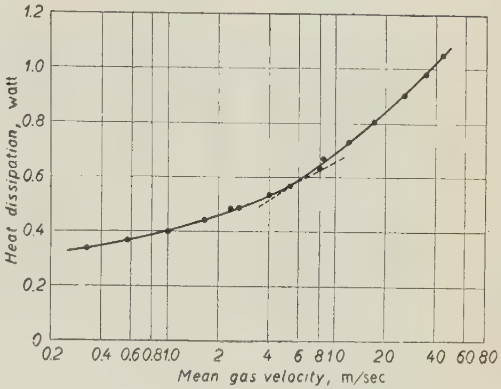

Fig. 11. Heat dissipation vs. gas velocity.

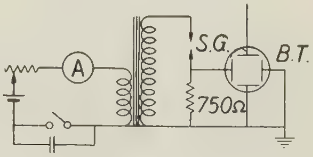

Fig. 12. Measuring system for discharge current.

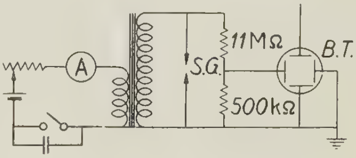

Fig. 13. Measuring system for discharge voltage.

When gas velocity is low enough for laminar flow, the inflammability increases with it similarly as that described above. But the inflammability decreases with increasing gas velocity above 5 m/s.

In order to find the transition point from laminar to turbulent flow, heat dissipation from a hot wire is measured. For this purpose a platinum wire of 0.05 mm diameter and 5 mm length is inserted into the ignition unit in place of the spark gap, its temperature being kept constant (at 250°C). The result of measurement shown in Fig. 11 reveals that the transition velocity is about 5 m/s, suggesting some unfavourable effect of turbulence on spark ignition.

Figs. 12 and 13, respectively, show the measuring systems for the discharge current and voltage of the ignition coil sparks by means of a Braun-tube oscilloscope. Examples of oscillograms are reproduced in Fig. 14. Fig. 15 shows the duration and current of the inductance component plotted against gas (air in this case) velocity. In this figure the

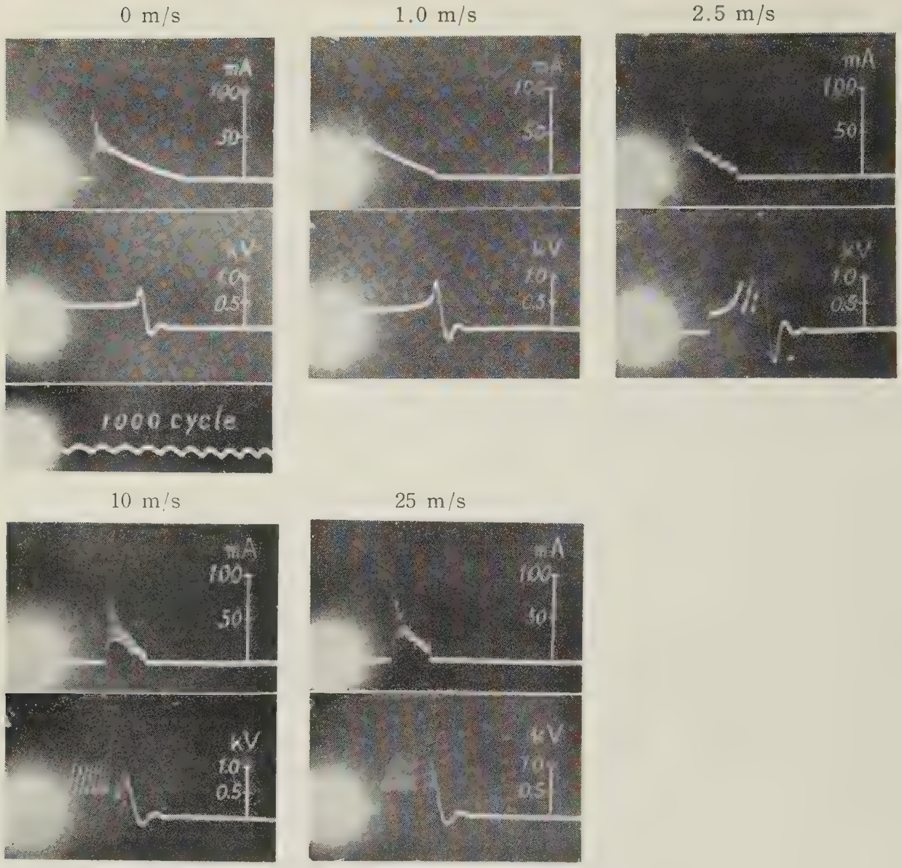

Fig. 14. Discharge current and voltage vs. gas velocity.
0.6 mm gap width, 2.5 A break current.

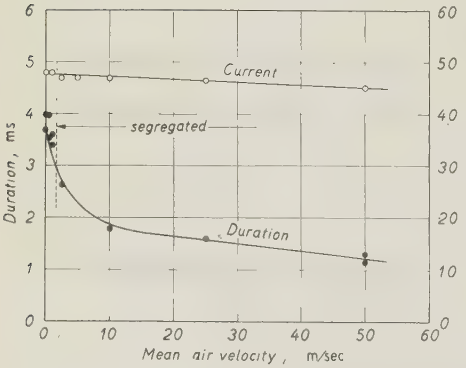

Fig. 15. Effect of gas velocity on spark characteristics.
0.6 mm gap width,
2.5 A break current.

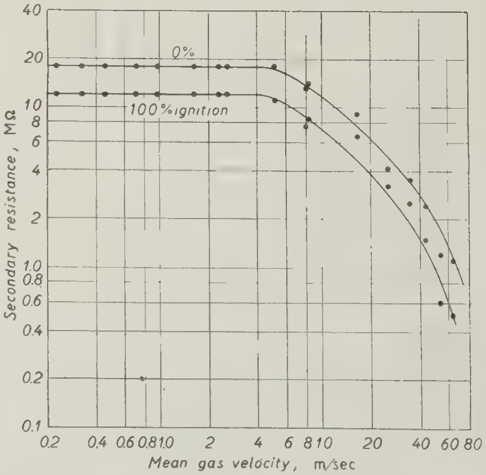

Fig. 16. Inflammability vs. gas velocity.
30% by volume city gas,
5.0 mm gap width.

current means the height of the mean line about which the initial oscillations occur.

Gas flows have some effects on the spark characteristics, especially in normal sparks as shown in Figs. 14 and 15. When gas velocity is low, its effect on a normal spark is not so remarkable, except that the duration is shortened and the voltage trace rises towards the end of discharge. As gas velocity increases, the

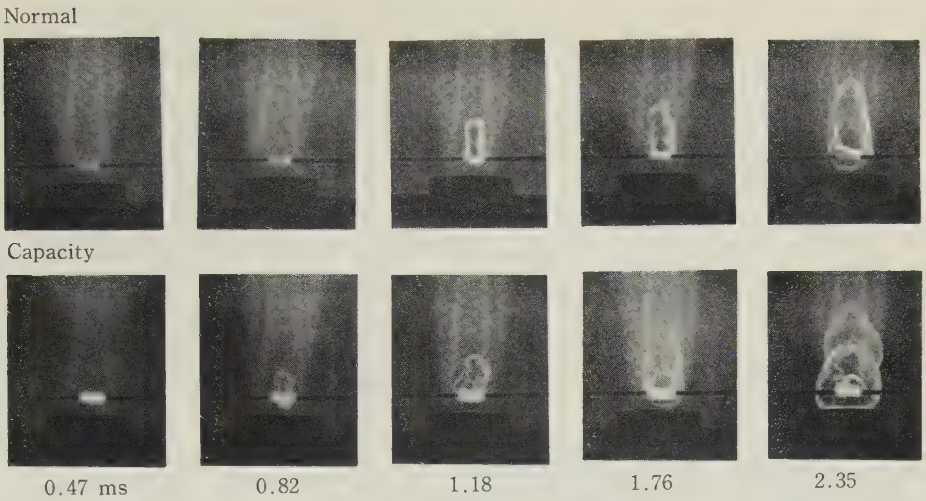

Fig. 17. Growth of initial flames.
2.9 m/s gas velocity, 40% by volume city gas, 3.5 mm gap width, 1.8 A break current.

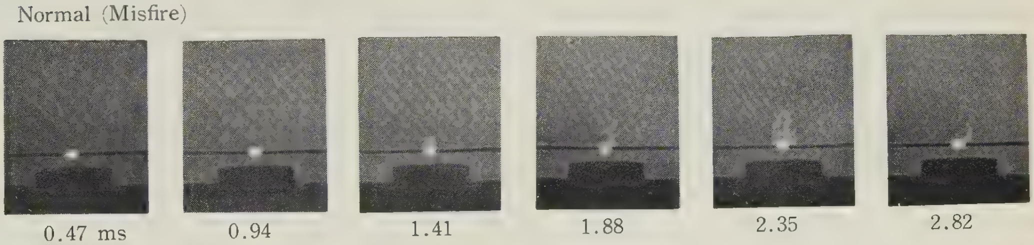

Fig. 18. Initial flames in misfire. 1.4 m/s, 40%, 1.5 mm, 1.5 A.

spark begins to segregate into successive parts, the number of which increases with gas velocity. The first part is the most energetic, and the energy of the following parts decreases gradually. So it may happen that they are scarcely available for ignition. But it is reasonable to suppose that the increased turbulence is the essential cause of hard ignition on the basis of the fact that the inflammability decreases with increasing gas velocity under turbulent condition with capacity sparks also.

As a special case, the spark gap is widened until the ends of electrodes are just on the inner surface of the ignition unit B. The spark energy is controlled by changing the series water resistance inserted into the the seconday circuit of the ignition coil, since the incendivity of this spark cannot be varied to the desired extent by adjusting the primary break current. From the result shown in Fig. 16, it is noted that the inflammability remains exactly constant under laminar condition. This is to be expected from the fact that the cooling effect of electrodes is masked by that of the pipe wall of the ignition unit. Under turbulent condition, the inflammability decreases with increasing gas velocity similarly as in the case shown in Fig. 10.

Figs. 17 and 18 are the examples of the instantaneous schlieren photographs of initial flames under laminar condition, the latter being the case of misfire. The initial flame at any instant is shifted downstream according to gas velocity on these photographs, and this suggests the reduction of cooling of initial flames by electrodes.

## § 4. Conclusion

The inflammability of gas mixtures is the lowest in the quiescent state and increases with gas velocity under laminar condition. The most appropriate explanation of this fact is probably that the initial flame is shifted downstream under the influence of gas flow and thereby the cooling effect of electrodes on it decreases with increasing gas velocity. The fact that the inflammability of flowing gases under turbulent condition decreases with increasing gas velocity is possibly due to the suppression of ignition by the increased eddy diffusivity.

### References

1) C. C. Swett, Jr.: NACA Research Memo. no. E9E17, August 1949.
2) S. Kumagai, T. Sakai and I. Kimura: Journal of the Faculty of Engineering, University of Tokyo, vol. 24, no. 1, January 1953, pp. 9–23.

---

# Short Notes

This section is intended to secure prompt publication of important discoveries in physics. The reports should not exceed 800 words in length. A figure of size 7 cm × 7 cm will be counted as 150 words.

J. PHYS. SOC. JAPAN **11** (1956) 604~605

## On the Uniaxial Anisotropy Induced by Magnetic Annealing in Ferrites

By Satoshi TANIGUCHI and Mikio YAMAMOTO

*Research Institute for Iron, Steel and Other Metals, Tohoku University, Sendai*

(Received January 26, 1956)

Quite recently, Bozorth *et al.*[1] have studied the effect of magnetic annealing in single crystals of cobalt zinc ferrite ($Co_{0.32}Zn_{0.24}Fe_{2.18}O_4$) and found that the induced uniaxial anisotropy, $F$, can be expressed as follows;

$$F=-K_u(\Sigma_i\alpha_i\beta_i)^2\ , \tag{1}$$

where $K_u$ is the anisotropy constant of the order of magnitude of about $10^6$ erg/cm³, and $\alpha_i$'s and $\beta_i$'s are the direction cosines of magnetic field present during annealing and of magnetization vector, respectively, with respect to the crystallographic axes. It seems, at first sight, that such magnitude and orientational dependence of the uniaxial anisotropy is puite different from those proposed previously by us[2] and by Néel[3] for metallic ferromagnetic solid solutions. However, they can also be interpreted by our theory modified slightly so as to be appropriate to the case concerned here, which will be shown in this note.

Now, ferrites, which have so far been found responsive notably to magnetic annealing, are those containing cobalt ferrite. Cobalt ferrite of the stoichiometric composition, however, shows a very small induced anisotropy[1], especially in the state heat-treated in *vacuo*[4], indicatiing that the presence of cation vacancies may be responsible for the induced uniaxial anisotropy as suggested by Iida *et al.*[4] Moreover, in cobalt zinc ferrite, non-magnetic $Zn^{2+}$ ions, which may be regarded as the same as cation vacancies magnetically, distribute on 8f sites and some of them probably distribute on 16c sites, too. So, we may consider, for simplicity, a mixed ferrite of the type

$$N_{n_f}M_{1-n_f}(N_{2n_c}M_{2(1-n_c)})O_4\ ,$$

where $N$ denotes a non-magnetic cation or cation vacancy, $M$ a magnetic cation, and $n_f$ and $n_c$ are the concentrations of $N$ on 8f and on 16c sites, respectively.

Let us consider the anisotropic distribution of $M$ and $N$ in the equilibrium state at a temperature, $\Theta$, below the Curie point. The probability $\omega_{ij}$ $(i, j=c, f)$ finding $N$ on one of $j$ sites in the nearest neighbors of $N$ on $i$ sites is given by

$$\omega_{ij}=(1/z_{ij})\exp\{-\varepsilon_{ij}C_{ij}B_i(\Theta)B_j(\Theta)(1-3\cos^2\phi_\Theta)/k\Theta\}\ , \tag{2}$$

where a constant of dipole interaction, $C_{ij}$, is expressed as $C_{ij}=C_{M_iM_j}+C_{N_iN_j}-(C_{M_iN_j}+C_{M_jN_i})$, and a numerical factor $\varepsilon_{ij}$ is $+1$ for $i=j$ or $-1$ for $i\neq j$. Moreover, $z_{ij}$ is the number of nearest neighbors in $j$ sites of $N$ on $i$ sites, $\phi_\Theta$ the angle between magnetization vector at the temperature $\Theta$ and a nearest neighbor direction, $k$ Boltzman's constant, and $B_i(\Theta)$ the averaged magnetization for $i$ sites at the temperature $\Theta$. Then the induced uniaxial anisotropy, $F$, at a temperature, $T$, is given by

$$F=(1/2)\sum z_{ij}n_j\omega_{ij}\varepsilon_{ij}C_{ij}B_i(T)B_j(T)(1-3\cos^2\phi_T), \tag{3}$$

where $\sum$ denotes the summation over all of the nearest neighbors on $i$ and on $j$ sites around all of $N$ on $i$ and on $j$ sites.

Since the large anisotropy of ferrite containing cobalt ferrite may be caused by a contribution from the interactions between 16c and 16c as well as between 16c and 8f sites, we can neglect in Eq. (3) the summation over $i=j=f$. Expanding $\omega_{ij}$ (Eq. (2)) into power series of $C_{ij}/k\Theta$, retaining only first order term of $C_{ij}$, further assuming reasonably $n_c \approx n_f (=n)$, $C_{cc}{}^2 \approx C_{cf}{}^2 (=C^2)$ and $B_c(\Theta)B_c(T) \approx B_f(\Theta)B_f(T)(=B(\Theta)B(T))$, we have the following expression:

$$F = -(5697/242)(N_m n^2 C^2 B^2(\Theta) B^2(T)/k\Theta) \times \{(\Sigma_i \alpha_i \beta_i)^2 - (174/633) \sum_{j>i} \alpha_i \alpha_j \beta_i \beta_j\}\ , \quad (4)$$

where $N_m$ is the number of molecules in unit volume. Evidently the second term in Eq. (4) is negligibly small. Thus we have got the induced anisotropy $F$ of the same form as Eq. (1). Moreover, the calculation of the magnetocrystalline anisotropy energy using the above model has shown that the induced uniaxial anisotropy and the magnetocrystalline one are the same in the order of magnitude.

Eq. (3) indicates that the orientational dependence of the uniaxial anisotropy depends on both the concentration of $N$ distributed among 16c and 8f sites and the kind of magnetic cations responsible for the anisotroy, so that it may vary with the kind of ferrites. For example, if the uniaxial anisotropy is caused by the anisotropic distribution of $M$ and $N$ on 16c sites alone, which may probably be the case of iron cobalt ferrite, the orientational dependence becomes the same as that of metallic face-centered substitutional solid solutions. It is to be added, further, that the occurence of a maximum of uniaxial anisotropy in iron cobalt ferrite solid solutions[1)4)] can also be explained in terms of Eq. (3).

## References

1) R. M. Bozorth, E. F. Tilden and A. J. Williams: Phys. Rev. **99** (1955) 1788.
2) S. Taniguchi and M. Yamamoto: Sci. Rep. Res. Inst. Tôhoku Univ. **A 6** (1954) 330.
S. Taniguchi: ibid. **A 7** (1955) 269.
3) L. Néel: J. de phys. rad. **15** (1954) 225.
4) S. Iida, H. Sekizawa and Y. Aiyama: J. Phys. Soc. Japan **10** (1955) 907.

---

J. Phys. Soc. Japan **11** (1956) 605~606

# Electron Bombardment Conductivity in Silver Bromide Single Crystal II

By Chiyoe Yamanaka, Hidetsugu Sakai
and Tokuo Suita

*Colledge of Engineering, Osaka University*

(Received December 26, 1955)

We have reported the experimental results[1)] concerning the motion of electrons and holes in single crystals of silver chloride. At the same time the electron mobility in AgCl [2)3)] was independently investigated by F. C. Brown.

Now we have studied the behaviors of electrons in AgBr single crystals at low temperatures by the method of electron bombardment.

The experimental apparatus for induced conductivity were almost same as reported before[1)4)]. With a field applied across a specimen a pulsed electron beam was focused to the front electrode. The induced current due to the excited electrons was amplified and detected by a distributed amplifier and a syncroscope.

Single crystals of AgBr were made by Kyropoulos method. Recrystalization was repeated five times, but it does not seem to be perfect. The dimensions of AgBr specimens were about 15×15 ×5 mm³. These specimens were kept in just below the melting point for about 24 hours and then gradualy cooled to room temperature in a period of 48 hours. Thin silver electrodes were attached to the specimen using silver-conducting paint.

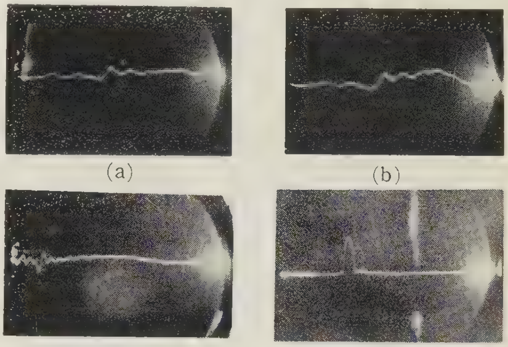
(a) (b)
(c) (d)

Fig. 1. Induced current patterns and electron beam form
(a) Sweep duration 2.1 μs; at 90°K, 660 V, 0.388 cm; $\mu = 221$ cm²/sec. V.
(b) Sweep duration 2.1 μs; at 90°K, 1150 V, 0.390 cm; $\mu = 159$ cm²/sec. V.
(c) Sweep duration 5.5 μs; at 195°K, 410 V, 0.380 cm; $\mu = 129$ cm²/sec. V.
(d) Sweep duration 2.1 μs; electron beam form.

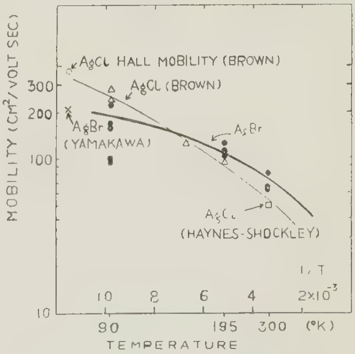

Fig. 2. Electron mobility in AgBr single crystal.

Fig. 1 shows typical patterns of the induced current due to 10 KV electron beam at the various temperatures and the electron beam form. From these patterns we can estimate the electron traversing time, during which the excited electrons go through the specimen. Electron mobility computed from the traversing times is shown in Fig. 2 with some reference data[2][3]. The computed mobilities at the liquid oxygen temperature are rather scattered. This may be caused to some internal strains which were formed in the cooling process. These results, as Brown[2] pointed out, do not agree with a theoretical calculation[6] with the assumption of electron scattering by the optical mode of lattice vibration. Our result shows that the electron mobility does not increase so remarkably at low temperatures as the theory predicts. This may be due to the fact that electrons are dominantly scattered by ionized impurities in this low temperature region. Space charge effect was also noticed when the electron beams were applied repeatedly. Hole pulses were observed in the reversed applied field. But they were too small to give a reasonable estimation.

Electron mobility in AgBr is almost of the same magnitude as in AgCl. Now we are studying the electron behaviors in more purified crystals avoiding the strain as possible.

### References

1) C. Yamanaka and T. Suita: Tech. Rep. of Osaka Univ. **5** (1955) 47.
2) F. C. Brown: Phys. Rev. **97** (1955) 355.
3) L. P. Smith: Semi-conducting Materials 114, 1951, London.
4) C. Yamanaka and T. Suita: J. Phys. Soc. Japan **10** (1955) 238.
5) K. A. Yamakawa: Phys. Rev. **82** (1951) 522.
6) H. Fröhlich and N. F. Mott: Proc. Roy. Soc. **A 62** (1946) 446.

---

J. PHYS. SOC. JAPAN **11** (1956) 606~607

## Electrical Conductivity of Iron Sulfides Single Crystals at the Temperature Range of $\alpha$-transformation

By Takahiko KAMIGAICHI

*Physical Laboratory, Faculty of Education, Hiroshima University, Hiroshima,*

Tadamiki HIHARA, Hideo TAZAKI

*Department of Physics, Faculty of Science, Hiroshima University, Hiroshima,*

and Eiji HIRAHARA

*Department of Applied Physics, Faculty of Engineering, Hiroshima University, Hiroshima*

(Received January 9, 1956)

In spite of many studies on the magnetic[1], the crystallographic[2] and the thermal[3] properties of iron sulfides in $\alpha$-transformation at about 140°C, the nature of this transformation has been still remained unexplained. One of the authors[4] has found an anomaly of the electrical conductivity in the synthetic polycrystal sample at the temperature of $\alpha$-transformation ($T_\alpha$), and his results show the same behaviors as those of the magnetic and the thermal measurements.

Recently, we could make a single crystal of the substance and measured the electrical conductivity for the differently oriented samples, obtaining a remarkable anisotropic property.

The single crystals were prepared as follows; first, pure iron (prepared by E. Merk) and pure sulfur (distilled from carbon bisulfide solution) were sealed in an evacuated terex tube, which was heated at about 600°C in a furnace, making a lump of the compound iron sulfide.

The lump was ground into powder and sealed in an evacuated thick silica tube, which was slowly moved in a furnace keeping the temperature at 1200°C.

Laue diffraction patterns of samples Nos. 3 and 5 are shown in Fig. 1. In each photograph, a beam of X-rays was parallel to the longitudinal axis of samples, along which an electric field would be applied in the measurement of the conduction. From the analysis of the patterns, it was found that the longitudinal axis of No. 3 aws parallel to $c$-plane (perpendicular to $c$-axis) and maked an angle 28° to $a$-axis of the sample and the longitudinal axis of No. 5 was parallel to $c$-axis.

The results of the measurements on electrical conductivity for the above mentioned samples were as follows (see Fig. 2). An electric field being applied along the length or the longitudinal axis of the sample, the sample No. 3 with the length

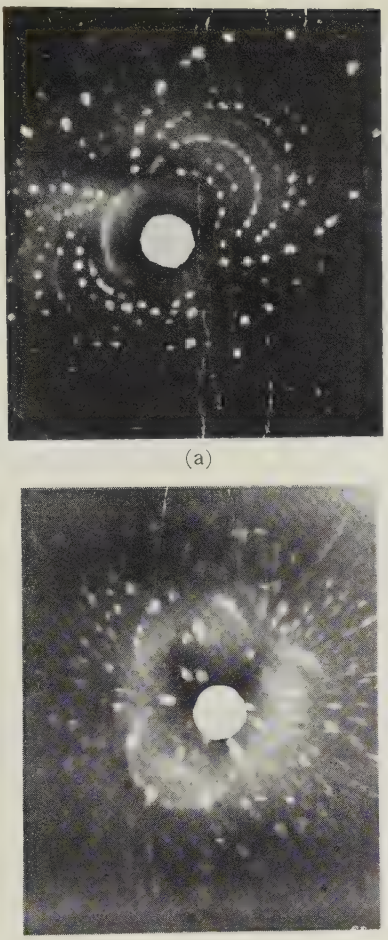

(a)

(b)

Fig. 1. Laue diffraction patterns of samples No. 3 (a) and No. 5 (b).
In the (a) a beam of X-rays was parallel to the *c*-plane of the sample and in the (b) was parallel to the *c*-axis.

parallel to the *c*-plane showed high conduction and a little anomaly at the temperature $T\alpha$ and the sample No. 5 with the length parallel to the *c*-axis showed low conduction on the low temperature side of $T\alpha$ and high conduction on the high temperature side, showing a remarkable anomaly at $T\alpha$.

The anomaly obtained above corresponds to those of the magnetic, the thermal and the crystallographic properties. The samples measured above, however, are nearly stoichiometric ones and the samples containing various amount of excess sulfur are now being prepared. The further measurements of the conductivity and of the magnetic susceptibility are ready now.

This work has been done by the financial aid of the Educational Ministry.

### References

1) R. Juze und W. Bitz: Z. Anorg. u. Allg. Chem. **205** (1932) 273.
H. Haraldsen: Z. Anorg. u. Allg. Chem. **231** (1937) 78, **246** (1941) 169.
2) R. Ueda, T. Ichinokawa and T. Mitsui: Busseiron Kenkyn (in Japanese) No. 33 (1950) 55.
F. Bertaut: Compt Rend. **254** (1952) 1295, Acta Cryst. **6** (1953) 557.
3) T. Hirone, S. Maeda and N. Tsuya: Journ. Phys. Soc. of Japan **9** (1954) 507.
4) T. Kamigaichi: Journ. Scie. Hiroshima Univ. **A 19** (1956) 499.

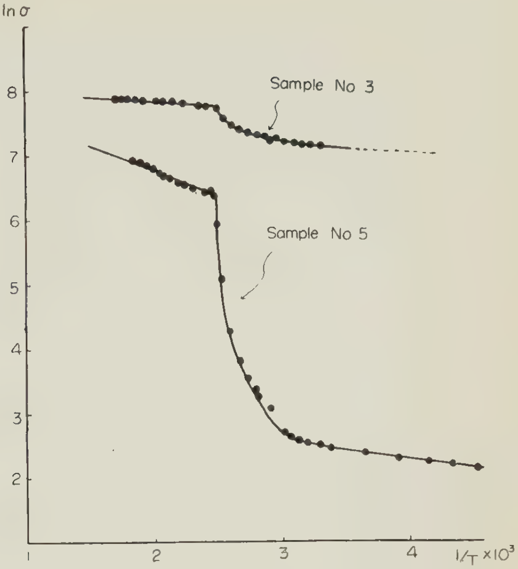

Fig. 2. Electrical conductivities of single crystals. Electric field was applied parallel to *c*-plane for the sample No. 3 and to *c*-axis for the sample No. 5.

---

J. Phys. Soc. Japan **11** (1956) 607~608

## On the Lithium Resonance in Lithium Sulfate Monohydrate $Li_2SO_4 \cdot H_2O$

(On the Quadrupole Effects)

Ay Miyuki MURAKAMI and Eiji HIRAHARA
*Department of Applied Physics, Faculty of Engineering, Hiroshima University, Hiroshima, Japan*

(Received February 6, 1956)

In the experiment on lithium-resonance in the single crystal of the substance, Pound¹⁾ observed already the triplet structure, rotating a crystal around the axis perpendicular to the *bc*-plane. As shown in Fig. 1, however, we have observed the five components structure of the Li-resonance line for this substance, in contradistinction to Pound's result, in the similar experimental condition.

Taking into account the X-ray analysis of the crystal structure, the Li-resonance lines of Li-ions lying close by water molecules are expected to be split by the electric field of the strongly polarized water molecules.

Assuming, for simplicity, the rotational symmetry of the mentioned electric field with the symmetry axis along the line jointing the Li-ion and the oxygen of water molecule (Li–O line), the conventional procedure of the first order perturbation gives, for the energy level splitting of Li with $I=3/2$,

$$\Delta\varepsilon=-\frac{2}{3}\mu H\pm\frac{e^2qQ}{8}\{3\cos^2\delta\cdot\cos^2(\varphi-\varphi_0)-1\} \qquad (1)$$

where $\varphi$ is the angle between the magnetic field and the reference line, $\varphi_0$ the angle between the reference line and the projection of the Li–O line on the plane in which the magnetic field sweeps, and $\delta$ the angle between the Li–O line and its projection mentioned above.

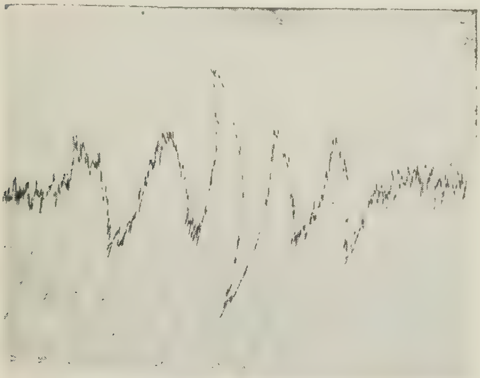

Fig. 1. The five components structure of the Li-resonance line. The sample is rotated around the axis normal to the $bc$-plane.

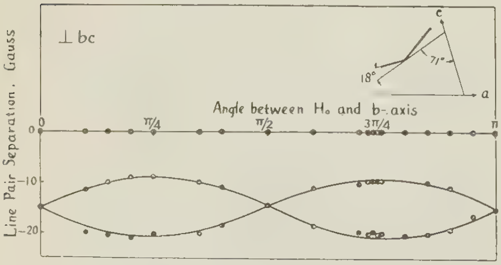

Fig. 2. The line pair separations when the crystal is rotated around the axis perpendicular to the $bc$-plane.

One of the results obtained is shown in Fig. 2, in which the crystal was rotated around the axis perpendicular to the plane $bc$. In the figure the abscissa represents the angle of rotation with respect to the magnetic field, and the ordinate the line pair separation of satellites appearing on both sides of the main Zeeman line which is represented by the middle horizontal line. The points in the figure denote the measured, values and the curves the calculated ones by the use of relation (1) for quadrupole splitting with suitable values $\delta$ and $\varphi_0$.

The orientation of an assumed symmetry axis of the surrounding electric field may be determined $\delta$ and $\varphi_0$, derived from the best-fitting of relation (1) to the experimental data in Fig. 2; and the result is shown at the upper right corner in the figure. The results obtained for $\delta$ and $\varphi_0$ on rotating the crystal around the various axes, however, are slightly at variance with each other. Consequently it seems to be clear that there are two different directions of the symmetry axis in the crystal, and the present results seem to favour the X-ray result by Ziegler²⁾ rather than the result by Larson and Helmholz³⁾.

In view of our experimental accuracy of ±2° for angles, the disagreements among the values of $\delta$ and $\varphi_0$ in the various rotations seem to be mainly due to the incorrectness of our assumption for the rotational symmetry of the surrounding electric field. In order to make clear this point, we are now continuing the measurements together with the calculations without the assumption of the rotational symmetry, which will shortly be reported in this journal.

We wish to thank to Prof. T. Muto of Tokyo University for his kind discussions.

## References

1) R. V. Pound: Phys. Rev. **79** (1950) 685.
2) G. E. Ziegler: Zeits. f. Krist. Physk. **89** (1934) 459.
3) A. C. Larson and L. Helmholz: J. Chem. Phys. **22** (1954) 2049.

---

J. PHYS. SOC. JAPAN **11** (1956) 608~609

# On the Low Temperature Conduction Phenomena in Semiconductors

By Shigeharu KOSHINO

*Department of Physics, Kyoto University, Kyoto*

(Received March 12, 1956)

Recently Fritzsche¹⁾ observed the complicated phenomena on germanium with the order of $10^{16}$ gallium atoms per $cm^3$ at very low temperature, that besides the usual two different temperature ranges there exists the intermediate range between them. They can not be interpreted by using the simple impurity band model presented by Hung.²⁾ In this note, we shall show that above mentioned phenomena as well as the usual phenomena can be interpreted phenomenologically by using the excited bands model which was first suggested by Erginsoy.3)

We consider only $n$-type sample which contains also the small concentration of acceptor atoms, and assume it has two excited donor bands. Let $E_1$, $E_2$ and $E_3$ denote the energy differences between the donor level and the lower edge of the first excited band, the second one, and the conduction band, respectively. If the distribution of electrons is governed by Boltzmann's law and the condition $N_d \gg N_a \gg n_1+n_2+n_3$ is satisfied, the concentration of electrons in the $i$ th band, $n_i$, is: $n_i = AK_i \times \exp(E_i/kT)$, where $A=N_d/N_a$, $N_d$ is the concentration of the donor atoms, $N_a$ the acceptor atoms, $k$ is Boltzmann's constant, $T$ is the absolute temperature and $K_i$ is the slow function of $T$ and $N_d$.

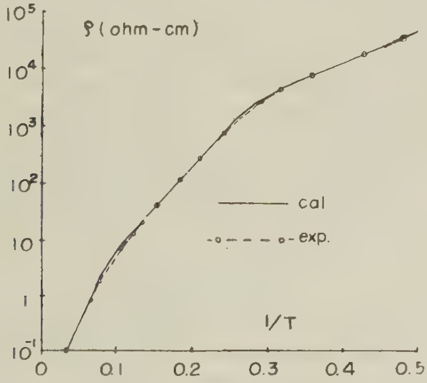

Fig. 1. log $\rho$ *versus* $1/T$.

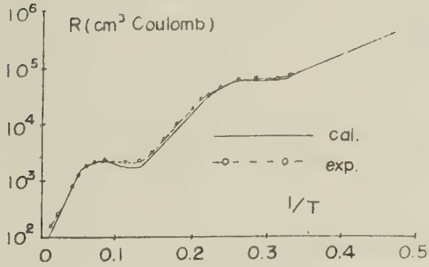

Fig. 2. log $R$ *versus* $1/T$.

Electrical resistance, $\rho$, and Hall coefficient, $R$, in the sample with three bands may be generally expressed:

$$\rho = (1/e)(n_1\mu_1 + n_2\mu_2 + n_3\mu_3)^{-1}$$

$$R = \frac{r_1 n_1 \mu_1^2 + r_2 n_2 \mu_2^2 + r_3 n_3 \mu_3^2}{e(n_1\mu_1 + n_2\mu_2 + n_3\mu_3)^2}$$

by analogy with the case of two kinds of carrier, where $e$ is the electronic charge, $r_i = \mu_i/\mu_{Hi}$, $\mu_i$ and $\mu_{Hi}$ are the drift mobility and Hall mobility, respectively, of electrons in the $i$ th band. If there exists the temperature range in which $n_2\mu_2 \gg n_1\mu_1 + n_3\mu_3$, then the curve of log $\rho$ *versus* $1/T$ can be diveded into three lines, and two maxima appear on the curve of log $R$ *versus* $1/T$. Such behaviors are shown in Figs. 1 and 2 with Fritzsche's experimental curves.1) In the calculation of our curves, we have assumed that the values of $K_i$'s and $\mu_i$'s are approximately constant because of their slow variation, and the values of parameters are determined as follows.

$$r_1 = r_2 = r_3 = 1, \quad E_1 = 1.0\times10^{-3}\,\text{eV.}, \quad E_2 = 2.9\times10^{-3}\,\text{eV.}, \quad E_3 = 6\times10^{-3}\,\text{eV.},$$

$$\mu_1 = 10\ \text{cm}^2\,(\text{volt sec})^{-1}, \quad \mu_2 = 1.6\times10^2\ \text{cm}^2\,(\text{volt sec})^{-1}, \quad \mu_3 = 2\times10^4\ \text{cm}^2\,(\text{volt sec})^{-1},$$

$$K_1 = 7\times10^{14}\ \text{cm}^{-3}, \quad K_2 = 1.5\times10^{16}\ \text{cm}^{-3}, \quad K_3 = 3.6\times10^{15}\ \text{cm}^{-3}.$$

It has been shown experimentally on Ga-doped Ge1) that the size of the intermediate range decreases with the value of $N_d$ and it disappears at $N_d = 2\times10^{16}$ atoms/cm$^3$. It is expected from the theoretical point of view. As the impurity concentration increases, the breadth of the second band and the mobility of electrons in it increases faster than those of the first band. Therefore the increase of $\mu_2 K_2$ will be faster than that of $\mu_1 K_1$.

The effects of other excited bands can not appear without much larger value of $N_d$. Practically, before reaching to this value the overlapping of bands will occur, then the effects of them will be impossible to appear.

### References

1) H. Fritzsche: Phys. Rev. **99** (1955) 406.
2) C. Hung: Phys. Rev. **79** (1950) 726.
3) C. Erginsoy: Phys. Rev. **80** (1950) 1104.

---

J. PHYS. SOC. JAPAN **11** (1956) 609~610

## Fermi Part $\eta_0$ of the TF Function for Free Positive Ion*

By Shigehiro KOBAYASHI

*Department of Physics, Kagawa University, Takamatsu*

(Received March 14, 1956)

According to Fermi1) the TF function for free positive ion $\phi$ can be approximated by that for free neutral atom $\phi_0$, as

$$\phi(x) = \phi_0(x) + k\eta_0(x),$$

$$\eta_0(x) = \left(\phi_0 + \frac{x}{3}\phi_0'\right)\int_0^x \frac{dx}{\left(\phi_0 + \frac{x}{3}\phi_0'\right)^2},$$

where $k$ is a constant depending upon the ionization degree $q$ roughly, as $k = -0.083\,q^3$.

Table I. Exact values of the Fermi part $\eta_0$ of the TF function for free positive ion.

| $x$ | $\eta_0$ | $\eta_0'$ |
|---|---|---|
| 0.0 | 0.00000 | 1.00000 |
| 0.1 | 0.10123 | 1.03060 |
| 0.2 | 0.20686 | 1.08460 |
| 0.3 | 0.31862 | 1.15277 |
| 0.4 | 0.43778 | 1.23208 |
| 0.5 | 0.56536 | 1.32103 |
| 0.6 | 0.70228 | 1.41873 |
| 0.7 | 0.84938 | 1.52464 |
| 0.8 | 1.00747 | 1.63843 |
| 0.9 | 1.17731 | 1.75991 |
| 1.0 | 1.35969 | 1.88895 |
| 1.2 | 1.7650 | 2.1696 |
| 1.4 | 2.2296 | 2.4805 |
| 1.6 | 2.7593 | 2.8222 |
| 1.8 | 3.3605 | 3.1954 |
| 2.0 | 4.0396 | 3.6012 |
| 2.2 | 4.8032 | 4.0406 |
| 2.4 | 5.6582 | 4.5149 |
| 2.6 | 6.6116 | 5.0253 |
| 2.8 | 7.6708 | 5.5730 |
| 3.0 | 8.8434 | 6.1594 |
| 3.2 | 10.137 | 6.7858 |
| 3.4 | 11.561 | 7.4538 |
| 3.6 | 13.122 | 8.1646 |
| 3.8 | 14.829 | 8.9198 |
| 4.0 | 16.693 | 9.7208 |
| 4.5 | 22.094 | 11.933 |
| 5.0 | 28.679 | 14.466 |
| 5.5 | 36.618 | 17.342 |
| 6.0 | 46.084 | 20.589 |
| 6.5 | 57.273 | 24.230 |
| 7.0 | 70.385 | 28.294 |
| 7.5 | 85.641 | 32.807 |
| 8.0 | 103.27 | 37.797 |
| 8.5 | 123.52 | 43.293 |
| 9.0 | 146.66 | 49.322 |
| 9.5 | 172.94 | 55.916 |
| 10.0 | 202.67 | 63.105 |
| 10.5 | 236.15 | 70.918 |
| 11.0 | 273.69 | 79.387 |
| 11.5 | 315.65 | 88.54 |
| 12.0 | 362.35 | 98.42 |
| 12.5 | 414.20 | 109.05 |
| 13.0 | 471.53 | 120.47 |
| 13.5 | 534.30 | 132·71 |
| 14.0 | 604.40 | 145.80 |
| 14.5 | 680.74 | 159.79 |
| 15.0 | 764.33 | 174.69 |
| 15.5 | 855.59 | 190.57 |
| 16.0 | 955.04 | 207.44 |
| 16.5 | 1063.2 | 225.43 |
| 17.0 | 1180.6 | 244.34 |
| 17.5 | 1307.7 | 264.43 |
| 18.0 | 1445.2 | 285.67 |
| 18.5 | 1593.6 | 308.11 |
| 19.0 | 1753.5 | 331.78 |
| 19.5 | 1925.6 | 356.72 |
| 20.0 | 2110.4 | 382.97 |
| 21.0 | 2521.2 | 439.57 |
| 22.0 | 2991.5 | 501.92 |
| 23.0 | 3527.1 | 570.4 |
| 24.0 | 4134.4 | 645.2 |
| 25.0 | 4819.9 | 727.0 |
| 26.0 | 5590.7 | 815.8 |
| 27.0 | 6454,1 | 912.2 |
| 28.0 | 7417.9 | 1016.6 |
| 29.0 | 8489.8 | 1129.3 |
| 30.0 | 9679.0 | 1250.7 |
| 31.0 | 10994. | 1381.2 |
| 32.0 | 12445. | 1521.3 |
| 34.0 | 15791. | 1831.8 |
| 36.0 | 19801. | 2185.5 |
| 38.0 | 24563. | 2586.3 |
| 40.0 | 30179. | 3037. |
| 45.0 | 48650. | 4412. |
| 50.0 | 74960. | 6188. |
| 60.0 | 160240. | 11220. |
| 70.0 | 307520. | 18710. |
| 80.0 | 544700. | 29300. |
| 90.0 | 906200. | 43700. |
| 100.0 | 1434000. | 62670. |

The values of $\eta_0(x)$ and $\eta_0'(x)$ were given previously by Fermi, Miranda[2], Amaldi[3] and Gombás[4]. The present author has recalculated them anew using the exact values of $\phi_0$ and $\phi_0'$ obtained recently by us[5]. The results are listed in Table I. The values obtained have slight discrepancy with those given by Miranda, as $\eta_0$ (Kobayashi) <or> $\eta_0$ (Miranda) for $x$ <or> ca. 4.5 respectively.

The author wishes to express his sincere thanks to Professors Gombás and Umeda for their suggestion of this calculation.

## References

1) E. Fermi: Mem. Acc. Italia **1** (1930) 1.
2) C. Miranda: Mem. Acc. Italia **5** (1934) 283.
3) E. Fermi and E. Amaldi: Mem. Acc. Italia **6** (1934) 117.
4) P. Gombás: Die statistische Theorie des Atoms und ihre Anwendungen (Wien, 1949) Tab. 2 and 54.
5) S. Kobayashi, T. Matsukuma, S. Nagai and K. Umeda: J. Phys. Soc. Japan **10** (1955) 759.

---

* Supported by the Scientific Research Expenditure of the Ministry of Education.

---

J. Phys. Soc. Japan **11** (1956) 610~611

# The Temperature Dependence of the Optical Absorption of Zinc Selenide

By Hirosi Tubota, Hiromichi Suzuki
and On Matumura
*General Education Department,*
*Kyushu University*

(Received March 17, 1956)

By melting zinc and selenium together in stoichiometric proportions in an evacuated quartz tube at about 1350°C for about one hour, an yellow polycrystalline compound was obtained. According to X-ray analysis, the compound has the crystal structure of the zinc blende type and its lattice constant is 5.65 Å[1].

The optical absorption of the film of the selenide evaporated on a quartz plate (thickness of the film is about 1 $\mu$) was measured by using a combination of a quartz spectrograph of a medium size and a "Spekker" diaphragm photometer. It was proved by X-ray analysis that this film has also the same crystal structure as that of the original material.

From the absorption edges, the energy gaps ($E_G$) were determined for several temperatures. The results are shown in the following table:

| $T$(°K) | Absorption Edge (Å) | $E_G$ (ev) |
|---|---|---|
| 295 | 4780 | 2.59 |
| 398 | 5050 | 2.47 |
| 496 | 5230 | 2.38 |

Assuming that the temperature dependence of the energy gap is given by the formula $E_G=E_{GO}+\alpha T$, we also obtained the values of 2.9 ev for the energy gap at 0°K $E_{GO}$, and $-0.001$ ev/°K for the temperature coefficient $\alpha$. These values may be considered to be in good agreement with the ones obtained by Bube[2] from the photoconductive effect.

We should express our hearty thanks to Professor Atuyosi Okazaki for suggesting this work and for placing research facilities at our disposal. We are also indebted to Mr. Atsushi Okazaki for taking X-ray photographs.

### References

1) J. W. Mellor: *"A Comprehensive Treatise on Inorganic and Theoretical Chemistry."* Vol. **X** (1930) 777.
2) R. H. Bube: Phys. Rev. **98** (1955) 431.

---

J. PHYS. SOC. JAPAN **11** (1956) 611~612

## Note on Rayleigh's Problem for a Circular Cylinder with Uniform Suction and Related Unsteady Flow Problem

By Hidenori HASIMOTO

*Department of Physics, Faculty of Science, University of Tokyo*

(Received March 17, 1956)

Recently, Stewartson[1], Glauert and Lighthill[2] have made very interesting studies on the asymptotic boundary layer over a long circular cylinder, and have shown the utility of the solution for the corresponding unstead flow known by the name of Rayleigh's problem.

Continuing a series of studies on Rayleigh's problem[3], the author has obtained the solutions of this problem (B) for a circular cylinder with uniform suction and the related unsteady flow problem (A). In this note we want to give the outline of them.

(A) With cylindrical coordinates $(r, \varphi, z)$, a circular cylinder $r=a$ makes an arbitrary unsteady motion with velocity $W(t)$ parallel to the $z$-axis. Let the uniform and constant suction velocity from the surface be $u_0$ per unit area.

The Navier-Stokes equations of motion and continuity for the surrounding viscous fluid possess an exact solution for which the radial velocity component $u$ is

$$u=-u_0 r/a\,, \tag{1}$$

provided that $w$, the velocity component parallel to the $z$-axis, can be found as a function of $r$ and $t$ satisfying the equation:

$$\partial w/\partial t=\nu[\partial^2 w/\partial r^2+(\kappa+1)r^{-1}\partial w/\partial r]\,, \tag{2}$$

subject to the boundary conditions

$$w(a,t)=W(t) \quad \text{and} \quad w(\infty,t)=0\,, \tag{3}$$

where

$$\kappa=au_0/\nu \tag{4}$$

is the suction Reynolds number.

This is equivalent to a heat conduction problem from a $(\kappa+2)$-dimensional hypersphere of radius $a$ and has a solution

$$w=\left(\frac{a}{r}\right)^{\kappa/2}\frac{H_{\kappa/2}^{(2)}(\sqrt{i\omega/\nu}\,r)}{H_{\kappa/2}^{(1)}(\sqrt{i\omega/\nu}\,a)}e^{i\omega t} \tag{5}$$

for

$$W(t)=e^{i\omega t}\,, \tag{6}$$

where $H_{\kappa/2}^{(1)}$ is the Hankel function of order $\kappa/2$. The solution for the arbitrary functional forms of $W(t)$ can be given easily by Fourier synthesis.

(B) In Rayleigh's problem

$$w=0 \quad \text{for} \quad t<0 \tag{7}$$

and the solution is easily given by Laplace transform[4], as follows:

$$\frac{w}{W}=\frac{1}{2\pi i}\left(\frac{a}{r}\right)^{\kappa/2}\int_{\mathrm{Br}}\frac{e^{pt}}{p}\frac{K_{\kappa/2}(\sqrt{p/\nu}\,r)}{K_{\kappa/2}(\sqrt{p/\nu}\,a)}dp \tag{8}$$

$$=\left(\frac{a}{r}\right)^{\kappa}-\frac{2}{\pi}\left(\frac{a}{r}\right)^{\kappa/2}\times\int_0^\infty\frac{J_{\kappa/2}(sa)Y_{\kappa/2}(sr)-Y_{\kappa/2}(sa)J_{\kappa/2}(sr)}{J_{\kappa/2}^2(sa)+Y_{\kappa/2}^2(sa)}\frac{e^{-\nu s^2 t}}{s}ds \tag{9}$$

where $K_{\kappa/2}$ is the modified Bessel function of the second kind, $\kappa\cdot\mathrm{I}=\kappa$ or 0 according to $\kappa\gtrless 0$. When $\kappa=-1, 1, 3$ etc. (8) gives simple formulae[5]:

$$w/W=\mathrm{Erfc}\,R \quad (\kappa=-1), \quad =(a/r)\,\mathrm{Erfc}\,R \quad (\kappa=1),$$

$$=\frac{a^3}{r^3}\mathrm{Erfc}\,R+\left(\frac{a^2}{r^2}-\frac{a^3}{r^3}\right)\times\exp\{-(1-r/a)+\nu t/a^2\}\,\mathrm{Erfc}\,(R+\sqrt{\nu t}/a) \quad (\kappa=3) \tag{10}$$

where

$$R=(r-a)/(2\sqrt{\nu t})\,. \tag{11}$$

The quantity of the greatest practical interest is the frictional force per unit length $D$ which is given by

$$\frac{D}{2\pi\mu W}=-\frac{a}{W}\left(\frac{\partial w}{\partial r}\right)_{r=a}$$

$$=\kappa+\frac{4}{\pi^2}\int_0^\infty\frac{\exp(-\nu s^2t}{J_{\kappa/2}{}^2(sa)+Y_{\kappa/2}{}^2(sa)}\frac{ds}{s} \qquad (12)$$

$$=\frac{a}{\sqrt{\pi\nu t}}+\frac{\kappa+1}{2}+(\kappa^2-1)\left\{\frac{\sqrt{\nu t}}{4\sqrt{\pi}a}-\frac{\nu t}{8a^2}+O\left(\frac{(\nu t)^{3/2}}{a^3}\right)\right\} \qquad (13)$$

$$\sim\begin{cases}\kappa\cdot\mathrm{I}+[2^{|\kappa|-1}\Gamma(|\kappa|/2)]^{-1}(a/\sqrt{\nu t})^{|\kappa|}+\cdots & (\kappa>0)\\ 1/\{-\gamma-\ln(a/\sqrt{4\nu t})\}+\cdots & (\kappa=0)\end{cases}$$

$$\sqrt{\nu t}\gg a. \qquad (14)$$

They show the effect of the suction on the boundary layer growth very well and is in contrast with the solution for a flat plate

$$\frac{D}{2\pi\mu W}=\frac{u_0}{2\nu}+\frac{1}{\sqrt{\pi\nu t}}\exp\{-(u_0{}^2/4\nu)t\}+\frac{|u_0|}{2\nu}\mathrm{Erfc}\left(\frac{|u_0|\sqrt{t}}{2\sqrt{\nu}}\right), \qquad (15)$$

## References

1) K. Stewartson: Quart. Appl. Math. **13** (1955) 113.
2) M. B. Glauert and M. J. Lighthill: Proc. Roy. Soc. **230** (1955) 188.
3) H. Hasimoto: J. Phys. Soc. Japan **6** (1951) 400; **9** (1954) 611; **10** (1955) 397.
4) Carslaw and Jaegar: Conduction of Heat in Solids. Oxford (1947) 280.
5) Erdelyi: Tables of Integral Transforms **1** (1954) 233, McGraw-Hill.

---

J. PHYS. SOC. JAPAN **11** (1956) 612~613

# Note on the Electron Spin Resonance of the $V_1$-center*

## — Calculation of the Electronic $g$-value —

By Teturo INUI, Susumu HARASAWA
*Department of Applied Physics, Faculty of Engineering, University of Tokyo*
and Yukio OBATA
*Department of Physics, Faculty of Science, University of Tokyo*

(Received April 7, 1956)

The recent experiment[1] on the $V_1$-center seems to persuade us to change its picture that it is a pure antimorph to the F-center. We are led to conclude that the resonance patterns obtained are to be attributed to a complex consist of two $Cl^-$-ions which approach together to form into $Cl_2{}^{--}$ in the vicinity of a positive vacancy. As such a system has tendency to attract a hole, something like a $Cl_2{}^-$ molecular ion will result. Calculations have been made of the electronic $g$ value and hf. splittings of the patterns. In this note only the result on $g$ value for the case of KCl will be stated briefly.

Though the real circumstance is surely complicated, being many electron system in the crystal with positive vacancies, we assume such a system can be substituted by a "pseudo-molecule" $Cl_2{}^-$, a hole $e^+$ trapped by a $Cl^- - Cl^-$ pair.

According to the correlation diagram, the ground state of this "pseudo-molecule" is

$$(1s\sigma_g)^2\cdots(3p\pi_g)^4(3p\sigma_u),$$

and the next excited state connected by the spin-orbit interactian is

$$(1s\sigma_g)^2\cdots(3p\pi_u)^3(3p\pi_g)^4(3p\sigma_u)^2.$$

We shall use LCAO-MO approximation. The ground state function is of the form,

$$\Phi_0=(1/\sqrt{2(1+a^2)})[\{p_z(A)+p_z(B)\}-a\{S(A)-S(B)\}] \qquad (1)$$

and the excited state wave functions are given by

$$\Phi_x=(1/\sqrt{2})[p_x(A)+p_x(B)], \qquad (2)$$

$$\Phi_y=(1/\sqrt{2})[p_y(A)+p_y(B)]. \qquad (3)$$

Treating the spin-orbit coupling as a perturbation, the wave functions belonging to Kramers' doublet are calculated to be

$$\left.\begin{aligned}\Psi_1&=[1-\xi_0{}^2]\Phi_0\alpha+\xi_1\Phi_x\beta+i\xi_2\Phi_y\beta,\\ \Psi_2&=[1-\xi_0{}^2]\Phi_0\beta-\xi_1\Phi_x\alpha+i\xi_2\Phi_y\alpha\end{aligned}\right\} \qquad (4)$$

where $\alpha$ and $\beta$ are the usual spin functions, and $\xi_0$, $\xi_1$, and $\xi_2$ are given by the following:

$$\left.\begin{aligned}\xi_0{}^2&=[\lambda^2/8(1+a^2)][1/\Delta_1{}^2+1/\Delta_2{}^2],\\ \xi_1&=[\lambda/2\sqrt{1+a^2}\Delta_1][1+\lambda/2\Delta_2],\\ \xi_2&=[\lambda/2\sqrt{1+a^2}\Delta_2][1+\lambda/2\Delta_1],\end{aligned}\right\} \qquad (5)$$

in which $\lambda$ is the parameter of spin-orbit interaction, and $\Delta_1$, $\Delta_2$ are the energy differences of the first two excited states from the ground state respectively.

Using Peierls' technique[2], all the matrix elements of the Zeeman energy needed are reduced to those of purely atomic ones. Thus we get the following results for $g$-values;

$$g_z=g_0-[\lambda^2/(1+a^2)][(g_0/2)(1/\Delta_1{}^2+1/\Delta_2{}^2)-1/\Delta_1\Delta_2], \qquad (6a)$$

$$g_x=g_0-[2\lambda/(1+a^2)\Delta_2]-[\lambda^2/(1+a^2)][(g_0/2)(1/\Delta_1{}^2)+1/\Delta_1\Delta_2], \qquad (6b)$$

$$g_y=g_0-[2\lambda/(1+a^2)\Delta_1]-[\lambda^2/(1+a^2)][(g_0/2)(1/\Delta_2{}^2)+1/\Delta_1\Delta_2]. \qquad (6c)$$

The above results show that $\delta g_z$ is of the second order in $\lambda/\Delta$, while $\delta g_x$ and $\delta g_y$ are of the first order. So far as the experimental results are concerned, $\delta g_x$ and $\delta g_y$ are equal, i.e. the $g$-tensor has an axial symmetry. Hence we can put $\Delta_1=\Delta_2=\Delta$. The experimental result that $\delta g_{//}=0$ and $\delta g_\perp=0.04$ is well fitted if we set

$$-\lambda/\Delta=0.029\ , \qquad (7)$$

where we put the degree of $s$ mixture, $a^2/(1+a^2)$, equal to 0.3 after Känzig. The transitions between the ground and these excited states are optically forbidden. However the order of magnitude of $\Delta$ will not differ very much from the peak wave number of the $V_1$ band. The latter taken from the experiment is 28100 cm$^{-1}$.[3] The order of magnitude of $\lambda$ may be given by the 2/3 of the doublet separation of $(3s)^2(3p)^5$ state of Cl atom which is 881 cm$^{-1}$. Thus we have

$$-\lambda/\Delta=0.021\ , \qquad (8)$$

which is to be compared to (7).

In conclusion, we should like to thank Professors M. Ueta, T. Nagamiya and Y. Uemura for their valuable discussions.

### References

1) W. Känzig: Phys. Rev. **99** (1955) 1890.
2) R. E. Peierls: Zeits. f. Physik **80** (1933) 763.
3) W. Duering and J. Markam: Phys. Rev. **88** (1952) 1043.

---

* A preliminary account on this note has been reported by one of the authors (T.I.) as a part of the invited paper to the General Meeting of Physical Society of Japan on Oct. 14, 1955. Private communication to T.I. from Professor M. Ueta, who collaborated with Känzig during his stay at the University of Illinois has made them possible to begin their theoretical study of this problem before the appearance of Känzig's paper (ref. 1).

---

## Errata

### Decrement of Blast Wave

By Akira SAKURAI

J. Phys. Soc. Japan **10** (1955) 1018

In figure, $\lambda=3\ (1-1.92)$ must be $\lambda=3\ (1-1.92y)$, and the indications of the Goldstine and von Neumann and of the Approximate theory curves should be interchanged.

# PROGRESS OF THEORETICAL PHYSICS

*(Founded by H. Yukawa in 1946)*

Published for the
**Research Institute for Fundamental Physics**
**The Physical Society of Japan**

Progress of Theoretical Physics Vol. 14, No. 6, December 1955

Positive Temperature Effect of Cosmic Rays ............................................ Satio HAYAKAWA, Kensai ITO and Yoshinosuke TERASHIMA..497

On Quantum Electrodynamics without Subsidiary Conditions ........... Shozi OZAKI..511

Some Remarks on the Reaction $K^- + d \rightleftarrows \Sigma^- + p$ ............... Kazuhiko NISHIJIMA..523

On the Interaction between Hyperons and Nucleons and the Hyperfragments.. ................................................ Kazuhiko NISHIJIMA..527

The Relativistic and Exchange Current Corrections to the Deuteron Magnetic Moment and the Thermal $N$-$P$ Capture Cross Section..Masao SUGAWARA..535

Low Energy Limits of Photon-Nucleon and Pion-Nucleon Collisions .................................. Sigeo HANAWA, Mikio NAMIKI and Shin CHIBA..551

Scattering Matrix in the Heisenberg Representation for a System with Bound States............................................. Abraham KLEIN..580

Tables of $U$ Coefficients ................. Hiroyuki MATSUNOBU and Hisao TAKEBE..589

Letters to the Editors:

Meson-Theoretical Potential in $N^{14}$..S. OTSUKI, T. SAWADA and S. SUEKANE..606

On the Relation between Hill-Wheeler's and Bohr-Mattelson's Description of the Nuclear Collective Model .................... T. MARUMORI..608

Errata: ............................................................................ 610

Price $ 1.25 per copy
$ 15.00 per year (postage inclusive)
Annual dues for foreign members (individual subscribers)
$ 12.00 (postage inclusive)
〃 for foreign members of the Physical Society of Japan
$ 10.00 (postage inclusive)

Application for members, subscriptions and orders for back mumbers should be sent, directly or through book-dealers, to

The Publication Office
in
**Yukawa Hall, Kyoto University, Kyoto, Japan**

JOURNAL OF THE PHYSICAL SOCIETY OF JAPAN Vol. 11, No. 6, JUNE, 1956

# Lattice Theory of Liquid State

By Ikuro SHIMOSE

*Faculty of Literature and Science, Yamaguchi University*

(Received November 30, 1955)

We develop the lattice theory of liquid state by using the cell model of lattice type with interstitial sublattices. The free energy, the pressure, and the quantities at the critical point are calculated in the degree of quasi-chemical approximation. The degree of agreement of the calculated values of $\tau_c, v_c/v_0$ and $p_c v_0/\varepsilon$ with their observed values is considerably improved as compared with those calculated values for the cell model of lattice type with no sublattice.

## § 1. Introduction

We shall mention the two principal methods by which the liquid state of the system consisting of many inert gas atoms (molecules) or saturated molecules can be statistically dealt with. One is the method of molecular distribution function developed by Kirkwood and his co-workers[1)], Green[2)], Rodriguez[3)], and others. In this method there exist the following defects; (i) the use of the so-called "superposition approximation", and (ii) the necessity of the enormous evaluation to solve the integral equation determining the distribution function. The other is the model-method (lattice theory or cell method) elaborated by Lennard-Jones and Devonshire[4)], Cernuschi and Eyring[5)], Ono[6)7)], Peek and Hill[8)], Rowlinson and Curtiss[9)], and others. By this method we are able to reach without great difficulty to the results, which can be compared with the observed values. However, all of the values of $\tau_c, v_c/v_0$ and $p_c v_0/\varepsilon$ (these quantities will be defined in the later articles) calculated by the above method are not in good agreement with their observed values. Then, the assumption about the structure of liquid state is intuitively introduced in this method. Furthermore, since the solidlike structure of crystal is used in this method, we may not be able to deal with the three phases (that is the vapor, liquid and solid phases) by this method. However, the work of Kirkwood[10)] has recently made clear how to reach to the model-method by the fundamental theory of statistical mechanics. By his work the model-method has come to be more and more promising. Then the existing theories for the improvement of the model-method are given as follows. In the first place, Mayer and Careri[11)] generalized Kirkwood's theory[10)] and developed the model-method (cell method) on the basis of the statistical mechanics. Nevertheless, the values obtained by them are in great disagreement with the observed values. Next, Janssens and Prigogine[12)], Pople[13)], and others extended the theory by using the cells, in which 2 molecules can exist. However, they did not give special consideration to the influence of the neighboring cells upon the cells including 2 molecules.

Recently, Kikuchi[14)] concretely calculated the equation of state for a lattice gas (triangular lattice type) with 3 interstitial sublattices in the degree of Bragg-Williams' approximation[15)], and showed that the liquid phase, together with the vapor and the solid phases, can exist in this system, though the intermolecular potential used was unnatural. Then we[16)] numerically calculated the equation of state of a lattice gas (square lattice type) with more sublattices by another method in the degree of Bragg-Williams' approximation[15)], and showed that the stable liquid phase results from a natural potential between molecules.

In this paper, we extend the lattice theory developed by Ono[6),7)] and others to the case for the cell model of lattice type with interstitial sublattices. Hereby, we intend to improve the degree of agreement of the calculated values of the quantities with their observed values.

## § 2. Partition Function

We consider a face-centered cubic lattice composed of $n^3L$ lattice points ($n$ is a integer), in which the distance between nearest neighbors is $a/n$. We can divide the above $n^3L$ lattice points into $n^3$ face-centered cubic lattices, in each of which the distance between nearest neighbors is $a$. We define each of the $n^3$ lattices as "sublattice". Then we divide all the lattice points into $L$ groups (or cells) so that each group may contain $n^3$ lattice points, each of which respectively belongs to each of $n^3$ sublattices and all of which either directly or indirectly are connected with each other at a distance $a/n$. Now we consider the system composed of $N$ molecules. We assume that each of $N$ molecules is confined to any of the above cells and the distance between the centers of nearest cells is $a$.

Then we assume the potential energy $\varphi(r)$ between any two molecules to be of the following form, where $r$ is the distance between two molecules.

(i) If two molecules occupy the adjacent cells,

$$\varphi(r)=4\varepsilon\left\{\left(\frac{r_0}{r}\right)^{12}-\left(\frac{r_0}{r}\right)^{6}\right\}, \tag{1}$$

(ii) if two molecules occupy the remoter cells than adjacent ones,

$$\varphi(r)=0,$$

where $r_0$ and $\varepsilon$ are the distance and energy characteristics of the potential. Furthermore, we assume that any cell does not include more than one molecule. Now the partition function $Z$ of the system at the absolute temperature $T$ is given by

$$Z=(2\pi mkT/h^2)^{3N/2}\cdot Z_{\text{con}}, \tag{2}$$

where $m$ is the mass of a molecule, $k$ Boltzmann's constant, $h$ Planck's constant. $Z_{\text{con}}$ is the configuration partition function of the system and is given by the following sum of integrals over each cells.

$$Z_{\text{con}}=\sum\int dv_1\cdots\int dv_N \exp(-E/kT). \tag{3}$$

The sum in Eq. (3) is over all the possible arrangements of $N$ molecules in $L$ cells. $dv_i$ is the volume element of the $i$th molecule, $E$ the total potential energy of the system. Then we define a pair of any two molecules as "molecular pair", which respectively belong to two adjacent cells. In one of the molecular configurations mentioned above we denote the number of molecular pairs by $Yz$, where $z$ is the number of nearest neighbors and 12 for a face-centered cubic lattice. Thereupon, we give the total potential energy $E$ by

$$E=\varphi(a)Yz+\sum_{i=1}^{N}u_i, \tag{4}$$

where $u_i$ is the value of the potential energy of the $i$th molecule at any position in its cell above the center of its cell. As the approximate value of $u_i$ we use the value of the potential energy of the $i$th molecule surrounded by the neighboring molecules at the centers of their own cells. We write

$$\int_{v_i}\exp(-u_i/kT)dv_i=s_i n^3 v_1, \tag{5}$$

where $v_1$ is the volume per a lattice point and is given by $a^3/\sqrt{2}\,n^3$. $s_i$ is a parameter for the free volume. Then $Z_{\text{con}}$ is given by

$$Z_{\text{con}} =(n^3v_1)^N\sum_{Y}G(L,N,Y)\exp(-\varphi(a)Yz/kT)\cdot\prod_{i=1}^{N}s_i \tag{6}$$

$G(L, N, Y)$ means the number of the possible cases where $N$ molecules are distributed among $L$ cells in such a way that the number of molecular pairs is $Yz$. And the relation

$$\sum_{Y}G(L,N,Y)=\frac{L!}{N!\,(L-N)!} \tag{7}$$

holds. Then we write $\prod_{i=1}^{N}s_i=s^N$ and assume that $s$ depends on $x$ and $Y$, where $x$ is molecular density and is defined by $x=N/L$.

We can calculate the value of $Z_{\text{con}}$ in Eq. (6) by the "quasichemical method"[17]. Corresponding to the ordinary configuration partition function $Z_{\text{con}}$ for given $N$, the (configuration) grand partition function $\Xi$ for given absolute activity $\lambda$ is given by

$$\Xi=\sum_{N}\sum_{Y}G(L,N,Y)\xi_a{}^N s^N \eta_a{}^{Yz}, \tag{8}$$

where $\xi_a=n^3v_1\lambda$ and $\eta_a=\exp(-\varphi(a)/kT)$. If we denote the greatest term in Eq. (8) by $\Xi^*$ and $N, Y, s$ in this term by $N^*$, $Y^*, s^*$ respectively, we have

$$\Xi=\Xi^*=G(L,N^*,Y^*)\xi_a{}^{N^*}(s^*)^{N^*}\eta_a{}^{Y^*z}. \tag{9}$$

Then, denoting the average values of $N, Y, s$ in the grand canonical ensemble by $\overline{N}, \overline{Y}, \overline{s},$ respectively, it follows that $\overline{N}=N^*$, $\overline{Y}=Y^*$ $\overline{s}=s^*$. Further, if we write

$$\left.\begin{aligned}\xi^L&=\xi_a{}^{N^*}, & s_0{}^L&=(s^*)^{N^*},\\ \gamma^L&=G(L,N^*,Y^*), & \eta^{1/2Lz}&=\eta_a{}^{Y^*z}\end{aligned}\right\} \tag{10}$$

in Eq. (9), we have

$$\Xi=\Xi^*=\gamma^L\xi^L s_0{}^L\eta^{(1/2)Lz}. \tag{11}$$

Now, if we regard assembly as a pair of two neighboring cells, in a field due to the remaining cells, we have

$$\Xi=\Xi^*_2=\{(\eta^{(0)})^{2(z-1)}+2\delta_1 s^*\xi_u(\eta^{(0)}\eta^{(m)})^{z-1}+\delta_2(s^*)^2\xi_a{}^2(\eta^{(m)})^{2(z-1)}\eta_a\}\times\gamma^{L-2}\xi^{L-2}s_0{}^{L-2}\eta^{(1/2)Lz-2z+1}\,. \tag{12}$$

Here, $\eta^{(0)}$ is the geometric mean contribution to the facter $\eta^{(1/2)Lz}$ in $\Xi^*$, of a pair of the neighboring cells, of which the first is not occupied; $\eta^{(m)}$ the above contribution, when the first cell is occupied. $\delta_1$ and $\delta_2$ are parameters depending on the molecular configuration in the two neighboring cells. For the cell model of the lattice type with sublattices, the relation $\delta_1{}^2>\delta_2$ holds from the form of intermolecular potential (Eq. (1)), though $\delta_1{}^2=\delta_2$ for the cell model with no sublattice. From Eq. (12) we obtain

$$\frac{\frac{1}{2}(L-2\overline{N}+2\overline{Y})}{(\eta^{(0)})^{2(z-1)}}=\frac{\overline{N}-2\overline{Y}}{2\delta_1 s^*\xi_a(\eta^{(0)}\eta^{(m)})^{z-1}}=\frac{\overline{Y}}{\delta_2(s^*)^2\xi_a{}^2(\eta^{(m)})^{2(z-1)}\eta_a}\,. \tag{13}$$

If we write $\overline{X}=\overline{N}-2\overline{Y}$ in Eq. (13), we have

$$\frac{\overline{X}^2}{(L-\overline{N}-\overline{X})(\overline{N}-\overline{X})}=\frac{1}{\delta\eta_a}\,, \tag{14}$$

where $\delta=\delta_2/\delta_1{}^2(<1)$.

Applying Fowler-Guggenheim's method[17], we obtain

$$Z_{\text{con}}=\frac{L!}{N!(L-N)!}(n^3v_1s)^N\times\left[\frac{x(\beta+1-2x)}{(1-x)(\beta-1+2x)}\right]^{(Nz/2)}\left[\frac{(1-x)(\beta+1)}{(\beta+1-2x)}\right]^{(Lz/2)}, \tag{15}$$

$$\beta^2=1-4x(1-x)\alpha\,, \tag{16}$$

$$\alpha=1-\delta\eta_a\,. \tag{17}$$

Here, $\alpha$ depends on $x$ for the cell model with sublattices, though does not depend on $x$ for the cell model with no sublattice. From Eqs. (2) and (15) the Helmholtz free energy (per mole) $A$ of the system is given by

$$\frac{A}{RT}=-\frac{1}{N}\log Z=-\frac{3}{2}\log\left(\frac{2\pi mkT}{h^2}\right)+\frac{1}{x}\{x\log x+(1-x)\log(1-x)\}-\frac{1}{kT}\log(n^3v_1s)+\frac{z}{2x}\left\{x\log\frac{\beta-1+2x}{x(\beta+1)}+(1-x)\log\frac{\beta+1-2x}{(1-x)(\beta+1)}\right\}, \tag{18}$$

where $R$ is gas constant (per mole).

## §3. Pressure, Second Virial Coefficient, and Quantities at Critical Point

From Eq. (18) the pressure $p$ of the system is given by

$$\frac{pV}{RT}=-V\left(\frac{\partial}{\partial V}\right)_T\left(\frac{A}{RT}\right)=-x\frac{\partial}{\partial x}\log s-\frac{1}{x}\left\{\log(1-x)+\frac{z}{2}\log\frac{\beta+1-2x}{(1-x)(\beta+1)}\right\}-\frac{zx(1-x)}{(1-\alpha)(\beta+1)}\cdot\frac{\partial\alpha}{\partial x}\,, \tag{19}$$

where $V$ is the volume (per mole) of the system. For sufficiently small density (or $x$), when we neglect the infinitesimal terms of higher order than $x$, we have

$$\frac{pV}{RT}=1+\frac{B}{V}\,.$$

$B$ is the second virial coefficient and is given by

$$B=\frac{1}{2}Nv_0q\left\{1+z\alpha-2\frac{\partial}{\partial x}\log s-\frac{z}{1-\alpha}\frac{\partial\alpha}{\partial x}\right\}, \tag{20}$$

where $x=N/L=Nv_0q/V$ and $v_0=r_0{}^3$.

At the critical point of the vapor-liquid transition the following two conditions are satisfied.

$$V\left(\frac{\partial}{\partial V}\right)_T\left(\frac{pV}{RT}\right)=\frac{pV}{RT}\,, \tag{21}$$

$$V^2\left(\frac{\partial^2}{\partial V^2}\right)_T\left(\frac{pV}{RT}\right)=0\,. \tag{22}$$

$p_c, \tau_c, v_c$ (respectively the values of $p, \tau\ (=kT/\varepsilon)$, $v(=V/N)$ at the critical point) are determined from Eqs. (19), (21) and (22).

## §4. Values of $s$ and $\delta$

For $x=0$, we obtain $s=1$ from the fact that all the neighboring cells of any molecule are vacant. For $x=1$, all the neighboring cells (the number is $z$) of any molecule are occupied. By using the procedure of Lennard-Jones and Devonshire[4], we obtain

Table I.

| | $\tau_c$ | $v_c/v_0$ | $p_cv_0/\varepsilon$ | $p_cv_c/\varepsilon\tau_c$ | $\overline{\omega}$ |
|---|---|---|---|---|---|
| Observed value | 1.28 | 3.09 | 0.121 | 0.293 | |
| Lennard-Jones and Devonshire | 1.30 | 1.77 | 0.434 | 0.591 | 0.000 |
| Cernuschi and Eyring | 2.74 | 2.00 | 0.469 | 0.342 | 0.455 |
| Ono | 0.75<br>(1.10)7),† | 2.00 | 0.128 | 0.342 | 0.455 |
| Peek and Hill | 1.18 | 3.25 | 0.261 | 0.719 | 0.175 |
| This paper | 1.35 | 3.33 | 0.120 | 0.296 | 0.593 †† |

† This value is calculated by considering the interactions with the remoter molecules than nearest neighbors.
†† $s=0.600$, $\delta=0.728$.

$$\left.\begin{aligned}&(s)_{x=1}=2\pi\sqrt{2}\int_0^{y_0} y^{1/2}\exp\left\{-\frac{z}{\tau}[q^{-4}l(y)-2q^{-2}n(y)]\right\}dy\,,\\&y=r^2/a^2\,,\qquad y_0=(3/4\pi\sqrt{2})^{2/3}=0.3054\,,\\&l(y)=(1+12y+25.2y^2+12y^3+y^4)(1-y)^{-10}-1\,,\\&n(y)=(1+y)(1-y)^{-4}-1\,,\\&q=a^3/r_0^3\sqrt{2}\,,\end{aligned}\right\}\tag{23}$$

where it is assumed that $n^3$ (the number of sublattices) is sufficiently great. Then, from Eq. (14) we obtain

$$\overline{\omega}=\frac{2(1-x)}{\beta+1}\,,\tag{24}$$

where $z\overline{\omega}$ is the average number of vacant cells around any one molecule. Hereupon, we assume the relations

$$s=(s)_{x=1}+(1-(s)_{x=1})\overline{\omega}\tag{25}$$

and

$$s\delta=s-2(1-(s)_{x=1})/z\,.\tag{26}$$

From Eqs. (16), (17), (24), (25), (26), we can evaluate the values of $s$, $\alpha$, $\beta$, $\delta$ and $\overline{\omega}$ for the given value of $x$ and $\tau$.

## § 5. Numerical Calculation

For the values of $r_0$ and $a$ we use respectively $3\cdot 83\times 2^{-(1/6)}$Å and 4.04Å (the values of argon). These values were already used in Ono's theory6),7). The above value of $a$ (4.04 Å) is determined from the molar volume of liquid argon at 88°K, where the cell model of lattice type with no sublattice is assumed. Using these values, we obtain $q=1.174$ from Eq. (23). Thus we can evaluate the values of $\tau_c, v_c/v_0$, and $p_cv_0/\varepsilon$ from Eqs. (19), (21) and (22). The values obtained are given in Table I. Herein are tabulated also the observed values18) of $\tau_c$, $v_c/v_0$, $p_cv_0/\varepsilon$, $p_cv_c/\varepsilon\tau_c$ (the mean values for Ne, A, N), and the calculated values obtained by the methods of Lennard-Jones and Devonshire4), Cernuschi and Eyring5), Ono6), Peek and Hill8). We shall see from Table I that all the calculated values by the method of this paper are in good agreement with the observed values. Then the value of the second virial coefficient (at the critical temperature) calculated from Eq. (20) is $B/(2/3)\pi Nr_0^3=-2.12$. The above value calculated from the exact formula19) is $-1.63$. The above values††† calculated by the methods of Cernuschi and Eyring, Ono, Peek and Hill are between $-1.0$ and $-1.2$. Accordingly, the method of this paper for the second virial coefficient shows little sign of improvement in the degree of agreement of the calculated value with the exact value. Probably this means that the cell method is not so adequate for gases of rather small density.

## § 6. Conclusion

For the lattice theory of the liquid state we used the cell model of lattice type with interstitial sublattices. This model has the possibility of realization of the three phases (that is the vapor, liquid, and solid phases), though the cell models heretofore in use may realize but the two phases. The degree of agreement of the calculated values of $\tau_c$, $v_c/v_0$ and $p_cv_0/\varepsilon$ with their observed values was considerably improved as compared with those calculated values for the cell model of lattice type with no sublattice. Of course, it is to be desired that the purely statistical method should be used as Mayer and Careri[11] did. However, also the improvement of the lattice theory by such an intuitive model as shown in this paper may have some meaning in the transition period before the time when the good agreement with the observed value will be able to be obtained by the above purely statistical method.

---

††† These values were calculated by Rowlinson and Curtiss9).

The author wishes to express his sincere thanks to Professor A. Harasima, Tokyo Institute of Technology, for his valuable discussions.

## References

1) J. G. Kirkwood, V. A. Lewinson and B. J. Alder: J. Chem. Phys. **20** (1952) 929.
2) H. S. Green: Proc. Roy. Soc. **A 189** (1947) 103.
3) A. E. Rodriguez: Proc. Roy. Soc. **A 196** (1949) 73.
4) J. E. Lennard-Jones and A. F. Devonshire: Proc. Roy. Soc. **A 163** (1937) 53; **165** (1938) 1.
5) F. Cernuschi and H. Eyring: J. Chem. Phys. **7** (1939) 547.
6) S. Ono: Memoirs Fac. Eng. Kyushu Univ. **10** (1947) 190.
T. Sato and S. Ono: J. Phys. Soc. Japan **4** (1949) 103.
7) T. Sato and S. Ono: J. Phys. Soc. Japan **6** (1951) 410.
8) H. M. Peek and T. L. Hill: J. Chem. Phys. **18** (1950) 1252.
9) H. S. Rowlinson and C. F. Curtiss: J. Chem. Phys. **19** (1951) 1519.
10) J. G. Kirkwood: J. Chem. Phys. **18** (1950) 380.
11) J. E. Mayer and G. Careri: J. Chem. Phys. **20** (1952) 1001.
G. Careri: J. Chem. Phys. **20** (1952) 1114.
12) P. Janssens et I. Prigogine: Physica **16** (1950) 895.
13) J. A. Pople: Phil. Mag. **42** (1951) 459.
14) R. Kikuchi: J. Chem. Phys. **19** (1951) 1230.
15) W. L. Bragg and E. J. Williams: Proc. Roy. Soc. **A 145** (1934) 699.
16) I. Shimose: J. Phys. Soc. Japan **10** (1955) 860.
17) R. H. Fowler and E. A. Guggenheim: "*Statistical Thermodynamics*" (Cambridge University Press, London, 1939) 246–53, 358–64, 437–43.
18) International Critical Tables.
19) J. E. Lennard-Jones: Proc. Roy. Soc. **A 106** (1924) 463.

Journal of the Physical Society of Japan Vol. 11, No. 6, June, 1956

# Growth Spirals on Crystals of $WO_3$

By Sigetosi TANISAKI

*Faculty of Literature and Science, Yamaguchi University*

(Received December 22, 1955)

Growth spirals were observed on the (001) and {111} surfaces of $WO_3$ crystals which were prepared by sublimation. Spirals on (001) are of 'circular symmetry', but spirals on {111} are of a characteristic shape which is explained by crystal structure. It was found that in any one region of the crystal the dislocations were not only predominantly of the same sign but also had the same strength. The movement of dislocation has been illustrated. Besides these spirals the layer formation from edges or corners of crystals was observed.

## § 1. Introduction

The growth spirals, which were predicted by Frank's theory[1] on crystal growth by screw dislocation mechanism, were observed on the crystal faces of beryl, carborundum, cadmium iodide and other materials[2]. Similar observations on crystals of wolfram trioxide, $WO_3$, which is one of the ferroelectric materials[3], are to be reported in this paper. With relation to the ferroelectricity the crystal structure of this material was studied by several workers[4]. $WO_3$ has monoclinic structure in room temperature, and this structure changes to an orthorhombic form at 350°C and to a tetragonal form at 750°C. There is a transition point at 910°C, but the crystal has still the tetragonal form in the temperature range up to 1200°C. The crystal structure has not been determined above 1200°C. Besides these, another transition near −50°C is known. This material has the domain structure in room temperature, whose boundaries are (110) and (100) twin planes. As the crystal cools through the transition temperature at 750°C and 350°C, the twinning takes place in the (110) and (100) planes respectively.

## § 2. Preparation of Crystals

Powder of purified wolframic acid was heated in silica tube above 1300°C for several hours in the electric furnace as shown in Fig. 1 and cooled down in furnace. The temperature of the sample was known by the correction of reading of the thermocouple. Then the powder of wolframic acid changed to $WO_3$ crystallites and on the surface of lump of these crystallites the green crystals with surfaces of area $1\sim2$ mm² were obtained, which were ascertained to be $WO_3$ by the X-ray powder method. These $WO_3$ single crystals seem to have grown by sublimation on account of the temperature gradient caused vertically in the silica tube by the structure of furnace. Fig. 2 shows an example of such crystals. This crystal has a rectangular (001) plane and several {111} planes, and on {111} the domain boundaries, (110) and (100), are observed. The habits of the crystals depend on the temperature of crystal growth. At relatively low temperature (below about 1400 °C) the crystals with the predominant {111} surfaces were obtained while at higher temperature the crystals grew usually into forms of thin platelets having only (001) surface well developed. These indices were determined by X-ray rotation photographs and the measurements of facial angles.

## § 3. Observation and Discussion

On (001) and {111} surfaces of such crystals several types of growth spirals were observed by the metallurgical microscope. The growth spiral was not observed on the crystal surfaces of other kinds. In $WO_3$, most of spirals are of dotted curves which are composed of many spots, perhaps pits, along the edges of the growth layers. Such cases were already observed on other crystals[5].

a) *Spirals on* (001)

The typical spirals as shown in Fig. 3 and 4 were observed on (001). Several straight lines on crystal surface of Fig. 3 are (110) domain boundaries and many faint parallel lines in Fig. 4 are (100) boundaries. In these photographs spirals develop across the domain

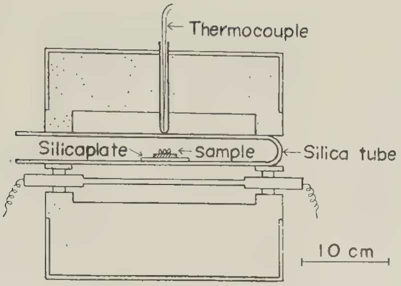

Fig. 1. Structure of electric furnace.

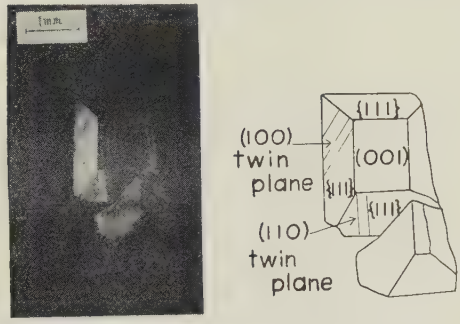

(a) (b)

Fig. 2. Example of a single crystal.

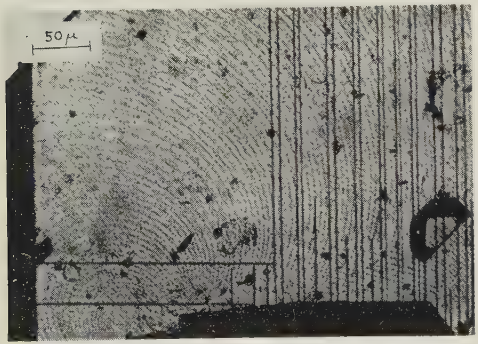

Fig. 3. Spirals and (110) domain boundaries on (001).

boundaries, and this shows that the domain structure was built up after the growth of crystals. Fig. 5 shows many dislocations of the same sign appeared on the surface of a thin tabular crystal which had grown in the following state. This crystal grew on the (001) surface of another larger crystal with a rotation of 38° about the common $c$ axis. It seemed that the above mentioned dislocation pattern was caused by the strain which had been appeared in the crystal on account of this special condition of growth.

### b) *Spirals on* {111}

An example of the growth spirals observed on {111} is shown in Fig. 6. Fig. 7 shows

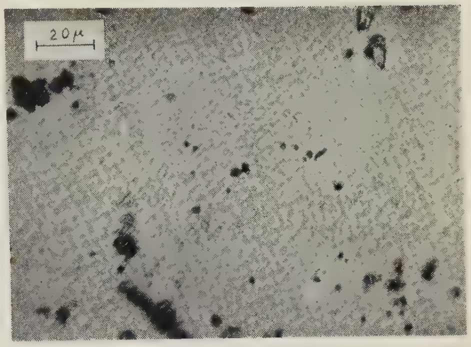

Fig. 4. Spiral and (100) domain boundaries on (001).

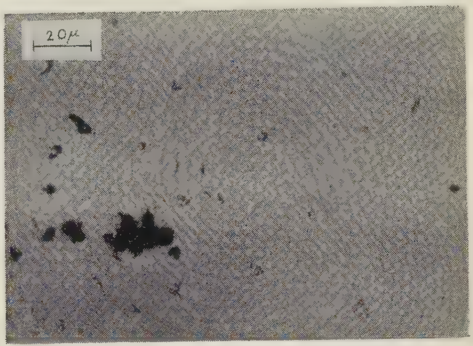

Fig. 5. Many dislocations of the same sign on (001).

the interaction of spirals originating from three dislocations of the same sign at a distance of separation greater than the radius of critical nucleus $\rho_c$. Fig. 8 shows many screw dislocations of the same sign at a distance of separation less than $\rho_c$. The formation of closed loops due to two dislocations of the opposite sign has not been observed. It seems to be characteristic in general on $WO_3$ crystals that in any one region of the crystal there is a large predominance either of right handed or left handed screw dislocations. Such observations were reported only on SiC⁶⁾. The closed loops, produced by the movement of dislocation from the centre of the spiral before growth ceased, are illustrated in Fig. 9.

Besides these spirals the layer structure as shown in Fig. 10 was sometimes observed on {111}. This layer structure seems to be related to crystal growth as observed in ionic crystals⁷⁾ and sintered metal oxides⁸⁾. But it is characteristic in $WO_3$ that layers always start, not from the centres, of faces, but from the edges or corners of crystals. The layer edges are roughly semicircular on small

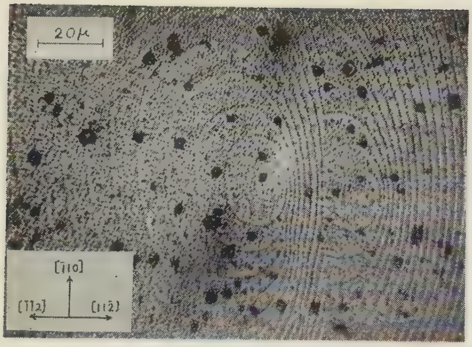

Fig. 6. Two spirals observed on a {111} surface.

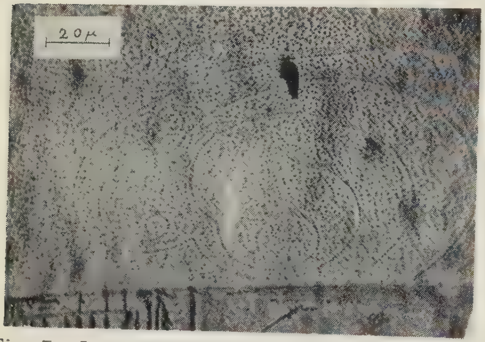

Fig. 7. Interaction of spirals originating from three dislocations.

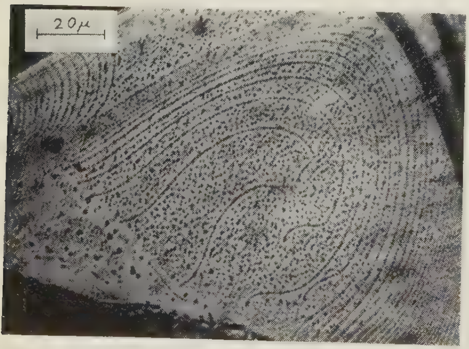

Fig. 8. Many dislocations of the same sign.

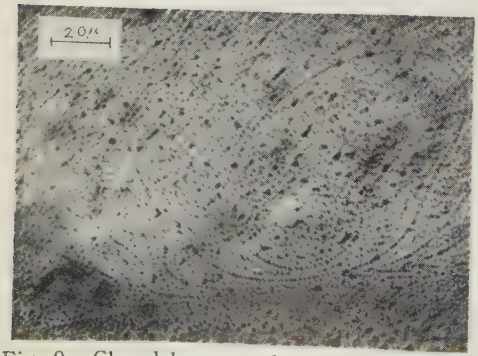

Fig. 9. Closed loops produced by the movement of dislocation.

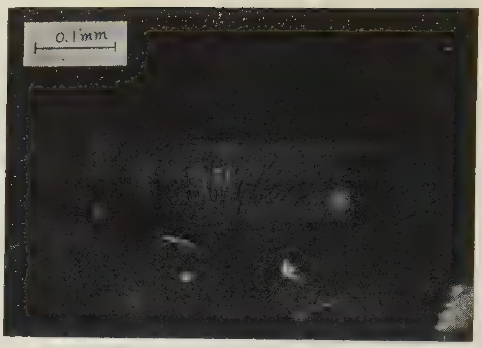

Fig. 10. Layer structure spreading from the edge of a crystal.

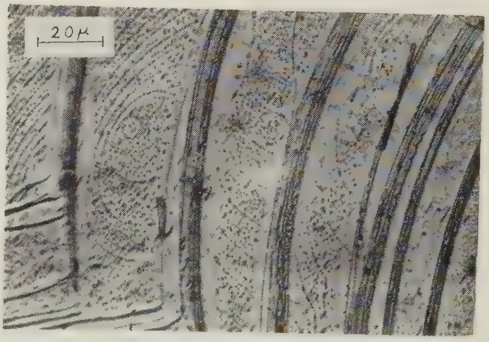

Fig. 11. Spirals appeared on each layer.

faces. But when large crystals were observed, the development of each layer was irregular and relatively wide layers were observed. In such cases the growth spirals described above were observed on relatively wide layers as shown in Fig. 11. Therefore the crystal growth seems to proceed by two mechanism, the layer formation and the spiral growth of each layer. The formation of layer structure depends on the conditions of temperature, impurities and others, but it was not studied in this experiment.

### c) *Shape of spiral*

The $WO_3$ single crystals prepared by the method mentioned above seem to grow from the vapour by sublimation, and so the polygonal spiral has not been observed. The growth spiral on (001) has ‘circular symmetry’, but the shape of spirals on {111} is so characteristic that the orientation of the crystals can be determined approximately from this shape only. The spiral on {111} is elongated in [$\bar{1}$10] direction and the distances between two neighbouring steps in [11$\bar{2}$] direction from the centre of spiral are always narrower than in [$\bar{1}\bar{1}$2]. Fig. 6 is a good example of this form of spirals. This characteristic shape of spirals on {111} is to be explained from the crystal structure in the temperature of growth. Three structures of this material in the temperature range between room temperature and 1200°C, monoclinic, orthorhombic and tetragonal, can be described as a distorted cubic structure of the $ReO_3$ type. The structure in the temperature of crystal growth has not been known, but judging from the structure in lower temperature it may be assumed that it is also approximately a cubic structure of the $ReO_3$ type. The ideal cubic form would contain one molecule per unit cell. In the monoclinic form there are four molecules per unit cell, and each of the $a$ and $b$ axis lengths is approximately twice the length expected for $a$ in the cubic cell. The $c$ axis length is approximately the same in all lattices. In this paper all the indices of planes and directions refer to this monoclinic lattice for convenience. Then the assumed structure is represented as being built up of the atomic layers parallel to {111}, one of which is shown in Fig. 12. Each layer is stacked upon another with the displacement shown by the arrow in this figure, and one period of this stacking contains six such layers and the repeated distance is about 9.2 Å. Accordingly, the stacking of atoms in $[\bar{1}\bar{1}2]$ direction is different from that in $[11\bar{2}]$, and so the velocities of advance of the growth steps differ in each direction. This results the above characteristic shape of spirals.

d) *Step height*

The successive arms of the spirals originating from any two dislocations can join with each other only if the step heights of the two spirals are the same, *i.e.*, the two dislocations are of the same strength. This is the general behaviour of the spirals on $WO_3$ crystals as shown in Fig. 3, 5, 6 and 7. This shows that the dislocations of the same strength tend to appear in any one region of the crystals.

For the measurement of the step height, the multibeam interferometry has been widely used in other crystals. The same method was tried preliminarily to this crystal, but the shift of Fizeau fringe at an individual step could not be observed, and the method of determination of the average step height from the bend of fringe could not be applied to $WO_3$, for the crystal surface is not flat but zigzag on account of its twin structure, especially the fine (100) twinning.

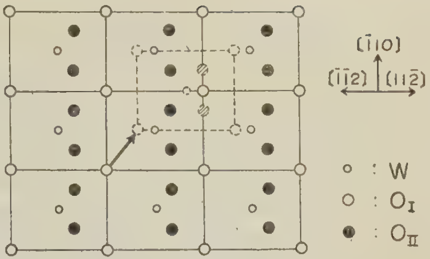

Fig. 12. Elementary atomic layer parallel to {111}. W and $O_I$ is in one plane, $O_{II}$ is in another plane. The latter is $d/12$ higher than the former, where $d$ is the repeated distance of {111}, about 9.2 Å.

In conclusion the author wishes to express his hearty thanks to Prof. K. Tanaka of Kyoto University, Prof. S. Shimose and Prof. M. Tokuhisa of Yamaguchi University for their continual interests and encouragements, and to Mr. Y. Shinnaka for his helpful discussions. His thanks are also due to Prof. E. Takahasi of Yamaguchi University for his kindness to have allowed him to use the microscope in his laboratory.

## References

1) F. C. Frank: Disc. Far. Soc. **5** (1949) 48, 67.
W. K. Burton, N. Cabrera and F. C. Frank: Phil. Trans. Roy. Soc. **A 243** (1951) 299.
2) For example, A. J. Forty: Advances in Physics **3** (1954) 1.
3) B. T. Matthias: Phys. Rev. **76** (1949) 430.
4) H. Bräkken: Z. Krist. **78** (1931) 484.
K. Hirakawa: "Busseiron Kenkyu" **26** (1950) 42 (in Japanese).
R. Ueda and T. Ichinokawa: Phys. Rev. **82** (1951) 563.
K. Hirakawa: J. Phys. Soc. Japan **7** (1952) 331.
W. L. Kehl, R. G. Hay and D. Wahl: J. Appl. Phys. **23** (1952) 212.
S. Sawada: Phys. Rev. **91** (1953) 1010.
R. Ueda and J. Kobayashi: Phys. Rev. **91** (1953) 1565.
5) A. J. Forty: Phil. Mag. **43** (1952) 481.
S. Amelinckx and E. Votava: Naturwiss. **41** (1954) 422.
6) A. R. Verma: "Crystal Growth and Dislocations" (1953).
7) C. W. Bunn and H. Emmett: Disc. Far. Soc. **5** (1949) 119.
8) K. Nonaka and others: "Nagoya Kôgyô Gizyutu Sikenzyo Hôkoku" **4** (1955) 30, 284 (in Japanese).
K. Kubo and others: Met. Phys. **1** (1955) 116 (in Japanese).

JOURNAL OF THE PHYSICAL SOCIETY OF JAPAN Vol. 11, No. 6, JUNE, 1956

# On the Domain Structure of Rochelle Salt Crystal

By Terutaro NAKAMURA

*Department of Physics, University of Tokyo*

(Received February 11, 1956)

The effect of the condition of crystallization on the domain pattern was studied by a polarization microscope. Slow crystallization at the temperatures between two Curie points gave domains parallel to the $b$-axis, whereas above the upper Curie point they were parallel to the $c$-axis. On raising temperature through the upper Curie point, monoclinicity decreased gradually, without any change of domain width, until the domain pattern disappeared at $24.25° \pm 0.2°$C, where a marked pyroelectricity and a maximum of permittivity were observed. The pyroelectric effect continued to exist up to a temperature a little higher. Annealing crystals in the atmosphere of appropriate humidity had no effect on the domain formation. This fact, together with the fact that the crystallization between two Curie points brought about the splitting into domains seems to show that the domain formation is mainly governed by elastic energy rather than electrostatic energy. Explanations of observed phenomena are presented.

## §1. Introduction

By a simple analogy to ferromagnetism, rochelle salt crystal was supposed to split up into ferroelectric domains between two Curie points, since the early days of the study. It was first predicted theoretically by Jaffe[1] that domain structure must actually be existing in rochelle salt. His careful analysis of the physical properties of rochelle salt crystal led him to the conclusion that in ferroelectric temperature range it must belong to monoclinic symmetry $P2_1$, although it "appears" to posses the orthorhombic symmetry $P2_12_12$ as in non-ferroelectric range. His hypothesis was that every domain has the monoclinic symmetry and has spontaneous strain $y_z$, but, as a whole, crystal appears to show orthorhombic symmetry by forming laminated twin structure. X-ray studies by Miyake[2] and Ubbelohde[3] presented experimental suppots of Jaffe's theory independently. Furuichi and Mitsui[4] observed domain structure directly by the use of polarization microscope, providing the conclusive evidence to Jaffe's theory.

A theory about shape and size of the ferromagnetic domain was discussed extensively by Kittel[5], concluding that the domain structure which minimizes exchange energy, anisotropy energy, magnetoelastic energy, and magnetostatic energy must be realized. The ferroelectric domain structure, however, cannot be discussed in parallel. The most important differences between ferromagnetic and ferroelectric cases lie in the following two points. Firstly, there is the possibility of charge neutralization by means of free charges in the atmosphere in the case of ferroelectrics. Secondly, piezoelectric effect or electrostriction of ferroelectrics is considerably larger than the values of magnetostriction of ferromagnetic materials. It is consequently very likely that the formation of ferroelectric domains is largely governed by elastic energy, rather than electrostatic energy, whereas the formation of ferromagnetic domains is governed by magnetostatic energy.

It is also very likely that the imperfections on surfaces and in the interior give remarkable effects on domain structure. These situations are much complicated, and the problem seems to be beset with difficulties in understanding the phenomena conclusively. The present study was designed to secure informations about ferroelectric domain formation as possible, and several points of interest have come to light during the course of our experiments.

## §2. Variety of Domain Pattern

A variety of domain patterns, as already reported[6,7], can be observed using polarization microscope. Domain patterns can be assorted into five types as follows:

(1) Laminated domains parallel to *a*- and *c*-axes.
(Let us call them *c*-axis domains or simply *c*-domains in the present paper.)

(2) Laminated domains parallel to *a*- and *b*-axes.
(Let us call them *b*-axis domains or simply *b*-domains.)

(3) Co-existence of *b*-axis domains and *c*-axis domains.

(4) A part of crystal forms a large domain.

(5) Peculiar types of domain structure.

Domain patterns were studied by controlling temperature or controlling speed of crystallization. Crystallization was done by both evaporation method at constant temperature using drying agents and cooling method at constant speed of crystallization utilizing the temperature dependence of solubility. Observation were made on *a*-plate crystals, which had grown from seeds of *a*-plate placed between parallel glass plates immersed in the saturated solution, so that the domain structure of the crystal, just grown, was able to be observed without applying mechanical stresses resulted from cutting. Domain patterns were also studied by applying some physical treatments.

### § **2.1.** *b*-axis Domain, *c*-axis Domain, and their Co-existence.

According to simple analogy to ferromagnetism, ferroelectric crystal must split up into domains, making the electrostatic energy small. If this is the case, it must be inferred that a crystal which has been crystallized at temperatures between two Curie points should give a single domain crystal, because the crystallization is carried out in the conductive solution and electrostatic energy will be zero.

Experiments turned out that crystallization at temperature between two Curie points also gave poly-domain crystals, supporting the view that the formation of ferroelectric domains is largely governed by elastic energy, rather than electrostatic energy.

Crystallization at temperatures between two Curie points gave domains parallel to the *b*-axis, whereas the crystals which were crystallized above the upper Curie point gave domains parallel to the *c*-axis when cooled down to temperatures between two Curie points. Crystallization started at 26°C, completed at 22°C gave the crystal of the domain pattern rather complicated. Namely, the part crystallized at temperatures above the upper Curie point was composed of *c*-axis domains, the part crystallized in ferroelectric temperature range *b*-axis domains, and the transient part *b*- and *c*-axis domains coexisting. These facts clearly indicate that for rochelle salt crystals, which have grown at temperatures above the upper Curie point, *c*-axis domains are more stable, whereas for crystals grown below the upper Curie point *b*-axis domains are stable. It was also found that *b*-domain crystals yielded a tendency to change into *c*-domain crystals in the long time. Possible explanations of the phenomena will be presented later in § 5.

Cracking a *b*-domain crystals with a knife edge also caused *c*-axis domains co-existing with *b*-axis domains due to a high mechanical stress. Coexistence of *b*- and *c*-axis domains was also observed near flaws, which were present in the portion where the crystallization had taken place rapidly.

### § **2.2.** Large Domains

Large domains of the order of magnitude 1 mm$^2$ are sometimes observed in crystals which are supposed to have been subject to high internal stress in the course of crystal growth. The width of large domains is some hundreds times as large as that of usual domain. The large domain splits up into usual *c*-axis domains, when craked by a knife edge.

### § **2.3.** Peculiar Type of Domain Structure I.

Observation with microscope revealed that the flaws present in a rochelle salt crystal was composed of nearly spherical small holes, the order of magnitude (1/100)mm in diameter, which were filled with saturated solution. The existence of the liquid in the hole was deduced from the bubbles observed in the hole. Peculiar type of domain structure as shown in Fig. 1, as has been reported⁶⁾, is frequently observed around a small hole, which composes the flaw. It will be shown in § 5 that this type of domain structure must be due to stress concentration around the hole.

### § **2.4.** Peculiar Type of domain Structure II.

Another peculiar type of domain structure

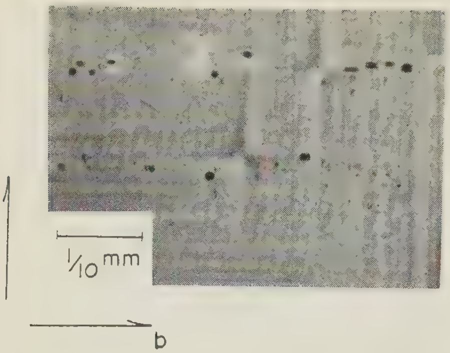

Fig. 1. Peculiar type (I) of domain structure around a hole filled with saturated solution.

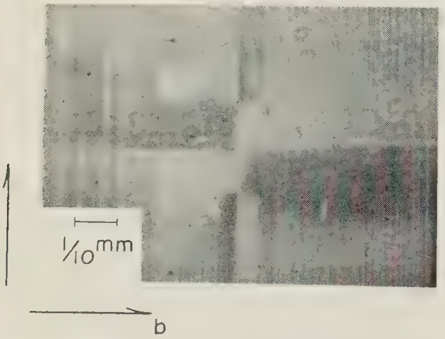

Fig. 2. Peculiar type (II) of domain structure around a group of fine crystals, which has been crystallized by a certain treatment.

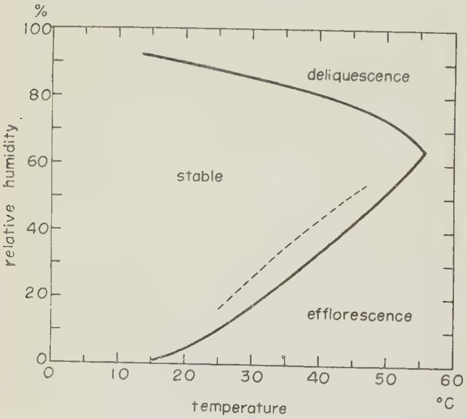

Fig. 3. Stable region of rochelle salt crystal in relation to temperature and humidity. Dotted line shows the boundary for effloresced crystals. (according to Kawai[8].)

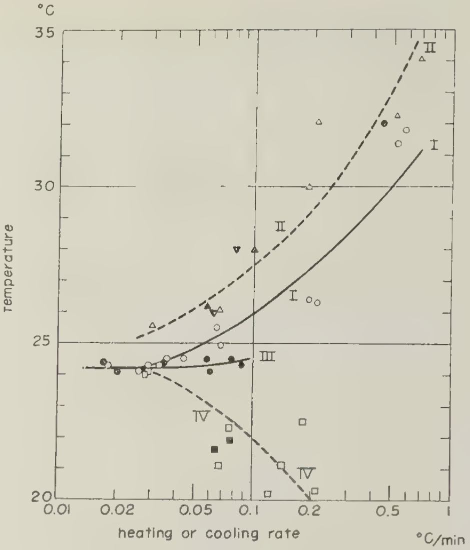

Fig. 4. Effect of heating or cooling rate on
(I) ○ (III) ● the temperature at which domain structure disappears (on heating),
(IV) □ ■ the temperature at which domain structure appears (on cooling),
(II) △ ▲ the temperature at which pyroelectric effect ends (on heating),
and (II) ▼ the temperature at which pyroelectric effect starts (on cooling);
where solid symbols denote the cases of applying an a.c. field.

as shown in Fig. 2 was observed around a group of fine crystals produced by a treatment described below. In the first place thin *a*-plate crystals of rochelle salt were kept at 40°～45°C in a humidistat, of which humidity was kept constant by $CaCl_2$ for about one day, resulting in the roughness of the surface by efflorescence, as can be understood from Fig. 3. A close observation of the surface by the use of a microscope, lines parallel to *c*-axis were observed, in agreement with results obtained by Sakisaka[9], indicating that cracks in *c*-direction exist. The second process followed, keeping the crystals at also 40°～45°C in the humidistat, which confines the air of humidity 70% at 10°～15°C, for several days. The surface then underwent deliquescence to a small extent, as can be assumed from Fig. 3[8]. The aquous solution of rochelle salt resulted from deliquescence will fill the crack, and will crystallize in the crack forming a group of fine crystals in decreasing temperature. Around the group of fine crystals this type of domain structure was observed. It will be shown in § 5 that this type of domain structure must be due to stress distribution around the crack filled with group of fine crystals.

## § 3. Pyroelectric Effect; Temperature Dependence of Domain Structure and Permittivity

It is well known that a marked pyroelect-

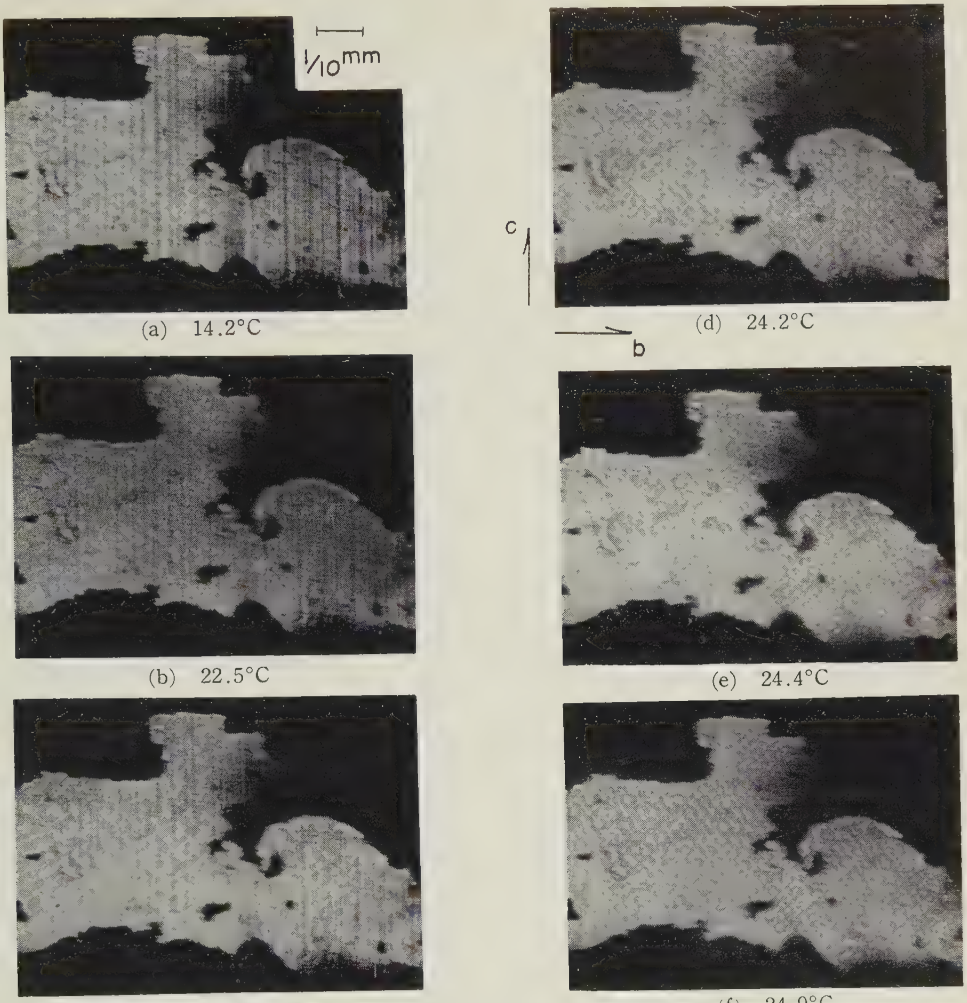

(a) 14.2°C (d) 24.2°C

(b) 22.5°C (e) 24.4°C

(c) 24.0°C (f) 24.9°C

Figs. 5. Temperature dependence of domain pattern.

ricity is observed in rochelle salt, in raising temperature from the ferroelectric temperature range through the upper Curie point. It is clear that there should exist a close relation between the domain structure and pyroelectric effect as has been pointed out by Jaffe[1]. However, two possible processes are conceivable, by which the domain structure disappears at the transition point, being accompanied by pyroelectric effect: Firstly the process that domain width varies in accordance with pyroelectric effect, and at Curie point domain structure disappears abruptly; secondly the process that the domain width and domain distribution are indepedent on temperature, but the monoclinicity, i.e. the deviation from the orthorhombic symmetry, decreases gradually in accordance with pyroelectric effect, until the domain structure becomes invisible. In order to determine which process actually takes place, temperature dependence of domain pattern was observed, and the measurement of pyroelectric effect was also carried out simultaneously, raising temperature from ferroelectric range through the upper Curie point.

On the surface of *a*-plate crystals of the rectangular shape 1 cm×2 cm with thickness 0.6 mm, which were cut out from large crystals, silver foil of thickness of the order of magnitude 0.08 $\mu$ was applied by means of absolute alcohol. At the center of the foil, a hole of area of the order of magnitude 1 $\mathrm{mm}^2$ was made, and domain pattern of that portion was observed. Under and over the

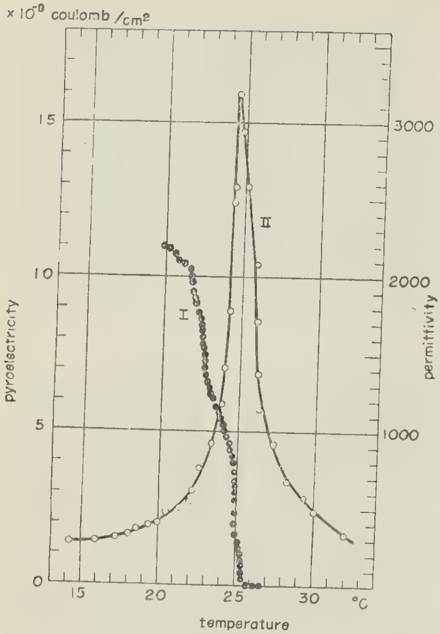

Fig. 6. Temperature dependence of permittivity and pyroelectric effect.

silver-foiled crystal two thin metal electrodes with circular holes were placed. Whole system of the microscope was set in a thermostat. The temperature of the specimen was measured by copper-constant an thermocouple, placed in the vicinity of the specimen, held between plates of rochelle salt crystal of the same size as the specimen, and covered by the same metal plate as electrodes.

The temperature, at which the domain structure disappears, have been plotted against the rate of raising temperature in Fig. 4, curve I. The temperature, at which the pyroelectric effect ends, have been also plotted against the rate of raising temperature in Fig. 4, curve II. Fig. 4 summarizes the results for good many specimens. It should be noted here that the temperature, at which the domain structure disappears, and the temperature, at which the pyroelectric effect ends, largely depend on the rate of raising temperature, as can be seen by curves I, II in Fig. 4. The rate of raising temperature lower than 0.04 deg/min. gave essentially the same temperature for the domain structure to disappear.

The domain patterns at various temperatures are shown in Figs. 5, the rate of raising temperature being 0.03 deg/min. In raising temperature from about 10°C very slowly, no change of domain pattern was observed at first, and pyroelectric effect was also scarecely deteced. In raising temperature furthermore, pyroelectric effect increased gradually, whereas domain pattern showed no change until 22°C was reached. Above 22°C, difference of the brightness between adjacent domains decreased, indicating that the monoclinicity decreased. Simultaneously large pyroeletric effect was observed, indicating that decrease of monoclinicity evidently corresponds to pyroelectric effect. The pyroelectric effect v.s. temperature has been plotted in Fig. 6, curve I. The domain pattern became invisible at 24.25°±0.2°C, whereas pyroelectricity continued to exist up to a temperature a little higher.

The temperature dependence of permittivity was also studied, observing domain pattern simultaneously. Permittivity measurement was made using a bridge circuit at frequency 700 cps, applying 5 volts/cm. In Fig. 6, curve II permittivity has been plotted against temperature. In raising temperature very slowly (heating rate $<0.04$ deg/min.), the temperature dependence of domain pattern was just the same as shown in Figs. 5, and a peak of the permittivity was observed at the critical temperature for the domain structure to become invisible.

The a.c. field applied in measuring permittivity may affect the temperature at which domain structure disappears or the temperature at which pyroelectric effect ends. Our close studies showed that the temperature at which domain structure disappears was affected by the a.c. field as shown in Fig. 4, curve III; i.e. transition occurred at lower temperature than without a.c., when the rate of raising temperature is larger than 0.04 deg/min. The pyroelectrity, however, also continued to exist up to a little higher temperature than domain structure disappearance, even when the a.c. field is applied. Thus it seems to be concluded that the application of a.c. field makes it easy for the transition to occur, whereas it has no effect on the temperature at which pyro-electric effect ends. No proper under standing of this phenomenon is not yet reached.

## § 4. Effect of Electrostatic Energy on the Domain Formation

As mentioned above, the formation of ferroelectric domains seems to be mainly governed by elastic energy, rather than electrostatic energy. This view is supported by our finding that crystallization in ferroelectric temperature range never shows a tendency to become single domain crystal but gives poly-domain crystal. However, Mitsui and Furuichi[6)] reported that a specimen, which had been kept at a high temerature for a long time and then cooled down to a temperature between two Curie points, showed a domain structure largely different from the initial one, i.e. domain width is markedly smaller, the relation between domain width $w$ and thickness $D$ was represented as $w=k\sqrt{D}$. This experimental data led them to conclude that the formation of the ferroelectric domains is governed also by electrostatic energy.

This experiment by Mitsui and Furuichi, however, did not pay satisfactory attention to the effect of humidity. Therefore, similar experiments controlling not only temperature but also humidity were carried out. Specimens of thickness 0.6 mm were kept at 40°∼45°C for 2 or 3 days in a humidistat. As Fig. 3 shows, at these temperatures a crystal undergoes efflorescence at relative humidity lower than about 40% and it undergoes deliquescence at relative humidity higher than about 80%.

Experiments were carried out with the results as follows. In the case, where $CaCl_2$ was used for keeping the humidity constant in the humidistat, domain width markedly decreased in agreement with Mitsui and Furuichi's result; the crystal effloresced a little, surfaces were rough, number of small cracks parallel to $c$-axis were present, and many powders of dehydrated rochelle salt were observed on the surfaces. In the case of using $H_2SO_4$ of concentration 37.5%, which keeps relative humidity 64% at 50°C, there was no notable change in domain width, the crystal surfaces were smooth, in contrast with the result of experiments in dried air. This clearly shows that domain formation is not governed by electrostatic energy, for stable crystals in a atmosphere of relative humidity 64%.

For understanding the decrease of domain width in a dried atmosphere, two main possibilities will be conceivable. First, in dried atmosphere, the electrostatic energy may prevail, so that "annealing" should cause domain structure of notably decreased width; second, the efflorescence of the crystal may affect the domain structure, resulting in the decrease of domain width.

Similar experiments with short-circuited crystals were carried out, by holding crystals in mercury, or wrapping them with tin foil, or wrapping silver-foiled crystal with tin foil, the surface of the crystal being dried in the atmosphere of the relative humidity lower than 35%. High electric field, if existing in the space between the crystal and the electrodes, is confined within a very small space, resulting in low electrostatic energy as a whole.

The experiments turned out that domain width decreased markedly in agreement with the results in the case of the crystals, which were not short-circuited in a dried atmosphere, the surface being rough by the dehydration. It seems likely that the decrease of domain width in a dried atmosphere should be attributed to the efflorescence of the crystal surface.

This series of experiments supports the view that domain formation is not governed essentially by electrostatic energy.

## § 5. Theoretical Analysis and Discussion

In the present section interpretations of peculiar types of domain structure as Figs. 1 and 2 are presented in the first place.

The first type is observed around holes which are filled with saturated solution. Stress distribution around the circular hole, in which hydrostatic pressure $p$ is existent, can be obtained as two dimentional problem of elastic body, by finding a suitable Airy stress function $F$, provided for brevity that elastic constants are isotropic. This stress function must satisfy the differential equation:

$$\left(\frac{d}{dr^2}+\frac{1}{r}\frac{d}{dr}\right)\left(\frac{d}{dr^2}F+\frac{1}{r}\frac{d}{dr}F\right)=0, \quad (5.1)$$

and must yield stresses or displacements which satisfy the boundary conditions of the problem. The stresses are given by the following relations:

$$Y_y=\frac{\partial^2 F}{\partial z^2}, \quad Y_z=-\frac{\partial^2 F}{\partial y \partial z}, \quad Z_z=\frac{\partial^2 F}{\partial y^2}. \qquad (5.2)$$

The Airy stress function appropriate for the problem is:

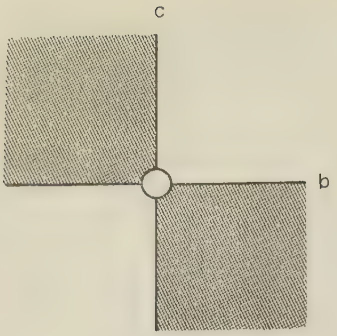

Fig. 7. The sign of $Y_z$-stress field around a hole filled with saturated solution.

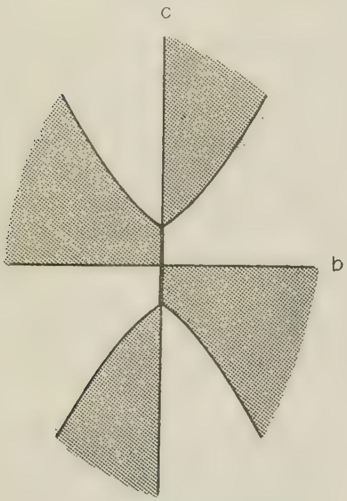

Fig. 8. The sign of $Y_z$-stress field around a crack, filled with a group of fine crystals.

$$F=c_1 \log r+c_2 r^2\,, \tag{5.3}$$

constants $c_1$, $c_2$ are determined as:

$$c_1=-a^2 p\,,$$
$$c_2=0\,,$$

by means of boundary conditions:

$$\sigma_r=-p \quad \text{at} \quad r=a$$
$$\sigma_r=0 \quad \text{at} \quad r\to\infty$$

where $a$ denotes the radius of the hole. Thus stress $Y_z$ is obtained as:

$$Y_z=-\frac{\partial^2 F}{\partial y \partial z}=-a^2\frac{p}{r^2}\sin 2\theta\,. \tag{5.4}$$

The absolute value of $Y_z$ dies off inversely as the second power of the distance from the conter of the circle and the sign of $Y_z$ is shown in Fig. 7.

If a crystal is cooled from above the upper Curie point under the influence of stress $Y_z$ expressed by (5.4), it must split up into domains, so that the portion subject to positive $Y_z$ should have positive $y_z$ and vice versa, resulting in the peculiar type of domain structure shown in Fig. 1.

The second type is observed around a group of fine crystals which have been crystallized by the treatment described in § 2. Fine crystals are situated in a crack, of which shape can be approximated by very thin ellipse. Stress distribution of the similar problem as the previous one can be obtained by the use of elliptic coordinate:

$$y=c \sinh \xi \sin \eta$$
$$z=c \cosh \xi \cos \eta\,.$$

The Airy stress function $F$ must satisfy the differential equation:

$$\Delta\Delta F=0\,, \tag{5.5}$$

and yield stresses which satisfy the boundary conditions:

$$\tau_{\xi\eta}=0,\quad \sigma_\xi=-p, \quad \text{at the boundary} \quad \xi=0$$
$$\sigma_\xi=0 \quad \text{at} \quad \xi\to\infty\,.$$

where the equation of boundary $\xi=\alpha$ was put $\xi=0$, because $\alpha\doteq 0$. These boundary condition were adopted because the group of fine crystals crystallized in the crack will result no shear stress but normal stresses. The Airy stress function appropriate for this problem is:

$$F=A(e^{-2\xi}+\cos 2\eta)+B\xi\,, \tag{5.6}$$

where integration constants $A$, $B$ are determined as:

$$A=\frac{B}{2}=-\frac{cp^2}{4}\,.$$

$Y_z$ is obtained as:

$$Y_z=-\frac{p}{4(\cosh^2\xi-\cos^2\eta)^2}\times[\varphi(\xi,\eta)\sin 4\eta+\psi(\xi,\eta)\sin 2\eta]\,, \tag{5.7}$$

$$\varphi(\xi,\eta)=-\frac{1}{2}(1+R)\sinh 2\xi\,,$$

$$\psi(\xi,\eta)=-e^{-2\xi}\sinh 2\xi+e^{-2\xi}-\sinh 2\xi-1 -2R\sinh\xi(e^{-2\xi}\sinh\xi-\cosh\xi-\sinh\xi)\,,$$

where

$$R=(\cosh^2\xi+\cos^2\eta)/(\cosh^2\xi-\cos^2\eta)\,.$$

Amount of stress $Y_z$ near both ends of major axis of very thin ellipse must be extremely high and dereases in increasing the distance from the group of the fine crystals, and the sign of $Y_z$ is shown in Fig. 8.

If a crystal is cooled from above the upper Curie point under the influence of stress $Y_z$ expressed in (5.7), it must split up into domains, so that the portion subject to positive $Y_z$ should have positive $y_z$ and vice versa, resulting in the peculiar type of domain structure shown in Fig. 2.

Now we are on the step to give tentative explanations for the phenomena that rochelle salt crystals which have grown at temperatures above the upper Curie point give $c$-axis domains when cooled down to ferroelectric temperature range, and that $b$-domain crystals show a tendency to change into $c$-domain crystals.

Observation of the crystal by throwing light at a certain angle of incidence yields large number of groups of fine lines. As reported by Sakisaka$^{10)}$ those are cylindrical fine holes, parallel to crystallographic $c$-axis, the order of magnitude $1\sim10\,\mu$ in diameter, hollow or filled with saturated solution. It may be noted here that those fine holes are present even when the crystallization is carried out in the best condition, whereas flaws which has been remarked in § 2.1 take place at the portion where speed of crystallization is too high. If a domain wall intersect cylindrical fine holes parallel to $c$-axis, the energy of the domain wall will be small$^{11)}$. Therefore, it may be inferred that the existence of cylindrical fine holes parallel to $c$-axis prefers $c$-domains rather than $b$-domains, when cylindrical holes are existent in a certain distribution. This may provide one of possible explanations of the facts cited above.

There appears to be another possible explanation to account for the phenomena. Let us suppose that crystals contain great number of screw dislocations especially parallel to $c$-axis. This assumption may be not found unreasonable, because, according to Frank, for a dislocation of large Burgers' vector there exists a state of equibrium in which the core of the dislocation is an empty tube$^{12)}$ and then cylindrical fine holes parallel to $c$-axis is possible to be dislocations with large Burger's vector. Provided that there are great many screw dislocations in $c$-direction, there should exist stress field in the vicinity of them.

Let us first consider the crystal at a temperature above the upper Curie point. The strain component $y_z$ at a point $(r, \theta)$ is given by

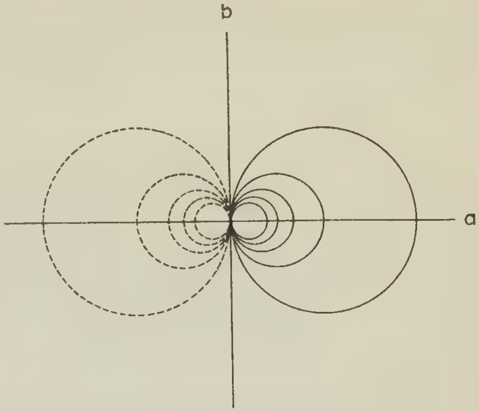

Fig. 9. Contours of strain $y_z$ around a screw dislocation, above the upper Curie point; solid line denotes positive, dotted line negative strain.

$$y_z = \frac{b}{2\pi r}\cos\theta\,, \tag{5.8}$$

provided for brevity that elastic constants are isotropic, where $\theta$ denotes the angle measured from $a$-axis in (001) plane, $r$ denotes the distance from the screw dislocation parallel to $c$-axis. Our discussion is only confined to the region $r \geqq r_0$, where $r_0$ is critical radius for which the theory of elasticity applies. Contours for the stain $y_z$ are circles in Fig. 9, as can be seen from (5.8). A portion near the screw dislocation is largely polarized even above the upper Curie point, because the strain $y_z$ must be accompanied by polarization according to Mueller's theory$^{13)}$. The region, in which the polarization is larger than spontaneous polarization $P_s$ ($=2.5\times10^{-7}$ coulomb/cm² at 0°~10°C), is obtained from (5.8):

$$r < \frac{b}{2\pi y_{zs}}\cos\theta\,, \tag{5.9}$$

where $y_{zs}$ shows the spontaneous strain at 0°~10°C:

$$y_{zs} = 8\times10^{-4}\,.$$

The region expressed by (5.9) is a circular cylinder of diameter $0.12\,\mu$, provided that the modulus of the Burgers' vector $b$ is equal to the lattice constant in $c$-direction, 6.17 A.

Cooled through the upper Curie point, crystals must split up into domains. Then, the portions in the vicinity of dislocations, which have been largely polarized at temperatures above the upper Curie point, may provide nuclei of domains, which will grow into *c*-axis domains. This is another possible explanation of the phenomena.

## § 6. Summary and Conclusions

Effect of the condition of crystallization on the domain pattern was studied, temperature dependence of the domain pattern and its relation to pyroelectric effect and to permittivity were also studied. What governs the formation of ferroelectric domains was investigated.

The findings are summarized in the following.

(1) Crystallization at temperatures between two Curie points gave domains parallel to *b*-axis. (*b*-axis domains)

(2) Crystallization at the temperature above the upper Curie point gave *c*-axis domains. The *b*-axis domains yielded a tendency to change into *c*-axis domains.

(3) On raising temperature through the upper Curie point, monoclinicity decreased gradually until the domain pattern disappeared, without any change of domain width. This process showed good correspondence with pyroelectric effect. The domain pattern became invisible at 24.25°±0.2°C, the peak value of permittivity being attained at the same temperature. The pyroelectric effect, however, continued to exist up to some higher temperature.

(4) Annealing crystals in the atmosphere, where rochelle salt remains stable, showed no effect on domain structure. The effect of annealing crystals short-circuited in dried atmosphere was quite similar to that of annealing free crystals in the dried atmosphere. These results, together with the fact that the crystallization in ferroelectric temperature region, immersed in the conducting solution, brought about the splitting up into domains, may support the view that the domain formation is mainly governed by elastic energy, rather than electrostatic energy.

(5) It was revealed that the peculiar types of domain structure as shown in Figs. 1 and 2 were due to stress distributions around a hole filled with saturated solution and around a crack filled with a group of fine crystals, respectively.

(6) If a domain wall interesects cylindrical fine holes parallel to *c*-axis, the domain wall energy will be small, giving a possible explanation of the phenomena, described above in (2).

(7) Suppose the existence of screw dislocations parallel to *c*-axis, then some portions in the vicinity of them should be largely polarized. Therefore, on cooling through the upper Curie point, nuclei of domains may be formed, which will grow into *c*-axis domain, giving another possible explanation of the phenomena cited above in (2).

The author wishes to express his gratitude to Prof. H. Takahasi, for his valuable discussions and suggestions rendered during the course of this work. He is also indebted to Dr. M. Marutake for supplying him samples of rochelle salt, to Prof. Y. Sakisaka and Prof. G. Matsuura for their helpful discussions. Progress of this study was facilitated by a Grant in Aid for Fundamental Scientific Research from the Ministry of Education.

### References

1) H. von R. Jaffe: Phys. Rev. **51** (1937) 43.
2) S. Miyake: Proc. Phys-math. Soc., Japan **23** (1941) 377; 810.
3) A. R. Ubbelohde and I. Woodward: Proc. Roy. Soc., London A **185** (1946) 448; **188** (1947) 358.
4) J. Furuichi and T. Mitsui: Phys. Rev. **80** (1950) 93.
5) C. Kittel: Rev. Mod. Phys. **21** (1949) 541.
6) T. Mitsui and J. Furuichi: Phys. Rev. **90** (1953) 193.
7) M. Marutake: J. Phys. Soc. Japan **7** (1952) 25.
8) H. Kawai: Nippon Sugaku Butsuri Gakkai Shi **17** (1943) 270 (in Japanese).
9) Y. Sakisaka: Sci. Rep. of Saitama Univ. **1** (1952) 50.
10) Y. Sakisaka: unpublished, short remarks appeared in ibid. **1** (1952) 50; **1** (1953) 63.
11) R. Abe: J. Phys. Soc. Japan **11** (1956) 104.
12) F. C. Frank: Acta Cryst. **4** (1951) 497.
13) For example see: W. G. Cady, Piezoelectricity (McGraw-Hill Book Co. Inc., New York, 1946), p. 582.

JOURNAL OF THE PHYSICAL SOCIETY OF JAPAN Vol. 11, No. 6, JUNE, 1956

# Electronic Structure of the Exciton

## I. Localized Exciton in KCl

By Toshinosuke MUTO and Hiroshi OKUNO

*Institute of Science and Technology, University of Tokyo, Tokyo*

(Received February 14, 1956)

The present situation of the exciton problem is discussed briefly. The localized excitons of KCl in both optical and X-ray absorption have been worked by using Wannier-Slater's equation for the perturbed lattice, which may be considered to essentially correspond to the quantum-analogue of von Hippel's semi-classical model of the exciton. The perturbing potential fields in Wannier-Slater's equation are evaluated numerically by the use of Hartree's data and then the best-fit analytical functions are constructed with fair accuracy. The solutions of the equation are worked by the variational method. The result for the optical exciton is observed to be in fair agreement with the experiment. As for the X-ray exciton, the quantitative comparison with our results can hardly be carried out at present, since the position of the bottom of conduction band can not be measured accurately on the X-ray absorption spectra. On the basis of our results for X-ray exciton, however, some discussions on the characteristic structure near the absorption edge in KCl are presented.

### § 1.

As is well-known in the ultraviolet absorption in alkali halide crystals, the first absorption band without photocurrent can not be appropriately taken into account by the usual band theory of solids, but has been ascribed, by Frenkel¹⁾, to a new electronic state, i.e., the exciton state, in which an ejected electron by an incident photon has been bound in the field of a positive hole left after the light absorption and, further, a coupled pair of electron and positive hole, i.e., a quasi-neutral atom in excited state is capable of wandering from one cell of the lattice to another throughout the crystal. Recently, the detailed behavior of such exciton, i.e., its mobility in colored alkali halides has been actually measured by Taft and Apker²⁾ in their beautiful experiments of the external photoelectric effect. Furthermore, Inchauspe³⁾ has successfully found some experimental evidence about the exciton localized near a vacant lattice site or a $F$-center in alkali halides. In the present article the exciton consisted of an electron coupled by a positive hole in the state of a valence band shall be called "optical exciton" for the reason that it has been usually observed in the ultraviolet absorption. In fact, such exciton states have actually been observed, though qualitatively, not only in the ultraviolet absorption of many insulating crystals⁴⁾, but also in their $X$-ray absorption and emission spectra according to the recent experimental observations. As was already stressed by Mott and Cauchois⁵⁾ and Parratt and Jossem⁶⁾ in their interpretations of $X$-ray spectra of the alkali halide crystals, the appearance of the remarkably sharp peeks in both $X$-ray absorption and emission spectra in the insulating crystals seems to provide strong support for the existence of the different kind of exciton states from those in the optical region, just below the bottom of both conduction and valence bands, in which an ejected electron by a photon is trapped in the field of a positive hole left in the $X$-ray level. Such kind of exciton shall be called "$X$-ray exciton" for the reason that it has been observed experimentally in the $X$-ray region. Furthermore, Friedel⁷⁾ has discussed theoretically the possible effect of an optical exciton upon the ultraviolet absorption in metallic crystals, according to which whether the effect of an exciton is observable or not seems to be essentially governed by the amount of screening of a positive hole by the nearby crystal electron during the electronic transitions. In view of the above situations both experimental and theoretical, the exciton may be considered to make its appearance, to a more or less amount, quite generally in almost all the crystals with or without lattice defects, and, to provide a useful data for elucidating the detailed structure of electronic states in the crystal which can not be satisfactorily dealt with by the usual band theory, particularly allowing for the situation that the band theory can hardly be proceeded, at present, along Hartree's original procedure of self-consistent field method developed in atomic structure.

Among the theoretical investigations of the exciton problem which have been carried out so far, we have two different approaches to this problem the inter-relation of which seems not to be worked out from a unified standpoint; one is due to von Hippel[8)], de Boer[9)] and Dexter[10)] whose works did concern with a localized exciton, and another due to Frenkel[11)], Peierls[12)], Slater and Shockley[13)] who have dealt with the moving exciton or excitation wave. In the former work the energies of localized excitons in alkali halide crystals have been quantitatively computed on the basis of classical, atomic model in which an electron is removed from a halogen ion to a neighbouring metal ion. They have obtained good agreement with the experiments on the position of the first absorption bands in alkali halides. Dexter[14)] has discussed the transition probability to a localized exciton state through ultraviolet absorption by the use of his perturbation procedure developed in the *F*-center problem but not worked the energies of the localized exciton. On the other hand, the characteristics of a moving exciton or excitation wave have been qualitatively discussed by the mentioned authors only for the oversimplified crystal model but, for the actual crystals, the quantitative work about exciton seems to be still lacking at present in spite of the rather accumulated data in the experimental observations. Generally speaking, the theoretical treatment of a moving exciton is considered to become essentially many electron problem in which the configuration interaction plays decisive role as shown in Slater and Shockley's work[15)], whereas, the idea involved in von Hippel's classical treatment of localized exciton seems to be based upon one electron problem. The mutual relation between both treatments of exciton seems to remain still unclarified, at least quantitatively, though it is intuitively speculated.

In view of the above mentioned situations of the exciton problem, it seems to be highly desirable to attempt to work quantitatively the electronic structure of excitons, appearing in both optical and *X*-ray absorptions. Now, in the present article (Part I), the electronic states of the localized excitons in both optical and *X*-ray regions shall be dealt with for KCl by the use of Wannier-Slater's equation for the perturbed lattice, the content of which may be considered to correspond to a quantum-analogue of von Hippel's model of a localized exciton. The quantitative discussions of the moving exciton or excitation wave in KCl shall be worked out in the next paper (Part II), taking into account the configuration interaction based upon the basic set of Bloch orbital or its modified form, together with the discussions on the relation to a localized exciton treated here and the interaction with lattice vibration.

## § 2.

According to Slater-Koster's theory[16)] of the perturbed lattice, the wave function of an electron in the perturbed periodic field is described in terms of the complete set of Wannier functions,

$$\Psi(\vec{r})=\sum_{n,j}\psi_n(\vec{R}_j)a_n(\vec{r}-\vec{R}_j)\,, \qquad (1)$$

in which $a_n(\vec{r}-\vec{R}_j)$ represents Wannier function, around a lattice point $\vec{R}_j$, belonging to a band $n$. The unknown coefficients $\psi_n(\vec{R}_j)$ and the energy of the perturbed state are determined by the Schrödinger wave equation of an electron in the perturbed periodic field, i.e.,

$$(H_0+V(\vec{r}))\Psi(\vec{r})=E\Psi(\vec{r})\,, \qquad (2)$$

where $V(\vec{r})$ is the perturbation to the unperturbed Hamiltonian $H_0$ of the periodic field problem. Putting (1) into (2), the conventional manipulation leads to the difference equations to be satisfied by the coefficient $\psi_n(\vec{R}_j)$. The differential equation approach to such set of difference equations has been shown to arise from considering the coefficients as a continuous function of space variable $\vec{r}$ under the assumption that the perturbation $V(\vec{r})$ varies rather slowly over the spread of Wannier functions and, further, the perturbation do not result in mixing of the Wannier functions of different bands and different unit cells, that is, the perturbed states are mainly determined by the diagonal components of the matrix of $V(\vec{r})$ with respect to Wannier functions belonging to a single band under consideration. The derived differential equation to be satisfied by $\psi(\vec{r})$ can be written as

$$E_0(-i\nabla)\psi(\vec{r})+V(\vec{r})\psi(\vec{r})=E\psi(\vec{r})\,, \qquad (3)$$

which is called Wannier-Slater's fundamental equation for the perturbed state. $E_0(-i\nabla)$ is obtained by replacing wave number vector $\vec{k}$ by the operator $-i\nabla$ in the energy band $E_0(\vec{k})$ of the periodic potential problem, i.e., the eigenvalue of unperturbed system $\boldsymbol{H}_0$. The merit of Slater-Wannier's equation lies in the fact that the solution for the energy of perturbed levels can be easily obtained without the explicit use of Wannier functions of the periodic field as in the case of the ordinary perturbation theory and all the effect of expansion into the Wannier functions are concisely involved in the differential operator $E_0(-i\nabla)$.

Now, according to Tibbs and others[17)], the levels in the lower part of the conduction band of alkali halides have been shown to become of *s*-symmetry, on account of which we may safely suppose for $E_0(-i\nabla)$ to take the following form near the band bottom.

$$E_0(-i\nabla)=E_0-\frac{\hbar^2}{2m^*}\left(\frac{\partial^2}{\partial x^2}+\frac{\partial^2}{\partial y^2}+\frac{\partial^2}{\partial z^2}\right), \qquad (4)$$

where $E_0$ represents the energy of conduction band bottom and $m^*$ the effective mass of an electron in its neighbourhood. The substitution of (4) into (3) leads to

$$-\frac{\hbar^2}{2m^*}\Delta\psi(\vec{r})+V(\vec{r})\psi(\vec{r})=E'\psi(\vec{r})\,, \qquad (5)$$

where $E'=E-E_0$, i.e., the energy of perturbed state measured from the conduction band bottom. Our next task is to solve Wannier-Slater's equation (5) by introducing the explicit form of the perturbation potential $V(\vec{r})$ appropriate for our exciton problem.

## § 3.

As is well-known, the optical exciton is produced by removing one $3p$ electron from a chlorine ion $Cl^-$ and the *X*-ray exciton appearing in the *K*-absorption by removing one 1s electron from a chlorine ion $Cl^-$ or a potassium ion $K^+$. To find the potential function $V(\vec{r})$ for each removed electron, it will be instructive to proceed in the following way. The Hamiltonian of an additional electron introduced into a perfect crystal of KCl is $\boldsymbol{H}_0$. Then, removing a $3p$ electron from a chlorine ion $Cl^-$ for the optical exciton and a 1s electron from a chlorine ion $Cl^-$ or a potassium ion $K^+$ for the *X*-ray exciton, we shall investigate how the potential field for the additional electron is changed, which change in the potential represents $V(r)$ in Eq. (5) of our exciton model. The additional potential field will be consisted of three parts,

$$V(\vec{r})=V_1(\vec{r})+V_2(\vec{r})+V_3(\vec{r})\,, \qquad (6)$$

where, for the optical exciton, $V_1$ is the negative of the potential field due to a $3p$ electron of a $Cl^-$ ion, and $V_2$ arises just from the changes in the wave functions of the other electrons in the chlorine atom. $V_3$ is due to the changes in the wave functions of all the surrounding electrons, assuming the short times of electronic transition compared with the necessary for the surrounding nuclei to move according to the Franck-Condon principle. $V_3$ can be taken into account approximately by introducing the effective dielectric constant $\kappa$ into $V_1+V_2$. $V_2$ can be approximately neglected for the optical exciton since the outer screening by an electron may reasonably be supposed to become quite small compared with the inner screening of the atom.

By using Dexter's wave function for the $Cl^-$ $3p$ electron,

$$\phi_{3p}(r)=[r/(24)^{1/2}(A/2)^{5/2}](e^{-r/A}-23.2e^{-r/B}) \qquad (7)$$

($A=a_H/1.1$, $B=a_H/8$ and $a_H$=Bohr's radius)

which have been found by curve-fitting to Hartree's data, we are able to compute $V_1+V_2+V_3$ for the optical exciton as follows.

$$\begin{aligned} V_0(r)=V_1+V_2+V_3&=-\frac{1}{\kappa}\int\phi_{3p}{}^2(r')d\tau'/|\vec{r}-\vec{r}'| \\ &=\frac{N^2}{\kappa}\left[\frac{1}{\alpha^2}\{e^{-\alpha\gamma}(r^2+ar+b+cr^{-1})-cr^{-1}\}\right. \\ &\quad-\frac{\bar{a}}{\beta^2}\{e^{-\beta\gamma}(r^2+a'r+b'+c'r^{-1})-c'r^{-1}\} \\ &\quad\left.+\frac{\bar{b}}{\gamma^2}\{e^{-\gamma r}(r^2+a''r+b''+c''r^{-1})-c''r^{-1}\}\right], \qquad (8)\end{aligned}$$

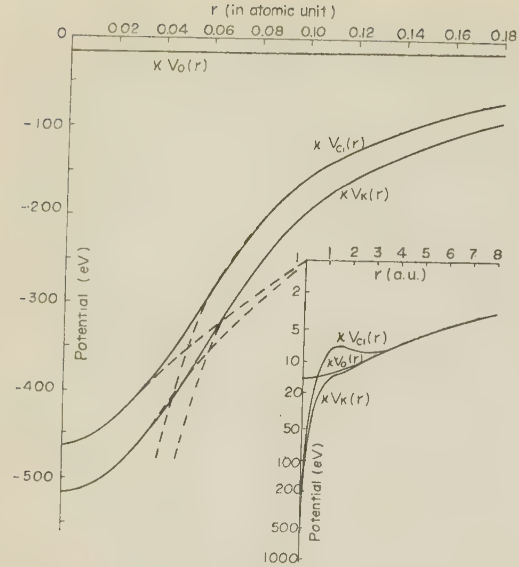

Fig. 1. Potential $V(r)$ for both optical and X-ray excitons, which is computed by using the Hartree data.

in which the atomic units are used and

$$N=[(24)^{1/2}(1/2.2)^{5/2}]^{-1},$$

$$\alpha=1.1\times 2,\qquad \beta=1.1+8,\qquad \gamma=8\times 2,$$

$$\bar{a}=23.2\times 2,\qquad \bar{b}=(23.2)^2,$$

$$a=6\alpha^{-1},\qquad b=18\alpha^{-2},\qquad c=24\alpha^{-3}$$

$$a'=6\beta^{-1},\qquad b'=18\beta^{-2},\qquad c'=24\beta^{-3},$$

$$a''=6\gamma^{-1},\qquad b''=18\gamma^{-2},\qquad c''=24\gamma^{-3}. \quad (9)$$

The general behavior of $(V_1+V_2+V_3)$ is described graphically in Fig. 1.

For the $X$-ray exciton around a Cl atom, we have, along the similar reasoning as above,

$V_1+V_2=$the potential due to a Cl$^-$ ion lacking one 1s electron minus the potential due to a Cl$^-$.

In the chlorine ion lacking one 1s electron, the wave functions of electrons outside of 1s orbit will be affected considerably due to the increase by one unit of the effective nuclear charge and the resulting potential field may be reasonably supposed to resemble the potential field within the neutral argon atom A. In the inside of 1s orbit, however, the potential field will be mainly governed by the electric charges of both the remaining 1s electron and the chlorine nucleus. Along the above considerations, $(V_1+V_2)$ in the outside region of 1s orbit is assumed to be approximately given by the difference of the Hartree fields of a neutral argon atom A and chlorine ion Cl$^-$, while, in the inside region of 1s orbit, to be governed by the minus of the potential determined by the charge distribution of the remaining 1s electron in the chlorine atom. The behavior of $(V_1+V_2)$ is graphically represented in Fig. 1 by using the Hartree data[19]. Since we shall adopt the variational method to solve the Wannier-Slater's equation (5) for our model of $X$-ray exciton, the following set of analytical forms of potential functions has been constructed by curve-fitting to the numerical data described in the figure.

$$\begin{aligned}
V_1+V_2&=a+br^2+cr^3+dr^4, && \text{for } 0\leqq r\leqq 0.1,\\
&=a'r+b'+c'r^{-1}+d'r^{-2}, && \text{for } 0.1\leqq r\leqq 1.0,\\
&=a''+b''r+c''r^2+d''r^2e^{-kr}, && \text{for } 1.0\leqq r\leqq 2.0,\\
&=-1+a'''(7-r)^2+b'''(7-r)^4+c'''(7-r)^6, && \\
& && \text{for } 2.0\leqq r\leqq 7.0\\
&=-r^{-1}, && \text{for } 7.0\leqq r, \quad (10)
\end{aligned}$$

in which the atomic units are used as above.

$$a=-17,\qquad b=2625.6,$$

$$c=-13040,\qquad d=-18156.3,$$

$$a'=-0.21315,\quad b'=0.31320,$$

$$c'=-0.37904,\quad d'=-0.02102,$$

$$a''=-0.552,\qquad b''=0.498,$$

$$c''=-0.128,\qquad d''=-0.2307,$$

$$a'''=5.41808.10^{-4},\quad b'''=2.068515.10^{-4},$$

$$c'''=1.5595.10^{-5},\qquad k=0.67465. \qquad (11)$$

Taking account of the effect from $V_3$ through introducing the effective dielectric constant $\kappa$ in the above expression, we have finally

$$V_{Cl}(r)=\frac{1}{\kappa}(V_1+V_2)\,, \qquad (12)$$

as a potential function in our model of $X$-ray exciton around a chlorine ion.

Similarly, for the $X$-ray exciton around a K$^+$ ion, we have

$V_1+V_2=$the potential due to a K$^+$ ion lacking one 1s electron minus the potential due to a K$^+$ ion.

Following the quite similar reasoning as above, $(V_1+V_2)$ in the outside region of 1s orbit of a K atom is assumed to be given by the difference of the Hartree fields of a doubly ionized calcium ion Ca$^{++}$ and a singly ionized potassium ion K$^+$, whereas, in the inside region of 1s orbit, it is determined by the minus of the charge distribution of a remaining 1s electron within a $K^+$ ion. The behavior of $(V_1+V_2)$ is shown graphically in Fig. 1, using the Hartree data[20] and the best fitted analytical functions to the curve in the figure are found to become of the following form in atomic units.

$$
\begin{aligned}
V_1+V_2 &= \bar{a}+\bar{b}r^2+\bar{c}r^3+\bar{d}r^4, &&\text{for } 0\leqq r\leqq 0.1,\\
&= \bar{a}'r+\bar{b}'+\bar{c}'r^{-1}+\bar{d}'r^{-2}, &&\text{for } 0.1\leqq r\leqq 1.0,\\
&= \bar{a}''r+\bar{b}'', &&\text{for } 1.0\leqq r\leqq 3.5,\\
&= -r^{-1}, &&\text{for } 3.5\leqq r,
\end{aligned}
$$

and (13)

$$
\begin{aligned}
&\bar{a}=-19, \quad \bar{b}=1938.25,\\
&\bar{c}=2750, \quad \bar{d}=-108125,\\
&\bar{a}'=0.50685, \quad \bar{b}=-0.74780,\\
&\bar{c}'=-0.27364, \quad \bar{d}'=-0.03742,\\
&\bar{a}''=0.1068, \quad \bar{b}''=-0.6588.
\end{aligned}
\tag{14}
$$

Allowing for the contribution from $V_3$, we get, for the $X$-ray exciton around a potassium ion $K^+$,

$$V_K(r)=(1/\kappa)(V_1+V_2)\ . \tag{15}$$

In (10) and (13) the accuracies of the curve-fitting to the numerical data are observed to lie within the limit of five to one percent in all ranges of $r$.

## § 4.

Since the mentioned potential field of an electron trapped in an exciton is taken to be spherically symmetric, the exciton levels are classified as $s, p, d, \cdots$ as usual. In addition, the energy values $E'$ in (5) are measured from the bottom of conduction band according to the Wannier-Slater's approximation. In order to solve (5) by variational method, we have attempted to evaluate the energies of the ground and first-excited states assuming the following trial functions of $s$- and $p$- symmetry.

$$\psi_s(r)=N(Z)e^{-rZ/a_H} \quad \text{for the ground state,} \tag{16}$$

and

$$\psi_p(r)=N(Z)re^{-rZ/a_H} \quad \text{for the first-excited state,} \tag{17}$$

respectively, in which the variational parameter is taken to be an effective nuclear charge $Z$ and $N(Z)$ the normalization factor. Besides $Z$, the effective mass $m^*$ near the bottom of conduction band and the effective dielectric constant $\kappa$ are regarded as adjustable parameters. According to the available data, the effective mass near the bottom of conduction band of alkali halides seems to become of about (0.6∼1) times electron mass, whereas, the value of effective dielectric constant seems to be highly questionable since the values depend sensively upon the spacial extent of the wave function and the time required for the electronic transition as was frequently discussed in the literature[21]. Generally speaking, however, the concerned value of effective dielectric constant for our exciton model will presumably lie in the range of the normal bulk value for the high frequency region 2.13 to unity, or it may be a little closer to unity, allowing for a rather limited size of exciton wave function and the short period of the absorbed radiation. In view of the above situation we have numerically worked the energy values $E'$ corresponding to a number of different values for the effective mass and the dielectric constant for both cases of ground and excited levels of optical and $X$-ray excitons.

The substitution of (16) and (17) into (5) leads to

$$
\begin{aligned}
E' &= \int \psi(\vec{r})\left[-\frac{\hbar^2}{2m^*}\Delta+V(r)\right]\psi(\vec{r})dV\\
&= \frac{Z^2}{2\sigma}+\frac{4Z^3}{\kappa}\int_0^\infty V(r)r^2e^{-2Zr}dr
\end{aligned}
$$

(in atomic units) (18)

for the ground state and

$$= \frac{Z^2}{2\sigma}+\frac{4Z^5}{3\kappa}\int_0^\infty V(r)r^4e^{-2Zr}dr$$

(in atomic units) (19)

for the first-excited state, respectively, $m^*$ being replaced by $\sigma\cdot m$. The variational procedure to solve the equation (5) has been proceeded as follows. After the explicit calculation of the above energy integral by putting each of the potential functions (8), (12) and (15) into (18) and (19) (refer to Appendix), the numerical calculations of $E'(Z)$ corresponding to each of the assigned values of $m^*$ and $\kappa$ have been carried out, some of which are represented graphically in Fig. 2. The required energies of both ground and first-excited states of the excitons are determined by the minimum positions on the energy curves, the results of which are given in Tables I and II.

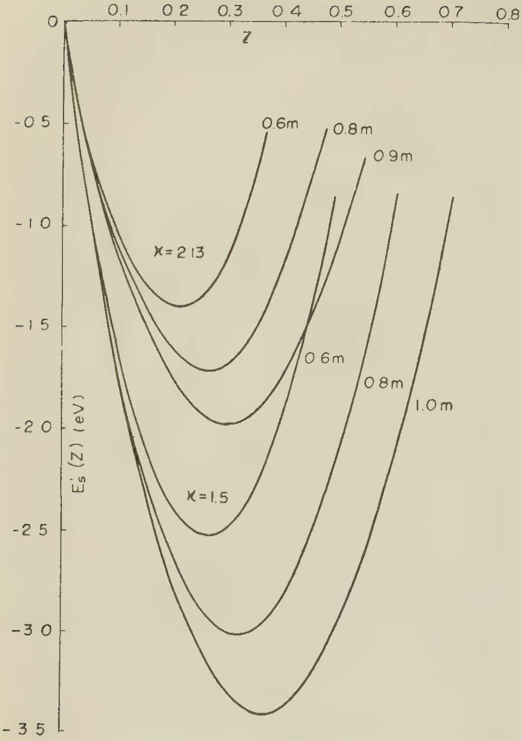

(a)

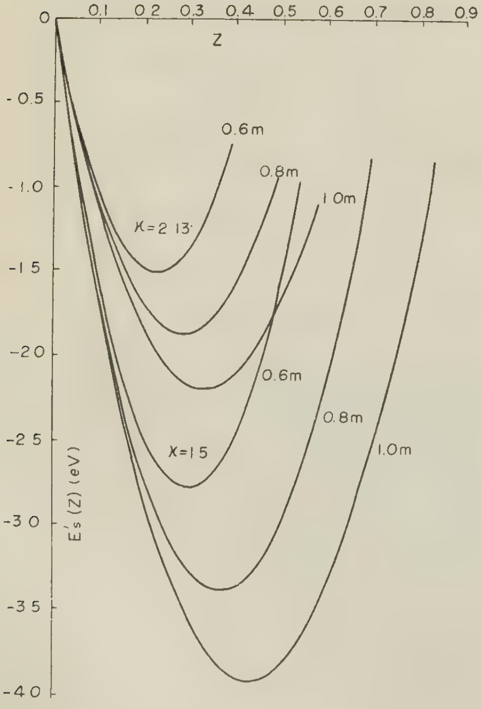

(b)

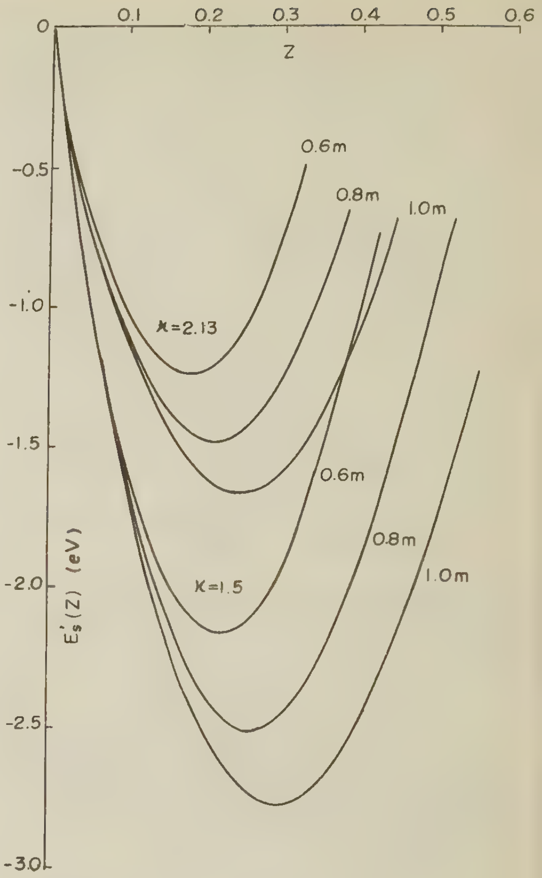

(c)

Fig. 2. $E_s'(Z)$.

a) Ground state of optical exciton.
b) Ground state of X-ray exciton around a potassium ion.
c) Ground state of X-ray exciton around a chlorine ion.

## § 5.

The ultraviolet absorption spectra of the alkali halides have been extensively investigated by Hilsch and Pohl and their colleagues[22], and by Schneider and O'Bryan[23], the absorption coefficient being very large, of the order of $10^5$ to $10^6$ cm$^{-1}$ for wave lengths for which the absorption reaches its greatest value. For the case of KCl, the absorption curve has been observed to consist of two peaks in the long wave length side, which are usually considered respectively the series limit (1310 Å) and the exciton peak (1620 Å). In the absorption of light in the region of the series limit, an electron is considered to be taken from the filled valency band and set free in the conduction band, thus the positive hole

Table I. Ground State Energies of Excitons.

a) Optical Exciton, $E_s'(Z)$ (ev)

| $\kappa$<br>$\sigma$ | 1.0 | 1.5 | 2.13 | 4.68 |
|---|---|---|---|---|
| 0.5 | | | −1.23(0.20) | −0.29(0.11) |
| 0.6 | −4.86(0.33) | −2.54(0.27) | −1.41(0.21) | −0.34(0.115) |
| 0.7 | | | −1.57(0.23) | −0.39(0.14) |
| 0.8 | −5.62(0.40) | −3.02(0.315) | −1.72(0.27) | −0.44(0.15) |
| 0.9 | | | −1.86(0.28) | −0.48(0.16) |
| 1.0 | −6.23(0.45) | −3.40(0.36) | −1.97(0.30) | −0.51(0.17) |
| b) X-ray Exciton around K⁺, $E_s'(Z)$ (ev) | | | | |
| 0.5 | | | −1.31(0.20) | |
| 0.6 | −5.52(0.40) | −2.79(0.295) | −1.51(0.225) | |
| 0.7 | | | −1.70(0.25) | |
| 0.8 | −6.57(0.49) | −3.39(0.37) | −1.88(0.285) | |
| 0.9 | | | −2.04(0.31) | |
| 1.0 | −7.43(0.55) | −3.92(0.415) | −2.19(0.33) | |
| c) X-ray Exciton around Cl⁻, $E_s'(Z)$ (ev) | | | | |
| 0.5 | | | −1.10(0.16) | |
| 0.6 | −3.99(0.29) | −2.15(0.23) | −1.24(0.185) | |
| 0.7 | | | −1.36(0.205) | |
| 0.8 | −4.53(0.33) | −2.51(0.27) | −1.47(0.22) | |
| 0.9 | | | −1.57(0.24) | |
| 1.0 | −4.90(0.36) | −2.78(0.30) | −1.66(0.25) | |

$\kappa=2.13$ and 4.68 represent the bulk dielectric constants for high frequency- and static fields, respectively.

Table II. $p$-State Energies of Excitons.

a) Optical Exciton, $E_p'(Z)$ (ev)

| $\kappa$<br>$\sigma$ | 1.5 | 2.13 | 2.5 |
|---|---|---|---|
| 0.6 | −0.89(0.19) | −0.45(0.14) | −0.33(0.12) |
| 0.8 | −1.17(0.225) | −0.59(0.18) | −0.44(0.16) |
| 1.0 | −1.44(0.31) | −0.73(0.22) | −0.54(0.20) |
| b) X-ray Exciton around K⁺, $E_p'(Z)$ (ev) | | | |
| 0.6 | −0.90(0.20) | −0.45(0.145) | −0.33(0.11) |
| 0.8 | −1.19(0.265) | −0.60(0.185) | −0.42(0.16) |
| 1.0 | −1.48(0.315) | −0.74(0.23) | −0.54(0.21) |
| c) X-ray Exciton around Cl⁻, $E_p'(Z)$ (ev) | | | |
| 0.6 | −0.88(0.19) | −0.44(0.14) | −0.33(0.13) |
| 0.8 | −1.14(0.245) | −0.58(0.18) | −0.44(0.16) |
| 1.0 | −1.39(0.30) | −0.72(0.22) | −0.53(0.20) |

being created inside the crystal which will be responsible for photoconduction together with the conduction electron. On the other hand, the first peak or the exciton peak in the fundamental absorption is considered to give rise to the electronic transition from the filled valency band to the exciton level. Therefore, the energy difference between two peaks of the fundamental absorption, i.e, 9.4 ev−7.6ev =1.8 ev is interpreted to give the energy difference of the exciton level from the bottom of a conduction band. According to Abraham, the broadening of the peak seems to be mainly ascribed to the thermal effect since only one state of the exciton band is allowed by selection rule and further the observed broadenings show very sensitive dependencies upon temperature.

Looking at Table I, the observed value of the exciton ground state from the band bottom is found in between those corresponding to $m^*=0.8\,\text{m}$ and $m^*=0.9\,\text{m}$ with $\kappa=2.13$ and, consequently, our interpolated value, 1.83 ev of the ground state energy of an optical exciton corresponding to $m^*=0.85\,\text{m}$ and $\kappa=2.13$, is found to be fair agreement with the observed value mentioned above. The assigned values of $m^*$ and $\kappa$ seems to be quite reasonable allowing for the other physical data.

In Table II, the first exciton level of $p$-type is seen to lie at 0.6∼0.7 ev below the conduction band, corresponding to the same values of $m^*$ and $\kappa$, although the electronic transition to such excited level of an optical exciton has not been observed with sufficient intensity in the absorption band. The situation may be qualitatively understood as follows. The wave functions of the exciton states become, according to (1), (16) and (17),

$$\Psi_s(\vec{r})=N(Z)\sum_j e^{-ZR_j/a_H}a_s(\vec{r}-\vec{R}_j) \qquad (20)$$

for the ground state and, for the first excited state,

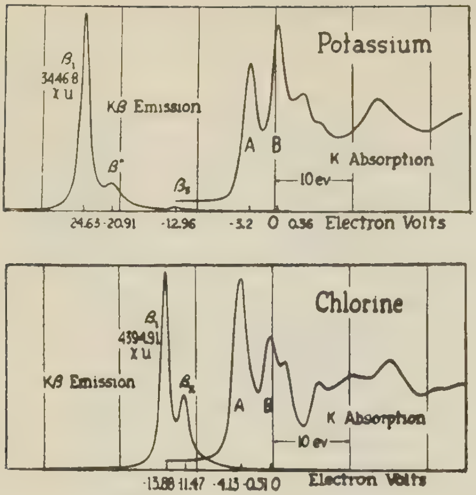

Fig. 3. Experimental results of X-ray absorption and emission spectra in KCl.
(L. G. Parratt and E. L. Jossem: Phys. Rev. **97** (1955) 916.

$$\Psi_p(r)=N(Z)\sum_j R_j e^{-ZR_j/a_H} X_j/R_j a_s(\vec{r}-\vec{R}_j) \tag{21}$$

respectively, in which $a_s(\vec{r}-\vec{R}_j)$ represents the Wannier function belonging to the conduction band. Thus, the wave function of an exciton in ground state behaves strongly concentrated around the chlorine ion in which a positive hole is localized, whereas, the wave function corresponding to an excited state is a little pushed away from the same ion compared with the former, the dominant portion being located somewhat outwards. Such different behaviors of the respective wave functions will be supposed to lead to the different overlappings of both wave functions, belonging to an upper state (exciton level) and a lower state in the valency band in the electronic transition, giving rise to sensitive influences upon the transition probabilities. The quantitative computations of the mentioned transition probabilities, however, shall be postponed in the next report since it is required, for such problem, to calculate the wave functions of both conduction and valence bands in KCl.

Next we shall proceed to discuss the comparison of our results with Parratt and Jossem's observation of *X*-ray absorption spectra in KCl[24]. In the Fig. 3 which is the reproduction of the experimental results, the strong peaks are clearly observed near the edge of the absorption spectra in both chlorine and potassium ions, which structure seems not to be explained by the conventional band theory of solids, but to be reasonably ascribed to the *X*-ray exciton level below the conduction band, as was discussed qualitatively by Parratt and Jossem. Since the position of the bottom of a conduction band is not entirely recognizable in the observed contour for either chlorine or potassium, the relative locations in energy of the exciton peaks from the band bottom can not be determined on the reliable basis. In addition, the following complicated situation seems to happen to occur in determining experimentally the location of the band bottom as was stressed by Parratt and Jossem. If the band bottom in KCl is supposed as the bottom of 4s chlorine band, the pottassium 1s electron may go happily to the bottom of this band because of the symmetry exchange effect, but the chlorine 1s electron may prefer to go to a higher level having *p*-symmetry near the chlorine ion. Hence we may expect the 1s absorption continium for potassium to be a little lower than for chlorine, and consequently the shapes of the absorption spectra may be considered to be different in the two cases as was observed experimentally. In spite of the above situation, Parratt and Jossem have tentatively taken the energy position of the band bottom as 4.13 ev and 3.2 ev as measured from the first absorption peaks for the chlorine and potassium, respectively. Strictly speaking, their choice of the band bottom seems not to be convincing as far as the experimental data concern.

On the other hand, on comparing our results with the experiments, a highly questionable parameter in our calculation is the effective dielectric constant responsible for the polarization of the surrounding medium. Unfortunately, the reliable computation of the electric polarization due to the local change of charge distribution seems to be lacking at present. For the *X*-ray exciton, the mentioned effective dielectric constant will presumably become closer to unity in comparison with that of the optical exciton mainly due to both the rather limited spread of the corresponding wave function and the extremely short period of *X*-ray radiation. Taking tentatively 0.8 m for the effective mass and 1.5 for $\kappa$ according to the above consideration, the energy position of a *X*-ray exciton around a potassium ion will become 3.39 ev as measured from the bottom of a conduction band, as shown in Table I, which should be compared with the experimentally assigned value of 3.2 ev as mentioned above. If our assumed value of $\kappa$ were approximately correct, the position of the bottom of a conduction band might be situated near a *B* peak of the absorption contour in the potassium (Fig. 3). The mentioned values of parameters will lead to about 2.5 ev for the position of *X*-ray exciton around a chlorine ion as measured from the band bottom, in contradistinction to 4.13 ev, the value assigned rather arbitrarily by Parratt and Jossem. In the absorption contour in chlorine, therefore, the band bottom might be expected to be located near the valley between *A* and *B* peaks in Fig, 3. The remarkable difference between the shapes of the absorption spectra near the edge in both cases, i.e., the reversed intensity-ratio of *A* and *B* peaks in $K^+$ compared with that in $Cl^-$ will presumably make plausible our assignment of the bottom mentioned above, together with the above consideration of the symmetry character of wave functions near the bottom of conduction band. Furthermore, the transition to the excited *p*-type level of *X*-ray exciton will be supposed to become sufficiently small according to the similar considerations to the case of optical exciton, allowing for the observed result that there is no peak between *A* peak and our assigned band bottom. The observed *B* peak on the absorption contour (Fig. 3) will presumably be ascribed to the state density fluctuation in the conduction band or to the energy dependency of transition matrix involved.

According to Parratt and Jossem, the remarkably sharp peaks in the *X*-ray *K* emmision bands are reasonably attributable to a *X*-ray exciton appearing just below the valency band, which will be dealt with in a similar way to the case mentioned above through expanding the wave function of a perturbed lattice into the Wannier functions belonging to the valency band.

Regarding the validity of the assumption (§ 2) involved in the derivation of the Wannier-Slater's differential equation, it should be remarked that the slowly varying portion of the perturbing potential (Fig. 1) for both optical and *X*-ray excitons has actually given dominant contribution in determining the wave functions and the corresponding energies of our exciton problem, which shows the approximate validity of the assumption of slowly varying $V(r)$ for the differential equation approach.

Finally, a few words should be added on the criticism of our treatment of a localized exciton. In fact, our present calculation of a localized exciton has been worked in terms of a one electron picture by using Wannier-Slater's equation, the result of which seems to show favourable agreements with the experimental observations as described above. In a one electron approximation, however, the exchange interaction of an electron trapped within a localized exciton with the remaining electrons in a valency band has been approximately disregarded. In order to correct for such situation, we must start with many-electron treatment of a localized exciton in which the determinantal wave functions are set up, corresponding to the configurations consisting of one electron in a localized exciton state and the remaining electrons in a valency band having one hole, and the configuration interactions are taken into consideration in the usual way. The actual computations of these problems are now in progress and, since the mentioned procedure is closely related with that of a moving exciton, we shall, in the next report, come to this question in connection with a further discussion of both localized and moving excitons.

One of the authors gratefully acknowledges the financial support from Research Institute, Fuji Photo Film Co., Ltd., for our present work.

## Appendix

Optical exciton.
Ground state,

$$E_s' = \frac{Z^2}{2\sigma} + \frac{4Z^3}{\kappa} + \int_0^\infty V_0(r) r^2 e^{-2Zr} dr$$

$$=\frac{Z^2}{2\sigma}+\frac{4Z^3N^2}{\kappa}\left[\frac{1}{\alpha^2}\left\{\frac{4!}{(\alpha+2Z)^5}+\frac{3!a}{(\alpha+2Z)^4}+\frac{2!b}{(\alpha+2Z)^3}+\frac{c}{(\alpha+2Z)^2}-\frac{c}{(2Z)^2}\right\}\right.$$
$$-\frac{\bar{a}}{\beta^2}\left\{\frac{4!}{(\beta+2Z)^5}+\frac{3!a'}{(\beta+2Z)^4}+\frac{2!b'}{(\beta+2Z)^3}+\frac{c'}{(\beta+2Z)^2}-\frac{c'}{(2Z)^2}\right\}$$
$$\left.+\frac{\bar{b}}{\gamma^2}\left\{\frac{4!}{(\gamma+2Z)^5}+\frac{3!a''}{(\gamma+2Z)^4}+\frac{2!a''}{(\gamma+2Z)^3}+\frac{c''}{(\gamma+2Z)^2}-\frac{c''}{(2Z)^2}\right\}\right].$$

Excited state,

$$E_p'=\frac{Z^2}{2\sigma}+\frac{4Z^5}{3\kappa}\int_0^\infty V_0(r)^4e^{-2Zr}dr$$
$$=\frac{Z^2}{2\sigma}+\frac{4Z^5N^2}{3\kappa}\left[\frac{1}{\alpha^2}\left\{\frac{6!}{(\alpha+2Z)^7}+\frac{5!a}{(\alpha+2Z)^6}+\frac{4!b}{(\alpha+2Z)^5}+\frac{3!c}{(\alpha+2Z)^4}-\frac{3!c}{(2Z)^4}\right\}\right.$$
$$-\frac{\bar{a}}{\beta^2}\left\{\frac{6!}{(\beta+2Z)^7}+\frac{5!a'}{(\beta+2Z)^6}+\frac{4!b'}{(\beta+2Z)^5}+\frac{3!c'}{(\beta+2Z)^4}-\frac{3!c'}{(2Z)^4}\right\}$$
$$\left.+\frac{\bar{b}}{\gamma^2}\left\{\frac{6!}{(\gamma+2Z)^7}+\frac{5!a''}{(\gamma+2Z)^6}+\frac{4!b''}{(\gamma+2Z)^5}+\frac{3!c''}{(\gamma+2Z)^4}-\frac{3!c''}{(2Z)^4}\right\}\right].$$

$X$-ray exciton around a potassium ion.

Ground state,

$$E_s'=\frac{Z^2}{2\sigma}+\frac{4}{\kappa}\left[e^{-0.2Z}\left\{\frac{2!a}{2^3}\sum_{n=3}^{\infty}A(n)+\frac{4!b}{2^5Z^2}\sum_{n=5}^{\infty}A(n)+\frac{5!c}{2^6Z^3}\sum_{n=6}^{\infty}A(n)+\frac{6!d}{2^7Z^4}\sum_{n=7}^{\infty}A(n)\right\}\right.$$
$$+\frac{3!a'}{2^4Z}\left\{e^{-0.2Z}\sum_{n=0}^{3}A(n)-e^{-2Z3}\sum_{n=0}^{3}B(n)\right\}+\frac{2!b'}{2^3}\left\{e^{-0.2Z}\sum_{n=0}^{2}A(n)-e^{-2Z}\sum_{n=0}^{2}B(n)\right\}$$
$$+\frac{c'}{2^2}Z\left\{e^{-0.2Z}\sum_{n=0}^{1}A(n)-e^{-2Z}\sum_{n=0}^{1}B(n)\right\}+\frac{d'}{2}Z^2\left\{e^{-0.2Z}A(o)-e^{-2Z}B(o)\right\}$$
$$+\frac{3!a''}{2^4Z}\left\{e^{-2Z}\sum_{n=0}^{3}B(n)-e^{-7Z}\sum_{n=0}^{3}D(n)\right\}+\frac{2!b''}{2^3}\left\{e^{-2Z}\sum_{n=0}^{2}B(n)-e^{-7Z}\sum_{n=0}^{2}D(n)\right\}$$
$$\left.-\frac{1}{2}Ze^{-7Z}\sum_{n=0}^{1}D(n)\right].$$

Excited state,

$$E_p'=\frac{Z^2}{2\sigma}+\frac{4}{3\kappa}\left[e^{-0.2Z}\left\{\frac{4!a}{2^5}\sum_{n=5}^{\infty}A(n)+\frac{6!b}{2^7Z^2}\sum_{n=7}^{\infty}A(n)+\frac{7!c}{2^8Z^3}\sum_{n=8}^{\infty}A(n)+\frac{8!d}{2^9Z^4}\sum_{n=9}^{\infty}A(n)\right\}\right.$$
$$+\frac{5!a'}{2^6Z}\left\{e^{-0.2Z}\sum_{n=0}^{5}A(n)-e^{-2Z}\sum_{n=0}^{5}B(n)\right\}+\frac{4!b'}{2^5}\left\{e^{-0.2Z}\sum_{n=0}^{4}A(n)-e^{-2Z}\sum_{n=0}^{4}B(n)\right\}$$
$$+\frac{3!c'}{2^4}Z\left\{e^{-0.2Z}\sum_{n=0}^{3}A(n)-e^{-2Z}\sum_{n=0}^{3}B(n)\right\}+\frac{2!d'}{2^3}Z^2\left\{-e^{-2Z}\sum_{n=0}^{2}A(n)-e^{2Z}\sum_{n=0}^{2}B(n)\right\}$$
$$+\frac{5!a''}{2^6Z}\left\{e^{-2Z}\sum_{n=0}^{5}B(n)-e^{-7Z}\sum_{n=0}^{5}D(n)\right\}+\frac{4!b''}{2^5}\left\{e^{-2Z}\sum_{n=0}^{4}B(n)-e^{-7Z}\sum_{n=0}^{4}D(n)\right\}$$
$$\left.-\frac{3!}{2^4}Ze^{-7Z}\sum_{n=0}^{3}D(n)\right].$$

$X$-ray exciton around a chlorine ion.

Ground state,

$$E_s'=\frac{Z^2}{2\sigma}+\frac{4}{\kappa}\left[e^{-0.2Z}\left\{\frac{2!\bar{a}}{2^3}\sum_{n=3}^{\infty}A(n)+\frac{4!\bar{b}}{2^5Z^2}\sum_{n=5}^{\infty}A(n)+\frac{5!\bar{c}}{2^6Z^3}\sum_{n=6}^{\infty}A(n)+\frac{6!\bar{d}}{2^7Z^4}\sum_{n=7}^{\infty}A(n)\right\}\right.$$
$$+\frac{3!\bar{a}}{2^4Z}\left\{e^{-0.2Z}\sum_{n=0}^{3}A(n)-e^{-2Z}\sum_{n=0}^{3}B(n)\right\}+\frac{2!\bar{b}'}{2^3}\left\{e^{-0.2Z}\sum_{n=0}^{2}A(n)-e^{-2Z}\sum_{n=0}^{2}B(n)\right\}$$

$$
\begin{aligned}
&+\frac{\bar{c}}{2^2}Z\left\{e^{-0.2Z}\sum_{n=0}^{1}A(n)+e^{-2Z}\sum_{n=0}^{1}B(n)\right\}+\frac{\bar{d}'}{2}Z^2\left\{e^{-0.2Z}A(o)-e^{-2Z}B(o)\right\}\\
&+\frac{2!\bar{a}''}{2^3}\left\{e^{-2Z}\sum_{n=0}^{2}B(n)-e^{-4Z}\sum_{n=0}^{2}C(n)\right\}+\frac{3!\bar{b}''}{2^4Z}\left\{e^{-2Z}\sum_{n=0}^{3}B(n)-e^{-4Z}\sum_{n=0}^{3}C(n)\right\}\\
&+\frac{4!\bar{c}''}{2^5Z^2}\left\{e^{-2Z}\sum_{n=0}^{4}B(n)-e^{-4Z}\sum_{n=0}^{4}C(n)\right\}+\frac{4\bar{d}''Z^3}{(k+2Z)^5}\left\{e^{-(k+2Z)}\sum_{n=0}^{4}\frac{(k+2Z)^n}{n!}-e^{-2(k+2Z)}\sum_{n=0}^{4}\frac{2^n(k+2Z)^n}{n!}\right\}\\
&+e^{-14Z}\left[-7\left\{\frac{1}{2!}Z^2(e^{10Z}E(o)-1)\right\}-\left\{\frac{1!}{2^2}Z\left(e^{10Z}\sum_{n=0}^{1}E(n)-1\right)\right\}\right.\\
&+7\bar{a}'''\left\{\frac{2!}{2^3}\left(e^{10Z}\sum_{n=0}^{2}E(n)-1\right)\right\}+\bar{a}'''\left\{\frac{3!}{2^4Z}\left(e^{10Z}\sum_{n=0}^{3}E(n)-1\right)\right\}\\
&+7\bar{b}'''\left\{\frac{4!}{2^5Z^2}\left(e^{10Z}\sum_{n=0}^{4}E(n)-1\right)\right\}+\bar{b}'''\left\{\frac{5!}{2^6Z^3}\left(e^{10Z}\sum_{n=6}^{5}E(n)-1\right)\right\}\\
&\left.+7\bar{c}'''\left\{\frac{6!}{2^7Z^4}\left(e^{10Z}\sum_{n=0}^{6}E(n)-1\right)\right\}+\bar{c}'''\left\{\frac{7!}{2^7Z^4}\left(e^{10Z}\sum_{n=0}^{7}E(n)-1\right)\right\}\right]-\frac{1!}{2^2}Ze^{-14Z}\sum_{n=0}^{1}F(n)\Bigg].
\end{aligned}
$$

Excited state,

$$
\begin{aligned}
E_p'=&\frac{Z^2}{2\sigma}+\frac{4}{3\kappa}\left[e^{-0.2Z}\left\{\frac{4!\bar{a}}{2^5}\sum_{n=5}^{\infty}A(n)+\frac{6!\bar{b}}{2^7Z^2}\sum_{n=7}^{\infty}A(n)+\frac{7!\bar{c}}{2^8Z^3}\sum_{n=8}^{\infty}A(n)+\frac{8!\bar{d}}{2^9Z^4}\sum_{n=9}^{\infty}A(n)\right\}\right.\\
&+\frac{5!\bar{a}'}{2^6Z}\left\{e^{-0.2Z}\sum_{n=0}^{5}A(n)-e^{-2Z}\sum_{n=0}^{5}B(n)\right\}+\frac{4!\bar{b}'}{2^5}\left\{e^{-0.2Z}\sum_{n=0}^{4}A(n)-e^{-2Z}\sum_{n=0}^{4}B(n)\right\}\\
&+\frac{3c'}{2^4}Z\left\{e^{-0.2Z}\sum_{n=0}^{3}A(n)-e^{-2Z}\sum_{n=0}^{3}B(n)\right\}+\frac{2!\bar{d}'}{2^3}Z\left\{e^{-0.2Z}\sum_{n=0}^{2}A(n)-e^{-2Z}\sum_{n=0}^{2}B(n)\right\}\\
&+\frac{4!\bar{a}''}{2^5}\left\{e^{-2Z}\sum_{n=0}^{4}B(n)-e^{-4Z}\sum_{n=0}^{4}C(n)\right\}+\frac{5!\bar{b}''}{2^6Z}\left\{e^{-2Z}\sum_{n=0}^{5}B(n)-e^{-4Z}\sum_{n=0}^{5}C(n)\right\}\\
&+\frac{6!\bar{c}''}{2^7Z^2}\left\{e^{-2Z}\sum_{n=0}^{6}B(n)-e^{-4Z}\sum_{n=0}^{6}C(n)\right\}+\frac{6!\bar{d}''Z^5}{(k+2Z)^7}\left\{e^{-(k+2Z)}\sum_{n=0}^{6}\frac{(k+2Z)^n}{n!}-e^{-2(k+2Z)}\sum_{n=0}^{6}\frac{2^n(k+2Z)^n}{n!}\right\}\\
&+e^{-14Z}\left[-343\left\{\frac{1}{2}Z^4(e^{10Z}E(o)-1)\right\}-147\left\{\frac{1!}{2^2}Z^3\left(e^{10Z}\sum_{n=0}^{1}E(n)-1\right)\right\}\right.\\
&-(21-343\bar{a}''')\left\{\frac{2!}{2^3}Z^2\left(e^{10Z}\sum_{n=0}^{2}E(n)-1\right)\right\}-(1-147\bar{a}''')\left\{\frac{3!}{2^4}Z\left(e^{10Z}\sum_{n=0}^{3}E(n)-1\right)\right\}\\
&+(21\bar{a}'''+343\bar{b}''')\left\{\frac{4!}{2^5}\left(e^{10Z}\sum_{n=0}^{4}E(n)-1\right)\right\}+(\bar{a}'''+147\bar{b}''')\left\{\frac{5!}{2^6Z}\left(e^{10Z}\sum_{n=0}^{5}E(n)-1\right)\right\}\\
&+(21\bar{b}'''+343'''\bar{c})\left\{\frac{6!}{2^7Z^2}\left(e^{10Z}\sum_{n=0}^{6}E(n)-1\right)\right\}+(\bar{b}'''+147\bar{c}''')\left\{\frac{7!}{2^8Z^3}\left(e^{10Z}\sum_{n=0}^{7}E(n)-1\right)\right\}\\
&\left.+21\bar{c}'''\left\{\frac{8!}{2^9Z^4}\left(\sum_{n=0}^{8}E(n)-1\right)\right\}+\bar{c}'''\left\{\frac{2^{10}Z^5}{9!}\left(e^{10Z}\sum_{n=0}^{9}E(n)-1\right)\right\}\right]-\frac{3!}{2^4}Ze^{-14Z}\sum_{n=0}^{3}F(n)\Bigg].
\end{aligned}
$$

$$
A(n)=\frac{(0.2Z)^n}{n!},\qquad B(n)=\frac{(2Z)^n}{n!},\qquad C(n)=\frac{(4Z)^n}{n!},\qquad D(n)=\frac{(7Z)^n}{n!}
$$

$$
E(n)=\frac{(-10Z)^n}{n!},\qquad F(n)=\frac{(14Z)^n}{n!}.
$$

## References

1) J. Frenkel: Phys. Rev. **37** (1931) 17; Phys. Zeits. d. Sowj. **8** (1935) 185, **9** (1936) 158.

2) L. Apker and E. Taft: Phys. Rev. **79** (1950) 964, **81** (1951) 698, **82** (1951) 814.
M. Hebb: Phys. Rev. **81** (1951) 702.
D. L. Dexter and W. R. Heller: Phys. Rev. **84** (1951) 377.

3) N. Inchauspe: (in press) The authors thank Prof. Ueta for his kindness of showing them

Inchauspe's work before its publication.
4) e.g. F. Seitz: Rev. Mod. Phys. **23** (1953) 328, Article contributed to Proceeding of Photographic Sensitivity of Japan (now in press).
5) N. F. Mott and J. Cauchois: Phil. Mag. **40** (1950) 1260.
6) L. G. Parratt and E. L. Jossem: Phys. Rev. **97** (1955) 916.
7) J. Friedel: Proc. Phys. Soc. **65** (1952) 769, Phil. Mag. **43** (1952) 153.
8) von Hippel: Zeits. f. Phys. **101** (1936) 680.
9) de Boer: Electron Emission and Absorption Phenomena (Cambridge, 1935) p. 242.
10) D. L. Dexter: Phys. Rev. **83** (1951) 435.
11) J. Frenkel: loc. cit.
12) R. Peierls: Ann. d. Phys. **13** (1932) 905.
13) J. C. Slater and W. Shockley: Phys. Rev. **50** (1936) 705.
G. H. Wannier: Phys. Rev. **52** (1937) 191.
W. R. Heller and A. Marcus: Phys. Rev. **84** (1951) 809.
I. M. Dykman and S. I. Pekar: A. N. USSR **83** (1952) 825.
14) D. L. Dexter: loc. cit.
15) J. C. Slater and W. Shockley: loc. cit.
16) J. C. Slater and G. F. Koster: Phys. Rev. **95** (1954) 1167.
G. F. Koster: ibid. **95** (1954) 1436.
C. Kittel and J. W. Mitchell: Phys. Rev. **96** (1954) 1488.
17) S. R. Tibbs: Trans. Farad. Soc. **35** (1939) 1471.
18) D. L. Dexter: loc. cit.
19) D. R. Hartree and W. Hartree: Proc. Roy. Soc. **A 166** (1938) 450.
20) D. R. Hartree and W. Hartree: Proc. Roy. Soc. **A 164** (1938) 167.
21) F. Seitz: Modern Theory of Solids.
N. F. Mott and R. W. Gurney: Electronic Processes in Ionic Crystals.
22) R. Hilsch and R. W. Pohl: Zeits. f. Phys. **59** (1930) 812.
H. Fesefeldt: ibid. **64** (1930) 623.
23) E. G. Schneider and H. M. O'Bryan: Phys. Rev. **51** (1937) 293.
24) L. G. Parratt and E. L. Jossem: loc. cit.
J. W. Trischka: Phys. Rev. **67** (1945) 318.

---

JOURNAL OF THE PHYSICAL SOCIETY OF JAPAN Vol. 11, No. 6, JUNE, 1956

# Calculation of the Cohesive Energy of Zincblende*

By Sumitada ASANO and Yasuo TOMISHIMA

*Department of Physics, Faculty of Science, Okayama University*

(Received February 20, 1956)

The cohesive energy of zincblende has been calculated quantum mechanically by introducing a covalency correction into the usual pure ionic binding. The cohesive energy per ion-pair thus obtained is 1.46 in atomic unit which is very near the observed value 1.36 derived by means of Born-Harber's energy cycle, and is certainly greater than the value calculated for purely ionic binding by about 60%.

This method of calculation would be generally applicable not only for sphalerite-type crystals but also for wurzite-type ones.

## §1. Introduction

According to the current view, covalent binding coexists with ionic binding in ZnS-type crystals**. This is evidenced by several well-known experimental facts: For example, their crystal structure belongs to $T_d$-group or $C_{6v}$-group, which is not familiar with purely ionic crystals; the cohesive energy which is calculated by using Born-Mayer's equation is, in general, smaller than that which is derived from Born-Haber's energy cycle¹⁾; the electronic polarizability of the anion in these crystals varies in a wide range with the kind of the partner cation[2]; the effective charge of the constituent ions in them are estimated to be considerably smaller on account of relatively small differences between the experimental values of their static and optical dielectric constants[3].

---

* The fundamental idea on which the calculation of this paper is based was briefly reported at the regular meeting, held at Tottori in July, 1955, of the Chugoku-Shikoku-Branch of the Physical Society of Japan.

** The term "ZnS-type crystals" is used here in a broad sense that it covers not only cub- and hex-ZnS but also all the sphalerite-type and wurzite-type crystals, for example, ZnSe, CdS and CdSe etc.

Here in this paper, the cohesive energy of zincblende, which is one of the most typical ZnS-type crystals, is calculated by adding a covalent bond to the usual ionic binding.

## § 2. Formulation of the Wave Function

In totally ionic state the electron configurations of the constituent ions in zincblende are $S^{2-}(3s^2 3p^6 : {}^1S_0)$ and $Zn^{2+}(3d^{10} : {}^1S_0)$. In totally covalent state it will be assumed that the electron configurations of the constituent ions are $S^{2+}(3s^1 3p^3 : {}^5S)$ and $Zn^{2-}(3d^{10} 4s^1 4p^3 : {}^5S)$, their polarities being interchanged[4], and that the valence orbitals $s^1p^3$ of each of them form four lobe-like orbitals jutting out tetrahedrally as shown by Slater-Pauling theory[5], the two electrons in two overlapping lobe-like orbitals between adjacent ions form a covalent bond. Although the free $Zn^{2-}$-ion cannot be realized, the above assumption in zincblende might be supported by the experimental fact that a Zn-atom can form complex ions, such as $[Zn(NH_3)_4]^{2+}$ and $[Zn(CN)_4]^{2-}$ etc, which have the tetrahedral structure[6]. The real state of the crystal may be assumed to be intermediate between the two extreme cases of the totally ionic and totally covalent states.

Similary to the case of diamond, whose cohesive energy has been calculated by introducing an ionic state correction into the totally covalent bonding state[7], the normalized two-electron wave function constructed from the two bonded lobes may be assumed to have the following form:

$$\varphi_{ij}(k,l)=\frac{1}{[1+2A^2]^{1/2}}\{u_i(k)u_i(l) + A[u_i(k)v_j(l)+v_j(k)u_i(l)]\} \times\frac{1}{\sqrt{2}}[\alpha(k)\beta(l)-\beta(k)\alpha(l)] \tag{2.1}$$

where $u_i$ and $v_j$ are the space parts of the lobes of S- and Zn-ions respectively, $\alpha$ and $\beta$ spin-functions, and the arguments $k$ and $l$ designate the $k$th and $l$th sets of the electron coordinates respectively. The quantity given by the first term inside the curly brackets corresponds to the totally ionic state, in which the two valence electrons are on the S-atom, whereas that in square brackets corresponds to the covalent state, in which the two valence electrons are shared by the two lobes forming a bonding pair. The adjustable parameter $A$ measuring the relative proportions of these two states will be so determined as to minimize the energy for the observed value of the lattice parameter. The space parts of the two bonded valence orbitals will be taken to be the orthogonalized ones*. Each core-orbital of S- and Zn-atom ($1s$, $2s$ and $2p$ orbitals in S-atom and $1s$, $2s$, $2p$, $3s$, $3p$ and $3d$ orbitals in Zn-atom) is regarded to be filled with two electrons of opposite spins.

Let us designate the space parts of the ion-core orbitals of S-atom by $u_i^0$ and those of Zn-atom by $v_i^0$ with $u_i^0=u_j^0$ and $v_i^0=v_j^0$, the corresponding wave functions $\varphi_{ij}$'s of the two electrons are given by

$$\begin{aligned}\varphi_{ij}(k,l)&=u_i^0(k)u_j^0(l)[\alpha(k)\beta(l)-\beta(k)\alpha(l)]/\sqrt{2}\,,\\ \varphi_{ij}(k,l)&=v_i^0(k)v_j^0(l)[\alpha(k)\beta(l)-\beta(k)\alpha(l)]/\sqrt{2}\,.\end{aligned} \tag{2.2}$$

We note that $\varphi$'s defined by (2.1) and (2.2) are antisymmetric with respect to the interchange of their electron coordinates, that is,

$$\varphi_{ij}(k,l)=-\varphi_{ij}(l,k)\,. \tag{2.3}$$

They also constitute an orthonormal system, since

$$\begin{aligned}&(\varphi_{ij}(k,l)\,|\,\varphi_{ij}(k,l))_{kl}=1\,;\\ &(\varphi_{ij}(k,l)\,|\,\varphi_{i'j'}(k,m))_k=0\,,\\ &\text{pair } i,j\neq\text{pair } i',i'\,,\\ &\qquad 1\neq k \text{ and } m\neq k\,,\end{aligned} \tag{2.4}$$

where the double subscript $k, l$ means the integrations over the $k$th and $l$th electron coordinates and the subscript $k$ the integration over the $k$th coordinate only.

The total electronic wave function of the crystal, $\Psi$, may be written in the form

$$\Psi=2^{-N'/2}\sum_p(-1)^p P\varphi_{1,2}(1,2)\varphi_{3,4}(3,4)\cdots\varphi_{N'-1,N'}(N'-1,N')\,, \tag{2.5}$$

where $N'$ is the total number of the electrons (including ion-cose electrons) in the crystal. The permutation should be made only for the electron coordinates. Because of the antisymmetry of the $\varphi$'s, each factor in $\Psi$ is repeated

---

* The orthogonalization is made in the way to be described in § 4.

$2^{N'/2}$ times by operating all the permutations, so that, by multiplying by the factor $2^{-N'/2}$, $\Psi$ can be given as a sum of $2^{-N'/2}\,N'!$ independent terms.

## § 3. Energy Expression

The spin-independent Hamiltonian for the zincblende lattice is given by

$$H=\sum_{k=1}^{N}O_1(k)+\sum_{k=1}^{N}\sum_{l<k}O_2(k,l)+\sum_{k=1}^{N}\sum_{n=1}^{N'-N}O_2(k,n)+\sum_{n=1}^{N'-N}\sum_{m<n}O_2(n,m)$$
$$+\sum_{n=1}^{N'-N}O_1(n)+\sum_{L=1}^{N/4}\sum_{L'<L}Z_LZ_{L'}/|\boldsymbol{R}_L-\boldsymbol{R}_{L'}|\,, \tag{3.1}$$

where, in atomic unit,

$$O_1(k)=-\frac{1}{2}\Delta_k-\sum_{L=1}^{N/4}Z_L/|\boldsymbol{r}_k-\boldsymbol{R}_L|\,, \tag{3.2}$$

$$O_2(k,l)=1/|\boldsymbol{r}_k-\boldsymbol{r}_l|\,, \tag{3.4}$$

where $\boldsymbol{r}_k$ and $\boldsymbol{r}_l$ are the vectors specifying the $k$th and the $l$th valence electron coordinates, $\boldsymbol{R}_L$ and $\boldsymbol{R}_{L'}$ the $L$th and $L'$th lattice points, and $\boldsymbol{r}_n$ and $\boldsymbol{r}_m$ the $n$th and the $m$th core-electron coordinates. $Z_L$ is the nuclear charge at the $L$th lattice point, i.e. $Z_L=16$ or 30 according as the atom located there is S or Zn. $N$ is the total number of valence electrons in the crystal. The subscripts on the operators $O_1$ and $O_2$ mean that they involve coordinates of one or two electrons.

Using (2.1)-(2.5) and (3.1)-(3.3), we obtain the following expression for $(\Psi|H|\Psi)/(\Psi|\Psi)$.

$$\begin{aligned}
&(\Psi|H|\Psi)/(\Psi|\Psi)\\
&=\frac{2(1+A^2)}{1+2A^2}\left[\sum_{i=1}^{N/2}(u_i|O_1|u_i)+\sum_{i=1}^{N/2}\sum_{n=1}^{N'-N}\overset{\textcircled{1}}{C(ii;nn)}-\frac{1}{2}\sum_{i=1}^{N/2}\sum_{n=1}^{N'-N}C(in;ni)\right]\\
&+\frac{2A^2}{1+2A^2}\left[\sum_{j=1}^{N/2}(v_j|O_1|v_j)+\sum_{j=1}^{N/2}\sum_{n=1}^{N'-N}\overset{\textcircled{2}}{C(jj;nn)}-\frac{1}{2}\sum_{j=1}^{N/2}\sum_{n=1}^{N'-N}C(jn;nj)\right]\\
&+\frac{4A}{1+2A^2}\left[\sum_{i=1}^{N/2}(u_i|O_1|v_j)+\sum_{i=1}^{N/2}\sum_{n=1}^{N'-N}\overset{\textcircled{3}}{C(ij;nn)}-\frac{1}{2}\sum_{i=1}^{N/2}\sum_{n=1}^{N'-N}C(in;nj)\right]\\
&+\frac{1}{1+2A^2}\sum_{i=1}^{N/2}\overset{\textcircled{4}}{C(ii;ii)}+\frac{2A^2}{1+2A^2}\sum_{i=1}^{N/2}\overset{\textcircled{5}}{[C(ii;jj)+C(ij;ij)]}\\
&+\frac{4A}{1+2A^2}\sum_{i=1}^{N/2}\overset{\textcircled{6}}{C(ii;ij)}\\
&+\frac{4A^2(1+A^2)}{(1+2A^2)^2}\sum_{i=1}^{N/2}\sum_{i<k}\overset{\textcircled{7}}{\left[C(ii;ll)+C(jj;kk)-\frac{1}{2}C(il;li)-\frac{1}{2}C(jk;kj)\right]}\\
&+\frac{8A(1+A^2)}{(1+2A^2)^2}\sum_{i=1}^{N/2}\sum_{\substack{k\\(k\neq i)}}\overset{\textcircled{8}}{\left[C(ij;kk)-\frac{1}{2}C(ik;kj)\right]}\\
&+\frac{8A^3}{(1+2A^2)^2}\sum_{j=1}^{N/2}\sum_{\substack{l\\(l\neq j)}}\overset{\textcircled{9}}{\left[C(ij;ll)-\frac{1}{2}C(il;lj)\right]}\\
&+\frac{4(1+A^2)^2}{(1+2A^2)^2}\sum_{i=1}^{N/2}\sum_{i<k}\overset{\textcircled{10}}{\left[C(ii;kk)-\frac{1}{2}C(ik;ki)\right]}\\
&+\frac{4A^4}{(1+2A^2)^2}\sum_{j=1}^{N/2}\sum_{j<l}\overset{\textcircled{11}}{\left[C(jj;ll)-\frac{1}{2}C(jl;lj)\right]}\\
&+\frac{16A^2}{(1+2A^2)^2}\sum_{i=1}^{N/2}\sum_{i<k}\overset{\textcircled{12}}{\left[C(ij;kl)-\frac{1}{4}C(jk;li)-\frac{1}{4}C(jl;ki)\right]}\\
&+\sum_{L=1}^{N/4}\sum_{L<L'}\overset{\textcircled{13}}{\Gamma_{LL'}}+\sum_{L=1}^{N/4}\overset{\textcircled{14}}{S_L}
\end{aligned}\tag{3.4}$$

Since the integral of the type $(u_iu_k|O_2|v_jv_l)$ can be considered as the Coulomb integral between the charge densities $u_iv_j$ and $u_kv_l$, it is denoted by $C(ij; kl)$. The subscripts $i$ and $k$ are used for lobes, $u$'s, belonging to S-atoms, while the subscripts $j$ and $l$ are for lobes, $v$'s, belonging to Zn-atoms. The subscript $n$ is used for ion-core orbitals, disregarding whether they belong to S-atoms or Zn-atoms. The indices $i$ and $j$, when they appear in the same summand, designate a bonded pair, and the same is for the indices $k$ and $l$. So the summation should be extended only over all the sets of bonded pair orbitals $(ij)$ or $(kl)$, even when $i$ or $k$ stands singly under the summation sign. The upper limit $N'-N$ for summations means that the summations are taken over all the ion-core orbitals in the crystal and summations whose upper limit is $N/2$ are to be extended over all the $u$-lobes or $v$-lobes. $\Gamma_{LL'}$ denotes the interaction between the ion-cores* at the $L$th and $L'$th lattice points. $S_L$ is the self-energy of core-electrons of the atom at the $L$th lattice point; however, we need not calculate the values of $S_L$'s by selecting the reference level of the cohesive energy appropriately, so that the last term in (3.4) will henceforth be omitted.

When $A=0$ (purely ionic state), only the first, fourth, tenth and thirteenth terms take non-zero values and the other terms vanish. When $A$ assumes a non-zero value, that is, when covalent bonds are introduced, we can take the point of view that new charge densities

$$\rho_A=\sum_{i=1}^{N/2}\rho_{ij}=\sum_{i=1}^{N/2}[4A/(1+2A^2)]u_iv_j\,, \qquad (3.5)$$

$$\rho_Z=\sum_{j=1}^{N/2}\rho_{jj}=\sum_{j=1}^{N/2}[2A^2/(1+2A^2)]v_j^2\,, \qquad (3.6)$$

appear, while the charge densities

$$\rho_S{}^0=\sum_{i=1}^{N/2}\rho_{ii}{}^0=\sum_{i=1}^{N/2}2u_i^2$$

on $u$-lobes in the totally ionic state decrease to

$$\rho_S=\sum_{i=1}^{N/2}\rho_{ii}=\sum_{i=1}^{N/2}[2(1+A^2)/(1+2A^2)]u_i^2\,, \quad (3.2)$$

and the terms in (3.4) give the energy associated with these new charge densities. Since $u_i$ and $v_j$ were assumed to be mutually orthogonal, the net charge of $\rho_{ij}$ i.e. $\rho_A$ is zero.

The first part of the first term consists of the kinetic energy of the valence electrons belonging to S-atoms and the Coulomb interactions between the nuclear charges and the charge densities $\rho_S$. Similarly the first part of the second term gives the kinetic energy of the valence electrons added to Zn-atoms by covalency correction and the Coulomb interactions between the nuclear charges and the charge densities $\rho_Z$. The first part of the third term gives the change in kinetic energy resulting from covalency correction and the Coulomb interactions between the nuclear charges and the charge densities $\rho_A$. The second parts of the first, second and third terms give the Coulomb interactions between the core-electron charges and $\rho_S$, $\rho_Z$ and $\rho_A$, respectively. The Coulomb interaction between two different charge densities of the type $\rho_{ii}$ is included in the tenth term, that of $\rho_{jj}$ in the eleventh term, and that of $\rho_{ij}$ in the twelveth term. The Coulomb interaction between the two of the three charge densities $\rho_S$, $\rho_Z$ and, $\rho_A$, excluding the interactions between the charge densities on the same bond such as $C(ii; jj)$, $C(ii; ij)$ and $C(jj; ij)$, is involved in the seventh, eighth and nineth terms.

As regards the interactions between the charge densities on one pair of bonded lobes, the fourth term, the first part of the fifth term, and the sixth term correspond to the Coulomb interactions between the charge density $\rho_{ii}{}^0/2=u_i^2$ (which is still adhered to the S-atom even in the totally covalent state $(A=\infty)$) and the charge densities

$$\rho_{ii}{}^R=\rho_{ii}-\frac{\rho_{ii}{}^0}{2}\left(=\frac{1}{1+2A^2}u_i^2\right),$$

$\rho_{jj}$ and $\rho_{ij}$ respectively. The remainder of charge density, $\rho_{ii}{}^R$, after subtracting $u_i^2$ from $\rho_{ii}$ on a $u$-lobe has no interaction with the charge densities $\rho_{ij}$ and $\rho_{jj}$. Likewise $\rho_{jj}$ has no interaction with $\rho_{ij}$. Accordingly we may regard the charge density $\rho_{ij}$ as interacting with charge densities $\rho_{kk}$'s and $\rho_{ll}$'s in the crystal, except that the S-atom and Zn-atom adjoining $\rho_{ij}$ have holes, cut into their outer electronic charge densities, through which $\rho_{ij}$ can "see" some of the ion-core charge of these two atoms. The charge density $\rho_{jj}$ is also in similar situation for the electronic charge densities of the S-atoms. The interaction between $\rho_{jj}$ and the ion-core charge of the adjacent S-atom is attractive. According to calculation, the interaction between $\rho_{ij}$ and the core-charge of the adjoinig S-atom is also strongly attractive, countervailing the slightly repulsive interaction between $\rho_{ij}$ and the core-charge of the Zn-atom adjoining it. In this way, $\rho_{ij}$ and $\rho_{jj}$ tend to bind the adjacent S- and Zn-atoms together, as far as the interaction of $\rho_{ij}$ and $\rho_{jj}$ with their ion-core charges is concerned, although new positive Coulomb interactions between $\rho_{jj}$ and $\rho_{kk}$'s occur by the covalency correction.

---

* The ion-core hereafter means the core-electron and nucleus altogether.

The above situation may be visualized as follows: If the double summations in the first and second parts of the seventh term, and the first parts of the eighth and the nineth terms are extended so as to included the interactions between the charge densities on the same bond such as $C(ii;\, jj)$, $C(ii;\, ij)$ and $C(jj;\, ij)$, and if the new added terms are subtracted from the first part of the fifth term and the sixth term, then we obtain

$$-\frac{2A^2}{(1+2A^2)^2}\sum_{i=1}^{N/2} C(ii;\, jj) -\frac{4A}{(1+2A^2)^2}\sum_{i=1}^{N/2} C(ii;\, ij) -\frac{8A^3}{(1+2A^2)^2}\sum_{i=1}^{N/2} C(jj;\, ij)\,. \tag{3.8}$$

The first term in (3.8) corresponds to the Coulomb interactions between $\rho_{jj}$'s and the holes ($-\rho_{ii}^{R}$'s) in the electronic charge densities on the S-atoms adjoining them and the second term to those between $\rho_{ij}$'s and these holes. The third term corresponds to the Coulomb interactions between $\rho_{ij}$'s and the holes ($-\rho_{jj}$'s) in the electronic charge densities on the Zn-atoms adjoining them. (Calculation shows that $C(ii;\, jj)$ has a relatively large positive value, and $C(ii;\, ij)$ and $C(jj;\, ij)$ have also small positive values.)

## § 4. Energy per Ion-pair

In actual calculations, it is convenient to derive the energy expression per ion-pair from that for the total energy. In this process, the following approximations will be made.

We regard the Coulomb interaction between two atoms, the distance between which is equal to or larger than that from a particular atom to its next nearest-neighbour, as the interaction between two points having charge $e_S$ or $e_Z$, which are the effective charges of the constituent S-atom and Zn-atom in the crystal, respectively and are given from (3.6) and (3.7) by

$$e_S = -e_Z = -2\frac{1-2A^2}{1+2A^2} \tag{4.1}$$

Further we may neglect the Coulomb interaction between two different charge densities $\rho_{ij}$, such as $C(ij;\, kl)$, because each of these charge densities has zero net charge. The Coulomb interactions between $\rho_{ij}$ and atoms located at distances equal to or larger than the distance from a particular atom to its next nearest-neighbour, may also be omitted. Applying this approximation, all the Coulomb terms in (3.4), except those between the nearest-neighours, can be combined together into a single term by using the Madelung constant.

Among the exchange or exchange type integrals in (3.4), the following four kinds are taken into account: $C(ij;\, ji)$ in which valence orbitals $i$ and $j$ make a bonded pair. $C(ik;\, ki)$ or $C(jl;\, lj)$ in which valence orbitals $i$ and $k$ ($j$ and $l$) belong to a same S- (Zn-) atom. $C(in;\, ni)$ or $C(jm;\, mj)$ in which core orbital $n$ ($m$) and valence orbital $i$ ($j$) belong to a same S- (Zn-) atom. $C(im;\, mi)$ or $C(jn;\, nj)$ in which core orbital $m$ ($n$) belongs to the Zn- (S-) atom towards which the valence orbital $i$ ($j$) of the adjacent S- (Zn-) atom points. And all other exchange and exchange type integrals are completely negligible according to order estimation.

Allowing the above simplification and neglection, we can express the energy per one ion-pair, $E_p$, in the following form;

$$\frac{1}{4}E_p = \frac{2(1+A^2)}{1+2A^2}\Bigg[\left(u^i\middle|-\frac{\Delta}{2}\middle|u_i\right) - \overset{①}{Z_s}\left(u_i\middle|\frac{1}{r}\middle|u_i\right) + I\Big[u_i^2,\, \sum_{n}(u_n^0(\boldsymbol{r}))^2\Big] - Z_z\sum_{\beta=1}^{4}\left(u_i\middle|\frac{1}{r_\beta'}\middle|u_i\right) + \sum_{\beta=1}^{4} I\Big[u_i^2,\, \sum_{m}(v_m^0(\boldsymbol{r}_\beta'))^2\Big] - \frac{1}{2}J_{i\alpha} - \frac{1}{2}J_{i\beta}\Bigg]$$

$$
\begin{aligned}
&+\frac{2A^2}{1+2A^2}\Bigg[\left(v_j\left|-\frac{\Delta}{2}\right|v_j\right)\overset{\textcircled{2}}{-Z_z}\left(v_j\left|\frac{1}{r'}\right|v_j\right)+I\,[v_j^2,\sum_m(v_m{}^0(\boldsymbol{r}'))^2]\\
&\qquad -Z_s\sum_{\alpha=1}^{4}\left(v_j\left|\frac{1}{r_\alpha}\right|v_j\right)+I\sum_{\alpha=1}^{4}[v_j^2,\sum_n(u_n{}^0(\boldsymbol{r}_\alpha))^2]-\frac{1}{2}J_{j\beta}-\frac{1}{2}J_{j\alpha}\Bigg]\\
&+\frac{1}{1+2A^2}\Big[C(ii;ii)+4\overset{\textcircled{3}}{A}C(ii;ij)+2A^2[C(ii;jj)+C(ij;ji)]\Big]\\
&+\frac{6(1+A^2)^2}{(1+2A^2)}\Big[C(ii;kk)\overset{\textcircled{4}}{-}\frac{1}{2}C(ik;ki)\Big]\\
&+\frac{6A^4}{(1+2A^2)^2}\Big[C(jj;ll)\overset{\textcircled{5}}{-}\frac{1}{2}C(jl;lj)\Big]\\
&+\frac{24A(1+A^2)}{(1+2A^2)^2}\Big[C(ij;kk)\overset{\textcircled{6}}{+}\sum_{p=1}^{4}C(ij;k_pk_p)\Big]\\
&+\frac{24A^3}{(1+2A^2)^2}\Big[C(ij;ll)\overset{\textcircled{7}}{+}\sum_{p=1}^{4}C(ij;l_pl_p)\Big]\\
&+\frac{4A}{1+2A^2}\Bigg[\left(u_i\left|-\frac{\Delta}{2}\right|v_j\right)\overset{\textcircled{8}}{-}Z_s\sum_{\alpha=1}^{4}\left(u_i\left|\frac{1}{r_\alpha}\right|v_j\right)-Z_z\sum_{\beta=1}^{4}\left(u_i\left|\frac{1}{r_\beta{}'}\right|v_j\right)\\
&\qquad +\sum_{\alpha=1}^{4}I[u_iv_j,\sum_n(u_n{}^0(\boldsymbol{r}_\alpha))^2]+\sum_{\beta=1}^{4}I[u_iv_j,\sum_m(v_m{}^0(\boldsymbol{r}_\beta{}'))^2]\Bigg]\\
&+\frac{6A^2(1+A^2)}{(1+2A^2)^2}\Big[C(ii;ll)\overset{\textcircled{9}}{+}\sum_{p=1}^{4}C(ii;l_pl_p)+C(jj;kk)+\sum_{p=1}^{4}C(jj;k_pk_p)\Big]\\
&+\left(\frac{1-2A^2}{1+2A^2}\right)^2\frac{4-\overset{\textcircled{10}}{\alpha_M}}{d}\overset{\textcircled{11}}{+}\Gamma_{\alpha\beta}\,. \qquad (4.2)
\end{aligned}
$$

We call two atoms, a S-atom and a Zn-atom constituting given ion-pair, the "central S-atom" and the "central Zn-atom" respectively, and the line joining the two central atoms the "central axis" of the ion-pair. $\boldsymbol{r}$ and $\boldsymbol{r}'$ in (4.2) are the vectors pointing respectvely from the central S-atom and Zn-atom to the running point of integration, while $\boldsymbol{r}_\alpha$ and $\boldsymbol{r}_\beta{}'$ the vectors pointing respectively from one of the neighbouring S-aloms and Zn-atoms surrounding the central Zn-atom and S-atom to the running point. (Then $\boldsymbol{r}_2\equiv\boldsymbol{r}$, $\boldsymbol{r}_2{}'=\boldsymbol{r}'$. cf. Fig. 1) The summation $\sum_n(\boldsymbol{u}_n{}^0)\boldsymbol{r}))^2$ and $\sum_m(v_m{}^0(\boldsymbol{r}'))^2$ extend over all the orbitals of the core-electrons in S-atom and Zn-atom respectively, and the arguments of these expressions automatically indicate to which atom the core-electrons belong. The notation

$$I[u_i^2,\sum_m(v_m{}^0(\boldsymbol{r}_\beta{}'))^2]$$

denotes the Coulomb integral of the type

$$\int(u_i(\boldsymbol{r}))^2\cdot\sum(v_m{}^0(\boldsymbol{r}_\beta{}'))^2/r_{12}\cdot d\boldsymbol{r}d\boldsymbol{r}_\beta{}'\,,$$

where $r_{12}$ designates the distance between the two running points of integration. The indices $i$ and $j$ or lobes $u_i$ and $v_j$ correspond to the bonded pair on the central axis. The indices $k$ and $l$ designate one of the other lobes belonging to the central S-atom and Zn-atom respectively. The indices $k_p$ and $l_p$ correspond to one of the lobes on the neigh-

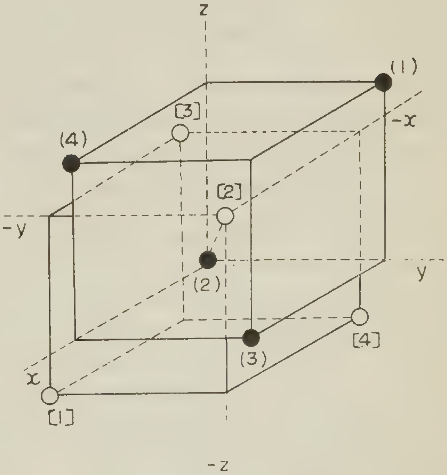

Fig. 1. Sketch of an ion-pair surrounded with six nearest-neighbours in the lattice of zincblende.
(2): Central S-atom [2]: Central Zn-atom
(1), (3) and (4): Non-central S-atoms
[1], [3] and [4]: Non-central Zn-atoms
Line (2)-[2]: Central axis of ion-pair.

bouring three non-central S-atoms and Zn-atoms, respectively. The summations with respect to $p$ should be extended over four lobes belonging to one of these non-central atoms. The summations with respect to $\alpha$ and $\beta$ are to be taken over the four neighbouring S-atoms and Zn-atoms surrounding the central Zn-atom and S-atom respectively. $J_{i\alpha}$ and $J_{j\beta}$ are the exchange integrals between $u_i$ and the core-orbitals in the central S-atoms and between $v_j$ and core orbitals in the central Zn-atom, whereas $J_{i\beta}$ and $J_{j\alpha}$ are the exchange integrals between $u_i$ and the core-orbitals in the central Zn-atom and between $v_j$ and core-orbitals in the central S-atom respectively. $\Gamma_{\alpha\beta}$ is the Coulomb interaction between the ion-core of the central S-atom and that of the central Zn-atom. It consists of two negative Coulomb interactions between the nuclear charge of one atom and the core-electron charge of another atom, and *vice versa*; and two positive Coulomb interactions between the core-electron charges and between the nuclear charges. $Z_s(=16)$ and $Z_z(=30)$ are the nuclear charges of a S-atom and a Zn-atom respectively, $\alpha_M$ is the Madelung constant (=1.6381) for a zincblende-type crystal, and $d$ the lattice parameter i.e. the length of the central axis (=2.33 Å).

The lobe-like four $u$'s on the central S-atom and the four $v$'s on the central Zn-atom in the crystal may be written in the forms,

$$\begin{aligned} u_1&=\tfrac{1}{2}[g^s+g_x{}^p-g_y{}^p-g_z{}^p]\\ u_2&=\tfrac{1}{2}[g^s+g_x{}^p+g_y{}^p+g_z{}^p]\\ u_3&=\tfrac{1}{2}[g^s-g_x{}^p-g_y{}^p+g_z{}^p]\\ u_4&=\tfrac{1}{2}[g^s-g_x{}^p+g_y{}^p-g_z{}^p]\ , \end{aligned} \tag{4.3}$$

and

$$\begin{aligned} v_1&=\tfrac{1}{2}[k^s-k_x{}^p+k_y{}^p+k_z{}^p]\\ v_2&=\tfrac{1}{2}[k^s-k_x{}^p-k_y{}^p-k_z{}^p]\\ v_3&=\tfrac{1}{2}[k^s+k_x{}^p+k_y{}^p-k_z{}^p]\\ v_4&=\tfrac{1}{2}[k^s+k_x{}^p-k_y{}^p+k_z{}^p] \end{aligned} \tag{4.4}$$

respectively. Where $g^s$; $g_x{}^p$, $g_y{}^p$ and $g_z{}^p$ are the 3$s$-orbital and the three 3$p$-orbitals on the S-atom, and $k^s$; $k_x{}^p$, $k_y{}^p$ and $k_z{}^p$ the 4$s$-orbital and the three 4$p$-orbitals on the Zn-atom in the crystal. As is shown in Fig. 1, the suffixes of $u_1$, $u_2$, $u_3$ and $u_4$ indicate the number of the neighbouring four Zn-atoms towards which the lobe of S-atom $u_i$ points, and just the same for $v_j$. So the lobes $u_2$ and $v_2$ form a bonded pair.

In deriving (3.4), it was assumed that the $u$'s and $v$'s are all mutually orthogonal, and this condition is fullfild if $g$'s and $k$'s are so. We may construct a set of mutually orthogonal $g$'s and $k$'s from the non-orthogonal orbitals $f$'s (3$s$- and 3$p$-orbitals of a free $S^{2-}$-ion) and $h$'s (4$s$- and 4$p$-orbitals of a virtual $Zn^{2-}$-ion in free state), by applying the orthogonality correction first given by Landshoff[8] and later generalized byLöwd in[9]. According to Landshoff, orthogonality correction is given by

$$\varphi_\mu=\phi_\mu\left[1+\frac{3}{8}\sum_\alpha(S_{\mu\alpha})^2\right]-\frac{1}{2}\textstyle\sum_\alpha\phi_\alpha S_{\alpha\mu}\ ,$$

$$S_{\mu\nu}=(\phi_\mu|\phi_\nu)-\delta_{\mu\nu}\ ;\qquad \delta_{\mu\nu}=\begin{matrix}1 & \mu=\nu\\ 0 & \mu\neq\nu\end{matrix} \tag{4.5}$$

where the $\varphi$'s are mutually orthogonal orbitals constructed from the $\phi$'s, which are non-orthogonal. $\varphi$'s are normalized (if the $\phi$'s are) to terms of order $(S_{\mu\nu})^3$ and are mutually orthogonal to the extent that $3/4\cdot\sum_\alpha S_{\mu\alpha}S_{\alpha\nu}$ and higher order terms are negligible. In our case $\varphi$'s are to be identified with $g$'s and $k$'s, and $\phi$'s with $f$'s and $h$'s.

It should be noted that, by introducing these orthogonality corrections, the orbitals in the crystal, $g$'s and $k$'s, are distorted in obedience to the lattice symmetry and belong to certain irreducible representations of the point group $T_d$, as was pointed out by Schmidt[7].

Unfortunately, we could not find the Hartree's self-consistent solutions for free states except the 4$s$-orbital $h^s$ of a free Zn-atom[10], so the orbitals of a free $S^{2-}$-ion, $f^s$ and $f^p$'s, were derived from those of a free $Cl^-$-ion[11], and 4$p$-orbitals, $h^p$'s, of a virtual free $Zn^{2-}$-ion from those of a free $As^+$-ion by means of scale changes of radial coordinates[12], using the screeniging constant given by Pauling-Sherman[13].

For the sake of simplicity, it is assumed that the orbitals of the core-electrons of a S-atom and a Zn-atom in the crystal are completely indentical with those in the free atoms. That is, the orbitals of the core-electrons are subjected to negligible deformations by being brought into the crystal. Accordingly, for the core-orbitals of the both atoms the wave functions of the free atoms are used without any modification. The core electron wave functions of a free Zn-atom could be find in the cited reference[10] and those of a S-atom were derived from those of $Cl^-$-ion[11] by the above mentioned procedure.

All the terms in (4.2) may be numerically evaluated. The details in numerical calculation will shortly be published in the Research Notes of the Department of Physics, Faculty of Science, Okayama University. Restricting ourselves to only main energy contributions, we may give the following description of the situation with increasing $A$ value.

A large increase of a positive energy with increasing $A$ value occurs from the nineth term in (4.2), which corresponds to the Coulomb interactions between the new charge densities $\rho_{jj}$'s added by covalency correction and $\rho_{kk}$'s remaining on the $u$-lobes. But the eighth term contributes a negative energy. With incresing $A$ value, the magnitude of this negative term increases rapidly and then decreases slowly, passing through a peak point. This depression of the energy overcomes the increase of the positive energy chiefly ascribable to the nineth term, in a range of comparatively small $A$ value.

As the resultant effect, $E_p$ given by (4.2) has a minimum at $A=0.22$. The energy depression from the totally ionic state which is given by putting $A=0$ in (4.2) is $-0.52$ in atomic unit. (1 atomic unit of energy equals 27.07 eV or 623.96 Kcal/mol.) Fig. 2 shows the dependence of the energy per ion-pair upon the parameter $A$.

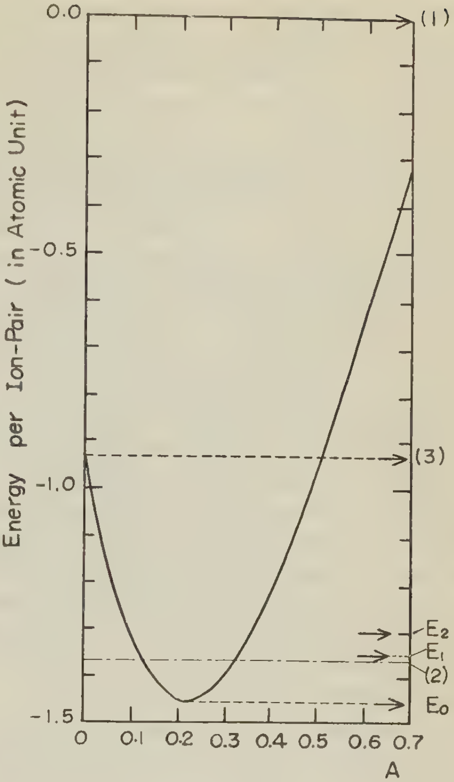

Fig. 2. Dependence of energy of zincblende upon the parameter $A$.

(1): Reference Level ($S^{2-}$, $Zn^{2+}$)
(2): Monatomic Gas Level (S, Zn)
(3): Totally Ionic Level ($S^{2-}+Zn^{2+}$) $A=0$
$E_0$: Level obtained by the present model ($A=0.22$)
$E_1$: Level derived from BH energy cycle.
$E_2$: Level calculated by using BM equation.

## § 5. Conclusions

The ion gas state which consists of free $S^{2-}$-ions and free $Zn^{2+}$-ions is selected as the reference level of the cohesive energy. It corrresponds to the case that $A=0$ and $d\to\infty$ in (4.2). The energy per one ion-pair at the reference level, $E_{p\infty}$, is given by

$$\frac{1}{4}E_{p\infty}=2\left[\left(u_i\left|-\frac{\varDelta}{2}\right|u_i\right)-Z_s\left(u_i\left|\frac{1}{r}\right|u_i\right)\right.$$
$$\left.+I[u_i^2,\sum_n(u_n^0(\boldsymbol{r}))^2]-\frac{1}{2}J_{i\alpha}\right]$$
$$+C(ii;ii)+6\left[C(ii;\,kk)-\frac{1}{2}C(ik;\,ki)\right].\quad(5.1)$$

In this expression, for $u_i$ and $u_k$ the valence orbitals on a free $S^{2-}$-ion which are given by replacing $g$'s with $f$'s in (4.3), are to be used. The value $E_{p\infty}$ is evaluated to be $-13.35$ in atomic unit*. The energy of the reference level is above the totally ionic level [$A=0$ and $d$ is finite] by 0.94 in atomic unit per ion-pair. The total energy depression from the reference level at $A=0.22$ amounts to $-1.46$ in atomic unit per ion-pair.

The observed cohesive energy of zincblende derived by means of Born-Haber's energy cycle is 1.36 in atomic unit per ion-pair

---

* As is easily understood, $E_{p\infty}$ is the total energy of eight electrons in the $M$-shell of a free $S^{2-}$-ion and should be compared with the ionization energy $E_i$ required to strip these electrons. $E_i$ is however equal to $9.76-0.13=9.63$ in atomic unit, where 9.76 is the ionization energy to remove the six electrons from a neutral S-atom[14] and $-0.13$ the electron affinity of a $S^{2-}$-ion.[15] This discrepancy will be due to the fact that the states of the core-electrons remain fixed to those in the free $S^{2-}$-ion in the calculation of $E_{p\infty}$, whereas the former must be greatly altered from the latter, in reality, as a result of ionization.

(=851 Kcal/mol)[15], and that calculated by means of Born-Mayer's equation is 1.31 (=816 Kcal/mol)[16] as shown in Fig. 2. Besides, the energy level of the monatomic gas state (=−1.37/atom-pair, in atomic unit, below the reference level) calculated from the ionization voltage 33.61 eV ($Zn \rightarrow Zn^{2+}$)[14] and the electron affinity of a $S^{2-}$-ion −3.44 eV[15] is shown in the same figure. The effective charge on the constituent ions which is calculated from (4.1) by putting $A=0.22$, is $2 \times 0.83$ in atomic unit. This is considerably larger than $2 \times 0.48$, which is estimated from the theory of dielectric constant of ionic crystals[3]. The calculated energy difference between the reference level and the totally ionic state (=−0.94), that is, the energy depression due to purely ionic binding, is nearly comparable to the cohesive energies of predominantly ionic alkali-earth sulphide crystals. For example, the calculated cohesive energies per ion-pair of CaS, SrS and BaS are equal to 1.17, 1.09 and 1.03 in atomic unit, respectively[17].

The above comparison between the calculated and the observed values seems to show that our model for ZnS-type crystals would be reasonable. The eighth term in (4.2), which consists of the change in kinetic energy resulting from the covalency correction and the Coulomb interactions between charge density $\rho_{ij}$ and the ion-core charges of the nearest-neighbouring four S-atoms and four Zn-atoms, contributes conspicuously to the depression of energy, and then renders the crystal more stable than predominantly ionic crystals. It should be noted that this effect may appear first by introducing covalency correction into the usual ionic binding. Owing to this stability the crystals of this type have been used as a durable host-crystal of phosphor.

In order to clarify thoroughly the true aspects in the zincblende lattice, it is necessary to know the numerical factor of each energy term in (4.2) at various values of the interionic distance $r$ and to determine $A$ so as to minimize the energy at every particular value of $r$. Survey of the physical meaning of each energy term stated in § 3 and its energy contribution at the observed value of $r$ ($r=d$), suggests that the most important energy contribution to the binding in crystals of this type can be classified in the following three main parts, provided we assume that the variations of the forms of the valence orbitals and of $A$ minimizing the energy are neglegible for a small change of $r$, compared with those of the main energy parts which are explicitly dependent on $r$*.

(1) The total Coulomb interaction between constituent ions in the crystal. Its magnitude is considerably decreased owing to the decrease of the effective charge on them, compared with that in the case where the crystal is assumed to be purely ionic. This long-range interaction may be expressed approximately in the form $-\alpha_M (Zes)^2/r$, where $s$ indicates the ratio of the effective charge to the usual ionic charge.

(2) A short-range type interaction which may be expected to be strongly attractive. It originates from the interactions between the charge densities $\rho_{ij}$'s and the charge densities on the neighbouring ions around them, and from the negative change in kinetic energy caused by the covalency correction as well as from the interactions given in (3.8). (Although $\rho_{ij}$'s interact with the charge densities on all the ions in the crystal, we may regard this interaction as effective only in short range because of zero net charge of each $\rho_{ij}$ as stated in § 3.) Setting aside the question of the $r$-dependence of this negative short-range type interaction, it amends the above-mentioned decrease in the magnitude of the negative long-range Madelung term.

(3) A short-range exchange interaction between the electrons of a particular ion and the ion-core electrons of the neighbouring ions around it, which is involved in the third parts of the first and second terms in (3.4). This interaction will operate repulsively and may be expressed approximately in the form $ae^{-br}$ or $br^{-n}$ as in the usual manner.

In trying to deal with the problems on the ZnS-type crystals phenomenologically by means of an equation analogous to the Born-Mayer-type one, the former would be obtained by modifying the latter so as to be suited for the above-stated features.

The method of the calculation used in this paper would be generally applicable not only for the other sphalerite-type crystals but also for wurzite-type ones by modifying the expansion forms of wave functions in accordance with the crystallographical symmetry $C_{6v}$ instead of $T_d$.

---

* An energy term in which the orbitals belonging two different ions are concerned is called here "explicitly dependent on $r$".

### Acknowledgement

The authors express their sincere thanks to Dr. L. A. Schmid for sending to them a bulky copy of his thesis which contains the details in the method of numerical calculations and is greatly helpful to this work. They also wish to thank Professor T. Nagamiya who read the manuscript and gave them valuable advices, and Professor K. Umeda for his continuous interest and encouragement.

This work was partly supported by a Grant in Aid for Fundamental Scientific Research from the Ministry of Education of Japan, which was given to one of the authors (T), a member of the Research Group for the Study of Atomic and Molecular Structure.

### References

1) F. Seitz: *Modern Theory of Solids* (McGraw-Hill Co. N. Y. 1940) p. 83.
2) J. R. Tessman, A. H. Kahn and W. Shockley: Phys. Rev. **92** (1953) 890.
3) B. Szigeti: Trans. Faraday Soc. **45** (1949) 155.
4) H. J. Emeléus and J. S. Anderson: *Modern Aspects of Inorganic Chemistry* (D. Van Nostrand Co. N. Y. 1952) pp. 80, 177.
B. D. Saksena: Phys. Rev. **81** (1951) 1012.
5) L. Pauling: J. Am. Chem. Soc. **53** (1931) 1367.
J. C. Slater: Phys. Rev. **37** (1931) 481.
6) H. J. Emeléus and J. S. Anderson: *loc. cit.* p. 142.
7) L. A. Schmid: Phys. Rev. **92** (1953) 1373. *Calculation of Cohesive Energy of Diamond* (1953) (Thesis).
8) R. Landshoff: ZS. f. Phys. **102** (1936) 201.
9) P. O. Löwdin: J. Chem. Phys. **18** (1950) 365.
10) W. Hartree and D. R. Hartree: Phys. Rev. **59** (1941) 299.
11) D. R. Hartree and W. Hartree: Proc. Roy. Soc. **A 156** (1936) 45.
12) D. G. Bell, D. M. Hum, L. Pincherle, D. W. Sciama and P. M. Woodward: Proc. Roy. Soc. **A 217** (1953) 71.
13) L. Pauling and J. Sherman: ZS. f. Krist. **81** (1932) 1.
14) Landolt-Börnstein: *Physikalisch-Chemische Tabellen* (J. Springer, Berlin, 1931) Erg.-Bd. II, p. 567.
15) F. Seitz: *loc. cit.* p. 83.
16) J. Sherman: Chem. Rev. **11** (1932) 93.
17) J. E. Mayer and M. McC. Maltbie: ZS. f. Phys. **75** (1932) 748.

JOURNAL OF THE PHYSICAL SOCIETY OF JAPAN Vol. 11, No. 6, JUNE, 1956

# Effect of Self-diffusion on the Ortho-para Conversion in Oxiygen Contaminated Solid Hydrogen

By Kazuko MOTIZUKI and Takeo NAGAMIYA
*Department of Physics, Osaka University*

(Received March 2, 1956)

When self-diffusion takes places rapidly in solid hydrogen contaminated with oxygen, the ortho-para conversion rate is enhanced. The ortho-concentration follows the diffusion equation including the effect of the oxygen; by finding the steady state solution of this equation and using values of the relaxation time, $\tau$, associated with the self-diffusion, which were measured recently by Rollin and Watson, we can conclude that below 4°K the effect of the self-diffusion is negligible and above 8°K the self-diffusion is so rapid that it smoothes out the ortho-concentration around each oxygen molecule. The rate of ortho-para conversion above 8°K is calculated assuming a uniform ortho-concentration throughout the crystal.

In our previous report[1)] the ortho-para conversion rate for pure and oxygen cotaminated solid hydrogen was calculated assuming the effect of self-diffusion to be negligible. Rollin and Watson[2)] have recently measured the width of the proton magnetic resonance in solid hydrogen as a function of temperature and found an appreciable narrowing of it in the neighbourhood of 10°K, which indicates an increase in the self-diffusion. They estimated the life time, $\tau$, which a molecule spends on one lattice site before jumping to another, to be as follows:

| $T$(°K) | 1° | 4° | 10° | 11° | 12° |
|---|---|---|---|---|---|
| $\tau$(sec) | $7.5\times10^{62}$ | $7.5\times10^{5}$ | $3\times10^{-6}$ | $6\times10^{-7}$ | $1.6\times10^{-7}$ |

If self-diffusion takes place rapidly enough in solid hydrogen contaminated with oxygen, ortho-molecules diffuse into the action spheres of the oxygen molecules, change to para, and leave the spheres, so that the conversion rate must be greatly enhanced.

Consider the case where the ortho-para conversion due to the mutual interactions among ortho-molecules are negligible and the crystal lattice can be replaced by a continuum. The ortho-concentration $c(r, t)$ ($r$ is the distance from a given oxygen molecule) follows the equation.

$$\frac{\partial c(r,t)}{\partial t}=D\Delta c(r,t)-k_{\text{oxy.}}(r)c(r,t)\,, \qquad (1)$$

where $D$ is the diffusion constant and is approximately equal to $a^2/4\tau$, $a$ being the intermolecular distance in the lattice, and $k_{\text{oxy.}}(r)$ is the rate of conversion due to an oxygen molecule; this was calculated in our previous paper and was found to be $b/r^{12}$ ($b$=250 per hour when $r$ is measured in units of $a$). We transform the variables $t, r$ into $r', t'$ by

$$t=\frac{1}{D}\left(\frac{b}{D}\right)^{1/5}t', \quad r=\left(\frac{b}{D}\right)^{1/10}r', \qquad (2)$$

and find

$$\frac{\partial c(r',t')}{\partial t'}=\Delta c(r',t')-\left(\frac{1}{r'}\right)^{12}c(r',t'). \qquad (3)$$

It is not easy to solve this equation completely. However, the steady state solution can be found easily in the form of a path integral, taking $(1/r')^{10}$ as a new variable instead of $r'$ (see Appendix). The solution which vanishes at $r'=0$ can be expanded in inverse powers of $r'$ as

$$\left[1+\frac{1}{90}\left(\frac{1}{r'}\right)^{10}+\frac{1}{90\times380}\left(\frac{1}{r'}\right)^{20}+\cdots\right] -0.71\frac{1}{r'}\left[1+\frac{1}{110}\left(\frac{1}{r'}\right)^{10}+\cdots\right], \qquad (4)$$

or, approximately

$$1-0.71\left(\frac{b}{D}\right)^{1/10}\frac{1}{r}. \qquad (5)$$

The value of $r$ determined by putting (5) equal to 1/2 gives a measure of the radius at which the ortho-concentration becomes appreciably different from its value at infinity (or, within which one finds practically para-molecules only). This value of $r$ is calculated to be:

| | | | |
|---|---|---|---|
| $r/a=20$ for | $\tau=1.1\times10^{12}$ sec | $T=3.5$°K | ca |
| 4.9 | $7.5\times10^{5}$ | 4° | |
| 2 | $1.1\times10^{2}$ | 5° | ca |
| 1 | $1.0\times10^{-1}$ | 6° | ca |
| 0.5 | $1.0\times10^{-4}$ | 8° | ca |
| 0.2 | $1.1\times10^{-8}$ | 12° | ca |

Since values of $r$ smaller than $a$ are meaningless, we are in such cases in the situation that the self-diffusion is rapid enough to smooth out the ortho-concentration around the oxygen molecule. On the other hand, if the value of $r$ is greater than $2.7a$, which measures the distance at which the conversion rate due to the oxygen molecule equals that due to the mutual interactions among ortho-molecules (see our previous paper), the effect of diffusion can be neglected; in such a case our previous calculation can be applied. Looking at the above table, we see that the former cases occur above 8°K and the latter cases below 4°K.

We now go over to calculating the rate of ortho-para conversion above 8°K. The ortho-concentration can be assumed to be uniform throughout the crystal. It can be found by solving the equation

$$\frac{dc}{dt}=\alpha\sum_i(b/r_i^{12})c-k_{\mathrm{hydr.}}c^2\,, \tag{6}$$

where $\alpha$ is the molar concentration of oxygen and the summation is to be extended over the lattice points surrounding each oxygen molecule. The solution of this equation is

$$c(t)=\frac{\alpha c_0\sum_i(b/r_i^{12})}{[\alpha\sum_i(b/r_i^{12})+c_0k_{\mathrm{hydr.}}]\exp[\alpha\sum_i(b/r_i^{12})t]-c_0k_{\mathrm{hydr.}}}\,.$$

$$(c_0=\text{initial ortho-concentration}) \tag{7}$$

Solid curves in Fig. 1 show this function of $t$ for normal hydrogen ($c_0=75\%$) with $\alpha=0.1\%$ and $\alpha=0.01\%$; the corresponding broken curves are for the case where the diffusion is negligible. The values of $b$ and $k_{\mathrm{hydr.}}$ used for this calculation are those obtained theoretically in our previous paper.

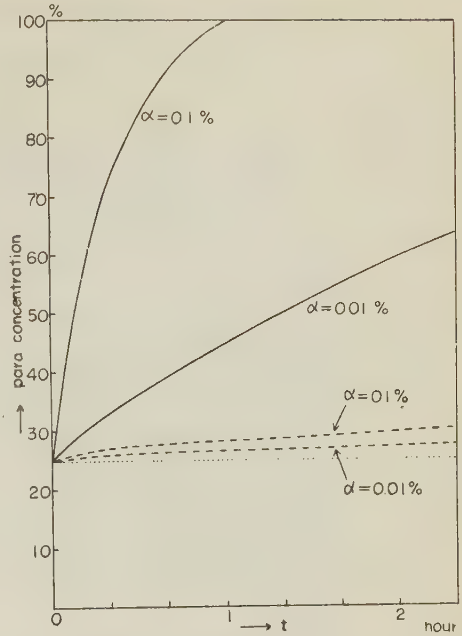

Fig. 1. The average concentration of para-molecules in normal hydrogen as a function of time for various values of the molar oxygen concentration, α. Full curves were calculated with the use of Eq. (7), broken curves are the results obtained in our previous paper.

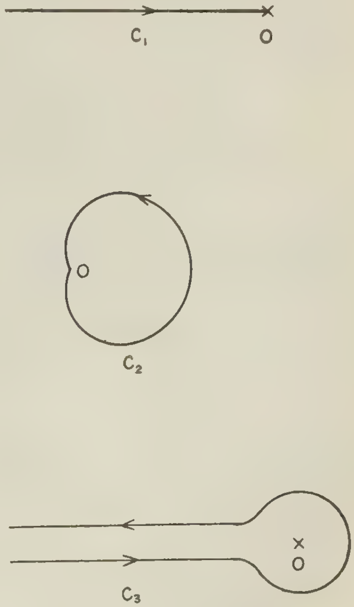

Fig. 2. Integration paths.

### Appendix Steady state Solution of Eq. (3)

Writing $(1/r')^{10}=x$, the steady state equation symmetrical around the oxygen molecule can be written

$$100x\frac{d^2c}{dx^2}+90\frac{dc}{dx}-c=0\,.$$

The solution of this equation can be found in the form of a path integral

$$\int_C \zeta^{-11/10} \exp\left(x\zeta + \frac{1}{100\zeta}\right) d\zeta\,,$$

where the path $C$ can be any one of the three shown in Fig. 2. Path $C_1$ gives the required solution since it gives a vanishing value of the integral at $x$=infinity, or $r'=0$. On the other hand, integrals along paths $C_2$ and $C_3$ can be expanded in powers of $x$:

$$\int_{C_2} \zeta^{-11/10} \exp\left(x\zeta + \frac{1}{100\,\zeta}\right) d\zeta$$

$$= 2i \sin\frac{\pi}{10} \cdot (100)^{1/10} \Gamma\left(\frac{1}{10}\right)$$

$$\times\left(1 + \frac{1}{90}x + \frac{1}{90\times 380}x^2 + \cdots\right),$$

$$\int_{C_3} \zeta^{-11/10} \exp\left(x\zeta + \frac{1}{100\,\zeta}\right) d\zeta$$

$$= -2i \sin\frac{\pi}{10} \Gamma\left(-\frac{1}{10}\right)$$

$$\times x^{1/10}\left(1 + \frac{1}{110}x + \cdots\right).$$

Now, the integral along $C_1$ is a combination of the integrals along $C_2$ and $C_3$:

$$\int_{C_1} = (1 - e^{-22\pi i/10})^{-1}\left[\int_{C_3} - \int_{C_2}\right].$$

Thus we find (4), where 0.71 is the value of

$$\frac{-\Gamma\left(-\frac{1}{10}\right)}{(100)^{1/10}\Gamma\left(\frac{1}{10}\right)}.$$

## References

1) K. Motizuki and T. Nagamiya: J. Phys. Soc. Japan **11** (1956) 93.
2) B. V. Rollin and E. Watson: Conférence de Physique des bases Températures, Paris (1955) 474.

---

# Errata

## Theory of the Ortho-para Conversion in Solid Hydrogen

By K. MOTIZUKI and T. NAGAMIYA

J. Phys. Soc. Japan **11** (1956) 93

There are a number of printer's errors in our first paper entitled as above, of which some might lead to misunderstandings. They are:

| page | column | line | incorrect | correct |
|---|---|---|---|---|
| 95 | left | 19th | of one of | If one of |
| 95 | right | 3rd | in units of | in units of $\hbar$ |
| 95 | right | 4th | $\sqrt{1}$ | $\sqrt{-1}$ |
| 97 | right | 30th | motion | mention |
| 98 | left | 20th | same | sum |
| 98 | Eq. (4.3) | | $\sum_i [1-\exp(-k_{\text{oxy}})R_i)t_0$ | $\sum_i [1-\exp(-k_{\text{oxy}}(R_i)t)]$ |
| 98 | right | 15th | (6.6) if | (4.5) is |
| 99 | caption to Fig. 1. | | Eq. (4.4), Curve C Eq. (4.9). | Eq. (4.3), Curve B Eq. (4.4), Curve C Eq. (4.8). |
| 99 | caption to Fig. 2. | | (5.11) | (4.11) |
| 99 | right | 3rd | Dr. Yoshida | Dr. Yosida |
| 103 | Eq. (B.11) | | $\left[\frac{\sin(R_0\omega/v)}{R_0\omega/v}\right]$ | $\left[1-\frac{\sin(R_0\omega/v)}{R_0\omega/v}\right]$ |
| 103 | 6th line from Eq. (B.11) | | $h\omega_r/k$ | $\hbar\omega_r/k$ |

JOURNAL OF THE PHYSICAL SOCIETY OF JAPAN Vol. 11, No. 6, JUNE, 1956

# The Soft X-ray Spectroscopy of the Solid State by the Electronic Differentiating Method:

## Aluminium $L_3$

By Gunji SHINODA, Tatsuro SUZUKI and Susumu KATO

*Laboratory for Applied Physics, Faculty of Engineering,*
*Osaka University, Higashinoda, Osaka, Japan*

(Received January 23, 1956)

A method was developed of observing soft X-ray emission spectra directly on the screen of a cathode-ray oscilloscope. Soft X-rays emitted from metals were detected by a photoelectric device which works under retarding voltages having saw-tooth wave form. The photoelectric current was differentiated three times by electronic differentiating circuits. The saw-tooth wave voltage corresponds to the reciprocal of wavelength, while the differentiated photoelectric current represents the intensity of soft X-ray emission. Using this method we obtained the emission spectra in about 1/100 sec. exposure without serious contamination of the anticathode. As an example, the structure of the $L_3$ emission spectrum of Al was studied.

## § 1. Introduction

The soft *X*-ray spectroscopy of solids has been developed by many investigators, for instance, Siegbahn and Magnusson[1], O'Bryan and Skinner[2] and recently by Piore, Harvey, Gyorgy and Kingstone[3] and Rogers and Chalklin[4]. All of their works have been carried out with spectrographs having diffraction gratings, although in some recent works the photographic plate has been replaced by a photomultiplier or a Geiger counter.

There is another method of soft *X*-ray spectroscopy, which does not use gratings but is based on the photoelectric effect of *X*-rays. This method was tried by several workers (Compton and Thomas[5], and Skinner[6],) about thirty years ago, but was not successful because of the inevitable inaccuracy in the process of graphical differentiation of observed curves. When, however, we apply electronic differentiating circuits to this method, the above-mentioned inaccuracy may be eliminated, and moreover we may gain even some advantages because the contamination of the *X*-ray source may be completely avoided by virtue of the very short time required for the experiment.

The present authors previously reported on a measuring system of this kind, in which the electronic differentiation was applied to the change of photoelectric current with the change of bombarding potential of the *X*-ray tube[7]. In the present paper a different system is reported in which the electronic differentiations are carried out on the change of photoelectric current with the change of retarding potential against photoelectrons while the bombarding potential of the *X*-ray tube is kept constant. As an example of application, the structure of the emission line of Al $L_3$ was studied.

## § 2. Experimental Procedures

Fig. 1 shows the *X*-ray tube used by us. When we apply a retarding potential $V$ between the photoelectric surface and the collector, the photoelectric current $I$ detected by the collector will be given by Fowler-DuBridge's formula[8][9] for the monochromatic incident rays

$$I=\alpha A T^2 \phi(x)\,, \qquad (1)$$

where

$\alpha$: a constant proportional to the intensity of *X*-rays, and dependent on the photoelectric yield,

$A=4\pi mk^2/h^3$ ,

$\phi(x)$: Fowler's function given by

$$\phi(x)=\frac{\pi^2}{6}+\frac{x^2}{2}-\left(e^{-x}-\frac{e^{-2x}}{2^2}+\frac{e^{-3x}}{3^2}-\cdots\right) \qquad \text{for} \quad x\geq 0$$

$$=e^{x}-\frac{e^{2x}}{2^2}+\frac{e^{3x}}{3^2}-\cdots \qquad \text{for} \quad x\leq 0,$$

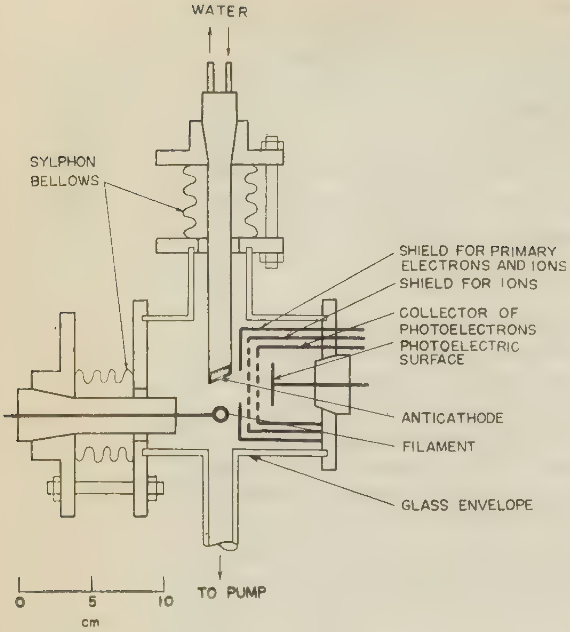

Fig. 1. Soft X-ray tube.

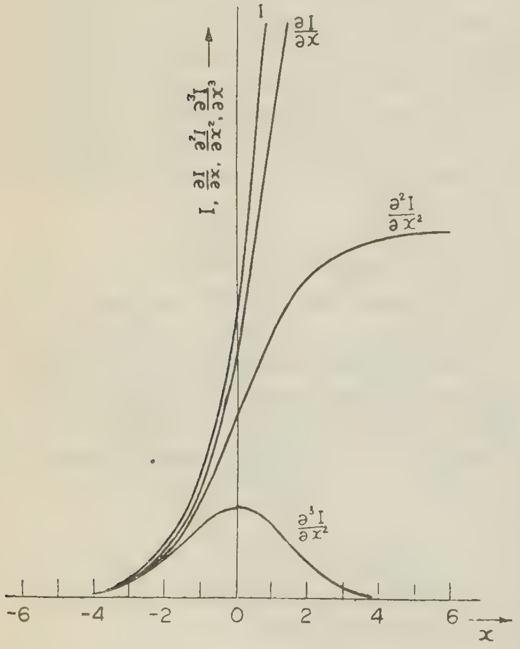

Fig. 2. Curves representing I, $\partial I/\partial x$, $\partial^2 I/\partial x^2$ and $\partial^3 I/\partial x^3$.

and $x=(V_m-V)e/kT$, $V_m$ being given by Einstein's formula $V_m e=h\nu-\varphi e$. $m$, $e$, $h$ and $k$ are electronic mass, electronic charge, Planck's constant and Boltzmann's constant, $T$ the absolute temperature, $\varphi$ the work function of the photoelectric surface.

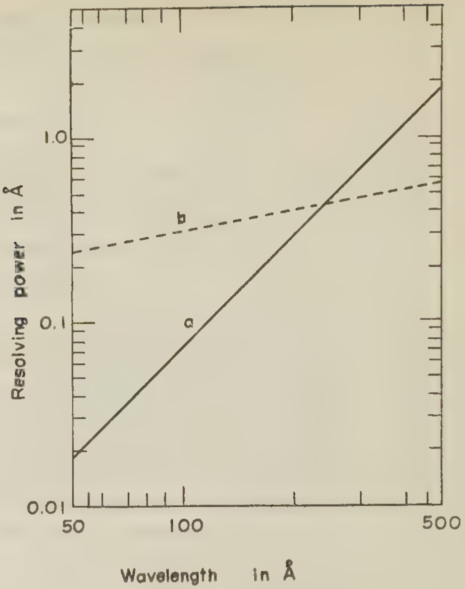

Fig. 3. Resolving power of the differentiating method at $T=293°\mathrm{K}$ (a), and the diffraction grating method by Skinner[11] (b).

The photoelectric surface and the collector, shown in Fig. 1 shall be plane parallel. Moreover the photoelectric current should not be saturated. These are the fundamental assumptions for Eq. (1).

The first derivative of Eq. (1) $\partial I/\partial x$ gives distributions of the "normal energy"* of emitted photoelectrons, and the second derivative $\partial^2 I/\partial x^2$ gives the distribution of normal components of velocities of photoelectrons, and the third derivative

$$\left.\begin{aligned}\frac{\partial^3 I}{\partial x^3}&=\alpha A T^2\phi'''(x)=\alpha A T^2\left\{\begin{matrix}(1+e^{-x})^2\\ e^{-x}\end{matrix}\right\}\\ &\qquad\qquad\text{for}\quad x\geq 0\\ &=\alpha A T^2\left\{\begin{matrix}e^{x}\\ (1+e^{x})^2\end{matrix}\right\}\\ &\qquad\qquad\text{for}\quad x\leq 0\end{aligned}\right\}\qquad(2)$$

gives the function shown in Fig. 2. This is an even function of $x$. At $x=0$, the height of the curve is proportional to the intensity of the incident rays. Thus, the photoelectric current differentiated three times can reproduce the spectral intensity curve of $X$-ray lines. If we apply a potential due to this

---

* If the collector has a potential $V$, negative to the photoelectric surface, only those electrons reach the collector which emerge from the photoelectric surface with velocity component $v_n$ normal to the surface, such that $\frac{1}{2}mv_n^2=E_n\geq Ve$. $E_n$ is called for brevity the "normal energy".

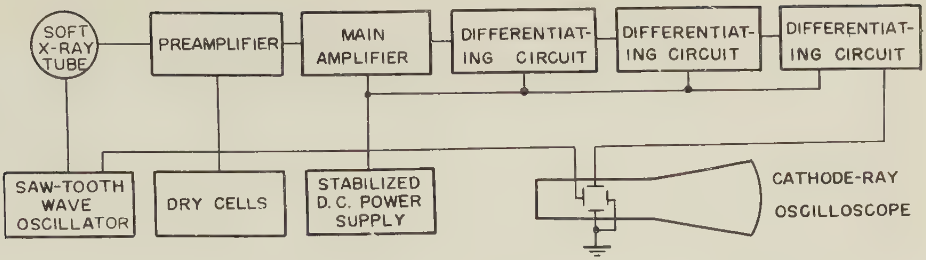

Fig. 4. Electronic Circuit of the experiment.

current to the ordinate of a cathode-ray oscilloscope and a saw-tooth retarding potential to the abscissa we can observe directly the spectral intensity *vs* wavelength curve on the fluorescent screen.

The resolving power of this method, or the half-value width of the curve, is given by

$$\Delta\lambda \fallingdotseq \frac{3.25\,kT}{ch}\lambda^3 \qquad (3)$$

where $\lambda$ is the wavelength of the incident $X$-rays, $c$ the light velocity. Fig. 3 shows the resolving power of this method in comparison with that due to a diffraction grating[10]. We can see that on the short wavelength side the resolving power is superior to that of the diffraction grating.

## § 3. Electronic Circuit

Fig. 4 shows the electronic circuits used. The preamplifier has two 6AK5 tubes. For the first stage of the preamplifier a tube having the smallest grid current was selected and this was used with a sufficiently low anode voltage. The electric power was supplied by several dry cells. In this way an electric current as low as $10^{-12}$ ampere was amplified satisfactorily. According to the recent study of Hinteregger and Watanabe[11], the photoelectric yield of Ni, Pt and W for 1000 Å is fairly large and attains to about $10^{-1}$, and in fact we have obtained fairly large photoelectric currents of about $10^{-9}$ ampere for an $X$-ray tube current of 10 mA.

The main amplifier has satisfactorily high gain with low distortions. The differentiating circuits are *RC* types having cathode followers to avoid any distortion in the voltage wave form. The negative feed back was inserted to improve reliability of this electronic differentiation.

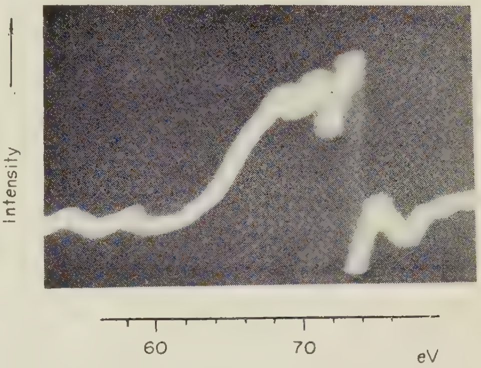

Fig. 5. The emission-spectral curve of Al $L_3$ observed on the screen of cathode-ray oscilloscope.

The saw-tooth wave generator shows good linearity at about 100 c.p.s. All the powers are supplied through an electronic voltage stabilizer.

## § 4. The Result of the Experiment for Pure Al

Fig. 5 is the emission-spectral curve of Al $L_3$ observed on the screen of cathode-ray oscilloscope, the photoelectric surface being Ni. The bombarding potential was about 800 V and the tube current was 10 mA. The purity of Al was 99.99% and the material was attached to the anticathode as a thick plate. The tube was evacuated by a high speed oil diffusion pump and pressures of the order of $10^{-6}$ mmHg could be obtained. The emission-spectral curves was obtained within multiples of 1/100 sec with saw-tooth waves of 100 c.p.s. The time of exposure was 1/50 sec. Therefore, in Fig. 5 two cycles are superimposed. The average empirical band width obtained from Fig. 5 and several other photographs, which are not shown here, is 13.0±1 eV and the reduced band width is 10.5± eV.

The empirical band width obtained from the $K$ and $L_3$ spectra of Al by previous investigators are 13±1 eV, Farineau[12]; 11.3±2 eV, Karlsson and Siegbahn[13]; 12.2±2 eV, Yoshida[14]; 10±1 ev, Cauchois[15] (all from the $K$ band), and 13.2±0.4 eV Skinner[10] (from the $L_3$ band).

## § 5. Discussion

### (a) *Experimental method*

As stated in a previous section, there are two possible types of spectroscopy by the electronic method according to whether the saw-tooth wave voltage is applied as the bombarding potential of the $X$-ray tube or as the retarding potential to the photoelectric surface.

In the first method, the available photoelectric current is fairly large because the photoelectric collector is kept at a positive potential to the photoelectric surface and the electronic differentiation is done only once. In the second method the photoelectric current is produced against the retarding potential and the electronic differentiation must be done three times. Thus, the trouble due to the circuit is much more scanty in the first method than in the second method. On the other hand, in the soft $X$-ray region the bombarding potential of the $X$-ray tube in the first method is very low, namely at most 100 V, so that the electrons cannot penetrate deep enough into the material of the anticathode, then the results may be affected by the surface condition of the anticathode. The $M_{23}$ emission curves of Cu observed by the first method showed two types of emission curves[16], one probably corresponding to the energy distribution of the higher electronic levels in Solid Cu and the other to the surface contamination. As in the experiment by Compton and Thomas[5] who observed photoelectric current against applied bombarding voltage curves similarly to those in our first method, some unexpected discontinuities may occur under certain surface conditions. In the second method, however, the bombarding potential can be taken high, namely several hundred or thousand volts, and thus these disturbances may be avoided. There fore the latter method as described in this paper appears to be the more advantageous one.

The theoretical value of the resolution of the second method is shown in Fig. 3. The band width of Al $L_3$ measured from several emission curves varies in about 2 eV *i.e.* 5 Å and is not so good as theoretical one. Perhaps it may be caused by the mixing of the various energy components besides the "normal energy" in the photoelectric current or by the secondary electron emission. According to the Fowler-DuBridge's formula, the distribution function of the "normal energy" and "total energy" are very different. The third derivative of the former gives the spectral intensity curves of incident $X$-rays, but the latter does not. The second derivative of the "total energy" has some similalities to the third derivative of the "normal energy" but is not symmetrical and the difference between them increases with increase of the incident wavelength, so it can not represent true spectral distribution*. Thus, any mixing of various energy components other than "normal energy" must be avoided. The secondary electrons emitted from the collector flow reversely to the photoelectrons because of the electric field which has been applied by the retarding potential, so a certain amount of the photoelectric current would be reduced by the secondary emission.

In spite of these effects the shapes of the emission curves were not influenced seriously.

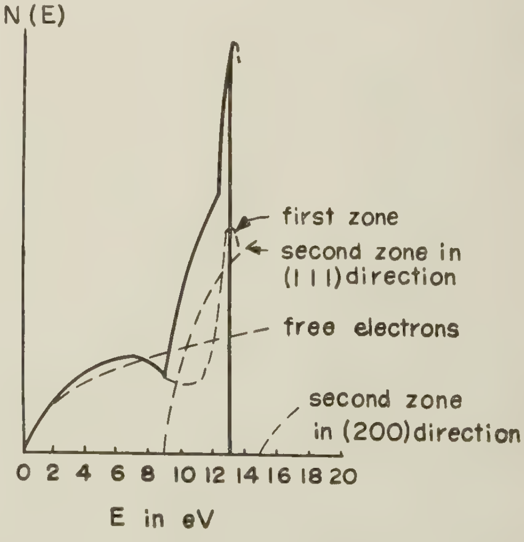

Fig. 6. The $N(E)$ curve for Al. (after Matyás[18])

---

* An experiment for visible light was reported by Sziklai & Schroeder[17] already. In their method the spectra were obtained by differentiating two times. To obtain the true spectral distribution curves differentiation must be done three times as is pointed out here.

### (b) *The $L_3$ emission spectrum of* Al

From the band theory of metals we can expect that in crystals of trivalent elements such as Al there are always considerable overlapping from the first Brillouin zone. The $L_3$ emission spectrum of Al shown in Fig. 5 clearly shows the sign of this fact. The $N(E)$ curve for Al has been worked out by Matyás[18)] who took into account the symmetry of the *s* and *p* functions of the valence electrons. According to his theory, Al is an element in which the first zone is nearly filled, and electrons, slightly more than one per atom, are contained in the second zone. The $N(E)$ curve obtained in his work is shown in Fig. 6. We can see that there is no serious contradiction between the theory and the experimental results obtained by us and Skinner[10)].

## References

1) M. Siegbahn and T. Magnusson: Zeits. f. Phys. **62** (1930) 435.
2) H. M. O'Bryan and H. W. B. Skinner: Phys. Rev. **45** (1934) 370.
3) E. R. Piore, G. G. Harvey, E. M. Gyorgy and R. H. Kingston: Rev. Sci. Instr. **23** (1952) 8.
4) J. L. Rogers and F. C. Chalklin: Proc. Roy. Soc. **B 67** (1954) 348.
5) K. T. Compton and C. H. Thomas: Phys. Rev. **28** (1926) 601.
6) H. W. B. Skinner: Proc. Roy. Soc. **A 135** (1932) 84.
7) G. Shinoda, T. Suzuki and S. Kato: Technology Reports of the Osaka University **4** (1954) 1.
8) R. H. Fowler: Phys. Rev. **38** (1931) 45.
9) L. A. DuBridge: Phys. Rev. **43** (1933) 727.
10) H. W. B. Skinner: Phil. Trans. Roy. Soc. **A 239** (1940) 95.
11) H. E. Hinteregger and K. Watanabe: J.O.S.A. **43** (1953) 604.
12) J. Farineau: Ann. Phys., Paris **10** (1938) 20.
13) H. Karlsson and M. Siegbahn: Zeits. f. Phys. **88** (1934) 76.
14) S. Yoshida: Sci. Pap. Inst. Phys. Chem. Res. Tokyo, **28** (1936) 43.
15) Y. Cauchois: Acta Cryst. **6** (1953) 352.
16) G. Shinoda, T. Suzuki and S. Kato: Phys. Rev. **95** (1954) 840.
17) G. C. Sziklai and A. C. Schroeder: J. App. Phys. **17** (1946) 763.
18) R. Matyás: Phil. Mag. **39** (1948) 429.

JOURNAL OF THE PHYSICAL SOCIETY OF JAPAN Vol. 11, No. 6, JUNE, 1956

# The Magnetic Properties of Chromium-Tellurium-Selenium System*

By Ichiro TSUBOKAWA

*The Research Institute for Iron, Steel and Other Metals,*
*Tohoku University, Sendai*

(Received February 28, 1956)

The change of magnetic properties due to the replacement of tellurium by selenium in CrTe, which has NiAs structure, was investigated. Ferromagnetism is observed in the concentration range from $x=0$ to $x=0.8$, where $x$ is defined by $Cr(Te_{1-x}Se_x)$. The compounds outside this range are para- or antiferromagnetic. In the paramagnetic range of temperature the Curie-Weiss law is found to be valid. It was also found that the Curie-Weiss constant is independent of concentration in the neighbourhood of CrTe and CrSe respectively, and varies abruptly at the transition concentration from ferro- to antiferromagnetic state. A short discussion are given.

## §1. Introduction

Several compounds between the chalcogen group and the element of iron group crystallize in nickel arsenide type and in such compounds various types of magnetism have been found. It is considered that the complicated behaviours of their magnetic properties would be attributed to the various possible distribution of the magnetic moment of cations in the crystals. Such distributions are supposed to be caused by the exchange interactions with the first, second and third neighbouring cations. Therefore, it follows that, in general, a different magnetic coupling will occur by replacing one component by another kind of atom of the same chemical group: in such crystals it is expected that a somewhat different type of spin ordering will be formed by introducing a different type of interaction between cations due to the replacement of cations or anions by another kind of them. From this point of view, we intend to investigate the change in magnetic behaviour of the ternary system in which the cation or anion of the binary system is replaced by another kind of cations or anions. In the present paper, as first trial to such cases, experimental results and a short discussion of the effect of replacing tellurium in CrTe by selenium are given.

## §2. Preparation of Specimens and Experimental Procedures

The specimens used for the measurement were made by the solid reaction which was always used to prepare such compounds: chromium (99.9%) as well as tellurium and selenium purified twice by vacuum distillations were crushed into powders finer than those of 100 mesh, and were mixed in such a way that the compound $Cr(Te_{1-x}Se_x)$ was found, where

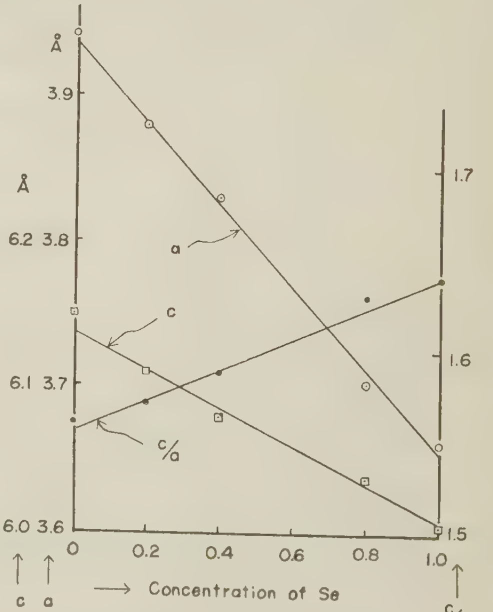

Fig. 1. The curves of lattice constants $a$, $c$ and axial ratio $c/a$ as a function of selenium content.

---

* This investigation was carried out at Hirone's laboratory of the Institute, and was supported in part by the Grant-in-Aid of Fundamental Scientific Research of Ministry of Education. The magnetic measurement at very low temperature was performed by using the Collins Helium Cryostat in the Research Institute above cited.

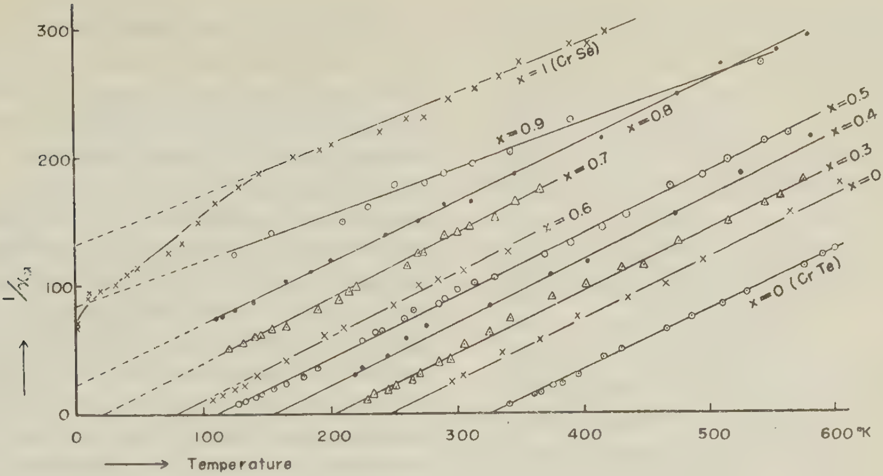

Fig. 2. The curves of reciprocal of the magnetic susceptibility, $1/\chi_M$, versus temperature.

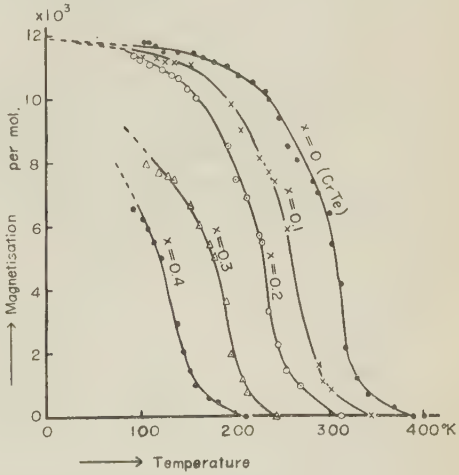

Fig. 3. The curves of magnetization per mol, $M$, versus temperature.

$x$ was taken as every 0.1 interval from zero to unity. The mixtures of the planned composition were sealed respectively in an evacuated silica tube and heated at about 1000°C. for 48 hours or more, thereafter, the products were cooled down to the room temperature.

In order to investigate the solubility of CrSe in CrTe, the prepared specimens were examined by *X*-ray analysis. Powder photographs showed monophase pattern of the crystal structure of NiAs type for any concentration of selenium. The lattice constants $a, c$ and axial ratio $c/a$ are shown in Fig. 1. As is shown, these lattice constants and the axial ratio change linearly with the concentration of selenium. It can be seen from these results that both the tellurides and selenides of chromium form perfect solid solutions in all proportions.

The apparatus used for measuring the magnetic properties was a magnetic balance of automatically recording type[1]. The mass of specimens used was several milligrams for the measurement of ferromagnetic region and several hundred milligrams for the measurement of para- and antiferromagnetic region respectively. In some cases the specimens were enclosed in evacuated silica or glass capsules to prevent the evaporation of anions at higher temperatures.

## § 3. Results and Discussions

It was once reported by Haraldsen and Kowalski[2], and by Guillaud[3], that CrTe is ferromagnetic, the Curie point of which is at about 30°C. And for CrSe the susceptibility was measured by Haraldsen and Kowalski[2] in the temperature range from the boiling point of liquid nitrogen to 630°K. According to their results the reciprocal of the susceptibility changes linearly with rise of temperature. In the present investigation we measured the susceptibility at temperatures ranging from liquid helium temperature to about 1100°K. The reciprocal of the susceptibility, $1/\chi_M$, is plotted against temperature, $T$, in Fig. 2. A breaking point was found at about 15°K. The origin of this breaking point is not clear but it can be considered that the Cr-Se-Cr interaction is small if we assume there exsists the antiferromagnetic or ferrimagnetic Curie point

Table I. The Curie-Weiss constants, the numbers of effective Bohr magneton and the spin quantum numbers are indicated as a function of selenium content.

| $x$ | | $C_M$ | $\mu_{eff}$ | $S$ |
|---|---|---|---|---|
| 0 | (CrTe) | 2.08 | 4.08 | 1.60 |
| 0.1 | | | | |
| 0.2 | | 1.96 | 3.97 | 1.55 |
| 0.3 | | 2.00 | 4.00 | 1.57 |
| 0.4 | | 2.02 | 4.03 | 1.58 |
| 0.5 | | 2.02 | 4.03 | 1.58 |
| 0.6 | | 2.00 | 4.00 | 1.57 |
| 0.7 | | 1.94 | 3.94 | 1.53 |
| 0.8 | | 2.06 | 4.08 | 1.60 |
| 0.9 | | 2.82 | 4.76 | 1.94 |
| 1.0 | (CrSe) | 2.88 | 4.83 | 1.97 |

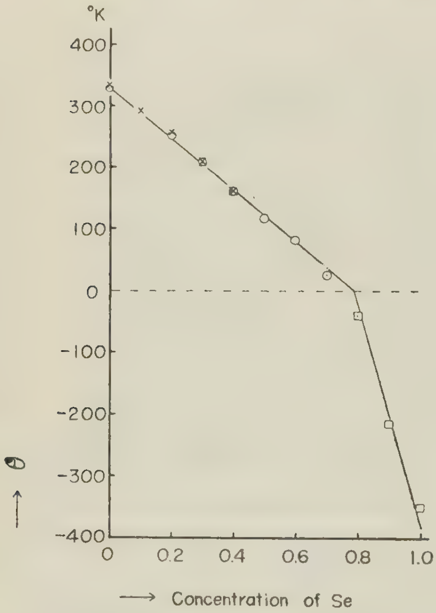

Fig. 4. Paramagnetic and ferromagnetic Curie point. ⊙ and ⊡ indicate the paramagnetic Curie point and × indicates the ferromagnetic one respectively.

below 1°K. Therefore, it may be assumed that the Curie point will be lowered by replacing the tellurium of CrTe by selenium. Under such an idea we measured the magnetic properties of every specimen in the temperature range from 100°C. to the boiling point of liquid nitrogen.

( I ) According to the present measurement the magnetic property of CrTe prepared by the above mentioned method was ferromagnetic and its Curie point was about 35°C., thus we confirmed the former result of Haraldsen and Kowalski[2], and Guillaud[3].

In Fig. 3 the magnetization per mol, $M$, in this system is plotted against temperature, $T$, ranging from the boiling point of liquid nitrogen to 100°C. The magnetic field used for the measurement was 3500 Oe. As can be seen from the figure, in this temperature range the ferromagnetic Curie point of CrTe was lowered, as expected above, with an increase of the selenium content, and finally when the selenium content exceeded 40%, the spontaneous magnetization was not observed. From the saturation magnetization of CrTe at absolute zero, which was determined by an extrapolation from the measured thermomagnetic curve shown in Fig. 3, the magnetic moment per atom of chromium is obtained as 2.2 $\mu_\beta$. This value lies a little lower than the observed data of the former investigators[2),3)] and smaller than the spin magnetic moment of $Cr^{2+}$ (4 $\mu_\beta$) and $Cr^{3+}$ (3 $\mu_\beta$).

The magnetizations per mol, $M$, for, $x=0$, 0.1, 0.2 are almost the same value near the liquid nitrogen temperature, and it will be so at obsolute zero. Hence by replacing tellurium by selenium, the type of magnetic interaction between the chromium ions is not changed and only exchange coupling is weakened by the replacement of tellurium by selenium.

( II ) From the measured magnetic susceptibility per mol in the paramagnetic region we obtained the relation between the reciprocal of susceptibility and temperature, as shown in Fig. 2. It can be seen from the figure that $1/\chi_M$ decreased linearly with the fall of temperature: the susceptibility changes with the temperature according to the Curie-Weiss law, $\chi_M=C_M/(T-\theta)$ where $-\theta$ is the asymptotic Curie point.

For the tellurium rich side, the paramagnetic Curie point ($\theta$) nearly coincides with the ferromagnetic Curie point, the concentration dependence of which is shown in Fig. 4. On the basis of these facts, it should be concluded that the type of spin ordering at the tellurium rich side is ferromagnetic. The paramagnetic Curie point reaches zero at the concentration $x \doteqdot 0.8$. From the above mentioned coincidence of ferro- and paramagnetic Curie points at the tellurium rich side, it follows also that the ferromagnetic Curie point vanishes at the same concentration $x \doteqdot 0.8$.

At the selenium side paramagnetic Curie point takes a negative value, as shown in Fig. 4. The compound at the selenium side will be weakly paramagnetic or antiferromagnetic. As shown in Table I the estimated Curie-Weiss constant from the $1/\chi_M$ -$T$ relation is nearly independent of the concentration in the neighbourhood of CrTe and CrSe respectively, and changes abruptly at about $x=0.8$. This behaviour can also be seen from Fig. 4 directly: the inclination of the lines $1/\chi_M$ -$T$ can be classified into two groups, and the border content, $x_0$, of the two groups lies near 0.8. It is also remarkable that this concentration nearly coincides with the critical concentration of ferro- and paramagnetic transition. Now we can estimate the number of effective Bohr magneton, $\mu_{eff}$, from each value of $C_M$, assuming the Landé factor, $g$, is equal to two, and we obtain the spin quantum number, $S$, by $\mu_{eff}=\sqrt{4S(S+1)}$, the values being listed in the 2nd and 3rd columns in the table. $S$ takes a value near 3/2 for the CrTe side, and near 4/2 for the CrSe side, the former value does not differ so much from a value obtained from the saturation magnetization at ferromagnetic side.

From the values of $S$, one could assume that at the tellurium rich side the cation took $Cr^{3+}$ state and at selenium rich side $Cr^{2+}$ state, but this supposition seems to be not valid, because it indicates the higher electronegativity of tellurium than that of selenium. The evaluation of $S$, however, is based upon the assumption $g=2$, and it is desirable for the interpretation of this apparent difficulty to measure the Landé factors of these compounds.

## Acknowledgements

The author wishes to express his thanks to Profs. S. Maeda and N. Tsuya for their encouragement and valuable discussions. He also wishes to express his hearty thanks to Prof. T. Haseda who gave him valuable suggestions on the magnetic measurement at very low temperature.

## References

1) T. Hirone, S. Maeda and N. Tsuya: Rev. Sci. Instr. **25** (1954) 516.
2) H. Haraldsen and E. Kowalski: Z. Anorg. u. Allge. Chem. **224** (1935) 329.
3) C. Guillaud: Compt. Rend. **222** (1946) 1225.

JOURNAL OF THE PHYSICAL SOCIETY OF JAPAN Vol. 11, No. 6, JUNE, 1956

# The Magnetic Properties of $FeSe_x$ with the NiAs Structure*

By Tokutaro HIRONE and Shu CHIBA

*Research Institute for Iron, Steel and other Metals*
*Tohoku University, Sendai*

(Received March 8, 1956)

The thermal and X-ray analyses were carried out for iron-selenium system from 48.8 to 57.4 atomic percent of selenium, such range being previously reported to be ferrimagnetic. It was concluded from the experimental results that at room temperature the concentration range from 48.8 to 53.1% selenium is the two phase region $\alpha+\beta$; $\alpha$ has the PbO type structure and $\beta$ the NiAs type. These two phases transform through a eutectoid reaction into a $\gamma$ phase with the NiAs structure of slightly different lattice parameters in comparison with those of the $\beta$ phase, the eutectic temperature being 350°C. The solubility limit in iron side of the phase lies at 53.1% selenium. It is remarkable that the substance with stoichiometric concentration (50% Se) does not lie in the single phase region of NiAs type. It was also found that the ferrimagnetism of this binary system originates from the phase of NiAs type ($\beta$ phase) and the $\alpha$ phase is weakly paramagnetic or antiferromagnetic. The Curie point of the compound containing 53.1% selenium is 174°C and the spontaneous magnetization at absolute zero of temperature is 0.20 Bohr magneton. This magnitude of magnetization is explained by assuming a kind of the ordered arrangement of ferric ion in the crystal lattice.

## § 1. Introduction

The magnetic properties of some of the sulfides of the transition elements, such as $FeS_x$ (pyrrhotite)[1] etc, have been investigated by several authors. In these compounds the anion in the crystal lattice plays an important role to the superexchange interaction between the ions of the transition element. Therefore, it is interesting to clarify the change of the magnetic properties in such compounds due to the replacement of sulfer by another kind of anions with different electronegativity, such as selenium, while the cations remain unchanged. From this point of view, we have investigated the properties of $FeSe_x$ which has the NiAs structure similar to pyrrhotite, $FeS_x$. It has been reported that, according to the thermomagnetic measurements, $FeSe_x$ with the composition from $x=1.00$ to 1.35 is ferrimagnetic as $FeS_x$. However, the result of measurement showed a peculiar change of magnetism with the Se content, suggesting a possibility that some kind of phase change occurs in this region. For this reason, we investigated the phase diagram of Fe-Se system by means of X-ray and thermal analyses in the composition region in which ferrimagnetism is supposed to occur, and found the existence of the two phase region $\alpha+\beta$, in which $\alpha$ has the PbO structure and $\beta$ the NiAs type, and that the obseved ferrimagnetism is due to the latter. The thermal and thermomagnetic properties previously reported give us many clues to the explanation of the magnetism of $FeSe_x$. In the following sections, the experimental results and a short discussion on the spontaneous magnetization of this system will be given.

## § 2. Experimental Procedures

The specimens of $FeSe_x$ were prepared by the method similar to that in the previous paper[2]; A mixture of the powders of iron and selenium with the desired composition was enclosed in an evacuated silica tube and heated at 1000°C for 24 hours. In the present investigation, doubly sealed silica tubes were used in order to prevent the oxidation of these specimens due to the cracks of the silica tubes caused by the volume change of the specimens during cooling. $FeSe_x$ thus

---

* This investigation was supported in part by the Grant-in-Aid of Fundamental Scientific Research of Ministry of Education (1955-4022).

obtained had a silvery luster. The specimens for the measurement of specific heat and X-ray analyses were crushed to about 100 mesh by a mortar. The apparatus for the measurement of specific heat was the same as that previously reported[3]. The specific heat was measured in the range from room temperature to 500°C, with a heating rate of $1\sim2$ degree per minute. According to the results of thermal analysis, a eutectoid point was found at 350°C in the composition range from $x=1.00$ to 1.13 and such a eutectic reaction showed considerable relaxation. For the purpose of finding the adequate heat treatment three specimens were prepared as follows:

Specimen 1: quenched from a temperature above 500°C into water,
Specimen 2: annealed for 5 hours just below the eutectoid point, and
Specimen 3: annealed for 12 hours at the same point.

The specimen 1 had a broad peak at 350°C in the curve of specific heat versus temperature while the specimens 2 and 3 had a sharp one at the same temperature, and the excess heat absorption shown in such a peak by the specimen 1 was less than that in 2 or 3, while the difference between these for 2 and 3 was little. These facts show that a high temperature phase is predominant in the quenched specimens. Therefore, it may be concluded that an annealing during 5 hours is sufficient to develope the stable phase at the room temperature; all the specimens used for the thermal and X-ray analyses were annealed for 5 hours just below the eutectoid point.

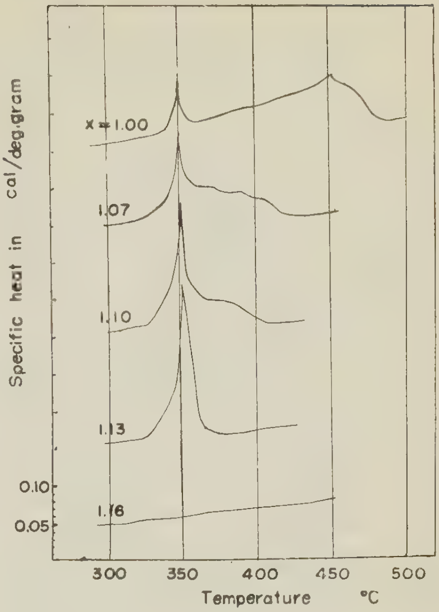

Fig. 1. The specific heat versus temperature curve of FeSe$_x$ from $x=1.00$ to 1.16 in the vicinity of the eutectoid point.

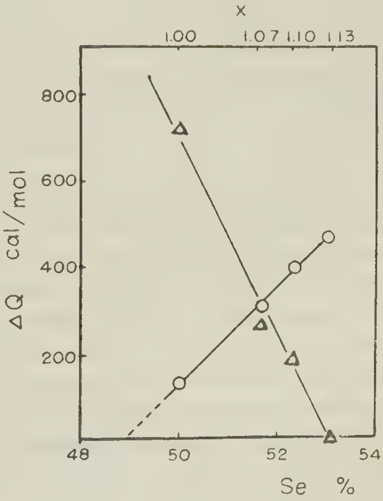

Fig. 2 —○— Total heat absorption at 350°C.
—△— Excess heat absorption above 350°C.

## § 3. The Study of the Phase Diagram

### a) Thermal Analysis

For the specific heat temperature curves of the specimens with compositions from $x=1.00$ to 1.35, a sharp peak was observed at 350°C.

The absorbed energy under the peak is about 200 cal/mol at $x=1.13$, whereas for $x$ greater than 0.13 it rapidly falls down and vanishes before $x$ reaches a value 1.16. For the specimens from $x=1.16$ to 1.35, such an anomalous heat absorption was not observed below 500°C. Another anomalous heat absorption was found for the specimens from $x=1.00$ to 1.13, For $x=1.00$ it occurs from 350 to 450°C and the absorbed energy reaches 750 col/mol and with increasing $x$ it decreases linearly and vanishes at about $x=1.13$.

### b) Phase Diagram

From the results of the thermal analysis above mentioned, a possible phase distribution in the measured temperature and composition range is proposed, the Röntogenographic confirmation of which will be given in next section. An estimated phase diagram is shown

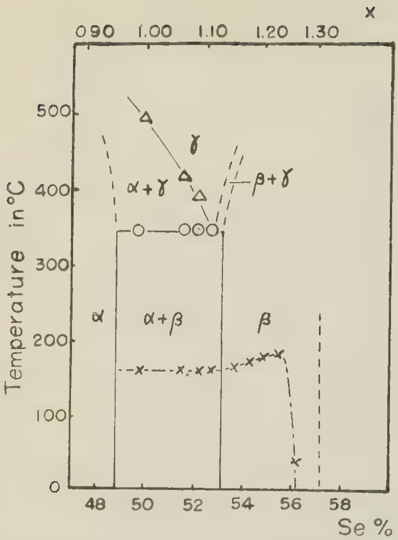

Fig. 3. The phase diagram of $FeSe_x$ system.

Table I.

| | $a$ | $c$ | $c/a$ |
|---|---|---|---|
| the β phase (at room temperature) $x=1.00$ | 3.548 | 5.733 | 1.616 |
| the γ phase (at about 500°C) $x=1.00$ | 3.610 | 5.928 | 1.642 |
| according to H. and K. (quenched from 500°C) $x=1.05$ | 3.618 | 5.927 | 1.638 |

in Fig. 3. From this figure it is seen that the specimens from $x=1.00$ to 1.13 are mixtures of two phases, which transform into the third phase $\gamma$ by eutectoidal reaction at 350°C. Furthermore, Fig. 2 shows that a eutectoid point exists at the close vicinity of the iron side solubility limit of the $\beta$ phase. The chain line shows a curve of the Curie point for various compositions which will be discussed in § 4. However it seems that this phase diagram is not the only one which can be deduced from the present data. It is also possible that the transformation $\beta \rightleftarrows \gamma$ is a kind of lattice transformation; in this case the two phase region $\beta+\gamma$ does not exist and the eutectoid reaction mentioned above should degenerate into the transformation $\beta \rightleftarrows \gamma$. However both cases are not easily distinguishable because of the narrow existence range of $\beta+\gamma$.

### c) X-ray Analysis

In the composition range from $x=1.00$ to 1.13, the observed X-ray diffraction lines could be classified into two groups, one of which was attributable to the phase NiAs structure, its intensity increasing with $x$, and another one to the phase of PbO structure, its intensity decreasing with increasing $x$. The structure above the eutectoid point in the same compounds was also determined by high temperature powder photographs and it was found that the crystal lattice also has the NiAs structure similar to that in the $\beta$ phase; but the lattice constants are differnt from each other as shown in Table I. It has been reported by Hägg and Kindström that the NiAs structure was found in a wide range of composition including stoichiometric ratio $x=1.00$ even at room temperature. According to them, the composition range from $x=1.00$ to 1.13 is a single phase region with the NiAs structure, contrary to the present analysis. In the third column the data for $x=1.05$ by Hägg and Kindström[4] is also shown for comparison. It is supposed that specimens used by them had a structure which is stable in the high temperature range above 350°C, since the lattice constants observed by them are numerically consistent with our results on the $\gamma$ phare. This difference may be due to the fact that the specimens used in the present investigation were annealed just below the eutectoidal point while those in the former were quenched from a higher temperature. In the present case the specimen $x=1.16$ shows a typical line distribution due to the NiAs structure. But, for the specimens from $x=1.20$ to 1.35, some lines split into double or triple ones, showing that the degree of symmetry decreases as $x$ increases from 1.16 to 1.35. For example, the $c$ axis of the crystal inclines gradually against base plane with increasing $x$. Such a line splitting was also comfirmed by Hägg and Kindström.

## § 4. Magnetic Properties and phase Diagram

As reported in the previous paper, the spontaneous magnetization of $FeSe_x$ at absolute zero is 7 gauss for $x=1.00$ and linearly increases to $x=1.13$. Moreover, by extrapolating the intensity of magnetization to the low concentration side of selenium, it was found that the magnetization vanishes at the solubility limit of the $\beta$ phase above mentioned. In the specimen $x=1.23$ it reaches 35 gauss, about 0.2 Bohr magneton per iron atom. The

Curie point takes a constant value 174°C in the same composition range, and it gradually increases from 174 to 192°C with increasing $x$ and then rapidly falls to 40°C at $x=1.30$. This fact shows that the ferrimagnetism of FeSe$_x$ originates from the $\beta$ phase with the NiAs structure and the $\alpha$ phase with PbO structure is weakly paramagnetic or antiferromagnetic. The region in which the observed spontaneous magnetization changes linearly corresponds to the two phase region from $x=1.00$ to 1.13. Moreover, in the investigation of specific heat of FeSe$_x$ near the Curie point, the linear change of heat absorption was obtained as shown Figs. 4 and 5, and the highest magnetic transformation energy was found at $x=1.20$.

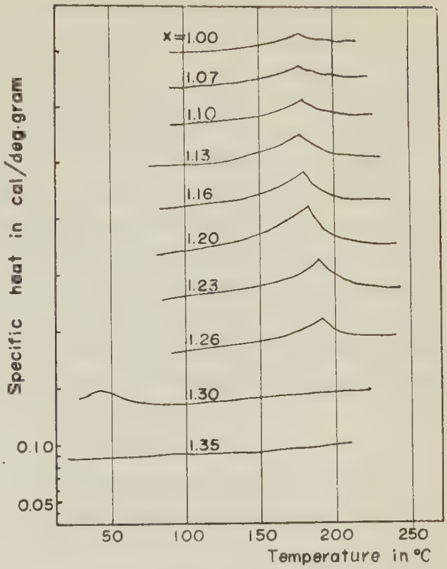

Fig. 4. The specific heat versus temperature curve of FeSe$_x$ from $x=1.00$ to 1.35 in the vicinity of the magnetic Curie point.

## § 5. Discussion

Now a discussion will be made about the origin of the ferrimagnetism of FeSe$_x$ found in the $\beta$ phase above mentioned. If the Se ions in the lattice of such a phase are assumed to be doubly ionized, then the cation sites are occupied mostly by ferrous and partly by ferric ions and vacant sites in the phase of excess Se atoms. Since the magnetic moment of free ferrous ion is 4 $\mu_B$, $\mu_B$ being the Bohr magneton, the Curie-Weiss constant for the paramagetic region of the substance takes a value *ca.* 3.00. The same constant estimated from the observed inverse susceptibility versus temperature curve is somewhat greater than the calculated value. This difference may be attributed to the assumed electronegativity of the selenium ions above mentioned. However, based on the above mentioned consideration, the determination of the possible distribution of ferric ions and vacancies which is consistent with the observed ferrimagnetism can be made. If the notation Fe$_{1-y}$ Se is adopted instead of FeSe$_x$, the number of ferric ion and vacancy is expected to be $2yN$ and $yN$ respectively, $N$ being the total number of anions. Then, if the lattice points for cations can be divided into two equivalent sublattices, and if (1) all the vacancies and ferric ions are selectively distributed in one of the sublattices* and (2) all the magnetic moments in the $A$ sublattice orient antiparallel with those in the $B$ sublattice, then the resultant magnetic moment per atom is given by $2y\ \mu_B$. Since $y$ takes a value 0.115 corresponding to a specimen $x=1.13$, the magnetization takes a value 0.23 $\mu_B$. This result shows a good agreement with the experimental value 0.20 $\mu_B$. Next, we shall consider the specific heat near the Curie point. The total heat absorption during the magnetic transformation, $\varDelta Q$, and the jump of specific heat at the Curie point, $\varDelta C$, can be expressed respectively by

$$\varDelta Q=\frac{3}{10}\frac{S^2+(1+S^2)}{(1+S)^2}T_c\varDelta C$$

$$\varDelta C=\frac{5S(1+S)}{S^2+(1+S)^2}R$$

where $S$ is the total spin moment of the cations, and $R$ the gas constant. If we put $S=2$, then $\varDelta Q$ and $\varDelta C$ become respectively

$$(\varDelta Q)_{calc}=900\ \text{cal/mol}$$

$$(\varDelta C)_{calc}=4.62\ \text{cal/deg mol}$$

while the observed values are as follows

$$(\varDelta Q)_{obs}=250\ \text{cal/mol}$$

$$(\varDelta C)_{obs}=4.4\ \text{cal/deg-mol}\ .$$

As for $\varDelta C$, the agreement is satisfactory, but $(\varDelta Q)_{obs}$ is smaller than $(\varDelta Q)_{calc}$. This is probably due to the difficulty in the evaluation of the total heat absorption from the specific heat curve observed. Also it is to be concluded that the ferrimagnetism of $FeSe_x$ is further confirmed by the thermomagnetic data above mentioned and as the ferrimagnetic behavior of this compound is found to be similar to that of $FeS_x$, the superexchange interaction between Fe–Se–Fe has the same order of magnitude as Fe–S–Fe in $FeS_x$ with antiferromagnetic ordering of spins.

---

* Such an assumption on the distribution of vacancies does not contradict with the experimental result obtained by Drs. A. Okazaki and K. Hirakawa (Tokyo Meeting of the Phys. Soc. of Japan in October, 1955).

The authors wish to express their cordial thanks to Profs, S. Maeda, N. Tsuya and S. Nagasaki for their valuable suggestions and discussions.

### References

1) H. Haraldsen: Z. Anorg. u. Allg. **246** (1941) 169 and 195.
T. Hirone, S. Maeda and N. Tsuya: J. Phys. Soc. Japan **9** (1954) 500, 503 and 736.
2) T. Hirone, S. Maeda and N. Tsuya: J. Phys. Soc. Japan **9** (1954) 496.
3) T. Hirone, S. Maeda, I. Tsubokawa and N. Tsuya: Sci. Rep. RITU A **5** (1953) 513.
4) G. Hägg and A. L. Kindström: Z. Phys. Chem. **22** (1933) 453.

---

Journal of the Physical Society of Japan Vol. 11, No. 6, June, 1956

# Nuclear Magnetic Resonance in Molecular Chlorine Compounds

By Yoshika Masuda
*Department of Physics, Kobe University*

(Received March 12, 1956)

We have measured the chemical shifts, the transverse- and longitudinal-relaxation times of chlorine nuclear magnetic resonance of such liquid chlorine compounds as $TiCl_4$, $VOCl_3$, $CrO_2Cl_2$, and $SiCl_4$, of which the quadrupole coupling constants were measured by Dehmelt by means of the pure quadrupole resonance experiment. Our results were considered in view of the correlation to quadrupole coupling constant. Line widths are nearly proportional to the square of the quadrupole coupling constant. The equality of the transverse relaxation time $T_2$ and the longitudinal relaxation time $T_1$ has been verified experimentally in these compounds. Solomon's method for the calculation of $T_1$ and $T_2$ was applied to a quadrupole relaxation. $T_1$ is exactly equal to $T_2$ in cases where quadrupole relaxation is essential, the molecular surroundings are isotropic, and further the extreme narrow conditions are well established. This result is identical to Wangsness and Bloch's. Experimental $T_1$ values are about ten times larger than the theoretical one and the reason of the discrepancy is discussed. In Appendix, estimation of chemical shift by $d$-electron is given.

## §1. Introduction

The nuclear magnetic resonance absorption is influenced by its electronic environment. A difference in the molecular structure in different molecules produces a "chemical shift" of resonance frequency. In a heavy atom having a large chemical shift, the paramagnetic term may be expected predominantly large. Ramsey¹⁾ pointed out the paramagnetic term for the atom represents the contribution set up by the orbital motion of the unbalanced $p$-electron. On the other hand, Townes and Dailey²⁾ pointed out the nuclear quadrupole coupling in molecules depends on the way in which valence electrons fill the $p$-type orbitals. Accordingly, it is interesting to note the close correlation between a chemical shift and a nuclear quadrupole coupling constant. This relation was examined in such liquid chlorine compounds as $TiCl_4$, $VOCl_3$, $CrO_2Cl_2$, and $SiCl_4$.

Pound³⁾ discussed the situation in which the electric quadrupole interaction causes the relaxation. But there were no experimental studies of this situation for liquid, since a large quadrupole interaction in liquid causes a relaxation width to such an extent as to make the detection of magnetic resonance impossible. Concerning this point, the chlorine molecular liquids here examined serve as suitable samples because they have appropriate and known magnitude of $e^2qQ$.

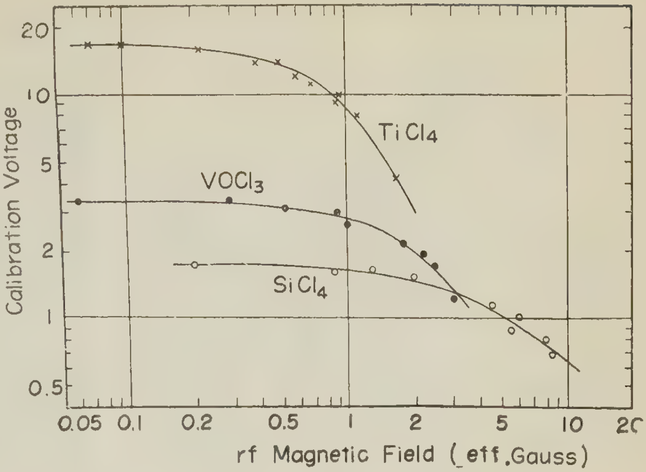

Fig. 1. Saturation Curve.

Wangsness and Bloch4) predicted that there exists equality between the longitudinal and the transverse relaxation time, in cases where quadrupole relaxation is essential, the molecular surroundings are isotropic, e.g., as in gaseous and liquid samples, and further their characteristic frequencies of interaction with the nuclei are large compared to the Larmor frequency. The predicted equality of $T_1$ and $T_2$ has been verified experimentally, and its value was also estimated theoretically using Solomon's method5).

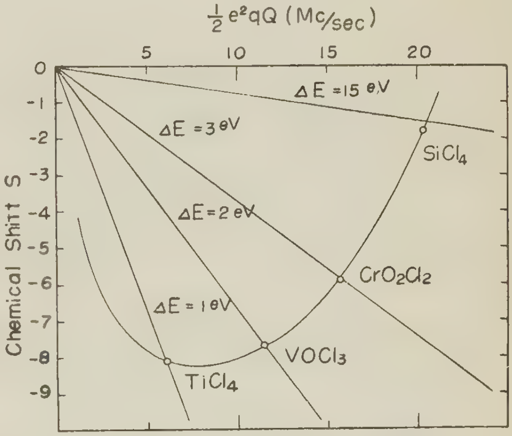

Fig. 2. Chemical Shift S.

## § 2. Experiment

The experimental procedures and equipments employed for the measurement of the chemical shift have been described6). The chemical shift is defined as

$$S=(H_s-H_r)/H_r \times 10^4 ,$$

where $H_s$ and $H_r$ are the magnetic fields necessary for resonance, at a fixed frequency, for the sample and reference, respectively. The reference was a dilute aqueous solution of the sodium chloride.

The magnetic resonance spectrometer consists of the autodyne detector, the calibrator7), and the vacuum tube voltmeter having the three-stage rf amplifier. For the measurement of short relaxation time as in our samples, a rf voltage as large as 80 volts across the sample coil is required and care must be taken not to reduce the sensitivity of the detector at such a high voltage. We adopted UY-807 as a detector tube and a choke coil of 100 H as a plate load. Rf field strength was estimated from the coil voltage by a standard method3) and the saturation curves thus obtained are shown in Figure 1. Assuming that the saturated intensity of the resonance obeys a simple $1/(1+x^2)$ law, $T_1$ was estimated by

$$x^2=\gamma^2 H_1^2 T_1 T_2 , \qquad (1)$$

where $2H_1$ is the amplitude of rf field.

## § 3. Results and Discussion

### i ) *Chemical Shift*

The chemical shift are plotted against the nuclear quadrupole coupling constants measured by Dehmelt8) at the liquid air temperature in Figure 2, where the 0-origin of the shift was taken at the resonance position of $Cl^-$. In these molecules chlorine atom is univalent and its bonding is mainly by $3p$ electron. When this orbit is hybridized by 3s orbit to the amount of $s$ and moreover the bonding contains an ionicity of degree $i$, the $e^2qQ$ in the direction of bonding is given by

$$e^2qQ=(1-s)(1-i)e^2q_0Q , \qquad (2)$$

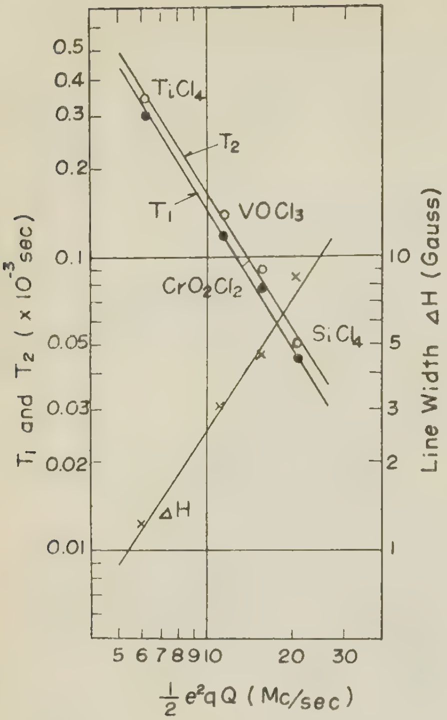

Fig. 3. $T_1$, $T_2$, and ΔH.

where $e^2q_0Q$ is the quadrupole coupling of a $3p$ orbit in the direction of bonding e.g. 110 Mc[2].

The chemical shift of univalent $p$-bonding state is given by Ramsey[1], Saika and Slichter[9] as:

$$S_0 = -\frac{2}{3}\frac{e^2\hbar^2}{m^2c^2}\left\langle\frac{1}{r^3}\right\rangle_{3p}\frac{1}{\Delta E}, \tag{3}$$

where $\langle 1/r^3\rangle_{3p}$ is the average of $1/r^3$ for $3p$ electron and $\Delta E$ is an appropriate mean of excitation energy of the molecule. Considering $s$-hybridization and ionicity, the shift is multiplied by $(1-s)(1-i)$ and the result is

$$S = -(1-s)(1-i)\frac{68.3}{\Delta E}\times 10^{-4}, \tag{4}$$

where the value of $\langle 1/r^3\rangle_{3p}$ was taken from the table of Barnes and Smith[10]. It is seen from Eqs. (3) and (4) that $S$ is proportional to $e^2qQ$ when $\Delta E$ is a constant irrespective of the kind of molecules. This contradicts to the experiment as shown in Figure 2 and the reason of this discrepancy will be considered below. The first is the effect of $d$-orbital. When the bond is hybridized by $3d$-orbit to the amount of $d$, the $e^2qQ$ is increased by $\{1+(2/7)d\}$* and the chemical shift by $(1+4d)$. (The derivation is given in the Appendix). $s$-orbit and $d$-orbit affect to $e^2qQ$ and to $S$ in a different manner. The second is the difference of $\Delta E$ for various compounds about which we can not say much. Aside from the effect of $d$-orbit, we may estimate $\Delta E$ from $e^2qQ$ and $S$ leading to the result of 1, 2, 3, and 13 eV for $TiCl_4$, $VOCl_3$, $CrO_2Cl_2$, and $SiCl_4$, respectively. The third is the difference of $e^2qQ$ between liquid and solid state to which we will mention in the next section.

### ii) *Transverse and Longitudinal Relaxation Time*

The line widths $\Delta H$ in gauss defined as the separation of maximum slope are plotted in Figure 3 as a function of the molecular quadrupole coupling constant $e^2qQ$. $\Delta H$ is nearly proportional to $(e^2qQ)^2$ and this fact indicates that the difference of $e^2qQ$ between liquid and solid state is not so large as to upset the order of magnitude of $e^2qQ$ of the compounds in question. The line shape is approximately Lorentzian and $T_2$ estimated from the formula $1/T_2=(\sqrt{3}/2)\gamma\Delta H$ are 0.35, 0.14, 0.092, and 0.052 msec for $TiCl_4$, $VOCl_3$, $CrO_2Cl_2$, and $SiCl_4$, respectively. Values of $T_1$ measured by saturation method are 0.31, 0.12, 0.08, and 0.046 msec for $TiCl_4$, $VOCl_3$, $CrO_2Cl_2$, and $SiCl_4$, respectively. The estimated error of these relaxation times is about 30 percent which is mainly due to the ambiguity of the absolute value of $H_1$. These values are also plotted in Figure 3 which shows that $T_1$ and $T_2$ is equal within experimental error.

Let us consider the relation between $T_1$ and $T_2$ and also its absolute value when the electric quadrupole interaction is dominant. Considering the molecular structure of our samples it is reasonable to assume that the electric field gradient at the Cl nucleus has an axial symmetry about its bonding axis. Owing to the Brownian motion of the molecule in the liquid, the orientation of the bonding axis fluctuates at random referring to the spin quantizing axis (external magnetic field) and thus the quadrupole relaxation will result. Transition probability caused by the quadrupole interaction $\mathscr{H}'=\mathbf{Q}\cdot\nabla\mathbf{E}$ and the lattice motion from the state $m_i$ to the state $m_j$, both being the eigenstates of $I_z$, is given by

---

* This formula is different from $(1+d)$ of Townes and Schawlow (Reference 11, p. 235). Our formula includes the effect not only of the normalization but also of the $e^2qQ$ produced by $d$-orbital.

$$U_{m_i m_j}=\frac{2\tau_c}{\hbar^2}\,\frac{\langle|\mathscr{H}'_{m_i m_j}|^2\rangle_{Av}}{1+(\omega_{m_i m_j}\tau_c)^2}\ , \qquad (5)$$

where $\omega_{m_i m_j}$ is the Zeeman frequency between $m_i$ and $m_j$, $\tau_c$ is the correlation time of molecular reorientation and $\langle\ \ \rangle_{Av}$ means the space average.

In the present case of spin 3/2, we write four normalized eigenfunctions of $\boldsymbol{I}_z$ as $\varphi(3/2)$, $\varphi(1/2)$, $\varphi(-1/2)$, and $\varphi(-3/2)$ of which the eigenvalues are $(3/2)\hbar$, $(1/2)\hbar$, $(-1/2)\hbar$, and $(-3/2)\hbar$, respectively. Their occupation numbers are denoted by $N_{3/2}$, $N_{1/2}$, $N_{-1/2}$, and $N_{-3/2}$, respectively.

We find the only non-vanishing upwards transition probabilities to be

$$\begin{aligned}U_{-3/2,\,-1/2}&=U_{1/2,\,3/2}\\&=\frac{\pi^2}{5}\left(\frac{e^2qQ}{h}\right)^2\frac{\tau_c}{1+\omega^2\tau_c^2}\equiv U_1\ , \qquad (6)\\U_{-3/2,\,1/2,}&=U_{-1/2,\,3/2}\\&=\frac{\pi^2}{5}\left(\frac{e^2qQ}{h}\right)^2\frac{\tau_c}{1+4\omega^2\tau_c^2}\equiv U_2\ .\end{aligned}$$

In the extreme narrow conditions ($\omega^2\tau_c^2\ll 1$), above probabilities are given by

$$U_1=U_2=\frac{\pi^2}{5}\left(\frac{e^2qQ}{h}\right)^2\tau_c\equiv U\ . \qquad (7)$$

If there are a total number of $N$ of spin systems to be distributed over the four states, then the following equations describe the shifting of the population $N_{m_i}$,

$$\dot N_{m_i}=\sum_{\substack{m_i\\ m_i\neq m_j}} U_{m_i m_j}(N_{m_j}-N_{m_i})+\text{const.}$$

$$\left(m_i,\, m_j=\frac{3}{2}\,,\ \frac{1}{2}\,,\ -\frac{1}{2}\,,\ -\frac{3}{2}\right). \qquad (8)$$

The macroscopic magnetic moment is proportional to $\langle \boldsymbol{I}_z\rangle$ which is given by

$$\begin{aligned}&(3/2)N_{3/2}+(1/2)N_{1/2}+(-1/2)N_{-1/2}\\&\qquad+(-3/2)N_{-3/2}=K\langle \boldsymbol{I}_z\rangle, \qquad (9)\end{aligned}$$

where $K$ is a constant. Accordingly, we get:

$$\begin{aligned}&d\langle \boldsymbol{I}_z\rangle/dt=-\langle \boldsymbol{I}_z\rangle(U_1+U_2)\\&\ +(1/2K)(N_{3/2}+3N_{1/2}-3N_{-1/2}-N_{-3/2})(U_1-U_2)\\&\ +\text{const.} \qquad (10)\end{aligned}$$

In the extreme narrow conditions, above formula is simplified as follows:

$$d\langle \boldsymbol{I}_z\rangle/dt=-2U(\langle \boldsymbol{I}_z\rangle-I_0)\ , \qquad (11)$$

where $I_0$ is the equilibrium value of the $z$-component of the spin $\boldsymbol{I}$. This shows that the nuclear spin $\boldsymbol{I}$ has simple decay with relaxation time:

$$\frac{1}{T_1}=2U=\frac{2\pi^2}{5}\left(\frac{e^2qQ}{h}\right)^2\tau_c\ . \qquad (12)$$

Now let us examine the relation between the $T_1$ defined by Eqs. (11), (12) and that of determined by the saturation factor. For spin greater than 1/2, the identity of both $T_1$'s is not self-evident. In the liquid state the Zeeman levels are not shifted by quadrupole coupling and the transitions between subsequent Zeeman levels have a same transition frequency $\nu_0$. When an external radio frequency $\nu_0$ is impressed, the transition probabilities between the states $m_j$ and $m_k$ are given by

$$\begin{aligned}&V_{3/2,\,1/2}=V_{-1/2,\,-3/2}=3p,\\&V_{1/2,\,-1/2}=4p\ , \qquad (13)\end{aligned}$$

where $p=(1/4)\gamma^2H_1^2\,g(\nu)$ and $g(\nu)$ is the shape function. For the time rate of change of the population we get the equation analogous to Eq. (8) where $U_{m_i m_j}$ is now replaced by $U_{m_i m_j}+V_{m_i m_j}$. For stationary state the population differences of subsequent levels $\Delta_{m'\to m}=N_{m'}-N_m$ in the case of extreme narrowing are given by

$$\begin{aligned}&\Delta_{-3/2\to-1/2}=\Delta_{-1/2\to1/2}=\Delta_{1/2\to3/2} \qquad (14)\\&\qquad=(N\Delta/D)(4+30\,P+36P^2)\ ,\end{aligned}$$

where $P=p/U$, $\Delta=h\nu_0/kT$, and $D=16+36\Delta+136\,P+216\,P\Delta+264\,P^2+216\,P^2\Delta+144\,P^3$. From Eq. (14) the saturation factor $S_{m'\to m}$ which is the ratio of $\Delta_{m'\to m}$ with and without rf is given by

$$\begin{aligned}&S_{-1/2\to-3/2}=S_{1/2\to-1/2}=S_{3/2\to1/2}\\&\qquad=(1+P)^{-1}. \qquad (15)\end{aligned}$$

Therefore the population difference of each level has the *same* saturation factor and the $T_1$ defined by the Eqs. (1) and (15) is given by

$$\frac{1}{T_1}=\frac{2\pi^2}{5}\left(\frac{e^2qQ}{h}\right)^2\tau_c\ . \qquad (16)$$

The above expression is identical to Eq. (12) from which we know the identity of $T_1$'s defined by a different way. Next we pass to the problem of the $T_2$.

The eigenfunctions of the transverse components of the spin operator $\boldsymbol{I}_x$ (or $\boldsymbol{I}_y$) may be written as $\Psi(\alpha)$, $\Psi(\beta)$, $\Psi(\gamma)$, and $\Psi(\delta)$ which have eigenvalues $(3/2)\hbar$, $(1/2)\hbar$, $-(1/2)\hbar$, and $-(3/2)\hbar$, respectively. They can be expanded by eigenfunctions of $I_z$ as follows:

$$\begin{aligned}
\Psi(\alpha)&=\frac{1}{\sqrt{8}}\left\{\varphi\left(\frac{3}{2}\right)+\sqrt{3}\,\varphi\left(\frac{1}{2}\right)+\sqrt{3}\,\varphi\left(-\frac{1}{2}\right)+\varphi\left(-\frac{3}{2}\right)\right\},\\
\Psi(\beta)&=\frac{1}{\sqrt{8}}\left\{\sqrt{3}\,\varphi\left(\frac{3}{2}\right)+\varphi\left(\frac{1}{2}\right)-\varphi\left(-\frac{1}{2}\right)-\sqrt{3}\,\varphi\left(-\frac{3}{2}\right)\right\},\\
\Psi(\gamma)&=\frac{1}{\sqrt{8}}\left\{\sqrt{3}\,\varphi\left(\frac{3}{2}\right)-\varphi\left(\frac{1}{2}\right)-\varphi\left(-\frac{1}{2}\right)+\sqrt{3}\,\varphi\left(-\frac{3}{2}\right)\right\},\\
\Psi(\delta)&=\frac{1}{\sqrt{8}}\left\{\varphi\left(\frac{3}{2}\right)-\sqrt{3}\,\varphi\left(\frac{1}{2}\right)+\sqrt{3}\,\varphi\left(-\frac{1}{2}\right)-\varphi\left(-\frac{3}{2}\right)\right\}.
\end{aligned}\tag{17}$$

We calculate the transition probabilities,

$$\begin{aligned}
W_{\alpha\beta}=W_{\gamma\delta}&=\frac{(e^2qQ)^2\tau_c}{40\,\hbar^2}\left[\frac{1}{1+\omega^2\tau_c^2}+\frac{1}{1+4\omega^2\tau_c^2}\right],\\
W_{\alpha\gamma}=W_{\beta\delta}&=\frac{(e^2qQ)^2\tau_c}{160\,\hbar^2}\left[3+\frac{4}{1+\omega^2\tau_c^2}+\frac{1}{1+4\omega^2\tau_c^2}\right].
\end{aligned}\tag{18}$$

In the extreme narrow conditions, above probabilities are given by

$$W_{\alpha\beta}=W_{\gamma\delta}=W_{\alpha\gamma}=W_{\beta\delta}=(1/20\hbar^2)(e^2qQ)^2\tau_c\equiv W. \tag{19}$$

For the occupation numbers $N_\alpha$, $N_\beta$, $N_\gamma$, and $N_\delta$, of the four states $\Psi(\alpha)$, $\Psi(\beta)$, $\Psi(\gamma)$, and $\Psi(\delta)$, we proceed with the similar method as for the longitudinal component $I_z$. In the extreme narrow case, the transverse relaxation time is given by

$$\frac{1}{T_2}=2W=\frac{2\pi^2}{5}\left(\frac{e^2qQ}{h}\right)^2\tau_c\,. \tag{20}$$

Accordingly, in the extreme narrow case we can see that $T_1$ is equal to $T_2$, and

$$\frac{1}{T_1}=\frac{1}{T_2}=\frac{2\pi^2}{5}\left(\frac{e^2qQ}{h}\right)^2\tau_c\,. \tag{21}$$

Inserting the measured values of $T_1$ and $e^2qQ$ into Eq. (16), we find the correlation time of $0.51\times10^{-11}$, $0.32\times10^{-11}$, $0.26\times10^{-11}$, and $0.29\times10^{-11}$ sec for $TiCl_4$, $VOCl_3$, $CrO_2Cl_2$, and $SiCl_4$, respectively. These values will be compared with those derived from the well known formula[12],

$$\tau=4\pi\eta a^3/3kT\,,$$

where $a$ is the radius of the molecule, and $\eta$ is the viscosity of the liquid at the temperature $T$. For $TiCl_4$, say, the radius $a$ will lie between $a_1$ which is the sum of the internuclear distance 2.18Å and the single-bonded chlorine covalent radius 0.99 Å and $a_2$ which is the sum of 2.18 Å and the Van der Waals radius of chlorine 1.81 Å. Using the value of $\eta=0.01$ poise we get

$$3.2\times10^{-11}<\tau(TiCl_4)<6.5\times10^{-11}.$$

Similar consideration gives for $SiCl_4$

$$2.7\times10^{-11}<\tau(SiCl_4)<5.6\times10^{-11}.$$

All these values are about ten times larger than those derived from the $T_1$. If this discrepancy is attributed to the difference of $e^2qQ$ between liquid and solid, the quadrupole coupling in liquid would be about one third of the coupling in solid. One of the reason of the decrease of $e^2qQ$ in liquid would be the molecular dimerization. Analysis of $X$-ray diffraction pattern of liquid $CCl_4$ revealed the presence of a kind of permanent or temporary associated molecules such that they orient themselves to each other with each one face of $CCl_4$[13]. This suggests similar situation for our samples although there is no explicit evidence of dimerization of $SiCl_4$ and so on. For the exact evaluation of the magnitude of $e^2qQ$ of molecules in liquid we may need further experimental studies.

## Acknowledgement

The author wishes to express his hearty thanks to Professor T. Kanda for his kind guidance and stimulating discussion throughout the course of this research. He is also indebted to Mr. K. Kuninobu who contributed to the experimental work as technical assistant. Part of this research was supported by the Scientific Research Fund granted by the Ministry of Education.

## Appendix

As there has been no reference on the chemical shift by $d$-electron we have given a brief account on the problem. First we consider an atom consisting of (closed shell) plus (one $d$-electron) covalently coupled to another atom. Taking a coordinate system $x', y', z'$ fixed to the molecule and taking $z'$ as a bonding direction, the wave function of the orbital part is

$$\Psi=\frac{1}{\sqrt{2}}\{\Psi_{d_{z'}}(1)A(2)+A(1)\Psi_{d_{z'}}(2)\}\ , \quad (21)$$

here $d_{z'}$, is the $d$-orbit directed to the $z'$-axes and $A$ is the orbit of the bonded atom. Let the coordinate system $x, y, z$, be fixed in space, $z$ be the direction of external magnetic field and $\beta$ be the angle between $z'$ and $z$. Transforming Eq. (21) to the $xyz$-system and taking the expectation value of the "chemical shift operator"$^{1)}$ $\sum_{j,k}(m_{z_j}/r_j^3)\cdot m_{z_k}$ we obtain for the chemical shift $S$

$$S=-3\frac{1}{\Delta E}\frac{e^2\hbar^2}{m^2c^2}\left\langle\frac{1}{r^3}\right\rangle_d \sin^2\beta\ .$$

Here $\langle 1/r^3\rangle_d$ is the mean of the $1/r^3$ of the $d$-orbit and $\Delta E$ is an appropriate average energy of the excitation states which have matrix element of the operator $m_z$ between the ground state. Taking the space average of $\sin^2\beta$ the final result is

$$S=-2\frac{1}{\Delta E}\frac{e^2\hbar^2}{m^2c^2}\left\langle\frac{1}{r^3}\right\rangle_d\ . \quad (22)$$

If we assume the $\Delta E$ and $\langle 1/r^3\rangle_d$ be the same as those of $p$-orbit the chemical shift is three times larger than the shift by $p$-electron.

Next we consider the effect of $d$-orbit hybridized to the $p$ orbit as in the case of the present problem. Taking the six electrons in which four are in the orbit $p_{x'}, p_{x'}, p_{y'}$, and $p_{y'}$ respectively, the fifth in $d$-hybridized $p$-orbit e.g. $(\sqrt{1-d}\,\Psi_{p_{z'}}+\sqrt{d}\,\Psi_{d_{z'}})$ and the last in the orbit A of neighbouring atom bonded to the atom under consideration, we can set up a wave function of 6-electron system by adding appropriate spin functions to the orbit. Calculation of the expectation value of the chemical shift operator gives the chemical shift of the molecule in random motion as follows:

$$S=-\frac{2}{3}\frac{1}{\Delta E}\frac{e^2\hbar^2}{m^2c^2}\left\langle\frac{1}{r^3}\right\rangle(1+4d)\ . \quad (23)$$

If we assume again $\Delta E$ and $\langle 1/r^3\rangle$ be the same as in the case of no hybridization we know that the shift is increased by $(1+4d)$.

## References

1) N. F. Ramsey: Phys. Rev. **78** (1950) 699, **86** (1952) 243.
2) C. H. Townes and B. P. Dailey: J. Chem. Phys. **17** (1949) 782, **20** (1952) 35.
3) R. V. Pound: Phys. Rev. **79** (1950) 123.
4) R. K. Wangsness and F. Bloch: Phys. Rev. **89** (1953) 728.
5) I. Solomon: Phys. Rev. **99** (1955) 559.
6) Y. Masuda and T. Kanda: J. Phys. Soc. Japan **9** (1954) 82.
7) G. D. Watkins: thesis, Harvard University, 1952 (unpublished).
8) H. G. Dehmelt: J. Chem. Phys. **21** (1953) 380.
9) A. Saika and C. P. Slichter: J. Chem. Phys. **22** (1954) 26.
10) R. G. Barnes and W. V. Smith: Phys. Rev. **93** (1954) 95.
11) C. H. Townes and A. L. Schawlow: Microwave Spectroscopy (McGraw-Hill, 1955).
12) Bloembergen, Purcell and Pound: Phys. Rev. **73** (1948) 679.
13) I. Nitta and T. Watanabe: Sci. Pap. I.P.C.R. **28** (1936) 277.

JOURNAL OF THE PHYSICAL SOCIETY OF JAPAN Vol. 11, No. 6, JUNE, 1956

# Auger Ejection of Electrons from Barium Oxide by Inert Gas Ions and the Cathode Fall in the Normal Glow Discharges

By Yoshiyuki TAKEISHI

*Tokyo Shibaura Electric Co., 72, Horikawa-chō, Kawasaki, Japan*

(Received January 12, 1956)

1. Total yield, $\gamma$, and energy distribution were calculated for electrons ejected from BaO by inert gas ions, on the basis of the theory of Auger neutralization. The method used here was similar to Hagstrum's one for tungsten. Total electron yield, $\gamma$, are found to be 0.481, 0.480, 0.476, 0.474, and 0.471 for $He^+$, $Ne^+$, $Ar^+$, $Kr^+$, and $Xe^+$ ions of several electron volts (ev), respectively. The electrons ejected from BaO have unexpectedly high energy and narrow distribution in comparison with those from tungsten observed by Hagstrum. In the case of $Ar^+$ ion, the calculated value of total electron yield, $\gamma$, is in good agreement with the Varney's measurements, and the high energy of ejected electrons is just as he expected.

2. The cathodic phenomena (cathode fall, width of Crookes dark space, and current density) in the normal glow discharges were observed for He, Ne, Ar, and Xe gases with BaO-coated cathode and tungsten, and were interpreted by the von Engel and Steenbeck's theory using the calculated values of $\gamma$ for BaO and the observed one by Hagstrum for tungsten.

## § 1. Introduction

Alkaline earth oxides and their solid solutions have been widely employing as the cathode of glow discharge tube filled with Ne and Ar gases by main reason of giving lower normal cathode fall. However, not only in Ne and Ar gases, but also in He and Xe, they give the lower normal cathode fall as shown in § 6. The same tendency will be expected for Kr gas, even though no observation has been made up to this time. We are interested in the fact that lower normal cathode fall is obtained with alkaline earth oxide cathode than with usual heavy metals, for example, tungsten and molybdenium. According to the theory of von Engel and Steenbeck, the cathode materials showing lower normal cathode fall are to have higher values of $\gamma$ (total yield of electrons per ion). Then, the calculations of total yield, $\gamma$, and the energy distribution of electrons ejected from BaO by each inert gas ion are attempted.

There have been two principal theories on the mechanism of ejection of electrons from cathode by an ion, that is, so-called the potential ejection theory and kinetic ejection theory. In the normal glow discharges, however, the electron ejection from cathode will be principally caused by the former mechanism, because the ions striking the cathode surface are of thermal energy, at most 10 ev. As a matter of fact, the recent experimental studies by Bradley1), Parker2), and Hagstrum3)-5), etc., have shown with various metals that the total yield, $\gamma$, is nearly independent of kinetic energy of incident ions up to several hundreds ev. Further the studies of Hagstrum5),6) have indicated that the values of $\gamma$ for tungsten increases with the ionization energy of inert gas atoms and with the charge and hence total ionization energy for each ion of inert gases, and the observed values of $\gamma$ and energy distributions can be almost completely explained on the basis of the theory of potential ejection. These facts seem to justify the mechanism of potential ejection, so our calculations should be based on the theory of potential ejection.

Up to this time, the theoretical studies on the electronic transition between metal and an ion or an excited atom of inert gas, have been carried out by Massey7), Oliphant and Moon8), Shekhter9), Cobas and Lamb10), and Hagstrum6)*. After these studies, four types of electronic transition are considered to be possible, that is, resonance neutralization, resonance ionization, Auger de-exitation, and Auger neutralization. Which transition will be possible, depends on the electronic structures of the concerned metal and atom.

---

* Among these papers, we can not read the Shekhter's one because there is no one in Japan, although we know the same results of his calculations quoted in Hagstrum's paper. And only Shekhter and Hagstrum have treated Auger neutralization up to this time.

Here we refer to the electronic band structure of BaO, the physical state of which will be reported in § 6. The following model is adapted as the electronic band structure: the width of conduction band, or electron affinity is 0.6 ev which is suggested by Narita[11], the energy gap between the impurity level and the bottom of conduction band is 0.8~1.0 ev, the top of filled band is 5.1 ev or more below the vacuum level and the width of it is 6~9 ev[12].

According to this band structure of BaO and the ionization and the excitation energies of each inert gas atom (refer to Table I), even though the latters vary with the distance of atom from BaO surface (refer to § 4), the only possible process of electronic transition is *Auger neutrarization* for any inert gas ion and no other process do play a role. Then, it may be assumed through the following calculations that both of two electrons in BaO concerned with Auger neutralization are conduction electrons.

In this paper, after the discussions on the general theory of Auger neutralization (§ 2) and on the explicit expression in the case of He$^+$ ion and BaO (§ 3), we shall calculate the total yield, $\gamma$, and the energy distributions of ejected electrons for each inert gas ion using the approximate methods developed by Hagstrum (§ 4), and shall compare the results for Ar$^+$ ion with the Varney's measurements (§ 5). Next, our observations on the cathode fall, the width of Crookes dark space, and the current density in the normal glow discharges in inert gases (except Kr) with BaO-coated and tungsten cathodes will be interpreted by the theory of von Engel and Steenbeck, using the calculated values of $\gamma$ for BaO and the observed one by Hagstrum for tungsten (§ 6).

## § 2. General Theory of Auger Neutralization

### (a) *Auger neutralization caused by an ion at the distance, s, from the crystal surface.*

According to the time independent perturbation theory developed by Dirac*, transition probability per unit time (transition coefficient) is given by

$$2\pi\hbar^{-1}|\langle E'\beta''|V|\alpha'\rangle|^2 , \qquad (1)$$

where $\alpha'$ and $\beta''$ are the dynamical variables which represent the initial state and the final state, respectively, $E'$ is the energy of initial state, and $V$ is the perturbing potential.

Table I. Table of ionization energy ($E_i$) and excitation energy ($E_e$), in ev, of inert gas atom.

| Atom. | $E_i$ | $E_e$ |
|---|---|---|
| He | 24.58 | 19.81 |
| Ne | 21.56 | 16.61 |
| Ar | 15.76 | 11.55 |
| Kr | 14.00 | 9.91 |
| Xe | 12.13 | 8.31 |

These values are quoted from Hagstrum's paper. $E_e$'s are the energies to be excited from ground state to metastable state which are such state; $2s^3S$ for He, $ns[1^1/_2]^\circ$ with $n=3, 4, 5$ and 6 for Ne, Ar, Kr and Xe respectively.

This theory is applied to Auger neutralization as follows. In the process of Auger neutralization, the interaction between an ion and two conduction electrons causes the electron 1 to neutralize the ion directly into the ground state and the other conduction electron 2 to be excited into the positive energy continium above the conduction band. Now, the energies of the electron 1 and the electron 2 at initial state and the energy of the excited electron 2 at final state are defined as $\mathcal{E}_1=\hbar^2/2m\cdot\boldsymbol{k}_1^2$, $\mathcal{E}_2=\hbar^2/2m\cdot\boldsymbol{k}_2^2$, and $\mathcal{E}_k=\hbar^2/2m\cdot\boldsymbol{K}^2$, respectively, measured from the bottom of conduction band, where $\boldsymbol{k}$ and $\boldsymbol{K}$ are the wave number vectors. And we define $n_c(\mathcal{E})$ as the electron density function (state density × distribution function) in the conduction band, and $\rho$ $(\mathcal{E}_k)$ as the density of final state at $\mathcal{E}_k$. $\rho(\mathcal{E}_k)$ is represented, as usual, by $c\sqrt{\mathcal{E}_k}$ where $c$ is a constant. $|\langle E'\beta''|V|\alpha'\rangle|^2$ in Eq. (1) may be written as

$$|H|^2\delta(\mathcal{E}_k-\mathcal{E}_1-\mathcal{E}_2+\mathcal{E}_0-E_i'(s)) ,$$

where $H$ represents the matrix element, $\delta$ is the Dirac's $\delta$-function, $E_i'(s)$ is defined as the effective ionization energy of concerned atom at a distance, $s$, from the crystal surface, and $\mathcal{E}_0$ is the energy difference between the bottom of conduction band and the vacuum level. Here, the effective ionization energy has been first defined by Hagstrum (refer to § 4).

---

* e.g. Dirac: The Principles of Quantum Mechanics, third edition, (1948), sec. 46.

Thus, the transition rate for a process of Auger neutralization is given by

$$2\pi\hbar^{-1}n_c(\mathcal{E}_1)n_c(\mathcal{E}_2)\rho(\mathcal{E}_k)|H|^2 \times\delta(\mathcal{E}_k-\mathcal{E}_1-\mathcal{E}_2+\mathcal{E}_0-E_i'(s))\,d\mathcal{E}_1d\mathcal{E}_2d\mathcal{E}_k\sin\theta d\theta d\varphi\,, \tag{2}$$

where $\sin\theta\, d\theta d\varphi=d\Omega$ is the element of solid angle within which the direction of the wave number vector $\boldsymbol{K}=\hbar^{-1}\sqrt{2m\mathcal{E}_k}$, lies. Therefore, the total transition rate, $\lambda(s)$, for all processes occuring when the ion is at a distance, $s$, from the surface is

$$\lambda(s)=2\pi\hbar^{-1}\int_0^{2\pi}\int_0^{\pi}\int_{\mathcal{E}_c}^{\infty}\int_0^{\mathcal{E}_c}\int_0^{\mathcal{E}_c}n_c(\mathcal{E}_1)n_c(\mathcal{E}_2)\rho(\mathcal{E}_k)|H|^2 \times\delta(\mathcal{E}_k-\mathcal{E}_1-\mathcal{E}_2+\mathcal{E}_0-E_i'(s))\,d\mathcal{E}_1d\mathcal{E}_2d\mathcal{E}_k\sin\theta d\theta d\varphi\,, \tag{3}$$

where $\mathcal{E}_c$ is the width of conduction band. The matrix element is assumed to be independent of azimuthal angle $\varphi$ and to depend only on the angle $\theta$ with the surface normal.

Then, the distribution in energy, $N_0(\mathcal{E}_k)$, of electrons which escape from the crystal is

$$N_0(\mathcal{E}_k)=2\pi\hbar^{-1}\rho(\mathcal{E}_k)\int_0^{2\pi}\int_0^{\theta_c}\int_0^{\mathcal{E}_c}\int_0^{\mathcal{E}_c}n_c(\mathcal{E}_1)n_c(\mathcal{E}_2)|H|^2 \times\delta(\mathcal{E}_k-\mathcal{E}_1-\mathcal{E}_2+\mathcal{E}_0-E_i'(s))d\mathcal{E}_1d\mathcal{E}_2\sin\theta d\theta d\varphi\,, \tag{4}$$

where $\theta_c$ is the maximum value of $\theta$ for which escape of the excited electron over the surface potential barrier is possible.

The total yield, $\gamma$, of electrons ejected from the crystal by an ion at a distance, $s$, from the surface is given by

$$\gamma=2\pi\hbar^{-1}\int_0^{2\pi}\int_0^{\theta_c}\int_{\mathcal{E}_0}^{\infty}\int_0^{\mathcal{E}_c}\int_0^{\mathcal{E}_c}n_c(\mathcal{E}_1)n_c(\mathcal{E}_2)\rho(\mathcal{E}_k)|H|^2 \times\delta(\mathcal{E}_k-\mathcal{E}_1-\mathcal{E}_2+\mathcal{E}_0-E_i'(s))d\mathcal{E}_1d\mathcal{E}_2d\mathcal{E}_k\sin\theta d\theta d\varphi \tag{5}$$

$$=\int_{\mathcal{E}_0}^{\infty}N_0(\mathcal{E}_k)d\mathcal{E}_k \tag{6}$$

$$=\int_0^{\infty}N(E_k)dE_k\,, \tag{6'}$$

where $E_k=\mathcal{E}_k-\mathcal{E}_0$.

### (b) *The probability of transition caused by an ion in moving toward the surface.*

If $P(s, v_0)\, ds$ is defined as the probability that the ion, having started from infinity with constant speed, $v_0$, normal to the surface, will undergo transition in $ds$ at $s$, it is represented by following equation from the definition of $\lambda(s)$:

$$P(s, v_0)ds=[\lambda(s)/v_0]\left[1-\int_s^{\infty}P(s, v_0)ds\right]ds\,. \tag{7}$$

The solution of this integral equation is

$$P(s, v)=C\exp\int\{1-d/ds[v_0/\lambda(s)]\}\lambda(s)/v_0ds \tag{8}$$

where $C$ is a constant of integration.

From the theoretical studies of several authors7)−9), it is allowed to assume

$$\lambda(s)=A\exp(-as)\,, \tag{9}$$

where $A$ and $a$ are numerical constants. With this expression for $\lambda(s)$, $P(s, v_0)$ is found to be

$$P(s, v_0)=C\exp[-(A/a.\,v_0)\exp(-as)-as]\,, \tag{10}$$

where $C$ is a constant.

From Eqs. (8) and (10) under the condition of large $s$,

we find

$$C=A/v_0\,.$$

Therefore

$$P(s, v_0)=(A/v_0)\exp[-(A/av_0)\exp(-as)-as]\,. \tag{11}$$

This expression has been derived by Cobas and Lamb10).

The distance at which $P(s, v_0)$ function becomes maximum is easily derived from Eq. (11) as follows:

$$s_m=(1/a)\ln(A/av_0)\,. \tag{12}$$

This relation shows that $s_m$ is larger for the ion with lower velocity.

Hagstrum has pointed out the following important result: if it is assumed that Eq. (9) holds to $s=0$, the probability that the ion will undergo transition in comming from infinity to the surface ($s=0$) is

$$\int_0^{\infty}P(s, v_0)ds=1-\exp[-\exp(\ln(Aav_0))]\,. \tag{13}$$

From this equation, it follows,

$$\lim_{v_0\to 0}\int_0^{\infty}P(s, v_0)ds=1\,. \tag{14}$$

Therefore, for the ion of lower velocity, the transition probability of Auger neutralization is very nearly unity. This is consistent with the observation by him that very few ions (~0.1%) are reflected when their energy is less than 100 ev.

## § 3. Expression of $\lambda(s)$ in the case of He⁺ ion and BaO.

Here we will discuss the explicit expression of $\lambda(s)$ in the case of $He^+$ ion and BaO.

(a) The electron density function $n_c(\mathcal{E})$ in the conduction band of BaO is given by

$$n_c(\mathcal{E})=g_c(2mc)^{3/2}/2\pi^2\hbar^3 \exp(-E_0/kT)\sqrt{\mathcal{E}}$$
$$\times\exp(-\mathcal{E}/kT) \qquad (15)$$
$$=c_1(T)\sqrt{\mathcal{E}}\exp(-\mathcal{E}/kT)\,, \qquad (15')$$

where $c_1(T)=g_c(2mc)^{3/2}/2\pi^2\hbar^3\exp(-E_0/kT)$ is a constant dependent on only $T$ and $E_0$ is the energy difference between the bottom of the conduction band and Fermi level and $k$ is Boltzmann's constant and $g_c$ is the degeneracy except those of spin.

(b) The state density of positive energy continium above the conduction band may be expressed as usual, thus,

$$\rho(\mathcal{E}_k)=(2m)^{3/2}/2\pi^2\hbar^3\sqrt{\mathcal{E}_k} \qquad (16)$$
$$=c_2\sqrt{\mathcal{E}_k}\,, \qquad (16')$$

where $c_2=(2m)^{3/2}/2\pi^2\hbar^3$ is a constant and here the degeneracy of spin is included.

(c) The expression of matrix element $H$.

The wave function of initial state is consisted of:

(i) the wave function of ground state of $He^+$;

$$\psi_{1s}(\boldsymbol{r}_3)=1/\sqrt{\pi}\,(Z'/a_0)^{3/2}\exp(-Z'\boldsymbol{r}_3/a_0)\,,[13] \qquad (17)$$

where $Z'=1.69$ and $a_0$ is Bohr's radius.

(ii) the wave function of conduction electron 1; $\exp(i\boldsymbol{k}_1\boldsymbol{r}_1)$,

(iii) the wave function of conduction electron 2; $\exp(i\boldsymbol{k}_2\boldsymbol{r}_2)$, where $\boldsymbol{k}=\hbar^{-1}\sqrt{2m\mathcal{E}}$.

The wave function of final state is consisted of:

(i) the wave function of ground state of He atom; $\psi_{1s}(\boldsymbol{r}_3)\psi_{1s}(\boldsymbol{r}_1)$ where $\psi_{1s}(\boldsymbol{r})$ is the same expression for Eq. (17).

(ii) the wave function of excited electron; $\exp(i\boldsymbol{K}\boldsymbol{r}_2)$, where $\boldsymbol{K}=h\sqrt{2m\mathcal{E}_k}$.

In the wave functions of conduction electron and excited electron, normalization factors are omitted.

Next the perturbing potential $V$ may be written as;

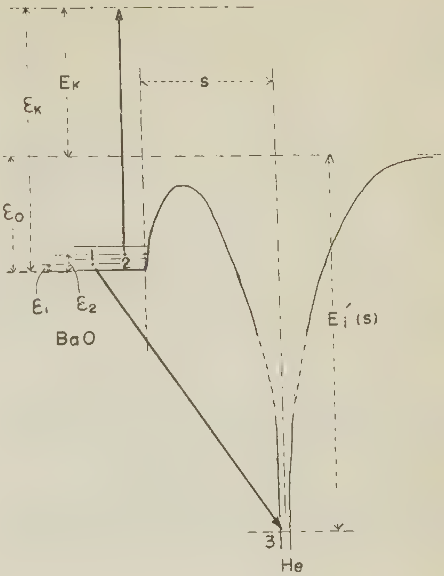

Fig. 1. Schematic diagram illustrating Auger neutralization of He⁺ ion at BaO surface. The electronic transition is indicated by the full arrows.

$$V=-e^2\left\{\frac{1}{|\boldsymbol{r}_1-\boldsymbol{r}_3|}+\frac{1}{|\boldsymbol{r}_2-\boldsymbol{r}_3|}+\frac{1}{|\boldsymbol{r}_1-\boldsymbol{r}_2|}\right\}.$$

However, the last term seems to be not accurate, and should be corrected by the knowledge of electron-electron interaction, or plasma oscillation, etc. We will not discuss further on this point.

From these expressions, it follows that

$$H=\iiint\{\psi_{1s}(\boldsymbol{r}_3)\psi_{1s}(\boldsymbol{r}_1)-\psi_{1s}(\boldsymbol{r}_1)\psi_{1s}(\boldsymbol{r}_3)\}\exp(-i\boldsymbol{K}\boldsymbol{r}_2)$$
$$\times(-e^2)\cdot\left\{\frac{1}{|\boldsymbol{r}_1-\boldsymbol{r}_3|}+\frac{1}{|\boldsymbol{r}_2-\boldsymbol{r}_3|}+\frac{1}{|\boldsymbol{r}_1-\boldsymbol{r}_2|}\right\}$$
$$\times\{\exp(i\boldsymbol{k}_1\boldsymbol{r}_1)\exp(i\boldsymbol{k}_2\boldsymbol{r}_2)-\exp(i\boldsymbol{k}_2\boldsymbol{r}_2)\exp(i\boldsymbol{k}_1\boldsymbol{r}_1)\}$$
$$\times\psi_{1s}(\boldsymbol{r}_3)d\tau_1 d\tau_2 d\tau_3\,. \qquad (18)$$

The antisymmetrization contained in this representation is not exact. It should be modified by Slater function about the wave functions of all conduction electrons and excited electron, but this correction seems to have little effect upon the results.

If these expressions of $n_c(\mathcal{E}_1)$, $n_c(\mathcal{E}_2)$, $\rho(\mathcal{E}_k)$, and $H$ are inserted to Eq. (3), the representation of $\lambda(s)$ can be obtained.

## § 4. Calculations by Approximate methods

It is very troublesome to carry out the above calculations exactly, so we adapt the approximate methods developed by Hagstrum for tungsten by which he has succeeded in the explanation of his experimental results for tungsten.

The essential quality of this methods lies in diving the Auger process in several elemental processes, regarding the matrix element as a constant. Several probability functions are defined as follows: $P_k(\mathcal{E}_k, s)d\mathcal{E}_k$ is the probability that the excited electron produced in the process of Auger neutralization caused by an ion at a distance $s$ will have energy within the interval $d\mathcal{E}_k$ at $\mathcal{E}_k$; $P_\Omega(\mathcal{E}_k, \theta)d\Omega$, is the probability that the excited electron of energy, $\mathcal{E}_k$, has its velocity vector lying within a solid angle $d\Omega=\sin\theta d\theta d\varphi$; the probability $P(s, v_0)ds$ is the one defined previously in § 2, (b); $P_e(\mathcal{E}_k)$ is the probability that an excited electron of energy, $\mathcal{E}_k$, will escape over the surface barrier. From these probability distribution functions, the energy distributions of excited electrons and ejected electrons and hence the total yield, $\gamma$, of ejected electrons are obtained easily with some further approximations.

At first total transition rate $\lambda(s)$ is rewritten

$$\lambda(s)=2\pi\hbar^{-1}c_3\iiiint\!\!\int n_c(\mathcal{E}_1)n_c(\mathcal{E}_2)\rho(\mathcal{E}_k)P_\Omega(\mathcal{E}_k, \theta)\times\delta(\mathcal{E}_k-\mathcal{E}_1-\mathcal{E}_2+\mathcal{E}_0-E_i'(s))\times d\mathcal{E}_1 d\mathcal{E}_2 d\mathcal{E}_k \sin\theta d\theta d\varphi\ , \tag{19}$$

where $|H|^2$ is considered to be constant and represented by $c_3$ and $\mathcal{E}_c$ is replaced by $\mathcal{E}_0$, because both are same for BaO.

The probability distribution function $P_k(\mathcal{E}_k, s)$ is given by

$$P_k(\mathcal{E}_k, s)=\frac{\rho(\mathcal{E}_k)\iint n_c(\mathcal{E}_1)n_c(\mathcal{E}_2)\delta(\mathcal{E}_k-\mathcal{E}_1-\mathcal{E}_2+\mathcal{E}_0-E_i'(s))d\mathcal{E}_1 d\mathcal{E}_2}{\iiint n_c(\mathcal{E}_1)n_c(\mathcal{E}_2)\rho(\mathcal{E}_k)\delta(\mathcal{E}_k-\mathcal{E}_1-\mathcal{E}_2+\mathcal{E}_0-E_i'(s))d\mathcal{E}_1 d\mathcal{E}_2 d\mathcal{E}_k}\ , \tag{20}$$

since

$$\int_0^{2\pi}\int_0^{\pi} P_\Omega(\mathcal{E}_k, \theta)\sin\theta d\theta d\varphi=1 \text{ at all } \mathcal{E}_k\ .$$

Replacing the denominator by $c_4^{-1}$, a constant, it follows,

$$P_k(\mathcal{E}_k, s)=c_4\rho(\mathcal{E}_k)\iint n_c(\mathcal{E}_1)n_c(\mathcal{E}_2)\delta(\mathcal{E}_k-\mathcal{E}_1-\mathcal{E}_2+\mathcal{E}_0-E_i'(s))d\mathcal{E}_1 d\mathcal{E}_2\ . \tag{20$'$}$$

Next, using the probability distributions $P_k(\mathcal{E}_k, s)$ and $P(s, v_0)$, the distribution in energy, $N_i(\mathcal{E}_k)$, of electrons excited in the process of Auger neutralization is obtained as

$$\begin{aligned}N_i(\mathcal{E}_k)&=\int_0^{\infty}\int_0^{2\pi}\int_0^{\pi} P(s, v_0)P_k(\mathcal{E}_k, s)P_\Omega(\mathcal{E}_k, \theta)\sin\theta d\theta d\varphi ds\\&=\int_0^{\infty} P(s, v_0)P_k(\mathcal{E}_k, s)ds\ .\end{aligned} \tag{21}$$

(a) Here, the following approximations are adapted in our calculations.

*Approximation I.*

“The distance, $s$, in the probability distribution, $P_k(\mathcal{E}_k, s)$, is taken as $s_m$ at which $P(s, v_0)$ becomes maximum and which is constant at the given velocity of ion (Eq. (12))”.

This is suggested by the fact that $P(s, v_0)$ is large only in a relatively small range of $s$ (refer to Fig. 5).

Basing upon this Approximation,

$$\begin{aligned}N_i(\mathcal{E}_k)&=P_k(\mathcal{E}_k, s_m)\int_0^{\infty} P(s, v_0)ds\\&=P_k(\mathcal{E}_k, s_m)\ ,\end{aligned} \tag{22}$$

since $\int_0^{\infty} P(s, v_0)ds\simeq 1$, as mentioned already in § 2 (b).

*Approximation II*

“The variation of ionization energy caused by the interaction with the crystal is neglected, so $E_i'(s)=E_i$, a constant”. According to this approximation, $P_k(\mathcal{E}_k, s)$ becomes independent of $s$, and

$$N_i(\mathcal{E}_k)=P_k(\mathcal{E}_k)\,. \qquad (23)$$

The consequences without these approximations will be discussed in the subsection (b) and (c) in this section.

Thus, $N_i(\mathcal{E}_k)$ is given by

$$N_i(\mathcal{E}_k)=c_i\rho(\mathcal{E}_k)\iint_0^{\mathcal{E}_0} n_c(\mathcal{E}_1)n_c(\mathcal{E}_2) \times\delta(\mathcal{E}_k-\mathcal{E}_1-\mathcal{E}_2+\mathcal{E}_0-E_i)d\mathcal{E}_1 d\mathcal{E}_2\,. \qquad (23)'$$

In order to calculate this integration, it is convenient to use Auger transform defined as follows[14]:

$$\left.\begin{aligned} T(\mathcal{E})&=\int_0^{\mathcal{E}} n_c(\mathcal{E}-\Delta)n_c(\mathcal{E}+\Delta)d\Delta\,,\quad 0<\mathcal{E}<\mathcal{E}_0/2 \\ T(\mathcal{E})&=\int_0^{\mathcal{E}_0-\mathcal{E}} n_c(\mathcal{E}-\Delta)n_c(\mathcal{E}+\Delta)d\Delta,\quad \mathcal{E}_0/2<\mathcal{E}<\mathcal{E}_0 \\ &=0,\qquad \mathcal{E}<0,\qquad \mathcal{E}>\mathcal{E}_0, \end{aligned}\right\} \qquad (24)$$

where $\mathcal{E}=\frac{1}{2}(\mathcal{E}_1+\mathcal{E}_2)$ and $\Delta=\frac{1}{2}(\mathcal{E}_1-\mathcal{E}_2)$.

Using Eq. (15)′, $T(\mathcal{E})$ are calculated as follows:

$$T(\mathcal{E})=c_1(T^2)\cdot\pi/4\mathcal{E}^2\exp(-2\mathcal{E}/kT),\quad 0<\mathcal{E}<\mathcal{E}_0/2 \qquad (25)$$

$$\begin{aligned} &=c_1(T)^2/2\{(\mathcal{E}_0-\mathcal{E})(2\mathcal{E}\mathcal{E}_0-\mathcal{E}_0^2)^{1/2} \\ &\quad+\mathcal{E}^2\sin((\mathcal{E}_0-\mathcal{E})/\mathcal{E})\} \\ &\quad\times\exp(-2\mathcal{E}/kT),\quad \mathcal{E}_0/2<\mathcal{E}<\mathcal{E}_0. \end{aligned} \qquad (25)'$$

In the present case, only Eq. (25) may be used, because at several hundreds degree in Kelvin the conduction electrons in BaO populate only near the bottom of conduction band.

Thus, from Eqs. (25), (23)′ and (16)′, $N_i(\mathcal{E}_k)$ is obtained as

$$N_i(\mathcal{E}_k')=c_5(T)\mathcal{E}_k'^{5/2}\exp(-2\mathcal{E}_k''/kT) \qquad (26)$$

where $\mathcal{E}_k'=\mathcal{E}_k-\mathcal{E}_k(\text{min.})$, $\mathcal{E}_k(\text{min.})=E_i-\mathcal{E}_0$, and $c_5(T)=c_1(T)^2\pi/4c_2c_4$. Here we take the cathode temperature as 500°K, which seems to be not so far from the practical temperature of the cathode of glow discharge tube filled with Ar gas. At this temperature, $N_i(\mathcal{E}_k')$ has the form in Fig. 2. In this calculation, the value of the width of conduction band is taken as 0.6 ev, as mentioned previously in Introduction. In Fig. 2, the total areas under the curve of $N_i(\mathcal{E}_k')$ are normalized to one electron per incident ion. Because, from Eq. (21),

$$\int_0^\infty N_i(\mathcal{E}_k)d\mathcal{E}_k=\int_0^\infty P(s,v_0)ds\simeq1\,, \qquad (27)$$

since

$$\int_0^\infty P_k(\mathcal{E}_k,s)d\mathcal{E}_k=1\,.$$

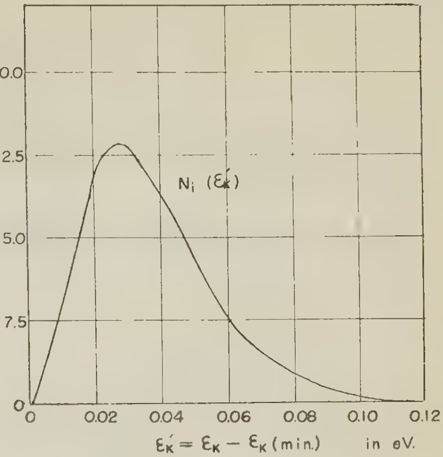

Fig. 2. Distributions in kinetic energy inside BaO, $N_i(\varepsilon_k)$, of electrons excited by Auger neutralization of the singly charged inert gas ions. Here two approximations are used. Areas under $N_i(\varepsilon_k')$ curve are normalized to one electron per incident ion. The forms of $N_i(\varepsilon_k')$ are common for each inert gas ion. Only the values of $\varepsilon_k(\text{min})$ are different.

The forms of $N_i(\mathcal{E}_k')$ are common for each inert gas ion and only $\mathcal{E}_k(\text{min.})$s are different.

Next, the energy distribution, $N_0(\mathcal{E}_k)$, of electrons which escape from BaO surface is obtained by.

$$\begin{aligned} N_0(\mathcal{E}_k)&=\int_0^{2\pi}\int_0^{\theta_c}\int_0^\infty P(s,v_0)P_k(\mathcal{E}_k,s)P_\Omega(\mathcal{E}_k,\theta) \\ &\qquad\times ds\sin\theta d\theta d\varphi. \\ &=N_i(\mathcal{E}_k)\cdot P_e(\mathcal{E}_k)\,. \end{aligned} \qquad (28)$$

Here we defined the probability of escape, $P_e(\mathcal{E}_k)$, as

$$P_e(\mathcal{E}_k)=\int_0^{2\pi}\int_0^{\theta_c} P_\Omega(\mathcal{E}_k,\theta)\sin\theta d\theta d\varphi\,, \qquad (29)$$

where $\theta_c$ represents the maximum value of $\theta$ for which escape of the excited electron over the surface barrier is possible. This critical angle $\theta_c$ is given by

$$\theta_c=\cos^{-1}(\mathcal{E}_0/\mathcal{E}_k)^{1/2}\,. \qquad (30)$$

If the angular distribution of excited electrons is isotropic, $P_\Omega(\mathcal{E}_k,\theta)$ is a constant and equal to $1/4\pi$. So, by the Eq. (29),

$$\begin{aligned} P_e(\mathcal{E}_k)&=\tfrac{1}{2}[1-(\mathcal{E}_0/\mathcal{E}_k)^{1/2}]\,,\quad \mathcal{E}_k>\mathcal{E}_0 \\ &=0,\qquad \mathcal{E}_k<\mathcal{E}_0. \end{aligned} \qquad (31)$$

However it seems to be probable that the angular distribution is not isotropic*. It has been suggested* by C. Herring that the matrix element $H_1$ for $\theta<\theta_c$ may be greater than the matrix element $H_2$ for $\theta>\theta_c$, here $H_1$ and $H_2$ are also assumed constant. Hagstrum obtained the next expression of $P_e(\varepsilon_k)$, taking into account this circumstance.

$$P_e(\varepsilon_k)=\frac{1}{2}\left[\frac{1-(\varepsilon_0/\varepsilon_k)^{1/2}}{1-(1-1/f)(\varepsilon_0/\varepsilon_k)^{1/2}}\right],\quad \varepsilon_k>\varepsilon_0\,,$$
$$=0\,,\qquad \varepsilon_k<\varepsilon_0\,, \tag{32}$$

where

$$f=|H_1/H_2|^2\,.$$

The value of the parameter, $f$, has not been estimated theoretically, but he has determined it as $f=2.2$ by fitting the theoretical $\gamma$ for tungsten for He$^+$ ions of 40 ev to the experimental $\gamma$. In our calculations also this value will be adapted.

These escape probability functions $P_e(\varepsilon_k)$ with $f=1$ (Eq. (31)), and with $f=2.2$ (Eq. (32)) are plotted in Fig. 3 as curves 1 and 2, respectively.

From the distribution in energy, $N_i(\varepsilon_k)$, of the excited electrons and the escape probability function, $P_e(\varepsilon_k)$, the energy distribution, $N_0(\varepsilon_k)$, of the ejected electrons is easily obtained by Eq. (28). The forms for all inert gas ions are common and are almost similar to the forms of $N_i(\varepsilon_k)$, because $N_i(\varepsilon_k)$, as shown in Fig. 2, is distributed within the limited range of $\varepsilon_k$(0.12 ev) and in this range, $P_e(\varepsilon_k)$ has practically a constant value for each inert gas ion. Therefore we will omit the figures of $N_0(\varepsilon_k)$. However $\varepsilon_k'$ in the abscissa of Fig. 2 is of course replaced by $E_k'$ which equals $E_k-E_k$(min.), here $E_k=\varepsilon_k-\varepsilon_0$, and $E_k$(min.) $=E_i-2\varepsilon_0$.

The values of $\varepsilon_k$(min.), $\varepsilon_k^0$, and $\varepsilon_k$(max.) in the distribution, $N_i(\varepsilon_k)$, and those of $E_k$(min.), $E_k^0$, and $E_k$(max.) in $N_0(E_k)$ are shown in Table II, where $\varepsilon_k^0$ and $E_k^0$ are the energies at which $N_i(\varepsilon_k)$ and $N_0(E_k)$ become maximum, respectively. And $\varepsilon_k$(max.)s and $E_k$(max.)s are the energy extremes the excited electrons and ejected electrons possess inside the crystal and outside the crystal, respectively. However, correctly speaking, $\varepsilon_k$(max.) and $E_k$(max.) are not maximum energy, but the values above which $N_i(\varepsilon_k)$ and $N_0(E_k)$ have not appreciable values.

Finally the total electron yield, $\gamma$, per incident ion for the Auger neutralization process is obtained by integrating $N_0(E_k)$ over $E_k$. Thus

$$\gamma=\int_0^\infty N_0(E_k)dE_k\,. \tag{33}$$

In the present case, however, the value of $\gamma$ for each inert gas ion is nearly equal to $P_e(\varepsilon_k^0)$, because $P_e(\varepsilon_k)$ is practically constant over the range of energy $\varepsilon_k$, within which $N_i(\varepsilon_k)$ has appreciable value. The error which results from this approximation will be negligible.

(b) Removal of the *Approximation II.*

This removal means the inclusion of the effects of the variation in the ionization energy of concerned inert gas atom near the BaO surface. Here, this effects will be briefly discussed after Hagstrum.

The variation, $dE_i'(s)=E_i-E_i'(s)$, in the ionization energy is caused by the difference between two interaction energy, $E(i-c)$ and $E(n-c)$, where the former is the one between ion and BaO and the latter between normal atom and BaO. So, it follows,

$$dE_i'(s)=E(n-c)-E(i-c)\,. \tag{34}$$

It is sufficient for the interaction energy, $E(i-c)$, to consider only the Coulombic image potential, $-3.6/s$ ev, and the repulsive interaction potential, $B_i\exp(-b_is)$, between pairs of ions, where $B_i$ and $b_i$ are constant, although there are three types of ions. Then,

$$E(i-c)=-3.6/s+B_i\exp(-b_is)\,. \tag{35}$$

Such representation of the repulsive interaction is based on the quantum mechanical investigations by Born and Mayer[15].

On the other hand, as the interaction energy between normal atom and BaO, $E(n-c)$, only the repulsive potential may be considered, so

$$E(n-c)=B_n\exp(-b_ns)\,, \tag{36}$$

where $B_n$ and $b_n$ are constant. This representation is suggested by the theoretical studies of Slater and, Mayer and Bleick[16].

In both cases of $E(i-c)$ and $E(n-c)$, the van der Waals interaction energies are considered to be negligible small.

Thus, $dE_i'(s)$ is given by

$$dE_i'(s)=B_n\exp(-b_ns)-B_i\exp(-b_is)+3.6/s\,. \tag{37}$$

The curves of $dE_i'(s)$ as a function of dis-

---

* For detailed discussions, see reference 6), Chap. VI.

Table II. Results of calculations in § 4 (a).

| Ion | $N_i(\varepsilon_k)$ | | | $N_0(E_k)$ | | | $\gamma$ | |
|---|---|---|---|---|---|---|---|---|
| | $\varepsilon_k$ (min.) | $\varepsilon_k^0$ | $\varepsilon_k$ (max.) | $E_k$ (min.) | $E_k^0$ | $E_k$ (max.) | $f=1$ | $f=2.2$ |
| He$^+$ | 23.98 | 24.01 | 24.10 | 23.38 | 23.41 | 23.50 | 0.421 | 0.481 |
| Ne$^+$ | 20.96 | 20.99 | 21.08 | 20.36 | 20.39 | 20.48 | 0.415 | 0.480 |
| Ar$^+$ | 15.16 | 15.19 | 15.28 | 14.56 | 14.59 | 14.68 | 0.401 | 0.476 |
| Kr$^+$ | 13.40 | 13.43 | 13.52 | 12.80 | 12.83 | 12.92 | 0.394 | 0.474 |
| Xe$^+$ | 11.53 | 11.58 | 11.62 | 10.93 | 10.96 | 11.05 | 0.386 | 0.471 |

tance $s$ are plotted in Fig. 4, where the used values of $B_n, b_n, B_i$ and $b_i$ are those which Hagstrum has estimated from various data of above authors. These curves indicate the decrease in ionization energies of inert gas atoms at distance $s$.

The distance, $s_0$, at which the ion "touches" the BaO surface may be defined as

$$s_0=r_1/2+r_2/2\ , \tag{38}$$

where $r_1$ is the radius of inert gas ion and $r_2$ half the distance between Ba$^{++}$ and O$^{--}$ in BaO crystal. The values of $s_0$ for all inert gas ions are tabulated in Table III.

Next, we will estimate the distance $s_m$ at which the transition probability function $P(s, v_0)$ becomes maximum. $s_m$ is given by

$$s_m=(1/a)ln(A/a\cdot v_0)\ . \tag{12}$$

The plot of $P(s, v_0)$ as a function of $a(s-s_m)$ is quoted in Fig. 5 from Hagstrum's paper.

The numerical value of $A$ and $a$ can be obtained principally by the calculation of $\lambda(s)$. However, in our case, this calculation is very troublesome. Then as a value of $a$, we will use $2\times10^8\ \text{cm}^{-1}$, which is estimated by Hagstrum from the theoretical studies of several authors, and he has determined the values of $A$ for this value of $a$, using the experimental data for tungsten. Those are $7.1\times10^{16}$, $4.8\times10^{16}$, $1.1\times10^{17}$, $1.2\times10^{17}$, and $2.1\times10^{17}\ \text{sec}^{-1}$, for He, Ne, Ar, Kr, and Xe, respectively. With these values of $a$ and $A$, $s_m$ for ions of 1 ev and 10 ev are determined from Eq. (12) and are listed in Table III. Then the decrease in ionization energy, $dE_i'(s_m)$, at the distance $s_m$ can be estimated for each inert gas atom from the curves in Fig. 4 and the values in Table III. We tabulate these in Table IV.

Consequently, the distributions, $N_i(\mathcal{E}_k)$ and $N_0(E_k)$, are shifted bodily to lower energy side by $dE_i'(s_m)$. However the forms of $N_i(\mathcal{E}_i)$ and $N_0(E_k)$ are not affected and the values of total yield, $\gamma$, are scarcely affected.

Table III. The distance, $s_0$, at which the ion "touches" the BaO surface and $s_m$ at which the transition probability of Auger neutralization becomes maximum, for the ions of velocities of 1 ev and 10 ev.

| Atom. | $s_0$ (in A) | $s_m$ (in A) | |
|---|---|---|---|
| | | $v_0=1$ ev | $v_0=10$ ev |
| He | 2.03 | 3.1 | 2.6 |
| Ne | 2.53 | 3.3 | 2.8 |
| Ar | 3.03 | 3.9 | 3.4 |
| Kr | 3.28 | 4.1 | 3.5 |
| Xe | 3.58 | 4.5 | 3.9 |

Table IV. The decrease in ionization energy at the distance $s_m$.

| | | He | Ne | Ar | Kr | Xe |
|---|---|---|---|---|---|---|
| $dE_i'(s_m)$ in ev. | $v_0=1$ ev | 1.2 | 1.1 | 0.9 | 0.9 | 0.8 |
| | $v_0=10$ ev | 1.5 | 1.3 | 1.2 | 1.1 | 1.0 |

### (c) Removal of the *Approximations I and II.*

When the *Approximations* I and II are removed, the distribution, $N_i(\mathcal{E}_k)$, is reduced to Eq. (21), thus

$$N_i(\mathcal{E}_k)=\int_0^\infty P(s, v_0)P_k(\mathcal{E}_k, s)ds\ . \tag{21}$$

Using Eqs. (11), (20), and (25), it follows

$$N_i(\mathcal{E}_k)=c_4\cdot c_1\cdot\pi/4\rho(\mathcal{E}_k)A/av_0\int_0^\infty \times\exp\left[-(A/av_0)\exp(-as)-as\right] \times\mathcal{E}^2\exp(-2\mathcal{E}/kT)ds\ , \tag{36}$$

where

$$\mathcal{E}=\mathcal{E}_k+\mathcal{E}_0-E_i+B_i\exp(-b_is)-B_n \times\exp(-b_ns)-3.6/s\ . \tag{37}$$

In this case, $N_i(\mathcal{E}_k)$ functions become broader than those calculated in subsection (a), because $\mathcal{E}$ in Eq. (36) is a function of $s$ and the ex-

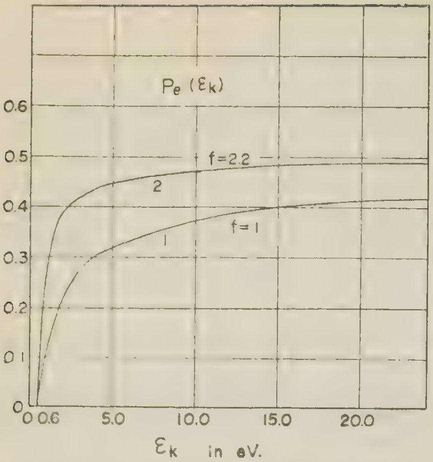

Fig. 3. Two escape probability functions, $P_e(\mathcal{E}_k)$. The curve 1 corresponds to an isotropic distribution of velocity vectors of excited electrons inside BaO crystal. Curve 2 is a plot of Eq. (32) with $f=2.2$.

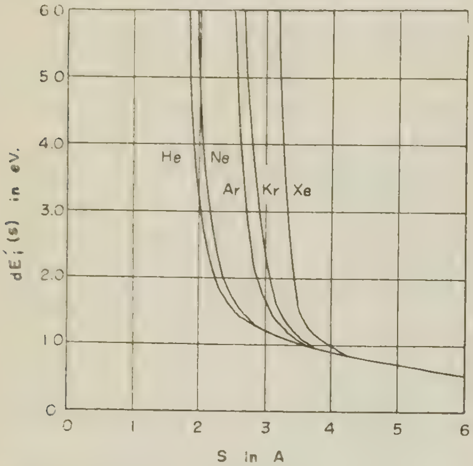

Fig. 4. The plots of $dE_i'(s)$, the change in the ionization energy near the BaO surface, as a function of distance from the surface. This is similar to the Fig. 23 in Hagstrum's paper.

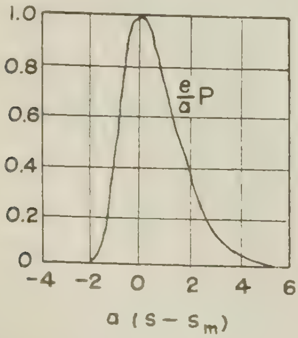

Fig. 5. The plots of $P(s, V_0)$, as a function of $a(s-s_m)$. Here,
$P(s, v_0)=a \exp\{-\exp[-a(s-s_m)]-a(s-s_m)\}$. which is easily derived from Eq. (11). This figure is quoted from Hagstrum's paper.

ponential function in the integrand has finite width on the $s$ scale, as shown in Fig. 5.

Consequently, the values of $\mathcal{E}_k$(min.) and $E_k$ (min.) are shifted toward the lower energy side, $\mathcal{E}_k$(max.) and $E_k$(max.) toward the high energy side, and $\mathcal{E}_k^0$ and $E_k^0$ are lowered. However, these shifts seem to be small, although this calculation has not been carried out here.

The $N_i(\mathcal{E}_k)$ functions will also be broadened by the fact that the initial and the final states of the process have finite life times, the effects of which have been studied by Hagstrum for metal. However we omit the discussion on this point, here.

(d) Above results of our calculations of total electron yield, $\gamma$, for BaO are very characteristic when they are compared with those of molybdenium, tantalum and tungsten observed by Varney[17] and Hagstrum[3)-5)]. These are compared in Table V. The calculated values of $\gamma$ for BaO are very greater than those for above metals and do not change with the kind of gases.

The energies of electrons ejected from BaO are also higher and the distributions are narrower than those from tungsten, molybdenium, and tantalum observed by Hagstrum[3)-5)].

These characteristic results for BaO are thought to be caused by the fact that the width of conduction band or electron affinity of BaO is very small, that is only 0.6 ev.

Table V. Comparison with the values of $\gamma$ for three metals.

| | $He^+$ | $Ne^+$ | $Ar^+$ | $Kr^+$ | $Xe^+$ | observer |
|---|---|---|---|---|---|---|
| Mo | 0.25 | — | — | — | — | Hagstrum |
| Mo | — | 0.20 | 0.083 | 0.053 | — | Varney |
| Ta | 0.14 | — | — | — | — | Hagstrum |
| W | 0.293 | 0.213 | 0.094 | 0.047 | 0.018 | Hagstrum |
| BaO | 0.481 | 0.480 | 0.476 | 0.474 | 0.471 | calculation |

The values observed by Hagstrum are for the ions of 40 ev. The velocities of ions in the experiments of Varney are not obvious but seem to be thermal velocities or at most 5 ev. This will be discussed in next section.

## § 5. Comparison with Varney's Measurements

Up to this time, the direct measurements of total electron yield $\gamma$, and the energy distribution of electrons ejected from BaO by inert gas ion beams in high vacuum have not been made. The only datum has been obtained for the case of $Ar^+$ ion indirectly by Varney[17] with a pulsed Townsend discharge tube.

The observed value of $\gamma$ for activated BaO-coated cathode, by him, is 0.5 for $Ar^+$ ion. This is in good agreement with the result of our calculation, that is, 0.476.

The bases upon which the comparison can be justified are as follows.

(a) The physical state of BaO-coated cathode used by him may be not exactly similar to the one used by us which will be reported in following section. However, both cathodes produced by his method which seems to be conventional activationmethod* and by our method give the same discharge characteristics relating to $\gamma$ in glow discharges in He, Ne, Ar, and Xe gases.

(b) The results of our calculations should be compared with the direct measurements by ion beams. However, the values of $\gamma$ for molybdenium cathod measured by the method similar to the case of BaO-coated cathode which are reported in his paper, are similar to the values expected from the direct measurement**.

(c) The energy of ion which is the object of our study is several ev. In his experiments the energies of $Ar^+$ ions which strike the cathode surface are not obvious, but can be estimated as follows. From the recent experimental study of Warren[18], the velocity of $He^+$ ion in He gas is given by $v_+=8.2\times10^4\sqrt{E/p}$ cm. sec$^{-1}$, where $E$ is the strength of electric field in volt cm$^{-1}$ and $p$ is the gas pressure in mmHg. So the energy of $He^+$ ion is$\sim$1 ev for $E/p=100$ volt cm$^{-1}$ mm Hg$^{-1}$ and is$\sim$5 ev for $E/p=400$, which is the maximum value used in Varney's experiments. The velocity of other inert gas ions may be considered to be lower than $He^+$ ion, for the same value of $E/p$. Therefore, the energies of $Ar^+$ ions which strike the BaO-coated cathode in his experiments are not far from thermal energy or at most several ev.

Next, the calculated result that the electrons ejected from BaO have very higher energies than those for metals is just as he expected. In his experiments the electron yield, $\gamma$, decreases generally at lower $E/p$, but for BaO-coated cathode its behavior differs from those for molybdenium cathode; the formers definitely do not pass through the origin, whereas the latters essencially do so. He thought that the tendency of such decrease at lower $E$ and higher $p$ would be resulted from the significant reflection of electrons by gas atoms in close proximity to the cathode and not from the dependency upon the kinetic energy of ion. Moreover he stated that the difference between such tendencies for BaO-coated cathode and molybdenium is attributed to a different distribution of electrons for the ejected electrons from the BaO surface than for the metal surface, and he expected that the velocities of electrons from BaO will have higher energy than the pure metal.

In the following section, we will discuss the calculated results from a view point of the cathodic phenomena in the normal glow discharges.

## § 6. Cathode Fall, Width of Crookes Dark Space, and Current Density in the Normal Glow Discharges in He, Ne, Ar, and Xe Gases Using BaO-coated Cathode and Tungsten

In this section the observations of the cathode fall, the width of Crookes dark space, and current density in the normal glow discharges in He, Ne, Ar, and Xe gases using BaO-coated cathode and tungsten will be reported and it will be shown how these observed phenomena can be explained by the von Engel and Steenbeck's theory using the calculated values of $\gamma$ for BaO and the observed one by Hagstrum for tungsten.

### (a) *Observations*

The BaO-coated cathode used are made by the following methods: $BaCO_3$ coated on Ni plate is decomposed in vacuum to BaO by suddenly heating up to about 1000°C. In this course of decomposition, basic carbonate, $BaO\cdot BaCO_3$, is formed and this is melted (m.p. $\sim$800°C) and finally crusty BaO crystal, which is semi-transparent crystal, is formed. Such process is not observed in the cases of (Ba Sr) $CO_3$ and (Ba Sr Ca)$CO_3$. This cathode is very easily activated in glow discharge in any inert gas. The usual activation method † using a high frequency discharge in Ar gas is not demanded here. By the reason of this physical state, it is adequate to adapt the Narita's model for the electronic band structure, which has been used in above calculations. However, the both BaO-coated cathodes made by our method and by the usual method give the same discharge characteristics, so it is allowed to compare the results of calculations with Varney's measurements (in the preceding section).

---

* e.g. J. P. Molnar: Phys. Rev. **83** (1951) 942, foot note.

** The detailed discussions on this point are done in Varney's paper.

† e.g. Molnar: Phys. Rev. **83** (1951) 842, foot note.

The form of BaO-coated cathode is of a dish, the diameter of which is 10 mm, and the anode (Ni) has the form similar to the cathode. As tungsten cathode, a ribbon of 2×10 mm is used and in this case, the anode is Ni plate of 7×14 mm. The distance between cathode and anode is 10 mm in both cases. These discharge tubes are heated six hours at 400°C in vacuum. The tungsten cathode is flushed to over 2000°C in order to remove the surface contaminations. Both anodes are outgasssed by heating with an induction furnace. The pressure in the tubes before filling gases is $\sim 2 \times 10^{-6}$ mmHg. During the measurements liquid oxygen is used on the traps in the case of He, Ne, and Ar gases and dry ice in ether ($-80$°C) is used in the case of Xe gas. The He, Ne, and Ar gases are made in our company and are spectroscopically pure, and Xe gas is the products of L'AIR LIQUIDE Co., in France.

( i ) *Normal Cathode Fall.*

The d.c. tube drops (voltages) between anode and cathode in the normal glow discharges are measured after sufficient stabilization of the cathodes. The tube drop seems to be nearly equal within a few volts to the normal cathode fall. For BaO-coated cathode, the tube drop is same, even if the anode approaches to 0.5 mm from the cathode in each inert gas (except Kr gas). For tungsten cathode, this is not confirmed. In the following, we call the cathode fall, $V_{cn}$, in stead of the tube drope. The observed values of $V_{cn}$ are listed in Table VI. In this Table, the normal cathode falls for molybdenium cathode, observed by Jurriance, Penning, and Moubis[19], are shown for comparison.

( ii ) *The Width of Crooks Dark Space in the Normal Glow Discharges.*

We measured roughly the width between the cathode surface and the negative glow, although the edge of negative glow is not very obvious. For BaO-coated cathode, this dark space is too narrow to measure in any inert gas of He, Ne, Ar, and Xe. The widths measured roughly for tungsten cathode are reported in Table VI. The error of those values is within 0.1 mm.

Table VI. The normal cathode fall, $V_{cn}$ in volt, and the Width of Crookes dark space, $d_n$, in mm.

| Cathode | | He | Ne | Ar | Kr | Xe |
|---|---|---|---|---|---|---|
| Tungsten | $V_{cn}$ | 121 | 114.5 | 117 | — | 250? |
| | $p$ | 20.0 | 36.0 | 10.0 | — | 6.6 |
| | $d_n$ | $\sim 0.4$ | $<0.2$ | $\sim 0.2$ | — | $\sim 0.3$ |
| Molybdenium | $V_{cn}$ | 109.5 | 107 | 103.6 | 120 | 134.4 |
| | $p$ | 42 | 40 | 10 | 5.8 | 5.4 |
| | $d_n$ | — | — | — | — | — |
| BaO-coated cathode | $V_{cn}$ | 80.5 | 73.5 | 56 | — | 46.5 |
| | $p$ | 15.1 | 15.0 | 13.9 | — | 6.6 |
| | $d_n$ | $\sim 0$ | $\sim 0$ | $\sim 0$ | — | $\sim 0$ |

$p$ is the gas pressure in mm Hg. The data for molybdenium are of Penning et al.[19] $V_{cn}$ for tungsten cathode in Xe gas is not accurate and it seems to be lower than 250 volts.

(iii) *The Current Density in the Normal Glow Discharges.*

The current density is estimated roughly by dividing the anode current by the apparent areas of the cathode surface covered with glow. The ratios of the current densities for BaO-coated cathode and tungsten are nearly equal to 1, 1.5, $2\sim3$, and $>5$ in He, Ar, and Xe gases, respectively. These observed ratios are shown in Table IX.

( b ) ***Discussions.***

Here, we will discuss the above observed results, basing upon the theory of von Engel and Steenbeck on the normal glow discharges. This theory seems to be not necessarily accurate, because various assumptions are contained. However, the assumption that the electric field in the Crookes dark space is linear seems to be confirmed by the recent studies of Warren[18]. Also, in his experiments, it is shown that the ions produced in negative glow do not contribute to those ions which strike the cathode surface, in the normal glow discharges, which is also the assumption used in their theory.

According to the theory of von Engel and Seenbeck, the normal cathode fall, $V_{cn}$, the width of Crookes dark space, $d_n$, and the current density, $j_n$, are given by following equations;

$$V_{cn}=3.0\cdot B/A\cdot\ln(1+1/\gamma)\,,\quad \text{volts}, \qquad (38)$$

$$d_n=8.2\cdot\ln(1+1/\gamma)/Ap,\ \text{mm}. \qquad (39)$$

$$j_n=5.92\times10^{-14}AB^2(k_+p)p^2 \times(1+\gamma)/\ln(1+1/\gamma),\ A/cm^2\,. \qquad (40)$$

where $p$ is the gas pressure in mmHg and $k_+$ is the mobility of an ion. $A$ and $B$ are constant and are defined as

$$\alpha/p=A\exp(-Bp/E)\,. \qquad (41)$$

This equation represents the relation between the ionization coefficient, $\alpha$, and the field strength by gas pressure, $E/p$ (volt cm$^{-1}$mm Hg$^{-1}$). Correctly speaking, $A$ and $B$ are the function of $E/p$, but it is permitted to consider these as constant within a limited range of $E/p$. The values of $A$ and $B$ estimated from Townsend and Mc Callum's experiment for He gas and Kruithoff's one for Ne, Ar, and Xe gases are listed in Table VII.

Table VII. The values of A, B and C in Eqs. (38), (39), (40) and (38′).

| | A (cm·mmHg$^{-1}$) | B (volt·cm$^{-1}$·mmHg$^{-1}$) | C | $E/p$ (volt·cm$^{-1}$·mmHg$^{-1}$) |
|---|---|---|---|---|
| He | 1.74 | 45 | 173 | 25∼ 97 |
| Ne | 4.8 | 116 | 168 | 100∼400 |
| Ar | 13.9 | 195 | 97.5 | 100∼600 |
| Xe | 18.6 | 234 | 86.6 | 100∼400 |

The values of A and B are appropriate to this range of $E/p$. The data from which A and B are determined are of Townsend and McCallum[21)], and of Kruithoff[22)].

(i) *Normal Cathode Fall.*

If $3.0\cdot A/B\cdot\log_{10}e$ is replaced by $C$, Eq. (38) reduces to

$$V_{cn}=C\log(1+1/\gamma)\,. \qquad (38)'$$

The values of $C$ are shown in Table VII. Using the calculated values of $\gamma$ for BaO, the observed one by Hagstrum for tungsten and $C$ listed in Table VII, normal cathode fall $V_{cn}$ (cal.) is obtained from Eq. (38)′. Inversely, the values of $\gamma$ (named $\gamma''$) are calculated by Eq. (38) using the observed values, $V_{cn}$ (ob.) and the values of $C$ in Table VII. Moreover, if the values of $C$ are determined by the observed values, $V_{cn}$(ob.) and $\gamma$, for tungsten, according to Eq. (38), $\gamma$ (named $\gamma'$) and $V_{cn}$ (named $V_{cn}'$(cal.)) are also calculated for BaO from the observed $V_{cn}$(ob.) and the calculated $\gamma$, respectively. These values are all reported in Table VIII [A] and [B]. These calculated values based on Eq. (38) are in rough agreement with the observed normal cathode fall, $V_{cn}$(ob.) for both cathodes and with the calculated values of $\gamma$ for BaO, except $V_{cn}$ and $\gamma$ for tungsten in Xe gas. This exception seems to be resulted from the error in the observation of $V_{cn}$. The question about the correctness of this observation with tungsten cathode in Xe gas comes out from the fact of difference with the one for molybdenium cathode (Table VI), even though $V_{cn}$s for both cathodes in other gases are alike and this resemblance can be understood from the similar electronic structure of both metals.

Table VIII. [A] and [B].

[A] Tungsten Cathode.

| | He | Ne | Ar | Xe |
|---|---|---|---|---|
| $V_{cn}$(ob.) in volt | 121 | 114.5 | 117 | 250 |
| $p$ in mmHg | 20 | 36 | 10 | 6.6 |
| γ(ob.) | 0.293 | 0.213 | 0.094 | 0.018 |
| $V_{cn}$(cal.) in volt | 110.8 | 128 | 102 | 152 |
| $d_n$(ob.) in mm | ∼0.4 | <0.2 | ∼0.2 | ∼0.3 |
| $d_n$(cal.) in mm | 0.35 | 0.09 | 0.14 | 0.27 |
| γ″(cal.) | 0.25 | 0.27 | 0.067 | 0.0016 |
| $V_{cn}$(cal.)/$d_n$(cal.)$p$ | 165 | 420 | 710 | 850 |
| $V_{cn}$(ob.)/$d_n$(cal.)$p$ | 173 | 375 | 835 | |

[B] BaO-coated Cathode.

| | He | Ne | Ar | Xe |
|---|---|---|---|---|
| $V_{cn}$(ob.) in volt | 80.5 | 73.5 | 56 | 46.5 |
| $p$ in mmHg | 15.1 | 15.0 | 13.9 | 6.6 |
| γ(cal.) | 0.481 | 0.480 | 0.476 | 0.471 |
| $V_{cn}$(cal.) in volt | 86.6 | 84.5 | 48.8 | 43.3 |
| $d_n$(ob.) in mm | ∼0 | ∼0 | ∼0 | ∼0 |
| $d_n$(cal.) in mm | 0.33 | 0.13 | 0.04 | 0.07 |
| $V_{cn}'$(cal.) in volt | 92.5 | 74.5 | 55.8 | |
| γ′(cal.) | 0.6 | 0.48 | 0.46 | 0.42 |
| γ″(cal.) | 0.52 | 0.57 | 0.37 | 0.42 |
| $V_{cn}$(cal.)/$d_n$(cal.)$p$ | 165 | 420 | 710 | 850 |
| $V_{cn}$(ob.)/$d_n$(cal.)$p$ | 161 | 350 | 900 | 890 |

(ii) *Width of Crookes Dark Space.*

According to Eq. (39), this width can be calculated with the constant, $A$, and the pressure, $p$ and $\gamma$. These calculated widths and the observed one are compared in Table VIII [A] and [B]. It is obvious from Eq. (39)

that the BaO-coated cathode having higher values of $\gamma$ gives the width narrower than the tungsten cathode having lower values of $\gamma$. However, these widths observed for BaO-coated cathode seem to be far narrower than the values expected from the calculations. This discrepancy can not be easily explained, but it seems to be resulted from the fact that the theory of von Engel and Steenbeck does not take into account the initial velocities of electrons ejected from BaO surface, nevertheless the ejected electrons from BaO-coated cathode have too high energies in any inert gas to neglect, which is the results of our calculations in previous sections. In the case of tungsten cathode, both widths of the calculated and the observed are similar qualitatively. The great differences between both widths for BaO-coated cathode and for tungsten are explained at least from the difference in the values of $\gamma$.

From Eqs. (38) and (39), $V_{cn}/d_n p$, which represents the mean electric field (by pressure) in Crookes dark space, is given by $V_{cn}/d_n p = 3.0/8.2\cdot 10^{-1}\cdot B$ (volt cm$^{-1}$ mmHg$^{-1}$), a constant for a given gas. These values and those obtained with the observed values of $V_{cn}$(ob.) are compared in Table VIII [A] and [B].

(iii) *Current Density*.

Now we shall name the current density, $j_n$, for BaO-coated cathode as $j_{n_1}$, and the one for tungsten as $j_{n_2}$. According to Eq. (40), the ratio of $j_{n_1}$ and $j_{n_2}$ is given by

$$j_{n_1}/j_{n_2}=(1+\gamma_1)\ln(1+1/\gamma_2)/(1+\gamma_2)\ln(1+1/\gamma_1), \tag{42}$$

where $\gamma_1$ is the value of $\gamma$ for BaO and $\gamma_2$ the one for tungsten. As is shown in this equation this ratio, $j_{n_1}/j_{n_2}$, is determined by only the values of $\gamma$ in each inert gas. The calculated values of the ratio, $j_{n_1}/j_{n_2}$, using Eq. (42) are listed in Table IX. Both ratios of the observed one and the calculated accord with each other qualitatively in any inert gas.

(iv) From these investigations, it is permissible to say that the observed cathodic phenomena can be explained at least qualitatively by the theory of von Engel and steenbeck using the calculated values of $\gamma$ for BaO and the observed one by Hagstrum for tungsten. In other words, our calculations in preceding sections seem to be justified at least qualitatively, even though the discussions in this section are rather crude. And if this fact is not accidental, the essential mechanism of electron from cathode by an ion in the normal glow discharges, should be that of potential ejection discussed in preceding sections.

Table IX. The ratios of $j_{n_1}$ (for BaO-coated cathode) and $j_{n_2}$ (for tungsten).

| gas | $j_{n_1}/j_{n_2}$ observation | $j_{n_1}/j_{n_2}$ calculation |
|---|---|---|
| He | ~1 | 1.47 |
| Ne | ~1.5 | 1.85 |
| Ar | 2~3 | 2.86 |
| Xe | >5 | 4.45 |

## § 7. Conclusions

The results of our calculations based on the theory of Auger neutralization are in good agreement with the observed value of $\gamma$ by Varney and meet his expectations about the energies of ejected electrons in the case of $Ar^+$ ion. However, it is not exactly confirmed by only this fact that the possible type of electronic transition is only Auger neutralization. The proof must be done in comparison with the direct measurements which will give the informations not only about the mechanism and the estimation of the assumptions and the approximations used in the calculations, but also about the electronic structure of BaO. We will achieve this direct measurement in future.

On the other hand, the observed cathodic phenomena seem to be explained by von Engel and Steenbeck's theory using the calculated values of $\gamma$, even though the discussions are rather crude. However, in order to confirm definitely the essential of cathodic phenomena concerned with $\gamma$ in normal glow discharges, we expect the experiments on the other discharge phenomena relating to $\gamma$ and at the same time the construction of the precise theory on the glow discharges in which energy of ejected electrons from cathode is taken into account.

In conclusion, the author is very grateful to Mr. Kiyoshi Nomura and Mr. Reiji Satō for their interests and kind supports in this work, and his thanks are also due to the members of Matsuda Research Laboratory for their discussions. He is greately indebted to

Mr. Kin-ichi Nōga who has kindly advised and closely read and criticized this work in manuscript. The author wishes to express his sincere appreciation to Prof. Masasi Yasumi and Mr. Hitoshi Komo-oka of University of Tokyo, and Mr. Takashi Tamikado of Tokyo Institute of Technology, for their kind and continuous encouragements.

### References

1) R. C. Bradley: Phys. Rev. **93** (1954) 719.
2) J. H. Parker: Phys. Rev. **93** (1954) 1148.
3) H. D. Hagstrum: Phys. Rev. **89** (1953) 244.
4) H. D. Hagstrum: Phys. Rev. **91** (1953) 543.
5) H. D. Hagstrum: Phys. Rev. **96** (1954) 325.
6) H. D. Hagstrum: Phys. Rev. **96** (1954) 336.
7) H. S. W. Massey: Proc. Cambridge Phil. Soc. **26** (1930) 386; **27** (1931) 469.
8) M. L. E. Oliphant and P. B. Moon: Proc. Roy. Soc. (London) **A 127** (1930) 388.
9) S. S. Shekhter: J. Expl. Theoret. Phys. (U.S.S.R.) **7** (1937) 750.
10) A. Cobas and W. E. Lamb: Phys. Rev. **65** (1944) 327.
11) S. Narita: J. Phys. Soc. Japan **8** (1953) 331.
12) e.g. R. L. Sproul and W. W. Tyler: Semi-Conducting Materials, Butterworths Scientific Publication, London, 1951, p. 122.
13) H. Bethe: Handbuch der Physik, XXIV, Kap. 3, p. 365.
14) H. D. Hagstrum: Ref. 6), Chap. III and J. J. Lander: Phys. Rev. **91** (1953) 1382.
15) e.g. F. Seitz: The Modern Theory of Solids, McGraw-Hill, New York, 1940, Chap. II.
16) e.g. F. Seitz: loc. cit. Chap. VII.
17) R. N. Varney: Phys. Rev. **93** (1954) 1156.
18) R. Warren: Phys. Rev. **98** (1955) 1650; **93** (1955) 1658.
19) T. Jurriance, F. M. Penning and J. H. A. Moubis: Phil. Res. Rep. 537·525·83.
20) A. von Engel and Steenbeck: Elektrische Gasentladungen, Bd. 2, 1934.
21) J. S. Townsend and S. P. McCallum: Phil. Mag. **17** (1934) 678.
22) A. A. Kruithoff: Physica **7** (1940) 519.

JOURNAL OF THE PHYSICAL SOCIETY OF JAPAN Vol. 11, No. 6, JUNE, 1956

# The Forces acting on Two Circular Cylinders of arbitrary Radii placed in a Uniform Stream at Low Values of Reynolds Number

By Hiroomi FUJIKAWA

*Junior College of Engineering, University of Osaka Prefecture,*
*Neyagawa nr. Osaka*

(Received January 26, 1956)

The steady slow motion of a viscous fluid past two parallel circular cylinders $C_1$, $C_2$ of arbitrary radii is discussed on the basis of Oseen's linearized equations of motion, confining ourselves to the case when their axes are perpendicular to a uniform flow. The forces acting on the cylinder $C_1$ are calculated to the first approximation.

By performing detailed numerical calculations, a discussion is made on the manner in which the forces acting on the cylinder $C_1$ is modified by the presence of the other cylinder $C_2$.

It is thus found that, as the radius of the cylinder $C_2$ increases, the drag on the cylinder $C_1$ decreases, while the lift increases. It is also found that the cylinder $C_1$ experiences smaller drag when the two cylinders are in tandem orientation than when they are placed side by side in a uniform stream. Especially, when the cylinder $C_1$ is situated behind the cylinder $C_2$, it experiences smaller drag than when it is situated in front of $C_2$.

## § 1. Introduction and Summary

In a previous paper[1], the writer investigated the forces acting on two equal circular cylinders placed side by side in a uniform stream of small Reynolds numbers and obtained the results that the drag acting on one of the cylinders is smaller than that acting on a single circular cylinder of equal radius placed in an unbounded stream and also that the two cylinders repulse each other.

Now, it is interesting to generalize the orientation of two circular cylinders as well as their dimension and to investigate the forces acting on one cylinder with the intention of discussing the interference effect due to the presence of the other cylinder. In the present paper, therefore, the writer treats the steady slow motion of a viscous fluid past a circular cylinder $C_1$ accompanied by the other cylinder $C_2$ of arbitrary radius and investigates the manner in which the forces acting on the cylinder $C_1$ are modified by the dimension and orientation of the cylinder $C_2$.

Expansion formulae for the forces acting on the cylinder $C_1$ in powers of the Reynolds number $R$ are obtained to the first approximation, which correspond to Lamb's approximation for the case of a single circular cylinder in an unbounded stream. Making use of these formulae, detailed numerical calculations are carried out in four cases in which the ratio of the distance between the axes of the two cylinders to the radius of the cylinder $C_1$ takes the values 20, 100, 400 and 1000. The values of the ratio of radii of the two cylinders have been taken to be 0.5, 1.0 and 2.0 and the azimuthal angle giving the orientation of the cylinder $C_2$ relative to $C_1$ has been taken to be 0°, 45°, 90°, 135° and 180°.

After numerical calculations, it is shown that the individual cylinder experiences a smaller drag when the two cylinders are in tandem orientation than when they are placed side by side. It is also found that, on increasing the radius of the cylinder $C_2$, the drag acting on the cylinder $C_1$ decreases; on the other hand, the lift (i.e. the force acting in a direction perpendicular to the uniform stream) increases as the radius of the cylinder $C_2$ increases.

Further, it is found that the lift is not always a repulsive force but is of an attractive nature in some cases of orientation. As for the distance-effect on the forces acting on the cylinder $C_1$, the results are quite similar in all cases and are quite the same as the results in the previous paper[1]. Namely, as the cylinder C$_2$ recedes away from the cylinder C$_1$, the drag on the latter tends to increase to values for a single circular cylinder in an unbounded stream; while the lift on the cylinder C$_1$ decreases monotonously and tends to zero, but for fairly small values of Reynolds number, the lift increases first and then decreases.

## § 2. Conjugate Complex Velocity for the Perturbation Flow

We consider two infinitely long circular cylinders C$_1$. C$_2$, of radii $a$ and $b$ respectively, placed in a steady uniform stream of velocity $U$ of an incompressible viscous fluid in such a manner that their axes are parallel and perpendicular to the uniform stream.

Let $O_1x_1$, $O_1y_1$ and $O_2x_2$, $O_2y_2$ be the rectangular co-ordinate axes in the plane of fluid motion, the axes of $x_1$ and $x_2$ being taken along the direction of the uniform stream at infinity and the origins $O_1$ and $O_2$ coinciding with the centres of the cylinders C$_1$ and C$_2$ respectively. If we denote the distance $O_1O_2$ between the axes of the two cylinders by $h$ and the angle between the $x_1$-axis and the central line $O_1O_2$ by $\omega$, we have

$$\left.\begin{aligned} & z_1=z_2+h\,e^{i\omega},\\ \text{with}\qquad & z_1=x_1+iy_1=r_1\,e^{i\theta_1},\\ \text{and}\qquad & z_2=x_2+iy_2=r_2\,e^{i\theta_2}.\end{aligned}\right\}\tag{2.1}$$

As it is already obtained in the previous paper[1], the conjugate complex velocity $W$ for the perturbation flow due to the presence of the two cylinders in the uniform stream is, to the first approximation, written in the following form:

$$W=W_h^{(1)}+W_u^{(1)}+W_h^{(2)}+W_u^{(2)},\tag{2.2}$$

with

$$\left.\begin{aligned} W_h^{(1)}&=A_0r_1^{-1}\exp(-i\theta_1)+\cdots,\\ W_u^{(1)}&=\exp(kr_1\cos\theta_1)\{B_0K_0(kr_1)\\ &\qquad+\bar{B}_0K_1(kr_1)\exp(-i\theta_1)+\cdots\},\\ W_h^{(2)}&=A_0^*r_2^{-1}\exp(-i\theta_2)+\cdots,\\ W_u^{(2)}&=\exp(kr_2\cos\theta_2)\{B_0^*K_0(kr_2)\\ &\qquad+\bar{B}_0^*K_1(kr_2)\exp(-i\theta_2)+\cdots\},\end{aligned}\right\}\tag{2.3}$$

where $A_0$, $B_0$, $A_0^*$, $B_0^*$ etc. are arbitrary complex constants as

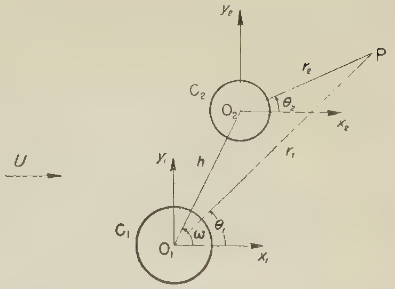

Fig. 1.

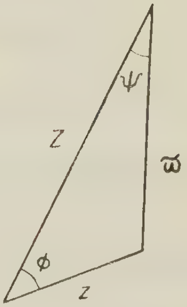

Fig. 2.

$$\left.\begin{aligned} &A_0=a_0+i\alpha_0, &&B_0=b_0+i\beta_0, &&\cdots\cdots,\\ &A_0^*=a_0^*+i\alpha_0^*, &&B_0^*=b_0^*+i\beta_0^*, &&\cdots\cdots,\end{aligned}\right\}\tag{2.4}$$

$K_n(kr)$ is the modified Bessel function of the second kind[†], and $k$ is connected with the kinematic viscosity $\nu$ as

$$k=U/2\nu\,.\tag{2.5}$$

## § 3. Fulfilment of the Boundary Conditions

We now proceed to the consideration of the boundary conditions at the surfaces of the two cylinders. As the resultant complex velocity $U+W$ must be zero on the surfaces of the cylinders, the required boundary conditions may be written as

$$(W)_{r_1=a}=-U\,,\tag{3.1}$$

and

$$(W)_{r_2=b}=-U\,.\tag{3.2}$$

In order to apply these conditions to $W$ given by (2.2), we expand $W$ in a Fourier series in $\theta_1$ and $\theta_2$ on the surfaces of the cylinders C$_1$ ($r_1=a$) and C$_2$ ($r_2=b$) respectively.

---

[†] The definition of the modified Bessel function used here is identical with those in G. N. Watson's *"A Treatise on the Theory of Bessel Functions"* (Cambridge, 1922).

We shall begin with a Fourier expansion of $W$ on the surface of the cylinder $C_1$. Fortunately, the first term $W_h^{(1)}$ has already the required form:

$$[W_h^{(1)}]_{r_1=a}=\frac{A_0}{a}\exp(-i\theta_1)+\cdots. \tag{3.3}$$

Assuming $h\gg a$, and using the relations (2.1), $W_h^{(2)}$ can be immediately expanded as

$$[W_h^{(2)}]_{r_1=a}=-A_0{}^*h^{-1}\exp(-i\omega)\left\{1+\frac{a}{h}\exp(i(\theta_1-\omega))+\cdots\right\}. \tag{3.4}$$

Further, making use of the formula

$$\exp(kr\cos\theta)=\sum_{n=-\infty}^{\infty}I_n(kr)\exp(-in\theta), \tag{3.5}$$

$W_u^{(1)}$ can be easily expanded in the following form:

$$[W_u^{(1)}]_{r_1=a}=\sum_{n=-\infty}^{\infty}I_n(ka)\{B_0K_0(ka)+\overline{B}_0K_1(ka)\exp(-i\theta_1)+\cdots\}\exp(-in\theta_1). \tag{3.6}$$

Finally, we proceed to obtain the expansion of $W_u^{(2)}$ on the surface of the cylinder $C_1$ ($r_1=a$). For this purpose, it is convenient to use the following addition theorem†:

$$\left.\begin{aligned}&K_\nu(\tilde{\omega})\exp(\pm i\nu\psi)=\sum_{m=-\infty}^{\infty}K_{\nu+m}(Z)I_m(z)\exp(\pm im\phi),\\ \text{where}\quad&\tilde{\omega}^2=Z^2+z^2-2Zz\cos\phi.\end{aligned}\right\} \tag{3.7}$$

Thus, taking $\tilde{\omega}=kr_2$, $z=kr_1=ka$, $Z=kh$, $\phi=\omega-\theta_1$ and $\psi=\pi-\omega+\theta_2$, we get

$$\left.\begin{aligned}&K_\nu(kr_2)\exp(i\nu\theta_2)=\exp\{i\nu(\omega-\pi)\}\sum_{m=-\infty}^{\infty}K_{\nu+m}(kh)I_m(ka)\exp\{im(\omega-\theta_1)\},\\ &\qquad\qquad(\nu=0,\ \pm1,\ \pm2,\ \cdots).\end{aligned}\right\} \tag{3.8}$$

Therefore, combining these with (2.1) and (3.5), we obtain the expansion in the following form;

$$\left.\begin{aligned}&[W_u^{(2)}]_{r_1=a}=\sum_{n=-\infty}^{\infty}(B_0{}^*\lambda_{n,0}+\overline{B}_0{}^*\lambda_{n,-1}+\cdots\cdots)\exp(-in\theta_1),\\ \text{where}\quad&\\ &\lambda_{n,\nu}=(-1)^\nu\exp(-kh\cos\omega)\sum_{m=-\infty}^{\infty}I_m(ka)I_{n-m}(ka)K_{\nu+m}(kh)\exp\{i(\nu+m)\omega\}\\ &\qquad\qquad(\nu=0,\ \pm1,\ \pm2,\ \cdots).\end{aligned}\right\} \tag{3.9}$$

Thus, substituting (3.3), (3.4), (3.6) and (3.9) into (2.2), we arrive at the Fourier expansion of $W$ on the circular cylinder $C_1$.

In a similar manner, we can obtain the expansion of $W$ in a Fourier series in $\theta_2$ on the cylinder $C_2$ ($r_2=b$). That is,

$$\left.\begin{aligned}&[W_h^{(1)}]_{r_2=b}=A_0h^{-1}\exp(-i\omega)+\cdots\cdots,\\ &[W_u^{(1)}]_{r_2=b}=\sum_{n=-\infty}^{\infty}(B_0\lambda^*_{n,0}+\overline{B}_0\lambda^*_{n,-1}+\cdots\cdots)\exp(-in\theta_2),\\ &[W_h^{(2)}]_{r_2=b}=A_0{}^*b^{-1}\exp(-i\theta_2)+\cdots\cdots,\\ &[W_u^{(2)}]_{r_2=b}=B_0{}^*K_0(kb)\sum_{n=-\infty}^{\infty}I_n(kb)\exp(-in\theta_2)\\ &\qquad+\overline{B}_0{}^*K_1(kb)\sum_{n=-\infty}^{\infty}I_{n-1}(kb)\exp(-in\theta_2)+\cdots\cdots,\\ \text{where}\quad&\\ &\lambda^*_{n,\nu}=\exp(kh\cos\omega)\sum_{m=-\infty}^{\infty}(-1)^mI_m(kb)I_{n-m}(kb)K_{\nu+m}(kh)\exp\{i(\nu+m)\omega\}\\ &\qquad\qquad(\nu=0,\ \pm1,\ \pm2,\ \cdots).\end{aligned}\right\} \tag{3.10}$$

---

† See, for example, G. N. Watson, *A Treatise on the Theory of Bessel Functions* (Cambridge, 1922), § 11.3, p. 361.

According to the boundary conditions (3.1) and (3.2), every coefficients of $\exp(in\theta_1)$ and $\exp(in\theta_2)$ in the expansions should vanish except for the constant terms ($n=0$), which must be equal to $-U$.

Thus, we have, from (3.1),

$$-A_0{}^*h^{-1}\exp(-i\omega)+B_0I_0(ka)K_0(ka)+\overline{B}_0I_1(ka)K_1(ka)+B_0{}^*\lambda_{0,0}+\overline{B}_0{}^*\lambda_{0,-1}+\cdots=-U\,, \tag{3.11}$$

and

$$A_0a^{-1}+B_0I_1(ka)K_0(ka)+\overline{B}_0I_0(ka)K_1(ka)+B_0{}^*\lambda_{1,0}+\overline{B}_0{}^*\lambda_{1,-1}+\cdots\cdots\cdots\cdots=0\,. \tag{3.12}$$

Also, from (3.2), we get

$$A_0h^{-1}\exp(-i\omega)+B_0\lambda^*_{0,0}+\overline{B}_0\lambda^*_{0,-1}+B_0{}^*I_0(kb)K_0(kb)+\overline{B}_0{}^*I_1(kb)K_1(kb)+\cdots\cdots=-U\,, \tag{3.13}$$

and

$$A_0{}^*b^{-1}+B_0\lambda^*_{1,0}+\overline{B}_0\lambda^*_{1,-1}+B_0{}^*I_1(kb)K_0(kb)+\overline{B}_0{}^*I_0b(k)K_1(kb)+\cdots\cdots\cdots\cdots=0\,. \tag{3.14}$$

## §4. Approximate Solution for the Case $ka\ll1$, $kb\ll1$ and $(kh)^{-1}=O(1)$

The system of simultaneous equations (3.11)–(3.14) for determining the constants $A_0$, $A_0{}^*$, $B_0$, $B_0{}^*$ etc. having been derived, we can obtain the required solution satisfying all the boundary conditions.

Eliminating $A_0$ and $A_0{}^*$ from these equations and separating real and imaginary parts, we have the system of equations for determining $B_0(=b_0+i\beta_0)$, $B_0{}^*(=b_0{}^*+i\beta_0{}^*)$ etc.:

$$\left.\begin{aligned}
&C_{11}b_0+C_{12}\beta_0+C_{13}b_0{}^*+C_{14}\beta_0{}^*+\cdots\cdots=-U\,,\\
&C_{21}b_0+C_{22}\beta_0+C_{23}b_0{}^*+C_{24}\beta_0{}^*+\cdots\cdots=0\,,\\
&C_{31}b_0+C_{32}\beta_0+C_{33}b_0{}^*+C_{34}\beta_0{}^*+\cdots\cdots=-U\,,\\
&C_{41}b_0+C_{42}\beta_0+C_{43}b_0{}^*+C_{44}\beta_0{}^*+\cdots\cdots=0\,,\\
&\cdots\cdots\cdots\cdots\cdots\cdots\cdots\cdots\cdots\cdots\,.
\end{aligned}\right\} \tag{4.1}$$

The coefficients $C_{ij}$ are given as follows:

$$\left.\begin{aligned}
&C_{11}=I_0(ka)K_0(ka)+I_1(ka)K_1(ka)+(b/h)\{(p^*_{1,0}+p^*_{1,-1})\cos\omega+(q^*_{1,0}+q^*_{1,-1})\sin\omega\}\,,\\
&C_{12}=(h/b)\{(p^*_{1,0}-p^*_{1,-1})\sin\omega-(q^*_{1,0}-q^*_{1,-1})\cos\omega\}\,,\\
&C_{13}=(kh)^{-1}\cos\omega+p_{0,0}+p_{0,-1}\,,\\
&C_{14}=(b/h)\{I_1(kb)K_0(kb)-I_0(kb)K_1(kb)\}\sin\omega+q_{0,-1}-q_{0,0}\,,\\
&C_{21}=-(b/h)\{(p^*_{1,0}+p^*_{1,-1})\sin\omega-(q^*_{1,0}+q^*_{1,-1})\cos\omega\}\,,\\
&C_{22}=I_0(ka)K_0(ka)-I_1(ka)K_1(ka)+(b/h)\{(p^*_{1,0}-p^*_{1,-1})\cos\omega+(q^*_{1,0}-q^*_{1,-1})\sin\omega\}\,,\\
&C_{23}=-(kh)^{-1}\sin\omega+q_{0,0}+q_{0,-1}\\
&C_{24}=(b/h)\{I_1(kb)K_0(kb)-I_0(kb)K_1(kb)\}\cos\omega+p_{0,0}-p_{0,-1}\,,\\
&C_{31}=-(kh)^{-1}\cos\omega+p^*_{0,0}+p^*_{0,-1}\,,\\
&C_{32}=(a/h)\{I_0(ka)K_1(ka)-I_1(ka)K_0(ka)\}\sin\omega-q^*_{0,0}+q^*_{0,-1}\,,\\
&C_{33}=I_0(kb)K_0(kb)+I_1(kb)K_1(kb)-(a/h)\{(p_{1,0}+p_{1-1})\cos\omega+(q_{1,0}+q_{1,-1})\sin\omega\}\,,\\
&C_{34}=-(a/h)\{(p_{1,0}-p_{1,-1})\sin\omega-(q_{1,0}-q_{1,-1})\cos\omega\}\,,\\
&C_{41}=(kh)^{-1}\sin\omega+q^*_{0,0}+q^*_{0,-1}\,,\\
&C_{42}=(a/h)\{I_0(ka)K_1(ka)-I_1(ka)K_0(ka)\}\cos\omega+p^*_{0,0}-p^*_{0,-1}\,,\\
&C_{43}=(a/h)\{(p_{1,0}+p_{1,-1})\sin\omega-(q_{1,0}+q_{1,-1})\cos\omega\}\,,\\
&C_{44}=I_0(kb)K_0(kb)-I_1(bk)K_1(kb)-(a/h)\{(p_{1,0}-p_{1,-1})\cos\omega+(q_{1,0}-q_{1,-1})\sin\omega\}\,,
\end{aligned}\right\} \tag{4.2}$$

where we have put

$$\lambda_{n,\nu}=p_{n,\nu}+iq_{n,\nu}\,,\qquad \lambda^*_{n,\nu}=p^*_{n,\nu}+iq^*_{n,\nu}\,, \tag{4.3}$$

$p_{n,\nu}$, $q_{n,\nu}$, $p^*_{n,\nu}$ and $q^*_{n,\nu}$ being all real.

However, it is very difficult to solve the equations (4.1) exactly. In the first place, let us consider the case where $ka \ll 1$, $kb \ll 1$ and $(kh)^{-1} = O(1)$. In this case the coefficients $C_{ij}$ given by (4.2) can be expanded as follows:

$$\left.\begin{aligned}
&C_{11}=S_a+O(k^2b^2)\,, \quad C_{12}=O(k^2b^2)\,, && C_{13}=\tau^{-1}(K_0+Q\cos\omega)+O(k^2a^2)\,,\\
&C_{14}=-\tau^{-1}Q\sin\omega+O(k^2a^2)\,, && C_{21}=O(k^2b^2)\,,\\
&C_{22}=-(1-S_a)+O(k^2b^2)\,, && C_{23}=-\tau^{-1}Q\sin\omega+O(k^2a^2)\,,\\
&C_{24}=\tau^{-1}(K_0-Q\cos\omega)+O(k^2a^2)\,, && C_{31}=\tau(K_0-P\cos\omega)+O(k^2b^2)\,,\\
&C_{32}=\tau P\sin\omega+O(k^2b^2)\,, && C_{33}=S_b+O(k^2a^2)\,,\\
&C_{34}=O(k^2a^2)\,, && C_{41}=\tau P\sin\omega+O(k^2b^2)\,,\\
&C_{42}=\tau(K_0+P\cos\omega)+O(k^2b^2)\,, && C_{43}=O(k^2a^2)\,,\\
&C_{44}=-(1-S_b)+O(k^2a^2)\,,
\end{aligned}\right\} \tag{4.4}$$

where

$$\left.\begin{aligned}
&S_a=\frac{1}{2}-\gamma-\log\frac{ka}{2}\,, \qquad S_b=\frac{1}{2}-\gamma-\log\frac{kb}{2}\,,\\
&P=(kh)^{-1}\tau^{-1}-K_1\,, \qquad Q=(kh)^{-1}\tau-K_1 \quad\text{and}\quad \tau=\exp(kh\cos\omega)\,,
\end{aligned}\right\} \tag{4.5}$$

$\gamma$ being the Eulerian constant, and the argument $kh$ of the modified Bessel function $K_n$'s has been omitted for brevity.

Inserting (4.4) in (4.1), we obtain the solutions for $b_0$, $\beta_0$, $b_0{}^*$, $\beta_0{}^*$ etc. After some straightforward calculations, we get

$$\left.\begin{aligned}
&\frac{b_0}{U}=\frac{\Delta_1}{\Delta}+O(k^2a^2)\,, \qquad \frac{\beta_0}{U}=\frac{\Delta_2}{\Delta}+O(k^2a^2)\,,\\
&\frac{b_0{}^*}{U}=\frac{\Delta_3}{\Delta}+O(k^2a^2)\,, \qquad \frac{\beta_0{}^*}{U}=\frac{\Delta_4}{\Delta}+O(k^2a^2)\,,\\
&\cdots\cdots\cdots\cdots\cdots\cdots\cdots\cdots\cdots\cdots\cdots\cdots\,,
\end{aligned}\right\} \tag{4.6}$$

where

$$\left.\begin{aligned}
\Delta={}&S_aS_b\{(1-S_a)(1-S_b)+PQ\sin^2\omega-(K_0+P\cos\omega)(K_0-Q\cos\omega)\}\\
&+(1-S_a)(1-S_b)\{PQ\sin^2\omega-(K_0-P\cos\omega)(K_0+Q\cos\omega)\}\\
&+(K_0{}^2-P^2)(K_0{}^2-Q^2)-PQ\sin^2\omega\,,\\
\Delta_1={}&-S_b\{(1-S_a)(1-S_b)+PQ\sin^2\omega-(K_0+P\cos\omega)(K_0-Q\cos\omega)\}\\
&+\tau^{-1}\{(1-S_a)(1-S_b)(K_0+Q\cos\omega)\\
&-(K_0{}^2-Q^2)(K_0+P\cos\omega)\}+PQ\sin^2\omega\,,\\
\Delta_2={}&\sin\omega[Q(1-S_b)\{\tau^{-1}S_a-(K_0-P\cos\omega)\}\\
&+P\{\tau^{-1}(K_0{}^2-Q^2)-S_b(K_0-Q\cos\omega)\}]\,,\\
\Delta_3={}&-S_a\{(1-S_a)(1-S_b)+PQ\sin^2\omega-(K_0+P\cos\omega)(K_0-Q\cos\omega)\}\\
&+\tau\{(1-S_a)(1-S_b)(K_0-P\cos\omega)-(K_0{}^2-P^2)(K_0-Q\cos\omega)\}\\
&+PQ\sin^2\omega\,,\\
\Delta_4={}&-\sin\omega[P(1-S_a)\{\tau S_b-(K_0+Q\cos\omega)\}\\
&+Q\{\tau(K_0{}^2-P^2)-S_a(K_0+P\cos\omega)\}]\,,
\end{aligned}\right\} \tag{4.7}$$

the functions $S_a$, $S_b$, $P$, $Q$ and $\tau$ being given by (4.5).

Further, solving Eq. (3.12) for $A_0=a_0+i\alpha_0$ and separating the real and imaginary parts, we get

$$\left.\begin{aligned}
&a_0/a=-b_0(ka)^{-1}\,,\\
&\alpha_0/a=\beta_0\{I_0(ka)K_1(ka)-I_1(ka)K_0(ka)\}-b_0{}^*(q_{1,0}+q_{1,-1})-\beta_0{}^*(p_{1,0}-p_{1,-1})+\cdots,
\end{aligned}\right\} \tag{4.8}$$

Inserting (4.6) into (4.8) and expanding the right-hand sides in power series of $ka$, up to the order of $ka$, we have

$$a_0/a = -U\Delta_1(ka\Delta)^{-1} + O(ka)\,, \qquad \alpha_0/a = U\Delta_2(ka\Delta)^{-1} + O(ka)\,, \tag{4.9}$$

where $\Delta$, $\Delta_1$ and $\Delta_2$ are given by (4.7).

In a similar manner, Eq. (3.14) determines the constant $A_0^* = a_0^* + i\alpha_0^*$. But it is unnecessary for the calculation of the forces acting on the cylinder $C_1$ and therefore its explicit expression is not given here.

## § 5. The Forces on the Cylinder

The force acting on the cylinder $C_1$ ($r_1 = a$) may be considered as composed of the drag $D$ and the lift $L$ in the directions of the $x_1$ and $y_1$-axes respectively. As already shown in the previous paper[1)], these forces are expressed as

$$D = 2\pi\rho U a_0 \quad \text{and} \quad L = 2\pi\rho U\alpha_0\,, \tag{5.1}$$

where $\rho$ is the density of the fluid concerned.

Therefore, making use of the expressions (4.9) for $a_0$ and $\alpha_0$, we can finally obtain expansion formulae for the drag and lift. Thus, correct as far as terms of the order of $R^{-1}$, we have

$$C_D = \frac{D}{2\rho U^2 a} = -\frac{4\pi\Delta_1}{R\Delta} + O(R)\,, \tag{5.2}$$

$$C_L = \frac{L}{2\rho U^2 a} = \frac{4\pi\Delta_2}{R\Delta} + O(R)\,, \tag{5.3}$$

where as before

$$\left.\begin{aligned}
\Delta = {} & S_a S_b\{(1-S_a)(1-S_b) + PQ\sin^2\omega - (K_0 + P\cos\omega)(K_0 - Q\cos\omega)\} \\
& + (1-S_a)(1-S_b)\{PQ\sin^2\omega - (K_0 - P\cos\omega)(K_0 + Q\cos\omega)\} \\
& + (K_0{}^2 - P^2)(K_0{}^2 - Q^2) - PQ\sin^2\omega\,, \\
\Delta_1 = {} & -S_b\{(1-S_a)(1-S_b) + PQ\sin^2\omega - (K_0 + P\cos\omega)(K_0 - Q\cos\omega)\} \\
& + \tau\{(1-S_a)(1-S_b)(K_0 + Q\cos\omega) \\
& - (K_0{}^2 - Q^2)(K_0 + P\cos\omega)\} + PQ\sin^2\omega\,, \\
\Delta_2 = {} & \sin\omega[Q(1-S_b)\{\tau^{-1}S_a - (K_0 - P\cos\omega)\} \\
& + P\{\tau^{-1}(K_0{}^2 - Q^2) - S_b(K_0 - Q\cos\omega)\}]\,, \\
\text{with} \qquad & \\
& S_a = \frac{1}{2} - \gamma - \log\frac{R}{8}\,, \qquad S_b = \frac{1}{2} - \gamma - \log\left(\frac{R}{8}\frac{b}{a}\right), \\
& P = (2/R_h)\tau^{-1} - K_1\,, \qquad Q = (2/R_h)\tau - K_1\,, \qquad \tau = \exp(\tfrac{1}{2}R_h\cos\omega)\,, \\
& R = 4ka = 2Ua/\nu \quad \text{and} \quad R_h = 2kh = Uh/\nu\,,
\end{aligned}\right\} \tag{5.4}$$

the argument $R_h/2$ of the modified Bessel function $K_n$'s having been dropped for simplicity. The quantities $R$ and $R_h$ are the Reynolds numbers referring to the diameter $2a$ of the cylinder $C_1$ and the distance $h$ between the two cylinders respectively.

It may be mentioned here that when the distance $h$ tends to infinity, i.e. $R_h \to \infty$, all the modified Bessel functions $K_n(R_h/2)$ ($n = 0, 1, \cdots$) tend to zero, and the above formulae reduce to

$$C_D = 4\pi/RS_a \qquad \text{and} \qquad C_L = 0\,. \tag{5.5}$$

As should be expected, the result is in perfect agreement with the formula obtained by H. Lamb for the case of a single circular cylinder in an unbounded stream.

## § 6. Special Cases

In the preceding section we have obtained the expansion formulae for the drag and lift acting on one of the two circular cylinders placed in any orientation. In this section, we shall give the results for some special cases of interest.

At first, we shall consider the case when the direction of flow at infinity is parallel to the central line of the cylinders (Figs. 3 and 4).

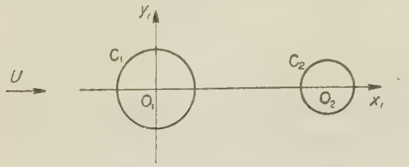

Fig. 3. ($\omega=0$)

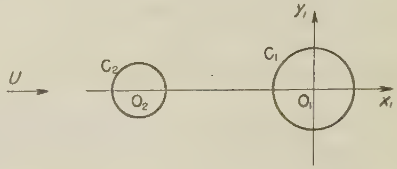

Fig. 4. ($\omega=\pi$)

For this case, we have only to put $\omega=0$ or $\pi$ in the various formulae. Thus, for $\omega=0$, we obtain

$$\left.\begin{aligned} b_0&=-U\Delta_0^{-1}\{S_b-\exp(-kh)(K_0+Q_0)\}+O(k^2a^2)\,, & \beta_0&=0\,,\\ b_0^*&=-U\Delta_0^{-1}\{S_a-\exp(kh)(K_0-P_0)\}+O(k^2a^2)\,, & \beta_0^*&=0\,, \end{aligned}\right\} \tag{6.1}$$

where

$$\left.\begin{aligned} \Delta_0&=S_aS_b-(K_0-P_0)(K_0+Q_0)\,,\\ P_0&=(kh)^{-1}\exp(-kh)-K_1\,,\\ Q_0&=(kh)^{-1}\exp(kh)-K_1\,, \end{aligned}\right\} \tag{6.2}$$

the argument $kh$ of the modified Bessel functions $K_0$ and $K_1$ having been omitted for brevity.

Also, for $\omega=\pi$ we get

$$\left.\begin{aligned} b_0&=-U\Delta_0^{-1}\{S_b-\exp(kh)(K_0-P_0)\}+O(k^2a^2)\,, & \beta_0&=0\,,\\ b_0^*&=-U\Delta_0^{-1}\{S_a-\exp(-kh)(K_0+Q_0)\}+O(k^2a^2)\,, & \beta_0^*&=0\,, \end{aligned}\right\} \tag{6.3}$$

where the functions $\Delta_0$, $P_0$ and $Q_0$ are given by (6.2).

Therefore, we have

$$\left.\begin{aligned} C_D&=4\pi(R\Delta_0)^{-1}\{S_b-\exp(-\tfrac{1}{2}R_h)(K_0+Q_0)\}+O(R) \quad \text{for} \quad \omega=0\,,\\ C_D&=4\pi(R\Delta_0)^{-1}\{S_b-\exp(\tfrac{1}{2}R_h)(K_0-P_0)\}+O(R) \quad \text{for} \quad \omega=\pi\,, \end{aligned}\right\} \tag{6.4}$$

and

$$C_L=0 \quad \text{for} \quad \omega=0 \quad \text{or} \quad \omega=\pi\,, \tag{6.5}$$

where as before

$$\left.\begin{aligned} &\Delta_0=S_aS_b-(K_0-P_0)(K_0+Q_0)\,,\\ &S_a=\frac{1}{2}-\gamma-\log\frac{R}{8}\,, \qquad S_b=\frac{1}{2}-\gamma-\log\left(\frac{R}{8}\frac{b}{a}\right),\\ &P_0=(2/R_h)\exp(-\tfrac{1}{2}R_h)-K_1\,, \qquad Q_0=(2/R_h)\exp(\tfrac{1}{2}R_h)-K_1\,, \end{aligned}\right\} \tag{6.6}$$

the argument $R_h/2$ of the modified Bessel functions $K_0$ and $K_1$ having been omitted for brevity.

The result (6.5) is also expected from symmetry without any calculation.

We next consider the case when the direction of flow at infinity is perpendicular to the central line of two cylinders (Fig. 5). Putting $\omega=\pi/2$ in (4.6) and (4.7), we have

$$\left.\begin{aligned} b_0&=-U\Delta_*^{-1}\{M(S_b-K_0)-P_1^2\}+O(k^2a^2)\,,\\ \beta_0&=-UP_1\Delta_*^{-1}\{M-(1-S_b-K_0)\}+O(k^2a^2)\,,\\ b_0^*&=-U\Delta_*^{-1}\{M(S_a-K_0)-P_1^2\}+O(k^2a^2)\,,\\ \beta_0^*&=UP_1\Delta_*^{-1}\{M-(1-S_a-K_0)\}+O(k^2a^2)\,, \end{aligned}\right\} \tag{6.7}$$

where

$$\left.\begin{aligned}\Delta_* &= M\{S_aS_b-(K_0^2-P_1^2)\}-P_1^2\,,\\ M &= (1-S_a)(1-S_b)-(K_0^2-P_1^2)\,,\\ P_1 &= (kh)^{-1}-K_1\,,\end{aligned}\right\} \qquad (6.8)$$

the argument $kh$ of the modified Bessel functions $K_0$ and $K_1$ having been omitted.

Therefore, we obtain

$$\left.\begin{aligned}C_D &= 4\pi(R\Delta_*)^{-1}\{M(S_b-K_0)-P_1^2\}+O(R)\,,\\ C_L &= -4\pi P_1(R\Delta_*)^{-1}\{M-(1-S_b-K_0)\}+O(R)\,,\end{aligned}\right\} \qquad (6.9)$$

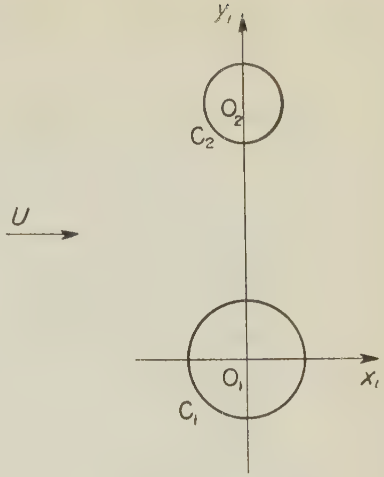

Fig. 5. ($\omega=\pi/2$)

where as before

$$\left.\begin{aligned}&S_a=\frac{1}{2}-\gamma-\log\frac{R}{8}\,,\qquad S_b=\frac{1}{2}-\gamma-\log\left(\frac{R}{8}\,\frac{b}{a}\right),\\ &\Delta_*=M\{S_aS_b-(K_0^2-P_1^2)\}-P_1^2\,,\\ &M=(1-S_a)(1-S_b)-(K_0^2-P_1^2)\,,\qquad P_1=2/R_h-K_1\,,\end{aligned}\right\} \qquad (6.10)$$

the argument $R_h/2$ of the modified Bessel functions $K_0$ and $K_1$ having been omitted for brevity.

In particular, for $a=b$, we have

$$C_D=\frac{4\pi}{R}\,\frac{S-1-K_0}{(S+K_0)(S-1-K_0)+P_1^2}+O(R)\,,\quad C_L=-\frac{4\pi}{R}\,\frac{P_1}{(S+K_0)(S-1-K_0)+P_1^2}+O(R)\,, \qquad (6.11)$$

where

$$S=\frac{1}{2}-\gamma-\log\frac{R}{8}\,. \qquad (6.12)$$

Except for the difference in sign of $C_L$†, these expansion formulae (6.11) are in perfect agreement, up to the first term, with the formulae obtained in the previous paper$^{1)}$.

## §7. Approximate Solution for the Case $ka\ll1$, $kb\ll1$ and $kh\ll1$

The preceding analysis has been carried out under the assumption that $ka\ll1$, $kb\ll1$ and $(kh)^{-1}=O(1)$. But, when $kh\ll1$ for sufficiently small $k$, the values of $K_n(kh)$ $(n=0, 1, \cdots)$ in (4.2) become very large and therefore the analysis for small values of $k$ should be reconsidered.

However, as was noted in the previous paper$^{1)}$, detailed examination of the coefficients $C_{ij}$ in Eq. (4.1) shows that the correct expansion for this case just agrees with the one which is obtained by considering formally the case $kh\ll1$ in the preceding results (5.2)~(5.4).

Thus, putting

$$\sigma=\log\frac{b}{a}\qquad\text{and}\qquad\kappa=\log\frac{h}{a}-\frac{1}{2}\,, \qquad (7.1)$$

we obtain the results:

---

† In the present paper, we have calculated the forces acting on the cylinder $C_1$ for the case of $\omega=90°$, while in the previous paper we have treated the case of $\omega=270°$.

$$\left.\begin{aligned}
&C_D=-\frac{4\pi\Delta_1}{R\Delta}+O(R)\,,\qquad C_L=\frac{4\pi\Delta_2}{R\Delta}+O(R)\,,\\
&\text{where}\\
&\Delta=\{(2\kappa-\sigma)S-\kappa(\kappa+2)+\sigma\}\{(2\kappa-\sigma+2)S-(\kappa+1)^2\}\\
&\qquad-\cos^2\omega\{\sigma+2(\kappa+1)(\kappa-\sigma)\}+O(R^2)\,,\\
&\Delta_1=-(\kappa-\sigma+1)\{(2\kappa-\sigma)S-\kappa(\kappa+2)+\sigma\}+\cos^2\omega\{\sigma S+(\kappa+1)(\kappa-2\sigma)\}\\
&\qquad+\frac{R}{8}\frac{h}{a}\cos\omega[S^2(\sigma-2\kappa+2)+S\{3\kappa^2+(1-\sigma)\kappa-(3+(5/2)\sigma)\}\\
&\qquad-(\kappa^2-\sigma)(\kappa+(3/2))+1-\cos^2\omega\{4S^2-S(7+6\kappa+\sigma)\\
&\qquad+3(\kappa+1)^2+\sigma-\kappa+(1/2)\}+\cos^4\omega]+O(R^2)\,,\\
&\Delta_2=-\sin\omega\cos\omega\{\sigma S+(\kappa+1)(\kappa-2\sigma)\}\\
&\qquad-\frac{R}{8}\frac{h}{a}\sin\omega[(S-\kappa-(1/2))\{(2\kappa-\sigma+2)S-(\kappa+1)(\kappa+2)\}\\
&\qquad-\cos^2\omega\{4S^2-S(7+6\kappa+\sigma)+3(\kappa+1)^2+(1/2)\}+\cos^4\omega]+O(R^2)\,.
\end{aligned}\right\}\quad(7.2)$$

If we put $\omega=90°$ and $\sigma=0$ $(a=b)$ in (7.2), we get

$$\left.\begin{aligned}
C_D&=\frac{4\pi}{R(2S-\kappa-1)}+O(R)\,,\\
C_L&=-\frac{\pi}{4\kappa}\frac{h}{a}\frac{2S-2\kappa-1}{2S-\kappa-1}+O(R)\,.
\end{aligned}\right\}\quad(7.3)$$

Except for the difference in sign of $C_L$*, these results agree, up to the first term, with those which were obtained in the previous paper$^{1)}$.

At sufficiently small Reynolds number $R$, (7.2) also gives

$$\left.\begin{aligned}
C_D&\sim-\frac{4\pi}{R\log R}\frac{(2\kappa-\sigma)(\kappa-\sigma+1)-\sigma\cos^2\omega}{(2\kappa-\sigma)(2\kappa-\sigma+2)}\,,\\
C_L&\sim\frac{4\pi}{R\log R}\frac{\sigma\sin\omega\cos\omega}{(2\kappa-\sigma)(2\kappa-\sigma+2)}\,.
\end{aligned}\right\}\quad(7.4)$$

It may be noted here that, when the radii of the two cylinders are equal,

$$C_D\sim-\frac{2\pi}{R\log R}\,,\qquad(7.5)$$

which is independent of the value of $\omega$.

## § 8. Numerical Discussions

Making use of the formulae (5.2), (5.3), (6.4) and (6.9), the writer has calculated the values of $C_D$ and $C_L$ for various small values up to unity of the Reynolds number $R$ as well as for various values of the azimuthal angle $\omega$, the distance ratio $h/a$ and the ratio of radii $b/a$. The results are given in Tables I∼XII† and some of them are also plotted against $R$ in Figs. 6∼11.

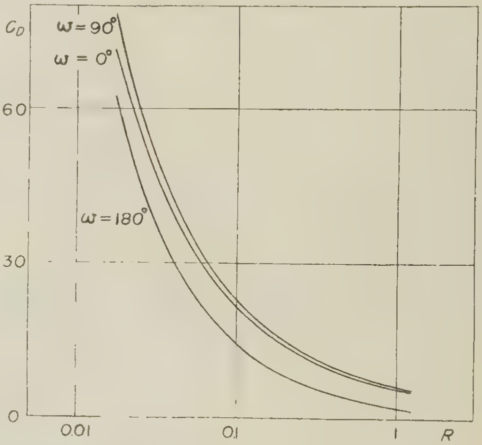

Fig. 6. $(h/a=20,\ b/a=2.0)$

From these tables and figures, it will readily be seen that, as the Reynolds number $R$ increases, all the values of $C_D$ for various cases decrease monotonously and the interference effects due to the presence of the cylinder $C_2$ become imperceptible. It is also found that the value of $C_D$ for the case of $\omega=90°$ is greater than any other values for the cases of $\omega=0°$, 45°, 135° or 180° and the value for $\omega=180°$ is smaller than the one for $\omega=0°$ (Fig. 6).

As for the variation of the drag coefficient $C_D$ with the ratio $b/a$ for a given Reynolds number $R$ as well as for the given values of the ratio $h/a$ and of the azimuthal angle $\omega$, it is seen that the value of $C_D$ decreases with the increase of the ratio $b/a$ (Figs. 7 and 8).

---

* It will be noted that the distance between the axes of the cylinders is here denoted by $h$, while in the previous paper we denoted it by $2h$.

† In Table XII and Fig. 10, negative values of $C_L$ mean that the $y$-component force acting on the cylinder $C_1$ is of attractive nature.

Table I. Values of $C_D$ ($h/a=20$, $b/a=0.5$)

| $R$ | $\omega=0°$ | $\omega=45°$ | $\omega=90°$ | $\omega=135°$ | $\omega=180°$ |
|---|---|---|---|---|---|
| 0.01 | 131 | 134 | 136 | 130 | 124 |
| 0.02 | 76.4 | 77.7 | 79.0 | 74.5 | 69.7 |
| 0.04 | 45.6 | 46.2 | 46.9 | 43.4 | 39.5 |
| 0.06 | 34.1 | 34.5 | 35.0 | 32.0 | 28.5 |
| 0.08 | 27.9 | 28.2 | 28.6 | 26.0 | 22.8 |
| 0.1 | 24.0 | 24.2 | 24.6 | 22.2 | 19.1 |
| 0.2 | 15.3 | 15.3 | 15.7 | 14.04 | 11.42 |
| 0.4 | 9.92 | 9.87 | 10.26 | 9.39 | 7.13 |
| 0.6 | 7.85 | 7.78 | 8.11 | 7.64 | 5.56 |
| 0.8 | 6.72 | 6.65 | 6.94 | 6.69 | 4.73 |
| 1.0 | 6.02 | 5.95 | 6.19 | 6.09 | 4.22 |

Table II. Values of $C_D$ ($h/a=20$, $b/a=1.0$)

| $R$ | $\omega=0°$ | $\omega=45°$ | $\omega=90°$ | $\omega=135°$ | $\omega=180°$ |
|---|---|---|---|---|---|
| 0.01 | 121 | 125 | 129 | 121 | 113 |
| 0.02 | 71.2 | 73.1 | 75.2 | 69.4 | 63.3 |
| 0.04 | 42.9 | 43.8 | 44.9 | 40.6 | 35.7 |
| 0.06 | 32.3 | 32.9 | 33.6 | 30.1 | 25.7 |
| 0.08 | 26.6 | 27.0 | 27.6 | 24.4 | 20.4 |
| 0.1 | 23.0 | 23.2 | 23.8 | 20.9 | 17.1 |
| 0.2 | 14.78 | 14.81 | 15.3 | 13.36 | 10.11 |
| 0.4 | 9.71 | 9.64 | 10.11 | 9.07 | 6.19 |
| 0.6 | 7.70 | 7.61 | 8.03 | 7.45 | 4.74 |
| 0.8 | 6.61 | 6.51 | 6.87 | 6.57 | 3.96 |
| 1.0 | 5.93 | 5.82 | 6.14 | 6.02 | 3.47 |

Table III. Values of $C_D$ ($h/a=20$, $b/a=2.0$)

| $R$ | $\omega=0°$ | $\omega=45°$ | $\omega=90°$ | $\omega=135°$ | $\omega=180°$ |
|---|---|---|---|---|---|
| 0.01 | 107 | 113 | 120 | 109 | 97.0 |
| 0.02 | 63.6 | 66.7 | 70.1 | 62.5 | 54.1 |
| 0.04 | 39.0 | 40.4 | 42.2 | 36.7 | 30.3 |
| 0.06 | 29.7 | 30.6 | 31.8 | 27.2 | 21.6 |
| 0.08 | 24.7 | 25.2 | 26.3 | 22.2 | 17.0 |
| 0.1 | 21.5 | 21.8 | 22.7 | 19.1 | 14.16 |
| 0.2 | 14.05 | 14.11 | 14.76 | 12.33 | 8.05 |
| 0.4 | 9.34 | 9.26 | 9.86 | 8.53 | 4.60 |
| 0.6 | 7.44 | 7.31 | 7.84 | 7.11 | 3.25 |
| 0.8 | 6.39 | 6.23 | 6.69 | 6.35 | 2.45 |
| 1.0 | 5.73 | 5.53 | 5.88 | 5.86 | 1.87 |

Table IV. Values of $C_D$ ($h/a=100$, $b/a=0.5$)

| $R$ | $\omega=0°$ | $\omega=45°$ | $\omega=90°$ | $\omega=135°$ | $\omega=180°$ |
|---|---|---|---|---|---|
| 0.01 | 151 | 154 | 158 | 147 | 135 |
| 0.02 | 89.2 | 91.0 | 93.1 | 85.6 | 76.9 |
| 0.04 | 53.6 | 54.3 | 55.9 | 51.2 | 44.4 |
| 0.06 | 39.8 | 40.3 | 41.6 | 38.4 | 32.6 |
| 0.08 | 32.3 | 32.6 | 33.7 | 31.5 | 26.3 |
| 0.1 | 27.5 | 27.7 | 28.7 | 27.1 | 22.4 |
| 0.2 | 16.8 | 16.8 | 17.32 | 17.06 | 13.73 |
| 0.4 | 10.54 | 10.54 | 10.75 | 10.86 | 8.73 |
| 0.6 | 8.20 | 8.21 | 8.33 | 8.43 | 6.84 |
| 0.8 | 6.97 | 6.97 | 7.05 | 7.14 | 5.81 |
| 1.0 | 6.20 | 6.21 | 6.27 | 6.34 | 5.21 |

Table V. Values of $C_D$ ($h/a=100$, $b/a=1.0$)

| $R$ | $\omega=0°$ | $\omega=45°$ | $\omega=90°$ | $\omega=135°$ | $\omega=180°$ |
|---|---|---|---|---|---|
| 0.01 | 146 | 150 | 154 | 142 | 129 |
| 0.02 | 87.0 | 89.1 | 91.4 | 83.0 | 73.1 |
| 0.04 | 52.6 | 53.5 | 55.3 | 50.0 | 42.2 |
| 0.06 | 39.3 | 39.8 | 41.3 | 37.7 | 31.0 |
| 0.08 | 31.9 | 32.3 | 33.5 | 31.0 | 25.0 |
| 0.1 | 27.2 | 27.4 | 28.5 | 26.7 | 21.2 |
| 0.2 | 16.7 | 16.7 | 17.29 | 17.00 | 13.02 |
| 0.4 | 10.48 | 10.49 | 10.73 | 10.88 | 8.24 |
| 0.6 | 8.16 | 8.17 | 8.32 | 8.46 | 6.43 |
| 0.8 | 6.94 | 6.94 | 7.04 | 7.16 | 5.46 |
| 1.0 | 6.18 | 6.18 | 6.26 | 6.36 | 4.84 |

Table VI. Values of $C_D$ ($h/a=100$, $b/a=2.0$)

| $R$ | $\omega=0°$ | $\omega=45°$ | $\omega=90°$ | $\omega=135°$ | $\omega=180°$ |
|---|---|---|---|---|---|
| 0.01 | 140 | 144 | 149 | 135 | 120 |
| 0.02 | 84.1 | 86.5 | 89.5 | 79.7 | 68.1 |
| 0.04 | 51.4 | 52.4 | 54.5 | 48.4 | 39.3 |
| 0.06 | 38.6 | 39.1 | 40.9 | 36.7 | 28.7 |
| 0.08 | 31.4 | 31.8 | 33.3 | 30.3 | 23.2 |
| 0.1 | 26.8 | 27.1 | 28.4 | 26.3 | 19.6 |
| 0.2 | 16.5 | 16.5 | 17.28 | 16.9 | 11.96 |
| 0.4 | 10.39 | 10.41 | 10.73 | 10.91 | 7.45 |
| 0.6 | 8.10 | 8.11 | 8.32 | 8.51 | 5.70 |
| 0.8 | 6.88 | 6.89 | 7.04 | 7.21 | 4.73 |
| 1.0 | 6.13 | 6.13 | 6.26 | 6.40 | 4.08 |

Therefore, when the cylinders of arbitrary radii in tandem orientation are moving slowly with equal velocity in a viscous fluid, they experience a smaller drag than when they are moving side by side; and, the greater the value of the radius of the one cylinder is, the smaller becomes the value of the drag acting on the other cylinder. In particular, when the cylinders are of equal radius, the front cylinder experiences a greater drag than the rear cylinder.

On the other hand, the variation of the lift coefficient $C_L$ with the Reynolds number $R$ and the azimuthal angle $\omega$ are somewhat complicated. When the Reynolds number is not so small, the values of the coefficient $C_L$ for the case of $\omega=90°$ are greater than those for the cases of $\omega=45°$ and 135° and, since the coefficient $C_L$ takes a negative value in all cases, the cylinder $C_1$ experiences a repulsive force[†] (Fig. 10).

However, when the Reynolds number $R$ becomes fairly small, the value of $C_L$ for the case of $\omega=45°$ becomes greater than the cor-

---

[†] However, as is noted in a previous footnote, the values of the coefficient $C_L$ for repulsive force are given by positive numbers, while those for attractive force are given by negative numbers.

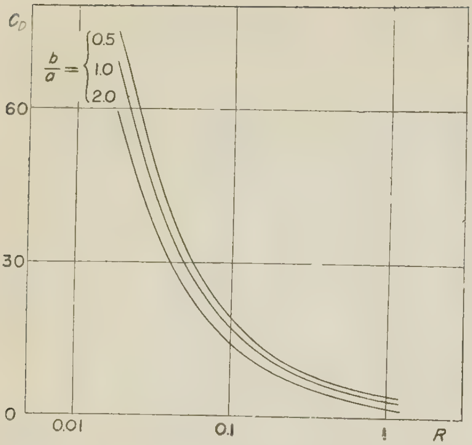

Fig. 7. ($h/a=20$, $\omega=180°$)

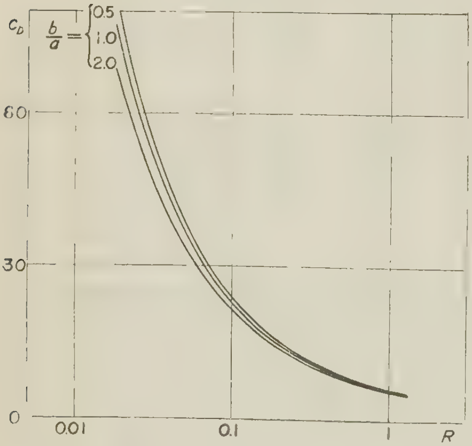

Fig. 8. ($h/a=20$, $\omega=0°$)

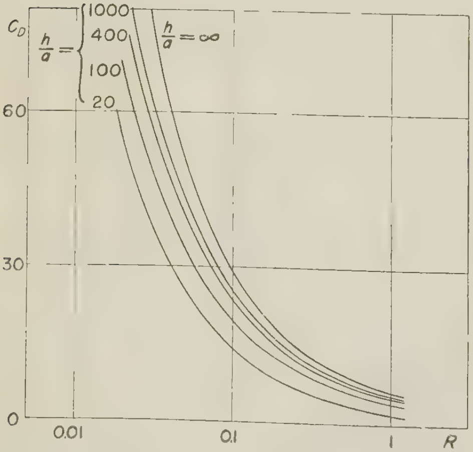

Fig. 9. ($b/a=2.0$, $\omega=180°$)

responding value for the case of $\omega=90°$. As for the case of $\omega=135°$, the coefficient $C_L$ changes its sign at a certain value of $R$ and therefore for smaller values of $R$ the cylinder

Table VII. Values of $C_D$ ($\omega=0°$)

| $h/a$ | 400 | | | 1000 | | | ∞ |
|---|---|---|---|---|---|---|---|
| $b/a$ / $R$ | 0.5 | 1.0 | 2.0 | 0.5 | 1.0 | 2.0 | — |
| 0.01 | 172 | 170 | 167 | 182 | 181 | 180 | 190 |
| 0.02 | 100 | 99.3 | 98.3 | 104 | 103 | 103 | 106 |
| 0.04 | 58.1 | 57.8 | 57.5 | 59.3 | 59.2 | 59.0 | 60.2 |
| 0.06 | 42.4 | 42.3 | 42.0 | 43.0 | 43.0 | 42.9 | 43.5 |
| 0.08 | 34.0 | 33.9 | 33.7 | 34.4 | 34.3 | 34.3 | 34.7 |
| 0.1 | 28.7 | 28.6 | 28.5 | 29.0 | 28.9 | 28.9 | 29.2 |
| 0.2 | 17.2 | 17.2 | 17.1 | 17.3 | 17.3 | 17.3 | 17.4 |
| 0.4 | 10.70 | 10.68 | 10.66 | 10.74 | 10.73 | 10.72 | 10.76 |
| 0.6 | 8.30 | 8.29 | 8.27 | 8.32 | 8.31 | 8.31 | 8.33 |
| 0.8 | 7.03 | 7.02 | 7.01 | 7.05 | 7.04 | 7.04 | 7.06 |
| 1.0 | 6.26 | 6.25 | 6.23 | 6.27 | 6.26 | 6.26 | 6.27 |

Table VIII. Values of $C_D$ ($\omega=90°$)

| $h/a$ | 400 | | | 1000 | | | ∞ |
|---|---|---|---|---|---|---|---|
| $b/a$ / $R$ | 0.5 | 1.0 | 2.0 | 0.5 | 1.0 | 2.0 | — |
| 0.01 | 179 | 178 | 177 | 188 | 188 | 188 | 190 |
| 0.02 | 104 | 104 | 103 | 106 | 106 | 106 | 106 |
| 0.04 | 59.9 | 59.9 | 59.8 | 60.1 | 60.1 | 60.1 | 60.2 |
| 0.06 | 43.4 | 43.4 | 43.4 | 43.5 | 43.5 | 43.5 | 43.5 |
| 0.08 | 34.7 | 34.7 | 34.6 | 34.7 | 34.7 | 34.7 | 34.7 |
| 0.1 | 29.2 | 29.2 | 29.2 | 29.2 | 29.2 | 29.2 | 29.2 |
| 0.2 | 17.4 | 17.4 | 17.4 | 17.4 | 17.4 | 17.4 | 17.4 |
| 0.4 | 10.76 | 10.76 | 10.76 | 10.76 | 10.76 | 10.76 | 10.76 |
| 0.6 | 8.33 | 8.33 | 8.33 | 8.33 | 8.33 | 8.33 | 8.33 |
| 0.8 | 7.06 | 7.06 | 7.06 | 7.06 | 7.06 | 7.06 | 7.06 |
| 1.0 | 6.28 | 6.28 | 6.27 | 6.28 | 6.28 | 6.28 | 6.27 |

Table IX. Values of $C_D$ ($\omega=180°$)

| $h/a$ | 400 | | | 1000 | | | ∞ |
|---|---|---|---|---|---|---|---|
| $b/a$ / $R$ | 0.5 | 1.0 | 2.0 | 0.5 | 1.0 | 2.0 | — |
| 0.01 | 149 | 144 | 139 | 159 | 156 | 152 | 190 |
| 0.02 | 85.6 | 83.2 | 80.0 | 91.4 | 89.7 | 87.5 | 106 |
| 0.04 | 50.0 | 48.6 | 46.8 | 53.1 | 52.2 | 51.0 | 60.2 |
| 0.06 | 36.8 | 35.8 | 34.5 | 38.9 | 38.3 | 37.4 | 43.5 |
| 0.08 | 29.7 | 28.9 | 27.8 | 31.3 | 30.8 | 30.1 | 34.7 |
| 0.1 | 25.2 | 24.5 | 23.6 | 26.5 | 26.1 | 25.5 | 29.2 |
| 0.2 | 15.3 | 14.95 | 14.37 | 16.0 | 15.8 | 15.4 | 17.4 |
| 0.4 | 9.66 | 9.40 | 8.97 | 10.05 | 9.88 | 9.60 | 10.76 |
| 0.6 | 7.54 | 7.32 | 6.93 | 7.82 | 7.68 | 7.43 | 8.33 |
| 0.8 | 6.41 | 6.21 | 5.83 | 6.64 | 6.51 | 6.27 | 7.06 |
| 1.0 | 5.72 | 5.52 | 5.13 | 5.92 | 5.79 | 5.54 | 6.27 |

$C_1$ experiences an attractive force. But, both the repulsive and attractive forces increase as the value of the radius of the second cylinder increases (Fig. 11).

Lastly, we shall refer to the variation of the coefficients $C_D$ and $C_L$ with the distance ratio $h/a$. As is noted in the previous paper[1], for given values of the Reynolds number $R$

Table X. Values of $C_L$ ($\omega=45°$)

| $h/a$ | 20 | | | 100 | | |
|---|---|---|---|---|---|---|
| $b/a$ \ $R$ | 0.5 | 1.0 | 2.0 | 0.5 | 1.0 | 2.0 |
| 0.01 | 7.76 | 9.74 | 12.82 | 13.14 | 14.76 | 16.82 |
| 0.02 | 5.93 | 7.21 | 9.15 | 8.86 | 9.97 | 11.39 |
| 0.04 | 4.60 | 5.48 | 6.78 | 5.25 | 5.96 | 6.89 |
| 0.06 | 3.94 | 4.66 | 5.73 | 3.51 | 4.02 | 4.70 |
| 0.08 | 3.49 | 4.13 | 5.06 | 2.52 | 2.91 | 3.43 |
| 0.1 | 3.16 | 3.74 | 4.58 | 1.91 | 2.21 | 2.64 |
| 0.2 | 2.14 | 2.57 | 3.20 | 0.758 | 0.902 | 1.113 |
| 0.4 | 1.252 | 1.55 | 2.02 | 0.316 | 0.389 | 0.507 |
| 0.6 | 0.877 | 1.113 | 1.51 | 0.201 | 0.256 | 0.350 |
| 0.8 | 0.695 | 0.902 | 1.258 | 0.154 | 0.201 | 0.286 |
| 1.0 | 0.600 | 0.794 | 1.104 | 0.130 | 0.174 | 0.258 |

Table XI. Values of $C_L$ ($\omega=90°$)

| $h/a$ | 20 | | | 100 | | |
|---|---|---|---|---|---|---|
| $b/a$ \ $R$ | 0.5 | 1.0 | 2.0 | 0.5 | 1.0 | 2.0 |
| 0.01 | 4.02 | 4.67 | 5.59 | 8.57 | 9.57 | 10.86 |
| 0.02 | 3.79 | 4.42 | 5.31 | 7.00 | 7.87 | 9.00 |
| 0.04 | 3.47 | 4.07 | 4.93 | 5.10 | 5.79 | 6.70 |
| 0.06 | 3.24 | 3.82 | 4.65 | 3.90 | 4.46 | 5.22 |
| 0.08 | 3.06 | 3.61 | 4.41 | 3.07 | 3.54 | 4.18 |
| 0.1 | 2.90 | 3.43 | 4.22 | 2.47 | 2.87 | 3.42 |
| 0.2 | 2.30 | 2.78 | 3.50 | 1.092 | 1.300 | 1.61 |
| 0.4 | 1.63 | 2.02 | 2.66 | 0.453 | 0.560 | 0.734 |
| 0.6 | 1.25 | 1.59 | 2.18 | 0.288 | 0.367 | 0.506 |
| 0.8 | 1.03 | 1.35 | 1.93 | 0.219 | 0.288 | 0.418 |
| 1.0 | 0.898 | 1.21 | 1.82 | 0.186 | 0.250 | 0.383 |

Table XII. Values of $C_L$ ($\omega=135°$)

| $h/a$ | 20 | | | 100 | | |
|---|---|---|---|---|---|---|
| $b/a$ \ $R$ | 0.5 | 1.0 | 2.0 | 0.5 | 1.0 | 2.0 |
| 0.01 | -3.61 | -5.06 | -7.44 | -4.31 | -4.95 | -5.81 |
| 0.02 | -2.08 | -2.83 | -4.08 | -2.14 | -2.44 | -2.85 |
| 0.04 | -1.143 | -1.52 | -2.15 | -0.876 | -0.994 | -1.149 |
| 0.06 | -0.781 | -1.021 | -1.424 | -0.391 | -0.441 | -0.503 |
| 0.08 | -0.584 | -0.753 | -1.037 | -0.131 | -0.144 | -0.158 |
| 0.1 | -0.457 | -0.583 | -0.792 | 0.026 | 0.036 | 0.054 |
| 0.2 | -0.167 | -0.200 | -0.247 | 0.279 | 0.336 | 0.422 |
| 0.4 | 0.040 | 0.067 | 0.136 | 0.255 | 0.317 | 0.420 |
| 0.6 | 0.146 | 0.206 | 0.357 | 0.193 | 0.247 | 0.345 |
| 0.8 | 0.216 | 0.305 | 0.551 | 0.154 | 0.203 | 0.299 |
| 1.0 | 0.269 | 0.386 | 0.777 | 0.132 | 0.179 | 0.282 |

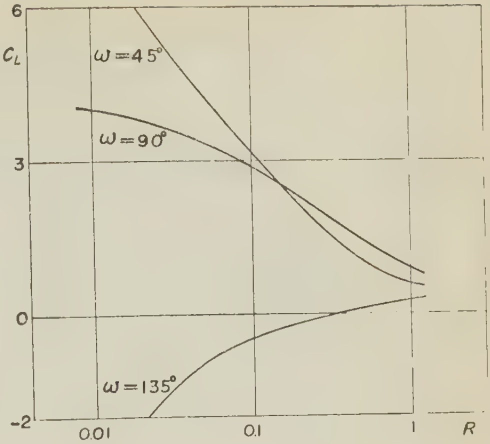

Fig. 10. ($h/a=20$, $b/a=0.5$)

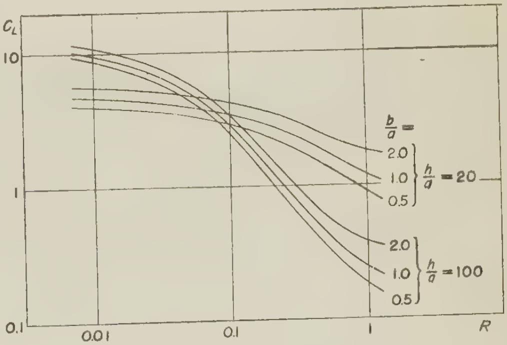

Fig. 11. ($\omega=90°$)

as well as for given values of the azimuthal angle $\omega$ and the ratio of radii $b/a$, the value of $C_D$ increases monotonously with the increase of the ratio $h/a$ and tends to the values for the case of a single circular cylinder in an unbounded stream††; however, the variation of the coefficient $C_L$ with the ratio $h/a$ is somewhat complicated. When the Reynolds number is not so small, it decreases with the increase of the ratio $h/a$ and ultimately tends to zero, but, when the Reynolds number becomes fairly small, the values of $C_L$ increases first and then decreases.

## Acknowledgements

The present problem has been carried out at the suggestion of Professor S. Tomotika. The writer wishes to express his sincere gratitude to him for his helpful suggestions and continual encouragement throughout this work and especially for his kind inspection of the manuscript. Also, the writer is much indebted to Professor K. Tamada for his invaluable advices throughout the present investigation and also for his important criticism of the final manuscript. The writer's thanks are also due to the Ministry of Education for a grant-in-aid for fundamental scientific research.

## Reference

1) H. Fujikawa: J. Phys. Soc. Japan **11** (1956) 558.

†† The values of $C_D$ for a single circular cylinder in an unbounded stream have been calculated from (5.5) and tabulated in Tables VII, VIII and IX under the heading ∞ for the sake of reference.

JOURNAL OF THE PHYSICAL SOCIETY OF JAPAN Vol. 11, No. 6, JUNE, 1956

# Experimental Investigation on the Transition of Laminar Separated Layer

By Hiroshi SATO

*Institute of Science and Technology, University of Tokyo*

(Received February 20, 1956)

Transition of two-dimensional separated layer was investigated in detail. Mean velocity distribution of laminar layer shows a similar profile and agrees with Lin's calculation. In the transition region, hot-wire anemometer survey of velocity fluctuation revealed the existence of sinusoidal wave, the frequency of which lies in the unstable zone predicted by stability theory. Transition points determined by layer thickness and by fluctuation measurements are in good coincidence. A simple empirical relation was derived for transition distance.

## § 1. Introduction

In order to compare results of stability calculation in shear layer with experiments, a long range program was planned. It involves detailed measurements in jets, wakes, separated layers etc. As a first step, the present experiment is concerned with a separated laminar boundary-layer which is also termed "laminar half jet". It relates with the laminar separation of boundary-layer on aerofoil or cylinder and also with the base-pressure problem at low Reynolds number.

Such a flow field was investigated experimentally by Linke and Fage and Johansen1)2). Making detailed mean velocity survery, they showed the extent of shear layer and determined the transition point. Linke was interested in the separation on circular cylinder at various Reynolds numbers, and Fage and Johansen observed the separated layer from bluff bodies.

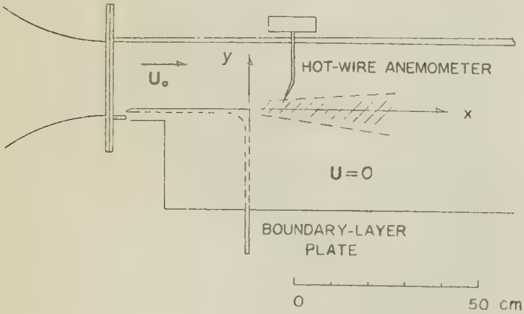

Fig. 1. Test-section arrangement.

In the present experiment, velocity fluctuation was measured in detail. There are many unknown effects on the boundary-layer separation, for instance, geometrical shape near separation point, pressure distribution, separation point fluctuation and others. For making these effects as small as possible, a combination of flat plate and perpendicular flat-end was used. Flow is two-dimensional without pressure gradient, and boundary-layer before separtion has Blasius-type velocity distribution.

Lessen treated the stability of boundary-layer between two parallel flows theoretically using a linearized equation of small perturbation3). A similar solution for mean velocity distribution was derived and one branch of neutral stability curve was calculated. Lin extended the theory into the compressible flow using essentially the same fundamental equation4). Such theoretical results will be compared with experiments. Liepmann and Laufer reported measurements in a fully developed turbulent half jet5). Their results will also be refered to as an extreme of transition region.

## § 2. Equipment and Procedure

### Wind-Tunnel

Experiments were all made in a 20 cm by 60 cm low turbulence wind-tunnel at Institute of Science and Technology. The original closed test-section for boundary-layer research was replaced by an open channel which is spanned by a boundary-layer plate (Fig. 1). The mixed flow established in the test-section re-enters a return duct which is about 2.5 meters downstream of boundary-layer plate. At first, such an arrangement was thought inadequate because the entrance of return duct might disturb the flow. But, as described later, influences were found negligible at the transition region.

Wind speed at test-section can be changed from 1 to 30 m/s and longitudinal free-stream turbulence level is about 0.03 percent at 5 m/s and 0.08 percent at 10 m/s.

### Boundary-layer Plate

Three kinds of boundary-layer plate were used. Each one consists of a flat top-plate and a perpendicular end-plate. The trailing edge is sharp having inclination of 90 degrees. The surface of wooden top-plate was carefully polished and sharpened properly at the leading edge. Plates denoted by I, II and III are 42 mm, 150 mm and 360 mm long respectively and end-plates are all 270 mm long.

For Plate I, another top-plate was added in order to maintain the main-stream parallel and to establish Blasius-type velocity profile at the trailing edge. Between two top-plates, boundary-layer suction was applied. Boundary-layer of forward top-plate was completely removed. Two-dimensional suction was realized by placing a high pressure-drop screen in the suction box. The gap of suction were determined purely experimentally. The two-dimensionality of separated layer was proved to be satisfactory. For two other boundary-layer plates, no suction was necessary.

### Range of Experiment

Among many stream conditions which may influence the separated layer transition, three are the most important. They are thickness of layer, velocity and turbulence of main-stream. In the presnt experiment, main-stream velocity was changed from 3 to 15 m/s. Using three boundary-layer plates of different length, Reynolds number based on momentum thickness at trailing edge covers from 70 to 380. Effects of main-stream turbulence will be examined systematically in the future.

### Mean Velocity and Fluctuation Measurements

Hot-wire anemometer was exclusively used for mean velocity and fluctuation measurements. A fine Pitot-tube was used at first for mean velocity survey but whole data were discarded when great inaccuracy was found near the still-air boundary. Platinum-Rhodium wire, 5 microns in diameter and about 2 mm in length was operated between 100°C and 200°C by the constant current method. Errors in measuring longitudinal mean velocity $U$ at the layer boundary were reduced by placing hot-wire perpendicular ($z$-direction) and parallel ($x$-direction) to the main stream. By proper subtraction of two readings, the influences of lateral component of mean velocity and large velocity fluctuation were cancelled.

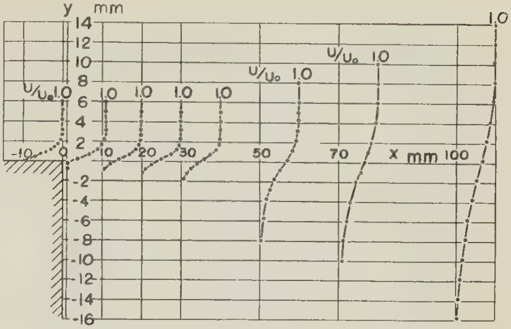

Fig. 2. Mean velocity distribution, Plate II, $U_0=10.0$ m/s.

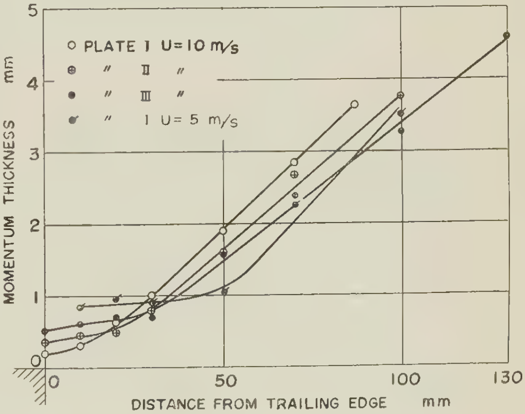

Fig. 3. Momentum thickness increase.

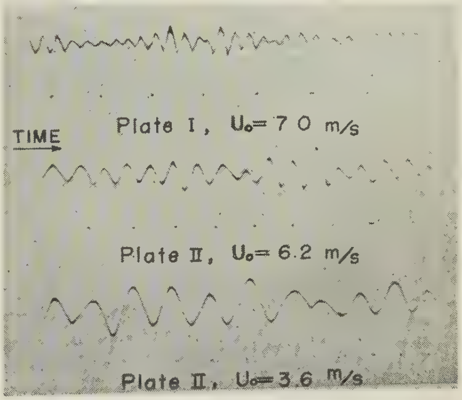

Fig. 4. $u$-fluctuation records for various wind speeds. Time interval between dots 0.01 sec.

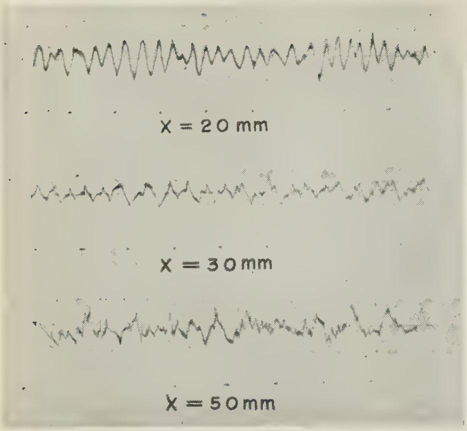

Fig. 5. $u$-fluctuation records for various $x$-stations, with Plate I, $U_0=7.0$ m/s and $y=0$. Time interval between dots 0.01 sec.

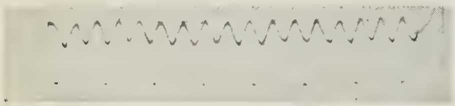

Fig. 6. Sound excited $u$-fluctuation with $U_0=10.0$ m/s. Time interval between dots 0.01 sec.

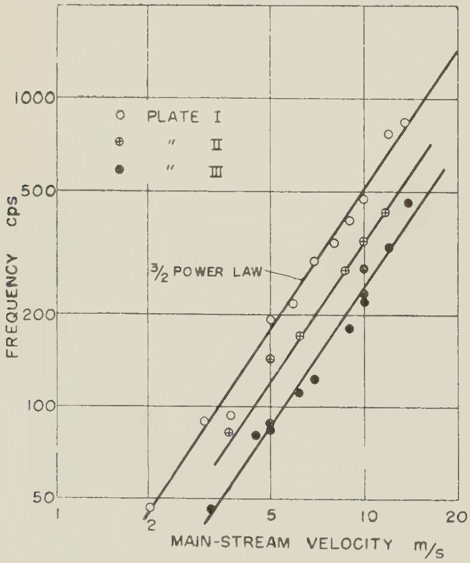

Fig. 7. Sinusoidal fluctuation frequency.

A detailed description is found in reference 6.

The output signal from hot-wire is amplified by a conventional compensated amplifier[7]. Compensated frequency response is flat from 20 to 20,000 cps and noise level is equivalent to 50 microvolts input at hot-wire time constant of 1 millisecond. Output from amplifier was recorded by an electromagnetic oscillograph when necessary. Frequency respose of recorder itself is flat up to 1000 cps.

Only $u$, the longitudinal velocity fluctuation was measured so far. The hot-wire was placed parallel to the trailing edge ($z$-direction) except a few special measurements. It was moved in $x$- and $y$-directions by micrometer screws and $y$-position was determined by a precision dial gage. Accuracy of $y$-positioning at different $x$-stations is approximately 0.1 mm, while relative position in the same $x$-station was read within 0.01 mm.

## § 3. Experimental Results

### Mean Velocity Distribution

At first, the two-dimensionality of flow field was studied. At various $x$-stations, mean velocity survey was made at five different $z$-stations. Data showed a good agreement confirming the two-dimensionality for mean velocity distribution.

Fig. 2 shows an example of distribution with Plate II at main-stream velocity 10.0 m/s. The boundary-layer before separation is of Blasius type and a similar velocity profile is established in a short distance after separation.

As a measure of layer thickness, momentum thickness $\theta$ which is defined by

$$\theta=\int_{-\infty}^{\infty}\frac{U}{U_0}\left(1-\frac{U}{U_0}\right)dy\ ,$$

is plotted in Fig. 3. The accuracy of calculating $\theta$ is not so high, since it involves the integral from infinity to infinity. Probable error may be in the order of 10 percent. In Fig. 3, the thickness increases gradually at first and at a certain point, the gradient becomes steeper. The point might be the trasition point. The linearity of thickness and $x$ characterizes the turbulent layer as shown by Liepmann and Laufer[5]. Details on transition point will be found in the next chapter.

### Sinusoidal Velocity Fluctuations

An interesting finding in the present experiment is the existence of sinusoidal velocity fluctuation in the transition region of separated layer. After the laminar boundary-layer separates at the trailing edge, it remains laminar in some distance and then occurs the velocity fluctuation which is a regular sinusoidal wave. Fig. 4 shows some examples of such fluctuations. Frequency increases with wind speed, while for a certain wind speed, frequency is nearly constant throughout whole field in which the sinusoidal wave exists. It is difficult to tell exactly where the region of sinusoidal fluctuation is, because the wave changes its form as it goes downstream. It is illustrated in Fig. 5. Records at three $x$-stations show the change of wave-from before a typical turbulence pattern is established.

At first, such a fluctuation was considered as the result of some external disturbances rather than inherent velocity fluctuation in separated layer. Influences of periodical wake from fan-blades, organ pipe resonance of air column in wind-tunnel, disturbance by diffuser duct in downstream and vibration of hot-wire support which were carefully checked did not explain such a high-level sinusoidal fluctuation. In fact, the fluctuation level can be several percent of main-stream velocity. Turbulence in main-stream is low and shows no periodical natures. Influence of external disturbance was felt only when the separated layer was excited by sound from loudspeaker. When the frequency of sound coinsides with that of velocity fluctuation, the amplitude of fluctuation increases remarkably and waveform is purely sinusoidal as shown in Fig. 6. The detailed study concerning excitation effects will be reported in the near future.

In Fig. 7, the frequency is plotted against wind speed. Because of some irregularities of sinusoidal wave, errors of 10 percent is probable in frequency measurements from oscillograghic records. As shown in the figure, frequency is nearly proportional to 3/2 power of main-stream velocity. This is understandable from a simple dimensional reasoning. The frequency might relate to wind speed and layer thickness. Using main-stream velocity $U_0$ and momentum thickness $\theta$, frequency $f$ might be expressed by $f=\text{const.}\ U_0/\theta$. $\theta$ for laminar layer is expressed by $\theta=\text{const.}\ (\nu x/U_0)^{1/2}$ from which $f=\text{const.}\ (\nu x)^{1/2}U_0^{3/2}$.

In Fig. 8, records at three $y$-position are reproduced. At $y=0$, it is fully turbulent, while traces at layer boundary show the intermittency. There is still a slight difference between two wave-forms, upper one at the main-stream boundary and lower one at the still-air boundary.

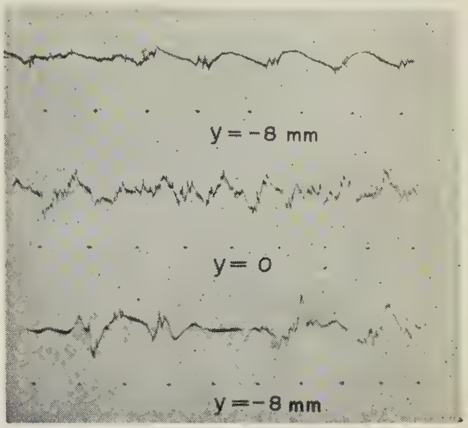

Fig. 8. $u$-fluctuation records at various $y$-positions, with Plate I, $U_0=7.0$ m/s and $x=100$ mm. Time interval between dots 0.01 sec.

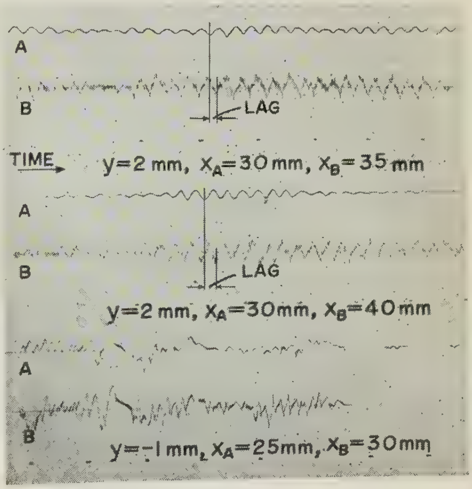

Fig. 9. Simultaneous records with two hot-wires at different $x$-stations. Time interval between dots, 0.01 sec.

Fig. 9 shows a simultaneous record by two hot-wires in the layer. When two wires are placed several millimeters apart in $x$-direction, phase lag of two sinusoidal waves is clearly observed. When they are placed apart in $y$-direction, two waves are in phase. These facts mean that the sinusoidal wave travels in $x$-direction with a certain wave velocity. From such records, time lag is plotted in Fig. 10, taking $x=30$ mm as an origin. Wave velocity corresponds to the gradient of straight line. Points at different $y$-position come roughly on a single straight line suggesting a constant wave velocity throughout the layer. For the theoretical line by Lessen and Lin, discussion will be presented in the following chapter.

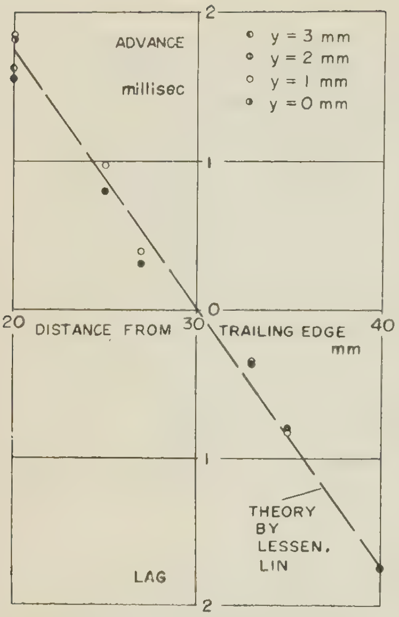

Fig. 10. Time lag of sinusoidal fluctuation.

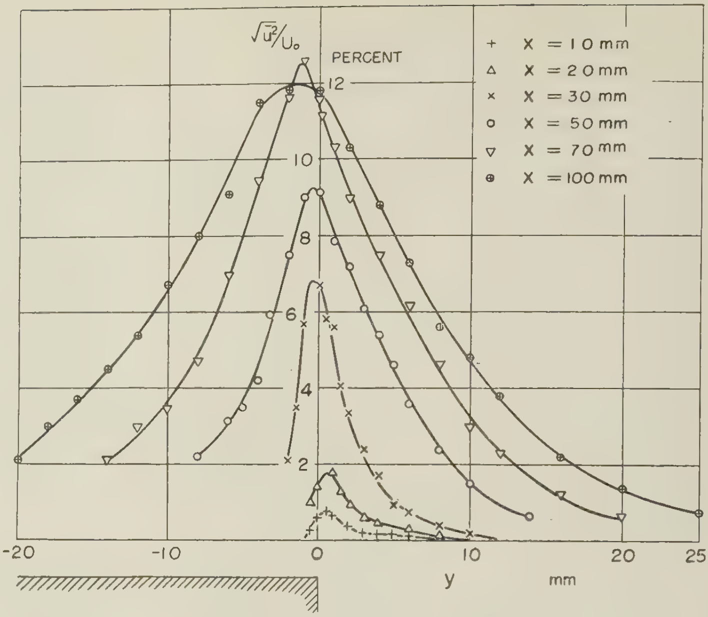

Fig. 11. Turbulence level distribution, Plate II, $U_0=10.0$ m/s.

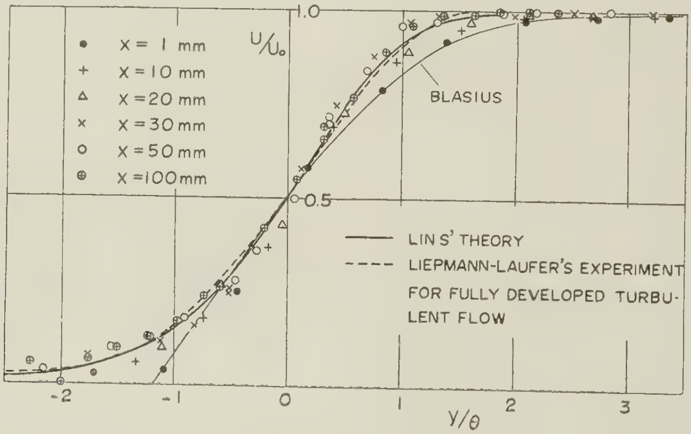

Fig. 12. Non-dimensional plot of mean velocity distribution, Plate II, $U_0=10.0$ m/s.

### Turbulence Energy

An example of turbulence level distribution is shown in Fig. 11. There is a sudden increase of energy at the transition region. Distribution for large $x$, tends to a similar profile, keeping a constant peak value and spreading in $y$-direction. In the case of Fig. 11, the layer is supposed to be fully turbulent at $x=100$ mm by many reasons which will be mentioned later.

## § 4. Discussion

### Mean Velocity

In Fig. 12, mean velocity distribution of Fig. 2 is plotted non-dimesionally using momentum thickness $\theta$ and fixing the point of $U/U_0=0.5$ as $y/\theta=0$. A theoretical curve calculated by Lin is shown together with Blasius profile on a flat plate. The distribution changes from Blasius profile to a similar distribution which is established approximately at $x=20$ mm. Since the similarity of mean velocity distribution is assumed in the course of stability theory, it must be checked by experiments before detailed comparison is made. In the present experiment, similarity was almost proved in the laminar seperated layer. In the same figure, experimental results in fully developed turbulent half jet by Liepmann and Laufer are added. By a non-dimensional plot, two curves—Lin's calculation for laminar and experimental for turburent layer—show so slight difference that it is difficult to point out the transition point from mean velocity distribution itself. This is a great contrast with the case of boundary-layer near solid wall.

**Sinusoidal Wave**

The sinusoidal fluctuation found in separated layer seems to be essentially the same as the one reported by Schubauer and Skramstad with the name of laminar boundary-layer oscillation. In separated layer, however, there are no ways of justifying the use of same word since no positive reasons are found why the layer is laminar.

Stability of free boundary-layer was treated theoretically by Lessen[3]. He solved Orr-Sommerfeld equation numerically and calculated one branch of neutral stability curve for Reynolds number from 16 to infinity. Lin also attacked the same problem with compressibility effects. Numerical results were given only for infinite Reynolds number[4]. Comparisons of experimental data with those theories are shown in Figs. 10 and 13.

In stability theory, perturbation stream fuction is expressed by

$$\phi(y) \exp i\alpha(x-ct) , \qquad (1)$$

where $\alpha$ is wave number, and separating $c=c_r+ic_i$, real part $c_r$ is the wave velocity and imaginary part $c_i$ is the rate of amplification of small disturbance. If $c_i$ is zero, the disturbance is in neutral stability, that is, it is neither amplified nor damped.

Comparison for wave velocity is found in Fig. 10. Wave velocity corresponds to the gradient of straight line. Theoretical values for neutral stability are,

Lin: $c_r=0.576$
for Reynolds number=infinity

Lessen: $c_r=0.584$
for Reynolds number=280

Both value is very close and agrees reasonably well with experiments. Because the experimental velocity fluctuation is not in neutral stability, it should be compared with theoretical values for same amplification rate. Unfortunately, complete calculation has not reported yet. Since $c_r$ seems to change little with the value of $c_i$, such a comparison as Fig. 10 may still have some significance.

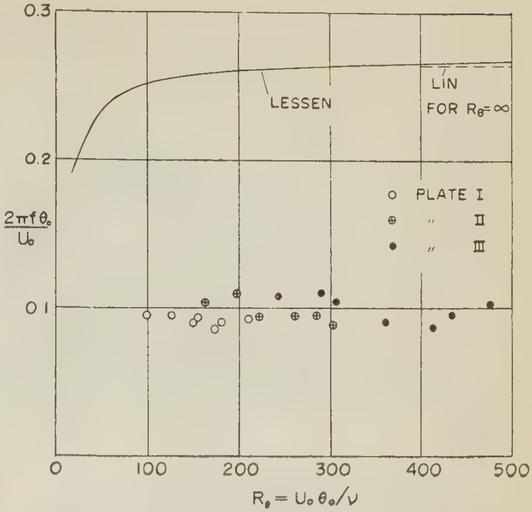

Fig. 13. Non-dimensional plot of sinusoidal fluctuation. $\theta_0$: momentum thickness at trailing edge.

For wave number, fluctuation frequency was compared, because it can be measured more easily and accurately. Relation between wave number and frequency is given by

$$\frac{2\pi f\theta}{U_0} = 1.16\,\alpha c_r , \qquad (2)$$

in which $f$ is frequency and momentum thickness for laminar layer is assumed to be expressed by

$$\theta = 1.16\sqrt{\nu(x+x_s)/U_0} , \qquad (3)$$

where $U_0$ is main-stream velocity and $x_s$ is co-ordinate of virtual origin of layer. Eq. 3 was given by Lin theoretically. In Fig. 13, Lessen's thoretical curve is expressed by a full-line and experimental data for three boundary-layer plates are plotted. For $\theta$, values at trailing edge is used for simplicity because the thickness of laminar layer does not change so much. Experimental data seem to lie in the unstable zone or probably on the curve of maximum amplification. This can not be stated with certainty, because the second branch of neutral stability curve and curves for various amplification rates have not been calculated. Lin's theoretical value for infinite Reynolds number is added with some corrections*.

---

* A slight numerical mistake in Lin's final expression for wave number was pointed out by T. Tatsumi.[9]

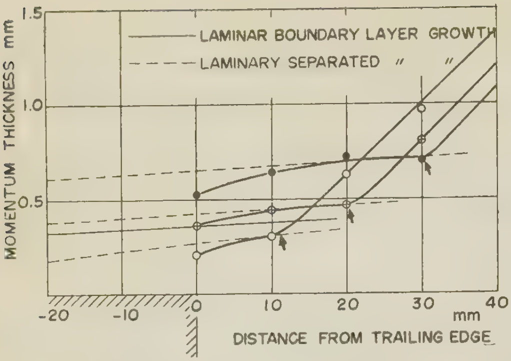

Fig. 14. Detail of momentum thickness increase near trailing edge. Arrows indicate transition points.

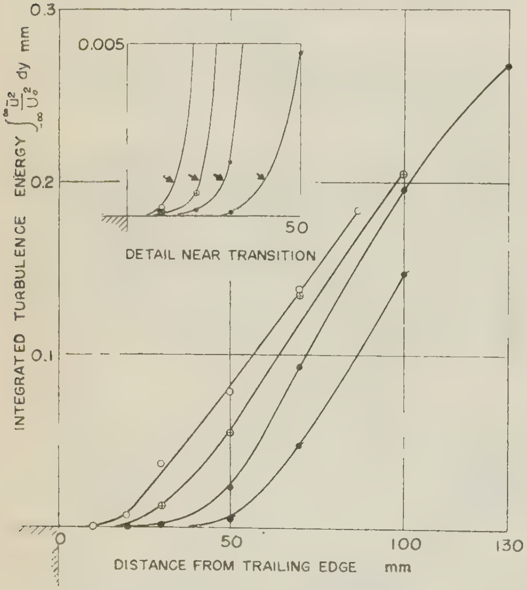

Fig. 15. Integrated energy increase. Arrows indicate transition.

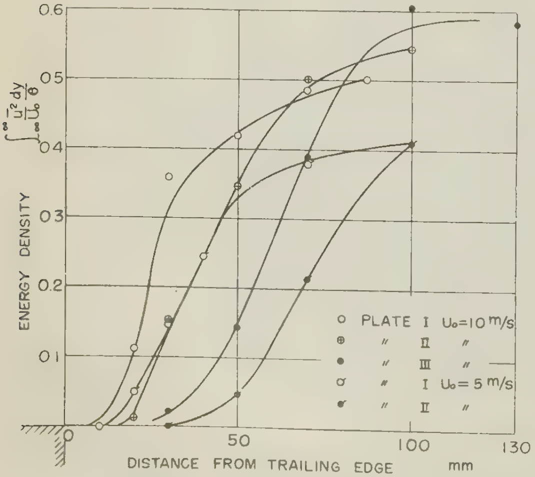

Fig. 16. Energy density.

## Position of Transition

There are many ways for locating transition point. Actually, trasition does not occur at a "point" but the layer changes gradually from laminar to turbulent. Therefore, "transition region" should be the word. In this paper "transition point" is used just for the sake of simplicity.

From mean velocity survey, transition is observed. As described before, velocity distribution itself can not be used. The difference of thickness increase of laminar and turbulent layer was used by Linke for locating the trasition point[1]. He assumed that the thickness of laminar layer increased proportional to the square root of distance from a virtual origin and defined the transition point where this law broke down. The same method was applied to the present case. Fig. 14 shows the detail of thickness increase near transition point. Transition points are determined as indicated by arrows. Broken lines show the growth of separated layer, while a full line is for boundary-layer near solid wall. Transition distance $x_t$ for various flow conditions are tabulated in Table I.

Table I.

| Plate | $U_0$ m/s | $\frac{U_0\theta_0}{\nu}$ | From thickness $x_t$ mm | $\frac{U_0x_t}{\nu}$ | $\frac{x_t}{\theta_0}$ | From turbulence $x_t$ mm | $\frac{U_0x_t}{\nu}$ | $\frac{x_t}{\theta_0}$ |
|---|---|---|---|---|---|---|---|---|
| I | 10.0 | 180 | 12 | 8,000 | 44 | 13 | 8,600 | 48 |
| II | 10.0 | 280 | 20 | 13,300 | 47 | 21 | 14,000 | 50 |
| III | 10.0 | 430 | 30 | 20,000 | 46 | 29 | 19,000 | 45 |
| III | 5.0 | 280 | 44 | 15,000 | 52 | 40 | 13,000 | 47 |

Another way of locating transition point is from turbulence measurements. If there is velocity fluctuation in a flow, it should be called turbulent. When the fluctuation is sinusoidal, however, it is not necessarily called turbulent because it is not irregular fluctuation. In order to avoid the complexity of definition, we call any fluctuation as turbulence at the present. In Fig. 15, turbulence energy integrated in $y$-direction is plotted. Transition can be observed by a sudden increase of energy. Values of transition distance are added in Table I. Comparing two columns of different methods, values are in good coincidence. This may prove the validity of rather indirect method by Linke for determining the transition point. Table I also shows that the transition distance is 40 to 50 times of momentum thickness at the trailing edge within the range of present experiment. This may be interesting from a practical view point.

In Fig. 19, energy density is plotted. It is defined as the integrated energy divided by momentum thickness. It is zero at the beginning and increases with $x$-distance approaching nearly a constant value for each wind speed. When the miximum value is reached, the layer may be considered as "fully developed turbulent". Taking into account of the value obtained by Liepmann and Laufer, energy density for fully developed turbulent separated layer seems to be proportional to the square root of main-stream velocity.

## §5. Concluding Remarks

In the laminnar separated layer, a similar, velocity distribution is established and it agrees reasonably well with theoretical calculations. The momentum thickness is proportional to the square root of distance from a virtual origin when the layer is laminar and proportional to distance when turbulent.

Sinusoidial velocity fluctuation in transition region seems to correspond to the unstable wave which is predicted by stability theory.

Transition distance from separation point is 40 to 50 times of momentum thikness at the separation point.

The author wishes to express his appreciation to Professor Itiro Tani for constant advices and encouragements and thank to Professor Tomomasa Tatsumi for valuable suggestions in the theoretical phase. Acknowledgement is extended to Messrs Y. Onda and S. Kyoya who assisted in carring out the experimental program.

This work was finacially supported by the Scientific Research Fund of the Ministry of Education.

## References

1) W. Linke: Physik. Zeits. **32** (1931) 900-914.
2) A. Fage and F. C. Johansen: Proc. Roy. Soc. **A 116** (1927) 170-197 also Brit. ARC R & M 1104 (1927).
3) M. Lessen: NACA Tech. Rep. 979 (1950).
4) C. C. Lin: NACA Tech. Note 2887 (1953).
5) H. W. Liepmann and J. Laufer: NACA Tech. Note 1257 (1947).
6) to be published.
7) H. Sato, Y. Kobashi, M. Iuchi, K. Yamamoto and Y. Onda: Rep. Inst. Sci. Tech. Univ. Tokyo **8** (1954) 271-283.
8) G. B. Schubauer and H. K. Skramstad: NACA Tech. Rep. 909 (1948).
9) T. Tatsumi: private communication.

JOURNAL OF THE PHYSICAL SOCIETY OF JAPAN Vol. 11, No. 6, JUNE, 1956

# The Flow past a Flat Plate accompanied with an Unsymmetric Dead Air at Mach Number 1

By Takeo SAKURAI

*Department of Physics, Faculty of Science, University of Tokyo*

(Received March 13, 1956)

The flow past a flat plate accompanied with an unsymmetric dead air, especially the flow past such a flat plate with a small angle of attack at Mach number 1, is investigated, using Imai's WKB method. Comparing the results with those of Guderley and of Truitt, it is ascertained that these agree fairly well with each other. It may be concluded that the dead air model is useful for the study of the transonic flow.

## §1. Introduction

Recently, Guderley investigated the flow past a flat plate with a small angle of attack at Mach number 1, using the hodograph method as simplified by the transonic approximation1). Assuming that the flow condition in the expansion region from the leading edge has very little influence upon the flow over the pressure side, he succeeded in determining the pressure distribution over the pressure side in a relatively simple analytical expression.

If the angle of attack is small enough, however, it is also expected that the flow condition in the expansion region from the trailing edge has little influence upon the flow over the pressure side. Hence, we may safely neglect the influence of both the expansion regions from the leading and the trailing edges. As Guderley stated, however, the character of the free stream singularity being determined, it is essential to represent the stagnation point as a branch-point of the stream lines. Thus, the flow conditions which are essential to determine the pressure distribution over the pressure side may be summarised as follows:

i) *The stagnation point is a branch-point of the stream lines.*

ii) *At the leading and the trailing edges the sonic velocity is reached.*

As the simplest model that retains the above-mentioned properties, we shall adopt the flow past a flat plate accompanied with an unsymmetric dead air at Mach number 1.

Besides the above significance, the dead air model has further advantage that it can be regarded as an inviscid limit of the real viscous fluid. In fact, if the angle of attack is finite, the flow separates from the leading and the trailing edges; in such a case the dead air model is more reliable than the model of the continuous flow. But, if the angle of attack is small enough, Guderley's solution, which is the continuous flow type, is expected to be highly reliable. Hence, we must examine the accuracy of our results comparing with those of Guderley in the case of vanishingly small angle of attack, and to such an examination the present study is mainly directed.

The flow past a flat plate accompanied with an unsymmetric dead air was studied extensively by Hida2), using the exact hodograph equation and expanding the results in power series of $M_\infty{}^2$. However, his results do not seem to be reliable for the case of Mach number 1, because his results cannot contain the law of transonic similarity6).

It must be remarked that the idea of the dead air model was already applied by Prof. Imai4) to the case of a finite wedge at Mach number 1. The boundary conditions are almost the same in both cases except the unsymmetric nature of our problem.

In the course of the study, we have become aware of the similar study by Truitt7). His results are also compared with ours.

## §2. Basic Relations

According to Imai's WKB method3),5), the exact equation for the two-dimensional steady irrotational flow of an inviscid compressible fluid can be approximated as follows:

For purely subsonic flow

$$\left(\frac{\partial^2}{\partial\tau^2}+\frac{\partial^2}{\partial\theta^2}\right)\psi=0\,, \tag{2.1}$$

and for transonic flow

$$\left(\frac{\partial^2}{\partial\tau^2}+\frac{\partial^2}{\partial\theta^2}\right)\psi=-\frac{5}{36}\frac{1}{\tau^2}\psi\,, \tag{2.2}$$

where

$$\tau=-\int_1^q \mu\frac{dq}{q}\,, \tag{2.3}$$

$$\mu=\sqrt{1-M^2}\,, \tag{2.4}$$

$$\Psi=K^{-1/4}\psi\,, \tag{2.5}$$

$$K=\left(\mu\frac{\rho_0}{\rho}\right)^2, \tag{2.6}$$

and $(q, \theta)$ are the magnitude and the direction of the velocity vector, $M$ the local Mach number, $\Psi$ the stream function, $\rho$ the density and $\rho_0$ the stagnation density.

The correspondence between the physical and the hodograph planes is expressed as follows:

$$dx+idy=q^{-1}e^{i\theta}[d\Phi+i(\rho_0/\rho)d\Psi]\,, \tag{2.7}$$

$$\frac{\partial\Phi}{\partial\tau}=K^{1/2}\frac{\partial\Psi}{\partial\theta}\,,\qquad \frac{\partial\Phi}{\partial\theta}=-K^{1/2}\frac{\partial\Psi}{\partial\tau}\,, \tag{2.8}$$

where $(x, y)$ are the Cartesian coordinates and $\Phi$ is the velocity potential.

For the adiabatic gas, we have

$$\mu=\left(\frac{1-q^2}{1-a^2q^2}\right)^{1/2}, \tag{2.9}$$

$$\tau=\tanh^{-1}\mu-a^{-1}\tanh^{-1}a\mu\,, \tag{2.10}$$

$$K=(1-q^2)(1-a^2q^2)^{-1/a^2}\,, \tag{2.11}$$

$$a^2=\frac{\gamma-1}{\gamma+1}\,, \tag{2.12}$$

where $\gamma$ is the ratio of the specific heats, and the unit of the magnitude of the velocity is taken to be the critical velocity $c^*$, at which the fluid velocity is equal to the local velocity of sound.

## § 3. The Boundary Value Problem in the Hodograph Plane

In order to formulate the boundary-value problem for the dead air model, let us consider the flow field in the hodograph plane (Fig. 1).

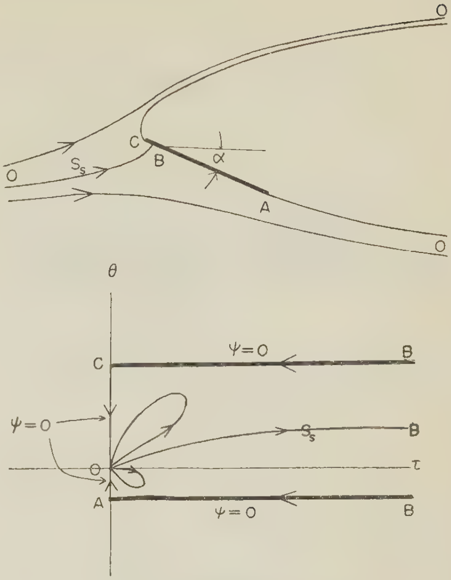

Fig. 1.

All stream lines start from the infinity upstream of the physical plane with the sonic velocity, which corresponds to the singular point O in the hodograph plane. Among the stream lines which start from O, the stagnation stream line $S_s$ has the special character. As one proceeds along the stagnation stream line towards the flat plate, the inclination of the velocity vector will increase, and its magnitude will decrease. At the stagnation point B, the magnitude of the velocity vector vanishes, and the stream line bifurcates into two branches. One of these two branches then follows the lower side of the flat plate towards the leading edge C and the other towards the trailing edge A, these branches corresponding to the straight lines BC and BA respectively in the hodograph plane. At the leading and the trailing edges, the magnitude of the velocity vector attains to the sonic velocity, and the stream lines separate from the plate to form the free stream lines, which correspond to the straight lines CO and AO respectively in the hodograph plane. The correspondence between the physical and the hodograph planes for other stream lines is obtained quite analogously, and it is easily seen that the flow field in the hodograph plane is bounded by the stagnation stream lines.

The boundary condition in the hodograph plane is, as usual, $\psi=0$ on the stagnation stream lines.

## § 4. The Method of Solution

Let us consider the transformation

$$\tau=\alpha\tau_s\,,\quad \theta=\alpha\theta_s\,, \tag{4.1}$$

$$\tau_1=\alpha k\,, \tag{4.2}$$

where $\tau_1$ corresponds to $q_1$, the magnitude of the velocity of the undisturbed flow, and $\alpha$ the angle of attack of the flat plate. The basic

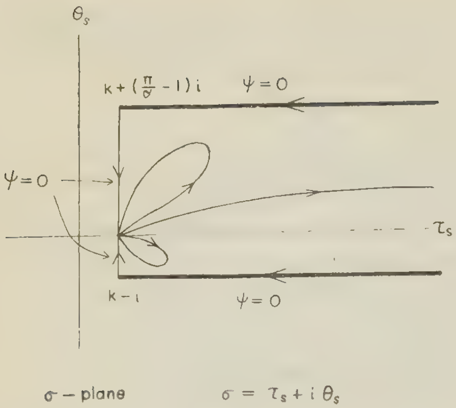

Fig. 2.

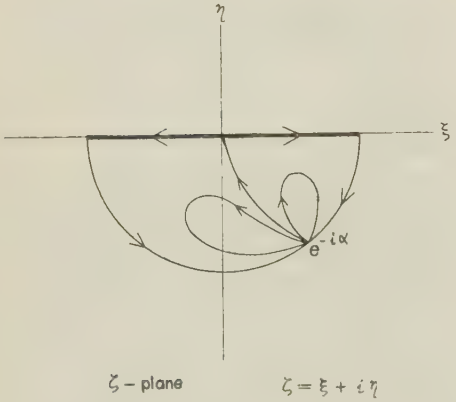

Fig. 3.

equations (2.1) and (2.2) remain unchanged for the transformation (4.1), yielding

$$\left(\frac{\partial^2}{\partial\tau_s^{\,2}}+\frac{\partial^2}{\partial\theta_s^{\,2}}\right)\psi=0\ , \tag{4.3}$$

and

$$\left(\frac{\partial^2}{\partial\tau_s^{\,2}}+\frac{\partial^2}{\partial\theta_s^{\,2}}\right)\psi=-\frac{5}{36}\frac{1}{\tau_s^{\,2}}\psi\ . \tag{4.4}$$

We first solve (4.3) and (4.4) with the boundary conditions as shown in Fig. 2, then, making $k$ and $\alpha$ tend to zero in the solution, we obtain the solution of our problem. For the sake of simplicity we shall omit the suffix $s$ hereafter.

Since the solutions of Eq. (4.3) represent the incompressible flow in the $\sigma$-plane (Fig. 2), we can solve the above boundary-value problem by the usual method of conformal mapping. By means of a relation

$$\zeta=e^{\alpha(k-i)}e^{-\alpha\sigma}\ , \tag{4.5}$$

the flow field in the $\sigma$-plane (Fig. 2) is mapped onto the flow field in the $\zeta$-plane (Fig. 3).

By superposing the dipole and the quadrupole solutions, we can easily obtain the complex velocity potential for the flow in the $\zeta$-plane,

$$\begin{aligned}w(\zeta)&=N\zeta\left\{\frac{e^{i\alpha}}{(\zeta-e^{i\alpha})^2}+\frac{e^{-i\alpha}}{(\zeta-e^{-i\alpha})^2}\right\}\\&\quad+iN\frac{\cos\alpha}{\sin\alpha}\left\{\frac{e^{i\alpha}}{\zeta-e^{i\alpha}}-\frac{e^{-i\alpha}}{\zeta-e^{-i\alpha}}\right\}\\&=\frac{2N}{\sin\alpha}\sum_{n=1}^{\infty}(n\sin\alpha\cos n\alpha-\cos\alpha\sin n\alpha)\zeta^n\ .\end{aligned} \tag{4.6}$$

Substituting (4.5) into Eq. (4.6), and then taking the imaginary part, we can obtain the solution as follows:

$$\psi(\tau,\theta)=\frac{2N}{\sin\alpha}\sum_{n=1}^{\infty}(\cos\alpha\sin n\alpha-n\sin\alpha\cos n\alpha)\times\frac{e^{-\alpha n\tau}}{e^{-\alpha nk}}\sin\alpha n(\theta+1)\ . \tag{4.7}$$

The right-hand side of (4.7) is the expanded form by the particular solutions $e^{-\alpha n\tau+i\alpha n\theta}$ of (4.3) in the rectangular domain. Therefore, if we replace the particular solutions of Eq. (4.3) by those of (4.4), i.e.;

$$\frac{e^{-\alpha n\tau}}{e^{-\alpha nk}}\sin\alpha n(\theta+1)\rightarrow\frac{\tau^{1/2}K_{1/3}(\alpha n\tau)}{k^{1/2}K_{1/3}(\alpha nk)}\times\sin\alpha n(\theta+1)\ , \tag{4.8}$$

in (4.7), we can obtain the solution for (4.4) as follows:

$$\psi(\tau,\theta)=\frac{2N}{\sin\alpha}\sum_{n=1}^{\infty}(\cos\alpha\sin n\alpha-n\sin\alpha\cos n\alpha)\times\frac{\tau^{1/2}K_{1/3}(\alpha n\tau)}{k^{1/2}K_{1/3}(\alpha nk)}\sin\alpha n(\theta+1)\ . \tag{4.9}^*$$

Substituting the solutions (4.7) and (4.9) into the relations (2.7) and (2.8), we obtain the flow in the physical plane. We are interested only in the pressure distribution over the pressure side BA of the plate (Fig. 1), on which the boundary conditions $\theta=-1$ and $\psi=0$ are prescribed. There, the relation (2.7) takes the form,

$$dl=q^{-1}K^{1/4}\left(\frac{\partial\psi}{\partial\theta}\right)_{\theta=-1}d\tau\ , \tag{4.10}$$

where $l$ is the length measured from the trailing edge along the side AB.

Thus, we obtain

---

* It is easily proved that (4.9) satisfies the boundary conditions by putting $\tau=k_1$ or $\theta=-1$, $(\pi/\alpha)-1$ in (4.9).

$$dl=\frac{2N}{\sin\alpha}q^{-1}\mathrm{K}^{1/4}$$
$$\times\sum_{n=1}^{\infty}(\cos\alpha\sin n\alpha-n\sin\alpha\cos n\alpha)$$
$$\times\frac{e^{-\alpha n\tau}}{e^{-\alpha nk}}(\alpha n)d\tau \qquad (4.11)$$

from (4.7), and

$$dl=\frac{2N}{\sin\alpha}q^{-1}K^{1/4}$$
$$\times\sum_{n=1}^{\infty}(\cos\alpha\sin n\alpha-n\sin\alpha\cos n\alpha)$$
$$\times\frac{\tau^{1/2}K_{1/3}(\alpha n\tau)}{k^{1/2}K_{1/3}(\alpha nk)}(\alpha n)d\tau \qquad (4.12)$$

from (4.9).

The pressure distribution $\tau(l)$, the pressure coefficient $C_p$, and the location $x_c$ of the centre of pressure for the flat plate are given by the formulae,

$$\frac{l}{L}=\int_0^\tau dl\bigg/\int_0^\infty dl\,, \qquad (4.13)$$
$$C_p=\int_0^\infty c_p dl\bigg/\int_0^\infty dl\,, \qquad (4.14)$$
$$x_c=\int_0^\infty \frac{l}{L}c_p dl\bigg/\int_0^\infty c_p dl\,, \qquad (4.15)$$

where $c_p$ is the local pressure coefficient:

$$c_p=\frac{p-p_\infty}{\frac{1}{2}p_\infty q_\infty}=\frac{2}{\gamma M_\infty^2}\left(\frac{p}{p_\infty}-1\right). \qquad (4.16)$$

Here we make further approximations which correspond to the usual transonic approximations

$$q^{-1}\doteqdot 1\,, \qquad (4.17)$$
$$K^{1/4}\doteqdot\left[\frac{3}{2}(\gamma+1)\right]^{1/6}\left(\frac{\rho_0}{\rho^*}\right)^{1/2}\alpha^{1/6}\tau^{1/6}, \qquad (4.18)$$
$$c_p\doteqdot\left(\frac{\gamma+1}{2}\right)^{-1/3}(3\alpha\tau)^{2/3}\,, \qquad (4.19)$$

where $\rho_0$ is the density of the fluid at rest, and $\rho^*$ is the density at the sonic state. Then we have from (4.11)

$$\frac{l}{L}=\int_0^\tau \tau^{1/6}T_{10}(\tau)d\tau\bigg/\int_0^\infty \tau^{1/6}T_{10}(\tau)d\tau\,, \qquad (4.20)$$
$$\tilde{C}_p=\left[\int_0^\infty \tau^{5/6}T_{10}(\tau)d\tau\bigg/\int_0^\infty \tau^{1/6}T_{10}(\tau)d\tau\right]$$
$$\times 2^{1/3}\times 3^{2/3}\,, \qquad (4.21)$$
$$x_c=\int_0^\infty \frac{l}{L}\tau^{5/6}T_{10}(\tau)d\tau\bigg/\int_0^\infty \tau^{5/6}T_{10}(\tau)d\tau\,, \qquad (4.22)$$

where

$$T_{10}(\tau)=N_{10}\sum_{n=1}^{\infty}(\alpha n)\frac{e^{-\alpha n\tau}}{e^{-\alpha nk}}$$
$$\times(\cos\alpha\sin n\alpha-n\sin\alpha\cos n\alpha)\,, \qquad (4.23)$$

and from (4.12)

$$\frac{l}{L}=\int_0^\tau \tau^{1/6}T_{20}(\tau)d\tau\bigg/\int_0^\infty \tau^{1/6}T_{20}(\tau)d\tau\,, \qquad (4.24)$$
$$\tilde{C}_p=\left[\int_0^\infty \tau^{5/6}T_{20}(\tau)d\tau\bigg/\int_0^\infty \tau^{1/6}T_{20}(\tau)d\tau\right]$$
$$\times 2^{1/3}\times 3^{2/3}\,, \qquad (4.25)$$
$$x_c=\int_0^\infty \frac{l}{L}\tau^{5/6}T_{20}(\tau)d\tau\bigg/\int_0^\infty \tau^{5/6}T_{20}(\tau)d\tau\,, \qquad (4.26)$$

where

$$T_{20}(\tau)=N_{20}\sum_{n=1}^{\infty}(\cos\alpha\sin n\alpha-n\sin\alpha\cos n\alpha)$$
$$\times\frac{\tau^{1/2}K_{1/3}(\alpha n\tau)}{k^{1/2}K_{1/3}(\alpha nk)}(\alpha n)\,, \qquad (4.27)$$

and $\tilde{C}_p$ is the modified pressure coefficient;

$$\tilde{C}_p=C_p\times(\gamma+1)^{1/3}\alpha^{-(2/3)}\,, \qquad (4.28)$$

where $N_{10}$ and $N_{20}$ are the constants which are derived from $N$.

In the above formulae, $T_{10}(\tau)$ and $T_{20}(\tau)$ are the only terms which depend upon $\alpha$ and $k$. Hence, in order to obtain their limiting forms for $k\to 0$ and $\alpha\to 0$, we have only to investigate the behaviour of $T_{10}(\tau)$ and $T_{20}(\tau)$ in this case. Using the formulae,

$$\lim_{k\to 0}e^{-\alpha nk}=1\,, \qquad (4.29)$$
$$\lim_{k\to 0}\{k^{1/2}K_{1/3}(\alpha nk)\}^{-1}=\frac{3^{1/2}\Gamma(2/3)}{2^{1/3}\pi k^{1/6}}(\alpha n)^{1/3}\,, \qquad (4.30)$$

and noting that the summation reduces to the integral in the limit $\alpha\to 0$, we have

$$T_1(\tau)=\lim_{\alpha\to 0}(\lim_{k\to 0}T_{10}(\tau))$$
$$=N_1\int_0^\infty xe^{-\tau x}(\sin x-x\cos x)dx\,, \qquad (4.31)$$
$$T_2(\tau)=\lim_{\alpha\to 0}(\lim_{k\to 0}T_{20}(\tau))$$
$$=N_2\tau^{1/2}\int_0^\infty x^{4/3}K_{1/3}(\tau x)(\sin x-x\cos x)dx\,, \qquad (4.32)$$

where $N_2$ and $N_3$ are the constants derived from $N_{10}$ and $N_{20}$. The integrals in the above formulae are easily evaluated, obtaining

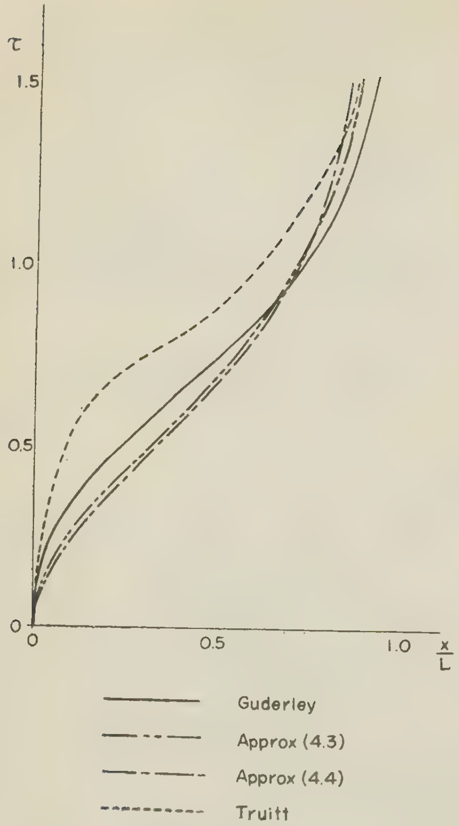

Fig. 4.

$$T_1(\tau)=N_1\frac{8\tau}{(\tau^2+1)^3}, \tag{4.33}$$

$$T_2(\tau)=N_2\frac{55\times\pi^{1/2}\times 2^{1/3}}{18}\,\Gamma(5/6)\,\frac{\tau^{5/6}}{(1+\tau^2)^{17/6}}, \tag{4.34}$$

where the formulae

$$\int_0^\infty x\sin x\, e^{-\tau x}dx=\frac{2\tau}{(\tau^2+1)^2}\,{}^{8)}, \tag{4.35}$$

$$\int_0^\infty x\cos x\, e^{-\tau x}dx=\frac{\tau^2-1}{(\tau^2+1)^2}\,{}^{9)}, \tag{4.36}$$

$$\int_0^\infty x^{\nu+1}K_\nu(\tau x)\sin x\,dx$$

$$=\pi^{1/2}(2\tau)^\nu\Gamma\{(3/2)+\nu\}(1+\tau^2)^{-(3/2)-\nu}\,{}^{10)}, \tag{4.37}$$

$$\frac{d}{dx}K_{1/3}(\tau x)=\frac{1}{3x}K_{1/3}(\tau x)-\tau K_{4/3}(\tau x), \tag{4.38}$$

have been used.

Substituting (4.33) and (4.34) into (4.20)–(4.27) we have

$$\frac{l}{L}=\int_0^\tau\frac{\tau^{7/6}}{(\tau^2+1)^3}d\tau\Big/\int_0^\infty\frac{\tau^{7/6}}{(\tau^2+1)^3}d\tau, \tag{4.39}$$

$$\tilde{C}_p=2^{1/3}\times 3^{2/3}\times\int_0^\infty\frac{\tau^{11/6}}{(\tau^2+1)^3}d\tau\Big/\int_0^\infty\frac{\tau^{7/6}}{(\tau^2+1)^3}d\tau, \tag{4.40}$$

$$x_c=\int_0^\infty\frac{l}{L}\frac{\tau^{11/6}}{(\tau^2+1)^3}d\tau\Big/\int_0^\infty\frac{\tau^{11/6}}{(\tau^2+1)^3}d\tau, \tag{4.41}$$

for the purely subsonic approximation (4.3), and

$$\frac{l}{L}=\int_0^\tau\frac{\tau}{(\tau^2+1)^{17/6}}d\tau\Big/\int_0^\infty\frac{\tau}{(\tau^2+1)^{17/6}}d\tau, \tag{4.42}$$

$$\tilde{C}_p=2^{1/3}\times 3^{2/3}$$

$$\times\int_0^\infty\frac{\tau^{5/3}}{(\tau^2+1)^{17/6}}d\tau\Big/\int_0^\infty\frac{\tau}{(\tau^2+1)^{17/6}}d\tau, \tag{4.43}$$

$$x_c=\int_0^\infty\frac{l}{L}\frac{\tau^{5/3}}{(\tau^2+1)^{17/6}}\Big/\int_0^\infty\frac{\tau^{5/3}}{(\tau^2+1)^{17/6}}d\tau, \tag{4.44}$$

for the transonic approximation (4.4).

The integrals in these formulae are easily evaluated analytically, except the numerators of (4.39) and (4.41), which are integrated numerically using Simpson's rule. The simplicity of the calculations is the greatest merit of the dead air model.

## § 5. Results

The results are represented in Table I and in Fig. 4, together with those of Guderley and of Truitt. These agree fairly well with each other. As mentioned in § 1, our chief purpose is to examine the accuracy of our results comparing with those of Guderley at the small angle of attack, which seems to have been affirmed. Thus, as far as the pressure side is concerned, it may by concluded that the dead air model is highly reliable even in the case of a small angle of attack.

Table I.

| | $\tilde{C}_p$ | $x_c$ |
|---|---|---|
| Guderley | 2.12 | 0.35 |
| Truitt | — | 0.38 |
| Approx. (4.3) | 2.23 | 0.38 |
| Approx. (4.4) | 2.20 | 0.37 |

**Acknowledgement**

The writer wishes to express his cordial thanks to Prof. Isao Imai for his kind guidance and encouragement. The author is also indebted to Dr. Hidenori Hasimoto for his invaluable advice and discussions in the course of study.

**References**

1) G. Guderley: Journ. Aero. Sci. **21** (1954) 261.
2) K. Hida: Unpublished.
3) I. Imai: Journ. Math. Phys. **28** (1949) 173.
4) I. Imai: Journ. Aero. Sci. **19** (1952) 496.
5) I. Imai: Journ. Phys. Soc. Japan **9** (1954) 1009.
6) Th. v. Kármán: Journ. Math. Phys. **26** (1947) 182.
7) R. W. Truitt: Journ. Aero. Sci. **21** (1954) 713.
8) A. Erdélyi: *Theory of Integral Transforms*, Vol. 1 (1954) 72.
9) A. Erdélyi: ibid. 14.
10) A. Erdélyi: ibid. 105.

---

# Short Notes

This section is intended to secure prompt publication of important discoveries in physics. The reports should not exceed 800 words in length. A figure of size 7 cm × 7 cm will be counted as 150 words.

J. Phys. Soc. Japan **11** (1956) 715~716

## On the Frequency Dependence of the Fatigue of Metals

By Takeo Yokobori

*Department of Mechanical Engineering, Tohoku University, Sendai, Japan*

(Received April 16, 1956)

The theory of tatigue fracture suggested by the author[1] predicts that the number of cycles for fracture is proportional to the frequency of the applied stress. The data recently reported by Head and cooperators,[2] however, have shown some discrepancy for this predicted frequency dependence. The following points may be suggested in explaining this discrepancy.

It is likely that some type of microscopic void has already been formed in the periphery of the obstacle before the initiation of the fatigue crack as proposed in the reference (1). The conclusion may be predicted by the fact the calculated value of the stress concentration factor $q_1$ induced by the obstacle itself fitted to the data is considerably large[1][3]. Thus, the total number of repeated cycles for fracture, $N_t$ is expressed as follows:

$$N_t = N_0 + N_i + N_g \qquad (1)$$

where

$N_0$ = the cycles required for the initiation of the microscopic void in the periphery of the obstacle against which dislocations pile up. The process may be determined by such a process as proposed by Fujita[4].

$N_i$ = the repeated cycles during which the fatigue crack as suggested in the reference (1) initiates as nucleation process after the stress has been repeated $N_0$ cycles.

$N_g$ = the repeated cycles during which the crack grows up and the specimen fractures.

In the case of some steels, especially harder steel, $N_i$ was assumed to have the major part of the total fatigue life, and the theoretical S-N relation was in good agreement with the data[1]. In the case of non-ferrous metals such as used by Head and cooperators[2], however, near-by Frank-Read sources[5] may be operated and the stress concentration at the apex of the fatigue crack may be relaxed. Consequently, in such a case $N_g$ may have the major part of the fatigue life. On the other hand, such growth process may be described by the Head's mechanism[6], and, therefore, the total life for fracture will be little affected by the frequency of the applied stress in such a case.

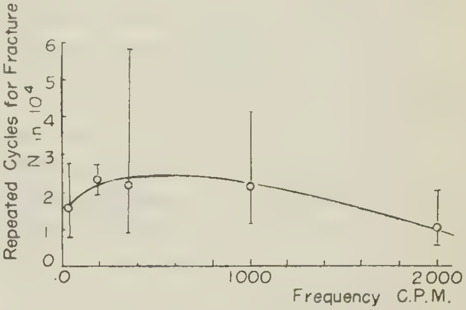

Fig. 1. 0.41% carbon steel, stress range = 38.4 kg/mm². (mean stress = 0) Ono's rotary bending test.

Another reason for the discrepancy may be as follows: The temperature of the specimen increases as the frequency increases. $N_i$ decreases with the increase of the temperature of the specimen as suggested by the theory[1] other things being equal. Hence, it may be understood that $N_i$ decreases with the increase of frequency above some limit. The experimental data on harder steel predict such effect as shown in Fig. 1.

The author wishes to express hearty thanks to Professor M. Hirata in Tokyo University for useful advise and discussion.

## References

1) T. Yokobori: J. Phys. Soc. Japan **10** (1955) 368.
2) A. K. Head: J. Phys. Soc. Japan **11** (1956) 468.
3) T. Yokobori: J. Appl. Mech. (to be published)
4) F. E. Fujita: Science Reports of the Research Institutes, Tohoku University, A **6**, No. 6 (1954) 565 (in English).
5) F. C. Frank and W. T. Read: Phys. Rev. **79** (1950) 722.
6) A. K. Head: Phil. Mag. **44** (1953) 925.

---

J. PHYS. SOC. JAPAN **11** (1956) 716~717

# Electrical Properties of Stannous Telluride SnTe

By Kimio HASHIMOTO and Kazuyosi HIRAKAWA

*Department of Physics, Faculty of Science, Kyusyu University, Hukuoka*

(Received April 16, 1956)

The electrical resistivity $\rho$, the Hall coefficient $R$ and the thermoelectric power $d\Theta/dT$ of stannous telluride SnTe have been measured between about 100° and 1000°K. The procedure of the perparation of the compound $SnTe_x$ is as follows: a mixture of granular tin (high purity Merck) and tellurium (99.998%, obtained from the Nihon Kōgyō K.K.) with a desired proportion was sealed in an evacuated silica tube, and was heated at 850°C for 15 hours and cooled, and then some samples were twice purified by zone melting in vacuum. From X-ray analysis, the crystal structure of the sample of stoichiometric composition was found to be the face-centred-cubic type (probably NaCl type)[1] with a lattice constant of 6.32 Å at room temperature.

Table I. Resistivity, Hall coefficient and thermoelectric power of $SnTe_x$ at room temperature.

| Sample No. | $x$ | $\rho\times10^4$ (ohm·cm) | $R\times10^3$ $\left(\frac{cm^3}{coulomb}\right)$ | $d\Theta/dT$ $\left(\frac{\mu V}{°C}\right)$ | $R/\rho$ $\left(\frac{cm^2}{volt\cdot sec}\right)$ | $1/eR\times10^{-20}$ $(cm^{-3})$ |
|---|---|---|---|---|---|---|
| 1* | 1.00 | 1.35 | +10.1 | — | 75 | 6.2 |
| 2* | 1.01 | 1.38 | + 7.58 | +33.3 | 55 | 8.3 |
| 3* | 0.99 | 0.49 | +14.6 | +29.2 | 297 | 4.3 |
| 4* | 1.10 | 1.12 | +13.4 | — | 120 | 4.7 |
| 5** | 1.00 | 1.37 | +11.9 | +29.1 | 87 | 5.2 |
| 6*** | 1.00 | 1.26 | + 7.45 | — | 59 | 8.4 |

* Polycrystalline,
** Zone-melt, polycrystalline,
*** Zone-melt, single crystalline.

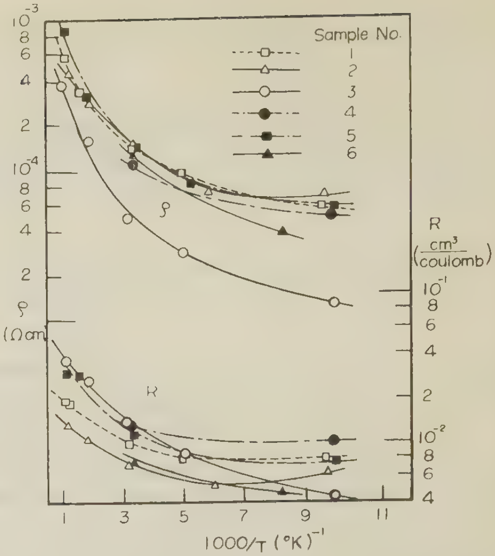

Fig. 1. Resistivity $\rho$ and Hall coefficient $R$ of SnTe as a function of the inverse absolute temperature.

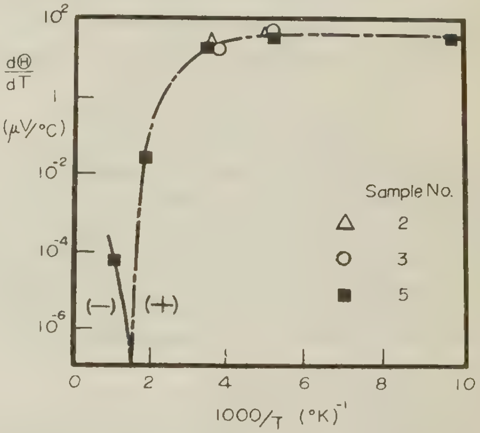

Fig. 2. Thermoelectric power $d\Theta/dT$ of SnTe as a function of the inverse absolute temperature.

In Table I, the observed data of $\rho$, $R$ and $d\Theta/dT$ at room temperature are summarized, and the values of the Hall mobility $R/\rho$ and the carrier concentration $1/eR$ are also shown. The temperature dependence of $\rho$, $R$ and $d\Theta/dT$ are shown in Figs. 1 and 2, respectively. As shown in Fig. 1, the values of $\rho$ and $R$ for all samples, except for the sample 3, have almost the same values at each temperature.

It should be noted that the temperature coefficients of both $\rho$ and $R$ are positive for all samples in the whole temperature range.

The thermoelectric power at room temperature is in good agreement with the value +26.0 μV/°C obtained by Haken[2)], and the change of the sign of the thermoelectric power is found at about 250°C.

Several attempts to explain the above results of SnTe are now being carried on.

### References

1) R. Wyckoff: *Crystal Structures* (Interscience Publishers, Inc., New York, 1948), Vol. I.
2) W. Haken: Ann. Phys. **32** (1910) 291.

---

J. Phys. Soc. Japan **11** (1956) 717

## Mechanism for Self-Diffusion in Metallic Lithium

By Tadanobu KOJIMA

*Department of Physics, Faculty of Science, Osaka University*

(Received March 12, 1956)

Activation energy of self-diffusion in metallic lithium was calculated for various mechanisms. In the case of an interstitial atom, we have taken the trial wave functions for the conduction electrons of the form

$$\varphi_k=\psi_k(1+\beta e^{-\alpha r}), \qquad (1)$$

where $\psi_k$ is the Bloch function of a conduction electron in a perfect crystal, $\alpha$ and $\beta$ are variational parameters, and then orthogonalized them to the wave functions of the interstitial core electrons. It is essentially important to take account of this non-orthogonality between the wave functions; a simple Huntington-Seitz[1)] type calculation without this correction yields a negative formation energy. In the case of a vacancy, each trial function of the form (1) was modified so as to eliminate an oscillating part of the original Bloch function within the vacancy cell. The variational parameters and the positions of the ions surrounding a given lattice defect were determined so as to minimize the total energy of the crystal. Our calculated energy is about 1.0 ev for the formation of an interstitial atom and less than 0.1 ev for its migration. For the vacancy, we have obtained a value of 0.4 ev for its formation and 0.3 ev for its migration. Holcomb and Norberg[2)] measured a value of 0.6 ev for the activation energy by nuclear magnetic resonance technique, which is in good agreement with our theoretical value, 0.4+0.3 =0.7 ev. Ring mechanisms should here be excluded since they need at least 2 ev.[3)] We may conclude that the dominant mechanism of diffusion in lithium, and presumably in all other alkali metals, is due to the formation and migration of vacancies. The same mechanism may also predominate in other b.c.c. metals such as $\alpha$-iron for which the formation of interstitials should be more unfavorable because of the strong ion-core repulsions. A full account of this work with further refinements will be published in this journal.

### References

1) H. B. Huntington and F. Seitz: Phys. Rev. **61** (1942) 315.
H. B. Huntington: Phys. Rev. **91** (1953) 1092.
2) D. F. Holcomb and R. E. Norberg: Phys. Rev. **98** (1954) 1074.
3) H. R. Paneth: Phys. Rev. **80** (1950) 708.

---

J. Phys. Soc. Japan **11** (1956) 717~718

## On the Inductive Reactance and Negative Resistance in the Transistor

By Jiro YAMAGUCHI

*Faculty of Engineering, Osaka University*

(Received February 13, 1956)

The inductive reactance in the transistor shown in Fig. 1 which has been previously explained[1)], is interpreted from another point of view as follows: In the $n$-region of the transistor in Fig. 1 the boundary condition is given as

$$p=p_n+p_0+p_1e^{j\omega t} \quad \text{at} \quad x=0$$
$$\text{and} \quad p=p_d \quad \text{at} \quad x=d.$$

Combining this with the recombination equation

$$\partial p/\partial t=(p_n-p)/\tau_p+D\partial^2 p/\partial x^2$$

leads to the solution for the a.c. part of hole current

$$J_p(x)=qD_p\Gamma_1 p_1\frac{\exp(j\omega t)}{2\sinh(\Gamma_1 d)}[\exp\Gamma_1(d-x)+\exp\Gamma_1(x-d)]$$

where $\Gamma_1=(1+j\omega\tau_p)^{1/2}/L_p$

and the other symbols are defined as reference (2). Let $J_e$ and $J_c$ be $J_p(x)$ at $x=0$ and $x=d$, respectively and $J_b=J_e-J_c$. When $\omega\tau_p>1$ and $\Gamma_1 d<1$, each component of hole current is described as below

$$J_e=qD_p(p_1/d)(1+j\omega\tau_p d^2/2L_p^2)\exp(j\omega t),$$
$$J_c=qD_p(p_1/d)\exp(j\omega t)$$
$$\text{and} \quad J_b=qD_p p_1 j\omega\tau_p(d/2L_p^2)\exp(j\omega t).$$

The bulk resistance of $n$-region is assumed to be $R_b$, the applied a.c. voltage is the sum of $v_0$ and $J_b(R_b+Z)$, the former being the potential difference across the barrier. From the vector diagram of a.c. voltage and current in case of $Z=R$ (Fig. 2), it is concluded that $J_e$ lags the applied voltage, consequently the inductive reactance appears, if $(R_b+R)$ is appropriately large. The lagging

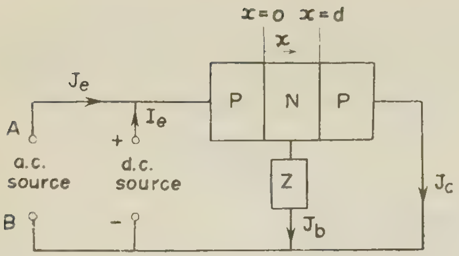

Fig. 1. Electric connection diagram studied.

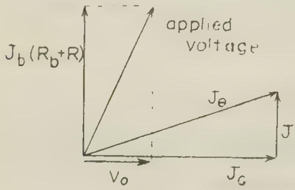

Fig. 2. Vector diagram of a.c. voltage and current.

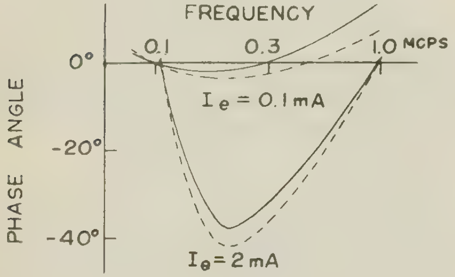

Fig. 3. Phase angle versus a.c. frequency, $Z$ in Fig. 1 being $R$. (Full lines for $Z=0$. Dotted lines for $Z=50\,\mathrm{k\Omega}$.)

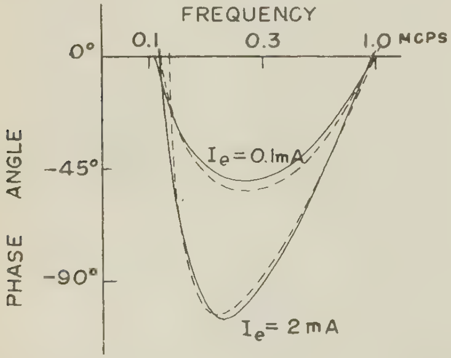

Fig. 4. Phase angle versus a.c. frequency, $Z$ in Fig. 1 being $L$. (Full lines for grown type. Dotted lines for alloyed type.)

angle shown in Fig. 3 is measured by the Lissajous figure of a.c. voltage versus current on the cathode-ray oscilloscope.

Assuming $Z$ in Fig. 1 to be inductive reactance, Fig. 2 suggests that the negative resistance would arise. Fig. 4 shows the experimental results of the lagging angle versus a.c. frequency. The magnitude of negative resistance comes up to 500 ohms without difficulty.

Using the negative resistance mentioned above, we can easily obtain the electric oscillation by connecting a condenser across the terminals A and B of Fig. 1. In an ordinary alloyed transistor the oscillation is of sine wave form and attains to 0.8 volt across the condenser terminals, and its frequency varies from about 100 kcps to 300 kcps according to the magnitude of inductance and capacitance.

The author expresses his sincere thanks to M. Kajiwara and H. Haruki for their experimental helps.

### References

1) Y. Kanai: J. Phys. Soc. Japan **10** (1955) 718.
2) W. Shockley: B.S.T.J. **28** (1949) 487.

---

J. Phys. Soc. Japan **11** (1956) 718~719

## On the Interpretation of Magnetic Torque Reversal

By Sōshin Chikazumi

*Department of Physics and Chemistry,*
*Gakushuin University,*
*Mejiro, Tokyo, Japan*

(Received March 29, 1956)

It was first found by Nesbitt, Williams and Bozorth[1)] that the torque of $Fe_2NiAl$ crystal at first decreases and finally reverses its sign when the intensity of the magnetic field is increased. Similar behavior was also found on the model which consists of three perpendicular rods of magnetic material. Basing upon this fact they concluded that the torque reversal is due to the fine precipitate particles elongated along ⟨100⟩ directions. The torque reversal have also been observed for Alnico 5 by Nesbitt and Williams[2)] and recently for Co-ferrite by Williams, Heidenreich and Nesbitt[3)]. The latter investigators found also that torque reversal did not occur in the material which is insensitive to the magnetic annealing. In their works they interpreted the torque reversal as an evidence of the presence of elongated precipitates. I should like to point out, however, that the torque reversal can be explained as a result of usual magnetic annealing irrespective of the mechanism of the induced anisotropy.

When the material in question is cooled without magnetic field, the intrinsic magnetizations would be stabilized in their directions during cooling. If the crystal anisotropy constant $K_1$ is positive, the stabilized directions are ⟨100⟩. Now we shall give attention at first to the $x$-domain in which the intrinsic magnetization are stabilized in $x$ direction. When the field is applied in $(\beta_1, \beta_2, \beta_3)$ direction, the energy density is given as a function of direction of intrinsic magnetization $(\alpha_1, \alpha_2, \alpha_3)$ by

$$E_x = -K_u\alpha_1^2 - HJ_s(\alpha_1\beta_1+\alpha_2\beta_2+\alpha_3\beta_3)\ , \qquad (1)$$

where the first term represents the uniaxial anisotropy induced by the intrinsic magnetic annealing.

The direction of intrinsic magnetization can be solved by minimizing Eq. (1) under the restriction $\alpha_1^2+\alpha_2^2+\alpha_3^2=1$. By assuming that $HJ_s \gg K_u$, thus we have approximately

$$\left.\begin{aligned} \alpha_1 &= \beta_1+2(\beta_1\beta_2^2+\beta_1\beta_3^2)(K_u/HJ_s) \\ \alpha_2 &= \beta_2-2\beta_2\beta_1^2(K_u/HJ_s) \\ \alpha_3 &= \beta_3-2\beta_3\beta_1^2(K_u/HJ_s) \end{aligned}\right\} \qquad (2)$$

Putting Eq. (2) into Eq. (1), we have an energy density as a function of direction cosines of applied field as

$$E_x = -HJ_s - K_u\beta_1^2 - \frac{4K_u^2}{HJ_s}(\beta_1^2\beta_2^2+\beta_1^2\beta_3^2)\ . \qquad (3)$$

The similar expression can be obtained for $y$- or $z$-domains. By averaging them, we have finally

$$E = -HJ_s - \frac{K_u}{3} - \frac{8K_u^2}{3HJ_s}(\beta_1^2\beta_2^2+\beta_2^2\beta_3^2+\beta_3^2\beta_1^2). \qquad (4)$$

The last term in Eq. (4) express an anisotropy energy having a similar functional form as that of crystal anisotropy energy. Together with the crystal anisotropy energy $K_1(\beta_1^2\beta_2^2+\beta_2^2\beta_3^2+\beta_3^2\beta_1^2)$, we find the coefficient of the anisotropy energy to be $(K_1 - 8K_u/3HJ_s)$, whose sign is reversed when the field $H$ becomes larger than $8K_u/3K_1J_s$. This means the torque reversal, because the torque is equal to the first derivative of an anisotropy energy. When $K_1<0$, the similar reversal of anisotropy energy (from positive to negative) would also be calculated in the same way.

Thus we can conclude that the torque reversal are related to the effect of usual magnetic annealing, but not particularly to the precipitation particles.

## References

1) E. A. Nesbitt, H. J. Williams and R. M. Bozorth: J. Appl. Phys. **25** (1954) 1014.
2) E. A. Nesbitt and H. J. Williams: J. Appl. Phys. **26** (1955) 1217.
3) H. J. Williams, R. D. Heidenreich and E. A. Nesbitt: J. Appl. Phys. **27** (1956) 85.

---

J. Phys. Soc. Japan **11** (1956) 719∼720

# A Remark on the Excitement of the Electrodes when a Positive Joshi Effect Inversion is Observed under Continuous Discharge

By Bogdan Sujak

*Institute of Experimental Physics, Boleslaw Bierut University, Wroclaw, Poland*

(Received March 12, 1956)

Joshi's theory of the instantaneous and reversible photovariation (enhancement $+\Delta i$ and diminution $-\Delta i$) of the current $i$ under silent electrical discharge in some of gases, contemplates emission of photoelectrons from activated adsorptionlike ionic and molecular layer on the electrodes as primary. Capture of slow photoelectrons by the electronegative atoms or molecules is leading to a negative space charge and the negative effect $-\Delta i$. When the electrons escape capture and cause an increase in the current $i$, the positive effect $+\Delta i$ is observed1)2).

Many experiments on this problem, showing the surface dependence of the Joshi effect were done by Mohanty and coworkers1)-9). These authors works cleared that the inversion of the Joshi effect (from $+\Delta i$ to $-\Delta i$) can be observed when increasing only one of the two parameters: 1. the illuminating light intensity, 2. the frequency of the illuminating light, when a suitable voltage is put on across the electrodes covered with a dielectric layer. Mohanty4) observed also, that the positive Joshi effect $+\Delta i$ changes sign to the negative $-\Delta i$ under continuous exposure to discharge (aging). This phenomenon of inversion is described by Mohanty to increased cathode emissivity due to a progressive diminution in the surface workfunktion through disappearence of the adsorbed gas layer by desorption or/and chemical interaction5).

The recent works on the induced emissivity of electrons from oxides of metals10-13) and dielectric layers14-18) showe that one is obliged to take in acount not only the electrode surface-gas interface as the seat of the residual electrons deposited by the antecedent half cycle, but also some of generated imperfections in the insulating layer. The increasing emissivity partly can also be seen as due to a progressive increase of the imperfections concentration in the excited cathode. On this imperfections the Mohanty's residual electrons seems to form some color centres22) like F- and F'-centres, at least in the cases when alkaline halides were used6-9). In the first stage the color centres are generating during the gas discharge being so the source of the additional free electrons (the primary of the inversion effect) when photoionised. In this way the color centres should take part in the observed inversion of the positive Joshi effect under continuous discharge in respect to progressive increasing of their concentration in the surface layer.

To confirme the mentioned point of view I give the schematic graph of the inversion effect with "aging" under continuous discharge⁴⁾ in comparison with a schematic graph of the progressive change of photoelectric emission from a KCl layer observed by me and due to color centres generated by continuous discharge.¹⁸⁾ The quantum yield of the emission of photoelectrons from the color centres produced in the examined surface layer of alkaline halides depends to their concentration¹⁸⁻²¹⁾. Therefore, when a Siemens' glass tube containing finely powdered potasium chloride is used a generating of color centres takes place in a KCl layer on the glass walls, and the Joshi effects, as well as, its inversion from positive to negative is more pronounced.

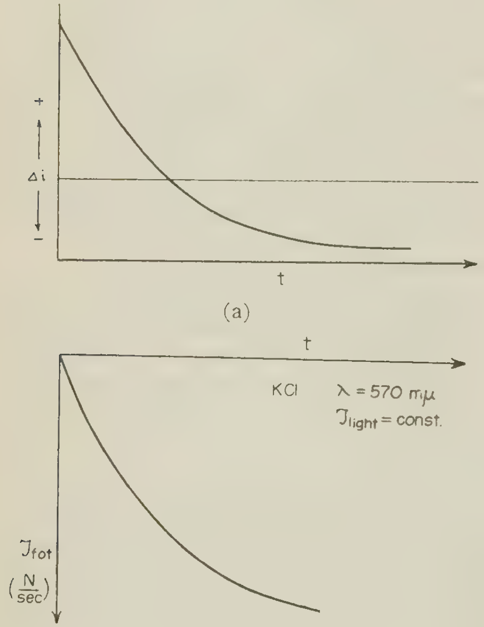

(a)

(b)

Fig. 1. (a) Inversion of the positive Joshi effect during "aging" under discharge.⁴⁾
(b) The progressive change of the photoelectrons emission from KCl layer abserved by the author (schematicly), due to the progressive excitement of the layer by continuous discharge. The exciting discharge was interrupted when photoelectrons measured with a G.M. counter.¹⁸⁾

It must be cleared, that a generation of color centres in a glass surface may also take place²³⁾ and so cooperate in the inversion of Joshi effect, when clean glass "electrodes" are used. The author's preliminary observations of the induced emission of photoelectrons under visible light from excited glass (cleaned up or with a layer of dirt) show that it is especially large, when the glass surface is first mechanicaly deformed—scratched. The emissivity was induced in atmospheric air by bombarding the glass with sparks of a small Tessla coil. The photoelectrons were measured with an open, atmospheric Geiger counter as used by Kramer. The study on the induced emissivity from glass is carried on.

The author wishes to thank Prof. Dr. J. Nikliborc for stimulating discussions on the solid state problems and Dr. S. R. Mohanty for his kind help in the literature problem on the Joshi effect.

## References

1) S. R. Mohanty: J. Chem. Phys. **22** (1954) 1010.
2) S. R. Mohanty: Z. Phys. **140** (1955) 370.
3) S. R. Mohanty: J. Phys. Soc. Japan **9** (1954) 578.
4) S. R. Mohanty: Z. Phys. Chem. Neue Folge **4** (1955) 233.
5) S. R. Mohanty: Nuovo Cimento **2** (1955) 1107.
6) S. R. Mohanty, J. Yayaraman and V. G. Krishna Rao: J. Scient. and Ind. Res. **13 B** (1954) 526.
7) S. R. Mohanty: J. Phys. Soc. Japan **10** (1955) 163.
8) S. R. Mohanty: J. Scient. and Ind. Res. **13 B** (1954) 145.
9) S. R. Mohanty: J. Scient. Res. Banaras Indu Univ. **5** (1954–55) 11.
10) A. Bohun: Czechosl. Journ. Phys. **5** (1955) 429.
11) A. Bohun, K. Karpiskova and A. Duskova: Czechosl. Journ. Phys. **5** (1955) 100.
12) L. Grunberg and K. H. R. Wright: Proc. Roy. Soc. London **232** (1955) 402.
13) K. H. Seeger: Z. Phys. **141** (1955) 221.
14) A. Bohun: Czechosl. Journ. Phys. **4** (1954) 139.
15) A. Bohun: Czechosl. Journ. Phys. **5** (1955) 64.
16) B. Sujak: Acta Phys. Pol. **12** (1953) 241.
17) B. Sujak: Acta Phys. Pol. **14** (1955) 263.
18) B. Sujak: Zeszyty Naukowe U.B.B. **1 B** (1956) 151.
19) L. Apker and E. Taft: Phys. Rev. **79** (1950) 964.
20) L. Apker and E. Taft: Phys. Rev. **81** (1951) 698.
21) L. Apker and E. Taft: Phys. Rev. **83** (1952) 479.
22) F. Seitz: Rev. Mod. Phys. **26** (1954) 7.
23) K. Przibram: Verfärbung und Lumineszenz, Springer Verlag-Wien 1953 pp. 73–76.

# Errata

## Note on Rayleigh's Problem for a Circular Cylinder with Uniform Suction and Related Unsteady Flow Problem

By Hidenori HASIMOTO

J. Phys. Soc. Japan **11** (1956) 611-612

| line | | | |
|---|---|---|---|
| 5 left | unstead | should be read | unsteady |
| (1) | $u=-u_0r/a$ | 〃 | $u=-u_0a/r$ |
| (9) | $\left(\frac{a}{r}\right)^{\kappa}$, $-\nu s2t$ | 〃 | $\left(\frac{a}{r}\right)^{\kappa\cdot\boldsymbol{I}}$, $-\nu s^2t$ |
| (12) | $=\kappa+\cdots$, $\exp(-\nu s^2t$ | 〃 | $=\kappa\cdot\boldsymbol{I}+\cdots$, $\exp(-\nu s^2t)$ |
| (14) | $(\kappa>0)$ | 〃 | $(\kappa\neq0)$ |
| (15) | $\frac{D}{2\pi\mu W}$, Erfc | 〃 | $\frac{D}{\mu W}$, Erf |

# PROGRESS OF THEORETICAL PHYSICS

*(Founded by H. Yukawa in 1946)*

Published for the
**Research Institute for Fundamental Physics**
**The Physical Society of Japan**

Progress of Theoretical Physics Vol. 15, No. 2, February 1956

Populations and Evolution of Stars ........................................ Mitsuo TAKETANI, Takeo HATANAKA and Shinya OBI.. 89

Theory of Electron Multiplication in Silicon ........................Jiro YAMASHITA.. 95

Supernova Origin of Cosmic Rays ..................................Satio HAYAKAWA..111

Pion Theory of Nuclear Forces .......................................... Kazuhiko INOUE, Shigeru MACHIDA, Mitsuo TAKETANI and Toshiyuki TOYODA..122

Intermediate Coupling Meson Theory of Nuclear Forces, II ..................................Yukihisa NOGAMI and Hiroichi HASEGAWA..137

Quantum Statistical Mechanics of Electron-Phonon System ........ Hiroshi ICHIMURA..151

On a Regular Formulation of Quantum Field Theory, I
—*Non-Relativistic Theory*—..............................Ken-iti GOTO..167

Letters to the Editors:

On Solutions of He$^3$ and He$^4$...............S. K. TRIKHA and V. S. NANDA..178

Note on the Decay Interactions of Hyperons and Heavy Mesons...... .....................................M. KAWAGUCHI and K. NISHIJIMA..180

Note on the Decays of $\Sigma$ Particles........M. KAWAGUCHI and K. NISHIJIMA..182

On the Energy Dissapation of Conduction Electrons undergoing Elastic Scattering by Impurities ..................T. YAMAMOTO and K. OKADA..184

Interaction of Antinucleons in Matter, I .... J. IWADARE and S. HATANO..185

Errata ..........................................................................187

Price $ 1.25 per copy
$ 15.00 per year (postage inclusive)
Annual dues for foreign members (individual subscribers)
$ 12.00 (postage inclusive)
〃 for foreign members of the Physical Society of Japan
$ 10.00 (postage inclusive)

Application for members, subscriptions and orders for back numbers should be sent, directly or through book-dealers, to

The Publication Office
in
**Yukawa Hall, Kyoto University, Kyoto, Japan**

JOURNAL OF THE PHYSICAL SOCIETY OF JAPAN Vol. 11, No. 7, JULY, 1956

# Transformations of Various Centres among Each Other in Coloured Alkali-halide Crystals

By Hisao YAGI

*Department of Physics, University of Kyoto*

(Received December 20, 1955)

Photo-thermal transformations among various centres in coloured alkali-halide crystals are studied here collectively.

## §1. Introduction

In general, there are photo-thermal transformations among various centres in coloured alkali-halide crystals. For instance, Seitz¹⁾ and Petroff²⁾ have shown that by exposure to F-light, the F-band is reduced and the M-band is at first formed and then the M-band is reduced and the R- and N-bands are enhanced. Conversely, by heating the crystal having the F-, R-, M- and N-bands, the R-, M- and N-bands are all reduced and only the F-band is enhanced. In the present paper we have studied photo-thermal transformations among V-, K-, F-, R-, M- and N-centres.

## §2. Experimental Procedures

NaCl, KCl, KBr and LiF crystals used in these experiments were grown in our laboratory³⁾ by Kyropoulos' method, and perfectly annealed at 400°C. In order to subject the crystals to electrolysis, they were mounted in a furnace in a way as shown in Fig. 1. A crystal was supported between two iron rods which served as a part of the electrical circuit supplying the current for electrolysis. (This is called "pointed-electrode method".) The one rod (A) is sharply pointed at one end and acts as cathode. The other (B) contacts the crystal with the carbon plates covered with platinum foil and acts as anode. Current is supplied by a 450 volt power supply with a 500 KΩ resister.

After inserting a crystal in the furnace, the temperature of the furnace was raised up to 450°C∼500°C and current was supplied and colour cloud was made electrolytically in the crystal. This coloured condition is called "F-coloured". Then the temperature of the furnace was brought down to 350°C∼400°C and the coloured cloud in the crystal was removed by reversing the polarity of the current. This coloured condition is called "K-coloured". For the purpose of the irradiation with X-rays, use was made of a Mazda Sealex tube, operated at a voltage of 30 KV D.C. and a current of 8 mA. The crystals used were always freshly cleaved on all sides at the last possible moment before starting experiments.

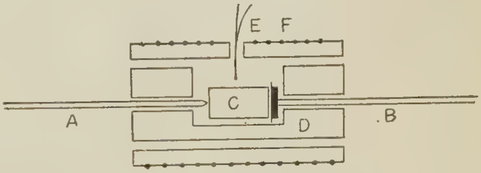

Fig. 1. Arrangement for subjecting crystals to electrolysis.
A: cathode, B: anode, C: crystal, D: holder, E: thermocouple, F: furnace.

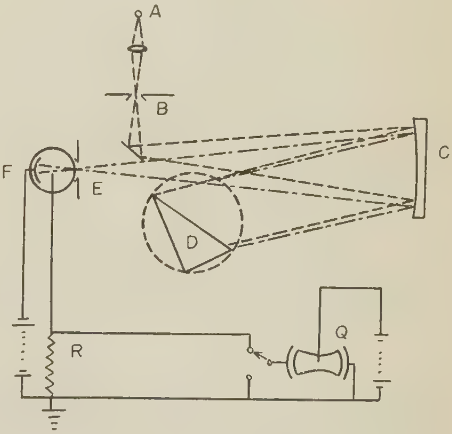

Fig. 2. Arrangement for measuring absorption.
A: light source, B: 1st slit, C: collimator mirror, D: prism, E: 2nd slit, F: photocell, R: $10^{10}$ ohms, Q: quadrant electrometer.

The absorption spectra of the crystals were obtained with a large apertured glass-prism spectraphotometer with 1.5 meter focal length objective and a quartz-prism spectrophotometer of medium size. Monochromatic light from the second slit was measured photo-

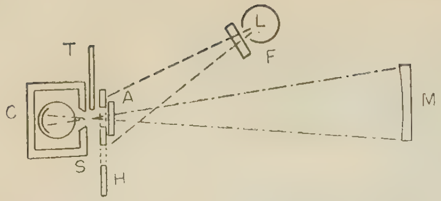

Fig. 3. Arrangement for bleaching crystals.
A: sample, L: bleaching light source, F: filter,
H: holder, T: shutter, S: 2nd slit,
M: collimator, C: photocell.

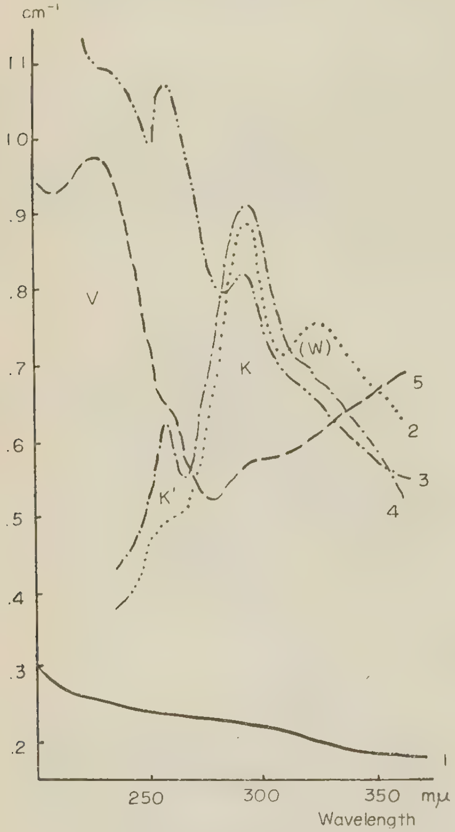

Fig. 4. Absorption bands of coloured NaCl.
1. Original crystal. 2. K-coloured in vacuum.
3. F-coloured in vacuum. 4. K-coloured in air.
5. X-ray coloured.

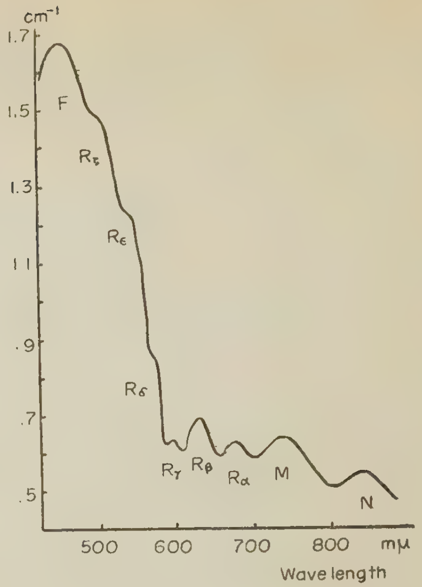

Fig. 5. Absorption bands of X-ray coloured NaCl.

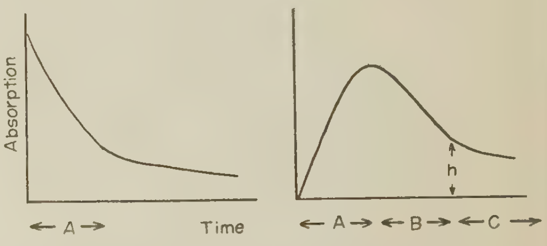

(a) Reduced band by bleaching (b) Enhanced band by bleaching

Fig. 6. Changes of the absorption coefficient of bands by bleaching (schematic).

electrically by Sb, Rb, or Cs photocells and a Dolezaleck quadrant electrometer (sensitivity: 1500 D/V) connected as shown in Fig. 2.

For light source, a projection lamp (10 volts, 80 watts) was used for visible region and a hydrogen discharge tube (6000 volts, 1 Amp.) for ultraviolet region. RCA photomultiplier tubes 1P–28 and 1P–22 were also used in place of photocells.

For light bleaching, the apparatus as shown in Fig. 3 was constructed inside the spectrometer. For bleaching light source, a projection lamp (10 V., 80 W.) was used for visible region, while a mercury lamp (110 volts, 5 Amp.) was used for ultraviolet region. Suitable filters were set between the light source and samples. When samples were bleached, the bleaching light source was put on and the shutter was closed. After bleaching, the bleaching light source was put off and the shutter was opened. The light source for the photometer was put on and the absorption spectrum was measured.

## § 3. Results

The aspects of absorption spectra of $V_2$-, K-, K′-, F-, R-, M- and N-centres described in this paper are shown in Figs. 4 and 5. The author has studied only $V_2$-bands in the X-rayed crystals. However, precise characters of V-bands produced by other methods were studied previously by Uchida and Nakai⁴⁾. K- and K′-centres are those which were observed and investigated by Uchida, Ueta and Nakai⁵⁾. The characters of R-bands were described precisely by the author in the previous paper⁶⁾. New absorption bands⁷⁾ except $V_2$-, K-, K′-, F-, R-, M- and N-bands were found according to the differences of coloured conditions and stress of crystals, i.e. according to the differences of the history of crystals. In the present paper, however, will be studied transformations among familiar $V_2$-, K-, K′-, F-, R-, M. and N-bands found in the crystals which were well annealed according to the above-described conditions.

When irradiated by the light lying in a band, the change of the absorption coefficient of that band generally becomes as shown in Fig. 6 (a). After the time " A ", the decrease of the absorption coefficient becomes very small. On the other hand, the change of the absorption coefficient of enhanced band becomes as shown in Fig. 6 (b). In this case, after the time " A ", absorption of this band is reduced and after the time " B ", the absorption coefficient becomes nearly constant. In the case of crystals irradiated by X-rays, the time " A " is about 1.5 minutes and the time " B " is nearly 5∼10 minutes. In the case of crystals coloured electrolytically the time " A " is 5∼10 minutes and the time " B " is 30∼60 minutes. The value of $h[=\{(\kappa-\kappa_0)/\kappa_0\}\times 100]$ in the figure depends on the kind of crystal, the temperature of crystal as well as on the observed absorption band, and it may become positive, zero or negative according to circumstances.

The relationships between photo-thermal transformaions among various centres are shown in Table I, which was obtained from Tables II∼VIII and Fig. 7 and is applicable to every alkali-halide crystals. In Tables II∼VIII are given the numerical values of $\{(\kappa-\kappa_0)/\kappa^0\}$

Table I. Photo-transformations of various centres in coloured alkali-halide crystals.

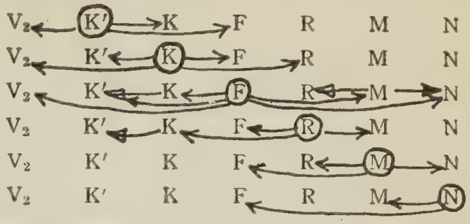

Note: ○ shows the bleached centre.
↛ shows the thermal-transformation.

Table II. K′-bleaching in KBr.

| Bleaching time in minutes | Centres | | | |
|---|---|---|---|---|
| | $V_2$ | K′ | K | F |
| 1 | 40 | −13 | 108 | 1.1 |
| 3 | 84.5 | −18 | 168 | 4.2 |
| 5 | 73.5 | −20 | 177 | 3.5 |
| 10 | 51.5 | −26 | 134 | 2.3 |
| 20 | 30 | −33 | 116 | 1.4 |
| 30 | 18 | −39 | 114 | 1.3 |
| 60 | 14 | −45 | 110 | 1.1 |

Thin Ag film was used as the filter of bleaching light.

Table III. K-bleaching in KBr.

| Bleaching time in minutes | Centres | | | | | | |
|---|---|---|---|---|---|---|---|
| | $V_2$ | K′ | K | F | $R_\alpha$ | M | N |
| 3 | 24 | 55 | −27 | 12 | 16 | 0 | 0 |
| 5 | 17 | 48 | −32 | 10 | 11 | 0 | 0 |
| 10 | 17 | 49 | −34 | 8.6 | 8.5 | 0 | 0 |
| 20 | 0 | 39 | −36 | 3 | 3 | 0 | 0 |
| 30 | 0 | 34 | −37 | 3 | 3 | 0 | 0 |

Mazda UV-Dl filter was used.

Table IV. F-bleaching in NaCl.

| Bleaching time in minutes | Centres | | | | | | | | | |
|---|---|---|---|---|---|---|---|---|---|---|
| | K′ | K | F | $R_\alpha$ | $R_\beta$ | $R_\gamma$ | $R_\delta$ | $R_\zeta$ | M | N |
| 1 | 34 | 38 | −1.5 | 0 | 0 | 0 | 0 | 0 | 11 | 9 |
| 3 | 46 | 32 | −3.9 | 20 | 15 | 17 | 16 | 14 | 2 | 15 |
| 5 | 10 | 27 | −4.8 | −1.7 | 8 | 8 | 8 | 5.7 | 1 | 15 |
| 10 | 7 | 21 | −7.5 | −10 | −3.5 | 5 | 5.3 | 3.3 | −2 | 7 |
| 20 | 6 | 12 | −10.5 | −15 | −13 | 0 | 5 | 2 | −2.7 | 4 |
| 30 | 6 | 4 | −12.2 | | −14 | −1 | 5 | 2 | −3.5 | 3 |

Table V. F-bleaching in KBr.

| Bleaching time in minutes | Centres | | | |
|---|---|---|---|---|
| | $V_2$ | K′ | K | F |
| 1 | 16.5 | 22 | 100 | −12 |
| 3 | 9.5 | 132 | 54 | −20 |
| 5 | 7 | 100 | 42 | −32 |
| 10 | 0 | 82 | 33 | −36 |
| 20 | − 7 | 75 | 17 | −48 |
| 30 | − 9 | 70 | 9.5 | −54 |
| 60 | −11 | 70 | 5 | −56 |

Table VI–a. K→F bleaching.

| Bleaching time in minutes | Crystal | | |
|---|---|---|---|
| | KBr | KCl | NaCl |
| 1 | | 20 | |
| 3 | 12 | 22 | 50 |
| 5 | 10 | 20 | 45 |
| 10 | 8.6 | 18 | 40 |
| 20 | 3 | 16 | 35 |
| 30 | 3 | 15 | 30 |

Table VI–b. F→K→K′ bleaching.

| Bleaching time in minutes | Crystal | KBr | | KCl | | NaCl | |
|---|---|---|---|---|---|---|---|
| | Bands | K′ | K | K′ | K | K′ | K |
| 1 | | 22 | 100 | 13 | 19 | 34 | 38 |
| 3 | | 132 | 54 | 20 | 17 | 46 | 32 |
| 5 | | 100 | 42 | 10 | 15 | 10 | 27 |
| 10 | | 82 | 33 | 6 | 10 | 7 | 21 |
| 20 | | 75 | 17 | 6 | 6 | 6 | 12 |
| 30 | | 70 | 9.5 | 6 | 5 | 6 | 4 |
| 60 | | 70 | 5 | 6 | − 5 | 5 | −12 |

Table VII. M-bleaching in LiF.

| Bleaching time in minutes | Centres | | | |
|---|---|---|---|---|
| | F | $R_\beta$ | M | N |
| 3 | 8 | 10 | −20 | 90 |
| 5 | 8 | 7 | −25 | 80 |
| 10 | 4 | 4 | −28 | 60 |
| 20 | 2 | 1 | −30 | 44 |
| 30 | 2 | 0 | −32 | 44 |

Table VIII. N-bleaching in LiF.

| Bleaching time in minutes | Centres | | | |
|---|---|---|---|---|
| | F | R | M | N |
| 3 | 5 | 0 | 20 | −30 |
| 5 | 1 | 0 | 15 | −40 |
| 10 | −0.5 | 0 | 12 | −50 |
| 20 | −1 | 0 | 10 | −55 |
| 30 | −3 | 0 | 10 | −60 |

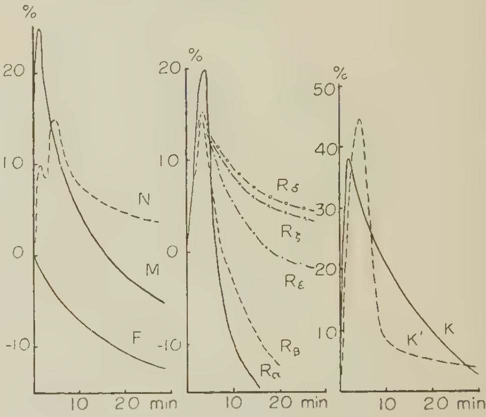

Fig. 7. Changes of the absorption bands of coloured NaCl exposed to F-light.

×100, where $\kappa_0$ is the initial absorption coefficient and $\kappa$ is the absorption coefficient after bleaching. Photo-transformations of R-bands were described in the previous paper⁶⁾. As shown in Table VI, the K→F photo-transformation is the easiest in NaCl, while in KBr the F→K→K′ photo-transformation is the easiest.

A. *Thermal Transformation.*

In Petroff's experiment, bands in the side of the longer wavelength than that of F-band were treated. We have therefore extended experiment to the region of the shorter wavelength than the F-band. Changes of the absorption of $R_\gamma$-, $R_\beta$-, F-, K- and K′-bands of KBr crystal heated from 20°C up to 150°C are shown in Fig. 8. Absorptions of F- and K′-bands in KBr crystal are reached a maximum at 120°C∼130°C. The temperature corresponding to the highest efficiency of thermal trasformation was 250°C in NaCl and 200°C in KCl.

B. *Photo-thermal Transformation*

By exposure to F-light, the K-band in coloured KBr crystal is enhanced suddenly to arrive at a point (a) shown in Fig. 9 and reduces to (b), and then to (c) slowly. If the bleaching light was put off at (a), the path of change of the absorption was as shown a→b′ and b′→c′. This action is only thermal.

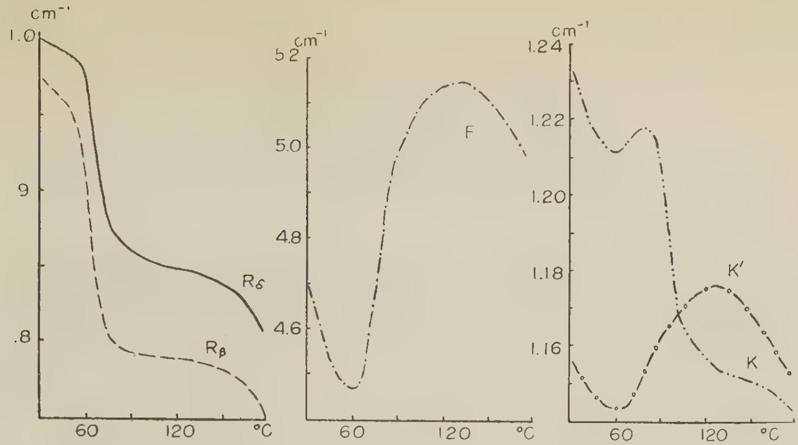

Fig. 8. Thermal transformation of the absorption bands of coloured KBr crystal.

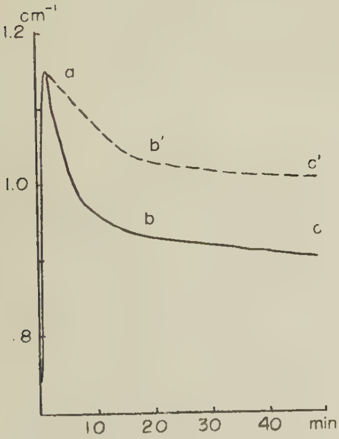

Fig. 9. Absorption of the K-band in KBr crystal exposed to F-light.

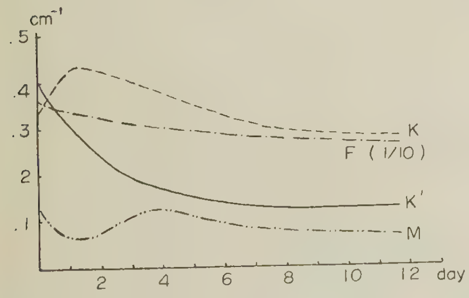

Fig. 10. Thermal equiliblium of the absorption band of coloured NaCl crystal.

Moreover, since lines bc and b′c′ are nearly parallel, the region bc may be of the thermal action.

C: *Thermal Equilibrium*

Fig. 10 shows the change of absorptions of K′-, K-, F- and M-bands of NaCl crystal, kept in dark room immediately after X-ray irradiation. This fact shows most probably the existence of thermal equilibrium among each centre.

## § 4. Discussion

In the F→K⇸K′ and $\mathrm{F}\rightarrow\mathrm{M}-\genfrac{}{}{0pt}{}{\nearrow\mathrm{R}}{\searrow\mathrm{N}}$ transformations, the F→K and F→M trasformations are both direct photo-trasformations, but the K⇸K′ and $\mathrm{M}-\genfrac{}{}{0pt}{}{\nearrow\mathrm{R}}{\searrow\mathrm{N}}$ transformations are thermal transformations inculded in the photo-transformation. Therefore, as is shown in the above example, the photo-transformation is always subject to the thermal-transformation, and after the both transformations are performed, each centre reaches its equilibrium state.

In conclusion, the author wishes to express his cordial thanks to Professor Yôichi Uchida for his kind advices during the course of this work.

### References

1) F. Seitz: Rev. Mod. Phys. **18** (1946) 384.
2) S. Petroff: ZS. f. Phys. **127** (1950) 443.
3) Y. Uchida and H. Yagi: J. App. Phys. Japan **16** (1947) 65 (in Japanese).
4) Y. Uchida and Y. Nakai: J. Phys. Soc. Japan **9** (1954) 928.
5) Y. Uchida, M. Ueta and Y. Nakai: J. Phys. Soc. Japan **6** (1951) 107.
Y. Uchida, and H. Yagi: J. Phys. Soc. Japan **7** (1952) 109.
6) H. Yagi: J. Phys. Soc. Japan **11** (1956) 430.
H. Yagi and Y. Uchida: Memoirs Coll. Sci., Univ. of Kyoto **A 27** (1956) (in press).
7) H. Yagi: Memoirs Coll. Sci., Univ. of Kyoto **A 27** (1956) (in press).

JOURNAL OF THE PHYSICAL SOCIETY OF JAPAN Vol. 11, No. 7, JULY, 1956

# A Note on the Extended Theory of the Junction Transistor

By Toshio MISAWA

*Central Labs., Matsushita Elec. Ind. Co., Ltd.*
*Kadoma-cho, Kitakawachi-gun, Osaka-fu*

(Received March 5, 1956)

In obtaining the current voltage relation of a junction transistor, one solves continuity equations for minority carriers with appropriate boundary conditions. There are two kinds of boundary condition which have been extended so as to apply to the high injection level operation of a junction transistor. One is in terms of the electrostatic potential and the other is in terms of the quasi-Fermi levels. Taking into account the effect of the base spreading resistance, it is shown that they can be equivalently used in describing the dc and the low frequency performances of a junction transistor but at medium frequencies the quasi-Fermi level approach is preferable. The small signal ac conductances and capacitances which are related to the emitter junction have another correction factor that saturates to 1/2 at high injection levels. Conductances and capacitances are calculated as functions of the emitter current by using the latter boundary condition.

## § 1. Introduction

Shockley founded the general theory of the junction transistor and developed the detailed theory for low injection level operation[1),2)]. Later the theory was extended by Rittner[3)] to include the high injection level operation where the concentration of the injected minority carriers into the base region become comparable to the thermal equilibrium concentration of the majority carriers, which is the case in the usual operation of the junction transistor. Some authors treated the problem concerning the current amplification factor at high level[4),5)]. In treating this problem the present writer extended the low level theory differently in a certain point from Rittner did[5)]. In this note we shall show the new scheme is preferable to Rittner's and calculate components in the equivalent circuit of a transistor according to the new scheme. Before going into details, we shall present a summary of Shockley's theory and the line of reasonings which will be followed in the following sections.

The basis of Shockley's theory is that the flow of carriers in a transistor is determined by their behavior in the minority region*; according to Cutler's nomenclature[6)], the current in a junction transistor is not "emission controlled" but "diffusion controlled". Shockley introduces the concept of the quasi-Fermi levels or imrefs for electrons and holes, $\varphi_n$ and $\varphi_p$[7)]. Namely, even while current flows, electrons in the conduction and the valence bands are considered to interact enough with each other in the respective band to have Fermi levels although the Fermi levels are different for the conduction and the valence bands and according to the position in a semiconductor. And he assumes that imrefs are nearly constant not only in the majority region but also even in the barrier layer[1),2)]. Constancy of the imrefs in the barrier layer is used to obtain the boundary condition for the continuity equation. Negligibility of the barrier layer impedance to the carrier flow compared to the minority region impedance is due to the fact that the lifetime of the injected carriers is larger in transistor materials, and can be justified as will be shown in the Appendix B. It should be noted that in the diffusion theory of rectification at a metal-semiconductor contact the imref for majority carriers changes in the barrier layer[8)], namely the carrier densities across the barrier layer is governed by the Boltzmann factor with *thermal equilibrium* potential height[9)], and the majority carrier flow is impeded by the barrier layer, which corresponds to the zero lifetime in metals. Sometimes, especially at high injection level operation of a transistor, the majority region impedance plays an important role and the imref drop in the majority region is comparable to that in the minority region. This drop can be easily estimated from the relation between the current density and the carrier concentration as is shown latter.

---

* We shall call a region as the majority or the minority region of the carrier according to whether the carrier under consideration is of majority or of minority in that region.

The behavior of carriers in the minority region is treated by solving the continuity equation for them under the assumption of electrical neutrality. The solution gives the current density as a function of the carrier densities on sides of barrier layers, which form the boundary condition for the continuity equation and can be expressed as functions of the differences there between the imrefs for electrons and holes.

The external voltage applied to a transistor is the difference between the Fermi levels in the contact electrodes. The value of an imref on a side of the barrier layer of a junction is different from the Fermi level in the electrode metal, which contacts to the region that is of majority for the imref under consideration, by the drop in the majority region. When we neglect the imref drops in the majority regions and equate the difference between the imrefs for electrons and holes on a side of the junction to the bias across the junction, we have to do with the so-called intrinsic transistor. Combining this fact with the solution of the continuity equation, which gives the current density as a function of the differences between the imrefs for electrons and holes on sides of barrier layers as mentioned in the preceeding paragraph, the current voltage relation of the intrinsic transistor is obtained. On the above bases Shockley developed the detailed theory of the junction transistor which is valid at low injection level. In solving the continuity equation in the minority region he assumed that carriers flow only by diffusion, which simplified the continuity equation, and in expressing the carrier density on a side of a barrier layer in terms of the difference between imrefs, he made an assumption that the majority carrier density is not appreciably change by the minoritiy carrier injection, which simplified the boundary condition. Under these assumptions he obtained the first term in Taylor's expansion of the transistor characteristics.

Rittner³⁾ and Webster⁴⁾ pointed out the low level assumption is not valid in the base region in the usual operation of a transistor. Rittner³⁾ extended Shockley's theory by taking into account the electric field in solving the continuity equation in the base region, which was shown to be important at high level, and by using the boundary condition which applies up to the high level case. He obtained the boundary condition*, which gives the carrier density in terms of the "potential difference"** across the barrier layer, by using the "standard assumption of rectifier theory" and assigning to the majority carrier density the value different from the thermal equibrium one by the amount of injected minority carriers (conductivity modulation).

The extension of the boundary condition is also possible along Shockley's line, i.e., in terms of imrefs. (Say B.C.I.) This is the other extension mentioned above and is different from Rittner's which may be named as the boundary condition in terms of the electrostatic potential. (Say B. C. II.) It was pointed out that the two B.C.'s give different emitter characteristics at high level⁵⁾. As will be shown later, the difference comes from the fact that, at high level, the "potential difference" across the junction becomes different from the difference between imrefs for electrons and holes on a side of the barrier layer at a given injection level. The fact is that the choice of the intrinsic transistor is different for two cases. In order to obtain the characteristics of a transistor as a whole, one must take into account the imref drops in the majority regions when B. C. I is used and the potential drops there when B. C. II is used.

It is well known experimentally¹⁰⁾,¹¹⁾ that the base resistance plays an important role both in dc and ac characteristics and is attached to the intrinsic transistor which is given by the theory. As far as dc characteristics are concerned, there is no experimental means to divide the applied voltage into the IR drop in the base spreading resistance and the effective part in biasing the junction. One can regard the imref drop or the potential drop in the base region equivalently as the IR drop in the base spreading resistance. We may use B. C. I or B. C. II with equal qualification in describing the dc characteristics of a transistor when the proper choice of the base resistance is made. It can be shown that the usual base spreading resistance which is obtained by integrating the resistivity of the material for given geometry[12] should be used along with B. C. I and another term must be added to this when we deal with B. C. II.

---

* Private communication from E. S. Rittner, to whom the writer expresses his sincere thanks.

** We shall call the deviation of the potential barrier height across the junction from its thermal equilibrium value as "potential difference" across the junction for simplicity of terminology.

In the ac operation, the base spreading resistance can be determined by the multi-frequency measurement of the small signal parameters[10),13)]. From the fact that the difference between the "potential difference" across the junction and the difference between imrefs comes from the electrical neutrality condition, which is established in a very short time compared with the involved time interval[14)], it is conclnded that the IR drop, which is developed on the purely resistive base resistance, is the imref drop, not the potential drop and one must use B. C. I to compute the admittances in the equivalent circuit.

In the followings § 2 re-presents the derivation of both B. C.'s and the difference between them, and clarifies the origin of the difference. After it is shown in § 3 that the both B. C.'s are equivalently used in describing the dc operation of a transistor we shall explain in § 4 the preferability of B. C. I to B. C. II in the ac operation. In the Appendix A, rewriting of Rittner's calculation is made by using B. C. I and a numerical example is given for the transistor in Reference 3). It will be assumed that the electrical neutrality condition is preserved expect in the barrier layer of the junction, as has usually been done[3),15)], although this may introduce an over-correction as Swanson pointed out[15)]. We shall treat only the case of a $p$-$n$-$p$ unit.

## § 2. Extended Boundary Conditions in Terms of the Imrefs and of the Electrostatic Potential

Shockley's boundary condition can be extended to the case of high injection level by taking into account the deviation of the majority carrier density from its thermal equilibrium value, which results from the electrical neutrality condition.

Electron and hole densities, $n$ and $p$, are expressed in terms of the imrefs for them, $\varphi_n$ and $\varphi_p$, and of the electrostatic potential, $\psi$, by

$$n=n_i \exp\left[q(\psi-\varphi_n)/kT\right], \qquad (1)$$

$$p=n_i \exp\left[q(\varphi_p-\psi)/kT\right], \qquad (2)$$

where $n_i$ is the electron density of the intrinsic semiconductor. Upon inserting the formula for the electrical neutrality condition,

$$p-p_0=n-n_0, \qquad (3)$$

where the subscript 0 means thermal equilibrium, into the proudect of Eqs. (1) and (2), we obtain the relations between $\varphi_p-\varphi_n$ and $n$ or $p$,

$$n(n-n_0+p_0)=n_i^2 \exp\left[q(\varphi_p-\varphi_n)/kT\right], \qquad (4)$$

$$(p-p_0+n_0)p=n_i^2 \exp\left[q(\varphi_p-\varphi_n)/kT\right]. \qquad (5)$$

On the emitter side of the emitter junction the density of injected electrons is negligible[3),4)] compared to the hole density and Eq. (4) is

$$\begin{aligned} n_{E1}&=(n_i^2/p_{E0}) \exp\left[q(\varphi_p-\varphi_n)_{E1}/kT\right] \\ &=n_{E0} \exp(q\delta\varphi'_E/kT), \end{aligned} \qquad (6)$$

while on the base side of the emitter junction where the injection level is high[3),4)] Eq. (5) reads

$$p_{B1}(p_{B1}+n_{B0})=n_i^2 \exp\left[q(\varphi_p-\varphi_n)_{B1}/kT\right],$$

or

$$\frac{p_{B1}}{n_{B0}}\left(1+\frac{p_{B1}}{n_{B0}}\right)=\frac{p_{B0}}{n_{B0}} \exp\left[q\delta\varphi_E'/kT\right]. \qquad (7)$$

Here the subscripts $E$, $B$ and 1 imply the emitter, the base regions and the sides of the emitter junction, $\delta\varphi_E'$ is the value of $\varphi_p-\varphi_n$ on sides of the emitter junction and smaller than the bias applied to the emitter terminal, $\delta\varphi_E$, by the imref drop for holes in the emitter region, $\delta\varphi_{pE}$, plus that for electrons in the base region, $\delta\varphi_{nB}$,

$$\delta\varphi_E'=\delta\varphi_E-\delta\varphi_{pE}-\delta_{nE}. \qquad (8)$$

Following the custom, $\delta\varphi_{pE}$ in Eq. (8) will be neglected in the following discussion*. Equation (7) is different from Shockley's and shows that the hole injection into the base region becomes smaller than his as injection level rises. On the other hand Eq. (6) is the low level formula.

---

* From the ac measurement on the alloy junction transistor Giacoletto (Reference 10) pointed out the possible importance of $\delta\varphi_{pE}$, but his discussion seems to be short of consistency.

Rittner assumed that even while current flows the drop in carrier density across the junction is still given by a boltzmann factor involving the *altered* potential barrier, namely,

$$n_{E1}=n_{B1}\exp[q(V_E-\phi)/kT]\,, \tag{9}$$

$$p_{B1}=p_{E1}\exp[q(V_E-\phi)/kT]\,, \tag{10}$$

where $\phi$ is the thermal equilibrium height of the potential barrier across the emitter junction and $V_E$ is the "potential difference" across it. This assumption is equivalent to the constancy of imrefs within the barrier layer as is easily seen from Eqs. (1) and (2)[5]. Paying attention to the conductivity modulation, he obtained

$$n_{E1}=n_{E0}(1+p_{B1}/n_{B0})\exp(qV_E/kT)\,, \tag{11}$$

$$p_{B1}=p_{B0}\exp(qV_E/kT)\,. \tag{12}$$

$V_E$ is smaller than the bias voltage, $\delta\varphi_E$, by the potential drop in the base region, $\delta\psi_B$,

$$V_E=\delta\varphi_E-\delta\varphi_B\,. \tag{13}$$

In this case Eqs. (11) and (12) shows that the hole injection into the base region remains the same as at low level while the electron injection into the emitter region is increased compared with the low level one. The situation is opposite to that given by Eqs. (6) and (7).

The apparent difference stems from the difference between $\delta\varphi_E'$ and $V_E$ at a given injection level. When the injection level in the base region rises, Eq. (1) on the base side of the emitter junction is

$$\begin{aligned} n_{B1}&=n_{B0}+p_{B1}\\ &=n_i\exp[q\{\delta\psi+(\psi-\varphi_n)_{B0}\}/kT]\\ &=n_{B0}\exp(q\delta\psi/kT) \end{aligned} \tag{14}$$

and the value of $\psi-\varphi_n$ there deviates from its thermal equilibrium value by the amount given by

$$\delta\psi=(kT/q)\ln(1+p_{B1}/n_{B0})\,. \tag{15}$$

In Shockley's low level theory the value of $\psi-\varphi_n$ was equal to its thermal equilibrium value because $p_{B1}$ was much smaller than $n_{B0}$. Since the value of $\varphi_p-\psi$ on the emitter side of the emitter junction remains as it had been before the bias was applied, the "potential difference" across the emitter juntion is smaller than $(\varphi_p-\varphi_n)_{E1}$ for a given injection level by the amount of $\delta\psi$,

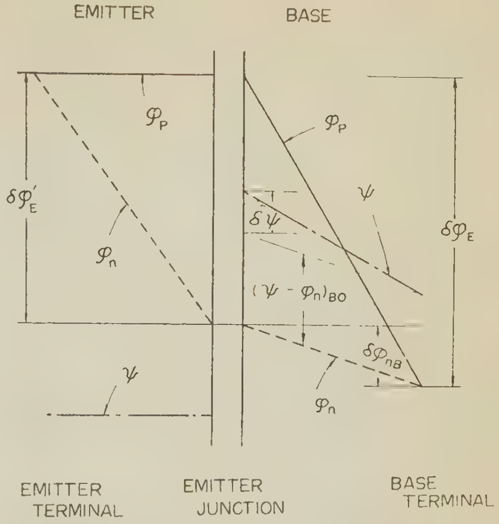

Fig. 1. Electrostatic potential-imref diagram from the emitter to the base terminals, only schematical.

$$V_E=\delta\varphi_E'-\delta\psi\,. \tag{16}$$

The potential drop in the base region is equal to the imref drop, $\delta\varphi_{nB}$, plus $\delta\psi$,

$$\delta\psi_B=\delta\psi+\delta\varphi_{nB}\,. \tag{17}$$

The situation is illustrated in Fig. 1, which shows schematically the behaviors of the imrefs and the electrostatic potential from the emitter to the base terminals*. As pre-

---

* For the fast recombination type contact, in the bulk of semiconductor beneath which the carrier densities assume the values in thermal equilibrium, it is apparent that, at the base terminal, the imrefs for electrons and holes coincide and are positioned at the same level of energy with respect to the electrostatic potential as in thermal equilibrium. The diagram is correct even for the non-injection type contact under which the carrier densities may or may not be equal to thermal equilibrium ones but the imref gradient for minority carriers always vanishes, for in the heavily doped region between the bulk of semiconductor and metal, which is the feature of the contact of this type and supresses the minority carrier flow, the imrefs behave as in the region of semiconductor just under the former type contact. It should be noted that in Eq. (17) we are only concerned with the deviations from the thermal equilibrium values. As for the definition and the physical realization of the above mentioned types of contact to semiconductor, see W. C. Waltz: Bell Lab. Rec. **33** (1955) 260. By the way the possibility in the case of the fast recombination type contact that since the imref gradient for holes is favorable to the flowing-out hole current (see Eq. (22) for the relation between imref gradient and current density.) the hole current might contribute to the base current which has been and

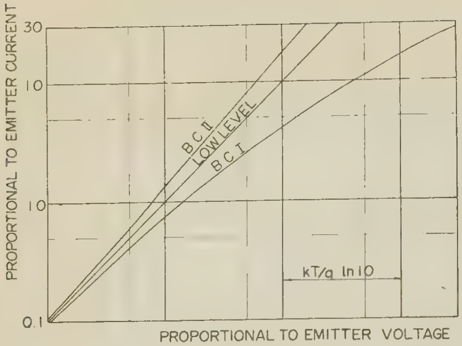

Fig. 2. Semi-log plot of theoretical relations between current and voltage at the emitter junction. The scale of the abscissa is linear with voltage, its origin being dependent on the resistivity of the base material.

viously pointed out[5)], Eqs. (6) and (7) are obtained when Eq. (16) is inserted into Eqs. (11) and (12).

## § 3. DC Operation

In order to obtain the current voltage relation of a junction transistor, we must solve the continuity equations in minority regions and express various currents as functions of the carrier densities on the sides of the emitter and the collector junctions. As the number of injected holes into the base region becomes comparable to that of electrons in thermal equilibrium, the drift hole current by that electric field which sweeps electrons from collector to emitter against their unfavorable concentration gradient can not be neglected. This is because the drift current is directly propotional to the carrier density. It was shown[3),4)] that the hole flow across the emitter junction is doubled by the field compared with the value given by the low level formula. Rittner[3)] calculated the recombination current, which gives the difference between the hole currents across the emitter and the collector junctions, by the perturbation method. It is smaller than the low level formula gives since it becomes easier for holes to travel across the base region owing to the field and the chance for recombination decreases. We can use Shockley's solution in emitter and collector regions.

By combining the expressions thus obtained with B. C.'s in § 2, the emitter current, $I_E$, and the collector current, $I_C$, are expressed in terms of $\delta\varphi_E'$ and $\delta\varphi_C'$ or $V_E$ and $V_C$. Here $\delta\varphi_C'$ and $V_C$ are given by Eqs. (8) and (13) with the subscript $E$ exchanged with $C$. $\delta\varphi_C'$ is equal to the value of $\varphi_p-\varphi_n$ on sides of the collector junction since $\varphi_n$ is nearly constant across the base region, while $V_C$ is the "potential difference" across the collector junction subtracted by $\delta\psi$ since $\psi$ changes by $\delta\psi$ across the base region as previously shown[5)]. When the collector is negatively biased by a few volts, $\delta\varphi_C'$ and $V_C$ are related to $I_E$ and $I_C$ only through the base width. This is Early effect[16)]. Reserving the detailed calculations for the Appendix A, we show in Fig. 2 the current voltage relation at the emitter junction which sensitively reflects the effect of the high level injection. Here the emitter current was approximated by its hole component. When B. C. II is used, the emitter current is twice as large as the low level theory gives at high level limit. This is due to the field in the base region. On the other hand B. C. I gives smaller emitter current than the low level theory does. This is because the effect of the field is overshadowed by the decrease of hole injection.

The apparent difference between the two schemes is reconciled by considereing the base spreading resistance. In analysing the measured relation between current and voltage at the emitter junction, the surplus voltage above the theoretical one for a given value of the emitter current is regarded as the IR drop in the base spreading resistance and the base resistance is obtained by dividing this surplus voltage by the observed base current[10)]. Thus the base resistance obtained from the dc measurement is

$$r_{BB'}=\delta\varphi_{nB}/I_B \tag{18}$$

when B. C. I is used and

---

will be considered to be made up only of the electron current is rejected on the following basis. We consider various sections through the base contact. $\varphi_p$ decreases in the base region from its emitter end to its collector end and really goes so further below $\varphi_n$ at the collector end (Reference 5)) that the total hole current through the base terminal vanishes. In other words there exist a hole current from the base region adjacent to the emitter to the base terminal and at the same time a hole current from the base terminal to the collector end of the base region. This means only that more or less fraction of the holes which are injected through the emitter junction takes a long way near the base terminal.

$$r_{BB''}=\delta\psi_B/I_B$$
$$=(\delta\varphi_{nB}+\delta\psi)/I_B \tag{19}$$

when B. C. II is used. In the latter case the base resistance is larger than that in the former case by

$$r_{B'B''}=\delta\psi/I_B\ . \tag{20}$$

Fig. 3 shows the calculated values of $r_{B'B''}$ of the transistor in Reference 3) as a function of the emitter current. $r_{B'B''}$ is about 1800 ohms at low level and decreases as the emitter current increases. A similar behavior was already discussed about the spreading resistance of the point contact rectifier[15),17)]. Any way two B. C.'s can describe the dc characteristic with equal qualification.

Now we shall consider the meaning of the base resistance, $r_{BB'}$, given by Eq. (18). According to Shockley[1)] the imref gradient is associated with the current density by the same equation as that which relates the potential gradient with the current density in an ordinary conductor,

$$J_n=-\sigma_n\,\mathrm{grad}\,\varphi_n\ , \tag{21}$$
$$J_p=-\sigma_p\,\mathrm{gran}\,\varphi_p\ , \tag{22}$$

where $\sigma_n$ and $\sigma_p$ are the conductivities due to electrons and holes respectively. Hence $r_{BB'}$ is obtained from conductivity and geometry of the base region in the same way as a usual resistance is calculated. The base resistance which has appeared in the literature[12)] should be used along with B. C. I. It was pointed out[5)] that the increase in $\sigma_n$ due to the conductivity modulation at high injection level leads to a decrease in $r_{BB'}$.

## § 4. AC Performance

The behavior of a junction transistor at very low frequencies is described by the equations which are obtained by differentiating the dc formulae. Upon differentiating the expressions for the emitter and the collector currents with the emitter bias, $\delta\varphi_E$, and the collector bias, $\delta\varphi_C$, and changing the independent variables into $\delta\varphi_E'$ and $\delta\varphi_{C'}$, we can easily find that the small signal low frequency equivalent circuit of a transistor becomes as shown Fig. 4, where symbols developed by Giacoletto[18)] are used, and each element is

$$g_{eeb'}=\partial I_E/\partial\delta\varphi_E'\ , \tag{23}$$
$$g_{ecb'}=\partial I_E/\partial\delta\varphi_C'\ , \tag{24}$$
$$g_{ceb'}=\partial I_C/\partial\delta\varphi_E'\ , \tag{25}$$

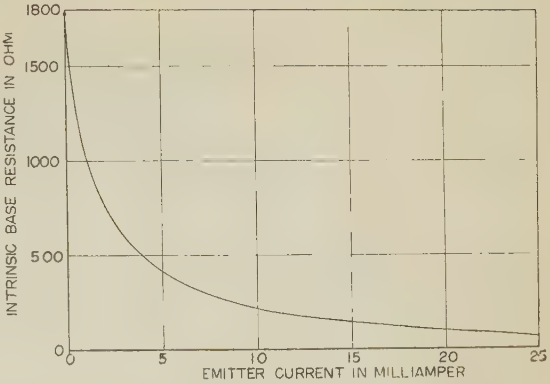

Fig. 3. Variation of the "intrinsic base resistance" with the emitter current for the transistor in Reference 3).

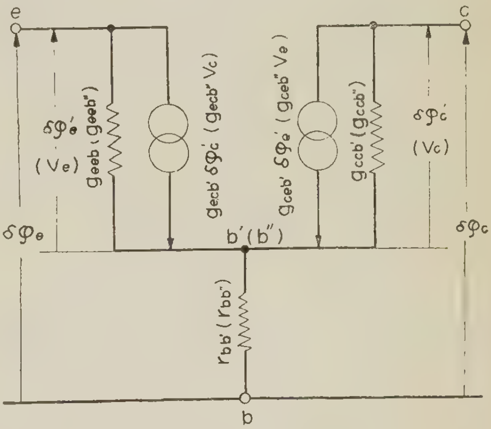

Fig. 4. Small signal equivalent circuit at very low frequencies.

$$g_{ccb'}=\partial I_C/\partial\delta\varphi_C'\ , \tag{26}$$
$$r_{bb'}\ =\partial\delta\varphi_{nB}/\partial I_B\ . \tag{27}$$

The derivative of a current, $I$, with respect to $\delta\varphi_E'$ is rewritten as

$$\frac{\partial I}{\partial\delta\varphi_E'}=\frac{\partial I}{\partial n_{E1}}\frac{\partial n_{E1}}{\partial\delta\varphi_E'}+\frac{\partial I}{\partial p_{B1}}\frac{\partial p_{B1}}{\partial\delta\varphi_E'}\ , \tag{28}$$

where

$$\frac{\partial n_{E1}}{\partial\delta\varphi_E'}=\frac{qn_{E1}}{kT}\ , \tag{29}$$

$$\frac{\partial p_{B1}}{\partial\delta\varphi_E'}=\frac{qp_{B1}}{kT}\left(\frac{1+p_{B1}/n_{B0}}{1+2p_{B1}/n_{B0}}\right) \tag{30}$$

as are obtained from Eqs. (6) and (7). The factor with parentheses in Eq. (30) is a correction due to the extended B. C. and varies from unity to one half as level rises. Derivatives with respect to $\delta\varphi_C'$ are

$$\frac{\partial I}{\partial\delta\varphi_C'}=\frac{\partial I}{\partial w}\frac{\partial w}{\partial\delta\varphi_C'}\ , \tag{31}$$

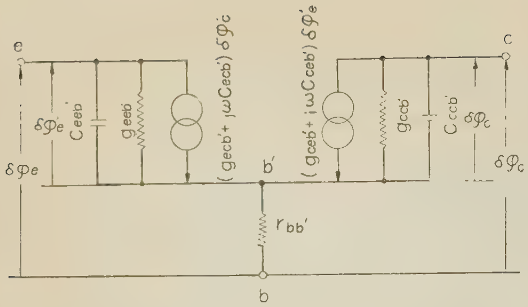

Fig. 5. Small signal equivalent circuit at medium frequencies.

which shows Early effect. The deviation of the continuity equation from low level theory is reflected in the first factor of each term in Eq. (28) and of Eq. (31). When we regard the derivatives in Eqs. (23)-(26) as functions of the emitter current through the parameters, $n_{B1}$ and $p_{B1}$, the third correction foctor comes in implicitly. For the emitter current at a given value of $p_{B1}$ is almost doubled at high level limit. These three factors determine the variation of elements in the equivalent circuit with the emitter current.

When B. C. II is used, similar discussions are valid with $b'$, $\delta\varphi_E'$, $\delta\varphi_C'$, and $\delta\varphi_{nB}$ exchanged with $b''$, $V_E$, $V_C$ and $\delta\varphi_{nB}+\delta\psi$. For example, the base spreading resistance, $r_{bb''}$, is

$$r_{bb''}=\partial(\delta\psi+\delta\varphi_{nB})/\partial I_B\ , \tag{32}$$

and the correction factor due to B. C. appears in the expression corresponding to Eq. (29) instead of in that to Eq. (30).

At medium frequencies, it is a common practice to associate a capacitance with each element but the base spreading resistance, as shown in Fig. 5. These capacitances are obtained by solving the time-dependent continuity equation which contains the effect of the electric field and inserting the extended boundary condition. But this orthodox method is not easily accessible. These capacitances are mainly due to the charge of holes stored in the base region, $Q$, and actually at low level there exist the relations[11),19)]

$$C_{eeb'}+C_{ceb'}=\partial Q/\partial\delta\varphi_E'\ , \tag{33}$$

$$C_{ecb'}+C_{ccb'}-C_{Tc}=\partial Q/\partial\delta\varphi_C'\ , \tag{34}$$

where $C_{Tc}$ is the collector junction capacitance. If these relations hold up to high level, some of the capacitances can be calculated from dc formulae, and fortunately it has been experimentally ascertained[10)] that these two are sufficient to describe the characteristics at medium frequencies.

In this frequency range it is apparent that the behavior of a transistor differs whether one uses B. C. I or B. C. II. As each element in the equivalent circuit can be directly measured by the multi-frequency method[10)], it becomes an important problem whether one should use B. C. I or B. C. II, or whether the base resistance is given by Eq. (27) or Eq. (32). It can be concluded that B. C. I is preferable to B. C. II and $r_{bb'}$ is really measured. We compare the transient after application of a small increment of the emitter current to the base-grounded transistor with the same process in the equivalent circuit with $r_{bb'}$ or $r_{bb''}$ as a base resistance. In the equivalent circuit of Fig. 5 the voltage which appears between the emitter and the base terminals immediately after the application of the step current is the IR drop in the base resistance, since there is a diffusion capacitance between the emitter and the internal base. On the other hand in the transistor the application of the step current means a constant-rate feeding of holes into the base region through the emitter junction*. At first the number of the injected holes is not appreciable. $\delta\varphi_E'$, $V_E$ and $\delta\psi$, which are all in the same phase with $p_{B1}$, do not increase immediately. Only electrons which are to neutralize the charge of these holes come into the case region through the base terminal. This entails an immediate increase in $\delta\varphi_{nB}$ according to Eq. (21)** and this is the very IR drop mentioned above. Threfore the base resistance is the derivative of the imref drop with respect to the base current. The important fact is that $\delta\psi$, which appears in Eq. (32), is in the same phase with the hole density in the base region and does not increase immediately.

---

* We speak only of the incremental part.

** $\delta\varphi_{nB}$ may decrease gradually after this sudden increase in accordance with the gradual increase of holes in the base region owing to the resulting conductivity modulation, i.e., $\partial\delta\varphi_{nB}/\partial I_B$ may be inductive to some extent. But this inductance is negligible as the conductivity-modulated part is only a small fraction of the base region which contributes to the base spreading resistance, or more rigorously speaking, $\delta\varphi_{nB}$ is in the same phase with $I_B$ as long as $\Delta r_{BB'}\cdot I_B$ is small compared with $r_{BB'}\cdot\Delta I_B$, where $\Delta r_{BB'}$ is the decrease in $r_{BB'}$ when $I_B$ increases by $\Delta I_B$.

When we use B. C. I instead of B. C. II, those conductances and capacitances which were obtained by differentiating with $V_E$ must be multiplied by

$$\frac{\partial V_E}{\partial \delta\varphi_E'} = \frac{1+p_{B1}/n_{B0}}{1+2p_{B1}/n_{B0}}, \tag{35}$$

which varies from unity to one half as injection level rises. For the quantities which were the derivatives with respect to $V_C$, there is no need for change. The dimensionless quantities, such as injection efficiency and current amplification factor are independent of which B. C. is used, when considered as functions of the emitter current, because $\delta\varphi_E'$ or $V_E$ enters only as a parameter5).

## § 5. Conclusion

Under the assumption that the electrical neutrality condition is preserved in homogeneous regions of a junction transistor, the following were shown: The boundary conditions in terms of the electrostatic potential and of the imrefs are equivalently used in describing dc and low frequency operations of the transistor with the appropriate choice of the base spreading resistance. But at higher frequencies we must use the latter boundary condition. When we use the latter in stead of the former, some of the conductances and capacitances as functions of the emitter current are multiplied with a correction factor which saturates to 1/2 at high level limit.

## Acknowledgement

The writer expresses his sincere thanks to Mr. K. Akiyama and Mr. T. Kondo of these Laboratories for their deep interest in the present study.

## Appendix A

In this Appendix, we shall calculate the characteristics of a junction transistor, using the boundary condition in terms of imrefs and following Rittner's perturbation method3). After dc formulae are presented in [1], ac formulae will be derived from them and numerical values for the transistor in Reference 3) will be given in [2]. The calculations are based on various simplifying assumptions, but may serve as an aid to know the tendency of the variation of the junction transistor characteristics with the emitter current.

### [1] *DC Formulae*

DC formulae are derived after the principle in § 3. They are:

Electron current through the emitter junction,

$$I_{nE} = \frac{A_E q D_n n_{E0}}{L_{nE}} \left[ \frac{n_{B0}}{p_{B0}} P(P+1) - 1 \right], \tag{A 1}$$

where $A_E$ is the cross section area of the emitter junction, $D$ the diffusion constant, $L$ the diffusion length and $P = p_{B1}/n_{B0}$, which may be called an injection level parameter, is related to $\delta\varphi_E'$ by Eq. (7), or

$$P(1+P) = (p_{B0}/n_{B0}) \exp(q\delta\varphi_E'/kT). \tag{A 2}$$

Hole current through the emitter junction,

$$I_{pE} = \frac{A_B q D_p n_{B0}}{w} [2P - \ln(1+P)], \tag{A 3}$$

where $A_B$ is an effective cross section area of the base region10) and is equal to $A_E$ and $A_C$, the cross section area of the collector junction, in the grown-junction transistor; or if we define the emitter current parameter, $Z$, as

$$Z = I_{pE}/(A_B q D_p n_{B0}/w), \tag{A 4}$$

$$Z = 2P - \ln(1+P). \tag{A 5}$$

Current due to the surface recombination in the base region of the grown-junction transistor,

$$I_{SRG} = A_{SR} q s n_{B0} [P(P+1)/Z - 1], \tag{A 6}$$

where $A_{SG}$ is the area of the free surface of the base region and the surface recombination velocity, $s$, is assumed to be constant3),4).

Current due to the surface recombination in the base region of the alloy junction transistor,

$$I_{SRA} = {}_{SA} q s n_{B0} P, \tag{A 7}$$

where $A_{SA}$ is the effective recombination area4).

Current due to the volume recombination in the base region,

Table I. Derivatives which appear in the expressions for the elements in the small signal equivalent circuit of a junction transistor. The last column is the high level limit of the ratio to the low level expression.

| derivative | expression | |
|---|---|---|
| $\frac{\partial I_{nE}}{\partial\delta\varphi_E'}$ | $\frac{A_E q\mu_n n_{EO}}{L_{nE}}\frac{n_{BO}}{p_{BO}} \cdot P(P+1)$ | $\infty$ |
| $\frac{\partial I_{pE}}{\partial\delta\varphi_E'}$ | $\frac{A_B q\mu_p n_{BO}}{w} \cdot P$ | $\frac{1}{2}$ |
| $\frac{\partial I_{SRG}}{\partial\delta\varphi_E'}$ | $\frac{1}{2}A_{SG}qsn_{BO}\frac{q}{kT} \cdot 2\frac{P}{Z}(1+P)\left(1-\frac{P}{Z}\right)$ | $\frac{1}{4}$ |
| $\frac{\partial I_{SRA}}{\partial\delta\varphi_E'}$ | $A_{SA}qsn_{BO}\frac{q}{kT} \cdot \frac{P(1+P)}{1+2P}$ | $\frac{1}{4}$ |
| $\frac{\partial Q}{\partial\delta\varphi_E'}$ | $\frac{1}{2}A_B qn_{BO}w \cdot 2\frac{P}{Z}(1+P)\left(1-\frac{P}{Z}\right)$ | $\frac{1}{4}$ |
| $\frac{\partial I_{pE}}{\partial\delta\varphi_C'}$ | $-\frac{A_B qD_p n_{BO}}{w^2}\frac{\partial w}{\partial\delta\varphi_C'} \cdot Z$ | 1 |
| $\frac{\partial I_{SRG}}{\partial\delta\varphi_C'}$ | $\frac{1}{2}\frac{\partial A_{SG}}{\partial\delta\varphi_C'}qsn_{BO} \cdot 2\left[\frac{P(P+1)}{Z}-1\right]$ | $\frac{1}{2}$ |
| $\frac{\partial I_{SRA}}{\partial\delta\varphi_C'}$ | $\frac{\partial A_{SA}}{\partial\delta\varphi_C'}qsn_{BO} \cdot P$ | $\frac{1}{2}$ |
| $\frac{\partial I_{VR}}{\partial\delta\varphi_C'}$ | $\frac{1}{2}\frac{A_B qn_{BO}}{\tau_{pO}}\frac{\partial w}{\partial\delta\varphi_C'} \cdot \frac{2}{rZ}\left[P^2+\left(1-\frac{2}{r}\right)P-\frac{1}{r}\left(1-\frac{2}{r}\right)\ln(rP+1)\right]$ | $\frac{1}{2r}$ |
| $\frac{\partial Q}{\partial\delta\varphi_C'}$ | $\frac{1}{2}A_B qn_{BO}\frac{\partial w}{\partial\delta\varphi_C'} \cdot 2\left[\frac{P(P+1)}{Z}-1\right]$ | $\frac{1}{2}$ |

$$J_{VR}=\frac{A_B qwn_{B0}}{\tau_{p0}}\frac{1}{rZ}$$
$$\times\left[P^2+\left(1-\frac{2}{r}\right)P-\left(1-\frac{2}{r}\right)\ln(rP+1)\right], \tag{A 8}$$

where the life time of holes, $\tau_p$, was considered to vary with injection level and after Shockley-Read-Hall theory[20),21)] is expressed by

$$\tau_p=\tau_{p0}\frac{1+rp/n_0}{1+p/n_0}, \tag{A 9}$$

$\tau_{p0}$ being the low level lifetime and $r$ a factor by which the lifetime decreases at high level limit.

Saturation current through the collector junction,

$$I_{nC}=-A_C qD_n n_{C0}/L_{nC}\ . \tag{A 10}$$

Charge of holes stored in the base region,

$$Q=A_B qwn_{B0}[p(P+1)/Z-1]\ . \tag{A 11}$$

The terminal currents, i.e., the emitter, the collector and the base currents, are given by

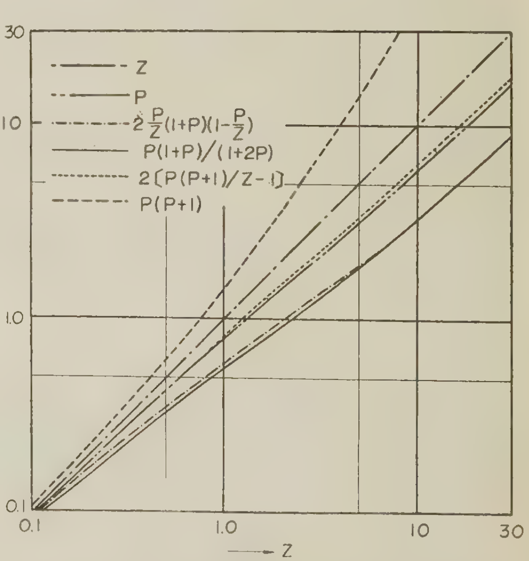

Fig. 6. Variation of factors which appear in derivatives of currents and charge with respect to $\delta\varphi'_E$ and $\delta\varphi'_C$.

$$L_E=I_{nE}+I_{pE}$$
$$\cong I_{pE}\ , \tag{A 12}$$
$$I_C=-I_{pE}+I_{VR}+I_{SR}-I_{nC}$$
$$\cong -I_{pE}+I_{SR}\ , \tag{A 13}$$
$$I_B=-(I_{nE}+I_{VR}+I_{SR}-I_{nC})$$
$$\cong -I_{nE}-I_{SR}\ , \tag{A 14}$$

where the flowing-in current was taken as of positive sign and the approximations are valid in a usual unit. Equation (A 12) was already illustrated in Fig. 2.

[2] *AC Formulae*

Derivatives of important currents and the charge of holes in the base region, with respect to $\delta\varphi_E'$ and $\delta\varphi_C'$ are tabulated in Table I and factors, which are independent of the material constant and the geometry of the transistor and were equal to $Z$ in the low level theory, are shown in Fig. 6 as function of $Z$ which is nearly proportional to $I_{pE}$. From Table I and the transformation equations which were worked out extensively by Giacoletto[18] we can calculate the variations of components in any equivalent circuit with the emitter current. As an example, we give the elements of the admittances in the common-emitter hybrid π equivalent circuit[10),18] which is shown in Fig. 7, in Table II. Here the numerical values are again for the transistor in Reference 3). As for other important quantities, the measure of the injection efficiency is[5]

$$\frac{\partial I_{nE}}{\partial I_{pE}}=\frac{\partial I_{nE}/\partial\delta\varphi_E'}{\partial I_{pE}/\partial\delta\varphi_E'}=\frac{\mu_n n_{B0} w}{\mu_p p_{E0} L_{nE}}(1+P)$$

and the alpha cut-off frequency, $\omega_{\alpha c}$, is

$$\omega_{\alpha c}\cong\frac{{}_e g_m}{{}_e C_{b'e}}=\frac{2D}{w^2}\,\frac{2}{Z}\,(1+P)\left(1-\frac{P}{Z}\right),$$

which is shown in Fig. 8 as a function of $Z$. Note that these two quantities are independent of the kind of B. C., as mentioned previously.

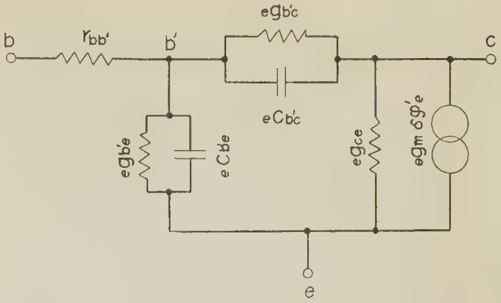

Fig. 7. Common-emitter hybrid π equivalent circuit.

Table II. Approximate expressions for the elements of the equivalent circuit shown in Fig. 7. Numerical values are for the transistor in Reference 3) with the collector biased by 5 volts, the collector junction being assumed to be of abrupt type for convenience sake.

| element | expression | numerical value |
|---|---|---|
| $I_E$ | | $0.87\,Z\ mA$ |
| ${}_e g_{b'e}$ | $\frac{\partial I_{SRG}}{\partial\delta\varphi_E'}+\frac{\partial I_{nE}}{\partial\delta\varphi_E'}$ | $\left[8.75\frac{P}{Z}(1+P)\left(1-\frac{P}{Z}\right)+1.17\,P(1+P)\right]\times10^{-4}\,\mho$ |
| ${}_e C_{b'e}$ | $\frac{\partial Q}{\partial\delta\varphi_E'}$ | $1.88\frac{P}{Z}(1+P)\left(1-\frac{P}{Z}\right)\times10^{-2}\mu F$ |
| ${}_e g_{b'c}$ | $\frac{\partial I_{SRG}}{\partial\delta\varphi_C'}$ | $2.68\left[\frac{P(1+P)}{Z}-1\right]\times10^{-7}\,\mho$ |
| ${}_e C_{b'c}$ | $C_{TC}+\frac{\partial Q}{\partial\delta\varphi_C'}$ | $4.42+5.90\left[\frac{P(1+P)}{Z}-1\right]\,\mu\mu F$ |
| ${}_e g_{ce}$ | $-\frac{\partial I_{pE}}{\partial\delta\varphi_C'}$ | $1.04\,Z\times10^{-5}\,\mho$ |
| ${}_e g_m$ | $\frac{\partial I_{pE}}{\partial\delta\varphi_E'}$ | $3.33\,Z\times10^{-2}\,\mho$ |

## Appendix B

In this Appendix we shall discuss the current through a *p-n* junction by taking into account the impedances of both the minority region and the barrier layer and with the density of injected minority carriers unknown, as Cutler did in a point contact rectifier[6]. It is found that the resulting expression for current is excellently approximated by that obtained under the assumption of constant imrefs within the barrier layer. In the latter half of the Appendix the imref drops in the barrier layer are estimated and it is shown that in the junction biased revereseely far more than a few tenth of a volt, the major part of the bias appears as an imref drop within the barrier layer, but with little effect on the above conclusion.

In the barrier layer, one must consider both the diffusion and the drift currents. The electron current is given by

$$J_n=-q\mu_n n\frac{d\psi}{dx}+qD_n\frac{dn}{dx}, \qquad \text{(A 15)}$$

where the positive direction of the $x$-axis is from the $p$- to $n$-regions. Upon integrating Eq. (A 15) across the barrier layer, the current is expressed by

$$n_2\exp(\varPsi_1-\varPsi_2)-n_1=\frac{J_n}{qD_n}\int_{x_1}^{x_2}\exp\{\varPsi_1-\varPsi(x)\}dx \qquad \text{(A 16)}$$

as a function of the carrier densities on the both sides of the junction, where the subscripts

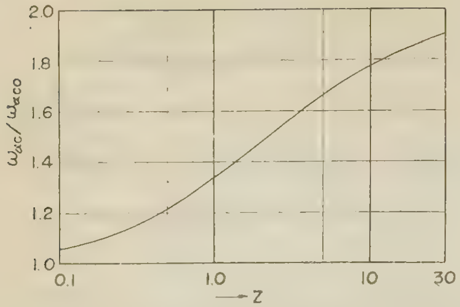

Fig. 8. Variation of the alpha cut-off frequency with emitter current. $\omega_{\alpha c0}$ is its low level value.

1 and 2 mean the negative and the positive sides of the junction, and $\Psi=q\psi/kT$. The solution in the $p$-region is[1)]

$$n_1-n_p=(J_n/qD_n)L_n\ , \qquad (\text{A }17)$$

where $n_p$ is the thermal equilibrium electron density in the $p$-region. Eliminating the unknown density of the injected electrons from Eqs. (A 16) and (A 17), one obtains the exact formula for the current,

$$n_2\exp(\Psi_1-\Psi_2)-n_p$$
$$=\frac{J_n}{qD_n}\left(L_n+\int_{x_1}^{x_2}\exp\{\Psi_1-\Psi(x)\}dx\right), \qquad (\text{A }18)$$

where $n_2$ may deviate from $n_n$, the thermal equilibrium electron density in the $n$-region, owing to the hole injection into the $n$-region. The second term in the right hand side of Eq. (A 18) is a measure of the distance over which $\Psi(x)$ does not deviates from $\Psi_1$, since $\Psi(x)>\Psi_1$. In the step junction where $p$- and $n$-regions have resistivities of the same order, therefore $\Psi(x)$ deviates from $\Psi_1$ appreciably within the $p$-region,

$$\int_{x_1}^{x_2}\exp\{\Psi_1-\Psi(x)\}dx\simeq L_{Dp}\sqrt{\pi}\ ,$$

where $L_{Dp}$ is the Debye length for the acceptor density, $N_a$, in the $p$-region,

$$L^2_{Dp}=\kappa kT/8\pi q^2N_a\ ,$$

and Schottky's exhaustion layer approximation was made. In transistor materials, $L_n$ is several orders of magnitude greater than $L_D$ and the second term in Eq. (A 18) can be neglected compared with the first. The resulting formula is Eq. (17) with

$$n_1=n_2\exp(\Psi_1-\Psi_2)\ , \qquad (\text{A }19)$$

which means the imref for electrons is constant within the barrier layer. Here one must be careful of the fact that, when the junction is biased highly negatively, the first term in the left side of Eq. (A 18) becomes comparable with the second term of the right side which is almost independent of bias, and Eq. (A 19) does not tell truth although combination of Eqs. (A 17) and (A 19) is a good approximation.

When the $n$-region is thinner than $L_p$ and its positive end has a hole density of $p_3$, the solution in the $n$-region is

$$p_2-p_3=(J_p/qD_p)w\ , \qquad (\text{A }20)$$

where $w$ is the thickness of the $n$-region, and the expression for the current is

$$p_1\exp(\Psi_1-\Psi_2)-p_3$$
$$=\frac{J_p}{qD_p}\left(w+\int_{x_1}^{x_2}\exp\{\Psi(x)-\Psi_2\}dx\right). \qquad (\text{A }21)$$

Again if $w$ is much larger than the Debye length for the donors in the $n$-region, the current is given by Eq. (A 20) with

$$p_2=p_1\exp(\Psi_1-\Psi_2)\ , \qquad (\text{A }22)$$

which shows the imref for holes is constant in the barrier layer.

The imref drop in the barrier layer is estimated as follows. Integrating the expression for current density

$$J_n=-q\mu_n n\frac{d\varphi_n}{dx}$$
$$=-qD_n n_i\exp(\Psi-\Phi_n)\frac{d\Phi_n}{dx}\ ,$$

where $\Phi_n=q\varphi_n/kT$, across the barrier layer and using Eq. (A 17), one obtains

$$\exp(\Phi_{n1}-\Phi_{n2})-1$$
$$=\frac{1}{L_n}\int_{x_1}^{x_2}\exp\{\Psi_1-\Psi(x)\}dx\cdot\left(1-\frac{n_p}{n_1}\right). \qquad (\text{A }23\text{ a})$$

When $1-(n_p/n_1)\lesssim 1$, which corresponds to the case of the positive and the small negative bias, $|\Phi_{n1}-\Phi_{n2}|\lesssim L_{Dp}/L_n$ and the imref drop is completely negligible. When $n_p/n_1\gg 1$, the imref drop may become appreciable and we set

$$n_1=n_p\exp(\delta\Phi+\Phi_{n2}-\Phi_{n1})\ , \qquad (\text{A }24)$$

where $\delta\Phi=q(\varphi_{p1}-\varphi_{n2})kT$ and is negative in the present case. Then Eq. (A 23 a) is

$$\exp(\Phi_{n2}-\Phi_{n1})$$
$$=1+\frac{1}{L_n}\int_{x_1}^{x_2}\exp\{\Psi_1-\Psi(x)\}dx\cdot\exp(-\delta\Phi) \qquad (\text{A }23\text{ b})$$

This shows that if the reverse bias, $|\delta\Phi|$, exceed $\ln(L_n/L_{Dp})$, which is of the order of ten, it is $\Phi_{n2}-\Phi_{n1}\sim-\delta\Phi$, or the major part of the bias appears as the imref drop within the barrier layer[22]. The imref is constant between $x_2$ and the point where

$$\Psi_1-\Psi(x)-\delta\Phi=0\ ,$$

or $\Phi(x)$ goes below $\Psi_2$ by the thermal equilibrium value of $\Psi_2-\Psi_1$, and it decreases by the amount almost equal to $\delta\Phi$ within the rest of the barrier layer.

Finally we shall check the constancy of the imref for holes within the emitter junction at high injection level. This is almost self-evident since the impedance of the base region is decreased only by a factor two at high level limit. If we insert Eq. (A 4) into the equation for holes corresponding to Eq. (A 23 a)

$$\exp(\Phi_{p1}-\Phi_{p2})-1 = \frac{Z}{P}\frac{1}{w}\int_{x_1}^{x_2}\exp\{\Psi(x)-\Psi_2\}dx\ , \qquad \text{(A 25)}$$

which shows that $\Phi_{p1}-\Phi_{p2}$ is only doubled at high level.

## References

1) W. Shockley: Bell Sys. Tech. J. **28** (1949) 435.
2) Shockley, Sparks and Teal: Phys. Rev. **83** (1951) 151.
3) Edmund S. Rittner: Phys. Rev. **94** (1954) 1161.
4) W. M. Webster: Proc. IRE **42** (1954) 914.
5) Toshio Misawa: J. Phys. Soc. Japan **10** (1955) 362.
6) Melvin Cutler: Phys. Rev. **96** (1954) 255.
7) Concerning the quasi-Fermi level, see, besides Shockley's papers, Y. Uemura: *Electronic Phenomena in Imperfect Crystals, Iwanami Lectures on Contemporary Physics*, vol. II H, (Iwanami Shoten, Tokyo, 1955), p. 71, (in Japanese) and E. Spenke: *Elektronische Halbleiter* (Springer-Verlag, Göttingen, 1955), p. 280.
8) J. B. Gunn: Proc. Phys. Soc. **67 B** (1954) 575.
9) N. F. Mott: Proc. Roy. Soc. **171 A** (1937) 27.
10) L. J. Giacoletto: RCA Rev. **15** (1954) 506.
11) R. L. Pritchard: Proc. IRE **42** (1954) 786.
12) J. M. Early: Bell. Sys. Tech. J. **32** (1953) 1271.
13) L. J. Giacoletto: RCA Rev. **14** (1953) 269.
14) W. van Roosbroeck: Bell Sys. Tech. J. **29** (1950) 560.
15) J. A. Swanson: J. Appl. Phys. **25** (1954) 314.
16) J. M. Early: Proc. IRE **40** (1952) 1401.
17) J. Bardeen and W. H. Brattain: Phys. Rev. **75** (1949) 1208.
18) L. J. Giacoletto: RCA Rev. **14** (1953) 28.
19) C. W. Mueller and J. I. Pankove: Proc. IRE **42** (1954) 42.
20) W. Shockley and W. T. Read: Phys. Rev. **87** (1952) 835.
21) R. N. Hall: Phys. Rev. **87** (1952) 387.
22) C. G. Garrett and W. H. Brattain: Phys. Rev. **99** (1955) 376.

JOURNAL OF THE PHYSICAL SOCIETY OF JAPAN Vol. 11, No. 7, JULY, 1956

# On the Electron Diffraction Patterns from the Oriented Silver Films

By Yasuyoshi WATANABE

*Osaka Industrial Research Institute, Ikeda, Osaka*

(Received September 20, 1955)

Rotation patterns of electron diffraction from oriented silver films prepared by condensation in *vacuo* onto heated NaCl crystal surface, were obtained by rotating the films about the [100] axis lying in the films. The intensity distribution along the hyperbolae appearing in the patterns was measured. The observed intensity was in good agreement with the intensity calculated on the assumption that the silver film is composed of parts of the parallel-growth structures, the twin structures, and the structures having defects proposed by Göttsche (Z. Phys. **134** (1953) 517). It was found by electronmicroscopy that the twin structures occur here and there on a submicroscopic scale, but the displacement of diffraction spots due to the twin faults was not detected.

## §1. Introduction

It has long been known since the experimental works of Lassen[1], Lassen and Brück[2] that thin silver films prepared by evaporation in *vacuo* on rocksalt cleavage faces kept at temperatures above 150°C have a definite oriented structure with crystallographic axes parallel to those of rock-salt substrate. The diffraction pattern contains abnormal spots corresponding to the intersections of the sphere of reflection with the body-diagonals of the body-centred reciprocal lattice. The abnormal spots become strong at the points dividing the reciprocal lattice period along body diagonals into six equal parts. While some of these points can be attributed to the reciprocal lattice points of the {111} twin lattices, the others can not. Here we shall call the diffraction spots corresponding to the formers the twin spots, and those corresponding to the latters the 1/6 spots.

In addition to works by electron diffraction method[3], studies on evaporated silver films were also made by other methods. Miwa and Annaka[4], for example, observed by the x-ray method abnormal patterns similar to those mentioned above from oriented silver films. Recently Ogawa, Watanabe and Fujita[5] observed in electronmicrographs of evaporated films linear stripes running parallel to the ⟨110⟩-axes lying in the plane of the films and they attributed the stripes to the twin lattices.

Although the abnormal diffraction patterns of silver film were studied by many workers cited above, so far the geometry of the patterns has been mainly studied. In the present study we have made the intensity measurement on the rotation photograph of oriented silver film. The observed result was compared with calculated intensities, by assuming that the silver film was composed of the parallel-growth structures, the twin structures, and the structures having defects (as shown in Fig. 9).

## §2. Experimental Procedures and Results

Silver metal was evaporated in *vacuo* onto freshly cleaved faces of NaCl crystals heated at about 300°C. The structure of the silver depends more or less on the thickness and the degree of vacuum during evaporation[6]. In the present experiment films of about 300 Å thick prepared at about $1\times10^{-3}$ mmHg pressure were used. They were well oriented and fairly strong mechanically. Each silver film isolated from the NaCl substrate in water was mounted on an aluminium sheet of 0.1 mm thick perforated with a hole of 0.3 mm in diameter. The aluminium sheet was electropolished beforehand so as to be able to catch the films flatly. The sample thus prepared was mounted on a sample holder in such a way that the center of the hole covered with the silver film is passed by the two rotation axes of the holder. Then, by means of one of the rotation axes, the [100] axis contained in the film plane was adjusted to coincide with the other rotation axis. The adjustment was confirmed by observing that two equivalent electron diffraction spots, e.g. (131)

and (131̄), appear at the same point on the fluorescent screen when the film was rotated about the [100] axis.

The electron diffraction apparatus was a modified electron-microscope supplied with highly stable accelerating potential and electron beam current. The accelerating potential of about 50,000 volts was applied throughout the experiment. The electron beam was made parallel only by passing through two small slits of 0.05 mm in diameter and no focussing coil was employed.

The sample was rotated through nearly 90° about the [100] axis during exposure with uniform angular velocity of one revolution per 2¾ minutes. The electron beam was normal to the axis of rotation. An example of the diffraction patterns thus obtained is reproduced in Fig. 1, the indexing of the pattern being shown in Fig. 2. There are found series of hyperbolic curves, on which the abnormal spots having fractional indices lie between the normal ones.

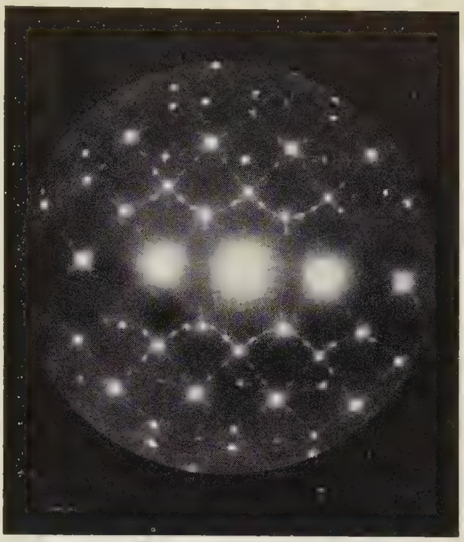

Fig. 1. Electron diffraction pattern from silver film rotated about the [100]-axis during exposure to the electron beam normal to the axis of rotation.

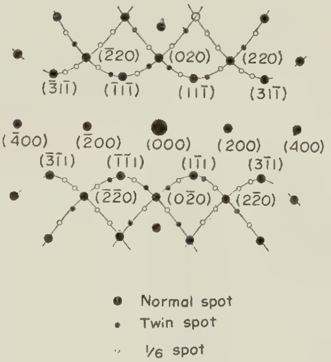

Fig. 2. Indexing of Fig. 1.

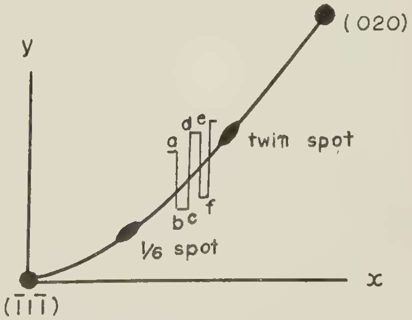

Fig. 3. Illustration of the path traced in the microphotometry of the intensity distribution along a hyperbola.

In order to obtain true scattering intensities against the general background along the hyperbolic curves, photographic densities were measured along the path as shown in Fig. 3. The plate was moved up and down with uniform speed relative to the light beam of a microphotometer, i. e. from *a* to *b* in the direction parallel to *y*-axis and from *c* to *d* in the inverse direction, and then from *e* to *f* in the same direction as from *a* to *b*, and so on. *ab*, *cd* and *ef* --- are separated by 1/10 mm from each other. The microphotometer curves thus obtained are shown in Fig. 4, where (a), (b) and (c) correspond to the diffraction patterns with decreasing exposure. *X*, *Y* and *Z* indicate the peaks of 1/6, twin and (020) spots respectively. From these curves the photographic densities along the hyperbolic curves were read and plotted against *x*-coordinate. The photographic density curves thus determined were transformed to intensity distribution curves by the use of the intensity vs. density curve. The latter was obtained by measuring the relation between the photographic density and the time of exposure for several definite Debye-Scherrer rings in the electron diffraction pattern of tin (Sn) film. In order to see the experimental error of the intensity distribution curve, the ratios of intensities obtained from corresponding points in Fig. 4 (b) and (c) have been evaluated and are plotted against *x*-coordinate in Fig. 5.

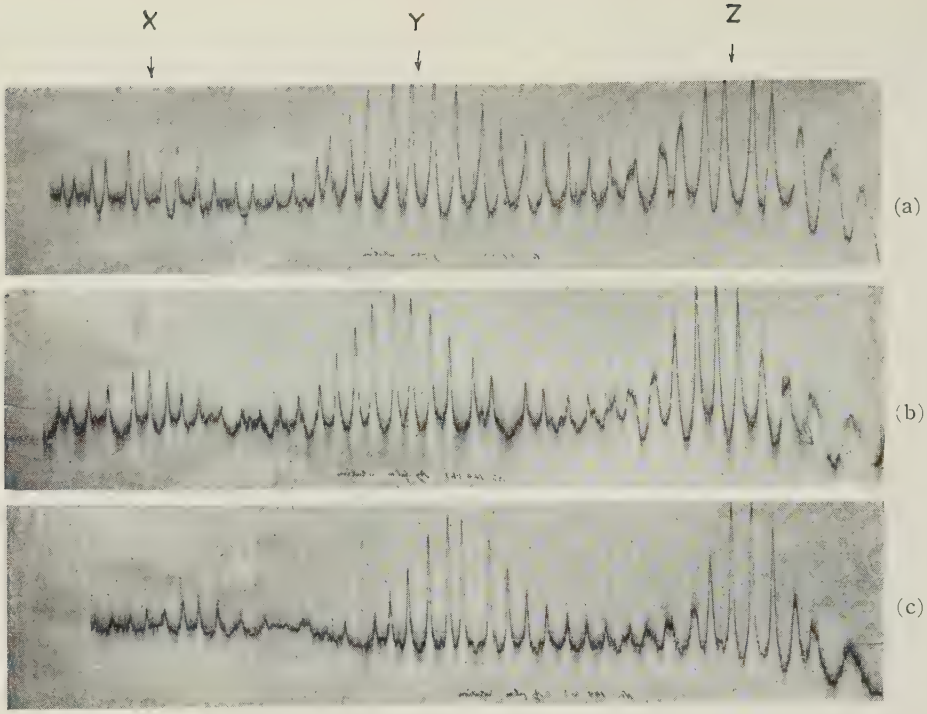

Fig. 4. Microphotometer curves along the paths as illustrated in Fig. 3. X, Y and Z indicate the peaks of 1/6, twin and normal spots respectively. (a), (b) and (c) correspond to the diffraction patterns of decreasing exposure.

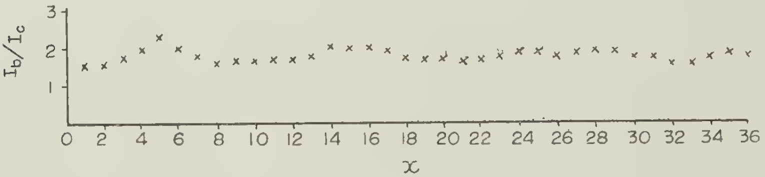

Fig. 5. Ratio of intensities obtained from corresponding points in Fig. 4 (b) and (c).

The ratio is roughly constant, indicating that the error is less than ±10%.

The intensity of a spot recorded in the rotation photograph must be corrected for the geometrical factor[7] $\cos\theta/\sqrt{\cos^2\varphi-\sin^2\theta}$, where $\theta$ is the Bragg angle, and $\varphi$ is the angle between the axis of rotation and the reflection plane. The corrected intensity is shown by the thick full line in Fig. 6.

It is easily proved that the intensity distribution along the hyperbola plotted against $x$-coordinate (in Fig. 6) indicates directly the intensity distribution along the corresponding {111}-rod of reciprocal lattice. The normal spot is the strongest and sharp. The 1/6 spot is weak and broad. The intensity of the streak between the (020) spot and the twin spot is found to be about twice as strong as that between the twin spot and the 1/6 spot. While, the intensity of the streak between the $(\bar{1}1\bar{1})$ spot and the 1/6 spot was found to be almost equal to that between the twin spot and the 1/6 spot. Similar relations were confirmed to hold for other streaks in the diffraction pattern.

Fig. 7 is the defocussed electron diffraction pattern of the oriented silver film. The figure shows that the normal diffraction patterns have almost continuous intensity distributions, while the twin patterns are rather spotty.

## § 3. Theoretical Interpretations

For convenient sake of theoretical treatment, let us take hexagonal axes in place of cubic ones in expressing the face-centred cubic

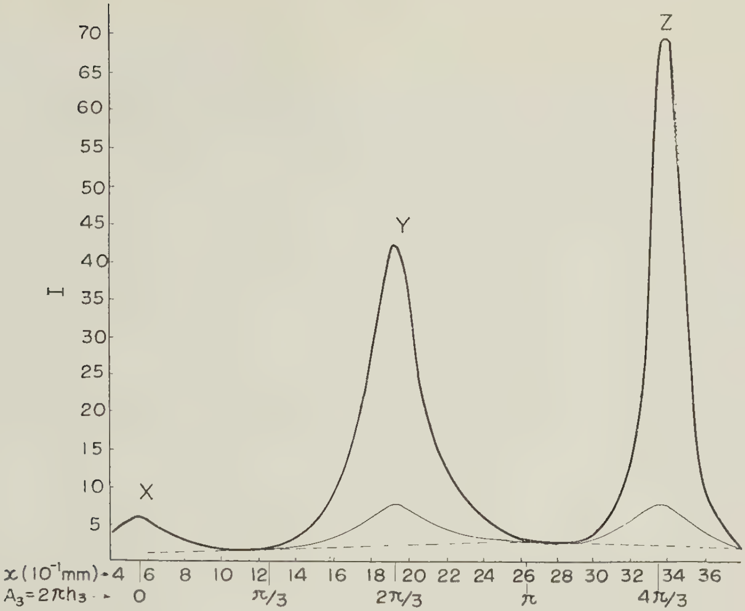

Fig. 6. Intensity distribution curves along the hyperbola. The thick full line is the observed intensity distribution corrected for the background and the geometical factor; the dashed line corresponds to the intensity distribution calculated from equation $I \propto (E - E' \cos A_3)^2$; and the thin full line corresponds to that from

$$I \propto (E - E' \cos A_3)^2 \frac{\sin^2 \frac{1}{2} N_3 A_3}{\sin^2 \frac{1}{2}(3A_3)} .$$

lattice of silver. The third axis $\boldsymbol{a}_3$ of the former, chosen parallel to the [111] axis of the latter, has the length 1/3 of the unit length of the [111] axis. The first axis $\boldsymbol{a}_1$ and the second axis $\boldsymbol{a}_2$ are taken parallel to $[01\bar{1}]$ and $[\bar{1}01]$ respectively both with the unit length one-half of the unit length of [011]. Hereafter Miller indices referred to the hexagonal axes will be expressed by $(h_1 h_2, h_3)$ and those referred to the cubic axes by $(k_1 k_2 k_3)$. For example, the normal spots (020) and $(\bar{1}1\bar{1})$, in Fig. 3, are expressed by $(\bar{1}0, 2/3)$ and $(\bar{1}0, \bar{1}/3)$ respectively when referred to the hexagonal axes, and the twin spot lying between them is $(\bar{1}0, 1/3)$ when referred to the same axes. The 1/6 spot in the same figure corresponds to $(\bar{1}0, 0)$. All points on this hyperbola satisfy the condition $1/3\,(h_1 - h_2) =$ *an integer* $\pm 1/3$.

We assume that the silver film is composed of the parallel-growth structures, the twin structures, and the structures having defects (as shown in Fig. 9). Then the diffraction pattern from the film can be thought of as superposition of the diffraction patterns due to the three structures, because these structures are considered as taking place at random over the entire film.

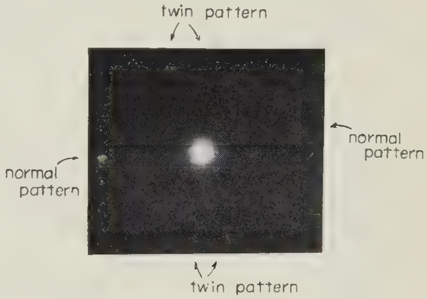

Fig. 7. Defocussed diffraction pattern from an oriented silver film.

a) First we shall study the diffraction due to the parallel-growth and the twin structures. Fig. 7 indicates that the twin structures actually occur here and there over the entire film. The twinning on the {111}-planes can be considered as a stacking fault of the {111}-layers. The diffraction from layer lattice having random stacking faults has been theoretically discussed in detail by many workers[8]. The growth fault, in which the

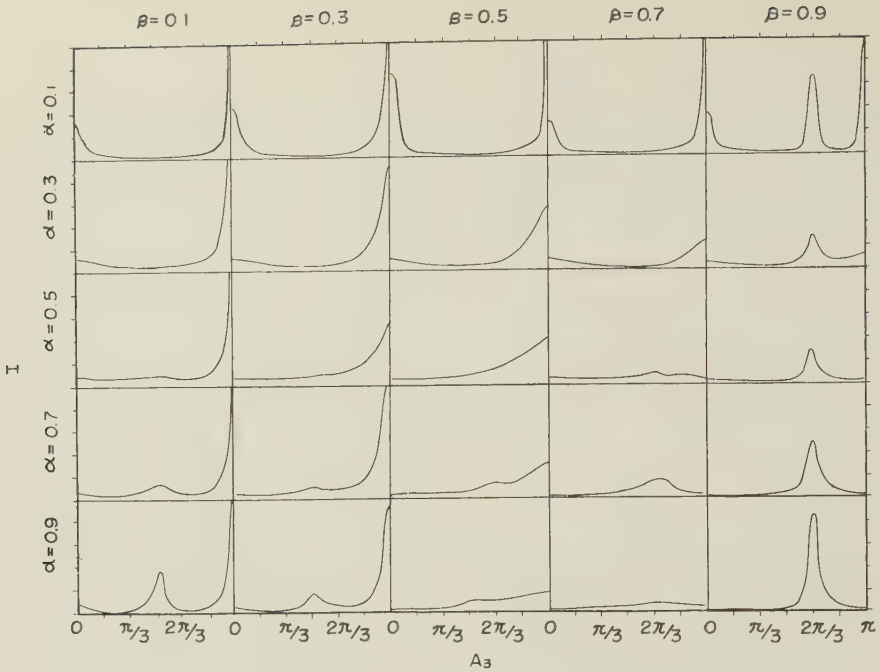

Fig. 8. Intensity distribution along the body-diagonal of reciprocal cubic lattice point row satisfying $1/3(h_1-h_2)=an\ integer \pm 1/3$, calculated by assuming the irregular stacking-sequence of {111} layers. Ordinate represents the intensity in arbitrary unit and abscissa represents $A_3(=2\pi h_3)$ over 0 to $\pi$. $\alpha$ and $\beta$ are defined as follows: the probability that the three layers stacking in hexagonal order are followed by a layer in hexagonal (or cubic) manner is $1-\alpha$ (or $\alpha$) and the probability that the three layers stacking in cubic order are followed by a layer in hexagonal (or cubic) manner is $1-\beta$ (or $\beta$).

ABCABC----- and the ACBACB----- stacking sequences occur equivalently to each other, is not the case, because the observed diffraction pattern (Fig. 6) is unsymmetrical across $2\pi h_3 = \pi$. Kakinoki, Komura and Hijiya[9] derived the expression of the diffraction intensity from the disordered cubic type crystal, assuming that the probability $\gamma$ of the fault from ABCABC----- to ACBACB----- is different from that $\gamma'$ of the reverse fault, from ACBACB----- to ABCABC-----. According to their result for reflections satisfying the condition $1/3(h_1-h_2) = integer \pm 1/3$, the positions of intensity maxima are displaced from the normal positions by a certain amount depending upon the probability of stacking fault. However, in the observed intensity distribution curve (Fig. 6) the displacement of the positions of maxima was not found out. Thus it is concluded within the limit of our experimental precision that the probability of the stacking fault $\gamma$ is less than 0.03 in our oriented films.

b) Next we shall interprete the 1/6 spots and the streaks along the hyperbolae. Cochrane[10] ascribed the streaks to shifts of atoms in the stacking layer and Menzer[11] ascribed it to an aperiodic lattice disturbance arising from the slight difference of the $\boldsymbol{a}_3$-spacing between cubic and hexagonal close packed arrangements. However, neither of these faults can explain the experimental fact that the streak is stronger in the region between the normal spot and the twin spot than in the region between the twin spot and the 1/6 spot or between the 1/6 spot and the normal spot.

The effect of the stacking faults mentioned in a) also gives streaks along the body-diagonals of reciprocal cubic lattice points satisfying $1/3(h_1-h_2) = integer \pm 1/3$. The expression for the streak intensity gives some peaks when correlation between neighbouring layers is present. When the correlation range is assumed to be three layers, the intensity distribution along the body-diagonals can be expressed graphically as shown in Fig. 8. It is seen from this figure that when the intensity distribution curve has a peak at $A_3 = 2\pi h_3 = 0$, it always has another stronger one at $A_3 = 2\pi h_3 = \pi$. However, it is not actually the case in the observed intensity distribution.

Menzer[11)] has pointed out that periodical defects are formed in a boundary region where two components of a twin crystal meet together as shown in Fig. 9. It is seen from the figure that, while layer $A$ is closely packed with atoms, other two layers $B$ and $C$ contain defects, and consequently the lattice has periodicity three times as large as the normal period along the $a_3$ axis. Menzer ascribed the 1/6 spot to these periodical defects. However, Fig. 9 illustrates only an ideal case. If stacking sequences of $A, B$ and $C$ are irregular, the defects having other periodicities or non-periodicity will also appear. Göttsche[12)] attributed the streak to this kind of non-periodical defects. Although in order to treat the diffraction intensity due to these kinds of structure, the lateral extension of the layers must be taken into account, Göttsche gave no further idea of it.

In the following consideration, we assume that atoms in a portion surrounding one or more of the defects are slightly displaced toward the defects, so that this portion is incoherent with remaining parts of the film. We call this portion the domain having defects*. Since the lateral extension of the domains of the parallel-growth and of the twin structures is said to be of the order of 1000 Å[5)], the extension of the domain containing only a single defect may be smaller than this length. Then, such a domain can not contribute to the diffraction intensity appreciably. However if defects are clustered closely as shown in Fig. 10, the domain becomes large and will contribute to appreciable intensity. Let us derive the expression for the intensity due to this kind of assumed structure.

The diffraction intensity for a layer lattice is generally given by[13)]

$$I = R \sum_{m_3=-(N_3-1)}^{+(N_3-1)} (N_3 - |m_3|)\overline{S_{j_3} S^*_{j_3+m_3}} \exp(im_3 A_3),$$

where

$$R = \frac{\sin^2 \frac{1}{2} N_1 A_1}{\sin^2 \frac{1}{2} A_1} \cdot \frac{\sin^2 \frac{1}{2} N_2 A_2}{\sin^2 \frac{1}{2} A_2},$$

and $A_\nu$ denotes $2\pi(\boldsymbol{a}_\nu \cdot \boldsymbol{k} - \boldsymbol{k}_0)$ or $2\pi h_\nu$, where $\boldsymbol{k}_0$ and $\boldsymbol{k}$ represent the wave vectors of the

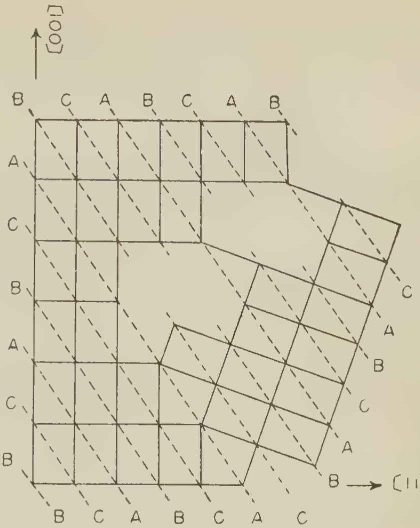

Fig. 9. Supposed structure of the evaporated silver film having periodical defects in the lattice.

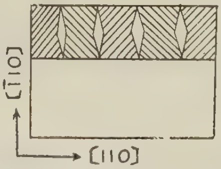

Fig. 10. Schematic illustration of the domains of the parallel-growth or twin structure (the lower white rectangle) and the structure having some defects (the upper hatched rectangle).

incident and the diffracted rays respectively and $\nu = 1, 2, 3$. The value of $R$ is large only when both $h_1$ and $h_2$ are integers. $N_1, N_2$ and $N_3$ are the numbers of translation along $\boldsymbol{a}_1$, $\boldsymbol{a}_2$ and $\boldsymbol{a}_3$ axes respectively, and $S_{j_3}$ and $S_{j_3}{}^*$ represent the structure factor of $j_3$th layer and its complex conjugate respectively; —— represents the average. When the correlation between neighbouring layers is absent, the formula is reduced to[13)]

$$I = R\left[N_3\left(\overline{|S_{j_3}|^2} - |\overline{S_{j_3}}|^2\right) + |\overline{S_{j_3}}|^2 \frac{\sin^2 \frac{1}{2} N_3 A_3}{\sin^2 \frac{1}{2} A_3}\right]. \tag{1}$$

Let us consider at first the structure as shown in Fig. 9. Each layer of this structure is composed of two layers which we shall denote by

---

* It is doubtful whether there are such clear-cut domains of distorted structure. Our idea is analogous to that in the theory of the mosaic structure of crystal.

$$\begin{matrix}A\\A\end{matrix},\quad \begin{matrix}B\\C\end{matrix}\ \text{or}\ \begin{matrix}C\\B\end{matrix}\ .$$

Then, this structure is expressed as follows:

$$\begin{matrix}\dot{A}BC\dot{A}BC\dot{A}BC\cdots\cdots\\ ACBACBACB\cdots\cdots\ .\end{matrix}$$

As the layer adjacent to layer A is always B or C in this case, each three layers $\begin{matrix}CAB\\BAC\end{matrix}$ can be treated as unit layer in evaluating the intensity formula (1). Since we can take the extension of B and C layers to be equal, the structure factor of the unit layer for $h_1, h_2$ $=$*integer* is given by*

$$\begin{aligned}S_{j_3}=E+\tfrac{1}{2}E\Big[&\exp 2\pi i\Big(\frac{h_1-h_2}{3}-h_3\Big)+\exp 2\pi i\Big(\frac{-h_1+h_2}{3}-h_3\Big)\\ &+\exp 2\pi i\Big(\frac{h_1-h_2}{3}+h_3\Big)+\exp 2\pi i\Big(\frac{-h_1+h_2}{3}+h_3\Big)\Big]\\ =E+2E'&\cos\Big\{2\pi\Big(\frac{h_1-h_2}{3}\Big)\Big\}\cos A_3\ ,\end{aligned}\qquad (2)$$

where $E$ and $E'$ denote the structure factors of an $\begin{matrix}A\\A\end{matrix}$ layer and a $\begin{matrix}B\\C\end{matrix}$ layer respectively. These layers is considered to contain distortions due to defects, therefore $E$ and $E'$ are both different from the normal atomic scattering factor.**. $E$ is always larger than $E'$, because the $\begin{matrix}B\\C\end{matrix}$ layer has defects and heavier distortion than the $\begin{matrix}A\\A\end{matrix}$ layer. For $1/3\,(h_1-h_2)$ $=$*an integer*$\pm 1/3$ equation (2) is reduced to

$$S_{j_3}=E-E'\cos A_3\ .$$

Therefore the diffraction intensity is given by

$$I=R(E-E'\cos A_3)^2\,\frac{\sin^2\frac{1}{2}N_3A_3}{\sin^2\frac{1}{2}(3A_3)}\ ,\qquad (3)$$

which gives sharp maxima at $3A_3=6\pi h_3=2\pi$ $\times$*integer*, or $h_3=1/3\times$*integer* with the intensity proportional to the factor $(E-E'\cos A_3)^2$.

If in the sequences of stacking layers of the distorted structure $\begin{matrix}CAB\\BAC\end{matrix}, \begin{matrix}ACB\\BCA\end{matrix}$ and $\begin{matrix}CBA\\ABC\end{matrix}$ are mixed at random with equal probability and no correlation is present among them, we have for $1/3(h_1-h_2)=$*integer*$\pm 1/3$

$$\begin{aligned}|\overline{S_{j_3}}|^2=\{&1/3(E-E'\cos A_3)\\ &\times[1+\exp(2\pi i/3)+\exp(-2\pi i/3)]\}^2=0\ ,\end{aligned}$$

and

$$\overline{|S_{j_3}|^2}=(E-E'\cos A_3)^2\ .$$

Then, the intensity formula (1) becomes

$$I=R\frac{N_3}{3}(E-E'\cos A_3)^2\ .\qquad (4)$$

This formula gives the streak along the body-diagonal of the reciprocal cubic lattice.

So far we have treated only the structure having periodicity three times as large as the normal spacing along $\boldsymbol{a}_3$ axis. We shall call this structure three-layer type. The structures having other periodicities or non-periodicity will be treated in the same way. We can show that, on the reciprocal lattice point row satisfying $1/3\,(h_1-h_2)=$ *an integer*$\pm 1/3$ these structures give the sharp maxima corresponding to $\mathrm{I}\propto(E-E'\cos A_3)^2\,\dfrac{\sin^2\frac{1}{2}N_3A_3}{\sin^2\frac{1}{2}pA_3}$, where $p$ is an integer determining the periodicity, and the streak corresponding to $\mathrm{I}\propto(E-E'\cos A_3)^2$, neglecting small constant term.

The 1/6 spot and the streak in Fig. 6, therefore, can be interpreted by the defects of three-layer type or non-periodical type. The fact that the scattering intensity between the normal and the twin spots is about twice stronger than the intensity between the twin and the 1/6 spots can be explained by assuming an appropriate value for $E'$ in equation $\mathrm{I}\propto$ $(E-E'\cos A_3)^2$. The intensity distribution calculated for $E'=0.25\,E$ is shown by the

---

* The general expression for the case where $h_1$ and $h_2$ are not both integers is not simple. However we are interested in the expression only for $h_1, h_2=$*integers*.

** Supposing that the number of defects is one per $N$ atoms of a perfect layer and the position of the atom in each unit cell of the distorted layer is simply expressed by $(1/3-\varepsilon, 2/3+\varepsilon)$ or $(2/3+\varepsilon, 1/3-\varepsilon)$, $E'$ becomes

$$\frac{N-1}{N}\,\frac{E_0\cos\{2\pi(1/3-\varepsilon)(h_1-h_2)\}}{\cos\{2\pi/3\,(h_1-h_2)\}}\ ,$$

where $E_0$ is the structure factor for a non-distorted layer.

dashed line in Fig. 6. It is normalized at $2\pi h_3=\pi$ so as to coincide with the observed intensity.

On the hyperbolae where the condition $1/3(h_1-h_2)=$ *an integer* is satisfied, for example the hyperbola passing through $(\bar{2}20)$ and $(\bar{3}1\bar{1})$, no twin spots are expected to appear. However, the scattering maxima due to the structure of three-layer type (simple or compound) are expected to occur from equation (1). By the help of (2) we obtain

$$I=R(E+2E'\cos A_3)^2\frac{\sin^2\frac{1}{2}N_3A_3}{\sin^2\frac{1}{2}(3A_3)}\,.$$

This equation gives two weak maxima of equal intensity at the points $h_3=1/3$ and $2/3$, corresponding to the positions of the 1/6 spots. The observed intensities of the two maxima, however, are neither equal nor weak. This discrepancy can be explained by the multiple reflection effect of electron beam. When the $(\bar{2}00)$-reflection is diffracted again through the same crystal, the new hyperbolae are superposed on the hyperbolae due to the primary beam. The new hyperbola passing through $(\bar{2}20)$ and $(\bar{3}1\bar{1})$ corresponds to the hyperbola which is due to the primary beam and passes through $(020)$ and $(\bar{1}1\bar{1})$. As the intensities of the abnormal spots on the new hyperbola are strong, the diffraction intensities along the hyperbola passing through $(\bar{2}20)$ and $(\bar{3}1\bar{1})$ can possess features similar to those on the hyperbola passing through $(020)$ and $(\bar{1}1\bar{1})$.

In the above discussion, to explain the result given by Fig. 6, $E'$ is assumed to be about 0.25 $E$. This value is apparently too small. However, since the evaporated silver film have developed from independent nuclei, the extension of layers will be often very small, leaving a great many vacant sites. Then the effect of defects mentioned above increases and as the result the value of $E'/E$ becomes small. When, moreover, the sideway displacements of atoms surrounding the defects are taken into account as mentioned before, the value of $E'/E$ becomes very much smaller.

c) The shapes of the normal and the twin peaks obtained by substracting the intensity due to the structures having defects as considered above are found to be symmetric. This fact supports the above interpretation for the diffraction pattern. The twin peak is broader than the normal peak, indicating that the dimension of the twin structure along the ⟨111⟩-direction is smaller than that of parallel-growth structure.

## Acknowledgement

The author expresses his sincere thanks to Professor Mitsuo Miwa of Tokyo University of Education for his guidance and encouragement throughout this work. He is indebted to Professor Ryozi Uyeda of Nagoya University and Professor Jiro Kakinoki of Osaka City University and Dr. Minoru Iwata of our laboratory for their kind discussions and also to Mr. Hideo Hayashi for his assistance in experiments.

## References

1) H. Lassen: Phys. Z. **35** (1934) 172.
2) H. Lassen and L. Brück: Ann. d. Phys. **24** (1935) 173.
3) F. Kirchner and H. Lassen: Ann. d. Phys. **24** (1935) 173.
L. Brück: Ann. d. Phys. **26** (1936) 233.
W. Cochrane: Proc. Phys. Soc. London **48** (1936) 723.
M. v. Laue: Ann. d. Phys. **26** (1936) 55; **29** (1937) 211.
M. v. Laue and K. H. Riewe: Z. f. Kristallogr. **95** (1936) 408.
F. Kirchner and O. Rüdiger: Ann. d. Phys. **30** (1937) 609.
F. Kirchner: Ann. d. Phys. **30** (1937) 619.
O. Goche and H. Wilman: Proc. Phys. Soc. London **51** (1939) 625.
R. Uyeda: J. Phys.-Math. Soc. Japan **24** (1942) 809.
H. Göttsche: Zeit. f. Phys. **134** (1953) 517.
4) M. Miwa and S. Annaka: J. Phys. Soc. Japan **9** (1954) 302.
5) S. Ogawa, D. Watanabe and E. Fujita: J. Phys. Soc. Japan **10** (1955) 429.
6) Y. Watanabe: J. App. Phys. Japan **23** (1954) 167 (in Japanese).
7) See, for example, Lonsdale: Crystals and X-rays (G. Bell & Sons Ltd., 1948) Chap. 5.
8) A. J. C. Wilson: Proc. Roy. Soc. **180** (1942) 277.
M. S. Paterson: J. App. Phys. **23** (1952) 805.
S. Hendricks and E. Teller: J. Chem. Phys. **10** (1952) 147.
H. Jagodzinski: Acta Cryst. **2** (1949) 201; **2** (1949) 208; **2** (1949) 298; **7** (1954) 17.
J. Kakinoki and Y. Komura: J. Phys. Soc. Japan **7** (1952) 30; **9** (1954) 169; **9** (1954) 177.
H. Gevers: Natuurwet. Tijdschr. **35** (1953) 25: Acta Cryst. **7** (1954) 337.
9) J. Kakinoki, Y. Komura and K. Hijiya: X-rays **8** (1955) 67 (in Japanese)
10) W. Cochrane: *loc. cit.*
11) G. Menzer: Naturwissen. **26** (1938) 385; Z. f. Kristallogr. **99** (1938) 378;
12) O. Göttsche: *loc. cit.*
13) H. Jagodzinski: *loc. cit.*

JOURNAL OF THE PHYSICAL SOCIETY OF JAPAN Vol. 11, No. 7, JULY, 1956

# Anomalous Enhancement of X-ray Reflection Intensity at the Boundary of Ground and Etched Regions on Crystal Surface

By Norio KATO

*Kobayasi Institute of Physical Research, Kokubunji, Tokyo*

(Received March 14, 1956)

The anomalous effect reported by Fukushima (E. Fukushima; *Acta Cryst.* 459 (1954) **7**), *i.e.* a large enhancement of X-ray reflection intensity at the boundary of etched and ground regions in quartz crystal slab, is studied by a double crystal spectrometer. The difference can not be found in line width of reflection curves at the ground region and at the boundary region. Lattice bending is not detected at the boundary. It is not larger than 10″, if it exists. The anomalous enhancement is erased by etching the crystal surface for several seconds. This anomalous effect can be observed also in $NaClO_3$ crystal and calcite but the enhancement is very small in the latter crystal. It is concluded that the anomalous enhancement is due to a reduction of primary extinction caused by elastic distortion accumulated at the boundary region.

## § 1. Introduction

It has long been known[1] that the reflected intensity of *X*-rays from crystals is greatly changed by surface treatments. Investigations on this subject have given us many valuable informations about the actions of surface treatments on crystal texture. When surfaces of highly perfect crystal are ground or polished, the integrated reflection intensity of *X*-rays increases enormously. When such surfaces are etched by a suitable method the reflection intensity decreases to the initial value. This variability of intensity can be explained by the extinction effect which is very sensitive to the degree of perfectness of crystals. Darwin[2] classified the extinction effect into two, *i.e.* primary and secondary extinction, although such a classification is not always distinctive in real crystals.

Recently, Fukushima[3] found in quartz plates that the reflected intensity at the boundary between the etched and ground region was enormously larger than that at the ground region. He used *Z*-cut plate having the boundary line parallel to the *Y*-plane. He showed that:

( i ) The large enhancement can be observed only for low order reflections.

( ii ) No enhancement can be observed for the reflections from the net plane perpendicular to the boundary and from that parallel to the crystal surface.

To explain these results, Fukushima assumed that there exists a zone containing large strain gradient in the direction parallel to the crystal surface and perpendicular to the boundary.

The result ( i ) suggests that this phenomenon is intimately related to the reduction of extinction effect as the result of lattice distortions at the boundary region. In his experiment, however, the nature of the distortion was not made clear since the observations were carried out by a single crystal spectrometer. To clarify this point the present author studied reflection curves of *X*-rays from quartz, sodium chlorate crystal and calcite in detail by a double crystal spectrometer. Studies on these crystals may be interesting because it has been revealed by Sakisaka[4] that quartz and sodium chlorate crystal belong to the same class of texture while calcite to a different class.

## § 2. Experimental Procedures

( a ) *Preparation of specimens*

( i ) *Quartz*

Specimen plates were prepared from Brazillian quartz which had no twin, no colour and no the other optical faults. The plates were ground manually with 600 mesh alundum on a glass plate. After grinding they were washed with water and dried. Next, a half of one surface of each plate was covered with paraffin and it was immersed into 48% hydrofluoric acid. After etching for about 30 min., the paraffin was removed from the plates by melting it in hot water. As the results of these treatments the boundary was produced between the etched and ground surface.

( ii ) *$NaClO_3$ crystal*

$NaClO_3$ single crystals were obtained from aqueous solution by the evaporation method in a thermostat. {100}-plates were prepared from them by polishing with very fine emery paper. The boundary was made by the similar procedure as in quartz. In this case the crystal surface was covered with organic film and etched with pure methyl alcohol.

(iii) *Calcite*

The plates were prepared from Iceland spar. They were cleaved and polished by very fine emery paper. Etching was carried out in 2% HCl solution.

( b ) *X-ray measurements*

Mo $K\alpha$ was used throughout all the experiments. The experiments on quartz and $NaClO_3$ crystal were carried out by means of a double crystal spectrometer. Incident *X*-rays were monochromatized by calcite which is set in an approximate (1, −1) position to the specimen. The separation of $K\alpha$-doublet and the width of each line were about 0.15 mm and 0.10 mm respectively at the place of specimen. The height of collimating slits was 8 mm. The primary intensity of the monochromatized *X*-rays was measured by an ionization chamber and a string electrometer. The *X*-rays reflected by specimens were measured by a G.M. counter and an electronic scaler.

The measurements on calcite were carried out by a single crystal spectrometer. In this case the width of primary beam was about 0.10 mm at the place of specimen. The intensity of reflected *X*-rays was measured by a G.M. counter.

The geometrical arrangement of specimen relative to incident *X*-rays was similar to that reported by Fukushima[3]. Specimen mounted on a crystal holder was moved horizontally in an increment of 0.2–0.05 mm. The holder was placed on the crystal table of spectrometer with a vertical rotation axis. The angles of rotation were read to 5″ in the double crystal spectrometer and to 30″ in the single crystal spectrometer.

The reflection curve was obtained at each horizontal position of crystal. For every specimen the peak values of reflection curves were plotted against the horizontal positions of crystal. This curve will be called the *p-x* curve in the present paper.

( c ) *The angular position of the crystal holder relative to the incident beam.*

To determine whether bending of the lattice takes place at the boundary or not, we must know the angular position of crystal relative to the incident beam, when the orientation of crystals satisfies the Bragg condition exactly. This was determined by a combination of the double crystal spectrometer and an optical system of mirror and telescope (cathetometer) as shown in Fig. 3 (a). A mirror $MM'$ was mounted on the crystal holder $H$ in parallel with the crystal surface $SS'$. An oblique cross drawn on a paper $PP'$ was placed at the cathetometer and distance $l$ between the two cross points $A$ and $B$ of a vertical wire with the mirror image of oblique cross was read by a telescope. Then rotation angle of the mirror $\varDelta\theta$ is given by variation of the vertical distance $\varDelta l$ as

$$\varDelta\theta=\frac{\cot\varphi}{2L}\varDelta l$$

where $L$ is the distance of the mirror and the telescope, and $\varphi$ is the angle between the two crossed lines. Since it is possible to take $L$, $\varDelta l$ and $\varphi$ as 1 m, 0.05 mm and 70° respectively, the minimum detectable angle is estimated to be approximately 2.5″. However, reproducible accuracy was in an order of 10″, probably due to waving of the mirror surface.

## § 3. Experimental Results

( a ) *Quartz*

( i ) *p-x curves and reflection curves*

Preliminary experiments were carried out for several plates. Among these plates a *Y*-cut plate was studied especially in detail. The boundary was made along the *z*-axis and the observations were carried out on the reflection from *X*-plane which was perpendicular to the crystal surface.

Fig. 1 shows the *p-x* curve of this specimen.

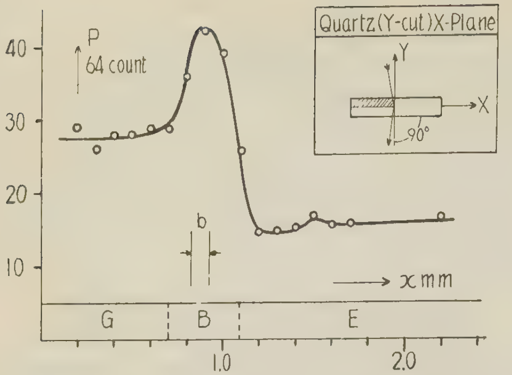

Fig. 1. Peak values of reflection curve against horizontal positions of quartz plate (*p*-*x* curve). *G*, *B* and *E* correspond to the ground region, the boundary region and the etched region respectively. b represents the width of the incident X-rays

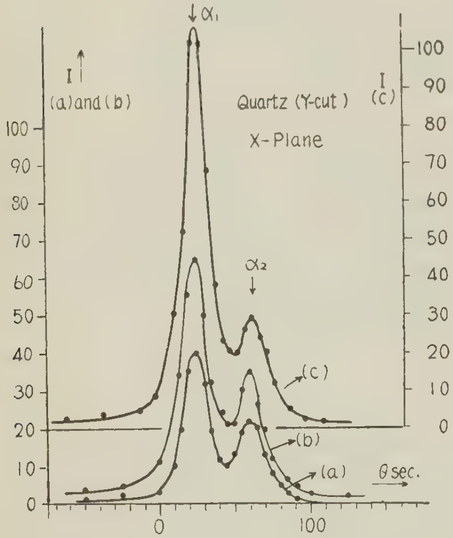

Fig. 2. The reflection curves of quartz plate. (a), (b) and (c) correspond to the etched and ground region and the boundary respectively.

Some of the reflection curves of this plate are shown in Fig. 2. The curves (a), (b) and (c) correspond to the etched region, the ground region and the boundary region respectively. The two peaks in each curve correspond to the *Kα*-doublet. The width at half value and the integrated intensity of the individual curve were obtained graphically assuming that it can be expressed by Hoyt's formula⁵⁾ of the same half width. The results are given in Table I.

In the other specimens, which were proved to be more imperfect by inspecting their reflection curves, the *p*-*x* curves were not so different from the above results.

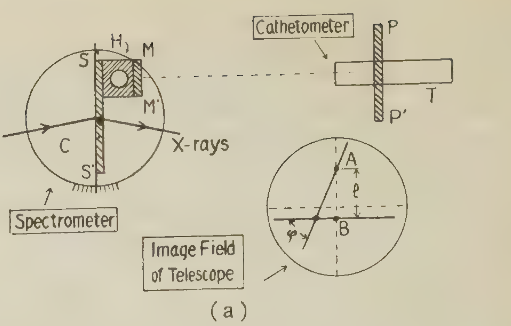

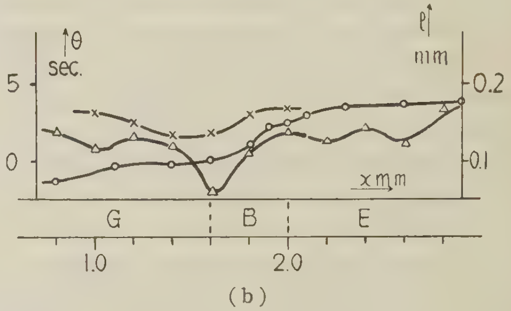

Fig. 3 (a). Schematic diaphragm of a combination of the double crystal spectrometer and an optical system of mirror and telescope (cathetometer).
*C*: Crystal table of spectrometer. *H*: Crystal holder. *SS'*: Crystal of specimen. *MM'*: Mirror. T: Telescope. *PP'*: Paper on which two crossed lines are drawn.
In the image field of the telescope, the full lines show the oblique cross and the dotted lines the cross wire of the telescope.
*AB*=*l*: The vertical distance between the image of the two crossed lines.

Fig. 3 (b). Angular position (*θ*) of crystal at which Bragg relation is satisfied strictly. Ordinate, *l*, is explained in the legend of Fig. 3 (a). *θ* was obtained from *l* in terms of calibrated scale. Abscissa shows horizontal positions. These curves were obtained under the different conditions of attachment of the mirror.

### (ii) *Bending of lattice at the boundary*

If crystal lattice bends at the boundary,* the crystal must be rotated by the angle of the bending in order to satisfy the Bragg condition. Therefore, the angular position of the crystal holder relative to the incident beam was measured by the method described in § 2 (c). The experimental results are shown in Fig. 3 (b). The ordinate shows the angles of rotation at which the reflection curve attains its peak value and the abscissa, the horizontal positions of the crystal. Letters *G*, *B* and *E*

---

* Similar situations are expected when crystal lattice is expanded or compressed.

Table I.

| | Intensity | | | Line width | | |
|---|---|---|---|---|---|---|
| | *G* | *B* | *E* | *G* | *B* | *E* |
| Quartz | 21.0 | 36.0 | 15.3 | 21.5″ | 18.6″ | 19.7″ |
| NaClO$_3$ | 23.7 | 35.8 | 5.2 | 33″ | 34″ | 26″ |
| Calcite | 20 | 27 | 13 | — | — | — |

The integrated intensity of reflection and the line width at half value of reflection curve for various substances.

show the ground region, the boundary region, and the etched region respectively. These results indicate that the bending of the crystal lattice is not larger than about 10″.

(iii) *Variations of the anomalous effect by etching*

To study the variation of the anomalous effect with time of etching, a half of the ground surface was etched for from 1 sec. to 30 min., and *p-x* curves were obtained successively. In this case, paraffin was not removed throughout the experiments. The results are shown in Fig. 4 (a).

Next, the boundary was made on a plate by the usual method (*cf.* § 2 (a)) and the plate was immersed in HF acid for about 1 sec.. The *p-x* curves before and after the etching are shown in Fig. 4 (b). From these results, it is clear that the anomalous region is made and removed easily by shallow etching. It is also to be noted that the enhancement of intensity at the ground region is diminished by etching of very short time.

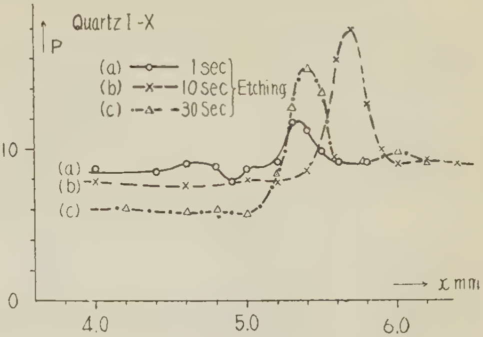

(a)

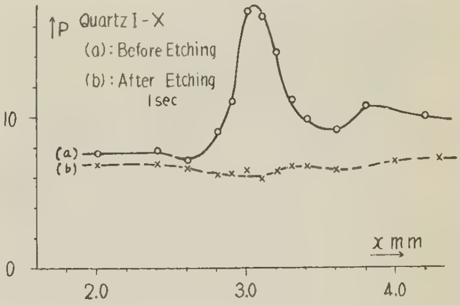

(b)

Fig. 4 (a). Variation of $p$–$x$ curves with the time of etching to make the boundary.

Fig. 4 (b). Change of the boundary effect by etching.

(iv) *Order of grinding and etching*

In the above experiments, the boundary was produced according to the procedure described in § 2. The reverse procedure, *i.e.* grinding a half portion after etching the whole surface, gave also the similar enhancement at the boundary. But this procedure was not adopted usually since special cautions were necessary to make up the sharp boundary by grinding.

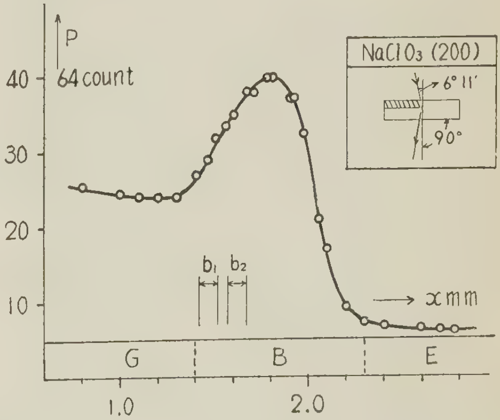

Fig. 5. $p$–$x$ curves of NaClO$_3$ crystal. $b_1$ and $b_2$ represent the line width of $K$-$\alpha$ doublet of incident X-rays.

(b) *NaClO$_3$ crystal*

The observations were carried out on the (200) plane which was perpendicular to the crystal surface. The boundary was made parallel to the [010]-direction. The *p-x* curve is shown in Fig. 5. The reflection curves are given in Fig. 6. From these figures, the width at half value and the integrated reflection intensities were obtained (Table I). In this case the reflection curves of *Kα*-doublet coalesce with each other since Bragg angle of the first crystal (6°43′) are nearly equal to that of the second crystal (6°11′). Therefore, the true width at half value may be smaller than the tabulated value by an order of the sepa-

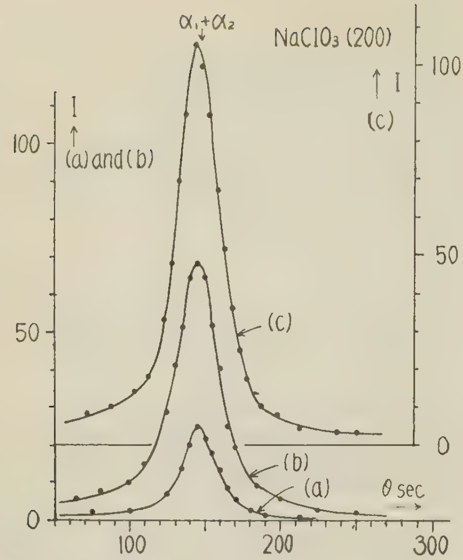

Fig. 6. The reflection curves of $NaClO_3$ crystal. (a), (b) and (c) correspond to the etched and ground region and the boundary respectively.

ration angle of the doublet, 6.5″. The other specimens also gave the similar result.

(c) *Calcite*

In the case of calcite, the studies were performed by a single crystal spectrometer, because large and thin specimen suitable to measure the intensity with double crystal spectrometer could not be prepared. The observations were carried out on the (211) plane. One of the results is shown in Fig. 7(a). The enhancement of *X*-ray intensity at the boundary can be detected also in this substance, but it is less predominant compared with the cases of quartz and $NaClO_3$.

## § 4. Comparisons of the Results from the Various Crystals.

(i) *Width of the region of anomalous intensity*

For quartz and calcite the width of the region of anomalous intensity is estimated to be about 0.2 mm (*cf.* Fig. 1 and 7(a)). For $NaClO_3$ crystals, the width is apparently larger than that of quartz as shown in Fig. 5. However, this difference is only due to the fact that the incident beam used for $NaClO_3$ crystal is effectively broader. Though the width of the incident beam is about 0.1 mm in the case of quartz, the effective width of the incident beam amounts to 0.25 mm in $NaClO_3$ crystal, because both of the $K\alpha$-doublet contribute to the peak values of reflection curve. Therefore, the width of the anomalous region of $NaClO_3$ is supposed to be comparable with that of quartz.

(ii) *Integrated intensity at the anomalous region*

The integrated reflection intensity at the boundary is about 1.7 and 1.5 times that of the ground region for quartz and $NaClO_3$ crystal respectively (Table I). For $NaClO_3$ crystal it would be larger if $K\alpha$-doublet could be separated since $K\alpha$-line is reflected from the etched region at the position where the total reflected intensity of $K\alpha$-doublet is maximum.

For calcite the enhancement is still appreciable but not so remarkable as for quartz and $NaClO_3$. The intensity at the boundary is about 1.35 times that at the ground region. In this case, however, the experiments were carried out by single crystal spectrometer and the angle between the examined net plane and the crystal surface is peculiar, being 74°55′. Therefore, the difference in the geometrical condition of the incident beam or in the angle between the net plane and the surface might be the cause of the smallness of the anomalous effect. To test these possibilities *Y*-net plane inclined 60° to the surface of a *Y*-cut quartz plate was examined under the same condition of the incident beam (Fig. 7(b)). For this specimen the intensity of the boundary was about 1.9 times that of the ground region. Therefore the difference of the anomalous enhancement in Fig. (a) and (b) can not be attributed to the geometrical conditions.

## § 5. Discussions and Conclusions

Concerning the reflection curves of quartz and $NaClO_3$ crystal (Fig. 2 and 6 and Table I), the following points are to be noted.

(a) For good crystals of quartz the line width of the reflection curve at the ground region and that at the boundary region are almost equal to that at the etched region. Moreover, experiments show that no bending of lattice takes place at the boundary.

(b) For $NaClO_3$ crystals the line width at the polished region and that at the boundary are slightly larger than that at the etched region. However, the remarkable difference of the integrated intensity can not be explained by such a slight increase of line width. The difference of the line width between the polished region and the boundary region is not discernible.

These results indicate that the misorientation of crystal at the boundary is very small and not larger than that at the polished or ground region. Thus it is concluded that the anomalous enhancement is caused mainly by reduction of the primary extinction.

Sakisaka[4] found in his experiments of reflection case that quartz and $NaClO_3$ crystal are in a similar state of distortion when their surfaces are ground or polished. When the crystals are ground with fine carborundum, both the line width and the peak value increase, but with the increase cf coarseness of carborundum the peak value decreases after attaining its maximum value. On the other hand, he found that for calcite the line width increases with the coarseness of carborundum and the peak value decreases from beginning even when its surfaces are treated with very fine emery paper. These results mean that for good crystal of quartz and $NaClO_3$ both the primary and the secondary extinction effects are remarkable and only the primary extinction is reduced by fine grinding. While, for calcite, only the secondary extinction is predominant and is reduced even by slight treatments*.

Therefore, the large enhancement for $NaClO_3$ as well as for quartz and the small enhancement for calcite, may be understood as reasonable if the enhancement at the boundary is caused by an anomalous reduction of the primary extinction. The difference of the boundary effect in these substances is due to the difference in their crystalline texture itself.

*The state of lattice distortion at the boundary and the ground regions*

It is well known that the reduction of primary extinction is due to lattice distortions. The anomalous reduction at the boundary cannot be explained in a satisfactory way at the present stage of investigation, and full discussions of the phenomena at the boundary are postponed to a later date. We can consider, however, that the nature of distortion at the boundary is the same for both the ground region and the boundary region, but that the degree of distortion is more intense at the boundary than at the ground region for substances such as quartz and $NaClO_3$. This consideration is supported by the following facts.

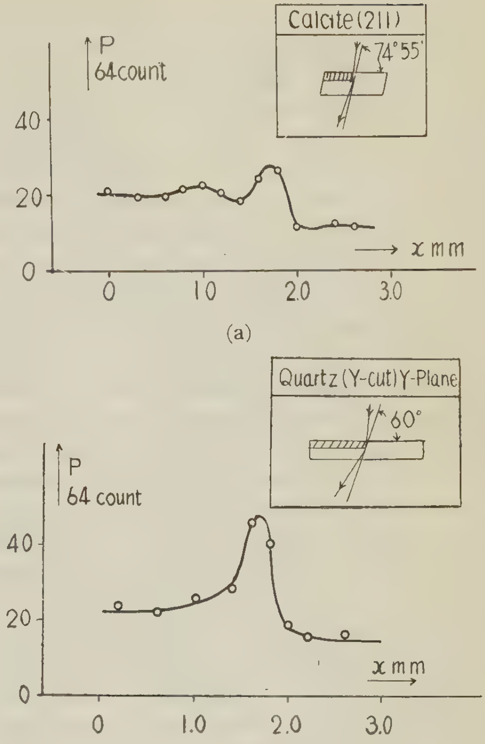

(a)

(b)

Fig. 7.

(a) Difference in the line width is not detected between the boundary and the ground region.

(b) The intensity enhancement at the boundary and the ground region are erased simultaneously by a short etching.

(c) The *p-x* curves are independent of the order of grinding and etching.

The crystalline state of the ground surface in substance such as quartz is infered as follows. The thickness of the distorted region beneath the ground surface which contributes to the intensity enhancement may be of an order of 0.1 mm. This is concluded from the fact that the absolute integral intensity of reflection at the ground surface is comparable with the calculated value for an ideally mosaic crystal of such an order of thickness. As described before, this intensity enhancement, is diminished by etching for several seconds. If crystal is assumed to be dissolved homogeneously by the etching, the thickness of the surface layer removed by such a shallow etching is estimated to be about several Ångstroms. This fact indicates that the permanently destroyed region is very thin compared with the region responsible for the intensity enhancement, especially in transmission experiments.*

---

* For the quartz crystals used by Sakisaka, it seems that the secondary extinction effect was not so remarkable in comparison with the primary extinction effect. The line width was 45″ for untouched crystals. It was 10″ for untouched crystals of calcite.

From the above considerations the author supposes the ground surfaces to be as follows. By grinding numerous cracks are produced on the surfaces and crystal is prevented to join by debris in the cracks. As theresults, elastic strain is present in the layer of considerable thickness. This layer contributes to the enhancement of *X*-ray reflection, at least, in transmission experiments. By a slight etching, the debris in the cracks are removed and most of cracks disappear. Thus elastic strain is removed from the region lying beneath the permanently destroyed very thin layer.

## § 6. Acknowledgement

The author wishes to say his thanks to Professor E. Fukushima for his suggestion and valuable discussions on this work and Professor Ryozi Uyeda for his kind advices. He says his thanks also to Mr. M. Imai in Hitachi Central Research Laboratory who prepared G. M. counter for him, and to the late F. Ootake for his assistance throughout this experiments. This work was defrayed from the grant in Aid for Fundamental Scientific Research of the Educational Ministry.

## References

1) The important literatures are described in the following two articles.
R. W. James: *The optical principles of the diffraction of X-rays* 1948, Chap. VI.
E. G. Armstrong: J. Bell Syst. Tech. **25** (1946) 136.
2) C. G. Darwin: Phil. Mag. **27** (1914) 315; **27** (1914) 675.
3) E. Fukushima: *Acta Cryst.* **7** (1954) 459.
4) Y. Sakisaka: Proc. Math.-Phys. Soc. Japan: **12** (1930) 189.
5) A. Hoyt: Phys. Rev. **40** (1932) 477.
6) R. M. Bozorth and F. E. Haworth: Phys. Rev. **45** (1934) 821.

---

* In this experiments the time of etching to remove the effect of grinding was an order of second, while Bozorth and Hawarth⁶⁾ and Armstrong¹⁾ found in their reflection experiments that it is about 2 min. in 48% HF acid. This fact is apparently curious because in transmission experiment deeper region is effective than in reflection experiment. However, the author infers that a slight etching is sufficient to remove the elastic strain in the deeper region and more etching is necessary to remove the permanently distorted surface layer.

JOURNAL OF THE PHYSICAL SOCIETY OF JAPAN Vol. 11, No. 7, JULY, 1956

# Proton Magnetic Resonance Absorption Spectra of Long Chain Normal Primary Alcohol of Probable Carbon Number 32

By Hachiro KOMATSU

*Institute of Science and Technology, University of Tokyo,*
*Komaba-machi, Meguro-ku, Tokyo*

(Received August 15, 1955; Revised April 10, 1956)

Proton magnetic resonance absorption from long chain normal primary alcohol of probable carbon number 32 was observed between 120°K and its melting point 355°K. Its absorption line width and second moment were constant below 260°K, being 15.5 gauss and 26.5 gauss$^2$, respectively. From 260°K to the transition point, the line width decreases gradually with increasing temperature and, at the transition point, abruptly decreases to 4.6 gauss. The narrowing of the absorption line below the transition point is considered to be due to the torsional vibration of the molecules around the carbon chain axis. The relation between the dielectric anomaly below the transition point observed by Takamatsu and the molecular motion revealed from nuclear resonance studies is discussed.

## § 1. Introduction

Quite recently, Takamatsu[1] has observed experimentally a small but definite dielectric anomaly in higher normal primary alcohol extracted from Carnauba wax, whose carbon number is probably 32, below the rotational transition point, together with the usual large anomaly due to molecular rotation, which is quite the same in character as that observed in tetradecyl, hexadecyl, octadencyl, or dococyl alcohols[2][3][4][5].

The aim of the present paper is to investigate the behaviors of the molecules in this higher alcohol through proton magnetic resonance, and to discuss its results in relation to the dielectric behaviors revealed by Takamatsu's experiment.

Investigations on the rotation of molecules in aliphatic compounds through proton resonance are not entirely novel, and among them Andrew's work on paraffins[6] and Kojima and Ogawa's work on hexadecyl (cetyl) alcohol[7] should be noted. Their results confirm the existence of molecular rotation, hitherto concluded from dielectric[3] as well as X-ray[8][9][10] and specific heat measurements[11].

The result of our experiment has shown that even at the temperature below the rotational transition point, not only OH radicals but also the whole part of the molecule have some degree of freedom.

## § 2. Experimental Procedure

The detector was a Pound-Knight-Watkins type of radio-frequency spectrometer[12][13]. Electromagnet used in the present experiment was charged by a motor generator. The field current was controlled by feeding back the deviation of the voltage across a manganin resistor put in series with the magnet coil, from a standard voltage. Then the current through the magnet was automatically stabilized to one part in twenty thousands. The field strength of the magnet was near 2400 gauss in 3 cm gap, the diameter of the pole pieces being 15 cm. The inhomogeneity within the volume occupied by the samples was less than 0.1 gauss which was, in most cases, negligible compared with the width of the resonance line.

Magnetic field was modulated sinusoidally at 230 cps with half amplitudes ranging from 0.1 to 1.0 gauss. The frequency of the R. F. oscillator was fixed to a constant value and the magnetic field was slowly swept through the resonance at the rate of 2 gauss/min. by regulating the current through a subsidiary coil wound around the pole of the magnet[14]. The output of the resonance signal was fed into a phase-sensitive detector[15] with a time constant of 8 sec. for the broad lines and of 0.4 sec. for the narrow lines. The derivative of the absorption curve was recorded by a recording milliammeter. Bias mag-

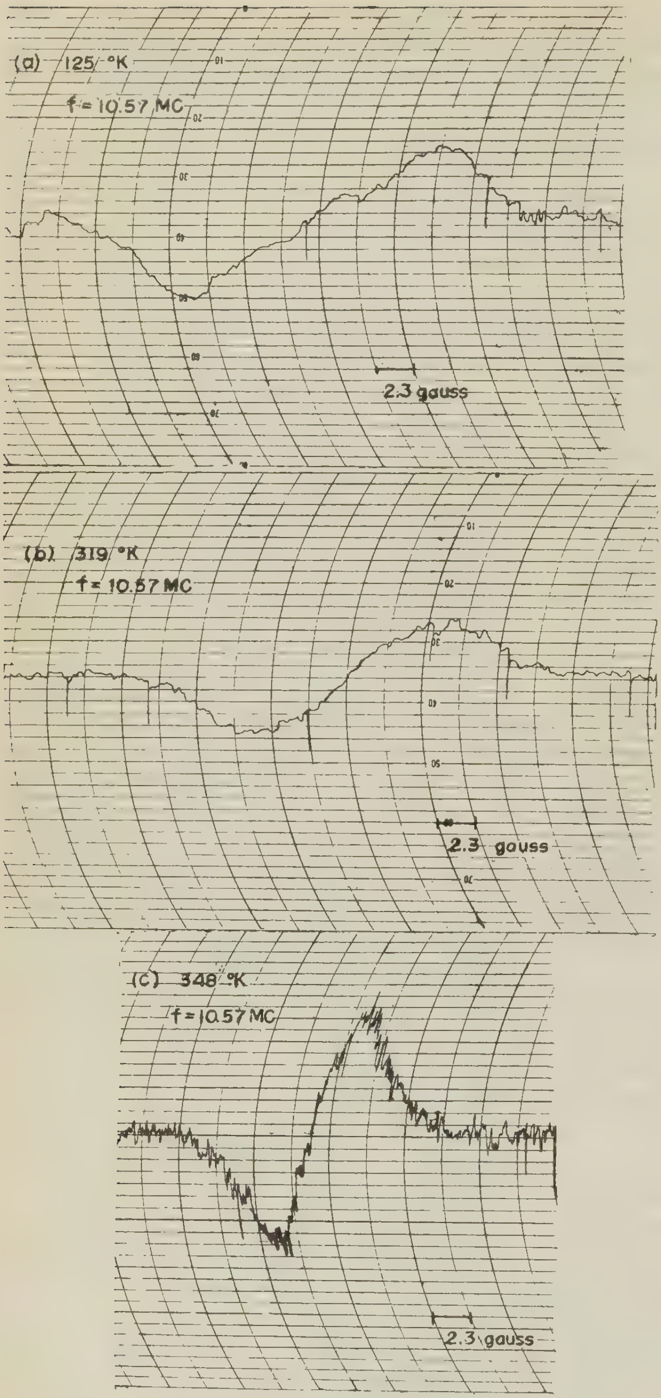

Fig. 1. Experimental recordings of the derivative of the nuclear magnetic resonance absorption.

netic field was calibrated by the proton resonance in water.

The cooling of the sample was achieved in a conventional way[14)], using a Dewer flask of 18 mm in inside and 29 mm in outside diameter at the lower part which was to be inserted between pole-pieces. It was not silvered in order to prevent a drop in Q values of the coil. The temperature range from 150°K to 210°K was covered using liquid oxygen as coolant, from 210°K to room temperature by a mixture of dry ice and ethyl alcohol. Higher temperature was attained by heaters only. Temperature of the sample was measured by a copper-constantan thermojunction located near the sample.

The sample was offered from Takamatsu. It was dried in a desiccator with phosphorus pentoxide and then enclosed in a thin glass tube of 7 mm outside diameter.

## § 3. Experimental Results

At the lowest temperature attained, 125°K, the derivative of the resonance line of higher normal alcohol of probable carbon number 32 was as shown in Fig. 1 (a). As the result of the repeated recordings, there were observed small humps inside of the maximum and minimum derivatives of the resonance line, which were not observed in normal paraffins[6)] and polyethylene[16)]. The line width and the second moment were 15.5±0.5 gauss and 26.5±1.0 gauss$^2$, respectively. Here the line width was defined as the separation between maximum slopes on the absorption curve. These values and also the line shape remained unchanged up to about 260°K. From 260°K to 342°K (the rotational transition point of the sample), the line width decreased gradually with increasing temperature. An example of the derivative of the resonance line at 319°K is given in Fig. 1 (b). There was found no fine structure of a sharp central peak as reported in some normal alcohols[6)7)]. At 342°K, the line width decreased abruptly to 4.6±0.5 gauss. The derivative of the resonance line at 348°K is given in Fig. 1 (c), which seems to indicate a central peak, though very small. There was no further variation in line width and line shape up to 355°K. At 355°K, the sample melted and the line became very narrow.

When the sample was cooled from its liquid state, the behaviors of the resonance indicated no recognizable hysteresis, with only the exception of the presence of fairly strong central peak at the temperature ranging a few degrees below the freezing point. The variation of the line width as a function of temperature was plotted in Fig. 2.

## § 4. Discussions

### (1) *Rigid Lattice*

The crystal structure of the normal higher primary alcohol has not hitherto been made definite. X-ray analysis gave approximately the same *a* and *b* spacings as other normal alcohols and paraffins, and long chain axis was found to be normal to a basal plane at room temperature[1]. Though the structure above transition point has not been determined by X-ray analysis, it is anticipated, from its dielectric[1] as well as from specific heat anomaly[17], that the crystal structure will be similar to that of cetyl alcohol. Wilson and Ott[18] have examined the long spacing of alcohols, and have concluded that *c*-spacing of the unit cell corresponds to the length of the molecules, arrayed end to end, OH groups being closely situated, and O–O interval along *c*-axis is estimated to be 1.46 Å, assuming C–C distance 1.27 Å along *c*-axis obtained by Müller. Recently, Smith[19] has determined the precise crystal structure of the normal paraffins of odd carbon number from single crystal X-ray analysis. According to his result, C–C distance mentioned above must be increased by 0.005 Å. If we accept Smith's data instead of Müller's, the similar estimation of O–O interval along *c*-axis results in the value 1.15 Å. Although nothing more precise can be said at present about the crystal structure of the alcohol, we shall tentatively assume it to be something like that as shown in Fig. 3, the black circles showing the site to which each oxygen atom belongs, the supposed hydrogen bonds being expressed by the dotted line. In this model, the chain of the hydrogen bond is assumed to be formed nearly in the direction of *b*-axis, and the length of the hydrogen bond becomes 2.72 Å, in accordance with the values 2.70 Å and 2.75 Å, observed in resorcinol[20]. The C–O–H bond angles seem to have reasonable value 90°–110°. The following discussions on the resonance line of the rigid lattice state are based on this model of the crystal structure.

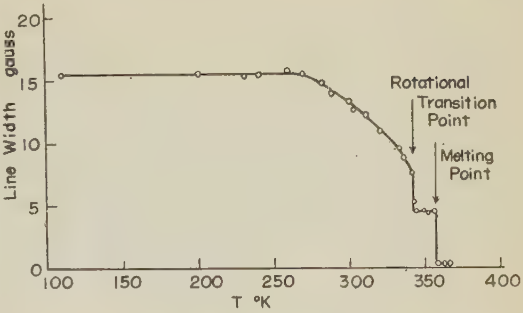

Fig. 2. Temperature dependency of line width.

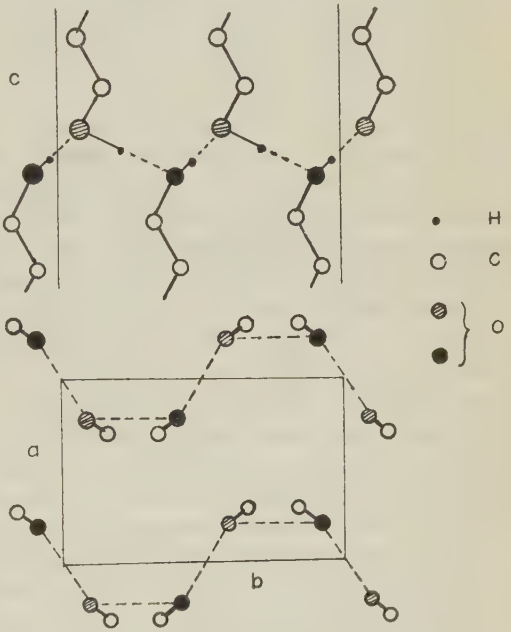

Fig. 3. Supposed structure of alcohol.

As described in § 3, there was a pair of humps inside of the maximum and minimum derivatives of the resonance line. This may be interpreted as due to the proton resonance in the end groups OH of alcohol molecules. This view is supported by the following consideration. The hump has been subtracted in the derivative curve, so as to leave the normally shaped derivative as was observed

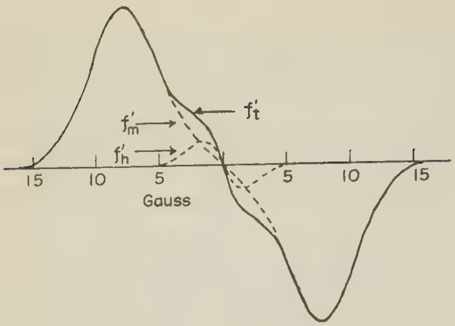

Fig. 4. Derivative of the resonance at 125°K. Rigid curve $f_t'$ shows experimental; dotted curves, $f_m'$, the contribution from protons in paraffin chains: $f_h'$, the contribution from protons in OH groups.

in normal paraffin in rigid lattice state[6], as shown in Fig. 4. The intensity ratio of the main part of the resonance line to the hump was evaluated to be approximately 80–50, as above separation accompanies by some ambiguities. This value should be compared with the number ratio 65 of the protons included in $CH_3(CH_2)_{31}$ group to those in OH group.

Although it is desirable to compare the experimental line shape with the theoretical, it is hardly possible to solve many proton interaction problem exactly. Therefore, as usual, the experimental second moment of the resonance was compared with the theoretical one, calculated from geometrical arrangement of magnetic nuclei. Andrew[6] has already estimated the second moment of the normal paraffin of carbon number $n$, on the basis of the crystal structure determined by Muller[21], his result being $[26.3+19.1/(n+1)]$ gauss². In the present case, the second moment of the normal alcohol is estimated as $[26.3+5.3/(n+1)]$ gauss², where $CH_3(CH_2)_{n-1}$ contribution is estimated from the result of Andrew's, and additional OH contribution is calculated, assuming that a proton in the OH group lies on the O···O line in the model previously described, and 0.96 Å apart from one of two oxygen atoms. For $n=32$, the calculated second moment is 26.4 gauss², which is in good agreement with the experimental value of 26.0 gauss² for temperature below 260°K. The additional OH contribution to the second moment is found to be $4.9/(n+1)$ gauss². For $n=32$, this value amounts to 0.15 gauss², which is in qualitative agreement with the experimental value of 0.03–0.06 gauss², estimated from the formula

$$\int_{-\infty}^{\infty} f_h \cdot h^2 dh \Big/ \int_{-\infty}^{\infty} f_t dh \,,$$

where $f_h$ and $f_t$ are the shape function in the experimental resonance line of the hump and of the total, respectively. Thus, at temperatures below 260°K, the molecules are effectively stationary and the hump in the derivative of the resonance line is regarded to be presumably due to the absorption due to OH groups in the compound.

(2) *Rotational Phase*

Molecular motion in the crystal lattice, if its reorientation frequency exceeds the value corresponding to the half width of the resonance line, makes the central part of the line narrower and sharper, and the tails, though very weak, will extend far from the centre. This tails are so weak that we cannot usually observe them above the noise background, and the second moment estimated from the observed data would correspond only to the contribution from the central part, which is made much smaller by molecular motion. Generally speaking, the central part is essentially due to the secular part of dipolar interaction, and the broadened weak tails, due to the non-secular part. But the rigorous treatment of the motional narrowing for the combined magnetic nuclei has not been presented, as far as we know. So we will discuss the problem on the basis of the conventional second moment argument as follows.

For the molecular rotation around the long chain axis of the normal paraffins, it has been found by Andrew[6] that the second moment is reduced from the rigid lattice of $[26.3+19.1/(n+1)]$ gauss² to $[9.4-11.6/(n+1)]$ gauss² if all the molecules are set in rotation simultaneously. For the normal alcohols, the rigid lattice value of $[26.3+5.3/(n+1)]$ gauss² must reduce itself to $[9.4-4.8/(n+1)]$ gauss². For $n=32$, the calculated second moment is 9.3 gauss², if all the molecules are assumed to rotate simultaneously. This value must be further reduced to 8.3 gauss² due to lattice expansion above the trasition point. The experimental value of 7.0 gauss² above the transition point is in agreement with the above estimated theoretical value, as far as some ambiguities of the theoretical evaluation are concerned. It, therefore, may safely be concluded that, above the transition point, all the molecules in the normal alcohol of carbon number 32 are rotating around their long chain axis as is often the case in other members of primary normal alcohols and paraffins.

(3) *Transition Region*

As is easily seen from Fig. 2, there is a gradual narrowing of the width, followed by a rather sudden one, between the rigid lattice and free rotational phases mentioned above. Although any reliable quantitative discussion seems to be hardly possible at present, it may be of some interest to go into further detail, because of the fact that the recently obtained dielectric data suggest strongly the existence of the independent relaxation mechanism beside the one, which is associated to molecular rotation.

Takamatsu[1)] found a definite Debye type dispersion below the rotational transition point 342°K, which was also confirmed by Shishikura[17)] through the specific heat measure ment, and there is no doubt that this dispersion is *not* due to the so called molecular rotation. Takamatsu tentatively ascribed this to the torsional vibration of the molecule, which is also expected generally in long chain compounds from the specific heat consideration[22)].

Our results seem to be entirely consistent with his conclusion, and the obvious narrowing of proton resonance between 260°K and the rotational transition point 342°K, will presumably correspond not to the molecular rotation, but to the torsional vibration of the molecule.

It was not entirely certain, from the dielectric observation alone, whether the long chain is fixed and the OH group only is allowed to librate, or the whole chain is subject to torsional vibration. Our result is obviously sufficient to support the view that the latter is to be the case.

## § 5. Acknowledgements

The author wishes to express his sincere thanks to Professor Y. Kakiuchi for his kind interest and helpful advice during the course of this investigation. He also wishes to thank Professor T. Muto for his helpful advice of the manuscript. He is greatly indebted to Mr. T. Takamatsu for giving him a sample, and letting him know the experimental results on the dielectric investigation on the same sample before publication.

## References

1) T. Takamatsu: J. Phys. Soc. Japan **10** (1955) 1049.
2) W. O. Baker and C. P. Smyth: J. Amer. Chem. Soc. **60** (1938) 1229.
3) J. D. Hoffman and C. P. Smyth: J. Chem. Soc. **71** (1949) 431.
4) K. Higashi and M. Kubo: Sci. Rep. I.P.C.R. **36** (1939) 286.
5) Y. Kakiuchi, H. Komatsu and S. Kyoya: J. Phys. Soc. Japan **6** (1951) 321.
6) E. R. Andrew: J. Chem. Phys. **18** (1950) 607.
7) S. Kojima and S. Ogawa: J. Phys. Soc. Japan **8** (1953) 283.
8) A. Müller: Proc. Roy. Soc. **A 127** (1930) 417, **A 138** (1932) 514.
9) J. D. Bernal: Nature **129** (1932) 870.
10) K. Sano and Y. Kakiuchi: J. Phys. Soc. Japan **4** (1949) 178.
11) Y. Kakiuchi, T. Suzuki and T. Sakurai: J. Phys. Soc. Japan **5** (1950) 369.
12) R. V. Pound and W. D. Knight: Rev. Sci. Inst. **21** (1950) 219.
13) G. Watkins: Thesis, Harvard University (1952)
14) H. S. Gutowsky, L. H. Meyer and R. E. McClure: Rev. Sci. Inst. **24** (1953) 644.
15) N. A. Schuster: Rev. Sci. Inst. **22** (1951) 254.
16) C. W. Wilson and G. E. Pake: J. Poly. Sci. **10** (1953) 503.
17) R. Shishikura: J. Phys. Soc. Japan **10** (1955) 903.
18) D. A. Wilson and E. Ott: J. Chem. Phys. **2** (1934) 239.
19) A. E. Smith: J. Chem. Phys. **21** (1953) 2229.
20) J. M. Robertson: Proc. Roy. Soc. **A 157** (1936) 79.
J. M. Robertson and A. R. Ubbelohde: Proc. Roy. Soc. **A 167** (1938) 122.
21) A. Müller: Proc. Roy. Soc. **A 120** (1928) 437.
22) Y. Kakiuchi: J. Phys. Soc. Japan **6** (1951) 313.

JOURNAL OF THE PHYSICAL SOCIETY OF JAPAN Vol. 11, No. 7, JULY, 1956

# On the Interionic Contributions to the Specific Heat of Cobalt Ammonium Tutton Salt $Co(NH_4)_2(SO_4)_2 6H_2O$ at Very Low Temperatures

By Tutô NAKAMURA and Norikiyo URYÛ

*Department of Physics, Faculty of Science,*
*Kyusyu University, Hukuoka*

(Received March 12, 1956)

The specific heat of cobalt ammonium sulfate $Co(NH_4)_2(SO_4)_2 \cdot 6H_2O$ in the liquid helium temperature region is investigated theoretically. The possible contributions to it are the dipole-dipole and the exchange interactions between $Co^{2+}$ ions and the hyperfine interactions within each ion. Our investigation is to obtain the first two contributions. The dipole-dipole interactions are given by use of the anisotropic $g$-factors determined from the paramagnetic resonance. And the exchange interactions are determined by modifying the isotropic exchange interactions by the wave functions of the lowest Kramers doublet, where we took into account only the interactions with the first and second neighbouring ions. The result obtained from the moment expansion method gives $C_v T^2/R = 30.2 \times 10^{-4}$ which is in good agreement with the experimental value $27 \times 10^{-4}$. Here $C_v$ is the interionic (dipole-dipole and exchange) part of the specific heat at moderately high temperatures, $T$ the absolute temperature and $R$ the gas constant.

## § 1. Introduction

The magnetic properties of the cobalt Tutton salt have been studied by many authors[1-4]. According to their results, the cobalt Tutton salt shows a large deviation from the Curie law in the neighbourhood of room temperatures. And further, the measurements of the magnetic susceptibilities of single crystal tell us that it shows a large magnetic anisotropy. These magnetic behaviours of cobalt Tutton salt have qualitatively been interpreted by Van Vleck[5] and Schlapp and Penney[6].

A cobalt ion $Co^{2+}$ is surrounded by six water molecules nearly in octahedral arrangement. The crystalline electric field arising from these water molecules is then nearly cubic around the cobalt ion. This crystalline field splits the orbital level of $Co^{2+}$, which is seven fold degenerate in its free state, into a singlet and two triplets, where a triplet is the lowest orbital level and the next level is again a triplet widely separated from the lowest. The lowest level is then of degeneracy twelve inclusive of spin, because the spin quantum number of a $Co^{2+}$ is $S=3/2$. The octahedral arrangement of six water molecules surrounding a cobalt ion is, however, elongated along an axis passing through two opposite water molecules. Then the combined actions of a small tetragonal field and the spin-orbit coupling split the above mentioned degenerate level into six Kramers doublets. If the energy separation between the lowest Kramers doublet and the next one is comparable with $kT$ of room temperature, we might expect a large deviation from the Curie law, where $k$ is the Boltzmann constant and $T$ the absolute temperature. And further, the orbital angular momentum distorted by the crystalline field considerably survives in the lowest Kramers doublet and also connects the lowest level with the different upper ones for its different components. These situations bring about a large magnetic anisotropy, if the energy separation between the lowest Kramers doublet and the next one is rather small. Thus the large magnetic anisotropy of cobalt salt is closely related to the large deviation from the Curie law for the magnetic susceptibility at room temperatures, as pointed out by Van Vleck[5].

Now, at low temperatures where almost only the lowest Kramers doublet is populated, the Curie law becomes again valid and the anisotropic Curie constants tell us the Landé $g$-factors of the lowest Kramers doublet.

These $g$-factors can, however, be determined from the paramagnetic resonance experiments. Thus Bleaney and Ingram⁷⁾ studied the paramagnetic resonance absorption of cobalt salts and determined, for example, the $g$-factors of cobalt ammonium sulfate as $g_{\parallel}=6.45$ and $g_{\perp}=3.06$, where $g_{\parallel}$ is the $g$-factor parallel to the tetragonal axis and $g_{\perp}$ the perpendicular one. Another interesting feature of the paramagnetic resonance experiments is the appearance of hyperfine structure in the spectrum, which arises from the interaction between the electron spin and the nuclear one.

The magnetic and thermal properties of Co-Tutton salts in the temperature regions of liquid helium have been studied by Garrett⁸⁾. The magnetic susceptibilities are in good agreement with the $g$-factors from the paramagnetic resonance data. And further, Garrett extracted the interionic contributions to the specific heat, $C_v$, by the method of magnetic relaxation. In the regions of temperature not so low, $C_v$ should be proportional to $1/T^2$, and hence $C_vT^2$ should be constant in these temperature regions. Thus Garrett gave $C_vT^2/R$ as $43\times10^{-4}(°\mathrm{K})^2$, where $R$ is the gas constant. Malaker also gave it a similar value $42.5\times10^{-4}$ ⁹⁾. This magnetic specific heat arises from three kinds of interactions, the hyperfine interaction, the magnetic dipolar interaction and the exchange one. The first of them is the intra-ionic interaction, whereas the others are the inter-ionic ones. Hence, the value of $C_vT^2/R$ extrapolated to the limiting case of infinite dilution corresponds to the hyperfine contribution to it. Thus Benzie and Cooke found the hyperfine part of $C_vT^2/R$, $(C_vT^2/R)_{\mathrm{hfs}}$, to be $16.6\times10^{-4}$ ¹⁰⁾, while Malaker took the same procedure and obtained $(C_vT^2/R)_{\mathrm{hfs}}=16.1\times10^{-4}$ ⁹⁾. This value can also be obtained from the hyperfine structure of paramagnetic resonance spectrum. Thus Bleaney estimated $(C_vT^2/R)_{\mathrm{hfs}}$ as $16\times10^{-4}$ ¹¹⁾, in excellent agreement with its experimental values.

Then the remaining part of $C_vT^2/R$ is attributed to the magnetic dipolar and exchange interactions. However, its analysis is not so easy because of the fact that the magnetic ion has a strong anisotropy and the magnetic lattice is also of low symmetry. A treatment of such a system was given by Opechowski¹²⁾. On the assumption that both magnetic dipolar and exchange interactions are anisotropic, he tried to correlate the susceptibility data and the magnetic specific heat of copper potassium sulfate observed by De Klerk¹³⁾. But, he did not give any explicit form of the interactions mentioned above. Due to this situation, unfortunately, no unambiguous conclusion was obtained.

Now Abragam and Pryce succeeded in determining the crystalline electric field so as to explain the $g$-factors obtained from the paramagnetic resonance experiments¹⁴⁾. Using the wave functions of the lowest Kramers doublet given by them, we get the anisotropic exchange interactions between the neighbouring cobalt ions, which are given by the semi-diagonal part of the isotropic exchange interactions. Then, if we assume the exchange interactions to be effective up to the second neighbours, the anisotropic exchange interactions thus obtained involve only two parameters. To determine these two parameters we use the values of the Weiss constants given by Garrett. Next the magnetic dipolar interactions can be obtained from the $g$-factors of the lowest Kramers doublet whose values were already mentioned. An application of the method of $1/T$-expansion to the interionic Hamiltonian thus obtained gives the interionic part of free energy in powers of $1/T$, whence the specific heat $C_v$ can be calculated. It proves to be proportional to $1/T^2$ at high temperatures. Finally we get the interionic contributions to $C_vT^2/R$. The theoretical value of $C_vT^2/R$ thus estimated is $30.2\times10^{-4}$, in good agreement with the experimental value.

## § 2. The Lattice Constants of $(NH_4)_2Co(SO_4)_26H_2O$

The salt $(NH_4)_2Co(SO_4)_26H_2O$ belongs to the Tutton group crystallographically. The Tutton salts form a monoclinic series, in which the three crystallographic axes $(a, b, c)$ are very closely in the ratio (3, 4, 2). According to the $X$-ray analysis performed by W. Hofmann¹⁵⁾ the unit cell contains two molecules, the one is derived from the other by a translation from the point (0, 0, 0) to (1/2, 1/2, 0) followed by a reflexion in the $ac$-plane. Although the detailed structures of $(NH_4)_2$Mg Tutton salt and $(NH_4)_2$Zn Tutton salt are well investigated, we have no available data of $(NH_4)_2$-Co Tutton salt

According to the analysis made by Hofmann

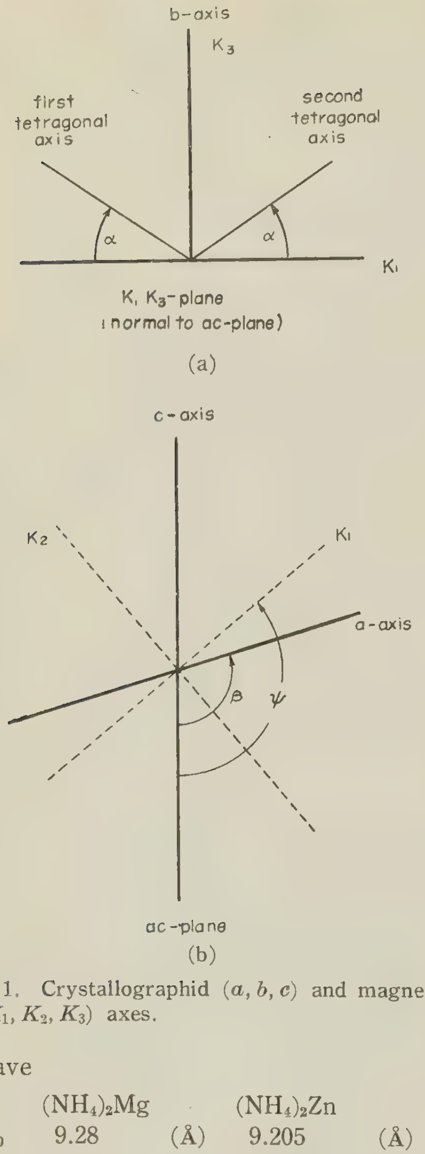

(a)

(b)

Fig. 1. Crystallographid $(a, b, c)$ and magnetic $(K_1, K_2, K_3)$ axes.

we have

| | $(NH_4)_2Mg$ | | $(NH_4)_2Zn$ | |
|---|---|---|---|---|
| $a_0$ | 9.28 | (Å) | 9.205 | (Å) |
| $b_0$ | 12.57 | | 12.475 | |
| $c_0$ | 6.20 | | 6.225 | |
| $\beta$ | 107°06′ | | 106°52′ | |

where $\beta$ is the angle which the $a$-axis makes with the $c$-axis in the anti-clockwise direction. Now, the ionic radii of $Mg^{2+}$, $Zn^{2+}$ and $Co^{2+}$ are respectively given by

$Mg^{2+}$: 0.78 Å
$Zn^{2+}$: 0.83
$Co^{2+}$: 0.82 .

Hence it may be reasonable to assume that the lattice constants of $(NH_4)_2Co$ Tutton salt are closer to those of $(NH_4)_2Zn$ Tutton salt than to those of $(NH_4)_2Mg$ Tutton salt. Thus, in the present calculation, we shall take the lattice constants of $(NH_4)_2Zn$ Tutton salt in place of those of $(NH_4)_2Co$ Tutton salt.

To discuss the magnetic behaviours, it is further necessary to have another constants which determine the directions of the magnetic principal axes $K_1$, $K_2$ and $K_3$. As was mentioned in § **1**, each $Co^{2+}$ ion is surrounded by six water molecules, and these water molecules form an elongated octahedron. The tetragonal axis of $Co^{2+}$ ion coincides with the elongated direction, but two $Co^{2+}$ ions contained in a unit cell have the tetragonal axes of different orientations. The parameters which determine the magnetic principal axes are an angle $\alpha$ (the angle that the tetragonal axis makes with the $ac$-plane) and another angle $\psi$ (the angle that the plane containing the different tetragonal axes of the two $Co^{2+}$ ions in a unit cell makes with the $c$-axis). These situations can be seen in Fig. 1, where we can also see the relation of the magnetic principal axes to the ionic principal ones. According to the paramagnetic resonance experiments made by Bleaney and Ingram, $\alpha$ and $\psi$ are given by

$$\psi=130°, \quad \alpha=34° .$$

In order to enable us to draw a fair picture of the unit cell, a view of the unit crystal structure is shown in Fig. 2, in which the $b$-axis is normal to the plane of the paper.

## § 3. Hamiltonian of the Assembly of $Co^{2+}$ Spins

Let us search for the interactions between $Co^{2+}$ spins in the lowest Kramers doublet. We assume that both magnetic dipolar and exchange interactions are effective. The expressions for them in the absence of the crystalline field are well known. These are, however, greatly modified by a crystalline field. And it is the object of the present section to inquire into such a modification.

First, the Hamiltonian due to the magnetic dipolar interaction, $\mathscr{H}_{\rm dip}$, is given by

$$\mathscr{H}_{\rm dip}=\sum_{i>k} r_{ik}^{-3}[\boldsymbol{\mu}_i\boldsymbol{\mu}_k-3(\boldsymbol{\mu}_i\cdot\boldsymbol{t}_{ik})(\boldsymbol{\mu}_k\cdot\boldsymbol{t}_{ik})] . \qquad (1)$$

Here $\boldsymbol{\mu}_i$ is the magnetic moment vector of the $i$-th magnetic ion

$$\boldsymbol{\mu}_i=\mu_0(\boldsymbol{L}_i+2\boldsymbol{S}_i) , \qquad (2)$$

where $\mu_0$ is the Bohr magneton, $\boldsymbol{L}_i$ and $\boldsymbol{S}_i$ denote respectively the orbital and spin angular momentum operators of the $i$-th ion with

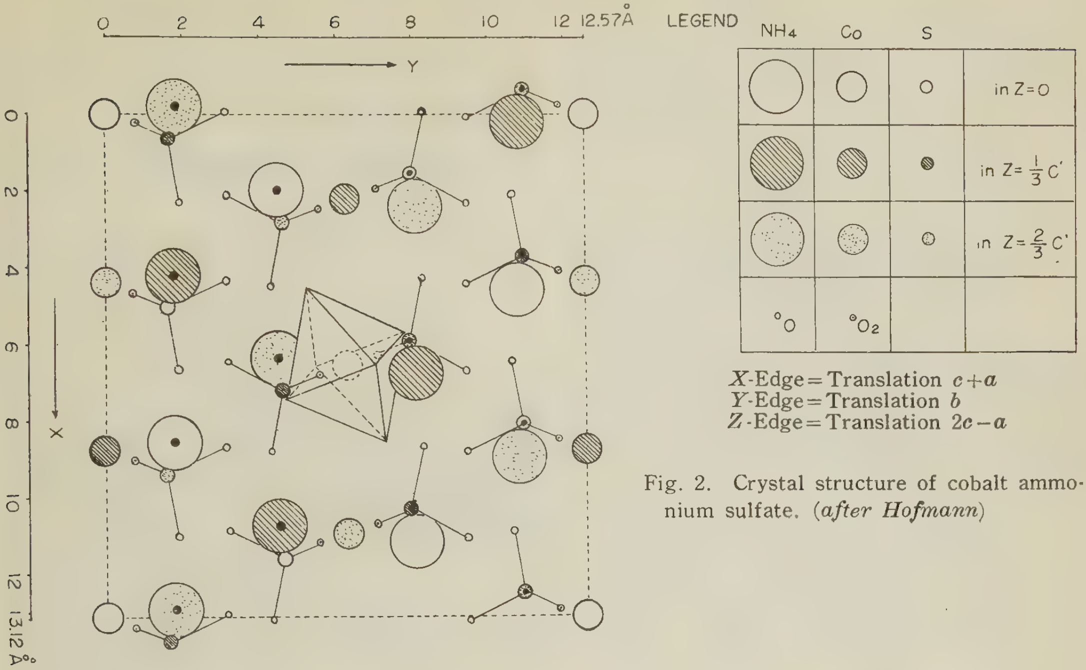

*X*-Edge = Translation $c+a$
*Y*-Edge = Translation $b$
*Z*-Edge = Translation $2c-a$

Fig. 2. Crystal structure of cobalt ammonium sulfate. (*after Hofmann*)

$L=3$ and $S=3/2$, and $\boldsymbol{t}_{ik}$ a unit vector connecting two lattice points $i$ and $k$. Secondly the Hamiltonian due to the exchange interaction, $\mathscr{H}_{\rm ex}$, is given by

$$\mathscr{H}_{\rm ex}=-2\sum_{i>k} J_{ik}\boldsymbol{S}_i\cdot\boldsymbol{S}_k\,. \qquad (3)$$

It may be noted that these operators are of course defined in the coordinates system common to all ions, which is conveniently taken as the system of magnetic principal axes $x$, $y$ and $z$ as can be seen in Fig. 3.

The degeneracy of the ground state of a $Co^{2+}$ ion in the free state is greatly removed by the crystalline field and the spin-orbit interaction, and we have the Kramers doublets. The first excited Kramers doublet is separated from the ground one by the order of spin-orbit coupling parameter, $\lambda$, and according to a theory developed by Abragam and Pryce the separation is about 245 cm$^{-1}$. Then it is sufficient to consider the lowest doublet only, because our temperature region is in the neighbourhood of 1°K. We should now restrict the Hamiltonians (1) and (3) within the sub-space subtended by the wave functions belonging to the lowest Kramers doublet.

Introducing the effective spin operator $\boldsymbol{\sigma}$ concerning the lowest doublet, $(\mu_i)$ is written as

$$(\mu_i)_\lambda=\mu_0\sum_{\mu} g_{\lambda\mu}{}^i\sigma_{\mu_i}\,. \qquad (4)$$

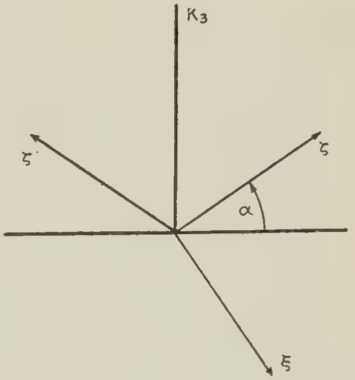

Fig. 3. Magnetic ($K_1, K_2, K_3$) and ionic ($\xi, \eta, \zeta$) axes.

Here $(\mu_i)$ denotes the semi-diagonal part of $\mu_i$ within the subspace corresponding to the lowest doublet and the suffixes $\lambda$ and $\mu$ represent $x, y$ and $z$. By using (4) the semi-diagonal part of $\mathscr{H}_{\rm dip}$ is written

$$\mathscr{H}_{\rm dip}=\mu_0^2\sum_{i>k} r_{ik}^{-3}\Big(\sum_{\lambda\nu\mu} g_{\lambda\mu}{}^i g_{\lambda\nu}{}^k\sigma_{\mu i}\sigma_{\nu_k} -3\sum_{\lambda\mu}\sum_{\nu\nu'} t_{ik}{}^\lambda t_{ik}{}^\mu g_{\lambda\nu}{}^i g_{\mu\nu'}{}^k\sigma_{\nu_i}\sigma_{\nu'_k}\Big)\,; \qquad (5)$$

Here we take the macroscopic magnetic principal axes $K_1$, $K_2$ and $K_3$ as our coordinate ones. These axes do not correspond to the microscopic magnetic principal ones, and owing to this situation the calculations become considerably complicated.

Since the quantity $g$ transforms as a tensor and the principal axes of $g$ defined in Eq. (4) coincide with the ionic principal ones (which are denoted by $\xi, \eta$ and $\zeta$), we can get the non-zero components of $g$ in the system of magnetic principal axes as follows:

$$
\begin{aligned}
&g_1 \equiv g_{xx} = g_{\parallel} \cos^2\alpha + g_{\perp} \sin^2\alpha \,, \\
&g_2 \equiv g_{yy} = g_{\perp} \,, \\
&g_3 \equiv g_{zz} = g_{\parallel} \sin^2\alpha + g_{\perp} \cos^2\alpha \,, \\
&g_4 \equiv g_{zx} (g_{\parallel} - g_{\perp}) \sin\alpha \cos\alpha \,,
\end{aligned}
\tag{6}
$$

where $g_{\xi\xi} = g_{\eta\eta} = g_{\perp}$ and $g_{\zeta\zeta} = g_{\parallel}$. The ions with these $g$-factors will be called ion I. Further, the components of $g$ of an ion of another type (i.e. an ion whose tetragonal axis is $\zeta'$ in Fig. 3) are the same as (6) except $g_{zx}$, which is now given by

$$
g_{zx} = -(g_{\parallel} - g_{\perp}) \sin\alpha \cos\alpha = -g_4 . \tag{7}
$$

The ions with these $g$-factors will be called ion II. Since the value of $g_{\parallel}$ and $g_{\perp}$ are obtained from the paramagnetic resonance experiments, we get an explicit expression for $\mathscr{H}_{\text{dip}}$.

We shall next consider $\mathscr{H}_{\text{ex}}$. In order to get the semidiagonal part of it within the lowest doublet we should obtain appropriate wave functions of the lowest doublet.

Assuming an appropriate crystalline field with a cubic term of fourth order and tetragonal terms of second order and fourth order, Abragam and Pryce solved the orbital problem of $\text{Co}^{2+}$. Their procedure is in the following. The lowest two orbital levels are a doublet and a singlet, where the doublet is lower. Since the second excited level is widely separated from the first excited one, they introduce an effective orbital angular momentum operator $\boldsymbol{l}'$ with $l' = 1$, where the orbital Landé factors have numerical values difference from unity and are of the tetragonal symmetry. The effect of the spin-orbit coupling may be treated within the manifold of $l' = 1$. Although the resulted secular problem is of order twelve, it is factorized to six parts, which are classified according to $m_l' + M_S$. Two parts of them whose values of $m_l' + M_s$ are equal in magnitude and opposite in sign to each other, prove to be identical with each other. Here $m_l'$ denotes an eigenvalue of the $\zeta$-component of $\boldsymbol{l}'$ and $M_s$ that of the $\zeta$-component of $\boldsymbol{S}$. Then the lowest level is contained in the secular problem with $m_l' + M_s = \pm 1/2$.

Thus, the lowest wave functions defined by

$$
\sigma_{\zeta} \psi_{1/2} = \frac{1}{2} \psi_{1/2} \,, \quad \sigma_{\zeta} \psi_{-1/2} = -\frac{1}{2} \psi_{-1/2} \,, \tag{8}
$$

are given by

$$
\begin{aligned}
\psi_{1/2} &= a\psi\left(-1, \frac{3}{2}\right) + b\psi\left(0, \frac{1}{2}\right) \\
&\quad + c\psi\left(1, -\frac{1}{2}\right), \\
\psi_{-1/2} &= a\psi\left(1, -\frac{3}{2}\right) + b\psi\left(0, -\frac{1}{2}\right) \\
&\quad + c\psi\left(-1, \frac{1}{2}\right),
\end{aligned}
\tag{9}
$$

where $\psi$'s in the right-hand side of (9) denote $\psi(m_l', M_s)$, The coefficients $a, b$ and $c$ can be computed by use of the crystalline parameters well chosen by Abragam and Pryce. The result is obtained as

$$
a = -0.8959, \quad b = 0.2772, \quad c = -0.3471. \tag{10}
$$

The lowest wave functions thus obtained can successfully interpret the $g$-values observed by paramagnetic resonance. We shall therefore use their result here.

We shall now write $\mathscr{H}_{\text{ex}}$ as

$$
\mathscr{H}_{\text{ex}} = \sum_{i>k} (\mathscr{H}_{\text{ex}})_{ik} .
$$

In the case when $i$ and $k$ are ions of the same kind, the calculations are very simple. In the system of ionic principal axis we have a matrix representation of $(\mathscr{H}_{\text{ex}})_{ik}/(-J_{ik})$ in the following;

$$
\begin{array}{c|cccc}
 & ++ & +- & -+ & -- \\
++ & A^2/2 & 0 & 0 & 0 \\
+- & 0 & -A^2/2 & 4B^2 & 0 \\
-+ & 0 & 4B^2 & -A^2/2 & 0 \\
-- & 0 & 0 & 0 & A^2/2
\end{array} ,
$$

where $A = 3a^2 + b^2 - c^2$, $B = b^2 + \sqrt{3}\,ac$.

It can easily be expressed in terms of $\boldsymbol{\sigma}$:

$$
\begin{aligned}
(\mathscr{H}_{\text{ex}})_{ik} = {} & J_{\parallel}(i, k) \sigma_{\zeta i} \sigma_{\zeta k} + J_{\perp}(i, k) \\
& \times (\sigma_{\xi i} \sigma_{\xi k} + \sigma_{\eta i} \sigma_{\eta k}) \,,
\end{aligned}
\tag{11}
$$

where $J_{\parallel}(i, k)$ and $J_{\perp}(i, k)$ are given by

$$
\begin{aligned}
J_{\parallel}(i, k) &= -2J_{ik}(3a^2 + b^2 - c^2)^2 \,, \\
J_{\perp}(i, k) &= -8J_{ik}(b^2 + \sqrt{3}\,ac)^2 \,.
\end{aligned}
\tag{11a}
$$

To transform (11) from the system of ionic principal axes to that of magnetic principal ones, we consider two cases separately. In the case when both ions are of the type I, we use the following relations:

$$
\sigma_{\xi} = \sigma_x \sin\alpha - \sigma_z \cos\alpha \,,
$$

$$\sigma_\eta=\sigma_y\ ,$$

$$\sigma_\zeta=\sigma_x\cos\alpha+\sigma_z\sin\alpha\ . \tag{12}$$

Then (11) becomes

$$(\mathscr{H}_{\mathrm{ex}})_{ik}=\sum_{\lambda\mu}J_{ik}{}^{\lambda\mu}\sigma_{\lambda i}\sigma_{\mu k}, \tag{13}$$

where the non-vanishing components of $J_{ik}{}^{\lambda\mu}$ are given by

$$\begin{aligned}J_{ik}{}^{xx}&=J_{\parallel}\cos^2\alpha+J_{\perp}\sin^2\alpha\ ,\\ J_{ik}{}^{yy}&=J_{\perp}\ ,\\ J_{ik}{}^{zz}&=J_{\parallel}\sin^2\alpha+J_{\perp}\cos^2\alpha\\ J_{ik}{}^{zx}&=J_{ik}{}^{xz}=(J_{\parallel}-J_{\perp})\sin\alpha\cos\alpha\ .\end{aligned} \tag{14}$$

In the case when both ions are of the type II, we have only to replace $\cos\alpha$ by $-\cos\alpha$ in the above equations, and then for a pair of ions II, which will be hereafter denoted by Greek letters $\alpha,\beta\cdots$, $J_{\alpha\beta}{}^{\lambda\mu}$ takes the same forms as (14), except that the last equation should be replaced by

$$J_{\alpha\beta}{}^{zx}=J_{\alpha\beta}{}^{xz}=-(J_{\parallel}-J_{\perp})\sin\alpha\cos\alpha\ . \tag{15}$$

The exchange interaction for a pair of ions of different types is more complicated. We shall now consider it. First we transform the exchange Hamiltonian

$$(\mathscr{H}_{\mathrm{ex}})_{i\alpha}=-2J_{i\alpha}S_iS_\alpha$$

in the system of magnetic principal axes into that in the system of ionic principal ones, where the inverse transformation of (12) (I ions) or another one with $\cos\alpha$ in Eq. (12) replaced by $-\cos\alpha$ (II ions) can be used. Then we have

$$\begin{aligned}(\mathscr{H}_{\mathrm{ex}})_{i\alpha}=-2J_{i\alpha}\{&-\cos 2\alpha\, S_{\xi i}\cdot S_{\xi\alpha}+S_{\eta i}S_{\eta\alpha}\\ &-\cos 2\alpha\, S_{\zeta i}S_{\zeta\alpha}+\sin\alpha\cos\alpha\\ &\times(S_{\zeta i}S_{\xi\alpha}-S_{\xi i}S_{\zeta\alpha})\}\ .\end{aligned} \tag{16}$$

and a matrix representation of $(\mathscr{H}_{\mathrm{ex}})_{i\alpha}/(-J_{i\alpha})$ in the system of the ionic principal axes are given by

$$\begin{array}{c|cccc} & ++ & +- & -+ & -- \\ \hline ++ & -\frac{1}{2}A^2\cos 2\alpha & & & \\ +- & \frac{1}{2}AB\sin 2\alpha & \frac{1}{2}A^2\cos 2\alpha & & \\ -+ & -\frac{1}{2}AB\sin 2\alpha & 2B^2(1-\cos 2\alpha) & \frac{1}{2}A^2\cos 2\alpha & \\ -- & -2B^2(1+\cos 2\alpha) & \frac{1}{2}AB\sin 2\alpha & -\frac{1}{2}AB\sin 2\alpha & -\frac{1}{2}A^2\cos 2\alpha \end{array}$$

It can again be written in terms of $\sigma_i$ and $\sigma_\alpha$. The result is

$$\begin{aligned}(\mathscr{H}_{\mathrm{ex}})_{i\alpha}=J_a\sigma_{\zeta i}\sigma_{\zeta'\alpha}&\\ +J_b(\sigma_{\zeta i}\sigma_{-\alpha}-\sigma_{-i}\sigma_{\zeta'\alpha}+\sigma_{\zeta i}\sigma_{+\alpha}-\sigma_{+i}\sigma_{\zeta'\alpha})&\\ +J_c(\sigma_{-i}\sigma_{-\alpha}+\sigma_{+i}\sigma_{+\alpha})+J_d(\sigma_{-i}\sigma_{+\alpha}+\sigma_{+i}\sigma_{-\alpha})&\ ,\end{aligned} \tag{17}$$

where

$$\sigma_\pm=\sigma_\xi\pm i\sigma_\eta\ , \tag{17a}$$

and

$$\begin{aligned}J_a&=2J_{i\alpha}(3a^2+b^2-c^2)^2\cos 2\alpha\ ,\\ J_b&=-J_{i\alpha}(3a^2+b^2-c^2)(b^2+\sqrt{3}\,ac)\sin 2\alpha\ ,\\ J_c&=2J_{i\alpha}(b^2+\sqrt{3}\,ac)^2\,(1+\cos 2\alpha)\ ,\\ J_d&=-2J_{i\alpha}(b^2+\sqrt{3}\,ac)^2\,(1-\cos 2\alpha)\ .\end{aligned} \tag{18}$$

Expressing (17) in terms of the spin operators $\sigma_x$, $\sigma_y$ and $\sigma_z$ in the system of magnetic principal axes, we can represent $(\mathscr{H}_{\mathrm{ex}})_{i\alpha}$ as

$$(\mathscr{H}_{\mathrm{ex}})_{i\alpha}=\sum_{\lambda\mu}J_{i\alpha}{}^{\lambda\mu}\sigma_{\lambda i}\sigma_{\mu\alpha}\ , \tag{19}$$

where $J_{i\alpha}{}^{\lambda\mu}$'s become

$$\begin{aligned}J_{i\alpha}{}^{xx}&=-J_a\cos^2\alpha+2J_b\sin 2\alpha+2J_c\sin^2\alpha\\ &\quad+2J_d\sin^2\alpha\ ,\\ J_{i\alpha}{}^{yy}&=2(J_d-J_c)\ ,\\ J_{i\alpha}{}^{zz}&=J_a\sin^2\alpha+2J_b\sin 2\alpha-2J_c\cos^2\alpha\\ &\quad-2J_d\cos^2\alpha\ ,\\ J_{i\alpha}{}^{zx}&=-J_{i\alpha}{}^{xz}=-1/2J_a\sin 2\alpha-2J_b\cos 2\alpha\\ &\quad-J_c\sin 2\alpha-J_d\sin 2\alpha\ .\end{aligned} \tag{20}$$

## § 4. Specific Heat

In the absence of the external magnetic field, we may write down the total Hamiltonian as

$$\mathscr{H}=\sum_{s>t}\mathscr{H}_{st}\ . \tag{21}$$

Making use of the $(1/kT)$-expansion method devised by Van Vleck[16], we obtain the specific heat, $C_v$, per gramm ion of $Co^{2+}$ in the hhig temperature regions as

$$\frac{C_vT^2}{R}=\frac{1}{4k^2}\left\{\sum_{s=k,\alpha}\langle(\mathscr{H}_{is})^2\rangle_{\mathrm{AV}}+\sum_{s=k,\beta}\langle(\mathscr{H}_{\alpha s})^2\rangle_{\mathrm{AV}}\right\} \tag{22}$$

A pair Hamiltonian $\mathscr{H}_{st}$ can be separated into two parts

$$\mathscr{H}_{st}=(\mathscr{H}_{\mathrm{dip}})_{st}+(\mathscr{H}_{\mathrm{ex}})_{st}\,, \tag{23}$$

and so the quantity $(C_vT^2/R)$ can be divided into three parts

$$\left(\frac{C_vT^2}{R}\right)=\left(\frac{C_vT^2}{R}\right)_{\text{dip-dip}}+\left(\frac{C_vT^2}{R}\right)_{\text{dip-ex}}+\left(\frac{C_vT^2}{R}\right)_{\text{ex-ex}}. \tag{24}$$

We shall consider them separately.

Let us first evaluate $(C_vT^2/R)_{\text{dip-dip}}$. Paying our attention to the spin quantum number of $\sigma$ equal to 1/2, we get the following results after somewhat troublesome calculations

$$\left(\frac{C_vT^2}{R}\right)_{\text{dip-dip}}=\frac{\mu_0^4}{32\,k^2}(F_1+F_2)\,, \tag{25}$$

where

$$F_r=P_rA_r+\sum_{\lambda\mu}Q_{r\lambda\mu}B_{r\lambda\mu}+\sum_{\lambda}R_{r\lambda}C_{r\lambda}\,,$$
$$r=1,2, \tag{26}$$

$r=1$ corresponds to the part arising from $(\mathscr{H}_{st})^2$ between ions of the same type and $r=2$ to that between ions whose types are different with each other. Here $P_r$, $Q_{r\lambda\mu}$ and $R_{r\lambda}$ are given by the following

$$\begin{aligned}
&P_1=(g_1^2+g_4^2)^2+(g_3^2+g_4^2)^2+2(g_1+g_3)^2g_4^2+g_2^4,\\
&Q_{1xx}=9\,(g_1^2+g_4^2)^2 \qquad (=Q_{2xx})\,,\\
&Q_{1yy}=9g_2^2 \qquad (=Q_{2yy})\,,\\
&Q_{1zz}=9\,(g_3^2+g_4^2)^2 \qquad (=Q_{2zz})\,,\\
&Q_{1xy}=18g_2^2(g_1^2+g_4^2) \qquad (=Q_{2xy})\,,\\
&Q_{1yz}=18g_2^2(g_3^2+g_4^2) \qquad (=Q_{2yz})\,,\\
&Q_{1zx}=18[(g_3^2+g_4^2)(g_1^2+g_4^2)+2g_4^2(g_1+g_3)^2]\,,\\
&R_{1x}=-6[(g_1^2+g_4^2)^2+g_4^2(g_1+g_3)^2],\\
&R_{1y}=-6g_2^4 \qquad (=R_{2y}\ )\,,\\
&R_{1z}=-6[(g_3^2+g_4^2)^2+g_4^2(g_1+g_3)^2]\,.
\end{aligned} \tag{27}$$

On the other hand, $P_r$, $Q_r$ and $R_r$ between ions whose types are different with each other are given by

$$\begin{aligned}
&P_2=(g_1^2+g_4^2)^2+(g_3^2+g_4^2)^2-2(g_1+g_3)^2g_4^2+g_2^4\,,\\
&Q_{2zx}=18[(g_1^2+g_4^2)(g_3^2+g_4^2)-2g_4^2(g_1+g_3)^2]\,,\\
&R_{2x}=-6[(g_1^2+g_4^2)^2-g_4^2(g_1+g_3)^2]\,,\\
&R_{2z}=-6[(g_3^2+g_4^2)^2-g_4^2(g_1+g_3)^2]\,,
\end{aligned} \tag{28}$$

and the others are all identical with (27). And further $A$, $B$ and $C$ are the lattice sums defined by

$$\begin{aligned}
&A_1=\sum_{\beta}1/r_{\alpha\beta}^6\,, \qquad A_2=\sum_{k}1/r_{\alpha k}^6,\\
&B_{1\lambda\mu}=\sum_{\beta}(t_{\alpha\beta}^{\lambda})^2(t_{\alpha\beta}^{\mu})^2/r_{\alpha\beta}^6\,,\\
&B_{2\lambda\mu}=\sum_{k}(t_{\alpha k}^{\lambda})^2(t_{\alpha k}^{\mu})^2/r_{\alpha k}^6\,,\\
&C_{1\lambda}=\sum_{\beta}(t_{\alpha\beta}^{\lambda})^2/r_{\alpha\beta}^6\,,\\
&C_{2\lambda}=\sum_{k}(t_{\alpha k}^{\lambda})^2/r_{\alpha k}^6\,.
\end{aligned} \tag{29}$$

Calculation of $(C_vT^2/R)_{\text{ex-ex}}$ is rather easy and its result becomes

$$\left(\frac{C_vT^2}{R}\right)_{\text{ex-ex}}=\frac{1}{32\,k^2}\sum_{s=\alpha,k}\sum_{\lambda\mu}(J_{is}^{\lambda\mu})^2\,. \tag{30}$$

Finally we shall calculate $(C_vT^2/R)_{\text{dip-ex}}$. For simplicity we shall take into account the exchange interactions up to the second neighbours. Noting that the first neighbours of an ion are two ions of the similar type and the second neighbours of it four ions of the dissimilar type, we get

$$\left(\frac{C_vT^2}{R}\right)_{\text{dip-ex}}=\frac{\mu_0^2}{32k^2}(2H_1+4H_2)\,, \tag{31}$$

$$\begin{aligned}
H_1=2/r_{ik}^3\{&(1-3\,t_x^2)\\
&\times(g_1^2J_{ik}^{xx}+g_4^2J_{ik}^{zz}+2g_1g_4J_{ik}^{zx})\\
&+(1-3\,t_y^2)g_2^2J_{ik}^{yy}+(1-3\,t_z^2)\\
&\times(g_3^2J_{ik}^{zz}+g_4^2J_{ik}^{xx}+2g_3g_4J_{ik}^{zx})\}\,,\\
H_2=2/r_{i\alpha}^3\{&(1-3\,t_x^2)\\
&\times(g_1^2J_{i\alpha}^{xx}-g_4^2J_{i\alpha}^{zz}+2g_1g_4J_{i\alpha}^{zx})\\
&+(1-3\,t_y^2)g_2^2J_{i\alpha}^{yy}+(1-3\,t_z^2)\\
&\times(g_3^2J_{i\alpha}^{zz}-g_4^2J_{i\alpha}^{xx}+2g_3g_4J_{i\alpha}^{xz})\}\,,
\end{aligned} \tag{32}$$

where we took into account the situations that the first two neighbours lie in the $xy$-plane and there are neighbours with the components of $t_\lambda$ equal in magnitude to each other.

## § 5. The Curie-Weiss Constants

We are now prepared to evaluate numerically the contribution to the specific heat coming from the exchange and magnetic dipolar interactions. But we cannot estimate the parts due to the exchange interaction without knowing the magnitude of $J_{ik}$. To obtain some informations about it, we shall make use of the data of the magnetic susceptibilities.

Let us calculate the magnetic susceptibility along a direction to which a magnetic field is applied. If we denote the magnetic moment operator of the ion along this direction by $\mathscr{H}_s'$, the total Hamiltonian is written

$$\mathscr{H}=\sum_{s>t}\mathscr{H}_{st}+\sum_s\mathscr{H}_s'H\,. \tag{33}$$

The magnetic susceptibility $\chi$ along this direction is then calculated by the method of Van Vleck. The result is

$$\begin{aligned}\chi=\frac{N}{2kT}\Big[&\{\langle(\mathscr{H}_i')^2\rangle_{\mathrm{AV}}+\langle(\mathscr{H}_\alpha')^2\rangle_{\mathrm{AV}}\}\\&-\frac{1}{2kT}\Big\{\sum_{s=\alpha,k}\langle\mathscr{H}_i'\mathscr{H}_{is}\mathscr{H}_s'\rangle_{\mathrm{AV}}\\&+\sum_{s=\beta,k}\langle\mathscr{H}_\alpha'\mathscr{H}_{\alpha s}\mathscr{H}_s'\rangle_{\mathrm{AV}}\Big\}+\cdots\Big]\\\simeq{}&\frac{C}{T-\Theta}\,,\end{aligned} \tag{34}$$

where

$$C=\frac{N}{2k}\{\langle(\mathscr{H}_i')^2\rangle_{\mathrm{AV}}+\langle(\mathscr{H}_\alpha')^2\rangle_{\mathrm{AV}}\}\,, \tag{34a}$$

$$\begin{aligned}\Theta=-\frac{1}{k}\Big\{&\sum_{s=\alpha,k}\langle\mathscr{H}_i'\mathscr{H}_{is}\mathscr{H}_s'\rangle_{\mathrm{AV}}\\&+\sum_{s=\beta,k}\langle\mathscr{H}_\alpha'\mathscr{H}_{\alpha s}\mathscr{H}_s'\rangle_{\mathrm{AV}}\Big\}\\&\div\{\langle(\mathscr{H}_i')^2\rangle_{\mathrm{AV}}+\langle(\mathscr{H}_\alpha')^2\rangle_{\mathrm{AV}}\}\,.\end{aligned} \tag{34b}$$

Now we should like to obtain $\chi$'s along the magnetic principal axes. But, in order to make the comparison with the experimental data, it is rather desirable to evaluate the Weiss constants (34b) along the principal axes than the magnetic susceptibility (34) itself, because the anisotropic Weiss constants have been determined by Garrett.

( i ) Let us first calculate the Weiss constant along the magnetically simplest direction, that is $K_2$-axis. For simplicity we shall use an abbreviation such as

$$\mathscr{H}_{st}=\sum_{\lambda\mu}C_{st}^{\lambda\mu}\sigma_{\lambda s}\sigma_{\mu t}\,, \tag{35}$$

where $C_{st}^{\lambda\mu}$'s are easily obtained from $(\mathscr{H}_{\mathrm{ex}})_{st}$ and $(\mathscr{H}_{\mathrm{dip}})_{st}$. In the present case $\mathscr{H}_s'$ is given by

$$\mathscr{H}_s'=g_2\mu_0\sigma_{ys}\,, \tag{36}$$

and so the following relations are obtained:

$$\begin{aligned}\langle\mathscr{H}_s'\mathscr{H}_{st}\mathscr{H}_t'\rangle_{\mathrm{AV}}&=(1/16)g_2^2\mu_0^2C_{st}^{yy}\,,\\\langle(\mathscr{H}_s')^2\rangle_{\mathrm{AV}}&=(1/4)g_2^2\mu_0^2\,.\end{aligned} \tag{37}$$

Thus

$$\Theta_2=-\frac{1}{4k}\sum_t C_{st}^{yy}\,. \tag{38}$$

Or, writting down $C_{st}^{yy}$ explicitly by use of (5), (13) and (19), we have

$$\sum_t C_{st}^{yy}=2J_{ik}^{yy}+4J_{i\alpha}^{yy}+g_2^2\mu_0^2(G_{1y}+G_{2y})\,, \tag{39}$$

where $G_{1y}$ and $G_{2y}$ are defined by

$$\begin{aligned}\sum_k(1-3\,[t_{ik}^\lambda]^2)/r_{ik}^3&=\mathrm{G}_{1\lambda}\,,\\\sum_\alpha(1-3\,[t_{i\alpha}^\lambda]^2)/r_{i\alpha}^3&=G_{2\lambda}\,,\end{aligned} \tag{40}$$

and we have taken into account the exchange interactions up to the second neighbours.

( ii ) Let us next calculate the Weiss constant along $K_1$ axis. In this case the magnetic moment operators $\mathscr{H}_i'$ and $\mathscr{H}_\alpha'$ are given by

$$\begin{aligned}\mathscr{H}_i'&=\mu_0(g_1\sigma_{xi}+g_4\sigma_{zi})\,,\\\mathscr{H}_\alpha'&=\mu_0(g_1\sigma_{x\alpha}-g_4\sigma_{z\alpha})\,.\end{aligned} \tag{41}$$

The present calculations are more complicated than the case along $K_2$-axis, the procedure remaining essentially unaltered. The result is

$$\Theta_1=(\Theta_1)_{\mathrm{ex}}+(\Theta_1)_{\mathrm{dip}}\,, \tag{42a}$$

$$\begin{aligned}(\Theta_1)_{\mathrm{ex}}=\frac{-1}{4k}\,\frac{1}{g_1^2+g_4^2}&\\\times\{2g({}_1^2J_{ik}^{xx}&+g_4^2J_{ik}^{zz}+2g_1g_4J_{ik}^{zx})\\+4\,(g_1^2J_{i\alpha}^{xx}&-g_4^2J_{i\alpha}^{zz}-2g_1g_4J_{i\alpha}^{xz})\}\,,\end{aligned} \tag{42b}$$

$$\begin{aligned}(\Theta_1)_{\mathrm{dip}}=\frac{-1}{4k}\,\frac{1}{g_1^2+g_4^2}&\{(g_1^2+g_4^2)^2(G_{1x}+G_{2x})\\&+g_4^2(g_1+g_3)^2(G_{1z}-G_{2z})\}\,.\end{aligned} \tag{42c}$$

(iii) The magnetic susceptibility along $K_3$-axis can be calculated in the same way as that along $\mathrm{K}_1$-axis. The magnetic moment operators corresponding to (41) are given by

$$\begin{aligned}\mathscr{H}_i'&=\mu_0(g_3\sigma_{zi}+g_4\sigma_{xi})\,,\\\mathscr{H}_\alpha'&=\mu_0(g_3\sigma_{z\alpha}-g_4\sigma_{x\alpha})\,,\end{aligned} \tag{43}$$

and the final results are

$$\Theta_3=(\Theta_3)_{\mathrm{ex}}+(\Theta_3)_{\mathrm{dip}}\,, \tag{44a}$$

$$\begin{aligned}(\Theta_3)_{\mathrm{ex}}=\frac{-1}{4k}\,\frac{1}{g_3^2+g_4^2}&\\\times\{2(g_3^2J_{ik}^{zz}&+g_4^2J_{ik}^{xx}+2\,g_3g_4J_{ik}^{zx})\\+4\,(g_3^2J_{i\alpha}^{zz}&-g_4^2J_{i\alpha}^{xx}+2g_3g_4J_{i\alpha}^{xz})\}\,,\end{aligned} \tag{44b}$$

$$\begin{aligned}(\Theta_3)_{\mathrm{dip}}=\frac{-1}{4k}\,\frac{1}{g_1^2+g_4^2}&\{(g_3^2+g_4^2)^2(G_{1z}+G_{2z})\\&+g_4^2(g_1+g_3)^2(G_{1x}-G_{2x})\}\,.\end{aligned} \tag{44c}$$

It may be noted that the Curie constants $C_i$ along each directions are respectively given by

$$C_1=N\mu_0^2(g_1^2+g_4^2)/4k\ ,$$
$$C_2=N\mu_0^2 g_2^2/4k\ ,$$
$$C_3=N\mu_0^2(g_3^2+g_4^2)/4k\ . \qquad (45)$$

## § 6. Result

As the first step the exchange integrals, $J_{st}$'s, should be evaluated from the observed Weiss constants. On assuming the exchange interactions to be effective up to the second neighbours, we have two exchange integrals and then denote them respectively by $J_{ik}=J_{\alpha\beta}\equiv J_1$ (for the first neighbours) and $J_{i\alpha}=J_{\alpha i}\equiv J_2$ (for the second neighbours). We should then estimate $J_{st}{}^{\lambda\mu}$ in terms of $J_1$ and $J_2$. $J_{ik}{}^{\lambda\mu}$'s are obtained from (11a) and (14), and $J_{i\alpha}{}^{\lambda\mu}$'s from (18) and (20). The coefficients $a, b$ and $c$ appearing in those expressions are given by (10). The results are tabulated in Table I.

Table I. The numerical values of $J_{st}{}^{\lambda\mu}$.
(The common factor $-J_1$ or $-J_2$ is omitted)

| $(\lambda, \mu)$ | $(s, t)$ | |
|---|---|---|
| | $(i, k)$ | $(i, \alpha)$ |
| $(xx)$ | 8.63 | 5.03 |
| $(yy)$ | 3.03 | 3.03 |
| $(zz)$ | 5.58 | 1.97 |
| $(zx)$ | 3.78 | 1.46 |
| $(xz)$ | 3.78 | −1.46 |

Next, the $g$-values are obtained from (6), in which $\alpha=34°$, by use of $g_{\parallel}$ and $g_{\perp}$ observed by Bleaney and Ingram. The tensorial $g$-values thus obtained are given in Table II.

Table II. The numerical values of $g_{\lambda\mu}$.

| $g_{\parallel}$ | $g_{\perp}$ | $g_1$ | $g_3$ | $g_4$ |
|---|---|---|---|---|
| 6.45 | 3.05 | 5.39 | 4.11 | 1.58 |

Further it is necessary to know the numerical values of $G_{r\lambda}$. We have obtained them from the method of direct sum over magnetic ions up to about 47 Å from an ion. The results are listed in Table III, together with the numerical values summed up to about 20 Å which give some suggetions about the accuracy of the present results.

As is well known, the eipole sum depends on the shape of sample. Usually, this dipole sum is divided into two parts. The one is over lattice points inside a large sphere, and the other over lattice points outside it. In the spherical sample, however, the latter part proves to vanish identically because the famous Lorentz field and the demagnetizing field are equal in magnitude and opposite in direction to each other in this case. Now, the usual magnetic measurements are made by spheroidal sample. In his paper concerning the copper Tutton salt[17], Garrett corrected the magnetic susceptibilities of spheroidal sample so as to obtain the corresponding susceptibilities of spherical sample. His magnetic data concerning the copper Tutton salt were obtained by such a way. We cannot see from reference 8 any note on the shape correction of the magnetic susceptibility of Co Tutton salt, but the shape correction must have been made in this substance.

Table III. The numerical values of $G_{r\lambda}(\times 10^{-22})$ (in $cm^{-3}$).*

| | up to 20 Å | up to 47 Å |
|---|---|---|
| $G_{1x}$ | −0.3979 | −0.4097 |
| $G_{1y}$ | −0.7322 | −0.7398 |
| $G_{1z}$ | 1.1300 | 1.1629 |
| $G_{2x}$ | 0.3681 | 0.3670 |
| $G_{2y}$ | 0.4974 | 0.4982 |
| $G_{2z}$ | −0.8656 | −0.8670 |

* The authors wish to express their thanks to Mrs. O. Nagai and R. Hatakeyama for checking the numerical values in this table.

We can now theoretically get the values of the Weiss constants $\Theta_\lambda$ by substituting these numerical values into Eqs. (42), (38) and (44), that is

$$\Theta_\lambda=a_\lambda+b_\lambda+b_\lambda J_1+c_\lambda J_2\ , \qquad (46)$$

where $a_\lambda, b_\lambda$ and $c_\lambda$ are given in Table IV. Now we have two undetermined parameters, $J_1$ and $J_2$, whereas we have three Weiss constants $\Theta_\lambda$ owing to the experiments by Garret. Thus we estimate $J_1$ and $J_2$ from these $\Theta_\lambda$'s by the method of least squares. Then we estimate the values of $\Theta_\lambda$ by use of $J_1$ and $J_2$ thus obtained.

Table IV. The numerical values of $a_\lambda$, $b_\lambda$ and $c_\lambda$.

| $\lambda$ | $a_\lambda\times 10^2$ | $b_\lambda$ | $c_\lambda$ |
|---|---|---|---|
| 1 | −2.039 | 5.21 | 5.26 |
| 2 | +0.350 | 1.52 | 3.03 |
| 3 | +0.503 | 4.25 | 0.10 |

The values of $\Theta_\lambda$ estimated in such a way serve to suggest the reliability of the estimations of $J_1$ and $J_2$. These results are tubulated in Table V.

Table V. The numerical values of $\Theta_\lambda$ and the estimated values of $J_1$ and $J_2$.

| | exp. | theoret. |
|---|---|---|
| $\Theta_1$ | −0.005°K | −0.010°K |
| $\Theta_2$ | −0.017 | −0.008 |
| $\Theta_3$ | +0.050 | +0.053 |
| $J_1/k$ | | +0.0116 |
| $J_2/k$ | | −0.00956 |

Having estimated the exchange integrals $J_1$ and $J_2$, we are now prepared to estimate the specific heat. First, we estimate $(C_vT^2/R)_{\text{dip-dip}}$ from Eqs. (25), (26), (27), (28) and (29). Here $P, Q$ and $R$ appearing in (26) are estimated with the help of (27) and $g$-values of Table II. The result can be seen in Table VI.

Table VI. The numerical values of $P$, $Q$ and $R$.

| $r$ | 1 | 2 |
|---|---|---|
| $P_r$ | 1904 | 1007 |
| $Q_{rxx}$ | 8932 | |
| $Q_{ryy}$ | 779 | |
| $Q_{rzz}$ | 3388 | |
| $Q_{rxy}$ | 5275 | |
| $Q_{ryz}$ | 3249 | |
| $Q_{rzx}$ | 19074 | 2930 |
| $R_{rx}$ | −7300 | −4609 |
| $R_{ry}$ | − 519 | |
| $R_{rz}$ | −3604 | − 913 |

Table VII. The numerical values of $A$, $B$ and $C$ ($\times 10^{-44}$)(in $cm^{-6}$).

| $r$ | 1 | 2 |
|---|---|---|
| $A_r$ | 0.4648 | 0.3040 |
| $B_{rxx}$ | 0.0954 | 0.0294 |
| $B_{ryy}$ | 0.1512 | 0.0266 |
| $B_{rzz}$ | 0.0120 | 0.0982 |
| $B_{rxy}$ | 0.1000 | 0.0061 |
| $B_{ryz}$ | 0.0016 | 0.0269 |
| $B_{rzx}$ | 0.0015 | 0.0419 |
| $C_{rx}$ | 0.1970 | 0.0774 |
| $C_{ry}$ | 0.2528 | 0.0595 |
| $C_{rz}$ | 0.0151 | 0.1671 |

The numerical values of lattice sums (29) are listed in Table VII. With the help of Tables VI and VII and Eqs (25) and (26), we get the numerical values of $(C_vT^2/R)_{\text{dip-dip}}$ equal to $17.8\times10^{-4}$. Secondly, $(C_vT^2/R)_{\text{ex-ex}}$ is estimated from (30) with the help of $J_1$ and $J_2$ of Tables I and V, and then obtain it as $16.9\times10^{-4}$. Finally we estimate $(C_vT^2/R)_{\text{dip-ex}}$. By using Tables I, II and the numerical values of $t_{is}{}^\lambda$, it can be estimated from (31) and (32) as follows.

$$(C_vT^2/R)_{\text{dip-ex}} = -10^{-2}k^{-1}(2.1\ J_1+1.3\ J_2). \quad (47)$$

Substituting the numerical values of $J_1$ and $J_2$ in Table V into the above equation, we get the value of $(C_vT^2/R)_{\text{dip-ex}}$ equal to $-4.5\times10^{-4}$.

Thus we get the inter-ionic contributions to the specific heat, which give $C_vT^2/R$ equal to $30.2\times10^{-4}$ in good agreement with the experimental value $27\times10^{-4}$ (see Table VIII).

Table VIII. The numerical value of $(C_vT^2/R)\times10^4$.

| | | | |
|---|---|---|---|
| theoret. | 30.2 | dip-dip | 17.8 |
| | | dip-ex | − 4.5 |
| | | ex-ex | 16.9 |
| exp. | 27 | | |

This work was supported by the grant for Scientific Researches from Education Ministry.

## References

1) L. C. Jackson: Trans. Roy. Soc. (London) **A 224** (1924) 1.
2) I. I. Rabi: Phys. Rev. **29** (1927) 184.
3) B. W. Bartlett: Phys. Rev. **41** (1932) 818.
4) K. S. Krishnan, N. C. Chakravarty and S. Banerjee: Phil. Trans. Roy. Soc. (London) **A 232** (1933) 99.
5) J. H. Van Vleck: Phys. Rev. **41** (1932) 208.
6) R. Schlapp and W. G. Penney: Phys. Rev. **42** (1932) 666.
7) B. Bleaney and D. J. E. Ingram: Proc. Roy. Soc. **A 208** (1951) 143.
8) C. G. B. Garrett: Proc. Roy. Soc. (London) **A 206** (1951) 242.
9) S. F. Malaker: Phys. Rev. **84** (1951) 133.
10) R. J. Benzie and A. H. Cooke: Nature **164** (1949) 837.
11) B. Bleaney: Phys. Rev. **78** (1950) 214.
12) W. Opechowski: Physica **14** (1948) 237.
13) De Klerk: Physica **12** (1946) 513.
14) A. Abragam and M. H. L. Pryce: Proc. Roy. Soc. **A 206** (1951) 173.
15) W. Hofmann: Z. fur Krist. **78** (1931) 279.
16) J. H. Van Vleck: J. Chem. Phys. **5** (1937) 320.
17) C. G. B. Garrett: Proc. Roy. Soc. **A 203** (1950) 375.

JOURNAL OF THE PHYSICAL SOCIETY OF JAPAN Vol. 11, No. 7, JULY, 1956

# Note on the Magnetic Anisotropy of the Cobalt Ammonium Tutton Salt $Co(NH_4)_2(SO_4)_2 \cdot 6H_2O$

By Norikiyo URYÛ

*Department of Physics, Faculty of Science,*
*Kyusyu University, Hukuoka*

(Received March 12, 1956)

Magnetic anisotropy of cobalt ammonium Tutton salt in the temperature region from about 10°K to 300°K is studied, where we used the wave functions obtained by Abragam and Pryce. The temperature dependence of the effective Bohr magneton is also studied. The agreements of the present theoretical results with the experimental ones are excellent.

## § 1. Introduction

The magnetic behaviour of cobalt ammonium Tutton salt has been experimentally studied by many investigators, such as Jackson¹⁾, Rabi²⁾, Krishnan³⁾, Bose⁴⁾, and Bleaney and Ingram⁵⁾. And now we have sufficient data of its magnetic susceptibility, which shows remarkable anisotoropy, and we are now interested in the evalution of this magnetic anisotropy.

As is usually considered, the atomic origins of magnetic anisotropy are such as (1) the dipolar interactions between magnetic ions, (2) anisotoropic exchange interactions and (3) the anisotropic $g$-factors caused by a crystalline field. However, our temperature regions are at rather high temperatures, where the interionic interactions are ineffective because of a large separation between magnetic ions. Then we may take exclusively the third type into account as the origin of the magnetic anisotropy of cobalt Tutton salt.

The electron configuration $3d^7$ of a cobalt ion has $^4F_{9/2}$ as the lowest level in its free state and the next level $^4P$ lies at a distance of about 14000 cm$^{-1}$ from the lowest one. Under a crystalline field of the cubic symmetry the seven-fold degenerate $F$-state splits into a one-fold and two three-fold degenerate orbital levels, but in the case of $Co^{2+}$, contrary to the cases of $Cr^{3+}(^4F_{3/2})$ and $Ni^{2+}(^3F_4)$, a triplet orbital level is the lowest one. This situation in the case of $Co^{2+}$ gives rise to a greater anisotropy than in the cases of $Cr^{3+}$ and $Ni^{2+}$, as was pointed out by Van Vleck⁶⁾.

Recently, Abragam and Pryce⁷⁾ determined appropriate crystalline parameters to interpret the anisotropy of $g$-values in the lowest Kramers doublet. A similar attempt has been also tried by Kambe, Koide and Usui⁸⁾, whose purpose consists in a consistent interpretation of the anisotoropies of both $g$-values and magnetic susceptibilities by a well chosen parameter, but they could not successfully attain their aim. Although the result obtained by Abragam and Pryce is in excellent agreement with the experiments as long as the lowest Kramers doublet is concerned, the magnetic susceptibilities have not been examined over any wide range of temperatures, where many Kramers doublets are effective. We use the wave functions of Kramers doublets given by Abragam and Pryce to calculate the magnetic susceptibilities over such a temperature region. The result thus obtained is in excellent agreement with the observed magnetic anisotropy.

As was described in the preceding paper, the magnetic anisotropy is closely related to a deviation from the Curie law, which can conveniently be described in terms of the temperature dependence of the effective Bohr magneton. Then, we calculate the effective Bohr magneton for a powdered sample. Its temperature dependence is in good agreement with experimental data.

## § 2. Results of Abragam and Pryce

As was described in § 1, the lowest level of $Co^{2+}$ under a cubic crystalline field is a triplet. It can then be regarded as a orbital state with the orbital quantum number $l'=1$, where the Landé factor of orbital angular momentum may be replaced by an effective value of it. Then, a tetragonal field causes an anisotoropy of the effective Landé factor, whose symmetry should naturally be tetragonal. Thus the part of the orbital angular momentum operator, $\boldsymbol{L}$, which is semi-diagonal in the manifold of the lowest triplet, can be written

$$L_x=-\alpha' l_x' \ , \quad L_y=-\alpha' l_y' \ , \quad L_z=-\alpha l_z' \ , \tag{1}$$

where $l_x'$, $l_y'$ and $l_z'$ are the components of the angular momentum operator with a quantum number equal to unity and the tetragonal axis is taken as $z$-axis.

In solving an orbital problem, Abragam and Pryce assumed an appropriate crystalline field with a cubic term of fourth order and tetragonal terms of second order and fourth order, where they also took into account $^4P$ state. As a result they obtained

$$\alpha=1.128 \ , \qquad \alpha'=1.503 \ . \tag{2}$$

And then, the orbital part of Hamiltonian in the manifold of the lowest triplet, $\mathscr{H}_{\text{orb.}}$, becomes

$$\mathscr{H}_{\text{orb.}}=\Delta(1-l_z'^2) \ . \tag{3}$$

Here $\Delta$ is a positive value equal to 1090 cm$^{-1}$, and hence the lowest orbital state is doubly degenerate. If we take into account spin states of the ion and introduce the spin-orbit coupling $\lambda LS$, the Hamiltonian now becomes:

$$\mathscr{H}=\Delta(1-l_z'^2)-\alpha'\lambda(l_x'S_x+l_y'S_y)-\alpha\lambda l_z'S_z \ . \tag{4}$$

Here the spin-orbit coupling parameter $\lambda$ of $Co^{2+}$ is equal to $-180$ cm$^{-1}$.

Our Hamitonian gives rise to six Kramers doublets, whose energy values can be obtained in the following way. If we classify the energy levels obtained from (4) according to the eigenvalues of $l_z'+S_z$, which is commutable with $\mathscr{H}$, the eigenvalue problem (4) can be factorized as follows:

$$\begin{pmatrix} \frac{3}{2}\alpha\lambda & -\sqrt{\frac{3}{2}}\alpha'\lambda & 0 \\ -\sqrt{\frac{3}{2}}\alpha'\lambda & \Delta & -\sqrt{2}\alpha'\lambda \\ 0 & -\sqrt{2}\alpha'\lambda & \frac{1}{2}\alpha\lambda \end{pmatrix} \quad \left(m=\pm\frac{1}{2}\right)$$

$$\begin{pmatrix} \Delta & -\sqrt{\frac{3}{2}}\alpha'\lambda \\ -\sqrt{\frac{3}{2}}\alpha'\lambda & -\frac{1}{2}\alpha\lambda \end{pmatrix} \quad \left(m=\pm\frac{3}{2}\right)$$

$$\left(\Delta-\frac{3}{2}\alpha\lambda\right) \qquad \left(m=\pm\frac{5}{2}\right) . \tag{5}$$

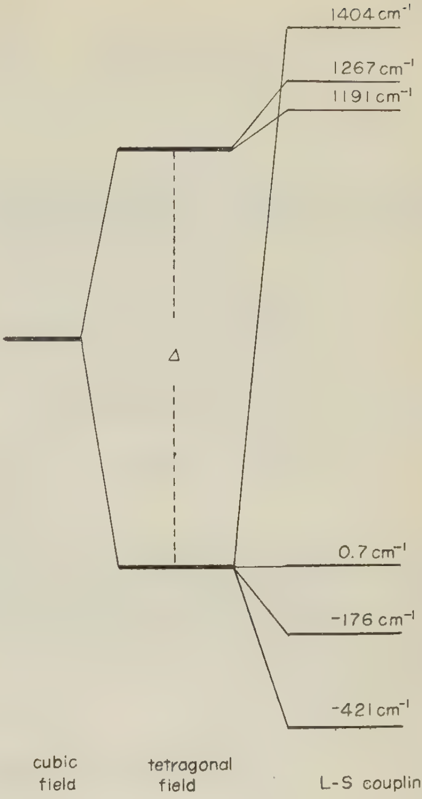

Fig. 1. Level diagram of the lowest six Kramers doublets.

Solving each eigenvalue problem thus obtained, we get six energy eigenvalues as is schematically drawn in Fig. 1.

## § 3. Magnetic Susceptibility

In our temperature regions, we have only to take into account the lowest three levels. These states can be described by the following wave functions

$E=-421$ cm$^{-1}$:

$$\psi_{1/2}=\alpha\psi\left(-1,\ \frac{3}{2}\right)+b\psi\left(0,\ \frac{1}{2}\right)+c\psi\left(1,\ -\frac{1}{2}\right),$$

$$\psi_{-1/2}=a\psi\left(1,-\frac{3}{2}\right)+b\psi\left(0,-\frac{1}{2}\right)+c\psi\left(-1,\ \frac{1}{2}\right),$$

$E=-176$ cm$^{-1}$:

$$\psi'_{1/2}=a'\psi\left(-1,\ \frac{3}{2}\right)+b'\psi\left(0,\ \frac{1}{2}\right)+c'\psi\left(1,-\frac{1}{2}\right),$$

$$\psi'_{-1/2}=a'\psi\left(1,-\frac{3}{2}\right)+b'\psi\left(0,-\frac{1}{2}\right)$$
$$+c'\psi\left(-1,\ \frac{1}{2}\right),$$

$E=0.7\,\mathrm{cm}^{-1}$:

$$\psi_{3/2}=a''\psi\left(0,\frac{3}{2}\right)+b''\psi\left(1,\frac{1}{2}\right),$$

$$\psi_{-3/2}=a''\psi\left(0,-\frac{3}{2}\right)+b''\psi\left(-1,-\frac{1}{2}\right), \tag{6}$$

in which $\psi_m$ denotes the eigenfunction with an eigenvalue, $m$, of $l_z'+S_z$ and $\psi(m_l', M_S)$ the eigenfunction with an eigenvalue, $m_l'$, of $l_z'$ and with an eigenvalue, $M_S$, of $S_z$. Here the coefficients $a, b, c, \cdots$ etc. are given by

$a=-0.8959$ $a'=-0.4020$ $a''=-0.2911$
$b=0.2772$ $b'=-0.1626$ $b''=0.9567$
$c=-0.3471$ $c'=0.9011$

Using the well-known formula of Van Vleck[9]

$$\chi_x=\frac{B\mu_0^2}{kT}\sum_n\sum_{m,m'}|(n,m|L_x+2S_x|n,m')|^2\exp(-E_n/kT)$$
$$+2B\mu_0^2\sum_{m,m}\sum_{\substack{n',m'\\ n'\neq n}}\frac{|(n,m|L_x+2S_x|n',m')|^2}{E_{n'}-E_n}\exp(-E_n/kT),$$
$$x=x,\,y,\,z, \tag{7}$$
$$B=N/\sum_n\exp(-E_n/kT), \tag{8}$$

we can now calculate the magnetic susceptibility at any temperature below about 400°K. Here $n$ refers to one of the Kramers doublets and $m$ to a wave function pertaining to the Kramers doublet, and then $E_n$ denotes the energy value of the Kramers doublet $n$. And further $N$ is the number of magnetic ions and $\mu_0$ the Bohr magneton. The calculated result is the following:

$$\chi=\chi_1+\chi_2, \tag{9}$$
$$\chi_{1x}=\frac{B\mu_0^2}{kT}\{G_{1x}+G'_{1x}\exp(-\Theta_1/T)+G''_{1x}\exp(-\Theta_2/T)\}, \tag{10}$$
$$\chi_{2x}=2B\mu_0^2\{G_{2x}+G'_{2x}\exp(-\Theta_1/T)+G''_{2x}\exp(-\Theta_2/T)\},$$
$$x=x,\,y,\,z, \tag{11}$$

where $\Theta_1$ and $\Theta_2$ are respectively given by

$$k\Theta_1=245\,\mathrm{cm}^{-1}\quad\text{or}\quad\Theta_1=352.48°\mathrm{K},$$
$$k\Theta_2=422\,\mathrm{cm}^{-1}\quad\text{or}\quad\Theta_2=607.13°\mathrm{K}. \tag{12}$$

Here $G_{rx}$, $G'_{rx}$ etc. $(r=1, 2)$ are given by

$$G_{1x}=G_{1y}=8(-1/\sqrt{2}\cdot bc\alpha'+\sqrt{3}\,ac+b^2)^2,$$
$$G'_{1x}=G'_{1y}=8(-1/\sqrt{2}\cdot b'c'\alpha'+\sqrt{3}\,a'c'+b'^2)^2,$$
$$G''_{1x}=G''_{1y}=0,$$
$$G_{1z}=2\{(a^2-c^2)\alpha+3a^2+b^2-c^2\}^2,$$
$$G'_{1z}=2\{(a'^2-c'^2)\alpha+3a'^2+b'^2-c'^2\}^2,$$
$$G''_{1z}=2\{-b''^2\alpha+3a''^2+b''^2\}^2, \tag{13}$$
$$G_{2x}=G_{2y}=+\frac{2}{245}(\delta_2+2\gamma_2)^2+\frac{2}{422}(\delta_3+2\gamma_3)^2,$$
$$G'_{2x}=G'_{2y}=-\frac{2}{245}(\delta_2+2\gamma_2)^2+\frac{2}{177}(\delta_4+2\gamma_4)^2,$$
$$G''_{2x}=G''_{2y}=-\frac{2}{422}(\delta_3+2\gamma_3)^2-\frac{2}{177}(\delta_4+2\gamma_4)^2,$$
$$G_{2z}=+\frac{2}{245}(\delta_1+2\gamma_1)^2,$$
$$G'_{2z}=-\frac{2}{245}(\delta_1+2\gamma_1)^2,$$
$$G''_{2z}=0. \tag{14}$$

Here $\delta_j$ and $\gamma_j$ are given by the expressions written down in the Table I, where their numerical values are also tabulated. The numerical values of $G_{1x}$'s and $G_{2x}$'s are listed in Table II.

## § 4. Comparison with Experiment

In the preceding section we calculated the ionic susceptibility. In order to get the magnetic susceptibility of a sample, we should take into account the facts that a unit cell of Tutton salt contains two divalent ions whose tetragonal axes are different in orientation, as can be seen in Fig. 1b of the preceding paper. Let us denote the magnetic susceptibilities along the principal magnetic axes $K_1$, $K_2$ and $K_3$ by $\chi_1$, $\chi_2$ and $\chi_3$ respectively. Then we have

Table I.

| | Expression | Numerical value |
|---|---|---|
| $\delta_1$ | $\alpha(aa'-cc')$ | 0.7591 |
| $\delta_2$ | $-\alpha'(bc'+b'c)/\sqrt{2}$ | −0.3255 |
| $\delta_3$ | $-\alpha'(aa''+bb'')/\sqrt{2}$ | −0.5591 |
| $\delta_4$ | $-\alpha'(a'a''+b'b'')/\sqrt{2}$ | 0.0409 |
| $\gamma_1$ | $(3aa'+bb'-cc')/2$ | 0.6741 |
| $\gamma_2$ | $(\sqrt{3}ac'+2bb'+\sqrt{3}a'c)/2$ | −0.6234 |
| $\gamma_3$ | $(\sqrt{3}a''b+2b''c)/2$ | −0.4020 |
| $\gamma_4$ | $(\sqrt{3}a''b'+2b''c')/2$ | 0.9031 |

Table II. The numerical values of $G_{1x}$'s and $G_{2x}$'s.

| $r$ | 1 | 2 |
|---|---|---|
| $G_{rx}$, $G_{ry}$ | 4.1218 | +0.0290 |
| $G_{rx}'$, $G_{ry}'$ | 1.5862 | +0.0184 |
| $G_{rx}''$, $G_{ry}''$ | 0 | −0.0474 |
| $G_{rz}$ | 19.6407 | +0.0362 |
| $G_{rz}'$ | 2.1395 | −0.0362 |
| $G_{rz}''$ | 0.0376 | 0 |

Table III. Numerical values of $\chi_1-\chi_2$, $\chi_1-\chi_3$ and $\chi$ (mean susceptibility). The experimental values are Jackson's data corrected.

| T°K | $(\chi_1-\chi_2)\times10^6$ | | $(\chi_1-\chi_3)\times10^6$ | | $\chi\times10^6$ | |
|---|---|---|---|---|---|---|
| | exp. | calc. | exp. | calc. | exp. | calc. |
| 290 | 3023 | 4522 | 1541 | 2465 | 9590 | 9540 |
| 200 | | 8280 | | 4513 | | 13780 |
| 100 | | 20420 | | 11130 | | 24920 |
| 77.2 | 25500 | 26850 | 13000 | 14630 | 30300 | 30490 |
| 50 | | 41280 | | 22500 | | 43040 |
| 20.3 | 94400 | 99880 | 51900 | 54440 | 93600 | 94090 |
| 16.7 | 120000 | 121100 | 64800 | 66020 | 111000 | 112600 |
| 14.5 | 137000 | 139300 | 74300 | 75930 | 124000 | 128500 |

$$\begin{aligned}\chi_1&=\chi_x\sin^2\alpha+\chi_z\cos^2\alpha\,,\\ \chi_2&=\chi_y\,,\\ \chi_3&=\chi_x\cos^2\alpha+\chi_z\sin^2\alpha\,,\end{aligned}\tag{15}$$

where $\alpha=34°$ according to the measurements by Bleaney and Ingram.

The temperature variations of the magnetic anisotropy, $\chi_1-\chi_2$ and $\chi_1-\chi_3$, thus obtained are plotted in Fig. 2 and the mean magnetic susceptibility, $\chi$, is also plotted in Fig. 3. These numerical values are tabulated in Table III.

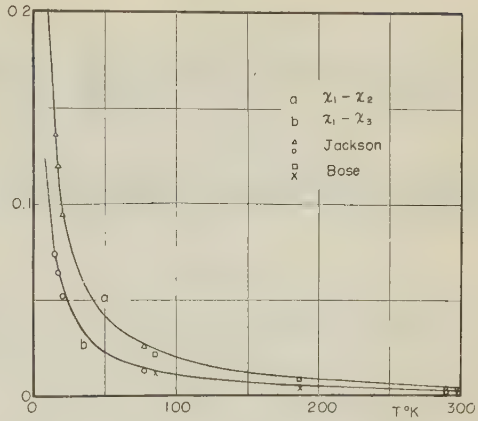

Fig. 2. Temperature variations of $\chi_1-\chi_2$ and $\chi_1-\chi_3$.

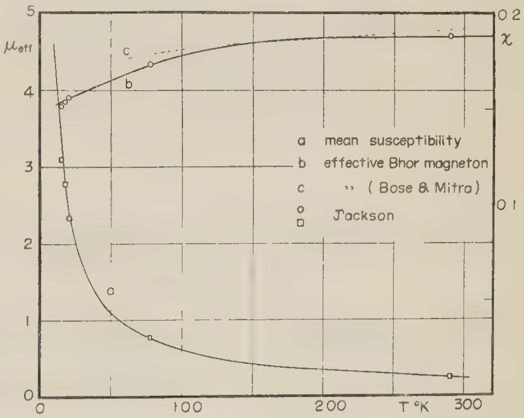

Fig. 3. Temperature variations of the mean magnetic susceptibility and the effective Bohr magneton.

As was already mentioned in § **1**, several investigators have studied the cobalt Tutton salt experimentally. Above all, Jackson's experiments cover the widest range of temperatures, whereas other investigators have merely reported a few measurements at rather high temperatures. According to Krishnan, however, Jackson's values are not correct because he erroneously deduced $\chi_1-\chi_2$ from the measured data. With the help of the reliable data given by Krishnan at 30°C, corrected values of $\chi_1-\chi_2$ and $\chi_1-\chi_3$ prove to be obtained through multiplying Jackson's data by appropriate factors (1.976 for $\chi_1-\chi_2$ and 1.822 for $\chi_1-\chi_3$). For the mean susceptibility the correction is not so serious (difference at 30°C is about only 3%). These values thus corrected are tabulated in Table III.

Next, we calculate the temperature dependence of the effective Bohr magneton number

$$\mu_{\text{eff}}=\sqrt{\frac{3\chi kT}{N\mu_0^2}} \tag{16}$$

which serves to see a deviation from the Curie law. Here $\chi$ is the mean magnetic susceptibility. The result can be seen in Fig. 3, where the experimental data are also plotted. Bose and Mitra proposed an empirical formula for $\mu_{\text{eff}}$[10])

$$\bar{\mu}^2_{\text{eff}}-15=A+BT+\frac{C}{T}\,, \tag{17}$$

$$A=5.06\,,\qquad B=0.0115\,,\qquad C=-74.7\,,$$

which should be regarded as good approximate formula at moderately high temperatures. A curve obtained from (17) are also plotted in Fig. 3. The agreement of our calculated results with experimental ones seems to be excellent. Thus we may conclude that the magnetic properties of cobalt ammonium Tutton salt can be satisfactorily explained from the theory of Abragam and Pryce.

In conclusion the author wishes to express his sincere thanks to Dr. T. Nakamura for his kind interest in this work.

### References

1) L. C. Jackson: Trans. Roy. Soc. (London) **A 224** (1924) 1.
2) I. I. Rabi: Phys. Rev. **29** (1927) 184.
3) K. S. Krishnan, N. C. Chakravarty and S. Banerjee: Phil. Trans. Roy. Soc. (London) **A 232** (1933) 99.
4) A. Bose: Ind. Jour. Phys. **22** (1948) 276.
5) B. Bleaney and D. J. E. Ingram: Proc. Roy. Soc. **A 208** (1951) 143.
6) J. H. Van Vleck: Phys. Rev. **41** (1932) 208.
7) A. Abragam and M. H. L. Pryce: Proc. Roy. Soc. **A 206** (1951) 173.
8) K. Kambe, S. Koide and T. Usui: Prog. Theor. Phys. **7** (1952) 15.
9) J. H. Van Vleck: *The Theory of Electric and Magnetic Susceptibilities.* Oxford, Clarendon Press, 1932.
10) A. Bose and S. C. Mitra: Ind. Jour. Phys. **27** (1953) 95.

---

JOURNAL OF THE PHYSICAL SOCIETY OF JAPAN Vol. 11, No. 7, JULY, 1956

# Hyperfine Structure of the Spectrum of Cu I and Test of the Hyperfine Structure Formulas

By Kiyoshi MURAKAWA

*Institute of Science and Technology, Komaba-machi, Meguro-ku, Tokyo*

(Received March 1, 1956)

The hyperfine structure (hfs) of the levels $3d^94s^2\,{}^2D_{5/2}$ and ${}^2D_{3/2}$ was measured and compared with the usual hfs formulas for $d$-electrons, and a discrepancy between theory and experiment was found. This can be phenomenologically interpreted by assuming that the values of $\langle 1/r^3\rangle$ are different for $3d_{5/2}$- and $3d_{3/2}$-electrons, namely $\langle 1/r^3\rangle=7.4$ and $8.0$ for $3d_{5/2}$- and $3d_{4/2}$-electrons respectively, where $r$ is measured in unit of hydrogen atom radius.

## §1. Introduction

The hyperfine structure (hfs) of the levels $3d^94s^2\,{}^2D_{5/2,\,3/2}$ of Cu I was studied by several workers[1-5]. But the hfs of ${}^2D_{5/2}$ has never been treated carefully. Since this configuration is a $d$-electron hole, we can express the hfs interval factor by the formula for a single $d$-electron. From the general formula[6]*

$$\left.\begin{matrix} a' \\ a'' \end{matrix}\right\}=\frac{2l(l+1)}{j(j+1)}\langle 1/r^3\rangle F\,1.585\left(\frac{\mu}{I}\right)\times 10^{-3}\ \text{cm}^{-1}\,, \tag{1}$$

$$a'''=-\frac{1}{2l+1}\langle 1/r^3\rangle G\,1.585\left(\frac{\mu}{I}\right)\times 10^{-3}\ \text{cm}^{-1}\,, \tag{2}$$

we get

$$a(d_{5/2})=\frac{48}{35}\langle 1/r^3\rangle F_2'\,1.585\left(\frac{\mu}{I}\right)\times 10^{-3}\ \text{cm}^{-1}\,, \tag{3}$$

$$a(d_{3/2})=\frac{48}{15}\langle 1/r^3\rangle F_2''\,1.585\left(\frac{\mu}{I}\right)\times 10^{-3}\ \text{cm}^{-1}\,, \tag{4}$$

---

* In the present paper we write merely $\langle 1/r^3\rangle$ instead of $\langle 1/r^3\rangle_{\text{Av}}$ for the sake of brevity.

$a(d_{5/2}, d_{3/2})$

$$= -\frac{1}{5}\langle 1/r^3\rangle G_2\, 1.585\left(\frac{\mu}{I}\right) \times 10^{-3}\,\mathrm{cm}^{-1}\,. \qquad (5)$$

Here $r$ is expressed in unit of the hydrogen atom radius (usually denoted as $a_H$).

It is the purpose of the present work to test the validity of the formulas (3) and (4) by studying the hfs of the Cu I lines λ 5782, λ 5700 and λ 5105.

The spectrum of Cu I was excited by a liquid-air cooled hollow cathode discharge tube, and a Fabry-Perot etalon was used in order to resolve the hfs. Fig. 1 reproduces some of the interference patterns that were obtained.

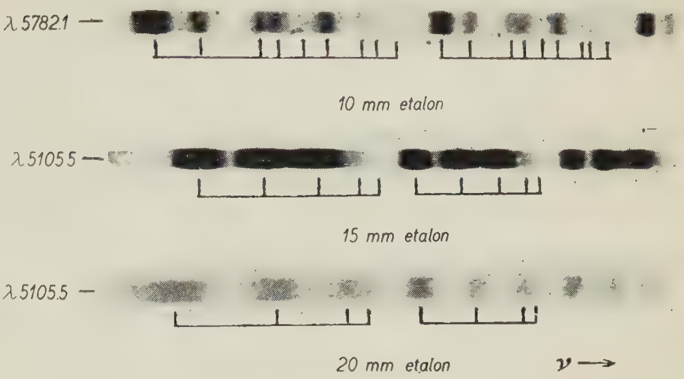

Fig. 1. Reproduction of some interference patterns of the spectrum of Cu I.

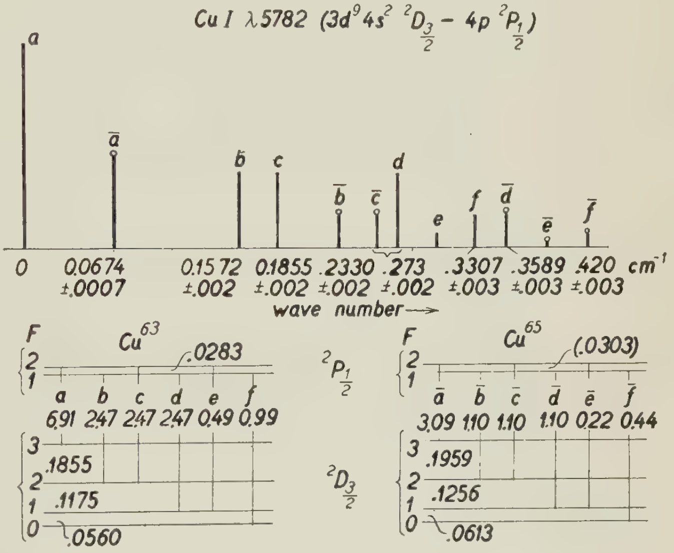

Fig. 2. Hfs of Cu I λ 5782.

## § 2. Experimental Result

The measured hfs of the above-mentioned three lines are shown schematically in Figs. 2, 3 and 4.

Natural copper is known to consist of two odd isotopes 63 and 65 with abundances 69.09% and 30.91% respectively[7]. Each of them has the nuclear spin[1] 3/2. The ratio of their nuclear magnetic moments was measured by Pound[8]:

$$\mu(\mathrm{Cu}^{65})/\mu(\mathrm{Cu}^{63}) = 1.0711 \pm 0.0002 \qquad (6)$$

The ratio of the nuclear quadrupole moments given in the literature[9] is

$$Q(\mathrm{Cu}^{65})/Q(\mathrm{Cu}^{65}) = 1.081 \pm 0.003\,. \qquad (7)$$

On the basis of the above-mentioned spin and the isotopic abundance Ritschl[1] detected an isotope shift in the lines λ 5782, λ 5700 and λ 5105. His interpretation (with a slightly modified form) will be employed here.

**a.** λ 5782 ($3d^9\,{}^2D_{3/2} - 4p\,{}^2P_{1/2}$). All the hfs components were measured relative to the strongest one, their positions being shown in Fig. 2 together with the maximum deviation of the individual measurements. The hfs splitting of ${}^2P_{1/2}$ of Cu$^{65}$ was calculated from that of Cu$^{63}$ using the ratio (6). However that of ${}^2D_{3/2}$ of Cu$^{65}$ was not, in order to test the accuracy of the measurement. The measured ratio

$$A^{63}({}^2D_{3/2})/A^{65}({}^2D_{3/2}) = 0.0643/0.0605$$
$$= 1.063 \pm 0.017$$

would be in agreement with the nuclear induction ratio (6).

**b.** λ 5700 ($3d^9\,{}^2D_{3/2} - 4p\,{}^2P_{3/2}$). See Fig. 3. The resolution of the group of components $c$, $d$, and $e$ was not complete, so their positions were determined by means of a photometer and a comparator. From these measurements the hfs of the upper level ${}^2P_{3/2}$ could be determined and was used in interpreting the hfs of λ 5105.

**c.** λ 5105 ($3d^9\,{}^2D_{5/2} - 4p\,{}^2P_{3/2}$). See Fig. 4.

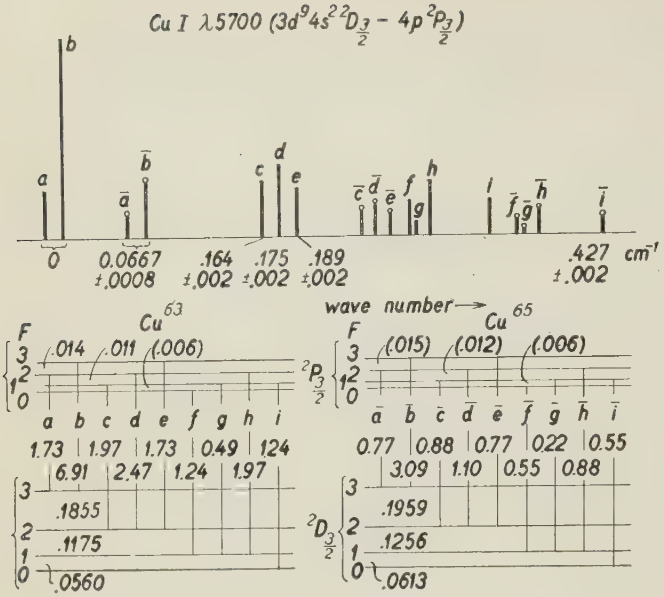

Fig. 3. Hfs of Cu I λ5700.

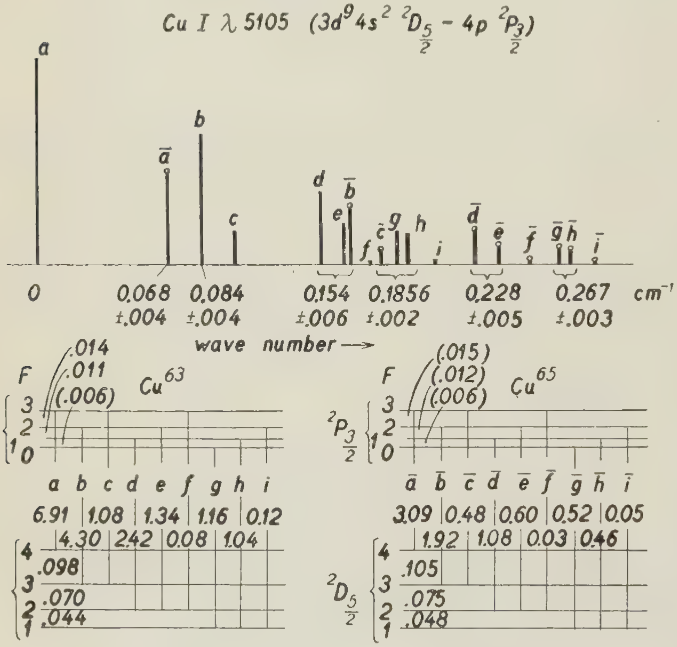

Fig. 4. Hfs of Cu I λ5105.

Although the structure is not so favorable for measurement, the hfs splitting of the lower level $^2D_{5/2}$ could be determined with fair accuracy, and will be discussed later on.

Expressing the position of the hfs levels of a term by the usual formula

$$E=E_0+\frac{A}{2}+BC(C+1)\,,$$

$$C=F(F+1)-I(I+1)-J(J+1)\,,$$

all the hfs constants $A$ and $B$ that were determined in the present work are listed in Table I.

Wagner[5] gives $A^{63}(^2D_{3/2})=0.0597\ \mathrm{cm}^{-1}$, $A^{65}(^2D_{3/2})=0.0644\ \mathrm{cm}^{-1}$. The latter value is in agreement with that given here. The former value seems to the present author to be a little too low. Further Wagner gives $A^{63}(^2D_{5/2})=0.0256\ \mathrm{cm}^{-1}$, $A^{65}(^2D_{5/2})=0.0274\ \mathrm{cm}^{-1}$. These values seem to have been calculated on the basis of the usual hfs formula [see (7)], so they are not in agreement with those of the present work.

## § 3. Discussion of the Result

We are now in a position to test the validity of the formulas (3) and (4) for a single $d$-electron. For the sake of brevity we will discuss only the hfs of $\mathrm{Cu}^{63}$.

If the values of $\langle 1/r^3\rangle$ are the same for $d_{5/2}$- and $d_{3/2}$-electrons, we can eliminate $\langle 1/r^3\rangle$ from (3) and (4) and get

$$a(d_{5/2})=\frac{3}{7}\frac{F_2'}{F_2''}a(d_{3/2})\,. \qquad (7)$$

For Cu I, we have $F_2'/F_2''=0.993$. Putting $a(d_{3/2})=0.0605\ \mathrm{cm}^{-1}$ in the expression (7), we get $a(d_{5/2})=0.0259\pm0.0003\ \mathrm{cm}^{-1}$, whereas the observed value is $a(d_{5/2})=0.0238\pm0.0010\ \mathrm{cm}^{-1}$. The discrepancy is far beyond the experimental error. This discrepancy between theory and experiment can be phenomenologically interpreted by assuming that the values of $\langle 1/r^3\rangle$ are different for $d_{5/2}$- and $d_{3/2}$-electrons.

Putting the value $\mu(\mathrm{Cu}^{63})/I=1.4842$ and the observed values of $a$'s in the formulas (3) and (4), we get

$$\langle 1/r^3\rangle=7.4 \quad \text{for a} \quad d_{5/2}\text{-electron,} \qquad (8)$$

$$\langle 1/r^3\rangle=8.0 \quad \text{for a} \quad d_{3/2}\text{-electron.} \qquad (9)$$

Differentiation of $\langle 1/r^3\rangle$ for $d_{5/2}$- and $d_{3/2}$-electrons causes differentiation of the effective charge $Z_d{}^*$ through the formula

Table I. Hfs constants of some terms of Cu I, ($\mathrm{cm}^{-1}$)*.

| | $\mathrm{Cu}^{63}$ | $\mathrm{Cu}^{65}$ |
|---|---|---|
| $3d\,4s^2\,{}^2D_{3/2}$ | $A=0.0605\pm0.0005$<br>$B=0.15_4\times10^{-3}$ | $A=0.0643\pm0.0005$<br>$B=0.12_4\times10^{-3}$ |
| $3d\,4s^2\,{}^2D_{5/2}$ | $A=0.0238\pm0.0010$<br>$B\approx0.05\times10^{-3}$ | $A=(0.0255)$<br>$B\approx0.05\times10^{-3}$ |
| $4p\,{}^2P_{1/2}$ | $A=0.0141\pm0.004$ | $A=(0.0151)$ |
| $4p\,{}^2P_{3/2}$ | $A=0.0050\pm0.0004$<br>$B\approx-0.04\times10^{-3}$ | $A=0.0053\pm0.0004$<br>$B\approx-0.03\times10^{-3}$ |

* Numbers in parentheses were calculated using the ratio of the nuclear magnetic moments (6).

$$\langle 1/r^3\rangle=\zeta/(5.822\,Z^*)\,, \tag{10}$$

$\zeta$=spin-orbit interaction parameter expressed in $\mathrm{cm}^{-1}$,

namely, we get ($\zeta_d=816\,\mathrm{cm}^{-1}$ for Cu I)

$$Z_d^*=19.0=29-10.0 \quad \text{for a } d_{5/2}\text{-electron}, \tag{11}$$

$$Z_d^*=17.4=29-11.6 \quad \text{for a } d_{3/2}\text{-electron}. \tag{12}$$

The other value of $\langle 1/r^3\rangle$ to be compared is 7.52 of Sternheimer[10] who calculated it from the Hartree-Fock wave functions. This is in agreement with the weighted mean of (8) and (9).

It would be important to test the usual formula (1) in the case of a single $p$-electron. Perl, Rabi and Senitzky[11] studied the hfs of $3p\,{}^2P_{3/2}$ and $3p\,{}^2P_{1/2}$ of Na I and obtained $a(p_{1/2})=94.45\pm0.5$Mc/sec, $a(p_{3/2})=19.06\pm0.36$Mc/sec, and showed that these values satisfy the usual formula (1), namely $a(p_{1/2})/a(p_{3/2})=5.0$ within the experimental error. we can therefore asume that the values of $\langle 1/r^3\rangle$ are the same for $p_{1/2}$- and $p_{3/2}$-electrons.

The phenomenological proposition that $\langle 1/r^3\rangle$ is larger for a $d_{3/2}$- than for a $d_{5/2}$-electron is given here only on the basis of the hfs measurement of Cu I, but it may be remarked that this assumption can suppress a greater part of the discrepancy between theory and experiment observed in the $d$-electron hfs of V I[12] and in a vast amount of data of $d$-electron hfs of the spectra of the elements in the neighbourhood of Cu.

The properties of the remaining hfs factor (namely $a'''$) of the $d$-electron will be described in another paper.

## References

1) R. Ritschl: Z. f. Physik **79** (1932) 1.

2) H. Schuler u. T. Schmidt: Z. f. Physik **100** (1936) 113. The conclusion of these authors that $a(d_{3/2})$ and $a(d_{3/2})$ follow the usual hfs formula is apparently incorrect.

3) P. Brix: Z. f. Physik **126** (1949) 725.

4) H. Kopfermann, A. Steudel, S. Wagner u. W. Walcher: Nachrichten Akad. Gottingen Math.-Phys. Kl. (1953), Nr. 1.

5) S. Wagner: Z. f. Physik **141** (1955) 122.

6) See, for example, H. Casimir: Verh. Teylers Tweede Genootschap, Haarlem **11** (1936).

7) M. G. Inghram, D. C. Hess and R. J. Hayden: quoted by G. T. Seaborg and I. Perlman, Rev. Mod. Phys. **20** (1948) 585.

8) R. V. Pound: Phys. Rev. **73** (1948) 523.

9) H. Krüger u. U. Meyer-Berkhout: Z. f. Physik **132** (1952) 171.
See also B. Bleaney, K. D. Bowers and D. J. E. Ingram: Proc. Phys. Soc. London **64** (1951) 758.

10) R. M. Sternheimer: Phys. Rev. **95** (1954) 736.

11) M. L. Perl, I. I. Rabi and B. Senitzky: Phys. Rev. **98** (1955) 611.

12) K. Murakawa: J. Phys. Soc. Japan **11** (1956) 422.

JOURNAL OF THE PHYSICAL SOCIETY OF JAPAN Vol. 11, No. 7, JULY, 1956

# Isotope Shift in the Spectra of Ne II and W I

By Kiyoshi MURAKAWA

*Institute of Science and Technology, Komaba-machi, Meguro-ku, Tokyo*

(Received March 1, 1956)

(I) The isotope shift in the transition $3s-3p$ in the spectrum of Ne II ($Ne^{22}-Ne^{20}$) was observed, using a liquid-air cooled hollow cathode. The shift in the doublet spectrum of the $^3P$ system was found to be of the order of 0.2 $cm^{-1}$ and larger than that in the quartet spectrum or the $^1D$ system.

(II) The component due to the rare isotope $W^{180}$ was detected in the line $\lambda$ 4269 of the spectrum of W I, and the ratio of the distances of the neighboring even isotopes was found to be $\Delta(186-184):\Delta(184-182):\Delta(182-180)=1:1.206\pm0.010:0.88\pm0.07$.

## §1. Isotope Shift in the Spectrum of Ne II

Several years ago[1)] isotope shift ($Ne^{22}-Ne^{20}$) in the spectrum of Ne II[2)] was studied, using a water-cooled hollow cathode. A large isotope shift was observed in the $3s-3p$ transition in the doublet spectrum of the $^3P$ system.

In the present work a liquid-air cooled hollow cathode was used and interference patterns that are sharper than before could be obtained. The quartz etalon which the author had used in the study of the ultraviolet lines was returned early in 1955 to Professor Kiuchi from whom it was kindly lent to the author, so an uviol etalon and two quartz Lummer plates were used in order to resolve the hyperfine structure (hfs). Fig. 1 reproduces a typical example of the isotope shift in the spectrum of Ne II.

In all cases where the isotope shift was actually detected, the $Ne^{20}$ component was found to lie to the higher frequency side of the $Ne^{22}$ component, the abundance ratio being $Ne^{22}:Ne^{20}=9:1$.

Using a hot hollow cathode, Suwa[3)] found a wing structure in the spectrum of Ne II, as shown qualitatively in Fig. 2a. [This phenomenon is characteristic of Ne II, because no such structure was detected in the lines (in the red and ultraviolet region) of Ne I, even when a hot hollow cathode was used.] Of course the $Ne^{22}$ component would have a wing structure, but this would have been masked by the broad $Ne^{20}$-structure.

When the cathode was cooled with water, it was found that the wing denoted as $w$ in Fig. 2b still exists and partly superposes on the $Ne^{22}$-component in the case of the $3s-3p$ transition of the $^3P$ system. This makes the apparent isotope shift somewhat larger than actual in the case of the same transition. Therefore the isotope shift for the lines $\lambda\lambda$ 3727, 3713, 3392, 3378 and 3323 published by Murakawa and Suwa[1)] must be corrected

Table I. Isotope shift in the spectrum of Ne II.

| $\lambda$ (A) | Transition* | Isotope shift ($cm^{-1}$) | Isotope shift ($cm^{-1}$) previous work** |
|---|---|---|---|
| 3766.3 | $3s\,^4P_{3/2}(^3P)-3p\,^4P_{5/2}(^3P)$ | $0.15_0\pm0.019$ | |
| 3727.1 | $3s\,^2P_{1/2}(^3P)-3p\,^2D_{3/2}(^3P)$ | $0.193\pm0.008$ | $0.22_7$ |
| 3713.1 | $3s\,^2P_{3/2}(^3P)-3p\,^2D_{5/2}(^3P)$ | $0.203\pm0.008$ | $0.23_3$ |
| 3709.6 | $3s\,^4P_{3/2}(^3P)-3p\,^4P_{1/2}(^3P)$ | $0.14_9\pm0.015$ | |
| 3694.2 | $3s\,^4P_{5/2}(^3P)-3p\,^4P_{5/2}(^3P)$ | $0.15_0\pm0.015$ | 0.15 |
| 3664.1 | $3s\,^4P_{5/2}(^3P)-3p\,^4P_{3/2}(^3P)$ | $0.14_8\pm0.015$ | |
| 3568.5 | $3s\,^2D_{5/2}(^3D)-3p\,^2F_{7/2}(^1D)$ | $0.16_2\pm0.016$ | $0.13_5$ |
| 3392.8 | $3s\,^2P_{1/2}(^3P)-3p\,^2P_{3/2}(^3P)$ | $0.221\pm0.006$ | $0.25_7$ |
| 3378.3 | $3s\,^2P_{1/2}(^3P)-3p\,^2P_{1/2}(^3P)$ | $0.221\pm0.006$ | $0.25_1$ |
| 3355.1 | $3s\,^4P_{3/2}(^3P)-3p\,^4D_{3/2}(^3P)$ | $0.16_0\pm0.016$ | |
| 3345.5 | $3s\,^2D_{5/2}(^1D)-3p\,^2P_{3/2}(^1D)$ | $0.15_2\pm0.015$ | $0.15_4$ |
| 3334.9 | $3s\,^4P_{5/2}(^3P)-3p\,^4D_{7/2}(^3P)$ | $0.14_3\pm0.016$ | |
| 3323.8 | $3s\,^2P_{3/2}(^3P)-3p\,^2P_{3/2}(^3P)$ | $0.219\pm0.006$ | $0.26_0$ |
| 3319.8 | $3s\,^2D_{3/2}(^1D)-3p\,^2P_{1/2}(^1D)$ | $0.13_6\pm0.022$ | $0.16_6$ |

* Reference 2. ** Reference 1.

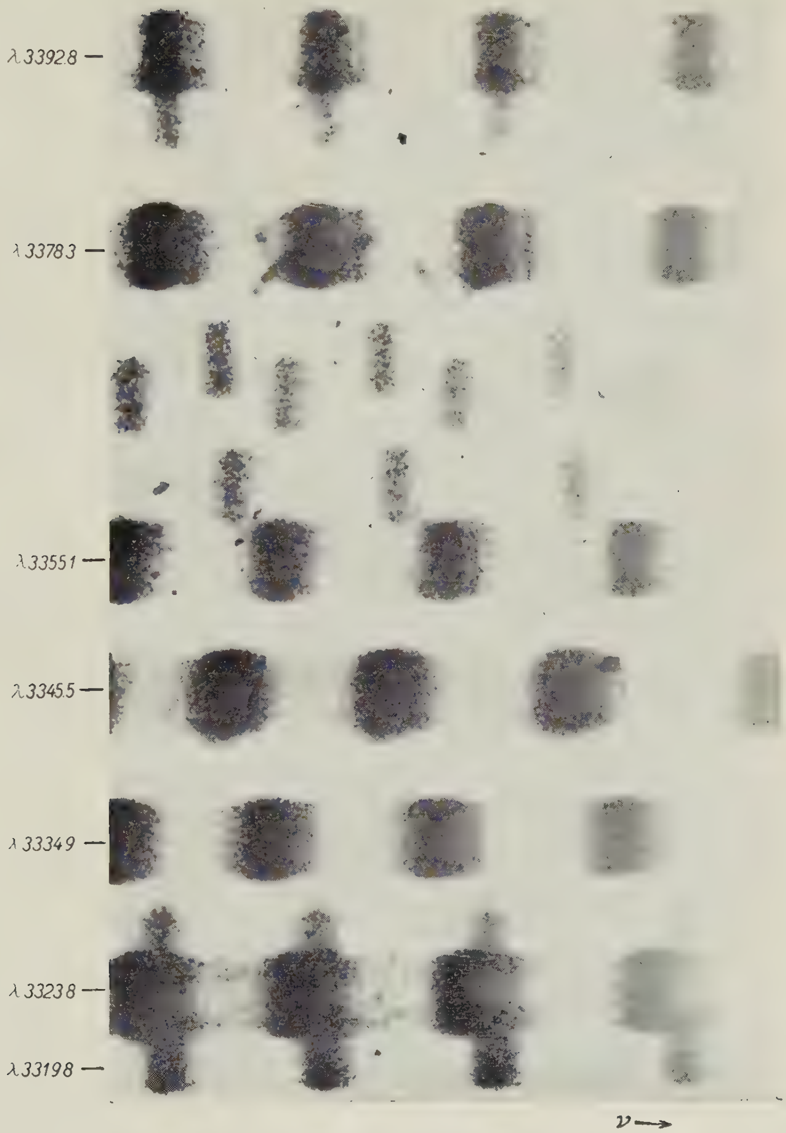

quartz Lummer plate (thickness 4.4 mm)

Fig. 1. Enlargement of interference patterns of the spectrum of Ne II.

for this wing.

When the cathode is cooled with liquid-air, the hfs gets naturally sharper, but it is not certain whether the wing disappears in this case altogether. Probably a weak wing would still exist but is difficult to detect positively. However a considerable scatter among individual data of isotope shift would point to possible existence of a weak wing structure.

The isotope shift measured in the present work is listed in Table I. As was mentioned in the previous work, largest shift is observed in the $3s-3p$ transition of the doublet spectrum of the $^3P$ system.

## § 2. Isotope Shift of $W^{180}$ in the Spectrum of W I

Using an enriched isotope ($W^{180}$ 4.95%, $W^{182}$ 50.75%, $W^{183}$ 15.28%, $W^{184}$ 17.89%, $W^{186}$ 11.14 %), Vreeland and Murakawa[4] observed in the hfs of some lines of W I the component due to $W^{180}$, but the existence of $W^{183}$ was, as it now seems, very unfavorable for measurement of the isotope shift. Since in that work an aluminium hollow cathode coated with tungsten oxide was used, the strong alumi-

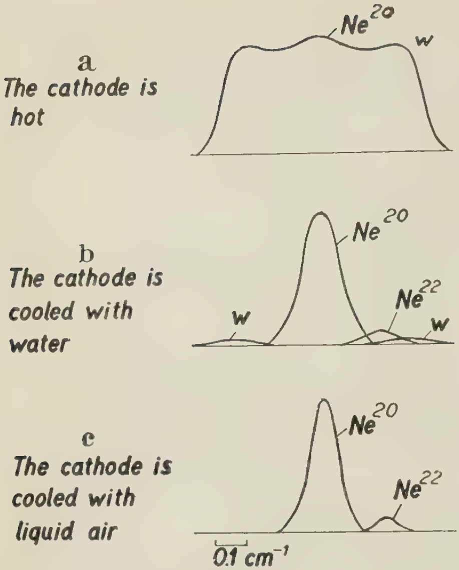

Fig. 2. Qualitative illustration of the hfs of the lines of the transition $3s-3p$ of the doublet spectrum of the $^3P$ system in Ne II.

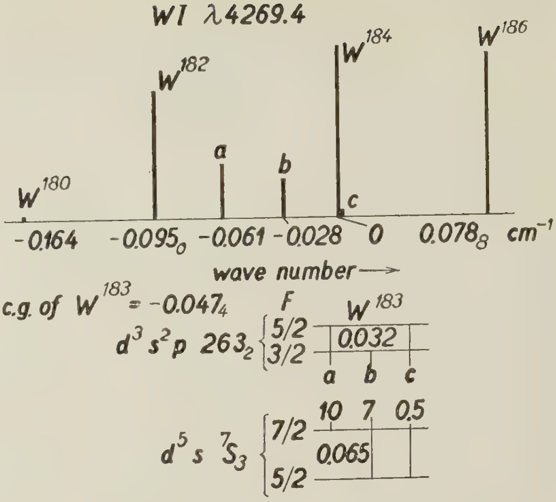

Fig. 3. Hfs of W I λ4269.4.

nium hydride band masked the important line λ4269. In the present work (using natural tungsten) the hollow cathode was of pure tungsten, so no disturbing band appeared. Since, however, the abundance of $W^{180}$ in natural tungsten is only 0.2%, a considerable time was spent in obtaining a clear interference spectrogram. Finally several plates just showing the existence of $W^{180}$-component in λ4269 and λ3817.5 were obtained. The result of measurement of λ4269 is shown in Fig, 3. That of λ3817.5 is approximately the same, but less accurate. Except the position of $W^{180}$, the positions of other components were taken from the previous publication of the author[5]. From the hfs of λ4269, we get the ratio of the distances of the neighboring even isotopes:

$$\Delta(186-184) : \Delta(184-182) : \Delta(182-180)$$
$$=1 : 1.206\pm0.010 : 0.88\pm0.07 .$$

Since in the line λ4269 none of the even isotopes is affected by the odd isotope $W^{183}$, the ratio given here would be the most accurate one available at present.

## References

1) K. Murakawa and S. Suwa: Phys. Rev. **74** (1948) 1535.
2) The classification of the spectrum of Ne II was published by T. L. de Bruin and C. J. Bakker, Z. f. Physik **69** (1931) 19.
3) S. Suwa: J. Phys. Soc. Japan **4** (1949) 179.
4) J. A. Vreeland and K. Murakawa: Phys. Rev. **83** (1951) 229.
5) K. Murakawa: J. Phys. Soc. Japan **8** (1953) 215.
6) The term notation was taken from O. Laporte and J. E. Mack, Phys. Rev. **63** (1943) 246.

JOURNAL OF THE PHYSICAL SOCIETY OF JAPAN Vol. 11, No. 7, JULY, 1956

# Fine Structure of $J=1\leftarrow 0$ Transition due to Internal Rotation in Methyl Alcohol

By Tetsuji NISHIKAWA*

*Department of Physics, Faculty of Science,*
*University of Tokyo, Tokyo, Japan*

(Received April 7, 1956)

The fine structure of $J=1\leftarrow0$ lines in various isotopic species of methyl alcohol has been explained by a combination method of Itoh's theory for a rigid asymmetric hinded rotor and Kivelson's theory for a nonrigid symmetric hindered rotor. All lines have been fitted within errors of 2 Mc by this method. From the analysis the height of potential barrier to internal rotation for $CH_3OD$ has been determined to be 371±5 $cm^{-1}$. The molecular structure of methyl alcohol has also been calculated and discussed.

## §1. Introduction

The microwave spectra of various isotopic species of methyl alcohol have been studied by Venkateswarlu, Edwards, and Gordy[1]. The $J=1\leftarrow0$, $K=0\leftarrow0$ lines have been observed in the ground torsional state, $n=0$, and the first two excited states, $n=1$ and $n=2$. Hindered internal rotations of the molecules split all of these lines into doublets, corresponding to the degenerate and non-degenerate sublevels which are designated here by $\mu=1$ and $\mu=0$**, respectively.

Three types of perturbations should be considered to explain these fine structures of the spectra. One is the perturbation energy due to the off-diagonal element, $H^{JK\mu n}_{JK+1\mu n'}$, which was previously calculated by Burkhard and Dennison[2], based upon a model of a rigid symmetrical top, $CH_3$, attached at an arbitrary angle to a rigid asymmetric framework, OH. This perturbation energy is sensitively dependent on the barrier height of internal rotation and the physical angle between the CO axis and the methyl axis. Swalen[3] tried to explain the splitting of ground vibrational state, $n=0$, from this effect and to determine the barrier height and the molecular structure, but his approximation used seems to be inappropriate to this molecule.

The other perturbation is the centrifugal distortion including the effects of internal rotations upon the other vibrations and hence upon the rotational constants. The third perturbation is the effect of repulsion between methyl and hydroxyl groups, which varies with the angle of internal rotation, $x$. The last two effects have been treated by Kivelson[4] for symmetric hindered rotors and successfully applied to explain the similar fine structure of the $J=1\leftarrow0$ line of methyl silane. Recently, Hecht and Dennison[5] have examined the theory similar to that given by Kivelson incorporating the asymmetry existing in methyl alcohol. Details of their theory and calculation have not yet been found***. However, since the methyl alcohl is only slightly asymmetric (asymmetry parameter, $\kappa\simeq-0.98$), Kivelson's theory for symmetric rotors can be applicable with additional treatment of the effect of asymmetry in a rigid hindered rotor. This combination method will be found to give better agreements between the experimental and calculated values, though it is rather semiempirical than Hecht and Dennison's method.

## §2. Rigid Hindered Rotor Model

The diagonal element $H^{JK\mu n}_{JK\mu n}$ of Hamiltonian, on the basis of a simplified model consisting of a rigid hydroxyl and a rigid methyl groups, includes the energy of the overall rotation of the molecule, which depends only on $J$ and $K$, and the energy of internal rotation, which depends on $K, \mu, n$, but not on $J$. Fine structure for $J=0\leftarrow 1$, $K=0\leftarrow 0$, $\mu\leftarrow\mu$, $n\leftarrow n$ lines, therefore, can not be expected from the diagonal element.

---

* Present adress: Institute for Nuclear Study, University of Tokyo, Tanashimachi, Tokyo, Japan.

** The definition of $\mu$ will be found in ref. (6). $\mu$ is related to the quantum number $\tau$, which is used by Dennison and others[2], by $\mu=-(K+\tau-1)$ mod. 3.

*** After sending our results, we have received a copy of their work. Their results are closely agree with ours, while they have pointed out that the term $G_v$, which we have named as centrifugal distortion term, also includes the effect of Coriolis force. Further, they have taken into account some small off-diagonal terms due to Coriolis interaction. The author thanks to them for their kind information.

The Hamiltonian, however, has off-diagonal elements

$$H^{JK\mu n}_{JK\mu n'}\ (n'\neq n),\ H^{JK\mu n}_{JK+1\mu n'},\ \text{and}\ H^{JK\mu n}_{JK+2\mu n'}\,.$$

Because the last matrix element is not existent for $J=1,0$ and $K=0$ levels, the fiirst two off-diagonal elements should be considered in explaining the fine structure splittings in this case. These matrix elements have first been obtained by Burkhard and Dennison[2] in the form

$$H^{JK\mu n}_{JK\mu n'}=-\frac{h^2D^2}{8\pi^2 I_1(I_yI_1-D^2)}\int_0^{2\pi}(P^{K\mu n}(x))^*\frac{d^2}{dx^2}P^{K\mu n'}(x)dx \tag{1}$$

$$H^{JK\mu n}_{JK+1\mu n'}=\frac{h^2D\sqrt{(J+K+1)(J-K)}}{8\pi^2 2(I_yI_1-D^2)}\int_0^{2\pi}\left[\frac{e^{-ix}}{i}(P^{K\mu n}(x))^*\frac{d}{dx}P^{K+1\mu n'}(x)\right.$$
$$\left.-\frac{1}{2}e^{-ix}(P^{K\mu n}(x))^*P^{K+1\mu n'}(x)\right]dx \tag{2}$$

where the definition of $P^{K\mu n}(x)$ is in reference (2). $I_y$ is the moment of inertia of the molecule about the axis passing through the center of mass of the molecule and perpendicular to the methyl axis in the COH plane. $I_1$ is defined as $I_1=I_z-I_2$, $I_z$ and $I_2$ being the moments of inertia of the molecule and the methyl group along their axes parallel to the methyl axis, respectively. $D$ is the product of inertia of the molecule in the COH plane. The magnitude of $D$ is considerably sensitive to the physical angle between CO axis and methyl axis.

Burkhard and Dennison's expression, however, is inadequate to calculate thepe rturbation energy which produces the fine structure, since they have the matrix elements between states of different vibrational quantum numbers. If we take into account only the matrix elements which are diagonal in vibrational quantum number, $n$, this perturbation energy seems to give a splitting of several megacycles for the ground torsional state of normal methyl alcohol. This estimation is not good enough, since the contribution from matrix elements between different $n$ states gives the frequency shifts of the same order.

Recently, Itoh[6], and Hecht and Dennison[7] have succeeded, in different ways, to eliminate the matrix elements between the different $n$ states by a suitable transformation of the axis. The only appreciable off-diagonal matrix element $H^{JK\mu n}_{JK+1\mu n}$ is expressed by

$$H^{JK\mu n}_{JK+1\mu n}=\frac{h^2D(2K+1)\sqrt{(J+K+1)(J-K)}}{8\pi^2 2(I_y^2+D^2)}\int_0^{2\pi}(Q^{K\mu n}(x))^*Q^{K+1\mu n}(x)dx \tag{3}$$

where $Q^{K\mu n}(x)=e^{-iKx}P^{K\mu n}(x)$. It is noted that the factor involving molecular constants is $D/I_y^2+D^2$ in equation (3), and it is $D/I_yI_1-D^2$ in equation (2). Since $I_y$ is about thirty times larger than $I_1$ in the normal methyl alcohol, the splitting of $J=1\leftarrow 0$ line in the ground torsional state can be calculated to be only 0.02 Mc for normal methyl alcohol, using the barrier height ($\approx$375 cm$^{-1}$) and the molecular structure which have been obtained by Ivash and Dennison[8]. This calculated value is too small compared with the observed value, 4.59 Mc. Calculated splittings for the excited torsional states tend to be much smaller. The frequency shift due to this effect were also found to be less than 0.1 Mc for the isotopic species, $C^{13}H_3O^{16}H$ and $C^{12}D_3O^{16}H$.

This situation is considerably different in the case of $C^{12}H_3O^{16}D$ and $C^{13}H_3O^{16}D$. The splittings of about 10 Mc for $n=0$, and 2 or 3 Mc for $n=1$, are calculated from the morecular structure, which has been obtained by Venkateswarlu and Gordy[9] assuming no effect of torsional vibration. Because the values of

$D$ of these species are about ten times larger than those of other isotopic species and also because the energy difference, $E^{0\mu n}-E^{1\mu n}$, which is the denominator in the perturbation calculation, decreases to about one fifth of that of $C^{12}H_3O^{16}H$ in the ground state. Therefore, the perturbation energy due to $H^{JK\mu n}_{JK+1\mu n}$ should be taken into account in the case of $C^{12}H_3O^{16}D$ and $C^{13}H_3O^{16}D$. The magnitude of the calculated frequency shift can be found in the third column of Table II. However, the calculation shows that the fine structure of $CH_3OD$ lines also cannot be correctly explained by this perturbation energy alone.

## § 3. Nonrigid Hindered Rotor Model

It has been found that the rigid hindered rotor model can not explain the fine structure of $J=1\leftarrow 0$ lines of methyl alcohol. It would be necessary to take into account the interactions of the other vibrational modes with the torsional vibrations. The effect of these interactions have been examined by Kivelson[4)] for the symmetric internal rotor and the frequencies of $J=1\leftarrow 0$, $K=0\leftarrow 0$, $\mu\leftarrow\mu$, $n\leftarrow n$ lines were given by the relation,

$$\nu=2[B_v+F_v(\mu, n|1-\cos 3x|\mu, n)+G_v(\mu, n|\Pi^2|\mu, n)] \qquad (4)$$

where $B_v$ is the usual rigid rotor rotational constant, $G_v$ is a centrifugal distortion term, $F_v$ is a parameter that arises from the mutual repulsion of the two functional groups that rotates with respect to each other, and $\Pi$ is the angular momentum of internal rotation.

As was shown in § 2, the effect of asymmetry on the fine structures of $J=0\leftarrow 1$ lines for $C^{12}H_3O^{16}H$, $C^{13}H_3O^{16}H$, and $C^{12}D_3O^{16}H$ is expected to be negligibly small so that the fine structures of these lines may be calculated from Kivelson's formula, equation (4). There are four constants to be determined, $B_v$, $F_v$, $G_v$, and $\alpha=\frac{2\pi^2 cV_0I_2(I_yI_1-D^2)}{h(I_yI_z-D^2)}$ *, where $V_0$ is the height of potential barrier. Since the torsional and vibrational interactions are not so sensitively dependent on the barrier height and the molecular structure, we can used $\alpha$ estimated from the approximate values of $V_0$ and $\frac{I_2(I_yI_1-D^2)}{I_yI_z-D^2}$ which were formerly given by Ivash and Dennison[8)] or Venkateswarlu and Gordy[9)]. Values of $\alpha$ for $C^{12}H_3O^{16}H$, $C^{13}H_3O^{16}H$, and $C^{12}D_3O^{16}H$ were taken as 3.4, 3.4**, and 3.8, respectively. $B_v$, $F_v$, and $G_v$ were calculated from the observed frequencies of arbitrary selected three lines. Using these four constants, the calculated frequencies of unassumed lines show very good agreements to the observed ones for all three isotopic species as shown in Table I. The values of $B_v$, $F_v$, and $G_v$ used in the calculation are listed in Table III.

Table I. Comparison of observed and calculated frequencies for $C^{12}H_3O^{16}H$, $C^{13}H_3O^{16}H$, and $C^{12}D_3O^{16}H$. The errors involved in observed frequencies were reported to be less than 0.5 Mc unless otherwise stated. Frequencies in parentheses were used to determine the constants $B_v$, $F_v$ and $G_v$.

| Molecule | $n$ | $\mu$ | Cal. freq. in Mc | Obs. freq. in Mc |
|---|---|---|---|---|
| $C^{12}H_3O^{16}H$ | 0 | 0 | (48372.60) | 48372.60 |
| | 0 | ±1 | 48376.96 | 48377.09 |
| | 1 | 0 | 48257.57 | 48257.49 |
| | 1 | ±1 | (48247.89) | 48247.89 |
| | 2 | 0 | (48192.12) | 48192.12 |
| | 2 | ±1 | 48177.92 | 48178.0 ±1.0 |
| $C^{13}H_3O^{16}H$ | 0 | 0 | (47205.20) | 47205.20 |
| | 0 | ±1 | 47209.65 | 47209.63 |
| | 1 | 0 | 47094.49 | 47094.11 |
| | 1 | ±1 | (47083.82) | 47083.82 |
| | 2 | 0 | (47030.16) | 47030.16 |
| | 2 | ±1 | 47018.00 | 47019.5 ±1.0 |
| $C^{12}D_3O^{16}H$ | 0 | 0 | (39066.21) | 39066.21 |
| | 0 | ±1 | 39069.32 | 39069.25 |
| | 1 | 0 | 38982.54 | 38982.88 |
| | 1 | ±1 | (38972.05) | 38972.05 |
| | 2 | 0 | (38928.89) | 38928.89 |
| | 2 | ±1 | 38923.77 | 38923.97 |

The above method of calculation for $C^{12}H_3C^{16}H$, $C^{13}H_3O^{16}H$, and $C^{12}D_3O^{16}H$ should be slightly modified for $C^{12}H_3O^{16}D$ and $C^{13}H_3O^{16}D$. The effect of asymmetry must be taken into account for the latters. The frequency shift due to the asymmetry can be calculated from equation (3) for rigid hindered rotor, because it depends less on the other vibrations than torsion. With the corrections of asymmetry effect thus calculated, equation (4) for nonrigid symmetric hindered rotor can also be applied to $C^{12}H_3O^{16}D$ and $C^{13}H_3O^{16}D$.

Since the effect of asymmetry on the fine structure is sensitive to $V_0$, it has been

---

* $\alpha=2\pi^2 cV_0I_1I_2/hI_z$ in a symmetric hindered rotor, in which $D=0$. See also ref. (6).

** The isotopic substitution in C affects $\alpha$ less.

Table II. Comparison of observed and calculated frequencies for $C^{12}H_3O^{16}D$ and $C^{13}H_3O^{16}D$. Frequencies in parentheses were used to determine the constants $B_v$, $F_v$ and $G_v$.

| Molecule | $\alpha$ | $n$ | $\mu$ | Freq. shift due to the asymmetry in Mc | Calc. Freq. in Mc ($\nu_{calc.}$) | Obs. Freq. in Mc ($\nu_{obs.}$) | $\nu_{calc.}-\nu_{obs.}$ |
|---|---|---|---|---|---|---|---|
| $C^{12}H_3O^{16}D$ | 5.3 | 0 | 0 | − 5.88 | 45358.98 | 45359.43 | −0.45 |
| | | 0 | ±1 | −22.07 | (45344.30) | 45344.30 | — |
| | | 1 | 0 | + 1.21 | (45265.78) | 45265.78 | — |
| | | 1 | ±1 | + 3.25 | 45259.25 | 45259.44 | −0.19 |
| | | 2 | 0 | − 0.40 | (45193.36) | 45193.36 | — |
| | | 2 | ±1 | − 0.08 | 45187.74 | 45189.46 | −1.72 |
| | 5.4 | 0 | 0 | − 6.54 | 45358.30 | | −1.13 |
| | | 0 | ±1 | −21.92 | (45344.30) | | — |
| | | 1 | 0 | +1.36 | (45265.78) | | — |
| | | 1 | ±1 | +3.66 | 45260.20 | | +0.76 |
| | | 2 | 0 | − 0.45 | (45193.36) | | — |
| | | 2 | ±1 | − 0.09 | 45187.14 | | −2.32 |
| | 5.5 | 0 | 0 | − 7.24 | 45357.86 | | −1.57 |
| | | 0 | ±1 | −22.05 | (45344.30) | | — |
| | | 1 | 0 | + 1.53 | (45265.78) | | — |
| | | 1 | ±1 | + 4.10 | 45261.25 | | +1.81 |
| | | 2 | 0 | − 0.49 | (45193.36) | | — |
| | | 2 | ±1 | − 0.11 | 45186.32 | | −3.14 |
| $C^{13}H_3O^{16}D$ | 5.3 | 0 | 0 | − 5.50 | 44241.40 | 44241.43 | −0.03 |
| | | 0 | ±1 | −20.24 | (44228.26) | 44228.26 | — |
| | | 1 | 0 | + 1.13 | (44151.09) | 44151.09 | — |
| | | 1 | ±1 | + 3.07 | 44143.47 | 44144.06 | −0.59 |
| | | 2 | 0 | − 0.37 | (44079.30) | 44079.30 | — |
| | | 2 | ±1 | − 0.08 | 44075.52 | 44076.55 | −1.03 |
| | 5.4 | 0 | 0 | − 6.23 | 44241.18 | | −0.25 |
| | | 0 | ±1 | −20.59 | (44228.26) | | — |
| | | 1 | 0 | + 1.31 | (44151.09) | | — |
| | | 1 | ±1 | + 3.53 | 44144.69 | | +0.63 |
| | | 2 | 0 | − 0.43 | (44079.30) | | — |
| | | 2 | ±1 | − 0.09 | 44074.50 | | −2.05 |
| | 5.5 | 0 | 0 | − 6.92 | 44240.81 | | −0.62 |
| | | 0 | ±1 | −20.78 | (44228.26) | | — |
| | | 1 | 0 | + 1.47 | (44151.09) | | — |
| | | 1 | ±1 | + 3.96 | 44145.78 | | +1.72 |
| | | 2 | 0 | − 0.48 | (44079.30) | | — |
| | | 2 | ±1 | − 0.10 | 44073.66 | | −2.89 |

calculated taking three different values of $\alpha$, 5.3, 5.4 and 5.5, which correspond to $V_0=371$, 378, and 385 $cm^{-1}$, respectively. Because the effect is also sensitive to $D$, which are not accurately known, it had to be calculated for different values of the parameter $D/(I_y^2+D^2)$, in order to find the optimum set of constants. The calculated frequencies for each value of $\alpha$ are compared with the observed frequencies in Table II, when $D/(I_y^2+D^2)$ has been taken to give the best fit to the experimental data. The agreement is particularly good when $\alpha=5.3$, or $V_0=371\ cm^{-1}$. The set of constants, $B_v$, $F_v$, $G_v$ and $D/(I_y^2+D^2)$ for each $\alpha$ used in the calculations are given in Table III. The maximum discrepancy is only the order of 1 Mc/sec even in $n=2$ which is the magnitude expected from the accuracy of the aproximation used.

Table III. Molecular parameters used in calculations.

| Molecule | $\alpha$ | $2B_v$ in Mc | $F_v$ in Mc | $G_v$ in Mc | $\frac{D}{I_y^2+D^2}$ in Mc |
|---|---|---|---|---|---|
| $C^{12}H_3O^{16}H$ | 3.4 | 48449.20 | −71.341 | −3.5361 | — |
| $C^{13}H_3O^{16}H$ | 3.4 | 47279.76 | −69.758 | −3.3452 | — |
| $C^{12}D_3O^{16}H$ | 3.8 | 39121.69 | −54.901 | −2.3354 | — |
| $C^{12}H_3O^{16}D$ | 5.3 | 45423.96 | −65.927 | −2.6709 | 895 |
| | 5.4 | 45423.56 | −65.672 | −2.6413 | 935 |
| | 5.5 | 45423.60 | −65.490 | −2.6782 | 975 |
| $C^{13}H_3O^{16}D$ | 5.3 | 45304.50 | −64.922 | −2.4596 | 867 |
| | 5.4 | 45304.84 | −64.750 | −2.5119 | 915 |
| | 5.5 | 45304.96 | −64.568 | −2.5523 | 955 |

Table IV. Molecular structure of methyl alcohol.

| | Present work* | Venkateswarlu and Gordy | Ivask and Dennison |
|---|---|---|---|
| $d_{OH}(A)$ | 0.953 | 0.956 | 0.937 |
| $d_{CO}(A)$ | 1.427 | 1.427 | 1.434 |
| $d_{CH}(A)$ | 1.096 | 1.096 | 1.093 (assumed) |
| $\angle$HCH | 109°4′ | 109°2′ | 109°30′ |
| $\angle$COH | 108°24′ | 108°52′ | 105°56′ |
| $\theta$** | 3°18′ | 3°20′ | 3°9′ |

* On the probable values of errors involved in the molecular parameters, see ref. (9).

** $\theta$ is the angle between the CO axis and the methyl axis.

Table V. $B_v$ and $D/I_y^2+D^2$ calculated from the molecular parameters. The values in right columns were taken from Table III for comparison.

| Molecule | $2B_v$ in Mc | | $\frac{D}{I_y^2+D^2}$ in Mc | |
|---|---|---|---|---|
| $C^{12}H_3O^{16}H$ | 48449 | 48449 | 78 | — |
| $C^{13}H_3O^{16}H$ | 47267 | 47280 | 87 | — |
| $C^{12}D_3O^{16}H$ | 39124 | 39122 | 88 | — |
| $C^{12}H_3O^{16}D$ | 45422 | 45424 | 836 | 895 ($\alpha=5.3$) |
| $C^{13}H_3O^{16}D$ | 44290 | 44305 | 800 | 867 ($\alpha=5.3$) |

Table VI. $F_v$ and $G_v$ of methyl silane and methyl mercaptan.

| Molecule | $F_v$ in Mc | $G_v$ in Mc |
|---|---|---|
| $C^{12}H_3Si^{28}H_3$* | −65.322 | −0.8824 |
| $C^{12}H_3Si^{28}D_3$* | −52.868 | −0.8012 |
| $C^{12}H_3S^{32}H$** | −61.41 | −0.980 |
| $C^{13}H_3S^{32}H$** | −58.82 | −0.937 |
| $C^{12}D_3S^{32}H$** | −47.33 | −0.718 |
| $C^{12}H_3S^{32}D$** | −58.83 | −0.839 |

* from ref. (4).

** from ref. (10).

## §4. Molecular Constants and Discussions

$B_v$ in eq. (4) can approximately be expressed by[6,7].

$$B_v = \frac{h}{16\pi^2}\left(\frac{1}{I_x}+\frac{I_y}{I_y^2+D^2}\right), \tag{5}$$

where $I_x$ is the moment of inertia about the axis perpendicular to COH plane. The molecular structure has been calculated so that it gives the best fit to the values of $B_v$ for various isotopic species and also fits the moments of inertia $I_1$, $I_2$, and the product of inertia $D$ in $C^{12}H_3O^{16}H$ obtained by Ivash and Dennison[8]. The calculated molecular structure is given in Table IV, together with the structure determined by Ivash and Dennison and with those by Venkateswarlu and Gordy. Present structure is very close to the latter but lies between two.

The calculated frequencies of the effective rotational constants $B_v$ from the present structure are given in Table V with the values of $D/(I_y^2+D^2)$ for various isotoropic species. The values of $D(I_y^2+D^2)$ is not so sensitive to the molecular structure for $C^{12}H_3O^{16}D$ and $C^{13}H_3O^{16}D$ as for $C^{12}H_3O^{16}H$. The calculated $D/(I_y^2+D^2)$ of $CH_3OD$ are somewhat smaller than those obtained from the fine structure analysis, and the difference between them decreaces as $\alpha$ or $V_0$ decreaces. Also from this point, the height of potential barrier of 371±5 cm$^{-1}$ for $C^{12}H_3O^{16}D$ and $C^{13}H_3O^{16}D$ seems to be most reasonable. This value agrees within probable errors to the value of 374.8 cm$^{-1}$ determined by Ivash and Dennison from the analysis of the spectrum of $C^{12}H_3O^{16}H$. The disagreement of the order of ten megacycles still remains between the observed and calculated values of $B_v$, while it is not unaccountable considering the approximation used.

The values of $F_v$ and $G_v$ in Table III are compared with those of methyle silane[4] and of methyl mercaptain[10] in Table VI. The values are not different from each other for all these molecules. It seems interesting to calculate these coefficients from the molecular parameters. Recently, Kivelson[11] has presented a method to calculate $F_v$ from the nature of the forces constituting the barrier to internal rotation. $G_v$ can also be calculated from the vibrational frequencies and rotational constants assuming some molecular potential constants. These calculation, however, seems to be formidable task and uncertain.

## § 5. Acknowledgement

The author express his hearty thanks to Prof. K. Shimoda for his continuous encouragement and interest during the course of this work and to Mr. T. Itoh for his valuable discussions and advices.

### References

1) P. Venkateswarlu, H. D. Edwards and W. Gordy: J. Chem. Phys. **23** (1955) 1195.
2) D. G. Burkhard and D. M. Dennison: Phys. Rev. **84** (1951) 408.
3) J. D. Swalen: J. Chem. Phys. **23** (1955) 1739.
4) D. Kivelson: J. Chem. Phys. **22** (1954) 1733.
5) K. T. Hecht and D. M. Dennison: Symposium on Molecular Structure and Spectroscopy held in July, 1955 at the Ohio State University.
6) T. Itoh: J. Phys. Soc. Japan **11** (1956) 264.
7) K. T. Hecht and D. M. Dennison: cited in C. H. Townes and A. L. Shawlow: Microwave Spectroscopy of Gases, Mc Graw-Hill (1955) p. 324.
8) E. V. Ivash and D. M. Dennison: J. Chem. Phys. **21** (1953) 1804.
9) P. Venkateswarlu and W. Gordy: J. Chem. Phys. **23** (1955) 1200.
10) T. Kojima and T. Nishikawa: to be published.
11) D. Kivelson: J. Chem. Phys. **23** (1955) 2230.

---

JOURNAL OF THE PHYSICAL SOCIETY OF JAPAN Vol. 11, No. 7, JULY, 1956

# On the Eigenvalue Problem in Terms of a Complete Set of the Casimir Operators

By Hajime NARUMI

*Yukawa Laboratory, Institute for Chemical Research, Kyoto University*

(Received December 14, 1955)

The existence of the group of contact transformations, regarded as the so-called continuous Schrödinger group whose elements commute with Hamiltonian, is intimately related not only to the problem of degeneracy, as shown by Jauch and Hill, but also to the problem of quantization. In the present paper, it is shown that on the basis of representations of the Lie ring generated by the operators which have a certain definite correspondence with a set of independent integrals of the equations of motion in Newtonian mechanics, an energy eigenvalue problem can be constructed in terms of a complete set of the Casimir operators. It is further pointed out that this quantization procedure is, in spite of various restrictions, applicable to quantum-mechanical systems having the continuous Schrödinger group, and then the degree of degeneracy in regard to the angular momentum can be obtained simultaneously.

## § 1. Introduction

It is well known that the degeneracy of the energy spectra in quantum mechanics is essentially related not only to the symmetry properties of the Schrödinger equation which are associated with the symmetry operators of the elements of the rotation-reflection group and of the symmetric group of the permutations of identical particles in many body problems, but also to the existence of the continuous group generated by contact transformations under which Hamiltonian is invariant. The existence of the latter Schrödinger group was shown by Fock[1] who derived the Balmer formula of the hydrogen like atom by identifying the Schrödinger equation in the momentum space with an integral equation for spherical harmonics in four dimensions, and Bargmann[2] gave the formal relationship of the Lenz-Pauli integral with the above group for the same system. By generalizing their considerations, Jauch and Hill[3] further developed the relation between the general contact-transformation theory and the problem of degeneracy. In fact it was shown that this type of degeneracy was based upon the structure of the continuous Schrödinger group, that is to say, the degree of degeneracy of the energy level in question was nothing but the degree of each representation of the finite transformations (generated by a certain unitary operator with the finite parameters) of the group, where the eigenfunctions belonging to each level were regarded as the bases.

Originally, however, the problem of degeneracy is in close relation with the eigenvalue problem in quantum mechanics, which is also related intimately to the existence of the transformation group in the corresponding classical theory. In the present paper, therefore, we shall first comment briefly on the structure and representations of the Lie ring generated by the operators, which commute with Hamiltonian and which have a certain definite correspondence with the independent integrals of the equations of motion in classical mechanics; moreover it will be shown that an eigenvalue problem as well as the degeneracy problem can be developed in terms of a complete set of operators, which were introduced by Casimir⁹⁾ in order to prove the full reducibility of the representation of a semi-simple Lie group.

For example, the problem of spin degeneracy in the system of several identical particles⁴⁾, however, belongs to the problem of the former Schrödinger group mentioned above, and on the contrary the dynamical problem of the spin angular momentum of a particle cannot be derived from the present type of quantization procedure in non-relativistic approximation, since the spin of the particle is substantially one of the quantities peculiar to quantum mechanics, having no classical correspondence, while the present theory rests on the basis of the method of *classical analogy* in itself. Accordingly such a problem will possibly be brought in our theory by introducing the model of a rotating rigid body⁵⁾.

Nevertheless we have to point out with Jauch and Hill that the classical problems which lend themselves to the quantization procedure are restricted in various points. For example, we have no general method for finding the classical integrals mentioned above, and further there is such a case as follows: the correspondence between contact transformations in classical and quantum mechanics is ambiguous, as for an example of the two-dimensional anisotropic oscillator. With all these restrictions, however, it will be shown that our procedure is applicable in general to quantum-mechanical problems, as far as it is possible to find the continuous Schrödinger group for a given system.

## § 2. The Classical Integrals and the Continuous Schrödinger Group

Under the necessity of developing our theory we must begin with a brief argument of the transformation theory of Newtonian mechanics. Suppose now that the linearly independent integrals, called *classical integrals*, of the equations of motion of the form

$$F_\lambda(q_k;\,p_k)=\text{ a constant}\qquad(\lambda=1,2,\cdots,r;\ k=1,2.\cdots,n)\tag{2.1}$$

on the energy surface for a given Hamilton function $H(q_k;p_k)$ could be obtained, where $n$ is the degree of freedom of this system, then each $F_\lambda$ can be used to generate a one-parameter group of contact transformations, where the $q$'s and $p$'s are the coordinates and the conjugate momenta for the system and we restrict ourselves to the problem in which the integrals are not explicit functions of the time.

Let us consider the following infinitesimal transformations:

$$\left.\begin{aligned} p_k' &= p_k+\sum_{\lambda=1}^{r}\eta_\lambda(F_\lambda,p_k)=p_k-\sum_{\lambda=1}^{r}\eta_\lambda\frac{\partial F_\lambda}{\partial q_k}\\ q_k' &= q_k+\sum_{\lambda=1}^{r}\eta_\lambda(F_\lambda,q_k)=q_k+\sum_{\lambda=1}^{r}\eta_\lambda\frac{\partial F_\lambda}{\partial p_k}\end{aligned}\right\}\tag{2.2}$$

generated by the $rF_\lambda$'s; then they constitute a set of contact transformations due to the invariancy of the Poisson bracket made from $p'$ and $q'$. Thereupon introducing the infinitesimal operators of contact transformations

$$X_\lambda=\sum_{k=1}^{n}\left(\frac{\partial F_\lambda}{\partial p_k}\frac{\partial}{\partial q_k}-\frac{\partial F_\lambda}{\partial q_k}\frac{\partial}{\partial p_k}\right),\tag{2.3}$$

these operators generate a *r-parameter Lie group* under the complete integrability condition including the first fundamental theorem of Lie, and then they satisfy the second fundamental theorem:

$$X_\lambda X_\mu-X_\mu X_\lambda=\sum_{\nu=1}^{r}c_{\lambda\mu}{}^{\nu}X_\nu\,.\tag{2.4}$$

By making use of the Jacobi identity, the theorem (2.4) is reduced to the following form by the Poisson bracket notation:

$$[F_\lambda, F_\mu] = \sum_{\nu=1}^{r} c_{\lambda\mu}{}^{\nu} F_\nu \,, \qquad (2.5)$$

where the $r^3$ coefficients $c_{\lambda\mu}{}^{\nu}$ are called the *structure constants* of the Lie group, and they have the following relation, called the third fundamental theorem:

$$\left.\begin{aligned} & c_{\lambda\mu}{}^{\nu} + c_{\mu\lambda}{}^{\nu} = 0 \,, \\ & \sum_{\sigma=1}^{r} (c_{\lambda\mu}{}^{\sigma} c_{\sigma\nu}{}^{\tau} + c_{\mu\nu}{}^{\sigma} c_{\sigma\lambda}{}^{\tau} + c_{\nu\lambda}{}^{\sigma} c_{\sigma\mu}{}^{\tau}) = 0 \,. \end{aligned}\right\} \qquad (2.6)$$

It is clear that the relation (2.5) is the necessary and sufficient condition that (2.2) generates the group of contact transformations, and it is shown that the structure constants of the group are at most functions of the total energy, as far as related to the contact transformation group on the energy surface. Strictly speaking, the relation (2.5) is the condition of a group germ (a local group), but in case the integrals are defined within a closed region on the energy surface, the group germ may be capable of blossoming fourth into a full group. Moreover the energy surface in question is either closed or unbounded according to the energy region. The former group is a compact Lie group, while the latter is non-compact, but it can be regarded as locally compact.

Now let us transfer the above considerations upon the classical contact transformations to the corresponding quantum-mechanical unitary transformations; then we have the problem of determining quantum-mechanical operators $\boldsymbol{F}_\lambda$ which correspond to the classical integrals $F_\lambda$. It is possible under the following well-known procedure to get over this problem: the $\boldsymbol{F}_\lambda$'s must be the Hermite operators, so that it may be necessary for them to be well-ordered or to be symmetrized in $p$'s and $q$'s, and $F_\lambda$ must be regarded as the limiting case of $\boldsymbol{F}_\lambda$ when $\hbar$ tends to zero. But in general cases the transition to quantum operators is not unique. As is pointed out by Dirac[6], the method of defining general functions of non-commuting observables in quantum mechanics has a certain limitation: if the generating function of the transformation is not real, the analogy between classical and quantum contact transformations is not perfect. In fact we are confronted with such difficulty in a simple example of the two-dimensional anisotropic oscillator: there exists a group of contact transformations which is isomorphic with the three-dimensional rotation group, but the corresponding Schrödinger group cannot be found directly. In such a case the limiting relation (in case $\hbar$ tends to zero) of the Lie group comes into question, or it may be originated in the fact that $\boldsymbol{F}_\lambda$ $(\lambda=1, 2, \cdots, r)$ alone cannot constitute a complete set, but more other independent integrals must be found quantum-mechanically.

In spite of these circumstances the integral property of the $\boldsymbol{F}_\lambda$'s is expressed by their commutability with Hamiltonian, and on the basis of the well-known correspondence relation of the Poisson bracket between classical and quantum mechanics, we can obtain the following quantum operator relation on the analogy of the classical form (2.5):

$$[\boldsymbol{F}_\lambda, \boldsymbol{F}_\mu] = -i\hbar \sum_{\nu=1}^{r} c_{\lambda\mu}{}^{\nu} \boldsymbol{F}_\nu \,, \qquad (2.7)$$

where the structure constants $c_{\lambda\mu}{}^{\nu}$ may be operators at most depending on the Hamiltonian alone, and in principle they need not be identical with the classical constants. If there is no ambiguity with respect to an order for non-commuting observables, it is expected that both the structure constants in (2.5) and (2.7) are clearly the same. Consequently all the operators $\boldsymbol{F}_\lambda$ are also independent of each other, and they have an isomorphic correspondence to a set of the classical integrals. In fact this is realized in the example of the hydrogen atom or the isotropic harmonic oscillator, and in case the classical contact transformations generate a one-parameter group, the one-to-one correspondence can be formally established between them, since there is no necessity for having respect to the commutation relation. In this way the Schrödinger group, whose elements commute with Hamiltonian, can be given as a continuous group of contact transformations generated by the integral operator $\boldsymbol{F}_\lambda$ satisfying the relation (2.7).

## § 3. The Lie Ring Generated by the Integral Operators

The so-called Heisenberg ring[7] made from a set of the power series of the non-commuting operators $\boldsymbol{p}_k$ and $\boldsymbol{q}_k$ $(k=1, 2, \cdots, n)$ can be regarded at same time as a function group* with infinite order or Lie ring generated by the operations of the Poisson bracket. Our problem is, however, restricted to dynamical systems expressed by a definite Hamiltonian, so the Lie ring $\mathfrak{R}_F$ generated by the integral operators $\boldsymbol{F}$ which satisfy the relation of the Poisson bracket

$$[\boldsymbol{H}, \boldsymbol{F}] = 0 \tag{3.1}$$

has a finite order. Therefore such ring $\mathfrak{R}_F$ is nothing but a permissible sub-ring of the full Heisenberg ring with common operator domain. On the other hand, the classical analogue

$$[H, F] = \sum_{k=1}^{n} \left( \frac{\partial H}{\partial p_k} \frac{\partial F}{\partial q_k} - \frac{\partial H}{\partial q_k} \frac{\partial F}{\partial p_k} \right) = 0 \tag{3.2}$$

being the first order homogeneous differential equation, there should be the $(2n-1)$ independent integrals (not always linearly independent, but having no functional relation with each other), which also generate a function-group, or a sub-ring of the full commutative ring $\mathfrak{R}_K$. Besides it is understood that the ring $\mathfrak{R}_K$ is not always isomorphic with the Heisenberg ring from the fact mentioned in the preceding section.

For our purpose let us consider a function-group $\mathfrak{G}_F$ regarding the ring $\mathfrak{R}_F$ as a sub-ring, then the order $r$ of $\mathfrak{R}_F$ is never lower than $(2n-1)$, since linearly independent elements in $\mathfrak{R}_F$ is not always independent of each other in $\mathfrak{G}_F$; furthermore the Lie ring $\mathfrak{R}_F$ is not necessarily unique as a sub-ring of $\mathfrak{G}_F$. Actually in case of the $n$-dimensional isotropic harmonic oscillator as shown in the appendix of this paper there exists the Lie ring regarded as the generator not only of the $n$-dimensional unimodular unitary group, but also of the $(n+1)$-dimensional rotation group.

According to the fundamental theorem of the Lie ring, it should be resolved into a direct sum of the maximal soluble ideal and the semi-simple Lie ring**, but due to the hermiticity of the operators the former must be Abelian. As the irreducible representation of the Abel ring (the commutative ring) has the degree of one, the degree of the irreducible representation of $\mathfrak{R}_F$ cannot be higher than that of the irreducible representation of the semi-simple sub-ring in consequence of the existence of this ideal. Accordingly our attention may be focussed upon the semi-simple Lie ring for our subject.

## § 4. The Representation of the Semi-Simple Lie Group and a Complete Set of the Casimir Operators

Considering the representation space of the semi-simple Lie ring, by the reduction to the eigenspace of a regular element every irreducible representation of $\mathfrak{R}_F$ is uniquely determined by its *highest weight* $\boldsymbol{m}=(m_1, m_2, \cdots m_l)$, $l$ the rank of the above ring. It was shown by Weyl under the unitary restriction that the representations of every semi-simple Lie group are fully reducible, while in order to extend a purely infinitesimal proof of the full reducibility for the three-dimensional rotation group to any semi-simple Lie group, Casimir introduced the operator$^{9)}$

$$\boldsymbol{G} = \sum_{\lambda,\mu} g^{\lambda\mu} \boldsymbol{F}_\lambda \boldsymbol{F}_\mu = \sum_{\lambda,\mu} g_{\lambda\mu} \boldsymbol{F}^\lambda \boldsymbol{F}^\mu \,, \tag{4.1}$$

where

$$g_{\lambda\mu} = \sum_{\alpha,\beta=1} c_{\lambda\beta}{}^{\alpha} c_{\mu\alpha}{}^{\beta} \,, \tag{4.2}$$

and as $\det(g_{\lambda\mu}) \neq 0$ is the necessary and sufficient condition for the semi-simplicity, $(g^{\lambda\mu}) = (g_{\lambda\mu})^{-1}$ can be determined from (4.2). Besides the following theorems for the Casimir operator are easily proved: this operator does not depend upon any selection of the bases in the representation space, and commutes with every element $\boldsymbol{F}_\lambda$. Then by the Schur lemma for the irreducible representation the above operator can be reduced to a scalar matrix in an irreducible space, and a highest weight determines an eigenvalue of the Casimir operator:

$$G' = (\boldsymbol{mm}) + \sum_{\alpha}{}^{+} (\alpha \boldsymbol{m}) \,, \tag{4.3}$$

where the summation extends over positive roots only. But conversely an eigenvalue of $\boldsymbol{G}$ cannot always determine a highest weight uniquely.

To solve this problem we must construct a complete set of the $l$ operators which are commutative with every operator of $\mathfrak{R}_F$ and whose eigenvalues characterize the irreducible representations. In fact these operators satisfy the relation

---

* If all the Poisson brackets made from $r$ functions of $2n$ independent variables $(q_k;\, p_k)$ can be expressed as functions of the $r$ functions, these functions are called to form a function group.

** An ideal $\mathfrak{R}'=[\mathfrak{R}, \mathfrak{R}]$ for the sub-ring $\mathfrak{R}'$ of the Lie ring $\mathfrak{R}$ is said to be *soluble*, if $[\mathfrak{R}', \mathfrak{R}']=\mathfrak{R}''$, $\ldots, \mathfrak{R}^{(n)}=0$, its maximal one is called the *radical*, and the Ling $\mathfrak{R}$ which the radical $= 0$ is nothing but the *semi-simple* Lie ring.

$$[F_\lambda, F^\mu]\frac{\partial G}{\partial F^\mu}=c_\lambda{}^{\mu\nu}F_\nu\frac{\partial G}{\partial F^\mu}=c_{\nu\lambda}{}^\mu F^\nu\frac{\partial G}{\partial F^\mu}=0\ , \tag{4.4}$$

then due to the invariants of the adjoint group a complete set of the operators $G_1, G_2, \cdots, G_l$ can be obtained, and by making choice of an eigenvector with respect to a highest weight each eigenvalue

$$G_i'=f_i(m_1, m_2,\cdots, m_l),\ (i=1, 2,\cdots, l) \tag{4.5}$$

characterizes an irreducible representation, determined from possible values* of the highest weight $(m_1, m_2, \cdots, m_l)$.

In this way we can find the irreducible representations mathematically possible, but can all Casimir operators be ever expressed in terms of Hamiltonian $H(q_k, p_k)$? For this question we will find the following theorem:

Every Casimir operator is commutative with every element of the Lie ring $\mathfrak{R}_F$, but is not always a constant of motion. Therefore let $p$ be the number of constants of motion in the set of the $l$ operators, then the highest weight of an irreducible representation which can actually realize is given by $(m_1, m_2, \cdots, m_p, 0,\cdots, 0)$.

## § 5. Energy Eigenvalues and Their Degrees of Degeneracy

The set of Casimir operators derived from each subring of the semi-simple Lie ring $\mathfrak{R}_F$ makes a complete set of observables according to Dirac's terminology. Therefore this fact means that it is possible by the canonical transformation to transform from $q$-diagonal representation to $G$-diagonal representation, where Hamiltonian has necessarily a certain functional relation with the Casimir operators. As the latter are used to give a definite value (a scalar matrix) in each representation space, energy eigenvalues can be found out from this functional relation, and at the same time the degrees of degeneracy of each energy level can be settled by the highest weights mentioned above. This will be shown by the following examples.

1) *The two-dimensional isotropic harmonic oscillator*

For the Hamilton function of this system given by

$$H=\frac{1}{2m}(p_1{}^2+p_2{}^2)+\frac{k}{2}(q_1{}^2+q_2{}^2) \tag{5.1}$$

the following three classical integrals can be found readily:

$$\left.\begin{aligned}F_1&=\frac{1}{2}(q_1p_2-q_2p_1)\\ F_2&=\frac{1}{4\sqrt{mk}}\{(p_1{}^2-p_2{}^2)+mk(q_1{}^2-q_2{}^2)\}\\ F_3&=\frac{1}{2\sqrt{mk}}(p_1p_2+mkq_1q_2)\end{aligned}\right\} \tag{5.2}$$

The Poisson bracket relation generated by the above integrals is

$$[F_\lambda, F_\mu]=F_\nu,$$
$$(\lambda, \mu, \nu\text{: cyclic between 1, 2, and 3}). \tag{5.3}$$

As each $F_\lambda$ does not include any term of the product $p_kq_k$, there is no ambiguity with respect to an order of non-commuting observables in the transition to quantum mechanics. Then the commutation relation is given by

$$[F_\lambda, F_\mu]=-i\hbar F_\nu\ , \tag{5.4}$$

where the structure constants of the Lie group in quantum theory are identical with classical one, and the Schrödinger group of this system is isomorphic with the two-dimensional unimodular unitary group as well as the three-dimensional rotation group.

Now by expressing the Casimir operator in terms of the Hamiltonian $H$ we obtain

$$G=-\frac{1}{2}\sum_{\lambda=1}^{3}F_\lambda{}^2=\frac{1}{4}\{(H/h\nu)^2-1\} \tag{5.5}$$

with the fundamental frequency $\nu=\sqrt{k/m}/2\pi$, where the eigenvalue of $G$ is generally given by $j(j+1)$, provided $j=n/2\,(n=0, 1, 2, \cdots)$, since the Casimir operator of this case is the ordinary one introduced for the three-dimensional orthogonal group. Then

$$G'=\frac{n}{2}\left(\frac{n}{2}+1\right)=\frac{1}{4}\{(H'/h\nu)^2-1\} \tag{5.6}$$

where $H'$ means the energy eigenvalue. Consequently

$$H'=(n+1)h\nu \tag{5.7}$$

can be obtained with the degree of degeneracy, $2j+1=n+1$, of each energy level, which is plain also from the consideration of the Schrödinger group of this system mentioned above.

---

* Whether it takes every integral value or every odd half integral value depends on the property of the semi-simple Lie ring.

2 ) *The hydrogen like atom*

The six integral operators commutative with the non-relativistic Hamiltonian

$$\boldsymbol{H}=\boldsymbol{p}^2/2m+Ze^2/r^2 \qquad (5.8)$$

of this system are, as well-known, the Lenz-Pauli vector integral

$$\boldsymbol{A}=\frac{1}{2mZe^2}(\boldsymbol{M}\times\boldsymbol{p}-\boldsymbol{p}\times\boldsymbol{M})+\frac{\boldsymbol{r}}{r} \qquad (5.9)$$

in addition to the orbital angular momentum operator $\boldsymbol{M}=\boldsymbol{r}\times\boldsymbol{p}$, where $m$, $\boldsymbol{p}$, and $e$ are the electron mass and momentum, and the elementary charge, respectively; $r$, the distance between a given nucleus and electron; $Ze$, the nuclear charge. For the negative energy state the Balmer formula was formerly derived by Hulthèn¹¹⁾ using the commutation relation of the above integral (5.9) and it was already shown that the Schrödinger group of this system was isomorphic with the four-dimensional rotation group, while from our point of view the set composed of the above six operators might be regarded as a semi-simple group of the rank 2, therefore there must exist a set of two Casimir operators. But in this case it can be found that only one Casimir operator of these has the following functional relation with the Hamiltonian:

$$\boldsymbol{G}=-\tfrac{1}{2}\sum_{\lambda=1}^{4}\boldsymbol{F}_\lambda{}^2=-(Z^2e^4m/2\hbar^2H)-1\,. \qquad (5.10)$$

Each highest weight characterizing the irreducible representations of the Lie group is $(0,0),(1,0),\cdots,(k,0),\cdots$, and then the degrees of their representations are $1^2, 2^2, \cdots, (k+1)^2, \cdots$, respectively. The eigenvalue of the Casimir operator determined by a given highest weight $(k,0)$ must be given by $k(k+2)$, which is also connected with the eigenvalue of angular momentum in the four-dimensional Euclid space. Consequently by subtituting $n$ for $k+1$ the relation (5.10) can be reduced to

$$n^2-1=-(Z^2e^4m/2\hbar^2H_n')-1\ ,$$

or

$$H_n'=-Z^2e^4m/2\hbar n^2 \quad (n=1,2,\cdots)\ , \qquad (5.11)$$

which is the well known Balmer formula, and then each eigenvalue is accompanied with the degree of degeneracy $(k+1)^2=n^2$ as mentioned above.

On the other hand it is known that the Schrödinger group of the positive energy state of this system is isomorphic with the four-dimensional Lorentz group. In the case of the continuous eigenvalue we must find an infinite continuous (unitary) representation of a non-compact Lie group, which will be developed in the subsequent paper¹²⁾.

## § 6. Concluding Remarks

Apart from such various restrictions as already mentioned above, our quantization procedure based on classical contact transformations is applicable to any quantum-mechanical systems, as far as the continuous Schrödinger group can be found. One of our remaining problems is the consideration of the correspondence relation between classical and quantum contact transformations, where the problem of the two-dimensional anisotropic oscillator will be also treated, although in some fundamental problems the above correspondence relation can be undoubtedly obtained. In relation to this point some considerations about the Schrödinger group of the $n$-dimensional isotropic oscillator will be added in the following appendix.

One of further applications of our procedure is to the perturbation theory, where the problem of the splitting of degenerate energy levels by the addition of a perturbed term to the original Hamiltonian can be settled, provided that the perturbed Hamiltonian is commutative with $F_\lambda\,(\lambda=1,2,\cdots,q<r)$ of a sub-ring of $\Re_F$. As a special case let us consider the perturbed term which has a symmetry expressed by a finite or continuous point group, such as molecular and crystalline fields, then it can be shown generally that the original representation space with a certain degree is resolved at the appearance of the term into several direct-sum spaces of irreducible representations of the point group with lower degree in general. In fact this reduction can be completed by making use of the group characters. For example, the term splitting by an applied or inner field in atoms, molecules, and crystals is possible to be formulated from this general point of view.

In this way it can be pointed out that the present method has the possibility to find the energy eigenvalue accompanied with the corresponding degree of degeneracy in term of a complete set of the Casimir operators for all difficulties on the basis of the method of classical analogy.

In conclusion the author should like to express his cordial thanks to Professor H.

Yukawa and Professor M. Kotani for their kind interest and continual encouragement, and also to Mr. S. Matsuo for his served verification. The present work was supported in part by the Grant for Scientific Researches from the Education Ministry of Japan.

## Appendix

*The Schrödinger group of the n-dimensional isotropic oscillator*

The integral operators derived from the classical integrals are commutative with the Hamiltonian

$$\boldsymbol{H}=-\tfrac{1}{2}\sum_{k=1}^{n}(\boldsymbol{p}_k{}^2+\beta\boldsymbol{q}_k{}^2) \tag{A.1}$$

for a reduced constant $\beta$, and they can be given by

$$\left.\begin{aligned}
\boldsymbol{F}_{1,\lambda}{}^{\lambda'} &= \frac{1}{i\hbar}(\boldsymbol{q}_{\lambda'}\boldsymbol{p}_\lambda-\boldsymbol{q}_\lambda\boldsymbol{p}_{\lambda'})\\
\boldsymbol{F}_{2,\lambda}{}^{\lambda'} &= \frac{1}{i\hbar\sqrt{\beta}}(\boldsymbol{p}_{\lambda'}\boldsymbol{p}_\lambda+\beta\boldsymbol{q}_{\lambda'}\boldsymbol{q}_\lambda)\\
\boldsymbol{F}_{3,\lambda} &= \frac{1}{2i\hbar\sqrt{\beta}}\{(\boldsymbol{p}_{\lambda'}{}^2-\boldsymbol{p}_\lambda{}^2)+\beta(\boldsymbol{q}_{\lambda'}{}^2-\boldsymbol{q}_\lambda{}^2)\}
\end{aligned}\right\} \tag{A.2}$$

where $1\leqq\lambda'\leqq\lambda-1\ (\lambda=1, 2, \cdots, n)$. Now let $\mathfrak{R}_\lambda$ be a set of all the integrals with no larger suffices than $\lambda$, then it can be shown that $\mathfrak{R}_\lambda$ is isomorphic with a $\lambda$-dimensional unimodular unitary group, whose elements are a set of operators generated by infinitesimal transformations.

The commutation ralations of the operators $\boldsymbol{F}^{\lambda'}_{1,\lambda}$, $\boldsymbol{F}^{\lambda'}_{2,\lambda}$ and $\boldsymbol{F}_{3,\lambda}$ $(2\leqq\eta, \iota, \kappa\leqq\lambda;\ 1\leqq\eta'\iota'\leqq\eta-1, \iota-1)$ can be obtained as follows:

$$\left.\begin{aligned}
[\boldsymbol{F}^{\eta'}_{1\eta}, \boldsymbol{F}^{\iota'}_{1\iota}] &= \delta_{\eta\iota}\boldsymbol{F}^{\iota'}_{1\iota'}+\delta_{\eta'\iota'}\boldsymbol{F}^{\iota}_{2\iota}+\delta_{\eta\iota'}\boldsymbol{F}^{\iota}_{2\eta'}\\
&\quad+\delta_{\eta'\iota}\boldsymbol{F}^{\iota'}_{1\eta},\\
\boldsymbol{F}^{\eta}_{1\eta} &= 0\ ,\\
[\boldsymbol{F}^{\eta'}_{2\eta}, \boldsymbol{F}^{\iota'}_{2\iota}] &= \delta_{\eta\iota}\boldsymbol{F}^{\eta'}_{2\iota'}+\delta_{\eta'\iota'}\boldsymbol{F}^{\eta}_{1\iota}+\delta_{\eta\iota'}\boldsymbol{F}^{\iota'}_{1\iota}\\
&\quad+\delta_{\eta'\iota}\boldsymbol{F}^{\eta}_{1\iota'},\\
[\boldsymbol{F}_{3\eta}, \boldsymbol{F}_{3\iota}] &= 0\ ,\\
[\boldsymbol{F}^{\eta'}_{1\eta}, \boldsymbol{F}^{\iota'}_{2\iota}] &= \delta_{\eta'\iota'}\boldsymbol{F}^{\eta}_{2\iota}-\delta_{\eta\iota}\boldsymbol{F}^{\eta'}_{2\iota'}-\delta_{\eta'\iota}\boldsymbol{F}^{\eta}_{2\iota'}\\
&\quad-\delta_{\eta\iota'}\boldsymbol{F}^{\eta'}_{2\iota},\\
\boldsymbol{F}^{\iota}_{2\eta} &= \boldsymbol{F}^{\eta}_{2\iota}\ ,\\
\boldsymbol{F}^{\eta}_{2\eta}-\boldsymbol{F}^{\eta}_{2\iota} &= 2(\boldsymbol{F}_{3,\eta+1}+\boldsymbol{F}_{3,\eta+2}+\cdots+\boldsymbol{F}_{3\iota}),\ (\eta<\iota)\\
[\boldsymbol{F}^{\eta'}_{1\eta}, \boldsymbol{F}_{3\iota}] &= \delta_{\eta\iota}\boldsymbol{F}^{\eta'}_{2\iota}-\delta_{\eta\iota-1}\boldsymbol{F}^{\eta'}_{2\iota-1}-\delta_{\eta'\iota}\boldsymbol{F}^{\eta}_{2\iota}\\
&\quad+\delta_{\eta'\iota-1}\boldsymbol{F}^{\eta}_{2\iota-1}\ ,\\
[\boldsymbol{F}^{\eta'}_{3\eta}, \boldsymbol{F}_{3\iota}] &= -\delta_{\eta\iota}\boldsymbol{F}^{\eta'}_{1\iota}+\delta_{\eta\iota-1}\boldsymbol{F}^{\eta'}_{2\iota-1}-\delta_{\eta'\iota}\boldsymbol{F}^{\eta}_{1\iota}\\
&\quad+\delta_{\eta'\iota-1}\boldsymbol{F}^{\eta}_{2\iota-1},
\end{aligned}\right\} \tag{A.3}$$

where $\delta$ means the Kronecker delta. As the suffices of the right sides are never larger than those of the left sides in the above commutation relations, it can be understood that $\mathfrak{R}_\lambda$ constitutes the bases of a Lie group. On the other hand let us take two types of matrix, $M^{r'}_{1r}$ and $M^{r'}_{2r}$, whose elements are $+1$ and $-i$ for the $r$-th row and the $r'$-th column, and $-1$ and $+i$ for the $r'$-th row and the $r$-th column, respectively, and 0 for all the other remaining elements, the last one $M_{3r}$, whose elements are $+i$ for the $r$-th row and column, and $-i$ for the $(r-1)$-th row and column, and 0 for all the other elements. Then a set of $(r^2-1)$ matrices with no larger suffices than $\lambda$:

$$\begin{aligned}
&M^1_{12};\ M^1_{22};\ M_{32}\ ,\\
&M^1_{13};\ M^2_{13};\ M^1_{23}, M^2_{23};\ M_{33}\\
&\qquad\cdots\cdots\\
&M^1_{1\lambda}, M^2_{1\lambda}, \cdots, M^{\lambda-1}_{1\lambda};\ M^1_{2\lambda}, M^2_{2\lambda}\cdots, M^{\lambda-1}_{2\lambda}; M_{3\lambda}
\end{aligned} \tag{A.4}$$

constitutes the characteristic matrices of the $\lambda$-dimensional unimodular unitary group. It can be shown readily that the commutation relations constructed by all of the above matrices $\mathfrak{R}_\lambda'$ are equivalent to (A.3). Therefore $\mathfrak{R}_\lambda'$ has the same structure constants as $\mathfrak{R}_\lambda$, and then we can understand that the group generated by $\mathfrak{R}_\lambda$ is isomorphic with the $(\lambda^2-1)$-parameter $\lambda$-dimensional unimodular unitary group. If we substitute $n$ for $\lambda$, it can be found that the Schrödinger group of the $n$-dimensional isotropic oscillator is isomorphic with the $(n^2-1)$-parameter $n$-dimensional unimodular unitary group as well as the $(n+1)$-dimensional rotation group.

## References

1) V. Fock: Zeits. f. Phys. **98** (1935) 145.
2) V. Bargmann: ibid. **99** (1936) 578.
3) J. M. Jauch and E. L. Hill: Phys. Rev. **57** (1940) 641.
4) H. Narumi: Prog. Theor. Phys. **3** (1948) 202.
5) N. Rosen: Phys. Rev. **82** (1951) 621.
6) P. A. M. Dirac: Rev. Mod. Phys. **17** (1949) 195.
7) G. Falk: Zeits. f. Phys. **130** (1951) 51, **131** (1952) 470.
8) H. Narumi and T. Nakau: Bull. Inst. Chem. Res. Kyoto Univ. **26** (1951) 26; **27** (1951) 29.
9) H. Casimir: Proc. Roy. Acad. Amsterdam **34** (1931) 144.
H. Casimir and B. L. van der Waerden: Math. Ann. **111** (1935) 1.
10) G. Racah: Rendiconti dell'Academia Nazionale dei Lincei **8** (1950) 108; Lectures on *Group Theory and Spectroscopy* (unpublished).
11) L. Hulthèn: Zeits. f. Phys. **86** (1933) 21.
12) H. Narumi and S. Matsuo: Bull. Inst. Chem. Res. Kyoto Univ. **33** (1955) 265.

JOURNAL OF THE PHYSICAL SOCIETY OF JAPAN Vol. 11, No. 7, JULY, 1956

# A Sphere Theorem on the Stokes Equation for Axisymmetric Viscous Flow

By Hidenori HASIMOTO

*Department of Physics, Faculty of Science, University of Tokyo*

(Received April 5, 1956)

A theorem is presented which gives the perturbation stream function $\tilde{\Psi}(r, \theta)$ when a sphere $(r=a)$ is introduced into an unlimited viscous fluid in axisymmetric motion obeying the Stokes equation, of which the stream function is $\Psi(r, \theta)$, where $(r, \theta, \varphi)$ are the polar coordinates.

$\tilde{\Psi}(r, \theta)$ is given by

$$\tilde{\Psi}(r, \theta)=\tilde{\Psi}_1(r, \theta)+a^2\tilde{\Psi}_2(r, \theta) ,$$

$$\tilde{\Psi}_1(r, \theta)=\left(a-\frac{r^2}{a}\right)\frac{\partial}{\partial R}\phi_1(R, \theta)-\left(\frac{3}{2}\frac{r}{a}-\frac{1}{2}\frac{r^3}{a^3}\right)\phi_1(R, \theta) ,$$

$$\tilde{\Psi}_2(r, \theta)=\left(a-\frac{r^2}{a}\right)\frac{\partial}{\partial R}\phi_2(R, \theta)-\left(\frac{1}{2}\frac{r}{a}+\frac{1}{2}\frac{r^3}{a^3}\right)\phi_2(R, \theta) ,$$

$$\phi_2(r, \theta)=-\frac{\sin\theta}{4\sqrt{r}}\int_0^r \sqrt{r}\,\omega(r, \theta)\,dr , \quad \phi_1(r, \theta)=\Psi(r, \theta)-r^2\phi_2(r, \theta) ,$$

where $\omega$ is the vorticity, and $R=a^2/r$.

This gives the stream sheets directly without recourse to manipulation of spherical harmonics, and is very simple when $\Psi(r, \theta)$ is irrotational, i.e. $\omega=\phi_2=0$.

As examples of the applications of this theorem, the stream functions for uniform flow, source flow and parabolic flow past a sphere are derived.

## § 1. Introduction

Let $\Psi(r, \theta)$ be the Stokes stream function for an unlimited viscous fluid in axisymmetric motion, where $(r, \theta, \varphi)$ are the polar coordinates. The axis of symmetry is taken to be the polar axis $(\theta=0, \pi)$. We also use the Cartesian coordinates $(x, y)$ in the meridian plane given by $x=r\cos\theta$ and $y=r\sin\theta$ $(0\leqq\theta\leqq\pi,\ y\geqq0)$.

If we introduce a sphere whose equation is $r=a$, the flow is disturbed, and its stream function becomes

$$\Psi(r, \theta)+\tilde{\Psi}(r, \theta) . \qquad (1.1)$$

The undisturbed flow $\tilde{\Psi}(r, \theta)$ may contain singularities, but we assume that they all lie outside the sphere $r=a$.

In this note we want to give formulae to determine the perturbed term $\tilde{\Psi}$ in terms of an arbitray $\Psi$, assuming the Stokes equation of motion to be valid in the field of flow.

The corresponding formulae for the irrotational motion of an inviscid fluid are well-known, as the sphere theorem of Weiss(1) (for the velocity potential) and Butler(2) (for the Stokes stream function). The circle theorem of Milne-Thomson(3) for the complex potential in the two dimensional flow is also famous.

In the case of a viscous fluid we know a very interesting general formula due to Faxén(4), which asserts that the force $\boldsymbol{F}$ on a sphere placed in any kind of unlimited steady flow is expressed by

$$\boldsymbol{F}=6\pi\mu a\boldsymbol{V}_0+\pi a^3(\mathrm{grad}\,p)_0 , \qquad (1.2)$$

where $\mu$ is the viscosity, and $\boldsymbol{V}_0$ and $(\mathrm{grad}\,p)_0$ are respectively the velocity and the pressure gradient vectors of the undisturbed flow at the centre of the sphere. The Stokes equation is, of course, assumed to be valid.

On the other hand, the expressions for the flow field are very complicated on account of its generality and tensor forms.

By confining the problem to the axisymmetric motion and using the Stokes stream function, we obtain a very simple expression for the perturbed term, which has a close resemblance to Butler's formula, being simpler than Weiss' formula.

## § 2. Fundamental Equation and Its Solutions

Using the Stokes stream function $\Psi(r, \theta)$, the Stokes equation for the axisymmetric steady slow motion of an incompressible viscous fluid is expressed as follows[5]:

$$DD\Psi(r, \theta)=0\,, \tag{2.1}$$

or

$$D\zeta=0\,, \tag{2.1'}$$

where $D$ is an operator defined as:

$$D=\frac{\partial^2}{\partial r^2}+\frac{1}{r^2}M\,,$$

$$M=\sin\theta\,\frac{\partial}{\partial\theta}\left(\frac{1}{\sin\theta}\,\frac{\partial}{\partial\theta}\right), \tag{2.2}$$

and

$$\zeta(r, \theta)=-D\Psi(r, \theta)=r\sin\theta\,\omega(r, \theta)\,, \tag{2.3}$$

$\omega$ being the vorticity; $\partial v/\partial x-\partial u/\partial y$.

We want to call the solution $\psi(r, \theta)$ of the equation

$$D\psi(r, \theta)=\left(\frac{\partial^2}{\partial r^2}+\frac{1}{r^2}M\right)\psi=0 \tag{2.4}$$

"irrotational", because it represents the irrotational flow.

Introducing (2.4) and its derivative with respect to $r$ into the expression

$$\frac{\partial^2}{\partial r^2}\left(r\frac{\partial\psi}{\partial r}\right)=r\,\frac{\partial}{\partial r}\left(\frac{\partial^2\psi}{\partial r^2}\right)+2\,\frac{\partial^2\psi}{\partial r^2}\,, \tag{2.5}$$

we obtain

$$\frac{\partial^2}{\partial r^2}\left(r\,\frac{\partial\psi}{\partial r}\right)=\frac{2}{r^2}M\psi-\frac{1}{r}M\frac{\partial\psi}{\partial r}-\frac{2}{r^2}M\psi$$

$$=-\frac{1}{r^2}M\left(r\frac{\partial\psi}{\partial r}\right). \tag{2.6}$$

This gives the following lemma:

Lemma I. If $\psi$ is irrotational, $r(\partial\psi/\partial r)$ is also irrotational, i.e.

$$D\{r(\partial\psi/\partial r)\}=0\,. \tag{2.7}$$

Using this lemma we can prove the following lemma:

Lemma II. If $\psi$ is irrotational,

$$DD(r^2\psi)=0\,. \tag{2.8}$$

This can be easily proved by taking into account that

$$D(r^2\psi)=r^2\frac{\partial^2\psi}{\partial r^2}+4r\frac{\partial\psi}{\partial r}+2\psi+M\psi$$

$$=4r\frac{\partial\psi}{\partial r}+2\psi \tag{2.9}$$

and (2.7).

According to this lemma and lemma I, the solution $\Psi$ of (2.1) can be written in the form

$$\Psi=\psi_1+r^2\psi_2\,, \tag{2.10}$$

making use of $\psi_1$ and $\psi_2$ which satisfy the equations

$$D\psi_1=0 \quad\text{and}\quad D\psi_2=0\,. \tag{2.11}$$

We can find $\psi_1$ and $\psi_2$ from $\Psi$, as

$$\psi_2(r, \theta)=\frac{-1}{4\sqrt{r}}\int_0^r r^{-1/2}\zeta(r, \theta)dr\,, \tag{2.12}$$

$$\psi_1(r, \theta)=\Psi(r, \theta)-r^2\psi_2(r, \theta)\,. \tag{2.13}$$

We want to prove that $\psi_1$ and $\psi_2$ determined by (2.12) and (2.13) satisfy (2.11) when $\Psi$ satisfies (2.1). Now, using

$$\int_0^r r^{-1/2}M\zeta dr=-\int_0^r r^{3/2}\frac{\partial^2\zeta}{\partial r^2}dr$$

$$=-r^{3/2}\frac{\partial\zeta}{\partial r}+\frac{3}{2}\,r^{1/2}\zeta-\frac{3}{4}\int_0^r r^{-1/2}\zeta dr\,, \tag{2.14}$$

we obtain

$$D\psi_2=-\frac{1}{4}\left[\frac{1}{r}\,\frac{\partial\zeta}{\partial r}-\frac{3}{2}\,\frac{\zeta}{r^2}+r^{-5/2}\left(\frac{3}{4}+M\right)\right.$$

$$\left.\times\int_0^r r^{-1/2}\zeta dr\right]=0\,. \tag{2.15}$$

The proof for $\psi_1$ is obvious if we note (2.3), (2.9), (2.12) and

$$D(r^2\psi_2)=2\psi_2+4r\,\frac{\partial\psi_2}{\partial r}=-\zeta\,. \tag{2.16}$$

Here we also cite the following lemma, which was presented by Butler[2]:

Lemma III. If $\psi(r, \theta)$ is irrotational, then so is $r\psi(R, \theta)$, i.e.

$$D[r\psi(R, \theta)]=0\,, \tag{2.17}$$

where

$$R=a^2/r\,.$$

## § 3. The Sphere Theorem

Let all the singularities of $\Psi(r, \theta)$ be in the region external to the sphere $r=a$, and suppose that $\Psi=0$ at the origin.

Then, our sphere theorem for the disturbed flow by the introduction of the sphere $r=a$, asserts for the perturbation stream function $\tilde{\Psi}(r, \theta)$:

Theorem I. When the undisturbed flow $\Psi(r, \theta)$ is irrotational, i.e.

$$D\Psi(r, \theta)=0\,, \tag{3.1}$$

then

$$\tilde{\Psi}(r,\theta)=\left(a-\frac{r^2}{a}\right)\frac{\partial}{\partial R}\Psi(R,\theta)-\left(\frac{3}{2}\frac{r}{a}-\frac{1}{2}\frac{r^3}{a^3}\right)\Psi(R,\theta)\,, \qquad (3.2)$$

where

$$R=a^2/r\,.$$

Theorem II. When the undisturbed flow is rotational, i.e.

$$D\Psi(r,\theta)=-\zeta(r,\theta)\neq 0\,, \qquad (3.3)$$

then

$$\tilde{\Psi}(r,\theta)=\tilde{\Psi}_1(r,\theta)+a^2\tilde{\Psi}_2(r,\theta)\,, \qquad (3.4)$$

where

$$\tilde{\Psi}_1(r,\theta)=\left(a-\frac{r^2}{a}\right)\frac{\partial}{\partial R}\psi_1(R,\theta)-\left(\frac{3}{2}\frac{r}{a}-\frac{1}{2}\frac{r^3}{a^3}\right)\psi_1(R,\theta)\,, \qquad (3.5)$$

$$\tilde{\Psi}_2(r,\theta)=\left(a-\frac{r^2}{a}\right)\frac{\partial}{\partial R}\psi_2(R,\theta)-\left(\frac{1}{2}\frac{r}{a}+\frac{1}{2}\frac{r^3}{a^3}\right)\psi_2(R,\theta)\,, \qquad (3.6)$$

with

$$\psi_2(r,\theta)=-\frac{1}{4\sqrt{r}}\int_0^r r^{-1/2}\zeta(r,\theta)dr\,, \qquad (3.7)$$

$$\psi_1(r,\theta)=\Psi(r,\theta)-r^2\psi_2(r,\theta)\,. \qquad (3.8)$$

In these two cases, we can prove easily;

i) $DD\tilde{\Psi}(r,\theta)=0$ ,

ii) $\Psi+\tilde{\Psi}=0$ and $\partial[\Psi+\tilde{\Psi}]/\partial r=0$ at $r=a$,

iii) $\tilde{\Psi}(r,\theta)$ has no singularities in the region $\infty>r>a$,

iv) the perturbation velocity tends to zero as $r\to\infty$.

We shall begin with the proof of Theorem I,

i) Rearranging (3.2) with $R=a^2/r$ as

$$\tilde{\Psi}(r,\theta)=\frac{r}{a}\left\{R\frac{\partial}{\partial R}\Psi(R,\theta)-\frac{3}{2}\Psi(R,\theta)\right\}-\frac{r^2}{a^2}\left[\frac{r}{a}\left\{R\frac{\partial}{\partial R}\Psi(R,\theta)-\frac{1}{2}\Psi(R,\theta)\right\}\right], \qquad (3.9)$$

and using the Lemmas I, II, and III we see that $DD\tilde{\Psi}=0$, which proves i).

ii) At $r=a$, $R$ is equal to $a$, and $\partial R/\partial r=-1$. Then

$$\tilde{\Psi}(a,\theta)=-\Psi(a,\theta)\,, \qquad (3.10)$$

and

$$\left[\frac{\partial\tilde{\Psi}}{\partial r}\right]_{r=a}=-2\left[\frac{\partial}{\partial R}\Psi(R,\theta)\right]_{R=a}-\left[\frac{\partial}{\partial r}\Psi(R,\theta)\right]_{r=a}=-\left[\frac{\partial}{\partial r}\Psi(r,\theta)\right]_{r=a}\,, \qquad (3.11)$$

which prove ii).

iii) The singularity of $\tilde{\Psi}(r,\theta)$ at $(r,\theta)$ $(r>a)$ comes from the singularity of $\Psi(r,\theta)$ at $(a^2/r,\theta)$, where $\Psi$ is regular from the assumption. iii) is thus proved.

iv) Since the velocity components

$$u=\frac{1}{y}\frac{\partial\Psi}{\partial y} \quad\text{and}\quad v=-\frac{1}{y}\frac{\partial\Psi}{\partial x} \qquad (3.12)$$

are finite at the origin,

$$\Psi(r,\theta)=O(y^2)=O(r^2\sin^2\theta) \qquad (3.13)$$

near the origin. This shows that

$$\Psi(R,\theta)=O\left(\frac{\sin^2\theta}{r^2}\right)=O\left(\frac{y^2}{r^4}\right) \qquad (3.14)$$

as $r\to\infty$. Introducing (3.14) into (3.2) we obtain

$$\tilde{\Psi}(r,\theta)=O(r\sin^2\theta)=O\left(\frac{y^2}{r}\right) \quad\text{as}\quad r\to\infty. \qquad (3.15)$$

The velocity components derived from (3.15) tend to zero as $r\to\infty$, which proves iv).

The proof of Theorem II proceeds similarly, except for iv) which we can prove as follows.

On account of the regularity and the symmetry of the flow field

$$u\sim u_0(x)+u_1(x)y^2+O(y^4)\,,$$
$$v\sim v_1(x)y+O(y^3)\,, \qquad (3.16)$$
$$\omega\sim O(y)=O(r\sin\theta)\,,$$

near the origin. These show that

$$\zeta=O(r^2\sin^2\theta) \quad\text{and}\quad \psi_2(r,\theta)=O(r^2\sin^2\theta)$$

from (3.7). Introducing these into (3.8), $\psi_1(r,\theta)$ is also shown to be of the order $O(r^2\sin^2\theta)$ near the origin.

Thus, we have only to prove that the velocity derived from (3.6) tends zero as $r\to\infty$. Introducing

$$\psi_2(R,\theta)=O(r^{-2}\sin^2\theta)$$

and

$$\frac{\partial}{\partial R}\Psi_2(R,\theta)=O(r^{-1}\sin^2\theta) \text{ as } r\to\infty\,, \qquad (3.17)$$

into (3.6), we obtain

$$\tilde{\Psi}_2(r,\theta)=O(r\sin^2\theta) \quad\text{as}\quad r\to\infty\,, \qquad (3.18)$$

which proves iv), taking account of the result $\tilde{\Psi}_1(r,\theta)=O(r\sin^2\theta)$ as derived from $\psi_1(r,\theta)$ by the same formula as that for $\tilde{\Psi}(r,\theta)$ in the irrotational case.

## § 4. Examples

i) Uniform Flow past a Sphere.

The stream function for the uniform flow with velocity $U$ is expressed by

$$\Psi(r,\theta)=\frac{1}{2}Uy^2=\frac{1}{2}Ur^2\sin^2\theta\ . \tag{4.1}$$

In this case $D\Psi=0$. Using Theorem I we obtatin

$$\frac{1}{U}\tilde{\Psi}(r,\theta)=\left[\left(a-\frac{r^2}{a}\right)\frac{a^2}{r}-\left(\frac{3}{2}\frac{r}{a}-\frac{1}{2}\frac{r^3}{a^3}\right)\frac{1}{2}\frac{a^4}{r^2}\right]\sin^2\theta=\left[\frac{a^3}{4r}-\frac{3}{4}ar\right]\sin^2\theta\ , \tag{4.2}$$

which is the well-known Stokes formula.

ii) A Sphere in the Flow due to a Point Source or Sink.

The stream function for a point source (or sink) of strength $\kappa$ at $r=l>a$, $\theta=\pi$, is expressed by

$$\Psi(r,\theta)=\frac{\kappa}{4\pi}(1-\cos\Theta)=\frac{\kappa}{4\pi}\left[1-\frac{r\cos\theta+l}{r_1}\right], \tag{4.3}$$

where

$$r_1\cos\Theta=r\cos\theta+l\ ,\quad r_1=\sqrt{r^2+2rl\cos\theta+l^2}\ . \tag{4.4}$$

In this case $\Psi(R,\theta)$ and $\partial\Psi(R,\theta)/\partial R$ are

$$\Psi(R,\theta)=\frac{\kappa}{4\pi}\left(1-\frac{lr+a^2\cos\theta}{\rho}\right),\qquad \frac{\partial}{\partial R}\Psi(R,\theta)=\frac{\kappa}{4\pi}\frac{la^2r^2\sin^2\theta}{\rho^3}\ , \tag{4.5}$$

where

$$\rho=\sqrt{l^2r^2+2la^2r\cos\theta+a^4}\ .$$

Introducing (4.5) into Theorem I we obtain

$$\tilde{\Psi}(r,\theta)=\frac{\kappa}{4\pi}\left[\frac{la^3}{\rho^3}\left(r^2-\frac{r^4}{a^2}\right)\sin^2\theta-\frac{1}{2}\left(\frac{3r}{a}-\frac{r^3}{a^3}\right)\left(1-\frac{lr+a^2\cos\theta}{\rho}\right)\right]. \tag{4.6}$$

iii) Parabolic Flow.

As an example of the rotational flow, let us consider the parabolic flow

$$u=\alpha y^2=\alpha r^2\sin^2\theta\ ,\qquad v=0\ . \tag{4.7}$$

$\Psi(r,\theta)$ and $\zeta(r,\theta)$ are given respectively by

$$\Psi(r,\theta)=\frac{1}{4}\alpha y^4=\frac{1}{4}\alpha r^4\sin^4\theta\ , \tag{4.8}$$

and

$$\zeta(r,\theta)=y\omega(r,\theta)=-2\alpha y^2=-2\alpha r^2\sin^2\theta\ . \tag{4.9}$$

Introducing (4.9) into (3.7) and (3.8) we obtain for $\psi_2(r,\theta)$ and $\psi_1(r,\theta)$

$$\psi_2(r,\theta)=-\frac{\sin^2\theta}{4r^{1/2}}\int_0^r(-2\alpha r^{3/2})dr=\frac{1}{5}\alpha r^2\sin^2\theta\ , \tag{4.10}$$

$$\psi_1(r,\theta)=\alpha r^4\Theta\ ,\qquad \Theta=\frac{1}{4}\sin^4\theta-\frac{1}{5}\sin^2\theta\ . \tag{4.11}$$

Then (3.5) and (3.6) give

$$\tilde{\Psi}_1(r,\theta)=\alpha\left[\left(a-\frac{r^2}{a}\right)\frac{4a^6}{r^3}-\left(\frac{3}{2}\frac{r}{a}-\frac{1}{2}\frac{r^3}{a^3}\right)\frac{a^8}{r^4}\right]\Theta=\alpha\left(\frac{5a^7}{2r^3}-\frac{7a^5}{2r}\right)\Theta\ , \tag{4.12}$$

and

$$a^2\tilde{\Psi}_2(r,\theta)=\alpha a^2\left[\left(a-\frac{r^2}{a}\right)\frac{2a^2}{r}-\left(\frac{1}{2}\frac{r}{a}+\frac{1}{2}\frac{r^3}{a^3}\right)\frac{a^4}{r^2}\right]\times\frac{1}{5}\sin^2\theta$$

$$=\alpha\left(\frac{3a^5}{2r}-\frac{5a^3r}{2}\right)\times\frac{1}{5}\sin^2\theta\ . \tag{4.13}$$

Adding (4.12) and (4.13) the perturbed term for the stream function is expressed by

$$\tilde{\Psi}(r,\theta)=-\frac{\alpha}{2}\left(a^3r-\frac{2a^5}{r}+\frac{a^7}{r^3}\right)\sin^2\theta-\frac{\alpha}{8}\left(\frac{7a^5}{r}-\frac{5a^7}{r^3}\right)\sin^4\theta\ . \tag{4.14}$$

In conclusion the author expresses his cordial thanks to Professor Isao Imai for the continual guidance and encouragement throughout this work. This work was supported by the Scientific Research Fund of the Ministry of Education of Japan.

### References

1) P. A. Weiss: Proc. Cambr. Phil. Soc. **40** (1944) 259.
2) S. F. J. Butler: Proc. Cambr. Phil. Soc. **49** (1953) 168.
3) L. M. Milne-Thomson: Proc. Cambr. Phil. Soc. **36** (1940) 246.
4) H. Faxén: Arkiv. Mat. Astro. Fysik. **20** (1927) 5.
5) H. Lamb: Hydrodynamics (6th ed., 1932), p. 602.

---

JOURNAL OF THE PHYSICAL SOCIETY OF JAPAN Vol. 11, No. 7, JULY, 1956

# On the Transverse Vibration of an Elliptic Plate with Clamped Edge

By Yoshio SHIBAOKA
*Institute of Polytechnics, Osaka City University*

(Received March 31, 1956)

The transverse vibration of a uniform thin elliptic plate with clamped edge is solved in an exact manner by the use of Mathieu functions and modified Mathieu functions. The relationship between the frequency of the fundamental mode of vibration and the eccentricity of the elliptic plate is shown graphically. Also, an approximate formula for the said relationship is derived correct to the fourth power of the eccentricity, which may be adequately used in case when the eccentricity is not so large.

## § 1. Introduction

It is well known that the transverse vibration of a circular plate subject to a variety of boundary conditions can be solved exactly by the use of Bessel functions and modified Bessel functions. The transverse vibration of a square plate has also been discussed by several authors, with satisfactory results, under various boundary conditions, and especially for the case of a square plate with four clamped edges Professor Tomotika has given an exact solution1),2).

On the other hand, the problem of the transverse vibration of a thin elliptic plate has been attacked by McLachlan3),4). By careful examination of his analysis it has been found however that he has made serious errors. McLachlan has considered that any one normal mode of vibration of an elliptic plate can be expressed, as in the case of a circular plate, by only one particular solution of the differential equation governing the vibration of the plate, but this is not the case for the transverse vibration of an elliptic plate; all appropriate particular solutions should be summed up to express even one normal mode of vibration. Otherwise, the prescribed boundary conditions cannot be satisfied.

In the present paper, the fundamental normal mode of the transverse vibration of a uniform thin elliptic plate with clamped edge is investigated in an exact manner by the use of Mathieu functions and modified Mathieu functions. After carrying out rather laborious calculations the relationship between the frequency of the fundamental mode of vibration and the eccentricity of the elliptic plate is shown graphically. Also, an approximate formula for the said relationship is derived correct to the fourth power of the eccentricity, which may be adequately used in case when the eccentricity is not so large.

## § 2. General Solution of the Fundamental Equation

Let the rectangular coordinate-axes $(x, y)$ be taken in the middle plane of an elliptic plate of uniform small thickness, $d$, in such a way that the origin coincides with the centre of the plate and the axes are along the major and minor axes of the ellipse respectively. We denote the density, Young's modulus, and Poisson's ratio of the material of the plate, which is assumed to be homogeneous and isotropic, by $\rho$, $E$, and $\sigma$ respectively.

Then, if $W$ be the transverse displacement of a point on the middle plane, the differential equation for the transverse vibration of the plate with small amplitude is given by

$$\left.\begin{aligned}&\frac{\partial^4 W}{\partial x^4}+2\frac{\partial^4 W}{\partial x^2\partial y^2}+\frac{\partial^4 W}{\partial y^4}+\frac{1}{c^4}\frac{\partial^2 W}{\partial t^2}=0\,,\\ &\text{with}\\ &c^2=Ed^2/\{12\rho(1-\sigma^2)\}\,.\end{aligned}\right\}\quad(1)$$

When the plate vibrates in a normal mode, the displacement is of the form

$$W=\zeta\cos\omega t\,,\qquad(2)$$

where $\zeta$ is a function of $x, y$, and $\omega$ is the circular frequency. If we insert (2) into (1) and write $k_1{}^4=\omega^2/c^2$ for simplicity, we get a partial differential equation for $\zeta$, namely:

$$\frac{\partial^4\zeta}{\partial x^4}+2\frac{\partial^4\zeta}{\partial x^2\partial y^2}+\frac{\partial^4\zeta}{\partial y^4}-k_1{}^4\zeta=0\,,\qquad(3)$$

or

$$\left(\frac{\partial^2}{\partial x^2}+\frac{\partial^2}{\partial y^2}+k_1{}^2\right)\left(\frac{\partial^2}{\partial x^2}+\frac{\partial^2}{\partial y^2}-k_1{}^2\right)\zeta=0\,.\qquad(4)$$

The solution of this equation is given by

$$\zeta=\zeta_1+\zeta_2\,,\qquad(5)$$

where $\zeta_1$ and $\zeta_2$ satisfy respectively the differential equations:

$$\frac{\partial^2\zeta_1}{\partial x^2}+\frac{\partial^2\zeta_1}{\partial y^2}+k_1{}^2\zeta_1=0\qquad(6)$$

and

$$\frac{\partial^2\zeta_2}{\partial x^2}+\frac{\partial^2\zeta_2}{\partial y^2}-k_1{}^2\zeta_2=0\,.\qquad(7)$$

Denoting the focal length of the ellipse by $2h$, we now introduce the elliptic coordinates $(\xi, \eta)$ defined as:

$$x+iy=h\cosh(\xi+i\eta)\,.$$

Then, equations (6) and (7) become respectively

$$\frac{\partial^2\zeta_1}{\partial\xi^2}+\frac{\partial^2\zeta_1}{\partial\eta^2}+2k^2(\cosh 2\xi-\cos 2\eta)\zeta_1=0\,,\qquad(8)$$

$$\frac{\partial^2\zeta_2}{\partial\xi^2}+\frac{\partial^2\zeta_2}{\partial\eta^2}-2k^2(\cosh 2\xi-\cos 2\eta)\zeta_2=0\,,\qquad(9)$$

where

$$2k=k_1h=\sqrt{\omega/c}\,h\,.$$

If we restrict our attention to those normal modes of vibration in which the displacement is symmetrical about both axes, as in the case of the fundamental normal mode under consideration, the appropriate particular solutions of equations (8) and (9) can be expressed in terms of Mathieu functions $\mathrm{ce}_{2m}(\eta, q)$, $\mathrm{ce}_{2m}(\eta, -q)$ and modified Mathieu functions $\mathrm{Ce}_{2m}(\xi, q)$, $\mathrm{Ce}_{2m}(\xi, -q)$. Thus,

$$\zeta_1{}^{(2m)}=C_{2m}\mathrm{Ce}_{2m}(\xi, q)\mathrm{ce}_{2m}(\eta, q)\,,\qquad(10)$$

$$\zeta_2{}^{(2m)}=\bar{C}_{2m}\mathrm{Ce}_{2m}(\xi, -q)\mathrm{ce}_{2m}(\eta, -q)\,,\qquad(11)$$

with

$$q=k^2=\frac{\omega}{4c}h^2\,,\qquad(12)$$

where $m$ takes any positive integral value, zero inclusive, and $C_{2m}$, $\bar{C}_{2m}$ are arbitrary constants.

Hence, summing up all these particular solutions, a formal general solution of equation (3) can be written in the form:

$$\begin{aligned}\zeta&=\sum_{m=0}^{\infty}\{\zeta_1{}^{(2m)}+\zeta_2{}^{(2m)}\}\\&=\sum_{m=0}^{\infty}\{C_{2m}\mathrm{Ce}_{2m}(\xi, q)\mathrm{ce}_{2m}(\eta, q)+\bar{C}_{2m}\mathrm{Ce}_{2m}(\xi, -q)\mathrm{ce}_{2m}(\eta, -q)\}\,.\end{aligned}\qquad(13)$$

Now, after some calculations we have

$$\mathrm{ce}_{2m}(\eta, -q)=\sum_{l=0}^{\infty}D_{2m,2l}\mathrm{ce}_{2l}(\eta, q)\,,\qquad(14)$$

where

$$D_{2m,2l}=(-1)^m \sum_{p=0}^{\infty} (-1)^p A_{2p}^{(2m)} A_{2p}^{(2l)} s_p\,, \qquad s_0=2\,, \qquad s_p=1 \qquad (p\neq 0)\,.$$

Thus, eliminating the functions $\mathrm{ce}_{2m}(\eta, -q)$ from the right-hand side of (13) by the use of this relation, we have

$$\begin{aligned}\zeta &= \sum_{m=0}^{\infty} [C_{2m}\mathrm{Ce}_{2m}(\xi, q)\,\mathrm{ce}_{2m}(\eta, q)+\overline{C}_{2m}\mathrm{Ce}_{2m}(\xi,-q) \sum_{l=0}^{\infty} D_{2m,2l}\,\mathrm{ce}_{2l}(\eta, q)] \\ &= \sum_{m=0}^{\infty} [C_{2m}\mathrm{Ce}_{2m}(\xi, q)+ \sum_{l=0}^{\infty} \overline{C}_{2l}D_{2l,2m}\mathrm{Ce}_{2l}(\xi, -q)]\,\mathrm{ce}_{2m}(\eta, q)\,. \end{aligned} \tag{15}$$

If the clamped edge of the elliptic plate be expressed by $\xi=\xi_0$, the boundary conditions at this edge are given by

$$(\zeta)_{\xi=\xi_0}=0\,, \qquad (\partial\zeta/\partial\xi)_{\xi=\xi_0}=0\,, \tag{16}$$

and substituting the expression (15) for $\zeta$ into these conditions, we have

$$\left.\begin{aligned} &\sum_{m=0}^{\infty} [C_{2m}\mathrm{Ce}_{2m}(\xi_0, q) + \sum_{l=0}^{\infty} \overline{C}_{2l}D_{2l,2m}\mathrm{Ce}_{2l}(\xi_0, -q)]\,\mathrm{ce}_{2m}(\eta, q)=0\,, \\ &\sum_{m=0}^{\infty} [C_{2m}\mathrm{Ce}'_{2m}(\xi_0, q)+ \sum_{l=0}^{\infty} \overline{C}_{2l}D_{2l,2m}\mathrm{Ce}'_{2l}(\xi_0, -q)]\,\mathrm{ce}_{2m}(\eta, q)=0\,. \end{aligned}\right\} \tag{17}$$

In order that these two relations should be satisfied for all values of $\eta$ between $-\pi/2$ and $\pi/2$, we must have, for any positive integral value of $m$, zero inclusive,

$$\left.\begin{aligned} &C_{2m}\mathrm{Ce}_{2m}(\xi_0, q)+ \sum_{l=0}^{\infty} \overline{C}_{2l}D_{2l,2m}\mathrm{Ce}_{2l}(\xi_0, -q)=0\,, \\ &C_{2m}\mathrm{Ce}'_{2m}(\xi_0, q)+ \sum_{l=0}^{\infty} \overline{C}_{2l}D_{2l,2m}\mathrm{Ce}'_{2l}(\xi_0, -q)=0\,. \\ &\qquad\qquad (m=0,\,1,\,2,\,3,\cdots\cdots) \end{aligned}\right\} \tag{18}$$

If we eliminate the constants $C_{2m}$'s from these equations, we get a system of simultaneous linear equations for determining the constants $\overline{C}_{2l}$'s. Thus,

$$\sum_{l=0}^{\infty} a_{lm}\overline{C}_{2l}=0\,, \qquad (m=0,\,1,\,2,\,3,\cdots) \tag{19}$$

with

$$a_{lm}=D_{2l,2m}\{\mathrm{Ce}_{2l}(\xi_0, -q)\mathrm{Ce}'_{2m}(\xi_0, q) -\mathrm{Ce}'_{2l}(\xi_0, -q)\mathrm{Ce}_{2m}(\xi_0, q)\}\,. \tag{20}$$

The solution of this system of simultaneous linear equations would in general yield the result that all the $\overline{C}_{2l}$'s are zero; but if a certain special relationship exists between the dimensions of the plate and the frequency $\omega$ of vibration, namely, if the relation obtained by eliminating all the $\overline{C}_{2l}$'s from the system of simultaneous linear equations (19) exists, we can obtain a displacement in the normal mode of vibration, and with the aid of the said relationship the frequency of vibration can be determined as a function of the dimensions of the plate, the elastic constants and density of the material of the plate.

By eliminating all the $\overline{C}_{2l}$'s from (19), we have the required relationship as:

$$\Delta=\begin{vmatrix} a_{00} & a_{10} & a_{20} & a_{30} & \cdots\cdots \\ a_{01} & a_{11} & a_{21} & a_{31} & \cdots\cdots \\ a_{02} & a_{12} & a_{22} & a_{32} & \cdots\cdots \\ a_{03} & a_{13} & a_{23} & a_{33} & \cdots\cdots \\ \cdots & \cdots & \cdots & \cdots & \cdots\cdots \\ \cdots & \cdots & \cdots & \cdots & \cdots\cdots \end{vmatrix}=0\,. \tag{21}$$

If we obtain the numerical values of the root $q$ of this infinite determinantal equation, the numerical value of $\sqrt{\frac{\omega}{c}}\,a$ can be obtained from the relation:

$$\sqrt{\frac{\omega}{c}}\,a=2\frac{\sqrt{q}}{\varepsilon}\,, \tag{22}$$

which follows immediately from (12), where $a$ and $\varepsilon$ are respectively a half-length of the major axis and the eccentricity of the ellipse.

When $a$, $\varepsilon$ and $c$ are fixed the only variable remaining in the determinant $\Delta$ is $q$, which is connected with the frequency of vibration $\omega$

by the relation (22), so that the smallest root of $\Delta=0$ will give the frequency of the fundamental normal mode of vibration with which we are mainly concerned in the present paper.

The solution expressed by (21) is, however, merely formal. To find out where it can be used to determine the actual value of the frequency of the fundamental normal mode of vibration we must examine its convergence. For this purpose we may form, as in Professor Tomotika's treatment of the transverse vibration of a square plate clamped at its four edges1), a series of finite determinants $\Delta_1, \Delta_2, \Delta_3, \cdots \Delta_N$ by taking 1, 2, 3, $\cdots N$ rows and columns starting at the left-hand top corner of $\Delta$, so that $\Delta_1=a_{00}$, $\Delta_2=\begin{vmatrix} a_{00} & a_{10} \\ a_{01} & a_{11} \end{vmatrix}$, etc. If it is found that the smallest roof of $\Delta_N=0$ converges to a definite limit as $N$ increases, this root gives the required frequency of the fundamental normal mode of vibration of the elliptic plate under consideration.

## § 3. A 'Rayleigh' Value of the Frequency

Before proceeding further to the numerical computations of the roots of the equations $\Delta_N=0\ (N=0, 1, 2, \cdots)$, we shall here calculate an approximate value of the frequency of the fundamental mode of vibration by applying the well-known Rayleigh's principle and assuming the transverse displacement W of the plate in the form:

$$\mathrm{W}=\mathrm{W}_0\left(1-\frac{x^2}{a^2}-\frac{y^2}{b^2}\right)^2 \cos\omega t\,, \tag{23}$$

where $b$ is a half-length of the minor axis of the ellipse.

In this case, the kinetic energy $T$ and the potential energy $V$ of the plate become respectively

$$\left.\begin{aligned} T&=\frac{\pi}{10}\,\rho\, dab\,\omega^2\,\mathrm{W}_0^2 \sin^2\omega t\,,\\ V&=\frac{\pi}{9}\,\frac{E}{1-\sigma^2}\,d^3ab\left(\frac{3}{a^4}+\frac{2}{a^2b^2}+\frac{3}{b^4}\right)\mathrm{W}_0^2\cos^2\omega t\,,\end{aligned}\right\} \tag{24}$$

Thus, equating the mean value of $T$ to that of $V$ we easily get a 'Rayleigh' value for the frequency of the fundamental normal mode of transverse vibration of the elliptic plate. Denoting it by $\omega_{\mathrm{R}}$ we have

$$\omega_{\mathrm{R}}=\sqrt{\frac{10}{3}}\sqrt{\frac{1}{a^4}+\frac{2}{3a^2b^2}+\frac{1}{b^4}}\sqrt{\frac{E}{\rho(1-\sigma^2)}}\,d. \tag{25}$$

Substituting this in (12) we get the corresponding Rayleigh value of $q$, which will be denoted by $q_{\mathrm{R}}$, as a function of the eccentricity $\varepsilon$ of the ellipse in the form:

$$q_{\mathrm{R}}=\sqrt{\frac{5}{6}}\,\frac{\varepsilon^2}{1-\varepsilon^2}\sqrt{3\varepsilon^4-8\varepsilon^2+8}\,. \tag{26}$$

Using this formula the values of $q_{\mathrm{R}}$ have been calculated in three cases in which the value of the ratio $a/b$ is equal to 5/4, 2/1 and 3/1 respectively, the corresponding values of the eccentricity $\varepsilon$ being 0.6, 0.866 and 0.943 respectively. The values of $q_{\mathrm{R}}$ thus calculated are shown in Table I.

## § 4. Search for Roots of $\Delta=0$

The writer has calculated the smallest roots $q$ of $\Delta_1=0$, $\Delta_2=0$ and $\Delta_3=0$ in three cases in which the values of $a/b$ are equal to 5/4, 2/1 and 3/1 respectively, with a view to finding out whether they converge to a definite limit.

Table I. Values of $q_{\mathrm{R}}$.

| $a/b$ | $\varepsilon$ | $q_{\mathrm{R}}$ |
|---|---|---|
| 5/4 | 0.6 | 1.205 |
| 2/1 | 0.866 | 5.259 |
| 3/1 | 0.943 | 13.18 |

To this end, the values of $\Delta_1, \Delta_2$ and $\Delta_3$ have been calculated for different values of $q$ close to the Rayleigh values tabulated in Table I, and then plotting these values of $\Delta_1, \Delta_2$ and $\Delta_3$ against $q$, the roots of equations $\Delta_1=0$, $\Delta_2=0$ and $\Delta_3=0$ have been determined graphically as shown in Figs. 1, 2 and 3*. The results are as shown in Table II.

It may be added here that for the numerical calculations of the modified Mathieu functions $\mathrm{Ce}_{2n}(\xi_0, q)$ and $\mathrm{Ce}_{2n}(\xi_0-q)$ contained

---

* The values of $\Delta_4$ have also been calculated in case when $a/b$ is equal to 3/1 and the root of $\Delta_4=0$ has been obtained.

Table II. Roots of $\Delta_N=0$.

| $a/b$ | $\varepsilon$ | Root of $\Delta_1=0$ | Root of $\Delta_2=0$ | Root of $\Delta_3=0$ | Root of $\Delta_4=0$ |
|---|---|---|---|---|---|
| 5/4 | 0.6 | 1.23 | 1.185 | 1.185 | — |
| 2/1 | 0.866 | 6.33 | 5.16 | 5.15 | — |
| 3/1 | 0.943 | 17.0 | 12.66 | 12.63 | 12.63 |

Table III. Values of $\sqrt{\omega/c}\,a$.

| $a/b$ | $\varepsilon$ | $\sqrt{\omega/c}\,a$ |
|---|---|---|
| 5/4 | 0.6 | 3.62 |
| 2/1 | 0.866 | 5.25 |
| 3/1 | 0.943 | 7.54 |

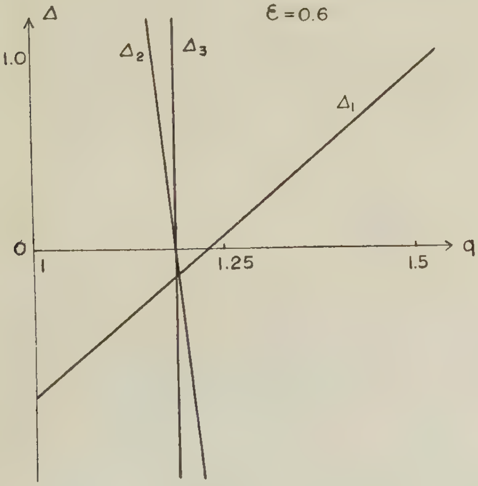

Fig. 1.

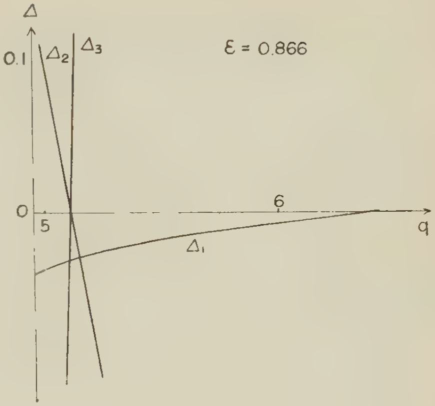

Fig. 2.

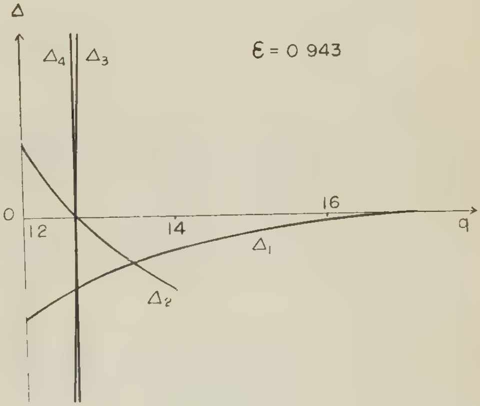

Fig. 3.

in the elements $a_{ln}$'s of the determinant $\Delta$ use has been made of the following product series expressions because of their rapid convergency:

$$\left.\begin{aligned} \mathrm{Ce}_{2n}(\xi_0, q) &= \frac{p_{2n}}{A_0^{(2n)}}\sum_{r=0}^{\infty}(-1)A_{2r}^{(2n)}J_r(v_1)J_r(v_2)\,, \\ \mathrm{Ce}_{2n}(\xi_0, -q) &= \frac{p_{2n}'}{A_0^{(2n)}}\sum_{r=0}^{\infty}(-1)^r A_{2r}^{(2n)}I_r(v_1)I_r(v_2), \end{aligned}\right\}$$

where

$$v_1=\sqrt{q}\;e^{-\xi_0}\,, \qquad v_2=\sqrt{q}\;e^{\xi_0}\,,$$

$$p_{2n}=(-1)^n p_{2n}'=\mathrm{ce}_{2n}(0,q)\,\mathrm{ce}_{2n}\left(\frac{\pi}{2}\,,\,q\right)\Big/A_0^{(2n)}\,,$$

$\xi_0$ being connected with the value of $a/b$ as:

$$\cosh\xi_0=\frac{a}{\sqrt{a^2-b^2}}=\frac{1}{\varepsilon}\,.$$

From Figs. 1, 2, 3 and Table II it will be seen that as $N$ increases, the roots $q$ of equation $\Delta_N=0$ converge to 1.185 when $a/b=5/4$, to 5.15 when $a/b=2/1$ and to 12.63 when $a/b=3/1$. Thus, substituting these limiting values of $q$ into (22), we obtain ultimately the most probable values of $\sqrt{\dfrac{\omega}{c}}\;a$ as shown in Table III below.

The curve of $\sqrt{\omega/c}\;a$ plotted against the eccentricity $\varepsilon$ is shown by a thick-lien curve in

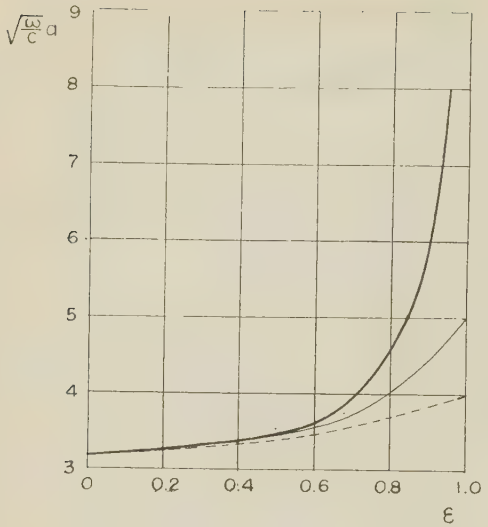

Fig. 4.

Fig. 4, where is also shown the well-known value of $\sqrt{\omega/c}\ a$ equal to 3.1961 for a circular plate ($\varepsilon=0$) with clamped edge[5].

## § 5. An Expansion Formula for $\sqrt{\frac{\omega}{c}}\,a$ in Powers of $\varepsilon$

When an elliptic plate differs only slightly from a circular plate, its eccentricity $\varepsilon$ is very small, and accordingly $q$ is also very small, as will be seen from the relation $q=\frac{1}{4}(\sqrt{\omega/c}\ a)^2\varepsilon^2$ which follows immediately from (22). In such a case, $\sqrt{\omega/c}\,a$ can be expanded in a power series of $\varepsilon$.

We have obtained such an expansion formula for $\sqrt{\frac{\omega}{c}}\,a$ correct to the order of $\varepsilon^4$. To this end we have expanded the elements $a_{ij}$'s of the determinant $\Delta$ into series correct to the order of $q^2$. After rather lengthy but straightforward calculations we have

$$\sqrt{\frac{\omega}{c}}\,a=u_0+u_1\varepsilon^2+u_2\varepsilon^4\,, \tag{27}$$

where $u_0$ is the value of $\sqrt{\omega/c}\ a$ for the fundamental normal mode of transverse vibration of a circular plate of radius $a$ with clamped edge and is given by the smallest root of the equation:

$$J_0'(u_0)I_0(u_0)-J_0(u_0)I_0'(u_0)=0\,,$$

$J$ and $I$ being the Bessel function and the modified Bessel function of the first kind respectively. Thus, we have

$$u_0=3.1961\,. \tag{28}$$

Both the coefficients $u_1$ and $u_2$ can be expressed in terms of the Bessel functions and the modified Bessel functions of the first kind with argument $u_0$. Using the value 3.1961 of $u_0$, we have calculated the numerical values of $u_1$ and $u_2$, obtaining

$$u_1=0.7991\,,\qquad u_2=0.7892\,. \tag{29}$$

Thus, we have finally

$$\sqrt{\frac{\omega}{c}}\,a=3.1961+0.7991\,\varepsilon^2+0.7892\varepsilon^4\,. \tag{30}$$

The values calculated by using this expansion formula are shown by a thin-line curve in Fig. 4, while those calculated by a formula obtained by ignoring the last term in the same formula are shown by a dotted-line curve. It will be seen that the expansion formula (30) is particularly useful for calculating the numerical values of $\sqrt{\frac{\omega}{c}}\,a$ in case when the plate is nearly circular.

## § 6. Summary

The fundamental normal mode of transverse vibration with small amplitude of a uniform elliptic plate clamped at its edge is investigated in an exact manner. An exact formal solution of the partial differential equation governing the transverse vibration of the plate is obtained by the use of Mathieu functions and modified Mathieu functions. Carrying out detailed numerical calculations in three cases in which the eccentricity $\varepsilon$ of the ellipse is equal to 0.6, 0.866 and 0.943 respectively, the relationship between $\sqrt{\omega/c}\ a$ and $\varepsilon$ is shown graphically, where $\omega$ is the circular frequency, $a$ a half-length of the major axis of the ellipse and

$$c=\sqrt{Ed^2/12\rho(1-\sigma^2)}$$

$E$, $\sigma$ and $\rho$ being respectively Young's modulus, Poisson's ratio and the density of the material of the plate and $d$ being the thicknesss of the plate.

An expansion formula for $\sqrt{\omega/c}\,a$ is then derived correct to the order of $\varepsilon^4$, and it is shown that such an expansion formula is particularly useful for calculating the value of $\sqrt{\omega/c}\ a$ in case when an elliptic plate differs only slightly from a circular plate.

### Acknowledgements

The present problem has been suggested by Professor S. Tomotika. The writer wishes to express his best thanks to him for his kind guidance throughout the present work. The writer's thanks are also due to Professor K. Tamada for his many valuable advices and to Professor T. Okuda for his encouragement.

### References

1) S. Tomotika: The transverse vibration of a square plate clamped at four edges. Phil. Mag. [7] **21** (1936) 745-760.
2) S. Tomotika: On the transverse vibration of a square plate with four clamped edges. Report Aeron. Res. Inst., Tokyo Imp. Univ., **10** (1935) 299-328.
3) N. W. McLachlan: Vibrational problem in elliptic coordinates. Quart. Appl. Math. **5** (1947) 289.
4) N. W. McLachlan: *Theory and application of Mathieu functions.* (Oxford Univ. Press, 1947) 309-311.
5) H. Carrington: The frequencies of vibration of flat circular plates fixed at the circumference. Phil. Mag. [6] **50** (1925) 1261-1265.

---

# Short Notes

This section is intended to secure prompt publication of important discoveries in physics. The reports should not exceed 800 words in length. A figure of size 7 cm × 7 cm will be counted as 150 words.

J. PHYS. SOC. JAPAN **11** (1956) 803~804

## On a Change of Dielectric Property of $(Ba_{0.5}\cdot Sr_{0.5})TiO_3$ Ceramics due to the Thermal Treatment

By Shoichiro NOMURA
*Institute of Science and Technology, University of Tokyo*

(Received April 30, 1956)

$(Ba\cdot Sr)TiO_3$ ceramics show not only an aging effect but also a small fluctuating effect in the dielectric property, specimen by specimen, which are interpreted to be brought about by a redistribution of unstable domains to a stable state[1]. In order to make clear these phenomena, we have investigated the change of the dielectric property of barium-strontium titanate ceramics by thermal treatment, and found that the dielectric property was varied appreciably.

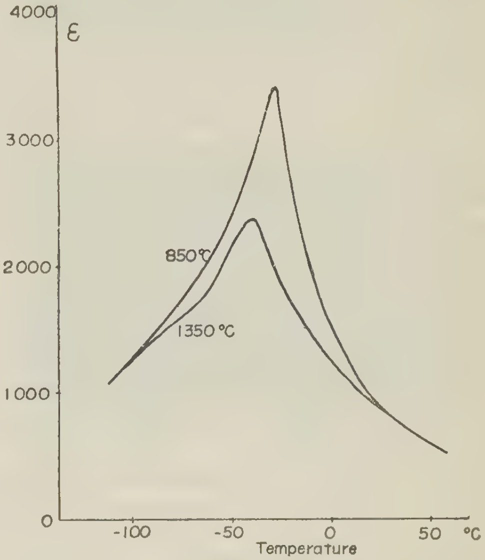

Fig. 1. Dielectric constant versus temperature curve.

In the first, we sintered enough $(Ba_{0.5}\cdot Sr_{0.5})TiO_3$ ceramics at 1350°C, then took it out of the furnace rapidly, and cooled it to room temerature during a few minutes. We call this treatment as "rapid air-cooling". This specimen was cut into several pieces. They were heated again at several temperatures, being lower than 1350°C, for about 10 hours, and then were cooled rapidly, as in the case of 1350°C. Fig. 1 shows the dielectric constant-temperature characteristics for the samples rapidly air cooled at 850°C and 1350°C. Fig. 2 shows a relation of the Curie temperature of $(Ba_{0.5}\cdot Sr_{0.5})TiO_3$ ceramics with the air-cooling temperature. The Curie temperature increases as the temperature of heat treatment decreases and becomes nearly constant below 1100C°. The determination of the Curie temperature as the peak positon on the perpermittivity-temperature curve contains some uncertainty, which is 2~3°C in our case. There occurred a remarkable change also in the dielectric hysteresis loop. For barium titanate, we performed the same experiment, but did not find any noticeable change of the Curie temperature, although the

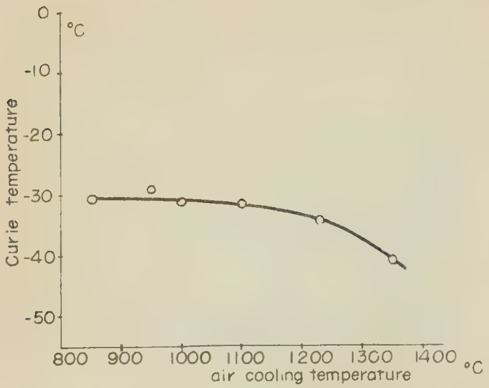

Fig. 2. Change of Curie temperature due to rapid air-cooling.

value of dielectric constant changed in some degree.

It may be considered that there are two causes that bring about such phenomena, one of them being a macroscopic one, such as an effect due to thermal stress and grain growth, and the other a microscopic one, which is an arrangement of $Ba^{2+}$ and $Sr^{2+}$ ions in the crystal lattices. It is well known that the value of dielectric constant is depressed by thermal stress and is influenced by grain size[2)], and so there may occur such phenomena even in barium titanate. The change of the ionic arrangement, however, may be realized only in the case of solid solution, and it would be expected on the stand point of thermodynamical consideration, that the degree of order of the arrangement of $Ba^{2+}$ and $Sr^{2+}$ ions in the crystal lattices becomes less, when the temperature of heat treatment is high. This state corresponds to the one having high energy compared with the one prepared at lower temperature. As this state is quenched by the treatment of the rapid air-cooling, the crystal lattice will show large microscopic distortion at low temperature. We are now investigating in detail these problems.

We wish to express our hearty thanks to Assist. Prof. S. Sawada for his encouragement.

### References

1) W. P. Mason: J. Acous. Soc. Am. **27** (1955) 73.
2) L. Egerton and S. E. Koonce: J. Am Cer. Soc. **38** (1955) 412.

---

J. PHYS. SOC. JAPAN **11** (1956) 804~805

## Nuclear Spins of Dy 163 and Dy 161

By Kiyoshi MURAKAWA

*Institute of Science and Technology,*
*Komaba-machi, Meguro-ku, Tokyo*

(Received May 23, 1956)

In 1953 Kamei and the author[1)] studied the hyperfine structure (hfs) of the spectrum of dysprosium, and it was found that $Dy^{163}$ and $Dy^{161}$ have the same nuclear spins and that their magnetic moments are approximately equal. In the hfs of the unclassified line Dy II λ 3968 six components out of eight were ascribed to $Dy^{163}$ and $Dy^{161}$, and it was deduced that their nuclear spins were probably 7/2, assuming that the components of $Dy^{103}$ coincided exactly with those of $Dy^{161}$.

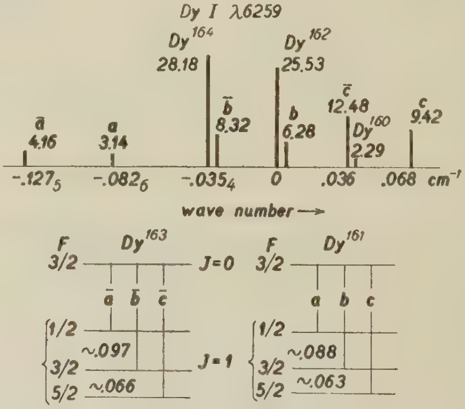

Fig. 1. Hfs of Dy I λ 6259. In the transition scheme it is assumed that the level with $J=1$ is the deeper. If this is the higher, the hfs level scheme must be reversed.

A critical review regarding λ 3968 shows that this assumption is valid only to a very rough approximation, so all that we can conclude unambiguously about the spins is that the spins of $Dy^{163}$ and $Dy^{161}$ must be larger than 1/2. In order to find them exactly, classified lines must be studied.

In these three years the classification of the spectrum of Dy I has been undertaken from time to time (but not continuously) in this laboratory, and it has been found that the hfs of the line λ 6259 that was studied previously[1)] can be interpreted as due to a transition $J=1 \longleftrightarrow J'=0$, as shown in Fig. 1.

The intensity ratio of the components $c$ and $a$ was measured to be int. $c$/int. $a=3.2\pm0.4$, from which we conclude that the nuclear spin of $Dy^{161}$ is 3/2. Since it was found previously that the spins of $Dy^{163}$ and $Dy^{161}$ are equal, we conclude that the spin of $Dy^{163}$ is 3/2.

From the splittings of the level with $J=1$ in λ 6259 we find the ratio of the magnetic moments

$$\mu(\mathrm{Dy}^{163})/\mu(\mathrm{Dy}^{161})=1.07\pm0.05\ ,$$

and the ratio of the quadrupole moments

$$Q(\mathrm{Dy}^{163})/Q(\mathrm{Dy}^{161})\approx 1\ .$$

In a recent work Mottelson and Nilsson²⁾ predict a spin of 5/2 (instead of 3/2) for $\mathrm{Dy}^{161}$, but since this is sensitive to their assumed deformation according to their calculation, the discrepancy between theory and observation does not seem to be serious.

### References

1) K. Murakawa and T. Kamei: Phys. Rev. **92** (1953) 325.
2) B. R. Mottelson and S. G. Nilsson: Phys. Rev. **99** (1955) 1615.

---

J. PHYS. SOC. JAPAN **11** (1956) 805~806

## Radio Frequency Absorption in Barium Chlorate

By Shoji KOJIMA, Kiyoe KATO, Shoichi ANNAKA
*Tokyo University of Education, Otsuka, Tokyo*

(Received May 18, 1956)

Several substances give rise radio-frequency absorption lines which are called piezoelectric lines¹⁾⁻⁶⁾. Among these substances $\mathrm{Ba(ClO_3)_2\cdot H_2O}$ was interesting in that it could produce nuclear quadrupole absorption too. On the other hand, according to the result obtained by Kartha⁷⁾ with the method of X-ray analysis the crystal is monoclinic with space group of $C^6_{2h}$, which can not have piezoelectric properties. It is very important for the interpretation of the absorption to determine whether the substances are piezoelectric or not.

The apparatus used for the detection of absorptions was a superregenerative oscillator working in the frequency range between 25 Mc and 30 Mc. At first, in the sample of $\mathrm{Ba(ClO_3)_2\cdot H_2O}$ the nuclear quadrupole resonance of chlorine isotope 35 was observed at 29.38 Mc, but the piezoelectric absorption was not detected. However, after the sample was heated in several hours at about 150°C, it gave rise the piezoelectric absorption and the quadrupole absorption disappeared. By this heat treatment the weight of the sample was decreased about five percent. The heated sample recovered the initial properties after it was kept several months in open air.

Disappearing of the quadrupole resonance by the heat treatment seemed to be caused by the increase of internal stress due to dehydration. Appearing of the piezoelectric absorption by the heat treatment supports the previous conclusion²⁾³⁾ that the absorption relates closely to imperfection of crystal.

If the absorption were only observed in piezoelectric substances, the sample should be changed by heating. In order to study the structure of crystal Debye-Scherrer photographs were taken for the natural sample and the heated sample with Cu K$\alpha$ radiation which was filtered by a nickel foil. The obtained patterns are reproduced in Fig. 1. The lines of the heated sample are in accord with those of the natural sample which have correspondence with the observations of Kartha. The change of intensity is attributed to change of size of grains. The agreement of the lines suggests that the structure of the crystal did not change at heating. By this result we must conclude that the absorption is observed in non-piezoelectric substance too.

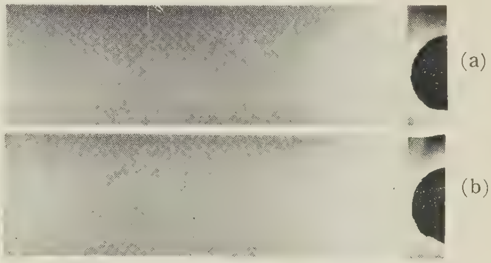

Fig. 1. Debye-Scherrer patterns of $\mathrm{Ba(ClO_3)_2\cdot H_2O}$. (a) natural sample (b) heated sample (1 hour at 150°C).

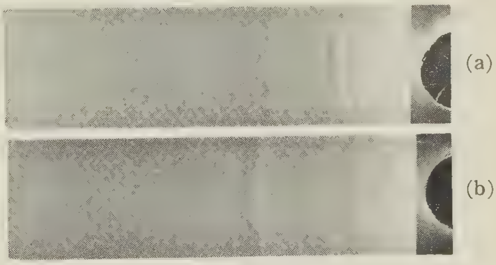

Fig. 2. Debye-Scherrer patterns of $\mathrm{CuSO_4\cdot 5H_2O}$. (a) natural sample (b) heated sample (1 hour at 55°C).

We have also found the absorption in $\mathrm{CuSO_4\cdot 5H_2O}$, $\mathrm{CaSO_4\cdot 2H_2O}$ and $\mathrm{SrCl_2\cdot 6H_2O}$ with some heat treatment. In view of the crystal structures⁸⁾ these substances seem to be non-piezoeletric before heating. Among them we have studied $\mathrm{CuSO_4\cdot 5H_2O}$ with X-rays. Debye-Scherrer patterns were taken on the natural sample which did not give rise the absorption and on the heated sample which gave rise it. In this case apparent change of pattern was observed as shown in Fig. 2. As a result we can not necessarily say that the studied sample was non-piezoelectric. At present, the certain indication is the case of $\mathrm{Ba(ClO_3)_2\cdot H_2O}$ alone.

We wish to thank professor Sudo for valuable discussions on the structure of crystals.

### References

1) R. Livingston: Ann. N.Y. Acad. Sci. **55** (1952) 800.
2) S. Kojima, K. Tsukada, S. Ogawa and A. Shimauchi: Phys. Rev. **92** (1953) 1571, **95** (1954) 1705.
3) S. Kojima, K. Tsukada, S. Ogawa, A. Shimauchi and N. Matsumiya: J. Phys. Soc. Japan **10** (1655) 265.
4) J. Duchesne and A. Monfils: J. Chem. Phys. **23** (1955) 762.
5) J. Duchesne and A. Monfils: Comptes Rendus Paris **241** (1955) 794.
6) Y. Yokogawa and I. Tatsuzaki: J. Phys. Soc. Japan **11** (1956) 85.
7) G. Kartha: Proc. Indian Acad Sci. **36** (1952) 501.
8) R. W. G. Wyckoff: "The Structure of Crystal" Int. Pub. Inc. N. Y. (1948).

---

## Errata

### Diffraction of Electromagnetic Waves by Circular Plate and Hole

Yûkichi NOMURA and Shigetoshi KATSURA

J. Phys. Soc. Japan **10** (1955) 285

P. 299 $r/a$ in Fig. 6, 7, 8 and 9 should be read $(r/a)^2$.

### The Effect of Frequency on the Fatigue of Metals

Alan K. HEAD

J. Phys. Soc. Japan **11** (1956) 468

Fig. 1 1200 C.P.M. should be read 12000 C.P.M.

JOURNAL OF THE PHYSICAL SOCIETY OF JAPAN Vol. 11, No. 8, AUGUST, 1956

# A Calculation of Physical Constants of Ceramic Barium Titanate

By Masakazu MARUTAKE

*Kobayasi Institute of Physical Research, Kokubunji, Tokyo*

(Received February 20, 1956)

The dielectric, piezoelectric and elastic constants of polycrystalline ceramics at room temperature are calculated by averaging those values of single crystals on the assumption that the ceramic is composed of spherical crystallites. The calculated values are in good agreement with observed ones, showing that the piezoelectric effects in each single crystal (especially $d_{15}$ at room temp.) play a great part in determining the properties of the ceramic.

Also the method is shown for calculating elastic constants of polycrystals which consist of spherical crystallites in all directions, with the calculated values of metals (Au, Ag, Cu, Fe etc.) in the cubic system.

The "destressing factor", which gives the relations between the internal stress of the sphere and the stress in the surrounding medium, is defined and calculated.

## § 1. Introduction

Barium titanate single domain crystals are well known to be highly anisotropic in the ferroelectric range, the dielectric constant along the $z$-axis, for instance, being much smaller than along the $x$-axis in the tetragonal phase¹⁾, and hence to show large piezoelectric effects²⁾³⁾. When the aggregate of these crystallites makes up a ceramic, its physical properties are considered to be some kind of averages of those of crystallites over all orientations. The averaging process may, however, be made in many ways, as Devonshire pointed out⁴⁾, and the shape of the grain boundaries must be taken into account.

On the dielectric constants of polycrystals, a calculation was made by Bruggeman⁵⁾ in 1935 under various conditions of aggregation; and he showed that in both the aggregate of spherical crystallites and the laminar aggregate where the planes of laminae are oriented uniformly in all directions, dielectric constants averaged are approximately equal and in good agreement with experimental values in polycrystals. On the elastic constants, however, it seems that such calculations were not made except that Bruggeman also studied in an insufficient way⁶⁾, and simple averaging processes have been used in calculating the elastic constants of polycrystalline metals⁷⁾.

Furthermore, barium titanate shows large piezoelectric effects, and each crystallite reacts on each other piezoelectrically in ceramics, and hence the dielectric constant and the elastic constants of ceramics cannot be derived independently without taking account of these piezoelectric interactions.

In this paper, the elastic constants of polycrystals are firstly considered which are aggregates of non-piezoelectric single crystals and the values of polycrystalline metals in the cubic system are calculated (§ 3). Then by the same method, the dielectric, the elastic and the piezoelectric constants of BaTiO$_3$ ceramics are calculated (§ 4). In these calculations, it is assumed that the polycrystal consists of crystallites each of which has a spherical form and the axes of which are oriented uniformly in all directions. In the case of BaTiO$_3$, the domain structures are not considered, but each spherical crystallite is assumed to be a single domain, the motion of the domain boundaries being hence neglected.

Outlines of the calculation (in the case of BaTiO$_3$ ceramics) are as follows. Consider an arbitrary sphere (a crystallite) to be placed in the isotropic medium which has the same dielectric and elastic constants as those of the ceramic. The sphere, then, has dielectric and elastic constants different from those of the surrounding medium, so that the electric field and the elastic stress in the interior of the sphere are different from those of the medium which are equal to applied ones. The electric field and the mechanical stress in the sphere are calculated, respectively, in § 2 and § 3, and the electric polarization and the mechanical strain in the sphere, which are variable as the orientation of the crystallographic axes, are averaged over all orientations.

Following notations (in CGS esu.) are used:

$E$: electric field
$P$: polarization
$\kappa$: dielectric susceptibility
$\varepsilon$: dielectric constant
$T$: stress
$S$: strain
$c$: elastic constant
$s$: elastic compliance coefficient
$d$: piezoelectric modulus
$O-xyz$: a coordinate system which has an origin at the center of the sphere and has axes parallel to the crystallographic ones of each crystallite
$O\text{-}x'y'z'$: a coordinate system which is fixed to the medium or to the ceramic

$$\begin{array}{c|ccc} & x & y & z \\ \hline x' & l_1 & l_2 & l_3 \\ y' & m_1 & m_2 & m_3 \\ z' & n_1 & n_2 & n_3 \end{array}$$

: direction consines between two coordinate systems

The suffixes $o$ and $i$ denote, respectively, the surrounding medium and the interior of the sphere, and the suffix $*$ denotes an averaged value which is a physical constant of the ceramic; thus, for example, $T_{05}$ denotes a shear component in the surrounding medium with respect to the coordinate axes fixed to the sphere, $P_{i3}'$ is a component of the polarization in the interior of the sphere along the $z'$-axis fixed to the medium, and $s_{44}^{*E}$ is an elastic compliance coefficients at the constant electric field of the ceramic.

## § 2. Electric Field in the Interior of the Sphere

### (i) Internal Field

Let us consider a sphere of radius $a$ which is placed in the medium. If the sphere is uniformly polarized ($P_i$) and in the medium the polarization is $P_0$ and the electric field is $E_0$ except near the sphere, the electric field $E_i$ in the interior of the sphere is calculated as follows.

Near the sphere, the electric field is equal to $E_0$ plus the field which is produced by the dipole $A$ placed at the center of the sphere. Then, if the boundary conditions — the continuity of the tangential components of the electric field, and the continuity of the normal components of the electric displacements—are satisfied, $A$ and $E$ are easily calculated.

$$A=\frac{4\pi}{3}a^3\frac{3}{2\varepsilon^*+1}(P_i-P_0)\ , \qquad (2.1)$$

$$E_i-E_0=\frac{4\pi}{2\varepsilon^*+1}(P_0-P_i)\ , \qquad (2.2)$$

where $P_0$ and $P_i$ include the polarization produced by the piezoelectric effects in addition to the dielectric polarization; and when non-piezoelectric, Eq. (2.2) is reduced to the well known formula.

Eq. (2.2) gives the internal field $E_i$, or

$$E_i-E_0=\alpha(P_0-P_i)\ , \qquad (2.3)$$

where

$$\alpha=\frac{4\pi}{2\varepsilon^*+1}\ . \qquad (2.4)$$

We shall call $\alpha$ the " depolarising factor ".

### (ii) Dielectric Constants of Polycrystals

Next, we shall consider the dielectric constant of the polycrystal (non-piezoelectric) which is an aggregate of spheres of various dimensions. This problem was previously solved by Bruggeman[5)] in the most general case. Here the same problem is considered rather in a different way because it is analogous to the method for calculating the elastic constants in § 3. For simplicity, only the case is considered where the crystallite belongs to the tetragonal or hexagonal system, namely $\varepsilon_1=\varepsilon_2\neq\varepsilon_3$.

If the electric field is parallel to the $z'$-axis, the polarization is given by

$$\left.\begin{aligned} P_{i1}&=\kappa_1 E_{i1}\ ,\\ P_{i2}&=\kappa_1 E_{i2}\ ,\\ P_{i3}&=\kappa_3 E_{i3}\ ;\end{aligned}\right\} \qquad (2.5)$$

$$\left.\begin{aligned} P_{01}'&=P_{02}'=0\ ,\\ P_{03}'&=\kappa^* E_{03}'\ ;\end{aligned}\right\} \qquad (2.6)$$

where the surroundings of an arbitrary sphere of the crystallite are replaced by an isotropic medium which has a dielectric constant $\varepsilon^*$.

Then, by transforming the coordinate axes, we obtain from Eqs. (2.3), (2.5) and (2.6)

$$\left.\begin{aligned} P_{i1}&=\frac{n_1\kappa_1(1+\alpha\kappa^*)}{1+\alpha\kappa_1}E_{03}'\ ,\\ P_{i2}&=\frac{n_2\kappa_1(1+\alpha\kappa^*)}{1+\alpha\kappa_1}E_{03}'\ ,\\ P_{i3}&=\frac{n_3\kappa_3(1+\alpha\kappa^*)}{1+\alpha\kappa_3}E_{03}'\ .\end{aligned}\right\} \qquad (2.7)$$

Accordingly, by transforming the coordinate axes again,

$$P_{i3}'=n_1P_{i1}+n_2P_{i2}+n_3P_{i3}$$
$$=\left\{\frac{(n_1^2+n_2^2)\kappa_1}{1+\alpha\kappa_1}+\frac{n_3^2\kappa_3}{1+\alpha\kappa_3}\right\}(1+\alpha\kappa^*)E_{03}' . \tag{2.8}$$

We can average $P_{i3}'$ by considering that the crystallographic axes of every sphere are uniformly oriented.

Namely,

$$\langle P_{i3}'\rangle_{AV}=\left(\frac{2}{3}\frac{\kappa_1}{1+\alpha\kappa_1}+\frac{1}{3}\frac{\kappa_3}{1+\alpha\kappa_3}\right)\times(1+\alpha\kappa^*)E_{03}' , \tag{2.9}$$

because

$$\langle n_1^2\rangle_{AV}=\langle n_2^2\rangle_{AV}=\langle n_3^2\rangle_{AV}=1/3 .$$

And as

$$\langle P_{i3}'\rangle_{AV}=\kappa^*E_{03}' ,$$

we obtain

$$\kappa^*=\left(\frac{2}{3}\frac{\kappa_1}{1+\alpha\kappa_1}+\frac{1}{3}\frac{\kappa_3}{1+\alpha\kappa_3}\right)(1+\alpha\kappa^*) . \tag{2.10}$$

Eq. (2.10) can be solved by simple calculations, and

$$\varepsilon^*=\frac{1}{4}(\varepsilon_1+\sqrt{\varepsilon_1^2+8\varepsilon_1\varepsilon_3}) . \tag{2.11}$$

This result is identical with Bruggeman's formula⁵⁾.

## § 3. Mechanical Stress in the Interior of the Sphere

In this section we shall consider the mechanical stress, in the same way as we discussed the electric field in § 2.

### ( i ) Internal Stress

In the case of the mechanical stress, we cannot solve rigorously the internal stress in the sphere which is placed in the isotropic medium except when the hydrostatic pressure is applied, because the sphere is not uniformly strained. We can, however, consider that the strains in the interior of the sphere are approximately uniform and can calculate the stresses in this approximation.

### (a) Elongation

If the sphere is uniformly elongated along the $z$-axis (the elongation is denoted by $S_{i3}$) and in the medium the elongation and the tension are zero except near the sphere, the tension components ($T_{i1}$, $T_{i2}$ and $T_{i3}$) in the interior of the sphere is calculated as follows. Near the sphere in the medium, the tension is produced by the tension source $B$ placed at the center of the sphere approximately. The definition of the "tension source" and the stress and strain which are produced by the tension source are shown in the Appendix. Then, if the following boundary conditions,

(1) the continuity of 3 stress components perpendicular to the boundary plane,

(2) the continuity of 3 strain components parallel to the boundary plane,

are satisfied, $T_{i1}$, $T_{i2}$ and $T_{i3}$ can be calculated.

$$\left.\begin{aligned}T_{i1}&=T_{i2}=-\beta_\perp S_{03} ,\\ T_{i3}&=-\beta_{\parallel}S_{03}\end{aligned}\right\} \tag{3.1}$$

where

$$\left.\begin{aligned}\beta_\perp&=\mu\frac{\lambda+6\mu}{3\lambda+8\mu} ,\\ \beta_{\parallel}&=10\,\mu\frac{\lambda+2\mu}{3\lambda+8\mu} ;\end{aligned}\right\} \tag{3.2}$$

where $\lambda$ and $\mu$ are Lamé's elastic constants of the medium, and we shall call $\beta_\perp$ and $\beta_{\parallel}$ "destressing factors" for the elongation. The destressing factors are analogous to the depolarizing factor $\alpha$, but it is to be noted that two factors are defined—$\beta_{\parallel}$ along the direction of the elongation, and $\beta_\perp$ perpendicular to it.

Or, by the superposition principle, Eq. (3.1) can be shown in more general form.

$$\left.\begin{aligned}T_{i1}-T_{01}&=\beta_{\parallel}(S_{01}-S_{i1})+\beta_\perp(S_{02}-S_{i2})+\beta_\perp(S_{03}-S_{i3}) ,\\ T_{i2}-T_{02}&=\beta_\perp(S_{01}-S_{i1})+\beta_{\parallel}(S_{02}-S_{i2})+\beta_\perp(S_{03}-S_{i3}) ,\\ T_{i3}-T_{03}&=\beta_\perp(S_{01}-S_{i1})+\beta_\perp(S_{02}-S_{i2})+\beta_{\parallel}(S_{03}-S_{i3}) .\end{aligned}\right\} \tag{3.3}$$

### (b) Shearing Strain

If we put

$$S_{01}-S_{i1}=-(S_{02}-S_{i2})=\sigma , \tag{3.4}$$

and other strain components are zero, the stress components are given from Eq. (3.3) as follows.

$$\left.\begin{aligned}T_{i1}-T_{01}&=(\beta_{\parallel}-\beta_\perp)\sigma ,\\ T_{i2}-T_{02}&=-(\beta_{\parallel}-\beta_\perp)\sigma .\end{aligned}\right\} \tag{3.5}$$

Now, if we rotate the coordinate axes by $-\pi/4$ around the $z$-axis, we can obtain strain and stress components with respect to the new coordinate system.

$$\left.\begin{aligned} &S_{06}-S_{i6}=2\sigma\ , \\ &T_{i6}-T_{06}=(\beta_{\parallel}-\beta_{\perp})\sigma\ , \\ &\text{Other components}=0. \end{aligned}\right\} \tag{3.6}$$

Accordingly, we obtain for the shearing strain

$$\frac{T_{i4}-T_{04}}{S_{04}-S_{i4}}=\gamma\ , \tag{3.7}$$

and

$$\gamma=\frac{\beta_{\parallel}-\beta_{\perp}}{2}=\frac{\mu}{2}\,\frac{9\lambda+14\mu}{3\lambda+8\mu}\ . \tag{3.8}$$

Hereafter $\gamma$ shall be called the destressing factor for the shearing strain.

This factor $\gamma$ was previously studied by Bruggeman⁶⁾, and by his method $\gamma$ can be calculated as

$$\gamma=\frac{\mu}{2} \quad \text{(Bruggeman)}\ .$$

This is not consistent with Eq. (3.8), and is not correct, because he calculated in the case of the torsional strain where the strain is not uniform.

### (c) Hydrostatic Compression

In the case of the hydrostatic pressure, we can put

$$\left.\begin{aligned} &S_{i1}=S_{i2}=S_{i3}\ , \\ &S_{01}=S_{02}=S_{03}\ , \\ &S_{01}-S_{i1}=\sigma\ ; \\ &T_{i1}=T_{i2}=T_{i3}\ , \\ &T_{01}=T_{02}=T_{03}\ . \end{aligned}\right\} \tag{3.9}$$

Then from Eqs. (3.3)

$$\frac{T_{i1}-T_{01}}{S_{01}-S_{i1}}=\delta\ , \tag{3.10}$$

and

$$\delta=\beta_{\parallel}+2\beta_{\perp}=4\mu\ . \tag{3.11}$$

$\delta$ is the destressing factor for the hydrostatic compression, and this is consistent with the result calculated by Bruggeman⁶⁾ with no approximation.

### (ii) Elastic Constants of Polycrystals

Now we can calculate the elastic constants of the aggregate of spherical crystallites with various dimensions and with various orientations when the crystal is non-piezoelectric. For simplicity, we shall consider only the case where the crystal belongs to the cubic system.

If the stress is a pure tension along $z'$-axis (namely, stress components except $T_{03}'$ are zero), the strain components are given by

$$\left.\begin{aligned} &S_{i1}=s_{11}T_{i1}+s_{12}(T_{i2}+T_{i3})\ , \\ &S_{i2}=s_{11}T_{i2}+s_{12}(T_{i3}+T_{i1})\ , \\ &S_{i3}=s_{11}T_{i3}+s_{12}(T_{i1}+T_{i2})\ , \\ &S_{i4}=s_{44}T_{i4}\ , \\ &S_{i5}=s_{44}T_{i5}\ , \\ &S_{i6}=s_{44}T_{i6}\ ; \end{aligned}\right\} \tag{3.12}$$

and

$$\left.\begin{aligned} &S_{01}'=S_{02}'=s_{12}{}^{*}T_{03}'\ , \\ &S_{03}'=s_{11}{}^{*}T_{03}'\ , \\ &S_{04}'=S_{05}'=S_{06}'\ , \end{aligned}\right\} \tag{3.13}$$

The surroundings of an arbitrary sphere of the crystallite are replaced by an isotropic medium which has elastic compliance coefficients $s_{11}{}^{*}$, $s_{12}{}^{*}$ and $s_{44}{}^{*}$ (or Lamé's constants $\lambda$ and $\mu$). Then, by transforming coordinate axes and by averaging, in the similar way to the case of evaluating dielectric constants, we obtain (in detail $v$. ref. (8))

$$\left.\begin{aligned} s_{11}{}^{*}=&\frac{1}{5\varDelta}[(3g_1+2g_2)+\{(3g_1+2g_2)\beta_{\parallel}+(2g_1+8g_2)\beta_{\perp}\}s_{11}{}^{*} \\ &+\{(2g_1+8g_2)\beta_{\parallel}+(8g_1+12g_2)\beta_{\perp}\}s_{12}{}^{*}] \\ &+\frac{s_{44}}{5(1+\gamma s_{44})}(1+2\gamma s_{11}{}^{*}-2\gamma s_{12}{}^{*})\ , \\ s_{12}{}^{*}=&\frac{1}{5\varDelta}[(g_1+4g_2)+\{(g_1+4g_2)\beta_{\parallel}+(4g_1+6g_2)\beta_{\perp}\}s_{11}{}^{*} \\ &+\{(4g_1+6g_2)\beta_{\parallel}+(6g_1+14g_2)\beta_{\perp}\}s_{12}{}^{*}]\ , \\ &-\frac{s_{44}}{10(1+\gamma s_{44})}(1+2\gamma s_{11}{}^{*}-2\gamma s_{12}{}^{*})\ , \\ s_{44}{}^{*}=&2(s_{11}{}^{*}-s_{12}{}^{*}) \\ =&\left(\frac{4}{5}\,\frac{g_1-g_2}{\varDelta}+\frac{3}{5}\,\frac{s_{44}}{1+\gamma s_{44}}\right)(1+\gamma s_{44}{}^{*})\ ; \end{aligned}\right\} \tag{3.14}$$

where

$$\left.\begin{aligned}&\varDelta=\begin{vmatrix}L, & M, & M\\ M, & L, & M\\ M, & M, & L\end{vmatrix}, \quad g_1=\begin{vmatrix}s_{11}, & M, & M\\ s_{12}, & L, & M\\ s_{12}, & M, & L\end{vmatrix}, \quad g_2=\begin{vmatrix}s_{12}, & M, & M\\ s_{11}, & L, & M\\ s_{12}, & M, & L\end{vmatrix};\\ &L=1+\beta_{\|}s_{11}+2\beta_{\perp}s_{12}\,,\\ &M=s_{11}\beta_{\perp}+s_{12}\beta_{\perp}+s_{12}\beta_{\|}\,.\end{aligned}\right\} \qquad (3.15)$$

Averaged elastic constants are given implicitly by Eqs. (3.14) (Namely, $\beta$ and $\gamma$ are averaged values.), and they are to be calculated by the successive approximation.

In Table II and III, the numerical values calculated in this way are shown in comparison with other averaged values which were calculated from the average of the elastic compliance coefficients $s$'s and the average of the elastic constants $c$'s. Constants of single crystals in Table I were used in the calculation which were quoted from Mason and McSkimin's paper[7].

The agreement with the experimental values[9] is not very good, but is better than other calculations. This calculation, however, is rather laborious and is not considered to be an efficient and appropriate method.

Table I. Elastic complience coefficients of single crystals (in $10^{-12}$cm$^2$/dyne).

| Metal | $s_{11}$ | $s_{12}$ | $s_{44}$ |
|---|---|---|---|
| Au | 2.33 | −1.07 | 2.38 |
| Ag | 2.32 | −0.993 | 2.29 |
| Cu | 1.49 | −0.625 | 1.33 |
| Fe | 0.757 | −0.282 | 0.862 |
| Al | 1.59 | −0.58 | 3.52 |
| Pb | 9.30 | −4.26 | 6.94 |
| W | 0.257 | −0.073 | 0.660 |

Table II. Elastic compliance coefficients $s_{11}^*$ of polycrystals (in $10^{-12}$cm$^2$/dyne).

| Metal | Calculated from $\langle s_{11}'\rangle$ | Calculated from $\langle c_{11}'\rangle$ | Present calculation | Observed value |
|---|---|---|---|---|
| Au | 1.45 | 1.12 | 1.24 | 1.25 |
| Ag | 1.45 | 1.14 | 1.26 | 1.27 |
| Cu | 0.91 | 0.69 | 0.77 | 0.81 |
| Fe | 0.51 | 0.44 | 0.47 | 0.48 |
| Al | 1.43 | 1.42 | — | 1.42 |
| Pb | 5.26 | 3.53 | — | 6.18 |
| W | 0.26 | 0.26 | 0.26 | — |

Table III. Elastic compliance coefficients $s_{44}^*$ of polycrystals (in $10^{-12}$cm$^2$/dyne).

| Metal | Calculated from $\langle s_{44}'\rangle$ | Calculated from $\langle c_{44}'\rangle$ | Present calculation | Observed value |
|---|---|---|---|---|
| Au | 4.15 | 3.18 | 3.57 | 3.61 |
| Ag | 4.02 | 3.06 | 3.46 | 3.48 |
| Cu | 2.49 | 1.84 | 2.08 | 2.20 |
| Fe | 1.35 | 1.13 | 1.22 | 1.22 |
| Al | 3.85 | 3.82 | — | 3.75 |
| Pb | 15.03 | 9.84 | — | 17.8 |
| W | 0.66 | 0.66 | 0.66 | — |

## § 4. Physical Constants of Barium Titanate Ceramics

The dielectric constants $\mathcal{E}^*$ and the elastic com-pliance coefficients $s_{11}^*$ and $s_{12}^*$ of polycrystalline ceramic BaTiO$_3$ can be calculated by using $\alpha$, $\beta$ and $\gamma$ derived in § 2 and § 3. BaTiO$_3$ single crystal, however, shows piezoelectric effects, and the calculation is more complicated. In this calculation, it is assumed that the form of the single crystal is spherical, and that each crystallite consists of a single domain. The ignorance of the domain structures may seem to be a very crude approximation, but the diameters of crystallites are observed to be less than *ca.* 10 microns and it is possible that there exist many single domain crystallites; furthermore in this calculation of averaging, the assumption of spherical domain may be considerabled to be a sufficient approximation.

The piezoelectric moduli $d_{31}^*$, $d_{33}^*$ and $d_{15}^*$ of the prepolarized ceramic can be also calculated in the similar way, when the distribution of the orientations of crystallites is determined. In the fully polarized ceramic, it is considered, 180° reversals of the polar axes are complete, but 90° rotations does not remain after the polarizing d.c. electric field is removed because 90° rotations accompany the mechanical strain. Accordingly it is assumed that in the prepolalized ceramic all 180° reversals of the polar axes take place in favor of the polarizing field, namely the $z$-axes are oriented uniformly within right angles around the $z'$-axis (*v.* the notations in § 1.). Though prepolarized ceramics have tetragonal symmetry, anisotropies in their dielectric and elastic constants are very small[10], and in this calculation they are assumed to be isotropic with regard to their dielectric and elastic properties. (The calculation was only made on the numerical values at room temperature.)

The piezoelectric equations in each crystallite are

$$\left.\begin{aligned}
P_{i1}&=\kappa_1{}^T E_{i1}+d_{15}T_{i5}\ ,\\
P_{i2}&=\kappa_1{}^T E_{i2}+d_{15}T_{i4}\ ,\\
P_{i3}&=\kappa_3{}^T E_{i3}+d_{31}T_{i1}+d_{31}T_{i2}+d_{33}T_{i3}\,;\\
S_{i1}&=d_{31}E_{i3}+s_{12}{}^E T_{i1}+s_{11}{}^E T_{i2}+s_{13}{}^E T_{i3}\ ,\\
S_{i2}&=d_{31}E_{i3}+s_{12}{}^E T_{i1}+s_{11}{}^E T_{i2}+s_{13}{}^E T_{i3}\ ,\\
S_{i3}&=d_{33}E_{i3}+s_{13}{}^E T_{i1}+s_{13}{}^E T_{i2}+s_{33}{}^E T_{i3}\ ,\\
S_{i4}&=d_{15}E_{i2}+s_{44}{}^E T_{i4}\ ,\\
S_{i5}&=d_{15}E_{i1}+s_{44}{}^E T_{i5}\ ,\\
S_{i6}&=s_{66}T_{i6}\ .
\end{aligned}\right\} \tag{4.1}$$

The internal electric field and the internal mechanical stress are given by

$$\left.\begin{aligned}
E_{i1}&=E_{01}+\alpha(P_{01}-P_{i1})\ ,\\
E_{i2}&=E_{02}+\alpha(P_{01}-P_{i2})\ ,\\
E_{i3}&=E_{03}+\alpha(P_{03}-P_{i3})\,;\\
T_{i1}&=T_{01}+\beta_{||}(S_{01}-S_{i1})\\
&\qquad+\beta_{\perp}(S_{02}-S_{i2})+\beta_{\perp}(S_{03}-S_{i3})\ ,\\
T_{i2}&=T_{02}+\beta_{\perp}(S_{01}-S_{i1})\\
&\qquad+\beta_{||}(S_{02}-S_{i2})+\beta_{\perp}(S_{03}-S_{i3})\ ,\\
T_{i3}&=T_{03}+\beta_{\perp}(S_{01}-S_{i1})\\
&\qquad+\beta_{\perp}(S_{01}-S_{i2})+\beta_{||}(S_{03}-S_{i3})\ ,\\
T_{i4}&=T_{04}+\gamma(S_{04}-S_{i4})\ ,\\
T_{i5}&=T_{05}+\gamma(S_{05}-S_{i5})\ ,\\
T_{i6}&=T_{06}+\gamma(S_{06}-S_{i6})\ .
\end{aligned}\right\} \tag{4.2}$$

From Eqs. (4.1) and (4.2), $P_{i1}$, $P_{i2}$, $P_{i3}$ and $S_{i1}$, $S_{i2}$, $\cdots$, $S_{i6}$ can be solved as functions of $E_{01}$, $E_{02}$, $E_{03}$; $P_{01}$, $P_{02}$, $P_{03}$ and of $T_{01}$, $T_{02}$, $\cdots$, $T_{06}$; $S_{01}$, $S_{02}$, $\cdots$, $S_{06}$. (The solution is complicated, including 4th order determinants.) Then, for instance, if $E_{03}'$ is given, $\langle P_{03}'\rangle_{AV}$, $\langle S_{i1}\rangle_{AV}$ and $\langle S_{i3}\rangle_{AV}$ can be solved by transforming the coordinate axes twice (*cf.* § 2) and by averaging over all orientations. Hence,

$$\kappa^*=\frac{\langle P_{03}'\rangle_{AV}}{E_{03}'}\ ,\qquad d_{31}^*=\frac{\langle S_{i1}'\rangle_{AV}}{E_{03}'}$$

$$\text{and}\quad d_{33}^*=\frac{\langle S_{i3}'\rangle_{AV}}{E_{03}'}$$

can be calculated. In the same way all constants in Table V are calculated.

Table IV. Dielectric, piezoelectric and elastic constants of $BaTiO_3$ single crystal.

| | | Bond *et al.*[3] | Merz *et al.*[1][2] | Devonshire[4] | Value used in this calculation |
|---|---|---|---|---|---|
| Elastic compliance coefficient (in$10^{-12}$cm$^2$/dyne) | $s_{11}{}^E$ | 1.2 | — | 1.1 | 1.0 |
| | $s_{12}{}^E$ | −0.12 | — | −0.2 | −0.1 |
| | $s_{13}{}^E$ | — | — | −0.9 | −0.7 |
| | $s_{33}{}^E$ | — | — | 2.3 | 2.0 |
| | $s_{44}{}^E$ | — | — | 5.5 | 4.0 |
| | $s_{66}{}^E$ | — | — | 0.75 | 0.7 |
| Dielectric constant | $\varepsilon_1{}^T$ | — | 4500 | 4400 | 4500 |
| | $\varepsilon_3{}^T$ | — | 215 | 225 | 250 |
| Piezoelectric modulus (in $10^{-6}$ CGS esu.) | $d_{31}$ | −3.1 | −1.0 | −1.5 | −2.0 |
| | $d_{33}$ | 9.5 | 3.0 | 5.0 | 6.0 |
| | $d_{15}$ | — | — | 40 | 30 |

Table V. Dielectric, piezoelectric and elastic constants of the polycrystalline ceramic $BaTiO_3$.

Dielectric constant $\varepsilon^*$.

| Calculated value | | | | Observed value |
|---|---|---|---|---|
| $\langle\varepsilon\rangle_{AV}$ | $1/\langle 1/\varepsilon\rangle_{AV}$ | Bruggeman's formula(2.11) | Present calculation | |
| 3100 | 680 | 2500 | 1500 | 1600 |

Elastic compliance coefficients $s_{11}^*$ and $s_{44}^*$. (in $10^{-12}$cm$^2$/dyne)

| | Calculated value | | | Observed value |
|---|---|---|---|---|
| | $\langle s\rangle_{AV}$ | From $\langle c\rangle_{AV}$ | Present calculation | |
| $s_{11}^*$ | 1.06 | 0.73 | 0.8 | 0.78 |
| $s_{44}^*$ | 3.23 | 2.08 | 2.1 | 2.1 |

Piezoelectric moduli $d_{31}^*$, $d_{33}^*$ and $d_{15}^*$. (in $10^{-6}$ CGS esu.)

| | Calculated valued | | Observed value |
|---|---|---|---|
| | $\langle d\rangle_{AV}$ | Present calculation | |
| $d_{31}^*$ | −3.8 | −2.1 | −2.0 |
| $d_{33}^*$ | 8.5 | 5.1 | 5.4 |
| $d_{15}^*$ | 9.5 | 6.0 | 8.0(?) |

The numerical values of the constans of the single crystal are shown in Table IV. All values, however, have not been measured as yet, and calculated values by Devonshire[4] are also referred.

Table V shows the calculated values in comparison with other averaged values. The agreement with observed values is considered to be good by taking account of our crude approximations, though the calculated values of piezoelectric moduli are a little smaller by considering that the specimens are not perfectly polarized. (The observed values[11] of the dielectric and the elastic constants are corrected ones for zero porosity[12][13], because usually porous ceramic specimens (porosity: *ca.* 8%) are used.)

## § 5. Discussion and Summary

In § 4 the dielectric, elastic and piezoelectric constants of ceramic $BaTiO_3$ were calculated, and were shown to be in fairly good agreement with experimental values. It may be concluded that the properties of the ceramic are averages of those of the single crystal, and that the motions of the domain boundaries can be neglected for small amplitudes except at very low frequencies. (That this is the case was recently confirmed by Little[14] experimentally from the observations of the motions of the domain boundaries.) Accordingly, there need not exist any relations among piezoelectric moduli $d_{31}{}^*$, $d_{33}{}^*$ and $d_{15}{}^*$, while the ratio of $d_{33}{}^*$ to $d_{31}{}^*$ is expected to be equal to 2, for instance, according to Mason's electrostrictive theory[11]. Experimentally it was observed to be 2.7.

It should be noted that the dielectric constant $\varepsilon^*$ is smaller than averaged values without considerations of piezoelectric reactions (*cf.* the calculated value from Bruggeman's formula in Table V), and that the large value of $d_{15}$ (at room temperature) of the single crystal plays a great part in reducing the value of $\varepsilon^*$. Also, large piezoelectric moduli $d_{31}{}^*$, $d_{33}{}^*$ and $d_{15}{}^*$ are mainly due to the large value of $d_{15}$. In this sense the measurement of $d_{15}$ of the single crystal is desirable.

The method for calculating the elastic constants of polycrystals (§ 3) is very complicated and may not be appropriate for the applications, yet the destressing factors $\beta$, $\gamma$ and $\delta$ are considered to be useful in some other cases (*e.g.* the calcuclation of the elastic constants of porous materials[13]).

### Appendix. Tension Source

In the isotropic bodies, the following displacements can exist as shown from the elastic theory.

$$\left.\begin{aligned} u&=B\left(\frac{x}{r^3}-\frac{3xz^2}{r^5}\right),\\ v&=B\left(\frac{y}{r^3}-\frac{3yz^2}{r^5}\right),\\ w&=B\left(\frac{\lambda-\mu}{\lambda+\mu}\frac{z}{r^3}-\frac{3z^3}{r^5}\right); \end{aligned}\right\} \tag{A.1}$$

where $u$, $v$ and $w$ are displacements respectively along the $x$-, $y$- and $z$-axis. Eqs. (A. 1) represent a solution when the "dipole or force" or the "tension source" is applied at the origin of the coordinate system ($O$-$xyz$). The tension source is defined as follows.

When two forces $(0,\ 0,\ F)$ and $(0,\ 0,\ -F)$ are applied respectively at the points $(0,\ 0,\ \Delta z)$ and $(0,\ 0,\ -\Delta)$, and

$$\lim_{\Delta z\to 0} F\Delta z=B\ , \tag{A.2}$$

we shall call the pair of forces the tension source and $B$ the magnitude of the tension source.

Eqs. (A.1) can be derived from the solution shown in Love's text-book[15].

The stress components can be calculated from Eqs. (A.1).

$$\left.\begin{aligned} X_\nu&=-2\mu\left(\frac{3\lambda+2\mu}{\lambda+\mu}\frac{x}{r^4}-12\frac{xz^2}{r^6}\right)B\ ,\\ Y_\nu&=-2\mu\left(\frac{3\lambda+2\mu}{\lambda+\mu}\frac{y}{r^4}-12\frac{yz^2}{r^6}\right)B\ ,\\ Z_\nu&=-2\mu\left(\frac{2(3\lambda+2u)}{\lambda+\mu}\frac{z}{r^4}-12\frac{z^3}{r^6}\right)B\ . \end{aligned}\right\} \tag{A.4}$$

Here, only the stress components $(X_\nu,\ Y_\nu,\ Z_\nu)$ in the spherical surface of radius $r$ $(=\sqrt{x^2+y+z^2})$ and are shown.

The solution given by Eqs. (A.1) and (A.3) is rigorous except at the origin, and in order to satisfy the boundary conditions when a uniformly deformed sphere of radius $a$ is inserted at the origin, it is necessary that Eqs. (A.1) and (A.3) are averaged over the boundary plane (or the surface of the sphere of radius $a$). Namely, by expanding Eqs. (A.1) and (A.3) by the spherical surface functions and by taking the first terms, we obtain at the surface of the sphere

$$\left.\begin{aligned} u&=\frac{2}{5}B\frac{x}{a^3}\ ,\\ v&=\frac{2}{5}B\frac{y}{a^3}\ ,\\ w&=-\frac{2}{5}B\frac{2\lambda+7\mu}{\lambda+\mu}\frac{z}{a^3}; \end{aligned}\right\} \tag{A.4}$$

$$\left.\begin{aligned} X_\nu &= -\frac{2}{5}\,\mu\frac{3\mu-2\mu}{\lambda+\mu}\,\frac{x}{a^4}\,B\,,\\ Y_\gamma &= -\frac{2}{5}\,\mu\frac{3\lambda-2\mu}{\lambda+\mu}\,\frac{y}{a^4}\,B\,,\\ Z_\nu &= \ \ \frac{4}{5}\,\mu\frac{3\lambda+8\mu}{\lambda+\mu}\,\frac{z}{a^4}\,B\,. \end{aligned}\right\} \qquad (A.5)$$

The approximate solution given by Eqs. (A. 4) and (A.5) now satisfies the boundary conditions and by taking account of the superposition principle, we can derive equations (3.1) and (3.2). (The derivation of the destressing factor is shown in more detail in ref. (8) pp. 137–140.)

**Notes added in proof**: (1) Recently F. Kulscar (J. Am. Cer. Soc. **39** (1956) p. 13) and W. R. Cook, Jr. (*ibid.* p. 17) observed the domain structures in $BaTiO_3$ ceramic. This suggests that the assumption of the laminar aggregate is more appropriate, but physical constants of the spherical aggregate may not differ sensibly from those of the laminar aggregate as was shown by Bruggeman[5] in the case of the dielectric constant.

(2) Recently M. McQuarrie (J. Am. Cer. Soc. **39** (1956) 54) suggested some questions on the domain processes in $BaTiO_3$ ceramics. This paper is an answer to his questions though not satisfactory.

### References

1) W. J. Merz: Phys. Rev. **76** (1949) 1221.
2) M. E. Caspari and W. J. Merz: Phys. Rev. **80** (1950) 1082.
3) W. L. Bond, W. P. Mason and H. J. McSkimin: Phys. Rev. **82** (1951) 442.
4) A. F. Devonshire: Phil. Mag. **40** (1949) 1040, **42** (1951) 1065.
5) D. A. G. Bruggeman: Zeits. f. Phys. **92** (1934) 561; Ann. d. Phys. **24** (1935) 636.
6) D. A. G. Bruggeman: Ann. d. Phys. **29** (1937) 160.
7) W. P. Mason and H. J. McSkimin: J .Acous. Soc. Am. **19** (1947) 464; J. App. Phys. **19** (1949) 464; J. App. Phys. **19** (1948) 940, **20** (1949) 228.
8) M. Marutake: Bull. Kobayasi Inst. Phys. Res. **5** (1955) 135 (in Japanese).
9) Kaye and Laby: *Physical and Chemical Constants* (Longmans, Green and Company, New York) p. 29.
10) D. S. Moseley: J. Acous. Soc. Am. **27** (1955) 947.
M. Marutake and T. Ikeda: Unpublished.
11) W.P. Mason: *Piezoelectric Crystals and their Application to Ultrasonic* (1950) Chap. XII.
12) D. F. Rushman and M. A. Strivens: Proc. Phys. Soc. **59** (1947) 1011.
13) M. Marutake and T. Ikeda: J. Phys. Soc. Japan. **11** (1956) 814.
14) Elizabeth A. Little: Phys. Rev. **98** (1955) 978.
15) A. E. H. Love: *The Mathematical Theory of Elasticity*. 4th Ed. (1934) p. 185.

---

JOURNAL OF THE PHYSICAL SOCIETY OF JAPAN Vol. 11, No. 8, AUGUST, 1956

# Elastic Constants of Porous Materials, Especially of $BaTiO_3$ Ceramics

By Masakazu MARUTAKE and Takuro IKEDA
*Kobayasi Institute of Physical Research, Kokubunji, Tokyo*

(Received February 20, 1956)

The effective elastic constants of porous materials are calculated on the assumption that spherical pores are dispersed uniformly, and are compared with observed values of $BaTiO_3$ ceramics sintered at different temperatures. The agreement of the calculations with the experiments is not very good, and the form factors of pores are discussed.

## §1. Introduction

Recently many kinds of electro-mechanical transducers in the polycrystalline ceramic form were devised, such as barium titanate (piezoelectric) and ferrite (magnetostrictive). These ceramic materials, prepared by sintering, are invariably porous to a certain extent. It is, therefore, considered that the studies of the physical properties of such porous materials are necessary in the practical application.

On the dielectric properties, Rushman and Strivens[1] studied theoretically and experimentally.

On the other hand, the elastic properties of porous materials, it seems, have not been studied as yet, and we took up this problem in this paper. Firstly, the general formulae were derived for calculating the elastic constants as functions of the porosity, and then they were compared with the experiments. As samples of porous materials, $BaTiO_3$ ceramics were exclusively used, which were sintered at different temperatures in order that they may have different porosities.

## § 2. Theoretical

The following notations are used:

$v$ : porosity (volume fraction of pores)
$s_{11}$, $s_{44}$ : elastic compliance coefficients
$\lambda$, $\mu$ : Lamé's elastic constants
$E\left(=\frac{1}{s_{11}}\right)$ : Young's modulus
$N\left(=\frac{1}{s_{44}}\right)$ : rigidity
$K$ : volume elastic constant
$\varepsilon$ : dielectric constant

The suffix $*$ represents the constant when there are no pores, and the suffix $P$ represents the constant of the porous material.

Outlines of the calculation are as follows. The whole body of the porous material is assumed to be an aggregate of spherical grains with various dimensions, and the surroundings of an arbitrary sphere (grain) which has elastic constants $s_{11}{}^*$, $s_{44}{}^*$ are replaced by the averaged homogeneous medium which has elastic constants $s_{11}{}^P$, $s_{44}{}^P$. Then the stresses in the interior of the sphere are different from those in the medium because the elastic constants are different. The internal stress in each sphere can be calculated by the destressing factor which was introduced by one of the authors[2], and the averaged value of the internal stress in each sphere is equal to the external stress applied on the porous material as a whole. (In the interior of the pores which intervene among spherical grains, the internal stress vanishes.)

This approximation gives the results identical with those calculated by assuming that all pores have spherical forms and dispersed uniformly in the body, as will be shown in the followings.

### (i) Rigidity

We shall consider that the shearing stress $T_{04}$ is applied. (The same notations are used as in the reference 2).) Then, the strain $S_{04}$ in the material (or the medium which surrounds each sphere) is given by

$$S_{04}=s_{44}{}^P T_{04}\,. \tag{1}$$

In the sphere,

$$S_{i4}=s_{44}{}^* T_{i4}\,. \tag{2}$$

And by using the destressing factor $\gamma$ [(3.8) in ref. 2)],

$$\frac{T_{i4}-T_{04}}{S_{04}-S_{i4}}=\gamma^P=\frac{\mu^P}{2}\,\frac{9\lambda^P+14\mu^P}{3\lambda^P+8\mu^P}\,. \tag{3}$$

From Eqs. (1), (2) and (3)

$$T_{i4}=\frac{1}{s_{44}{}^P}\cdot\frac{1+\gamma^P s_{44}{}^P}{1+\gamma^P s_{44}{}^*}\cdot S_{04}\,. \tag{4}$$

Accordingly, by considering that the stress vanishes in the interior of the pore,

$$s_{44}{}^P=\frac{S_{04}}{<T_{i4}>_{AV}}$$
$$=1\Big/\left\{(1-v)\,\frac{1}{s_{44}{}^P}\cdot\frac{1+\gamma^P s_{44}{}^P}{1+\gamma^P s_{44}{}^*}\right\},$$

hence,

$$s_{44}{}^P=s_{44}{}^*\left\{1-v\left(1+\frac{1}{\gamma^P s_{44}{}^*}\right)\right\}\,. \tag{5}$$

Or, if $v \ll 1$,

$$\left.\begin{aligned} N^P&=\frac{1}{s_{44}{}^P}=N^*\left\{1-v\left(1+\frac{N^*}{\gamma}\right)\right\}, \\ \gamma&=\frac{\mu^*}{2}\,\frac{9\lambda^*+14\mu^*}{3\lambda^*+8\mu^*}\,. \end{aligned}\right\} \tag{6}$$

Eqs. (6) are formulae for calculating the rigidity of the porous material.

### (ii) Volume Elastic Constant

The volume elastic constant of the porous material can be calculated in the same way as rigidity, by using the destressing factor $\delta$ for the hydrostatic compression[2]. The result is

$$\left.\begin{aligned} K^P&=K^*\left\{1-v\left(1+\frac{3K^*}{\delta}\right)\right\}, \\ \delta&=4\mu^*\,. \end{aligned}\right\} \tag{7}$$

This result can be obtained rigorously, as Bruggeman showed[3], on the assumption that the pores of the spherical form are dispersed in the body.

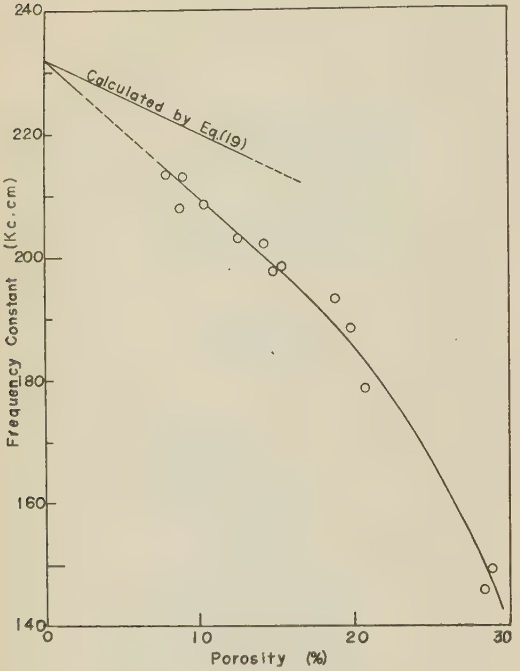

Fig. 1. The frequency constant for the longitudinal vibration.

### (iii) Young's Modulus

Young's modulus $E$ can be calculated from $N$ and $K$ by using the following relation.

$$\frac{1}{E}=\frac{1}{3N}+\frac{1}{9K}\,. \tag{8}$$

And after simple calculations (from (6) and (7)),

$$\left.\begin{aligned} E^P&=E^*\left\{1-v\left(1+\frac{E^*}{k}\right)\right\}\,,\\ k&=1\Big/\left(\frac{1}{3\gamma}+\frac{1}{3\delta}\right)\\ &=4\mu^*\frac{9\lambda^*+14\mu^*}{11\lambda^*+26\mu^*}\,. \end{aligned}\right\} \tag{9}$$

Eqs. (9) are formulae for calculating Young's modulus of the porous material.

### (iv) Dielectric Constant

The dielectric susceptibility $\kappa$ can be also calculated in the same way as rigidity by using the depolarizing factor $\alpha$[2]. Namely,

$$\frac{E_{i1}-E_{01}}{P_{01}-P_{i1}}=\alpha^P=\frac{4\pi}{2\varepsilon^P+1}\,. \tag{10}$$

In the sphere,

$$P_{i1}=\kappa^*E_{i1} \tag{11}$$

In the medium which surrounds the sphere,

$$P_{01}=\kappa^PE_{01}\,. \tag{12}$$

And in the pore, the polarization vanishes. From Eqs. (10), (11) and (12),

$$P_{i1}=\kappa^*\frac{1+\alpha^P\kappa^P}{1+\alpha^P\kappa^*}E_{01}\,, \tag{13}$$

and

$$\langle P_{i1}\rangle_{AV}=(1-v)P_{i1}\,.$$

Hence,

$$\kappa^P=\kappa^*(1-v)\frac{1+\alpha^P\kappa^P}{1+\alpha^P\kappa^*}\,. \tag{14}$$

If $v\ll 1$,

$$\kappa^P=\kappa^*\{1-v(1+\alpha\kappa^*)\}\,. \tag{15}$$

Or

$$\varepsilon^P=\varepsilon^*\left\{1-\frac{3(\varepsilon^*-1)}{2\varepsilon^*+1}v\right\}\,. \tag{16}$$

Eq. (16) is identical with the result which is derived from Wiener's formula, as discussed by Rushman and Strivens[1].

## § 3. Experimental

BaTiO$_3$ ceramics were prepared as follows. First, the mixtures of BaCO$_3$ and TiO$_2$ (equimolecular proportions) were prefired at 1200°C and the products were crushed and milled. Then, a series of specimens having different porosities were made by pressing the powders and by sintering them at different temperatures ranging between 1000°C and 1450°C.

The porosity was determined by measuring the density $\rho^P$. Namely,

$$\rho^P=\rho^*(1-v)\,, \tag{17}$$

where

$$\rho^*=6.0\,\mathrm{g/cm^3}$$

is the $X$-ray density, and $\rho^P$ was determined by weighing the specimen ground to a regular shape.

Samples were not very pure, and Curie temperature of them is 110°C. All the measurements were made at 27°C.

### (i) Young's Modulus

The resonant frequency of the longitudial vibration of the bar (*ca.* $23\times3.5\times2.5\,\mathrm{mm^3}$) was measured by the self-resonance method. Namely, the piezoelectric vibrations were excited by applying the electric field perpendicular to the length of the bar, and the electric current was measured. Then the resonant frequency is that at which the maximum electric current is produced. In Fig. 1, the observed values of the frequency constant (the resonant frequency of the unit length) are shown together with calculated values in the following way.

The frequency constant $f^P$ of the bar is given by

$$f^P=\frac{1}{2}\sqrt{\frac{E^P}{\rho^P}}\,. \tag{18}$$

By substituting Eqs. (9) and (17),

$$\begin{aligned} f^P&=\frac{1}{2}\sqrt{\frac{E^P}{\rho^*}}\sqrt{\frac{1-v(1+E^*/k)}{1-v}} \\ &=f^*\left(1-\frac{E^*}{2k}v\right) \end{aligned} \tag{19}$$

The values of $f^*$ and $E^*$ were determined from the observed values by the extrapolation to zero porosity. From these values together with the observed values of the rigidity $N^*$ (*v.* Eq. (23)), $\lambda$, $\mu$ and $k$ were calculated.

$$\left.\begin{aligned} f^*&=232\ \text{kc·cm}\,, \\ E^*&=1.29\times10^{12}\ \text{dyne/cm}^2\,, \\ \lambda^*&=1.07\times10^{12}\quad ,, \quad , \\ \mu^*&=0.48\times10^{12}\quad ,, \quad , \\ k&=1.30\times10^{12}\quad ,, \quad . \end{aligned}\right\} \tag{20}$$

Mason reported[4] that

$$\left.\begin{aligned} \lambda&=5.2\times10^{11}\ \text{dyne/cm}^2\,, \\ \mu&=4.5\times10^{11}\quad ,, \quad ; \end{aligned}\right\}$$

for the samples having porosity *ca.* 8%. The disagreement between his results and ours may partly be due to the impurities.

### (ii) Rigidity

The resonant frequencies of the torsional vibrations of the specimens of cylindrical forms (length 17 mm; diameter 3.4 mm) were measured by the "composite-bar method"[5] used previously by F.C. Rose[6]. Namely, the specimen is attached to the quartz (with equal cross-section) in which the torsional vibration is excited piezoelectrically. The resonant frequency of the specimen can be calculated from the resonant frequency of the quartz alone and that of the composite-bar. In Fig. 2, the observed values are shown with calculated ones.

In the case of the torsional vibration, the frequency constant $f^P$ is given by

$$\begin{aligned} f^P&=\frac{1}{2}\sqrt{\frac{N^P}{\rho^P}} \\ &=f^*\left(1-\frac{N^*}{2\gamma}\right). \end{aligned} \tag{21}$$

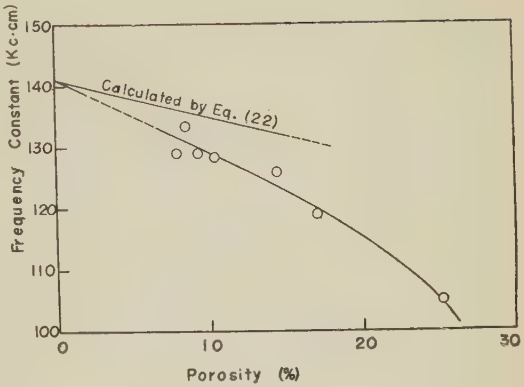

Fig. 2. The frequency constant for the torsional vibration.

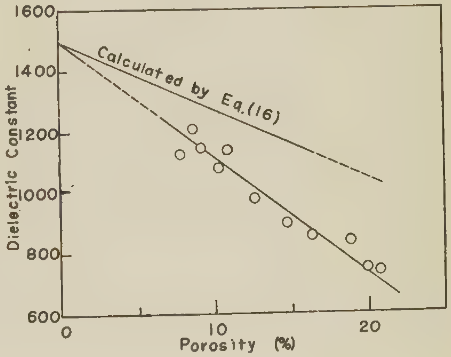

Fig. 3. Dielectric constant.

Following values were obtained from this experiment.

$$\left.\begin{aligned} f^*&=141\ \text{kc·cm}\,, \\ N^*&=0.48\times10^{12}\ \text{dyne/cm}^2\,, \\ \gamma^*&=0.56\times10^{12}\quad ,, \quad . \end{aligned}\right\} \tag{22}$$

### (iii) Dielectric Constant

The dielectric constants were also measured at the frequency of about 1 Mc/sec. The results are shown in Fig. 3, and $\varepsilon^*=1500$.

## § 4. Discussions

Young's modulus, the rigidity and the dielectric constant of the porous material were calculated in Eqs. (9), (10) and (16). In the case of $BaTiO_3$ ceramics, however, the observed values are not in good agreement with these formulae as shown in Fig. 1, 2 and 3. The discrepapancy shows the similar tendency in every masurement, and is considered mainly due to the shape of pores.

Namely, we calculated in § 2 on the assumption that the ceramic is composed of spherical grains the surroundings of which are replaced by the isotropic medium having the same elastic and dielectric constants as the porous ceramic. In real porous ceramics, however, the pores intervene among all grains and have plane forms; accordingly, the surroundings are rich in pores and the replacement of them by the averaged medium is not correct.

In other words, our assumptions are equivalent that all pores have spherical forms and are dispersed in the non-porous body, as shown in the calculation of the volume elastic constant and the dielectric constant in (ii) and (iv) in § 2. And the shape of the pores, or the form factor, as Rushman and Strivens discussed1), has to be considered, but it is a very difficult problem and we cannot calculate for the general case.

Meanwhile, anomalously large values of the dielectric constants in $BaTiO_3$ ceramics were reported recently7)8) for ceramics which are composed of very small grains (*ca.* 1 $\mu$ in diameter), and it is possible that elastic anomalies are also observed in these samples. It may appear to suggest that dielectric and elastic properties depend much on the sintering conditions, but these anomalies are considered rather due to the anomalies of the crystallite itself which has small dimensions9). In our case, however, each grain has a diameter of 10 $\mu$ or so and the effects of dimensions are not necessary to be considered.

This work was supported by the Scientific Research Expenditure of the Ministry of Education.

### References

1) D. F. Rushman and M. A. Strivens: Proc. Phys. Soc. **59** (1947) 1011.
2) M. Marutake: J. Phys. Soc. Japan **11** (1956) 807.
3) D. A. G. Bruggeman: Ann. d. Phys. **29** (1937) 160.
4) W. P. Mason: *Piezoelectric Crystals and their Application to Ultrasonics.* (1950) p. 295.
5) O. Nomoto and T. Ikeda: J. Acous. Soc. Japan **9** (1953) 83 (in Japanese).
6) F. C. Rose: Phys. Rev. **49** (1936) 50.
7) H. Kniepkamp u. W. Heywang: Zeits. f. angew. Phys. **6** (1954) 385.
8) L. Egerton and S. E. Koonce: J. Amer. Cer. Soc. **38** (1955) 412.
9) M. Anliker, H. R. Brugger and W. Känzig: Helv. Phys. Acta **27** (1954) 99.
W. Känzig: Phys. Rev. **98** (1955) 549.

---

JOURNAL OF THE PHYSICAL SOCIETY OF JAPAN Vol. 11, No. 8, AUGUST, 1956

# Irreversible Production of Entropy and the Absorption of Sound*

By Otohiko NOMOTO
*Kobayasi Institute of Physical Research, Kokubunzi, Tokyo*

(Received March 7, 1956; Received in amended form on May 25, 1956)

Molecular absorption of sound was ascribed to the irreversible production of entropy due to the heat conduction under finite temperature difference between the external and the internal degrees of freedoms of the molecules. Absorption formula was obtained in this manner and was found to be in agreement with the known formulas obtained by other methods.

## § 1. Introduction

The formula for molecular absorption and dispersion of sound have been obtained by various methods; kinetic theory method originated by Bourgin1), irreversible thermodynamics method originated by Herzfeld and Rice2), statistical thermodynamics method of

---

* The text in Japanese of this paper will be published in "Bulletin of the Kobayasi Institute of Physical Research."

Kneser[3)], phenomenological method of Issakovich[4)], and others. Many works have been performed since these earlier works (cf. Markham, Beyer and Lindsay (17) and the introduction of the previous paper[5)] for detailed references), though the equivalence of these various methods is not always demonstrated.

Of these various methods, the irreversible thermodynamics method have the advantage of being simple. The earlier papers in this category, including that of Herzfeld and Rice, are phenomenological, and not necessarily connected with the theory of thermodynamics intimately; and even in recent years many authors employ phenomenological relaxation equations because of its simplicity for practical applications. The previous paper[5)] by the present author was one such attempt.

It is, however, necessary to establish the "irreversible thermodynamics theories of acoustic relaxation" on the recent developments of the irrreversible thermodynamics and connect the relaxation equation (equation of irreversibility) with the rate of production of entropy. Such efforts are being made by Damköhler[6)], Meixner[7)-16)] and Eckart (unpublished lecture, cited in Markham, Beyer and Linday[17)]) (cf. also De Groot[18)] for a treatment of relaxation phenomena on the basis of irreversible thermodynamics.)

Here we intend to make a more straight forward derivation of the absorption formula by calculating the amount of entropy production directly.

When entropy $\Delta S$ is produced in an irreversible process, there accompanies a decrease in free energy by $T\Delta S$. In case of sound absorption, the entropy production must take place, because of the conversion of ordered motion of the fluid particles into heat. So the absorption coefficient of sound is obtainable from calculation of the irreversible production of entropy. If the rate of irreversible production of entropy is $\Delta S$/cycle/mole, the rate of decrease of free energy is $T\Delta S$/cycle/mole. If the energy of the sound wave is $E$/mole, the intensity absorption coefficient per wavelength is given by $T\Delta S/E$, and the amplitude absorption coefficient per wavelength by

$$\alpha\lambda = T\Delta S/2E\,. \tag{1.1}$$

In case of the molecular absorption of sound, the thermal equilibrium is not established between the internal and the external degrees of freedoms of the molecules, and there takes place a heat conduction between the both degrees of freedoms under finite temperature difference. This accompanies an irreversible production of entropy. We can obtain the absorption coefficient in this manner.

As this method is quite general, it may be applied also for obtaining absorption coefficients of sound due to other mechanisms.

## § 2. Irreversible Production of Entropy Accompanying an Instantaneous Volume Change

Consider one mole of gas (or liquid) contained in a cylinder to be subjected to a sudden adiabatic compression. The work of compression is used at first only for increasing the energy of the external degrees of freedom of the molecules (external system) of the gas, because the energy of the internal degrees of freedom of the molecules (internal system) does not change instantaneously. Here the content of the "energy of the external system" and that of the "energy of the internal system" is also dependent on the time scale of the experiment. If the compression takes place during an interval of time which is shorter than the relaxation time of the rotational energy of the molecules, the "energy of the external system" is the translational energy of the molecules, while the "energy of the internal system" consists of the rotational and the vibrational energies. When, however, the time required for compression is longer than the relaxation time of the rotational energy of the molecules, but shorter than the relaxation time of the vibrational energy, the "energy of the external system" is the sum of the translational and the rotational energies, and the "energy of the internal system" is the vibrational energy of the molecules. As the rotational and the vibrational relaxation times are usually of different order of magnitude and the both relaxation frequencies can be separated in acoustic experiments, we will consider the case of one relaxation time for the sake of simplicity.

A sudden decrease of volume by $|\Delta v|$ ($\Delta v<0$) accompanies an instantaneous increase in pressure by $\Delta p_\infty$, which gradually relaxes to the equilibrium increment $\Delta p_0$ with a relaxation time $\tau$. By periodic repetition of sudden com-

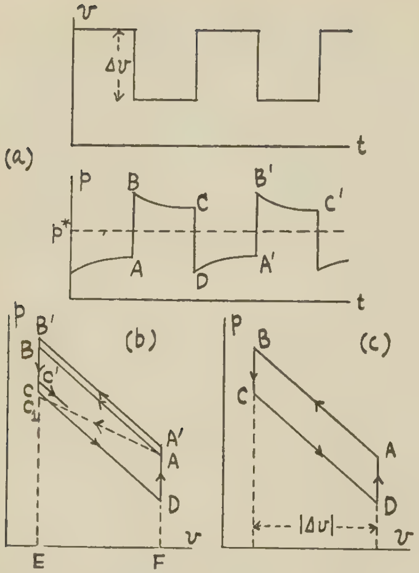

Fig. 1. Change of pressure accompanying an instantaneous periodic volume change of a fluid.

pression and expansion the volume and pressure undergo changes as illustrated in Fig. 1 (a), and the work required per each compression is equal to the area ABEF in the *pv*-diagram, Fig. 1 (b), while the work obtained in expansion is only CEFD. The difference between the work of compression and that of expansion, ABCD in the *pv*-diagram, is irreversibly converted into heat per cycle. If the time interval between the compression and the following expansion is sufficiently long, the pressure relaxes from $p+\Delta p_\infty$ to $p+\Delta p_0$ during this time interval, so that we have

$$\oint p dv = -(\Delta p_\infty - \Delta p_0)\Delta v \qquad (\Delta v < 0) \qquad (2.1)$$

as the work lost per cycle. This is the usual manner of computing the loss.

Strictly speaking, the periodic adiabatic volume change of Fig. 1 (a) does not accompany a completely periodic change of pressure, because the internal energy increases by

$$\oint dU = -\oint p\, dv$$

in this change. This results in the increase in temperature (and pressure) of the fluid and the new equilibrium state after an adiabatic cycle becomes $A'$ in place of $A$ (cf. Fig. 1 (b)). The new cycle begins from $A'$ along $A'B'C'\cdots$, and the straight line representing the mean pressure $p^*$ becomes somewhat inclined to the horizontal, slightly increasing with time. This corresponds to the temperature rise by the absorption of sound. The quantity $\delta p = AA'$, however, is a small quantity of the second order if $\Delta p_0$ and $\Delta p$ are small quantities of the first order. This is to be shown later.

Now we can compress the fluid in a quasi-static, adiabatic process from the state $A$ to the state $C_1$ along the dotted line in Fig. 1 (b), and expand it in a quasi-static adiabatic process along the same path from $C_1$ to $A$. In this case, there accompanies no loss of mechanical work per each cycle. Here the state $C_1$ is of equal volume with $C$, but of slightly lower pressure. The difference, however, is a small quantity of the second order in $\Delta p_0$ and $\Delta p_\infty$. As the two processes $AB$ and $AC_1$ are both adiabatic, fluids in states $B$ and $C_1$ are of equal entropy as that in state $A$; thus $S_{C1} = S_A = S_B$. Only the state $B$ is not an equilibrium state, because the "external system" of the molecules and the "internal system" are not in equilibrium. No loss of mechanical work, however, is produced in the state $B$ as yet, because we can bring the fluid in the original state $A$ by instantaneous expansion from $B$ along the same path $BA$ and thus regaining the same work as used in compression.

The entropy increases in the relaxation stage $BC$, $C$ being a state of equal internal energy but of higher entropy than $B$. The entropy production is given by (2.14) as is to be shown later; i.e.,

$$S_c - S_B = \frac{1}{2}\frac{C_i}{T^2}\Delta T_0 \Delta T_\infty\,, \qquad (2.2)$$

where $C_i$ means the molar specific heat of the "internal system", and $\Delta T_0$ and $\Delta T_\infty$ are the temperature increments in states $B$ and $C$, respectively. On the other hand we can bring the fluid in state $C_1$ to that in state $C$ by supplying heat under constant volume. This gives as the entropy increase

$$\begin{aligned} S_c - S_{c1} &= C_{v0}\int_{T+\Delta T_0'}^{T+\Delta T_0} \frac{dT}{T} \\ &= C_{v0}\log\left[1+\frac{\Delta T_0 - \Delta T_0'}{T+\Delta T_0'}\right] \\ &\doteqdot C_{v0}\frac{\Delta T_0 - \Delta T_0'}{T}\,, \end{aligned} \qquad (2.3)$$

where $C_{v0}$ is the molar specific heat at constant volume (and at sufficiently low frequency), and $\Delta T_0'$ denotes the temperature increment in the state $C$. As $S_{C1}=S_B$, we have from (2.2) and (2.3)

$$\Delta T_0-\Delta T_0'=\frac{C_i}{C_{v0}}\,\frac{\Delta T_0\Delta T_\infty}{T}\,. \tag{2.4}$$

This indicates that the temperature difference between the two states $C$ and $C_1$ is a small quantity of the second order, if the temperature increments $\Delta T_0$ and $\Delta T_\infty$ are small quantities of the first order. This holds true also concerning the pressure difference. So we can omit the difference between the states $C$ and $C_1$ in usual acoustic problems. The pressure difference between $A$ and $A'$ is twice the pressure difference between $C$ and $C_1$ and is also a second order small quantity. In this case, the $pv$-diagram becomes a cyclic figure as illustrated in Fig. 1 (c).

Thus we see that the loss is produced along the path $BC$ and $DA$ while the pressure relaxes. In practice, after the fluid is instantaneously compressed along the path $AB$ and then the pressure relaxed along $BC$, we can bring it in the original state A by a quasi-static adiabatic expansion along $CA$. In this case, the loss is equal to the area of the triangle $ABC$, i.e., half the value corresponding to the parallelogram $ABCD$.

Pressure relaxes along $BC$ and $DA$ because there takes place a heat conduction from the external degrees of freedom of the molecules to the internal degrees of freedom and vice versa. If the temperature of the external degrees of freedom is $T+\Delta T$, and that of the internal degrees of freedom $T+\Delta T_i$, $\Delta T$ and $\Delta T_i$ being functions of the time, we have

$$\Delta T>\Delta T_i \tag{2.5}$$

in case of $BC$.

If a quantity of heat $d'q$ is transferred from the external to the internal degrees of freedom under this temperature difference, the entropy production is

$$\begin{aligned} ds&=\frac{-d'q}{T+\Delta T}+\frac{d'q}{T+\Delta T_i}\\ &=\frac{d'q}{T^2}(\Delta T-\Delta T_i)>0 \end{aligned} \tag{2.6}$$

Now the temperature of the internal degrees of freedom increases by $d\Delta T_i$ accompanying this heat transfer, i.e.,

$$d'q=C_i d\Delta T_i, \tag{2.7}$$

where $C_i$ means the internal specific heat per mole of the fluid. The total entropy production during the relaxational stage $BC$ is

$$\Delta s=\frac{C_i}{T^2}\int_0^{\Delta T_0}(\Delta T-\Delta T_i)d\Delta T_i\,, \tag{2.8}$$

where $\Delta T_0$ means the equilibrium increment of temperature corresponding to the new equilibrium state after compression. The temperature increment is $\Delta T_\infty$ immediately after the instantaneous compression, but it gradually relaxes to the equilibrium value $\Delta T_0$ by transferring heat to the internal degrees of freedom. Thus a heat quantity $C_i\Delta T_i$ is transferred till the temperature of the internal degrees of freedom attains $T+\Delta T_i$, while the temperature of the external degrees of freedom becomes $T+\Delta T$ by this moment, where

$$\Delta T=\Delta T_\infty-(C_i/C_a)\Delta T_i=\Delta T_\infty-(C_i/C_{v\infty})\Delta T_i\,. \tag{2.9}$$

Here $C_a$ means the specific heat at constant volume (per mole) of the external degrees of freedom of the molecules. As this corresponds to the specific heat at sufficiently high frequency, it is usual to write it $C_{v\infty}$ in the theory of the molecular absorption of sound, while we denote the molar specific heat at constant volume for the quasi-static process, i.e., at sufficiently low frequency, with $C_{v0}$. This is related to $C_{v\infty}$ by

$$C_{v0}=C_{v\infty}+C_i\,. \tag{2.10}$$

Substituting (2.9) and (2.10) into (2.8) we have

$$\Delta s=\frac{C_i}{T^2}\int_0^{\Delta T_0}\left(\Delta T-\frac{C_{v0}}{C_{v\infty}}\Delta T_i\right)d\Delta T_i\,. \tag{2.11}$$

This becomes by integration

$$\Delta s=\frac{C_i}{T^2}\left(\Delta T_\infty\Delta T_0-\frac{C_{v0}}{2C_{v\infty}}\Delta T_0^{\,2}\right). \tag{2.12}$$

We have, on the other hand, from the conservation of heat quantity the relation

$$C_{v\infty}\Delta T_\infty=C_{v0}\Delta T_0\,, \tag{2.13}$$

and this simplifies (2.12) as

$$\Delta s=\frac{1}{2}\,\frac{C_i}{T^2}\,\Delta T_0\Delta T_\infty\,. \tag{2.14}$$

As the amount of entropy production is the same also in case of the pressure relaxation along $DA$ after an instantaneous expansion, the entropy production per one cycle is twice the above value, i.e.,

$$\Delta S=2\Delta s=(C_i/T^2)\Delta T_0\Delta T_\infty\,. \tag{2.15}$$

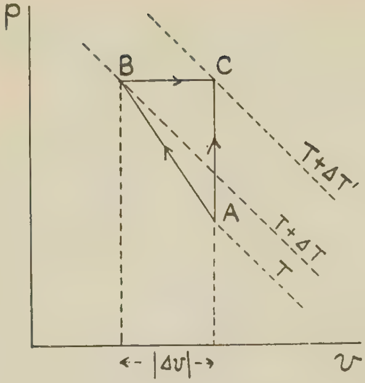

Fig. 2. *pv*-diagram of a fluid in an adiabatic volume change.

This accompanies an decrease in free energy by an amount

$$T\Delta S=(C_i/T)\Delta T_0\Delta T_\infty\,. \tag{2.16}$$

Now this must be equal to the loss in mechanical energy per cycle given by (2.1). We will show this in the following. We have

$$\Delta p_\infty=\left(\frac{\partial p}{\partial \rho}\right)_\infty \Delta\rho=-\left(\frac{\partial p}{\partial \rho}\right)_\infty \frac{M\Delta v}{v^2} \tag{2.17}$$

in (2.1), where $M$ means the molecular weight, $\rho$ the density, and $v$ the molar volume of the fluid. As the sound velocity at sufficiently high frequency is

$$V_\infty{}^2=(\partial p/\partial \rho)_\infty\,, \tag{2.18}$$

we have

$$\Delta p_\infty=-(V_\infty{}^2M/v^2)\Delta v\,. \tag{2.19}$$

Similarly, we have

$$\Delta p_0=-(V_0{}^2M/v^2)\Delta v\,, \tag*{(2.20)*}$$

where

$$V_0{}^2=(\partial p/\partial \rho)_0 \tag{2.21}$$

means the sound velocity at sufficiently low frequency. We have accordingly

$$-(\Delta p_\infty-\Delta p_0)\Delta v=(M/v^2)(V_\infty{}^2-V_0{}^2)(\Delta v)^2. \tag{2.22}$$

We have further the relations:

$$V_\infty{}^2=(\partial p/\partial \rho)_T(C_{p\infty}/C_{v\infty})\,, \tag{2.23}$$

and

$$V_0{}^2=(\partial p/\partial \rho)_T(C_{p0}/C_{v0}) \tag{2.24}$$

where $C_{p0}$ and $C_{p\infty}$ mean the molar specific heats at constant pressure at sufficiently low frequency and at sufficiently high frequency respectively, these being related by

$$C_{p0}=C_{p\infty}+C_i\,. \tag{2.25}$$

By employing (2.23), (2.24) with (2,25) and (2.10), we have

$$V_\infty{}^2-V_0{}^2=V_0{}^2\left(\frac{C_{p\infty}C_{v0}}{C_{v\infty}C_{p0}}-1\right)$$
$$=V_0{}^2C_i(C_{p0}-C_{v0})/C_{p0}C_{v\infty}\,. \tag{2.26}$$

Now we will consider of the relation between the volume change and the temperature increment in an adiabatic compression. In the *pv*-diagram of Fig. 2, suppose the volume of a fluid is reduced by $|\Delta v|$ $(\Delta v<0)$ and the temperature increased by $\Delta T$ in an adiabatic compression from $A$ to $B$. The increment of internal energy (in the thermodynamical meaning) in this process is

$$U_B-U_A=W=-\int_v^{v-\Delta|v|}pdv=p|\Delta v|=-p\Delta v \tag{2.27}$$

If this fluid is heated from $A$ to $C$, a state with the same pressure as $B$, under constant volume and supplying a heat quantity $Q$, the temperature increases by $\Delta T'$ and the increase in internal energy is

$$U_c-U_A=Q=C_v\Delta T'\,. \tag{2.28}$$

The expansion at constant pressure from the state $B$ to state $C$ on the other hand, requires a heat quantity $Q'$ and the internal energy changes in this process by

$$U_C-U_B=Q'-p|\Delta v|$$
$$=C_p(\Delta T'-\Delta T)+p\Delta v\,, \tag{2.29}$$

while the amount of expansion is

$$-\Delta v/v=|\Delta v|/v=\alpha(\Delta T'-\Delta T)\,, \tag{2.30}$$

where $\alpha$ means the expansion coefficient.

Subtracting (2.29) from (2.28) we have

$$U_B-U_A=C_v\Delta T'-C_p(\Delta T'-\Delta T)-p\Delta v \tag{2.31}$$

and equating this with (2.23),

$$C_v\Delta T'-C_p(\Delta T'-\Delta T)=0\,.$$

This gives

$$\frac{\Delta T'}{\Delta T}=\frac{C_p}{C_p-C_v}=\frac{\gamma}{\gamma-1}\,, \tag{2.32}$$

where $\gamma$ means the ratio of the specific heats. Substituting this into (2.30) we have the relation between the amount of adiabatic compression and the temperature increment:

$$\Delta v/v=-\alpha\Delta T/(\gamma-1)\,. \tag{2.33}$$

As the ratio of the specific heats is related to the sound velocity and the expansion coefficient by

---

* Strictly Speaking, $\Delta p_0$ represents the pressure increment at $C_1$ in Fig. 1 (b), but not that in $C$, though the difference is a second order small quantity.

$$\gamma = 1 + T\alpha^2 V^2 M / C_p \,, \tag{2.34}$$

we can write (2.33) also as

$$\Delta v / v = -(C_p / T\alpha V^2 M) \Delta T \,. \tag{2.35}$$

The relations (2.33) and (2.35) are valid for a quasi-static adiabatic compression (of a liquid or a gas) as well as for an instantaneous one*, though we have to use the corresponding values of $C_p$, $C_v$ and $\gamma$ for each case. Multiplying (2.33) and (2.35) side by side we have

$$(\Delta v)^2 = \frac{C_v C_p v^2}{MTV^2(C_p - C_v)} (\Delta T)^2 \,. \tag{2.36}$$

Especially, considering the case of a quasi-static adiabatic compression we have

$$(\Delta v)^2 = \frac{C_{v0} C_{p0} v^2}{MTV_0^2(C_{p0} - C_{v0})} (\Delta T_0)^2 \,. \tag{2.37}$$

When (2.26) and (2.37) is substituted into (2.22) we have

$$-(\Delta p_\infty - \Delta p_0)\Delta v = \frac{C_i C_{v0}}{TC_{v\infty}} (\Delta T_0)^2 \,. \tag{2.38}$$

This becomes by (2.13) as

$$-(\Delta p_\infty - \Delta p_0)\Delta v = (C_i / T)\Delta T_0 \Delta T_\infty \,. \tag{2.39}$$

This is in accordance with (2.16), i.e., we have

$$T\Delta S = -(\Delta p_\infty - \Delta p_0)\Delta v \,. \tag{2.40}$$

## § 3. Molecular Absorption of Sound

Now we will consider the case of the molecular absorption of sound. After an instantaneous compression of volume as illustrated in Fig. 1, the energy of the internal degrees of freedom of the molecules undergoes an change

$$\Delta E_i = \Delta E_i^0 (1 - e^{-t/\tau}) \,. \tag{3.1}$$

This gives a differential equation for the time change of the energy of the internal system

$$\frac{\partial(E_i)}{\partial t} = \frac{1}{\tau} (\Delta E_i^0 - \Delta E_i) \,. \tag{3.2}$$

The same time change takes place also in the sound wave, due to the difference in value of $\Delta E_i$ from the equilibrium value $\Delta E_i^0$. Generally speaking, there is an instantaneous variation of a quantity accompanying the density change. This, however, being zero in case of $E_i$, i.e.,

$$(\partial(\Delta E_i)/\partial(\Delta\rho))_\infty = 0 \,,$$

we have

$$\frac{d(\Delta E_i)}{dt} = \frac{\partial(\Delta E_i)}{\partial t} + \left( \frac{\partial(\Delta E_i)}{\partial(\Delta\rho)} \right)_\infty \frac{\partial(\Delta\rho)}{\partial t}$$
$$= \frac{\partial(\Delta E_i)}{\partial t} \,. \tag{3.3}$$

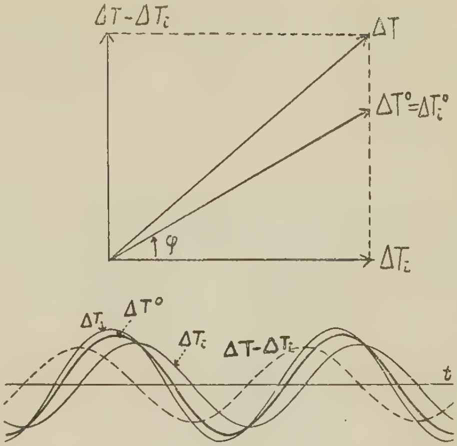

Fig. 3. Phase relations of $\Delta T_i^0$, $\Delta T_i$ and $\Delta T - \Delta T_i$.

Thus we have to solve

$$\frac{d(\Delta E_i)}{dt} = \frac{1}{\tau} (\Delta E_i^0 - \Delta E_i) \tag{3.4}$$

for the sine wave of the form exp ($i\omega t$). The solution is

$$\Delta E_i = \Delta E_i^0 / (1 + i\omega\tau) \,. \tag{3.5}$$

As the internal temperature (=temperature of the internal degrees of freedom of the molecules) is related with $E_i$ by

$$\Delta T_i = \Delta E_i / C_i \,, \tag{3.6}$$

we have the same type solution as (3.50) also for $\Delta E_i$, i.e.,

$$\Delta T_i = \Delta T_i^0 / (1 + i\omega\tau) \,, \tag{3.7}$$

where $\Delta T_i^0$ means the increment of the internal temperature corresponding to the equilibrium state, i.e., for zero frequency. (3.7) can also be written as

$$\Delta T_i = \frac{e^{-i\varphi}}{(1 + \omega^2\tau^2)^{1/2}} \Delta T_i^0 \,. \tag{3.8}$$

where

$$\varphi = \tan^{-1} \omega\tau \,. \tag{3.9}$$

We see that $\Delta T_i$ is lagging $\Delta T_i^0$ by angle $\varphi$ in phase (cf. Fig. 4)**.

Now the energy of the external system relaxes after an instantaneous volume change illustrated in Fig. 1, according to the equation

---

* As to (2.35) for example, the frequency-dependent factor is $(C_p / V^2)\Delta T$, which becomes $(C_{p0} / V_0^2) \Delta T_0$ for a quasi-static process. This, however, is equal to $(C_{p\infty} / V_\infty^2)\Delta T_\infty$ by (2.13), (2.23) and (2.24).

** The vector of $\Delta T$ is placed on a diagonal of a rectangle with vectors $\Delta T_i$ and $(\Delta T - \Delta T_i)$ as two adjacent sides, and the vector of $\Delta T^0 (= \Delta T_i^0)$ is placed on one side of this rectangle because $|\Delta T_i| = |\Delta T^0| \cos\varphi$.

$$\Delta E_a=\Delta E_a^\infty+(\Delta E_a^0-\Delta E_a^\infty)(1-e^{-t/\tau})$$
$$=\Delta E_a^0+(\Delta E_a^\infty-\Delta E_a^0)e^{-t/\tau}\,, \tag{3.10}$$

and we have as the differential equation of the time variation:

$$\frac{\partial(\Delta E_a)}{\partial t}=-\frac{1}{\tau}(\Delta E_a-\Delta E_a^0)\,. \tag{3.11}$$

As the external temperature (=temperature of the external degrees of freedom of the molecules) is proportional to the energy of the external degrees of freedom by

$$\Delta T=\Delta E_a/C_a\,, \tag{3.12}$$

$\Delta T$ satisfies an equation of the same type as (3.11), i.e.,

$$\frac{\partial(\Delta T)}{\partial t}=-\frac{1}{\tau}(\Delta T-\Delta T^0)\,. \tag{3.13}$$

In case of a sound wave, we have also an instantaneous variation of $\Delta T$ following the variation of the density, i.e.,

$$\frac{d(\Delta T)}{dt}=\frac{\partial(\Delta T)}{\partial t}+\left(\frac{\partial(\Delta T)}{\partial(\Delta\rho)}\right)_\infty\frac{\partial(\Delta\rho)}{\partial t}\,. \tag{3.14}$$

As we have

$$\frac{\partial(\Delta T)}{\partial(\Delta v)}=-\frac{\gamma-1}{v\alpha}$$

by (2.33), we have

$$\frac{\partial(\Delta T)}{\partial(\Delta\rho)}=-\frac{v^2}{M}\frac{\partial(\Delta T)}{\partial(\Delta v)}=\frac{v(\gamma-1)}{M\alpha}=\frac{\gamma-1}{\alpha\rho}$$
$$=\frac{C_p-C_v}{C_v\alpha\rho} \tag{3.15}$$

and accordingly,

$$\left(\frac{\partial(\Delta T)}{\partial(\Delta\rho)}\right)_\infty=\frac{C_{p\infty}-C_{v\infty}}{\alpha\rho C_{v\infty}}=\frac{C_{p0}-C_{v0}}{\alpha\rho C_{v\infty}} \tag{3.16}$$

and

$$\left(\frac{\partial(\Delta T)}{\partial(\Delta\rho)}\right)_0=\frac{C_{p0}-C_{v0}}{\alpha\rho C_{v0}}\,. \tag{3.17}$$

This gives

$$\Delta T^0=(C_{p0}-C_{v0})\Delta\rho/\alpha\rho C_{v0}\,. \tag{3.18}$$

Substituting (3.18) and (3.16) into (3.14) we have

$$\frac{d(\Delta T)}{dt}=-\frac{1}{\tau}\left(\Delta T-\frac{C_{p0}-C_{v0}}{\alpha\rho C_{v0}}\Delta\rho\right)$$
$$+\frac{C_{p0}-C_{v0}}{\alpha\rho C_{v\infty}}\frac{d(\Delta\rho)}{dt}\,. \tag{3.19}$$

Assuming sinusoidal variations of the form exp $(i\omega t)$ for both $\Delta T$ and $\Delta\rho$, we have as the solution of this equation

$$\Delta T=\frac{(C_{p0}-C_{v0})(C_{v\infty}+i\omega\tau C_{v0})}{C_{v0}C_{v\infty}(1+i\omega\tau)}\Delta\rho\,, \tag{3.20}$$

or, expressed in terms of $\Delta T^0$ by (3.18),

$$\Delta T=\frac{C_{v\infty}+i\omega\tau C_{v0}}{C_{v\infty}(1+i\omega\tau)}\Delta T^0\,. \tag{3.21}$$

As the temperatures of the external and the internal systems are different, we have heat conduction between them. If a heat quantity $d'q$ is transferred between the two systems, there takes place an entropy production

$$ds=-\frac{d'q}{T+\Delta T}+\frac{d'q}{T+\Delta T_i}=\frac{d'q}{T^2}(\Delta T-\Delta T_i)\,. \tag{3.22}$$

New we have by (3.7) and (3.21) as the temperature difference

$$\Delta T-\Delta T_i=\frac{i\omega\tau}{1+i\omega\tau}\frac{C_{v0}}{C_{v\infty}}\Delta T^0=\frac{i\omega\tau}{1+i\omega\tau}\Delta T^\infty\,. \tag{3.23}$$

This can also be written as

$$\Delta T-\Delta T_i=\frac{\omega\tau\exp\{i(\pi/2-\varphi)\}}{(1+\omega^2\tau^2)^{1/2}}\frac{C_{v0}}{C_{v\infty}}\Delta T^0 \tag{3.24}$$

This means that the wave of the temperature difference $(\Delta T-\Delta T_i)$ is leading the wave of the equilibrium temperature $(\Delta T^0)$ by $(\pi/2-\varphi)$ in phase. The temperature for equilibrium state is of course common for the external and the internal degrees of freedom, i.e.,

$$\Delta T^0=\Delta T_i^0\,. \tag{3.25}$$

So we see that wave of $(\Delta T-\Delta T_i)$ is leading the wave of $\Delta T_i$ by $\pi/2$ (cf. Fig. 3).

If the transfer of heat quantity $d'q$ takes place in a time interval $dt$, the rate of production of entropy is

$$\frac{ds}{dt}=\frac{1}{T^2}(\Delta T-\Delta T_i)\frac{d'q}{dt} \tag{3.26}$$

by (3.22). As

$$d'q=C_i d(\Delta T_i) \tag{3.27}$$

this becomes

$$\frac{ds}{dt}=\frac{C_i}{T^2}(\Delta T-\Delta T_i)\frac{d(\Delta T_i^*)}{dt} \tag{3.28}$$

or

$$\frac{ds}{dt}=(i\omega C_i/T^2)(\Delta T-\Delta T_i)\Delta T_i^*\,, \tag{3.29}$$

where the quantity with asterisk means the conjugate complex quantity. (As both $\Delta T-\Delta T_i$ and $\Delta T_i$ are complex quantities in this case, we have to make one of them the conjugate complex in making the product of them. This cancels the phase factor $\exp i(\pi/2-\varphi)$. This is also to be seen when we notice that $d(\Delta T)/dt$ and $(\Delta T-\Delta T_i)$ are in phase.) Substituting (3.24) and (3.8) into (3.29) we have

$$\frac{ds}{dt}=\frac{C_i}{T^2}\frac{\omega^2\tau}{1+\omega^2\tau^2}\frac{C_{v0}}{C_{v\infty}}(\varDelta T^0)^2 . \qquad (3.30)$$

Integrating this for the time interval of half period $(\theta/2)$, we have

$$\frac{1}{2}\varDelta S=\int_0^{\theta/2}\frac{ds}{dt}\,dt . \qquad (3.31)$$

As $\varDelta T^0=\Re(\varDelta T_0{}^0 e^{i\omega t})=\varDelta T_0{}^0\cos\omega t$, we obtain as the integral

$$\frac{1}{2}\varDelta S=\frac{\omega^2\tau}{1+\omega^2\tau^2}\frac{C_i}{T^2}\frac{C_{v0}}{C_{v\infty}}\frac{1}{2}\frac{\theta}{2}(\varDelta T_0{}^0)^2 . \quad (3.32)$$

After each half cycle the sign of the temperature difference $\varDelta T-\varDelta T_i$ is reversed. But the sign of $d(\varDelta T_i)/dt$ becomes reversed at the same time and the entropy production becomes twice the above value in one cycle. So the decrease of free energy in each cycle is

$$T\varDelta S=\frac{C_i}{T}\frac{C_{v0}}{C_{v\infty}}\frac{\theta}{2}\frac{\omega^2\tau}{1+\omega^2\tau^2}(\varDelta T_0{}^0)^2 . \qquad (3.33)$$

As

$$\theta=1/\nu=2\pi/\omega , \qquad (3.34)$$

where $\nu$ means the frequency, this becomes also as

$$T\varDelta S=\pi\frac{C_i}{T}\frac{C_{v0}}{C_{v\infty}}\frac{\omega\tau}{1+w^2\tau^2}(\varDelta T_0{}^0)^2 . \qquad (3.35)$$

Now the intensity of a plane progressive sound wave is known to be

$$I=(\varDelta p)^2/2\rho V , \qquad (3.36)$$

where $\varDelta p$ means the pressure amplitude. So the energy of sound per one mole of fluid is

$$E=\frac{1}{2}\frac{(\varDelta p)^2}{\rho V^2}v , \qquad (3.37)$$

where $v$ means the molar volume. Now we can obtain the expression of the pressure amplitude

$$\varDelta p=-(V^2M/v^2)\varDelta v , \qquad (3.38)$$

quite in a similar manner as in obtaining (2.19) and (1.20). Here $V$ means the velocity of sound at frequency $\nu=\omega/2\pi$. Employing (3.38), we have

$$E=\frac{1}{2}\frac{M^2V^2}{\rho v^3}(\varDelta v)^2=\frac{1}{2}\frac{MV^2}{v^2}(\varDelta v)^2 , \qquad (3.39)$$

and substituting (2.37) for $(\varDelta v)^2$,

$$E=\frac{1}{2}\frac{C_{v0}C_{p0}V^2}{TV_0{}^2(C_{p0}-C_{v0})}(\varDelta T_0{}^0)^2 . \qquad (3.40)$$

Free energy $T\varDelta S$ being lost per each cycle from the total energy of sound $E$, the absorption coefficient per wavelength becomes by (3.35), (3.40) and (1.1) as

$$\alpha_\lambda=\frac{T\varDelta S}{2E}=\pi C_i\frac{V_0{}^2}{V^2}\frac{C_{p0}-C_{v0}}{C_{p0}C_{v\infty}}\frac{\omega\tau}{1+\omega^2\tau^2} , \quad (3.41)$$

or,

$$\alpha_\lambda=\pi\frac{(C_{p0}-C_{v0})C_i\omega\tau}{C_{p0}C_{v\infty}(1+\omega^2\tau^2)}\frac{V_0{}^2}{V^2} . \qquad (3.42)$$

By employing further the dispersion formula (cf. Nomoto (5), eq. (3.28)).

$$V^2=V_0{}^2\left[1+\frac{(C_{p0}-C_{v0})C_i\omega^2\tau^2}{C_{p0}C_{v\infty}(1+\omega^2\tau^2)}\right] \qquad (3.43)$$

the absorption coefficient becomes as

$$\alpha_\lambda=\pi\frac{(C_{p0}-C_{v0})C_i\omega\tau}{C_{p0}C_{v\infty}+C_{v0}C_{p\infty}\omega^2\tau^2} . \qquad (3.44)$$

This is in accordance with the previous result (cf. Nomoto (5), eq. (3.27)).

In employing further the relaxation time of the internal specific heat $\beta$ in place of the relaxation time of the energy of the internal degrees of freedom $\tau$, by the substitution

$$\tau=\beta C_{v\infty}/C_{v0} , \qquad (3.45)$$

and putting $C_{p0}-C_{v0}=R$, we obtain the familiar absorption formula (Kneser's formula) for gases.

## Appendix

Another derivation of eq. (2.29)

This relation can be obtained also directly from the equations of thermodynamics. The change of internal energy $U$ in an adiabatic process is

$$\begin{aligned}-p dv=dU&=(\partial U/\partial T)_s dT\\ &=(\partial U/\partial v)_T dv+(\partial U/\partial T)_v dT\\ &=(\partial U/\partial v)_T dv+C_v dT . \end{aligned}\qquad (1)$$

As

$$C_p-C_v=[(\partial U/\partial v)_T+p](\partial v/\partial T)_p , \qquad (2)$$

we have

$$(\partial U/\partial v)_T=\frac{C_p-C_v}{(\partial v/\partial T)_p}-p , \qquad (3)$$

and substituting this into (1), we have

$$\left\{\frac{C_p-C_v}{\alpha v}-p\right\}dv+C_v dT=-p dv.$$

Accordingly,

$$\frac{C_p-C_v}{\alpha v}dv+C_v dT=0 . \qquad (4)$$

This gives

$$\left(\frac{\partial v}{\partial T}\right)_s=-\frac{C_v dv}{C_p-C_v}=-\frac{\alpha v}{\gamma-1} , \qquad (5)$$

or,

$$\frac{dv}{v} = -\frac{\alpha}{\gamma-1} dT, \qquad (6)$$

in accordance with (2.33).

**Acknowledgement**

The author expresses his sincere thanks to the referee of the Physical Society of Japan for very valuable suggestions.

## References

1) D. G. Bourgin: Phil. Mag. **7** (1929) 821; Phys. Rev. **34** (1929) 521; **42** (1932) 721; J. Acous. Soc. Amer. **4** (1932) 108; **5** (1933) 57; Phys. Rev. **50** (1936) 355.
2) K. F. Herzfeld and F. O. Rice: Phys. Rev. **31** (1928) 691.
3) H. O. Kneser: Ann. Phys. **11** (1931) 761; Ergebnisse der Exakt. Naturwiss. **22** (1949) 121.
4) M. A. Issakovich: Propagation of waves in a liquid possessing Maxwell viscosity. C. R. (Doklady) URSS **23** (1939) 783.
5) O. Nomoto: Phenomenological theory of the molecular absorption and dispersion of sound in fluids and the relation between the relaxation time of the internal energy and the relaxation time of the internal specific heat. J. Phys. Soc. Japan, in printing.
6) G. Damköhler: Isentropische Zustandsänderungen in dissoziierenden Gasen und die Methode der Schalldispersion zur Untersuchung sehr schneller homogener Gasreaktionen. Zeits. Elektrochem. **48** (1942) 62; 116.
7) J. Meixner: Absorption und Dispersion des Schalles in Gasen mit chemisch reagierenden und anregbaren Komponenten. Ann. Phys. **43** (1943) 470.
8) J. Meixner: Der Begriff der inneren Temperatur in der Dynamik von Gasen mit mehratomigen Molekülen. Zeits. Phys. **124** (1948) 129.
9) J. Meixner: Thermodynamik und Relaxationserscheinungen. Zeits. Naturforsch. **4a** (1949) 594.
10) J. Meixner: Thermodynamische Betrachtungen zur Schallabsorption und Druckviskosität in homogenen Medien. Colloquium over ultrasonore trillingen, Brussels (1951) 107.
11) J. Meixner: Allgemeine Theorie der Schallabsorption in Gasen und Flüssigkeiten unter Berücksichtigung der Transporterscheinungen. Acustica **2** (1952) 101.
12) J. Meixner: Stromungen von fluiden Medien mit inneren Umwandlungen und Druckviskosität. Zeits. Phys. **131** (1952) 456.
13) J. Meixner: Thermodynamische Theorie der elastischen Relaxation. Zeits. Naturforsch. **9a** (1954) 654.
14) J. Meixner: Thermodynamische Erweiterung der Nachwirkungstheorie. Zeits. Phys. **139** (1954) 30.
15) J. Meixner: On the thermodynamic theory of the second viscosity. Proc. Roy. Soc. **226A** (1954) 51.
16) J. Meixner: Zur Nachwirkungstheorie der elastischen Relaxation. Zeits. angew. Phys. **6** (1954) 215.
17) J. J. Markham, R. T. Beyer and R. B. Lindsay: Absorption of sound in fluids. Rev. Modern Physics **23** (1951) 353.
18) S. R. de Groot: "Thermodynamics of irreversible processes" (1952) p. 51.

JOURNAL OF THE PHYSICAL SOCIETY OF JAPAN Vol. 11, No. 8, AUGUST, 1956

# Theory of the Ultrasonic Absorption in Aqueous Solutions
## (I) Introduction and General Theory*

By Otohiko NOMOTO

*Kobayasi Institute of Physical Research, Kokubunzi, Tokyo*

(Received March 30, 1956)

The origin of the anomalous ultrasonic absorption in aqueous solutions has been attributed to the rearrangement process between the associated and the single molecules of water and the solute molecules accompanying the acoustic cycle. The excess pressure of sound wave changes the existence ratio between the associated and the single molecules of water and gives rise to the molecular rearrangement. This process accompanies a change in configurational entropy, the entropy increasing in the compressed volume element. This entropy increase is approximately reversible, becoming perfectly reversible in the quasi-stationary limit. This reversible increase $\Delta S$ in entropy, however, requires a heat quantity $T\Delta S$ ($T$=absolute temperature), which must be supplied by the volume element itself. Thus the specific heat apparently increases by an amount $C_m$, which corresponds to the specific heat of the internal degrees of freedom of the molecules by the molecular absorption of sound. The main part of $\Delta S$ is due to the diffusion of the solute molecules into the groups of single water molecules formed by the collapse of the associated molecules of water under excess pressure, the relaxation time of this diffusion corresponding to the relaxation time of the internal energy in the molecular absorption of sound. General formula of the anomalous ultrasonic absorption in aqueous solutions has been obtained along these lines and under appropriate assumptions.

## § 1. Introduction

It is known that the ultrasonic absorption coefficient in many of the aqueous solutions exhibits a peak at intermediate concentration, the peak value being higher than that of the both component liquids up to 100 times in some cases. The following are the liquids which exhibit absorption peaks in aqueous solutions:

Acetone (Bajouline and Merson[1], Willard[2], Willis[3], Burton[4]);
ethanol (Willis[3], Burton[4], Storey[5]);
*n*-propanol (Burton[4]);
iso-propanol (Burton[4]);
tartiary butanol (Burton[4]);
ethyl cellosolve (ethyl glycol ether) (Burton[4]);
butyl cellosolve (butyl glycol ether) (Burton[4]);
etc.

Although there are also liquids which do not exhibit peaks of sound absorption in aqueous solutions, for example, dioxane, methyl cellosolve (methyl glycol ether), etc., the absorption coefficients in these solutions are higher than the straight line connecting the absorption values of the both component liquids; and when the background absorption assumed as straight line is subtracted, absorption peak is revealed at an intermediate concentration. This is contrary to the case of molecular absorption, where the absorption *vs.* molar fraction curve is concave upwards and the absorption value is lower than the straight line connecting the absorption coefficients of the two component liquids.

The aqueous methanol solution exhibits an almost linear dependency of sound absorption on concentration at ordinary temperature. An absorption peak, however, is observed at a lower temperature (−10°C), and presumably also at −32°C (Sette[6]).

Table I summarizes the results of measurements mainly due to Burton[4]. As is to be seen in the table, these mixtures also exhibit peaks of sound velocity at intermediate concentrations, the concentration of the velocity

---

* The text in Japanese of this paper will be published in "Bulletin of the Kobayasi Institute of Physical Research".

Table I. Concentration of the velocity maximum, concentration of the absorption maximum, and the value of the absorption maximum of ultrasonic waves in aqueous solutions (mainly after measurements of Burton[4])

| Solutes | Molar fraction of the solute at the velocity maximum | Molar fraction of the solute at the absorption maximum | Values of the absorption maximum $(\alpha/\nu^2)_{\max}$ | Temperature (°C) | Temperature coefficient of sound absorption | Temperature range investigated | Author of the temperature dependence |
|---|---|---|---|---|---|---|---|
| methanol | 0.19 | (—) | $(—)\times10^{-17}$ | 27° | negative | −32°~10°C | Sette[6] |
| | — | 0.3 | 110 | −10°(Sette) | | | |
| ethanol | 0.12 | 0.27 | 190 | 27° | negative | 0°~25° | Storey[5] |
| *n*-propanol | 0.05 | 0.14 | 960 | 25° | negative | −7°~27° | Sette[6] |
| iso-propanol | 0.075 | 0.19 | 720 | 25° | | | |
| tert. butanol | 0.045 | 0.11 | 3850 | 27° | | | |
| acetone | 0.07 | 0.38 | 220 | 27.5° | negative | 20°~38° | Bjouline-Merson[1] |
| methyl glycol ether | 0.14 | (0.2) | (43) | 28° | | | |
| ethyl glycol ether | 0.10 | 0.22 | 220 | 28.5° | | | |
| butyl glycol ether | 0.02 | 0.09 | 3500 | 28.5° | | | |
| dioxane | 0.09 | (0.3) | (60) | 23° | | | |
| glycol | 0.50 | (0.5) | (20) | 28° | | | |
| phenol | 0.06 | 0.05~0.07 | 50 | 70° (Cevolani-Petralia[7][16]) | | | |

peak being lower than that of the absorption peak for each mixture. The table shows the concentration (molar fraction of the second component) for the velocity peak, that for the absorption peak, and the value of the absorption peak $(\alpha/\nu^2)_{\max}$, where $\alpha$ means the amplitude absorption coefficient per unit length and $\nu$ the frequency. The values in the parentheses indicate the peak values of the excess absorption obtained by subtracting the linear beckground. The temperature of observation of the absorption coefficients is also indicated. When the measurements are available over a range of temperatures, the sign of the temperature coefficient is also included. As is to be seen in the table, the temperature coefficient of absorption is always negative, the absorption coefficient decreasing rapidly with increasing temperature. This is a second point which distinguishes the sound absorption in aqueous solutions from the molecular absorption. For example, the absorption coefficient in aqueous ethanol solution decreases by a factor of 3.5 between 0° and 25°C (Storey[5]).

Next we will consider of the relaxation time. The fact that the value of $\alpha/\nu^2$ is almost independent of the frequency within experimental errors (±20%) in aqueous acetone solutions, as tabulated below, indicates that the relaxation time is of the order of 100 Mc/sec or higher.

| | | |
|---|---|---|
| Willis | 3.84 Mc<br>6.40 Mc<br>11.50 Mc<br>19.20 Mc | $(\alpha/\nu^2)_{\max}=190\times10^{-17}$ |
| Willard* | | $170\times10^{-17}$ |
| Bajouline-Merson | 19 Mc<br>26 Mc<br>29.5 Mc<br>38 Mc | $150\times10^{-17}$ |

In case of ethanol solutions, Storey's measurement[5] by the pulse technique (accuracy ±1%) at 22.5 Mc, 37.5 Mc, and 52.5 Mc, and at temperatures 0°, 10° and 25°C indicates that the concentration of maximum absorption is independent of the frequency, though slightly dependent on the temperature, shifting towards higher alcohol concentration with increasing temperature. By assuming single relaxation time and writing

$$\frac{\alpha}{\nu^2}=\frac{A}{1+(\nu/\nu_m)^2}, \tag{1.1}$$

Storey has found out that

$$\left.\begin{array}{l}\nu_m=103\pm5\ \text{Mc/sec at }0°\text{C and }22\%\ \text{(molar fraction),}\\ \text{and}\\ \nu_m=145\pm10\ \text{Mc/sec at }25°\text{C and }25\%\ \text{(molar fraction).}\end{array}\right\} \tag{1.2}$$

For aqueous propanol solutions, Sette[6] has obtained the peak values at 13.9% (molar fraction) and 24.5°C:

---

* Frequency not clearly indicated, but measurement made with one or more of the following four frequencies: 6.57, 10.31, 19.7 and 31.0 Mc/sec.

$$\left.\begin{array}{l}(\alpha/\nu^2)_{\max}=835\times10^{-17}\text{cgs}\ ,\\ \text{and}\\ (\alpha/\nu^2)_{\max}=582\times10^{-17}\text{cgs}\ .\end{array}\right\}$$

This gives by (1.1) the relaxation frequency

$$\nu_m=53.6\ \text{Mc/sec}\ (24.5°\text{C};\ 13.9\%)\ . \tag{1.3}$$

For aqueous phenol solutions, there is a measurement by Cevolani and Petralia⁷⁾ at 70°C. In this case, exact calculation is difficult because of the small magnitude of the absorption peak and the relatively high and inclined background. The approximate values of the excess absorption obtained from Cevolani-Petralia's graphs, however, are as follows:

$$\left.\begin{array}{l}(\alpha/\nu^2)_{\max}=39\times10^{-17}\text{cgs}\quad \text{at}\quad 9\ \text{Mc}\ ,\\ \text{and}\\ (\alpha/\nu^2)_{\max}=22\times10^{-17}\text{cgs}\quad \text{at}\ 33\ \text{Mc}\ ,\end{array}\right\}$$

and we obtain

$$\nu_m=35\ \text{Mc/sec}\ (70°\text{C};\ 5\sim7\%) \tag{1.4}$$

in this case.

These results give clues in constructing the theory to be described below.

There are known also some non-aqueous mixtures which exhibit absorption peaks at intermediate concentrations. These are the solutions containing nitrobenzene, ethanol, propanol, butanol, phenol or acetic acid as one of the component liquids. Although these mixtures have the common feature of having negative temperature coefficient of sound absorption as in the case of aqueous solutions, the absorption mechanism seems to be a little different for aqueous and non-aqueous solutions. So we will not treat the non-aqueous solutions in this paper.

Although it is commonly supposed that the anomalous ultrasonic absorption in aqueous solutions is related to the associated nature of the water molecules, no concrete and satisfactory theory is hitherto available for explaining the absorption coefficient. For example, Pinkerton¹⁵⁾ has pointed out that the maximum of absorption in aqueous ethanol solution occurs in a mixture containing roughly four water molecules to every alcohol molecule, and assumes (after suggestion of E. Bauer) that the absorption arises from the breakdown of this complex. Also Storey⁵⁾ holds this view by pointing out (after Bauer) that the heat of mixing of ethanol and water attains maximum at 20% (molar fraction) alcohol and that the curve representing the freezing point. *vs.* concentration of this mixture has a discontinuity of slope at 20% alcohol. No formulation of the exact absorption mechanism, however, is proposed.

So we intend to treat this problem in the following.

## § 2. Mechanism of Anomalous Ultrasonic Absorption

We have seen that the ultrasonic absorption in aqueous solutions are higher than that of the constituent liquids by factors attaining up to 100 in some cases. It seems that the anomalous part of absorption is related with the associated structure of water and its variation with the acoustic cycle. Water is known to be an associated liquid consisting of the associated molecules and the single ones which are in mutual thermal equilibrium. The associated molecules are supposed to be nearly in the tridymite structure of the ice crystal with four nearest neighbours, while the single molecules are considered to be nearly in the closest packed structure with twelve nearest neighbours. The associated molecules are of larger molar volume (per monomer), while the single molecules are of smaller molar volume.

Excess pressure in sound wave transforms some of the associated molecules into single ones and this process requires a finite relaxation time of the order of $2\times10^{-12}$ sec at room temperature. This gives rise to an excess ultrasonic absorption in pure water, as was discussed in detail by Hall⁸⁾. We will adopt the manners of thinking and the results of the Hall's theory in this paper. This mechanism, however, cannot explain the appearance at intermediate concentration of the absorption maximum in aqueous solutions.

We propose a new mechanism of ultrasonic absorption in aqueous solutions in this paper, the "**relaxation of molecular rearrangement**" or "**diffusion relaxation mechanism**". We will describe of this mechanism in the following. We have to begin with the consideration of the structure of the aqueous solution. The aqueous solution consists of the molecules of the solvent water in the associated and the single states and those of the solute substance. Generally speaking, the solute molecules may

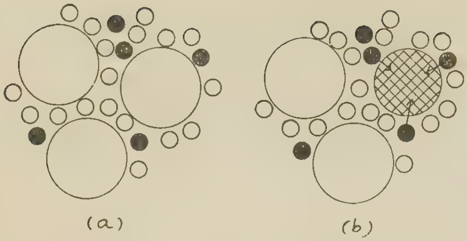

Fig. 1. Schematical model of the aqueous solution (a), and the molecular rearrangement induced by an excess pressure (b).

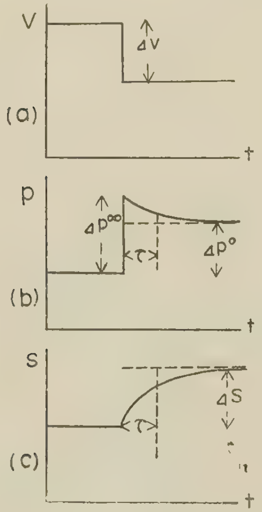

Fig. 2. Relaxation of pressure and the increase in configurational entropy after an instantaneous compression of an aqueous solution.

be also in the associated and the single states, as in the case of alcohol. There may exist also the mutual association between the molecules of solute and water. It is, however, not easy to estimate all of these effects quantitatively, and there is involved moreover a danger of missing the true importance of the various factors when a too complex model is employed. So we omitted the association of the solute and the mutual association between solute and water in this paper, and only the association of water is taken into account.

As is to be seen later (cf. part (II) of this paper; § 5, eq. (5.12)), our theory requires that the average magnitude of the associated molecules are very large, containing about 8000 monomers ($H_2O$–molecules) in case of pure water. It is essentially different from the degree of association in other liquids as alcohols, in which the associated molecules consists mainly of trimers or tetramers. This is one of the reason to suppose that the mechanism of anomalous sound absorption in aqueous solutions is different from that in other associated mixtures.

So we will consider the model of the aqueous solution as illustrated in Fig. 1, (a) schematically. The great white circles in the figure indicate the associated molecules of water, the smaller white circles the single water molecules, and the small black circles the solute molecules.

Excess pressure in sound wave crushes some of the associated water molecules and transforms them into groups of single molecules. Here we assume that some of the associated moleculer collapse as a whole and transform entirely into single molecules, while the others remain unchanged.

Then the excess pressure produces the groups of single water molecules as illustrated in Fig. 1, (b) by great white circles with networks, in which the density of the solute molecule is zero. So there takes place a molecular rearrangement by diffusion process as illustrated by arrows in the figure.

This diffusion accompanies an irreversible entropy production, $\Delta S_{\text{irr}}$, and therefore, the sound absorption. It, however, is not easy to estimate the irreversible production of entropy directly. So we will take an indirect course and proceed as follows.

This molecular rearrangement process accompanies an increase in configurational entropy $\Delta S$ (per mole) as is to be shown later (cf. § 4). It, however, must be remarked that this entropy increase $\Delta S$ is not entirely irreversible. ($\Delta S$ is different from $\Delta S_{\text{irr}}$ as is to be shown below.) On the contrary, this increase in configurational entropy is approximately reversible, becoming completely reversible if the increase of pressure is quasi-static. This is analogous to the fact that the heat conduction is reversible in the quasi-static limit. (cf. further Saito and Sugita[10].) As the total process is adiabatic in an acoustic cycle, the heat quantity $T\Delta S$ required for the increase of the configurational entropy (where $T=$ absolute temperature) must be supplied by the volume element itself, because the increase of configurational entropy is nearly reversible. This results in the decrease in temperature, and therefore, also in pressure of the volume element here considered. (The circumstance is similar as in the case of adiabatic demagnetization process in obtaining low temperatures.)

Consider an aqueous solution contained in a cylinder with adiabatic walls and equipped with a piston. When this liquid is instantaneously compressed, the volume undergoes a change as illustrated in Fig. 2, (a). The corresponding change of pressure, however, becomes as Fig. 2, (b), the pressure increasing by $\varDelta p^{\infty}$ at first, but relaxing to the valne $\varDelta p^0$ with the relaxation time of the molecular rearragnement process. Here we neglected the relaxation time for collapse of the associated molecules of water because it is short ($2\times 10^{-12}$sec) as compared to the relaxation time of the molecular rearrangement (of the order of $10^{-9}$sec). This gives rise to the absorption of sound.

Thus the existence of the molecular rearrangement process accompanying the acoustic cycle means that the energy is stored in the form of the (configurational entropy) × (temperature) similarly as the energy is stored as molecular vibrational or rotational energy in case of the molecular absorption of sound. So there exists a specific heat $C_m$ due to molecular rearrangement process corresponding to the internal specific heat $C_i$.

Generally speaking, the total entropy change of the system consists of three parts, (a) the part $\varDelta S^c$ due to uniform compression, (b) the part $\varDelta S^t$ due to the change of thermal motion, and (c) the configurational entropy change $\varDelta S$ here considered. Here we are dealing with the excess part of the ultrasonic absorption and we have omitted $\varDelta S^c$ because the contribution of this to ultrasonic absorption is considered to be included in the absorption of component liquids. $\varDelta S^c$ consists of the parts belonging to the two component liquids, the part $\varDelta S^c_F$ belonging to the solute is presumably in phase with the pressure change and does not contribute to sound absorption. The part $\varDelta S^c_w$ belonging to pure water have a part not in phase with the pressure change because the compression in water accompanies the breaking of hydrogen bonds, which requires a relaxation time of the order of $10^{-12}$sec. The main part of ultrasonic absorption in pure water, however, is due to the energy change rather than the entropy change. Referring to Fig. 2, part of the work of compression is changed into thermal motion while the other part is used to reduce $\varDelta S^c$. After elapse of time interval of the order of $10^{-12}$sec, however, we have only to deal with $\varDelta S^t$ and $\varDelta S$.

We will consider of the process at constant volume, i.e., after the compression is finished. The part $\varDelta S^t$ due to the thermal motion compensates with the other parts if the process is adiabatic and quasi-static. In this case, the entropy relation

$$\varDelta S+\varDelta S^t=0 \qquad (2.1)$$

coincides with the energy relation

$$T\varDelta S-C_m\varDelta T=0\,, \qquad (2.2)$$

because here the heat quantity $\varDelta Q=C_m\varDelta T$ must be transferred from the thermal motion to increase the configurational entropy.

If, however, the system is not in equilibrium, i.e., not isentropic, the entropy relation becomes

$$\varDelta S+\varDelta S^t=\varDelta S_{\mathrm{irr}}\,, \qquad (2.3)$$

where $\varDelta S_{\mathrm{irr}}$ means the irreversible entropy production, while the energy relation after an instantaneous compression of Fig. 2 remains the same:

$$T\varDelta S-C_m\varDelta T^0=0\,, \qquad (2.4)$$

where $\varDelta T^0$ means the equilibrium increment of temperature.

The circumstance is quite similar to the case of molecular sound absorption. In this case we have to deal with the heat conduction between the external system (translational degrees of freedom of the molecules) and the internal system (vibrational degrees of freedom of the molecules) which are at different temperatures. (cf. Nomoto[9]).

In our present case the configurational entropy increases by absorption of heat from the thermal motion of the volume element. The volume element gives the same quantity of heat as the "configurational degree of freedom" receives. The entropy decrease $\varDelta S^t$, however, is smaller in this case because the temperature is higher in the translational degrees of freedoms. We have to deal with the heat conduction between the "thermal motion" and the "configurational degrees of freedoms". $C_m$ (defined by (2.4)) corresponds to the internal specific heat $C_i$ in the molecular absorption of sound, and the temperature of the "configurational degrees of freedom" is to be defined by

$$\Delta T_m=\Delta Q_m/C_m\ , \qquad (2.5)$$

where $\Delta Q_m$ means the quantity of heat transferred to the "configurational degree of freedom".

We can obtain the irreversible entropy production in the relaxation stage of Fig. 2 quite in a similar manner as in the case of molecular absorption. This becomes $(C_m/T^2)(\Delta T^0\Delta T^\infty/2)$. As two relaxation stages are present in one cycle (once from the thermal motion to the configurational system and vice versa), the total entropy production during an rectangular wave cycle is

$$\Delta S_{\text{irr}}=\frac{C_m\Delta T^0\Delta T^\infty}{T^2}\ , \qquad (2.6)$$

where $\Delta T^0$ and $\Delta T^\infty$ are the equilibrium and the instantaneous increment of pressure corresponding to the volume change of Fig. 2.

We will describe a quantitative theory along these ideas in the following.

## § 3. Variation of the Numbers of the Associated and the Single Molecules of Water Accompanying the Acoustic Cycle

In order to obtain the sound absorption coefficient by the above mentioned mechanism, it is required to calculate the increment of the configurational entropy $\Delta S$ induced by the excess pressure of sound. In computing $\Delta S$, it becomes necessary in turn to know the existence ratio between the associated and the single molecules of solvent water in aqueous solutions, and their variation with pressure. Also the magnitude of the associated molecules of water and its concentration dependence is required. The existence ratio of the associated molecules at various concentrations can be obtained from the adiabatic compressibility of the solution (velocity of sound in the solution) under appropriate assumptions. This is to be described in a separate paper (Nomoto[14]). Here we consider the variation in numbers of the associated and the single molecules of water in aqueous solutions.

### (a) Pure Water

First we will consider the case of pure water. The associated and the single molecules of water are in thermal equilibrium. If we denote the numbers of moles of the associated and the single molecules of water in one mole ($n_w=1$) of water by $n_a$ and $n_s$ respectively, we have

$$n_a+n_s=n_w=1\ . \qquad (3.1)$$

Here and in the following, the numbers of moles are always calculated in molecular weight of the monomers.

Writing the reaction equation between the molecules

$$-\dot{n}_s=k_2n_s-k_1n_a\ , \qquad (3.2)$$

after Hall[8], we have at equilibrium ($\dot{n}_s=0$),

$$n_{a0}k_{10}=n_{s0}k_{20}\ , \qquad (3.3)$$

and for small deviations from equilibrium

$$-\Delta\dot{n}_s=k_{20}\Delta n_s+n_{s0}\Delta k_2-k_{10}\Delta n_a-n_{a0}\Delta k_1\ . \qquad (3.4)$$

Here the quantities with suffix zero indicate the equilibrium values. The ratio between the numbers of moles of the single and the associated molecules is given by

$$\frac{n_{s0}}{n_{a0}}=\frac{\exp(-F_s/RT)}{\exp(-F_a/RT)}=e^{-\Delta F/RT}, \qquad (3.5)$$

where

$$\Delta F=F_s-F_a \qquad (3.6)$$

indicates the difference between the free energies per mole of the associated and the single water molecules, and $R$ the universal gas constant. As we have

$$\Delta n_a=-\Delta n_s \qquad (3.7)$$

by (3.1), we have from (3.4) by assuming sinusoidal variations $\exp(i\omega t)$ for all the quantities with $\Delta$, the following relation

$$\Delta n_s=\frac{-k_{20}n_{s0}\Delta(\Delta F/RT)}{i\omega+k_{10}+k_{20}}\ . \qquad (3.8)$$

And if this variation is due to the sinusoidal variation of pressure $\Delta p$ in the sound wave, we have

$$\Delta n_s=-\frac{k_{20}n_{s0}\{\partial(\Delta F)/\partial p\}\Delta p}{RT(i\omega+k_{10}+k_{20})}\ . \qquad (3.9)$$

Or, expressed in terms of the relaxation time

$$\tau_w=1/(k_{10}+k_{20})\ , \qquad (3.10)$$

and by assuming the pressure variation of the free energy simply as

$$\partial(\Delta F)/\partial p=-\Delta v=-(v_a-v_s) \qquad (3.11)$$

after Hall, where $v_a$ and $v_s$ mean the molar volumes of water consisting of the associated molecules of water and the single molecules of water respectively, we have

$$\Delta n_s=\frac{n_w(v_a-v_s)\Delta p}{2RT\{1+\cosh(\Delta F/RT)\}}\frac{1}{1+i\omega\tau_w}\ . \qquad (3.12)$$

Also it is to be written as

$$\Delta n_s = -\frac{n_a(v_a - v_s)\Delta p}{RT\{1+\exp(\Delta F/RT)\}}\frac{1}{1+i\omega\tau_w}\,. \qquad (3.12\text{a})$$

This indicates that $\Delta n_s$ mole of associated water molecules collapse and change into single molecules under excess pressure $\Delta p$.

Although it is usual in these treatments to employ the equation of the form (3.12), we have to employ (3.12a) in the following, in order to treat also the aqueous solutions, as will be discussed soon below.

### (b) Aqueous Solutions

Now we will consider the aqueous solutions. In an aqueous solution, there are the associated and the single molecules of water and the solute molecules in mutual equilibrium. There is $n_w$ mole of solvent water in one mole of an aqueous solution containing $n_F$ mole of the solute. The solvent water consists of $n_s$ mole of the single water molecules and $n_a$ mole of the associated water molecules, i.e.,

$$n_w = n_s + n_a = 1 - n_F\,. \qquad (3.13)$$

The ratio $n_s/n_w$ in solution, however, is not the same as in pure water and is also dependent on the concentration. The associated molecules are partly collapsed and reduced in magnitude by the influence of the solute molecules and the number of mole of the single water molecules is increased. This is to be concluded from the occurence at intermediate concentration of the velocity peak (and the minimum of the compressibility) in aqueous solutions, and the variation of the existence ratio of $n_s:n_a$ can be evaluated from the sound velocity data. The method of estimation is described elsewhere Nomoto[14] and we will employ the result afterwards.

Although the three sorts of molecules, the associated and the single molecules of water, and the solute molecules, are in mutual equilibrium in aqueous solutions, it is too complex for practical calculation. So we will consider a simplified schematical model by assuming that the single water molecules can be divided into two classes, one part ($n_s^{(1)}$mole) in thermal equilibrium with the associated molecules, and the other part ($n_s^{(2)}$mole) in equilibrium with the molecules of the solute, i.e.,

$$n_s = n_s^{(1)} + n_s^{(2)}\,. \qquad (3.14)$$

We have assumed further that the number of that part of the single water molecules in equilibrium with the solute molecules does not change under excess pressure, i.e.,

$$\Delta n_s^{(2)} = 0\,, \qquad (3.15)$$

while that part of the single water molecules in equilibrium with the associated water molecules is considered to increase under excess pressure in the same ratio as in case of pure water, i.e., following (3.12a). As

$$\Delta n_s = \Delta n_s^{(1)} + \Delta n_s^{(2)} = \Delta n_s^{(1)} \qquad (3.16)$$

after (3.15), $\Delta n_s$ is given by (3.12a) also for aqueous solutions. The relaxation time $\tau_w$ being of the order of $2\times10^{-12}$sec at room temperature, we have $\omega\tau_w \ll 1$ for ultrasonic waves of usual frequencies (up to 100 Mc/sec), and (3.12a) becomes simply as

$$\Delta n_s = \frac{n_a(v_a - v_s)\Delta p}{RT\{1+\exp(\Delta F/RT)\}}\,. \qquad (3.17)$$

We will employ this relation in the following.

## §4. Entropy Change due to Molecular Rearrangement

It is not easy to obtain the configurational entropy of the aqueous solution exactly even for the simple liquid model as here employed. First we will perform the calculation, ignoring the difference in magnitude of the various kinds of the molecules constituting the solution. Moreover, we will treat the single molecules and the associated molecules of water as different kinds of molecules. Next we calculate the entropy by assuming the single molecule of water and the solute molecule as two kinds of linear polymers each constituting of one kind of atoms of mutually different species.

### (a) Calculation Ignoring the Difference in Sizes of the Molecules

If the number of the single water molecules, the associated water molecules and the solute molecules in one mole of solution be denoted by $m_s$, $m_a$ and $m_F$ respectively, these are related with the molar fraction by

$$\left.\begin{aligned} m_s &= n_s N_L\,, \\ m_a &= n_a N_L/Z\,, \\ m_F &= n_F N_L\,, \end{aligned}\right\} \qquad (4.1)$$

where $N_L$ means the Loschmidt number, and $Z$ the average number of monomers constituting an associated water molecule.

Ignoring the difference in magnitude of the molecules, we have as the configurational entropy per mole of the solution,

$$S=k\log W$$
$$=k[(m_F+m_s+m_\alpha)\log(m_F+m_s+m_\alpha)$$
$$-m_F\log m_F-m_s\log m_s-m_\alpha\log \mathrm{m}_\alpha]\,, \tag{4.2}$$

where $k$ means the Boltzmann constant. This becomes by (4.1) as

$$S=R[(n_F+n_s+n_\alpha/Z)\log(n_F+n_s+n_\alpha/Z)$$
$$-n_F\log n_F-n_s\log n_s-(n_\alpha/Z)\log(n_\alpha/Z)], \tag{4.3}$$

where $R=kN_L$ is the universal gas constant. The configurational entropy remains the same also immediately after collapse of the associated molecules by the excess pressure, because at this moment all the single molecules newly produced by the sudden collapse of the associated molecules are considered to be still in the original groups, in which they formed the associated molecules.

After establishment of the new equilibrium with $n_s+\Delta n_s$ moles of single water molecules and $n_\alpha+\Delta n_\alpha=n_\alpha-\Delta n_s$ moles of the associated molecules, the entropy is given by

$$S+\Delta S=R\Big[\Big(n_F+n_s+\Delta n_s+\frac{n_\alpha}{Z}-\frac{\Delta n_s}{Z}\Big)$$
$$\times\log\Big(n_F+n_s+\Delta n_s+\frac{n_\alpha}{Z}-\frac{\Delta n_s}{Z}\Big)$$
$$-n_F\log n_F-(n_s+\Delta n_s)\log(n_s+\Delta n_s)$$
$$-\Big(\frac{n_\alpha}{Z}-\frac{\Delta n_s}{Z}\Big)\log\Big(\frac{n_\alpha}{Z}-\frac{\Delta n_s}{Z}\Big)\Big]\,,$$

and the increment of entropy becomes by retaining terms up to the first order in $\Delta n_s$,

$$\Delta S=R\Big[\Big\{\log\Big(n_F+n_s+\frac{n_\alpha}{Z}\Big)-\log n_s\Big\}$$
$$-\frac{1}{Z}\Big\{\log\Big(n_F+n_s+\frac{n_\alpha}{Z}\Big)-\log\frac{n_\alpha}{Z}\Big\}\Big]\Delta n_s\,. \tag{4.4}$$

As is to be shown later (Part II of this paper, § 5), $Z$ is very large and is of the order of 8000 for pure water; it becomes smaller in solutions but still larger than 1000 for most part of the concentration range. So the terms in $(n_\alpha/Z)$ and $(\Delta n_s/Z)$ in this equation can be omitted within an error of 1% or less. So we will employ an approximate expression

$$S=R[\log(n_F+n_s)-\log n_s]\Delta n_s \tag{4.5}$$

in the following.

Employing (3.17) for $\Delta n_s$, we have

$$T\Delta S=f\Delta p\,, \tag{4.6}$$

where

$$f=\frac{(v_\alpha-v_s)n_\alpha\log(1+n_F/n_s)}{1+\exp(\Delta F/RT)}\,. \tag{4.7}$$

Fig. 3 shows the factor of this expression

$$\varphi=n_\alpha\log(1+n_F/n_s) \tag{4.8}$$

as function of $n_F$ and for various values of the existence ratio $n_s/n_w$ as parameters. As is to be seen from the figure, $\varphi$, and accordingly also $f$ is the larger, smaller the value of $n_s/n_w$.

### (b) Calculation Regarding the Molecules as Linear Polymers

We omit the associated molecules of water from the beginning as above, considering of the small numbers, i.e., large $Z$, and take into account the difference in magnitude of the single water molecule and the solute molecule assuming each of them as a linear polymer (with or without ramification, but without cross linking) each consisting of a single kind of atoms. In practice the water molecules consists of the atoms of H and O, and a solute atom may consist of the atoms of C, H, O, etc., and there are common kinds of atoms, as well as different ones, in the consituent atoms of water and solute. It is, however, very complex to compute the entropy by considering these actual molecules. So we assumed, for the sake of simplicity, that the single molecule of water consists of three atoms of one kind ($S$), and the solute molecule consists of some atoms of the other kind ($F$), equal in number with the actual constituting atoms. For this simplified model we can apply the result of calculations by Guggenheim[12)13)] on the entropy of mixing of two kinds of linear polymers (with or without ramification, but without cross linking) each consisting of one kind of atoms. (Of course this calculation is based on the assumption that the molecules are located on lattice-points as in usual statistical mechanical calculations.)

Let the number of moles of the molecules of type $S$ and type $F$ be denoted respectively by $n_s$ and $n_F$, and the number of sites (lattice-points) per one molecules of these types by $r_s$ and $r_F$. If the number of nearest neighbours of a lattice point is $z$, there are $zr_s$ pairs connecting $r_z$ atoms of a molecule of $S$-type to their nearest neighbours. As a pair is commonly possessed by the two atoms constituting the pair, the number of pairs belonging to an $S$-type molecule is $zr_s/2$. Out of these $zr_s/2$ pairs, $(r_s-1)$ belongs to the interior of the molecule, i.e., they connect two atoms belonging to one $S$-type molecule. So the number of the pairs with one end occupied by an atom of $S$-type molecule and the other end not occupied by a constituting element of the same molecule becomes

$$\frac{1}{2}zq_s=\frac{1}{2}zr_s-(r_s-1)\,. \tag{4.9}$$

We have similarly

$$\frac{1}{2}zq_F=\frac{1}{2}zr_F-(r_F-1) \tag{4.10}$$

as the number of pairs with one end occupied by an atom of $F$-type and the other end not occupied by an element of the same molecule.

The entropy of mixing for two kinds of linear polymers is given by Guggenheim as

$$\begin{aligned}\frac{S^*}{R}=n_s\log\frac{r_sn_s}{r_sn_s+r_Fn_F}&\\+\frac{1}{2}zq_sn_s\log\frac{q_s(r_sn_s+r_Fn_F)}{r_s(q_sn_s+q_Fn_F)}&\\+n_F\log\frac{r_Fn_F}{r_sn_s+r_Fn_F}&\\+\frac{1}{2}zq_Fn_F\log\frac{q_F(r_sn_s+r_Fn_F)}{r_F(q_sn_s+q_Fn_F)}&\,.\end{aligned} \tag{4.11}$$

Here the asterisk is added in order to distinguish from the result of case (a).

We can obtain from this the entropy increase corresponding to an increase in number of moles of the single molecules of water by $\Delta n_s$. Retaining terms up to the first order in $\Delta n_s$, and employing (4.13) and (4.14), we have

$$\begin{aligned}\Delta S^*=R\Delta n_s\Big[\log\left(1+\frac{r_Fn_F}{r_sn_s}\right)&\\+\frac{1}{2}zq_s\log\frac{r_s(q_sn_s+q_Fn_F)}{q_s(r_sn_s+r_Fn_F)}\Big]&\,.\end{aligned} \tag{4.12}$$

This gives an expression corresponding to (4.7) in case (a),

$$\begin{aligned}f^*=\frac{(v_a-v_s)n_a}{1+\exp(\Delta F/RT)}\Big[\frac{1}{2}zq_s\log\left(1+\frac{q_Fn_F}{q_sn_s}\right)&\\-\left(\frac{1}{2}zq_s-1\right)\log\left(1+\frac{r_Fn_F}{r_sn_s}\right)\Big]&\,.\end{aligned} \tag{4.13}$$

## § 5. Apparent Specific heat due to Molecular Rearrangement Process

If the temperature of the solution is raised by $\Delta T$ by the external work of compression $-p\Delta v(\Delta v<0)$, we can write

$$-p\Delta v=C_s\Delta T\,, \tag{5.1}$$

where $C_s$ means the proportionality factor. There exists, generally, a relation between the amount of volume reduction and the increase of temperature by an adiabatic compression of a fluid (liquid or gas), namely

$$\frac{\Delta v}{v}=-\frac{\vartheta}{\gamma-1}\Delta T\,, \tag{5.2}$$

(cf. Nomoto[9]; eq. (2.29)), where $\vartheta$ means the thermal expansion coefficient and $\gamma(=C_p/C_v)$ the ratio of the specific heats. We have accordingly,

$$C_s=\frac{\vartheta}{\gamma-1}\frac{pM}{\rho}\,. \tag{5.3}$$

Here $M$ means the mean molecular weight and $\rho$ the density.

Now we will denote the apparent molar specific heat due to the molecular rearrangement process by $C_m$, then we have by (4.6) the relation:

$$T\Delta S=f\Delta p=C_m\Delta T\,, \tag{5.4}$$

where $f$ is given by (4.7) and $\Delta T$ means the same temperature increment as given in (5.2). This means that out of the external work of compression $\Delta W=-p\Delta v$, an amount $\Delta Q=T\Delta S$ is used for the configurational entropy increase due to the molecular rearrangement process, the ratio being

$$\frac{\Delta Q}{\Delta W}=\frac{T\Delta S}{-p\Delta v}=\frac{f\Delta p}{-p\Delta v}=-\frac{f}{p}\left(\frac{\partial p}{\partial v}\right)_s\,. \tag{5.5}$$

Now the sound velocity in any substance is given by

$$V^2=\left(\frac{\partial p}{\partial \rho}\right)_s=-\frac{M}{\rho^2}\left(\frac{\partial p}{\partial v}\right)_s\,. \tag{5.6}$$

So we have, by substituting (5.1), (5.3) and (5.6) into (5.5)

$$C_m=\frac{f}{p}\frac{\rho^2}{M}V^2C_s=\frac{f\vartheta\rho V^2}{\gamma-1}\,. \tag{5.7}$$

As we have further the relation

$$\gamma=1+\frac{T\vartheta^2V^2}{c_p}=1+\frac{TM\vartheta^2V^2}{C_p}\,, \tag{5.8}$$

where $c_p$ means the specific heat at constant pressure, and $C_p$ the molar specific heat at constant pressure, we can also write

$$C_m=\frac{\rho C_p}{TM\vartheta}f\,, \tag{5.9}$$

where $f$ is given by (4.7), or

$$C_m{}^*=\frac{\rho C_p}{TM\vartheta}f^* \tag{5.10}$$

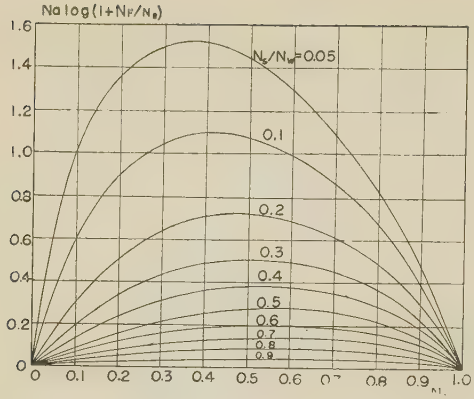

Fig. 3. Dependence of $\varphi=n_a \log(1+n_F/n_s)$ on $n_F$ and $n_s/n_w$.

where $f^*$ is given by (4.13). The mean molecular weight $M$ involved in these equation are given by

$$M=(1-n_F)M_w+n_F M_F \ . \tag{5.11}$$

## § 6. Ultrasonic Absorption Coefficient

The occurrence of the molecular rearrangement between the single molecules of water and the solute molecules implies an apparent increase in molar specific heat $C_v$ by an amount $C_m$ given by (5.11) or $C_m$ given by (5.12). The specific heat $C_{v0}$ for quasi-stationary process includes $B_m$, while the specific heat for instantaneous change $C_{v\infty}$ does not include $C_m$. Therefore,

$$C_{v0}=C_{v\infty}+C_m \ . \tag{6.1}$$

After an instantaneous compression, the increase of entropy $\varDelta S$ takes place with relaxation time $\tau$, as illustrated in Fig. 2. Now the quantity $T\varDelta S$ corresponds to the internal energy $E_i$ in case of the molecular absorption of sound, by (5.4); and $C_m$ corresponds to the internal specific heat (per mole) $C_i$. Thus $\tau$ means the relaxation time of the internal energy, and the relaxation time of the internal specific heat becomes

$$\beta=\tau\frac{C_{v0}}{C_{v\infty}}=\tau\frac{C_{v0}}{C_{v0}-C_m} \tag{6.2}$$

(cf. Nomoto[11]).

There accompanies, therefore, an excess ultrasonic absorption and dispersion as in the case of the thermal relaxation process of the molecular vibrational or rotational energy and the absorption coefficient is to be obtained immediately from the known results of the thermal relaxation process. The relaxational specific heat in this case being $C_m$, the amplitude absorption coefficient per wavelength becomes

$$\alpha_\lambda=\alpha\lambda=\pi\frac{(C_{p0}-C_{v0})C_m\omega\tau}{C_{p0}C_{v\infty}+C_{v0}C_{p\infty}\omega^2\tau^2} \tag{6.3}$$

(cf. Nomoto[9], eq. (3.44) or Nomoto[11], eq. (3.27)), where $C_{p0}$ and $C_{p\infty}$ mean the molar specific heat at constant pressure at sufficiently low frequency and at sufficiently high frequency respectively. Here we have

$$C_{p0}=C_{p\infty}+C_m \ . \tag{6.4}$$

We have from (6.3)

$$\frac{\alpha}{\nu^2}=\frac{2\pi^2(C_{p0}-C_{v0})C_m\tau}{V(C_{p0}C_{v\infty}+C_{v0}C_{p\infty}\omega^2\tau^2)} , \tag{6.5}$$

where $V$ means the sound velocity.

Now writing simply $C_v$ and $C_v$ in place of $C_{p0}$ and $C_{v0}$ respectively, and substituting (5.9) for $C_m$, (6.5) becomes

$$\frac{\alpha}{\nu^2}=\frac{2\pi^2\rho\vartheta v}{C_p}\frac{C_v}{C_v-C_m}f\frac{\tau}{1+\dfrac{C_v(C_p-C_m)}{C_p(C_v-C_m)}\omega^2\tau^2} , \tag{6.6}$$

where $f$ is given by (4.7). When the magnitude of the molecules are taken into account, we have to use $f^*$ (eq. (4.13)) instead of $f$.

At sufficiently low frequencies, we have $\omega\tau\ll 1$, and we have as the "*frequency independent*" absorption coefficient

$$\left(\frac{\alpha}{\nu^2}\right)_0=\frac{2\pi^2\vartheta\rho v}{C_p}\frac{C_v}{C_v-C_m}f\tau , \tag{6.7}$$

or,

$$\left(\frac{\alpha^*}{\nu^2}\right)_0=\frac{2\pi^2\vartheta\rho v}{C_p}\frac{C_v}{C_v-C_m{}^*}f^*\tau \ . \tag{6.8}$$

As the relaxation time is of the order of $10^{-9}$ sec for aqueous solutions (cf. § 1), the approximate formulas (6.7) and (6.8) are valid within an accuracy of 1% up to 20 Mc/sec. as far as the frequency dependence is concerned.

## § 7. Relaxation Time of Molecular Rearrangement

When some of the associated molecules of water collapse under excess pressure and the groups of single molecules are produced, the molecular rearrangement takes place among the three kinds of molecules, the associated and the single molecules of water and the solute molecules. We have seen, however, that the associated molecules of water may be omitted within an accuracy of 1% in calculating the configurational entropy change $\Delta S$ (cf. § 4). So the molecular rearrangement process may be also regarded as taking place between the molecules of solute and the single water molecules. As the solute molecules does not exist at first within the group of the single water molecules newly formed by the sudden collapse of an associated molecule of water under excess pressure, the solute molecules diffuse into the newly formed group of single water molecules from the surroundings, as illustrated in Fig. 1, (b).

Also there being no solute molecule inside of the associated molecules of water, the solute molecules are mixed with the single molecules of water, and the associated molecules of water are to be regarded as mere obstacles in this mixture. So the density of the solute molecules dissolved in the single water molecules is given by

$$n_0 = \kappa \frac{n_F}{n_s + n_F} = \kappa \frac{n_F}{n_w - n_a}, \tag{7.1}$$

$\kappa$ being a proportionality factor. If the concentration is expressed in units of molecules/cm$^3$, we have

$$n_0 = \frac{n_F N_L}{v - n_a v_a}, \tag{7.2}$$

where $v$ and $v_a$ mean the molar volume of the solution and the associated molecules of water respectively.

Although there are also the associated molecules of water as illustrated in Fig. 1, (b), this model is not convenient for practical calculation. So we replace it by a homogeneous model as represented in Fig. 4, in which the surrounding medium is assumed to be a homogeneous solution of concentration $n_0$ of solute molecules in single water molecules.

Then we have to solve the equation of diffusion

$$\frac{\partial(nr)}{\partial t} = D \frac{\partial^2(nr)}{\partial r^2}, \tag{7.3}$$

where $D$ is the diffusion coefficient and $r$ the distance from center of the sphere, under the initial condition

$$(n)_{t=0} = f(r). \tag{7.4}$$

The solution becomes

$$n = \frac{1}{\sqrt{\pi}\, r} \left[ \int_{-(r/2\sqrt{Dt})}^{\infty} \exp(-\beta^2) \times (r + 2\sqrt{Dt}\,\beta) f(r + 2\sqrt{Dt}\,\beta)\, d\beta \right.$$
$$\left. - \int_{(r/2\sqrt{Dt})}^{\infty} \exp(-\beta^2) \times (-r + 2\sqrt{Dt}\,\beta) f(-r + 2\sqrt{Dt\beta})\, d\beta \right]. \tag{7.5}$$

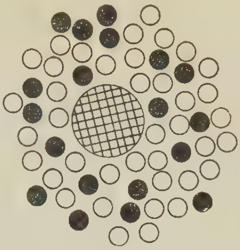

Fig. 4. Homogeneous model of aqueous solution surrounding a group of single water molecules produced under excess pressure.

Especially, when the initial condition is given by

$$\left. \begin{array}{ll} n = 0 & \text{for} \quad r = 0 \sim r_0, \\ \text{and} & \\ n = n_0 & \text{for} \quad r = r_0 \sim \infty \end{array} \right\} \text{at } t = 0, \tag{7.6}$$

the solution becomes

$$n = n_0 - \frac{n_0}{\sqrt{\pi}} \left[ \int_0^{(r_0 - r)/2\sqrt{Dt}} \exp(-\beta^2)\, d\beta + \int_0^{(r_0 + r)/2\sqrt{Dt}} \exp(-\beta^2)\, d\beta - \frac{\sqrt{Dt}}{r} \left\{ \exp\left( -\frac{(r_0 - r)^2}{4Dt} \right) - \exp\left( -\frac{(r_0 + r)^2}{4Dt} \right) \right\} \right]. \tag{7.7}$$

The velocity of diffusion towards interior of the sphere is obtained from this. Especially, the velocity at the surface of the sphere is given by

$$V_0 = -(\partial n / \partial r)_0 = \frac{n_0}{\sqrt{\pi}} \left[ \frac{\sqrt{Dt}}{r_0^2} \left\{ 1 - \exp(-r_0^2/Dt) \right\} - \frac{1}{2\sqrt{Dt}} \left\{ 1 + \exp(-r_0^2/Dt) \right\} \right]. \tag{7.8}$$

Strictly speaking, the relaxation time $\tau$ is the time required for the increase of the configurational entropy attaining to $(1 - 1/e)$ of the increase in the equilibrium state. We will, however, postulate for simplicity's sake that this is given by the time required for the mean concentration inside the sphere attaining to $(1 - 1/e)$ of the equilibrium concentration $n_0$. Moreover, the original spherical group of single water molecules formed by the sudden collapse of an associated water molecule becomes larger as the solute molecules diffuse into this sphere.

When, however, we suppose the original boundary of the sphere ($r=r_0$) as fixed in space, we can regard the expansion of the sphere as diffusing out of the single molecules, too. So we will suppose for simplicity's sake the original boundary of the sphere as fixed in space, and calculate the number of the solute molecules diffusing into this sphere in the following, for the above solution is valid under this condition only. Then we have the relation

$$\int_0^\tau 4\pi r_0^2 D V_0\, dt = \frac{4}{3}\pi r_0^3 n_0 (1-1/e)\ . \qquad (7.9)$$

Substituting the value of $V_0$ and performing the calculation by integration by parts, (7.9) becomes as

$$\frac{1}{e}=\frac{1}{\sqrt{\pi}}\Big[2\int_0^\alpha \exp(-x^2)\,dx$$
$$-3\alpha\Big\{1-\frac{1}{3}\exp(-\alpha^2)\Big\}+2\alpha^3\{1-\exp(-\alpha^2)\}\Big]. \qquad (7.10)$$

where

$$\alpha=r_0/\sqrt{D\tau}\ . \qquad (7.11)$$

By solving (7.11) numerically by employing tables of error integrals we obtain

$$\alpha=1.130\ . \qquad (7.12)$$

This gives the expression of the relaxation time

$$\tau=0.783\, r_0^2/D \qquad (7.13)$$

by (7.11). In this equation, $r_0$ means the radius of the group of single water molecules and $D$ the diffusion coefficient. In the following we will write $r_0$ simply as $r$, and denote with $r_0$, $D_0$ and $\tau_0$ the values of $r$, $D$ and $\tau$ at zero concentration respectively. Then we have,

$$\tau=0.783\, r^2/D\ , \qquad (7.14)$$

at any concentration.

If the number of the monomers ($H_2O$-molecules) composing an associated molecule is

$$Z=s^3\ , \qquad (7.15)$$

the radius of the associated water-molecule is equal to

$$r'=sL_a\ ,$$

where $L_a$ means the effective diameter of the monomer composing the associated molecule, defined by

$$(4/3)\pi L_a^3=v_a/N_L\ , \qquad (7.16)$$

the effective volume (=the volume including the clearance) of the monomer composing an associated molecule being $v_a/N_L$. So we have

$$r'=sL_a=s\left(\frac{3}{4\pi}\frac{v_a}{N_L}\right)^{1/3}. \qquad (7.17)$$

When the associated molecule of radius $r$ collapses under excess pressure and becomes a spherical group of single water molecules, the effective volume of the monomer becomes $v_s/N_L$ (=the effective volume of the single molecule), and the effective diameter of the monomer becomes $L_s$ (=the effective diameter of the single molecule), so that the radius of the spherical group becomes

$$r=sL_s=s\left(\frac{3}{4\pi}\frac{v_s}{N_L}\right)^{1/3}. \qquad (7.18)$$

This gives the value of $r$ in eq. (7.14).

In practice there may be other agitations than thermal fluctuations after an collapse of associated molecules under excess pressure of the ultrasonic wave, and the diffusion coefficient may be somewhat larger than the static value. This will make the relaxation time somewhat shorter than predicted by (7.14). On the other hand, the use of the homogeneous solution model of Fig. 4 in place of the heterogeneous model of Fig. 1, (b) will give a shorter relaxation time, i.e., the real relaxation time will be longer than the calculated one. It is, however, not certain whether a more detailed calculation under detailed assumptions will make the approximation better. So we will employ the above result without any correction.

Strictly speaking, the diffusion equation is not (7.3) written for the number of molecules per volume, but

$$\frac{\partial(cr)}{\partial t}=D\frac{\partial^2(cr)}{\partial r^2} \qquad (7.19)$$

written for the concentration $c$ in molarity. As the molarity is related to the weight fraction $p$ by

$$p=\frac{M_F c}{1000\rho} \qquad (7.20)$$

and as the weight fraction is related to the molar fraction $n_F$ with

$$n_F=\frac{m_F}{m_w+m_F}\ ,$$

where

$$m_w=(1-p)/M_w;\quad \text{and}\quad m_F=p/M_F,$$

we have

$$n_F = \frac{M_w c}{1000\rho - (M_F - M_w)c} \tag{7.21}$$

So the equation of diffusion for $n_F$, or that written for $n_0$ as in (7.2) must be somewhat different from (7.3). This effect was also omitted because of the same reason as above stated.

In practical calculations, we have determined the quantity $s$ (or the radius $r$) from (7.14) employing experimental value of the relaxation time, and used this for computing the absorption coefficient by (6.7) and (6.8). So the omission of various detailed assumptions will not influence the absorption coefficient so much. Only this effect will influence the determination of the values of $r$ and $r'$.

## § 8. Conclusion

As above stated, there accompanies a variation of the existence ratio between the associated and the single molecules of water due to excess pressure by the ultrasonic propagation in aqueous solutions, and this variation gives rise to the molecular rearrangement among the associated and the single molecules of water and the solute molecules. A relaxational molar specific heat $C_m$ given in (5.9) or (5.10)) accompanies this rearrangement process. In this equation $f$ is a function proportional to the change of configurational entropy due to molecular rearrangement and is given by (4.7), becoming (4.13) in case the difference in magnitudes of the molecules are taken into account. The absorption coefficient of sound at low frequency (practically up to 20 Mc/sec) is given by (6.7) (or (6.8)). The quantity $\tau$ involved in this equation means the relaxation time of molecular rearrangement and as a matter of fact equal to the relaxation time for the diffusion of the solute molecules into the groups of single molecules formed by the collapse of associated molecules under excess pressure. This is given by (7.14).

By employing these formulas it is possible to calculate the ultrasonic absorption coefficient ($\alpha/\nu^2$), specific heat of the molecular rearrangement $C_m$, relaxation time $\tau$, etc., if the various physical quantities involved in these formulas, the physical constants of the aqueous solution (density $\rho$, thermal expansion coefficient $\vartheta$, sound velocity $V$, specific heat at constant pressure $c_p$, ratio of the specific heats $\gamma$, diffusion coefficient $D$), the existence ratio between the associated and the single molecules of water, $n_a : n_s$, and the magnitude of the associated molecules ($s$) are known as function of the concentration $n_F$.

Practical calculations for aqueous solutions of some alcohols are to be described in part (II) of this paper.

### Acknowledgements

The author wishes to express his sincere thanks to Dr. M. Sugita and Dr. N. Saito for their illuminating discussions throughout this work.

This work was financially supported by the Grant for Scientific Research of the Ministry of Education for the 1954 fiscal year.

### References

1) P. Bajouline et J. M. Merson: Absorptions des ondes ultra-acoustiques dans un mélange acétone-eau. C. R. (Doklady) URSS. **24** (1939) 690.

2) G. W. Willard: Ultrasonic absorption and velocity measurements in numerous liquids. J. Acous. Soc. Amer. **12** (1941) 438.

3) F. H. Willis: Measurements of ultrasonic Absorption and velocity in liquid mixtures. J. Acous. Soc. Amer. **19** (1947) 242.

4) C. J. Burton: A study of ultrasonic velocity and absorption in liquid mixtures. J. Acous. Soc. Amer. **20** (1948) 186.

5) L. R. O. Storey: Ultrasonic absorption in mixtures of ethyl alcohol and water. Proc. Phys. Soc. **65B** (1952) 943.

6) D. Sette: Structural effects in the ultrasonic absorption of liquid mixtures, Nuovo Cimento **1** (1955) 800.

7) M. Cevolani e S. Petralia: Assorbimento di ultrasuoni in sistemi di liquidi parzialmente miscibili. Nuovo Cimento **2** (1955) 186.

8) L. Hall: The origin of ultrasonic absorption in water. Phys. Rev. **73** (1948) 775; **71** (1947) 318.

9) O. Nomoto: Irreversible production of entropy and the absorption of sound. J. Phys. Soc. Japan, in printing.

10) N. Saito and M. Sugita: Energy dissipation and entropy production in irreversible process of dilute systems. J. Phys. Soc. Japan **7** (1952) 554.

11) O. Nomoto: Phenomenological theory of the molecular absorption and dispersion of sound and the relation between the relaxation time of the internal energy and the relaxation time

of the internal specific heat. J. Phys. Soc. Japan, in printing.
12) E. A. Guggenheim: Statistical thermodynamics of mixtures with zero energies of mixing. Proc. Roy. Soc. **183A** (1944) 203.
13) E. A. Guggenheim: "Mixtures" (1951) p. 197.
14) O. Nomoto: State of association of water molecules in aqueous solutions as deduced from sound velocity data. J. Phys. Soc. Japan, in printing.
15) J. M. M. Pinkerton: On the interpretation of ultrasonic absorption measurements in liquids. Colloquium over ultrasonore trillingen, Brussels. (1951) 117.
11) M. Cevolani e S. Petralia: Velocita di ultrasuoni in sistemi di liquidi parzialmente miscibili. Nuovo Cimento **1** (1955) 705–716.

---

JOURNAL OF THE PHYSICAL SOCIETY OF JAPAN Vol. 11, No. 8, AUGUST, 1956

# Magnetoresistance Effect of Lead Sulphide Group of Semiconductors
## I. Measurements on Natural Specimens of Lead Sulphide

By Taizo IRIE

*Scientific Research Institute*

(Received April 6, 1956)

The magnetoresistance effect of lead sulphide was measured on natural specimens at various angles between the direction of the electric field and the magnetic field. The results were quantitatively consistent with the existing phenomenological theory. The magnetoresistance constants for weak magnetic field, introduced by Seitz, were determined. Some discussions are given in the light of the electronic theory based on the approximation of spheroidal energy surface. The magnetoresistance mobility and the Hall mobility agree to the order of magnitudes and also show similar temperature dependency.

### § 1. Introduction

Since the study of the magnetoresistance effect on the single crystals of germanium had been performed by Pearson and Suhl,[1] the experimental and theoretical investigations of this effect have been carried out by many investigators. It is, now, known that measurements of the magnetoresistance at various directions of the current and the magnetic field with respect to the crystal axis give some information on the energy band structures. The lead sulphide group of semiconductors; lead sulphide, -selenide, and- telluride, are one of the groups of typical semiconductors of great interest, and it is, obviously, important to investigate the magnetoresistance effect on these substances too. Until recent years, however, only a few works have been done concerning the magnetoresistance effect on these substances[2]. Therefore, we intended to carry out a systematic experiment on the magnetoresistance effect of the single crystals of lead sulphide group. In the present paper, some experimental results on natural specimens of lead sulphide are presented.

### § 2. Experimental Procedures

The specimens of single crystals possessing desired orientations, as shown in Fig. 1, and having the dimension of about 5 mm × 2 mm × 1 mm were cut of natural galena and their uniformity checked by using a moving probe to search for any variation of resistance along the length. Some characters of our samples are given in Table I. Current electrodes and potential electrodes were applied by mean of the cathode sputtering of gold films at the end surfaces and the top surfaces of the sample respectively. The probes are tungsten wires of 0.2 mm diameters which are pressure contacted to the potential electrodes. The magnetoresistance measurements were made by determining the current and the potential drop between the two probes, with and with-

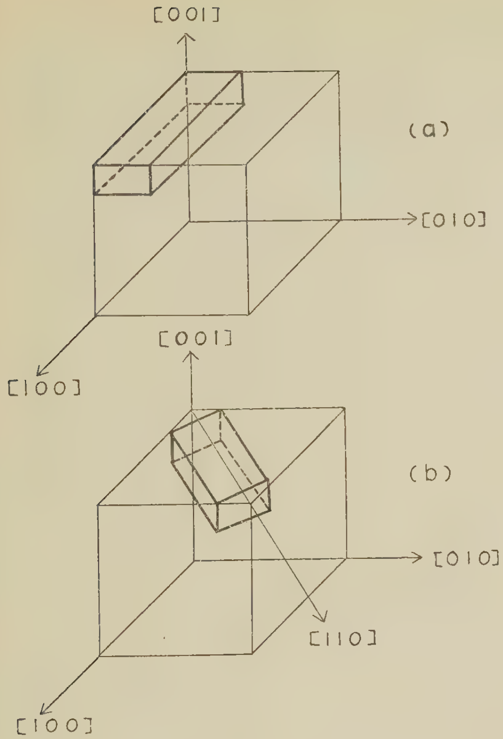

Fig. 1. Orientations of samples cut out of natural galena
(a): Sample cut with its length along the [100] axis
(b): Sample cut with its length along the [110] axis

out the application of the magnetic field, the direction of which being changed by rotating the electromagnet about the axis of the sample holder. To maintain the temperature of the sample constant during the measurements, the sample holder was put in an evacuated pyrex tube which was immersed in refrigerant contained in a tailed Dewar Vessel as shown in Fig. 2. All measurements were made by the use of direct current and at a temperature of 200°K or 93°K. Hall voltages appearing across the potential probes were canceled out by averaging the values of two potential drop measurements with magnetic field in forward and reversed directions and the thermoelectromotive forces which appeared were also measured and corrected. It was ascertained that the changes of the resistance caused by applying the magnetic field were independent of the magnitudes of the current flowing through the sample, within the experimental error.

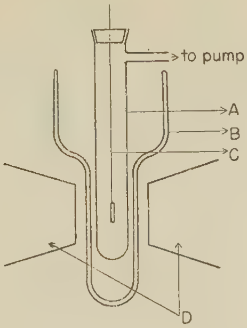

Fig. 2. Experimental arrangement.
A: pyrex glass tube
B: tailed Dewar Vessel
C: sample holder
C: magnet pole piece

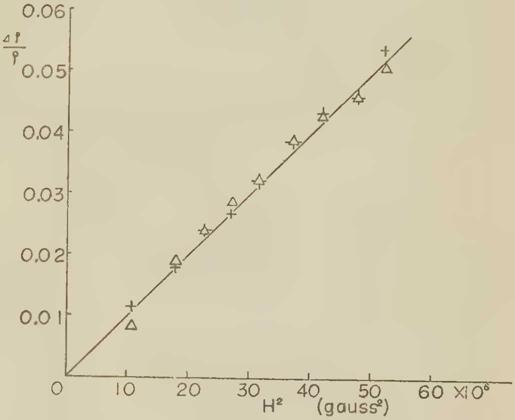

Fig. 3. $\Delta\rho/\rho$ vs. $H^2$, transversal orientation, sample #A No. 2, T=108°K

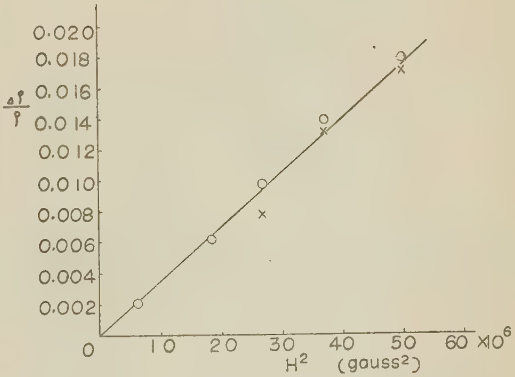

Fig. 4. $\Delta\rho/\rho$ vs. $H^2$, transversal orientation, sample #B No. 1, T=93°K

## § 3 Experimental results

(1) Field dependency

The transversal magnetoresistance when the current was flowing along the [100] direction was measured as a function of magnetic field strength. It was found that the magnetoresistive ratios were proportional to the square of the magnetic field strength within the ex-

Table I Characteristic properties of the natural lead salfide sumples.

| Sample | Source | Direction of cut | $T$ (°K) | $\rho_0$ (Ω-cm) | $R$ $\left(\frac{\text{cm}^3}{\text{coulomb}}\right)$ | $n$ $\left(\frac{1}{\text{cm}^3}\right)$ | $\mu_H$ $\left(\frac{\text{cm}^2}{V\cdot\text{sec}}\right)$ | $\mu_B$ $\left(\frac{\text{cm}^2}{V\cdot\text{sec}}\right)$ | Equation used for calculation of $\mu_B$ | Uniformity (%) |
|---|---|---|---|---|---|---|---|---|---|---|
| #A No. 2 (*p*-type) | Budō Mine | [100] | 300 | 1.32 | 319 | $2.3\times10^{16}$ | 205 | 500 | Eq. (2)** | ~3 |
| | | | 200 | 0.84 | 356* | $2.1\times10^{16}$ | 360 | 1000 | Eq. (2) | |
| | | | | | | | | 800 | Eq. (3) | |
| | | | 93 | 0.23 | 352* | $2.1\times10^{16}$ | 1308 | 3680 | Eq. (2) | |
| | | | | | | | | 2500 | Eq. (3) | |
| #A No. 4 (*p*-type) | Bodō Mine | [110] | 200 | 1.76 | 549 | $1.4\times10^{16}$ | 264 | | | ~5 |
| #B No. 1 (*n*-type) | Ani Mine | [100] | 200 | *** | | | | 1350 | Eq. (2) | |
| | | | | | | | | 1280 | Eq. (3) | |
| | | | | | | | | 780 | Eq. (4) | |
| | | | 93 | | | | | 5650 | Eq. (2) | |
| | | | | | | | | 5350 | Eq. (3) | |
| | | | | | | | | 3030 | Eq. (4) | |
| #B No. 2 (*n*-type) | Ani Mine | [100] | 300 | 0.91 | 124 | $6\times10^{16}$ | 117 | *** | | |
| | | | 200 | 0.63 | 208 | $3.6\times10^{16}$ | 282 | | | |
| #B No. 3 (*n*-type) | Ani Mine | [110] | 200 | 0.19 | 61 | $1.2\times10^{17}$ | 273 | | | ~10 |

* This value is measured at 138°K.

** For the sample #A No. 2, Eq. (4) gives imaginary value of $\mu_B$ because of the fairly large value of the longitudinal effect.

*** The lack of the data of sample #B No. 1 and #B No. 2 is due to the breakage of the sample before measurements.

$T$: temperature

$\rho_0$: specific resistivity

$R$: Hall coefficient

$n$: number of charge carriers calculated by $n=\pm\frac{3\pi}{8e}\frac{1}{R}$

$\mu_H$: Hall mobility

$\mu_B$: magnetoresistance mobility calculated using Eqs. (2), (3) and (4).

perimental error in the range of temperature and magnetic field used. The typical behaviors are shown in Fig. 3 and 4. Different marks in each curve indicate measurements at reversed current directions.

(2) Dependency on the angle between the current and the magnetic field.

Measurements were made with the magnetic field kept at various directions with respect to the fixed direction of the current, which was always along the length of the sample. In Figs. 5~8, $\Delta\rho/\rho H^2$, the magnetoresistive ratios divided by the square of magnetic field strength, are plotted against $\theta$, the angle of rotation of magnetic field*. When the direction of the current is in the [100] axis and the width of the sample is parallel to the axis of rotation of the magnetic field, $\Delta\rho/\rho H^2$ varies approximately as $A+B\sin^2\theta$ as shown in Figs. 5 and 6, where $A$ and $B$ are constants. For the samples cut with its length along [110], measurements were made only at 200°K. These results are shown in Figs. 7 and 8 for a *p*- and an *n*-type sample res-

---

* In these figures, except Fig. 7, different marks in each curve indicate measurements at reversed current direction. In Fig. 7 the average values of measurements at reversed current directions were plotted to cancel out the spurious voltages, which seems to occur in this case, because, when the direction of the current was reversed, the voltage drop between the probes changed their amounts beyond the value expected from the measured thermoelectromotive force. However, a rough measurement under the condition of absence of such spurious voltages gave the similar results.

Table II

| Sample | Direction of current | Direction of magnetic field | $\Delta\rho/\rho H^2$ | Theory* |
|---|---|---|---|---|
| #A No. 2 | [100] | [100] | $1.15\times10^{-11}$ | $b+c+d$ |
| #A No. 2 | [100] | [010] | $3.91\times10^{-11}$ | $b$ |
| #A No. 4 | [110] | [001] | $3.28\times10^{-11}$ | $b$ |
| #A No. 4 | [110] | [1$\bar{1}$0] | $2.78\times10^{-11}$ | $b+\frac{1}{2}d$ |
| #A No. 4 | [110] | [110] | $1.64\times10^{-11}$ | $b+c+\frac{1}{2}d$ |

Table III

| Sample | Direction of current | Direction of magnetic field | $\Delta\rho/\rho H^2$ | Theory* |
|---|---|---|---|---|
| #B No. 1 | [100] | [100] | $0.69\times10^{-11}$ | $b+c+d$ |
| #B No. 1 | [100] | [010] | $6.9\ \times10^{-11}$ | $b$ |
| #B No. 3 | [110] | [001] | $2.205\times10^{-11}$ | $b$ |
| #B No. 3 | [110] | [1$\bar{1}$0] | $2.205\times10^{-11}$ | $b+\frac{1}{2}d$ |
| #B No. 3 | [110] | [110] | $1.17\times10^{-11}$ | $b+c+\frac{1}{2}d$ |

* $\Delta\rho/\rho H^2=b+c(\sum_{i=1}^{3}\iota_i\eta_i)^2+d\sum_{i=1}^{3}\iota_i^2\eta_i^2$

where $\iota_i$, $\eta_i$ are direction cosines of $j$ and $H$ respectively. See reference (1).

pectively. Two curves in each figures show the results obtained with different mounting of the sample; in one case, the axis of rotation being parallel to the width and in the other parallel to the length of the sample. The experimentally determined values of $\Delta\rho/\rho H^2$ for some directions of current and magnetic field are listed in Tables II and III for $p$- and $n$-type samples respectively. Using these data, we can calculate the magnetoresistance constants for weak magnetic field introduced by Seitz[3)] in his equation,

$$j=\sigma_0 E+\alpha[E\times H]+\beta H^2\cdot E \\ +\gamma(E\cdot H)H+\delta T\cdot E \qquad (1)$$

where $j$ is the current density, $E$ and $H$ the electric and magnetic field, $\sigma_0$ the conductivity in the absence of the magnetic field, $-\alpha/(\sigma)^2$ the Hall coefficient, $T$ a diagonal tensor with elements $H^2{}_1$, $H^2{}_2$, and $H^2{}_3$, and $\beta$, $\gamma$, and $\delta$ the small-field magnetoresistance constants. Though it is desirable to determine $\beta$, $\gamma$, and $\delta$ using the values in all five rows in Tables II and III respectively, we determined the values of these constants from the values in the lower three rows in the Tables, i.e. the values obtained on the sample cut along [110] direction, because of the appreciable difference of the mobility between the sample cut along [110] direction and the sample cut along [100] direction. The values obtained are, for $p$-type sample at 200°K,

$$\beta=-2.4\times10^{-11}\,,\ \gamma=+1.2\times10^{-11},\ \text{and} \\ \delta=+0.56\times10^{-11},$$

and, for $n$-type sample at 200°K,

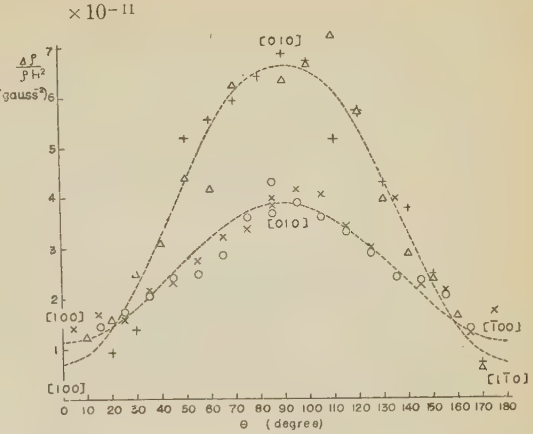

Fig. 5. $\Delta\rho/\rho H^2$ vs. angle $\theta$, T=200°K, current is along [100] and axis of rotation is along [010]. Certain cardinal directions of H are indicated in the figure.

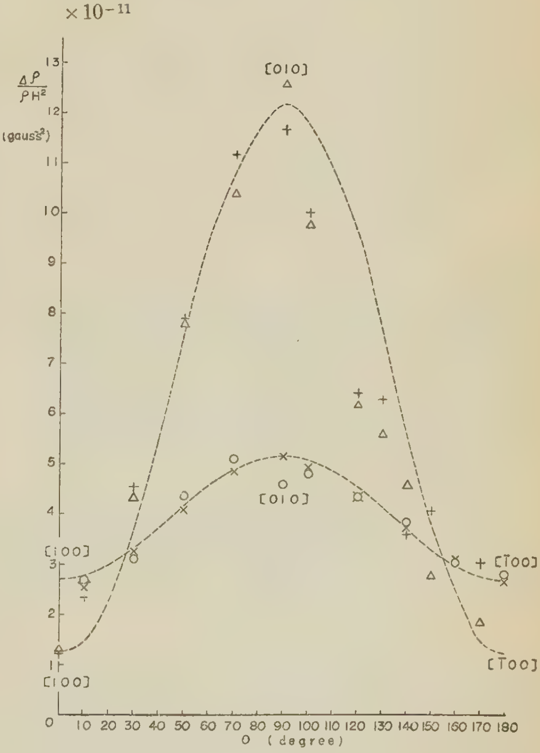

Fig. 6. $\Delta\rho/\rho H^2$ vs. angle $\theta$, T=93°K, current is along [100] and axis of rotation is along [010]. Certain cardinal directional of H are indicated in the figure.

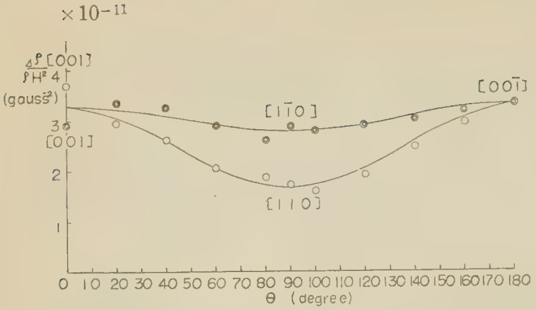

Fig. 7. $\Delta\rho/\rho H^2$ vs. angle $\theta$, Sample ♯A No. 4. $T=200°K$. Certain cardinal directions of $H$ are indicated in the figure.

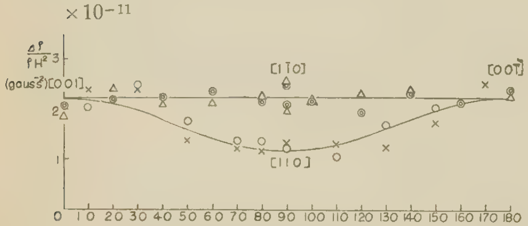

Fig. 8. $\Delta\rho/\rho H^2$ vs. angle $\theta$, Sample ♯B No. 3, $T=200°K$. Certain cardinal direction of $H$ are indicated in the figure.

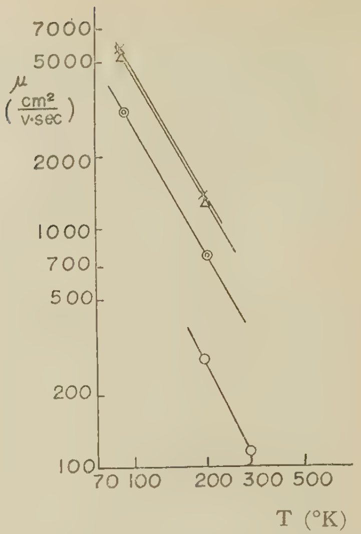

Fig. 9. Mobility vs. T, $n$=type sample.

× $\mu_B$ calculated by Eq. (2) } Sample ♯B No. 1
△ $\mu_B$ calculated by Eq. (3) } Sample ♯B No. 1
◎ $\mu_B$ calculated by Eq. (4) } Sample ♯B No. 1
○ $\mu_H$ Sample ♯B No. 3

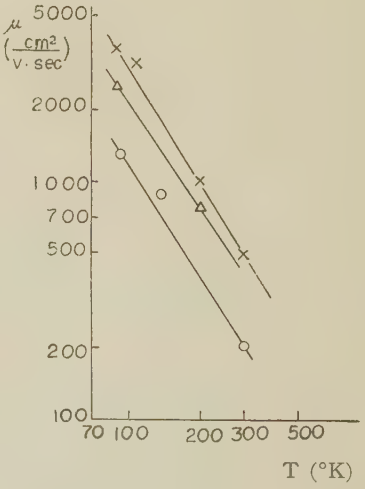

Fig. 10. Mobility vs. T, $p$-type sample.

× $\mu_B$ calculated by Eq. (2) } Sample ♯A No. 2
△ $\mu_B$ calculated by Eq. (3) } Sample ♯A No. 2
○ $\mu_H$ } Sample ♯A No. 2

$\beta=-1.7\times10^{-10}$, $\gamma=+1.1\times10^{-10}$, and $\delta=0$.

Using these constants, values of $\Delta\rho/\rho H^2$ for any other angle $\theta$ could be calculated using the relation deduced from the phenomenological theory. The curves shown in Figs. 5 and 6 were thus obtained. It can be seen that the observed points lie well on the curves.

(3) Mobility

For the simple case of isotropic materials having a mean free path independent of energy, the mobility is related to the transversal magnetoresistive ratio as

$$\Delta\rho/\rho H^2=3.8\times10^{-17}\mu^2 \qquad (2)$$

where $\mu$ is the mobility of the carriers in cm²/volt. sec and $H$ the magnetic field strength in gauss. Values of the mobility calculated by this formula on the samples ♯A No. 2 and ♯A No. 4 are given in colum 10 of Table I. It must be noted, however, that Eq. (2) is only valid when there is no longitudinal effects, while our results showed that there exist small longitudinal effects, which are certainly beyond experimental errors for $p$-type material. Following Estermann and Foner,[4] a simple correction for the longitudinal effects may be made by putting

$$\Delta\rho/\rho=f(H)+g(H)\sin^2\theta \qquad (3)$$

or more rigolously, the relation

$$\mu^2=2.62\times10^{16}\left[\left(\frac{\sigma^0-\sigma_H{}^t}{\sigma_0 H^2}\right)-6.65\left(\frac{\sigma^0-\sigma_H{}^l}{\sigma_0 H^2}\right)\right] \qquad (4)$$

derived by them[4] from the phenomenological theory developed by Seitz, may be used, where $\sigma_H{}^t$ and $\sigma_H{}^l$ are the conductivity in the magnetic field $H$ for the transversal orientation and for the longitudinal orientation, respectively. Mobility calcutated by Eqs. (3) and (4) are also included in Table I. In Figs. 9 and 10, these values are plotted against the reciplocal of the absolute temperature in logarithmic scale as well as the Hall mobility. It is seen that in the $p$-type sample the values of the magnetoresistance mobility and the Hall mobility coincides in the order of magnituds but the absolute magnitude differ by a factor of 2~3 as with the results of Putley[2)] on lead tellulide and selenide. This fact may be due to the nonspherical form of energy surface or the anisotropy of the collision frequency. In the $n$-type sample, unfortunately we could not make comparison between the Hall mobility and the magnetoresistance mobility on the same sample because of the breakage of the sample. The values of mobility in either $p$-type and $n$-type samples are somewhat smaller than the ones obtained by Brebrick and Scanlon[5)] and by Putley[2)]. Furthermore, the temperature dependency of the mobility we have obtained varied as $T^{-1.8}$ and did not obey the $T^{-5/2}$ law as is usually accepted. This can be seen from Figs. 9 and 10 in which the mobility are plotted against the reciplocal of the absolute temperature in logarithmic scale. These results may indicate that some forms of impurity scattering are present.

## § 4. Discussion

According to the theory developed by Shibuya[6)] assuming the spheroidal energy surfaces near the extremums, there exist certain relations among the magnetoresistance constants. Those are, when the extremums are found along the six [100] axes in the Brillouin zone,

$$\beta+\gamma+\delta=0, \qquad \delta>0, \tag{5}$$

when the extremums are found along the twelve [110] axes,

$$\beta+\gamma-\delta=0, \qquad \delta<0, \tag{6}$$

and when the extremums are found along the eight [111] axes,

$$\beta+\gamma=0, \qquad \delta<0. \tag{7}$$

In the case of an isotropic material having a spherical energy surface, the next relation holds:

$$\beta+\gamma=0, \qquad \delta=0 \tag{8}$$

In our case, the relations (5) and (8) are nearly satisfied for $p$- and $n$-type sample respectively, although the longitudinal effects are not completely absent in both samples.

At this stage of our experiments, the experimentally determined values of magnetoresistance constants are not accurate enough to discuss in detail, but it seems safe to conclude that (a) the magnetoresistance in single crystals of lead sulphide, cut out of natural galena, approximately conforms with the phenomenological relation, (b) in $p$-type samples, though not much can be said from our results as to the energy surfaces of valence band, our experimental results seem to prefer the model where the energy extremums are located along the [100] axes in the Brillouin zone to the one having the extremums along the [110] axes if we must choose between the two, and (c) the experimental results in $n$-type samples seem to show that the conduction band has nearly spherical energy surface. Non-zero longitudinal effect may be attributed to the anisotropy of collision frequency which may not has cubical symmetry when expressed in terms of the electron wave number.

A calculation performed by D. G. Bell and others[7)] shows that the constant energy surface of the valence band of lead sulphide has extremums near the points at the twelve equivalent positions along the [110] direction in the Brillouin zone. The inconsistency with the experimental results is not surprising, however, as their calculation is based on the approximations of cellular method.

Further experiments on the synthetic single crystals of lead sulphide group are intended.

### Acknowledgement

The author is deeply indebted to Professor K. Hayase and Mr. R. Otsuka of Waseda University for furnishing galena from which the single crystals used were cut out.

He wishes to express his sincere thanks to Dr. J. Yamashita and to Dr. M. Shibuya for their helpful discussions and also to Dr. K. Shinohara and Mr. R. Uno for their continual encouragement.

### References

1) G. L. Pearson and H. Suhl: Phys. Rev. **83**, (1951) 768.

2) E. Hirahara and M. Murakami: Bulletin of the Faculty of Engineering, Hiroshima University, **4** (1955) 259.
E. H. Putley: Proc. Phys. Soc. B. **68** (1955) 22.
3) F. Seitz Phys. Rev. **79** (1950) 372.
4) I. Esterman and A. Foner: Phys. Rev. **79** (1950) 365.
5) R. F. Brebrick and W. W. Scanlon: Phys. Rev. **96** (1954) 598.
6) M. Shibuya: Phys. Rev. **95** (1954) 1385.
7) D. G. Bell, D. M. Hum, L. Pincherle, D. W. Sciama and P. M. Woodwerd: Proc. Roy. Soc. **217** (1953) 71.

---

JOUNAL OF THE PHYSICAL SOCIETY OF JAPAN Vol. 11, No. AUGUST, 1956

# Phase Diagram of Iron-Cobalt-Oxygen System. (I) Experimental Study*,**

By Shūichi IIDA

*Department of Physics*
*Faculty of Science, University of Tokyo*

(Received November 7, 1955)

Phase diagram of iron-cobalt-oxygen has been established experimentally in certain temperature, pressure, and composition ranges (900°C～1400°C, $10^{-4}$～760 mm Hg, $Fe_{1-x}Co_x$～Oxygen, $0 \leqq x \leqq 1/3$). In these ragges, when the temperature and the mixing ratio of metallic elements are fixed, it has been found that spinel phase is stable below a certain critical pressure of oxygen. Above this pressure, precipitates of hematite are formed in the spinel matrix, resulting in an abrupt increase of the total oxygen content in the solid phases. The phase boundary was determined by observing the change of the oxygen pressure in a sealed tube, which resulted from the oxidation or reduction of the specimen. Results of several measurements of specific heat on heating from 100°C to 750°C, the variations in oxygen content during heat-treatment, and the change of lattice constants at room temperature with heat-treatment, are presented. Curves of lattice constants *vs* composition of metallic constituents have a minimum at compositions intermediate between magnetite and cobalt ferrite. It has been concluded that the diffusion rate of ions in these oxides varies exponentially in passing through the temperature range around 300°C. No result has been obtained which are favourable for the existence of structural change in the temperature range from 200°C to 400°C (effective range for magnetic anneal), for all these ferrites.

## §1. Introduction

It was discovered in 1933 by Kato and Takei[1] that the magnetic properties of the solid solution of magnetite and cobalt ferrite show a remarkable response to the magnetic field applied during cooling. This study led to the invention of O. P. magnet[2][3][4]. This magnet is a magnetically oriented ceramic material, which is a solid solution of magnetite and cobalt ferrite with the ratio of 1:3. Further investigations have been performed on the same ferrite system by several investigators[5][6][7]. In all these studies, chief attention has been paid to the strong response to magnetic anneal of this material. Some mechanisms were suggested by Sugiura[5], Guil-

---

* Portions of this work were presented at the 1952 Kyoto Meeting of the Physical Society of Japan.

** This research was financially supported by the Scientific Research Expenditure of the Department of Education.

laud[6], and Néel[8] on this phenomenon*. Since 1950, the author has made experimental and theoretical studies of this phenomenon in cooperation with several collaborators. In these studies, it was found that the degree of oxidation of specimens is correlated essentially with this phenomenon[9]. This fact, combined with several other evidences, has led to the conclusion that the uniaxial anisotropy in these ferrites is related intimately to the directional order between cobalt ion and cation vacancy. Now, in these studies, a considerable effort has been made to establish the phase diagram of iron-cobalt-oxygen. On the phase diagram of iron-oxygen, many investigations[10][11], including the extensive work by Darken and Gurry[12], have been made. On the other hand, on the phase diagram of iron-cobalt-oxygen, we know only the studies made by Robin and Bénard[13][14]. Robin and Benard's study, however, was very limited, being made in an air atmosphere and in the temperature range from 500°C to 1000°C. Therefore, it is quite necessary to extend the study to wider pressure ranges, and to higher temperatures.

The study consists of two parts: experimentals and theoreticals. The present paper presents the experimental part of the study. The theoretical part of the study, a statistical treatment, will be given in the forthcoming paper[15]. In §2, preparation of specimens are described, in §3, the explanation of the phase diagram above 900°C is given, and then, measurement of specific heats, measurement of lattice constants, and observation of the variation in oxygen contents during heat-treatments, are described in §4, 5, and 6 respectively.

## §2. Specimens

Two methods were used for the preparation of specimens.

(1). The specimens used in the determination of the phase diagram in §3 were prepared by 'wet method'. The mixtures of the chlorides of constituent metals in the desired proportions were dissolved in water and were neutralized with potassium hydroxide. The resulting precipitates were heated up to 800°C in air to remove the moisture.

(2). The other specimens were prepared by 'nitric acid method'. The mixtures of constituent metals in the desired proportions were dissolved in nitric acid. The solutions were then dried with an infra-red ray lamp and heated up to 800°C in air in a furnace to remove the residual nitrate and moisture.

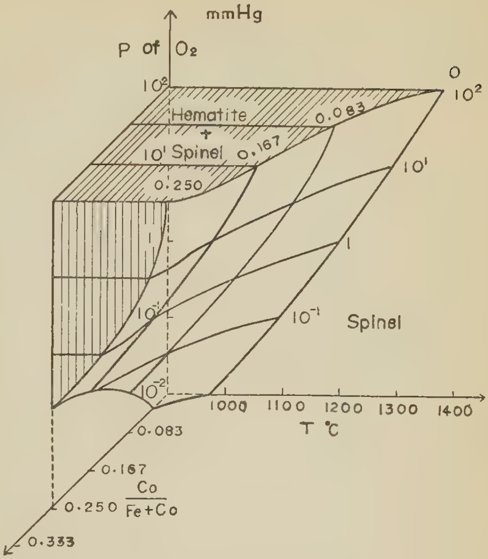

Fig. 1. Schematic phase diagram of iron-cobalt-oxygen. Curved surface illustrates phase boundary between single phase field of spinel and two phase field of spinel with hematite.

## §3. Phase Diagram

We have determined the phase diagram of iron-cobalt-oxygen by observing the change of oxygen pressure in a sealed tube containing specimen, in the temperature range from 900°C to 1400°C and in the pressure range from $10^{-4}$ to 760 mm Hg of oxygen. The results are as follows:

The phase diagram can be represented in a three-dimentional space. The coordinates are composition of metallic constituents, temperature, and oxygen pressure. Fig. 1 shows such a diagram schematically. Hereafter, the composition Co/Fe+Co will be denoted by $r$. In the ranges investigated, the space is divided by a curved surface into a spinel phase field and a two phase field consisting of hematite

---

* *Note added in proof*—Williams and others have reported recently [J. Appl. Phys. 27 (1956) 85] that the response is due to the tendency of the precipitated particles to grow preferentially along the magnetic field direction. Though the conclusion has been deduced from magnetic torque measurements and electron diffraction datterns, it seems that the evidences are not convincing enough. There are several facts which seem difficult to be explained by their mechanism. The detailed discussion will be given in forthcoming papers.

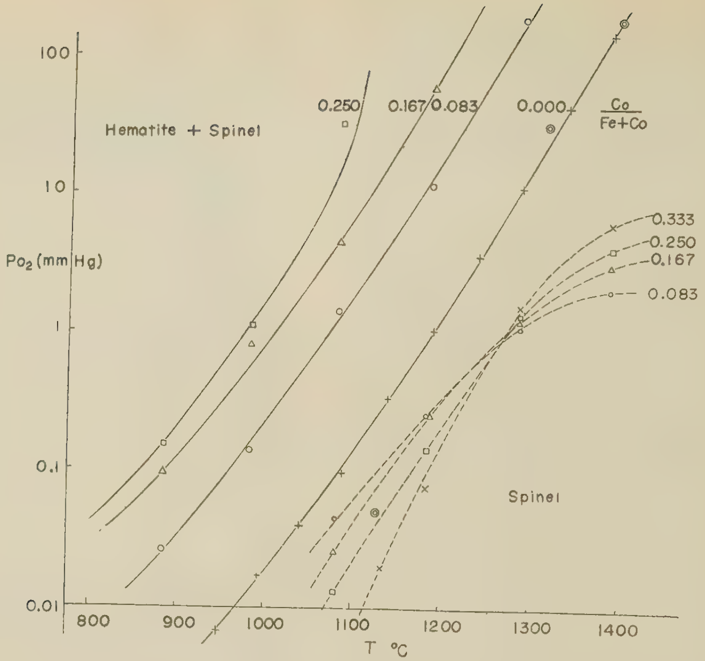

Fig. 2. Projection of phase diagram of iron-cobalt-oxygen on oxygen pressure-temperature plane. Solid line shows the location of phase boundary between spinel field and spinel with hematite field for each composition indicated. Dotted line means the partial vapour pressure of CoO evaporating from spinel matrix having each composition indicated.

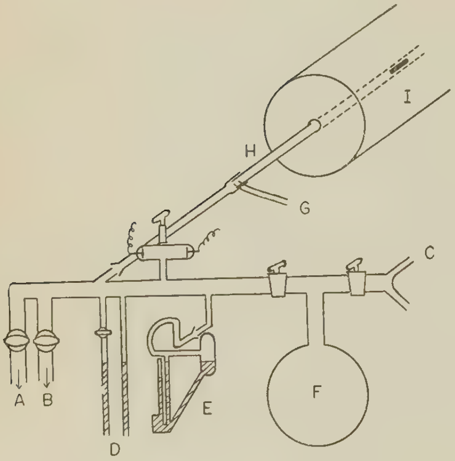

Fig. 3. Apparatus used for the determination of phase diagram; A, to fore-pump; B, to oil diffusion pump; C, to oxygen tank; D, mercury manometer; E, Moser's guage; F, reservoir; G, Pt-PtRh junction; H, alumina tube; I, furnace.

phase and spinel phase. In the figure, the two-phase field corresponds to the higher pressure region. As seen in the figure, for a certain composition of metallic constituents, the phase boundary is found to be the intersection line between the curved surface and a constant composition plane. By projecting these intersection lines into the temperature-pressure plane, we can illustrate the phase diagram on an oxygen pressure-temperature plane. Fig. 2 shows the experimental results projected on the same plane in such a manner. Full lines indicate the intersection lines corresponding to various compositions. The points shown by double circles are the results obtained by Darken and Gurry[12] for iron-oxygen system. They coincide well with our results at higher temperatures, but not at lower temperatures. Robin and Bénard's data[13] should give the cross section of our phase diagram at the oxygen pressure of 159 mmHg (the partial pressure of oxygen in air). They are in good accordance with our results. The dotted lines lying in the low pressure area in the figure indicate the values of the partial pressure of CoO evaporating from the ferrite phases. This conclusion is deduced mainly from our statistical analysis[15]. Experimentally, when we lower the oxygen pressure in a tube containing the specimen below the corresponding critical pressures, the specimen loses oxygen rapidly. The detailed discussion will be given later.

The experimental procedure is as follows. Five specimens having the composition $r$ of 0.000, 0.083, 0.167, 0.250, and 0.333 were prepared by wet method as described in § 2. Apparatus for the measurements is shown in Fig. 3. About 5 grams of a specimen was firstly put into a small porcelain crucible, and was placed at the sealed end of the air-tight alumina tube which was set in a silicon-carbide furnace. After the tube was filled with oxygen gas at 760 mmHg, the specimen was heated up to 1400°C, kept 10 minutes at the pressure reduced so that the oxide was transformed into spinel phase completely, and then cooled to the temperature at which the critical pressure should be determined. In the high temperature range above 900°C, the degree of oxidation of the specimen responds sensitively to the change in the pressure of oxygen atmosphere or to that in the temperature. The specimen is oxidized further with the increase of the oxygen pressure. The rate of oxidation becomes abruptly large after the oxygen pressure has crossed over the phase boundary in Fig. 2. The actual measurements were carried out at constant temperature. The specimen was first annealed at the oxygen pressure just below the critical pressure (which had been estimated roughly before the measurement). After the equilibrium was established, the pressure was raised abruptly to just above the critical pressure by introducing an adequate amount of oxygen, and the following spontaneous variation of the oxygen pressure in the sealed tube was observed. The initial decrease of the pressure is considered to be due to the fact that a slight amount of hematite was precipitating in the spinel matrix. The variation of the pressure ceased apparently after a certain time interval. The oxygen pressure in such a state is defined as the critical pressure $P_-$. The pressure was next raised to a pressure several times higher than $P_-$, and the specimen was annealed at that pressure for an adequate time interval. Then, the pressure was abruptly reduced to just below the critical pressure, and the following variation of the pressure was observed until it ceased. Thus we obtained another critical pressure $P_+$. In general, $P_+$ was not equal to $P_-$, for much longer time would be necessary to attain a complete equilibrium state. Therefore, the critical pressure was determined approximately by putting $P=\sqrt{P_-\cdot P_+}$.

The measurements were repeated at several temperatures ranging from 1400°C to 900°C. The ratio $P_+/P_-$ was closely equal to unity at higher temperatures, but became up to 2 at 1000°C. In these measurements, the accuracy of the measurements became doubtful with an increase in the content of cobalt. Of course, there was not such a critical pressure for the specimen with $r=0.333$ (corresponding to pure cobalt ferrite). It should be noted that even in the single spinel phase field, the specimen is oxidized or reduced to some extent, when the pressure or the temperature is altered.

Besides the critical pressures for the hematite precipitation, we have found another critical pressures for all specimens containing cobalt. For instance, for specimen with $r=0.333$, it was difficult to lower the oxygen pressure below 3 mmHg at 1400°C. If we could reduce the pressure below 3 mmHg, the specimen would lose oxygen rapidly. Such critical pressures were measured by the same way as before. They are shown in Fig. 2 by a series of dotted curves. Because of the experimental difficulties, the accuracy of the measurements became worse below 1200°C.

X-ray powder patterns were taken for the specimens which had been quenched from 1400°C after annealed at the same temperature for an hour in a high vacuum by steady pumping. The patterns have shown clearly the splitting of lines (222), (400), (440), and (444) of spinel structure. This indicates the existence of wüstite type crystal, which is supposed to be CoO. We conclude from these evidences and our statistical analysis of the iron-cobalt-oxygen system that the presence of the lower critical pressure is due to the rapid evaporation of oxygen and CoO from spinel matrix, which occurs when the pressure of the surrounding atmosphere becomes smaller than the partial vapour pressure of CoO which can be in equilibrium with the spinel at the temperature. The reaction will be represented approximately by the following equation:

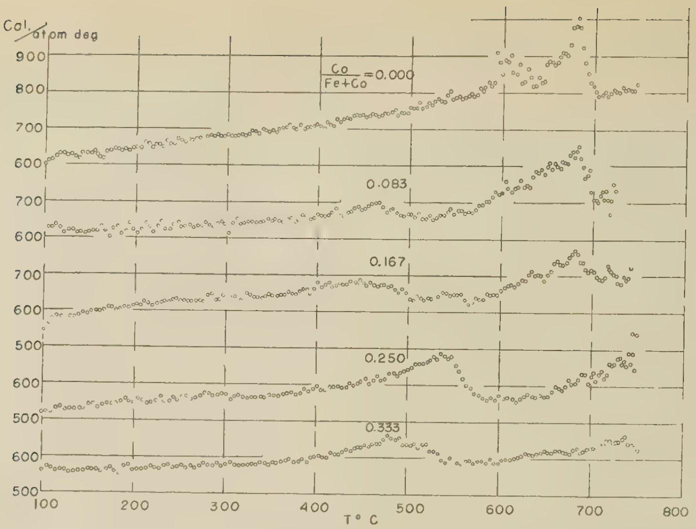

Fig. 4. Specific heat curves on heating for specimens having various compositions after annealing for an hour at 1000°C at oxygen pressure of 0.1~0.05 mmHg.

$$Co_xFe_{3-x}O_4 \longrightarrow y\,CoO\uparrow + \left(1-\frac{y}{3}\right)$$

$$\times\, Co_{\frac{3(x-y)}{3-y}}Fe_{\frac{3(3-x)}{3-y}}O_4 + \frac{y}{6}O_2\uparrow\ . \qquad (1)$$

The details of the statistical analysis of the phenomena will be published in the forthcoming paper.

## § 4. Specific Heat

Using a modified type of Takagi-Nagasaki's adiabatic calorimeter[16)17)], specific heats were measured from 100°C to 800°C for five specimens having the composition $r=0.000$, 0.083, 0.167, 0.250, and 0.333 with the oxygen pressure maintained at about $10^{-3}$ mmHg. The oxides prepared by the nitric acid method were pressed to a pot shape and prefired at 1000°C for an hour at the oxygen pressure of about 0.1~0.05 mmHg*.

The results are shown in Fig. 4. It should be noted that the small thermal conductivity of the specimen might introduce errors of more than five percent in the absolute values of the specific heat at higher temperatures, though the relative values are reliable even at these temperatures. Hematite phase is present in the iron-rich specimens as seen from the anti-ferromagnetic anomaly of hematite at 780°C. Considering from the data of the phase diagram, it can be admitted that the preparation of the specimens was inadequate to complete the spinel phase. The specific heats in the neighbourhood of 300°C (the effective temperature range for magnetic anneal) are not anomalous for all specimens.

The specimen with $r=0.250$ was cooled from 400°C to 200°C in four days, and the measurements of specific heat on heating were again performed. However, no anomalous change was observed.

## § 5. Variation of Lattice Constant with Heat-treatment

In the measurements described in § 3, we observed that at higher temperatures the iron-cobalt ferrites are oxidized or reduced reversibly by changing the pressure or the temperature, even in the single spinel phase field. In these ferrites, it is considered that the main imperfections present are vacant sites of cation created by further oxidation of divalent iron or cobalt. The general representation of the composition will be

$$Fe^{++}_{1-x-y}Co^{++}_{x-z}Fe^{+++}_{2+y}Co^{+++}_{z}O^{--}_{4+y/2+z/2}\ . \qquad (2)$$

Here, the absence of tetravalent cobalt ion is tentatively assumed. Accompanied with oxidation, the lattice constants exhibit continuous changes of the order of $10^{-2}$~$10^{-1}$ percent. These phenomena have been studied with a counter type *x*-ray spectrometer by observing {800} reflection of spinel for *Kα* radiation of iron.

---

* This preparation procedure is used in the industrial production of O. P. magnet, and these specimens have been prepared by Mr. H. Nakamura at Mitsubishi Electric Mfg. Company. It is to be noted, however, that the preparation was performed before the establishment of the phase diagram.

The study was first made for a stoichiometric cobalt ferrite ($r=0.333$). About 3.5 grams of a powder specimen, contained in a small Pt crucible with a lid, was inserted into an air-tight tube and heat-treated several times in the oxygen at various pressures. After each heat-treatment, the change in weight of the specimen was weighed by a balance, and the change of the lattice constant was determined.

The heat-treatments were made successively on the same specimen. The results are shown in Fig. 5, where the attached numbers show the sequence of the measurements. The specimen was

(1), cooled in furnace from 1200°C at the oxygen pressure of 40 mmHg;

(2), cooled in furnance from 1300°C at the oxygen pressure of 800 mmHg;

(3), annealed for 15 minutes at 1300°C at about 1.5 mmHg, and cooled in furnace with the oxygen pressure being adjusted to just above the partial vapour pressure of CoO for $r=0.333$ in Fig. 2;

(4), quenched rapidly from 1300°C at 1.2 mm Hg by taking off the furnace;

(5), annealed for 30 minutes at 1300°C in vacuum by steady pumping, and quenched by taking off the furnace.

It should be noticed that the amount of reduction of oxygen shown by point (5) in Fig. 5 will not be accurate. For some part of it might be attributed to CoO lost out of the crucible in vapour form. Actually, in heat-treatment (5), a rapid reduction of oxygen was observed during the annealing, which was considered to be associated with a rapid evaporation of CoO as explained in § 3. In general, the lattice constants of the oxides of this kind decrease as the degree of oxidation increases, that is, as the concentration of cation vacancy increases. This appears also in the present case of cobalt ferrite as shown in the figure.

For specimens having $r$ less than 0.333, great care must be taken of the pressure of oxygen during heat-treatment. Fig. 6 shows the variation in lattice constant of iron-cobalt ferrites with composition.

Curves (a), (b), and (c) are the results for three different series of specimens obtained after the heat-treatments attempted to be as identical as possible. The specimens had been cooled in furnace from 1400°C in the single phase spinel field common to all specimens by keeping the oxygen pressure at just below

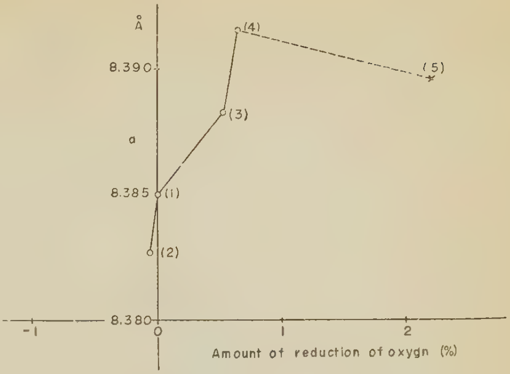

Fig. 5. Variation of lattice constant of cobalt-ferrite plotted against the variation of oxygen content.

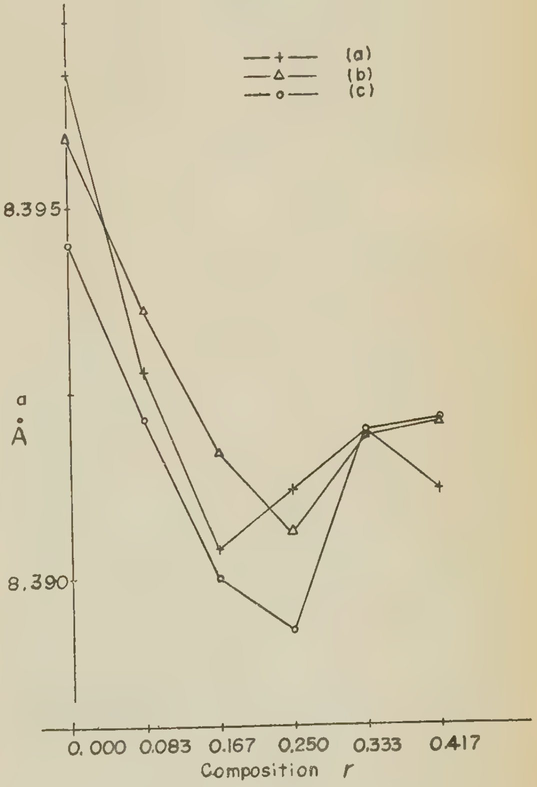

Fig. 6. Variation of lattice constant with composition. Specimens were cooled from 1400°C with the oxygen pressure being adjusted at just below the critical pressure for hematite precipitation from magnetite. Curves (a), (b), and (c) show the scattering of experiment.

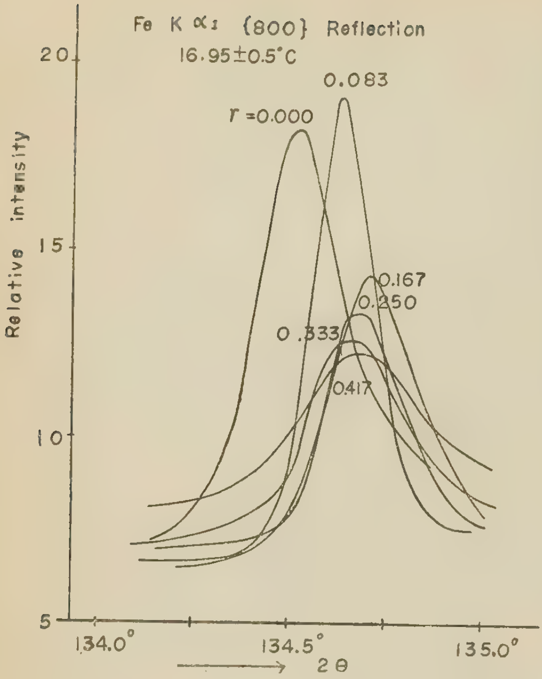

Fig. 7. Line profile of {800} reflection for iron-cobalt ferrites having various compositions.

the critical pressure line for the precipitation of hematite from magnetite shown in Fig. 2. In the procedure, the tube containing specimens was pumped out by an oil diffusion pump below 800°C, as the critical pressure became lower than $10^{-3}$ mmHg below this temperature. We believe that large differences among the curves in Fig. 6 are arising from the difficulty of controlling the oxygen pressure at below 800°C; slight and undetectable leakage would result in a considerable scattering of the measured values of the lattice constants.

However, it is evident that there is a minimum of lattice constant at a certain composition between magnetite and cobalt ferrite. It was shown by our statistical analysis for iron-cobalt ferrites[15] that the concentration of cation vacancy in cobalt ferrite increases steeply with the addition of magnetite. This increase in the concentration of vacancy will result in the steep decrease of lattice constant. Therefore, the existence of a minimum in Fig. 6 can be explained by the fact that the lattice constant of stoichiometric (i.e. vacancy-less) magnetite is larger than that of stoichiometric cobalt ferrite, and that there is a steep decrease of lattice constant with small addition of magnetite to cobalt ferrite. The measurements were repeated for specimens cooled with the oxygen pressure controlled to just below the precipitation pressure lines in Fig. 2 for $r=0.083$ and 0.167. In these cases, hematite phase appeared in the iron-rich specimens and the lattice constants decreased considerably. However, the minimum was also observed in each case at an intermediate composition.

The line profiles taken for {800} reflection in the measurements to get curve (a) in Fig. 6 are shown in Fig. 7. It is well-known that iron-cobalt ferrites have magnetostriction constants ranging from $8\times10^{-5}$ for magnetite (with the anisotropy constant $K_1<0$) to $-6\times10^{-4}$ for cobalt ferrite ($K_1>0$). The broadening of the line width towards cobalt-rich specimens is certainly due to the splitting of the line by the magnetostrictive distortion of the crystallites. However, the broadening as seen in the magnetite specimen compared with the specimen with $r=0.083$ will be due to the inhomogeneous oxidation of the former. It should be noted that the lattice constants and the line profiles of these specimens are very sensitive to heat-treatment and oxygen pressure even at room temperature. It was observed that the line widths of these specimens became broad after a day's exposure to air at room temperature. This fact show that the surface of these specimens is easily oxidized in air.

## § 6. Variation in Oxygen Content During Heat-treatment

Now we extend the study in §3 to the lower temperature range by observing the variation of the pressure of a sealed space containing specimen in a course of heating or cooling.

In Fig. 8, we show oxygen pressure-temperature curves for cobalt ferrite specimen ($r=0.333$), under various circumstances. They are

(1), cooling curve in furnace after sealed at 2 mmHg at 1300°C;

(2), reheating curve of the specimen after ground into fine powder at room temperature;

(3), heating curve of the fine powedered specimen ground at room temperature after cooled in furnace from 1300°C with the oxygen pressure of 760 mmHg;

(4), 'blank' heating curve without specimen. Here, the rate of about 5 deg/min was used on heating. The change in oxygen content of the specimen can be determined approximately by the change in pressure, and its order of magnitude is given by a extra scale in the figure.

The curves show that even pure cobalt ferrite is oxidized or reduced reversibly in cooling or heating. It agrees with the implication of Fig. 5. It is infered from the curves that the oxygen ions become chemically active in this ferrite at about 300°C on heating. Some years before, Takagi and Sawaguchi* have measured at room temperature the lattice constant of cobalt ferrite quenched from various temperatures. They have reported that the lattice constant shows some discontinuous change at about 500°C. The phenomenon might be explained as resulting from the change in the degree of oxidation of the cobalt ferrite. It might be caused by the combination of the effect of the rate of oxidation of their specimen in air with the quenching speed used. Above 500°C, the rate of oxidation is so large that there would be no difference in the degree of oxidation among the states of the specimens with altering quenching temperatures.

In Fig. 9, the results of the same kind of measurements for specimens $r=0.167$ and 0.000 are shown:

(1), cooling curve for powder specimen with $r=0.167$ after cooling from 1300°C to 1000°C with the oxygen pressure being adjusted at just below the hematite precipitation line for $r=0.167$ in Fig. 2;

(2), reheating curve of the specimen after ground into fine powder at room temperature;

(3), heating curve of hematite specimen ($r=0.000$) after cooling from 1300°C with the oxygen pressure of 760 mmHg and ground into fine powder at room temperature.

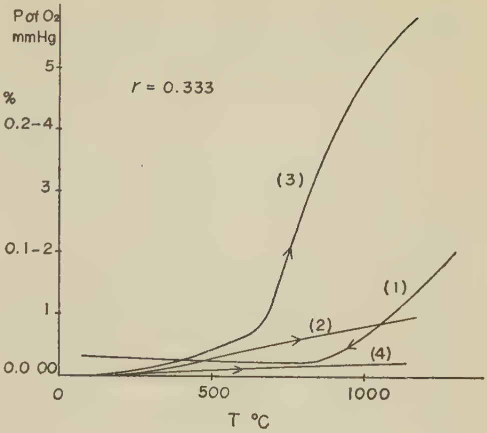

Fig. 8. Variation of oxygen pressure of sealed tube containing cobalt ferrite specimen, during heat-treatment; (1), cooling curve from 1300°C and from at 2 mmHg; (2), reheating curve of the specimen after treatment (1); (3), reheating curve of the specimen after cooling from 1300°C with oxygen pressure of 760 mmHg; (4), heating curve without specimen.

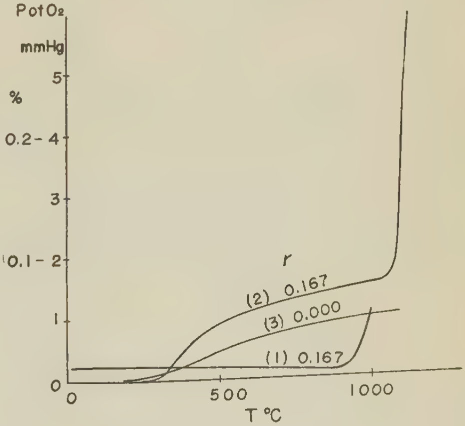

Fig. 9. Variation of oxygen pressure of sealed tube containing specimen during heat-treatment; (1), cooling curve from 1000°C for specimen with $r=0.167$; (2), reheating curve of the specimen after treatment (1); (3), heating curve for specimen with $r=0.000$ (hematite) after cooling from 1300°C with oxygen pressure of 760 mmHg.

A rapid reduction in pressure observed from 1000°C to 900°C on curve (1), will be due to the precipitation of hematite. Although there is no anomalous change of pressure below 900°C on this curve, we can see a slight enhancement of oxidation in this temperature range, compared with curve (1) in Fig. 8. We can deduce from curve (2) some interesting conclusions. There is somewhat anomalous reduction starting from about 300°C, which corresponds to the most sensitive temperature range for the magnetic annealing. However, from the fact that curve (2) lies sufficiently above curve (1) at temperatures above 400°C, and that there is no anomaly in curve (1) in this temperature, we must suppose that the specimen had been oxidized further at room temperature when it had been ground in air atmosphere. The conclusion is consistent with the results from x-ray studies in §5. Accordingly, it must be presumed that the diffusion rate of ions in these oxides increases exponentially at about 300°C on heating, which results in rapid reduction of oxygen from the surface of specimen powder from this temperature on, if the surface have been oxidized at room temperature in air. Another anomalous reduction beginning from 1070°C is undoubtedly due to the transformation of hematite into spinel phase. We consider that the total amount of anomalous reduction around 300°C is so small that it is difficult to account for the anomaly as arising from the reduction over the whole volume of the individual particles rather than at their surfaces. By comparing curve (3) with other curves in Fig. 9 and Fig. 8, we can see that all anomalous reductions shown in Fig. 9 and Fig. 8 are related closely to the presence of cobalt ions.

---

* Unpublished data,

## §7. Conclusion

The phase diagram for iron-cobalt ferrites has been established above 900°C. Below 900°C, all results have been explained by a simple extrapolation of the phase diagram above 900°C and by the assumption that the diffusion rate of the constituent ions in these oxides varies exponentially in passing through the neighbourhood of 300°C. The assumption is supported by magnetic relaxation experiments in these ferrites, electric resistivity-temperature curves[18], and by the experiment by Vernon and others[19] who measured the rate of oxidation of iron.

We have not been able to find any structual anomaly in the solid solutions of magnetite and cobalt ferrite. Though we have found that the lattice constant of cobalt ferrite decreases steeply with the addition of magnetite, it shows only that the vacancy concentration in cation sites increases rapidly with the addition of divalent iron ions to the ferrite. It must be emphasized that in the solid solution of magnetite and cobalt ferrite, the process of oxidation in air goes on to some extent even at room temperature.

## Acknowledgement

The writer wishes to express his sincere thanks to Professor Seiji Kaya for his constant encouragement. He also wishes to express his gratitude to Mr. Hiroshi Nakamura of the Mitsubishi Electric Mfg. Company for his kind preparation of the earlier specimens, and to Mr. Kazuo Kanematsu for his helpful assistance.

## References

1) Y. Kato and T. Takei: J. Inst. Elect. Engrs. (Japan) **53** (1933) 408.
2) Y. Kato, T. Takei, N. Kawai and Aikawa: J. Chem. (Japan) **55** (1934) 584.
3) T. Takei: Elect. Chem. (Japan) **5** (1937) 411.
4) N. Kawai: Thesis to Tokyo Univ.
5) I. Sugiura: J. Appl. Phys. (Japan) **19** (1950) 198. 231; **20** (1951) 98.
6) C. Guillaud: Rev. Mod. Phys. **25** (1953) 64.
7) R. M. Bozorth, E. F. Tilden and A. J. Williams: Phys. Rev. **99** (1955) 1788.
8) L. Néel: J. de Phys. **15** (1953) 225.
9) S. Iida, H. Sekizawa and Y. Aiyama: J. Phys. Soc. Japan **10** (1955) 907.
10) J. W. Greig, E. Posnjak, H. E. Merwin and R. B. Sosman: Am. J. of Sci. **30** (1935) 239.
11) J. Smiltens: J. Chem. Phys. **20** (1952) 990.
12) L. S. Darden and R. W. Gurry: J. Am. Chem. Soc. **67** (1946) 1398; **68** (1946) 798.
13) J. Robin and J. Bénard: C. R. **234** (1952) 734, 956.
14) J. Robin: C. R. **236** (1953) 204.
15) S. Iida: to be published.
16) S. Nagasaki and Y. Takagi: J. Appl. Phys. Japan. **17** (1948) 104.
17) S. Iida: J. Phys. Soc. Japan. **7** (1952) 373.
18) S. Iida, H. Sekizawa and Y. Aiyama: to be published.
19) W. H. J. Vernon, E. A. Calnan, C. J. B. Clews and T. J. Nurse: Proc. Roy. Soc. **216** (1953) 375.

JOURNAL OF THE PHYSICAL SOCIETY OF JAPAN Vol. 11, No. 8, AUGUST, 1956

# Change of Magnetic Susceptibility of Transition Metals and Alloys at their Melting Points

By Yasuaki NAKAGAWA

*Department of Physics, Faculty of Science, University of Tokyo*

(Received March 16, 1956)

The magnetic susceptibility of Mn, Fe, Co, Ni and their alloys has been measured through their melting points up to 1600°C. In general, the susceptibility of transition metals shows a decrease or an increase on melting, depending on whether the interatomic interactions favour parallel alignment of atomic magnetic moments or not, indicating that the interactions are always weaker in liquid than in solid. Although some Fe alloys of face-centred cubic lattice form exceptions to the above simple rule, they are also explained on the basis of the Bethe-Slater exchange interaction curve together with the volume increase on melting.

It is to be noted that a remarkable supercooling of liquid, often exceeding one hundred degrees, has been observed during the course of these susceptibility measurements.

## § 1. Introduction

Although various experimental and theoretical investigations on the magnetic properties of transition metals have been carried out, there are only a few reports which deal with the properties in the liquid state.

In 1917, Terry1) measured the paramagnetic susceptibility of ferromagnetic elements above the Curie point up to the temperature slightly above the melting point. More recently, Fallot2) reported that the susceptibility of nickel did not change on melting, in agreement with Terry's result. This remarkable result seems to indicate that both the number of electrons contributing to the magnetic moment and the interactions between them are unaltered by the liquid-solid transformation.

On the other hand, concerning the studies of non-ferromagnetic elements, Grube and Winkler3), and Isobe4) observed that the paramagnetic susceptibility of manganese was almost independent of temperature in both liquid and solid states at higher temperatures, and increased discontinuously on melting. Its temperature-independent paramagnetism has been explained either as antiferromagnetism in the Heitler-London treatment, or as well-known Pauli paramagnetism in the band theory of metals. Either theory may be applicable to the liquid state with some modifications. However, detailed discussions are impossible because of the lack of experimental data.

For non-transition metals showing weak para- or dia-magnetism, Shimizu5) discussed the change of susceptibility on melting, in connection with the difference in volume between solid and liquid. The magnetic susceptibility of these metals is related to conduction electrons in a very broad band.

The present work is concerned with the transition metals, for which *d*-electrons play an important role in the magnetic properties. The results obtained on these metals in the liquid state will be discussed on the basis of the current theories of magnetism in the solid state.

## § 2. Experimental Method

The measurements of susceptibility were made by Faraday's method using a ring balance similar to that described by Sucksmith6). If an isotropic substance of mass $m$ and susceptibility $\chi$ is placed in a non-uniform field $H$, the force exerted in a direction $z$ at right angle to the field is given by the expression $F=m\chi H(dH/dz)$. The displacement of the specimen due to the force was so small that no correction was necessary for it.

The magnetic field of about 4000 oersteds was produced by a Weiss-type electromagnet. $H(dH/dz)$, as a function of $z$, had a maximum value (*ca.* $2\times10^6$ oe$^2$. cm$^{-1}$.) at the position of the specimen.

In order to obtain the absolute value of susceptibility, a specimen of pure nickel was used as the standard material. In measuring

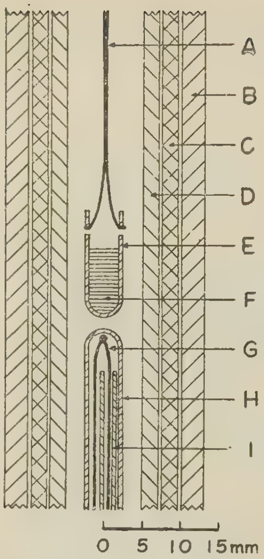

Fig. 1. High temperature furnace.

A: Suspender (Mo-wire). B: Shielding tube (porous alumina). C: Heating element (silicon carbide). D: Air-tight tube (half-fused alumina). E: Crucible (half-fused pure alumina). F: Specimen. G: Thermo-couple (Pt-PtRh). H: Protecting tube (half-fused alumina). I: Insulating tube (porous alumina).

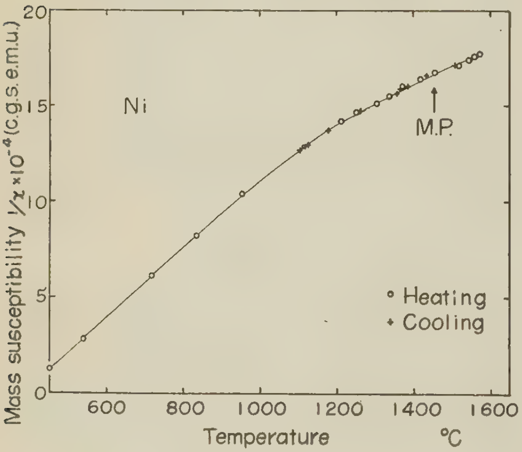

Fig. 2. Ni.

the relative values of susceptibility at different temperatures, an accuracy of 1 per cent was obtained, while the error of the absolute value might amount to 5 per cent for the worst case.

The furnace used to produce the high temperatures up to 1600°C is shown in Fig. 1. The heating element was a cylinder of sintered silicon carbide, which was 'siliconized' at both ends to lower the contact resistance. Direct current, instead of alternating current, was supplied for heating in order to avoid the mechanical vibration caused by the strong magnetic field. Two water-cooled copper plates were inserted between the furnace and the pole-pieces to protect the latter against the heat.

Temperature, measured with a Pt-PtRh thermo-couple, was calibrated *in situ* at four transition temperatures of pure iron: ferromagnetic Curie point (770°C), $\alpha-\gamma$ transformation point (900°C), $\gamma-\delta$ transformation point (1400°C) and melting point (1540°C), where the magnetic susceptibility shows abrupt changes. For this purpose the susceptibility measurements for iron were frequently repeated during the full course of investigation. Since, however, very accurate data of these transition temperatures have not been found in literature, the accuracy of the absolute values of the temperature given in this paper may be about ±10°C, though the accuracy of the relative values was much higher.

Specimens weighing about 500 mg were used for measurements. A small alumina crucible, containing the specimen, was suspended by a thin molybdenum wire, which was fixed to the bottom of a ring balance. In order to prevent evaporation and oxidation of the specimen, it was placed in an air-tight tube filled with purified argon, the pressure of which was about 1 atm. Although slight evaporation, oxidation and reaction with the crucible were found after the measurements at high temperatures, the curve for the magnetic susceptibility *vs* temperature obtained during cooling was in close agreement with that obtained during heating, except in the case of manganese. Therefore, it could be supposed that most specimens were not severely contaminated during the measurements at high temperatures.

## § 3. Experimental Results

Curves obtained for the reciprocal of magnetic susceptibility per gram $1/\chi$ *vs* temperature $T$ are shown in Figs. 2–11. The change of susceptibility at the melting point is listed in Table 1, together with the observed melting point. Details will be given below.

### Pure Metals

(a) Ni. The susceptibility was measured of both commercial electrolytic Ni of 99% purity and spectroscopically pure Ni (99.99%) supplied by Electrotechnical Laboratory*. However, there was no appreciable difference between them. As shown in Fig. 2, the $1/\chi$ *vs* $T$ curve is concave towards the $T$-axis at higher temperatures, showing remarkable deviation from the Curie-Weiss law. The susceptibility shows no change at the melting point within the experimental error, in agreement with Terry's[1] and Fallot's[2] results.

(b) Co. Fig. 3 shows the result for Co of 99.99% purity, obtained from Johnson, Matthey & Co. The susceptibility decreased slightly on melting, while the gradient of $1/\chi$ *vs* $T$ curve remained unaltered in disagreement with Terry's[1] result. During cooling, the discontinuous change of susceptibility at the melting point was not observed, supposedly due to considerable supercooling of the liquid state.

Such remarkable supercooling of liquid was often observed in other metals and alloys in case of our measurements, which will be discussed in the later section.

(c) Fe. The result for Fe of 99.99% purity, also supplied by Electrotechnical Laboratory**, is shown in Fig. 4. It is well known that the susceptibility of face-centred cubic phase ($\gamma$-Fe) is much smaller than that of body-centred cubic phases ($\alpha$- and $\delta$-Fe). On passing through the melting point, the value of susceptibility was markedly reduced and approached the value corresponding to the extension of the curve in $\gamma$-region. This agrees fairly well with the result obtained by Terry[1], whose measurements in liquid were limited to the temperature only a few degrees above the melting point. The gradient of $1/\chi$ *vs* $T$ curve in the liquid state was larger than that in $\gamma$-phase and smaller than that in $\delta$-phase.

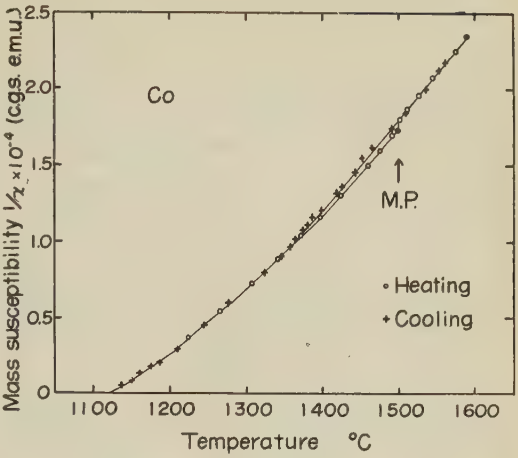

Fig. 3. Co.

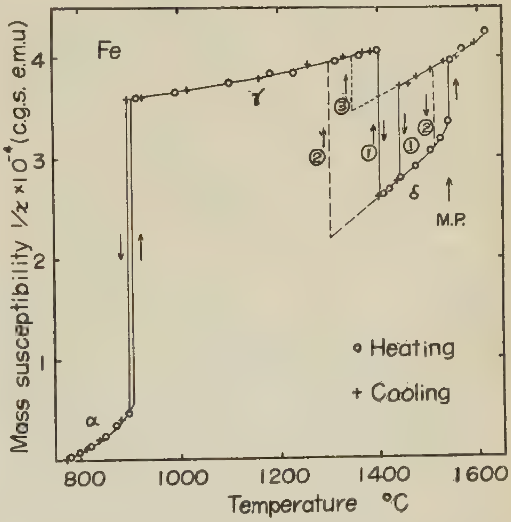

Fig. 4. Fe.
① Liquid is supercooled, but $\delta$-phase is not supercooled.
② Both liquid and $\delta$-phase are supercooled.
③ Liquid is supercooled to $\gamma$-region.

It was observed in our experiments during cooling that the liquid state was supercooled to a temperature about one hundred degrees below the melting point. Subsequently a sudden increase in susceptibility occured on solidification, accompanied by an increase in temperature resulting from the release of latent heat. After reaching the equilibrium state the susceptibility curve coincided with that obtained during heating. The measurements on Fe were repeated ten times for the purpose of temperature calibration as mentioned previously. The different measurements were in close agreement except in the amount of supercooling indicated. In a few cases the liquid was supercooled to the $\gamma$-region, as shown in Fig. 4 with a dotted line; it seems that the liquid solidified directly to face-centred cubic lattice. In other cases, where the supercooling of liquid was not so extensive, $\delta$-phase was also supercooled to a temperature about one hundred degrees below the $\gamma-\delta$ transformation point, as shown in Fig. 4 with a dashed line.

(d) Mn. The result for the electrolytic Mn

---

*, ** The author is indebted to messrs. T. Nagashima and S. Goseki, research members of Electrotechnical Laboratory, for the supply of Ni and Fe of high purity.

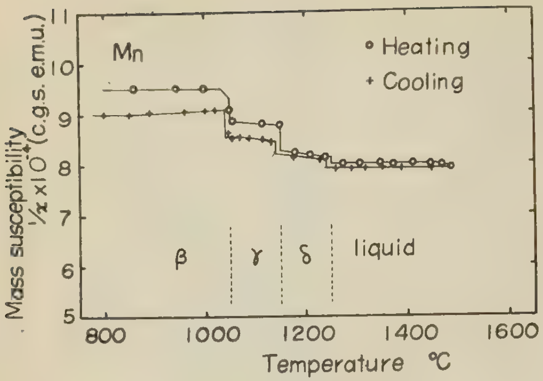

Fig. 5. Mn.

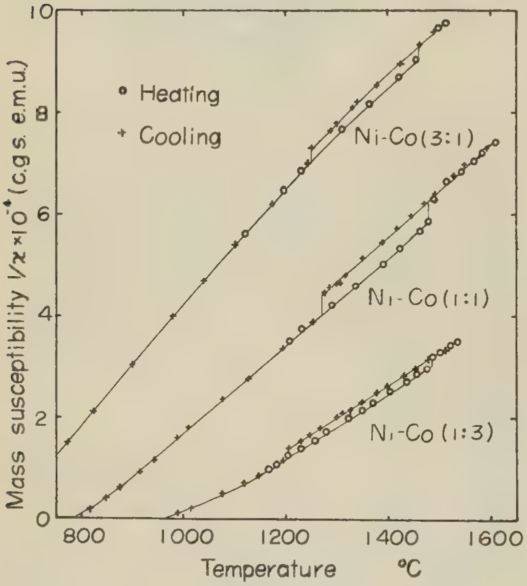

Fig. 6. Ni–Co.

of 99% purity is shown in Fig. 5. The susceptibility was almost independent of temperature in each phase at higher temperatures: $\beta$-phase (600°–1050°C), $\gamma$-phase (1050°–1150°C), $\delta$-phase (1150°–1250°C) and liquid phase. The discontinuous increase in susceptibility was observed during heating at every transformation temperature. The susceptibility measured during cooling was slightly larger than that of heating, probably owing to the contamination of the specimen. Previously, Grube and Winkler[3)] reported that there was no appreciable change of susceptibility on melting, while Isobe's[4)] measurement indicated much larger increase than ours.

It is to be noted that the crystal structure of $\gamma$-Mn and $\delta$-Mn are face-centred cubic and body-centred cubic respectively, as confirmed recently by Basinski and Christian[7)] using a high temperature X-ray camera.

**Alloys**

Among the various binary alloys consisting of 3*d*-transition elements, those of homogenious solid solutions with (1:1) or (3:1) atomic compositions were selected for investigation*. The alloys were prepared by melting two component metals together in a vacuum induction furnace. Only Mn alloys were melted in argon atmosphere to prevent the evaporation of Mn. The materials were less pure than those used for the previous measurements on metallic elements. The purities reported by suppliers were as follows: Cu 99.5%; Ni 99%; Co 98.5%; Fe 99.5%; Mn 99%; Cr. 99.3%; V, commercial ferro-vanadium with 49.3% V. As the composition of specimens was not directly determined by chemical analysis but calculated from mixing ratio, an error of a few per cent is possible in the indicated compositions.

(a) Ni-Co alloys. There is an unbroken series of solid solutions with face-centred cubic structure in this system. As shown in Fig. 6 the magnetic behaviour in the liquid state is quite similar to that in the solid state. There is a slight decrease in susceptibility on melting in every alloy investigated.

(b) Ni-Fe alloys. The alloys investigated are face-centred cubic at higher temperatures. Since Fig. 7 shows that the susceptibility increases on melting for the alloys containing 25% and 50% Ni and decreases for the alloy containing 75% Ni, it may be that there is no change of susceptibility on melting for a composition of about 65% Ni, where the ferromagnetic Curie point shows a maximum in the Ni-Fe system.

(c) Co-Fe alloys. At higher temperatures, the alloys investigated are face-centred cubic. As the ferromagnetic body-centred cubic phase appears below 950°C, the reciprocal value of susceptibility decreases rapidly, as shown in Fig. 8. The increase in susceptibility of these alloys on melting corresponds to the fact that the molten Fe has larger values of susceptibility than face-centred cubic Fe.

---

* The references to the phase diagrams of the alloys are found in: R. M. Bozorth: "*Ferromagnetism*" (1951); Amer. Soc. Metals: "*Metals Handbook*" (1948). As can be seen in these diagrams, deviations between solidus and liquidus lines are small at the compositions that we have chosen for the specimens in most cases. This is why the melting occurs at a fairly definite temperature.

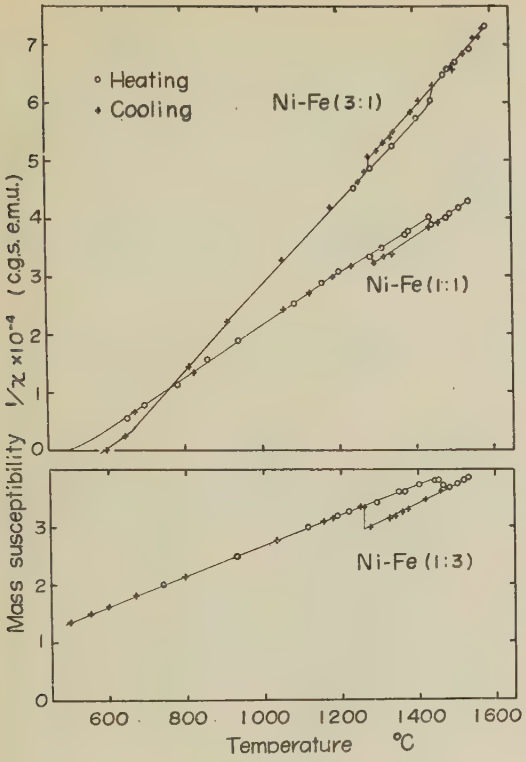

Fig. 7. Ni-Fe.

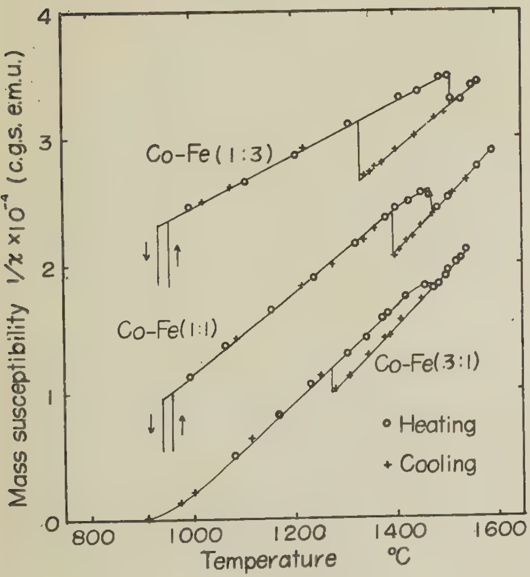

Fig. 8. Co–Fe.

(d) Ni-Cu, Ni-Mn and Ni-Cr alloys with (3:1) composition. The results for these face-centred cubic alloys are shown in Fig. 9. The $1/\chi$ *vs* $T$ curves for Ni-Mn and Ni-Cu (3:1) are considerably concave towards the $T$-axis, while the susceptibility of Ni-Cr (3:1) is nearly independent of temperature. On melting, an increase in susceptibility was observed in every case.

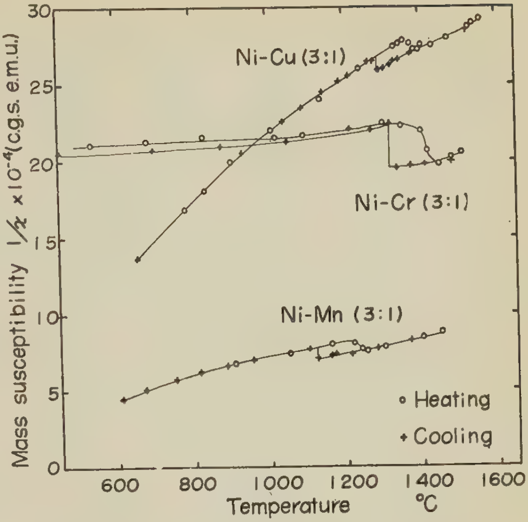

Fig. 9. Ni–Cu, Ni–Mn, Ni–Cr.

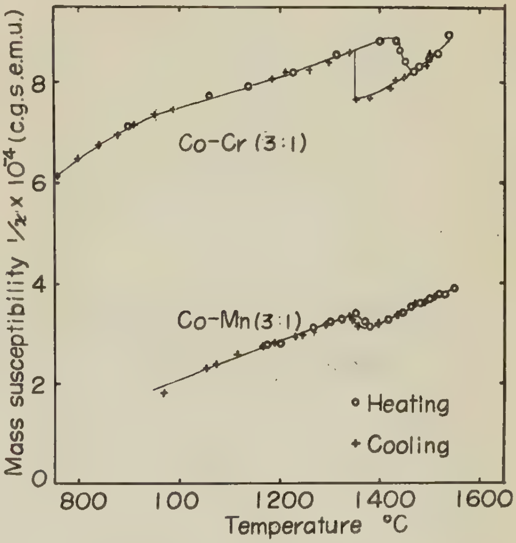

Fig. 10. Co–Mn, Co–Cr.

(e) Co-Mn and Co-Cr alloys with (3:1) composition. The susceptibility of these alloys also increases on melting, as shown in Fig. 10. They are face-centred cubic at higher temperatures. However, Co-Cr (3:1) transforms to the hexagonal close-packed structure below 900°C, where an anomaly of susceptibility was observed. It is interesting that the susceptibility curve for Co-Mn (3:1) is somewhat similar to that for Fe-rich alloys of face-centred cubic lattice.

(f) Fe-Mn, Fe-Cr and Fe-V alloys with

Table I

| Group | Material | $T_m$ (°C) | $\Delta T$ (°C) | $\Delta\chi$ ($10^{-6}$emu/g) | $\Delta\chi/\chi_s$ (%) | $C_l/C_s$ | Characteristics of group |
|---|---|---|---|---|---|---|---|
| 1 *a* | Co | 1500 | 100? | −1.5 | −3 | 1.0 | Susceptibility following Curie-Weiss law |
| | Ni-Co (1:3) | 1485 | 205 | −1.9 | −6 | 1.0 | |
| | Ni-Co (1:1) | 1480 | 210 | −1.4 | −8 | 1.0 | |
| | Ni-Co (3:1) | 1460 | 210 | −0.3 | −3 | 1.0 | |
| 1 *b* | Mn | 1250 | 0 | +0.3 | +2 | 1.0 | Susceptibility depending weakly on temperature |
| | Mn (γ)* | — | — | +1.0 | +9 | 1.0 | |
| | Ni-Cr (3:1) | 1410 | 90 | +0.8 | +18 | 1.0 | |
| 1 *b′* | Ni-Cu (3:1) | 1380 | 90 | +0.16 | +5 | 1.3 | Susceptibility being expressed by, $\chi=\alpha+C/(T-\theta)$ where $\alpha$ has fairly large value |
| | Ni-Mn (3:1) | 1220 | 100 | +1.2 | +10 | 1.0 | |
| | Co-Mn (3:1) | 1360 | 0 | +4.1 | +14 | 0.8 | |
| | Co-Cr (3:1) | 1440 | 100 | +1.1 | +10 | 0.6 | |
| 1 *c* | Ni | 1455? | ? | 0.0 | 0 | 1.0 | Being intermediate between (1 *a*) and (1 *b′*) |
| 2 *a* | Fe | 1540 | 190 | −6.2 | −20 | 1.5 | Susceptibility following Curie-Weiss law; Body-centred cubic structure just below melting point |
| | Fe-Cr (3:1) | 1510 | 30 | −2.4 | −14 | 2.3 | |
| | Fe-V (3:1) | 1475 | 0 | −2.3 | −15 | 3.4 | |
| 2 *b* | Fe (γ)* | — | — | +1.6 | +7 | 0.4 | Susceptibility following Curie-Weiss law ($\theta$ is negative or slightly positve); Face-centred cubic structure just below melting point |
| | Fe-Ni (3:1) | 1460 | 200 | +2.0 | +8 | 0.8 | |
| | Fe-Co (3:1) | 1510 | 180 | +2.3 | +8 | 0.6 | |
| | Fe-Mn (3:1) | 1440 | 220 | +1.9 | +9 | 0.6 | |
| 3 *a* | Fe-Ni (1:3) | 1445 | 165 | −0.5 | −3 | 1.0 | Being similar to (1 *a*) |
| 3 *b* | Fe-Ni (1:1) | 1440 | 150 | +1.2 | +5 | 1.0 | Being similar to (2 *b*) |
| | Fe-Co (1:3) | 1470 | 200 | +1.9 | +4 | 0.9 | |
| | Fe-Co (1:1) | 1470 | 75 | +3.8 | +10 | 0.8 | |

$T_m$: Melting point; mean value of liquidus and solidus temperature in case of alloys.
$\Delta T$: Maximum amount of supercooling observed.
$\Delta\chi=\chi_l-\chi_s$; $\chi_l$ and $\chi_s$ are values of susceptibility at $T_m$ in liquid and solid states, respectively.
$C_l$ and $C_s$ are values of $dT/d(1/\chi)$ at $T_m$ in liquid and solid states, respectively.
(If the susceptibility follows the Curie-Weiss law, $C_l$ and $C_s$ coincide with the Curie constants in liquid and solid states, respectively.)
When the susceptibility shows gradual change on melting, extrapolated values at $T_m$ are taken for $\chi_l$, $\chi_s$, $C_l$ and $C_s$.
* The values of susceptibility in γ-range are extrapolated to $T_m$ for comparison with those in liquid state.

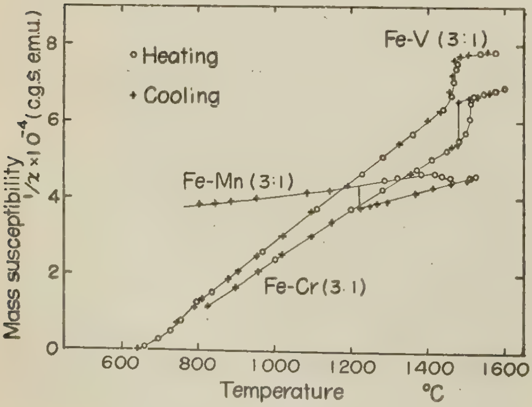

Fig. 11. Fe–Mn, Fe-Cr, Fe-V.

(3:1) composition. The results are shown in Fig. 11. The magnetic behaviour and the crystal structure of Fe-Mn (3:1) are similar to those of Fe-rich alloys with Ni or Co. Among many alloys investigated, only Fe-Cr and Fe-V (3:1) are body-centred cubic at higher temperatures. The magnetic behaviour of these alloys on melting is similar to that of δ-Fe.

## § 4. Discussion

As the magnetic behaviour of Fe and its alloys at their melting points is somewhat unusual, the metals and alloys investigated are classified into following groups:

1. The metals and alloys not containing Fe,
2. Fe and Fe-rich alloys,

3. Fe-poor alloys.

Then, each group is further divided into subgroups *a*, *b* and *c*. depending on whether the susceptibility shows a respective decrease, increase or no change on melting. This classification is listed in Table I.

The susceptibility of Co and Ni-Co alloys (group 1*a*) is approximately expressed by the Curie-Weiss law,

$$\chi = C/(T-\theta)\ , \qquad (1)$$

in the liquid state as well as in the solid state. There is no difference in the Curie constant *C* between liquid and solid, whereas the paramagnetic Curie temperature $\theta$ is lower in liquid than in solid. This fact indicates that the atomic magnetic moments remain unaltered, while the exchange interaction becomes weaker on melting.

On the other hand, the susceptibility of Mn and Ni-Cr (3:1) (group 1*b*) is weakly dependent on temperature in both liquid and solid. The weakly temperature-dependent paramagnetism has been explained by Néel⁸⁾ and Zener⁹⁾ on the basis of the theory of antiferromagnetism.*

When the antiferromagnetic interactions are weakened, the susceptibility should increase. Therefore, the increase in susceptibility on melting, observed in this case, is explained by the assumption that the interatomic interactions are weaker in liquid than in solid, which is consistent with the assumption used previously in the case of group 1*a***.

In cases where the $1/\chi$ *vs* $T$ curve is concave towards the $T$-axis, the susceptibility is expediently expressed by

$$\chi = \alpha + C/(T-\theta)\ , \qquad (2)$$

where $\alpha$ is weakly dependent on temperature, and the second term corresponds to the Curie-Weiss law (1). The former may increase while the latter may decrease on melting, as mentioned above. The suscptibility of Ni (group 1*c*) is expressed by (2), and shows no change on melting. In this case the increase in $\alpha$ may just compensate the decrease in $C/(T-\theta)$***. The susceptibility of alloys of Ni or Co with non-ferromagnetic metals (group 1*b′*) is also expressed by (2), and shows an increase on melting. In this case the increase in $\alpha$ may predominate over the decrease in $C/(T-\theta)$.

In the expression (2), it is assumed that the Curie-Weiss paramagnetism and the weakly temperature-dependent paramagnetism coexist without mutual interference. This assumption may be justified by Pauling's valence-bond theory¹¹⁾, which states that there are two kinds of *d*-orbitals in a transition metal, one being 'atomic' the other being 'bonding' (hybridized with *s*- and *p*-orbitals). It may be reasonable to suppose that the electrons in the 'atomic' orbitals show the Curie-Weiss paramagnetism, while those in the 'bonding' orbitals show the weakly temperature-dependent paramagnetism.

It is to be remarked here that Grube and Winkler³⁾¹⁴⁾ measured the susceptibility of Mn-Pd and Ni-Mo alloys up to a temperature above their melting points, and Uchida and Kondoh¹⁵⁾ measured that of Ni-Te. The susceptibility of these alloys is also expressed by (2) and shows an increase on melting, similar to that of group 1*b′* investigated by us.

Although the susceptibility of Fe and Fe-rich alloys (group 2) shows a peculiar behaviour in connection with the allotropy in their solid state, we have no difficulty in explaining the change of their susceptibility on melting. It has been supposed that the interatomic interactions are ferromagnetic in the body-centred cubic Fe, while antiferro-

---

* Since the antiferromagnetic long-range order is impossible in the liquid state because of the absence of the regular lattice, the constant paramagnetism cannot be explained on the ordinary theory of antiferromagnetism. However, it may be explained on the basis of Pauling's valence-bond theory of metals¹¹⁾: if the valence-bond of 3*d*-electrons in the 'bonding' orbitals is weak enough to be affected by the external magnetic field, these electrons will contribute to the susceptibility as in case of antiferromagnetism.

** According to Kriessman and Callen,¹⁰⁾ the band theory of metals is more suitable to account for the weakly temperature-dependent paramagnetism of the transition metals. On the basis of this theory, the increase in susceptibility on melting can be also explained as follows: the susceptibility associated with the electrons in an unfilled *d*-band is proportional to the density of states at Fermi surface, and thus inversely proportional to the band width, under the assumption that the band shape remains unaltered. The band width may be narrower in liquid than in solid, since the interatomic interactions may be weaker. It follows that the susceptibility is larger in liquid than in solid.

*** The magnetic behaviour of Ni in the solid state is more consistently explained by two bands model¹²⁾¹³⁾ (3*d*- and 4*s*-band) in the collective electron theory of ferromagnetism. However, it may be difficult to apply this model to the liquid state.

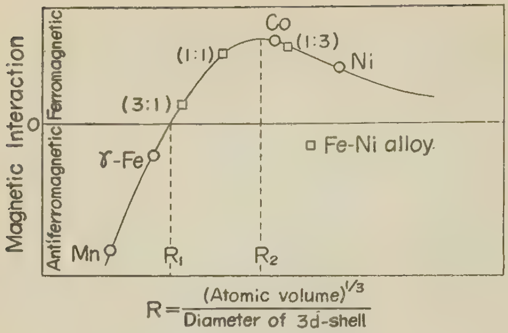

Fig. 12. Interaction Curve.

magnetic in the face-centred cubic. Therefore, the susceptibility of the former must decrease on melting and that of the latter must increase, as mentioned above.

On the other hand, the magnetic behaviours of Fe poor alloys (group 3) in the liquid state cannot be explained so simply, although these alloys seem to be intermediate between Fe-rich alloys and the alloys such as Ni-Co. Every Fe-poor alloy investigated is face-centred cubic at higher temperatures, and their susceptibility is expressed by the Curie-Weiss law (1) with a positive value of $\theta$. On melting, the susceptibility shows an increase in some cases and a decrease in others. In the former cases, it must be supposed that the interatomic interactions are stronger in liquid than in solid, contrary to all other cases mentioned previously. However, it will be satisfactorily explained as follows.

According to Bethe and Slater, the exchange interaction varies with the ratio $R$ of the interatomic distance to the diameter of $3d$-sell. In order to treat the liquid and solid together, we use the cubic root of atomic volume instead of the interatomic distance. The ratio $R$ is larger in liquid than in solid because of the increase in volume on melting*. Fig. 12 shows the interaction curve similar to that drawn by Bozorth[17] following Slater's calculation.

If $R>R_2$ or $R<R_1$ (see Fig. 12), the interactions will be weakened on melting, although it is ferromagnetic in the former case and antiferromagnetic in the latter, justifying the assumption used previously in the case of group 1. On the other hand, if $R_1<R<R_2$, the interaction is ferromagnetic and stronger in liquid than in solid, as supposed in some cases of Fe-poor alloys. Thus the Bethe-Slater interaction curve is satisfactorily consistent with the fact that an alloy of Fe with 65% Ni, having a maximum Curie temperature in the Fe-Ni system, is expected to show no change of susceptibility at its melting point. This alloy may correspond to the maximum point ($R=R_2$) on the interaction curve.

It is assumed in this discussion that the atomic magnetic moments remain unaltered on melting. However, this assumption may be invalid in the cases of Fe-rich alloys, since the Curie constants of these alloys show variation of some amount at their melting points.

## On the Supercooling of Liquid

Up to the year 1950, it had been supposed that the metals with simple crystal structure, like those investigated here, could not be supercooled more than a few degrees. Recently, however, Turnbull[18] observed that very small particles (50–500 $\mu$ in diameter) of molten metals were supercooled by about 15–25% of their absolute melting temperature, regardless of whether their crystal strucure is simple or complex. He supposed that the extensive supercooling is in principle possible with all liquids because of the nucleation difficulty. The nucleation probability, calculated by the classical statistics, is able to account for the observed supercooling. His theory was supplimented by Frank[19] and Borelius[20].

However, there may be a 'catalyst' of nucleation in the material, suppressing the supercooling. The probability of catalytic nucleation may be much larger in bulky material than in a small droplet. It has been thus explained that most of metals are difficult to supercool extensively in bulk, as believed up to this time (see Frank's paper).

On the contrary, the experimental results, presented here, show that most of transition metals and alloys are supercooled remarkably in bulk; the weights of the specimens were about 500 mg. The magnetic susceptibility was measured during cooling at temperature intervals of about 20 degrees. Temperature was changed step by step, the cooling rate being about 5 degrees per minute on the average. The amounts of maximum supercooling observed, $\Delta T$, are listed in Table 1. When $\Delta T$ was one hundred degrees, the supercooling state could be retained for twenty minutes.

---

* There have been only a few available data on the volume change on melting of the transition metals and alloys. It is undoubted, however, that the volume of a face-centred cubic metal shows an increase of about 4% on melting.[16]

It was observed previously by Bardenheuer and Bleckmann[21] that a bulky specimen of Fe could be supercooled over one hundred degrees. This is the only report on the extensive supercooling of transition metals in bulk, so far as the author knows.

## § 5. Conclusion

The magnetic behaviours of transition metals and alloys in the liquid state are fairly similar to those in the solid state. There may be little difference in short-range structure between liquid and solid, as the magnetic properties are mainly affected by the short-range interactions. The observed change of susceptibility at the melting point is explained in connection with the volume increase on melting.

When the susceptibility follows the Curie-Weiss law, its change on melting depends on the difference in interatomic interactions, under the assumption that the atomic magnetic moments remain unaltered. If the interatomic distance is larger than that corresponding to a maximum interaction on the Bethe-Slater exchange interaction curve, the interaction becomes weaker on melting because of the volume increase, and thus the susceptibility shows a decrease. If the interatomic distance is smaller than that, the susceptibility shows an increase on melting, regardless of whether the exchange interaction is positive or negative.

For Fe and Fe-rich alloys, however, it has been observed that not only the paramagnetic Curie temperature but also the Curie constant changes at their melting points, indicating that the atomic magnetic moments do not remain unaltered.

When the susceptibility is nearly independent of temperature, it shows always an increase on melting. This case may be considered to be similar to the above-mentioned case where the exchange interaction is negative.

In some cases, the susceptibility is expressed as a sum of two terms: one being temperature-independent and the other corresponding to the Curie-Weiss law. The change at the melting point depends on which term predominates over the other.

It is to be noted that the unexpectedly remarkable supercooling of liquid was observed for most of the metals and the alloys during the course of our susceptibility measurements.

The author wishes to express his sincere thanks to Professor S. Kaya for his kind discussions and encouragement.

### References

1) E. M. Terry: Phys. Rev. **9** (1917) 394.
2) M. Fallot: J. Phys. Rad. **5** (1944) 153.
3) G. Grube and O. Winkler: Z. Elektrochem. **42** (1936) 815.
4) M. Isobe: Sci. Rep. Res. Inst. Tôhoku Univ. **A 3** (1951) 78.
5) Y. Shimizu: Sci. Rep. Tôhoku Imp. Univ. **25** (1937) 921.
6) W. Sucksmith and R. R. Pearce: Proc. Roy. Soc. **A 167** (1938) 189.
7) Z. S. Basinski and J. W. Christian: Proc. Roy. Soc. **A 223** (1954) 554.
8) L. Néel: Ann. de Phys. **5** (1936) 232.
9) C. Zener: Phys. Rev. **81** (1951) 440.
10) C. J. Kriessman and H. B. Callen: Phys. Rev. **94** (1954) 837.
11) L. Pauling: Phys. Rev. **54** (1938) 899.
12) H. Watanabe: J. Phys. Soc. Japan **3** (1948) 317.
13) E. P. Wohlfarth: Proc. Roy. Soc. **A 195** (1949) 434.
14) G. Grube and O. Winkler: Z. Elektrochem. **44** (1938) 423.
15) E. Uchida and H. Kondoh: J. Phys. Soc. Japan **11** (1956) 21.
16) O. Kubaschewski: Trans. Faraday Soc. **45** (1949) 931.
17) R. M. Bozorth: *Ferromagnetism* (1951) 444.
18) D. Turnbull and R. E. Cech: J. Appl. Phys. **21** (1950) 804.
19) F. C. Frank: Proc. Roy. Soc. **A 215** (1952) 43.
20) G. Borelius: Ark. f. Fys. **6** (1953) 191.
21) P. Bardenheuer and R. Bleckmann: Stahl u. Eisen **61** (1941) 49.

JOURNAL OF THE PHYSICAL SOCIETY OF JAPAN Vol. 11, No. 8, AUGUST, 1956

# On the Absorption Spectra of Complex Ions, III
# The Calculation of the Crystalline Field Strength

By Yukito TANABE

*Department of Applied Physics, Faculty of Engineering, Tokyo University*

and Satoru SUGANO*

*Institute of Broadcasting N. H. K., Setagaya, Tokyo*

(Received March 7, 1956)

A molecular calculation of the crystalline field parameter *Dq* in chrome alum has been carried out on the basis of the generalized crystalline field model suggested in the previous papers I and II (Journ. Phys. Soc. Japan. 9 (1954) 753, 766). The deformation of the electron cloud of $Cr^{3+}$ is taken into consideration by making the 3d orbital of $Cr^{3+}$ orthogonal to ligand orbitals.

The result shows that Kleiner's value of *Dq* with a wrong sign is corrected. This improvement is due to the large resonance energy between the 3d orbitals of the central ion and the ligand orbitals, which appears only in the molecular treatment. However, the model $Cr^{3+}$–$6H_2O$ cannot explain the observed change in the values of the spin orbit coupling constant $\lambda$ and the *B*-value. A possible way to get over this difficulty is considered.

## § 1. Introduction

The crystalline field model has been successfully used not only in the interpretation of the specific heat and magnetic susceptibility of paramagnetic complex salts, but also in the analysis of paramagnetic resonance absorption experiments. Recent analyses show that this model with suitable modification[1,2] is also applicable to the excited states, because it is found that the optical absorption bands and lines of these ionic complexes are satisfactorily explained on this basis.

However, in those treatments the quantity *Dq*, which represents the strength of the crystalline field and is to be evaluated theoretically within the frame of the crystalline field approximation, was left as a parameter and was adjusted so as to give the best fit to the experimental data. The theoretical work hitherto made is therefore of more or less empirical nature, and it seems of some value to determine the value of *Dq* on purely theoretical ground and compare it with the empirically determined one in order to confirm the adequacy of this model.

Although Van Vleck[3] and Polder[4] tried, many years ago, to calculate *Dq* with a rather crude model—a point charge or dipole model—and gave seemingly good results, a more elaborate calculation recently performed by Kleiner[5] has revealed serious difficulty. He calculated the crystalline field of chrome alum taking the overlap effect of electron clouds between the central $Cr^{3+}$ ion and the octahedrally coordinated water molecules into consideration. The treatment was exactly based on the crystalline field model of Bethe[6] and Van Vleck, according to which, in making complex, 3*d* electrons of $Cr^{3+}$ are considered just to come under the influence of the electrostatic field due to both the nuclear charges and average electron distribution of ligands, and the effect of electron transfer between the central metal ion and ligands is entirely put out of consideration. Unfortunately his result gave the crystalline field with the wrong sign—*Dq* with the minus sign. As he pointed out, this was due to the imperfect screening of the nuclear field of ligands by their electrons and was an inevitable difficulty as far as we use the naive crystalline field model. Moreover, if we consider the effect of the exchange field due to electrons of ligands, which was not included in Kleiner's calculation, the result would become worse (see § 4,5). As shown by recent quantitative arguments, there are several other difficulties in the old crystalline field model. One of them is that we must choose the Slater integrals $F_2$ and $F_4$ much smaller than those of the free ions in order to explain the observed spectra of the complex ion, whereas these two parameters are considered equal to those of the free ions in the old crystalline field theory. This suggests the deformation of $3d$ orbitals of metal ions in ionic complexes. Another failure of the old model was pointed out by Owen[2]. It is that in complex ions we must assume smaller values of the spin orbit coupling constant than those in the free ions in order to explain the $g$-values observed in the paramagnetic resonance absorption in a consistent way with the optical absorption data of these ionic complex ions. This is also to be interpreted as due to the deformation of orbitals.

---

* Present adress: Department of Physics, Faculty of Science, Tokyo University.

All these facts suggest that one may get a better result if one treats the $[Cr(H_2O)_6]^{3+}$ complex as a whole molecule or, in other words, if one considers the effect of the deformation of atomic orbitals due to molecular formation.

We shall examine here the effect of overlapping of orbitals adopting the ionic model for $[Cr(H_2O)_6]^{3+}$ complex, because this model is nothing but the old crystalline field model if the non-orthogonality of orbitals is neglected, and is therefore covenient for a comparative study with the latter.

## §2. Model and Method of Calculation

To facilitate the comparison with Kleiner's results, we adopt the same model for $[Cr(H_2O)_6]^{3+}$ as that used by him. The ion is assumed to be composed of a central $Cr^{3+}$ ion and octahedrally coordinated six water molecules, of which the nuclei of oxygen in the latter being situated 1.97 Å (3.73 a.u.) apart from the $Cr^{3+}$. The water molecule is assumed to consist of an $O^{2-}$ ion and double positive charges (protons) which are uniformly distributed on the circle of radius 0.76 Å (1.43 a.u.) with centre on the $Cr^{3+}-O^{2-}$ axis and in the plane perpendicular to this axis (Fig. 1.). The justification of this model has been discussed in detail by Kleiner.

In treating $[Cr(H_2O)_6]^{3+}$ as a molecule, either the Heitler-London method or the molecular orbital method may be employed. As mentioned in the previous paper (I), it is promising to take the orbital mixing of the central metal ion's orbital and those of the ligands into account and determine the mixing ratio by the variation principle. But this MO method has several difficulties in practice to perform to a satisfactory degree. Namely, we must determine the atomic orbitals to be used, especially $4s$ and $4p$ orbitals of the central metal ion; we must assume a suitable field with exchange due to core elecrons. In order to settle these points, it seems, as the result obtained here suggests, necessary to make an S.C.F. calculation, which needs a rather tedious evaluation of many molecular integrals even if we neglect many centre integrals and thus is almost impossible in the present stage. A more empirical approach is therefore favoured if we adopt the MO method.

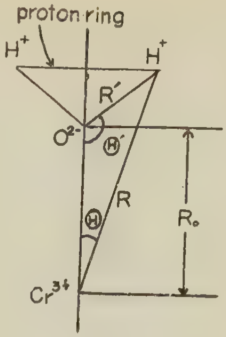

Fig. 1. The relative positions of $Cr^{3+}$, $O^{2-}$ and protons.
$R_0=1.97$ Å $\Theta'=127.5°$ $R'\sin\Theta'=0.76$ Å

On the other hand, although the ionic model (a special structure in the valonce-bond theory), which has been assumed hitherto and will also be assumed here is surely insufficient in describing the electronic structure of a molecule, it does not seem inappropriate for such a loosely bound complex as treated here, and moreover because of its simplicity we need only few integrals to be evaluated besides those calculated by Kleiner. It thus enables us to carry out the calculation entirely on non-empirical ground.

Therefore, with the hope that we could reach some definite conclusion within the frame of the adopted model and get some insight into the nature of the electronic structure of the complex ion for further progress, we shall discuss the problem with the Heitler-London method (purely ionic model) in this paper and the MO method will be considered only briefly in the last section.

The expectation that Kleiner's result would be improved if molecular theoretical calculation (even though based on purely ionic model) were carried out comes from the following: When we neglect the orbital overlap* between the metal ion and ligands in the Heitler-London method, we cannot expect the correct order of $e$ and $f_2$ level, calculated position of $e$ level lying lower than that of $f_2$ level contrary to the observation, because $e$ orbital lies stretched towards ligands and is more stabilized than $f_2$ orbital by the field of ligand nuclei which is not screened perfectly. But if the orbital overlap is taken into account, we can expect that the so-called Heisenberg exchange integrals, i.e. exchange integrals between non-orthogonal orbitals, would improve the result giving the correct order of $e$ and $f_2$ levels because they are negative and surely larger for $e$ than $f_2$ orbital.

## § 3. Derivation of the Expression for 10 *Dq*

According to the model described in § 2, the electron configuration of $[Cr(H_2O)_6]^{3+}$ is considered to be $Cr^{3+}$ ($K$, $L$, $(3s)^2$, $(3p)^6$, $(3d)^3$)—$6O^{2-}$ ($K$, $L$), where $K$ and $L$ stand for closed $K$ and $L$ shells respectively.

To take the overlap between the orbitals of the central metal ion and ligands into account properly, we proceed as follws. We first make the core orbitals $\phi^c$ orthogonal to each other, the resulting orthonormalized set $\varphi^c$ being thus given by

$$\varphi_i^c=\sum_j \phi_j^c(1+s)_{ji}^{-1/2}\,, \quad (i=1,2,\cdots,n)$$

$$(1+s)_{ji}=\int d\tau\phi_j^{c*}\phi_i^c\,, \tag{3.1}$$

where $n$ is the total number of core orbitals. Then we construct the following functions $\varphi$ from $3d$ orbitals $\phi$ of the central metal ion and $\varphi^c$:

$$\varphi_k=N_k^{-1/2}\left\{\phi_k-\sum_j^n \varphi_j^c(\varphi_j^c|\phi_k)\right\}\,, \quad (k=1,2,\cdots,5)$$

$$N_k=1-\sum_j^n |(\varphi_j|\phi_k)|^2\,. \tag{3.2}$$

These $\varphi$ are orthogonal to $\varphi^c$ and thus to core orbitals $\phi^c$, but not orthogonal among themselves. Then we choose $\phi$ and $\varphi^c$ so that they make the bases of the irreducible representations of the octahedral group. Five $\varphi_k$ functions are now split into two groups: The $e$-group orbitals $u$, $v$ which are the bases for the representation $E$, and the $f_2$-group orbitals $\xi$, $\eta$, $\zeta$ which are those for the representation $F_2$. These five functions are obviously orthogonal to each other.

One can easily show by constructing Slater determinants that we may use the orbitals $\varphi^c$, $\varphi$ instead of $\phi^c$, $\phi$, because the space that is spanned by the set of Slater determinants constructed from the former orbitals is just spanned by the Slater determinants of the same type which is obtained by replacing $\varphi^c$, $\varphi$ in those determinants by $\phi^c$, $\phi$. We therefore use these orbitals $\varphi^c$, $\varphi$ to obtain the expression of 10 $Dq$ in the following.

It is well known that the strength of the crystalline field which we are going to evaluate is given by the relation,

$$10\,Dq=\mathcal{E}_e-\mathcal{E}_{f_2}\,,$$

i.e., the difference of one-electron energies of $e$ and $f_2$ orbitals. Further consideration shows that, in the case of chrome alum, the quantity 10 $Dq$ should be the energy separation between two states ${}^4A_2(f_2^3)$ and ${}^4F_2(f_2^2e)$. Thus

$$10\,Dq=E(f_2^2e;\ {}^4F_2)-E(f_2^3;\ {}^4A_2)\,, \tag{3.3}$$

which is expressed as

$$\begin{aligned}10\,Dq=&\textstyle\sum'_{(\xi)}(\xi|h_0|\xi)+(v|h_0|v)+J(\xi\eta)-K(\xi\eta)\\&+\textstyle\sum'_{(\xi)}\{J(\xi v)-K(\xi v)\}\\&-\textstyle\sum_{(\xi)}(\xi|h_0|\xi)-\frac{1}{2}\sum_{(\xi\xi')}\{J(\xi\xi')-K(\xi\xi')\}\,,\end{aligned} \tag{3.4}$$

where the summation in the first and second lines runs over $\xi$, $\eta$, while that in the third line should run over $\xi$, $\eta$, $\zeta$, because ${}^4F_2$ and ${}^4A_2$ are the states in which three electrons with parallel spins are in the orbitals $\xi$, $\eta$, $v$ and $\xi$, $\eta$, $\zeta$ respectively. $J(\xi\eta)$ and $K(\xi\eta)$ are respectively coulomb and exchange integrals between two orbitals $\xi$ and $\eta$, and

$$(\xi|h_0|\xi)=\int d\tau_1\xi^*(1)h_0\xi(1)\,,$$

$h_0$ being the sum of the kinetic energy and the potential energy of an electron in the field of the core electrons and the nuclei of both the central metal ion and ligands. The right-hand side of (3.4) may be simply written as the difference of the orbital energy as follows;

---

* It must be noted that this is different from the neglect of the charge overlap in the naive crystalline field model, which leads to the point charge or dipole model. In fact, Kleiner's paper dealt with the effect of this charge overlap and showed that inclusion of this made the situation worse.

$$10\,Dq=(v|h|v)-(\zeta|h|\zeta)=\varepsilon_e-\varepsilon_{f_2}\,, \qquad (3.5)$$

$$h=h_0+\int d\tau_2 r_{12}^{-1}(|\xi(2)|^2+|\eta(2)|^2)$$
$$-\int d\tau_2 r_{12}^{-1}(\xi^*(2)\xi(1)+\eta^*(2)\eta(1))P_{12}\,, \qquad (3.6)$$

where $P_{12}$ denotes the permutation operator of the electron 1 and 2, and the second and third term in (3.6) represent the coulomb and exchange energy operator due to two electrons in the orbitals $\xi$ and $\eta$ respectively.

For the orbitals $(u, v)$ and $(\xi, \eta, \zeta)$, we use the following functions;

$$u=\varphi_u\,,\quad v=\varphi_v\,,$$
$$\xi=\varphi_\xi\,,\quad \eta=\varphi_\eta\,,\quad \zeta=\varphi_\zeta\,,$$
$$\varphi_\gamma=N_\gamma^{-1/2}(\phi_\gamma-\delta_\gamma\psi_\gamma)\,, \qquad (3.7)$$

where

$$(u_0=)\phi_u=P_{3d}(r)/r\cdot Y_{20}(\theta\varphi)\,,$$
$$(v_0=)\phi_v=2^{-1/2}\cdot P_{3d}(r)/r\cdot\{Y_{22}(\theta\varphi)+Y_{2-2}(\theta\varphi)\}\,,$$
$$(\xi_0=)\phi_\xi=i2^{-1/2}\cdot P_{3d}(r)/r\cdot\{Y_{21}(\theta\varphi)+Y_{2-1}(\theta\cdot\varphi)\}\,,$$
$$(\eta_0=)\phi_\eta=-2^{-1/2}P_{3d}(r)/r\cdot\{Y_{21}(\theta\varphi)-Y_{2-1}(\theta\varphi)\}\,,$$
$$(\zeta_0=)\phi_\zeta=-i2^{-1/2}P_{3d}(r)/r\cdot\{Y_{22}(\theta\varphi)-Y_{2-2}(\theta\varphi)\}\,. \qquad (3.8)$$

$\psi_\gamma$ are molecular orbitals constructed from $2s$, $2p$ atomic orbitals of six ligands (we assume that $1s$ orbitals may be treated as shrunk into the respective nuclear positions) and, if we number the ligands as in Fig. 2, they are given by

$$\psi_v=\mu_s\chi_{sv}+\mu_\sigma\chi_{\sigma v}\,,$$
$$\psi_\zeta=\mu_\pi\chi_{\pi\zeta}\,,$$
$$\chi_{sv}=2^{-1}(s_1+s_4-s_2-s_5)\,,$$
$$\chi_{\sigma v}=2^{-1}(\sigma_1+\sigma_4-\sigma_2-\sigma_5)\,,$$
$$\chi_{\pi\zeta}=2^{-1}(y_1-y_4+x_2-x_5)\,, \qquad (3.9)$$

where $s_i$, $\sigma_i$, $x_i$, $y_i$ are all orbital functions of $O^{2-}$ at the position $i$; $s_i$ the $2s$-function, $\sigma_i$ the $2p\sigma$-function directed to the origin (metal ion), $x_i$ and $y_i$ the $2p\pi$-functions stretched along in the direction of $x$ and $y$ axes respectively.

In our treatment $\delta_v$, $\delta_\zeta$, $\mu_s$, $\mu_\sigma$ and $\mu_\pi$ are determined from the equations

$$\delta_v\mu_s=(\phi_v|\chi_{sv})\,,$$
$$\delta_v\mu_\sigma=(\phi_v|\chi_{\sigma v})\,,\qquad(\delta_\gamma>0)$$
$$\delta_\zeta\mu_\pi=(\phi_\zeta|\chi_{\pi\zeta})\,, \qquad (3.10)$$

and

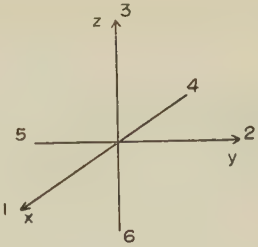

Fig. 2.

$$\mu_s^2+\mu_\sigma^2=1\,,\qquad \mu_\pi=1\,. \qquad (3.11)$$

In (3.9), (3.10) and (3.11) the overlaps between ligand orbitals are neglected as is done throughout this paper. $N_v$ and $N_\zeta$ are then given by

$$N_v=1-\delta_v^2\,,$$
$$N_\zeta=1-\delta_\zeta^2\,. \qquad (3.12)$$

For the evaluation of matrix elements, we decompose $h$ into several terms as follows:

$$\left.\begin{aligned}
&h=h_\alpha+\sum_{i=1}^{6}V_i+\varDelta V\,,\\
&h_\alpha=-\tfrac{1}{2}\varDelta+V_\alpha\,,\\
&V_\alpha=V_{\mathrm{core}}+V(\xi\eta)\,,\\
&V(\xi\eta)=\int d\tau_2 r_{12}^{-1}(|\xi_0(2)|^2+|\eta_0(2)|^2)\\
&\qquad-\int d\tau_2 r_{12}^{-1}(\xi_0^*(2)\xi_0(1)+\eta_0^*(2)\eta_0(1))P_{12}\,,\\
&\varDelta V=\int d\tau_2 r_{12}^{-1}\sum_{ij}\phi_i^c(2)\phi_j^c(2)R_{ji}\\
&\qquad+\int d\tau_2 r_{12}^{-1}{\sum}'_{(\xi)}(|\xi(2)|^2-|\xi_0(2)|^2)\\
&\qquad-\int d\tau_2 r_{12}^{-1}\sum_{ij}\phi_i^c(2)\phi_j^c(1)R_{ji}P_{12}\\
&\qquad-\int d\tau_2 r_{12}^{-1}{\sum}'_{(\xi)}(\xi^*(2)\xi(1)-\xi_0^*(2)\xi_0(1))P_{12}\,,\\
&R_{ji}=-[s/(1+s)]_{ji}\,,
\end{aligned}\right\} \qquad (3.13)$$

where $\varDelta V$ represents the change of the field from the mere superposition of the field of the $Cr^{3+}$ ion and six ligands due to molecular formation, which we neglect throughout the following. In (3.13), $h_\alpha$ is the Hartree-Fock Hamiltonian for a $Cr^{3+}$ free ion and $V_i$ represents the potential energy including the exchange potential due to the $H_2O$ molecule at the position $i$. $V_{\mathrm{core}}$ means the potential energy due to core electrons and the nucleus of the $Cr^{3+}$ ion. The summation $\sum_{ij}$ on the right-hand side of the expression of $\varDelta V$ extends over all core orbitals $i$, $j$ and $\sum'_{(\xi)}$ means the summation over the orbitals $\xi$, $\eta$.

## § 4. Evaluation of Matrix Elements and Results

We are now going to evaluate the matrix elements which appear in the expression of the orbital energy

$$\begin{aligned} N_\gamma(\varphi_\gamma|h|\varphi_\gamma) &= (\phi_\gamma|h_\alpha|\phi_\gamma)+(\phi_\gamma|\sum V_i|\phi_\gamma) \\ &+\delta_\gamma^2\{(\psi_\gamma|-\tfrac{1}{2}\Delta+\sum V_i|\psi_\gamma)+(\psi_\gamma|V_\alpha|\psi_\gamma)\} \\ &-2\delta_\gamma\{(\phi_\gamma|h_\alpha|\psi_\gamma)+(\phi_\gamma|\sum V_i|\psi_\gamma)\}\,, \qquad (4.1) \end{aligned}$$

for $\gamma=v$ and $\zeta$.

For the calculation of these elements, we shall use Slater type functions with the orbital exponent 3.85 for the $2s$ and $2p$ orbitals in $\psi_\gamma$ and Hartree's function of Cr$^{2+}$[7] for $\phi$ instead of using that of Cr$^{3+}$ which is not available at present.

(i) Overlap Integrals:

Overlap integrals between $\phi_\gamma$ and $\chi_{\alpha\gamma}$ are listed below. The values marked with asterisk are those caluculated with the $2s$ function with node which is orthogonalized to the $1s$ function of O$^{2-}$. Nodeless $2s$ function was used for simplicity whenever it does not introduce serious error.

$\delta_\gamma$, $\mu_\alpha$ and $N_\gamma$ are easily found by means of (3.10), (3.11) and (3.12). For the sake of comparison we have also calculated the overlap integrals using the $3d$ wave function of Cr$^{3+}$ which is extrapolated from those of Cr (Porter)[8] and Cr$^{2+}$ (Mooney)[7]. We shall use them only to make a rough estimation of resonance integrals in the last section because the extrapolated function is not so reliable.

(ii) $(\phi_\gamma|h_\alpha|\phi_\gamma)$:

We replace this matrix element by Hartree's orbital energy $\mathcal{E}_d$ of the $d$-electron for Cr$^{3+}$. The calculated and observed (ionization potential) $\mathcal{E}_d$ for Cr$^{2+}$ and Cr$^{3+}$ are as follows:

| | Calc. | (in a.u.) | Obs. |
|---|---|---|---|
| Cr$^{2+}$ | −0.898 | | −1.137 |
| Cr$^{3+}$ | —— | | −1.822 |

For Cr$^{3+}$, unfortunately, there is no Hartree field calculation and we have no reliable value of $\mathcal{E}_d$. However, since the quantity with which we are concerned is given by the difference $(\varphi_v|h|\varphi_v)-(\varphi_\zeta|h|\varphi_\zeta)$ and is not so sensitive to the value of $\mathcal{E}_d$, we may well take a moderate value $\mathcal{E}_d=-1.5$ instead of the non-empirically calculated value of this matrix element.

Table I. The overlap Integrals.

| $\gamma$ | $\alpha$ | $(\phi_\gamma\|\chi_{\alpha\gamma})$ | | $\mu_\alpha$ | | $\delta_\gamma$ | |
|---|---|---|---|---|---|---|---|
| | | Cr$^{2+}$ | Cr$^{3+}$ | Cr$^{2+}$ | Cr$^{3+}$ | Cr$^{2+}$ | Cr$^{3+}$ |
| $v$ | $s$ | 0.279*<br>0.285 | 0.236 | 0.746*<br>0.752 | 0.705 | 0.374*<br>0.378 | 0.335 |
| $v$ | $\sigma$ | 0.249 | 0.238 | 0.666*<br>0.659 | 0.709 | | |
| $\zeta$ | $\pi$ | 0.191 | 0.158 | 1 | 1 | 0.191 | 0.158 |

Table II. The calculated values of $(\phi_\gamma|\sum V_i|\phi_\gamma)$.

| $\gamma$ | $(\phi_\gamma\|\sum V_i\|\phi_\gamma)_{\text{coul.}}$ | $(\phi_\gamma\|\sum V_i\|\phi_\gamma)_{\text{exch.}}$ | $(\phi_\gamma\|\sum V_i\|\phi_\gamma)_{\text{total}}$ |
|---|---|---|---|
| $v$ | 0.744 | 0.137 | 0.606 |
| $\zeta$ | 0.769 | 0.038 | 0.731 |

(iii) $(\phi_\gamma|\sum V_i|\phi_\gamma)$:

This matrix element consists of two terms, namely the coulomb and exchange energy terms. They were numerically calculated (Appendix I*a*, I*b*) and are listed in Table II. The difference of two coulomb energy terms $(\phi_v|\sum V_i|\phi_v)_{\text{coul.}}$ and $(\phi_\zeta|\sum V_i|\phi_\zeta)_{\text{coul.}}$ is essentially Kleiner's $10\,Dq$ and is found to be negative. As is easily understood, the exchange energy term is larger for the $v$ type orbital $\phi_v$ than for $\phi_\zeta$, so that the contribution of the exchange energy term to $10Dq$ makes the discrepancy between the observed and calculated value greater. Thus we see that the classical calculation completely fails to give the correct sign of the crystalline field strength.

(iv) $(\psi_\gamma|-\frac{1}{2}\Delta+\sum V_i|\psi_\gamma)$:

It is convenient to divide this matrix element into two parts in the following way;

$$\begin{aligned} &(\psi_\gamma|-\tfrac{1}{2}\Delta+\sum V_i|\psi_\gamma) \\ &\quad=(\psi_\gamma|-\tfrac{1}{2}\Delta+\sum V_i(\mathrm{O}^{2-})|\psi_\gamma) \\ &\quad+(\psi_\gamma|\sum V_i(\text{proton})|\psi_\gamma)\,. \qquad (4.2) \end{aligned}$$

Throughout our calculation, we shall neglect the differential overlap of orbitals between the different ligands and also ignore the dipole field due to other ligands which comes from both terms in (4.2). The first term then can be calculated from orbital energies of $2s$ and $2p$ electrons of O$^{2-}$. These orbital energies were determined by extrapolation from the Hartree-Fock orbital energies of O$^{3+}$, O$^{2+}$, O$^{+}$ and O[9]):

$$\mathcal{E}_{2s}=-0.48_5\ ,\quad \mathcal{E}_{2p}=+0.33_5\ .$$

The second term was analytically calculated using the following expansion formula for $V_i$ (proton);

$$V_i(\text{proton}) = -2\sum P_l(\cos\theta)P_l(\cos\Theta')\begin{cases} R'^{\,l}/r^{l+1} & \text{for } R'>r \\ r^l/R'^{\,l+1} & \text{for } R'<r, \end{cases} \tag{4.3}$$

where we took the origin at the position of the oxygen nucleus. For the definition of $R'$ and $\Theta'$ see Fig. 1; $R'=1.81$, $-\cos\Theta'=0.607$.

Table III shows the numerical values thus determined together with the corresponding observed ionization potentials of a water molecule[10], where $x$) and $y$) distinguish the two kinds of $\pi$-orbitals: $x$) the one stretched along the $x$ axis in the plane including two protons and $y$) the other along the $y$ axis perpendicular to this plane (the origin is taken at the position of oxygen nucleus and the $z$ axis passes through the midpoint of the line connecting two protons). In our model of uniformly distributed change on a ring, there is no need to distinguish them.

(v) $(\psi_\gamma|V_\alpha|\psi_\gamma)$:

For the term $V_{\text{core}}$ in $V_\alpha$, we use an approximate analytical expression

$$V_{\text{core}} = -(6+30.15\exp(-3.71r))/r\ , \tag{4.4}$$

which is in good agreement with Hartree's $V_{\text{core}}$ in the region $r>0.9$ where the integrand in question is appreciable. We can thus calculate $(\psi_\gamma|V_{\text{core}}|\psi_\gamma)$ analytically.

The exchange energy term in $(\psi_\gamma|V_\alpha|\psi_\gamma)$, $\int d\tau_2 r_{12}^{-1}(\xi_0{}^*(2)\xi_0(1)+\eta_0{}^*(2)\eta_0(1))P_{12}$ was discarded, because the result will not be greatly affected by this approximation.

All these calculated values are given in Table IV.

(vi) $(\phi_\gamma|h_\alpha|\psi_\gamma)+(\phi_\gamma|\sum V_i|\psi_\gamma)$:

The first term $(\phi_\gamma|h_\alpha|\psi_\gamma)$ was replaced by $\mathcal{E}_\alpha(\phi_\gamma|\psi_\gamma)$. The second term $(\phi_\gamma|\sum V_i|\psi_\gamma)$ is divided into parts, namely the coulomb and exchange parts according to the terms which appear in $V_i$. The coulomb part comes from the potential energy due to the oxygen nucleus field perfectly screened by 1*s* electrons and the proton field, beside the repulsive coulomb field due to 2*s* and 2*p* electrons of $O^{2-}$, while the exchange part comes from the exchange potential term due to 2*s* and 2*p* electrons.

Table III. The calculated value of $(\phi_{1\alpha}{}^c|-\frac{1}{2}\Delta+V_1|\phi_{1\alpha'}{}^c)$, together with the corresponding observed values.

| $\phi_{1\alpha}{}^c$ | $\phi_{1\alpha'}{}^c$ | $(\phi_{1\alpha}{}^c\|-\frac{1}{2}\Delta+V_1\|\phi_{1\alpha'}{}^c)$ | Corresponding observed ionization potentials of a water molecule |
|---|---|---|---|
| $s_1$ | $s_1$ | −1.556 | −1.174 |
| $\sigma_1$ | $\sigma_1$ | −0.747 | −0.624 |
| $s_1$ | $\sigma_1$ | +0.243 | |
| $y_1$ | $y_1$ | −0.731 | −0.661$^{x)}$<br>−0.466$^{y)}$ |

The calculation of $(\phi_\gamma|V_1(\text{proton})|\psi_\gamma)$ was made by making use of the expansion formula (4.3), this time taking the origin at the position of chromium nucleus (Appendix II c).

It was found in calculating $(\phi_\gamma|\sum V_i(O^{2-})|\psi_\gamma|_{\text{coul.}}$ (Appendix II*a*), that it makes a great difference to the result whether we use 2*s* function with or without node, because the contribution of the nuclear field near the oxygen nucleus is too large; thus, if we use the nodeless 2*s* function, the value of $(\phi_\gamma|V_1(O^{2-})|s_1)$ is about one-half of that calculated with the function with node. In this case, therefore, 2*s* function with node was employed. (see § 4—( i )).

The term $(\phi_\gamma|V_1(O^{2-})|\varphi_{1\alpha}{}^c)_{\text{exch.}}$ can be expressed in the form $(\phi_\gamma|V_{1,\text{exch.}}(\alpha)|\varphi_{1\alpha}{}^c)$. Using these exchange potentials $V_{1,\text{exch.}}(\alpha)$, $(\phi_\gamma|\sum V_i|\psi_\gamma)_{\text{exch.}}$ were calculated in an analogous way to the case of $(\phi_\gamma|\sum V_i|\psi_\gamma)_{\text{coul.}}$ (Appendix II*b*).

Now we summarize the values of various matrix elements which appear in (4.1) in Table VI, together with the required orbital energies $\mathcal{E}_v$ and $\mathcal{E}_\zeta$. In the third column, the

Table IV.

| $\phi_{1\alpha}{}^c$ | $\phi_{1\alpha'}{}^c$ | $(\phi_{1\alpha}{}^c\|V_{\text{core}}\|\phi_{1\alpha'}{}^c)$ | $(\phi_{1\alpha}{}^c\|V(\xi\eta)\|\phi_{1\alpha'}{}^c)$ | $(\phi_{1\alpha}{}^c\|V_\alpha\|\phi_{1\alpha'}{}^c)$ |
|---|---|---|---|---|
| $s_1$ | $s_1$ | −1.612 | 0.502 | −1.110 |
| $\sigma_1$ | $\sigma_1$ | −1.716 | 0.486 | −1.230 |
| $s_1$ | $\sigma_1$ | −0.326 | 0.032 | −0.294 |
| $y_1$ | $y_1$ | −1.561 | 0.488 | −1.073 |

Table V.

| $\gamma$ | $\varphi_{1\alpha}{}^c$ | $(\phi_\gamma \vert V_1(\text{proton}) \vert \varphi_{1\alpha}{}^c)$ | $(\phi_\gamma \vert V_1(O^{2-}) \vert \varphi_{1\alpha}{}^c)_{\text{coul.}}$ | $(\phi_\gamma \vert V_1(O^{2-}) \vert \varphi_{1\alpha}{}^c)_{\text{exch.}}$ |
|---|---|---|---|---|
| $v$ | $s_1$ | $-0.0317$ | 0.368<br>(0.201) | 0.573<br>(0.583) |
| $v$ | $\sigma_1$ | $-0.0338$ | 0.340 | 0.404 |
| $\zeta$ | $y_1$ | $-0.0252$ | 0.261 | 0.260 |

The values in brackets are those calculated with nodeless $2s$ function.

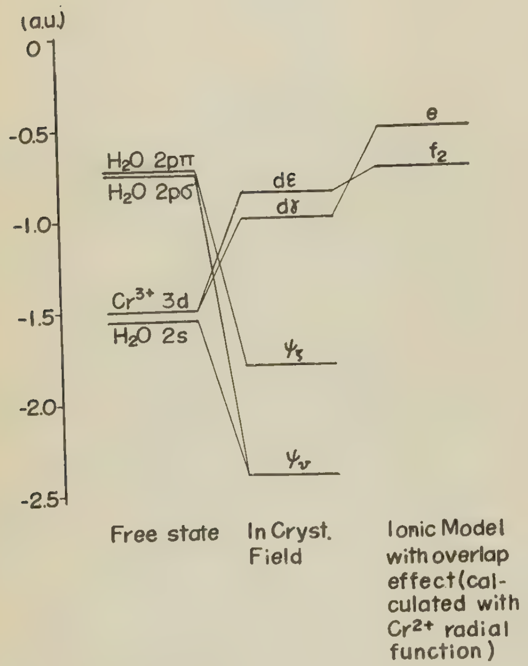

Fig. 3. The location of energy levels in three stages of calculation.

values at the left are those calculated here and the values at the right are those obtained using Mulliken's formula[11];

$$(\phi_\gamma|h|\psi_\gamma)=F_\gamma 2^{-1}(\phi_\gamma|\psi_\gamma)\{(\phi_\gamma|h|\phi_\gamma)+(\psi_\gamma|h|\psi_\gamma)\}, \tag{4.5}$$

in which we assume $F_\zeta=2.00$, $F_v=1.67$ after Wolfsberg and Helmholtz[12]. These values are given only for the purpose of comparison.

## § 5. Discussion

For the convenience of comparison, we indicate in Fig. 3 the location of relevant energy levels in three stages of calculation.

The lines in the left column of this figure represent from up to down the orbital energies of $2p\pi$, $2p\sigma$ and $2s$ electron of free $H_2O$ calculated with the model described in § 2, and $3d$ electron of free $Cr^{3+}$ ion.

Those in the middle column are the values of the diagonal elements $(\phi_\gamma|h|\phi_\gamma)$ and $(\psi_\gamma|h|\psi_\gamma)$. The difference of the former energies $(\phi_v|h|\phi_v)-(\phi_\zeta|h|\phi_\zeta)$ is exactly $10Dq$ calculated according to the naive crystalline field model, i.e., $10Q$ calculated by Kleiner plus the strength of the crystalline exchange field due to six ligands. As was already mentioned, in this stage the $e$ level lies lower than the $f_2$ level, which means that the sign of the crystalline field strength is negative in contradiction to the observation.

The right column shows the positions of the $e$ and $f_2$ levels determined under the assumption of the purely ionic model taking the orbital overlap effect mentioned in § 2 and § 3 into account. Here the $e$ level is brought up higher than the $f_2$ level, while the position of the latter is not seriously altered from that in the middle column. This is just what we expected qualitatively in § 2, namely the $e$ orbital has higher energy because it has a larger exchange integral with the ligand orbital (exchange integral between non-orthogonal orbitals), or, in the language of molecular orbital theory, the $e$ level is pushed upward from its original position, because the orbital has a larger resonance integral than $f_2$ orbital with the ligand orbital.

The value in question in the final stage is $10Dq=5.9$ ev, which is of correct sign as we saw, but is too large compared with the value 2.15 ev determined empirically. We shall therefore discuss the possible explanation of this disagreement in the following.

In the first place, we used the radial function of $Cr^{2+}$ for the $3d$ orbital in the evaluation of molecular integrals instead of using that of $Cr^{3+}$, only because Hartree's solution for the latter is not available at present. If we had used the radial function of $Cr^{3+}$ in the calculation, the overlap between $3d$ and ligand orbitals would have been smaller, because the $3d$ electrons of $Cr^{3+}$ are more tightly bound to the chromium nucleus than those of $Cr^{2+}$

and as the result the value of $10Dq$ would have been smaller than the value obtained here. We estimate this effect—the change in the final result caused by the use of $Cr^{3+}$ wave function instead of $Cr^{2+}$ function-roughly in the following way. The change of the contribution from the difference of the terms $N_\gamma^{-1}(\phi_\gamma|h|\phi_\gamma)\,(\gamma=v,\zeta)$ is shown to be small, because $(\phi_\gamma|h_\alpha|\phi_\gamma)$ is already that of $Cr^{3+}$ and the effect of the change in $(\phi_\gamma|\sum V_i|\phi_\gamma)$ is small as Kleiner has found out. The change of the contribution from the difference of the terms $N_\gamma^{-1}\delta_\gamma^2(\psi_\gamma|h|\psi_\gamma)$ we may safely estimate to be of the order of 0.1 ev. So that they are of minor importance compared to the change of the contribution from the difference of resonance integral term. We tentatively estimate the values of the resonance integral $(\phi_\gamma{}^{3+}|h|\chi_\alpha)$assuming that they are reduced from those of $(\phi_\gamma{}^{2+}|h|\chi_\alpha)$ by a factor $(\phi_\gamma{}^{3+}|\chi_\alpha)/(\phi_\gamma{}^{2+}|\chi_\alpha)$. This estimation is based upon the formula (4.5), where the change in the diagonal elements is ignored. Thus, using the values of overlap integral for $Cr^{3+}$ listed in Table I we obtain 3.7 ev. for $10\,Dq$.

In the second place, we have neglected many centre integrals besides those integrals corresponding to the interaction of the electron in one ligand with the dipole field due to other ligands, which are two centre integrals. The error originating from the neglect of latter integrals estimated to be smaller than 1 ev. and if we included this effect the discrepancy of the calculated value of $10\,Dq$ from the empirical one would become slightly larger. As to the error arising from the neglect of many centre integrals, we can not say anything definite at present.

In the third place, we have neglected $\varDelta V$ in the expression (3.13). In fact this change of the field is the first thing to be considered when we undertake an S. C. F. calculation in the MO method, although we are not sure at present how our result will be altered if we include this effect in our calculation.

Considering all these possible errors, it may be concluded that the calculated value of $10Dq$ which differs from the observed one by few electron volts is not very unsatisfactory, but further considerations on the change of the values of Slater integrals and the spin-orbit coupling constant $\lambda$ in complexes mentioned in §1 seem to show that the model on which our calculation is based is still an unsatisfactory one as is seen below.

Table VI.

| $\gamma$ | $(\phi_\gamma\|h\|\phi_\gamma)$ | $(\psi_\gamma\|h\|\psi_\gamma)$ | $(\phi_\gamma\|h\|\psi_\gamma)$ | | $\varepsilon_\gamma$ |
|---|---|---|---|---|---|
| $v$ | $-0.894$ | $-2.411$ | $-1.054$ | $-1.033$ | $-0.515$ |
| $\zeta$ | $-0.769$ | $-1.804$ | $-0.334$ | $-0.493$ | $-0.734$ |

The empirically determined reduction of $B$-value $(B=F_2-5F_4)$ is about 80% and that of $\lambda$ 60% for $[Cr(H_2O)_6]^{3+}$ complex ion. We will examine here if it is possible to explain this reduction with the model we adopted.

It is easily seen from the previous papers (I, II) that the $B$ value for Cr alum is given by

$$(3+\gamma)B'=K(\xi\zeta)\ , \quad \gamma=C'/B'=4\ , \qquad (5.1)$$

where $B'$ means the $B$-value in the complex ion. When we denote the absolute value of the decrement of $B$ by $\varDelta B$: $B'=B-\varDelta B$, the ratio of the reduction is approximately given by the following, as far as we neglect the terms of higher powers of $\delta_\gamma$, $\delta_\gamma{}^n (n>2)$;

$$1-\varDelta B/B=N_\zeta{}^{-2}(1-4\delta_\zeta A/B)\ , \qquad (5.2)$$

$$A=(\phi_\xi\psi_\zeta|r_{12}{}^{-1}|\phi_\zeta\phi_\xi)\ ,$$

$$B=4.2\times10^{-3}\ \ (920\ \mathrm{cm}^{-1})\ .$$

Numerical calculation shows that $A=0.515\times10^{-3}$ (Appendix III), which is too small to explain the observed reduction ratio, namely this value of $A$ leads to the result $1-\varDelta B/B=0.98$.

Nor can reduction of the spin orbit coupling constant $\lambda$ be explained, because, according to Owen[2)], $\lambda$ in complex is reduced from $\lambda$ in free ions by a factor $(N_\zeta N_v)^{-1}$ i.e. the product of squares of normalization constants of two orbitals, which is, however, larger than unity in our case.

The mixing ratio of $\phi_\gamma$ to $\psi_\gamma$ determined assuming purely ionic model thus fails to explain the change of $B$ and $\lambda$ values in complexes. We now ask what it would be if we determine the mixing ratio by variation principle adopting the same molecular Hartree-Fock field Hamiltonian $h$ (4.1) as was used here, namely if we made the simple MO calculation in which the change of field due to orbital deformation is neglected. (Although this procedure is meaningless in strict sense, because the field is that of ionic model, it may point the direction in which we should start.) The eigenvalues and the corresponding mixing ratio determined in this way are given below for each calculation with $Cr^{2+}$ and the extrapolated $Cr^{3+}$ radial $3d$ functions. In this calculation, all the values of the matrix elements and the mixing ratio of $2s$ and $2p\sigma$ functions in $\psi_v$ were set equal to the values employed in the former calculation.

Table VII. $\varphi_\gamma=\alpha\phi_\gamma+\beta\psi_\gamma$.

| | | $Cr^{2+}$ | | $Cr^{3+}$ | |
|---|---|---|---|---|---|
| $\gamma$ | | $\beta/\alpha$ | $\varepsilon_\gamma$ | $\beta/\alpha$ | $\varepsilon_\gamma$ |
| $v$ | antibonding orbit | $-0.454$ | $-0.501$ | $-0.409$ | $-0.598$ |
| | bonding orbit | 10.48 | $-2.424$ | 11.77 | $-2.381$ |
| $\zeta$ | antibonding orbit | $-0.025$ | $-0.734$ | $-0.015$ | $-0.746$ |
| | bonding orbit | $-9.324$ | $-1.804$ | $-11.37$ | $-1.804$ |

As shown above, this calculation also fails to explain the observed reduction of $B$ and $\lambda$ because $\alpha$ becomes larger than unity for antibonding states. The revel separation between two antibonding states $\varepsilon_v-\varepsilon_\zeta$ becomes slightly larger than the result of the former calculations. These circumstances together with those in the calculation with the ionic model seem to indicate that the field in which the electron moves is not well approximated by formula $Cr^{3+}-6H_2O$.

Another point to be considered is the model of water molecule. $O^{2-}$ model has several unfavourable features in order to obtain a good result with molecular treatments, namely the orbitals $2s$, $2p\sigma$, etc., are too diffuse (large overlap), therefore repel the electron in the $d$ orbital too strong, and as the result make the $e$ orbital energy too high. Moreover, the model gives the dipole moment of three times as large as that of a free water molecule, although these were favourable for Kleiner's calculation.

We tried here to improve Kleiner's result on the basis of ionic model taking the orbital overlap into consideration. But the result obtained is again negative exactly in the opposite sense to Kleiner's.

A possible way out of this difficulty seems to be found in the use of a more diffuse $3d$ function and take the change of field into account. The use of more diffuse $d$-orbital, although the effect of which we can express by means of a large hybridization between orbitals of metal and ligands to some extent, is not only supported by the reason that it would give the correct tendency to the value of $B$ and $\lambda$, but also by recent semi-empirical calculation by Kuroda and Itoh[13] which assumed Pauling's neutrality principle[14] from the beginning. Their calculation was based on the model $Cr\text{-}(H_2O^{1/2+})_6$ and the $d$ function used as an atomic orbital was that of neutral Cr. This calculation, although rather crude, could give a reasonable value of $\varepsilon_v-\varepsilon_\zeta$. Though we are not yet sure whether their and our results support the neutrality principle of Pauling, we may say that a more elaborate calculation with $3d$ function with variable orbital exponent and a variable mixing parameter is necessary and desired strongly in order to understand the electronic structure of the complex salts.

In conclusion we should like to express our sincere thanks to Prof. M. Kotani for his encouragement and valuable advices, and to Prof. K. Kambe of University of Electro-communication who kindly read and criticised the manuscript. We are also indebted to the members of Kotani Laboratory for their helpful discussions and support during this work.

## Appendix I

### Coulomb and Exchange Integrals $(\phi_\gamma|\sum V_i|\phi_\gamma)$

(a) $(\phi_\gamma|\sum V_i|\phi_\gamma)_{\text{coul.}}$ : Owing to the symmetry of $\sum V_i$, we have

$$(\phi_v|\sum V_i|\phi_v)=6Q+Q_0\,,\qquad (\phi_\zeta|\sum V_i|\phi_\zeta)=-4Q+Q_0\,, \tag{A.1}$$

where $Q$ is the field strength calculated by Kleiner and

$$\begin{aligned}Q_0&=\frac{6}{5}\sum_\gamma(\phi_\gamma|V_1|\phi_\gamma)\\ &=-48\Big(\int_0^{R_0}dr\,P_{3d}^2(r)/R_0+\int_{R_0}^\infty dr\,P_{3d}^2(r)/r\Big)-12\Big(\int_0^{-R'\cos\Theta'}dr\,P_{3d}^2(r)/(-R'\cos\Theta')+\int_{-R'\cos\Theta'}^\infty dr\,P_{3d}^2(r)/r\Big)\\ &\quad+60\Big(\int_0^{R_0}dr\,P_{3d}^2(r)/R_0+\int_{R_0}^\infty dr\,P_{3d}^2(r)/r\Big)+\int_0^\infty dr\,P_{3d}^2(r)(6/4\pi)\int d\omega\,V_c(r')\,.\end{aligned} \tag{A.2}$$

$R_0$, $R'$ and $\Theta'$ are defined in Fig. 1.

The first row on the right-hand side of (A2) is the contributions from the oxygen nuclei and the second row is those from the proton charges, while the third row represents those from the electrons of $O^{2-}$ under the assumption of complete screening plus the correction due to imperfect screening by $L$ shell electrons, where $r'$, $\omega$ are respectively the distance from the oxygen nuclei and the solid angle around it, and

$$-3V_c(r')=ae^{-t'}(t'^3+6t'^2+18t'+24)\,,\qquad t'=ar',\quad \tau=aR_0,\quad a=3.85\,. \tag{A.3}$$

In accordance with the above, the last integral is written in terms of the variables $t=ar$ and $t'$ after carrying out the integration with respect to the azimuthal angle and expressing the angle variable by $\tau$, $t$ and $t'$, thus

$$-(1/\tau)\int_0^\infty dt\,P_{3d}^2(t)/t\int_{|t-\tau|}^{t+\tau}dt'\,e^{-t'}(t'^3+6t'^2+18t'+24)\,,$$

or if we add part of the first term in the third row to this,

$$\begin{aligned}&12\left(\int_0^{R_0}drP_{3d}^2(r)/R_0+\int_{R_0}^\infty drP_{3d}^2(r)/r\right)+\int_0^\infty drP_{3d}^2(r)(6/4\pi)\int d\omega V_c(t')\\&=(1/\tau)\int_0^\infty dtP_{3d}^2(t)/t\int_{|t-\tau|}^{t+\tau}dt'V_0(t')\\&V_0(t')=6-e^{-t'}(t'^3+6t'^2+18t'^2+24)\,.\end{aligned} \tag{A.4}$$

The other integrals in (A1) are also rewritten in the variable $t$.

The integration with respect to $t$ was carried out by Simpson's rule taking the interval $\Delta t=0.8$ and from $t=0$ up to $t=28.8$, where $P_{3d}(t)$ becomes sufficiently small, while that with respect to $t'$ was done taking $\Delta t'=0.4$.

Thus 0.759 is obtained as the value of $Q_0$, which was unnecessary in Kleiner's calculation but is not in ours.

(b) $(\phi_\gamma|\sum V_i|\phi_\gamma)_{\text{exch.}}$: For the exchange terms we have

$$(\phi_v|\sum V_i|\phi_v)=3\sum_{u_0v_0}(u_0|V_3|u_0)_{\text{exch}}\qquad(\phi_\zeta|\sum V_i|\phi_\zeta)=2\sum_{\xi_0\eta_0\zeta_0}(\xi_0|V_3|\xi_0)_{\text{exch}} \tag{A.5}$$

The integrals on the right-hand sides of the above equalities can be written as suitable linear combinations of the following exchange integrals between $\phi(3dm|\mathbf{r})=(P_{3d}(r)/r)Y_{2m}(\theta,\varphi)$ and the oxygen atomic orbital at the position 3: $\phi_3(nlm|\mathbf{r}')=(P_{nl}(r')/r')Y_{lm}(\theta',\varphi')$ (The coordinate axes $x', y', z'$ at the point 3 are chosen in the direction of $x, y$ and $-z$ so that $\theta'=\pi-\theta$ and $\varphi'=(\pi/2)-\varphi$ .),

$$\int d\tau_1\,d\tau_2\phi^*(3dm|\mathbf{r}_1)\phi_3^*(nlm'|\mathbf{r}_2')(1/r_{12})\phi_3(nlm'|\mathbf{r}_1')\phi(3dm|\mathbf{r}_2) \tag{A.6}$$

which we write simply $(dm\,lm'||lm'\,dm)$, or $(dm, lm')$.

In order to calculate (A6) we expand the atomic orbitals $2p\sigma(l=1, m'=0)$, $2p\pi^\pm(l=1, m'=\pm1)$ and $2s(l=0)$ in spherical harmonics around the position of Cr nucleus in the following way

$$\begin{aligned}&\phi_3(2p\sigma|r')=\sum Y_{l0}(\theta\varphi)F_l(2p\sigma|r)/r\qquad \phi_3(2p\pi^\pm|r')=\sum Y_{l\mp1}(\theta\varphi)F_l(2p\pi|r)/r\\&\phi_3(2s|r')=\sum Y_{l0}(\theta\varphi)F'_l(2s|r)/r\end{aligned} \tag{A.7}$$

The functions $F$'s expressed in the variable $t$ defined in (A3) were calculated from the tables of $I_{l+1/2}$ and $K_{l+1/2}$[15,16] and tabulated with the intterval of $\Delta t=0.2$ up to 14.4.

(A7) carried into (A6) gives

$$(dm, lm')=\sum_\alpha\int dr_1dr_2P_{3d}(r_1)A_\alpha(2m, lm'|r_1)P_{3d}(r_2)A_\alpha(2m, lm'|r_2)(r_<^\alpha/r_>^{\alpha+1})\,, \tag{A.8}$$

where $r_<, r_>$ are respectively the smaller and the larger of $r_1, r_2$, and

$$\begin{aligned}&A_\alpha(2mp\sigma|r)=\sum F_l(2p\sigma|r)(2m|C_\mu^{(\alpha)}|lo)\,,^{17)}\qquad A_\alpha(2mp\pi^\pm|r)=\sum F_l(2p\pi|r)(2m|C_\mu^{(\alpha)}|l\mp1)\,,\\&A_\alpha(2m\,s|r)=\sum F_l(2s|r)(2m|C_\mu^{(\alpha)}|lo)\,.\end{aligned}$$

These were calculated easily from the tables of F's and tabulated as far as $\alpha=6$.

The double integration were carried out first with the interval $\Delta t=0.2$ and then with $\Delta t=0.4$ by Simpson's rule.

The convergence with respect to $\alpha$ is not always rapid, but those integrals which converge slowly seem to be very small so that they would not cause serious errors in the result, if we neglect terms with higher $\alpha$. The behavior of the terms in the series (A8) with increasing $\alpha$ is shown in Table A1.

Table A1.

| $\alpha$ | $(d\sigma, p\sigma)$ | $(d\pi, p\sigma)$ | $(d\delta, p\sigma)$ |
|---|---|---|---|
| 0 | $836.8\times10^{-5}$ | | |
| 1 | 628 | 73.6 | |
| 2 | 464 | 100.0 | 15.2 |
| 3 | 192 | 54.4 | 8.0 |
| 4 | 78.4 | 22.4 | 3.2 |
| 5 | 30.4 | 8.0 | |
| 6 | 12.0 | 3.2 | |
| | 2183.2 | 260.8 | 26.4 |

| $\alpha$ | $(d\sigma, p\pi^-)$ | $(d\pi, p\pi^-)$ | $(d\delta, p\pi^-)$ |
|---|---|---|---|
| 0 | $\times10^{-5}$ | 265.6 | |
| 1 | 19.2 | 131.2 | 8.0 |
| 2 | 43.2 | 43.2 | 5.6 |
| 3 | 54.4 | 9.6 | 2.4 |
| 4 | 48.0 | 1.6 | |
| 5 | 34.4 | | |
| 6 | 21.6 | | |
| | 222.4 | 451.1 | 16.0 |

| $\alpha$ | $(d\pi, p\pi^+)$ | $(d\delta, p\pi^+)$ |
|---|---|---|
| 0 | $\times10^{-5}$ | |
| 1 | | |
| 2 | 5.6 | |
| 3 | 12.0 | 0.8 |
| 4 | 12.0 | 0.8 |
| 5 | 8.8 | 0.8 |
| 6 | 5.6 | 0.8 |
| | 43.2 | 3.2 |

| $\alpha$ | $(d\sigma, s)$ | $(d\pi, s)$ | $(d\delta, s)$ |
|---|---|---|---|
| 0 | $796.0\times10^{-5}$ | | |
| 1 | 533.6 | 46.4 | |
| 2 | 318.4 | 62.4 | 7.2 |
| 3 | 151.2 | 38.4 | 4.8 |
| 4 | 61.6 | 17.6 | 1.6 |
| 5 | 23.2 | 7.2 | 0.8 |
| 6 | 8.0 | 2.4 | 0.0 |
| | 1892.2 | 174.4 | 14.4 |

The calculated values of the integrals are given in Table A2.

Table A2.

$(d\delta, p\sigma) = 2.6\times10^{-4}$

$(d\pi, p\sigma) = 26.1$

$(d\sigma, p\sigma) = 218.3$

$(d\delta, p\pi^+) = 0.4\times10^{-4}$

$(d\pi, p\pi^+) = 4.3$

$(d\sigma, p\pi^+) = 22.2$

$(d\delta, p\pi) = 1.6\times10^{-4}$

$(d\pi, p\pi) = 45.1$

$(d\sigma, p\pi^-) = 22.2$

$(d\delta, s) = 1.4\times10^{-4}$

$(d\pi, s) = 17.5$

$(d\sigma, s) = 189.2$

Collecting these appropriately we have finally

$$\sum_{u_0 v_0} (u_0|\sum V_i|u_0)_{\text{exch}} = 458.1\times10^{-4} \qquad \sum_{\xi_0\eta_0\zeta_0} (\xi_0|\sum V_i|\xi_0)_{\text{exch}} = 192.0\times10^{-4}$$

## Appendix II

### Coulomb and Exchange Integrals $(\phi_\gamma|\sum V_i|\phi_\gamma)$

If many center integrals are neglected, we have

$$(\phi_v|\sum V_i|\phi_v) = 2\mu_s(\phi_v|V_1|s_1) + 2\mu_\sigma(\phi_v|V_1|\sigma_1), \qquad (\phi_\zeta|\sum V_i|\phi_\zeta) = 2(\phi_\zeta|V_1|y_1). \tag{A.10}$$

(a) $(\phi_\gamma|V_1(\mathrm{O}^{2-})|\varphi_{1\alpha}{}^{c})_{\text{coul}}$ :

We take the co-ordinate axes $x', y', z'(r', \theta', \varphi')$ at the position 1 in the direction of $z, y, -x$ of Fig. 2 and take the axes $x, y, z\,(r, \theta, \varphi)$ newly in the direction of $y, z, x$ of Fig. 2, so that $\theta' = \pi - \theta$ and $\varphi' = \pi/2 - \varphi$.

The integration with respect to $\varphi$ can be easily carried out and then expressing the angle variable by $\tau$, $t$ and $t'$ as in App. I we obtain

$$(\phi_v|V_1(\mathrm{O}^{2-})|s_1) = (\sqrt{15\pi}\, N_{2s}/48a^2\tau^3)\int_0^\infty dt P_{3d}(t) \sum A_{sm}(t) F_m(t)/t^2\,,$$

$$(\phi_v|V_1(\mathrm{O}^{2-})|\sigma_1) = (\sqrt{5\pi}\, N_{2s}/32a^2\tau^3)\int_0^\infty dt P_{3d}(t) \sum A_{\sigma m}(t) F_m(t)/t^2\,,$$

$$(\phi_\zeta|V_1(\mathrm{O}^{2-})|y_1) = (\sqrt{5\pi}\, N_{2s}/16a^2\tau^3)\int_0^\infty dt P_{3d}(t) \sum A_{\pi m}(t) F_{\pi m}(t)/t^2\,, \tag{A.11}$$

where

$$N_{2s}=\sqrt{a^5/96\pi}\ , \qquad F_m(t)=\int_{|t-\tau|}^{t+\tau} dt' t'^m e^{-(t'/2)}V_0(t')\ ,$$

$$\begin{cases} A_{s1}=(\tau^2-t^2)^2+2(\tau^2+t^2)^2\ , \\ -A_{s3}/6=\tau^2+t^2\ , \\ A_{s5}=1\ , \end{cases} \qquad \begin{cases} A_{\sigma 0}=(\tau^2-t^2)A_{s1}\ , \\ A_{\sigma 2}=(\tau^2-t^2)^2+2(\tau^2+t^2)^2-6(\tau^2-t^2)(\tau^2+t^2)\ , \\ -A_{\sigma 4}/3=2(\tau^2+t^2)-(\tau^2-t^2)\ , \\ A_{\sigma 6}/3=1\ , \end{cases}$$

$$\begin{cases} -A_{\pi 0}=(\tau^2+t^2)(\tau^2-t^2)^2\ , \\ A_{\pi 2}=A_{s1}\ , \\ A_{\pi 4}=A_{s3}/2\ , \\ A_{\pi 8}=1\ . \end{cases}$$

The numerical integration was done in the same way as described in Appendix I. Although all the numerical tables used for the integration are limited in the parameter range from 0 to 28.8, they converge nicely in its range and the magnitude of the resulting error will be negligible.

As stated in § 4, suprisingly large discrepancy arises whether we use the $2s$ wave function with or without node, because of the large contribution of the nuclear field near the oxygen nucleus, while the effect arising from the change of $V_0$ due to the node is not so serious for the result. The $2s$ radial function with node is given by

$$(2s \text{ with node})=1.016(2s \text{ without node})-7.701\ \exp(-7.7r). \tag{A.12}$$

As far as we adopt the same form of $V_0$ calculated with the nodelass $2s$ function, $(\phi_v|V_1(\mathrm{O}^{2-})|e^{-7.7r})$ which now appears can be calculated, using (A11) with suitable modification of the numerical factor, if we replace $F_m(t)$ in the expression of (A11) by $F_{m-1}'(t)$, which is defined as

$$F_m'(t)=\int_{|t-\tau|}^{t+\tau} dt' t'^m e^{-t'} V_0(t'). \tag{A.13}$$

(b) $(\phi_\gamma|V_1(\mathrm{O}^{2-})|\varphi_{1\alpha}{}^c)_{\mathrm{exch}}$ :

This matrix element can be written as

$$(\phi_\gamma|V_1(\mathrm{O}^{2-})|\varphi_{1\alpha}{}^c)_{\mathrm{exch}}=\sum_{\beta=2s,2p\sigma,2p\pi}\int d\tau_1 d\tau_2 \phi_\gamma(1)\varphi_{1\beta}{}^c(2)(1/r_{12})\varphi_{1\beta}{}^c(1)\varphi_{1\alpha}{}^c(2)\ , \tag{A.14}$$

The results of the integration with respect to the coordinate of the electron 2 are already given by Barnett and Coulson[16] and therefore, using their results, $(\phi_\gamma|V_1(\mathrm{O}^{2-})|\varphi_{1\alpha}{}^c)_{\mathrm{exch}}$ are written in the form of $(\phi_\gamma|V_{\mathrm{exch}}|\varphi_{1\alpha}{}^c)$ as follows;

$$\begin{aligned} &(\phi_v|V_1|s)_{\mathrm{exch}}=(\phi_v|V_{\mathrm{I}}|s_1)/12\ , \qquad (\phi_v|V_1|\sigma_1)_{\mathrm{exch}}=(\phi_v|V_{\mathrm{II}}|\sigma_1)/12\ , \\ &(\phi_\zeta|V_1|y_1)_{\mathrm{exch}}=(\phi_\zeta|V_{\mathrm{II}}|y_1)/12\ , \end{aligned} \tag{A.15}$$

where $V_{\mathrm{I}}$ and $V_{\mathrm{II}}$ are functions of $t'$ and are given by

$$\begin{aligned} &t^2V_{\mathrm{I}}(t)=tj_3(t)+3j_5(t)\ , && j_5(t)=40-(40+40t+20t^2+6t^3+t^4)e^{-t}\ , \\ &t^3V_{\mathrm{II}}(t)=tj_5(t)+3j_7(t)+6j_3(t)\ , && j_7(t)=144-(144t+72t^2+24t^3+6t^4+t^5)e^{-t}\ , \\ &j_3(t)=24-(24+18t+6t^2+t^3)e^{-t}=18+V_0(t)\ , && j_8(t)=-24+4t^2+(24+24t+8t^2+t^3)e^{-t}\ . \end{aligned}$$

With the same procedure taken in Appendix II (a), we get the following formulae for the numerical calculation;

$$\begin{aligned} &(\phi_v|V_1(\mathrm{O}^{2-})|s_1)_{\mathrm{exch}}=(\sqrt{15\pi}\,N_{2s}/192\,a^2\tau^3)\int_0^\infty dtP_{3d}(t)\sum A_{sm+1}(t)G_m\mathrm{I}(t)\ , \\ &(\phi_v|V_1(\mathrm{O}^{2-})|\sigma_1)_{\mathrm{exch}}=(\sqrt{5\pi}\,N_{2s}/128\,a^2\tau^4)\int_0^\infty dtP_{3d}(t)\sum A_{\sigma m+2}(t)G_m\mathrm{II}(t)\ , \\ &(\phi_\zeta|V_1(\mathrm{G}^{2-})|y_1)_{\mathrm{exch}}=(\sqrt{5\pi}\,N_{2s}/64\,a^2\tau^4)\int_0^\infty dtP_{3d}(t)\sum A_{\pi m+2}(t)G_m\mathrm{II}(t)\ , \end{aligned} \tag{A.17}$$

where

$$G_m\mathrm{I}(t)=\int_{|t-\tau|}^{t+\tau} dt' t'^m e^{-(t'/2)}V_{\mathrm{I}}(t'), \qquad G_m\mathrm{II}(t)=\int_{|t-\tau|}^{t+\tau} dt' t'^m e^{-(t'/2)}V_{\mathrm{II}}(t')\ .$$

Although the effect of a node in the $2s$ wave function is not serious in this case, because the exchange integral does not include the nuclear field of the oxygen, we calculated $(\phi_v|V_1(\mathrm{O}^{2-})\,|\,2s_{1\ \mathrm{w,\ node}})_{\mathrm{exch}}$ exactly in the same way as described in Appendix II (a). The effect due to the change of $V_{\mathrm{I}}(t')$ from that calculated with the nodeless $2s$ function was estimated to be negligible so that this was also ignored.

(c) Evaluation of $(\phi_\gamma|V_{(\mathrm{proton})}|\psi_\gamma)$.

We expand $V_{1(\mathrm{proton})}$ around the position of the metal nucleus, then

$$V_{1(\mathrm{proton})}=2\sum_{k=0}^{\infty}\{r^k/R^{k+1}\ \text{or}\ R^k/r^{k+1}\}P_k(\cos\theta)A_k\,, \tag{A.18}$$

$$A_k=P_k(-\cos\Theta),\quad \cos\Theta=0.9587,\quad R=5.04,$$

where $r, \theta$ are referred to the coordinates newly adopted in Appendix II (a), and $R$, $\Theta$ are shown in Fig. 1.

Using the expansion formulae of $2s, 2p\sigma$ and $2p\pi$ orbitals around the same centre as described in Appendix I (b), we get

$$(\Phi_v|V_{1(\mathrm{prot.})}|s_1)=\sqrt{3}\sum A_kC_{kl}^0\{F_{kl}(2s)/r^{k+1}+F_{kl}'(2s)R^k\}\,,$$

$$(\phi|V_{1(\mathrm{prot.})}|\sigma_1)=\sqrt{3}\sum A_kC_{kl}^0\{F_{kl}(2p\sigma)/R^{k+1}+F_{kl}'(2p\sigma)R^k\}\,,$$

$$(\phi\zeta|V_{1(\mathrm{prot.})}|y_1)=2\sum A_kC_{kl}^1\{F_{kl}(2p\pi)/R^{k+1}+F_{kl}'(2p\pi)R^k\}\,,$$

$$F_{kl}(\alpha)=\int_0^R drP_{3d}(r)F_l(\alpha|r)\,,$$

$$F'_{kl}(\alpha)=\int_R^\infty pr\rho(r)F_l(\alpha|r)\,,$$

where $C_{kl}^m$ is $C^k(2m;lm)$ of Condon and Shortley.

Each term in the sum is numerically calculated up to $k=6$, where the convergence of the sum seems good in all cases (Table A3).

Table A 3.

| $k$ | $(\Phi_v\|V_{1(\mathrm{prot.})}\|s_1)$ | $(\Phi_v\|V_{1(\mathrm{prot.})}\|\sigma_1)$ | $(\Phi\zeta\|V_{1(\mathrm{prot.})}\|y_1)$ |
|---|---|---|---|
| 0 | $570.4\times10^{-4}$ | $501.4\times10^{-4}$ | $383.2\times10^{-4}$ |
| 1 | −316.1 | −213.3 | −189.5 |
| 2 | 170.7 | 65.1 | 81.9 |
| 3 | −83.5 | − 12.1 | − 30.1 |
| 4 | 38.6 | − 6.0 | 8.5 |
| 5 | −16.2 | 7.7 | − 1.2 |
| 6 | 5.8 | − 4.8 | − 0.5 |
|  | 369.7 | 338.0 | 252.3 |

## Appendix III

### Deviation from the Atomic *B*-Value, $\Delta B$.

From (5.1), the magnitude of the deviation $\Delta B$ can be obtained using the equation

$$7N\zeta^2\Delta B=7B(N\zeta^2-1)+4\delta\zeta(\xi_0\zeta_L||\zeta_0\xi_0)-2\delta\zeta^2\{(\xi_0\zeta_L||\zeta_L\xi_0)+(\xi_0\zeta_L||\zeta_0\xi_L)+(\xi_0\zeta_0||\zeta_L\xi_L)\}$$
$$+4\delta\zeta^3(\xi_0\zeta_L||\zeta_L\xi_L)-\delta\zeta^4(\xi_L\zeta_L||\zeta_L\xi_L)\,, \tag{A.20}$$

where we have used the abbreviation

$$\xi_L=\phi_\xi=1/2(z_1-z_4+x_3-x_6)\,,\qquad \zeta_L=\phi_\zeta=1/2(x_2-x_5+y_1-y_4)\,.$$

If $\delta\zeta$ is small, (5.2) is obtained only retaining the first two terms of (A20). Further, using the ligand orbital at the position 3, we obtain

$$(\xi_0\zeta_L||\zeta_0\xi_0)=(\zeta_0x_3||\xi_0\zeta_0)+(\eta_0x_3||\xi_0\eta_0)\,, \tag{A.21}$$

and

$$(\zeta_0x_3||\xi_0\zeta_0)=i/2\{(d\delta p\pi^-||d\pi+d\delta)-(d\delta p\pi^+||d\pi-d\delta)\}\,,$$
$$(\eta_0x_3||\xi_0\eta_0)=-i/2(d\pi p\pi^+||d\pi-d\pi)\,, \tag{A.22}$$

From (A.7), $(dm'p\pi^\pm||dm''dm)$ reduces to

$$(dm'p\pi^\pm||dm''dm)=+i\sum_k(2m'|C_\mu^{(k)}|2m'')\int_0^\infty dr_2P_{3d}^2(r_1)\int_0^\infty dr_1P_{3d}(r_2)A_k(2m2p\pi^\pm|r_2)r_<^k/r_>^{k+1}\,, \tag{A.23}$$

which vanishes unless $m'-m''=m\pm1$.

By means of (A23) and the numerical tables of A's, we obtain

$$(\zeta_0 x_3||\xi_0\zeta_0)=0.439\times10^{-4} \qquad (\eta_0 x_3||\xi_0\eta_0)=4.77\times10^{-4}$$

## Errata of Part I.

i). P. 758 Table I.
$1/\sqrt{1}$ of $(F_1\beta F_1\beta|F_1F_1Ev)$ should be read as $1/\sqrt{2}$.

ii). P. 760 Table III.
$-12Dq-6B+3B$ of the column $d\varepsilon^3(^2E)d\gamma^4$ of $^2E$ should be read as $-12Dq-6B+3C$.

iii). P. 761 Table III.
$^4F_4$ at the top of the first line should be read as $^4F_1$.

iv). p. 762 Table III.
In the table of the energy matrix $^1F_1$, $d\varepsilon^3(^2F_2)d\gamma^3$, $d\varepsilon^4(^1F_2)d\gamma^2(^1E)$ and $d\varepsilon^5d\gamma$ should be shifted so as to be above $5\sqrt{3}\,B$, $3B$ and $\sqrt{6}$ B respectively.

## Errata of Part II.

i). P. 771. The 12th line: "The line (though..." should be read as "The lines of $[Fe(H_2O)_6]^{3+}$ (though...".

---

## References

1) Y. Tanabe and S. Sugano: Journ. Phys. Soc. Japan. **9** (1954) 753, 766 cited as I, II respecvely.
2) J. Owen: Proc. Roy. Soc: **227A** (1955) 183.
3) J. H. Van Vleck: J. Chem. Chys. **7** (1939) 72.
4) D. Polder: Physica **IX** (1942) 709.
5) W. H. Kleiner: J. Chem. Phys. **20** (1952) 1784.
6) H. A. Bethe: Ann. d. Phys. **3** (1929) 133.
7) R. L. Mooney: Rhys. Rev. **55** (1939) 557.
8) A. Porter: Manchester Memoirs, **LXXIX** (1934–35) 75.
9) D. R. Hartree, W. Hartree and B. Swirles: Phil. Trans. Roy. Soc. **238A** (1939) 229.
10) R. S. Mulliken: J. Chem. Phys. **3** (1935) 506.
11) R. S. Mulliken: Journ. Phys. Chem. **56** (1952) 295.
12) M. Wolfsberg and L. Helmholtz: J. Chem. Chem. Phys. **20** (1952) 837.
13) Y. Kuroda and K. Itoh: Nippon Kagaku Kaishi (in Japanese). **76** (1955) 545, 762, 766, 934.
14) L. Pauling: Report of International Conference, Paris, 1948, p. 2.
15) C. W. Jones: A short Table for the Bessel Functions $I_{l+1/2}(x)$, $2/\pi K_{l+1/2}(x)$, Cambridge University Press, 1952.
16) M. P. Barnett and C. A. Coulson: Phil. Trans. Roy. Soc. London. **243** (1951) 221.
17) G. Racah: Phys. Rev. **62** (1942) 438.

JOURNAL OF THE PHYSICAL SOCIETY OF JAPAN Vol. 11, No. 8, AUGUST, 1956

# On the Hypersonic Viscous Flow Past Slender Bodies of Revolution

By Michiru YASUHARA

*Institute of Science and Technology, University of Tokyo*

(Received March 12, 1956)

A similar solution of the hypersonic viscous flow past slender bodies of revolution is deduced for a special case when the radial coordinate of the body surface at section $x$ is proportional to $x^{3/4}$, where the radial coordinote have the comparable order value with the thickness of the boundary layer. Here, "similar" is used in the direct meaning that distributions in the boundary layer keep the similar form lengthwise. Calculations are accomplished for the region of strong interaction between the boundary layer and the shock wave. From several calculations it may be expected that if the thickness of the body becomes small, the thickness of the layer in which the longitudinal velocity component $u$ is rapidly decreased also becomes small, and in the major part of the boundary layer, only the normal component $v$ is increased. Further if the thickness of the body is increased, then, the height of the shock wave, the pressure on the wall, and the shear stress at the wall are also increased while the boundary layer thickness is decreased. The nose region is excluded by the reason that the ordinary boundary layer theory will be invalid there.

## § 1. Introduction

Recently, many studies have been made on thehypersonic flow over two dimensional slender bodies. From these studies and experiments, it has been suggested that, the flow will be affected so much by the retarding action caused by the boundary layer, that viscous effect cannot be neglected. The shock wave grown from or before the leading edge of the body will become close to the body surface and have a great influence on the flow patterns between itself and the body especially in the neighbourhood of the leading edge. Even in the case of a flat plate, the flow direction near the plate is changed by the viscous effect and a shock wave is formed from or before the leading edge. It was suggested first by Tsien and further confirmed by Stewartson¹⁾ that the flow field between the shock wave and the body can be divided into two regions as shown in Fig. 1.

In the region (A) in contact with the plane of the flate plate, viscous effects are important, and the pressure change across it is so small that the boundary layer theory may be used to describe the flow. In this region the gas is extremely hot in comparison with the uniform flow before the shock wave and has small density. Between the shock wave and (A) there is a region (B) in which the effect of viscosity is small or negligible but large entropy changes occur near the contact surface with (A). This layer is called "inviscid layer".

The flow in the region far behind the leading edge where the shock wave has decayed and interaction between the shock wave and the boundary layer is weak was studied by Lees and Probstein²⁾. The region in which the interaction is strong was first attacked by Shen, Li and Nagamatsu³⁾, assuming that the shock wave coincides with the outer edge of (A), and they found that there is a similar solution throughout (A). Stewartson¹⁾ has discussed also the problem more accurately considering the existence of (B) to avoid the contradiction with physical phenomena and shown that there is a similar solution throughout (A) and (B) without inconsistency.

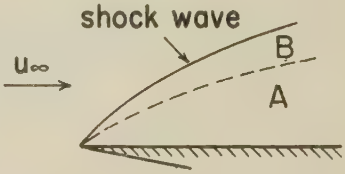

Fig. 1. Hypersonic Flow on the Flat Plate.

Recently, corresponding problems for three-dimensional slender bodies have been considered with many interests from the practical needs of the aeronautical engineering. It is easily shown by using Mangler's[4] transformation that the boundary layer induced on the axi-symmetric body is equivalent to the boundary layer on a flat plate provided only that the thickness of the layer is small compared with the radius of the body. But there is a real possibility that such is not the case.

For such regions in the incompressible flow, Seban and Bond[5], Kelly[6], Stewartson[7], and Glauert and Lighthill[8], have calculated the boundary layer over slender circular cylinder, and Wuest[9] has given asymptotic solutions over cylindrical bodies with uniform suction for several cases of the body form.

For the flow of the compressible fluid, there are only few studies, especially for the case where the thickness of the body is comparable with that of the boundary layer. It is easy to consider, as one of calculating method for such cases, the perturbation technique starting from the solution by Mangler's transformation, which however, perhaps may be restricted within the range of order one of the ratio of boundary layer to body thickness.

The purpose of this paper is to give a contribution to the investigation of the effect of slenderness of the body with axial symmetry on the flow pattern at hypersonic flights, especially for the region of strong interaction between the boundary layer and the shock wave assumed to be attached to the nose of the body. Then investigation given in the present paper is an extension of Stewartson's idea to the axi-symmetric flow.

## § 2. Equations of Motion and Solutions

### 2–1. General Equations of Motion

Let us consider a slender body of revolution occupying the positive half of the $x$-axis, the fluid flowing along it with uniform velocity $u_\infty$ at infinity, and a shock wave assumed to be attached to the nose of the body, and the boundary layer assumed to have comparable thickness with that of the body, as shown in Fig.2. Then, using cylindrical coordinates $(x,r)$ where $r$ represents the radial distance from $x$-axis, consider the following equations of motion between the shock wave and the body.

$$\frac{\partial(\rho u)}{\partial x}+\frac{1}{r}\frac{\partial(\rho v r)}{\partial r}=0\,, \qquad (1)$$

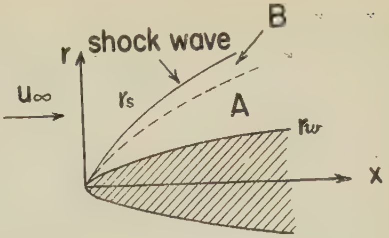

Fig. 2. Hypersonic Flow on the Slender Bodies of Revolution.

$$\rho u\frac{\partial u}{\partial x}+\rho v\frac{\partial u}{\partial r}=-\frac{\partial p}{\partial x}+\frac{1}{r}\frac{\partial}{\partial r}\left(\mu r\frac{\partial u}{\partial r}\right), \qquad (2)$$

$$\rho u\frac{\partial v}{\partial x}+\rho v\frac{\partial v}{\partial r}=-\frac{\partial p}{\partial r}\,, \qquad (3)$$

$$\rho u\frac{\partial(C_pT)}{\partial x}+\rho v\frac{\partial(C_pT)}{\partial r}-u\frac{\partial p}{\partial x}-v\frac{\partial p}{\partial r}=\frac{1}{r}\frac{\partial}{\partial r}\left\{\lambda r\frac{\partial(C_pT)}{\partial r}\right\}+\mu\left(\frac{\partial u}{\partial r}\right)^2, \qquad (4)$$

$$\frac{p}{p_\infty}=\frac{\rho}{\rho_\infty}\cdot\frac{T}{T_\infty}\,, \qquad (5)$$

where $P_\infty$, $\rho_\infty$, and $T_\infty$ represent quantities at infinity. Following the model previously stated, two regions (A) and (B) are considered. Then, Eq. (1) is valid everywhere, Eq. (2) is valid in the boundary layer (A) and in the inviscid layer (B), Eq. (3) is valid in the inviscid layer, and effects of momentum change of $r$-component on $p$ must be negligible in the boundary layer, Eq. (4) is valid in both regions and Eq. (5) is valid everywhere. There are many terms neglected in these equations, but it may be shown that in both regime their effects are negligible if $r_s \ll x$, where

$$r_s=r_s(x) \qquad (6)$$

expresses the equation of the position of the shock wave. Throughout the present paper, suffix $\infty$, $s$, and $w$ represent quantities at infinity, just behind the shock wave, and on the wall, respectively, and assumptions are made that,

$$C_p=\text{const.},\quad P_r=1\quad \frac{\mu}{\mu_\infty}=C\cdot\frac{T}{T_\infty} \qquad (7)$$

Where $C$ represents Chapman-Rubesin's coefficient[10].

If it is assumed that, just behind the shock wave Rankine-Hugoniot's conditions are satisfied, then next relations can be obtained as the boundary conditions along the shock wave.

$$u_s-u_\infty=u_\infty \mathrm{O}(dr_s/dx)^2$$

$$v_s=\frac{2u_\infty}{(\gamma+1)}\frac{dr_s}{dx}\left\{1-\frac{1}{M_\infty{}^2(dr_s/dx)^2}\right\}$$

$$\frac{p_s}{p_\infty}=\frac{2\gamma}{(\gamma+1)}M_\infty{}^2\left(\frac{dr_s}{dx}\right)^2-\frac{\gamma-1}{\gamma+1}$$

$$\frac{\rho_s}{\rho_\infty}=\frac{(\gamma+1)M_\infty{}^2(dr_s/dx)^2}{(\gamma-1)M_\infty{}^2(dr_s/dx)^2+2} \tag{8}$$

under the condition

$$dr_s/dx \ll 1$$

While on the body surface, velocity must vanish and the surface is assumed to be thermally insulated;

$$u=0\,,\quad v=0\,,\quad \frac{\partial T}{\partial y}=0 \tag{9}$$

at $r=r_w$, $x>0$, where $y$ represents the normal distance from the surface. Then the equations (1) to (5) have a simple integral

$$\frac{T}{T_\infty}=1+\frac{(\gamma-1)}{2a_\infty{}^2}(u_\infty{}^2-u^2-v^2) \tag{10}$$

Where "$a$" represents the velocity of sound.

Further if a stream function $\psi$ is defined by

$$\rho_\infty\frac{\partial\psi}{\partial r}=\rho ur \tag{11}$$

$$\rho_\infty\frac{\partial\psi}{\partial x}=-\rho vr \tag{12}$$

Eqs. (1)~(4) are transformed into the form with independent variables $x$ and $\psi$.

$$\frac{\partial v}{\partial x}=-\frac{r}{\rho_\infty}\frac{\partial p}{\partial\psi} \tag{13}$$

$$\frac{\rho}{2}\frac{\partial}{\partial x}(u^2+v^2)=-\frac{\partial p}{\partial x}+\frac{\rho u}{\rho_\infty}\frac{\partial}{\partial\psi}\left(\frac{\mu\rho ur^2}{\rho_\infty}\frac{\partial u}{\partial\psi}\right) \tag{14}$$

$$\frac{\partial}{\partial\psi}\left(\frac{v}{u}\right)=\frac{\partial}{\partial x}\left(\frac{\rho_\infty}{\rho ur}\right) \tag{15}$$

$$\rho u\frac{\partial(C_pT)}{\partial x}-u\frac{\partial p}{\partial x}=\frac{\rho u}{\rho_\infty}\frac{\partial}{\partial\psi}\left\{\frac{\mu\rho ur^2}{\rho_\infty}\frac{\partial(C_pT)}{\partial\psi}\right\}+\mu\left(\frac{\rho ur}{\rho_\infty}\frac{\partial u}{\partial\psi}\right)^2 \tag{16}$$

It is noted that $\psi$ is a continuous function of $x$ and $r$, and equals to $u_\infty r^2/2$ in the undisturbed fluid, which is easily known from Eq. (11).

In terms of the new coordinates $(x, \psi)$.

$$u=0\,,\quad v=0\,,\quad \frac{\partial T}{\partial\psi}=0 \tag{17}$$

at $\psi=0$ for all $x$, and just behind the shock wave, Eq. (8) must be satisfied.

### 2-2. Inviscid Layer

In the present paper, attention is paid for the nature of the flow only when $M_\infty=u_\infty{}'a_\infty$ is large, and it is assumed that the shock wave is thin and the conditions on it are given by Eqs. (8). These relations are now used as the boundary conditions to specify the flow in the inviscid layer.

The fundamental equations are given by putting $\mu=0$ in Eqs. (13)–(16), where $r$ should be considered as a dependent variable. From the last two of these it follows that

$$\frac{p}{p_\infty}=S(\psi)\cdot\left(\frac{\rho}{\rho_\infty}\right)^\gamma, \tag{18}$$

where $S$ is related in a simple way to the entropy, and may be determined from the conditions at the shock wave, just behind which $\psi=u_\infty r_\infty{}^2/2$ since $\psi$ is continuous though the shock wave exists. From the definition of $\psi$, it is easily known

$$\frac{v}{u}=\left(\frac{\partial r}{\partial x}\right)_\psi, \tag{19}$$

therefore Eqs. (13) and (15) become, respectively,

$$\frac{\partial}{\partial x}\left(u\frac{\partial r}{\partial x}\right)=-\frac{r}{\rho_\infty}\frac{\partial p}{\partial\psi},$$

$$\frac{\partial r}{\partial\psi}=\frac{\rho_\infty}{\rho ur}. \tag{20}$$

Just behind the shock wave, it is known that $u$-$u_\infty$ may be neglected in comparison with $u_\infty$ as seen from the first of Eqs. (8), and in Eqs. (20) $u$ may be replaced by $u_\infty$. After introducing Eq. (18) and $u=u_\infty$ into Eq. (20), next relations are obtained:

$$u_\infty\frac{\partial^2 r}{\partial x^2}=-\frac{r}{\rho_\infty}\frac{\partial p}{\partial\psi},$$

$$u_\infty r\frac{\partial r}{\partial\psi}=\left\{S(\psi)\cdot\frac{p_\infty}{p}\right\}^{1/\gamma}, \tag{21}$$

with the boundary conditions

$$r=r_s,\quad p=p_s\quad \text{at}\quad \psi=\frac{u_\infty r_s{}^2}{2}. \tag{22}$$

If a new variable $\eta$ defined by

$$\eta=\frac{2\psi}{u_\infty r_s{}^2(x)} \tag{23}$$

is introduced instead of $\psi$, then $\eta=1$ at the shock wave and $\eta=0$ when $\psi=0$. Further $R(\eta, x)$ and $P(\eta, x)$ are introduced by

$$r=r_s(x)R(\eta, x)$$

$$\frac{p}{p_\infty}=\frac{2\gamma M_\infty{}^2}{(\gamma+1)}\left(\frac{dr_s}{dx}\right)^2 P(\eta, x) \tag{24}$$

In terms of $R$ and $P$, it is easily known that Eq. (21) have similar solutions when $r_s \sim x^n$ or $\sim e^{\alpha x}$ in the meaning that the distributions are derivable from ordinary differential equations.

Next, the appropriate form of $R$ may be determined by the matching procedure, which will be presented in 2–3, from which the equation of the shock wave is assumed to be

$$r_s=\vartheta x^{3/4}(1+\alpha x^{1/2}+\cdots) \qquad (25)^*$$

Above expression corresponds only to the case when $r_w \sim x^{3/4}(1+\beta x^{1/2}+\cdots)$ as shown in 2–3.

Then, using Eqs. (8), $S$ can be expressed in terms of $\psi$ by

$$S(\psi)=\frac{9\gamma M_\infty{}^2\vartheta^2}{8(r+1)}\left(\frac{\gamma-1}{r+1}\right)^\gamma\left(\frac{2\psi}{u_\infty\vartheta^2}\right)^{-1/3}$$

$$\times\left[1+\left(\frac{2\psi}{u_\infty\vartheta^2}\right)^{1/3}\left\{4\alpha+\frac{8(3\gamma-1)(\gamma+1)}{9\gamma(\gamma-1)M_\infty{}^2\vartheta^2}\right\}+\cdots\right] \tag{26}$$

or in terms of $\eta$ and $x$,

$$\left\{\frac{(\gamma+1)S}{2\gamma M_\infty{}^2(dr_s/dx)^2}\right\}^{1/\gamma}=\frac{(\gamma-1)}{(r+1)}\eta^{-1/3\gamma}\{1+O(x^{1/2})\} \tag{27}$$

Expanding $R$ and $P$ in power series of $x^{1/2}$, i.e.

$$R(\eta, x)=R_0(\eta)+O(x^{1/2})$$

$$P(\eta, x)=P_0(\eta)+O(x^{1/2}) \tag{28}$$

and introducing into (24) and (21), we obtain the equations to determine $R_0$ and $P_0$ as follows,

$$\frac{3}{(\gamma+1)}R_0\frac{dP_0}{d\eta}+2\eta\frac{dR_0}{d\eta}+3\eta^2\frac{d^2R_0}{d\eta^2}-\frac{R_0}{4}=0$$

$$\frac{(\gamma-1)}{(r+1)}\cdot\eta^{-1/3\gamma}P_0{}^{-1/\gamma}=2R_0\frac{dR_0}{d\eta} \tag{29}$$

with $R_0=P_0=1$ at $\eta=1$, etc..

These equations can be integrated numerically for given value of $\gamma$. Results when $\gamma=1.4$ are, at $\eta=0$

$$R_{0E}=0.8688, \quad P_{0E}=0.8387 \tag{30}$$

etc., where suffix $E$ represent quantities at $\eta=0$. As functions of $\eta$ singularities in $R$ and $P$ only occur at $\eta=0$ from Eqs. (29) and so if the equations for $R$ and $P$ are valid anywhere in $0<\eta\leq 1$, they are valid in the whole interval. Hence by assuming that the flow is inviscid just behind the shock wave, it can be deduced that it must be inviscid everywhere except in the immediate neighbourhood of $\psi=0$, so that viscous terms can only be important there. It is clear that there must be a viscous layer because the inviscid solution does not satisfy the boundary conditions at $\psi=0$, and further since $\psi$ is a measure of the mass of fluid, almost all the fluids behind the shock wave are confined in the inviscid layer.

From Eqs. (29) it can be seen that near $\eta=0$, $\partial P/\partial\eta$ is bounded while

$$\frac{\partial R}{\partial\eta}\sim\eta^{-1/3\gamma}$$

therefore as $\eta\to 0$

$$\frac{\partial}{\partial r}\left(\frac{p}{p_\infty}\right)=\frac{2rM_\infty{}^2ur}{(\gamma+1)\frac{1}{2}u_\infty r_s{}^2}\left(\frac{1}{S}\cdot\frac{p}{p_\infty}\right)^{1/\gamma}\frac{\partial P}{\partial\eta}\to 0$$

because $S\sim\psi^{-1/3}$ when $\eta\sim 0$.

Thus the pressure gradient tends to zero as the boundary layer is approached from above. Further near $\eta=0$

$$\frac{T}{T_\infty}=\frac{p/p_\infty}{\rho/\rho_\infty}\sim O\left(\frac{\rho}{\rho_\infty}\right)^{-1}\sim O(S^{1/\gamma})\sim O(\eta^{-1/3\gamma})$$

when $x$ is small, therefore $T$ must be increased rapidly near the end of the inviscid layer, and $\rho$ and $u$ must be decreased rapidly, all of of which we must have for the boundary layer theory.

### 2–3. Boundary Layer

As shown in the previous section, the variation of $p$ across the boundary layer in the immediate neighbourhood of $\psi=0$ is so small that in it $p$ may be assumed to be a function of $x$ only. Therefore the relevant equations of motion in this layer are Eqs. (1) and (2) with boundary conditions $u=0$ at $r=r_w(x)$ or at $\psi=0$, and $u=u_B$ outside the boundary layer $r=r_B$ or $u\to u_B$ as $\psi\to\infty$ because $\psi$ is still small in comparison with $\psi_0$ when $u$ is not sensibly different from $u_\infty$, where $\psi_0$ denotes the value of $\psi$ at matching point between inviscid and boundary layer, and suffix $B$ denotes quantities outside the boundary layer. It is noted that this boundary condition may be replaced by $u\to u_\infty$ as $r\to r_E$ where $r_E$ corresponds to $r$ at $\eta=0$ in the inviscid layer solution. The discussion of the adoptability of such condition is as follows.

---

* The power $m$ of $x^m$ in the series expansion when the leading term is $x^{3/4}$ is found to be 1/2 similarly as in the two dimensional case.

First, $\eta=0$ corresponds to a stream line in the inviscid layer solution, which is seen from Eq. (19) easily, and

$$v_B=v_{\eta=0}=u_\infty\left(\frac{\partial r}{\partial x}\right)_{\eta=0}=u_\infty\frac{dr_F}{dx} \tag{31}$$

While $v$ component of the velocity at the edge of the boundary layer in the boundary layer solution becomes, from Eq. (15) with the aid of Eq. (10)

$$v=u\frac{\partial}{\partial x}\int_0^\psi\frac{\rho_\infty}{\rho ur}d\psi=\frac{(\gamma-1)}{2}M_\infty{}^2u$$
$$\times\frac{\partial}{\partial x}\left\{\frac{p_\infty}{p}\int_0^\psi\frac{1}{r}\left(\frac{u_\infty}{u}-\frac{u}{u_\infty}\right)d\psi\right\}, \tag{32}$$

because in the boundary layer

$$1\ll\frac{(\gamma-1)}{2a_\infty{}^2}(u_\infty{}^2-u^2).$$

To find the value of $v$ at the edge of the boundary layer, the upper limit may be replaced by $\infty$ in Eq. (32), since when $\psi$ is large on the scale of the boundary layer $u-u_\infty$ is exponentially small. Therefore

$$v_B=\frac{(\gamma-1)}{2}M_\infty{}^2u_\infty\frac{d}{dx}$$
$$\times\left\{\frac{p_\infty}{p}\int_0^\infty\frac{1}{r}\left(\frac{u_\infty}{u}-\frac{u}{u_\infty}\right)\right\}d\psi \tag{33}$$

since $u=u_\infty$ there. Further from Eq. (11) the boundary layer is definite and

$$r_B=\frac{(\gamma-1)}{2}M_\infty{}^2\frac{p_\infty}{p}\int_0^\infty\frac{1}{r}\left(\frac{u_\infty}{u}-\frac{u}{u_\infty}\right)d\psi. \tag{34}$$

Comparing (34) with Eq. (33), next relation is obtained.

$$v_B=u_\infty\frac{dr_B}{dx}. \tag{35}$$

According to Eq. (35) the outer edge of the boundary layer is also a stream line of the inviscid layer, and therefore the assumption previously described may be acceptable, and further it is clear that the mass of fluid in the boundary layer is negligible in comparison with that in the inviscid layer.

Now, in the present paper Kármán-Pohlhausen's approximation will be accepted to discuss the boundary layer. Thus, conditions used are

$$u=0,\quad v=0,\quad \left(\frac{\partial T}{\partial r}\right)_w=0\quad\text{at}\quad r=r_w(x) \tag{36}$$

and complementary conditions

$$u=u_B,\quad \left(\frac{\partial u}{\partial r}\right)=\left(\frac{\partial^2u}{\partial r^2}\right)=\cdots=0$$
$$\text{at}\quad r=r_w+\delta$$

Where $r_w+\delta$ correspond to $r_B$ approximated in the Kármán-Pohlhausen sence, and $u_B$ is the velocity outside the boundary layer to be replaced by $v_\infty$ finally. Then, integrating Eqs. (1) and (2) over the boundary layer and combining these results, the momental integral relation is obtained. Further for computational purposes, if $r'$ is used instead of $r$,

$$r'=r-r_w(x) \tag{37}$$

then, the relation is reduced to

$$\frac{r_w\mu_w}{\rho_\infty u_\infty{}^2}\left(\frac{\partial u}{\partial r'}\right)_{r'=0}=\frac{2}{(\gamma-1)M_\infty{}^2}\frac{d}{dx}$$
$$\times\left\{\delta\frac{p_B}{p_\infty}\int_0^1\frac{u/u_B}{\{1+(u/u_B)\}}(r_w+r')d\left(\frac{r'}{\delta}\right)\right\}$$
$$-\frac{(\frac{1}{2}\delta^2+r_w\delta)}{\gamma M_\infty{}^2}\frac{d}{dx}\left(\frac{p_B}{p_\infty}\right) \tag{38}$$

after terms smaller order than $1/M_\infty{}^2$ is neglected.

Above relation, for the case of $r_w=\text{const.}$ and $\delta/r_w\to0$ have been used by Shen, Li and Nagamatsu$^{3)}$ for their hypersonic viscous flow problems on the two dimensional flat plate.

Now, next parameters are used in the boundary layer,

$$u/u_B=f(\xi)\quad \xi=r'/\delta \tag{39}$$

and $\Lambda$ is introduced by

$$f''(0)=-\Lambda. \tag{40}$$

Then, the velocity profile approximated by a polynomial series can be obtained. It is well known in the case of incompressible fluid past flat plate, the quartic function give plausible results and higher power do not improve in accuracy any more. But this may be inconclusive in the present problem. According to several numerical results, if the thickess of the body is decreased compared with that of the boundary layer, that is when

$$\varepsilon=\frac{r_w}{\delta} \tag{41}$$

become small, then it may happen that the velocity profiles become unreasonable physically for smaller value of $\varepsilon$, and the higher power may give the velocity profile plausible for small $\varepsilon$. In the present paper the sextic polynomial is used from the result of comparison with that of the quartic as shown later.

Then, Eq. (2) at the wall becomes, with the aid of the boundary condition $(\partial T/\partial r)_w=0$,

$$\frac{dp_B}{dx}=\frac{\mu_w}{r_w}\frac{u_\infty}{\delta^2}\left\{\delta\left(3+\frac{\Lambda}{10}\right)-r_w\Lambda\right\}$$

or,

$$-\Lambda+\frac{1}{\varepsilon}\left(3+\frac{\Lambda}{10}\right)=\frac{\delta^2(dp_B/dx)}{\mu_w u_\infty}. \tag{42}$$

Further when $F(\Lambda)$ and $F_1(\Lambda)$ are introduced by

$$F(\Lambda)\equiv\int_0^1\frac{1}{1+f(\xi)}d\xi$$

$$F_1(\Lambda)\equiv\int_0^1\frac{\xi}{1+f(\xi)}d\xi \tag{43}$$

Eq. (38) and (42) become, respectively,

$$-\Lambda+\frac{1}{\varepsilon}\left(3+\frac{\Lambda}{10}\right)=\frac{2\delta^2 p_\infty}{(\gamma-1)C\mu_\infty u_\infty M_\infty{}^2}\frac{d}{dx}\left(\frac{p_B}{p_\infty}\right) \tag{44}$$

$$\frac{(\gamma-1)C\mu_\infty M_\infty{}^2}{2\rho_\infty u_\infty}\cdot\varepsilon\left(3+\frac{\Lambda}{10}\right)$$
$$=\frac{2}{(\gamma-1)M_\infty{}^2}\frac{d}{dx}\left[\frac{p_B}{p_\infty}\delta^2\left\{\frac{1}{2}-F_1+\varepsilon(1-F)\right\}\right]$$
$$-\frac{\delta^2}{\gamma M_\infty{}^2}\frac{d}{dx}\left(\frac{p_B}{p_x}\right)\left(\frac{1}{2}+\varepsilon\right). \tag{45}$$

Now, the confirmation that the form of the shock wave assumed in Eq. (25) is consistent, will be done here,. If $r_s\sim x^n$ when $x$ is small, then since $R_0$ and $P_0$ are functions of $\eta$ only, at the inner edge of the inviscid layer, $p_B\sim x^{2(n-1)}$ and $r_B\sim x^n$ from Eqs. (24) and (28). While in the boundary layer, three cases according to the order of $\varepsilon$ are considered.

**Case 1.** $\varepsilon=\text{const.}$

In this case, from Eqs. (44) and (45), if $p_B\sim x^{2(n-1)}$, then

$$\delta\sim 1/\sqrt{dp_B/dx}\sim x^{3/2-n}$$

to allow the existence of the similar solution in both the inviscid layer and the boundary layer, or more directly to keep $\Lambda$ as a constant as have been obtained by Li-Nagamatsu in the flat plate case by a similar method. Therefore for consistency of $r_B$ and $r_B=r_w+\delta$, $n=(3/2)-n$, whence $n=3/4$, so that $\delta\sim x^{3/4}$ and $r_w\sim x^{3/4}$. The existence of such $n$ was first demostrated by Li and Nagamatsu in the boundary layer solution on the flat plate.

**Case** 2. $\varepsilon\sim x^k$, $k>0$

In this case, as $r_B=\delta(1+\varepsilon)\sim\delta$ and then

$$\delta\sim 1/\sqrt{(dp_B/dx)}\cdot\varepsilon\sim x^{(3/2)-n-(k/2)}$$

and $n=(3/2)-n-(k/2)$ whence $n=(3-k)/4$, so that $\delta\sim x^{(3-k)/4}$ and $r_w\sim x^{(3+3k)/4}$. The characteristic properties of these cases are that near the leading edge of the body, the inverse flow is caused, which can be estimated from the deduced condition,

$$F_1=\frac{1}{2}+\frac{\gamma-1}{2\gamma}.$$

If $k=1/3$ is chosen as a special case, $\delta\sim x^{2/3}$, $r_s\sim x^{2/3}$ and $r_w\sim x$ which corresponds to the flow around a pointed body of revolution.

**Case** 3. $\varepsilon\sim x^{-q}$, $q>0$

In this case, as $r_B=\delta(1+\varepsilon)\sim\varepsilon\delta$ and then

$$\delta\sim 1/\sqrt{dp_B/dx}\sim x^{(3/2)-n}$$

and $(3/2)-n-q=n$ whence $n=(3-2q)/4$, so that $\delta\sim x^{(3+2q)/4}$, $r_w\sim x^{(3-2q)/4}$ and $r_s\sim x^{(3-2q)/4}$. The value of $q$ must be smaller than 3/2, from physical consideration.

In the present paper "Case 1." only is chosen as the most typical case because they afford the similar solution, and several numerical calculations are presented. Discussions for real possibility of "Case 2, and 3." are not presented in this paper.

## 2-4. Matching Procedure

Now, it may be effected a match between the inviscid solution at $\psi=0$ with the boundary layer solution at $\psi=\infty$ or in the approximate meaning at $r=r_w+\delta$. Discussions for such boundary conditions may be referred to Stewartson's paper.

It was shown in 2-2 that if the equation of the shock wave is given by Eq. (25), then at the inner edge of inviscid layer ($\psi=0$), $p_B/p_\infty$ and $r_B$ are represented by Eqs. (24), (28), and (30).

On the other hand, at the outer edge of the boundary layer $r_B=r_w+\delta$, $p_B/p_\infty$ and $\delta$ must be satisfied by Eqs. (44) and (45), therefore solutions to match at the boundary between both layers can be obtained by making these values represented by the same expresions, say, $p_B/p_\infty=p_B/p_\infty$ and $r_B=r_w+\delta$.

If the leading terms of series expansion only are written down for simplicity, introducing the inviscid layer solutions at the inner edge $\eta=0$ into Eqs. (44) and (45), equations to determine $\vartheta$ and $\Lambda$ can be obtained. These are,

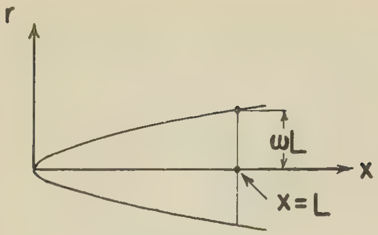

Fig. 3. Coordinates of the Body Surface.

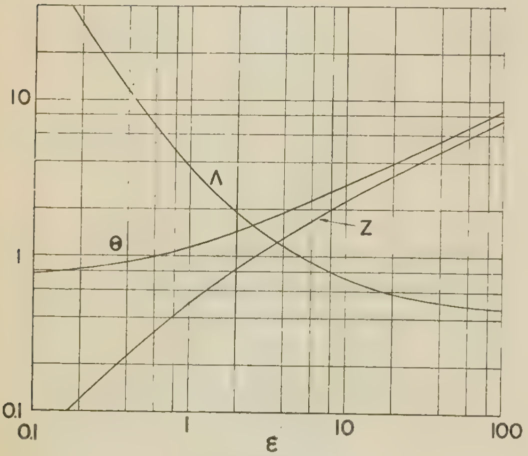

Fig. 4. Relations Between $\varepsilon$ and $\Theta$, $\Lambda$, $z$.

$$-\Lambda+\frac{1}{\varepsilon}\left(3+\frac{\Lambda}{10}\right)=-\frac{9P_0R_0{}^2\rho_\infty u_\infty}{8(\gamma^2-1)C\mu_\infty M_\infty{}^2}\frac{\vartheta^4}{(1+\varepsilon)^2},$$

$$\frac{(\gamma-1)}{2}\frac{C\mu_\infty M_\infty{}^2}{\rho_\infty u_\infty}\varepsilon\left(3+\frac{\Lambda}{10}\right)$$
$$=\frac{9\gamma P_0R_0{}^2\{\frac{1}{2}-\mathrm{F}_1+\varepsilon(1-F)\}}{4(\gamma^2-1)(1+\varepsilon)^2}\vartheta^4$$
$$+\frac{9P_0R_0{}^2(\frac{1}{2}+\varepsilon)}{16(\gamma+1)(1+\varepsilon)^2}\vartheta^4, \qquad (46)$$

From Eqs. (46), with the aid of Eqs. (43), $\Lambda$ and $\vartheta$ can be obtained for given $\gamma$ and $\varepsilon$ numerically. Once when $\Lambda$ and $\vartheta$ are determined, where $\vartheta$ is of the form

$$\vartheta=\theta\cdot\left(\frac{M_\infty{}^2C\mu_\infty}{\rho_\infty u_\infty}\right)^{1/4}\equiv\theta\cdot N^{1/4} \qquad (47)$$

$\delta$, $p_B/p_\infty$ etc. become, respectively

$$\delta=\frac{R_0\theta}{(1+\varepsilon)}N^{1/4}x^{3/4}+\mathrm{O}(x^{5/4})\equiv\Delta N^{1/4}x^{3/4}+\cdots$$
$$r_w+\delta=R_0\theta N^{1/4}x^{3/4}+\mathrm{O}(x^{5/4})\equiv R_BN^{1/4}x^{3/4}+\cdots$$
$$r_s=\theta N^{1/4}x^{3/4}+\mathrm{O}(x^{5/4})\equiv R_sN^{1/4}x^{3/4}+\cdots \qquad (48)$$
$$p_w/p_\infty=\frac{9\gamma P_0\theta^2M_\infty{}^2}{8(\gamma+1)}N^{1/2}x^{-1/2}+\mathrm{O}(1)$$
$$\equiv P_wM_\infty{}^2N^{1/2}x^{-1/2}+\cdots$$
$$r_w=\frac{R_0\varepsilon\theta}{(1+\varepsilon)}N^{1/4}x^{3/4}+\mathrm{O}(x^{5/4})\equiv R_wN^{1/4}x^{3/4}+\cdots$$

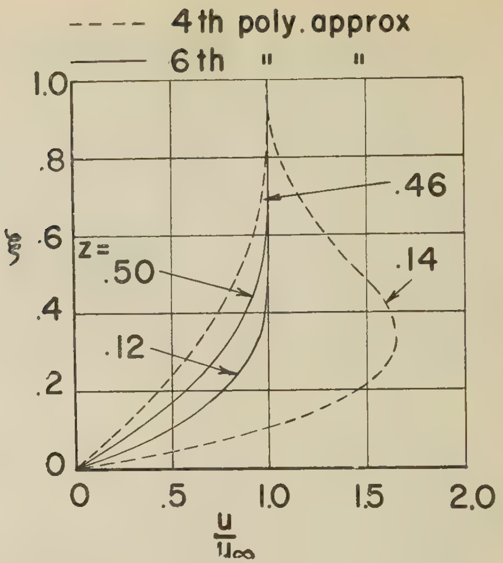

Fig. 5. Comparison of Velocity Profiles.

$$\frac{\tau_w}{\rho_\infty u_\infty{}^2}=\frac{(\gamma-1)(1+\varepsilon)\{3+(\Lambda/10)\}}{2R_0\theta}N^{3/4}x^{-3/4}$$
$$+\mathrm{O}(x^{-1/4})\equiv S_wN^{3/4}x^{-3/4}+\cdots$$

where $\tau_w$ represents the shear stress on the wall.

It is convenient to express above quantities as the functions of the body profile represented by

$$r_w=\omega\left(\frac{L}{x}\right)^{1/4}x+\cdots \qquad (49)$$

where $L$ shows the reference length, and $\omega L$ is the radius of the body surface at section $x=L$ as shown in Fig. 3. The relation between $\varepsilon$ and $\omega$ is given by

$$\frac{\varepsilon\theta(\varepsilon)}{1+\varepsilon}=\frac{\omega}{R_0(0)}\left(\frac{\rho_\infty u_\infty L}{M_\infty{}^2C\mu_\infty}\right)^{1/4}\equiv\frac{z}{R_0(0)} \qquad (50)$$

Fig. 4 shows values of $z$, $\Lambda$, and $\theta$ for given values of $\varepsilon$ when $\gamma=1.4$. If the value of $z$ is given numerically, then the corresponding value of $\varepsilon$ is also known from this figure, and therefore coefficints of $\delta$, $r_s$ and $p_w/p_\infty$ can be calculated as functions of $z$.

It is required to determine the region of validity of Eqs. (1)~(5) and of the division of flow field into a boundary layer and an inviscid layer, which may be referred to Stewartson's paper, who found that the region is restricted by the condition $(r_s/x)^2\ll1$. Further, the flow field may be divided into inviscid and viscous fields if, in terms of $\psi$, the thickness of the viscous layer is much thinner than that of the inviscid field. The condition for this is also the same. Therefore the results of the present paper are to be taken under the conditions

$$\frac{M_\infty^2 C\mu_\infty}{\rho_\infty u_\infty} \ll x \ll \frac{M_\infty^6 C\mu_\infty}{\rho_\infty u_\infty}$$

$$\omega^4 \frac{L}{x} \ll 1 \tag{51}$$

The lower bound is also the lower bound for the validity of the assumption of a continuum. In addition, the error caused by the Kármán-Pohlhausen approximation should be estimated, which is not presented in this paper beyond to point out that when $z$ become small, higher power polynomial may give more plausible curve than lower one as shown in Fig. 5.

## § 3. Numerical Results and Discussions

As described in the last of the preceding section, numerical errors are not estimated, however, comparisons of results obtained from several different power polynomials in the case of a flat plate show that the higher power polynomials give the more over-estimated values in comparison with Stewartson's results, which are considered to have small errors only.

From these properties of the polynomial approximations, it may be estimated that when the Mach number of the main stream is increased, the lower power are better, while if the slenderness of the body increased, the higher power may be required, that is, the velocity profiles in the boundary layer are functions of the Mach number and the slenderness of the body. All of which should be evaluated by comparisons with the exact solutions.

Results of numerical calculations based on the sextic approximation for the velocity profile, are shown in Figs. 4, 6, and 7.

Fig. 4 shows relations between values of $\Lambda$, $\theta$, or $z$ and $\mathcal{E}$ in log-log scale. If tendencies of these curves only are concerned without discussing the range of validity of these values, it is noted that

$$\lim_{\mathcal{E}\to\infty} \Lambda = 0.441$$

and further it is expected that the value of $\Lambda$ may be increased as $\mathcal{E}$ becomes small, which means that the velocity profile in the boundary layer may become almost uniform except only the vicinity of the body surface. Such property for axisymmetrical flows is well known in cases of the incompressible fluid. Further

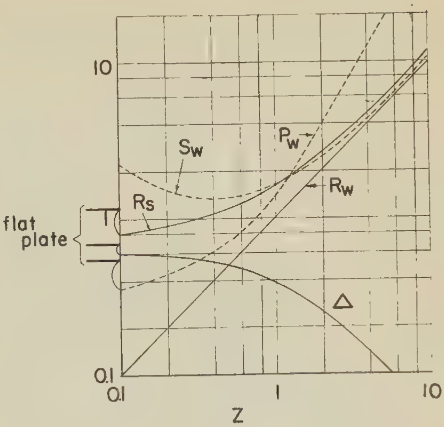

Fig. 6. Effects of Slenderness Parameter $z$.

$$\lim_{\mathcal{E}\to\infty} \frac{\theta^4}{(1+\mathcal{E})^2} = 0.594$$

or $\theta \sim \mathcal{E}^{1/2}$ as $\mathcal{E}\to\infty$, so that

$$z = \frac{R_0(0)\mathcal{E}\cdot\theta(\mathcal{E})}{(1+\mathcal{E})} \sim \mathcal{E}^{1/2}$$

therefore curves of $\theta$ and $z$ tend to become parallel for large values of $\mathcal{E}$, and, it is expected that the value of $\theta$ may tend to be diminished as $\mathcal{E}\to 0$. But such tendencies should not be continued to $\theta\to 0$ as expected from the physical considerations, because if $\theta$ tend to zero, also the contour of the shock wave become closer and closer to the body surface, while the shock wave cannot become close to the body surface beyond the Mach wave determined by $M_\infty$.

In Fig. 6 coefficients defined in Eq. (48) are plotted as functions of $z$, the slenderness parameter. From the figure it is known that, if the thickness of the body become large, the value of $z$ also become large, therefore pressure coefficient $R_w$, shock coefficient $R_s$, shear stress coefficient $S_w$ also become large, while the boundary layer thickness coefficient $\Delta$ become small. On the contrary, if the thickness of the body become small, then $P_w$ and $R_S$ become small, and further $\Delta$ will also become small as proportional to $R_s$ though not shown explicitly in the figure, while the shear stress will tend to be increased. It is remarkable that $S_w$ and $\Delta$ have extremum values. For comparisons with flat plate case, values of coefficient of shock, pressure on the

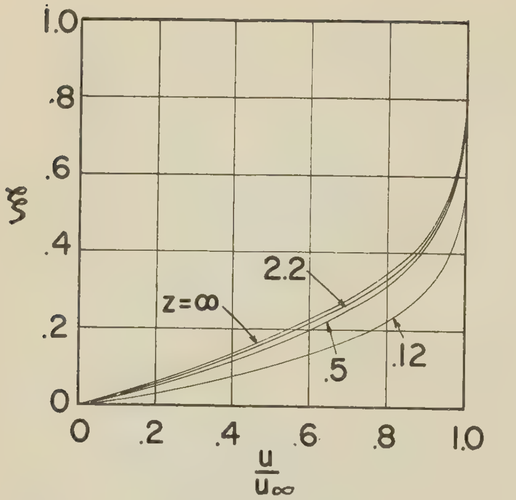

Fig. 7. Velocity Profiles in the Boundary Layer.

wall, and boundary layer thickness in the case of the flow over a flat plate are also shown.

Fig. 7 show velocity profiles in the boundary layer, from which it may be expected that if the thickness parameter $z$ of the body decreased, then the thickness of the layer in which $u$ is rapidly changed, also decreased, and therefore this region may become to be confined in the vicinity of the body, and in the major part of the boundary layer, only $v$ is increased.

All of those results are restricted by the fact that only the first term of expansion in power series are considered, therefore these results can not be taken as the complete description of the flow.

## § 4. Conclusion

A similar solution of the hypersonic viscous flow past slender bodies of revolution is deduced for a special case when $r_w \sim x^{3/4}$, where $r_w$ represents the radial coordinate of the body surface. The calculation was accomplished for the region of strong interaction between the boundary layer on the body surface, and the shock wave caused by the retarding action of the boundary layer. The nose region is excluded because the region of validity in the present paper does not contain this region.

Only similar solutions when $r_w \sim x^{3/4}$ are chosen to calculate numerically by the reason that these solutions have the most typical characteristics of the problem.

Several numerical examples are represented in Figs. 4, 6 and 7 from which it may be expected that if the thickness of the body become small, then the hight of the shock wave, pressure on the wall, and the thickness of the boundary layer are also diminished while the shear stress is increased, and further, the layer in which velocity $u$ is rapidly changed, become to be thin in comparison with the thickness of the boundary layer, and in the major part of the boundary layer, $v$ component only is changed. While if the thickness of the body increased, the hight of the shock wave, the pressure on the wall, the shear stress on the wall are also increased while the thickness of the boundary layer are diminished.

The author would like to acknowledge his gratitude for the cordial guidance and discussions on the work described in this paper given by Prof. Uchida.

### References

1) K. Stewartson: Jour. Aero. Sci., **22** (1955) 303-309.
2) L. Lees and R. F. Probstein: Princeton Univ. Aero. Engi. Lavo. Rep, No. 195, (1952).
3) T. Y. Li, and H. T. Nagamatsu, Contract No. PA-04-495-Ord-19, Memorandum No. 1314, 1930, GALCIT Pasadena, California, 1952.
4) L. Howarth, Modern Developments in Fluid Dynamics, High Speed Flow, Vol. 1, pp. 382-386, Oxford at the Clarendon Press, 1953.
5) R. A. Seban and R. Bond: Aero. Sci., Vol. 18, No. 10, Oct. 1951, pp. 671-675.
6) H. R.. Kelly, Jour. Aero. Sci., Vol. 21, No. 9, Sept. 1954, p. 634.
7) K. Stewartson: Quart. Appl. Math., Vol. 8, No. 2, July 1955. pp. 113-122.
8) M. B. Glauert and M. J. Lighthill: Proc. Roy. Soc. London, Vol. 230, Series A, No. 1181, June 1955, pp. 188-203.
9) W. Wuest: Inge. Arch., 23 Band, Drittes Heft, 1955, pp. 198-208.
pp. 198-208.
10) D. Chapman and M. Rubesin: Aero. Sci., Vol. 16, No. 9, Sept. 1949, pp. 547-565.

JOURNAL OF THE PHYSICAL SOCIETY OF JAPAN Vol. 11, No. 8, AUGUST, 1956

# Temperature Dependence of Velocity and Attenuation of Ultrasonic Waves in High Polymers

By Yasaku WADA and Keiji YAMAMOTO

*Department of Applied Physics, Faculty of Engineering, Tokyo University, Tokyo*

(Received April 12, 1956)

Measurements of velocity and attenuation of ultrasonic waves are carried out for polystyrene, polymethyl methacrylate, phenol resin, polyethylene, nylon 6 and other commercial resins in the temperature from −60°C to 90°C and at frequencies of 100 kc, 1.46 Mc, 4.38 Mc and 7.30 Mc. A correlation between sound velocity in the megacycle range and density is pointed out for glassy polymers. In the case of linear polymers, the temperature coefficient of ultrasonic velocity, $\beta$, exhibits a relatively abrupt change in the glass trasition region at the temperature $T_m$, which is independent of frequency of sound agrees with the transition point associated with thermal expansion. The ratio of $\beta$ to volume expansion coefficient $\alpha$ is found to be constant below and above $T_m$ for each polymer. These facts indicate that the change in $\beta$ at $T_m$ should be ascribed to the temperature dependence of intermolecular free volume. For some polymers a change in $\beta$ and a peak of loss factor are observed at lower temperatures.

## §1. Introduction

As well known, linear amorphous polymers such as polystyrene show a transition from a rubbery state to a glassy state in a relatively narrow temperature range. The transition is attributed to a freezing-in of the segmental motion of the long chain polymers. If measurements of specific volume as a function of temperature are made through the transition region, the curves generally show an abrupt change in slope at the temperature, which is usually called the "apparent second order transition point". This transition occurs also for partly crystalline polymers such as nylon.

Recently, some authors have reported[1-5] that the temperature dependence of velocity of ultrasonic waves exhibits a relatively abrupt change of slope in this transition region. But a full explanation of the mechanism of this phenomenon is not yet available.

In the present paper, the temperature dependence of ultrasonic velocity and attenuation has been measured for polystyrene, polymethyl methacrylate, nylon 6, polyethylene, and phenol resin, the first three of which exhibit the second order transition within the temperature range studied. The measurements have been also carried out for other commercial plastics, such as polyvinyl chloride, celluloid and ebonite.

## §2. Experimental Procedures

The pulse technique was employed for measurements in the megacycle range. A schematic diagram of the apparatus is shown in Fig. 1. A pulsed compressional wave is generated and received in a liquid tank by a pair of crystal transducers, X-cut quartz plates 2 mm in thickness and being used in fundamental frequency and in third and fifth harmonics. A total reflection angle, $\theta$, of longitudinal sound wave at a liquid-polymer interface is observed by rotating a sample plate of 4.5 mm thickness inserted in the path of the beam. The velocity in the sample, $u$, can be given by[6]

$$u=u_l \operatorname{cosec}\theta\ , \tag{2.1}$$

where $u_l$ is the velocity in the liquid. The above formula is based on the assumption that the thickness of the plate is at least several times larger than the wave length of sound. This assumption is satisfied in the present experiment. The attenuation in a sample can be calculated by observing the amplitude change of the received pulse when the sample is inserted in the sound field perpendicularly to the beam.

Water is used as a transmitting liquid. In case of nylon, however, liquid paraffin is used instead of water to avoid the swelling. Though some of the other polymers, polymethyl methacrylate for example, absorb water to some extent, no appreciable change is observed in sound velocity when a sample has been immersed in water for a month. Measurements are made in the temperature range from 0°C to 90°C. Cautions have to be paid to the rate of temperature variation which should be as slow as less than 0.2°C/min to obtain a reproducible result.

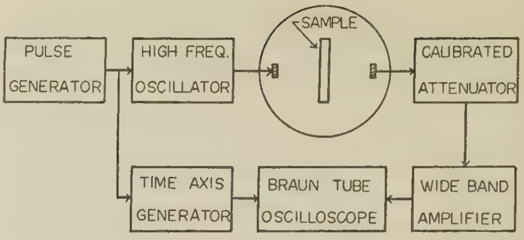

Fig. 1. Schematic diagram of the pulse system

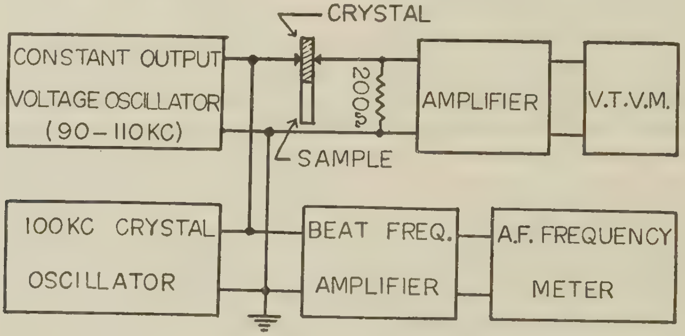

Fig. 2. Block diagram of the composite oscillator system

For measurements at 100 kc/s, the above-mentioned pulse method is not available and the composite oscillator method[7] was employed to study sound velocity and loss factor of polymers. A composite cylinder, made by cementing the specimen of 3 mm square cross section to an X-cut quartz rod of identical cross section, is set into longitudinal vibration, the nodal point of the quartz rod being supported. The length of the specimen should be adjusted by trial so that the resonant frequencies of the quartz and the specimen lie within ten percent.

The composite bar with its holder is placed in a test tube of 25 mm diameter which is immersed in a Dewar's vessel containing water (0–90°C) or alcoholl-dry ice mixture (0- −60°C). Measurements of frequency and temperature are made after a steady state has been reached at each temperature.

It should be noted here that the velocity in the infinite medium is obtained by the pulse method and, on the other hand, the so-called "bar velocity" is given by the composite oscillator method. Sound velocity is related to Young's modulus $E$ as

$$u_{inf.}=\sqrt{\frac{E}{\rho}\cdot\frac{(1-\rho)}{(1+\sigma)(1-2\sigma)}} \qquad (2.2)$$

and

$$u_{bar}=\sqrt{\frac{E}{\rho}} \qquad (2.3)$$

respectively, where $\rho$=density and $\sigma$=Poisson's ratio. It is impossible to reduce one to the other unless $\sigma$ is known. In the present study, however, the reduction is not necessary because only the slope of velocity *vs.* temperature curves comes into question.

The attenuation of sound waves, $\varDelta$ in db/cm, is related to the loss factor $\tan\delta$, as

$$\varDelta=\frac{27.3\tan\delta}{\lambda}, \qquad (2.4)$$

where $\lambda$ is wave length in cm.

The linear thermal expansion of polymers is measured by the optical lever method, a specimen being immersed in water or liquid paraffin tank. Specimens cut from the same piece of materials have been used throughout the present study.

## § 3. Experimental Results

Figs. 3–5 show the data given by the pulse technique. A change in slope of velocity *vs.* temperature curve is observed at the glass transition temperature for polystyrene, polymethyl methacrylate, nylon 6, polyvinyl chloride, celluloid and ebonite. The attenuation of these polymers is found to begin to in-

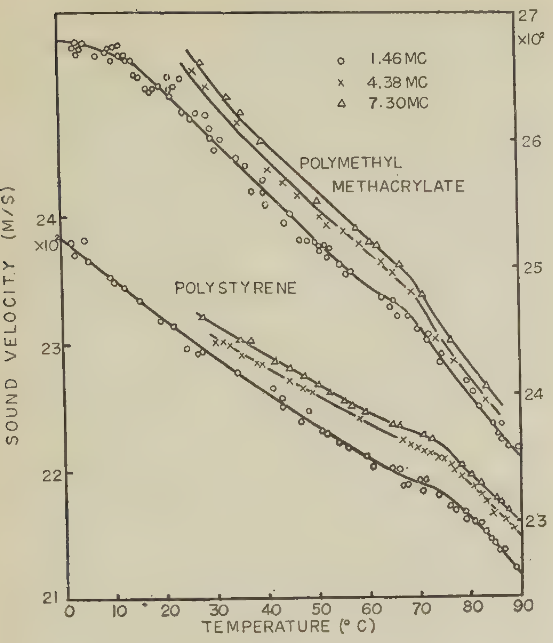

Fig. 3. Sound velocity in polystyrene (left scale) and polymethyl methacrylate (right scale)

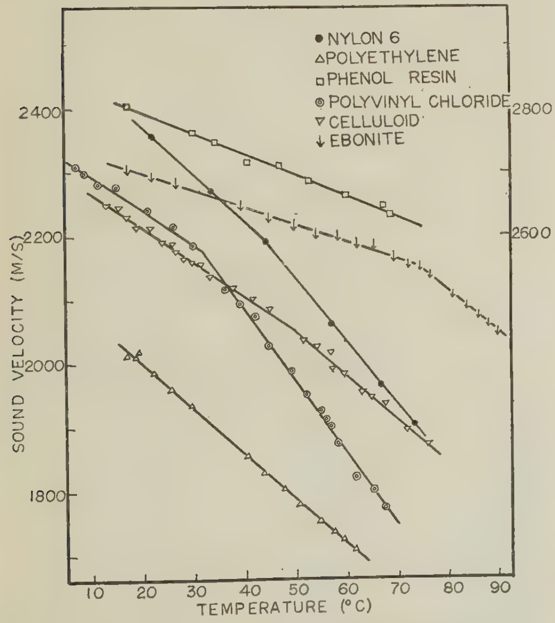

Fig. 4. Sound velocity in several polymers at 1.46 Mc/s (use the right scale only for phenol resin.)

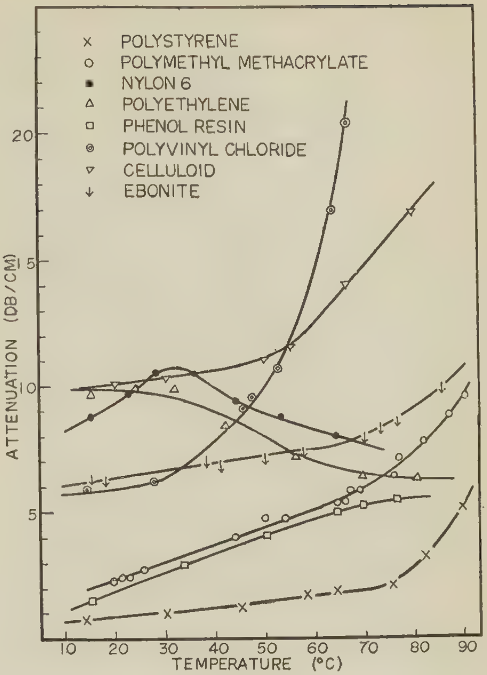

Fig. 5. Attenuation of sound in polymers at 1.46 Mc/s

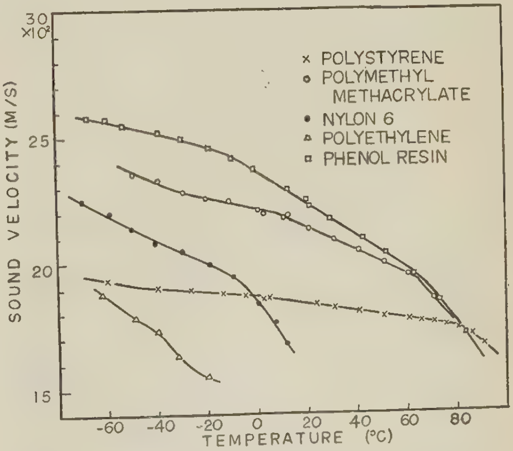

Fig. 6. Sound velocity in polymers at 100 kc/s

crease rapidly at this temperature, with the exception of nylon 6. As can be seen in the case of polystyrene and polymethyl methacrylate (Fig. 3) the slope of the curves does not vary so much with frequency, though a slight increase with frequency is found in sound velocity. Polymethyl methacrylate shows another discontinuity of slope at 10°C (Fig. 3) which is also observed in the thermal expansion curve and in Fig. 6.

Figs. 6 and 7 show the data given by the composite oscillator method. Except polystyrene and polymethyl methacrylate, the damping of the specimen becomes so great that measurements can no longer be carried out up to the glass transition temperature with this method. But on the other hand, measure-

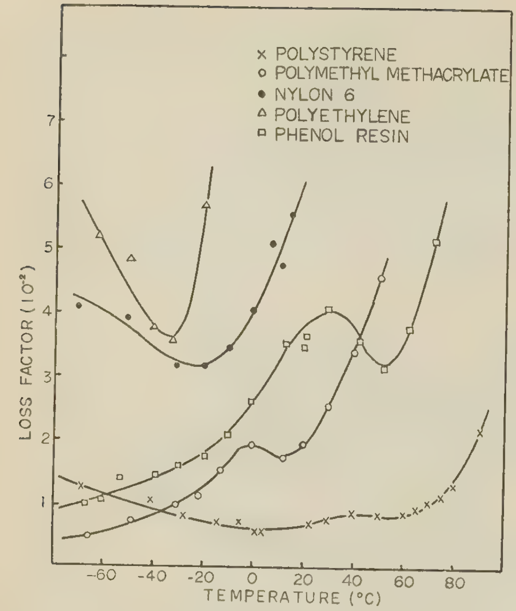

Fig. 7. Loss factor in polymers at 100 kc/s

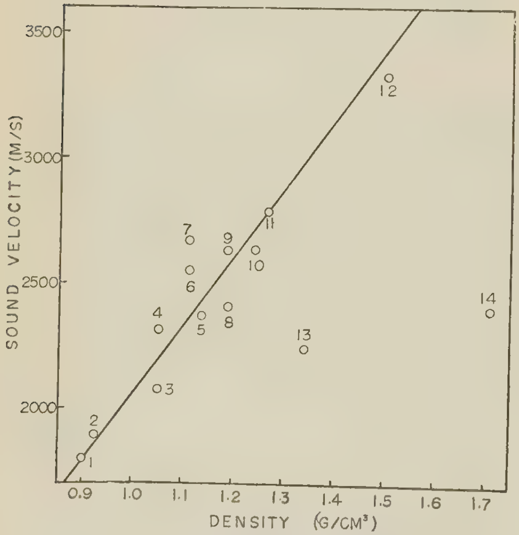

Fig. 8. Correlation between ultrasonic velocity in the megacycle range and density at room temperature. 1 Polyisobutylene, 2 Polyethylene, 3 Polyisobutyl methacrylate, 4 Polystyrene, 5 Nylon 6, 6 Nylon 6-10, 7 Nylon 6-6, 8 Polyvinyl acetate, 9 Polymethyl methacrylate, 10 Polyvinyl formal, 11 Phenol resin, 12 Melmac resin, 13 Polyvinyl chloride, 14 Polyvinylidene chloride.

ments below 0°C become possible and a discontinuity in slope of velocity curves is observable at lower temperatures.

As is seen in Fig. 7, the loss factor curves for polystyrene, polyethylene and nylon 6 indicate the possible existence of peaks above and below the temperature range studied. Polymethyl methacrylate and phenol resin have a marked peak of loss factor at 0°C and 30°C respectively, which is found to be extremely sensitive to the amount of absorbed water. Only the results for the specimen in equilibrium with room humidity (ca. 60% R. H.) are presented here. A more detailed study along these lines is now in progress and will be presented in another paper.

## § 4. Relation Between Ultrasonic Velocity and Density of Glassy Polymers

It is a well known fact for a group of organic liquids with similar molecular weight that a liquid of larger density has in general larger ultrasonic velocity too, with the exception of halogenated hydrocarbons. An example of this law is shown in Table I. This law can be qualitatively understood by the theory developed by Kincaid-Eyring[8], Kittel[9] and Collins.[10] According to Kincaid-Eyring's theory, the velocity of ultrasonic waves in a liquid, $u_l$, is closely related to intermolecular free volume per unit volume, $v_f$, and is given by

$$u_l=\sqrt{\gamma \frac{RT}{M}} \cdot v_f^{-\frac{1}{3}} , \tag{4.1}$$

where $\gamma$ is the ratio of specific heats, $R$ the gas constant, $T$ the absolute temperature and

Table I. Density and ultrasonic velocity of organic liquids with similar molecular weight[11] (20°C)

| Liquid | Molecular weight | Density (g/cc) | Sound velocity (m/s) |
|---|---|---|---|
| *n*-Heptane | 100.2 | 0.684 | 1162 |
| *n*-Octane | 114.2 | 0.703 | 1194 |
| *n*-Hexyl alcohol | 102.2 | 0.820 | 1322 |
| *p*-Xylene | 106.2 | 0.860 | 1330 |
| *m*-Xylene | 106.2 | 0.863 | 1340 |
| Ethyl benzene | 106.2 | 0.868 | 1338 |
| *o*-Xylene | 106.2 | 0.871 | 1360 |
| *m*-Toluidine | 107.2 | 0.989 | 1620 |
| *o*-Toluidine | 107.2 | 0.998 | 1634 |
| Ethyl bromide | 109.0 | 1.428 | 892 |

$M$ the molecular weight. Organic liquids composed of carbon, oxygen, nitrogen and hydrogen atoms will have, in a rough approximation, an identical density in the limiting state of $v_f=0$. Hence, at room temperature, a liquid of larger density must have smaller free volume and thus larger ultrasonic velocity.

In case of high polymers, an analogous behaviour can be found between ultrasonic velocity and density. In Fig. 8 the correlation between ultrasonic velocity in the megacycle range and density at room temperature is plotted for a series of glassy polymers, among which linear amorphous polymers, partly crystalline polymers and three-dimensional polymers are included. Some of the data involved in Fig. 8 have been compiled from the results of the present work and the others from those of other authors. As can be readily seen, a polymer of larger density has, in general, larger ultrasonic velocity as in case of the organic liquids and the points represented in Fig. 8 fall approximately on a straight line with the exception of halogenated polymers. It may be also of interest to note that a velocity *vs.* density point of low class paraffins lies on the extension of this line, too.

The above fact seems to favour the following statement that ultrasonic velocity in the megacycle range depends chiefly on the intermolecular free volume as in case of a liquid. From the relaxational theory of viscoelasticity of polymers, this may be reasonale because kinetic motions of a chain element with a extremely short relaxation time alone can contribute to the propagation of sound in the megacycle range and the unit of molecular motions may be restricted to such a small part of a chain molecule as a liquid molecule of low molecular weight. Cross-linkings and crystallinity may have effect on this type of dynamic elasticity only through the variation of free volume. In fact, it has been recently observed[12-13] that many polymers, including crystalline polymers, have an almost identical spectrum of relaxation times at room temperature in the time scale of the order of $10^{-6}$ second and less.

## § 5. Relation Between Temperature Coefficient of Ultrasonic Velocity and Thermal Expansion Coefficient

As has been seen in the foregoing section, the ultrasonic velocity in high polymers seems to be closely related to intermolecular free volume in their glassy state. On this assumption, the temperature dependence of ultrasonic velocity may be considered to be caused by the increase of free volume with temperature, and the discontinuity of temperature coefficient of ultrasonic velocity at the transition point may be attributed to the change of thermal expansion coefficient[14].

In case of liquids, the ratio $n$ of temperature coefficient of ultrasonic velocity, $\beta$, to volume expansion coefficient, $\alpha$, is approximately 3 for orgainc liquids[15] and 2 for liquified gases and takes a rather scattered value for molten metals. The value of $n$ depends on the type of intermolecular potential[16].

The values of $n$ are computed in Table II for high polymers. Though $n$ varies from polymer to polymer, it may be seen that $n$ is kept constant below and above the transition point for each polymer. This result contributes evidence for the statement that the molecular mechanism of elastic deformation in ultrasonic waves is the same in nature below and above the transition point and only the increase of free volume causes the decrease of ultrasonic velocity.

Table II. Temperature coefficient of sound velocity at 1.46 Mc/s ($\beta$) and volume expansion coefficient ($\alpha$).

| Polymer | Temp. range (°C) | $\beta(10^{-4}/°C)$ | $\alpha(10^{-4}/°C)$ | $n=\beta/\alpha$ |
|---|---|---|---|---|
| Polystyrene | 0–65 | 9.4 | 2.2 | 4.3 |
| | 75–95 | 23.8 | 5.3 | 4.5 |
| Polymethyl methacrylate | 25–60 | 14.5 | 3.4 | 4.3 |
| | 75–95 | 24.2 | 5.1 | 4.7 |
| Nylon 6 | 10–35 | 32 | 2.6 | 12.5 |
| | 45–60 | 49 | 3.9 | 12.5 |
| Polyethylene | 10–70 | 26 | 7.9 | 3.3 |
| Phenol resin | 10–70 | 11.5 | 2.8 | 4.2 |
| Polyvinyl chloride | 0–30 | 28 | 3.4 | 8.3 |
| | 40–70 | 57 | 5.7 | 10.0 |
| Celluloid | 10–45 | 25 | 2.6 | 9.6 |
| | 55–80 | 36 | 4.0 | 9.0 |
| Ebonite | 20–70 | 12.3 | 2.1 | 5.8 |
| | 80–95 | 31 | 5.7 | 5.4 |

It must be noted here, however, that this conclusion should not hold far above the transition temperature where a polymer becomes soft enough, because the values of $n$ in Table II have been predicted from the data up to some twenty degrees higher than the transition point. In rubbery or viscous state, some of the segmental motions may occur even in high frequency sound waves and *n* will become much greater.

## § 6. Frequency Dependence of the Transition Point

On the basis of the foregoing considerations, it appears reasonable to say that the break point in ultrasonic velocity *vs.* temperature curves agrees with the apparent second order transition point observed in thermal expansion curves and is independent of frequency of ultrasonic waves used. As can be seen in Table III, this assumption seems to be verified within the limit of accuracy of experiment.

Table III. Transition point from thermal expansion and sound velocity (°C)

| Polymer | Thermal expansion | Sound velocity | | | |
|---|---|---|---|---|---|
| | | 100 kc | 1.46 Mc | 4.38 Mc | 7.30 Mc |
| Polystyrene | 73 | 79 | 76 | 75 | 74 |
| Polymethyl methacrylate | 68 | 64 | 67 | 67 | 68 |
| Nylon 6 | 40 | — | 43 | — | — |
| Polyvinyl chloride | 39 | — | 35 | — | — |
| Celluloid | 45 | — | 48 | — | — |
| Ebonite | 73 | — | 74 | — | — |

Values of the transition temperature hitherto obtained by other workers from sound velocity-temperature curve are given in Table IV. Although these temperatures are somewhat at variance, they are not inconsistent with the idea that the transitions are independent of frequency.

Table IV. Transition point from sound velocity measurements.

| Polymer | Transition point (°C) | Frequency (Mc) | Reference* |
|---|---|---|---|
| Polymethyl methacrylate | 72 | 0.5 | 2 |
| | 74.5 | 1 | 2 |
| | 75 | 2 | 2 |
| | 75 | 5 | 2 |
| | 60 | 0.1 | 4 |
| | 61 | 1.1–5.7 | 3 |
| | 68 | 0.3–0.7 | 5 |
| Polystyrene | 70 | 0.1 | 4 |
| | 70 | 1.1–5.7 | 3 |

* Numbers refer to references at the end of the paper.

## § 7. Conclusion

A rough correlation has been found between ultrasonic velocity in the megacycle range and density of glassy polymers: namely, a polymer of larger density has larger ultrasonic velocity, too. For linear polymers, a discontinuity of slope of ultrasonic velocity *vs.* temperature curve was observed at glass transition temperature. This break point agrees with the apparent second order transition point determined from the thermal expansion measurement and is independent of frequency of sound in the range from 100 kc to 7.3 Mc. In this case, the ratio of temperature coefficient of velocity to volume expansion coefficient was found to be constant below and above the transition point.

These behaviours can be qualitatively understood from the assumption that the velocity of ultrasonic waves in the megacycle range should be determined, in the first approximation at least, by the intermolecular free volume in an analogous way as a liquid.

For some polymers, a break in the velocity *vs.* temperature curve was observed at lower temperatures, too.

In conclusion, the authors wish to express sincere thanks to Prof. Y. Suge for his continual encouragements and to Mr. M. Oda for his technical assistance.

## References

1) T. F. Protzman: J. Appl. Phys. **20** (1949) 628.
2) J. L. Melchor and A. A. Petrauskas: Ind. Eng. Chem. **44** (1952) 716.
3) M. Krishnamurthi and G. Sivarama: Nature **174** (1954) 132.
4) S. V. Subrahmanyan: J. Chem. Phys. **22** (1954) 1562.
5) P. Hatfield: Nature **174** (1954) 1186.
6) W. C. Schneider and C. J. Burton: J. Appl. Phys. **20** (1949) 48.
7) J. Zacharias: Phys. Rev. **44** (1933) 116.
8) J. F. Kincaid and H. Eyring: J. Chem. Phys. **6** (1938) 620.
9) C. Kittel: J. Chem. Phys. **14** (1946) 614.
10) F. C. Collins and M. H. Navidi: J. Chem. Phys. **22** (1954) 1254.
11) The data have been compiled from L. Bergmann's book: Der Ultraschall, 6. Auflage (1954) 375.
12) K. Fujino and H. Kawai: Textile Research J. **25** (1955) 722.
13) J. D. Ferry and E. R. Fitzgerald: Proc. 2nd Int. Congress of Rheology (1954) 144.
14) R. N. Work: J. Appl. Phys. **27** (1956) 69.
15) R. Rao: Indian J. Phys. **14** (1940) 109.
16) T. Kishimoto and O. Nomoto: J. Phys. Soc. Japan **9** (1954) 59.

# Short Notes

This section is intended to secure prompt publication of important discoveries in physics. The reports should not exceed 800 words in length. A figure of size 7 cm × 7 cm will be counted as 150 words.

J. Phys. Soc. Japan **11** (1956) 893～894

## Recovery Process in the Evaporated Metal Films

By Y. Mizushima and O. Ochi

*Electrical Communication Laboratory, Nippon Telegraph and Telephone Public Corporation, Tokyo*

(Received March 31, 1956)

Metal films evaporated in vacuo on substrates at low temperatures are known to possess unstable excess resistivity, which anneals out at sucessively raised temperatures[1]. The extra resistivity is found to follow Mathiesen's rule just as in the radiation-induced excess resistivity. The present authors report on the behaviors of the excess resistivities of evaporated films of Cu (99.99%) and Ag (99.98%) and Au (99.95%) prepared on glass substrates at the liquid oxygen temperature in high vacuum.

Following the method of analysis given by Overhauser[2], the film was annealed in a bath kept at desired temperature for about 10 min., and the temperature was raised stepwise. The resistivity change was recorded throughout. From the rate of recoveries, the activation energies of the resistivity recovery were obtained (Fig. 1～3). The influence of the length of annealing time at each sucessive stage of temperature is shown in Fig. 2 for the case of Ag film. When a longer time, say about 1 hour, was spent in each stage of annealing, the region of smaller activation energy is shortened. This means that the only flat portion of the spectrum has a physical meaning, and that it is dangerous to adopt the activation energy where it is a function of temperature. One can see, by comparing our result with the result of Overhauser, that in evaporated films the imperfections having lower energy process may be relatively not so abundant as those having unique energies, as in radiation-damaged metals.

From the form of the spectrum, recoveries may be devided roughly in three stages, in each of which the recovery is expressed as

$$d(r-r_0)/dt=-\mathrm{A}(r-r_0)^n ,$$

where $r-r_0$, $t$, $n$ means excess resistivity, annealing time and order of reaction, respectively, all notations in this paper following Overhauser. In the experiment on Cu, the first region, corresponding to lower energies, is from −183°C to −78°C, the second region up to −9°C, and the third up to 31°C. The value of $n$, bringing the best fit to the experimental curves, is 9.6, 4.0 and 1.26 for each region, respectively.

In evaporated films of metals of f.c.c. type, the number of vacancies is assumed to be very much larger than that of interstitials. This resembles the quenched state of metals from higher temperature, but is somewhat different from the radiation-damaged state in which interstitials and vacancies are made equally in numbers. Therefore it is supposed that the unique energy process in our experiment is attributed to the behavior of vacancies, and that the interstitials are annihilated sooner at lower temperatures, although this view is not yet exactly confirmed at present[3]. One can regard the movement of vacancies as a first-order

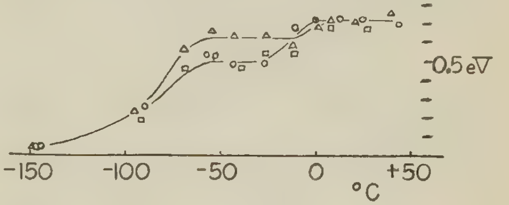

Fig. 1. Spectrum of activation energies of the excess resistivities in Cu films. Annealing time in each stage is somewhat different in two curves.

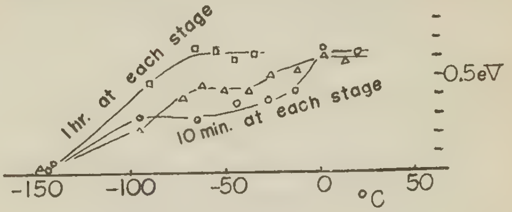

Fig. 2. Spectrum of activation energies of the excess resistivities in Ag films. There are shown three curves, in which annealing time in each stage is different with the other, from 10 min. to 1 hr.

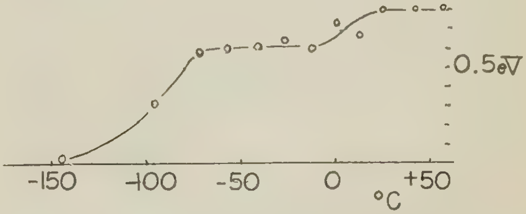

Fig. 3. Spectrum of activation energies of the excess resistivity in Au film.

process including extra term representing lattice stresses. This process is expressed, following Overhauser, by

$$df/dt=-cf\cdot\exp(bf)\,,$$

where $f$ means the density of vacancies.

In our experiment, virgin films condensed at low temperatures will contain naturally large stresses, and by heat-treatment $n$ will diminish approaching 1. Therefore, one can obtain true energies relating to the vacancy migration, nearly free from lattice stresses, only in the last recovery region. These values can be compared with the other studies. The energy thus obtained is 0.7 eV for Cu, 0.6 eV for Ag and 0.8 eV for Au.

### References

1) R. Suhrmann and G. Barth: Z. Phys. **103** (1936) 10.
2) A. W. Overhauser: Phys. Rev. **90** (1953) 393.
3) J. W. Glen: Adv. in Phys. **4** (1955) 381.

---

J. PHYS. SOC. JAPAN **11** (1956) 894~895

## Galvanomagnetic Effects of a Heavily Doped Germanium Crystal*

By Wataru SASAKI

*Electrotechnical Laboratory, Nagatacho, Tokyo*

and Yasuo KANAI

*The Electrical Communication Laboratory, Nippon Telegraph and Telephone Public Corporation, Musasinosi, Tokyo*

(Received May 22, 1956)

Galvanomagnetic effects of a heavily doped n-type germanium crystal have been measured between 1.3°K and 280°K. The specimen used was cut in the *bridge* shape with its current axis along the [100] direction.

Table I shows the electrical registivity $\rho$, the Hall constant $R$ at the magnetic field of $1.0\times10^4$ gauss, and the Hall mobility $\mu_R=R/\rho$ at various temperatures. It seems that the resistivity increases slowly and monotonically as the temperature is lowered, while the Hall constant first increases with decreasing temperature, then goes through a maximum and takes a constant value between 4.2°K and 1.3°K which coincides with the room temperature value. The Hall mobility first increases with decreasing temperature then goes through a maximum and shows values smaller than the room temperature value under 4.2°K. These observations are explained qualitatively by the impurity band conduction suggested by Hung and Gliessmann[1].

Table I.

| Temperature °K | Resistivity ohm-cm | Hall constant cm³/coul | Hall mobility cm²/volt-sec |
|---|---|---|---|
| 280 | $1.14\times10^{-2}$ | 21.6 | $1.90\times10^3$ |
| 80 | $1.32\times10^{-2}$ | 30.1 | $2.28\times10^3$ |
| 4.2 | $2.61\times10^{-2}$ | 21.2 | $0.80\times10^3$ |
| 1.3 | $2.71\times10^{-2}$ | 20.4 | $0.76\times10^3$ |

The relative increase of the resistivity $\Delta\rho/\rho=\{\rho(H)-\rho(0)\}/\rho(0)$ as a function of magnetic field $H$ is shown in Fig. 1. At the room and the liquid air temperatures the resistivity increases under the magnetic field, while at the liquid helium temperatures the resistivity decreases with the increase in magnetic field and goes through a minimum at about $1.5\times10^4$ gauss. This *magneto-conductive* effect is seen both in the transverse and longitudinal directions of magnetic field relative to electric current, and is far more temperature sensitive compared with the resistivity or the Hall constant in the liquid helium temperature region.

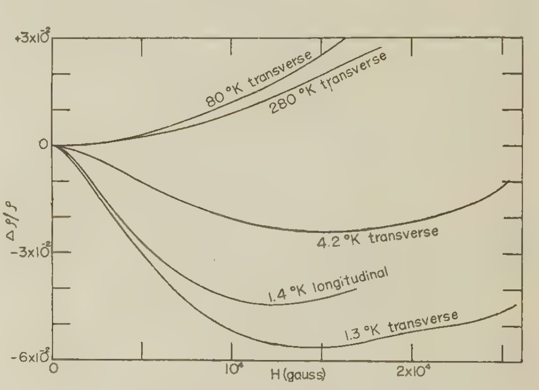

Fig. 1. The relative increase of resistivity in magnetic field.

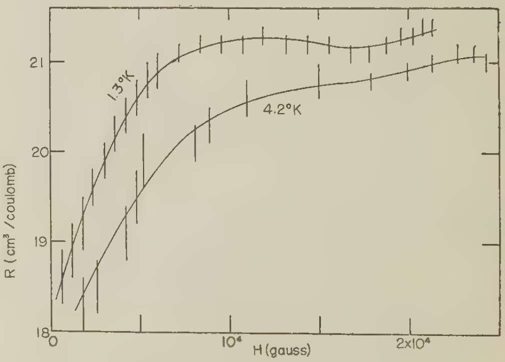

Fig. 2. The variation of Hall constant in magnetic field.

Fig. 2 shows the Hall constant as a function of magnetic field at the temperature where *magneto-conductive* phenomenon is observable. The Hall constant increases slightly with increasing magnetic field and approaches a constant value at about $1.0 \times 10^4$ gauss. This variation, with the *magneto-conductive* phenomenon described above, may be interpreted as transfer of electrons from the impurity band to the empty conduction band.

We are grateful to Professor T. Fukuroi and his coworkers for the hospitalities given in using the helium apparatus at the Research Institute for Iron, Steel and Other Metals of Tohoku University, and also to Mr. A. Amaya for the preparation of germanium crystals.

### Reference

1) C. S. Hung and J. R. Gliessmann: Phys. Rev. **96** (1954) 1226.

---

* This work was carried at the Research Institute for Iron, Steel and Other Metals, Tohoku University.

---

J. Phys. Soc. Japan **11** (1956) 895~896

## Influence of Magnetic Field on the Precipitation Process of Ferromagnetic Phase in Cu–Fe Alloy (I)

By Tadayasu Mitui
*Department of Physics, Faculty of Science, University of Hokkaido, Sapporo, Japan*

(Received June 4, 1956)

In the previous work1), we have investigated experimentally an influence of a magnetic field on a process of precipitation of a ferromagnetic phase of Cu–Co alloy for the purpose of establishing the origin2)3) of the induced magnetic anisotropy of the permanent magnet of precipitate alloy. Now, we have examined the Cu-Fe alloy including ca. 2 weight % of iron. The samples were prepared in the form of polycrystalline disks which were 14.0 mm in diameter and 4.6 mm in thickness. The samples were prepared by water-quenching after solid solution-treatment at ca. 900°C. After the isothermal tempering in the uniform magnetic field of ca. 5000 Oe at 700°C, the induced uniaxial anisotropy was measured by the torsion method in the uniform magnetic field of 10000 Oe as we previously reported.

The experimental results are as follows:

(1) For a quenched sample tempered for ca. 5.0 hrs. isothermally at 700°C in a uniform magnetic field of ca. 5000 Oe, no uniaxial anisotropy was observed because of a very weak ferromagnetic behavior. Moreover, for the same sample tempered 17.0 hrs. in the same manner, the torque curve of twofold rotational symmetry was obtained and then the value of the uniaxial anisotropy became ca. $9 \times 10^2$ ergs/cm³, as shown in Fig. 1.

(2) For successive and isothermal heat treatments, the anisotropy of the sample increased with the increasing tempering times as shown in Fig. 2. Moreover, hardness measurements were made on a Vickers' hardness tester using 200 gr. after the same heat treatment, as shown in Fig. 2. The hardness showed maximum after a sharp increase in the initial stage of tempering. This means that the nucleation and the growth of precipitates occured at this stage. The magnetic property showed, however, that the precipitates were not remarkably ferromagnetic for a considerable time after the precipitation began its growth.

According to the study of R. B. Gordon and M. Cohen4), it is possible that the precipitate stays for some time as a transition phase with f.c.c. If there is a period of transition phase, one should expect that it transforms to the stable, ferromagnetic, b.c.c. phase ultimately. Moreover, it is interesting to note that the transformation in the precipitation does not affect the hardness, but affects remarkably the magnetic anisotropy.

Further we are studying the effect of magnetic field on the variously heat-treated alloys.

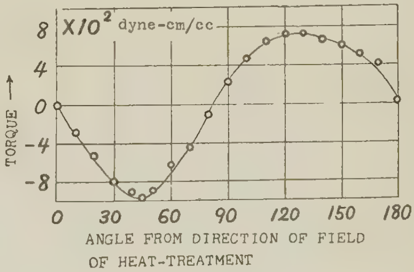

Fig. 1. Torque magnetometer curve.

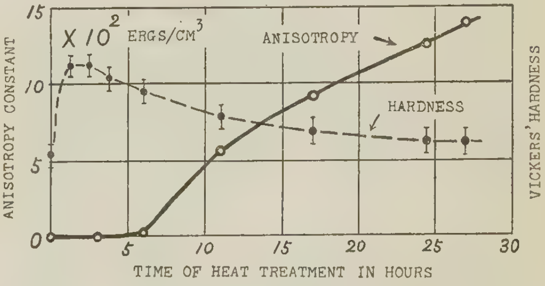

Fig. 2. Anisotropy and Hardness as dependent on time of magnetic heat treatment at 700°C.

### References

1) S. Miyahara and T. Mitui: J. Fac. Sci. Hokkaido Univ. **4** (1953) 275.
T. Mitui and S. Miyahara: J. Phys. Soc. Japan **10** (1955) 1023.
2) R. D. Heidenreich and E. A. Nesbitt: J. App. Phys. **23** (1952) 352.

E. A. Nesbitt and R. D. Heidenreich: J. App. Phys. **23** (1952) 366.

3) L. Néel: Compt. rend. **225** (1947) 109; J. Phys. et Rad. **15** (1954) 225.

4) R. B. Gordon and M. Cohen: Age Hardening of Metals, A.S.M., (1940) 161.

---

J. PHYS. SOC. JAPAN **11** (1956) 896

## Paramagnetic Resonance Absorption in Copper Hexapyridine Nitrate

By Hidetaro ABE and Mieko OHTSUKA

*Institute of Science and Technology,*
*University of Tokyo*

(Received June 5, 1956)

Single crystals of unhydrous copper hexapyridine nitrate were examined at room temperature by the method of paramagnetic resonance absorption using 6.5 mm and 3.23 cm wavelengths. From the chemical analysis, their composition was determined as $Cu(C_5H_5N)_6 \cdot (NO_3)_2$. In any direction of applied field H, there appears one group of resonance lines. $g$-value corresponding to the center of this group can be expressed by an axially symmetric tensor whose principal values are observed to be $g_{//}=2.25\pm0.02$ and $g_{\perp}=2.05\pm0.02$ for both frequencies. Around the direction of H giving $g_{//}$, four component peaks can be seen as shown in Fig. 1. The positions of peaks vary with the direction of the applied field as shown in Fig. 2. Since $g$-value corresponding to the center of peaks, spacings between the component lines, and line-widths do not depend on the frequency, the structure may be ascribed to the hfs from the copper nucleus. ($I=3/2$) The hfs constants can be deduced as $|A|=190\pm5$ oer. and $|B|<15$ oer. The observed line width for a single hyperfine component is 150±20 oer. at both frequencies. This agrees well with the calculated dipole width from the effective lattice constants estimated from the molecular weight[1].

From these results, the followings can be concluded;

(1) The hfs constant $A$ of this crystal is fairly larger than that of hydrated copper salts (e.g. in copper Tutton salts it ranges from 100 to 130 oer.[2])

(2) The spin-lattice relaxation in this crystal is small even at room temperature.

(3) This crystal contains either only one inequivalent ion, $Z=1$, or more ions whose crystalline axes only slightly deviate from each other.

The direction of the predominant hfs constant $A$ coincides with that of the principal $g$-value, $g_{//}$, which may be the predominant axis of the tetragonal crystalline field.[4] Furthermore the observed $g$-values give reasonable magnitude of hfs constants using the same constants $P=2\gamma\beta\beta_N/\overline{(r^3)}$ and $\kappa$ as those of Tutton salts.[5] These facts support the preceding analysis by one of the authors[3] (H.A.) applying the theory of Abragam and Pryce[4] for some of the copper complex compounds in which the copper ion is surrounded by a quasi-square coordination of nitrogen atoms. In the pyridine derivative of the copper sulfate such structures do not appear.

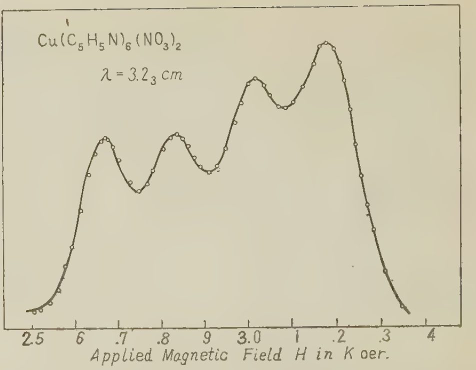

Fig. 1. The absorption curve integrated from the readings of phase-detector with a magnetic field along the axial direction, the direction giving $g_{//}$, and at room temperature.

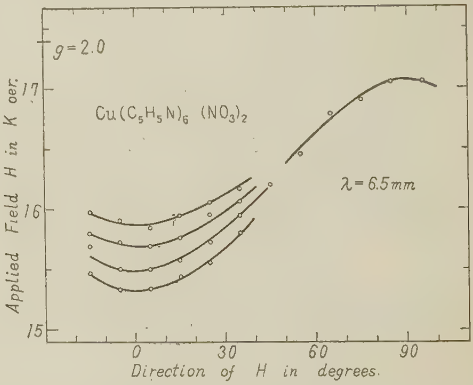

Fig. 2. Peak positions as a function of orientation for $H$, the angle being measured from the axial direction.

### References

1) H. Kumagai et al: Jour. Phys. Soc. Japan **9** (1954) 369.

2) K. D. Bowers and J. Owen: Rept. Prog. Phys. **18** (1955) 352.

3) H. Abe and K. Ôno: Jour. Phys. Soc. Japan **11** (1956) in press.

4) A. Abragam and M. H. L. Pryce: Proc. Roy. Soc. **A 205** (1951) 135.

5) A. Abragam and M. H. L. Pryce: Proc. Roy. Soc. **A 206** (1951) 164.

J. PHYS. SOC. JAPAN **11** (1956) 897

# Interaction of Dislocations with Atomic Order in Solid Solution

By Kôji SUMINO and Mikio YAMAMOTO

*Research Institute for Iron, Steel and Other Metals, Tôhoku University, Sendai*

(Received June 11, 1956)

In general, when solid solutions such as superlattice and precipitation alloys, in which interatomic interactions must be taken into account, undergo the phase change, they exhibit the volume change, which may be attributed to the difference between the length of the like atom-pair and that of the unlike one. In such solid solutions, we can expect a mechanism of interaction of dislocations with solute atoms, which is different from those so-far proposed1). If a dislocation exists in such a solid solution, its stress field may naturally couple with the strain originating from the difference in the length of atom-pairs. Hence the atomic order varies as a function of the place from the value in the absence of the stress field, and the atomosphere of such atomic configuration may lock the dislocation.

For example, for superlattice alloys, following Iwata's treatment2), we can obtain the long-range order parameter, $s$, and short-range order parameter in the $k$th direction of the nearest neighbors of an atom, $\sigma_k$'s ($k=1, 2, \ldots z/2$, $z$ is the number of the nearest-neighbors), as the function of the order parameter in the absence of the stress field, $s_0$ and $\sigma_0$, of the place concerned, and of the atomic concentration. Putting $\sigma_k=\sigma_0+\sigma_k'$, the interaction energy of a dislocation per unit length, $E$, is given as

$$E=-R\iint\Big(\sum_{ij} P_{ij}\,\Gamma_{ij}(\sigma_k')\Big)dx\,dy\,. \qquad (1)$$

Here, $P_{ij}$'s $(i, j=x, y, z)$ are the tensor components of the stress due to the dislocation, and $\Gamma_{ij}$'s the components of the tensor defined by

$$\Gamma_{ij}(\sigma_k')=\sum_{k=1}^{z/2}\sigma_k'\,\alpha_{ki}\,\alpha_{kj}\;,$$

where $\alpha_{ki}$'s are the direction cosines of the $k$th nearest-neighbor direction, and $R$ a constant which characterizes a linear relation between the contribution from the $k$th atom-pairs to the dilatation in the $k$th direction and $\sigma_k$. The locking force for the motion of the dislocation is, then, given by the maximum value of

$$F=R(\partial/\partial x_0)\Big(\iint\sum_{ij} P_{ij}(x-x_0, y)\,\Gamma_{ij}(x, y)\,dx\,dy\Big)\,, \qquad (2)$$

and the calculation shows that it amounts to a surely observable magnitude.

(a) edge dislocation

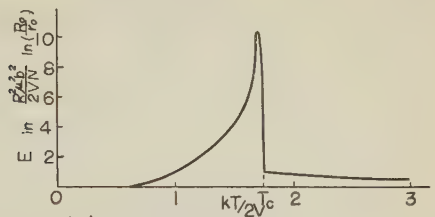

(b) screw dislocation

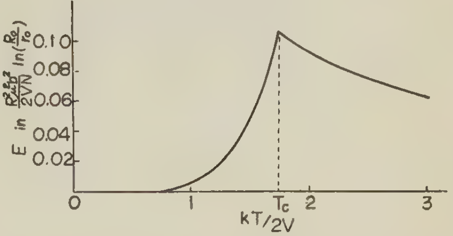

Fig. 1. Interaction energies between dislocations of the edge and screw types and atomic order as dependent on the temperature in $\beta$-brass type crystal.
$k$; Boltzmann constant, $V$; ordering energy, $N$; Avogadro number, $\mu$; rigidity modulus, $b$; Burgers vector of the dislocation, $T_c$; Curie temperature, $R_0$ and $r_0$; upper and lower limits of integrals for the radius direction from the dislocation line.

Interaction energies, $E$, for the edge and screw dislocations in $\beta$-brass type crystal as calculated from Eq. (1) are plotted against the temperature, $T$, in Fig. 1 (a) and (b). It is almost clear that the characteristic features shown in Fig. 1 are also retained for $Cu_3Au$ type superlattices. A peak in Fig. 1 (a), thus, seems to correspond to a peak of the critical shear stress near the Curie point of $Cu_3Au$ as observed recently by Ardley3).

## References

1) A. H. Cottrell: *Report on Strength of Solids* (Phys. Soc. London (1948)), 30.
H. Suzuki: Sci. Rep. RITU **A 4** (1952) 455.
A. H. Cottrell, S. C. Hunder and F. R. N. Nabarro: Phil. Mag. **44** (1953) 1064.
J. C. Fisher: Acta Met. **2** (1954) 9.

2) T. Iwata: Nippon Kinzoku Gakkai-Si **19** (1955) 95 (in Japanese).

3) G. W. Ardley: Acta Met. **3** (1955) 525.

J. PHYS. SOC. JAPAN **11** (1956) 898

# Some Experiments on the Germanium Surface Layer

By Makoto KIKUCHI
*Electrotechnical Laboratory, Tokyo, Japan*

(Received June 14, 1956)

Four-probe method for measuring resistivity[1] has been applied to n-type germanium single crystal on which thin p-type layer was formed by heat treatment. In this case, apparent resistivity $\rho_a$,

$$\rho_a = \frac{V_s}{I} 2\pi s \qquad (1)$$

is very high ($V_s$, $I$ are shown in Fig. 1, and $s$ is the separation of the probes.).

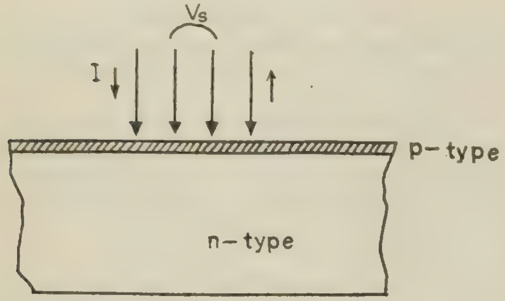

Fig. 1. Four probes and the specimen.

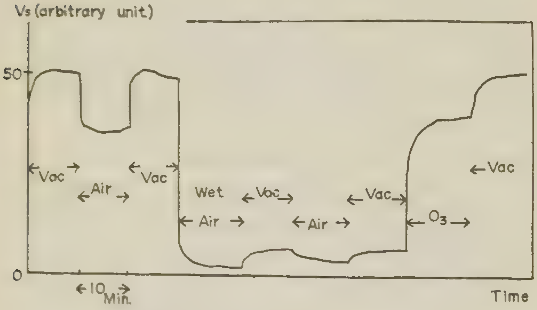

Fig. 2. $V_s$ *vs.* ambient. (Short-time effect and the effect of wet air and $O_3$.)

It has been found that $V_s$ for fixed $I$ is quite dependent on the ambient atmosphere. The sample mounted on the four probe apparatus was placed in a vacuum bell-jar, and $V_s$ was measured varying the ambient atmosphere. Some of the typical and reproducible results are shown in Fig. 2.

They can be summarized as follows:

(1) Long-time effect

If the sample is kept in vacuum or air for relatively long time, $V_s$ shows maximum and gradually decreases to some equilibrium value. When $O_3$ is introduced after the vacuum condition, $V_s$ increases and saturates instead of showing maximum. $V_s$ increases when $O_3$ is again pumped out and the maximum is higher than the maximums found in vacuum in the foregoing cycling. These haviors may be characterized as the "long-time effect."

(2) Short-time effect (Fig. 2)

If the ambient cycling is performed before the falling down from the maximum occurs, $V_s$ shows different type of variation as shown in Fig. 2.

$V_s$ in vacuum is higher than that in air. In this case, $V_s$ decreases when $O_3$ is introduced after the vacuum condition in the vac.-air cycling, to a value even lower than that in air. (not shown in the figure.)

An interesting result is given in Fig. 2. $V_s$ shows remarkable decrease when wet air is introduced, and it does not show much increase in the next vacuum condition. When $O_3$ is introduced, however, $V_s$ goes up very fast. This seems to show that $O_3$ is quite efficient in wiping out the influence of wet air.

Considering a simple equivalent circuit for the structure of our sample, it can be seen that the increase of $V_s$ corresponds to the decrease of the conductance $G_s$ of the p-type layer. Therefore, the variation of $V_s$ may be attributed to the variation of $G_s$. Majority of the experimental results are consistent with the physical picture based on the usual energy scheme of the surface whicn takes into account the n-type inversion layer on the p-type layer.

Detailed discussion of these experiments will be given elsewhere in near future[2].

## References

1) Valdes: Proc. I.R.E. **42** (1954) 420.
2) Bulletin of the Electrotechnical Lab.

JOURNAL OF THE PHYSICAL SOCIETY OF JAPAN Vol. 11, No. 9, SEPTEMBER, 1956

# The Angular Distribution of $\alpha$-particles from the Reaction $^{19}F(p\alpha)^{16}O^*(\pi)^{16}O$

By Akira ISOYA*, Kazuo GOTO**, and Teruo MOMOTA

*Department of Physics, Faculty of Science, University of Tokyo*

(Received May 19, 1956)

The angular distribution of $\alpha$ -particles from the reaction $^{19}F(p\alpha)^{16}O^*(\pi)^{16}O$ has been measured at fourteen energies between 800 kev and 1400 kev. The $\alpha$ -particles were detected and identified by coincidence with nuclear pair-electrons. The data were analyzed to give coefficients in the expansion formula $\sigma(\theta)=a_0+a_1\cos\theta+a_2\cos^2\theta+a_3\cos^3\theta+a_4\cos^4\theta$. The spins of the levels of the compound nucleus $^{20}$Ne were assigned from the evidence of anomalies in the coefficients. For the resonances at 843-, 1126-, 1355-kev $J=2$ and for that at 1250 kev $J=1$.

## §1. Introduction

The states of the compound nucleus $^{20}$Ne resulting from the reaction $^{19}F+p$ are classified into two types according to the even-odd characters of their spin and parity[1]. The state with even spin and even parity or odd spin and odd parity, insofar as their assignments are known, decays with emission of an $\alpha$-particle to the ground state and/or the pair-emitting, first excited state of $^{16}$O. Transitions to higher excited states of $^{16}$O accompanying successive $\gamma$-ray emission have not been observed. On the other hand the state with even spin and odd parity or odd spin and even parity decays by emission of an $\alpha$-particle only to higher excited states of $^{16}$O. Transitions to the ground or to the first excited state (both $0^+$) are inhibited by the law of conservation of angular momentum and parity. Up to the present day, many experimental results have been accumulated which enable one to make conclusive assignments to most states belonging to the latter type, while for the states of the former type available informations are scarce and values of the spin are not assigned yet except for a few cases.

Assignment of spin, J, to the states of $^{20}$Ne of the former type can be accomplished most reliably by measuring the angular distribution of $\alpha$-particles. The angular distribution of the full energy group ($\alpha_0$) which leaves $^{16}$O in the ground state has been measured at various proton energies by several investigators[2][1], but strong interference effect of neighbouring levels complicated the analysis of data and made it difficult to draw a unique conclusion in the energy region around 1 Mev. The angular distribution of $\alpha$-particles of the next largest energy ($\alpha_\pi$) leading to the pair-emitting state has not been measured by reason that this group is generally obscured by much more intense groups of $\alpha$-particles ($\alpha_1$, $\alpha_2$, and $\alpha_3$) from the compound states of another type, above all the $\alpha_1$-group leading to the second excited state of $^{16}$O, the energy of which is very close to that of $\alpha_\pi$. This group $\alpha_\pi$, however, seems to be better suited for the analysis because the yield curve of nuclear pair-electrons ($\pi$) emitted successively shows resonance peaks somewhat more prominent compared with those of $\alpha_0$. In the present investigation, the angular distribution of $\alpha_\pi$ was measured by singling out $\alpha_\pi$ from groups of $\alpha$-particles by means of the coincidence counting between $\alpha_\pi$ and $\pi$. The procedure is correct because the directional correlation is not to exist between $\alpha_\pi$ and $\pi$ owing to the nature of a 0-0 transition characteristic of the pair-emitting process. A result at $E_p=843$ kev which was obtained in the early stage of this study has been reported[3]. The present paper contains the measurements of the angular distributions measured at fourteen proton energies between 800 kev and 1400 kev with a view that the nature of a resonance level manifests itself remarkably in the variation of the angular distribution coefficients in the neighbourhood of its resonance energy.

---

* Now at The Institute of Nuclear Study, University of Tokyo.

** Now at The University of Rochester, Rochester, New York, U.S.A.

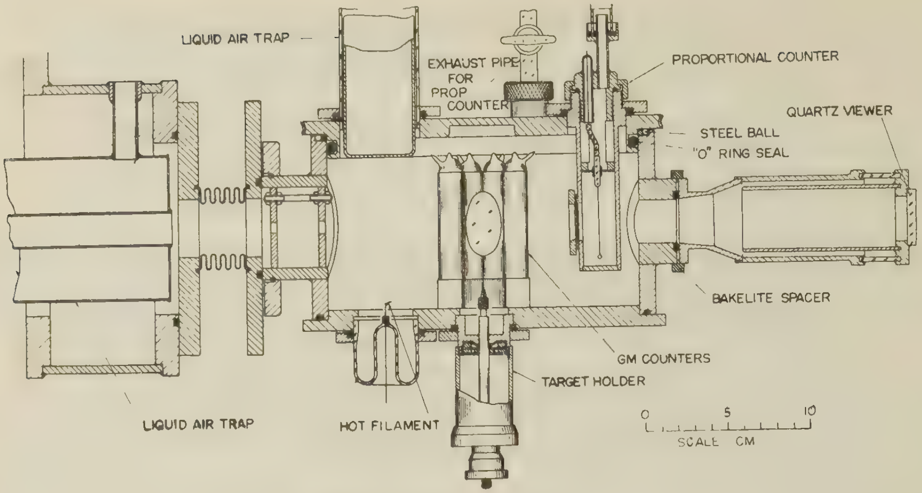

Fig. 1. Reaction chamber.

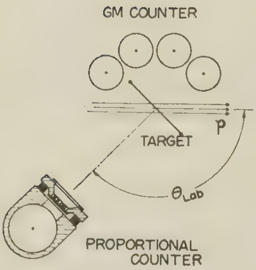

Fig. 2. Arrangement of target and detectors.

## § 2. Equipment and Experimental Procedure

As detectors for $\alpha$-particles and pair-electrons a proportional counter and GM counters were used respectively. Because the proportional counter was exposed to flux of protons elastically scattered from the target, it was necessary to keep the proportional counter from paralysis by using a target as light and thin as possible. Under usual operating conditions normal pulses of scattered protons could be excluded by the discriminator because the pulse height of proton was made much smaller than that of low energy $\alpha$-particles. Among the five groups of $\alpha$-particles ($\alpha_0$, $\alpha_\pi$, $\alpha_1$, $\alpha_2$, $\alpha_3$) those accompanying successive $\gamma$-rays ($\alpha_1$, $\alpha_2$, $\alpha_3$) might have contributed some appreciable number of coincidence counts if the sensitivity of the GM counters to $\gamma$-rays had not been small enough. Thus care ought to be taken to reduce the amounts of matter in the region of the target and the detectors to a minimum, so as to minimize the production of secondary electrons. The use of thin-wall GM counters was appropriate for this purpose. The effect due to internal pair-electrons associated with $\gamma$-ray transitions could not be excluded by this method. But the probability of this process was generally so small ($\sim$1/1000) that its contribution could be neglected except at the restricted region of $\gamma$-ray resonance.

Fig. 1 is a schematic diagram of the apparatus used in this experiment. The proton beam, the energy spread of which is about 0.2%, from a stabilized electro-static generator enters the reaction chamber through a beam defining slit of 3 mm in width and 6 mm in height. After penetrating a thin-backed target the beam is collected in a long Faraday cage. To reduce the disturbing effect on counters due to soft $x$-rays or back-scattered protons from the Faraday cage it is placed as far as possible from the detectors. Alignment of the beam is facilitated by quartz viewer at the bottom of the Faraday cage. The inner surface of the quartz plate is made conductive with a thin layer of aluminium to avoid sparking due to accumulation of charge. The degree of broadening of the beam spot on the quartz viewer by the insertion of the target gives a quick estimation of the target thickness.

### Detectors

A cylindrical proportional counter is set, with its accessories (a gas-filling system and a pre-amplifier), on the upper lid of the chamber, which is rotatable by means of a "O"-ring seal. Thus the counter can be set at any angles with respect to the beam direction. The inner diameter of the counter wall is 2 cm. The anode is made of tungsten wire of 0.24 mm in diameter, which is finished electrolytically. The window on the side wall is covered with a formvar film, which is supported by a perforated plate. The effective area of the window is 75% of the total area of 8 mm in width and 20 mm in height. The inner surface of the formvar film is made conductive by evaporating a thin coat of aluminium. A preliminary test with a filling gas of argon showed that pulse heights of $\alpha$-particles from a polonium source were uniform within about 15%. The distance from the target to the counter window is 6 cm, and the solid angle subtended at the target by the effective area of the window is 1/450 of a total sphere. The angular spread is about 8°. The angular resolution available with this geometry is sufficient for taking the distribution function, the complexity of which is not higher than $\cos^4\theta$. (See the following section on correction.) In the actual run the counter was filled with pure hydrogen gas of 16 cm Hg pressure introduced through a palladium tube. The use of hydrogen gas of low pressure seems to be effective in preventing the counter from paralysis by reason of large mobility of ions.

In front of the proportional counter an absorber composed of mica and aluminium foils was placed, the thickness of which was adjusted so as to make the pulse-height of $\alpha_\pi$ maximum. The best result was obtained with an absorber of about 8 mg/cm² thickness, which reduced the original energy of $\alpha_\pi$, 2 to 2.5 Mev, to several hundred kev which corresponded to the maximum energy loss per unit length of path. The pulse height of $\alpha_\pi$ attained with this arrangement was about eight times as large as those of elastically scattered protons and still about twice as large as the largest pulse produced by multiply scattered protons of low energies. Although these normal proton pulses could be removed by the discriminator as mentioned above, it was observed that even with the thinnest target available a large pile-up of scattered protons occured, which produced many pulses of the size comparable to those of $\alpha_\pi$ and their frequency increased near the forward direction. Furthermore the uniformity of pulse height was impaired by the counter paralysis. These effects became more serious at low energies. By this reason the measurements could not be extended below 800 kev.

Four cylindrical thin-wall GM counters for detection of $\pi$-electrons are fixed on the bottom lid of the chamber. They are connected in parallel and placed around the target as closely as possible, because the cross-section of the $\pi$-formation is fairly small ($\sigma_R \sim$a few $m$ barns). The diameter of the cathode and the wire of each counter are 15 mm and 0.8 mm respectively. The length of the active volume is 3 cm. The total acceptance solid angle subtended by the set of these counters is 0.19 of a total sphere. If the fact that pair of electrons are emitted with an angular correlation $W \doteqdot 1+0.85\cos\theta$[4], is taken into account, the counting probability is estimated to be about 0.33 per reaction. This value is slightly overestimated, because of the absorption of low energy electrons in the counter wall. The thickness of aluminium wall of the counter is 0.4 mm, which is thin enough to reduce the $\gamma$-ray conversion to a tolerable amount, but on the other hand thick enough to absorb soft $x$-rays from the target. The over-all efficiency of GM counters, for 6 Mev $\gamma$-rays was estimated experimentally to be about 0.1% (See the following paragraph).

### Targets

The target was made by evaporating SiO and $AlF_3$ successively onto a thin formvar-film (~10 $\mu g$/cm² thick), stretched on an elliptic frame made of thin piano-wire. The coating of SiO[5] of several $\mu g$/cm² in thickness formed a satisfactorily rugged base for the target material. For most measurements the thickness of $AlF_3$ was of the order of 1 kev in stopping power. This target could withstand the proton bombardment upto a few $\mu$ A per cm². Thicker target was found to be less durable under the bombardment. During bombardment the target was supplied with electrons from a hot filament to avoid damage due to accumulation of charge. The carbon deposit on the target was reduced to a negligible amount by the use of two liquid air traps; the one was set in the chamber and the other located at the entrance of it. The target was set at an angle of 45° with respect

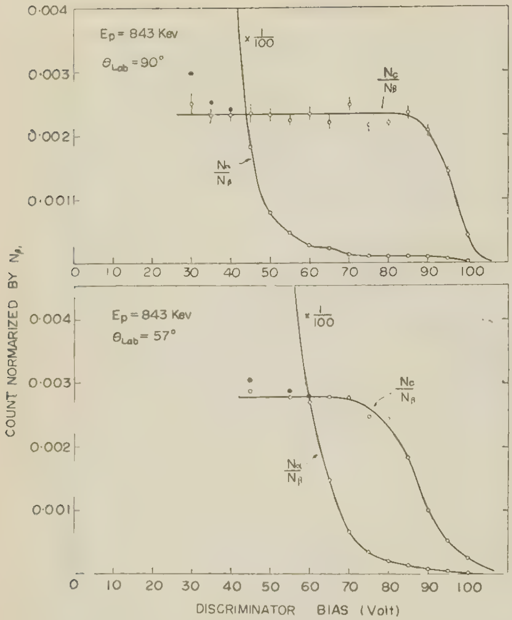

Fig. 3. Integral bias curves of the total ($N_\alpha$) and coincidnece ($N_c$) pulses of the proportional counter at two angles with respect to the beam direction at $E_p$=843 kev. The counts are normalized by the count of the *GM* counters ($N_\beta$). The coincidence counts which are not corrected for the chance coincidence are indicated by dots. $N_\alpha$ consists of five groups of α-particles ($\alpha_0, \alpha_\pi, \alpha_1, \alpha_2, \alpha_3$) and scattered protons. The large rise at low bias value is attributed to pile-up of scattered protons. The height of a single pulse due to scattered proton is about 15 volts. Comparison of two curves indicates that uniformity of the pulse height is disturbed at the forward angles.

to the beam direction. Those α-particles emitted to angles less than 90° against the beam direction penetrate the target and suffer small angle scattering. However, the amount of deflection is judged to be small because α-particles of 2 Mev or so are deflected by nearly the same amount as protons of 1 Mev. The mean deflection angle of the latter was estimated to be about 0.2∼0.4 degrees from the broadening of the proton beam observed at the quartz viewer when the target was placed in the position.

### Coincidence Counting and Errors

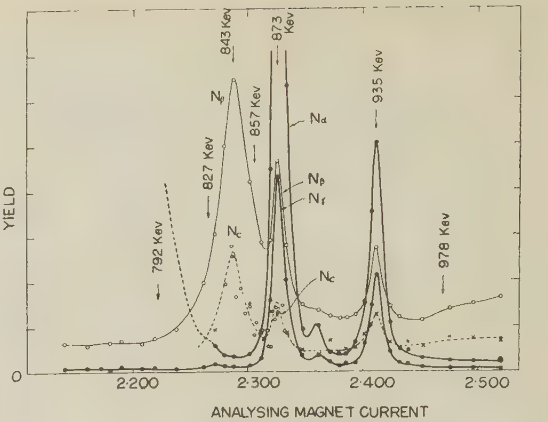

Fig. 4. Yield curves measured simultaneously with the proportional counter ($N_\alpha$), the *GM* counter ($N_\beta$) and the γ-ray counter ($N_\gamma$) in the neighbourhood of the 843 kev resonance. The coincident counting rate ($N_c$) is also shown. The proton energies where the angular distribution was measured and the resonance energies of γ-rays are indicated on the curves.

The pulses of both detectors were fed into linear amplifiers and discriminators. Both output, shaped in their wave forms, were mixed in a coincidence circuit, the resolving time of which was 0.45 $\mu$ sec. The delay time in the GM counters was estimated to be of the order of 0.1 $\mu$ sec from the size of the counter. Its fluctuation is considered to be of the same order. Integral bias curves of the total and coincidence pulses of the proportional counter pulses taken at two counter angles, with the proton energy $E_p$=843 kev are shown in Fig. 3. These curves indicate performance of the coincidence circuit and the grade of uniformity of the height of $\alpha_\pi$-pulses. The pulse shapes and the pulse height distribution were observed in the course of measurements with an oscilloscope to monitor the operating condition of the proportional counter and to check whether the discriminator bias was proper.

Fig. 4 shows the yield curves of pair-electrons, α-particles and γ-rays taken simultaneously with the detectors mentioned above and a γ-ray counter placed just beneath the chamber, together with a rough measurement of the coincidence counting rate in the neighbourhood of the 843 kev resonance. In the yield curve taken with the thin-walled GM counters in the chamber ($N_\beta$) are seen peaks due to γ-rays or internal pair-electrons at the strong resonances of 873.5 and 935 kev. By comparing the count of α-particles at the resonance peak with the corresponding count of GM counters, the γ-ray sensitivity of the set of the GM counters including the effect of internal pair creation is estimated to be about 0.001 per reaction. The count $N_\beta$ includes small amount of soft $x$-rays from the target, which is estimated to be about one percent of the total count at 843 kev with the target used in this case. The number of counts of the proportional counter shows an abrupt increase below 800 kev, which is ascribed in pile-up of pulses of scattered protons. This increase is nearly proportional to $(E_p)^{-10}$ or $(E_p)^{-11}$. This abrupt change is explained by the fact that the discriminator bias is set at about five times of the normal pulse height of elastically scattered protons and the intensity of scattered protons is proportional to $(E_p)^{-2}$.

The time required to take the coincidence counts with a statistical error of 3% was about 10 minutes at angles and energies, where the counting rate of the proportional counter was not high and the speed of measurement was limited only by the maximum beam intensity tolerable for the target. The correction for chance coincidence was a few percent or less. At forward angles, however, much more time was required, because the beam intensity ought to be reduced to avoid the paralysis of the proportional counter and to prevent the increase of the chance coincidence rate. The chance coincidence count was estimated from the average counting rate by the following formula:

Chance coincidence count in $t$ sec$=2\tau N_\alpha N_\beta k/t$,

where $\tau$ is the resolving time of the coincidence circuit and $N_\alpha$ and $N_\beta$ are the counts in $t$ seconds of the proportional counters and the set of GM counters respectively. $k$ is the shape factor of fluctuation of the bombarding current. In spite of considerably large variation of the current, $k$ could be safely taken to be 1*. The systematic error due to this procedure is much less than the statistical error for most cases.

The true coincidence count was normalized with respect to the count of GM counters $N_\beta$. This procedure made the data insensitive to the effect due to change in the target conditions and the efficiency of GM counters and /or drifts in the proton energy. Some variations in the normalized yield of $\alpha_\pi$ were observed from target to target probably owing to variation in the yield of soft $x$-rays. The ratio of $N_\beta$ to the collector beam current served as a check on the constancy of conditions in the target and/or the detectors. In order to check occurence of systematic errors, the whole range of angles was swept in irregular order. The main factor of the error was the insufficient statistical accuracy, amounting to 3%∼5%. The errors of geometrical origin, misalignment of the proton beam and off-centering of the target position, never exceed 2%. The finite acceptance solid angle of the proportional counter brings about attenuation in the coefficients of the angular distribution. For $a_4$, that is, the coefficient of $\cos^4\theta$ term, this correction is generally the largest and amount to about 5%, which is considerably small compared to the statistical error of $a_4$.

Magnitude of the systematic error due to $\alpha-\gamma$ coincidences can be estimated by the following consideration: The average count due to $\alpha-\gamma$ coincidence and that due to $\alpha_\pi-\pi$ coincidence are given approximately by $N_{\alpha_\gamma}\cdot\eta_\gamma$ and $N_\beta\cdot\eta_\alpha$ respectively, where $N_{\alpha_\gamma}$ and $N_\beta$ are the count of proportional counter due to $\alpha$-particles associated with $\gamma$-rays and that of the GM counter respectively, and $\eta_\gamma$ and $\eta_\alpha$ are the detection probabilities of the GM counters for $\gamma$-rays and of the proportional counter for $\alpha$-particles respectively. From the measurements mentioned above $\eta_\gamma \doteqdot 0.001$ and $\eta_\alpha=1/450$. Thus the ratio of the average count of $(\alpha_\gamma-\gamma)$ coincidence to that of $(\alpha_\pi-\pi)$ is given by

$$\frac{N_{\alpha_\gamma}\eta_\gamma}{N_\beta\eta_\alpha} \doteqdot 0.45\frac{N_{\alpha_\gamma}}{N_\beta} < 0.45\frac{N_\alpha}{N_\beta},$$

where $N_\alpha$ is the average count of the proportional counter. The magnitude of the quantity at the right hand side is one to three percent except for measurements at the proton energies near the 843 kev resonance (857-, 827- 792-kev). At these unfavourable cases the count due to scattered protons is so large that $N_{\alpha_\gamma}$ is a small fraction of $N_\alpha$, and the estimation mentioned above is improper. Approximate average counting rates due to $\alpha-\gamma$ coincidence at these proton energies can be estimated from the behaviour of the yield curve of $\gamma$-

---

* In the case where the chance coincidence is predominantly due to pile-up pulses of scattered protons, the rate of which varys roughly as the fifth power of the proton current

$$k=\frac{\langle I^6\rangle_{\mathrm{AV}}}{\langle I^5\rangle_{\mathrm{AV}}\langle I\rangle_{\mathrm{AV}}}.$$

Although the mean proton current level measured with a DC microammeter wae kept constant to within 5∼10% during a run, the instantaneous current was not constant, because it had a fiarly large AC component. If the variation is assumed sinusoidal and its amplitude is put to be 0.5 of the mean current, $k\sim1.3$.

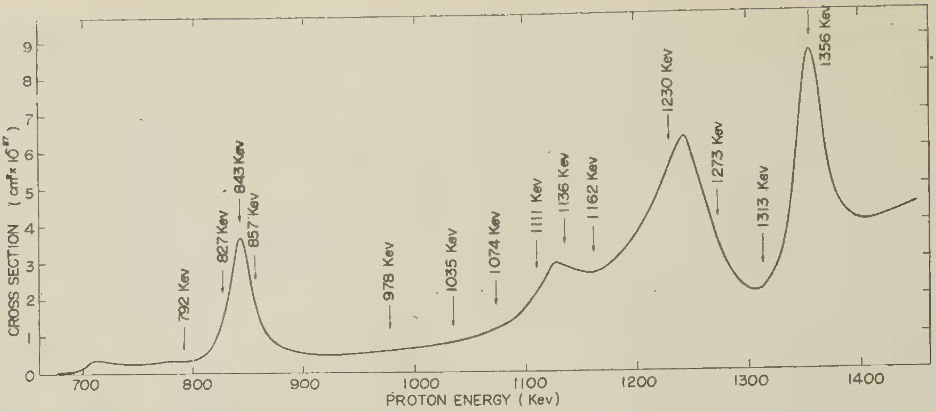

Fig. 5. Yield curve of nuclear pair electrons from the reaction $^{19}F(p\alpha_\pi)\,^{16}O^*(\pi)\,^{16}O$. The proton energies where the angular distribution was measured are indicated by arrows.

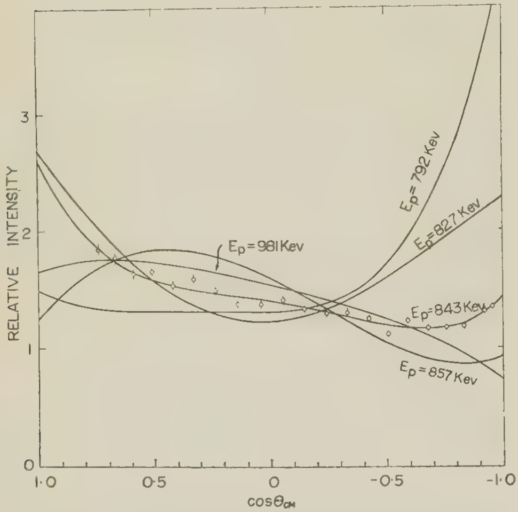

Fig. 6. Angular distribution curves in the center-of-mass system of α-particles from the reaction $^{19}F(p,\alpha_\pi)\,^{16}O^*$ at $E_p$=792-, 827-, 843- and 859-kev. Measured points and their statistical accuracies are indicated only in a few cases. The full curves as drawn according to the expressions, which are not corrected for the finite acceptance solid angle of the proportional counter:

$W(\theta)=1-0.05\cos\theta+0.35\cos^2\theta-0.75\cos^3\theta+0.55\cos^4\theta$ for $E_p=792$ kev

$W(\theta)=1-0.07\cos\theta+1.20\cos^2\theta+0.24\cos^3\theta-0.20\cos^4\theta$ for $E_p=827$ kev

$W(\theta)=1+0.23\cos\theta-0.21\cos^2\theta+0.20\cos^3\theta+0.65\cos^4\theta$ for $E_p=843$ kev

$W(\theta)=1+0.63\cos\theta-0.41\cos^2\theta-0.53\cos^3\theta+0.10\cos^4\theta$ for $E_p=857$ kev

$W(\theta)=1+0.33\cos\theta-0.08\cos^2\theta-0.03\cos^3\theta-0.14\cos^4\theta$ for $E_p=981$ kev

rays or α-particles and the energy dependence of the total coincident counting rate (See Fig. 4). The ratios of the $\alpha-\gamma$ coincidence counts to the $\alpha_\pi$-$\pi$ coincidence counts are estimated

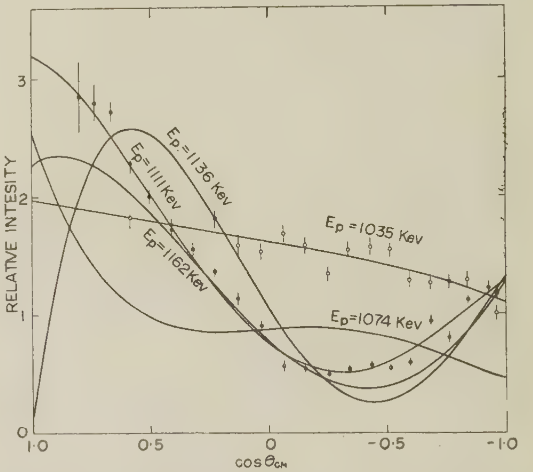

Fig. 7. Angular distribution curves in the center-of-mass system of α-particles from the reaction $^{19}F(p,\alpha_\pi)\,^{16}O^*$ at $E_p$=1035-, 1074-, 1111-, 1136- and 1162-kev. Measured points and their statistical accurracies are indicated only in a few cases. The full curves are drawn according to the expressions, which are not corrected for the finite acceptance solid angle of the proportional counter:

$W(\theta)=1+0.22\cos\theta-0.02\cos^2\theta+0.05\cos^3\theta-0.03\cos^4\theta$ for $E_p=1035$ kev

$W(\theta)=1-0.14\cos\theta-0.15\cos^2\theta+1.39\cos^3\theta+0.90\cos^4\theta$ for $E_p=1074$ kev

$W(\theta)=1+2.11\cos\theta+3.24\cos^2\theta-0.85\cos^3\theta-1.28\cos^4\theta$ for $E_p=1111$ kev

$W(\theta)=1+3.08\cos\theta+1.88\cos^2\theta+3.64\cos^3\theta-2.25\cos^4\theta$ for $E_p=1136$ kev

$W(\theta)=1+2.32\cos\theta+1.96\cos^2\theta-1.68\cos^3\theta-0.67\cos^4\theta$ for $E_p=1162$ kev

to be at most a few percent. Thus the errors due to the presence of $\alpha-\gamma$ coincidence are generally less than statistical errors.

## § 3. Results

The excitation function of pair-electrons measured with the set of GM counters is shown in Fig. 5. It is proportional to the total cross section of the $(p, \alpha_\pi)$ process because pair-electrons are emitted isotropically. It is corrected for the contribution of the soft x-rays from the target. The correction was made by assuming that the yield of soft x-rays increase as the fourth power of the proton energy and by adjusting its magnitude so that energy dependence of the yield of pair-electrons might agree with those given by Phillips and Heydenburg[6] and by Devons, Goldring, and Lindsey[7]. The absolute magnitude of the cross section of the $(p, \alpha_\pi)$ process was estimated relative to that of the $(p, \alpha\,\gamma)$ process at 935 kev given by Chao et al[8] by assuming the acceptance solid angles of the both counters as quoted in the preceeding section. The energy scale was caribrated by resonances at 873.5, 935.3, 1137, 1290, 1346, and 1372 kev[1,8], appearing in the yield curve of α-particles taken simultaneously with the proportional counter. The proton energies where the angular distribution was measured are indicated by arrows in the figure.

The measured distribution were transformed to the center-of-mass system as to both angles and counter solid angles and then fitted to a power series of cos θ containing upto the fourth power, because the higher order terms were not expected to appear in the energy

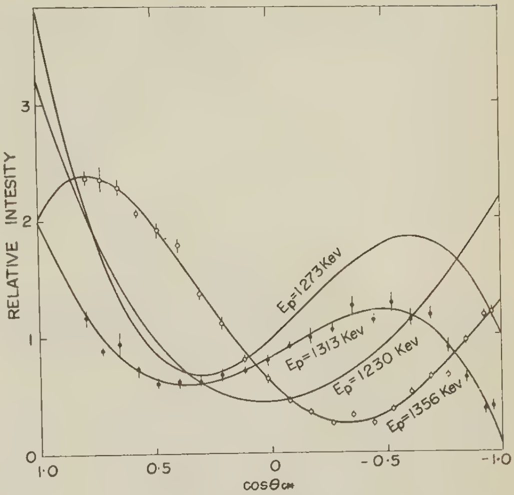

Fig. 8. Angular distribution curves in the center-of-mass system of α-particles from the reaction $^{19}F(p, \alpha_\pi)\,^{16}O^*$ at $E_p$=1230, 1273-, 1313- and 1356-kev. Measured points and their statistical accuracies are indicated only in a few cases. The full curves are drawn according to the expressions, which are not corrected for the finite acceptace solid angle of the proportional counter:

$W(\theta)=1-0.29\cos\theta+4.54\cos^2\theta+1.43\cos^3\theta+0.56\cos^4\theta$ for $E_p$=1230 kev

$W(\theta)=1-1.75\cos\theta+1.43\cos^2\theta+3.16\cos^3\theta-0.005\cos^4\theta$ for $E_p$=1273 kev

$W(\theta)=1-1.32\cos\theta+0.56\cos^2\theta+2.48\cos^2\theta-0.32\cos^4\theta$ for $E_p$=1313 kev

$W(\theta)=1+3.38\cos\theta+4.26\cos^2\theta-2.77\cos^3\theta-2.50\cos^4\theta$ for $E_p$=1356 kev

Table I. Angular distributions of the $^{19}F(p\alpha_\pi)^{16}O^*$ reaction and level assignments.

| Bombarding energy or Resonance energy (kev) | $^{20}$Ne level assignment | Coefficients of the angular distribution $W(\theta)=a_0+a_1\cos\theta+a_2\cos^2\theta+a_3\cos^3\theta+a_4\cos^4\theta$ | | | | |
|---|---|---|---|---|---|---|
| | | $a_0$ | $a_1$ | $a_2$ | $a_3$ | $a_4$ |
| 792 | | 1±0.05 | −0.04±0.11 | 0.33±0.31 | −0.77±0.19 | 0·58±0.37 |
| 827 | | 1±0.03 | −0.07±0.09 | 1.21±0.24 | 0.25±0.14 | −0.21±0.28 |
| 843 (res) | 2⁺ * | 1±0.01 | 0.23±0.03 | −0.23±0.07 | 0.21±0.04 | 0.68±0.08 |
| 857 | | 1±0.03 | 0.64±0.06 | −0.42±0.16 | −0.55±0.09 | 0.10±0.17 |
| 981 | | 1±0.03 | 0.34±0.06 | 0.09±0.17 | −0.03±0.09 | −0.15±0.19 |
| 1035 | | 1±0.02 | 0.22±0.05 | −0.02±0.12 | 0.05±0.07 | −0.03±0.14 |
| 1074 | | 1±0.02 | −0.14±0.05 | −0.17±0.13 | 1.43±0.08 | 0.95±0.15 |
| 1111 | | 1±0.03 | 2.12±0.08 | 3.30±0.23 | −0.88±0.15 | −1.29±0.17 |
| 1126 (res) | 2⁺ | | | | | |
| 1136 | | 1±0.02 | 3.05±0.04 | 1.95±0.12 | 3.75±0.06 | −2.36±0.13 |
| 1162 | | 1±0.04 | 2.36±0.09 | 1.90±0.24 | −1.73±0.13 | −0.70±0.25 |
| 1230 | | 1±0.03 | −0.31±0.11 | 4.54±0.31 | 1.48±0.20 | 0.59±0.39 |
| 1250 (res) | 1⁻ | | | | | |
| 1273 | | 1±0.03 | −1.81±0.07 | 1.44±0.18 | 3.26±0.11 | −0.005±0.21 |
| 1313 | | 1±0.03 | −1.37±0.07 | 0.56±0.20 | 2.56±0.11 | −0.34±0.23 |
| 1356 (res) | 2⁺ | 1±0.03 | 3.45±0.09 | 4.39±0.23 | −2.85±0.14 | −2.62±0.28 |

* This assignment is different from that given by E. U. Baranger[10].

region concerned. The results are shown in Figs. 6, 7 and 8. The measured points and their statistical errors are plotted only in a few cases. It is to be noted that areas under the distribution curves are common for all curves because $N_c/N_\beta$, corrected for transformation of coordinate system, are plotted as ordinates and

$$\int_{-1}^{1} N_c/N_\beta d(\cos\theta)$$

depends only on the acceptance solid angle of the proportional counter. Small amount of soft x-ray background in $N_\beta$ introduces some deviation from this rule. The coefficients corrected for the finite solid angle of the counter are given in Table I, with their statistical errors which were calculated by the method described in the appendix.

Analysis of the experimental results has been done, and the structure of the overlapping compound levels was revealed in the energy region concerned. The spin of the compound levels assigned are given in Table I. The analysis will be published in the near future by one of the authors (A. I.) in this Journal.

The authors wish to thank the members of Van de Graaff group at the University of Tokyo for their cooperation.

### Appendix

The statistical error $\tilde{a}_i$ in the coefficient $a_i$ was calculated according to the following formula, which was derived in a manner similar to that used by P. M. Endt[9]:

$$\frac{\tilde{a}_i}{\alpha_0}=\frac{1}{N^{1/2}}\left[\sum_{m,n} C_{im}C_{in}(2m+1)(2n+1)\right.$$
$$\left.\times\sum_{r=0}^{r\leq m,n}\frac{A_{m-r}A_{n-r}A_r}{(2m+2n-2r+1)A_{m+n-r}}\cdot\frac{\alpha_{m+n-2r}}{\alpha_0}\right]^{1/2},$$

with

$$Ar=\frac{1\cdot 3\cdot 5\ldots.(2r-1)}{\gamma!}, \text{ and } A_0=1,$$

where $N$ denotes the sum of $N_c$'s taken at various angles, $\alpha_m$ $(m=0, 1, 2,\ldots.)$ is a coefficient in the expansion of angular distribution function into a series of Legendre's polynomials, and $C_{im}$ represents one of the numerical constants which relate $\alpha_m$'s with $a_i$'s as follows:

$$a_i=\sum_{m=0} C_{im}\alpha_m .$$

In the present case, where $a_i$'s and $\alpha_m$'s with $i$ or $m$ upto 4 are taken into consideration,

$$a_0=\alpha_0-\frac{1}{2}\alpha_2+\frac{3}{8}\alpha_4,$$
$$a_1=\alpha_1-\frac{3}{2}\alpha_3,$$
$$a_2=\frac{3}{2}\alpha_2-\frac{15}{4}\alpha_4,$$
$$a_3=\frac{5}{2}\alpha_3,$$
$$a_4=\frac{35}{8}\alpha_4$$

and the expression for the statistical error becomes

$$\frac{\tilde{a}_0}{\alpha_0}=\frac{1.87}{N^{1/2}}\left(1-0.364\frac{\alpha_2}{\alpha_0}+0.234\frac{\alpha_4}{\alpha_0}\right)^{1/2},$$
$$\frac{\tilde{a}_1}{\alpha_0}=\frac{4.33}{N^{1/2}}\left(1-0.061\frac{\alpha_4}{\alpha_0}\right)^{1/2},$$
$$\frac{\tilde{a}_2}{\alpha_0}=\frac{11.7}{N^{1/2}}\left(1+0.052\frac{\alpha_2}{\alpha_0}+0.047\frac{\alpha_4}{\alpha_0}\right)^{1/2},$$
$$\frac{\tilde{a}_3}{\alpha_0}=\frac{6.61}{N^{1/2}}\left(1+0.267\frac{\alpha_2}{\alpha_0}+0.182\frac{\alpha_4}{\alpha_0}\right)^{1/2},$$

and

$$\frac{\tilde{a}_4}{\alpha_0}=\frac{13.1}{N^{1/2}}\left(1+0.260\frac{\alpha_2}{\alpha_0}+0.162\frac{\alpha_4}{\alpha_0}\right)^{1/2}$$

respectively.

### References

1) F. Ajezenberg and T. Lauritzen: Rev. Mod. Phys. **27** (1955) 77.
2) C. Y. Chao: Phys. Rev. **80** (1950) 1035.
Y. Asano: Proc. Phys. Math. Soc. Japan **25** (1943) 432.
3) A. Isoya, K. Goto and T. Momota: J. Phys. Soc. Japan **10** (1955) 1022.
4) S. Devons and G. R. Lindsey: Nature **164** (1949) 539.
5) G. A. Sawyer: Rev. Sci. Instr. **23** (1952) 604.
6) G. C. Philips and N. P. Heydenburg: Phys. Rev. **83** (1951) 184.
7) S. Devons, G. Goldring and G. R. Lindsey: Proc. Phys. Soc. **A 67** (1954) 134.
8) Chao, Tollestrup, Fowler and Lauritsen: Phys. Rev. **79** (1950) 108.
9) P. M. Endt: Physica **18** (1952) 421.
10) Hagedorn, Fowler and Lauritsen: Phys. Rev. **99** (1955) 138.
E. U. Baranger: Phys. Rev. **99** (1955) 145.

JOURNAL OF THE PHYSICAL SOCIETY OF JAPAN Vol. 11, No. 9, SEPTEMBER, 1956

# An X-ray Study of Ordering Processes in CuAu Single Crystals

By Makoto HIRABAYASHI and Shiro OGAWA

*The Research Institute for Iron, Steel and Other Metals,*
*Tohoku University, Sendai*

(Received May 2, 1956)

Ordering processes in the CuAu alloy were studied by X-rays using single crystals. Characteristic diffuse scattering effects, which may be regarded as similar phenomena to those in the partially ordered CoPt alloy, were observed at early stages of the ordering. The change in X-ray diffraction pattern during aging was discussed on the basis of kinetics of the ordering reaction.

## § 1. Introduction

In copper-gold alloys near the composition CuAu, the solid solution possessing face-centered cubic lattice exists above about 410°C, while at lower temperatures the equilibrium state is complicated by the existence of two crystallographic structures in the ordered state. Below 380°C, the ordered structure is face-centered tetragonal (CuAu I), the atomic plane parallel to one of the cube faces of the original cubic cell being composed alternately of gold and of copper atoms alone. The superstructure formed between 380°C and 410°C is an orthorhombic structure (CuAu II) made out of ten cells of the CuAu I.[1] Thus, the disorder-to-order transformation in CuAu is so complex that its reaction is accompanied by the change in the crystal structure associated with the volume contraction.

The kinetics of the ordering in the alloy CuAu has been investigated by many workers in detail by means of the calorimetric[2], resistometric[3], metallographic[4] and X-ray studies. Källbäck, Nyström and Borelius[5] have found that, from X-ray studies in polycrystalline specimens, the tetragonal phase grows gradually and continuously from the disordered cubic phase in the temperature range from 225°C to 325°C but at higher temperatures the change is discontinuous. Harker[6] has also indicated that the ordering of CuAu is a continuous process in the range of temperature from 180°C to 300°C, and has proposed for the intermediate state of ordering reaction successive alternate layers on (111) planes of the three orientations of the tetragonal lattice separated by layers of the cubic structure. Early workers[7] have also investigated the transformation from the disordered phase to the tetragonal ordered phase by X-rays using single crystals. However, far less work has been done of the kinetics of early stages of ordering at lower temperatures. The work described in this paper deals with only the ordering process from the quenched disordered state to CuAu I below 200°C, and not with the ordering process from the disordered phase to CuAu II directly or passing through CuAu I.

The problem of how the ordering initially takes place in a disordered alloy quenched from above the transition temperature is very important and interesting, but has not yet been clearly solved. As discussed by Lipson[8], it seems that there are at least two ways in which an initial stage of ordering is produced. In the first way it may be considered that the ordering starts at particular points in a disordered matrix and spreads outwards from these. This process is regarded as the formation and growth of small ordered nuclei in a similar way to the heterogeneous precipitation in alloys. It is another possibility of ordering that the development of order is essentially a homogeneous increase in short range order throughout the crystal, so that the ordering process starts at all points in the crystal simultaneously. This homogeneous process is suggested from the X-ray study of $Cu_3Au$ crystal by Edmunds and Hinde[9] and examined through the optical demonstration of Taylor and coworkers[10]. On the other hand, the heterogeneous process is also supported by many investigators.

If the ordering of CuAu starts heterogeneously, so that the ordered tetragonal nuclei (coherent with the matrix) form on particular atomic planes of the disordered solid solution, the anisotropic lattice distortion will be caused by the difference of lattice parameters between the ordered and disordered structures. It will be expected that some diffuse X-ray diffraction effects arise from such non-uniform lattice strain as mentioned above. In fact Newkirk *et al.*[11] found characteristic diffuse diffraction effects at an early stage of the ordering of the alloy CoPt, which forms a tetragonal ordered structure with an atomic distribution analogous to that of CuAu I. From X-ray and microscopic observations they concluded that thin platelets of the ordered nuclei lie on {110} planes of the disordered matrix.

The present investigation is undertaken to examine the diffuse scattering effects at various stages of the ordering process in single crystals of CuAu. The two different possibilities on the formation of order mentioned above will be discussed in the light of the present experimental results.

## § 2. Experimental Procedure

### a) *Preparation of Specimens*

The CuAu alloys were prepared from electrolytic copper (99.9%) and pure gold. The metals were melted under flux in a crucible made from high purity graphite electrode and then sucked up into thin ceramic tubes of about 1 mm in diameter. The single crystals of a few centimeters in length were grown by the Tammann-Bridgman method from these small ingots and then homogenized by holding for several hours below the solidus temperature in vacuum. After homogenization the diameter of the specimens was reduced to 0.1∼0.2 mm by etching in aqua regia or $HCl+CrO_3$ aqueous solution.

### b) *Heat Treatment*

Two single crystals were sealed in evacuated glass tubes. To obtain the disordered state, the crystals were heated at temperatures above the transition point for a period of 1 or 2 hours and quenched in ice water. After this treatment various stages of the ordering process were attained by keeping them at 100°C or 200°C for various durations of annealing and by quenching immediately into ice water.

### c) *X-ray Examination*

After taking the back reflection Laue photographs either a [100] or a [110] direction of the original cubic crystal was precisely kept vertically on the goniometer head of an X-ray camera. Some series of stationary crystal photographs were taken, the azimuthal angle being successively varied around the vertical axis, and sometimes oscillation photographs were also taken. In each case the photographing was carried out with a cylindrical cassette of 10 cm in diameter using Eastman-Kodak films or Fuji industrial high speed films. Unfiltered Fe or Cu radiations were used. The experimental conditions were, for example, as follows; for a rotating-anode X-ray tube (Tokuda Seisakusho Co.) the applied voltage, the anode current and the exposure time were 40 kV, 80 mA and 30 min respectively, and for a usual stationary tube with Wehrnelt grid they were 40 kV, 15 mA and 3 hr respectively. For simplicity only the diffractions on the zero-layer line were noticed.

## § 3. Experimental Results

In the first place, initial quenched states were studied by taking Laue photographs. The specimen quenched from 450°C or 500°C gave no appreciable diffuse diffraction. By keeping it for several days at room temperature the X-ray pattern did not show any change. In a Laue photograph taken immediately after being quenched from 700°C, however, the diffuse scattering faintly appeared about certain Laue reflections. If the initial ordering is characterized by such a diffraction effect, this shows that the ordering rate increases with increasing quenching temperature. This fact agrees with the experimental results for $Cu_3Au$[12], and is interpreted as an evidence of freezing of the vacancies which exist in thermal equilibrium at the higher temperatures.

Fig. 1 is an example of the back reflection Laue photographs showing strong diffuse diffraction, as shown by an arrow. This pattern corresponds to a partially ordered state, i.e. the crystal was heated at 100°C for a period of four hours after being quenched from 500°C. Thus, the diffuse diffraction effect becomes stronger as the ordering proceeds even at relatively low temperatures. From Laue patterns alone, however, it will be very difficult to obtain precise informations about the

Table I.

| Annealing temperature C° | Annealing time min | Observed relpoints surrounded by diffuse scattering | Unfiltered characteristic radiation |
|---|---|---|---|
| 100 | 30 | 200, 220, 222, 400 | Fe–K |
| | 150 | 111, 200, 220, 311, 222, 400 | |
| | 300 | 220, 420 | Cu–K |
| 200 | 5 | 220, 311, 420 | |
| | 20 | 111, 200, 220, 311, 222 | Fe–K |
| 250 | 2 | 200, 220, 311 | Cu–K |

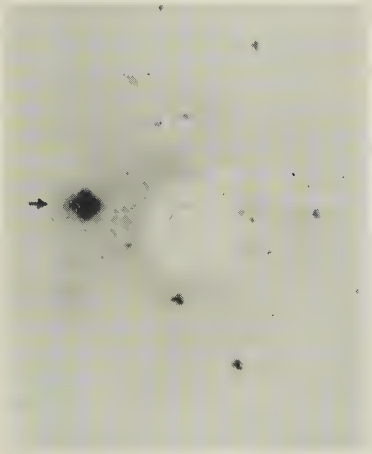

Fig. 1. Back reflection Laue photograph showing diffuse scattering, as noted by an arrow.

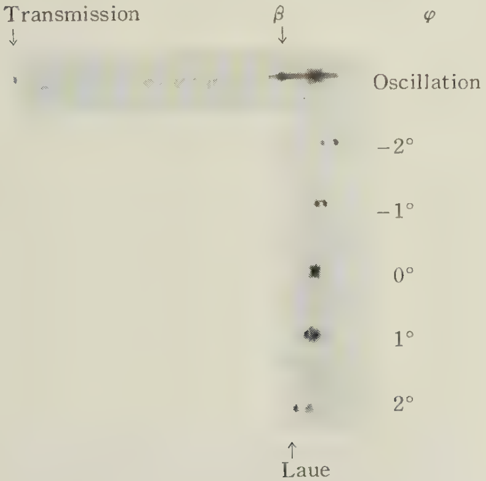

Fig. 2. Diffuse reflections about the (220) relpoint of CuAu crystal annealed at 100°C for 30 min. Crystal was rotated around [001]. Unfiltered FeK radiation was used.

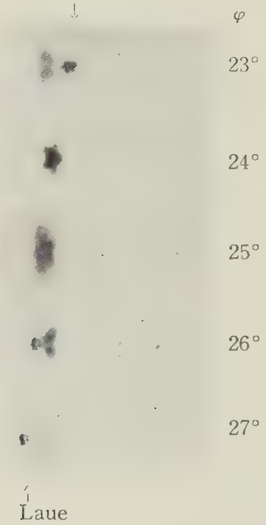

Fig. 3. Diffuse reflections about the (222) relpoint of the alloy annealed at 100°C for 30 min. Crystal was rotated around [0$\bar{1}$1]. FeK radiation was used.

configuration of the diffuse regions in reciprocal space. Therefore, we investigated mainly by means of the stationary crystal method. In Table I we summarized the heat treatments after quenching from 500°C and the observed relpoints* surrounded by diffuse scattering. The observed results for each stage of the ordering will be described below.

a) *Annealing at 100°C for 30 min.*

Fig. 2 is an oscillation photograph and a series of stationary crystal photographs showing the diffuse diffraction about the (220) relpoint of the cubic crystal with the [001]

---

* Hereafter we use the term "relpoint", "relrod" or "relplane" in place of point, rod or plane in the reciprocal lattice.

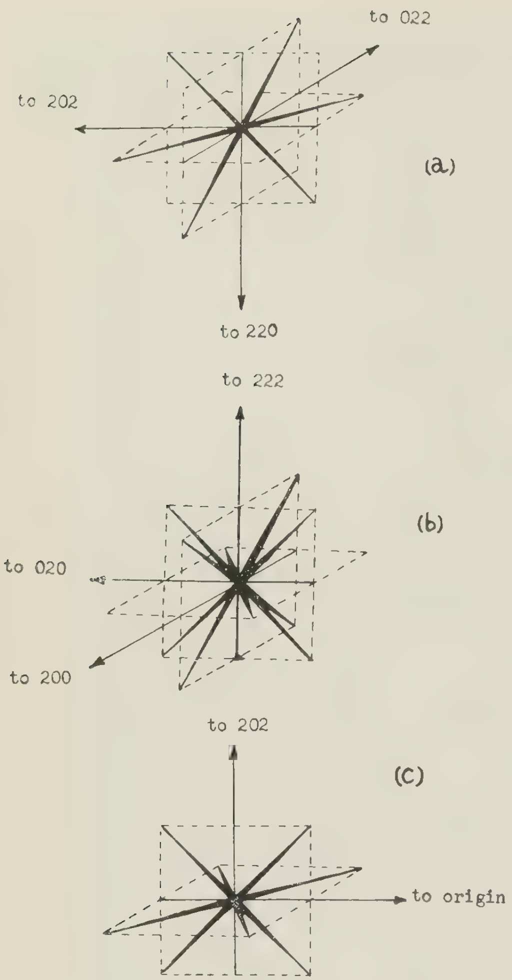

Fig. 4. Distribution of relrods about the relpoints.
(a): (222), (b): (220), (c): (200).

axis vertical. The direction of the incident radiation lies in the (001) plane and $\varphi$ is the angle between this direction and the horizontal [010] direction of the cubic crystal. It will be found that the diffuse reflection is composed of streaks or spots besides Laue spots, and especially that the diffuse streaks in the oscillation photograph make an angle of about 45° with the equatorial line.

The series in Fig. 3 shows another example of similar diffuse pattern around the (222) relpoint. It may be noticed that this pattern is quite similar to the diffuse pattern about the $(\bar{1}11)$ relpoint reported by Newkirk *et al.* at an early stage of ordering of a CoPt crystal (see Fig. 6 of reference (11)). They have concluded that " there are three ⟨110⟩ rods at this (reciprocal) point all in the same plane and at an angle of 60° from each other ". This conclusion is also just true for the present case. According to the present study, the configuration of relrods through the (222) relpoint is schematically shown in Fig. 4a. Fig. 4b depicts the diffuse scattering around the (220) relpoint, corresponding to five relrods in ⟨110⟩ directions. From the diffuse pattern about four relpoints, i.e. (200), (220), (222) and (400), it might be thought that the features of the appearance of diffuse scattering are almost analogous to the case of the CoPt crystal. In this ordering stage, however, the diffuse diffraction effect about the (200) relpoint was so weak that the complete information of the rods distribution in reciprocal space was difficult to obtain. Neither superlattice reflection nor tetragonal reflection appeared in any photograph.

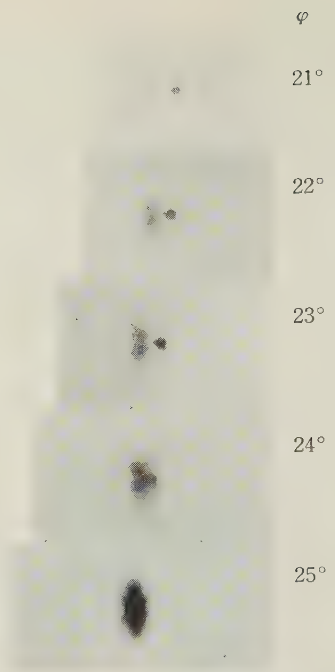

Fig. 5. Diffuse reflections about the (222) relpoint of the alloy annealed at 100°C for 150 min. $[0\bar{1}1]$ was vertical. Fe K radiation was used.

b) *Annealing at 100°C for 150 min.*

The crystal annealed at 100°C for 150 min gave relatively strong diffuse diffraction pattern, as shown in Figs. 5 and 6. By comparing Fig. 5 with Fig. 3, it is easily found that the number of relrods passing through the relpoint does not change, but the length and intensity of them increase with increasing time of annealing. Fig. 6 shows another series of more distinct and characteristic diffuse patterns. This series of stationary crystal photographs showing the diffuse pattern around the (311) relpoint can well be interpreted, in the same way as the case of (220), by the intersection of five ⟨110⟩ relrods with the sphere of reflection. The diffuse pattern around the (400) relpoint clearly shows the existence of four ⟨110⟩ relrods, of which the distribution is the same as of the (200) relpoint shown schematically in Fig. 4c.

It can be concluded that all of the relrods pass through the relpoints and are symmetrical with regard to these points. But the number of them varies between three to five with the indices of relpoints, as described in Table II. Such features have also been reported, but not completely explained, by Newkirk and coworkers[11)]*. This point will be again discussed later. Even in this annealing stage, one could not observe any superlattice reflection and any splitting of spots due to the formation of the tetragonal structure.

Table II. Number of ⟨110⟩ relrods around the relpoints.

| Relpoint | 111 | 200 | 220 | 311 | 222 | 400 |
|---|---|---|---|---|---|---|
| Number of relrods | 3 | 4 | 5 | 5 | 3 | 4 |
| Type of relrods distribution* | a | c | b | b | a | c |

* a, b and c are referred to Fig. 4.

c) *Annealing at 200°C for 5 min.*

The diffuse scatterings around three relpoints (220), (311) and (420) were observed using unfiltered Cu K radiation. The crystal used was so imperfect that the diffuse diffraction could not be interpreted so exactly as in the other cases where another specimen was used. It was found, however, that the characteristic diffuse scatterings became rather broader than those in 100°C annealing.

d) *Annealing at 200°C for 20 min.*

In this stage of annealing, it appears that there coexist the tetragonal reflections with the cubic ones, being surrounded by the diffuse scatterings. For example, this coexistence is shown in this pattern of (222) in Fig. 7, where $[0\bar{1}1]_{\text{cub.}}$ axis was kept as vertical. The oscillation photogragh shows that the surface of the sphere of reflection happens to pass across four major relpoints**, among which two lie in the equatorial plane or the $(0\bar{1}1)$ relplane and the other two just above and below it.

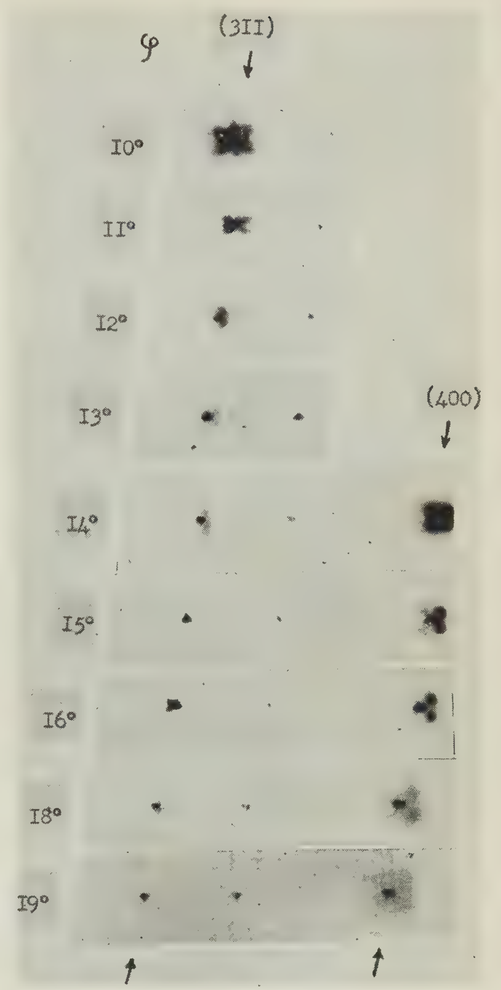

Fig. 6. Diffuse reflections about the (311) and (400) relpoints of the alloy annealed at 100°C for 150 min. $[0\bar{1}1]$ was vertical. Fe K radiation was used.

During the transition from cubic to tetragonal,

---

* Newkirk and coworkers found that there exist five ⟨110⟩ relrods about the (200) relpoint, though the (400) relpoint is surrounded by four relrods.

** In Fig. 7, one may see the extra reflections, as shown by the arrow, besides the cubic and tetragonal ones. It is considered that these extra spots are due to thin surface layer of gold, produced by preferential attacking of etching reagent, because the specimen was etched by aqua regia for dissolving thin oxide film produced in the course of annealing, and only copper but none of gold was probably attacked by this etching.

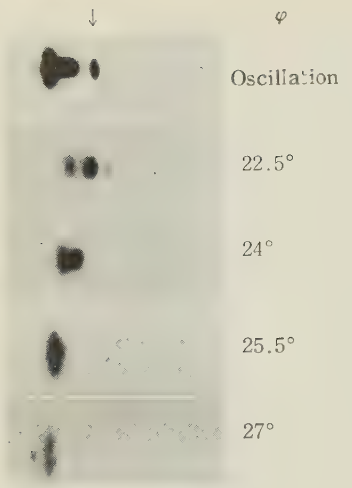

Fig. 7. Diffuse reflections about the (222) relpoint of the alloy annealed at 200°C for 20 min. $[0\bar{1}1]$ was vertical. Cu K radiation was used. The ar rowshows extra spot due to gold.

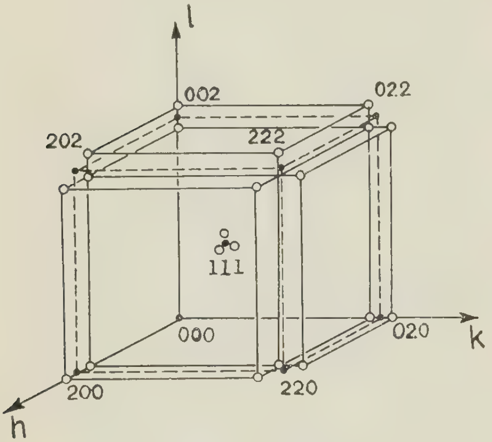

Fig. 8. Reciprocal lattice derived from the coexistence of the face-centered cubic and the face-centered tetragonal structures.

it is possible that, under no external influence, the tetragonal $c$-axis equally distributes in each of three original cubic axes. Thus, as the reciprocal lattice in this state we have to consider the superposition of the original cubic lattice and three tetragonal lattices, as shown in Fig. 8. Among the three $(222)_{\text{tet.}}$ relpoints, one is on the $(0\bar{1}1)_{\text{cub.}}$ relplane passing through the origin, while the other two are above and below this plane, being separated from this by the same distance which depends upon the axial ratio. In this oscillation photograph taken by keeping $[0\bar{1}1]_{\text{cub.}}$ vertical, therefore, such a pattern as seen in the top of Fig. 7 should be expected. It is to be noticed, however, that the actual splittings due to the tetragonal phase are not distinctly separated but seem rather continuous. The fact suggests that there are a number of ordered tetragonal regions with various of axial ratio in the cubic matrix. A rough estimate indicates that the axial ratio $c/a$ is larger than 0.95.

By comparing Fig. 5 and Fig. 7, it will be seen that the characteristic diffuse scatterings surrounding the (222) relpoint of the cubic structure spread out with the progress of ordering and Laue reflections are also considerably broader at 200°C than those at earlier stages of ordering. Such features were also observed on the other relpoints.

Further we investigated certain states under different annealing conditions, such as 250°C, 2 min and 100°C, 300 min. In these both stages, the diffraction patterns show diffuse tetragonal splittings of normal reflections and superlattice reflections, which are both more intense than those at earlier stages as mentioned above. No relrod was observed in any other direction than ⟨110⟩ at each state of ordering.

## §4. Discussions

### a) *Interpretation of the Diffuse Diffraction Effects*

In general, it is very difficult to obtain a unique interpretation of the diffuse diffration phenomena of X-rays. As has already been reported by many workers, the age-hardening alloys, such as Al-Cu, Al-Ag and so on, give characteristic diffuse scattering patterns in early stages of the precipitation process, and the similar phenomenon has recently been observed[13] also in the solid solution of NaCl and CaCl$_2$. Such diffraction effects have been ascribed to the formation of small plate-like zones with different concentration of solute atoms or molecules in the homogeneous matrix.

The unit cell of the ordered structure CuAuI is about 5% shorter in the one axial direction and about 2% longer in the other two axial directions than the disordered structure. Thus the unit cells of the two structures have appreciably different dimensions, and hence corresponding interplanar distances are not the same. It is probable, therefore, that the diffuse X-ray effects reported here arise mainly from the lattice distortion associated with the ordering reaction, as already mentioned in § 1. From evaluation[12] of the coherent strain of conjugate planes between the disordered and ordered phases, it was concluded that the contained strain is minimum, if the $(101)_{\text{tet.}}$ plane in the ordered phase is chosen as the conjugate plane with a $(110)_{\text{cub.}}$ type plane in the disordered phase. If we stand on the basis of the nucleation or fluctuation process on the initial ordering, it follows, from the consideration mentioned above and the microscopic examinations[4], that the thin layers of the ordered nuclei begin to form coherently on {110} matrix planes at the earliest stage of ordering.

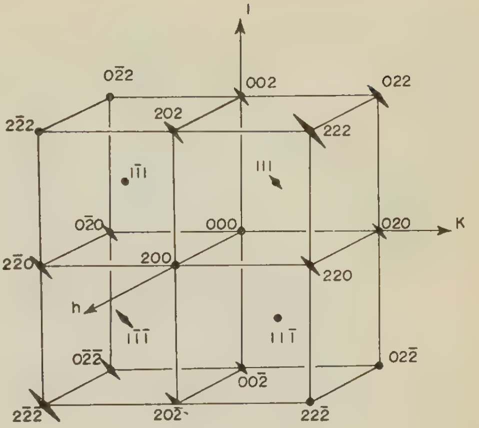

Fig. 9. Distribution of ⟨110⟩ rods in the reciprocal lattice for a single orientation of the plate-like ordered nuclei.

Thus the rod-like distribution of diffuse intensity weight in reciprocal space, running along ⟨110⟩ direction through relpoints belonging to the matrix cubic phase, will be qualitatively interpreted by the lattice strain caused by a number of thin plate-like ordered regions lying on {110} planes of the matrix. From the cubic symmetry of this phase, there is the six equivalent planes (110), (101), (011), $(\bar{1}10)$, $(\bar{1}01)$ and $(0\bar{1}1)$, and so the distribution of relrods around each relpoint corresponding to the actual crystal must be constructed by a superposition of contributions from these six planes. Analyzing sets of such relrods, we can obtain the fundamental rod distribution due to single orientation of the ordered nuclei. Fig. 9 shows the distribution of the $[0\bar{1}1]$ relrods near the origin of the reciprocal lattice due to the contribution from a $(0\bar{1}1)$ plane. Both the intensity of rod, indicated qualitatively by its thickness, and the length of rod are symmetrical with respect to the relpoint, and both of them increase with the distance of the relevant relpoint from the origin of the reciprocal lattice. From this figure it is noted that the $[0\bar{1}1]$ relrods appear only about some of relpoints and are absent at the relpoints (200), $(1\bar{1}1)$, $(0\bar{2}2)$, $(2\bar{2}2)$ *etc.*. Although no attempt to examine around the origin was undertaken, an absence of relrod about this point should be expected if the diffuse diffractions are caused by the lattice distortion. Thus, it results that the intensity of $[0\bar{1}1]$ relrod is missing or very weak at every relpoint with the indices having the relation $k+l=0$. Although the cause of this fact remains unexplained, it is obvious that the observed results summarized in Table II are well explained from this relation. The average lattice strain, estimated from the relrod length, is relatively larger than the case of the partially ordered crystal of CoPt. And it is probably reasonable, for the dilatation change of CuAu crystal associated with the transformation is larger than that of the CoPt crystal.

The usual theory of the size effect of small crystals may be also an alternative explanation of the diffuse scatterings, but this can not explain the fact that the length of relrods increases with increasing duration of annealing at 100°C or 200°C, because it has to mean the gradual decreasing of the thickness of ordered plate-like regions as the ordering proceeds.

We found recently the analogous diffuse diffraction effects at early stages of the ordering process in the alloy $CuAu_3$ and the results will be published elsewhere.

### b) *Ordering Processes in CuAu*

As Brinkman *et al.*[12] already noticed, lattice imperfections, particularly vacancies, interstitials and dislocations, may be responsible for the ordering process of the alloy quenched from high temperatures. Even if the alloy is annealed at sufficiently low temperatures, interstitial atoms or vacant lattice sites will migrate and contribute to the atomic ordering, thus ordered nuclei may be first of all formed in the vicinity of such lattice defects.

In contrast to $Cu_3Au$, in which the ordering occurs at least in two steps, it appears from

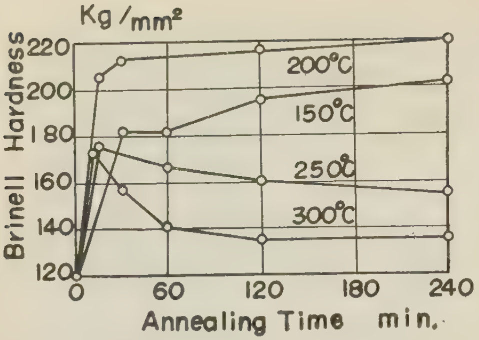

Fig. 10. Age-hardening curves for a CuAu alloy. The alloy was rapidly cooled from 500°C before annealing. (After L. Nowack)

many investigations[3] that the ordering in CuAu may be essentially a single process with a well defined activation energy, provided the temperature is not too near the critical point. One would consider, therefore, that during the early state of ordering in CuAu a number of nuclei of the ordered phase are formed by the interaction between lattice imperfections and atomic ordering and continuously grow within the disordered matrix in such a way that their flat surfaces are parallel to the {110} planes of the cubic phase. It is noteworthy here, however, the changes in such mechanical properties as Young's modulus[14] and hardness[15] accompanying the ordering take place in two stages. In Fig. 10, we show the time variation of hardness obtained by Nowack. It may be noted that the order-hardening at various temperatures occurs in a similar way to the age-hardening in the precipitation process. The initial rise in hardness at 150°C and 200°C will neither be caused by the strain due to such successive layers of the tetragonal and cubic structures as proposed by Harker[6] nor by the short-range order hardening by Fisher[16], but probably by the local lattice strain as described above. This fact can be closely connected with the fact that some ferromagnetic superlattices such as CoPt[17] and FePt[18] of a similar type to CuAuI have considerably high coercive forces at an initial stage of ordering. As the ordering further proceeds, twinning, Harker's successive layer structure, self-deformation and recrystallization will occur to relieve the lattice strains, which become so large that the original cubic crystal bends appreciably wavily. Especially for coarse-grained specimens, a grain boundary fracture was often observe after repeated heat-treatments in the present work.

In conclusion, the writers wish to express their thanks to Mr. T. Haga for his helpful assistance in experimental procedures. This work has been supported partly by the fund of the Ministry of Education in Aid of Scientific Researches.

## References

1) C. H. Johansson and J. O. Linde: Ann. Physik **25** (1936) 1.
2) J. Nyström: Arkiv Fysik **2** (1950) 151.
G. Borelius, L. E. Larsson and H. Selberg: *ibid.* **2** (1950) 161.
3) G. Borelius: J. Inst. Met. **74** (1949) 17.
G. J. Dienes: J. Appl. Phys. **22** (1951) 1020.
M. Hirabayashi: J. Japan Inst. Met. **B 15** (1951) 565.
4) J. L. Haughton and R. J. M. Payne: J. Inst. Met. **46** (1931) 457.
G. C. Kuczynski, R. F. Hochman and M. Doyama: J. Appl. Phys. **26** (1955) 871.
5) O. Källbäck, J. Nyström and G. Borelius: Ing. Vetensk. Akad. No. 157 (1941).
6) D. Harker: Trans. Am. Soc. Metals **32** (1944) 210.
7) W. Gorsky: Zeit. f. Phys. **50** (1928) 64.
K. Ohshima and G. Sachs: *ibid.* **63** (1930) 210.
U. Dehlinger and L. Graf: *ibid.* **64** (1930) 359.
8) H. Lipson: Progress in Metal Physics **2** London 1950.
9) I. G. Edmunds and R. M. Hinde: Proc. Phys. Soc. **B 65** (1952) 716.
10) C. A. Taylor, R. M. Hinde and H. Lipson: Acta Cryst. **4** (1951) 261.
11) J. B. Newkirk, R. Smoluchowski and A. H. Geisler: Acta Cryst. **4** (1951) 507.
12) J. A. Brinkman, C. E. Dixon and C. J. Meechan: Acta Met. **2** (1954) 38.
13) S. Miyake and K. Suzuki: J. Phys. Soc. Japan **9** (1954) 702.
K. Suzuki: *ibid.* **10** (1955) 794.
14) W. Köster: Zeit. Metallk. **32** (1940) 145.
15) L. Nowack: *ibid.* **22** (1930) 94.
16) J. C. Fisher: Acta Met. **2** (1954) 9.
17) J. B. Newkirk, A. H. Geisler, D. L. Martin and R. Smoluchowski: Trans. A.I.M.E. **188** (1950) 1249. J. Met. (October 1950).
18) H. Lipson, D. Shoenberg and G. V. Stupart: J. Inst. Met. **67** (1941) 333.

JOURNAL OF THE PHYSICAL SOCIETY OF JAPAN Vol. 11, No. 9, SEPTEMBER, 1956

# Electrical Properties of $Bi_2Te_3$

By Shigenobu SHIGETOMI,
*Kurume University*
and Sigeyasu MORI
*Meizen Senior High School, Kurume*

(Received March 17, 1956)

The conductivity, the Hall coefficient and the thermoelectric power of the compound $Bi_2Te_3$ have been measured over the temperature range from 100°K to 750°K. The specimens used show electrical conduction of $p$-type at room temperature and the hole mobility temperature dependence is represented by the relation $\mu_h = 1.2\times10^8\,T^{-2\cdot3}$. It is found that the forbidden energy gap $E_G$ is 0.21 eV at 0°K, and the effective masses of holes and electrons are, respectively, 1.26 $m$ and 1.07 $m$, and the mobility ratio $b$ is about 1.7.

## § 1. Introduction

The semiconducting properties of many intermetallic compounds have recently been investigated. From the measurements of the conductivity, the thermoelectric power and the magnetic susceptibility, Honda and Sone[1], and Endo[2] have found that the intermetallic compound $Bi_2Te_3$ exists and Haken[3] has reported that the compound $Bi_2Te_3$ is of $p$-type from the measurement of the Hall effect at room temperature and Moss[4] has investigated the photoconductivity. We have studied in detail its semiconducting properties: the resistivity, the Hall effect and the thermoelectric power. During the preparation of this paper, a short report by Harman *et al*[5] appeared, which however, to has not reference to the Hall effect of $Bi_2Te_3$.

## § 2. Experimental Procedure

The starting materials used are bismuth obtained from the Merck Company and tellurium from the Saganoseki Refining Campany. The bismuth is "extra pure" (free from arsenic) and the tellurium has the purity of 99.997 percent. By melting Bi and Te together in stoichiometric proportion or in 0.2 % excess of one component in an evacuated silica tube at the temperature 600∼700°C for a few hours, the polycrystalline compound was obtained, and then by applying zone melting to the compound in an evacuated silica tube, a large single crystal, whose melting point is about 580°C, was prepared. The crystal cleaves well and the cleavage surface has a metallic lustre. Laue photographs show that the cleavage plane is perpendicular to the $c$-axis of the hexagonal crystal[6], and the lattice constants are $a=6.79$ Å, $c/a=1.40$. From the ingot we cut out a specimen along the cleavage plane with the dimension of about $8\times2\times1$ mm. The Hall effect and the electrical conductivity were simultaneously measured with the conventional d.c. method in the temperature range from −170°C to 450°C. It is found that the Hall effect is a linear function of magnetic field strength up to 8000 gauss, so that field strength of 4000 gauss was chosen for all measurements. The probes of manganin wire welded to the specimen. The thermoelectric power and electrical conductivity were simultaneously measured in the range from room temperature to 450°C. The thermoelectric voltage was measured with the same probes as those used for conductivity measurement, and then the temperature difference between two probes were measured with two pairs of chromel-alumel thermocouples in contact with them. The actual temperature difference was kept in a few degrees.

## § 3. Experimental Results

All samples, including the samples of 0.2% excess Te and 0.2% excess Bi, showed $p$-type conduction at room temperature. In stoichiometric samples the Hall coefficient reversed its sign at 435°K, namely above this temperature the samples showed $n$-type conduction. The thermoelectric power of stoichiometric samples showed $p$-type conduction at room temperature and also its sign changed

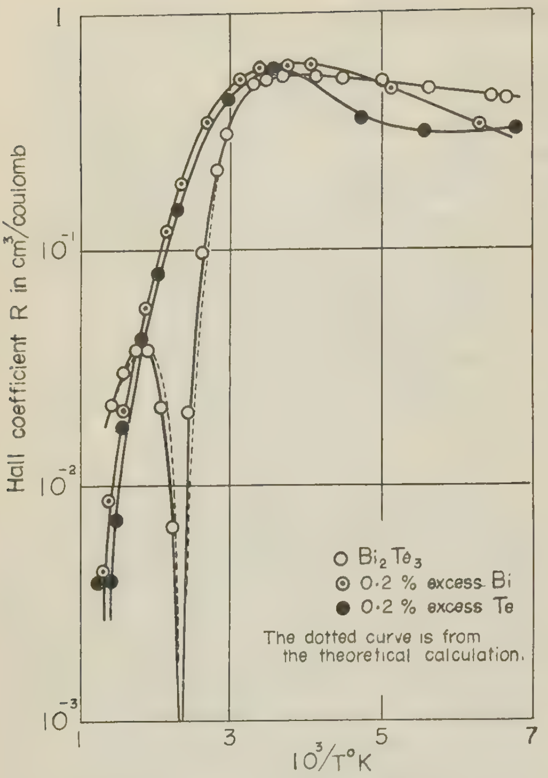

Fig. 1. Hall coefficient in stoichiometric and 0.2 % excess samples *versus* absolute temperature.

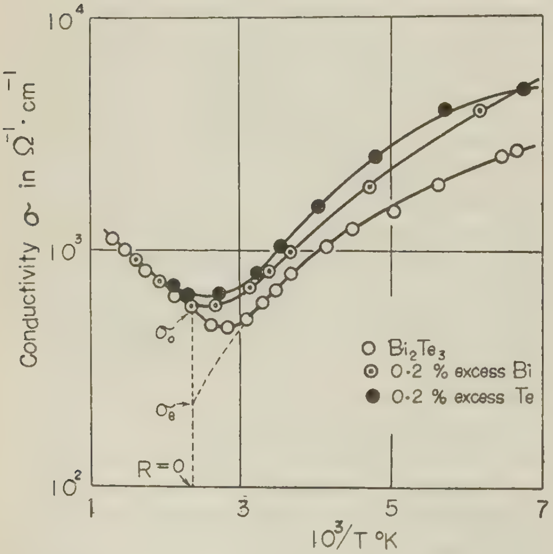

Fig. 2. Conductivity in stoichiometric and 0.2% excess samples *versus* absolute temperature.

at nearly the same temperature as the Hall coefficient. These results are illustrated in Figs. 1~3.

## § 4. Discussions

The following discussions are made for the stoichiometric samples 7SP1, 7SP2 and 7SP3 for which the experimental data are shown in Figs. 1~3.

As the Hall coefficient $R$ is approximately constant in the low temperature range as shown in Fig. 1, it is reasonable to assume that in this range the "saturation" hole concentration $p_s$ is equal to the acceptor concentration. Then from the relation $R=3\pi/8p_se$, we get the acceptor concentration $p_s=1.4\times10^{19}$ cm$^{-3}$.

In Fig. 2, if the saturation conductivity line in the low temperature range is extraporated to the temperature for which the Hall coefficient falls to zero, a conductivity $\sigma_e$ is obtained, whereas the actual conductivity is $\sigma_0$. Then we have $\sigma_e/\sigma_0=b/b-1$ 7), where $b$ is a ratio of electron to hole mobility. The values of $\sigma_e$ and $\sigma_0$ can be read from Fig. 2. Thus we get $b=1.7$ for the present sample.

The conductivity $\sigma$ is given by the well-known relation

$$\sigma=e\mu_h(bn+p)\,, \tag{1}$$

where $n$ is the density of electrons (that is, number/cm$^3$) in the conduction band, $p$ the density of holes in the filled band, $\mu_h$ the hole mobility and $e$ the charge on the electron.

By using the relation

$$n=p-p_s\,, \tag{2}$$

the equation (1) can be expressed in the form

$$p=\left(\frac{\sigma}{e\mu_h}+bp_s\right)\Big/(b+1)\,. \tag{3}$$

If we consider only the exhaustion range, the degeneracy temperature $T_{\text{deg}}$ for the present sample can be estimated from the formula8)

$$T_{\text{deg}}=\left(\frac{3}{\pi}\right)^{2/3}\frac{h^2}{8km}p^{3/2}\,.$$

where $k$ is Boltzmann's constant, $m$ the free electron mass and $h$ Planck's constant. Using the value $p=p_s=1.4\times10^{19}$ cm$^{-3}$, we get $T_{\text{deg}}=240$°K. In the lower temperatures, where the specimen becomes degenerate, we have $\mu_h=R\sigma$, and in the higher temperatures, where the specimen is non-degenerate, we have $\mu_h=(8/3\pi)R\sigma$ for the case of lattice scattering. Using these formulae with the observed values of $R$ and $\sigma$ in the exhaustion range, we can evaluate the value

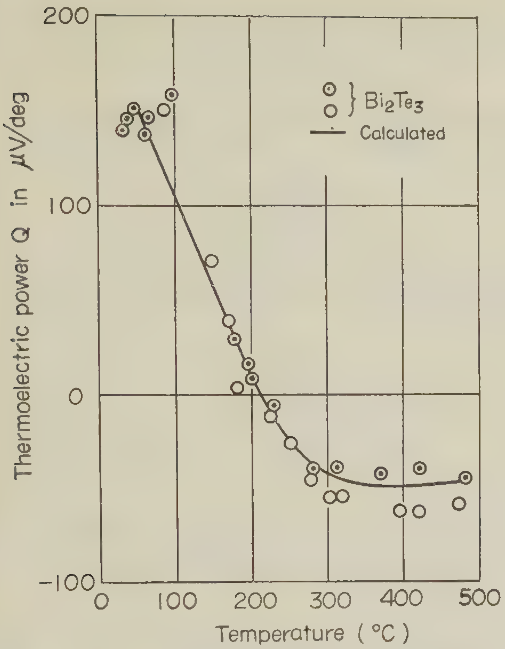

Fig. 3. Thermoelectric power *versus* temperature (°C) for samples 7SP2 and 7SP3.

of $\mu_h$ which is plotted against temperature in Fig. 4 which shows that the above assumption of lattice scattering is appropriate for the present sample. Thus we can approximately express $\mu_h$ as the function of temperature as follows:

$$\mu_h = 1.2\times10^8 T^{-2.3}\ \mathrm{cm^2/volt\cdot sec}\ . \qquad (4)$$

If the relation (4) can be assumed, the hole density $p$ can be obtained from the equation (3), and then the electron density $n$ from the equation (2). These results are shown in Fig. 5. Using the values of $n$ and $p$ obtained above, we can calculate the Hall coefficient $R$ in the intrinsic and the transition ranges by using the following formula:

$$R = -\frac{3\pi}{8e}\,\frac{nb^2-p}{(nb+p)^2}\ . \qquad (5)$$

The values are shown in Fig. 1, which shows that the calculated values are in good agreement with the observed ones.

The product $np$ at any temperature is independent of impurity concentration and is given by following formula[9]:

$$\frac{np}{T^3} = 4\left(\frac{2\pi mkT}{h^2}\right)^3\left(\frac{m_e m_h}{m^2}\right)^{3/2}\exp\left(-\frac{E_G}{kT}\right), \qquad (6)$$

where $m_e$ and $m_h$ are, respectively, the effective mass of electrons and holes, $m$ is the free electron mass and $E_G$ the energy gap between filled and conduction bands. By using values of $n$ and $p$ given in Fig. 5, the plot of $\ln np/T^3$ versus $1/T$ is shown in Fig 6. Substituting the relation $E_G(T) = E_G(0) - \beta T$ into the equation (6) and comparing it with Fig. 6, we obtain

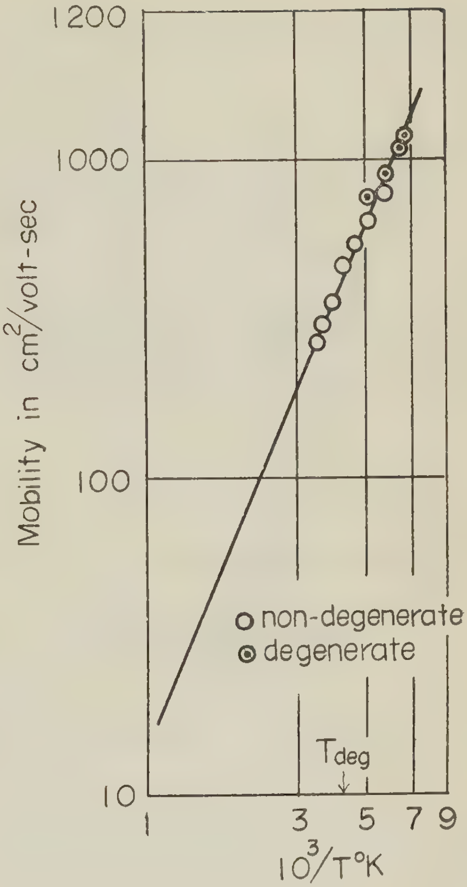

Fig. 4. Carrier mobility *versus* absolute temperature for sample 7SP1.

$$E_G(0) = 0.21\ \mathrm{eV}$$

and

$$4\left(\frac{2\pi mkT}{h^2}\right)^3\left(\frac{m_e m_h}{m^2}\right)^{3/2}\exp\left(-\frac{\beta}{k}\right)$$
$$= 5.35\times10^{32}\ . \qquad (7)$$

The equation (7) contains two unknown parameters, $\beta$ and $(m_e m_h/m^2)$. The quantity $\beta$ can be calculated from the thermoelectric power in the intrinsic range as below. In the intrinsic range the thermoelectric power $Q$ is expressed by the formula[10]

$$Q = -\frac{k}{e}\,\frac{b-1}{b+1}\left(\frac{E_G(0)}{2kT} + 2 - \frac{\beta}{2k}\right). \qquad (8)$$

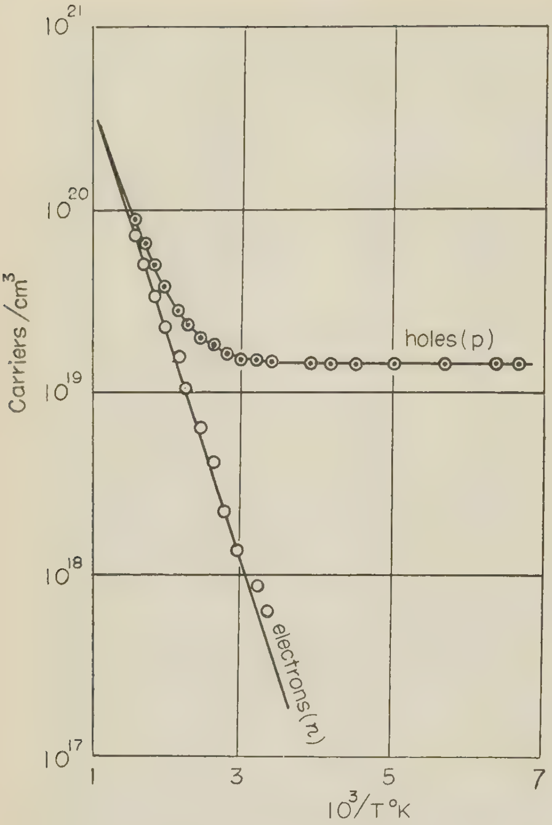

Fig. 5. Densities of conduction electrons and holes in sample 7SP1 *versus* absolute temperature.

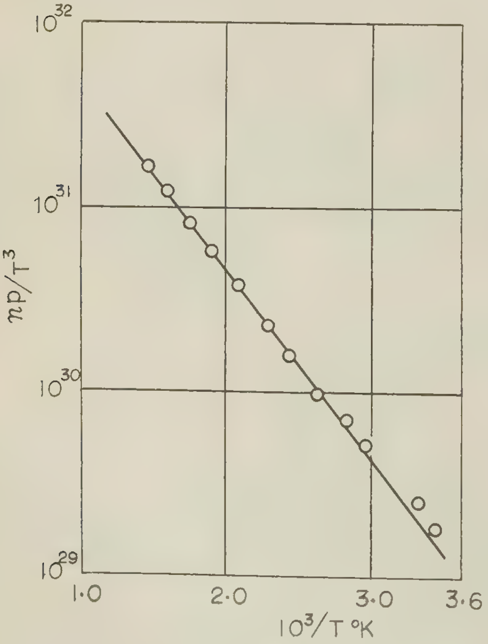

Fig. 6. The value of $np/T^3$ *versus* absolute temperature for sample 7SP1.

Using $b=1.7$, $E_G(0)=0.21$ eV and the observed value $Q$ in the intrinsic range, we get

$$\beta=2.4\times10^{-4}\ \text{eV/deg}\ .$$

Substituting this value of $\beta$ into the equation (7) we obtain

$$\frac{m_e m_h}{m^2}=1.35\ . \qquad (9)$$

On the other hand, in the transition range the thermoelectric power may be written in the form[11]

$$Q=-\frac{R}{e(nb+p)}\Bigg[2(nb-p)$$
$$-nb\ln\left\{\frac{nh^3}{2(2\pi m_e kT)^{3/2}}\right\}+p\ln\left\{\frac{ph^3}{2(2\pi m_h kT)^{3/2}}\right\}\Bigg]. \qquad (10)$$

We can find the temperature $T=488°\text{K}$ for $Q=0$ in Fig. 3 and the values of $n$ and $p$ for this temperature in Fig. 5. Making use of these values and relation (9) together with the value $b=1.7$ in the equation (10), we get the following values for the effective masses of electrons and holes:

$$m_e=1.07\,m \quad \text{and} \quad m_h=1.26\,m\ .$$

Then we can calculate the thermoelectric power $Q$ in the transition range by using the above obtained values for $m_e$ and $m_h$ in the equation (10), and the calculated values are also included in Fig. 3 which shows good agreement between the observed and the calculated values.

If we may assume the well-known relation for the mobility ratio[12],

$$b=\left(\frac{m_h}{m_e}\right)^{5/2}, \qquad (11)$$

the combination of the equations (9) and (11) yields the following values for the effective masses of electrons and holes:

$$m_e=1.04\,m \quad \text{and} \quad m_h=1.29\,m\ .$$

The above values for $m_e$ or $m_h$ derived by two different ways seem to be in good agreement with each other within the experimental errors.

We should express our hearty thanks to Prof. Atuyosi Okazaki and Assistant Prof. Toshihiro Okada of the Faculty of Science, Kyusyu University, for their guidance and for placing research facilities at our disposal, and also to Mr. Atushi Okazaki for taking X-ray photographs and to Mr. Kimio Hashimoto, Mr. Sizuo Asanabe, Mr. Kazuyosi

Hirakawa, Mr. Yoshiro Moriguchi and Mr. Yutaka Koga for their assistance in the present experiment.

We are also much obliged to the Saganoseki Refining Company for the supply of pure tellurium.

## References

1) K. Honda and T. Sone: Science Reports of Tohoku Imperial University, First Series **2** (1913) 1.
2) H. Endo: *ibid.* **14** (1925) 479.
3) W. Haken: Ann. Phys. **32** (1910) 291.
4) T. S. Moss: Proc. Phys. Soc. **63 A** (1950) 176.
5) T. C. Harman, S. E. Miller and H. L. Goering: Bulletin of the Amer. Phys. Soc. Programme, November (1955) 35.
6) E. Dönges: Z. anorg. u. allgem. Chem. **265** (1951) 56.
7) W. Shockley: "*Electrons and Holes in Semiconductors*" (1950) p. 218.
8) W. Shockley: *ibid.* p. 242.
9) W. Shockley: *ibid.* p. 245.
10) V. A. Johnson and K. Lark-Horovitz: Phys. Rev. **92** (1953) 226.
11) V. A. Johnson and K. Lark-Horovitz: *ibid.*
12) G. L. Pearson and J. Bardeen: Phys. Rev. **75** (1949) 865.

---

JOURNAL OF THE PHYSICAL SOCIETY OF JAPAN Vol. 11, No. 9, SEPTEMBER, 1956

# A Note on the Ground State of Antiferromagnetism

By Hiroshi TAKETA
*Yamaguchi Medical School, Ube, Japan*
and Tutô NAKAMURA
*General Education Department, Kyusyu University, Hukuoka, Japan*

(Received April 28, 1956)

Kasteleijn's method of obtaining the ground state of antiferromagnetism is generalized to the cases of two and three dimensional lattices. According to our generalization, the ground state of the three dimensional antiferromagnetic Heisenberg model with the spin quantum number equal to one half is paramagnetic in the absence of anisotropy energy. The magnetization of sublattices is calculated as a function of the degree of anisotropy. With increasing coordination numbers the anisotropy energy necessary for establishing the antiferromagnetic state decreases rapidly.

## §1. Introduction

A method of studying the ground state of an antiferromagnetic linear chain with the spin quantum number equal to one half has been presented by Hulthén[1] and Kasteleijn[2]. In particular Kasteleijn studied the anisotropic exchange Hamiltonian

$$\mathscr{H}=(1-a)J\sum_{(jk)}(S_j^+S_k^-+S_j^-S_k^+)+2J\sum_{(jk)}S_j^zS_k^z\ , \qquad (1)$$

where $-J$ is the exchange integral with the negative sign, $a$ an anisotropic parameter. $S_j^x$, $S_j^y$, $S_j^z$ are the usual spin operators of the $j$-th lattice point and

$$S_j^\pm=S_j^x\pm iS_j^y \qquad (2)$$

And $\sum_{(jk)}$ denotes the summation over nearest-neighbour lattice points $j$ and $k$. According to his result, the ground state of (1) is paramagnetic in the absence of anisotropic parameter. He obtained a critical value of an anisotropic parameter $a$ at which the system becomes aniferromagnetic.

It is now interesting to inquire into the situation in two and three dimensional lattices on the line of Kastelejn's method. Recently, Marshall took up this problem and calculated the ground level of the isotropic exchange Hamiltonian[3]. As in the case of linear chain problem, where his result is of course identical with Kasteleijn's one, the ground levels obtained by him are lower than those from the spin wave theory[4]. Then Kasteleijn's procedure may give more accurate value for the ground level than that the spin wave theory gives. Further, Marshall came to conclusion that the ground state predicted by his procedure should be paramagnetic even in the three dimensional lattices. This is in contradiction with the conclusion from the spin wave theory, according to which the spontaneous magnetization of a sublattice should occur even in the square lattice.

We have considered the same problem independently of Marshall. The essence of Kasteleijn's method consists in the calculation of the *transition probability*. Since it becomes more difficult in two and three dimensional problems than in the linear chain problem, a certain approximate procedure is necessary. The correlation among spin neighbouring to a spin pair, which is neglected in our procedure, is partly taken into account in Marshall's one. But our procedure is much simpler than his. Then we can obtain a general expression for the ground levels of the linear, square, simple cubic and body centred cubic lattices on the line of our procedure. Further, Marshall confined his investigation to the ground state of the isotropic exchange Hamiltonian. However, it seems to be worth while to study the ground state of the anisotropic exchange Hamiltonian of the type (1). Then, we calculated the spontaneous magnetization of sublattices as a function of the anisotropic parameter $a$ for two and three dimensional lattices. The result is that the critical value of $a$ at which the system becomes antiferromagnetic decreases rapidly with increasing coordination number of lattices.

As is mentioned above, our method is less accurate in its approximation than Marshall's. As a result, the ground levels obtained from our procedure are higher than those from the spin wave theory, accordingly than those from Marshall's procedure, although both our result and Marshall's one reduce to Kasteleijn's result in the case of linear chain.

## § 2. Kasteleijn's Method

Let us confine our consideration to the crystal lattices where we can divide the whole lattice points into two sublattices, A and B, in such a way that a lattice point belonging to one sublattice is surrounded by the nearest neighbours belonging to another sublattice.

Following Kasteleijn, let us take the coordinate system of a spin belonging to a sublattice so as to coincide with that of a spin belonging to another sublattice rotated around the quantized axis, that is the $z$-axis, by the angle $\pi$. Then we can write (1) as

$$\begin{aligned}\mathscr{H}=-(1-a)J\textstyle\sum_{(jk)}(S_j^+S_k^-+S_j^-S_k^+)\\ +2J\textstyle\sum_{(jk)}S_j^zS_k^z\,. \qquad (3)\end{aligned}$$

Our problem is to find the eigenfunction $\psi$ of $\mathscr{H}$ corresponding to the ground level, which we may write as

$$\Psi=\textstyle\sum_\lambda a_\lambda\psi_\lambda \qquad (4)$$

Here $\psi_\lambda$ is a normalired wave function expressed as a product of $\alpha_i$'s or $\beta_i$'s defined by

$$S_i^z\begin{pmatrix}\alpha_i\\ \beta_i\end{pmatrix}=\begin{pmatrix}1/2 & 0\\ 0 & -1/2\end{pmatrix}\begin{pmatrix}\alpha_i\\ \beta_i\end{pmatrix}. \qquad (5)$$

We shall now classify $\psi_\lambda$'s into several groups, each of which is specified by the following parameters.

the number of + spins on the A sublattice: [↑ on A]. [↓ on A], [↑ on B], and [↓ on B] are defined in the same way. And

the number of neighbouring pairs of + spin on the A sublattice and + spin on the B sublattice: [↑ on A; ↑ on B]. [↑ on A; ↓ on B] [↓ on A; ↑ on B], and [↓ on A; ↓ on B] are defined in the same way. Of course, these eight parameters are not independent of each other. It can easily be proved that we have only three independent parameters. For we have the following relations.

$$\begin{aligned}&[\uparrow\text{ on A}]+[\downarrow\text{ on A}]=N\\ &[\uparrow\text{ on B}]+[\downarrow\text{ on B}]=N\,. \qquad (6a)\end{aligned}$$

$$\begin{aligned}&[\uparrow\text{ on A};\uparrow\text{ on B}]+[\uparrow\text{ on A};\downarrow\text{ on B}]=z[\uparrow\text{ on A}],\\ &[\downarrow\text{ on A};\uparrow\text{ on B}]+[\downarrow\text{ on A};\downarrow\text{ on B}]=z[\downarrow\text{ on A}],\\ &[\uparrow\text{ on A};\uparrow\text{ on B}]+[\downarrow\text{ on A};\uparrow\text{ on B}]=z[\uparrow\text{ on B}],\\ &[\uparrow\text{ on A};\downarrow\text{ on B}]+[\downarrow\text{ on A};\downarrow\text{ on B}]=z[\downarrow\text{ on B}]. \qquad (6b)\end{aligned}$$

where $N$ is the number of lattice points belonging to each sublattice and $z$ the number of nearest neighbours. But the number of independent relations in (6b) is only three. If we confine our consideration to the case where there is no magnetic field, the total magnetization of the system should be equal to zero:

$$[\uparrow\text{ on A}]+[\uparrow\text{ on B}]=[\downarrow\text{ on A}]+[\downarrow\text{ on B}], \qquad (7)$$

which gives us another relation. Let us introduce two independent parameters, $\sigma$ and $x$, defined by

$$\begin{aligned}&[\uparrow \text{ on A}]-[\uparrow \text{ on B}]=[\downarrow \text{ on B}]-[\downarrow \text{ on A}]=N\sigma,\\ &[\uparrow \text{ on A}; \ \uparrow \text{ on B}]=[\downarrow \text{ on A}; \downarrow \text{ on B}]=Nzx.\end{aligned} \tag{8}$$

Then we can easily show

$$\begin{aligned}&[\uparrow \text{ on A}]=[\downarrow \text{ on B}]=(N/2)(1+\sigma)\ ,\\ &[\downarrow \text{ on A}]=[\uparrow \text{ on B}]=(N/2)(1-\sigma)\ ,\\ &[\uparrow \text{ on A}; \downarrow \text{ on B}]=(Nz/2)(1+\sigma-2x)\ ,\\ &[\downarrow \text{ on A}; \uparrow \text{ on B}]=(Nz/2)(1-\sigma-2x)\ .\end{aligned} \tag{9}$$

Thus our basic wave functions $\psi_\lambda$'s with fixed parameters $\sigma$ and $x$ are grouped together. We shall then assume that the probability amplitudes $a_\lambda$'s are equal to each other for $\psi_\lambda$'s belonging to such a group. It will be convenient to introduce the following functions

$$\varPhi(\sigma,\ x)=\sum\nolimits_\lambda\psi_\lambda(\sigma, x)/\sqrt{W(\sigma, x)}\ , \tag{10}$$

in which $\psi_\lambda(\sigma, x)$ denotes $\psi_\lambda$ with fixed values of $\sigma$ and $x$. Here the summation runs over all $\psi_\lambda$ with fixed $\sigma$ and $x$, whose number is denoted by $W(\sigma, x)$. Hence $\varPhi(\sigma, x)$ is a normalized wave function. Using the assumption stated above, the function (4) may be written as

$$\psi=\sum\nolimits_{\sigma,x}b(\sigma, x)\varPhi(\sigma, x)\ , \tag{11}$$

which is a trial function taken up by Kasteleijn.

We should next determine $b(\sigma, x)$ so as to minimize $(\varPsi|\mathscr{H}|\varPsi)$. For this purpose let us look for the matrix elements of $\mathscr{H}$ with respect to $\varPhi(\sigma, x)$. First, we can easily get

$$\begin{aligned}\sum\nolimits_{(jk)}S_j{}^zS_k{}^z\varPhi(\sigma, x)=1/4\ (&[\uparrow \text{ on A}; \uparrow \text{ on B}]\\ &+[\downarrow \text{ on A}; \downarrow \text{ on B}]-[\uparrow \text{ on A}; \downarrow \text{ on B}]\\ &-[\downarrow \text{ on A}; \uparrow \text{ on B}])\\ &=(Nz/4)(4x-1)\varPhi(\sigma, x)\ .\end{aligned} \tag{12}$$

Secondly we shall consider the matrix element of $\sum_{(jk)}(S_j{}^+S_k{}^-+S_j{}^-S_k{}^+)$, which operates on anti- parallel pairs of spins and interchanges their spin states. As a result a $\psi_\lambda(\sigma, x)$ is transformed into a $\psi_{\lambda'}(\sigma', x')$. The number of $\psi_{\lambda'}(\sigma', x')$ thus generated is equal to the number of antiparallel spin pairs. Then

$$\begin{aligned}(\varPhi(\sigma'', x'')|&\sum\nolimits_{(jk)}(S_j{}^+S_k{}^-+S_j{}^-S_k{}^+)|\varPhi(\sigma, x))\\ &=\{W(\sigma, x)W(\sigma'', x'')\}^{-1/2}\\ &\quad\times\sum\nolimits_{\lambda',\sigma',x'}(\sum\nolimits_{\lambda''}\psi_{\lambda''}(\sigma'', x'')|\psi_{\lambda'}(\sigma', x'))\\ &=(W(\sigma, x)/W(\sigma'', x''))^{1/2}F_{\sigma,x}^{\sigma'',x''}\ .\end{aligned} \tag{13}$$

The summation $\sum_{\lambda', \sigma', x'}$ in the second line of the above equation runs over $\psi_{\lambda'}(\sigma', x')$ which is generated as the effect of operating our operator on $\varPhi(\sigma, x)$. Hence $W(\sigma, x)F_{\sigma,x}^{\sigma''',x'}$ denotes the number of transitions from the spin configurations with $(\sigma, x)$ to those with $(\sigma'', x'')$. By use of the relation of detailed balancing

$$W(\sigma, x)F_{\sigma,x}^{\sigma'',x''}=W(\sigma'', x'')F_{\sigma'',x''}^{\sigma,x}, \tag{14}$$

we rewrite (13) as

$$\begin{aligned}(\varPhi(\sigma'', x'')|&\sum\nolimits_{(jk)}(S_j{}^+S_k{}^-+S_j{}^-S_k{}^+)|\varPhi(\sigma, x))\\ &=\{F_{\sigma,x}^{\sigma'',x''}F_{\sigma'',x''}^{\sigma,x}\}^{1/2}\end{aligned} \tag{15}$$

With the help of (11), (12) and (13), an eigenvalue equation $\mathscr{H}\varPsi=E\varPsi$ leads to

$$\begin{aligned}(NzJ/2)(4x-1)b(\sigma, x)-(1-a)J&\sum\nolimits_{\sigma'',x''}\\ \times\{F_{\sigma,x}^{\sigma''x''}\ F_{\sigma'',x''}^{\sigma,x}\}^{1/2}&b(\sigma'', x'')\\ =Eb(\sigma, x)&\end{aligned} \tag{16}$$

where we regard the ortho-normal condition of $\varPhi(\sigma, x)$: $(\varPhi(\sigma, x)|\varPhi(\sigma'', x''))=\delta_{\sigma\sigma''}\delta_{xx''}$. Now, the lowest eigenvalue $E$ will occur near certain value of $\sigma$ and $x$, where $b(\sigma, x)$ shows a sharp maximum. Since $\sigma''$ and $x''$ respectively differ from $\sigma$ and $x$ by the order of the magnitude of $1/N$, we may replace $b(\sigma'', x'')$ by $b(\sigma, x)$ in the neighbourhood of that peak. Hence we get

$$\begin{aligned}E=(NzJ/2)(4x-1)-(1-a)\,J&\sum\nolimits_{\sigma'',x''}\\ \times\{F_{\sigma,x}^{\sigma'',x''}F_{\sigma'',x''}^{\sigma,x}\}&\end{aligned} \tag{17}$$

## § 3. Calculation of the Transition Probability

As in the case of Kasteleijn's procedure, the essence of the present procedure consists in the method of calculating the *transition probability* $F_{\sigma,x}^{\sigma''x''}$. As can easily be seen from (13), $F_{\sigma,x}^{\sigma'',x''}$ corresponds to the average number of $\psi_{\lambda'}(\sigma', x')$ with given $\sigma'$ and $x'$ generated from operation of $\sum_{(jk)}(S_j{}^+S_k{}^-+S_j{}^-S_k{}^+)$ on a $\psi_\lambda(\sigma, x)$. The operator $S_j{}^+S_k{}^-$ interchanges $-$ spin on the $j$-th lattice point and $+$ spin on the $k$-th one. The differences of the values of $\sigma$ and $x$, $\varDelta\sigma$ and $\varDelta x$, before and after this interchange depend on the spin configuration of neighbours. If the number of $+$ spins neighbouring to the $j$-th spin is equal to $m$ except the $k$-th one, and the number of those neighbouring to the $k$-th spin is equal to $n$ except the $j$-th one, we have

$$\varDelta\sigma=2/N,\quad \varDelta x=(m-n)/Nz\ , \tag{18}$$

where we assume that the $j$-th spin belongs to A sublattice and the $k$-th one to $B$ sublattice.

To find the *transition probability* we must know the probability of finding the spin configuration stated above when the $j$-th and the $k$-th lattice points are respectively occupied by $-$ and $+$ spins. But we cannot find out this probability without making some assumptions. We shall now neglect the correlation among spin states of $2(z-1)$ spins neighbouring to the $j$-th and the $k$-th spins. Then we can express the probabilities corresponding to various spin configurations in terms of $\sigma$ and $x$.

The following expressions of probabilities can easily be proved: when the $j$-th lattice point is occupied by $+$ spin, the probability of finding $+$ spin on one of its neighbours is

$$2x/(1+\sigma)\,,$$

and the probability of finding $-$ spin on one of its neighbours is

$$(1+\sigma-2x)/(1+\sigma)\,.$$

When the $j$-th lattice point is occupied by $-$ spin, the probability of finding $+$ spin on one of its neighbours is

$$(1-\sigma-2x)/(1-\sigma)\,,$$

and the probability of finding $-$ spin on one of its neighbours is

$$2x/(1-\sigma)\,.$$

In the same way, we can obtain the probability of finding a spin state on a neighbour of the $k$-th spin when the $k$-th spin is in a given state.

Accordingly, the probability of finding a spin configuration responsible for a transition (18) may approximately be given by

$$\left(\frac{1-\sigma-2x}{1-\sigma}\right)^m\left(\frac{2x}{1-\sigma}\right)^{z-m-1} \times\left(\frac{2x}{1-\sigma}\right)^n\left(\frac{1-\sigma-2x}{1-\sigma}\right)^{z-n-1}. \tag{19}$$

But we have equivalent spin configurations which cause the transition (18). First, the number of spin configurations with given $m$ and $n$ is equal to

$$\binom{z-1}{m}\binom{z-1}{n}. \tag{20}$$

Secondly, the spin configurations with a given value of $m-n$ lead to the same kind of transition. Hence we sum up (19) multiplied by (20) over $m$ and $n$ under a restriction $m-n=\lambda$ to obtain the total probability of finding the spin configurations responsible for a transition (18). Multiplying the probability thus obtained by [↓ on A; ↑ on B], we finally get the *transition probability* $F_{\sigma,x}^{\sigma',x'}$:

$$F_{\sigma,x}^{\sigma'x'}=(Nz/2)(1-\sigma-2x)\sum_{m-n=\lambda} \times\binom{z-1}{m}\binom{z-1}{n}\left(\frac{1-\sigma-2x}{1-\sigma}\right)^m \times\left(\frac{2x}{1-\sigma}\right)^{z-m-1}\left(\frac{2x}{1-\sigma}\right)^n\left(\frac{1-\sigma-2x}{1-\sigma}\right)^{z-n-1}, \tag{21}$$

where

$$\sigma'=\sigma+2/N\,,$$
$$x'=x+\lambda/Nz\,, \tag{22}$$

After simple calculations (21) can be written

$$F_{\sigma,x}^{\sigma'x'}=(Nz/2)\,\frac{(1-\sigma-2x)^z(2x)^{z-1}}{(1-\sigma)^{2(z-1)}} \times\left(\frac{1-\sigma-2x}{2x}\right)^\lambda\binom{2z-2}{\lambda+z-1}. \tag{23}$$

Next the effect of $S_j^-S_k^+$ is to interchange $+$ spin on the $j$-th lattice point and $-$ spin on the $k$-th one. In the complete parallel with the above procedure we obtain

$$F_{\sigma,x}^{\sigma''x''}=(Nz/2)\,\frac{(1+\sigma-2x)^z(2x)^{z-1}}{(1+\sigma)^{2(z-1)}} \times\left(\frac{2x}{1+\sigma-2x}\right)^\lambda\binom{2z-2}{\lambda+z-1}, \tag{24}$$

where

$$\sigma''=\sigma-2/N\,,$$
$$x''=x-\lambda/Nz\,. \tag{25}$$

Since $\sigma'$ and $x'$ differ from $\sigma$ and $x$ by the order of the magnitude of $1/N$, we have

$$F_{\sigma,x}^{\sigma'',x''}\simeq F_{\sigma',x'}^{\sigma,x}\,, \tag{26}$$

which is correct to the order of the magnitude of $1/N$. Taking into account (23), (24) and (26), we get

$$\begin{aligned}&\textstyle\sum_{\sigma',x'}(F_{\sigma,x}^{\sigma',x'}F_{\sigma',x'}^{\sigma,x})^{1/2}+\sum_{\sigma'',x''}(F_{\sigma,x}^{\sigma'',x''}F_{\sigma'',x''}^{\sigma x})^{1/2}\\ &=Nz\frac{(2x)^{z-1}}{(1-\sigma^2)^{z-1}}\sum_{\lambda=-(z-1)}^{z-1}\binom{2z-2}{\lambda+z-1}\\ &\quad\times(1-\sigma-2x)^{(z+\lambda)/2}(1+\sigma-2x)^{(z-\lambda)/2}\\ &=Nz\frac{(2x)^{z-1}}{(1-\sigma^2)^{z-1}}(1-\sigma-2x)^{1/2}(1+\sigma-2x)^{1/2}\\ &\quad\times\{(1+\sigma-2x)^{1/2}+(1-\sigma-2x)^{1/2}\}^{2(z-1)}\,. \end{aligned}\tag{27}$$

## § 4. Result

Expression (17) can now be written

$$E=\frac{1}{2}NzJ(4x-1)-(1-a)NzJ\left(\frac{2x}{1-\sigma^2}\right)^{z-1}$$
$$\times\{(1-2x)^2-\sigma^2\}^{1/2}$$
$$\times\{(1+\sigma-2x)^{1/2}+(1-\sigma-2x)^{1/2}\}^{2(z-1)} \quad (28)$$

with the help of (27). This eigenvalue should correspond to the lowest one. Namely $E$ should satisfy

$$\partial E/\partial x=0\ ,\quad \partial E/\partial\sigma=0\ , \quad (29)$$

which are respectively written as

$$-2+(1-a)\left(\frac{2x}{1-\sigma}\right)^{z-1}$$
$$\times\{(1+\sigma-2x)^{1/2}+(1-\sigma-2x)^{1/2}\}^{2(z-1)}$$
$$\times\left[\frac{z-1}{x}\{(1-2x)^2-\sigma^2\}^{1/2}-2(1-2x)\right.$$
$$\left.\times\frac{1}{\{(1-2x)^2-\sigma^2\}^{1/2}}-2(z-1)\right]=0\ , \quad (30)$$

and

$$4(z-1)^2\sigma^2p^4-\sigma^2$$
$$\times\{(z-1)(z-3)\sigma^4+6(z-1)^2\sigma^2+(z^2-1)\}p^2$$
$$+\sigma^4\{(z-2)^2\sigma^4+2((z-1)^2-1)\sigma^2+z^2\}=0 \quad (31)$$

where $p=1-2x$. The minimum condition of $E$ requires

$$\frac{\partial^2E}{\partial\sigma^2}>0\ ,\left(\frac{\partial^2E}{\partial x^2}\right)\left(\frac{\partial^2E}{\partial\sigma^2}\right)-\left(\frac{\partial^2E}{\partial x\partial\sigma}\right)>0\ . \quad (32)$$

We must solve above two equations (30) and (31) under the condition (32). We search for this solution for square, simple cubic, and body-centred cubic lattices separately. When $a=0$, we have a solution $\sigma=0$ (i.e. the magnetization of a sublattice is zero) for all cases, and the energy values are as follows.

| $2E/NzJ$ for | the present paper | Marshall | Kubo |
|---|---|---|---|
| square lattice | $-1.282$ | $-1.3119$ | $-1.294$ |
| simple cubic lattice | $-1.181$ | $-1.203$ | — |
| body centred cubic lattice | $-1.133$ | $-1.157$ | $-1.138$ |

In order that we have a magnetization of each sublattice, the anisotropic parameter $a$ must be larger than a certain critical value. This critical value is

$$a=\begin{cases}0.108 \text{ for square lattice,}\\ 0.046 \text{ for simple cubic lattice,}\\ 0.024 \text{ for body centred cubic lattice.}\end{cases}$$

If $a$ is larger than this value, we have non-zero solutions of $\sigma$, and in Fig. 1 we show these solutions as the functions of $a$.

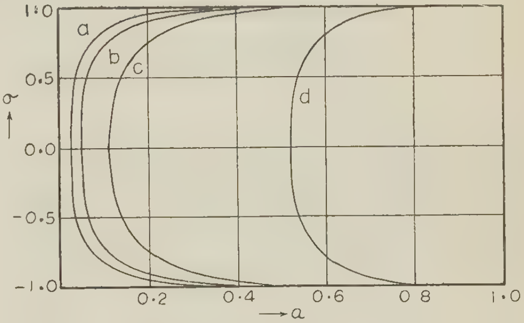

Fig. 1. Curves for σ versus $a$.
a: body centred cubic lattice b: simple cubic lattice c: square lattice d: linear chain (after Kasteleijn).

## References

1) L. Hulthén: Arkiv Mat. Astro. Fys. **26 A** (1938).
2) P. W. Kasteleijn: Physica **18** (1952) 104.
3) W. Marshall: Proc. Roy. Soc. London **232** (1955) 48.
4) R. Kubo: Rev. Mod. Phys. **25** (1953) 344.

JOURNAL OF THE PHYSICAL SOCIETY OF JAPAN Vol 11, No. 9, SEPTEMBER, 1956

# Solid State Reaction between Barium Titanate and Strontium Titanate

By Shoichiro NOMURA

*Institute of Science and Technology, University of Tokyo*

(Received May 7, 1956)

The first stage of the sintering process between barium titanate and strontium titanate powders, which are responsible for the formation of solid solution, was investigated. We measured the variation of permittivity *vs.* temperature characteristics and crystal structure of the mixtures, with sintering conditions. The shift of the effective Curie temperature and the broadening of diffracted lines were observed in the transient states of the reaction. A diffusion mechanism was introduced in order to interpret these phenomena qualitatively.

## § 1. Introduction

In the last few years, solid solutions of barium titanate and other alkaline earth titanates have been investigated as materials to be used for capacitors and electromechanical transducers. The most familiar substances among them are solid solutions of barium titanate, strontium titanate and lead titanate, whose properties are varied considerably by changing the ratio of their compositions.¹⁾ Usually these solid solutions are made from the mixtures by a so-called sintering process. The phenomena of sintering fall into the classification of solid state reactions. In many cases, the term "sintering" is employed in the following sense: sintering is the extension of the contact areas between powder particles in the solid state, by the transport of material across or around pores, under appropriate conditions of time, temperature, pressure and atmosphere. But, in a broad sense, sintering concerns any interaction such as adherence or other related interdiffusion phenomena, which occur individually or simultaneously.

There are many papers on sintering mechanisms for several oxides,²⁾,³⁾ but there seems to be few papers, in which the formation of solid solutions has been mainly investigated. It is noteworthy that the reaction to make solid solution is not always the same one as so-called sintering. Sintering phenomena may occur even between two sorts of powder particles, which are impossible to react into a solid solution. A solid solution may be made only by migration of ions through contact areas of particles, even without occurrence of decrease of porosity.

The purpose of this investigation is to discuss the first stage of the sintering process between barium titanate and strontium titanate powders, which are responsible for the formation of the solid solution, under various firing conditions. For that, the variations of permittivity temperature characteristics and crystal structure due to the firing condition have been studied. In our case, the firing temperature was not very high, so that the decrease of porosity in samples was out of question. Although the details of the reaction are so complicated, the ionic diffusion plays the main role in making the solid solution. We shall find later the activation energy for ionic diffusion in barium strontium titanate from our experimental data under certain assumptions. That will contribute a preliminary knowlege to the investigation of the atomic arrangement in the lattice of solid solution.

## § 2. Preparation of Samples

First, we made separately barium titanate and strontium titanate ceramics by the usual method.¹⁾ The grade of purity of barium carbonate, strontium carbonate and titanium dioxide we used was extra chemical pure. Then the ceramics were pulverized, and large powder particles were excluded by a sieve, its mesh size being 1/150 inch. Photo. 1 shows microscopic views of the sifted powders; (a) is barium titanate and (b) is strontium titanate. The powders of barium titanate and strontium titanate were mixed together in 1:1 molar ratio, pressed into a disk by an Amsler type pressing machine and fired under several different conditions. The firing temperature and

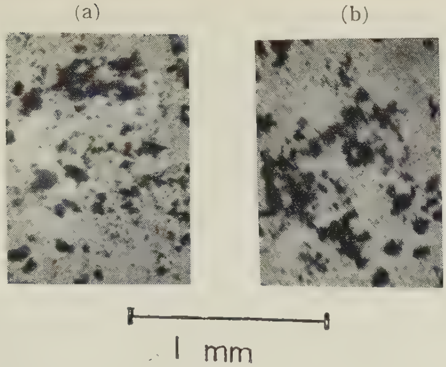

Photo. 1. Microscopic views of $BaTiO_3$ and $SrTiO_3$ powders.

time were varied from 800°C to 1350°C and 30 minutes to 53 hours respectively. The furnace we used for sintering is a BSH–2 type 4.2KW siliconit electric furnace. The temperature control was carried out by utilizing the steady state of the furnace and its fluctuation during the sintering process was within about ±5°C. No marked shrinkage was observed for samples fired below 1220°C, but their mechanical strength increased with the firing temperature. We measured the permittivity of these samples from −130°C to 80°C and investigated their structures by the X-ray analysis at room temperature.

## § 3. Permittivity-Temperature Characteristics

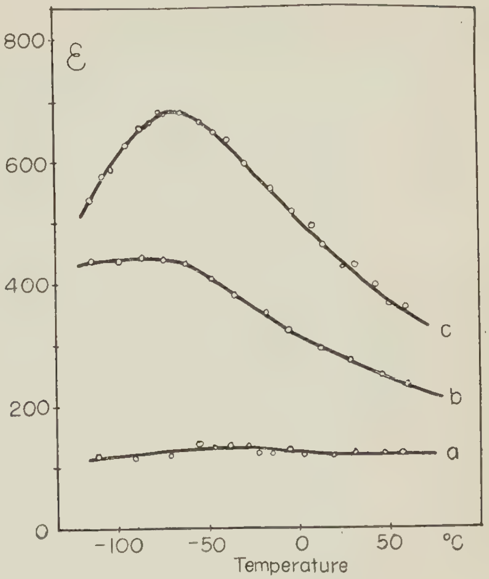

Fig. 1. Permittivity-temperature curves for $(Ba_{0.5}\cdot Sr_{0.5})\ TiO_3$ sintered at 1120°C.

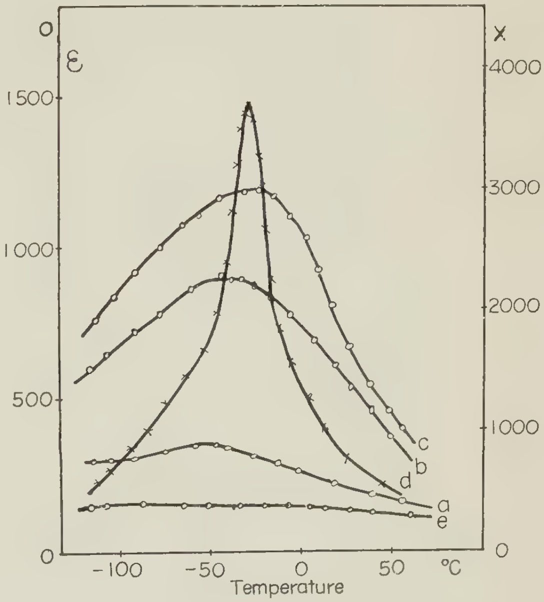

Fig. 2. Permittivity-temperature curves for $(Ba_{0.5}\cdot Sr_{0.5})\ TiO_3$ sintered at 1020°C, 1220°C and 1350°C.

The resonance method at 1043 kC was used for the measurement of permittivity. Fig. 1 shows the permittivity *vs.* temperature curves for a sample sintered at 1120°C, where the firing times for (a), (b) and (c) are 3.5, 24 and 53 hours respectively. The values of the permittivity is very small because of high porosity. Fig. 2 shows a case of 1220°C. The firing time for (a), (b) and (c) are 1.5, 8 and 20 hours respectively. The curves for samples sintered at 1020°C and 1350°C are also indicated in this figure. The bulk density for these samples is nearly constant, so that the difference in the value of permittivity shown in Figs. 1 and 2 is not always due to the decrease of porosity. The peak of permittivity shifts to the high temperature side, as the firing temperature becomes higher and the firing time becomes longer, and this phenomenon may be illustrated by the dispersion of the Curie temperature of each powder particle. Although the concentration of $Ba^{2+}$ ions and $Sr^{2+}$ ions are equal on the average in the samples, this relation doesn't hold in each powder particle. Before firing, some particles don't contain any $Ba^{2+}$ ions and others any $Sr^{2+}$ ions. In the final state of firing, on the contrary, a homogeneous distribution of ions will be brought about microscopically. As the permittivity *vs.* temperature

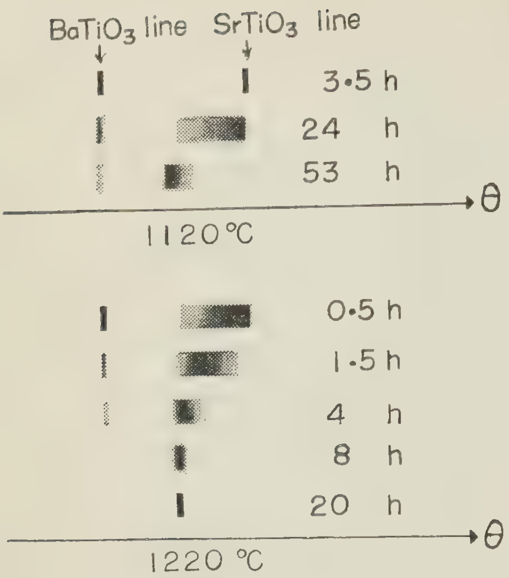

Fig. 3. Schematic diagram showing the change of (211) diffracted lines of $(Ba_{0.5}\cdot Sr_{0.5})\,TiO_3$ sintered at 1120°C and 1220°C.

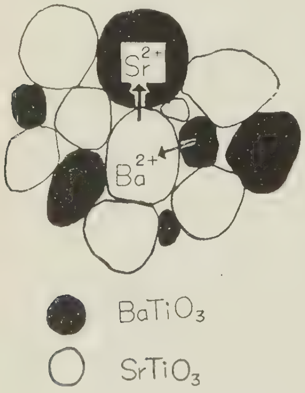

Fig. 4. Schema of mixed state of $BaTiO_3$ powders.

curve is considered to represent a resultant of contributions from each part of the sample, having different characteristics, which depend on the constituents, we may estimate the rate of the reaction by the permittivity measurement. We will discuss these points further in Sec. 5.

## § 4. X-ray Analysis

The most direct evidence for the presence of barium strontium titanate solid solution is obtained by the X-ray diffraction method. When the solid state reaction has not yet occurred, both diffracted lines of barium titanate and strontium titanate will be observed, and they will tend into single lines corresponding to those of barium-strontium titanate after the solid state reaction has finished completly. On the other hand, broad diffracted lines and diffuse scattering will be observed, if the reaction is not yet complete and consequently a non-uniform distribution of $Ba^{2+}$ and $Sr^{2+}$ ions is realized in the crystal. In order to check this situation, we paid our attention mainly to the behavior of (211) lines. It is not adequate for our analysis to adopt too low or too high index lines, since, in the former case, the separation between lines of barium titanate and strontium titanate are small and, in the latter case, the lines of barium titanate split into multiplets, its structure being tetragonal.[4)]

We carried out our analysis for the samples sintered at 1020°C, 1120°C and 1220°C. For the ones sintered at 1020°C, only the diffracted lines corresponding to those of barium titanate and strontium titanate were observed, but for the ones sintered at 1120°C and 1220°C, we recognized the broadened diffracted lines. Fig. 3 is a schematic diagram showing the change of (211) diffracted lines due to the prolongation of the sintering time in case of the samples sintered at 1120°C and 1220°C. When the firing time is short, we have, of course, only the separated lines of barium titanate and strontium titanate. When the firing time is prolonged, the line of strontium titanate begins to broaden and becomes a band corresponding to$(Ba_xSr_{1-x})TiO_3(0.5>x\geq 0)$, the line of barium titanate remaining at its initial position. The breath of the band increases and that of the line of barium titanate does not change noticeably; the intensity of the former increases and that of the latter decreases. At the final stage, however, the breadth of the band decreases again and at last the band and the line mingle into a single line corresponding to $(Ba_{0.5}Sr_{0.5})TiO_3$. We measured the intensities of the diffracted lines by a microphotometric method, but it was very difficult to estimate the intensity, because of the strong diffuse scattering masking them.

At 1250°C or more higher temperature, the rate of the reaction was very rapid, because of the macroscopic flow, which was responsible for the decrease of porosity. It is of no interest in our present investigation, so we made it out of our description.

## § 5. Discussion and Conclusion

To make solid solution from barium titanate and strontium titanate powders, the positions of $Ba^{2+}$ ions and $Sr^{2+}$ ions in the perovskite lattices should be exchanged in any way. As the reaction is not accompanied with the increase of bulk density, we may suppose that the migration of ions occurs mainly by the mechanism of ionic diffusion. In the first, it is necessary to create contact surfaces between powders as shown in Fig. 4. There are many investigations of the growing mechanisms of the interfaces, which are considered as the first stage of sintering phenomenon.[2),3)] Various types of material transport, such as viscous flow, evaporation, condensation, surface diffusion and volume diffusion may occur during the initial stage of the process. As the decrease of free energy of the mixture may be caused not only by that of surface energy, but also by the increase of entropy due to the random distribution of $Ba^{2+}$ and $Sr^{2+}$ ions, the interface growth and the migration of ions through them will occur simultaneously.

It is well known that a solid state reaction, accompanied by a chemical change, for instance, $BaCO_3+TiO_2 \rightarrow BaTiO_3+CO_2$, begins even at very low temperatures compared with usual sintering ones,[5)] in which the binding energy doesn't change at all. Our case of $BaTiO_3+SrTiO_3 \rightarrow 2(Ba_{0.5}Sr_{0.5})TiO_3$, ought to be treated as an intermediate one between these two cases. Whatever mechanism would occur in the initial stage, we can estimate the activation energy for the ionic diffusion from the observed rate of the reaction in the following way, if the main part of this reaction is the ionic diffusion.

Let us suppose that the ions diffuse through the contact surfaces, as shown in Fig. 4. The equation for diffusion is given as

$$\partial c/\partial t = div(D \cdot grad\ c) \tag{1}$$

where $c$ is the concentration of ions and $D$ is the diffusion constant.

If $D$ is independent on the concentration of the constituent of the lattices, the above equation is written as

$$\partial c/\partial t = D \cdot \Delta c \text{ or } \partial c/\partial(D \cdot t) = \Delta c. \tag{2}$$

Then a general solution of this equation may be expressed in the form

$$c(x,y,z,t) = \Phi(x,y,z,D \cdot t) \tag{3}$$

If we find that the rates of reactions are the same for two different firing conditions $T_1$, $t_1$ and $T_2$, $t_2$, the next relation can be established

$$D_{T_1} \cdot t_1 = D_{T_2} \cdot t_2 \tag{4}$$

Here we shall adopt the well known equation

$$D_T = D_0 e^{-\phi/kT} \tag{5}$$

for the temperature dependence of the diffusion constant $D$, where $\phi$ is the activation energy. Then, using the equation (4), we get the activation energy, from the observed value of $T_1$, $t_1$ and $T_2$, $t_2$. When the firing time is too short or the difference of $T_1$ and $T_2$ is large, however, the equation (4) perhaps will fail to hold, because only the interface growth is predominant in the former and the conditions of the interfaces are too different in the latter.

From our results of X-ray analysis and permittivity measurement, we may put

$$D_{1393} \cdot 50 = D_{1493} \cdot 4 \tag{6}$$

and obtain 4.5 eV as the value of the activation energy, which is very large compared with that in univalent ionic crystals. Supposing that the migration of ions may occur by that of vacancies in the crystals, we may say this is not so unreasonable value. It is noticeable, however, that the relation (4) shows appreciable deviation when applied to the whole range of the reaction. In the above derivation, the other transport mechanisms of ions except diffusion were not considered and the activation energy was assumed to be independent on the concentration of the diffusing constituents. If the effect of the increasing of the contact areas between powders were considered, we would find a smaller value for the activation energy.

As pointed out in Sec. 4, any line corresponding to $(Ba_x \cdot Sr_{1-x})TiO_3(1 > x \geq 0.5)$ was not observed in our firing process. This fact suggests us that the values of the diffusion coefficient for $Ba^{2+}$ and $Sr^{2+}$ ions are strongly affected by the constituent of the lattices and large $Ba^{2+}$ ions diffuse more easily than small $Sr^{2+}$ ions. Perhaps the concentration of ions in the crystals will be changed with the firing time as shown in Fig. 5, where (a) is the initial state in which the reaction has not yet begun, (b) and (c) are the transient states and

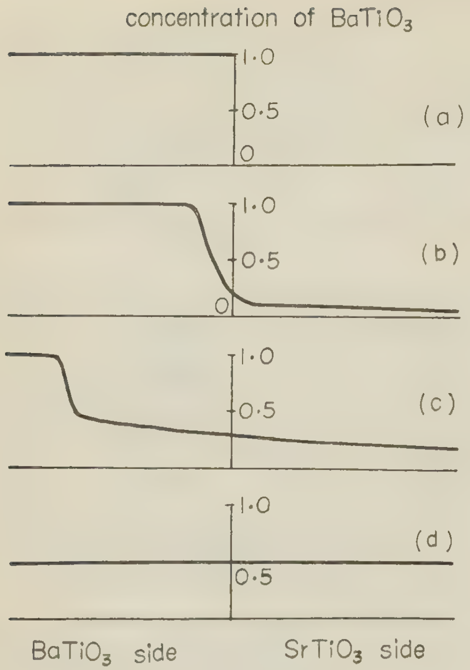

Fig. 5. Change of the concentration of ions in the powder particle due to the firing.

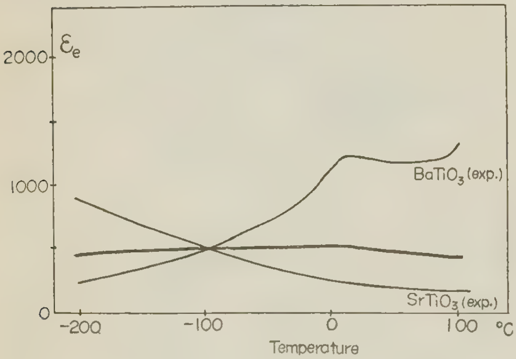

Fig. 6 (a). Effective dielectric constant calculated by

$$\log \varepsilon_e = \frac{1}{2} \log \varepsilon_{\mathrm{BaTiO_3}} + \frac{1}{2} \log \varepsilon_{\mathrm{SrTio_3}} .$$

(d) is the final state, in which the reaction finished completely. (b) and (c) may correspond to the case of 0.5 h. and 1.5 h. in Fig. 3 respectively. Our X-ray data lead us to consider that the fraction of the portion corresponding to $(Ba_x \cdot Sr_{1-x})TiO (1 > x \geqslant 0.5)$ is very small compared with the other.

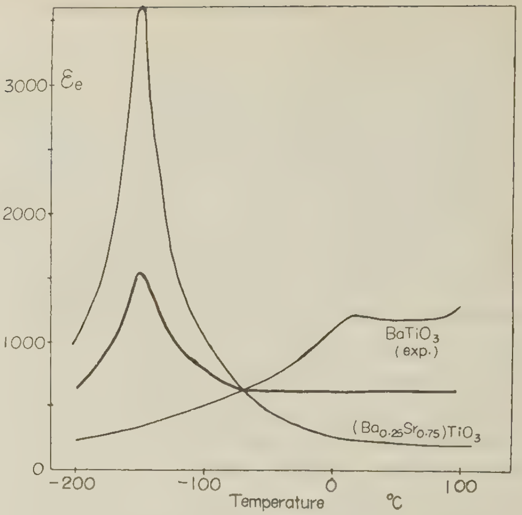

Fig. 6 (b). Effective dielectric constant calculated by

$$\log \varepsilon_e = \frac{1}{3} \log \varepsilon_{\mathrm{BaTiO_3}} + \frac{2}{3} \log \varepsilon_{\mathrm{(Ba_{0.25} \cdot Sr_{0.75})TiO_3}} .$$

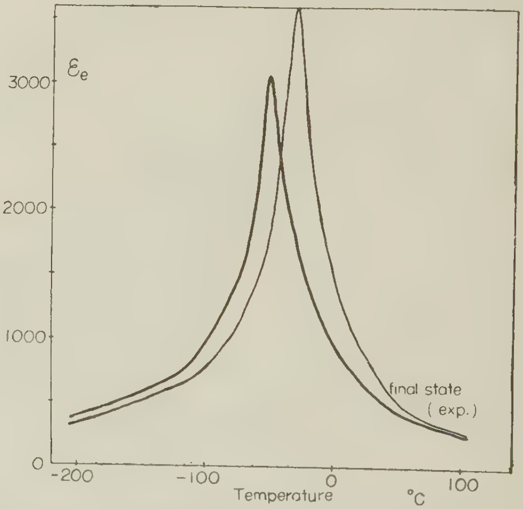

Fig. 6 (c). Effective dielectric constant calculated by

$$\log \varepsilon_e = \frac{1}{10} \log \varepsilon_{\mathrm{BaTiO_3}} + \frac{9}{10} \log \varepsilon_{\mathrm{(Ba_{0.445} \cdot Sr_{0.555})TiO_3}} .$$

The observed change of permittivity-temperature characteristics due to the firing condition may be interpreted qualitatively by this model in the following way. Let us apply so-called "Lichtenecker's" formula for calculating the effective permittivity of solid solutions. Then, in the initial state (a) of Fig. 5, it is given by

$$\log \varepsilon_e = \frac{1}{2} \log \varepsilon_{\mathrm{BaTiO_3}} + \frac{1}{2} \log \varepsilon_{\mathrm{SrTiO_3}} \qquad (7)$$

which is shown in Fig. 6 (a). A broad maximun on this curve is observed in Fig. 1 (a) or Fig. 2 (e). Fig. 6 (b), in which the effective permittivity is calculated by

$$\log \varepsilon_e = \frac{1}{3} \log \varepsilon_{\mathrm{BaTiO_3}} + \frac{2}{3} \log \varepsilon_{\mathrm{(Ba_{0.25} \cdot Sr_{0.75})TiO_3}} \quad (8)$$

may correspond to the state of Fig. 5 (b), and Fig. 1 (b) or Fig. 2 (a) show the similar characteristics. The one near the final state is shown in Fig. 6 (c), where only 1/10 fraction of barium titanate remains unreacted. In this region, the effective Curie point shifts to the high temperature side with the increase of the firing time. This coincides with our experimental data. As the effect of porosity and the detailed distribution of concentration of solid solutions have not considered in this calculation, any quantitative comparison with the experimental data would be impossible.

As long as the Curie temperature varies with the firing time, it means that the reaction is yet incomplete. This fact shows us that we must pay our attention to the firing conditions in making solid solution having uniform structure and stable characteristics. The ratio of two firing times, which are appropriate to the realization of the similar distributions of the concentration, $t_1 : t_2$, is known to be equal to $l^2{}_1 : l^2{}_2$, if the linear dimensions of the particles are $l_1$, and $l_2$ respectively. Accordingly, it is more efficient, in the firing, to use fine powder rather than to prolong the firing time. Furthermore, from rough calculations using the simple model stated above, it is found that a very long firing time is necessary to get completely uniform distribution of ions, so that the higher firing temperature has to be used for this purpose, even if we don't want to get dense ceramics. The cause of the previously reported fact that the two phases of barium·strontium titanate soild solution co-exist at the Curie temperature may be perhaps attributed to the non-uniform distribution of $Ba^{2+}$ and $Sr^{2+}$ ions.⁶⁾ But this problem will be solved thoroughly only when the atomic arrangement in the solid solution in the ceramic state becomes clear.

The author is grateful to Assist. Prof. S. Sawada of Tokyo University for his helpful discussion.

## References

1) S. Sawada and S. Nomura: Rep. Inst. Sci. & Tech. Univ. Tokyo **4** (1950) 1.
2) D. R. Wilder and E. S. Fitzimmons: J. Am. Cer. Soc. **38** (1955) 66.
3) R. F. Walker: J. Am. Cer. Soc. **38** (1955) 187.
4) S. Miyake and R. Ueda: J. Phys. Soc. Jap. **1** (1946) 32.
5) K. Shinriki and T. Kubo: J. Chem. Soc. Jap. Ind. Chem. Sec. **57** (1954) 621.
6) H. D. Megaw: Nature **157** (1946) 20.

JOURNAL OF THE PHYSICAL SOCIETY OF JAPAN Vol. 11, No. 9, SEPTEMBER, 1956

# Structural Study of Iron Selenides FeSe$_x$. I
# Ordered Arrangement of Defects of Fe Atoms

By Atsushi OKAZAKI and Kinshiro HIRAKAWA

*Department of Physics, Faculty of Science,*
*Kyusyu University, Fukuoka, Japan*

(Received May 17, 1956)

The ordered arrangements of the defects of iron atoms in FeSe$_x$ have been studied for several compositions by X-ray analysis. These defects tend to assume an ordered arrangement as in the case of pyrrhotite FeS$_{1.14}$. New phases are found in the region ($x=8/7\sim4/3$) which have been considered as the single phase region. If we choose the orthohexagonal and pseudo-orthohexagonal unit cells for $x=8/7$ and 4/3, respectively, the unit cell dimensions of the superstructure resulting from this ordering are twice as large as that of the fundamental structure along the $a$- and $b$-axes, and three times along the $c$-axis for $x=8/7$, and on the other hand, twice only along the $c$-axis for $x=4/3$.

## §1. Introduction

From X-ray analysis with powder method, Hägg and Kindström[1)] have found that iron selenide FeSe$_x$ has two phases in the range $x\cong1\sim4/3$ at room temperature, namely the phase of the PbO type structure for $x\cong1\sim8/7$ (the $\alpha$-phase) and of the NiAs type structure for $x\cong8/7\sim4/3$ (the $\beta$-phase). In the $\beta$-phase region, the lattice parameters decrease gradually as the excess Se content ($x>1$) increases. They have concluded that the decrease of the parameters might be ascribed to the formation of vacant lattice points of Fe atoms i.e. the defects of Fe atoms, although there have been some discrepancy between the values of the X-ray and the pycnometrical densities.

Recently, Hirone, Maeda and Tsuya[2)] have found that FeSe$_x$ has ferrimagnetic properties similar to those of iron sulphides FeS$_x$[3)].

The ferrimagnetism of pyrrhotite Fe$_7$S$_8$ has been considered to come out from the ordered arrangement of the defects of Fe atoms. The existence of the ordering was suggested by Néel and verified by Bertaut[4)] by X-ray analysis with single crystal method. In the NiAs type structure* Fe atoms are arranged in layers perpendicular to the hexad axis, alternating with layers of S atoms. Bertaut has found that the defects are restricted to the alternate iron layers and distributed in such a way as to be as widely dispersed as possible. The ferrimagnetism based on the superexchange interaction between Fe atoms in these layers requires not only the existence of the defects of Fe atoms, but also that the number of Fe atoms in one of these layers is different from that in the next iron layers.

The similarity between the ferrimagnetism of FeS$_x$ and that of FeSe$_x$ suggests the fact that the defects of Fe atoms are arranged orderly also in FeSe$_x$. Therefore, it should be interesting to study the ordering of the defects in FeSe$_x$ in order to establish relations between the magnetic properties and the crystal structures. In this paper, the results of X-ray analysis obtained for the single crystals of the $\beta$-phase at room temperature are described. The $\alpha$-phase crystals have not been studied because good specimens were not available. A paper treating their magnetic properties will be published in near future.

## §2. Crystal Preparation

Single crystals were prepared for $x=8/7$, 7/6, 6/5, 5/4 and 4/3 by the following methed: the powdered mixture of electrolytic iron reduced by hydrogen and redistilled 99.997% selenium in proper proportions was sealed in an evacuated silica tube. In the case of Fe$_7$Se$_8$, for example, the mixture was heated to 1150°C and kept at the temperature for 70 hours, and then cooled gradually down to room temperature taking 5 days. Also in the other cases the similar heat treatments were carried out.

---

* E. F. Bertaut[4)] showed that pyrrhotite was only pseudo-hexagonal with a monoclinic unit cell ($\beta=89°33'$).

All of these crystals have metallic lustre. The plane perpendicular to the $c$-axis is the cleavage plane in the case of $Fe_7Se_8$, but not so in the other cases as will be described in § 4. In general, however, it was not easy to find out these cleavage surfaces when the ingot was broken.

The compositions of these crystals were ascertained by chemical analysis and density measurements. Chemical analysis* with a small quantity (about 15 mg) of $Fe_7Se_8$ showed that the specimen contained 38.15% iron and 60.71% selenium in weight per cent.**, corresponding to $Fe_7Se_{7.90}$. On the other hand, the X-ray density of $Fe_7Se_8$ (6.37 g cm$^{-3}$) is in good agreement with the pycnometric value (6.42 g cm$^{-3}$). Since, also for the other compositions, the density values by the two methods are in good agreement with each other as shown in Fig. 1 and Table I, we have avoided the trouble to carry out chemical analysis except for the case of $Fe_7Se_8$.

According to the present study there is no such discrepancy between the two values as observed by Hägg and Kindström, whose result is also shown in Fig. 1 for comparison.

## § 3. Experimental

All X-ray data were obtained from Laue and oscillation (or rotation) photographs. For the latter method, iron filtered Co $K$-radiation was used and the camera radius was $4.99_0$ cm. The exposure time were 1.5~2 hours for 30° oscillation photographs, 3~4 hours for rotation photographs, when applied voltage was ~30 kV, and beam current (focused by electrostatic lens) ~15 mA.

The specimens for X-ray diffraction were cut from the single crystals along the cleavage surfaces in the cases of $Fe_7Se_8$, $Fe_5Se_6$, $Fe_4Se_5$ and $Fe_3Se_4$. In the case of $Fe_6Se_7$ the cleavage surface was not found.

The specimens were coated with thin wax to prevent the oxidation. Their dimensions were of the order of magnitude 0.5 mm. Sufficiently clear diffraction patterns were obtained from $Fe_7Se_8$, and $Fe_3Se_4$, but not from the others.

The linear absorption coefficient of $FeSe_x$ ($x$=8/7~4/3) is larger than 600 cm$^{-1}$, so that the shape of the specimen should be regulated for the absorption correction. In the present case, however, this caution has not been taken, because the fundamental crystal structure (for instance the NiAs type for $Fe_7Se_8$) is well known and the considerable information about the superstructure is available even without the accurate intensity data.

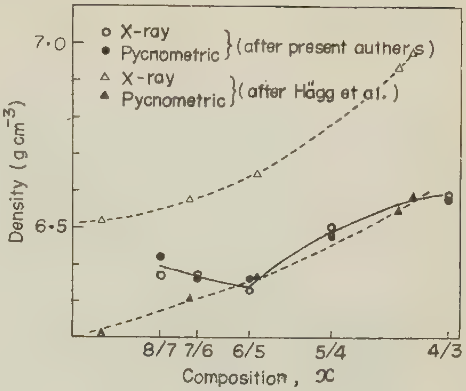

Fig. 1. Density versus composition.

Table I. Density of $FeSe_x$.

| $x$ | 8/7 | 7/6 | 6/5 | 5/4 | 4/3 |
|---|---|---|---|---|---|
| X-ray | 6.37 | 6.37 | 6.33 | 6.50 | 6.59 |
| pycnometric | 6.42 | 6.36 | 6.36 | 6.48 | 6.58 |

## § 4. Structure Determination

### (a) $Fe_7Se_8$

On the rotation photographs about the $a$- and $c$-axes of the single crystal of $Fe_7Se_8$, there are many weak spots besides the strong ones corresponding to the NiAs type structure. Their intensities are of the order of one hundredth of those of the strong ones. These weak spots are due to the superstructure, since they appear not only on the layer lines made by the strong ones, but also on those corresponding to the unit cell dimensions twice along the $a$-axis and thrice along the $c$-axis as large as those of the fundamental NiAs type structure. We may assume, thus, that the superstructure is due to the ordered arrangement of the defects of Fe atoms similar to the case of pyrrhotite $Fe_7S_8$ [4]. The splitting of the spots due to the monoclinic deformation of the fundamental lattice as in the case of $Fe_7S_8$ is not found in $Fe_7Se_8$.

---

* We are indebted to Dr. K. Kumada, Faculty of Agriculture, Tokyo University, for chemical analysis.

** Deficit of 1.14% is attributed to impurities and experimental error.

Table II. Distances between the neighbouring defects in Å.

| | $Fe_7Se_8$ | | $Fe_7S_8$ |
|---|---|---|---|
| | type (i) | type (ii) | |
| in the same (001) layer | 7.23 | 7.23 | 6.86 |
| in the next (001) layer | 6.91 | 5.88<br>& 6.91 | 6.71 |

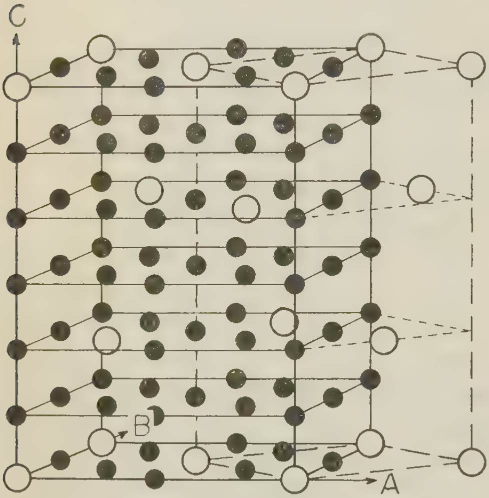

Fig. 2. Unit cell of $Fe_7Se_8$. Open and solid circles represent defects and Fe atoms respectively. Se atoms are omitted for clarity.

These rotation photographs are reporduced in Photo. 1.

We can choose for the superstructure the following orthorhombic unit cell containing six chemical units $Fe_7Se_8$.

$$A=\sqrt{3}B=12.5_3, \quad B=2a=7.23_4,$$
$$\text{and} \quad C=3c=17.6_5 \text{ Å}.$$

The capital and small letters designate the unit cell lengths of the super and fundamental lattices, respectively.

All the spots appearing on the oscillation photographs, taken with the oscillation range 20° and 30° about the $B$- and $C$-axes, respectively, could be indexed on the basis of the above orthorhombic lattice. For all the observed $hkl$ reflections, $h+k$ were even. This extinction rule is satisfied in the orthorhombic system only in the case of the space groups $D_2^6-C222$, $C_{2v}^{14}-Cm2m$ and $D_{2h}^{19}-Cmmm$.

Since an extremely inhomogeneous distribution of the defects is improbable, the only plausible arrangements of the six defects of Fe atoms in the unit cell are as follows:

$$\text{(i)} \quad \left(0, 0, 0; \frac{1}{2}, \frac{1}{2}, 0\right)$$
$$+\frac{1}{4}, \frac{1}{4}, \frac{1}{3}; \frac{1}{4}, \frac{3}{4}, \frac{2}{3}, \quad \text{or}$$
$$\text{(ii)} \quad \left(0, 0, 0; \frac{1}{2}, \frac{1}{2}, 0\right) \pm \left(0, \frac{1}{2}, \frac{1}{3}\right).$$

For the type (i), the calculated structure factor* $F_c(hkl)=0$ if $l=3n$ ($n$; integers) and $h$ and $k$ are odd. For the type (ii), on the other hand, $|F_c(hkl)| \neq 0$ for all the reflections which obey the above extinction rule. Moreover, $|F_c(hkl)|$ is larger for $l=3n$ than for $l \neq 3n$.

The observed intensities favour the type (i), that is, the reflections for which $l=3n$ and $h$ is odd are not observed or very faint for smaller indices. For larger ones (about 10), however, the intensities become the same order of magnitude as those of other superstructure spots. This fact is explainable when we assume slight displacements of Fe and Se atoms from their original positions due to the appearance of the defects. The magnitude of the displacement will be of the order of one hundredth of the unit cell dimensions**. The same diffraction patterns were obtained from different specimens.

The distances between the neighbouring defects for the type (i) and (ii) are given in Table II, and are compared with those in $Fe_7S_8$. The comparison suggests that if the "$A$-likes-$B$" type ordering is the case as in $Fe_7S_8$ 5), the structure of the type (i) may be more stable.

From these considerations, it seems that the structure of the type (i) is more probable. The most probable structure of $Fe_7Se_8$ is shown in Fig. 2, whose space group is $D_2^6-C222$. (When we choose the hexagonal unit cell as shown by broken lines, the space group is $C_6^4-P6_2$ or $C_6^5-P6_4$.)

### (b) $Fe_3Se_4$

$Fe_3Se_4$ is monoclinic, whose Laue symmetry is $C_{2h}-2/m$. The lattice parameters of the unit

---

* We assume that the atomic structure factor of the defect is equal to that of Fe atom.

** If this is the case, the extinction rule for the fundamental NiAs type structure must be also violated. The weak spots whose indices correspond to the prohibited reflections for the fundamental lattice are observed. But at present we cannot distinguish whether these are due to the fundamental or superstructure lattice.

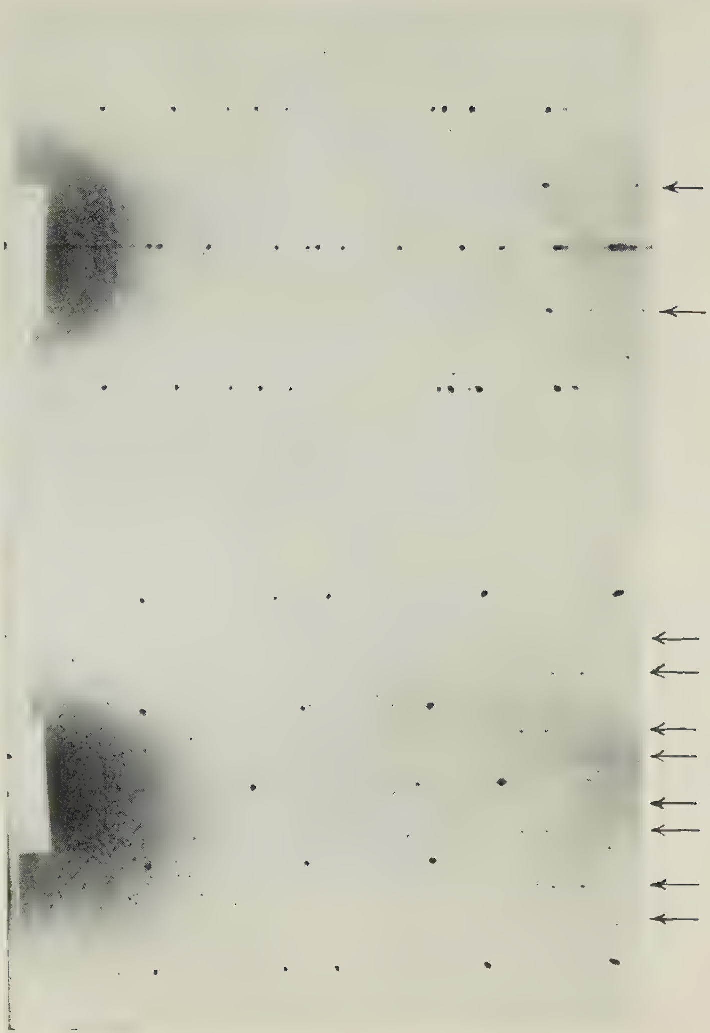
(a)

(b)

Photo. 1. Rotation photographs of $Fe_7Se_8$:
(a) about the B-axis,
(b) about the C-axis. Each arrow indicates the location of the layer lines made by weak spots alone.

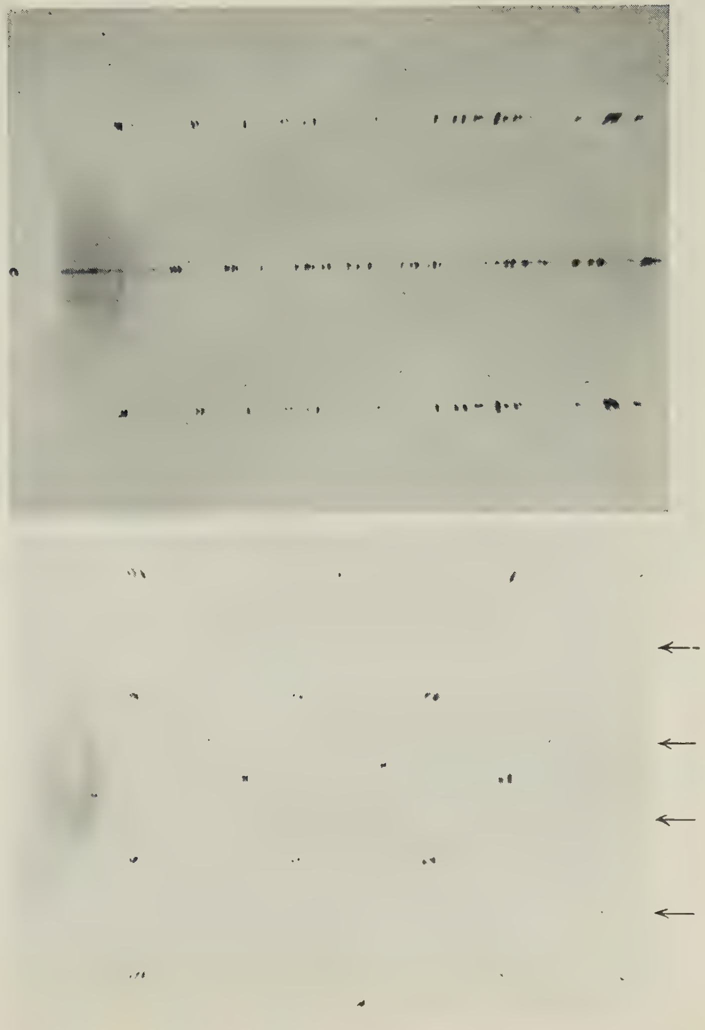
(a)

(b)

Photo. 2. Rotation photographs of $Fe_3Se_4$:
(a) about the B-axis,
(b) about the C-axis. Each arrow indicates the location of the layer lines made by weak spots alone.

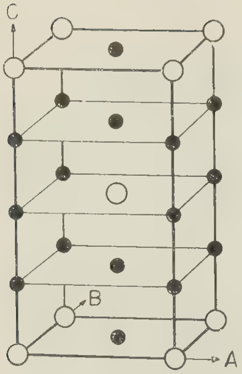

Fig. 3. Unit cell of $Fe_3Se_4$. Open and solid circles represent defects and Fe atoms, respectively. Se atoms are omitted for clarity.

cell containing two chemical units, $Fe_3Se_4$, are

$$A=6.16_7,\quad B=3.53_7,\quad C=2c=11.1_7\,\text{Å}\quad \text{and}\quad \beta=92.0°.$$

The rotation photographs about the $C$-axis is the most characteristic, since the splitting of the spots corresponding to the monoclinic deformation of the fundamental lattice and the deviation of $A/B$ from the value $\sqrt{3}$ are observed and, furthermore, many weak spots corresponding to $C=2c$ are found. These weak spots may be probably due to the superstructure resulting from the ordered arrangement of the defects of Fe atoms as in the case of $Fe_7Se_8$. On the rotatation photographs about the $A$- and $B$-axes, such weak spots are not observed except on the layer lines made by the strong ones. Two of these rotation photographs are reproduced in Photo. 2.

All the reflections on the oscillation photographs taken with the oscillation range 30° about each axis could be indexed on the basis of the monoclinic lattice. For all the observed $hkl$ reflections, $h+k+l$ were even. Therefore the lattice made of the defects should be body centred as shown in Fig. 3. (The reflections for which $h+k+l=$even were observed without exception.)

From this structure, it is expected that $Fe_3Se_4$ cleaves along the $(\bar{1}01)$ planes. The calculated value of the angle between the $(\bar{1}01)$ plane and the $A$- or $C$-axis is in good agreement with that determined by observing the shadow image of the specimen.

(c) $Fe_4Se_5$

Although the diffraction pattern of $Fe_4Se_5$ shows asterism in general, one among several specimens examined gave pattern sufficiently clear for the analysis of the superstructure.

$Fe_4Se_5$ is monoclinic, whose Laue symmetry is $C_{2h}-2/m$ as in the case of $Fe_3Se_4$, and the lattice parameters of the unit cell containing two chemical units, $Fe_{3.2}Se_4$, are

$$A=6.21_6,\quad B=3.59_2,\quad C=2c=11.3_2\,\text{Å},\quad \text{and}\quad \beta=91.5°.$$

The rotation photographs about the three axes are quite the same as those of $Fe_3Se_4$ except for the systematic displacements of the spots resulting from the differences of the lattice parameters. By the oscillation photographs in the range of 30° about the $B$-axis, the same extinction rule as in the case of $Fe_3Se_4$ was confirmed.

In $Fe_4Se_5$ it seems, therefore, that the ordered defects in the structure of $Fe_3Se_4$ are occupied at random by the excess Fe atoms. If this is the case, the intensity of the superstructure spots should decrease to $(4/5)^2=0.64$ compared with that of $Fe_3Se_4$. Although, because of the difference of the absorption effect depending on the shape of the specimen, the quantitative comparison over the whole range of scattering angle was not carried out, the intensity decrease by the factor of about 0.5 was confirmed by visual estimation on eight high angle reflections ($\theta>60°$).

Also in this case, the cleavage plane is the $(\bar{1}01)$ plane.

(d) $Fe_5Se_6$

In this case the diffraction patterns are highly obscure. We could not find the sufficiently good specimen to analyse the superstructure thoroughly, although the existence of the superstructure was sure as described below.

On the rotation photographs about each axis of the specimen whose pattern was relatively clear, we found many weak spots corresponding to the unit cell dimensions twice as large as those of the fundamental structure. But by closer examination of this pattern it was revealed that the specimen examined was composed of several crystals having orientations slightly different from one another. This was also confirmed by Laue photograph taken with the incident beam parallel to the $B$-axis, since this photograph was similar to that of $Fe_4Se_5$ except for the splitting of spots. This splitting remained after dividing the specimen into two pieces whose dimensions were 0.1×0.1×0.2 mm and 0.1×0.2×0.4 mm.

The other specimens giving spots as clear as those of the above-mentioned one gave also the same patterns.

We may assume that $Fe_5Se_6$ is fairly unstable in accordance with the fact, that in the course of the crystal preparation, the silica tube exploded four times out of six although the preparation condition had been varied, and that near the composition $x=6/5$ the density is minimum throughout the $\beta$-phase.

The lattice parameters of the fundamental sturucture are estimated as follows:

$a=6.24$, $b=3.61$, $c=5.84$ Å and

$\beta$: probably 90.0°∼90.5°.

(e) $Fe_6Se_7$

Also in this case it is difficult to find the specimen giving sufficiently clear diffraction pattern for the analysis of the superstructure. Two kinds of specimens whose diffraction patterns were different from each other were obtained from the same ingot.

In the first case, on the rotation photographs about three axes, we found many weak spots similar to those of $Fe_5Se_6$. Unlike the case of $Fe_5Se_6$, these were not contributed from more than one crystal, but the extinction rule could not be obtained, because superstructure spots at higher angle were weak and with asterism. Within the definition the splitting of the fundamental structure spots may be attributed only to the deviation of $A/B$ from $\sqrt{3}$, without any monoclinic deformation.

In the second case, the rotation photographs about the $C$-axis was quite the same as that of $Fe_7Se_8$ except for the systematic displacement of the spots due to the differences of the cell dimensions, and these spots were markedly clear compared with those in the first case. By the oscillation photographs in the range of 30° about this axis, the existence of the same extinction rule as in the case of $Fe_7Se_8$ was confirmed. (The intensity of the superstructure spots is smaller than expected from the composition as compared with $Fe_7Se_8$.)

Therefore $Fe_6Se_7$ seems to be a mixture of the crystals with the $Fe_7Se_8$ type structure and probably of those with the $Fe_5Se_6$ type one although the structure of the latter is

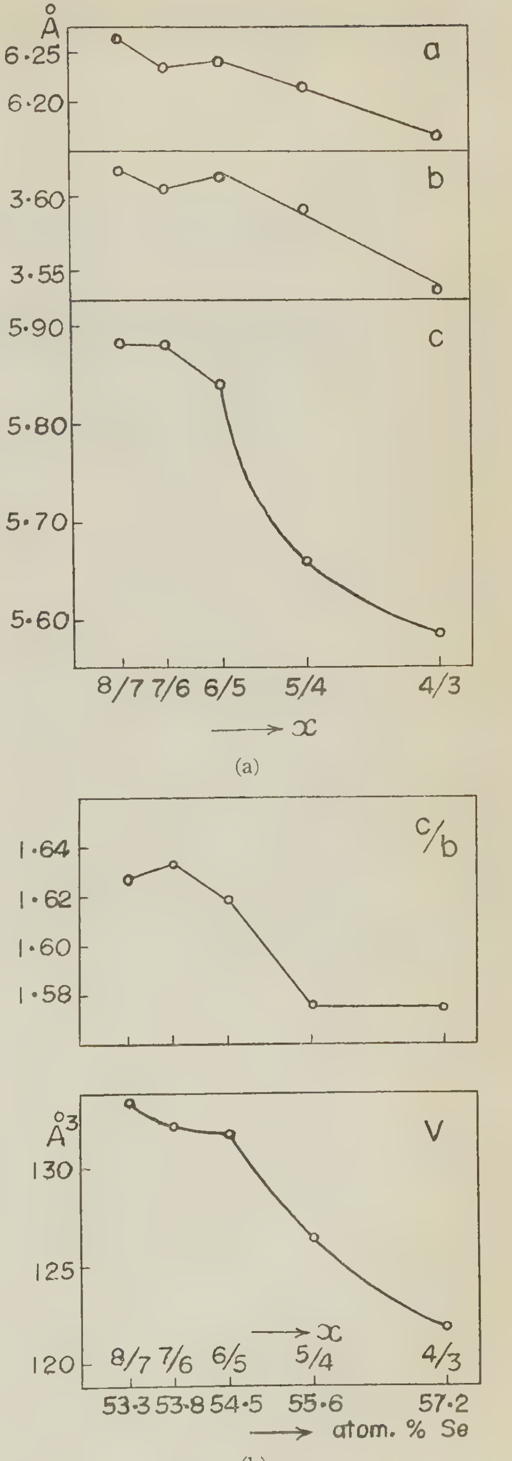

(a)

(b)

Fig. 4. (a) Measured lattice parameters of fundamental unit cells versus composition.
(b) $c/b$ (average of $c/b$ and $\sqrt{3}\,c/a$) and volume of fundamental unit cell versus composition.

unknown.

The unit cell dimensions of the fundamental structure obtained in the first case are as follows:

$$a=6.23,\quad b=3.61,\quad \text{and}\quad c=5.88\,\text{Å}.$$

## § 5. Conclusions

It is found that the defects of Fe atoms in $FeSe_x$ are arranged orderly in the region $x=8/7\sim4/3$.

For $x=8/7$, all the distances between the neighbouring defects are almost equal to $2a$, that is, these defects are distributed as widely as possible similarly to the case of $Fe_7S_8$, but the structure of $Fe_7Se_8$ shown in Fig. 2 differs from that of $Fe_7S_8$ in the following respects: the former is hexagonal with $C=3c$ while the latter is only pseudo-hexagonal with $C=4c$. In the region $x=8/7\sim7/6$, further defects corresponding to these compositions may now appear in those layers perpendicular to the $C$-axis, in which for the case of $Fe_7Se_8$ we can not find any defect. When $x$ increases beyond 7/6, the periodicity of $C=3c$ vanishes and that of $C=2c$ becomes dominant. In the region $x=5/4\sim4/3$, the structure becomes the $Fe_3Se_4$ type with $C=2c$, and the excess defects to the composition may probably be occupied at random by Fe atoms. In $Fe_3Se_4$, the defects are arranged along the $B$-axis without any intervenient Fe atom and each of the rows of those defects parallel to the $B$-axis is surrounded by six neighbouring rows of defects with almost the same distances (Fig. 3).

According to the different types of the ordering mentioned above, the $\beta$-phase region may be divided at least into two regions, that is, $x=8/7\sim7/6$ and $x=6/5\sim4/3$, although the arrangement of the defects near $x=6/5$ are unknown. This may be also supported by the measurement of the lattice parameters and the volume of the fundamental unit cell, which are shown in Fig. 4.

The authors are much indebted to Assist. Prof. T. Okada for his encouragement and valuable comments. They also wish to express their cordial thanks to Dr. N. Tsuya for the communication of the results obtained at his laboratory prior to publication. The present investigation was supported by the Scientific Research Expenditure of the Ministry of Education.

### References

1) G. Hägg and A. L. Kindström: Z. Phys. Chem. **22** (1933) 453.
2) T. Hirone, S. Maeda and N. Tsuya: J. Phys. Soc. Japan **9** (1954) 496.
3) H. Haraldsen: Z. anorg. allg. Chem. **246** (1941) 169 and 195.
4) E. F. Bertaut: Acta Cryst. **6** (1953) 557.
5) L. Néel: Rev. Mod. Phys. **25** (1953) 58.

JOURNAL OF THE PHYSICAL SOCIETY OF JAPAN Vol. 11, No. 9, SEPTEMBER, 1956

# Determination of Elastic Constants of Metals and Alloys by Temperature Diffuse Scattering of X-Rays

By Shoichi ANNAKA

*Physics Department, Tokyo University of Education*

(Received March 27, 1956)

A new simple but fairly accurate method for the determination of elastic constants of cubic crystals from the observation of the temperature diffuse scattering of x-rays has been developed. The elastic constants of silver, copper-zinc and silver-copper alloys were determined by this method. Diffuse scattering due to the disorder of atoms as well as due to the thermal motion of atoms were considered in the case of alloys. In silver-copper alloy, the abnormal diffuse scattering, probably due to the former cause, was found along the [001] direction from the (004) reciprocal lattice point. The elastic constants obtained were as follows:

|  | $c_{11}$ | $c_{12}$ | $c_{44}$ |
|---|---|---|---|
| Ag | $1.2_1\times10^{12}$ | $0.89_9\times10^{12}$ | $0.42_6\times10^{12}$ dyne/cm$^2$ |
| $Cu_{82}Zn_{18}$ | $1.5_6\times10^{12}$ | $1.1_4\times10^{12}$ | $0.68_7\times10^{12}$ |
| $Ag_{95}Cu_5$ |  |  | $0.42_7\times10^{12}$ |

## § 1. Introduction

Theories and experiments of the temperature diffuse scattering of x-rays have been developed by many workers[1] and it has been shown that elastic constants and elastic spectra of crystals could be obtained by measuring of the temperature diffuse scattering[2][3]. Wooster and his collaborators, for example, determined elastic constants of some cubic crystals accurately and proved that this method was one of the important method of obtaining the elastic constants of crystals[4][5]. Recent development of the Geiger-Müller counter technique has much facilitated the application of this method.

In the present work, we have attempted to obtain the elastic constants of some metals and alloys of cubic structure from the temperature diffuse scattering of x-rays. But in the case of certain alloys, we have to take account of the fact that the diffuse scattering of x-rays is also produced by the disorder of atoms due to such causes as difference in atomic radii[6], order-disorder transformation[7], etc. Furthermore, the temperature factor in the intensity formula of Bragg reflection is not known usually for alloys.

Taking these factors into consideration, we have determined the elastic constants of Ag, $Cu_{82}Zn_{18}$ (the equilibrium phase) and $Ag_{95}Cu_5$ (the non-equilibrium phase) at room temperature by measuring the temperature diffuse scattering of x-rays*.

## § 2. Experimental Procedure

A copper target x-ray tube was operated at about 30 kv so that half-wave length component could be neglected. The intensity of x-ray beam was monitored by an air-filled ionization chamber and was controlled by regulating the input power manually. A small bent monochromator of lithium fluoride crystal was used. The diffuse scattering of x-rays from single crystal sample was observed by a halogen-filled Geiger-Müller counter and the absolute intensity was determined by measuring the Compton scattering from paraffin wax at the scattering angle of 120°.

The single crystal sample were prepared by cooling slowly the molten metal and alloy in quartz tubes. But the sample of silver-copper alloy was quenched from equilibrium temperature to room temperature. The (001) faces cut out of the samples were first polished mechanically and then electrolytically. The area of these flat faces were about 1×1 cm². Laue photographs taken at several points on each face gave good crystalline reflections.

The intensities of the diffuse scattering were measured in [100], [001] and [10$\bar{1}$] directions around the (004) reciprocal lattice point and at three points along each direction. Before applying the observed intensities to the calculation of the elastic constants necessary corrections were applied.

---

* All compositions are expressed by atomic per cent in the present paper.

The first set of the corrections, for white radiation and mosaic structure, were done along [001] and [100] directions respectively after Ramachandran and Wooster[2]. However, these corrections are very difficult for points too near to the (004) point. The observation point, therefore, was chosen to be reasonably remote from the (004) point.

The second correction is the skew correction which is due to the angle of incidence and reflexion being unequal.

After applied the above corrections, the three intensity values $I_1, I_2$ and $I_3$ along the direction concerned are plotted against $1/R^2$ on a graph and connected by a smooth curve, where $R$ is the absolute of the wave vector $\boldsymbol{R}$. This curve is not linear generally since all corrections are not yet completed. By extraporating the curve, the intensity of the diffuse scattering I, corrected up to for white radiation, mosaic structure and skew effect, can be obtained at any point near to the (004) point. The nearer is the point in consideration to the (004) point, the less is the error due to using the value of structure factor and temperature factor corresponding to the (004) point in the intensity formula, in place of the values corresponding to the point concerned. The above procedure of obtaining the extrapolated diffuse scattering intensity I is also important as the intensity formula which is used to obtain the elastic constants is valid only for the small wave vector $\boldsymbol{R}$. However, in order to be used in calculating the elastic constants, the extrapolated value should be subjected to further corrections as follows.

The correction for the Compton scattering is calculated theoretically. For example, the next formula was used for silver[5].

$$I_c = I_0 \frac{e^4}{m^2c^4} \frac{1+\cos^2\varphi}{2} \frac{\Omega}{2\mu\tau} 4(47-\sum f^2)/B^3 \tag{1}$$

where the notations except the usual ones have the following meaning:

$\varphi$: the total deflection angle of the x-ray beam,
$\mu$: the absorption coefficient of the sample,
$\tau$: the volume of the unit cell,
$\Omega$: the solide angle subtended at the face of the sample by the observation slit,
$\sum f^2$: the incoherent scattering function,
B: the Breit-Dirac correction factor.

The most important correction in our method is for the divergence of scattered x-rays. The divergence of x-rays for the incident x-rays, however, may be neglected because the distance between monochromator and collimating slit was long enough in our experiment. Vertical and horizontal dimensions of the slit in front of the Geiger-Müller counter were 3 mm and 1 mm respectively. The distance between the slit and the sample was 5.5 cm. The calculation of the correction factor was done in the following way on the assumption that all of the observed diffuse scattering were the first order temperature diffuse scattering.

(*a*) *Correction for vertical divergence*

By Figs. 1, 2, 3 and 4 we explain the successive method of the correction [10$\bar{1}$] direction around the (004) reciprocal lattice point in silver. In Fig. 1 *o* indicates the (004) point in the reciprocal lattice space whose origin is *o′*. The intensity curve *add′* is so drawn that the distance from the (004) point to any point of the curve, *od* for example, is proportional to the intensity of the diffuse scattering observed at the same distance from the (004) point of each direction. The line *aa′* indicates the length of the slit which corresponds to *p′q′* in Fig. 3. By using Fig. 1 the intensity expected to be observed at the point *b* of the slit at an angle $\theta$ to the horizontal line *oa* can be obtained on the basis of the usual theory that the intensity of the temperature diffuse scattering is proportional to $1/R^2$ in the neighbourhood of the reciprocal lattice point. This intensity is plotted against the angle $\theta$ as shown in Fig. 2. As the irradiated area of the sample face was chosen equal to that of the slit, when viewed from the direction of the slit, and lay on the same horizontal plane as the slit (Fig. 3), we could simply evaluate the intensity of the diffusely reflected x-rays from any point of the irradiated area of the sample face in the following way. When we want, for example, to obtain the intensity from the point *z*, we have simply to add the areas *oabco* and *oab′c′o* of Fig. 2. The value of this sum is plotted as ordinate *tt′* in Fig. 4. Thus the height of the curve *rt′s* shows the intensity I entering into the slit from each point of the irradiated area on the crystal face.

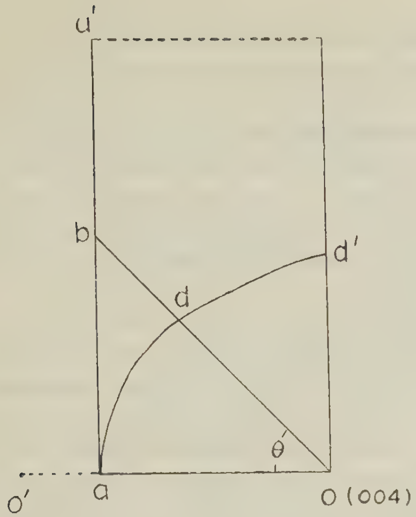

Fig. 1. Diagram showing intensity curve *add′* and vertica lslit length *aba′* in the reciprocal lattice space whose origin is *o′*.

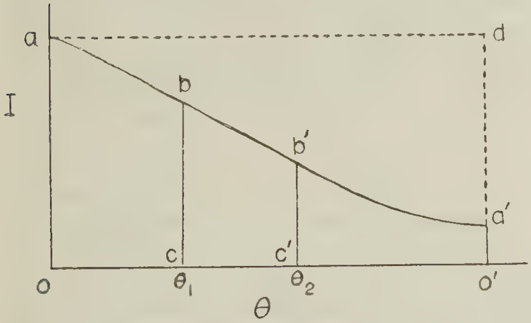

Fig. 2. Diagram showing the intensity I to be observed at a point of the observation slit at an angle $\theta$ to the horizontal line.

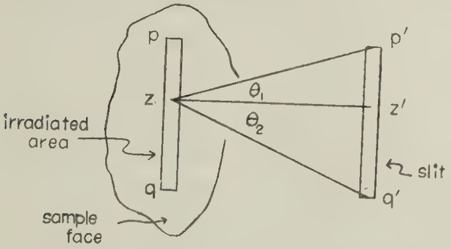

Fig. 3. Schematic diagram of the diffuse beam diverging from the point $z$ on the irradiated area of the sample face and falling on the slit $p'q'$. The line $zz'$ is horizontal.

The ratio of the area *oado′* of Fig. 2 to the mean height $I_m$ of the curve *rt′s* of Fig. 4 is the correction factor for the vertical divergence.

(*b*) *Correction for horizontal divergence*

The horizontal divergence correction was done in the same way as for the vertical one.

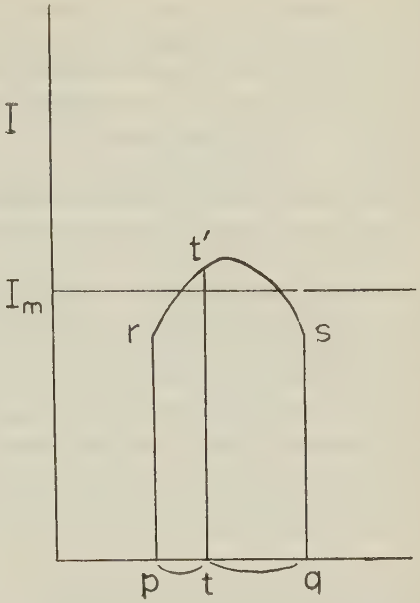

Fig. 4. Diagram showing the relative intensity of the scattered x-rays entering into the slit from any point of the face of the sample. $I_m$ is the mean intensity entering into the observation slit. The line *pq* shows the vertical length of the irradiated area.

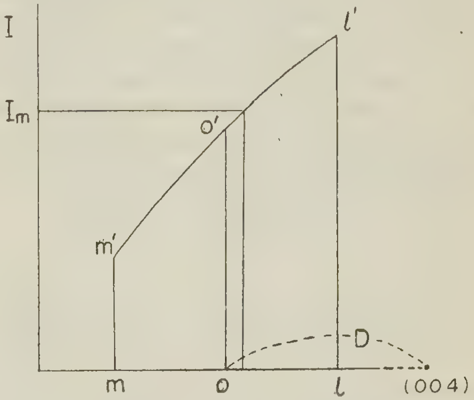

Fig. 5. Diagram showing the divergence correction along the *R* direction. The line *lm* is the horizontal breadth of the observation slit, *o* being the center of the slit. $I_m$ is the mean value of the intensity entering into the slit.

But in this case the horizontal edge of the slit is not perpendicular to $\boldsymbol{R}$ in the reciprocal lattice space. If the edge is almost parallel to $\boldsymbol{R}$, the correction factor can be obtained from the following simple consideration. In Fig. 5 *lm* corresponds to the horizontal breadth 2a of the slit in the reciprocal lattice space and the curve *l′o′m′* is so drawn that its ordinate is proportional to the inverse of the squire of the distance $R$ or the intensity of the temperature diffuse scattering of the point in consideration near the reciprocal lattice point (004). The mean value of the intensity entering into the slit at the distance $D$ from the (004) point in the reciprocal lattice space is that of the mean height of the curve, which is $K/(D^2-a^2)$, where $K$ is a proportional constant. The correction factor therefore is $(D^2-a^2)/D^2$.

Applying the corrections (*a*) and (*b*) for several directions, we could obtain the more exact intensity curve than the one *add'* in Fig. 1. By using the new curve the same procedure as described above was repeated until the changes of the correction factors became sufficiently small. After these procedures we can obtain the correction factors provided the intensity curve are approximately correct.

The alloys studied have imperfections due to the difference of radii of constituent atoms. The diffuse scattering due to this kind of imperfection was estimated by the Huang's formula⁶⁾. As the intensity of this diffuse scattering was very weak compared with that of the temperature diffuse scattering in our cases, the approximate values of the former diffuse scattering were subtracted from the above corrected values of the observed diffuse scattering, only in [001] directions around (004) reciprocal lattice points. The intensity $I_i$ of this diffuse scattering was calculated for [001] direction by using the next formula:

$$I_i=I_0\frac{4e^4}{m^2c^4}\frac{1+\cos^2\varphi}{2}\frac{3\Omega}{2\mu\tau R^2}f^2e^{-2M}(p-p^2)$$
$$\times\left(\frac{\Delta d}{d}\right)^2\left(\frac{\sin\theta}{\lambda}\right)^2\left\{\cos 2\pi dR+5\frac{\sin 2\pi dR}{2\pi dR}\right\}, \tag{2}$$

where the notations except the ones in Eq. (1) are as follows:

$f$: the atomic scattering factor corrected for dispersion,
$p$: the atomic concentration,
$d$: the lattice constant,
$\Delta d$: the difference of the lattice constants of solute and solvent metals,
$e^{-2M}$: the temperature factor.

The evaluation of the small constant background which is not corrected above can be obtained after Ramachandran and Wooster²⁾. When the diffuse scattering intensities at three points in one direction are plotted against $1/R^2$ after applied the above mentioned corrections, these three points can be connected by a straight line approximately. The value of the background is given by the intercept of the line with the ordinate. This constant contribution to the extrapolated diffuse scattering intensity, however, could be neglected within the experimental error in our case except the one to the weak intensity in [001] direction.

The temperature factors for the alloys are not well known. We have therefore obtained the factors by comparing the intensities of the temperature diffuse scattering near (002) and (004) reciprocal lattice points at room temperature. We observe the diffuse intensities $I_{(002)}$ and $I_{(004)}$ at the positions corresponding to the same wave vector $\boldsymbol{R}$. By the corrections except that for the divergence, which is the same for either intensity, we can obtain the value of the ratio $I_{(002)}/I_{(004)}$ in the following formula:

$$I_{(002)}/I_{(004)}=\frac{1}{4}\,\frac{1+\cos^2\varphi}{1+\cos^2\varphi'}\,\frac{f^2}{f'^2}\,\frac{\exp(-2M)}{\exp(-2M')}, \tag{3}$$

where the values of $\varphi$, $f$ and $M$ correspond to the (002) point and $\varphi'$, $f'$ and $M'$ to the (004) point. The mean-square amplitude of vibration can be obtained from the above formula.

Applying the various methods for corrections described above for the observed diffuse scattering, we finally obtained the true intensities of the temperature diffuse scattering. The theoretical expressions for the temperature diffuse scattering were given by James¹⁾, Laval⁸⁾, Born⁹⁾ and others. In the case of small wave vector $\boldsymbol{R}$, thermal waves in a crystal are almost the same as elastic sound waves. Therefore, the intensity $I_a$ of the first order diffuse scattering for small $\boldsymbol{R}$ can be given by the following formula and the second order diffuse scattering can be corrected by the Wooster's method.

$$I_a=I_0\frac{e^4}{m^2c^4}\frac{1+\cos^2\varphi}{2}\frac{\Omega}{2\mu\tau}D \tag{4}$$

where

$$D=\frac{kT}{\tau}|F_T|^2\frac{q^2}{R^2}\sum_{\alpha=1}^{3}\frac{\cos^2(\boldsymbol{q}\cdot\boldsymbol{\xi}_\alpha)}{\rho V_\alpha^2},$$

$k$: the Boltzmann's constant,
$F_T$: the structure factor at temperature $T$,

$\rho$: the density of the crystal,

$\boldsymbol{q}$: the vector joining the (004) point and the origin of the reciprocal lattice space,

$\xi_\alpha$: the amplitude of the acoustical wave for $\alpha$ component of the wave vector $\boldsymbol{R}$,

$V_\alpha$: the velocity of the acoustical wave for $\alpha$ component of the wave vector $\boldsymbol{R}$.

$D$ shows the intensity reflected by a unit cell. For cubic crystals,

$$\sum_{\alpha=1}^{3}\frac{\cos^2(\boldsymbol{q}\cdot\xi_\alpha)}{\rho V_\alpha^2}$$

can be reduced to the next formula:

$$\begin{aligned}\sum_{\alpha=1}^{3}\frac{\cos^2(\boldsymbol{q}\cdot\xi_\alpha)}{\rho V_\alpha^2}=&[h^2\{c_{44}^2+c_{44}(c_{11}-c_{44})(v^2+\omega^2)+(c_{11}+c_{12})(c_{11}-c_{12}-2c_{44})v^2w^2\}\\&+k^2\{c_{44}^2+c_{44}(c_{11}-c_{44})(w^2+u^2)+(c_{11}+c_{12})(c_{11}-c_{12}-2c_{44})w^2u^2\}+l^2\\&\times\{c_{44}^2+c_{44}(c_{11}-c_{44})(u^2+v^2)+(c_{11}+c_{12})(c_{11}-c_{12}-2c_{44})u^2v^2\}-2hk(c_{12}+c_{44})\\&\times\{c_{44}+(c_{11}-c_{12}-2c_{44})w^2\}uv-2kl(c_{12}+c_{44})\{c_{44}+(c_{11}-c_{12}-2c_{44})u^2\}vw\\&-2lh(c_{12}+c_{44})\{c_{44}+(c_{11}-c_{12}-2c_{44})v^2\}wu]\\&+(h^2+k^2+l^2)[c_{11}c_{44}^2+c_{44}(c_{11}+c_{12})(c_{11}-c_{12}-2c_{44})(u^2v^2+v^2w^2+w^2u^2)\\&+(c_{11}+2c_{12}+c_{44})(c_{11}-c_{12}-2c_{44})^2u^2v^2w^2]\,,\end{aligned}\tag{5}$$

where $h, k$ and $l$ are direction cosines of $\boldsymbol{q}$ to the orthogonal cubic axes and $u, v$ and $w$ direction cosines of $\boldsymbol{R}$ to the same axes. $c_{11}$, $c_{12}$ and $c_{44}$ are the elastic constants. We have evaluated the above formula (5) for three directions and obtained the three independent elastic constants.

## § 3. Result

### (*a*) *Silver*

The observed intensities corrected for mosaic structure, white radiation and skew effect were plotted against $1/R^2$ as shown in Fig. 6. The extrapolated values of the corrected intensities were obtained at the point $1/R^2=0.5$, where $R$ was measured in cm in the reciprocal lattice space which had been drawn to the scale of $1/\lambda=49.7$ cm. The values of the intensities in Fig. 6 shows the number of counts of the Geiger-Müller counter when that of the total scattering of paraffin is 290. The curves in Fig. 6 become straight line after all corrections as mentioned in § 2. For example, the relationship between the corrected intensity for the [100] direction and $1/R^2$ is shown in Fig. 7, whose intensity scale is the same as in Fig. 6. The temperature factor was calculated by using the mean-square amplitude of atomic vibration given by Lonsdale[11]. The elastic constants obtained are shown in Table I together with the corresponding values obtained by other method[12].

Table I. Elastic Constants of Silver (in *dyne*/*cm*²).

| | Ag present author | Ag Röhl |
|---|---|---|
| $c_{11}\times10^{12}$ | $1.2_1$ | 1.18 |
| $c_{12}\times10^{12}$ | $0.89_9$ | 0.879 |
| $c_{44}\times10^{12}$ | $0.42_6$ | 0.437 |

### (*b*) *Copper-zinc alloy* ($Cu_{82}Zn_{13}$)

The alloy examined was in equilibrium at room temperature. The observed intensities corrected for the same effects as in silver were plotted against $1/R^2$ as shown in Fig. 8. The intensity scale of the figure is the same as in Fig. 6. But the total scattering of paraffin wax in this case is 200. The curves in Fig. 8 become straight lines after all corrections as in silver. The mean-square amplitude of atomic vibration obtained by the method described in § 2 was 0.03 cm$^{-16}$ instead of 0.021 cm$^{-16}$ for pure copper. The amplitude of atomic vibration thus obtained will contain the effect of the irregularity due to the difference in atomic radii of constituents. The elastic constants obtained are shown in Table

Table II. Elastic Constants of Copper and Copper-Zinc Alloy (in *dyne*/*cm*²).

| | Cu Gaffney and Overton | $CuZn_{4.59}$ Neighbours and Smith | $CuZn_{18}$ present author | $CuZn_{28}$ Masima and Sachs |
|---|---|---|---|---|
| $c_{11}\times10^{12}$ | 1.7 | 1.63 | $1.5_6$ | 1.5 |
| $c_{12}\times10^{12}$ | 1.23 | 1.19 | $1.1_4$ | 1.16 |
| $c_{44}\times10^{12}$ | 0.752 | 0.742 | $0.68_7$ | 0.72 |

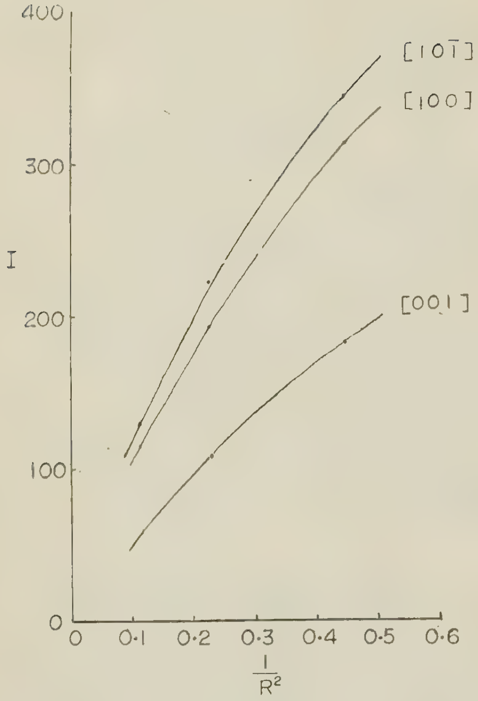

Fig. 6. Variation of the intensity of the diffusely scattered x-rays in silver with $1/R^2$, which was corrected for white radiation, mosaic structure and skew effect.

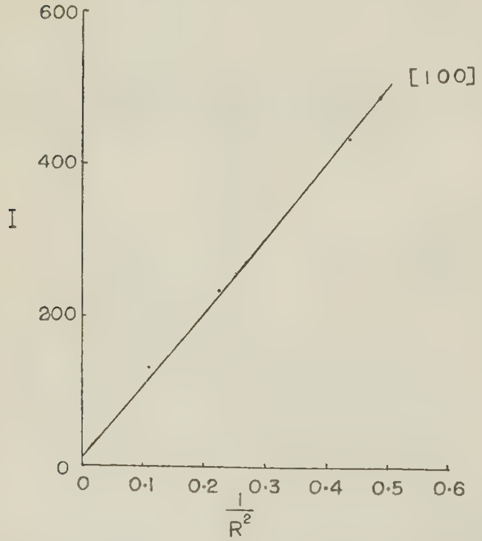

Fig. 7. Variation of the intensity of the diffusely scattered x-rays along the [100] direction in silver with $1/R^2$, for which all correctons were applied.

II, where the elastic constants of some related metal and alloys are also shown for reference[13][14][15].

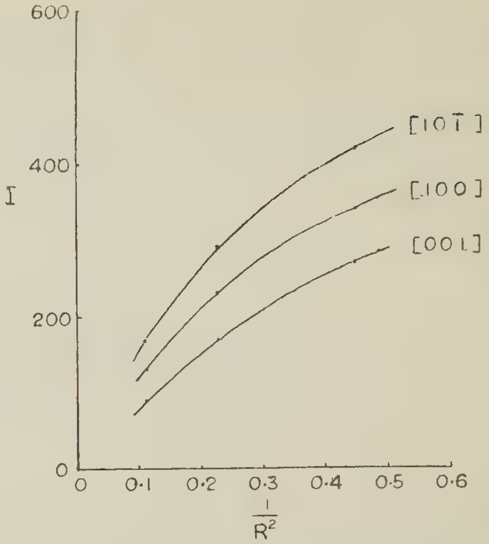

Fig. 8. Variation of the intensity of the diffusely scattered x-rays in copper-zinc alloy with $1/R^2$, which was corrected for white radiation, mosaic structure and skew effect.

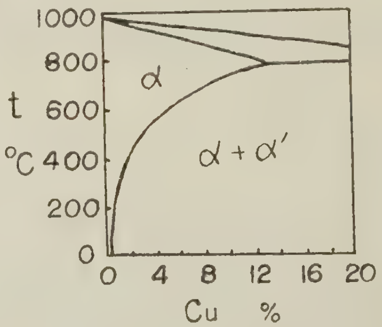

Fig. 9. Phase diagram of silver-copper system at lower copprecomposition.

(c) *Silver-copper alloy* ($Ag_{95}Cu_5$)

The alloy examined (the α phase) was not in equilibrium at room temperature as shown in Fig. 9. The intensities corrected for the same effects as in silver were plotted against $1/R^2$ as shown in Fig. 10. The intensity scale is the same as that for the copper-zinc alloy. This figure is entirely different from that of silver, namely the intensity along the [001] direction is much larger than that along the [$10\bar{1}$] direction, whereas the reverse is the case in silver. In this figure only the curve for the [100] direction becomes a straight line after all corrections. Moreover it was found that the intensity along the [001] direction varied more or less from sample to sample and did not vary like those of the other direc-

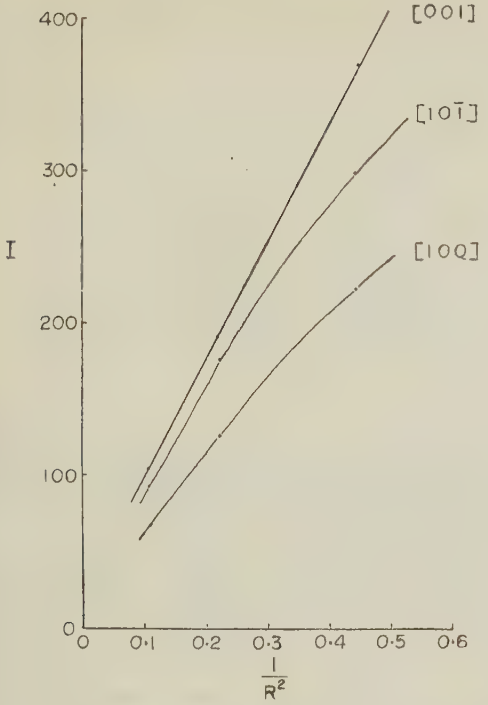

Fig. 10. Variation of the intensity of the diffusely scattered x-rays in silver-copper alloy with $1/R^2$ which was corrected for white radiation, mosaic structure and skew effect.

tions with temperature. This abnormality seems to be due to the disorder of atoms along the [001] direction in the non-equilibrium alloy*. As the diffuse scattering due to this imperfection was considered to be small in the [100] direction, we calculated approximately the elastic constants $c_{44}$, which was $0.42_7 \times 10^{12}$ *dyne/cm*$^2$. In this case the mean-square amplitude was 0.035 cm$^{-16}$ instead of 0.026cm$^{-16}$ for pure silver$^{11)}$.

## § 4. Conclusion

A simple method of obtaining the elastic constants of metals and alloys of cubic structure by observing the temperature diffuse scattering of x-rays has been described. The accuracy of the method depends mainly upon that of the measurement of weak x-ray beam by a Geiger-Müller counter and the correction for the divergence of x-rays. Even for the diffusely scattered x-rays it was not difficult to obtain the absolute value of the intensity within the experimental error of 3%. A method to test the accuracy of the correction for the divergence of x-rays is to calculate the intensity entering into the slit at any direction by using the finally obtained intensity curve and to compare it with the experimental value. In the present case, the error of the elastic constants thus obtained was within 5%.

In the case of alloys, the diffuse scattering due to the disorder of atoms was also taken into consideration.

In conclusion, the author wishes to express his sincere thanks to Prof. Mitsuo Miwa for his continuous encouragement and valuable discussion. He is also indebted to the Ministry of Education for financial aids.

### References

1) K. Lonsdale: Rep. Phys. Soc. Progr. Phys. **9** (1943) 256.
W. H. Zachariasen: Theory of X-Ray Diffraction in Crystals. (Wiley, London, 1946).
R. W. James: The Optical Principle of the Diffraction of X-Rays. (Bell, London, 1948).
2) G. N. Ramachandran and W. A. Wooster: Acta Cryst. **4** (1951) 335.
3) E. H. Jacobsen: Phys. Rev. **97** (1955) 654.
4) G. N. Ramachandran and W. A. Wooster: Acta Cryst. **4** (1951) 431.
5) E. Prince and W. A. Wooster: Acta Cryst. **6** (1953) 450.
6) K. Huang: Proc. Roy. Soc. **A 190** (1947) 102.
7) J. M. Cowley: J. App. Phys. **21** (1950) 24.
8) J. Laval: Bull. Soc. Fr. Min. **64** (1941) 1.
9) M. Born: Rep. Phys. Soc. Progr. Phys. **9** (1943) 293.
10) H. A. Jahn: Proc. Roy. Soc. **A 179** (1942) 320.
11) K. Lonsdale: Acta Cryst. **1** (1948) 142.
12) H. Röhl: Ann. d. Phys. **16** (1933) 887.
13) J. R. Neighbours and C. S. Smith: Acta Met. **2** (1954) 591.
14) J. Gaffney and W. C. Overton: Phys. Rev. **95** (1954) 602.
15) M. Masima and G. Sachs: Z. f. Phys. **50** (1928) 161.
16) R. Glocker: Materialprüfung mit Röntgenstrahlen. (J. Springer, Berlin, 1936)

---

* The disorder of atoms seemed to grow more with the progress of annealing and gave rise to the splitting of some spots and streaks of diffraction patterns at last. Further study on this anomaly is now in progress.

JOURNAL OF THE PHYSICAL SOCIETY OF JAPAN Vol. 11, No. 9, SEPTEMBER, 1956

# Temperature Dependence of Anisotropy Energy of Ferromagnetics

By Tadao KASUYA
*Physical Institut, Nagoya University*

(Received February 20, 1956)

The temperature dependence of anisotropy energy of ferromagnetics was calculated by the spin wave method which assumes the existence of only pseudodipole interaction which included some restricted long range forces. The temperature dependence obtained is $(M/M_0)^{16}$, a result which is in fairly satisfactory agreement with the experimental $(M/M_0)^{20}$ law, and is an improvement on Van Vleck's result $(M/M_0)^3$. This small discrepancy is discussed from the standpoint of s-d interaction.

## §1. Introduction

The theory of anisotropy energy of ferromagnetics based on Heisenberg's model was developed by Van Vleck[1]. According to his theory, in substances having spin 1/2, the only force causing anisotropy is pseudo-dipole interaction, which gives correct direction of the magnetization in Ni. In substances having a spin value greater than 1, these is quadrupole interaction, and in Fe, it is believed that as the origin of anisotropy the quadrupole interaction is more dominant than pseudo-dipole interaction. He also calculated the temperature dependence of anisotropy energy which dependence, however, is too weak to explain the experimental result. Experimentally, the temperature dependence of anisotropy energy in Fe is about $(M/M_0)^{10}$, and in Ni, about $(M/M^0)^{20}$. Van Vleck' used the molecular field approximation to simplify his calculation, and the discrepancies between the theory and the experimental result must first be attributed to this approximation. Quadrupole interaction affects the anisotropy energy in the first order, and the situation is fairly simple. Van Vleck calculated on a more rigorous basis, taking into account the nearest neighbours' interaction, while Zener[2] calculated by using the classical model as a random motion, and recently Keffer[3] by the spin-wave method explained these calculations very beautifully. His calculations show that in low temperatures the quadrupole interaction gives temperature dependence of anisotropy energy as $(M/M_0)^{10}$ which is very satisfactory compared with the experimental result for Fe. On the other hand, pseudo-dipole interaction effect appears only in the second order perturbation, and the situation becomes more difficult. Recently Tessman[4] calculated the anisotropy energy of the ground state by the spin-wave method, but here temperature dependence has not yet been obtained.

In this paper we calculate temperature dependence of anisotropy energy due to pseudo-dipole interaction by the spin wave method. The result is fairly satisfactory as compared with the experimental result for Ni. The small discrepancy is discussed according to the concept of *s-d* interaction which has recently been developed by the author[5].

## §2. Hamiltonian and Free Energy

We consider the Hamiltonian as containing the exchange interaction and the pseudo-dipole interaction, that is

$$\mathscr{H}=-\sum_n\sum_m J(R_{nm})\boldsymbol{S}_n\boldsymbol{S}_m+\sum_n\sum_m D(R_{nm})\times\{\boldsymbol{S}_n\boldsymbol{S}_m-3(S_n\boldsymbol{r}_{nm})(\boldsymbol{S}_m\boldsymbol{r}_{nm})\}\,, \qquad (1)$$

where $\boldsymbol{r}_{nm}$ is the unit vector in the direction of $\boldsymbol{R}_{nm}$.

We introduce the spin-wave operator by the method of Holstein-Primakoff[6]

$$\left(\begin{array}{l} S_n{}^+=(2S)^{1/2}(1-a_n{}^*a_n/2S)^{1/2}a_n \\ S_n{}^-=(2S)^{1/2}a_n{}^*(1-a_n{}^*a_n/2S)^{1/2} \\ S-S_n{}^z=a_n{}^*a_n \end{array}\right.$$

$$\left(\begin{array}{l} a_n=N^{-1/2}\sum_q \exp(-i\boldsymbol{q}\boldsymbol{R}_n)a_q \\ a_n{}^*=N^{-1/2}\sum_q \exp(i\boldsymbol{q}\boldsymbol{R}_n)a_q{}^* \end{array}\right. \qquad (3)$$

and expanding to the first order in each term, we have

$$\begin{aligned} H=E_0&+\sum_q A_q a_q{}^*a_q \\ &+\sum_q C_q a_q{}^*a_{-q}+\text{c.c.} \\ &+\sum_{q_1}\sum_{q_3}\sum_{q_2} B_{q_1}a_{q_1}{}^*a_{q_2}{}^*a_{q_3} \\ &\times\delta(\boldsymbol{q}_1+\boldsymbol{q}_2-\boldsymbol{q}_3,\ \text{mod}\ \boldsymbol{K})+\text{c.c.}\,, \end{aligned} \qquad (4)$$

where

$$E_0=-NS^2\sum_n\{J(R_n)-D(R_n)(1-3\,r_n{}^{z2}\}\,, \tag{5}$$

$$A_q=2S\sum_n[J(R_n)\{1-\exp(i\boldsymbol{q}R_n)\}$$
$$-\frac{1}{2}D(R_n)(1-3r_n{}^{z2})\exp(i\boldsymbol{q}\boldsymbol{R}_n)$$
$$-D(R_n)(1-3\,r_n{}^{z2})]\,, \tag{6}$$

$$C_q=-(3/2)S\sum_n D(R_n)r_n{}^{+2}\exp(i\boldsymbol{q}\boldsymbol{R}_n)\,, \tag{7}$$

$$B_q=3(2S/N)^{1/2}\sum_n D(R_n)r_n{}^z r_n{}^+\exp(i\boldsymbol{q}\boldsymbol{R}_n)\,. \tag{8}$$

and ***K*** is the principal wave vector of the reciprocal lattice. We consider a cubic crystal, therefore the last terms of (5) and (6) vanish.

Next, we operate a unitary transformation to reduce the third and the fourth terms of (4). Writing new operators as $\boldsymbol{\alpha}_q{}^*$ and $\boldsymbol{\alpha}_q$, we have

$$H=\exp(-i\mathrm{S}/\hbar)\mathscr{H}\exp(i\mathrm{S}/\hbar)\,, \tag{9}$$

where we put

$$\mathrm{S}=i\hbar\sum_q(C_q/2A_q)\boldsymbol{\alpha}_q{}^*\boldsymbol{\alpha}_{-q}{}^*+\text{c.c.}$$
$$+i\hbar\sum_{q_1}\sum_{q_2}\sum_{q_3}B_{q_1}/(A_{q_1}+A_{q_2}-A_{q_3})$$
$$\times\delta(\boldsymbol{q}_1+\boldsymbol{q}_2-\boldsymbol{q}_3,\ \mathrm{mod}\ \boldsymbol{K})\boldsymbol{\alpha}_{q_1}{}^*\boldsymbol{\alpha}_{q_2}{}^*\boldsymbol{\alpha}_{q_3}+\text{c.c.} \tag{10}$$

Then, picking up only the diagonal terms of the first order, we have

$$H=E_0-\sum_q|C_q|^2/2A_q+\sum_q(\mathcal{E}_q{}^0+\varDelta_q)\boldsymbol{\alpha}_q{}^*\boldsymbol{\alpha}_q\,, \tag{11}$$

where $\mathcal{E}_q{}^0$ is the isotropic term

$$\mathcal{E}_q{}^0=2S\sum_n J(R_n)\{1-\exp(i\boldsymbol{q}\boldsymbol{R}_n)\}\,, \tag{12}$$

and $\varDelta_q$ is the anisotropic term

$$\varDelta_q=-2\sum_n D(R_n)(1-3\,r_n{}^{z2})\exp(i\boldsymbol{q}\boldsymbol{R}_n)$$
$$-\frac{|C_q|^2}{A_q}-\frac{1}{2}\sum_{q_1}\sum_{q_2}\frac{|B_{q_1}+B_{q_2}|^2}{A_{q_1}+A_{q_2}-A_q}$$
$$\times\delta(\boldsymbol{q}_1+\boldsymbol{q}_2-\boldsymbol{q},\ \mathrm{mod}\ \boldsymbol{K})\,. \tag{13}$$

Eq. (11) is the basic Hamiltonian for our calculation.

The free energy is written

$$F=-\kappa T\ \ln\,[\mathrm{Tr}\exp(-H/\kappa T)]. \tag{14}$$

Using the Hamiltonian (11), and dividing the isotropic terms and the anisotropic terms, we have

$$F=F_{iso}+F_{aniso}\,, \tag{15}$$

$$F_{iso}=E_0+\kappa T\sum_q\ln\,[1-\exp(-\mathcal{E}_q{}^0/\kappa T)]\,, \tag{16}$$

$$F_{aniso}=-\frac{1}{2}\sum_q\frac{|C_q|^2}{A_q}+\kappa T\sum_q\ln$$
$$\times\frac{1-\exp[-(\mathcal{E}_q{}^0+\varDelta_q)/\kappa T]}{1-\exp(-\mathcal{E}_q{}^0/\kappa T)}\,. \tag{17}$$

Now we are interested only in the anisotropic part. Using approximations mentioned above and assuming $\kappa T\gg\varDelta_q$, Eq. (17) becomes

$$F_{aniso}=-\frac{1}{2}\sum_q\frac{|C_q|^2}{A_q}+\sum_q\varDelta_q n_q$$
$$-\frac{1}{2\kappa T}\sum_q\varDelta_q{}^2 n_q{}'\,, \tag{18}$$

where

$$n_q=[\exp(\mathcal{E}_q{}^0/\kappa T)-1]^{-1}\,, \tag{19}$$

$$n'_q=[\{\exp(\mathcal{E}_q{}^0/\kappa T)-1\}\{1-\exp(-\mathcal{E}_q{}^0/\kappa T)\}]^{-1}. \tag{20}$$

In $\varDelta_q$ in (13), the second and the third terms are higher in order compared to the first term, so that we can neglect them in the third term of (18).

## § 3. Calculations

Now we calculate each term of (18).

We assume in the following calculation that the pseudo-dipole interaction $D(R)$ is not limited to short range force but includes as well long range force, while $A_q$, $B_q$ and $C_q$ in (6), (7) and (8) have such properties that they can be expanded in power series of $q^2$ and, as is easily seen, begin with the term $q^2$. This assumption is correct for short range forces and also for *s-d* interaction as regards exchange interaction.

### (*i*) *The first term*

This term was calculated for pure dipole by Tessman and also for pseudo-dipole interaction between nearest neighbors. The tecknique of our calculation is the same as his.

Substituting $\mathcal{E}_q{}^0$ for $A_q$ the first term becomes

$$-\frac{9}{16}S\sum\frac{\sum_n\sum_m D(R_n)D(R_m)r_n{}^{+2}r_m{}^{-2}\exp(i\boldsymbol{q}\boldsymbol{R}_{nm})}{\sum_n J(R_n)-\sum_n J(R_n)\exp(i\boldsymbol{q}\boldsymbol{R}_n)}\,, \tag{21}$$

By the above assumption, the contribution from $q$ near the maximum value is predominantly large in the summation over $q$, and thus we can neglect the second term of the denominator when it is compared to the first term. Then the summation of (21) is straightforward. Using the relation

$$\sum_q \exp(i\boldsymbol{q}\boldsymbol{R}_n)=0 \quad \text{when} \quad R_n \neq 0 \tag{22}$$

(21) becomes

$$-(9/16)(NS/J(0))\sum_n D^2(R_n)(1-2r_n^{z2}-r_n^{z4})\,, \tag{23}$$

where

$$J(q)=\sum J(R_n)\exp(i\boldsymbol{q}\boldsymbol{R}_n)\,. \tag{24}$$

Next, we transform the coordinates from the direction of the magnetization into the direction of the principal axis of the cubic crystal, and performing the summation over the direction by fixing the distance $R_n$, we have

$$\langle r^{z2}\rangle_n=1/3\,, \tag{25}$$

$$\langle r^{z4}\rangle_n=\langle r_\xi^4\rangle_n-2(\langle r_\xi^4\rangle_n-3\langle r_\eta^2 r_\zeta^2\rangle_n)\Gamma \tag{26}$$

where $\langle\ \rangle_n$ means the average in directions, fixing the distance $R_n$, while $r_\xi$, $r_\eta$ and $r_\zeta$ are direction cosines of $\boldsymbol{R}_n$ referring to the principal axis $\xi$, $\eta$ and $\zeta$, and

$$\Gamma=\alpha_\xi^2\alpha_\eta^2+\alpha_\eta^2\alpha_\zeta^2+\alpha_\zeta^2\alpha_\xi^2\,. \tag{27}$$

Here $\alpha_\xi$, $\alpha_\eta$ and $\alpha_\zeta$ are direction cosines of the magnetization referring to the principal axis $\xi$, $\eta$, and $\zeta$.

Thus (23) becomes

$$-(3/16)(NS/J(0))\sum_n D^2(R_n)(1-3\langle r_\xi^4\rangle_n)$$
$$-(9/8)(NS/J(0))\sum_n D^2(R_n)(3\langle r_\eta^2 r_\zeta^2\rangle_n-\langle r_\xi^4\rangle_n)\Gamma. \tag{28}$$

(*ii*) *The second term*

As mentioned in the preceding section, among the terms of $\Delta_q$, the first term is lower in order than are the second and third terms. Since $n_q$ is isotropic, however, the contribution to anisotropy energy by the first term is exactly zero.

By the above assumption, we can expand $\Delta_q$ in a power series of $q^2$ where, in our approximation, only the first terms, that is, the constant terms, should be picked up. Thus the contribution of the second term of $\Delta_q$ is zero in our approximation, and only the third term is considerable.

In our approximation the third term of (18) becomes

$$\Delta_0\sum_q n_q=NS\Delta_0(M_0-M)/M_0\,, \tag{29}$$

where $M_0$ and $M$ are respectively the magnetizations of the system at the absolute zero and the finite temperature we are considering. For $\Delta_0$ we have

$$\Delta_0=-\frac{9}{N}\sum_{q'}$$
$$=\frac{\sum_n\sum_m D(R_n)D(R_m)r_n^z r_n^+ r_m^z r_m^- \exp(i\boldsymbol{q}'\boldsymbol{R}_{um})}{\sum_n J(R_n)-\sum_n J(R_n)\exp(i\boldsymbol{q}'\boldsymbol{R}_n)}\,.$$

The technique of calculation for (30) is the same as that for (21) and

$$\Delta_0=-3NS\{(M_0-M)/M_0J(0)\}\sum_n D^2(R_n)$$
$$\times(1-3\langle r_\xi^4\rangle_n)+18\,NS\{(M_0-M)/M_0J(0)\}$$
$$\times\sum_n D^2(R_n)(3\langle r_\eta^2 r_\zeta^2\rangle_n-\langle r_\xi^4\rangle_n)\Gamma. \tag{31}$$

(*iii*) *The third term*

As stated in section 2, we can neglect in $\Delta_q$ the second and third terms, and thus $\Delta_q^2$ is proportional to $q^4$. By partial integration, we can easily see that this is a higher order term than the second term of (18) and should be neglected in our approximation.

Thus the anisotropy constant $K_1$ is obtained as

$$K_1=-\frac{9}{8}\frac{NS}{J(0)}\sum_n D^2(R_n)(3\langle r_\eta^2 r_\zeta^2\rangle_n-\langle r_\xi^4\rangle_n)$$
$$\times\left(\frac{M}{M_0}\right)^{16}, \tag{32}$$

using

$$1-16\frac{M-M_0}{M_0}=\left(\frac{M}{M_0}\right)^{16}, \tag{33}$$

in our approximation.

## § 4. Discussions

The result that $K_1$ is proportional in low temperatures to $(M/M_0)^{16}$ agrees fairly well with the experimental result $(M/M_0)^{20}$ for Ni. On the other hand, the result of Van Vleck gives only a very low power law, that is, about $(M/M_0)^3$. This very low power law of Van Vleck's is owing to his having used the molecular field method which does not include the most important term for temperature variation as does our treatment.

The remaining discrepancy between our result and the experimental result seems to be caused, in part, by neglecting the second term of the denominator of (21) and (30) in our approximation, and, in part, by assumptions cited at the beginning of § 3 but not justified in cases of long rang forces. In fact, as is shown in our other papers, *s*-*d* interaction plays a very important role in many phenomena, even for ferromagnetic transition metals such as Ni, Fe, etc.

Finally, we must point out the restriction mentioned in § 2, that is, $\kappa T \gg \Delta_q$. In fact, when $q$ approaches zero, $\Delta_q$ does not approach zero; it approaches finite value $\Delta_0$. Therefore, spin-waves of quite long wave length have negative energy. This means that the perturbation method is not applicable to such long wave excitation since in actuality the mixing of such spin-waves may occur. This mixing seems to give rise to the line width of the microwave resonance absorption of ferromagnetics. We will treat with these phenomena in another paper.

I express my deep appreciation to Prof. Ariyama for his encouragement in this work. The authors is particularly indebted to Prof. Nagamiya, Associated Prof. Yoshida and staff members of Nagamiya Laboratory who have made available the unpublished manuscript of F. Keffer.

### References

1) J. H. Van Vleck: Phys. Rev. **52** (1937) 1178.
2) C. Zener: Phys. Rev. **96** (1954) 1335.
3) F. Keffer: Phys. Rev. **100** (1955) 1692.
4) J. R. Tessman: Phys. Rev. **96** (1954) 1192.
5) T. Kasuya: Busseiron Kenkyu.
6) T. Holstein and H. Primakoff: Phys. Rev. **58** (1940) 1098.

---

JOURNAL OF THE PHYSICAL SOCIETY OF JAPAN Vol. 11, No. 9, SEPTEMBER, 1956

# Paramagnetic Resonance Spectra of Some Cupric Salts (I)

By Hidetaro ABE and Kazuo ÔNO

*Institute of Science and Technology, University of Tokyo*

(Received March 14, 1956)

The paramagnetic resonance spectra of some ammine, ethylenediammine, and pyridine derivatives of hydrated cupric salts were examined, using their single crystals and microwaves of $\lambda = 32 \sim 5$ mm. In the cases of $[Cu(NH_3)_4]$ $SO_4 \cdot H_2O$ and $[Cu(en)_2]$ $Cl_2 \cdot xH_2O$, detailed analysis of spectra was performed using the structural data from x-ray analysis given by Mazzi. In the other cases, analysis was discussed under an assumption of inequivalent magnetic units. Results thus obtained are fully explained by the treatments given by Abragam and Pryce with modified $\lambda$, the spin-orbit coupling coefficient, so the forces acting between the central copper ion and the surrounding nitrogen atmos are supposed to be mainly ionic rather than covalent, as in the cases of usual hydrates. Exchange energies between copper ions are also discussed.

## § 1. Introduction

Many papers on paramagnetic resonance absorption in cupric salts already appeared. We were interested in paramagnetic resonance experiments on copper complex salts besides its ordinary hydrates, because the hypothesis of "covalent structure" with hybridized (3d) $(4s)(4p)^2$ bonds was early introduced by Pauling[1] in coplaner complexs of divalent copper.

So we examined single crystals of ammine, ethylenediammine and pyridine derivatives of hydrated salts of copper by the usual method of paramagnetic resonance absorption with microwaves of $\lambda = 32 \sim 5$ mm.

Detailed measurements were achieved in

copper tetrammine sulfate monohydrate
$[Cu(NH_3)_4]SO_4 \cdot H_2O$,
copper diethylenediammine dichloride
$[Cu(en)_2]Cl_2 \cdot x(H_2O)$
copper pyridine sulfate*
$[Cu(py)_m]SO_4 \cdot nH_2O$ and
copper pyridine nitrate*
$[Cu(py)_m](NO_3)_2 \cdot nH_2O$

where (en) means ethylenediammine ($NH_2CH_2 \cdot CH_2NH_2$) and (py) pyridine ($NC_5H_5$), respectively. The composition of latter two compounds with asterisk is not yet chequed chemically.

A preliminary report on single crystals of copper tetrammine sulfate monohydrate, which is abbreviated hereafter as *c.t.s.*, was read in 1952[2]. In that report, strong exchange coupling between copper ions was pointed out from small line width and from the fact that only single peak was observed in any direction of the static field even at our upper most frequency ($\lambda \sim 5.4$ mm) whereas more than one ion is expected in unit cell (rhombic system). Though the results contain some interesting features, the more detailed discussion on the resonance data, at that time, was impossible, by the lack of x-ray analysis on this salt.

Recently an explanation with covalent bonding hypothesis was suggested by Okamura and Date[3] for the paramagnetic spectra observed in two salts of copper tetrammine group. As their results do not agree with ours both in g-value and in line width beyond experimental errors, we carefully repeated the resonance measurements and obtained results consistent with our earlier ones. Appropriate analysis of experimental data with assumed molecular arrangements was discussed[4] and a report was prepared. Recently, however, x-ray analysis in two of these crystals was carried out by Mazzi[5][7] and by Zemann[6], so our resonance data can now be analysed by their structural results.

Miduno et al also examined[8] the paramagnetic resonance in some salts of this group and their results agree with ours. Lancaster and Gordy[9] have examined, on the other hand, paramagnetic resonance on some cupric salts in powder form. Their g-values for *c.t.s.* and for copper tetrapyridine nitrate are too much smaller than our results. As their work, however, was a preliminary survey, as pointed out by Weidner and Whitmer in technical side, we may ignore this disagreement.

## § 2. Preliminary Discussion: Peak observed under strong exchange coupling

Generally speaking, it is said under a strong exchange coupling that peaks originated from the inequivalent ions in unit cell would be unified to a single peak which appears at a field given approximately by their arithmetrical mean. In the case of two inequivalent ions in unit cell, the g-value of the unified peak is given by

$$g=\frac{1}{2}(g'+g'') \qquad (1)$$

where $g'$ and $g''$ stand for the $g$-values which may be expressed by each ion when the exchange coupling becomes negligible. This situation was shown theoretically by Anderson[13] and experimentally by the following authors; In the case of $CuSO_4 \cdot 5H_2O$ by Bagguley and Griffiths[10] using microwaves down to $\lambda=8.5$ mm and by one of the authors (K.O.)[11] down to $\lambda=5.4$ mm and in $K_2CuCl_4 \cdot 2H_2O$ by our group[12].

The ground state of a free $Cu^{++}$ ion, $(3d)^9$, is $^2D$. In crystal, it is subjected to several interactions. The theory of the crystalline fields was worked out by Polder[14] and by Abragam and Pryce[15]. Interactions may be shown by the following Hamiltonian

$$\mathscr{H}=\mathscr{H}_x+\lambda(\boldsymbol{L}\cdot\boldsymbol{S})+\beta\boldsymbol{H}(\boldsymbol{L}+2\boldsymbol{S}) \qquad (2)$$

and are treated by the usual perturbation method, where $\mathscr{H}_x$ means the interactions from the surrounding ions in crystal, considered as an effective crystalline electric field, $\lambda(\boldsymbol{L}\cdot\boldsymbol{S})$ the term of spin-orbit coupling and the next is the interaction with a magnetic field applied externally. By a cubic field the orbital levels are spilit into a low-lying doublet and a triplet several thousands $cm^{-1}$ higher. Furthermore, these levels are completely removed by a interplay of lower symmetry crystalline field and the spin-orbit coupling, remaining Kramers' degeneracy. This yields, in our case of tetragonal symmetry, the $g$-values for the external magnetic field parallel and perpendicular to the tetragonal axis, $g_{//}$ and $g_\perp$, respectively, as

$$\begin{aligned}(g_{//}-2)&=-\frac{8\lambda}{E_4-E_3}\\(g_\perp-2)&=-\frac{2\lambda}{E_5-E_3}\end{aligned} \qquad (3)$$

where $E_3$ is the energy of the lowest orbital level, and $E_4$ and $E_5$ are those of higher levels split from the upper triplet as shown in Fig. 1. They may be approximately expressed as

$$\begin{aligned}(g_{//}-2)&\fallingdotseq-\frac{8\lambda}{\Delta E}\\(g_\perp-2)&\fallingdotseq-\frac{2\lambda}{\Delta E}\end{aligned} \qquad (4)$$

where $\Delta E$ represents a mean energy difference between the ground state and the upper levels from the triplet. Eq. (4) gives rise to an approximate relation

$$(g_{//}-2)/(g_{\perp}-2) \fallingdotseq 4 \qquad (5)$$

On the other hand, $g$-value for each ion, when an external field is applied in a direction making angle $\theta$ from the tetragonal axis of crystalline field, will be given by

$$g^2 = g_{//}^2 \cos^2\theta + g_{\perp}^2 \sin^2\theta \qquad (6)$$

so the principal values of $g$-tensor shown by the unified peak are

$$\begin{cases} g_1 = g_{\perp} \\ g_2 = \{g_{//}^2 \sin^2\alpha + g_{\perp}^2 \cos^2\alpha\}^{1/2} \\ g_3 = \{g_{//}^2 \cos^2\alpha + g_{\perp}^2 \sin^2\alpha\}^{1/2} \end{cases} \qquad (7)$$

where $2\alpha$ means an angle between two tetragonal axes of inequivalent ions, assuming unit cell contains two ions inequivalent in space but identical in their situation. $g$-values so defined are in an increasing order $g_1 < g_2 < g_3$ in general.

## § 3. Experimental Procedures

Measurements were made by the usual method at room temperature with microwaves having wavelengths of 32, 11, 6.5 and 5.4 mm. The experimental apparatus is the same as described elsewhere[12], although for 3 cm band the layout has been simplified as like as for shorter wavelengths. Special cares were taken for the determination of $g$-values. Exciting current of each electromagnet which produces static magnetic field was supplied by a set of storage batteries provided only for its use. The reading scale of precision meter for the exciting current was calibrated by means of proton resonance. It was driven under the same condition as it was calibrated in order to avoid errors caused by the hysteresis. A speck of the organic free radical $\alpha$-diphenyl $\beta$-picryl hydrazyl[16][17] measured simultaneously with the studying crystal gave a mark of $g=2.0036$.

In order to determine the principal values of $g$-tensor, we must rotate sample crystal in such a manner as the direction of static magnetic field may pass through the principal axes of $g$-tensor. Desired axis of $g$-tensor, however, often deviates from the plane in which the static field is rotated. This deviation may amount to even several degrees by sum-up effect of the following reasons: (1) The error in cutting or grinding the desired plane, especially when the external shape of crystal is not suitable for this plane or when the nature of crystal (e.g. perfect cleavarage) prevents these treatments. (2) Rough setting of sample to the mount by polystyrene cement. (3) Imperfect setting of resonant cavity in the gap of polepieces.

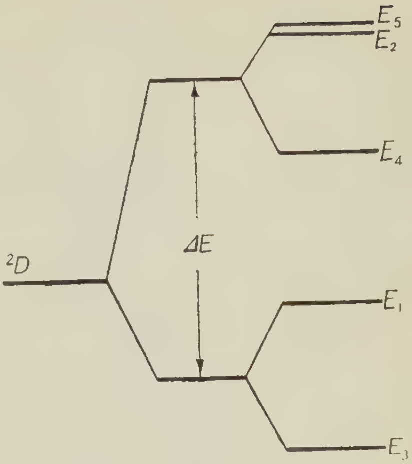

Fig. 1. Schematic energy levels of Cu ion in crystalline electric field.

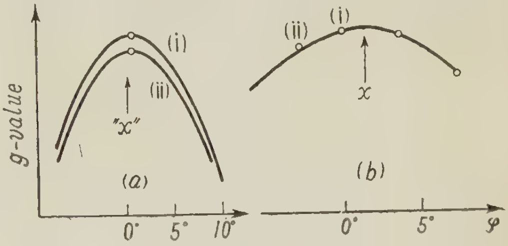

Fig. 2. Curves of $g$-values to determine its principal value.

To avoid errors from these origins we adopt the following treatment with some indifference to crystal form. For instance, let us assume to determine the $g$-value $g_3$ for $x$-axis, one of the three mutually perpendicular axes. For convenience, we can assume $g_3$ is the maximum value without loss of generality. We cut a sample crystal with $xy$-plane as correct as we can, which we call the "$xy$-plane". We set this sample with this "$xy$-plane". Measurements of $g$-value or of magnetic field for the peak absorption give such a curve shown as (i) in Fig. 2 (a.). Then we change the setting angle $\varphi$ of this sample by $2\sim3$ degrees around the $y$-axis by insertion of a

Table I. Observed $g$-values and line widths at $\lambda=32$ and 11 mm.

| Sample | $g_3$ | $g_2$ | $g_1$ | $\Delta H$ in oer |
|---|---|---|---|---|
| $[Cu(NH_3)_4]SO_4\cdot H_2O$ | $2.181\pm0.005$<br>$(=g_c)$ | $2.104\pm0.006$<br>$(=g_b)$ | $2.054\pm0.003$<br>$(=g_a)$ | 20 (for $a$)~31 (for $c$) |
| $[Cu(en)_2]Cl_2\cdot xH_2O$* | $2.244\pm0.010$ | $2.057\pm0.010$ | $2.050\pm0.004$ | ≈120 (for $g_2$ and $g_1$) |
| $[Cu(py)_m]SO_4\cdot nH_2O$** | $2.314\pm0.010$ | $2.081\pm0.006$ | $2.072\pm0.004$ | ≈60↔80 (for $g_1$ and $g_2$) |
| $[Cu(py)_m](NO_3)_2\cdot nH_2O$** | $2.161\pm0.008$ | $2.124\pm0.015$ | $2.056\pm0.004$ | ≈160 (for $g_1$) |

* $x=1$ or 2.
** Chemical formula is not yet examined.

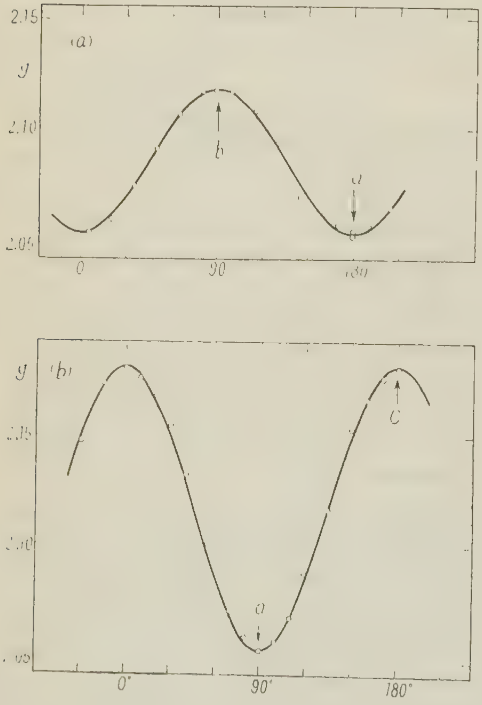

Fig. 3. Variation of $g$-values with the angle of the static magnetic field H in $Cu(NH_3)_4SO_4\cdot H_2O$ with $\lambda=32$ mm.
(a) ab-plane (b) ac-plane

polystyrene speck. We have a different maximum $g$-value near at the "$x$"-direction as shown (ii) in Fig. 2 (a). Repetition of these procedures gives a group of curves. Maximum $g$-value of each curve plotted against the angle $\varphi$ gives such a curve as Fig. 2 (b). The greatest maximum thus obtained should be taken as the correct value for $g_3$. Determination of $g_2$ and $g_1$ is done with the same procedure as above. Cares may be taken for the determination of $g_2$, because it is a saddle point of the $g$-tensor.

## § 4. Results and Discussions

### a) *Copper tetrammine sulfate monohydrate (c.t.s.)*: $[Cu(NH_3)_4](SO_4)\cdot H_2O$

The samples of this crystal under observation were obtained by the usual manner: An excess $NH_3$ is added to aqueous solution of cupric sulfate, the colour of which changes from blue to violet. Many crystals are slowly precipitated with alcohol. They are in dark violet.

They have rhombic symmetry[18] and easily grow along its $a$-axis. Crystallographic data are

$$a:b:c=0.5903:1:0.8892\,.$$

When exposed in air, they loose ammonia easily and decompose slowly. But, even after 2 years' storage in alcohol within open vessel, the main part of a single crystal shows the same properties as the newly prepared samples for the paramagnetic resonance experiments, though its outer part is removed out. Samples of wedge shape having the largest dimension of 10 ~ 20 mm and the thickness of several mm were chosen and ground, taking care of cleavage.

In all directions we observe only one peak. One of the results of $g$-value in *c.t.s.* is shown in Fig. 3. In this rhombic crystal, the principal axes of $g$-tensor coincide with the axes of crystalline form. Precise measurements at the three principal axes through the above-mentioned treatments give the $g$-values listed in Table I. It is rather easy to determine the $g$-values in this crystal, since the absorption is very sharp and strong in its intensity.

According to the result of x-ray analysis by Mazzi[5], unit cell has a dimension of

$$a=7.07,\ b=12.12 \text{ and } c=10.66\,\text{kx}\ (\pm1\%)$$

and it contains 4 formula molecules. But from the magnetic point of view, they mean

2 inequivalent molecules; $Z=2$. Schematic constitution projected on the *bc*-plane is shown in Fig. 4, in which $\cdots H_2O\cdots Cu\cdots H_2O\cdots Cu\cdots$ chain extends clearly along the *c*-axis in the *bc*-plane. The line joining $H_2O$—$H_2O$ makes an angle of $\alpha$ from the *c*-axis. Angle $\alpha$ obtained by x-ray data is $26°20'\pm4°$. Cu atom is surrounded by nitrogen atoms of ammine group $NH_3$ as shown in Fig. 5 which make normal square co-ordination. So a tetragonal symmetry would be fairly assumed to the crystalline field acting on the central $Cu^{++}$ ion, which leads to a tetragonal symmetry in *g*-tensor. We then assume that the axial direction of crystalline field coincides with the $H_2O$—$H_2O$ direction.

The best fit is given between observed *g*'s and estimated ones using Eq. (7) when parameters $g_{//}$, $g_{\perp}$ and $\alpha$ are chosen as in Table II within the experimental errors. The agreement in $g_b$ and $g_c$ is fairly well, and *g*-values in Table II yield an approximate relation, Eq. (5), which may infer that the assumption of tetragonal symmetry in crystalline field is adequate. The colour of $CuSO_4\cdot5H_2O$ i. e. $[Cu(H_2O)_4]SO_4\cdot H_2O$ is blue and $[Cu(NH_3)_4]SO_4\cdot H_2O$ is violet. Then, it may be deduced that the optical absorption band of the latter crystal indicates a larger level difference than that of the former. Data of their optical absorption[19] in aqueous solution are reproduced in Fig. 6. If we assume the absorption peak of this data corresponds to $\Delta E$ i.e. energy difference between ground state and orbital upper levels in crystal, we have

$$\Delta E \text{ for } Cu(OH_2)_4\cdot SO_4\cdot H_2O \cong 12\ 300\ \text{cm}^{-1}$$

$$\Delta E \text{ for } Cu(NH_3)_4\cdot SO_4\cdot H_2O \cong 14\ 200\ \text{cm}^{-1}.$$

To explain Eq. (4), in case of $CuSO_4\cdot5H_2O$, we had to adopt $\lambda=-700\ \text{cm}^{-1}$ from $g_{//}$ and $\lambda=-370\ \text{cm}^{-1}$ from $g_{\perp}$. This disagreement between $\lambda$'s may be deduced from the existence of rhombic part in crystalline field in copper sulfate. As a measured value for the free $Cu^{++}$ ion[20], we have $\lambda=-852\ \text{cm}^{-1}$. In

Table II. The principal *g*-values, $g_{//}$ and $g_{\perp}$, and the angle $\alpha$ to be given to a molecule of copper tetrammine sulfate monohydrate in order to have the best fit with the observed *g*-values ($g_a$, $g_b$ and $g_c$).

| | $g_{//}$ | $g_{\perp}$ | $\alpha$ | $g_b$ | $g_c$ |
|---|---|---|---|---|---|
| Calc. | 2.200 | 2.060* | 26° | $2.08_7$ | 2.171 |
| | $2.22_2$ | $2.05_5$* | 30° | $2.09_7$ | 2.181 |
| Obs. | — | $2.05_4$<br>±0.003<br>($g_a$) | 26°20′±4°<br>from x-ray data | 2.104<br>±0.006 | 2.181<br>±0.005 |

* According to our assumption, $g_a$, the observed *g*-value at the *a*-axis, was used as $g_{\perp}$.

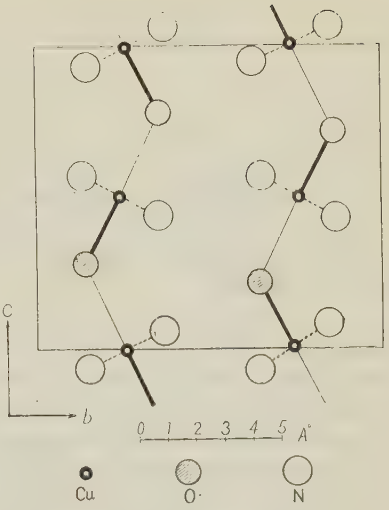

Fig. 4. Projection of the unit cell of $Cu(NH_3)_4SO_4\cdot H_2O$ on its (100) plane. After F. Mazzi[5]

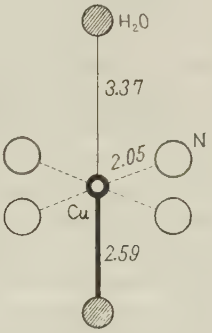

Fig. 5. Atomic configuration surrounding a Cu ion in $Cu(NH_3)_4SO_4\cdot H_2O$.

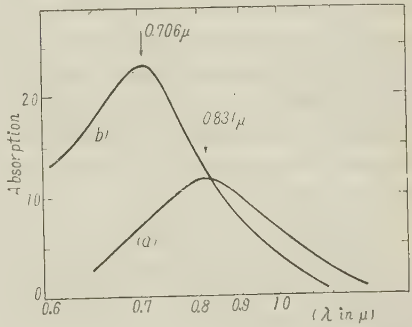

Fig. 6. Optical absorption spectra by aqueous solution of (a) $CuSO_4\cdot5H_2O$ and (b) $Cu(NH_3)_4SO_4\cdot H_2O$. After Dreisch and Trommer[19].

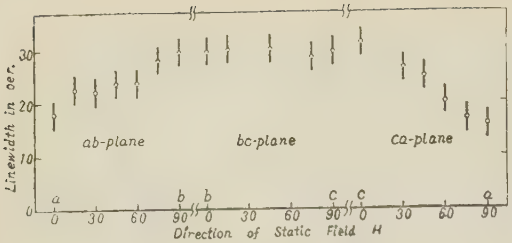

Fig. 7. Absorption line-width $\Delta H_{\frac{1}{2}}$ in $Cu(NH_3)_4SO_4 \cdot H_2O$ at $\lambda = 3.2$ cm.

crystalline state, the $\lambda$ for ions is lowered to some extent from a value in free ion state. After this report was completed, we knew that Owen tried to explain this reduction of $\lambda$ by the admixture of covalent bonding[29]. In case of $Cu(NH_3)_4 \cdot SO_4 \cdot H_2O$, $\lambda = -390\ \mathrm{cm}^{-1}$ is necessary to explain both $g_{//}$ and $g_{\perp}$ deduced from experimental data, which is reasonable compared with the case of the hydrate.

Roughly speaking, the observed line-shape is Lorentzian, though it is difficult to say rigorously about its line-shape because of its sharpness. At $\lambda = 32$ mm, the full width is 20 oer (for $a$-axis), 31 oer (for $c$-axis) and an intermediate value (for $b$-axis). The variation in line width at $\lambda = 32$ mm is shown in Fig. 7. The vertical lines indicate the range of our errors which were estimated to be 3 oer. Width observed at $\lambda = 5.4$ mm does not differ appreciably from that by 32 mm wave beyond the experimental errors; i.e. the width is independent on the measuring frequency within our limits of errors ($\lambda = 32 \sim 5$ mm).

The estimated dipolar width[21] $\Delta H_{dip}$ is approximately 360 oer. According to Anderson's definition[22)13], dipolar contribution $H_p^2$ to the width, assuming that unit cell is a cube of $a^3$ cm$^3$, is given by

$$H_p^2 = 5.1 \times (g\beta n)^2 \cdot S(S+1) \qquad (8)$$

where $n = a^{-3}$ is the density of spins per cm$^3$. In our case of *c.t.s.*, $H_p^2$ is estimated to be $2.4 \times 10^4$ oer$^2$.

On the other hand, the Curie temperature $\Theta$ deduced from the Curie-Weiss' law

$$\chi = \frac{C}{T + \Theta} \qquad (9)$$

is reported[23] to be about 15°. This corresponds to an exchange energy $2J = 7\ \mathrm{cm}^{-1}$ by Weiss molecular field equation

$$2J = \frac{3k\Theta}{Z_n \cdot S(S+1)} \qquad (10)$$

where 6 is given to $Z_n$, approximate number of the nearest neighbours. According to the expression by Anderson and Weiss, the exchange field is given as

$$H_{ex} = \sqrt{2.83}\,\frac{J}{g\beta}[S(S+1)]^{1/2} \qquad (11)^*$$

Then in our case $H_{ex} = 5.2 \times 10^4$ oer. So the full line width $\Delta H$ for the extreme-narrowed line by exchange is given by

$$\Delta H = 2[(10/3)H_p^2]/H_{ex} \qquad (12)$$

which gives us $\Delta H = 3.1$ oer. in our present case. This is too much smaller than our experimental width 20 oer., at the direction of the $a$-axis where two inequivalent ions in unit cell are placed under the same situation; $g' = g''$. This disagreement is attributable to the neglect of the hyperfine structure and of the spin-lattice relaxation. This circumstance is also observed in $K_2CuCl_4 \cdot 2H_2O$[12].

The line width becomes the smallest when $H$ is applied along the $a$-axis i.e. the direction perpendicular to the tetragonal axes of both ions. This situation was already experienced in $CuSO_4 \cdot 5H_2O$.

When the anisotropy of $g$-tensor is taken into account, the line width under extremely narrowing case becomes greater than that given by Eq. (12) which is valid only when the $g$-tensor is isotropic. Theory for this case is treated by Anderson[13].

The similar fact was also obtained in copper Tutton salt[24] in which it is well ascribed to the unresolved nuclear hyperfine structure. In our extremely narrowing case, this hfs effect also contributes to the line width[22] through a field expressed as $H_H$ in an equation,

$$\Delta H = 2[(10/3)H_p^2 + H_H^2]/H_{ex} \qquad (13)$$

Since $H_H$ gives its maximum value at the axial direction of crystalline field where $g$-value reaches to its maximum[30], $g_{//}$, the variation of line width is reasonable also from the view-point of hyperfine structure.

The contribution to the line width of *c.t.s.* from the spin-lattice relaxation must be smaller than the smallest observed width, 20 oer. It should be noted that this crystal has such a small spin-lattice relaxation at room temperature, compared with the case of hydrates. Some of the copper Tutton salts are the examples of the latter group. The contribution to their line width from the spin-lattice relaxation is estimated, at room temperature, to be 150 oer. which means that their spin-lattice relaxation time $\tau_{SL}$ is $2\times10^{-9}$ sec.31)

---

* There is a misprint in Eq. (28 a) of Anderson's report[22], the factor 2.83 must be read as $\sqrt{2.83}$.

The experimental facts (e.g. the line-shape is close to be Lorentzian, the width is very sharp and they are independent on measured frequency) suggest us the exchange interaction between $Cu^{++}$ ions in this crystal should be very large. The mechanism for this strong exchange coupling becomes clear by the $\cdots Cu \cdots H_2O \cdots Cu \cdots$ structure in Fig. 4.

### b) *Copper diethylenediammine chloride*: $[Cu(en)_2]Cl_2 \cdot xH_2O$.

This crystal was prepared by the usual way; by adding excess ethylenediammine to an aqueous solution of $CuCl_2$ followed by slow precipitation25). Thin blade-shape crystals (e.g. 10×10×0.5 mm) easily grow and they are bright blue, slightly nearer to violet than that of $CuSO_4 \cdot 5H_2O$. Absorption intensity of their paramagnetic resonance is strong and only one peak is observed in any direction of static field. Data obtained are listed also in Table I. Two principal axes of $g$-tensor are in the wide face of the blade-shape crystal, which correspond to $g_1$ and $g_3$ in the table. This wide face seems to be the {010} plane observed by Mazzi7) who gave crystallographic data as a monoclinic system*):

$$a:b:c:=0.819:1:0.401 \text{ and } \beta=111°20'.$$

By his x-ray analysis, unit cell of this crystal

$$a_0=12.48\pm0.01\text{Å},\ b_0=15.22\pm0.03\text{Å},$$
$$c_0=6.23\pm0.01\text{Å} \text{ and } \beta=111°20':$$

contains 4 unit molecules (i.e. $Z=4$) and belongs to the space group $P_{2_1/a}$. The molecule of this crystal is somewhat curious as shown in Fig. 8. Copper atom is surrounded by 4 nitrogen atoms of two ethylenediammines which make square co-ordination. Perpendicular to this plane of nitrogens, there is one chlorine atom 2.89Å apart from Cu atom, while on the other side there is one oxygen atom of water 2.68Å apart. Although the x-ray analysis shows that the unit cell of this crystal contains 4 inequivalent molecules, i.e. $Z=4$, from the view-point of magnetic absorption, there are only two inequivalent orientations of molecules in unit cell, which are in mirror positions with the *ac*-plane in each other. If we assume the Cl–Cu–$OH_2$ direction is the axis of crystalline field, it makes an angle of 6°10′ with the *ac*-plane and we shall call this angle $\alpha$. From the molecular shape of this crystal, crystalline field acting on the Cu ion can be assumed to be tetragonal. Hence we can deduce $g_\perp = g_1 = 2.050\pm0.004$ directly. Then, we can deduce $g_{//}=2.250$ with $g_3=2.248$, $g_2=2.05_3$ and $\alpha=6°10'$ which are in close agreement with the measured values shown in Table I. On the contrary any manipulation with $g_{//}<g_\perp$ can not explain the observed data. This means that the usual treatment with crystalline electric field and with usual sign of deformation as in $CuSO_4 \cdot 5H_2O$ is adequate for this salt.

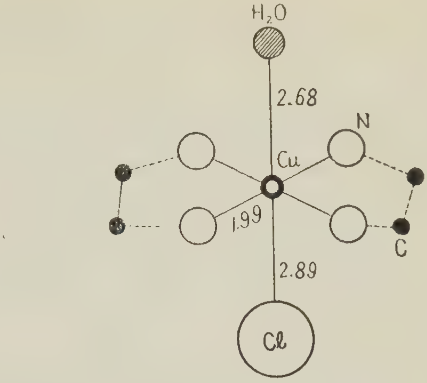

Fig. 8. Atomic configuration surrounding a $Cu^{++}$ ion in $Cu(en)_2Cl_2 \cdot xH_2O$. where $x=1$ or 2. After F. Mazzi7)

"Apparent" line width was measured in the directions of the principal axes of $g$-tensor. It is larger when it is observed in the direction giving larger $g$-value than that in the direction of smaller $g$-value. In the directions giving $g_2$ and $g_1$, it was observed as about 120 oer. From these data of line widths, we expect as an exchange field $H_{ex}$ a value about 1/5 times of that of $Cu(NH_3)_4 \cdot SO_4 \cdot H_2O$. Then for the temperature $\Theta$, we expect, though we have not yet any available data, ~3° for $Cu(en)_2Cl_2 \cdot xH_2O$. Here, the term "apparent width" means that obtained without correction of cavity tuning, though we put some cares to reduce the dispersion effect by using

---

* Mazzi determined the number of hydration $x$ of this crystal is one, as $Cu(en)_2Cl_2 \cdot H_2O$ although Werner et al25) thought $x=2$ namely $Cu(en)_2Cl_2 \cdot 2H_2O$. We have no data around this point, so we remain this number as $x$.

Table III. Results of our measurements.

| | Principal $g$-values | | $H_{ex}$ in oer | | Number of inequivalent ions in unit cell |
|---|---|---|---|---|---|
| | $g_{//}$ | $g_{\perp}$ | from line width*** | from $\Theta$ of $\chi$ | |
| $[Cu(NH_3)_4]SO_4 \cdot H_2O$ | 2.22 | $2.05_5$ | ~7500 | 52000 | $Z=2$ (from x-ray data) |
| $[Cu(en)_2]Cl_2 \cdot xH_2O$* | 2.25 | 2.05 | ~1500 | — | $Z=2$ (from x-ray data) |
| $[Cu(py)_m]SO_4 \cdot nH_2O$ | $2.31_5$ | $2.07_5$ | ~1500 | — | $Z=1$ is assumed** |
| $[Cu(py)_m](NO_3)_2 \cdot nH_2O$ | $2.22_5$ | $2.05_5$ | ~ 600 | — | $Z=2$ is assumed** |
| $[Cu(OH_2)_4]SO_4 \cdot H_2O$ | 2.46 | 2.06 | ~3000 | 2400[a)]<br>6200[b)] | $Z=2$ (from x-ray data) |

* $x=1$ or 2.

** Chemical composition is not yet examined.

*** Here, influences on the line width by the hfs and by the spin-lattice relaxation are neglected.

a) T. H. Gaballe and W. F. Giauque: Jour. Amer. Chem. Soc. **74** (1952) 3513.

b) K. S. Krishnan and A. Mookerji: Phys. Rev. **54** (1938) 841.

a small enough sample to the case. So it may happen that the correct width is somewhat smaller than this "apparent" width.

c) *Copper pyridine sulfate*:

$[Cu(py)_m] \cdot SO_4 \cdot nH_2O$

The crystals for this study were prepared by slow precipitation through vaporization from aqueous solution of copper sulfate added by somewhat excess pyridine. Since they are not yet chemically analyzed, the number of pyridine and water in a molecule is remained as $m$ and $n$, respectively. They grow in a shape of elongated rectangular hexahedron which may lead to an assumption of rhombic or tetragonal system. They have a colour of blue as that of $CuSO_4 \cdot 5H_2O$ but more plain one. Three principal axes of $g$-tensor are along the three edges of the external form. The line width depends on the direction of static field as the preceding two crystals do. It is 60 ~ 80 oer. in directions of $g_1$ and $g_2$. The apparent $g$-value seems approximately to have an axial symmetry. Then we may choose $g_{//}=2.31_5$ and $g_{\perp}=2.07_5$ within our experimental errors. If there are, however, more than one inequivalent $Cu^{++}$ ions in unit cell having $g$-tensor of rhombic symmetry, the above results must be changed to make $g_{//}$ larger and $g_{\perp}$ smaller, as in the case of $K_2CuCl_4 \cdot 2H_2O$ observed at longer wavelength[12)]. Again they can be fairly explained by Eq. (5). The line width infers an exchange energy of 1/5 of that in *c.t.s.*, by which we may expect $\Theta \approx 3°$.

d) *Copper pyridine nitrate*:

$[Cu(py)_m] \cdot (NO_3)_2 \cdot nH_2O$

The crystals under examination were obtained by the same way as in its sulfate except starting from $Cu(NO_3)_2 \cdot 3H_2O$. They grow in rhombic symmetry and are transparent. The colour of them resembles to that of concentrated aqueous solution of copper nitrate.

In all direction of $H$, we have only one peak. We assume that unit cell of this crystal contains two formula molecules, i.e. $Z=2$, and the crystalline field acting on the copper ion has an axial symmetry. Then we have the following parameters using Eq. (7) and observed $g$-values listed in Table I:

$$g_{//}=2.22_5,\ g_{\perp}=2.05_5 \text{ and } \alpha=38°40'$$

which are reasonable values. The minimum line width is about 160 oer. at $\lambda=11$ mm.

## § 5. Conclusion

The measurements reported in this paper have yielded, together with the x-ray analysis of atomic arrangement, informations on the nature of bonding between Cu and N atoms in some metal complexes. Observed $g$-values can be explained out by the Polder's treatment with coefficient $\lambda$ somewhat reduced and by assumption of strong exchange coupling which may be reasonable from the fact of their sharp absorption. $g_{//}$ and $g_{\perp}$ thus deduced from our experimental data are listed in Table III.

Values for the two former samples in this table are reliable. Those for the following two cases, however, are less reliable, because, for these two cases with asterisks, we have not yet confirmed their chemical compositions and we assume, by the lack of x-ray analysis, the number of inequivalent ions and the axial symmetry of $g$-tensor belonging to individual ions. Generally speaking about these results, $g_{//}$ in these compounds is considerably smaller than that in $CuSO_4 \cdot 5H_2O$. Since Eq. (4) gives larger $\Delta E$ for smaller $(g_{//}-2)$, it may be concluded that $\Delta E$ for these compounds is considerably larger than that of usual hydrates. The colour of these compounds also indicates this circumstance. However, the coplaner structure of four squarely co-ordinated nitrogen atoms does not necessarily support the covalent bonding hypothesis. The reason why $g_{//}$ for copper diethylenediammine chloride is larger than that of *c.t.s.* may probably due to the change in distance between Cu and N atoms (from 2.05Å in *c.t.s.* to 1.99 Å in $Cu(en)_2Cl_2 \cdot xH_2O$). It may be also affected by the difference in radicals to which the nitrogen atoms belong and the difference in atoms which locate perpendicularly to these co-ordinated nitrogens. Without regard to these rather minor facts, the observed $g$-values can be well explained by Eq. (7) resulted from the "crystalline electric field" assumption which treats the effects of surrounding atoms as a rigid charge distribution.

The theory with covalent bonding has been shown to explain the experimental results in cases of palladium (4d) and platinum (5d) group compounds[26] and of $K_3Fe(CN)_6$[27]. In cases of our Cu compounds, however, it is impossible to give a reasonable explanation for our experimental results under a standpoint of $g_{//} < g_{\perp}$. So theories giving $g_{//}=2.00$ is not adequate to explain the resonance absorption in $Cu\text{-}N_4$ group. By the electronegativity consideration, considerable portion of covalency may be expected, especially in the case of $Cu\text{-}N_4$ group. Sometimes the forces between the copper ion and the surrounding atoms were supposed to be covalent rather than electrostatic, even in the hydrates of copper. To explain the anomalies of the hfs in the copper Tutton salts, treatment on covalent bonding hypothesis was attempted by Abragam and Pryce[15][28]. The strong square bond constructed by hybridizing the $dsp^2$ orbitals makes an electron in a state $p_z$ responsible for the magnetic properties of the salt. This structure leads to $g_{//}=2$ and $g_{\perp} \gtrsim 2$ and to a different symmetry properties from the ionic structure which can be expected no resonance between them. So the explanation by covalent bonding hypothesis had been rejected.

It may contain, at the present state, only a few importance to discuss the detailed character of Cu bonding in crystal, whereas the effects produced by the attached atoms or molecules (e.g. $OH_2$, $NH_3$, etc.) are remained for theory which treats them as an effective static crystalline field.

The authors wish to express their sincere thanks to Professor Hiroo Kumagai for his continuous encouragement. They wish to thank Professors J. Zemann and F. Mazzi for their communications and Professor R. D. Myers for the marker radical.

## References

1) L. Pauling: Nature of the Chemical Bond (Cornell University Press, Ithaca, 1940).
2) H. Abe and J. Shimada: Report, "Paramagnetic resonance in some copper salts using 8 mm wave," at the annual meeting of the Physical Society of Japan held at Kyoto, October 1952.
3) T. Okamura and M. Date: Phys. Rev. **94** (1954) 314.
4) H. Abe: Report, "Paramagnetic resonance in some copper salts," at the annual meeting of the Physical Society of Japan held at Ôsaka, November, 1954.
5) F. Mazzi: Acta Cryst. **8** (1955) 137.
6) J. Zemann: Experientia **4** (1948) 2.
7) F. Mazzi: Rend. Soc. Mineral. Italiana **9** (1953) 148.
8) Z. Miduno, O. Matumura, K. Hakuda and K. Horai: Report given at the annual meeting of the Physical Society of Japan held at Ôsaka, November 1954. To be published in Mem. Fac. Sci. Kyushu Univ. **B 2** (1955) No. 1.
9) F. W. Lancaster and W. Gordy: Jour. Chem. Phys. **19** (1951) 1181 and *ibid* **20** (1952) 740.
10) D. M. S. Bagguley and J. H. E. Griffiths: Proc. Roy. Soc. **A 201** (1950) 366.
11) K. Ôno and M. Ohtsuka: To be published in Jour. Phys. Soc. Japan.
12) H. Abe, K. Ôno, I. Hayashi, J. Shimada and K. Iwanaga: Jour. Phys. Soc. Japan **9** (1954) 814
13) P. W. Anderson: Jour. Phys. Soc. Japan **9** (1954) 316.
14) D. Polder: Physica **9** (1942) 709.
15) A. Abragam and M. H. L. Pryce: Proc. Roy. Soc. **A 206** (1951) 164.
16) A. N. Holden, C. Kittel, F. R. Merritt and W. A. Yager: Phys. Rev. **77** (1950) 147.
17) C. H. Townes and J. Turkevitch: Phys. Rev. **77** (1950) 148.
18) P. Groth: *Chemische Kristallographie* Vol,

**2**, 438 (Leipzig, 1908).
19) Th. Dreisch and W. Trommer: Zeit. Phys. Chem. **B 37** (1937) 37.
20) O. Laporte: Zeit. Phys. **47** (1928) 761.
21) J. H. Van Vleck: Phys. Rev. **74** (1948) 1168.
22) P. W. Anderson and P. R. Weiss: Rev. Mod. Phys. **25** (1953) 269.
23) C. J. Gorter: *Paramagnetic Relaxation* (Elsevier, 1947) p. 115.
24) B. Bleaney, R. P. Penrose and B. I. Plumpton: Proc. Roy. Soc. **A** 198 (1949) 406.
25) A. Werner and W. Sprück: Zeit. anorg. Chem. **21** (1899) 233.
26) J. H. E. Griffiths, J. Owen and I. M. Ward: Proc. Roy. Soc. **A 219** (1953) 526.
27) B. Bleaney and D. J. E. Ingram: Proc. Phys. Soc. **A 65** (1952) 953.
28) A. Abragam: Physica **17** (1951) 209.
29) J. Owen: Proc. Roy. Soc. **A 227** (1955) 183.
30) A. Abragam and M. H. L. Pryce: Proc. Roy. Soc. **A 205** (1951) 135.
31) D. M. S. Bagguley and J. H. E. Griffiths: Proc. Phys. Soc. **A 65** (1952) 594.

---

Journal of the Physical Society of Japan Vol. 11, No. 9 September, 1956

# Zeeman Splitting of Nuclear Quadrupole Resonance Line of Iodine

By Kineo Tsukada

*Tokyo University of Education, Otsuka Tokyo*

(Received April 12, 1956)

Zeeman patterns of the nuclear Quadrupole resonance line of $I^{127}$ were studied with a single crystal of iodine at medium and weak magnetic fields. The asymmetry parameter of coupling, $\eta$, and the angle between bond axis of the iodine molecule and crystallographic $c$ axis, $\varphi$, were determined from the pattern at a medium magnetic field of about 120 gauss. The result was $\eta=-0.16\pm0.01$ at 14°C when crystallographic $b$ axis was chosen as $x$ axis and $\varphi=31°38'\pm60'$. The absolute value of $\eta$ is in accord with the value obtained by the two resonance frequencies, i.e. $0.151\pm0.001$ at 11°C. $\varphi$ agrees with that obtained by the X-ray diffraction, 32°4′. At a weak magnetic field, Zeeman patterns of the fine structure of iodine were examined at three directions of magnetic field against the iodine crystal, i.e. the $b$ axis, the $c$ axis and the direction of 60° from the $b$ axis in the $bc$ plane. Behaviour of the superregenerative detector used for these N.Q.R. measurements was studied and the observed shape of the resonance line is discussed.

## § 1. Introduction

The pure quadrupole spectrum of $I^{127}$ in solid iodine has been measured by Dehmelt1), Pound2) and Kamei3). The absolute value of the asymmetry parameter, $\eta$, which is expressed by $\eta=(q_{xx}-q_{yy})/q_{zz}$ with respect to the principal axis system $(x, y, z)$ of field gradient tensor was determined from the two resonance frequencies. The obtained value of $\eta$, 0.151), was explained as a result of intermolecular coupling by Townes and Dailey4) and Gordy et al5). The sign of $\eta$ can be determined only by analysis of Zeeman patterns of the pure quadrupole resonance line. This analysis, also, can present data concerning crystal structure. We studied the Zeeman patterns of solid iodine, so as to check the theory of the Zeeman effect, to determine the sign of $\eta$ and to obtain some information of the structure of the crystal.

In the course of this experiment, we found a fine structure6) in the lower frequency absorption line of solid iodine at zero magnetic field. This fine structure was not explained by multiple absorption lines due to crystallographically nonequivalent atoms, but by splitting due to electron coupled nuclear spin-spin interaction7). With an external weak magnetic field below 40 gauss, the lines of the fine structure were shifted independently and the separations between the lines were different from what the theory of Zeeman effect predicted. The variations of the lines were measured with increasing magnetic field.

For all measurements, the superregenerative spectrometer was used because of its high sensitivity and stability against external electric or mechanical disturbances. When it was used under unsuitable conditions, however, the detected line was broadened and, sometimes, had an additional hump on the side of the line. This hump might be mistaken for a fine structure. We examined in some detail the behaviour of the superregenerative detector. These results are described in the Appendix.

## § 2. Calculations of First-Order Zeeman Patterns

By Zeeman effect on the nuclei of spin 5/2, a single resonance line, corresponding to the transition $m_z=\pm 1/2 \leftrightarrow \pm 3/2$, splits into four lines. The frequencies of these lines are expressed by

$$\nu_{I,II}=\nu_0\pm\frac{1}{2}S,\quad \nu_{III,IV}=\nu_0\pm\frac{1}{2}s,\quad \cdots\cdots(1)$$

where

$$\nu_0=(3Qq_{zz}/20\,h)(1+1.093\,\eta^2)\,.$$

The theory of the first-order Zeeman effect8)9) gives

$$\left.\begin{matrix}S\\ s\end{matrix}\right\}=\frac{0.8\,\mu}{\mathrm{h}}H\left[\left\{4\eta^2+(2.25-4.75\eta^2)\left(\frac{H_z}{H}\right)^2\right\}^{1/2}\right.$$
$$\pm\left\{2.25+4.833\eta^2-6\eta\left(\frac{H_x{}^2-H_y{}^2}{H^2}\right)\right.$$
$$\left.\left.-(2+5.506\eta^2)\left(\frac{H_z}{H}\right)^2\right\}^{1/2}\right]\cdots\cdots\cdots\cdots(2)$$

where $H_x$, $H_y$ and $H_z$ are the components of the magnetic field referred to the principal axis system of the field gradient tensor and $\mu$ is the magnetic moment of iodine nucleus, $1.4185\times10^{-23}$ erg gauss$^{-1}$. The relative intensities** of the four lines in the Zeeman pattern are dependent upon the direction of the magnetic field against the principal axes of the field gradient tensor.

Solid iodine forms a orthorhombic crystal of a layer-like structure. The lattice constants are as follows10)*: $a=4.7761$ A, $b=7.2501$ A and $c=9.7711$ A at 19°C. The positions of atoms are shown in Fig. 1. Bonds of all molecules are perpendicular to the $b$ axis. Half of them are oriented $+32°4'$ from the $c$ axis and the other half $-32°4'$. Corresponding to the two classes of molecules, two sets of the principal axis systems of the field gradient tensor ($x_1$, $y_1$, $z_1$) and ($x_2$, $y_2$, $z_2$) must be taken into account, where $x_1$ and $x_2$ axes lie along the crystallographic $b$ axis and, the $z_1$ and $z_2$ axes along the molecular bonds of each class. If the intermolecular coupling is taken into account, the $z$ axis will be slightly different from the molecular bond (§ 6).

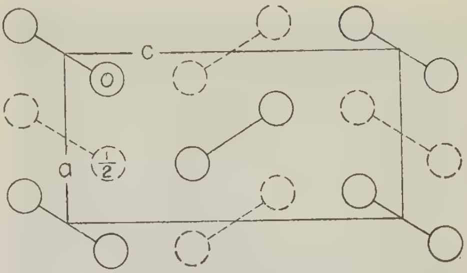

Fig. 1. A projection of the orthorhombic structure of solid iodine upon its crystallographic b-face.

In order to calculate the Zeeman patterns, it is convenient to use coordinate axes, $\xi$, $\eta$ and $\zeta$, which fit on the $c$, $a$ and $b$ axis, respectively. Generally the Zeeman patterns consist of eight lines, four of which are due to the molecules of one class and the other four to those of the other class. When the magnetic field is applied parallel to the $\zeta\xi$ or $\zeta\eta$ plane, the molecules of the two classes give rise same patterns, so only four lines will appear. In this case components of the applied magnetic field $H$ are expressed by

$$H_x=H\cos\theta\,,\quad H_y=\pm H\sin\theta\sin\varphi$$

and $H_z=H\sin\theta\cos\varphi$ for $H$ in $\zeta\xi$ plane,

$$H_x=H\cos\theta\,,\quad H_y=-H\sin\theta\cos\varphi$$

and $H_z=\pm H\sin\theta\sin\varphi$ for $H$ in $\zeta\eta$ plane, where $\theta$ is angle between the direction of the magnetic field and the $\zeta$ axis, $\varphi$ is between the $z$ and $\xi$ axes and double signs, ±, correspond to the two classes. With Eq. (2) we can calculate the separation of lines. These

---

* Notation $a_0$, $b_0$ and $c_0$ in the literature (10) correspond to $b$, $c$ and $a$ in this report respectively.

** The calculation of the variation of the relative intensities was given by H. Krüger and Meyer-Berkhout, Z. Physik **132** (1952) 221. See also, Eq (16) in the reference (9).

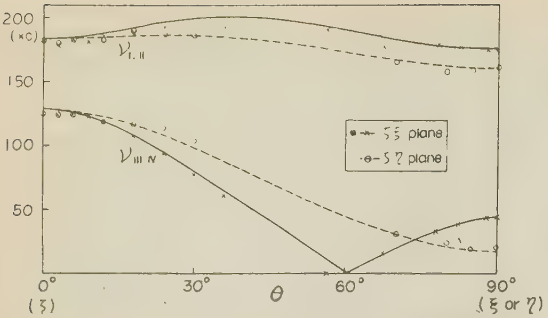

Fig. 2. The Zeeman splittings when the magnetic field lies on the $\zeta\xi$ or $\zeta\eta$ planes. The values are reduced to those of 100 gauss.

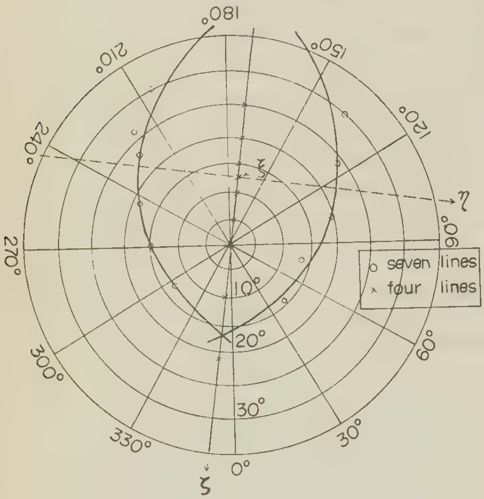

Fig. 3. Gnomonic projection of the magnetic field where seven lines were observed. Three lines of them were due to the molecules of one class, in which $s=0$, and the other four lines were due to the molecules of the other class.

results are shown in Fig. 2.

The value of the asymmetry parameter, $\eta$, can be determined by analysis of the pattern for $\theta=0$, because the pattern of this direction is not so sensitive to $\theta$ and the doublet separation, $(\nu_{I,II}-\nu_{III,IV})$, depends rather strongly on $\eta$. In this case

$$\nu_1-\nu_0=0.8566\times10^3H \times\{-2\eta+(2.25-6\eta+4.833\eta^2)^{1/2}\}\cdot\cdot(3)$$

$$\nu_{IV}-\nu_0=0.8566\times10^3H \times\{2\eta+(2.25-6\eta+4.833\eta^2)^{1/2}\}\cdot\cdot\cdot(4)$$

These equations give

$$\nu_I-\nu_{IV}=-3.426\eta H\ \ (\text{kc})\cdots\cdots\cdot(5)$$

When $\eta$ is negative and small, the value of $(\nu_{IV}-\nu_0)$ is almost independent of $\eta$ and equal to $1.285H$ kc. Intensity ratio[11] of $\nu_{I,II}$ to $\nu_{III,IV}$ at $\theta=0$ is calculated by considering the direction of magnetic field $H$ and the radio frequency field $H_r$. When $H_r$ is parallel to the $\zeta$ axis or the $\xi\eta$ plane, intensity of $\nu_{I,II}$ or $\nu_{III,IV}$ is zero respectively. Intermediate value of this ratio is obtained when $H_r$ is pointed to direction between the two extreme values.

The value of the angle between the $z$ and $\xi$ axes, $\varphi$, can be determined from the angle between the two directions of the triplet patterns in the $\zeta\xi$ plane, in which directions $s=0$ in Eq. (2), for all molecules. But experimentally, it is more easily decided from projection of the direction of applied magnetic field to the $\xi$ plane, in which $s=0$ for one of two classes of molecules. This projection is shown in Fig. 3. Angle $\theta_t$ between those two directions in the $\xi\eta$ plane, in which $s$ of Eq. (2) for one of two classes of molecules is equal to zero, is given by

$$\cos(\theta_t+2\varphi)=0.0588+1.330\eta-1.674\eta^2\cdot\cdot(6)$$

## § 3. Experimental Procedure

Iodine can be liquefied at about 120°C in a sealed tube. A single crystal of about 30 gr. was made by the method of "pointed bottom crucible"[12]. The spectrometer was a super-regenerative type[9] and the pattern was observed on C.R.O.. The frequency separation of the split lines was measured in such a way that the quench frequency was changed and one of the side bandes of the wave meter signal was used as a marker of the frequency. Magnetic field was produced by a Helmholtz coil. Instead of rotating the crystal, the magnet was rotated. The crystal axes were determined by study of the Zeeman patterns. Two planes, in which four lines were observed, were searched. One of these, containing triplet lines, was the $\zeta\xi$ plane and the other was the $\zeta\eta$ plane. These axes were further confirmed with intensity variation[11] of the absorption line at zero magnetic field, when the single crystal was rotated against $H_r$. All measurements were carried out at 14°C.

## § 4. Results at a Medium Magnetic Field

In order to study the general aspect of the Zeeman patterns, we have set the magnetic field to be parallel to the $\zeta\xi$ and $\zeta\eta$ planes, where molecules of the two classes inclined same angle against the magnetic field. The field used was of 120 gauss for almost all measurments. In this region of field strength, fine structure could not be seen in each split line $\nu_I$, $\nu_{II}$, $\nu_{III}$ or $\nu_{IV}$ and their frequency separations and intensity distribution were almost symmetric against the frequency of center of the fine structure at zero field (§ 5). The half values of the separations of lines, $(\nu_I-\nu_{II})/2$ and $(\nu_{III}\sim\nu_{IV})/2$ were plotted against $\theta$. The result is reproduced in Fig. 2, where the separations are reduced to value for 100 gauss. The theoretical curves with $\eta=-0.16$ and $\varphi=32°4'$ are also shown in the figure. At $\theta=0$, $(\nu_I-\nu_{II})/2$ was I82 kc at 100 gauss and $(\nu_I-\nu_{IV})/2$ was 57 kc. So $\eta=-0.166$ with Eq. (5), and $\eta=-0.155$ with Eq. (3). Using these values, we determined $\eta=-0.16\pm0.01$. In the case of positive sign of $\eta$, half of separation of the outer lines, $(\nu_I-\nu_{II})/2$, is approximately equal to $1.285H$ kc. So, at $\theta=0$, the splitting will be much smaller than that shown in Fig. 2. Photographes of the Zeeman patterns at $\theta=0$ were shown in Fig. 4 for two directions of the *rf* field $H_r$ against $H$. As mentioned above, four lines are observed, (upper photograph). However, in a special direction of the radio frequency field, two of them disappear, (lower photograph).

In Fig. 3, Gnomonic projection of the direction of the applied magnetic field nearly to the $\xi$ plane, in which seven lines were observed, is shown. Three lines are due to one of the two classes of molecules for which $s=0$ and four lines due to the other class. In this figure, calculated curves, with $\eta=-0.16$ and $\varphi=31°38'$, are shown. The observed value of $\theta_t$ in Eq. (6) was $38°6'\pm2°$. Using this value of $\theta_t$ and $-0.16$ of $\eta$, the value of $\varphi$ was determind as $31°38'\pm60'$.

## § 5. Zeeman Patterns of the Fine Structure

At a magnetic field weaker than about 40 gauss, fine structure was observed. Frequency separations and photographes of the patterns at 0°, 60° and 90° of $\theta$ in the $\zeta\xi$ plane are shown in Figs. 5*, 6*, 7* and 8. In the figures, full curves show behaviour of the line predicted by the theory of the first-order Zeeman effect if it has no fine structure. The $O$ point of the ordinate in frequency scale was decided so that observed points at the

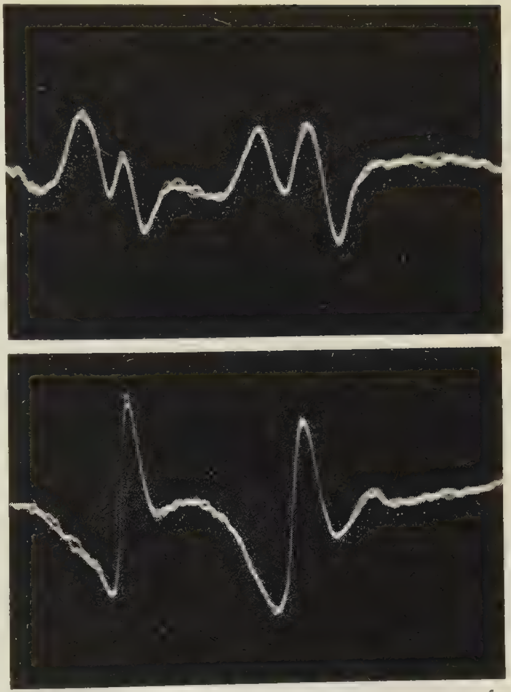

Fig. 4. Photographes of the Zeeman patterns for two different angles between $H$ and $H_r$. $\theta=0°$ and $H=60$ gauss.

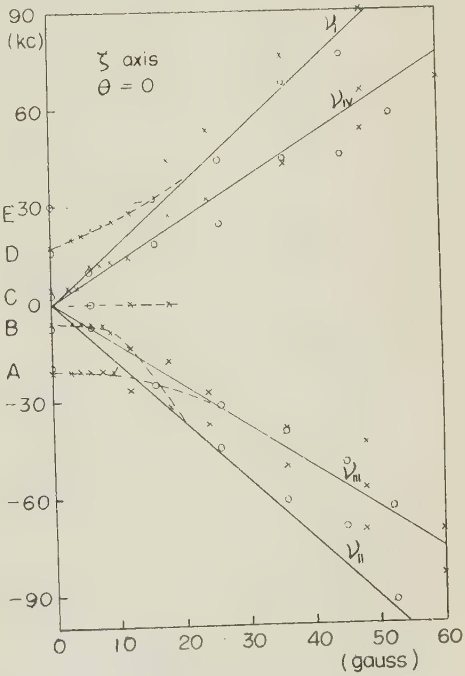

Fig. 5. Observed Zeeman pattern of the fine structure as a function of the magnetic field parallel to the $\zeta$ axis.

---

* In these figures, the points denoted by a open circles were measured by the author and the points denoted by crosses were measured by Ogawa and Minematsu with another crystal. Both measurements were consistent within experimental erra.

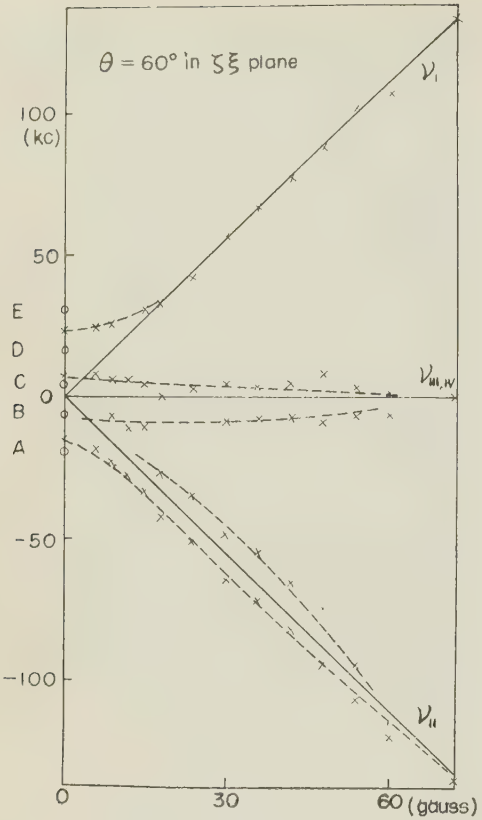

Fig. 6. Observed Zeeman pattern of the fine structure as a function of the magnetic field. The direction of the field is in the $\zeta\xi$ plane and $\theta=60°$.

medium magnetic field were in accord with the full curves. This point at zero magnetic field was on the middle between *B* and *C* lines, which were much more intensive than *A*, *D* or *E*, and rather close to *C*, 4 kc apart from this line to lower frequency side.

It was rather difficult in some places to determine how each line in the zero field pattern shifted and split with increasing magnetic field, because each line had width of about 10 kc and such a shape which seemed to be further resolved. As shown in the figures, however, the lines *A*, *B*, *C*, *D* and *E* approached gradually to the asymptotes $\nu_I$, $\nu_{II}$, $\nu_{III}$ and $\nu_{IV}$, which were predicted by the calculation in § 2, with increasing magnetic field. On the way, some of them split or crossed. When the magnetic field was applied parallel to the $\zeta$ axis, the pattern at more than about 20 gauss was nearly in accord with the full curves and, for other directions in Figs. 6 and 7, a little stronger field was

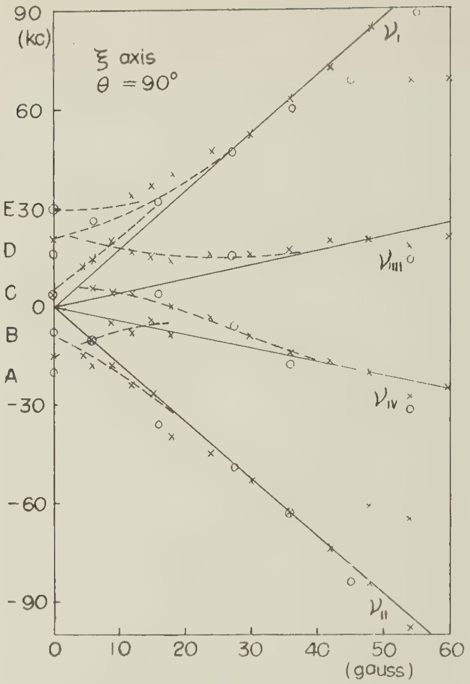

Fig. 7. Observed Zeeman pattern of the fine structure as a function of the magnetic field parallel to the $\xi$ axis.

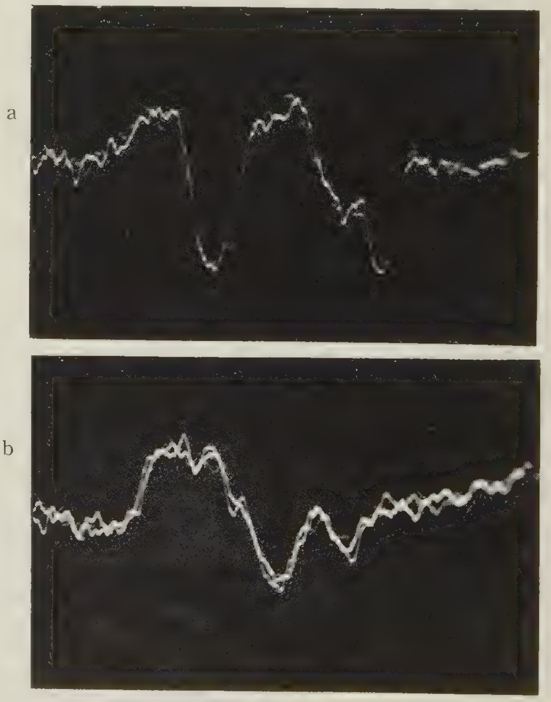

Fig. 8. Photographes of Zeeman pattern of the fine structure.

a. the direction of the magnetic field is the $\zeta$ axis and $H=19$ gauss.

b. the direction of the magnetic field is the $\xi$ axis and $H=6$ gauss.

necessary. Line width of the medium field pattern observed on the C.R.O. was slightly increased with magnetic field because of inhomogenuity of the field and deviation of its direction from the $\zeta\xi$ or $\zeta\eta$ plane. But line width of each line at 50 gauss was about 25 kc and this value was much narrower than total width of the zero field pattern, 50 kc.

## § 6. Discussion

As shown in Figs. 2 and 3, general tendencies of distribution of observed points in a medium magnetic field are in accord with the theory. In this case, fluctuation of the observed points seems to be mainly caused in measuring the intensity and direction of the applied magnetic field. The asymmetry parameter, $\eta$, determined through the Zeeman effect, $-0.16\pm0.01$, at 14°C was well consistent with the value of $0.151\pm0.001$ which was obtained with two resonance frequencies of 331.61 and 644.39 Mc at 11°C. From these results, theory of the first-order Zeeman effect were well confirmed and the known crystal structure of iodine were also consistent with the present result. Minus sign of $\eta$ was favourable for the discussion about intermolecular origin[4)5)] of $\eta$. The bond switching model[4)9)] suggests that the principal axis of field gradient tensor, $z$, does not coincide with the molecular axis $z_0$. The angle between the $z$ and $z_0$ axes, $\Theta$, is given by Eq. (18) and (20) of reference (9). In solid iodine $\Theta_{cal}=0°30'$*. Observed value of the angle between the principal axis $z$ and the crystallographic $c$ axis, was $31°38'\pm60'$ and the value of the angle between the molecular axis $z_0$ and the $c$ axis obtained by the X-ray diffraction was $32°4'$[10)]. Therefore, $\Theta_{obs}$ was $0°26'$, but this was comparable to magnitude of error both in the X-ray diffraction data and in the present measurements.

As already reported[6)], the electron coupled nuclear spin-spin interaction[7)] seems to be the origin of the fine structure. In this case, it is expected that, in a weak magnetic field, the patterns are very different from those predicted by the ordinary Zeeman theory and, when the Zeeman splitting is comparable with the zero field splitting, this anomalous charactor decreases, because of decoupling of spin-spin interaction. As shown in Fig. 5, each line approached to the asymptote calculated with the first-order Zeeman theory at about 20 gauss, where overall calculated splitting was 70 kc. This was comparable with the extent of the zero field splitting, 50 kc.

## § 7. Acknowledgements

The encouragement and guidance of Professor Shoji Kojima are gratefully acknowledged. The author is indebted to Dr. Shizuko Ogawa and Miss Midori Minematsu for their measurements of the Zeeman patterns of the fine structure, (Figs. 5, 6 and 7).

## Appendix

When the superregenerative detector is used as a spectrometer for N.Q.R., it is frequently experienced that deformed or broadened shapes of spectral lines are observed. Characteristics of the superregenerative spectrometers[9)], which were used in preceding experiments, were measured and examined. The results were summarized as follows.

1) Spectral lines must be observed in the region where oscillation of the *rf* oscillator is coherent in successive quench cycles. When spectral lines are observed in the region in which the oscillation is incoherent in successive quench cycles, their line shape will be broadened. Because incoherency makes the frequency components of the oscillation to have continuous distribution.

2) Quenching of the superregenerative oscillator yields a large frequency modulation for the oscillation of the oscillator. As a result, the detected spectral line has a shape of mixing of absorption and dispersion.

### § 1. Coherency of Oscillation

If the amplitude of oscillation, of which frequency is $f$, is modulated with frequency $f_q$, many side bands are observed in addition to the center frequency $f$. In the case of the superregenerative detector, $f_q$ corresponds to the frequency of the quench oscillator. However, if the oscillation of the *rf* oscillator is incoherent in successive quench cycles, i.e. the oscillation stops in every quench cycles, it consists of a train of pulses, and phases of the oscillations in pulses are random* with respect to each other, since we assume that each oscillation is started by noises. In this case the discrete side bands cannot be observed, and frequency components have a continuous distribution centered at $f$, as shown by a Fourier integral of a pulse of oscillation. If the oscillation is partially incoherent, i.e. the oscillation does not always stop in every quench cycles, each of a center line and side bands has frequency distribution, of which width depends on duration of the coherent part of the oscillation. When the quench voltage is sufficiently large, the *rf* oscillation is interrupted at a region of each negative half cycle of quenching oscillation. In this region the *rf* voltage in the tank circuit decayes as $V_c \exp(-\pi ft/Q)$, where $V_c$ is the *rf* voltage at the instant when the oscillation is interrupted. If this decayed *rf* voltage at the beginning of the next quench cycle is higher than noise voltage, $V_n$, the oscillation will be always coherent, even though the quench voltage is large. Therefore, in order to be coherent for the large quench voltage, the quench frequency must be higher than some critical value. The critical quench frequency, $f_c$, is derived as

---

* The value of $\Theta$ which was given in the reference (4), 4°9′, seems to be erroneous.

$$V_c \exp\left(-\frac{\pi}{2}\frac{1}{Q}\frac{f}{f_c}\right) = \sqrt{\overline{V_n^2}}\,, \quad \cdots\cdots(6)$$

where $\sqrt{\overline{V_n^2}}$ is rms value of the noise voltage induced in the tank circuit, and equal to $\sqrt{kT/C}$[13])

The existence of the critical quench frequency was confirmed by experiment. The broadening of the resonance line was observed at the large quench voltage, of which frequency was lower than $f_c$. In a case of $f=200$ Mc, $f_c$ was measured as about 200 kc. Eq. (6) was satisfied with these values. In the region where the broadening was observed, a rushing noise could be heard in a receiver of the wave meter. This noise may be due to incoherency of the oscillation. For $f_q$ lower than $f_c$, with increasing quench voltage $V_q$, the observation showed that the width of the spectral line became broader and its intensity decreased. In the course of these observations, a small hump was observed on a side of the line. In Fig. 10c, an example of the broadened line was shown. In this case, strong rushing noise was heard outside of the frequency region of the resonance. About the center of the resonance, sometimes, the rushing noise could not be heard and there was hysterysis of frequency of the *rf* oscillator for the direction of the frequency sweep. In this region it may be possible that the emission due to resonance in preceding quench cycle makes the oscillation of the next quench cycle to start and, in such a case, no rushing noise is heard.

## § 2. Frequency Modulation

In the superregenerative spectrometer, a mixed shape of absorption and dispersion types is observed. This mechanism may be supposed as follows. In addition to the amplitude modulation, the frequency modulation is inevitable because of variation of the working conditions of the oscillator tubes with quench voltage. Observed frequency excursion from the carrier frequency $f$ often amounted to several hundred kilocycles at $f=270$ Mc. In such a case, the *rf* voltage in the tank circuit, $V(t)$, may be expressed in a form with amplitude and frequency modulation as

$$\begin{aligned} V(t) &= V_0\left\{1+\sum_{n=1}^{\infty} a_n \cos(2\pi n f_q t+\phi_n)\right\} \\ &\quad \times \cos\left\{2\pi f t+\sum_{m=1}^{\infty} b_m \sin(2\pi m f_q t+\varphi_m)\right\}, \\ &= V_0\left\{1+\sum_{n=1}^{\infty} a_n \cos(2\pi n f_q t+\phi_n)\right\} \\ &\quad \times [J_0(b_1)\pm J_1(b_1)\cos\{2\pi(f\pm f_r)t\} \\ &\quad + J_2(b_1)\cos\{2\pi(f\pm 2f_q)t\}\pm\cdots], \quad \cdot\cdot(7) \\ &= \sum_{n=-\infty}^{\infty} A_n \cos\{2\pi(f+nf_q)t+\Phi_n\}. \quad \cdot\cdot(8) \end{aligned}$$

In Eq. (7) $\varphi_1$ is neglected.

If the resonance frequency of the sample is equal to the frequency of the center line, $f$, the only component which participates in the resonance is $A_0\cos(2\pi ft+\Phi_0)$ because the frequency of the induced voltage in the tank circuit is $f$. The induced voltage $\Delta V$ is given by[14])

$$\Delta V = 4\pi q Q(\chi''+i\chi')V\,, \quad \cdots\cdots\cdots(9)$$

where $q$ is the effective filling factor and

---

* It is possible by the suitable conditions of quenching that the phase difference between the *rf* oscillation and the quench oscillation is always constant at the start of each quench cycle. In such a case the frequency spectra of the oscillation consist of line spectra of which frequencies are $nf_q$ ($n$ is a positive integer).

$V=A_0\cos(2\pi ft+\Phi_0)$. The receiver detects only changes in magnitude of the vector $(\overrightarrow{V}(t)+\overrightarrow{\Delta V})$ as shown in Fig. 9.

The locus of $\overrightarrow{\Delta V}$ is a circle[14]. Therefore the shape of the detected signal depends upon the angle $\Phi_0$ between $V(t)$ and $A_0$ in the vector diagram. The sensitive time of the superregenerative detector is limited only in the small part of a quench cycle, i.e., beginning of the growth of $rf$ oscillation. In this small part of quench cycle, the amplitude of $V(t)$ is much smaller than $A_0$ and the angle $\Phi_0$ can be considered to be constant. $\Phi_0$ is approximately given as

$$\Phi_0=\tan^{-1}\{a_1\sin\phi_1 J_1(b_1)/J_0(b_1)\} \\ +\tan^{-1}\{2\sin(2\pi f_q t)J_1(b_1)/J_0(b_1)\}\,. \quad \cdot\cdot(10)$$

In the case of $\Phi_0=0$ or $\pi/2$, the center line is of pure absorption or dispersion type, respectively. When $V(t)$ is modulated only in amplitude, $\Phi_0$ is equal to zero and the pure absorption line will be obtained. $b_1$, which is necessary for $\Phi_0=\pi/2$, is nearly equal to one if $a_1=\sin\phi_1=\sin 2\pi f_q t=1$. It was possible to obtain a pure absorption or dispersion pattern by adjusting $V_q$, $f_q$ or plate voltage of the $rf$ oscillator. Such examples are shown in Fig. 10.

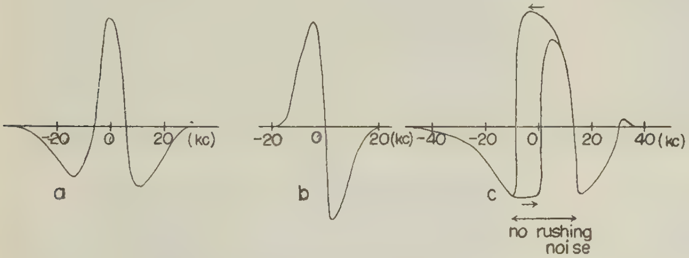

Fig. 10. Derivative curves of the resonance lines of $Br^{79}$ in $pBr_2C_6H_4$ at 268.03 Mc.

a. pure dispersion line.
b. pure absorption line.
c. broadened line. The arrows show the direction of the frequency sweep.

It was confirmed by the frequency measurement that, in suitable conditions, $b_1$ was equal to one.

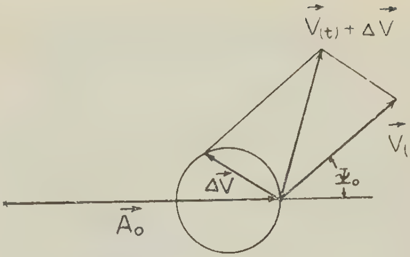
$\overrightarrow{V}_{(t)}+\overrightarrow{\Delta V}$
$\overrightarrow{V}_{(t)}$
$\Phi_0$
$\overrightarrow{\Delta V}$
$\overrightarrow{A}_0$

Fig. 9. Diagram of the voltages in the tank circuit.

If the resonance is of a damped oscillator type, the ratio of width between maximum deflections in the dispersion curve to that between maximum slopes in the absorption curve is 1.73. This ratio is smaller for a Gaussian type. In $p$-dibromobenzen, $pBr_2C_6H_4$, measured ratio was 1.8, for resonance of $Br^{79}$, as shown in Fig. 10. The absorption curve were measured also by the autodyne spectrometer for the comparison. The result agreed completely with that of the damped oscillator type. Because the sensitivity of the superregenerative detector is nonlinear for the magnitude of signal, so discussion for the exact line shape will be difficult except the line width, but the valuable information about the line shape will be obtained by the measurement of the ratio of width of a dispersion curve to that of a absorption curve, as discussed above.

## References

1) H. G. Dehmelts: Z. Physik **130** (1951) 346.
2) R. V. Pound: Phys. Rev. **82** (1951) 343.
3) T. Kamei: J. Phys. Soc. Japan **7** (1952) 649.
4) C. H. Townes and B. P. Dailey: J. Chem. Phys. **20** (1952) 35.
5) H. Robinson, H. G. Dehmelt and W. Gordy: J. Chem. Phys. **22** (1954) 511.
6) S. Kojima and K. Tsukada: J. Phys. Soc. Japan **10** (1955) 591.
7) N. F. Ramsey: Phys. Rev. **91** (1953) 303.
8) R. Bershon: J. Chem. Phys. **20** (1952) 1505.
9) S. Kojima, K. Tsukada, S. Shimauchi and Y. Hinaga: J. Phys. Soc. Japan **9** (1954) 795.
10) R. W. G. Wyckoff: "Crystal Structures", Interscience Publishers, Inc., New York (1948).
11) M. G. Cohen: Phys. Rev. **96** (1954) 1278.
12) S. Kojima, K. Tsukuda and Y. Hinaga: J. Phys. Soc. Japan **10** (1955) 498.
13) G. E. Valley and H. Wallman: "Vacuum tube amplifiers" McGraw-Hill Book Company, Inc., New York (1948).
14) N. Bloembergen: Nuclear Magnetic Relaxation, Thesis, Leiden (1948).

JOURNAL OF THE PHYSICAL SOCIETY OF JAPAN Vol. 11, No. 9, SEPTEMBER, 1956

# Structure of Nuclear Quadrupole Resonance Line
# I. Solid Iodine

By Shoji KOJIMA, Shizuko OGAWA, Shigeo HAGIWARA,
Yoshihito ABE and Midori MINEMATSU

*Department of Physics, Tokyo University of Education*
*Otsuka, Tokyo*

(Received May, 14, 1956)

The complex structure of the line which was found in the nuclear quadrupole resonance in solid iodine was studied with recording instruments. The recorded pattern of the low-frequency line spreaded in the range of about 80 kc and resolved into five lines at least. The pattern changed considerably when the radiofrequency field was orientated with respect to the crystallographic axes. The structure was explained to be caused by the electron-coupled spin-spin interaction.

## § 1. Introduction

By earlier observations of nuclear quadrupole resonance in solid iodine, two absorption lines were found and their frequencies were reported as 332 Mc and 644 Mc at room temperature.[1][2][3] Recently, Tsukada and one of the present authors (S.K.) revealed that the low-frequency line had a fine structure.[4]* Their experiment was carried out with a method of low-cut amplifier and oscilloscope, which gave a intermediate pattern between a true absorption curve and its derivative curve.

One of the aim of the present work was to study the fine structure of the line precisely with the aid of recording instruments. As a result, not only accurate derivative curves were obtained, but also a dependence of the intensity of absorption upon the direction of the radio-frequency field was clarified.

For the high-frequency line such structure has not yet been observed.[4][5] A precise study for the line was attempted with a recording cavity spectrometer and it was found that the shape of the high-frequency line was slightly asymmetric.

These results are interpreted from the stand point of the electron-coupled spin-spin interaction.

## § 2. Experimental Procedures

a) *Experiment for the low-frequency line.*

The main part of the apparatus was a super-regenerative oscillator with a transmission line tuned circuit, which was essentially the same as that reported proviously.[6] A frequency modulation of small amplitude was applied for the oscillator, and the method of narrow band amplifier and phase-sensitive detector was employed. Since the modulation amplitude was reduced to a fairly small fraction of the line width, the recording meter gave a derivative curve. A block diagram of the circuit is shown in Fig. 1. The modulation frequency was 160 cps and the band width of the amplifier was about 5 cps. The time constant of the recording was about 0.8 sec for most experiments. The frequency sweep at the rate of 17 kc/min was established with a capacitor which was derived by a phono-motor. For a frequency scale, signals of a UHF signal-generator were occasionally recorded.

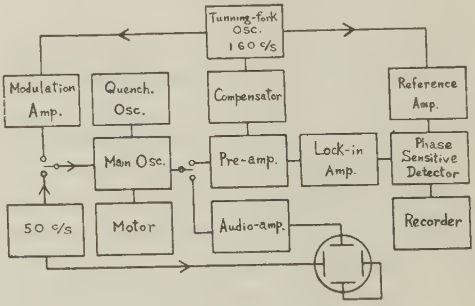

Fig. 1. Block diagram of apparatus.

A single crystal of iodine of about 30 gr was prepared by a method of pointed bottom crucible.[6] The sample was located within the rf coil of two turns of the tuned circuit.

For the determination of the crystallographic

---

* More recently, Watkins and Walker discussed the shape of the absorption line.[5]

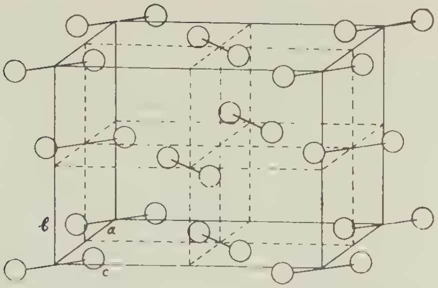

Fig. 2. Crystal structure of iodine.

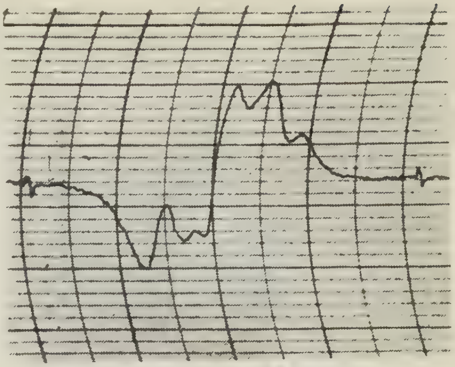

(d) $\theta=45°$.

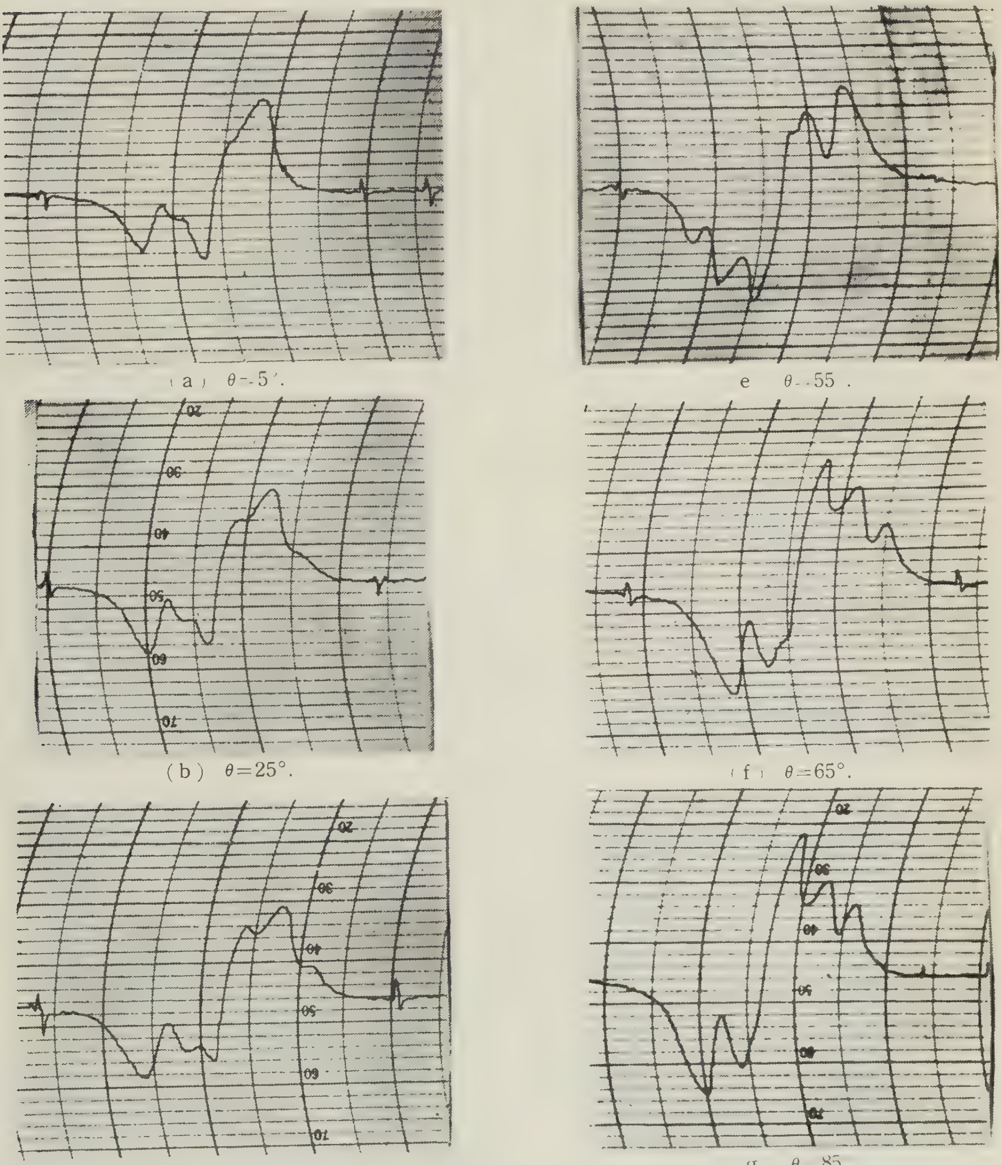

(a) $\theta=5°$.

(e) $\theta=55°$.

(b) $\theta=25°$.

(f) $\theta=65°$.

(c) $\theta=35°$.

(g) $\theta=85°$.

Fig. 3. Derivative curves of low frequency resonance line of $I^{127}$ at seven orientations of the rf field in the $b-c$ plane. $\theta$ is the angle between the rf magnetic field and the crystallographic $c$ axis. Frequency in creases from the left to the right.

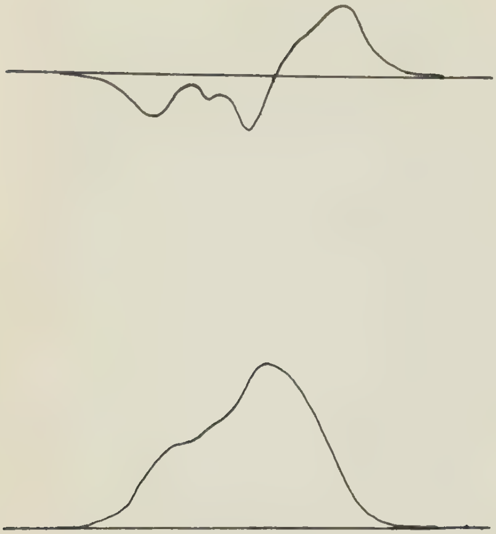

(a) θ=0°.

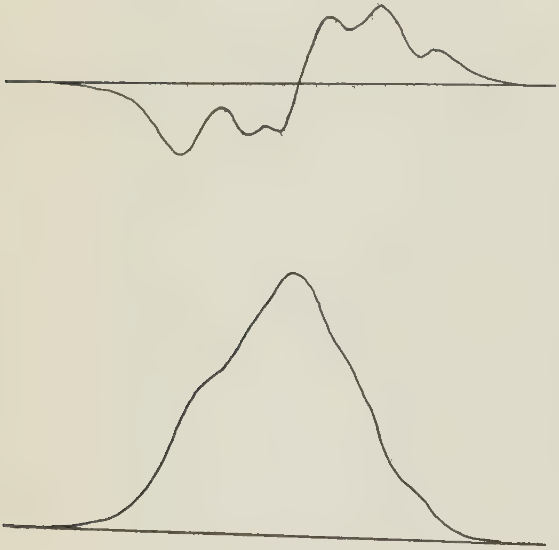

(b) θ=45°.

axes of iodine the Zeeman splittings of the line were used, since the relation between the splitting and the orientation of axes was already known[7]. The effective direction of the rf magnetic field was also determined from the intensities of the Zeeman components by using the relation that the molecules parallel to the rf field did not give rise the absorption. Then the sample was carefully mounted in such a way that the crystallographic *a* axis was perpendicular to the rf field.

Crystalline iodine is known to consist of distinct diatomic molecules which are arranged on layers as shown in Fig. 2.[8]

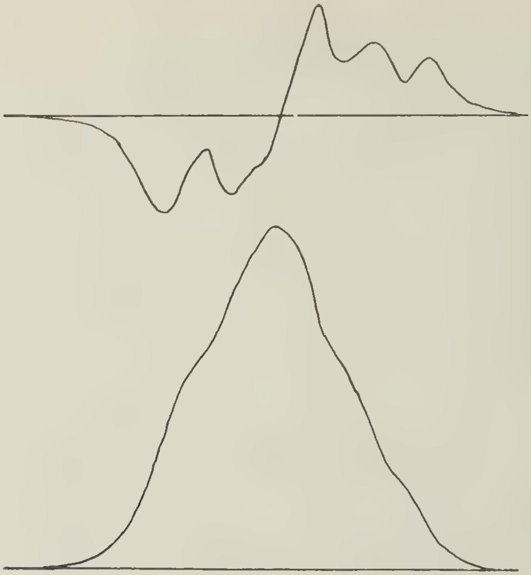

(c) θ=90°.

Fig. 4. Shapes of the low frequency line. The upper curves are the corrected derivative curves. The lower curves are the integrated curves.

Thus, there are two sets of molecules, in each of which molecular bonds are parallel. When the rf field is in the direction perpendicular to the *a* axis or to the *c* axis, it makes same angle against the axes of molecules of the both sets.

b) *Experiment for the high-frequency line.* The main part of the apparatus was the coaxial cavity spectrometer which was described elsewhere.[9] The out put of this apparatus was fed into a set of narrow band amplifier, phase-sensitive detector and recording meter. The frequency sweep of the rate of 20 kc/min was achieved with the stub which was equipped perpendicularly to the modulation stub and derived electrically with a relaxation oscillator of a long period. The sample used for most of the experiments was a polycrystalline block shaped like a doughnut.

## § 3. Results of Experiments

Derivative curves of the low-frequency line of the nuclear quadrupole resonance of iodine were recorded at the various orientations of the rf field in the range between the directions of the *b* axis and the *c* axis of the crystal. One example of the series of recordings are reproduced in Fig. 3, where the angles between the rf field and the *c* axis of 5°, 25°, 35°, 45°, 55°, 65° and 85° correspond to the angles between the rf field and the molecular bonds of 32°08′, 39°37′, 45°04′, 53°05′, 60°50′, 68°57′ and 85°46′ respectively. Two small signals appeared at both ends of the recordings are the frequency markers, the separation of which is 132 kc. The series of recordings illustrates the change of structure of the line clearly. The recorded curve at the angle of 53°05′ shows the most complex structure, which is resolved at least into five lines. Whereas the curve at the angle of 32°08′ is obscure for the 4th and 5th lines and the curve at the angle of 85°46′ for the 3rd line.

The integrated curves were calculated from the recorded derivative curves. The obtained curves which were taken from another set of recordings are reproduced in Fig. 4. The change of height of the integrated curves is mainly due to the fact that the absorption is caused by the perpendicular component of the rf field with respect to the bond axes. The integral curves do not illustrate the structure so clearly as the derivative curves do, but it is evident that the low-frequency resonance line of iodine is composed of several lines.

A recording of the high-frequency line of the nuclear quadrupole resonance of iodine is reproduced in Fig. 5. This recording was taken for the polycrystal of iodine. Although the high-frequency line has less clear structure than that of the low-frequency line, its asymmetric shape suggests that it is also composed of lines.

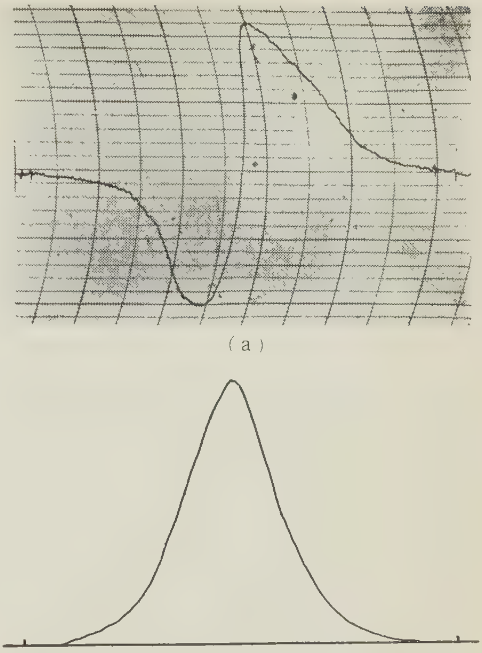

Fig. 5. Shape of the high-frequency line. (a) Recording of derivative curve. (b) Integrated curve.

## § 4. Discussion

It was shown by the present experiment that the nuclear quadrupole resonance line in solid iodine was composed of several lines whose spreading was about 80 kc. It was also known that these lines displayed anomalous Zeeman effect for weak magnetic field.[4)7)] What is the origin of this complex structure of the line?

Multiple resonance lines are often experienced in pure quadrupole spectra. Such multiplet was first observed by Dehmelt on the doublet of iodine resonance in $SnI_4$.[10)] The most complex case was found by Livingston on the multiplet of chlorine resonance in $CCl_4$, which consisted of fifteen lines.[11)] These multiplets were explained from non-equivalent positions of the nuclei in the crystal lattice. Since crystalline iodine has a simple structure as shown in Fig. 2, it can not give rise multiplets due to this effect.

In nuclear magnetic resonances in solid some structures of lines are frequently observed. Pake first observed such structure of the proton resonance in $CaSO_4 2H_2O$.[12)] This structure was explained with the direct nuclear spin-spin interaction. This mechanism is valid for the nuclear quadrupole resonance. However, the splitting due to this effect amounts to about 3 kc for the iodine molecule. It is too small to account for the observed effect.

Recently, nuclear magnetic octapole moment of iodine was discovered by Jaccarino *et al.*[13)] But in solid there are no magnetic field to couple this moment.

Electric hexadecapole interaction of iodine was first taken into account by Wang.[14)] This interaction, however, only shifts the energy levels. Therefore, it can not be the origin of splitting.

In nuclear magnetic resonances in gases and liquids, a multiplet structure due to electron-coupled nuclear spin-spin interaction is known. This effect was first suggested by Ramsey and Purcell for the nuclear magnetic

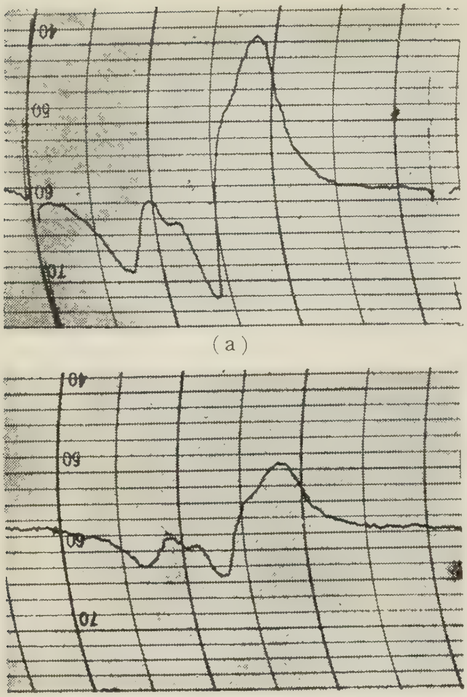

(a)

(b)

Fig. 6. Derivative curves of low-frequency resonance line of $I^{127}$. (a) Rf field was applied to be parallel to the *a* axis. (b) Parallel to the *c* axis.

resonances of gaseous HD.[15)16)] On the other hand, Gutowsky, McCall, Slichter and McNeil[17)] and Hahn and Maxwell[18)] found in liquid a multiplet of the nuclear magnetic resonance in independent experiments. This multiplet was completely explained by Gutowsky *et al* and Hahn and Maxwell[20)] with this indirect spin-spin interaction.[19)] This interaction was expressed by the from $A\boldsymbol{I}_1\cdot\boldsymbol{I}_2$, where $\boldsymbol{I}_1$ and $\boldsymbol{I}_2$ were the spins of chemically non-equivalent nuclei. Between the equivalent nuclei this interaction vanished. In iodine crystal all nuclei are equivalent. But the indirect spin-spin coupling in the case of nuclear quadrupole resonance remains because of the different form of unperturbed part of the Hamiltonian. Itoh calculated this interaction for the solid iodine and obtained the form:

$$A\boldsymbol{I}_1\cdot\boldsymbol{I}_2+B(\boldsymbol{I}_{1x}\cdot\boldsymbol{I}_{2x}+\boldsymbol{I}_{1y}\cdot\boldsymbol{I}_{2y}) \tag{1}$$

where $\boldsymbol{I}_1$ and $\boldsymbol{I}_2$ were the nuclear spins of two iodine atoms. The constants $A$ and $B$ were expressed by

$$A=\frac{2}{\Delta E}\left[\beta\gamma\left\{\frac{8\pi}{3}\alpha|\psi(0)^2+\frac{4}{5}(1-\alpha)<\frac{1}{r^3}>\right\}\right]^2 \tag{2}$$

$$B=\frac{2}{\Delta E}\left[\beta\gamma\left\{\frac{8\pi}{3}\alpha|\psi(0)^2-\frac{2}{5}(1-\alpha)<\frac{1}{r^3}>\right\}\right]^2 \tag{3}$$

where $\alpha$ was the s-character of the I–I bonds, $\beta$ and $\gamma$ were the gyromagnetic ratio of the electron and the nucleus respectively, and $\Delta E$ was the mean energy difference of excited levels from the $^1\Sigma_0$ ground state. When the s-character was about 20% or 30%, this theory yielded a result which agreed with the observed separation of the line.

Itoh and Kambe calculated the pattern of the line taking into account asymmetry parameter of the field gradient tensor. This calculation gave fifteen lines for the transition of $m_z=1/2 \leftrightarrow 3/2$. These fifteen lines would form the observed patterns on account of their finite line width. The comparison between their theory and the present experiment will be given elsewhere.[21)]

Very recently Watkins and Walker found a similar pattern of the resonance line in solid iodine.[5)] Their interpretation is completely same as ours. Thus, the electron-coupled spin-spin interaction seems to be most important for the origin of the observed structure of the resonance line.

The change of pattern which occurs when the orientation of the rf field is varied seems to be unreasonable so far as molecules of iodine are concerned. On molecules the change of inclination of the rf field with respect to the bond axis gives the change of intensity of absorption but not the change of pattern. On iodine crystals, however, a finite value of the asymmetry parameter of the field gradient tensor indicates that the direction of the crystallographic *b* axis which is one of the principal axes of the tensor, say $x$ axis is not equivalent to the direction of another principal axis, say $y$ axis*. This asymmetry may yield the change of pattern. If this interpretation is true, the rf fields parallel to the *a* axis and parallel to the *c* axis will give rise same pattern for the reason that these directions are both perpendicular to the $x$ axis. The intensity of absorption, however, will be different, since these two directions have different inclination with respect to the plane perpendicular to the bond. This expectation was verified by observation. The recordings were obtained for the both directions of the rf field by the apparatus with smaller gain than the case shown in Fig. 3. The pattern at the rf field parallel to the *a* axis excellently agrees with the patterns at the field parallel to the *c* axis which are given in Fig. 6*b* and Fig. 3*a*. As a result the change of pattern can be accounted for the existence of asymmetry of the field gradient tensor.

---

* The $z$ axis is taken along the bond axis. With respect to this coordinate system $\eta=-0.15$[7)].

Such structure can also be observed in solid bromine and ICl.[5] The study of solid bromine will be reported in paper II in this series.

## Acknowledgements

The authers wish to thank Dr. T. Itoh and Dr. K. Kambe for valuable discussions on the origin of the structure of line. They also thank Dr. K. Tsukada and Dr. A. Shimauchi for the aid in construction of the oscillator. The present work was partially supported by the Scientific Research Expenditure of the Ministry of Education.

## References

1) H. G. Dehmelt: Z. Physik **130** (1951) 346.
2) R. V. Pound: Phys. Rev. **82** (1951) 343.
3) T. Kamei: J. Phys. Soc. Japan **7** (1952) 649.
4) S. Kojima and K. Tsukada: J. Phys. Soc. Japan **10** (1955) 591.
5) G. D. Watkins and R. M. Walker: Bull. Am. Phys. Soc. Ser. III **1** (1956) 11.
6) S. Kojima, K. Tsukada, A. Shimauchi and Y. Hinaga: J. Phys. Soc. Japan **9** (1954) 795.
7) K. Tsukada: J. Phys. Soc. Japan **11** (1956) 950.
8) R. W. G. Wykoff: "*Crystal structures*" Int. Sci. Pub. Inc., New York (1940).
9) S. Kojima, A. Shimauchi, S. Hagiwara and Y. Abe: J. Phys. Soc. Japan **10** (1955) 930.
10) H. G. Dehmelt: Z. Physik 130 (1951) 356.
11) R. Livingston: J. Phys. Chem. **57** (1953) 496.
12) G. E. Pake: J. Chem. Phys. **16** (1948) 327.
13) V. Jaccarino, J. G. King, R. A. Satten and H. H. Stroke: Phys. Rev. **94** (1954) 1798.
14) Wang: Phys. Rev. **99** (1955) 566.
15) N. F. Ramsey and E. M. Purcell: Phys. Rev. **85** (1952) 143.
16) N. F. Ramsey: "*Nuclear Moment*" J. Wiley & Sons, Inc., New York (1953).
17) H. S. Gutowsky, D. W. McCall, C. P. Slichter and McNeil: Phys. Rev. **82** (1951) 748.
18) E. L. Hahn and D. E. Maxwell: Phys. Rev. **84** (1952) 1246.
19) H. S. Gutowsky, D. W. McCall and C. P. Slichter: J. Chem. Phys. **21** (1953) 279.
20) E. L. Hahn and D. E. Maxwell: Phys. Rev. **88** (1952) 1070.
21) T. Itoh and K. Kambe: to be published shortly in this Journal.

JOURNAL OF THE PHYSICAL SOCIETY OF JAPAN Vol. 11, No. 9, SEPTEMEB, 1956

# Rotational Intensity Distribution of the OH Band

By Masayoshi NINOMIYA

*Department of Physics, Faculty of Science, University of Tokyo*

(Received February 10, 1956)

The anomaly of the rotational intensity distribution of the OH band excited by vacuum discharge is explained as due to the existence of two unstable excited states of $H_2O$ molecules, through which a radical OH in the excited states ($^2\Sigma$) is produced. It is shown that the intensity distribution of the band excited by electrons with known energies depends upon the energy of impinging electrons in the electron impact experiments. The feature of the distribution of the band intensities from molecules excited by usual electric discharge can be understood as to be determined by the energy distribution of electrons in discharge tubes.

## §1. Introduction

An OH band spectrum $^2\Sigma-{}^2\Pi$ ($\lambda$ 3064 Å) observed in a glow-discharge tube containing water vapor shows anomalous intensity distribution. Besides first intensity maximum, which is expected from thermal equilibrium, this spectrum has a second maximum near $K=19$. Bonhoeffer and Pearson¹⁾ and Oldenberg²⁾ have explained it as follows: Dissociation of a molecule $H_2O$ and excitation of a radical OH occur simultaneously with collision of an electron,

$$\left.\begin{array}{c} H_2O+e\rightarrow OH^*(^2\Sigma)+H+e \\ OH^*\rightarrow OH(^2\Pi)+h\nu \end{array}\right\} \qquad (1)$$

The excited radical OH* receives a rotational moment as a reaction from the dissociated H atom, and consequently many radicals are produced in higher rotational states. Experiments show, however, that the intensity distribution depends considerably on conditions of the excitation³⁾⁴⁾, and we can not explain it considering only molecular collisions within the life time of the excited radical.

There have been two explanations of this dependence of intensity distribution on discharge conditions. The first one is the following: The excited radicals OH* may be formed not only by electron collisions with water molecules, but also by re-excitations of produced radicals OH in ground state. The emitted spectrum from re-excited radicals should have a thermal intensity distribution. Hence the frequency of each kind of OH* formation, and therefore the intensity distribution, may depend on conditions of the discharge. Actually Frost and Oldenberg⁵⁾ have observed ultraviolet absorption spectrum of the normal OH immediately after stop of the electric discharge and the existence of the normal OH in a discharge tube has recently been ascertained also by observations of microwave absorption⁶⁾.

The second explanation is the following: There are two unstable excited states of a $H_2O$ molecule ($^1A_1{}^*$ and $^3B_2$), through which $H_2O$ dissociates into a H atom and an excited OH* radical. The rotational moments received by OH are different according to unstable states of the water molecule, from which OH* is produced. The excitation cross-sections to $^1A_1{}^*$ and $^3B_2$ vary differently with velocities of impinging electrons. Hence according to the variation of the energy distribution of electrons in the discharge tube the intensity distribution of the OH band changes⁷⁾.

Several years ago the author⁸⁾ made an experiment on the electron impact with known velocities for the purpose of clarifying these phenomena. He observed that the intensity distribution of the OH band did not change between 25 and 200 V and concluded that the re-excitation of normal OH radicals was a cause for the variation of the intensity distribution. But later the fact that the band intensity is linearly proportional to the discharge current and the fact that the intensity distribution is independent of the current intensity have been confirmed. Hence it has become difficult to consider that there-excitation of OH would play an important role, because the frequency of the reaction,

$$H_2O\rightarrow H_2O^*\xrightarrow{H}OH^*\xrightarrow{h\nu}OH\,, \qquad (2)$$

may be proportional to the discharge current and for the reaction,

$$H_2O \rightarrow OH,\ OH \rightarrow OH^* \xrightarrow{h\nu} OH\,, \qquad (3)$$

that may not be the same.

In order to solve this inconsistency, the author made an electron-impact experiment in region of lower electron energy than 25 V. In the following results on this experiment and several facts in vacuum discharges will be reported.

## § 2. Experimentals

### *a*) *Vacuum Discharge*

Discharge tubes of 2, 6, 17.5, and 25 mm inner diameters were used. They had two Al-electrodes in their side tubes and a window of quartz-plate. The electrical discharge was maintained by a 50—∞ transformer. Water vapor was let flow continuously from ice, cooled adequately by liquid air, into the discharge tube through a controled leak and was pumped out from the other end of the tube. The pressure of water vapor in the discharge tube was measured by a McLeod gauge and a Pirani gauge.

The $(O, O)$ band of OH was photographed end on by a Hilger E-1 spectrograph. In order to examine the effect of the self-absorption of the emitted quanta due to the normal OH radicals, spectra from a quartz discharge tube were observed end on and from side, but there was no difference between them. So it was unnecessary to consider this effect throughout the present work.

The line intensity was recorded by a Riken-B-type microphotometer and was corrected by the method of intensity marks.

Typical intensity distributions of the $Q_1$-branch in the $(O, O)$ band are presented in Fig. 1, which show two maxima at about $K=2\sim3$ and $K=19$. Characteristics are the same in other branches. In the usual plot of the logarithm of the intensity $I$ devided by the intensity factor $A$ *versus* the rotational energy $E$, the linear relation, indicating the Maxwell-Boltzmann distribution among rotational states, holds only in the region of small rotational quantum numbers, as shown in Fig. 2. For large quantum numbers the curve indicates that more radicals than expected from the equilibrium exist.

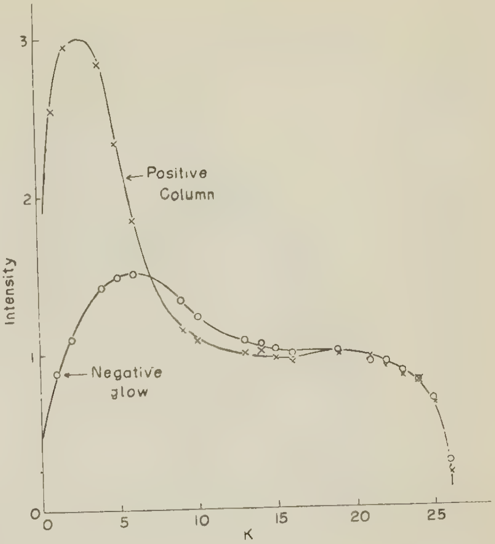

Fig. 1. Rotational intensity distribution of OH $(O, O)$ band excited by glow discharge.

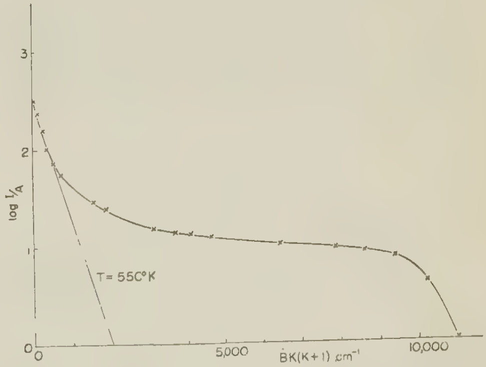

Fig. 2. Logarithmic plot of rotational intensity distribution of OH $(O, O)$ band in a positive column.

The ratio of the heights of two intensity peaks varies with conditions of the discharge. If we take the ratio $X$ of the intensities of $Q_1(2)$ and $Q_1(19)$, which are isolated and not hindered by other lines, $X$ depends on the pressure in the discharge tube as shown in Fig. 3. In Fig. 3 results obtained in the tubes of several diameters are shown. They agree qualitatively with Broida's experimental results.

The radii $R$ of the discharge tubes also have an influence upon $X$, the larger the $R$ the larger the $X$, as shown in Fig. 3. If we take $Rp$ as abscissa instead of $p$ the values of $X$ trend to be on a curve although incompletely.

Intensity distributions depend upon types of the discharge. For example, in Fig. 1 are shown two distributions observed at the positive column and at the negative glow of the same discharge. Horie et al.[3] have also published their results on the positive column, condensed discharge, low voltage arc, and high frequency ring discharge.

The relations between the discharge current and the intensities of $Q_1(2)$ and $Q_1(19)$ are linear in a considerably wide range 20~3000 mA/cm²; and therefore the ratio $X$ does not change with the current intensity (Fig. 4).

In order to see an effect of the re-excitation of free OH radicals on the intensity distribution of the OH band, the author observed the spectra from a tube of 6-mm diameter which coated by KCl or contained Cu pieces, and compared them with that from an ordinary 6–mm tube under same pressure and current. But any difference could not be found. Since KCl and Cu work as catalyser for recombination of OH, it seems that free OH radicals have not an important effect on the intensity distribution.

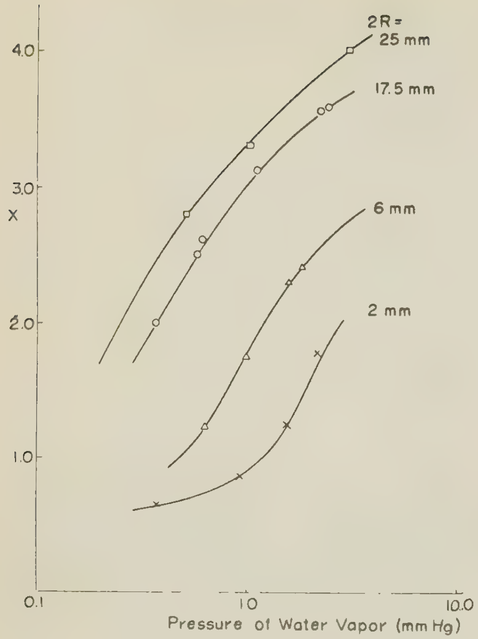

Fig. 3. $X$: ratio of intensities of $Q_1(2)$ and $Q_1(19)$ *versus* pressure in various discharge tubes.

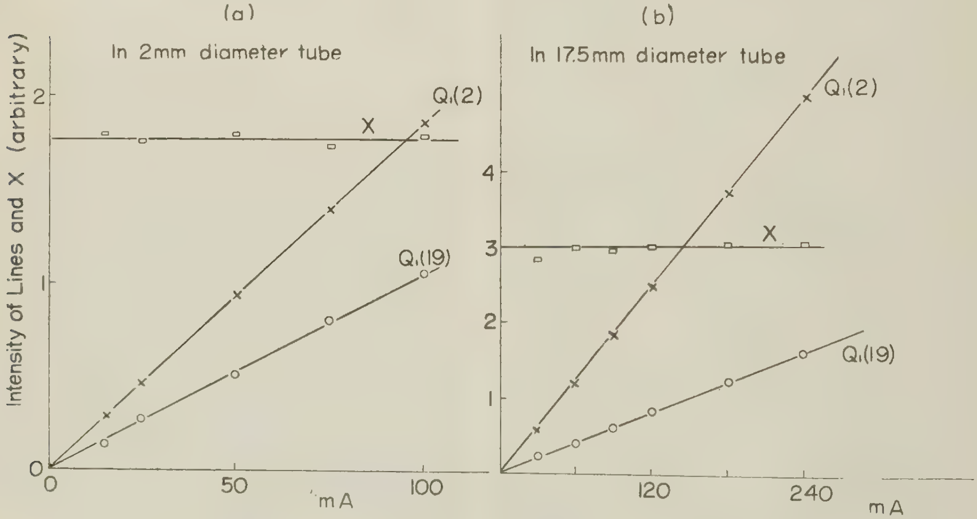

Fig. 4. The intensities of $Q_1(2)$ and $Q_1(19)$ and the ratio $X$ *versus* discharge current.

*b) Electron Impact*

The apparatus used in this experiment had four electrodes and was similar to a tube described by Bernard[10]. There were an oxide-coated Pt-cathod, an accelerating grid, and an equi-potential space between a second grid and a Faraday cage, which were maintained at a desired voltage. In low voltage experiments the voltage of the accelerating electrode was 35 V, and then the electrons were retarded to desired voltages. The pressure in the tube was about 0.01 mmHg, controled by cooling and by a leak cock. The light from the field-free space was photographed by a Hilger E–1, spectrograph; the intensities were measured in the same way as the case of vacuum-discharge experiment. Since a long time of exposure was necessary to get a good spectrogram by E–1, and it was very difficult to keep other experimental conditions than voltage constant for long a time, it was unsuitable for getting the excitation probabilities at various voltages.

The rotational intensity distributions of the $(O, O)$ band of OH excited by 75 V and 15 V electrons are represented in Fig. 5. The intensities at small $K$ of the spectrum by 15 V excitation are higher than those by 75 V.

In Fig. 6 the quantity $X$, intensity of $Q_1(2)$ divided by intensity of $Q_1(19)$, *vs.* the electron voltage is plotted. It shows that $X$ is almost constant over about 20 V, but varies greatly below this voltage.

The relations between the electron current and line intensities were linear. Since the electron current was weak and flow of water vapor was considerably rapid, it was not necessary to consider the existence of OH in the ground state in these experiments.

As is clear from the above two figures, the intensity distribution of OH band excited by the electron impact varies with the electron energy, and the band excited by lower energy electrons has stronger line intensities at low rotational quantum numbers. Therefore it may be natural to consider that there are two unstable excited states of $H_2O$, whose excitation probabilities are different functions of the electron velocity.

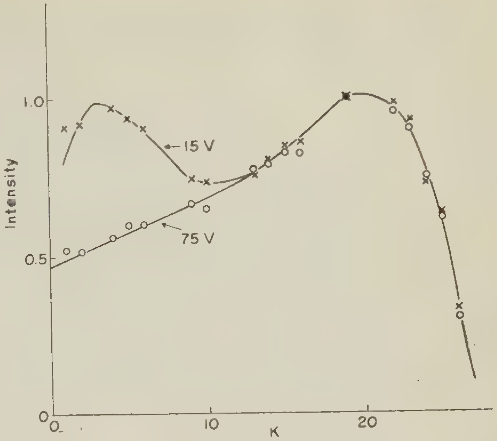

Fig. 5. Rotational intensity distribution of OH band excited by known energy electron.

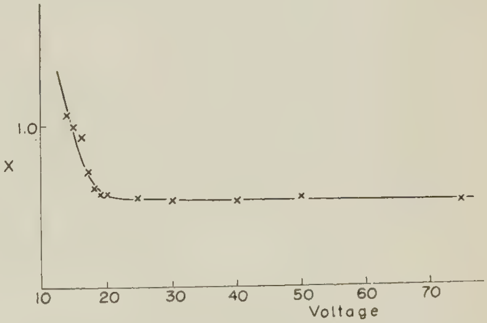

Fig. 6. Relation between $X$ and energy of impinging electron.

## § 3. Discussions

As described in the preceding section, the intensity distributions vary with the impinging electron energy when the potential is lower than 25 V. But at higher potential than this voltage the variation of the intensity distribution with the electron energy is too small to be observed obviously. If we assume according to Niira's theory two unstable excited states, ${}^1A_1{}^*$ and ${}^3B_2$, through which excited OH radicals $({}^2\Sigma)$ are produced, the excitation ${}^1\mathrm{A}_1$ (normal state)$\rightarrow{}^3B_2$ can occur only with the exchange collision of electrons. Then its cross-section decreases rapidly for higher energy of electrons. Therefore at the region higher than 25 V we may observe the intensity distribution excited only by the transition:

$$\mathrm{H_2O}({}^1A_1)\rightarrow\mathrm{H_2O}^*({}^1A_1{}^*)\rightarrow\mathrm{OH}^*({}^2\Sigma)\rightarrow\mathrm{OH}({}^2\Pi)\,.$$

Let us call this distribution $f_a$. Let us further define $f_e=f-f_a$, where $f$ is the distribution at lower energy multiplied by a factor so as to make intensity coinside with that of $f_a$ at $K=19$. Then $f_e$ is practically a normal distribution for the rotational temperature 600°K. The line intensity at $K=19$ for the normal distribution of 600°K are very weak and so the operation adjusting intensities at $K=19$ is reasonable. Hence if we assume that the spectrum for the other transition,

$$\mathrm{H_2O}({}^1A_1)\rightarrow\mathrm{H_2O}^*({}^3B_2)\rightarrow\mathrm{OH}^*({}^2\Sigma)\rightarrow\mathrm{OH}({}^2\Pi)\,,$$

be a normal distribution, we may consider $f_e$ as the distribution for the latter transition.

If we make the same operation in the case of vaccum discharge, $f_d-f_a$ is also practically a normal distribution for rotational temperature 600∼1200°K, when $f_d$ is a distribution excited by the vaccum discharge. Therefore we may consider that the other part of the band than the part due to the transition, ${}^1A_1\rightarrow{}^1A_1{}^*$, has a normal intensity distribution; but it is uncertain whether this part is for the transition, ${}^1A_1\rightarrow{}^3B_2$, only. However, we can show the fact that $X$ becomes 3∼4 when the electron temperature is about 15,000°K under following assumptions: If the variation of cross-sections for the transition ${}^1A_1 \rightarrow {}^3B_2$ with impinging electron energies is similar to that of the exchange collision of helium and the excitation voltage is 10 eV, the same as that of ${}^1A_1 \rightarrow {}^1A_1^*$, and the maximum value of this cross-section is 1/3 compared with that of ${}^1A_1 \rightarrow {}^1A_1^*$. As these assumptions are reasonable, we may consider that the band spectrum observed in a discharge tube comes from two transitions ${}^1A_1 \rightarrow {}^1A_1^*$ and ${}^1A_1 \rightarrow {}^3B_2$.

When slower electrons are abundant, the frequency of the transition ${}^1A_1 \rightarrow {}^3B_2$ is large compared with that of ${}^1A_1 \rightarrow {}^1A_1^*$, and so $X$ becomes large. The dependency of the intensity distribution on the pressure or the radius of tubes as shown in Fig. 3, can be understood as due to the variation of the electron temperature, since it decreases as $Rp$ decreases⁹⁾.

The rotational temperature of $f_d - f_a$ and consequently the position of the intensity maximum for small $K$ change with conditions of the discharge as described by Broida⁴⁾, especially up to 2,000°K and $K_{\max}=8$ in negative glow. These may be understood by considering that the rotational moment of $H_2O$ is maintained at least partly as the rotational moment of OH after dissociation.

The linear relation between the band intensity and the discharge current is natural according to this interpretation.

We can write the ratio of the re-excitation of free OH and the excitation of $H_2O$ as

$$\frac{N_{\mathrm{OH}}}{N_{\mathrm{H_2O}}} \cdot \frac{\int C_{\mathrm{OH}} V \exp.\left(-\frac{eV}{kT_e}\right) dV}{\int C_{\mathrm{H_2O}} V \exp.\left(-\frac{eV}{kT_e}\right) dV},$$

where $N_{\mathrm{OH}}$ and $N_{\mathrm{H_2O}}$ are concentrations of OH and $H_2O$, $C$ are cross-sections of excitation by electrons of energy of eV, and $T_e$ is the electron temperature in discharge. As the excitation voltage of OH is only 4 eV compared with 10 eV of $H_2O$, the above integral for OH is large compared with that for $H_2O$. But under the assumption that $C_{\mathrm{OH}}$ is equal to $C_{\mathrm{H_2O}}$ except movement of the excitation voltage to 4 eV, we can show that the above ratio becomes larger than 0.1 when $N_{\mathrm{OH}}/N_{\mathrm{H_2O}}$ is more than 0.01 and $T_e$ is 15,000°K. According to Frost and Oldenberg the concentration of OH was the order of 0.1% in their intermittent discharge; and we can estimate it below 1% in our experiment; so re-excitation of OH does not play important role. However, as Townes et al.⁶⁾ have observed larger concentration of OH by microwave absorption, this excitation mechanism of OH will become important in case of such a high concentration of OH, if $T_e$ is not very high.

According to Niira OH dissociated from ${}^3B_2$ of $H_2O$ would receive larger rotational moment compared with that from ${}^1A_1^*$; but on the contrary our experiments show that OH from ${}^1A_1^*$ receives larger moment. Whether OH from ${}^1A_1^*$ or from ${}^3B_2$ receives larger moment is determined by the potential surface of $H_2O$ and especially the energy of excitation to ${}^1A_1^*$ and ${}^3B_2$. So more accurate calculations are desired.

## Acknowledgement

The author takes his opportunity with pleasure to express his sincere thanks to Prof. T. Tanaka and Prof. Z. Koana for their interest and encouragement through this work. He wishes also to thank to Prof. K. Niira and Prof. T. Horie for their kind discussions and useful suggestions on this matter.

## References

1) K. F. Bonhoeffer and T. G. Pearson: Zeits. für Phys. Chem. **14** (1931) 3.
2) O. Oldenberg: Phys. Rev. **46** (1934) 210.
3) T. Horie, T. Nagura, and Y. Honda: Busseiron Kenkyu **23** (1950) 18. (in Japanese)
4) H. P. Broida and W. R. Kane: Phys. Rev. **89** (1953) 1053.
5) A. A. Frost and O. Oldenberg: Journ. Chem. Phys. **4** (1936) 642.
6) T. M. Sanders, Jr., A. L. Schawlow, C. C. Doumanis, and C. H. Townes: Journ. Chem. Phys. **22** (1954) 245.
7) K. Niira: J. Phys. Soc. Japan, **4** (1949) 230; **7** (1952), 193.
8) M. Ninomiya: J. Phys. Soc. Japan **4** (1949) 275.
9) L. B. Leob: Fundamental Processes of Electrical Discharge in Gases (John Wiley & Sons, New York, 1939)
10) R. Bernard: Ann. de Phys. **13** (1940) 5.

JOURNAL OF THE PHYSICAL SOCIETY OF JAPAN Vol. 11, No. 9, SEPTEMBER, 1956

# Optical Properties of Magnesium Fluoride Films

By Nobuyoshi MORITA

*Scientific Research Institute, Tokyo*

(Received February 17, 1956)

Transmittance and reflectance of magnesium fluoride films deposited on optical glass and fused quartz are measured as functions of wavelength between 3500Å and 6000Å. Film deposited on fused quartz kept above 240°C shows remarkable scattering as compared with that of film deposited on optical glass under the same condition. This difference is explained by the affinity of film to substrate surface. Index of refraction is determined from wavelength of transmittance extremes and film-thickness. The aging effect can not be observed. The causes of porosity of films are discussed.

## § 1. Introduction

Much work has been done in the past on the optical and structural properties of films prepared by evaporation. The properties of these films often differ from those of bulk material, and moreover there are considerable variations among films deposited under varying conditions. The optical property of magnesium fluoride films is also one of those investigated by several workers[1,2,3,4], and it was found by some of them that the refractive index of the films was considerably smaller than that of bulk material and changed with time. Besides the refractive index of film, optical phenomena such as scattering of light by film are worthy of investigation as useful means of film structure analysis. Some investigators[5,6] have found the existence of some evidence which seems to show that transmittance and reflctance of fluoride films deviate from the values obtained from interference theory. However, no detailed observation has been reported concerning intensity of scattered light by fluoride film.

It is the object of the present investigation to correlate the observed optical properties of films such as scattering loss and refractive index with the film structure, and to survey some factors which might cause the variation of film structure.

## § 2. Experimental

Films were prepared in vaccum by evaporating a known amount of material from molybdenum boat heated by electric current. Metal trap cooled by mixture of dry-ice and alcohol was set between evaporating chamber and 5″ oil diffusion pump to prevent contamination of oil vapor on substrate surface. Optically polished plan-parallel plates of crown glass (BK7) and fused quartz, 1 cm × 1 cm in size and 2 mm in thickness, were used as substrate. In order to know the effects of substrate on film structure, a crown glass and a fused quartz plate were arranged horizontally side by side 25 cm above the molybdenum boat. Film was deposited on a part of substrate in shape of rectangle of 5 mm in width. To degas the adsorbed molecules from the surface, the substrate was heated at 350°C for an hour in high vacuum, then the film was deposited on the substrate keeping it at various temperatures. Temperature of substrate was measured by a copper-constantan thermocouple inserted in a hole drilled at the side of substrate. Film was deposited at the rate between 30Å/sec and 60Å/sec. The pressure during deposition was $5\times10^{-5}$ mmHg or less.

The thickness of the film was measuredby the method of multiple-beam interferometry[7]. The transmittance $T_R$ and reflectance $R_R$ of the coated portion relative to the uncoated portion of the plate were measured by using monochromater and photomultiplier tube. These measurements were carried out within 6 hours after deposition. True transmittance $T$ and reflectance $R$ of the film were calculated by the following formulas[8]

$$R=\frac{R_R 2/(1+r)-(T_R/(1+r))^2}{1-(T_R\cdot r/(1+r))^2}r\,,$$

$$T=T_R\frac{1-Rr}{1+r}\,,$$

where $r$ is the reflection coefficient of the substrate surface. The values of $(1-T-R)$

Table I.

| Specimen | Substrate | Substrate temperature | Film-thickness |
|---|---|---|---|
| G1H | optical glass | 240°C | 596 mμ |
| Q1H | fused quartz | 〃 | 610 〃 |
| G2L | optical glass | room temperature | 533 〃 |
| Q2L | fused quartz | 〃 | 534 〃 |
| G6H | optical glass | 400°C | 829 〃 |
| Q6H | fused quartz | 〃 | 835 〃 |
| G7H | optical glass | 350°C | 1090 〃 |
| Q7H | fused quartz | 〃 | 1095 〃 |
| G10L | optical glass | room temperature | 697 〃 |
| Q10L | fused quartz | 〃 | 687 〃 |

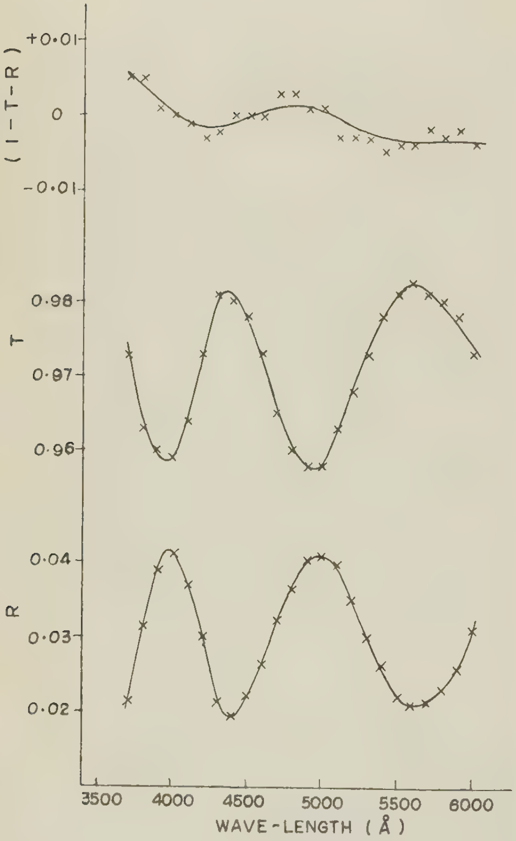

Fig. 1. T, R, (1–T–R) vs. wavelength for the film GIOL.

indicate the relative amount of light lost in the film due to scattering or absorption within the film.

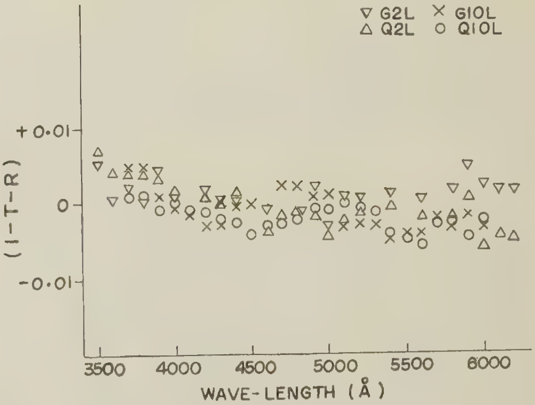

Fig. 2. (1–T–R) vs. wavelength for the films deposited on the substrate kept at room temperature.

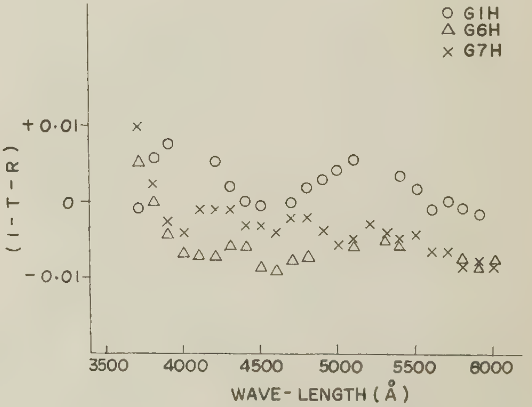

Fig. 3. (1–T–R) vs. wavelength for the films deposited on optical glass kept at higher temperatures.

## § 3. Results

### 1) Loss by scattering in the film

Five pairs of specimens were used to determine the relative amount of light lost in the film. Film-thickness, kind of substrate and its temperature during deposition are shown in Table I. The specimens prepared at the same time have the same number in the table. Typical results observed of $T$, $R$ and (1–$T$–$R$) are shown in Fig. 1. The values of (1–$T$–$R$)

Table II.

| Specimen | Substrate | Substrate temperature | Film-thickness |
|---|---|---|---|
| Q11L | fused quartz | room temperature | 395 mμ |
| Q12H | 〃 | 350°C | 358 〃 |
| G13H | optical glass | 320°C | 470 〃 |
| G15H | 〃 | room temperature | 350 〃 |
| G16H | 〃 | 350°C | 362 〃 |

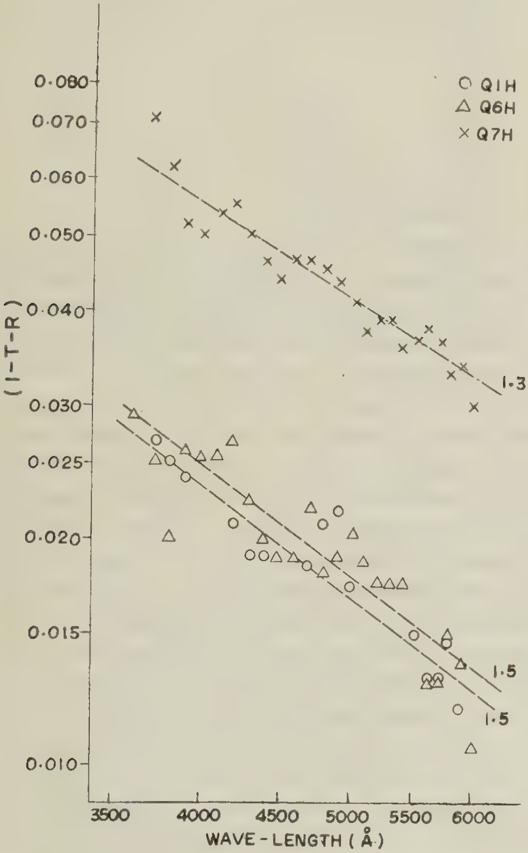

Fig. 4. (1–T–R) vs. wavelength for the films deposited on fused quartz kept at higher temperatures.

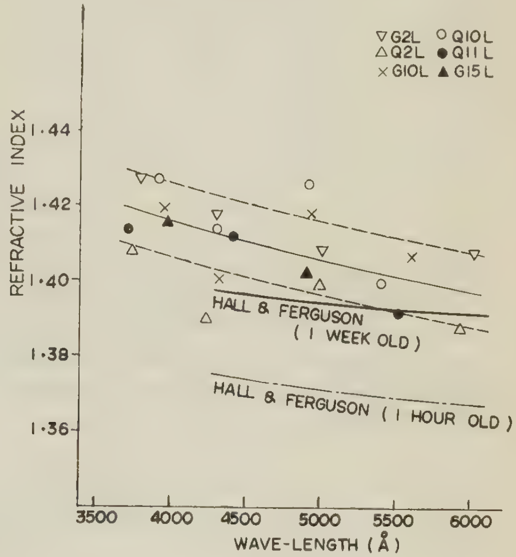

Fig. 5. Refractive index vs. wavelength for the films deposited on substrate kept at room temperature. The results of Hall and Ferguson are also shown.

for various specimens are shown in Figs. 2, 3 and 4. As seen from Fig. 2, the relative amount of light lost in films deposited on substrate kept at room temperature was found to be below 1%, and showed a slight increase towards shorter wavelength and no variation with the kind of substrate. On the other hand, the films deposited at higher substrate temperatures showed marked variation from substrate to substrate. Namely, the values of (1–$T$–$R$) for the films deposited on optical glass were always about 1%, as seen in Fig. 3, but the films deposited on fused quartz showed loss of light of several percent, as shown in Fig. 4. So the loss of light in the film deposited on fused quartz kept at a higher temperature must be due to the scattering of light in the film and not due to the absorption.

### 2) Refractive index of the film

Five specimens in addition to those listed in Table I were used to determine the refractive index of the film. Film-thickness, kind of substrate and substrate temperature of the five specimens are shown in Table II. Transmittance of normally incident light upon the non-absorbing plan-parallel film attains extreme value at the wavelength which satisfies the following condition,

$$n_f t = m\lambda/4 \tag{1}$$

where $t$ is the film-thickness, $n_f$ the refractive index of the film, and $m$ an integer. The refractive indices calculated from Eq. (1) are

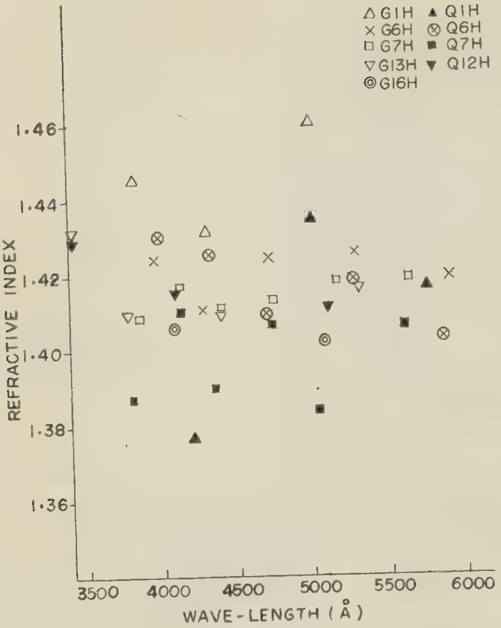

Fig. 6. Refractive index vs. wavelength for the films deposited on substrate kept at higher temperatures.

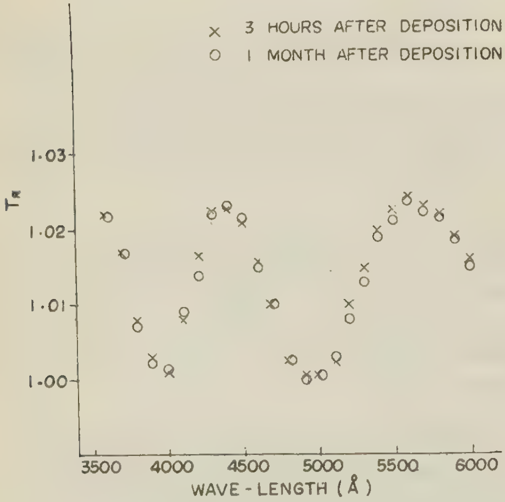

Fig. 7. Transmittance vs. wavelength for the specimen G1OL, measured immediately after deposition and a month after deposition.

shown in Figs. 5 and 6, for the films deposited on substrate kept at room temperature and at higher temperatures, respectively. The latter fluctuates more extensively than the former. This fact must have close connection with the variation of scattering loss among the specimens deposited on substrate kept at higher temperatures.

Table III.

| Specimen | Film-thickness | |
|---|---|---|
| | measured immediately after deposition | measured a month after deposition |
| G1H | 597 mμ | 596 mμ |
| Q1H | 611 〃 | 610 〃 |
| G2L | 533 〃 | 534 〃 |
| Q6H | 835 〃 | 834 〃 |
| G10L | 697 〃 | 693 〃 |
| Q11L | 392 〃 | 386 〃 |
| Q12H | 358 〃 | 360 〃 |
| G14H | 471 〃 | 470 〃 |

### 3) Aging effect

In order to find out if the films change their properties with time, transmittance of the coated plates was measured again a month after deposition, and also the film-thickness was measured at another border of the film strip 5 mm apart from the border at which the film-thickness was measured immediately after deposition. The results are shown in Fig. 7 and Table III. The film-thickness of most specimens in Table III showed no change beyond experimental error with age, except a few specimens which were deposited on substrate kept at room temperature. Transmittance also suffered no change during a month as shown in Fig. 7 for the specimen G10L. Therefore, even if we take the contraction of film-thickness for the specimen G10L into account, the increase of refractive index does not exceed 0.6%, which is smaller than the value 1.8% reported by J. F. Hall and W. F. Ferguson[4].

## § 4. Estimation of the Error of Observation

For the determination of film-thickness, about thirty lines of Fizeau fringes were measured along one border of a film strip 10 mm in length, and these measurements were repeated several times under different seperation between two silvered plates. The error of the mean value of film-thickness thus obtained was less than ±20Å. This error in film-thickness corresponded to an uncertainty between ±0.002 and ±0.008 in refractive index. The slit width of the spectrometer for transmittance measurement was 20Å at the wavelength of 4360Å, and the wavelengths of transmittance extremes were accurate to ±20Å, which corresponded to an uncertainty between ±0.005 and ±0.008 in refractive index. The absolute values of transmittance and reflectance of the films were accurate to within ±0.004, the error being caused by the divergency of nearly parallel beam and the relative position of incident beam to the sensitive surface of photomultiplier tube. Therefore, the values of $(1-T-R)$ were accurate to within ±0.008.

## § 5. Discussion of the Results

The refractive indices obtained from the films deposited on substrate kept at room temperature showed the variation of ±0.01 from the most probable dispersion curve obtained therefrom, as shown in Fig. 5. The results obtained by J. F. Hall and W. F. Ferguson[4] are also plotted on the same figure. They obtained the refractive indices from the values of minimum reflectance. Their films were porous in structure and showed the aging effect, namely in case of thicker films (ca. 8000Å), it took about a week to reach their ultimate indices. J. L. Rood[1] estimated the refractive index as 1.35 from the minimum reflectance value and also reported the aging effect. The cause of discrepancy between these results seems to lie in the difference of film structure. The film deposited on the substrate which had not been degased, and particularly in low vacuum, would often show dark interference color, which is the evidence of lower index of the film. Such films usually are aged and poor in tenacity.[9] In their observations of the structure of antimony films, H. Levinstein[10] found that if the surface was contaminated by grease, the film consisted of aggregates, whilst if a freshly-formed surface was used, the film formed was continuous within the resolution limit of some 100Å. In the present experiment, the substrate surface was outgased sufficiently before deposition by heating it in high vacuum and was protected afterwards from contamination of the vapor of diffusion pump oil by cooled trap. The film obtained showed scarcely any aging effect both in film-thickness and in transmittance vs. wavelength curve, and may be thought not porous. The refractive indices for such films is expected to show the values proper to magnesium fluoride. The values of refractive indices obtained by the author were in agreement within the error of ±0.01 with the values of aged films obtained by F. J. Hall and W. F. Ferguson.

Films deposited on fused quartz kept at a higher temperature scattered several percent of incident light at shorter wavelength. This phenomenon indicates that such a film consists of aggregates, the size of which is of the order of wavelength. G. Bauer[11] calculated the intensity of light scattered by a dielectric sphere of varying diameter as a function of wavelength, and found that Rayleigh's scattering formula can be applied up to the size of 500Å, and for larger particles the exponent of wavelength in the scattering law becomes smaller. In Fig. 4, plotted in double logarithm, the intensity of scattered light is shown to be proportional to $\lambda^{-1.3\sim-1.5}$ instead of $\lambda^{-4}$. Therefore one can estimate the size of aggregates to be considerably larger than 500Å.

Films deposited on substrate kept at higher temperatures showed remarkable difference from substrate to substrate in the scattered light intensity. The fact that whilst the film deposited on optical glass showed no detectable scattering of light even at a thickness of 1 μ, the film deposited on fused quartz aggregated, indicates that the number of nuclei on fused quartz substrate is insufficient to build thick continuous film at a higher temperature. The optical glass used as substrate contained $B_2O_3$, $K_2O$, $Na_2O_3$, and BaO besides 70% of $SiO_2$. These oxides except $SiO_2$ in glass substrate may be thought to bind with fluoride molecules more tightly than $SiO_2$, and so the film deposited on glass does not aggregate. Whilst film deposited on fused quartz kept at room temperature would often crack and peal off from the substrate when the film becomes as thick as 1 μ, film deposited on optical glass at the same time showed no such phenomena. This difference might also be explained by the weak affinity of $SiO_2$ to magnesium fluoride molecules compared with that of other oxides.

As seen from the comparison of Fig. 6 with Fig. 5, the values of refractive indices obtained for the films deposited on substrate kept at higher temperatures showed larger variations than those obtained for the films deposited on substrate kept at room temperature. This fact also indicates that the surface of the film deposited on substrate kept at a higher temperature is considerably rough, and Eq. (1) can not be applied for such a film.

## § 6. Summary

It was found that films deposited on fused quartz kept at a higher temperature showed remarkable scattering, whilst films deposited at the same time on optical glass kept at the same temperature showed no detectable scattering. This could be explained by the tightliness of film to substrate surface.

The refractive indices of magnesium fluoride were obtained from the film-thickness and transmittance extremes, and the dispersion curve was obtained within the error of ±0.01.

The change of film-thickness and transmittance vs. wavelength curve by aging was examined. The aging effect was scarcely detectable in nearly all the specimens. The causes of porous films being deposited which may sinter in age, as reported by some workers, were considered.

In conclusion, the author wishes to express his hearty thanks to Dr. K. Shinohare for his kind encouragement and guidance.

## References

1) J. L. Rood: J. Opt. Soc. Am. **39** (1949) 854.
2) L. G. Schultz and E. J. Scheibner: J. Opt. Soc. Am. **40** (1950) 761.
3) N. Morita: J. Sci. Res. Inst. **46** (1952) 127.
4) J. F. Hall and W. F. Ferguson: J. Opt. Soc. Am. **45** (1955) 74.
5) P. Bousquet: C. R. Acad. Sci. Paris **238** (1954) 1485.
6) C. N. R. S.: J. Phys. et Radium **11** (1950) 305.
7) S. Tolansky: Multiple-Beam Interferometry of Surfaces and Films. Clarendon Press, Oxford, (1948).
8) G. Kuwabara and K. Ishiguro: J. Phys. Soc. Japan **7** (1952) 72.
9) N. Morita, J. Sci. Res. Inst. **44** (1950) 130.
10) H. Levinstein: J. Appl. Phys. **20** (1949) 306.
11) G. Bauer: Ann. d. Physik **19** (1934) 434.

---

JOURNAL OF THE PHYSICAL SOCIETY OF JAPAN Vol. 11, No. 9, SEPTEMBER, 1956

# On the Expansion Formula of Atomic Orbitals in Spherical Harmonics around Another Center

By Yukito TANABE

*Department of Applied Physics, Faculty of Engineering, Tokyo University*

(Received March 26, 1956)

A general formula for the expansion coefficient of one atomic orbital in spherical harmonics around another center, which is useful in numerical evaluation of molecular integrals, is derived and applied to the evaluation of certain two center integrals.

## § 1. Introduction

In the non-empirical treatment of the electronic structure of molecules, one has to evaluate several molecular integrals between atomic orbitals centered around different points of the space, and it is often convenient (especially in the evaluation of many center integrals) to expand an atomic orbital

$$\psi_b = Y_{bl'm'}(\theta_b\phi_b)g(r_b)/r_b$$

centered around point $B$ in the spherical harmonics $Y_{alm}(\theta_a\phi_a)$ around another point $A$. This problem is treated in a well-known paper by Barnett and Coulson[1] and is also discussed by Löwdin[2]. In the former, the expansion coefficients $f_{lm}(r_a|\psi_b)/r_a$ are given for $l'=0, 1, 2$ for the case of analytical (Slater type) radial function $g(r)=r^m \exp(-\alpha r)$ while in the latter a method convenient for numerically given $g(r)$ is investigated. In calculating these expansion coefficients, both of these authors use the method of recurrence relations and hence explicit expressions for the arbitrary $l, l'$ an $g(r)$ have not been stated. It is the purpos of this paper to derive a general expansio formula which would enable us to calculate them directly, and to apply it to the evaluation of certain two center integrals in terms of the coefficient function.

## § 2. The Expansion Formula

$A$ and $B$ are denoted for the two centers, the distance of which is written as $R$. Taking an arbitrary point $P$ in space, we denote the distances $PA$ and $PB$ as $r_a$ and $r_b$ respectively, and set

$$\rho_a = r_a/R\,, \qquad \rho_b = r_b/R\,. \tag{1}$$

The angles $\angle PBA$ and $\angle PAB$ are denoted as $\beta$ and $\alpha$ respectively, while the polar angles of the vector $BA$ are $\omega$, $\psi$. (see Fig. 1)

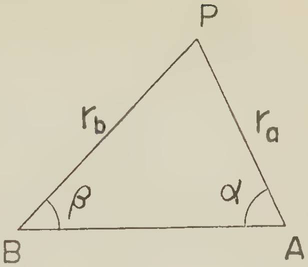

Fig. 1.

As is well known, the atomic orbital function $\psi_b = Y_{bl'm'} g/r_b$* with its center at point $B$ is expanded in the spherical harmonics $Y_{alm}(\theta_a\phi_a)$ around point $A$ under appropriate conditions:

$$Y_{bl'm'} g/r_b = \sum_{lm} Y_{alm} f_{lm}(r_a \,|\, gl'm')/r_a \tag{2}$$

where

$$f_{lm}(r_a \,|\, gl'm')/r_a = \int Y^*{}_{almz} Y_{bl'm'z} g/r_b \, d\Omega_a \tag{3}$$

The suffix $z$ attached to $Y_{alm}$, $Y_{bl'm'}$ in the above expression indicates that these spherical harmonics are "quantized" with respect to $z$ axis.

Now these functions can be written in terms of the spherical harmonics referred to the coordinate system, having the $BA$ direction as $z$ axis (this new $z$ axis is called $z_0$ axis in the following), that is, in terms of the spherical harmonics quantized with respect to $z_0$ axis. If we denote the rotation which brings this new axis to the $z$ axis by $R$, this relation proceeds as follows:

$$Y_{lmz} = RY_{lmz_0} = \sum_{m''} Y_{lm''z_0} D^{(l)}(R)_{m''m}\,, \tag{4}$$

where $D^{(l)}(R)_{m''m}$ is the $m''m$ element of $2l+1$ dimentional irreducible representation matrix of the rotation $R$. If we carry this into the expression (3), we get

$$\sum_{m''m'''} \int Y^*_{alm''z_0} Y_{bl'm'''z_0} g/r_b \times d\Omega_a D^{(l)*}(R)_{m''m} D^{(l')}(R)_{m'''m'}\,. \tag{5}$$

When we use the following property of the representation matrix

$$D^{(l)*}(R)_{m''m} = (-)^{m''+m} D^{(l)}(R)_{-m'',\,-m} \tag{6}$$

and the relation between the Wigner coefficients and the matrix $D$:

$$D^{(l)}(R)_{-m''-m} D^{(l')}(R)_{m'''m'} = \sum_{k\bar{q}q} (l-m''l'm''' \,|\, k\bar{q}) D^{(k)}(R)_{\bar{q}q} \times (kq \,|\, l-m,\, l'm')\,, \tag{7}$$

(5) can further be transformed:

$$\sum_{kq} \int \sum_{m_0} (-)^{m_0} Y^*_{alm_0} Y_{bl'm_0} (l-m\,.\, l'm_0 \,|\, k\,0) \; g/r_b d\Omega_a D^{(k)}(R)_{0q} (-)^m (kq \,|\, l-m,\, l'm')\,. \tag{8}$$

where we have used the fact that the integral is non-vanishing only when $m''=m'''$ (this can be easily seen when we carry out the integration with respect to the azimuthal angle $\phi_a$ around $z_0$ axis.). As is well known, $D^{(k)}(R)_{0q}$ can be expressed in terms of the spherical harmonics whose arguments are $\omega$, $\psi$:

$$D^{(k)}(R)_{0q} = \sqrt{\frac{4\pi}{2k+1}}\, Y_{kq}(\omega\psi) = C^{(k)}_q(\omega\psi) = C^{(k)}_q(\overrightarrow{BA}) = (-)^{(k)} C^{(k)}_q(\overrightarrow{AB})\,. \tag{9}$$

so that we have

$$\sum_{kq} \int (g/r_b) \sum_{m_0} (-)^{m_0} Y^*_{alm_0} Y_{bl'm_0} (l-m_0 l'm_0 \,|\, k_0) \times d\Omega_a C^{(k)}_q(\overrightarrow{BA}) (-)^m (kq \,|\, l-ml'm')\,. \tag{10}$$

Here we change the integration variable from $\alpha' = \pi - \alpha$, $\phi_a$ to $r_b$, $\phi_a$ by means of the following relation

$$\cos\alpha' = (r_b{}^2 - r_a{}^2 - R^2)/2Rr_a \tag{11}$$

then the volume element can be written as

$$d\Omega_a = (r_b/Rr_a) dr_b d\phi_a\,. \tag{12}$$

and therefore, we have, after carrying out the integration with respect to $\phi_a$ and changing the argument of $\Theta_{alm_0}$ from $\cos\alpha'$ to $\cos\alpha$

$$f_{lm}(r_a \,|\, gl'm') = \sum_{kq} (1/R) \int_{|R-r_a|}^{R+r_a} dr_b g(r_b) \times \Big[\sum_m \Theta_{al-m}(\cos\alpha) \Theta_{bl'm}(\cos\beta) (-)^m (l-ml'm \,|\, k_0)\Big] \times (-)^l C^{(k)}_q(\overrightarrow{BA}) (-)^m (kq \,|\, l-ml'm')\,. \tag{13}$$

---

* For the definition of the sphericl harmonics we adopt that of Condon and Shortley[3]:

$$Y(lm) = \Theta(lm)\Phi(m)\,.$$

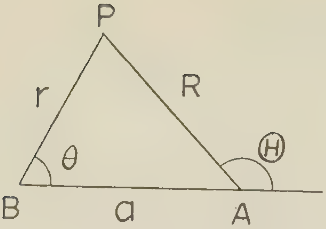

Fig. 2.

Thus we have separated $f$ into two parts, i.e., that depends upon $m, m'$ (the part which relys upon the choice of the quantization axis) and that does not depend upon them. Our purpose is to express explicitly the quantity in the bracket

$$\sum_m \Theta_{alm}(\cos\alpha)\Theta_{bl'm}(\cos\beta)(-)^m(l-ml'm|k_0) \equiv \frac{1}{2}S(ll'k;\rho_a\rho_b) \tag{14}$$

in terms of $\rho_a$ and $\rho_b$.

As can be seen immediately, $S$ vanishes unless we have the so-called triangular condition

$$|l-l'|\leq k\leq l+l' \tag{15}$$

between $l, l'$ and $k$, owing to the Wigner coefficient in the expression (14). Furthermore, consideration on the parity of both sides of the expansion formula shows that it also vanishes unless

$$l+l'+k=2g=\text{even integer} \tag{16}$$

Therefore we set

$$S=(-)^{g-k}\sqrt{(2l+1)(2l'+1)}(l0l'0|k0) \times\rho_a{}^{-l}\rho_b{}^{-l'}\sigma(ll'k;\ \rho_a\rho_b)\,, \tag{17}$$

where the Wigner coefficient $(l0l'0|k0)$ ensures the condition (15) and (16).

As will be shown in the Appendix, the function $\sigma(ll'k;\ \rho_a\rho_b)$ can be expressed in terms of Appell's hypergeometric function of two variables[4)]

$$F_4(\alpha\beta\gamma\gamma';xy)=\sum_{mn}\frac{(\alpha)_{m+n}(\beta)_{m+n}}{(\gamma)_m(\gamma')_n m!n!}x^my^n \tag{18}$$

in the following way

$$\sigma(ll'k;\ \rho_a\rho_b)=(-)^{g-k}\frac{\Pi(l-\frac{1}{2})\Pi(l'-\frac{1}{2})}{g!\,\Pi(l+l'-g-\frac{1}{2})} \times F_4(-g,g-l-l'+\tfrac{1}{2},-l+\tfrac{1}{2},-l'+\tfrac{1}{2};\ \rho_a{}^2\rho_b{}^2) \tag{19}$$

where

$$(\alpha)_m=\Gamma(\alpha+m)/\Gamma(\alpha) \tag{20}$$

and

$$\left.\begin{aligned}\Pi(n-1/2)&=\Gamma(n+1/2)/\Gamma(1/2)\\&=(n-1/2)(n-3/2)\cdot\cdot3/2\cdot1/2\,,\\ \Pi(-n-1/2)&=(-)^n/\Pi(n-1/2)\,,\end{aligned}\right\}(n>0)$$
$$\Pi(-1/2)=1\,. \tag{21}$$

The right hand side of (19) is not an infinite series because $\alpha=-g$ is a negative integer. If we put (19) into (17) and write out the function $F_4$ explicitly,

$$S=\sigma_{ll'k}\rho_a{}^{-l}\rho_b{}^{-l'} \times\sum_{p,q}\frac{\Pi(p+q+k-g-\frac{1}{2})}{(g-p-q)!}\frac{\Pi(l-p-\frac{1}{2})}{p!}\frac{\Pi(l'-q-\frac{1}{2})}{q!} \times\rho_a{}^{2p}\rho_b{}^{2q}\,, \tag{22}$$

where

$$\sigma_{ll'k}=(-)^{g-k}\sqrt{(2l+1)(2l'+1)}(l0l'0|k0)\,, \tag{23}$$

and the summation in (22) is taken over all values of $p$ and $q$ for which the factorial notation has a meaning $(0!=1)$.

Thus we get the following result for the coefficient

$$f_{lm}(r_a|gl'm')=\sum_k(1/2R)\int_{|R-r_a|}^{R+r_a}S(ll'k;\ \rho_a\rho_b) \times g(r_b)dr_b(-)^lC_q^{(k)}(\overrightarrow{BA})(-)^m(kq|l-ml'm')\,. \tag{24}$$

or if we put

$$F_l^{(k)}(r_a|gl')=(1/2R) \times\int_{|R-r_a|}^{R+r_a}\rho_a{}^{-l}\rho_b{}^{-l'}\sigma(ll'k;\ \rho_a\rho_b)g(r_b)dr_b\,, \tag{25}$$

then

$$f=\sum_k F_l^{(k)}(r_a|gl')\sigma_{ll'k} \times(-)^{l'}C_q^{(k)}(\overrightarrow{AB})(-)^m(kq|l-ml'm')\,, \tag{26}$$

or

$$=\sum_k F_l^{(k)}(r_a|gl')(-)^g(2k+1) \times(-)^lC_q^{(k)*}(\overrightarrow{AB})(lm|C_q^{(k)}|l'm')\,. \tag{27}$$

When the $z$ axis coincides with the direction of $\overrightarrow{BA}$ or $\overrightarrow{AB}$,

$$f=\sum_k F_l^{(k)}(r_a|gl')\sigma_{ll'k} \times(-)^l \text{ or } (-)^{l'}(-)^m(k0|l-ml'm)\delta(mm')\,. \tag{28}$$

Comparing this with Löwdin's[2)] definition of $\alpha_k(NLM|ar)$, that is, (Fig. 2)

$$P_L{}^M(\cos\Theta)f_{NL}(R)/R =\sum P_k{}^M(\cos\theta)\alpha_k(NLM|a,r)\,, \tag{29}$$

we find

$$\alpha_k(NLM\,|\,a,r)=(2k+1)\sqrt{\frac{(k-M)!\,(L+M)!}{(k+M)!\,(L-M)!}}$$
$$\times\sum_k(-)^{g-k}(k0L0\,|\,p0)(-)^M(k-MLM\,|\,p0)$$
$$\times F_k^{(p)}(r\,|\,f_{NL}L)/r\,. \tag{30}$$

It is interesting to observe that the general formulae (22), (24) obtained include both the classical Hobson's formula[6] for solid spherical harmonics and the formula recently obtained by Nosawa[7] in the study of the wave potential as its special case.

Some of the elementary properties of the function follow at once from the definition:

1) $S(ll'k;\ \rho_a\rho_b)$ is defined for the values of $\rho_a$ and $\rho_b$ in the region of

$$|\,\rho_a-\rho_b\,|\leq 1\leq\rho_a+\rho_b \tag{31}$$

and is symmetrical with respect to $l\rho_a$ and $l'\rho_b$,

$$S(ll'k;\ \rho_a\rho_b)=S(l'lk;\ \rho_b\rho_a) \tag{32}$$

2) For $\rho_a+\rho_b=1$. it reduces to a constant

$$S(ll'k;\ \rho_a\rho_b)=(-)^{g-k}\sigma_{ll'k}$$

and similarly, for $\rho_a=\rho_b+1$,

$$=(-)^{g-l}\sigma_{ll'k} \tag{33}$$

and also for $\rho_b=\rho_a+1$,

$$=(-)^{g-l'}\sigma_{ll'k}$$

3) If we take a limit, $\rho_b\to1$, $\rho_a\to0$ in such a way that $\lim\,(1-\rho_b)/\rho_a=\cos\alpha$, then

$$S\to(-)^{g-k}\sigma_{ll'k}P_l\,(\cos\alpha)\,.$$

In a similar way if we take $\rho_a\to1$, $\rho_b\to0$ and at the same time $\lim\,(1-\rho_a)/\rho_b=\cos\beta$

$$\to(-)^{g-k}\sigma_{ll'k}P_{l'}\,(\cos\beta)\,, \tag{34}$$

and if $\rho_a\to\infty$, $\rho_b\to\infty$ in such a way $\rho_b-\rho_a=\cos\theta$

$$\to(-)^{g-l'}\sigma_{ll'k}P_k\,(\cos\theta)\,.$$

## § 3. Evaluation of Certain Two Center Integrals.

Now we turn to the evaluation of certain two center integrals in terms of the $S$ function. The method is not new, being essentially that of Barnett-Coulson and Lowdin.[2] The purpose of this section, therefore, is to show how all these integrals can be concisely expressed in terms of $S$ functions.

a) The Overlap Integrals

The overlap integrals betweens $\psi_a=Y_{alm}f_a/r_a$ and $\psi_b=Y_{bl'm'}g_b/r_b$ can readily be calculated from (24):

$$\int\psi_a{}^*\psi_b d\tau$$
$$=\sum_k(1/2R)\iint f^*(r_a)g(r_b)S(ll'k;\rho_a\rho_b)dr_adr_b$$
$$(-)^lC_q^{(k)}(\overrightarrow{BA})(-)^m(kq\,|\,l-ml'm')\,. \tag{35}$$

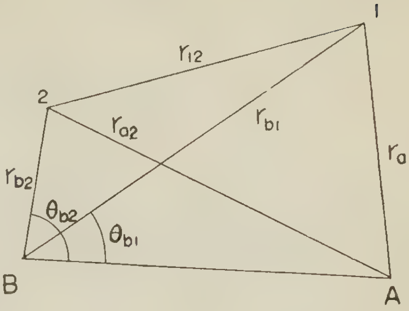

Fig. 3.

b) The Coulomb Integrals

The following relation can easily be established in the same way as (10).

$$(l_am_al_bm_b\,|\,1/r_{12}\,|\,l_a'm_a'l_b'm_b')$$
$$=\sum_{k\lambda_1\lambda_2}J_k(l_al_a'\lambda_1\,,\,l_bl_b'\lambda_2)(-)^{l_a+l_a'}C_q^{(k)}(\overrightarrow{BA})$$
$$(-)^{m_a}(l_a-m_al_a'm_a'\,|\,\lambda_1\mu_1)$$
$$(-)^{m_b}(l_b-m_bl_b'm_b'\,|\,\lambda_2\mu_2)$$
$$\times(\lambda_1\mu_1\lambda_2\mu_2\,|\,kq) \tag{36}$$

where

$$J_k(l_al_a'\lambda_1\,,\,l_bl_b'\lambda_2)$$
$$=\sum_{\substack{m_am_a'\\m_bm_b'}}(l_am_al_bm_b\,|\,1/r_{12}\,|\,l_a'm_a'l_b'm_b')$$
$$(-)^{m_a}(l_a-m_al_a'm_a'\,|\,\lambda_1\mu_1)$$
$$(-)^{m_b}(l_b-m_bl_b'm_b'\,|\,\lambda_2\mu_2)$$
$$\times(\lambda_1\mu_1\lambda_2\mu_2\,|\,k0)(-)^{l_a+l_a'}\,, \tag{37}$$

and the axis of quantization is in the direction of $\overrightarrow{BA}$ in the latter.

In order to evaluate this we expand $1/r_{12}$ in the following way. (For the notations, see Fig. 3)

$$1/r_{12}=\sum_{lm}(-)^mC_m{}^{(l)}(\theta_{b1}\,,\,\phi_{b1})$$
$$\times C_{-m}{}^{(l)}(\theta_{b2}\,,\,\phi_{b2})r_<{}^l/r_>{}^{l+1}$$

$r_<$, $r_>$ being smaller and larger respectively of $r_{b_1}$ and $r_{b_2}$. Then we have

$$J_k = \sum_{\substack{m_a m_a' \\ m_b m_b' \\ lm}} \int dr_{a_1} f^* f' \int d\Omega_1 Y^*_{l_a m_a} (-)^m C_m^{(l)}(\theta_{b_1}\phi_{b_1}) Y_{l_a' m_a'} (-)^{m_a} (l_a - m_a l_a' m_a' \mid \lambda_1 \mu_1)$$

$$\times \int dr_{b_2} g^* g' (r_<^{\,l} / r_>^{\,l+1}) \int d\Omega_2 Y^*_{l_b m_b} C_{-m}^{(l)}(\theta_{b_2}\phi_{b_2}) Y_{l_b' m_b'} (-)^{m_b} (l_b - m_b l_b' m_b' \mid \lambda_2 \mu_2)$$

$$\times (-)^{l_a + l_a'} (\lambda_1 \mu_1 \,,\ \lambda_2 \mu_2 \mid k0) \,. \tag{39}$$

If we carry the integration with respect to $\Omega_2$ and use the following relation

$$\sqrt{2l+1}\,(l_b m_b \mid C_{-m}^{(l)} \mid l_b' m_b') = (-)^{l_b - l - m_b - m} (l_b \| C^{(l)} \| l_b')^* (l_b - m_b l_b' m_b' \mid lm) \tag{40}$$

we get,

$$\sum_{m_a m_a'} \int dr_{a_1} f^* f' \int d\Omega_1 Y^*_{l_a m_a} Y_{l_a' m_a'} C_{\mu_2}^{(\lambda_2)}(\theta_{b_1}\phi_{b_1}) (-)^{m_a} (l_a - m_a l_a' m_a' \mid \lambda_1 \mu_1)$$

$$\times \int dr_{b_2} g^* g' (r_<^{\,\lambda_2} / r_>^{\,\lambda_2+1}) (-)^{\lambda_2 + l_b} (l_b \| C^{(\lambda_2)} \| l_b') / \sqrt{2\lambda_2 + 1}$$

$$\times (\lambda_1 \mu_1 \lambda_2 \mu_2 \mid k0) (-)^{l_a + l_a'} \,. \tag{41}$$

We then use the following formula between three spherical harmonics

$$Y^*_{l_a m_a} Y_{l_a' m_a'} = \sum_{lm} Y_{lm} (-)^{m_a - l_a'} (l_a \| C^{(l)} \| l_a') (l_a - m_a l_a' m_a' \mid lm) / \sqrt{4\pi} \,, \tag{42}$$

for the product of spherical harmonics in (41) and carry out the summation over $m_a m_a'$. The only nonvanishing terms are those for which $(lm) = (\lambda_1 \mu_1)$. Therefore

$$\sum_{\mu_1 \mu_2} \int dr_{a_1} f^* f' \int d\Omega_1 Y_{\lambda_1 \mu_1}(\theta_{a_1}\phi_{a_1}) Y_{\lambda_2 \mu_2}(\theta_{b_1}\phi_{b_1}) (\lambda_1 \mu_1 \lambda_2 \mu_2 \mid k0)$$

$$\times \int dr_{b_2} g^* g' (r_<^{\,\lambda_2} / r_2^{\,\lambda_2+1}) (-)^{\lambda_2 + l_b - l_a'} (-)^{l_a + l_a'} / (2\lambda_2 + 1)$$

$$\times (l_a \| C^{(\lambda_1)} \| l_a') (l_b \| C^{(\lambda_2)} \| l_b') \,, \tag{43}$$

Finally we obtain the following result from (14).

$$J_k = (-)^{l_a + l_b + k} (l_a \| C^{(\lambda_1} \| l_a') (l_b \| C^{(\lambda_2)} \| l_b') / 2R$$

$$\times \int_0^\infty dr_{a_1} f^* f' \int dr_{b_1} S(\lambda_1 \lambda_2 k;\ r_{a_1}/R \,,\ r_{b_1}/R) (r_{b_1}/r_{a_1})$$

$$\times \int_0^\infty dr_{b_2} g^* g' (r_<^{\,\lambda_2} / r_>^{\,\lambda_2+1}) / (2\lambda_2 + 1) \tag{44}$$

As is clear from the above expression, $J_k$ vanishes unless all of the triads $l_a l_a' \lambda_1$, $l_b l_b' \lambda_2$, $\lambda_1 \lambda_2 k$ satisfy (15) and (16).

Similar results would have been obtained if we used the expansion formula of $1/r_{12}$ with respect to $A$ instead of (38).

### c) Hybrid Integrals

Again we set

$$(l_a m_a l_b m_b \mid 1/r_{12} \mid l_b' m_b' l_b'' m_b'') = \sum_{k \lambda_1 \lambda_2} L_k (l_a l_b' \lambda_1 \,,\ l_b l_b'' \lambda_2) (-)^{l_a} C_q^{(k)} (\overrightarrow{BA})$$

$$(-)^{m_a} (l_a - m_a l_b' m_b' \mid \lambda_1 \mu_1) (-)^{m_b} (l_b - m_b l_b'' m_b'' \mid \lambda_2 \mu_2) (\lambda_1 \mu_1 \lambda_2 \mu_2 \mid kq) \,, \tag{45}$$

and calculate

$$L_k = \sum_{m_a m_b m_b' m_b''} (l_a m_a l_b m_b \mid 1/r_{12} \mid l_b' m_b' l_b'' m_b'')$$

$$\times (-)^{m_a} (l_a - m_a l_b' m_b' \mid \lambda_1 \mu_1) (-)^{m_b} (l_b - m_b l_b'' m_b'' \mid \lambda_2 \mu_2) (\lambda_1 \mu_1 \lambda_2 \mu_2 \mid k0) (-)^{l_a} \tag{46}$$

---

* $(l \| C^{(k)} | \, l') = (-)^{g-l} \sqrt{(2l+1)(2l'+1)} \, C_{ll'k}/2$, $\quad l + l' + k = 2g =$ even integer.

$C_{ll'k} = \int_0^1 P_l(\cos\omega) P_{l'}(\cos\omega) P_k(\cos\omega) \, d(\cos\omega)$ .

Here it is convenient to use the expansion of $1/r_{12}$ with respect to the center B. The result is

$$L_k=(-)^{l_b+\lambda_2}(l_b\|C^{(\lambda_2)}\|l_b'')/2R\sum_l\int_0^\infty dr_{a_1}f^*(r_{a_1})\int dr_{b_1}g'(r_{b_1})S(l_alk;\, r_{a_1}/R\, r_{b_1}/R)$$

$$\times\int_0^\infty dr_{b_2}g^*g''(r_<^{\lambda_2}/r_>^{\lambda_2+1})/\sqrt{2\lambda_2+1}$$

$$\times\{(l\|C^{(\lambda_2)}\|l_b')/\sqrt{2l+1}\}(l_a\,,\, l_b'\lambda_2(l)k\,|\,l_al_b'(\lambda_1)\lambda_2k)\,, \tag{47}$$

where $l_al_b'\lambda_1$, $\lambda_1\lambda_2k$ must satisfy (15), while $l_al_b''\lambda_2$ must satisfy both (15) and (16), and $l_a+l_b'+k+\lambda_2$ must be an even integer in order that $L_k$ does not vanish. The transformation matrix $(l_a\,,\, l_b'\lambda_2(l)k|l_al_b'(\lambda_1)\lambda_2k)$ can be written in terms of Racah coefficient in the following way[8]

$$\sqrt{(2l+1)(2\lambda_1+1)}\,W(l_al_b'k\lambda_2;\,\lambda_1l) \tag{48}$$

and is simply evaluated.

The author wishes to thank Professors T. Inui and M. Kotani for their kind advice and encouragement, and he is also indebted to Professor S. Sueoka who read and criticized the manuscript.

## Appendix

Because the proof the author has obtained for the formula (22) is a little awkward, though elementary, only an outline of it shall be sketched here.

If we express $\Theta(lm)$ on the right hand side of (14) by linear combination of the product of $\Theta(l-1\,,m')$ and $\Theta(1\,,\sigma)$ by means of the formula

$$\Theta(lm)=\sum_{m'\sigma}\Theta(l-1.m')\Theta(1\sigma)(l-1m'1\sigma\,|\,lm)\sqrt{2(2l+1)/3l} \tag{A.1}$$

we get the following recurrence formula for $S(ll'k;\,\rho_a\rho_b)$ (to simplify this we write it as $S(ll'k)$ below)

$$S(ll'k)=\sum_{k'}\{\cos\alpha S(l-1l'k')(k'0\,|\,0\,|\,k0)-\sqrt{2/k'(k'+1)}\sin\alpha DS(l-1l'k')(k'1\,1-1\,|\,k0)\}$$

$$\times\sqrt{(2l+1)/l}(l-1\,l'(k')\,1\,k\,|\,l-1\,1\,(l)l'k$$

$$-\sqrt{2/k(k+1)}\sum_{k'}(\cot\alpha+\cot\beta)\sin\alpha S(l-1\,lk')(k'\,|\,k)(k1\,1-1\,|\,k0)$$

$$\times\sqrt{(2l+1)}/l\,(l-1\,l'(k)1\,k\,|\,l-1\,1\,(l)l'k) \tag{A.2}$$

where

$$(k+1\,|\,k)=2[(g-l+1)(g-l')(g+\tfrac{1}{2})(g-k-\tfrac{1}{2})/(2k+1)(2k+3)]^{1/2}\,, \tag{A.3}$$

$$(k-1\,|\,k)=2[(g-l+\tfrac{1}{2})(g-l'-\tfrac{1}{2})g(g-k)/(2k-1)(2k+1)]^{1/2}\,,$$

and

$$\cos\alpha=(\rho_a^2-\rho_b^2+1)/2\rho_a\,,\quad \cos\beta=(\rho_b^2-\rho_a^2+1)/2\rho_a \tag{A.4}$$

and

$$\rho_a\sin\alpha D=(\rho_b^2-\rho_a^2+1)/2\cdot\rho_a\frac{\partial}{\partial\rho_a}-(\rho_a^2-\rho_b^2+1)/2\cdot\rho_b\frac{\partial}{\partial\rho_b}$$

$$\rho_a(\cot\alpha+\cot\beta)\sin\alpha=1 \tag{A.5}$$

This recurrence formula for $S(ll'k)$ leads to the following formula for $\sigma(ll'k)$

$$\sigma(ll'k)=\left\{(\rho_a^2-\rho_b^2-1)\left[\rho_a\frac{\partial}{\partial\rho_a}-l+1\right]+(\rho_a^2-\rho_b^2+1)\left[\rho_b\frac{\partial}{\partial\rho_b}-l'-k-1\right]\right\}\sigma(l-1l'k+1)$$

$$\times(g-k)\left(g-l+\frac{1}{2}\right)\Big/l(k+1)(2k+1)$$

$$+\left\{(\rho_a{}^2-\rho_b{}^2-1)\left[\rho_a\frac{\partial}{\partial\rho_b}-l+1\right]+(\rho_a{}^2-\rho_b{}^2+1)\left[\rho_b\frac{\partial}{\partial\rho_b}-l'+k\right]\right\}\sigma(l-1l'k-1)$$

$$\times\left(g+\frac{1}{2}\right)(g-l')/lk(2k+1)$$

$$+\{(\sigma\,|\,l-1l'k+1)+\sigma(l-1l'k-1)\}$$

$$\times 4(g-k)\left(g-l+\frac{1}{2}\right)\left(g+\frac{1}{2}\right)(g-l')/lk(k+1)(2k+1) \qquad \text{(A.6)}$$

Now if we could find out the expression for $\sigma(0l'l')$ for an arbitrary $l'$, all $\sigma(ll'k)$ for which the triad $(ll'k)$ satisfies (15) and (16) would be determined by means of the above formula. As is directly verified by substituting, $\sigma(ll'k)$ given by (19) satisfies (A6) and reduces to the following expression when we set $l=0$ $k=l'$:

$$\sigma(0l'l')=\sum_{pq}(-)^p\frac{\Pi\,(p+q-\frac{1}{2})\,\Pi\,(l'-q-\frac{1}{2})}{(l'-p-q)!\;p!q!\;\Pi\,(p-\frac{1}{2})}\rho_a{}^{2p}\rho_b{}^{2q}$$

which is nothing but $\rho_b{}^{l'}P_{l'}(\cos\beta)=\rho_b{}^{l'}S(0l'l';\,\rho_a\rho_b)/\sigma_{0l'l'}$ expanded to the powers of $\rho_a$ and $\rho_b$ as is shown below.

Because, by definition

$$P_{l'}(x)=\frac{1}{2^{l'}l'!}\sum_r(-)^{l'-r}\binom{l'}{r}\frac{(2r)!}{(2r-l')!}x^{2r-l'}$$

and if we set

$$x=(\rho_b{}^2-\rho_a{}^2+1)/2\rho_b$$

$$P_{l'}=\frac{1}{2^{l'}l'!}\sum_{rmn}(-)^{l'-r}\binom{l'}{r}\frac{(2r)!}{(2r-l')!}(-)^n\frac{(2r-l')!}{m!n!(2r-l'-m-n)!}\frac{\rho_b{}^{2m}\rho_a{}^{2n}}{(2\rho_b)^{2r-l'}}$$

or

$$=\frac{\rho_b{}^{-l'}}{l'!}\sum_{rpq}(-)^{l'-r}\binom{l'}{r}\frac{(2r)!}{p!(p+r-l')!(r-p-q)!}\frac{(-)^p}{2^{2r}}\rho_a{}^{2p}\rho_b{}^{2q}$$

while we have

$$\frac{1}{l'!}\sum_r(-)^{l'-r}\binom{l'}{r}\frac{(2r)!}{(r+q-l')!\;(r-p-q)!}\frac{1}{2^{2r}}=\sum_r(-)^{l'-r}\frac{\Pi(r-\frac{1}{2})}{(l'-r)!\;(r+q-l')!\;(r-p-q)!}$$

$$=(-)^q\sum_r(-)^s\frac{\Pi\,(s+l'-q-\frac{1}{2})}{s!\;(q-s)!\;(s+l'-p-2q)!}=(-)^q\frac{\Pi\,(-p-\frac{1}{2})\,\Pi\,(l'-q-\frac{1}{2})}{q!\;(l'-p-q)!\;\Pi\,(-p-q-\frac{1}{2})}$$

(by Van der Monde's theorem)

$$=\frac{\Pi\,(p+q-\frac{1}{2})\,\Pi\,(l'-q-\frac{1}{2})}{(l'-p-q)!\;q!\;\Pi\,(p-\frac{1}{2})},$$

so that finally

$$\rho_b{}^{l'}P_{l'}=\sum_{pq}(-)^p\frac{\Pi\,(p+q-\frac{1}{2})\,\Pi\,(l'-q-\frac{1}{2})}{(l'-p-q)!\;p!\;q!\;\Pi\,(p-\frac{1}{2})}\rho_a{}^{2p}\rho_b{}^{2q}$$

and this coincides with (A7).

Thus (19) or (22) is proven.

Finally it can be remarked that though the recurrence formula (A6) is not convenient in actual calculation of $\sigma(ll'k)$ of higher $l$, much simpler relations can be derived from the recurrence formulae which hold for the hypergeometric function $F_4(\alpha\beta\gamma\gamma';\,xy)$.

---

## References

1) M. P. Barnett and C. A. Coulson: Phil. Trans. Roy. Soc. London **243** (1951) 221.

2) P. O. Löwdin: A Theoretical Investigation into Some Properties of Ionic Crystals, thesis (Almquist and Wicksell, Uppsala, 1948).

3) E. U. Condon and G. H. Shortley: The Theory of Atomic Spectra (Cambridge, 1935).

4) P. Appell and J. Kampé de Feriet: Fonctions Hypergéométriques et Hypersphériques (Gauthier-Villars, Paris, 1926).

5) G. Racah: Phys. Rev. **62** (1942) 438.

6) E. W. Hobson: The Theory of Spherical and Ellipsoidal Harmonics (Cambridge, 1931).

7) T. Nozawa: Busseiron Kenkyu (in Japanese) **78** (1954) 75.

8) G. Racah: Phys. Rev. **63** (1943) 368.

JOURNAL OF THE PHYSICAL SOCIETY OF JAPAN Vol. 11, No. 9, SEPTEMBER 1956

# The Flow due to Impulsive Motion of a Wedge, II

By Akira SAKURAI*

*Department of Applied Mathematics*
*Weizmann Institute of Science, Rehovot, Israel*

(Received April 14, 1956)

As a continuation of the previous study on the impulsive motion of an advancing wedge (J. Phys. Soc. Japan **10**, 221 (1955)), we now consider the case in which the wedge is receding. The general features of both cases are similar. We now have rarefaction waves instead of the shock waves which played a fundamental role in the previous paper. The two limiting cases of small, and almost blunt, vertex angles are discussed analytically. The former is essentially the same as the corresponding case of the advancing wedge. On the other hand, the latter presents new features.

## § 1. Introduction

In a previous paper[1)], the author studied the transient flow in a gas generated by a wedge which was moved instantaneously from rest to a constant velocity $u_0$ in the direction of negative $X$-axis as shown in Fig. 1a, and found that this flow was similar to that in the case of diffraction of a shock wave by the wedge.

The purpose of the present paper is to consider a closely related problem, namely the case of a wedge receding to the direction of the $X$-axis (Fig. 1b). This problem is very similar to the first one. Rarefaction waves, and in particular the centred wave, play a fundamental role in the problem as did the shock waves in the previous problem.

After discussions on some properties of the flow field in § 2, two limiting cases of $\delta_1=\delta_2=\delta\ll 1$ and $\delta_1$, $\delta_2\approx\pi/2$ are studied analytically in § 3 and § 4 respectively.

## § 2. Some Properties of Flow Field

Just as in the first paper[1)], the concept of the pseudo-steady state of the flow due to lack of a particular scale to measure time or space is also useful in the present problem, and the flow field can be represented by the two independent variables $X/t$ and $Y/t$ only.

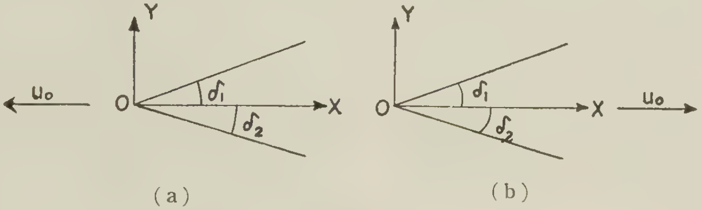

(a) (b)

Fig. 1.

By considerations similar to those in § 1 of the first paper[1)], we may show that the part of the wedge, where the effect from the apex O does not reach, behaves as if an infinite plane rigid wall moved obliquely, and the flow generated by this wall is the same as that generated by the wall receding normal to its surface at a constant velocity $u_0 \sin\delta_1$ for the upper surface, and $u_0 \sin\delta_2$ for the lower surface, respectively.

The flow due to the wall receding normal to the surface with a velocity $u_p$ is well known and can be represented by centred rarefaction waves[2)]: the front of the rarefaction wave propagates in the direction of negative $\xi$-axis with the sound velocity $c_0$ of the undisturbed region (Fig. 2; the $\xi$-axis is fixed in space, and $\xi=0$ is coincident with the initial position of the wall); the distributions of the particle velocity $u$, the sound velocity $c$, the pressure $p$ and the density $\rho$ behind the front of the wave are represented by

---

* Weizmann Fellow, on leave from Tokyo Electrical Engineering College.

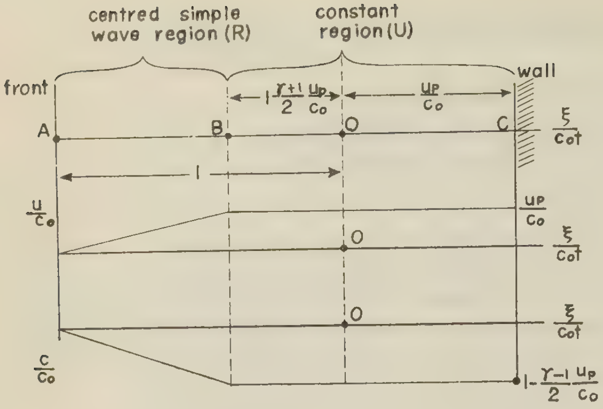

Fig. 2

$$\frac{u}{c_0}=\begin{cases}\dfrac{2}{\gamma+1}\left(1+\dfrac{\xi}{c_0t}\right), \\ \qquad -\left(1-\dfrac{\gamma+1}{2}\dfrac{u_p}{c_0}\right)\geqq\dfrac{\xi}{c_0t}\geqq-1, \\ \dfrac{u_p}{c_0}\quad, \\ \qquad \dfrac{u_p}{c_0}\geqq\dfrac{\xi}{c_0t}\geqq-\left(1-\dfrac{\gamma+1}{2}\dfrac{u_p}{c_0}\right),\end{cases} \tag{1}$$

$$\frac{c}{c_0}=1-\frac{\gamma-1}{2}\frac{u}{c_0}\geqq0,$$

$$\frac{p}{p_0}=\left(\frac{c}{c_0}\right)^{\frac{2\gamma}{\gamma-1}},\quad \frac{\rho}{\rho_0}=\left(\frac{c}{c_0}\right)^{\frac{2}{\gamma-1}}, \tag{2}$$

where $p_0$, $\rho_0$ are quantities of the undisturbed state and $\gamma$ is the ratio of the specific heats.

These relations are illustrated in Fig. 2.

For the velocity $u_p>2c_0/(\gamma-1)$, the expansion is complete and there remains a region of vacuum between the wall and the wave.

The fact that equations (1) and (2) all involve only $\xi/c_0t$ corresponds to the above-mentioned pseudo-steady state of the flow field.

It is more convenient for us to use a $\xi'$-axis fixed to the moving wall, where

$$\xi'=\xi-u_pt.$$

Thus, equations (1) and (2) are transformed into

$$\frac{u}{c_0}=\begin{cases}\dfrac{2}{\gamma+1}\left(1+\dfrac{\xi'}{c_0t}\right)-\dfrac{\gamma-1}{\gamma+1}\dfrac{u_p}{c_0}, \\ \qquad -\left(1+\dfrac{u_p}{c_0}\right)\leqq\dfrac{\xi'}{c_0t}\leqq-\left(1-\dfrac{\gamma-1}{2}\dfrac{u_p}{c_0}\right), \\ 0\quad, \\ \qquad -\left(1-\dfrac{\gamma-1}{2}\dfrac{u_p}{c_0}\right)\leqq\dfrac{\xi'}{c_0t}\leqq0,\end{cases} \tag{3}$$

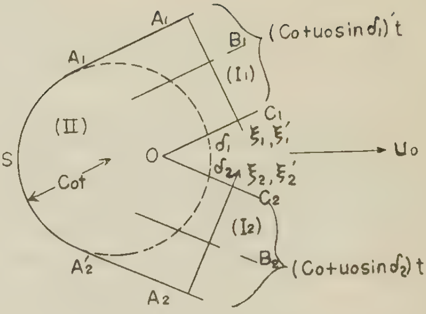

Fig. 3

$$\frac{c}{c_0}=1-\frac{\gamma-1}{2c_0}(u+u_p),$$

$$\frac{p}{p_0}=\left(\frac{c}{c_0}\right)^{\frac{2\gamma}{\gamma-1}},\quad \frac{\rho}{\rho_0}=\left(\frac{c}{c_0}\right)^{\frac{2}{\gamma-1}}. \tag{4}$$

Returning to our present problem, it will be seen that in the regions ($I_1$), ($I_2$) (Fig. 3) having appropriate distances from the apex O, two rarefaction waves parallel to the walls propagate with the front velocity $c_0$, and the distributions of velocities, sound velocities, etc., behind them are represented by (1), (2) or (3), (4), if we use $\xi_1$, $\xi_1'$, $u_1$, $c_1$, $p_1$, $\rho_1$, $u_0\sin\delta_1$ for the upper surface and $\xi_2$, $\xi_2'$, $u_2$, $c_2$, $p_2$, $\rho_2$, $u_0\sin\delta_2$ for the lower surface respectively in place of $\xi$, $\xi'$, $u$, $c$, $p$, $\rho$, $u_p$. As for the region (II) (affected by the apex O), it may be asserted that the front of it also propagates with the velocity $c_0$. Then the front of the whole domain affected by the motion of the wedge may be formed from the three parts: $A_1A_1'$, a straight line parallel to $OC_1$, $A_1'SA_2'$, a circular arc of radius $c_0t$ and $A_2'A_2$, a straight line parallel to $OC_2$ where $A_1'$, $A_2'$ are contact points of $A_1A_1'$, and $A_2A_2'$ on the circle, respectively.

## § 3. The Case of a Wedge with Small Vertex Angle

The essential feature of this case is the same as in the corresponding case in § 2 in the first paper[1]. The deviation of pressure $p'$ from the undisturbed one $p_0$ is determined by the same wave equation as equation (3) in the first paper[1],

$$\frac{\partial^2p'}{\partial t^2}=c_0^2\left(\frac{\partial^2p'}{\partial X'^2}+\frac{\partial^2p'}{\partial Y'^2}\right), \tag{5}$$

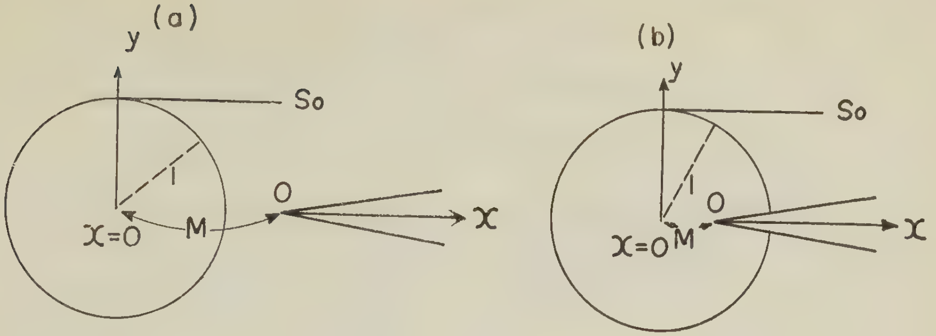

Fig. 4

where

$$X'=X-u_0t,\quad Y'=Y.$$

Utilizing the concept of pseudo-steady state of the flow field, equation (5) can be reduced to the conical flow equation

$$(1-x^2)p_{xx}-2xyp_{xy}+(1-y^2)p_{yy}=2(xp_x+yp_y), \tag{6}$$

where

$$x=X'/(c_0t),\quad y=Y'/(c_0t),\quad p=p'/(\rho_0u_0c_0).$$

As we have done in § 2 of the first paper1), we must distinguish between the different configurations according as $M>1$ or $M<1$. The first case is trivial, since the apex O of the wedge has no effect on the wall of the wedge as is shown in Fig. 4a, and the values of $p$ on the walls are simply $-\delta_1$ for the upper surface and $-\delta_2$ for the lower surface. On the other hand, the circumstance of the second case $M<1$ is precisely the same as in the corresponding case in the first paper1) and the flow field for $\delta_1=\delta_2=\delta$ is obtained from equations (14), (17) and (18) in the first paper1) simply by replacing $\delta$ by $-\delta$.

## § 4. The Case of Almost Blunt Wedge Angle

The flow in the case of $\delta_1$, $\delta_2\approx\pi/2$ or $\varepsilon_1$, $\varepsilon_2\ll 1$ ($\varepsilon_1=\pi/2-\delta_1$, $\varepsilon_2=\pi/2-\delta_2$) is not far different from that generated by a plane wall shown in § 2, and the flow field is expected to be approximated by a small perturbation from the state expressed by equations (4) and (3). Some difficulties arise from the fact that the original unperturbed solution (3) and (4) has a singularity at the boundary (B in Fig. 2) between two regions. We must find the perturbed solutions separately in both regions and connect them on the boundary to make the physical quantities continuous there.

Since the flow is irrotational, the basic equations of the field are

$$\frac{\partial c^2}{\partial t}+\frac{\partial\Phi'}{\partial X'}\frac{\partial c^2}{\partial X'}+\frac{\partial\Phi'}{\partial Y'}\frac{\partial c^2}{\partial Y'}+(\gamma-1)c^2\left(\frac{\partial^2\Phi'}{\partial X'^2}+\frac{\partial^2\Phi'}{\partial Y'^2}\right)=0, \tag{7}$$

$$\frac{\partial\Phi'}{\partial t}+\frac{1}{2}\left\{\left(\frac{\partial\Phi'}{\partial X'}\right)^2+\left(\frac{\partial\Phi'}{\partial Y'}\right)^2\right\}+\frac{1}{\gamma-1}c^2=\frac{1}{2}u_0^2+\frac{1}{\gamma-1}c_0^2, \tag{8}$$

where $\Phi'$ is the velocity potential.

Utilizing the concept of the pseudo-steady state of the flow field and putting

$$x=\frac{X'}{c_0t},\quad y=\frac{Y'}{c_0t},\quad \Phi=\frac{\Phi'}{c_0^2t},\quad \Psi=\left(\frac{c}{c_0}\right)^2,\quad M=\frac{u_0}{c_0}, \tag{9}$$

equations (7) and (8) are reduced to

$$(\Phi_x-x)\Psi_x+(\Phi_y-y)\Psi_y+(\gamma-1)\Psi(\Phi_{xx}+\Phi_{yy})=0, \tag{10}$$

$$\Phi-x\Phi_x-y\Phi_y+\frac{1}{2}(\Phi_x^2+\Phi_y^2)+\frac{1}{\gamma-1}\Psi=\frac{1}{2}M^2+\frac{1}{\gamma-1}. \tag{11}$$

The solution of equations (10) and (11), which is equivalent to equation (3) and (4), is obtained by putting $\Phi_0$, $\Psi_0$ for $\Phi$, $\Psi$ where $\Phi_0$, $\Psi_0$ are functions of $x$ only. In this case, equations (10) and (11) are reduced to

$$(\Phi_{0x}-x)\Psi_{0x}+(\gamma-1)\Psi_0\Phi_{0xx}=0, \tag{12}$$

$$\Phi_0-x\Phi_{0x}+\frac{1}{2}\Phi_{0x}+\frac{1}{\gamma-1}\Psi_0=\frac{1}{2}M^2+\frac{1}{\gamma-1}, \tag{13}$$

and their solutions $\Phi_0$ and $\Psi_0$ are expressed as

$$\Phi_0=\frac{1}{\gamma+1}(x+M+1)^2-Mx,\quad \Psi_0=(x-\Phi_{0x})^2,$$
$$-(M+1)\leqq x\leqq-\left(1-\frac{\gamma-1}{2}M\right),$$
$$\Phi_0=\frac{1}{\gamma+1}\left(\frac{\gamma+1}{2}M\right)^2+M\left(1-\frac{\gamma-1}{2}M\right),$$
$$\Psi_0=\left(1-\frac{\gamma-1}{2}M\right)^2,\quad -\left(1-\frac{\gamma-1}{2}M\right)\leqq x\leqq 0. \tag{14}$$

In the region $x\leqq-(M+1)$, the state is undisturbed and $\Phi_0=M(M+1)$, $\Psi_0=1$. Now we put

$$\Phi=\Phi_0+\varphi,\quad \Psi=\Psi_0+\psi, \tag{15}$$

and assume that $\varphi$, $\psi$ are small throughout the region. Inserting (15) into (10) and (11), and utilizing the relations (12) and (13), we have

$$\Psi_{0x}\varphi_x-(x-\Phi_{0x})\psi_x-y\psi_y$$
$$+(\gamma-1)(\Psi_0\Delta\varphi+\Phi_{0xx}\psi)=0, \tag{16}$$
$$(\gamma-1)\{\varphi-(x-\Phi_{0x})\varphi_x-y\varphi_y\}+\psi=0, \tag{17}$$

neglecting small quantities. Eliminating $\psi$ from (16) and (17), we have

$$\{\Psi_0-(x-\Phi_{0x})^2\}\varphi_{xx}+(\Psi_0-y^2)\varphi_{yy}-2(x-\Phi_{0x})y\varphi_{xy}$$
$$+\{\Psi_{0x}/(\gamma-1)+\gamma(x-\Phi_{0x})\Phi_{0xx}\}\varphi_x$$
$$+(\gamma-1)\Phi_{0xx}(y\varphi_y-\varphi)=0. \tag{18}$$

$\psi$ is determined by equation (17), using the solution $\varphi$ of equation (18).

Because of the different behaviours of $\Phi_0$, $\Psi_0$ in the different regions of $x$ as shown in equation (14), the equation (18) has different forms in different regions of $x$. In the region ($R$) (say);

$$-(1+M)\leqq x\leqq-\left(1-\frac{\gamma-1}{2}M\right),$$

equation (18) becomes

$$\{(x-\Phi_{0x})^2-y^2\}\varphi_{yy}-2(x-\Phi_{0x})y\varphi_{xy}$$
$$+2(x-\Phi_{0x})\varphi_x+(\gamma-1)\Phi_{0xx}(y\varphi_y-\varphi)=0.$$

Introducing a new variable $x_1$:

$$-x_1=x-\Phi_{0x}=\mu^2x-2a/(\gamma+1),$$
$$1\geqq x_1\geqq a,\quad a=1-(\gamma-1)M/2,$$
$$\mu^2=(\gamma-1)/(\gamma+1), \tag{19}$$

this equation is reduced to

$$(2\mu^2)^{-1}(x_1{}^2-y^2)\varphi_{yy}-x_1y\varphi_{x_1y}+x_1\varphi_{x_1}+y\varphi_y-\varphi=0. \tag{20}$$

In the region ($U$) (say):

$$-\left(1-\frac{\gamma-1}{2}M\right)\leqq x\leqq 0\quad\text{or}\quad -a\leqq x\leqq 0,$$

equation (18) becomes

$$(a^2-x^2)\varphi_{xx}-2xy\varphi_{xy}+(a^2-y^2)\varphi_{yy}=0. \tag{21}$$

Equation (21) is exactly the same as the conical flow equation of Busemann, as expected; on the other hand, equation (20) has an unusual appearance, but we can nevertheless solve it. To do this, we put

$$y\varphi_y-\varphi=F.$$

Then, equation (20) is reduced to

$$(2\mu^2y)^{-1}(x_1{}^2-y^2)F_y-x_1F_{x_1}+F=0, \tag{22}$$

and its characteristic equation is

$$\frac{dx_1}{-x_1}=\frac{dy}{(2\mu^2y)^{-1}(x_1{}^2-y^2)}=\frac{dF}{-F}.$$

Two integrals of this equation are readily found as

$$Fx_1{}^{-1}=c_1,\quad \{x_1{}^2-(1-2\mu^2)y^2\}x_1{}^{-1/\mu^2}=c_2,$$

where $c_1$, $c_2$ are arbitrary constants.

The complete solution of equation (22) is obtained by setting an abritrary functional relation between $c_1$, $c_2$ as

$$c_1=f_1(c_2).$$

Then we have

$$F=y\varphi_y-\varphi=x_1f_1(x_1{}^{-1/\mu^2}\{x_1{}^2-(1-2\mu^2)y^2\}).$$

The final solution $\varphi$ of equation (20) is readily obtained and we get

$$\varphi=y\left\{\int\frac{x_1}{y^2}f_1(Z)\,dy+f_2(x_1)\right\},$$
$$Z=x_1{}^{-1/\mu^2}\{x_1{}^2-(1-2\mu^2)y^2\}, \tag{23}$$

where $f_2(x_1)$ is an arbitrary function of $x_1$.

$X'$, $Y'$ components of perturbation velocity, $u$ and $v$, are obtained by differentiating $\varphi$ with respect to $x$ and $y$ respectively and we have

$$\frac{u}{c_0}=\varphi_x=-\mu^2\varphi_{x_1}=-\mu^2y\left[\int\frac{1}{y^2}\left\{f_1(Z)+\frac{1-2\mu^2}{\mu^2}x_1{}^{-1/\mu^2}(y^2-x_1{}^2)f_1'(Z)\right\}dy+f_2'(x_1)\right], \tag{24}$$

$$\frac{v}{c_0}=\varphi_y=\int\frac{x_1}{y^2}f_1(Z)\,dy+\frac{x_1}{y}f_1(Z)+f_2(x_1)\,. \tag{25}$$

The pressure $p$ is given by $\psi$ in equation (17).

Equcation (21) becomes hyperbolic in the region $r=\sqrt{x^2+y^2}>a$ and elliptic in $r<a$ and the solutions for $u$, $v$, $p$ in the respective regions are as follows[3]:

$$\left.\begin{aligned} \frac{u}{c_0} &= \varphi_x = \int^{\sigma+\theta} f(\tau)\cos\tau d\tau + \int^{\sigma-\theta} F(\tau)\cos\tau d\tau, \\ \frac{v}{c_0} &= \varphi_y = \int^{\sigma+\theta} f(\tau)\sin\tau d\tau - \int^{\sigma-\theta} F(\tau)\sin\tau d\tau, \\ \frac{p'-p}{\rho' c_0^2} &= \varphi - x\varphi_x - y\varphi_y = -a\left(\int^{\sigma+\theta} f(\tau)d\tau + \int^{\sigma-\theta} F(\tau)\, d\tau\right), \\ x &= r\cos\theta, \quad y = r\sin\theta, \quad \sigma = \cos^{-1}(a/r). \end{aligned}\right\} \text{for } r<a, \tag{26}$$

and

$$\left.\begin{aligned} &\frac{u}{c_0} = \varphi_x = R_e\{W_2(\zeta)\}, \quad \frac{v}{c_0} = \varphi_y = R_e\{W_3(\zeta)\}, \quad \frac{p'-p}{\rho' c_0^2} = \varphi - x\varphi_x - y\varphi_y = R_e\{W_1(\zeta)\} \\ &-2\zeta a W_2'(\zeta) = (\zeta^2+1)W_1'(\zeta), \quad -2i\zeta a W_3'(\zeta) = (\zeta^2-1)W_1'(\zeta), \\ &\zeta = \xi + i\eta = Re^{i\theta}, \quad z = x+iy = re^{i\theta}, \quad R = (a-\sqrt{a^2-r^2})/r, \end{aligned}\right\} \text{for } r<a, \tag{27}$$

where $p'$, $\rho'$ are the undisturbed values in the region $(U)$ and given by $p_0 a^{2\gamma/(\gamma-1)}$, $\rho_0 a^{2/(\gamma-1)}$ respectively, using equations (4), (9), (14) and (19). $f$, $F$, $W_1$, $W_2$, $W_3$ are all functions to be determined by the boundary conditions.

Now, the velocity must be continuous at the boundary between regions $(R)$ and $(U)$; namely,

$$u\text{ (of }(R)) = u\text{ (of }(U)), \quad v\text{ (of }(R)) = v\text{ (of }(U)) \quad \text{at the boundary.} \tag{28}$$

Since $x_1=-x=a$ on the boundary, we have from equation (26), $\sigma=\pi+\theta$ there. Then, using equations (24), (25) and (26), boundary conditions (28) yield

$$-\mu^2 y\left[\int \frac{1}{y^2}\left\{f_1(Z_a) + \frac{1-2\mu^2}{\mu^2} a^{-1/\mu^2}(y^2-a^2) f_1'(Z_a)\right\} dy + f_2'(a)\right] = \int^{2\theta+\pi} f(\tau)\cos\tau d\tau + \text{const.},$$

$$\int \frac{a}{y^2} f_1(Z_a)dy + \frac{a}{y} f_1(Z_a) + f_2(a) = \int^{2\theta+\pi} f(\tau)\sin\tau d\tau + \text{const.},$$

where $Z_a = a^{1/\mu^2}\{a^2-(1-2\mu^2)y^2\}$. Differentiating these equations with respect to $y$, we get

$$\begin{aligned} -\mu^2 &\left[\int \frac{1}{y^2}\left\{f_1(Z_a) + \frac{1-2\mu^2}{\mu^2} a^{-1/\mu^2}(y^2-a^2) f_1'(Z_a)\right\} dy \right. \\ &\left. + \frac{1}{y}\left\{f_1(Z_a) + \frac{1-2\mu^2}{\mu^2} a^{-1/\mu^2}(y^2-a^2) f_1'(Z_a)\right\} + f_2'(a)\right] \\ &= -2f(2\theta+\pi)\cos 2\theta \frac{d\theta}{dy}, \\ &-2a^{1-1/\mu^2}(1-2\mu^2) f_1'(Z_a) = -2f(2\theta+\pi)\sin 2\theta \frac{d\theta}{dy}. \end{aligned} \tag{29}$$

Eliminating $f(2\theta+\pi)$ and utilizing the relation $\tan 2\theta = 2ay(a^2-y^2)^{-1}$, the above equations are reduced to

$$\int \frac{1}{y^2}\left\{f_1(Z_a) + \frac{1-2\mu^2}{\mu^2} a^{-1/\mu^2}(y^2-a^2) f_1'(Z_a)\right\} dy + \frac{1}{y} f_1(Z_a) + f_2'(a) = 0.$$

If we differentiate this equation again with respect to $y$, we get simply

$$f_1'(Z_a) = 0,$$

and

$$f_1(Z_a) = A \ (=\text{const.})$$

Then equations (24) and (25) are reduced to

$$u/c_0 = -\mu^2\{-A + yf_2'(x_1)\}, \quad v/c_0 = f_2(x_1). \tag{30}$$

Referring to the two regions where the apex O has no effect, $u=0$ and $v=-\mathcal{E}_1 u_0$ for the upper region and $u=0$, $v=\mathcal{E}_2 u_0$ for the lower region, and so equations (30) are simplified and we have

$$\frac{u}{c_0} = 0, \quad \frac{v}{c_0} = \begin{cases} -\mathcal{E}_1 M, & y>0 \\ \mathcal{E}_2 M, & y<0, \end{cases} \tag{31}$$

$f$ is given by equation (29) and also vanishes and

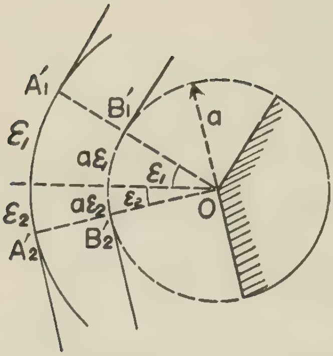

Fig. 5

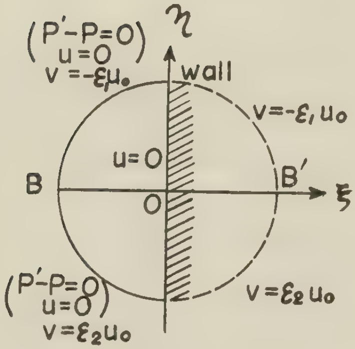

Fig. 6

$$f(\tau)=0.$$

By considering the condition $u=0$ on the wall where $\theta=\pm\pi/2$, we have from equation (26)

$$0=\text{const.}+\int^{\sigma\mp\pi/2} F(\tau)\cos\tau d\tau$$

and we get $\qquad F(\tau)=0.$

Then the flow in the region $r>a$ in $(U)$ becomes the same as in equation (31). Accordingly the state is not disturbed in the region $(R)$ and $r>a$ in $(U)$ except on the line $y=0$. This rather curious result is, however, also acceptable from another point of view. Because, as we can see from Fig. 5, the breadth of the region which is affected by the apex O is represented by $\overline{A_1'A_2'}$ and is, of the order of $\varepsilon_1$, $\varepsilon_2$. In this first order theory which we are now considering, this region must be reduced to the line $y=0$, where the solution becomes singular.

Now the remaining problem is to find the functions $W_1(\zeta)$, $W_2(\zeta)$, $W_3(\zeta)$ in $r<a$, satisfying the following boundary conditions on the circle $r=a$ and on the surface of the wall:

$$v=-\varepsilon_1 u_0,\ \text{on}\ |\zeta|=1\ (r=a),\ \pi>\theta\geqq\pi/2,$$
$$v=\ \varepsilon_2 u_0\ ,\ \text{on}\ |\zeta|=1\ (r=a),\ 3\pi/2\geqq\theta>\pi,$$
$$u=\ 0\ ,\ \text{on}\ \xi=0,\ |\eta|\leqq 1, \qquad (32)$$

they are shown in Fig. 6.

Because of unknown singularities of $p'-p$ and $u$ at B, we cannot use the values of $u$ and $p'-p$ as a boundary condition, though they are zero on the semicircle except at B. But we shall later verify that our solution gives the correct boundary values.

Since $u=0$ on the wall, $v$ must be symmetrical about the $\eta$-axis and so the function $W_3(\zeta)$ can be obtained easily by constructing a function of which the real part takes the constant values $-\varepsilon_1 M$, $\varepsilon_2 M$ on each semicircle. Then we get

$$W_3(\zeta)=\frac{M}{2\pi i}\Bigl[-\varepsilon_1\Bigl\{2\log\frac{-1-\zeta}{1-\zeta}-\log(-1)\Bigr\}$$
$$+\varepsilon_2\Bigl\{2\log\frac{1-\zeta}{-1-\zeta}-\log(-1)\Bigr\}\Bigr]. \qquad (33)$$

Differentiating this with respect to $\zeta$, we have

$$W_3'(\zeta)=\frac{2(\varepsilon_1+\varepsilon_2)M}{\pi}\cdot\frac{i}{1-\zeta^2}.$$

Then $W_1(\zeta)$, $W_2(\zeta)$ are obtained by equation (27) as

$$W_1(\zeta)=-\frac{4(\varepsilon_1+\varepsilon_2)Ma}{\pi}\int\frac{\zeta}{(1-\zeta^2)^2}d\zeta$$
$$=-\frac{2(\varepsilon_1+\varepsilon_2)Ma}{\pi}\frac{1}{1-\zeta^2}+C, \qquad (34)$$
$$W_2(\zeta)=\frac{2(\varepsilon_1+\varepsilon_2)M}{\pi}\int\frac{1+\zeta^2}{(1-\zeta^2)^2}d\zeta$$
$$=\frac{2(\varepsilon_1+\varepsilon_2)M}{\pi}\frac{\zeta}{1-\zeta^2}+C', \qquad (35)$$

where $C$, $C'$ are constants and are determined by the conditions $(p'-p)/c_0^2\rho'=R_e(W_1)=0$, $u/c_0=R_e(W_2)=0$ on the circle except at B, B′. By putting $\zeta=i$ for example, we have

$$C=(\varepsilon_1+\varepsilon_2)Ma/\pi,\quad C'=0. \qquad (36)$$

Now the values of $(p'-p)/\rho' c_0^2$ and $u/c_0$ on the circle are given by

$$\left(\frac{p'-p}{\rho' c_0^2}\right)_{R=1}=R_e\{W_1(e^{i\theta})\}$$
$$=R_e\left\{\frac{(\varepsilon_1+\varepsilon_2)Ma}{\pi}\frac{-1-e^{2i\theta}}{1-e^{2i\theta}}\right\},$$
$$\left(\frac{u}{c_0}\right)_{R=1}=R_e\{W_2(e^{i\theta})\}$$
$$=R_e\left\{\frac{2(\varepsilon_1+\varepsilon_2)M}{\pi}\frac{e^{i\theta}}{1-e^{2i\theta}}\right\},$$

and it is easily verified that they reduce to zero except at B, B′ where $W_1$ and $W_2$ have simple poles as we can see from equations (34) and (35).

Thus we can find $p$, $u$, $v$ in the field by taking real parts of equations (34), (35) and (33), and in particular the pressure distribution on the wall is given by

$$\frac{p'-p}{\rho' c_0^2}=\frac{(\mathcal{E}_1+\mathcal{E}_2)Ma}{\pi}\,\frac{1-\eta^2}{1+\eta^2}\,,$$

which is reduced to

$$\frac{p'-p}{\rho' c_0^2}=\frac{(\mathcal{E}_1+\mathcal{E}_2)Ma}{\pi}\sqrt{1-\left(\frac{y}{a}\right)^2}\,,$$

by use of equation (27), where $a$ is $1-(\gamma-1)\times M/2$ by equation (19).

### References

1) A. Sakurai: J. Phys. Soc. Japan **10** (1955) 221.
2) Courant-Friedrichs: *Supersonic Flow and Shock Waves* (Interscience Publishers, 1948) pp. 104–106.
3) R. Sauer: *Einführung in die theoretische Gasdynamik* (Springer, 1951) pp. 158–160.

---

JOURNAL OF THE PHYSICAL SOCIETY OF JAPAN Vol. 11, No. 9, SEPTEMBER, 1956

# Heat Loss from a Partially Insulated Solid Body

By Joseph GILLIS

*Department of Applied Mathematics, Weizmann Institute of Science, Rehovoth, Israel*

(Received April 14, 1956)

We investigate the problem of a thermally conducting solid, initially at a uniform temperature, part of whose surface is insulated. The uninsulated part of the surface radiates heat into a medium at zero temperature. We deal especially with the case in which the insulated and uninsulated regions cannot be represented as distinct coordinate surfaces in variables in terms of which the conduction equation is separable.

An integral equation is derived for the boundary values of the temperature and solutions of this equation are obtained in two special cases, viz. a semi-infinite solid insulated except for a single infinite strip, and the same solid insulated except for two equal parallel infinite strips at a considerable distance apart. In both cases we show that the solution can be represented for large values of the time $t$, by a series of inverse powers of $\log t$. In case the strips are very narrow we obtain closed expression which approximate the sums of the series.

## § 1. Introduction

We propose to investigate the problem of heat loss from a conducting body part of whose surface is thermally insulated and such that from the uninsulated parts heat is radiated into a medium which remains throughout at zero temperature. The central difficulty of the problem arises when the insulated and uninsulated portions of the surface cannot be represented as distinct coordinate surfaces in variables in terms of which the fundamental equation is separable. We shall show how the most general case can be reduced to an integral equation in which the boundary conditions are taken care of automatically. All the results obtained apply, of course, to any diffusion process with suitable definitions of the quantities involved.

Feshbach [1), cf. also 2)] has discussed a similar problem in connection with the Helmholtz equation, using a Green's function to reduce the problem to an integral equation. Our chief concern in this paper will be the study of the time-dependence of the solution, and to demonstrate methods for calculating this dependence in some special cases. A particular difficulty arises when large values of the time are in question, since the various iteration procedures often useful for integral equations now either diverge or else converge so slowly as to be of no practical value. This is related to the fact that the kernel of the integral equation, regarded as a function of the time, has an essential singularity at the upper limit of integration, a fact which is, in turn, related to the irreversibility in time of the diffusion equation.

## § 2. Derivation of Integral Equation

We begin by considering a slightly more general problem. Let S denote the surface of a solid body, D, and suppose that the emissivity of the surface S is $h(x, y, z)$ where $h$ varies with position. The whole body is initially at constant temperature $V$ and we denote by $\phi(x, y, z, t)$ the temperature at the point $(x, y, z)$ of D at any subsequent time $t$.

Then, $\phi$ has to satisfy the following equations:

( i ) $$\nabla^2\phi=\frac{1}{k}\frac{\partial\phi}{\partial t} \tag{2.1}$$

in the interior of D, where $k$ is assumed to be a constant.

(ii) $$\frac{\partial\phi}{\partial n}=-h(x, y, z)\phi \tag{2.2}$$

on S, where $n$ is the outward normal to the surface.

(iii) $$\phi(x, y, z, 0)\equiv V \tag{2.3}$$

throughout D.

To begin with, consider the same set of equations except that (2.2) is replaced by

$$\frac{\partial\phi}{\partial n}=-\psi(x, y, z, t)\ , \tag{2.2'}$$

where $\psi$ is taken to be a known function. The system (2.1), (2.2′) and (2.3) can be solved by a Green's function. In fact, we require a function $G(x,y,z;\ t|x', y', z';\ \tau)$ which denotes the temperature at $(x, y, z, t)$ due to an instantaneous unit point-source at $(x', y', z', \tau)$ and such that $\partial G/\partial n$ is zero for $(x, y, z)$ on S. This function can always be constructed [3), p. 291] and it is then easily seen that

$$\phi(x, y, z, t)=\int_D \phi(x',y',z',0)\cdot G(x', y', z';\ t|x, y, z;\ 0)dx'dy'dz'$$
$$-k\int_0^t d\tau\int_S G(x',y',z';t\,|\,x,y,z,\tau)\cdot\psi(x', y', z', \tau)dS' \tag{2.4}$$

satisfies (2.1), (2.2′) and (2.3) where the surface integral in (2.4) is taken with respect to the variables $(x', y', z')$. The first integral on the right-hand side is, by (2.3), equal to

$$V\int_D G(x', y', z';\ t|x, y, z;\ 0)dx'dy'dz'. \tag{2.5}$$

But the integrand in (2.5) represents, by definition, the temperature distribution which would obtain in D after the action of the instantaneous point-source and in the absence of any heat loss through S. The integral must therefore be constant and equal to unity. Hence

$$\phi(x, y, z, t) =V-k\int_0^t d\tau\int_S G(x, y, z;\ t|x', y', z';\ \tau)\cdot\psi(x',y',z', \tau)dS'\ . \tag{2.6}$$

We now consider the problem in which S consists of two parts, $S_1$, $S_2$ such that

$$h(x,y,z)=\begin{cases} h \text{ on } S_1\,, \\ 0 \text{ on } S_2\,, \end{cases} \tag{2.7}$$

where $h$ is a constant. In equation (2.6) we can replace $\psi$ by the unknown function $h(x',y',z')\phi(x', y', z', \tau)$ and we get the equation

$$\phi(x, y, z, t) =V-hk\int_0^t d\tau\int_{S_1} \phi(x', y', z', \tau)\cdot G(x, y, z;\ t|x', y', z';\ \tau)dS'\ . \tag{2.8}$$

It we now let the point $(x, y, z)$ approach the boundary from the interior of D, then (2.8) becomes an integral equation for the boundary values of $\phi$. Since our main concern in this paper is the study of the rate of heat loss, it will be sufficient by (2.2) and (2.7) to calculate the value of $\varphi$ on $S_1$. The proviso that $(x, y, z)$ approach S from the interior of D is necessary, since (2.8) does not hold for $(x, y, z)$ outside the body.

## § 3. Specialization of Problem

In what follows we shall consider only the special case in which D is the semi-infinite solid $x<0$. Then it is easily verified that

$$G=[4\pi k(t-\tau)]^{-3/2}\exp\left[-\frac{(y-y')^2+(z-z')^2}{4k(t-\tau)}\right]\left\{\exp\left[-\frac{(x-x')^2}{4k(t-\tau)}\right]+\exp\left[-\frac{(x+x')^2}{4k(t-\tau)}\right]\right\} \tag{3.1}$$

satisfies all the requirements. On the boundary we have $x'=0$ and so our integral equation for $\phi$ becomes

$$\phi(y,z,t)=V-\frac{1}{4}hk^{-1/2}\pi^{-3/2}\int_0^t d\tau\int_{S_1}(t-\tau)^{-1/2}\phi(y',z',\tau)\exp\left[-\frac{(y-y')^2+(z-z')^2}{4k(t-\tau)}\right]dy'dz'. \qquad (3.2)$$

Moreover we shall confine our attention to the case in which $S_1$ consists of infinitely long parallel strips of finite width, i.e. such that

$$|y-\delta_i|\leq\alpha_i \qquad (i=1,2,\cdots). \qquad (3.3)$$

Clearly $\phi$ is then independent of $z$ and so the $z'$ integration in (3.2) can be carried out immediately. We then get

$$\phi(y,t)=V-\frac{h}{2\pi}\int_0^t d\tau\int_{y'\varepsilon S_1}(t-\tau)^{-1}\exp\left[-\frac{(y-y')^2}{4k(t-\tau)}\right]\phi(y',\tau)dy'. \qquad (3.4)$$

In what follows we shall consider ways of estimating $\phi$ for some special systems of $\delta_i$, $\alpha_i$.

## § 4. Initial Behaviour

We begin with the case where $S_1$ consists of the single strip

$$|y|\leq\alpha. \qquad (4.1)$$

Then (3.4) can be written

$$\phi(y,t)=V-\frac{h}{2\pi}\int_0^t d\tau\int_{-\alpha}^{\alpha}(t-\tau)^{-1}\exp\left[-\frac{(y-y')^2}{4k(t-\tau)}\right]\phi(y',\tau)dy'. \qquad (4.2)$$

The $\tau$ integral on the right-hand side of (4.2) is the convolution of $\phi(y',t)$ with $t^{-1}\exp[-(y-y')^2/4kt]$. We take Laplace transforms with respect to $t$ and write

$$f(y,p)=\int_0^\infty e^{-pt}\phi(y,t)dt. \qquad (4.3)$$

The convergence of the integral in (4.3) is assured for all $p>0$, since $\phi$ is bounded by the initial temperature, $V$. Moreover the Laplace transform of $t^{-1}\exp[-(y-y')^2/4kt]$ is $2K_0[\sqrt{p/k}(|y'-y|)]$ [cf. 4), p. 146], where $K_0$ is the modified Bessel function of the second kind. Hence

$$f(y,p)=\frac{V}{p}-\frac{h}{\pi}\int_{-\alpha}^{\alpha}K_0\left[\sqrt{\frac{p}{k}}\,|y'-y|\right]f(y',p)dy'. \qquad (4.5)$$

We are looking for an expansion of $\phi$ which is to be valid for small $t$, and for this we need an expansion of $f(y,p)$ valid for large $p$. This is readily obtained from the standard iteration procedure. Consider first $|y|<\alpha$, and write $f=V/p$ for the first approximation. Then the next approximation gives

$$f(y,p)=\frac{V}{p}-\frac{hV}{\pi p}\int_{-\alpha}^{\alpha}K_0\sqrt{\frac{p}{k}}\,|y'-y|\Big]dy' \qquad (4.6)$$

$$=\frac{V}{p}-\frac{hV\sqrt{k}}{\pi p^{3/2}}\left\{\int_0^{\sqrt{p/k}(\alpha+y)}K_0(\zeta)d\zeta+\int_0^{\sqrt{p/k}(\alpha-y)}K_0(\zeta)d\zeta\right\}. \qquad (4.7)$$

But for large $p$, each of the integrals on the right-hand side of (4.7) is $\frac{1}{2}\pi+O(e^{-M_1\sqrt{p}})$ for some positive $M_1$ (cf. 4), p. 205], and so

$$f(y,p)\sim Vp^{-1}+Vhk^{1/2}p^{-3/2} \quad \text{for} \quad |y|<\alpha. \qquad (4.8)$$

Again, if $|y|>\alpha$, it is easily seen that (4.5) becomes

$$f(y,p)=Vp^{-1}-(Vhk^{1/2}/\pi p^{3/2})\int_{\sqrt{p/k}(|y|-\alpha)}^{\sqrt{p/k}(|y|+\alpha)}K_0(\zeta)d\zeta=Vp^{-1}+O(e^{-M_2\sqrt{p}}) \qquad (4.9)$$

for some positive $M_2$ [4)].

We insert the approximation (4.8) into (4.5) and repeat the iteration. Since the integrals in (4.7) are each $\frac{1}{2}\pi+o(p^{-N})$ for every positive $N$ while that in (4.9) is, analogously, simply

$o(p^{-N})$, it follows that, to the order of $p$ in question, the integrals cannot change the situation. Hence, for sufficiently large $p$,

$$f(y,p)\sim Vp^{-1}-h[Vp^{-1}-Vhk^{1/2}p^{-3/2}]\sqrt{\frac{k}{p}}=Vp^{-1}-Vh\sqrt{k}\,p^{-3/2}+Vh^2kp^{-2}, \tag{4.10}$$

while (4.9) still holds for $|y|>\alpha$.

Inverting (4.10) and (4.9), we get [4), p. 233]

$$\left.\begin{aligned}\phi(y,t)/V&\sim 1-2h\sqrt{\frac{kt}{\pi}}+h^2kt \quad \text{for} \quad |y|<\alpha\,,\\ \text{and}\qquad &\sim 1 \qquad\qquad\qquad\qquad \text{for} \quad |y|>\alpha\,.\end{aligned}\right\} \tag{4.11}$$

The above argument can clearly be continued and it follows that for $|y|<\alpha$ and small $t$, the $y$ dependence of the surface temperature is $o(t^N)$ for every positive $t$. Similary, for $|y|>\alpha$, the surface temperature remains at $V+o(t^N)$. This is in accordance with the physical reality that, initially, all the lines of flow are normal to the surface. It follows that, for small $t$, any gaps in the insulation, whatever their shape and number, will radiate independently and that the temperature in each such gap will be given by (4.11). It is clear from (4.11) that the time range for which these considerations are valid is given by $h\sqrt{kt}\ll 1$.

The problem of large values of $t$ is less amenable to treatment by means of (4.5). The logarithmic singularity of the function $K_0$ at the origin makes it very difficult to use (4.5) effectively for small $p$. We shall therefore use other methods to deal with the case $t\gg 1$.

## § 5. Large Values of $t$. $S_1$ consists of a Single Strip

In order to obtain some insight into the general behaviour of the solutions of (3.4) when $t$ is large, we again consider the case in which $S_1$ consists of the single strip $-\alpha\leq y\leq\alpha$ and we therefore have to deal with (4.2). Our first interest is to find the order of magnitude of $\phi$ as a function of $t$ as $t\to\infty$. To this end we make the approximation of ignoring the dependence of $\phi$ on $y$ as the latter varies over $S_1$ and write $\phi(0,t)=\chi(t)$. Then (4.2) become

$$\chi(t)=V-(h/\pi)\int_0^t\int_0^\alpha (t-\tau)^{-1}\chi(\tau)\exp\left[-\frac{y'^2}{4k(t-\tau)}\right]dy'\,d\tau\,. \tag{5.1}$$

Now the left-hand side of (5.1) tends to zero as $t\to\infty$ and so the double integral on the right-hand side must tend to $\pi V/h$. This implies that the rate at which $\chi$ tends to zero must just balance the order of infinity of

$$\int_0^t\int_0^\alpha (t-\tau)^{-1}\exp\left[-\frac{y'^2}{4k(t-\tau)}\right]dy'\,d\tau\,.$$

The latter integral

$$=\int_0^\alpha dy'\int_{(y'^2/4kt)}^\infty \sigma^{-1}e^{-\sigma}\,d\sigma=\int_0^\alpha E_1(y'^2/4kt)\,dy'\,. \tag{5.2}$$

Now, for large $t$, the integrand in (5.2)$\sim -\log(y'^2/4kt)=\log t-2\log y'+O(1)$ [5), p. 143]. Hence

$$\int_0^t\int_0^\alpha \exp\left[-\frac{y'^2}{4k(t-\tau)}\right](t-\tau)^{-1}dy'\,d\tau\sim\alpha\log t+O(1) \quad \text{as} \quad t\to\infty\,. \tag{5.3}$$

This suggests that $\chi(t)$ should behave like $(\log t)^{-1}$ as $t\to\infty$, a fact which will be established more precisely below. However, we note at this point an important difference from the case in which the entire surface of the semi-infinite solid can radiate (i.e. $S_2=0$, $\alpha=\infty$). It is known [3), p. 53] that the surface temperature for large values of $t$ is then $O(t^{-1/2})$. The essential distinction between the two cases lies in that the double integral in (5.3) has a different order of magnitude, as a function of $t$, according as $\alpha$ is finite or infinite. In fact, in the latter event, we have

$$\int_0^t\int_0^\infty \exp\left[-\frac{y'^2}{4k(t-\tau)}\right](t-\tau)^{-1}\,dy'\,d\tau=2\sqrt{\pi kt}\,. \tag{5.4}$$

Before proceeding further we shall make some simplifying changes of variables. We write

$$\eta=y/\alpha,\quad \eta'=y'/\alpha,\quad t_1=kt/\alpha^2,\quad \tau_1=k\tau/\alpha^2,\quad S(\eta,\,t_1)=\phi(y,\,t)/V \quad\text{and}\quad U(t_1)=\chi(t)/V\,.$$

This makes all our quantities dimensionless, and equation (4.2) becomes

$$S(\eta,\,t_1)=1-(\alpha h/2\pi)\int_{-1}^1\int_0^{t_1}(t_1-\tau_1)^{-1}\exp\left[-\frac{(\eta-\eta')^2}{4(t_1-\tau_1)}\right]S(\eta',\,\tau_1)d\eta'\,d\tau_1 \tag{5.5}$$

while (5.1) becomes

$$U(t_1)=1-(\alpha h/\pi)\int_0^1\int_0^{t_1}(t_1-\tau_1)^{-1}\exp\left[-\frac{\eta'^2}{4(t_1-\tau_1)}\right]U(\tau_1)d\eta'\,d\tau_1. \tag{5.6}$$

In view of the considerations discussed above, we begin by trying in (5.6) a solution of the type $A(\log t_1)^{-1}$. This would lead to

$$\begin{aligned}A(\log t_1)^{-1}&=1-(\alpha hA/\pi)\int_0^{t_1}\int_0^1\exp\left[-\frac{\eta'^2}{4(t_1-\tau_1)}\right]\frac{d\eta'\,d\tau_1}{(t_1-\tau_1)\log\tau_1}\\&=1-(\alpha hA/\pi)\int_0^1 d\eta'\int_0^{t_1}\frac{1}{s}\,e^{-\eta'^2/4s}\,\frac{ds}{\log(t_1-s)}\\&=1-(\alpha hA/\pi)\int_0^1 d\eta'\int_0^{t_1}\frac{1}{s}\,e^{-\eta'^2/4s}\left\{(\log t_1)^{-1}+(\log t_1)^{-2}\left[\frac{s}{t_1}+\frac{s^2}{2t_1^2}+\cdots\right]\right.\\&\qquad\left.+(\log t_1)^{-3}\left[\frac{s}{t_1}+\frac{s^2}{2t_1^2}+\cdots\right]^2+\cdots\right\}ds\,.\end{aligned} \tag{5.7}$$

But it is easily verified that, for large $t_1$,

$$\left.\begin{aligned}&\int_0^{t_1}s^{r-1}e^{-\eta'^2/4s}\,ds=\frac{t_1{}^r}{r}+O(t_1{}^{r-1})\quad(r\neq 0)\,,\\ \text{and}\qquad&\\&\int_0^{t_1}\frac{1}{s}e^{-\eta'^2/4s}\,ds=\log t_1+[\log 4-\gamma-2\log|\eta'|]+o(1)\,,\end{aligned}\right\} \tag{5.8}$$

where $\gamma$ is Euler's constant.

From (5.7) and (5.8) we get

$$A(\log t_1)^{-1}=1-(\alpha hA/\pi)\int_0^1 d\eta'\{1+O(1/\log t_1)\}\,. \tag{5.9}$$

This suggests the possibility of expansion in an asymptotic series of descending powers of $\log t_1$. With this in view we accordingly go back to (5.5) and write

$$S(\eta,\;t_1)=\sum_{r=1}^\infty\sum_{s=0}^\infty A_{rs}(\log t_1)^{-r}\eta^s, \tag{5.10}$$

and shall seek constants $A_{rs}$ to satisfy (5.5). But, by the argument of (5.7) and (5.8) we have, for any real $\theta$,

$$\begin{aligned}\int_0^{t_1}(\log t_1)^{-r}\exp\left[-\frac{\theta^2}{4(t_1-\tau_1)}\right]\frac{d\tau_1}{t_1-\tau_1}&=\int_0^{t_1}\frac{1}{s}e^{-\theta^2/4s}\left\{(\log t_1)^{-r}\right.\\&\quad\left.+r(\log t_1)^{-r-1}\left[\frac{s}{t_1}+\frac{s^2}{2t_1^2}+\cdots\right]+\frac{r(r+1)}{2}(\log t_1)^{-r-2}\left[\frac{s}{t_1}+\frac{s^2}{2t_1^2}+\cdots\right]^2+\cdots\right\}ds\\&=(\log t_1)^{-r}\{\log t_1+[\log 4-\gamma-2\log|\theta|]+O(t_1^{-1})\}\\&\quad+\frac{r\pi^2}{6}(\log t_1)^{-r-1}+\frac{1}{2}r(r+1)G(\log t_1)^{-r-2}+\cdots,\end{aligned} \tag{5.11}$$

where

$$G=\sum_{n=1}^{\infty}\frac{1}{n^3}+2\sum_{1\leq i<j}\frac{1}{ij(i+j)}\sim 3.0068\,.$$

Hence, if we substitute (5.5) from (5.10) and write $L_r(t_1)$ for $(\log t_1)^{-r}$ we get

$$\begin{aligned}&\sum_{r=1}^{\infty}\sum_{s=0}^{\infty}A_{rs}\eta^s L_r(t_1)\\ &\quad=1-\frac{\alpha h}{2\pi}\sum_{r=1}^{\infty}\sum_{s=0}^{\infty}A_{rs}\int_{-1}^{1}\{L_{r-1}(t_1)+[\log 4-\gamma-2\log|\eta'-\eta|]L_r(t_1)\\ &\qquad+\frac{1}{6}r\pi^2L_{r+1}(t_1)+\frac{1}{2}r(r+1)GL_{r+2}(t_1)+\cdots\Big\}\eta'^s d\eta'\\ &\quad=1-\frac{\alpha h}{\pi}\sum_{r\geq 1}\sum_{s\geq 0}A_{rs}\Big\{\Big[L_{r-1}(t_1)+(\log 4-\gamma)L_r(t_1)+\frac{1}{6}r\pi^2L_{r+1}(t_1)\\ &\qquad+\frac{1}{2}r(r+1)GL_{r+2}(t_1)\Big]\frac{1+(-1)^s}{2(s+1)}-L_r(t_1)\int_{-1}^{1}\eta'^s\log|\eta'-\eta|\,d\eta'\Big\}\,.\end{aligned}\tag{5.12}$$

Now it will be shown in § 7 (a) that, for $|\eta|\leq 1$,

$$\begin{aligned}\int_{-1}^{1}\eta'^s\log|\eta'-\eta|\,d\eta'=\frac{1}{s+1}\Big\{&(1-\eta^{s+1})\log(1-\eta)+[(-1)^s+\eta^{s+1}]\log(1+\eta)\\ &-\frac{2}{s+1}\Big(\eta^s+\frac{1}{3}\eta^{s-2}+\frac{1}{5}\eta^{s-4}+\cdots\Big)\Big\}=F_s(\eta)\quad\text{(say)}\,,\end{aligned}\tag{5.13}$$

and hence

$$F_{2n}(\eta)=-\frac{2}{(2n+1)^2}+\sum_{r=1}^{\infty}\frac{\eta^{2r}}{r(2r-2n-1)}\,,\qquad F_{2n+1}(\eta)=2\sum_{r=1}^{\infty}\frac{\eta^{2r-1}}{(2r-1)(2r-2n+3)}\,,\tag{5.14}$$

and so, for $|\eta|\leq 1$,

$$\begin{aligned}\sum_{r=1}^{\infty}\sum_{s=0}^{\infty}A_{rs}\eta^sL_r(t_1)=1-\frac{\alpha h}{\pi}\sum_{r=1}^{\infty}\sum_{s=0}^{\infty}A_{rs}\Big[&L_{r-1}(t_1)+(\log 4-\gamma)L_r(t_1)+\frac{1}{6}r\pi^2L_{r+1}(t_1)\\ &+\frac{1}{2}r(r+1)GL_{r+2}(t_1)+\cdots\Big]\frac{1+(-1)^s}{2(s+1)}-\frac{\alpha h}{2\pi}\sum_{r=1}^{\infty}\sum_{s=0}^{\infty}A_{rs}F_s(\eta)L_r(t_1).\end{aligned}\tag{5.15}$$

But it is clear from symmetry that $S$ is an even function of $\eta$, and hence we need consider only even values of $s$. It will therefore be taken for granted in what follows that $A_{rs}$ is aero for odd $s$, which permits us to rewrite (5.15) more simply as

$$\begin{aligned}&\sum_{r=1}^{\infty}\sum_{s=0}^{\infty}A_{r,2s}\eta^{2s}L_r(t_1)\\ &\quad=1-\lambda\sum_{r=1}^{\infty}\sum_{s=0}^{\infty}\frac{A_{r,2s}}{2s+1}\Big[L_{r-1}(t_1)+\mu L_r(t_1)+\frac{1}{6}r\pi^2L_{r+1}(t_1)+\frac{1}{2}r(r+1)GL_{r+2}(t_1)+\cdots\Big]\\ &\qquad-\frac{1}{2}\lambda\sum_{r=1}^{\infty}\sum_{s=0}^{\infty}A_{r,2s}L_r(t_1)\Big\{\frac{2}{(2s+1)^2}-\sum_{p=1}^{\infty}\frac{\eta^{2p}}{p(2p-2s-1)}\Big\}\,,\end{aligned}\tag{5.16}$$

where $\lambda=\alpha h/\pi$ and $\mu=\log 4-\gamma\sim 0.8091$.

Next compare the coefficients of the individual terms $\eta^sL_r(t_1)$ beginning with the terms $s>0$. We have from (5.16)

$$A_{r,2s}=\frac{1}{2}\lambda\sum_{q=0}^{\infty}\frac{A_{r,2q}}{s(2s-2q-1)}\,.\tag{5.17}$$

Now (5.17) is an infinite set of homogeneous linear equations in the unknown $A$'s, and the system can be investigated in the usual way to determine the ratios of the successive $A_{r,2s}$ for fixed $r$. We note, however, that the coefficients in (5.17) are independent of $r$ and so therefore are the ratios. It follows that we can write

$$A_{r,2s}=\chi_rA_{1,2s}=\chi_rB_s\quad\text{(say)},\tag{5.18}$$

where the quantities depend only on the suffixes indicated, and $\chi_1=1$. The significance of (5.18) is that to the accuracy of the representation (5.10) the space and time variables are separable. In fact

$$S(\eta,\ t_1)=\sum_{r=1}^{\infty}\chi_r L_r(t_1)\sum_{s=0}^{\infty}B_s\eta^s. \tag{5.19}$$

To get an estimate of the $B$'s we shall make the approximation of neglecting terms corresponding to $s>3$. Equations (5.17) now become

$$\left.\begin{aligned}B_1&=\frac{1}{2}\lambda\left[B_0-B_1-\frac{1}{3}B_2-\frac{1}{5}B_3\right],\\ B_2&=\frac{1}{2}\lambda\left[\frac{1}{6}B_0+\frac{1}{2}B_1-\frac{1}{2}B_2-\frac{1}{6}B_3\right],\\ B_3&=\frac{1}{2}\lambda\left[\frac{1}{15}B_0+\frac{1}{9}B_1+\frac{1}{3}B_2-\frac{1}{3}B_3\right].\end{aligned}\right\} \tag{5.20}$$

The three equations (5.20) are sufficient to determine the ratios $B_0{:}B_1{:}B_2{:}B_3$ and we get

$$\frac{B_0}{\dfrac{45}{\lambda^3}+\dfrac{165}{4\lambda^2}+\dfrac{14}{\lambda}+\dfrac{16}{9}}=\frac{B_1}{\dfrac{45}{2\lambda^2}+\dfrac{3}{5\lambda}+\dfrac{8}{15}}=\frac{B_2}{\dfrac{15}{4\lambda^2}+\dfrac{8}{\lambda}+\dfrac{16}{15}}=\frac{B_3}{\dfrac{3}{2\lambda^2}+\dfrac{3}{\lambda}+\dfrac{16}{9}}=\omega\ \ \text{(say)}. \tag{5.21}$$

Incidentally we see from (5.20) why equations (5.17), in spite of their form, do not in fact lead to an eigenvalue problem for $\lambda$. At whichever point we choose to break off the $B_s$ sequence in (5.17) we shall always have one equation fewer than the number of unknowns, so that we can solve for the ratios of the latter. It is clear, of course, from physical considerations that there cannot be preferred values of $\lambda$, and that the problem must have a unique solution whatever $\lambda$ may be.

We now have to determine $\omega$, and for this we consider the term independent of $\eta$ and of $t_1$ in (5.16), containing

$$0=1-\lambda\sum^{\infty}\frac{A_{1s}}{s+1}=1-\lambda\sum_{s=0}^{\infty}\frac{B_s}{2s+1}. \tag{5.22}$$

From (5.21) and (5.22) we deduce that

$$\frac{1}{\omega\lambda}=\frac{424}{175}+\frac{66}{35\lambda}+\frac{348}{7\lambda^2}+\frac{45}{\lambda^3}. \tag{5.23}$$

The next step is to investigate the values of $\chi_r$ ($r=2, 3, \cdots$). For this purpose we put $\eta=0$ in (5.16) and use (5.18) and (5.22), obtaining

$$\begin{aligned}B_0\sum_{r=1}^{\infty}\chi_r L_r(t_1)&=1-\lambda\sum_{r=1}^{\infty}\chi_r[L_{r-1}(t_1)+\mu L_r(t_1)+\cdots]\sum_{s=0}^{\infty}\frac{B_s}{2s+1}\\ &=1-\sum_{r=1}^{\infty}\chi_r\left[L_{r-1}(t_1)+\mu L_r(t_1)+\frac{1}{6}r\pi^2L_{r+1}(t_1)+\frac{1}{2}r(r+1)GL_{r+2}(t_1)+\cdots\right].\end{aligned} \tag{5.24}$$

Comparing coefficients of the successive $L_r$'s we get

$$\left.\begin{aligned}&0=1-\chi_1, &&B_0\chi_1=-\mu\chi_1-\chi_2,\\ &B_0\chi_2=-\frac{1}{6}\pi^2\chi_1-\mu\chi_2-\chi_3, &&B_0\chi_3=-G\chi_1-\frac{1}{3}\pi^2\chi_2-\mu\chi_3-\chi_4.\end{aligned}\right\} \tag{5.25}$$

The first of these equations was already known, but the subsequent equations give

$$\chi_2=-(B_0+\mu),\quad \chi_3=(B_0+\mu)^2-\frac{\pi^2}{6},\quad \chi_4=-(B_0+\mu)^3+\frac{\pi^2}{2}(B_0+\mu)-G, \tag{5.26}$$

where $B_0$ is given by (5.21) and (5.23). We are thus able to estimate the time dependence of the surface temperature up to the term in $(\log t_1)^{-4}$, and the process could clearly be continued further if necessary.

To evaluate the rate of heat loss from the body we note that, by the boundary conditions, the only such loss is by radiation from the area $|y| \leq \alpha$ and it is there proportional to the surface temperature. It follows that the rate of heat loss per unit $z$ is proportional to

$$\int_{-\alpha}^{\alpha} \phi(y,\ t)dy = 2\alpha V \int_0^1 S(\eta,\ t_1)d\eta = 2\alpha V \sum_{s=0}^{\infty} \frac{B_s}{2s+1} \sum_{r\geq 1} \chi_r L_r(t_1) = \frac{2\alpha V}{\lambda} \sum_{r\geq 1} \chi_r L_r(t_1)\ , \tag{5.27}$$

by (5.19) and (5.22). But $\lambda = \alpha h/\pi$ and so we can write the rate of heat loss at time $t$ per unit $z$ as

$$R(t) = (2\pi VK/h) \sum_{r=1}^{\infty} \chi_r L_r(t_1) = (2\pi VK/h) M_\lambda(t_1) \text{ (say)}\ , \tag{5.28}$$

where $t_1 = kt/\alpha^2$ and $K$ is a constant of the materials involved. The function $M_\lambda$ is easily evaluated numerically. We note incidently that, when $\lambda$ is very small, it follows from (5.21) and (5.23) that $B_0 \sim \lambda^{-1}$ and so, by (5.26), $\chi_r \sim (-1/\lambda)^{r-1}$. Hence

$$M_\lambda(t_1) = [1+o(\lambda)]L_1(t_1) \sum_{r=1}^{\infty} (-1/\lambda)^{r-1} L_{r-1}(t_1) = \frac{1+o(\lambda)}{\log t_1 + \lambda^{-1}}\ , \tag{5.29}$$

provided that $\log t_1 > \lambda^{-1}$, and, in this case,

$$R(t) \sim 2\alpha VK/\{1+(\alpha h/\pi) \log (kt/\alpha^2)\}\ . \tag{5.30}$$

In particular this is the solution for the case of a very narrow slit $S_1$ (i.e. $\alpha \ll 1$), provided that $t > \frac{\alpha^2}{k} e^{\pi/\alpha h}$.

## § 6. S₁ Consists of Two Equal Strips

We shall conclude by considering the case in which $S_1$ consists of two equal parallel strips at a considerable distance apart,

$$S^+ :\ |y-d| \leq \frac{1}{2}\alpha\ , \qquad \text{and} \qquad S^- :\ |y+d| \leq \frac{1}{2}\alpha\ . \tag{6.1}$$

The total area exposed, per unit $z$, is the same as in the case discussed in § 5 and we shall investigate the dependence of $R(t)$ on $d$. It is assumed that $d \gg \alpha$. We again write $\eta = y/\alpha$, $t_1 = kt/\alpha^2, \cdots$ etc. and also $\delta = d/\alpha$. The integral equation for $S$ now becomes

$$S(\eta,\ t_1) = 1 - \frac{\alpha h}{2\pi} \int_0^{t_1} \frac{d\tau_1}{t_1 - \tau_1} \left[ \int_{-\delta-1/2}^{-\delta+1/2} + \int_{\delta-1/2}^{\delta+1/2} \right] \exp\left[ -\frac{(\eta-\eta')^2}{4(t_1-\tau_1)} \right] S(\eta',\ \tau_1)d\eta'\ . \tag{6.2}$$

We again assume for $S$ an expansion of the type (5.10). More precisely we shall write

$$\left.\begin{aligned} S(\eta,\ t_1) &= \sum_{r\geq 1} \sum_{s\geq 0} A_{rs} (\log t_1)^{-r} (\eta-\delta)^s \quad \text{in} \quad S^+ \\ \text{and} \qquad & \\ &= \sum_{r\geq 1} \sum_{s\geq 0} A_{rs} (\log t_1)^{-r} (-\eta-\delta)^s \quad \text{in} \quad S^-. \end{aligned}\right\} \tag{6.3}$$

It is clear that this expansion has all the necessary symmetry requirements in $\eta$ though we shall no longer have $A_{rs} = 0$ for odd $s$. Now let us take $\eta$ in $S^+$. Substituting from (6.3) into (6.2) gives, on writing $\eta = \delta + \zeta$, $\eta' = \delta + \zeta'$ in $S^+$ and $\eta' = -\delta + \zeta'$ in $S^-$,

$$\begin{aligned} \sum_{r\geq 1} \sum_{s\geq 0} A_{rs} \zeta^s L_r(t_1) &= 1 - (\alpha h/2\pi) \sum_{r,s} A_{rs} \left\{ \int_{-1/2}^{1/2} [L_{r-1}(t_1) + (\mu - 2 \log|\zeta-\zeta'|) L_r(t_1) + \cdots] \zeta'^s d\zeta' \right. \\ & \qquad \left. + (-1)^s \int_{-1/2}^{1/2} [L_{r-1}(t_1) + (\mu - 2 \log|\zeta-\zeta'+2\delta| L_r(t_1) + \cdots] \zeta'^s d\zeta' \right\} \\ &= 1 - \lambda \sum_{r,s} \frac{A_{r,2s}}{2^{2s}(2s+1)} \left[ L_{r-1}(t_1) + \mu L_r(t_1) + \frac{1}{6} r\pi^2 L_{r+1}(t_1) + \cdots \right] \\ & \qquad + \lambda \sum_{r,s} A_{rs} L_r(t_1) \int_{-1/2}^{1/2} \zeta'^s \{\log|\zeta-\zeta'| + (-1)^s \log|\zeta-\zeta'+2\delta|\} d\zeta'\ . \end{aligned} \tag{6.4}$$

We shall write

$$E_n(\zeta)=\int_{-1/2}^{1/2}\zeta'^n \log|\zeta-\zeta'|\,d\zeta'=\sum_{p=0}^{\infty} e_{np}\zeta^p\,, \quad \left(|\zeta|\leq\frac{1}{2}\right) \tag{6.5}$$

and

$$G_{n,\delta}(\zeta)=\int_{-1/2}^{1/2}\zeta'^n \log|\zeta-\zeta'+2\delta|\,d\zeta'=\sum_{p=0}^{\infty} q_{n,p}(\delta)\zeta^p. \quad \left(|\zeta|\leq\frac{1}{2}\,,\quad \delta\geq\frac{1}{2}\right) \tag{6.6}$$

The actual evaluation of the coefficients $e_{np}$, $g_{n,p}(\delta)$ will be deferred to § 7 so as not to confuse the main argument. Then

$$\begin{aligned}\sum_{r\geq1}\sum_{s\geq0} A_{rs}\zeta^s L_r(t_1)=1-\lambda\sum_{r,s}\frac{A_{r,2s}}{2^{2s}(2s+1)}\Big[L_{r-1}(t_1)+\mu L_r(t_1)+\cdots\Big]&\\ +\lambda\sum_{r,s}\sum_{p=0}^{\infty}A_{rs}[e_{sp}+(-1)^s g_{s,p}(\delta)]L_r(t_1)\zeta^p.&\end{aligned} \tag{6.7}$$

As in the case of the single strip we begin by comparing coefficients of $\zeta^p L_r(t_1)$ for $p>0$. This leads to

$$A_{rp}=\lambda\sum_{s=0}^{\infty}A_{rs}[e_{sp}+(-1)^s g_{sp}(\delta)]\,. \tag{6.8}$$

As before we see that the coefficients in this infinite set of equations for the $A_{rp}$ are independent of $r$. Hence the ratios of the successive $A_{rp}$'s ($p=1, 2, \cdots$) are independent of $r$ and we can write

$$A_{rp}=\chi_r A_{1p}=\chi_r C_p \quad \text{(say)}\,, \tag{6.9}$$

where, again as before, $\chi_1=1$. Again, putting $\zeta=0$ in (6.7), we get

$$\begin{aligned}\sum_r C_0\chi_r L_r(t_1)=1-\lambda\sum_s\frac{C_{2s}}{2^{2s}(2s+1)}\sum_r\chi_r\{L_{r-1}(t_1)+\mu L_r(t_1)+\cdots\}&\\ +\lambda\sum_r\chi_r L_r(t_1)\sum_{s\geq0}C_s[e_{s0}+(-1)^s g_{s0}]\,.&\end{aligned} \tag{6.10}$$

Since the left-hand side of (6.10) has no term independent of $t_1$, we must have

$$1-\lambda\chi_1\sum_s\frac{C_{2s}}{2^{2s}(2s+1)}=0\,, \tag{6.11}$$

and hence

$$\begin{aligned}C_0\sum_r\chi_r L_r(t_1)&=1-\sum_r\chi_r\left\{L_{r-1}(t_1)+\mu L_r(t_1)+\frac{1}{6}r\pi^2 L_{r+1}(t_1)+\cdots\right\}\\ &\quad+\lambda\sum_r\chi_r L_r(t_1)\sum_{s\geq0}C_s[e_{s0}+(-1)^s g_{s0}]\\ &=1-\sum_r\chi_r\{L_{r-1}(t_1)-\mu L_r(t_1)+\cdots\}+\lambda D\sum_r\chi_r L_r(t_1)\quad\text{(say)}\,,\end{aligned} \tag{6.12}$$

i.e.

$$(C_0-\lambda D+\mu)\sum_{r=1}^{\infty}\chi_r L_r(t_1)=1-\sum_{r=1}^{\infty}\chi_r\left[L_{r-1}(t_1)+\frac{r\pi^2}{6}L_{r+1}(t_1)+\cdots\right]. \tag{6.13}$$

We now compare coefficients of corresponding $L_r$'s, obtaining

$$\left.\begin{aligned}0&=1-\chi_1\,,\\ (C_0-\lambda D+\mu)\chi_1&=-\chi_2\,,\\ (C_0-\lambda D+\mu)\chi_2&=-\frac{\pi^2}{6}\chi_1-\chi_3\,,\\ (C_0-\lambda D+\mu)\chi_3&=-G\chi_1-\frac{\pi^2}{3}\chi_2-\chi_4\,,\quad\text{etc.}\end{aligned}\right\} \tag{6.14}$$

and hence

$$\left.\begin{aligned}
\chi_1&=1\,,\\
\chi_2&=-(C_0-\lambda D+\mu)\,,\\
\chi_3&=(C_0-\lambda D+\mu)^2-\frac{1}{6}\pi^2\,,\\
\chi_4&=-(C_0-\lambda D+\mu)^3+\frac{1}{2}\pi^2(C_0-\lambda D+\mu)-G\,.
\end{aligned}\right\} \tag{6.15}$$

Now the rate of heat loss from S⁺ is

$$KV\alpha\int_{-1/2}^{1/2}S(\eta,\,t_1)d\eta=KV\alpha\sum_{r,s}\frac{A_{r,2s}}{2^{2s}(2s+1)}L_r(t_1)=\frac{KV\alpha}{\lambda}\sum_r\chi_rL_r(t_1)\,. \tag{6.16}$$

The same is true for S⁻ and hence the total rate of loss of heat is

$$R_\delta(t)=\frac{2KV\alpha}{\lambda}\sum_r\chi_rL_r(t_1)=\frac{2\pi\,VK}{h}\sum_r\chi_rL_r(t)\,. \tag{6.17}$$

Hence the estimation of $R_\delta(t)$ depends entirely on the $\chi_r$'s and these, by (6.15), can be expressed in terms of $C_0$, $D$. We can get a reasonable estimate of $C_p$ by solving (6.8) with the approximation that all the $C_p$ for $p>4$ are negligible. We take the asymptotic values of $g_{sp}(\delta)$ valid for large $\delta$ and obtain, when $\delta\gg1$,

$$\begin{aligned}
\frac{C_0}{\dfrac{1}{\lambda^2}+\dfrac{3}{4\lambda}+\dfrac{1}{6}}=\frac{C_2}{\dfrac{2}{\lambda}+\dfrac{4}{9}}=\frac{C_4}{\dfrac{4}{3}\left(\dfrac{1}{\lambda}+2\right)}&=\frac{30\delta\left(\dfrac{1}{\lambda}+\dfrac{2}{3}\right)^2C_1}{\left(\dfrac{1}{\lambda}+\dfrac{1}{3}\right)\left(\dfrac{15}{\lambda^2}+\dfrac{14}{\lambda}+\dfrac{32}{9}\right)}\\
&=\frac{45\delta\left(\dfrac{1}{\lambda}+\dfrac{2}{3}\right)^2C_3}{2\left(\dfrac{15}{\lambda^2}+\dfrac{14}{\lambda}+\dfrac{32}{9}\right)}=\frac{\dfrac{15}{\lambda}}{\dfrac{15}{\lambda^2}+\dfrac{14}{\lambda}+\dfrac{32}{9}}\,.
\end{aligned} \tag{6.18}$$

while

$$D=\frac{\log\delta}{\lambda}-\frac{15}{\lambda}\,\frac{\dfrac{1}{\lambda^2}+\dfrac{182}{225\lambda}+\dfrac{2{,}927}{16{,}200}}{\dfrac{15}{\lambda^2}+\dfrac{14}{\lambda}+\dfrac{32}{9}}+O(\delta^{-2})\,. \tag{6.19}$$

If $\delta$ is very large while $\lambda$ is very small, then we see, by an argument similar to that used to establish (5.30) that

$$R_\delta(t)\sim2\alpha VK/\{1+(\alpha h/\pi)\log(kt/\alpha^2\delta)\}\,. \tag{6.20}$$

Comparison with (5.30) shows the effect of having two " half-slits " at a distance apart $2\delta$ times their combined width as compared with that of a single " full-width " slit.

## § 7. Derivation of Formulae

### a) *Proof of* (5.14)

Since $|\eta|\le1$,

$$\begin{aligned}
F_n(\eta)&=\int_{-1}^{\eta}\eta'^n\log(\eta-\eta')d\eta'+\int_{\eta}^{1}\eta'^n\log(\eta'-\eta)d\eta'\\
&=\int_0^{1+\eta}(\eta-\zeta)^n\log\zeta\,d\zeta+\int_0^{1-\eta}(\eta+\zeta)^n\log\zeta\,d\zeta\\
&=\phi_n(\eta)+(-1)^n\phi_n(-\eta)\qquad\text{(say).}
\end{aligned} \tag{7.1}$$

Now

$$\begin{aligned}
\phi_n(\eta)&=\sum_{r=0}^{n}(-1)^r\eta^{n-r}\binom{n}{r}\int_0^{1+\eta}\zeta^r\log\zeta\,d\zeta\\
&=\sum_{r=0}^{n}(-1)^r\binom{n}{r}\eta^{n-r}\\
&\quad\times\left\{\frac{(1+\eta)^{r+1}}{r+1}\log(1+\eta)-\frac{(1+\eta)^{r+1}}{(r+1)^2}\right\}\\
&=A_n(\eta)\log(1+\eta)-B_n(\eta)\,,
\end{aligned} \tag{7.2}$$

where

$$A_n(\eta)=\eta^n(1+\eta)\sum_{r=0}^{n}\binom{n}{r}\left(-\frac{1+\eta}{\eta}\right)^r\frac{1}{r+1}\,, \tag{7.3}$$

and

$$B_n(\eta)=\eta^n(1+\eta)\sum_{r=0}^{n}\binom{n}{r}\left(-\frac{1+\eta}{\eta}\right)^r\frac{1}{(r+1)^2}\,. \tag{7.4}$$

Now

$$\sum_{r=0}^{n}\binom{n}{r}\left(-\frac{1+\eta}{\eta}\right)^rx^r=\left(1-\frac{1+\eta}{\eta}x\right)^n\,. \tag{7.5}$$

Hence

$$A_n(\eta)=\eta^n(1+\eta)\int_0^1\left(1-\frac{1+\eta}{\eta}\,x\right)^n dx$$
$$=\frac{1}{n+1}\left[\eta^{n+1}+(-1)^n\right], \tag{7.6}$$

while

$$B_n(\eta)=\eta^n(1+\eta)\int_0^1\frac{dx}{x}\int_0^x\left(1-\frac{1+\eta}{\eta}t\right)^n dt$$
$$=\frac{\eta^{n+1}}{n+1}\int_0^1\frac{1}{x}\left[1-\left(1-\frac{1+\eta}{\eta}\,x\right)^{n+1}\right]dx\,. \tag{7.7}$$

Hence

$$B_n(\eta)+(-1)^nB_n(-\eta)$$
$$=\frac{1}{n+1}\int_0^1\frac{[\eta(1-x)+x]^{n+1}-[\eta(1-x)-x]^{n+1}}{x}dx$$
$$=\frac{2}{n+1}\sum_{r\leqq\frac{1}{2}n}\eta^{n-2r}\binom{n+1}{2r+1}\int_0^1 x^{2r}(1-x)^{n-2r}dx$$
$$=\frac{2}{n+1}\sum_{r\leqq\frac{1}{2}n}\eta^{n-2r}\binom{n+1}{2r+1}B(2r+1,\,n-2r+1)$$
$$=\frac{2}{n+1}\sum_{r\leqq\frac{1}{2}n}\frac{\eta^{n-2r}}{2r+1}\,. \tag{7.8}$$

Equation (5.14) is now an immediate consequence of (7.1), (7.6) and (7.8).

b) *The functions* $E_n(\zeta)$, $G_{n,\delta}(\zeta)$

From (6.5), if $|\zeta|\leq 1/2$,

$$E_n(\zeta)=\int_{-1/2}^{1/2}\zeta'^n\log|\zeta'-\zeta|d\zeta'$$
$$=\frac{1}{2^{n+1}}\int_{-1}^{1}\eta^n\log\left|\frac{\eta}{2}-\zeta\right|d\eta$$
$$=\frac{1}{2^{n+1}}\left\{\int_{-1}^{1}\eta^n\log|\eta-2\zeta|d\eta-\log 2\int_{-1}^{1}\eta^n d\eta\right\}$$
$$=-\frac{1+(-1)^n}{n+1}\,\frac{\log 2}{2^{n+1}}+\frac{1}{2^{n+1}}F_n(2\zeta)\,. \tag{7.9}$$

Again

$$G_{n,\delta}(\zeta)=\int_{-1/2}^{1/2}\zeta'^n\log(\zeta-\zeta'+2\delta)d\zeta'\,,$$
$$\text{since } |\zeta|\leq\tfrac{1}{2},\quad \delta\geqq 1$$
$$=\int_{-1/2}^{1/2}\zeta'^n\log(2\delta+\zeta)d\zeta'-\sum_{r=1}^{\infty}\int_{-1/2}^{1/2}\frac{\zeta'^{n+r}}{r(2\delta+\zeta)^r}d\zeta'$$
$$=\frac{1+(-1)^n}{2^{n+1}(n+1)}\log(2\delta+\zeta)$$
$$-\sum_{r=1}^{\infty}\frac{1+(-1)^{n+r}}{r(r+n+1)}\,\frac{1}{2^{n+r+1}(2\delta+\zeta)^r}\,. \tag{7.10}$$

To use (7.10) we note that

$$\sum_{r=1}^{\infty}\frac{x^r}{r(n+r+1)}=\frac{1}{n+1}\sum_{r=1}^{\infty}x^r\left(\frac{1}{r}-\frac{1}{n+r+1}\right)$$
$$=\frac{1}{(n+1)x^{n+1}}\left[x+\frac{x^2}{2}+\cdots+\frac{x^{n+1}}{n+1}\right]$$
$$-\frac{1}{n+1}(1-x^{-n-1})\log(1-x)\,. \tag{7.11}$$

$G_{n,\delta}(\zeta)$ and the coefficients of its expansion can now be obtained immediately.

## References

1) H. Feshbach: Phys. Rev. **65** (1944) 307.
2) W. Karush and G. Young: J. Appl. Phys. **23** (1952) 1191.
3) H. S. Carslaw and J. C. Jaeger: *Conduction of Heat in Solids* (Oxford, 1948).
4) A. Erdelyi: *Tables of Integral Functions*, I. (New York, 1954).
5) A. Erdelyi: *Higher Transcendental Functions*, II. (New York, 1953).
6) N. W. McLachlan: *Bessel Functions for Engineers* (Oxford, 1955).

JOURNAL OF THE PHYSICAL SOCIETY OF JAPAN Vol. 11, No. 9, SEPTEMBER, 1956

# Note on the Drag on a Circular Cylinder moving with Low Speeds in a Semi-infinite Viscous Liquid bounded by a Plane Wall

By Yorisaburo TAKAISI

*Department of Physics, Faculty of Education, Ehime University, Matuyama*

(Received April 14, 1956)

The steady slow motion of a circular cylinder in a semi-infinite viscous liquide bounded by a plane wall is discussed on the basis of Stokes' equations of motion, assuming that the cylinder is moving parallel to the bounding wall. It is shown that the components of velocity satisfying the boundary conditions on the bounding plane wall as well as at the surface of the cylinder, satisfy also automatically the conditions at infinity. A second approximation for the drag on the circular cylinder is obtained. As far as higher order terms are neglected, it is in perfect agreement with the first approximation obtained recently by the present writer on the basis of Oseen's linearized equations of motion.

## § 1. Introduction

In a recent paper[1], the present writer has made, on the basis of Oseen's linearized equations of motion, an investigation on the steady motion with low speed $U$ of a circular cylinder in a semi-infinite viscous liquid parallel to its bounding wall, by developing an analysis similar to that in Faxén's treatment of the sphere problem[2][3]. Thus, it was found that the drag on the cylinder is of the so-called Stokes' type in the case of sufficiently small Reynolds numbers $R\ (=Ud/\nu)$ and $R^*\ (=Ub/\nu)$, where $d$ is the diameter of the cylinder, $b$ is the distance between its centre and the wall, and $\nu$ is the kinematic viscosity of the liquid concerned.

As is well-known, by using Stokes' equations of motion it is impossible to satisfy all the conditions for the steady motion produced by the translation of a circular cylinder through an infinite mass of liquid. The above results suggest, however, that, in a semi-infinite viscous liquid bounded by a plane wall, Stokes' equations of motion are also effective for the steady motion of a circular cylinder, and to this enquiry the present note is directed. Thus, a second approximation for the drag on the cylinder is obtained.

## § 2. Method of Solution

As in the previous paper, suppose that a cylinder of radius $a$ is moving, with constant slow velocity $U$, from right to left in a semi-infinite viscous liquid at rest parallel to its bounding plane wall. Referring to rectangular coordinates $Ox$, $Oy$ with its origin at the centre of the cylinder, where the $x$- and $y$-axes are taken parallel and perpendicular to the wall respectively, the fluid at infinity flows, with constant velocity $U$, past the cylinder at rest in the positive direction of the $x$-axis (Fig. 1). In this case the bounding wall should also move, with the same velocity $U$, from left to right in its own plane, so as to satisfy the boundary conditions.

Using the stream function $\psi$, Stokes' equations of motion for the two-dimensional steady motion of a viscous liquid are expressed as follows:

$$\Delta\Delta\psi=0\,, \tag{2.1}$$

where $\Delta=\partial^2/\partial x^2+\partial^2/\partial y^2$.

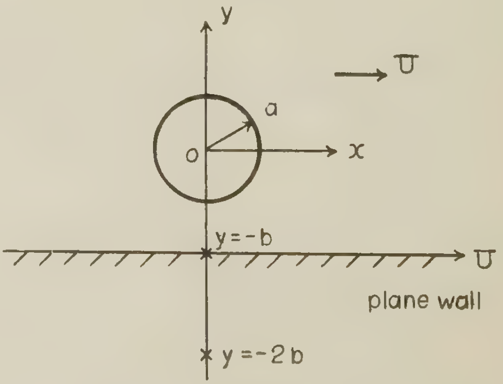

Fig. 1.

The solution of (2.1) can be written in the form

$$\psi=\psi_1+\psi_2\,, \tag{2.2}$$

where

$$\Delta\psi_1=0\,, \tag{2.3}$$

$$\Delta\Delta\psi_2=0\,. \tag{2.4}$$

The solutions satisfying (2.3) and (2.4) are given respectively by

$$\psi_1=A_0\ln r+\sum_{n=1}^{\infty}A_n r^{-n}\cos n\theta+B_0\theta+\sum_{n=1}^{\infty}B_n r^{-n}\sin n\theta\,, \tag{2.5}$$

$$\psi_2=a_0 r\ln r\cos\theta+\sum_{n=1}^{\infty}a_n r^{-n+1}\cos(n+1)\theta+b_0 r\ln r\sin\theta+\sum_{n=1}^{\infty}b_n r^{-n+1}\sin(n+1)\theta\,, \tag{2.6}$$

where $x=r\cos\theta$, $y=r\sin\theta$. As mentioned already, the boundary conditions at infinity for unbounded liquid are not satisfied with the first two terms in $\psi_2$.

If we confine ourselves to the approximation of order $(a/b)^2$ in the expression of the drag on the cylinder, it suffices to take only the first four and six terms in (2.5) and (2.6) respectively. We then have

$$\begin{aligned}u=\frac{\partial\psi}{\partial y}&=A_0\frac{y}{r^2}-A_1\frac{2xy}{r^4}+B_0\frac{x}{r^2}+B_1\left(\frac{1}{r^2}-\frac{2y^2}{r^4}\right)+a_0\frac{xy}{r^2}-a_1\left(\frac{4y}{r^2}-\frac{4y^3}{r^4}\right)\\&-a_2\left(\frac{10xy}{r^4}-\frac{16xy^3}{r^6}\right)+b_0\left(\ln r+\frac{y^2}{r^2}\right)+b_1\left(\frac{2x}{r^2}-\frac{4xy^2}{r^4}\right)+b_2\left(\frac{3}{r^2}-\frac{18y^2}{r^4}+\frac{16y^4}{r^6}\right),\end{aligned} \tag{2.7}$$

$$\begin{aligned}v=-\frac{\partial\psi}{\partial x}&=-A_0\frac{x}{r^2}+A_1\left(\frac{1}{r^2}-\frac{2y^2}{r^4}\right)+B_0\frac{y}{r^2}+B_1\frac{2xy}{r^4}-a_0\left(1+\ln r-\frac{y^2}{r^2}\right)\\&-a_1\frac{4xy^2}{r^4}+a_2\left(\frac{1}{r^2}-\frac{14y^2}{r^4}+\frac{16y^4}{r^6}\right)-b_0\frac{xy}{r^2}+b_1\left(\frac{2y}{r^2}-\frac{4y^3}{r^4}\right)+b_2\left(\frac{6xy}{r^4}-\frac{16xy^3}{r^6}\right).\end{aligned} \tag{2.8}$$

Now, $\ln r$ can be expressed in an integral form as:

$$\ln r=-\frac{1}{2}\int_{-\infty}^{\infty}\frac{1}{|\alpha|}e^{i\alpha x-|\alpha||y|}d\alpha+C\,, \tag{2.9}$$

where $C$ is an appropriate constant so chosen as to make the integral convergent.

Making use of (2.9) and its derivatives with respect to $x$ and $y$, we obtain integral expressions for the components of velocity in the forms:

$$\begin{aligned}u=&\frac{1}{2}\int_{-\infty}^{\infty}\left(A_0\frac{y}{|y|}-iB_0\frac{\alpha}{|\alpha|}+iA_1\alpha\frac{y}{|y|}-B_1|\alpha|\right)e^{i\alpha x-|\alpha||y|}\,d\alpha\\&+\frac{1}{2}\int_{-\infty}^{\infty}\left\{\left(-b_0\frac{1}{|\alpha|}-2a_1\frac{y}{|y|}-2ib_1\frac{\alpha}{|\alpha|}+3ia_2\alpha\frac{y}{|y|}-3b_2|\alpha|\right)\right.\\&\qquad\left.+\left(-ia_0\frac{\alpha}{|\alpha|}+2a_1|\alpha|-2ia_2\alpha|\alpha|\right)y+(b_0+2ib_1\alpha+2b_2\alpha^2)|y|\right\}e^{i\alpha x-|\alpha||y|}\,d\alpha\,,\\v=&-a_0-\frac{1}{2}\int_{-\infty}^{\infty}\left(-iA_0\frac{\alpha}{|\alpha|}-B_0\frac{y}{|y|}+A_1|\alpha|+iB_1\alpha\frac{y}{|y|}\right)e^{i\alpha x-|\alpha||y|}\,d\alpha\\&-\frac{1}{2}\int_{-\infty}^{\infty}\left\{\left(-a_0\frac{1}{|\alpha|}+a_2|\alpha|+ib_2\alpha\frac{y}{|y|}\right)+(-a_0-2ia_1\alpha-2a_2\alpha^2)|y|\right.\\&\qquad\left.-\left(ib_0\frac{\alpha}{|\alpha|}-2b_1|\alpha|+2ib_2\alpha|\alpha|\right)y\right\}e^{i\alpha x-|\alpha||y|}\,d\alpha\,,\end{aligned} \tag{2.10}$$

where the constant $C$ has been omitted, for it can be added whenever it is necessary.

Further, by Fourier expansion, we obtain from (2.7) and (2.8),

$$\begin{aligned}w=u-iv=&\,b_0\left(\frac{1}{2}+\ln r\right)-ia_0\left(\frac{1}{2}-\ln r\right)+e^{-i\theta}\left(\frac{B_0}{r}+i\frac{A_0}{r}\right)+e^{i\theta}\left(\frac{b_1}{r}+i\frac{a_1}{r}\right)\\&+e^{-2i\theta}\left\{\left(-\frac{1}{2}b_0+\frac{B_1}{r^2}\right)+i\left(\frac{1}{2}a_0-\frac{A_1}{r^2}\right)\right\}+e^{2i\theta}\left(\frac{b_2}{r^2}+i\frac{a_2}{r^2}\right)+\cdots.\end{aligned} \tag{2.11}$$

In order to satisfy the boundary conditions on the bounding plane wall as well as at the surface of the cylinder, we now superpose, as done by Faxén in the case of sphere problem, a flow due to images, which is defined as:

$$\begin{aligned}
u^* &= \frac{1}{2}\int_{-\infty}^{\infty} f_1(\alpha)\Bigl(1-\frac{i\alpha}{|\alpha|}-|\alpha|+i\alpha\Bigr)e^{i\alpha x-|\alpha|(y+2b)}\,d\alpha \\
&\quad+\frac{1}{2}\int_{-\infty}^{\infty} f_2(\alpha)\Bigl\{\Bigl(-\frac{1}{|\alpha|}-2-2i\frac{\alpha}{|\alpha|}-3|\alpha|+3i\alpha\Bigr) \\
&\qquad\qquad+\Bigl(1-\frac{i\alpha}{|\alpha|}+2|\alpha|+2i\alpha+2\alpha^2-2i\alpha|\alpha|\Bigr)(y+2b)\Bigr\}e^{i\alpha x-|\alpha|(y+2b)}\,d\alpha\,, \\
v^* &= -\frac{1}{2}\int_{-\infty}^{\infty} f_1(\alpha)\Bigl(-1-\frac{i\alpha}{|\alpha|}+|\alpha|+i\alpha\Bigr)e^{i\alpha x-|\alpha|(y+2b)}\,d\alpha-\frac{1}{2}\int_{-\infty}^{\infty} f_2(\alpha)\Bigl\{\Bigl(-\frac{1}{|\alpha|}+|\alpha|+i\alpha\Bigr) \\
&\qquad\qquad+\Bigl(-1-i\frac{\alpha}{|\alpha|}-2i\alpha+2|\alpha|-2\alpha^2-2i\alpha|\alpha|\Bigr)(y+2b)\Bigr\}e^{i\alpha x-|\alpha|(y+2b)}\,d\alpha\,,
\end{aligned}\qquad(2.12)$$

where $b$ denotes the distance of the centre of the cylinder from the wall (see Fig. 1), and $f_1(\alpha)$ and $f_2(\alpha)$ are unknown functions to be determined by the under-mentioned boundary conditions.

The boundary conditions to be satisfied on the bounding plane wall $y=-b$ as well as at the surface of the cylinder are as follows:

(i) $$(u+u^*)_{y=-b}=0\,,\qquad (v+v^*)_{y=-b}=0\,,\qquad(2.13)$$

(ii) $$(w+w^*)_{r=a}=-U\,,\qquad(2.14)$$

where $w^*=u^*-iv^*$.

It will become clear later in § 4 that the boundary conditions at infinity are satisfied automatically by the components of velocity, which satisfy the above-mentioned conditions.

## § 3. Determination of the Functions $f_1(\alpha)$ and $f_2(\alpha)$

Inserting the values of $(u,\ v)$ and $(u^*,\ v^*)$ as given respectively by (2.10) and (2.12) into (2.13), we can express the functions $f_1(\alpha)$ and $f_2(\alpha)$ so far undetermined in terms of the unknown constants $A_0,\ B_0,\ \cdots,\ b_2$ as:

$$\begin{aligned}
f_1(\alpha) &= \frac{1}{2(1-|\alpha|)(1+2i\alpha+2\alpha^2)}\Bigl\{b_0\frac{1}{2|\alpha|}-a_1+ib_1\frac{\alpha}{|\alpha|}+ia_2\alpha+b_2|\alpha| \\
&\quad+\Bigl(ib_0\frac{\alpha}{|\alpha|}-2ia_1\alpha-2b_1|\alpha|-2a_2\alpha^2+2ib_2\alpha|\alpha|\Bigr)b \\
&\quad+(|\alpha|+i\alpha)\Bigl[-2A_0|\alpha|+B_0\Bigl(\frac{1}{2|\alpha|}+1\Bigr) \\
&\quad+A_1\Bigl(\frac{1}{2}+|\alpha|\Bigr)-2B_1\alpha^2-\frac{1}{2}b_0+a_1|\alpha|+a_2\Bigl(\frac{1}{2}+|\alpha|\Bigr)-3b_2\alpha^2 \\
&\quad+b\{A_0(1+2\alpha^2)-2B_0|\alpha|-2A_1\alpha^2+B_1(|\alpha|+2\alpha^2|\alpha|)+3b_0|\alpha|-6a_1\alpha^2-4b_1|\alpha|-6a_2\alpha^2 \\
&\quad+b_2(|\alpha|+8\alpha^2|\alpha|)\}+b^2\{-b_0(1+2\alpha^2)+2a_1(|\alpha|+2\alpha^2|\alpha|)+4b_1\alpha^2+4a_2\alpha^2|\alpha|-2b_2(\alpha^2+2\alpha^4)\}\Bigr] \\
&\quad+(|\alpha|-i\alpha)\Bigl[A_0\Bigl(\frac{1}{2|\alpha|}+1\Bigr)+2B_0|\alpha|+2A_1\alpha^2+B_1\Bigl(\frac{1}{2}+|\alpha|\Bigr)+b_1|\alpha|+3a_2\alpha^2+b_2\Bigl(\frac{1}{2}+|\alpha|\Bigr) \\
&\quad+b\{-2A_0|\alpha|-B_0(1+2\alpha^2)-A_1(|\alpha|+2\alpha^2|\alpha|) \\
&\quad-2B_1\alpha^2-2b_0+4a_1|\alpha|-6b_1\alpha^2-a_2(|\alpha|+8\alpha^2|\alpha|)-6b_2\alpha^2\} \\
&\quad+b^2\{2b_0|\alpha|-4a_1\alpha^2+2(|\alpha|+2\alpha^2|\alpha|)b_1+2a_2(\alpha^2+2\alpha^4)+4b_2\alpha^2|\alpha|\}\Bigr]\Bigr\}\,,
\end{aligned}\qquad(3.1)$$

$$\begin{aligned}
f_2(\alpha) &= \frac{1}{1+2i\alpha+2\alpha^2}\Bigl\{(|\alpha|+i\alpha)\Bigl[-A_0-B_1|\alpha|-\frac{1}{2}b_0\frac{1}{|\alpha|}+a_1-2b_2|\alpha|+b(b_0-2a_1|\alpha|+2b_2\alpha^2)\Bigr] \\
&\qquad+(|\alpha|-i\alpha)[B_0+A_1|\alpha|+b_1+2a_2|\alpha|-b(2b_1|\alpha|+2a_2\alpha^2)]\Bigr\}\,,
\end{aligned}\qquad(3.2)$$

and also we have a relation

$$a_0=0\,. \tag{3.3}$$

Inserting these expressions into (2.12) and after some lengthy calculations, we obtain, neglecting all terms higher than $\mathcal{E}^3$,

$$\begin{aligned} w^* = {} & \frac{1}{4}\frac{A_0}{b}\mathcal{E}^2-\frac{B_2}{b^2}\left(\frac{1}{4}-\frac{3}{8}\mathcal{E}^2\right)-b_0\left(\frac{1}{2}+\frac{1}{8}\mathcal{E}^2+\ln 2b\right)-\frac{a_1}{b}\left(1-\frac{1}{2}\mathcal{E}^2\right)+\frac{b_2}{b^2}\left(\frac{3}{4}-\frac{3}{4}\mathcal{E}^2\right) \\ & +i\left\{-\frac{B_0}{b}\left(1-\frac{1}{4}\mathcal{E}^2\right)-\frac{A_1}{b^2}\left(\frac{3}{4}-\frac{3}{8}\mathcal{E}^2\right)+\frac{b_1}{b}\left(1-\frac{1}{2}\mathcal{E}^2\right)+\frac{a_2}{b^2}\left(\frac{3}{4}-\frac{3}{4}\mathcal{E}^2\right)\right\} \\ & +i\mathcal{E}e^{-i\theta}\left(-\frac{1}{2}\frac{A_0}{b}-\frac{1}{2}\frac{B_1}{b^2}-\frac{1}{2}\frac{a_1}{b}+\frac{1}{2}\frac{b_2}{b^2}\right) \\ & +\mathcal{E}e^{i\theta}\left\{\frac{1}{4}\frac{B_0}{b}+\frac{1}{2}\frac{A_1}{b^2}-\frac{b_1}{b}-\frac{3}{2}\frac{a_2}{b^2}+i\left(-\frac{1}{4}\frac{A_0}{b}-\frac{1}{2}\frac{B_1}{b^2}+\frac{1}{2}b_0-\frac{a_1}{b}+\frac{3}{2}\frac{b_2}{b^2}\right)\right\} \\ & +\mathcal{E}^2e^{-2i\theta}\left\{-\frac{1}{8}\frac{A_0}{b}-\frac{3}{16}\frac{B_1}{b^2}+\frac{1}{16}b_0-\frac{1}{4}\frac{a_1}{b}+\frac{3}{8}\frac{b_2}{b^2}+i\left(\frac{1}{8}\frac{B_0}{b}+\frac{3}{16}\frac{A_1}{b^2}-\frac{1}{4}\frac{b_1}{b}-\frac{3}{8}\frac{a_2}{b^2}\right)\right\} \\ & +\mathcal{E}^2e^{2i\theta}\left\{\frac{1}{8}\frac{A_0}{b}+\frac{3}{8}\frac{B_1}{b^2}-\frac{3}{16}b_0+\frac{3}{4}\frac{a_1}{b}-\frac{27}{16}\frac{b_2}{b^2}+i\left(\frac{1}{8}\frac{B_0}{b}+\frac{3}{8}\frac{A_1}{b^2}-\frac{3}{4}\frac{b_1}{b}-\frac{27}{16}\frac{a_2}{b^2}\right)\right\}, \end{aligned} \tag{3.4}$$

where $\mathcal{E}=r/b$.

## § 4. Determination of the Constants $A_0$, $B_0$, $\cdots$, and $b_2$

The constants $A_0$, $B_0$, $\cdots$, and $b_2$ can be determined by inserting (2.11) and (3.4) into (2.14), and we have, after some calculations,

$$\left.\begin{aligned} & B_0=A_1=b_1=a_2=0\,, \qquad A_0\sim \mathrm{O}(\mathcal{E}_0^3)\sim 0\,, \\ & B_1=\left(\frac{1}{2}-\frac{1}{16}\mathcal{E}_0^2\right)a^2b_0\,, \qquad a_1=-\frac{1}{2}a\mathcal{E}_0b_0\,, \qquad b_2=\frac{3}{16}a^2\mathcal{E}_0^2b_0\,, \end{aligned}\right\} \tag{4.1}$$

and

$$b_0=\frac{U}{\ln(2b/a)-(1/4)\mathcal{E}_0^2}\,, \tag{4.2}$$

where $\mathcal{E}_0=a/b$.

Making use of (3.3), (4.1) and (4.2), we have finally the expressions for the components of velocity, which satisfy the boundary conditions on the bounding plane wall $y=-b$ exactly, and the conditions at the surface of the cylinder to the order of $(a/b)^2$, in the forms:

$$\begin{aligned} (u+u^*)/b_0 = {} & \frac{1}{2}\frac{a^2}{r^2}\left(1-\frac{1}{8}\mathcal{E}_0^2\right)\left(1-\frac{2y^2}{r^2}\right)+\frac{2ay}{r^2}\left(1-\frac{y^2}{r^2}\right)\mathcal{E}_0 \\ & +\ln r+\frac{y^2}{r^2}+\frac{3}{16}\frac{a^2}{r^2}\left(3-\frac{18y^2}{r^2}+\frac{16y^4}{r^4}\right)\mathcal{E}_0^2 \\ & +\left(\frac{1}{2}-\frac{1}{16}\mathcal{E}_0^2\right)\frac{a^2}{r_1^2}\left\{-1+\frac{2(y+2b)^2+12(y+b)(y+2b)}{r_1^2}-\frac{16(y+b)(y+2b)^3}{r_1^4}\right\} \\ & -\ln r_1-\frac{(y+2b)^2+2b(y+b)}{r_1^2}+\frac{4b(y+b)(y+2b)^2}{r_1^4} \\ & +\frac{1}{2}\frac{a}{r_1}\mathcal{E}_0\left\{\frac{4(y+2b)}{r_1}-\frac{4(y+2b)^3+24b(y+b)(y+2b)}{r_1^3}+\frac{32b(y+b)(y+2b)^3}{r_1^5}\right\} \\ & +\frac{3}{16}\frac{a^2}{r_1^2}\mathcal{E}_0^2\left\{-3+\frac{18(y+2b)^2+12(y+b)(y+4b)}{r_1^2}\right. \\ & \left.-\frac{16(y+2b)^4+16(y+b)(y+2b)^3+192b(y+b)(y+2b)^2}{r_1^4}+\frac{192b(y+b)(y+2b)^4}{r_1^6}\right\}, \end{aligned}$$

$$(v+v^*)/b_0=\left(1-\frac{1}{8}\mathcal{E}_0^2\right)\frac{a^2xy}{r^4}+\frac{2a\mathcal{E}_0xy^2}{r^4}-\frac{xy}{r^2}+\frac{3}{8}\frac{a^2xy}{r^4}\left(3-\frac{8y^2}{r^2}\right)\mathcal{E}_0^2$$

$$
\begin{aligned}
&+\left(\frac{1}{2}-\frac{1}{16}\varepsilon_0^2\right)\frac{a^2}{r_1^2}\left\{\frac{2x(y+2b)-4x(y+b)}{r_1^2}+\frac{16x(y+b)(y+2b)^2}{r_1^4}\right\}+\frac{xy}{r_1^2}-\frac{4bx(y+b)(y+2b)}{r_1^4}\\
&+\frac{1}{2}\frac{a}{r_1}\varepsilon_0\left\{\frac{4xy(y+2b)+8bx(y+b)}{r_1^3}-\frac{32bx(y+b)(y+2b)^2}{r_1^5}\right\}\\
&+\frac{3}{16}\frac{a^2}{r_1^2}\varepsilon_0^2\left\{-\frac{6xy}{r_1^2}+\frac{16xy(y+2b)^2+16x(y+b)(y+2b)^2+96bx(y+b)(y+2b)}{r_1^4}\right.\\
&\left.-\frac{192bx(y+b)(y+2b)^3}{r_1^6}\right\}, \qquad (4.3)
\end{aligned}
$$

where $r_1^2=x^2+(y+2b)^2$.

As mentioned already, it it easily verified that the conditions at infinity are satisfied automatically by (4.3).

## § 5. The Drag experienced by the Cylinder

Now, by integrating the fluid stresses over the circular cylinder, it is easily shown that the drag $D$ experienced by the cylinder per its unit length can be expressed as:

$$D=4\pi\mu b_0\,, \qquad (5.1)$$

where $\mu$ is the viscosity of the liquid concerned.

Hence, if use is made of (4.2), we have

$$D/\mu U=\frac{4\pi}{\ln(2b/a)-1/4\cdot(a/b)^2}\,. \qquad (5.2)$$

As far as the term involving $(a/b)^2$ is neglected, this formula is in perfect agreement with the first approximation obtained recently by the present writer on the basis of Oseen's linearized equations of motion.

As an addendum, in the recent analysis, there is a lift on the circular cylinder perpendicular to the bounding wall, however, no lift appears in this case.

## § 6. Summary

The steady slow motion of a circular cylinder in a semi-infinite viscous liquid bounded by a plane wall is discussed on the basis of Stokes' equations of motion, assuming that the cylinder is moving parallel to the bounding wall. It is shown that the components of velocity satisfying the boundary conditions on the bounding plane wall as well as at the surface of the cylinder, satisfy also automatically the conditions at infinity. Thus, a second approximation for the drag on the circular cylinder is obtained. As far as the term involving $(a/b)^2$ is neglected, the drag on the cylinder is in perfect agreement with the first approximation obtained recently by the present writer on the basis of Oseen's linearized equations of motion.

In conclusion, the writer wishes to express his cordial thanks to Professor S. Tomotika for his continual encouragement and also for his kind inspection of the manuscript.

### References

1) Y. Takaisi: J. Phys. Soc. Japan **10** (1955) 407.
2) H. Faxén: Diss. Uppsala (1921).
3) H. Faxén: Ann. d. Phys. **68** (1922) 89.

JOURNAL OF THE PHYSICAL SOCIETY OF JAPAN Vol. 11, No. 9, SEPTEMBER, 1956

# Note on the Drag on a Circular Cylinder moving with Low Speeds in a Viscous Liquid between Two Parallel Walls

By Yorisaburo TAKAISI

*Department of Physics, Faculty of Education, Ehime University, Matuyama*

(Received April 14, 1956)

The steady slow motion of a circular cylinder in a viscous liquid bounded by two parallel plane walls is discussed on the basis of Stokes' equations of motion, confining ourselves to the case when the cylinder is moving midway between the bounding walls. A second approximation for the drag experienced by the cylinder is then calculated and compared with White's experiments. But the disagreement existing between the first approximation obtained recently by the present writer on the basis of Oseen's linearized equations of motion and White's empirical formula, when the values of the ratio (distance between the walls/diameter of the cylinder) are smaller than 20, has hardly been removed. As far as higher order terms are neglected, the second approximation is in perfect agreement with the first approximation.

## §1. Introduction

In quite a recent paper[1)], the present writer has made, on the basis of Oseen's linearized equations of motion, an investigation on the steady motion with low speed $U$ of a circular cylinder in a viscous liquid bounded by the parallel plane walls, confining ourselves to the case when the cylinder is moving midway between the bounding walls. Thus, the drag experienced by the cylinder was calculated to Lamb's approximation, and compared with White's experiments[2)] on wires falling in viscous liquids between two vertical plates. Allowing for some experimental errors, it was seen that the coincidence of our theoretical results with White's experimental ones is fairly well, provided the values of the ratio $b/a$ are greater than 20, where $a$ is the radius of the cylinder and $2b$ is the distance between the two walls.

When the ratio $b/a$ is smaller than 20, the disagreement between the theoretical results and the empirical ones became remarkable. Therefore, we should perhaps proceed with approximation one step or more, but the analysis based upon Oseen's equations of motion would then become lengthy and difficult. For this purpose, however, Stokes' equations of motion seem effective, as in the case of the steady slow motion of a circular cylinder in a semi-infinite viscous liquid bounded by a plane wall[3)], and to this enquiry the present note is directed.

## § 2. Method of Solution

As in the previous paper, suppose that a cylinder of radius $a$ is moving, with constant slow velocity $U$, from right to left in a viscous liquid at rest, which is bounded by parallel plane walls. Referring to rectangular coordinate-system $Ox$, $Oy$ with its origin at the centre of the cylinder, where the $x$- and $y$-axes are taken parallel and perpendicular to the walls respectively, the liquid at infinity flows with constant velocity $U$, past the cylinder at rest in the positive direction of the $x$-axis (Fig. 1). In this case the bounding plane walls should also move with the same

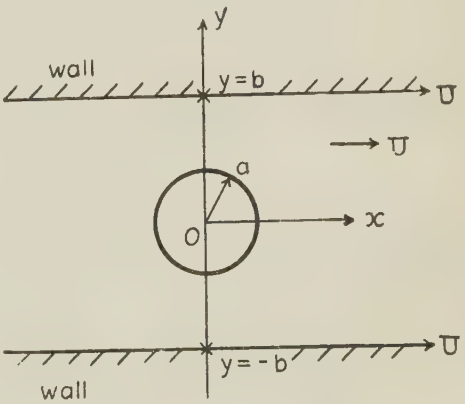

Fig. 1.

velocity $U$ from left to right in their own planes, so as to satisfy the boundary conditions.

Using the stream function $\psi$, Stokes' equations of motion for the two-dimensional steady motion of a viscous liquid are expressed as follows:

$$\Delta\Delta\psi=0\,, \tag{2.1}$$

where

$$\Delta=\partial^2/\partial x^2+\partial^2/\partial y^2.$$

The solution of (2.1) can be written in the form

$$\psi=\psi_1+\psi_2\,, \tag{2.2}$$

where

$$\Delta\psi_1=0\,, \tag{2.3}$$

$$\Delta\Delta\psi_2=0\,. \tag{2.4}$$

If we confine ourselves to the approximation of order $(a/b)^2$ in the expression of the drag on the circular cylinder, the solutions satisfying (2.3) and (2.4) are given simply by;

$$\begin{aligned}\psi_1=&A_0\ln r+A_1r^{-1}\cos\theta\\&+B_0\theta+B_1r^{-1}\sin\theta\,,\end{aligned} \tag{2.5}$$

$$\begin{aligned}\psi_2=&a_0\,r\ln r\cos\theta+a_1\cos 2\theta+a_2r^{-1}\cos 3\theta\\&+b_0r\ln r\sin\theta+b_1\sin 2\theta+b_2r^{-1}\sin 3\theta\,,\end{aligned} \tag{2.6}$$

where $x=r\cos\theta\,,\quad y=r\sin\theta\,.$

In a special case when the cylinder is moving midway between two bounding plane walls, we may put, due to the symmetry of the flow,

$$A_0=A_1=a_0=a_1=a_2=0\,.$$

Moreover, referring to the analysis in the case of a semi-infinite viscous liquid bounded by a plane wall[3], we may also put

$$b_1=0\,.$$

Now, $\ln r$ can be expressed in an integral form as:

$$\ln r=-\frac{1}{2}\int_{-\infty}^{\infty}\frac{1}{|\alpha|}e^{i\alpha x-|\alpha||y|}d\alpha+C\,, \tag{2.7}$$

where $C$ is an appropriate constant so chosen as to make the integral convergent. Making use of (2.7) and its derivatives with respect to $x$ and $y$, we obtain integral expressions for the components of velocity in the forms:

$$\left.\begin{aligned}u=\frac{\partial\psi}{\partial y}=&-\frac{1}{2}\int_{-\infty}^{\infty}B_1|\alpha|e^{i\alpha x-|\alpha||y|}d\alpha\\&+\frac{1}{2}\int_{-\infty}^{\infty}\left\{\left(-\frac{1}{|\alpha|}+|y|\right)b_0+(-3|\alpha|+2\alpha^2|y|)b_2\right\}e^{i\alpha x-|\alpha||y|}d\alpha\,,\\v=-\frac{\partial\psi}{\partial x}=&-\frac{1}{2}i\int_{-\infty}^{\infty}B_1\alpha\frac{y}{|y|}e^{i\alpha x-|\alpha||y|}d\alpha\\&-\frac{1}{2}i\int_{-\infty}^{\infty}\left\{-\frac{\alpha}{|\alpha|}yb_0+\left(\alpha\frac{y}{|y|}-2\alpha|\alpha|y\right)b_2\right\}e^{i\alpha x-|\alpha||y|}d\alpha\,,\end{aligned}\right\} \tag{2.8}$$

where the constant $C$ has been omitted, for it can be added whenever it is necessary.

Further, by Fourier expansion, we get

$$w=u-iv=b_0\left(\ln r+\frac{1}{2}\right)+e^{-2i\theta}\left(-\frac{1}{2}b_0+\frac{1}{r^2}B_1\right)+e^{2i\theta}\frac{b_2}{r^2}\,. \tag{2.9}$$

In order to satisfy the boundary conditions on the bounding plane walls as well as at the surface of the cylinder, we may now superpose, as done by Faxén[4)5)] in the case of the sphere problems, flows due to images, which are defined as:

$$\left.\begin{aligned}u^*=&-\frac{1}{2}\int_{-\infty}^{\infty}|\alpha|f_1(\alpha)e^{i\alpha x-|\alpha|y}d\alpha+\frac{1}{2}\int_{-\infty}^{\infty}f_2(\alpha)\left(-\frac{1}{|\alpha|}-3|\alpha|+y+2\alpha^2y\right)e^{i\alpha x-|\alpha|y}d\alpha\,,\\v^*=&-\frac{1}{2}i\int_{-\infty}^{\infty}\alpha f_1(\alpha)e^{i\alpha x-|\alpha|y}d\alpha-\frac{1}{2}i\int_{-\infty}^{\infty}f_2(\alpha)\left\{-\frac{\alpha}{|\alpha|}y+(\alpha-2\alpha|\alpha|y)\right\}e^{i\alpha x-|\alpha|y}d\alpha\,;\end{aligned}\right\} \tag{2.10}$$

$$\left.\begin{aligned}u^{**}=&-\frac{1}{2}\int_{-\infty}^{\infty}|\alpha|f_3(\alpha)e^{i\alpha x+|\alpha|y}d\alpha-\frac{1}{2}\int_{-\infty}^{\infty}f_4(\alpha)\left(\frac{1}{|\alpha|}+3|\alpha|+y+2\alpha^2y\right)e^{i\alpha x+|\alpha|y}d\alpha\,,\\v^{**}=&\frac{1}{2}i\int_{-\infty}^{\infty}\alpha f_3(\alpha)e^{i\alpha x+|\alpha|y}d\alpha+\frac{1}{2}i\int_{-\infty}^{\infty}f_4(\alpha)\left(\frac{\alpha}{|\alpha|}y+\alpha+2\alpha|\alpha|y\right)e^{i\alpha x+|\alpha|y}d\alpha\,,\end{aligned}\right\} \tag{2.11}$$

where $f_n(\alpha)$'s are unknown functions to be determined by under-mentioned boundary conditions.

The boundary conditions on the bounding walls $y=b$ and $y=-b$ as well as at the surface of the cylinder are as follows:

$$(u+u^*+u^{**})_{y=b}=0\,, \quad (v+v^*+v^{**})_{y=b}=0\,; \tag{2.12}$$

$$(u+u^*+u^{**})_{y=-b}=0\,, \quad (v+v^*+v^{**})_{y=-b}=0\,; \tag{2.13}$$

and

$$(w+w^*+w^{**})_{r=a}=-U\,, \tag{2.14}$$

where $w^*=u^*-iv^*\,,\quad w^{**}=u^{**}-iv^{**}\,.$

## § 3. Determination of the Functions $f_n(\alpha)$'s and the Constants $B_1$, $b_0$ and $b_2$

Inserting the values of $(u, v)$, $(u^*, v^*)$ and $(u^{**}, v^{**})$ as given respectively by (2.8), (2.10) and (2.11) into (2.12) and (2.13), we can express the functions $f_n(\alpha)$'s so far undetermined in terms of the unknown constants $B_1$, $b_0$ and $b_2$ as:

$$\begin{aligned} f_1(\alpha)=f_3(\alpha)=&\frac{1}{(1+2\alpha^2)(e^{2b|\alpha|}-e^{-2b|\alpha|}-4b|\alpha|)}\times[\{1+4\alpha^2+2b|\alpha|+4b\alpha^2|\alpha|+(1+2\alpha^2)e^{-2b|\alpha|}\}B_1\\ &+(1-2b^2-2b|\alpha|-4b^2\alpha^2-e^{-2b|\alpha|})b_0+(1+2b|\alpha|+6\alpha^2-4b^2\alpha^2-8b^2\alpha^4+e^{-2b|\alpha|})b_2]\,, \end{aligned} \tag{3.1}$$

$$\begin{aligned} f_2(\alpha)=f_4(\alpha)=&\frac{1}{(1+2\alpha^2)(e^{2b|\alpha|}-e^{-2b|\alpha|}-4b|\alpha|)}\\ &\times\{-2\alpha^2B_1+(-1+2b|\alpha|+e^{-2b|\alpha|})b_0+(-4\alpha^2+4b\alpha^2|\alpha|+2\alpha^2e^{-2b|\alpha|})b_2\}\,. \end{aligned} \tag{3.2}$$

Inserting these expressions into (2.10) and (2.11), and after some calculations, we obtain, neglecting all terms higher than $\varepsilon^3$,

$$\begin{aligned} w^*+w^{**}=&\Bigg\{-\ln 2b+\varepsilon^2e^{-2i\theta}\left(-\frac{1}{16}\right)+\varepsilon^2e^{2i\theta}\left(-\frac{1}{16}\right)\Bigg\}b_0\\ &-\int_0^\infty\frac{d\xi}{1-4\xi e^{-2\xi}-e^{-4\xi}}\\ &\times\Bigg\{\Bigg[\left(-\frac{1}{\xi}+4-4\xi-\varepsilon^2\xi+2\varepsilon^2\xi^2\right)e^{-2\xi}+\left(\frac{2}{\xi}-4-\varepsilon^2\xi\right)e^{-4\xi}-\frac{1}{\xi}e^{-6\xi}\\ &\qquad+\varepsilon^2e^{-2i\theta}\left\{\left(\frac{1}{4}\xi-\xi^2\right)e^{-2\xi}+\left(-\frac{1}{2}\xi+\xi^2\right)e^{-4\xi}+\frac{1}{4}\xi e^{-6\xi}\right\}\\ &\qquad+\varepsilon^2e^{2i\theta}\left\{\left(\frac{5}{4}\xi-3\xi^2+2\xi^3\right)e^{-2\xi}+\left(-\frac{3}{2}\xi+\xi^2\right)e^{-4\xi}+\frac{1}{4}\xi e^{-6\xi}\right\}\Bigg]b_0\\ &+[(-2\xi+4\xi^2-2\varepsilon^2\xi^3)e^{-2\xi}+2\xi e^{-4\xi}+\varepsilon^2e^{-2i\theta}\xi^3e^{-2\xi}\\ &\qquad+\varepsilon^2e^{2i\theta}\{(2\xi^3-2\xi^4)e^{-2\xi}-\xi^3e^{-4\xi}\}]\frac{B_1}{b^2}\\ &+[(-6\xi+12\xi^2-8\xi^3-4\varepsilon^2\xi^3+4\varepsilon^2\xi^4)e^{-2\xi}+(6\xi+2\varepsilon^2\xi^3)e^{-4\xi}\\ &\qquad+\varepsilon^2e^{-2i\theta}\{(2\xi^3-2\xi^4)e^{-2\xi}-\xi^3e^{-4\xi}\}\\ &\qquad+\varepsilon^2e^{2i\theta}\{(5\xi^3-8\xi^4+4\xi^5)e^{-2\xi}-4\xi^3e^{-4\xi}\}]\frac{b_2}{b^2}\Bigg\}\,, \end{aligned} \tag{3.3}$$

where $\varepsilon=r/b$. The integrals in (3.3) have been evaluated numerically.

Finally, the constants $B_1$, $b_0$ and $b_2$ can be determined by inserting (2.9) and (3.3) into (2.14), obtaining

$$B_1=\left(\frac{1}{2}-0.4311\varepsilon_0{}^2\right)a^2b_0\,, \qquad b_2=0.2358\,\varepsilon_0{}^2a^2b_0\,, \tag{3.4}$$

and

$$b_0=\frac{U}{\ln(b/a)-0.9156+1.7243\,\varepsilon_0{}^2}\,, \tag{3.5}$$

where $\varepsilon_0=a/b\,.$

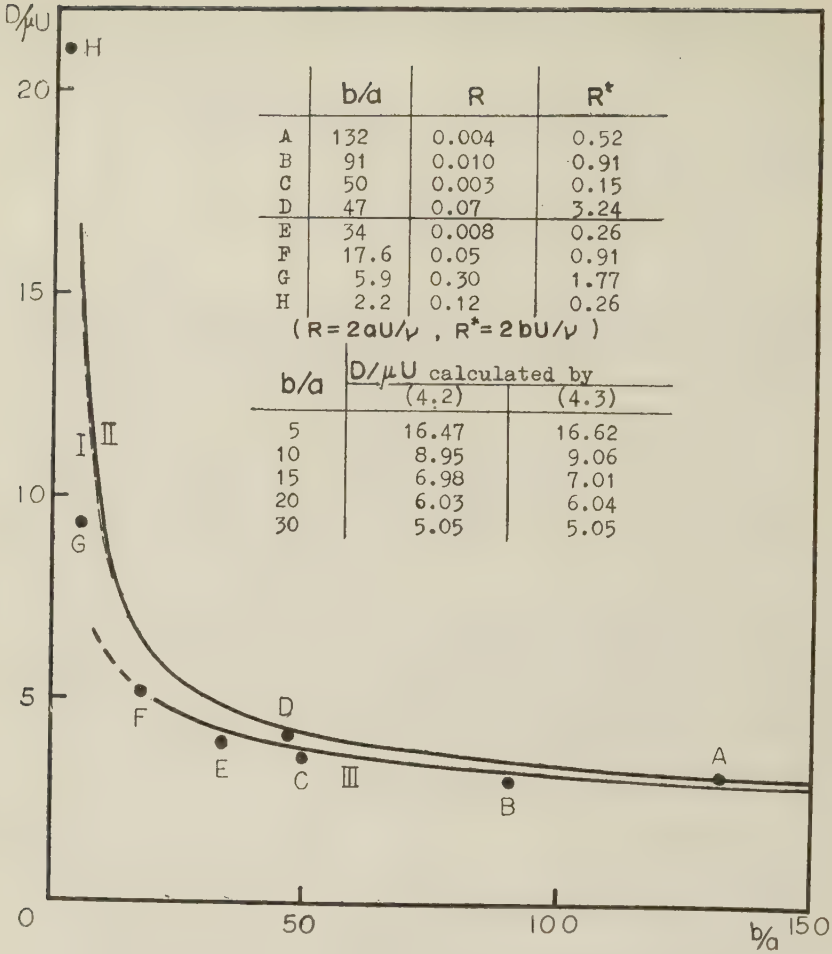

| | b/a | R | R* |
|---|---|---|---|
| A | 132 | 0.004 | 0.52 |
| B | 91 | 0.010 | 0.91 |
| C | 50 | 0.003 | 0.15 |
| D | 47 | 0.07 | 3.24 |
| E | 34 | 0.008 | 0.26 |
| F | 17.6 | 0.05 | 0.91 |
| G | 5.9 | 0.30 | 1.77 |
| H | 2.2 | 0.12 | 0.26 |

$(R=2aU/\nu\ ,\ R^*=2bU/\nu)$

| b/a | D/μU calculated by | |
|---|---|---|
| | (4.2) | (4.3) |
| 5 | 16.47 | 16.62 |
| 10 | 8.95 | 9.06 |
| 15 | 6.98 | 7.01 |
| 20 | 6.03 | 6.04 |
| 30 | 5.05 | 5.05 |

Fig. 2. Curve I ; $D/\mu U$ calculated by (4.2): second approximation,
Curve II ; 〃 〃 (4.3): first approximation,
Curve III; 〃 〃 (4.4): empirical formula,
● $A, B, \cdots, H$; data obtained by White's experiments.

## § 4. Discussion of the Result

Now, by integrating the fluid stresses over the cylinder, it is easily shown that the drag $D$ experienced by the circular cylinder per its unit length can be expressed as:

$$D=4\pi\mu b_0\,, \tag{4.1}$$

where $\mu$ is the viscosity of the liquid concerned.

Hence, if use is made of (3.5), we have

$$D/\mu U=\frac{4\pi}{\ln(b/a)-0.9156+1.7243(a/b)^2}\,. \tag{4.2}$$

The first approximation for the drag obtained recently by the present writer on the basis of Oseen's linearized equations of motion is

$$D/\mu U=\frac{4\pi}{\ln(b/a)-0.9156}\,. \tag{4.3}$$

As far as the term involving $(a/b)^2$ is neglected, the formula (4.2) is in perfect agreement with (4.3).

By carrying out experiments on wires falling in viscous liquids midway between two vertical plates, White obtained the data, corrected properly for end-effects, which are shown in Fig. 2 by points $A, B, \cdots, G$ and $H$. Excluding, due mainly to experimental uncertainities—perhaps 20% in error—, the data shown by $G$ and $H$, White obtained an empirical formula for the drag in the form:

$$D/\mu U=\frac{6.4}{\log(b/a)}\,. \tag{4.4}$$

The values of $D/\mu U$ have been calculated by the above three formulae (4.2), (4.3) and (4.4), and they are shown for comparison by curves I, II and III respectively in Fig. 2.

The disagreement existing between the values of $D/\mu U$ calculated by the emprical formula (4.4) and the theoretical one (4.3) for values of $b/a$ smaller than 20, has hardly been removed even by (4.2). We should perhaps find the reason for the disagreement elsewhere.

In conclusion, the writer wishes to express his cordial thanks to Professor S. Tomotika for his continual encouragement and also for his kind inspection of the manuscript.

### References

1) Y. Takaisi: J. Phys. Soc. Japan **10** (1955) 685.
2) C. M. White: Proc. Roy. Soc. **A 186** (1946) 472.
3) Y. Takaisi: J. Phys. Soc. Japan **11** (1956) 1004
4) H. Faxén: Diss. Uppsala (1921).
5) H. Faxén: Ann. d. Phys. **68** (1922) 89.

# Short Notes

This section is intended to secure prompt publication of important discoveries in physics. The reports should not exceed 800 words in length. A figure of size 7 cm × 7 cm will be counted as 150 words.

J. PHYS. SOC. JAPAN **11** (1956) 1004~1005

## Electrical Properties of Cd-Sb

By Takeshi MIYAUCHI and Harunobu KIMURA
*Junior College of Engineering,*
*University of Osaka Prefecture*

(Received March 12, 1956)

Justi and Lautz[1),2)] reported that Cd-Sb is a semiconducting material. We also studied its electrical properties. The result shows some discrepancies from their reports. Specimens used in this work are of resistivity of the order of 0.1 ohm-cm at room temperature and p-type. The n-type Cd-Sb cannot yet be produced, though the reason is not known in details.

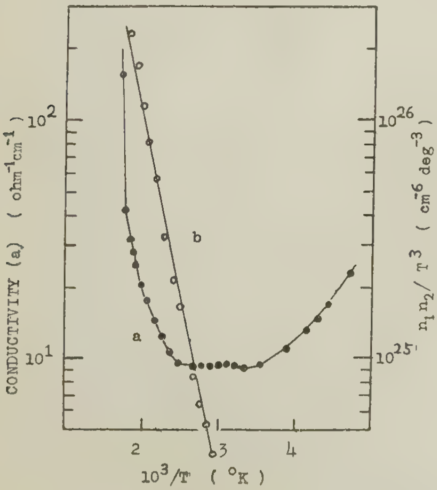

Fig. 1.

A typical curve of the conductivity versus temperature is shown in Fig. 1-a. The conductivity increases rapidly from about 120°C with increasing temperature. However, as an ionic conduction takes place at temperatures above 300°C, all measurements cannot be practised at temperatures higher than 280°C. So, in order to define the width of the forbidden band $\Delta E$, we make use of the equation:

$$n_1 n_2 = 2.33 \cdot 10^{31} (m^*)^3 T^3 \exp(-\Delta E/kT) \text{ cm}^{-6}, ^{3)} \quad (1)$$

where $m^* = (m_1 m_2)^{1/2}/m_0$, $m_1$ and $m_2$ are the effective masses of electron and hole, respectively, $m_0$ the free electron mass, $n_1$ and $n_2$ the densities of electrons and holes in bands.

From measurements of the Hall effect, we may estimate the mobility to be 1100±200 cm²/volt sec for hole. Assuming the mobility ratio to be $c \simeq 1$ from a reason that the thermoelectric power in the intrinsic range tends to zero but never becomes negative (Fig. 2), and also assuming that each mobility yields to $T^{-3/2}$ law at high temperatures, the carrier densities are obtained. The result is shown in Fig. 1-b, where the curve has a fairly well linearity. From this curve and Eq. (1), we may estimate $\Delta E$ to be $0.3 \pm 0.05$ ev and $m^*$ to be $0.15 \pm 0.05$.

The thermoelectric power is measured and the result indicates an expected transition from the extrinsic to the intrinsic range at reasonable temperature. (Fig. 2) The plots give the experimental values and the rigid line is calculated by

$$Q = -\frac{k}{e(n_1 c + n_2)} \Big[ 2(n_1 c - n_2) - n_1 c \ln \left\{ \frac{n_1 h^3}{2(2\pi m_1 kT)^{3/2}} \right\} + n_2 \ln \left\{ \frac{n_2 h^3}{2(2\pi m_2 kT)^{3/2}} \right\} \Big], ^{4)} \quad (2)$$

$Q$ being the thermoelectric power. The calculated curve is drawn by taking $m_1$ and $m_2$ as $0.1\,m_0$, and fairly agrees with the experimental data.

It may surely be said from Fig. 1-b and Fig. 2 that the effective masses of carriers are relatively small ($0.1$-$0.2\,m_0$). The energy gap is about half of, and the mobility is three times larger than those given in Reference 2). We could not find any rectification (at room temperature) in our samples, and n-type specimens are not found at all, while in the reference are reported weak rectification and existence of n-type, which exists sparsely in the p-type sample. The low mobility may be due to partial compensation by mixture of n-type. We wish to thank the editors of the Physical Society for several valuable advices.

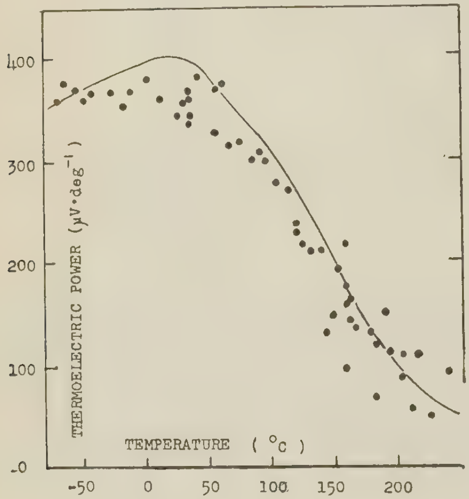

Fig. 2.

## References

1), 2) E. Justi and G. Lautz: Z. Naturforschg. **7a** (1952) 191 and 602.
3) W. Shockley: "Electrons and Holes in Semiconductors" 333.
4) V. A. Johnson and K. Lark-Horovitz: Phys. Rev. **92** (1953) 226.

---

J. Phys. Soc. Japan **11** (1956) 1014~1015

# The Effect of Adsorbed Water on the Phosphorescence of Sodium Acetate

By Kikusaburo Osada
*Faculty of Engineering, Nagoya University*

(Received April 26, 1956)

It was reported in the previous paper1) that the brightness of phosphorescence of sodium acetate depends on the treatment of the crystal. Further experiments were carried out to obtain the quantitative relations by means of photographic photometry.

The specimen was recrystallized thrice, dried in a desiccator, and divided into several parts. When they are put *in vacuo* instantly, they phosphoresce weakly with nearly equal brightness. Five specimens were prepared. One of them was kept *in vacuo* and the others were exposed to air for 1.5 hrs. Immediately afterwards one of the latters was put *in vacuo*, and the other three were treated in a similar manner after drying in a desiccator for one, two, and four days respectively. The afterglow of their phosphorescence was photographed and its density was measured with microphotometer. The brightness of phosphorescence decreases with increasing time of predrying in a desiccator as shown in Fig. 1. $(I-I_\infty)/(I_0-I_\infty)$ is shown in the ordinate, where $I$ is the brightness of partly dried specimen, $I_0$ that of undried, and $I_\infty$ that of unexposed to air.

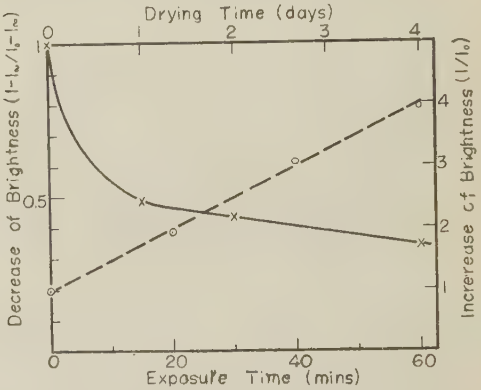

Fig. 1. Decrease of brightness with the time of drying in a desiccator (—) and increase with the time of exposure to air (- - -).

Further, to measure the relation between the brightness and the exposure time in air, another four specimens were prepared. One of them was kept unexposed to air, while the others were exposed for 20, 40, and 60 mins. respectively. The brightness is proportional to the exposure time as shown in Fig. 1. $(I/I_0)$ is shown in the ordinate, where $I$ is the brightness of an exposed specimen, and $I_0$ that of an unexposed one.

In the first case, on account of deliquescence, the crystal may adsorb water homogeneously during exposure to air, but may lose it slowly again when it is put in a desiccator. The quantity of the water adsorbed decreases with increasing time of drying in a desiccator. In the second case, the adsorbed water increases with exposure to air. When assumed that the brightness is proportional to the quantity of water which the specimen holds before it is put *in vacuo*, the variation of the brightness should be similar to that of the adsorbed water in the usual drying phenomena[2]. From the experimental results, this assumption is supported.

When the water vaporizes quickly *in vacuo*, the crystal may become imperfect. The larger is the quantity of the adsorbed water prior to the drying *in vacuo*, the more imperfect is the crystal. Therefore, we may conclude that the brightness of the phosphorescence increases with the imperfections of the crystal.

These results seem to give some quantitative support to the previous conclusion[1], that the phosphorescence of sodium acetate is due to the imperfections of the crystal.

## References

1) K. Osada: J. Phys. Soc. Japan **11** (1956) 425.
2) I. Osida: *Evaporation and Drying*, (Kawade Shobo, Tokyo, 1950) p. 75. (in Japanese)

---

J. Phys. Soc. Japan **11** (1956) 1015~1016

# Proton Magnetic Resonance in Polyisoprene, Polychloroprene and Polyisobutylene

By Hazime Kusumoto*

*Institute of Science and Technology, University of Tokyo, Tokyo, Japan*

(Received June 27, 1956)

The proton magnetic resonance has been observed in polyisoprene, polychloroprene and polyisobutylene from liquid nitrogen temperature to room temperature. The apparatus used has been described elsewhere[1] and all the samples were commercial ones, namely, crepe rubber (polyisoprene), Neoprene W (polychloroprene) and Vistanex (polyisobutylene). The results are summarized in Fig. 1 and Fig. 2.

The line width variation of the crepe rubber was very similar to that of 30-minute cured natural rubber reported by Gutowsky and Meyer.[2] However, it should be noticed in connection with vulcanization mechanism that the decreasing of the line width began at 130°K, which was lower than the temperature of onset of the line width decreasing, 143°K, in the vulcanized rubber.[2] In the rigid state its experimental line width and second moment were 9.5 gauss and 18.4 $\text{gauss}^2$, respectively, which were consistent with the values of the vulcanized rubber.[1,2]

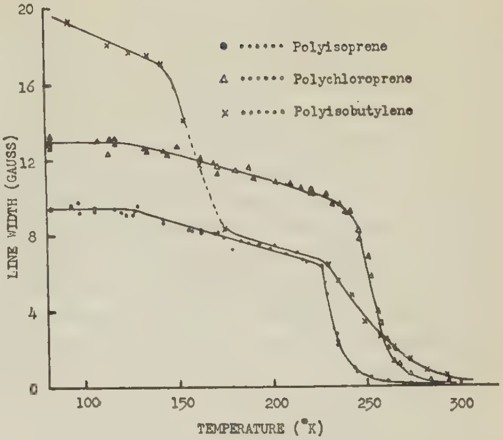

Fig. 1. The line widths *vs* temperature for polyisoprene, polychloroprene and polyisobutylene.

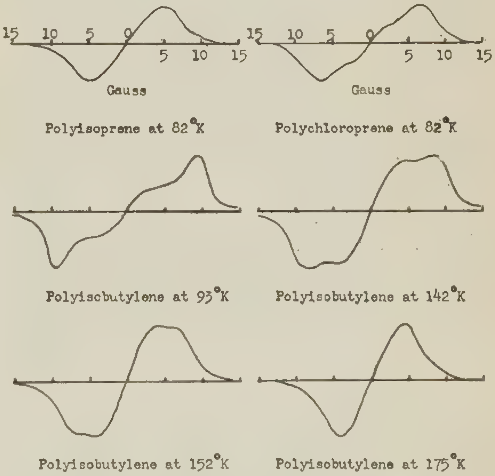

Polyisoprene at 82°K

Polychloroprene at 82°K

Polyisobutylene at 93°K

Polyisobutylene at 142°K

Polyisobutylene at 152°K

Polyisobutylene at 175°K

Fig. 2. The absorption line derivatives for polyisoprene, polychloroprene and polyisobutylene at various temperatures.

The neoprene had line width, 13.0 gauss, and second moment, 22.0 $\text{gauss}^2$ in rigid state, where the line had small inner peak separated by about 4 gauss. The over-all features of the variation of the outer peak separation are comparable to those of natural rubber as shown in Fig. 1. Polychloroprene monomer has a chlorine atom in place of the methyl group in polyisoprene monomer. The chlorine has only negligible contribution to dipolar broadening compared with the meteyl group. So, it would be expected that polychloroprene might have narrower line width and smaller second moment in rigid state than crepe rubber in proton magnetic resonance. Therefore, the results would suggest that intermolecular broadening might contribute considerably to the line width and the second moment. The inner peak would be due to the isolated proton in the monomer. The inner peak was weakened with increasing temperature and was not observed above about 250°K. Since polychloroprene had no methyl group, the rotation of which causes gradual narrowing of the line width in low temperature range in the case of natural rubber[2], there might be certain type of molecular motion above 130°K.

Polyisobutylene had sharp outer peak and broad inner peak at 91°K. The separation of the outer peak was 19.3 gauss and that of the inner peak was about 6 gauss in that temperature. The outer peak separation appears to be increasing still with decreasing temperature below 91°K. The experimental second moment was about 37 gauss$^2$ at that temperature. The features of the resonance in polyisobutylene as shown in Fig. 1 and Fig. 2 are very different from those found with natural rubber[1][2], Nylon[3] and Teflon[4]. The line width and the second moment would be attributed mainly to the two methyl groups in the monomer and the inner peak might be due to the ethylene group.

The author wishes to express thanks to Prof. K. Oshima for his helpful discussions.

## References

1) K. Oshima and H. Kusumoto: J. Chem. Phys. **24** (1956). 915
2) H. S. Gutowsky and L. H. Meyer: J. Chem. Phys. (1953) 21, 2122.
3) W. P. Slichter: J. Appl. Phys. **26** (1955) 1099.
4) J. A. S. Smith: Discussion of the Faraday Soc. No. 19, (1955) 207.

* Present address, Department of Chemistry, University of Illinois, Urbana, Illinois, U.S.A.

---

J. Phys. Soc. Japan **11** (1956) 1016~1017

# Anomalous Line Broadening of Paramagnetic Resonance Lines in $Cu(NH_3)_4SO_4H_2O$ at Liquid Helium Temperatures

by Muneyuki Date

*Research Institute for Iron, Steel and Other Metals, Tohoku University, Sendai*

(Received July 6, 1956)

Recently, we observed the paramagnetic resonance absorption of $Cu(NH_3)_4SO_4H_2O$ at liquid helium temperatures. As described in a previous paper[1], the magnetic resonance of $Cu(NH_3)_4^{++}$ group shows two interesting differences from that of $Cu(H_2O)_4^{++}$. One of them is the small values of *g*-factor compared with that of the latter and the other is the anomalous sharpness of resonance lines in the case of $Cu(NH_3)_4^{++}$ group. Experiments were also repeated by H. Abe[2], Z. Mizuno et al[3]. independently. They expressed the opinion that it is not necessary to introduce a covalent bond configuration in the case of $Cu(NH_3)_4^{++}$ as well as in the case of $Cu(H_2O)_4^{++}$ in contradiction to our assertion. Recently, however, Carlson and Spence repeated this experiment[4] and the results of their analysis show that the ground state of $Cu(NH_3)_4^{++}$ group has a covalent bond configuration in addition to the usual $(3d)^9$ configuration of the cupric ion. Although it is unplausible[5] to consider that the ground state of $Cu(NH_3)_4^{++}$ group consists of the covalent bond configuration only, it may be reasonable that the ground state of both $Cu(H_2O)_4^{++}$ and $Cu(NH_3)_4^{++}$ groups contain, more or less, the covalent bond configuration as a constituent of the ground state wave function[6] and this fact is more conspicuous in the case of $Cu(NH_3)_4^{++}$ group. The existence of the covalent bond configuration is also confirmed by the results of Raman spectra and other experiments. The detailed discussion on this point will be published later.

We carried out paramagnetic resonance experiment of $Cu(NH_3)_4^{++}$ group at liquid helium temperature, using the microwave of 9800 MC/sec. It is interesting to investigate the magnetic resonance of this group at liquid helium temperature because of the following reason. As described above, the resonance line width of this group at room temperature shows extreme narrowing effect and this may be considered as the exchange narrowing as in the usual case. Accordingly, there is a possibility that the antiferromagnetic transition point may be found above the adiabatic demagnetization temperatures as in the case of $CuCl_2 \cdot 2H_2O$. This expectation was not answered, but the anomalous broadening was observed in $Cu(NH_3)_4SO_4H_2O$. Fig. 1. shows the experimental results. The resonance

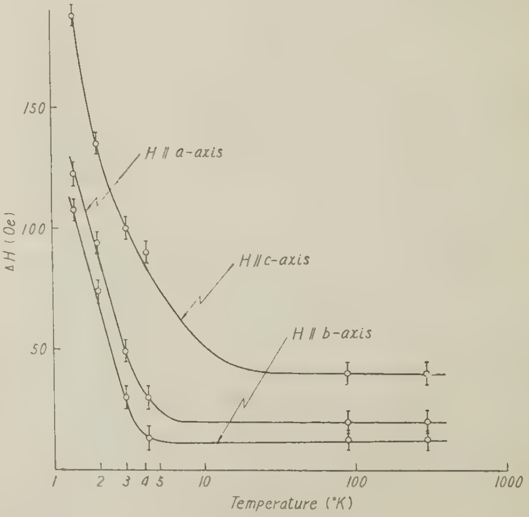

Fig. 1. Temperature dependence of paramagnetic resonance lines in $Cu(NH_3)_4SO_4H_2O$ at 9800 MC/sec. Abcissa shows the temperature in logarismic scale and ΔH represents the full width at the half maximum point.

lines become broad when temperature is decreased. The reason of this phenomena is not yet clear. One possibility of explanation is that the broadening occurs just above the antiferromagnetic transition (Néel Point) and if so, the Néel point of the salt might lie near 1°K. It must also be noticed that the anomalous broadening of this type is observed in DPPH[7)-9)], the famous free radical, in the liquid helium temperature region. The experiments were also made with regard to $Cu(NH_3)_4(NO_3)_2$ and $Cu(NH_3)_4Cl_2H_2O$, but no broadening effect was observed.

Finally, the author wishes to express his cordial thanks to Dr. T. Fukuroi, Professor of low temperature physics, for his stimulations during the course of this work. The present research was subsidized by the Research Grant from the Ministry of Education in Japan.

## References

1) T. Okamura and M. Date: Phys. Rev. **94** (1954) 314.
2) H. Abe: unpublished.
3) Z. Mizuno, O. Matumura, K. Hukuda and K. Hōrai: Memoirs of the Faculty of Science, Kyushu Univ. **2** (1956) 13.
4) E. H. Carlson and R. D. Spence: J. Chem. Phys. **24** (1956) 471.
5) This is comfirmed by the Data of the X ray analysis of $Cu(NH_3)_4SO_4H_2O$ which is recently published by F. Mazzi (Act. Cryst. **8** (1955) 138).
6) J. Owen: Proc. Roy. **A227** (1955) 183.
7) R. T. Weidner and C. A. Whitmer: Phys. Rev. **91** (1953) 1279.
8) L. S. Singer and E. G. Spencer: J. Chem. Phys. **21** (1953) 939.
9) L. S. Singer and C. Kikuchi: J. Chem. Phys. **93** (1955) 1738.

*Note added after writing*: H. J. Gerritzen (Thesis, Leiden, 1955, p. 84) observed a similar broadening below 3°K in the same salt with 21000 Mc/sec wave.

---

J. PHYS. SOC. JAPAN **11** (1956) 1017~1018

# Oscillatory Galvanomagnetic Effects in *n*-type Indium Antimonide*

By Yasuo KANAI
*Electrical Communication Laboratory, Musashinoshi, Tokyo*
and Wataru SASAKI
*Electrotechnical Laboratory, Nagatacho, Tokyo*

(Recieved June 7, 1956)

The galvanomagnetic effects of the tellurium-doped *n*-type indium antimonide (InSb) were measured as a function of the magnetic field strength (H) in the temperature range from room temperature to 1.3°K. In the above temperature range, the resistivity ($\rho$) and Hall coefficient (R) of the samples were temperature independent[1)] and had the constant value of about $6\times10^{-4}$ ohm-cm and 10 cm³/coulomb respectively, and furthermore, R was nearly constant up to 26 kilogauss. At very low temperatures, the magneto-resistance ($\Delta\rho/\rho(O)=\rho(H)/\rho(O)-1$) was about several per cent at 5~20 kilogauss for both the transverse and longitudinal effects, and in the stronger magnetic field a saturation behavior was found only in the longitudinal effect.

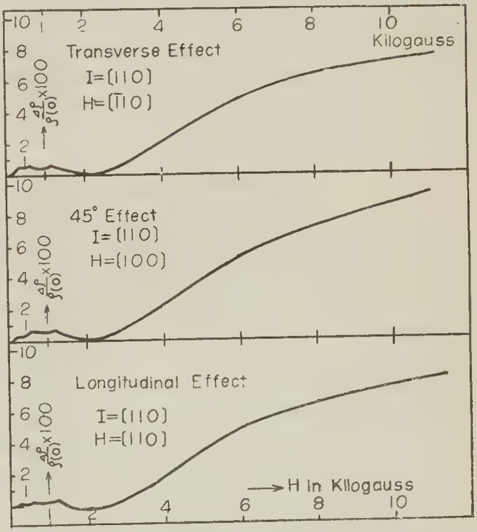

Fig. 1. Magnetoresistance ($\Delta\rho/\rho(O)$) as a function of magnetic field strength (H) for a single crystal of *n*-type InSb, at 1.3°K.

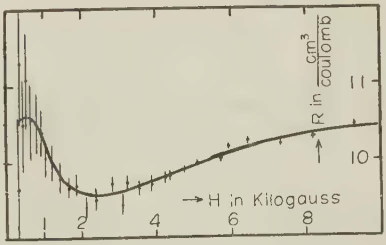

Fig. 2. Hall coefficient (R) as a function of H for the same crystal as its $\Delta\rho/\rho$ (O) is shown in Fig. 1, at 1.3°K.

In the course of precise measurements of the galvanomagnetic effects of an *n*-type InSb at very low temperatures, an anomalous behaviour was found in a weak magnetic field. As was shown in Figs. 1 and 2, the curves of $\Delta\rho/\rho(O)$ and R versus H seemed to have an oscillatory character. Furthermore, Fig. 1 shows that this oscillatory character was isotropic under the rotation of magnetic field in a (100) plane.

The oscillatory galvanomagnetic effects were found already for Bi, Sb, and graphite etc[2]., and these phenomena may be explained by the same theory as the de Haas-van Alphen effect. If the oscillatory galvanomagnetic effects of $n$-type InSb are caused by the same reason as the de Haas-van Alphen effect, then the theoretical value of the period of oscillations of $\Delta\rho/\rho(O)$ and R versus 1/H curves would be calculated[3] as $4.6\times10^{-6}$ gauss$^{-1}$, while the experimental value is approximately $1\times10^{-3}$ gauss$^{-1}$.

Further systematic investigation on this oscillatory effects is now under planing.

We are grateful to Professor T. Fukuroi and his corworkers for the hosipitality given in using the helium apparatus at the Research Institute for Iron, Steel and Other Metals of Tohoku University, and also to Mr. R. Nii for the x-ray determination of the crystal axis.

### References

1) Y. Kanai: J. Phys. Soc. Japan. **10** (1955) 718.
2) For instance, M. C. Steele: Phys. Rev. **99** (1955) 1751. The bibliography of the oscillatory galvanomagnetic effects of metals was cited in his paper.
3) For instance, A. H. Wilson: "The Theory of Metals." 2nd edition (1953) 171. It should be noticed that this theoretical value is independent of the effective mass and is determined only by the number of carriers, if the energy surface has spherical symmetry.

---

* This work was carried at the Research Institute for Iron, Steel and Other Metals, Tohoku University.

---

J. Phys. Soc. Japan. **11** (1956) 1018~1091

# The Zero-Time Correction in Free Diffusion Experiments

By Hiroshi Fujita

*Physical Chemistry Laboratory, Department of Fisheries, University of Kyoto, Maizuru, Japan*

(Received July 16, 1956)

The "height-area ratio" diffusion coefficient $D_A$ obtained in free diffusion experiments on dilute solutions is defined by

$$D_A=(\Delta C)^2/4\pi t(\partial C/\partial x)^2_{max}, \tag{1}$$

where $\Delta C$ is the difference in concentration across the diffusing boundary, and $(\partial C/\partial x)_{max}$ is the maximum height of the concentration gradient curve. It is usually observed that experimental $D_A$ values drift with time and follow for sufficiently large values of $t$ an empirical equation of the form:

$$D_A=D_A(\infty)(1+\Delta t/t)\ . \tag{2}$$

The value of $\Delta t$ is obtained from the slope of a $D_A$ *vs.* $1/t$ plot, and called the zero-time correction. The cause of the drift of $D_A$ with time may be attributed primarily to the deviation of the experimentally obtainable initial condition from the ideally sharp boundary as assumed in the theory. The purpose of this note is to consider the physical meanings of $D_A(\infty)$ and zero-time correction $\Delta t$ for the case in which $D$ does not depend on $C$.

The starting equation is a general solution to the Fick diffusion equation for unidimensional free diffusion experiments on a two-component system, i.e.,

$$C(x,t)=\frac{1}{2\sqrt{\pi Dt}}\int_{-\infty}^{\infty}f(\xi)\exp\left[-\frac{(x-\xi)^2}{4Dt}\right]d\xi\ , \tag{3}$$

where $f(x)$ is the initial concentration distribution in the cell. It is assumed that $f(x)$ is represented by

$$f(x)=\begin{cases}C_1 & (-\infty<x<-\lambda)\\ C_1+(\Delta C)\phi(x) & (-\lambda<x<\varepsilon)\\ C_2 & (\varepsilon<x<\infty)\end{cases} \tag{4}$$

where $\phi(x)$ is an arbitrary function of $x$ such that $\phi(-\lambda)=0$ and $\phi(\varepsilon)=1$. Provided the values of $\lambda$ and $\varepsilon$ are chosen sufficiently small, Eq. (4) represents an initial solute distribution which is slightly deviated from the ideal form as generally assumed in the theoretical treatment of the unidimensional free diffusion.

Substitution of Eq. (4) in Eq. (3) yields, after some calculations,

$$\frac{\partial C}{\partial x}=\frac{\Delta C}{2\sqrt{\pi Dt}}\left\{\exp\left[-\frac{(x-\varepsilon)^2}{4Dt}\right]-\frac{1}{2Dt}\right.$$
$$\left.\times\int_{-\lambda}^{\varepsilon}(x-\xi)\phi(\xi)\exp\left[-\frac{(x-\xi)^2}{4Dt}\right]d\xi\right\}\ . \tag{5}$$

The equation for $(\partial C/\partial x)_{max}$ can be obtained from Eq. (5) and is expanded to give

$$(\partial C/\partial x)_{max}=\frac{\Delta C}{2\sqrt{\pi Dt}}\left\{1-\frac{1}{Dt}\left(\frac{\varepsilon P}{2}-\frac{p^2}{4}-\frac{Q}{2}\right)\right.$$
$$\left.+O\left(\frac{1}{D^2t^2}\right)\right\}, \tag{6}$$

where $P$ and $Q$ are

$$P=\int_{-\lambda}^{\varepsilon}\phi(\xi)d\xi\ ,\qquad Q=\int_{-\lambda}^{\varepsilon}\xi\phi(\xi)d\xi\ . \tag{7}$$

Introduction of Eq. (6) in Eq. (1) and expansion leads to

$$D_A=D\left\{1-\frac{1}{Dt}\left(\varepsilon P-\frac{1}{2}P^2-Q\right)+O\left(\frac{1}{D^2t^2}\right)\right\} \tag{8}$$

comparison of which with Eq. (2) provides

$$D_A(\infty)=D\,, \tag{9}$$

$$\varDelta t=(\varepsilon P-1/2P^2-Q)/D. \tag{10}$$

Thus, it is found that the $D_A$ value extrapolated to infinite time gives actually the diffusion coefficient $D$ for the given system, and that the zero-time correction depends not only on the blurring of the initial boundary but also on the reciprocal of $D$.

Let us consider a simple case in which $\phi(x)$ is given by a straight line such that

$$\phi(x)=(\lambda+x)/(\varepsilon+\lambda)\ \ (-\lambda<x<\varepsilon)\,. \tag{11}$$

Simple calculation gives for $\varDelta t$ an equation of the form:

$$\varDelta t=(\varepsilon+\lambda)^2/24D\,. \tag{12}$$

The sum $\varepsilon+\lambda$ is the thickness of the blurred initial boundary. By way of example, assume that $D=1\times10^{-5}$ cm.$^2$/sec. and $\varDelta t=10$ sec. The thickness of the initial diffused layer is calculated to be about 0.05 cm., which is expected to be of the order of magnitude as obtained in precision free diffusion experiments with such as the Gouy diffusiometer.

# PROGRESS OF THEORETICAL PHYSICS

*(Founded by H. Yukawa in 1946)*

Published for the
**Research Institute for Fundamental Physics**
**The Physical Society of Japan**

---

Progress of Theoretical Physics Vol. 15, No. 3, March 1956

On the One Pion Exchange Potential ........................................ ....................Kichiro HIIDA, Junji IWADARE and Shigeru MACHIDA..189
Electromagnetic Radiation from Electron Plasma ............................ ..................................Satio HAYAKAWA and Noboru HOKKYO..193
Deuteron Stripping Reactions and Nuclear Shell Structure .................... ..........................................Sueji OKAI and Mitsuo SANO..203
Effect of Hard Core on the Binding Energies of $H^3$ and $He^3$, I ............... ................. Takashi KIKUTA, Masao MORITA and Masami YAMADA..222
On the Use of Feynman Amplitudes in the Quantum Field Theory.........Ziro MAKI..237
A Collective Description of the Surface Oscillation of Atomic Nuclei ——*Extension of Tomonaga's Method to Three Dimensional Nucleus*——.................. Tatsuoki MIYAJIMA and Taro TAMURA..255
Coulomb Interactions and the Diamagnetism of Free Electrons.....Hideo KANAZAWA..273

Letters to the Editors:

Interaction of $\pi$-Mesons with $\pi$-Mesons.............................Z. KOBA..294
Surface Tension of Liquid He$^4$ and Liquid He$^3$ ...................... ......................................S. K. TRIKHA and O. P. RUSTGI..296
On the Renormalization Theory of Quantum Electrodynamics......... .....................................S. KAMEFUCHI and H. UMEZAWA..298
On the Elementarity of the Weak Boson-Fermion Interaction, I....... ..................................S. ÔNEDA, S. HORI and A. WAKASA..300
On the Elementarity of the Weak Boson-Fermion Interaction, II...... ..................................S. ÔNEDA, S. HORI and A. WAKASA..302
On K-Meson Decays and the Universal Interactions.................. ..................................S. ÔNEDA, S. HORI and A. WAKASA..304
Theory of Antiferromagnetic Resonance in CuCl$_2$·2H$_2$O ........T. NAGAMIYA..306

---

Price $ 1.25 per copy
$ 15.00 per year (postage inclusive)
Annual dues for foreign members (individual subscribers)
$ 12.00 (postage inclusive)
" for foreign members of the Physical Society of Japan
$ 10.00 (postage inclusive)

Application for members, subscriptions and orders for back numbers should be sent, directly or through book-dealers, to

The Publication Office
in
**Yukawa Hall, Kyoto University, Kyoto, Japan**

JOURNAL OF THE PHYSICAL SOCIETY OF JAPAN Vol. 11, No. 10, OCTOBER, 1956

# On the Interaction of Cosmic Radiation with Materials at 32 m.w.e. and 200 m.w.e. Underground

By S. HIGASHI, I. HIGASHINO, M. ODA, T. OSHIO, H. SHIBATA,
K. WATANABE and Y. WATASE

*Osaka City University, Osaka*

(Received May 7, 1956)

Penetrating showers produced in lead and some other phenomena have been studied at 32 m.w.e. and 200 m.w.e. below the top of the atmosphere and at sea level with a counter hodoscope. As much cares as possible were taken to avoid uncertainties of the counter hodoscope study. The threshold energy of the penetrating showers observed was estimated as about 7 Bev taking into account the geometrical condition of the apparatus. The cross section for the penetrating showers at 32 m.w.e. was concluded as $(2.8\pm0.7)\ 10^{-31}$ cm$^2$/nucleon and about ten times bigger cross section was obtained at 200 m.w.e. Those events which were interpreted as the mixed shower coming from the earth above the apparatus were also studied. The energy involved in this phenomena has been estimated to be very high and the cross section was suggested. Occasionally two or more penetrating particles have traversed the apparatus in parallel with each other without being accompanied with soft components. The intimate association of air showers with these events was concluded.

## §1. Introduction

The existence of the cosmic radiation below ground has been confirmed up to 3000 m.w.e. underground[1]. Many observations have established accurate intensity-depth relation of the cosmic ray particle up to, say, 1000 m.w.e. so far. K. Greisen[2], Hayakawa and Tomonaga[3], George[4] and Barret et al[5] have discussed on the interrelation among intensity-depth relation, various ways of losing energy of charged particles and the energy spectrum of the mu-meson in the atomosphere. These discussions gave us fairly strong reason to believe that the particles are mainly mu-mesons, which enter the ground from the atmosphere and traverse the earth losing their energies primarily by ionization processes, and some secondary particles which are supposed to be in equilibrium with the mu-meson.

Nuclear interactions have been observed by various investigators[5-10] at more than ten meters below ground, since Braddick and Hensby[11] had reported their observation. George and Evans[10] have observed the stars in nuclear emulsions which were exposed at 20 m.w.e., 34 m. w. e. and 60 m. w. e. below ground. Since the occurence of stars decreased very slowly by the increase of the depth, they concluded that the stars were produced by mu-mesons and the cross section for the nuclear interaction is the order of $10^{-30}$ cm$^2$/nucleon. They have considered that the stars containing a fast secondary particle is produced by a simple scattering of the mu-meson by a nucleon in the nucleus and the star containing at least two of fast secondary particles are the example of pi-meson production by the mu-meson. There have been some trials to explain latter processes as an electromagnetic meson production and they seemed to have succeeded in explaining the order of the magnitude of the cross sections. The explanation was unavoidably vague, however, since the nature of the electromagnetic meson production for higher energy involved in the process than the order of Bev is scarcely known. More difinite and quantitative informations are needed for further discussions on the matter. Particularly, it is very important to know the cross section as a function of the energy of incident mu-mesons and the energy involved in the nuclear process, i.e. so-called threshold energy. It seems to be very difficult, however, to measure the incident energy of the interaction since the elasticity of the interaction underground is expected to be very large and, hence, the incident energy may not correspond well to the size of the interaction.

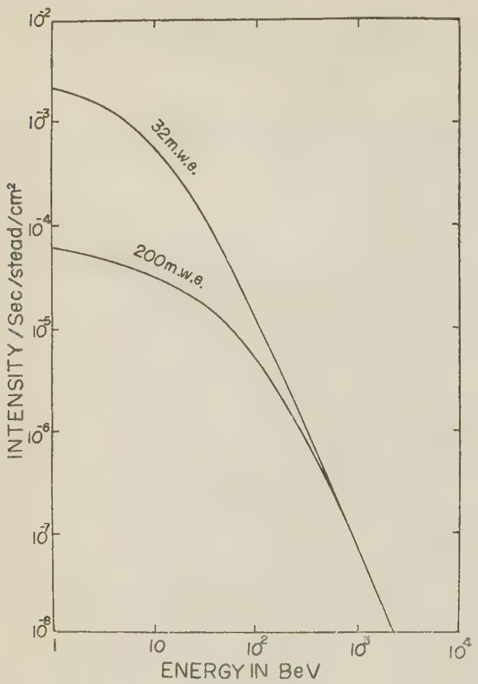

Fig. 1. The energy spectrum of mu-mesons at 32 m.w.e. and 200 m.w.e. below the top of the atmosphere calculated with the intensity-depth relation underground and the energy-range relation of the mu-meson.

The intensity-depth relation is well known and we can deduce the energy spectra of mu-mesons at various depths from this relation and the range-energy relation of mu-mesons which is not very doubtful except at extremely high energy. The energy distributions thus obtained at 32 m. w. e. and 200 m. w. e. are presented in Fig. 1. General features of the distributions are that the lower energy part decreases more rapidly than the higher energy part by the increase of the depth. Thus it it very likely that informations on the depth dependence of the cross section may help the discussions as an alternative of its energy dependence. Argan et al[8)] have measured cross sections for penetrating showers which involve the energy of at least 2 Bev at 50 m.w.e. and 200 m.w.e. underground with a counter hodoscope. They have discussed on their experimental results and concluded that the results are not inconsistent with the theoretical interpretation of the nuclear interactions underground by George and Evans.

Present authors had located a counter hodoscope in a tunnel and observed during the period of 1952–1953 at two different depths the penetrating shower produced in a lead layer. The nuclear interactions underground are very rare and the average energy of mu-mesons underground is very high and, hence, occurence of high energy cascade shower is very frequent compared with penetrating showers. This is serious in counter experiments of the penetrating shower. And one has to be very careful to avoid false interpretations of the hodoscope pictures. It will be shown by the absorption measurement of the secondary particle that the lead absorber of at least 20 cm thick is necessary to distinguish the penetrating shower from its mixture with the cascade shower by the appearance of the picture. Also an auxiliary counter tray which will be described later was found to be helpful for this purpose. One had to be careful of the chance of successive cascade showers being misinterpreted as locally produced penetrating showers. With these cares the cross sections of the penetrating shower were estimated for 32 m.w.e. and 200 m. w. e. below the top of the atmosphere without big dangers of taking something else as the penetrating shower. A sort of Monte Carlo method was applied to estimate the detecting efficiency of the apparatus as a function of the multiplicity of the shower. And it was concluded that the showers of small multiplicity are often missed and the multiplicity of usually observed showers is at least 4 corresponding to about 7 Bev of the energy involved in the shower if the relation of the multiplicity and the energy is similar to that of the showers at mountain altitude.

Observations have been done for showers coming out from the earth above the apparatus. A part of these were obviously cascade showers developed in the earth and the rest of them contained at least three penetrating particles each and were considered to be mixed showers produced in the earth. Also data will be presented for cases where two or more penetrating particles traverse the apparatus in parallel with each other. Their association with air showers was studied and will be discussed.

The tunnel was rent by Japanese Government Railways and is located at Yaizu, Shizuoka. The rock above the points of observation is mostly alkali basalt whose density is 2.7±0.1 with mean atomic number 11. The densities were measured by direct weighing of samples of the rock as well as by means of the measurement of gravities in and above the tunnel.

## § 2. Experimental Arrangement

One of counter arrangements which were used in the course of the experiment is shown in Fig. 2. Counters of trays C, D, E and part of A are of 4 cm diameter and of 40 cm effective length and those of B and part of A are of 2 cm diameter and the same effective length of the former. Each counter is connected to a corresponding neon bulb which is arranged on a panel so as to duplicate the whole arrangement. Neon bulbs are usually lit and the electronics is prepared so that the bulbs are turned off except those which correspond to discharged counters always when it is triggered and the panel is photographed. Thus one can have the hodoscope picture of the arrangement for any desired triggerings. $\Sigma$ is a lead producer of local showers whose thickness was 10 cm in most cases and $\Sigma'$ and $\Sigma''$ are also lead layers used as absorbers of secondary particles of local showers. The thickness of $\Sigma'$ was fixed at 5 cm. The thickness of $\Sigma''$ had been varied from 0 to 20 cm in order to take absorption curves of secondery particles of the local shower produced in $\Sigma$. Counters of B and D are separated from each other by lead plates of 1 cm thickness to reduce the chance of knock-on electrons discharging the counter.

The condition of triggering could easily be changed. As it is often very difficult to tell the difference between appearances of hodoscope pictures of big shower and two small showers occured successively, we had to investigate the occurence of very small showers including knock-ons with triggering in favor of those events. In most period of the observation the hodoscope was triggered whenever at least any two of interior ten counters of B, any two of interior eight of C and any one of interior seven of D were discharged in coincidence within 20 microseconds. The electronics was examined at least once a day. Because of natural activities underground, the discharge rate of the counter was not reduced much and hence we had to be careful of chance coincidences. So artificial master pulses were occasionally generated and the panel was photographed to see the chance discharge rate of each counter.

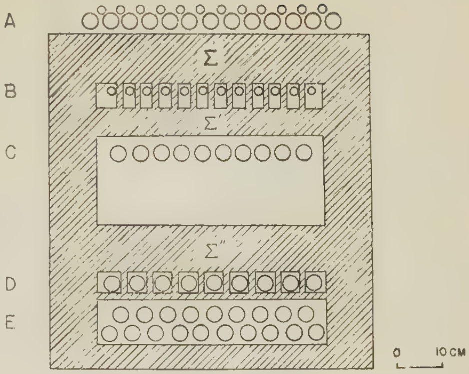

Fig. 2. Schematic diagram of the counter arrangement located underground. Shadowed section is lead. $\Sigma$ is the producer of the local shower. $\Sigma'$ and $\Sigma''$ are the absorbers of secondary particles of the local shower.

Events ($A \leq 2$, $B \geq 2$, $C \geq 2$, $D \geq 2$) were selected as the candidate of the penetrating shower locally produced in lead. If we observe the penetrating shower at sea level or at mountain altitude, we regard these events as the penetrating shower without much worry of mistake. But cosmic ray underground has comparatively big chance of high energy bremsstrahlung and so the high energy cascade shower may compete with the penetrating shower in such an arrangement if the amount of the absorber is not sufficient. The tail of the cascade shower is composed of low energy photons which have much larger absorption mean free path than cascade electrons and which discharge a counter by a probability of about a few percent per photon. If one can indicate the counter discharged by photons, one may drop most of the cascade showers of high energy from the competition with the penetrating shower. The tray E placed under D works for this purpose. The low energy photon which discharges the counter mostly by the photoelectric effect at the wall of the counter does not have much energy left to discharge E counter or, even if it has, probability of discharging two counters on the path of the photon is very small. On the other hand, the secondary particle of the penetrating shower scarcely misses E counter after having penetrated the absorber and discharged D counter. So, if we require discharges of D counter and E counter on a line of the secondary particle to select the penetrat-

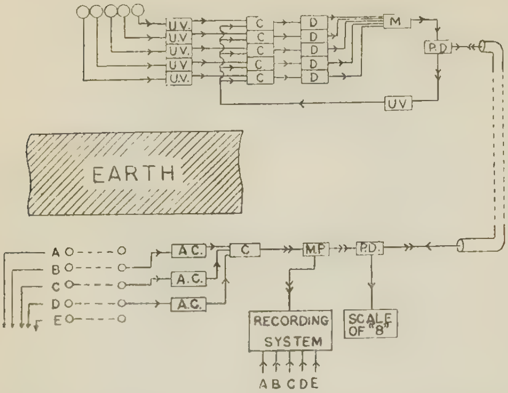

Fig. 3. The block diagram of the electronics. U.V. is the univibrator; C is the conventional coincidence circuit; M is the mixer; A.C. is "any *m* of *n* coincidence" circuit; M.P. is the master pulse generator; P.D. is the circuit to give incoming pulses directions shown by the arrows in the figure. D is the delay circuit. The time of delay is different for each of five channels so that the number of discharges is counted by the number of pulses in series.

ing shower from hodoscope pictures, dangers of the misinterpretation are much reduced.

An air shower monitoring counter tray was placed in a period of the observation on the ground surface above the apparatus. It consists of ten counters each of which is 4 cm diameter and 40 cm effective length. Whenever the hodoscope was triggered by an event the master pulse was sent to the air shower electronics. The master pulse opened the gate circuit of the electronics for the air shower tray and the informations of discharges of the air shower counters which were coincident with the event underground were sent back to the recording circuit. The tray was separated into five groups and the number of discharged groups was indicated on hodoscope panel. The block diagram of the whole electronics is shown in Fig. 3.

## § 3. Experimental Results

Most of hodoscope pictures $A \leq 2$, $B \geq 2$, $C \geq 2$, $D \geq 1$ were to be interpreted as shower produced in $\Sigma$. These events were named "local shower". Events $A \geq 3$ which corresponded to the cases of at least three particles entering the apparatus were named "earth shower". Records of events or single particles whose axes incline from the vertical line by more than thirty degrees were not taken for the analysis to avoid the complication of various corrections including that of the change of the detecting efficiency of the apparatus for large incident angle. The local shower of $D \geq 2$ and $D=1$ will be called p. s. and c. s. respectively.

*a*) *Single particle*

Hodoscope records which were regarded as single penetrating particles were counted of records obtained by the triggering $B \geq 1$, $C \geq 1$, $D \geq 1$. Intensities of the penetrating particles in the apparatus thus obtained are as follows at various points.

| | |
|---|---|
| 32 m.w.e. below the top of the atmosphere; | $(1.35 \pm 0.09)\ 10^3$/hour |
| 200 m.w.e.; | $(56.8 \pm 2.4\ )$ /hour |
| sea level; | $(4.95 \pm 0.38) 10^3$/hour. |

The knock-ons or the small showers produced at lead layers discharge another counter which is usually adjacent to the discharged counter on the track of the particle. Probabilities of those for each trey are given in the following;

| | 32 m. w. e. | 200 m. w. e. |
|---|---|---|
| B | $0.94 \pm 0.12\%$ | $1.29 \pm 0.10\%$ |
| C | $3.25 \pm 0.51\%$ | $4.16 \pm 0.52\%$ |
| D | $0.89 \pm 0.13\%$ | $1.81 \pm 0.34\%$ |
| E | $3.3\ \pm 1.1\ \%$. | |

The chance of two adjacent counters being discharged in a tray is about an order of magnitude less.

*b*) *c. s.* ($A \leq 2$, $B \geq 2$, $C \geq 2$, $D=1$)

Rates of this events are as follows;

| | |
|---|---|
| 32 m. w. e. | $(1.68\ \pm 0.09\ )$/hour |
| 200 m. e. w. | $(0.204 \pm 0.009)$/hour |
| sea level | $(6.6\ \ \pm 0.7\ \ )$/hour. |

Changes of the rates were not observed by the change of $\Sigma''$ from 0 to 20 cm. They decreased very rapidly by the increase of the thickness of $\Sigma'$. Absolute values of the rates agree with the calculation of the rate of the cascade shower which originate to the bremsstrahlung of high energy mu-meson. Thus it was concluded that almost all of the events were cascade showers.

*c*) *p. s.* ($A \leq 2$, $B \geq 2$, $C \geq 2$, $D \geq 2$)

Most of records p. s. were traceable assuming that they are penetrating showers. Some of them were not traceable unless we considered complicated secondary phenomena and were discounted in the analysis. This neglection did not influence the conclusion of the present accuracy. Certainly a part of p. s. must be the cascade shower particularly when the amount of the absorber is not large enough. The least amount of the absorber which is enough to descriminate the cascade showers from the records p. s. was estimated as follows. Rates of p. s. are presented in Fig. 4 for various thicknesses of the absorber. One notices a knee of the curve around 15～20 cm lead of the absorber. A calculation can be done for the frequency of the cascade shower which start from the bremsstrahlung of mu-meson at $\Sigma$ and which may discharge the counter tray giving a hodoscope picture of p.s. Christy-Kusaka's[12] formula and Greisen's[13] calculation were used. As is seen from the results of this calculation drawn in Fig. 4, the frequency of the cascade shower decreases more and more rapidly by the increase of the thickness of the absorber. Also one should not see too much importance in good agreement between the calculated curve and the experimental results at the left side of curves, one may safely conclude that 20 cm thickness of the absorber is enough to exclude the cascade showers from p.s. for both depths.

Tray E was supposed to have a role in distinguishing the penetrating showers in p. s. Indeed, rates of p. s. with $E\leq 1$ rapidly decrease by the increase of thickness of the absorber following the expectation for the cascade shower and, on the other hand, p. s with $E\geq 2$ shows very small decrement for more than 20 cm thick of the absorber as shown in Fig. 5. In the following p. s. of $E\geq 2$ for the absorber of more than 20 cm thickness are tabulated.

| | B=2<br>C=2<br>D=2 | B=2<br>C≥3<br>D=2 | B=2<br>C≥3<br>D≥3 | B≥3<br>C≥3<br>D=2 | B≥3<br>C≥3<br>D≥3 | period of observation |
|---|---|---|---|---|---|---|
| 32 m.w.e. | 19 | 13 | 4 | 21 | 8 | 964.2 hrs |
| 200 m.w.e. | 1 | 4 | 0 | 7 | 3 | 899.5 hrs |

When a c. s. and a knock-on or a small shower occur succeedingly on the path of the mu-meson, the hodoscope picture may look like a p. s. The rate of those was calculated from the rate of c. s. and the probability of producing knock-ons or small showers. Almost all of B=2, C=2, D=2 and a considerable fraction of B=2, C≥3, D=2 may be ascribed to this process. It was calculated that B≥3, C≥3, D=2 and B≥3, C≥3, D≥3 may be regarded as the penetrating shower with only small correction of successive events. Corrected rates of the penetrating showers

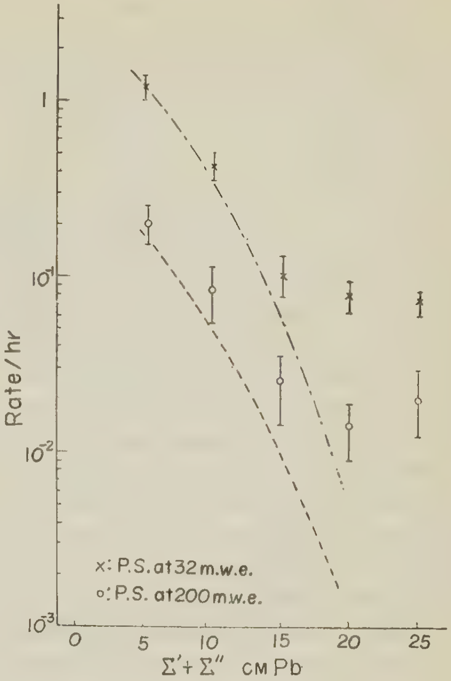

Fig. 4. Rates of coincidences $A\leqslant 2$, $B\geqslant 2$, $C\geqslant 2$, $D\geqslant 2$ for various thicknesses of the absorber. The curves represent results of the calculation for the cascade shower which starts from the bremsstrahlung in lead of mu-meson.

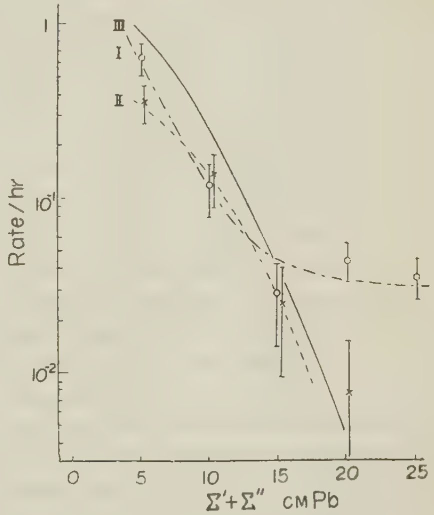

Fig. 5. Rates of coincidences $A\leqslant 2$, $B\geqslant 2$, $C\geqslant 2$, $D\geqslant 2$, $E\geqslant 2$ (I) and $A\leqslant 2$, $B\geqslant 2$, $C\geqslant 2$, $D\geqslant 2$, $E=1$ (II) at 32 m.w.e. (III) is the result of the calculation for the cascade shower.

which show the hodoscope picture of $B\geq3$, $C\geq3$, $D\geq2$ $E\geq2$ are as follows;

| | |
|---|---|
| 32 m.w.e. | $(2.3\ \pm0.6)\,10^{-2}$/hour |
| 200 m.w.e. | $(1.0\ \pm0.35)\,10^{-2}$/hour |
| sea level | $(1.15\pm0.19)$ /hour . |

*d*) *Earth shower*

Records of $A\geq3$ were interpreted as showers produced in the earth. Inspection of the pictures seem to show that events are vaguely to be classified into two groups; 1) only one penetrating particle is involved in the process being associated with soft components, 2) three or more penetrating particles are associated with soft components. Most of 1) are supposed to belong the cascade shower produced in the earth by the mu-meson. 2) may represent nuclear interactions occurred in the earth somewhere close to the apparatus. The rates of 2) are;

| | |
|---|---|
| 32 m. w. e. | $(2.4\pm0.6)\,10^{-2}$/hour |
| 200 m. w. e. | $(2.0\pm0.4)\,10^{-2}$/hour . |

*e*) *p. p. p.*

A certain number of records showed the cases that two or more penetrating particles had traversed the apparatus simultaneously in parallel with each other. Also a fraction of the events may physically belong to the previous classification, namely the nuclear interaction in the earth, general features of the pictures suggest that majority of these events may be physically different phenomena. So, this phenomena were called "p. p. p." following Amaldi et al[8]. The frequency of the p.p.p. is presented as follows;

| | |
|---|---|
| 32 m. w. e. | $0.029\ \pm0.005$ /hour |
| 200 m. w. e. | $0.0020\pm0.0014$/hour . |

During the period of 717 hours the air shower tray was put on the ground above the observing station 32 m. w. e. underground. In this period 89 cases were interpreted as the earth shower with two cases of the association with the discharge of the air shower tray. 15 cases were interpreted as the p.p.p. 14 cases were not necessarily to be classified as the p. p. p. but can be interpreted as the cases where one of the penetrating particles aimed the side of the apparatus so that the parallelism was not well confirmed or one of the particles had stopped in the lead layer or had scattered or had produced the secondary interaction in the lead. A part of records of the latter cases show rather complicated shape and were taken as the p. p. p. only because they may be the p. p. p. associated with secondary events such as the stop, scattering or big interaction in the lead in order not to miss the possible p. p. p. The above mentioned 15 cases and 14 cases are listed as a) and b) respectively in the following. The number of discharged air shower counters are also given.

| number of discharged groups of air shower counters | 0 | 1 | 2 | 3 | 4 | 5 |
|---|---|---|---|---|---|---|
| (a) | 8 | 4 | 1 | 1 | 1 | |
| (b) | 12 | 1 | | | | 1 |

Of nine p.p.p. associated with the discharge of the air shower tray two knock-ons were observed along the tracks of the particles. This number of knock-ons is consistent with the knock-on probabilities at each lead layer previously given. Twenty p. p. p. were not associated with the discharge of the air shower tray. Nine cases of them were that one of the particles did not reach E tray either by scattering out or the stop in the lead layer. Three cases were of complicated shape and may be interpreted as the p. p. p. associated with big interactions in the lead. Thirteen knock-ons were counted along the tracks of the particles. These are too much to be interpreted as the electromagnetic interactions of the particle.

## § 4. Discussions and Conclusions

The cross section for the nuclear interaction of the mu-meson certainly depends not only on the depth but also on the experimental definition of the interaction. If the experimental equipment is to favor the interactions of higher energy, the cross section turns out to be smaller than that measured with, for instance, the emulsion. Thus, the cross section is desired to be presented, if possible, in connection with the lowest energy of the interaction to be observed by the equipment. Present criterion of selecting penetrating showers ($B\geq3$, $C\geq3$, $D\geq2$, $E\geq2$) simply means a requirement that at least three particles penetrate five centimeters of lead and at least two of them penetrate about 20 cm or more of lead. However, the geometry of the apparatus complicates the situation; the secondary particle may miss to hit the counter or two particles hit one counter so that one of them may not show up. Analytical calculation of these geometrical consideration is not very easy and the following means were taken for this purpose.

Imitations of showers were made on paper on the basis of the Monte Carlo method. The producer was divided into thirty six sections and numbered. Multiplicity ($n_s$) distribution and the angular distribution of shower particles were assumed to obey $n_s^{-\gamma}$ and $\cos^n\theta$ where $\theta$ is the angle between the shower particle and the vertical line. The distribution curves were divided into sections of the same areas and also numbered. By using a random number table, locations of the origins of showers and multiplicity were determined and then $\theta$ and the azimuthal angle of the shower particle with respect to the vertical line were determined. Thus a group of imitations of showers were made which follow the assumed distributions. Absorption mean free path was assumed as about 300 g/cm². Hodoscope pictures which would have been presented by these showers were compared with those experimentally obtained and $n=20$ or about 15 degrees of average angle of shower particles and $\gamma\sim 2$ were concluded. And the probabilities ($\eta$) of penetrating showers presenting $D\geqq 2$ are obtained for various multiplicities. The overall detecting efficiency for the penetrating shower of $n_s>2$ is about 20%. The total number of the shower is expressed by

$$\sum_{n_s-2}^{\infty} \eta(n_s)\cdot f(n_s)$$

where $f(n_s)$ is the multiplicity distribution and $\eta(n_s)$ is the detecting efficiency as a function of $n_s$ given above. This expression may be approximated by omitting $\eta(n_s)$ and taking a different number of the smallest multiplicity; i.e. $\sum_{n_s\simeq 4\sim 5}^{\infty} f(n_s)$. $n_s\cong 4\sim 5$ may correspond to about 7 Bev of energy involved in the shower if we may assume an equality of the shower underground and at mountain altitude. This energy may be called the threshold energy of the interaction in this apparatus.

The cross section of the penetrating shower $\sigma(x, \mathcal{E}_m)$ was defined as a function of the depth and the threshold energy ($\mathcal{E}_m$) of the shower observed as;

$$\sigma(x, \mathcal{E}_m)=f(x, \mathcal{E}_m)/I(x)\cdot N\cdot X\,,$$

where $f(x, \mathcal{E}_m)$; the rate of showers

$I(x)$; the intensity of incident particles

$N$ ; Loschmidt number

$X$ ; thickness of the producer $\Sigma$ in g/cm².

Thus cross sections of the penetrating showers whose threshold energy is 7 Bev are concluded;

$\sigma$(32 m. w. e.); $(2.8\pm 0.7)\,10^{-31}$ cm²/nucleon

$\sigma$(200 m. w. e.); $(2.9\pm 1.1)\,10^{-30}$ cm²/nucleon.

Cross sections for 2) type of the earth showers are expressed as;

$$\sigma(x)=f(x, \mathcal{E}_m)\cdot s/R\cdot N\cdot S\cdot I(x)\,,$$

where

$R$ ; the average range of the secondary particle

$S$ ; the area which primary mu-mesons of these earth showers aim

$s$ ; the effective area of the apparatus

$I(x)$; flux of mu-mesons in the apparatus.

$R$ is presumably assumed as 300 g/cm². Since the apparatus was located four meters beneath the roof of the tunnel and $s$ is about 40×40 cm². $S$ is much larger than $s$ unless the secondaries of the shower were ejected in a very narrow cone. For assumptions of the average spread angle, corresponding $S$ and $\sigma(x)$ calculated by the formula are tabulated in the following.

| average spread angle | $S$ m² | $\sigma$ (32) cm²/nucleon | $\sigma$ (200) cm²/nucleon | $n_s$ | $\mathcal{E}_m$ Bev |
|---|---|---|---|---|---|
| 15° | $\sim 4$ | $\geqq 2.5\times 10^{-33}$ | $\geqq 6\times 10^{-32}$ | $\gtrsim 70$ | $\gg 100$ |
| 10° | $\sim 2$ | $\geqq 5\times 10^{-33}$ | $\geqq 1.2\times 10^{-31}$ | $\gtrsim 30$ | $\gg 100$ |
| 5° | $\sim 2/3$ | $\geqq 1.5\times 10^{-32}$ | $\geqq 3.6\times 10^{-31}$ | $\gtrsim 10$ | $\gtrsim 100$ |

The total number of penetrating secondaries $n_s$ which should have been produced to present at least two particles on the apparatus are estimated in the sixth column. Threshold energy of events $\mathcal{E}_m$ is crudely estimated from $n_s$ on the basis of assumption that the relation of $n_s$ and the energy is given by Fermi's[14)] theory. $n_s\gtrsim 70$ may not be the case because the intensity of the particle of such a high energy is too small to explain the occurrence of the events. Thus the cross section of the order of $10^{-32}$ cm²/nucleon and $10^{-31}$ cm²/nucleon are suggested for this event at 32 m. w. e. and 200 m.w.e. respectively whose involved energies are larger than 100 Bev.

Since about one third of the p. p. p. is associated with the discharge of the air shower tray whereas only one hundredth or one fiftieth is so for earth showers or other events as was described before, the strong relation between the p. p. p. and the air shower is obvious. As was mentioned above, the p.p.p. associated with the air shower show knock-ons of reasonable frequency but the p. p. p. not associated with the air shower show much more knock-ons than expected from the knock-on probability and scatterings or stops in the lead. So it is presumed that the former p.p.p. is composed of mu-mesons and at least a part of the latter is composed of strongly interacting particles, say pi-mesons. Thus the former is reasonably interpreted that after the electronic component of the air shower being rapidly absorbed in the earth the mu-meson component remains as the skeleton of the air shower and turns out to be the p.p.p. The probability of a counter of area $s$ being discharged by the density $\Delta$ is $(1-\exp(-\Delta\cdot s))$. Therefore, the most probable electron density $\Delta_n$ of the case where $n$ of $m$ counters of area $s$ each are discharged is obtained by solving the following formula;

$$\frac{\partial}{\partial\Delta}\left\{\binom{m}{n}(\exp(-\Delta\cdot s))^{m-n}(1-\exp(-\Delta\cdot s))^{n}\right\}=0$$

$s$ is 160 cm² and $m=5$ for the air shower counter tray on the ground. Thus we obtain $\Delta_1\sim7/m^2$, $\Delta_2\sim16/m^2$, $\Delta_3\sim29/m^2$, $\Delta_4\sim50/m^2$, $\Delta_5>50/m^2$. $n$ was $1\sim4$ for eight cases of nine p.p.p. and for five of them $n=1$. At first sight it may seem strange that the density of the electrons on the ground is too low to give rather high density of mu-mesons underground from our conventional knowledge that the density of mu-mesons in the air shower is about a percent or less of the density of the electrons. This is understandable if we suppose that the mu-mesons in the air shower are distributed in a circle more or less uniformly whereas the electrons have a sharp lateral distribution around the core of the air shower. Thus, when one observe the air shower on the ground, the dense core is usually caught. And the core is not necessarily important for the p. p. p. but rather the tail of the air shower where the electron density is low but the mu-meson density remains relatively high may mostly contribute to the p.p.p.

The air shower tray was not set on the ground for the observations at 200 m. w. e. and, hence, the previous classification of the p.p.p. is not possible. Barret et al. had taken the decoherence curve of the meson showers at 1600 m. w. e. Their result shows that about a half of the p. p. p. might have been due to the mu-meson component of the air shower. Considering this and the present result that about one third or more of the p.p.p. at 32 m. w. e. is due to the air shower, it is presumed that about the same fraction of the p. p. p. at 200 m.w.e. is also due to the air shower.

The conclusions are summarized as follows;

1) Cross section of nuclear interactions in lead by the cosmic ray particle underground, the threshold energy of which is estimated as 7 Bev, are $(2.8\pm0.7)\cdot10^{-31}$ cm²/nucleon for 32 m. w. e. and $(2.9\pm1.1)\cdot10^{-30}$ cm²/nucleon for 200 m. w. e.
2) The cross section of the nuclear interactions in the earth, the threshold energy of which is larger than 100 Bev, is the order of magnitude of $10^{-32}$ cm²/nucleon for 32 m. w. e. and about one order larger for 200 m. w. e.
3) Mu-meson components of the air shower present two of them simultaneously in the area of 0.16 m² at 32 m. w. e. by the frequency of about once per hundred hours mostly giving the electron density about $10\sim50/m^2$ on the ground. At 200 m. w. e. the frequency may be reduced by a factor of ten.

Comparisons of present conclusions with other studies and a discussion on the interpretation of nuclear interaction underground will be presented elsewhere.

## § 5. Acknowledgements

The author wish to thank Professor S. Hayakawa for many helpful discussions, and Professor J. Hatsuta and Mr. Y. Yoshimura of Kyoto University and Professor J. Iwatsu and Mr. T. Takenaka of Osaka City University for estimating the density of the earth by means of the measurement of the gravity. Professor T. Kubozoe of National Defence University who had been a staff of Osaka City University had contributed to the technical part of the works.

The authors are grateful to Mr. T. Shiota and the Institute for Food Chemistry for their financial aids.

## References

1) Y. Miyazaki: Phys. Rev. **76** (1949) 1733.

Y. Nishina, Y. Sekido, Y. Miyazaki and T. Masuda: Phys. Rev. **59** (1941) 401.

2) K. Greisen: Phys. Rev. **76** (1949) 1718; **73** (1948) 521.

3) S. Hayakawa and S. Tomonaga: Prog. Theor. Phys. **4** (1949) 287.

4) E. P. George: Progress in Cosmic Ray Physics (Amsterdam, 1952).

5) P. H. Barret, M. L. Bollinger, G. Cocconi, Y. Eisenberg and K. Greisen: Rev. Mod. Phys. **24** (1952) 133.

6) M. Annis, H. C. Wilkins and J. D. Miller: Phys. Rev. **94** (1954) 1038.
G. Cocconi and V. Cocconi-Tongiorgi: Phys. Rev. **84** (1951) 29.
R. D. Sard, M. F. Crouch, D. R. Jones, A. M. Conforto and B. F. Stearns: Nuovo Cimento **8** (1951) 326.

7) E. P. George and P. Trent: Nature **164** (1948) 838, 248.

8) P. E. Argan, A. Gigli and S. Sciuti: Nuovo Cimento **11** (1954) 530.
E. Amaldi, C. Castagnoli, A. Gigli and S. Sciuti: Nuovo Cimento **9** (1952) 969, 453.

9) H. J. J. Braddick and B. Leontic: Phil. Mag. **45** (1954) 1287.
A. Lovati, A. Mura, C. Succi and G. Tagliaferri: Nuovo Cimento **10** (1953) 1201.

10) E. P. George and J. Evans: Proc. Phys. Soc. **63** (1950) 1248; **64** (1951) 195.

11) H. J. J. Braddick and G. Hensby: Nature **144** (1939) 1012.

12) R. F. Christy and S. Kusaka: Phys. Rev. **59** (1941) 405.

13) K. Greisen: Phys. Rev. **75** (1949) 1071.

14) E. Fermi: Phys. Rev. **81** (1951) 683.

---

JOURNAL OF THE PHYSICAL SOCIETY OF JAPAN Vol. 11, No. 10, OCTOBER, 1956

# A Quantum-statistical Theory of Transport Processes[*]

By Hazime MORI

*Department of Applied Physics, Faculty of Engineering*
*Kyushu University, Fukuoka*[**]

(Received July 4, 1956)

A quantum-statistical method of finding molecular expressions for kinetic coefficients is formulated so as to be applicable to the case where the external disturbance which made a system deviate from equilibrium can not be taken as a definite additive term in the Hamiltonian of the system, such as the heat conduction and the viscous flow. This method provides an extension of the fluctuation-dissipation theorem to such quantum-mechanical systems. A quantum-statistical expression for the entropy of a non-equilibrium system is defined so as to be consistent with Gibbs' relation, and is shown to give a quantum-statistical basis for the thermodynamics of irreversible processes. Two ways of application of our method to each special system are shown; one is concerned with deriving the phenomenological equations of motion, and the other with calculating the entropy production of the system. Thus, quantum-statistical expressions are obtained for the relaxation time of an energy transfer between two sub-systems and that of momentum relaxation phenomena, and for the coefficients of thermo-electricity.

## §1. Introduction

According to Kirkwood's program[1], the principal objectives of the statistical mechanics of transport processes are the formulation of phonomenological equations of motion such as the equations of hydrodynamics from the standpoint of molecular dynamics, the investigation of the limits of validity of empirical linear relations such as Fourier's law between heat flow and temperature gradient, the determination of kinetic coefficients such as the coefficient of thermal conductivity from known properties of molecules, and the molecular interpretation of the linear stimulus-response theory.

---

[*] The main contents of the present paper was published in Japanese (Busseiron Kenkyu **90** (1955) 25; 93; **92** (1956) 24).

[**] Present address, Department of Chemistry, Metcalf Research Laboratory, Brown University, Providence 12, R. I., U.S.A.

Kirkwood's theory[1] of transport processes has given some great insights into these problems. His theory is concerned with classical systems and is intended to be so general as to be applicable to the transport phenomena in liquids and dense gases. One of the most important results is the molecular expression for the friction constant $\zeta$ of a Brownian particle in an isotropic equilibrium fluid,

$$\zeta=(1/6kT)\int_{-\tau_c}^{\tau_c} dt\langle\dot{\boldsymbol{P}}(0)\cdot\dot{\boldsymbol{P}}(t)\rangle^0, \qquad (1.1)$$

where $\dot{\boldsymbol{P}}(t)$ means the time derivative of the momentum $\boldsymbol{P}(t)$ of the Brownian particle at time $t$, $\langle\cdots\rangle^0$ the average over a canonical ensemble at the temperature $T$ of the system and $\tau_c$ the decay time of the correlation function $\langle\dot{\boldsymbol{P}}(0)\cdot\dot{\boldsymbol{P}}(t)\rangle^0$.

Eq. (1.1) establishes a quantitative correlation between dissipation and equilibrium fluctuations. An intuitive interpretation of such a connection may be that an irreversible process is a transfer of energy from a macroscopic degree of freedom to microscopic degrees of freedom, while fluctuation is the transfer of energy in the reverse direction, and the course of the transfer of energy is characterized by the kinetic coefficient.

This idea, on the ground of which Nyquist[2] derived the well-known relation about thermal noises in electrical circuits, has been developed in a fluctuation-dissipation theorem by Callen, Welton[3] and Takahasi[4], which relates the response of a system to a small external disturbance with the spontaneous fluctuations of the system. They treated systems whose Hamiltonian depends linearly on a small perturbation induced by a driven change of some external parameter, $X(t)$, as follows:

$$H(t)=H+X(t)Q\ , \qquad (1.2)$$

where $Q$ is the generalized force associated with the external coordinate $X$. This theorem has more extensively been discussed by Callen and Greene[5]. Kubo and Tomita[6] have presented a clear-cut method for this problem in their theory of magnetic resononce absorption to obtain generalizations of Takahasi's theory[4] for classical systems to quantum-mechanical systems. This method is general and rigorous enough to provide a satisfactory quantum-statistical formulation of the linear stimulus-response theory. Thus, on the basis of the fluctuation-dissipation theorem, we may calculate the values of kinetic coefficients from the molecular standpoint. Actually, this program has been carried out by Green[7], Kubo, Tomita[6] and Nakano[8] in respective interesting cases. Kubo and Tomita's method, however, may be strictly limited to the case where the external disturbance can be taken as a definite additive term in the Hamiltonian like Eq. (1.2).

On the contrary, there are many important phenomena which are not the case, such as the heat conduction and the viscous flow. Green[9] has defined a complete set of macroscopic variables to be a set of functions of the representative point in the phase space of a dynamical system which is such that their present values completely determine their expected future values. On the basis of Onsager's[10][11] postulate that the average regression of spontaneous fluctuations obeys the same laws as the corresponding irreversible processes, he has derived the phenomenological equations of motion of the set, which provide a generalization of the fluctuation-dissipation theorem to the latter case. Yamamoto[12] has derived Green's results from Liouville's equation for the phase-space distribution function by use of Kirkwood's[1] time-smoothing procedure. These theories, however, may be limited to classical systems and may not straightforward be generalized to quantum-mechanical systems.

The principal purpose of the present paper is, therefore, to give a quantum-statistical formulation of the general theory of transport phenomena which gives a microscopic basis for the phenomenological equations of transport and provides molecular expressions for the kinetic coefficients involved in such equations. At present, it seems, however, that one has no systematic method of approach to this problem. Hence, in § 2 we begin with quantum-statistical inspection of the assumptions underlying the phenomenological theory of transport processes to integrate some of the ideas latent in Kirkwood's[1] general theory of transport processes and the other theories of irreversible processes into such a form as to be convenient for our treatment. It will be shown there that, in order to obtain molecular expressions for the kinetic coefficients, we have only to investigate the time behavior of the statistical ensemble of the system in question for a short time interval under a given initial condition. The short time interval is much shorter than the relaxation time for the system to attain an equilibrium state, but far longer than a characteristic molecular time. The magnitude of the time interval depends on the phenomena in question, and is, in the corresponding case, of the same order as that of the short time interval used in the time-smoothing procedure introduced by Kirkwood[1] to obtain an adequate macroscopic description of the secular variations of observable properties of a non-equilibrium system. The initial condition means that, at the beginning of that time interval, the distribution of the system is approximated by a coarse-grained distribution corresponding to the macroscopic state of the system, which may be in a close relation with Gibbs'[13] coarse-graining procedure in phase space.

In § 3, we shall embody the thus obtained lines of thought in a concrete formulation to derive macroscopic equations of motion. Our fundamental assumption made there is that the initial distribution can be approximated by such a form as $\rho_t = Z^{-1}\exp(-K)$. This form makes our quantum-mechanical analysis possible. Most of interesting systems will be shown to satisfy not only this assumption but also a relation $\dot{K} = (1/kT)\sum_h J_h X_h(t)$, where $X_h(t)$'s are the thermodynamic forces[11] and $J_h$'s such dynamical variables that a kind of averages of them are the thermodynamic fluxes. The reason for our introduction of this assumption has an intimate correlation with why Green[9] has defined a complete set of macroscopic variables. Thus, we shall obtain macroscopic equations of motion whose classical limit are essentially identical with Green's phenomenological equations of motion. These equations will be applied to an energy transfer between two subsystems at different temperatures to obtain a molecular expression for the relaxation time (§ 4), and also applied to momentum relaxation phenomena (§ 5).

In § 6, we shall deal with a statistical-mechanical expression for the entropy of non-equilibrium states, which will be done on the basis of quantum statistics. The expression for the entropy, whicn is consistent with Gibbs' relation in the thermodynamics of irreversible processes[11], provides an entropy production having the same structure as the entropy production in the thermodynamics. Thus, a kind of averages of $J_h$'s will be shown to be the thermodynamic fluxes, and linear relations between these fluxes and thermodynamic forces will be derived. The coefficients appearing in these linear relations satisfy Onsager's[10] reciprocal relations. These linear relations will be applied to the phenomena of thermo-electricity to give molecular expressions for the kinetic cofficients of these phenomena (§ 7). The expression for the electrical conductivity is identical with Nakano's[8] expression.

## § 2. Preliminary Discussions

We shall inspect the assumptions underlying the phenomenological treatment of transport processes[11] from the statistical-mechanical standpoint to find out an approach to the statistical-mechanical theory of transport processes.

As a simple illustration, we consider an energy transfer between two sub-systems I and II at the different temperatures $T_{\text{I}}$ and $T_{\text{II}}$ respectively, such as the energy transfer between the spin system and the crystalline lattice in the paramagnetic relaxation or between the ion and electron systems in the gas discharge plasma. The change with time of the temperature of the sub-system I, is described by

$$\delta T_{\text{I}}/\delta t = -(1/\tau_r)(T_{\text{I}} - T_{\text{II}})\,. \tag{2.1}$$

The relaxation time $\tau_r$ is usually independent of the temperature diference $\Delta T \equiv T_{\text{I}} - T_{\text{II}}$, so far as the total system is departing slightly from thermal equilibrium. Introducing the specific heat $C_{\text{I}}$ and the internal energy $E_{\text{I}}$ of the subsystem I, Eq. (2.1) can be written in the alternative form more convenient for the following treatment,

$$\delta E_{\text{I}}/\delta t = -(C_{\text{I}}/\tau_r)(T_{\text{I}} - T_{\text{II}})\,. \tag{2.2}$$

The statistical ensemble of quantum-mechanical system can be described by the density operator $\rho(t)$, which obeys the equation of motion

$$i\hbar\dot{\rho}(t) = [H, \rho(t)]\,, \tag{2.3}$$

where $[A, B] \equiv AB - BA$. $H$ is the Hamiltonian of the total system and hereafter will be assumed to be a constant of motion. The formal integration of Eq. (2.3) is readily shown to be given by

$$\rho(t+s)=U(s)\,\rho(t)\,U^*(s) \tag{2.4}$$

with

$$U(s)\equiv\exp(-isH/\hbar)\,. \tag{2.5}$$

Therefore, the expectation value of the observable $F$ which does not depend explicity on the time can be written as

$$\begin{aligned}\langle F\rangle(t+s)&=\mathrm{Tr}\,\rho(t+s)F\\&=\mathrm{Tr}\,\rho(t)F(s)\,,\end{aligned} \tag{2.6}$$

where

$$F(s)\equiv U^*(s)FU(s) \tag{2.7}$$

is the Heisenberg representation of the observable $F$ following the equation of motion

$$i\hbar\dot{F}(s)=[F(s),H] \tag{2.8}$$

Thus, the internal energy $E_{\mathrm{I}}(t)$ can be expressed as

$$E_{\mathrm{I}}(t)=\mathrm{Tr}\,\rho(t)\,H_{\mathrm{I}}\,, \tag{2.9}$$

$H_{\mathrm{I}}$ being the Hamiltonian of the subsystem I. To obtain a molecular expression for the relaxation time $\tau_r$, we have only to investigate the time behavior of the total system for a short time interval between $t$ and $t+\tau$ from the microscopic standpoint, because statistical-mechanical calculation of the rate of change with time of the internal energy $E_{\mathrm{I}}$,

$$\delta E_{\mathrm{I}}/\delta t\equiv(E_{\mathrm{I}}(t+\tau)-E_{\mathrm{I}}(t))/\tau \tag{2.10}$$

$$=\frac{1}{\tau}\int_0^\tau ds\frac{d}{ds}\langle H_{\mathrm{I}}\rangle(t+s) \tag{2.11}$$

$$=\frac{1}{\tau}\int_0^\tau ds\,\mathrm{Tr}\,\rho(t)\dot{H}_{\mathrm{I}}(s)\,, \tag{2.12}$$

and comparison between thus obtained equation and the right-hand side of Eq. (2.2) may give us a molecular expression for $\tau_r$. Here, it will become clear from the following consideration that the time interval $\tau$ has to be finite and hence Eq. (2.10) has to be strictly a quotient of differences. In Eqs. (2.10), (2.11) and (2.12), the unknown quantities are the following:

(1) *the initial distribution* $\rho(t)$

(2) *the lower limit of the time interval* $\tau$

It is clear that $\tau\ll\tau_r$ has to be satisfied.

In the phenomenological theory, the following is usually assumed:

(A1) The subsystems I and II are, approximately, themselves in internal thermal equilibrium with the temperatures $T_{\mathrm{I}}(t)$ and $T_{\mathrm{II}}(t)$, respectively, at the time $t$ (*The assumption of local equilibrium*).

Hence, we may approximate the initial distribution $\rho(t)$ by the local equilibrium distribution,

$$\rho(t)\doteqdot\rho_t\equiv Z^{-1}\exp\left(-\frac{H_{\mathrm{I}}}{kT_{\mathrm{I}}}-\frac{H_{\mathrm{II}}}{kT_{\mathrm{II}}}\right), \tag{2.13}$$

which is a statistical-mechanical expression of the assumption (A1). For the validity of (A1), it may be necessary that the velocity of the progress of heat transfer should be slow and hence

(A2) $|\Delta T|\ll T_{\mathrm{I}},\ T_{\mathrm{II}}$,

which is also necessary for the process to be linear dissipative. Moreover, the interaction energy $H'$ between two subsystems is usually assumed to be small,

(A3) $|H'|\ll|H_{\mathrm{I}}|,\ |H_{\mathrm{II}}|$ .

The process we are concerned with is irreversible, so that, as is well-known in the usual thermodynamics, it is impossible to define the changes with time of the thermodynamic quantities, such as the temperature and the entropy, continuously along the path of the natural development with time of the system, because it is possible only to do so along the paths of the quasi-static and reversible processes. Hence, the short time interval $\tau$ in Eq. (2.10) must be finite, so far as the initial distribution $\rho(t)$ of Eq. (2.12) is replaced by the local equilibrium distribution $\rho_t$, (2.13). Here, let us remember that one can not obtain any transport properties, such as the heat conduction and the viscous flow, from the maxwell-Boltzmann equation in the kinetic theory of gases, as far as the local equilibrium is assumed for the velocity distribution function. In accordance with these circumstances, the following procedure is implicitly assumed[14)] in the phenomenological theory;

(A4) The local equilibrium is assumed at discrete values of time whose neighboring values are separated by a short time interval $\tau$, and then these local equilibrium points are connected by the quasi-static processes with the help of the procedure of the virtual brake processes.

Eq. (2.1) and (2.2) should be difference equations in such a meaning, and the change with time of the internal energy $E_{\mathrm{I}}$ along the natural path for the time interval $\tau$ may be pressed in the kinetic coefficient $\tau_r$. These circumstances will be clearer in § 6, where the temporal behavior of the entropy of the system will in detail be investigated from the statistical-mechanical point of view. The physical meaning of the lower limit of $\tau$ can not become clear within the domain of the phenomenological theory. As will be discussed later on, it has to be far longer than a finite time interval, $\tau_c$, characterizing the molecular randomness of the system, and hence the time interval $\tau$ must be bounded by the inequalities

$$\tau_c \ll \tau \ll \tau_r \,. \tag{2.14}$$

For instance, in the case of transport equations in gases of such low density that molecular motion can be adequately analyzed in terms of binary collisions, the time interval $\tau_c$ is of the order of magnitude of the mean free time of molecules. Such interpretation for the time derivative in the transcriptions from statistical-mechanical to macroscopic equations is usually used in deriving Onsager's reciprocal relations about kinetic coefficients[10)11)] and also will play an important part in our theory.

From the above investigation, we see that, in order to obtain a molecular expression for the relaxation time $\tau_r$, the approximation (2.13) may be taken at the discrete values of time whose neighboring values are separated by such a finite time interval $\tau$ as bounded by the inequalities (2.14).

## § 3. General Formulation (I)—Phenomenological Equations of Motion

In this section, we shall embody the above-mentioned lines of thought in a concrete formulation to develop a quantum-statistical method of deriving the phenomenological equations of motion of interesting macroscopic variables, which, at the same time, provides molecular expressions for the kinetic coefficients involved in such equations. We shall not, however, go so far into the complication of general treatments of irreversible processes, but shall confine ourselves to the simple case of the linear theory, which assumes that the system is departing slightly from thermal equilibrium and the rate of change with time of the average value of a macroscopic observable of the system is linear with respect to certain small parameters describing the departure of the system from the thermal equilibrium.

In order to obtain molecular expressions for the kinetic coefficients appearing in the phenomenological equations of transport, we shall, as stated in the preceding section, have only to investigate the change with time of the density operator for a short time interval ($t \sim t+\tau$) with the initial distribution $\rho(t)$ suitably defined according to the physical conditions of the system under consideration.

To carry out this scheme generally, we shall now consider a system whose initial distribution can be approximated as

$$[A1] \qquad \rho(t) \doteq \rho_t \equiv Z^{-1} \exp(-K) \,, \tag{3.1}$$

where $K$ is an operator explicitly dependent on the time $t$ and $Z$ the normalization factor. The explicit form of the factor $K$ depends upon every special system and should be determined according to the physical condition of the system in question. For the example mentioned in the preceding section, we find that $K = H_{\mathrm{I}}/kT_{\mathrm{I}} + H_{\mathrm{II}}/kT_{\mathrm{II}}$.

The state of the system changes with time according to the Hamiltonian $H$ and will, in a sufficiently long time, attain a thermal equilibrium state which is described by a stationary distribution

$$\rho_0 \equiv Z_0^{-1} \exp(-\beta \bar{H})$$

with

$$[H, \bar{H}] = 0 \,, \tag{3.2}$$

which is consistent with Eq. (3.1). We shall suppose that the deviation of the initial distribution (3.1) from the equilibrium distribution (3.2) is very small, that is,

$$[A2] \qquad |R| \ll |\bar{H}| \quad \text{for} \quad K \equiv \beta(\bar{H}+R) \,. \tag{3.3}$$

This assumption may be satisfied by the so-called linear dissipative systems as will be seen later on.

Now, we shall first investigate the temporal behavior of the system at an arbitrary time after the initial time $t$. With the help of the well-known expansion formula.

$$\begin{aligned} &\exp(-\beta(A+B)) \\ &\quad = \Big\{1 - \int_0^\beta d\lambda \exp(-\lambda A) B \exp(\lambda A) \\ &\qquad + \int_0^\beta d\lambda_1 \int_{\lambda_1}^\beta d\lambda_2 \exp(-\lambda_1 A) B \\ &\qquad \times \exp((\lambda_1 - \lambda_2) A) B \exp(\lambda_2 A) + \cdots \Big\} \\ &\qquad \times \exp(-\beta A) \,, \end{aligned}$$

we find the first order approximation to $\rho_t$ given by Eq. (3.1),

$$\rho_t=\Bigl\{1-\int_0^\beta d\lambda \exp(-\lambda\overline{H})\,(R-\langle R\rangle^0)\times\exp(\lambda\overline{H})\Bigr\}\rho_0+\boldsymbol{O}(R^2). \tag{3.4}$$

In this expression and in the following, the averages over the equilibrium distribution $\rho_0$ are expressed as

$$\langle A\rangle^0\equiv\mathrm{Tr.}\ \rho_0 A\,. \tag{3.5}$$

If one retains the first order in $R$ alone, the last expression of Eq. (2.6) is written as

$$\langle F\rangle(t+s)-\langle F\rangle^0=-\Phi_{F,R}(s)+\beta\langle F\rangle^0\langle R\rangle^0\,, \tag{3.6}$$

where

$$\Phi_{F,G}(s)\equiv\int_0^\beta d\lambda\,\langle\exp(\lambda\overline{H})F(s)\exp(-\lambda\overline{H})G\rangle_0 \tag{3.7A}$$

$$=\int_0^\beta d\lambda\,\langle G\exp(-\lambda\overline{H})\,F(s)\exp(\lambda\overline{H})\rangle^0 \tag{3.7B}$$

$$=\Phi_{G,F}(-s)\,. \tag{3.7C}$$

The expression (3.7$B$) is readily obtained from (3.7$A$) by changing the integration variable $\lambda$ to $\beta-\lambda$. The above mathematical technique is the same as has been used in Kubo and Tomita's[6] theory of magnetic resonance absorption. Eq. (3.6) completely determines the temporal behavior of the average value $\langle F\rangle(t+s)$ after the initial time $t$ and is of great use in the cases where the $R$-factor can be expressed in a handy definite terms, such as the magnetic resonance absorption[6], the electrical conduction[8] and the energy transfer between two modes. However, the transport phenomena in continuous systems[11], which are usually described by macroscopic differential equations of transport such as the equations of hydrodynamics, are not the case.

Therefore, we shall next derive a macroscopic equation for the change with time of the average value $\langle F\rangle(t)$. Differentiation of Eq. (3.6) with respect to $s$ gives

$$\frac{d}{ds}\langle F\rangle(t+s)=\Phi_{F,\dot{R}}(s) \tag{3.8}$$

with

$$\dot{R}\equiv(i\hbar)^{-1}\,[R,H]\,, \tag{3.9}$$

because of $\Phi_{\dot{F},G}(s)=-\Phi_{F,\dot{G}}(s)$. As will be seen in the later sections and the subsequent articles, we have the following linear combination in most of interesting cases:

[$A3$] $$\dot{R}=\sum_{h=1}^{n}J_hX_h(t)\,, \tag{3.10}$$

where $J_h$'s are dynamical quantities independent of the statistical state of the system and $X_h(t)$'s parameters characterizing the macroscopic state of the system at the time $t$. For the example mentioned in the preceding section, we find that $J_h=\dot{H}_h$ and $X_h(t)=-(T_h-T_0)/T_0$. Then, substitution of Eq. (3.10) into Eq. (3.8) gives

$$\frac{d}{ds}\langle F\rangle(t+s)=\sum_{h=1}^{n}\Phi_{F,J_h}(s)X_h(t)\,. \tag{3.11}$$

The quantities $X_h(t)$'s will be shown to be the thermodynamic forces in the thermodynamics of irreversible processes[11], which give rise to the occurrence of irreversible phenomena. The fluxes in thermodynamics will be identified with the values of dynamical quantities $J_h$'s averaged in a certain manner. These circumstances will be visualized in connection with the calculation of the entropy production as shown in the later section.

The macroscopic rate of change with time of the average value $\langle F\rangle(t)$ is, as stated in the preceding section, given by

$$\frac{\delta}{\delta t}\langle F\rangle(t)\equiv\frac{1}{\tau}\int_0^\tau ds\frac{d}{ds}\langle F\rangle(t+s)\,. \tag{3.12}$$

Although this definition of the macroscopic time rate has been introduced according to the rather technical demand, it may be equivalent to the time-smoothing procedure first introduced by Kirkwood[1] to obtain an adequate macroscopic description of the secular variations of observable properties of a physical system. By using a mathematical identity

$$\frac{d}{ds}\langle F\rangle(t+s)=\frac{d}{dt}\langle F\rangle(t)+\int_0^s ds'\frac{d^2}{ds'^2}\langle F\rangle(t+s')\,, \tag{3.13}$$

for Eq. (3.12) and substituting Eq. (3.11) into thus obtained equation, we obtain

$$\frac{\delta}{\delta t}\langle F\rangle(t)=\sum_{h=1}^{n}\Bigl\{\Phi_{F,J_h}(0)+\int_0^\tau ds\Bigl(1-\frac{s}{\tau}\Bigr)\Phi_{\dot{F},J_h}(s)\Bigr\}X_h(t)\,. \tag{3.14}$$

This equation is certainly valid for arbitrary observables which do not explicity depend on the time, so far as the assumptions [$A1$], [$A2$] and [$A3$] concerning the macroscopic state of the system are statisfied. However, in order that this equation can provide an adequate macroscopic description of the secular variation of the observable $F$, it is necessary that the time interval $\tau$ should be able to be selected to disappear from the right-hand side. This fact may impose a restriction on the property of the observable $F$. These circumstances were in detail discussed by Kirkwood[1], M.S. Green[9] and Yamamoto[12].

After a lapse of sufficiently long time to attain thermal equilibrium:

$$\lim_{s\to\infty}\langle F\rangle(t+s)=\langle F\rangle^0\,, \tag{3.15}$$

we obtain

$$\lim \Phi_{F,J_h}(s)\ =0\,,$$

with the help of Eqs. (3.6) and (3.10). Although this limiting property of $\Phi_{F,J_h}(s)$ is naturally required from physical reasons, it is rather difficult to prove it rigorously. In fact, a logical justification is the most essential point of any rigorous theory of irreversible processes, which is beyond of the scope of this article. It is worth mentioning, however, that in the classical limit, $\Phi_{F,G}(s)$ becomes a phase coefficient of correlation connecting $G$ and $F(s)$, $\beta\langle G(t)\,F(t+s)\rangle^0$, and then this limiting property represents the basic idea of molecular chaos[15] which is of great importance in the foundation of the statistical-thermodynamic theory of equilibrium states from the ergodic theory. Therefore, we may define a decay time $\tau(\dot{F},J_h)$ after which the function $\Phi_{\dot{F},J_h}(s)$ effectively vanishes out, as follows:

$$\Phi_{\dot{F},J_h}(s)\simeq 0\quad\text{for}\quad s>\tau(\dot{F},J_h)\,. \tag{3.16}$$

By introducing the largest value of $\tau(\dot{F},J_h)$'s $(h=1\cdots n)$, $\tau(\dot{F})$, we then obtained, with the help of Eq. (3.11),

$$\frac{d^2}{ds^2}\langle F\rangle(t+s)\simeq 0\quad\text{for}\quad s>\tau(\dot{F})\,, \tag{3.17}$$

which means that, if the approximation (3.1) is made at the initial time $t$, the acceleration of $\langle F\rangle(t+s)$ will effectively vanish in the time $\tau(\dot{F})$.

Now, we shall assume the following relation:

$$[A4]\qquad \tau(\dot{F})\ll\tau\ll\tau_r\,, \tag{3.18}$$

where $\tau_r$ is a time in which the average value $\langle F\rangle(t)$ is appreciably reduce to the equilibrium value $\langle F\rangle^0$, or the decay time of the relaxation function $\Phi_{F-\langle F\rangle^0,R-\langle R\rangle^0}(s)$. Taking such a time interval $\tau$, Eq. (3.14) can be reduced to the macroscopic equation of motion of the observable $F$,

$$\frac{\delta}{\delta t}\langle F\rangle(t)=\sum_{h=1}^{n}\{\Phi_{F,J_h}(0)+L(\dot{F},J_h)\}X_h(t)\,, \tag{3.19}$$

with

$$L(\dot{F},J_h)\equiv\int_0^{\tau(\dot{F})}ds\Phi_{\dot{F},J_h}(s) \tag{3.20A}$$

$$=\int_0^{\tau(\dot{F})}ds\int_0^{\beta}d\lambda$$

$$\times\langle J_h\exp(-\lambda\overline{H})\,\dot{F}(s)\exp(\lambda\dot{H})\rangle^0\,, \tag{3.20B}$$

which provides molecular expressions for the kinetic coefficients $L(\dot{F},J_h)$'s. The assumption $[A4]$ is the most essential point of our theory, and may, in the cases of $J_h=\dot{G}$, appear to be correlated to the complicated problem of Kirkwood[1][12], that is, whether the integral $\int_0^{\tau}ds(1-s/\tau)\Phi_{\dot{F},\dot{G}}(s)$ possesses a plateau value nearly independent of the time interval $\tau$ in the region bounded by the inequalities (3.18). Further investigation concerning this point will be postponed for later treatment. The magnitude of the time interval $\tau_c$ depends upon every special phenomenon. For example, in deriving the equations of transport in dilute gases, the mass current density and the energy density are taken as $F$, and then $\tau(\dot{F})$'s are of the order of magnitude of the mean free time of molecules, as will be shown in subsequent article.

## § 4. Energy Transfer Between Two Modes

By making use of our method mentioned in the last section, we shall derive a molecular expression for the relaxation time of the energy transfer between two subsystems which was, in § 2, taken up as a simple illustration in inspecting the phenomenological theory of transport processes, and also discuss the correlation function of the energy of the subsystem I.

The system will naturally approach to a thermal equilibrium state which is described by the stationary density operator,

$$\rho_0=Z_0^{-1}\exp(-H/kT_0) \tag{4.1}$$

with

$$H\equiv H_{\text{I}}+H_{\text{II}}+H'\,, \tag{4.2}$$

which is the total Hamiltonian of the system. Since the deviation of the system from the thermal equilibrium is small, the initial distribution $\rho(t)$ can, as stated in § 2., approximated as

$$\rho(t) \doteqdot \rho_t \equiv Z^{-1} \exp\left(-\frac{H_{\mathrm{I}}}{kT_{\mathrm{I}}}-\frac{H_{\mathrm{II}}}{kT_{\mathrm{II}}}-\frac{H'}{kT_0}\right), \tag{4.3}$$

which is consistent with the equilibrium distribution (4.1). Therefore, the $R$-factor defined in Eq. (3.3) is in this case written as

$$R=-\frac{T_{\mathrm{I}}-T_0}{T_0}H_{\mathrm{I}}-\frac{T_{\mathrm{II}}-T_0}{T_0}H_{\mathrm{II}}, \tag{4.4}$$

which satisfys

$$|R| \ll |H| \tag{4.5}$$

on account of the condition

$$|T_{\mathrm{I}}-T_0|, \quad |T_{\mathrm{II}}-T_0| \ll T_0 . \tag{4.6}$$

Therefore, the thermodynamic forces and the fluxes defined by Eq. (3.10) are, respectively, given by

$$X_h(t)=-(T_h-T_0)/T_0 \tag{4.7}$$

and

$$J_h=\dot{H}_h . \tag{4.8}$$

Thus, the assumptions [$A1$], [$A2$] and [$A3$] are satisfied, so that we obtain, with the help of Eq. (3.6),

$$\begin{aligned}\langle H_{\mathrm{I}}\rangle(t+s)-\langle H_{\mathrm{I}}\rangle^0 &= -\Phi_{H_{\mathrm{I}}-\langle H_{\mathrm{I}}\rangle^0,\, H_{\mathrm{I}}}(s)X_{\mathrm{I}}(t) \\ &\quad -\Phi_{H_{\mathrm{I}}-\langle H_{\mathrm{I}}\rangle^0,\, H_{\mathrm{II}}}(s)X_{\mathrm{II}}(t)\end{aligned} \tag{4.9}$$

with

$$\Phi_{F,G}(s)\equiv\int_0^\beta d\gamma\langle\exp(\lambda H)F(s)\exp(-\lambda H)\,G\rangle^0, \tag{4.10}$$

where $\beta\equiv 1/kT_0$ .

The loss of energy of the sub-system I almost changes into the gain of energy of the sub-system II, so that we can assume

$$\dot{H}_{\mathrm{I}}+\dot{H}_{\mathrm{II}}=-\dot{H}'\simeq 0 ,$$

to obtain

$$\Phi_{F,\dot{H}_{\mathrm{I}}}(s)+\Phi_{F,\dot{H}_{\mathrm{II}}}(s)\simeq 0 , \tag{4.11}$$

where a condition, $s<\tau_r$, may be necessary.

If the function $\Phi_{\dot{H}_{\mathrm{I}},\dot{H}_{\mathrm{I}}}(s)$ appreciably vanishes for values of $s$ greater than $\tau(\dot{H}_{\mathrm{I}})$, i. e.,

$$\Phi_{\dot{H}_{\mathrm{I}},\dot{H}_{\mathrm{I}}}(s)\simeq 0 \quad \text{for} \quad s>\tau(\dot{H}_{\mathrm{I}}) , \tag{4.12}$$

and, in addition to that, a relation

$$\tau(\dot{H}_{\mathrm{I}})\ll\tau\ll\tau_r \tag{4.13}$$

is satisfied, we obtain, by the use of Eqs. (3.19) and (4.11),

$$\frac{\delta}{\delta t}\langle H_{\mathrm{I}}\rangle(t)=-\frac{L(\dot{H}_{\mathrm{I}},\dot{H}_{\mathrm{I}})}{T_0}(T_{\mathrm{I}}-T_{\mathrm{II}}) , \tag{4.14}$$

with

$$L(\dot{H}_{\mathrm{I}},\dot{H}_{\mathrm{I}})\equiv\int_0^{\tau(\dot{H}_{\mathrm{I}})} ds\ \Phi_{\dot{H}_{\mathrm{I}},\dot{H}_{\mathrm{I}}}(s) , \tag{4.15}$$

because of the relation, $\Phi_{F,\dot{F}}(0)=0$, which is readily obtained from the symmetry property, $\Phi_{F,F}(s)=\Phi_{F,F}(-s)$, being a result of (3.7$C$).

Thus, comparison between the right-hand side of Eq. (2.2) and that of Eq. (4.14) gives

$$\begin{aligned}1/\tau_r &= L(\dot{H}_{\mathrm{I}},\dot{H}_{\mathrm{I}})/T_0C_{\mathrm{I}} \\ &= \frac{1}{2T_0C_{\mathrm{I}}}\int_{-\tau(\dot{H}_{\mathrm{I}})}^{\tau(\dot{H}_{\mathrm{I}})} ds\int_0^\beta d\lambda\langle\dot{H}_{\mathrm{I}}\dot{H}_{\mathrm{I}}(s+i\hbar\lambda)\rangle^0\end{aligned} \tag{4.16}$$

for the relaxation time $\tau_r$ to establish the equilibrium of the energy partition between the subsystems I and II. Eq. (4.16) is, in the second order approximation with respect to $H'$, identical with Kubo and Tomita's[6] expression, if the region of integration $(-\tau(\dot{H}_{\mathrm{I}}) \sim \tau(\dot{H}_{\mathrm{I}}))$ is extended to the region $(-\infty\sim\infty)$.

We shall here add a remark about the relaxation function of the energy of the subsystem I. For simplicity, let us suppose that $C_{\mathrm{I}}\ll C_{\mathrm{II}}$ so that $T_{\mathrm{II}}=T_0$. Then, Eq. (2.2) is integrated to give

$$\begin{aligned}\langle H_{\mathrm{I}}\rangle(s)-\langle H_{\mathrm{I}}{}^0\rangle \\ = -T_0C_{\mathrm{I}}X_{\mathrm{I}}(0)\exp(-s/\tau_r) \quad \text{for} \quad s\gg\tau(\dot{H}_{\mathrm{I}}) ,\end{aligned}$$

which is compared with Eq. (4.9) to give

$$\begin{aligned}\Phi_{H_{\mathrm{I}}-\langle \Pi_{\mathrm{I}}\rangle^0}(s) \\ = \Phi_{H_{\mathrm{I}}-\langle H_{\mathrm{I}}\rangle^0,\, H_{\mathrm{I}}}(0)\exp(-s/\tau_r) \quad \text{for} \quad s\gg\tau(\dot{H}_{\mathrm{I}})\end{aligned} \tag{4.17}$$

because

$$\langle(H_{\mathrm{I}}-\langle H_{\mathrm{I}}\rangle^0)^2\rangle^0=kT_0{}^2C_{\mathrm{I}} . \tag{4.18}$$

Thus, the correlation function $\Phi(s)$ in this case drops exponentially to zero.

## § 5. Momentum Relaxation Phenomena

We shall next investigate momentum relaxation phenomena, such as the electrical conduction and the friction of a Brownian particle in a fluid in equilibrium, which are the examples of historical significance in the statistical mechanics of transport phenomena.

We shall tade up the electrical conduction. It is well-known, that, when the applied constant electric field has been cut off, the average value of the total momentum $\boldsymbol{P}$ of the conduction electron system in a metal changes with time according to the equation

$$\frac{\delta}{\delta t}\langle \boldsymbol{P}\rangle+\frac{1}{\tau_r}\langle \boldsymbol{P}\rangle=0\,. \tag{5.1}$$

The relaxation time $\tau_r$ is related with the electrical conductivity by the relation

$$\tau_r=(m/Ne^2)\sigma\,, \tag{5.2}$$

where the mass and the charge of an electron were denoted by $m$ and $-e$, respectively, and the number of conduction electrons in the metal by $N$, and the metal was taken to be a unit volume.

We shall clarify the condition under which Eq. (5.1) can be justified, from the standpoint of our method and shall derive an expression for the conductivity in terms of molecular constants.

The equilibrium state which the system will attain is described by the canonical density operator

$$\rho_0=Z_0^{-1}\exp(-\beta H)\,, \tag{5.3}$$

with

$$H=H_e+H_1+H'\,, \tag{5.4}$$

where $H_e$ and $H_1$ are, respectively, the Hamiltonians for the conduction electrons and for the lattice vibrations, and $H'$ the interaction energy between them. $H_e$ may be written down as

$$H_e=\sum_{i=1}^{N}p_i^2/2m+U\,, \tag{5.5}$$

where $U$ is the sum of the interaction energy between the electrons and the interaction energy between the electrons and the undisturbed crystalline lattice.

The average velocity of the conduction electron is given by

$$\boldsymbol{v}(t)=\langle \boldsymbol{P}\rangle(t)/Nm\,. \tag{5.6}$$

As in the usual theory of electrical conduction, we shall assume that the lattice vibrations are always in complete equilibrium and the electron system always keeps thermal equilibrium with the lattice vibrations. Then, the approximate expression for the initial distribution of the system in the sense stated in § 3, may be given by

$$\rho(t)=Z^{-1}\times\exp\left[-\beta\left(\sum_{1=i}^{N}\frac{(\boldsymbol{p}_i-m\boldsymbol{v})^2}{2m}+U+H_1+H'\right)\right], \tag{5.7}$$

which implies that the distribution of the electrons in the momentum space may be approximated by a Fermi distribution the center of the Fermi sphere of which displaces from the origin by $m\boldsymbol{v}$. Therefore, the $R$-factor defined in Eq. (3.3) is given by

$$R=-\boldsymbol{P}\cdot\boldsymbol{v}+(Nm/2)v^2\,, \tag{5.8}$$

whence $J$- and $X$-factors defined in Eq. (3.10) be taken as

$$J=\boldsymbol{P},\quad X(t)=-\boldsymbol{v}(t)\,. \tag{5.9}$$

Thus, with the help of Eq. (3.19), we readily obtain

$$\frac{\delta}{\delta t}\langle \boldsymbol{P}\rangle=-(\tau_r^{-1})\cdot\langle \boldsymbol{P}\rangle \tag{5.10}$$

with

$$(\tau_r^{-1})_{xy}\equiv\frac{1}{Nm}\int_0^{\tau(\dot{P})}ds\times\int_0^{\beta}d\lambda\,\langle \dot{P}_y\dot{P}_x(s+i\hbar\lambda)\rangle^0\,, \tag{5.11}$$

where such an interval $\tau$ that $\tau(\dot{P})\ll\tau\ll\tau_r$, was assumed to exist.

In the classical limit, $\hbar=0$, Eq. (5.11) becomes

$$(\tau_r^{-1})_{xy}=\frac{\beta}{Nm}\int_0^{\tau(\dot{P})}ds\,\langle\{\dot{P}_y\dot{P}_x(s)\}\rangle^0\,, \tag{5.12}$$

where we have, for convenience, defined the symmetrized product $\{AB\}\equiv(AB+BA)/2$. This equation may be used in order to derive Kirkwood's[1] expression for the friction constant of a Brownian particle in an equilibrium fluid. To do this, in the above equations, we have only to regard $m$ and $\boldsymbol{P}$ as the mass and the momentum of the Brownian particle, respectively, and to take $N=1$. Then, $H_e$ and $H_1$ represent the Hamiltonian of the Brownian particle and that of the equilibrium fluid, respectively, and $H'$ the interaction energy between them. Thus, we obtain, in an isotropic case,

$$\zeta=m/\tau_r=\beta\int_0^{\tau(\dot{P})}ds\,\langle\dot{P}_x\dot{P}_x(s)\rangle^0 \tag{5.13}$$

for the friction constant $\zeta$ to dissipate the macroscopic energy of the Brownian particle into the random motion of the fluid. This expression is essentially identical with Kirkwood's[1] one.

As remarked by Kubo and Tomita[6] in the case of magnetic resonance absorption, Eq. (5.12) holds also in the quantum-mechanical system under such a condition that the energy differences $E_m - E_n$ of the various levels of the system connected by matrix elements of $\boldsymbol{P}$ should be much smaller than $kT(\equiv 1/\beta)$, i.e.,

$$|E_m - E_n| \ll kT\,. \tag{5.14}$$

Of course, $\boldsymbol{P}$ should then be treated as the quantum-mechanical operator and there the symmetrized product represents the quantum-mechanical counterpart of the classical one.

Next, we shall, in such an approximation, deal with the electrical conductivity, which can, in an isotropic case, be expressed as

$$\sigma^{-1} = \frac{\beta}{(Ne)^2}\,\frac{1}{2}\int_{-\tau(\dot{P})}^{\tau(\dot{P})} ds\,\langle\{\dot{P}_x \dot{P}_x(s)\}\rangle^0\,. \tag{5.15}$$

We shall now observe that the Heisenberg operator $F(s)$ of an observable $F$ can be expanded in a Fourier series of the form,

$$F(s) = \sum_{\omega} F(\omega)\exp(i\omega s) \tag{5.16}$$

with

$$F^*(\omega) = F(-\omega)\,, \tag{5.17}$$

where $F(\omega)$ is the matrix formed from all the matrix elements $\langle m|F|n\rangle$ of $F$ which are accompanied by the energy difference $\hbar\omega \equiv E_m - E_n$. As to these harmonic components, we obtain the well-known relation

$$\langle\{F^*(\omega)F(\omega')\}\rangle^0 = 0 \text{ for } \omega \neq \omega' \tag{5.18}$$

where we have assumed that the decay time of the correlation function,

$$\Psi_{F,F}(s) \equiv \langle\{FF(s)\}\rangle^0\,, \tag{5.19}$$

is finite. This relation means that the different harmonic components are uncorrelated to each other. Thus, we obtain

$$\Psi_{\dot{P}_x\dot{P}_x}(s) = \sum_{\omega}\langle\{\dot{P}_x^*(\omega)\dot{P}_x(\omega)\}\rangle^0 \exp(i\omega s)\,. \tag{5.20}$$

It is due to the destructive interference between the various harmonic components oscillating with the different frequencies that the correlation function $\Psi_{\dot{P}_x,\dot{P}_x}(s)$ vanishes for the values of $s$ greater than $\tau(\dot{P})$. To obtain detailed informations about this situation, we should inspect the $\omega$-dependence of the spectrum $\Psi_{\dot{P}_x,\dot{P}_x}(\omega) = \langle\{\dot{P}_x^*(\omega)\dot{P}_x(\omega)\}\rangle^0$. Simply, let us assume, however, that, similarly to the almost pure random process, the spectrum $\Psi(\omega)$ is constant in such a wide region of $\omega$ that $|\omega| < \pi/\tau(\dot{P})$, that is, a white spectrum[16]. Then, we obtain

$$\sigma^{-1} = (\pi\beta/(Ne)^2)\sum_{\omega}\langle\{\dot{P}_x^*(\omega)\dot{P}_x(\omega)\}\rangle^0\delta(\omega)\,, \tag{5.21}$$

which is, in the second order approximation with respect to $H'$, identical with Nakano's[8] equation, in which the asymptotic form of the after-effect function, $\Phi_{P_x,P_x}(t) \propto \exp(-t/\tau_r)$, has been taken into account, because $\langle P_x^2\rangle^0 = NmkT$. As has been shown by Nakajima[17] and Nakano[8], straightforward calculation of the expression (5.21) leads to the Bloch-Grüneisen formula for the electrical conductivity of simple metals.

## § 6. General Formulation (II)—*Entropy Production*

As is well-known, the entropy plays an important part in the thermodynamical theory of irreversible processes[11], the starting point of which is usually to calculate the irreversible production of entropy during the evolution of the irreversible process in question. The calculation reposes upon the acceptance of Gibbs' relation for the entropy $S_\text{I}$ of each uniform part of the system,

$$T_\text{I} dS_\text{I} = dE_\text{I} + p_\text{I} dV_\text{I} - \sum_i \mu_\text{I}^i\, dN_\text{I}^i\,, \tag{6.1}$$

where $E_\text{I}$ is the internal energy, $V_\text{I}$ the volume, $p_\text{I}$ the pressure, $N_\text{I}^i$ the number of molecules and $\mu_\text{I}^i$ the chemical potential of the component $i$ of the part. The relation (6.1) is thus assumed to be valid even outside thermal equilibrium. However, this is not yet justified from the molecular-theoretical point of view except for a particular model.

Therefore, it is undoubtedly necessary to seek for a statistical-mechanical expression of the entropy of a non-equilibrium state, which may not only clarify the meaning of the assumption (6.1) but also serve to find out molecular expressions for kinetic coefficients. Although the generalized $H$-theorem investigated by Gibbs and others[13] gave a great insight into the statistical mechanics of irreversible processes, many difficulties should be overcome until the generalized $H$-function can be taken as the entropy. Therefore, in this section, we shall investigate this problem by means of our method.

To do this, we again consider the heat transfer between two subsystems at different temperatures already mentioned in § 2. If the local equilibrium is assumed at a time $t$, the entropy of the system at that time can be given by

$$S(t)=-k\,\mathrm{Tr}\,\rho_t\ln\rho_t \tag{6.2}$$

by virtue of the statistical mechanics of equilibrium states, where $\rho_t$ is the local equilibrium distribution (2.13). According to the assumption (A4) stated in § 2., this equation (6.2) may be taken at discrete values of time whose neighboring values are separated by the short time interval $\tau$. Hence, we can obtain

$$\delta S(t)/\delta t=(1/T_{\mathrm{I}})\delta E_{\mathrm{I}}/\delta t+(1/T_{\mathrm{II}})\delta E_{\mathrm{II}}/\delta t\ , \tag{6.3}$$

where $\delta/\delta t$ means the macroscopic time derivative defined in Eq. (2.10). Of course, this equation can also be obtained from the application of Gibbs' equation to our system. In fact, Gibbs' relation, which means that the entropy of the subsystem I, $S_{\mathrm{I}}$, is supposed to depend explicitly only on the energy $E_{\mathrm{I}}$, may be regarded to be founded on the above-mentioned assumption (A4).

First of all, we shall seek for such a statistical-mechanical expression for the entropy of the system at an arbitrary time as is consistent with Eqs. (6.2) and (6.3). By inserting Eq. (2.11) into the right-hand side of Eq. (6.3) and comparing thus obtained equation with an alternative form of the left-hand side of Eq. (6.3),

$$\frac{\delta}{\delta t}S(t)=\frac{1}{\tau}\int_0^\tau ds\frac{d}{ds}S(t+s)\ , \tag{6.4}$$

we can readily obtain, for $s<\tau$,

$$\frac{d}{ds}S(t+s)$$
$$=\frac{1}{T_{\mathrm{I}}}\frac{d}{ds}\langle H_{\mathrm{I}}\rangle(t+s)+\frac{1}{T_{\mathrm{II}}}\frac{d}{ds}\langle H_{\mathrm{II}}\rangle(t+s)\ , \tag{6.5}$$

which is integrated to give

$$S(t+s)=-k\,\mathrm{Tr}\,\rho(t+s)\ln\rho_t \tag{6.6}$$

for $s<\tau$, which is consistent with Eq. (6.2). The local equilibrium distribution $\rho_t$ depends explicitly on the time $t$ only through the temperatures $T_{\mathrm{I}}(t)$ and $T_{\mathrm{II}}(t)$, which hardly change for the short time interval $\tau$, so that Eq. (6.6) can be obtained as a good approximation of

$$S(t+s)=-k\,\mathrm{Tr}\,\rho(t+s)\ln\rho_{t+s}\ , \tag{6.7}$$

which is valid for an arbitrary magnitude of $s$. Thus, we find Eq. (6.7) to provide a statistical-mechanical expression for the entropy of the non-equilibrium system.

It is clear from the way of derivation that Eq. (6.7) is generally valid beyond a special example of the energy transfer between two subsystems, so far as the distribution $\rho_t$ is chosen to be consistent with Gibbs' relation corresponding to the system we are concerned with.

Next, we shall demonstrate the following relations:

$$\begin{aligned} &S(t+s)>S(t)\ , \quad \text{if} \quad \rho(t+s)\neq\rho_{t+s}\\ &S(t+s)=S(t)\ , \quad \text{otherwise,}\end{aligned} \tag{6.8}$$

under the initial condition

$$\rho(t)=\rho_t\ . \tag{6.9}$$

The first equation of (6.8) shows that the value of the entropy $S(t+s)$ will be larger at the later time $t+s$ than at the initial time $t$, and will serve for the statistical-mechanical proof of the famous fact that the entropy production is always positive definite. Moreover, it is worth mentioning in connection with (A4) in § 2 that Eqs. (6.8) tell us that the assumption of local equilibrium can at most be made only at the discrete values of time in the statistical-mechanical formulation of the irreversible processes. Since from Eq. (2.4)

$$\mathrm{Tr}\,\rho(t)\ln\rho(t)=\mathrm{Tr}\,\rho(t+s)\ln\rho(t+s)\ , \tag{6.10}$$

we obtain, with the help of the initial condition (6.9),

$$S(t+s)-S(t)$$
$$=k\,\mathrm{Tr}\,\rho(t+s)\left(\ln\rho(t+s)-\ln\rho_{t+s}\right)\ . \tag{6.11}$$

As is easily seen from Neumann's definition of density operator, a set of state vectors diagonalizing $\rho(t+s)$ always exists so that, denoting the set by $\{|m\rangle\}$, the right-hand side of Eq. (6.11) can be written down as

$$k\sum_m\langle m|\rho(t+s)|m\rangle(\ln\langle m|\rho(t+s)|m\rangle$$
$$-\langle m|\ln\rho_{t+s}|m\rangle)\ ,$$

where the matrix elements of operator $A$ in that representation are denoted by $\langle m|A|m\rangle$'s. To treat this expression, we shall first make use of the following lemma[18] concerning a Hermitian operator $A$:

$$\langle m|\ln A|m\rangle\leq\ln\langle m|A|m\rangle\ , \tag{6.12}$$

which is a simple consequence of a property of the concave function $\varphi(a_n)\equiv\ln a_n$ ,

$$\text{mean}\quad\varphi(a_n)\leq\varphi(\text{mean }a_n)\ ,$$

because

$$\langle m|A|m\rangle=\sum_n a_n|\langle n|m\rangle|^2\ ,\quad \sum_n|\langle n|m\rangle|^2=1\ ,$$

$$\langle m|\ln A|m\rangle=\sum_n \ln a_n|\langle n|m\rangle|^2\ ,$$

where $\langle n|m\rangle$ is the matrix of the unitary transformation from the set $\{|m\rangle\}$ to the set of the eigenvectors of $A$. This lemma gives

$$\begin{aligned}&S(t+s)-S(t)\\&\quad\geqq k\sum_m \langle m|\rho(t+s)|m\rangle(\ln\langle m|\rho(t+s)|m\rangle\\&\qquad-\ln\langle m|\rho_{t+s}|m\rangle)\ .\end{aligned}\tag{6.13}$$

Secondly, we make use of the following well-known relation:

$$x(\ln x-\ln y)-x+y>0\tag{6.14}$$

for any pair of quantities $x$ and $y$ which cannot assume negative values and cannot equal each other. Hence, by subtracting $\sum\langle m|\rho(t+s)|m\rangle$ from and adding $\sum\langle m|\rho_{t+s}|m\rangle$ to the right-hand side of Eq. (6.13) we find that $S(t+s)>S(t)$, if $\rho(t+s)\neq\rho_{t+s}$. Thus, the first equation of Eq. (6.8) has been proved. The second equation can easily be obtained from Eq. (6.10).

From the foregoing discussion, one may notice that there is an intimate relation between the entropy (6.7) and the generalized $H$-function. But, before going into the investigation of the relation, we shall calculate the irreversible production of entropy of such a system that its initial distribution, $\rho_t$, satisfys the assumptions [$A$1], [$A$2] and [$A$3] stated in § 3. To do this, we may confine ourselves to the consideration of the temporal behavior of the entropy for the short time interval ($t\sim t+\tau$). For this time interval, the entropy (6.7) can be written, in good approximation, as

$$S(t+s)=k\,\mathrm{Tr}\,\rho(t+s)\,K+C\ ,\tag{6.15}$$

with the help of Eqs. (6.6) and (3.1), where $C$ is a trivial constant term. Evidently, Eq. (3.6) can be applied to Eq. (6.15) to give

$$S(t+s)\fallingdotseq-\frac{1}{T}\varPhi_{R,R}(s)+C'\ ,$$

which is differentiated with respect to $s$ to give

$$\begin{aligned}\frac{d}{ds}S(t+s)&=-\frac{1}{T}\varPhi_{\dot R,R}(s)\\ \frac{d^2}{ds^2}S(t+s)&=\frac{1}{T}\varPhi_{\dot R,\dot R}(s)\end{aligned}\tag{6.16}$$

for $s<\tau$, where $T\equiv1/k\beta$ expresses the temperature of the final equilibrium state to which the system approaches. Therefore, the macroscopic time derivative of the entropy, (6.4), can be written, with the help of the mathematical identity (3.13), as

$$\frac{\delta}{\delta t}S(t)=\frac{1}{T}\int_0^\tau ds\left(1-\frac{s}{\tau}\right)\varPhi_{\dot R,\dot R}(s)\tag{6.17}$$

because of the relation

$$\varPhi_{\dot R,R}(0)=0\ ,\tag{6.18}$$

which is readily obtained from Eq. (3.7$C$).

By the use of Eq. (3.10), the function $\varPhi_{\dot R,\dot R}(s)$ can be written in terms of the fluxes $J_h$'s as follows:

$$\varPhi_{\dot R,\dot R}(s)=\sum_h\sum_k\varPhi_{J_h,J_k}(s)X_h(t)X_k(t)\ ,\tag{6.19}$$

where $X_h(t)$'s are parameters characterizing the macroscopic state of the system at the time $t$. Now, we define a decay time $\tau(J_h,J_k)$ in which the function $\varPhi_{J_h,J_k}(s)$ effectively vanishes out, that is,

$$\varPhi_{J_hJ_k}(s)\simeq0\quad\text{for}\quad s>\tau(J_h,J_k)\ ,\tag{6.20}$$

which, as already stated in § 3., may represent the basic idea of molecular chaos. By introducing the largest value of $\tau(J_h,J_k)$'s ($h$, $k=1\cdots n$), $\tau_c$, we then obtain

$$\varPhi_{\dot R,\dot R}(s)\simeq0\quad\text{for}\quad s>\tau_c,\tag{6.21}$$

which leads to a remarkable conclusion that, if the coarse-graining assumption (6.9) is made at the initial time $t$, the acceleration of the entropy $S(t+s)$ will effectively vanish in the time $\tau_c$ in the case of $\tau_c\ll\tau_r$.

Now, we shall assume, in accordance with Eq. (3.18), that

$$\tau_c\ll\tau\ll\tau_r\ .\tag{6.22}$$

Then, by substituting Eq. (3.10) into the left $\dot R$ of Eq. (6.17), the entropy production is to be written as

$$\frac{\delta}{\delta t}S(t)=\frac{1}{T}\sum_h((J_h))X_h\geqq0\tag{6.23}$$

with

$$((J_h))\equiv\int_0^{\tau_c}ds\,\varPhi_{J_h,\dot R}(s)\ ,\tag{6.24}$$

which may by regarded as a kind of average value of the dynamical flux $J_h$. It is a direct consequence of Eq. (6.8) that the value of $\delta S(t)/\delta t$ should always be non-negative. One may notice that Eq. (6.23) has the same standard form as the entropy production in the thermodynamical theory of irreversible processes[11]. Hence, we find that $((J_h))$ and

$X_h$ are, respectively, the conjugated thermodynamic fluxes and forces. Substitution of Eq. (3.10) into Eq. (6.24) thus gives the linear relations,

$$((J_h)) = \sum_{k=1}^{n} L(J_h, J_k) X_k(t), \quad (h=1\cdots n) \tag{6.25}$$

with

$$L(J_h, J_k) \equiv \int_0^{\tau_c} ds\, \Phi_{J_h, J_k}(s) \tag{6.26 A}$$

$$= \int_0^{\tau_c} ds \int_0^{\beta} \delta\lambda \, \langle J_k \exp(-\lambda \overline{H}) J_h(s) \times \exp(\lambda \overline{H}) \rangle^0 \,, \tag{6.26B}$$

which provides quantum-statistical expressions for the phenomenological coefficients in the thermodynamics. To state a symmetry property of $(J_h, J_k)$ briefly, we now suppose that any enternal magnetic field is not applied to our system, so that the Hamiltonian $H$ and also $\overline{H}$ in $\rho_0$ are invariant to the reversal of the direction of the time axis. Therefore, if $F$ and $G$ change their sign (then being called odd variables) or remain invariant (even variables) with the reversal of time, we have, as prove by Kubo and Tomita[6] in the case of the magnetic relaxation function,

$$\Phi_{F,G}(s) = \varepsilon_{F,G}\, \Phi_{F,G}(-s) \tag{6.27}$$

with

$$\varepsilon_{F,G} = \begin{cases} 1, & \text{if } F \text{ and } G \text{ are the same kind of variables} \\ -1, & \text{otherwise.} \end{cases}$$

Combining with (3.7$C$), we thus obtain

$$\Phi_{F,G}(s) = \varepsilon_{F,G}\ \Phi_{G,F}(s) \,, \tag{6.28}$$

which is applied to Eq. (6.26) to give the Onsager reciprocal relations

$$L(J_h, J_k) = \varepsilon_{J_h, J_k} L(J_k, J_h) \,. \tag{6.29}$$

Thus, we see that the quantum-statistical expression (6.7) for the entropy of the non-equilibrium system may provide a microscopic basis for the thermodynamics of irreversible processes[11].

Now, we turn to discussion of a relation of the expression (6.7) to the generalized $H$-theorem. For brevity, we again take up the energy transfer between two sub-systems as in the beginning of this section. Then, denoting the set of the simultaneous eigenvectors of $H_{\text{I}}$ and $H_{\text{II}}$ by $\{|m\rangle\}$, Eq. (6.7) can be written as

$$S(t+s) = -k \sum_m \langle m|\rho(t+s)|m\rangle \ln P_m(t+s) \tag{6.30}$$

with

$$P_m(t) \equiv \langle m|\rho_t|m\rangle = Z^{-1} \exp\left(-\frac{E_{\text{I}}{}^m}{kT_{\text{I}}(t)} - \frac{E_{\text{II}}{}^m}{kT_{\text{II}}(t)}\right), \tag{6.31}$$

where $E_{\text{I}}{}^m$ and $E_{\text{II}}{}^m$ are the eigenvalues of $H_{\text{I}}$ and $H_{\text{II}}$, respectively. $P_m(t)$ may be regarded as the coarse-grained probability in the sense of Gibbs[13] even if the original definition is done in a manner somewhat different from ours. By the use of the coarse-grained probability, the $H$-function $(\times(-k))$ is usually defined as

$$S'(t+s) = -k \sum_m P_m(t+s) \ln P_m(t+s) \,, \tag{6.32}$$

which is never equal to Eq. (6.30). We find, however, that, in the derivation of the $H$-theorem, not Eq. (6.32) but Eq. (6.30) is always used. Eq. (6.30) has the essential connection with the generalized $H$-theorem, so that the relations (6.8) may be regarded only as a direct consequence of the $H$-theorem. But, the representation diagonalizing $\rho_{t+s}$ does not generally remain invariant with the lapse of time, and in such a case the usual method of proof of the $H$-theorem cannot be applied to Eq. (6.7). On the countrary, the above method may be more general and just fit for Eq. (6.7). The inequality (6.12) corresponds to the Klein lemma[18] and therefore represents the quantum effect which is usually called the quantum-mechanical spreading of fine-grained probability. It is well-known that the inequality (6.14) means the inhomogenous redistribution of fine-grained probability which is also present in the classical statistisc.

## § 1. Cross-phenomena between Electrical and Thermal Conduction

When the electrical and thermal conduction occur simultaneously, they interfere with each other and give rise to new effects, that is, the thermoelectric effects. Then, the averages of the electric and heat current densities are given, respectively, by[11][19]

$$\bar{j} = S^{(1)}(\boldsymbol{H})\left(\boldsymbol{E} + \frac{T}{e} \nabla \frac{\mu}{T}\right) + S^{(2)} \frac{1}{T} \nabla T$$

$$\bar{q} = S^{(3)}(\boldsymbol{H})\left(\boldsymbol{E} + \frac{T}{e} \nabla \frac{\mu}{T}\right) + S^{(4)}(\boldsymbol{H})\ \frac{1}{T} \nabla T, \tag{7.1}$$

where $-e$ is the charge of an electron, $\boldsymbol{E}$ the applied electric field, $\boldsymbol{H}$ the external magnetic field, $T$ the local temperature and $\mu$ the local chemical potential. The coefficients satisfy the symmetry relations

$$S_{xy}^{(1)}(\boldsymbol{H})=S_{yx}^{(1)}(-\boldsymbol{H}),\quad S_{xy}^{(4)}(\boldsymbol{H})=S_{yx}^{(4)}(-\boldsymbol{H})$$
$$S_{xy}^{(2)}(\boldsymbol{H})=-S_{yx}^{(3)}(-\boldsymbol{H}) \tag{7.2}$$

which represent the Onsager reciprocal relation. These phenomena have always served as touchstones for the various theories of irreversible phenomena. For this reason and also because of the particular importance of the phenomena in question, we shall here reformulate the equation (7.1) to find quantum-statistical expressions for the kinetic coefficients by means of the method stated in the preceding section.

For brevity, let us suppose the applied electric field to have been cut off. The local equilibrium distribution of the system may then be given by

$$\rho_t=Z^{-1}\exp\left(-\int\beta(\boldsymbol{x})\{H(\boldsymbol{x})-\mu(\boldsymbol{x})n(\boldsymbol{x})\}\,d\boldsymbol{x}\right), \tag{7.3}$$

where $n(\boldsymbol{x})$ is the local number density of conduction electrons and $\beta(\boldsymbol{x})\equiv1/kT(\boldsymbol{x})$. $H(\boldsymbol{x})$ is the sum of the local energy density of conduction electrons and that of lattice vibrations. We have here assumed that the electron system locally keeps thermal equilibrium with lattice vibrations. Therefore, if the coarse-graining procedure (6.9) is made at the initial time $t$, the assumption [$A1$] stated in § 3 is satisfied. The equilibrium distribution of the system is given by

$$\rho_0=Z_0^{-1}\exp\left(-\beta(H-\mu N)\right), \tag{7.4}$$

where $H$ is the total Hamiltonian of the system, $N$ the total number of electrons. Hence, the $R$-factor,

$$R=-\int\{(1-\beta(\boldsymbol{x})/\beta)H(\boldsymbol{x})$$
$$-(\mu-\beta(\boldsymbol{x})\mu(\boldsymbol{x})/\beta)\,n(\boldsymbol{x})\}d\boldsymbol{x}\,, \tag{7.5}$$

satisfies the assumption [$A2$], so far as the system is departing but slightly from the equilibrium.

In order to find the conjugated dynamical fluxes and thermodynamic forces of the system, we shall first notice the equation of continuity and the law of conservation of energy,

$$\dot{n}(\boldsymbol{x})=(1/e)\nabla\cdot\boldsymbol{j}(\boldsymbol{x})$$
$$\dot{H}(\boldsymbol{x})=-\nabla\cdot(\boldsymbol{q}(\boldsymbol{x})+\boldsymbol{q}'(\boldsymbol{x}))\,, \tag{7.6}$$

where $\boldsymbol{q}'$ is the heat current density of lattice vibrations and will hereafter be neglected because it is usually very small in comparison with the heat current density of electrons, $\boldsymbol{q}$. From the definition of $\dot{R}$, (3.9), we thus obtain

$$\dot{R}=\int\left(-\boldsymbol{q}(\boldsymbol{x})\cdot\frac{1}{T}\nabla T+\boldsymbol{j}(\boldsymbol{x})\cdot\frac{T}{e}\nabla\frac{\mu}{T}\right)d\boldsymbol{x} \tag{7.7}$$

For simplicity, we shall now suppose that the gradients of the temperature and the chemical potential are almost uniform. Then, Eq. (7.7) can be written as

$$\dot{R}=-\boldsymbol{Q}\cdot\frac{1}{T}\nabla T+\boldsymbol{J}\cdot\frac{T}{e}\nabla\frac{\mu}{T}\,, \tag{7.8}$$

which gives

$$J_h=\boldsymbol{J},\,\boldsymbol{Q}$$
$$X_h=\frac{T}{e}\nabla\frac{\mu}{T}\,,\;-\frac{1}{T}\nabla T \tag{7.9}$$

for the conjugated dynamical fluxes and thermodynamic forces. Here, $\boldsymbol{J}$ and $\boldsymbol{Q}$ are, respectively, the total electric current and the total heat current, being expressed as

$$\boldsymbol{J}=-(e/m)\sum_{i=1}^{N}\boldsymbol{p}_i$$
$$\boldsymbol{Q}=\sum_{i=1}^{N}\frac{p_i^2}{2m}\frac{\boldsymbol{p}_i}{m}\,, \tag{7.10}$$

where, in the second expression, the terms due to the interaction between electrons are neglected as usual. Thus, from Eq. (6.25), we obtain

$$((\boldsymbol{J}))=L(\boldsymbol{J},\boldsymbol{J})\cdot\frac{T}{e}\nabla\frac{\mu}{T}-L(\boldsymbol{J},\boldsymbol{Q})\cdot\frac{1}{T}\nabla T$$
$$((\boldsymbol{Q}))=L(\boldsymbol{Q},\boldsymbol{J})\cdot\frac{T}{e}\nabla\frac{\mu}{T}-L(\boldsymbol{Q},\boldsymbol{Q})\cdot\frac{1}{T}\nabla T \tag{7.11}$$

for the thermodynamic fluxes corresponding to the dynamical fluxes $\boldsymbol{J}$ and $\boldsymbol{Q}$. These equations are compared with Eqs. (7.1) to give

$$S_{xy}^{(1)}(\boldsymbol{H})=\int_0^{\tau_c}ds\int_0^{\beta}d\lambda\langle J_yJ_x(s+i\hbar\lambda)\rangle^0$$
$$S_{xy}^{(2)}(\boldsymbol{H})=-\int_0^{\tau_c}ds\int_0^{\beta}d\lambda\langle Q_yJ_x(s+i\hbar\lambda)\rangle^0$$
$$S_{xy}^{(3)}(\boldsymbol{H})=\int_0^{\tau_c}ds\int_0^{\beta}d\lambda\langle J_yQ_x(s+i\hbar\lambda)\rangle^0 \tag{7.12}$$
$$S_{xy}^{(4)}(\boldsymbol{H})=-\int_0^{\tau_c}ds\int_0^{\beta}d\lambda\langle Q_yQ_x(s+i\hbar\lambda)\rangle^0$$

with the help of Eq. (6.26), where the system was taken to be a unit volume. The right-hand sides of Eqs. (7.12) satisfy the symmetry relations (7.2) as a direct consequence of Eq. (6.29) or that of the straightforward extention of it to the system in the external magnetic field. Eqs. (7.12) provide the molecular expressions for the various kinetic coefficients of thermoelectric phenomena. The definition of the time interval $\tau_c$ is evident from Eq. (6.20). Similar results to Eqs. (7.12) have been obtained by Kubo, Yokota and Hashitsume[20] independently from the author by means of a new method.

$S^{(1)}(\boldsymbol{H})$ is nothing but the electrical conductivity and becomes identical with Nakano's expression

$$\sigma_{xy}=\int_0^\infty ds\int_0^\beta d\lambda\,\langle \dot{J}_y \dot{J}_x(s+i\hbar\lambda)\rangle^0\,, \quad (7.13)$$

if $\tau_c$ is extended to the infinity by taking into account that, for values of $s$ greater than $\tau_c$, the integrand vanishes out. A way of deriving the alternative expression (5.11) for the electrical conductivity from this equation is as follows. For simplicity, let us consider an isotropic case. Since $\Phi_{\dot{J}_x,\,J_x}(0)=0$, we obtain

$$\begin{aligned}\Phi_{J_x,\,J_x}(s)&=\Phi_{J_x,\,J_x}(0)-\int_0^s (s-s')\Phi_{\dot{J}_x,\,\dot{J}_x}(s)'ds'\\ &=\Phi_{J_x,\,J_x}(0)-s\int_0^{\tau(\dot{P})}\Phi_{\dot{J}_x,\,\dot{J}_x}(s')ds'\end{aligned}$$

for $\tau_r\gg s\gg\tau(\dot{P})$. If the after-effect function $\Phi_{J_x,\,J_x}(s)$ can be described in terms of one relaxation time, $\tau_r$, as usual[8], that is,

$$\Phi_{J_x,\,J_x}(s)=\Phi_{J_x,\,J_x}(0)\exp(-s/\tau_r) \quad \text{for} \quad s\gg\tau(\dot{P})\,, \qquad (7.14)$$

we readily obtain, by making a comparison between the two above equations at such a time $s$ that $\tau(\dot{P})\ll s\ll\tau_r$,

$$\sigma^{-1}=\left(\frac{m}{Ne^2}\right)^2\int_0^{\tau(\dot{P})} ds\int_0^\beta d\lambda\langle \dot{J}_x \dot{J}_x(s+i\hbar\lambda)\rangle^0\,, \qquad (7.15)$$

which provides Eq. (5.15). Eq. (7.14) may be equivalent to Eq.(5.1) and hence the acceptance of it may correspond to the procedure that approximation (5.7) is made at discrete values of time whose neighboring values are separated by such a time interval $\tau$ that $\tau(\dot{P})\ll\tau\ll\tau_c$. Moreover, both $\tau_c$ and $\tau_r$ are of the order of magnitude of the mean free time of electrons.

## § 8. Summary and Some Remarks

In our formulation of the quantum-statistical theory of transport processes, our particular intention was to establish the fluctuation-dissipation theorem which relates kinetic coefficiens, such as the coefficients of heat conductivity and viscosity, with the equilibrium fluctuation of the system in question. This was done by investigating the time behavior of the system for the short time interval under the condition that the initial distribution can be approximated by such a distribution as satisfies the assumptions [*A*1], [*A*2] and [*A*3] characterizing the macroscopic state of the system. Thus, the macroscopic time derivative (3.12) led to the phenomenological equation of motion (3.19), which provided the molecular expressions for the kinetic coefficients. The quantum-statistical expressin (6.7) for the entropy of the non-equilibrium sytem was shown to lead to the entropy production (6.23), which gave a molecular basis for the thermodynamics of irreversible processes. Thus, Eq. (6.26) served for the general proof of the fluctuation-dissipation theorem.

This approach can readily be carried out for any linear dissipative processes, even if the suitable initial distribution is found out. For example, for the transport phonomena in liquid, we can take as

$$K=\int\beta(\boldsymbol{x})\Big\{E(\boldsymbol{x})+p(\boldsymbol{x})-\sum_i\mu^i(\boldsymbol{x})n^i(\boldsymbol{x})\Big\}dV\,,$$

which is consistent with Gibbs' relation (6.1). But, in this case, we are usually concerned with the "local" entropy[11], which is of particular convenience in discussing the viscous flow. The detailed analysis will be postponed for later article, but it is here worth while to state the results briefly. It tells us that the coefficients of shear and bulk viscosities of an isotropic liquid are, respectively, given by

$$\eta=\eta_{xy;xy}\quad(x\neq y)$$
$$\phi=\eta_{xx;xx}-\frac{4}{3}\eta\,,$$

where

$$\eta_{xy;x'y'}\equiv\frac{1}{2}\int_{-\infty}^{\infty}ds\int_0^\beta d\lambda\langle\pi_{xy}\pi_{x'y'}(s+i\hbar\lambda)\rangle^0$$

with

$$\pi\equiv\sum_{i=1}^N\frac{1}{m_i}(\boldsymbol{p}_i\boldsymbol{p}_i-\langle\boldsymbol{p}_i\boldsymbol{p}_i\rangle^0)+\sum_i\sum_j(\boldsymbol{r}_{ij}\boldsymbol{F}_{ij}-\langle\boldsymbol{r}_{ij}\boldsymbol{F}_{ij}\rangle^0)\,,$$

where $r_{ij} \equiv x_i - x_j$, and $F_{ij}$ is the intermolecular force exerted on the $i$-th molecule by the $j$-th molecule. This equation can be applied to the quantum gases to give results consistent with Chapman and Enskog's theory in the high temperature and with Tomonaga's[21)] results for the extremely degenerate Fermi gas, as will be given in subsequent paper by H. Nishimura and the author.

The present theory is based on the repeated use of the coarse-graining assumption (6.9) after each of a long succession of short time intervals. Therefore, it must be desirable to justify this procedure from a more fundamental basis. Van Hove[22)] has recently presented an approach to such a problem for quantum-mechanical systems whose approach to equilibrium is produced by a perturbation, which may require a further investigation.

### Acknowledgement

The author would like to express appreciation to Professor N. Watanabe for encouragement, and to Professor S. Ono of the University of Tokyo for helpful discussions and encouragement. The author is also greatly indebted to Professor T. Yamamoto of the Kyoto University and Professor N. Hashitsume of the Ochanomizu University and Professor T. Nakamura of the Kyushu University for much valuable discussions and kind advices. This study was partially financed by the Scientific Research Fund of the Ministry of Education.

### References

1) J. G. Kirkwood: J. Chem. Phys. **14** (1946) 180.
2) H. Nyquist: Phys. Rev. **32** (1928) 110.
3) H. B. Callen and T. A. Welton: Phys. Rev. **83** (1951) 34.
4) H. Takahasi: J. Phys. Soc. Japan **7** (1952) 439.
5) H. B. Callen and R. F. Greene: Phys. Rev. **86** (1952) 702; **88** (1952) 1387.
6) R. Kubo and K. Tomita: J. Phys. Soc. Japan **9** (1954) 888.
7) M. S. Green: J. Chem. Phys. **19** (1951) 1036.
8) H. Nakano: Prog. Theor. Phys. **15** (1956) 77; Busseiron Kenkyu (in Japanese) **84** (1955) 25; **88** (1955) 53.
9) M. S. Green: J. Chem. Phys. **20** (1952) 1281; **22** (1954) 398.
10) L. Onsager: Phys. Rev. **37** (1931) 405; **38** (1931) 2265.
L. Onsager and S. Machlup: *ibid.* **91** (1953) 1505.
11) S. R. de Groot: *Thermodynamics of Irreversible Processes* (Amsterdam, 1951).
12) T. Yamamoto: Prog. Theor. Phys. **10** (1953) 11.
13) R. C. Tolman: *Principles of Statistical Mechanics* (Oxford, 1938) § 51, § 106.
14) T. Sakai: *Principles of Thermodynamics* (in Japanese, Tokyo, 1947) § 27.
15) A. I. Khinchin (translated by G. Gamow): *Mathematical Foundations of Statistical Mechanics* (New York, 1949) § 13.
16) M. C. Wang and G. E. Uhlenbeck: Rev. Mod. Phys. **17** (1945) 323.
17) S. Nakajima: Busseiron Kenkyu (in Japanese) **88** (1955) 45.
18) K. Husimi: Proc. Phys. Math. Soc. Japan **22** (1940) 264.
19) A. H. Wilson: *The Theory of Metals* (Cambridge, 1953) Chapter VIII.
20) R. Kubo and M. Yokota: Busseiron Kenkyu (in Japanese) **89** (1955) 99.
R. Kubo, N. Hashitsume and M. Yokota: *ibid.* **91** (1955) 32.
21) S. Tomonaga: Zeits. f. Phys. **110** (1938) 573.
22) L. Van Hove: Physica **XXI** (1955) 517.

JOURNAL OF THE PHYSICAL SOCIETY OF JAPAN Vol. 11, No. 10, OCTOBER, 1956

# Non-additive Intermolecular Potential in Gases
## I. van der Waals Interactions

By Yukio MIDZUNO and Taro KIHARA

*Department of Physics, Faculty of Science, University of Tokyo*

(Received July 6, 1956)

The potential energy of van der Waals interactions between three spherically symmetric atoms at large separations has been investigated both by perturbation theory and by variation method. Without using any particular atomic models the van der Waals interaction is derived, from second- and third-order perturbations, in the form

$$-\mu_{12}r_{12}^{-6}-\mu_{23}r_{23}^{-6}-\mu_{31}r_{31}^{-6}+\nu(r_{12}r_{23}r_{31})^{-3}(3\cos\theta_1\cos\theta_2\cos\theta_3+1),$$

where $r_{ij}$ is the distance between $i$th and $j$th atoms, $\theta_i$'s are inner angles of a triangle formed by the three atoms. An approximate relation between $\mu$ and $\nu$ is found by variation method:

$$\nu=\frac{2R_1R_2R_3(R_1+R_2+R_3)}{(R_1+R_2)(R_2+R_3)(R_3+R_1)},$$

in which

$$\frac{1}{R_1}=\frac{1}{\mu_{12}\alpha_3}+\frac{1}{\mu_{31}\alpha_2}-\frac{1}{\mu_{23}\alpha_1}\quad \text{etc},$$

$\alpha_i$ being the polarizability of the $i$th atom. In case three atoms are identical the relation reduces to $4\nu=3\alpha\mu$. The accuracy of this simple relation is sufficient; for example the error is 1.8% for atomic hydrogen. The relation will be applied in a subsequent paper to the equation of state of rare gases.

## § 1. Introduction

The intermolecular potential is usually assumed to be additive. It was recently shown, however, that the potential may not be considered to be strictly additive[1)2)]. Hence it is desired to treat many-molecule systems without postulating potential additivity.

The simplest system for which the non-additivity of the intermolecular potential plays a role is a system composed of three rare-gas atoms, which we will treat. In the present paper van der Waals interactions for a system of three distant atoms are considered both by perturbation theory and by variation method. The result will be applied, in the next paper, to the third cluster integral of gases.

The intermolecular potential derived from second-order perturbation, which was first given by F. London[3)], is additive. The potential from third-order perturbation is a non-additive correction and was first calculated by Y. Muto[4)] and by Axilrod and Teller[5)] both for a simplified atomic model. It is important to note that the assumption we make in the present paper is only the spherical symmetry of atoms.

## § 2. Perturbation Theory

Let us consider a system composed of three spherically symmetric neutral atoms located at $\boldsymbol{r}_1$, $\boldsymbol{r}_2$ and $\boldsymbol{r}_3$. Let $r_{ij}=|\boldsymbol{r}_i-\boldsymbol{r}_j|$. Each atom is assumed to be sufficiently separated from another so that only dipole interactions should be considered as the origin of intermolecular forces.

Under this assumption the total Hamiltonian of the system is divided into two parts,

$$H=H^0+J, \tag{1}$$

with the unperturbed Hamiltonian $H^0$ for three independent atoms and the interaction $J$ which can be treated as a small perturbation. The interaction $J$ is a sum of three dipole-dipole interactions between pairs:

$$J=J(12)+J(23)+J(31).$$

The first term, for example, is given by

$$J(12)=\boldsymbol{p}(1)\cdot T(12)\cdot\boldsymbol{p}(2),$$

$$T(12)=\frac{\boldsymbol{1}-3\boldsymbol{e}_{12}\boldsymbol{e}_{12}}{r_{12}^{3}},$$

$$\boldsymbol{e}_{12}=\frac{\boldsymbol{r}_1-\boldsymbol{r}_2}{r_{12}},$$

where $\boldsymbol{p}(i)$ is the electric dipole of $i$th atom at $\boldsymbol{r}_i$.

Let us denote by $E_n$ the eigenvalues of $H^0$, $E_0$ being the unperturbed energy of the ground state, and denote by $J_{nm}$ the $nm$ matrix element of $J$ in the representation in which $H^0$ is diagonal, $E_n\delta_{nm}$. Then the energy $W$ of the ground state is given, up to the third-order perturbation, by

$$W=E_0+W_2(r_{12},\, r_{23},\, r_{31})+W_3(r_{12},\, r_{23},\, r_{31})\ , \tag{2}$$

$$W_2=\sum_{n\neq 0}\frac{J_{on}J_{no}}{E_0-E_n}\ , \tag{3}$$

$$W_3=\sum_{n,m\neq 0}\sum\frac{J_{on}J_{nm}J_{mo}}{(E_0-E_n)(E_0-E_m)}\ , \tag{4}$$

where use has been made of the fact that $J_{oo}$ vanishes.

The unperturbed Hamiltonian $H^0$ is a sum of three parts

$$H^0=H(1)+H(2)+H(3)\ ,$$

$H(i)$ being the Hamiltonian for the $i$th molecule. Let $\mathcal{E}_\rho(1)$, $\mathcal{E}_\sigma(2)$ and $\mathcal{E}_\tau(3)$ be eigenvalues of $H(1)$, $H(2)$ and $H(3)$ respectively, $\mathcal{E}_0(i)$ being the unperturbed energy of the ground state of the $i$th atom, so that

$$E_n=\mathcal{E}_\rho(1)+\mathcal{E}_\sigma(2)+\mathcal{E}_\tau(3)$$

for $n\equiv(\rho,\, \sigma,\, \tau)$, in particular

$$E_0=\mathcal{E}_0(1)+\mathcal{E}_0(2)+\mathcal{E}_0(3)\ .$$

The $\rho\sigma\tau$, $\rho'\sigma'\tau'$ matrix element of $J$ vanishes unless

$$\rho=\rho',\ \sigma\neq\sigma',\ \tau\neq\tau'$$

or $\qquad \rho\neq\rho',\ \sigma=\sigma',\ \tau\neq\tau'$

or $\qquad \rho\neq\rho',\ \sigma\neq\sigma',\ \tau=\tau'\ .$

Therefore, the third-order perturbation $W_3$ is a sum of six terms of the type

$$\sum_{\sigma,}\sum_{\sigma,}\sum_{\tau\neq 0}\frac{\boldsymbol{p}_{0\rho}(1)\cdot T(12)\cdot\boldsymbol{p}_{0\sigma}(2)\boldsymbol{p}_{\sigma 0}(2)\cdot T(23)\cdot\boldsymbol{p}_{0\tau}(3)\boldsymbol{p}_{\tau 0}(3)\cdot T(31)\cdot\boldsymbol{p}_{\rho 0}(1)}{[\varDelta_\rho(1)+\varDelta_\sigma(2)][\varDelta_\rho(1)+\varDelta_\tau(3)]}$$

where

$$\varDelta_\rho(i)=\mathcal{E}_\rho(i)-\mathcal{E}_0(i)\ .$$

In this expression $\Sigma'\boldsymbol{p}_{o\sigma}(2)\boldsymbol{p}_{\sigma o}(2)$, summed over an orthonormal set which spans an irreducible representation space of the rotation group, is rotation invariant, i. e. unit tensor times $\Sigma'p_{xo\sigma}(2)p_{x\sigma o}(2)$, $p_x$ indicating the $x$-component of $\boldsymbol{p}$. Taking this fact into account we can reduce the expression to

$$\sum_{\rho,}\sum_{\sigma,}\sum_{\tau\neq 0}\frac{|p_{xo\sigma}(1)|^2|p_{xo\sigma}(2)|^2|p_{xo\tau}(3)|^2}{[\varDelta_\rho(1)+\varDelta_\sigma(2)][\varDelta_\rho(1)+\varDelta_\tau(3)]}\ \text{trace}\ T(12)\cdot T(23)\cdot T(31)\ .$$

Here the trace can be evaluated as follows

$$\begin{aligned}
&\text{trace}\ T(12)\cdot T(23)\cdot T(31)\\
&\quad=(r_{12}r_{23}r_{31})^{-3}\ \text{trace}\ [(1-3\boldsymbol{e}_{12}\boldsymbol{e}_{12})\cdot(1-3\boldsymbol{e}_{23}\boldsymbol{e}_{23})\cdot(1-3\boldsymbol{e}_{31}\boldsymbol{e}_{31})]\\
&\quad=3(r_{12}r_{23}r_{31})^{-3}[-2+3\{(\boldsymbol{e}_{31}\cdot\boldsymbol{e}_{12})^2+(\boldsymbol{e}_{12}\cdot\boldsymbol{e}_{23})^2+(\boldsymbol{e}_{23}\cdot\boldsymbol{e}_{31})^2\}\\
&\qquad-9(\boldsymbol{e}_{12}\cdot\boldsymbol{e}_{23})(\boldsymbol{e}_{23}\cdot\boldsymbol{e}_{31})(\boldsymbol{e}_{31}\cdot\boldsymbol{e}_{12})]\\
&\quad=3(r_{12}r_{23}r_{31})^{-3}(3\cos\theta_1\cos\theta_2\cos\theta_3+1)\ .
\end{aligned}$$

Here $\theta_1$, $\theta_2$, $\theta_3$ are inner angles of the triangle formed by the three atoms, for example,

$$\cos\theta_1=-\boldsymbol{e}_{31}\cdot\boldsymbol{e}_{12}=(r_{31}{}^2+r_{12}{}^2-r_{23}{}^2)/2r_{31}r_{12}\ ,$$

and use has been made of the relation

$$\cos^2\theta_1+\cos^2\theta_2+\cos^2\theta_3=1-2\cos\theta_1\cos\theta_2\cos\theta_3\ .$$

Thus we obtain finally

$$W_3(r_{12},\, r_{23},\, r_{31})=\nu(r_{12}r_{23}r_{31})^{-3}(3\cos\theta_1\cos\theta_2\cos\theta_3+1) \tag{5}$$

with

$$\nu=6\sum_{\rho,\sigma,\tau\neq0}\sum\sum\left\{\frac{1}{[\Delta_\tau(3)+\Delta_\rho(1)]\,[\Delta_\rho(1)+\Delta_\sigma(2)]}+\frac{1}{[\Delta_\rho(1)+\Delta_\sigma(2)]\,[\Delta_\sigma(2)+\Delta_\tau(3)]}\right.$$

$$\left.+\frac{1}{[\Delta_\sigma(2)+\Delta_\tau(3)]\,[\Delta_\tau(3)+\Delta_\rho(1)]}\right\}|p_{x0\rho}(1)|^2|p_{x0\sigma}(2)|^2|p_{x0\tau}(3)|^2$$

or

$$\nu=12\sum_{\rho,\sigma,\tau\neq0}\sum\sum\frac{[\Delta_\rho(1)+\Delta_\sigma(2)+\Delta_\tau(3)]\,|p_{x0\rho}(1)|^2|p_{x0\sigma}(2)|^2|p_{x0\tau}(3)|^2}{[\Delta_\rho(1)+\Delta_\sigma(2)][\Delta_\sigma(2)+\Delta_\tau(3)][\Delta_\tau(3)+\Delta_\rho(1)]}\ .$$

As regards $W_2$ the calculation is much simpler; the result being

$$W_2(r_{12},r_{23},r_{31})=-\mu_{12}r_{12}^{-6}-\mu_{23}r_{23}^{-6}-\mu_{31}r_{31}^{-6}, \tag{6}$$

where, for example,

$$\mu_{12}=6\sum_{\rho,\sigma\neq0}\sum\frac{|p_{x0\rho}(1)|^2|p_{x0\sigma}(2)|^2}{\Delta_\rho(1)+\Delta_\sigma(2)}\ .$$

This relationship was given by F. London.

The intermolecular potential $W_2$ from the second-order perturbation is additive; the potential $W_3$ from the third-order perturbation is a non-additive correction, which is positive (repulsive) for Max $(\theta_1, \theta_2, \theta_3)<117°$ and negative (attractive) for Max $(\theta_1, \theta_2, \theta_3)>126°$.

In the particular case of a system of three harmonic oscillators with angular frequencies $\omega_i$, the matrix elements $p_{x0\rho}(i)$ vanish except the 01 element $p_{x01}(i)$, for which $\Delta_1(i)=\hbar\omega_i$, $2\pi\hbar$ being Planck's constant $(i=1, 2, 3)$. Hence

$$\mu_{12}=\frac{2}{3}\frac{(p(1)^2)_{00}(p(2)^2)_{00}}{\hbar(\omega_1+\omega_2)}\ ,$$

$$\nu=\frac{4}{9}\frac{\omega_1+\omega_2+\omega_3}{\hbar^2(\omega_1+\omega_2)(\omega_2+\omega_3)(\omega_3+\omega_1)}$$
$$\times(p(1)^2)_{00}(p(2)^2)_{00}(p(3)^2)_{00}\ ,$$

where use has been made of the relationship $(p^2)_{00}=3(p_x^2)_{00}$.

For a harmonic oscillator with mass $m$, charge $e$ and angular frequency $\omega$, $(p^2)_{00}$ is given by $3\hbar e^2/2m\omega$, which is $3\hbar\omega/2$ times the polarizability $\alpha=e^2/m\omega^2$. We can therefore eliminate $\omega$ from the above expressions by use of the relation

$$\frac{3}{2}\hbar\omega=\frac{(p^2)_{00}}{\alpha}\ ,$$

obtaining

$$\mu_{12}=\frac{\pi_1\pi_2}{\pi_1+\pi_2}\alpha_1\alpha_2\ , \tag{7}$$

$$\nu=\frac{(\pi_1+\pi_2+\pi_3)\pi_1\pi_2\pi_3}{(\pi_1+\pi_2)(\pi_2+\pi_3)(\pi_3+\pi_1)}\alpha_1\alpha_2\alpha_3, \tag{8}$$

in which

$$\pi_i\equiv(p(i)^2)_{00}/\alpha_i\ .$$

In case three atoms are identical, the energy of the ground state is of the form

$$W=E_0-\mu(r_{12}^{-6}+r_{23}^{-6}+r_{31}^{-6})$$
$$+\nu(r_{12}r_{23}r_{31})^{-3}(3\cos\theta_1\cos\theta_2\cos\theta_3+1)\ . \tag{9}$$

For a system of three identical harmonic oscillators we have

$$\mu=\frac{1}{2}\alpha(p^2)_{00}\ , \tag{10}$$

$$\nu=\frac{3}{8}\alpha^2(p^2)_{00}\ , \tag{11}$$

from which we obtain a very simple relation

$$4\nu=3\alpha\mu\ . \tag{12}$$

The relations (7), (8), (10), (11), and (12) contain no model constant of the harmonic oscillator. In fact it can be shown that these relations hold for rare-gas atoms with the accuracy of the variation method. Details will be given in the next section.

It is to be noted that Y. Muto[4] derived the relation (9) with $\mu=(3/4)\hbar\omega\alpha^2$, $\nu=(9/16)\hbar\omega\alpha^3$ for harmonic oscillator model and Axilrod[5] derived (9) with $\mu=(3/4)V_i\alpha^2$, $\nu=(9/16)V_i\alpha^3$ for a particular atomic model with the ionization potential $V_i$. From these relations follows $4\nu=3\alpha\mu$ at once. The point which the present authors emphasize is that the relations (9) and (12) hold for any spherically symmetrical atom, the former exactly, the latter accurately enough.

## § 3. Variation Method

For the purpose of evaluating the energy $W$ of the ground state, variation method is usually more convenient than the perturbation method. A theorem will be first shown.

For a system of three identical harmonic oscillators the ground-state energy $W$ given by (2) coincides, up to the term proportional to the cube of the interaction $J$, with the result of variation calculation by use of the simplest trial function

$$\psi=(1+AJ)\psi_0\,. \tag{13}$$

Here $\psi_0$ is the unperturbed eigenfunction of the ground state and $A$ is the variation parameter assumed to be real.

In general, an upper limit for the ground-state energy obtainable with this trial function is given by the minimum of the expectation value of the Hamiltonian (1) for function $\psi$:

$$[(1+AJ)(H^0+J)(1+AJ)]_{00}/[(1+AJ)^2]_{00}\,.$$

This expression becomes, since $J_{00}=0$, $(H^0J)_{00}=(JH^0)_{00}=0$ and $(H^0)_{00}=E_0$,

$$[E_0+2A(J^2)_{00}+A^2(JH^0J)_{00}+A^2(J^3)_{00}]$$
$$/[1+A^2(J^2)_{00}]\,,$$

which is equal, up to the term proportional to $J^3$, to

$$E_0+2A(J^2)_{00}$$
$$-A^2[E_0(J^2)_{00}-(JH^0J)_{00}-(J^3)_{00}]\,.$$

This takes a minimum with respect to variation of $A$ when

$$A=(J^2)_{00}/[E_0(J^2)_{00}-(JH^0J)_{00}-(J^3)_{00}]\,,$$

the minimum being

$$E_0+\frac{[(J^2)_{00}]^2}{E_0(J^2)_{00}-(JH^0J)_{00}-(J^3)_{00}}\,.$$

This is equal, up to the term of $J^3$, to

$$E_0+\frac{[(J^2)_{00}]^2}{E_0(J^2)_{00}-(JH^0J)_{00}}+\frac{[(J^2)_{00}]^2(J^3)_{00}}{[E_0(J^2)_{00}-(JH^0J)_{00}]^2}\,. \tag{14}$$

It is easy to see that the expression (14) coincides with (2) for a system of three identical harmonic oscillators. Thus, for this particular system the lowest upper limit for the ground-state energy obtainable with (13) is exact up to the term corresponding to the third-order perturbation. It is therefore reasonable to adopt the trial function (13) also for real systems composed of identical molecules.

It will be shown in the following, by use of the trial function (13) and the expression (14), that the relations (10) and (12):

$$4\nu=3\,\alpha\mu\,,\quad 2\,\eta=\alpha(p^2)_{00} \tag{15}$$

hold for spherically symmetric atoms with accuracy of the variation method.

we must first calculate

$$(JH^0J)_{00}=(J(12)H^0J(12))_{00}$$
$$+(J(23)H^0J(23))_{00}+(J(31)H^0J(31))_{00}\,,$$

in which, for example,

$$(J(12)H^0J(12))_{00}$$
$$=(J(12)H(1)J(12))_{00}+(J(12)H(2)J(12))_{00}$$
$$+(J(12)H(3)J(12))_{00}\,.$$

The right-hand side of

$$(J(12)H(1)J(12))_{00}$$
$$=(\boldsymbol{p}(2)\cdot T(12)\cdot\boldsymbol{p}(1)H(1)p(1)\cdot T(12)\cdot\boldsymbol{p}(2))_{00}$$

can be transformed, by virtue of the spherical symmetry of the operator $H(1)$, into

$$\kappa\mathcal{E}_0(\boldsymbol{p}(2)\cdot T(12)\cdot\boldsymbol{p}(1)\boldsymbol{p}(1)\cdot T(12)\cdot\boldsymbol{p}(2))_{00}\,.$$

Here $\mathcal{E}_0$ is the unperturbed energy of the ground state of an atom, $3\,\mathcal{E}_0=E_0$; the coefficient $\kappa$ is a dimensionless constant of the atom. We thus obtain

$$(J(12)H(1)J(12))_{00}=\kappa\mathcal{E}_0(J(12)^2)_{00}\,,$$

furthermore

$$(J(12)H^0J(12))_{00}=(2\kappa+1)\mathcal{E}_0(J(12)^2)_{00}\,,$$

and finally $(JH^0J)_{00}=(2\kappa+1)\mathcal{E}_0(J^2)_{00}\,.$ (16)

Substituting (16) into (14) we have

$$3\mathcal{E}_0+\frac{(J^2)_{00}}{2(1-\kappa)\mathcal{E}_0}+\frac{(J^3)_{00}}{[2(1-\kappa)\mathcal{E}_0]^2}\,. \tag{17}$$

The matrix element $(J^2)_{00}$ and $(J^3)_{00}$ can be calculated in the same way as in the preceding section, the results being

$$(J^2)_{00}=\frac{2}{3}[(p^2)_{00}]^2(r_{12}{}^{-6}+r_{23}{}^{-6}+r_{31}{}^{-6})\,,$$

$$(J^3)_{00}=\frac{2}{3}[(p^2)_{00}]^3(r_{12}r_{23}r_{31})^{-3}$$
$$\times(3\cos\theta_1\cos\theta_2\cos\theta_3+1)\,,$$

($p\equiv|\boldsymbol{p}|$). Substituting these expressions into (17) we obtain the expression (9) with

$$\mu=-\frac{1}{3}\frac{[(p^2)_{00}]^2}{(1-\kappa)\mathcal{E}_0}\,,\qquad \nu=\frac{1}{6}\frac{[(p^2)_{00}]^3}{[(1-\kappa)\mathcal{E}_0]^2}\,. \tag{18}$$

In order to obtain (15), therefore, we need only to prove that the polarizability $\alpha$ of an atom is given by

$$\alpha=-\frac{2}{3}\frac{(p^2)_{00}}{(1-\kappa)\mathcal{E}_0}\,. \tag{19}$$

The Hamiltonian of an atom in an electric field $\boldsymbol{F}$ is given by $H(1)+\boldsymbol{F}\cdot\boldsymbol{p}$. By use of a trial function similar to (13) the energy gained

Table I.

| | $\alpha$ | $\chi_{\mathrm{mol}}$ | $(p^2)_{00}$ | $\mu=\frac{1}{2}\alpha(p^2)_{00}$ |
|---|---|---|---|---|
| He | 0.201 A$^3$ | $-$ 1.9$\times$10$^{-6}$ cm$^3$ | 1.55$\times$10$^{-11}$ erg A$^3$ | 0.156$\times$10$^{-11}$ erg A$^6$ |
| Ne | 0.390 | $-$ 7.2 | 5.9 | 1.15 |
| A | 1.62 | $-$19.4 | 15.8 | 12.8 |
| Kr | 2.46 | $-$28 | 23 | 28 |
| Xe | 3.99 | $-$43 | 35 | 70 |

by the interaction with the field is given by

$$\frac{[(\boldsymbol{F}\cdot\boldsymbol{pp}\cdot\boldsymbol{F})_{00}]^2}{\mathcal{E}_0(\boldsymbol{F}\cdot\boldsymbol{pp}\cdot\boldsymbol{F})_{00}-(\boldsymbol{F}\cdot\boldsymbol{p}H(1)\boldsymbol{p}\cdot\boldsymbol{F})_{00}}\,.$$

This expression is calculated, since

$$(\boldsymbol{F}\cdot\boldsymbol{p}H(1)\boldsymbol{p}\cdot\boldsymbol{F})_{00}=\kappa\mathcal{E}_0(\boldsymbol{F}\cdot\boldsymbol{pp}\cdot\boldsymbol{F})_{00}$$

and

$$(\boldsymbol{F}\cdot\boldsymbol{pp}\cdot\boldsymbol{F})_{00}=\frac{1}{3}(p^2)_{00}F^2\,,\quad F\equiv|\boldsymbol{F}|\,,$$

to be

$$\frac{(p^2)_{00}}{3(1-\kappa)\mathcal{E}_0}F^2\,,$$

from which (19) follows.

For rare-gas atoms $(p^2)_{00}$ can be evaluated from observed values of molar diamagnetic susceptibility $\chi_{\mathrm{mol}}$ by use of the relation

$$\chi_{\mathrm{mol}}=-\frac{L}{6m_ec^2}(p^2)_{00}\,,$$

where $m_e$ is the electron mass, $c$ light velocity, $L=6.0\times10^{23}$. Observed values of $\alpha$ and $\chi$ together with the derived values of $(p^2)_{00}$ and $\mu$ are given in Table I.

For atomic hydrogen

$$\mathcal{E}_0=-\frac{e^2}{2a_0}\,,\quad (p^2)_{00}=3e^2a_0^2\,,\quad \kappa=0\,,$$

where $e$ is the electron charge and $a_0$ is the Bohr radius.

Substituting these expressions into (18) and (19) we have

$$\mu=6e^2a_0^5,\quad \nu=18\,e^2a_0^8,\quad \alpha=4a_0^3\,.$$

A higher approximation by use of the trial function

$$\begin{aligned}\psi=[1+AJ+B&\\ &\times\{(p(1)+p(2))J(12)+(p(2)+p(3))J(23)\\ &+(p(3)+p(1))J(31)\}]\psi_0\end{aligned}$$

$(p(i)\equiv|\boldsymbol{p}(i)|)$ gives

$$\mu=\frac{84}{13}e^2a_0^5,\quad \nu=\frac{3618}{169}e^2a_0^8,\quad \alpha=\frac{9}{2}a_0^3\,.$$

From these values follow

$$\frac{4\nu}{3\alpha\mu}=\frac{268}{273}\quad\text{and}\quad\frac{2\mu}{\alpha(p^2)_{00}}=\frac{112}{117}\,.$$

Hence the accuracy of the relations $4\nu=3\alpha\mu$ and $2\mu=\alpha(p^2)_{00}$ is very high at least for hydrogen atoms.

We have been considering a system of three identical atoms. With regard to a system of unlike atoms we can similarly show that the relations (7) and (8) hold for any spherically symmetric atoms in the accuracy of the variation by use of the trial function

$$\psi=[1+AJ(12)+BJ(23)+CJ(31)]\psi_0$$

with three variation parameters. The generalization of the relation $4\nu=3\,\alpha\mu$ is

$$\nu=\frac{2R_1R_2R_3(R_1+R_2+R_3)}{(R_1+R_2)(R_2+R_3)(R_3+R_1)}\,,$$

in which

$$\frac{1}{R_1}=\frac{1}{\mu_{12}\alpha_3}+\frac{1}{\mu_{31}\alpha_2}-\frac{1}{\mu_{23}\alpha_1}\quad\text{etc.}$$

## References

1) T. Kihara: Revs. Modern Phys. **27** (1955) 412.
2) B. M. Axilrod: J. Chem. Phys. **19** (1951) 724.
3) F. London: Z. Phys. **63** (1930) 245.
4) Y. Muto: Nippon Sugaku-Buturigakukai-si **17** (1943) 629.
5) B. M. Axilrod and E. Teller: J. Chem. Phys. **11** (1943) 299.
B. M. Axilrod: J. Chem. Phys. **19** (1951) 719.

JOURNAL OF THE PHYSICAL SOCIETY OF JAPAN Vol. 11, No. 10, OCTOBER, 1956

# Non-additive Intermolecular Potential in Gases.
# II. Cluster Integrals

By Saburo KOBA, Shobu KANEKO and Taro KIHARA

*Department of Physics, Faculty of Science, University of Tokyo*

(Received July 6, 1956)

The van der Waals interaction discussed in Part I are applied to the equation of state of rare gases. The potential energy between three identical atoms is assumed to be

$$U(r_{12},r_{23},r_{31})=U(r_{12})+U(r_{23})+U(r_{31})+\nu(r_{12}r_{23}r_{31})^{-3}(3\cos\theta_1\cos\theta_2\cos\theta_3+1).$$

Here $r_{ij}$ is the distance between $i$th and $j$th atoms, $\theta_i$'s are inner angles of the triangle formed by the three atoms, and

$$U(r)=\lambda r^{-12}-\mu r^{-6}\,.$$

Use is made of a relation proved in Part I, $4\nu=3\alpha\mu$, in which $\alpha$ is the polarizability. For this model of the intermolecular potential we have calculated the third cluster integral including quantum effect. By virtue of the non-additive part of the intermolecular potential agreement between observed and calculated values is very good.

## § 1. Introduction

The equation of state of gases may be expressed in terms of cluster integrals $b_l$ by

$$Pv=kT\left(1+\frac{-b_2}{v}+\frac{4b_2{}^2-2b_3}{v^2}+\cdots\right)$$

or

$$Pv=kT\left(1+P\frac{-b_2}{kT}P+\frac{5b_2{}^2-2b_3}{(kT)^2}P^2+\cdots\right).$$

Here $P$ is the pressure, $v$ the volume per molecule, $k$ the Boltzmann constant, $T$ the temperature, and $b_l$'s are functions of the temperature. The second cluster integral $b_2$ depends on the intermolecular potential between two molecules; the third cluster integral $b_3$ refers to the potential between three molecules.

For practical calculation of the third cluster integral we have been assuming that the intermolecular potential be strictly additive, namely that the potential energy of a three-molecule system be equal to a sum of three potential energies between pairs. However, since there is a small disagreement between calculated and observed third cluster integrals an investigation of the effect of non-additivity is desired.

The non-additivity of the van der Waals interaction between three molecules was discussed in a previous article[1]. The aim of the present paper is to apply the result to the third cluster integral of single-component rare gases.

## § 2. Intermolecular Potential

Taking account of the fact that the negative potential energy between two molecules at a large separation is proportional to the sixth power of the distance, the intermolecular potential is usually assumed in the form

$$U(r)=\lambda r^{-12}-\mu r^{-6}\,. \tag{1}$$

Here $r$ is the intermolecular distance, $\lambda$ and $\mu$ are molecular constants. We also adopt this potential function for two-molecule systems.

The potential energy for a system of three molecules is then of the form

$$U(r_{12},r_{23},r_{31})=U(r_{12})+U(r_{23})+U(r_{31})+u(r_{12},r_{23},r_{31})\,, \tag{2}$$

$r_{ij}$ being the distance between $i$th and $j$th molecules. The last term $u(r_{12},r_{23},r_{31})$ indicates the effect of the potential non-additivity. It is expressed, at large separations at least, in the form

$$u(r_{12},r_{23},r_{31})=\nu(r_{12}r_{23}r_{31})^{-3}(3\cos\theta_1\cos\theta_2\cos\theta_3+1), \tag{3}$$

where $\theta_1,\theta_2,\theta_3$ are inner angles of the triangle formed by the three molecules, and $\nu$ is another constant. We assume this relation for all separations, not only for large separations.

Between $\mu$ and $\nu$ there exist a simple and useful relationship[1]

$$4\nu=3\alpha\mu\,, \tag{4}$$

$\alpha$ being the polarizability of the molecule.

The molecular constant $\lambda$ and $\mu$ can be determined from analysis of observed values for the second cluster integral. The other costant $\nu$ will be calculated with the help of (4) and by use of observed values of the polarizability.

## § 3. Cluster Integrals

Excepting the case of helium at very low temperatures the cluster integrals are expressed in the form of series in $\hbar^2/4mkT$,

$$b_l=b_l^{(0)}+\frac{\hbar^2}{4mkT}b_l^{(1)}+\left(\frac{\hbar^2}{4mkT}\right)^2 b_l^{(2)}+\cdots, \tag{5}$$

where $2\pi\hbar$ is Planck's constant, $m$ the mass of a molecule.

The first four terms of the second cluster integral are[2], for the intermolecular potential (1),

$$b_2^{(0)}=\frac{\pi}{6}\left(\frac{\lambda}{kT}\right)^{1/4}\sum_{t=0}^{\infty}\Gamma\left(\frac{2t-1}{4}\right)\frac{y^t}{t!},$$

$$b_2^{(1)}=-\frac{\pi}{6}\left(\frac{\lambda}{kT}\right)^{1/12}\sum_{t=0}^{\infty}\frac{36t-11}{3}\Gamma\left(\frac{6t-1}{12}\right)\frac{y^t}{t!},$$

$$b_2^{(2)}=\frac{\pi}{6}\left(\frac{\lambda}{kT}\right)^{-1/12}\sum_{t=0}^{\infty}\frac{3024t^2+4728t+767}{30}\Gamma\left(\frac{6t+1}{12}\right)\frac{y^t}{t!},$$

$$b_2^{(3)}=-\frac{\pi}{6}\left(\frac{\lambda}{kT}\right)^{-1/4}\sum_{t=0}^{\infty}\frac{53568t^3+303216t^2+491076t+180615}{70}\Gamma\left(\frac{2t+1}{4}\right)\frac{y^t}{t!},$$

where

$$y=\frac{\mu}{kT}\left(\frac{kT}{\lambda}\right)^{1/2}.$$

The classical limit of the third cluster integral is given by

$$b_3^{(0)}=\frac{4\pi^2}{3}\iiint\left[\exp\left(-\frac{U(r_{12},r_{23},r_{31})}{kT}\right)-\exp\left(-\frac{U(r_{12})}{kT}\right)-\exp\left(-\frac{U(r_{23})}{kT}\right)\right.$$
$$\left.-\exp\left(-\frac{U(r_{31})}{kT}\right)+2\right]r_{12}r_{23}r_{31}dr_{12}dr_{23}dr_{31},$$

where the integral is to be taken over all values of $r_{12}$, $r_{23}$, $r_{31}$, which form three sides of a triangle. We expand it into a series in $\nu$:

$$b_3^{(0)}=(b_3^{(0)})_{\nu=0}+\nu\left(\frac{\partial b_3^{(0)}}{\partial\nu}\right)_{\nu=0}+\cdots, \tag{6}$$

in which

$$(b_3^{(0)})_{\nu=0}=\frac{4\pi^2}{3}\iiint[f(r_{12},r_{23},r_{31})-f(r_{12})-f(r_{23})-f(r_{31})]r_{12}r_{23}r_{31}dr_{12}dr_{23}dr_{31},$$

$$f(r)=\exp[-U(r)/kT]-1,$$

$$f(r_{12},r_{23},r_{31})=\exp\left[-\frac{U(r_{12})+U(r_{23})+U(r_{31})}{kT}\right]-1$$

and

$$\left(\frac{\partial b_3^{(0)}}{\partial\nu}\right)_{\nu=0}=-\frac{4\pi^2}{3kT}\iiint\exp\left[-\frac{U(r_{12})+U(r_{23})+U(r_{31})}{kT}\right]\frac{3\cos\theta_1\cos\theta_2\cos\theta_3+1}{(r_{12}r_{23}r_{31})^2}dr_{12}dr_{23}dr_{31}.$$

Higher terms in the series expansion can be neglected except at very low temperatures.

Each term in (6) can be expanded in $y$. For the first term

$$(b_3^{(0)})_{\nu=0}=\left(\frac{\lambda}{kT}\right)^{1/2}\sum_{t=0}^{\infty}G_t y^t,$$

in which

$$G_t=4\pi^2\int_0^1\int_{1-\xi}^1 C_t\xi\eta d\eta d\xi\ ,$$

$$C_t=\frac{1}{12}\frac{1}{t!}\Gamma\left(\frac{t-1}{2}\right)[\langle 6\rangle^t\langle 12\rangle^{(1-t)/2}-\langle 6\rangle]\quad\text{for}\quad t\neq 1\ ,$$

$$C_1=\frac{1}{12}[\xi^{-6}\ln\xi^{-12}+\eta^{-6}\ln\eta^{-12}-\langle 6\rangle\ln\langle 12\rangle]\ .$$

For the second term

$$\left(\frac{\partial b_3{}^{(0)}}{\partial\nu}\right)_{\nu=0}=-\frac{1}{kT}\left(\frac{kT}{\lambda}\right)^{1/4}\sum_{t=0}^{\infty}H_t y^t\ ,$$

in which

$$H_t=\frac{\pi^2}{3}\frac{1}{t!}\Gamma\left(\frac{2t+1}{4}\right)\int_0^1\int_{1-\xi}^1\langle 6\rangle^t\langle 12\rangle^{-(2t+1)/4}\frac{3\cos\theta_1\cos\theta_2\cos\theta_3+1}{\xi^2\eta^2}d\eta d\xi\ .$$

Here the bracket notation has been used in the sense

$$\langle a\rangle\equiv 1+\xi^{-a}+\eta^{-a}$$

The values of $G_t$ and $H_t$ obtained by numerical integrations are given in Table I.

As regards the quantum correction $b_3{}^{(1)}$ we obtain

$$(b_3{}^{(1)})_{\nu=0}=\left(\frac{\lambda}{kT}\right)^{1/3}\sum_{t=0}^{\infty}I_t y^t\ ,$$

in which

$$\begin{aligned}I_t=-\frac{4\pi^2}{9}\frac{1}{t!}\Gamma\left(\frac{3t-2}{6}\right)\int_0^1\int_{1-\xi}^1&\{(3t+4)(3t-2)[\langle 12,12\rangle\langle 12\rangle^{(2-3t)/6-2}\langle 6\rangle^t-\langle 6\rangle]\\&-6t(3t-2)[\langle 12,6\rangle\langle 12\rangle^{(2-3t)/6-1}\langle 6\rangle^{t-1}-\langle 6\rangle]\\&+9t(t-1)[\langle 6,6\rangle\langle 12\rangle^{(2-3t)/6}\langle 6\rangle^{t-2}-\langle 6\rangle]\}\xi\eta d\eta d\xi\ .\end{aligned}$$

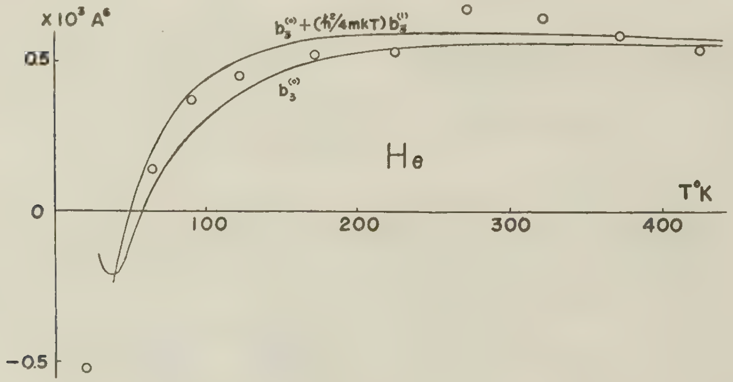

Fig. 1. The third integral of helium.

Here another bracket notation has been used in the sense

$$\begin{aligned}\langle a,b\rangle\equiv&\langle a+b+2\rangle\\&+(\xi^{-a-2}+\xi^{-b-2})(1+\xi^2-\eta^2)/4\\&+(\eta^{-a-2}+\eta^{-b-2})(1+\eta^2-\xi^2)/4\\&+(\xi^{-a-2}\eta^{-b-2}+\eta^{-a-2}\xi^{-b-2})(\xi^2+\eta^2-1)/4\ .\end{aligned}$$

The values of $I_t$ are also given in Table I.

The third cluster integral

$$b_3=\left[(b_3{}^{(0)})_{\nu=0}+\nu\left(\frac{\partial b_3{}^{(0)}}{\partial\nu}\right)_{\nu=0}+\cdots\right]$$

$$+\left[\frac{\hbar^2}{4mkT}(b_3{}^{(1)})_{\nu=0}+\cdots\right]$$

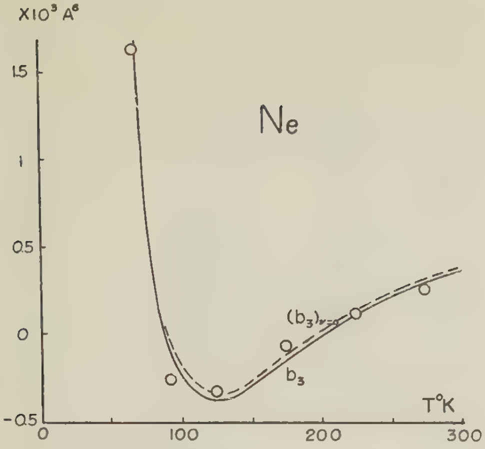

Fig. 2. The third cluster integral of neon.

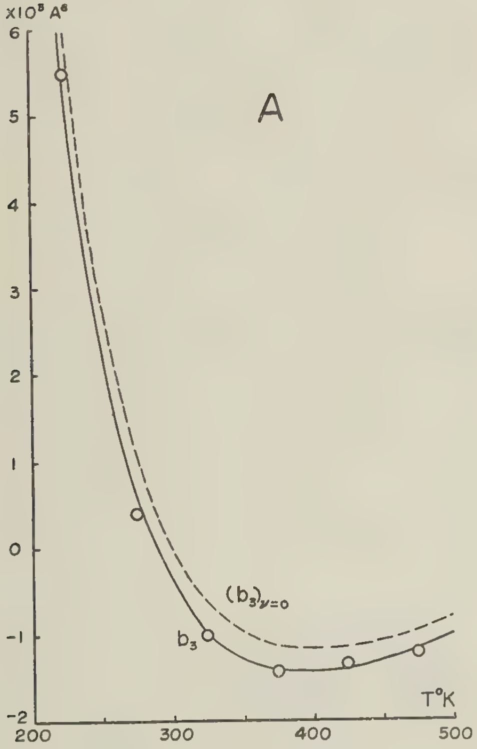

Fig. 3. The third cluster integral of argon.

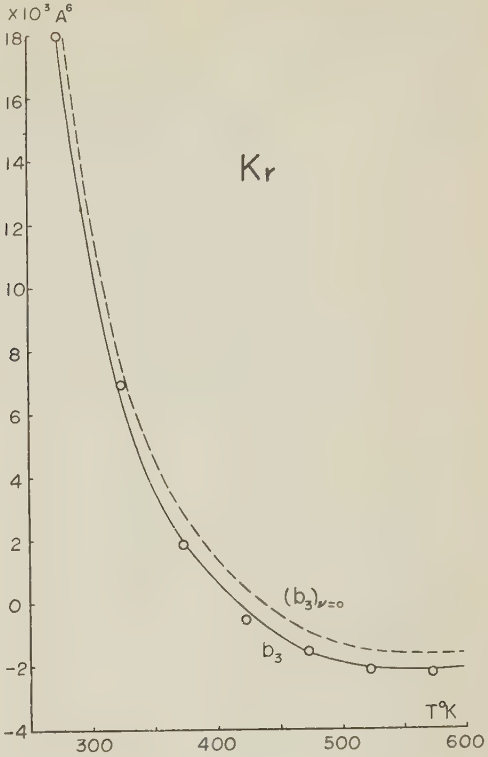

Fig. 4. The third cluster integral of krypton.

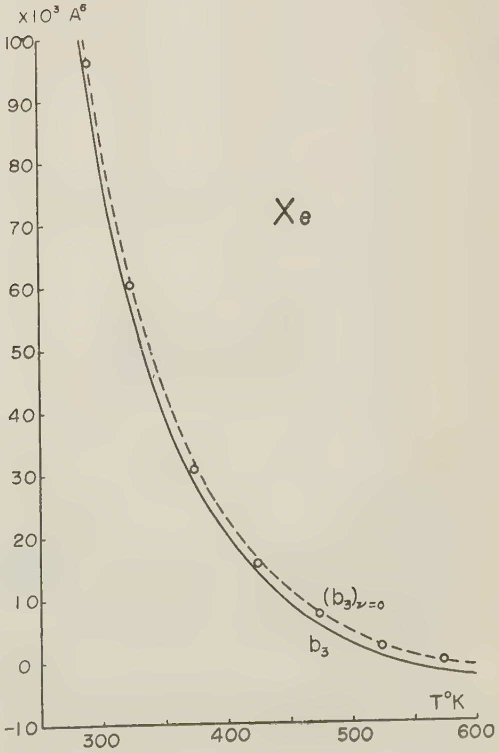

Fig. 5. The third cluster integral of xenon,

can be approximated, excepting the case of helium at very low temperatures, by a sum of three terms calculated above.

## § 4. Comparison with Experiment

Comparing the calculated and observed second cluster integral (given in Table II) we can determine two parameters $\lambda$ and $\mu$ of the intermolecular potential (1). This potential can be rewritten in the form

Table II. Observed values of the second and third cluster integrals.

| | $T$°K | $b_2$ A$^3$ | $b_3\times10^{-3}$ A$^6$ | Reference |
|---|---|---|---|---|
| He | 20.35 | + 4.6 | −0.52 | a |
| | 65.15 | − 15.6 | +0.14 | |
| | 90.15 | − 17.6 | +0.37 | |
| | 123 | − 18.9 | +0.45 | |
| | 173 | − 19.8 | +0.52 | |
| | 223 | − 19.8 | +0.53 | |
| | 273 | − 19.7 | +0.67 | b |
| | 323 | − 19.2 | +0.64 | |
| | 373 | − 18.8 | +0.58 | |
| | 423 | − 18.4 | +0.53 | |
| Ne | 65.2 | + 34.8 | +1.65 | c |
| | 90.6 | + 13.6 | −0.24 | |
| | 123 | − 0.2 | −0.30 | |
| | 173 | − 10.7 | −0.05 | |
| | 223 | − 15.1 | +0.14 | |
| | 273 | − 17.7 | +0.28 | |
| | 373 | − 19.7 | ... | |
| | 473 | − 21.7 | ... | |
| | 573 | − 22.8 | ... | |
| | 673 | − 22.8 | ... | |
| A | 173 | +106.8 | ... | c |
| | 223 | + 62.7 | +5.5 | |
| | 273 | + 36.7 | +0.4 | |
| | 323 | + 18.3 | −1.0 | |
| | 373 | + 7.1 | −1.4 | |
| | 423 | − 1.9 | −1.3 | |
| | 473 | − 7.8 | −1.2 | |
| | 573 | − 18.6 | ... | |
| Kr | 273 | +104.5 | +18.0 | d |
| | 323 | + 71.1 | + 7.0 | |
| | 373 | + 47.9 | + 1.9 | |
| | 423 | + 31.2 | − 0.5 | |
| | 473 | + 18.5 | − 1.5 | |
| | 523 | + 9.5 | − 2.1 | |
| | 573 | + 1.9 | − 2.2 | |
| Xe | 290 | +229 | +96 | e |
| | 323 | +184 | +60 | |
| | 373 | +135 | +31 | |
| | 423 | +100.9 | +15.6 | |
| | 473 | + 75.4 | + 7.2 | |
| | 523 | + 55.2 | + 2.4 | |
| | 573 | + 39.1 | − 0.3 | |

a. The values are taken from J. Otto: Handbuch d. Experimentalphysik, Bd. 8, Teil 2 (Akademische Verl. Leipzig, 1929) p. 144.
b. A. Michels and H. Wouters: Physica **8** (1941) 923.
c. L. Holborn and J. Otto: Z. Physik **33** (1925) 1.
d. Beattie, Brierley and Barriault: J. Chem. Phys. **20** (1952) 1615.
e. Beattie, Barriault and Brierley: J. Chem. Phys. **19** (1951) 1222.

Table I.

| $t$ | $G_t$ | $H_t$ | $I_t$ |
|---|---|---|---|
| 0 | 11.278 | 2.350 | +211.8 |
| 1 | −17.733 | 1.080 | −80.22 |
| 2 | + 3.498 | 0.557 | −40.42 |
| 3 | 1.492 | 0.268 | −33.80 |
| 4 | 0.571 | 0.1203 | −20.55 |
| 5 | 0.201 | 0.0505 | − 9.85 |
| 6 | 0.0662 | 0.0201 | − 4.75 |
| 7 | 0.0206 | 0.0076 | − 1.652 |
| 8 | 0.0062 | 0.0027 | − 0.586 |
| 9 | 0.00178 | ... | − 0.197 |
| 10 | 0.00049 | ... | − 0.063 |
| 11 | 0.00014 | ... | ... |

Table III.

| | $U_0/k$ °K | $r_0$ A | $\mu\times10^{11}$ erg A$^6$ |
|---|---|---|---|
| He | 10.8 | 2.88 | 0.170 |
| Ne | 35.8 | 3.09 | 0.86 |
| A | 119 | 3.83 | 10.4 |
| Kr | 173 | 4.03 | 20.4 |
| Xe | 224 | 4.56 | 55 |

$$U(r)=U_0\left[\left(\frac{r^0}{r}\right)^{12}-2\left(\frac{r^0}{r}\right)^6\right],$$

where $U_0$ is the depth of the potential minimum, and $r_0$ is the intermolecular distance correspoding to this minimum. The values of $U_0$, $r_0$ and $\mu$ for helium, neon, argon, krypton, and xenon are given in Table III.

The value of the model parameter $\mu$ is not far from the value of the asymptotic $\mu$ given in Part I. Hence it is self-consistent to use, for a system of three molecules, the asymptotic formula as a relation between model parameters.

The curves for third cluster integral thus calculated are compared in Figs. 1, 2, 3, 4, and 5 with observed values given in Table II. In the same Figs. also shown by broken curves the third cluster integrals calculated on the assumption of the potential additivity. Excepting xenon agreement is very good. Slight discrepancy for xenon is perhaps due to the fact that for the large xenon atom the potential (1) needs some modification, if it is not due to experimental errors.

## References

1) Y. Midzuno and T. Kihara: J. Phys. Soc. Japan (this issue).
2) See T. Kihara: Revs. Modern Phys. **27** (1955) 412.

JOURNAL OF THE PHYSICAL SOCIETY OF JAPAN Vol. 11, No. 10, OCTOBER, 1956

# Spiral Cleavage of Mica*

By Koreo KINOSITA and Jun NAKAYAMA**

*Department of Physics and Chemistry, Gakushuin University,*
*Mejiro, Tokyo*

(Received May 31, 1956)

We chanced on a slice of mica which was cleaved spirally. The spiral lamella was several hundredths mm thick. Detailed observations on the structure of this specimen including polarization microscopic and X-ray studies are described. A tentative explanation of the origin of this unusually thick growth-layer is proposed assuming that an external force, which was exerted during the formation of the crystal, caused the left and right halves of the crystal to make a small relative rotation around the $a$-axis.

## § 1. Introduction

When we were trying to prepare a $1/2\lambda$-plate of mica, we chanced upon a slice of mica which was cleaved spirally. The specimen perhaps belongs to *muscovite* from India. It had been cut out in the shape as illustrated in Fig. 1. There was a cleavage line starting from the centre of the uppermost surface and, terminating at the periphery. We inserted a needle at the point of intersection of the clevage line and the periphery, and let it go round along the periphery. When the needle came back to the starting point, it was found to be beneath the lamella, which at the beginning was under the needle. On continuing, we could trace the spiral for several turns. Then the spiral structure ended, and lamellae which could be cleaved perfectly followed. The spiral lamella was several hundredths mm. thick.

We thought that this specimen would be of particular interest to the workers in the theory of crystal growth and dislocations, and started a systematic investigation of the specimen.

## § 2. Observations

For the purpose of investigation, the specimen was cleaved into five sheets*, from No. 1 to No. 5, as illustrated in Fig. 2. Among the five sheets, No. 1 and No. 2 exhibit spiral structure. Originally they formed a single continuous spiral. Nos. 3, 4 and 5 are cleaved perfectly lamellarly.

### 1) *Sheets which are cleaved perfectly*

Fig. 3 is a photograph of Sheet No. 4. There is a straight edge running across the sheet and dividing it into two, the left half (L.H.) and the right half (R.H.). L.H. and R.H. meet at the edge with a small exterior angle of the order of 1°. The edge which is seen in Fig. 3 is a reentrant edge, and there is a corresponding entrant edge on the rear side of the sheet. A ribbon surface bounded by these edges is the crystal boundary between L.H. and R.H. It is inclined to the basal plane and looks bright when viewed at an appropriate angle. L.H. and R.H. are differ-

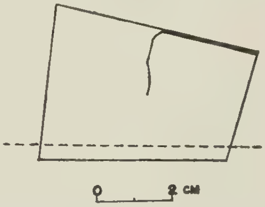

Fig. 1. Top view of the specimen.

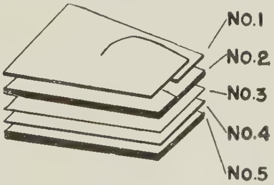

Fig. 2. The specimen has been cleaved into five sheets.

---

[*] This paper was presented at the Symposium on Crystal Plasticity and Dislocation at Nikko held on the occasion of the International Conference on Theoretical Physics, 1953. The publication in print has been delayed because something went wrong with the publication business.

[**] Now at the Research Laboratory, Asahi Glass Co.

[*] It is suspected that there was another sheet between No. 2 and No. 3, which had been broken and lost before the systematic investigation was started.

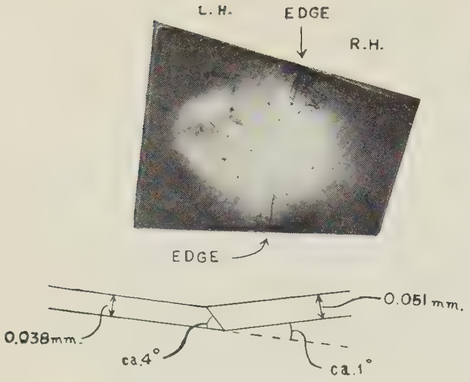

Fig. 3. Sheet No. 4.

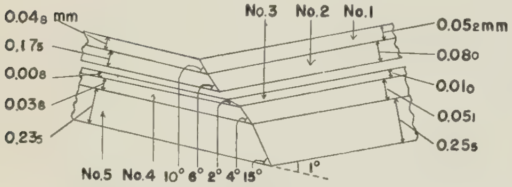

Fig. 4. Vertical section of all the sheets along the broken line in Fig. 1.

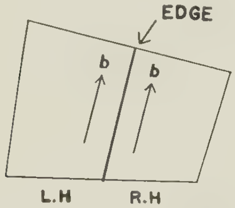

Fig. 5. Crystallographic orientation of L.H. and R.H.

ent in thickness.

No. 3 and No. 5 have essentially the same structure as No. 4. Detailed particulars are illustrated in Fig. 4, which shows the vertical section of all the sheets along the broken line in Fig. 1.

Investigations by X-ray and polarization microscope proved that L.H. and R.H. of Nos. 3, 4 and 5 are single crystals respectively. In other words, the specimen is a bicrystal. If we let the X-ray beam fall upon the boundary and take a Laue photograph, each of the Laue spots splits into two. The angle between the basal planes of L.H. and R.H. as estimated from the separation of the split spots is about 1.5°. Both halves have the *b*-axis in common, which is parallel to the edge dividing the both halves (Fig. 5).

Polarization micrographs reveal that there are interesting surface or internal patterns of a spiral nature in these sheets, by the inspection of which we can infer that L.H. and R.H. have grown as one body. The spiral-like pattern is especially well-developed in Sheet No. 3. This is shown in Fig. 6.

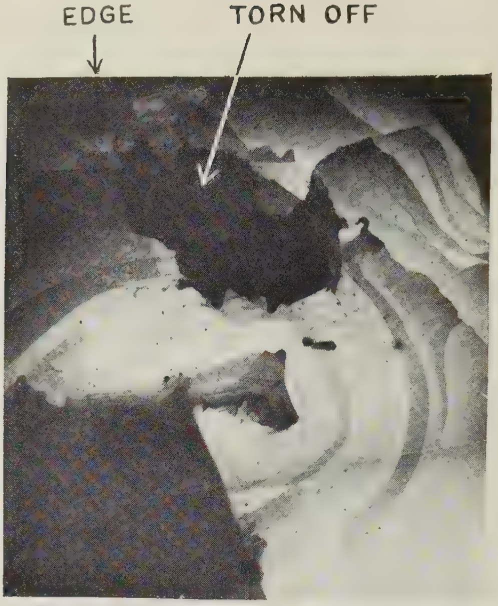

Fig. 6. Polarization micrograph of the central part of Sheet No. 3. This sheet is very thin, and has been torn in three places.

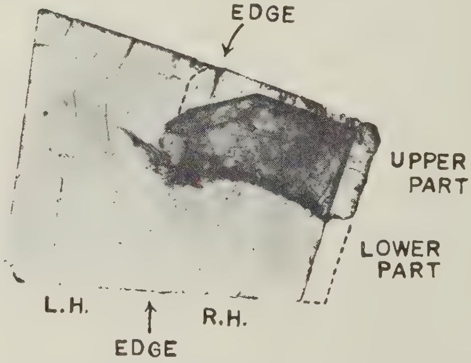

Fig. 7. Sheet No. 1. In order to demonstrate the spiral structure of the lamella, part of the hem of the uppermost surface has been cut away. Dotted line indicates the original periphery.

2) *Sheets which are cleaved spirally*

Fig. 7 is a photograph of No. 1, the uppermost sheet. The spiral nature of the lamella will be best seen in this photograph. Fig. 8 shows Sheet No. 2. This sheet consists of a spiral of about four turns.

For further description, it is convenient to discriminate the *upper* and *lower* parts of the sheet. The terms "upper" and "lower" will be used referring to Figs. 7 and 8. In the lower part of Nos. 1 and 2, the reentrant and entrant edges are nearly straight, and the boundary surface bounded by them makes a small angle with the basal plane, as was the case in Nos. 3, 4 and 5 (cf. Fig. 4). In the upper part of Nos. 1 and 2, however, the edge is no more straight, but is curved as is seen in Figs. 7 and 8. The axis of the spiral lies in the neighbourhood of the first bend of the edge. In the upper part, the boundary surface between L.H. and R.H. cannot be seen with the naked eye, because it is nearly perpendicular to the cleavage plane. This means that the boundary surface is *twisted* at the first bend of the edge (Fig. 9). Examination by Laue photograph proves that the basal planes of the crystals on both sides of the edge make a small angle in the upper part as well as in the lower part.

Fig. 10 (a) is a polarization micrograph of the central part of Sheet No. 1. The spiral pattern which is only faintly visible in the ordinary photograph (Fig. 7) shows itself beautifully. It is clearly seen that the spiral lines are the cleavage lines, or the boundaries of terraces on the surface. In this sheet, the inner spiral terrace is lower than the outer. A similar pattern is observed on the upper surface of Sheet No. 2 (Fig. 10(b)), which was facing No. 1. On the face of No. 2, the inner terrace is higher than the outer. Thus the spiral patterns on the two surfaces are perfectly-fitting.

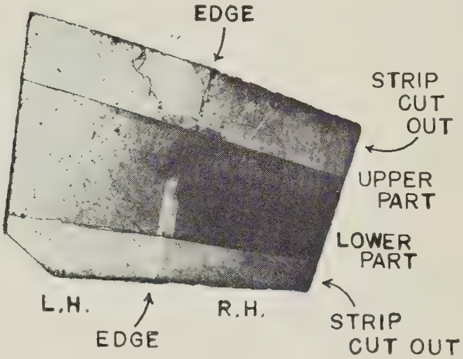

Fig. 8. Sheet No. 2. A spiral of *ca.* 4 turns. The sheet has a checkered appearance, because two narrow strips have been cut out. Boundary surface between L.H. and R.H. looks bright.

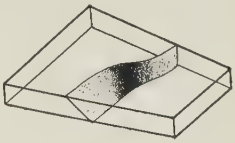

Fig. 9. The boundary surface is twisted at the bend of the edge (Sheets No. 1 and No. 2).

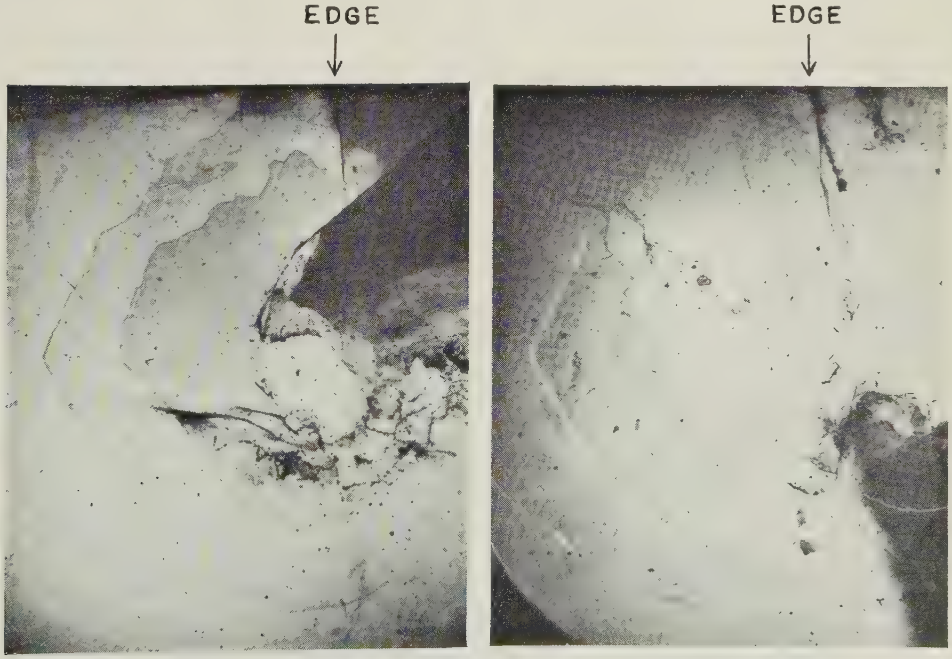

(a) Sheet No. 1. (b) Sheet No. 2.

Fig. 10. Polarization micrographs of Sheets No. 1 and No. 2. Central part.

It is difficult to locate the exact position of the spiral axis. Polarization microscopic study, as well as X-ray study, shows that the microscopic structures in its vicinity are very complicated (See Fig. 10 (a)).

Although the spiral is composed of a single continuous lamella, its thickness is not uniform. In the first place, there is variation of thickness due to spiral terraces on the surface, which was just mentioned. Secondly, there is an abrupt change of thickness at the boundary of L. H. and R.H., as is illustrated in Fig. 4.

## § 3. Discussions

The observations described above would at once stir up the association of the Frank mechanism of crystal growth.

It is true that there are difficulties in attributing the spiral structure of this specimen to the *growth due to screw dislocations**. In the first place, the thickness of the spiral lamella is too great. It amounts to $10^4$ times molecular height. In order that such a step can be realized, we have to assume as many screw dislocations concentrated at the axis of the spiral. Secondly, the thickness of the lamella is not uniform. There are difficulties in explaining the observed distribution of thickness.

Nevertheless, we are inclined to assume that the Frank mechanism did play the main part in the growth of this crystal. The surface or internal spiral patterns which are seen in Figs. 6 and 10 cannot but be the evidence of the intrinsic spiral nature of the crystal. Twisting of the crystal boundary at the apparent screw axis also indicates that numerous screw dislocations are concentrated there.

As to why such an extraordinary concentration of screw dislocations occurred, we suppose tentatively that an external force, which was exerted during the growth of the crystal, has caused it. If this caused the left and right halves of the crystal to make a small relative rotation around the *a*-axis, i.e. the axis which is perpendicular to the *b*-axis and lies in the basal plane, further growth could and would take place in a spiral manner.

The mechanism of the change of thickness is not clear. Before we go into this problem, more detailed examination of the distribution of thickness will be necessary.

We have searched for other specimens of mica which are cleaved spirally. We examined a lot of mica slices which had been classified as "inferior slices" and left in a mica condenser factory. A number of them showed an indication of incomplete spiral cleavage; we have not yet found, however, such a well-developed spiral structure as described here.

It is a pleasure for us to express our cordial thanks to the colleagues of the Department of Physics and Chemistry: to Prof. S. Yoshida and Mr. S. Kurokawa for their assistance in X-ray works, and to Profs. A. Ookawa and S. Chikazumi for useful discussions.

## Reference

1) S. Amelinckx: Nature **169** (1952) 580.

---

* Amelinckx[1] observed evidence of screw dislocation in mica. In his case, however, the step height was only 140 Å.

JOURNAL OF THE PHYSICAL SOCIETY OF JAPAN Vol. 11, No. 10, OCTOBER, 1956

# Point Contact of Pt and $\gamma$-$Cu_2S$

By Shin-ya MIYATANI

*Department of Physics, Faculty of Science, Niigata University*

(Received June 7, 1956)

Point contact between platinum needle and cuprous sulfide in its $\gamma$-phase ($<105$°C) shows d.c. characteristics which is apparently quite similar to those of metal-semiconductor rectifiers. This, however, must be attributed to ionic conduction in the semiconductor. A theoretical consideration shows that the $V-I$ characteristics are given by $eV/kT=\log(1+AI)$ as in the theory of rectification and that the time of relaxation depends on the effective contact area, $s$, electronic conductivity, $\sigma_h$, and ionic conductivity, $\sigma_i$, as $s\sigma_h/\sigma_i$. The experimental results show fairly good agreement with the theory.

## §1. Introduction

$Cu_2S$ is a p-type electronic semiconductor in which Cu ions are mobile[1,2,3]. It has two transition points at about 105°C and 470°C, being divided into three phases; $\gamma$ (below 105 °C), $\beta$, and $\alpha$ (above 470°C). In regard to the ionic conduction in the $\beta$ and $\alpha$ phases, we have reported in the previous papers[2,3]. Those results are illustrated in Fig. 1 somewhat schematically. The general features may be summed up as follows: The ionic conductivity, $\sigma_i$, is structure-insensitive, while the electronic conductivity, $\sigma_h$, varies widely according to the Cu/S ratio. The number of Cu ion vacancies in excess is equal to the number of free holes, since the change of the former is equal to that of the latter when the Cu atoms are removed from the sample. The ionic conductivity shows no jump at the $\alpha$-$\beta$ transition, whereas it changes discontinuously at the $\beta$-$\gamma$ transition.

When a voltage is applied between two electrodes, Cu ions move toward the cathode, but they do not deposit there and a stationary state is attained (*polarization process*). In the $\gamma$-phase, the ionic conductivity is very small and hence the time required for the polarization to build up becomes very long, as seen from the time constant given by[3,4)

$$\tau=\left(\frac{L}{\pi}\right)^2\frac{e}{pkT}\frac{\sigma_i+\sigma_h}{\sigma_i}, \qquad (1)$$

where $L$ is the length of the specimen, and $p$ is the mobility of holes. In order to make $\tau$ small, $L$ must be made small. In a thin sample, however, the boundary condition at the electrodes will give an important effect to the time constant of the polarization. In our present work, Pt point contact is used as one of the electrodes. With this layout, the relaxation time can be made comparatively small, though the process in this case is not exponential, and hence the accuracy of measurements is worse than the one-dimensional case taken up in the previous work.

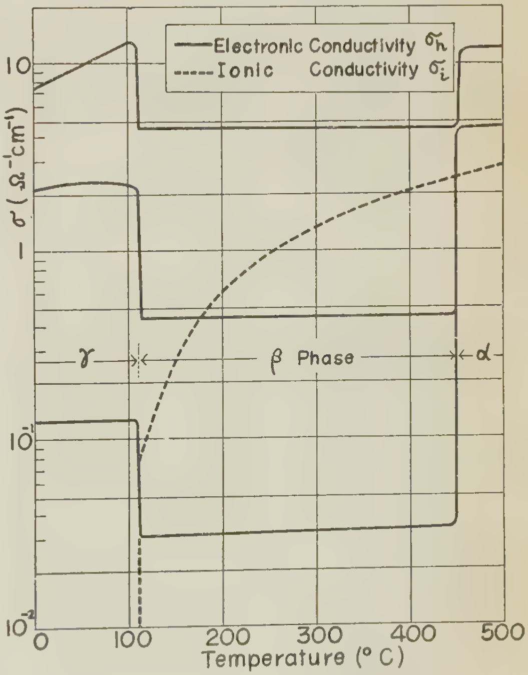

Fig. 1. $\sigma_h$ and $\sigma_i$ vs. Temperature.

## §2. The Diffusion Theory

At first, let us assume that the contact of Pt with $Cu_2S$ is semi-spherical for the sake of simplicity (Fig. 2). Next, it is assumed that the barrier layer does not exist, that is, the contact is ohmic. When a voltage is applied between Pt and the base metal (Pt), the concentration of Cu ion vacancies changes near the contact point, resulting in a change of the contact resistance. In the case of the constant current intensity, the potential drop changes with the time. Let us derive the diffusion equation in this case. The principle is the same with that used in our previous work. The current densities due to holes and ions are given by

$$i_h = -\sigma_h \frac{\partial}{\partial r}\left(\frac{\mu}{e} + \Phi\right), \tag{2}$$

$$i_i = -\sigma_i \frac{\partial \Phi}{\partial r} \tag{3}$$

respectively, where $\mu$ is the chemical potential of a hole, and $\Phi$ is the electrostatic potential. The chemical potential of an ion is assumed to be independent of the composition of $Cu_2S$ as assumed in our previous works for $Ag_2S$ and $\beta$-$Cu_2S$. When the concentration of holes is not too large (non-degenerate), $\mu$ is given by

$$\mu = kT \log n + \text{const.} \tag{4}$$

From Eqs. (2), (3), and (4), using the total current density, $i \equiv i_i + i_h$, we have

$$i_i = \frac{\sigma_i}{\sigma} i + \frac{\sigma_h}{\sigma} \sigma_i \frac{kT}{e} \frac{1}{n} \frac{\partial n}{\partial r}, \tag{5}$$

$$i_h = \frac{\sigma_h}{\sigma} i - \frac{\sigma_h}{\sigma} \sigma_i \frac{kT}{e} \frac{1}{n} \frac{\partial n}{\partial r}, \tag{6}$$

where $\sigma$ is the total conductivity; $\sigma \equiv \sigma_i + \sigma_h$. Further, we assume that the number of free holes is equal to the number of excess Cu ion vacancies. This assumption has been proved to be right in the case of $\beta$-$Cu_2S$. In our present case of $\gamma$-$Cu_2S$, it may not be right. But it may be approximately right at least in the case where the $\sigma_h$ does not depend upon the temperature. This is the case when the sample has rather small conductivity and the temperature is above the room temperature (Fig. 1). We shall discuss within such a limit. Then the equation of continuity for the ion vacancies is given by

$$2\pi r^2 \frac{\partial n}{\partial t} = \frac{\partial}{\partial r}\left(2\pi r^2 \frac{i_i}{e}\right), \tag{7}$$

where $n$ is the density of Cu ion vacancies which is equal to that of free holes. Substituting Eq. (5) into (7), and putting $\sigma_h/\sigma = 1$ ($\sigma_i/\sigma$ is smaller than $10^{-2}$), we have

$$r^2 \frac{\partial n}{\partial t} = \frac{\partial}{\partial r}\left\{\frac{\sigma_i}{e}\left(\frac{r^2 i}{\sigma} + \frac{kT}{e} \frac{1}{n} \frac{\partial n}{\partial r}\right)\right\}. \tag{8}$$

Now, $\sigma_i$ is almost independent of the composition as in the $\beta$ phase (see later experimental results), Eq. (8) can be reduced to

$$r^2 \frac{\partial n}{\partial t} = A \frac{\partial}{\partial r}\left\{\left(J + r^2 \frac{\partial n}{\partial r}\right)/n\right\},$$

$$A \equiv \frac{kT\sigma_i}{e^2}, \qquad J \equiv \frac{i r^2}{kTp} = \frac{I}{2\pi kTp}, \tag{9}$$

where $I$ is the total current intensity. The potential difference between Pt and the base metal is given by

$$V = \int_a^\infty \frac{i}{\sigma} dr = \frac{I}{2\pi ep} \int_a^\infty \frac{dr}{nr^2}, \tag{10}$$

where $a$ is the radius of the contact semi-sphere (Fig. 2).

The initial potential drop, $V_o$, is given by $I/2\pi\sigma_o a$, where $\sigma_o$ is the initial conductivity. The final stationary state is attained when the ionic current, $i_i$, decays out. Putting the right-hand side of Eq. (5) to be zero, we have

$$\frac{dn}{dr} = -\frac{J}{r^2}. \tag{11}$$

Integrating Eq. (11) and substituting it into Eq. (10) or (4), we obtain the stationary potential drop, $V_s$, given by

$$\frac{eV_s}{kT} = \log\left(1 + \frac{eI}{2\pi kTa\sigma_o}\right) \equiv \log\left(1 + \frac{J}{an_o}\right). \tag{12}$$

The change of the potential drops from $V_o$ to $V_s$ is given by solving Eq. (9). This equation is not linear and it is difficult to solve this exactly. If $I$ is sufficiently small, however, Eq. (9) may be approximated by

$$r^2 \frac{\partial n}{\partial t} = \frac{A}{n_o} \frac{\partial}{\partial r}\left(J + r^2 \frac{\partial n}{\partial r}\right), \tag{13}$$

which can be solved rather easily with the initial condition $n = n_o$, and the boundary condition

$$J + r^2 \frac{\partial n}{\partial r} = 0 \quad \text{at } r = a \text{ and } \infty.$$

The result is as follows:

$$n = n_o + J(1 - \mathfrak{F}(t, r))/r, \tag{14}$$

where

$$\mathfrak{F}(t, r) = \frac{2}{\pi} \int_o^\infty \exp\left(-\frac{y^2 At}{x^2 n_o a^2}\right) \frac{\sin y + (y/x)\cos y}{y(1 + (y/x)^2)} dy,$$

where $x = (r - a)/a$. Substituting Eq. (14) into Eq. (10), and remembering that $J$ is assumed to be small, we have

$$V=\frac{I}{2\pi\sigma_o}\int_a^\infty\left\{1-\frac{J}{r}(1-\mathfrak{F}(t,r))\right\}\frac{dr}{r^2}\ . \qquad (15)$$

Then we have

$$v\equiv\frac{V_s-V}{V_s-V_o}=-\int_a^\infty\mathfrak{F}(t,r)\frac{dr}{r^3}$$

$$=\frac{4}{\pi}\int_o^\infty\exp(-\eta^2\tau)(1+\eta^2)^{-1}\left\{1+\frac{\eta}{2}(\cos\eta+\eta\sin\eta)\right.$$

$$\left.\left(Si\,\eta-\frac{\pi}{2}\right)+(\eta\cos\eta-\sin\eta)Ci\,\eta\right\}d\eta\ , \qquad (16)$$

$$\tau\equiv\frac{At}{n_0a^2}\equiv\frac{kTp\sigma_i}{ea^2\sigma_h}t\ . \qquad (17)$$

Si $\eta$ and Ci $\eta$ can be referred to, e. g. Jahnke and Emde's book. When $\tau$ is sufficiently large, $v$ decreases as $1/\sqrt{\tau}$. Fig. 2 shows the calculated $v$-$\tau$ plot.

## § 3. Experimental Arrangements

The samples of $Cu_2S$ are prepared from Cu blocks and sulphur powder in proper proportion, which are together sealed into an evacuated hard glass tube and made to react at about 600°C. The conductivity of the samples obtained by this method is rather large. In order to obtain the samples with smaller conductivity, the cell $Pt|Cu_2S|CuI|Cu$ is used as shown in Fig. 3 (b): A specimen forming this cell is inserted in a glass tube which is evacuated by a diffusion pump and heated in a furnace and then sealed. By sending a current across the cell at about 340°C, the sample can be changed from S rich one to Cu-saturated one. (We wish to discuss about this cell in other paper in the future.)

When the temperature is required to be kept constant, the specimen tube is immersed in an oil bath thermostat. The method of measurements is as usual (Fig. 3).

## § 4. Experimental Results

### (a) *One-dimensional measurements of* $\sigma_i$[2,3,4]

If the conductivity is small and the temperature is near the transition point, the one-dimensional method can be carried out (Fig. 3 (a)). An example of measurements is illustrated in Fig. 4. The mobility of holes, p, is obtained by the use of Eq. (1). The number of holes in the $\gamma$ phase is almost equal to that of the Cu ion vacancies as in the $\beta$ phase, if Eq. (1) is valid even in the $\gamma$ phase. Then the theory described in § 2 may be used.

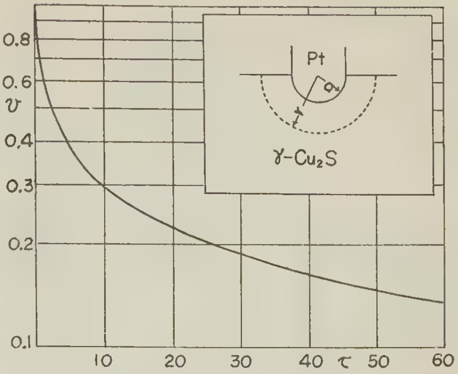

Fig. 2. $v$ vs. $\tau$.

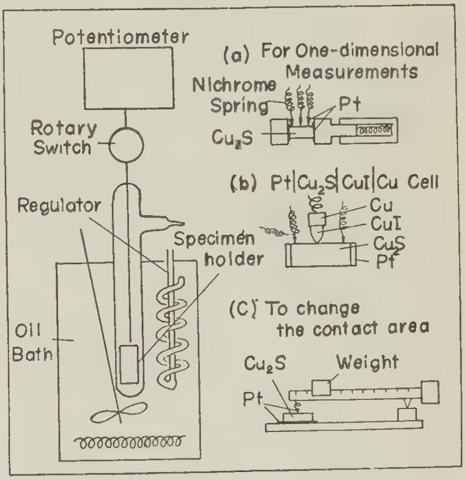

Fig. 3. Schematic diagram of apparatus.

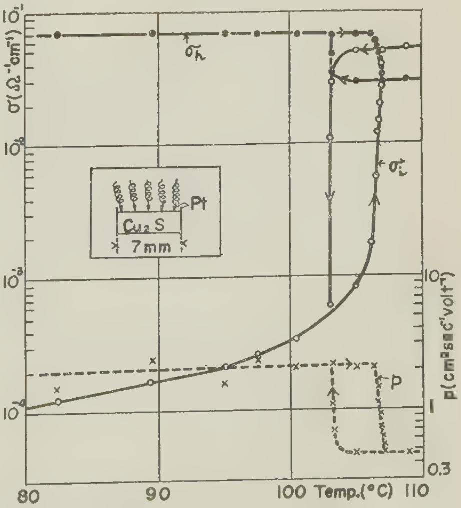

Fig. 4. $\sigma_h$, $\sigma_i$, and $p$ vs. Temperature.

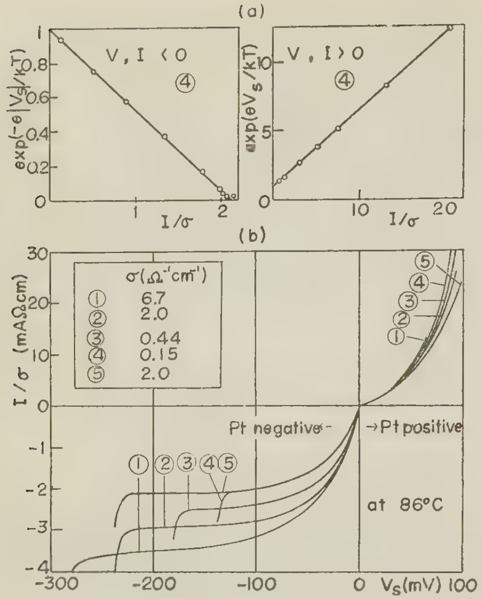

Fig. 5. Stationary $V$–$I$ characteristics.

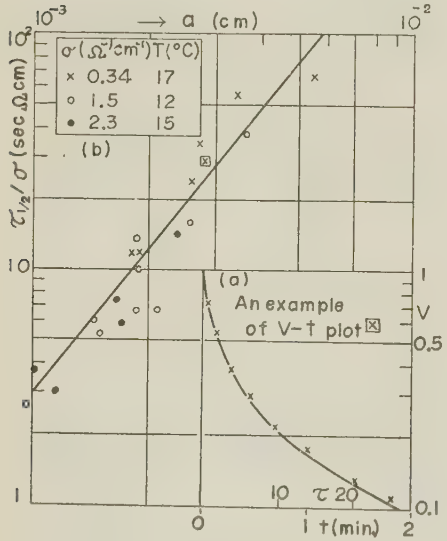

Fig. 6. (a) An example of $v$–$t$ plot, (b) $\tau_{1/2}/\sigma$ vs. $a$.

### (b) *Stationary characteristics of Pt point contact*

Fig. 5 (b) shows the results of a series of measurements. The numbers in small circles represent the order of measurements. The conductivity is changed by the use of CuI as mentione in § 3.

General features look like usual rectifiers, although there are important differences, that is, the direction of rectification is opposite and the time of relaxation is far larger, The experimental results are in good accordance with Eq. (12) both at positive $I$ and negative $I$ as shown in Fig. 5 (a), though the deviation from Eq. (12) becomes remarkable when $I/\sigma$ is too large. In the case of negative $I$, the deposition of Cu takes place at a certain potential, $V_d$, depending upon the Cu/S ratio, and hence the contact resistanse decreases suddenly. The potential, $V_d$, varies as $\sigma$ varies at a temperature, and decreases slightly as the temperature rises. It is approximately given by $eV_d = kT \log \sigma + f(T)$. The critical point of deposition is reached when the chemical potential of Cu atoms at the contacting point becomes equal to that in the Cu-saturated sample (the sample in equilibrium with Cu metal). Remembering our previous assumption that the chemical potential of Cu ion is independent of the Cu/S ratio, the above condition can be represented by

$$eV_d = \mu(\infty) - \mu(a) = kT \log \frac{n}{n_s} = kT \log \frac{\sigma}{\sigma_s}, \quad (18)$$

where suffix $s$ denotes the value in the Cu-saturated sample. Eq. (18) agrees with experimental results, justifying our viewpoint.

### (c) *The time rate of polarization*

Fig. 6 (a) shows an example of $v-t$ plot, where $v$ has been defined by Eq. (16). It corresponds to one with the same mark in Fig. 6 (b). In these measurements, $V_o$ is made smaller than 12 mV in order to compare the results with the theory. Then $(n(a)-n_o)/n_o = J/an_o = eV_o/kT < 0.5$ at the room temperture. Considering our poor accuracy of measurements, Eq. (13) may be applied within this voltage limit. As seen in the figure, $v$ has a rather long tail, making the measurements inaccurate. This is the same with the curve in Fig. 2. The curve in Fig. 6 (a) is the theoretical one properly adjusted by assuming that experimental $V_s$-value is not real stationary one, but corresponds to the value when $\tau=90$. For the sake of simplicity, the half-value period, $\tau_{1/2}$, that is, the time it takes for $v$ to be halved, is chosen as the measure of the time rate for polarization. The theoretical value of $\tau_{1/2}$ is given, from Fig. 2, by

$$\tau_{1/2} = 2.4 \frac{ea^2\sigma_h}{kTp\sigma_i}. \quad (19)$$

Fig. 6 (b) shows the exprimental $\tau_{1/2}/\sigma$ vs. $a$ plot, where $a$ is obtained by the relation $V_o = I/2\pi\sigma_o a$ mentioned already (see also Fig. 3

(c)). Although the experimental points are widely scattered, it can be said that $a$-dependence is just as expected from Eq. (19), and $\sigma_i$ is independent of $\sigma_h$. Using Eq. (19) and assuming $p=2\,\text{cm}^2\,\text{sec}^{-1}\,\text{volt}^{-1}$ (it is not too reliable), $\sigma_i$ can be estimated as $1.6\times10^{-5}\,\Omega^{-1}\,\text{cm}^{-1}$ at 15°C.

The time constant decreases as the temperature is raised, and, assuming $p$ is constant, the temperature dependence of $\sigma_i$ can be represented as

$$\sigma_i=B\exp(-eU/kT), \tag{20}$$

where $U$ is about 0.30 eV. It is the same with that in Fig. 4, when the temperature is lower than 95°C. By the use of the $\sigma_i$ value in Fig. 4, which has been obtained by the one-dimensional method, we have $B=2.4$. Using these values, we can estimate $\sigma_i$ at 15°C as $1.3\times10^{-5}\,\Omega^{-1}\,\text{cm}^{-1}$ which agrees well with the one obtained by the point contact measurements (Such a good agreement may be rather fortuitous).

## § 5. Discussions

(**a**) In our present work, the semi-spherical model is taken up for the sake of simplicity. The stationary $V$-$I$ characteristics are, however, independent of this simplification. Even with more complicated contact, the stationary potential, $V_s$, is given by

$$eV_s=\mu_c-\mu_0=kT\log\frac{n_c}{n_0},$$

where the suffix $c$ denotes the value at the contacting point. From the linearity of the equation which gives the gradient of $n$ ($i=-kTp\partial n/\partial s$) we can expect that $(n_c-n_0)/n_0$ is in proportion to the current intensity, resulting in the same equation with Eq. (12), where $a$ is not the radius, but some parameter. The radius, $a$, may, therefore, be regarded as "effective radius," and $2\pi a^2$ as "effective contact area." The time constant for the polarization to build up is, however, expected to depend more or less upon the condition of contact.

(**b**) In the case of Pt contact, the barrier layer can be neglected, since the contact resistance in the initial state is almost ohmic. In the case of other metals, e. g. Cu or Al, the barrier layer seems to be formed although it is rather unstable.

(**c**) The point contact of Pt and $Ag_2S$ shows similar characteristics[5]. The difference is that $Ag_2S$ is $n$-type and the interstitial Ag ions are mobile, and, hence, the $V$-I characteristics changes the sign of $V$- and $I$- axes, in comparison with the present case, as given by

$$-eV_s/kT=\log(1-J/an_o). \tag{21}$$

For positive $V$(Pt positive), sulphur seems to deposit, and for negative $V$, Ag deposits at certain potentials respectively. The experimental result shows a good accordance with Eq. (21) at least for posive $V$. In regard to the time constant, somewhat different diffusion equation from the present one should be used.

(**d**) As seen from Eq. (19), the change of potential due to polarization becomes measurable even if $\sigma_i/\sigma_h$ is very small, only if $a$ is sufficiently small. We imagine some of the creep phenomena of the usual rectifiers of the point contact type may be attributed to the ionic conduction as our present case.

Finally, the author wishes to express his sincere thanks to Mr. Y.Suzuki, Mr. I.Yokota and Mr. S.Endo for their kind discussions. This work was supported by the research grant of the Ministry of Education.

### References

1) E. Hirahara: J. Phys. Soc. Japan **6** (1951) 422.
2) S. Miyatani and Y. Suzuki: J. Phys. Soc. Japan **8** (1953) 680; J. Fac. Sci. Niigata Univ. Ser. I, **1**, No. 1 (1953) 1.
3) I. Yokota: J. Phys. Soc. Japan **8** (1953) 595.
4) S. Miyatani: J. Phys. Soc. Japan **10** (1955) 786.
5) Y. Suzuki and S. Endo: J. Fac. Sci. Niigata Univ. Ser. I, **1**, No. 3 (1956) 1.

JOURNAL OF THE PHYSICAL SOCITY OF JAPAN Vol. 11, No. 10, OCTOBER, 1956

# The Quadrupolar Effect in Alkali Halide Mixed Crystals

By Hazimu KAWAMURA, Eizo OTSUKA and Keiko ISHIWATARI
*Institute of Polytechnics, Osaka City University, Osaka*

(Received July 2, 1956)

Using NaBr–NaCl mixed crystals, we have observed the quadrupolar effect on the nuclear resonance absorption line of Na. The minority halogen plays the role of "impurity" or "solute" as in the case of alloys treated by Bloembergen and Rowland. The satellites of Na in NaCl are affected when the solute Br comes at the third halogen site counted from Na site, where the field gradient then becomes $q \sim 10^{21}$ cm$^{-3}$. From our analysis the antishielding factor $\lambda$ for Na is given as $\sim 10$. The asymmetric broadening of the central line due to the second order perturbation occurs when and only when the solute comes next to the Na nucleus. The specimen being a single crystal, the satellites of the second order arise at the definite positions depending upon the direction and strength of the external magnetic field. By measuring this shift of the resonance field, we see that the field gradients produced then at the Na site are nearly $1.4 \times 10^{23}$ cm$^{-3}$ and $2.0 \times 10^{23}$ cm$^{-3}$, when Br$^-$ and Cl$^-$ are the solute ion, respectively. On account of the segregation of the solute ions within the crystal, each Na site has rare chance to have more than one solute next to it.

## § 1. Introduction

The quadrupolar effects of imperfections on the nuclear resonance of ionic crystals, especially alkali halides, have already been investigated by some research workers. For example, Watkins[1)] and Watkins and Pound[2)] observed the resonance absorptions of the halogen ions in KBr and KI single crystals, whose nuclear spins are 3/2 and 5/2, respectively. Br and I have large electrical quadrupole moments and hence it is expected that there should be considerable interaction between their nuclear quadrupole moments and the random electric field gradients around the nuclei caused by the internal strains in the crystal. In fact it was shown that the portions which correspond to the satellite components of the absorption lines were almost completely smeared out, leaving only 0.4 and 0.28 fractions for Br and I, respectively, as the intensities compared with the total intensities expected for these nuclei. Furthermore, Watkins[1)] showed that the broadening to the central line due to the second order perturbation occurs after a strong plastic deformation in both crystals.

In the meantime, the quadrupolar effects have been observed also in metals. Bloembergen and Rowland[3)] confirmed that there arises considerable change in the satellite contribution in pure copper corresponding to cold-working and that by mixing zinc atoms so as to make $\alpha$-brass there occurs the second order broadening of the central line. The latter effect is attributed to the field gradients due to the local strains which are caused by the introduction of zinc atoms into copper. Further experiments were made by Rowland[4)] on aluminum containing zinc and magnesium as solute atoms and similar results were reported.

In the case of pure KBr and KI, the internal strains which are responsible for the local field gradients are considered chiefly due to dislocations and Watkins estimates the dislocation density from his own experimental results[1)]. While in the case of alloys, the excess charge and size effects of the solute atoms would be the dominant one and the influence of the dislocations only seems to be less effective compared with the case of KBr and KI. This will partly be explained by the difference of the magnitudes of the quadrupole moments and partly by the difference of the magnitudes of the field gradients in the cases of atomic and ionic displacements. So we naturally have the expectation that if we employ some ionic crystal and examine a nucleus with smaller quadrupole moment, say Na in NaCl or NaBr, the quadrupolar effect due to "impurity" might chiefly be observed. Such "impurity" can be achieved either by introducing divalent ions into the crystal thus producing excess charge effect around them, or by making a mixed crystal like NaBr-NaCl thus producing size effect around the solute ions, namely, the negative ions of the minority component. In this way, we shall be able to make an experiment similar to the case of alloys. We should, however, always keep in mind that there is a fundamental difference between these two cases. In the case of alloys, we are forced to employ powder in order to avoid the skin effect, but in dealing with alkali halides we can use single crystals for the resonance measurement. The availability of single crystals in the latter case indeed is a very strong merit, especially when we examine the asymmetric character of the absorption line which accompanies the second order broadening. This asymmetrical broadening at the plastically deformed single crystals of KBr and KI was found by Watkins. In his case, however, the chief role was played by the dislocations and therefore the asymmetry character should be independent of the angle between the crystalline axes and the external magnetic field. On the other hand, as we shall show later in this report, if the impurity is responsible for the broadening effect, the asymmetric character will have remarkable angular dependence, which turns out to be a strong tool in analizing the quadrupolar effect.

## § 2. Experimental Techniques

In our experiment the r–f oscillator and receiver were those of the Pound-Knight-Watkins type. The magnetic field was sinusoidally modulated with 30 cps and the signal thus detected was led through the phase-sensitive mixer-amplifier to the automatic recorder. The magnet was an electromagnet designed and made at the laboratories of the Tokyo College of Science and was drived with four six-volt storage batteries. The field strength was rather convenient nearly at 3,600 gauss and the r–f frequency was fixed at ~4 mc corresponding to this field strength in observing the Na-line. The sweep of the magnetic field was established by the natural drift due to the heating-up of the magnet and the scanning rate was adjusted through the velocity of the cooling water. The sinusoidal modulation was made 1.2 gauss peak to peak, small in comparison with the observed line width both for NaBr and for NaCl. All the samples were prepared at our laboratory and so shaped as to fit the r–f coil with 12 mm in diameter and 20 mm in height. The pure NaBr and pure NaCl, the latter being used as the standard for the intensity measurement, were annealed three to four hours long at about 50°C below their melting temperatures, and then cooled down at the rate of nearly 40°C per hour. While the NaBr-NaCl mixtures were left unannealed on account of the reason which will be stated in the later section and shaped soon after the crystallization. The compositions of the mixed crystals were determined by the density measurement, which showed some slight difference from the preliminary measurement before the crystalization. In order to establish the state of negligible saturation, the r–f oscillation level was made as low as 0.015 V. All the measurements were carried out at room temperature.

## § 3. Experimental Results and Their Analyses

For a crystal having the cubic symmetry there should be no quadrupolar effect; however, on account of the lattice vibrations, point defects or dislocations, which destroy the cubic symmetry, there arise nonzero electric field gradients and they couple with the quadrupole moment of the nuclei in question. The energy level of the nucleus with spin $I$ split into $2I+1$ levels specified by the magnetic quantum number $m$ and the energy difference between two adjacent levels is in the first approximation given by

$$\mathrm{W}_{m\to m-1} = h\nu_0-(2m-1)(1-3\cos^2\theta)3e^2qQ/8I(2I-1)\,, \tag{1}$$

here $\nu_0$ is the resonance frequency, $m$ the magnetic quantum number, $\theta$ the angle between $H$ and the axis of the electric field. Evidently for the transition $m=1/2\to m=-1/2$ the second term on the right-hand side of (1) vanishes; that is, this transition is unaffected by the first order perturbation and observed as the central line. While all other transitions give the so-called satellites. Now in case that

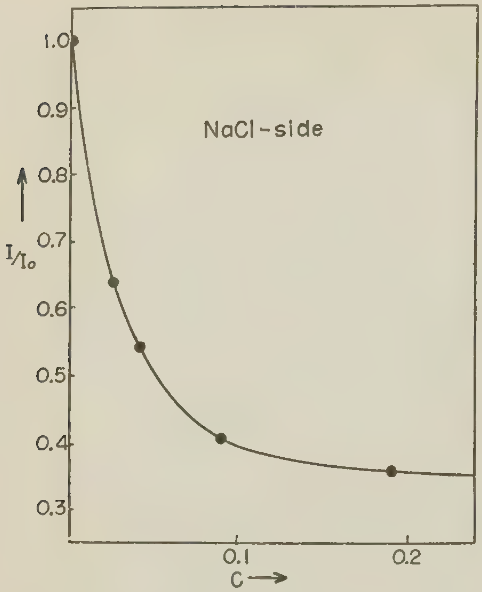

Fig. 1. The relative absorption intensity for $c\,\mathrm{NaBr}\cdot(1-c)\mathrm{NaCl}$.

the field gradients become so large that we have to consider the effect of the second order perturbation, the position of the central line also shifts according to the following formula:

$$h\Delta\nu = A(1-9\cos^2\theta)(1-\cos^2\theta)\,, \qquad (2)$$

where

$$A=\frac{9}{64}\cdot\frac{(2I+3)}{4I^2(2I-1)}\cdot\frac{e^4q^2Q^2}{h\nu}\,. \qquad (3)$$

As we shall see later, such second order effect in our case can occur only when the solute ion comes at the nearest neighbor position to the Na nucleus. The axis of the electric field gradient then lies in the direction connecting the Na ion and the solute negative ion. Hence by rotating the crystal we can vary the angle $\theta$ and see the corresponding change in the shift given by (2).

### 3·1) Intensity of the Absorption Line

First of all, in order to decide whether the intensity of the Na-line in a pure crystal is nearer to 1.0 or to 0.4, comparison was repeatedly made with the Na-line in the saturated solution of NaBr added by Mn and it was concluded that, differing from Br or I, Na in pure NaCl is very nearly 1.0 in its intensity. Second, comparison of the observed integrated intensities was made between a well-annealed and an oil-quenched crystal. Again, despite the repeated trials, little difference was seen and this led us to the conclusion that the defects produced by the quenching process, namely, vacancies and dislocations give no striking quadrupolar effect. By the NaCl powder sufficiently ground in the mortar, however, the intensity dropped nearly to 0.6 compared with that by a single crystal of pure NaCl.

Finally, by the mixed crystals, very striking intensity reductions were observed. Fig. 1 shows the relative intensity of the Na-line plotted against the solute ion concentration when $Br^-$ is the minority ion; i.e., when a small amount of NaBr is added to pure NaCl. The measurements in this case were made with the [100] axis of the crystal being parallel to the applied magnetic field. We see that the intensity drops, e.g., to 0.63 for 2.5 percent solute ion concentration and for 10 percent there hardly remains the satellite contribution, in other words, the intensity drops nearly to 0.4. Now we can make an analysis similar to that by Rowland for alloys for the region where the satellite contribution is still appreciable. Namely we put forward the assumption

$$I/I_0-0.4\propto(1-c)^n \qquad (4)$$

and construct a double logarithmic plot for both-hand sides. Here $c$ is the solute fraction, i.e., relative concentration of the minority halogen, and this being small compared with unity we may put $\ln(1-c)\sim -c$. The exponent $n$ signifies the number of the halogen sites included within the critical sphere which bounds the region around the Na nucleus and in which the solute ion can affect the satellites. The subtraction of the number 0.4 means, of course, the removal of the central line contribution for Na whose nuclear spin is 3/2. The available experimental points for this plot are only three in number, yet by the repitition of the measurement all these values were made as accurate as possible and we believe that they are quite reliable. From the slope of the straight line in Fig. 2, which shows the double logarithmic plot mentioned above, we obtain $n=38$. This is the number of the negative ion lattice sites which includes as far as the third halogen neighbors counted from the Na nucleus. It has indeed been surprising that such a sharp cut-off can be obtained in the case of a mixed ionic crystal.

Next we will mention briefly the case when $Cl^-$ is the minority ion; i.e., when a small amount of NaCl is added to pure NaBr crystal. The situation is quite analogous to the opposite side of the mixed crystal and we show in Fig. 3 the plot of intensity *vs.* solute ion concentration similar to Fig. 1. In this case of NaBr-side, however, the measurments were made with the [110] axis of the crystal being parallel to the external magnetic field with the intention of making the peak higher than in the case of the other direction. Moreover, the standard of the intensity is that of the pure NaCl on account of the fact that by our pure NaBr crystal the intensity did not reach 1.0, but remained less than 0.6. The reason is not clear but probably a considerable amount of impurities such as divalent metal ions would have affected the intensity of the Na-line in NaBr crystals*. In addition to this, a couple of sample at the side of the lower solute concentration had somewhat slant cylindrical axes so that there might have been some ambiguity in the measurement of peak intensity for these specimens. All these circumstances made the data for the NaBr-side less unambiguous than those for the NaCl-side and accordingly a very accurate analysis could not be made.

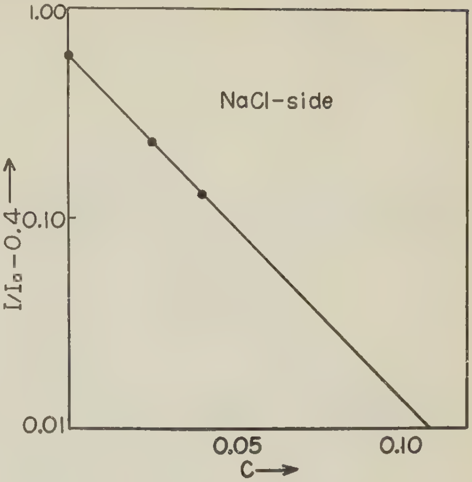

Fig. 2. The double logarithmic plot determining the number of halogen lattice sites within the critical sphere, which turns out to be 38 for the NaCl-side. Here the approximation $\ln(1-c)\sim -c$ has been made.

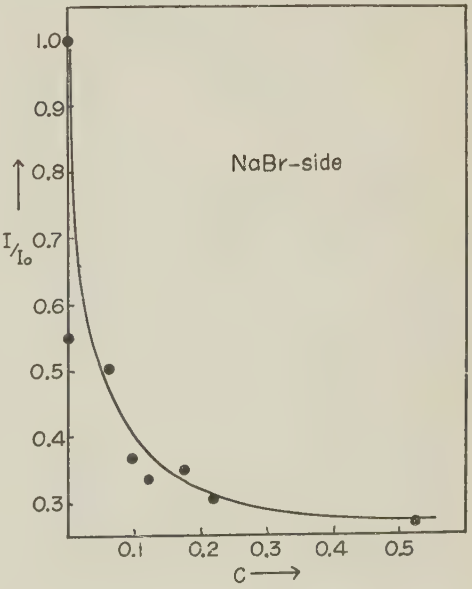

Fig. 3. The relative absorption intensity for $(1-c)\mathrm{NaBr}\cdot c\,\mathrm{NaCl}$.

### 3·2) Shapes of the Central Lines

As the solute concentration is increased, there appears asymmetry of the line in addition to the reduction of the intensity. This line asymmetry is most striking for $[100]//H$, rising sharply at the higher magnetic field side and having a long tail at the lower field side. For $[110]//H$, on the other hand, the line rises extremely slowly at the higher field side and drops rather gradually at the lower field side. This situation is shown in Fig. 4 by the integrated absorption curves. Needless to say, the asymmetry is far more pronounced by the recorded derivative curves. Such asymmetry character is well explained by considering Eq. (2) which gives the frequency shift due to the second order perturbation. To see this most clearly, we shall for simplicity assume that the second order broadening occurs only when the solute ion comes next to the Na nucleus and assume further that only one of the six nearest neighbor sites is occupied by such a solute ion. These two assumptions will later be justified. Now when the static magnetic field is applied along the [100] axis of the crystal, then, as can be seen from Eq. (2), there

---

* All the crystals used in this experiment were grown from commercially available reagents. The degree of purity for NaCl reagent was designated as "special", while no reagent of such high purity was obtainable for NaBr.

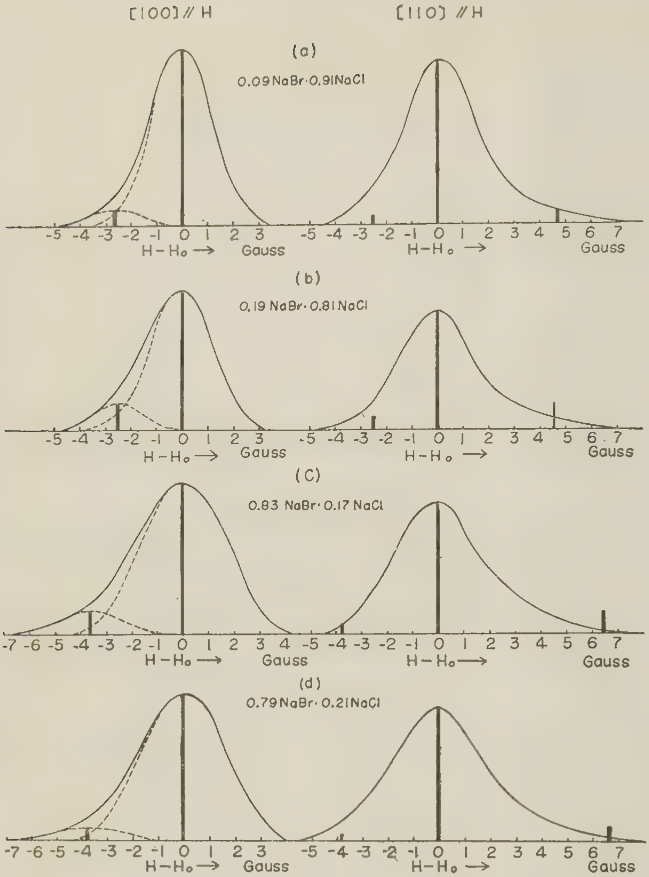

Fig. 4. The directional effect of the line asymmetry for the specimens with various compositions.

should be no shift at the two sites for which $\theta=0$ and should be a shift of $\Delta\nu=A/h$, or, in magnetic field unit, $\Delta H=-2\pi A/\gamma h$, at the four sites for which $\theta=\pi/2$.

By resolving the observed asymmetric line into two parts, as shown on the left sides of (a), (b), (c) and (d) in Fig. 4, the greater one corresponding to the unshifted central line portion for which responsible are the Na nuclei having none or one solute neighbor ion with $\theta=0$, while the other small peak appearing on the lower field side being associated with the Na nuclei having a solute neighbor with $\theta=\pi/2$, we are able to determine the magnitude of $\Delta H$ for the field strength employed; namely, the distance between the two separate peaks. In Table I are shown the values of $|\Delta H|$ thus determined and the intensity ratios $I_s/I_c$ of the two peaks, $I_s$ denoting the intensity of the shifted line, or the satellite of the second order, while $I_c$ the intensity of the unshifted, or the central line component. On account of the obtruding noise level at the far end of the line tail, the careful analysis for such small peak of the satellite is rather difficult; moreover, the determination of the relative peak intensity $I_s/I_c$ has to be obsessed with considerable error. Nevertheless the acquired values given in Table I suggest some interesting fact: If the solute ions are uniformly scattered all over the crystal, then the probability that a solute comes next to the Na nucleus with $\theta=\pi/2$ should be $4c(1-c)^5$ and hence $I_s/(I_c+I_s)\sim I_s/I_c$ has to be equal to this. The actual values of $I_s/I_e$, however, obviously are smaller than $4c(1-c)^5$ given in the last column of the table. The gap wider for the greater concentration of the solute. This fact suggests that the solute in no ways has uniform distribution in the crystal. More detailed discussions concerning this will be given in § 4. All values of $|\Delta H|$ listed here are those determined for $H_0=3,600$ gauss. As a characteristic of the quadrupolar effect, Eq. (3) gives the following relation between $\Delta H$ and $H$:

$$|\Delta H|=\frac{9\pi^2(2I+3)e^4q^2Q^2}{14\gamma^2h^24I^2(2I-1)H_0} \tag{5}$$

or, in short, $|\Delta H|$ is inversely proportional to $H_0$. Hence, changing the static field strength will make a simple criterion for this effect. Actually the magnitude of $\Delta H$ obtained for the 0.19 NaBr. 0.81 NaCl crystal under the application of the static field of $H_0=5350$ gauss dropped to about 1.8 gauss, thus providing consistency with the relation (5).

For the case of $[110]//H$, two out of the six nearest neighbor sites have $\theta=\pi/2$ and correspond to the same shift as in the case of $[100]//H$ discussed above, while the remaining four sites have $\theta=\pi/4$ and will make a shift toward the inverse side with the magnitude of $\Delta H=3.5\pi A/\gamma h$. Now that the satellites appear on both sides of the central line, the exact curve shape for the unshifted component is uncertain so that the separation of the

Table I. The shifts and relative intensities of the satellites for $[100]//H_0$, $H_0$ being fixed at 3,600 gauss.

| NaCl-side | | | |
|---|---|---|---|
| $c_{Br}$ | $\lvert\Delta H\rvert$ (gauss) | $I_s/I_c$ | $4c(1-c)^5$ |
| 0.025 | 2.5 | 0.08 | 0.088 |
| 0.04 | 2.6 | 0.12 | 0.130 |
| 0.09 | 2.6 | 0.10 | 0.225 |
| 0.19 | 2.7 | 0.20 | 0.265 |
| NaBr-side | | | |
| $c_{Cl}$ | $\lvert\Delta H\rvert$ (gauss) | $I_s/I_c$ | $4c(1-c)^5$ |
| 0.06 | 3.5 | 0.10 | 0.176 |
| 0.11 | 3.5 | 0.11 | 0.246 |
| 0.17 | 3.7 | 0.15 | 0.268 |
| 0.21 | 3.8 | 0.10 | 0.258 |

Table II. The shift and relative intensity of the satellite for the mixed crystal extremum, with $H_0//[100]$ and $H_0 \sim 3{,}600$ gauss.

| $c_{Br}$ | $\lvert\Delta H\rvert$ (gauss) | $I_s/I_c$ |
|---|---|---|
| 0.48 | 3.6 | 0.17 |

central line and the satellites is hardly possible. Thus we give merely the skeleton diagrams on the right side of Fig. 4, together with the experimental curves, derived by trusting the values of $\Delta H$ and $I_s/I_c$ obtained for the case of $[100]//H$. The fit between the experimental curves and the skeleton diagrams is hardly said to be very excellent; however, the characteristic of having the greater tail on the higher magnetic field side corresponding to the shift of $\Delta H = 3.5\pi A/\gamma h$ is common to all the experimental curves for the different values of $c$.

Finally, investigation was made of 50–50 crystal for the extreme case of mixing. A precise density determination later showed that the real composition of this specimen was 0.48 NaBr. 0.52 NaCl. The integrated absorption curves for this specimen are shown in Fig. 5 and the values of $\Delta H$ and $I_s/I_c$ similar to those given in Table I are listed in Table II for the direction $[100]//H$. The signal to noise ratio during the observation was poorest at this specimen so that the analysis by no means was easy.

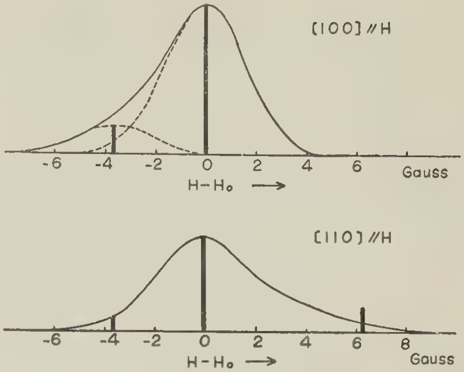

Fig. 5. The asymmetry characteristics of the absorption line for the mixed crystal extremum 0.48 NaBr·0.52 NaCl.

## § 4. Discussions

Various kinds of imperfections producing the electrical field gradients which are responsible for the quadrupolar effects in solids are considered. For example, dislocations, vacancies, lattice vibrations and impurities are always present even in the ordinary "pure" crystals. In the case of pure NaCl, however, we could meet with no appreciable quadrupolar effect unless we made sufficient grinding. Whereas by introducing a small amount of "impurity" into the crystal, we were at once able to produce a striking effect. Hence we were naturally led to the belief that the presence of "impurity", or solute ions, are chiefly responsible for the effect. Moreover, both $Cl^-$ and $Br^-$ being monovalent ions, the excess charge effect is out of question for the present and we can safely assume that the local strains due to the difference of the ionic radii of $Cl^-$ and $Br^-$ are playing the dominant role throughout. If we write $a_0$ and $a_i$ for the radii of the solvent and solute ions, the relative displacement of neighboring two ions placed at distance $r$ from the solute ion will in continuum model be given by[5]

$$\Delta a = (a_i - a_0)a^3/r^3\,, \tag{6}$$

where $a$ is the lattice constant. The change in field gradient corresponding to this compressional displacement will then be

$$\Delta(eq) = 6e(a_i - a_0)/r^3 a\,. \tag{7}$$

Substitute this into (1) and we have the frequency shift for the first order broadening:

$$h\Delta\nu = \frac{18e^2Q(a_i-a_0)}{r^3a}\,\lambda\,\frac{(2m-1)}{8I(2I-1)}(3\cos^2\theta-1) \tag{8}$$

The quantity $\lambda$ here is introduced in order to take into account the effect of all neighbors and the antishielding factor due to the distortion of the ion core around the nucleus by the fields gradient of the external charge. If $\Delta\nu$ is so widely spread out, then the satellites will become utterly unobservable. In our case, considering the signal to noise ratio, such a frequency range for which the satellites to vanish will be $\Delta\nu \sim 10\times10^3$ cps. By substituting 2 for the region of the values taken by $3\cos^2\theta - 1$ and putting $Q=0.1\times10^{24}$ cm² for Na[6], $a_0=1.80$ A, $a_i=1.95$ A, the ionic radii of $Cl^-$ and $Br^-$ respectively, and for $r$ taking the radius of the critical sphere obtained from the double logarithmic plot of (4), we get $\lambda \sim 10$ or $q \sim 10^{21}$ cm$^{-3}$ due to the olute at the third halogen site. Considering the crude nature of the estimation of $\Delta\nu$, this value for $\lambda$ offers a reasonable agreement with $1+|\gamma_\infty| = 5.5$ calculated by Das and Bersohn[7] who took the variational technique and also with the value 5.1 independently deduced by Sternheimer and Foley[8].

What is of further interest is the problem of the asymmetric broadening by the second order perturbation which is observed as we increase the solute ion concentration. In fact such a broadening is observed when the solute concentration becomes considerably high, say 10 percent, so that there is appreciable probability of finding a solute ion next to the Na nucleus. From this we have assumed that the condition for the second order broudening is provided only by the solute ions at the nearest neighbor sites. Now we shall justify this assumption. From Table I, it would not be much erraneous to put $|\Delta H| = 2.5$ gauss for the NaCl-side. Then from (3) we get $q_1 \sim 1.4 \times 10^{23}$ cm$^{-3}$ as the field gradient at the position of Na nucleus due to the solute ion placed next to it. The suffix indicates the first neighbor. Next, for the field gradient produced by a solute coming into the second negative ion neighbor site we obtain

$$q_2 = (r_1/r_2)^3 q_1 < 0.1\times10^{23}\text{cm}^{-3}\ .$$

This is less than a tenth of $q_1$ and indeed too small to give an observable frequency shift. Similarly for NaBr-side we obtain $q_1 \sim 2.0\times10^{23}$cm$^{-3}$.

Using these values of $q_1$ thus derived, we may again calculate the antishielding factor $\lambda$ both for the NaCl-side and for the NaBr-side. For the former we get $\sim 3.6$ and for the latter $\sim 4.3$ Both of them are smaller then the value obtained from the analysis of the first order effect or than the theoretical values deduced by Das-Bersohn and Sternheimer-Foley as well. This fact tells us of invalidity of using the continuum model for the case of the solute ion coming so near as next to the Na nucleus. Another assumption made at the beginning of the analysis was that not more than one solute ion come to the nearest neighbor position. It seems that such an assumption may become questionable as the solute ion concentration is increased. In fact, if the solute ions were scattered completely at random, then the probability of one, two and three of them coming next to the Na nucleus would be as follows.

Table III. The probabilities of finding one, two and three solutes next to the Na nucleus.

| $c$ | $P_1=6c(1-c)^5$ | $P_2=15c^2(1-c)^4$ | $P_3=20c^3(1-c)^3$ |
|---|---|---|---|
| 0.05 | 0.1891 | 0.0305 | 0.0021 |
| 0.10 | 0.3543 | 0.0948 | 0.0146 |
| 0.15 | 0.2452 | 0.1762 | 0.0415 |
| 0.20 | 0.4932 | 0.2458 | 0.0819 |

Exact quantitative prediction for the case of more than one solute neighbor is difficult, since the effects of ionic displacement and ion core deformation will now entangle the problem almost beyond saving. However, if we simply consider the solute like a point charge so that no such effects need be taken into account, then two solute appearing on the opposite sides of Na nucleus would give twice the field gradient as one solute neighbor, and those which appear at right angle through Na would give a field gradient the same as the case of one solute neighbor in magnitude and vertical to the plane of the three ions concerned. Thus these would make some contribution to the satellite peaks with different intensities and positions. We may as well further proceed to the case of three solute neighbors. However, out of twenty arrangements of these solute around the Na nucleus, merely eight will produce field gradient. Moreover, on account of lack of axial symmetry, the problem becomes still complicated. Remembering the very ambiguous nature of point charge substitution for actually deformed and displaced ions, we doubt the meaning of such tedious and rather foundless analysis and hence we would like to leave it undone. We are convinced that this will make no serious error, since $P_3$, the probability of finding three solute neighbors, itself is small compared with $P_1$ and $P_2$, which have similar meanings as $P_3$, as seen from Table III, and the actual intensity ratios will further be reduced on account of the existence of zero shift arrangements. Thus taking only one and two solute neighbor cases into account, we give in Fig. 6 the line shapes expected from the random distribution of the solute ions, (a) for $c=0.1$ and (b) for $c=0.2$, both with [100]//$H$ for simplicity. For comparison, the experimental curves are drawn in dotted lines, with $c=0.09$ and 0.19 for (a) and (b), respectively. The differences between them for both $c$ values are remarkable. Such differences indicate that the assumption of uniform distribution of solute ions should primarily be forsaken; in other words, the solute ions are subject to segregation in the crystal and the probability of more than one solute ion actually coming next to the Na nucleus is considered to be extremely small. This indication of segregation is connected with the preceding statement concerning the Table I, that for larger values of $c$ the actual values of $I_s/I_c$ are much smaller than the calculated ones listed in the last column of the table.

With the intention of changing the state of distribution of the solute ions, we annealed two specimens of mixed crystals having the compositions 0.19 NaBr. 0.81 NaCl and 0.79 NaBr. 0.21 NaCl at about 50 to 100°C below their melting points, though not so certain, for nearly three hours. The result, however, turned out to be negative and practically no change was detected. Probably the annealing would have been insufficient for producing the rearrangement of the negative ions.

Finally, mention should be made of the fact that the values of $\Delta H$ for the NaCl-side and for the NaBr-side differ rather greatly. As the general tendency, it is larger at the NaBr side. Since $\Delta H$ is proportional to the square of the field gradient, this means that the field gradient produced when $Cl^-$ is the solute ion is larger than that when $Br^-$ is considered to be the solute. This would be of much interest for further theoretical investigation.

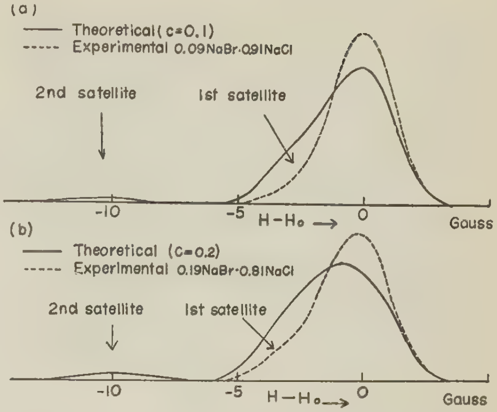

Fig. 6. Comparison of theoretical and experimental absorption lines for [100]//H.

## § 5. Conclusion

The chief results concerning the Na-line deduced from our present work are briefly summarized as follows:

1) The observed absorption intensity for the Na-line in pure NaCl is nearly 1.0, while that for pure NaBr less than 0.6. Both of them are little affected by quenching or annealing process.

2) The reduction of the satellites occurs as soon as a small amount of solute ions is added. The microscopic situation, if analized at the NaCl-side, is such that this occurs if the solute comes into the critical sphere which extends as far as the third negative ion neighbor site, where a solute will make the field gradient of order $q\sim10^{21}\text{cm}^{-3}$ at the Na nucleus concerned. The magnitude of the antishielding factor $\lambda$ for Na deduced from this analysis is $\sim$10 and agrees fairly well with Das-Bersohn and Sternheimer-Foley's calculations.

3) The asymmetric broadening of the central line due to the second order perturbation occurs when and only when the solute comes next to the Na nucleus. The specimen being a single crystal, the satellites of the second order arise at definite positions depending on the direction of the external magnetic field; thus the curve shape undergoes a remarkable angular dependence.

4) The observed magnitude of the second order shift $\Delta H$ gives $q_1\sim1.4\times10^{23}\text{cm}^{-3}$ when $Br^-$ is the solute ion and $\sim2.0\times10^{23}\text{cm}^{-3}$ when $Cl^-$ is the solute.

5) Inside a mixed crystal, the solute ions are in no ways uniformly distributed all over

the crystal, but subject to considerable segregation. Hence the probability of finding more than one solute ion in the nearest neighbor positions to the Na nucleus is very small.

In this report we have presented the results of the quadrupolar effect in the mixed crystal having different but equally-valenced negative ions. Further experiments in a similar fashion, for example, the quadrupolar effect caused by introducing divalent ions into the crystal or the investigations in a mixed crystal having different positive, not negative, ions are now being planned.

## § 6. Acknowledgements

The authors are greatly indebted to Professors J. Itoh and T. Nagamiya of the Osaka University for their continual advices and encouragements during the course of the present work. Thanks go also to Prof. T. Kanda of the Kobe University and Mr. T. Moriya of the Tokyo Metropolitan University who have benefitted us with many illuminating discussions.

## References

1) G. D. Watkins: Thesis, Harvard University 1952.
2) G. D. Watkins and R. V. Pound: Phys. Rev. **89** (1953) 658.
3) N. Bloembergen and T. J. Rowland: Acta Metallurgica **1** (1953) 731.
4) T. J. Rowland: Acta Metallurgica **3** (1955) 74.
5) N. Bloembergen: "*Defects in Crystalline Solids*", Report of the Conference held at Bristol, July, 1954.
6) M. L. Perl, I. I. Rabi and B. Senitzky: Phys. Rev. **98** (1955) 611.
7) T. P. Das and R. Bersohn: Phys. Rev. **102** (1956) 733.
8) R. M. Sternheimer and H. M. Foley: Phys. Rev. **102** (1956) 731.

---

JOURNAL OF THE PHYSICAL SOCIETY OF JAPAN Vol. 11, No. 10, OCTOBER, 1956

# Electron Diffraction Study on Thin Alloy Films of Aluminium-Silver System

By Denjiro WATANABE

*The Research Institute for Iron, Steel and Other Metals,*
*Tohoku University, Sendai*

(Received June 28, 1956)

Thin evaporated alloy films of the aluminium-silver system, mainly of hexagonal close packed phase and cubic $\beta'$-phase, were examined by electron diffraction. In the evaporated films, the h.c.p. lattice with an axial ratio of 1.63 was apt to be produced, which seemed to arise from the change of (111) stacking in the f.c.c. lattice, especially when the evaporation was carried out on to substrates at elevated temperatures, while the $\beta'$-phase was in general difficult to form by the evaporation only. The processes were also examined, through which the evaporated alloy films ultimately attained the equilibrium state after successive heat-treatments.

## § 1. Introduction

Electron diffraction studies on thin alloy films give us important and interesting informations in view of crystallography as well as metallography. For example, there are some experimental works[1-5] about the problem of ordering in copper-gold and copper-palladium alloy systems, carried out by such a method with considerable success. In order to contribute to studies on phase-diagrams, Takahashi *et al.*[6] have systematically examined many kinds of alloy films of the copper-aluminium system containing various intermetallic compounds with complex structures. About the aluminium-silver system, Boettcher[7] has carried out the electron diffraction work and the measurement of electrical resistance of vacuum evaporated alloy films to make clear the structure of films and its change due to the thermal treatments, discussing the diffusion process in such films. Recently, Göttsche[8] has also studied the above system by electron diffraction. He prepared alloy films containing 30 wt. per cent silver on heated rocksalt by vacuum evaporation and, in addition to a spot pattern due to the cubic phase, obtained two kinds of satellite spots around cubic spots, one kind of which is due to the hexagonal close packed $\gamma$-phase and the other due to lattice defects arising from the growth of $\gamma$-phase.

As the electron diffraction work on this alloy system seemed to be interesting and worth while investigating further, the present work has been undertaken. Alloys with various compositions, extending over the whole of the aluminium-silver system, were studied here. In Fig. 1, $\delta$- and $\alpha$-phases have the structure of face-centred cubic type, $\gamma$-phase ($Ag_2Al$) the structure of hexagonal close packed type, $\beta'$-phase ($Ag_3Al$) the structure of $\beta$-Mn type and $\beta$-phase the structure of body-centred cubic type. Among these phases, the hexagonal close packed $\gamma$-phase and the cubic $\beta'$-phase were chiefly examined by electron diffraction.

## § 2. Experimental Method

An electron diffraction camera of a hot cathode type and of a camera length 309 mm was used and a high voltage of about 50 KV was applied. Aluminium and silver were simultaneously evaporated *in vacuo* from fine wire (0.1~0.2 mm. in dia.) suspended in a tungsten filament onto cleavage surfaces of rocksalt maintained at various temperatures (from room temperature to 460°C) or sometimes onto collodion films supported on pin holes in nickel supporter maintained at room temperature. Quantities of evaporated metals were so controlled that alloy films formed had desired compositions. Because of alloying of aluminium with tungsten, the real compositions of the films may somewhat have shifted from those planned to silver-side, but they were difficult to determine accurately. The compositions described in the following sections are those planned. All films were heated at desired temperatures for desired periods in a copper tube and quenched by pouring water onto this tube[4].

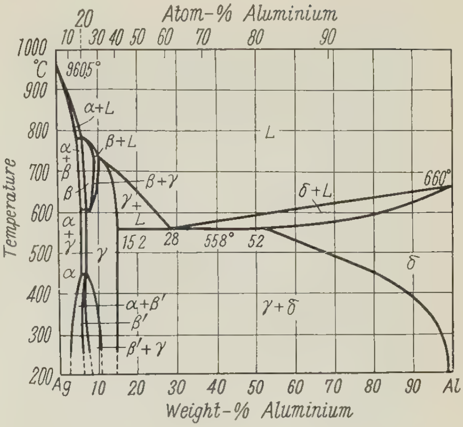

Fig. 1. Phase diagram of aluminium-silver system.

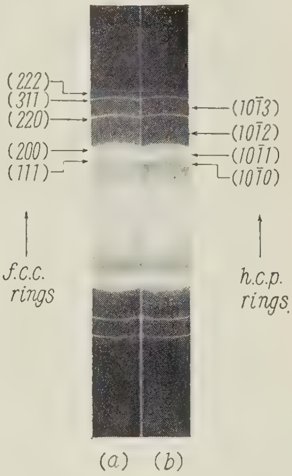

Fig. 2. Diffraction patterns of 60% Al–Ag film formed at room temperature,
(a) before thermal treatments (only f.c.c. rings),
(b) after heating at 100°C, 1 hr. (h.c.p. rings appeared).

## § 3. Experimental Results

From a standpoint of composition, the examined alloy films are classified into the following three groups: i) Alloy films containing aluminium more than 50 wt. per cent, ii) alloy films containing aluminium of about 20~40 wt. per cent, and iii) alloy films containing aluminium less than 15 wt. per cent. In the following sections all the concentration will be represented in weight per cent.

### i) *Results for the alloy films containing aluminium more than 50 per cent.*

Alloy films formed at room temperature

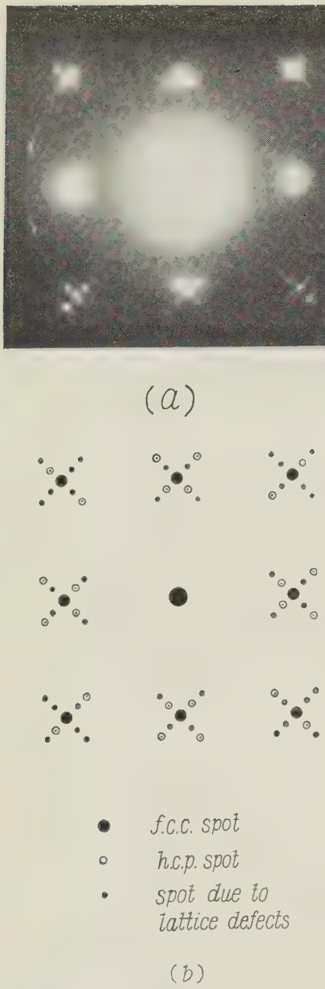

Fig. 3. (a) Diffraction pattern of 60% Al–Ag film formed at 450°C.
(b) Illustration of (a). Diffraction spots due to h.c.p. lattice and to lattice defects appeared owing to the rotation of crystallites (~15°) in the film.

showed comparatively sharp f.c.c. Debye rings ($a$=4.05±0.01 Å) in their diffraction patterns, where the background intensity was very strong (Fig. 2a). As the heating proceeded step by step from 100°C to 400°C *in vacuo*, h.c.p. rings began to appear faintly in addition to f.c.c. rings becoming very sharp and increased in intensity and sharpness with increasing temperature and heating duration, occasionally consisting of sharp fine spots, and at the same time the background intensity decreased (Fig. 2b). The lattice constants obtained from the h.c.p. rings slightly varied with thermal treatments; for example, an axial ratio $c/a$ of about 1.62 was obtained from very weak and diffuse h.c.p. rings appearing above about 100°C in a film containing about 60 per cent aluminium. With further annealings at 150~200°C for several hours these rings became sharp and strong and the lattice parameters progressively approached to the values, $a$=2.88 Å, $c$=4.59 Å, $c/a$=1.59, which agreed with X-ray results for $\gamma$-phase obtained by Westgren and Bradley (Table I).[9]

Alloy films formed at about 460°C containing 85~60 per cent aluminium gave patterns as shown in Fig. 3a. In these patterns, the f.c.c. diffraction spots are observed, accompanied with satellites bearing some resemblance to those due to twinned lattices in evaporated films of f.c.c. metals, such as silver, gold, copper, nickel and palladium. Fig. 3b is a schematic figure of Fig. 3a. Recently, Göttsche[8] has also obtained quite similar patterns using alloy films containing 30 per cent silver. According to him, some of these satellites were explained to be due to the h.c.p. lattice formed during the condensation of films, which arises only from the change of the stacking order of (111) plane in the f.c.c. lattice without any other change of the lattice. The other satellites are due to two kinds of lattice defect produced as a result of the formation of the hexagonal lattice. From these circumstances, it is understood that the orientation relationship between f.c.c.- and h.c.p.-lattice is such as: $\{111\}_{\text{f.c.c}}//(0001)_{\text{h.c.p.}}$, $\langle 110\rangle_{\text{f.c.c.}}//\langle 11\bar{2}0\rangle_{\text{h.c.p.}}$. The axial ratio $c/a$ for this hexagonal lattice should naturally be 1.63 and was so in Göttsche's case, while it was estimated to be 1.59 in the present case, $a$ and $c$ being 2.87 Å and 4.57 Å. This discrepancy will be discussed later.

Films formed at 350°C also showed patterns due to the f.c.c. $\delta$-lattice and to the h.c.p. lattice. In these films, a greater part of the h.c.p. crystals has such an orientation as $(0001)_{\text{h.c.p.}}//(001)_{\text{NaCl}}$, $\langle 11\bar{2}0\rangle_{\text{h.c.p.}}//\langle 110\rangle_{\text{NaCl}}$, and the remaining smaller part has such an orientation as $(0001)_{\text{h.c.p.}}//(111)_{\text{NaCl}}$ and $\langle 11\bar{2}0\rangle_{\text{h.c.p.}}//\langle 110\rangle_{\text{NaCl}}$, just as obtained at 460°C. The lattice parameters of $\delta$-lattice and of h.c.p. lattice were measured to be $a_\delta$=4.04 Å, $a_{\text{h.c.p.}}$=2.87 Å. $c_{\text{h.c.p.}}$=4.66 Å and $(c/a)_{\text{h.c.p.}}$=1.62, respectively.

Even when the specimens were heated at about 470~500°C (within the $\delta$-phase region) and quenched, the pattern due to the h.c.p.-phase ($c/a=1.61\pm0.01$) strongly remained, though intensities of the spots due to lattice defects decreased. This fact will be discussed later.

### ii) *Results for the alloy films containing about 20~40 per cent aluminium.*

Films containing about 40 per cent aluminium, condensed at room temperature, indicated almost similar behavior to those containing aluminium more than 50 per cent, condensed at room temperature, as described in the previous section, but films containing about 20 per cent aluminium already gave the h.c.p. rings having the lattice constants, $a=2.88$ Å, $c=4.59$ Å, $c/a=1.59$, in addition to the f.c.c. rings ($a=4.05\pm0.01$ Å) immediately after condensation, and the aspects of the patterns scarcely changed with further heat-treatments.

Films formed above 400°C showed very clear patterns due to the h.c.p. lattice and weak f.c.c. patterns, as shown in Fig. 4. The crystal orientation of h.c.p. lattice is the same as in films condensed at 350°C described in the previous section, i.e., $(0001)_{\text{h.c.p.}}//(001)_{\text{NaCl}}$ and $\langle 11\bar{2}0\rangle_{\text{h.c.p.}}//\langle 110\rangle_{\text{NaCl}}$, and such orientation faintly appeared also in films condensed at room temperature in the present composition range. The axial ratio is 1.59 in the present case, corresponding to the value of $\gamma$-phase saturated with aluminium, while it was 1.62 in films containing aluminium more than 50 per cent, condensed at 350°C.

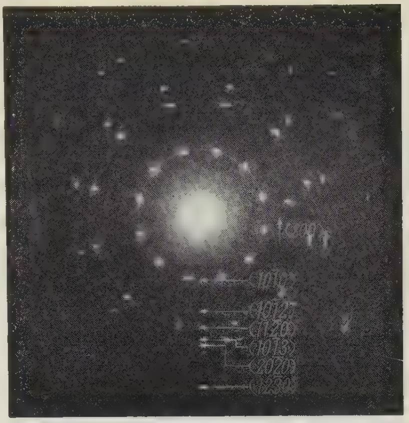

Fig. 4. Diffraction pattern of 20% Al–Ag film evaporated at 450°C. This pattern almost corresponds to h.c.p. $\gamma$-phase.

### iii) *Results for the alloy films containing aluminium less than 15 per cent.*

Films formed on the rocksalt substrate at room temperature containing about 10 per cent aluminium showed diffraction rings due to the f.c.c. lattice ($a=4.08$ Å, $\alpha$-phase). After being heated at 200°C for 7 hours, sharp rings corresponding to the $\beta'$-phase ($a=6.92$ Å) appeared in addition to rings of the $\alpha$-lattice, and hence it was found that the structure of this film tended to its equilibrium state by heat-treatment. When this film was again heated at 400~500°C, the rings due to the $\beta'$-lattice disappeared and only those due to the $\alpha$-lattice remained. This fact coincides with the phase diagram, provided that the composition shifted from the planned value to silver-side.

From the film formed on the rocksalt substrate at 200°C containing about 13 per cent aluminium, sharp rings due to the h.c.p. phase were obtained, accompanied with weak ones due to the f.c.c. $\delta$-phase ($a=4.04$ Å), as shown in Fig. 5a. In this case, the lattice parameters of $\gamma$-phase were measured to be $a=2.87$ Å, $c=4.57$ Å and $c/a=1.59$ respectively, and these almost coincide to those of aluminium-side of $\gamma$-phase. After being heated at 200~300°C for several hours, however, the lattice parameters changed to the values, $a=2.86$ Å, $c=4.62$ Å, $c/a=1.61$, indicating that the composition of $\gamma$-phase shifted from aluminium-side to more silver-side, and a sharp pattern due to $\beta'$-phase appeared (Fig. 5b) and the f.c.c. pattern vanished. At 400°C, a major part of the diffraction rings belonged to $\beta'$-lattice and only a few rings to h.c.p. lattice (Fig. 5c). The measured lattice constant of $\beta'$-lattice is 6.92 Å and well coincides to the X-ray result.[9] After being heated above 500°C, the component of this film changed to the h.c.p. lattice ($c/a=1.63$). The $\beta$-lattice again appeared by the successive annealings at about 200~250°C for several hours.

Films formed on the rocksalt substrate at 300°C containing about 10 per cent aluminium showed an oriented structure containing $\gamma$-lattice and $\beta'$-lattice (Fig. 6). The orientation relationship is such as $(0001)_{\gamma}//(111)_{\beta'}$. After being heated at 250°C (below the condensation temperature) for about 3 hours, a greater part of the pattern arose from the $\beta'$-phase and a smaller part from the $\alpha$-phase, as if the composition shifted with heating.

These behaviors of silver-rich films in the

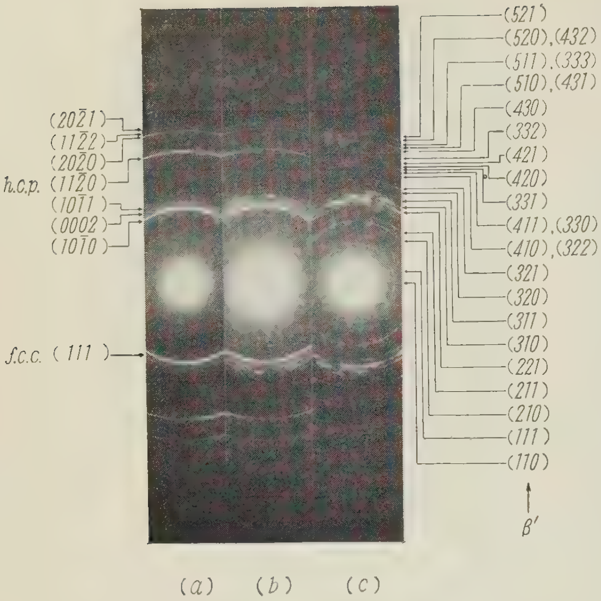

Fig. 5. Diffraction patterns of 13% Al–Ag film evaporated at 200°C.
(a) immediately after evaporation (before further heat-treatments). Strong h.c.p.-rings and weak f.c.c. rings ($a=4.04$ Å)
(b) annealed at 300°C, 3.5 hr. Continuous rings are due to γ-phase and spotty rings to β′-phase.
(c) annealed at 400°C, 2 hr. This pattern is almost due to β′-phase.

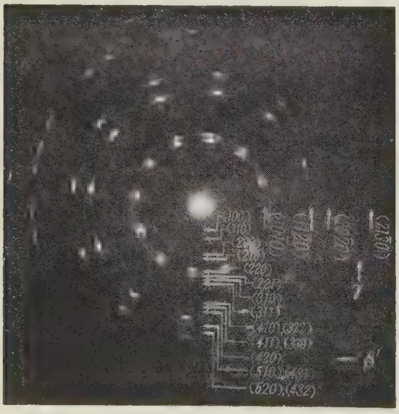

Fig. 6. Diffraction pattern of 10% Al–Ag film formed at 300°C. This pattern corresponds to h.c.p. γ-lattice and cubic β′-lattice.

course of successive heating will later be discussed.

## § 4. Discussions

In the present study, the axial ratio $c/a$ for the h.c.p. lattice changes between 1.63 and 1.59 with the film composition and the thermal treatment. According to the Westgren-Bradley's X-ray examination,[9] it has been known that the lattice parameters for the h.c.p. γ-phase in the equilibrium phase diagram vary with aluminium content as shown in Table I. The discrepancy between $c/a$ of 85 ∼60 per cent aluminium formed at about 460°C, 1.59, and that in the Göttsche's case, 1.63, seems to arise from the following reason; in the course of slow cooling of films from the condensation temperature to room temperature in the present case, the h.c.p. lattice formed at the time of condensation becomes nearly saturated with aluminium and the axial ratio results in 1.59, while films were quenched so quickly from 450°C immediately after the evaporation in Göttsche's experiment that the h.c.p. stacking built up in such a way as he suggested, having an axial ratio 1.63 corresponding to an ideal closest packing, still persisted (non-equilibrium state). If the evaporation is carried out at lower temperatures, e.g., at about 350°C, an axial ratio becomes about 1.63, even in the present experiment, because the slow-cooling effect after the condensation is insufficient in this case to make a stable γ-phase. From these facts, including the Göttsche's results, it can be considered that, in the films containing aluminium more than 50 per cent and not subject to heat-treatments after condensation, the h.c.p. lattice, having an axial ratio of 1.63, is consisted of ABABAB.... stacking simply translated from ABCABC.... stacking of the f.c.c. lattice by a simple shear. Such a lattice is not in equilibrium, but approaches to the equilibrium state on the phase diagram through the successive thermal treatments, i.e., γ-phase saturated with aluminium and having an axial ratio of 1.59 is formed by diffusion of atoms. Thus the h.c.p. lattice formed by simple shearing of (111) stacking should be distinguished from the h.c.p. γ-phase formed as a result of thermodynamical equilibrium and may have

Table I. Variation of lattice parameters for h.c.p. γ-phase with aluminium content.[9]

| Weight per cent of Al. | $a$(Å) | $c$(Å) | $c/a$ |
|---|---|---|---|
| 8.5 | 2.865 | 4.653 | 1.625 |
| 10.5 | 2.869 | 4.625 | 1.612 |
| 13.8 | 2.877 | 4.579 | 1.592 |
| 15.9 | 2.879 | 4.573 | 1.588 |

some connection with the intermediate state produced in the course of precipitation from supersaturated $\delta$-solid solution. It seems that the change in $c/a$ of the h.c.p. lattice in films formed at room temperature as described in § 3, (i), i.e., the change from 1.62 to 1.59, corresponds to the transition from the h.c.p. lattice due to simple shearing to the $\gamma$-lattice on the phase diagram, considering that there is an error of ±1% in the measured value of $c/a$.

In the present experiment it is noteworthy that the pattern due to the h.c.p. lattice ($c/a=1.61\pm0.01$) was already present immediately after the samples containing 85～70 per cent aluminium were quenched from temperatures of $\delta$-solid solution (470～500°C) and hence the supersaturated solid solution could not be produced in these alloy films by means of the present quenching method. Moreover, Winkelmann[10] has recently reported that, in the electron diffraction pattern of the thin evaporated aluminium-silver alloy film (38 per cent silver), hexagonal reflections clearly appeared immediately after the films was quenched from 530°C to $-10$°C. Therefore it seems to the present author that the h.c.p. lattice precipitates far faster in thin films than in bulk alloys or the quenching methods adopted by Winkelmann and by the present author are both not suitable for thin films.

In the composition range less than 15 per cent aluminium, it appears that the apparent composition of films immediately after being condensed at elevated temperatures seemed richer in aluminium than the equilibrium composition achieved by further heat-treatments. In this connection, it is reasonable to think that silver atoms are in general so quickly evaporated at the beginning of condensation that a greater part of film successively evaporated is composed of aluminium-rich crystals as already stated by Boettcher,[7] and that when the condensation is carried out at elevated temperatures such aluminium-rich parts approach to their equilibrium and $\delta$-, $\gamma$-, or $\beta'$-phases appear, as described in the previous section, in the course of cooling from condensation temperatures. The underlying silver-rich parts which are small in quantity compared with aluminium-rich parts do not give observable diffraction rings, probably because of the absorption effect.[11]

Here, the following remarks should be made. The fact that films formed at room temperature containing aluminium more than 50 per cent gave only f.c.c. $\delta$-rings accompanied with no other rings, as described in § 3, (i), is considered not to show that the film structure is in the quenched state (supersaturated solid solution), but to mean that the silver-rich parts which must be present do not give observable diffraction rings because of the absorption effect, as in the above-mentioned case.

Now, we return to the topic on the films containing aluminium less than 15 per cent. With further heat-treatments after detachment of films from substrates, the silver-rich parts react with the aluminium-rich parts through diffusion, and hence the aspect of diffraction pattern changes to some extent from aluminium-rich to silver-rich after sufficient annealings for homogenization. If the homogenization once occurs in this way, the film subjected to further various thermal treatments gives the patterns expected from the existing phase diagram, as already described in the previous section. We must pay attention also to the fact that the real composition of the film slightly shifted from those planned to silver-side due to alloying of aluminium with tungsten. In general, moreover, it seems that the $\beta'$ -lattice is difficult to be formed on the rocksalt substrate by the evaporation method alone also in the case of room temperature condensation and that the h.c.p.-lattice is easily formed especially in the case of elevated temperature condensation and the film structure approaches to an equilibrium state, increasing the quantity of $\beta'$-phase with successive heat-treatments. The films containing about 10 per cent aluminium condensed on collodion substrate, on the other hand, were nearly in the equilibrium state, indicating the very clear rings of $\beta'$-lattice, even when the evaporation was carried out at room temperature. This fact should be interpreted as follows; owing to the temperature rise of the collodion substrate of small heat capacity due to the radiation of filament, the initially inhomogeneous films immediately approached to nearly stable state, without further heat-treatments, while the temperature of rocksalt substrate did not rise appreciably due to large heat capacity.

On the whole, it can be concluded that the obtained results do not conflict with predictions from the existing phase diagram, if attention is paid to peculiar properties of films, e.g., such as those concerning their inhomogeneity after condensation, the hexagonal phase formation, etc.

In conclusion, the author wishes to express his sincere thanks to Prof. S. Ogawa for his kind guidance and ardent discussions. This work has been supported partly by the fund of the Ministry of Education in Aid of Scientific Researches.

### References

1) L. H. Germer, F. E. Haworth and J. J. Lander: Phys. Rev. **61** (1942) 614.
2) H. Raether: Z. angew. Phys. **4** (1952) 53.
3) S. Ogawa and D. Watanabe: J. Phys. Soc. Japan **7** (1952) 36.
4) S. Ogawa and D. Watanabe: J. Phys. Soc. Japan **9** (1954) 475.
5) D. Watanabe, M. Hirabayashi and S. Ogawa: Acta Cryst. **8** (1955) 510.
D. Watanabe and S. Ogawa: J. Phys. Soc. Japan **11** (1956) 226.
6) N. Takahashi, J. J. Trillat et A. Saulnier: Métaux **23** (1953) 185.
7) A. Boettcher: Z. angew. Phys. **2** (1950) 193.
8) H. Göttsche: Z. Phys. **134** (1953) 504.
9) A. F. Westgren and A. J. Bradley: Phil. Mag. **6** (1928) 280.
10) A. Winkelmann: Z. angew. Phys. **7** (1955) 7.
11) S. Yamaguchi: Z. Naturforsch. **11a** (1956) 255.

---

JOURNAL OF THE PHYSICAL SOCIETY OF JAPAN Vol. 11, No. 10, OCTOBER, 1956

# A Note on the Ferromagnetic Resonance in $\alpha$ Fe$_2$O$_3$

By Masao SHIMIZU

*Department of Physics, Faculty of Science*
*Tokyo Metropolitan University*

(Received May 22, 1956)

Microwave resonance formulas of a ferromagnet with a small hexagonal anisotropy in a basal plane besides with a uniaxial anisotropy are phenomenologically derived. The comparison with the resonance experiments on $\alpha$ Fe$_2$O$_3$ single crystals is made and they are satisfactorily explained. A few contradictions with the static measurements are pointed out.

## §1. Introduction

It is well known that $\alpha$ Fe$_2$O$_3$ shows a weak ferromagnetism[1-5] and recently ferromagnetic resonance experiments on $\alpha$ Fe$_2$O$_3$ single crystals have been performed at three laboratories[6-8]. Above the Morin transition temperature[9], which varies from 15°C to 50°C according to the samples and at which a sort of magnetic structure transition takes place, the common results are as follows. A strong resonance line having a width of about 500 oersted is observed with magnetic field perpendicular to the rhombohedral axis. This resonance field does not vary appreciably with temperature and the resonance line disappears completely below the Morin temperature. With larger deviations of the magnetic field from the basal plane the values of the resonance field become larger. This shows that the easy direction lies in the basal plane above the Morin temperature and is compatible with the static measurements[1-5] and the neutron diffraction experiments[10]. Neglecting a small anisotropy in the plane and the demagnetizing effect one obtains about 30000 oersted for the uniaxial anisotropy field $H_A$ from the usual resonance formula in the basal plane, $H_0{}^2=\omega^2/\gamma^2=H(H+H_A)$, where $H_0$ is the normal resonance field, $\omega/2\pi$ the microwave frequency, $\gamma=ge/mc$ the magneto-mechanical ratio and $H$ the resonance field in the plane.

As regards the small anisotropy in the basal plane, different observations have been reported. Anderson et al[6] obtained the resonance field, $H=(2270+60\sin 6\varphi)$ gauss, in the plane at 1.25 cm wavelength. Here $\varphi$ is the azimuthal angle of the magnetic field in the plane. Kumagai et al[7) did not clearly find the regular symmetry in the plane. Kojima[8) found a period of 180 degrees. These discrepancies may be attributable to the differences of the samples and the imperfections in the crystals. Kumagai et al[7) and Kojima[8) obtained the resonance fields at several wavelengths and from their results a natural resonance frequency of $\alpha$ $Fe_2O_3$ is found to be about 10000 Mc/sec in the plane. In order to calculate the natural resonance frequency in the case of the easy direction being in the basal plane, it is necessary to keep the small anisotropy energy in the plane in addition to the large uniaxial anisotropy. In the present paper the writer will derive the ferromagnetic resonance formula of $\alpha$ $Fe_2O_3$ assuming it to be a simple ferromagnet and keeping the hexagonal anisotropy energy in the plane so as to fit the experimental facts obtained by Anderson et al.

At shorter wavelengths, that is, higher resonance fields the experimental values of the resonance field in the basal plane are well explained within the experimental errors assuming proper values of the anisotropy energies. At lower fields (~1000 oe.) the calculated values of the resonance field are larger than the experimental ones. This discrepancy may be due to the fact the magnetization does not saturate at such lower magnetic fields. The resonance in the plane containing the rhombohedral axis is as well explained as already Anderson et al did. Finally the values of the anisotropy energies determined from the resonance data will be compared with the results of the static experiments. There are some inconsistencies between them and these cannot fully be settled here. Simultaneous resonance experiments and static measurements on the same $\alpha$ $Fe_2O_3$ single crystals are desirable.

The same discussions given in this note will be applicable to the pyrrhotite single crystal and other ferromagnetic crystals which have easy directions in the basal plane, but unfortunately resonance experiments on these crystals are scarce. It may necessitate higher magnetic field or shorter wavelength than the usual one because of their larger anisotropies[11).

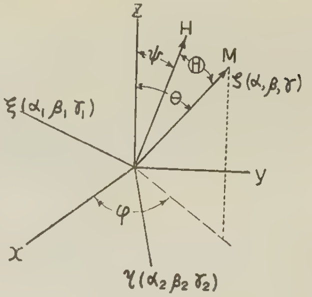

Fig. 1.

## § 2. Resonance Formulas

We take the rhombohedral axis as $z$-axis. Let the direction cosines of magnetic field $H$ and magnetization $M$ be $(\lambda, \mu, \nu)$ and $(\alpha, \beta, \gamma)$ respectively and their polar angles be $\psi$ and $\theta$ respectively, as shown in Fig. 1. The azimuthal angle on the $xy$ plane of the magnetization $M$ is $\varphi$. We assume the following anisotropy energy in $\alpha$ $Fe_2O_3$,

$$E_A=\frac{1}{2}H_AM[\gamma^2+K\gamma^4+K'(\alpha^6-15\alpha^4\beta^2+15\alpha^2\beta^4-\beta^6)], \quad H_A>0,\ K'>0. \qquad (1)$$

The third term in the square bracket is the same as $\sin^6\theta\times\cos 6\varphi$ and gives the hexagonal anisotropy in the basal plane. From this anisotropy one can obtain the $x, y, z$ components of the effective field,

$$\begin{aligned} H_x^e&=\lambda H-3H_AK'(\alpha^5-10\alpha^3\beta^2+5\alpha\beta^4), \\ H_y^e&=\mu H+3H_AK'(\beta^5-10\beta^3\alpha^2+5\beta\alpha^4), \\ H_z^e&=\nu H-H_A\gamma(1+2K\gamma^2). \end{aligned} \qquad (2)$$

Here we neglect the demagnetizing fields as the magnetization of $\alpha$ $Fe_2O_3$ is of the order of a few emu/cc. The equilibrium direction of the magnetization $M$ under the magnetic field applied along the direction $(\lambda, \mu, \nu)$ is obtained from the equations,

$$H_x^e/\alpha=H_y^e/\beta=H_z^e/\gamma. \qquad (3)$$

It is convenient to use new axes $\xi, \eta, \zeta$ instead of the $x, y, z$ axes, where the $\zeta$ axis is the direction of the magnetion $M$ in equilibrium and the $\xi$ and $\eta$ axes are orthogonal to each other and to the $\zeta$ axis. Let the direction cosines of $\xi$ and $\eta$ axes relative to the $x, y, z$ axes be $(\alpha_1, \beta_1, \gamma_1)$ and $(\alpha_2, \beta_2, \gamma_2)$ respectively. The components of the effective field with respect to the new axes are

$$H_\xi^e=\alpha_1H_x^e+\beta_1H_y^e+\gamma_1H_z^e,$$

$$H_\eta^e=\alpha_2H_x^e+\beta_2H_y^e+\gamma_2H_z^e\,,$$
$$H_\zeta^e=\alpha H_x^e+\beta H_y^e+\gamma H_z^e\,, \tag{4}$$

and the same can be said of the components of the magnetization. In static equilibrium, the components of the magnetization have values,

$$\overline{M}_\xi=\overline{M}_\eta=0\,,\quad \overline{M}_\zeta=M\,, \tag{5}$$

and the components of the effective field are

$$\overline{H}_\xi^e=\overline{H}_\eta^e=0\,,$$
$$\overline{H}_\zeta^e=H(\alpha\lambda+\beta\mu+\gamma\nu)-H_A\gamma^2(1+2K\gamma^2)$$
$$-3H_AK'(\alpha^6-15\alpha^4\beta^2+15\alpha^2\beta^4-\beta^6). \tag{6}$$

If there are small fluctuations of $M_\xi$ and $M_\eta$, that is, $\delta M_\xi$ and $\delta M_\eta$, the effective fields $\delta H_\xi^e$ and $\delta H_\eta^e$ appear in the directions of $\xi$ and $\eta$. From Eqs. (2), (4), (5), (6) these fields can be written as

$$\delta H_\xi^e=A_{11}\delta M_\xi+A_{12}\delta M_\eta\,,$$
$$\delta H_\eta^e=A_{21}\delta M_\xi+A_{22}\delta M_\eta\,, \tag{7}$$

where

$$A_{11}M=-15H_AK'\{(\alpha_1^2-\beta_1^2)(\alpha^4-6\alpha^2\beta^2+\beta^4)+8\alpha_1\beta_1(\alpha\beta^3-\alpha^3\beta)\}-H_A\gamma_1^2(1+6K\gamma^2)\,,$$
$$A_{22}M=-15H_AK'\{(\alpha_2^2-\beta_2^2)(\alpha^4-6\alpha^2\beta^2+\beta^4)+8\alpha_2\beta_2(\alpha\beta^3-\alpha^3\beta)\}-H_A\gamma_2^2(1+6K\gamma^2)\,,$$
$$A_{12}M=A_{21}M=-15H_AK'\{(\alpha_1\alpha_2-\beta_1\beta_2)(\alpha^4-6\alpha^2\beta^2+\beta^4)$$
$$+4(\alpha_1\beta_2+\alpha_2\beta_1)(\alpha\beta^3-\alpha^3\beta)\}-H_A\gamma_1\gamma_2(1+K\gamma^2)\,. \tag{8}$$

Thus the resonance condition with the anisotropy energy of Eq. (1) and an applied field in an arbitrary direction $(\lambda, \mu, \nu)$ is given by

$$H_0^2=\omega^2/\gamma^2=M^2(A_{11}A_{22}-A_{12}^2)-\overline{H}_\zeta^eM(A_{11}+A_{22})+\overline{H}_\zeta^{e2}\,. \tag{9}$$

The resonance formula (9) is rewritten by Eqs. (6) and (8) in terms of $\theta$, $\varphi$ and $\Theta$, $\Theta$ being an the angle between the magnetic field $H$ and the magnetization $M$, as follows,

$$H_0^2=\omega^2/\gamma^2=H^2\cos^2\Theta+HH_A\cos\Theta(1-3\cos^2\theta+6K\cos^2\theta$$
$$-10K\cos^4\theta-21K'\sin^6\theta\cos 6\varphi)$$
$$+H_A^2\cos^2\theta\{(2\cos^2\theta-1)+4K\cos^2\theta(3\cos^2\theta-2)+4K^2\cos^4\theta(4\cos^2\theta-3)\}$$
$$+6H_A^2K'\sin^6\theta\cos 6\varphi\{(4\cos^2\theta-3)+2K\cos^2\theta(5\cos^2\theta-9)\}$$
$$+9H_A^2K'^2\sin^8\theta(6\sin^4\theta\cos^2 6\varphi-25\cos^2\theta)\,. \tag{10}$$

Since $K'$ is assumed to be small, the resonance field $H$ is expanded in powers of $K'$, and we have

$$H\cos\Theta=\frac{1}{2}\sqrt{4H_0^2+H_A^2\sin^4\theta(1+6K\cos^2\theta)^2}$$
$$-\frac{1}{2}H_A(1-\cos^2\theta+6K\cos^2\theta-10K\cos^4\theta)$$
$$+\frac{1}{2}H_AK'\sin^6\theta\cos 6\varphi\left\{21+\frac{15H_A(1+\cos^2\theta)(1+6K\cos^2\theta)}{\sqrt{4H_0^2+H_A^2\sin^4\theta(1+6K\cos^2\theta)}}\right\}+O(K'^2)\,. \tag{11}$$

In the basal plane the above resonance formula takes a simpler form, because $\psi=\theta=\pi/2$ and, since the hexagonal anisotropy field in the plane, $3H_AK'$, is supposed to be much smaller than the magnetic field $H$, the magnetization is nearly parallel to the magnetic field in the plane, i.e. $\Theta=0$. Then we have from Eq. (10),

$$\omega^2/\gamma^2=H^2+HH_A(1-21K'\cos 6\varphi)-18H_A^2K'\cos 6\varphi+54H_A^2K'^2\cos^2 6\varphi\,, \tag{12}$$

and from Eq. (11)

$$H=\frac{1}{2}\{\sqrt{4H_0^2+H_A^2}-H_A\}+\frac{3}{2}H_AK'\cos 6\varphi(7+5H_A/\sqrt{4H_0^2+H_A^2})$$
$$+225H_0^2H_A^2K'^2(H_A^2+4H_0^2)^{-3/2}\cos^2 6\varphi+O(K'^3)\,. \tag{13}$$

A natural resonance frequency is obtained from Eq. (12) taking $\cos 6\varphi=-1$.

$$(\omega^2/\gamma^2)_{\text{natural}}=18H_A{}^2K'(1+3K')\,. \tag{14}$$

In the case of $\psi<\pi/2$, the magnetization deviates from the direction of the resonance field, as the uniaxial anisotropy field is supposed to be stronger than the ordinary resonance field, and we must take into account the equilibrium condition (3). If the component of the magnetic field on the basal plane is larger than the hexagonal anisotropy field in the plane we can take $\Theta=\theta-\psi$ and Eq. (3) becomes

$$H\cos\psi=H\sin\psi\cot\theta+H_A\cos\theta(1+2K\cos^2\theta)\,. \tag{15}$$

With this equation the resonance field is given by

$$\begin{aligned}H\sin\psi=&\frac{1}{2}\sin\theta\sqrt{4H_0{}^2+H_A{}^2\sin^4\theta(1+6K\cos^2\theta)^2}\\&-\frac{1}{2}H_A\sin^3\theta(1+6K\cos^2\theta)\\&+\frac{3}{2}H_AK'\sin^7\theta\cos6\varphi\{7+5H_A(1+\cos^2\theta)(1+6K\cos^2\theta)\\&\quad\times(4H_0{}^2+H_A{}^2\sin^4\theta(1+6K\cos^2\theta)^2)^{-1/2}\}+O(K'^2)\,.\end{aligned} \tag{16}$$

Table I. Resonance fields in the basal plane of $\alpha$ $Fe_2O_3$, $g=2$, $H_A=2.22\times10^4$ Oe., $K'=1.9\times10^{-4}$.

| Wavenumber cm$^{-1}$ | $H$ Oe. | $H_{\text{cal.}}$ Oe. | $\sqrt{H_0{}^2+H_A{}^2/4}-\frac{1}{2}H_A$, Oe. | $\frac{3}{2}H_AK'\left\{7+\frac{5H_A}{\sqrt{4H_0{}^2+H_A{}^2}}\right\}$ Oe. |
|---|---|---|---|---|
| 1.84 | 11380±100 | 11450 | 11510 | 60 |
| 1.55 | 8800±100 | 8800 | 8862 | 62 |
| 1.21 | 5980±100 | 5912 | 5977 | 65 |
| 0.90 | 3400± 50 | 3532 | 3600 | 68 |
| 0.65 | 1300± 70 | 1925 | 1996 | 71 |
| 0.31 | 0 | 411 | 486 | 75 |
| 0.16 | — | 51 | 130 | 79 |
| 0.12 | — | 0 | — | — |

It $\theta$ is eliminated from the above Eqs., the resononce field $H$ can be written as a function of $\psi$. Similar formulas to Eqs. (15) and (16) neglecting the hexagonal anisotropy have already been given by Anderson et al.[6)]

## § 3. Comparison with Experiments

As the experimental values of the resonance fields in the plane for $\alpha$ $Fe_2O_3$, which have been reported by Kumagai et al[7)] and are listed in the second column of Table I, are the minimum values in the plane, we take $\cos6\varphi=-1$ in the Eq. (13); the calculated values from Eq. (13) are given in Table I and Fig. 2, where we choose $g=2$ and $H_A=2.22\times10^4$ oersted in order to get the best agreement with the experimental values and $K'1.9\times10^{-4}$ in order that the hexagonal part of the resonance field becomes of the order of magnitude of the experiments (~60 oe). It

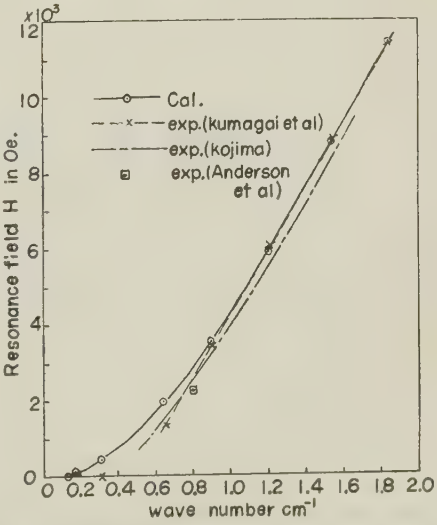

Fig. 2. The resonance fields in the basal plane as a function of wave number.

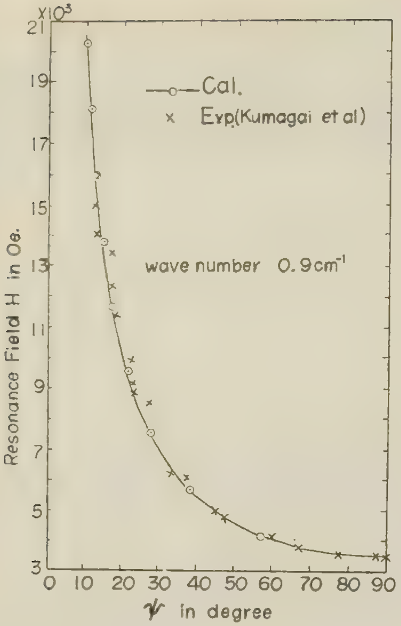

Fig. 3. The resonance fields at a wave number $0.9\,\mathrm{cm}^{-1}$ in the plane containing the rhombohedral axis as a function of the angle $\psi$ between the rhombohedral axis and the magnetic field.

should be noted that the magnitude of the hexagonal part of the resonance field depends slightly on the wavelength. The value of the natural resonance frequency thus obtained is 3640 Mc/sec. This is fairly low althongh we can get a much higher frequency if the value of $K'$ is assumed to be much larger.

In a range of shorter wavelengths the agreement is satisfactory within experimental errors. Discrepancies in a longer wavelength range might be due to that the magnetization is not saturated. In hysteresis measurements[1,5] on $\alpha$ $Fe_2O_3$ single crystals the magnetization in the plane is not saturated up to the range of 1000 to 2000 oersteds, in spite of the small anisotropy field ($3H_AK'\approx 13$ oersted) in the plane, and the coercive force is about 500 oersted. Wohlfarth[12] have estimated the anisotropy field in the plane to be roughly 1000 oersted from the hysteretic properties of powdered sample of $\alpha$ $Fe_2O_3$ assuming a trigonal anisotropy in the basal plane. This value seems to be too large toexplain a small variation of the resonance field in the plane and the natural resonance frequency. The large values of the magnetic field which are necessary to saturate the magnetization of $\alpha$ $Fe_2O_3$ may be due to imperfections in the crystal. A definite conclusion of this point and on the symmetry character in the plane cannot be got until further experiments on microwave resonance and static measurements on the same sample of $\alpha$ $Fe_2O_3$ single crystal are made.

Table II. Resonance fields in the vertical plane containing the rhombohedral axis at wave number $0.9\,\mathrm{cm}^{-1}$, $g=2$, $H_A=2.22\times10^4$ Oe., $K=1/24$, $K'=1.9\times10^{-4}$.

| $\psi$ | $H_{\mathrm{cal.}}$ Oe. | $H_{\mathrm{cal.}}\sin\psi$ Oe. | $H_{\mathrm{cal.}}\cos\psi$ Oe. | $\theta$ |
|---|---|---|---|---|
| 90° | 3532 | 3532 | 0 | 90° |
| 57°31′ | 4178 | 3525 | 2244 | 85° |
| 38°06′ | 5698 | 3515 | 4485 | 80° |
| 27°31′ | 7571 | 3498 | 6715 | 75° |
| 21°18′ | 9590 | 3484 | 8935 | 70° |
| 17°20′ | 11674 | 3478 | 11144 | 65° |
| 14°38′ | 13789 | 3484 | 13342 | 60° |
| 12°43′ | 15904 | 3504 | 15514 | 55° |
| 11°17′ | 18075 | 3534 | 17726 | 50° |
| 10°08′ | 20229 | 3561 | 19913 | 45° |

In the plane containing the rhombohedral axis the calculated values at a wave number $0.9\,\mathrm{cm}^{-1}$ are given in Table II where we use the values $g=2$, $H_A=2.22\times10^4$ oersted, $K'=1.9\times10^{-4}$ and $K=1/24$ so as to make $H\sin\psi$ $=$constant. These are graphically compared with the corresponding experimental values after Kumagai et al[7] at a wave number 0.9 $\mathrm{cm}^{-1}$ in Fig. 3.

As seen from the above discussions the uniaxial anisotropy field $H_A$ of $\alpha$ $Fe_2O_3$ is very strong (~22200 oersted). When a magnetic field weaker than $H_A$ is applied in the rhombohedral direction (difficult direction) and the magnetization $M$ is assumed to be saturated, $\alpha$ $Fe_2O_3$ is nearly paramagnetic in this direction and the susceptibility is expected to be $\chi=M/H_A$. Using the data $M=1.6$ emu/cc[4], we find $\chi=7.2\times10^{-5}$/cc. This value of the susceptibility is of the same order of magnitude as the experimental value $10.5\times10^{-5}$/cc[4]) which has been supposed by Neel[4] to be $\chi_\perp$ of the main antiferromagnetism of $\alpha$ $Fe_2O_3$ on which the weak ferromagnetism exists parasitically. It is desirable to make sure whether the experimental values of $\chi$ in the rhombohedral direction is due entirely to the antiferromagnetism or partly due to the ferromagnetism with a strong anisotropy. If the parasitic ferromagnetism is independent of the main antiferromagnetism the value of the susceptibility parallel to the rhombohedral axis will be greater than that measured in the basal plane under a sufficiently strong field. In the experiments[4),5)] however, this does not hold and these two values of the susceptibility of $\alpha$ $Fe_2O_3$ above the Morin temperature are nearly equal. The parasitic ferromagnetism is not independent of the antiferromagnetism. And so it is necessary to obtain the resonance formula based on a more reasonable model of the parasitic ferromagnetism in the main antiferromagnetism. This is a future problem.

The author wishes to express his sincere thanks to Professor T. Nagamiya and Dr. K. Yosida for their king advices and Mr. J. Kanamori for his valuable discussions. The present work has been supported by a Yukawa scholorship, with which the author was able to stay a few months in Osaka University.

### References

1) T. Townsend Smith: Phys. Rev. **8** (1916) 721.
2) R. Chevallier and S. Mathieu: Ann. Physik **18** (1943) 258.
3) L. Néel: Ann. Phys. **4** (1949) 249.
4) L. Néel et R. Pauthenet: Compt. rend. **234** (1952) 2172.
L. Néel: Revs. Mod. Phys. **25** (1953) 58.
5) H. Bizette: R. Chevallier et B. Tsai: Compt. rend. **236** (1953) 2043.
6) P. W. Anderson, F. R. Merritt, J. P. Remeika and W A. Yager: Phys. Rev. **93** (1954) 717.
7) H. Kumagai, H. Abe, K. Ono, I. Hayashi, J. Shimada and K. Iwanaga: Phys. Rev. **99** (1955) 1116.
8) Y. Kojima: Sci. Rep. R.I.T.U. **A 7** (1955) 591.
9) F. J. Morin: Phys. Rev. **78** (1950) 819.
10) C. G. Shull, W. A. Strauser and E. O. Wollan: Phys. Rev. **83** (1951) 333.
11) T. Fujimura and Y. Torizuka: J. Phys. Soc. Japan **11** (1956) 327.
12) E. P. Wohlfarth: Phil. Mag. **46** (1955) 1155.

---

JOURNAL OF THE PHYSICAL SOCIETY OF JAPAN Vol. 11, No. 10, OCTOBER, 1956

# On the Magnetic Properties of the System MnSb–CrSb*

By Tokutaro HIRONE, Seijiro MAEDA, Ichiro TSUBOKAWA
*The Research Institute for Iron, Steel and Other Metals,*
*Tohoku University, Sendai*
and Noboru TSUYA
*The Research Institute of Electrical Communication,*
*Tohoku University, Sendai*

(Received June 7, 1956)

The change of magnetic properties due to the replacement of manganese by chromium in manganese antimonide (MnSb), which is of the NiAs structure, was investigated. It was found that, with the increase of the concentration of chromium, the magnetic behaviour of these compounds $(Mn_{1-x}Cr_x)Sb$ changes as follows: (1) at $x=0$ (MnSb), the temperature-magnetization curve shows typical behaviour of ferromagnetic substance, (2) in the range $0.1\leqq x\leqq 0.7$, it deviates remarkably from the Weiss curve in proportion with the chromium content, and the temperature dependence of the reciprocal susceptibility above the Curie point is of a ferrimagnetic type. (3) In the range $0.8\leqq x\leqq 0.9$ a transition from ferrimagnetic to antiferromagnetic was observed, and finally (4) at $x=1$ (CrSb) a typical antiferromagnetism could be seen. A short discussion of such transitions is given.

## § 1. Introduction

It has been proposed[1)] that, if magnetic cations in an ionic crystal are replaced by another kind of magnetic cation, a new type of exchange coupling between the cations of different kinds will be introduced in addition to the original ones between the cations of the same kind, and that, in such a case, various types of the ordered arrangement of their magnetic moments, together with the transition among them, will be expected. If we made such binary systems of compounds by combining two kinds of ionic compounds of ferromagnetic and antiferromagnetic types, then it will be considered that their magnetic properties will change from ferromagnetic to antiferromagnetic due to the concentration change, and that the intermediate type of ordering of the magnetic moments of cations will occur. From these points of view, we have investigated magnetic properties of the binary system of manganese and chromium antimonide, both of them being of the same crystal structure of NiAs type, and the former being ferromagnetic and the latter antiferromagnetic. According to the present investigation, it was found that both compounds make perfect solid solutions in all proportions. In the following lines the results of the measurement of their magnetic properties and some discussions thereupon are given.

---

* This investigation was supported in part by the Grant-in-Aid of Fundamental Scientific Research of Ministry of Education.

## § 2. Preparation of the Specimens and the Measuring Apparatus

Eleven specimens having the concentration of $(Mn_{1-x}Cr_x)Sb$, where $x$ took the values from zero to unity in every interval of 0.1, were made by means of the ceramic method. The powders of manganese, chromium and antimony of below 100 mesh were mixed at the desired proportion, sealed in evacuated silica tubes respectively, and heated during about 24 hours at 1000°C. Then the reaction products were slowly cooled down in the furnace.

In order to confirm the mutual solubility of both antimonides, we examined all the specimens by means of the X-ray analysis. Powder photographs showed monophase patterns of crystal structure of NiAs type in all range of composition, and the lattice constants $a$, $c$ and axial ratio $c/a$ were determined. Fig. 1 shows the variation of the lattice constants $a$, $c$ as well as axial ratio $c/a$ with the chromium content $x$. As can be seen from the figure, one of the lattice constants $a$ is nearly constant throughout the range of chromium content,

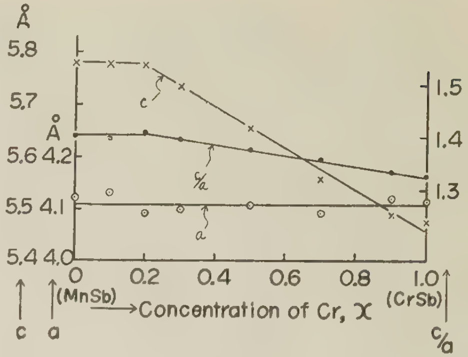

Fig. 1. The curves of lattice constants $a$, $c$ and axial ratio $c/a$ as a function of chromium content.

while another parameter $c$ and the axial ratio $c/a$ decrease linearly with increasing chromium content except the range $0 \leqq x \leqq 0.2$. So we may say that the reaction products form complete solid solution in the range $x \geqq 0.2$. The abrupt change of the slope of the $c$ *vs.* $x$ curve at $x=0.2$ shown in Fig. 1 would be somewhat strange from the above standpoint but we consider the samples in this range to be also the continuation of the solid solutions, since the compounds with $x \leqq 0.2$ and MnSb are of the same NiAs phase with the equal parameters, and as will be shown below, $1/\chi_M - T$ curves and the Curie point in the whole range show continuous change with composition. Hence we can presume in the whole range of $x$ these reaction products would make perfect solid solution.

The apparatus used for measurement of magnetic properties was an automatically recording magnetic balance²⁾.

## § 3. Experimental Results and Discussions

MnSb is a ferromagnetic with the Curie point of about 310°C³⁾ and CrSb is an antiferromagnetic with the Neel point of about 440°C.⁴⁾ Then, there must be a composition, which separates a ferromagnetic phase from an antiferromagnetic one. To see this, molar magnetizations $M$ and molar susceptibilities $\chi_M$ were measured as functions of temperature for samples of various compositions.

From the results of the measurement of magnetic susceptibility, the relation between $1/\chi_M$ and temperature $T$ was obtained, the result being shown in Fig. 2. Fig. 3 shows the result of the measurement of the field dependence of magnetization for a few

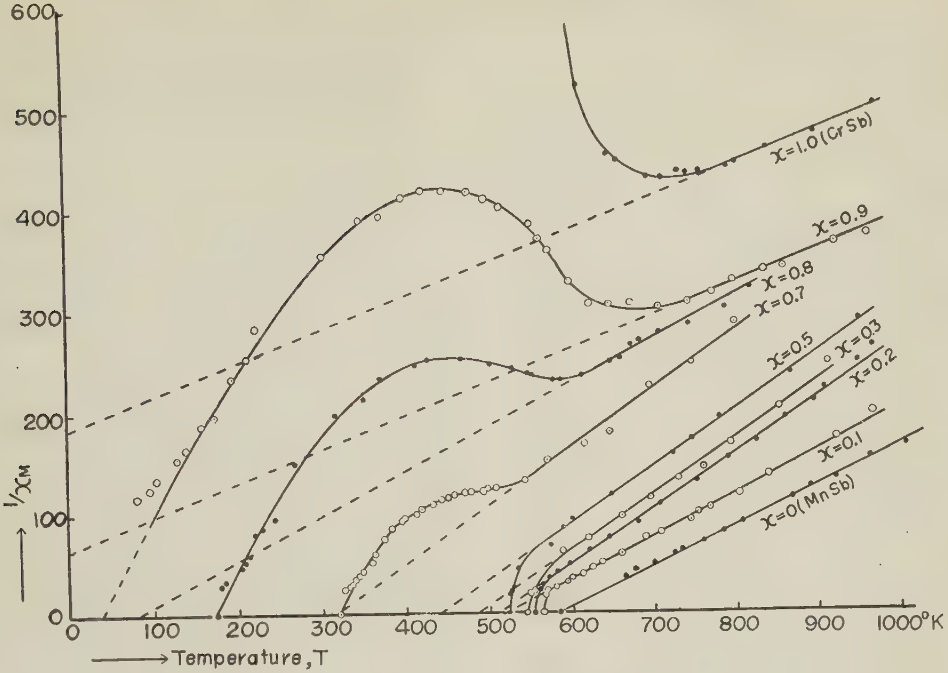

Fig. 2. The curves of reciprocal of the magnetic susceptibility, $1/\chi_M$, versus temperature.

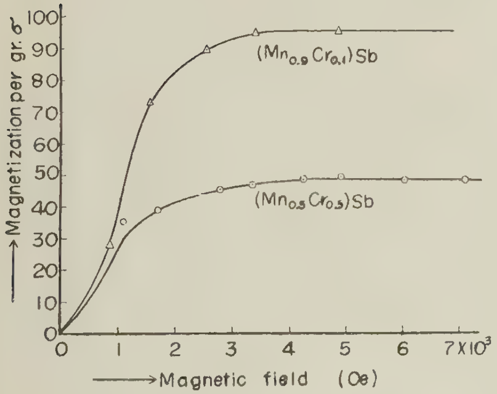

Fig. 3. The curves of magnetization per gr., $\sigma$, versus magnetic field.

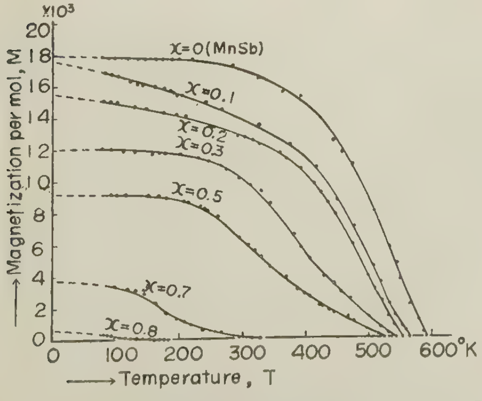

Fig. 4. The curves of magnetization per mol, $M$, versus temperature.

specimens. From this result, it can be concluded that the magnetization reaches saturation at about 4000 Oe. The relation between saturation magnetization $M_s$ and temperatue was also determined from such measurements, and the result is shown in Fig. 4. From these figures one can trace the whole behaviours of magnetic change of this binary system. For the manganese antimonide the reciprocal susceptibility decreases linearly with the fall of temperature until Curie point. It is also seen from Fig. 4 that the saturation magnetization below the Curie point changes nearly according to the Weiss curve. From these facts one can assume a ferromagnetic ordering of the magnetic moment for manganese antimonide. The extraplated saturation magnetization to absolute zero of temperature takes a value 3.49 $\mu$, $\mu_B$ being Bohr magneton, which is slightly smaller than the spin magnetic moment of 4 $\mu_B$ of $Mn^{3+}$. With the replacement of maganese with chromium, the Curie point decreases, and in addition, there appears a little bending of the $1/\chi_M$-T curve near the Curie temperature, like a ferrimagnetic substance. The deviation of the temperature-magnetization curve from the Weiss curve becomes the more significant, the higher the chromium concentrations. One of the peculiar features of

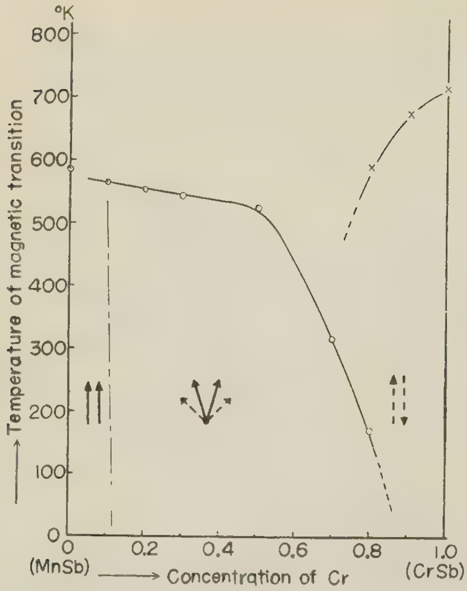

Fig. 5. Relation between temperature of magnetic transition and chromium content; ⊙ indicates the ferro- or ferrimagnetic Curie point and × indicates the antiferromagnetic one respectively. Chain line shows the border between ferro- and ferrimagnetic regions.

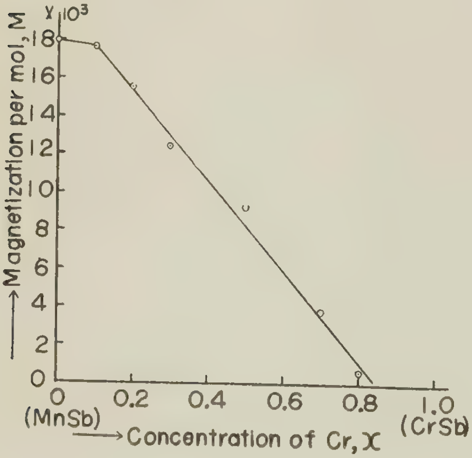

Fig. 6. The curves of saturation magnetization at the temperature of liquid nitrogen versus chromium content.

Table I. The ferro- and antiferromagnetic Curie point $T_f$ and $T_a$, asymptotic Curie point $\theta$, the number of effective Bohr magneton and the spin quantum numbers are indicated as a function of chromium content.

| $x$ | $T_f$ | $T_a$ | $\theta$ | $\mu_{eff}$ | $S$ |
|---|---|---|---|---|---|
| 0 (MnSb) | 587 (°K) | | 587(°K) | 4.48 | 1.80 |
| 0.1 | 565 | | 516 | 4.36 | 1.79 |
| 0.2 | 553 | | 506 | 3.83 | 1.48 |
| 0.3 | 543 | | 483 | 3.82 | 1.48 |
| 0.4 | | | | | |
| 0.5 | 523 | | 436 | 3.78 | 1.46 |
| 0.6 | | | | | |
| 0.7 | 315 | | 310 | 3.45 | 1.30 |
| 0.8 | 170 | 588 (°K) | 82 | 4.26 | 1.69 |
| 0.9 | | 673 | −190 | 4.91 | 2.01 |
| 1.0(CrSb) | | 713 | −550 | 4.92 | 2.02 |

these curves is that these have extraordinarily long tails near the Curie point. These behaviours can be seen as a characteristic property of a kind of ferrimagnetic spin ordering. For the further range with richer chromium, *viz.* $0.8 \leqq x \leqq 0.9$, the reciprocal susceptibility also decreases linearly with the fall of temperature, but at a certain temperature it reaches a minium. With a further cooling it increases slowly and, reaching a flat maximum at a certain temperature, it decreases again until Curie point. In the temperature range below the Curie point the spontaneous magnetization was observed, but the temperature dependence was quite different from that of the Weiss law. Finally CrSb was found to be antiferromagnetic; the curve of $1/\chi_M - T$ indicates the characteristics of antiferromagnetism, and the asymptotic Curie point, $\theta$, takes a negative value. Such a result coincides perfectly with the result formerly reported,[4] hence it can be seen that in the chromium rich side the transition of a type paramagnetic ⟶ antiferromagnetic ⟶ ferrimagnetic occurs, and that the antiferromagnetic Curie point converges to that of chromium antimonide with the decrease of manganese content. In such a case after extinction of spontaneous magnetization at ferrimagnetic Curie point, antiferromagnetic rearrangement of spins will occur.

In Fig. 5, the relations between such a ferromagnetic or antiferromagnetic Curie point and chromium content are shown. On the chromium rich side the antiferromagnetic Curie point falls with the addition of manganese and on the manganese rich side the ferro- or ferrimagnetic Curie point is lowered at first slowly and then more rapidly with the addition of chromium. In the composition range near $x=0.7$ both the ferri- and antiferromagnetic Curie points coexist as mentioned above. In Fig. 6, the change of saturation magnetization with the concentration of chromium is shown. As is shown, the saturation value does not vary appreciably with the addition of a small quantity of chromium to manganese antimonide (till 10%) but beyond a certain concentration it decreases linearly till it vanishes at $x\doteqdot 0.8$. We indicate in Table I the characteristic temperature of each magnetic curve, number of effective Bohr magneton and spin quantum number as a function of chromium content.

Such a change of magnetic behaviours in the solid solution system between ferromagnetic MnSb and antiferromagnetic CrSb will now be considered based on the idea of the triangular spin arrangement proposed by Yafet and Kittel[5]. In our case, the exchange coupling between manganese or chromium ions is supposed to be ferromagnetic or antiferromagnetic respectively, basing on their respective thermomagnetic properties. If we assume the exchange coupling between chromium and manganese ions to be ferromagnetic, the various types of magnetic behaviour can be explained satisfactorily. It is well known that the magnetic moments of cations in MnSb and CrSb are arranged parallel or antiparallel to $c$-axis respectively[3][6]. We indicate this behaviour by the symbols $\uparrow\uparrow$ or $\uparrow\downarrow$ as in Fig. 5. Replacing the manganese in MnSb by chromium, it can be considered that, for the low concentration range of chromium ion, the magnetic moments of both manganese and chromium ions will be almost parallel, because the saturation magnetization of the range $x\angle 0.1$ does not change remarkably. However, if the chromium content increases, it can be supposed that the orientation of the magnetic moment of chromium and manganese ions in this case takes different directions due to the antiferromagnetic interaction between a pair of chromium ions and ferromagnetic interaction between manganese and chromium ions. In the figure such a region is marked with ↖↖↗↗. It follows, from such a consideration, that a kind of ferrimagnetic behaviours in this composition range: on the chromium rich side, the antiferromagnetic interaction of chromium ions is predominant so that the type of spin ordering becomes antiferromagnetic. On the basis of the above mentioned idea and assuming appropriate values of interaction constants, one can reproduce the whole magnetic behaviours of this system completely. The details of the calculation will shortly be given by one of the present authors[7].

## References

1) C. Zener: Phys. Rev. **82** (1951) 403; P. W. Anderson and H. Hasegawa: Phys. Rev. **100** (1955) 675.
2) T. Hirone, S. Maeda and N. Tsuya: Rev. Sci. Instr. **25** (1954) 516.
3) C. Guillaud: *Thesis Strasbourg* (1943).
4) H. Haraldsen, T. Rosenqvist and F. Grønvold: Arch. Math. Naturvidensk **50** (1949) 95.
5) Y. Yafet and C. Kittel: Phys. Rev. **87** (1952) 290.
6) A. I. Snow: Phys. Rev. **85** (1952) 365, Rev. Mod. Phys. **25** (1953) 127.
7) T. Hirone and K. Adachi: *to be published shortly*.

JOURNAL OF THE PHYSICAL SOCIETY OF JAPAN Vol. 11, No. 10, OCTOBER, 1956

# On the Buckling of an Elliptic Plate with Clamped Edge I

By Yoshio SHIBAOKA

*Institute of Polytechnics, Osaka City University*

(Received April 30, 1956)

The buckling of a uniform thin elliptic plate with clamped edge whose periphery is subject to a uniform normal pressure in the plane of the plate is solved formally in an exact manner by the use of hyperbolic functions, circular functions, Mathieu functions and modified Mathieu functions. An approximate formula for the relationship between the critical buckling load and the eccentricity of the elliptic plate is derived correct to the fourth power of the eccentricity, which may be adequately used in case when the eccentricity is not so large.

## § 1. Introduction

It is well known that the buckling of a circular plate whose periphery is subject to a uniform radial pressure can be solved exactly by the use of Bessel functions[1)2)]. The buckling of a square plate or rectangular plate has also been discussed by several authors, with satisfactory results, under various boundary conditions[3)], and especially Professor Tomotika[4)] has given a useful result for the buckling of a square plate when its four edges are subject to a uniform shearing force. On the other hand, the buckling of a thin elliptic plate compressed uniformly along the normal on its periphery has been attacked by S. Woinovsky-Krieger by the use of the Rayleigh-Ritz method[5)].

In the present paper, the fundamental normal mode of the buckling of a uniform thin elliptic plate with clamped edge is discussed formally in an exact manner in case when its periphery is subject to a uniform normal pressure. However, postponing detailed numerical discussions to a future work, only an approximate formula giving the relationship between the critical buckling load and the eccentricity of the elliptic plate is here derived correct to the fourth power of the eccentricity, which may be adequately used in case when the eccentricity is not so large.

## § 2. General Solution of the Fundamental Equation

Let the rectangular coordinate axes $(x, y)$ be taken in the middle plane of an elliptic plate of uniform small thickness, $d$, in such a way that the origin coincides with the centre of the plate and the axes are along the major and minor axes of the ellipse respectively. We denote Young's modulus and Poisson's ratio of the material of the plate, which is assumed to be homogeneous and isotropic, by $E$ and $\sigma$ respectively.

Then if $w$ be the transverse displacement of a point on the middle plane, the differential equation for determining the deflection of the buckled plate subject to a uniform normal pressure $P$ per unit length on its periphery is given by

$$\left.\begin{aligned} &D\left(\frac{\partial^4 w}{\partial x^4}+2\frac{\partial^4 w}{\partial x^2\partial y^2}+\frac{\partial^4 w}{\partial y^4}\right)\\ &\qquad=-P\left(\frac{\partial^2 w}{\partial x^2}+\frac{\partial^2 w}{\partial y^2}\right),\\ &\text{with}\\ &\qquad D=Ed^3/\{12(1-\sigma^2)\}\,. \end{aligned}\right\}\tag{1}$$

If, for simplicity, we write $k_1{}^2=P/D$, equation (1) becomes

$$\left(\frac{\partial^2}{\partial x^2}+\frac{\partial^2}{\partial y^2}\right)^2 w+k_1{}^2\left(\frac{\partial^2}{\partial x^2}+\frac{\partial^2}{\partial y^2}\right)w=0\,,\tag{2}$$

or

$$\left(\frac{\partial^2}{\partial x^2}+\frac{\partial^2}{\partial y^2}\right)\left(\frac{\partial^2}{\partial x^2}+\frac{\partial^2}{\partial y^2}+k_1{}^2\right)w=0\,.\tag{3}$$

The solution of this equation is given by

$$w=w_1+w_2\,,\tag{4}$$

where $w_1$ and $w_2$ satisfy respectively the differential equations:

$$\frac{\partial^2 w_1}{\partial x^2}+\frac{\partial^2 w_1}{\partial y^2}=0\,,\tag{5}$$

and

$$\frac{\partial^2 w_2}{\partial x^2}+\frac{\partial^2 w_2}{\partial y^2}+k_1{}^2 w_2=0\,.\tag{6}$$

Denoting the focal length of the ellipse by $2h$, we now introduce the elliptic coordinates $(\xi, \eta)$ defined as:

$$x+iy=h\cosh(\xi+i\eta)\,.$$

Then, equations (5) and (6) become respectively

$$\frac{\partial^2 w_1}{\partial\xi^2}+\frac{\partial^2 w_1}{\partial\eta^2}=0\,, \tag{7}$$

$$\frac{\partial^2 w_2}{\partial\xi^2}+\frac{\partial^2 w_2}{\partial\eta^2}+2k^2(\cosh 2\xi-\cos 2\eta)w_2=0\,, \tag{8}$$

where

$$2k=k_1h=\sqrt{P/D}\;h\,.$$

If we restrict our attention to normal modes of buckling in which the displacement is symmetrical about both axes, as in the case of the fundamental normal mode of buckling under consideration, the appropriate particular solutions of equations (7) and (8) can be expressed in terms of hyperbolic function $\cosh 2m\xi$, circular function $\cos 2m\eta$ and Mathieu function $\mathrm{ce}_{2m}(\eta, q)$, modified Mathieu function $\mathrm{Ce}_{2m}(\xi, q)$. Thus,

$$w_1{}^{(2m)}=C_{2m}\cosh 2m\xi\cos 2m\eta\,, \tag{9}$$

$$w_2{}^{(2m)}=\overline{C}_{2m}\mathrm{Ce}_{2m}(\xi, q)\,\mathrm{ce}_{2m}(\eta, q)\,, \tag{10}$$

with

$$q=k^2=\frac{P}{4D}h^2, \tag{11}$$

where $m$ takes any positive integral value, zero inclusive, and $C_{2m}$, $\overline{C}_{2m}$ are arbitrary constants. Hence, summing up all these particular solutions, a formal general solution of equation (3) can be written in the form:

$$\begin{aligned} w&=\sum_{m=0}^{\infty}\{w_1{}^{(2m)}+w_2{}^{(2m)}\}\\ &=\sum_{m=0}^{\infty}\{C_{2m}\cosh 2m\xi\cos 2m\eta\\ &\quad+\overline{C}_{2m}\mathrm{Ce}_{2m}(\xi, q)\mathrm{ce}_{2m}(\eta, q)\}\,. \end{aligned} \tag{12}$$

Now by the use of the well-known relation

$$\mathrm{ce}_{2m}(\eta, q)=\sum_{l=0}^{\infty}A_{2l}{}^{(2m)}\cos 2l\eta\,, \tag{13}$$

we eliminate the functions $\mathrm{ce}_{2m}(\eta, q)$ from the right-hand side of (12). Then, we have

$$\begin{aligned} w&=\sum_{m=0}^{\infty}\{C_{2m}\cosh 2m\xi\cos 2m\eta\\ &\quad+\overline{C}_{2m}\mathrm{Ce}_{2m}(\xi, q)\sum_{l=0}^{\infty}A_{2l}{}^{(2m)}\cos 2l\eta\}\\ &=\sum_{m=0}^{\infty}\{C_{2m}\cosh 2m\xi\\ &\quad+\sum_{l=0}^{\infty}\overline{C}_{2l}A_{2m}{}^{(2l)}\mathrm{Ce}_{2l}(\xi, q)\}\cos 2m\eta\,. \end{aligned} \tag{14}$$

If the clamped edge of the elliptic plate be expressed by $\xi=\xi_0$, the boundary conditions at this edge are given by

$$(w)_{\xi=\xi_0}=0\,, \quad \left(\frac{\partial w}{\partial\xi}\right)_{\xi=\xi_0}=0\,, \tag{15}$$

and substituting the expression (14) for $w$ into these conditions, we have

$$\left.\begin{aligned} &\sum_{m=0}^{\infty}\{C_{2m}\cosh 2m\xi_0\\ &\quad+\sum_{l=0}^{\infty}\overline{C}_{2l}A_{2m}{}^{(2l)}\mathrm{Ce}_{2l}(\xi_0, q)\}\cos 2m\eta=0\,,\\ &\sum_{m=0}^{\infty}\{2mC_{2m}\sinh 2m\xi_0\\ &\quad+\sum_{l=0}^{\infty}\overline{C}_{2l}A_{2m}{}^{(2l)}\mathrm{Ce}_{2l}'(\xi_0, q)\}\cos 2m\eta=0\,. \end{aligned}\right\} \tag{16}$$

In order that these two relations should be satisfied for all values of $\eta$ between $-\pi/2$ and $\pi/2$, we must have, for any positive integral value of $m$, zero inclusive,

$$\left.\begin{aligned} &C_{2m}\cosh 2m\xi_0+\sum_{l=0}^{\infty}\overline{C}_{2l}A_{2m}{}^{(2l)}\mathrm{Ce}_{2l}(\xi_0, q)\\ &\quad=0\,,\\ &2mC_{2m}\sinh 2m\xi_0\\ &\quad+\sum_{l=0}^{\infty}\overline{C}_{2l}A_{2m}{}^{(2l)}\mathrm{Ce}_{2l}'(\xi_0, q)=0\,. \end{aligned}\right\} \tag{17}$$

If we eliminate the constants $C_{2m}$'s from these equations, we get a system of simultaneous linear equations for determining the constants $\overline{C}_{2l}$'s. Thus

$$\sum_{l=0}^{\infty}a_{lm}\overline{C}_{2l}=0\,, \quad (m=0,\,1,\,2,\,3,\,\cdots) \tag{18}$$

with

$$\begin{aligned} a_{lm}=A_{2m}{}^{(2l)}\{&2m\sinh 2m\xi_0\mathrm{Ce}_{2l}(\xi_0, q)\\ &-\cosh 2m\xi_0\mathrm{Ce}_{2l}'(\xi_0, q)\}\,. \end{aligned} \tag{19}$$

The solution of this system of symultaneous linear equations would in general yield the result that all the $\overline{C}_{2l}$'s are zero; but if a certain special relationship exists between the dimensions of the plate and the strength of the load $P$, namely, if the relation obtained by eliminating all the $\overline{C}_{2l}$'s from the system of simultaneous linear equation (18) exists, we can obtain a displacement in the normal mode of buckling, and with the aid of the said relationship the critical buckling load can be determined as a function of the dimensions of the plate and the elastic constants of the material of the plate.

By eliminating all the $\overline{C}_{2l}$'s from (18), we

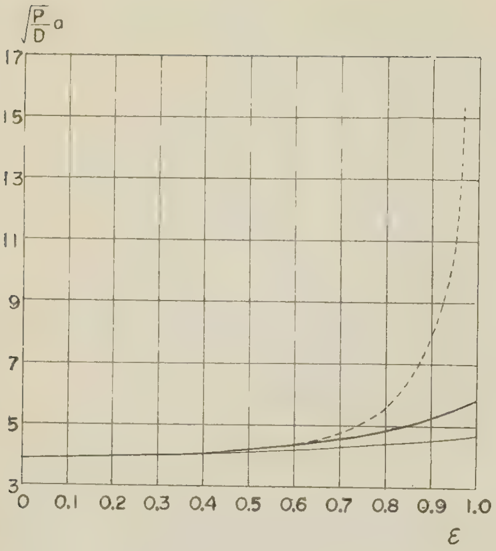

Fig. 1

have the required relationship as:

$$\Delta=\begin{vmatrix} a_{00} & a_{10} & a_{20} & a_{30} & \cdots \\ a_{01} & a_{11} & a_{21} & a_{31} & \cdots \\ a_{02} & a_{12} & a_{22} & a_{32} & \cdots \\ a_{03} & a_{13} & a_{23} & a_{33} & \cdots \\ \vdots & \vdots & \vdots & \vdots & \end{vmatrix}=0\,. \tag{20}$$

If we obtain the numerical value of the root $q$ of this infinite determinantal equation, the numerical value of $\sqrt{P/D}\,a$ can be obtained from the relation:

$$\sqrt{P/D}\,a=2\sqrt{q}/\varepsilon\,, \tag{21}$$

which follows immediately from (12), where $a$ and $\varepsilon$ are respectively a half length of the major axis and the eccentricity of the ellipse.

When $a$, $\varepsilon$ and $D$ are fixed the only variable remaining in the determinant $\Delta$ is $q$, which is connected with the critical buckling load $P$ by the relation (21), so that the smallest root of $\Delta=0$ will give the critical load of the fundamental normal mode of buckling, with which we are mainly concerned in the present paper.

The solution expressed by (20) is, however, merely formal. To find out whether it can be used to determine the actual value of buckling we must examine its convergence. For this purpose we may form, as in Professor Tomotika's treatment of the transverse vibration of a square plate clamped at its four edges⁶⁾, a series of finite determinants $\Delta_1$, $\Delta_2$, $\Delta_3$, $\cdots$, $\Delta_N$ by taking 1, 2, 3, $\cdots$, $N$ rows and columns starting at the left-hand top corner of $\Delta$, so that $\Delta_1=a_{00}$, $\Delta_2=\begin{vmatrix} a_{00} & a_{10} \\ a_{01} & a_{11}\end{vmatrix}$, etc. If it is found that the smallest root of $\Delta_N=0$ converges to a definite limit as $N$ increases this root gives the required critical load of the fundamental normal mode of buckling of the elliptic plate under consideration. However, we here restrict our attention to deriving only an expansion formula for $\sqrt{P/D}\,a$ in powers of $\varepsilon$ from the infinite determinant equation (20). Detailed numerical discussions of the roots of equation (20) will be carried out in a near future.

## § 3. An Expansion Formula for $\sqrt{P/D}\,a$ in Powers of $\varepsilon$

When an elliptic plate differs only slightly from a circular plate, its eccentricity $\varepsilon$ is very small, and accordingly $q$ is also very small, as will be seen from the relation $q=1/4\,(\sqrt{P/D}a)^2\varepsilon^2$ which follows immediately from (21). In such a case, $\sqrt{P/D}\,a$ can be expanded in a power series of $\varepsilon$.

We have obtained such an expansion formula for $\sqrt{P/D}\,a$ correct to the order of $\varepsilon^4$. To this end we have expanded the elements $a_{ij}$'s of the determinant $\Delta$ into series correct to the order of $\varepsilon^4$. After rather lengthy but straightforward calculations we have

$$\sqrt{P/D}\,a=u_0+u_1\varepsilon^2+u_2\varepsilon^4, \tag{22}$$

where $u_0$ is the value of $\sqrt{P/D}\,a$ for the fundamental normal mode of buckling of a circular plate of radius $a$ with clamped edge and is given by the smallest root of the equation:

$$J_1(u_0)=0\,,$$

$J_1$ being the Bessel function of the first kind¹⁾. Thus we have

$$u_0=3.8317\,.$$

Both the coefficients $u_1$ and $u_2$ can be expressed in terms of the Bessel functions with argument $u_0$. Using the value 3.8317 of $u_0$ we have calculated the numerical values of $u_1$ and $u_2$, obtaining

$$u_1=0.9579,\quad u_2=1.0382.$$

Thus we have finally

$$\sqrt{P/D}\,a=3.8317+0.9579\varepsilon^2+1.0382\varepsilon^4. \tag{23}$$

The value calculated by using this expansion formula are shown by a thick-line curve in Fig. 1, while those calculated by a formula obtained by ignoring the last term in the same formula are shown by a thin-line curve. The dotted-line curve in Fig. 1 shows the results which was obtained by S. Woinovsky-Krieger by the use of the Rayleigh-Ritz method⁵⁾. It will be seen that the expansion formula (23) is particularly useful for calculating the numerical values of $\sqrt{P/D}\,a$ in case when the plate is nearly circular.

## §4. Summary

The fundamental normal mode of buckling of a uniform elliptic plate clamped at its edge is investigated in an exact manner. A formal exact solution of the partial differential equation governing the buckling of the plate is obtained by the use of hyperbolic functions, circular functions, Mathieu functions and modified Mathieu functions. An expansion formula for $\sqrt{P/D}\,a$ in powers of $\varepsilon$ is derived correct to the order of $\varepsilon^4$, where $P$ is the strength of the critical load, $a$ a half length of the major axis of the ellipse and $D=\dfrac{Ed^3}{12(1-\sigma^2)}$, $E$ and $\sigma$ being respectively Young's modulus and Poisson's ratio of the material of the plate and $d$ being the thickness of the plate. Comparing graphically this relation with the results obtained by S. Woinovsky-Krieger it is shown that such an expansion formula is particularly useful for calculating the value of $\sqrt{P/D}\,a$ in case when an elliptic plate differs only slightly from a circular plate.

## Acknowledgement

The present problem has been suggested by Professor S. Tomotika. The writer wishes to express his best thanks to him for his kind guidance throughout the present work. The writer's thanks are also due to Professor K. Tamada for his many valuable advices and to Professor T. Okuda for his encouragement.

## References

1) Bryan, G. H.: Proc. London Math. Soc., **22** (1891) 54.
2) A. Nadai: Z. Ver. Deut. Ing., **59** (1915) 169,
3) G. I. Taylor: The buckling load for a rectangular plate with four clamped edges., Z. A. M. M., **13** (1933) 147.
4) S. Tomotika and I. Imai: On the elastic stability of a square plate under shearing forces at its clamped edges. (in Japanese). Umi to Sora, **13** (1938), 142–152.
5) S. Woinovsky-Krieger: The stability of a clamped elliptic plate under uniform compression. J. Appl. Mech. **4** (1937), 177.
6) S. Tomotika: The transverse vibration of a square plate clamped at four edges., Phil. Mag. [5], **21** (1936), 745–760.

JOURNAL OF THE PHYSICAL SOCIETY OF JAPAN Vol. 11, No. 10, OCTOBER, 1956

# The Drag on a Circular Cylinder placed in a Stream of Viscous Liquid midway between Two Parallel Planes

By Yorisaburo TAKAISI
*Department of Physics, Faculty of Education,*
*Ehime University, Matuyama*

(Received April 14, 1956)

The drag on a circular cylinder placed in slow stream of viscous liquid midway between two parallel planes was first obtained in numerical form for a special case by Bairstow, Cave and Lang as early as 1921 on the basis of Stokes' equations of motion. In 1923, Harrison obtained an analytical expression for the drag experienced by the cylinder using a kind of image method. But, no agreement can be found between these two results. In this paper, we treat the same problem based also upon Stokes' equations of motion using image methods which are developed by Faxén in the case of sphere problem. Our result is in good agreement with Harrison's.

## § 1. Introduction

The drag on a circular cylinder placed in slow stream of viscous liquid midway between two parallel planes has been calculated by some writers. In 1921 Bairstow, Cave and Lang[1] discussed the treatment of problems which require a solution of the differential equation $\Delta^2\psi=0$, and as a sample for illustration the slow motion of a viscous liquid past a circular cylinder in a parallel-walled channel was chosen. Thus, by using analytical and then partly numerical methods, they obtained the drag on the circular cylinder in numerical form for a special case in which $b/a=5$ and $U=1$, as:

$$D=2.26\,\pi\mu, \tag{1.1}$$

where $a$ is the radius of the cylinder, $2b$ is the destance between the two walls, $U$ is the free stream velocity in the middle of the channel, and $\mu$ is the viscosity of the liquid concerned.

In 1923, by developing quite a different analysis on the basis of Stokes' equations of motion and using a kind of image method, Harrison[2] obtained an analytical formula for the drag on the cylinder as:

$$D=\pi\mu U\frac{4(a/b)^2-8}{1.8584-3.5209(a/b)^2+2\ln(a/b)}\,. \tag{1.2}$$

For the special case in which $b/a=5$ and $U=1$, (1.2) reduces to

$$D=5.21\,\pi\mu\,. \tag{1.3}$$

The disagreement between (1.1) and (1.3) is too large to take it caused by neglecting higher order terms in the course of the analyses.

In this paper, we treat the same problem based also upon Stokes' equations of motion, using image methods which are developed by Faxén[3)4)] in the case of sphere problems. Thus, our result is compared with (1.1) and (1.3).

## § 2. Method of Solution

A cylinder of radius $a$ is fixed relative to the parallel walls of a channel so that the distance between its centre and each of the walls is $b$. Viscous liquid is forced through

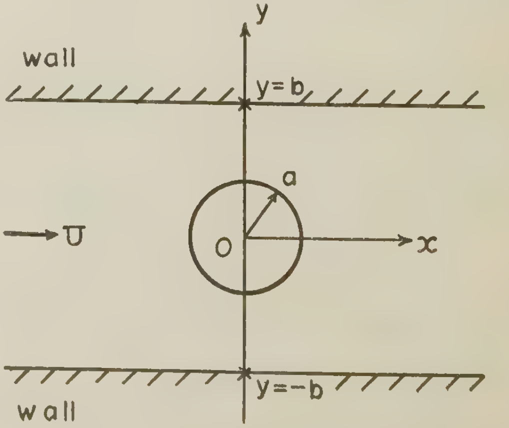

Fig. 1.

the channel in quantity sufficient to give slow constant velocity $U$ to the liquid in the centre of the channel at infinity.

Let $(x, y)$ be the rectangular coordinates having the origin at the cylinder, the axis of $x$ in the direction of the undisturbed velocity $U$ at infinity, and the axis of $y$ perpendicular to the parallel walls.

Using the stream function $\Psi$, Stokes' equations of motion are expressed as follows:

$$\Delta^2\Psi=0, \tag{2.1}$$

where $\Delta$ stands for $\partial^2/x^2+\partial^2/\partial y^2$.

In our present problem, the appropriate solution of (2.1) can be writen in the form

$$\Psi=\psi_0+\psi_1+\psi_2+\psi^*+\psi^{**}, \tag{2.2}$$

where $\psi_0$ is the stream function for the undisturbed stream in the channel; $\psi_1$ and $\psi_2$ are the stream functions for unbounded stream satisfying $\Delta\psi_1=0$ and $\Delta^2\psi_2=0$ respectively; and finally $\psi^*$ and $\psi^{**}$ are stream functions for image flows to be superposed in order to satisfy the boundary conditions on the bounding plane walls as well as at the surface of the cylinder. If we content ourselves with the approximation of order $(a/b)^2$ in the expression for the drag on the cylinder, the solutions for $\psi_0$, $\psi_1$ and $\psi_2$ reduce simply to

$$\psi_0=U\left(y-\frac{1}{3}\frac{y^3}{b^2}\right), \tag{2.3}$$

$$\psi_1=B_1\frac{y}{r^2}, \tag{2.4}$$

$$\psi_2=b_0 y\ln r+b_2\left(\frac{3y}{r^2}-\frac{4y^3}{r^4}\right), \tag{2.5}$$

where $x=r\cos\theta$, $y=r\sin\theta$.

We have from (2.3)

$$\left.\begin{aligned} u_0&=\frac{\partial\psi_0}{\partial y}\\ &=U\left(1-\frac{y^2}{b^2}\right),\\ v_0&=-\frac{\partial\psi_0}{\partial x}=0\,, \end{aligned}\right\} \tag{2.6}$$

or

$$\begin{aligned} w_0&=u_0-iv_0\\ &=U\left\{\left(1-\frac{1}{2}\frac{r^2}{b^2}\right)+\frac{1}{4}\frac{r^2}{b^2}e^{-2i\theta}+\frac{1}{4}\frac{r^2}{b^2}e^{2i\theta}\right\}. \end{aligned} \tag{2.7}$$

Now, $\ln r$ can be written in an integral form as:

$$\ln r=-\frac{1}{2}\int_{-\infty}^{\infty}\frac{1}{|\alpha|}e^{i\alpha x-|\alpha||y|}\,d\alpha+C, \tag{2.8}$$

where $C$ is an appropriate constant so chosen as to make the integral convergent. Making use of (2.8) and its derivatives with respect to $x$ and $y$, we obtain integral expressions for the components of velocity as:

$$\left.\begin{aligned} u&=\frac{\partial}{\partial y}(\psi_1+\psi_2)\\ &=-\frac{1}{2}\int_{-\infty}^{\infty}B_1|\alpha|\,e^{i\alpha x-|\alpha||y|}\,d\alpha\\ &\quad+\frac{1}{2}\int_{-\infty}^{\infty}\left\{\left(-\frac{1}{|\alpha|}+|y|\right)b_0\right.\\ &\quad\left.+(-3|\alpha|+2\alpha^2|y|)b_2\right\}e^{i\alpha x-|\alpha||y|}d\alpha,\\ v&=-\frac{\partial}{\partial x}(\psi_1+\psi_2)\\ &=-\frac{1}{2}i\int_{-\infty}^{\infty}B_1\alpha\frac{y}{|y|}e^{i\alpha x-|\alpha||y|}\,d\alpha\\ &\quad-\frac{1}{2}i\int_{-\infty}^{\infty}\left\{-\frac{\alpha}{|\alpha|}yb_0\right.\\ &\quad\left.+\left(\alpha_1\frac{y}{|y|}-2\alpha|\alpha|y\right)b_2\right\}e^{i\alpha x-|\alpha||y|}\,d\alpha, \end{aligned}\right\} \tag{2.9}$$

where the constant $C$ has been omitted, for it can be added whenever it is necessary. Further, by Fourier expansion, we get

$$\begin{aligned} w&=u-iv\\ &=b_0\left(\ln r+\frac{1}{2}\right)+e^{-2i\theta}\left(-\frac{1}{2}b_0+\frac{1}{r^2}B_1\right)\\ &\quad+\frac{b_2}{r^2}e^{2i\theta}. \end{aligned} \tag{2.10}$$

Components of velocities due to image flows may be written

$$\left.\begin{aligned} u^*&=\frac{\partial\psi^*}{\partial y}\\ &=\frac{1}{2}\int_{-\infty}^{\infty}\left\{-|\alpha|f_1(\alpha)\right.\\ &\qquad+f_2(\alpha)\left(-\frac{1}{|\alpha|}-3|\alpha|+y\right.\\ &\qquad\left.\left.+2\alpha^2y\right)\right\}e^{i\alpha x-|\alpha|y}\,d\alpha,\\ v^*&=-\frac{\partial\psi^*}{\partial x}\\ &=-\frac{1}{2}i\int_{-\infty}^{\infty}\left\{\alpha f_1(\alpha)\right.\\ &\qquad+f_2(\alpha)\left(-\frac{\alpha}{|\alpha|}y+\alpha\right.\\ &\qquad\left.\left.-2\alpha|\alpha|y\right)\right\}e^{i\alpha x-|\alpha|y}\,d\alpha, \end{aligned}\right\} \tag{2.11}$$

and

$$\left.\begin{aligned}
u^{**}&=\frac{\partial\psi^{**}}{\partial y}\\
&=-\frac{1}{2}\int_{-\infty}^{\infty}\Big\{|\alpha|f_3(\alpha)\\
&\qquad+f_4(\alpha)\Big(\frac{1}{|\alpha|}+3|\alpha|+y\\
&\qquad+2\alpha^2y\Big)\Big\}e^{i\alpha x+|\alpha|y}\,d\alpha,\\
v^{**}&=-\frac{\partial\psi^{**}}{\partial x}\\
&=\frac{1}{2}i\int_{-\infty}^{\infty}\Big\{\alpha f_3(\alpha)\\
&\qquad+f_4(\alpha)\Big(\frac{\alpha}{|\alpha|}y+\alpha\\
&\qquad+2\alpha|\alpha|y\Big)\Big\}e^{ix\alpha+|\alpha|y}\,d\alpha,
\end{aligned}\right\}\tag{2.12}$$

where $f_n(\alpha)$'s are unknown functions to be determined by under-mentioned boundary conditions.

The boundary conditions on the bounding plane walls $y=b$ and $y=-b$ as well as at the surface of the cylinder are as follows:

$$\left.\begin{aligned}
&(u_0+u+u^*+u^{**})_{y=b}=0,\\
&(v_0+v+v^*+v^{**})_{y=b}=0;
\end{aligned}\right\}\tag{2.13}$$

$$\left.\begin{aligned}
&(u_0+u+u^*+u^{**})_{y=-b}=0,\\
&(v_0+v+v^*+v^{**})_{y=-b}=0;
\end{aligned}\right\}\tag{2.14}$$

and

$$(w_0+w+w^*+w^{**})_{r=a}=0,\tag{2.15}$$

where $w^*=u^*-iv^*$, $w^{**}=u^{**}-iv^{**}$.

## § 3. Determination of the Functions $f_n(\alpha)$'s and the Constants $B_1$, $b_0$ and $b_2$

Inserting the values of $(u_0, v_0)$, $(u, v)$, $(u^*, v^*)$ and $(u^{**}, v^{**})$ as given respectively by (2.6), (2.9), (2.11) and (2.12) into (2.13) and (2.14), we can express the functions $f_n(\alpha)$'s so far undetermined in terms of unknown constants $B_1$, $b_0$ and $b_2$ as:

$$\begin{aligned}
f_1(\alpha)&=f_3(\alpha)\\
&=\frac{1}{(1+2\alpha^2)(e^{2b|\alpha|}-e^{-2b|\alpha|}-4b|\alpha|)}\\
&\quad\times[\{1+4\alpha^2+2b|\alpha|+4b\alpha^2|\alpha|\\
&\quad+(1+2\alpha^2)e^{-2b|\alpha|}\}B_1\\
&\quad+(1-2b^2-2b|\alpha|-4b^2\alpha^2-e^{-2b|\alpha|})b_0\\
&\quad+(1+2b|\alpha|+6\alpha^2-4b^2\alpha^2-8b^2\alpha^4\\
&\quad+e^{-2b|\alpha|})\,b_2]\,,
\end{aligned}\tag{3.1}$$

$$\begin{aligned}
f_2(\alpha)&=f_4(\alpha)\\
&=\frac{1}{(1+2\alpha^2)\,(e^{2b|\alpha|}-e^{-2b|\alpha|}-4b|\alpha|)}\\
&\quad\times\{-2\alpha^2B_1+(-1+2b|\alpha|+e^{-2b|\alpha|})\,b_0\\
&\quad+(-4\alpha^2+4b\alpha^2|\alpha|+2\alpha^2e^{-2b|\alpha|})\,b_2\}.
\end{aligned}\tag{3.2}$$

Inserting these expressions into (2.11) and (2.12), and after some calculations, we obtain, neglecting all terms higher than $\varepsilon^3$,

$$\begin{aligned}
&w^*+w^{**}\\
&=\Big\{-\ln 2b+\varepsilon^2e^{-2i\theta}\Big(-\frac{1}{16}\Big)+\varepsilon^2e^{2i\theta}\Big(-\frac{1}{16}\Big)\Big\}b_0\\
&-\int_0^{\infty}\frac{d\xi}{1-4\xi\,e^{-2\xi}-e^{-4\xi}}\\
&\times\Big\{\Big[\Big(-\frac{1}{\xi}+4-4\xi-\varepsilon^2\xi+2\varepsilon^2\xi^2\Big)e^{-2\xi}\\
&\quad+\Big(\frac{2}{\xi}-4-\varepsilon^2\xi\Big)e^{-4\xi}-\frac{1}{\xi}e^{-6\xi}\\
&\quad+\varepsilon^2e^{-2i\theta}\Big\{\Big(\frac{1}{4}\xi-\xi^2\Big)e^{-2\xi}\\
&\quad+\Big(-\frac{1}{2}\xi+\xi^2\Big)e^{-4\xi}+\frac{1}{4}\xi\,e^{-6\xi}\Big\}\\
&\quad+\varepsilon^2e^{2i\theta}\Big\{\Big(\frac{5}{4}\xi-3\xi^2+2\xi^3\Big)e^{-2\xi}\\
&\quad+\Big(-\frac{3}{2}\xi+\xi^2\Big)e^{-4\xi}+\frac{1}{4}\xi\,e^{-6\xi}\Big\}\Big]b_0\\
&\quad+\Big[(-2\xi+4\xi^2-2\varepsilon^2\xi^3)\,e^{-2\xi}+2\xi\,e^{-4\xi}\\
&\quad+\varepsilon^2e^{-2i\theta}\,\xi^3\,e^{-2\xi}\\
&\quad+\varepsilon^2e^{2i\theta}\{(2\xi^3-2\xi^4)\,e^{-2\xi}-\xi^3\,e^{-4\xi}\}\Big]\frac{B_1}{b^2}\\
&\quad+[(-6\xi+12\xi^2-8\xi^3-4\varepsilon^2\xi^3+4\varepsilon^2\xi^4)\,e^{-2\xi}\\
&\quad+(6\xi+2\varepsilon^2\xi^3)\,e^{-4\xi}\\
&\quad+\varepsilon^2e^{-2i\theta}\{(2\xi^3-2\xi^4)\,e^{-2\xi}-\xi^3\,e^{-4\xi}\}\\
&\quad+\varepsilon^2e^{2i\theta}\{(5\xi^3-8\xi^4+4\xi^5)\,e^{-2\xi}-4\xi^3\,e^{-4\xi}\}]\,\frac{b_2}{b^2}\Big\},
\end{aligned}\tag{3.3}$$

where $\varepsilon=r/b$. The integrals in (3.3) have been evaluated numerically.

Finally, the constants $B_1$, $b_0$ and $b_2$ can be determined by inserting (2.7), (2.10) and (3.3) into (2.15), obtaining

$$\left.\begin{aligned}
B_1&=-\frac{1}{4}a^2\varepsilon_0{}^2U+\Big(\frac{1}{2}-0.4311\,\varepsilon_0{}^2\Big)a^2b_0,\\
b_2&=-\frac{1}{4}a^2\varepsilon_0{}^2U+0.2358\,\varepsilon_0{}^2\,a^2b_0\,,
\end{aligned}\right\}\tag{3.4}$$

and

$$b_0=\frac{(\mathcal{E}_0^2-2)U}{1.8312-3.4486\,\mathcal{E}_0^2+2\ln\mathcal{E}_0}, \tag{3.5}$$

where $\mathcal{E}_0=a/b$.

## § 4. Discussion of the Results

Now, by integrating the fluid stresses over the circular cylinder, it is easily shown that the drag $D$ experienced by the cylinder per its unit length can be expressed as:

$$D=4\pi\mu b_0\,, \tag{4.1}$$

where $\mu$ is the viscosity of the liquid concerned.

Hence, if use is made of (3.5), we have

$$D=\pi\mu U\frac{4(a/b)^2-8}{1.8312-3.4486(a/b)^2+2\ln(a/b)}. \tag{4.2}$$

Putting $b/a=5$ and $U=1$ as in the case of Bairstow, Cave and Lang's calculation, (4.2) reduces to

$$D=5.14\,\pi\mu\,. \tag{4.3}$$

The present result is in good agreement with Harrison's, but not with Bairstow, Cave and Lang's.

A slight disagreement between the present result and Harrison's might perhaps arise from the conditions at the surface of the bounding plane walls. It is readily verified that the boundary conditions at the surface of the walls (2.13) and (2.14) are satisfield exactly by the present analysis, whereas in Harrison's analysis the conditions are satisfied only on a few lines parallel to the axis of the cylinder on the bounding walls.

In conclusion, the writer wishes to express his cordial thanks to Professor S. Tomotika for his continual encouragement and also for his kind inspection of the manuscript.

### References

1) L. Bairstow, B. M. Cave and E. D. Lang: Proc. Roy. Soc. **A 100** (1922) 394.
2) W. J. Harrison: Trans. Cambr. Phil. Soc. **23** (1924) 71.
3) H. Faxén: Diss. Uppsala (1921).
4) H. Faxén: Ann. d. Phys. **69** (1922) 89.

JOURNAL OF THE PHYSICAL SOCIETY OF JAPAN Vol. 11, No. 10, OCTOBER, 1956

# Experimental Studies on the Spectrum of Isotropic Turbulence behind Two Grids

By Hiroshi TSUJI

*Institute of Science and Technology,*
*University of Tokyo, Tokyo*

(Received June 12, 1956)

As a continuation of the previous work (Journ. Phys. Soc. Japan **10** (1955) 578), hot-wire measurements were made to determine the energy spectrum and decay of spectral components of turbulence behind two grids, the upstream grid having a larger mesh length than the downstream one, with a view to studying the characteristics of isotropic turbulence produced under various initial conditions and at high Reynolds numbers.

Similarity of the energy spectrum holds only for high-wave-number range, while the low-wave-number characteristics of turbulence depend on the initial conditions and exhibit no similarity. On the other hand, similarity of the spectrum of vorticity is observed over almost entire wave-number region for the turbulence either behind single or double grids unless high-wave-number disturbances are superposed. Therefore, Lin's decay law, $\overline{u^2}\sim[x^{-1}+const.]$, is expected to be valid for the turrblence either behind a single grid or with superposed disturbances of low wave numbers. Although superposed disturbances in high wave numbers destroy similarity of the spectrum, the disturbances decay out rapidly and the similarity spectrum is stable.

## §1. Introduction

When the Reynolds number of turbulence is large and the energy transfer between wave-number components plays an important role, the problem of isotropic turbulence has been treated by many authors by making plausible assumptions, such as the self-preservation of correlation function or the similarity of the spectrum during decay. The similarity spectrum, however, is expected to be only asymptotically correct for the large-wave-number range, its limit depending on the initial conditions and decreasing as the decay proceeds, and, therefore, the law of decay might also depend on the initial conditions. The importance of an experiment has been emphasized by Lin[1)2)] and Goldstein[3)] in order to find the dependence of the law of decay on the initial conditions in connection with the validity of the existing decay laws.

With a view to studying the characteristics of isotropic turbulence produced under various initial conditions, measurements were made on turbulence produced by two grids, the upstream grid having a larger mesh length than the downstream one. The results of decay and $g$-correlation measurements were presented in the preceding papers[4)5)].

As well known, the correlation and the spectrum have the Fourier transform relation to each other, and one of these quantities can be evaluated from the other. Nevertheless, the correlation is useful for understanding the large-scale physical process of turbulence during decay, while the spectrum for the small-scale process. Therefore, measurements were repeated on the energy spectrum and the decay of spectral components of turbulence produced by two grids, in order to investigate the similarity of the spectrum at high wave numbers of turbulence pertaining to various initial conditions. In this paper the results of these measurements are presented.

## §2. Experimental Equipment and Procedure

### *a*) *Experimental Equipment*

Wind tunnel, two grids (the mesh lengths, $M_1$ and $M_2$, of the first and second grids are 5 and 1 cm, respectively), traversing mechanism and compensating amplifier are the same as those described in detail in reference 5. However, a hot-wire used in the present experiment was nominally 0.0002-inch platinum, about 1 mm in length, etched from a Wollaston wire, instead of a 0.0003-inch wire used for the measurements of energy decay and correlation. Working temperature of the wire was about 300°C at heating current of 67 to 76 mA and the resistance of the wire was about 10.6 ohms. The time constant of the wire was then 0.7 to 0.5 milli-seconds.

In order to measure the spectrum of turbulent energy $\overline{u^2}$, the out put from the compensating amplifier was fed into a harmonic wave analyzer or into a variable-frequency parallel-T R-C band-pass filter.

The newly constructed harmonic wave analyzer was essentially the same as a Hewlett-Packard Model 300 A harmonic wave analyzer. The selectivity characteristics of our analyzer, however, were not so sharp, because high-Q coils were not available. This analyzer has an adjustable band width from 70 to 350 cycles per second and a frequency range from 70 to 18,000 cycles per second.

The tapered, parallel-T, R-C band-pass filter, which had been originally used by Hama[6] for the measurement of the spectrum of turbulence, was also used in this experiment. This instrument is a type recording nearly constant-percent band width, measuring the product of power spectrum times frequency. This has an obvious advantage in the high-frequency range where the energy of turbulence is very small. The selectivity characteristics of this analyzer are far from the optimum rectangular shape. The upper side of the selectivity curve is sufficiently steep and no appreciable error is attributable to the non-infinite slope for the spectrum measured in this investigation. Unfortunately, the lower side is not sufficiently steep[7][8], so that the non-cut-off characteristics of the filter provide erroneous results in the measurement of the spectrum especially in high-frequency range. In order to eliminate the influence of low-frequency components a simple capacitance-resistance low-cut network was added ahead of the filter. C and R were adjusted according to the tuning frequency of the filter. This filter has 30 tuning frequencies in the frequency range from 10 to 10,000 cycles per second.

The out-put signal from the selective amplifier of the harmonic wave analyzer or from the band-pass filter was fed into another amplifier in order to read the mean-square out put on a thermocouple milliammeter. In reading the out put, averages were taken over a period of 1 minute for the lower frequency range, accuracy being of the order of ±10 percent over most of the range. The accuracy is somewhat reduced near the low-frequency end below 50 cycles per second because of large-amplitude fluctuations and near the high-frequency end above 5,000 cycles per second because of low signal-to-noise ratio. The error due to a finite length of the wire increases as the scale of turbulent motions decreases and becomes significant at high wave numbers. No wire-length corrections were applied, however, because of lower accuracy in measurement in this range. The overall value of $\overline{u^2}$ served as a check and was good agreement with that calculated from the spectrum.

### b) *Measurement of Energy Spectrum*

Measurements were made of the one-dimensional energy spectrum $F(k)$, which is defined by

$$\overline{u^2}=\int_0^\infty \overline{u^2}F(k)dk\ ,$$

$k$ being the one-dimensional wave number, at a number of sections downstream of the second grid or a single grid for mean wind velocities of 5, 10 and 15 m/sec. The distance, $X$, between the two grids was 50, 200, 250, 350 or 450 cm.

### c) *Measurement of Decay of Spectral Components*

In order to study the process of decay in more detail, measurements were also made of the decay of the spectral components $\overline{u_k{}^2}$, which is defined by

$$\overline{u^2}=\int_0^\infty \overline{u_k{}^2}dk\ ,\quad \text{i.e.,}\quad \overline{u_k{}^2}=\overline{u^2}F(k)\ ,$$

for mean wind velocities of 10 and 15 m/sec behind the two grids or a single grid. The distance between the two grids was 50, 200, 250, 350 or 450 cm. Measurements were carried out by moving a hot-wire probe in the mean wind direction (longitudinally) and reading the out-put signal which passed through a filter of a fixed tuning frequency. For such a kind of measurement, however, the non-cut-off characteristics of the filter cause an appreciable effect which is apt to lead to an unreasonable

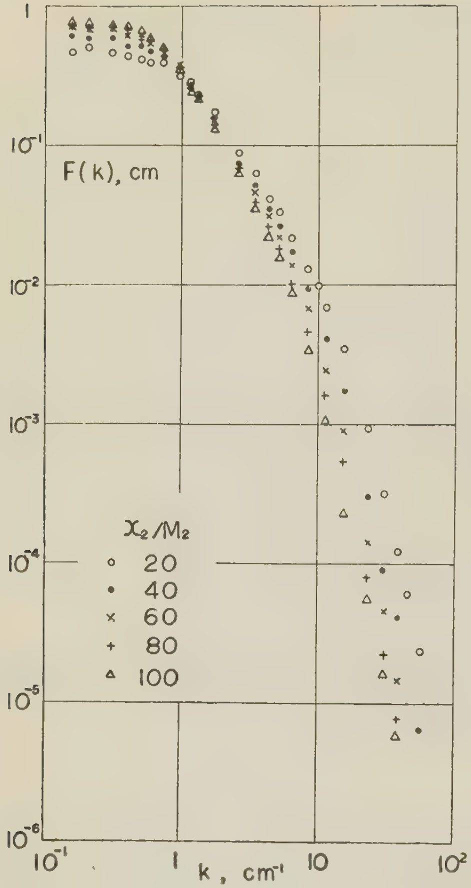

Fig. 1. Energy spectrum $F(k)$: Second grid alone, $U=10$ m/sec.

result in that the decay of the spectral components becomes slower as the frequency increases in the high frequency range.

*d) Determination of Microscale*

The microscale, or the dissipation length, $\lambda$, defined by the relation

$$\frac{1}{\lambda^2}=-\frac{1}{2}\left[\frac{\partial^2 g(r)}{\partial r^2}\right]_{r=0},$$

or

$$\frac{1}{\lambda^2}=\int_0^\infty k^2F(k)dk\ ,$$

where $g(r)$ is the lateral double velocity-correlation coefficient introduced by von Kármán and Howarth[9], can be measured by various methods: e.g., by the differentiation circuit[10][11], or by zero counting[12][13]. In this paper, however, the values of $\lambda$ were evaluated by integrating the $k^2F(k)$-curves, in view of investigating the similarity of the measured spectrum. When the mean wind velocity is large, the turbulence behind the second grid of fine mesh contains a large amount of high wave-number components at the very early stage of decay. Therefore, the $k^2F(k)$-curves do not close sufficiently at the high wave-number end up to which the measurements of the spectrum were carried out and it becomes difficult to evaluate the value of $\lambda$ with sufficient accuracy. As is well known, however, there exists the minimum wave length, i.e., the maximum wave number, of turbulence to be resolved by the hot-wire of finite length. If the minimum wave length, $l_{\min}$, of turbulence, which can be resolved by a hot-wire of 1 mm long, is assumed to be 2 mm, the maximum resolvable wave number, $k_{\max}$, of turbulence is

$$k_{\max}=2\pi n_{\max}/U=2\pi/l_{\min}=31.4\ \text{cm}^{-1}\ ,$$

in which $U$ is the mean wind velocity, and $n$ the frequency. Consequently, the maximum frequency limits for various wind velocities become as follows:

| $U$, m/sec | 5 | 10 | 15 | 20 |
|---|---|---|---|---|
| $n_{\max}$, kc/sec | 2.5 | 5 | 7.5 | 10 |

Therefore, it may be emphasized that the determination of the higher moments of spectrum, or, the mean square of higher time derivatives of $u$, of the turbulence which contains a large amount of the higher wave-number components becomes unreliable, even if the measuring equipments, such as the compensating amplifier and the differentiation circuit, had good frequency characteristics up to a very high frequency range.

## § 3. Experimental Results and Discussion

*a) Energy Spectrum*

The energy spectrum $F(k)$ behind a second grid alone for $U=10$ m/sec is shown in Fig. 1, in which $x_2$ is the distance downstream of the second grid. The observed spectrum agrees with those already obtained by many other authors, e.g., by Liepmann, Laufer and Liepmann[12], by Hama[6], etc. As is well known, $F(k)$ tends to a constant value $F(0)$ as $k$ tends to 0 and decreases rapidly as $k$ increases. The value of $F(0)$ increases as the decay time proceeds, corresponding to the increase in the integral scale $L=2\int_0^\infty g(r)dr$ during the decay. Any definite power law of spectrum cannot be observed over a finite wave-number range except at very high wave-

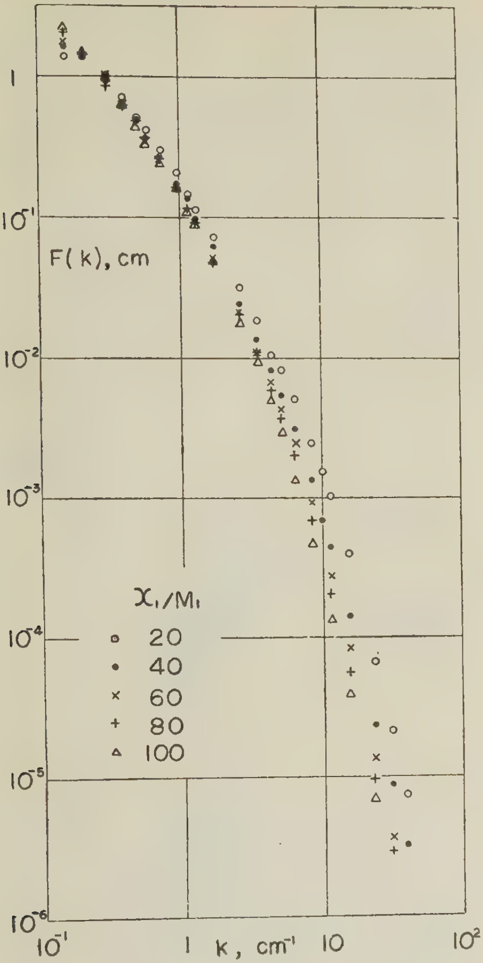

Fig. 2. Energy spectrum $F(k)$: First grid alone, $U=10$ m/sec.

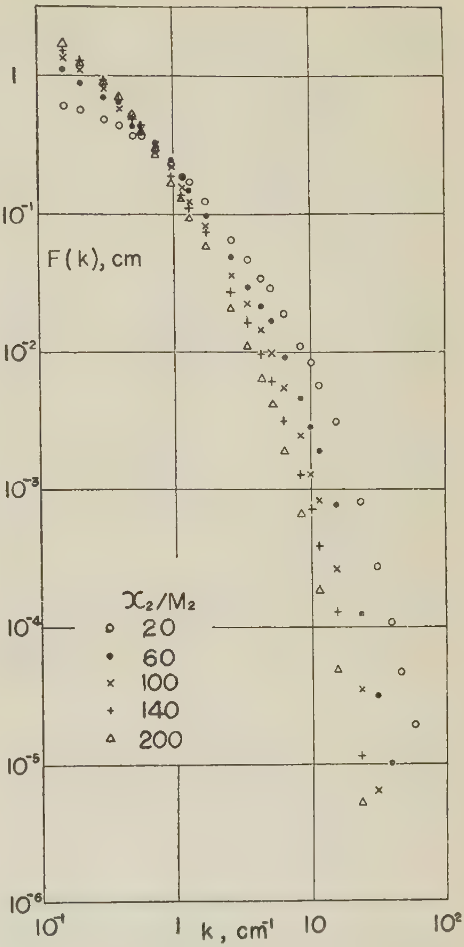

Fig. 3. Energy spectrum $F(k)$: $X=350$ cm, $U=10$ m/sec.

number region in these measured one-dimensional spectrum curves of $F(k)$, as was pointed out theoretically by the present author[14]. Moreover, no definite conclusions can be deduced about the power law of spectrum over the very high wave-number region of these observed spectrum, since the accuracy of the measurement is unfortunately insufficient because of low signal-to-noise ratio.

Results of the spectrum measurements behind the first grid alone for $U=10$ m/sec are presented in Fig. 2, in which $x_1$ is the distance downstream of the first grid. It is seen that the value of $F(k)$ at small $k$ is very large because of the large mesh length of the first grid.

Fig. 3 shows the spectrum $F(k)$ at various distances downstream of the two grids placed 350 cm apart for $U=10$ m/sec. The distance, $X$, between the two grids being large in this case, the high wave-number components of turbulence produced by the first grid have already decayed out and the low wave-number components are superposed on the turbulence produced by the second grid. Comparison of these results with those in Fig. 1 shows that the effect of the large-scale turbulence produced by the first grid predominates and the value of the spectrum at low wave numbers is much larger than that resulted from the second grid alone. The spectra $F(k)$ for $X=200$, 250 and 450 cm are found to be similar to those in Fig. 3.

Fig. 4 shows the spectrum $F(k)$ for $X=50$ cm and $U=15$ m/sec. In this case, $X$ is very small and the shapes of $F(k)$-curves quite resemble those for the first grid alone except at small values of $x_2/M_2$. This is due to the

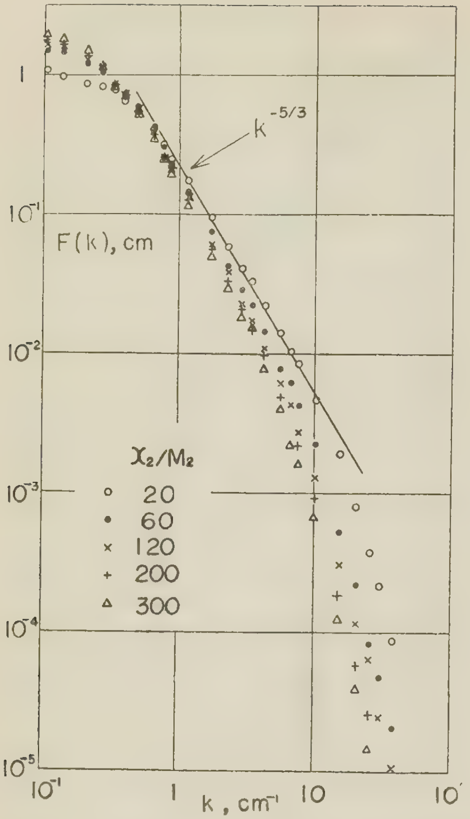

Fig. 4. Energy spectrum $F(k)$: $X=50$ cm, $U=15$ m/sec.

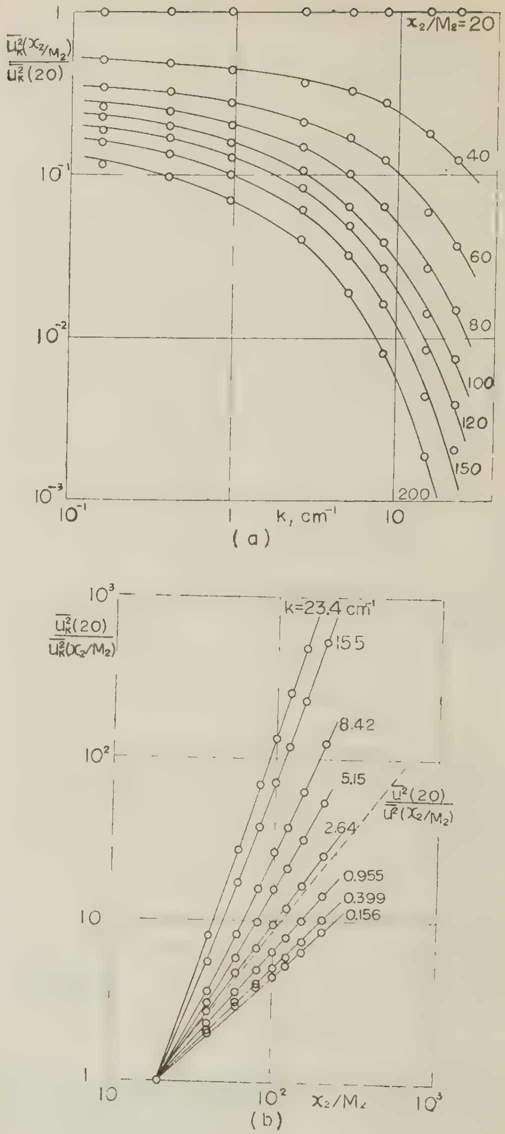

Figs. 5 (a) and (b). Decay of spectral components: Second grid alone, $U=10$ m/sec.

fact that the fine-scale turbulence produced by the second grid decays out rapidly and the large-scale turbulence produced by the first grid remains almost untouched. It is observed that $k^{-5/3}$ spectral law holds over a finite range of wave numbers for the spectrum at $x_2/M_2=20$. It was pointed out by the present author[14] that when high wave-number disturbances are superposed on the isotropic turbulence the power law might hold for the one-dimensional spectrum. The above experimental result shows that this is the case.

*b) Decay of Spectral Components*

The experimental results of the decay of spectral components behind the second grid alone for $U=10$ m/sec are shown in Figs. 5 (a) and 5 (b) in which $\overline{u_k^2}(x_2/M_2)/\overline{u_k^2}(20)$ is plotted against $k$ and $x_2/M_2$, the parameters being $x_2/M_2$ and $k$, respectively. The value of $n$ in the power law, $u_k^2(20)/\overline{u_k^2}(x_2/M_2)\sim(x_2/M_2)^n$, increases monotonically from the value smaller than 1 at low wave numbers to $\infty$ as $k$ increases. The decay of total energy $\overline{u^2}(x_2/M_2)/\overline{u^2}(20)$ is also plotted for the purposes of reference in this figure.

Figs. 6 (a) and 6 (b) show the decay of spectral components behind the first grid alone for $U=15$ m/sec.

Figs. 7 (a) and 7 (b) show the decay of spectral components behind the two grids placed 250 cm apart for $U=10$ m/sec. The decay of the high wave-number components is similar to that for the second grid alone, but the decay of the low wave-number components is very slow and the effect of the superposed large-scale turbulence produced by

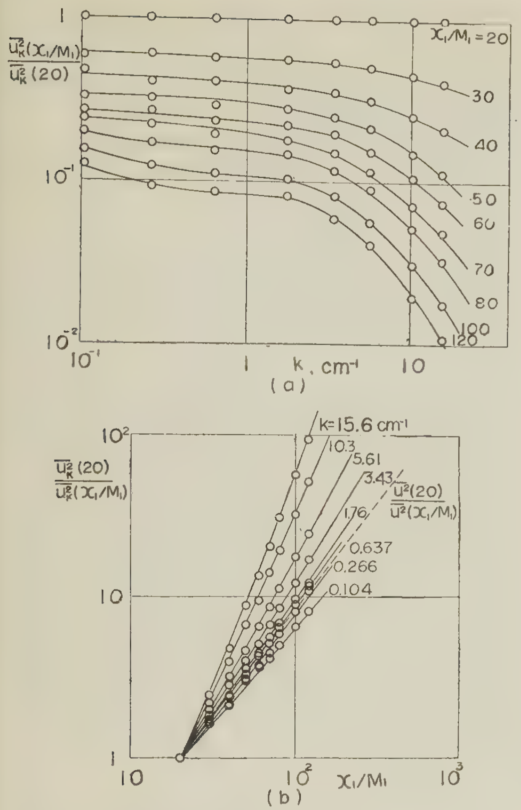

Figs. 6 (a) and (b). Decay of spectral components: First grid alone, $U=15$ m/sec.

the first grid appears considerably. Moreover, it is readily seen how the decay of the low wave-number components affects that of total energy $\overline{u^2}$. The decay curves for $X=200$, 350 and 450 cm are found to be similar to those in Figs. 7 (a) and 7 (b).

The decay of spectral components for $X=50$ cm and $U=10$ m/sec is shown in Figs. 8 (a) and 8 (b). For small $X$ such as this case, the turbulence produced by the second grid is superposed mainly on the high wave-number range of turbulence produced by the first grid. Therefore, the decay of spectral components over all wave-number range at the early stage of decay is influenced by the superposed disturbances. Since these superposed disturbances decay out rapidly, the decay of spectral components over all wave-number range tends to resemble that for the first grid alone.

### c) *Similarity of Spectrum $F(k)$*

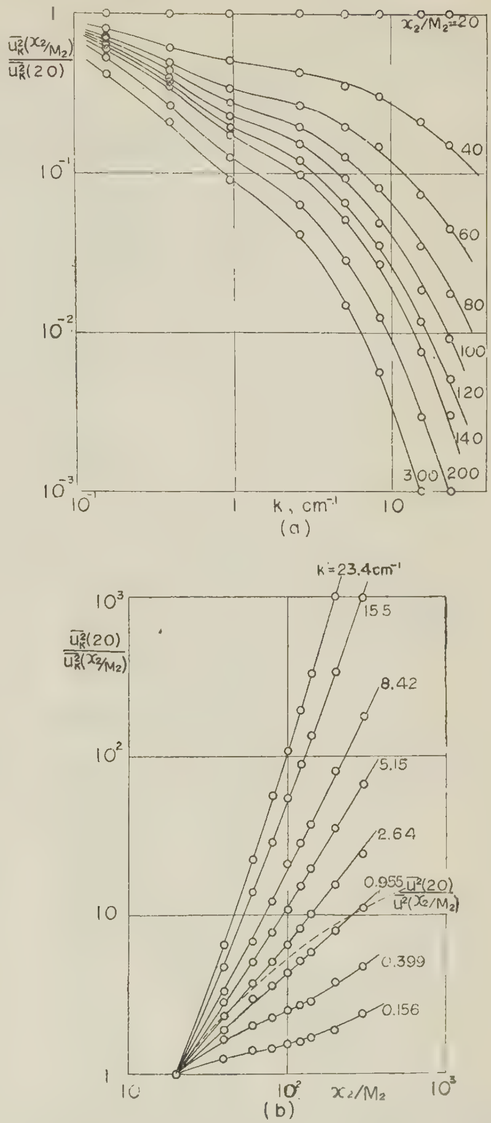

Figs. 7 (a) and (b). Decay of spectral components: $X=250$ cm, $U=10$ m/sec.

With the value of $\lambda$ determined by integrating the $k^2F(k)$-curves, the value of $F(\lambda k)/\lambda$ is replotted against $\lambda k$. Fig. 9 (a) shows $F(\lambda k)/\lambda$ for the second grid alone and $U=10$ m/sec. It is seen that the complete similarity holds in the wave-number range for $\lambda k>1$, the actual deviation from the similarity being observed for $\lambda k<1$. The value of $F(0)/\lambda$ decreases as the decay time proceeds. This tendency may be expected from the relation

$$F(0)/\lambda=2L/\pi\lambda\ ,$$

in which

$$L/\lambda=2\int_0^\infty g(r/\lambda)d(r/\lambda)\ ,$$

since the $g(r/\lambda)$-curves contract laterally outside the self-preserving region and $L/\lambda$ decreases as the decay time proceeds5)15). The same

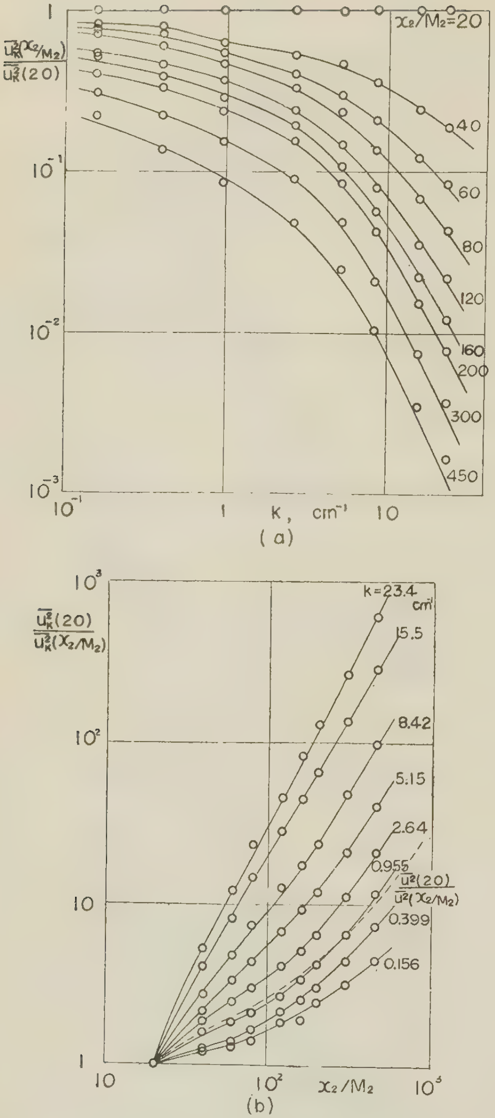

Figs. 8 (a) and (b). Decay of spectral components: $X=50$ cm, $U=10$ m/sec.

tendency is observed for the results of measurements for $U=5$, and 15 m/sec, and also for the first grid alone. However, it is seen generally that as the mesh Reynolds number $R_M=UM/\nu$ increases the wave-number range for which the similarity of spectrum holds becomes larger and the deviation from the similarity at low wave-number range decreases.

Fig. 9 (b) shows $F(\lambda k)/\lambda$ for $X=350$ cm and $U=10$ m/sec. Complete similarity seems to hold for $\lambda k$ larger than 1, and the effect of the superposed non-similar large-scale turbulence may be observed. It is to be noted that the value of $F(0)/\lambda$ increases with the increasing $x_2/M_2$, contrary to the tendency observed for the turbulence behind a single grid. This corresponds to the fact that the $g(r/\lambda)$-curves of any family outside the self-preserving region expand laterally as $x_2/M_2$ increases.

Fig. 9 (c) shows $F(\lambda k)/\lambda$ in the presence of two grids placed 50 cm apart for $U=10$ m/sec. In this case, the shape of $F(\lambda k)/\lambda$ resembles those with the first grid alone except at small values of $x_2/M_2$. For small value of $X$, the turbulence produced by the first grid is predominant, and the small-scale turbulence produced by the second grid is merely superposed on the high wave-number range of turbulence produced by the first grid for the latter of which the similarity of spectrum holds. The fact that the superposed small-scale turbulence decays rapidly and the spectrum curve tends to resemble the original one indicates the stability of spectrum. The experimental evidence thus supports Lin's theoretical discussion on the stability of spectrum2).

### d) *Similarity of Spectrum of Vorticity*

By plotting $\lambda k^2F(\lambda k)$ against $\lambda k$, the similarity of $k^2F(k)$ was also examined. The quantity $k^2F(k)$ is proportional to the spectrum of vorticity, $(\overline{\partial u/\partial x})^2$, and might be determined directly from the frequency analysis of the derivatives $du/dt$. In this paper, however, this was calculated from the measured energy spectrum $F(k)$. Figs. 10 (a), 10 (b) and 10 (c) show $\lambda k^2F(\lambda k)$ for the second grid alone, the two grids with $X=450$ cm and $X=50$ cm, respectively, and for $U=15$ m/sec. It is seen that the similarity of $\lambda k^2F(\lambda k)$ holds over almost entire wave-number region in Figs. 10 (a) and 10 (b), while the deviation from the similarity is observed in Fig. 10 (c). Hence, it may be concluded from these results that the effect of the deviation from the similarity will be negligible in the computation of the rate of energy dissipation for the turbulence either behind a single grid or two grids except for the case of small $X$. Therefore, Lin's decay law1)2)3), $\overline{u^2}=\alpha x^{-1}+\beta$, is expected to be valid for the turbulence behind a single grid or with superposed disturbances of low wave numbers. This decay law was already confirmed by the experimental results of the

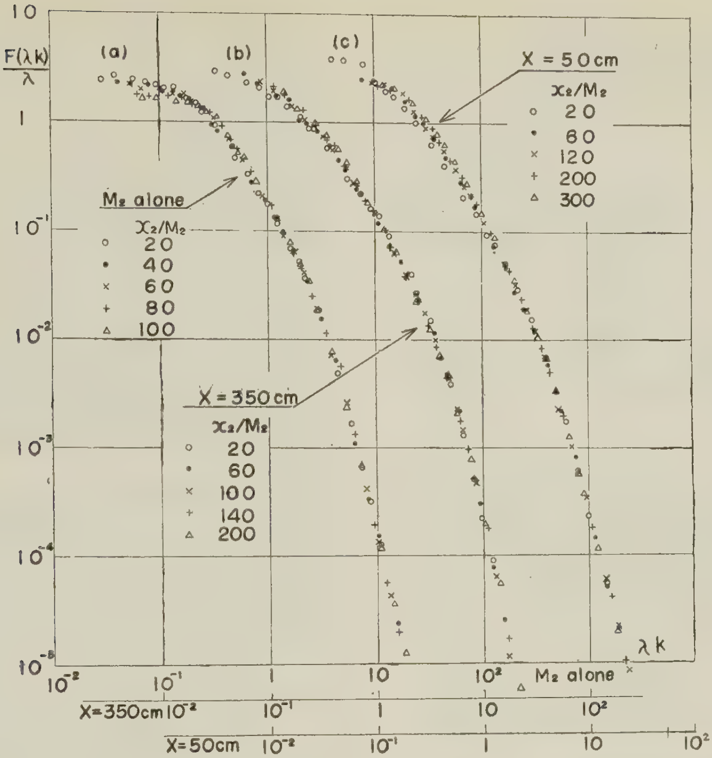

Figs. 9 (a), (b) and (c). Energy spectrum $F(\lambda k)/\lambda$: Second grid alone, two grids with $X=350$ cm and $X=50$ cm, respectively, and $U=10$ m/sec.

decay of energy as reported in the preceding papers[4)5)].

## § 4. Conclusion

The experimental investigation of the energy spectrum of the turbulence behind two grids confirms the following conclusions which have already been obtained in the preceding papers[4)5)] on the measurements of the energy decay and the correlation:

a) There exists no complete similarity of the energy spectrum nor the linear decay law, which may be deduced from the assumption of the complete similarity.

b) The low-wave-number characteristics of turbulence depend on the initial conditions and exhibit no similarity during decay, while the high-wave-number components are independent of the initial conditions and retain the similarity. The similarity of the spectrum of vorticity, on the other hand, is observed over almost entire wave-number range for the turbulence either behind a single grid or two grids except for the case in which the high-wave-number disturbances are superposed.

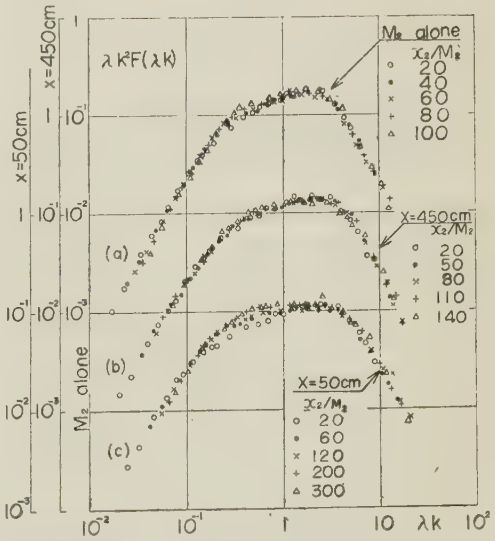

Figs. 10 (a), (b) and (c). Spectrum of vorticity $\lambda k^2 F(\lambda k)$: Second grid alone, two grids with $X=450$ cm and $X=50$ cm, respectively, and $U=15$ m/sec.

Therefore, Lin's decay law, $\overline{u^2}=\alpha x^{-1}+\beta$, which is derived under the assumption that the actual deviation from the similarity will be limited only for small values of wave number and hence the effect of the deviation will enter only in the calculation of energy but be negligible in the computation of the rate of energy dissipation, is valid for the turbulence either behind a single grid or with superposed disturbances of low wave numbers.

c) Superposed disturbances of high wave numbers destroy the similarity of spectrum, so that Lin's decay law cannot be relized. The disturbances, however, decay out rapidly and the similarity spectrum becomes stable.

The author would like to express his sincere thanks to Dr. F. R. Hama of University of Maryland for his suggestion of this problem and his continual guidance and encouragement in the course of this investigation, to Prof. I. Tani for his valuable advice and discussions, and to Mr. Y. Onda for his active assistance in conducting the experiments. This work is supported partly by the fund of the Ministry of Education in Aid of Scientific Research.

### References

1) C. C. Lin: Proc. Nat. Acad. Sci., U.S.A. **34** (1948) 540.
2) C. C. Lin: Proc. 4th Symp. Appl. Math. (1953) 19.
3) S. Goldstein: Proc. Camb. Phil. Soc. **47** (1951) 554.
4) H. Tsuji and F. R. Hama: Journ. Aero. Sci. **20** (1953) 848.
5) H. Tsuji: Journ. Phys. Soc. Japan **10** (1955) 578.
6) R. Hama: Rep. Inst. Sci. Tech. Univ. Tokyo **7** (1953) 145.
7) L. Stanton: Proc. I.R.E. **34** (1946) 447.
8) J. L. Bower: Electronics **20** (1947) 131.
9) Th. von Kármán and L. Howarth: Proc. Roy. Soc. London **A 164** (1938) 192.
10) A. A. Townsend: Proc. Camb. Phil. Soc. **43** (1947) 560.
11) G. K. Batchelor and A. A. Townsend: Proc. Roy. Soc. London **A 190** (1947) 534.
12) H. W. Liepmann, J. Laufer and K. Liepmann: NACA TN **2473** (1951).
13) H. W. Liepmann and M. S. Robinson: NACA TN **3037** (1953).
14) H. Tsuji: Journ. Japan Soc. Aero. Eng. **4** (1956) 210.
15) G. K. Batchelor and A. A. Townsend: Proc. Roy. Soc. London **A 193** (1948) 539.

---

JOURNAL OF THE PHYSICAL SOCIETY OF JAPAN Vol. 11, No. 10, OCTOBER, 1956

# Experimental Investigation of the Wake behind a Sphere at Low Reynolds Numbers

By Sadatoshi TANEDA

*Kobe University of Mercantile Marine*

(Received June 19, 1956)

Wakes produced by a sphere moving in a tank of water were photographically investigated at Reynolds numbers from 5 to 300. Main results obtained are as follows.

1. The critical Reynolds number at which the parmanent vortex-ring begins to form in the rear of a sphere is about 24.
2. The size of vortex-ring is nearly proportional to the logarithm of the Reynolds number.
3. The wake behind a sphere begins to oscillate at the rear of the permanent vortex-ring when Reynolds number of about 130 is reached.

## §1. Introduction

Up to the present, many theoretical and experimental investigations have been carried out concerning the viscous flow past a sphere. It is well known that when Reynolds number is sufficiently low, the theoretical calculations of the flow around a sphere can approximately be made by the methods of Stokes and Oseen or by other appropriate methods.[1][2][3]

However, the interest of the experimentalists have centered, in the past, mainly round the problem of the drag and no observation seems to have yet been made concerning the flow pattern for the case of Reynolds number lower than 150. (Reynolds number, $R$, is $Ud/\nu$; where $U$ is the model speed, $d$ is the diameter of the sphere and $\nu$ is kinematic viscosity.)

In the present report, detailed photographic observations of the velocity field in the wake immediately behind a sphere, at Reynolds numbers from 5 to 300, are described, together with some remarks about the apparatus and the experimental technique concerned.

## § 2. Apparatus and Experimental Method

The experiments were carried out with the glass water tank of 100 cm in length, 20 cm in breadth and 30 cm in depth. A general description of the appratus and an account of the experimental technique were given in the previous paper[4], and so need not be repeated here.

Various modifications, however, were made in the apparatus. In order to eliminate the very small vibrations of the carriage, the base of the gear box was separated from the foundation of the water tank, and the nut, which was attached to the carriage and engaged with the lead screw, was allowed "*play*" in a direction normal to the axis of the lead screw. As the result of a careful adjustment, a sufficiently smooth and uniform velocity of the carriage was obtained. Fig. 1 shows the general arrangement of the apparatus.

Steel ball-bearings of three different sizes were used as the model. The ball was attached to one end of a fine piano wire serving as a support. The piano wire was 0.5 mm in diameter and 15 mm in length, and it was fixed to the carriage through a steel needle. In Table I the size of the models are given.

The method of illumination was the same as in ultramicroscopy. A sheet of intense light from incandescent lamps behind a narrow slit was made to pass through a horizontal plane, containing the center of the sphere on it. The illuminated object was photographed from above with a camera fixed to the carriage.

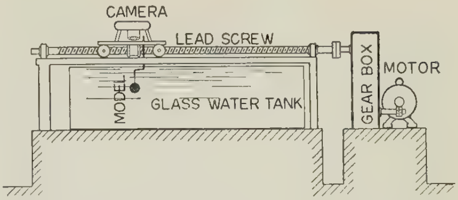

Fig. 1. Schematic diagram of the apparatus.

Table I.

| Sphere | | | |
|---|---|---|---|
| $d$(mm) | $d'$(mm) | $d'/d$ | $F_0/F$ |
| 19.82 | 0.5 | 1/40 | 1/190 |
| 15.08 | 0.5 | 1/30 | 1/330 |
| 9.52 | 0.3 | 1/32 | 1/840 |

$d$ : Diameter of the sphere
$d'$: Diameter of the support
$F_0$: Sectional area of the sphere
$F$ : Cross-sectional area of the water tank.

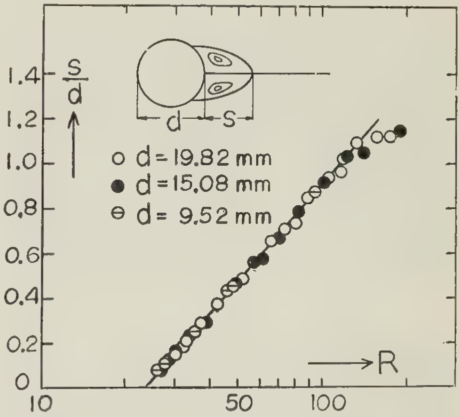

Fig. 2. Plot of $s/d$ against $\log R$. (Sphere)

## § 3. Critical Reynolds Number at which Permanent Vortex-Ring begins to Form

Concerning this problem there has been no experimental investigation except that by Nisi & Porter,[5] and little is known of the accurate value of the critical Reynolds number.

The present experiment was made by means of aluminium dust method. Before beginning the experiment, a great care was taken to allow the water to become sensibly still and to prevent small air bubbles from attaching to the surface of the sphere. Many photographs of the streamlines immediately behind the sphere were taken at various Reynolds numbers by making long duration of the exposure. In Photo 1 some of the photographs obtained are shown.

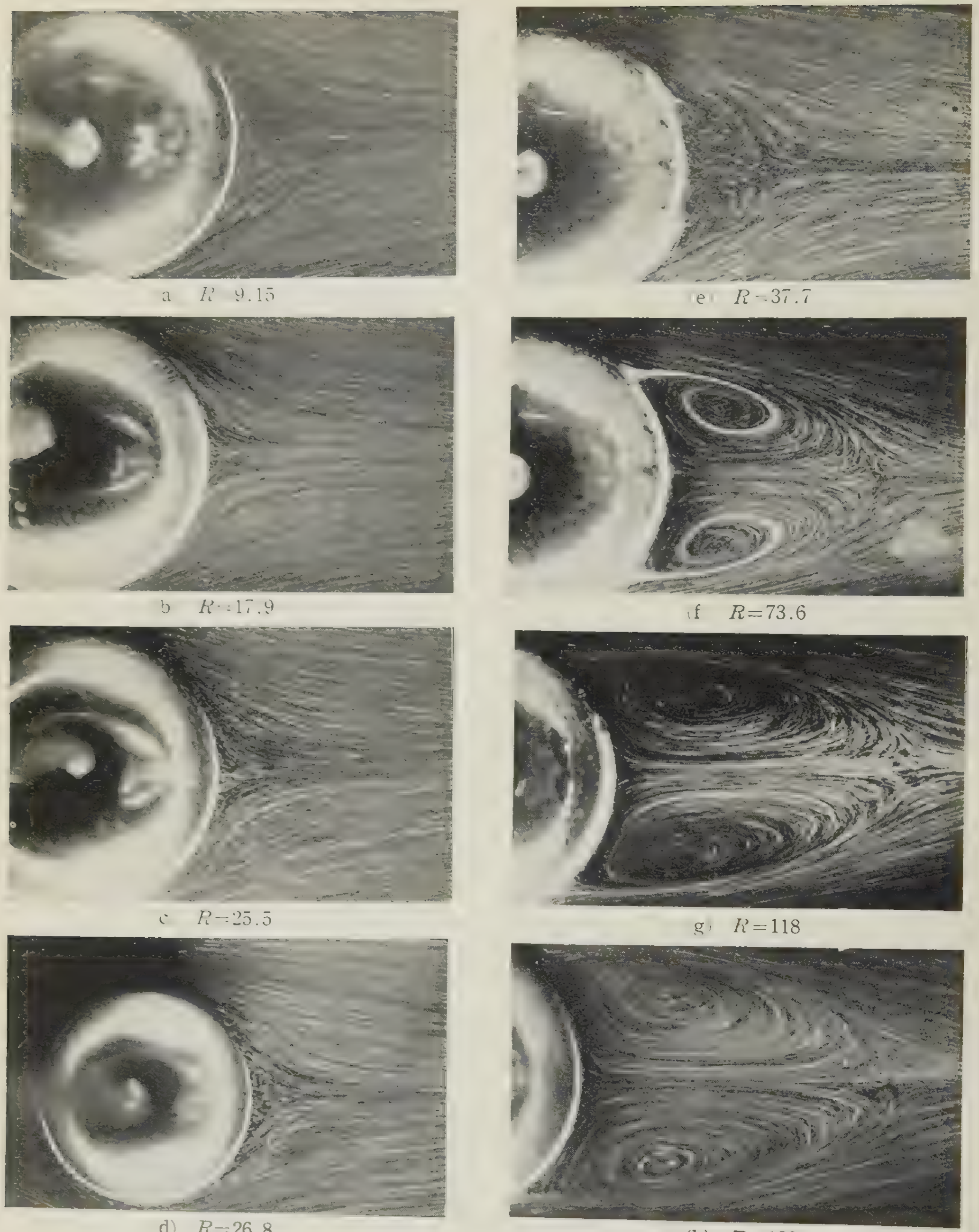

a) $R=9.15$

b) $R=17.9$

c) $R=25.5$

d) $R=26.8$

(e) $R=37.7$

(f) $R=73.6$

(g) $R=118$

(h) $R=133$

Photo 1. Photographs showing flow pattern in the wake immediately behind a sphere.

As is seen from the photographs, when the Reynolds number is lower than 22, the flow around the sphere is perfectly laminar and vortex-ring can be found nowhere. When Reynolds number of about 25 is reached, however, a small permanent vortex-ring appears in the neighborhood of the rear stagnation point. As the Reynolds number is increased further it grows and becomes more and more elongated in the flow direction. The size of vortex-ring is plotted against the Reynolds number in Fig. 2.

It is very difficult to determine the critical Reynolds number directly from the photographs for the following reasons: (1) the dimension of vortex-ring is still very small, (2) the vortex-ring appears in the neighborhood of the rear stagnation point where the velocity of the flow is extremely small. However, it can be estimated from Fig. 2 that the critical Reynolds number, at which the permanent vortex-ring begins to form, is about 24. It should be noticed that this value of Reynolds number 24 far exceeds the range in which approximations of Stokes or Oseen is valid.

The present experiments were carried out at $F_0/F<1/190$, where $F_0$ is the cross-sectional area of the sphere and $F$ is that of the tank. The influence of the tank wall was scarecely detected.

Furthermore, the influence of the support was also tested. It was observed that a slight asymmetry of the flow pattern was caused by the presence of the support; namely the separation point just behind the support was moved slightly forward. Of course, the smaller the diameter of the support was, as compared with that of the sphere, the less its influence was. In the present experiment the measurements were made at $d'/d<1/30$, where $d'$ is the diameter of the support and $d$ is that of the sphere, and it was confirmed that the support effect was nearly negligible in determining the critical Reynolds number.

## § 4. Relation between the Size of Vortex-Ring and the Reynolds Number

The permanent vortex-ring appears in the rear of a sphere at $R=24$ and, as the Reynolds number is increased, it grows and becomes more and more elongated in the flow direction.

As will be seen from Fig. 2 the size of vortex-ring is nearly proportional to the logarithm of the Reynolds number. On the other hand, in the case of a circular cylinder, as was shown in the previous paper, the size of twin-vortices is proportional to the Reynolds number itself. (see Fig. 3). Thus there is a conspicuous difference between the two cases of a sphere (three dimension) and a circular cylinder (two dimension).

The location of the center of the vortex-ring was also determined at various Reynolds numbers. When $R$ was small, it was rather difficult to locate photographically the accurate position of a vortex center. Therefore the measurements were made only at $R>50$. The results are shown in Fig. 4.

## § 5. Reynolds Number at which Vortex-Ring begins to Oscillate

The experiments concerning the oscillation of the permanent vortex-ring behind a sphere were carried out in the past by Schmiedel (1928)[6] and Möller (1938),[7] but comparatively little is known of the critical Reynolds number at which the oscillation begins.

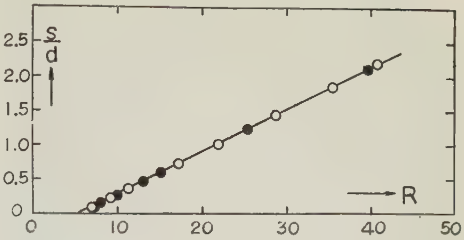

Fig. 3. Plot of $s/d$ against $R$. (Circular cylinder)

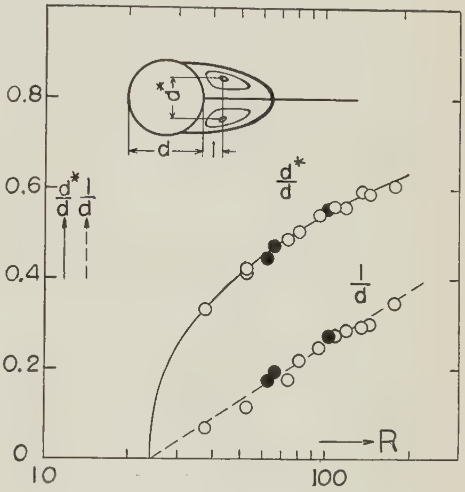

Fig. 4. Position of the vortex center.

As can be seen from the Photo 1, the permanent vortex-ring becomes larger as the Reynolds number is increased, but the flow of fluid around a sphere is sensibly stationary so far as Reynolds number is less than about 130.

When Reynolds number of about 130 is reached, however, the faint periodic pulsative motion with a very long period occurs at the rear of the vortex-ring. And as the Reynolds number is increased further, the oscillation becomes more and more conspicuous.

The flow behind the vortex-ring, however, was found to be perfectly laminar until Reynolds number of about 200 is reached. Moreover it was observed that the front-part of the vortex-ring was stably attached to the sphere up to $R=300$ or so.

The process of development of the wake behind a sphere is illustrated in Fig. 5.

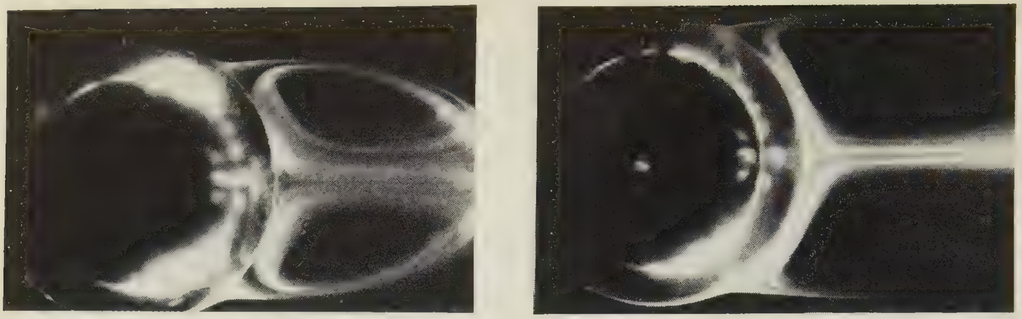

(a) $R=104$ (b) $R=202$

Photo 2. Photographs obtained by means of condensed milk method.

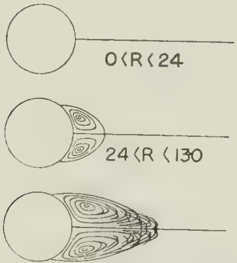

Fig. 5. Process of the development of the wake behind a sphere.

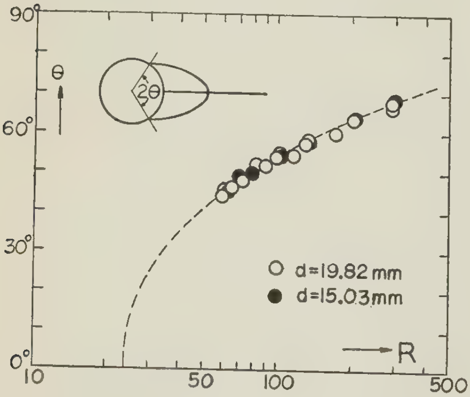

Fig. 6. Position of the separation.

As for the flow arround a sphere at Reynolds numbers exceeding 150, the detailed experiments have been reported by Möller in 1938.

## § 6. Position of Separation

The position at which the separation occurs was determined by examining the photographs at Reynolds numbers between about 60 and 300.

The experiments were made mainly by means of condensed milk method. When a sphere thinly coated with condensed milk is set in motion in water, the milk melts in the wake little by little and reveals the separation point clearly. When Reynolds number was small, it was considerably difficult to determine the separation point, because the streamlines in the immediate neighborhood of the separation point were not clear. Therefore the measurements were made at $R>60$.

The results are shown graphically in Fig. 6, and some of the records are shown in Photo 2.

In conclusion, the author wishes to express his thanks to Professor Hikoji Yamada of Research Institute for Applied Mechanics, for constant advice and encouragement in the course of this work.

### References

1) S. Tamotika and T. Aoi: Quart. Journ. Mech. App. Math. **3** (1950) 140.
2) M. Kawaguchi: J. Phys. Soc. Japan **10** (1955) 695.
3) T. Pearcey and B. McHugh: Phil. Mag. (7) **46** (1955) 783.
4) S. Taneda: J. Phys. Soc. Japan **11** (1956) 302.
5) H. Nisi and A. W. Porter: Phil. Mag. (6) **46** (1923) 754.
6) J. Schmiedel: Phys. Zeitschr. **29** (1928) 593.
7) W. Möller: Phys. Zeitschr. **39** (1938) 57.

JOURNAL OF THE PHYSICAL SOCIETY OF JAPAN Vol. 11, No. 10, OCTOBER, 1956

# On the Capacity of a Discrete Channel, II.
# Mathematical Expression of the Capacity of a Noisy Channel which is Expressible by Corresponding Two Multi-state Diagrams

By Saburo MUROGA
*Electrical Communication Laboratory*

(Received December 7, 1955)

In this paper, after some explanation of the use of Shannon's diagram to describe a Markoffian process, a noisy channel of a general character in which the transmitter has constraints on allowed sequences of symbols and is disturbed by a Markoffian noise is described by correlating two multi-state diagrams which correspond to the transmitter and the receiver, respectively. The set of probabilities of transitions from a symbol in the transmitting diagram to one in the receiving diagram specifies the stochastic character of transmission. Then a mathematical expression for the transmission rate is deduced. Finally, the problem of finding the channel capacity as the maximum of the transmission rate is discussed with some numerical example.

## § 1. Introduction

In the previous paper (Part I), a mathematical expression for the capacity of a noisy channel which is disturbed by noise symbol by symbol and is expressible by correlating two single-state diagrams, was dealt with[1]. The aim of the present paper is to discuss the capacity of a noisy channel of a more general character. That is, the channel is experssed by two multi-state diagrams, one for the transmitter and the other for the receiver, each line in the former corresponding to one in the latter under the disturbance of the noise.

A noisy channel expressed in this way is comprehensive and we can easily find examples which should be treated by such an expression. For example, a noisy channel with constraints on allowed sequences of symbols is no longer expressible by using the correspondence between two single-state diagrams. The second example is a noisy channel in which noise disturbs each sequence of several symbols, instead of each of symbols independently though symbols are transmitted indenpently of each other. Another example is a case where the transmitter is expressed by a multi-state diagram and noise disturbs each sequence of symbols, that is, cases like a teleprinter communication where a figure-blank signal and a letter-blank signal have some after-effects on following symbols, and a radio communication channel under influence of the fading where the receiver is provided with an automatic gain control in order to overcome disturbance influencing sequences of symbols. These channels can not be treated by a model of single-state diagrams in Part I.

## § 2. Shannon's Diagram

Shannon introduced elegantly a diagram consisting of a finite number of states connected by oriented lines, to express an information source and a channel with their statistical properties[2]. Some authors discussed its mathematical foundation[3),4)], so only its practical aspects will be mentioned here. A multiple Markoffian process for a source or a channel can be reduced to a simple Markoffian process by this diagram which offers a simpler form. So we shall extend his idea further.

This diagram will be called Shannon's diagram hereafter and the following classification may be convenient.

(a) *Shannon's diagram of the first kind.*

Assume we have a certain information source which generates $N$ letters, $L_1, L_2, \cdots$ and $L_N$. Now we will consider how to write a diagram to express the information source of a multiple Markoffian process where a

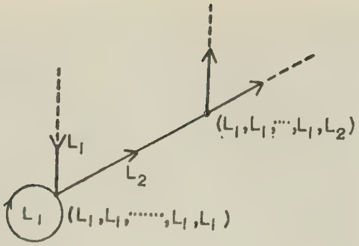

Fig. 1.

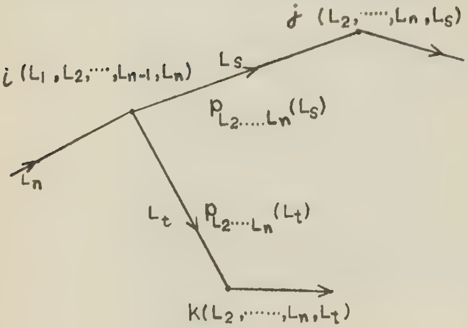

Fig. 2.

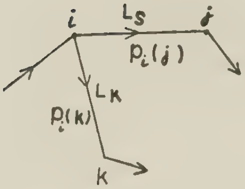

Fig. 3.

letter is generated with a probability depending on the preceding $n$ letters.

First let us label the states of the number of $N^n$ in a diagram, by $N^n$ coordinates, $(L_1, L_1, \cdots, L_1)$, $(L_1, L_1, \cdots, L_1, L_2)$, $\cdots$, $(L_N, L_N, \cdots, L_N)$, each of which is an arrangement of $n$ letters out of $N$ letters. Let us take any state among them and find another state as follows: an arrangement of the letters from the second to the $n$-th in the coordinate of the former state is just that of the letters from the first to the $(n$-$1)$ th in the coordinate of the latter state. Now draw a line from the former to the latter with an arrow in that direction and label it with the $n$-th letter of the coordinate of the latter state, as shown in Fig. 1. This letter should be considered to be generated when a source follows this line from the former state toward tha latter. Especially for a state with a coordinate where all letters are the same, the second state which should be searched by the above procedure coincides with itself, so we make a loop connected to this state, the coordinate of this state consisting of the same letters.

Next take a certain state, for example $(L_1, L_2, \cdots, L_n)$. As easily seen, when the source stands at this state, a sequence of letters $L_1, L_2, \cdots, L_n$ were generated in the past. Then attach a probability $p_{L_1\cdots L_n}(L_s)$ and a letter $L_s$ on a line going to the next state $(L_2, \cdots, L_n, L_s)$ from this state as in Fig. 2. $p_{L_1\cdots L_n}(L_s)$ is the transition probability that the letter $L_s$ follows the sequence of letters $L_1, \cdots, L_n$ in the original information source.

All of $N^n$ states should be numbered in this way. Here assume that two states in Fig. 2 are given numbers $i$ and $j$, respectively. The probability $P_{L_1\cdots L_n}(L_s)$ described above then is the transition probability $p_i(j)$ from the state $i$ to the state $j$. Then the diagram in Fig. 2 can be simplified into the one in Fig. 3. Of course

$$\sum_j p_i(j)=1 \tag{1}$$

must hold for all $i$'s.

Transition probabilities $p_i(j)$'s between states completely specify the statistical property of this information source[4]. When any state in this diagram can be reached from any other state by following a definite number of states, the diagram is called *irreducible.* Hereafter we shall be concerned only with such diagrams. Now let $f_i(n)$ be the probability that the first return to a state $i$ occurs after following just $n$ number of lines. The sum

$$f_i=\sum_{n=1}^{\infty} f_i^{(n)} \tag{2}$$

may be interpreted as the probability that the source ever returns to the state $i$. The state $i$ is called *recurrent* or *transient* according to whether a return to the state $i$ is certain or not (that is, according to whether $f_i=1$ or $f_i<1$). For a recurrent state $i$,

$$\mu_i=\sum_{n=1}^{\infty} nf_i^{(n)} \tag{3}$$

is the mean recurrence time. A recurrent state $i$ with infinite mean recurrence time is called a *null state.*

The state $i$ is called periodic with a period $t$ if a return to it is impossible except in $t, 2t, 3t, \cdots$ steps and $t>1$ is the greatest integer with this property.

A recurrent state which is neither a null

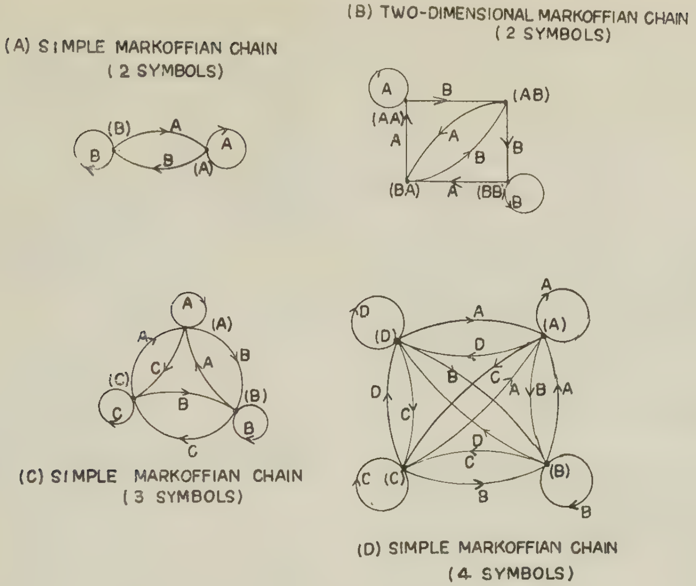

(A) SIMPLE MARKOFFIAN CHAIN
(2 SYMBOLS)

(B) TWO-DIMENSIONAL MARKOFFIAN CHAIN
(2 SYMBOLS)

(C) SIMPLE MARKOFFIAN CHAIN
(3 SYMBOLS)

(D) SIMPLE MARKOFFIAN CHAIN
(4 SYMBOLS)

Fig. 4.

state nor periodic is called *ergodic*. As in Shannon's theory, we will consider only on an ergodic source which consists of only ergodic states. The following theorem in the theory of the Markoffian chain is important for us: *In an irreducible diagram all states belong to the same class, that is, they are all transient, all recurrent null states, or all recurrent non-null states. If it is periodic, they have the same period.* This theorem will be useful for us to decide whether a diagram obtained by calculation of maximizing the transmission rate to get the capacity is ergodic or not. In a case of an ergodic source the probability $P(i)$ that the source takes a state $i$ is uniquely determined from $p_i(j)$ by the following equation:

$$\sum_i P(i)p_i(j)=P(j)\,, \qquad (4)$$

where $\sum P(i)=1$. The probability $P(i)$ for the state $i$, that is, the coordinate $(L_1, L_2, \cdots, L_{n-1}, L_n)$ in Fig. 2 is the multidimensional joint distribution probability $P(L_1, L_2, \cdots, L_{n-1}, L_n)$ that a sequence of letters, $L_1, L_2, \cdots, L_{n-1}, L_n$ take place in the original information source.

Fig. 4 shows some examples of the Shanon's diagram to express the Markoffian processes.

(b) *Shannon's diagram of the second kind.*

Diagrams explained in (a) may suffice for mathematical expression. However, simplification of such diagrams may be desirable for numerical calculation or its detailed discussion.

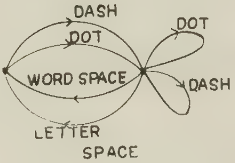

Fig. 5.

In the diagrams of the type in (a) all lines toward the same state generate the same symbol and there is only one line from a state toward other state in that direction and a state can have at most one loop. Such restrictions may be removed. Then numbers of lines and states will be reduced than those in (a).

Take a simple example of a diagram for the Morse Codes where neither word spaces nor letter spaces follow each other. In the diagram of Fig. 4 (d), states (B) and (C) should be merged into one state, after taking off two loops because of the above restriction and then states (A) and (B) into one state. Regarding the symbols A, D, B and C as the dash, the dot, the word space and the letter space respectively, we get the diagram of Fig. 5 which Shannon used.

To express the Markoffian process where preceding $n$ symbols affect the next one and where $N$ different symbols appear,

$N^n$ number of states are in general needed in the expression of (a), but number of states can be reduced in the extended expression of Shannon's diagram of the second kind. That is, if any sequences of symbols from the information source are allowed to be transmitted, this case will coincide with that of Part I since the number of states is reduced to only one, but if constraints are imposed on allowed sequences of symbols, the number of states will be reduced to at least $n$. However how many numbers can be reduced depends on the complexity of constraints on the diagram as seen in the above example.

Let $p_i(j, s)$ be the transition probability that a transition from a state $i$ toward a state $j$ takes place through the $s$-th line between the two states, and then the transition probability $p_i(j)$ from a state $i$ toward a state $j$ in the form described in (a) will be given by

$$p_i(j)=\sum_s p_i(j, s)\,. \tag{5}$$

Also the probability $p(i)$ that a state $i$ is occupied is determined by the set of linear equations:

$$\sum_i P(i) \sum_s p_i(j,s)=P(j)\,, \tag{6}$$

where $\sum\limits_i P(i)=1$. In short, we can calculate the probabilities as in the case (a), by regarding the bundle of all lines from a state toward the other as a single line.

## § 3. Construction of a Noisy Channel

When the information source is expressed by the Shannon's diagram, we shall receive sequences of symbols which can be expressed by the exactly same diagram, if there is no disturbance of noise. If there is noise, how shall the noisy channel affect on the diagram at the receiver? As an answer it may be proper to express the disturbance of noise by correspondence of two lines, of which the one is in Shannon's diagram for the transmitter and the other in that for the receiver.

Now assume that the information source is following the $s$-th line from a state $i$ toward a state $j$ in the diagram $D_t$ at the transmitter, provided that the diagram $D_r$ at the receiver stood at a state $\alpha$ when $D_t$ was at the state $i$. Then let $p_{ijs\alpha}(\beta\sigma)$ be the transition probability that $D_r$ moves toward the next state $\beta$ through the $\sigma$-th line from the state $\alpha$ in which it was, when $D_t$ moves to the state $j$ through the $s$-th line from the state $i$. That is, it is the conditional probability that indices $\beta$ and $\sigma$ take place under the condition that the indices $i, j, s$ and $\alpha$ had appeared. Since the indices $\beta$ and $\sigma$ may be thought independent of other values of $i, j, s$ and $\alpha$ but of the above ones, the statistical property of this noisy channel can be specified by this $p_{ijs\alpha}(\beta\sigma)$. A matrix

$$\underset{ijs}{\downarrow}\,[p_{ijs\alpha}(\beta\sigma)]^{\longrightarrow\alpha\beta\sigma} \tag{7}$$

will be called a *channel matrix* hereafter. For all $i, j, s$, and $\alpha$ where $p_{its\alpha}(\beta\sigma)\geq 0$,

$$\sum_{\beta\sigma} p_{ijs\alpha}(\beta\sigma)=1 \tag{8}$$

holds.

Though it may look somewhat troublesome to make provision of a diagram $D_r$ at the receiver, we receive sequences of symbols disturbed by noise over the communication system but we may not always be able to know momentary variation of noise itself explicitely. Therefore it is quite natural to seize the noise disturbance by making statistical correspondence of $D_t$ and $D_r$ rather than provision of a diagram for the noise itself.

Here $D_t$ may be interpreted as expressing the transmitter with a transducer in the communication system, and $D_r$ the receiver with a transducer.

By constructing of a noisy channel in this way we can deal with a channel in a wide sense and $p_{ijs\alpha}(\beta\sigma)$ specifies the statistical property of the noisy channel while $p_i(j)$ specifies that of the information source at the transmitter. As examples we can mention a case where noise disturbs every several symbols though the information source generates symbols independently of each other and a case where the transducer in the transmitter imposes constraints on allowed sequences of symbols. To thus expressed channel we can connect any ergodic source which passes through all states and lines in the diagram $D_t$. Stating it visually, $D_t$ is mapped on $D_r$ while the information source moves around in $D_t$, but noise varies the property of mapping in a probabilistic way.

Now we assume that $D_t$ and noise are ergodic and consequently $D_r$ is ergodic. Let us consider the product space of $D_t$ and $D_r$. In the product diagram of $D_t$ and $D_r$ in Fig. 6, the product state $(i, \alpha)$ of a state $i$ of $D_t$ and a state $\alpha$ of $D_r$ is shown. And let $p_{i\alpha}(j\beta s\sigma)$ be the transition probability that a transition from the product states $(i\alpha)$ to the product states $(j\beta)$ through a line $(s\sigma)$ takes place. It also can be written as follows:

$$p_{i\alpha}(j\beta s\sigma)=p_{i\alpha}(js)p_{ijs\alpha}(\beta\sigma) ,$$

but since any movement in $D_t$ at the transmitter can not be affected by that in $D_r$, $p_{i\alpha}(js)$ can be simply waitten as $p_i(js)$. Thus we have

$$p_{i\alpha}(j\beta s\sigma)=p_i(js)p_{ijs\alpha}(\beta\sigma) . \qquad (9)$$

Ergodicity of $D_t$ and noise implies that this product diagram is ergodic and that $D_r$ is consequently ergodic. Besides this ergodicity, the fact that transition between states in $D_t$ is entirely independent of that in $D_r$, requires that transition from the state $(i, \alpha)$ toward any other state $(j, \beta)$ in this product diagram is always possible as to the first indices $i$ and $j$, irrelevant of the second indices $\alpha$ and $\beta$, as far as transition from the state $i$ toward the other state $j$ in given $D_t$ is possible. Therefore properties which are required for the channel matrix $[p_{ijs\alpha}(\beta\sigma)]$ to be real are as follows; (i) The product diagram is ergodic, and (ii) trasition from a state $(i\alpha)$ toward other state $(j\beta)$ in it is always possible irrelevant of the indices $\alpha$ and $\beta$ as far as transition from a state $i$ toward $j$ is possible in $D_t$.

In general a probabilistic property of noise which disturbs a line $(i, j, s)$ in $D_t$ may not be independent of the noises that have disturbed the lines in the past history, but if independent, what property will the channel have? Suppose that there are $h$ different modes of noise disturbance (let us write it as $n(i, j, s)$) on the line $(i, j, s)$ in $D_t$; that is, $n^1(i, j, s)$, $n^2(i, j, s), \cdots$ and $n^h(i, j, s)$. One of them in general corresponds to "no noise", that is, a transmitted symbol is received without any change. These modes of noise disturbance are proper only to this line $(i, j, s)$, and generally to other lines there may be modes of noise disturbance of a number different from $h$ with reception of different symbols. For the line $(i, j, s)$ in $D_t$ we get $h$ different lines in $D_r$ by $h$ different modes of disturbance. That is, provided that $D_r$ was in a state $\alpha$ before transmission of a symbol for this line $(i, j, s)$, $h$ different lines which may not always be led to the same state $\beta$ will be possibly drawn starting from the state $\alpha$. Let probabilities of these mapping be $p_{ijs\alpha}(\beta_1\sigma_1)$, $p_{ijs\alpha}(\beta_2\sigma_2), \cdots$ and $p_{ijs\alpha}(\beta_h\sigma_h)$. But now since the mode of noise disturbance $n(i, j, s)$ is assumed to be independent of those having disturbed on the lines in the past, there are always the above $h$ different modes of noise disturbance, $n^1(i, j, s), \cdots, n^h(i, j, s)$ on the line $(i, j, s)$, whichever state of a particular $\alpha$ $D_r$ might be in.

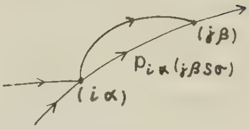

Fig. 6.

We can restate it as follows: For a channel where the modes of noise disturbance on a line $(i, j, s)$ in $D_t$ are independent of those that have disturbed the lines in the past history, when there are generated $h$ different lines starting from a state $\alpha$ in $D_r$ by noise disturbance on this line with probabilities $p_{ijs\alpha}(\beta_1\sigma_1), \cdots, p_{ijs\alpha}(\beta_h\sigma_h)$, respectively, lines of the same number $h$ even for other state $\alpha'$ are generated in $D_r$ with the same probabilities. That is: with appropriate renumbering of $k$'s for $\beta_k'$ and $\sigma_k'$, relations

$$p_{ijs\alpha}(\beta_k\sigma_k)=p_{ijs\alpha'}(\beta_k'\sigma_k') \quad (k=1, \cdots, h)$$

hold only for state $\alpha'$'s such that $D_r$ is at a state $\alpha'$ for $D_t$ being at the state $i$. It sometimes makes the property of the noisy channel simpler. A channel where disturbance of noise on a line in $D_t$ is not independent of those on other lines, can be expressed by a proper transformation with diagrams which have the above property and then its property of the channel would be simpler at the expense of some complexity of the diagrams.

## § 4. Transmission Rate and Dissemination

Let $P(i)$ be the probability that a state $i$ in $D_t$ is occupied and $p_i(js)$ be the conditional probability that the $s$-th line is followed toward a state $j$ from a state $i$. As shannon defined[2)], entropy per symbol for this diagram $D_t$ will be as follows:

$$H(x)=-\sum_{ijs} P(i)p_i(js)\log p_i(js) . \qquad (10)$$

Then let $P(\alpha)$ be the probability that a state $\alpha$ in $D_r$ is occupied and $p_\alpha(\beta\sigma)$ be the conditional probability that the $\sigma$-th line is followed toward a state $\beta$ from a state $\alpha$. Similarly for a diagram $D_r$ at the receiver:

$$H(y)=-\sum_{\alpha\beta\sigma} P(\alpha)p_\alpha(\beta\sigma)\log p_\alpha(\beta\sigma)\,. \tag{11}$$

For ergodic diagrams, $P(i)$ and $P(\alpha)$ are determined from $p_i(js)$ and $p_\alpha(\beta\sigma)$, respectively, so $H(x)$ and $H(y)$ are practically functions of only $p_i(js)$ and $p_\alpha(\beta\sigma)$, respectively.

Entropy per symbol for the joint distribution of corresponding symbols at the transmitter and the receiver, would be properly calculated from the product diagram in Fig. 6:

$$\begin{aligned} H(x,y)&=-\sum_{ijs\alpha\beta\sigma} P(i\alpha)p_{i\alpha}(j\beta s\sigma)\log p_{i\alpha}(j\beta s\sigma)\\ &=-\sum P(i\alpha)p_i(js)p_{ijs\alpha}(\beta\sigma)\log p_i(js)p_{ijs\alpha}(\beta\sigma)\\ &=-\sum_{ijs\alpha} P(i\alpha)p_i(js)\log p_i(js)\\ &\quad-\sum_{ijs\alpha\beta\sigma} P(i\alpha)p_i(js)p_{ijs\alpha}(\beta\sigma)\log p_{ijs\alpha}(\beta\sigma)\,. \end{aligned} \tag{12}$$

Using $H(x,y)=H(x)+H_x(y)$, the dissemination $H_x(y)$ is, from (12);

$$H_x(y)=-\sum_{ijs\alpha\beta\sigma} P(i\alpha)p_i(js)p_{ijs\alpha}(\beta\sigma)\log p_{ijs\alpha}(\beta\sigma)\,. \tag{13}$$

Using $H(x,y)=H(y)+H_y(x)$, the equivocation $H_y(x)$ will similarly be calculated.

Therefore transmission rate (entropy/symbol) for this channel would be defined as;

$$\begin{aligned} R=H(y)-H_x(y)&=-\sum_{\alpha\beta\sigma} P(\alpha)p_\alpha(\beta\sigma)\log p_\alpha(\beta\sigma)\\ &+\sum_{ijs\alpha\beta\sigma} P(i\alpha)p_i(js)p_{ijs\alpha}(\beta\sigma)\log p_{ijs\alpha}(\beta\sigma)\,. \end{aligned} \tag{14}$$

As a special case, if diagrams at both sides are independent of each other, we have

$$p_{ijs\alpha}(\beta\sigma)=p_\alpha(\beta\sigma)$$

and $P(i\alpha)=P(i)\cdot P(\alpha)$, and then $R=0$from (14).

Let time duration of a line $(i,j,s)$ in $D_t$ be $l(i,j,s)$ and that of a line $(\alpha\beta\sigma)$ in $D_r$ be $l(\alpha\beta\sigma)$. Since as an average time duration per symbol we get

$$\begin{aligned} T&=\sum_{ijs} P(i)p_i(js)l(ijs)\\ &=\sum_{\alpha\beta\sigma} P(\alpha)p_\alpha(\beta\sigma)l(\alpha\beta\sigma)\,, \end{aligned} \tag{15}$$

the transmission rate for this channel in entropy/second will be $R/T$ from (14) and (15).

Next we will mention important relations between probabilities in $D_t$ and $D_r$. As it is well known in the theory of the Markoffian process, in ergodic $D_t$ there is the following relation:

$$\sum_i P(i)p_j(j)=P(j)\,. \tag{17}$$

But since

$$P_i(j)=\sum_s p_i(js) \tag{18}$$

holds, (17) gives us

$$\sum_{si} P(i)p_i(js)=P(j)\,, \tag{19}$$

where

$$\left\{\begin{aligned} &\sum_i P(i)=1\\ &\sum_{js} p_i(js)=1\,. \end{aligned}\right. \tag{20}$$

As to $D_r$, similarly

$$\sum_{\beta\sigma} P(\alpha)p_\alpha(\beta\sigma)=P(\beta)\,,$$

where

$$\left\{\begin{aligned} &\sum_\alpha P(\alpha)=1\\ &\sum_{\beta\alpha} p_\alpha(\beta\sigma)=1\,. \end{aligned}\right. \tag{21}$$

As to the product diagram of Fig. 6 we can get an equation corresponding to (17) as follows:

$$\sum_{i\alpha} P(i\alpha)p_{i\alpha}(j\beta)=P(j\beta)\,. \tag{22}$$

Using

$$\begin{aligned} p_{i\alpha}(j\beta)&=\sum_{s\sigma} p_{i\alpha}(js\beta\sigma)\\ &=\sum_{s\sigma} p_i(j)p_{ijs\alpha}(\beta\sigma)\,, \end{aligned} \tag{23}$$

(22) will be

$$\sum_{i\alpha} P(i\alpha)\sum_{s\sigma} p_i(j)p_{ijs\alpha}(\beta\sigma)=P(j\beta)\,. \tag{24}$$

It means that we can determine $P(j\beta)$ from $p_i(j)p_{ijs\alpha}(\beta\sigma)$ if they are given, where $\sum_{i\alpha}P(i\alpha)=1$. Since $P(i\alpha)p_{i\alpha}(j\beta s\sigma)$ expresses the joint probability that two product states $P(i\alpha)$ and $P(j\beta)$ connected by the $(s\sigma)$-th line take place, what is summed over its $i$, $j$ and $s$ gives the joint probability that indices $\alpha$, $\beta$ and $\sigma$ appear in a successive order. That is, it gives

$$\sum_{ijs} P(i\alpha)p_{i\alpha}(j\beta s\sigma)=P(\alpha\beta\sigma)\,.$$

Therefore from (9) we get

$$\sum_{ijs} P(i\alpha)p_i(js)p_{ijs\alpha}(\beta\sigma)=P(\alpha\beta\sigma)\,. \tag{26}$$

Similarly to a case in Part I[1], we will introduce a set of characteristic equations as follows:

$$\sum_{\alpha\beta\sigma} X_{\alpha\beta\sigma}P(i\alpha)p_{ijs\alpha}(\beta\sigma) = \sum_{\alpha\beta\sigma} P(i\alpha)p_{ijs\alpha}(\beta\sigma)\log p_{ijs\alpha}(\beta\sigma) \qquad (27)$$

(for $i$, $j$ and $s$) .

This set of equations whose solutions $X_{\alpha\beta\sigma}$'s are auxiliary variables will be called as *Characteristic Equations*. It is an extended form of the previous case¹⁾. If we set $P(i\alpha)=1$, as a special case, these equations coincide with the previous case. Different from the previous case, $X_{\alpha\beta\sigma}$'s can not in general be determined uniquely from the channel matrix for (27) includes $P(i\alpha)$'s and therefore unfortunately $X_{\alpha\beta\sigma}$'s are functions of $P(i\alpha)$ and therefore unfortunately $X_{\alpha\beta\sigma}$'s are functions of $P(i\alpha)$ and moreover $p_i(js)$. But still it will be powerful for our analysis.

(27) gives us with multiplication of $p_i(js)$ and summation of it over $i$, $j$ and $s$;

$$\sum_{ijs\alpha\beta\sigma} X_{\alpha\beta\sigma}P(i\alpha)p_i(js)p_{ijs\alpha}(\beta\sigma) = \sum_{ijs\alpha\beta\sigma} P(i\alpha)p_i(js)p_{ijs\alpha}(\beta\sigma)\log p_{ijs\alpha}(\beta\sigma). \qquad (28)$$

Inserting (26) into this, the left side of this equation is

$$\sum_{\alpha\beta\sigma} X_{\alpha\beta\sigma}P(\alpha\beta\sigma)\ ,$$

while the right side is $-H_x(y)$. Thus we get the following:

**Theorem 1.** *Dissemination $H_x(y)$ can be expressed simply by the following*:

$$H_x(y) = -\sum_{\alpha\beta\sigma} X_{\alpha\beta\sigma}P(\alpha\beta\sigma)\ . \qquad (29)$$

*Then the transmission rate (entropy/symbol) for the noisy channel expressed by correspondence of two multi-state diagrams is*;

$$R = -\sum_{\alpha\beta\sigma} P(\alpha)p_\alpha(\beta\sigma)\log p_\alpha(\beta\sigma) + \sum_{\alpha\beta\sigma} X_{\alpha\beta\sigma}P(\alpha)p_\alpha(\beta\sigma)\ . \qquad (30)$$

These two formulae are extensions of those in Part I. As we shall see it later, mathematical expressions will be made simpler with $X_{\alpha\beta\sigma}$'s and it may be convenient to see their properties. Particulary when $X_{\alpha\beta\sigma}$'s can be calculated easily, they are very powerful for getting solutions.

From the above theorem, the transmission rate in entropy per second is

$$\frac{-\sum_{\alpha\beta\sigma} P(\alpha)p_\alpha(\beta\sigma)\log p_\alpha(\beta\sigma) + \sum_{\alpha\beta\sigma} X_{\alpha\beta\sigma}P(\alpha)p_\alpha(\beta\sigma)}{\sum_{\alpha\beta\sigma} P(\alpha)p_\alpha(\beta\sigma)l(\alpha\beta\sigma)}\ . \qquad (31)$$

## § 5. Channel Capacity

In order to get the greatest transmission rate of a noisy channel which was defined as its capacity by Shannon²⁾, we will try to get the maximum of (31), first, rather than its greatest value.

Lagrange's method is useful for our maximizing problem with constraints which are complex for $X_{\alpha\beta\sigma}$'s are functions of $P(i\alpha)$'s. Now let us enumerate all constraints. First, a set of characteristic equations (27) for defining $X_{\alpha\beta\sigma}$'s are necessary. Since our problem requires specification of probabilities for all lines $(i, j, s)$'s in $D_t$ so that the maximum may be given to the rate of the channel, $p_i(js)$'s should be specified and then other probabilities should be functions of $p_i(js)$'s. Therefore, (24) for $P(i\alpha)$ to be determined from $p_i(js)$ may be necessary. Also (26) for $P(\alpha\beta\sigma)$ to be determined from $P(i\alpha)$ and $p_i(js)$, and a constraint $\sum_{js} P_j(js)=1$ in $D_t$ are both necessary. (21) to characterize $D_r$ as an ergodic diagram, may be redundant since it is not independent of some other constraints but it will be included as a constraint for convenience of calculation. In order to obtain the maximum of (31) under these constraints, it may be enough to get simply the maximum value of the following:

$$\begin{aligned} V = {} & \frac{-\sum_{\alpha\beta\sigma} P(\alpha\beta\sigma)\log\{P(\alpha\beta\sigma)/\sum_{\gamma\sigma} P(\alpha\gamma\sigma)\} + \sum_{\alpha\beta\sigma} X_{\alpha\beta\sigma}P(\alpha\beta\sigma)}{\sum_{\alpha\beta\sigma} P(\alpha\beta\sigma)l(\alpha\beta\sigma)} \\ & + \sum_{ijs\alpha\beta\sigma} \delta_{ijs}[X_{\alpha\beta\sigma}P(i\alpha)p_{ijs\alpha}(\beta\sigma) - P(i\alpha)p_{ijs\alpha}(\beta\sigma)\log p_{ijs\alpha}(\beta\sigma)] \\ & + \sum_{\alpha} \eta_\alpha[\sum_{\beta\sigma} P(\alpha\beta\sigma) - \sum_{\beta\sigma} P(\beta\alpha\sigma)] \\ & + \sum_{j\beta} \nu_{j\beta}[\sum_{is\alpha\sigma} P(i\alpha)p_i(js)p_{ijs\alpha}(\beta\sigma) - P(j\beta)] \end{aligned}$$

$$+\sum_{\alpha\beta\sigma}\mu_{\alpha\beta\sigma}\Big[\sum_{ijs} P(i\alpha)p_i(js)p_{ijs\alpha}(\beta\sigma)-P(\alpha\beta\sigma)\Big]$$
$$+\sum_{i}\tau_i\sum_{js}p_i(js)+\gamma\sum_{\alpha\beta\sigma}P(\alpha\beta\sigma)\ , \tag{32}$$

where $\delta_{ijs}$, $\eta_\alpha$, $\nu_{j\beta}$, $\mu_{\alpha\beta\sigma}$, $\tau_i$ and $\gamma$ are undetermined constants. Let us maximize $V$, that is, (32) with respect to $P(\alpha\beta\sigma)$, $X_{\alpha\beta\sigma}$, $p_i(js)$ and $P(i\alpha)$. Then with a notation $C$ for the cpaacity to be calculated:

$$\frac{\partial V}{\partial P(\alpha\beta\sigma)}=\frac{1}{\sum_{\alpha\beta\sigma}P(\alpha\beta\sigma)l(\alpha\beta\sigma)}\Big[-\log\frac{P(\alpha\beta\sigma)}{\sum_{\gamma\sigma}P(\alpha\gamma\sigma)}+X\alpha\beta\sigma\Big]$$
$$-\frac{Cl(\alpha\beta\sigma)}{\sum_{\alpha\beta\sigma}P(\alpha\beta\sigma)l(\alpha\beta\sigma)}+\eta_\alpha-\eta_\beta-\mu_{\alpha\beta\sigma}+\gamma=0 \tag{33}$$

$$\frac{\partial V}{\partial X_{\alpha\beta\sigma}}=\frac{P(\alpha\beta\sigma)}{\sum_{\alpha\beta\sigma}P(\alpha\beta\sigma)l(\alpha\beta\sigma)}+\sum_{ijs}\delta_{ijs}P(i\alpha)p_{ijs\alpha}(\beta\sigma)=0 \tag{34}$$

$$\frac{\partial V}{\partial p_i(js)}=\sum_{\alpha\beta\sigma}\nu_{j\beta}P(i\alpha)p_{ijs\alpha}(\beta\sigma)+\sum_{\alpha\beta\sigma}\mu_{\alpha\beta\sigma}P(i\alpha)p_{ijs\alpha}(\beta\sigma)+\tau_i=0 \tag{35}$$

$$\frac{\partial V}{\partial P(i\alpha)}=\sum_{js\beta\sigma}\delta_{ijs}[X_{\alpha\beta\sigma}p_{ijs\alpha}(\beta\sigma)-p_{ijs\alpha}(\beta\sigma)\log p_{ijs\alpha}(\beta\sigma)]$$
$$+\sum_{j\beta}\nu_{j\beta}\sum_{s\sigma}p_j(js)p_{ijs\alpha}(\beta\sigma)-\nu_{i\alpha}+\sum_{j\beta\sigma}\mu_{\alpha\beta\sigma}\sum_{s}p_i(js)p_{ijs\alpha}(\beta\sigma)=0\ . \tag{36}$$

Comparison of (26) and (34) gives us

$$\delta_{ijs}=-p_i(js)/\sum_{\alpha\beta\sigma}P(\alpha\beta\sigma)l(\alpha\beta\sigma)\ . \tag{37}$$

Summing the equation (33) multiplied by $P(\alpha\beta\sigma)$ over $\alpha$, $\beta$ and $\sigma$, we obtain

$$\sum_{\alpha\beta\sigma}\mu_{\alpha\beta\sigma}P(\alpha\beta\sigma)=\gamma\ , \tag{38}$$

since its first term becomes equal to $C$.

Next, summation of (36) multiplied by $P(i\alpha)$ over $\alpha$, gives us an equation which will lead simply

$$\sum_{\alpha\beta\sigma}\mu_{\alpha\beta\sigma}P(\alpha\beta\sigma)=0\ , \tag{39}$$

Using (24) and (27). But comparison of this and (38) gives us

$$\gamma=0\ . \tag{40}$$

Then, (33) with (40) gives

$$\frac{P(\alpha\beta\sigma)}{\sum_{\gamma\sigma}P(\alpha\gamma\sigma)}=\exp\Big[-Cl(\alpha\beta\sigma)+X_{\alpha\beta\sigma}+(\eta_\alpha-\eta_\beta-\mu_{\alpha\beta\sigma})\sum_{\alpha\beta\sigma}P(\alpha\beta\sigma)l(\alpha\beta\sigma)\Big]\ , \tag{41}$$

summation of which over $\beta$ and $\sigma$ must be 1. That is,

$$\sum_{\beta\sigma}\exp\Big(-\eta_\beta\sum_{\alpha\beta\sigma}P(\alpha\beta\sigma)l(\alpha\beta\sigma)\Big)\cdot\exp\Big\{-C\cdot l(\alpha\beta\sigma)+X_{\alpha\beta\sigma}-\mu_{\alpha\beta\sigma}-\mu_{\alpha\beta\sigma}\sum_{\alpha\beta\sigma}P(\alpha\beta\sigma)l(\alpha\beta\sigma)\Big\}$$
$$=\exp\Big(-\eta_\alpha\sum_{\alpha\beta\sigma}P(\alpha\beta\sigma)l(\alpha\beta\sigma)\Big) \tag{42}$$

will be obtained. In order that these homogeneous equations (42) can have non-zero solutions, it is a necessary and sufficient condition that its coefficient determinant be zero. Then we obtain the following determinant;

$$\left|\sum_{\sigma}\exp\Big[-C\cdot l(\alpha\beta\sigma)+X_{\alpha\beta\sigma}-\mu_{\alpha\beta\sigma}\sum_{\alpha\beta\sigma}P(\alpha\beta\sigma)\cdot l(\alpha\beta\sigma)\Big]-\delta(\alpha\beta)\right|=0\ , \tag{43}$$

which will be called a *Capacity Equation*. The channel capacity $C$ can be solved as a function of $X_{\alpha\beta\sigma}$, $\mu_{\alpha\beta\sigma}$ and $P(\alpha\beta\sigma)$ as the largest positive root of this.

Camparison of an equation which is obtained by summing (35) multiplied by $p_i(js)$ over $j$ and $s$, and an equation which is obtained by summing (36) multiplied by $P(i\alpha)$ over $\alpha$ with (37), gives us

$$\tau_i = -\sum_{\alpha} \nu_{i\alpha} P(i\alpha) . \tag{44}$$

Inserting this into (35) we obtain the following (45).

After all, besides (41) and (43) we must solve the following five sets of equations:

$$\sum_{\alpha\beta\sigma} \mu_{\alpha\beta\sigma} P(i\alpha) p_{ijs\alpha}(\beta\sigma) = -\sum_{\alpha\beta\sigma} P(i\alpha) p_{ijs\alpha}(\beta\sigma)(\nu_{j\beta} - \nu_{i\alpha}) , \tag{45}$$

$$\sum_{j\beta s\sigma} \frac{p_i(js)}{\sum_{\alpha\beta\sigma} P(\alpha\beta\sigma) l(\alpha\beta\sigma)} [p_{ijs\alpha}(\beta\sigma) \log p_{ijs\alpha}(\beta\sigma) - X_{\alpha\beta\sigma} p_{ijs\alpha}(\beta\sigma)]$$
$$+ \sum_{j\beta} \nu_{j\beta} \sum_{s\sigma} p_i(js) p_{ijs\alpha}(\beta\sigma) - \nu_{i\alpha} + \sum_{j\beta\sigma} \mu_{\alpha\beta\sigma} \sum_{s} p_i(js) p_{ijs\alpha}(\beta\sigma) = 0 \tag{46}$$

and

$$\begin{cases} \sum_{ijs} P(i\alpha) p_i(js) p_{ijs\alpha}(\beta\sigma) = P(\alpha\beta\sigma) & (47) \\ \sum_{i\alpha s\sigma} P(i\alpha) p_i(js) p_{ijs\alpha}(\beta\sigma) = P(j\beta) & (48) \\ \sum_{\alpha\beta\sigma} X_{\alpha\beta\sigma} P(i\alpha) p_{ijs\alpha}(\beta\sigma) = \sum_{\alpha\beta\sigma} P(i\alpha) p_{ijs\alpha}(\beta\sigma) \log p_{ijs\alpha}(\beta\sigma) . & (49) \end{cases}$$

The latter three sets are relations between the probabilities $P(i\alpha)$, $p_i(js)$ and $P(\alpha\beta\sigma)$.

In a general form it seems somewhat complex, compared with the case of Part I, though it would be much simplified for most of practical cases as we shall see it later in a numerical example. However it should be noted as an indispensable condition that the probabilities $p_i(js)$, $P(i\alpha)$ and $p_\alpha(\beta\sigma)$ solved from the above equations are non-negative and to let $D_t$ and $D_r$ be both ergodic. Otherwise the value of $C$ can not express the channel capacity any more, so we must solve the maximizing problem without some lines and states in $D_t$ from the beginning of our calculation, analogous to the latter part in § 2 of Part I.

Now let us check solvability of the equations from (45) to (49). Since $\sum_{j\beta s\sigma} p_i(js) p_{ijs\alpha}(\beta\sigma) = 1$, the coefficient determinant of (46) as to the undetermined constants $\nu_{j\beta}$'s is zero. So the following set of equations, conjugate to (46), will be introduced;

$$\sum_{i\alpha} x_{i\alpha} \sum_{s\sigma} p_i(js) p_{ijs\alpha}(\beta\sigma) = x_{j\beta} . \tag{50}$$

This is exactly the same as (48). But (48) is always solvable as to $P(i\alpha)$ for the ergodicity of the product diagram. Then (50) can be always solved, leading to $x_{i\alpha} = P(i\alpha)$. Therefore from the theorem on the simultaneous linear equations[5], a necessary and sufficient condition for the solvability of (46) is that

$$\sum_{i\alpha} P(i\alpha) \left[ \sum_{j\beta s\sigma} \frac{p_i(js)}{\sum_{\alpha\beta\sigma} P(\alpha\beta\sigma) l(\alpha\beta\sigma)} [p_{ijs\alpha}(\beta\sigma) \log p_{ijs\alpha}(\beta\sigma) \right.$$
$$\left. - X_{\alpha\beta\sigma} p_{ijs\alpha}(\beta\sigma)] + \sum_{j\beta\sigma} \mu_{\alpha\beta\sigma} \sum_{s} p_i(js) p_{ijs\alpha}(\beta\sigma) \right] = 0 \tag{51}$$

holds. Since (51) is reduced to (39) for its first two terms vanish by (49), (46) is always solvable as to $\nu_{j\beta}$'s.

As to (49), if it does not have solutions, it must be dealt with directly as in § 4 of Part I[1] but we assumed existence of solutions for it.

Solvability of the remaining (45) as to $\mu_{\alpha\beta\sigma}$ and (47) as to $p_i(js)$ has connection with the rank of their coefficient determinants. When the rank is equal to the order of the determinants so that the numbers of lines and states in $D_t$ are equal to those in $D_r$, respectively, and that $|P(i\alpha) p_{ijs\alpha}(\beta\sigma)| \neq 0$, the discussion which we have made so far may suffice if the result is to let $D_t$ and $D_r$ be ergodic. If the rank is lower, our calculation will be more complex, though it may be dealt with, analogously to Part I where some conditions for their solvability should be included in (32) from the beginning. Here we will not go further.

Now we will check our result in a special case of the noiseless channel and show that it will be reduced to Shannon's determinant (page 9 of the reference (2)). For the noiseless channel, we have

$$\begin{cases} p_{ijs\alpha_i}(\beta_j\sigma_s)=1 & \\ p_{ijs\alpha}(\beta\sigma)=0 & \text{(for other } \alpha, \beta \text{ and } \sigma, \text{ except } \alpha_i, \beta_j \text{ and } \sigma_s) \end{cases} \tag{52}$$

where $\alpha_i$, $\beta_j$ and $\sigma_s$ are $\alpha$, $\beta$ and $\sigma$ in $D_r$ corresponding to $i, j,$ and $s$, respectively. Then, since the right side of (49) vanishes, we obtain $X_{\alpha\beta\sigma}=0$. As easily seen,

$$\begin{cases} P(i\alpha_i)\neq 0 & (=P(i)) \\ P(i\alpha)=0 & \text{for other } \alpha \text{ except } \alpha_i\,, \end{cases} \tag{53}$$

so (45) gives

$$\mu_{\alpha_i\beta_j\sigma_s}=\nu_{i\alpha_i}-\nu_{j\beta_j}\,. \tag{54}$$

And (46) where the brackt vanishes, gives.

$$\sum_{js}\nu_{j\beta_j}p_i(js)-\nu_{i\alpha_i}+\sum_{js}\mu_{\alpha_i\beta_j\sigma_s}p_i(js)=0\,. \tag{55}$$

So we have $\mu_{\alpha\beta\sigma}=\nu_{i\alpha}=0$. Finally (43) can be reduced to the following determinant which Shannon obtained for the noiseless channel:

$$\left|\sum_{\sigma}\exp(-C\cdot l(\alpha\beta\sigma))-\delta(\alpha\beta)\right|=0\,. \tag{56}$$

Thus, with a transformation $W=\exp(C)$ we can summarize the above as follows:

**Theorem 2.** *For the noisy channel whose channel matrix is* $[p_{ijs\alpha}(\beta\sigma)]$, *the capacity* $C=\log W$ *is given by the largest positive root of the following capacity equation*:

$$\left|\sum_{\sigma}W^{-l(\alpha\beta\sigma)}\exp\Big(X_{\alpha\beta\sigma}-\mu_{\alpha\beta\sigma}\sum_{\alpha\beta\sigma}P(\alpha\beta\sigma)l(\alpha\beta\sigma)\Big)-\delta(\alpha\beta)\right|=0\,, \tag{57}$$

*where* $X_{\alpha\beta\sigma}$, $\mu_{\alpha\beta\sigma}$ *and* $P(\alpha\beta\sigma)$ *are solved from* (41) *and* (45) *to* (49) *and satisfy the requirement to let* $D_t$ *and* $D_r$ *be ergodic. Especially, for the noiseless channel, the above equation is reduced to*:

$$\left|\sum_{\sigma}W^{-l(\alpha\beta\sigma)}-\delta(\alpha\beta)\right|=0\,. \tag{58}$$

The equation (57) is an extension of the determinant which Shannon obtained for the noiseless channel and it was shown now that the former can be reduced to the latter for the noiseless channel.

## § 5. Numerical Example

Now we will solve a simple numerical example. Suppose we have a transmitter which can be expressed by the diagram in Fig. 7. Four symbols A, B, C and D can be transmitted, and the time durations of A and B are one second each and those of C and D two seconds each. We number two states and six lines as shown in Fig. 7.

(a) *Capacity of the noiseless case*:

Since we receive a diagram exactly indentical to $D_t$ over the noiseless channel, the channel capacity $\log W$ is given by the largest positive root of the following determinant:

$$\begin{vmatrix} 2W^{-1}-1 & 2W^{-2} \\ 2W^{-1} & -1 \end{vmatrix}=0\,. \tag{59}$$

Solution of this equation of the third degree gives $W=2.594$. Then, the channel capacity is $\log_2 W=1.38$ bits/sec.

Let $P_a$ and $P_b$ be probabilities of the states $a$ and $b$, and $p(s)$ be probability that transi-

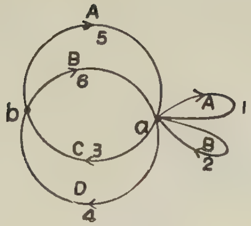

Fig. 7. Time durations of A and B; 1 sec.
Time durations of C and D; 2 sec.

| | | | $D_r$ | | | | | |
|---|---|---|---|---|---|---|---|---|
| | | | $a'$ | | | | $b'$ | |
| | | | $1'$ | $2'$ | $3'$ | $4'$ | $5'$ | $6'$ |
| $D_t$ | $a$ | 1 | 3/4 | 1/4 | 0 | 0 | 0 | 0 |
| | | 2 | 1/3 | 2/3 | 0 | 0 | 0 | 0 |
| | | 3 | 0 | 0 | 3/4 | 1/4 | 0 | 0 |
| | | 4 | 0 | 0 | 1/4 | 3/4 | 0 | 0 |
| | $b$ | 5 | 0 | 0 | 0 | 0 | 1/2 | 1/2 |
| | | 6 | 0 | 0 | 0 | 0 | 1/4 | 3/4 |

Fig. 8.

tion to the $s$-th line takes place. Thus we have;

$$\begin{cases} P_a=0.814 \\ P_b=0.186 \end{cases} \qquad \begin{cases} p(1)=p(2)=0.386 \\ p(3)=p(4)=0.114 \\ p(5)=p(6)=0.500 \end{cases} \tag{60}$$

(b) *Capacity of the noisy case*:

Now assume that the diagram $D_r$ at the receiver is exactly the same with $D_t$ of Fig. 7, being numbered in the same way, but that correspondence of $D_t$ and $D_r$ due to noise disturbance is expressed by the channel matrix of Fig. 8, where numbers of lines and states in $D_r$ are primed. The channel matrix satisfies the required property.

The characteristic equations (49) where $P(i\alpha)$ in both sides of each equation vanishes, give the following:

$$\begin{cases} \frac{3}{4}X_{1'}+\frac{1}{4}X_{2'} = \frac{3}{4}\log\frac{3}{4}+\frac{1}{4}\log\frac{1}{4} \\ \frac{1}{3}X_{1'}+\frac{2}{3}X_{2'} = \frac{1}{3}\log\frac{1}{3}+\frac{2}{3}\log\frac{2}{3} \\ \frac{3}{4}X_{3'}+\frac{1}{4}X_{4'} = \frac{3}{4}\log\frac{3}{4}+\frac{1}{4}\log\frac{1}{4} \\ \frac{1}{4}X_3'+\frac{3}{4}X_{4'} = \frac{3}{4}\log\frac{3}{4}+\frac{1}{4}\log\frac{1}{4} \\ \frac{1}{2}X_{5'}+\frac{1}{2}X_{6'} = \log\frac{1}{2} \\ \frac{1}{4}X_{5'}+\frac{3}{4}X_{6'} = \frac{3}{4}\log\frac{3}{4}+\frac{1}{4}\log\frac{1}{4} \end{cases} \tag{61}$$

whose solutions are

$$\begin{cases} X_{1'}=-0.2249\,k \\ X_{2'}=-0.3022\,k \\ X_{3'}=X_{4'}=-0.2442\,k \\ X_{5'}=-0.4147\,k \\ X_{6'}=-0.1874\,k \end{cases} \tag{11}$$

where $k=1/\log_{10}e$.

The equations (48) can be much simplified and give $\mu_{1'}=\mu_{2'}=0$ and $\nu_{aa'}=\nu_{bb'}$. The equation (46) do not give significant relations any more in this case. Now the capacity equation (43) is simply:

$$\begin{vmatrix} \exp(-0.2249\,k\text{-}C)+\exp(-0.3022\,k\text{-}C)-1 & 2\exp(-0.2442\,k\text{-}2C) \\ \exp(-0.4147\,k\text{-}C)+\exp(-0.1874\,k\text{-}C) & -1 \end{vmatrix}=0 \tag{63}$$

which gives $C=0.652$ bits/sec.

With the above $C$, $X_{\alpha\beta\sigma}$ and $\mu_{\alpha\beta\sigma}=0$, the equations (41) give the following probabilities;

$$\begin{cases} p(1')=0.379 \\ p(2')=0.317 \\ p(3')=p(4')=0.152 \end{cases} \qquad \begin{cases} p(5')=0.372 \\ p(6')=0.628 \end{cases} \tag{64}$$

These probabilities and the relations

$$\sum_{\beta\sigma} P(\alpha)p_{\alpha}(\beta\sigma)=P(\beta) \tag{65}$$

give $P(a')=0.767$ and $P(b')=0.233$.

As to the probabilities in $D_t$, the equations (47) and (48) give the following:

$$\begin{cases} P(1)=0.353 \\ P(2)=0.344 \\ P(3)=P(4)=0.152\,. \end{cases} \qquad \begin{cases} P(5)=0.488 \\ P(6)=0.512 \end{cases}$$

As our conclusion, values of the probabilities of the states in $D_t$ are equal to those in $D_r$ and the result recommends us more frequent use of the state $a$ than $b$. The line 5 is mapped onto the lines 5′ and 6′ in $D_r$ with the equal probabilities, so the line 6 at the transmitter should be used preferably rather than the line 5. Similarly the line 1 should be used more than the line 2.

## § 6. Conclusion and Acknowledgement

In this paper we have extended the treatment of a noisy channel in Part I. Naturally it may be somewhat complex but the introduction of the characteristic equations proves still powerful for our calculation. In the special case of the noiseless channel our extension leads to the determinant which Shannon obtained for calculation of the capacity.

The author wishes to acknowledge the constant encouragement and guidance of Mr. Zen'iti Kiyasu, Chief of the section to which he belongs and also the important suggestions of Assistant Professor Hidetosi Takahasi of Tokyo University with his careful reading of the original manuscript.

Also it is a pleasure for him to express indebtedness to Professor K. Kunisawa of Tokyo Institute of Technology for his useful advices, and Mr. H. Mine of Osaka University and Mr. N. Ikeno of his Laboratory for their illuminating discussions.

## References

1) S. Muroga: *On the capacity of a discrete channel I.—Mathematical expression of capacity of a channel which is disturbed by noise in its every one symbol and expressible in one state diagram*, J. Phys. Soc. Japan **8** (1953) 484.
2) C. E. Shannon and W. Weaver: *The mathematical theory of communication*, Univ. of Illinois Press, 1949.
3) K. Kunisawa: *The mathematical foundation of Shannon's information source and its application to binary coding*, Report of Stat. Appl. Res, UJSE, Vol. 2, No. 1, p. 1–23.
4) W. Feller: *An introduction to probability and its applications*, Vol. 1. John Wiley and Sons, 1950 Chaps. 15 and 16.
5) A. Duschek: *Vorlesungen über Höhere Mathematik II*, Springer, Wien 1950, p. 299.

# Short Notes

This section is intended to secure prompt publication of important discoveries in physics. The reports should not exceed 800 words in length. A figure of size 7 cm × 7 cm will be counted as 150 words.

J. PHYS. SOC. JAPAN **11** (1956) 1121

## On the Dielectric Anomaly of *n*-Higher Alcohols in the "Waxy State"

By Mitsuo IDA

*Department of Physics, Faculty of Science, Kanazawa University*

(Received July 23, 1956)

Of the dielectric anomaly of *n*-higher alcohols in the "way state" stable at temperatures just below the melting point, Hoffman and Smyth[1] attributed the origin to Maxwell-Wagner polarization. Meakins and Mulley[2] found abnormally large dielectric absorption and dispersion of the dielectric constant at low frequencies, at temperatures below that of the waxy state, and explained the facts by the presence of hydrogen-bonded chains of hydroxyl groups capable of reversing their directions. On the other hand Asai and his cooperators[3] considered that the high value of the dielectric constant of *n*-higher alcohols is only superficial and should be explained with Cole's theory[4] of the conductive dielectric.

If Asai's opinion is correct the dielectric constant of a *n*-higher alcohol must vary with electrode seperation of the condenser as Cole pointed out[5]. Therefore the present author measured the dielectric constant of cetyl alcohol and octadecyl alcohol with different electrode seperation from 1.2 mm to 6.7 mm at 2 Kc/s and 0.6 Kc/s, but could not find significant variation. So the dielectric anomaly at frequencies above 0.6 Kc/s does not seem to be a surface effect in the sense of Cole's theory but principally a volume property. For the purpose of studying the dielectric mechanism it is often useful to determine the relation of the real part $\varepsilon'$ and the negative imaginary part $\varepsilon''$ of the complex dielectric constant, and the author measured the two values in the waxy state and plotted a Cole-Cole diagram. The results were not the same in the heating and cooling stages. Fig. 1 is the diagram for the heating stage and consists of a circular arc with its center of little below the $\varepsilon'$ axis. If this diagram is correct the dielectric anomaly of *n*-higher alcohols in the heating stage ought to be attributed to the orientational polarization as was advocated by Meakins and Mulley rather than to Maxwell-Wagner polarization. Fig. 2 is the diagram for the cooling stage and shows conspicuous variation with temperature. This diagram can also be explained qualitatively if we assume that as the temperature becomes higher and the frequency lower the orientation of entire molecule becomes more likely to occur than that of the hydroxyl group alone.

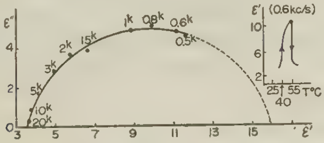

Fig. 1. Complex dielectric constants of octadecyl alcohol at the temperature shown in the $\varepsilon'-T$ curve of the heating stage.

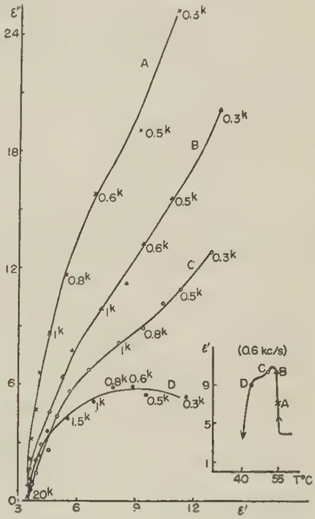

Fig. 2. Complex dielectric constants of octadecyl alcohol at the temperatures shown in the $\varepsilon'-T$ curve of the cooling stage.

The detail of this research will be published in the Science Reports of Kanazawa University.

The author wishes to express his sincere thanks to Professor H. Shoji for his kind guidance.

### References

1) J. D. Hoffman and C. P. Smyth: J. A. C. S. **71** (1949) 431.
2) R. J. Meakins and J. W. Mulley: Aust. J. Sci. Res. **A. 4** (1951) 365.
3) K. Asai, E. Yoda and S. Yamanaka: J. Phys. Soc. Japan **10** (1955) 634.
4) J. F. Jhonson and R. H. Cole: J. A. C. S. **73** (1951) 4536.
5) R. P. Auty and R. H. Cole: J. Chem. Phys. **20** (1952) 1309.

J. PHYS. SOC. JAPAN **11** (1956) 1122

# Surface Potential and Surface Conduction of Molybdenite

By Ichiro NAKADA

*Kobayashi Institute of Physical Research, Kokubunji, Tokyo.*

(Received June 23, 1956)

The measurements of surface potential and surface conduction of semiconductors in various gas ambients have given valuable information concerning their surface electronic states. With these measurements, Brattain, Bardeen and Morrison[1] have obtained a clear model of the surface space charge layer for germanium.

Now, we have made similar measurements on molybdenite since it is particulary suited for such experiments, because thin foils of single crystal can be cleaved easily from a natural crystal.

The measured samples are several microns in thickness with areal dimension of about $1 \times 1$ cm$^2$. At room temperature they are all $n$-type with Hall mobility of about 100 cm$^2$/volt, sec, and carrier density of about $10^{16}$/cm$^3$. These values are in the same order as those reported by Mansfield and Salam[2], though their samples are $p$-type.

The sample was placed in a vacuum vessel and $HNO_3$ and $NH_3$ ambients were cycled alternatively. The surface potential was measured by Kelvin method, in which the gold net was used as the reference electrode.

The typical result is shown in Fig. 1. For comparison, the change of surface potential on Al plate for the same reference electrode and gas cycling was also shown in the figure. The surface potential of molybdenite changes for different gas ambients in a rather complicated manner but the change with illumination has a clear relation to the ambient. In $HNO_3$ it increases with the illumination in a similar way to the case of $n$-Ge in the ambient of $O_3$ or dried air. For the case of $NH_3$ the effect is very small.

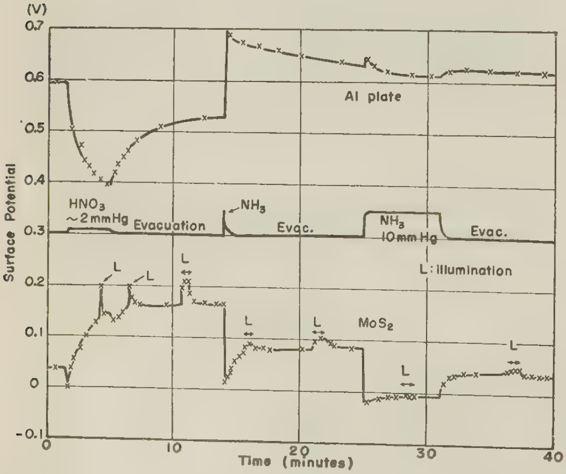

Fig. 1. The surface potential for different gas ambients.

Next the change of surface potential with illumination (i.e. surface photovoltage) and surface conduction were measured simultaneously. Here the surface potential change with illumination was measured by chopped light method and the surface conduction was deduced from D.C. conductivity. The typical result of one cycle is shown in Fig. 2.

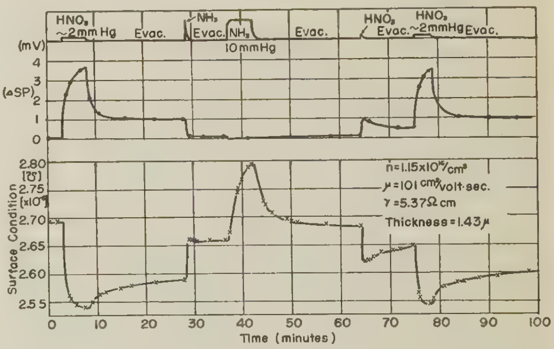

Fig. 2. Surface conduction and surface photovoltage for different gas ambients.

Apart from the quantitative details, we can interpret the result of Fig. 2 as follows.

In the ambient of $HNO_3$, adsorbed gas atoms would be charged negatively and might result in the formation of compensating positive space charges in the surface layer. For $n$-type semiconductors, decrease of surface conduction and increase of surface photovoltage can be easily explained by this model. The reverse would be the case for $NH_3$ ambient.

But from these results only, we could not deduce any detailed information about surface electronic states such as the energy levels and densities of the states.

## References

1) W. H. Brattain and J. Bardeen: Bell. Syst. Tech. Jour. **32** (1953) 1. S. R. Morrison: Jour. Phys. Chem. **57** (1953) 860. J. Bardeen and S. R. Morrison: Physical **20** (1955) 873.

1) R. Mansfield and S. A. Salam: Proc. Phys. Soc. **B66** (1953) 377.

J. PHYS. SOC. JAPAN **11** (1956) 1123

# Magnetic Anisotropy of the Iron Sulfide Single Crystal at $\alpha$-Transformation Temperature

By Takahiko KAMIGAICHI
*Physical Laboratory, Faculty of Education, Hiroshima University, Mihara*
Tadamiki HIHARA, Hideo TAZAKI
*Department of Physics, Faculty of Science, Hiroshima University, Hiroshima*
and Eiji HIRAHARA
*Department of Applied Physics, Faculty of Engineering, Hiroshima University, Hiroshima*

(Received July 2, 1957)

We have observed the anisotropy of electrical conductivity of iron sulfides single crystals at $\alpha$-transformation temperature ($T_\alpha$)¹⁾, and have now been studying the magnetic anisotropy of this substance at the same temperature range by using a magnetic balance. The samples of single crystals measured were prepared by the method mentioned in reference 1, and were made into a shape of parallelepiped, $3\times2\times2\,\text{mm}^3$. The symmetry axes of the single crystal were determined by the Laue method of X-ray diffraction. The samples measured contain an excess of sulfur $x=0.04$ in $FeS_{1+x}$.

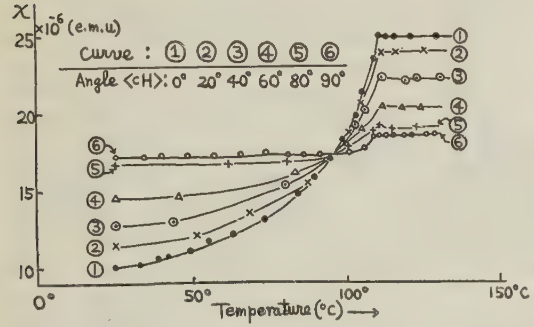

Fig. 1. Thermal variation of magnetic susceptibility of iron sulfide for various direction of external field *H*.

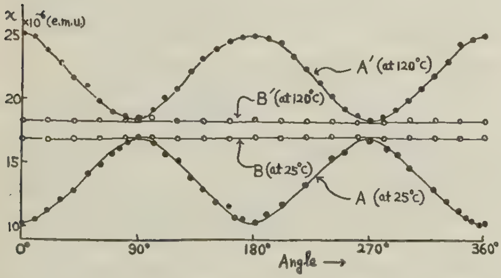

Fig. 2. Angle dependence of magnetic susceptibility of iron sulfide at constant temperatures.

The results recently obtained are shown in Figs. 1 and 2; curve 1 in Fig. 1 represents the thermal variation of magnetic susceptibility measured along the direction of the c-axis, and curve 6 the one along a direction in the c-plane, perpendicular to the c-axis. It was found that the thermal variations of the susceptibility depend upon a direction of external field H. The results obtained are shown by curves 1∼6 in Fig. 1, where angles indicated are those between the directions of H and the c-axis. The field H is in the plane including the c-axis. The angle dependence of susceptibility measured at constant temperature is shown by the curves *A* and *A′* in Fig. 2 for two temperatures 25°C and 120°C. When the crystal is rotated around the c-axis at the same temperatures, 25°C and 120°C, no dependence is observed as shown by curves *B* and *B′* in Fig. 2. The angles indicated on the abscissa in Fig. 2 are those between the directions of *H* and the c-axis for curves *A* and *A′*, while, those between the direction of *H* and a reference line in the c-plane for curves *B* and *B′*.

From the results described above, it seems that the anomalous thermal variation of the susceptibility of the substance is analogous to that of $\alpha$-$Fe_2O_3$.²⁾ Namely it is supposed that the direction of antiferromagnetism is fixed parallel to the c-axis at lower temperature than $T_\alpha$, whereas it rotates easily in the c-plane so as to be disposed perpendicularly to the external field *H* at the temperature above $T_\alpha$.

As for the cause of such a large difference in susceptibility between the values of curves 1 and 6 in the temperatures above $T_\alpha$, it might be explained by an anisotropic parasitic ferromagnetism depending on a direction in the c-plane, but its full explanation must be reserved untill more detailed experiments will be finished.

This work was financially supported by the Scientific Research Fund of the Ministry of Education.

## References

1) T. Kamigaichi T. Hihara, H. Tazaki and E. Hirahara: J. Phys. Soc. Japan **11** (1956) 606.
2) L. Néel: Rev. Mod. Phys. **25** (1953) 58.

J. PHYS. SOC. JAPAN **11** (1956) 1124~1125

## Photoconduction of Silver Chloride Crystals

By Noriaki ITOH and Tokuo SUITA

*Department of Electrical Engineering, College of Engineering, Osaka University*

(Received August 1, 1956)

The photoconductivity of silver halide crystals has been measured by several authors in D. C. fields[1,2]. However, the effects of dendrite formation and space charge seem to be serious, especially at room temperature. We measured the photoconductivity of AgCl with rectangular pulse voltage to minimize these secondary effects.

The measuring procedure we used, is as follows. The rectangular voltage pulse of 200 $\mu$ sec duration was applied to two specimens simultaneously and the current pulses through the specimens were put into the difference amplifier, which counterbalances the dark current and the charging and discharging current of both specimens. Photocurrent was measured by illumination of one specimen with 450 watts tungsten lamp through a liquid filter. The photoresponce occurs immediately after the beginning of illumination and no delay was observed as in D. C. measurements.

The specimens were cut from single crystals grown by Kyropoulos method. The electrodes were thin silver films developed on the surface of the specimens by photographic developer, and the specimens were illuminated through these electrodes.

In virgin specimens the photocurrent decreases with time at the beginning of illumination as shown in Fig. 1. This decrease ceases within about 100 seconds and cannot be observed at the subsequent illuminations at all. Therefore this decrease in the photocurrent seems to be due to photographic silver specks produced by illumination. These phenomena were observed also in the case of dielectric breakdown[3]: the breakdown voltage increases with illumination and saturates in a few minutes.

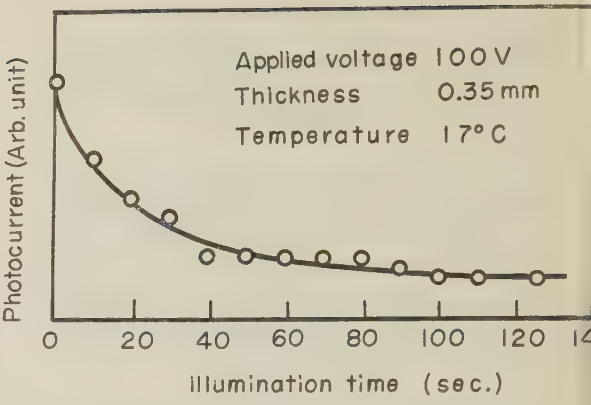

Fig. 1 The dependency of photocurrent on illumination time for a virgin specimen.

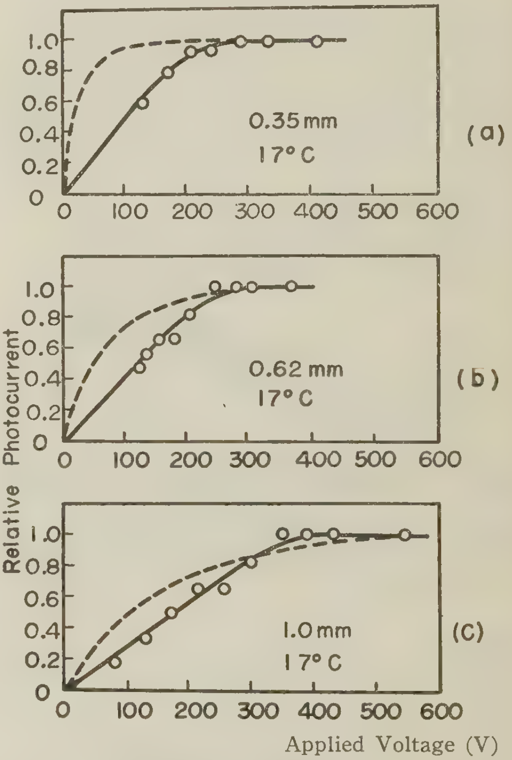

Fig. 2. The dependency of photocurrent on applied voltage.

—○—○— experimental results,
— — — calculated curve.

The dependency of photocurrent on the applied voltage for specimens illuminated more than 100 seconds is shown in Fig. 2. The photocurrent increases with increasing voltage for lower voltages and then saturates. Saturation effect may be explained by considering that "Schubweg" becomes comparable to the crystal thickness in higher fields. In our results, the saturation occurs at higher field strength than the calculated value[4] from the known value of mobility 50 cm$^2$/volt·sec and life time $10^{-6}$sec[5], and the discrepancy is larger for thinner specimens. Accordingly our results seem to show that the space charge lowers the effective field strength especially in the case of thinner specimens. More experiments are being carried out.

We wish to thank to Dr. E. Mizuki and other staffs of the research laboratory of Fuji Photofilm Co. for their supplying silver halide materials and for their valuable discussions. We also thank to Mr. A. Yonezawa for his devoted assistance to our experiments.

## References

1) W. Lehfeldt: Göttingen Nachrichten II, **1** (1935) 171.
2) S. Suzuki, Hakone Symposium on Photographic Sensitivity A**4** (1953).
3) T. Suita and N. Itoh: Jour. Phys. Soc. Japan **11** (1956) 474.
4) N. F. Mott, R. W. Gurney: *Electronic Processes in Ionic Crystals*, (Oxford 1940) p. 122.
5) C. Yamanaka and T. Suita: Tech. Rep. Osaka Univ. **5** (1955) 47.

---

J. PHYS. SOC. JAPAN **11** (1956) 1125

# On the Conducting Mechanism of Oxide Coated Cathode

By Hiroyuki MIZUNO
*Matsushita Electronics Corporation*
*Kyoto, Japan*

(Received August 20, 1956)

According to Loosjes-Vink theory, the conducting current of oxide cathode is carried mainly by conduction electrons which move from a granule to a granule in low temperature region (<800°K), while it is carried by electron gas emitted from granules in high temperature region (>800°K)[1].

If the conducting mechanism is such as above mentioned, the rectifying property between sleeve and coated oxide is naturally quite different in two regions. We can evaluate the differences as following.

### (A) Low temperature region

According Mott-Schottky, we can write the rectification equation as below.

$$I=I_s[\exp(eV/kT)-1] \qquad (1)$$

Where $I_s$ is given

$$I_s=\sigma\sqrt{8\pi ne(V_0-V)/\varepsilon}\cdot\exp(-eV_0/kT)\,. \qquad (2)$$

$$I_s=\sigma/d(V_0-V)\cdot\exp(-eV_0/kT) \qquad (3)$$

for Schottky's and Mott's cases respectively and $V$ is the voltage (positive value of $V$ being forward) applied across the contact boundary itself, $e$ the electronic charge, $kT$ is thermal energy, $n$ and $\sigma$ are the density of conducting electrons and conductivity in semi-conductors respectively, $\varepsilon$ is dielectric constant, $d$ is the thickness of barrier layer and the value $V_0$ is

$$V_0=(\zeta-\varphi)/e \qquad (4)$$

where $-\zeta$ and $-\varphi$ are Fermi-energies measured from vacuum state.

(a) **Forward direction flow** ($V>0$)

Considering $V\gg(kT)/e$, in usual cathode temperatures, we can induce next equation from Eq. (1).

$$\log I=\log I_s+(eV/kT) \qquad (5)$$

If the low conduction is attributed to the conducting electrons across the granules as proposed by Loosjes and Vink, it is supposed that the rectifying action between sleeve and coated oxide is to be predicated by Mott-Schottky's theory. There-fore the curves $\log I-(1/T)$ are to be linear and temperature dependencies of currents are to be changed with applied voltages which are applied from sleeve to coated oxide.

(b) **Reverse direction flow** ($V<0$)

When voltage is applied reversly and $|V|$ is larger than $kT/e$, we can obtain the following equation, neglecting schottky effect and $\exp(eV/kT)$ term compared with 1 in Eq. (1).

$$\log|I|=\log I_0+\{-(eV_0/kT)\} \qquad (6)$$

We can see easily from Eq (6) that the $\log I-(1/T)$ curves are to be linear and these tangents are to be independent of applied voltages.

### (B) High temperature region

If the high temperature conduction is due to the electron gas emitted from granules as proposed by Loosjes and Vink, the rectifying equation is evaluated as following.

(a) **Forward direction flow** ($V>0$)

From diode theory, we can get next equation.

$$\log\frac{I}{T^2}=\log A-\frac{e(\varphi+V_m)}{kT} \qquad (7)$$

From Eq (7) we can see that the $\log(I/T^2)-(1/T)$ curves are to be linear and the temperature dependencies are to be equal with different applied voltages in high temperature region for forward direction flow.

(b) **Reverse direction flow** ($V<0$)

We can find the following current equation theoretically in reverse field.

$$\log\frac{I}{T^2}=\log A-\frac{e(\varphi+|V|)}{kT} \qquad (8)$$

It is noted that the $\log(I/T^2)-(1/T)$ curves are to be linear and the temperature dependencies are changed by applied voltages.

Using rectifying theory, we proposed an approval method of Loosjes-Vink theory, but the experimental application of this consideration is left to future work.

## Reference

1) R. Loosjes and H. J. Vink: Philips. Res. Rep. **4** (1949) 449.

J. PHYS. SOC. JAPAN **11** (1956) 1126～1127

# Emitter Current Noise in Junction Transister

By Tatsuo YAJIMA

*Technical Research Laboratory,*
*Broadcasting Corporation of Japan, Tokyo*

(Received July 4, 1956)

While shot noise properties of junction transistors are becoming clear¹⁾²⁾, physical nature of 1/f noise has not been well understood. Here some output noise current behavior of junction transistors in common base connection is studied over the frequency range 80 c/s～300 kc/s including both shot and 1/f noise region. Particularly to clarify the effect of current amplification factor $\alpha_0$, a measure of recombination, measurements are made mainly on npn germanium grown junction tetrodes, for which $\alpha_0$ can be widely varied independently by the applied transverse electric field in base region.

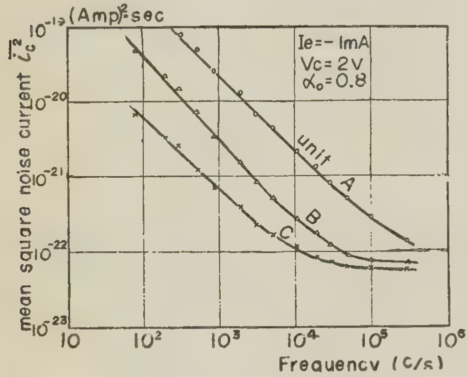

Fig. 1. Noise spectra of npn tetrodes.

Fig. 1 shows typical frequency spectra of mean square collector short circuit noise current measured on about 10 commercial units, including 3T201 and 3T203 made in Japan and 3N23B in U.S.A. The emitter sides are effectively open-circuited in a.c. during this study. For these units the noise due to collector saturation current $I_{co}$ (measured at $I_e=0$) is fairly low throughout the measured frequency range at relatively low collector voltages. Then observed noise can be attributed almost to emitter current $I_e$. The "bump" in spectrum as observed in pn junction diode³⁾ could not be detected.

Fig. 2a shows an example of $\alpha_0$– and current dependence of nearly flat spectrum component dominant at high frequency. The noise is nearly linear to $I_e$, and with decreasing $\alpha_0$, at first increases and then decreases through a maximum at about $\alpha_0=0.5$ for constant $I_e$. It is to be noted that the noise tends almost to zero for $\alpha_0\to1$ or 0. This outstanding behavior observed commonly agrees entirely with the low frequency partition noise formula¹⁾ $\overline{i_p^2}=2eI_e\alpha_0(1-\alpha_0)$ in its tendency. Measured absolute values are somewhat higher than the above formula, but agree within a factor 2 for all measured units. The predominance of partition noise in this situation can be explained by the shot noise equivalent circuit¹⁾ as in the study of junction triodes²⁾. So that this result may be regarded as the most direct experimental verification of partition noise in transistor. The fact that the high frequency performance of partition noise²⁾ could not be observed may be due to high $\alpha$ cut-off frequency (5～10 mc/s) of measured units.

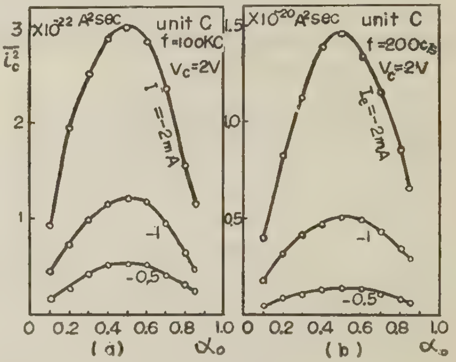

Fig. 2. Noise vs. $\alpha_0$ of npn tetrode
(a) flat component
(b) 1/f component.

The magnitudes of 1/f component are widely spread among different units as usual and proportional to $I_e^n$ where $n\sim2$ for small $I_e$ and $n<2$ for larger $I_e$. It is interesting, however, that $\alpha_0$ dependence of it shown in Fig. 2b is quite similar to the partition noise mentioned above. This feature was also common except for the anomalous one showing large leakage current between collector and second base.

There is a related phenomenon that the noise current sometimes shows slight but clear decrease with increasing collector voltage in the range where $I_{co}$ noise is sufficiently low. This is observed on many low noise junction transistors of various types having $\alpha_0$ close to unity and for wide frequency range. This seems curious at first sight, but the following explanation is possible; depletion layer widening of collector junction results in the increase of $\alpha_0$ and so the decrease of noise. Fig. 2b appears to confirm this point of view.

In this way we find that 1/f noise also has a component to be called "partition noise." Though detailed interpretations are left behind, the results may be a direct indication of that 1/f noise in junction transistor arises at least partly from the recombination process of injected carriers in the base and nearby surface.

The author wishes to thank Dr. K. Takeya and Mr. M. Kikuchi for their kind interest and valuable suggestions on this work.

### References

1) A. van der Ziel: J. Appl. Phys. **25** (1954) 815; Proc. I. R. E. **43** (1955) 1639
2) G. H. Hanson: J. Appl. Phys. **26** (1955) 1388
3) F. J. Hyde: Proc. Phys. Soc. **69B** (1956) 231

---

J. PHYS. SOC. JAPAN **11** (1956) 1127

## A Microscope Study of Etched Germanium Surfaces

by Makoto KIKUCHI and Seiichi DENDA
*Electrotechnical Laboratory, Tokyo Japan*

(Received July 30, 1956)

It was reported by Ellis[1] that there appeared small pits with closed terraces on germanium surface when certain etching solution was used. Recently, we have observed the same kind of etch pits using different kinds of solutions. Fig. 1 and Fig. 2 show the structure of the etch pits on (111) surfaces formed by No. 3 and No. 4 etching solutions, respectively.

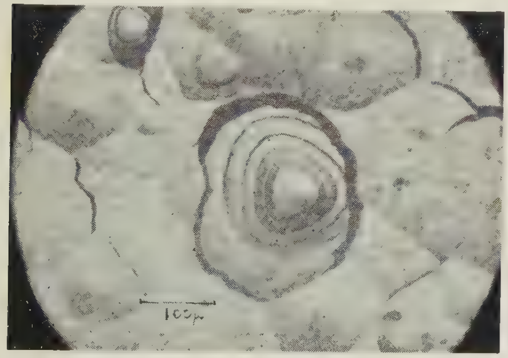

Fig. 1. Etch pits with terraces formed by No. 3 etch. (111) surface.

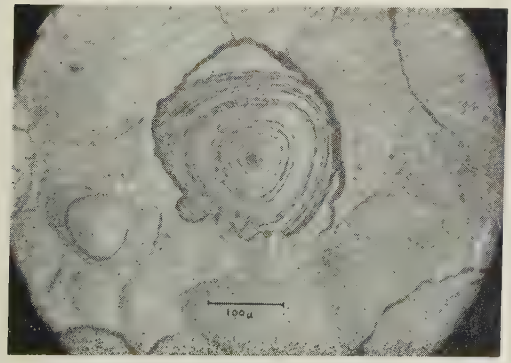

Fig. 2. Etch pits with terraces formed by No. 4 etch. (111) surface.

The composition of these etches are as follows:

No. 3 etch: 18 N $(HNO_3)$ 100 cc, 13 N (HCl) 100 cc, 30% $(H_2O_2)$ 30 cc. etching time 20 minutes.

No. 4 etch: 18 N $(HNO_3)$ 100 cc, 13 N (HCl) 100 cc, etching time 20 minutes.

Etch pits formed by CP-4 does not show the structure like this. When the etching solution is weakened (e. g. by replacing HF of CP-4 by HCl and omitting Br. etc), the etch pits become to show characteristic terrace structure. It seems likely that the number of terraces in the pits are increased as the solution is weakened.

Fig. 3 is a pit formed by No. 4 etch. As is shown, there is a group of small pits in the central portion of the bottom plateau, whose nature is not known at present.

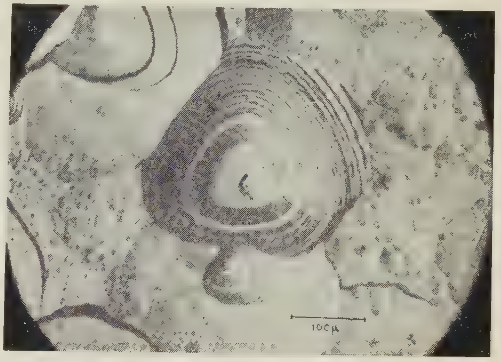

Fig. 3. Etch pit formed by No. 4 etch.

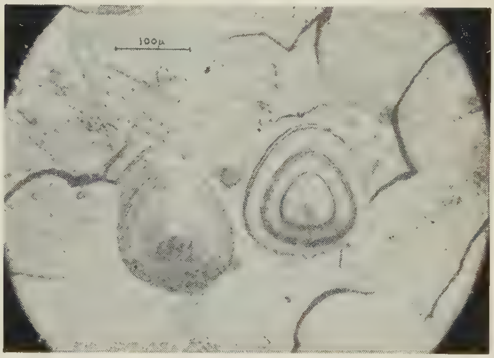

Fig. 4. A pair of etch pits formed by No. 4 etch.

In Fig. 4, a pair of pits of same size is shown. In most cases, it is observed that the terrace structure of these two pits does not appear in the same manner, one of them is fine and the other is rough

Further experiments are now being undertaken

### Reference

1) Ellis: J. A. P. **26** (1955) 1140.

# Errata

## Experimental Investigation on the Transition of Laminar Separated Layer

By Hiroshi SATO

J. Phys. Soc. Japan **11** (1956) 706

In Fig. 12, the scale of abscissa $y/\theta$ was in error. Numbers $-2$, $-1$, 0, 1, 2, 3, should be read $-4$, $-2$, 0, 2, 4, 6.

---

# Errata

## Structure of NQR Line I. Solid Iodine

By S. KOJIMA

J. Phys. Soc. Japan **11** (1956) 964

Figure 3(e) on page 965 has been inverted. Rotation of the photograph through 180° establishes agreement with other figures.

JOURNAL OF THE PHYSICAL SOCIETY OF JAPAN Vol 11., No. 11, NOVEMBER, 1956

# Observation of the High-Energy Proton-Proton Collision in Photographic Emulsion

By Shin-ichi KANEKO, Osamu KUSUMOTO and Shigeo MATSUMOTO
*Institute of Polytechnics, Osaka City University, Osaka.*

(Received August 10, 1956)

The tracing-back method has been applied to the detection of showers which could be regarded as those produced by single nucleon-nucleon collisions in a stack of stripped emulsions exposed at the stratosphere. The method consists in tracing star-producing tracks back along their passage through successive emulsion strips and in finding primary interactions. It enabled us to detect the interactions without any bias irrespective of the number of accompanying evaporation prongs.

A shower of the type $1+5_p$ detected by this method in a preliminary observation was analysed in terms of the single proton-proton collision. By the assumption of balance of transverse momenta for the charged outgoing particles alone, the incoming proton energy was estimated to be about 25 Gev and the inelasticity to be about 0.4. In this paper these results and another possible estimates has been presented together with a brief description of some features of the shower.

## § 1. Introduction

The phenomenon of multiple meson production in single nucleon-nucleon collisions at cosmic-ray energies has been studied by numerous workers making use of various experimental techniques. However, the results obtained are not necessarily in accordance with erch other[1].

Although the observations by nuclear emulsions make it possible to analyse particular showers which are under favourable conditions[2][3][4], it is not easy to observe a sufficient number of events for the statistical investigation. This difficulty is mainly due to the fact that the interaction of a high-energy nucleon with a hydrogen nucleus in emulsion is not accompanied, in general, by the emission of any heavily ionizing particle so that the event is likely to escape from detection by the usual area scanning method under a low magnification. These circumstances are in favour for the detection of high-energy showers since these emits, in general, a great number of shower particles into a narrow cone. But the method is not suited for the detection of low-energy showers. In fact, several showers which could be interpreted in terms of the single nucleon-nucleon collision were observed and analysed so far, but most of them were extremely energetic[2][3] ($\gtrsim$1000 Gev) or of remarkably high meson multiplicities[4]. It seems desirable, therefore, to search systematically free from detection bias for the meson showers due to single nucleon-nucleon collisions, in order to know the mechanism of multiple meson production at fairly low-energies (say, 10–100 Gev).

For this purpose, we have attempted a preliminary observation making use of a new method of searching which does not give any significant bias for detecting the showers. In this paper, we describe briefly the method of detection and the result of measurements on a particular shower which was detected by this method and was regarded as an example of single proton-proton interactions.

## § 2. The Tracing-Back Method

In a stack of stripped emulsions which was exposed at the stratosphere, numerous disintegration stars initiated by secondary N-radiations as well as those by primary protons were observed. If the size of the stack is so large that it is comparable with the mean free path of nuclear interactions of N-radiations in emulsions, an appreciable number of shower particles emerging from the primary interactions which have occurred in the stack can also give rise to nuclear disintegrations in the same stack. If we trace, under a high magnification, tracks of relativistic singly-charged particles—mostly protons and charged

$\pi$-mesons—producing nuclear disintegrations back in the opposite directions of their motion, then either we will attain to a primary interaction if the traced particle was that produced in the stack or we will leave the stack if the particle was that incident upon the stack. It is apparent that the primary interactions can be detected without any significant bias on the number of (heavy and thin) tracks associated with them. The interaction of nucleons with hydrogen nuclei should be detected approximately at the rate of the cross section of hydrogen relative to that of the other elements in emulsion assuming that the number of outgoing shower particles is independent on the mass number of the target nucleus. Then, the method seemed appropriate for searching for fairly low-energy nucleon-nucleon interactions.

In practice, we have adopted the following procedure. First, nuclear disintegration stars with three or more heavily ionizing prongs were searched by the usual area scanning method in the lower half region of plates exposed vertically. Then tracks associated with the stars which satisfied all of the following criteria were selected:

(i) The track lies in the upper hemisphere with respect to the star.

(ii) The grain density is less than 1.4 times the plateau value.

(iii) The direction of the track coincides nearly with the shower axis if it can be defined.

(iv) The dip angle of the track is less than a certain maximum value.

The possibility that selected tracks were due to relativistic secondary particles ejected upwards from the stars is diminished by imposing criteria (i), (ii), and (iii) upon the tracks, though it may not be ruled out perfectly. The maximum acceptable dip angle in criterion (iv) is determined from the requirement that the track can be traced easily from an emulsion strip to the next one and then it depends mainly upon the quantities of background tracks and random fogs. In the emulsions we have observed it was determined as $\cot^{-1}7$. The tracks which satisfied the above four criteria have been traced with oil immersion objectives back to the point of their production or incidence.

In this way, it has been found that we can detect efficiently any interaction of very small size as the types $0+2_p$ and $0+1_n$ (presumably an elastic proton-proton and neutron-proton collisions, respectively) which escape, of course, from the detection by the usual scanning method. Thus, we have detected the high-energy shower which will be described below in addition to several events which could be regarded as those produced by collisions of low-energy nucleons with hydrogen nuclei.

The tracing-back method has two additional advantages. The energy of a traced particle may be estimated from the size of the star it has produced—the original star—or sometimes from the scattering measurements because of the small dip of its track. This means that it may be possible to estimate the energy of at least one of the shower particles emerging from the parent interaction if it has been found by the tracing-back method. Furthermore, the fact that a traced particle has a small dip angle leads, in general, to the parent shower presenting a good geometrical condition especially when the traced track is nearly on the shower axis of the primary interaction. (The shower which will be described in the following sections is an example of these favourable cases.) This is in favour of a measurement of the primary shower. It appears also that the method enables us to study the process of successive interactions of N-radiations.

## § 3. Measurements of the Shower

In this preliminary observation, we have used a stack of Ilford G5 stripped emulsions, 600 microns thick and $6\times6$ inches wide, flown at an altitude of 70,000 feet during four hours at Bristol*. The shower *S* of the type $1+5_p$ shown in Fig. 1 has been detected by tracing back the primary particle (track 3) of the star *A* of the type $8+1_p$ which was found by the general scanning. The target diagram of the secondary particles emerging from shower *S* in the laboratory system is shown in Fig. 2. The primary and some of the secondary particles of the shower were dipping at angles much greater than $\cot^{-1}7$, but careful observations have made it possible to follow definitely

---

* A stack of greater size which has been exposed at a lower geomagnetic latitude can afford, of course, better facilities for detecting high-energy showers above 10 Gev because of a smaller amount of contamination of low-energy stars.

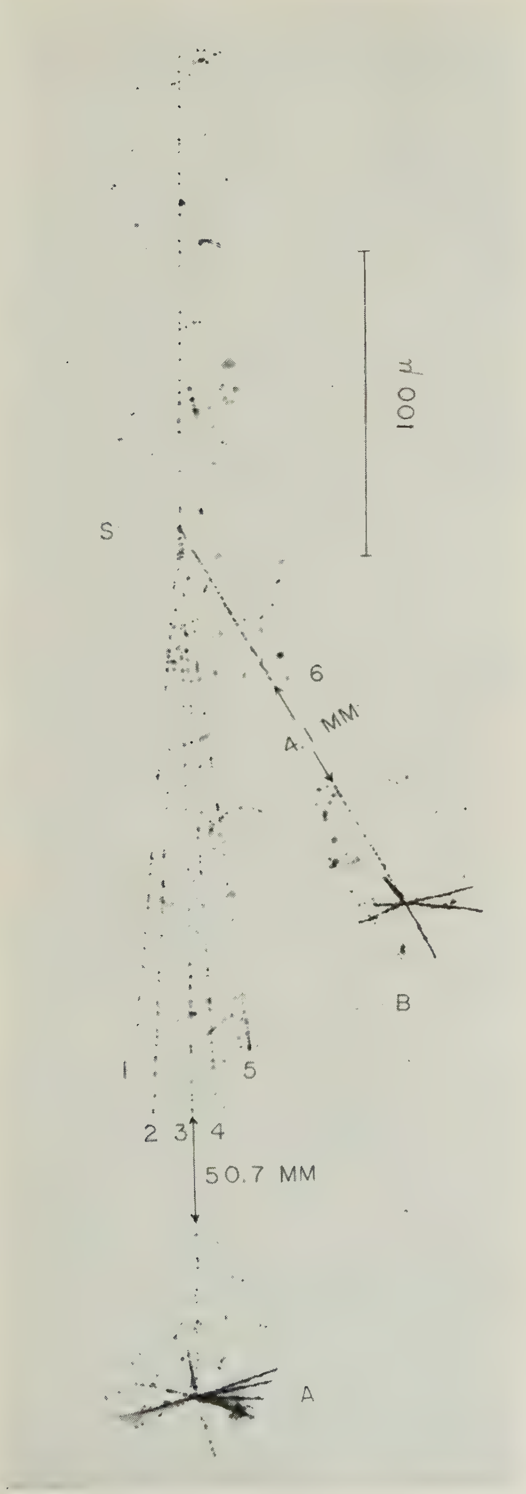

Fig. 1. Microphotograph of the shower, $S$, which could be regarded as a single proton-proton interaction at about 25 Gev together with those of the secondary nuclear disintegrations of the types $8+1_p$ and $6+0_p$ ($A$ and $B$).

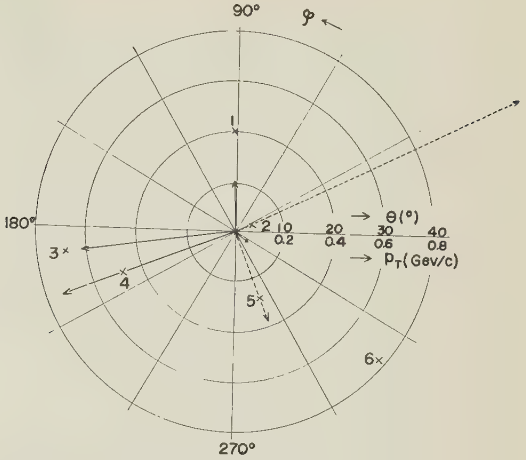

Fig. 2. The target diagram of the shower particles in the laboratory system and the transverse momentum diagram. The cross represents the polar angle $\theta$ and the azimuthal angle $\varphi$ of each shower particle. The radial vector represents the transverse momentum $p_T=p\sin\theta$ of the shower particle. The transverse momenta of particles 2 and 5 (the dotted vectors) were estimated from those measured directly on particles 1, 3, 4, and 6 (the full vectors) on the assumption of transverse momentum balance for the charged shower particles alone, $\sum_1^6 p_T=0$.

along these tracks from a plate to the next successively. Thus, it was found that shower particle 6 had given rise to nuclear disintegration $B$ of the type $6+0_p$ and that particles 1 and 4 had suffered a large angle single scattering of $\sim 20°$ and $\sim 3°$ at a point of their passage, respectively.

The blob density of the shower track was measured in some of the plates traversed by it, except for the layers within 50 microns from the emulsion surface and from the emulsion-glass interface, respectively. The plateau blob density was determined in each plate making use either of flat tracks of electrons having high energies ($\gtrsim 100$ Mev) in cascade showers or of primary protons ($\gtrsim 100$ Gev) giving rise to high-energy meson showers. The multiple Coulomb scatterings of shower particles 1, 3, 4. and 6 were measured in all of the plates traversed by them making use of the procedure recommended by the CERN standards[5]. The results of these measurements are shown in Fig. 3 and Table I. In Fig. 3 are also shown for comparison the experimental relations between the ionization and velocity of relativistic particles obtained

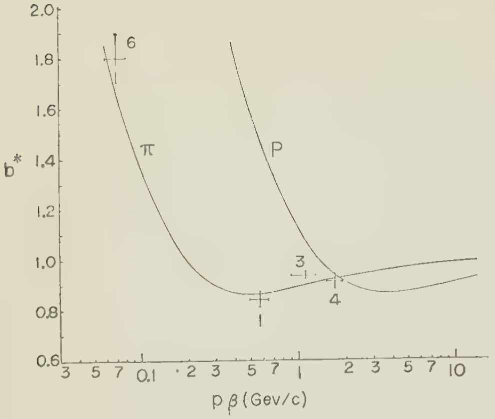

Fig. 3. The normalized blob densities and multiple scatterings measured on shower particles 1, 3, 4, and 6. The full curves are the experimental relations given by Stiller and Shapiro[6].

by Stiller and Shapiro[6]. Particles 1 and 6 were presumably $\pi$-mesons. No definite identification could be done for particles 3 and 4, but we have assumed in the following analysis that they were a $\pi$-meson and a proton, respectively.

Table I. The results of measurements of blob density and multiple scattering of four shower tracks together with their identities and secondary interactions.

| Shower particle | Track length per plate (mm) | Normalized blob density $b^*$ | Product of momentum and velocity $p\beta$ (Gev/c) | Identity | Secondary interaction |
|---|---|---|---|---|---|
| 1 | 11.3 | $0.84 \pm 0.03$ | $0.6 \pm 0.1$ | $\pi$ | ~20° scattering |
| 3 | 6.4 | $0.93 \pm 0.02$ | $1.1 \pm 0.2$ | $\pi(P)$ | $8+1_p$ |
| 4 | >50 | $0.91 \pm 0.03$ | $1.7 \pm 0.2$ | $P$ or $\pi$ | ~3° scattering |
| 6 | 0.8 | $1.8 \pm 0.1$ | $0.07 \pm 0.01$ | $\pi$ | $6+0_p$ |

The energies of shower particles 2 and 5 could not be measured directly since their tracks were dipping steeply to the surface of emulsion. In order to estimate their energies, we assumed tentatively that the transverse momenta of neutral particles emerging from the interaction have retained their balance independently of those of charged outgoing particles. This may, of course, not be the case, but the error resulting from this assumption seems to be small when a large number of particles were emitted. The resultant transverse momentum of all the charged shower particles should then vanish:

$$\sum_1^6 \boldsymbol{p}_T = 0\,, \qquad (1)$$

with

$$p_T = p \sin\theta\,,$$

where $\boldsymbol{p}$ and $\boldsymbol{p}_T$ are the momentum and its transverse component and $\theta$ denotes the polar angle of the secondary particle with respect to the primary direction in the laboratory system. The transverse momenta of shower particles 2 and 5 can then be determined graphically on the assumption of Equation (1) making use of the transverse momentum diagram shown in Fig. 2.

The momenta thus estimated are shown in the fourth column of Table II together with those measured directly for the other four particles. It should be noted that particle 2 is very energetic as compared with the other. It seems reasonable to assume, therefore, that particle 2 was a proton (presumably one of the colliding protons) and that the remainder, particle 5, turned out to be a $\pi$-meson.

## § 4. The Lorentz Transformation

According to the well-known formulas of Lorentz transformation, the momentum and the polar angle of a particle emerging from a proton-proton collision in the centre-of-mass system are represented in terms of the corresponding quantities in the laboratory system by the equations

$$\left.\begin{aligned} cp^* \cos\theta^* &= (cp\cos\theta - \beta_c U)(1-\beta_c^2)^{-1/2} \\ cp^* \sin\theta^* &= cp\sin\theta\,, \end{aligned}\right\} \qquad (2)$$

where $U$ is the total energy of the particle in the laboratory system, $\beta_c$ is the relative velocity of the two reference systems in units of the velocity of light, $c$, and the asterisk refers to the centre-of-mass system. Then, it follows

$$\beta_c = \frac{\overset{(p)}{\sum} cp\cos\theta + 1.5 \overset{(\pi)}{\sum} cp\cos\theta}{\overset{(p)}{\sum} U + 1.5 \overset{(\pi)}{\sum} U}\,, \qquad (3)$$

where $\overset{(p)}{\sum}$ and $\overset{(\pi)}{\sum}$ denote the sums over protons and charged π-mesons, respectively. The numerical factor 1.5 in the formula comes from the assumption that the neutral π-mesons emitted were equal, in number and energy, to the positive and negative π-mesons. It is thus found that $\beta_c=0.963$ for the present shower.

Table II. The angles and momenta of shower particles in the laboratory and center-of-mass systems.

| Shower particle | Assumed identity | Lab. system | | Azimuthal angle $\varphi$ (deg.) | C. m. system | |
|---|---|---|---|---|---|---|
| | | Polar angle $\theta$ (deg.) | Momentum $p$ (Gev/c) | | Polar angle $\theta^*$ (deg.) | Momentum $p^*$ (Gev/c) |
| 1 | π | 20 | 0.6 | 92 | 118 | 0.2 |
| 2 | $P$ | 3 | 21.4 | 26 | 25 | 3.0 |
| 3 | π | 35 | 1.1 | 188 | 135 | 0.9 |
| 4 | $P$ | 24 | 1.8 | 202 | 148 | 1.4 |
| 5 | π | 14 | 1.6 | 291 | 86 | 0.4 |
| 6 | π | 39 | 0.1 | 320 | 168 | 0.3 |

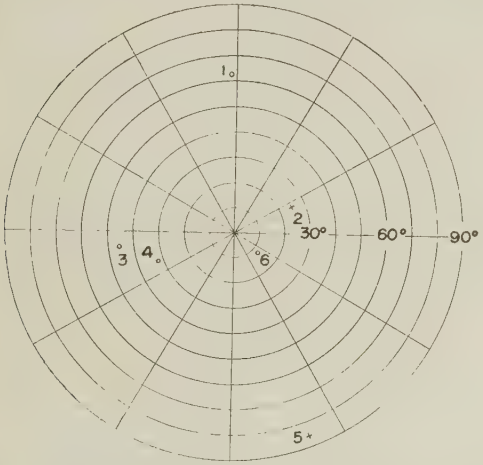

Fig. 4. The target diagram of the shower particles in the centre-of-mass system. The crosses and circles refer to those emitted into the forward and backward hemispheres, respectively.

The momenta and angles of the shower particles in the centre-of-mass system are determined using this value of $\beta_c$ and Equation (2). The results are shown in the sixth and the seventh columns of Table II. The target diagram in the centre-of-mass system is given in Fig. 4. The kinetic energy, $E_p$, of the incident proton in the laboratory system is estimated to be about 25 Gev by the equation

$$E_p=2Mc^2(\gamma_c^2-1)\,, \tag{4}$$

where $M$ is the rest mass of the proton and $\gamma_c=(1-\beta_c^2)^{-1/2}$ is the Lorentz factor of the centre-of-mass system. The inelasticity, $K$, is defined as the ratio of the energy lost in the collision—the total meson energy—to the available kinetic energy of the two colliding protons before the collision in the centre-of-mass system:

$$K=\frac{\gamma_c-(\gamma_{p1}^*+\gamma_{p2}^*)/2}{\gamma_c-1}\,, \tag{5}$$

where $\gamma_{p1}^*$ and $\gamma_{p2}^*$ are the Lorentz factors of the two protons after the collision in the centre-of-mass system. It is thus estimated to be about 0.41* using the values of the centre-of-mass momenta shown in Table II. The average momentum of the charged mesons in the centre-of-mass system is also found to be about 460 Mev/c.

## § 5. Discussion

Only one heavily ionizing track has been associated with the shower, but it has been shown that it is not a nuclear particle but a π-meson**. Neither visible nuclear recoil fragments nor slow electrons were observed. It seems likely, therefore, that the shower was produced by a collision of a high-energy proton

---

* It is to be noted that this value of the inelasticity agrees well with that estimated by the equation[7]

$$K=\frac{1.5n\gamma_c\sin\theta_{\max}}{2\mu(\gamma_c-1)}\,,$$

where $n$ is the number of charged mesons emitted, $\theta_{\max}$ is the limiting angle of the shower, and $\mu$ is the ratio of the rest mass of the proton to that of the π-meson.

** The fact that particle 6 (~40 Mev π-meson) gave rise to a small star $(6+0_p)$ is consistent with the observations of nuclear interactions initiated by artificially produced π-mesons[8]. Furthermore, it should be remembered that a neutron-proton collision observed at the Bevatron[9] has emitted a low-energy π-meson in addition to several relativistic particles in a similar way to the present shower.

with a hydrogen nucleus. Although a possibility of a peripheral collision with a heavier nucleous which was not accompanied by an evaporation of charged nuclear particles cannot be discarded, it seems reasonable to assume that bound nucleons other than the colliding partner inside the nucleus play only a minor role in the process of meson production. The possibility that the primary particle was a $\pi$-meson cannot also be rejected perfectly. However, most of $\pi$-mesons of energies 10–100 Gev produced nearly at the top of the atmosphere should have decayed in flight before their arrival at the stack, so that their intensity should be negligible as compared with that of protons of the same energies. The contribution of $\pi$-mesons produced locally in the materials surrounding the stack can also be neglected. It was assumed, therefore, that the shower was produced by a single proton-proton collision.

Concerning the scattering measurements of the shower particles, we should make allowance for a possible effect of the spurious scattering[10)11)] due to small local dislocations in processed emulsions. This effect seems likely to reduce the measured value of $p\beta$ of any high-energy track to a certain value (say, $p\beta \sim 2$ Gev/c). It might be possible to assume then that particles 3 and 4 were much more energetic than those estimated from the scattering measurements (Table I). However, it must be taken into account that the momentum measurement made on particle 4 is fairly reliable being free from the spurious scattering because of its very long track length per plate[11)] and that the energy measured on particle 3 is in accordance with the visible energy of star $A$ to which it gave rise. It seems probable then that the energies we have estimated are not seriously in error.

The particle idientifications made in Section 3 are, of course, not certain particulary for tracks 3 and 4. It may be possible, for instance, that they were a proton and a $\pi$-meson, respectively, in contrast with the assumption. It appears, however, that the results obtained are not seriously affected by this possible misidentification.

The primary energy and the inelasticity determined by the Lorentz transformation are based largely on the assumption of transverse momentum balance for the charged shower particles alone (Eq. (1)). It seems, then, necessary to make a few remarks on this estimate.

As an extreme case, it might be assumed that particle 2 had an energy of the same order of magnitude as those of the other particles. This assumption results in that two or more neutral particles having momenta similar to those of particles 3 and 4 should have been emitted in the azimuthal directions opposite to those of the latter particles in order to acquire balance of the transverse momenta (see Fig. 2) and that six or more mesons should have been produced in the collision. The primary energy is thus estimated to be at least 10 Gev*, since the recent observations at Berkeley show that the probability of occurrence of six or more meson production in $p-p$ or $n-p$ collisions seems to be very small at the Bevatron energies[9)12)]. It should be noticed that at the lower limit ($E_p \sim 10$ Gev) of this estimate the inelasticity of the collision turns out to be approximately unity which seems improbable to occur.

On the other hand, it is very unlikely that the primary particle was energetic far above 25 Gev, since it would result in a strong angular asymmetry of charged meson emissions into the forward and backward hemispheres in the centre-of-mass system.

These considerations seem, therefore, to be in favour of justifying the analysis given in Section 4, i.e., $E_p \sim 25$ Gev.

## § 6. Conclusions

Although the incoming proton energy has been estimated to be about 25 Gev, there seems to be an uncertainty within about ±15 Gev. Therefore, definite conclusions on the process of meson production cannot be drawn from this particular event, but it might be interesting to note some special features of the shower obtained by the above analysis.

The shower was accompanied by the emis-

---

* This lower limit agrees well also with the value estimated simply from the median angle, $\theta_{1/2}$, of the charged shower particles:

$$E_p = 2Mc^2\left(\frac{1}{\tan^2\theta_{1/2}} - 1\right).$$

However, the latter is based on the crude assumption that mesons are emitted symmetrically into the forward and backward hemispheres with the velocity equal to $\beta_c$. It cannot be stated, therefore, that the latter estimate is better than that given in Section 4.

sion of a low-energy $\pi$-meson. This fact suggests that the criterion for detecting the single nucleon-nucleon collision, no existence of any heavily ionizing prongs, which has usually been employed thus far is not necessarily correct; i.e., in some cases of single nucleon-nucleon collisions a slow $\pi$-meson giving rise to a heavy ionization may emerge from the interaction. In this connection, the tracing-back method described in Section 2 is available for detecting the showers irrespective of the number of accompanying heavy tracks.

If the energy estimation carried out in Section 4 is fairly satisfactory, i. e., $E_p \sim 25$ Gev, the kinetic energies of the two protons after the collision in the centre-of-mass system will be significantly different from each other (2.0 and 0.7 Gev). This fact relates closely to the marked angular asymmetry of charged meson emission in the centre-of-mass system as shown in Fig. 4. In this estimation the inelasticity turns out to be about 0.4.

On the other hand, if the primary energy was actually as low as 10 Gev, though this assumption is less probable than the above, then it can be said that we observed a low-energy shower with a remarkably high meson multiplicity ($\gtrsim 6$) resulting from an extreme loss of energies of the colliding protons.

### Acknowledgment

We wish to express our cordial thanks to Professor Y. Watase for invaluable suggestions on the approach to the subject of nucleon-nucleon collisions and continual encouragements in the course of this work. Thanks are also due to our colleagues, Messrs. S. Miyamoto, M. Teranaka and M. Takahata, for their generous cooperative efforts. The stack of stripped emulsions was obtained through the courtesy of Professors C. F. Powell, Y. Fujimoto, and S. Nakagawa. This study has been supported in part by a Grant in Aid for Fundamental Scientific Research from the Ministry of Education.

### References

1) For this discussion, see, for example, Y. Watase, K. Suga, Y. Tanaka and S. Mitani: Nuovo Cimento **2** (1955) 1183.
2) J. J. Lord, J. Fainberg and M. Schein: Phys. Rev. **80** (1950) 970.
3) V. D. Hopper, S. Biswas and J. F. Darby: Phys. Rev. **84** (1951) 457.
4) K. Gottstein and M. Teucher: Z. f. Naturf. **8a** (1953) 120.
5) Supple. Nuovo Cimento **11** (1954) 228.
6) B. Stiller and M. M. Shapiro: Phys. Rev. **92** (1953) 735.
7) G. Bertolino and D. Pescetti: Nuovo Cimento **12** (1954) 630; G. Bertolino: Nuovo Cimento **3** (1956) 141.
8) G. Bernardini and F. Levy: Phys. Rev. **84** (1951) 610.
9) W. B. Fowler, G. Maenchen, W. M. Powell, G. Saphir and R. W. Wright: Phys. Rev. **101** (1956) 911.
10) S. Biswas, B. Peters and Rama: Proc. Ind. Acad. Sci. **A41** (1955) 154.
11) E. Lohrmann and M. Teucher: Nuovo Cimento **3** (1956) 59.
12) R. W. Wright, G. Saphir, W. M. Powell, G. Maenchen and W. B. Fowler: Bull. Am. Phys. Soc. **30** (1955), No. 8, 18.

JOURNAL OF THE PHYSICAL SOCIETY OF JAPAN Vol. 11, No. 11, NOVEMBER, 1956

# Crystal Structure of Ferromagnetic Nickel Oxide*

By Yasumitsu SHIMOMURA, Morio KOJIMA and Shozo SAITO
*Department of Physics, University of Osaka Prefecture*

(Received July 30, 1956)

The determination of crystal structure was performed on the ferromagnetic nickel oxide obtained by the flame fusion method. Apart from a slight deviation of axial angle from 90°, it has a defect tetragonal structure belonging to the space group $I4_1/amd$ ($D_{4h}{}^{19}$), the lattice constants being $a=5.899_6$ kX. and $c=8.343_4$ kX. ($c/a=\sqrt{2}$) at $31._5$°C. Considering the deviation, the structure must be altered to a monoclinic one belonging to $C2/m$ ($C_{2h}{}^3$), the lattice constants being $a=5.104_4$ kX., $b=2.951_5$ kX., $c=2.948_2$ kX. and $\beta=125°11._4'$ at the same temperature as above. The details of the atomic arrangements in both cases are given in the last column of Table 8. The saturation magnetization estimated under an appropriate assumption for the spin alignment agrees fairly well with the observation. Thus the comparison of the present structure with that of the ordinary nickel oxide may give us a peek into one of the processes of transition from an antiferromagnetic state to a ferromagnetic one.

## § 1. Introduction

Nickel oxide crystals obtained by the flame fusion method sometimes exhibit fairly strong ferromagnetism. In almost all the cases, however, the magnetism must be ascribed to reduced nickel, the formation of which being naturally conceivable from the usage of hydrogen gas in the course of preparation. But in one case there has been produced a crystal exhibiting ferromagnetism indigenous to the oxide.

Dependence of its susceptibility on temperature observed by K. Igaki under an appropriate magnetic field is illustrated by the χ-curve in Fig. 1, which is said to be reproducible for several repetitions of heating and cooling. The curve indicates that the specimen is a typical ferromagnetic different clearly from nickel. On the other hand, dependence of magnetization on external field was observed by E. Uchida and H. Kondoh at room temperature, the results being the $\sigma_g$-curve in the same figure, from which the saturation magnetization can be estimated as $2.5_0$ gauss/gr.. In both measurements, no special regard was paid to the crystal orientation with respect to the external field.

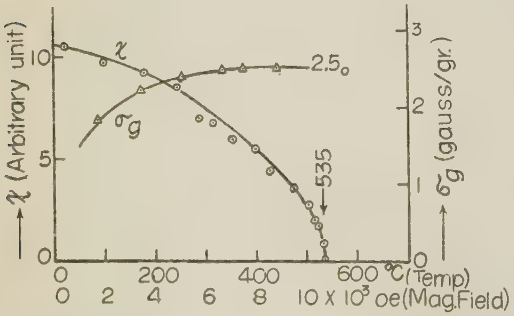

Fig. 1. Magnetic characteristics of ferromagnetic oxide.
χ-curve: Variation of susceptibility (in arbitrary unit) with temperature under the appropriate external field (after K. Igaki).
$\sigma_g$-curve: Magnetization curve at room temperature (after E. Uchida and H. Kondoh).

Though the magnetic characteristics can be considered fairly stable for heating in view of Igaki's measurement, some parts of the crystal lose the ferromagnetism when reheated at nearly the same temperature as that of its formation. Besides, the magnetization seems to be lowered by mechanical pulverization, the fact being confirmed also by Uchida and Kondoh through observation analogous to that for the $\sigma_g$-curve.

The present paper deals with the crystal structure of this ferromagnetic nickel oxide.

## § 2. Experimental

The starting material of the ferromagnetic crystal** was oxide powder formed by calcinating nickel sulphate, from which an antiferromagnetic crystal was also obtained in another course of preparation under nearly the same condition. The latter crystal was employed for comparison. Both crystals have not been subjected to chemical analysis on account of their limited quantity.

---

* The paper was read before the 10th and 11th annual meetings of the Physical Society of Japan held respectively on October 14, 1955 at Tokyo and on August 17, 1956 at Sendai.

** The crystals of nickel oxide in the present experiment were prepared by Y. Nakazumi, Tochigi Chemical Indust. Co. & Ltd., Osaka.

X-ray analysis was performed chiefly by the rotating or oscillating crystal method with a cylindrical film of 4 cm. in diameter and employed Cu$K$ radiations, which were monochromatized with a lithium fluoride crystal when necessary. The sample for this analysis was a cleaved cuboid with edges less than 0.5 mm., the size being sufficiently small to bathe in the incident beam in this experiment.

In order to determine the lattice constant presisely, the Bragg angles of Ni$K_\alpha$ reflexions from *{422}* planes (referred to the unit cell of NaCl type) of the oxide were measured in comparison with the reflexions of Cu$K_\alpha$ from (*331*) and (*420*) of nickel, whose lattice constant and thermal expansion coefficient are taken as $a=3.5170_7$ kX. and $1.37\times10^{-5}$/°C. at 15°C., respectively.[1] Although the standard nickel used was always in a powder state, the oxide sample was in two forms, cuboidal and powder. Pulverization was never adopted to obtain the latter for the reason mentioned in the previous paragraph. In the case of the measurement on the cuboidal specimen, use was made of the spots on the equator line in a rotation photograph.

The specific gravity was measured by the ordinary hydrostatic weighing method using distilled water or methyl alcohol as the immersion liquid.

## § 3. Results of Experiments

Considering the general appearance of the diffraction pattern of the ferromagnetic nickel oxide, the structure does not seem to differ so much from the deformed NaCl type of the antiferromagnetic one. For the moment, therefore, the description will be made with reference to this cell. The ferromagnetic crystal as well as the antiferromagnetic one is a crystal aggregate, individuals of which are mutually in a twin relation with parallel (*001*) planes.[2] The cell dimension and axial angles of the two were measured and are shown in Table I, where the values of specific gravity are also given. For the antiferromagnetic oxide, the observed value of specific gravity is in good agreement with the calculated one under the assumption that it has the stoichiometric composition. It must be

Table I. Cell dimensions, axial angles and specific gravities of nickel oxide crystals of two kinds.

| Specimen | Cell dimension & axial angle (Deformed NaCl type) | | | Specific gravity |
|---|---|---|---|---|
| | $a$($R_kX$.) | $\alpha$ | Temp. (°C.) | |
| Antiferromag. | $4.168_2$ | $90°3._6'$ | $30._0$ | $6.80_5$ |
| Ferromagnetic | $4.171_7$ | $90°3._8'$ | $31._5$ | $6.4_5$ |

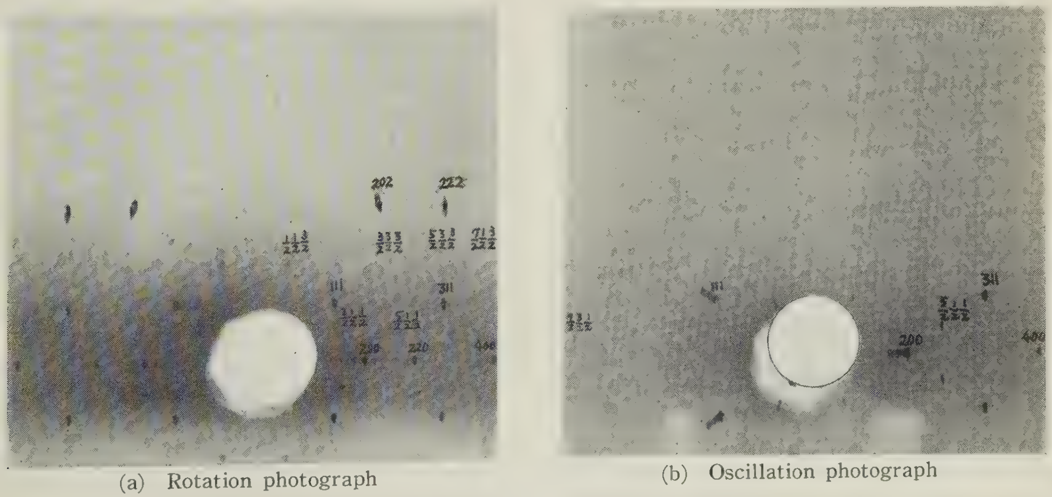
202
222
$\frac{1}{2}\frac{1}{2}\frac{3}{2}$
$\frac{3}{2}\frac{3}{2}\frac{3}{2}$
$\frac{5}{2}\frac{3}{2}\frac{3}{2}$
$\frac{7}{2}\frac{1}{2}\frac{3}{2}$
111
311
$\frac{3}{2}\frac{1}{2}\frac{1}{2}$
$\frac{5}{2}\frac{1}{2}\frac{1}{2}$
200
220
400
111
311
$\frac{3}{2}\frac{1}{2}\frac{1}{2}$
200
400

(a) Rotation photograph

(b) Oscillation photograph

Photo. 1. Rotation-, and oscillation-photographs. (Cu$K$)
Rotation-, and oscillation-axis: $c$ axis.
Indexings are made referring to the unit cell of NaCl type.

noticed that the ferromagnetic crystal has a definitely low density, though the accuracy of the measurement for this crystal is not so high as that for the antiferromagnetic one, because of the smaller size of the specimen.

However, the most important feature of this ferromagnetic crystal distinguished from the antiferromagnetic one is that it has extra weak reflexions other than those of NaCl type as shown in Photo. 1. These reflexions will surely be characteristic of the ferromagnetic oxide, because they disappear when the oxide loses the ferromagnetism on reheating at the formation temperature.

In spite of the presence of such extra reflexions, the Laue symmetry of the ferromagnetic oxide is apparently $m3m$ as in the case of the antiferromagnetic one. The true symmetry, however, might not be so high as this, considering the twinned structure mentioned above. Because, in this twinned structure, it is difficult technically to distinguish the component crystal which caused the reflexion concerned. For the present, however, treatment will be made following the apparent Laue symmetry.

According to the unit cell of NaCl type employed in Table I, there appear half-integers in many of the indices for the weak extra reflexions. Therefore, the edge length of the unit cell will hereafter be doubled (denoted by $\boldsymbol{a}_F$). The axial deformation is, for the present, neglected only for the reason of simplicity.

Table II. Results of observation by means of rotation (or oscillation) method.*

| | | General form *{hkl}* ** | Planes examined | Intensity ✱ |
|---|---|---|---|---|
| All even | N1 | *{4n, 4n, 4n}* | *{400}*, *{440}*, *{444}*, *{800}*, *{840}*, *{844}*. | *vvs* |
| | N2 | *{4n+2, 4n+2, 4n+2}* | *{222}*, *{622}*, *{662}*. | *vs* |
| | E1 | *{4n, 4n+2, 4n+2}* | *{220}*, *{422}*, *{620}*, *{642}*, *{822}*, *{660}*,<br>*{664}*, *{10,20}*, *{862}*. | *vw* |
| | E2 | *{4n, 4n, 4n+2}* | *{200}*, *{420}*, *{600}*, *{442}*, *{640}*, *{820}*,<br>*{644}*, *{842}*, *{10,00}*, *{860}*. | none |
| All odd | D1 | *{8n±3, 8n±3, 8n±3}* | *{333}*, *{533}*, *{553}*, *{555}*. | *w* |
| | | *{8n±1, 8n±1, 8n±3}* | *{311}*, *{511}*, *{731}*, *{751}*, *{931}*, *{951}*. | |
| | D2 | *{8n±1, 8n±3, 8n±3}* | *{331}*, *{531}*, *{551}*, *{733}*, *{753}*. | none |
| | | *{8n±1, 8n±1, 8n±1}* | *{111}*, *{711}*, *{911}*.† | |

* Indexings are made of $\boldsymbol{F}$-lattice, the lattice constant $a_F$ being twice that of NaCl type.

** $n$ is an integer, positive or negative, including zero and its value generally differs position by position even in the same braces.

✱ The letters $v$, $s$ and $w$ are the abreviations of 'very', 'strong' and 'weak', respectively.

† *{911}* reflexions can be observed very weak only by the small angle oscillation method.

The indices as well as the intensities of all the reflexions checked up by rotation or oscillation photographs can be classified as in Table II, where the conventional notation is given to each group of forms. The only exception to this classification is the *{911}* reflexions which were observed, though very weak, in small angle oscillation photographs. It can be directly derived from Table II that the reciprocal lattice of this crystal is composed of four kinds of $\boldsymbol{a}_F^*\boldsymbol{b}_F^*$-plane, i.e., A, B, C and D, the stacking along the $\boldsymbol{c}_F^*$ axis being mirror-symmetrical across the planes A as shown in Fig. 2, where (c) shows the projection of all the points onto the $\boldsymbol{a}_F^*\boldsymbol{b}_F^*$-plane. Here, $\boldsymbol{a}_F^*$, $\boldsymbol{b}_F^*$ and $\boldsymbol{c}_F^*$ are reciprocal vectors corresponding respectively to the edge vectors $\boldsymbol{a}_F$, $\boldsymbol{b}_F$ and $\boldsymbol{c}_F$ of the unit cell in the new lattice. The reciprocal lattice, thus, has a unit cell with three edges $8\boldsymbol{a}_F^*$, $8\boldsymbol{b}_F^*$ and $8\boldsymbol{c}_F^*$, respectively (larger square in Fig. 2 (c)), belonging to the point group $m3m$, which is natural consequence from the apparent symmetry.

Microphotometer plottings of *{440}*-, *{311}*- and *{511}*-spots in a rotation photograph

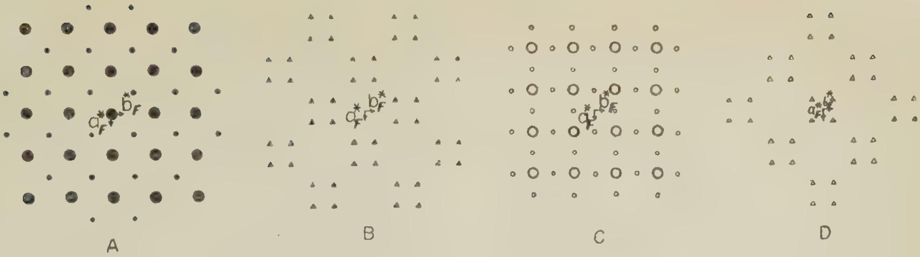

(a) Four kinds of $a_F^*\ b_F^*$ -planes

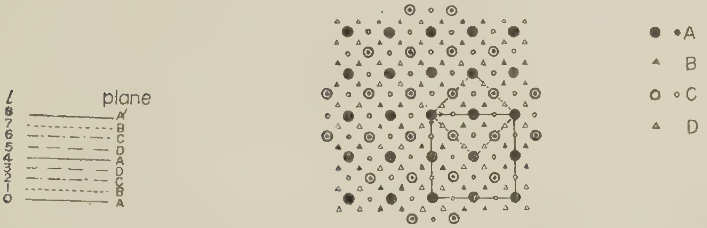

(b) Stacking of $a_F^*\ b_F^*$ -planes along $c_F^*$ axis

(c) Projections of all the points onto $a_F^*\ b_F^*$ -plane

Fig. 2. Reciprocal lattice of ferromagnetic nickel oxide.

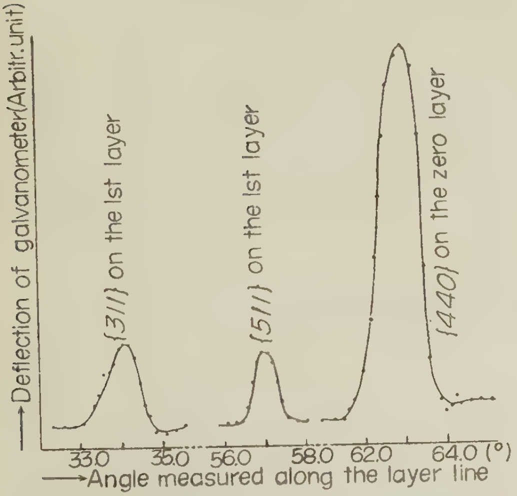

Fig. 3. Microphotometer plottings of three spots in a rotation photograph taken by Cu$K_\alpha$ radiation.

taken by Cu$K_\alpha$ radiations are given in Fig. 3, from which the relative intensities (I) can be obtained as given in the second column of Table III. After appropriate corrections for various factors other than extinction effects, the relative values of the structure amplitude ($\xi$) can be roughly estimated as in the third column. E1-reflexions were too weak to be traced.

Table III. Relative values of structure amplitudes of three reflexions. (Cu $K_\alpha$)

| {hkl} | relative intensity | relative $\|F\|$-value ($\xi$) | |
|---|---|---|---|
| | | obs. | calc. |
| {440} | 1 | 1 | 1 |
| {311} | 0.12 | $0.2_4$ | $0.2_0$ |
| {511} | $0.08_7$ | $0.2_5$ | $0.1_6$ |

## § 4. Determination of Crystal Structure

There are two difficulties in the determination of crystal structure of the ferromagnetic nickel oxide. One is the ambiguity in its Laue symmetry originated from the twinning in the specimen. The consideration will, however, be made according to Table II. The other difficulty is due to the situation that the accurate chemical composition of the sample is unknown. This can narrowly be escaped as follows. The lower value of specifiic gravity of ferromagnetic nickel oxide indicates that there is a defficiency of cation or, though less probable, anion in this oxide. The number of ions per unit cell for each case is calculated as in the **F**-column of Table IV, where the linear dimension of the cell is twice that of the NaCl type lattice.

Referring to this cell, the indices of all the reflexions detected are all even or all odd, as can be seen in Table II. The lattice must, therefore, be face-centred which will be hereafter called **F** lattice. Further, {0kl} reflexions are observed only for $k+l=4n$ (compare N1, E1 and E2). This shows the existence of a 'diamond glide plane' as a symmetry element.

Table IV. Summary of the conditions for the structure determination.

| | Condition | | | $F$ | $I$ |
|---|---|---|---|---|---|
| 1 | No. of atoms per cell | Assumption i | O | 32 | 16 |
| | | Ni-defficient | Ni | $29.9_6 \doteqdot 30$ | $14.9_8 \doteqdot 15$ |
| | | Assumption ii | O | $24.5_2 \doteqdot 24$ | $12.2_6 \doteqdot 12$ |
| | | O-defficient | Ni | 32 | 16 |
| 2 | Lattice type | | | Face centred | Body centred |
| 3 | New symmetry element | | | Diamond glide plane | |
| 4 | All odd reflexions * | | | 2 groups | — |

* The expression 'all odd' is referred to the $\boldsymbol{F}$-lattice.

Another feature characteristic of this oxide is that the reflexions with all odd indices are classified into two groups, D1 and D2, this being presumed to come from an accidental extinction. All the features mentioned here are summarized in Table IV, which will be set as the starting conditions for the structure determination. In this table, the apparent Laue symmetry $m3m$ is not taken into account, because it may be higher than the true symmetry as mentioned before.

Among the space groups in cubic system, there are only three, $Fd3$, $Fd3m$ and $Fd3c$, which satisfy Conditions 1, 2 and 3 in Table IV, but all of these space groups contradict Condition 4 even when the accidental extinctions are considered. Therefore, the cubic system must be excluded. Thus the Laue symmetry $m3m$ is only apparent.

Turning next to the tetragonal system, it can easily be recognized from Fig. 2 (c) that the tetragonal unit cell of the reciprocal lattice can be defined by three vectors $4\boldsymbol{a}_F^* + 4\boldsymbol{b}_F^*$, $-4\boldsymbol{a}_F^* + 4\boldsymbol{b}_F^*$ and $8\boldsymbol{c}_F^*$. As for the direct lattice, therefore, the unit cell may be considered to have the three edges

$$\boldsymbol{a}_I = (\boldsymbol{a}_F + \boldsymbol{b}_F)/2\,, \quad \boldsymbol{b}_I = (-\boldsymbol{a}_F + \boldsymbol{b}_F)/2\,, \quad \boldsymbol{c}_I = \boldsymbol{c}_F\,, \tag{1}$$

the lattice type being changed from $\boldsymbol{F}$ to the body-centred one which will hereafter be denoted by $\boldsymbol{I}$. Thus the starting conditions for the structure determination must be rewritten as in the $\boldsymbol{I}$-column of Table IV.

Now, in this tetragonal system, $I4_1md$, $I4_1cd$, $I\bar{4}2d$, $I4_1/amd$ and $I4_1/acd$ satisfy the first three conditions in Table IV, but $I4_1/amd(D_{4h}^{19})$ is the only one which does not conflict with the fourth one. This can be proved as follows.

For this system, the indices in Tables II must, of course, be transformed by Eq. (1).

Table V. Calculated structure factors of ferromagnetic nickel oxide as $I4_1/amd$ $(D_{4h}{}^{19})$.

| Group notation | $(h_I k_I l_I)$ * | Notation of $F$ | Perfect structure | Defect structure: General from | Defect structure: $N=15,\ \eta=0$ | Intensity (obs.) |
|---|---|---|---|---|---|---|
| $N_1$ | $(4n,\ 4n,\ 8n)$<br>$(4n+2,\ 4n+2,\ 8n+4)$ | $F_{N1}$ | $16f_{Ni}+12f_o$ | $16f_o+$<br>$(8p_c+8p_a+4p_b)f_{Ni}$ | $16f_o+15f_{Ni}$ | $vvs$ |
| | $(4n,\ 4n,\ 8n+4)$<br>$(4n+2,\ 4n+2,\ 8n)$ | $F'_{N1}$ | $16f_{Ni}+4f_o$ | $16f_o+$<br>$(8p_c+8p_a-4p_b)f_{Ni}$ | $16f_o+11f_{Ni}$ | |
| N2 | ↻$(4n,\ 4n+2,\ 8n\pm2)$ | $F_{N2}$ | $-16f_{Ni}+8f_o$ | $-16f_o+8(p_c+p_a)f_{Ni}$ | $-16f_o+13f_{Ni}$ | $vs$ |
| E1 | $(4n\pm1,\ 4n\pm1,\ 8n\pm2)$<br>↻$(4n,\ 4n+2,\ 4n)$ | $F_{E1}$ | $\pm4f_o$ | $+4p_o f_{Ni}$ | $\pm2f_{Ni}$ | $vw$ |
| E2 | $(4n,\ 4n,\ 4n+2)$<br>$(4n+2,\ 4n+2,\ 4n+2)$<br>$(4n\pm1,\ 4n\pm1,\ 4n)$ | $F_{E2}$ | 0 | 0 | 0 | none |
| D1 | ↻$(4n\pm1,\ 4n+2,\ 8n\pm1)$<br>↻$(4n,\ 4n\pm1,\ 8n\pm3)$ | $F_{D1}$ | $\pm(4+2\sqrt{2})f_o$ | $\pm\{4(p_c-p_a)+2\sqrt{2}p_b\}f_{Ni}$ | $\pm2\sqrt{2}f_{Ni}$ | $w$ |
| D2 | ↻$(4n\pm1,\ 4n,\ 8n\pm1)$<br>↻$(4n+2,\ 4n\pm1,\ 8n\pm3)$ | $F_{D2}$ | $\pm(4-2\sqrt{2})f_o$ | $\pm\{4(p_c-p_a)-2\sqrt{2}p_b\}f_{Ni}$ | 0 | none |

*: $n$ is an integer, positive or negative, including zero and its value generally differs position by position even in a same parentheses.

↻: Cyclic only for $h$ and $k$.

—: All the combinations of double signes on this line.

The corresponding tetragonal indices thus obtained are arranged in the second column of Table V, the notations in the first column being the same as those of Table II. Consider that, following the second assumption in Condition 1, sixteen nickel atoms occupy the positions of 16*h* where the parameters $x$ and $z$ are 1/2 and 1/4, respectively, referring to the second setting of the two in the 1952 International Tables (origin at center 2/m), and that twelve oxygen atoms situate at the points of both 4*b* and 8*c* or of both 4*a* and 8*d*, then the structure factor $F$ for each classified group is calculated as in the fourth column of Table V, which not only fulfil Condition 4 but also may give plausible intensities. The structure under such consideration is as illustrated in the upper left part of Table VIII, where the positions are given only for combination (4*b*, 8*c*, 16*h*), as the identical configuration is obtained for the other combination (4*a*, 8*d*, 16*h*).

The positions of 4*b*, 8*c*, 8*d* and 16*h* in every (*001*) plane of this structure are illustrated in Fig. 4, with respect to the ***I***-lattice as well as ***F***-lattice. It is clear that the distance between an anion and its neighbouring cations corresponds just to that in the ordinary nickel oxide as regards the oxygen in 8*c*, but as for 4*b*-ions, the distance is shorter by about 13%(i.e. $1-\sqrt{3}/2$). Such a large amount of shortening can hardly be accepted even if the diminution of coordination number is considered. Any adjustment in parameter values of 16*h* to give a plausible interatomic distance, however, results in a contradiction to Condition 4. The structure has been, so far, tacitly considered to be perfect (without any vacancy or interstitial atom).

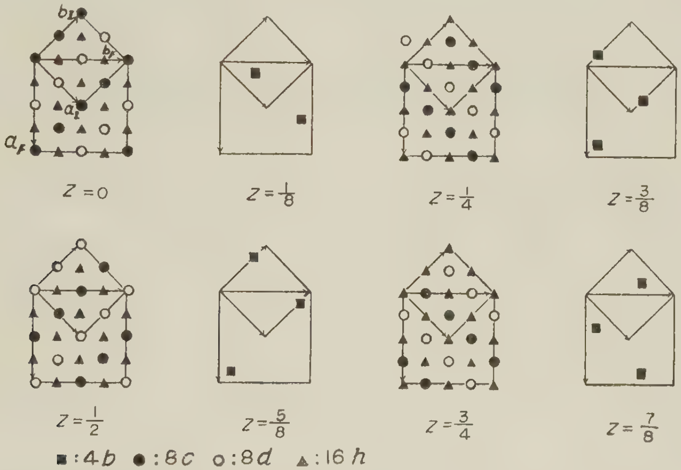

Fig. 4. Distribution of equivalent points in every (*001*) planes of ferromagnetic nickel oxide as $I4_1/amd$ ($D_{4h}^{19}$).

To avoid such a contradiction, we shall consider a defect lattice assigning ions as follows: 16 $O^{2-}$'s in 16*h*, $8p_c\mathrm{Ni}^{2+}$'s in 8*c*, $8p_d\mathrm{Ni}^{2+}$'s in 8*d* and $4p_b\mathrm{Ni}^{3+}$'s in 4*b*, where $p_c$, $p_d$ and $p_b$ are the distribution probabilities of nickel among cation sites (the upper half of the last column of Table VIII).* In this case, the structure factors turn into those in the fifth column of Table V, This structure has, of course, cation deficiency and therefore corresponds to Assumption 1 in Condition 1. Although, in this defect structure, all the interatomic distances are the same as those in the perfect one, it may be possible to assign to Ni atoms the narrow space of 4*b* because they may be there trivalent cations.

Now, the values of distribution probabilities must be estimated in order to determine the structure specifically. The number of cations per unit cell, $N$, can simply be expressed as follows:

---

* In accordance with the observation, such defects may not produce in diffraction patterns any detectable change other than in intensity (e.g. change in the shape of spots, occurence of diffuse scattering, etc.).

$$8p_c+8p_d+4p_b=N\,.$$

In the present case, $N$ amounts to 15, although it is not necessarily an integer owing to the defect. On the other hand, the relation

$$2\times 8p_c+2\times 8p_d+3\times 4p_b=2\times 16$$

results from the condition of charge neutrality. Next, put the ratio $|F_{D1}|:|F_{N1}|$ as $\xi$, which was determined for the two pairs as in Table III, the extinction effects being neglected for simplicity. Then we have

$$4(p_c-p_d)+2\sqrt{2}\,p_b=\xi K,$$

where $$K\equiv(Nf_{Ni}^{N1}+16f_{O}^{N1})/f_{Ni}^{D1}\,.$$

$f_{Ni}^{N1}$ and $f_{Ni}^{D1}$ are the atomic scattering factors of nickel for N1 and D1 reflexions, respectively, and $f_{O}^{N1}$ is that of oxygen for N1 reflexions. For the comparison among the structure factors of extra reflexions, we consider only the coefficients as follows:

$$\{4(p_c-p_d)+2\sqrt{2}\,p_b\}:\{4(p_c-p_d)-2\sqrt{2}\,p_b\}:4p_b=1:\eta:\zeta\,.$$

From the above four relations all the quantities in question can be expressed in terms of $N$ and $\eta$ as in the left column of Table VI, where the right column stands for the case $N=15$ and $\eta=0$. It is not unreasonable to regard $\eta$ as zero, because even the reflexions of *{911}* in Table II, the only one exception in D2, are extremely faint.* For these values of $N$ and $\eta$, the structure factors in the fifth column of Table V turn further into those in the next one, which may well explain the observed intensities (the last column). Moreover, $\xi$'s for two pairs, *{311}*/*{440}* and *{511}*/*{440}* (referring to **F**-lattice) can be calculated as in the last column of Table III for Cu$K_\alpha$ radiation under the consideration of anomalous dispersion, the agreement with the third column being rather good in view of the neglection of extinction effects. Thus the number of ions in each group of equivalent positions amounts to that shown in the parenthesis at the corresponding position in Table VIII.

Table VI. Distribution probabilities and $\xi$ and $\zeta$ as functions of $N$ and $\eta$.

| General form | $N=15$ $\eta=0$ * |
|---|---|
| $p_c=\frac{3}{16}N-2+\frac{16-N}{4\sqrt{2}}\frac{1+\eta}{1-\eta}$ | $p_c=\frac{1}{16}(13+2\sqrt{2})\doteqdot0.9893$ |
| $p_d=\frac{3}{16}N-2-\frac{16-N}{4\sqrt{2}}\frac{1+\eta}{1-\eta}$ | $p_d=\frac{1}{16}(13-2\sqrt{2})\doteqdot0.6357$ |
| $p_b=8-\frac{N}{2}$ | $p_b=\frac{1}{2}$ |
| $\xi=\frac{2\sqrt{2}}{K}\frac{16-N}{1-\eta}$ | $\xi=\frac{2\sqrt{2}}{K}$ |
| $\zeta=\frac{1}{\sqrt{2}}(1-\eta)$ | $\zeta=\frac{1}{\sqrt{2}}\doteqdot0.7071$ |

* In order to keep exact conformity with the saturation magnetization value under a certain assumption on the spin arrangement, $\eta$ should be $\eta=-0.01_2$, from which $p_c=0.98_6$ and $p_d=0.64_0$ result.

Now, it must be considered whether or not a 4*b*-site has sufficient space to accomodate a trivalent nickel ion. In what follows, the radii $r$'s of various ions will be distinguished from one another by suffixing with their respective chemical symbol, e.g., $r_{Ni^{2+}}$ etc. And further, of two sets of ionic radius values, Goldschmidt's and Pauling's, the former will be employed only for the reason of avoiding the tediousness of argument. Then, under the simple assumption that $r_{Ni^{3+}}/r_{Ni^{2+}}=r_{Fe^{3+}}/r_{Fe^{2+}}$ with $r_{Ni^{2+}}=0.78$ Å, $r_{Fe^{3+}}=0.67$Å and $r_{Fe^{2+}}=0.83$ Å, the radius of trivalent nickel ion can be estimated as $r_{Ni^{3+}}=0.60_9$ Å in the case of the coordination number 6. For the coordination number 4, the value turns out to be 0.56～0.59 Å according as Born exponent is 6～12, from which the radius sum $r_{Ni^{3+}}+r_{O^{2-}}=1.88\sim1.91$ Å results as in the second

---

* Formally, $\eta$ can be limited no more severely than $-0.4142\doteqdot1-\sqrt{2}<\eta\leqq17-12\sqrt{2}\doteqdot0.0296$ in view of the three additional conditions, $p_c\leqq1$, $F_{D1}>F_{B1}$ and $N=15$.

Table VII. Interatomic distance between cation in tetrahedral site and its neighbouring anion in both ferromagnetic nickel oxide and magnetite.

| Substance | $r_{M^{3+}}$ (Å) | * $r_{M^{3+}}+r_{O^{2-}}$ (Å) | $b\sim h$ dist. obs. (Å) | $b\sim h$ dist. / $(r_{M^{3+}}+r_{O^{2-}})$ |
|---|---|---|---|---|
| Ferromag. NiO | 0.56~0.59 | 1.88~1.91 | 1.81 | 0.96~0.95 |
| Magnetite * | 0.62~0.65 | 1.94~1.97 | 1.81 | 0.93~0.92 |

* $r_{O^{2-}}=1.32$ Å  * $a_{Fe_3O_4}=8.380$ kX.

line of Table VII, where the coordination number effect on $r_{O^{2-}}$ is neglected. Thus, the $b\sim h$ distance in the present structure, 1.81 Å, is shorter than the calculated one by 4~5 % (the last column). Although the difference is not so large as in the preceding perfect structure, it can never be negligible. Nevertheless, one may well accept this shortening if it is considered that in magnetite there is more severe situation about $8a$ ($8f$ according to Wyckoff's notation)-site as shown in the lowest line of Table VII, where the analogous calculation was performed on this iron oxide of inverse spinel type structure[3] with the lattice constant $a=8.380$ kX.[4] Moreover, this apparent tightness of the $4b$-ions can be relaxed

Table VIII. Crystal structure of ferromagnetic nickel oxide.

| Axial deformation | Space group and lattice constants | Atomic positions | Perfect [12 O's & 16 Ni's] | Defect [16 O's & $N$ (15) Ni's] |
|---|---|---|---|---|
| Neglected | $I\,4_1/amd$<br>$(D_{4h}^{19})$<br>$a=5.899_6$ kX.<br>$c=8.343_4$ kX.<br>$c/a=\sqrt{2}$<br>(31.₅°C.) | $4b$ | 4 $O_1$ | $4p_b(2.00_0)Ni_1$ |
| | | $8c$ | 8 $O_2$ | $8p_c(7.91_4)Ni_2$ |
| | | $8d$ | — | $8p_d(5.08_4)Ni_3$ |
| | | $16h$: $x=\frac{1}{2}$, $z=\frac{1}{4}$ * | 16 Ni | 16 O |
| Considered | $C2/m$<br>$(C_{2h}^3)$<br>$a=5.104_4$ kX.<br>$b=2.951_5$ kX.<br>$c=2.948_2$ kX.<br>$\beta=125°11._4'$<br>(31.₅°C.) | $2a$ | 2 $O_2$ | $2p_c(1.97_9)Ni_2$ |
| | | $2b$ | — | $2p_d(1.27_1)Ni_3$ |
| | | $2c$ | 2 $O_2$ | $2p_c(1.97_9)Ni_2$ |
| | | $2d$ | — | $2p_d(1.27_1)Ni_3$ |
| | | $4e$ | 4 $O_2$ | $4p_c(3.95_7)Ni_2$ |
| | | $4f$ | — | $4p_d(2.54_3)Ni_3$ |
| | | $4i_1$: $x=\frac{3}{8}$, $z=\frac{5}{8}$ | 4 $O_1$ | $4p_b(2.00_0)Ni_1$ |
| | | $4i_2$: $x=\frac{1}{4}$, $z=\frac{1}{4}$ | 4 Ni | 4 O |
| | | $4i_3$: $x=\frac{1}{4}$, $z=\frac{3}{4}$ | 4 Ni | 4 O |
| | | $8j$: $x=0$, $y=\frac{1}{4}$, $z=\frac{1}{4}$ | 8 Ni | 8 O |

* These parameters are referred to the second setting (origin at centre $2/m$) in the 1952 International Tables.

by the presence of vacancies in cation sites, especially in $4b$ itself. Besides, in this defect structure, differing from the perfect one, a further relaxation may be attained by suitable slight adjustment in parameters owing to the occupation of $16h$ sites by oxygen atoms which have a smaller scattering factor than nickel atoms. This may actually be the case, considering the occurrence of the weak but detectable reflexions of {*911*} in Table II. Due to rather qualitative data in the intensity measurements, accurate adjustment of parameters can hardly be made, but the deviations of $x$ and $z$ from their respective standard values, i.e., 1/2 and 1/4, can not exceed the order of one hundredth. Therefore, to a rough approximation, $x=1/2$ and $z=1/4$ are employed as the correct parameter values.

Thus, it can be concluded that, if the axial deformation of the lattice is neglected, the ferromagnetic nickel oxide has a defect tetragonal structure (deficient in nickel) belonging to the space group $I4_1/amd(D_{4h}^{19})$, the lattice constants being $a=5.899_6$ kX., $c=8.343_4$ kX. $(c/a=\sqrt{2})$ at $31._5$°C., which have been derived from $a$ in Table I through Eq. (1). The details are summarized in the upper half of Table VIII.

In deriving the above structure, the axial deviation from 90° has not been taken into consideration only for the sake of simplicity. Now the deviation must be considered. Then the symmetry must necessarily tend to $C2/m$ $(C_{2h}^3)$ and the edge vectors of unit cell ($\boldsymbol{a}_M$, $\boldsymbol{b}_M$ and $\boldsymbol{c}_M$) may be expressed as follows:

$$\begin{aligned}\boldsymbol{a}_M&=-\boldsymbol{a}_I-\boldsymbol{c}_I=-\tfrac{1}{2}\boldsymbol{a}_F-\tfrac{1}{2}\boldsymbol{b}_F-\boldsymbol{c}_F\\ \boldsymbol{b}_M&=\quad\boldsymbol{b}_I\qquad=-\tfrac{1}{2}\boldsymbol{a}_F+\tfrac{1}{2}\boldsymbol{b}_F\\ \boldsymbol{c}_M&=\quad\boldsymbol{a}_I\qquad=\tfrac{1}{2}\boldsymbol{a}_F+\tfrac{1}{2}\boldsymbol{b}_F\end{aligned}$$

The details of this monoclinic structure are also illustrated in the lower half of Table VIII, where it is assumed that no alteration occurs in any of the distribution probabilities when a group of equivalent positions in $I4_1/amd$ is divided into several ones in $C2/m$. Although $4b$ in $I4_1/amd$, which has no parameter, tends to $4i$ in $C2/m$ with definite parameter values ($x=3/8$ and $z=5/8$) formally, these values should be considered to have the same ambiguity as in those of the other sites.

## § 5. Discussion

From the survey in the preceding section, the preference of the defect structure over the perfect one is surely correct, this being further supported by the unacceptable degree of oxygen deficiency in the discarded structure.

The striking features of the ferromagnetic nickel oxide distinguished from the ordinary one are (1) that it has tetrahedral positions something like $8a$ ($8f$ according to Wyckoff's notation)-sites in magnetite and (2) that there is no equivalency between $8c$-, and $8d$-sites in $I4_1/amd$ $(D_{4h}^{19})$, this equivalency being one of the necessary conditions for NaCl-type. Indeed, the accidental extinction (Condition 4) is caused by the two features and the former feature is the origin of the E1-reflexions.

It is a well accepted fact that the oxygen-excess in nickel oxide is brought about by the production of cation vacancies which are distributed randomly among the cation sites in the structure of NaCl type. The structure here determined, however, can be said to deny such a uniform distribution of vacancies. It suggests that there exists not only a preferred distribution but also the production of interstitial cations with respect to the lattice of NaCl type. Thus, there must be a tendency of changing the symmetry even at the rather early stage of further oxidation of the stoichiometric oxide.

Referring to such a defect structure, the saturation magnetization of the present ferromagnetic nickel oxide will be estimated. There are four in spin alignments, if all the spins of magnetic atoms on the same crystallographic sites point to the same direction as with Néel's scheme for ferrites.⁵⁾ Among the four, the following arrangement will be adopted here, which gives the lowest magnetization. The spin of a trivalent nickel ion on the $4b$ site is parallel to that on the $8d$ site and is antiparallel to that on the $8c$ site, those on the $8c$ and $8d$ being thus antiparallel with each other. Then the atomic magnetic moment $\sigma_A$ can be expressed as

$$\sigma_A=(4p_b\times 3\mu_B+8p_d\times 2\mu_B-8p_c\times 2\mu_B)/N\ ,$$

where $\mu_B$ is a Bohr magneton, $2\mu_B$ and $3\mu_B$ being attached to a divalent nickel ion and a trivalent one, respectively. On the other hand, the saturation magnetization per gram, $\sigma_g$, should be related to $\sigma_A$ by the equation.

$$\sigma_g = \sigma_A L/(N W_{Ni}/16 + W_O)\ ,$$

where $L$ is Avogadro's number, $W_{Ni}$ and $W_O$ are the atomic weight of nickel and oxygen, respectively. Considering Table VI, $\sigma_g$ in gauss/gr. takes the form

$$\sigma_g = 31.46 - 29.67(1+\eta)/(1-\eta)$$

for $N=15$. As for the case $\eta=0$, $\sigma_g=1.7_9$ gauss/gr. is obtained. The coincidence with the value ($2.5_0$ gauss/gr.) estimated from the magnetization curve in Fig. 1 is not so satisfactory. Such a discrepancy, however, must not be seriously taken in view of the rather crude model employed here. Thus the crystal structure of the present ferromagnetic oxide seems to suggest one of the possible processes of transition from antiferromagnetic state to ferromagnetic one.

With the argument along the same line as mentioned here, the abnormally high saturation value of magnetization will result for the perfect structure owing to the equivalency throughout the nickel ions. This can be said also to show the preponderance of the defect structure over the perfect one.

One may well think of the reverse treatment of the above $\sigma_g$-equation. If use is made of the observed value of $\sigma_g$, which is more reliable in accuracy than the intensity data in X-ray analysis, $\eta$ seems to be determined more precisely as $\eta=0.06_8$ and $-0.01_2$, the latter value corresponding to the negative value of $\sigma_g$ with the same magnitude. Of these two values, the former must be ruled out because of the limitation about $\eta$ described in the preceding section, i.e.

$$-0.4142 < \eta \leqq 0.0296\ .$$

Thus, from $\eta=-0.01_2$, which can sufficiently explain the diffraction pattern, we obtain $p_c=0.98_8$ and $p_a=0.64_0$ (the remark in Table VI), the values being fairly close to those derived only from X-ray data. At the present stage of investigation, however, the latter must be preferred in view of the introduction of the *ad hoc* assumption concerning the spin arrangement in the derivation of the former.

Finally the following must be noticed. Although the ferromagnetic nickel oxide has a monoclinic structure, the symmetry is different from the monoclinic symmetry of the magnetic structure in antiferromagnetics of MnO type, to which the ordinary nickel oxide may belong.

## § 6. Conclusion

The ferromagnetic nickel oxide surely has a defect structure deficient in cation, although, as for the diffraction pattern only, it may be explained also by a perfect one with oxygen defficiency. The lattice of this crystal is deformed slightly just like the antiferromagnetic nickel oxide. When the deformation is neglected, the structure is tetragonal and belongs to the space group $I4_1/amd$ ($D_{4h}^{19}$), the lattice constants being $a=5.8996_6$ kX. and $c=8.343_4$kX. ($c/a=\sqrt{2}$) at $31._5$°C.. Strictly speaking, however, it should be monoclinic because of the detectable deviation of axial angle from 90°, the lattice constants being $a=5.104_4$ kX., $b=2.951_5$ kX., $c=2.948_2$ kX. and $\beta=125°\ 11._4'$ at the same temperature as above. Thus, the space group in this case, tends to $C2/m(C_{2h}^3)$. The detailed atomic distribution in the respective case is as illustrated in Table VIII.

The order of magnitude of saturation magnetization can well be explained by an appropriate spin alignment, where the distribution of magnetic atoms with different spin vectors submits to the symmetry of chemical cell (in the sense mentioned in § 5).

The atomic configuration in this structure can be derived from that of the ordinary nickel oxide by the preferred distribution of cation vacancies as well as the production of cation interstitials. Such modifications in the atomic arrangement, which can hardly be detected by the powder method, may cause ferrimagnetism in this oxide.

### Acknowledgement

The authors are indebted to Mr. Y. Nakazumi, Tochigi Chemical Industry Co. & Ltd., who prepared many crystals of nickel oxide in compliance with their request, the present specimens being picked out among these crystals. Thanks must also be extended to Dr. K. Igaki, Dr. E. Uchida and Mr. H. Kondoh for their magnetic observations kindly performed on the present oxide, and further to Mr. S. Minamigawa and Mr. T. Tsuru for their earnest assistances in the experiments.

Finally, the authors wish to express their deep gratitude to Prof. T. Nagamiya, Prof. T. Watanabe and Prof. Z. Nishiyama for kind advices and encouragements given to the present investigation.

The cost of this investigation was partly defrayed from the Grants from Scientific Research in the Ministry of Education.

### References

1) E. A. Owen and E. L. Yates: Phil. Mag. **21** (1936) 809.
2) Y. Shimomura and S. Saito: Bulletin of Univ. Osaka Pref. **A4** (1956) 111.
3) E. J. W. Verway and E. L. Heilmann: J. Chem. Phys. **15** (1947) 174.
4) G. Hägg: Zeits. phys. Chem. **B29** (1935) 95.
5) L. Néel: Ann. de Physique **3** (1949) 137.

---

JOURNAL OF THE PHYSICAL SOCIETY OF JAPAN Vol. 11, No. 11, NOVEMBER, 1956

# State of Association of Water Molecules in Aqueous Solutions as deduced from Sound Velocity Data*

By Otohiko NOMOTO

*Kobayasi Institute of Physical Research, Kokubunzi, Tokyo*

(Received April 12, 1956)

As the molecular compressibility $W(=M/\rho\beta^{1/7}$, where $M$=mean molecular weight, $\rho$=density, and $\beta$=adiabatic compressibility) in usual liquid mixtures is a linear function of the molar fractions of the constituent liquids within experimental errors, but slightly deviates from linearity in aqueous solutions (cf. Nomoto, J. Phys. Soc. Japan **8** (1953) 553), this deviation was attributed to the structure change of water molecules in aqueous solutions by the influence of the solute molecules. Computation of the molar fractions ($n_a$, $n_s$) of the associated and the single molecules of water in dependence on the concentration has been performed in aqueous solutions of methanol, ethanol, n-propanol, iso-propanol and acetone using existing ultrasonic data. It was revealed that the change of $n_a$ and $n_s$ by concentration is characteristic of each solution and widely different from one another.

## §1. Introduction

Concerning our theory of the anomalous absorption of ultrasonic waves in aqueous solutions[1),2)] to appear in near future it became necessary to know the state of association of water molecules in aqueous solutions and its variation in dependence on concentration of the solute. We have devised a method of estimating it from the concentration dependence of the adiabatic compressibility data to be obtained from ultrasonic velocity and density, and when the ultrasonic absorption coefficients are calculated by employing this result, it gives a semi-quantitative agreement with the experiments[2)]. So it is natural to conclude that this method of estimation is nearly correct. Also the other methods of estimation have been attempted in the early stage. For example, Jacobson's theory[3)] of the adiabatic compressibility of aqueous solutions was modified to give the degree of breaking of the hydrogen bonds and thus the molar fraction of the associated molecules of water. This method, however, proved to give no characteristic difference in the concentration dependence of the existence ratio of the associated molecules according to the different kinds of the solutes. The ultrasonic absorption curves for aqueous solutions of methanol, ethanol and $n$-propanol calculated by employing this latter estimation were not in agreement with experiments, the difference in magnitude of the absorption peaks between the three kinds of solutions being comparatively slight, and the concentration of the absorption peaks increasing in the order: methanol, ethanol, propanol,—a tendency, contrary to the experiment.

It is known from various experimental facts that water consists of associated molecules, and also the origin of the excess ultrasonic absorption in pure water is attributed to the structure change of water by excess pressure (cf. Hall4)).

---

* The text in Japanese of this paper will be published in "Bulletin of the Kobayasi Institute of Physical Research".

The ultrasonic velocity in pure water increases with increasing temperature up to 74°C. This trend is contrary to that of ordinary liquids, in which the sound velocity decreases with increasing temperature. The general temperature dependence of sound velocity in ordinary organic liquids is due to the increase in intermolecular distance, and therefore the compressibility, accompanying the temperature rise. In case of water, however, the compressibility consists of two parts, according to Hall4). The first part, the instantaneous compressibility $\beta_\infty$, is due to the reduction under pressure of the intermolecular distance as in ordinary liquids. The second part, the relaxational compressibility $\beta_r$, is due to the breaking of some of the associated water molecules under excess pressure, the more bulky associated molecules changing into the less voluminous single ones and thus reducing the volume. The temperature rise accompanies breaking of the hydrogen bonds and the reduction in the number of the associated molecules, and this in turn reduces the relaxational compressibility of water. This effect predominates the increase in usual or instantaneous compressibility due to the increase in the intermolecular distance up to the temperature of minimum compressibility (64°C). The maximum of sound velocity takes place at 74°, a slightly higher temperature than that of the minimum compressibility, due to the temperature change of the density.

It is supposed that the hydrogen bonds of water are partly destroyed in aqueous solutions by the influence of the solute molecules. This is to be concluded from the concentration dependence of the sound velocity in aqueous solutions. It is known that the ultrasonic velocity has a peak at some intermediate concentration in many aqueous solutions (cf. Sette's review article5), Nomoto6), etc.). According to Giacomini7),8), the peak value of the sound velocity in water-ethanol mixtures decreases with increasing temperature, the concentration of alcohol for velocity maximum decreasing at the same time. The circumstance is similar also in case of water-methanol mixtures (Pesce and Giacomini9)). Parshad10) has ascribed the increase in the sound velocity of water by the addition of alcohol to the breaking of the association of water by the influence of the alcohol molecules.

At higher temperatures, therefore, a smaller amount of alcohol becomes sufficient in breaking the association of water and the velocity peak is attained at smaller concentration of alcohol, though with a lower maximum value. The association of alcohol molecules is broken at the same time, though, according to Parshad's opinion, the association between water and alcohol does not take place. Parshad11) discussed also the cause of weak association in water and that of the breaking of association of water by alcohol12).

The first quantitative approach to the explanation of the adiabatic compressibility of aqueous solutions has been made by Jacobson3) based on these ideas. This paper describes a new method of estimating the existence ratio of the associated molecules of water in aqueous solutions.

## § 2. Concentration Dependence of the Molecular Compressibility in Aqueous Solutions and the Decrease of Compressibility in Aqueous Solutions

We6) have investigated the concentration dependence of the molecular sound velocity of Rao13)

$$R=(M/\rho)V^{1/3}\,, \tag{2.1}$$

and the molecular compressibility of Wada14)

$$W=(M/\rho)\beta^{-1/7}\,, \tag{2.2}$$

in liquid mixtures. Here $M$ means the mean molecular weight, $\rho$ the density, $V$ the sound velocity (in m/sec), and $\beta$ the adiabatic compressibility (in $10^{-12}$ cgs. units). It was revealed that the molecular compressibility is a linear function of the molar fraction for all the mixtures of organic liquids except in aqueous solutions, while the molecular sound velocity was linear for most of the non-aqueous mixtures, though it curves concavely upwards if the density of the constituent liquids are widely different. In aqueous mixtures, both $R$ and $W$ deviated slightly upwards from the straight line*. The linearity of $W$ in the case of organic mixtures is within 0.5%, and presumably within experimental errors.

---

* It was erroneously stated in the previous paper6) that only aqueous alcohol mixtures deviate from straight lines, but the linearity holds true for acetone-water mixture. Closer examination revealed that this is not the case.

Although the theoretical reason of this linear dependence is not clarified as yet, we may consider that experimentally the molecular compressibility is a perfectly linear function of the molar fraction in usual organic mixtures. The deviation from linearity in aqueous mixtures is to be ascribed to the partial destruction of the association of water in aqueous solutions. It is known that other organic liquids, as alcohols, etc., also form associated molecules. The degree of association, however, is slight, forming trimers or tetramers for example, and no great change in volume or compressibility may be involved.

In the case of water, on the other hand, it is to be concluded from our theory[1),2)] of the ultrasonic absorption in aqueous solutions that the associated molecules of water are very large, consisting of about 8000 monomers in the case of pure water. And the breaking of the associated molecules under excess pressure contributes not a small part of compressibility (the relaxational compressibility). So we will assume that the association of other constituent liquids than water does not change the molecular compressibility to such an extent as to exceed the fluctuation due to the experimental errors and attribute the deviation from linearity of the molecular compressibility in aqueous solutions to the change in association of the solvent water with concentration.

We denote the experimental value of the molecular compressibility with $W_{\mathrm{exp}}$, computed by (2.2) from the observed values of the density and compressibility and the mean molecular weight

$$M=(1-n_F)M_w+n_F M_F\ , \qquad (2.3)$$

where $M_w$ and $M_F$ are the molecular weights of water and the solute respectively and $n_F$ the molar fraction of the solute. On the other hand, we can obtain the calculated value of the molecular compressibility of the solution ($W_{\mathrm{cal}}$) by linear interpretation

$$W_{\mathrm{cal}}=(1-n_F)W_w+n_F W_F\ . \qquad (2.4)$$

from the molecular compressibility of pure water $W_w$ and that of the solute $W_F$. $W_{\mathrm{exp}}$ is larger than $W_{\mathrm{cal}}$ for aqueous solutions, as above mentioned.

This discrepancy, naturally, is ascribable to the different behaviour of both density and compressibility as compared to usual organic mixtures. For example, if a part of the associated molecules of water is broken by influence of the solute molecules in aqueous solutions, the volume must decrease or the density increase, and the compressibility must decreased. The total effect must be that $\rho\beta^{1/7}$ is somewhat decreased. It is, however, not possible to estimate the variation of density exactly, because the density varies in various manners with concentration even in usual organic mixtures. So we will attribute the cause of deviation from linearity of $W$ to the decrease of $\beta$. Suppose a hypothetical liquid mixture with the same mean molecular weight and same density $\rho_{\mathrm{exp}}$ at the same concentration $n_F$ with the aqueous solution, and obeying the linearity rule of the molecular compressibility (2.4). Then the compressibility of this hypothetical liquid mixture is to be computed from

$$W_{\mathrm{ca}}=M/\rho_{\mathrm{exp}}\beta_{\mathrm{cal}}{}^{1/7}\ . \qquad (2.5)$$

This is supposed to be an usual mixture without structure change as in aqueous mixture, so the value of $\beta_{\mathrm{cal}}$ is considered to be the normal compressibility value corresponding to this density and molecular weight (and the constants of the both constituent liquids). We can calculate $\beta_{\mathrm{cal}}$ from (2.5) and put

$$\Delta\beta=\beta_{\mathrm{cal}}-\beta_{\mathrm{exp}} \qquad (>0)\ , \qquad (2.6)$$

then the experimental value of the compressibility is

$$\beta_{\mathrm{exp}}=\beta_{\mathrm{cal}}-\Delta\beta\ , \qquad (2.7)$$

and smaller than the compressibility of the normal mixture by $\Delta\beta$. This is considered to be due to the partial destruction of the associated molecules of water in aqueous solutions.

Fig. 1 to Fig. 5 show the values of $\beta_{\mathrm{exp}}$ and $\beta_{\mathrm{cal}}$ in aqueous solutions of methanol, ethanol, *n*-propanol, iso-propanol and acetone as functions of the volume fraction $\phi$ (ratio between the volumes of the solute and the solution), values of $\beta_{\mathrm{exp}}$ and $\rho$ being taken from the Jacobson's paper.

The concentration is expressed in the volume fraction for the sake of comparison with Jacobson's theory, in which a linear dependence of the compressibility in ideal solutions on the volume fraction is postulated. The word "ideal solution" is not defined in Ja-

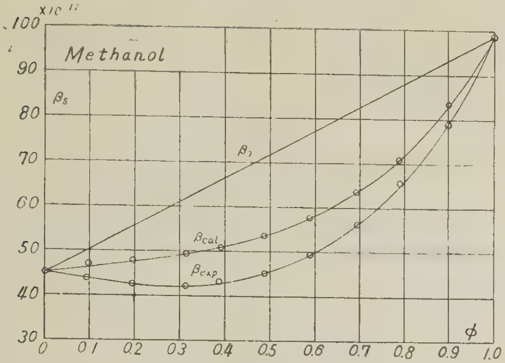

Fig. 1. Experimental value of the compressibility $\beta_{exp}$ and the hypothetical compressibility for normal mixture $\beta_{cal}$ in dependence on the volume fraction for aqueous methanol solution.

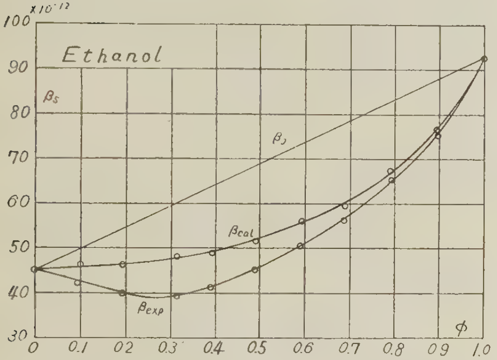

Fig. 2. Experimental value of the compressibility $\beta_{exp}$ and the hypothetical compressibility for normal mixture $\beta_{cal}$ in dependence on the volume fraction for aqueous ethanol solution.

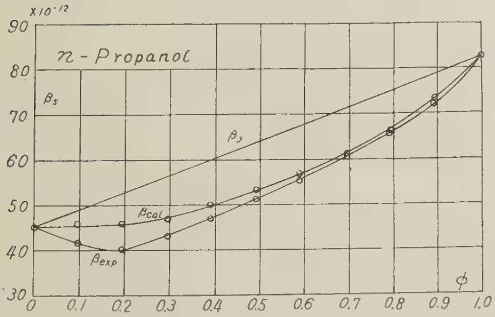

Fig. 3. Experimental value of the compressibility $\beta_{exp}$ and the hypothetical compressibility for normal mixture $\beta_{cal}$ in dependence on the volume fraction for aqueous $n$-propanol solution.

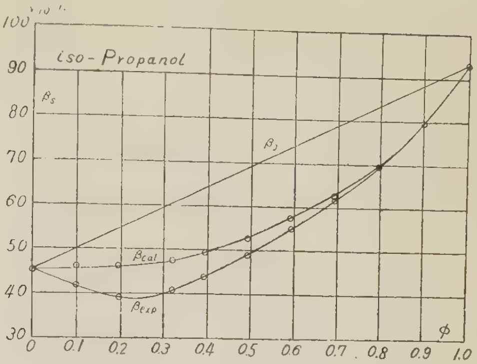

Fig. 4. Experimental value of the compressibility $\beta_{exp}$ and the hypothetical compressibility for normal mixture $\beta_{cal}$ in dependence on the volume fraction for aqueous iso-propanol solution.

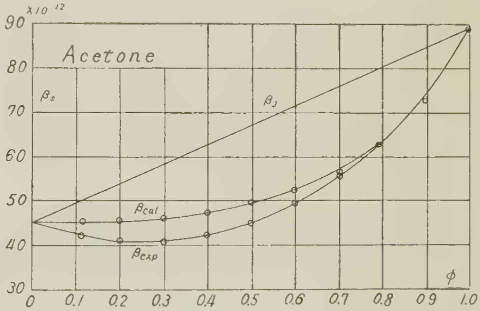

Fig. 5. Experimental value of the compressibility $\beta_{exp}$ and the hypothetical compressibility for normal mixture $\beta_{cal}$ in dependence on the volume fraction for aqueous acetone solution.

cobson's paper, but employed in the meaning of a liquid endowed with this characteristic.) Namely, the straight line denoted with $\beta_J$ in each figure represents the compressibility of the ideal solution of Jacobson and he has attributed the reduction of compressibility under this value to destruction of the hydrogen bonds of water.

As seen in the figures, our compressibility for normal mixtures (with the same density but without structure change) $\beta_{cal}$ is placed far below the straight line $\beta_J$, and thus makes the value of $\Delta\beta$ far smaller than in Jacobson's theory. One of the contradictory results of Jacobson's theory that the decrease in compressibility of the aqueous solution by complete destruction of the hydrogen bonds of water is about four times larger than the compressibility of water itself is ascribable to the assumption that the compressibility in the ideal solution is a linear function of the volume fraction.

We encounter the need of transforming the volume fraction into the molar fraction, in the course of the calculation. $\phi$ is transformed into the weight fraction $p$ by

$$p=\phi\rho_F/\rho\ , \tag{2.8}$$

where $\rho$ means the density of the solution, and then into the molar fraction by

$$n_F=m_F/(m_w+m_F)\ , \tag{2.9}$$

where

$$m_w=(1-p)/M_w\ ; \qquad m_F=p/M_w\ . \tag{2.10}$$

## § 3. Change of Number of Moles of the Associated Molecules of Water in Aqueous Solutions

The static compressibility $\beta_0$ of pure water consists of two parts, the instantaneous compressibility $\beta_\infty$ and the relaxational compressibility $\beta_r$, i.e.,

$$\beta_0=\beta_\infty+\beta_r\ , \tag{3.1}$$

$\beta_\infty$ being the ordinary compressibility due to the reduction of the intermolecular distance and $\beta_r$ being due to the decrease in volume of water by partial destruction of the associated molecules.

According to the theory of Hall[4] on the ultrasonic absorption in pure water, excess pressure $\Delta_p$ of the sound wave breaks some of the associated molecules of water and changes them into the single ones. The increase in the number of moles of single water molecules in $n_w$ moles of water constituting of $n_s$ moles of single molecules and $n_a$ moles of associated molecules is given by

$$\Delta n_s=\frac{n_w(v_a-v_s)\Delta p}{2RT\{1+\cosh(\Delta F/RT)\}}\frac{1}{1+i\omega\tau}\ , \tag{3.2}$$

where $v_a$ means the molar volume of associated molecules of water, $v_s$ that of single molecules of water, $\Delta F$ the difference in free energies (per mole) of single and associated molecules of water, $R$ the universal gas constant and $T$ the absolute temperature, $\omega$ is the circular frequency and $\tau$ the relaxation time of the order of magnitude of $2\times10^{-12}$ sec at room temperature.

As the existence ratio $n_a/n_s$ is changed by the influence of the solute molecules in aqueous solutions, it is not convenient to compute $\Delta n_s$ and $\beta_r$ based on the number of moles of water $n_w$. In writing (3.2), however, as

$$\Delta n_s=\frac{n_a(v_a-v_s)\Delta p}{RT\{1+\exp(\Delta F/RT)\}}\frac{1}{1+i\omega\tau}\ , \tag{3.3}$$

with reference to the number of moles of associated molecules $n_a$, this relation is considered to hold true also for aqueous solutions. We have from this the relaxational compressibility

$$\beta_r=\frac{n_a(v_a-v_s)^2}{vRT\{1+\exp(\Delta F/RT)\}}\ . \tag{3.4}$$

As this equation holds true both for aqueous solution and for pure water, we have the relation

$$\frac{\beta_r}{\beta_{r0}}=\frac{n_a v_w}{n_{a0}v}\ , \tag{3.5}$$

where $\beta_{r0}$ means the relaxational compressibility of pure water and $n_{a0}$ the value of $n_a$ for pure water.

If the existence ratio $n_a/n_w$ does not change with concentration, we have $n_a=n_w n_{a0}$, and the relaxational compressibility of this hypothetical solution becomes

$$(\beta_r)_{\text{cal}}=\beta_{r0}n_w\frac{v_w}{v}\ . \tag{3.6}$$

So we have

$$\beta_r=\frac{n_a}{n_w n_{a0}}(\beta_r)_{\text{cal}}=(\beta_r)_{\text{cal}}-\Delta\beta\ . \tag{3.7}$$

Accordingly

$$\frac{n_a}{n_w n_{a0}}=1-\frac{\Delta\beta}{\beta_r}\ . \tag{3.8}$$

If we put

$$n_a=n_w n_{a0}-\Delta n_a\ , \tag{3.9}$$

we have from (3.7),

$$\frac{\Delta n_a}{n_w n_{a0}}=\frac{\Delta\beta}{\beta_r}\ .$$

This becomes by (3.6) as

$$\frac{\Delta n_a}{n_{a0}}=\frac{\Delta\beta}{\beta_{r0}}\frac{v}{v_w}\ , \tag{3.10}$$

By employing this relation, we can obtain $\Delta n_a$ from $\Delta\beta$.

Figs. 6～10 show the values of $n_a$ and $n_s$ obtained by this method for the aqueous solutions of methanol, ethanol, $n$-propanol isopropanol and acetone in dependence on the concentration $n_F$. In these computations, we have employed the values of the existence ratios of the associated and the single molecules for pure water:

$$\left.\begin{aligned} n_{a0}&=0.825\ ,\\ n_{s0}&=0.175\end{aligned}\right\}\quad(20°\text{C})\ . \tag{3.11}$$

These values are obtained as follows. By assuming the values of the constants to be

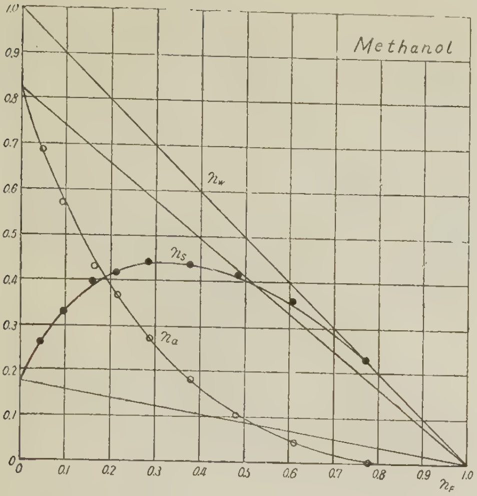

Fig. 6. Concentration dependence of the molar fractions of the associated and the single molecules of water in aqueous methanol solutions.

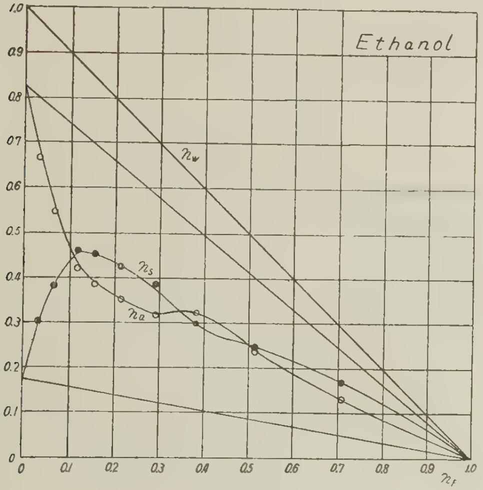

Fig. 7. Concentration dependence of the molar fractions of the associated and the single molecules of water in aqueous ethanol solutions.

$$\left.\begin{aligned}&v_a=19.6\,\text{cm}^3,\quad v_s=10.4\,\text{cm}^3,\\&\beta_r=27.8\times10^{-12}\,\text{cm}^2/\text{dyne}\,,\end{aligned}\right\}$$

we have from (3.3) as the value of the difference in the free energies between single and associated molecules of water

$$\Delta F=904\ \text{cal/mole}\,.$$

This gives the existence ratio by

$$n_{s0}/n_{a0}=\exp\left(-\Delta F/RT\right)\,.$$

Other assumptions on the values of the quantities $v_a$, $v_s$ and $\beta_r$ result in different values of the existence ratio $n_{s0}/n_{a0}$. Discussions on this respect are made elsewhere (Nomoto[2]).

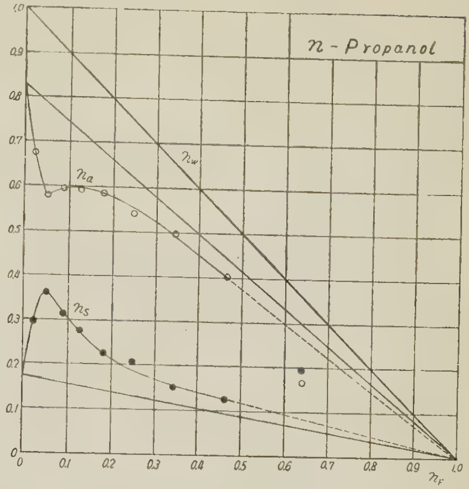

Fig. 8. Concentration dependence of the molar fractions of the associated and the single molecules of water in aqueous *n*-propanol solutions.

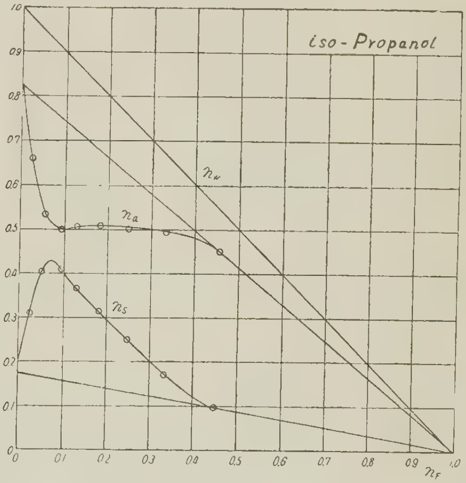

Fig. 9. Concentration dependence of the molar fractions of the associated and the single molecules of water in aqueous iso-propanol solutions.

The values of the constants here employed seemes to be the most adequate ones as judged from the result of our theory of the ultrasonic absorption in aqueous solutions.

In the first place, we can obtain $\Delta n_a$ by (3.10), then we have $n_a$ by (3.8), and $n_s$ by

$$n_s=n_w n_{s0}+\Delta n_a\,. \tag{3.12}$$

As is to be seen in the figures, the variation with concentration of $n_a$ and $n_s$ is widely different according to the different kinds of the solutes. The decrease of $n_a$ with increasing

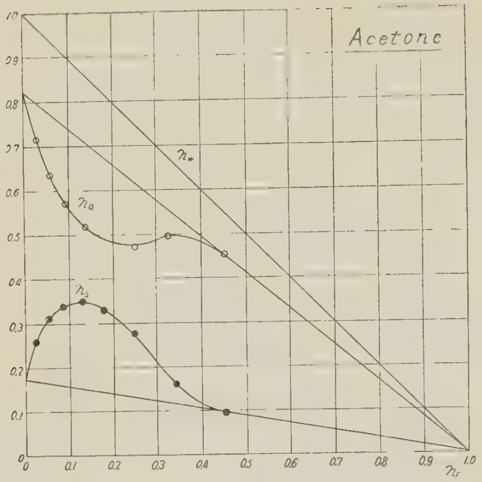

Fig. 10. Concentration dependence of the molar fractions of the associated and the single molecules of water in aqueous acetone solutions.

concentration is monotonous in aqueous methanol solution, while in the solutions of ethanol, $n$-propanol, iso-propanol and acetone, the decrease of $n_a$ with increasing concentration is rapid at first, but becomes more gradual in the intermediate concentration range, the $n_a$ vs. $n_F$-curve showing a nearly horizontal part and even a low maximum in this range.

Although these may seem strange at first sight, the ultrasonic absorption coefficient obtained by employing these curves are in fairly good agreement with experiments (cf. Nomoto[2]). The possibility of interpreting the non-monotonous decrease of $n_a$ not as a real one, but only as an apparent one due to the mutual association between water and the solute, is also excluded, because this does not give good absorption coefficients. So we have to conclude that these changes of $n_a$ and $n_s$ are real ones characteristic of each solution, although no theoretical explanations are available as yet.

This work was financially supported by the Grant for Scientific Research of the Ministry of Education for the 1954 fiscal year.

## References

1) O. Nomoto: Theory of the ultrasonic absorption in aqueous solutions. (I) Introduction and general theory. J. Phys. Soc. Japan **11** (1956) 827.
2) O. Nomoto: Theory of the ultrasonic absorption in aqueous solutions. (II) Ultrasonic absorption in aqueous alcohol solutions. J. Phys. Soc. Japan, in printing.
3) B. Jacobson: Arkiv för Kemi. **2** (1950) 177.
4) L. Hall: Phys. Rev. **73** (1948) 775.
5) D. Sette: Ricerca Scientifica **19** (1949) 1338–1379.
6) O. Nomoto: Molecular sound velocity and molecular compressibility of liquid mixtures. J. Phys. Soc. Japan **8** (1953) 553; Bull. Kobayasi Inst. Phys. Res. **2** (1952) 137.
7) A. Giacomini: Acta Pontificia Academia Scientarium **6** (1942) 87.
8) A. Giacomini: J. Acous. Soc. Amer. **19** (1947) 701.
9) B. Pesce ed A. Giacomini: Ricerca Scientifica **11** (1940) 619.
10) R. Parshad: J. Acous. Soc. Amer. **20** (1948) 60.
11) R. Parshad: J. Chem. Phys. **14** (1946) 348.
12) R. Parshad: J. Chem. Phys. **15** (1947) 418.
13) Rama Rao: Indian J. Phys. **14** (1940) 619.
14) Yasaku Wada: J. Phys. Soc. Japan **4** (1949) 280.

JOURNAL OF THE PHYSICAL SOCIETY OF JAPAN Vol. 11, No. 11, NOVEMBER, 1956

# The Measurement of Magnetostriction by means of Strain Gauge

By Hideo TAKAKI and Toshiro TSUJI

*Faculty of Science, University of Kyoto*

(Received July 21, 1956)

For the purpose of studying the relation of magnetostriction to technical magnetization, we used a strain gauge to measure the magnetostriction of long rod single crystals of 3.2% Si-Steel, and compared the results with those which had formerly been obtained on the same samples by using a mechano-optical lever. The latter method was applied in measuring the overall elongation of a rod sample, while the strain gauge recorded the local magnetostriction. In some of the samples, these two methods often gave remarkable difference in the results. This is mainly due to the fact that the sample is not uniformly magnetized, especially in lower magnetic field; the magnetostriction measured by the optical lever method showed only the mean change of length even if the magnetization is not uniform, while the result obtained by the strain gauge corresponds rather well to the local magnetization. The latter method is, therefore, more appropriate for relating the magnetostriction to the magnetization. We also determined the magnetostriction constants which are slightly different from the previous results.

## §1. Introduction

Goldman1) and many other authors2),3),4) observed the anisotropy of magnetostriction by rotating the sample in high magnetic field. For this purpose, the sample was prepared in the form of a disk or an oblate ellipsoid, and the magnetostriction was measured by means of the strain gauge bonded on the sample. This method has a notable advantage that it can be used on small single crystals which are hardly accessible by other methods.

But in the study of the relation between magnetostriction and technical magnetization it is more convenient to use a long rod single crystal, because we can measure its magnetization precisely and the corresponding longitudinal magnetostriction with increasing magnetic field parallel to the rod axis. To observe the change of length, extending over the greater part of rod sample, an optical lever method was used under the assumption that the magnetization is uniform. As a matter of fact, however, the magnetization of the sample is not uniform, and the previous results obtained by the optical lever method do not correspond to the local magnetization. When we use a small strain gauge which allows us to measure the local magnetostriction it is possible to obtain the correspondence between the magnetostriction and the magnetization.

In our study we have used the long rod single crystals of 3.2% Si-Steel and measured the magnetostriction by means of the strain gauge. The results were compared with those5) obtained by the optical lever method.

## §2. Experimental Technique

In measuring the magnetostriction we have used commercial strain gauges of type K-12 manufactured by the Kyowa Musen Kenkyusho. They are made of advance wire, 2 cm in effective length and also have the *gauge factor* equal to 2±0.03. This value was calibrated by measuring a known elastic bending of marble beam. The substance of the wire is in nonmagnetic phase at room temperature and it has a negligible magnetoresistance effect. The latter character was confirmed by the fact that the electrical resistance of the strain gauge itself does not vary with magnetic field, and enables us to use the strain gauge directly to measure the magnetostriction.

The change of electrical resistance of the strain gauge was measured by an ordinary Wheatstone Bridge in which all the arms are composed of the resistance equal to 120 Ω.

Two of these arms consist of the same strain gauge, an *active gauge* and a *dummy gauge*. The former is bonded on the sample to follow the longitudinal magnetostriction, the other on a brass tube, by using the Duco cement as adhesive. After inserting the sample into the brass tube, we set it in a water-cooling solenoid which keeps the inside temperature constant so that the error due to temperature variation may be neglected. A schematic circuit diagram is shown in Fig. 1.

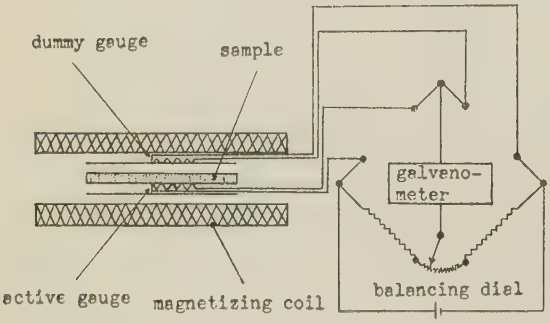

Fig. 1. Circuit diagram of magnetostriction measuring apparatus.

Procedure of the measurement is as follows; After balancing the Bridge circuit by a dial the sample is magnetized gradually in the solenoid, and the process of which follows the strain of active gauge together with the sample. An unbalanced current due to the change of electrical resistance of the strain gauge is immediately measured by the deflection angle of a mirror of galvanometer. In order to obtain high sensitivity we set up the scale of galvanometer keeping at a distance of 3 m from the mirror. With this arrangement a strain sensitivity of the order of $1.5\times10^{-7}$ per mm can be obtained.

Table I.

| Sample No. | Direction Cosines | | | $(\delta l/l)_{-\mathrm{Sat.Rem.}}\times10^6$ | |
|---|---|---|---|---|---|
| | $l$ | $m$ | $n$ | Authors. | Takaki and Nakamura. |
| 1 | 0.054 | 0.086 | 0.995 | 4.0 | 4.06 |
| 2 | 0.077 | 0.298 | 0.951 | 4.5 | 6.42 |
| 4 | 0.015 | 0.053 | 0.998 | 4.2 | 3.59 |
| 13 | 0.123 | 0.438 | 0.891 | 2.8 | 2.78 |
| 19 | 0.183 | 0.664 | 0.725 | − 4.5 | −1.47 |
| 39 | 0.436 | 0.615 | 0.657 | − 6.0 | −5.86 |
| 42 | 0.048 | 0.619 | 0.742 | − 5.2 | −1.71 |
| 49 | 0.561 | 0.567 | 0.603 | −10.1 | −6.37 |
| 50 | 0.108 | 0.134 | 0.985 | 5.0 | 7.22 |

## § 3. Experimental Results and Discussion

We have used the long rod single crystals of 3.2% Si-Steel, as shown in Table I. They were prepared from molten silicon steel in our laboratory[6)], using a vacuum *Tammann Furnace* which could attain high temperature with carbon heater. Takaki and Nakamura[5)] used these samples in their previous study of magnetostriction, where the longitudinal magnetostriction was measured by the optical lever method. Their results are reproduced here in Fig. 3 (B), Fig. 4 (B) and Fig. 5 (B). They also determined the magnetostriction constants of 3.2% Si-Steel from the following relation between magnetostriction and magnetization,

$$\left(\frac{\delta l}{l}\right)_{\mathrm{Sat.-Rem.}}=\left\{\frac{3}{2}\left(1-\frac{l^3+m^3+n^3}{l+m+n}\right)-3(m^2n^2+n^2l^2+l^2m^2)\right\}\lambda_{100}+3(m^2n^2+n^2l^2+l^2m^2)\lambda_{111}, \qquad (1)$$

where $(\delta l/l)_{\mathrm{Sat.-Rem.}}$ represents the difference between the magnetostrictions at the remanence and that at the saturation, and $l$, $m$ and $n$ are the direction cosines of rod axis with respect to the crystal axes. Equation (1) is based upon Kaya's relation which states that the domain distribution at the remanence is uniquely determined by the crystallographic orientation of the rod axis. Kaya's relation can be written in the form,

$$I_r/I_s=1/(l+m+n), \qquad (2)$$

where $I_r$ and $I_s$ are the remanent and the saturated magnetizations respectively. Although there is a good agreement between Kaya's theory and experiment in the case of these samples we cannot find the agreement for the overall magnetization of the rod sample, but only for its centre, because the rod sample is not uniformly magnetized in lower magnetic field. We obtained the different $I$–$H_{\mathrm{ext.}}$ curves corresponding to several positions in a rod sample, as shown in Fig. 2. In a weak field the sample has the maximum value of magnetization at the centre of rod and the magnetization decreases gradually with increasing distance from the centre. We found experimentally that in a very weak field the rod sample has the magnetization distribution given by

$$I_d=I_0\left\{1-\left(\frac{2d}{l}\right)^2\right\}, \qquad (3)$$

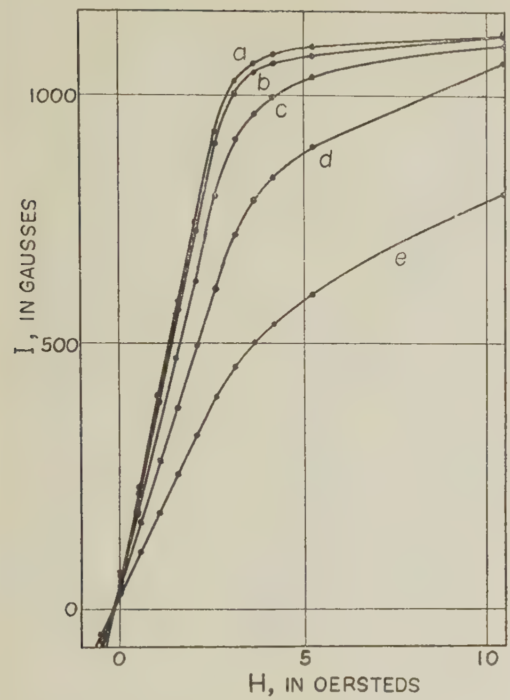

Fig. 2. Descending hysteresis curves of a rod single crystal of iron. *a* is the curve at the centre of rod, *b*, *c*, *d* and *e* are those which correspond to the positions apart from the centre $l/10$, $2l/10$, $3l/10$ and $4l/10$, respectively. ($l$ is the length of the sample.)

where $l$ is the length of rod, $d$ is the distance from the centre and $I_d$ is the magnetization at the distance of $d$. To a good approximation the decreasing of magnetization is proportional to $d^2$, when the coercive force of the sample is small enough. The magnetization of the sample becomes uniform with the increasing of magnetic field.

Neglecting the fact that the sample is not uniformly magnetized Takaki and Nakamura measured the magnetostriction, extending over the greater length of the rod sample. In other words, they obtained the mean magnetostriction curve which could not be coordinated to the measured magnetization.

In our case, however, we measured the local magnetostriction which corresponded well to the magnetization at the centre. With this result, we can determine the magnetostriction constants more precisely than before. Further we observed some local magnetostrictions at the other positions and compared the results with the previous ones.

Fig. 3 (A), Fig. 4 (A) and Fig. 5 (A) show the longitudinal magnetostrictions along the descending hysteresis curves for the samples having the rod axes nearly parallel to [100], [111] and [110] respectively. Every local magnetostriction curve was plotted against the magnetization at the centre of rod to be compared with the previous results.

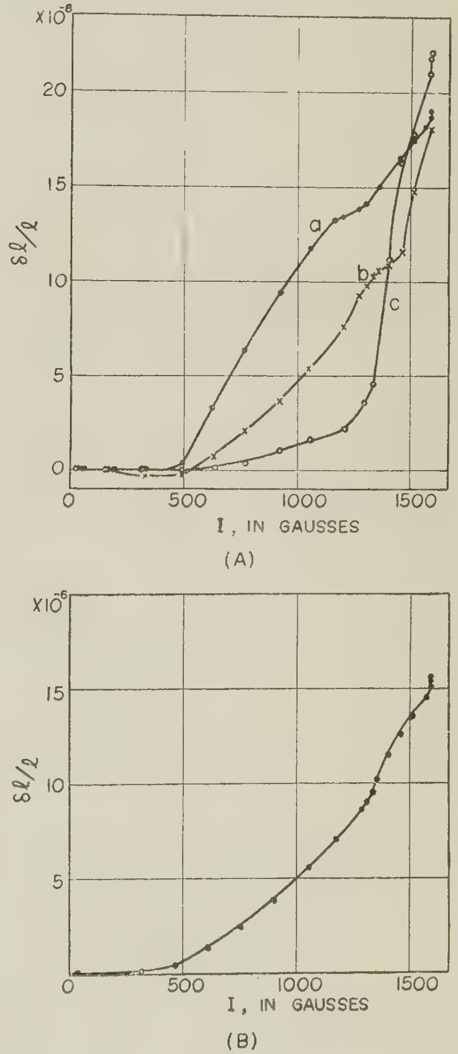

Fig. 3. (A) Magnetostriction curves along the descending hysteresis loop of a long rod single crystal of 3.2% Si-Steel (No. 59), having a rod axis nearly parallel to [100]. *a* is the local magnetostriction curve at the centre, just corresponding to *I*. *b* and *c* are those at the positions apart from the centre $l/4$ and $3l/8$, respectively.

(B) Previous curve obtained by optical lever method on the same sample as (A).

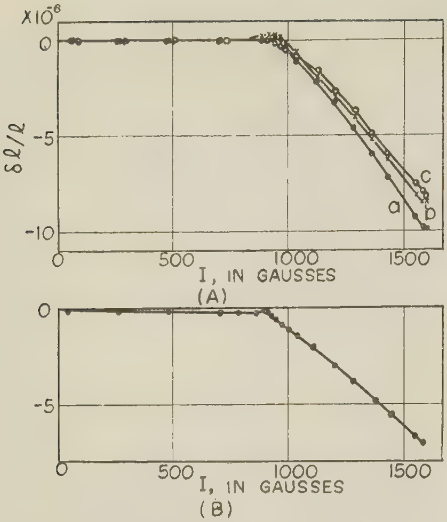

Fig. 4. (A) Magnetostriction curves along the descending hysteresis loop of a long rod single crystal of 3.2% Si-Steel (No. 49), having a rod axis nearly parallel to [111]. *a* is the local magnetostriction curve at the centre, just corresponding to *I*. *b* and *c* are those at the positions apart from the centre *l*/4 and 3*l*/8, respectively.

(B) Previous curve obtained by optical lever method on the same sample as (A).

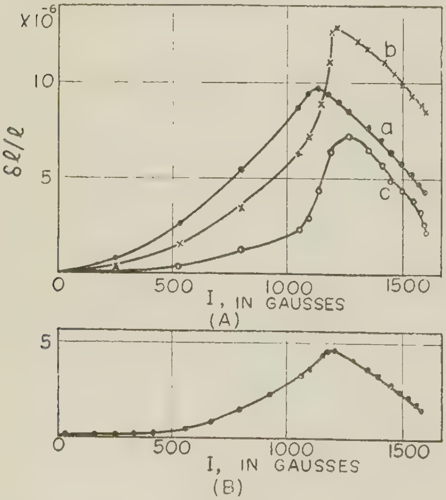

Fig. 5. (A) Magnetostriction curves along the descending hysteresis loop of a long rod single crystal of 3.2% Si-Steel (No. 42), having a rod axis nearly parallel to [110]. *a* is the local magnetostriction curve at the centre, just corresponding to *I*. *b* and *c* are those at the positions apart from the centre *l*/4 and 3*l*/8, respectively.

(B) Previous curve obtained by optical lever method on the same sample as (A).

In the case of [100] direction, as is shown in Fig. 3, the local magnetostriction curve depends largely on its position measured. On the other hand, in Fig. 4 we can find that all the curves are similar. A tentative explanation for these phenomena is as follows; Every sample is not uniformly magnetized in lower fields, so that the local magnetostriction curve depends considerably on the position when the sample is elongated by the redistribution of magnetic domains. And the previous curve in Fig. 3 (B) seems to be superposed on all the local magnetostrictions. But in the case where the change of length occurs only in higher magnetic fields we have similar curves, because the magnetization of the sample is more uniform.

Before this study it has been a problem why a sample like that in Fig. 3 shows the sharp elongation at the saturation. This is one of the typical effects caused by the superposition on all local magnetostrictions. That is to say, even when the centre of the sample attains the saturation the other positions, in particular the end of rod, is not saturated yet, and therefore, the previous curve, containing every part, has a sharp change near the saturation. But the local magnetostriction curve, just corresponding to *I*, has no sharp change any more.

Another typical case we observed is the sample which has a rod axis parallel to [110] and its magnetostriction curve has a maximum, as shown in Fig. 5. The curve of the centre which corresponds to *I* has a maximum at the remanence point of *I* on abscissa, while the previous curve in Fig. 5 (B) has it a little above the remanence. The latter is strongly affected by the superposition on every local magnetostriction. According to Becker's theory the sample must be shortened with *I* from the remanence as it has the rod axis nearly parallel to [110], and our result is in good agreement with the theory.

In this way we measured the magnetostrictions of the other six specimens, obtaining results as shown in Table I. We determined the magnetostriction constants as follows.

| | Present authors. | Takaki and Nakamura. | Carr and Smoluchowski. |
|---|---|---|---|
| $\lambda_{100}\times 10^6$ | $29.2\pm2.2$ | $32.0\pm1.8$ | 26.6 |
| $\lambda_{111}\times 10^6$ | $-(8.1\pm0.5)$ | $-(5.6\pm0.4)$ | $-5.4$ |

There are considerable differences between the values of $(\delta l/l)_{\mathrm{Sat.-Rem.}}$ obtained by two different methods. The apparent change of magnetostriction measured by the strain gauge is always larger than that measured by the optical lever method. But as to $(\delta l/l)_{\mathrm{Sat.-Rem.}}$, this is not the case. In the previous results $(\delta l/l)_{\mathrm{Sat.-Rem.}}$ of the samples having the rod axes nearly parallel to [100] must be too large by the effect of the superposition on every local change, while in the case of [110], $(\delta l/l)_{\mathrm{Sat.-Rem.}}$ must be shortened by the same effect. Then $\lambda_{100}$ becomes smaller and $\lambda_{111}$ is larger in absolute magnitude than those obtained by Takaki and Nakamura, both probable errors being the same order of magnitude. Carr and Smoluchowski also determined the magnetostriction constants of 3.03% Si-Steel by using a disk-shaped sample, and in their results $\lambda_{100}$ is closer to ours, while $\lambda_{111}$ is closer to the previous ones.

We wish to thank Mr. Y. Nakamura, Mr. J. Hayashi, Mr. S. Nakamura and Mr. T. Sugiyama for their helpful assistances throughout the work. The expense of this research has been partly defrayed by the Scientific Research Expenditure of the Ministry of Education.

### References

1) J. E. Goldman: J. de Phys. et Rad. **12** (1951) 471.
2) W. J. Carr and R. Smoluchowski: Phys. Rev. **83** (1951) 1236.
3) R. M. Bozorth and R. W. Hamming: Phys. Rev. **89** (1953) 865.
4) R. M. Bozorth and J. G. Walker: Phys. Rev. **89** (1953) 624.
5) H. Takaki and Y. Nakamura: J. Phys. Soc. Japan **9** (1954) 748.
6) H. Takaki, S. Nakamura, Y. Nakamura, J. Hayashi, K. Furukawa and M. Aso: J. Phys. Soc. Japan **9** (1954) 204.

---

JOURNAL OF THE PHYSICAL SOCIETY OF JAPAN Vol. 11, No. 11, NOVEMBER, 1956

# Radiative Collisions between Electronic and Molecular Beams

## I. Angular Momentum Distribution among OH* Radicals resulting from $H_2O$ Molecules

By Tadao HORIE, Takayuki NAGURA and Masamoto OTSUKA
*Faculty of Science, Osaka University*

(Received August 9, 1956)

The angular momentum distributions among the OH* radicals in radiative collisions between electronic and water molecular beams in the vacuum of $1\times10^{-4}$ mmHg lead to several predictions as regards the mechanism of the radiative decomposition of $H_2O$ as follows. (1) The relative number of the abnormally rotating OH* radicals to the thermally rotating ones, both coming out of water molecules excited by electron impacts, is on the average 10 to 1. (2) Two different kinds of singlet excited states of water molecules play leading parts in the radiative collisions; one is caused by the excitation of the oxygen (2*p*) electron up to the (3*s*) orbital, and the other by the simultaneous excitations of the oxygen (2*p*) and the hydrogen (1*s*) electrons up to their respective orbitals with higher principal quantum numbers. (3) The abnormally rotating OH* radicals result from the former and the thermally rotating ones from the latter. (4) The recoiling H atom flies off nearly in the direction of the H-H repulsion with the highest probability.

## §1. Introduction

The subject in this article is to study the rotational motion of the excited OH molecule which is born in an electrical discharge through water vapour and lives rather a long life as a physically stable molecule. In this molecule, a light particle, that is to say, the H atom may approximately be considered to be circling about the heavier O atom. The rotational energy distribution among molecules of this sort can be determined from the intensities of the rotational lines emitted from them. More than twenty years ago O. Oldenberg[1)] found for the first time that this rotational motion was too highly abnormal to be reconciled with any thermal rotation and proposed an interpretation that in the dissociation process of $H_2O$ the recoiling hydrogen atom might be expected to give angular momentum to the excited OH radical, leaving it with a highly excessive rotation, because of the triangular structure of the water molecule. For example, it is estimated from the temperature of water vapour in an electrical discharge that only one molecule in $10^{20}$ would have the rotational energy corresponding to the quantum number $K'$ of 26. Although it implys evidently much too small a concentration to be detected, the line $Q_1$ (26) due to the molecules rotating with such an abnormally high speed, contrary to expectation, comes out with a considerable intensity. This fact tells us that, in electrical discharges, any thermal equilibrium could not only be unestablished among the excited OH molecules, but also there should exist such abnormally rotating ones at an unexpectedly higher concentration.

After the discovery by O. Oldenberg, a great number of experiments have been carried out in order to approach to the mechanism of this abnormal rotation. These experiments may be classified into two categories as follows. The experiments falling under the first category have revealed how the abnormal rotation varies in different types of electrical discharges. In the experiments falling under the second, it has been studied in what manner a subsidiary condition such as diminution of discharge pressure or dilution with inert gases makes changes in the abnormal rotation in certain types of electrical discharges. First of all, several examples of electrical discharges and the corresponding references will be cited in the following table. Generally speaking from these experiments, the rotational intensity distribution for the (0, 0) band of OH has at all times two maxima in almost all of electrical discharges, as several examples of them are shown in Fig. 1, in which the intensity is plotted against the rotational quantum number, $K'$, of the excited state. The first one appers at lower $K'$ number, which may be called the *thermal maximum*. The second one appears at high $K'$ near 17, which may be called the *abnormal maximum*. The former is due to the excited OH molecules in a Maxwellian distribution corresponding to a gas temperature in an electrical discharge and consequently the $K'$ value of it varies from 2 to 8 in dependence on the type of discharge. On the contrary, the latter appears in any case near the $K'$ value of 17 and is surely due to the molecules rotating with abnormally high speeds corresponding to an extremely high temperature in comparison with the gas temperature. From the position of the abnormal maximum, the rotational temperature of these abnormally rotating molecules is estimated to be 14,000°K, even when the gas temperature is of the order of 600°K.

| Light source | Investigator | Reference |
|---|---|---|
| Geissler discharge | O. Oldenberg | (1) |
| | H. Wakeshima | (2) (3) |
| Low voltage arc | M. Ninomiya | (4) |
| Spark at low pressure | T. Horie, T. Nagura and M. Otsuka | (5) |
| High frequency glow discharge | M. Ninomiya | (4) |
| High frequency electrodeless ring discharge | H. P. Broida and W. R. Kane | (7) |
| | T. Horie | (6) |
| Sensitized fluorescence | E. R. Lyman | (8) |
| Electrical arc | E. R. Lyman | (9) |
| Hydrogen-oxygen flame | H. P. Broida and K. E. Shuler | (10) |
| | W. R. Kane and H. P. Broida | (11) |

In addition, the following features would seem to be noteworthy. The strength of the abnormal maximum relative to the thermal one changes fairly distinctly from one discharge to another. For instance, in a spark at low pressure the thermal maximum is quite predominant over the abnormal one, while in a high frequency discharge the abnormal maximum is well defined against the thermal one.

These variations may be dependent on the difference in the collision processes taking place in different discharge spaces. Consequently it looks quite important not only in analyzing the collision processes in discharge spaces, but also in studying the excited states of $H_2O$, to make it clear in what manner the water molecule is excited and then an abnormally rotating $OH^*$ molecule appears.

In order to obtain an insight into the mechanism of the abnormal rotation, in the experiments falling under the second category, the change in the rotational intensity distribution has been studied in detail by varying a subsidiary condition in a fixed discharge tube. O. Oldenberg[1)] and E. R. Lyman[9)] have examined the effect of the foreign gas He in Geissler discharges. H. Wakeshima[3)] has studied

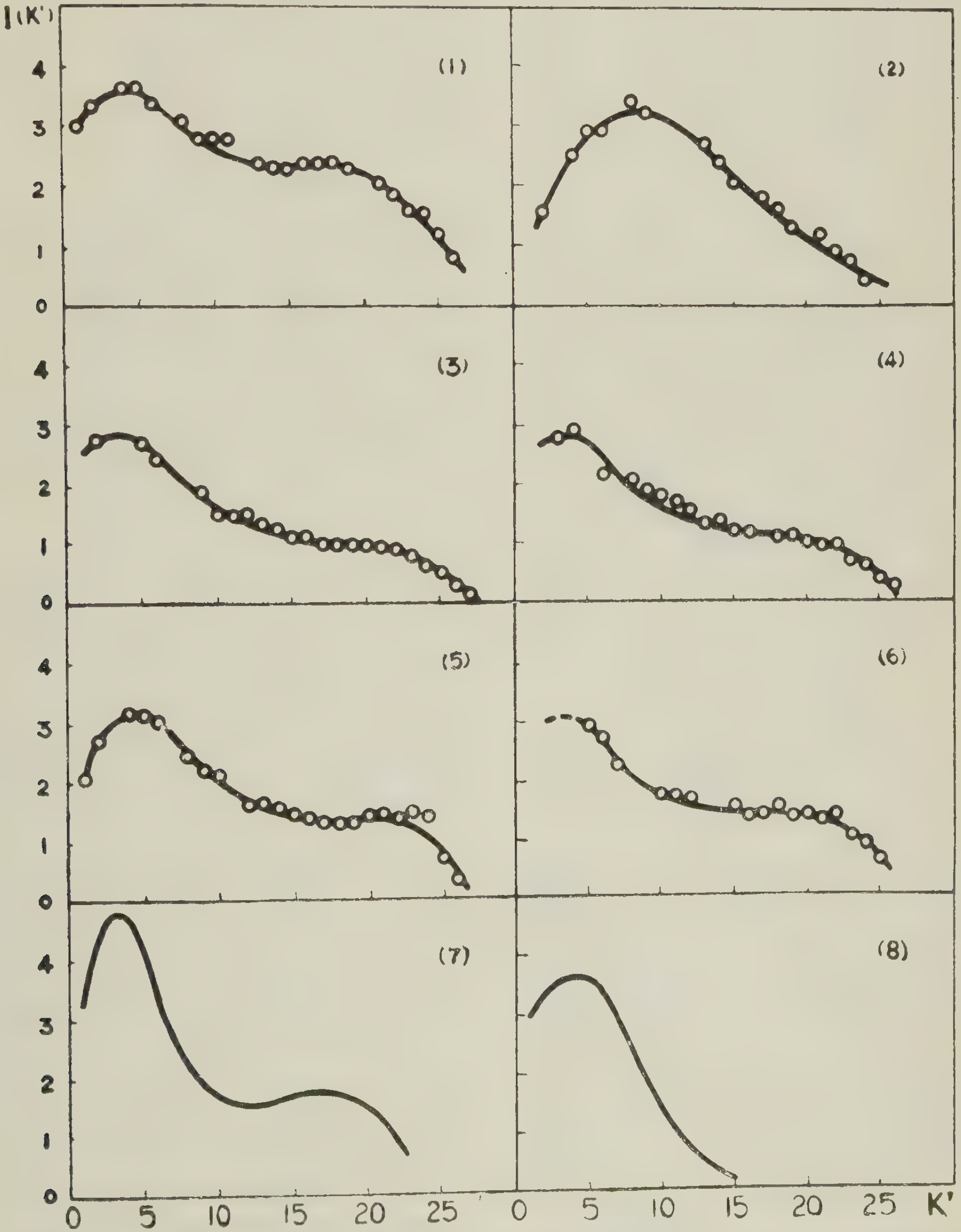

Fig. 1. Rotational intensity distributions in several kinds of light sources; (1) Geissler discharge, (2) Spark at low pressure, (3) (4) (5) (6) High frequency electrodeless ring discharge of 5 metres in wave-length, $P_1$, $P_2$, $Q_1$ and $Q_2$ branches respectively, (7) High frequency glow discharge, (8) Maxwellian distribution for 800°K.

the effect of the temperature of water vapour in a Geissler discharge. H. P. Broida and W. R. Kane[7) have investigated the effects of the pressure of water vapour and the dilution with inert gases in a high frequency electrodeless ring discharge. G. Hayakawa[13) and M. Ninomiya[4) have observed the effect of the grid potential in triode type discharge tubes filled with water vapour. W. R. Kane and H. P. Broida[11) have investigated a hydrogen-oxygen flame diluted with inert gases.

Notwithstanding that valuable data have already accumulated in abundance, the mechanism of this phenomenon has not yet been led to any complete understanding, and, what makes the matter worse, even different conclusions looking hard to be reconciled with one another are sometimes prone to be drawn out of different kinds of electrical discharges. What in the world is the reason for such a danger of confusion? It may certainly be caused by the complicated and incomprehensible character of the discharge. All sorts of collision processes are often intermingled with one another in a small space of electrical discharge. This may be the very reason why a small glass tube with electrodes enclosed into it is sometimes looked up to as a treasure box of collision processes, and at other times looked down upon as a waste box of them. Of all sorts of collisions among electrons, positive ions, atoms, molecules, excited atoms, excited molecules, metallic surfaces of electrodes and glass walls, which one does play the greatest part in the abnormal rotation considered in this article? It may in general be impossible to make a strict answer to this question. Even if a sort of collision process were tentatively assumed as most leading, it is quite ambiguous whether the remaining ones can be set aside from the question or not. The ambiguity like this seems to be unavoidable as far as electrical discharges are concerned.

At any rate, in a certain electrical discharge through water vapour, the collision of electrons with water molecules may perhaps play the most important role for the production of the abnormally rotating OH* molecules. That is,

$$\text{(A)} \qquad H_2O+e \rightarrow OH^*+H+e\ ,$$

where the asterisk means the excitation of the electronic state. As a secondary process of importance, the recombination collision between the atomic hydrogen and oxygen may sometimes need to be taken up as follows—

$$\text{(B)} \qquad H+O(+M) \rightarrow OH^*(+M)\ ,$$

where $M$ is a third body. Furthermore, the three body collision also may occasionally be obliged to be considered as follows—

$$\text{(C)} \qquad H+H+OH \rightarrow H_2+OH^*\ .$$

On the other hand, as an origin of the molecules giving the thermal maximum, the electronic excitation of the OH radicals at the ground state wandering about in a discharge tube may at times be necessary to be taken into account, namely—

$$\text{(D)} \qquad OH+e \rightarrow OH^*+e\ .$$

In addition, the experiment of hydrogen canal ray impact made by the authors[12) shows that the water molecule is rather intensively excited and dissociated by the collisions of the positive ions composed of proton, $H_2^+$ and $H_3^+$, leaving OH* molecules with fairly normal rotations. In any discussion about the rotational intensity distribution, would it not be worth while to take the following collision into consideration at all?

$$\text{(E)} \qquad H_2O+\textit{positive ion} \rightarrow OH^*+H\ .$$

Any ordinary discharge through water vapour, whatever sort of discharge it may be, doesn't make it possible to study the abnormal rotation without being shadowed by these ambiguities. Nevertheless, in almost all the studies on the abnormal rotation, some one of discharges has so far been utilized chiefly because it offers a sufficiently bright light source. The excited OH molecules emit a crowd of rotational lines with slight differences in wavelengths. In order to measure their intensities precisely, it is of imperative necessity to use a spectrograph with a dispersion which is good enough to separate the adjacent lines from one another as far as possible. The dispersion is usually increased at the sacrifice of the $f$-number of a spectrograph and so the light source is desired to be as bright as possible. Every one of electrical discharges just meets this requirement.

As the discovery of the abnormal rotation was born in an electrical discharge, it is quite natural that attentions should, to begin with, have long been payed to discharges. It looks, however, doubtful to succeed in drawing any more definite conclusions on the mechanism of the abnormal rotation out of the observations of electrical discharges alone, because the complete analysis of the discharge space has not yet been achieved. It may then be considered to be the only way left to the solution of this problem to investigate what kind of abnormal rotation is brought about by the simplified collisions between water molecules and electrons or protons with known velocities. Moreover, the synthesis of the conclusions derived from such elementary collision processes may also make it possible to understand much more fully the electrical discharge itself. Furthermore broadly speaking, the investigations of such elementary processes may contribute not only to physics of electrical discharges but also to many other different branches of physics, namely—the theory of molecular collision, the theory of molecular structure, the theory of chemical reaction, gas kinetic theory, atmospheric physics and astrophysics.

The principle of the present experiments of purely electronic collisions is as follows. A beam of electrons with nearly homogeneous energies and a beam of water molecules run across at right angles to each other in the vacuum of $1\times10^{-4}$ mmHg. The intensities of the rotational lines emitted from the excited OH molecules appearing at the intersection of the two beams are measured by a quartz Littrow-type spectrograph with two prisms and a recording microphotometer. The intensities of the rotational lines must be proportional to the intensities of the electronic and molecular beams. Hence it is prerequisite to study how to realize a powerful beam of electrons, an intense beam of molecules and a highly evacuated collision chamber. After years of preliminary tests, it has become possible to enhance the number of the excited OH molecules up to a desired amount. The molecular beam is projected into a collision chamber through an image slit via a source slit and then condensed on a metallic surface cooled by liquid air immediately after having run a short distance of ten millimetres or so. The electronic beam is emitted from an oxide-coated cathode in a specially designed electron-gun and focussed just in front of the image slit by electric and magnetic means. Both the hydrogen and oxygen gases appearing at the intersection of the two beams and the residual gases emanating from the metallic wall bombarded by electrons are rapidly evacuated by three oil diffusion pumps designed for use in high speed pumping.

## § 2. Experiment

The main purpose of this experiment is firstly to make sure of the intrinsic abnormal rotation due to purely electronic collisions of water molecules and secondly to see its dependence on the energy of colliding electrons. It may, therefore, be necessary that only the collision process between water molecules and electrons with energies lying within a definite narrow range, namely—

(A) $$H_2O+e\rightarrow OH^*+H+e\ ,$$

should be observed without being confused with all of the other collision processes, (B), (C), (D), (E) and so on as indicated in the last section. In order to realize such an idealized picture, the three axes at right angles to one another being taken in vacuo, in the direction of the $y$-axis the beam of electrons with nearly uniform velocities is shot and at the same time in the direction of the $z$-axis the beam of water molecules is projected. Nevertheless, at the intersection of these beams, various excitations of dissociated atoms may take place in company with (A) as follows:

(b) $$H_2O+e\rightarrow OH+H^*+e\ ,$$

(c) $$H_2O+e\rightarrow H^*+H+O+e\ ,$$

(d) $$H_2O+e\rightarrow H+H+O^*+e\ ,$$

and moreover miscellaneous ionizations as, for instance,

(e) $$H_2O+e\rightarrow H_2O^++2e\ ,$$

may also occur as have recently been discussed in detail by K. J. Laidler[16]. Quite fortunately, however, only the OH* in the process (A) emits a crowd of rotational lines in the neighbourhood of the wave-length 3060 Å, which is able to be detected in the direction of the $x$-axis**.

---

** A precise measurement of the excitation function by means of a molecular beam, a multiplier phototube and a lock-in amplifier is under preparation in our laboratory, and in the meantime, for simplicity, the process (A) comprehends all of the processes as follows, without distinction of electronic state in the recoiling H;

$$H_2O+e\rightarrow OH^*+H^*(n=2,3,4,\cdots)+e\ ,$$

and $$H_2O+e\rightarrow OH^*+H^++2e,$$

where $n$ is the principal quantum number.

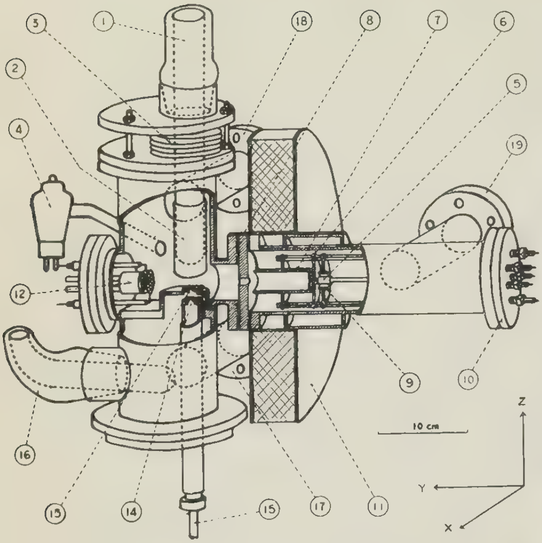

Fig. 2. The collision chamber.

The intensity of the rotational line emitted from the OH* molecule having an angular momentum corresponding to the rotational quantum number $K'$, $I(K')$, is proportional to the number of molecules per unit volume $N(K')$ and the transition probability $P(K', K'')$. Since $N(K')$ must be proportional to the number of collisions per unit volume per second at the intersection of the two beams, in order to make $I(K')$ measurable by rather short exposures, it is of imperative necessity to enhance the intensities of both the electronic and the molecular beams. An intense beam of electrons is obtained from a specially designed electron-gun with electric and magnetic focussing actions. As shown in Fig. 2, thermal electrons are emitted from an oxide-coated surface at the top of the nickel cap (5) with a diameter of 8 mm. The electrons drawn out of the cathode (5) by the probe electrode (6) are shot into the collision chamber through the accelerators (7) and (8) and brought to a focuss just in front of the so-called image slit (13), where they hit the molecular beam.

The beam of electrons passes through the spot in a bundle of 6 mm in diameter and its intensity is of the order of 50 mA under favourable conditions. The focussing of electrons is attained by the co-operation of the magnetic field due to the electromagnet (11) with the electric fields between the cathode (5), the screening electrode (9), the probe electrode (6), the accelerators (7) and (8). The energy distribution of the electron beam is measured by the electrodes (12) composed of a Faraday cage cooled by running water, a screen grid suppressing reflected and secondary electrons and a grid with varying potential of retardation. The separation of the thermal electron source from the image slit at a distance of fifteen centimetres is suitable to prevent the oxide-coated surface from being damaged by scattered molecules. All parts of the vacuum system are made of metal and connected with one another by rubber packings. A bird's-eye view of the collision chamber, a side-view of the whole apparatus and an inside view of the electron-gun are presented in Figs. (3), (4) and (5) respectively.

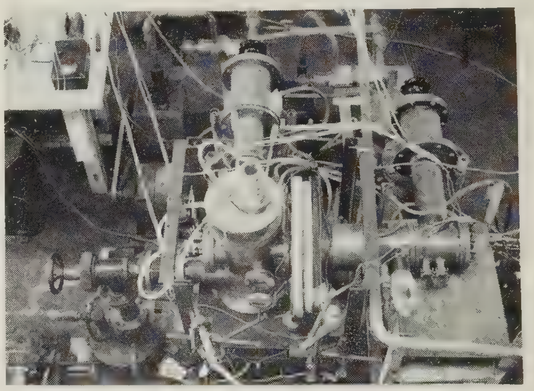

Fig. 3. A bird's-eye view of the collision chamber.

As the walls are all connected to the earth in order to ensure that the collision space may be free of electrical fields, the terminals of the electrodes in the electron-gun are all attached to the insulated disc (10). The most intense beams are obtained when the probe electrode is at the potentials ranging from 500 to 800 volts higher than the cathode. The addition of potentials, either accelerating or retarding, to the succeeding electrodes allows to change the energy of the beam from 1,000 down to 20 volts. Let $n(E)dE$ be the number of electrons which have energies lying in the range from $E$ to $E+dE$, and the number of such electrons passing per unit time through the spot where the collision takes place is proportional to $n(E)\sqrt{E}\,dE$. The curves in Fig. 6 show some examples of $n(E)\sqrt{E}$ *versus* $E$ for different combinations of potentials imposed on the electrodes, the screening electrode (9) being always kept at equipotential to the cathode (5). Although the shape of the curve more or less changes in dependence on the combination, the upper limit is always well defined and the lower side is somewhat diffuse. For instance, in the beam of 600 volts, the maximum is located at the $E$ value a little lower than the upper limit, while electrons of nearly 400 volts are also contained in some measure. Strictly speaking, therefore, the homogeneity of energies in a given beam is not complete, but the order of separation in the energy distributions for different accelerating potentials may be regarded as satisfactory for the present purpose.

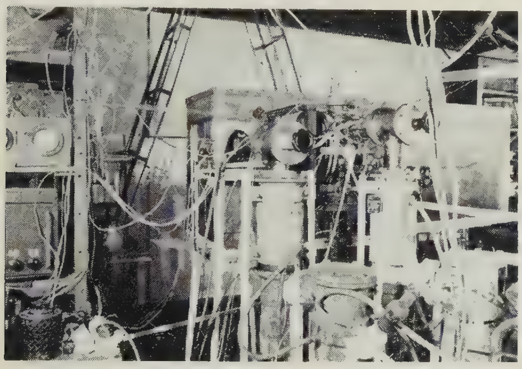

Fig. 4. A side-view of the whole apparatus.

The water molecules sent through the pipe (15) are projected into the collision chamber through the so-called source slit (14) and the image slit (13). Here are two requirements to be solved in order to enhance the intensities of the rotational lines. One is to make the molecular beam as strong as possible and the other is to keep the vacuum of the collision chamber as good as possible. Although they are at first sight contradictory to each other, this contradiction is avoided by the co-operations of the very rapid condensation of water molecules on the metallic surface (2) cooled by liquid air trap (1) with the high speed evacuation by the three pumps of oil diffusion type joined to the flanges (17), (18) and (19). The beam of water molecules shot through the image slit which is one half millimetre in width and five millimetres in length in the direction of the $x$-axis is condensed on the lower surface of the copper cylinder (2), immediately after having run a short distance of ten millimetres or so. The distance of flight is adjusted by the bellows (3). The scattered molecules in the collimator chamber between the source and the image slits are also rapidly removed by the condensation on the silvered surface of the liquid air trap (16) and an oil diffusion pump. According to R. G. J. Fraser "Molecular Rays" Cambridge, a pump having the effective speed at the collimator chamber of 10 litres per second at a pressure of $10^{-3}$ mmHg is equivalent on the average to a perfect condenser of rather less than 1 cm². In the present experiment, the effective areas of the cooled surfaces are about 200 cm² in (1) and about 100 cm² in (2). With keeping an eye on the ion gauge (4), the vacuum in the collision chamber is kept at the fixed pressure of $1\times10^{-4}$ mmHg, by adjusting the intensity of the molecular beam.

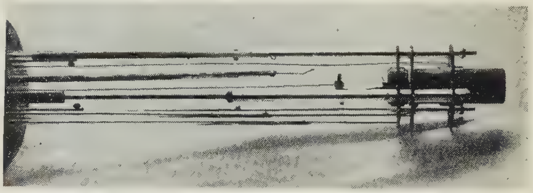

Fig. 5. An inside view of the electron-gun.

The intensity distributions of the rotational lines emitted in the direction of the $x$-axis are measured by the quartz Littrow-type spectrograph with one 30° and one 60° prism, the dispersion of which is 5.5 Å/mm, and the recording microphotometer with a phototube and a string electrometer. As the method of photographic photometry has already been described in detail elsewhere, only an example of microphotometric figure is given in Fig. 7.

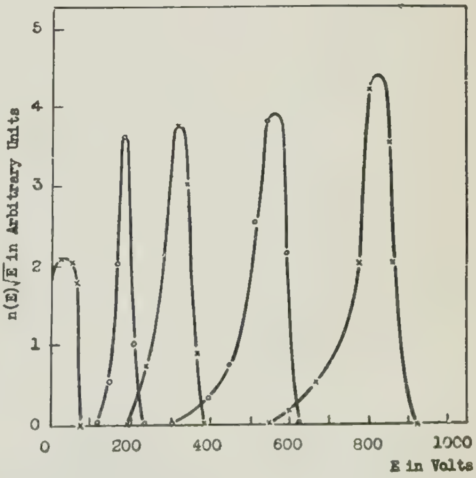

Fig. 6. Energy distributions in electron beams.

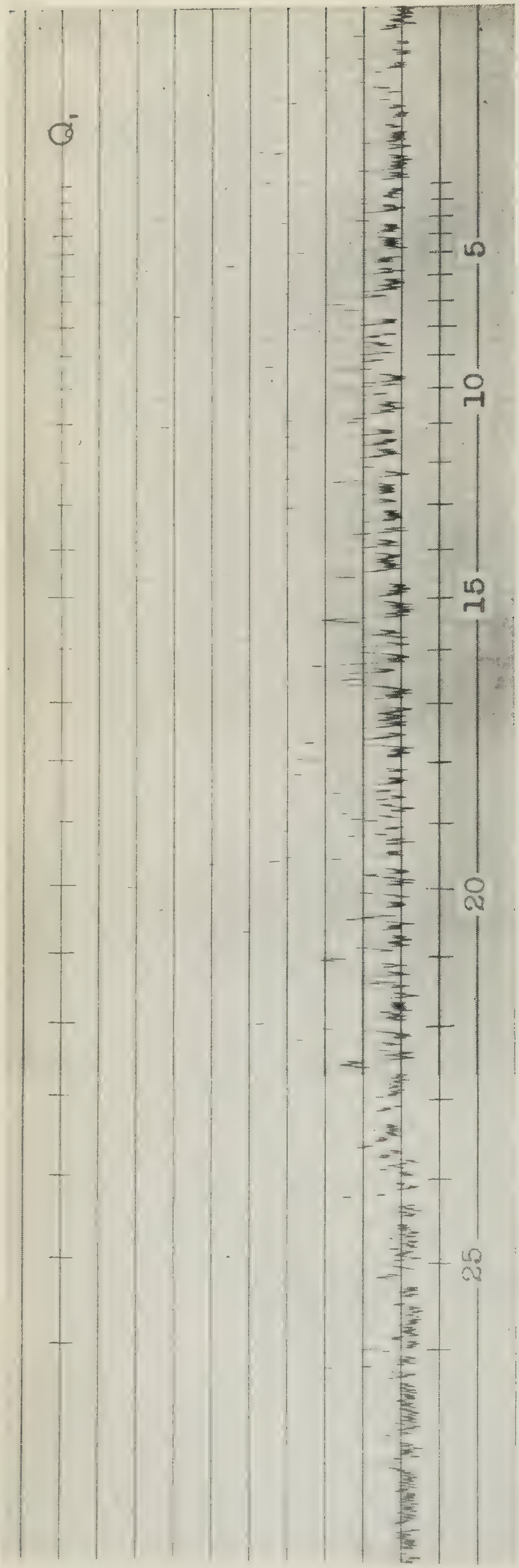

← Fig. 7. The microphotometric figure for 500 volts.

## § 3. Results

In the excited diatomic molecule, the different angular momenta—electron spin, electronic orbital angular momentum, angular momentum of nuclear rotation—form a resultant that is always designated $J'$. Since the electronic state of the OH* molecule is $^2\Sigma^+$, the resultant spin of the electrons is represented by the quantum number 1/2 and the resultant orbital angular mometum precesses at right angles about the internuclear axis. The nuclear rotation is essentially a motion of a light particle, the H atom, circling about the heavier O atom, the angular momentum of which is represented by the quantum number $K'$. A rotational level for a given $K'$ value splits into two levels corresponding to $J'=K'+1/2$ and $J'=K'-1/2$. Furthermore since the precession of the electronic orbital angular momentum is not uniform in the rotating molecule, on the average a non-zero component results in the direction of $K'$. The energy difference in the doublet splitting due to these causes, however, is so small in comparison with the rotational energy of the H atom that the $K'$ value itself is taken as the parameter to use in describing the intensity distribution among the rotational lines. Let $N(K')$, $I(K')$ and $P(K', K'')$ be the number of molecules per unit volume at the rotational state $K'$, the intensity of the rotational line emitted from these molecules and the transition probability from the excited $^2\Sigma^+$ state to the ground $^2\Pi$ state, and they are connected with one another as follows:

$$I(K')=CP(K', K'')N(K') , \qquad (1)$$

where $C$ is a constant. The rotational intensity distributions for different energies of impinging electrons are shown in Fig. 8, in which the energy of an electron beam is represented by the upper limit for the reason given in the last section.

The separation of rotational lines from adjacent ones is more favourable in the $Q_1$ branch than in any other branches. This is the reason why the present measurements are for the most part made in the $Q_1$ branch, which are shown by circles in Fig. 8. The rotational lines, however, lying in the region of the dotted lines are so close to their nearest neighbours that their reliabilities are judged

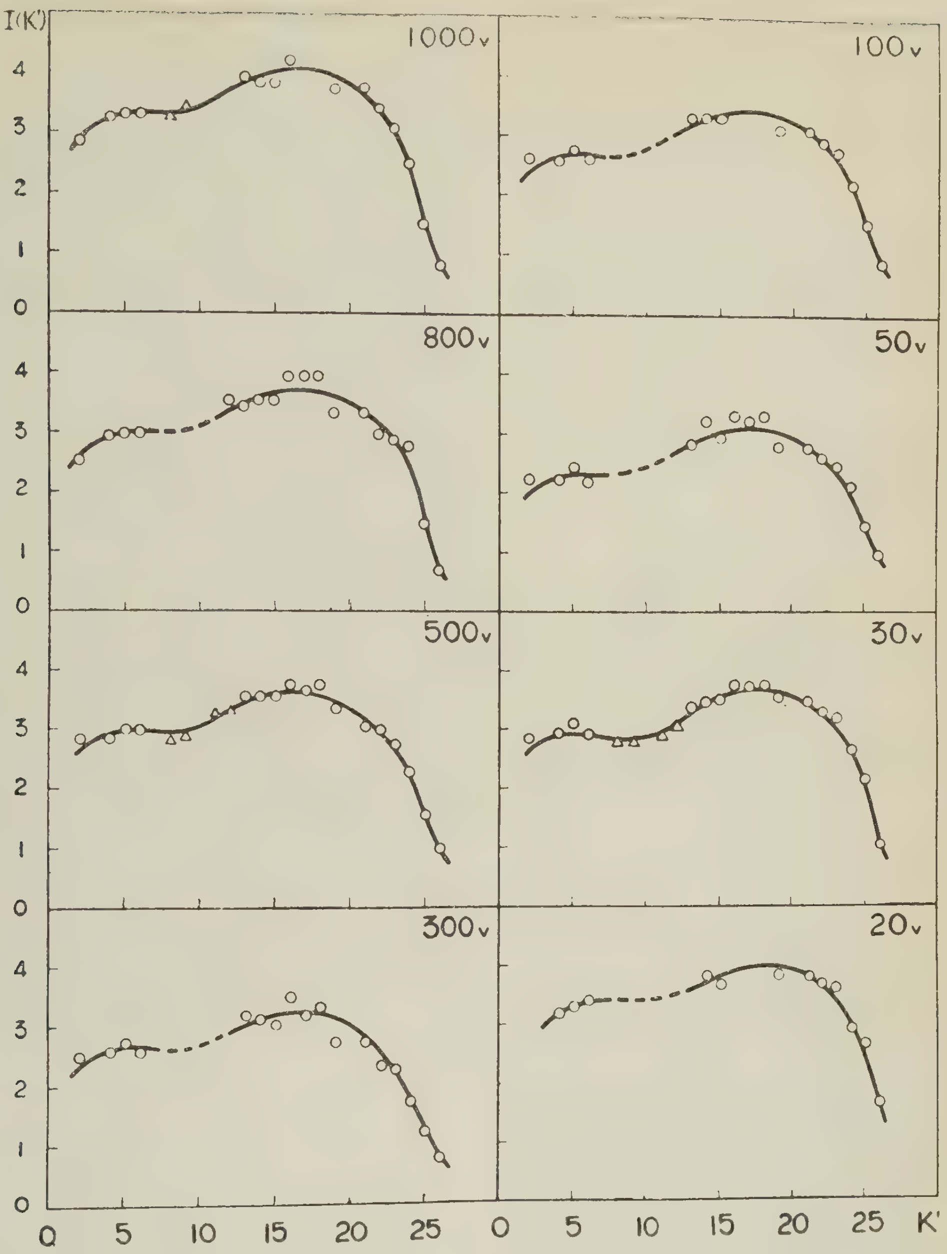

Fig. 8. The abnormal intensity distributions among rotational lines in purely electronic collisions of water molecules. The energy of electrons is indicated by the upper limit.

to be too low for intensity measurements. The judgements are made with reference to "A Spectrophotometric Atlas of the $^2\Sigma^+-{}^2\Pi$ Transition of OH" by A. M. Bass and H. P. Broida[14]. The points denoted by triangles are calculated by making use of well isolated lines of another branches as follows. The probability $P(K', K'')$ in the equation (1) can be replaced by the intensity factor $i(K', K'')$ which is equal to $(2K'+1)P(K', K'')$ and has already been evaluated by L. T. Earls[15], namely—

$$I(K')=Ci(K', K'')N(K')/(2K'+1) . \qquad (2)$$

As $I(K')/i(K', K'')$ is equal to $CN(K')/(2K'+1)$ which contains only $K'$, the values of log $\{I(K')/i(K', K'')\}$ for different branches can all be plotted in the same one curve against the initial rotational energy $B'K'(K'+1)$ as shown in Fig. 9. From these curves the triangular points mentioned above can be obtained by simple calculations.

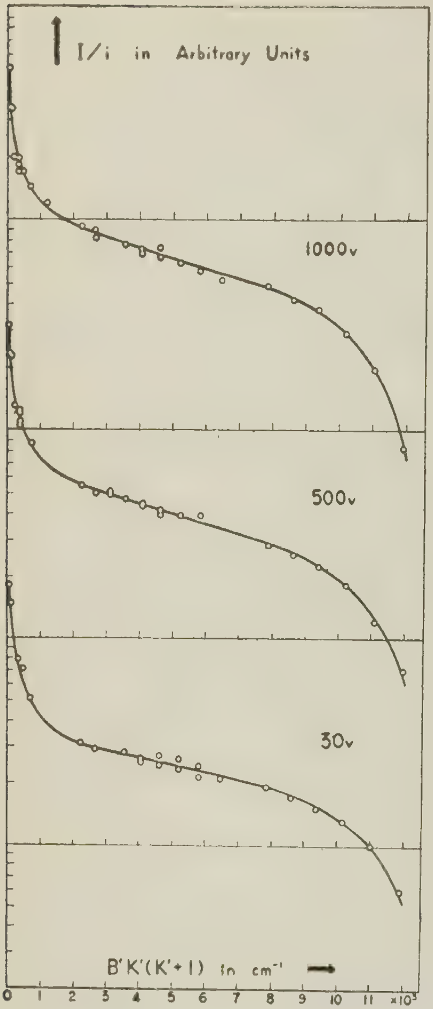

Fig. 9. $I(K')/i(K', K'')$ versus $B'K'(K'+1)$.

There may be involved in Fig. 8 the answers to the two questions which have long remained pending, namely—what features have the abnormal rotations due to purely electronic collisions and in what manner does the energy of impinging electrons exercise an influence upon them? The first answer tells us that almost all of the OH* molecules are abnormally rotating. The fact that the abnormal maximum is at all times predominant over the thermal maximum is standing in sharp contradiction to that in ordinary electric discharges as shown in Fig. 1. A question may arise as to whether the OH* molecules observed here are born in the process (A) or in the process (A′) as follows;

(A) $H_2O+e \rightarrow OH^*(1)+H+e$ ,

and

(A′) $H_2O+e \rightarrow OH+H^*+e$ ,

$OH+e \rightarrow OH^*(2)+e$ .

A further question may also arise whether either one of the two maxima is due to the OH*(2) molecules or not. If either one of these questions were the case, the intensities of the rotational lines should vary in a different manner from what would be expected in (A) in dependence on the intensity of the electron beam, because, contrary to the OH*(1) molecules, the OH*(2) may be expected to be proportional in number to the square of the intensity of the electronic beam. Both of the intensity distributions compared with each other in Fig. 10 were photographed on the same one photographic plate at the electron energy of 600 volts, one of which was taken by an exposure of 1 hour and an electron beam of 14 mA in intensity, while the other by an exposure of 3.5 hours and an electron beam of 4 mA in intensity. There may be any distinct difference neither in the intensity itself nor in the shape of intensity distribution curve. In conclusion, the predominant abnormal maximum may be the very feature characteristic of the OH* molecules produced in the simultaneous excitation and dissociation of water molecules by purely electronic collisions.

The second answer tells us that the rota-

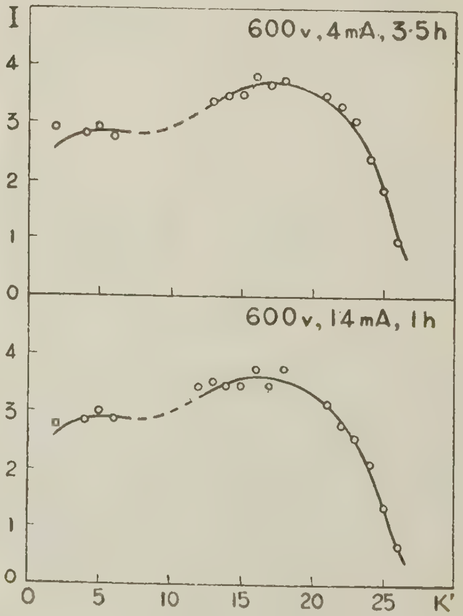

Fig. 10. Dependence on the intensity of electron beam.

tional intensity distribution does not show any appreciable change in dependence on the energy of impinging electrons in the wide range from 20 to 1,000 volts. This distribution, therefore, may be attributable to the nature characteristic of the excited states of water molecule taking part in the process (A) considered. According to J. J. Hopfield[17)], the absorption spectrum of water vapour exhibits three intense bands starting at about 1800 Å (6.9 eV), 1380 Å (9.0 eV) and 1250 Å (10 eV), each of them being called "A-band", "B-band" and "C-band" respectively. The total intensity of the (0, 0) band emitted from the OH* molecules in a triode-type discharge tube filled with water vapour has been measured by G. Hayakawa[13)] as a function of the grid potential, from which the excitation potential may be estimated to be in a range from 9 to 11 eV.

According to F. O. Ellison and H. Shull[18)], the ground state MO electronic configuration for $H_2O$ is written as follows:

$$(1a_1)^2(2a_1)^2(1b_2)^2(3a_1)^2(1b_1)^2\ ,\quad {}^1A_1\ .$$

The excitation of one of the outermost lying lone-pair electrons may give the lowest excited states as follows:

$$(1a_1)^2(2a_1)^2(1b_2)^2(3a_1)^2(1b_1)(3s)\ ,\quad {}^{1,3}B_1\ ,$$

which might be attributed to the A-band. The excited states resulting from the excitation of one of the bonding electrons $(3a_1)^2$ and $(1b_2)^2$, namely—

$$(1a_1)^2(2a_1)^2(1b_2)^2(3a_1)(1b_1)^2(3s)\ ,\quad {}^{1,3}A_1\ ,$$

and

$$(1a_1)^2(2a_1)^2(1b_2)(3a_1)^2(1b_1)^2(3s)\ ,\quad {}^{1,3}B_2\ ,$$

might contribute to the B- and C-band respectively as shown in Fig. 11. Either one or both of the last excited levels might also be attributed to the excited states concerning the process (A). After having been raised by electron impacts up to the excited states, ${}^{1,3}A_1$ or ${}^{1,3}B_2$, some water molecules would probably be decomposed spontaneously into recoiling H atoms and abnormally rotating OH* molecules. If the potential-energy surfaces for these excited states will have been elucidated, the path of the recoiling H atom will be known and the excess angular momentum accepted by the remaining H atom will also be determined.

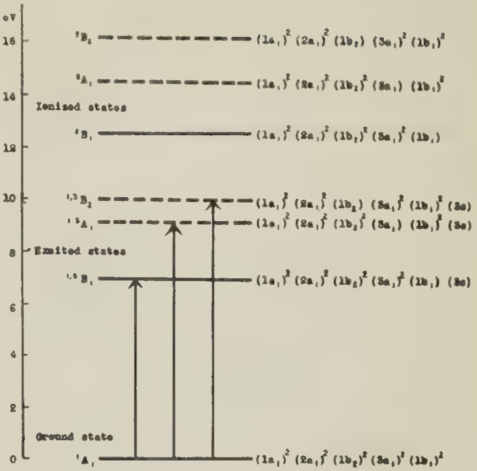
eV
16
14
12
10
8
6
4
2
0
Ionised states
Excited states
Ground state
${}^2B_2$ $(1a_1)^2(2a_1)^2(1b_2)(3a_1)^2(1b_1)^2$
${}^2A_1$ $(1a_1)^2(2a_1)^2(1b_2)^2(3a_1)(1b_1)^2$
${}^2B_1$ $(1a_1)^2(2a_1)^2(1b_2)^2(3a_1)^2(1b_1)$
${}^{1,3}B_2$ $(1a_1)^2(2a_1)^2(1b_2)(3a_1)^2(1b_1)^2(3s)$
${}^{1,3}A_1$ $(1a_1)^2(2a_1)^2(1b_2)^2(3a_1)(1b_1)^2(3s)$
${}^{1,3}B_1$ $(1a_1)^2(2a_1)^2(1b_2)^2(3a_1)^2(1b_1)(3s)$
${}^1A_1$ $(1a_1)^2(2a_1)^2(1b_2)^2(3a_1)^2(1b_1)^2$

Fig. 11. Energy level diagram for $H_2O$.

## § 4. Discussion

Since a LCAO MO treatment for the excited states of $H_2O$ is not yet available at present time, there is no help for it but to begin advancing discussions forwards by means of a tentative interpretation of the mechanism of the abnormal rotation as follows. In a model without regard to hybridizations, the $(2p)$ electrons of the oxygen atom are making electron-pair bonds with $(1s)$ electrons of the hydrogen atoms. If either one of the two $(2p)$ electrons is raised to the $(3s)$ orbital by an impinging electron, two different states may be taken place as shown in Fig. 12. In the singlet state, there remains no longer any directional character of bonding, owing to the spherical symmetry of the $(3s)$ orbital. If the bond strength between the hydrogen $(1s)$ and the oxygen $(3s)$ is not strong enough to allow this hydrogen atom to move along a circle about the oxygen atom until making a linear stable molecular form, this hydrogen atom may fly off in a certain direction intermediate between the radial and the tangential directions. Then the law of angular momentum conservation requires the remaining hydrogen atom to accept an excess angular momentum about the oxygen. On the other hand in the triplet state, owing to the anti-bonding character between the hydrogen $(1s)$ and the oxygen $(3s)$ electrons, the hydrogen atom may fly off in a direction nearly radial from the O, the remaining hydrogen atom being unnecessary to start any other excess rotation than its original rotation due to thermal agitation. These tentative considerations would seem to lead us to the expectation that the abnormally rotating OH* molecules come out of the singlet state and the OH* molecules with thermal rotations result from the triplet state.

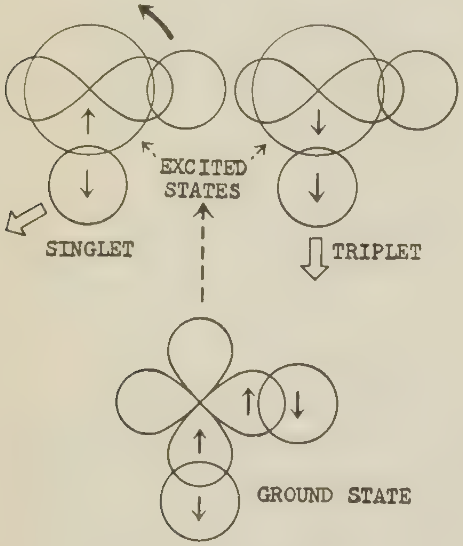

Fig. 12. A tentative interpretation of the abnormal rotation.

Some question, however, may arise especially as to the contribution of the triplet state, because the ground state of $H_2O$ is a singlet. Well known examples for transitions involving change of multiplicity from singlet ground state to triplet excited state are seen in He and Hg atoms. In He the transition is optically forbidden and the electron exchange collision plays a predominant role in electron-impact excitations. If it were the case with water molecule too, the rotational intensity distribution should be expected to show a remarkable change in dependence on the energy of impinging electrons, because the cross-section of the electron-impact excitation to the triplet state $Q(T)$ must be finite only in the vicinity of the excitation potential. On the contrary in Hg, the transition is optically allowed and $Q(T)$ remains finite up to higher energies of impinging electrons as well as the cross-section of the electron-impact excitation to the singlet state $Q(S)$ does. If it is the case with water molecule too, the rotational intensity distribution may be expected not to show any appreciable change in the relative height of the thermal maximum to the abnormal in dependence on the energy of impinging electrons. According to the experimental results presented in Fig. 8, it looks likely that the situation of the latter is similar to that of the electronic excitation of water molecules leading to both thermally and abnormally rotating hydroxyl radicals.

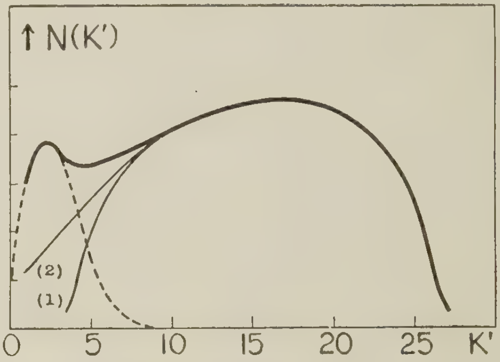

Fig. 13. $N(K')$ versus $K'$.

The ratio of $Q(S)$ to $Q(T)$ is estimated as follows. In Fig. 9 in the last section, the value of $I(K')/i(K', K'')$, that is, $N(K')/(2K'+1)$ is plotted against $B'K'(K'+1)$, all of them looking similar almost independently of the electron energy. The average distribution curve of $N(K')$ *versus* $K'$ is derived at once from them as shown in Fig. 13, in which the dotted curve corresponds to the Maxwellian distribution for 300°K and the rest (1) gives the distribution for the abnormally rotating molecules. The ratio of $Q(S)$ to $Q(T)$ is given by the ratio of the areas under the two different curves and nearly equals 5 to 1. So much weight, however, can not be placed upon this numerical value, because these curves can not be drawn without some ambiguities. For instance, if the total area is divided by a curve as shown by (2), the ratio increases up to 20 to 1. On the average, therefore, $Q(T)$ seems to be of the order of one tenth of $Q(S)$. Since the electron exchange plays only a minor role in exciting water molecules, a question may arise as to the reason why the contribution of the triplet state is so large.

If the thermally rotating OH* molecules were produced only in such a way as shown in Fig. 12, the triplet state considered here should not be of purely triplet character, but, due to spin-orbit interaction, contain an admixture of singlet character to some extent as in Hg. This is intuitively less probable and moreover there is no reason why the triplet state should be the only source of the thermally rotating OH* radicals. They may also be able to result from another kind of singlet state different from that discussed above. Actually in the present experiment, the path of the molecular beam looks reddish owing to the Balmer series, giving a fairly intensive lines due to excited hydrogen atoms as shown in the spectrogram of Fig. 14. These lines may be expected to appear from the processes as follows;

$$H_2O+e \rightarrow OH+H^*+e\ ,$$

and $$H_2O+e \rightarrow OH^*+H^*+e\ .$$

In the present model, the simultaneous excitations of the oxygen (2*p*) and the hydrogen (1*s*) electrons up to the oxygen (3*s*) orbital and a hydrogen orbital with a much higher principal quantum number respectively leads to a sudden increase of a great amount in the equilibrium distance of O–H. In the process of this kind, therefore, even in a singlet state, the recoiling H may fly off radially just in the same way as in the triplet state considered above. Accordingly, it looks more plausible that the thermally rotating OH* radicals result from such a species of singlet state under the condition of the present experiment.

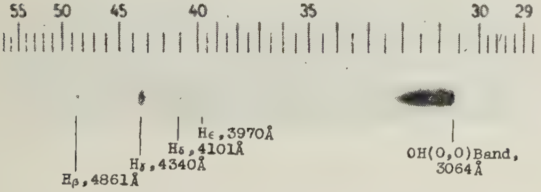

Fig. 14. The hydrogen Balmer series and the OH (0, 0) band emitted from the intersection of the two beams.

Let $\varDelta E$ be the potential difference of the hydrogen atom before and after leaving its original position, then the momentum after having been driven off is given by $\sqrt{2m\varDelta E}$, where $m$ is the mass of H. Let $\theta$ be the angle specifying the direction of recoiling as shown in Fig. 15, then we have

$$\sqrt{2m\varDelta E}\,a \sin\theta = h\sqrt{K'(K'+1)}/2\pi\ , \qquad (3)$$

where the right hand side represents the angular momentum accepted by the remaining hydrogen atom and $a$ is the O–H distance.

Let $K'_m$ be the maximum value corresponding to $\theta=90°$, then we have

$$\sqrt{2m\varDelta E}\,a = h\sqrt{K'_m(K'_m+1)}/2\pi\ . \qquad (4)$$

From (3) and (4) we have

$$\sin\theta = \sqrt{K'(K'+1)/K'_m(K'_m+1)}\ . \qquad (5)$$

It has been seen in Fig. 13 that the angular momentum distribution of molecular number for the abnormally rotating OH* radicals shows a maximum at the $K'$ value of 17 and exhibits a tail-end near 28. It may presumably be considered that the former of these rotational quantum numbers is closely related to the most probable direction for the recoiling H and the latter to the extreme value $K'_m$ defined as above. Putting these numerical values into the equation (5), we see that the most probable angle is equal to 37°52′, which is quite coincident with the angle ∠OHH of 37°45′, since the valence angle ∠HOH is, as is well known, 104°31′. Accordingly the recoiling hydrogen atom may be expected to be driven off nearly in the direction of the H–H repulsion with the highest probability.

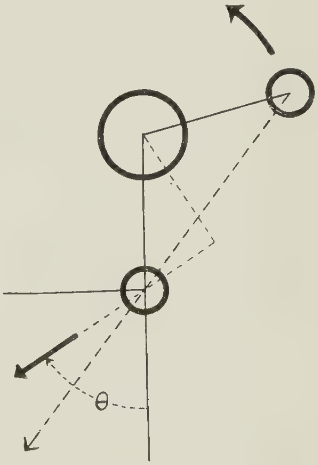

Fig. 15. The direction for the recoiling H atom.

It is a matter of course that the LCAO MO treatment including at least the (3*s*) orbital for the excited states of $H_2O$ should be desired to examine whether all of the conclusions derived in this section merely by the tentative interpretation of the abnormal rotation based upon a simple model of water molecule are plausible or not. When one succeeds in evaluating the potential-energy surfaces for the excited states of $^{1,3}A_1$ and $^{1,3}B_2$, contrary to the above expectation, it might be proved that only one of them, for instance a single excited state $^1A_1$, is enough for production of both the abnormally and thermally rotating OH* molecules. Some years ago K. Niira[19] drived the first spade into the laborious calculations of the potential-energy surfaces for the excited water molecule from the standpoint of the AO method, in which, unfortunately, the contribution of the oxygen (3*s*) orbital was not yet fully taken into consideration. In order to obtain much more detailed informations about the present problem, it seems, at any rate, to be keenly desired for the MO treatment of $H_2O$ to be promoted up to the higher excited states.

## § 5. Acknowledgments

More than ten years have already passed since the project of this research was planned. On the way of performance, it was often driven to the wall owing to the shortage of research fund. Fortunately, however, throughout the course of this work it has long been supported by the kind encouragements furnished by Prof. I. Nitta, Dean of the Faculty of Science, Prof. K. Husimi, Prof. T. Watanabe and all other members of the Department of Physics, whose supports are here gratefully acknowledged. The authors have pleasure in expressing their hearty thanks to Prof. T. Asada not only for placing the spectrographs and other facilities at their disposal but also for valuable suggestions. The authors wish to thank Prof. K. Niira for stimulating discussions on the theoretical interpretations of the experimental results. One of the authors, T. N., wishes to thank Prof. Y. Asano for giving oppotunities of taking part in this project and incessant encouragements. The authors are indebted to Dr. K. Matsui of Tokyo Shibaura Elec. Co., Ltd. for facilities provided as regards the pumping system when he was Manager at Himeji Factory. The authors wish to thank Dr. H. Morita and Dr. T. Misugi of Kobe Ind. Co., Ltd. for kind arrangements for materials for use in the electron-gun. The authors wish also to thank Dr. M. Iio, President of Iio Elec. Co., Ltd., for his kind services in trial construction of a part of the electron-gun. But for these valuable aids, the performance of this project must have been postponed till the farther distant future. Furthermore the authors wish not only to thank Drs. Y. Honda, Y. Nakajima, I. Yamada, K. Kawabe, T. Kiho, Y. Ito, H. Onishi, T. Iwai, N. Minami and M. Nakamura for their earnest assistances during their stays in the faculty as students or an assistant, but also to share the joy of setting the whole apparatus starting with them. Finally one of the authors wishes to express his sincere thanks to Emeritus Prof. T. Tanaka of University of Tokyo, Prof. R. S. Mulliken of the University of Chicago, and Prof. C. A. Coulson of the University of Oxford for their kind encouragements and valuable suggestions.

## References

1) O. Oldenberg: Phys. Rev. **46** (1934) 210.
2) H. Wakeshima: Proc. Phys. Math. Soc. Japan **24** (1942) 367.
3) H. Wakeshima: J. Phys. Soc. Japan **2** (1947) 12.
4) M. Ninomiya: J. Phys. Soc. Japan **4** (1949) 275.
5) T. Horie, T. Nagura and M. Otsuka: not yet published.
6) T. Horie: J. Phys. Soc. Japan **1** (1946) 6.
7) H. P. Broida and W. R. Kane: Phys. Rev. **89** (1953) 1053.
8) E. R. Lyman: Phys. Rev. **56** (1939) 466.
9) E. R. Lyman: Phys. Rev. **53** (1938) 379.
10) H. P. Broida and K. E. Shuler: J. Chem. Phys. **20** (1952) 168.
11) W. R. Kane and H. P. Broida: J. Chem. Phys. **21** (1953) 347.
12) T. Horie and M. Otsuka: J. Phys. Soc. Japan **9** (1954) 219.
13) G. Hayakawa: Proc. Phys. Math. Soc. Japan **26** (1944) 78.
14) A. M. Bass and H. P. Broida: National Bureau of Standards Circular 541 (1953).
15) L. T. Earls: Phys. Rev. **48** (1935) 423.
16) K. J. Laidler: J. Chem. Phys. **22** (1954) 1740.
17) J. J. Hopfield: Phys. Rev. **77** (1950) 560.
18) F. O. Ellison and H. Shull: J. Chem. Phys. **23** (1955) 2348.
19) K. Niira: J. Phys. Soc. Japan **7** (1952) 193.

JOURNAL OF THE PHYSICAL SOCIETY OF JAPAN Vol. 11, No. 11, NOVEMBER, 1956

# On the Magnetic Moment and g-Value of Complex Ions

By Hiroshi KAMIMURA

*Department of Physics, Faculty of Science, University of Tokyo*

(Received August 11, 1956)

Magnetic properties of complex salts containing paramagnetic ions of transition elements are studied on the crystalline field model. Strong cubic crystalline field splits $d$-orbital into $d\gamma$ and $d\varepsilon$, and the magnetism is due to incomplete $d\varepsilon$ shells. The crystalline field is assumed to have, besides cubic part, a component of tetragonal or trigonal symmetry, comparable in magnitude with spin-orbit interaction. Energy level structures, $g$-values of the ground state and magnetic susceptibilities are calculated for $(d\varepsilon)^n$ configurations $1 \leq n \leq 5$. The effective numbers of Bohr magnetons, which measure the magnetic susceptibility, are obtained as explicit functions of two parameters $x=\overline{r^2}A/7kT$ and $y=\lambda/2kT$, where $A$ is the coefficient of tetragonal or trigonal field, and $\lambda$ the constant of spin-orbit coupling. The result is applied to the discussion of magnetic properties of $K_3Fe(CN)_6$ and $K_3Mn(CN)_6$. In Appendix, it is shown that the result for the field of trigonal symmetry becomes equivalent to that for the field of tetragonal symmetry.

## § 1. Introduction

It is well known that the magnetic susceptibilities of some complex ions of the iron group transition elements differ considerably from those of simple salts containing the same metallic ions.* This has been explained by Van Vleck[2] as the effect of the break-down of the Russell-Saunders coupling caused by the very strong crystalline field. In the ferricyanides, for example, the $3d$ electron level splits into a higher doublet $d\gamma$ and a lower triplet $d\varepsilon$ under the influence of a large cubic field. The five $3d$ electrons of the central $Fe^{+++}$ ion must be housed in these $d\varepsilon$ states. Then the spins of two pairs of electrons cancel each other, and the ion shows the magnetic moment corresponding to one electron spin. According to this interpretation, magnetic moments of these complex ions are ascribed to the electron configurations $(d\varepsilon)^n$. This mechanism can account for the large reduction of magnetic moments of metallic ions in complex salts, but this simple theory usually predicts too low values of the magnetic moments, except in the case of $(d\varepsilon)^3$, as long as we take only spins into account. Moreover, the Curie's law is not obeyed in most of these paramagnetic complex salts, especially in lower temperatures. However, this discrepancy can be explained by taking into account the contribution of orbital magnetic moments, which are partly still alive in $d\varepsilon$-orbitals. This was pointed out by Kotani[3]. He calculated the magnetic moments for octahedral complex ions of the type $[MX_6]$ upon the assumption that the crystalline field has cubic symmetry. Usually, however, the macroscopic symmetry of paramagnetic crystal is monoclinic, rhombic, etc., and the local crystalline electric field, to which paramagnetic ions are subjected, is lower than cubic, even if the ligands would take strictly cubic arrangement. Moreover, in all cases where we have a degenerate orbital state for a cubic arrangement, some distortion should occur to remove the orbital degeneracy, in accordance with the theorem of Jahn-Teller[4]. Therefore, we may expect that the central magnetic ion is subjected to a crystalline field with symmetry lower than cubic.

From this standpoint, we are going to derive theoretical formulae for magnetic moments and $g$-values for electron configurations $(d\varepsilon)^n$ for all possible values of $n$, $1 \leq n \leq 5$ upon the assumption that the crystalline field is nearly cubic but has small tetragonal component or small trigonal component. For the field of rhombic symmetry, which is more general than the ones mentioned above, we can not obtain the expressions of magnetic moments and of $g$-values in closed forms.

---

* The first interpretation of this fact was given by Pauling[1] on the basis of the directed electron pair bond.

In the present study, we intend to derive results of more or less general character, which enable us to understand, at least qualitatively, the paramagnetic behaviour of the wide class of complex salts, rather than to carry out a detailed calculation for any particular substance.

This is the reason why we have assumed crystalline fields of tetragonal or trigonal symmetry and why we have put the crystalline field of rhombic symmetry aside in the present paper. In the present treatment the non-cubic part of the crystalline field contains a single parameter as far as we confine our attention to the crystalline field quadratic in the coordinates, and the effective number of Bohr magnetons is obtained as a function of two parameters, $x=\overline{r^2}A/7kT$ and $y=\lambda/2kT$, while $g$-values depend on a single parameter $t=\overline{r^2}A/\lambda$. This enables us to discuss the general behaviour of these quantities fairly easily. On the other hand, a detailed investigation about a particular complex salt will probably require a more careful formulation of the crystalline field, especially at low temperatures. Howard's calculation[5] of $K_3Fe(CN)_6$ is an example of the studies of this sort.

## § 2. General Procedure

If we neglect the exchange interaction between paramagnetic ions, each paramagnetic ion can assume its various substates according to Boltzmann's law, independently of other ions. Thus we have effectively "single ion problem," and the molar susceptibility can be calculated by the well-known formula[6]

$$\chi=\frac{L\sum\limits_{nm}[(E^{(1)}_{nm})^2/kT-2E^{(2)}_{nm}]\exp(-E^{(0)}_n/kT)}{\sum\limits_{nm}\exp(-E^{(0)}_n/kT)}\,, \tag{1}$$

where $L$ is Avogadro's number, $E^{(0)}_n$ is energy values under no applied magnetic field, $E^{(1)}_{nm}$ and $E^{(2)}_{nm}$ are coefficients of the 1st and 2nd order Zeeman energies respectively, defined by the relation

$$E_{nm}=E^{(0)}_n+E^{(1)}_{nm}H+E^{(2)}_{nm}H^2+\cdots\,. \tag{2}$$

On the other hand, the $g$-value can be derived from the coefficient of the 1st order Zeeman energy of the ground state.

In order to apply this general expression to the case of octahedral complex ions, we take the following Hamiltonian for the central ion

$$\mathscr{H}=\mathscr{H}_0+V_{\text{cubic}}+V' +\sum_i\{\lambda\boldsymbol{l}_i\cdot\boldsymbol{s}_i+\beta\boldsymbol{H}\cdot(\boldsymbol{l}_i+2\boldsymbol{s}_i)\}\,, \tag{3}$$

where $\mathscr{H}_0$ is the Hamiltonian of the free metallic ion without spin-orbit coupling, $V_{\text{cubic}}+V'$ is the electrostatic energy in the field of the neighbouring ions, $V_{\text{cubic}}$ having cubic symmetry and $V'$ tetragonal or trigonal symmetry, $\lambda$ is the constant of the spin-orbit interaction and $\boldsymbol{H}$ is the applied magnetic field.

Our calculation is based on the following assumptions:

(1) In the Hamiltonian (3) $V_{\text{cubic}}$ is dominant, that is, the cubic field is so strong that the level $d\gamma$ lies sufficiently high above $d\varepsilon$, and the central ion has the electron configuration $(d\varepsilon)^n$ only.

(2) $V'$ is of the form

$$V'=A\sum_i(3z_i^2-r_i^2)\,, \tag{4}$$

in the case of the field of tetragonal symmetry whose axis is $z$-axis, and

$$V'=2A\sum_i(x_iy_i+y_iz_i+z_ix_i)\,, \tag{4'}$$

in the case of the field of trigonal symmetry whose axis is in (1, 1, 1) direction. The general field of tetragonal or trigonal symmetry would contain other terms in addition to the ones mentioned above. We have neglected, however, these terms because these would be of higher orders.

(3) The tetragonal or trigonal term and the spin-orbit coupling are of comparable magnitude. The magnetic energy is always regarded as a small perturbation on these terms.

(4) The exchange coupling between paramagnetic ions is negligible.

## § 3. Calculation of Effective Magnetic Moments and $g$-values

We give in the following our results for each value of $n$ separately. As it is shown in Appendix, the results for the field of trigonal symmetry become equivalent to those for the field of tetragonal symmetry by replacing $A$ with $-A$. Consequently the results for trigonal symmetry may be obtained from the following results for the tetragonal symmetry by replacing $A$ with $-A$.

(1) In the absence of magnetic field the eigenvalues and degeneracies of each state are

found to be as follows:

(i) $(d\varepsilon)^1$

The sextet (orbital triplet with twofold spin degeneracy) level splits into three following Kramers' doublets.

$$E_1^{(0)}=\frac{2}{7}(\overline{r^2}A)-\frac{1}{2}\lambda \qquad \text{(doubly degenerate)},$$
$$E_2^{(0)}=-\frac{1}{7}(\overline{r^2}A)+\frac{1}{4}\lambda+\frac{3}{2}\sqrt{\frac{4}{49}(\overline{r^2}A)^2+\frac{2}{21}\lambda(\overline{r^2}A)+\frac{1}{4}\lambda^2} \qquad (\quad\text{〃}\quad), \qquad (5)$$
$$E_3^{(0)}=-\frac{1}{7}(\overline{r^2}A)+\frac{1}{4}\lambda-\frac{3}{2}\sqrt{\frac{4}{49}(\overline{r^2}A)^2+\frac{2}{21}\lambda(\overline{r^2}A)+\frac{1}{4}\lambda^2} \qquad (\quad\text{〃}\quad),$$

where $\overline{r^2}$ denotes $\int[f(r)]^2r^4dr$. Throughout our calculations, we have used the wave functions of the following form as unperturbed orbital wave functions:

$$\Psi_1=\sqrt{\frac{15}{4\pi}}\,f(r)yz/r^2\,,$$
$$\Psi_2=\sqrt{\frac{15}{4\pi}}\,f(r)xz/r^2\,,$$
$$\Psi_3=\sqrt{\frac{15}{4\pi}}\,f(r)xy/r^2\,.$$

These levels are shown graphically in Fig. 1. Six-fold degenerate level $d\varepsilon$ shown in (*a*) splits into three Kramers' doublets as shown in (*b*) when tetragonal field and spin-orbit interaction are taken into account, and (*c*) shows further splitting caused by the magnetic field applied along $z$-axis.

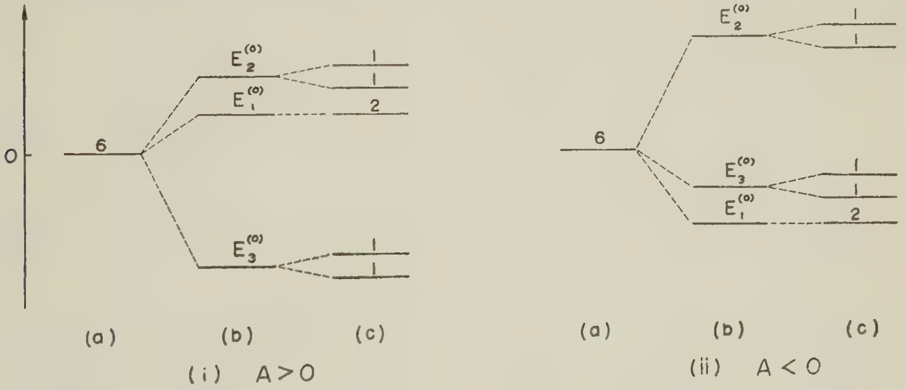

Fig. 1. A schematic energy-level diagram for $(d\varepsilon)^1$.

Assuming that $A$ is positive, the ground state is $E_3^{(0)}$, and as $A$ goes negative the ground state is $E_1^{(0)}$.

(ii) $(d\varepsilon)^5$

Since $(d\varepsilon)^6$ is a closed-shell configuration, energy levels for $(d\varepsilon)^5$ are obtained from formula (5) by reversing the signs of $A$ and $\lambda$, corresponding to a positive hole. In this case, the ground state is at

$$\frac{1}{7}(\overline{r^2}A)-\frac{1}{4}\lambda-\frac{3}{2}\sqrt{\frac{4}{49}(\overline{r^2}A)^2+\frac{2}{21}\lambda(\overline{r^2}A)+\frac{1}{4}\lambda^2}$$

irrespective of the sign of $A$.

(iii) $(d\varepsilon)^2$

Since Hund's rule holds in the present case[3)], the ground state belongs to $^3T_1$, which has nine-fold degeneracy. This nine-fold degeneracy is lifted partly by perturbation and we get the following levels:

$$E_1^{(0)}=-\frac{2}{7}(\overline{r^2}A)+\frac{1}{2}\lambda\,,$$
$$E_2^{(0)}=\frac{1}{7}(\overline{r^2}A)+\frac{1}{4}\lambda+\frac{1}{2}\sqrt{\left(\frac{6}{7}\overline{r^2}A-\frac{1}{2}\lambda\right)^2+2\lambda^2}\,,$$
$$E_3^{(0)}=\frac{1}{7}(\overline{r^2}A)+\frac{1}{4}\lambda-\frac{1}{2}\sqrt{\left(\frac{6}{7}\overline{r^2}A-\frac{1}{2}\lambda\right)^2+2\lambda^2}\,, \qquad (6)$$
$$E_4^{(0)}=-\frac{2}{7}(\overline{r^2}A)-\frac{1}{2}\lambda \qquad \text{(doubly degenerate)},$$

$$E_5^{(0)}=\frac{1}{7}(\overline{r^2}A)+\sqrt{\frac{9}{49}(\overline{r^2}A)^2+\frac{1}{4}\lambda^2} \qquad \text{(doubly degenerate)},$$

$$E_6^{(0)}=\frac{1}{7}(\overline{r^2}A)-\sqrt{\frac{9}{49}(\overline{r^2}A)^2+\frac{1}{4}\lambda^2} \qquad (\quad〃\quad).$$

These levels are shown graphically in Fig. 2. In this case the ground state is a doublet with energy $E_4^{(0)}$ for positive $A$ and a singlet with energy $E_3^{(0)}$ for negative $A$.

(iv) $(d\varepsilon)^4$

Energy levels for $(d\varepsilon)^4$ are obtained from $(d\varepsilon)^2$ by reversing the signs of $A$ and $\lambda$. The ground state is a singlet at

$$-\frac{1}{7}(\overline{r^2}A)-\frac{1}{4}\lambda-\frac{1}{2}\sqrt{\left(\frac{1}{2}\lambda-\frac{6}{7}\overline{r^2}A\right)^2+2\lambda^2}$$

irrespective of the sign of $A$.

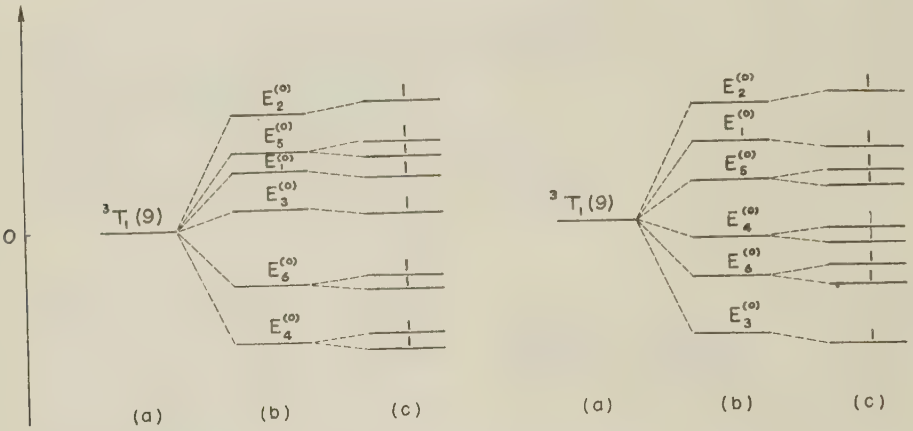

(i) $A>0$ (ii) $A<0$

Fig. 2. A schematic energy-level diagram for $(d\varepsilon)^2$.

(v) $(d\varepsilon)^3$

In this case the unperturbed state does not split, as long as we do not take account of the higher levels. Hence the orbital motion of electrons makes no contribution3).

(2) The $g$-values

We find the expressions for $g_{/\!/}$ and $g_\perp$ in the cases of $(d\varepsilon)^1$ and $(d\varepsilon)^5$.

(i) $(d\varepsilon)^1$

With positive $A$,

$$g_{/\!/}=2\left|\frac{1}{3\left(\frac{4}{49}t^2+\frac{2}{21}t+\frac{1}{4}\right)+\left(\frac{6}{7}t+\frac{1}{2}\right)\sqrt{\frac{4}{49}t^2+\frac{2}{21}t+\frac{1}{4}}}-1\right| \tag{7}$$

and

$$g_\perp=2\left|\frac{\frac{12}{49}t^2+\frac{1}{4}+\left(\frac{6}{7}t-\frac{1}{2}\right)\sqrt{\frac{4}{49}t^2+\frac{2}{21}t+\frac{1}{4}}}{3\left(\frac{4}{49}t^2+\frac{2}{21}t+\frac{1}{4}\right)+\left(\frac{6}{7}t+\frac{1}{2}\right)\sqrt{\frac{4}{49}t^2+\frac{2}{21}t+\frac{1}{4}}}\right|, \tag{8}$$

where $t=\overline{r^2}A/\lambda$.

With negative $A$, both $g_{/\!/}$ and $g_\perp$ give 0, because the doublet $E_1^{(0)}$ has no 1st order Zeeman energy both when the magnetic field is applied along $z$-axis and when the field is applied perpendicularly to $z$-axis.

(ii) $(d\varepsilon)^5$

Irrespective of the sign of $A$,

$$g_{//}=2\left|\frac{1}{3\left(\frac{4}{49}t^2+\frac{2}{21}t+\frac{1}{4}\right)-\left(\frac{6}{7}t+\frac{1}{2}\right)\sqrt{\frac{4}{49}t^2+\frac{2}{21}t+\frac{1}{4}}}-1\right| \tag{9}$$

and

$$g_{\perp}=2\left|\frac{\frac{12}{49}t^2+\frac{1}{4}-\left(\frac{6}{7}t-\frac{1}{2}\right)\sqrt{\frac{4}{49}t^2+\frac{2}{21}t+\frac{1}{4}}}{3\left(\frac{4}{49}t^2+\frac{2}{21}t+\frac{1}{4}\right)-\left(\frac{6}{7}t+\frac{1}{2}\right)\sqrt{\frac{4}{49}t^2+\frac{2}{21}t+\frac{1}{4}}}\right|. \tag{10}$$

The $g$-values for $(d\varepsilon)^1$ and $(d\varepsilon)^5$ are plotted in Figures 3 and 4 respectively, the variable parameter being $\overline{r^2}A/\lambda$.

Both $g_{//}$ and $g_{\perp}$ for $(d\varepsilon)^1$ converge to the same value 2, as the parameter $\overline{r^2}A/\lambda$ tends to infinity. On the other hand, $g_{//}$ and $g_{\perp}$ for $(d\varepsilon)^5$ converge to 4 and 0 respectively in the limit of large positive value of $\overline{r^2}A/\lambda$ and to the same value 2 in the limit of large negative value of $\overline{r^2}A/\lambda$.

$(d\varepsilon)^2$ will only give a paramagnetic resonance if $A$ is positive. In this case $g_{//}$ and $g_{\perp}$ give 2 and 0 respectively.

$(d\varepsilon)^4$ has a singlet ground state so that no resonance will be observed. This agrees with the experiment (see § 4).

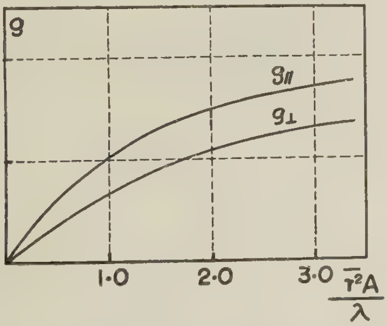

Fig. 3. The $g$-values for $(d\varepsilon)^1$ with positive $A$.

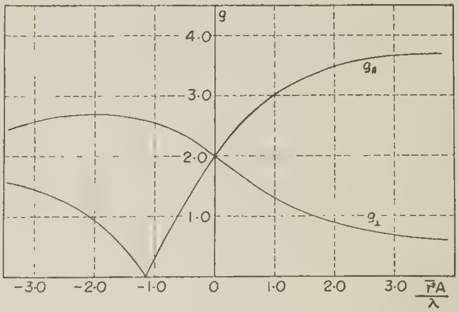

Fig. 4. The $g$-values for $(d\varepsilon)^5$.

(3) The magnetic moment

We give only our results for each value of $n$ separately. Now instead of susceptibility, we will use the effective Bohr magneton number $n_{\text{eff.}}$ which is connected with susceptibility through the relation $n^2_{\text{eff.}}=3kT\chi/L\beta^2$. We shall omit the diamagnetic term throughout our calculation. The experimental measurements of the susceptibilities of paramagnetic salts which we quote in the present paper are corrected for the diamagnetism.

(i) $(d\varepsilon)^1$

$$n^2_{\text{eff.}(//)}=\frac{3\left\{\frac{4y^2}{3\Lambda-(6x+y)\sqrt{\Lambda}}-1\right\}^2-\frac{4y^2}{\Lambda^{3/2}}+\left[3\left\{\frac{4y^2}{3\Lambda+(6x+y)\sqrt{\Lambda}}-1\right\}^2+\frac{4y^2}{\Lambda^{3/2}}\right]\exp(3\sqrt{\Lambda})}{1+\exp(3\sqrt{\Lambda})+\exp\left(-3x+\frac{3}{2}y+\frac{3}{2}\sqrt{\Lambda}\right)} \tag{11}$$

and

$$n^2_{\text{eff.}(\perp)}=\frac{3}{1+\exp(3\sqrt{\Lambda})+\exp\left(-3x+\frac{3}{2}y+\frac{3}{2}\sqrt{\Lambda}\right)}$$

$$\times\left[2\left\{\frac{4x^2-\frac{4}{3}xy+y^2-(2x-y)\sqrt{\Lambda}}{(-2x+y+\sqrt{\Lambda})\{3\Lambda-(6x+y)\sqrt{\Lambda}\}}\right.\right.$$

$$+\frac{4x^2-\frac{4}{3}xy+y^2+(2x-y)\sqrt{\Lambda}}{(-2x+y-\sqrt{\Lambda})\{3\Lambda+(6x+y)\sqrt{\Lambda}\}}\Bigg\}\exp\left(-3x+\frac{3}{2}y+\frac{3}{2}\sqrt{\Lambda}\right)$$

$$+\left\{\left(\frac{12x^2+y^2+(6x-y)\sqrt{\Lambda}}{3\Lambda+(6x+y)\sqrt{\Lambda}}\right)^2-2\frac{4x^2-\frac{4}{3}xy+y^2+(2x-y)\sqrt{\Lambda}}{(-2x+y-\sqrt{\Lambda})\{3\Lambda+(6x+y)\sqrt{\Lambda}\}}+\frac{(2x+y)^2}{3\Lambda^{3/2}}\right\}\exp(3\sqrt{\Lambda})$$

$$+\left(\frac{12x^2+y^2-(6x-y)\sqrt{\Lambda}}{3\Lambda-(6x+y)\sqrt{\Lambda}}\right)^2-2\frac{4x^2-\frac{4}{3}xy+y^2-(2x-y)\sqrt{\Lambda}}{(-2x+y+\sqrt{\Lambda})\{3\Lambda-(6x+y)\sqrt{\Lambda}\}}-\frac{(2x+y)^2}{3\Lambda^{3/2}}\Bigg], \tag{12}$$

where $\Lambda=4x^2+\frac{4}{3}xy+y^2$, $x=\frac{1}{7}\frac{\overline{r^2}A}{kT}$ and $y=\frac{1}{2}\frac{\lambda}{kT}$.

(ii) $(d\varepsilon)^2$

$$n^2_{\mathrm{eff.}(//)}=\frac{1}{2+e^{-2y}+e^{-\left(3x+\frac{3}{2}y+\frac{1}{2}\sqrt{u}\right)}+e^{-\left(3x+\frac{3}{2}y-\frac{1}{2}\sqrt{u}\right)}+2e^{-(3x+y+\sqrt{w})}+2e^{-(3x+y-\sqrt{w})}}$$

$$\times\Bigg[6+\left\{\frac{108y^2}{(v+\frac{1}{2}\sqrt{u})(2v^2+4y^2+v\sqrt{u})}+\frac{108y^2}{(v-\frac{1}{2}\sqrt{u})(2v^2+4y^2-v\sqrt{u})}\right\}e^{-2y}$$

$$-\frac{108y^2}{(v+\frac{1}{2}\sqrt{u})(2v^2+4y^2+v\sqrt{u})}e^{-\left(3x+\frac{3}{2}y+\frac{1}{2}\sqrt{u}\right)}-\frac{108y^2}{(v-\frac{1}{2}\sqrt{u})(2v^2+4y^2-v\sqrt{u})}e^{-\left(3x+\frac{3}{2}y-\frac{1}{2}\sqrt{u}\right)}$$

$$+6\left\{\left(2-\frac{3y^2}{2(w+3x\sqrt{w})}\right)^2-\frac{9y^2}{4w^{3/2}}\right\}e^{-(3x+y+\sqrt{w})}$$

$$+6\left\{\left(2-\frac{3y^2}{2(w-3x\sqrt{w})}\right)^2+\frac{9y^2}{4w^{3/2}}\right\}e^{-(3x+y-\sqrt{w})}\Bigg] \tag{13}$$

and

$$n^2_{\mathrm{eff.}(\perp)}=-\frac{6}{2+e^{-2y}+e^{-\left(3x+\frac{3}{2}y+\frac{1}{2}\sqrt{u}\right)}+e^{-\left(3x+\frac{3}{2}y-\frac{1}{2}\sqrt{u}\right)}+2e^{-(3x+y+\sqrt{w})}+2e^{-(3x+y-\sqrt{w})}}$$

$$\times\Bigg[-2\left\{\frac{(2y+3x+\sqrt{w})^2}{(3x+y+\sqrt{w})(4y^2+36x^2+12x\sqrt{w})}+\frac{(2y+3x-\sqrt{w})^2}{(3x+y-\sqrt{w})(4y^2+36x^2-12x\sqrt{w})}\right\}$$

$$+\left\{\frac{(2y-3x-\sqrt{w})^2}{(-3x+y-\sqrt{w})(4y^2+36x^2+12x\sqrt{w})}+\frac{(2y-3x+\sqrt{w})^2}{(-3x+y+\sqrt{w})(4y^2+36x^2-12x\sqrt{w})}\right\}e^{-2y}$$

$$+\left\{\frac{\{3y^2+2y(3x+\frac{1}{2}\sqrt{u})+4(3x+\frac{1}{2}\sqrt{u})(3x+\sqrt{w})\}^2}{2(\frac{1}{2}y+\frac{1}{2}\sqrt{u}-\sqrt{w})(4y^2+36x^2+12x\sqrt{w})(4y^2+2v^2+v\sqrt{u})}\right.$$

$$\left.+\frac{\{3y^2+2y(3x+\frac{1}{2}\sqrt{u})+4(3x+\frac{1}{2}\sqrt{u})(3x-\sqrt{w})\}^2}{2(\frac{1}{2}y+\frac{1}{2}\sqrt{u}+\sqrt{w})(4y^2+36x^2-12x\sqrt{w})(4y^2+2v^2+v\sqrt{u})}\right\}e^{-\left(3x+\frac{3}{2}y+\frac{1}{2}\sqrt{u}\right)}$$

$$+\left\{\frac{\{3y^2+2y(3x-\frac{1}{2}\sqrt{u})+4(3x-\frac{1}{2}\sqrt{u})(3x+\sqrt{w})\}^2}{2(\frac{1}{2}y-\frac{1}{2}\sqrt{u}-\sqrt{w})(4y^2+36x^2+12x\sqrt{w})(4y^2+2v^2+v\sqrt{u})}\right.$$

$$\left.+\frac{\{3y^2+2y(3x-\frac{1}{2}\sqrt{u})+4(3x-\frac{1}{2}\sqrt{u})(3x-\sqrt{w})\}^2}{2(\frac{1}{2}y-\frac{1}{2}\sqrt{u}+\sqrt{w})(4y^2+36x^2-12x\sqrt{w})(4y^2+2v^2-v\sqrt{u})}\right\}e^{-\left(3x+\frac{3}{2}y-\frac{1}{2}\sqrt{u}\right)}$$

$$+\left\{\frac{2(2y+3x+\sqrt{w})^2}{(3x+y+\sqrt{w})(4y^2+36x^2+12x\sqrt{w})}-\frac{(2y-3x-\sqrt{w})^2}{(-3x+y-\sqrt{w})(4y^2+36x^2+12x\sqrt{w})}\right.$$

$$
\begin{aligned}
&-\frac{\{3y^2+2y(3x+\frac{1}{2}\sqrt{u})+4(3x+\frac{1}{2}\sqrt{u})(3x+\sqrt{w})\}^2}{2(\frac{1}{2}y+\frac{1}{2}\sqrt{u}-\sqrt{w})(4y^2+36x^2+12x\sqrt{w})(4y^2+2v^2+v\sqrt{u})}\\
&\left.-\frac{\{3y^2+2y(3x-\frac{1}{2}\sqrt{u})+4(3x-\frac{1}{2}\sqrt{u})(3x+\sqrt{w})\}^2}{2(\frac{1}{2}y-\frac{1}{2}\sqrt{u}-\sqrt{w})(4y^2+36x^2+12x\sqrt{w})(4y^2+2v^2-v\sqrt{u})}\right\}e^{-(3x+y+\sqrt{w})}\\
&+\left\{\frac{2(2y+3x-\sqrt{w})^2}{(3x+y-\sqrt{w})(4y^2+36x^2-12x\sqrt{w})}+\frac{(2y-3x+\sqrt{w})^2}{(3x-y-\sqrt{w})(4y^2+36x^2-12x\sqrt{w})}\right.\\
&-\frac{\{3y^2+2y(3x+\frac{1}{2}\sqrt{u})+4(3x+\frac{1}{2}\sqrt{u})(3x-\sqrt{w})\}^2}{2(\frac{1}{2}y+\frac{1}{2}\sqrt{u}+\sqrt{w})(4y^2+36x^2-12x\sqrt{w})(4y^2+2v^2+v\sqrt{u})}\\
&\left.-\frac{\{3y^2+2y(3x-\frac{1}{2}\sqrt{u})+4(3x-\frac{1}{2}\sqrt{u})(3x-\sqrt{w})\}^2}{2(\frac{1}{2}y-\frac{1}{2}\sqrt{u}+\sqrt{w})(4y^2+36x^2-12x\sqrt{w})(4y^2+2v^2-v\sqrt{u})}\right\}e^{-(3x+y-\sqrt{w})}\Bigg], \qquad (14)
\end{aligned}
$$

where $u=(6x-y)^2+8y^2$, $v=3x-\frac{1}{2}y$ and $w=9x^2+y^2$.

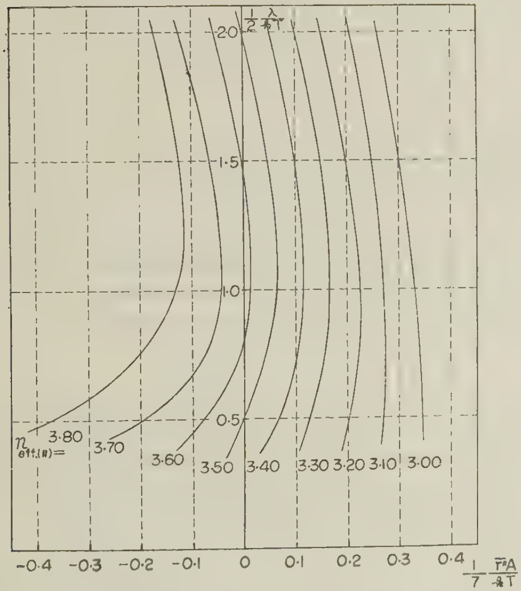

Fig. 5. $n_{\text{eff.}(\parallel)}$ for $(d\varepsilon)^4$.

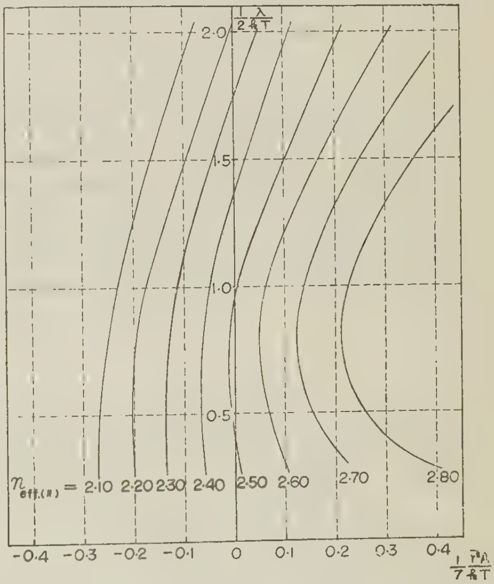

Fig. 6. $n_{\text{eff.}(\parallel)}$ for $(d\varepsilon)^5$.

(iii) $(d\varepsilon)^5$

The formulae for $(d\varepsilon)^5$ can be obtained from (11) and (12) by substituting $-x$ for $x$ and $-y$ for $y$.

(iv) $(d\varepsilon)^4$

The formulae for $(d\varepsilon)^4$ can be obtained from (13) and (14) by substituting $-x$ for $x$ and $-y$ for $y$.

The behaviour of $n_{\text{eff.}(\parallel)}$ in the cases of $(d\varepsilon)^4$ and $(d\varepsilon)^5$ is represented graphically in Figures 5 and 6.

## § 4. Discussion of the Result and Compairson with Experiment

We are going to discuss experimental results in the light of our theory. In this case it is desirable that there are experiments on complex salts in which each paramagnetic ion lies in the surrounding with exactly tetragonal or trigonal symmetry, but such experiments have not been reported.

At present, experiment on temperature dependence of susceptibility has been reported only both on $K_3Fe(CN)_6$ and on $K_3Mn(CN)_6$, which correspond to electron configurations $(d\varepsilon)^5$ and $(d\varepsilon)^4$ respectively.

In the following we shall discuss the results for each case separately.

$(d\varepsilon)^4$, $Mn^{3+}$. The magnetic susceptibility of potassium manganicyanide has been measured at temperature from 4.2°K to 300°K by Cooke and Duffus[7] for powdered specimen, while no paramagnetic resonance was detected by Bowers[8]. This agrees with our theory, as we mentioned in section 3.

Now we can not determine the symmetry of a crystalline field for this salt, because we have the experimental data only on the powdered specimen. By comparing with this experiment, however, we want to find the effect of the field with symmetry lower than cubic. We attempt to compare our theory, therefore, with experimental result by using the formula

$$n^2_{\text{eff.(average)}}=\frac{1}{3}n^2_{\text{eff.}(//)}+\frac{2}{3}n^2_{\text{eff.}(\perp)},$$

where $n^2_{\text{eff.}(//)}$ and $n^2_{\text{eff.}(\perp)}$ are given from the formulae (13) and (14) by substituting $-x$ for $x$ and $-y$ for $y$ respectively.

Best agreement is obtained by taking $\lambda/k=$ 410°K and $\overline{r^2}A/k=-287$°K. As is shown in Figure 7, the result of Kotani's calculation is improved by taking account of the field with lower symmetry.

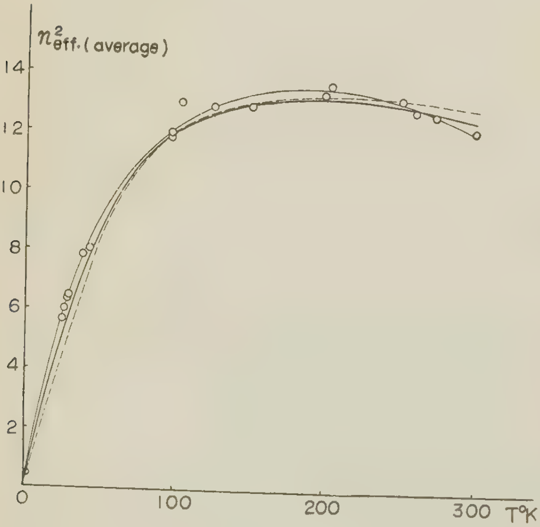

Fig. 7. Variation with temperature of the effective Bohr magneton number of potassium manganicyanide (powdered specimen). Experimental points are shown as circles. The solid curve represents the variation predicted by our theory. The broken curve shows the theoretical curve in the case of the field of cubic symmetry, taking $\lambda/k=410$°K.

The value obtained for $\lambda$ seems to be reasonable, since the spin-orbit coupling constant in the crystal may be smaller than the free ion value[9] ($\lambda/k=492$°K). A slight change (less than 10 percent) in parameter $A$ causes no appreciable difference in $n^2_{\text{eff.}}$.

$(d\varepsilon)^5$, $Fe^{3+}$. The susceptibility measurement on single crystal of $K_3Fe(CN)_6$, over the temperature range $T=300$°K to 90°K, was carried out by Jackson[10], while a single resonance line was found by Bleaney and Ingram[11]. The $g$-values have also rhombic symmetry, with values $a$-axis, 2.30; $b$-axis, 2.18; $c$-axis, 0.94. Here the accuracy is not very high because of the abnormally large line width.

Although the principal values of the magnetic susceptibility and of the $g$-value show that the symmetry of the local crystalline field to which the ion is subjected is rhombic, they suggest that the local field is very nearly axial in symmetry. Therefore, it is significant to use our theory in order to give a consistent and qualitative account of experimental results on the susceptibility and on the $g$-value.

If we want to place much weight in quantitative agreement, such a more detailed calculation as Howard[5] carried out will be required. Assuming the Hamiltonian of the form

$$\mathscr{H}=[Ax^2+By^2-(A+B)z^2]$$
$$+\lambda\boldsymbol{l}\cdot\boldsymbol{s}+\beta\boldsymbol{H}\cdot(\boldsymbol{l}+2\boldsymbol{s}),$$

Howard calculated the magnitude, anisotropy and temperature dependence of the principal magnetic susceptibilities of $K_3Fe(CN)_6$.

In his calculation, he set $A=E+\varDelta$ and $B=E-\varDelta$ and neglected the terms containing square or higher powers of $\varDelta$, assuming that $\varDelta$, the deviation from axial symmetry, is small compared with $E$, but as in the limit when $\varDelta=0$ and the crystalline field has axial symmetry the result of his theory does not reduce to that of our theory, his theory seems to require correction.

In comparing the results of our calculation with the experiment, $n^2_{\text{eff.}(c)}$ and $g_c$ have been taken as $n^2_{\text{eff.}(//)}$ and $g_{//}$ respectively. The values of the parameters are chosen to reproduce as nearly as possible both the correct magnitudes and correct temperature dependence of the susceptibilities. We thus obtained $\overline{r^2}A/k=-140$°K and $\lambda/k=700$°K, which yield $g_{//}=1.6$, $g_{\perp}=2.2$. Howard's theory has been revised by Bersohn[12], who finds that if the

$g$-values for the $a$- and $b$-axes are fitted, that for the $c$-axis comes to 1.5.

In figure 8 it may be seen that the magnitude and temperature dependence of the magnetic susceptibilities are fairly well reproduced by the theoretical results, but the experimental $g_c$ is much smaller than the value derived from our formula.

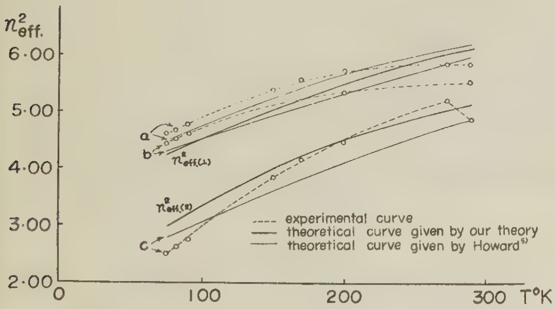

Fig. 8. Variation with temperature of the square of the effective Bohr magneton number $n_{\text{eff.}}$ corresponding to the principal axes $a$, $b$, $c$ of potassium ferricyanide.

If we adjust the parameters so as to get the good agreement with experiment for $n^2_{\text{eff.}(//)}$ and $g$-values, the experimental values for $n^2_{\text{eff.}(\perp)}$ show a large discrepancy with our theory.

The value obtained for $\lambda$ is fairly larger than $\lambda/k=635°\text{K}$, the value for the free $\text{Fe}^{3+}$ ion which was interpolated from the spectroscopic data of other iron group elements.

If we use the method of molecular orbital in this case, the orbital $g$-factor will be lower and the constant of the spin-orbit coupling will be reduced⁹⁾.

The discrepancy with experiment may be due to the following facts. Firstly, we have neglected the matrix elements connecting $d\gamma$ and $d\varepsilon$, because these elements are of higher order. Besides $(d\varepsilon)^n$, however, $(d\varepsilon)^{n-1}(d\gamma)$ or $(d\varepsilon)^{n-2}(d\gamma)^2$ may be included in some percentage in the ground state. Secondly, we have assumed the parameter $A$ is independent of temperature, though actually the parameter $A$ depends on temperature slightly.

The main purpose of the present paper is to explain, at least qualitatively, the paramagnetic behaviour of the wide class of complex salts. Unfortunately the available experimental data are not enough, but as was shown in this section the agreement of our theory with a few experiments is qualitatively fairly good.

It seems to us, however, that there is room for some refinements in our theory on the following ground.

In the present paper we have assumed the ideally ionic structure $\text{M}^{6-n}(\text{X}^-)_6$ for the complex ions of the type $[\text{MX}_6]^{-n}$, where M represents an iron group element and X represents a ligand such as CN, but actually the central ion has probably some covalent character. In other words, some of electrons which are assigned to X ions migrate into the central ion, and the amount of polarity is to be between $\text{M}^{6-n}(\text{X}^-)_6$ and $\text{M}^{-n}(\text{X})_6$.

We shall study this point by the use of molecular orbitals and we hope to obtain the clearer insight into the nature of intramolecular bonds in the complex ions.

## Acknowledgement

The author wishes to express his sincere thanks to Prof. M. Kotani for suggesting this problem and for his invaluable advice during the course of this work. The author is also very grateful to the members of Kotani Laboratory for their valuable discussions and the financial support.

## Appendix

In this appendix we prove that the results for the field of tetragonal symmetry become equivalent to those for the field of trigonal symmetry by changing the sign of the parameter $A$ denoting the coefficient of the quadratic term of a tetragonal crystalline potential.

It is known that within a manifold of states for which $\mathbf{L}$ is constant the matrix elements of potential operators are proportional to those of appropriate angular momentum operators¹³⁾.

For example, the matrix elements of the five quanties $3z^2-r^2$, $x^2-y^2$, $xy$, $yz$, $zx$ which we will now consider in detail are proportional to those of

$$3L_z^2-L^2,\ L_x^2-L_y^2,\ \tfrac{1}{2}(L_xL_y+L_yL_x),$$
$$\tfrac{1}{2}(L_yL_z+L_zL_y),\ \tfrac{1}{2}(L_zL_x+L_xL_z) \quad \text{(A1)}$$

within a manifold for which $\mathbf{L}$ is constant.

Now by comparing the corresponding matrix elements we can show that the matrix elements of the five quantities (A1) and of the components of $\mathbf{L}$ in the $d\varepsilon$ sub-space whose basic states diagonalize the potential of cubic field are proportional to those of the same expressions in the $p$ space whose basic states are real.

Thus

$$\left.\begin{aligned}
&[3L_z^2-L^2]_{d\varepsilon\text{ sub-space}}=-3[3L_z^2-L^2]_{p\text{ space}}\,,\\
&[L_x^2-L_y^2]_{d\varepsilon\text{ sub-space}}=-3[L_x^2-L_y^2]_{p\text{ space}}\,,\\
&[\tfrac{1}{2}(L_xL_y+L_yL_x)]_{d\varepsilon\text{ sub-space}}=3[\tfrac{1}{2}(L_xL_y+L_yL_x)]_{p\text{ space}}\,,\\
&[\tfrac{1}{2}(L_yL_z+L_zL_y)]_{d\varepsilon\text{ sub-space}}=3[\tfrac{1}{2}(L_yL_z+L_zL_y)]_{p\text{ space}}\,,\\
&[\tfrac{1}{2}(L_zL_x+L_xL_z)]_{d\varepsilon\text{ sub-space}}=3[\tfrac{1}{2}(L_zL_x+L_xL_z)]_{p\text{ space}}\,,
\end{aligned}\right\}\qquad\langle\mathrm{A2}\rangle$$

$$\left.\begin{aligned}
&[L_x]_{d\varepsilon\text{ sub-space}}=-[L_x]_{p\text{ space}}\,,\quad [L_y]_{d\varepsilon\text{ sub-space}}=-[L_y]_{p\text{ space}}\,,\\
&[L_z]_{d\varepsilon\text{ sub-space}}=-[L_z]_{p\text{ space}}\,,
\end{aligned}\right\}\qquad\langle\mathrm{A3}\rangle$$

where the components of the orbital angular momentum are represented in the $p$ space by the matrices

$$[L_x]_{p\text{ space}}=\begin{pmatrix}0&0&0\\0&0&-i\\0&i&0\end{pmatrix},\quad [L_y]_{p\text{ space}}=\begin{pmatrix}0&0&i\\0&0&0\\-i&0&0\end{pmatrix},\quad [L_z]_{p\text{ space}}=\begin{pmatrix}0&-i&0\\i&0&0\\0&0&0\end{pmatrix}.\qquad\langle\mathrm{A4}\rangle$$

In numbering the equation throughout this appendix, we will use an angular parentheses rather than a round one to enclose the number, in case the equation represents an equivalence between entire matrices rather than between ordinary algebraic quantities.

From the operator equivalence given in ⟨A2⟩ and ⟨A3⟩, it follows that the matrix of Hamiltonian (3) with (4) in the $d\varepsilon$ sub-space can be expressed by using the matrix of the orbital angular momentum in the $p$ space; that is,

$$\begin{aligned}
\mathscr{H}_{\text{tetragonal}}&=[V_{\text{cubic}}+\sum_i\{A(3z_i^2-r_i^2)+\lambda\boldsymbol{l}_i\cdot\boldsymbol{s}_i+\beta\boldsymbol{H}\cdot(\boldsymbol{l}_i+2\boldsymbol{s}_i)\}]_{D_2\text{ space}}\\
&=[V_{\text{cubic}}+\sum_i\{\alpha\overline{r^2}A(3l_{zi}^2-l_i^2)+\lambda\boldsymbol{l}_i\cdot\boldsymbol{s}_i+\beta\boldsymbol{H}\cdot(\boldsymbol{l}_i+2\boldsymbol{s}_i)\}]_{D_2\text{ space}}\\
&=\text{const.}+[\sum_i\{\alpha\overline{r^2}A(3l_{zi}^2-l_i^2)+\lambda\boldsymbol{l}_i\cdot\boldsymbol{s}_i+\beta\boldsymbol{H}\cdot(\boldsymbol{l}_i+2\boldsymbol{s}_i)\}]_{d\varepsilon\text{ sub-space}}\\
&=\text{const.}+\sum_i\{-3\alpha\overline{r^2}A(3l_{pzi}^2-l_{pi}^2)-\lambda\boldsymbol{l}_{pi}\cdot\boldsymbol{s}_i+\beta\boldsymbol{H}\cdot(-\boldsymbol{l}_{pi}+2\boldsymbol{s}_i)\}\,,
\end{aligned}\qquad\langle\mathrm{A5}\rangle$$

where $\alpha=-\dfrac{2}{21}$, $\overline{r^2}=\int[f(r)]^2r^4dr$ (see (5)), $\mathbf{l}_p$ is the orbital angular momentum, with the total value $\mathbf{l}_p^2=2$, and its components are represented by matrices ⟨A4⟩.

If we take $z'$-axis along the (1, 1, 1) direction, Hamiltonian (3) with (4′) becomes

$$\mathscr{H}_{\text{trigonal}}=V_{\text{cubic}}+\sum_i[A(3z_i'^2-r_i^2)+\lambda\boldsymbol{l}_i'\cdot\boldsymbol{s}_i'+\beta\boldsymbol{H}'\cdot(\boldsymbol{l}_i'+2\boldsymbol{s}_i')]\,,\qquad(\mathrm{A6})$$

where prime denotes the quantities whose components are taken along the $x'$, $y'$, $z'$-axis.

By using the fact that

$$[L_{z'}^2]_{d\varepsilon\text{ sub-space}}=[\tfrac{1}{3}(L_x+L_y+L_z)^2]_{d\varepsilon\text{ sub-space}}=3[L_{z'}^2]_{p\text{ space}}\qquad\langle\mathrm{A7}\rangle$$

the matrix of Hamiltonian (A6) in the $d\varepsilon$ sub-space whose basic states diagonalize the potential of cubic field can also be expressed by using the matrix of the orbital angular momentum in $p$ space, that is,

$$\begin{aligned}
\mathscr{H}_{\text{trigonal}}&=[V_{\text{cubic}}+\sum_i\{A(3z_i'^2-r_i'^2)+\lambda\boldsymbol{l}_i'\cdot\boldsymbol{s}_i'+\beta\boldsymbol{H}'\cdot(\boldsymbol{l}_i'+2\boldsymbol{s}_i')\}]_{D_2\text{ space}}\\
&=[V_{\text{cubic}}+\sum_i\{\alpha\overline{r^2}A(3l_{z'i}^2-l_i^2)+\lambda\boldsymbol{l}_i'\cdot\boldsymbol{s}_i'+\beta\boldsymbol{H}'\cdot(\boldsymbol{l}_i'+2\boldsymbol{s}_i')\}]_{D_2\text{ space}}\\
&=\text{const.}+[\sum_i\{\alpha\overline{r^2}A(3l_{z'i}^2-l_i^2)+\lambda\boldsymbol{l}_i'\cdot\boldsymbol{s}_i'+\beta\boldsymbol{H}'\cdot(\boldsymbol{l}_i'+2\boldsymbol{s}_i')\}]_{d\varepsilon\text{ sub-space}}\\
&=\text{const.}+\sum_i3\alpha\overline{r^2}A(3l_{pz'i}^2-l_{pi}^2)-\lambda\boldsymbol{l}_{pi}'\cdot\boldsymbol{s}_i'+\beta\boldsymbol{H}'\cdot(-\boldsymbol{l}_{pi}'+2\boldsymbol{s}_i')\}\,.
\end{aligned}\qquad\langle\mathrm{A8}\rangle$$

As Hamiltonian ⟨A5⟩ and ⟨A8⟩ are the same in structure except in the sign of $A$, they give the same eigenvalues except in the sign of $A$.

We have thus found that the elements of potential operators of the second degree in the $d\mathcal{E}$ sub-space are proportional to the matrix elements of similar operators in which $x$, $y$ and $z$ are everywhere replaced by $l_{px}$, $l_{py}$ and $l_{pz}$. This holds not only in $d\mathcal{E}$ sub-space but also for the representation $T_1$ and $T_2$ which arise from the single $f$ electron level under the influence of a cubic field.

### References

1) L. Pauling: J. Am. Chem. Soc. **53** (1931) 1367.
2) J. H. Van Vleck: J. Chem. Phys. **3** (1935) 807.
3) M. Kotani: J. Phys. Soc. Japan **4** (1949) 293.
4) H. A. Jahn and E. Teller: Proc. Roy. Soc. **A 161** (1937) 220; J. H. Van Vleck: J. Chem. Phys. **7** (1939) 72.
5) J. B. Howard: J. Chem. Phys. **3** (1935) 813.
6) J. H. Van Vleck: *The Theory of Electric and Magnetic Susceptibilities* (Clarendon Press, Oxford, 1932).
7) A. H. Cooke and H. J. Duffus: Proc. Phys. Soc. **A 68** (1955) 32.
8) K. D. Bowers: Proc. Phys. Soc. **A 65** (1952) 860.
9) K. W. H. Stevens: Proc. Roy. Soc. **A 219** (1953) 542.
10) L. C. Jackson: Proc. Roy. Soc. **A 140** (1933) 695.
11) B. Bleaney and D. J. E. Ingram: Proc. Phys. Soc. **A 65** (1952) 953.
12) R. Bersohn: Thesis, Harvard University (1949).
13) K. W. H. Stevens: Proc. Phys. Soc. **A 65** (1952) 209; B. Bleaney and K. W. H. Stevens: Reports on Progress in Physics **XIV** (1953) 108.

---

JOURNAL OF THE PHYSICAL SOCIETY OF JAPAN Vol. 11, No. 11, NOVEMBER, 1956

# On Rayleigh's Problem for a General Cylinder

By J. C. COOKE

*Department of Mathematics University of Malaya*

(Received June 5, 1956)

Rayleigh's problem, solved by Hasimoto for a general cylinder moving parallel to its length, is solved for small $\xi^2=4\nu t/R^2$, where $R$ is the radius of curvature of the section, in a series in $\xi$, by a different and more straightforward method which exhibits the velocity distribution at any point explicity. Five terms of the series are given and the skin friction is evaluated. This agrees to four terms with Hasimoto's result, which is as far as he gave the series.

## § 1. Introduction

Hasimoto[1,2], in two important papers, has solved in series the problem of an infinite cylinder of general section started from rest in a viscous fluid with speed $W$ parallel to the generators, this speed being afterwards maintained constant. It is also a heat conduction problem if the cylinder is maintained at a constant temperature $W$ when surrounded by an infinite medium whose initial temperature was zero. The first attempt at a solution was made by Batchelor[3], but he was only able to give the first two terms of the series for small time $t$ and the first term for large $t$. Hasimoto gave a series for the drag at small $t$ and another series for large $t$, but his solution cannot easily be used to calculate the actual velocity distribution in the fluid at any point in the case of small $t$.

It is the purpose of this note to solve the problem in this case, in a direct manner, in the form of a series which gives the velocity at any point of the fluid. The series for the skin friction comes out to be the same as that of Hasimoto.

Indeed this paper serves mainly as an appendex to Hasimoto's work, but gives perhaps a clearer physical picture of what actually happens in the fluid.

## § 2. The Problem

The equation to be solved for the velocity $w$, parallel to the generators is

$$\frac{\partial w}{\partial t}=\nu\Delta w\,,$$

with $w=W$ on the cylinder for $t>0$, $w=0$ everywhere when $t=0$, and $w=0$ at infinite distance from the cylinder.

Putting $\psi=w/W$ the equation to be solved is

$$\psi_t=\nu\Delta\psi\,, \tag{1}$$

with $\psi=1$ on the cylinder for $t>0$, $\psi=0$ when $t=0$, and $\psi=0$ at infinity.

## § 3. The Coordinate System

Proceeding slightly differently from Hasimoto we take an orthogonal coordinate system $y$, $z$, $\theta$ where $z$ is distance measured along the cylinder, the planes $z=$constant being right cross-sections. The surfaces $\theta=$constant are planes through the generators normal to the cylinder, and we shall take $\theta$ to be the angle a plane makes with some fixed plane belonging to the family. The cylinder belongs to a family of parallel surfaces $y=$constant; we take $y=0$ to be the given cylinder and $y$ to be distance along a normal to the cylinder. If in the section by the plane $z=$constant the radius of curvature of the curve $y=0$ is $R$, then we can take in general

$$ds^2=dy^2+dz^2+(R+y)^2d\theta^2\,.$$

We shall write $r=R+y$. $R$ is a function of $\theta$ only.

$\psi$ is of course independent of $z$. With this system the equation (1) becomes

$$\frac{1}{\nu}\frac{\partial\psi}{\partial t}=\frac{1}{r}\frac{\partial}{\partial y}\left(r\frac{\partial\psi}{\partial y}\right)+\frac{1}{r}\frac{1}{\partial\theta}\left(\frac{1}{r}\frac{\partial\psi}{\partial\theta}\right). \tag{2}$$

For flow due to a circular cylinder the equation is of the same form, except that there is no last term. This term thus represents the effect of the fact that the cylinder is not circular.

## § 4. Solution as a Series for Small $t$

We put

$$\xi=2(\nu t)^{\frac{1}{2}}/R,\quad \eta=\frac{1}{2}(\nu t)^{-\frac{1}{2}}y,\quad r=R+y\,, \tag{3}$$

$$\psi=f_0(\eta,\theta)+\xi f_1(\eta,\theta)+\xi^2 f_2(\eta,\theta)+\cdots \tag{4}$$

We substitute in equation (2), multiply by $4\nu t(=\xi^2R^2)$, and equate coefficients of powers of $\xi$. This is laborious but straightforward. Where $R/r$ and its square and cube appear we may use the relation

$$\frac{r}{R}=1+\xi\eta$$

and expand formally its inverse first, second and third powers. This expansion is formal only and can be avoided by multiplying the equation throughout by $(r/R)^3$, when the Binomial series become finite, but effectively the same results are obtained by either procedure, though they may *appear* different.

Proceeding in this way we obtain the following equations:—

$$f_0''+2\eta f_0'=0\,, \tag{5}$$

$$f_1''+2\eta f_1'-2f_1=-f_0'\,, \tag{6}$$

$$f_2''+2\eta f_2'-4f_2=\eta f_0'-f_1'\,, \tag{7}$$

$$\begin{aligned}f_3''+2\eta f_3'-6f_3=-f_2'+\eta f_1'-\eta^2 f_0'\\ +(a'-2a^2)f_1\,,\end{aligned} \tag{8}$$

$$\begin{aligned}f_4''+2\eta f_4-8f_4=-f_3'+\eta f_2'-\eta^2 f_1'\\ +\eta^3 f_0'-(6a^2-2a')f_2+(5a^2-2a')\eta f_1\,,\end{aligned} \tag{9}$$

where primes attached to each $f$ denote partial differentiation with respect to $y$, and $a=R'/R$, the prime here being a total differentiation with respect to $\theta$.

The boundary conditions, holding as they do for all $\xi$, lead to $f_0(0)=1$, $f_s(0)=0$ for $s\geq 1$, $f_s(\infty)=0$ for $s\geq 0$.

In the equations certain properties of the function $f$ appear. For instance equation (5), together with boundary conditions holding for all $\theta$, shows that $f_0$ is independent of $\theta$ and consequently its partial derivatives with respect to $\theta$ which occur multiplied by $\xi^2$ or $\xi^3$ do not appear in equation (7). In a similar way the partial derivatives of $f_1$ and $f_2$ with respect to $\theta$ do not appear in equations (8) and (9). The partial derivatives with respect to $\theta$ of $f_3$, $f_4$, etc. will greatly add to the complication in the equations for $f_5$, $f_6$, etc.

We notice further that the first three terms of the series are the same as if the last term in equation (2) were omitted. In other words they are the same functions as would be obtained if the cylinder were circular and of radius $R$. The was pointed out by Hasimoto, though Batchelor had shown that the first *two* terms were the same.

## § 5. Properties of the Error Function

Before solving the above equations we recapitulate here some properties of the Error function following Carslaw and Jaegar[4]. Using their notation we define

$$i^0 \operatorname{erfc} x = \operatorname{erfc} x = \frac{2}{\sqrt{\pi}} \int_x^\infty e^{-t^2} dt \,,$$

$$i^n \operatorname{erfc} x = \int_x^\infty i^{n-1} \operatorname{erfc} t dt \,,$$

where $n$ is a positive integer. Differentiation with respect to $x$ is equivalent to multiplying by $-i^{-1}$. We may extend this for negative $n$. Thus

$$i^{-1} \operatorname{erfc} x = -\frac{d}{dx} (\operatorname{erfc} x) = \frac{2}{\sqrt{\pi}} e^{-x^2} \,,$$

and so on.

The recurrence relation

$$2xi^{n-1} \operatorname{erfc} x = i^{n-2} \operatorname{erfc} x - 2ni^n \operatorname{exfc} x \,, \qquad (10)$$

given by Carslaw and Jaegar, holds for negative $n$ as well as positive, as does the formula

$$i^n \operatorname{erfc} 0 = \frac{1}{2^n \Gamma\left(\frac{1}{2} n+1\right)} \,. \qquad (11)$$

Note that $i^n \operatorname{erfc} \infty = 0$ for all integral $n$, positive or negative.

Finally we note that $y = i^n \operatorname{erfc} x$ is a solution of the differential equation

$$y'' + 2xy' - 2ny' = 0 \,.$$

The functions are tabulated by Carslaw and Jaegar for each $n$ between $-2$ and 6.

For convenience we shall sometimes write $i^n$ as an operator.

## § 6. The Solution of the Equations

The solution of equation (5), satisfying the boundary conditions, is

$$f_0 = \operatorname{erfc} \eta \,.$$

Hence $f_0'(0) = -2/\sqrt{\pi}$ by equation (11). Making use of this result and writing

$$f_1 = (Ai + Bi^{-1}) \operatorname{erfc} \eta \,,$$

which satisfies the boundary condition at infinity, we find on substituting in equation (6), that

$$-4Bi^{-1} \operatorname{erfc} \eta = i^{-1} \operatorname{erfc} \eta \,,$$

and so $B = -1/4$. Using the boundary condition $f_1(0) = 0$ and equation (11) we obtain $A = 1/2$. Hence the solution of equation (6) is

$$f_1 = \left(\frac{1}{2} i - \frac{1}{4} i^{-1}\right) \operatorname{erfc} \eta \,.$$

Hence

$$f_1'(0) = \left(-\frac{1}{2} + \frac{1}{4} i^{-2}\right) \operatorname{erfc} 0 = -\frac{1}{2} \,.$$

Continuing in this way we obtain

$$f_2 = \left(\frac{1}{2} i^2 - \frac{1}{8} + \frac{3}{32} i^{-2}\right) \operatorname{erfc} \eta \,,$$

and consequently $f_2'(0) = 1/8\sqrt{\pi}$;

$$f_3 = \left(\frac{9}{8} i^3 - \frac{1}{4} i - \frac{3}{64} i^{-1} - \frac{5}{128} i^{-3}\right) \operatorname{erfc} \eta$$

$$-R^3 \frac{d^2}{ds^2}\left(\frac{1}{R}\right)\left(\frac{3}{8} i^3 - \frac{1}{8} i + \frac{1}{32} i^{-1}\right) \operatorname{erfc} \eta$$

In the last equation we have used the result, easily proved, that

$$a' - 2a^2 = -R^3 \frac{d^2}{ds^2}\left(\frac{1}{R}\right) .$$

where $ds (= Rd\theta)$ is the element of length of a section of the cylinder.

Hence we have

$$f_3'(0) = -\frac{1}{32} - \frac{1}{32} R^3 \frac{d^2}{ds^2}\left(\frac{1}{R}\right) .$$

Again

$$f_4 = \left\{\left(\frac{13}{4} + \frac{13}{4} a' - \frac{17}{2} a^2\right) i^4 + \left(-\frac{25}{32} - \frac{27}{32} a' + \frac{35}{16} a^2\right) i^2 \right.$$

$$+ \left(\frac{3}{32} + \frac{7}{64} a' - \frac{1}{4} a^2\right) + \left(\frac{25}{254} - \frac{5}{128} a' + \frac{5}{48} a^2\right) i^{-2}$$

$$\left. + \frac{35}{2048} i^{-4}\right\} \operatorname{erfc} \eta \,.$$

Hence we may show that

$$\sqrt{\pi} \, f_4'(0) = \frac{25}{768} - \frac{7}{94} (a' - 2a^2) \,.$$

All the functions given here are tabulated by Carslaw and Jaegar except $i^{-3} \operatorname{erfc} \eta$ and $i^{-4} \operatorname{erfc} \eta$ which may be calculated directly, or or from equation (10).

## § 7. The Skin Friction

The skin friction $\tau$, is given by

$$\tau = -\mu \left(\frac{\partial w}{\partial y}\right)_{y=0} .$$

Hence we have

$$\frac{\tau}{\mu W} = -\frac{1}{2} (\nu t)^{-1/2} \{f_0'(0) + \xi f_1'(0) + \xi^2 f_2'(0) + \cdots\}$$

$$= \frac{1}{(\pi \nu t)^{1/2}} + \frac{1}{2R} - \left(\frac{\nu t}{\pi}\right)^{1/2} \frac{1}{4R^2}$$

$$+ \frac{\nu t}{8} \left\{\frac{1}{R^3} + \frac{d^2}{ds^2}\left(\frac{1}{R}\right)\right\}$$

$$- \frac{(\nu t)^{3/2}}{\pi^{1/2}} \left\{\frac{25}{96R^4} + \frac{7}{12R} \frac{d^2}{ds^2}\left(\frac{1}{R}\right)\right\} \cdots$$

which is Hasimoto's result with an additional term.

### References

1) H. Hasimoto: J. Phys. Soc. Japan **9** (1954) 611.
2) H. Hasimoto: J. Phys. Soc. Japan **10** (1955) 397.
3) G. K. Batchelor: Quart. J. Mech. and Appl. Math. **7** (1954) 179.
4) H. S. C. Carslaw and J. C. Jaegar: The Conduction of Heat in Solids, (1947) Oxford.

---

JOURNAL OF THE PHYSICAL SOCIETY OF JAPAN Vol. 11, No. 11, NOVEMBER, 1956

# Effective Use of Radiation and Thermal Shields in a Vacuum Furnace

By Yoshikazu ISHIKAWA and Shozo SAWADA

*Institute of Science and Technology, University of Tokyo, Tokyo, Japan*

(Received July 17, 1956)

A method for calculating the efficiency of several sheets of thick radiation shields with finite thermal conductivity is presented. It is shown that in case of shields having infinite conductivity, the efficiency and temperatures of the shields are expressed by simple formulas. It is shown by several examples of this method of calculations that the most important factors for the efficiency are found to be emissivity, thermal conductivity of the innermost shield and its position. Effectiveness of a shield with small conductivity, which we call 'thermal shield' in this paper, especially at high temperature is emphasized. Several experimental results are shown; they agree satisfactorily with the calculations.

## §1. Introduction

Recently, a group of compounds such as TiC or ZrC which have a high melting point and can only be sintered at very high temperatures (usually above 2000°C) have come to attract much attention from the view point of solid state physics, and a high temperature vacuum furnace is required to investigate these materials. In constructing the high temperature vacuum furnace, the heat efficiency must be good. Radiation shields are, as is well known, used for this purpose, and methods of calculating the efficiency of shields with infinite conductivity have been given by several authors.[1)2)3)4)] But no general considerations have been published under what conditions they are effective. This problem may become very important, especially when required temperature is very high.

Furthermore, when we use radiation shields with poor thermal conductivity, which we call 'thermal shield' and distinguish from 'radiation shield' which means a shield with infinite conductivity, it is naturally expected that they would give the better efficiency. It is therefore desirable to study how they are effective compared with radiation shields.

This paper describes at first a method of calculating the efficiency of several thick radiation shields with finite conductivity, and shows that in case of shields with infinite conductivity, the efficiency and their temperatures are expressed by very simple formulas. Then, applying them to some special cases, several conditions which are required in order to use the shields most effectively will be obtained.

## §2. Theoretical Calculation

Although the authors will treat here only a case where long cylindrical shields are concentrically placed surrounding a long co-axial heat source, corresponding to many practical cases, the idea can easily be extended to more general cases.

Suppose, as shown in Fig. 1, that a source and $n$ sheets of shields are kept in thermal equilibrium. Then, the equilibrium condition is expressed by

$$Q_n = Q^{01} = Q^1 = Q^{12} = \cdots = Q^{i-1i}$$

$$=Q^{i}=Q^{ii+1}=\cdots=Q^{n}=Q^{n\to}\,, \tag{1}$$

where $Q^{ii+1}$ means the total radiation flow per unit time and per unit length from the $i$-th shield to the $i+1$-th one and $Q^{i}$ is the heat flow in the $i$-th shield by conduction, which is easily calculated for the present case and is given by

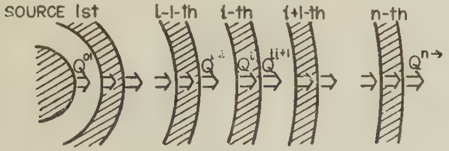

Fig. 1. Equilibrium diagram of the heat flow in a furnace.

$$Q^{i}=2\pi\kappa_i(T_i-T_i')/\log r_i'/r_i\,, \tag{2}$$

where $T_i$, $T_i'$ and $r_i$, $r_i'$ are respectively temperatures and radii of the inner and outer surfaces of the $i$-th shield and $\kappa_i$ is its thermal conductivity. $Q^{ii+1}$ can be calculated considering multiple reflections between $i$-th and $i+1$-th shields by the procedure of Braun and Busch, although some errors in their paper[4] must be corrected.

The radiation emitted from the outer surface of the $i$th shield per unit time is, according to the Stefan- Boltzmann's law, $q_0^{ii+1}=\sigma A_i'S_i'T_i'^4$ ($A_i'$ and $S_i'$ are emissivity and area of the outer surface and $\sigma$ is Stefan-Boltzmann's constant), which is diffusely reflected on the $i+1$-th shield which has an emissivity $A_{i+1}$. If we assume $f_{ii+1}$ times of the radiation which leaves the $i+1$-th shield is incident on the $i$-th shield, $f_{ii+1}(1-A_{i+1})q_0^{ii+1}$ comes back to the $i$-th shield and then $(1-A_i')(1-A_{i+1})f_{ii+1}q_0^{ii+1}$ is reflected again on the $i$-th shield and reaches the $i+1$-th shield. The radiation which dose not reach the $i$-th sield at the first reflection on the $i+1$-th shield is $(1-f_{ii+1})(1-A_{i+1})q_0^{ii+1}$. Then, the radiation which reaches $i+1$-th from $i$-th in the second process is given by

$$\begin{aligned}q_1^{ii+1}&=(1-A_i')(1-A_{i+1})f_{ii+1}q_0^{ii+1}\\&\quad+(1-f_{ii+1})(1-A_{i+1})q_0^{ii+1}\\&=(1-f_{ii+1}A_i')(1-A_{i+1})q_0^{ii+1}\\&\equiv c_{ii+1}q_0^{ii+1}\,.\end{aligned}$$

Repeating this procedure, the radiation from $i$-th to $i+1$-th in the $n+1$-th process is generally given by

$$q_n^{ii+1}=c_{ii+1}{}^{n}q_0^{ii+1}.$$

Then, the total radiation which $i+1$-th absorbs from $i$-th is

$$q^{ii+1}=A_{i+1}\sum_{n=0}^{\infty}q_n^{ii+1}=A_{i+1}q_0^{ii+1}\sum_{n=0}^{\infty}c_{ii+1}{}^{n}=\frac{A_{i+1}q_0^{ii+1}}{1-c_{ii+1}}$$

In the same manner, the radiation which $i$-th absorbs from $i+1$-th is found to be

$$q^{i+1i}=\frac{A_i'q_0^{i+1i}f_{ii+1}}{1-c_{ii+1}}\,.$$

Hence, $Q^{ii+1}$ defined above is given by

$$\begin{aligned}Q^{ii+1}=q^{ii+1}-q^{i+1i}&=\frac{A_{i+1}q_0^{ii+1}}{1-c_{ii+1}}-\frac{A_i'q_0^{i+1i}f_{ii+1}}{1-c_{ii+1}}\\&=\frac{\sigma A_i'A_{i+1}}{1-c_{ii+1}}(S_i'T_i'^4-S_{i+1}f_{ii+1}T_{i+1}^4)\,.\end{aligned} \tag{3}$$

$f_{ii+1}$ can be shown generally to be $S_i'/S_{i+1}$, if the $i+1$-th shield surrounds the $i$-th sheild completely and two surfaces concerned have curvatures of the same sign,[2] which is equal to $r_i'/r_{i+1}$ in our case. Putting this value and $S_i=2\pi r_i$ into Eq. (3), $Q^{ii+1}$ can be written as

$$Q^{ii+1}=\frac{2\pi\sigma(T_1'^4-T_{i+1}^4)}{\dfrac{B_i'}{r_i'}+\dfrac{B_{i+1}-1}{r_{i+1}}}\,, \tag{4}$$

where $B_i$ is the reciprocal of $A_i$.

Using Eqs. (1), (2) and (4), we obtain $2n$ simultaneous equations for $T_i$, $T_i'$ ($i=1, 2, \cdots, n$), the temperature of the source $T_0$ and the power $Q_n$ required to maintain the source at this temperature being two parameters. Or, on the contrary, if a boundary condition is given on the outer surface of the $n$-th shield, the efficiency and temperatures of shields are obtained numerically as functions of $T_0$.

When, as a special case, the shields have infinite conductivity, these equations can be reduced to

$$\begin{aligned}Q_n&=\frac{2\pi\sigma(T_0^4-T_1^4)}{\dfrac{B_0'}{r_0'}+\dfrac{B_1-1}{r_1}}=\cdots\frac{2\pi\sigma(T_{i-1}^4-T_i^4)}{\dfrac{B'_{i-1}}{r'_{i-1}}+\dfrac{B_i-1}{r_i}}\\&=\frac{2\pi\sigma(T_i^4-T_{i+1}^4)}{\dfrac{B_i'}{r_i'}+\dfrac{B_{i+1}-1}{r_{i+1}}}=\cdots\,,\end{aligned} \tag{5}$$

taking $T_i=T_i'$, which can be solved in a straight forward way and $Q_n$ is given by

$$Q_n=\frac{\sigma S_0(T_0^4-T_n^4)}{D_n}\,, \tag{6}$$

where $D_n$ is given by

$$D_n = r_0 \sum_{j=1}^{n} \left( \frac{B'_{j-1}}{r'_{j-1}} + \frac{B_j - 1}{r_j} \right),$$

and temperature of the $i$-th shield $T_i$ by

$$\frac{1-\left(\frac{T_i}{T_0}\right)^4}{1-\left(\frac{T_n}{T_0}\right)^4} = \frac{D_{ni}}{D_n}, \tag{7}$$

where $D_{ni}$ means the sum of the first $i$ terms of $D_n$.

## § 3. Special Examples

In order to find conditions to use radiation and thermal shields most effectively, the efficiency and temperatures of the shields are calculated for special examples using the above equations, and the results are shown in Figs. 2 ∼ 9. Hereafter, we use a notation $Q(n)$ to express the power required when $n$ sheets of shields are inserted in the furnace. As an outer vessel for keeping vacuum always serves as a shield at zero temperature* in practical cases, $Q(n)$ corresponds to $Q_{n+1}$ in the above paragraph. Then, the relative power which indicates the effectiveness in using $n$ sheets of shields is defined as

$$Q(n)/Q(0) = Q_{n+1}/Q_1 .$$

In calculations, the radiation shields were assumed to be thin and to have the same emissivity on their both sides, a condition which is approximately realized in practice.

1) *A radiation shield*

Formulas used in this case are written as

$$Q(1)/Q(0) = D_1/D_2$$

$$= \frac{B_0 + r_0/r_v(B_v - 1)}{B_0 + r_0/r_1(2B_1 - 1) + r_0/r_v(B_v - 1)},$$

$$T_1/T_0 = \left( \frac{D_2 - D_{21}}{D_2} \right)^{1/4}$$

$$= \left( \frac{r_0/r_1 B_1 + r_0/r_v(B_v - 1)}{B_0 + r_0/r_1(2B_1 - 1) + r_0/r_v(B_v - 1)} \right)^{1/4},$$

where $r_v$ and $B_v$ are respectively the radius and the reciprocal of emissivity of the vessel. Fig. 2 shows the relative power as a function of the position of the radiation shield where the diameter of the vessel is taken as a parameter. Broken lines in the figure show the

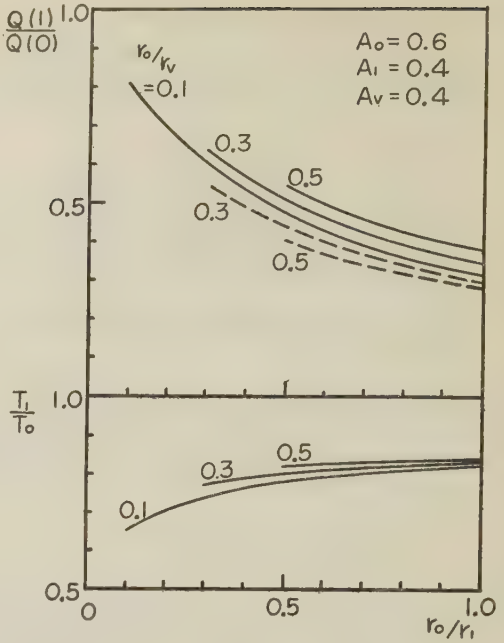

Fig. 2. Relative power and temperature of a radiation shield as a function of its position. $r_0/r_v$ is taken as a parameter. Broken lines represent $Q(1)$ divided by $Q(0)$ for $r_0/r_v = 0.1$. The values of emissivity assumed in the calculation are shown in the upper corner.

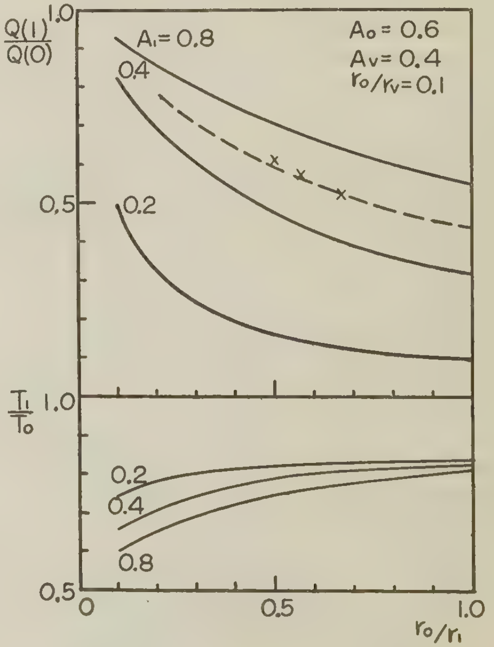

Fig. 3. Relative power and temperature of a radiation shield as a function of its position, when emissivity of the shield is taken as a parameter. × represents a experimental result for stainless steel shield. A broken line is a curve calculated assuming $A_0 = 0.5$, $A_1 = 0.5$, $A_v = 0.5$ and $r_0/r_v = 0.2$.

---

* In the calculation, the temperature of the outermost shield (the vacuum vessel) is assumed to be zero for simplicity, which does not introduce any appreciable errors when the temperature of the source is higher than 1000°K and the vacuum vessel is cooled by water.

power always divided by $Q(0)$ for $r_0/r_v=0.1$ in order to compare their absolute magnitude, because $Q(0)$ is not the same in three cases. The temperature of the shield is also shown as a function of its position. From Fig. 2, we can know that the dimension of the vessel does not affect so much the efficiency and that the effectiveness of the shield becomes less as the vessel becomes smaller, although the power required decreases in this case. Fig. 3 shows a case when emissivity of the radiation shields is changed, which is found to affect the efficiency greatly as is expected. Fig. 4 shows the fact that the variation of emissivity of the vessel dose not influence the efficiency so much as that of the radiation shield. In Fig. 5, we can see the change of the relative power with the variation of emissivity of the source, which shows that the use of a shield becomes more effective as emissivity increases, although then, as broken lines indicate, the power required increases. We may find, through these four cases, the position of the shield is very influential on the efficiency.

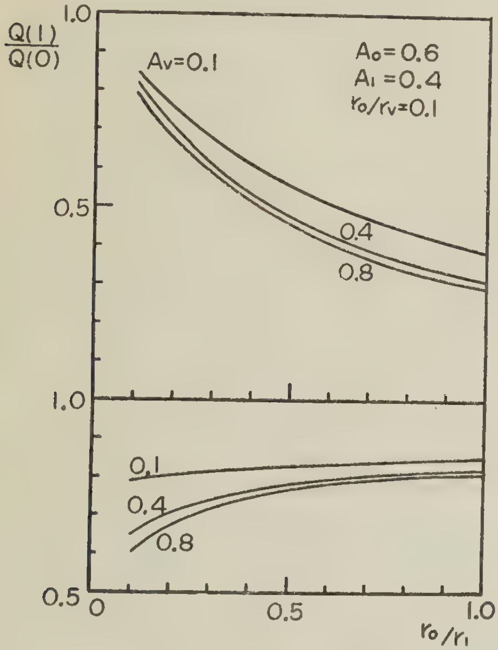

Fig. 4. Relative power and temperature of a radiation shield as a function of its position, when emissivity of the vessel is taken as a parameter.

2) *Two radiation shields*

In Fig. 6, the relative power, in a case of

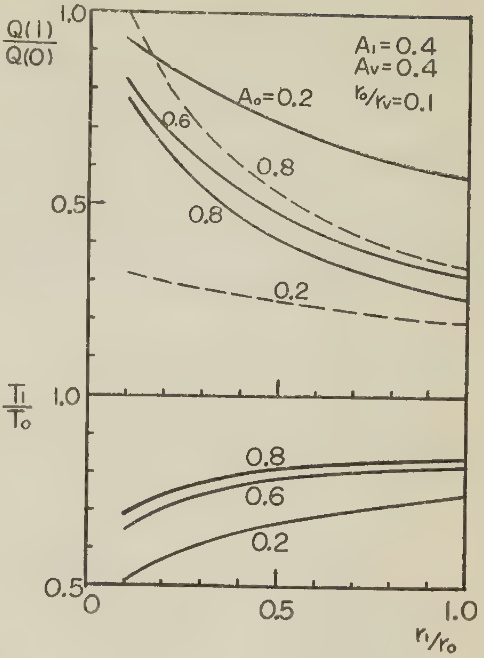

Fig. 5. Relative power and temperature of a radiation shield as a function of its position, when emissivity of the source is taken as a parameter. Broken lines represent $Q(1)$ always divided by $Q(0)$ for $A_0=0.6$.

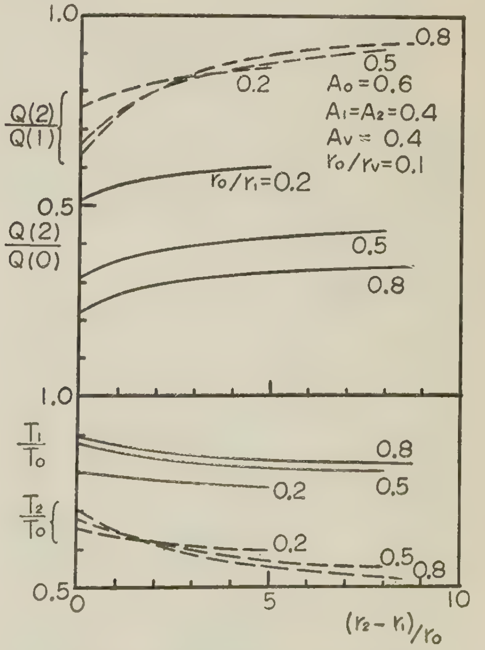

Fig. 6. Relative power and temperatures of two radiation shields as a function of the distance of the second shield from the first one. Solid lines in relative power correspond to $Q(2)/Q(0)$ and broken lines to $Q(2)/Q(1)$. Solid lines in temperature show that of the first shield and broken lines that of the second one. The position of the first shield $r_0/r_1$ is taken as a parameter.

using two shields, is shown as a function of the distance of the second shield from the first one. We may see that the position of the second shield does not affect the efficiency so much as the first one, and broken lines corresponding to $Q(2)/Q(1)$ indicate the effect of insertion of the second shield does not depend on the position of the first one. So we may expect that we need not too much concern the position of shields except the first one.

3) *Many radiation shields*

Figs. 7 (a), (b) show the change of the efficiency and temperatures of shields with the number of radiation shields, when shields are placed with the same interval, which indicates that it is not so effective to use more than five shields for the sake of a convergent property, especially so when emissivity of shields is small.

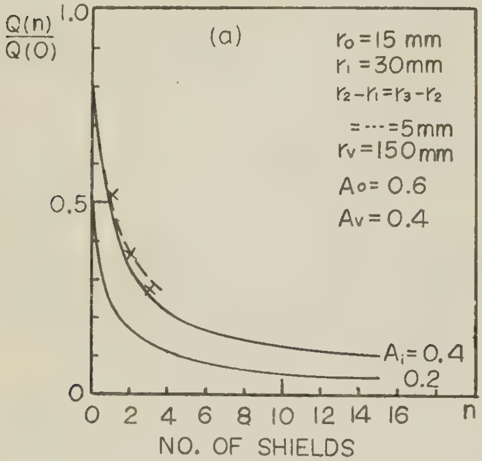

Fig. 7 (a). Relative power as a function of the number of radiation shields, when all shields are placed with the same interval. Emissivity of shields is taken as a parameter. × represents a experimental result. A broken line is a curve calculated.

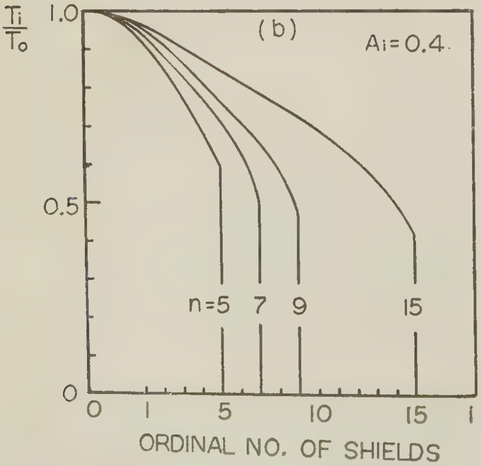

Fig. 7 (b). Temperatures of shields with $A_i=0.4$. The number of shields inserted in the furnace is taken as a parameter.

4) *Thermal shields*

Fig. 8 shows a case when a thermal shield having large emissivity is used, from which we can find, comparing with a case of radiation shields shown by chain lines in the figure, that a thermal shield is very preferable especially when high temperature is required. Fig. 9 shows the relative power in

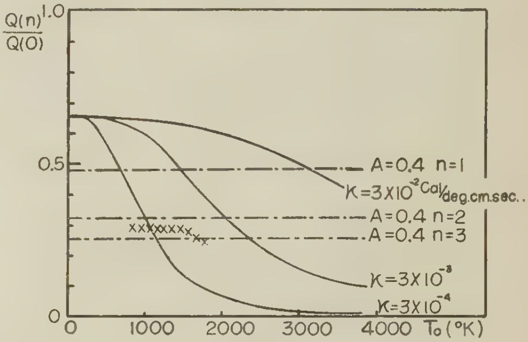

Fig. 8. Relative power as a function of the temperature of the source, when a thermal shield is used. A shield of 5 mm thickness with emissivity of 0.6 is placed at $r_0/r_1=0.5$ in the furnace $r_0/r_v=0.1$. Thermal conductivity is taken as a parameter. Chain lines show a case of thin radiation shields having emissivity of 0.4. × represents experimental values.

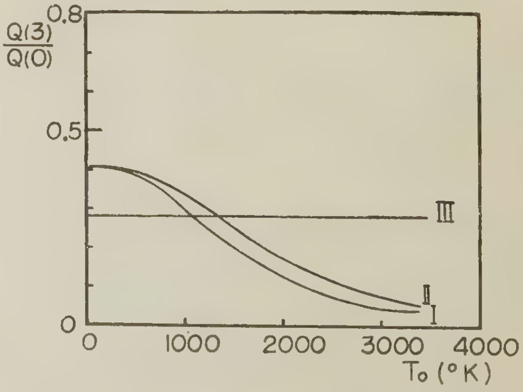

Fig. 9. Relative power as a function of the temperature of the source. I. Three thermal shields of 5 mm thickness with emissivity of 0.6 are placed at positions of $r_1=30$ mm, $r_2=40$ mm and $r_3=50$ mm in the furnace of $r_0=15$ mm and $r_v=150$ mm. II. The second and third shields are replaced by thin radiation shields having emissivity of 0.4. III. All are replaced by radiation shields with emissivity of 0.4.

the following three cases; the case I when three thermal shields of 5 mm thickness with emissivity $A=0.6$ are used, the case II when the second and third shields are replaced by thin radiation shields with $A=0.4$, and the case III when all are replaced by thin radiation shields with $A=0.4$. From this figure, together with Fig. 8, we might know that it is not so effective to set thermal shields in low temperature region of a furnace, and so it is nearly useless to insert more than one thermal shield in a vacuum furnace as insertion of many porous ceramics would necessarily decrease the degree of vacuum.

As far as there is only one thermal shield, numerical calculations are not tedious regardless of the number of other radiation shields.

## § 4. Comparision with Experimental Results

In order to check the above calculations, some experimental results are shown in Table I. They are also plotted in Figs. 3, 7 (a) and 8. Broken lines in these figures represent the calculated values. The furnace used in this experiment is composed of a longitudinal brass vacuum vessel 30 cm in length and 20 cm in diameter which is cooled by water and a molybdenum heater wound on a ceramic tube 20 cm in length and 4 cm in outer diameter, between which the shields were inserted. Temperature was measured by a Pt-PtRh thermo-junction placed in the middle of the ceramic tube. The relative power is the ratio of the power input required to maintain the source at 1300°C to the power required to maintain it at the same temperature without any shields as was defined in the above paragraph. In calculations, we assumed emissivity of the heater, the brass vessel and molybdenum- and stainless steel-shields are respectively 0.5, 0.5, 0.35 and 0.5, which values, though selected so as to fit experimental results, would not be unnatural.[5] Although the agreement is not 100 percent (see Table I and Figs. 3 and 7), because assumption made in deriving the above equations are only approximate and especially emissivity of the stainless steel shields is greatly affected by their surface conditions and can not always be the same as was assumed in the calculations, we may safely conclude that the tendency of the results obtained by the calculations are generally correct. This is also shown in Fig. 8, where we found that a ceramic shield coated by molybdenum on its inner side is very effective especially at high temperatures as was expected in the calculation.

Table I. Experimental results on efficiency in maintaining the furnace at 1300°C.

| Shielding materials | No. of shields | Condition used | $Q(n)/Q(0)$ experimental | $Q(n)/Q(0)$ calculated |
|---|---|---|---|---|
| molybdenum | 1 | $r_1=3$ cm | 0.41 | 0.415 |
| ceramics coated by molybdenum | 1 | $r_1=3$ cm<br>5 mm thickness | 0.28 | — |
| stainless steel | 1 | $r_1=3$ cm | 0.52 | 0.524 |
| stainless steel | 1 | $r_1=3.5$ cm | 0.57 | 0.564 |
| stainless steel | 1 | $r_1=4$ cm | 0.61 | 0.595 |
| stainless steel | 2 | $r_1=3$ cm<br>$r_2=3.5$ cm | 0.37 | 0.373 |
| stainless steel | 3 | $r_1=3$ cm<br>$r_2=3.5$ cm<br>$r_3=4$ cm | 0.27 | 0.297 |

$Q(n)$ is the power input required to maintain the heat source at 1300°C, and $Q(0)$ the power required to maintain it at the same temperature without any shields. In the calculation, emissivity of the heater, the vessel, molybdenum- and stainless steel-shields were assumed to be 0.5, 0.5, 0.35 and 0.5 respectively.

## § 5. Extension of Calculations

The above calculations can easily be extended to following two cases.

1. When a vessel is not cooled and no radiation comes back to it from outside, which corresponds to another extreme boundary condition, the above equations can be used

directly assuming that there exists one more outer shield with $A_{n+1}=1$ at zero temperature and at any position.

2. When the shields are spherical shells surrounding concentrically a spherical source, $Q^i$ and $f_{ii+1}$ must be replaced by

$$Q^i=\frac{4\pi\kappa_i(T_i-T_i')}{(1/r_i-1/r_i')},$$

$$f_{ii+1}=r_i'^2/r_{i+1}^2 .$$

$D_n$ in Eq. 6 is, therefore, given by

$$D_n=r_0^2\sum_{j=1}^{n}\left(\frac{B'_{j-1}}{r_{j-1}'^2}+\frac{B_j-1}{r_j^2}\right).$$

## § 6. Conclusions

The above considerations show that the factors which affect the efficiency greatly are emissivity, thermal conductivity of the innermost shield and its position. Thus in constructing a furnace, it is important to use this shield most effectively under the restriction usually imposed by its melting point and accurate measurements of emissivity and thermal conductivity of shielding materials at high temperatures are desired for this purpose.

The authors would like to express their hearty thanks to Prof. K. Murakawa for his kind criticism, to Profs. H. Kumagai and K. Oono for constructing the vacuum furnace. They thank also to Mrs. I. Tako for her assistance in the calculations.

## References

1) A. W. Lawson and R. Fano: Rev. Sci. Inst. **18** (1947) 727.
2) A. E. De Barr: Rev. Sci. Inst. **19** (1948) 569.
3) J. B. Garrison and A. W. Lawson: Rev. Sci. Inst. **19** (1948) 574.
4) A. Braun und G. Busch: Helv. Phys. Act. **9** (1946) 33.
5) International Critical Table **5** (1929) 242.

JOURNAL OF THE PHYSICAL SOCIETY OF JAPAN VOL. 11, NO. 11, NOVEMBER, 1956

# A Device for Calibration of Anemometers for Air Flow of Low Velocities

By Yoshirō Ōmori

*Department of Applied Physics, Faculty of Engineering, Kyōto University*

(Received April 10, 1956)

A device has been made to calibrate anemometers at low speeds (a few cm/s–2 m/s) of air streams. It consists of a wind-tunnel and a shaped nozzle, and anemometers are placed in the tunnel. The speed in the tunnel magnified by then nozzle is obtained from simple pressure measurement, and the initial speed is determined by conversion. Although the method is not new in principle, there are problems to be solved for actual use, and detailed experiments have been made to clear up the characteristics of the tunnel and the nozzle which will be suitable for the purpose, including the curvature and roughness of the surface of the nozzle, the length of the cylindrical part of the nozzle, the ratio of the sectional area of the nozzle to that of the upstream pipe etc.. As a result it has been found that the conversion chart may be applicable to nozzles of somewhat varying profiles when they are within some proper, fairly wide range as regards the above factors. This gives a convenient direction in constructing the device. The device constructed by taking such a result into consideration does not seem to be inferior in accuracy and is more convenient practically in comparison with the whirling-arm method.

## §1. Introduction

Anemometers like those of hot-wire type are conveniently used for measuring air streams of low speeds. But, exact calibration of such anemometers especially at very low speeds—down to a few cm/s—is considerably difficult. Usually the whirling-arm method is used as a standard method. Although the method is fairly accurate, the swirl produced by revolution of the arm and the draught in a room often give rise to misleading results. Moreover, in addition to the drawback that the method necessitates a large space, it is troublesome to attach anemometers and unless the anemometer is of a distant-reading type, the method is also inconvenient or even inapplicable to measurement.

Thus, the writer has intended to have a device which has accuracy of the same order at the whirling-arm method and is convenient for practice. For this purpose, wind tunnel is used to produce an air stream whose speed is obtained by measuring the pressure difference. Direct use of a pitot-static tube, however, cannot be made for low speeds such as less than 2 m/s, owing to the lack of accuracy of the pressure measurement and also to the indistinctness of its coefficient. Hence a method is adopted to magnify the speed by preparing a constriction, such as an orifice or a shaped nozzle and then to measure the magnified speed from the increased pressure difference, obtaining the initial speed by conversion. So, the method is not new in principle, but, there are some problems to be solved and so far the method has been left inapplicable to low speeds.

Detailed researches have hitherto been made about constrictions, and the rules, such as the V.D.I. Rules[1] and the B.S.I. Code[2], have been published and used generally. It is well known, however, that discharge coefficients of the constrictions vary, in general, with the Reynolds number, that is, although the coefficients become nearly constant at high Reynolds numbers, they vary distinctly when the Reynolds number decreases below a certain value. It is within the range of Reynolds numbers of constant discharge coefficients that the constrictions can be used according to the above results. Yet the range of air speeds we want to measure is rather low, and available data about the coefficients of constrictions seem to be wanting. So, the writer has intended to study constrictions for the application to air streams of such a range of small Reynolds numbers. In this connection, it may be noted that investigations have been made about new types of constrictions to keep discharge coefficients constant down to lower Reynolds numbers, and, for example, a cylindrical nozzle[3] has been devised. With such a nozzle, however, turbulence in flow is unavoidable and the measurements of flow velocity from the pressure difference seem to be accompanied by considerable errors, if the pressure difference and the quantity of flow are not calibrated directly.

Thus, a shaped nozzle having a rounded entrance has been selected for the present purpose, by the use of which turbulence was scarcely produced and the flow became parallel at the exit of the nozzle and the coefficient was obtained easily. Then, experiments have been carried out to examine the discharge coefficients by measuring distribution of air speed in the section of nozzles with various speeds, and it has been found that, if the form of the nozzle is proper, the change of the coefficient with air speed is not serious even for low Reynolds numbers, and, if once determined by precise preliminary experiments, this nozzle may be used with good accuracy for calibration at low speeds. The accuracy of the device for calibration of anemometers has been aimed at about 1%.

## § 2. Experimental Method and Results

### *a*) *Outline of the Method*

To get a stream-line flow of air of low speeds, it was decided to use a wind tunnel of suction type in a still room to avoid turbulence due to a driving blower. Generally, in a wind tunnel having an entrance of a rounded smooth profile, an air stream just behind the entrance has uniform velocity almost over the whole section except only a small part near the wall. Naturally, the present nozzle has this character. Thus, placing an anemometer at a point of uniform velocity in such a section of the tunnel, the calibration of the anemometer can be carried out by knowing the velocity at the nozzle from the pressure difference and by obtaining the velocity in the tunnel by conversion as explained later.

Fig. 1 illustrates the device schematically.

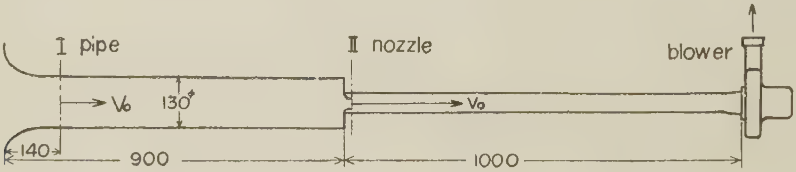

Fig. 1.

The sections of the wind tunnel near the entrance and the exit of the nozzle are both circular. If $V$ and $v$ and $R$ and $r$ denote respectively velocities and radii at those sections, and again, if $V_0$ and $v_0$ denote velocities at the central parts of the sections where the velocities are uniform, $V_0$ is related to $v_0$, as shown shortly after, as

$$V_0=K(r/R)^2 v_0\,, \qquad (1)$$

where $K$ is a correction factor with a value of nearly unity. One of the methods to determine the correction factor experimentally is to make a fluid such as water flow through the tunnel and correlate its rate of flow with the pressure difference at the nozzle, but this method requires contrivance of too large a scale to be available for the writer, so, instead of it the following method of measuring velocity distributions was adopted.

The quantities of flow at both sections are represented by $\rho_1\int_0^R 2\pi RVdR$ and $\rho_2\int_0^r 2\pi rvdr$ respectively, where $\rho_1$ and $\rho_2$ are densities at both sections. Now, if we put

$$\rho_1\int_0^R 2\pi RVdR=\alpha\rho_1\pi R^2 V_0\,,$$

and

$$\rho_2\int_0^r 2\pi rvdr=\beta\rho_2\pi r^2 v_0\,,$$

then

$$\left.\begin{aligned}\alpha&=\int_0^R 2\pi RVdR/\pi R^2 V_0\,,\\ \beta&=\int_0^r 2\pi rvdr/\pi r^2 v_0\,,\end{aligned}\right\} \qquad (2)$$

and we get, by the condition for continuity of flow,

$$\alpha\rho_1\pi R^2V_0=\beta\rho_2\pi r^2v_0\,, \tag{3}$$

or

$$V_0=\frac{\beta}{\alpha}\frac{\rho_2}{\rho_1}\left(\frac{r}{R}\right)^2v_0\,,$$

So, by putting

$$K=\frac{\rho_2}{\rho_1}\frac{\beta}{\alpha}=\frac{\rho_2\int_0^r 2\pi rv\,dr}{\pi r^2v_0}\Big/\frac{\rho_1\int_0^R 2\pi R\,dR}{\pi R^2V_0}\,, \tag{4a}$$

equation (1) is obtained. But, in the present case, the velocity $v_0$ at the nozzle is less than about 30 m/s, and therefore the change of density due to the decrease of the static pressure is very small, that is,

$$\frac{\Delta\rho}{\rho}=\frac{1}{\gamma}\frac{\Delta p}{p}\leq 0.38\%\,,$$

where $p$ and $\gamma$ denote respectively the static pressure and the ratio of the two specific heats of air. Also, in the present case the loss of the pressure head by the frictional resistance in the tunnel is very small. Thus, $K$ may be put as

$$K=\frac{\beta}{\alpha}=\frac{\int_0^r 2\pi rv\,dr}{\pi r^2v_0}\Big/\frac{\int_0^R 2\pi RV\,dR}{\pi R^2V_0}\,. \tag{4b}$$

Accordingly, $K$ is obtained by measuring velocity distributions at both sections.

*b) The forms and dimensions of the tunnel and the nozzles*

The sizes of anemometers to be calibrated now are assumed fairly small. As an example, a thermocouple anemometer[4] illustrated in Fig. 11 (a) is considered, and the part enclosed by dotted lines is inserted in the tunnel. Then a circular section of uniform velocity with diameter of 10 cm will be sufficient for the present purpose. Too large a tunnel needs much air and is liable to produce turbulence in the room, and consequently in the tunnel. And, since the boundary layer near the wall is estimated as 1–2 cm in thickness at low speeds the diameter of the tunnel was taken as 13 cm and the tunnel was manufactured of wood. So, the tunnel is of so small size that it will be called the " pipe " hereafter. To this pipe a nozzle was attached at a place about 90 cm distant from the inlet. The diameters of the nozzles were taken as 15 mm and 30 mm to measure the velocity in the tunnel from a few cm/s to 2 m/s. The velocity of 4–40 cm/s corresponds to about 3–30 m/s at the exit of the nozzle of 15 mm, and velocity of 20–200 cm/s corresponds to 3–30 m/s at that of 30 mm. These two nozzles were used according to the range of velocity to be calibrated. The profiles of the

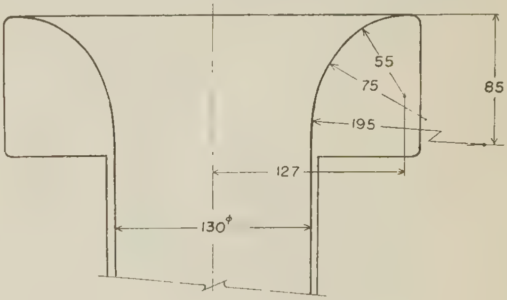

Fig. 2 (a)

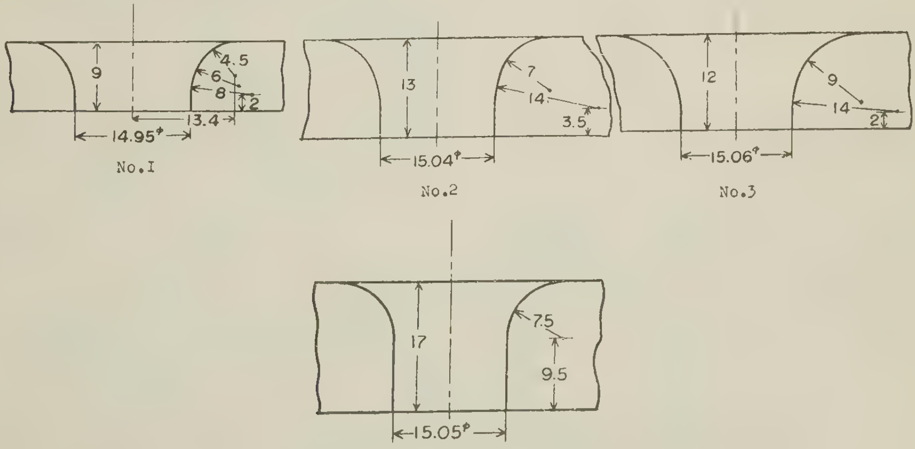

No.1 No.2 No.3 No.4

Fig. 2 (b)

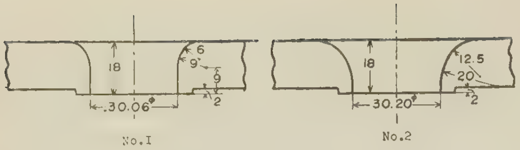

Fig. 2 (c)

pipe inlet and the nozzles are shown in Fig. 2. Several nozzles were made to study mainly the influence of profiles on the discharge coefficients. At first, the form prescribed by the V.D.I. Rules was aimed at, and the form of the nozzle of 30 mm (No. 1) was nearly the same as designed, but that of 15 mm (No. 1) differed distinctly owing to the difficulty of manufacturing. Profiles of other nozzles were designed differently from the Rules purposely, but also deviated more or less from the designed forms. The profiles of the manufactured nozzles were examined by impressing with modelling compound for dentists, and cutting the moulds through their middle planes. Profiles shown in Fig. 2 are close approximations substituted by one or more circular arcs. Degrees of roughness of the finished surfaces are shown roughly in Table.

| Nozzle | Degree of surface roughness | Length of cylindrical part (mm) | Material |
|---|---|---|---|
| 15mm, No. 1 | Polished a little and fairly smooth (superior to others) | 2 | cast iron |
| No. 2 | Having some cutting scratches and not so smooth | 3.5 | iron |
| No. 3 | Not polished, but fairly smooth | 2 | ,, |
| No. 4 | ,, ,, | 9.5 | ,, |
| 30mm, No. 1 | ,, ,, | 9 | ,, |
| No. 2 | ,, ,, | 2 | ,, |
| Inlet of pipe | Polished with sand paper and lacquered, and fairly smooth | | wood |

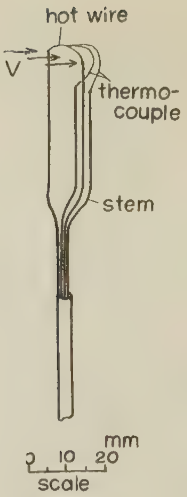

Fig. 3.

c) *Measurements of velocity distributions*

In order to find $\alpha$ and $\beta$, measurements of velocity distributions in the inlet of the pipe and at the nozzles were carried out as follows. The distribution in the pipe was observed with a thermocouple anemometer which, as shown in Fig. 3, consists of a hot wire of nichrome, a thermocouple of chromel and alumel attached to it, all 0.1 mm thick, and stems of piano wires 0.5 mm thick. The hot wire has a curved from (the radius is nearly equal to that of the pipe) and the thermocouple is placed back-ward the flow. The nichrome wire is heated by a fairly small electric current (300 mA) and the E.M.F. produced by the thermocouple is a measure of air flow. Calibration of it was made by the present apparatus as follows. Using the nozzles, the coefficients of which were predetermined, flow quantities in the pipe were measured and simultaneously E. M. F. distributions in the pipe were observed. First, by the relation of mean velocity and E.M.F. (indication in the central part of the pipe), approximate or relative velocity distribution curves are obtained. This curves were magnified to give flow quantities equal to that measured by the nozzle, from this a corrected relation of velocity and E.M.F. is given and then distribution curves were redrawn. By such a successive method, exact distribution curves were obtained. As described before, the thickness of boundary layer in this experiment is about 1 cm or a little more, and so disturbances due to the anemometer seems trifling. On the other hand, observations at the exits of the nozzles were made with a pitot tube manufactured of an injection needle. The dimension of the needle especially at the mouth is shown in Fig. 4. At the beginning of the experiments the needle shown by (b) in Fig. 4 was used for some time, but later it was chipped at its outside and the reformed needle shown by (c) was used throughout.

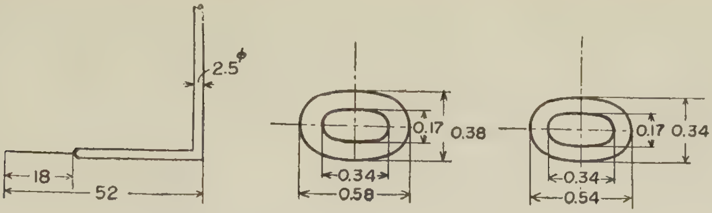

(a) (b) (c)

Fig. 4.

But observations with these two pitot tubes agreed well within experimental errors.

There are some problems about the measuement of the local velocity in a thin boundary layer with a pitot tube of finite dimension. But the slight errors in distribution curves cause errors in the discharge coefficients in less degree, and an error of as much as 1% will never happen in this case. From comparison of the coefficients of the nozzles of 15 mm and 30 mm and the pipe of 130 mm, shown later in Fig. 8, it is suggested that such errors will be very small. A pitot tube of smaller opening was one tried to use, but it was abandoned. The first and main reason is that it has a very large time lag, and the second reason is that such a small tube when used for flow of low velocity will not indicate the true total pressure as the law

$$p_{\text{pitot}}-p_{\text{static}}=\frac{1}{2}\rho v^2$$

holds only for Reynolds numbers larger than 30 at the opening.

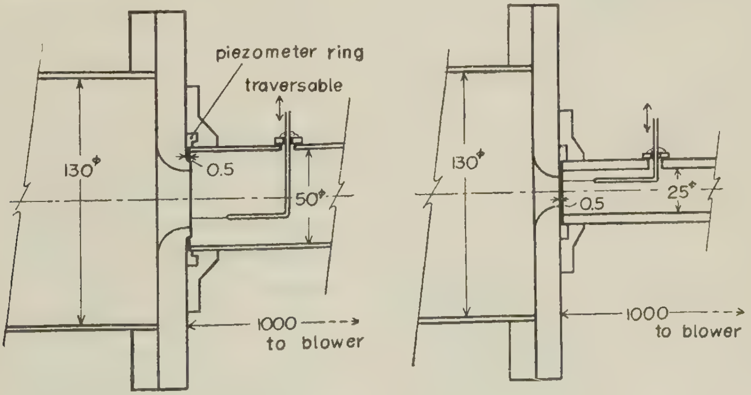

30 mm nozzle 15 mm nozzle

Fig. 5.

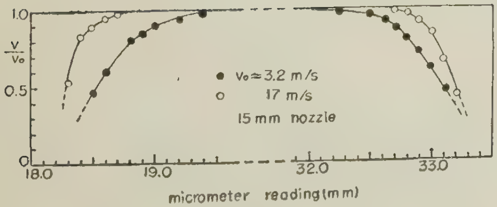

Fig. 6.

The pitot tube was attached to a spindle of a micrometer-head, and was traversed along diameters of the nozzle exits. The pressure of the pitot tube and the static pressure in a piezometer ring shown in Fig. 4 were observed differentially with a U-tube manometer and a reading-microscope of 1/100 mm scale. Fig. 5 shows the pitot tube inserted in the nozzel exit. An example of velocity distribution thus observed is shown in Fig. 6. For convenience of calculation, distribution curves are drawn showing $v/v_0$ at a point on a diameter. The abscissa means a distance between two diametral points equi-distant from the centre. Only observations of $v/v_0$ greater than 0.5 are used, as those less than 0.5 obtained near the wall are inaccurate owing to the mutual interference of the pitot tube and the wall. Examples are shown in

Figs. 7 (a), (b), (c). (a) gives the curves for the nozzle No. 1 of 30 mm, while (b) gives those for the nozzle No. 2 of 30 mm. (a) shows a group of unstable curves. This instability is perhaps due to vena contracta produced by a steep curvature of the profile of the nozzle. In the case of the nozzle of No. 2 (Fig. 7 (b)) the curves extra-polated to $v/v_0=0$ seem to converge to a point which closely agrees with the diameter of the nozzle measured previously. An example of the distribution curves of a nozzle of 15 mm is shown in Fig. 6 (c). The same results as in the case of the nozzle No. 2 of 30 mm are seen to hold for all the nozzles of 15 mm.

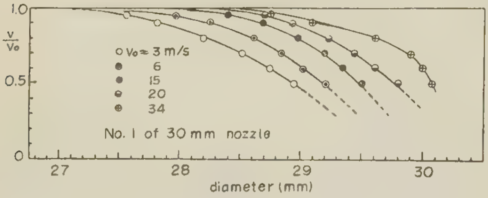

Fig. 7 (a)

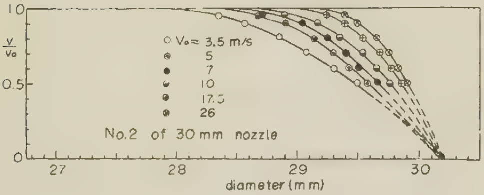

Fig. 7 (b)

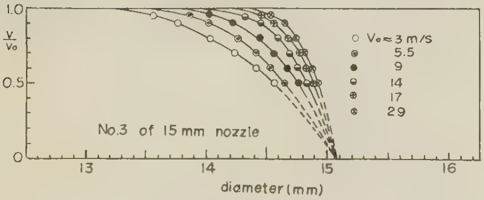

Fig. 7 (c)

From these results, it will be seen that, at low Reynolds numbers, when used the nozzle constructed according to the V.D.I. Rules produces unstable flow due to a steep curvature of the profile, and cannot be used in this case. (Naturally the V.D.I. Rules adopt this nozzle in a range of Reynolds numbers far greater than those in this case.) And nozzles having different profiles should be adopted in the range of low Reynolds numbers.

*d) Discharge coefficients α and β*

α and β are calculated from the observed distribution curves using Eq. (2). In practice, the integral calculations are replaced by summation such that

$$\alpha=\frac{\int_0^B 2\pi RVdR}{\pi R^2V_0}=\frac{\Sigma D_i\cdot\frac{V_i}{V_0}\cdot\Delta D_i}{D^2/2}, \qquad (5)$$

where $D$ is the diameter in the pipe and $D_i$ is the distance between two points on a diameter where velocities are equal to $V_i/V_0$.

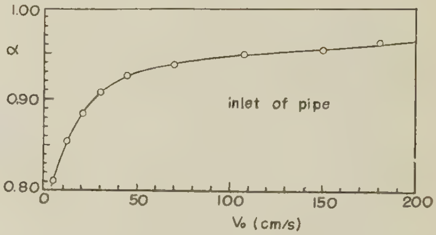

Fig. 8 (a)

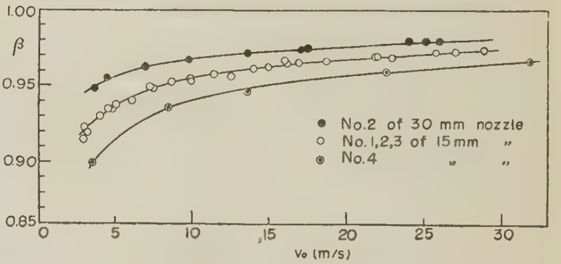

Fig. 8 (b)

Fig. 8 (a) shows α thus obtained plotted against central velocity $V_0$, and Fig. 8 (b) shows β plotted against $v_0$.

These discharge coefficients of nozzles, including the inlet of the pipe, are affected by various factors—profiles of the nozzles, diameters of both the nozzle and the pipes upstream and downstream, the roughness of surfaces, the velocity, the density and the viscosity of the fluid. If nozzles are all geometrically similar (including the roughness of the surfaces) the discharge coefficient may be expressed by

$$\beta=f\left(\frac{v_0d\rho}{\eta},\ \frac{d}{D}\right), \qquad (6a)$$

where $\rho$ and $\eta$ are respectively the density and the viscosity of the fluid at the nozzle. The inlet of the pipe is regarded as a nozzle. So, if the form is similar to that of the nozzle, the discharge coefficient will be expressed by the same function $f$ such that

$$\alpha=f\left(\frac{V_0D\rho}{\eta}\right). \qquad (6b)$$

Now the discharge coefficients $\alpha$ and $\beta$ for various nozzles and the pipe inlet are plotted against the Reynolds number in Fig. 9. It may be seen that all the points lie very closely on a single curve. Deviations of the points from the curve are of the same order as experimental errors. Hence, the following remarks will be made. With regard to the geometrical forms, these nozzles are fairly different from each other and cannot be considered as similar. Again, degrees of surface roughness are also different as shown in Table I, that is, one is polished and very smooth, while the other has cutting scratches. The fact that in spite of these differences in the form and roughess, all the points fall on a single curve within experimental errors shows, however, that considerable allowances may be given in designing and manufacturing the nozzle, that is, nozzles with profiles of gentle curvatures and with approximately smooth surfaces give very nearly equal discharge coefficients. But a nozzle with a profile of steep curvature such as No. 1 of 30 mm gives a quite different coefficient as seen from the curves of velocity distribution in Fig. 6 (a). A nozzle with a long cylindrical part such as No. 4 of 15 mm also gives a different coefficient since the distribution curves changes due to development of the boundary layer, so the cylindrical part must not be too long for the present purpose. Further, nozzles with and without a front or an upstream pipe show no observable difference in flow characteristics at exits, so it may be considered that if the ratio of diameters $d/D$ are fairly small, the discharge coefficient will hardly be affected by the existence of an upstream pipe.

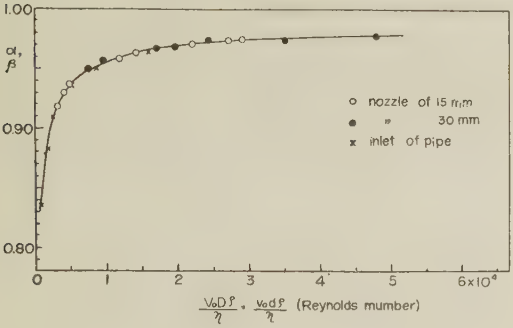

Fig. 9.

### e) *Measurements of static pressures—Use of the ring-piezometer*

In order to know $v_0$ at the exit of the nozle, it is necessary to measure the dynamic pressure—the difference between the total pressure and the static pressure. In the present case, the total pressure is equal to the atmospheric pressure, as the energy lost in the upstream pipe is very small. To measure the static pressure, usually a ring-piezometer is used, and the pressure in the ring space around the exit of the nozzle is regarded as the static pressure. But the pressure in the ring space will not always be equal to the true static pressure. The position and the form of the ring space and those of the pipe behind the nozzle may affect the pressure in it. If the discharge coefficients of the nozzles are determined by measuring flow quantity directly and comparing it with the pressure indicated by a ring-piezometer provided at a proper position, it matters little whether the indicated pressure is equal to the true static pressure or not. But it is not so in the present case, so the correct static pressure must be obtained. Then, experiments were carried out to examine the equality of the pressure in the ring space and the true static pressure.

For this purpose a small static tube was brought at the exit of the nozzle as shown in Fig. 10 (a), and the pressure of the static tube was compared with that in the ring space. Observations were made putting the hole of the static tube at various distances

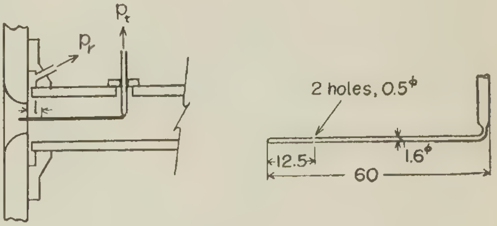

Fig. 10 (a)

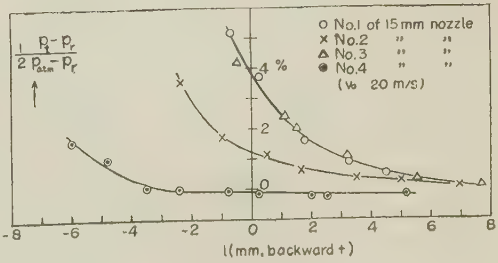

Fig. 10 (b)

from the exit. The results are shown in Fig. 10 (b). The errors converted to velocity i.el, $\Delta v_0/v_0$ or $\frac{1}{2}(p_t-p_r)/(p_{atm}-p_r)$ were plotted against the distance of the hold from the exit. These values undergo a little change with an increase of air velocity, but the change is negligible at fairly high velocity (15–30 m/s), and the figures show the values at this range.

Generally, a static tube will indicate a correct static pressure at high velocity, and if the flow along the static tube is parallel the indicated value may be regarded to be the true static pressure. As it may be seen in Fig. 10 (p), the pressure of the static tube changes continuously with its position along the axis and does not cease to change even at the cylindrical part and the exit with the nozzles No. 1, No. 2 and No. 3 of 15 mm. The pressure difference converted to velocity is about 4% at the exit in the case of No. 1. In the nozzle No. 4 having a longer cylindrical part, the pressure indication of the static tube becomes constant at the exit and agrees with that of the ring space. With other nozzles, No. 1, No. 2 and No. 3, this value is obtained at places several mms behind the exit.

It will be inferred that the flow at the exit is parallel, because these nozzles have cylindrical parts prolonged from curved entrances and the distribution curves show that no vena contracta seems to have occurred. Therefore, the static pressure may be unaltered through this part (the pressure decrease along the axis due to friction in such a short distance and that due to velocity increase may be both negligibly small), and the phenomena described above will be explained as due to the influence of the static tube itself. Thus, it is concluded that the finite dimension of the static tube itself makes it impossible to measure such local static pressures. Perhaps it may be only when the flow is parallel in some proper distance compared with the dimension of the static tube that the true static pressure is indicated. So, in this case the flow may be parallel in the neighbourhood of the exit, and the true static pressure may correspond to the pressure at the ring space in this device. Further, to ascertain the influence the following experiments were performed. An anemometer is calibrated by means of the nozzles No. 3 and No. 4, and it is examined by which pressure, either of the static tube or in the ring space, the calibration by No. 3 coincides with that by No. 4. The anemometer used for this purpose is a thermocouple anemometer shown in Fig. 11 (a). The temperature of the nichrome hot wire heated by a constant current is indicated by the e.m.f. of the thermocouple of chromel and alumel attached to it, thus the e.m.f. being the measure of the air velocity. The results of the calibration show, as it may be seen from Fig. 11 (b), that both curves agree with each other when the pressure in the ring space is used as the static pressure. Thus it may be concluded that in this device the pressure in the ring space is equal to the true static pressure.

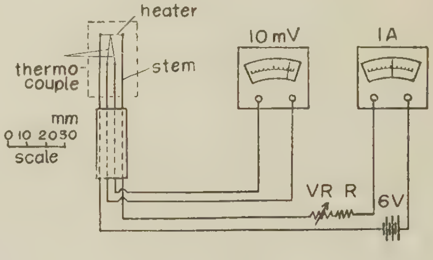

Fig. 11 (a)

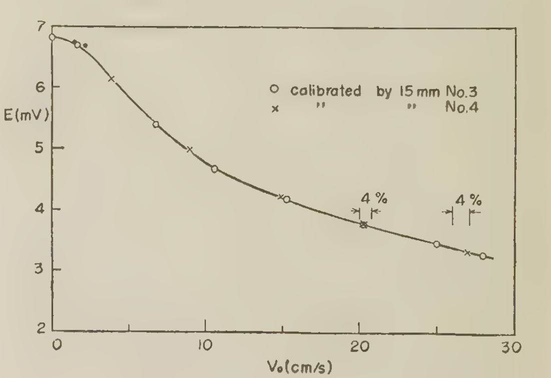

Fig. 11 (b)

### f) *Correction factor K*

By Eq. (4) $K$ is calculated as the ratio of $\beta$ to $\alpha$ when they satisfy Eq. (3), and when once $K$ is obtained as the function of $v_0$, $V_0$ is easily found by measuring $v_0$ and the ratio of two diameters. Calculation of $K$ is performed as follows. First, $K_1$, the ratio of $\beta$ to $\alpha$ corresponding to $v_0$ and apparent $V_0$, calculated with the ratio of two sectional areas and $v_0$, is obtained, this being the zeroth approximations value. Next, the ratio of $\beta$ to $\alpha$ corresponding to $v_0$ and $V_0$, calculated by the use of $K_1$, is calculated as the function of $v_0$, this is the first approximation value. By such a successive approximation the true value of $K$ can be obtained. Practically the first approximation value is sufficiently close to the true value. The value of $K$ of the second approximation is shown plotted against $v_0$ in Fig. 12. For the calibration, the nozzle of 15 mm is used for wind of low velocity of less than 40 cm/s, and the nozzle of 30 mm is used for wind of 20–200 cm/s. For higher velocity, if necessary, $V_0$ is measured directly by the pitot-static tube.

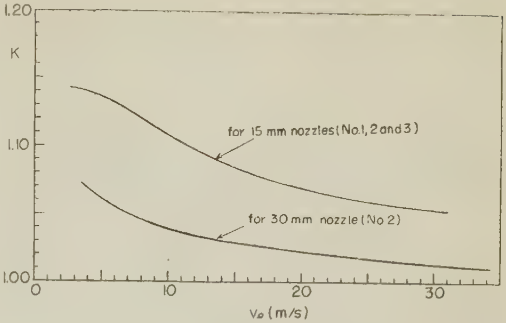

Fig. 12.

Fig. 13 (a) shows an example of calibration of the thermocouple anemometer. With a

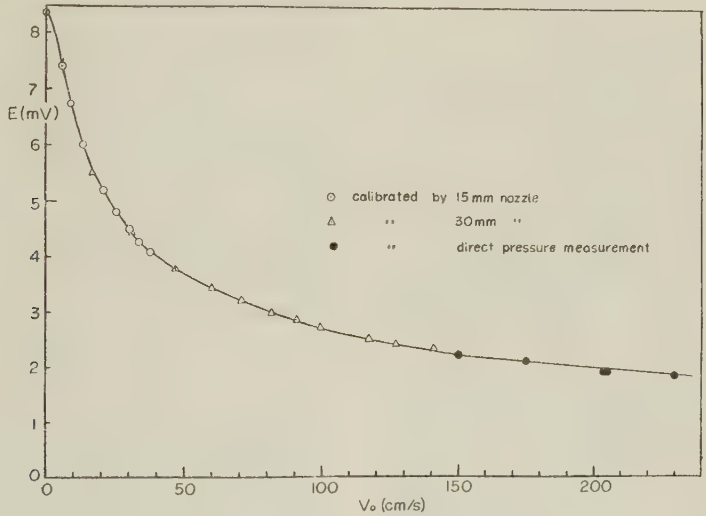

Fig. 13 (a)

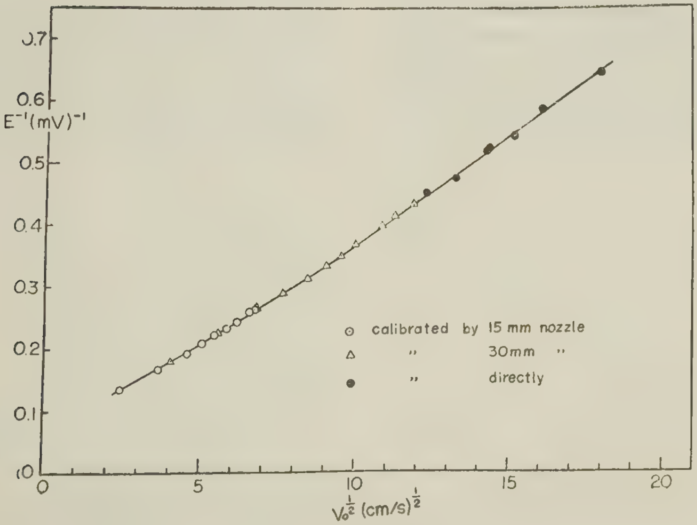

Fig. 13 (b)

constant heating current through the hot wire, the e.m.f. $E$ of the thermocouple is plotted against $V_0$. Those points observed by two nozzles of 15 mm and 30 mm respectively are seen to lie on a single curve which seems to be the continuation of a curve obtained by measurements with a pitot-static tube. If a similar relation holds with this anomometer as with a single hot-wire anemometer placed perpendicularly to the air stream, a linear relation is expected to hold between $E^{-1}$ and $V_0^{1/2}$ from King's investigations. Fig. 13 (b) shows the experimental results of $E^{-1}$ versus $V_0^{1/2}$. It may be seen that three sets of points lie very closely on a single curve and satisfy nearly a linear relation between $E^{-1}$ and $V_0^{1/2}$.

## § 3. Summary

A device was made to calibrate anemometers at low speeds of air stream—from a few cm/s to 2 m/s. The device consists of a wind tunnel and a nozzle which is selected from some nozzles to the purpose. The velocity in the tunnel is obtained by the measurement of static pressure at the exit of the nozzle and by the aid of a predetermined correction factor.

In connection with this device, the following properties have been found about the nozzles used in the experiments.

1) The discharge coefficient (it is defined here as the ratio of the mean velocity to the maximum velocity in the section) increases with increase of velocity or Reynolds number, and the change is a little larger in the range of low Reynolds numbers, but when it is once measured accurately, it may be used with sufficient reliability in this range.

2) By examination of nozzles having various profiles it has been inferred that for nozzles of gentle curvatures, so far as examined in the experiments, the discharge coefficients are represented by a single function of the Reynolds number even through profiles are not geometrically similar. But nozzles with profiles of too steep curvatures produce vena contracta and indicate unstable and variable coefficients.

3) The influence of the roughness of the nozzle surfaces on the discharge coefficients is not oberved if surfaces are fairly smooth.

4) When the ratio of the sectional area of the nozzle to that of the upstream pipe is small, the discharge coefficients do not change whether the upstream pipe is attached or not.

5) With nozzles having fairly long cylindrical part, the coefficients decrease owing to the development of boundary layers.

6) In this device the static pressure agree with the pressure in the ring space behind nozzle.

Lastly the writer wishes to express his cordial thanks to Prof. S. Kawata for his kindly instruction for the present research. Thanks are also due to the Ministry of Education for the financial support.

## References

1) Regeln für die Durchflussmessung mit genorm ten Düsen und Blenden (V.D.I., Durchfluss-Messregeln DIN 1952) 4th Edition (1937).

2) British Standard Institution, Flow Measurement, British Standard Code, B.S. (1943), 1042.

3) A. L. Jorssen and H. T. Newton; Discharge Measurements by Means of Cylindrical Nozzles, Trans. A.S.M.E., (July 1952), 826.

4) S. Kawata, Y. Ōmori and K. Nishimura; Characteristics of a Thermocouple Anemometer, Mem. Fac. Eng., Kyōto Univ., **14** (1952) 12.

# Short Notes

This section is intended to secure prompt publication of important discoveries in physics. The reports should not exceed 800 words in length. A figure of size 7 cm × 7 cm will be counted as 150 words.

J. PHYS. SOC. JAPAN **11** (1956) 1201

## A Possible Mechanism for the Fracture of Metals

By F. Eiichi FUJITA

*Japan Atomic Energy Research Institute*

(Received August 6, 1956)

It is generally accepted that pre-existing large stress-concentrators, such as the Griffith crack, are inconceivable in pure metal crystals because their expected dimension is too large. The size of the mechanically stable crack of penny-shape of radius $R$ and thickness $h$ in a crystal may be estimated by the following equation.

$$2\pi R^2\gamma \leqq \frac{\mu h^2}{2(1-\nu)} R \log \frac{R}{R_0} \qquad (1)$$

which determines whether or not the crack collapses to reduce its energy leaving a dislocation ring of the radius $R$ and the Burgers vector $h$, where $\gamma$ is the surface energy, $\mu$ rigidity modulus, $\nu$ Poisson's ratio, and $R_0$ the radius of dislocation core. Taking $h$ as a few atomic spacings, we have the value of $R$ of order $10^{-6}$ cm. Then, the stress concentration factor does not exceed about 20 which is unsatisfactory to cause fracture.

On the other hand, it is experimentally well known that the fracture of metals is generally accompanied with plastic flow. So that, many dislocation theories dealing with the fracture of metals have been proposed recently.1)-6) A possible mechanism to produce a long flat void proposed by the author6) is illustrated in Fig. 1 a and b. The cross-section of the void is $L(=n\lambda)$ in breadth and $h$ in height, where $n$ is the number of annihilated pairs of dislocations, and $\lambda$ the Burgers vector of each dislocation. Although this mechanism seems to give rise to the large stress-concentrator in plastically deformed metal crystals, the eventual size of the void will be unsatisfactory to cause fracture because of collapsing after a little further increase of $L$, as easily seen from the foregoing discussion.

Reexamination of Fig. 1 b, however, will lead us to expect another possible mechanism to cause fracture which is shown in Fig. 1 c: When some excess dislocations of either sign are squeezed into the void due to the concentrated stress excerted by the rear dislocations in one side, the state of the void may be regarded as a hollow dislocation of a large Burgers vector $n'\lambda$, where $n'$ is the number of excess dislocations contained. Approximating the crosssection of this void with an ellipse, we can calculate the stresses around the void by using complex stress functions in an elliptical coordinates.

The maximum tensile stress, occuring at the periphery near the tip of the void, is

$$\sigma_{\max} \simeq \frac{\mu n'\lambda}{\pi(1-\nu)} \cdot \frac{1}{(Lh)^{1/2}} \qquad (2)$$

When $n'\lambda$ becomes as large as $(Lh)^{1/2}$, the maximum stress will be of the order of $\mu/2\pi(1-\nu)$ which may be large enough to produce a crack from the tip of the void. However, the excess number of dislocations which the void can contain should be restricted within some extent, because the shear stress excerted ahead of the void increases as $n'$ increases and will finally cause the slip which will then diminish $n'$. This restricted amount of $n'$ can be estimated, assuming that the shear stress in the slip plane in front of the void cann't exceed the critical shear stress of the ideal crystal, and we may expect that $n'\lambda$ can become as large as $(Lh)^{1/2}$ before the critical shear stress is reached.

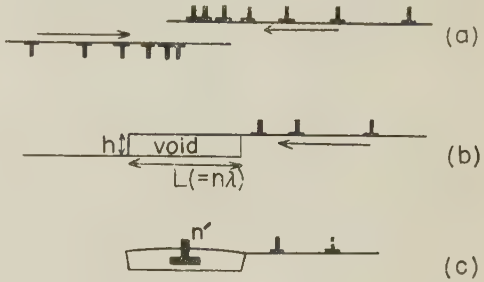

Fig. 1. A mechanism to produce a long flat void containing dislocations.

For example, taking $h$ as $1.2\times10^{-7}$ cm (about 4 atomic spacings) and $L$ as $3\times10^{-6}$ cm, we have the excess dislocations of about 10 which can be contained in the void and may produce a crack.

Another way of calculation for this mechanism is also possible by estimating the strain and surface energies associated with the void containing dislocations. The result of calculation also shows that this kind of void can produce a spreading crack even if it is considerably small in breadth $L$, say, of order $10^{-6}$ cm.

A full discussion including detailed calculations will be published elsewhere.

### References

1) N. F. Mott: Proc. Roy. Soc. **A 220** (1953) 1.
2) A. N. Stroh: Proc. Roy. Soc. **A 223** (1954) 404.
3) E. Orowan: Dislocations in Metals, AIME (1954).
4) A. Kochendörfer: Arch. Eisenhütt. **25** (1954) 351.
5) J. C. Fisher: Acta Met. **3** (1955) 109.
6) F. E. Fujita: Sci. Rep. RITU **A 6** (1954) 565.

J. Phys. Soc. Japan **11** (1956) 1202~1203

# Experimental Evidence of the Anisotropy of Hot Electrons in n-type Germanium

By W. Sasaki and M. Shibuya

*Electrotechnical Laboratory, Nagatacho, Tokyo*

(Received August 27, 1956)

One[1] of us made a rough estimation of the critical electric field strength $E_c$ where the deviation from Ohm's law occurs with the model of the spheroidal energy surfaces and found that we should introduce in the Shockley's[2] formula the numerical factor $A$ which depends on the direction of the current flow and is not smaller than 1. W. Sasaki, one of us, suggested that it might be quite difficult to detect directly this anisotropy factor $A$ by experiment, but it might be easier to detect the angle $\varepsilon$ between the current and field vectors. His idea was accepted by J. Bardeen, and C. T. Tomizuka tried to detect this effect using thin 1 cm square wafers of n-type germanium, but unfortunately he has not yet been able to get the decissive result.

In order to avoid the secondary deviations from Ohm's law due to carrier injection, we have designed specimens of the form shown in Fig. 1. Three samples $A$, $B$ and $C$ are cut from a highly homogeneous single crystal of n-type germanium furnished by M. Kikuchi and his colaborators in our labolatory. They are lying nearly, within the error of 5 degrees, in the (110) plane, and the current filaments are directed 0, 25 and 65 degrees from the cubic axis, in $A$, $B$ and $C$ respectively.

Using half microsecond pulses, the rising time of which is less than 0.1 microsecond, the floating transverse voltages are measured by an oscilloscope through an imput pulse transformer. The results obtained at 90°K, for an example, in the sample B are shown in Fig. 2, with the data of the current density. These transverse voltages appeared in the weak field in this figure are caused by the fact that we can not cut the transverse probes just perpendicular to the current filament. Eliminating these spurious voltages, we get the expected voltages caused by hot electrons. The signs and the order of magnitude of the angle between the current and field vectors are in pretty well accordance with the previous estimation in the region where the effects of the acoustical modes of vibration are predominant. The results are shown in Fig. 3, comparing with the theoretical curve. At the higher field where we must not neglect the contribution of the scattering by the optical modes, the experimental results may suggest another new anisotropic effect.

We are much indebted to K. Mizuguchi and Y. Matsukura who made an appropriate pulse amplifier

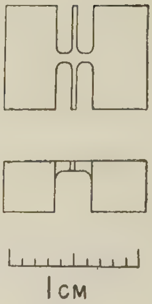

Fig. 1. Dimension of the sample B.

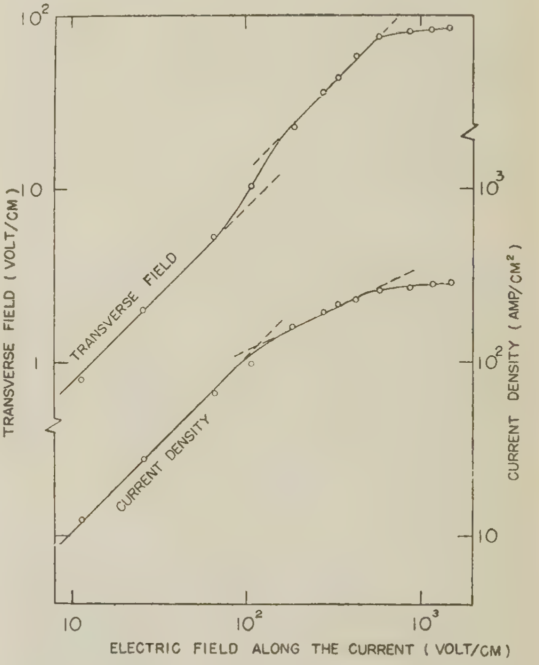

Fig. 2. Transverse field strength and the current density versus field strength in the current filament measured in the sample B.

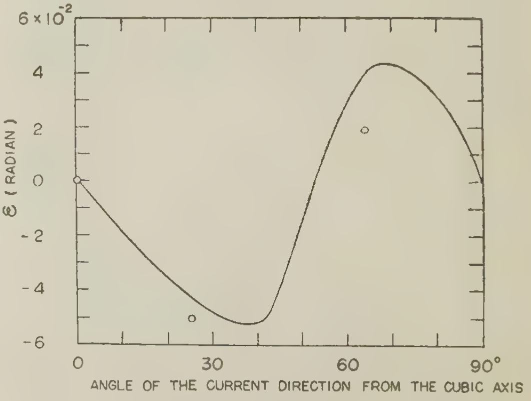

Fig. 3. Observed angle $\varepsilon$ between the current and field vectors of the three samples A, B and C are plotted comparing with the theoretical curve.

for this experiment, to Z. Ishii who determined the crystal axes of the samples by X-ray diffraction method and to G. M. Hatoyama under whom this work was done.

### References

1) M. Shibuya: Phys. Rev. **99** (1955) 1189.
2) W. Shockley: Bell System Tech. J. **30** (1951) 990.

---

J. PHYS. SOC. JAPAN **11** (1956) 1203

# Pressure Dependence of Sound Velocity in Organic Liquids

By Yasaku WADA

*Department of Applied Physics, Faculty of Engineering,*
*University of Tokyo, Tokyo*

(Received August 30, 1956)

M. R. Rao[1] has pointed out that the function $vu^{1/3}$ is almost independent of the temperature for many organic liquids, where $v$ is the specific volume and $u$ the sound velocity. This fact is considered to support the theory [2–4] that the sound velocity in liquids varies, in the first approximation at least, only with the intermolecular free volume and that the temperature dependence of the sound velocity is ascribed to the change of volume.

From the above consideration it may be reasonably concluded that the function $vu^{1/3}$ should be independent of pressure, too.[5] Recently some reliable data of the pressure dependence of sound velocity have been published for several organic liquids[6] and water[7–9] and it has become possible to discuss the problem. If $vu^{1/3}$ is independent of pressure $P$, it can be easily deduced that the ratio $n$ of the pressure coefficient of sound velocity to the isothermal compressibility $\beta$ should be a constant equal to 3. In Table I, the calculated values of $n$ are shown with the values of pressure coefficient of sound velocity and isothermal compressibility, computed from the initial slope of sound velocity-pressure curves and the volume-pressure curves respectively.[10]

Table I.

| Liquid | Temp. (°C) | $\frac{1}{u}\frac{\partial u}{\partial P}$ ($10^{-10}$cm²/dyn) | $\beta$ ($10^{-10}$cm²/dyn) | $n$ |
|---|---|---|---|---|
| Benzene | 25 | 2.96 | 0.97 | 3.0 |
| | 50 | 3.75 | 1.26 | 3.0 |
| | 70 | 4.42 | 1.53 | 2.9 |
| Carbon disulphide | 0 | 2.37 | 0.82 | 2.9 |
| | 25 | 2.62 | 0.92 | 2.8 |
| | 40 | 2.89 | 1.01 | 2.9 |
| Carbon tetrachloride | 25 | 3.51 | 1.09 | 3.2 |
| | 50 | 4.42 | 1.32 | 3.3 |
| Water | 0 | 1.23 | 0.51 | 2.4 |
| | 30 | 1.08 | 0.46 | 2.3 |
| | 50 | 1.02 | 0.45 | 2.3 |

As is seen in the table, the value of $n$ has proved to be 3 within the accuracy of the data for the organic liquids. Water has a rather smaller value of $n$, which may be attributed to the complicated structure of this liquid, especially to the strong association of molecules.

Taking the temperature $T$ and pressure as the independent thermodynamic variables, both $u$ and $v$ can be regarded as the function of them and it is not difficult to show the following relation:

$$\frac{1}{u}\left(\frac{\partial u}{\partial T}\right)_v=\alpha\left[\frac{1}{u}\left(\frac{\partial u}{\partial P}\right)_T\Big/\beta+\frac{1}{u}\left(\frac{\partial u}{\partial T}\right)_P\Big/\alpha\right],$$

where $\alpha$ is the thermal expansion coefficient. Substituting the experimental results above-mentioned, $(\partial u/\partial T)_v$ may be found to be zero. As $(\partial u/\partial P)_v$ can be shown also to be zero in the same way, it can be concluded that $u$ should depend only on one variable $v$.

### References

1) M. R. Rao: Indian J. Phys. **14** (1940) 109.
2) J. F. Kincaid and H. Eyring: J. Chem. Phys. **6** (1938) 620.
3) C. Kittel: J. Chem. Phys. **14** (1946) 614.
4) F. C. Collins and M. H. Navidi: J. Chem. Phys. **22** (1954) 1254.
5) Y. Wada: J. Phys. Soc. Japan **4** (1949) 280.
6) J. F. Mifsud and A. W. Nolle: J. Acous. Soc. Am. **28** (1956) 469.
7) G. Holton: J. Appl. Phys. **22** (1951) 1407.
8) A. H. Smith and A. W. Lawson: J. Chem. Phys. **22** (1954) 351.
9) T. A. Litovitz and E. H. Carnevalle: J. Appl. Phys. **26** (1955) 816.
10) The values of isothermal compressibility are based on Bridgman's data in International Critical Tables.

J. Phys. Soc. Japan **11** (1956) 1204~1205

## The Electron Density of the Thomas-Fermi Atom in Crystals

By Masao Atoji

*School of Chemistry, University of Minnesota, Minneapolis 14, Minn. U.S.A.*

(Received July 9, 1956)

The electron density of atoms in crystal is always modified by lattice vibrations even at absolute zero temperature. The time-averaged electron density $\overline{\rho(r)}$ of an atom in isotropic lattice vibrations is[1]

$$\overline{\rho(r)}=\int_0^\infty 4\pi s^2 f(s)\exp\left(-\frac{B}{4}s^2\right)\frac{\sin 2\pi rs}{2\pi rs}ds\,, \qquad (1)$$

where $s=2\sin\theta/\lambda$ is the distance in reciprocal space and $f(s)$ is the x-ray scattering factor of an atom at rest. $B=8\pi^2\overline{u^2}$ where $\overline{u^2}$ is the mean-square displacement of the atom from its average position. Altough Higgs[2] used the crystal space for obtaining $\overline{\rho(r)}$ of the carbon atom, the use of reciprocal space is directly connected with x-ray diffraction data such as $f(s)$ and $B$. For the Thomas-Fermi (*TF*) atom Umeda[3] obtained

$$f(s)=Z^{5/3}\sum_n \frac{\alpha_n\beta_n}{s^2+\beta_n Z^{2/3}}\,, \qquad (2)$$

where $\alpha_n$, $\beta_n$ are numerical constants and $Z$ is the atomic number, We have then

$$\begin{aligned}\overline{\rho(r)}=\frac{\pi^2Z^2}{2}\sum_n\frac{\alpha_n\beta_n^{3/2}}{Q_n}\exp(P_n)\\ \times\left\{\exp(-2Q_n)\cdot erfc\left(\sqrt{P_n}-\frac{Q_n}{\sqrt{P_n}}\right)\right.\\ \left.-\exp(2Q_n)\cdot erfc\left(\sqrt{P_n}+\frac{Q_n}{\sqrt{P_n}}\right)\right\},\qquad (3)\end{aligned}$$

where $P_n=B\beta_nZ^{2/3}/4$ and $Q_n=\pi\sqrt{\beta_n}Z^{1/3}r$. Accordingly, $\overline{\rho(r)}/Z^2$ of the *TF* atom is a function of $Z^{1/3}\sqrt{B}$ and $Z^{1/3}r$, so that $\overline{\rho(r)}$ of a *TF* atom can easily be applied to other *TF* atoms.

$$\overline{\rho(0)}=2\pi Z^2\sum_n\alpha_n\beta_n^{3/2}\left\{\sqrt{\frac{\pi}{P_n}}-\pi\exp(P_n)\cdot erfc(\sqrt{P_n})\right\}, \qquad (4)$$

is always finite. The electron density of a *TF* atom at rest is

$$\rho(r)=\pi^2Z^2\sum_n\frac{\alpha_n\beta_n^{3/2}}{Q_n}\exp(-2Q_n)\,. \qquad (5)$$

$\rho(r)/Z^2$ is then a function of $Z^{1/3}r$ only, and $\rho(0)=\infty$. However, owing to the lattice vibrations including those due to the zero-point energy, we would never be able to observe $\rho(r)$ in the electron density maps of crystals, even if the *TF* model were an exact treatment of the electron distribution of atoms.

$\overline{\rho(r)}$ of thec opper atom at absolute zero is shown in Fig. 1, where Rozental's three-term approximation[4] is used for Eq. (2) and $\overline{u^2}=0.0018$ Å² for the zero-point vibrations in the crystal[1]. $\rho(r)$ of the *TF* copper atom is also shown in Fig. 1. It is seen that the very small vibrations modify strikingly the electron density near the origin. From Fig. 2, it is seen that, when the thermal vibrations are appreciably large, the *TF* electron distribution of atoms tends to become identical to ones obtained from the Duncanson-Coulson wave functions[5),6)]. This is because the electronic orbitals are smoothed out by the thermal vibrations and the statistical treatment of the charge distribution becomes suitable even for lighter atoms. Fig. 2 shows that, if $\overline{u^2}>0.04$ Å², the electron distribution near the origin can be well represented by the *TF* model for the atoms with $Z\geq 9$.

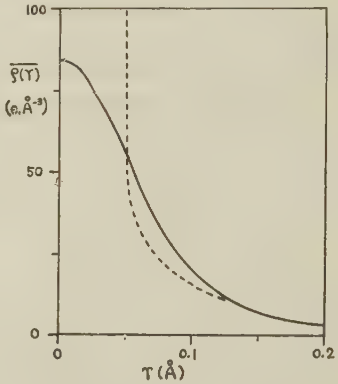

Fig. 1. The effect of the zero-point vibrations on the electron density of the *TF* copper atom. The physical limiting case ($B=0.14$ Å²) is shown by solid line and the mathematical limiting case ($B=0$), by broken line.

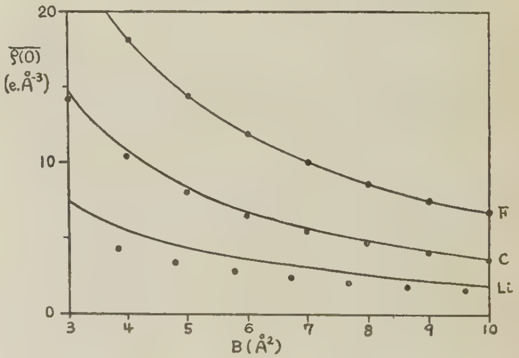

Fig. 2. The peak densities to atoms Li, *C* and *F* for 3 Å²$\leq B\leq$10 Å². The results obtained from the Duncanson-Coulson wave functions are shown by solid lines, and those from the *TF* method by ●.

### References

1) R. W. James: The Optical Principles of the Diffraction of X-rays, p. 193, Bell, London (1950).
2) P. W. Higgs: Acta Cryst. **6** (1953) 232.
3) K. Umeds: J. Faculty of Sci. Hokkaido Univ. II, **11** (1951) 57.
4) S. Rozental: Z. Phys. **98** (1935) 742.
5) W. E. Duncanson and C. A. Coulson: Proc. Roy. Soc. Edin. A**62** (1944) 37.
6) M. Atoji: Acta Cryst. to be published.

---

J. PHYS. SOC. JAPAN **11** (1956) 1205

## Bubble Chamber Study of Electric Breakdown of Liquid

By Shigeo NAGAO
*Engineering Faculty, Tohoku University, Sendai*

(Received September 12, 1956)

A bubble chamber is an apparatus to record the paths of ionizing particles, which was first developed by D. A. Glaser to get greater stopping power of particles than that of cloud chamber.[1] It is a vessel filled with a transparent liquid which is so highly superheated that an ionizing particle moving through it starts violent boiling by initiating the growth of a string of bubbles along its paths.

We applied this chamber to the study of electric breakdown of liquid as H. Raether applied cloud chamber to the study of gaseous discharge. Steel sphere electrode of 4 mm radius was placed in diethyl ether against needle electrode, 0.8 mm apart one another and both insulated from metal parts of chamber by teflon gaskets.

Several milliseconds after the expansion of the chamber began, rectangular pulse voltage with the duration of 1 msec. was applied between electrodes and xenon flash lamp with the duration of 0.6 msec. illuminated bubbles from right angle to the direction of the axis of electric field.

Fig. 1 shows pictures taken at 130°C with application of pulse voltages, when expansion ratio was about 1.06. Expansion without the application of voltage or voltage application without expansion did not generate any bubble. Distinct polarity effect of the picture of bubbles was not found and more bubbles seemed to be created near the sphere electrode than at the needle electrode without regard to the electric polarity of applied voltages. This fact may be due to the omission of degasing treatment of electrodes and poor purity of liquid used.

Breakdown voltages were greater than 25 KV in both case of polarity.

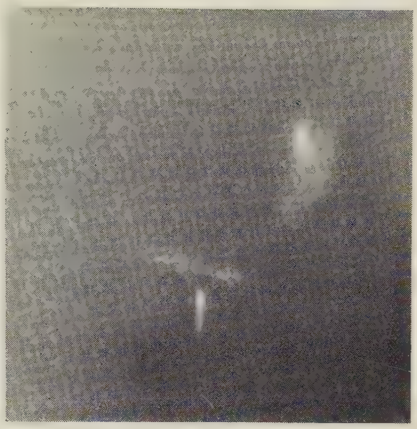

(a)

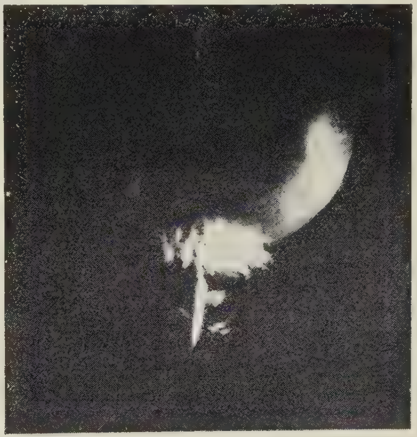

(b)

Fig. 1. (a) Negative needle. 18 KV.
(b) Positive needle. 21 KV.

The auther wishes to express his sincere thanks to Prof. Y. Toriyama for his supervision.

### Reference

1) D. Y. Glaser and D. C. Rahm: Phys. Rev. **97** (1955) 474

J. Phys. Soc. Japan **11** (1956) 1206~1207

## The Temperature Dependence of the Electrical Resistivity of the β-phase Titanium-Molybdenum Alloys

By Susumu Yoshida and Yûko Tsuya
*The Government Mechanical Laboratory,*
*Sumiyoshicho, Suginami-ku, Tokyo, Japan*

(Received August 2, 1956)

S. L. Ames and A. D. McQuillan[1] measured the electrical resistivity of β-phase Ti-Nb alloys containing more than 20 at. % Nb over the temperature range from −185°C to 900°C. They found that the temperature coefficient of resistivity becomes negative at low temperatures in the alloys containing less than 25 at.% Nb. F. R. Brotzen *et al.*[2] also found a negative temperature coefficient of resistivity in quenched Ti-V alloys containing from 15 to 20 wt.% V. Nb and V depress the transformation temperature of Ti and are soluble in β-Ti at high temperatures over the whole range of composition. In these alloy systems, the β-phase can be retained on quenching at concentrations above a critical amount of any of those addition elements. The present investigation was carried out on the Ti-Mo system which posseses the same characteristics as those of the above systems, over the temperature range from −190°C to 900°C and the concentration range from 12 to 30 wt.% Mo.

Commercially pure Ti sponge (99.5%<) and Mo wire (99.9%) were melted together in an argon arc furnace. Alloys containing 12, 14, 17, 25 and 30 wt.% Mo were prepared. They were rolled to 2 mm thick plates and specimens of 2 mm square section and 80 mm in length were cut from the plates. They were annealed in an evacuated silica tube at 950°C for 30 minutes or more. Then, pure argon was introduced into the tube and the specimens were quenched into water. It was ascertained by microscopic observation and X-ray diffraction that the β-phase was perfectly retained on quenching in these specimens. The experimental procedures of measuring electrical resistance at low and elevated temperatures and resistivity at room temperature were similar to those reported by Ames and McQuillan.

The results for each alloy are represented in Fig. 1 in terms of the ratio of the resistivity at a given temperature to the resistivity of the same alloy at 900°C. The dotted lines in the figure represent the temperature range at which the resistivity of the perfectly retained β-phase could not be obtained because of the decomposition of the β-phase. At relatively high temperatures and high Mo cocentrations, the resistivity-temperature curves are linear. The temperature coefficients of resistivity for 12~17 wt.% Molybdenum alloys become negative below 150°C in the same way as 20 and 25 at.% Nb alloys. Moreover, at lower temperatures, the resistivity-temperature curve for each of the above alloys shows a maximum and then again decreases with decreasing temperature. This anomalous behaviour of the resistivity-temperature curves depends considerably on the Mo cocentration. Both the magnitude of the maximum resistivity and the temperature where it appears increase with decreasing molybdenum concentration. The resistivity-temperature curves at low temperatures were identical when obtained by heating or cooling experiments and no hysteresis was observed. The resistance of 12 wt.% Mo alloy was measured 10 minutes after water quenching and thereafter for a weak, no change being observed.

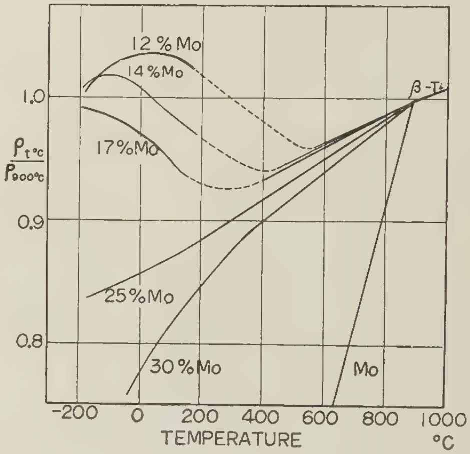

Fig. 1. Resistivity versus temperature curves. $\rho_{t\,°C}$, resistivity at $t$°C; $\rho_{900°C}$, resistivity at 900°C.

The anomalous behaviour of the resistivity-temperature curves observed in the Ti-Mo alloys bears a remarkable resemblance to those of the alloys which are commonly used for electrical resistance use, such as Ni-Cr, Ni-Cu, Ni-Cu-Zn and Cu-Mn alloys. H. Thomas[3] concluded that the anomalous behaviour of the latter group of alloys is due to some kind of a short range order caused by tempering. However, it seems difficult to attribute the behaviour of Ti-Mo alloys to the same origin, for temperature hysteresis and aging effect are lacking in this case. It may rather be attributed to a characteristic electronic structure of the β-phase Ti alloy with dilute concentration of the addition element or to some kind of intermediate structure formed during quenching.

In conclusion the authors wish to express their sincere thanks to Mr. Y. Tomono and Dr. T. Kawada for their kind advices.

## References

1) S. L. Ames and A. D. McQuillan: Acta Met. **2** (1954) 831.
2) F. R. Brotzen, E. L. Harmon Jr. and A. R. Troiano: Trans. Amer. Inst. Min. Met. Engrs. **179** (1955) 413.
3) H. Thomas: Zeits. f. Phys. **129** (1951) 219.

---

J. PHYS. SOC. JAPAN **11** (1956) 1207

# Microwave Spectra of Formaldehyde -$d_1$, -$d_2$

By Hiromasa HIRAKAWA, Takeshi OKA
and Koichi SHIMODA
*Department of Physics, Faculty of Science,*
*University of Tokyo*

(Received September 20, 1956)

Microwave spectra of formaldehyde-$d_1$, -$d_2$ molecules have been observed. To date 15 lines of $HDC^{12}O^{16}$, one line of $HDC^{13}O^{16}$ and 13 lines of $D_2C^{12}O^{16}$ have been measured and assigned as shown in Table I. Lawrance and Strandberg[1] used a semi-classical approach to handle the centrifugal distortion effect of $H_2CO$ molecule, and there seems to be some discrepancy between their results and the calculation based on the analysis given by Nielsen[2]. Further investigation to reinterpret all the spectra of formaldehyde and its available isotopic substitutions found in microwave[1][3] and infrared[4][5] region is now in progress.

## References

1) R. B. Lawrance and M.W.P. Strandberg: Phys. Rev. **83** (1951) 363.
2) H. H. Nielsen: Revs. Mod. Phys. **23** (1951) 90.
3) H. Hirakawa, A. Miyahara and K. Shimoda: J. Phys. Soc. Japan **11** (1956) 334.
4) G. Herzberg: *Infrared and Raman Spectra of Polyatomic Molecules* (1949) p. 300.
5) D. W. Davidson, B. P. Stoicheff and H. J. Bernstein: J. Chem. Phys. **22** (1954) 289.

Table I. Observed frequencies for formaldehyde -$d_1$, -$d_2$.

| Transition $J_{K_{-1},K_{+1}} \to J_{K_{-1},K'_{+1}}$ | Observed frequency (Mc/sec) | Intensity |
|---|---|---|
| 1) $HDC^{12}O^{16}$ | | |
| $1_{1,1} \to 1_{1,0}$ | 5346.64±0.03 | S |
| $2_{1,2} \to 2_{1,1}$ | 16038.06 | S |
| $5_{2,4} \to 5_{2,3}$ | 4489.08±0.03 | S |
| $6_{2,5} \to 6_{2,4}$ | 8922.59 | S |
| $7_{2,6} \to 7_{2,5}$ | 15907.38 | S |
| $10_{3,8} \to 10_{3,7}$ | 3283.09±0.03 | MS |
| $11_{3,9} \to 11_{3,8}$ | 5702.6* | MS |
| $12_{3,10} \to 12_{3,9}$ | 9412.51 | MS |
| $13_{3,11} \to 13_{3,10}$ | 14873.02 | MS |
| $16_{4,13} \to 16_{4,12}$ | 2946.67±0.03 | MW |
| $17_{4,14} \to 17_{4,13}$ | 4713.90 | MW |
| $18_{4,15} \to 18_{4,14}$ | 7322.35 | M |
| $19_{4,16} \to 19_{4,15}$ | 11074.30 | M |
| $23_{5,19} \to 23_{5,18}$ | 3330.66±0.04 | W |
| $24_{5,20} \to 24_{5,19}$ | 5018.25 | W |
| 2) $HDC^{13}O^{16}$ | | |
| $1_{1,1} \to 1_{1,0}$ | 5156.19±0.10 | WW |
| 3) $D_2C^{12}O^{16}$ | | |
| $1_{1,1} \to 1_{1,0}$ | 6096.10±0.02 | S |
| $2_{1,2} \to 2_{1,1}$ | 18287.90 | S |
| $4_{2,3} \to 4_{2,2}$ | 3687.28±0.04 | S |
| $5_{2,4} \to 5_{2,3}$ | 8519.10 | S |
| $6_{2,5} \to 6_{2,4}$ | 16759.64 | S |
| $8_{3,6} \to 8_{3,5}$ | 2850.62±0.03 | M |
| $9_{3,7} \to 9_{3,6}$ | 5536.98 | MS |
| $10_{3,8} \to 10_{3,7}$ | 10304.64 | MS |
| $13_{4,10} \to 13_{4,9}$ | 3079.48±0.03 | MW |
| $14_{4,11} \to 14_{4,10}$ | 5461.54 | M |
| $15_{4,12} \to 15_{4,11}$ | 9259.88 | M |
| $16_{4,13} \to 16_{4,12}$ | 15080.34 | M |
| $19_{5,15} \to 19_{5,14}$ | 4508.39±0.04 | W |

* The measurement of this line was difficult because it comes very near the strong HDO $4_{3,2} \to 4_{3,1}$ line.

J. PHYS. SOC. JAPAN **11** (1956) 1208

# On the Oscillating Cylinder Viscometer for Elastic Liquids II

By Ali A. K. IBRAHIM, Ph.D. London
*Physics Dept. Faculty of Science,*
*The University, Alexandria, Egypt*

(Received September 15, 1956)

Consider an elastic liquid of density $\rho$ in gm·cm$^{-3}$ dynamic viscosity $\eta_D$ in gm·cm$^{-1}$ sec and dynamic rigidity $N$ is inserted between two vertical, coaxial cylinders. If the outer cylinder (of inner diameter 2b in cm) is oscillating through very small angles about 1° say. at various frequencies $n$ in sec$^{-1}$, the liquid assumes an oscillatory motion and viscosity comes into play. Since the inner cylinder (of diameter 2a in cm, and moment of inertia I in gm·cm$^2$) is suspended by a torsion wire of restoring constant $\tau$ in gm·cm$^2$ sec$^{-2}$, then it experiences a shearing torque due to the liquid and a torque due to the suspension wire. As a result it acquires an angular acceleration. If $\theta_0$ is the angle of deflection of the inner cylinder, therefore, according to my theory1)

$$\tan\phi=\frac{2\omega\eta_D d(\gamma+d\rho)}{[(N/\omega)^2+\eta_D{}^2]e^{3d/R}-2Nd(\gamma+d\rho)} \tag{1}$$

where

$$\omega=2\pi n$$
$$d=(b-a)/2$$
$$R=(b+a)/2$$
$$\gamma=\frac{I\omega^2-\tau}{2\pi La^2\omega^2}$$

$L$ is the depth of immersion

$\phi$ is the phase angle by which the inner cylinder lags the outer cylinder.

Table I.

| Tan $\phi$ | |
|---|---|
| Experiment | Calculated from equ$^n$ (1) |
| 0.396 | 0.415 |

Markovitz et al2) have carried out Precise measurements on a 12–8 Percent solution (density=0.96 gm·cm$^{-3}$) of Vistanex polyisobutylne B–140, their results are listed below

$d=0.08$ cm.
$a=0.395$ cm.
$R=0.475$ cm.
$$\gamma=\frac{7.21\times4\pi^2(80)^2-140}{2\pi\times4.4(0.395)^2\times4\pi^2(80)^2}$$
$N=19200$ dyne cm$^{-2}$
$\eta_D=12.4$ Poise
$\omega=2\times\pi\times80$

Now, applying the above mentioned data, therefore, From the above table the given equation (1) may be regarded as a satisfactory description of the facts for elastic liquids. (The slight deviation is due to the end effect.)

## References

1) Ali A. K. Ibrahim (in preparation).
2) Markovitz et al. Rev. Sci. Inst. **23** (1952) No. 8.

---

J. PHYS. SOC. JAPAN **11** (1956) 1208

# *l*-type Doubling Spectra of HCN and DCN

By Hiromasa HIRAKAWA, Takeshi OKA
and Koichi SHIMODA
*Department of Physics, Faculty of Science,*
*University of Tokyo*

(Received September 20, 1956)

Microwave absorption lines corresponding to the direct transitions between $l$-type doublets of hydrogen cyanide have been reported by several authors.1)–4) This is the second note from our laboratory reporting one additional line of HCN ($J=7$) and three of DCN ($J=7, 8, 9$) in the frequency range between 10,000 and 17,000 Mc/sec. The observed frequencies $\nu$ are given in Table I. The $l$-type doubling constants $q=\nu/J(J+1)$ are in good agreement with those calculated from the formulae given before:4)

HCN: $q=224.478-0.002667\,J(J+1)$ Mc/sec
DCN: $q=186.193-0.002197\,J(J+1)$ Mc/sec.

Table I. Observed frequencies and $l$-type doubling constants for HCN and DCN.

1) HCN

| $J$ | $\nu$ (Mc/sec) | $q=\nu/J(J+1)$ | $q=224.478$ $-0.002667\,J(J+1)$ |
|---|---|---|---|
| 7 | 12562.46±0.03 | 224.330 | 224.329 |

2) DCN

| $J$ | $\nu$ (Mc/sec) | $q=\nu/J(J+1)$ | $q=186.193$ $-0.002197\,J(J+1)$ |
|---|---|---|---|
| 7 | 10419.88±0.03 | 186.069 | 186.070 |
| 8 | 13394.50 | 186.035 | 186.035 |
| 9 | 16739.42 | 185.994 | 185.995 |

## References

1) J. F. Westerkamp: Phys. Rev. **93** (1954) 716.
2) T. L. Weatherly and D. Williams: Phys. Rev. **87** (1952) 517.
3) R. J. Collier: Phys. Rev. **95** (1954) 1201.
4) A. Miyahara, H. Hirakawa and K. Shimoda: J. Phys. Soc. Japan **11** (1956) 335.

# PROGRESS OF THEORETICAL PHYSICS

(*Founded by H. Yukawa in 1946*)

Published for the

**Research Institute for Fundamental Physics**

**The Physical Society of Japan**

Progress of Theoretical Physics Vol. 15, No. 4, April 1956

Absorption Spectra of Unsymmetrical Cyanines...Gentaro ARAKI and Shigeru HUZINAGA..307

On the Wave Theory of Light in General Relativity, III—*Electromagnetic Four Potential*—........................Hyoitirô TAKENO ann Yoshio UENO..322

A Relativistic Field Theory of an Extended Particle, I..............Tadao NAKANO..333

A Statistical Theory of Linear Dissipative Systems, II..........Natsuki HASHITSUME..369

Letters to the Editors:

Some Relations between the Bound State Problem and Scattering Theory ............................................................N. FUKUDA..414

Note on the Nuclear Level of Spin 2⁺..........................M. SAKAI..416

On the Renormalization Cut-off.......................................... ..........H. UMEZAWA, S. KAMEFUCHI, Y. TOMOZAWA and M. KONUMA..417

Errata...................................................................................419

Progress of Theoretical Physics Vol. 15, No. 5, May 1956

The Atmospheric Effects on the Intensity of High Energy $\mu$-Mesons.......... ..........Takashi MURAYAMA, Kazuaki MURAKAMI, Ryokichi TANAKA and Shuzo OGAWA..421

Theory of Mass Reversal in the Quantized Field Theory.................... ........................ Tadashi OUCHI, Kei SENBA and Minoru YONEZAWA..431

Proposal for Experiments for Determination of Beta-Decay Interaction Theory of Triple Cascade Transition..............................Masato MORITA..445

Remarks on the Pion-Pion Interaction...................................Ziro KOBA..461

On the Relativistic Thomas-Fermi Atom..............................G. S. MURTY..473

The Statistical Mechanical Aspect of the H-Theorem, II...............Ei TERAMOTO..480

On the Universality of the Weak Interaction..........................Shuzo OGAWA..487

Interaction between Electrons in Two-Dimensional Free-Electron Model for Conjugated Systems.......................................Shigeru HUZINAGA..495

One-Center Expansion of Molecular Wave Function..............Shigeru HUZINAGA..501

Letters to the Editors:

On the Feynman's Theory of Polarons........................K. YAMAZAKI..508

Hydrodynamical Theory of the Multiple Production of Particles in High Energy Nucleon-Nucleus Collision..................C. ISO and M. SATO..510

Progress of Theoretical Physics Vol. 15, No. 6, June 1956

Orbits of an Electron in Static Electromagnetic Fields, I...............Giiti IWATA..513

Symmetry in Time and Tanikawa's Method of Superquantization in Regard to Negative Energy Fields ............................Satosi WATANABE..523

Deuteron Photodisintegration at High Energies.........................Ryozi SUZUKI..536

Elastic Scattering of Alpha-Particle by Heavy Elements .................... ................................ Nobuo ODA and Kichinosuke HARADA..545

The Theory of Radiative K Capture, I...............................Jiro YUKAWA..561

Interpretation on Nitrogen- and Proton-Induced Nuclear Reactions ........... .................Ryuzo NAKASIMA, Yoshihisa TANAKA and Ken KIKUCHI..574

Letters to the Editors:

Surface Rigidity and Shell Structure of Nuclei ........................................T. Marumori, S. Suekane and A. Yamamoto..582

Nuclear Quadrupole Moment and Rigidity of Nuclear Core ....................................T. Marumori, S. Suekane and A. Yamamoto..584

Rotational Excitation with Neutron Inelastic Scattering..........M. Yasuno..586

On the Hydrodynamical Description of the Behaviours of Elementary Particles..................................................M. Hamaguchi..588

Contents and Authors' Index to Volume 15.....................................i~vii

SUBJECT INDEX (1946–1955)..................................................1~63

---

Progress of Theoretical Physics Vol. 16, No. 1, July 1956

A Classical Theory of the Collective Description....................Yōiti Watanabe.. 1

Nuclear Magnetic Relaxation in Antiferromagnetics ....................Tōru Moriya..23

A Theory of Metallic Ferro- and Antiferromagnetism on Zener's Model...........................................................Tadao Kasuya..45

Electrical Resistance of Ferromagnetic Metals.......................Tadao Kasuya..58

Letters to the Editor:

The Decay Interaction of $K\mu_3$ and $Ke_3$ and Fermi Interaction ............S. Furuichi, T. Kodama, Y. Sugahara, M. Yonezawa and A. Wakasa..64

Interaction of $K^+$-Meson and Nucleon............................S. Minami..66

Nature of Nuclear Forces indicated by the Photodisintegration of the Deuteron, II.........................................S. H. Hsieh..68

---

Progress of Theoretical Physics Vol. 16, No. 2, August 1956

On the Quantum Mechanics-like Description of the Theories of the Brownian Motion and Quantum Statistical Mechanics ...........................................................Nobuhiko Saito and Mikio Namiki.. 71

Nucleon Magnetic Moments in Ps-Ps Intermediate Coupling Meson Theory ...................................Akira Kanazawa and Masao Sugawara.. 95

On Quantum-Mechanical Nuclear Dipole Vibrations..................Jun-ichi Fujita..112

Energy Loss of a Charged Particle Traversing Superconductors ..................................................Satio Hayakawa and Kazuo Kitao..131

Energy Loss of a Charged Particle Traversing Ionized Gas and Injection Energies of Cosmic Rays............Satio Hayakawa and Kazuo Kitao..139

Letters to the Editor:

An Attempt of Generalizing the Hypothesis of Charge Independence.....................................................O. Hara and Y. Fujii..149

A Conjecture on the Possible Existence of New Hyperons .......................................................O. Hara and Y. Fujii..150

Inelastic Scattering of Nucleons by Nuclei ................................R. Kajikawa, T. Sasakawa and W. Watari..152

On the Theory of Thermal Conductivity of Pure Metals at Low Temperatures..................................................P. G. Klemens..154

---

Price $ 1.25 per copy

$ 15.00 per year (postage inclusive)

Annual dues for foreign members (individual subscribers)

$ 12.00 (postage inclusive)

〃 for foreign members of the Physical Society of Japan

$ 10.00 (postage inclusive)

Application for members, subscriptions and orders for back numbers should be sent, directly or through book-dealers, to

The Publication Office

in

**Yukawa Hall, Kyoto University, Kyoto, Japan**

JOURNAL OF THE PHYSICAL SOCIETY OF JAPAN Vol. 11, No. 12, DECEMBER, 1956

# The Reaction $O^{16}(n, \alpha)C^{13}$

By Kiichi KIMURA, Isao KUMABE, Kozo MIYAKE,
Hiroshi OGATA and Kyoichi MIYASITA
*Department of Physics, Faculty of Science, University of Kyoto*

(Received August 30, 1956)

Using an ionization chamber filled with oxygen, the $O^{16}(n, \alpha)C^{13}$ reaction has been observed.

The chamber was irradiated with moderated Li-D fast neutrons with continuous energy spectrum, and the output pulses produced by the reaction were registered and the pulse height distribution was determined. We obtained eighteen resonances corresponding to the excited levels of $O^{17}$ at (9.66), (9.45), (9.21), 9.07, 8.90, 8.75, 8.52, (8.41), 8.27, 8.06, 7.93, 7.75, (7.57), (7.39), (7.28), (7.16), (7.09) and 6.89 Mev.

## § 1. Introduction

The present experiment has been undertaken to determine the excited states of $O^{17}$ using the $O^{16}(n, \alpha)C^{13}$ reaction.

The excited states of $O^{17}$ above 6.5 Mev were investigated by several workers. Burrows, Powell and Rotblat[1] investigated the energy levels of $O^{17}$. Measurements were made of the range in photographic emulsions of protons from the $O^{16}(d, p)O^{17}$ reaction and of alpha-particles from the $F^{19}(d, \alpha)O^{17}$ reaction. Eleven proton groups arising from the $O^{16}(d, p)O^{17}$ reaction and fourteen alpha-particle groups arising from the $F^{19}(d, \alpha)O^{17}$ reaction were identified. Excitation energies for thirteen $O^{17}$ states were calculated by averaging the results of the two reactions. Watson and Buechner[2] analyzed the energy spectrum of alpha-particles from the $F^{19}(d, \alpha)O^{17}$ reaction at 90 degrees to the incident deuteron beam, using an annular magnetic spectrograph with photographic detection. Alpha-particle groups corresponding to the ground state and ten excited levels of $O^{17}$ in the range of excitation from 0 to 6.9 Mev were identified.

Baldinger, Huber and Proctor[3] observed four resonances in the scattering of neutrons by $O^{16}$ using the ionization chamber. Hughes et al.[4] observed nine resonances in the scattering of neutrons by $O^{16}$.

Jones and Wilkinson[5] observed the neutron yield from the thin target of carbon bombarded by alpha-particles between 1 and 2 Mev. Strong resonances were observed at 1.066±0.005 and 1.344±0.010 Mev. These correspond to states of $O^{17}$ at 7.158±0.009 and 7.372±0.011 Mev. By similar method, Trumble[6] observed also strong resonances at 2.44, 2.66, 2.76 and 3.30 Mev in the alpha-particle energy range between 1.0 and 3.5 Mev, and Walton, Becker, Clement and Zucker[7] at 2.25, 2.44, 2.70, 2.78, 2.83, 3.09, 3.36 and 3.43 Mev between 1.6 and and 3.8 Mev.

Seitz and Huber[8] determined the cross section for the reaction $O^{16}(n, \alpha)C^{13}$ as a function of neutron energy by means of an ionization chamber filled with oxygen. Resonances were observed at 3.90 and 4.05 Mev in neutron energy. These correspond to excited states of $O^{17}$ at 7.81 and 7.95 Mev respectively.

Wilhelmy[9] observed $O^{16}(n, \alpha)C^{13}$ reaction using an ionization chamber filled with oxygen. The ionization chamber was irradiated by fast neutrons with continuous energy spectrum, and then the output pulses produced by the reactions were registered and the pulse height distribution was determined. He observed $\alpha+C^{13}$-recoils having energies $E_\alpha+E_C=0.65$, 0.85 and 1.5? Mev with Po-Be and Rn-Be neutrons. In our laboratory[10], experiment was carried out by similar method with Li-D neutrons and seven resonances were observed but no decisive conclusion could be obtained because of its poor statistics. Gierke[11] observed also $O^{16}(n, \alpha)C^{13}$ reaction. He observed thirty-two resonances corresponding to levels in $O^{17}$ between 6.8 and 12.8 Mev.

However, there are some discrepancies between the results obtained by the above workers. We have repeated the experiment with the improved condition and careful energy calibration, and obtained some reliable results.

## § 2. Experimental Apparatus and Procedure

The arrangement of the present measurement is shown schematically in Fig. 1.

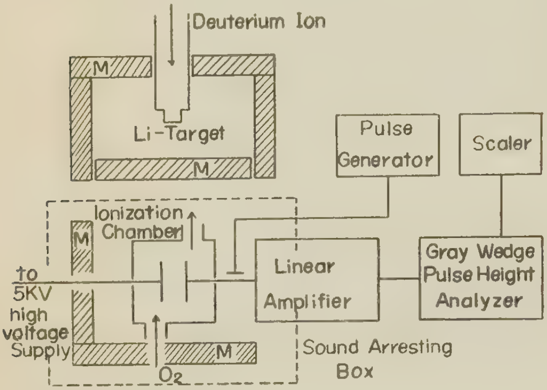

Fig. 1. The experimental arrangement shown schematically. M: Moderator (paraffin or graphite).

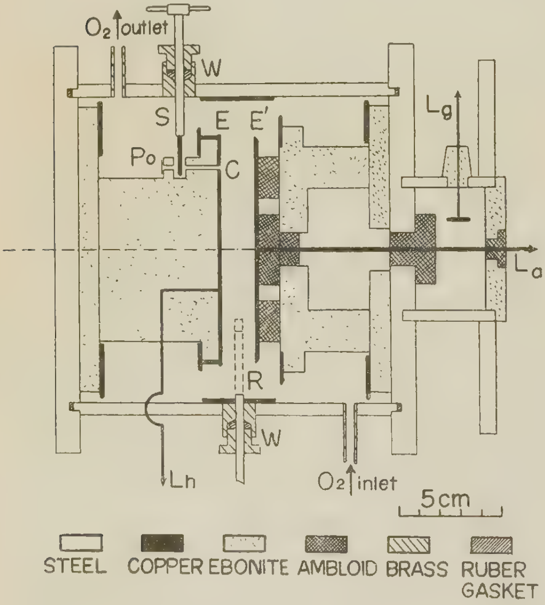

Fig. 2. The ionization chamber used. E, E′: Po: Polonium source mounted behind the collimator, C. S: Shutter. R: Po source supporting rod which is inserted to the position shown by the dotted-line with Po source, if necessary. Lh, La, Lg: Connected to the high voltage supply, linear amplifier and pulse generator, respectively. W: Wilson seal.

Neutrons were produced by bombarding a thick target of lithium metal with 310∼330 Kev unresolved deuteron beam of about 400 $\mu$A from the Cockcroft-Walton type accelerator, and the intensity was about 10 gram Ra-Be equivalent.

To moderate and smooth the energy spectrum of Li-D neutrons, paraffin or graphite plate of various thickness was inserted between the target and the ionization chamber, and the chamber was surrounded with paraffin or graphite plates.

Fig. 2 shows the ionization chamber used. It consists of a parallel plate condenser made of two copper disks of 2 mm in thickness and 11.3 cm in diameter. The depth of the chamber was designed to be 16 mm after the knowledge of the alpha-particle range of 3 Mev in N.T.P. oxygen gas. It was a good compromise between the disadvantage of the so-called wall effect and the demand for short collecting time, since the voltage required for a certain collecting time is proportional to the square of the chamber depth. Actually 5000 volt was applied to the high voltage electrode from a well-stabilized source, since the voltage was found to be the highest voltage practicable under the ordinary room humidity. The ebonite surfaces facing to the sensitive volume of the ionization chamber were covered with copper foil to shut out the recoil protons. Electrolytic oxygen dried by $CaCl_2$ was flowed through the chamber.

The energy calibration of the pulse height was carried out in two ways by comparison with the pulses of alpha-particles from polonium. One polonium source deposited carefully on a small silver plate was attached to the position of 27.75 mm behind the inner surface of the high voltage electrode, and alpha-particles were admitted into the chamber through the collimator of 27.75 mm in length and 2 mm in diameter. This polonium source was usually covered with the shutter. The other polonium source was inserted between the electrodes from the outside of the chamber when the energy calibration was carried out.

The linear amplifier used is a conventional resistance-capacity coupled type with five stages. This is a modification of the circuit developed by Kimura and Uemura[12] in our laboratory. Great care was demanded to suppress the noise and the gamma ray disturbance from the Li-D neutron source. For this purpose, for the input tube we used UZ-6001 selected carefully among many tubes of the same kind, which was operated with floating grid for the purpose of making the time constant of the input system greater than about one second, and to avoid microphonic noise the ionization chamber and the first and second stages were mounted in a sound arresting box. And the time constant has to be selected small enough to suppress the noise but not so small as to distort the linearity seriously. After several trials and theoretical calculations, we chose the value of $1.8\times10^{-3}$ sec for the clipping time constant between the first and second stages and much greater values of $1\times10^{-2}$ sec for the later stages. The ratio of the clipping time constant to the ion collecting time ($2.5\times10^{-4}$ sec) was 7.2. This ratio is not large enough to insure the strict proportionality between the ionization and the pulse height. The distortion, however, is not serious and the correction required is only about one percent. Thus we could obtain sufficiently good linearity and low noise level reduced to about 64 Kev in the energy scale.

For the adjustment of the gain and the linearity of the amplifier, a well-designed pulse generator proved to have satisfactory precision was used. The pulse was fed capacitively to the grid of first stage of the linear amplifier. The gain of the linear amplifier was checked every 10 or 15 minutes during the measurements.

The pulses were recorded in the decade scaler and the gray wedge pulse height analyzer[13] of which the time constant was $10^{-2}$ sec. A gelatin wedge obtained from "the Scientific Research Institute, Tokyo" was used, which has transmission range of 100∼1.

In the present experiment, counting rate was 50∼300 counts per minute.

## § 3. Energy Calibration

In order to determine the nuclear reaction energy by measuring the total ionization produced by charged particles in a pulsed ionization chamber with a linear amplifier, the following effects must be taken into consideration.

The first is the relation between the total ionization produced in the ionization chamber and the output pulse height. Thus, the time constant of the amplifier $\tau_e$ and the collecting time of ions $\tau_c$ were chosen $1.8\times10^{-3}$ and $2.5\times10^{-4}$ sec respectively, for the purpose of decreasing the variation of the reduction less than one percent that depends upon the relative magnitudes of $\tau_e$ and $\tau_c$[14].

The second is the recombination of ions produced in a chamber. This effect was negligible for the reaction particles, because the recombination was less than one percent for the particles except parallel ones with the electric field under our operated condition ($E$= 3100 volts/cm). However, the correction for the columnar recombination was required for collimated polonium alpha-particles used for the energy calibration of the pulse height because their tracks were parallel with the electric field.

The third is the relation between the amount of the total ionization and the energy of the particle. Now let $q$ be the charge of ions produced in a chamber and $e$ the charge of an electron. Then the energy of the particle $E$ is generally expressed by

$$E=Wq/e\,, \tag{1}$$

where $W$ denotes the average energy expended to produce one ion pair in gas by the particle. The ionization-energy relations in various gases and for various particles have been reported by many authors[15),16),17)], and it has been usually shown that $W$ increases considerably with the decreasing energy, and this variation is large at low energy. The empirical formula of $W$ for alpha-particles in air reported by Ishiwari et al.[18] is as follows,

$$W_\alpha(E)=W_{\rm Po}\left(0.948+\frac{0.119}{\sqrt{E}}\right), \qquad (E>1.5\ \text{Mev}) \tag{2}$$

where $W_{\rm Po}$ denotes $W$ for polonium alpha-particles, $E$ is expressed in Mev and this relation is tangentially extrapolated to 1.10 $W_{\rm Po}$ at zero energy in the region below 1.5 Mev. According to the measurements of $W$ for alpha-particles in air, nitrogen and oxygen[15),19),20),21),22)], there is constancy for the ratio $W_{\rm O_2}(E)/W_{\rm air}(E)$. Then it is considered that the formula (2) can be used for oxygen. Furthermore, from the knowledge[20),23),24)] of the reaction energy of $B^{10}(n, \alpha)Li^7$ reaction by the ionization chamber, it is deduced that $W$ for a heavy particle is equal to that of the alpha-particle with the same velocity. Therefore, $W_{\rm C}$ for the recoil nucleus $C^{13}$ from $O^{16}(n, \alpha)C^{13}$ reaction becomes as follows:

$$W_{\rm C}(E)=W_\alpha\left(\frac{m_\alpha}{m_{\rm C}}E\right), \tag{3}$$

where $m_\alpha$ and $m_{\rm C}$ denote masses of the alpha-particle and the nucleus $C^{13}$ respectively. Since the average ratio of the energy for the alpha-particle and the nucleus $C^{13}$ produced by the reaction is considered to be $m_C/m_\alpha$, the relation between reaction energy $Q$ and charge of ions $q_R$ produced by the reaction is expressed as follows:

$$\frac{q_R}{e}=\frac{E_\alpha}{W_\alpha(E_\alpha)}+\frac{E_C}{W_C(E_C)}$$

$$=\frac{\frac{m_C}{m_\alpha+m_C}Q}{W_\alpha\left(\frac{m_C}{m_\alpha+m_C}Q\right)}+\frac{\frac{m_\alpha}{m_\alpha+m_C}Q}{W_\alpha\left(\frac{m_\alpha}{m_\alpha+m_C}\frac{m_\alpha}{m_C}Q\right)}. \tag{4}$$

As shown in Fig. 3, the energy calibration of the pulse height was carried out by comparing the standard pulses with the pulses of polonium alpha-particles in two ways.

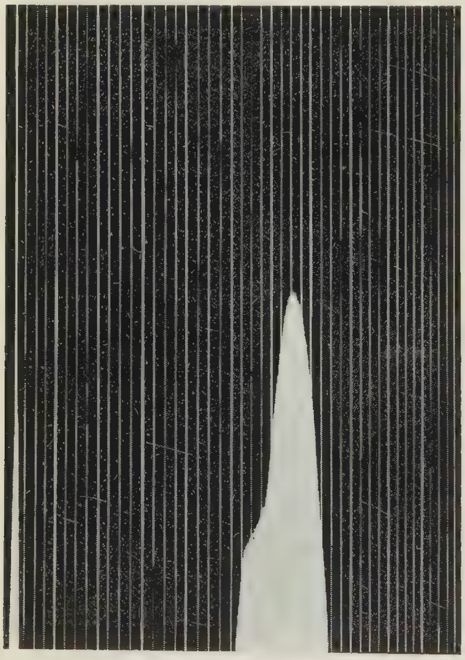

Fig. 3. The photograph of the pulse height distribution of the collimated polonium alpha-particles recorded in the gray wedge pulse height analyzer.

Figs. 4a and 4b show the pulse height distributions of polonium alpha-particles non-collimated and collimated respectively.

Now, let $q_a$ and $q_b$ be the charges of ions produced by non-collimated and collimated polonium alpha-particles respectively, and $q_s$ be the charge that equivalent to the standard pulse. Then, the ratios of the charges were measured as follows:

$$q_a/q_s\left(=\frac{E_{Po}/W_{Po}}{q_s/e}\right)=\frac{29.05\pm0.10}{8.55\pm0.05}, \tag{5a}$$

$$q_b\times f/q_s\left(=\frac{E_r/W(E_r)}{q_s/e}\times f\right)=\frac{24.30\pm0.10}{23.10\pm0.05}, \tag{5b}$$

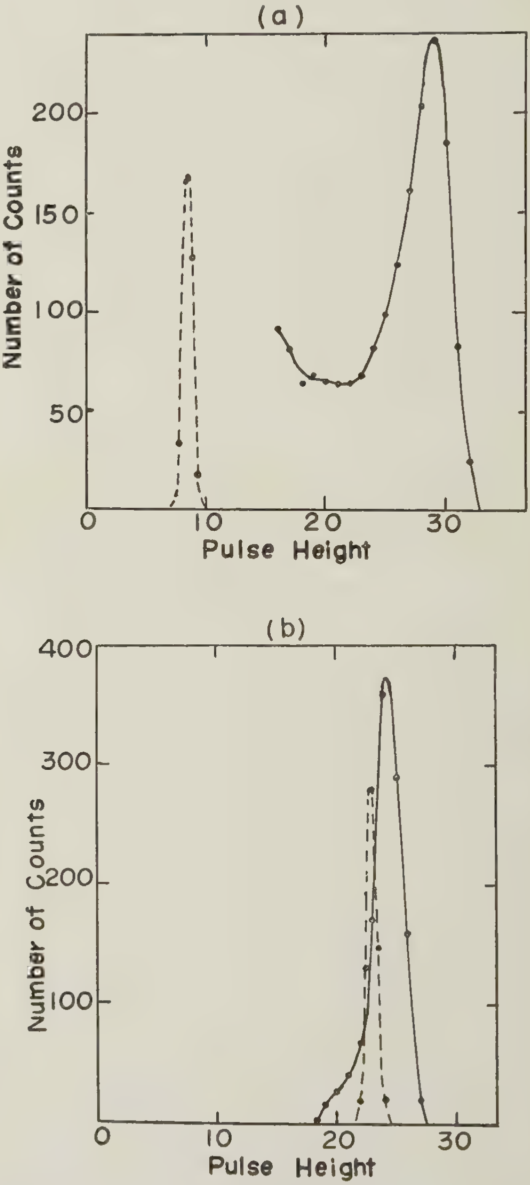

Fig. 4. The pulse height distributions of polonium alpha-particles (solid-lines) and standard pulses (dotted-line).

(a) Non-collimated polonium alpha-particles, $E_{Po}=5.3001$ Mev.

(b) Collimated polonium alpha-particles, $E_r=1.771$ Mev.

where $E_{Po}$ denotes the energy of polonium alpha-particles that is equal to $5.3006 \pm 0.0026$ Mev[25], $E_r$ denotes the residual energy of collimated polonium alpha-particles and $f$ denotes the columnar recombination factor. Let $R_c$ be the collimator length and $R_{Po}$ the range of polonium alpha-particle in air at 15°C and 760 mm Hg. Then the residual range $R_r$ in air at 15°C and 760 mm Hg. is expressed by

$$R_r = R_{Po} - R_C/\gamma\beta \ ,$$

where $\gamma = \frac{760}{288.15} \cdot \frac{T}{P}$ and $1/\beta (=1.060)$[15] denotes the stopping power of oxygen relative to the air. The room temperature and the atmospheric pressure were constant throughout the observation, namely 282.56°K and 751.56 mm Hg respectively, and the collimator length was 27.75 mm and $R_{Po}$ was 3.842 cm[26]. Thus, the value of $R_r$ was $0.876 \pm 0.005$ cm. According to the range energy relation reported by Bethe[27], $E_r$ became $1.771 \pm 0.010$ Mev.

Furthermore, according to the theory[28] the columnar recombination factor was calculated as follows:

$$f = 0.954_4 \ .$$

Therefore, putting these values into Eqs. (5a) and (5b), we obtain the following values for $q_s/e$ respectively.

$$q_s/e = (1.560 \pm 0.011) \frac{1}{W_{Po}} \ , \qquad (6a)$$

$$q_s/e = (1.552 \pm 0.011) \frac{1}{W_{Po}} \ . \qquad (6b)$$

These values obtained in two ways are in good agreement with each other within the limits of experimental errors.

If we take the values $(1.556 \pm 0.007)/W_{Po}$ for $q_s/e$, from Eqs. (2) and (4) uncorrected reaction energy, $Q' = \frac{q_R}{e} W_{Po}$, is expressed as follows.

$$\left.\begin{aligned} Q' &= \frac{\frac{13}{17} Q}{\left(0.948 + \frac{0.119}{\sqrt{\frac{13}{17} Q}}\right)} + \frac{\frac{4}{17} Q}{\left(1.1 - 0.03667 \times \frac{4}{17} \times \frac{4}{13} Q\right)} \ , \qquad \left(\frac{13}{17} Q \geqslant 1.5 \text{ Mev}\right) \\ Q' &= \frac{\frac{13}{17} Q}{\left(1.1 - 0.03667 \times \frac{13}{17} Q\right)} + \frac{\frac{4}{17} Q}{\left(1.1 - 0.03667 \times \frac{4}{17} \times \frac{4}{13} Q\right)} \ . \qquad \left(\frac{13}{17} Q < 1.5 \text{ Mev}\right) \end{aligned}\right\} \qquad (7)$$

Practically, the calculation of $Q$ from $Q'$ was carried out graphically.

## § 4. Preliminary Experiment

As the preliminary experiment, in order to determine the suitable observing condition seven experiments were carried out with various moderator conditions and in various energy ranges.

One example (Run 1) of the pulse height distribution is shown in Fig. 5. As can be seen in this figure, several peaks corresponded to reactions O+$n$ were observed. Table I summarizes the peak energies in the seven experiments. The moderator conditions and total counts are shown in the last row. Values shown in parentheses in Table I were of doubtful peaks. The mean values in the last column were calculated as a weighted mean. We found the moderator thickness 3.5 cm for the best condition.

## § 5. Results and Discussion

Since in the preliminary experiment the number of the registered pulses in each run was not yet sufficient, we could not conclude the reliable peak energies.

Therefore further three measurements having more counts were repeated.

One example (Run III) of the pulse height distribution is shown in Fig. 6. Table II summarizes the peak energies in the three measurements. Run I shows the mean values of the peak energies obtained in the preliminary experiment.

Run II and Run III show the results of the measurements for the determination of the peak energies in low (0.5∼2.5 Mev) and high (1.5∼3.0 Mev) energy ranges respectively.

Run IV shows the result using graphite instead of paraffin as the moderator.

Thus, the reliable nine peaks and doubtful nine peaks were obtained. Total count was

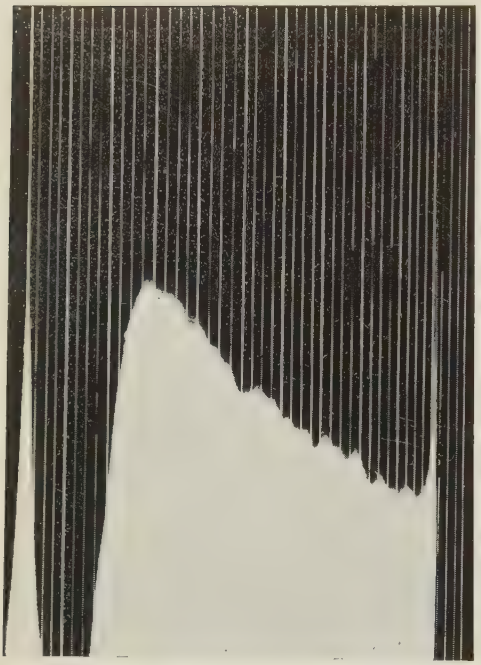

Fig. 5. The photograph of the pulse height distribution of the reaction $O^{16}+n$ recorded in the gray wedge pulse height analyzer.

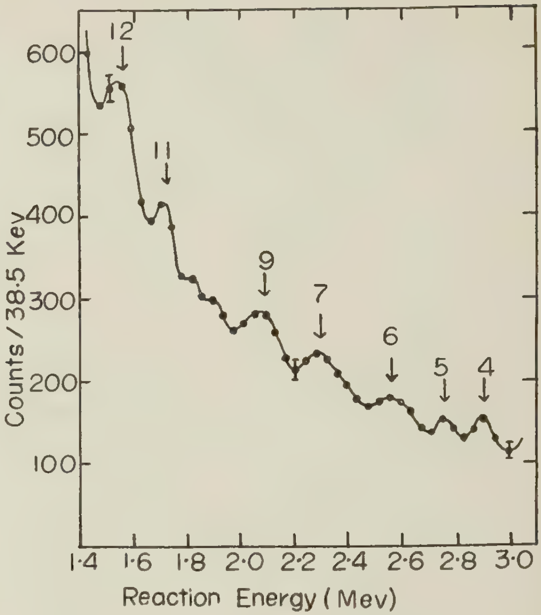

Fig. 6. A typical pulse height distribution of $O^{16}+n$ (Run III).

Table I. The peak energies (Mev) in the preliminary experiment. The total counts and the moderator thickness (cm) between the target and the chamber are shown in the last rows.

| | Run 1 | Run 2 | Run 3 | Run 4 | Run 5 | Run 6 | Run 7 | Mean |
|---|---|---|---|---|---|---|---|---|
| 1 | 3.56 | 3.50 | 3.54 | | | | | 3.54 |
| 2 | 3.28 | 3.31 | 3.38 | | | | | 3.32 |
| 3 | 3.03 | 3.07 | 3.06 | | | | | 3.06 |
| 4 | (2.87) | — | 2.88 | | | | | (2.88) |
| 5 | 2.74 | 2.72 | 2.70 | 2.72 | | | | 2.72 |
| 6 | (2.54) | — | — | — | | | | (2.54) |
| 7 | 2.37 | 2.33 | 2.40 | 2.35 | 2.33 | | | 2.37 |
| 8 | 2.23 | — | — | — | — | | | (2.23) |
| 9 | 2.09 | 2.06 | 2.11 | 2.08 | 2.04 | | | 2.08 |
| 10 | | 1.84 | 1.88 | 1.85 | 1.91 | | | 1.88 |
| 11 | 1.74 | | 1.69 | — | 1.75 | 1.73 | 1.73 | 1.74 |
| 12 | 1.56 | 1.53 | 1.51 | 1.57 | (1.55) | 1.48 | 1.53 | 1.53 |
| 13 | 1.33 | | | 1.36 | (1.33) | 1.32 | 1.35 | 1.34 |
| 14 | | | | — | (1.18) | 1.21 | — | (1.19) |
| 15 | | | | — | 1.05 | — | 1.05 | (1.05) |
| 16 | | | | 0.91 | — | 0.96 | 0.92 | 0.93 |
| 17 | | | | | | (0.87) | — | (0.87) |
| 18 | | | | | | $0.65_5$ | $0.65_5$ | $0.65_5$ |
| count | 5,833 | 14,783 | 13,071 | 16,481 | 22,851 | 10,123 | 15,141 | total count 98,283 |
| moderator thickness | 7 | 7 | 3.5 | 3.5 | 0 | 7 | 3.5 | |

Table II. Summary of the results.

| | Run I | Run II | Run III | Run IV | mean | $Q$ | $O^{17*}$ |
|---|---|---|---|---|---|---|---|
| 1 | 3.54 | | | | (3.54) | ($3.66_6$) | (9.66) |
| 2 | 3.32 | | | | (3.32) | (3.44) | (9.45) |
| 3 | 3.06 | | | | (3.06) | (3.18) | (9.21) |
| 4 | (2.88) | | 2.91 | 2.94 | 2.91 | 3.03 | 9.07±0.03 |
| 5 | 2.72 | | 2.76 | 2.75 | 2.74 | $2.85_5$ | 8.90±0.03 |
| 6 | (2.54) | | 2.60 | 2.58 | 2.58 | $2.69_5$ | 8.75±0.03 |
| 7 | 2.37 | 2.36 | 2.32 | 2.31 | 2.34 | 2.45 | 8.52±0.03 |
| 8 | (2.23) | (2.22) | — | — | ($2.22_5$) | ($2.33_5$) | (8.41) |
| 9 | 2.08 | 2.10 | 2.09 | 2.05 | 2.08 | 2.19 | 8.27±0.03 |
| 10 | 1.88 | $1.84_5$ | — | (1.85) | 1.86 | $1.96_5$ | 8.06±0.03 |
| 11 | 1.74 | 1.71 | 1.73 | 1.72 | $1.72_5$ | $1.82_5$ | 7.93±0.03 |
| 12 | 1.53 | 1.50 | $1.55_5$ | $1.55_5$ | $1.53_5$ | $1.63_5$ | 7.75±0.03 |
| 13 | 1.34 | 1.35 | | — | ($1.34_5$) | ($1.43_5$) | (7.57) |
| 14 | (1.19) | ($1.13_8$) | | — | (1.16) | ($1.24_5$) | (7.39) |
| 15 | 1.05 | ($1.03_5$) | | (1.07) | (1.06) | (1.13) | (7.28) |
| 16 | (0.93) | — | | — | (0.93) | (1.00) | (7.16) |
| 17 | (0.87) | ($0.88_4$) | | ($0.83_5$) | (0.86) | (0.93) | (7.09) |
| 18 | $0.65_5$ | $0.67_4$ | | | $0.66_5$ | (0.72) | 6.89±0.04 |
| count | 98,300 | 84,100 | 57,600 | 162,000 | total count 402,200 | | |

about $4 \times 10^5$.

Now let us consider by what reactions these peaks appear. There are three stable isotopes of mass number 16, 17 and 18 in natural oxygen. The following reactions give rise to the emission of charged particles when oxygen is bombarded with fast neutrons:

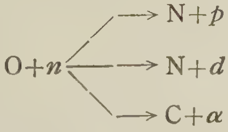

Because of the low relative abundance of $O^{17}$ and $O^{18}$ in natural oxygen, it is considered that the reaction rates of neutrons with $O^{17}$ and $O^{18}$ are sufficiently small as compared with that with $O^{16}$. Therefore, it will be seen that the peaks resulting from these reactions cannot be observed in the present experiment except the reaction $O^{17}(n, \alpha)C^{14}$ with thermal neutrons, of which cross section is fairly large ($\sigma_{\text{thermal}} = 0.46 \pm 0.11$ b[29]) and $Q = 1.825$ Mev[30]. It seems possible that the peak results from this reaction in the present experiment in which the thermal neutron flux is considerably intense.

For the reactions $O^{16}(n, p)N^{16}$ and $O^{16}(n, d)N^{15}$, since the threshold energies of these reactions are very high and the level density of $O^{17}$ in this region is very dense, we can exclude the possibility that the peak due to fast neutrons with continuous spectrum is observed. However, since the Li-D neutrons used have groups at 13.42 Mev, 10.90 Mev, ···, and $n-p$ scattering cross sections around these high energies are comparatively small, it seems possible that the groups are not completely flattened out by the moderator and remain in the neutron spectrum in the chamber, and then the corresponding peaks is observed in the results. Table III shows the reaction energies if the reactions take place by these neutron groups. Since the proton or deuteron emitted in the bombardment of $O^{16}$ by the neutron at 13.42 Mev has the energy of above 3 Mev, and its range in one atm. oxygen is considerably long as compared with the depth of the chamber used, it seems that peaks resulting from these reactions cannot be observed because of the very broad pulse height distribution as a result of the wall effect. And it seems that the peak resulting from the reactions with neutrons of 10.90 Mev cannot observed, because these neutrons corresponding to the broad first excited level of $Be^8$ shows the broad energy distribution. The peaks resulting from the reactions with neutrons of 9.74 Mev are scaled out in the present

Table III. The reaction energies (Mev) in the $O^{16}(n, p)N^{16}$ and the $O^{16}(n, d)N^{15}$ reaction due to the Li-D neutron groups used.

| | $Be^8$ excited state | Neutron energy | $O^{16}(n, p)N^{16}$ reaction energy | | | | $O^{16}(n, d)N^{15}$ reaction energy |
|---|---|---|---|---|---|---|---|
| | | | Ground state | First excited state (0.113) | Second excited state (0.300) | Third excited state (0.39) | |
| 1 | 0 | 13.42 | 3.803 | 3.690 | 3.503 | 3.412 | 3.536 |
| 2 | 2.90 | 10.90 | 1.283 | 1.170 | 0.983 | 0.892 | 1.016 |
| 3 | 4.2 | 9.74 | 0.123 | 0.010 | — | — | — |

Table IV. The excited levels of $O^{17}$ obtained by several workers and by us. *: The values after the correction of $W$ was carried out.

| | $O^{16}(n, \alpha)C^{13}$ | | | | | $C^{13}(\alpha, n)O^{16}$ | | | $O^{16}(n, n)O^{16}$ | $F^{19}(d, \alpha)O^{17}$<br>$O^{16}(d, p)O^{17}$ | |
|---|---|---|---|---|---|---|---|---|---|---|---|
| | Present exp. | Kimura et al. | Gierke | Wilhelmy | Seitz et al. | Walton et al. | Trumble et al. | Jones et al. | Baldinger et al. and Hughes | Watson et al. | Burrows et al. |
| 1 | (9.66) | | (9.57) | | | | | | (9.7) | | |
| 2 | (9.45) | | 9.34 | | | | | | (9.5) | | |
| 3 | (9.21) | | | | | | | | | | |
| 4 | 9.07 | | 9.09 | | | | | | | | 9.06 |
| | | | | | | 8.97 | | | 8.98 | | |
| 5 | 8.90 | | 8.84 | | | 8.91 | 8.87 | | | | |
| 6 | 8.75 | | 8.62 | | | 8.71 | | | 8.7 | | |
| 7 | 8.52 | | | | | 8.51 | | | 8.5 | | (8.59) |
| | | | | | | 8.47 | 8.45 | | | | |
| 8 | (8.41) | | | | | 8.41 | 8.38 | | | | |
| 9 | 8.27 | | 8.23 | | | 8.21 | 8.21 | | 8.28 | | 8.27 |
| 10 | 8.06 | | (7.98) | | | 8.06 | | | | | |
| 11 | 7.93 | | 7.85 | | 7.95 | | | | | | |
| 12 | 7.75 | 7.78* | 7.71 | | 7.81 | | | | 7.72 | | |
| | | | 7.63 | (7.62) | | | | | | | |
| 13 | (7.57) | 7.55* | 7.48 | | | | | | | | 7.51 |
| 14 | (7.39) | 7.40* | 7.35 | | | | | 7.372 | | (7.371) | |
| 15 | (7.28) | | | | | | | | 7.28 | | |
| 16 | (7.16) | 7.21* | 7.11 | | | | | 7.158 | | | |
| 17 | (7.09) | 7.05* | 6.99 | 7.01 | | | | | | (6.986) | |
| 18 | 6.89 | 6.87* | 6.89 | | | | | | | 6.869 | 6.89 |

experiment. Therefore we can exclude the possibilities that the peaks observed by us result from the reaction $O^{16}(n, p)N^{16}$ and $O^{16}(n, d)N^{15}$.

Thus, it seems that the peaks observed by us result only from the reaction $O^{16}(n, \alpha)C^{13}$. It is conceivable that the decay of the compound nucleus $O^{17}$ to an excited level of $C^{13}$ by alpha-emission is observed. Since the first excited level of $C^{13}$ is located at an energy of 3.09 Mev above the ground level, we can observe only the decay of a level of $O^{17}$ above 9.6 Mev to an excited level of $C^{13}$. On the other hand, the decays of the levels of $O^{17}$ above 9.6 Mev to the ground level of $C^{13}$ were few in the present experiment, because it has been observed that the ratio of number of the pulses corresponded to above 3.5 Mev to 0.7～3.5 Mev was about 1/20. Further, since the ground and first excited level spins of $C^{13}$ are $1/2^-$ and $1/2^+$, according to the consideration of spin, parity, Coulomb barrier and densely distributed levels, number of alpha-particles decaying to the first excited level of $C^{13}$ from the levels of $O^{17}$ above 9.6 Mev is considered to be comparable as or smaller than that to the ground level of $C^{13}$. Thus, the probability of the decay of $O^{17}$ to the excited level of $C^{13}$ is considered to be sufficiently small as compared with that to the ground level of $C^{13}$ in the present experiment. Since the Li-D neutron groups below 5.8 Mev have broad energy distributions, and their $n-p$ scattering cross sections are comparatively large, it is considered that no peaks of the reaction $O^{16}(n, \alpha)C^{13}$ (ground) corresponding to these neutron groups are observed.

Thus, it may be concluded that all the peaks observed by us are produced by the decay of $O^{17}$ to the ground level of $C^{13}$ by alpha-emission. The excited level of compound nucleus $O^{17}$ is shown in Table IV. These excitation energies were obtained by making use of values of 4.143 Mev and 6.344 Mev[30] for the neutron and alpha-particle binding energy in $O^{17}$. It seems probable that the eleventh peak is produced by the reaction $O^{17}(n, \alpha)C^{14}$. The fifth and sixth columns show the uncorrected and corrected reaction energies respectively. The probable errors of the excited levels of $O^{17}$ are also included in Table II, but errors due to the correction of $W$ are not included.

The excited levels of $O^{17}$ obtained by several workers and by us are summarized in Table IV.

The value of the energy of the level (4) in the present experiment is in good agreement with that obtained by Burrows et al..

For the six following levels the present values are in agreement with those obtained by Walton et al., although the values of the levels (6) and (9) are slightly higher than those obtained by them. The values of the levels (11) and (12) are slightly lower than those obtained by Seitz et al.. The value of the level (18) is in good agreement with that obtained by Burrows et al. and Watson et al.. The values of three levels in the other eight doubtful levels are in good agreement with those obtained by a few workers.

Since the result by Kimura et al.[10] agrees with ours if the correction of $W$ is carried out, the disagreement of Wilhelmy and Gierke's with ours might be also due to lack of the correction of $W$. Our values are in good agreement with those obtained with the inverse process $C^{13}(\alpha, n)O^{16}$.

The authors wish to express their cordial thanks to Mr. S. Fukushima of the Scientific Research Institute, Tokyo, for his kind prepation of the gray wedges, and Assistance Professor R. Ishiwari of the Institute for Chemical Research, University of Kyoto, for the constant interest. This work has been supported by the Scientific Research Expenditure of the Ministry of Education.

## References

1) H. B. Burrows, C. F. Powell and J. Rotblatt: Proc. Roy. Soc. (London) **A 209** (1951) 478.
2) H. A. Watson and W. W. Buechner: Phys. Rev. **88** (1952) 1324.
3) E. Baldinger, P. Huber and W. G. Proctor: Helv. Phys. Acta **25** (1952) 142.
4) Hughes et al.: A. E. C. Unclassified Report 2040 and Suppt. **2** (1953).
5) G. A. Jones and D. H. Wilkinson: Proc. Phys. Soc. (London) **A 66** (1953) 1176.
6) R. E. Trumble, Jr.: Phys. Rev. **94** (1954) 748 **A**.
7) R. B. Walton, R. L. Becker, J. D. Clement and M. S. Zucker: Phys. Rev. **99** (1955) 1649 **A**.
8) J. Seitz and P. Huber: Helv. Phys. Acta **28** (1955) 227.
9) E. Wilhelmy: Z. Physik **107** (1937) 769.
10) K. Kimura, R. Ishiwari, M. Sakisaka, I. Kumabe, S. Yamashita and K. Miyake: Bull. Inst. Chem. Res. Kyoto Univ. **29** (1952) 70.
11) G. Gierke: Z. Naturforsch. **8a** (1953) 567.
12) K. Kimura and Y. Uemura: Mem. Coll. Sci. Kyoto Univ. **A** 23 (1940) 1.
13) W. Bernstein, R. L. Chase and A. W. Schardt: R.S.I. **24** (1953) 437.
14) R. Ishiwari and K. Yuasa: Mem. Coll. Sci. Kyoto Univ. **A** 26 (1950) 151.
15) L. H. Gray: Proc. Camb. Phil. Soc. **40** (1944) 72.
16) T. E. Cranshow and J. A. Harvey: Can. Journ. Res. **A 26** (1948) 243.
17) W. P. Jesse, H. Forstal and J. Sadauskis: Phys. Rev. **77** (1950) 782.
18) R. Ishiwari, S. Yamashita, K. Yuasa and K. Miyake: J. Phys. Soc. Japan **11** (1956) 337.
19) R. W. Gurney: Proc. Roy. Soc. (London) **A 107** (1925) 332.
20) A. Stebler, P. Huber and H. Bichsel: Helv. Phys. Acta **22** (1949) 362.
21) T. E. Bortner and G. S. Hurst: Phys. Rev. **93** (1954) 1236.
22) R. Ishiwari: Private communication.
23) J. Rhodes, W. Franzen and W. E. Stephens: Phys. Rev. **87** (1952) 141.

24) G. C. Hanna: Phys. Rev. **80** (1950) 530.
25) G. H. Briggs: Rev. Mod. Phys. **26** (1954) 1.
26) M. G. Holloway and M. S. Livingston: Phys. Rev. **54** (1938) 18.
27) H. A. Bethe: Rev. Mod. Phys. **22** (1950) 213.
28) G. Jaffé: Ann. Physik **42** (1913) 303.
29) A. N. May and E. P. Hincks: Can. J. Research **25** (1947) 77.
30) F. Ajzenberg and T. Lauritsen: Rev. Mod. Phys. **27** (1955) 77.

---

JOURNAL OF THE PHYSICAL SOCIETY OF JAPAN Vol. 11, No. 12, DECEMBER, 1956

# On a Relation between Fluctuation-Dissipation Theorem and Irreversible Thermodynamics*

By Jun-ichi HORI

*Department of Physics, Hokkaido University, Sapporo, Japan*

(Received July 9, 1956)

It is first shown that, for some special simple impedances, the stochastic equation describing the fluctuation of macroscopic variables, which is suggested by the fluctuation-dissipation theorem, comes out to be equivalent to the Langevin equation appearing in ordinary irreversible thermodynamics. This does not mean, however, that the ordinary irreversible thermodynamics cannot describe any variables other than those with the simple impedances. It is secondly shown that, on the contrary, any macroscopic variable whose impedance is of the form

$$Z(i\omega)=z^{-1}/(i\omega)+z^{0}+(i\omega)z^{1}+\sum_{j} c_j/(i\omega-p_j)\ ,$$

can be described within the framework of the ordinary irreversible thermodynamics. This is proved by the fact that we can construct, starting from irreversible-thermodynamical equations and using the method of eliminating inner variables, a variable whose impedance is of the above-mentioned form and whose fluctuation-spectrum exactly coincides with that given by the fluctuation-dissipation theorem.

## §1. Introduction

The fluctuation-dissipation theorem, one of the fundamental results of the statistical mechanics of irreversible phenomena obtained by Takahasi[1] and Callen, Greene and Welton[2][3], gives the relation between the impedance or admittance of the macroscopic variables describing the physical system and the spectrum of their fluctuations in equilibrium state. This relation suggests that the fluctuation of the macroscopic variable $x(t)$ can be described by the equation of the form:

$$\mathscr{L}\{x(t)\}=f(t)\ , \qquad (1.1)$$

where $\mathscr{L}$ is the operator, which is the temporal representation of the impedance $Z(i\omega)$ of this variable, and $f(t)$ is the stochastic "force", whose spectrum is given by the theorem. In the classical case, which will be considered below, this spectrum is given by the real part of the impedance $Z(i\omega)$.

On the other hand, for the system to which the ordinary irreversible thermodynamics is applicable, the irreversible change of the variables characterizing the system is known to be described by linear homogeneous differential equations of the first or second order, and, moreover, as Hashitsume[4] and Onsager and Machlup[5] have shown, the fluctuations of these variables, either accompanying their irreversible change or occurring in an equilibrium state, can be taken into account by adding to these eqations the terms of random forces, thus converting them into the so-called Langevin stochastic equations.

---

* The contents of this paper were already reported in Japanese: Busseiron Kenkyu, No. 75 (1954) 36; No. 98 (1956) 26, 35.

The spectrum of fluctuations of these thermodynamic variables has definite forms determined by the respective Langevin equations. For example, in the one-dimensional case, the spectrum has either the form

$$F(i\omega)\sim 4D/(\beta^2+\omega^2)\,,$$

or the form

$$F(i\omega)\sim 4D/\{(\omega_0{}^2-\omega^2)^2+\beta^2\omega^2\}\,,$$

according as the equation is of the first or second order. On the contrary, the form of the spectrum given by the fluctuation-dissipation theorem is not restricted in such a way, and may have more general forms corresponding to infinitely many possibilities for the form of impedances.

In this paper it will first be shown (in § 2) that, for two special forms of impedances, (1.1) reduces to the Langevin equation which describes the fluctuation of the ordinary irreversible-thermodynamical variables. Thus, for these variables the fluctuation-dissipation theorem naturally leads us to the irreversible thermodynamics. The fluctuation-dissipation theorem may therefore lead us to a generalized irreversible thermodynamics which can describe the irreversible processes which are far more general than those dealt with in the ordinary irreversible thermodynamics.

This does not mean, however, that the ordinary irreversible thermodynamics completely loses its applicability to the variables with impedances other than the above-mentioned special ones. In fact, it can be shown, as will be seen in § 3, that any macroscopic variable whose impedance is of the form

$$Z(i\omega)=z^{-1}/(i\omega)+z^0+i\omega z^1+\sum_j c_j/(i\omega-p_j)\,, \quad (1.2)$$

can be described within the framework of ordinary irreversible thermodynamics. We prove this by constructing such variables upon the irreversible-thermodynamical basis, after the method used by Meixner[6] in his thermodynamic theory of viscoelasticity, that is, through introduction and subsequent elimination of appropriate "inner" variables. More precisely expressed, we first set up a system of Langevin equations of the first or second order which represents a many-dimensional irreversible-thermodynamical process, and subsequently eliminate all the variables but the particular one under examination, regarding them as the "inner" variables which should not appear explicitly in our description. Then we obtain a variable whose impedance is of the above-mentioned form and whose spectrum exactly coincides with that given by the fluctuation-dissipation theorem. This means that for such variables the irreversible-thermodynamical description is still possible, at least in principle. This is a natural result, since the fundamental assumption made in the derivation of the fluctuation-dissipation theorem requires that the resulting irreversible process should be essentially Markovian, i.e., that it may be represented as one-dimensional projection of a certain many-dimensional Markovian, hence many-dimensional irreversible-thermodynamical, process.

Most impedances that usually appear in our experience are either exactly of the form (1.2) or can be approximated sufficiently closely by such a form. Although impedances which contain higher order terms of $(i\omega)$ than the first are also possible to occur, their occurrence is very rare in practice (the case of the oscillator with radiation damping is well-known, but perhaps the only example). The impedance of the form (1.2) may therefore well be considered as a fairly general one covering almost all kinds of impedance. Thus it may be asserted that most of the macroscopic variables appearing in practice can be described within the framework of the ordinary irreversible thermodynamics, and that the fluctuation-dissipation theorem is, in a sense, a compact description of such variables, dispensed with the complexity due to extraneous inner variables.

## § 2. Derivation of the Langevin Equations in Irreversible Thermodynamics from Fluctuation-Dissipation Theorem

In this section it will be shown that for two special forms of thermodynamic impedances the fluctuation-dissipation theorem naturally leads us to the ordinary irreversible thermodynamics.

Consider the case in which $r$ extensive variables $x^1, x^2, \cdots, x^r$ fluctuate simultaneously. Let the Fourier transforms of the deviations of corresponding intensive variables $f_j(t)$ from their equilibrium values $F_j$ be $\beta_j(i\omega)$:

$$f_j(t)-F_j=(2\pi)^{-1/2}\int_{-\infty}^{+\infty} d\omega\beta_j(i\omega)\exp(i\omega t)\,, \quad (2.1)$$

and those of the responses $x^j(t)-X^j$ ($X^j$:

equilibrium values of the extensive variables) be $\alpha^j(i\omega)$:

$$x^j(t)-X^j=(2\pi)^{-1/2}\int_{-\infty}^{+\infty} d\omega\alpha^j(i\omega)\exp(i\omega t)\,. \quad (2.2)$$

The thermodynamic admittances $Y^{ij}(i\omega)$ and the thermodynamic impedances $Z_{ij}(i\omega)$ are defined by

$$i\omega\alpha^j(i\omega)=\sum_{i=1}^{r} Y^{ji}(i\omega)\beta_i(i\omega)\,, \quad (2.3)$$

and

$$\beta_j(i\omega)=\sum_{i=1}^{r} Z_{ji}(i\omega)i\omega\alpha^i(i\omega)\,, \quad (2.4)$$

respectively. Denoting the Fourier transforms of $Z_{ji}(i\omega)$ by $Z_{ji}(t)$, (2.4) can be transformed into its temporal representation:

$$f_j(t)=\sum_{i=1}^{r}\int_{-\infty}^{+\infty} Z_{ji}(\tau)x^i(t-\tau)d\tau\,, \quad (2.5)$$

where for simplicity the equilibrium values were all put equal to zero (this simplification will always be made in the following).

Callen and Greene[3] showed that the expansion of $Y^{ji}(i\omega)$ at the origin must have the form

$$Y^{ji}(i\omega)=i\omega\partial X^j/\partial F_i+O(\omega^2)\,, \quad (2.6)$$

in order that it is thermodynamically admissible. The same reasoning leads to the following form of the expansion of $Z_{ji}(i\omega)$ at the origin:

$$Z_{ji}(i\omega)=z_{ji}^{-1}/(i\omega)+z_{ji}^0+i\omega z_{ji}^1+O(\omega^2)\,,$$
$$z_{ji}^{-1}=\partial F_j/\partial X^i\,. \quad (2.7)$$

Now let us assume the simplest form satisfying this condition:

$$Z_{ji}(i\omega)=z_{ji}^{-1}/(i\omega)+z_{ji}^0\,,$$
$$z_{ji}^{-1}=\partial F_j/\partial X^i\,, \quad (2.8)$$

then (2.5) becomes

$$f_j(t)=\sum_{i=1}^{r}\{z_{ji}^{-1}x^i(t)+z_{ji}^0\dot{x}^i(t)\}\,, \quad (2.9)$$

Thus in this case the law which gives the causal relation between the intensive variables $f_j(t)$ and extensive ones $x^i(t)$ reduces to a system of linear differential equations of the first order. According to the fluctuation-dissipation theorem, the fluctuations in equilibrium state must be determined by the equations (2.9), whose left-hand sides are replaced by fluctuating forces $F_j(t)$ with spectra

$$\mathscr{F}_{ji}(i\omega)=-k(2\pi)^{-1/2}(Z_{ji}+Z_{ji}^*)\,. \quad (2.10)$$

In the present case, since the real parts of $Z_{ji}$ are constants $z_{ji}^0$, the spectra become

$$\mathscr{F}_{ji}(i\omega)=-(2/\pi)^{1/2}kz_{ji}^0=\text{const.}\,, \quad (2.11)$$

that is, $F_j(t)$ are white random forces. Thus (2.9) turns out to be a system of ordinary Langevin equations. In passing, we may point out that (2.11) requires the negativeness of $z_{ji}^0$ for $i=j$. We shall now show that this system of equations is equivalent to the one appearing in irreversible thermodynamics.

Owing to the identity of the canonical and the microcanonical ensembles in thermodynamics, the entropy of a non-equilibrium state $S'$ can be regarded as the same function of $x^i$ as the equilibrium entropy $S$ of $X^i$.[7] Hence

$$-\partial^2S'/\partial x^j\partial x^k=-\partial^2(S'-S)/\partial x^j\partial x^k$$
$$=-\partial^2S/\partial X^j\partial X^k=-\partial F_j/\partial X^k$$
$$=-\partial F_k/\partial X^j\,. \quad (2.12)$$

Denoting $-\partial^2S'/\partial x^j\partial x^k$ by $s_{jk}$, we have, according to (2.8),

$$z_{ji}^{-1}=\partial F_j/\partial X^i=-s_{ji}=-s_{ij}=z_{ij}^{-1}\,. \quad (2.13)$$

Let us develop the entropy deviation $\varDelta S=S'-S$ in power series of $(x^i-X^i)$'s, and neglect the terms of higher order than the second. Putting $X^i$'s equal to zero, this becomes:

$$\varDelta S=-\frac{1}{2}\sum_{j,k}^{r} s_{jk}x^jx^k\,. \quad (2.14)$$

From this follows the rate of entropy production:

$$\varDelta\dot{S}=-\sum_{j,k}^{r} s_{jk}x^j\dot{x}^k\,. \quad (2.15)$$

What gives the law of macroscopic irreversible decay is the system of equations (2.9), with the left-hand sides put equal to zero:

$$\sum_{j}^{r}\{-s_{kj}x^j(t)+z_{kj}^0\dot{x}^j(t)\}=0\,. \quad (2.16)$$

Substituting this into (2.15), we have

$$\varDelta\dot{S}=-\sum_{j,k}^{r} z_{kj}^0\dot{x}^j\dot{x}^k\,. \quad (2.17)$$

Now the affinities are given by

$$A_i=T(\partial\varDelta S/\partial x^i)=-T\sum_{j} s_{ij}x^j\,, \quad (2.18)$$

and the kinetic coefficients $L^{ij}$ are defined by

$$\dot{x}^i=\sum_{j} L^{ij}A_j; \quad (2.19)$$

we get therefore

$$-T\sum_{j} s_{kj}x^j=\sum_{j} L_{kj}\dot{x}^j\,, \quad (2.20)$$

where $L_{kj}$'s are the elements of the inverse matrix of $\{L^{kj}\}$. Comparing this with (2.16) it follows that

$$z^0_{ki} = -L_{ki}/T\,. \qquad (2.21)$$

Substituting this in (2.17), we obtain

$$\dot{\varDelta S} = (1/T)\sum_{j,k}^{r} L_{kj}\dot{x}^k\dot{x}^j\,. \qquad (2.22)$$

This coincides with the ordinary expression for the dissipation function.

Thus we see that, if we use the symbols of irreversible thermodynamics, the preceding system of Langevin equations is expressed as

$$-T\sum_j L^{kj}\mathscr{F}_j(t) = \sum_{i,j}\{TL^{kj}s_{ji}x^i\} + \dot{x}^k\,. \qquad (2.23)$$

If we further use the symbols

$$\varLambda^i_j = T\sum_k L^{ik}s_{kj}\,,$$

which have been employed by Hashitsume, and define that

$$p^k(t) = -T\sum_j L^{kj}\mathscr{F}_j(t)\,,$$

this turns out to be

$$\dot{x}^k + \sum_i \varLambda^k_i x^i = p^k(t)\,. \qquad (2.24)$$

Using the spectra of $F_j(t)$ and the relations (2.21), we get

$$\langle\mathscr{F}_i(t)\mathscr{F}_j(t+\tau)\rangle_{\mathrm{AV}} = 2kL_{ij}\delta(\tau)/T\,,$$

and consequently

$$\langle p^k(t)p^j(t+\tau)\rangle_{\mathrm{AV}} = 2kTL^{kj}\delta(\tau)\,. \qquad (2.25)$$

Thus it is shown that (2.24) coincides completely with the system of Langevin equations appearing in irreversible thermodynamics.

Next consider the more general case:

$$Z_{ij}(i\omega) = z^{-1}_{ij}/(i\omega) + z^0_{ij} + i\omega z^1_{ij}\,,$$
$$z^{-1}_{ij} = \partial F_i/\partial X^j\,. \qquad (2.26)$$

In this case the equations giving the relation between $x^i$ and $f_i$ are

$$f_i(t) = \sum_j^r\{z^{-1}_{ij}x^j(t) + z^0_{ij}\dot{x}^j(t) + z^1_{ij}\ddot{x}^j(t)\}\,. \qquad (2.27)$$

Inasmuch as the equations describing the fluctuations in equilibrium or the irreversible decay from a nonequilibrium state are (2.27) with left-hand sides replaced by the random forces $\mathscr{F}_i(t)$, whose spectra are again constants, (2.27) becomes the system of ordinary Langevin equations of the second order. We shall show that this is equivalent to the system of Langevin equations which Onsager and Machlup have obtained for the case including the velocity variables.

As the entropy deviation we assume, after Onsager and Machlup, the form:

$$\varDelta S = -\frac{1}{2}\sum_{i,j}s_{ij}x^ix^j - \frac{1}{2}\sum_{i,j}m_{ij}\dot{x}^i\dot{x}^j\,. \qquad (2.28)$$

From the same argument as before, it follows that

$$s_{ij} = -\partial^2\varDelta S/\partial x^i\partial x^j = -\partial F_i/\partial X^j$$
$$= -\partial F_j/\partial X^i = s_{ji} = -z^{-1}_{ij}\,. \qquad (2.29)$$

Differentiating (2.28) with respect to time we get

$$\dot{\varDelta S} = -\sum_{i,j}s_{ij}x^i\dot{x}^j - \sum_{i,j}m_{ij}\dot{x}^i\ddot{x}^j\,, \qquad (2.30)$$

which, using the equations giving the law of macroscopic irreversible decay

$$\sum_j^r s_{ij}x^j(t) = \sum_j^r\{z^0_{ij}\dot{x}^j(t) + z^1_{ij}\ddot{x}^j(t)\}\,, \qquad (2.31)$$

becomes

$$\dot{\varDelta S} = -\sum_{i,j}z^0_{ij}\dot{x}^j\dot{x}^i - \sum_{i,j}z^1_{ij}\ddot{x}^j\dot{x}^i - \sum_{i,j}m_{ij}\dot{x}^i\ddot{x}^j\,. \qquad (2.32)$$

Since only the real part of the impedance contributes to the energy dissipation, $\dot{\varDelta S}$ should not contain the coefficients $z^1_{ij}$. Also it should not contain $m_{ij}$, which have nothing to do with the mechanism of the irreversible change. Therefore we must put

$$m_{ij} = -z^1_{ij}\,, \qquad (2.33)$$

and

$$z^0_{ij} = -L_{ij}/T\,. \qquad (2.34)$$

Affinities are now given, from (2.31), by

$$A_i = \sum_j L_{ij}\dot{x}^j = -T\sum_j z^0_{ij}\dot{x}^j$$
$$= -T\sum_j s_{ij}x^j + T\sum_j z^1_{ij}\ddot{x}^j$$
$$= T\{\partial\varDelta S/\partial x^i + (d/dt)(\partial\varDelta S/\partial\dot{x}^i)\}\,, \qquad (2.35)$$

which, together with the expressions for entropy and dissipation function, coincide with the forms which Onsager and Machlup have given. If we further define

$$p_i(t) = -T\mathscr{F}_i(t)\,,$$

the irreversible process including fluctuations is now described by the system of Langevin equations:

$$\sum_j^r\{Ts_{ij}x^j + L_{ij}\dot{x}^j + Tm_{ij}\ddot{x}^j\} = p_i(t)\,,$$
$$\langle p_i(t)p_j(t+\tau)\rangle_{\mathrm{AV}} = 2kTL_{ij}\delta(\tau)\,, \qquad (2.36)$$

which is also of the form given by Onsager and Machlup.

We have thus shown that the fluctuation-dissipation theorem naturally leads us to the ordinary irreversible thermodynamics for the special forms of impedances.

## § 3. Irreversible-Thermodynamical Derivation of Fluctuation-Dissipation Theorem

In order to provide a thermodynamical basis for the theory of viscoelastic deformation of the matter, Meixner[6] showed that, by first introducing the "inner" variables which obey together with the variable under examination the equation of irreversible thermodynamics and afterwards eliminating them, the variable with viscoelastic impedance can be obtained. We shall show in this section that, starting not from the elastic relation between stress and strain but from the equation of irreversible thermodynamics itself containing the fluctuation term, we can construct a variable with a more general impedance, and that its fluctuation spectrum just coincides with what is given by the fluctuation-dissipation theorem.

Let $x(t)$ be the variable for which we should derive the impedance, and let us assume that this $x(=\xi^0)$, together with $n$ inner variables $\xi^\alpha(\alpha=1, 2\cdots, n)$, obeys the law of irreversible thermodynamics. Then the entropy deviation in a nonequilibrium state is

$$\varDelta S=-\frac{1}{2}s_{00}x^2-\sum_{\alpha=1}^{n}s_{0\alpha}x\xi^\alpha-\frac{1}{2}\sum_{\alpha,\beta}^{n}s_{\alpha\beta}\xi^\alpha\xi^\beta\,, \quad (3.1)$$

and the affinities for $x$ and $\xi^\alpha$ are given by

$$\left.\begin{aligned} A_0&=T(\partial\varDelta S/\partial x)=-Ts_{00}x-T\sum_\alpha s_{0\alpha}\xi^\alpha\,,\\ A_\alpha&=T(\partial\varDelta S/\partial\xi^\alpha)=-TS_{0\alpha}x-T\sum_\beta s_{\alpha\beta}\xi^\beta\,,\end{aligned}\right\} \quad (3.2)$$

respectively. The equations for irreversible change of $x$ and $\xi^\alpha$ are (using the summation convention for the summation from 0 to $n$),

$$dx/dt=L^{00}A_0+\sum_\beta L^{0\beta}A_\beta+p^0(t)=L^{0\beta}A_\beta+p^0(t)\,, \quad (3.3)$$

$$d\xi^\alpha/dt=L^{\alpha0}A_0+\sum_\beta L^{\alpha\beta}A_\beta+p^\alpha(t)=L^{\alpha\beta}A_\beta+p^\alpha(t)\,, \quad (3.4)$$

where $L^{\alpha\beta}(\alpha, \beta=0, 1, 2, \cdots, n)$ are kinetic coefficients, and $p^\alpha(t)(\alpha=0, 1, 2, \cdots, n)$ are fluctuating forces, whose correlation functions and spectra are given by

$$\left.\begin{aligned}\langle p^\alpha(t)p^\beta(t+\tau)\rangle_{\text{AV}}&=2kTL^{\alpha\beta}\delta(\tau)\,,\\ \mathscr{P}^{\alpha\beta}(i\omega)&=(2/\pi)^{1/2}kTL^{\alpha\beta}\,,\end{aligned}\right\} \quad (3.5)$$

respectively.

Solving (3.4) for $A_\alpha$, we obtain

$$A_\alpha=L_{\alpha\beta}(i\omega\xi^\beta)-L_{\alpha\beta}p^\beta(t)\,,$$

where $L_{\alpha\beta}$'s are the elements of the inverse matrix $\{L_{\alpha\beta}\}$ of $(n+1)\times(n+1)$ matrix $\{L^{\alpha\beta}\}$, and $(i\omega)$ represents the differential operator $d/dt$*. Introducing this equation into the second equation of (3.2), we get

$$\sum_\beta\{i\omega L_{\alpha\beta}+Ts_{\alpha\beta}\}\xi^\beta=-(i\omega L_{\alpha0}+Ts_{0\alpha})x+L_{\alpha\beta}p^\beta(t).$$

We define the $(n\times n)$ matrix $\{\varPhi_{\alpha\beta}\}$ by

$$\{i\omega L_{\alpha\beta}+Ts_{\alpha\beta}\}=\varPhi_{\alpha\beta}(i\omega)\,,$$

and denote the inverse matrix thereof by $\{\varPhi^{\alpha\beta}\}$, obtaining

$$\begin{aligned}\xi^\beta=&-\sum_\alpha\varPhi^{\alpha\beta}(i\omega)\{i\omega L_{\alpha0}+Ts_{0\alpha}\}x\\ &+\sum_\alpha\varPhi^{\alpha\beta}L_{\alpha\gamma}p^\gamma(t)\,.\end{aligned} \quad (3.6)$$

On the other hand, from (3.2) and (3.3),

$$\begin{aligned}i\omega x=&L^{00}(-Ts_{00}x-T\sum_\alpha s_{0\alpha}\xi^\alpha)\\ &+\sum_\alpha L^{0\alpha}(-Ts_{0\alpha}x-T\sum_\beta s_{\alpha\beta}\xi^\beta)+p^0(t)\,,\end{aligned}$$

which gives, with the help of (3.6),

$$\begin{aligned}&i\omega x+(L^{00}Ts_{00}+T\sum_\alpha L^{0\alpha}s_{0\alpha})x\\ &=TL^{0\alpha}\sum_{\beta,\gamma}s_{\alpha\beta}\varPhi^{\gamma\beta}(i\omega)(i\omega L_{\gamma0}+Ts_{0\gamma})x\\ &\quad-TL^{0\alpha}\sum_{\beta,\gamma}s_{\alpha\beta}\varPhi^{\gamma\beta}(i\omega)L_{\gamma\delta}p^\delta(t)+p^0(t)\,.\end{aligned} \quad (3.7)$$

Since $\{L_{\alpha\beta}\}$ and $\{s_{\alpha\beta}\}$ are both symmetric, they can be simultaneously diagonalized by a real matrix $\{T_\alpha{}^\beta\}$:

$$\sum_{\beta,\gamma}T_\alpha{}^\beta(Ts_{\beta\gamma}+i\omega L_{\beta\gamma})T_\varepsilon{}^\gamma=(1+i\omega\tau_\alpha)\delta_{\alpha\varepsilon}\,,$$

and consequently $\varPhi^{\gamma\beta}$ assumes the form

$$\varPhi^{\gamma\beta}(i\omega)=\sum_\delta T_\delta{}^\gamma T_\delta{}^\beta/(1+i\omega\tau_\delta)\,. \quad (3.8)$$

Hence it follows, in conjunction with (3.7), that

$$\begin{aligned}&i\omega x+(TL^{00}s_{00}+T\sum_\alpha L^{0\alpha}s_{0\alpha})x\\ &=TL^{0\alpha}\sum_{\beta,\gamma,\delta}s_{\alpha\beta}\frac{T_\delta{}^\gamma T_\delta{}^\beta}{1+i\omega\tau_\delta}(i\omega L_{\gamma0}+Ts_{0\gamma})x\\ &\quad-TL^{0\alpha}\sum_{\beta,\gamma,\delta}s_{\alpha\beta}\frac{T_\delta{}^\gamma T_\delta{}^\beta}{1+i\omega\tau_\delta}L_{\gamma\varepsilon}p^\varepsilon(t)+p^0(t)\,.\end{aligned} \quad (3.9)$$

From this it is clear that the impedance is given by

$$AZ(i\omega)=1+T(L^{00}s_{00}+\sum_\alpha L^{0\alpha}s_{0\alpha})/(i\omega)$$

---

* The symbolic method used here can be justified by the theory of Fourier transforms: see the reference [6].

$$-TL^{0\alpha}\sum_{\beta,\gamma,\delta} s_{\alpha\beta}\frac{T_\delta{}^\gamma T_\delta{}^\beta}{i\omega(1+i\omega\tau_\delta)}(i\omega L_{\gamma 0}+Ts_{0\gamma}),\tag{3.10}$$

which has the form

$$Z(i\omega)=z^{-1}/(i\omega)+z^0+\sum_j c_j/(i\omega-p_j),\tag{3.11}$$

where $p_j=-1/\tau_j$, which are all negative, inasmuch as $\tau_\delta$'s, the eigenvalues of the matrix $\{Ts_{\alpha\beta}\}^{-1}\{L_{\alpha\beta}\}$, are positive real. This corresponds to the physical realizability of $Z(i\omega)$. $A$ is the numerical factor to be determined below. The real part of this impedance is

$$A\,\mathrm{Re}\,Z(i\omega)$$
$$=1+TL^{0\alpha}\sum_{\beta,\gamma,\delta}\frac{s_{\alpha\beta}T_\delta{}^\gamma T_\delta{}^\beta(-L_{\gamma 0}+Ts_{0\gamma}\tau_\delta)}{1+\omega^2\tau_\delta{}^2}.\tag{3.12}$$

The spectrum $\mathcal{Q}(i\omega)$ of the fluctuating force

$$\left[-TL^{0\alpha}\sum_{\beta,\gamma,\delta} s_{\alpha\beta}\frac{T_\delta{}^\gamma T_\delta{}^\beta}{1+i\omega\tau_\delta}L_{\gamma\varepsilon}p^\varepsilon(t)+p^0(t)\right]\Big/A$$

corresponding to the impedance $Z(i\omega)$ is easily obtained by the use of (3.5):

$$\begin{aligned}A^2\mathcal{Q}(i\omega)=&(2/\pi)^{1/2}kT^3L^{0\alpha}L^{0\alpha'}\sum_{\beta,\gamma,\delta,\beta',\gamma',\delta'} s_{\alpha\beta}s_{\alpha'\beta'}\frac{T_\delta{}^\gamma T_\delta{}^\beta T_{\delta'}{}^{\gamma'} T_{\delta'}{}^{\beta'}}{(1+i\omega\tau_\delta)(1-i\omega\tau_{\delta'})}L_{\gamma\varepsilon}L_{\gamma'\varepsilon'}L^{\varepsilon\varepsilon'}\\&-(2/\pi)^{1/2}k\mathrm{T}^2L^{0\alpha}\sum_{\beta,\gamma,\delta} s_{\alpha\beta}\frac{T_\delta{}^\gamma T_\delta{}^\beta}{1+i\omega\tau_\delta}L_{\gamma\varepsilon}L^{\varepsilon 0}-(2/\pi)^{1/2}kT^2L^{0\alpha}\sum_{\beta,\gamma,\delta} s_{\alpha\beta}\frac{T_\delta{}^\gamma T_\delta{}^\beta}{1-i\omega\tau_\delta}L_{\gamma\varepsilon}L^{\varepsilon 0}\\&+(2/\pi)^{1/2}kTL^{00}.\end{aligned}$$

The second and third terms of this expression vanishes since $L_{\gamma\varepsilon}L^{\varepsilon 0}=\delta_\gamma{}^0=0$. The first term can be transformed as follows:

$$\begin{aligned}\text{The first term}&=(2/\pi)^{1/2}kT^3\sum_{\beta,\beta',\delta,\delta'}L^{0\alpha}L^{0\alpha'}s_{\alpha\beta}s_{\alpha'\beta'}\frac{T_\delta{}^\beta T_{\delta'}{}^{\beta'}\tau_\delta\delta_{\delta\delta'}}{(1+i\omega\tau_\delta)(1-i\omega\tau_\delta)}\\&=(2/\pi)^{1/2}kT^3\sum_{\alpha',\beta,\beta',\delta}L^{0\alpha}L^{0\alpha'}s_{\alpha\beta}s_{\alpha'\beta'}\frac{T_\delta{}^\beta T_\delta{}^{\beta'}\tau_\delta}{1+\omega^2\tau_\delta{}^2}\\&\quad+(2/\pi)^{1/2}kT^3L^{00}\sum_{\beta,\beta',\delta}L^{0\alpha}s_{\alpha\beta}s_{0\beta'}\frac{T_\delta{}^\beta T_\delta{}^{\beta'}\tau_\delta}{1+\omega^2\tau_\delta{}^2}.\end{aligned}\tag{3.13}$$

By virtue of the relations

$$\sum_{\beta'}T_\delta{}^{\beta'}L_{\beta'\alpha'}=\sum_\varepsilon\tau_\delta\delta_{\delta\varepsilon}S_{\alpha'}{}^\varepsilon,$$
$$T\sum_{\beta'}T_\delta{}^{\beta'}s_{\alpha'\beta'}=\sum_\varepsilon\delta_{\delta\varepsilon}S_{\alpha'}{}^\varepsilon,$$

and

$$L_{0\beta'}=-(1/L^{00})\sum_{\alpha'}L^{0\alpha'}L_{\alpha'\beta'},$$

where $\{S_\alpha{}^\beta\}$ is the inverse of $\{T_\alpha{}^\beta\}$, the first term of (3.13) becomes

$$\begin{aligned}&=(2/\pi)^{1/2}kT^2\sum_{\alpha',\beta,\delta,\varepsilon}L^{0\alpha}L^{0\alpha'}s_{\alpha\beta}\frac{T_\delta{}^\beta\delta_{\delta\varepsilon}S_{\alpha'}{}^\varepsilon\tau_\delta}{1+\omega^2\tau_\delta{}^2}\\&=(2/\pi)^{1/2}kT^2\sum_{\alpha',\beta,\beta',\delta}L^{0\alpha}L^{0\alpha'}s_{\alpha\beta}\frac{T_\delta{}^\beta T_\delta{}^{\beta'}L_{\beta'\alpha'}}{1+\omega^2\tau_\delta{}^2}\\&=-(2/\pi)^{1/2}kT^2L^{00}\sum_{\beta,\beta',\delta}L^{0\alpha}s_{\alpha\beta}\frac{T_\delta{}^\beta T_\delta{}^{\beta'}L_{0\beta'}}{1+\omega^2\tau_\delta{}^2}.\end{aligned}$$

Thus $\mathcal{Q}(i\omega)$ eventually reduces to

$$A^2\mathcal{Q}(i\omega)=(2/\pi)^{1/2}kTL^{00}\left[1+TL^{0\alpha}\sum_{\beta,\gamma,\delta}\frac{s_{\alpha\beta}T_\delta{}^\beta T_\delta{}^\gamma(-L_{0\gamma}+Ts_{0\gamma}\tau_\delta)}{1+\omega^2\tau_\delta{}^2}\right].\tag{3.14}$$

This coincides with (3.12) except for a numerical factor, that is, the spectrum of the fluctuating force corresponding to the variable constructed irreversible-thermodynamically as above is given by the real part of its impedance, just in accordance with the requirement of the fluctuation-dissipation theorem. The numerical factor $A$ should be determined so as to make this coincidence exact. Since fluctuation-dissipation theorem requires that

$$\mathscr{Q}(i\omega)=-(2/\pi)^{1/2}k\,\mathrm{Re}\,Z(i\omega)\,,$$

$A$ must be

$$A=-TL^{00}\,,$$

so that the coefficient $z^0$ in (3.11) must be

$$z^0=-1/TL^{00}\,.$$

This again coincides with the value that $z^0$ should have in the case involving no inner variables (where $1/L^{00}=L_{00}$).

It has thus been shown that for impedances of the form (3.11), the irreversible-thermodynamical description is still possible.

If we follow the similar procedure of elimination for the case where the velocity variables exist, using the definition of entropy (2.28) and of affinity which Onsager and Machlup have given for such cases, we obtain the impedance which has the term proportional to $i\omega$ and for which $p_j$'s become in general complex. These constants, however, cannot be obtained as above as the eigenvalues of a matrix, since there appear, in addition to $\{s_{\alpha\beta}\}$ and $\{L_{\alpha\beta}\}$, a new matrix $\{m_{\alpha\beta}\}$ which gives the quadratic form corresponding to the kinetic energy of the system. Consequently the equations become considerably complicated. Here therefore we shall content ourselves with the proof for the simplest case of one inner variable.

The entropy deviation and the affinities are given by

$$\begin{aligned}\Delta S=&-\frac{1}{2}s_{00}x^2-s_{01}x\xi-\frac{1}{2}s_{11}\xi^2\\&-\frac{1}{2}m_{00}\dot{x}^2-m_{01}\dot{x}\dot{\xi}-\frac{1}{2}m_{11}\dot{\xi}^2\,,\end{aligned}\tag{3.15}$$

and

$$\begin{aligned}A_0&=-T(s_{00}x+s_{01}\xi+m_{00}\ddot{x}+m_{01}\ddot{\xi})\,,\\A_1&=-T(s_{01}x+s_{11}\xi+m_{01}\ddot{x}+m_{11}\ddot{\xi})\,,\end{aligned}\tag{3.16}$$

respectively, and the Langevin equations take the form

$$dx/dt=L^{00}A_0+L^{01}A_1+p^0(t)\,,\tag{3.17}$$

$$d\xi/dt=L^{10}A_0+L^{11}A_1+p^1(t)\,,\tag{3.18}$$

where $p^0(t)$ and $p^1(t)$ are the fluctuating forces, whose correlation functions and spectra are given by

$$\left.\begin{aligned}\langle p^i(t)p^j(t+\tau)\rangle_{\mathrm{AV}}&=2kTL^{ij}\delta(\tau)\,,\\\mathscr{P}^{ij}(i\omega)&=(2/\pi)^{1/2}kTL^{ij}\,,\end{aligned}\right\}\tag{3.19}$$

respectively. Eliminating $A_0$ by making use of (3.17) and then $A_1$ with the aid of (3.16), (3.18) becomes

$$\begin{aligned}-\{Ts_{11}+Tm_{11}(i\omega)^2+L_{11}(i\omega)\}\xi&\\=\{Ts_{01}+Tm_{01}(i\omega)^2+L_{10}(i\omega)\}x&\\-(L_{10}p^0+L_{11}p^1)\,.&\end{aligned}$$

(3.17) can be written, in virtue of (3.16) and this relation, as

$$\begin{aligned}i\omega x+T\{L^{00}s_{00}+L^{01}s_{01}+(i\omega)^2(L^{00}m_{00}+L^{01}m_{01})\}x&\\=\frac{T\{L^{00}s_{01}+L^{01}s_{11}+(i\omega)^2(L^{00}m_{01}+L^{01}m_{11})\}}{Ts_{11}+Tm_{11}(i\omega)^2+L_{11}(i\omega)}\{Ts_{01}+Tm_{01}(i\omega)^2+L_{10}(i\omega)\}x&\\-\frac{T\{L^{00}s_{01}+L^{01}s_{11}+(i\omega)^2(L^{00}m_{01}+L^{01}m_{11})\}}{Ts_{11}+Tm_{11}(i\omega)^2+L_{11}(i\omega)}(L_{10}p^0+L_{11}p^1)+p^0\,,&\end{aligned}\tag{3.20}$$

which shows that the impedance should be

$$\begin{aligned}AZ(i\omega)=1+\frac{T(L^{00}s_{00}+L^{01}s_{01})}{i\omega}+i\omega T(L^{00}m_{00}+L^{01}m_{01})&\\-\frac{T\{L^{00}s_{01}+L^{01}s_{11}-\omega^2(L^{00}m_{01}+L^{01}m_{11})\}\{Ts_{01}-Tm_{01}\omega^2+L_{10}(i\omega))\}}{i\omega\{Ts_{11}-Tm_{11}\omega^2+L_{11}(i\omega))\}}&\end{aligned}\tag{3.21}$$

This clearly has the form (1.2). (That the impedance should have the form (1.2) can easily be shown also for the case of several inner variables. Complexity occurs only in the spectrum of the random term). The real part of (3.21) is

$$A\,\mathrm{Re}\,Z(i\omega)=1+\frac{T^2\{L^{00}s_{01}+L^{01}s_{11}-\omega^2(L^{00}m_{01}+L^{01}m_{11})\}\{L_{11}(s_{01}-m_{01}\omega^2)-L_{10}(s_{11}-m_{11}\omega^2)\}}{L_{11}{}^2\omega^2+(Ts_{11}-Tm_{11}\omega^2)^2}\tag{3.22}$$

On the other hand, the spectrum of the fluctuating force appearing on the right-hand side of

(3.20) becomes

$$(2/\pi)^{1/2}kT\left[\frac{T^2\{L^{00}s_{01}+L^{01}s_{11}-\omega^2(L^{00}m_{01}+L^{01}m_{11})\}^2}{(Ts_{11}-Tm_{11}\omega^2)^2+L_{11}{}^2\omega^2}(L_{10}{}^2L^{00}+2L_{10}L_{11}L^{01}+L_{11}{}^2L^{11})\right.$$
$$-\frac{T\{L^{00}s_{01}+L^{01}s_{11}-\omega^2(L^{00}m_{01}+L^{01}m_{11})\}}{Ts_{11}-Tm\omega^2+i\omega L_{11}}(L_{10}L^{00}+L_{11}L^{10})$$
$$\left.-\frac{T\{L^{00}s_{01}+L^{01}s_{11}-\omega^2(L^{00}m_{01}+L^{01}m_{11})\}}{Ts_{11}-Tm\omega^2-i\omega L_{11}}(L_{10}L^{00}+L_{11}L^{10})+L^{00}\right]. \qquad (3.23)$$

As before, the second and the third terms vanish identically and the first term can be transformed by the help of the relations between the elements of $\{L^{ij}\}$ and those of $\{L_{ij}\}$, so that we finally get the expression for the spectrum:

$$(2/\pi)^{1/2}kTL^{00}\left[\frac{T^2\{L^{00}s_{01}+L^{01}s_{11}-\omega^2(L^{00}m_{01}+L^{01}m_{11})\}}{(Ts_{11}-Tm_{11}\omega^2)^2+L_{11}{}^2\omega^2}\right.$$
$$\left.\times\{(s_{01}-m_{01}\omega^2)L_{11}-(s_{11}-m_{11}\omega^2)L_{10}\}+1\right], \qquad (3.24)$$

which just coincides with (3.22), provided that we put

$$A=-TL^{00}.$$

Thus it has been shown that for the impedances of the form (1.2), the irreversible-thermodynamical description is still possible, at least in principle.

## § 4. Conclusions

In the classical derivation of the fluctuation-dissipation theorem it is always assumed, as the fundamental postulate, that the average regression of the fluctuation coincides with the macroscopic irreversible decay (e.g., Callen and Greene [3]). As Onsager and Machlup⁵⁾ have pointed out, this is none other than the requirement that the process should be essentially Markovian. In one-dimensional Gaussian process this requires that the spectrum of the fluctuation be of the Lorentz-type. Since for general impedances the spectrum of the fluctuation is evidently not Lorentzian, the process cannot be one-dimensional Markov process in so far as we assume it to be Gaussian, the assumption which is physically most reasonable. Thus we are driven to consider it to be the one-dimensional projection of a certain many-dimensional Gaussian Markov process. Now since the ordinary irreversible-thermodynamical process with several variables constitutes a several-(but finite-) dimensional Gaussian Markov process, it is natural to expect that for impedances of the form (1.2) the process suggested by the fluctuation-dissipation theorem can be represented as its one-dimensional projection, in conformity with the fact that such a form of impedance implies the finite dimensionality of the process (finite number of relaxation times). This is just what was proved in § 3.

Almost all the variables that appear in practice are either exactly of the form (1.2) or can be approximated sufficiently closely by such a form. Thus we might conclude that most of the variables whose macroscopic behavior is described by their impedances and whose microscopic behavior is given by fluctuation-dissipation theorem can be described also by the ordinary irreversible thermodynamics.

The author wishes to express his sincere thanks to Prof. S. Ono for helpful advices concerning this paper. He is also partly indebted to the Ministry of Education for the financial aid.

## References

1) H. Takahasi: J. Phys. Soc. Japan **7** (1952) 439.
2) H. B. Callen and T. A. Welton: Phys. Rev. **83** (1951) 34.
3) H. B. Callen and R. F. Greene: Phys. Rev. **86** (1952) 702.
4) N. Hashitsume: Prog. Theor. Phys. **8** (1952) 461.
5) L. Onsager and S. Machlup: Phys. Rev. **91** (1953) 1505, 1512.
6) J. Meixner: Zeits. f. Naturforschung **9a** (1954) 654.
7) R. F. Greene and H. B. Callen: Phys. Rev. **83** (1951) 1231.

JOURNAL OF THE PHYSICAL SOCIETY OF JAPAN Vol 11., No. 12, DECEMBER, 1956

# On the Polygonization of Rock Salt Crystals

By Sukeaki HOSOYA, Seiya SATAKE* and Satio TAKAGI

(Received August 9, 1956)

*Institute of Physics, College of General Education, University of Tokyo*

Ionic crystals can be plastically bent under water to a great extent. This phenomenon has been known as Joffé effect, the mechanism being not fully elucidated. In the present work the X-ray diffraction method and etch pit techniques have been used in order to investigate the arrangement of crystallites in the bent and annealed rock salt. Both results show, with good correspondence, that the crystal consists of many polygonized crystallites which have the form like letter $L$, with small angle boundaries between the neighbours. The mean thickness of these crystallites was about $0.02\sim0.03$ mm, when the radius of curvature of bending was about 20 mm.

## § 1. Introduction

Rock salt crystals can be plastically deformed under water to a great extent, with the glide planes $\{110\}$ and with the glide directions $\langle 110\rangle$. This phenomenon has been known for many years as Joffé effect, being named after the first investigator[1], and it has been investigated by the X-ray diffraction, by optical observations, by mechanical measurements and by other methods[2]–[7].

Konobejewski and Mirer[3] obtained the elastic stress in the bent crystal, the thickness of the crystallites in bent and annealed crystals and other properties of the crystal, by observing the splitting of the Laue diffraction spots. Komar[5] measured the radius of curvature from the focusing pattern of the Laue diffraction spot. Earlier works are introduced in the textbook by Schmid and Boas[8] and in the one by Tertsch[9].

Recently Amelinckx[10],[11] optically observed the polygonized domains on the plane (100) (Fig. 1) of the bent and annealed crystal, using the Françon's method[12], and found the irregular boundaries along [101] and [10$\bar{1}$] directions on the (010) plane using the etch pit technique[11],[13].

We have found, however, more regular polygonized domains by the same technique, which well correspond to the Laue spot patterns.

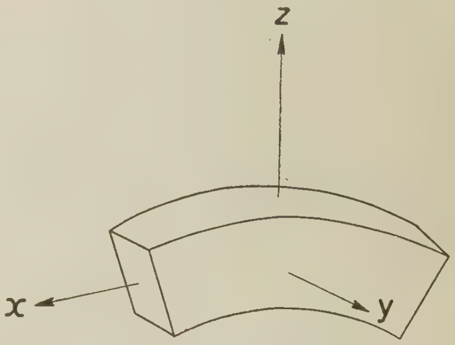

Fig. 1. The crystal axes as are referred in the text.

## § 2. Investigations by Laue Photographs

Rock salt crystals prepared from melt are cleaved into small samples which are usually about $25\times4\times3\,\mathrm{mm}^3$ in size. This sample is bent under lukewarm water to such an extent that the radius of curvature is usually about 20 mm. The crystal axes will be referred later as shown in Fig. 1, that is, the bending axis is the $y$-axis. The bent crystal can be cleaved along (010) plane even before being annealed.

One of the Laue photographs of bent and annealed crystals is shown in Fig. 2. The incident X-rays are parallel to the $y$-axis, each of the spots elongates more or less along concentric circles, and some of them split into many well defined subspots. The degree of elongation depends upon the azimuthal position of the spots around the incident spot. Further, the clearness of splitting also depends upon the azimuthal position of the spots. In Fig. 2, for instance, the spots right above the incident spot show the largest elongation and those right below the smallest elongation. The spots on the upper right ($\bar{h}kh$) and those on the lower left ($hk\bar{h}$) show most clear splitting and the

---

* Now at Musashi Technical College

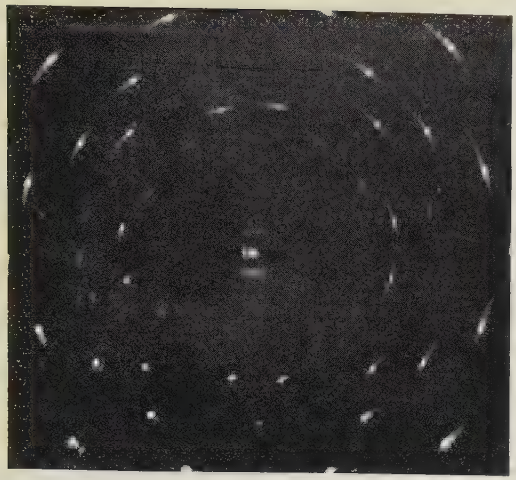

(a)

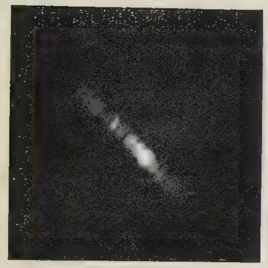

(b)

Fig. 2.
(a) Laue photograph of a bent and annealed rock salt crystal, incident beam being parallel to [010].
(b) Enlarged print of splitted $\bar{4}24$ spot.

spots on the upper left (hkh) and on the lower right ($\bar{h}k\bar{h}$) do not show any splitting. Others show intermediate splitting. The elongation of the spots is, of course, due to the bending of the crystal lattice, as was pointed out by some earlier investigators5),6). The elongation of the spot is largest at the convex side of the crystal, and is smallest at the concave side.

The splitting of the spots indicates that the bending is not continuous, but the crystal consists of many polygonized domains or crystallites the shape and the orientation of which are known from the azimuthal dependence of the splitting above mentioned. The results are schematically shown in Fig. 3. Each crystallite is a thin wedge shaped plate parallel to (101) (or to (10$\bar{1}$)).

The angle between the neighbouring crystallites can be easily measured on the Laue pattern. The average thickness of crystallites are known from the irradiated area of the specimen and the number of subspots in one Laue spot. The results are shown in Table I for example.

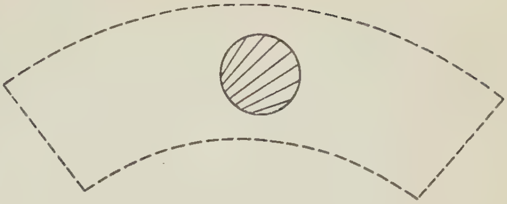

Fig. 3. The arrangements of the crystallites inferred from the Laue photograph. The dotted line shows the external form of the bent crystal.

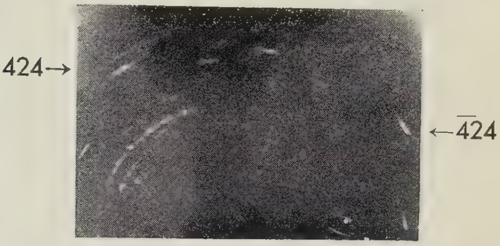

Fig. 4. Laue photograph showing the splitting of both hkh and $\bar{h}$kh spots, incident beam being parallel to [010].

Table I. Example of mean angle $\alpha$ between the neighbouring crystallites and mean thickness $d$ of a crystallite.

| | $\alpha$ | $d$ |
|---|---|---|
| From Laue photographs | 17′<br>24′ | 0.020 mm<br>0.028 |
| From Etch patterns | 27 | 0.026 |

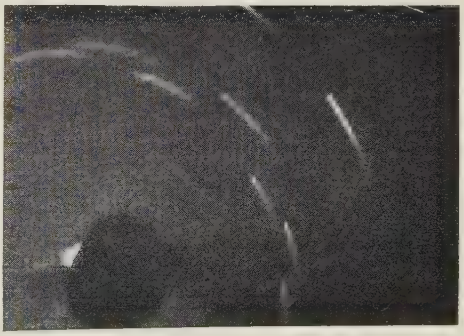

Fig. 5. Laue photograph of a bent rock salt crystal (not annealed), incident beam being parallel to [010].

Sometimes, both the spots hkh and hk$\bar{h}$ clearly split on a Laue photograph. An example is shown in Fig. 4. It is inferred that in this case the X-ray beam irradiated two kinds of areas at the same time, in one of which the wedge shaped crystallite plates were parallel to (101) and in another, to (10$\bar{1}$).

Before annealed, bent crystals give the Laue spots which already somewhat split into subspots, though the subspots are not well defined, as shown in Fig. 5. The polygonization, though incomplete, seems to occur before annealing.

## § 3. Investigations by Etching

By the etching technique[11), 13)] the boundaries between wedge-shaped crystallites can be observed on the (010) plane of the bent and annealed crystal. Fig. 6 shows that boundaries are not parallel but have a small angle and that crystallites have the form like letter L. From the angle between the neighbouring crystallites, the density of dislocations along the boundary is known to be in the order of $10^4\,\mathrm{mm}^{-1}$, assuming that the boundary consists of edge dislocations of the same sign only. It is reasonable, therefore, that the boundary in Fig. 6, is not a series of etch pits but apparently a continuous lines. The angle between boundaries and the breadth of crystallites are in the same order as the ones inferred by Laue photographs. An example is shown in Table I. Further, the Laue pattern in which both the hkh and hk$\bar{h}$ spots split, as shown in Fig. 4, could be obtained, when we intentionally irradiate both straight portion of the L-shaped crystallites. These facts mean the good correspondence between the results by X-ray diffraction and by etch patterns.

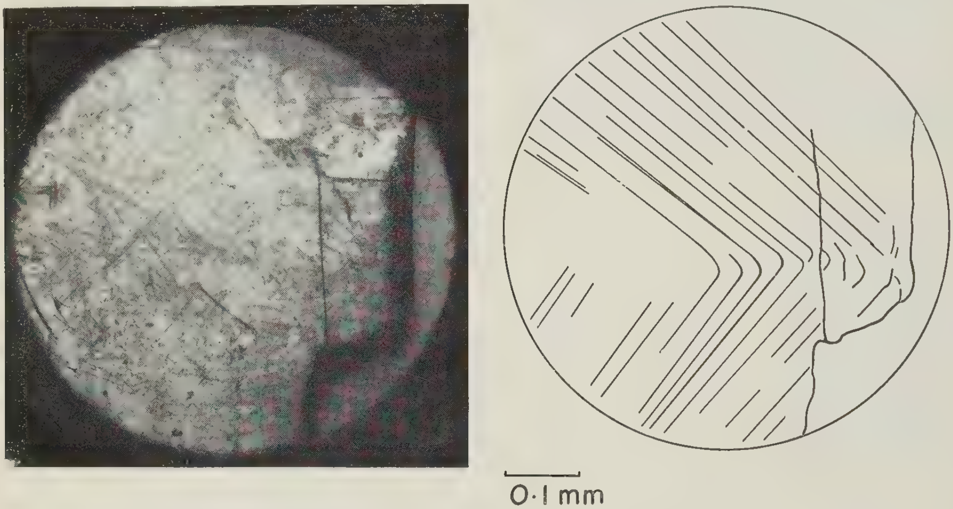

Fig. 6. The crystallite boundaries visualized by etching on the (010) plane.

## § 4. Conclusions

The results obtained by X-ray diffraction and etching clearly reveal the features of polygonized domains in bent and annealed rock salts, namely, the polygonized domains are wedge-shaped slabs, about 0.02∼0.03 mm in thickness and are parallel to one of {110} planes through the bending axis. This was also confirmed by the Laue photograph taken with incident beam parallel to the $z$-axis. Especially there were often found the L-letter-shaped polygonized domains, the corner of "L" being near the centre of the bent crystal slab, *i.e.*, near the neutral plane of bending. These will be further confirmed, as rather general features, in another work[14)] in which the colour centre colloids are used to visualize the boundaries inside the crystal.

This research was partly supported by the research grant of the Ministry of Education.

### References

1) A. Jeffé, M. W. Kirpitschewa and M. A. Lewitsky: ZS. f. Phys. **22** (1924) 285.
2) I. W. Obreimow and L. W. Schubnikoff: ZS. f. Phys. **41** (1927) 907.
3) S. Konobejwski and I. Mirer: ZS. f. Krist. **81** (1932) 69.
4) N. A. Brilliantow and I. W. Obreimow: Phys. ZS. d. Sowjetunion **6** (1934) 587.
5) A. Komar: ZS. f. Krist. **90** (1935) 467.

6) D. B. Gogoberidse: Phys. ZS. d. Sowjetunion **10** (1936) 826.
7) R. W. Cahn: J. Inst. Metals **76** (1949) 121.
8) E. Schmid and W. Boas: *Kristallplastizität* (Springer, Berlin, 1935), or *Plasticity of Crystals* (F. A. Fughes & Co., Ltd., 1950) in English version.
9) H. Tertsch: *Die Festigkeitserscheinungen der Kristalle* (Springer, Wien, 1949).
10) S. Amelinckx: Neture **173** (1954) 993.
11) S. Amelinckx: Ghent Dissertation, 1955 (in Dutch).
12) M. Françon: Rev. d'Optique **31** (1952) 65.
13) S. Amelinckx: Acta Metal. **2** (1954) 850.
14) S. Hosoya: J. Phys. Soc. Japan **11** (1956) 1231.

---

JOURNAL OF THE PHYSICAL SOCIETY OF JAPAN Vol. 11, No. 12, DECEMBER, 1956

# On the Polygonized Domain Pattern in Bent and Annealed NaCl Crystals Visualized by Colour Centre Colloids

By Sukeaki HOSOYA

*Institute of Physics, College of General Education, University of Tokyo*

(Received August 8, 1956)

Colour centre colloids have been used to visualize the dislocation networks in ionic crystals. The polygonization boundaries inside the crystal are also clearly seen by the decoration effect of the colloids. It has been found that these boundaries are usually *L*-letter-shaped in the strongly bent and annealed crystals. This polygonized structure is well corresponding to the results derived from etch pits and X-ray diffraction.

Polygonized boundaries were found to appear in the direction perpendicular to the glide planes when the crystal is annealed at 600°C or higher.

## § 1. Introduction

According to Smekal,¹⁾ the strained part of rock salt crystals is preferably coloured when irradiated with X-rays. Rexer²⁾ showed that Na colloids precipitate at the imperfections in NaCl crystals by the suitable heat treatment. From these facts, one would expect that the dislocation networks are to be visualized by colour centre colloids in the same way as Hedges and Mitchell³⁾ observed the networks in AgBr by the print-out effect. In fact, Amelinckx et al⁴⁾ succeeded in visualizing grain boundaries, dislocation lines, and dislocation networks, along this idea. In recent work, Amelinckx⁵⁾ obtained the regular networks and showed that their arrangements are well explained by the theory of Frank. The same work was being independently pursued in our laboratory. In the present paper, the macroscopic pattern of polygonized domain boundaries will be chiefly mentioned.

## § 2. Experimental Procedures and Results

The crystals used were produced from melt. The purity of material is about 99.9%. The procedure of making colour centre colloids is not essentially different from Rexer's method.²⁾ After a block of crystal, bent or not bent, is cleaved, one block is bored and then one or more holes are filled with Na metal and this block is put into contact with the other block as shown in Fig. 1. When the crystal is bent, the bending axis is taken to be the y-axis throughout this paper. The cleaved surface is preferable to be used in order to prevent Na from escaping as vapour or from oxydizing. Natural rock salt is usually too brittle to be bored by the dril. The crystal with Na in the hole was heated at 600–650°C for about 30–50 hours, then it was cooled in the air or in the electric furnace.

The crystal which was not deformed shows the irregular dislocation networks under the microscope with the cardioid condenser as shown in Fig. 2, as Amelinckx et al[4] reported. The temperature used when Na diffuses in the crystal seems to have been too low to get the regular dislocation networks.[5]

In bent crystals, on the other hand, dislocation lines concentrate at the small angle boundaries. Fig. 3 shows the regular L-letter-shaped small angle boundaries. The round white part is the hole which was filled with Na. Polygonization does not seem to be influenced by a hole bored, for the boundaries are not deformed in any way around the hole. In Fig. 4, however, some part of the crystal shows irregular patterns. It is reasonable, for this is the corner of the crystal which is different from other part of the crystal in strain distribution, and the irregular form of

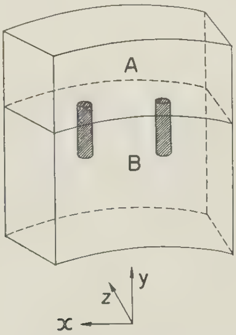

Fig. 1. The schematic picture of the crystal which is to be coloured. The hatched parts are the holes to be filled with Na metal. When the crystal is bent, the bending axis is taken to be the y-axis.

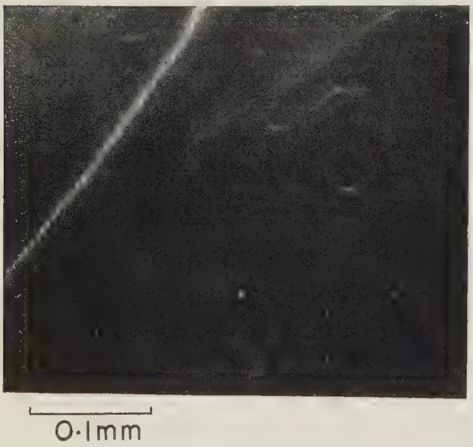

Fig. 2. Irregular dislocation networks in an annealed crystal.

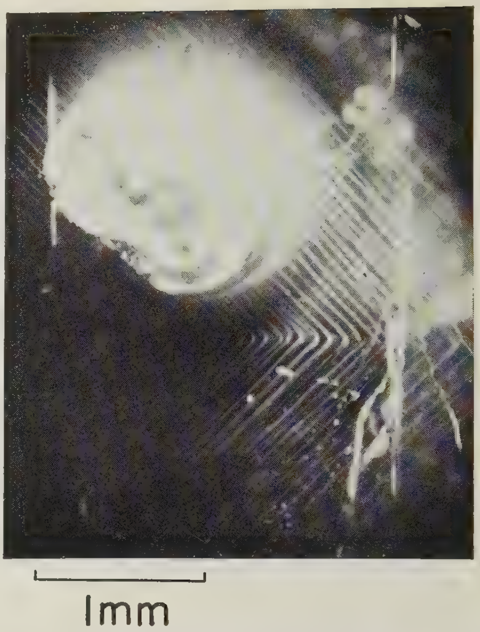

Fig. 3. Polygonized domains. The round white part is the hole which was filled with Na.

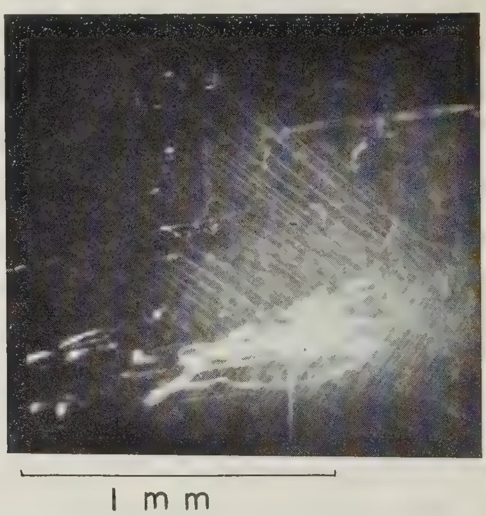

Fig. 4. (a) Polygonized domains. There is the irregular region.

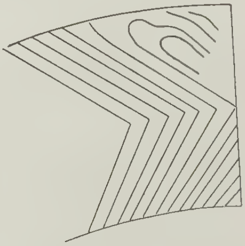

Fig. 4. (b) The irregular region is schematically shown.

domains appeared there while annealing.

The general features of polygonized domains were not essentially different, whether the crystal was annealed or not before the procedure of making colloids, because the annealing effect always accompanies the heat treatment for making colloids.

When the colloidal particles are suitable in size,[6] the domain pattern can be observed between the crossed nicols far more clearly than with the ultramicroscopic illumination.

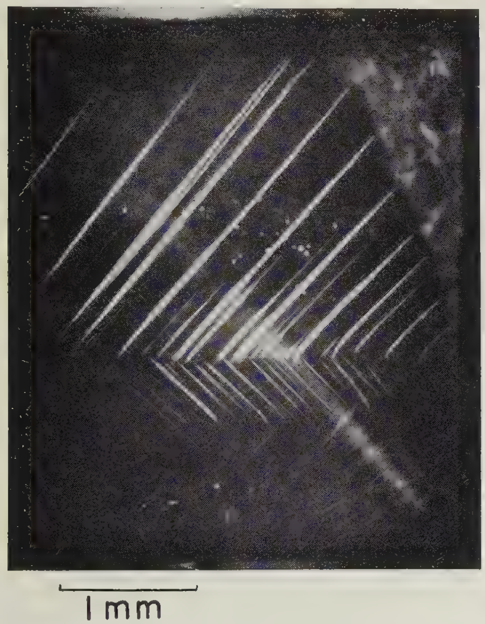

Fig. 5. The typical polygonized domain pattern.

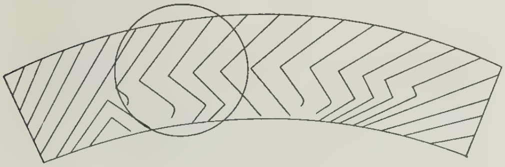

Fig. 6. The schematic pattern of polygonized domains.

The example is shown in Fig. 5, where the typical polygonized domains are seen. The neighbouring boundaries clearly seen have the angle 1.5 degrees in average outside the neutral plane. The less clear boundaries are observed between the clear ones. The density of these weak boundaries seems to depend upon the curvature of bending. In the extreme case that the bending is slight, this pattern of polygonized domains was not found.

The part shown in Fig. 5 is in the middle of the whole crystal, which has such a pattern as schematically shown in Fig. 6. This polygonization pattern may depend upon the strain distribution, therefore, upon the condition of bending. In the present work, the relation between this pattern and the bending condition was not investigated. It seems, however, that the middle part which is strongly bent from the beginning, has always the L-letter-shaped boundaries and the both ends which are not strongly bent have often the straight boundaries. Between these two regions, the transitional patterns are found.

These L-letter-shaped polygonized boundaries were already reported as the results by etch pits and X-ray diffraction.[7] Laue photographs suggest us that these boundaries are parallel to the y-axis and they go through the crystal at least in the range of a few mm's. In the present observation, such pattern as shown in Fig. 6 can be found in both A and B parts of the crystal (Fig. 1). Each clear line in Fig. 5 is the cross section of the polygonized boundaries. In most cases, however, it does penetrate the crystal; it is often about 1 mm in breadth along the y-axis. This can be known by changing the focus of the microscope. This fact may mean that all areas of boundaries are not always uniformly decorated. As expected, the boundary does not show the clear line, when it is observed from the direction of the x-axis.

On the neutral plane, small angle boundaries meet from both sides. They are not simply curved, but are connected with neighbouring boundaries in a complicated way, as Fig. 7 shows. The details can be followed by changing the depth of focusing plane.

The needle shaped inclusions which Amelinckx[5] reported as due to impurities were also observed in our case, when the undeformed crystal was heated at 700°C. Just outside the outer Liesegang ring the needles were in [010] and [001] directions (Fig. 8), but outside the inner ring they were in [010], [001] and [011] directions (Fig. 9). These inclusions were also observed in other equivalent direction.

## § 3. Polygonization Mechanism

When the wet crystal is bent between the crossed nicols, we can observe under the

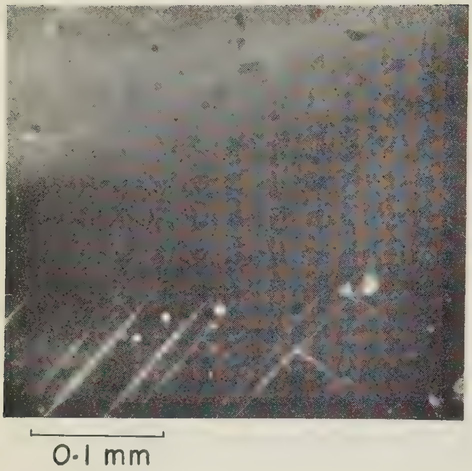

Fig. 7. The magnified pattern at the curved part.

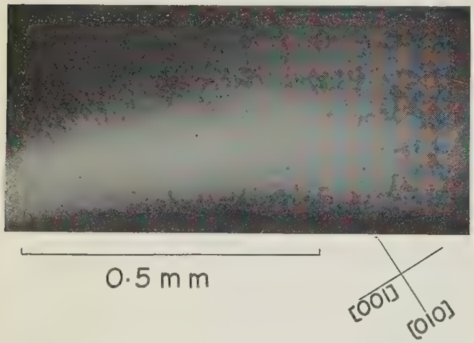

Fig. 8. The needle shaped inclusions with two directions.

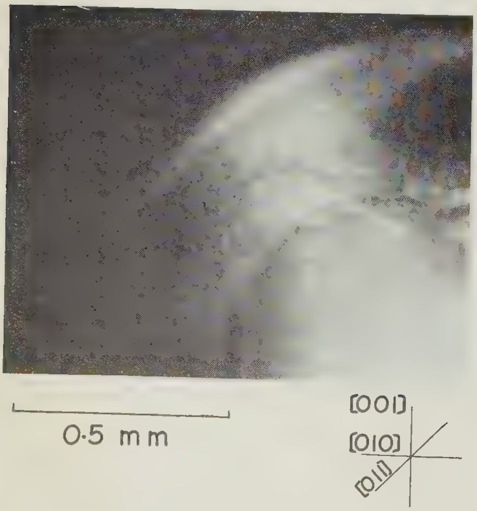

Fig. 9. The needle shaped inclusions with three directions.

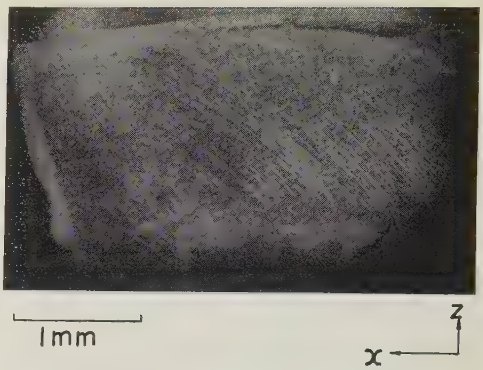

Fig. 10. Glide planes in a bent crystal observed between the crossed nicols from the y-direction.

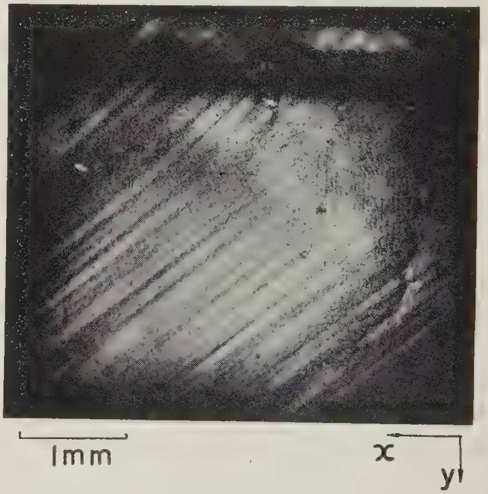

Fig. 11. Glide planes observed from the z-direction.

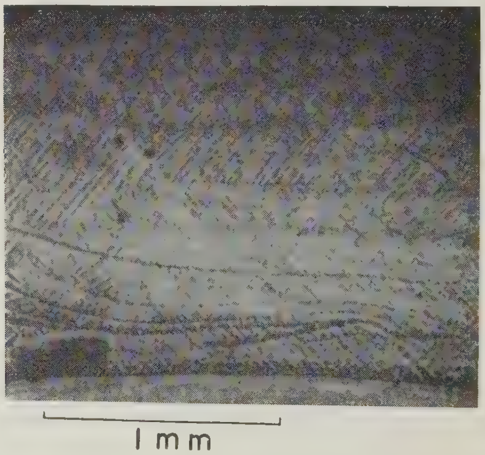

Fig. 12. Etch pit pattern on the (010) plane of a bent and annealed crystal.

microscope how glide planes appear.[8] In most cases, when we inspect the crystal from the direction of the y-axis, the two equivalent families of glide planes (101) and $(10\bar{1})$ appear mixing densely each other. The crystal shows, therefore, chequer pattern, even if it is cleaved along the x-z plane as thin as 1 mm or so. In a fortunate case, the crystal has herring-bone like glide planes as shown in Fig. 10. Namely either of two equivalent glide planes is dominant on both sides of neutral plane. When this crystal is observed from the z-direction between the crossed nicols, the stripes are seen in the $[1\bar{1}0]$ direction instead of the [100] direction as shown in Fig. 11. This will be mentioned in the next section.

After this crystal was annealed and etched, it showed the regular L-letter-shaped etch pit boundaries (Fig. 12), which were *perpendicular* to the herring-bones in Fig. 10 in direction. This perpendicularity can be also proved by inspecting the Laue photographs as follows. Such crystals as shown in Fig. 10 give the Laue pattern in which the spots already split to some extent, and this pattern inform us of the direction of diffuse grain boundaries.[7] On the other hand, the direction of glide planes in the irradiated part can be known by observing the crystal between the crossed nicols. It was found that this direction of glide planes and the direction of diffuse boundary inferred by Laue photographs are perpendicular. After the crystal is well annealed, it does not give any pattern like Fig. 10, and its Laue pattern informs us of the fact that the diffuse boundaries becomes definite, keeping the direction of the previous diffuse boundaries.

Thus the perpendicularity between the direction of polygonized boundaries and that of the glide planes were well confirmed. This means that the usual mechanism of polygonization[9] occurs.

In germanium, small angle boundaries are reported to arrange themselves parallel to the slip plane at a lower temperature and perpendicular to it at a higher temperature.[10] In our case, the temperature used can be thought to be higher (600–650°C). At a lower temperature, the clear pit line could not easily be obtained.

When the crystal is less homogeneous or it is bent to a little extent, the etch pit pattern is less regular as shown in Fig. 13, but the region with L-letter-shaped boundaries still partly exist.

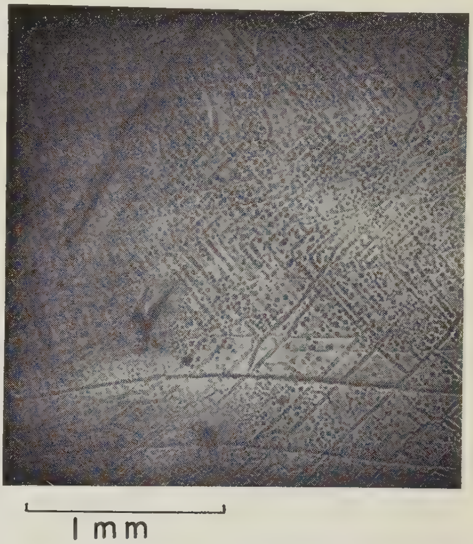

Fig. 13. The less regular etch pit pattern. The regular pattern is partly seen.

The crystal with chequer pattern of glide planes also shows the same type of etching pattern as seen in Fig. 12. This structure extends as thick as several mm's, which is proved by comparing the etch pit patterns on the several sections of cleaved crystal. This means that recrystalization or polygonization also proceeds in the direction along the y-axis.

## § 4. Discussions and Conclusions

By observing the glide planes in the bent crystal and the etch pit pattern after annealing, the usual mechanism of polygonization was concluded to occur at least at the temperature higher than 600°C. Then the polygonized domains in bent and annealed crystals usually have such pattern as shown in Fig. 6. The existence of Na colloids may not change the general pattern of polygonized domains, for the essential difference cannot be observed in Laue photographs of the crystal without them.

The observation after making colloids cannot be used for the investigation of a bent and non-annealed crystal, for the annealing inevitably accompanies the diffusion of Na metal.

The crystal with a pair of surfaces parallel to the (101) plane were cut out. Only one family of the glide planes parallel to (101) might appear, if it can be bent. This attempt was unsuccessful, because this crystal could not be bent before it broke.

The cleaved crystals usually show the chequer patterns, if it is observed between the crossed nicols from three crystal axes. The chequer pattern is clearest when seen from the y-direction.

These patterns will be propably explained as follows. When the crystal is bent around the y-axis, the four glide planes other than (101) and $(10\bar{1})$ also appear parallel to the x- or z-axis. Now, the pattern obtained with the crossed nicols depends upon the integral rotation of the polarizing light by the strained crystal. Therefore, in Fig. 11, for instance, the strain due to the glide planes (101) and $(10\bar{1})$ does not contribute and only the strain due to the plane $(1\bar{1}0)$ exclusively contributes. It is doubtless that the glide planes parallel to the y-axis is dominant and that the change of strain distribution is strongest. The above interpretation, therefore, seems to be supported by the fact that the stripes in Fig. 11 are not so sharp as those in Fig. 10.

After the crystal is annealed, it is reasonable that the domains extend in such a direction as release the strongest strain along the plones parallel to the bending axis. However, the fact cannot be simply explained that the crystal with two equivalent glide planes (101) and $(10\bar{1})$ everywhere also has the L-letter-shaped domains after it is annealed.

When the wet crystal is compressed, usually the chequer pattern appears. It was not investigated what pattern will appear after the compressed crystal is annealed.

The visualization of dislocation lines or networks might be also realized when the crystal is activated by the suitable fluorescent sensitizer. The activation centres may decorate the dislocations. The preliminary experiments were made with several crystals including NaCl sensitized by Mn and Pb, but they were not successful, perhaps chiefly because the fluorescent light was very weak. It may not be impossible if any crystal sensitized by the suitable impurities radiates intensive visible rays in the ultraviolet beam.

The author is heartily thankful to Asst. Prof. S. Takagi for his continuos interests since the early stage of this work. This research was party supported by the research grant of the Ministry of Education.

## References

1) A. Smekal: ZS. VDI. **72** (1928) 667, ZS. f. Phys. **55** (1929) 289.
2) E. Rexer: ZS. f. Phys. **76** (1932) 735.
3) J. M. Hedges and J. W. Mitchell; Phil. Mag. **44** (1953) 223, 357; H. Kanzaki: J. Phys. Soc. Japan **11** (1956) 120, 126.
4) S. Amelinckx, W. Van der Vorst, R. Gevers and W. Dekeyser: Phil. Mag. **46** (1955) 450.
5) S. Amelinckx: Phil. Mag. **1** (1956) 269.
6) E. Mollow: Nachr. Akad. Wiss. Göttingen (1932) 254, which is cited as 84) in Seitz: Rev. Mod. Phys. **26** (1954) 7.
7) S. Hosoya, S. Satake and S. Takagi: J. Phys. Soc. Japan **11** (1956) 1228.
8) I. W. Obreimow and L. W. Schubnikoff: ZS. f. Phys. **41** (1927) 907; F. Rinne: ZS. f. Krist. **61** (1925) 389; W. Schütze: ZS. f. Phys. **76** (1932) 135.
9) For instance, R. W. Cahn: Prog. in Metal Physics Vol. **2** (1950) 151.
10) F. L. Vogel: Acta Metal. **3** (1955) 95.

JOURNAL OF THE PHYSICAL SOCIETY OF JAPAN Vol. 11, No. 12, DECEMBER, 1956

# Thermal and Electrical Properties of Tungsten Oxide ($WO_3$)

By Shozo SAWADA

*Institute of Science and Technology, University of Tokyo*

(Received August 13, 1956)

Thermal and electrical properties of tungsten oxide were observed in a wide range of temperature. An entirely new anomaly was found at 1230°C, where the rate of sublimation increased abruptly. The amounts of anomalous heat were found to be 330, 450, 280 and 120 cal/mol at the 330°C, 740°C, 910°C and 1230°C transitions respectively, the entropy change being 0.55, 0.45, 0.23 and 0.08 cal/mol·deg at each of the transition temperatures. Any anomalous heat larger than 6 cal/mol was not observed near the −20°C transition point. At the mentioned transition points the anomalies of electrical properties were observed. The d.c. resistance decreases, on heating from room temperature, like a typical semiconductor with the activation energies of nearly 2.2, 0.3, 1.7 and 1.3 eV below 740°C, between 740°C and 910°C, between 910°C and 1230°C and above 1230°C, respectively, the small value as 0.3 eV between 740°C and 910°C being especially noticeable. A non-linearly of *I-V* relation was observed, indicating some anomalous electrical property of this substance.

## §1. Introduction

Since the discovery of ferroelectricity in barium titanate in 1942～1944, many studies have been made not only on barium titanate itself but also on the related substances. Nagasawa[1)] pointed out the possible existence of ferroelectricity in tungsten oxide, judging from the very high value of permittivity as ten thousand at room temperature. Okada et al.[2)] supported this point of view through the result of their measurements of permittivity and their observation of hysteresis loop of this substance. Matthias[3)] also reported independently the ferroelectric properties of tungsten oxide. In fact, the crystal structure of tungsten oxide, determined early by Bräkken[4)], resembles well to that of barium titanate; that is to say, the general aspect of the former may be obtained by omitting Ba ions and substituting W ions for Ti ions in the latter. The resemblance of crystal structures of these compounds, together with the position of W on the periodic table, will lead us to expect some interesting dielectric properties of tungsten oxide.

Afterwards, the electrical and thermal properties of tungsten oxide were investigated on ceramic samples[6),7)], the domain structure was observed on single crystals and further the effects of mechanical stress, temperature and electric field upon it were found to be similar to those observed on barium titanate single crystals[8)～15)]. Although such state of affairs may be said to support the possibility of ferroelectricity in tungsten oxide, the properties of tungsten oxide were re-studied from the stand-point of antiferroelectricity which has been found in lead zirconate and other substances of the $XYO_3$ type. Kehl et al.[17)] found that in tungsten oxide ions are arranged in an antiparallel manner along the c-direction above 740°C, and further Ueda and Kobayashi[18)] confirmed an antiparallel arrangement of ions in all of the a-, b- and c-directions at room temperature. However, it has not yet been determined whether tungsten oxide is ferro- or antiferro-electric. Of course, an antiparallel shift of ions alone does not necessarily give rise to antiferro-electricity, corresponding to the fact that a parallel shift is not a sufficient condition for ferroelectricity.

The two main points which make it difficult to proceed accurate measurements in tungsten oxide are its high electrical conductivity and rapid sublimation observed in this substance. Since, at room tenperature, tungsten oxide has electrical resistivity as low as some thousand ohm·cm in ceramics and some ten ohm·cm in single crystal, the dielectric measurement is rather difficult even at room temperature and becomes very difficult to make various measurements and especially to carry out the x-ray analysis at such high temperatures.

Since tungsten oxide, as is seen in the following, has a transition point also above 1000°C and, moreover, the measurements of dielectric properties and crystal structure, which provide the most useful means of determining ferroelectricity or antiferroelectricity of a substance, are very difficult at high temperatures, it does seem hardly possible to draw a final conclusion regarding ferro- or antiferroelectricity of this substance. On the other hand, the electrical conductivity of tungsten oxide has not yet been throughly investigated and it would be interesting to investigate the conductive properties of this substance in a wide range of temperatures for clarifying semiconductor characteristics.

The dilatometric measurements by Foëx[19] have discovered four transition points of tungsten oxide as −20°C, 330°C, 740°C and 910°C*, which are confirmed through the observations recently made with the interest in the resemblance of this substance to barium titanate. In addition, the author has found that almost all properties of tungsten oxide are anomalous at about 1230°C.

It might be emphasized that we know few examples of substance having so many transition points in a wide range of temperatures as in tungsten oxide. Hence it would be interesting to investigate the physical properties of this substance from the view-point of not only ferro- or antiferro-electricity but also of phase transition in general.

## § 2. Preparation of Samples

Raw material used in preparation of samples was of bright greenish yellow power of 99.9% purity. A ceramic sample was prepared by pressing powder into a disc, sintering it at 1100°C for two hours in a platinum or siliconit furnace. Nagasawa[1] has concluded that oxygen atoms do not escape on sintering in air. We also have found that a sintering in oxygen for two hours of a sample which had been sintered for two hours at 1100°C in air did not affect its properties, although reductive atmosphere always changed a sample into remarkably conductive one.

Single crystals were prepared by the sublimation method. Powder of about 15 g weight, packed in a silica tube, was heated up to about 1400°C, in a vertical kryptol furnace, and then crystals of 1 mm dimensions grew upon the lower surface of a silica disc which was suspended at a position a little apart from powder and kept at about 1000°C. We can also find good crystals on the surface of powder heated in a furnace in which an appropriate gradient of temperature is prepared.

## § 3. Thermal Properties

### 3.1 *Thermal Expansion*

The thermal expansion between −150°C and room temperature was measured by using a vertical dilatometer with an optical lever. On cooling, a remarkable contraction was observed at −50°C and, on heating, an expansion of the same amount at −20°C. This result agrees well with the previous ones[19), 25)], but in our case the amount of anomaly was larger.

The coefficient of linear thermal expansion between soom temperature and 850°C, determined by using a horizontal dilatometer, has already been reported[20), 21)]. A rather gradual expansion was observed near 330°C and a steep contraction at 740°C, the amount of the

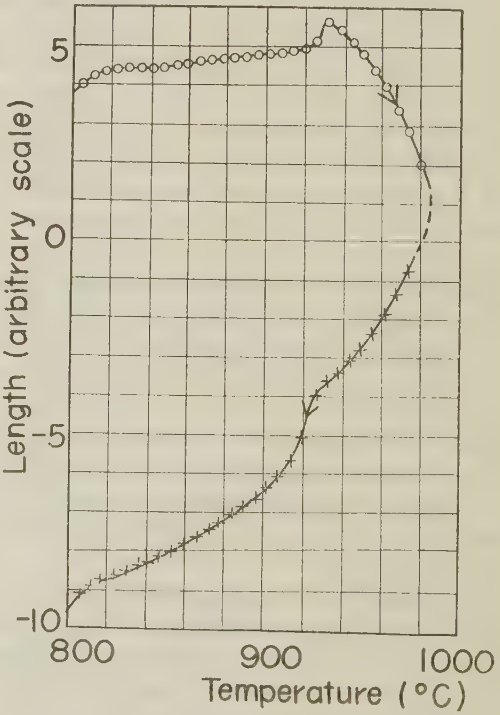

Fig. 1. Thermal expansion between 800°C and 1000°C.

---

* These values of transition temperature arc found on heating. The values lower by 10∼30°C than these are found on cooling.

latter being $\Delta l/l=1.2\times10^{-3}$. Although, at still higher temperatures, the absolute determination of coefficient of thermal expansion is impossible on account of apparent contraction due to the sublimation and sintering, we have shown a variation of length in Figs. 1 and 2 in an arbitrary scale. A distinct expansion is observed at 910°C and a slight contraction at 1230°C.

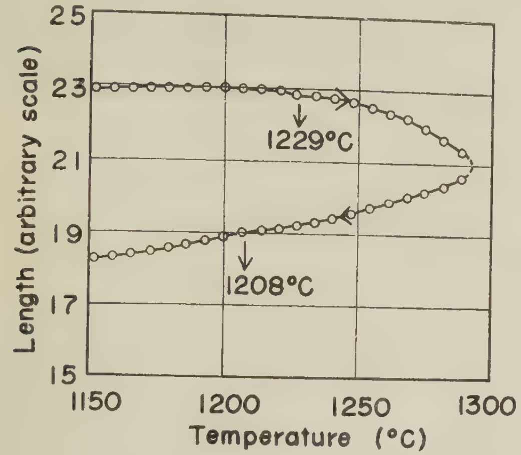

Fig. 2. Thermal expansion between 1150°C and 1300°C.

The anomalies at −20°C, 330°C, 740°C and 910°C agree well with those observed by Foëx[19)] in both sense and magnitude of upward or downward. The anomaly at 1230°C was found for the first time by our measurement and is seen to correspond to anomalies of other properties at the temperature, which will be mensioned in the following sections.

3.2 *Cooling Curve*

The cooling curve was observed between 700°C and 1400°C as a preliminary procedure for the measurement of specific heat. As is well-known, this is the most simple method to find out thermal anomalies not too small, though the amount of anomaly can hardly be measured accurately.

A ceramic disc was suspended in a platinum furnace by a Pt-Pt·Rh thermo-couple. Since a single cooling curve can not be observed in so wide range of temperatures, the range between 1400°C and 700°C was divided into five regions. Distinct anomalies were observed at 1195°C, 895°C and 730°C, respectively. Fig. 3 shows the result for a range of 14.5~12.0 mV (expressed by the thermoelectromotive force of the couple). The ordinate is the time interval necessary to cool the sample by 0.1 mV at each temperature.

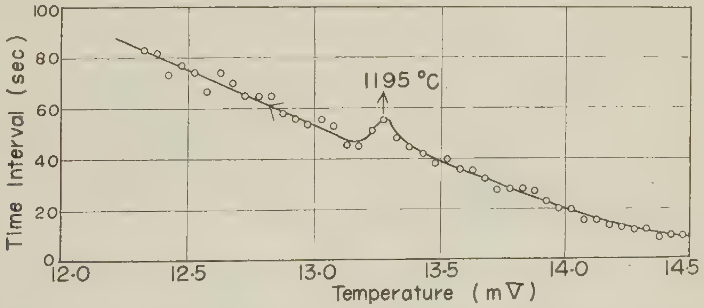

Fig. 3. Cooling curve between 14.5~12.0 mV.

3.3 *Specific Heat*

Although we have already reported the results of measurement on specific heat of tungsten oxide[7),20),21)], they were not so definite and not so self-consistent with each other owing to the variety of both sample and method, the defect of apparatus, etc. In view of our former experience, now we measured the specific heat of the same sample throughout by the same method between −170°C and 1300°C.

We have constructed four conduction calorimeters shown in Table I and adopted a new method of measurement in which the differ-

Table I.

| | |
|---|---|
| −170°C ~room temperature | cooper calorimeter for low temperatures |
| room temperature ~ 500°C | nickel calorimeter for moderate temperatures |
| 500°C ~ 1000°C | nickel calorimeter for high temperatures |
| 1000°C ~ 1300°C | platinum calorimeter for high temperature |

ence of temperatures of a sample vessel and an outer case was measured for the current of furnace varied following a definite rule, instead of the usual one in which the current of furnace is adjusted so as to keep constant the above temperature difference. The new method is much more reliable and much less laborious than the usual one especially at high temperatures. The details of calorimeters and measuring method have been reported in separate papers[26),27)]. The measurements below 1000°C was carried out in vacuum of $10^{-3}\sim 10^{-4}$ mmHg, and the one above 1000°C in air in order to avoid the reduction sublimation of the sample.

Fig. 4 (a), (b), (c) and (d) show the specific heat in the respective regions of temperatures. The value at low temperatures agrees well with that obtained by Seltz et al[22)]. Although a slight anomaly* which is only a little larger

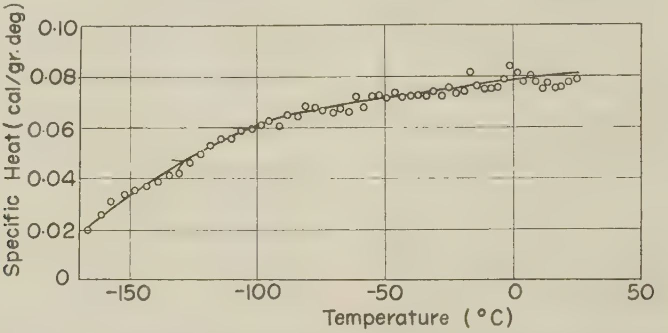

Fig. 4 (a). Specifiic heat between −170°C and room temperature.

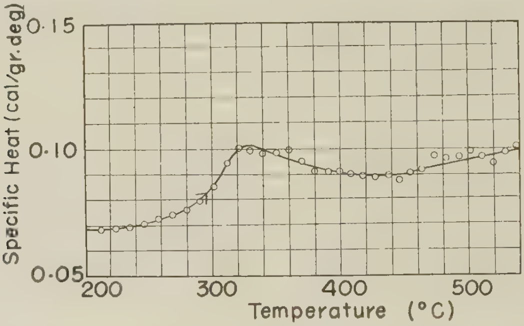

Fig. 4 (b). Specific heat between room temperature and 500°C.

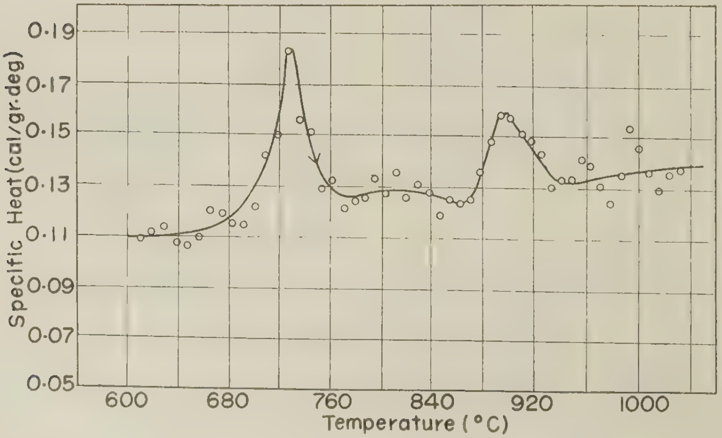

Fig. 4 (c). Specific heat between 500°C and 1000°C.

---

* About 6 cal/mol.

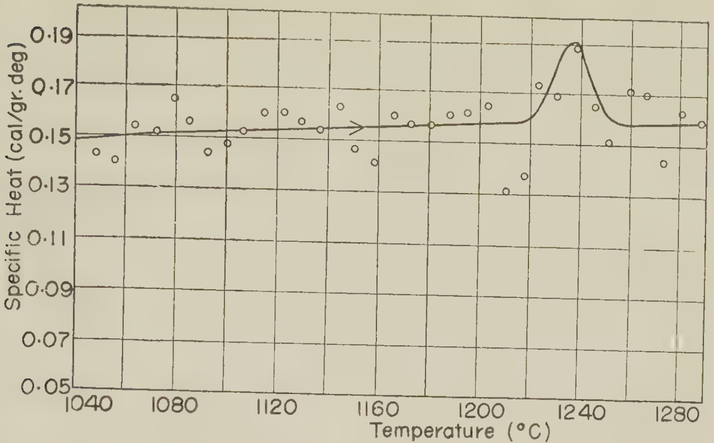

Fig. 4 (d). Specific heat between 1000°C and 1300°C.

than experimental error might be said to exist near −20°C, any noticeable anomaly corresponding to the remarkable one of thermal expansion was not observed. A gradual anomaly was observed near 330°C and the amount of anomalous heat was about 330 cal/mol, the change of entropy being 0.55 cal/mol·deg. Distinct anomalies were observed near 740°C and 910°C and the amounts of anomalous heat were 450 and 280 cal/mol, the change of entropy being 0.45 and 0.23 cal/mol·deg, respectively. Although the measurement above 1000°C is difficult and is less accurate, we can see a small but distinct anomaly of the order of 120 cal/mol at 1230°C and its change of entropy is 0.08 cal/mol·deg.

3.4 *Rate of Sublimation*

Tungsten oxide is volatile at temperatures above 1000°C and the rate of sublimation was measured quantitatively using a thermobalance. In Fig. 5 the abscissa is the reciprocal of absolute temperature and the ordinate shows the decrement of mass per unit time in an arbitrary scale. As is seen in the figure, the rate of sublimation increases abruptly at the 1230°C anomalous point. This fact makes it very difficult to determine the crystal structure by the x-ray analysis above this temperature.

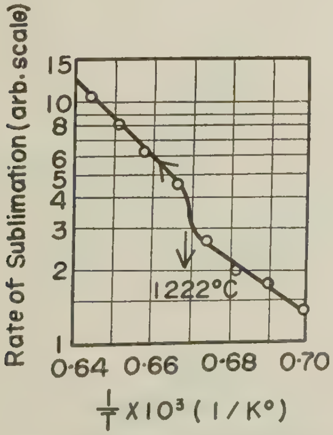

Fig. 5. Rate of sublimation *vs* temperature.

Adopting a formula as

$$v=v_0e^{-E/kT}$$

for the rate of sublimation $v$, we obtain

$$E=2.17\,eV \qquad T<1230°\text{C}\,,$$
$$E=3.22\,eV \qquad T>1230°\text{C}\,.$$

## § 4. Electrical Properties

### 4.1 *Permittivity and Loss*

Nagasawa[1] first payed attention to the high value of permittivity of tungsten oxide and Okada et al.[2] observed a peak on the permittivity *vs* temperature curve at 20°C. We observed a remarkable hysteresis phenomenon in the permittivity *vs* temperature relation[7]. On cooling from room temperature the permittivity decreased steeply and next gradually, whereas, on heating from −40°C, the permittivity increased and a maxium and a minimum were observed at about 40°C and 90°C, respectively. On the second cooling, only a monotonous decrease of permittivity was observed and, on the second heating, we had smaller value of permittivity than in the first one and a shrinkage of the maximum was especially noticeable. After repeating this process several time, no maximum or minimum were observed on heating. The original state was almost recovered after several or several ten days.

Hirakawa[6] also observed the same hysteresis phenomenon and found the decrease of permittivity with the increase of frequency. Further he observed a steep peak on the permittivity *vs* temperture curve at 710°C, by increasing the apparent resistance of a sample through putting it between nickel electrodes without sputtering[27].

Our present measurement of the permittivity has been carried out on a bar of the sample both ends of which were sharpened in order to decrease the capacity, between room temperature and 1300°C, using platinum electrodes pressed to the sample by a spring. Although sputtering was not applied upon the sample for avoiding the possible diffusion of metal atoms into the sample, reproducible results were always obtained by the use of this set of electrodes. The capacity and parallel resistance of a series circuit composed of the sample and an air condenser with adequate capacity were observed by a resonance method using 1043 KC and then the capacity and parallel resistance of the sample were calculated taking into account stray capacity and leakage due to the furnace and thermo-couple, etc. Fig. 6 (a) and (b) show the obtained result. The permittivity and specific resistance are given nearly by $\varepsilon=1500C_x$ and $\rho=1/100R_x$. Anomalies are seen at 330°C, 750°C, 910°C and 1230°C respectively for both capacity and parallel resistance.

It has been shown by an examination of Cole's figure[2] that a sample of tungsten oxide can not be substituted even at room temperature merely by a parallel circuit of a capacity and a resistance, so the physical meaning of thus obtained $C_x$, $R_x$, which were derived only formally, are rather ambiguous. It seems interesting, however, that contrary to our expectation the capacity does not increase so much and the resistance increases, between 740°C and 1240°C.

### 4.2 *Hysteresis Loop*

It has been reported by many authors[2), 3)] that the ferroelectric *E-D* hysteresis loop is observed in tungsten oxide at room temperature and that it tends to a linear relation with the rise of temperature. We also have observed the same phenomena in our repeated observations using 50 C and 1 MC. It is difficult, however, to draw any conclusion concerning this matter, since a bridge method should be used for the observation of hyster-

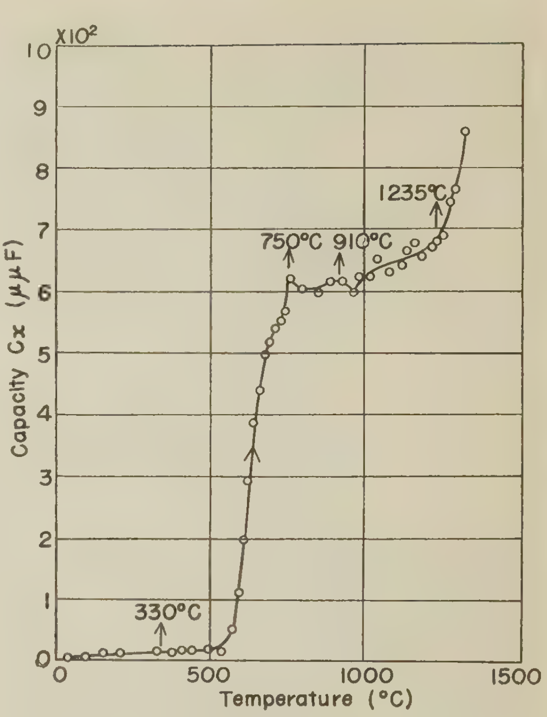

Fig. 6 (a). Permittivity *vs* temperature.

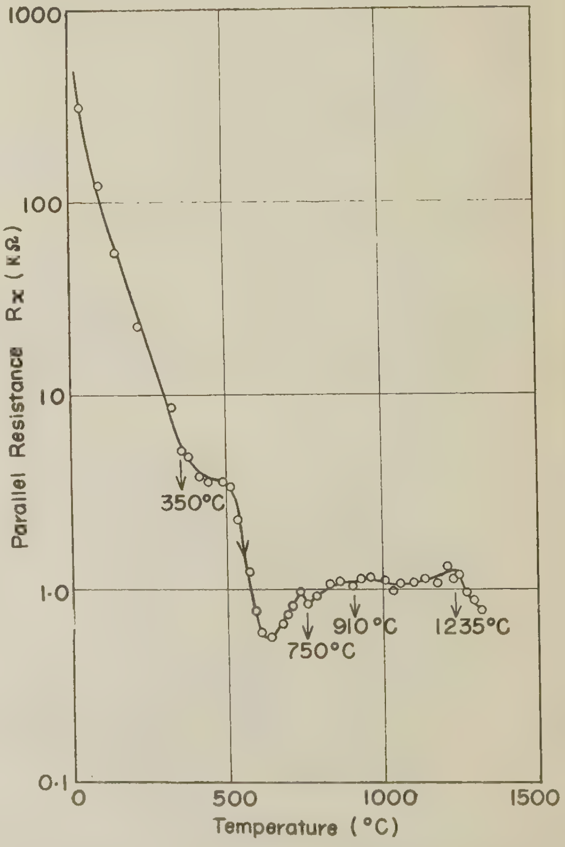

Fig. 6 (b). Parallel resistance *vs* temperature.

esis loop of tungsten oxide in order to cancel the d.c. conduction of the sample. Observations at low temperatures are much more reliable owing to the decrease of d.c. conduction. Hirakawa[6] has reported that a typical hysteresis loop observed at −100°C∼−70°C tends gradually to a straight line on heating and some degree of curvature is still retained above room temperature. The fact that the hysteresis loop is clearly observed at the low temperature phase leads us to consider that this phase is ferroelectric. A contradiction of the hysteresis loop observed far beyond −20°C to the result by the x-ray analysis that an antiparallel structure is realized at room temperature, could possibly be removed by considering that the transition process at −20°C does not rapidly occur due to relatively large relaxation time and then it is retained up to higher temperature.

### 4.3 *Non-linearity*

The anomalous dielectric property was observed through the measurement of the non-linearity of *I-V* relation at 1 MC. The impressed voltage was measured by the amplitude on a cathode ray oscilloscope and the current by a vacuo-junction. Fig. 7 (a), (b) and (c) show obtained *I-V* characteristics at several temperatures. An upward deviation was observed at intermediate voltage, a downward one at high voltage and the inflexion point was displaced to the low voltage side with the rise of temperature. Although a part of the upward deviation may be due to the Joule's heat, the downward one is to be thought as a characteristics property of tungsten oxide. Such property might be supposed

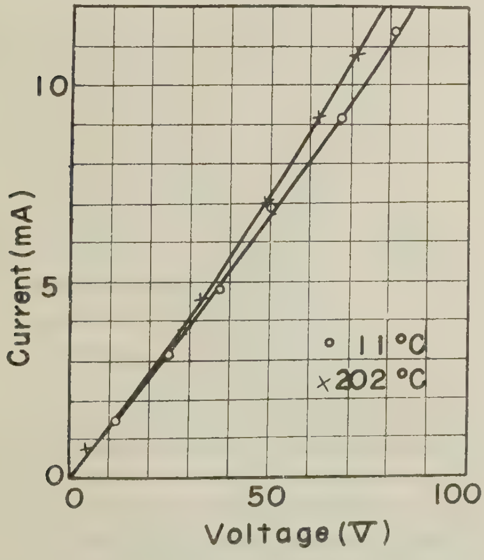

Fig. 7 (a). Non-linearity.

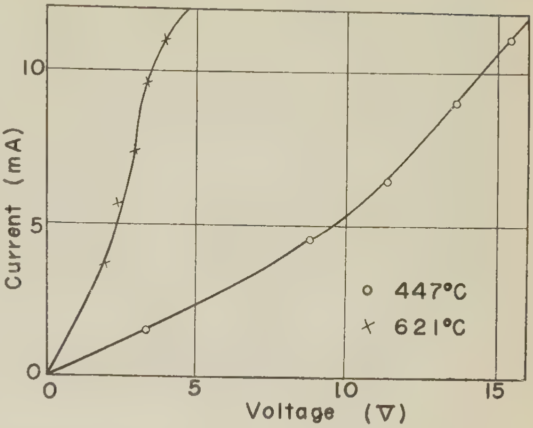

Fig. 7 (b). Non-linearity.

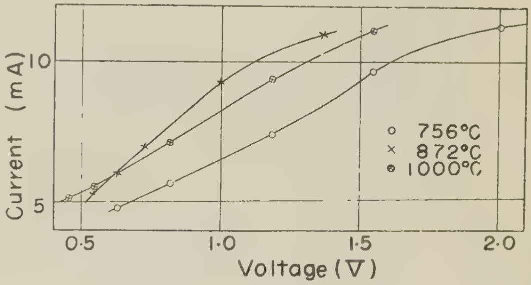

Fig. 7 (c). Non-linearity.

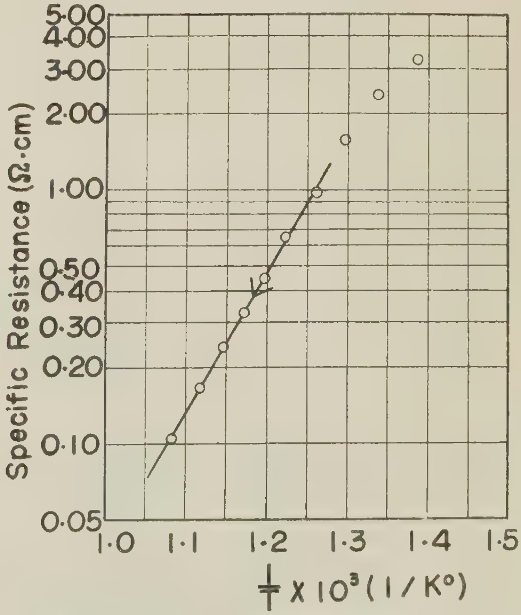

Fig. 8 (a). D. C. resistance below 700°C.

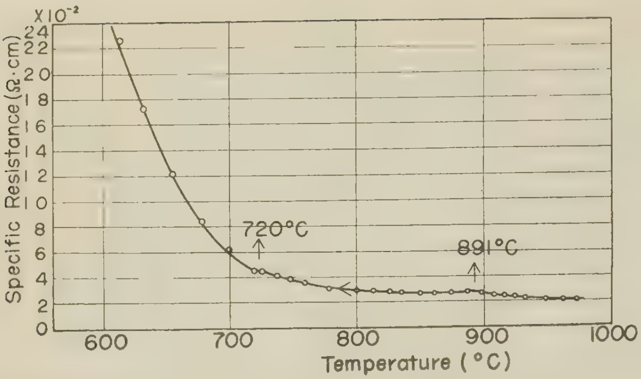

Fig. 8 (b). D. C. resistance between 600°C and 1000°C.

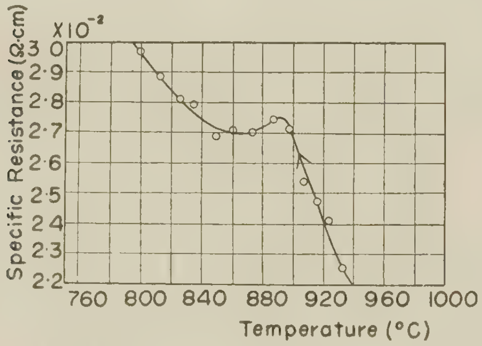

Fig. 8 (c). D. C. resistance near 910°C.

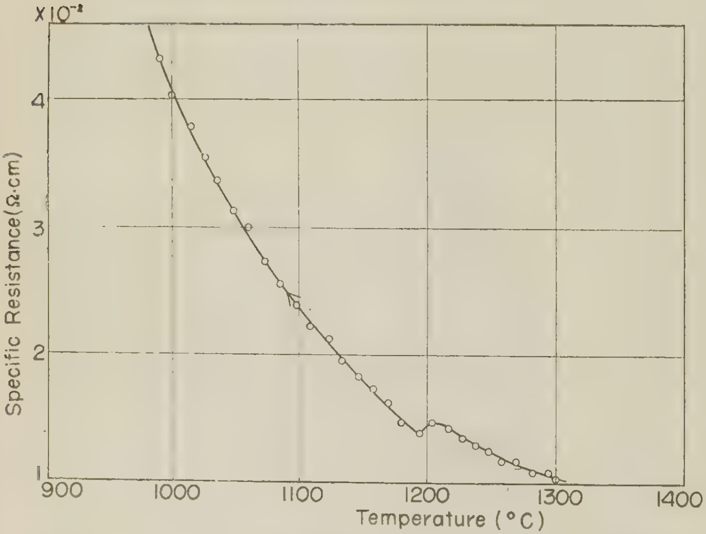

Fig. 8 (d). D. C. resistance between 1000°C and 1300°C.

to correspond to the ferro-electric property of this substance, but no remarkable change was observed at each transition temperature.

### 4.4 *D.C. Resistance*

The most reliacle data of electrical properties of tungsten oxide can be obtained for the d.c. resistance. We measured simultaneously the d.c. resistance and the thermo-electric power of a sample placed at a position in a furnace where there existed a temperature gradient of about 3°C. Fig. 8 (a), (b), (c) and (d) show the obtained value of d.c. resistance. A typical semi-conducting feature expressed by

$$\rho=\rho_0 e^{\phi/2kT}$$

is seen between room temperature and 700°C, the average value of activation energy $\phi$ between 500°C and 600°C being 2.2 eV. The decrease of resistance with the rise of temperature becomes abruptly slow at the 740°C transition. A maximum and knick are observed at 910°C and 1230°C respectively. Adopting the above formula, the activation energies between 740°C and 910°C, between 910°C and 1230°C and above 1230°C are found to be 0.3, 1.7 and 1.3 eV, respectively. Between 740°C and 910°C, the above formula does not hold so well and the small value of activation energy as 0.3 eV is especially noticeable.

The value of activation energy 2.2 eV near 550°C is nearly the same with that of the energy gap between the valence- and conduction-bands near this temperature, determined by the observation of optical absorption edge[23], indicating that tungsten oxide is an intrinsic semi-conductor in this range of temperature. The abrupt decrease of the rate of decrease of resistance above 740°C may be considered to be due to the creation of a new acceptor level by the change of lattice structure at this transition, which is also expected by the observation of optical absorption edge. The discrete level may be in an intimate relation with the crystal structure in which the corners of a cube are all vacant and some of the oxygen ions might occupy these vacancies at high temperatures.

The permittivity of single crystals is about ten times higher than that of ceramics, and d.c.- and a.c.-resistances of single crystals are about one tenth of those of ceramics, which fact seems to be due to the porosity of ceramics.

### 4.5 *Thermo-electric power*

Our temperature control was not sufficiently accurate to derive the temperature dependence of thermo-electric power, but it was found that the thermo-electric power is +0.33 mV/deg at 700°C and decreases monotonously from 300°C to 1300°C with a rate of $-1.3\times 10^{-4}$ mV/deg². This value agrees with that obtained by Hochberg[24] near room temperature. The thermo-electric power $Q$ of an intrinsic semiconductor is given by[28]

$$Q=-\frac{k}{e}\frac{c-1}{c+1}\left(\frac{E_0}{2kT}+2+\frac{a}{2k}\right),$$

where the energy gap $E_G$ between the valence- and conduction-bands is expressed by

$$E_G=E_0+aT$$

and $c$ by

$$c=\frac{\mu_1}{\mu_2},$$

$\mu_1$, $\mu_2$ being the mobilities of electrons and positive holes. Putting $a=-0.857\times 10^{-3}$ eV/deg[23] and $Q=0.35$ eV/°K at 550°C, we obtain

$$c=0.51$$

as the ratio of mobilities of electrons and holes. Then, using the well-known formulas for electrical conductivity $\sigma$ and number of electrons and holes per unit volume $n$

$$\sigma=ne(\mu_1+\mu_2)\ ,$$

$$n=Ne^{-E_G/2kT}$$

and assuming $N\approx 10^{22}/\mathrm{cm}^3$, we obtain the following values at 550°C:

$$n=3.1\times 10^{17}/\mathrm{cm}^3\ ,$$

$$\mu_1=12\ \mathrm{cm}^2/\mathrm{volt\cdot sec}\ ,$$

$$\mu_2=23\ \mathrm{cm}^2/\mathrm{volt\cdot sec}\ ,$$

which values do not seem unreasonable, but a fact that the mobility of holes is larger than that of electrons is noticeable.

It is well known that tungsten oxide is apt to be reduced. We really observed that the electrical resistance of a sample decreased by a factor of $10^4$ when it was kept at 1050°C in vacuum of $10^{-4}$ mmHg for three hours. Thus tungsten oxide is expected to be rather an *n*-type semiconductor. The observed value of thermo-electric power, however, shows that in unreduced tungsten oxide primary carriers of electricity are positive holes. The speculated band structures at 550°C and 750°C are shown in Fig. 9 (a) and (b) respectively. The mechanism of electrical conduction in tungsten oxide would become clearer by the measurement of Hall coefficient at each temperature.

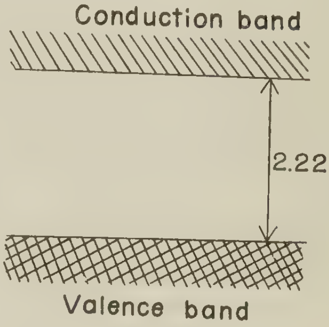

(a) 550°C

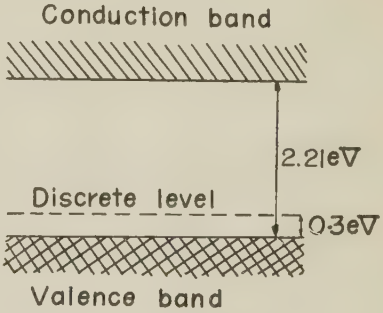

(b) 750°C.

Fig. 9. Speculated energy band scheme in $WO_3$.

The author wishes to express his sincere thanks to Prof. Seiji Kaya, Prof. Toshinosuke Muto and Prof. Kiichiro Ochiai for their kind advises and criticisms and to Mrs. Ine Tako for her continual assistance in the experiments.

## References

1) S. Nagasawa: Denki-kagaku **16** (1948) 13, 57; **17** (1949) 174.
2) T. Okada, K. Hirakawa and F. Irie: Busseiron Kenkyu No. 15 (1949) 49.
3) B. T. Matthias: Phys. Rev. **76** (1949) 430.
4) H. Brakken: Zeit. f. Krist. **78** (1931) 484.
5) K. Hirakawa and T. Okada: Mem. Fac. Sci.

Kyusyu Univ. Ser. **B 1** (1951) 1.
6) K. Hirakawa: Busseiron Kenkyu No. 33 (1950) 47.
7) R. Ando and S. Sawada: Rep. Inst. Sci. & Tech. Univ. Tokyo **4** (1950) 223.
8) K. Hirakawa: Busseiron Kenkyu No. 26 (1950) 42.
9) R. Ueda, T. Ichinokawa and J. Kobayashi: Busseiron Kenkyu No. 29 (1950) 75.
10) R. Ueda and T. Ichinokawa: Phys. Rev. **80** (1950) 1106.
11) R. Ueda and T. Ichinokawa: Journ. Phys. Soc. Jap. **6** (1951) 122.
12) S. Sawada and R. Ando: Rep. Inst. Sci. & Tech. Univ. Tokyo **4** (1950) 228.
13) R. Ueda and T. Ichinokawa: Busseiron Kenkyu No. 36 (1951) 64.
14) R. Ueda and T. Ichinokawa: Phys. Rev. **82** (1951) 563.
15) S. Sawada, R. Ando and S. Nomura: Phys. Rev. **82** (1951) 952.
16) E. Sawaguchi, G. Shirane and Y. Takagi: Journ. Phys. Soc. Japan **6** (1951) 333.
17) W. L. Kehl, R. G. Hay and D. Wahl: Journ. Appl. Phys. **23** (1952) 212.
18) R. Ueda and J. Kobayashi: Phys. Rev. **91** (1953) 1565.
19) M. Foëx: Compt. Rend. **220** (1945) 917; **228** (1949) 1335.
20) S. Sawada and R. Ando: Rep. Inst. Sci. & Tech. Univ. Tokyo **5** (1951) 143.
21) S. Sawada, R. Ando and S. Nomura: Phys. Rev. **84** (1951) 1054.
22) H. Seltz, F. J. Dunkerley and B. J. DeWitt: Journ. Amer. Chem. Soc. **65** (1943) 600.
23) T. Horie et al.: Ann. Rep. Sci. Works, Fac. Sci. Osaka Univ. **4** (1956) (in press).
24) B. M. Hokhberg and M. S. Somiskii: J. Exptl. Theoret. Phy. (U.S.S.R.) **7** (1937) 1099.
25) K. Hirakawa: Journ. Phys. Soc. Jap. **7** (1952) 331.
26) S. Sawada: Rep. Inst. Sci. & Tech. Univ. Tokyo **10** (1956) 107.
27) S. Sawada: Rep. Inst. Sci. & Tech. Univ. Tokyo **10** (1956) 115.
28) V. A. Johnson and K. Lark-Horovitz: Phys. Rev. **92** (1953) 226.

---

JOURNAL OF THE PHYSICAL SOCIETY OF JAPAN Vol. 11., No. 12, DECEMBER, 1956

# Microscopic and X-Ray Studies on Tungsten Oxide ($WO_3$)

By Shozo Sawada

*Institute of Science and Technology, University of Tokyo*

(Received August 13, 1956)

The domain structure of single crystals of tungsten oxide was observed between −130°C and 1200°C. An abrupt change of domain structure was observed at −50°C on cooling and it varied only gradually on heating, as reported (previously). No change was observed at the 910°C transition. The crystal structure was investigated in detail near 910°C and 1230°C respectively. No change of crystal symmetry except for only slight anomalies of lattice constants was observed at these two transitions. Ferroelectricity or antiferroelectricity and bond structure of this substance were discussed using the result of observations, and it was stressed that these would be in an intimate relation with each other.

## § 1. Introduction

In the previous paper[1], we have reported the anomalous behavior of thermal and electrical properties at each transition temperature of $WO_3$. Here, the results of our microscopic and X-ray studies shall be reported and some possible discussions of the characteristics of $WO_3$ will be made, allowing for the results of both present and former experiments.

## § 2. Observations of Domain Structure

### 2.1 *Observation at room temperature*

At room temperature we can observe the domain structure on single crystals using a polarized-light microscope. Most of plate crystals have the c-axis perpendicular to the plane of plate and in these crystals domain boundaries make an angle of 45° to the cleavage surfaces of crystals. This domain structure arises from the inequality of lattice constants *a* and *b*. Sometimes we have crystals having the c-axis on the plane of plate, in which the domain boundaries are parallel to the cleavage surfaces. Also single-domain crystals are not so rare.

These features of domain structure and the effect of mechanical stress upon them agree well with those which have been reported by many authors.[2][3]

2.2 *Observation at low temperatures*

Fig. 1 shows our low temperature stage for the observation of the domain structure at low temperatures. Cold air vaporized from liquid state is introduced into an outer vessel A covered by a rubber shield from an inlet P and then into an inner one B through a connector C. Using this stage, we can observe the domain structure between 20°C and −130°C continuously on both cooling and heating, under the consumption of liquid air of 2 l/hr at maximum.

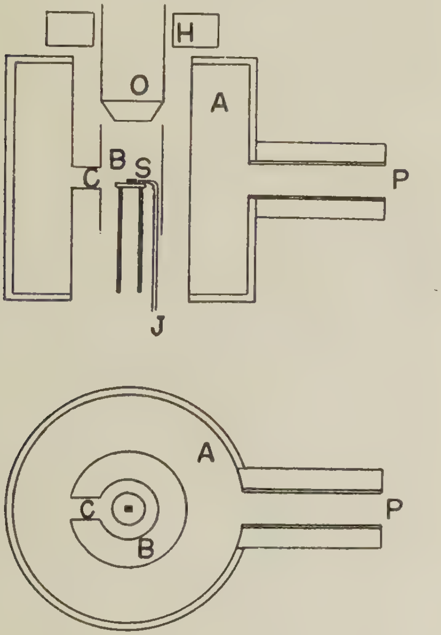

Fig. 1. Low temperature stage.

We observed a change of domain structure at low temperatures which agrees with that reported previously mainly on heating[4]—that is, at −50°C on cooling, each domain which had existed was split into minute ones by new parallel boundaries making 45° to the original boundaries, the latters vanishing at this temperature. On heating, this change is rather gradual. Although the new boundaries almost vanish at about −10°C, sometimes they remain faintly beyond room temperature. Matthias and Wood[5] have reported that the crystal structure of tungsten oxide below −50°C would be trigonal and the result of our observation of domain structure at low temperatures supports this supposition.

On the other hand, fine domain boundaries parallel to the cleavage surfaces are sometimes observed on virgin crystals which have never been cooled below room temperature. We can certainly say that these domain boundaries are due to the monoclinic structure below 330°C, since these vanish on heating up to 350°C. It cannot be ascertained, owing to their too minute dimensions, whether these domain boundaries are the same or not with those observed on crystals above −20°C on heating after cooling them below −50°C. It may be said, however, that the monoclinic and trigonal structures would be in an intimate relation.

2.3 *Observation at high temperatures*

The domain structure at high temperatures was observed up to 1200°C by using a micro-furnace under the objective. On heating, any change of the domain structure was not observed until 740°C, where the domain structure vanished suddenly on c-crystals and this corresponds to the transition from orthorhombic to tetragonal structure. On crystals having the c-axis on the plane of plate, such change was not observed and any change did not seem to occur up to 1200°C, but it is difficult to observe clearly the domain structure above 900°C owing to the radiation from crystals. The fact that there exists no change of the domain structure at 910°C is consistent with the fact that the crystal lattice does hardly change at this temperature. The observation above 1200°C was impossible for the sake of the rapid sublimation of crystals.

The color of crystals is yellowish red at temperatures immediately below 740°C and becomes suddenly dark red at this transition point. The fact that this phenomenon is also observed on crystals having the c-axis on the plane of plate in which the birefringence remains still above this temperature leads us to consider that the optical absorption edge which has already been displaced to the yellowish red region may jump to the infrared region at this transition point corresponding to the change of crystal structure. A detailed investigation of the dependence of the optical absorption edge upon temperature will be shortly reported by Horie et al.[6]

An application of electric field of several hundred V/cm upon crystals at room temperature does not change the domain structure at all, in which case the change of domain structure might be prevented by the coersive force too high at room temperature, even if tungsten oxide were ferroelectric; so it is desirable to apply an electric field upon crystals at temperatures near 740°C. We applied a d.c. voltage upon a crystal, then the crystal was heated by the Joule's heat and we could actually observe the effect of the applied d.c. electric field upon the domain structure of the crystal at high temperatures.[7] By this method, it was found that on a rectangular crystal with several domain boundaries inclined by 45° to the edges the d.c. electric field applied between two parallel edges had an effect to increase the area of one sort of domains by creating many new boundaries parallel to the original ones. The process was not quite reversal and the crystal was covered by a great number of domain boundaries after repeated applications of electric field.

Such change of the domain structure may hardly be ascribed to the thermal stress alone, supplied by the electrodes upon the crystal near 740°C, considering the slightness of the rise of temperature of the electrodes. Then the result of the above observation might show a possible existence of ferroelectricity in tungsten oxide below 740°C but such conclusion seems to be in contradiction to the result obtained by the X-ray analysis.

Hirakawa[8] observed a slight displacement of domain boundaries under the application of d.c. electric field of 1000 V/cm in the direction of 45° to the domain boundaries in the low temperature phase. Although this fact shows the ferroelectricity of this phase, it would be hardly possible to give any definite conclusion for the sake of very minute dimensions of domain.

## §3. Crystal Structure

Bräkken reported a crystal structure of tungsten oxide at room temperature in which W and O ions are shifted alternately in an antiparallel manner, by an equal amount, in the directions of both b- and c- axes. Recently Ueda and Kobayashi[18] have precisely studied the crystal structure of tungsten oxide at room temperature using a crystal having only two domains and obtained a result in which W ions are shifted in an antiparallel manner in the directions of a-, b- and c-axes, with the relative shift of 1:3.6:4.7, respectively and, on the other hand, O ions only in the b-direction. Both of these result suggest the possibility of antiferroelectricity in tungsten oxide at room temperature, which however, is in contradiction to the result of electrical measurements.

Although the crystal structure at the low temperature phase below −20°C has not yet been studied thoroughly, the preliminary report by Matthias and Wood[5] shows trigonal structure for the low temperature phase, which is not inconsistent with the result of observation of domain structure. If this phase is ferroelectric as is expected from the result of electrical measurements, it will be a phase similar to that of $BaTiO_3$ below −70°C.

Above room temperature, the crystal structure of tungsten oxide varies from monoclinic to orthorhombic at 330°C,[10] from orthorhombic to tetragonal at 740°C,[10],[11],[12] but no change has been observed at 910°C.[10],[12] On the other hand, Kehl et al.[12] have reported that ions are arranged in an antiparallel manner in the direction of c-axis above 740°C. In view of such situation, we have made precise measurement of the crystal structure by the powder photograph method using the CuK$\alpha$ ray in the neighborhood of 910°C and 1230°C respectively.

Since tungsten oxide sublimates very rapidly at high temperatures, the x-ray photographs should be taken as quickly as possible. As an intense source of x-ray, we have constructed a rotating anode type x-ray tube with an earthed cathode. Using this tube, the powder photograph of metals can be taken only in 10 sec and of oxides in 1∼2 min, the voltage and current being 50 kV and 30 mA, respectively. A detailed description about this tube will be reported in another paper.[19] We used a high temperature camera of 80 mm diameter with a splitted platinum heater, constructed at our laboratory.[21]

Fig. 2 shows the lattice constants near 910°C obtained by an analysis of (122), (131) lines. Although there is not any change of crystal symmetry at this transition, as reported by the previous authors,[10),12)] we can notice a slight anomaly of lattice constants. However, the amount of anomaly is only a little larger than experimental error and does not agree quantitatively with that obtained by the dilatometric measurement.

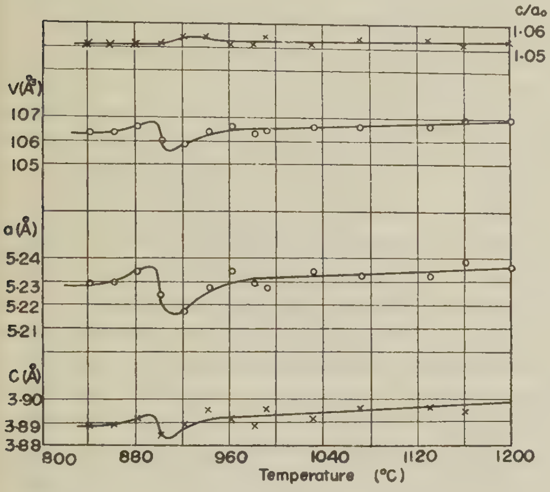

Fig. 2. Lattice constants near 910°C.

It was impossible to take a photograph near 1230°C by the ordinary method, even if the present intense source of x-ray is used, on account of the very rapid sublimation of the sample at such high temperatures, and some special device was necessary. A platinum wire was coated by powder until a rod of 2~3 mm diameter was obtained. As shown in Fig. 3, a vibration photograph with an amplitude of 90° was taken, the surface of the rod being always kept at the center of camera during the sublimation of the sample. Fig. 4 shows the result of an analysis of (122), (131) lines near 1230°C. Although there is no change of crystal symmetry, we have an anomaly of lattice constants which is also a little larger than experimental error. In this case, however, the result obtained by the x-ray analysis is not inconsistent with that by the dilatometric observation.

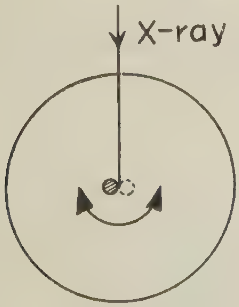

Fig. 3. Method of taking a photograph at high temperatures.

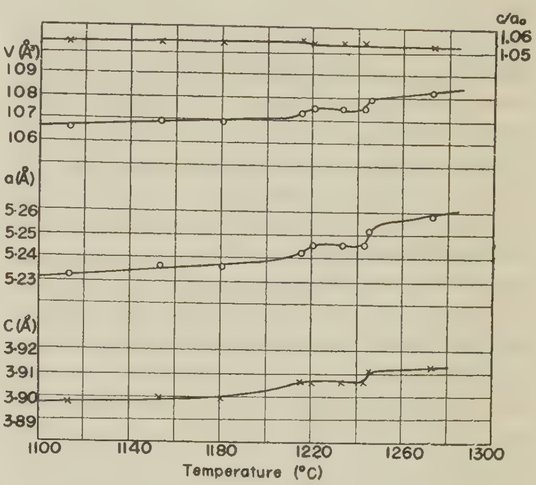

Fig. 4. Lattice constants near 1230°C.

The tetragonality of tungsten oxide is 1.05 and is less than that of $PbTiO_3$, 1.06, at room temperature, so it is not improbable to suppose that there may exist a transition from tetragonal to cubic below the melting point.* There was, however, no detectable anomaly on the cooling curve observed between 1400°C and 1230°C. Hence such transition point, if it existed, would be found very near the melting point and its identification by the x-ray analysis and other methods would prohibitively difficult owing to the fierce sublimation at such high temperatures.

## § 4. Discussions

### I. *Ferroelectricity and Antiferroelectricity*

Since an abrupt change of domain structure and a remarkable contraction are observed at −50°C on cooling, it is hardly doubtful that a new phase is realized from this temperature.

---

* The melting point of tungsten oxide is said to be 1437°C, but this value seems indefinite owing to its volatile property.

Although any detailed determination of crystal structure at this low temperature phase has not yet been made, this phase seems to be similar to that of $BaTiO_3$ realized below −70°C judging from the feature of domain structure and Matthias' preliminary investigation of crystal structure. The fact that the hysteresis loop is observed and domain boundaries are displaced by the application of d.c. field leads us to consider that this phase would be ferroelectric. A characteristic of the −50°C transition is the temperature hysteresis. This is noticeable in the permittivity, domain structure and hysteresis loop. Although any anomaly of specific heat is not observed in the neighborhood of −20°C on heating from below −100°C, there is a possibility that an anomaly of specific heat might be observed beyond room temperatures. An accurate measurement of specific heat between −100°C and 200°C is desired in order to clarify this point.

Although, according the precise determination of crystal structure by Ueda and Kobayashi,[18] ions are arranged in an antiparallel manner, we cannot still deny the possibility of ferroelectricity in the monoclinic phase between −20°C and 330°C, since the hysteresis loop is observed, the permittivity decreases with the d.c. biasing field[13] and the non-linearity of a.c. impedance is observed in this phase. The fact that the domain structure similar to that of $BaTiO_3$ is observed and it varies sensitively following the external mechanical stress is, of course, helpless in a criterion of ferro-, antiferro- and para-electricity. The ferroelectric behavior observed above room temperature may be due to the residual effect of the −20°C transition above room temperature or a forced transition[14],[15] from antiferroelectric state by applied electric field. Also a possibility of ferrielectricity should be taken into account. A crystal analysis by the x-ray method under the application of external electric field, if possible, would give us a more conclusive criterion.

Also the 330°C transition is rather gradual but the total amount of anomaly is not so small. Ionic positions in the orthorhombic phase between 330°C and 740°C are presumably supposed to be not so different from those in the monoclinic phase, although any determination of them has not yet been made. Thus the effect of d.c. field upon the domain structure observed between 500°C and 740°C seems to be due to the forced transition, but a small possibility that this orthorhombic phase might be again ferroelectric cannot be entirely denied.

Although there exist only slight anomalies of lattice constants and no change of crystal symmetry at 910°C and 1230°C, anomalies of all other properties are observed there. Here we might consider that there exist some slight change of axial angles, accompanied by minute shifts of component ions in the crystal or some other kinds of similar changes which cannot be ascertained by the present accuracy of powder photograph analysis. Even if it were approved, the discrepancy between the results obtained by the x-ray analysis and the dilatometric measurement at 910°C is still conflicting. It is easily supposed that the changes at 910°C and 1230°C would be very delicate, judging from the fact that the crystal structure above 1230°C is still non-cubic and the changes of entropy at 740°C, 910°C and 1230°C are 0.45, 0.23 and 0.08 cal/mol. deg. respectively.

Although the discrepancies among anomalies of each property similar to those of $WO_3$ have been observed in $NaNbO_3$[14],[15] they were recently removed by a precise determination of crystal structure by Francombe.[16] The fact that the arrangement of ions in tungsten oxide is similar to that in $NaNbO_3$ makes us expect that conflicting features of $WO_3$ mentioned above would be clarified by the more accurate x-ray analysis of this substance in future.

## II. *Bond Structure*

If all of six bonds ejected from each W ion were equivalent single bonds, the crystal

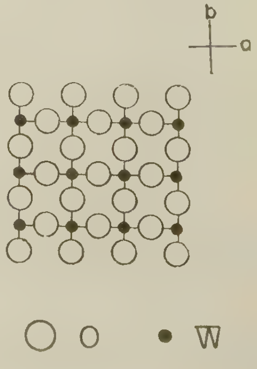

Fig. 5 (a). An ideal ionic lattice of $WO_3$.

structure would be a non-puckered cubic perovskite as shown in Fig. 5 (a). On the contrary, if three of them were double bonds and the other three were 'virtual' bonds, tungsten oxide would be a typical molecular crystal, as shown in Fig. (b) for example. In the real lattice of tungsten oxide, W–O seem to be in intermediate states between these. Each of the six bonds ejected from a W ion would have, in general, the different number of electrons upon it and accordingly the different bond length respectively. Thus the crystal would have a distorted structure as shown in Fig. 5 (c) and sometimes a puckered structure, which fact has been ascertained in experimental works. According to Ueda and Kobayashi,[18] the lengths of W–$O_{\pm X}$, W–$O_{\pm Y}$ and W–$O_{\pm Z}$ are 1.79, 1.88; 1.82, 1.95 and 1.71, 2.11 Å respectively. Since the bond length is generally considered to decrease with the increase of number of electrons existing upon it, this result shows that the greatest and the smallest densities of electrons are found in the c-direction and the intermediate ones in the a- and b-directions; which states of affairs might presumably be connected with the peculiar properties of $WO_3$. The many transition points of tungten oxide may be the temperatures where the feature of bonding changes successively.* That is, each anomaly seems to be of electronic origin, accompanied by the change of lattice. At 910°C and 1230°C, the accompanied change of lattice may be too slight to be ascertained by the accuracy of present x-ray analysis.

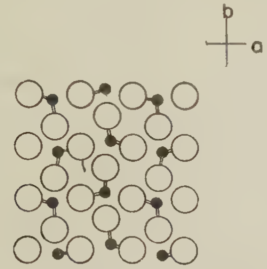

Fig. 5 (b). A molecular-crystal-like lattice of $WO_3$.

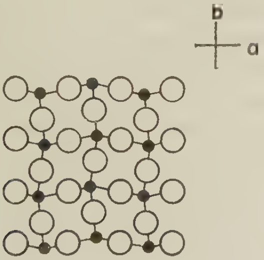

Fig. 5 (c). Real lattice of $WO_3$.

This view concerning the structure of tungsten oxide may be said to be similar to that of Megaw[17] in the point that the role of bonding is highly stressed in the discussion of ferroelectricity or antiferroelectricity and should await further experimental criticism before reaching a final conclusion, but here it should be pointed out that this model is able to interpret the volatility and electrical conductiveness of tungsten oxide.

The molecular-crystal-like property of tungsten oxide mentioned above would necessarily induce the volatility of this substance. The result that the activation energies of sublimation below and above 1230°C are 2.17 and 3.22 eV respectively, as mentioned in Sec. 2.4 of the previous paper.[1] indicates that the molecular crystal character as shown in Fig. 5 (b) is more probable below this temperature and the phase above this temperature has a structure more near to the one shown in Fig. 5 (a). It is reasonable that the more symmetrical structure is realized at high temperatures. A free molecule of tungsten oxide is supposed to have a pyramidal structure with $\alpha \approx 90°$ as shown in Fig. 6. It would be interesting to check this by the x-ray analysis and other methods.

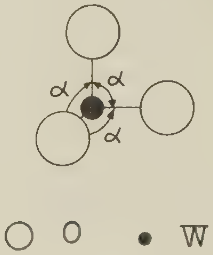

Fig. 6. An assumed form of a $WO_3$ molecule.

The resonance between the bonds containing the different number of electrons which is supposed to be realized in tungsten oxide would induce the transfer of electrons under the application of external electric field, which is thought to be the origin of high mobility of holes in tungsten oxide.

---

* Corresponding to the successive changes of bonding, the number of oxygen ions occupying the several kinds of interstitial sites would be also changed successively, but it would be hardly possible to discuss it in detail by the x-ray analysis.

If the displacement of ions in tungsten oxide were of the electronic origin, ferroelectricity or antiferroelectricity in tungsten oxide would be of the more complex character than in ordinary insulating substances, since the net transfer of electrons is induced by the external field.

Finally, we should like to say that tungsten oxide is really an interesting substance in its dielectric and conductive properties but these two are to be discussed simultaneously, not independently, in both experimental and theoretical investigations.

The author wishes to express his sincere thanks to Prof. S. Kaya, Prof. T. Muto and Prof. K. Ochiai for their kind advices and criticisms and to Prof. R. Ueda, Prof. J. Yamashita and Dr. J. Kobayashi for their continual discussions. The author wishes also to thank Mrs. I. Tako and Mr. S. Fujii for their continual assistance in the experiments.

## References

1) S. Sawada: Journ. Phys. Soc. Jap. **11** (1956) 1236.
2) K. Hirakawa: Busseiron Kenkyu No. **26** (1950) 42.
3) R. Ueda and T. Ichinokawa: Journ. Phys. Soc. Jap. **6** (1951) 122.
4) K. Hirakawa: Journ. Phys. Soc. Japan **7** (1952) 331.
5) B. T. Matthias and A. Wood: Phys. Rev. **84** (1951) 1255.
6) T. Horie et al.: Ann. Rep. Sci. Works, Fac. Sci. Osaka Univ. **4** (1956) (in press).
7) S. Sawada and R. Ando: Rep. Inst. Sci. & Tech. Univ. Tokyo **4** (1950) 223.
8) K. Hirakawa: Busseiron Kenkyu No. **38** (1951) 82.
9) H. Bräkken: Zeit. f. Krist., **78** (1931) 484.
10) J. Wyart and M. Foex: Compt. Rend. **232** (1951) 2459.
11) R. Ueda and T. Ichinokawa: Phys. Rev. **82** (1951) 563.
12) W. L. Kehl, R. G. Hay and D. Wahl: Journ. Appl. Phys. **23** (1952) 212.
13) A. Guntherschulze and H. Betz: Zeit. f. Phys. **71** (1931) 106.
14) G. Shirane, R. Newnham and R. Pepinsky: Phys. Rev. **96** (1954) 581.
15) L. E. Cross and B. J. Nicholson: Phil. Mag. **46** (1955) 453.
16) M. H. Francombe: Acta Cryst. **9** (1956) 256.
17) H. D. Megaw: Acta Cryst. **7** (1954) 187.
18) K. Kobayashi: Mem. Sch. Sci. & Eng. Waseda Univ. No. **18** (1954) 92.
19) S. Sawada, I. Tako and S. Fujii: Journ. Phys. Soc. Jap. (in press).
20) L. Pauling: Journ. Amer. Chem. Soc. **69** (1947) 542.
21) S. Sawada, S. Fujii and I. Tako: Rep. Inst. Sci. & Tech. Univ. Tokyo **10** (1956) 127.

JOURNAL OF THE PHYSICAL SOCIETY OF JAPAN Vol. 11., No. 12, DECEMBER, 1956

# Internal Friction and Critical Stress of Copper Alloys*

By Shuichiro TAKAHASHI

*Mining and Metallurgical Research Laboratory of Mitsubishi Metal Mining Co., Ltd. Omiya City, Saitama Prefecture*

(Received September 12, 1956)

The effects of strain amplitude on the internal friction and the Young's modulus of polycrystalline specimens of copper alloys (Cu－Zn, Cu－Al, Cu－P) with various concentrations of solute atoms have been investigated.

The results are:

1. The critical stress, up to which the internal friction and the Young's modulus are almost independent of strain amplitude, increases with concentration of solute atoms, showing a considerable harmony with the theoretical stress obtained by Mott.
2. The strain-independent part of the internal friction decreases as a power function of concentration of solute atoms, although its numerical value depends largely on the pre-treatment.
3. The strain-dependent part of the internal friction and the fractional change of Young's modulus are represented by two parallel fomulae, as in the theory of Nowick. But the factors of strain-dependencies seem to increase with concentration of solute atoms.
4. The internal friction and the Young's modulus are both almost independent of frequency in the range between 900 and 10,000 cps at at room temperatures.

## § 1. Introduction

Since the work of Read,1) the dependencies of internal friction and elastic modulus on strain ampliture have been discussed in terms of motion of dislocations. To explain the experimental results on copper and lead single crystals by Marx and Koehler,2) Koehler3) assumed pinned-down and broken-away dislocations. His theory led him to the conclusion that the internal friction and the elastic modulus are frequency-dependent. On the contrary, Nowick4) showed that they are both frequency-independent, and furthermore, that the change of internal friction ($\Delta Q^{-1}$) and the fractional change of elastic modulus ($-\Delta E/E_0$) are expressed by a common function of strain amplitude. This conclusion is based on his assumption of simple hysteresis. On the other hand, the present author5) has shown that the internal friction and the elastic modulus of zinc single crystals are both independent of strain amplitude up to a critical point, beyond which the former increases, while the latter decreases.

Keeping in mind such situation of the research of this field, the effects of strain amplitude on the internal friction and Young's modulus of copper alloys of various concentrations of solute atoms will be dealt with in the following. In carrying out the investigation of this kind, it would be most desirable that a series of single crystals of same orientation with various concentrations of solute atoms are prepared as specimens. However, if the internal friction of polycrystalline specimens is measured in kiloycle range and at room temperatures, the part of internal friction due to relaxational between stress and strain, which is caused by stress induced ordering,6) viscous flow in grain boundaries,7) or thermo-elastic effect,6) is supposed to be lower than the order of $10^{-5}$. Furthermore, if quenched or even chill cast specimens are chosen, the part of internal friction due to relaxation will become certainly negligible, since in them a large number of dislocations are not anchored by impurity atoms. Thus, it is expected possible to discuss the internal friction due to dislocations from experiments using polycrystalline specimens. The polycrystalline specimens used in the present work are of systems of Cu-Zn,

---

* The outline of this paper was read at the annual meeting of the Japan Institute of Metals, April, 1953.

Table I. Cu-Zn Alloys (cast)

| Specimen No., Concentration of Zn (analyzed) $C$ | Theoretical Critical Stress ($\times 10^5$ dyness/cm$^2$) $\mu\varepsilon^{4/3} C$ | Measured by 2 nods | | | | Measured by 3 nodes | | | |
|---|---|---|---|---|---|---|---|---|---|
| | | Experimental Critical Stress ($\times 10^5$ dynes/cm$^2$) $\sigma_C$ | Strain-independent Internal Friction $Q_0^{-1}$ | Factor of Strain-dependency of Internal Friction $\alpha$ | Factor of Strain-dependency of Fractional Change of Young's Modulus $\alpha'$ | Experimental Critical Stress ($\times 10^5$ dynes/cm$^2$) $\sigma_C$ | Strain-independent Internal Friction $Q_0^{-1}$ | Factor of Strain-depencency of Internal Friction $\alpha$ | Factor of Strain-depencency of Fractional Change of Young's Modulus $\alpha'$ |
| Zn 0 (tr.) | — | 1.54 | $2.20\times 10^{-3}$ | 1.08 | 0.72 | — | $2.24\times 10^{-3}$ | 1.08 | 1.21 |
| Zn 1 ($9.73\times 10^{-5}$) | 9.93 | 2.06 | $1.8\times 10^{-3}$ | 1.14 | 1.25 | 1.80 | $2.2\times 10^{-3}$ | 1.22 | 1.21 |
| Zn 2 ($3.89\times 10^{-4}$) | 39.8 | 2.57 | $1.4\times 10^{-3}$ | 1.26 | 1.33 | 4.25 | $1.4\times 10^{-3}$ | 1.33 | — |
| Zn 3 ($1.17\times 10^{-3}$) | 114 | 5.77 | $8.6\times 10^{-4}$ | 1.60 | 1.60 | 9.10 | $8.6\times 10^{-4}$ | 1.60 | 1.63 |
| Zn 4 ($3.11\times 10^{-3}$) | 302 | 10.9 | $7.2\times 10^{-4}$ | 1.95 | 2.10 | 27.4 | $6.0\times 10^{-4}$ | 2.35 | 2.35 |
| Zn 5 ($9.62\times 10^{-3}$) | 940 | 43.7 | $2.3\times 10^{-4}$ | 2.20 | 2.10 | 83.3 | $2.3\times 10^{-4}$ | 2.50 | 2.22 |
| Zn 6 ($2.98\times 10^{-2}$) | 2920 | 250 | $1.4\times 10^{-4}$ | 3.08 | 3.08 | 732 | $1.6\times 10^{-4}$ | 3.20 | 3.33 |
| Zn 7 ($9.70\times 10^{-2}$) | 9500 | 1990 | $9.8\times 10^{-5}$ | 4.21 | — | 2180 | $1.5\times 10^{-4}$ | 4.21 | — |

Table II. Cu-P Alloys (cast)

| Specimen No., Concentration of P (added) $C$ | Theoretical Critical Stress ($\times 10^5$ dynes/cm$^2$) $\mu \varepsilon^{4/3} C$ | Measured by 2 nodes | | | | Measured by 3 nodes | | | |
|---|---|---|---|---|---|---|---|---|---|
| | | Experimental Critical Stress ($\times 10^5$ dynes/cm$^2$) $\sigma_C$ | Strain-independent Internal Friction $Q_0^{-1}$ | Factor of Strain-dependency of Internal Friction $\alpha$ | Factor of Strain-dependency of Fractional Change of Young's Modulus $\alpha'$ | Experimental Critical Stress ($\times 10^5$ dynes/cm$^2$) $\sigma_C$ | Strain-Independent Internal Friction $Q_0^{-1}$ | Factor of Strain-dependency of Internal Friction $\alpha$ | Factor of Strain-dependency of Fractional Change of Young's Modulus $\alpha'$ |
| P 1 ($2.07 \times 10^{-5}$) | 0.87 | 1.67 | $1.75 \times 10^{-3}$ | 0.91 | 0.93 | 1.28 | $1.67 \times 10^{-3}$ | 1.05 | 1.05 |
| P 2 ($6.19 \times 10^{-5}$) | 2.61 | 4.0 | $9.8 \times 10^{-4}$ | 1.30 | 1.31 | 2.05 | $9.1 \times 10^{-4}$ | 1.50 | 1.38 |
| P 3 ($2.07 \times 10^{-4}$) | 8.77 | 2.95 | $7.75 \times 10^{-4}$ | 1.29 | 1.33 | 2.05 | $8.1 \times 10^{-4}$ | 1.50 | 1.54 |
| P 4 ($6.19 \times 10^{-4}$) | 26.1 | 9.35 | $5.23 \times 10^{-4}$ | 1.60 | 1.66 | 3.7 | $4.78 \times 10^{-4}$ | 1.68 | 1.70 |
| P 5 ($2.07 \times 10^{-3}$) | 87.7 | 12.8 | $2.73 \times 10^{-4}$ | 1.87 | 1.90 | 8.7 | $2.85 \times 10^{-4}$ | 2.10 | 2.00 |
| P 6 ($6.2 \times 10^{-3}$) | 262 | 54 | $2.05 \times 10^{-4}$ | 2.31 | 2.30 | 25.7 | $1.82 \times 10^{-4}$ | 2.35 | 2.42 |
| P 7 ($2.08 \times 10^{-2}$) | 880 | 170 | $1.82 \times 10^{-4}$ | 2.86 | 3.20 | 33.3 | $1.82 \times 10^{-4}$ | 2.35 | — |

Cu-Al, and Cu-P with various concentration of solute atoms.

## § 2. Measurement

The specimens were prepared by melting high purity electrolytic copper (99.99 wt. per cent) with desired amount of high purity aluminum (99.99 wt. per cent), high purity zinc (99.99 wt. per cent) or 15% P-Cu master alloy in graphite crucibles placed in a high frequency electric furnance. The demension of ingots was 10×10×200 mm or 20×20×150 mm. The ingots of the former dimension were used as the specimens "as cast." Those of the latter were thereafter forged down to the cross-section of 12×12 mm in the temperature ranging from 850° to 600°C, cut to the size of 10×10×200 mm, annealed at 800°C for 4 hrs, and finally quenched in water of 20°C. The chemical composition of the specimens added or analyzed are shown in Tables I and II.

The experiment consisted in the transversal vibration of the specimen bar in free-free modes at audio-frequencies (mainly about 1000 cps in the case of 2 nodes and about 2700 cps in the case of 3 nodes). The internal friction was measured either by resonance curve method or by the natural damping method. The frequency of a C-R-oscillator $f$, was adjusted by a variable condensor placed parallel to the main condensor so as to be resonant with characteristic frequency of the specimen $f_0$. The fractional change of Young's modulus was calculated from the value of capacity of the variable condensor at this resonance. The relative value of the strain amplitude was known from the gain of the receiving amplifier, which produced a constant vertical amplitude on the screen of a cathode-ray oscillograph. Its absolute value was calibrated by microscopic measurement for large strain amplitudes. All the measurements were performed in a stress range of $10^5$–$10^8$ dynes/cm² at room temperatures.

## § 3. Experimental Results

The obtained results for Cu-Zu, Cu-Al, and Cu-P alloys are shown in Fig. 1, 2, and 3, respectively. The curves in these figures are analogous to the curve for single crystal of zinc, obtained formerly by the present author.[5] A typical curve for Cu-Al (1.38 per cent Al) alloy is shown in Fig. 4.

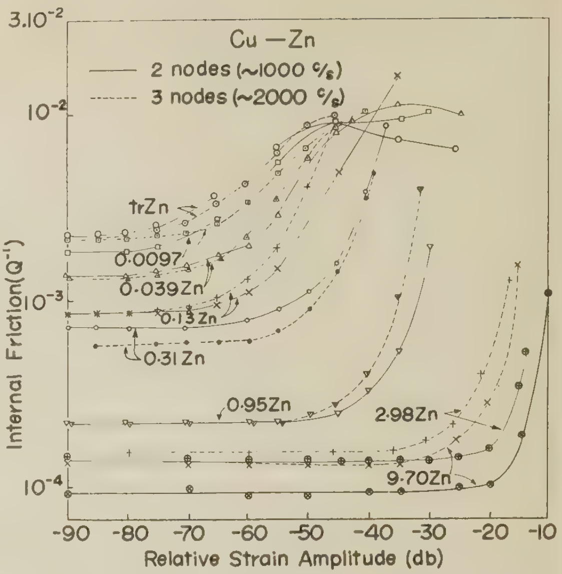

Fig. 1. Internal friction vs. relative strain amplitude for chill cast specimens of Cu-Zn alloys.

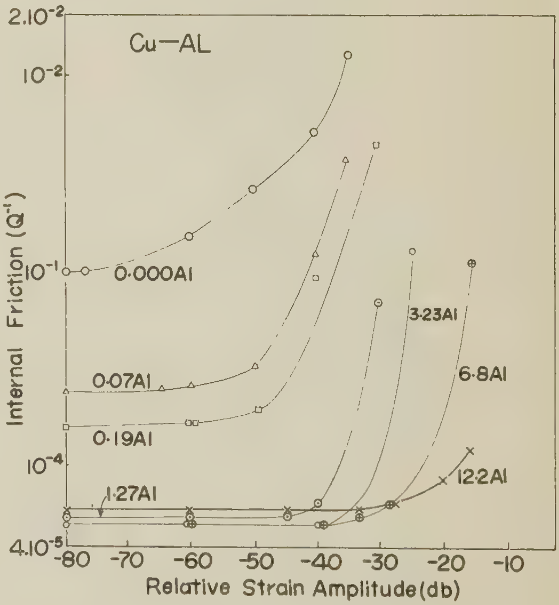

Fig. 2. Internal friction vs. relative strain amplitude for specimens of Cu-Al alloys, which were quenched from 800° after annealing for 270 mins.

The main features of these curves are summarized as follows:

1) Up to a critical strain amplitude the internal friction and the Young's modulus are almost independent of strain amplitude.

2) When the strain amplitude exceeds this

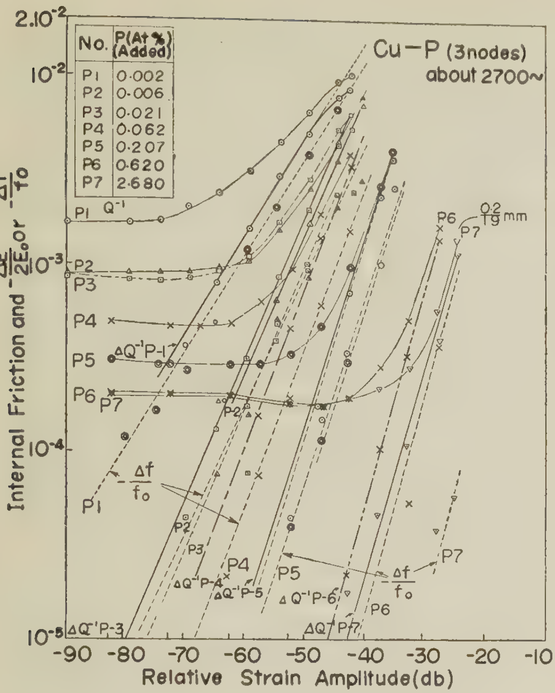

Fig. 3. Internal friction ($Q^{-1}$), strain-dependent internal friction ($\Delta Q^{-1}$), and fractional change of Young's Modulus $\left(-\frac{\Delta E}{2E_0}\right)$ or $\left(\frac{\Delta f}{f_0}\right)$ vs. relative strain amplitude for chill cast specimens of Cu–P alloys.

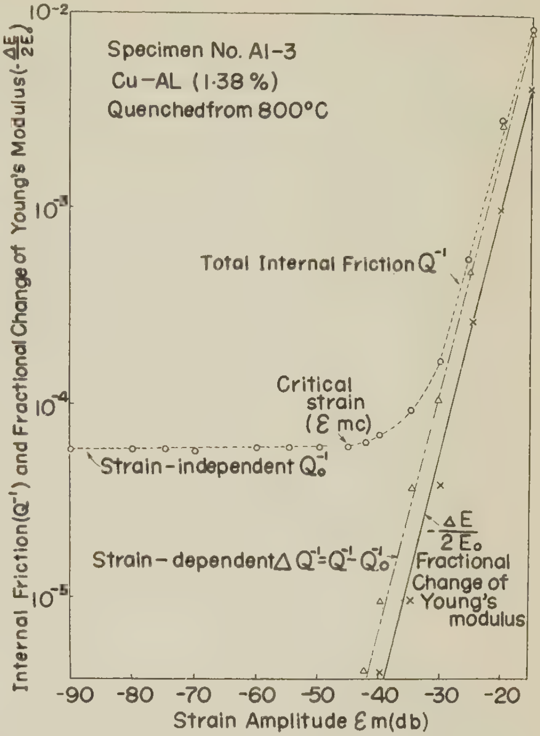

Fig. 4. Internal friction and fractional change of Young's Modulus vs. relave strain amplitude.

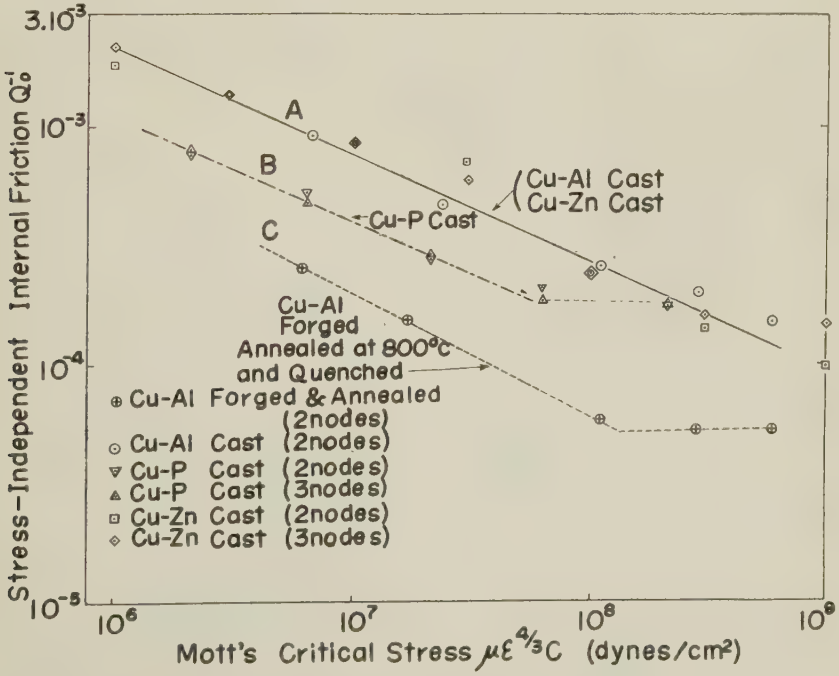

Fig. 5. Stress—independent internal friction v.s. content of solute atoms or critical stress calculated ($\mu\, \varepsilon^{4/3} C$).

critical point, the internal friction increases and Young's modulus decreases.

3) When the strain amplitude is further increased to another critical value, the internal friction begins to cease increasing (see curves for tr. 0.0097 and 0.039 Zn in Fig. 1). This behavior at the second critical point, however, is not observed for the specimens containing higher concentrations of solute atoms in the investigated strain range.

Within the strain range between the first and the second critical strains, the strain dependent part of the internal friction ($\Delta Q^{-1}=Q^{-1}-Q_0^{-1}$) and that of the fractional change of the Young's modulus ($-\Delta E/E_0$) are represented by two parallel straight lines within the experimental error (see Fig. 3 and Fig. 4). We get empirical expressions for $\Delta Q^{-1}$ and $\Delta E/E_0$:

$$\Delta Q^{-1}=Q^{-1}-Q_0^{-1}=\beta\varepsilon_m^{\alpha} \qquad (1)$$

and

$$\Delta E/E_0=(E-E_0)/E_0=\beta'\varepsilon_m^{\alpha'} \qquad (2)$$

where $Q_0^{-1}$ and $E_0$ are the respective strain independent parts, $\varepsilon_m$ is the strain, and $\beta$, $\beta'$, $\alpha$, and $\alpha'$, are constants. $\alpha$ and $\alpha'$ are the determing factors for the strain dependencies of the internal friction and the Young's modulus, respectively.

Tables I and II show, first, that $\alpha$ is approximately equal to $\alpha'$ for each alloy, and secondly, that they are almost constant, whether the frequency is 1000 cps or 2700 cps. It was confirmed that they remain almost unchanged in a wider frequency range of 900–10,000 cps.

The strain-independent internal friction $Q_0^{-1}$ for each alloy investigated decreases with increasing alloying content according to a power function, as shown in Fig. 5. It depends largly on the pretreatment of the specimen; it increases with the elevation of the quenching temperature, and decreases with prolongation of aging time at room temperature and at a temperature before recrystalization.

The critical strain amplitude ($\varepsilon_{mc}$), up to which the internal friction and the Young's modulus are almost independent of strain amplitude, increases with alloying content for each alloy system. The relation of the experimental critical stress, which is calculated from the critical strain and Young's modulus, to the concentration of the alloying element is shown in Fig. 6, whose abscissa is the

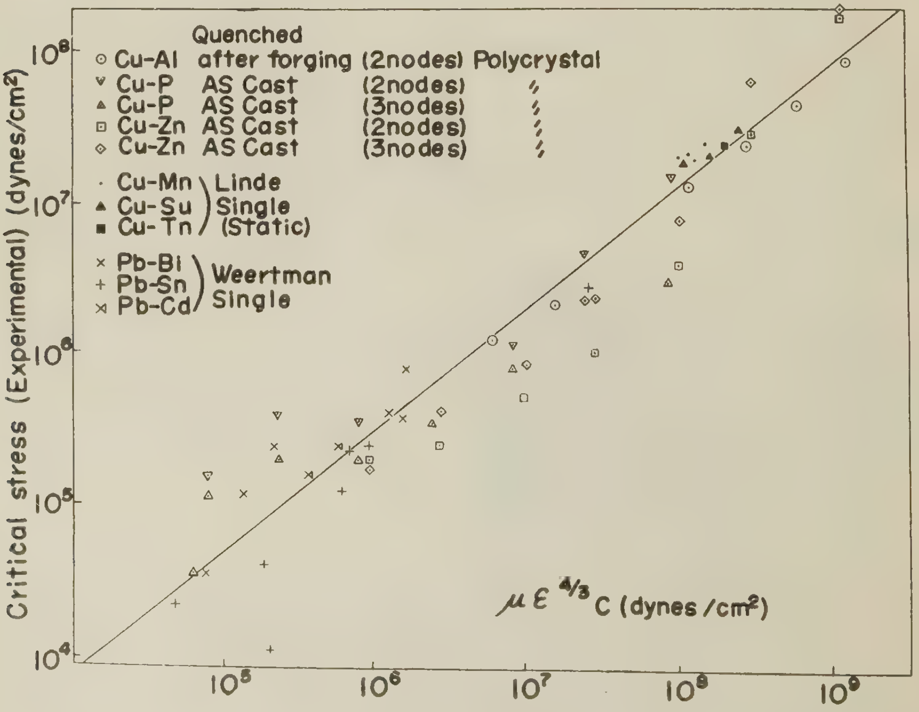

Fig. 6. Experimental stress v.s. calculated stress ($\mu\varepsilon^{4/3}C$).

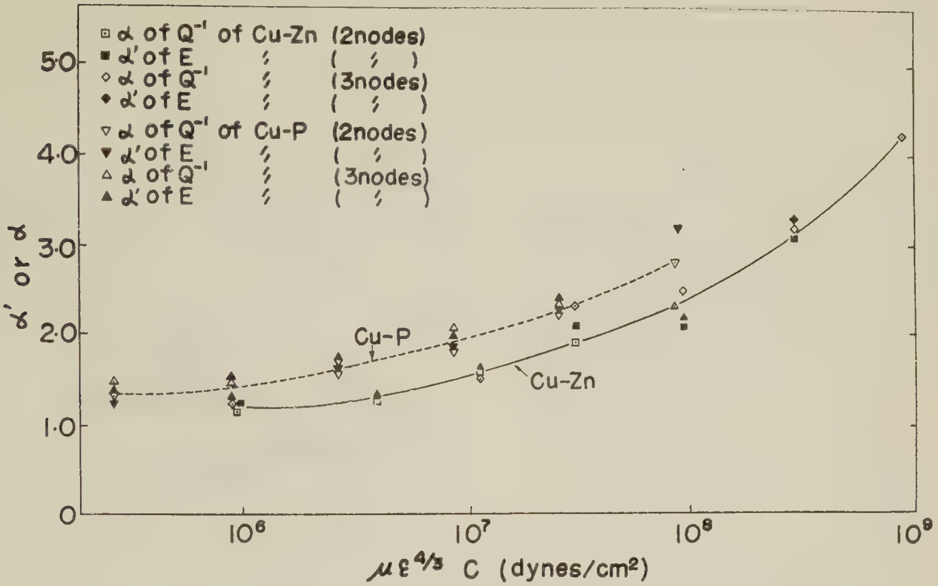

Fig. 7. Strain depedendet power of internal friction and Young's modulus v.s. concentration or critical stress calculated ($\mu\varepsilon^{4/3}C$).

theoretical stress[8] ($\mu\varepsilon^{4/3}c$) proposed by Mott, where $\mu$ is the shear modulus, $\varepsilon$ is $(1/a)\,da/dc$, a being the lattice parameter, and $c$ is the concentration of solute atoms. The relation of the strain dependency factors $\alpha$ and $\alpha'$ to the theoretical stress is Fig. 7. It is interesting that they are not constant, but increase with concentration of solute atoms, and that $\alpha$ and $\alpha'$ are very close to each other.

## § 4. Discussion

1) The cause of the observed internal friction

The internal friction due to the relaxation caused by stress induced ordering, viscous flow in grain boundaries, or thermo-elsatic effect is expressed by the equation[6]

$$Q_r^{-1}=\Delta_M f f_0/(f^2+f_0^2)\,, \qquad (3)$$

where $f$ is the measuring frequency, $f_0$ is the relaxation frequency which is equal to the inverse relaxation time, and $\Delta_M$ the relaxation strength. If $f$ is equal to $f_0$, the internal friction has its maximum value $Q^{-1}_{\max}$, and the relaxation strength $\Delta_M$ becomes $2Q^{-1}_{\max}$.

Many experiments on the relaxation phenomena, caused by stress-induced ordering or viscous flow in grain boundaries, have shown that the maximum internal friction of this kind does not exceed the order of $10^{-1}$. On the other hand, according to the analysis of the relaxation phenomena by Wert and Marx,[9] there is a relation connecting the measuring frequency, the activation energy $\Delta H$, and the temperature $T$ corresponding to the peak of the internal friction:

$$\Delta H=RT\ln(\nu/f)+T\Delta S, \qquad (4)$$

where $R$ is the gas constant, $\nu$ the atomic frequency, and $\Delta S$ the entropy of activation. The activation energy for diffusion of aluminum in copper is reported to be 37–40 Kcal/mol, that of zinc about 40 Kcal/mol. Although the data of the activation energy for phosphorus in copper are not available, it is supposed to be comparable to the above values for aluminum and zinc. By the use of the equations (3) and (4), it is concluded that when the internal friction is measured with a frequency of KC range at about room temperature, the internal friction due to the relaxation caused by stress induced ordering or viscous flow in grain boundaries does not exceed the order of $10^{-5}$.

As for the part of internal friction due to the relaxation caused by the thermo-elastic effect, it seems lower than $3.10^{-5}$ under the present experimental condition[6], for the grain sizes of the specimens are about 0.3–0.01 mm. Moreover, the present experiments at room temperatures show that the internal friction is almost independent of frequency in the range of 900–10,000 cps. Therefore, we are sure that the main mechanism underlying the internal friction observed in the present experiments lies in the motion of dislocations.

2) The mechanism of the internal friction due to the motion of dislocations

According to Koehler, the internal friction is frequency dependent, and its relation to strain amplitude is not the same as the relation of the fractional change of Young's modulus to strain amplitude. The present experiments, however, have shown that $\Delta Q^{-1}$ and $-\Delta E/E_0$ are represented by two parallel straight lines (Fig. 3 and 4), and that not only the internal friction of polycrystalline specimens but also that of single crystals are frequency independent in the range between 900 and 10,000 cps. Fig. 8 shows the internal friction of copper single crystals at room temperature obtained by Marx and the present author. Taking into accouut the difference between the purities of copper single crystals used by the different authors, the internal friction due to the motion of dislocations is most likely independent of frequency in the wider range of 900 to 260,000 cps. Thus, the present results are concluded to contradict Koehler's theory. They seem to be in favor of the Nowick's hysteresis theory. However, $\alpha$ and $\alpha'$ are not always constants but increase with concentration of solute atoms, as shown in Fig. 7.

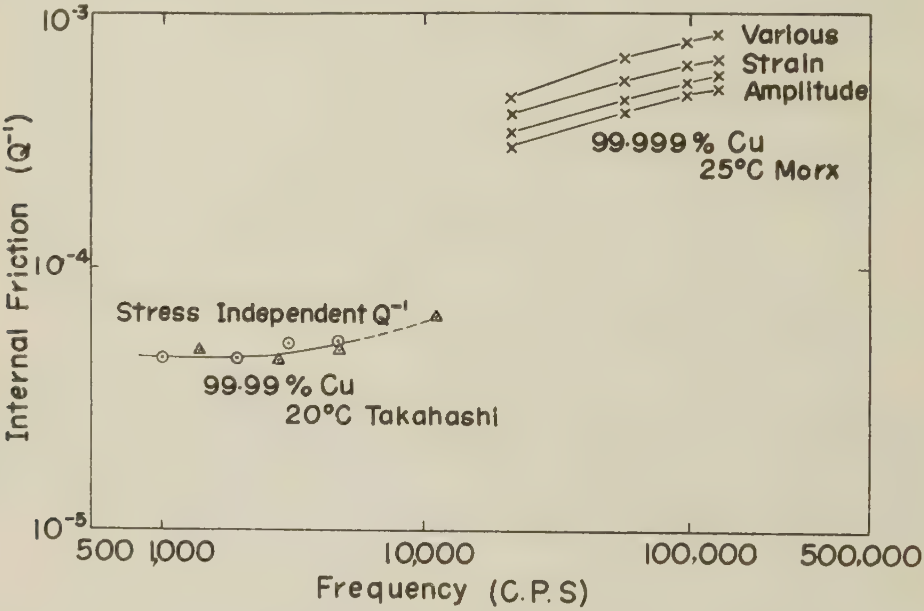

Fig. 8. Internal friction of Cu single crystals v.s. fregency.

3) Comparison of the critical stress with the the theoretical stress

When the maximum vibrational stress reaches a critical stress $\sigma_c$ which corresponds to the critical strain, a remarkable increase of the internal friction and a remarkable decrease of Young's modulus begin simultaneously to take place. This is supposed to correspond to the commencement of a large scale dislocation motion. In this regard we compare the empirical critical stresses to the Mott's theoretical stresses in Fig. 6, which includes also the results of the internal friction measurements by Weertman and Salkovits[10] for lead single crystals and those of static experiments by Linde, Lindell, and Stade[8] for copper single crystals. It seems that the points from the present experiments as well as those by other investigators stand approximately on a straight line, the value of the experimental critical stress being very close to that of Mott's theoretical critical stress for each point. The slight discrepancy between these two values is most likely ascribed to an inadequacy of the assumption regarding the coherent length of dislocation line. It is very interesting that present experiments have thus revealed micro-critical stress of polycrystalline specimens.

4) Effect of concentration of solute atoms

As to the stress-independent internal friction, it decreases with increaing concetration of solute atoms (Fig. 1, 2, 3 and 5), according to a power function, but the decrease is not so rapid as suggested by Weertman.$^{10)}$ It is also to be noted that the stress-independent internal friction depends largely on the pretreatment of the specimen.

Another interesting result is the strain-dependent part with factors $\alpha$ and $\alpha'$, which increase with the concentration of alloying element (Fig. 7). For explaining this phenomenon further investgation will be required.

The author wishes to express his sincere thanks to Prof. K. Iwase, Kyoto and Tòhoku Universities, for his kind guidance, and to Dr. Y. Imai, Director of our Laboratory, for his support and permission to publish this paper. He is grateful to Mr. H. Sawada, Manager of the 3rd Research Division, and Mr. A. Masuda for their continous interests, supports, and examining the manuscript. The author also thanks Mr. H. Konno for this continuous help.

### References

1) T. A. Read: Phys. Rev. **58** (1940) 371.
2) J. Marx and J. S. Koehler: *A Symposium on the Plastic Deformation of Crystalline Solids*, Mellon Institute (1950) 171.
3) J. S. Koehler: Imperfection in Nearly Perfect Crystals, 197.
4) A. S. Nowick: *A Symposium on the Plastic Deformation of Crystalline Solids*, Mellon Institute (1950) 155.
5) S. Takahashi: J. Appl. Phys. **23** (1952) 866.
6) C. Zener: *Elasticity and Anelasticity of Metals*, The University of Chicago Press (1948).
7) T. S. Kê: Phys. Rev. **73** (1948) 267.
8) A. H. Cotrell: *Dislocations and Plastic Flow in Crystals* (1954) 131.
9) C. Wert and J. Marx: Act. Met. **1** (1953) 113.
10) J. Weertman: J. Appls. Phys. **26** (1955) 202.

---

JOURNAL OF THE PHYSICAL SOCIETY OF JAPAN Vol. 11., No. 12, DECEMBER, 1956

# The Bond Orbital Approximation for $\pi$-electron System in Benzene

By Eiko AIHARA and Kazuo NIIRA

*Department of Physics, Tokyo Institute of Technology, Oh-okayama, Tokyo*

(Received August 14, 1956)

The electronic energies of $\pi$-electron system in benzene molecule have been calculated by the bond orbital (BO) method for singlet states. Configuration interactions (CI) have not been taken into account. All the levels other than ${}^1B_{2u}$ and ${}^1E_{2g}$ calculated by the present method are higher than the levels calculated by the MO method without CI. In the MO method, however, the order of levels is changed and coincides with the observed order, by including CI. In the BO method the order of levels would not be changed by including CI, since the BO method without CI already gives the correct order.

## §1. Introduction

There are two methods in common use for the quantitative study of electronic states in molecules. They are the "Method of molecular orbitals (MO)" and the "Method of valence-bond structures (VB)." The former, the MO method, which fails to give the simple relation between the chemical bonds and the molecular stabilities, is inconvenient to discuss the bond properties such as bond energies, bond dipoles and bond force constants. On the other hand, the VB method is closely related to the concept of chemical bonds, but has the difficult problem of non-orthogonalities. The method to be described in this paper, the band orbital (BO) method, is based upon the concept of chemical bonds and has an advantage of making easier to deal with the non-orthogonality problem.

To study the nature of the approximation of the BO method, we have calculated the electronic energies of the $\pi$-electron system in benzene molecule by this method, where numerical values of molecular integrals have been taken from the paper by Parr, Craig and Ross[1].

## § 2. Bond Orbitals and Electronic Configurations

The bond orbitals of the $\pi$-electrons in the benzene molecule are defined as follows:

$$\tau_k=\{2(1+S_{12})\}^{-1/2}(\chi_k+\chi_{k+1}) , \quad (k=1, 2, \cdots 6) \qquad (1)$$

$$\omega_k=\{2(1-S_{12})\}^{-1/2}(\chi_k-\chi_{k+1}) , \qquad (2)$$

$$\tau_{Dj}=\{2(1+S_{14})\}^{-1/2}(\chi_j+\chi_{j+3}) , \quad (j=1, 2, 3) \qquad (3)$$

$$\omega_{Dj}=\{2(1-S_{14})\}^{-1/2}(\chi_j-\chi_{j+3}) , \qquad (4)$$

where $S_{12}=\int\chi_1\chi_2 d\tau$ , $S_{14}=\int\chi_1\chi_4 d\tau$ and $\chi_k$ is the $2p\pi$ AO on the $k$-th carbon atom. $\tau_k$ and $\tau_{Dj}$ ($\omega_k$ and $\omega_{Dj}$) are bonding (antibonding) type BO's.

Electronic configurations which are taken into account in our calculation are given in Table I. In this Table the second column represents the total electronic wave functions which are constructed by forming the antisymmetrized products of one electron functions in the third column.

Table I. Electronic Configurations.

| Class | Wave Function | Configuration | Symmetry Type |
|---|---|---|---|
| (A) | $\Psi_{K1}$ | $\tau_1)^2\ \tau_3)^2\ \tau_5)^2$ | $A_{1g},\ B_{2u}$ |
| | $\Psi_{K2}$ | $\tau_2)^2\ \tau_4)^2\ \tau_6)^2$ | |
| | $\Psi_{D1}$ | $\tau_{D1})^2\ \tau_2)^2\ \tau_5)^2$ | |
| (B) | $\Psi_{D2}$ | $\tau_{D2})^2\ \tau_3)^2\ \tau_6)^2$ | $A_{1g},\ E_{2g}$ |
| | $\Psi_{D3}$ | $\tau_{D3})^2\ \tau_1)^2\ \tau_4)^2$ | |
| | $\Psi_{D1}{}^1$ | $\tau_{D1})\ \omega_{D1})\ \tau_2)^2\ \tau_5)^2$ | |
| (C) | $\Psi_{D2}{}^2$ | $\tau_{D2})\ \omega_{D2})\ \tau_3)^2\ \tau_6)^2$ | $B_{1u},\ E_{1u}$ |
| | $\Psi_{D3}{}^3$ | $\tau_{D3})\ \omega_{D3})\ \tau_1)^2\ \tau_4)^2$ | |
| | $\Psi_{K1}{}^1$ | $\tau_1)\ \omega_1)\ \tau_3)^2\ \tau_5)^2$ | |
| | $\Psi_{K1}{}^3$ | $\tau_3)\ \omega_3)\ \tau_1)^2\ \tau_5)^2$ | |
| (D) | $\Psi_{K1}{}^5$ | $\tau_5)\ \omega_5)\ \tau_1)^2\ \tau_3)^2$ | $E_{2g},\ B_{1u},$ |
| | $\Psi_{K2}{}^2$ | $\tau_2)\ \omega_2)\ \tau_4)^2\ \tau_6)^2$ | $E_{1u},\ A_{2g}$ |
| | $\Psi_{K2}{}^4$ | $\tau_4)\ \omega_4)\ \tau_2)^2\ \tau_6)^2$ | |
| | $\Psi_{K2}{}^6$ | $\tau_6)\ \omega_6)\ \tau_2)^2\ \tau_4)^2$ | |
| | $\Psi_{D1}{}^2$ | $\tau_2)\ \omega_2)\ \tau_{D1})^2\ \tau_5)^2$ | |
| | $\Psi_{D1}{}^5$ | $\tau_5)\ \omega_5)\ \tau_{D1})^2\ \tau_2)^2$ | |
| (E) | $\Psi_{D2}{}^3$ | $\tau_3)\ \omega_3)\ \tau_{D2})^2\ \tau_6)^2$ | $E_{2g},\ B_{1u},$ |
| | $\Psi_{D2}{}^6$ | $\tau_6)\ \omega_6)\ \tau_{D2})^2\ \tau_3)^2$ | $E_{1u},\ A_{2g}$ |
| | $\Psi_{D3}{}^1$ | $\tau_1)\ \omega_1)\ \tau_{D3})^2\ \tau_4)^2$ | |
| | $\Psi_{D3}{}^4$ | $\tau_4)\ \omega_4)\ \tau_{D3})^2\ \tau_1)^2$ | |

Table II. Mean Energy of the Electronic Configuration ($\Psi$).

| Class | Mean Energy[a)] | (eV) |
|---|---|---|
| (A) | $W(\Psi_{K1})$[b)] | 3.36 |
| (B) | $W(\Psi_{D1})$ | 12.44 |
| (C) | $W(\Psi_{D1}{}^1)$ | 18.48 |
| (D) | $W(\Psi_{K1}{}^1)$ | 25.95 |
| (E) | $W(\Psi_{D1}{}^2)$ | 48.25 |

a) The origin of the energy is chosen to the energy value of the ground configuration by the MO method without CI.

b) $W(\Psi)=\int\Psi\mathscr{H}\Psi d\tau\Big/\int\Psi^2 d\tau$, where $\mathscr{H}$ is the total Hamiltonian.

The wave functions in the same class have equal mean energies. The configurations classified in (A) and (B) correspond to Kekulé structures 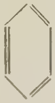 and Dewar structures 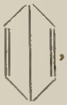, respectively. The configurations in (C), (D) and (E) give rise to both singlet and triplet states, but we consider only the singlet states. Further, we neglect the configurations which include two or more antibonding type BO's ($\omega_k$ or $\omega_{Dj}$).

## § 3. Calculated Result and Discussion

Table II shows the mean energy of the electronic configuration in each class. The difference between the mean energy $W(\Psi_{K1})$ in the Table II and the energy of the ground state calculated by the MO method without CI is supposed to be the delocalization energy in $\pi$-electron system in benzene by Mulliken and Parr[2].

The configurations classified in (E) will not be taken into account in the following calculation, since their mean energies are much higher than others (see Table II).

The electronic wave function of correct symmetry is constructed by forming the linear combination of $\Psi$'s in the same class. When there are several linear combinations of the same symmetry type, we take the one giving the lowest energy.

Table III. Energy Levels Calculated by the BO Method.

| Class | Level | Energy Value (eV)[a] |
|---|---|---|
| (A) | ${}^1A_{1g}$ | 1.69[b] |
| (D) | ${}^1A_{2g}$ | 23.27 |
| (C) | ${}^1B_{1u}$ | 14.43 |
| (A) | ${}^1B_{2u}$ | 5.86 |
| (C) | ${}^1E_{1u}$ | 21.52 |
| (B) | ${}^1E_{2g}$ | 9.61 |

a) The origin of the energy is the same as in the Table II.

b) When CI between the configurations classified in (A) and (B) is taken into account, the value of 1.69 eV is lowered to 1.04 eV.

Table III shows the result of our calculation where non-orthogonalities between the BO's are completely taken into account. CI's between the different classes are not taken into account.

In Fig. 1 our result is compared with the result of the MO method by Parr, Craig and Ross[1].

It may be seen from the Fig. 1 that all the levels other than ${}^1B_{2u}$ and ${}^1E_{2g}$ calculated by the BO method are higher than the levels calculated by the MO method without CI. In the MO method, however, the level ${}^1E_{2g}$ is so much lowered by CI that the order of the levels is changed to coincide with the observed order. On the other hand, in the BO method the order of levels would not be changed by CI, since the BO method without CI already gives the same order as the MO method with CI does (see Fig. 2).

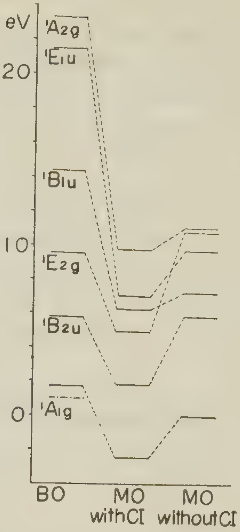

Fig. 1. The result of our calculation is compared with the calculation of the MO method by Parr, Craig and Ross[1]. Broken line (${}^1A_{1g}$ of BO method) represents the result of the CI between the configurations classified in (A) and (B). The origin of the energy is the same as in Table II.

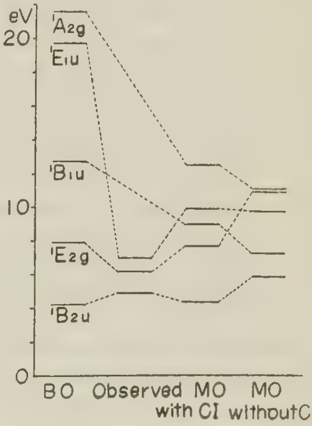

Fig. 2. Relative energy of lower excited levels of benzene for ground state ${}^1A_{1g}$.

In addition we may expect that the levels ${}^1B_{1u}$, ${}^1E_{1u}$ and ${}^1A_{2g}$ would be considerably lowered by including CI's between the configurations classified in (C), (D) and (E) (see Table I and II).

Therefore we can conclude that the BO method without CI is the rather better approximation than the MO method without CI for the lower excited states of benzene. However, when we want to concern only with the quantitative study of the ground state, the MO method is more useful at least for the case of $\pi$-electron system.

The BO method would be better approximation for $\sigma$-electron systems such as in methane than for $\pi$-electron systems, since $\sigma$-electrons are more localized in the region of a particular bond.

This work is indebted to the Ministry of Education for its research grant.

### References

1) R. S. Parr, D. P. Craig and I. G. Ross: J. Chem. Phys. **18** (1950) 1561.
2) R. S. Mulliken and R. S. Parr: J. Chem. Phys. **19** (1951) 1271.

---

JOURNAL OF THE PHYSICAL SOCIETY OF JAPAN Vol. 11., No. 12, DECEMBER, 1956

# Influence of Illumination from Outside on an A-Hg Discharge Tube

By Toshizo NAKAYA
*Department of Physics, Faculty of Science, Osaka University*

(Received April 26, 1956)

It has been discovered by the author that a faint illumination of ultraviolet ray or a visible light from a light source thrown on the discharge space of low pressure A-Hg discharge tubes increases the starting potential to a remarkable extent. This effect only takes place when there exist relatively high wall temperature of 40~90°C (i.e. high density of Hg atoms) and relatively high pressure of argon gas (a few mm Hg). When the intensity of illumination exceeds a certain value, the starting potential shows a somewhat saturated constant voltage. This effect is sensitive to radiations of any wave-length widely ranging from ultraviolent to visible light. An addition of a small quantity of $H_2$ gas suppresses this effect. The part of the tube that is sensitive to radiation is found on the anode side. According to the hypothesis by the author, under such condition that both the pressure of *A* gas and the density of Hg atoms are adequate, there seems to exist a region where metastable molecules of mercury are indispensable for starting a glow discharge as a principal source of ions. In the strength of the assumptions based on the hypothesis by the author, most of the experimental results can be explained fairly well.

## Part I. Experimental Researches

### I. Introduction

It has been proved, in various cases, that the characteristic quantities of the discharge in rare gases or metal vapours are affected when the discharge tube is illuminated from outside by the light from a second discharge tube filled with gas of the same kind.

The fact that the life and the density of metastable atoms decrease if illuminated with a light of gas of the same kind was first proved by Meissner and Graffunder[1] using neon and argon.

The attempt to research into the effect of illumination on the starting potential in rare gas mixtures was first made by Penning.[2][3][4][5] In his experiments, it was proved that the sparking potential of the tube filled with a few mm Hg of neon gas mixed with a small quantity of argon gas increases when illuminated intensely with neon light.

A further study in the influence of illumination on the characteristics of the positive column of low current (a few mA) discharge in the mixture of mercury and a rare gas is being made by Kenty.[6] He has discovered that strong illumination by the light of mercury (transmissible through glass) nearly doubles the tube voltage as well as the λ2537 output, and also nearly doubles the electron temperature, but the illumination by the light of the pure rare gas that is contained in the mixture (A, Kr, Xe) has no such effect.

Similar experiments to prove that the illumination of the positive column of a glow discharge in pure rare gases with the light of gas of the same kind affects the V–I characteristic, lowering the value of current (0.1∼1.0 mA), were carried out by Meissner and Pierson⁷⁾ using neon and helium, and by Meissner and Miller⁸⁾ using argon, krypton and xenon.

The results of the experiments by these researchers would be to a certain extent explained by means of the understanding that these phenomena arise from the destruction of metastable atoms by illumination. But, there exists another observation on the discharge that is called Joshi-effect.

Joshi discovered that an electrodeless discharge current in a Siemens' ozoniser filled with $Cl_2$ gas is lowered by illumination from outside.⁹⁾ After his discovery of this effect, similar experiments have been carried out as regards other gases, such as $I_2$, $Br_2$, $N_2$, $O_2$, $H_2$, air, $H_2O$, toluol etc., by Ramaiah, Subrahmanyam, Bhatawdekar, Saxena, Mohanty.¹⁰⁾⁻²⁵⁾ As the results of their studies, it has become known that this effect has connection with the electron-affinity of the gases, (i.e. the order of the degrees of the current decrease by illumination is $Cl_2 > Br_2 > I_2 > O_2$ etc.), that its behaviour is markedly increased by ageing, and that this effect is not selective in the wavelength of available radiation. On the strength of these experimental results, Joshi set up a hypothesis that the effect is attributed to the photoelectric effect of the particles adsorbed on the surface of the wall of the tube, i.e. negative ions that are formed by excited neutral particles capturing photoelectrons reduce the current mainly in the form of a space-charge.

It has been discovered by the author of this report that a faint illumination of ultraviolet ray or a visible light from a light source thrown on the discharge space of low pressure A–Hg discharge tubes increases the starting potential to a remarkable extent. This effect only takes place when there exist relatively high wall tempreature of 40∼90°C (i.e. high density of Hg atoms) and relatively high pressure of A gas (a few mm Hg).

## II. Experimental Methods

The starting potential is decided by gradually increasing the D.C. voltage applied to the discharge tube through 200 KΩ resistance

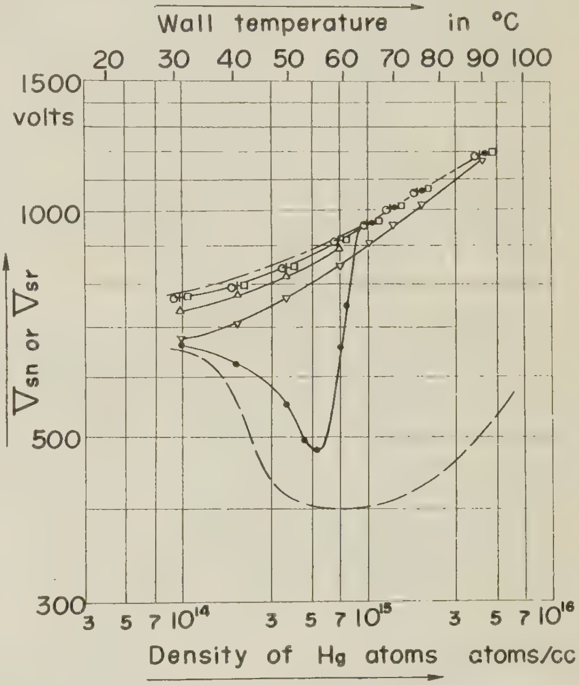

Fig. 1. Starting potentials (*Vsn*) without illumination and ($_{i}Vsr$) under illuminations as a function of the density of Hg atoms.

● *Vsn*: not illuminated.

▽ $_{1}Vsr$: illuminated by the light of 15 watt germicidal lamp placed at a distance of 25 cm.

○ $_{2}Vsr$: illuminated by the light of the same germicidal lamp, of which ultra-violet light is eliminated by means of inserting a glass filter, placed at a distance of 25 cm.

△ $_{3}Vsr$: illuminated by the same germicidal lamp placed at a distance of 100 cm.

□ $_{4}Vsr$: illuminated by the same germicidal lamp, with a glass filter, placed at a distance of 100 cm.

+ $_{5}Vsr$: illuminated by a 100 watt incandescent lamp placed at a distance of 100 cm.

——— represents the value of (*Vsn*) after ageing, and – – – – represents the value of (*Vsr*)*sat* after ageing.

until the discharge space suddenly begins to glow and becomes conducting and the tube voltage drops, and the voltage necessary to produce this phenomenon is defined to be the starting potential of glow discharge.

As the vapour pressure of mercury in the discharge tube is decided by the wall temperature, the tube to be illuminated was set in a furnace so that any desired temperature from the room temperature up to about 100°C could be obtained. All the measurements were made in a dark room, because as will be described later even faint indirect sun-light through windows has considerable effect on the starting potentials.

Measurements were carried out on the hot cathode tubes as well as cold cathode ones. Tubes with various electrode separations, of different tube diameters, and of different argon pressures, and those made of quartz, and of soda lime glass, and of glass transmitting ultra-violet ray were tried.

In the case of the hot cathode type, owing to the existence of constant electron supply before starting discharge, the starting potentials give constant readings and show less fluctuation than those of the cold cathode type. Hence, the results of the experiment will be described, in the main, in connection with the experiments with the tubes of a hot cathode.

## III. Experimental Results

### § 1. *General behaviours of the starting potentials with and without illumination*

The example given in Fig. 1 in which D.C. source is used with a tube of a hot cathode (inner diameter 23 mm, electrode separation 30 cm, argon pressure 4 mmHg and made of glass transmitting λ2537), illustrates general behaviours of starting potentials with and without illumination.

Following abbreviations will be used.

(*Vsn*): starting potential without illumination.

(*Vsr*): starting potential under illumination.

The results in Fig. 1 are derived from the measurement made immediately after exhaust of the discharge tube and, natually, before ageing. As will be described in § 5, broken lines in Fig. 1 represent the results after ageing. Thus, the measurements shown in Fig. 1 do not give the correct values. But this example is serviceable to explain general behaviours of starting potentials under various conditions.

It is seen that $_2Vsr={}_4Vsr={}_5Vsr=(Vsr)sat$ in all regions of wall temperature. In the region lower than 63°C, the effect of illumination in raising the starting potential is seen, i.e. $(Vsr)sat>(Vsn)$.

So long as the illumination is weak, *Log*(*Vsr*) rises almost in proportion to *Log*(*intensity*), but when the intensity of illumination exceeds a certain value, which varies with the kind of light sources, (*Vsr*) shows a somewhat saturated constant voltage (*Vsr*)*sat*. Further-

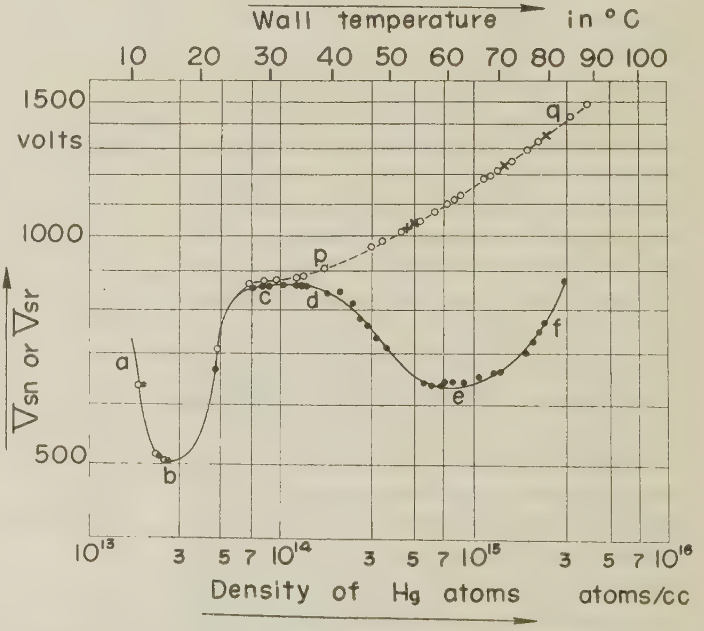

Fig. 2. Starting potentials as a function of wall temperature.

● *Vsn*: not illuminated.

○ $_1Vsr$: illuminated by a 100 watt high pressure Hg arc lamp enveloped in a glass globe, placed at a distance of 100 cm.

+ $_2Vsr$: illuminated by a 100 watt incandescent lamp placed at a distance of 100 cm.

× $_3Vsr$: illuminated by a 100 watt incandescent lamp placed at a distance of 200 cm.

Note that $_1Vsr={}_2Vsr={}_3Vsr=(Vsr)sat$, and also that in the region lower than 30°C, the effect of illumiation on raising the starting potential can not be noticed.

more, when illuminated with a strong light, no matter whether its source is incandescent lamp, iron arc, copper arc, aluminium spark, indirect sunlight, neon light or even argon light, $(Vsr)sat$ gives the same value in the saturated voltage as in the case of mercury light. An appreciation of $(Vsr)$ above this value has never been seen in a wide range of intensities of illumination.

It is seen in all regions of wall temperature that ${}_1Vsr<{}_3Vsr<(Vsr)sat$. This is believed to be due to an effect of $\lambda 2537$ that lowers the starting potential superposing up to $(Vsr)sat$. Therefore in the region higher than 63°C, where $(Vsn)$ is equal to $(Vsr)sat$, $({}_1Vsr)$ and $({}_3Vsr)$ are even lower than $(Vsn)$.

## § 2. *Relation to the wall temperature*

The effect of illumination on raising the starting potential is observed only when the tube is kept at relatively high wall temperature of 40~90°C (i.e. high density of Hg atoms).

Fig. 2 illustrates an example of how the starting potentials of a tube of a hot cathode (inner diameter 22 mm, electrode separation 26 cm, argon pressure 15 mm Hg and made of soda lime glass) behave with changing wall temperature. It is seen that there are two distinguishable parts, one lower than 30°C and the other higher than 30°C, and only in the latter region can the effect of illumination on raising the starting potential be seen. (This is the region that was discovered by the author). The behaviour of $(Vsn)$ suggests that the ionization processes in starting a glow discharge in these two parts are likely to be different. Experimental researches will be described hereinafter only in relation to the region of wall temperature above 30°C.

## § 3. *Relation to the argon pressure*

The argon pressure of at least higher than a certain value is required for the effect to take place, and the higher the argon pressure is, the more sensitive the tube becomes to visible light of long wave-length.

In order to study the relation of starting characteristics to the argon pressure, experiments were carried out on discharge tubes of the same size and description as Fig. 2 with various argon pressures. The results are given in Fig. 3. It should be pointed out that all the curves of $(Vsr)sat$ show the following relation:

$$Log((Vsr)sat) \propto Log(density\ of\ Hg\ atoms).$$

In this sense the $(Vsn)$ curve of (1) (argon pressure of 0.7 mm Hg) may be considered to correspond to the $(Vsr)sat$ curves of other cases, (suggesting that they are the same ionization process in starting).

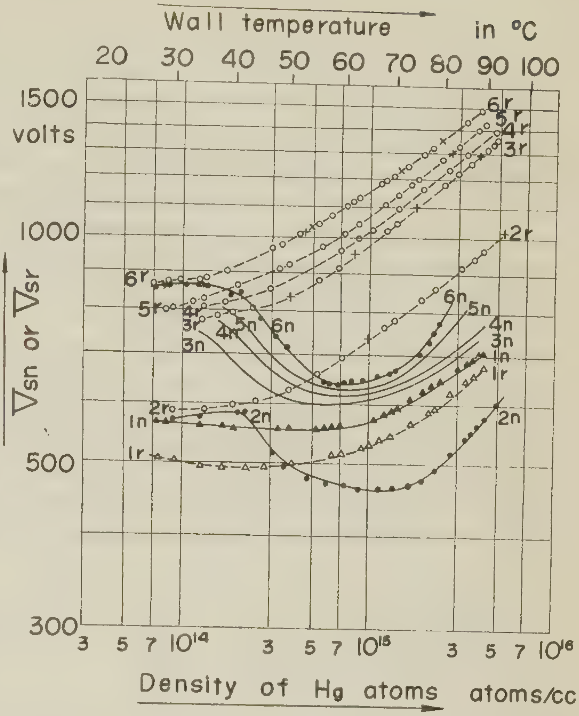

Fig. 3. Relation of $(Vsn)$ and $(Vsr)$ to the argon pressure. Suffix $n$ and $r$ mean $(Vsn)$ and $(Vsr)$ respectively.

○ or △: illuminated by a 100 watt high pressure Hg arc lamp enveloped in a glass globe placed at a distance of 100 cm.
+: illuminated by a 100 watt incandescent lamp placed at a distance of 100 cm.
×: illuminated by a 100 watt incandescent lamp placed at a distance of 200 cm.

As illustrated in the figure, $(Vsr)$ in these cases give the values of $(Vsr)sat$.
(1) argon pressure of 0.7 mm Hg, (2) 2.6 mm Hg, (3) 7.5 mm Hg, (4) 8.5 mm Hg, (5) 10.0 mm Hg, (6) 15.0 mm Hg.
Note that in the case of (1), the argon pressure is too low for the effect of illumination on raising the starting potential to take place, and, contrary to this, the effect of illumination with visible light on lowering the starting potential is noticed.

## § 4. *Relation to the illuminated part of the tube*

### 4.1 *Partial illumination screening the anode side, (aVsp)*

The part of the tube that is sensitive to illumination from outside has been found to be on the anode side. Furthermore, when the intensity of illumination is strong enough to give (*Vsr*)*sat*, there exists a definite critical point of the screening distance.

In order to investigate the distribution of sensitive parts in full, the relation of the starting potential, (*aVsp*), to the size of the part of the tube screened was examined. In this connection, (*aVsp*) means the starting potential of the tube illuminated partially, screening the anode side in the manner shown in Fig. 4. Measurements in Fig. 4 are obtained on a tube (inner diameter 23 mm, electrode separation 44 cm, argon pressure 4 mm Hg, a hot cathode, and made of glass that transmits λ2537). The light source is a 15 watt germicidal lamp placed at various distances from the tube to be illuminated in order to obtain various illuminating intensities.

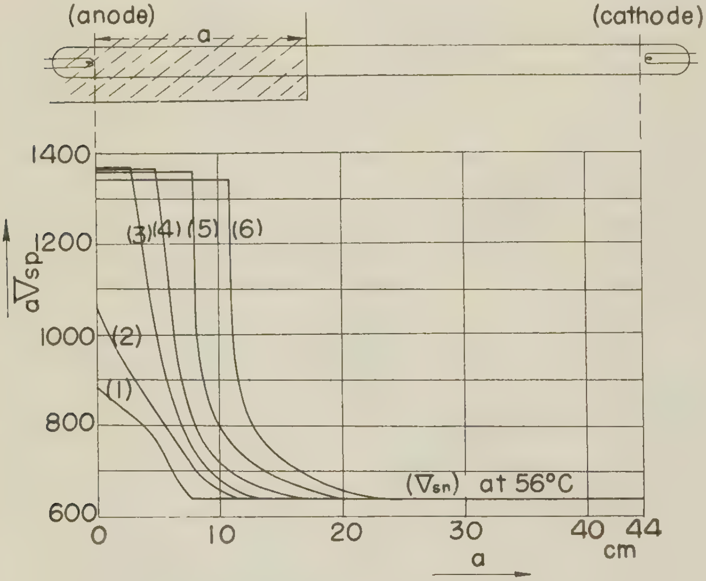

Fig. 4. The part of the tube that is sensitive to illumination to raise the starting pstential. A 15 watt germicidal lamp as the light source is placed at various distances; (1) 300 cm, (2) 200 cm, (3) 150 cm, (4) 120 cm, (5) 100 cm, (6) 50 cm.

In the case of the curves (1) and (2), (*aVsp*) decreases with increase of the screening distance *a*, and is reduced to (*Vsn*), if *a* is increased very much. On the other hand, curves (3), (4), (5) and (6) denote the state that the intensities of illumination are strong enough to give (*Vsr*)*sat*. In these cases, if the screening distance *a* is below a certain length, the starting potential continues to give the same value, (*Vsr*)*sat*, regardless of the screening distance *a*. But, if the screening distance becomes larger than the critical distance, (*aVsp*) decreases rapidly to (*Vsn*). The fact that (*Vsr*)*sat* of curves (5) and (6) are lower than those of curves (3) and (4), is considered to be due to the lowering effect of λ2537 as mentioned in § 1.

It is seen in Fig. 4 that the stronger the intensity of illumination is, the larger becomes the critical distance, (see curves (3) (4) (5) (6)). Therefore, comparison of the effects of different light sources may be quantitatively deduced from comparison of such distances. This comparison was made actually on the same tube in Fig. 1 keeping its wall temperature constant at 53°C, and it was proved that a D.C. 15 watt germicidal lamp at a distance of 4 m from the illuminated tube, and a D.C. 20 watt white fluorescent lamp at a distance of 2 m and a 100 watt incandescent lamp at a distance of 1 m had all the same effect on this illuminated tube, (these give the same critical distance of 12 cm). From this result, it is concluded that the ultraviolet ray has a greater effect than the visible light.

### 4.2 *Partial illumination screennig the cathode side, (cVsp)*

In the same way as in the measurements of (*aVsp*) above described, the starting potential (*cVsp*) was measured, screening the cathode side and illuminating the exposed anode side uniformly. The behaviour of curve (*cVsp*) is quite different from that of (*aVsp*). (*cVsp*) shows a constant value independent of the screening distance *c* and is always the same as the starting potential that is shown when only a small portion close to the anode is illuminated.

In consideration of the behaviours of both (*aVsp*) and (*cVsp*), it may be assumed that if the intensity of light is strong enough to give (*Vsr*)*sat* and the locally illuminated part lies within the critical screening distance, the starting potential gives the same constant (*Vsr*)*sat* as in the case of illuminating the whole tube. In fact this assumption was verified by experiment throwing a beam of light 5 mm broad on a part of the tube. If the intensity of illumination is strong and the breadth of the part locally illuminated is not too small (about 5 mm), the value of the starting potential does not change with the breadth of the beam of light.

### 4.3 *Relation of the critical screening distance to the wall temperature*

The result shown in Fig. 4 was obtained by varying the illuminating intensity at a constant wall temperature of 56°C. Fig. 5 shows how (*aVsp*) as a function of screening distance *a* under constant illuminating intensity behaves at varied wall temperatures. The illuminated tube that was used in the experiment was the same one used in Fig. 1 (but after ageing), and the light source was a 100 watt high pressure Hg arc lamp enveloped in a glass globe at the distance of 100 cm.

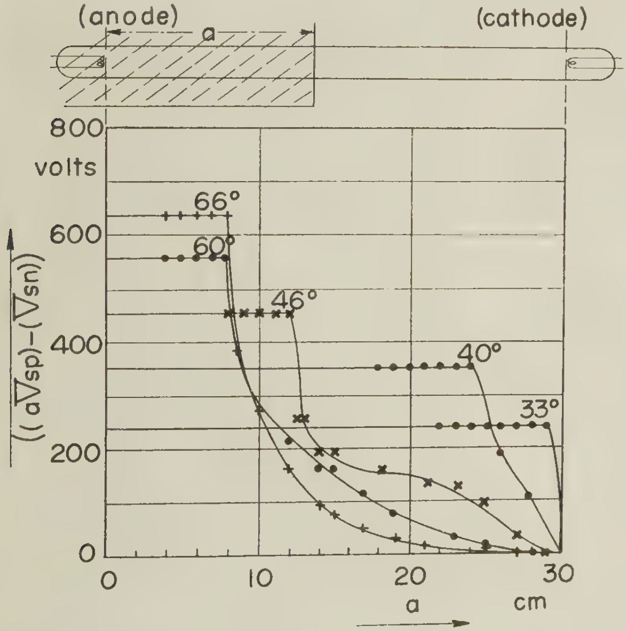

Fig. 5. Relation of the critical screening distance to the wall temperature.

(*Vsr*) in these cases give the values of (*Vsr*)*sat*. It is noted that the critical screening distance extends as the wall temperature is lowered, just as the illuminating intensity seemingly increases, and at the temperature of 33°C it extends as much as only 1 cm from the cathode.

## § 5. *On the illuminating light source*

### 5.1 *Wave-length of effective radiation*

It is of interest that Hg light has a greater effect to raise the starting potential than the light of A (the basic gas in A–Hg). This is one of the points that are different from the Penning's observation2)3)4)5) that the starting potential in Ne–A mixture would be raised when illuminated by intense light of Ne, the basic gas. Furthermore, strangely enough, while such light sources as Ne light and A light consist of line spectra which cannot be absorbed by Hg $(6^3P_{2,0})$, these light sources are proved to give (*Vsr*)*sat* of the same value as that in the case of Hg light. Generally speaking, however, ultra-violet light is far more effective than visible light, which is proved even in the experiments with mercury light, iron arc, copper arc, aluminium spark, neon light and argon light.

The results in Fig. 6 were obtained in the experiment with the same tube as the one used in Fig. 1 (though after ageing), to test different light sources.

A–Hg discharge tubes of this kind can be used as a sensitive detector for visible light, to say nothing of ultra-violet ray, or a relay to control the electric current by a light. The following observations were made with a tube that is the same one used in Fig. 1 (before ageing) keeping its wall temperature constant at 53°C.

*Log*(*Vsr*) is found to rise almost in proportion to *Log*(*intensity*) and in the sun-light of 50∼ 60 Lux the starting potential rises nearly twice as much as (*Vsn*). (*Vsn*) of this tube is 495 volts, but sun-light of 1 Lux which comes into the dark room through windows raises the starting potential as much as 57 volts or so. Under these circumstances keeping the voltage value across the tube be-

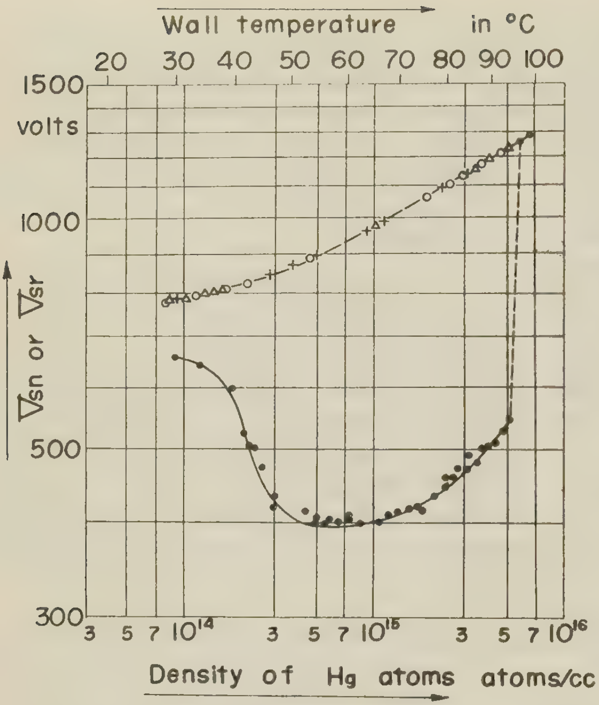

Fig. 6. Coincidence of the values of (*Vsr*)*sat* under various light sources.
● : (*Vsn*)
○ : (*Vsr*)*sat* under illumination by the neon light.
△ : (*Vsr*)*sat* under illumination by the argon light.
+ : (*Vsr*)*sat* under illumination by the incandescent lamp.

(The effect of ageing is also seen by comparison of the value of (*Vsn*) in this figure with the value of (*Vsn*) in Fig. 1, before ageing).

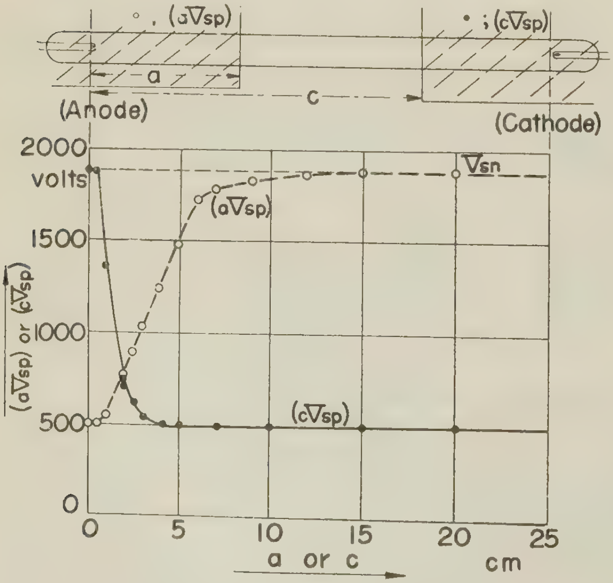

Fig. 7. Effect of λ2537 on lowering the starting potential. (*aVsp*) and (*cVsp*) as a function of screening distance *a* and *c* respectively are given on a tube that contains only one drop of mercury and no argon gas, (at 28°C).

tween 495 volts and 552 volts, if the sun light is shut off by closing the windows, the tube immediately starts a glow discharge. A similar experiment can be made with a match fire at a distance of 2 m.

### 5.2 *Effect of λ2537 on lowing the starting potential*

An example of the effect of λ2537 on lowering the starting potential was given in § 1. However, when the pressure of argon gas is relatively high (a few mm Hg), this effect is put out of sight by another effect which raises the starting potential. But it becomes noticeable as the argon pressure is reduced and becomes very prominent when there is no argon gas.

In Fig. 7, (*aVsp*) and (*cVsp*) as a function of screening distances *a* and *c* are given on a tube that contains only one drop of mercury and no argon gas, (inner diameter 23 mm, electrode separation 25 cm, with a hot cathode, and made of glass that transmits λ2537). The light source is a 15 watt germicidal lamp placed at a distance of 100 cm from the tube. This tube is very ensitives to λ2537 in lowering the starting potential, and the degree of (*Vs*) decline, namely {(*Vsn*–(*Vsr*)}, increase consistently with the rise of the wall temperature (i.e. with the increase of the density of Hg atoms). It is interesting to see that, in this case also, the anode side is sensitive to λ2537.

### 5.3 *Effect of λ2537 on raising the starting potential*

Contrary to the phenomenon described in § 5.2, λ2537 is one of the most effective radiations among Hg arc spectra to raise the starting potential.

By using a filter that transmits only λ2537 and the light that has nearly the same wave-length, it was possible to test the remarkable effect of λ2537 on raising the starting potential with a very satisfactory result. A 100 watt high pressure Hg arc lamp enveloped in a glass globe that transmits λ3650 is an intense light source of λ3650 and visible triplet lines, but its effect is found to be very poor as compared with a 15 watt germicidal lamp which is placed at a very long distance. As long as λ2537 is contained, even en extremely faint Hg arc is sufficiently effective to raise the starting potential.

### 5.4 *Effect of visible light on lowering the starting potential*

It has been observed that, in special cases, illumination of the discharge space by visible light lowers the starting potential. One of its examples is seen from curves (1) in Fig. 3 (argon pressure of 0.7 mm Hg) where the illumination has no effect on raising the starting potential. In this case the tube is illuminated by a 100 watt high pressure Hg arc lamp enveloped in a glass globe or a 100 watt incandescent lamp.

The distribution of parts of this tube sensitive to visible light lowering the starting potential was studied in the same manner as in § 4. And it was found that, in this case also, the anode side is more sensitive than the cathode side. The curve of (*cVsp*) shows that the starting potential is lowered in the same degree as long as a small part adjacent to the anode is exposed to illumination. But the curve of (*aVsp*) shows that the declining effect of starting potential is decreased as the screening distance *a* increases.

## § 6. *Effect of impurities in the gas*

### 6.1 *Variation of* (*Vsn*) *and* (*Vsr*) *by ageing*

As described in § 1, the results shown in Fig. 1 are obtained from the measurement before ageing, and the broken lines represent the values of (*Vsn*) and (*Vsr*) after ageing (the same values as in Fig. 6), in which the effect of illumination on raising the starting potential can be observed in all regions of wall temperature. Furthermore, it is note-worthy that (*Vsr*)*sat* after ageing is almost equal, within the tolerance of the experimental error, to the abnormally high value of (*Vsn*) before ageing in the region of wall temperature that is higher than 63°C. The measurement of the result shown in Fig. 6 was taken three monthes after the measurement of the result shown in Fig. 1 had been taken, and it is supposed that the filament heating voltage and other experimental conditions changed more or less in the meantime. Another example of similar case was experienced by accident while experimenting with a tube in which a trace of impurities must have remained after having taken the gas out.

### 6.2 *Effect of addition of $H_2$ gas*

In order to investigate whether metastable atoms of mercury have anything to do with starting discharge, i.e. the effect of impurities in the gas which are supposed to destroy metastable Hg atoms, an experiment was carried out. And it was found that an addition of a small quantity of $H_2$ gas suppresses the effect of illumination.

For this purpose, a small quantity of $H_2$

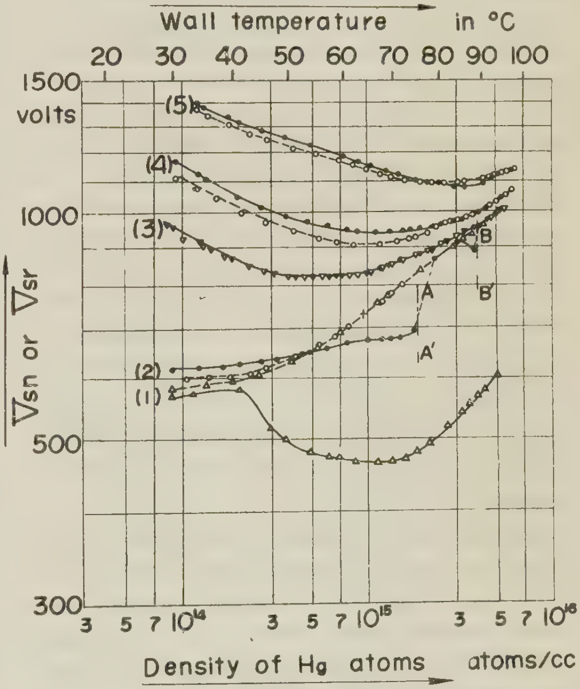

Fig. 8. Effect of addition of $H_2$ gas on changing (*Vsn*) and (*Vsr*).

(1) ▲ *Vsn*, △ *Vsr*: before adding $H_2$ gas. (*Vsr*) in this case gives the value of (*Vsr*)*sat*.

(2) ● *Vsn*, ○ *Vsr*: after adding a small quantity of $H_2$ gas. Measurements were taken while raising the wall temperature, at *A*--*A'* a small quantity of $H_2$ gas was added again, and at *B*--*B'* some more $H_2$ gas was added once again.

(3) ▼ *Vsn*, ▽ *Vsr*: after the measurement of (2) had been finished.

(4) ● *Vsn*, ○ *Vsr*: after adding more $H_2$ gas.

(5) ● *Vsn*, ○ *Vsr*: after adding more $H_2$ gas once again.

gas was added to a discharge tube, (the same type as in Fig. 2 and Fig. 3, and the argon pressure of 2.7 mm Hg), by a side tube through a palladium tube which was connected with this tube. The results are given in Fig. 8. The light source is a 100 watt high pressure Hg arc lamp enveloped in a glass globe, at a distance of 100 cm from the tube. Curve (1) was measured before adding $H_2$ gas. Such behaviours of starting potentials suggest that at a given temperature there exist two separate values of starting potential that arise from two different ionization processes in starting a glow discharge, and the one with the lower value is (*Vsn*) which, if illuminated from outside, is raised to the level of the higher one.

Curve (2) was obtained after adding a small quantity of $H_2$ gas by means of heating the palladium tube by gas flame. Measurements were taken while raising the wall temperature from 20°C, and at the temperature A--A′ shown in the figure, a small quantity of $H_2$ gas was added again, so as to raise (*Vsn*) to the level of (*Vsr*)*sat*, but in the course of raising the wall temperature making discharges repeatedly, lower value of (*Vsn*) began to appear again, and, therefore, at B--B′ more $H_2$ gas was added to raise (*Vsn*) to (*Vsr*)*sat*. Thus, in the region above B--B′ the effect to illumination to raise the starting potential disappeared completely. It seems that the effect of illumination from outside is similar to that of $H_2$ gas which is expected to destroy metastable Hg atoms.

Measurement of curve (3) was made on the tube by which the measurement of (2) had been finished and the wall temperature had been brought down to 20°C, while raising the wall temperature again from 20°C. It is seen that the measurement of curve (3) in the region higher than B--B′ shows an exactly same curvature as that of curve (2). But, in the region of 30∼90°C, values of (*Vsn*) and (*Vsr*) are very much higher than those of (*Vsr*)*sat* in curve (2). Measurements after adding $H_2$ gas once again are given in curves (4) and (5). In the cases of (3), (4) and (5), while the effect of illumination on raising the starting potential cannot be seen, the effect of visible light on lowering the starting potential is seen.

## §7. *Lasting effect of illumination*

A strange phenomenon is that the effect of illumination persistently lasts for several minutes or even hours, and keeps the starting potential higher than the normal voltage (*Vsn*) even after the illumination has been discontinued. This persistently lasting effect can be seen only in the case of D.C. measurement. Furthermore, it is very prominent in the case of a tube of cold cathode type having disproportionally large electrode separation to its diameter. However, this lasting effect is not so noticeable in the case of the tube with a hot cathode, and when the distance of the electrode separation of the tube is incongruously short compared with its diameter.

### 7.1 *Relation to the voltage across the tube during illumination*

The lasting effect seems to depend on the intensity and the duration of illumination, and also on the D.C. voltage across the tube during illumination.

In order to obtain qualitative data about this effect, an experiment has been carried out with a tube of a cold cathode (inner diameter 18 mm, electrode separation 41 cm, and made of fused quartz), using a light source of a 15 watt germicidal lamp at a distance of 250 cm. Following abbreviations will be used,

| | |
|---|---|
| (*Vs*)*aft*: | starting potential measured after the discontinuation of illumination. |
| (*Udur*); | voltage across the tube during illumination. |
| (*Uaft*); | voltage across the tube during the lapse of time after the discontinuation of illumination (until the measurement of starting potential) |

Before taking the data, preliminary experiments were made on the relation of (*Vs*)*aft* to the condition of the illumination (i.e. illuminating intensity and the duration of illumination). And in this case (*Vs*)*aft* was found to give a somewhat saturated constant value which is decided by the value of (*Udur*) when illuminated for 20 sec. or longer. Thus, the duration of illumination was fixed at 30 sec.

The results obtained under conditions are given in Fig. 9, in which (*Vs*)*aft* is given as a function of (*Udur*) at different wall temperatures. While these measurements of (*Vs*)*aft* were taken after the lapse of about 30 sec.

after the illumination had been discontinued, owing to the persistency of this lasting effect, these values of (*Vs*)*aft* did not change so much, ((*Vs*)*aft* kept on giving the same value for one minute).

It is seen in Fig. 9 that if the value of (*Udur*) is low, the starting potential (*Vs*)*aft* does not differ much from (*Vsn*) which is the value when the tube has never been exposed to illumination, but if the value of (*Udur*) is high, it rises in proportion to (*Udur*). This shows that the electric field across the tube during illumination plays an important role for the tube to produce this lasting effect.

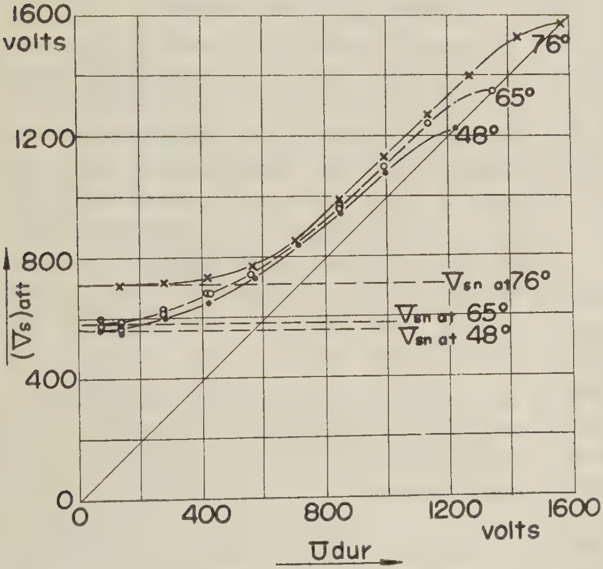

Fig. 9. Lasting effect of illumination. (*Vs*)*aft* is given as a function of (*Udur*) at different wall temperatures.

### 7.2 *Relation to the voltage across the tube after discontinuation of the illumination*

The measurements in Fig. 9 were made under the condition that (*Uaft*) was kept at the same value as (*Udur*). But the value of (*Vs*)*aft* also fluctuates according to the value of (*Uaft*). In case (*Uaft*) is kept at the same value as (*Udur*), the decline of (*Vs*)*aft* with the lapse of time is very slow, but it becomes very rapid if (*Uaft*) is reduced to a certain lower value after discontinuation of the illumination.

Thus it is concluded that (*Uaft*) plays an important part for the tube to keep up this lasting effect. Accordingly, in case the A.C. source is used, this lasting effect of illumination becomes unnoticeably small.

## § 8. *Experiments with A.C. source*

The effect of illumination on raising the starting potential of an A–Hg discharge tube was first discovered by the author as a phenomenon that the intermittent discharge in a tube of a cold cathode provided with A.C. source, which was visible to the naked eye, was stopped by a faint illumination of ultraviolet ray, when the tube was kept at 50∼60°C. The following observations were made with a tube of a cold cathode (the same tube that was used in Fig. 9).

When the voltage across the tube is gradually increased, in a certain region, feeble and intermittent but successive discharges that are visible to the naked eye, can be seen. Under this condition, illumination from outside can stop such discharge instantaneously. Furthermore, as the tube is provided with A.C. source and the lasting effect of illumination as described in §7 is not appreciable, as soon as the illumination is cut off, the discharge begins to starts again. Its response to putting-on and shutting-off of the illumination is instantaneous and repetitive, but when the voltage across the tube is raised and a stable glow discharge once gets started, even an intense radiation cannot stop the discharge.

It is considered that the surfaces of the two electrodes of the tube of a cold cathode type are not of equal condition. Thus, the current of a feeble intermittent discharge has, according to oscilloscopic observation, a somewhat rectified wave form. When the current of this intermittent discharge is relatively large, illumination from outside is effective only on one side of the tube and only on a limited part adjoining the electrode (which is assumed to be the anode in those half cycles). In case the current is very small, illumination is almost equally effective on all parts of the tube.

This tube is extremely sensitive to ultraviolet radiation. Even an extremely faint ultra-violet ray, such as reflection from the wall of a room, the intensity of which is too faint to be measured, is enough to stop the intermittent visible discharge, but the discharge starts again as soon as the illumination from outside is cut off.

This phenomenal truth may probably be

applied as a sensitive detector of ultra-violet ray or a visible light which can convert, with high efficiency, a variation in the light to a variation in the current.

### § 9. *Relation to the shape of the tube*

The effect of illumination to raise the starting potential is not appreciable in the case of the tubes with plane paralleled electrodes or wire-cylinder electrodes, but it is prominent in the case of a tube that is long and narrow in shape. Furthermore, the farther apart the electrode separation is, the larger does the ascent of the starting potential by illumination become.

One of the effects of filament heating is that it lowers the values of (*Vsn*) and (*Vsr*)*sat*, but, at the same time, the light from the filament causes the value of (*Vsn*) to rise. These experimental results are dependent on the shape of the discharge tube.

## Part II. Theoretical Considerations

### I. Introduction

The breadth of absorption spectra of atoms is made broader by the Doppler-broadening, the pressure-broadening of two kinds of self-broadening and foreign gas broadening, and other kinds of broadening. Even taking these kinds of broadening into account, absorption spectra of metastable atoms of A or Hg have very narrow lines, and it can hardly be imagined that these metastable atoms can absorb the sufficient radiations from incandescent lamp, or sun-light to have any appreciable effect on the starting potentials. In fact, that Ne light gives (*Vsr*)*sat* of the same value as in the case of Hg light cannot be explained on the basis of understanding that it is metastable atoms of A or Hg that absorb the radiation. According to the author's experiment, the understanding that the effect that is described in Part I is due to the photo-electric effect of the particles adsorbed on the wall does not explain the relation of this effect to the wall temperature and the argon pressure and the impurities in the gas.

It is commonly believed that the ionization process in starting a glow discharge in an A–Hg discharge tube of such a low pressure can be explained by the Penning-effect which explains that normal Hg atoms are ionized by metastable A atoms.1)2)3) For larger admixtures, of course, also the ionization of admixed gas atoms by electrons may take place, (in our case, i.e. A–Hg, ionization of Hg atoms by electrons may take place).

According to the investigations made by the author of this report, under a certain condition there seems to exist a region where metastable Hg$_2$ molecules act an important role in starting a glow discharge as a principal source of ions. In the strength of the assumptions based on the hypothesis by the author, most of the experimental results described in Part I can be explained fairly well.

### II. Hypotheses of the Author

In order to explain the experimental results in the Part I, the author has put forward the following hypotheses:

1) When the density of Hg atoms and the pressure of A gas are relatively high, the region of low order current before starting a glow discharge seems to be favourable to the formation of metastable molecules of mercury ($6^1S_0+6^3P_{2,0}$) through the following ternary collision:

$$\mathrm{Hg}^*+\mathrm{Hg}+\mathrm{A}\rightarrow\mathrm{Hg}_2^*+\mathrm{A}$$

2) Under such condition that both the pressure of A gas and the density of Hg atoms are adequate, there exists a region where metastable Hg$_2$ molecules act an important role in starting a glow discharge as the principal source of ions by way of stepwise ionization (from normals to $\mathrm{Hg}_2^+$ ions through metastables).

These two hypotheses 1) and 2) will be discussed in III and IV respectively.

### III. Formation of Metastable Hg$_2$ Molecules in A–Hg Mixtures

### § 1. *Process of the formation of Hg$_2$ molecules*

#### 1.1 *Ternary collision involving A atom*

Owing to its dissociation energy being as small as 0.07 e.v., Hg ($6^1S_0+6^1S_0$) molecule cannot exist stably in a discharge (thermal energy at 100°C, KT=0.03 e.v.). But excited Hg atoms ($6^3P_{2,1,0}$, $6^1P_1$, $7^3S_1$, $7^1S_0$ etc.), combined with other normal Hg atoms, can form stable excited molecules. Fig. 10 is the energy level diagram of Hg$_2$ molecule by Mrozowski.4) (though, according to the study made by McCoubrey,5) the curve of ($^3\Sigma^-_{ou}$ has to be revised). Metastable atoms ($6^3P_2$) forms ($^3\Pi_{1u}$) and ($^3\Pi^-_{ou}$) molecules, the latter being metastable. The transition from $Hg_2(^3\Sigma^-_{ou})$ ($6^1S_0+6^3P_0$) to the ground state ($^1\Sigma^+_g$) is not entirely forbidden, but according to the study in the band fluorescence of $Hg_2$ molecules made by Holstein, Alpert and McCoubrey,⁶⁾ the life of ($^3\Sigma^-_{ou}$) state is known to be 1.8 millisec or thereabout.

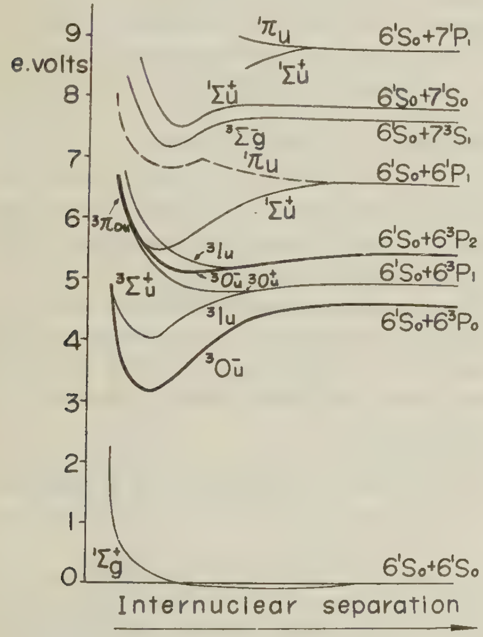

Fig. 10. Energy level diagram of $Hg_2$ obtained by Mrozowski.

The formation of molecules of mercury by a two-body collision is a very rare case, because an average time ($10^{-8}$ sec) that elapses before an excited molecule radiates is much larger as compared with the duration of collision ($10^{-13}$ sec), during which the electron has to jump down to form a stable molecule. On the other hand, at relatively high pressure, the formation of molecule by ternary collision without radiation of light occurs much more frequently. The fraction of two-body collisions which are also ternary collisions is proportional to the pressure of the third body, while in the case of two-body collision, the fraction of collisions causing the formation of molecule is independent of the pressure. When collisions occur, in order to form a stable excited $Hg_2$ excess energy that is relatively large as shown in Fig. 10, must be taken off. Presumably, A atoms take off this excess energy as the kinetic energy.

### 1.2 *Frequency of conversion of Hg* into Hg*₂*

In several cases, the formation of molecule through ternary collision have been posturated as one of the processes of destruction of metastable atoms and ions in an after-glow, when there is relatively high density of gas, (more than 10 mm Hg).

One of the examples is seen in the study made by Colli⁷⁾ who hypothesized the following reaction: $A^*+2A\rightarrow A_2^*+A$. Another example was furnished by Burkop,⁸⁾ $He^*+2He\rightarrow He_2^*+He$. A similar reaction was hypothesized also by Biondi,⁹⁾¹⁰⁾ $Hg^++2Hg\rightarrow Hg_2^++Hg$. In his study, the conversion frequency in this reaction was estimated in the order of $10^{-31}(n_{Hg})^2$. He also hypothesized the following reaction in He–Hg mixture, $Hg^++Hg+He\rightarrow Hg_2^++He$. According to his experiment, the conversion frequency in this reaction is of the order of $10^{-31}(n_{Hg}\cdot n_{He})$.

A case that is most similar to the reaction hypothesized by the author is the study made by McCoubrey who studied the band fluorescence of mercury vapour in a resonance tube containing Hg vapour only.⁵⁾ In his experiment which was carried out at the temperature of 200°C, the formation of $Hg_2^*$ molecule was hypothesized as arising from the following reaction, $Hg^*(6^3P_0)+2Hg(6^1S_0)\rightarrow Hg_2^*(^3\Sigma^-_{ou})+Hg(6^1S_0)$. And the conversion frequency of this reaction was estimated at $100\times10^{-32}(n_{Hg})^2$.

In McCoubrey's case: $Hg^*+Hg+Hg^{200}$, at 200°C.

In the author's case: $Hg^*+Hg+A^{40}$.

$\sigma_{Hg}=3.01\times10^{-8}$ cm, $\sigma_A=2.98\times10^{-8}$ cm, where $\sigma_{Hg}$, $\sigma_A$ are the collision diameters. Choosing tentatively a temperature of 100°C, and taking into account the variation of the mean velocity according to the temperature and the mass of the third body, the converting rate for the author's case is 1.77 times. While in the case of McCoubrey, the second and third bodies are atoms of the same kind, in the author's case they are atoms of different kinds. Therefore, the probability of the formation of molecule may be reduced to about one half of this value. At any rate, in the author's case involving A atoms, at the tentatively chosen temperature of 100°C, the conversion frequency may not be so far off the value of the order of $10^{-30}(n_{Hg}\cdot n_A)$.

Theoretical treatment of the ternary collision has been discussed by Wigner[11] as well as by several other authors, but the discussions in detail on this problem are beyond the scope of the present work.

### 1.3 *Function of argon gas*

The following processes are supposed to be pursued in the destruction of metastable Hg* atoms, (excepting the destruction by collisions with electrons).

1) Diffusion to the wall resulting in de-excitation by collision against glass wall.

2) Two-body collision with neutral atoms resulting in; a) excitation to a higher radiating state nearby, b) de-excitation to a lower state, c) collision-induced radiation.

3) Collision between two metastable atoms resulting in; a) ionization of one of the atoms and de-excitation of the other, b) formation of ion of molecule.

4) Ternary collision with two neutral atoms resulting in formation of stable excited molecule, $Hg^*+Hg+A$ (or Hg)$\rightarrow Hg_2^*+A$ (or Hg).

Owing to difference in the energy between metastable states and nearby radiating states being large, as compared with the thermal energy, the reaction (2a) may be energetically impossible. According to the study made by Stuart[12] or that made by Zemansky,[13] the quenching cross sections ($6^3P_1\rightarrow 6^3P_0$) of A and He are very small. Therefore, it is presumed that the probability of the reaction (2b) taking place is very small. Some of the evidences of this have been enumerated by Kenty.[14] The reaction (2c) is presumed not likely to occur, because unstable excited molecule (HgA)* must radiate before its dissociation. The reaction (3a) is hypothesized also by Biondi[10] in his study on an afterglow, and this reaction is energetically possible when both of the two metastable atoms are $6^3P_2$, but the reaction of this kind and the reaction (3b) become significantly large only when the density of metastable atoms is high, and, therefore, these reactions can be ignored in this case under review.

The rate of change of the density of metastable Hg atoms as a result of diffusion to the wall is $\frac{\partial m}{\partial t}=\left(\frac{D}{p}\right)\nabla^2 m$. Here $D$ is the diffusion coefficient for Hg* atoms at one mm Hg, and $p$ is the pressure of gas in mm Hg, (in the present case, $p$ stands for the pressure of argon gas, the basic gas). Therefore, the average time, $\omega$, that elapses before $6^3P$ atoms are destroyed by diffusion to the wall is given as $\frac{1}{\omega}=\frac{D}{p\Lambda^2}$. Where $\Lambda$ is the diffusion length of the container and for a cylinder vessel of radius $R$ and length $L$ is given by

$$\Lambda=\left[\left(\frac{\pi}{L}\right)^2+\left(\frac{2.4}{R}\right)^2\right]^{-1/2}.$$

On the other hand, the average time, $T$, that elapses before $6^3P$ atoms are converted into metastable $Hg_2(6^3P+6^1S_0)$ molecules, is given as $\frac{1}{T}=p\theta n_{Hg}$. Here $\theta$ is the conversion frequency of Hg* into $Hg_2^*$ through ternary collision under the argon pressure of one mm Hg, $n_{Hg}$ is the density of normal Hg atoms, and $p$ is the pressure of argon gas.

Therefore, it is assumed that A atoms serve to reduce the wall loss of metastable Hg atoms,[15][16] and at the same time assist the formation of metastable $Hg_2$ molecules. (see Appendix).

## § 2. *Spectroscopic studies of $Hg_2$ molecule*

### 2.1 *Relation of the density of $Hg_2$ molecule to the current*

The spectra of the light of super-high pressure Hg arc lamp have been studied precisely by Asada and Yoshinaga.[17] Their experiments were carried out under the following conditions: high current of 0.7∼1.5 A passes through the tube of 1.5 mm in inner diameter and, thereby, the temperature in the discharge tube is raised considerably, and the vapour pressure of mercury becomes as high as 66∼140 atm. Under these circumstances, markedly diffused line spectra and band spectra, which are emitted by $Hg_2$ molecules, have been observed.

Spectroscopic experiments have been carried out on the same tubes that were used in Fig. 3. When the wall temperature of the tube is raised above 90°C, the green radiation of the positive column, under excitation by a low current of a few mA, which has been rather faint, greatly increases its intensity, and the higher the pressure of argon gas is, the stronger becomes the brightness of this green light. Contrary to the case of the super-high pressure Hg arc lamp, in the case of the low pressure A–Hg discharge tube, the ratio of the brightness of this green light that is emitted by $Hg_2$ molecules,15) and visible triplet is greatly enlarged by a decrease in the current.

Another similar phenomenon is seen in the fact, which is observed with naked eye, that at the axis of the tube, the intensity of line spectrum emitted by Hg atoms is greatest, and the farther away from the axis, the stronger becomes the relative intensity of green continuum. The gradual variation along the radial direction of the ratio of brightness of this green continuum and line spectrum is also seen in the spectroscopic data obtained by Takeyama.18) This occurence is likely to be attributed to a decrease in the current density in radial direction. Therefore, it may be presumed that the smaller is the current density, the more favourable the condition becomes to form metastable $Hg_2$ molecules.

This fact endorses the hypotheses of the author advantageously, because it is naturally assumed that when the current is reduced to the extremity, the region of low order current before starting a glow discharge (in other words, the region of Townsend discharge) is favourable for formation of metastable $Hg_2$ molecules.

### 2.2 *Spectrograms of $Hg_2$ molecule*

The results in Figs. 11, 12 and 13 were obtained on the same tube that was used in Fig. 2 (argon pressure 15 mm Hg).

The spectrograms of green continuum given in Fig. 12 was obtained under the same condition, at 100°C, that was employed in the measurement of visible triplet given in Fig. 11. The tube had a negative characteristic and the differences in the voltage across the tube were as follows.

| (mA) | 1, | 2, | 3, | 5, | 7, | 10, | 14 |
|---|---|---|---|---|---|---|---|
| (volts) | 70.0, | 71.5, | 73.2, | 71.5, | 70.0, | 68.0, | 66.0 |

The spectral distributions agree sufficiently which the distribution obtained by Volkringer19) and by Kenty.15) The photographic plates were exposed for 10 hours in all cases. It is seen that, in a region of relatively low density of the current, while the visible triplet emitted from the positive column of the tube increases in proportion to the second power of the current in the tube, (this means an increase of the density of metastable Hg atoms proportional to the current density),16) the increase in the intensity of green continuum is disproportionally slow to the increase of the current.

However, to estimate the density of $Hg_2$ molecules as a function of the current, by measuring the intensity of this green continuum, meets with difficulties that the spectral distribution of the green continuum varies with the changes in the argon pressure, the density of Hg atoms and the current,15)19) (see Fig. 13). Therefore, if these factors were

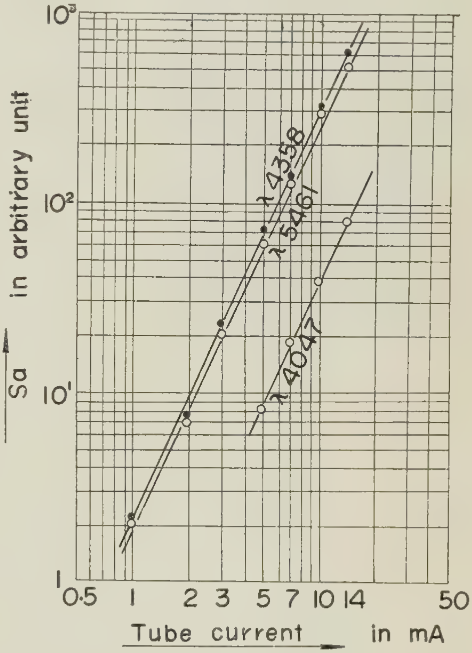

Fig. 11. Out-put of visible triplet as a function of current in the tube.

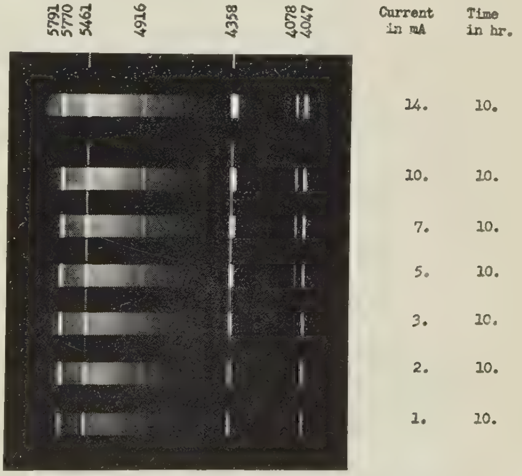

Fig. 12. Intensity of green continuum as a function of the current, (at 100°C).

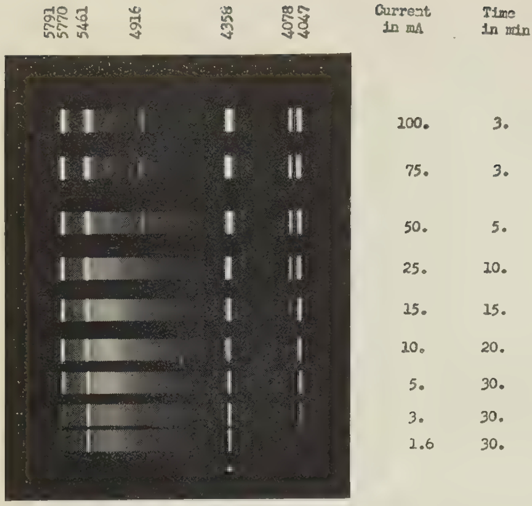

Fig. 13. Variation of spectral distribution with the current. (at 137°C).

altered considerably, the measurement would no longer mean anything.

The intensity of green continuum was measured also as a function of the density of Hg atoms, by changing the wall temperature, at constant current of 5 mA, (the differences in the voltage across the tube were not more than 5 %). The intensity of green continuum was found to increase approximately to the second power of the density of Hg atoms.

Fig. 13 illustrates how the spectral distribution changes with the variation of the current over a wide range of 1.5~100 mA, at constant wall temperature of 137°C, (the differences in the voltage across the tube are not more than 10 %).

## IV. Ionization in A–Hg Mixtures

### §1. *Classification of processes of ionization*

Processes of ionization which are supposed to occur in discharges in A–Hg mixtures are as follows:

$$\begin{array}{llll}
A^*(4^3P_{2,0}) & + Hg(6^1S_0) & \longrightarrow Hg^+ + A(3^1S_0) + e & \cdots(1)\\
A^*(4^3P_{2,0}) & + e & \longrightarrow A^+ + 2e & \cdots(2)\\
Hg^*(6^3P_{2,0}) & + e & \longrightarrow Hg^+ + 2e & \cdots(3)\\
Hg_2^*({}^3\Pi_{ou}^-, 3\Sigma_{ou}^-) & + e & \longrightarrow Hg_2^+ + 2e & \cdots(4)\\
A^*(4^3P_{2,0}) & + A^*(4^3P_{2,0}) & \longrightarrow A^+ + A(3^1S_0) + e & \cdots(5)\\
Hg^*(6^3P_2) & + Hg^*(6^3P_2) & \longrightarrow Hg^+ + Hg(6^1S_0) + e & \cdots(6)\\
Hg^*(6^3P_{2,0}) & + Hg^*(6^3P_2, 6^3P_0?) & \longrightarrow Hg_2^+ + e & \cdots(7)\\
A(3^1S_0) & + e & \longrightarrow A^+ + 2e & \cdots(8)\\
Hg(6^1S_0) & + e & \longrightarrow Hg^+ + 2e & \cdots(9)
\end{array}$$

These processes of ionization may be classified into the following four types:

1) Ionization by Penning-effect, Eq. (1).
2) Stepwise ionization through metastables, Eq. (2), Eq. (3) and Eq. (4).
3) Collision between two metastable atoms resulting in
   a) ionization of one of the atoms and de-excitation of the other, Eq. (5) and Eq. (6).
   b) formation of ion of molecule, Eq. (7).
4) Direct ionization of normal atoms, Eq. (8) and Eq. (9).

The type of collisions of Eq. (5), Eq. (6) and Eq. (7) can also take place in an afterglow when provided with high pressure of gas.[9)10)20)] But in this case under review, this process may be excluded as being less important.

### 1.1 *Ionization by Penning-effect*

The Penning-effect occurs in gas mixtures when the ionization potential of mixed gas atom is lower than the excitation potential of metastable state of the basic gas atom, for instance, in such cases as Ne–A,[1)] A–Hg,[2)] A–$I_2$,[2)] Ne–Hg,[2)] Ne–A,[2)] or A–NO.[3)] The efficiency of ionization by Penning-effect is very high only when the proportion of the basic gas and the admixed gas is adequate, and it diminishes rapidly when the percentage of added gas either decreases or increases. One of the examples is seen in the study made by Penning,[1)] in which the starting potentials in Ne–A mixtures show their lowest at 0.1~0.01 %.

It is well known that the cross section in the destruction of metastable A atoms by normal Hg atoms is very large. According to the study made by Phelps and Molnar in an after-glow,[20] the average cross section is $3\times 15^{-15}$ cm$^2$ (which is relatively large in the order of magnitude, compared with other cases of Penning's reaction).

Thus, it is commonly believed that the ionization process in starting a glow discharge in a low pressure A–Hg discharge tube like an ordinary germicidal lamp, can be explained by the reaction in Eq. (1). In Fig. 2, the region of wall temperature of lower than 30°C must doubtlessly be such a region that contributions from the ionization by Penning effect are predominant.

### 1.2 *Stepwise ionization*

Even in the case that the Penning-effect is predominant in starting a discharge, if the stepwise ionization once takes place, the efficiency of ionization greatly increases resulting in a decline of the electron temperature and, consequently, the number of the electrons that have sufficiently high energy to excite normal A atoms up to a metastable state decreases, and at the same time the temperature of the tube goes up causing an increase in the density of Hg atoms until finally this stepwise ionization of metastable Hg atoms becomes predominant. This is the phenomenon that can be seen in a positive column after a glow discharge has started.

According to the study made by Kenty[15] or that made by Barnes,[21] under the conditions that the current is relatively large (more than 10 mA) and the pressure of argon gas is relatively small (a few mm Hg) and the wall temperature is not so high (room temperature), the ionizations that occur in a positive column of A–Hg discharge are mainly the stepwise ionization of metastable Hg atoms, (Eq. (3)).

On the other hand, it has also been found out by Kenty and Larson,[15] that under the conditions that the current is small (0.5 mA) and the pressure of rare gas is high (more than 50 mm Hg) and the wall temperature is high (higher than 60°C), stepwise ionization of metastable $Hg_2$ molecules, (Eq. (4)), is predominant in a positive column of glow discharge.

## § 2. *Appearance of such a region as $Hg_2^*$ is indispensable for starting*

### 2.1 *Electron energy blance*

When the energy distribution of electrons is steady and the electron current $i$ flows through the gas under the influence of a steady electric field, the energy $idU$ which is gathered from the field while passing through the potential difference $dU$, is equal to the sum of the energy lost by electrons in collisions with gas atoms and the energy that is to be

Table I.

| | | 1 | 2 | 3 |
|---|---|---|---|---|
| | | A | Hg | $Hg_2$ |
| $d$ | direct ionization of normal atoms | $\eta_{1d}V_{1d}$ (8) | $(k_2\alpha)\eta_{2d}V_{2d}$ (9) | — |
| $k$ | excitation of normal atoms | $\sum_k \varepsilon_{1k}V_{1k}$ (10) | $(k_2\alpha)\sum_k \varepsilon_{2k}V_{2k}$ (11) | — |
| $s$ | stepwise ionization of metastable atoms or molecules | $(c_1i)\eta_{1s}V_{1s}$ (2) | $(k_2\alpha)(c_2i)\eta_{2s}V_{2s}$ (3) | $(k_3\alpha^2)(c_3i)\eta_{3s}V_{3s}$ (4) |
| $l$ | stepwise excitation of metastable atoms or molecules | $(c_1i)\sum_l \xi_{1l}V_{1l}$ (12) | $(k_2\alpha)(c_2i)\sum_l \xi_{2l}V_{2l}$ (13) | $(k_3\alpha^2)(c_3i)\sum_l \xi_{3l}V_{3l}$ (14) |
| $\lambda$ | elastic collision | $k_1\lambda_1\overline{V}$ | $(k_2\alpha)k_2\lambda_2\overline{V}$ | |
| | kinetic energy of newly formed electrons | $\eta_t\overline{V}$ | | |

given to the newly formed electrons to keep the mean energy of electrons remaining the same. This leads to the energy balance equation.[22]

The possible electronic collisions with gas atoms in A–Hg mixtures are given in Table 1, in which the suffix 1, 2 and 3 represent A, Hg and $Hg_2$ respectively. For example, $i\eta_{1d}V_{1d}dU$ represents the energy lost in the direct ionization of normal A atom with the coefficient of $\eta_{1d}$ and the ionization potential of $V_{1d}$. The terms concerning normal $Hg_2$ molecules are left in blank because of the smallness of its density. The terms concerning metastable $Hg_2$ molecules are proportional to $\alpha^2$, just as the terms concerning Hg atoms are proportional to $\alpha$, where $\alpha$ is the ratio of the density of Hg atoms to the density of A atoms which remains constant. It may be assumed that, in a region of low order current, the densities of mestastable atoms and molecules are, roughly speaking, proportional to the current. Therefore, in the table, the densities of metastables are shown as $(c_1 i)$, $(k_2\alpha)(c_2 i)$ and $(k_3\alpha^2)(c_3 i)$ respectively, where $k_i$ and $c_i$ are constants. The transitions corresponding to each term are illustrated in Fig. 14. $\lambda_i$ is the average fraction of the energy lost by electron in an elastic collision with gas atom. A certain fraction of $\sum_k \varepsilon_{ik}V_{ik}$ that are excitations up to various states, is the excitation up to metastable states. $\eta_t$ represents the total ionization coefficient which involves the direct and stepwise ionizations and the ionization by Penning-effect. In connection with the energy balance equation, the total sum of all terms in this table should be equal 1.

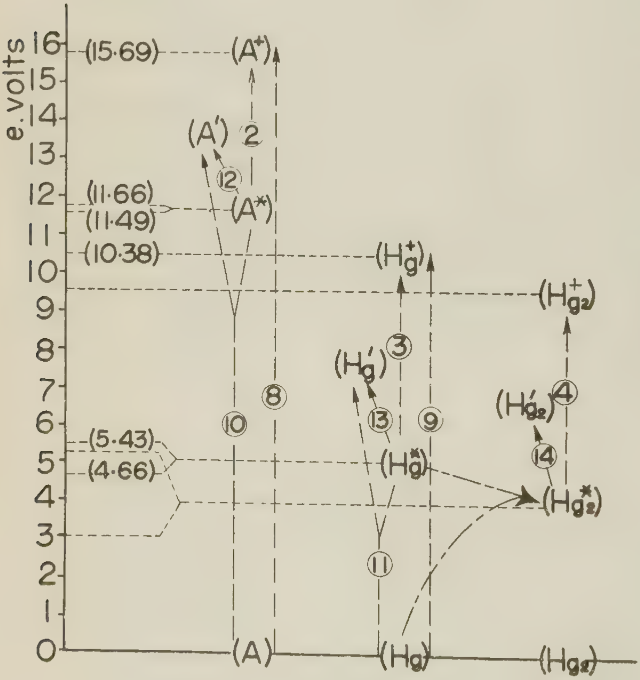

Fig. 14. Ionization processes in A–Hg mixtures.

### 2.2 *Variation of $\eta_t$ with the density of Hg atoms*

If the value of $E/p_0$ is low, most of the energy acquired by the electrons from the electric field is consumed in the elastic collisions with gas atoms. If the field strength is increased, other terms such as excitation and ionization become larger in the energy loss, and at the same time the fraction consumed in the kinetic energy of newly formed electrons becomes noticeable.

One example shown in Fig. 2 may serve to illustrate clearly that the region where metastable $Hg_2$ molecules are indispensable for starting a glow dischrage, takes shape in the course of changing the value of $\alpha$. In this case, $\alpha$ is the ratio of the density of Hg atoms, which varies with wall temperature, to that of A atoms which remains constant 15 mmHg. The value of $\alpha$ at the regions shown in this figure are as follows:

(a — b) $5\times10^{-5}$—$1\times10^{-4}$,
(b — c) $1\times10^{-4}$—$3\times10^{-4}$,
(d–e–f) $6\times10^{-4}$—$7\times10^{-3}$.

When the current density is not large, the density of radiating atoms is small. However, because of the life of $6^3P_1$ state elongated by imprisonment of λ2537, even the density of $6^3P_1$ atoms becomes significantly large as the density of normal Hg atoms increases.[23][24][25]

The contributions from each term shown in Fig. 14 may be supposed as follows:

1) When $\alpha$ is extremely small, only (8), (10), (2) and (12) take place. The stepwise ionization (2) of metastable A atoms which are produced by a certain fraction of (10) is the principle ion source in starting.

2) (a—b); Beside (8), (10), (2) and (12) only

(9) and (11) can barely take place. But ions are principally supplied by the Penning-effect, i.e. metastable A atoms which are produced by ac ertain fraction of (10) effectively ionize mormal Hg atmos.

3) (b—c); Ionization by the Penning-effect is predominant. But the electron energy is wasted greatly in (11) which results in a rise of the starting potential. The density of metastable Hg atoms is not yet appreciable and the ionizations in (9) and (3) are negligibly small.

4) (d–e–f); The energy loss in (11) is large. But owing to the high density of Hg atoms, metastable Hg atoms of appreciable density are brought about by a certain fraction of (11). The most of these metastable Hg atoms are converted into metastable $Hg_2$ molecules through ternary collisions. It is supposed that thus, (4) and (14) become appreciable and cause formation of the region, where metastable $Hg_2$ molecules are important as the principal ion source for starting a glow discharge.

5) (p—q); This curve represents the value of (*Vsr*)*sat*. Ionizations may owe principally to (9), i.e. the direct ionization of normal Hg atoms, (as will be described later in V. § 5).

## V. Interpretation of the Experimental Results in the Part I

### § 1. *Effect of illumination on raising the starting potential*

According to the energy level diagram of $Hg_2$ molecule shown in Fig. 10, metastable $Hg_2$ molecules ($^3\Pi^-_{ou}$, $^3\Sigma^-_{ou}$) can be photo-excited up to higher radiating states by absorbing the light of any wave-length ranging from ultra-violet to visible light. In this manner, the illumination on to the discharge space diminishes the number of metastable $Hg_2$ molecules which are the principal source of ions for starting a glow discharge.

### § 2. *Saturated starting potential*, (*Vsr*)*sat*

When the intensity of illumination is strong enough to destroy nearly all the metastable $Hg_2$ molecules, the ionization process in starting is forced to take a different course from that of (*Vsn*). In a region of low order current before starting a glow discharge, the density of metastable $Hg_2$ molecules is small and even when the intensity of illumination is not so strong, this phenomenon can be brought about.

As to the ionization process in (*Vsr*)*sat*, the following two processes can be assumed;

1) Direct ionization of normal Hg atoms by electrons.

2) Ionization of normal Hg atoms by metastable A atoms, (Penning-effect).

However, as described in § 5.1 of Part I, it is proved that the value of (*Vsr*)*sat* as illuminated by A light is equal to that as illuminated by other light sources, such as Hg light and incandescentl amp, (see Fig. 6). This fact means that the ionization process of (*Vsr*)*sat* is not what is mentioned in 2), because metastable A atoms are destroyed by A light. Therefore, the ionization process of (*Vsr*)*sat* must be what is defined in 1), (as described in IV § 2.2 of Part II).

### § 3. *Relations to the argon pressure and the wall temperature*

The relations of (*Vsn*) to the argon pressure and the wall temperature were fully discussed in III and IV of Part II.

When the argon pressure is lower than a certain limit that is necessary to form sufficiently numerous metastable $Hg_2$ molecules, the ionization process of (*Vsn*) is forced to take a different course from that of stepwise ionization of metastable $Hg_2$ molecules. This means that the ionization process of (*Vsn*) when argon pressure is lower than a certain limit resembles that of (*Vsr*)*sat*, (see (*Vsn*) curve of (1) in Fig. 3).

The appreciation of (*Vsn*) and (*Vsr*)*sat* with the increase of argon pressure, (in Fig. 3), may be due to an increase of the loss of electron energy by the elastic collision with A atoms.

### § 4. *On the illuminating light sources*

The fact that ultra-violet light is far more effective than visible light may be attributed to metastable $Hg_2$ molecules having strong absorbing power in ultra-violet region.

#### 4.1 *Effect of λ2537 on lowering the starting potential*

The density of normal Hg atoms in the region of wall temperature of 40∼90°C, is too low to bring about the selective reflection of λ2537.[26] Consequently, λ2537 (without selfreversing) can penetrate into the discharge space and produce Hg($6^3P_1$). The formation of ions may perhaps come about as follows; some of these photo-excited $6^3P_1$ will accidentally turn into $6^3P_2$ by absorbing λ4358, or by absorbing λ4047 after having once been accidentally knocked down to $6^3P_0$ by collisions with A atoms or Hg atoms. Thereafter, these metastable atoms ($6^3P_2$, $6^3P_0$) are ionized by electron collision. In this manner, the effect of λ2537 on lowering the starting potential takes place.

### 4.2 *Effect of λ2537 on raising the starting potential*

The light of λ2537 from a germicidal lamp has two different kinds of radiations: one is broad and self-reversed line, such as the radiation that is emitted by a hot arc, and the other is narrow and unreversed line, such as the radiation that is emitted by a resonance tube. The light of λ2537 must be narrow to be absorbed by normal Hg atoms, and, therefore, the self-reversed light of λ2537 is nothing but a simple ultra-violet light that effectively raises the starting potential.

According to the energy level diagram of $Hg_2$ molecule (Fig. 10), the wave-length that corresponds to the transition from $Hg_2$ ($6^3P_0+6^1S_0$) to $Hg_2$ ($7^3S_1+6^1S_0$) is not far off from λ2537. This may give an explanation to the fact that the light of Hg arc involving λ2537 has a remarkable effect on raising the starting potential, (§5.3 of Part I).

## §5. *Influence of impurities in the gas*

### 5.1 *Effect of ageing*

According to the studies made by Kenty, during the discharge in mercury vapour, impurities in the gas such as $H_2$, $N_2$, $O_2$, $CO_2$ and CO, which powerfully destroy metastable atoms and molecules of mercury,[15)27)] combined with Hg atoms, form the chemical compounds such as HgH, $Hg_3N_2$ and HgO, and these chemical compounds are derived to the glass wall and adsorbed there.[28)] In this manner, these impurities in the gas are cleaned up during discharge.

These experimental results lead to an assumption that the change in the character of the tube through ageing may be due to cleaning up of the impurities in the gas. Thus it is clearly explained that the value of $(Vsn)$ before ageing is almost equal to that of $(Vsr)sat$ after afeing, because the effect of illumination resembles the effect of impurities in the gas in the sense that both two effects destroy metastable $Hg_2$ molecules and thereby prevent the starting potential from taking a lower value.

### 5.2 *Addition of $H_2$ gas*

Even a small quantity of $H_2$ gas can powerfully destroy all of $6^3P_2$, $6^3P_1$ and $6^3P_0$ through the following process, (Cario-Franck Process),[29)]

$$Hg^*+H_2 \longrightarrow (HgH)^*+H$$
$$(HgH)^* \longrightarrow Hg+H$$

Thus, $Hg^*(^3P)+H_2(^1\Sigma_g^+) \longrightarrow Hg(^1S_0)+2H(^2S)$

Therefore, the experimental result in §6.2 is one of the direct proofs of the hypothesis that metastable Hg atoms act an important part in the ionization process in starting a glow discharge.

## §6. *On the illuminated part and the lasting effect*

It is the part near the anode of the tube that is sensitive to illumination from outside, (§4 of Part I). This may be for the reason that the density of metastable atoms increases in proportion to the current density and, on the other hand, the nearer to the anode the part is, the higher is the electron-current density there, and naturally the density of metastable Hg atoms is high at the part near the anode and, as the consequence, the density of metastable $Hg_2$ molecules is likewise high there.

However, the phenomenon that there exist a critical point of screening distance (§4.1), the lasting effect of illumination (§7) and the dependence of this effect of illumination on the shape of the tube (§9) are probably related to the mechanism in starting a glow discharge on such a low pressure discharge tube that is long and narrow in shape, i.e. whether it is the Townsend mechanism[30)] or the streamer mechanism[31)32)33)] or both.[34)35)36)]

In spite of the numerous studies made by other researchers on this problem, it still remains insolved; therefore, this work has kept this matter aside and has taken the ionization process in A-Hg mixtures only as the object of its study.

## Acknowledgements

This work has been carried out under the direction of Professor Tsunesaburo Asada of Osaka University, and the author wishes to express his sincere appreciation of the professor's kind and untiring interest and encouragement. He also wishes to express his hearty thanks to Professor Masaru Shoda of Osaka University, Mr. Tetsuo Mamuro and the members of Asada Laboratory for their kind co-operation extended to him and for taking part in the discussion on many occasions. The author is also extremely grateful to late Dr. F. M. Penning of the Philips Research Laboratories, to Dr. Carl Kenty of the Research Laboratories of General Electric Company, to Dr. N. A. Ramaiah of Delhi University, to Dr. A. V. Phelps of the Research Laboratories of Westinghouse Electric Company, and to Dr. L. B. Loeb of California University for the kind interest they have taken in his work, providing him with many valuable references, which proved him to be very useful in promoting the study.

### References for Part I

1) K. W. Meissner and W. Graffunder: Ann. d. Phys. **84** (1927) 1009.
2) F. M. Penning: Phil. Mag. **11** (1931) 961.
3) F. M. Penning: Zeit. f. Phys. **57** (1929) 723.
4) F. M. Penning: Proc. Amsterdam **32** (1929) 341.
5) F. M. Penning: Physica **11** (1931) 183.
6) C. Kenty: Phys. Rev. **80** (1950) 95.
7) K. W. Meissner and R. H. Pierson: Proc. Indiana Acad. Sci. **59** (1950) 269.
8) K. W. Meissner and W. F. Miller: Phys. Rev. **92** (1953) 896.
9) S. S. Joshi: Trans. Faraday Soc. **25** (1929) 127.
10) N. A. Ramaiah: J. Sci. Res. Banaras Hindu Univ. **1** (1950-51) 91.
11) N. A. Ramaiah and S. N. Kaveeshwar: J. Sci. Res. Banaras Hindu Univ. **2** (1951–52) 1.
12) N. A. Ramaiah: J. Sci. Indust. Res. **10B** (1951) 27.
13) N. A. Ramaiah: J. Phys. Chem. **56** (1952) 218.
-15) N. A. Ramaiah: J. Sci. Indust. Res. **11B** (1952) 392.
16) A. P. Saxena and N. A. Ramaiah: J. Chem. Phys. **20** (1952) 1342.
17) M. G. Bhatawdakar: J. Chem. Phys. **21** (1953) 365.
18) N. A. Ramaiah: M. G. Bhatawdekar and N. Subrahmanyam, J. Chem. Phys. **21** (1953) 1160.
19) N. Subrahmanyam and N. A. Ramaiah: Zeit. f. Phys. **138** (1954) 151.
20) S. R. Mohanty, J. Jayaraman and G. V. G. Krishna Rao: J. Phys. Soc. Japan **9** (1954) 576.
21) S. R. Mohanty, T. S. Nagarjuman, R. Srinivasan and G. Srinivasan: J. Phys. Soc. Japan **10** (1954) 163.
22) N. Subrahmanyam and N. A. Ramaiah: J. Sci. Indust. Res. **12B** (1953) 641.
23) N. Subrahamanyam and N. A. Ramaiah: Zeit. f. Phys. **135** (1953) 274.
24) A. P. Saxena and N. A. Ramaiah: J. Chem. Phys. **12A** (1953) 130.
25) N. A. Ramaiah: J. Chem. Phys. **22** (1954) 1507.

### References for Part II

1) F. M. Penning: Physica **10–11** (1934) 1007.
2) F. M. Penning: Zeit. f. Phys. **46** (1929) 335.
3) F. M. Penning: Zeit. f. Phys. **72** (1931) 338.
4) For example, W. Finkelnburg: Kontinuerliche Spectren (Verlag. Julius Springer, Berlin, 1938).
5) A. O. McCoubrey: Phys. Rev. **93** (1954) 1249.
6) T. Holstein, D. Alpert and A. O. McCoubrey: Phys. Rev. **76** (1949) 1256.
7) L. Colli: Phys. Rev. **95** (1954) 892.
8) E. H. S. Burkop: Proc. Phys. Soc. **A67** (1954) 276.
9) M. A. Biondi: Phys. Rev. **88** (1952) 660.
10) M. A. Biondi: Phys. Rev. **90** (1953) 730.
11) E. Wigner: J. Chem. Phys. **5** (1937) 724.
12) H. A. Stuart: Zeit f. Phys. **32** (1925) 262.
13) M. W. Zemansky: Phys. Rev. **36** (1930) 919.
14) C. Kenty: Phys. Rev. **42** (1932) 823.
15) C. Kenty and D. A. Larson: Phys. Rev. **89** (1953) 180.
16) C. Kenty: J. Appl. Phys. **21** (1950) 1309.
17) T. Asada and H. Yoshinaga: Butsurigaku-koenshu **2** 195 (Gakujutsu-kenkyukaigi, 1942).
18) H. Takeyama: J. Sci. Hiroshima Univ. Ser. **A15** (1952) 235.
19) H. Volkringer: Ann. de Phys. **14** (1930) 5.
20) A. V. Phelps and J. P. Molnar: Phys. Rev. 89 (1953) 1202.
21) B. T. Barnes: Phys. Rev. **86** (1952) 351.
22) M. J. Druyvesteyn and F. M. Penning: Rev. Mod. Phys. **12** (1940) 87.
23) T. Holstein: Phys. Rev. **72** (1947) 1212.
24) T. Holstein: Phys. Rev. **83** (1951) 1159.
25) T. Holstein: D. Alpert and A. O. McCoubrey, Phys. Rev. **76** (1949) 1257.
26) J. M. Hansen and H. W. Webb: Phys. Rev. **72** (1947) 332.
27) C. Kenty: Phys. Rev. **80** (1950) 95.
28) C. Kenty and J. R. Cooper: Trans. Electrochem. Soc. **87** (1945) 397.
29) A. C. G. Mitchell and M. W. Zemansky: Resonance Radiation and Excited Atoms (The Macmillan, New York, 1934).
30) For example, 22) and 31).
31) L. B. Loeb and J. M. Meek: The Mechanism

of the Electrical Spark (Stanford Univ. Press, 1941).
32) L. B. Loeb and R. A. Wijsman: J. Appl. Phys. **19** (1948) 797.
33) L. B. Loeb: Phys. Rev. **94** (1954) 227.
34) L. H. Fisher and B. Bederson: Phys. Rev. **81** (1951) 109.
35) L. B. Loeb: Phys. Rev. **81** (1951) 287.
36) H. W. Bandel: Phys. Rev. **93** (1954) 649.

### Appendix

In case that the wall temperature is 100°C and the argon pressure is 15 mm Hg, (under these conditions the spectrograms in § 2 are taken), conversion frequency into metastable $Hg_2$ molecules is given as follows; as described in III § 1.2, $\frac{1}{T}$ is of the order of $10^{-30}(n_{Hg}\cdot n_{A})$. the density of A atoms is $5.3\times10^{17}$ atoms/cc, the density of Hg atoms is $7.1\times10^{15}$ atoms/cc, therefore, $T$ is assumed in the order of $10^{-2}\sim10^{-3}$ sec. On the other hand, when the argon pressure is 15 mm Hg and the diameter of the tube is 22 mm, $\omega$ is assumed in the order of $10^{-2}$ sec., deriving from the results that were obtained, in a fluorescent lamp, by Kenty.16)

---

JOURNAL OF THE PHYSICAL SOCIETY OF JAPAN Vol. 11, No. 12, DECEMBER, 1956

# Boundary-Layer Transition by Roughness Element

By Itiro TANI and Hiroshi SATO
*Institute of Science and Technology, University of Tokyo*

(Received September 1, 1956)

Measurements were made on the boundary layer along a flat plate in a two-dimensional low turbulence wind tunnel. A fine rod was attached to the plate as a two-dimensional roughness element, and the resulting transition from laminar to turbulent flow was investigated by hot-wire equipment.

The transition was found to differ in marked contrast according as the height of roughness element $k$ is small or large as compared with the thickness of boundary layer $\delta_k$ at the element. When $k/\delta_k$ is small, the boundary-layer flow separates at the element, but reattaches to the plate at some distance producing scarcely any disturbance. Transition occurs in the reattached boundary layer. A sinusoidal velocity fluctuation, characteristic of the laminar-boundary-layer oscillation, is observed at a distance downstream from the roughness element. When $k/\delta_k$ is large, transition occurs in the separated layer before it reattaches to the plate. Within the separated layer, a sinusoidal fluctuation is observed having the frequency pertinent to the separated layer from a sharp corner.

For a given roughness element at a given position on the plate, the transition moves forward and the transition Reynolds number continues to decrease as the free-stream velocity is increased. At a certain value of $k/\delta_k$ the transition reaches the element, and the transition Reynolds number begins to increase as the free-stream velocity is further increased. The minimum of the transition Reynolds number was found to correspond approximately to the demarcation of the two types of transition mentioned above.

## § 1. Introduction

A number of experimental investigations have been made concerning the transition of boundary layer by roughness elements. The senior author, in collaboration with Hama and Mituisi1), 2), has carried out systematic measurements on the effect of a single two-dimensional roughness element (a cylindrical wire) on the boundary layer with zero pressure gradient. The value of the critical roughness height was found to be predictable by an empirical formula suggested from Taylor's theory of transition due to free-stream turbulence. Measurements were also made on two-dimensional roughness elements of various shapes by Fage[3] and Cowled[4], both of whom attempted to obtain the method of predicting transition induced by roughness. A better correlation of the data was obtained by Dryden[5], who analyzed the existing data including those of references 1 and 2 and plotted the transition Reynolds number against the ratio of the roughness height to the boundary-layer thickness at the roughness element. After that, the senior author[6] extended the experiments and found that Dryden's method of representation could be used also for the boundary layer with a favorable pressure gradient, provided the transition Reynolds number was defined by the equivalent flat-plate distance from the leading edge.

Measurements were also carried out by various authors on three-dimensional roughness elements, such as cylinders, cones and spheres, with a view to determining their effect on transition[3],[4],[7],[8],[9]. A great difference was pointed out by Klebanoff, Schubauer and Tidstrom[9] between the effects of two-dimensional and three-dimensional roughness elements.

Thus the step seems to have been reached in that the transition due to roughness can be predicted sufficiently accurately for most practical purpose. Much is left, however, to be explained concerning the fundamental mechanism of this type of transition. Undoubtedly, a detailed study of flow in the neighborhood of a roughness element and of stability in its wake should be made before a thorough understanding of the phenomenon can be gained.

Liepmann and Fila[10] investigated conditions at a two-dimensional roughness element in some detail, and gave a certain considerations on the stability of the laminar layer separated at the element. Their measurements were concerned, however, only with the mean velocity distribution. For a three-dimensional roughness element Schubauer and Klebanoff[11] made interesting observations by using spark excitation. They revealed the existence of the turbulent "patch," which was essentially similar to the turbulent "spot" as found by Emmons[12] and Mitchner[13] on the water table.

Recently the junior author[14] made some experiments on the transition of a two-dimensional separated layer, and investigated the detailed structure of the transition region. The informations obtained in these experiments seem to give a clearer insight into the roughness problem, in which the boundary layer separates from the roughness element.

In view of these circumstances, the investigation described in this paper was undertaken by observing the mean and fluctuating velocities in the neighborhood of a two-dimensional roughness element on a flat plate placed in a low-turbulent stream, the purpose being the detailed study of the transition due to roughness under as simple a condition as possible. The work was conducted at the Institute of Science and Technology, University of Tokyo, with the financial support of the Ministry of Education by the Scientific Research Fund. The authors are grateful to Mr. M. Iuchi and Mr. S. Kyoya for assisting them in carrying out the experiments.

## § 2. Symbols

| | |
|---|---|
| $k$ | height of two-dimensional roughness element |
| $f$ | frequency of sinusoidal velocity fluctuation |
| $U$ | mean velocity in $x$-direction at any point in the boundary layer |
| $U_0$ | mean velocity of free stream |
| $u$ | $x$-component of velocity fluctuation |
| $x$ | distance parallel to the plate, measured from leading edge in the direction of free stream |
| $x_k$ | value of $x$ at roughness element |
| $x_t$ | value of $x$ at transition position |
| $y$ | distance measured normal to the plate |
| $z$ | distance parallel to the plate, measured from centerline, and normal to the direction of free stream |
| $\delta$ | boundary-layer thickness, $=5.16(\nu x/U_0)^{1/2}$ |
| $\delta_k$ | boundary-layer thickness at roughness element |
| $\delta_t$ | boundary-layer thickness at transition position |
| $\nu$ | coefficient of kinematic viscosity |
| $\theta$ | momentum thickness of boundary layer |

## § 3. Equipment and Procedures

All the measurements were made in the 60 cm × 20 cm low turbulence wind tunnel at the Institute of Science and Technology. A laminar boundary layer was established on an aluminum plate spanned vertically in the test section, in which the longitudinal turbulence level was about 0.05 per cent. By adjusting the wall opposite to the plate, it was possible to maintain the static pressure constant to within one per cent of the dynamic pressure except near the leading edge of the plate.

The two-dimensional roughness element was a cylindrical rod cemented individually to the plate at a distance 50 cm or 100 cm from the leading edge. The diameters of the rods were 0.9 mm and 2.0 mm. The height of roughness was approximately equal to the diameter of the rod.

A hot-wire anemometer with a compensating amplifier was used for measuring mean velocity and longitudinal fluctuating velocity. The hot-wire was operated by the constant current method, and was traversed in the $x$- and $y$-directions, where $x$ and $y$ are measured parallel to the free stream and perpendicular to the plate, respectively. The precision of positioning were 0.5 mm and 0.02 mm in the $x$- and $y$-directions, respectively. The compensated frequency response of the amplifier was flat from 20 to 20,000 cycles per second. Wave pattern of velocity fluctuation was observed by photographing the screen of the cathode-ray oscillograph with a moving-film camera.

An examination was first made on the transverse contamination originating from the intersection of the boundary-layer plate and the top and bottom walls of the test section. Observation at various $z$-stations ($z$ being the lateral distance from the centerline of the plate) revealed the contamination effect as shown in Fig. 1. Two kinds of lines of contamination are drawn for various free-stream velocities, the one corresponding to the beginning of velocity fluctuation, while the other to the condition where the intermittency factor of fluctuation is 0.5. Thus the laminar flow in the boundary layer is maintained only in the V-shaped region, and the two-dimensionality is more or less doubtful at a great distance downstream from the leading edge.

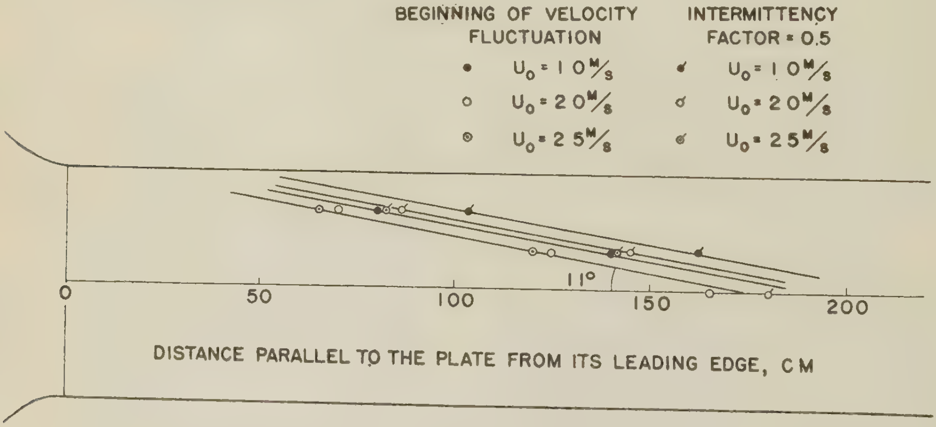
BEGINNING OF VELOCITY FLUCTUATION
● $U_0 = 10$ M/S
○ $U_0 = 20$ M/S
◎ $U_0 = 25$ M/S
INTERMITTENCY FACTOR = 0.5
$U_0 = 10$ M/S
$U_0 = 20$ M/S
$U_0 = 25$ M/S
11°
0
50
100
150
200
DISTANCE PARALLEL TO THE PLATE FROM ITS LEADING EDGE, CM

Fig. 1. Transverse contamination on the plate in the 60 cm × 20 cm wind tunnel.

## § 4. Results and Discussion

It appears from the results of measurements that the transition differs in marked contrast according as the height of roughness element $k$ is small or large as compared with the thickness of boundary layer $\delta_k$ at the position of the element (The thickness of boundary layer is defined as three times the displacement thickness, that is, $\delta_k = 5.16(\nu x_k/U_0)^{1/2}$, where $\nu$ is the kinematic viscosity, $U_0$ the free-stream velocity, and $x_k$ the distance of the roughness element from the leading edge of the plate). The difference will be illustrated below in terms of mean velocity profile, intensity of velocity fluctuation, oscillogram of velocity fluctuation, etc.

### a. Mean velocity profile

Typical examples are shown in Fig. 2 for the distribution of mean velocity, $U/U_0$, across several sections downstream of the roughness element. When $k/\delta_k$ is small, as shown in (a), all the profiles are approximately of Blasius type accompanying a thin region of separation close to the surface of the plate. The separated region extends over a considerable range, beyond which the flow reattaches to the surface as a laminar boundary layer having the Blasius profile. Transition is observed to occur in the reattached boundary layer, so that the velocity profile changes gradually from the Blasius type to turbulent-boundary-layer type.

When $k/\delta_k$ is large, as shown in (b), the velocity profiles are those characteristic of the separated layer. Transition occurs in the sepa-

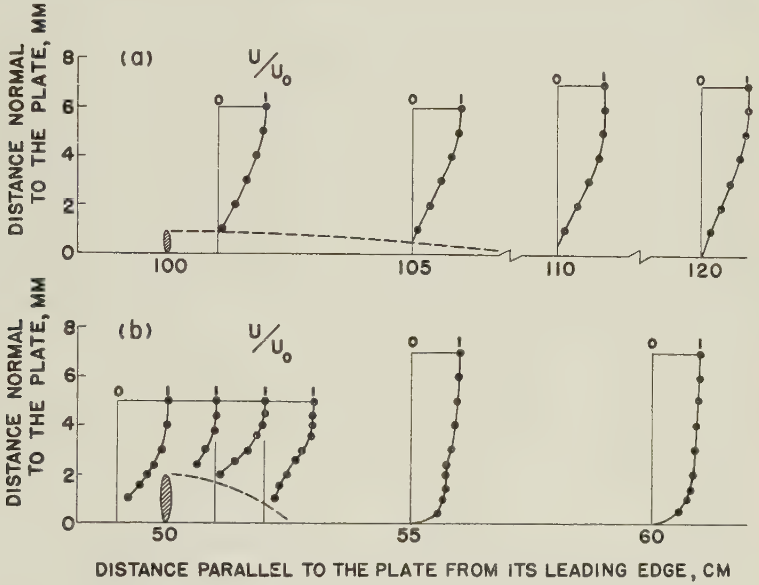

Fig. 2. Distribution of mean velocity downstream of roughness element.
(a) $U_0=10$ m/s, $k=0.9$ mm, $x_k=100$ cm, $k/\delta_k=0.15$.
(b) $U_0=20$ m/s, $k=2.0$ mm, $x_k=50$ cm, $k/\delta_k=0.64$.

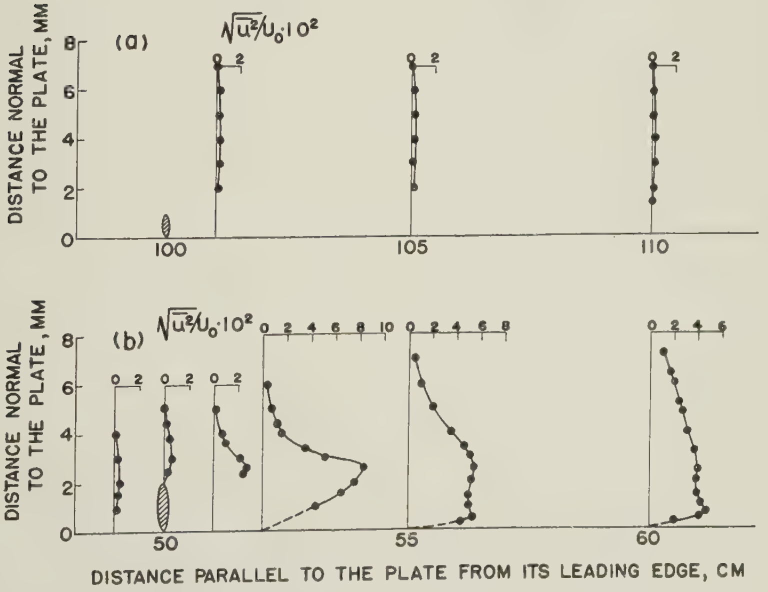

Fig. 3. Distribution of intensity of velocity fluctuation downstream of roughness element.
(a) $U_0=10$ m/s, $k=0.9$ mm, $x_k=100$ cm, $k/\delta_k=0.15$.
(b) $U_0=20$ m/s, $k=2.0$ mm, $x_k=50$ cm, $k/\delta_k=0.64$.

rated layer, thus causing the flow to reattach to the surface at a rather short distance. Fully developed turbulent profiles are established soon after the reattachment.

**b. Intensity of velocity fluctuation**

In the present experiment only the longitudinal component $u$ of the velocity fluctuation was measured, and the term "intensity" is used to denote the root-mean-square of $u$ in terms of the free-stream velocity. Typical examples are shown in Fig. 3 for the distribution of intensity of velocity fluctuation, for the case (a) when $k/\delta_k$ is small, and (b) when $k/\delta_k$ is large. In the former case, the velocity fluctuation is almost non-existent except for a weak sinusoidal oscillation. In the latter case, the intensity of fluctuation is of considerable amount, indicating the earlier transition to turbulence. It should be noted that the maximum value of intensity at the station $x=52$ cm occurs at about $y=2.5$ mm, which approximately corresponds to the point of maximum velocity gradient. This is in contrast to the case of natural transition, in which the turbulence seems to be produced in the immediate neighborhood of the surface. The point of maximum intensity moves on toward the surface until a turbulent boundary layer in energy equilibrium is established.

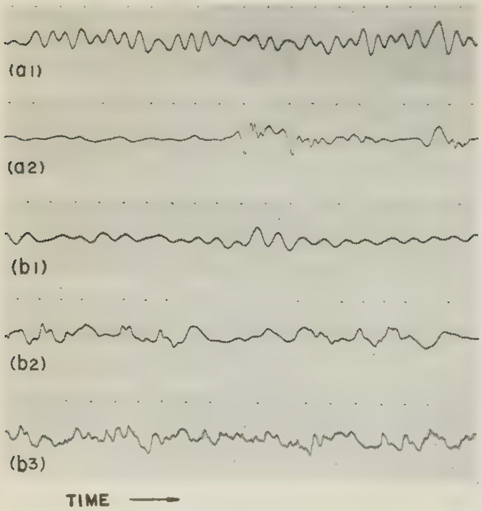

Fig. 4. Oscillographic records of velocity fluctuation. Time interval between dots is 0.01 seconds. Amplitude is not in scale.
(a1)(a2) $U_0=10$ m/s, $k=0.9$ mm, $x_k=50$ cm.
(b1)(b2)(b3) $U_0=5$ m/s, $k=2.0$ mm, $x_k=50$ cm.
(a1) $x=60$ cm, $y=0.5$ mm.
(a2) $x=75$ cm, $y=0.5$ mm.
(b1) $x=55$ cm, $y=4$ mm.
(b2) $x=60$ cm, $y=2$ mm.
(b3) $x=100$ cm, $y=2$ mm.

**c. Oscillogram of velocity fluctuation**

The velocity fluctuations, as detected in the region downstream of the roughness element, are shown on the oscillograms in Fig. 4. The first two records, (a1) and (a2), refer to the case $U_0=10$ m/s, $k=0.9$ mm, $x_k=50$ cm and $k/\delta_k=0.21$; these were taken at two stations $x=60$ cm and 75 cm, respectively. The record (a1) is approximately sinusoidal, the predominant frequency being that of the laminar-boundary-layer oscillation, which has been predicted from stability theory and first discovered by the experiments of Schubauer and Skramstad[15]. The record (a2) shows the appearance of intermittent bursts of large amplitude at the downstream station. These bursts develop a further distance downstream into an irregular high-frequency fluctuations, characteristic of turbulence. This process of transition is quite the same as that of the natural transition preceded by a laminar-boundary-layer oscillation. The remaining three records, (b1), (b2) and (b3), refer to the case $U_0=5$ m/s, $k=2.0$ mm, $x_k=50$ cm and $k/\delta_k=0.34$. These records were taken at three stations, $x=55$ cm, 60 cm and 100 cm, respectively. With such a large value of $k/\delta_k$, a sinusoidal fluctuation first make its appearance, but of the frequency somewhat higher than that corresponding to the above-mentioned

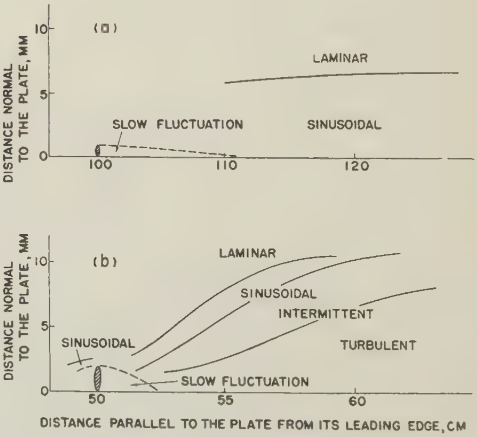

Fig. 5. Nature of velocity fluctuation.
(a) $U_0=10$ m/s, $k=0.9$ mm, $x_k=100$ cm, $k/\delta_k=0.15$.
(b) $U_0=20$ m/s, $k=2.0$ mm, $x_k=50$ cm, $k/\delta_k=0.64$.

laminar-boundary-layer oscillation. As the distance downstream increases, the wave pattern gradually changes and finally develops into the pattern of fully developed turbulence. The sinusoidal fluctuation of higher frequency seems to correspond to the velocity profile of the separated layer.

### d. Nature of velocity fluctuation

From a number of oscillographic records, the nature of velocity fluctuation is represented on a map as shown in Fig. 5. When $k/\delta_k$ is small, only a laminar-boundary-layer oscillation is present in the reattached boundary layer. A slow irregular fluctuation of small amplitude is observed in the separated region. When $k/\delta_k$ is large, a laminar-boundary-layer oscillation appears just in front of the roughness element. But this fluctuation disappears a short distance downstream the element, and is superseded by another sinusoidal fluctuation of higher frequency, which develops into turbulence at a distance downstream. Region of intermittency exists at the outer edge of the turbulence region. A slow irregular fluctuation is observed in the separated region.

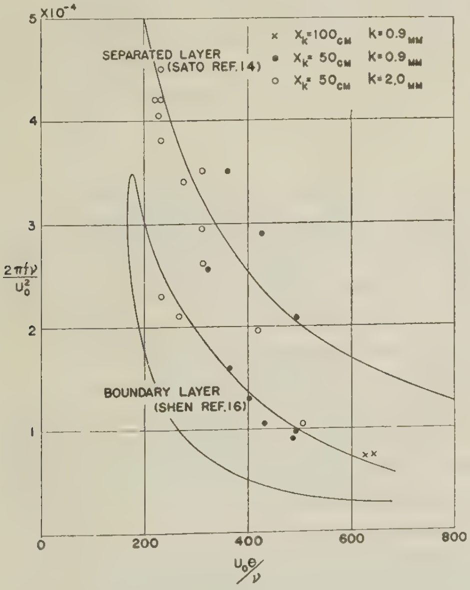

Fig. 6. Non-dimensional frequency of sinusoidal fluctuation.

### e. Frequency of sinusoidal fluctuation

In Fig. 6, the frequency of the sinusoidal fluctuation $f$, made non-dimensional in terms of the free-stream velocity and kinematic viscosity, is plotted against the Reynolds number, based on the free-stream velocity and momentum thickness of boundary layer $\theta$, the latter of which is obtained by integrating $(U/U_0)(1-U/U_0)$ with respect to $y$ throughout the layer at the position of the measurement. The momentum thickness is used in preference to the displacement thickness by reason of being applicable both for attached and separated layers.

In the same figure are also drawn two curves, the one of which is given by the neutral stability relation calculated by Shen[16] for the boundary layer having the Blasius profile, and the other by the empirical relation $2\pi f\theta/U_0=0.1$ as found by the junior author[14] for the separated flow from a sharp corner. With the values of $k$ and $x_k$ fixed, the observed frequency is first located somewhere near the first curve (boundary layer), and then approaches the second curve (separated layer), as the value of $k/\delta_k$ is increased. It is thus evident that the sinusoidal fluctuation leading to turbulence is of different nature according as $k/\delta_k$ is small or large.

As a matter of course, it is rather difficult to determine a definite value of $k/\delta_k$, below which the sinusoidal fluctuation is of the boundary-layer type, and above which it is of the separated-layer type. It seems nevertheless possible to draw at least a broad line of demarcation between the two types of fluctuation by examining a great number of oscillographic records. This has really been done, and the critical value of $k/\delta_k$ was found to depend on the ratio $x_k/k$, $x_k$ being the distance of the roughness element measured from the leading edge. This result will be mentioned in the following paragraph.

### f. Transition Reynolds number

In Fig. 7, the transition Reynolds number $U_0\delta_t/\nu$ is plotted as a function of the ratio $k/\delta_k$; $\delta_t$ is the thickness of the boundary layer at the transition point, which is defined as the point where the intermittency factor of velocity fluctuation attains the value 0.5. For comparison the data previously obtained by the senior author[6] and by Schubauer's group[17] are included. The correlation of data is very good and represented by a hyperbola $(U_0\delta_t/\nu)(k/\delta_k)=840$ except for very small values of $k/\delta_k$. As suggested in reference 6, the transition for very small values of $k/\delta_k$ is affected by free-stream turbulence and other external disturbances rather than by roughness itself.

The Reynolds number based on the boundary-layer thickness at the roughness element, $U_0\delta_k/\nu$, can be written in the form $26.6(x_k/k)\cdot(k/\delta_k)$. Therefore, when plotted against $k/\delta_k$, it is represented by a straight line having the slope $26.6(x_k/k)$. Three of such straight lines corresponding to the value of $x_k/k$ pertinent to the present experiment are drawn in Fig. 7. As pointed out by Dryden[5], these lines represent the limiting case $x_t=x_k$, that is, the case when transition occurs at the roughness element. As a matter of fact, the experimental points begin to depart from the hyperbola as $x_t$ approaches $x_k$, and then approach the straight line having the pertinent value of $x_k/k$.

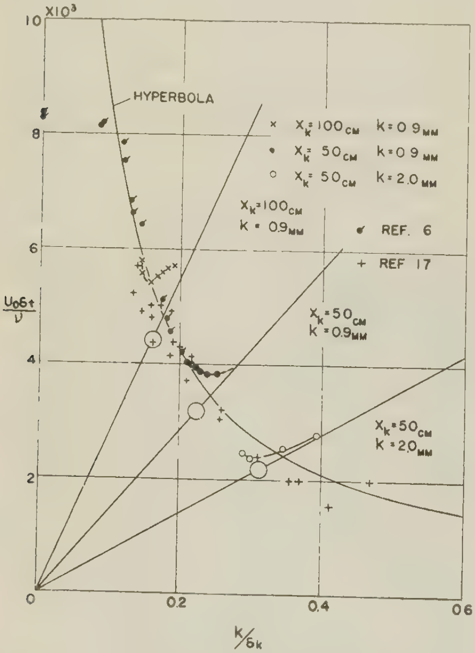

Fig. 7. Transition Reynolds number. Large circles denote demarcation of two types of transition.

The critical values of $k/\delta_k$ mentioned in the preceding paragraph are also shown by large circles on the straight lines. It is interesting to note that the critical points on the straight lines are very close to the intersections of the hyperbola with the straight lines. It should be added in this respect that, if the critical point is interpreted as the establishment of the separated-layer type transition, a simple calculation based on the assumptions concerning the mechanism of separated layer predicts the critical points to lie on a hyperbola on a plot of $U_0\delta_k/\nu$ versus $k/\delta_k$.

## § 5. Conclusion

It is concluded from the foregoing discussions that the transition induced by a roughness element differs in marked contrast according as the height of roughness element $k$ is small or large as compared with the thickness of boundary layer $\delta_k$ at the element. When $k/\delta_k$ is small, the boundary-layer flow separates at the roughness element, but attaches to the surface of the plate at some distance producing scarcely any disturbance. Transition occurs in the reattached boundary layer. Thus the mechanism of transition appears to be essentially the same as that of the natural transition. As a matter of fact, a sinusoidal velocity fluctuation, characteristic of the laminar-boundary-layer oscillation, is observed at a distance downstream from the roughness element. The transition for this case may be called the transition of laminar-boundary-layer type.

When $k/\delta_k$ is large, the separated layer becomes unstable before it reattaches to the surface. Within the separated layer, a sinusoidal fluctuation is observed having the frequency pertinent to the velocity profile of the flow separated from a sharp corner. The regular fluctuation is then amplified and develops downstream into an irregular high-frequency fluctuation characteristic of turbulence. Fully developed turbulent velocity profile is established soon after the reattachment of the separated layer. The transition for this case may be called the transition of laminar-separated-layer type.

As shown by Dryden, the experimental data are well represented by a single curve of the transition Reynolds number $U_0\delta_t/\nu$ versus the ratio $k/\delta_k$, provided that the transition occurs downstream from, but not too close to, the position of the roughness element. As the transition approaches the element, the experimental points begin to depart from this curve and then approach the other curves representing the condition $\delta_t=\delta_k$.

If we consider the free-stream velocity is increased with a given roughness element placed on the plate at a given distance from the leading edge, the transition position moves gradually forward, resulting a decrease in the transition Reynolds number $U_0\delta_t/\nu$ along the above-mentioned curve of $U_0\delta_t/\nu$ versus $k/\delta_k$. At a certain value of $k/\delta_k$ the transition position reaches the element, and the transition Reynolds number begins to increase as the free-stream velocity is further increased. It is one of the important findings of the present investigation that the minimum of the transition Reynolds number approximately corresponds to the demarcation of the two types of transition. In other words, the transition Reynolds number continues to decrease as the free-streem velocity is increased, so long as the transition is of the laminar-boundary-layer type. On the other hand, the transition Reynolds number increases with the free-stream velocity after the transition becomes that of the laminar-separated-layer type. Discrimination of the two types of transition yields an explanation for the success of Dryden's representation for transition occurring downstream from the element. The purpose of the present investigation seems to have been attained, since the apparently complex phenomenon of the transition due to roughness has been decomposed into those of simpler types, the transition of laminar-boundary-layer type and the transition of laminar-separated-layer type.

## References

1) I. Tani, R. Hama and S. Mituisi: *On the Permissible Roughness in the Laminar Boundary Layer*, Rep. Aero. Res. Inst., Tokyo Imp. Univ., No. 199, 1940.
2) I. Tani and R. Hama: *Experiments on the Permissible Roughness in the Laminar Boundary Layer along a Flat Plate* (in Japanese), Wartime Report I–4, March 1945; I. Tani, R. Hama and S. Mituisi: *On the Effect of a Single Roughness Element on Boundary-Layer Transition*, Rep. Inst. Sci. Tech., Tokyo Univ. **8** (1954) 125.
3) A. Fage: *The Smallest Size of a Spanwise Surface Corrugation Which Affects Boundary-Layer Transition on an Aerofoil*, ARC Rep. & Memo. No. 2120, 1943.
4) E. H. Cowled: *The Effects of Surface Irregularities on Transition in the Laminar Boundary Layer*, Aero. Res. Lab., Rep. A86, Melbourne 1954; *Experimental Determination of the Critical Heights of Surface Irregularities*, Aero. Res. Lab., Aerodyn. Note 138, Melbourne 1954.
5) H. L. Dryden: *Review of Published Data on the Effect of Roughness on Transition from Laminar to Turbulent Flow*, J. Aero. Sci. **20** (1953) 477.
6) I. Tani, M. Iuchi and K. Yamamoto: *Further Experiments on the Effect of a Single Roughness Element on Boundary-Layer Transition*, Rep. Inst. Sci. Tech., Tokyo Univ. **8** (1954) 171.
7) L. K. Loftin, Jr.: *Effects of Specific Types of Surface Roughness on Boundary-Layer Transition*, NACA Wartime Report L–48.
8) N. Gregory and W. S. Walker: *The Effect on Transition of Isolated Surface Excrescences in the Boundary Layer*, ARC 13436, 1950.
9) P. S. Klebanoff, G. B. Schubauer and K. D. Tidstrom: *Measurements of the Effect of Two-dimensional and Three-dimensional Roughness Elements on Boundary-Layer Transition*, J. Aero. Sci. **22** (1955) 803.
10) H. W. Liepmann and G. H. Fila: *Investigations of Effects of Surface Temperature and Single Roughness Elements on Boundary-Layer Transition*, NACA Tech. Rep. No. 890, 1947.
11) G. B. Schubauer and P. S. Klebanoff: *Contributions on the Mechanics of Boundary-Layer Transition*, NACA Tech. Note No. 3489, 1955.
12) H. W. Emmons: *The Laminar-Turbulent Transition in a Boundary Layer*, J. Aero. Sci. **18** (1951) 490.
13) M. Mitchner: *Propagation of Turbulence from an Instantaneous Point Disturbance*, J. Aero. Sci. **21** (1954) 350.
14) H. Sato: *Experimental Investigation on the Transition of Laminar Separated Layer*, J. Phys. Soc. Japan **11** (1956) 702.
15) G. B. Schubauer and H. K. Skramstad: *Laminar-Boundary-Layer Oscillations and Transition on a Flat Plate*, NACA Tech. Rep. No. 909, 1948.
16) S. F. Shen: *Calculated Amplified Oscillations in the Plane Poiseuille and Blasius Flows*, J. Aero. Sci. **21** (1954) 62.
17) H. L. Dryden: *Effects of Roughness and Suction on Transition from Laminar to Turbulent Flow*, Mémoires sur la Mécanique des Fluides, Publications Scientifiques et Techniques du Ministère de l'Air, Hors série, pp. 49–59, Paris 1954.

JOURNAL OF THE PHYSICAL SOCIETY OF JAPAN Vol. 11, No. 12, DECEMBER, 1956

# On the Space Charge affected by the Magnetic Field. Part II

By Yoshio YASUOKA

*Japan Radio Co., Ltd., Research Section, 930 Kamirenjaku, Mitaka, Tokyo*

(Received October 26, 1955)

In the previous paper, the author investigated the cathode back heating power and the anode dark current in a coaxial diode acted on by a magnetic field. The present paper gives a more advanced treatment, taking into account the effect of the magnetic field on the scattered electrons. As a result, values have been obtained which is much nearer to the experimental values and the agreement is considered satisfactory.

## §1. Introduction

In the previous paper[1)], in order to investigate the behaviour of electrons forming the space charge of high density in a magnetic field, the author made special coaxial diodes and performed experiments with the magnetic field applied parallel to the diode axis. The cathode back heating and the anode dark current were observed and their close correlation was determined.

On the assumption that the both are caused by the same source, that is, the excess energy electrons produced in the outermost sheath of the space charge, the calculation was carried out neglecting the effect of the magnetic field on the scattered electrons. The result was in fairly good agreement with the experiment. But in that case, the experimental values of the back heating power turned out to be about twice as large as the calculated value.

In this report, the calculation is extended to take into account the effect of the magnetic field on the scattered electrons. As a result, the calculated values approach more closely to the experimental values, the ratio becoming 1.3 and being almost constant over a wide range of the anode voltage. Considering that the calculation was two-dimensional, the agreement should be considered to be satisfactory.

## §2. Calculation of the Anode Dark Current when the Effect of the Magnetic Field is Taken into Account

The author, as described in the previous report, supposes that the cathode back heating and the anode dark current are principally caused by the scattered electrons in the outermost sheath of electron cloud. If no scattering exists, the electrons forming electron cloud are restricted between the cathode and a surface of radius $r_s$, which is determined by the electric and the magnetic fields. However, the orbital energies of electrons at $r_s$ are transformed into those of random motions, as shown in Fig. 1, when $u$ and $v$ denote the radial (positive when directed toward the anode) and tangential velocity components of these random motions respectively.

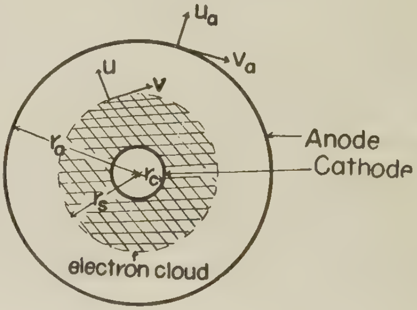

Fig. 1

The velocity distribution function of random motions should necessarily be Maxwellian:

$$f(u,\ v)=\frac{m}{2\pi\, kT}\varepsilon^{-m(u^2+v^2)/2kT}\,. \tag{1}$$

Thus the total random current toward the anode from $r_s$-surface is expressed by

$$\begin{aligned} i_T&=2\pi r_s lNe\int_0^\infty\int_{-\infty}^\infty uf(u,\ v)\,dudv \\ &=2\pi r_s lNe\sqrt{\frac{kT}{2\pi m}}\,, \end{aligned} \tag{2}$$

where $l$ is the axial length and $N$ the space charge density at $r_s$-surface. If the effect of magnetic field on scattered electrons is neglected, $i_T$ becomes the anode dark current itself, since all the scattered electrons toward the anode are caught by the anode.

When the effect of the magnetic field on the scattered electrons is taken into account, some of them can not reach the anode but must come back to $r_s$-surface. Putting this returing current as $i_B$, the anode dark current $i_a$ is given by:

$$i_a = i_T - i_B. \tag{3}$$

If an electron starting from $r_s$ with the velocity components $u$ and $v$ arrives at the anode with $u_a$ and $v_a$, the energy and the angular momentum relations are:

$$e(V_a - V_s) + \frac{m}{2}(u^2+v^2) = \frac{m}{2}(u_a^2+v_a^2), \tag{4}$$

and

$$v_a = r_a\left\{\frac{eB}{2m}\left(1-\frac{r_s^2}{r_a^2}\right)+\frac{r_s}{r_a^2}v\right\}, \tag{5}$$

where $V_a$ and $V_s$ are the potentials at the anode and $r_s$-surface against the cathode respectively, and $r_a$ is the anode radius.

From (5) and (4), we obtain:

$$u_a^2 - u^2 + r_a^2\left\{\frac{eB}{2m}\left(1-\frac{r_s^2}{r_a^2}\right)+\frac{r_s}{r_a^2}\right\}^2 - v^2 = \frac{2e(V_a-V_s)}{m}, \tag{6}$$

In order that the electron may not be caught by the anode and return to $r_s$-surface, the conditions $u_a^2<0$, and $u>0$ must be satisfied. The former conditions is rewritten:

$$A_1^2 + (u^2+v^2) - r_a^2\left\{\omega_0 K_1 + \frac{r_s}{r_a^2}v\right\} < 0. \tag{7}$$

Putting

$$\frac{2e(V_a-V_s)}{m} = A_1^2, \qquad \frac{eB}{2m} = \omega_0,$$
$$1-\frac{r_s^2}{r_a^2} = K_1; \tag{8}$$

$$\omega_0 r_s - \sqrt{\frac{K_1\cdot\omega_0^2 r_a^2 - A_1^2 - u^2}{K_1}} = v_1,$$
$$\omega_0 r_s + \sqrt{\frac{K_1\cdot\omega_0^2 r_a^2 - A_1^2 - u^2}{K_1}} = v_2, \tag{9}$$

and

$$\sqrt{K_1\cdot\omega_0^2\, r_a^2 - A_1^2} = u_1\,,$$

the above conditions become:

$$v_2 > v > v_1,$$

and

$$u_1 > u > 0. \tag{10}$$

Then

$$i_B = 2\pi r_s l N e \int_0^{u_1}\int_{v_1}^{v_2} u\cdot f(u,v)\, dv du. \tag{11}$$

With $D = 2r_s lN$ and $\frac{m}{2kT} = h^2$, (11) is rewritten:

$$i_B = De\, h^2 \int_0^{u_1}\int_{v_1}^{v_2} u\cdot\varepsilon^{-h^2(u^2+v^2)}\, dv du$$

Carrying out the integration,

$$i_B = \frac{De}{2h}\sqrt{\pi}\left[\frac{1}{2}\left\{\phi(RL+S)+\phi(RL-S)\right\} - \frac{\varepsilon^{\beta_1^2}}{2d_1}\cdot\{\phi(SL+R)-\phi(SL-R)\}\right], \tag{12}$$

where

$$\phi(x) = \frac{2}{\sqrt{\pi}}\cdot\int_0^x \varepsilon^{-x^2}\, dx,$$
$$L = \sqrt{1-\frac{A_1^2}{\omega_0^2(r_a^2-r_s^2)}}, \tag{13}$$
$$S = h\omega_0 r_s, \quad R = h\omega_0 r_a \quad \beta_1 = h^2 A_1^2,$$
and $$d_1 = \frac{r_s}{r_a}.$$

From (2)

$$i_T = \frac{De}{2h}\sqrt{\pi}. \tag{14}$$

Thus

$$i_a = i_T\left[1-\frac{1}{2}\left\{\phi(RS+S)+\phi(RL-S)\right\} - \frac{\varepsilon^{\beta_1^2}}{2d_1}\left\{\phi(SL+R)-\phi(SL-R)\right\}\right] \tag{15}$$
$$= i_T\cdot\Theta = \frac{De}{2h}\cdot\Theta.$$

### § 3. Calculation of the Back Heating Power when the Effect of the Magnetic Field is Taken into Account

The calculation of the back heating power of electrons scattered at $r_s$-surface can be performed by a process similar to that of the anode dark current.

As in II, if an electron with the velocity components $u$ (positive when directed to the cathode) and $v$ at $r_s$ reaches the cathode with $u_c$ and $v_c$, the relations among the velocity components are:

$$u_c^2 + r_c^2\left\{\frac{v}{d_2 r_c} - \omega_0 K_2\right\}^2 - (u^2+v^2) + A_2^2 = 0, \tag{16}$$

and

$$A_2^2 = \frac{2e(V_s-V_c)}{m}, \tag{17}$$

where

$$d_2=\frac{r_c}{r_s}, \qquad K_2=\frac{r_s^2}{r_c^2}-1,$$

and $V_c$ is the potential at the cathode.

In order that the electron may reach the cathode, the conditions $u_c^2>0$ and $u>0$ must be satisfied.

Putting

$$\omega_0 r_s-\sqrt{\frac{K_2\omega_0^2 r_c^2-A_2^2+u^2}{K_2}}=v_3$$

and

$$\omega_0 r_s+\sqrt{\frac{K_2\omega_0^2 r_c^2-A_2^2+u^2}{K_2}}=v_4, \tag{18}$$

the above conditions become:

$$v_3<v<v_4 \quad \text{for} \quad v,$$

and

$$u^2+K_2\omega_0^2 r_c^2-A_2^2>0 \quad \text{for } u. \tag{19}$$

If

$$K_2\omega^2 r_c^2-A_2^2>0, \tag{20}$$

then

$$u>0,$$

or if

$$K_2\omega_0^2 r_c^2-A_2^2<0, \tag{21}$$

then

$$u>\sqrt{A_2^2-K_2\omega_0^2 r_c^2}. \tag{22}$$

The equation $K_2\omega_0^2 r_c^2=A_2^2$ can be re-written:

$$e(V_s-V_c)=\frac{m}{8}\left(\frac{e}{m}B\right)^2 r_s^2\left(1-\frac{r_c^2}{r_s^2}\right)^2.$$

Thus (21) means the condition that all the electrons starting from $r_s$-surface should arrive at the cathode, which is the same as that for the case neglecting the effect of the magnetic field on the scattered electrons. Therefore, it is sufficient to consider only the case which satisfies the condition (20). Hence the back heating power $W_b$ becomes:

$$W_b=2\pi r_s Nel\int_0^\infty\int_{v_3}^{v_4} u\left\{\frac{1}{2}m(u^2+v^2)-e(V_s-V_c)\right\} f(u,v)\,dv\,du$$

$$=\frac{Dh^2m}{2}\int_0^\infty\int_{v_3}^{v_4} u(u^2+v^2-A_2^2)\times\varepsilon^{-h^2(u^2+v^2)}\,dv\,du \tag{23}$$

By integration we obtain:

$$W_b=\frac{3}{8}\cdot\frac{eDm}{h^3}\varepsilon^{-h^2A_2^2}\sqrt{\pi}\cdot d_2\cdot\Big[1-\frac{1}{2}\phi(\delta_1)$$

$$+\frac{1}{2}\phi(\delta_2)+\frac{1}{3\sqrt{\pi}}(\delta_1\varepsilon^{-\delta_1^2}-\delta_2\varepsilon^{-\delta_2^2})$$

$$+\frac{\varepsilon^{h^2A_2^2}}{d_2}\frac{1}{3\sqrt{\pi}}\Big\{(3-2\beta_1^2)(\phi(\gamma_1)-\phi(\gamma_2))$$

$$-\gamma_1\varepsilon^{-\gamma_1^2}+\gamma_2\varepsilon^{-\gamma_2^2}\Big\}\Big]$$

$$=\frac{3}{8}\cdot\frac{eDm}{h^3}\cdot\varepsilon^{-h^2A_2^2}\sqrt{\pi}\cdot d_2\cdot\Psi$$

$$=W_T\cdot\Psi, \tag{24}$$

where

$h\omega_0 r_c=t$

$$\delta_1=t+\frac{P_1}{(1-d_2^2)^{1/2}}, \qquad \delta_2=t-\frac{P_1}{(1-d_2^2)^{1/2}},$$

$$\gamma_1=S+\frac{P_1}{K_2}, \qquad \gamma_2=S-\frac{P_1}{K_2}, \tag{25}$$

$$a_1=h\omega_0(r_s+r_c), \qquad b_1=h\omega_0(r_s-r_c),$$

$$\beta_2=h^2A_2^2 \quad \text{and} \quad P_1=a_1b_1-\beta_2^2.$$

In (24), $W_T$ means the back heating power when the effect of the magnetic field on the scattered electrons is neglected (the electron density $N$ being yet undertermined), so $\Psi$ is the corresponding correction factor.

Electrons from the cathode describe the orbit determined by the electric and the magnetic fields, and at $r_s$ their orbital energies are transformed into those of random motions, hence

$$Ne(V_s-V_c)=3/2\,NKT. \tag{26}$$

The value $r_s$ for the given electric and magnetic fields can be obtained graphically from the following relations:

$$V_a-V_c=\frac{1}{8}\frac{e}{m}B^2r_s^2\left[\left(1-\frac{r_c^2}{r_s^2}\right)^2+2\left(1-\frac{r_c^4}{r_s^4}\right)ln\left(\frac{r_a}{r_s}\right)\right], \tag{27}$$

From (27) we obtain the potential difference $V_s-V_c$ between the cathode and $r_s$-surface:

$$V_s-V_c=\frac{1}{8}\frac{e}{m}B^2r_s^2\left(1-\frac{r_c}{r_s^2}\right)^2. \tag{28}$$

In order to eliminate the undetermined electron density $N$, we use (15), that is,

$$\frac{r_slN}{h}\sqrt{\pi}=\frac{i_a}{e}\frac{1}{\Theta}.$$

Then

$$W_{b_0}=\frac{3}{4}\frac{i_a}{e}\cdot\frac{m}{h^2}\cdot\varepsilon^{-h^2A_2^2}d_2\frac{\Psi}{\Theta}$$

$$=\frac{1}{8}\frac{e}{m}r_cr_s\left(1-\frac{r_c^2}{r_s^2}\right)^2\varepsilon^{-3/2}\cdot B^2\cdot i_a\frac{\Psi}{\Theta}$$

$$= W_{b_0}\frac{\Psi}{\Theta}, \tag{29}$$

where

$$W_{b_0} = \frac{1}{8}\frac{e}{m} r_c r_s \left(1 - \frac{r_c^2}{r_s^2}\right)^2 \cdot \mathcal{E}^{-3/2} \cdot B^2 \cdot i_a, \tag{30}$$

which means the back heating power, when the effect of the magnetic field on the scattered electrons is neglected.

## §4. Comparison with Experiment

Fig. 2 shows the anode dark current and the back heating power as ordinates and the anode voltage as abscissa, when the coaxial diode of the anode radius 3 mm, cathode radius 1.15 mm and the anode length 5 mm is used.

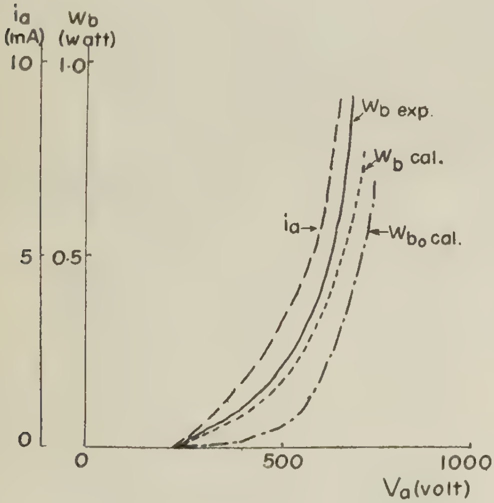

Fig. 2

In the figure, the broken and the solid lines show the experimental value of anode dark current $i_a$ and that of back heating power $W_{b\,\mathrm{exp}}$ respectively, and further the dotted and the chain lines the calculated value $W_{b\,\mathrm{cal}}$ when the effect of the magnetic field on the scattered electrons is taken into account and $W_{b_0\,\mathrm{cal}}$ when it is neglected.

When the ratios of $W_{b\,\mathrm{exp}}$ to $W_{b_0\,\mathrm{cal}}$ and $W_{b\,\mathrm{exp}}$ to $W_{b\,\mathrm{cal}}$ are denoted by $\alpha_1$ and $\alpha_2$ respectively, the following table is otained:

| $Va$ (Volt) | $\alpha_1$ | $\alpha_2$ |
|---|---|---|
| 500 | — | 1.33 |
| 560 | 1.95 | 1.33 |
| 617 | 2.11 | 1.32 |
| 680 | 2.33 | 1.34 |

In fact the electrons at $r_s$ are expected to be scattered in the axial direction as well (though in the present calculation, it has been neglected on the assumption of infinite axial length of the diode) and the outermost sheath to have some thickness instead of being a mere surface. When these are taken into consideration, the shown agreement of the calculation with the experiment are to be regarded as satisfactory.

The calculation neglecting the effect of the magnetic field on the scattered electrons is still useful to see the general behaviour of the back heating power.

In conclusion, the author wishes to express his thanks to Prof. I. Takahashi, Prof. S. Kojima, Prof. S. Okamura, Prof. S. Mito and Dr. S. Nakajima for their valuable advices and constant encouragement, and also wishes to thank Mr. C. Shibata and Mr. N. Suehiro for their assistance.

### References

1) Y. Yasuoka: J. Phys. Soc. Japan **10** (1955) Dec.
2) G. B. Collins: Microwave Magnetron.
3) K. R. Spangenberg: Vacuum Tubes.
4) J. C. Slater: Microwave Electronics.
5) L. Brillouin: Phys. Rev. **26** (1938) Mar.
6) E. G. Linder: Proc. I. R. E. **26** (1938) Mar.

# Short Notes

This section is intended to secure prompt publication of important discoveries in physics. The reports should not exceed 800 words in length. A figure of size 7 cm × 7 cm will be counted as 150 words.

J. Phys. Soc. Japan **12** (1956) 1296~1297

## Cation Arrangement and Magnetic Properties of Copper Ferrite-Chromite Series

by Syohei Miyahara and Haruyuki Ohnishi
*Department of Physics, Faculty of Science, Hokkaido University, Sapporo, Japan*

(Received October 5, 1956)

Crystal structure and magnetic properties of copper ferrite-chromite series are studied. The specimens were prepared from powders of pure cupric oxide, ferric oxide and chromic oxide by heating at 1000°C for several hours, then pressed in a mold and sintered at 900°C, and then treated in two manners: quenched (q) and slowly cooled (s) by the rate of 1°C per minute. Chemical analysis shows that each specimen coincides with the pre-arranged stoichiometric composition within two percent. Preliminary X-ray test confirms the compounds to have perfect spinel structure except for a few specimens which show slightly tetragonal distortion as stated later.

In general the spinels of copper ferrites-chromites are expressed as $(Cu_xFe_{1-x})[Cu_{1-x}Fe_{1+x-t}Cr_t]O_4$, where ( ) and [ ] mean respectively the tetrahedral and octahedral positions of cations in a spinel. To determine the cation arrangements of the series, intensities of the Debye-Scherrer patterns must be carefully measured. For this purpose filtered $K_\alpha$ radiations of Co, Mn and Cu were used. Patterns in each film were microphotometered and compared with the intensity scale provided preliminary to the same film. On the calculation of intensilies the Lorentz, polarization and geometrical factors were considered. In addition the depression of atomic scattering factors in the region of anormalous dispersion and a absorption due to the geometry and the sort of specimens were also considered. Here the difference of the atomic scattering factors of Fe and Cr ions is very small so that the arragement of Cu ions was only taken into account. The intensity ratios (400)/(220) and (400)/(422) are chosen to this aim because of the sensitiveness to the variation of the atomic arrangement. In the case of specimens with tetragonal symmentry (400)/(202) ratio is used instead of (400)/(220) ratio.

Thus the values of $x$ i.e. the amounts of Cu ions in tetrahedral position were determined to various values of $t$ i.e. the chromium contents. We see that $x$ increases monotonously from 0.18 to 0.9 for (q) and from 0.05 to 0.9 for (s) specimens. For the Cu ferrite ($t=0$) these values agree with Bertaut's results. Tetragonal distorsion detected in the (s) specimens of Cu ferrite diminishes with increase of Cr and disappears at $t=0.4$, further addition of Cr beyond $t=1.4$, however, causes again the tetragonal distortion both for (q) and for (s) specimens. From intensity relations it is found that the axial ratio c/a of Cu chromite is less than unity (0.91) contrary to the case of Cu ferrite. Hence Goodenough's explanation to the latter is not apllicable to the former.

The magnetization of the specimens were measured by Gouy's method under various temperatures. Maximum field strength used is 7000 Oe, which is thought to be enough strong to saturate the specimens. It is found that the Curie-temperature is lowered almost linealy to the Cr contents $t$. By extrapolation of the magnetization vs. temperature curves the saturation magnetic moments at 0°K of the series with various Cr contents are obtained. The value for copper chromite ($t=2$) agrees with the one obtained by MacGuire and his collaboraters. On the other hand we can get theoretically the saturation magnetic moments of these series from Néel's theory of ferrimagnetism. The agreement of the experiment and the theory is good only for the case $t=0$. For the specimens including Cr, on the contrary, dicrepancy of the experimental value and theoretical one assuming magnetic moment of Cr ion $3\mu_B$ becomes greater as shown in Fig. 1.

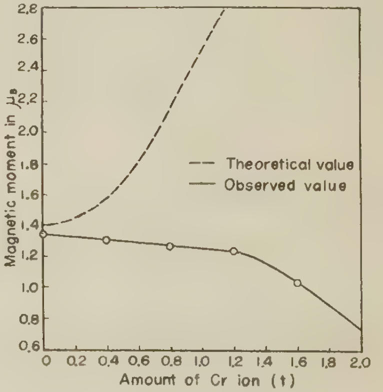

Fig. 1.

Detailed report including further discussion will be soon published.

### References

1) E. F. Bertaut: Compt. Rend. **230** (1950) 213 and J. Phys. Rad. **12** (1951) 252.

2) L. Néel: Ann. Physiques **3** (1948) 137.
3) D. Coster and K. S. Knol: Proc. Roy. Soc. **A 138** (1933) 459.
4) J. B. Goodenough and A. L. Loeb: Phys. Rev. **98** (1955) 391.
5) T. R. MacGuire, L. N. Howard and J. S. Smart: Ceramic Age **60** (1952) 22.

---

J. Phys. Soc. Japan **11** (1956) 1297

# A Method of Growing CdS Single Crystals by Sublimation

By S. Ibuki and K. Awazu

*Engineering Laboratory, Mitsubishi Elec.* Mfg. *Co., Ltd. Amagasaki, Hyogo*

(Received August 30, 1956)

Several methods of growing CdS single crystals have been reported as follows;

1. Growth by chemical reaction of Cd vapor with $H_2S$ gas in an inert gas atomosphere1).
2. Growth by chemical reaction of Cd vapor with S vapor in an inert gas atomosphere2).
3. Recrystallization of CdS powders in vacuum at high temperature3).
4. Recrystallization of CdS powders in a vessel which contains only $H_2S$ gas at high temperature4).

We report here another method utilizing the condensation of the sublimated vapor from CdS polycrystalline powders heated in $N_2$ gas flow onto the surface of an inserted cooling pipe.

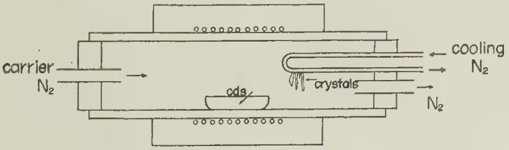

Fig. 1. Experimental arrangement.

Our apparatus is shown schematically in Fig. 1.

The crystal growth is performed in a quartz combustion tube. At first, $N_2$ gas is flowed through the tube, and the electric furnace is heated up. When the temperature of the center of the combustion tube is raised to about 1050°C to 1150°C, we insert a quartz boat containing CdS powders into the center of the combustion tube and then insert a pipe in which $N_2$ gas is flowing, from the exist side. As CdS in the boat gradually sublime, and the CdS-vapor deposits on the cooling pipe and the crystal growth starts only on the surface region of the cooling pipe where the temperature is between 900°C and 1000°C. After a few hours the size of the single crystal reaches to 10–20 mm long and 2–10 mm wide. Crystals grown are most commonly thinplates and ribbons which exhibit striations perpendicular to the length of crystals. When the temperature of the furnace is higher,there are some tendencies to develope twins with two or three wings. Some examples of crystals obtained are shown in Fig. 2, the max. size of which is about 20×12×0.3 or 25×3×0.1 mm.

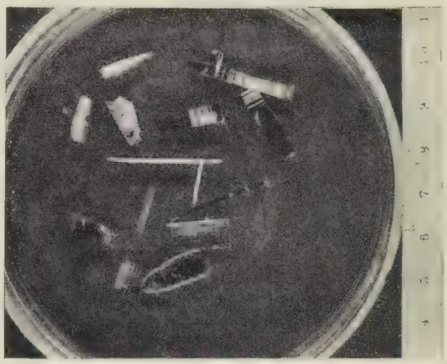

Fig. 2. Grown crystals.

It is necessary to clean perfectly the quartz combustion tube, the quartz boat and cooling pipe. The characteristics of grown crystals greatly depends on the purity of CdS polycrystalline powders in the quartz boat.

For controlling the crystal shape and size, it is essential to precisely adjust the flow velocity of carrier gas, the temperature of combustion tube and the size and temperature gradient of cooling pipe.

## References

1) R. Frerichs: Phys. Rev. **72** (1947) 595.
2) M. E. Bishop and S. H. Liebson: J. A. P. **24** (1953) 660
3) A. Halperin and G. F. J. Gorlick: Proc. Phys. Soc. **68B** (1955) 758
4) S. J. Czyzak et. al.: J.A.P. **23** (1952) 932.

J. Phys. Soc. Japan **11** (1956) 1298

# Double Hysteresis Loop of $(Pb_{\lambda}Ca_{1-\lambda})TiO_3$ Ceramics

By Etsuro SAWAGUCHI, Takeshi MITSUMA
and Zensho ISHII

*Electrotechnical Laboratory, Tanashi, Tokyo*

(Received September 26, 1956)

Dielectric and structural properties of $(Pb_{\lambda}Ca_{1-\lambda})TiO_3$ system have been examined. We have found so-called double hysteresis loop on the curve of electric displacement *vs* applied field. This sort of double hysteresis loop seems to be different from what is observed in $PbZrO_3$[1] and $BaTiO_3$[2].

X-ray Debye-Scherrer photographs of the solid solution were taken at room temperature. It has been concluded that the crystal structure at room temperature is tetragonal between $\lambda=1.0$ and *ca.* 0.6, while it is pseudo-cubic between $\lambda=0.6$ and 0. The result is shown in Fig. 1.

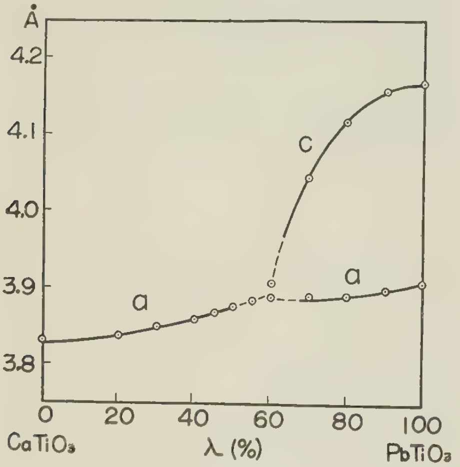

Fig. 1. Lattice spacing of $PbTiO_3$-$CaTiO_3$ system at room temperature.

At compositions between $\lambda=1.0$ and 0.7, the crystals are surely ferroelectric, but the hysteresis loops observed at room temperature are nearly straight lines. This is due to very strong coercive force. At compositions near $\lambda=0.6$, a typical ferroelectric hysteresis loop is observed.

In the sample $\lambda=0.5$, we have noticed many interesting behaviour on the hysteresis loop. Immediately after we quenched the sample in a silicone oil of room temperature from 200°C, which is sufficiently above the Curie point of *ca.* 80°C, the shape of the loop was like that of ferroelectrics. It changed gradually, however, and at some ten minutes after the quenching, it showed a shape of double hysteresis loop as shown in Fig. 2. During the course, no electric field was applied on the sample, except for a few second for taking photographs, during which an 50 cps a.c. field of 15 kv/cm was applied to display the loop on a cathod ray oscilloscope.

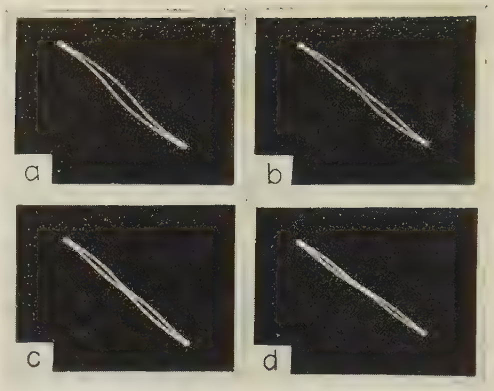

Fig. 2. Hysteresis loops of $(Pb_{0.5}Ca_{0.5})TiO_3$ observed at 30°C. a) at 10 seconds after the quenching; b) 5 minutes; c) 20 minutes; d) 4 hours.

The loop was affected remarkably by an electric field applied on the sample. When an a.c. field of 15 kv/cm was held for a few ten minutes, the double hysteresis character changed gradually into a ferroelectric one. After removing the field, the loop recovered gradually the original double hysteresis form. On the other hand, d.c. field treatment made the loop asymmetric. At first, d.c. field of 4 kv/cm was applied on the sample for 2 minutes at room temperature. Then even after the removal of the d.c. field, the shape of the loop was asymmetric. The effect was large when the d.c. field treatment was given just after the quenching of the sample.

The concavity that was clearly found on the loop (Fig. 2) became obscure with falling temperature of the sample. At temperatures below −30°C the double hysteresis character was hardly noticed on the loop.

It is well known that double hysteresis loop observed in $PbZrC_3$[1] and $BaTiO_3$[2] can be explained as a result of forced phase transition. But, the case of $(Pb_{0.5}Ca_{0.5})TiO_3$ would not be explained with the same mechanism, for we could not detect any evidence of occurence of the forced phase transition on the Debye-Scherrer photograph. It should be noteworthy to mention that a loop with very similar form to Fig. 2d have been observed by K. Kambe in $BaTiO_3$ ceramic[3] at 50°C, where a forced phase transition can hardly be expected to occur. Studies are going on to find the new kind of mechanism.

## References

1) G. Shirane, E. Sawaguchi and Y. Takagi: Phys. Rev. **84** (1951) 476.
2) W. J. Merz: Phys. Rev. **91** (1953) 513.
3) K. Kambe: J. Phys. Soc. Japan. **8** (1953) 15.

J. PHYS. SOC. JAPAN **12** (1956) 1299

# On the Pulse Breakdown of Plastic Films at Higher Temperatures

by Yoshio INUISHI

*Faculty of Engineering, Osaka University*

(Received July 13, 1956)

Pulse breakdown of "Mylar"* and polyethylene films were studied to examine high-temperature breakdown3),4) theries of amorphous substances.

Nearly square wave-shaped pulses were generated by the switching tube circuit. Extremely long pulses or *d-c* step voltages were shaped by manual operation of switch connected to a *d-c* source. Majority of pulse experiments were done in low repetition rate (1 pulse/10 sec.) and 10 trials were done at each voltage to minimize space charge and heating effect due to repetition. Samples were coated with aquadag on both sides and inserted between well polished brass electrodes. Whole electrode systems were immersed in xylene medium to avoid surface corona.

Figure 1 shows the pulse width dependency of the breakdown strength of Mylar films at several ambient temperatures. At lower temperatures the pulse width dependency is slight except for longer pulse (≳milliseconds). These phenomena cannot be explained by the classical thermal breakdown theory and should be electronic in their nature3),4). At longer pulse (≳several seconds) breakdown stress decreases very remarkably by the presence of high humidity as is shown in the dotted line in Fig. 1. Scattering of data becomes larger in longer pulses in comparison with shorter pulses. Accordingly, the decrease of breakdown stress at longer pulse might be mainly due to secondary effects such as local heating1) or ionic plus electronic space charge2). At higher temperatures both short pulse breakdown value and long pulse or *d-c* value decrease with increasing temperature as seen in Fig. 1. This decrease is much more remarkable in longer pulse than in shorter pulse. The decrease of breakdown strength with increasing temperature at short pulse ($\mu S$ range) cannot be explained by the above-mentioned secondary effects, and should be considered as an increase in conduction electron density due to impurity electron3) or valence band electron ionization4) at higher temperatures, since time lags can be extremely short in these cases.

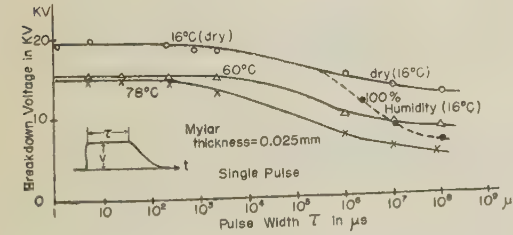

Fig. 1.

Fig. 2 shows the similar relation for polyethylene. Dotted line shows values for high reception rate (60 c/s) which are similar to single pulse values. This fact tells us that secondary factors such as local heating and space charge are negligible at short pulses. The same data are shown in Fig. 3 as the relations between temperature and breakdown strength for various pulse width in case of polyethylene. As is seen there, it is not adequate to compare various idealized high temperature breakdown theories with *d-c* experimental value which seems to be affected deeply by secondary factors1),5) such as local heating or space charge effect.

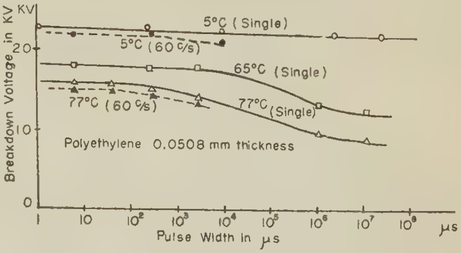

Fig. 2.

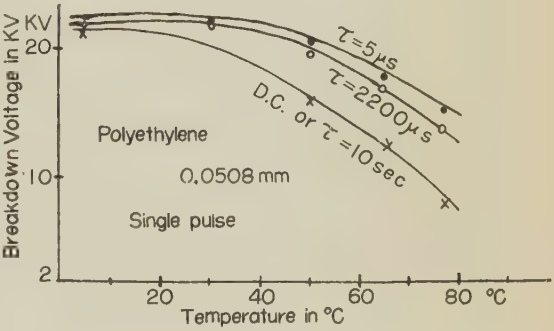

Fig. 3.

The secondary factors at *d-c* breakdown of Mylar have been investigated extensively by the author and D. A. Powers at the Laboratory for Insulation Research of M. I. T. and will be published in the near future.

## References

1) Keller: Physica **17** (1951) 511.
2) von Hippel and Alger: Phys. Rev. **76** (1949) 127; T. Suita: Tech. Rept. Osaka Univ. **1** (1951) 51.
3) Fröhlich: Proc. Roy. Soc. **A 188** (1947) 521.
4) Lehovec: Phys. Rev. **96** (1954) 921.
5) Vermeer: Physica **20** (1954) 313.

---

* Mylar is the commercial name of Dupont co. product of Polyethylene terephtalate.

J. Phys. Soc. Japan **11** (1956) 1300–1301

# Note on Superexchange Interactions and Magnetic Lattices, of the Rhombohedral Sesquioxides

By Shūichi IIDA

*Department of Physics, Faculty of Science, University of Tokyo*

(Received September 22, 1956)

Quite recently Y. Y. Li[1] has pointed out that there are three configurations responsible to the superexchange interactions M-O-M in the rhombohedral sesquioxides ($\alpha Fe_2O_3$, $Cr_2O_3$), in which the dominant interaction in $\alpha Fe_2O_3$ has negative sign while the same in $Cr_2O_3$ has positive sign. It has been stated by him that the dominant interaction alone does not cover the three-dimentional magnetic lattice and the interaction present in pseudo-molecular group should be considered as the next effective interaction.

However, it should be pointed out here that Li has missed the presence of another configuration responsible to the superexchange interaction. All of the interactions with close contacts of oxygen and cations are listed in Table I using the same notation as Li's. The distances of $M_1-M_2$ and the angle $\angle M_1OM_2$ are again calculated for $\alpha Fe_2O_3$ after the data used by Li ($a$=5.427A[3], $\alpha$=55°16′[3], $u$=0.105[4], $v$=0.295*). The actual ion arrangement is also shown in Fig. 1, as seen from [111] axis. Interaction (a)′ was dropped in Li's Table. (a)′ is important because it has the smallest *M-O* distances and a fairly large interaction angle.

Considering the presence of (a)′, the interpretation of the magnetic coupling in the rhombohedral sesquioxides might be different from that by Li's theory. It must be noticed that the coupling caused by (a) and (a)′ covers the three-dimentional magnetic lattice. In $\alpha Fe_2O_3$, the actual magnetic structure can be established by assuming that the dominant interactions are only in (a) and (a)′ and that both have negative sign. In $Cr_2O_3$, the situation is not so simple. An explanation might be possible that the effective superexchange interactions are also in (a) and (a)′, and (a) has positive sign while (a)′ has negative sign. There is some reason to expect that the sign of the superexchange interaction in this case depends on the equality of the two M-O distances. In (a) the two M-O distances are different and consequently, the Anderson term (positive sign) is dominant. Whereas in (a)′, the two M-O distances are equal and therefore, the Anderson-Hasegawa term[5] (negative sign) might be more effective that the Anderson term.

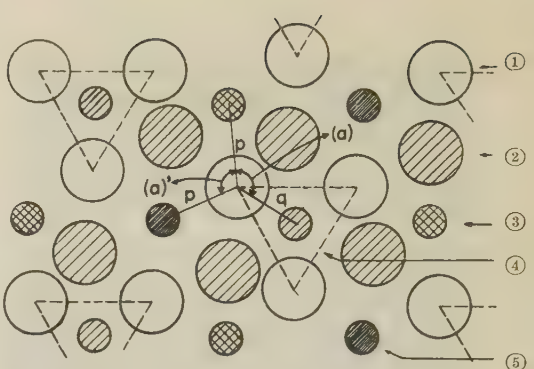

① Oxygen ion in basic layer.
② Oxygen ion in upper layer.
③ Cation belonging to lower pseudo-molecule.
④ Pseudo-molecule in basic layer.
⑤ Cation belonging to upper pseudo-molecule.

Fig. 1. The $Cr_2O_3$ lattice as seen from [111] axis. The large circles are the oxygen ions and the small ones, the cations. (a) and (a)′ superexchange interactions are shown in the figure.

We hope quantitative calculations are made to determine the total effect of the Anderson and Anderson-Hasegawa terms in (a) and (a)′ for $Cr_2O_3$.

## References

1) Y. Y. Li: Phys. Rev. **102** (1956) 1015.
2) B. N. Brockhouse: J. Chem. Phys. **21** (1953) 961.
3) B. T. M. Willis and H. P. Rooksby: Proc. Phys. Soc. (London) B. **65** (1952) 950.
4) R. W. G. Wyckoff: Crystal structures (Inter-

Table. I. The configurations of $M_1-O-M_2$ with close contacts between M and O. The distance of $M_1-M_2$ and the angle $\angle M_1OM_2$ are calculated for $\alpha$ $Fe_2O_3$. n is the number of oxygen ions forming the same triangular configuration with the same pair of cations. The notations A′, A″,···are defined in Li's paper.

| | | n | spin coupling in | | $M_1-O$ | $O-M_2$ | Fe−Fe | ∠FeOFe |
|---|---|---|---|---|---|---|---|---|
| | | | $Cr_2O_3$ | $\alpha Fe_2O_3$ | | | | |
| (a) | A′−O−C | 1 | ↑↑ | ↑↓ | $q$ | $p$ | 3.70 A | 132°41′ |
| (a)′ | B′−O−A″ | 1 | ↓↑ | ↑↓ | $p$ | $p$ | 3.37 A | 116°59′ |
| (b) | C−O−B′ | 2 | ↑↓ | ↑↑ | $p$<br>$q$ | $q$<br>$p$ | 2.97 A | 94°20′ |
| (c) | A′−O−B′ | 3 | ↑↓ | ↑↓ | $q$ | $q$ | 2.89 A | 88°23′ |

science Publications, Inc., New York, 1948), Vol. 1.
5) P. W. Anderson and H. Hasegawa: Unpublished (but see: T. Nagamiya, K. Yosida and R. Kubo, Advances in Physics **4** (1955) p. 64).

---

* Wyckoff's table[4] gives $v=0.292$. We do not know the original paper which gives $v=0.295$ (the value is used by Li).

---

J. PHYS. SOC. JAPAN **12** (1956) 1301

# On the Piezoelectric Effect of Silk Fibers

Eiichi FUKADA
*Kobayasi Institute of Physical Research*
*Kokubunji, Kitatama, Tokyo*

(Received August 31, 1956)

The piezoelectric effects in the various high polimeric materials as cellulose, collagen etc. have been already reported[1][2]. The piezoelectric effect in the silk fibers could be observed in the same way.

A number of native silk fibers were orientated in parallel to make the bundles. After drying for weeks in a decicater containing calcium chloride, they were immersed into the alcohlic solution of shellac, and dried in the air in order to evaporate the alcohol. These bundles were gathered and compressed at about 120°C so that the shellac melts and binds the silk fibers very closely. The solid block of orientated silk fibers was thus obtained.

The piezoelectric effect was observed most distinctly when the pressure was applied on the bundle of silk fibers in the direction making the angle of 45 degrees with the orientation axis of fibers. The behavior is quite similar to the case of wood, ramie bundles or bone. When the shearing force acts on the fibers to make them slip each other, the electrical polarization appears in the direction perpendicular to the plane of force.

The value of the piezoelectric constant of silk fibers was obtained by the measurement of the converse piezoelectric effect. It amounts to about $1.5\times10^{-8}$c.g.s.e.s.u., which is surprisingly high, compared with the piezoelectric constant of quartz crystal, $d_{11}=6.5\times10^{-8}$c.g.s.e.s.u.

The origin of the effect might be due to the crystalline properties of silk fibroin, which is known to be highly crystallized. The symmetry of unit cell of fibroin micelle is monoclinic, which is capable to yield the piezoelectric effect. The piezoelectric effect of silk fiber bundle will be the summary of contribution from a number of fibroin micelle which are distributed regularly in the fiber. If the layer composed of cerisin were removed from the silk fiber before the preparation of specimens, the larger piezoelectric effect could be observed.

## References

1) E. Fukada: J. Phys. Soc. Japan **10** (1955) 149.
2) E. Fukada and I. Yasuda: J. Phys. Soc. Japan, in print.

---

J. PHYS. SOC. JAPAN **12** (1956) 1301

# Frequency Shift in Ammonia Absorption

By Kiyokata MATSUURA, Yoshikazu SUGIURA
and G. M. HATOYAMA
*Electrotechnical Laboratory, Nagata-cho, Tokyo*

(Received October 16, 1956)

It had been widely accepted that the frequency of the centre of microwave absorption lines of Ammonia do not change appreciably with the state of the ammonia gas, provided the pressure is sufficiently low.

During the course of researches on atomic clock, we have found that the frequency of the centre of ammonia (3,3) absorption line does change apparently with the state of the gas.

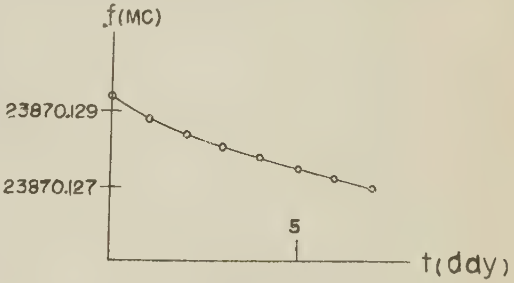

Fig. 1.

Fig. 1 shows an example of the variation of absorption frequency with the time lapsed after the gas is filled in the absorption cell. The absorption cell was about 23 m long, $K$-band wave-guide, filled with ammonia to an extent giving the half-value width of the line of about 200 Kc, and then left standing. The errors in the relative value of the frequencies does not exceed ±100 cps, or, 1 part in $2\times10^8$.

The difference between the frequency of the ammonia line measured immediately after filling the gas and that measured 2 days later amounted to 400±100 cps, from some ten measurements. This means a shift of about $2\times10^{-8}$ per day. This rate will depend, naturally, on experimental conditions.

This effect seems to be quite serious in designing an atomic clock based on the absorption of microwaves in ammonia. Experiments are going on to find out the nature of the phenomenon.

*Please Rush! and subscribe to*

# SUPPLEMENT
# PROGRESS OF THEORETICAL PHYSICS
# No. 3

Dear Subscriber,

We are publishing "SUPPLEMENT No. 3" to Progress of Theoretical Physics, which contains details of the recent researches made after the War by a Group of Japanese physicists, who developed the research on nuclear forces continuously, in close connection with the theory of meson field.

We should like to suggest that you place an order NOW so that we will be able to furnish you with a copy immediately upon publication.

Address to: Publication Office, Progress of Theoretical Physics, Yukawa Hall, Kyoto University, Kyoto, Japan.
Price: per part (postage inclusive)
overseas......$ 1.50; inland......¥ 500.
Date of Issue: November 20, 1956.

§ Please send checks on banks in dollars or pounds, or UNESCO book coupons, making them payable to the Publication Office, Progress of Theoretical Physics.

Yours sincerely,

PROGRESS OF THEORETICAL PHYSICS
Publication Office
Yukawa Hall, Kyoto University.

---

## Supplement of the Progress of Theoretical Physics

This supplemen is published for the purpose of surveying the development of theoretical physics in Japan. Each issue is devoted to a specified subject and contains either the reprints of papers by Japanese physicists which were published in various journals or the review articles on current topics.

**No. 1. Meson Theory I.** (*Formalism and Models*)
Price $ 1.50 (inland ¥ 500.00) Published in Nov. 1955

**No. 2. Meson Theory II.** (*Intermediate and Strong Coupling Theories*)
Price $ 1.50 (inland ¥ 500.00) Published in Jan. 1956

**No. 3. Meson Theory III.** (*Nuclear Forces*)

*Following issues are in preparation:*

**No. 4. Beta Disintegration.**

**No. 5. Meson Theory IV.** (*Scattering and Production of Mesons*)

**No. 6. Quantum Electrodynamics.**

**No. 7. Theory of Cosmic Rays.**

# Contents

## (Vol. 11)

### No. 1.

Itaru NONAKA, Susumu MORITA, Nawoyuki KAWAI, Toshiyuki ISHIMATSU, Shigeru SUEMATSU, Kenji TAKESHITA, Yutaka NAKAJIMA and Yoshihisa WAKUDA: On the Neutrons from the $N^{14}(d, n)O^{15}$ Reaction .................................. 1
Shoichiro KOIDE: A Lattice Theory of Quantum Fluids .......................... 7
Akira HARASIMA and Yoshihisa SHIMURA: Quantum Effects in the Theory of Surface Energy .................................................................. 14
Enji UCHIDA and Hisamoto KONDOH: Magnetic Properties of Nickel Telluride ........ 21
Enji UCHIDA, Hisamoto KONDOH and Nobuo FUKUOKA: Magnetic and Electrical Properties of Manganese Telluride .............................................. 27
Kei YOSHIDA and Tôru MORIYA: The Effects of Covalency on the Nuclear Magnetic Resonance in Ionic Crystals ................................................ 33
Kenjiro KAMBE and John F. OLLOM: Dipolar Broadening of the Central Line of a Magnetic Resonance for Half-integral Spin .................................. 50
Hiroshi KIMURA: On the Plastic Deformation of $\alpha$-brass Single Crystals by Compression .................................................................. 53
Kenzo YAMAMOTO and Takayoshi OKUDA: On the Floating Probe Method for the Measurement of Ionized Gas ............................................... 57
Hirosi HASUNUMA and Jiro NARA: On the Sheen Gloss ............................ 69
Saburo MIYAKE, Kensaku HINOTANI and Kan-ichi NUNOGAKI: A Cloud Chamber Study of the Cosmic-Ray Hard Showers ............................................. 76

### No. 2

Kazuko MOTIZUKI and Takeo NAGAMIYA: Theory of the Ortho-Para Conversion in Solid Hydrogen ................................................................ 93
Ryuji ABE: On Ferroelectric Barkhausen Pulses of Rochelle Salt ................... 104
Hiroshi WATANABE: Experimental Evidence for the Collective Nature of the Characteristic Energy Loss of Electrons in Solids—Studies on the Dispersion Relation of Plasma Frequency— ............................................ 112
Hiroshi KANZAKI: Observation of Dislocations in Silver Halides. Part I. Annealed Crystals .................................................................. 120
Hiroshi KANZAKI: Observation of Dislocations in Silver Halides. Part II. Strained Crystals .................................................................. 126
Susumu YOSHIDA: Electron Diffraction and Microscope Study of the Surface Structure of Copper Single Crystals ................................................ 129
J. SHIMADA, H. ABE and K. ÔNO: Paramagnetic Resonance Absorption in Copper Formate ................................................................... 137
Atsuo NISHIOKA and Ryuzo KOYAMA: Apparent Molecular Weight of Polytrifluorochloroethylene ........................................................... 139
Hideo TAKAMI: A Study of the Compressible Flow past a Cherry Profile ........... 145
Hakuro OGUCHI: Supersonic Jet with the Ambient Pressure corresponding to its Constant Pressure Point ........................................................ 155
Hiroshi FUJITA: On the Error of the Finite Difference Method in 1-dimensional Boundary Value Problems ........................................................... 160
Masao SUGAWARA: The Time Lag and other Undesirable Phenomena observed in Vacuum Photo-tubes at Weak Illumination I ....................................... 169

### No. 3

Hisashi MATSUDA: Focusing Properties of a large Mass Spectrograph newly constructed at Osaka University .............................................. 183
Shigeo NAKAGAWA, Eiji TAMAI, Humiaki HUZITA and Kiyoaki OKUDAIRA: On the Analysis of the Slow Particles Emitted from Cosmic-Ray Starts (I) ........... 191
Saburo MIYAKE: A High Pressure Cloud Chamber for Cosmic Ray Observation ...... 195
Ikuro SHIMOSE: Statistical Theory of Phase Transition III. Application to Vapor-Liquid-Solid Equilibrium ................................................... 202
Jiro SHIGETA: Oriented Overgrowth of Evaporated Crystallites. Fluoride Crystallites on Cleavage Surfaces of Single Crystals ....................................... 206

Tôru MORIYA, Kazuko MOTIZUKI, Junjiro KANAMORI and Takeo NAGAMIYA: On the Magnetic Anisotropy of FeF$_2$ and CoF$_2$ ... 211

Denjiro WATANABE and Shiro OGAWA: On the Superstructure of the Ordered Alloy Cu$_3$Pd I. Electron Diffraction Study ... 226

Eiji HIRAHARA and Miyuki MURAKAMI: Nuclear Magnetic Resonance Experiment on the Single Crystal of Lithium Sulfate Monohydrate, Li$_2$SO$_4$H$_2$O ... 239

Hiroshi MIZUTANI: Determination of the End-to-End Distance of High Polymer Molecule in Solution ... 245

Akira OKAYA: A Theoretical Analysis of the Magnetic Hyperfine Structure of the Microwave Spectrum of C$_{2v}$ Molecules ... 249

Akaira OKAYA: The Microwave Hyperfine Spectrum of Formaldehyde ... 258

Takashi ITOH: Molecular Structure of Methylamine ... 264

Masao SUGAWARA: The Time Lag and Other Undesirable Phenomena Observed in Vacuum Photo-tubes at Weak Illumination II ... 271

Masahumi NAGASE: Diffraction of Elastic Waves by a Spherical Surface ... 279

Sadatoshi TANEDA: Experimental Investigation of the Wakes behind Cylinders and Plates at Low Reynolds Numbers ... 302

Hiroji MITSUHASHI and Tadahisa NAKAYAMA: Apparatus for the Study of Spectral Response of Photoelectric Surface ... 308

Jiro OISHI, Mitsuru AWANO and Takeshi MOCHIZUKI: New Determination of the Temperature of Gold and Silver Points on the Thermodynamic Temperature Scale ... 311

Shoji KOJIMA and Kiyoe KATO: Statistical Study of Electron Avalanches in Gaseous Discharge ... 322

**No. 4**

Ryutaro ISHIWARI, Sukeaki YAMASHITA, Kazunori YUASA and KOZO MIYAKE: On the Ionization-energy Relation for Alpha-particles in Air ... 337

Seizabro KAGEYAMA: The Multiple Scattering of Fast Electrons ... 348

Akio YOSHIMORI and Yoshiharu KITANO: Theory of the Lattice Vibration of Graphite 352

Taro KIHARA, Yukio MIDZUNO and Shobu KANEKO: Virial Coefficients and Intermolecular Potential for Small Nonspherical Molecules ... 362

S. C. SAXENA: On the Two Schemes of Approximating the Transport Coefficients (Chapman—Cowling and Kihara) ... 367

Akio KOBAYASHI and Shinji KAWAJI: Adsorption and Surface Potential of Semiconductors, Part II. Surface Vacancies and its Reaction with Oxygen on ZnS .. 369

Hiroshi FUJIWARA: On the Application of the Thomas-Fermi-Dirac Method to the Study of the Residual Resistance of Binary Alloys containing Foreign Atoms in small Concentrations ... 376

Hideji SUZUKI, Susumu IKEDA and Sakae TAKEUCHI: Deformation of Thin Copper Crystals ... 382

Yasuhiro SHINNAKA: On the Metastable Transition and the Crystal Structure of Ammonium Nitrate (Tetragonal Modification) ... 393

Mieko TAKAGI: Electron-Diffraction Study of the Structure of Supercooled Liquid Bismuth ... 396

Jean Jacques TRILLAT, Nobuzo TERAO, Léa TERTIAN et Henri GERVAIS: Application de la Méthode de Décapage Ionique en Diffraction Electronique: Etude de la Structure de Dépôts Thermiques d'Or sur des Supports Cristallisés ou Amorphes 406

Misazo YAMAMOTO: The Visco-elastic Properties of Network Structure I. General Formalism ... 413

Kiyoshi MURAKAWA: The Quadrupole Moment of V$^{51}$ ... 422

Kikusaburo OSADA: Phosphorescence of Sodium- and Potassium-Acetates ... 425

Hisao YAGI: On the Absorption of Light by Colour-centres in the Region between F-band and M-band ... 430

Fumio TAMAKI: A Divergent Shock Tube for Obtaining Supersonic Flows ... 434

Kim, CHUL-SOO: Experimental Studies of Supersonic Flow past a Circular Cylinder .. 439

Hideo TAKAMI: A Study of the Compressible Flow past Tomotika-Tamada's Profiles .. 446

Yasoo MATUNOBU: Application of Imai's Transonic Approximation Method to the Compressible Flow past a Kaplan Bump ... 452

Hirohide MIWA: A Direct Reading Counting Rate Ratio Meter .................... 458

**No. 5**

Shobu KANEKO and Taro KIHARA: Second Virial Coefficient of Helium from the Square-well Potential .................... 471
Tokuo SUITA and Noriaki ITOH: Dielectric Breakdown and Pulse Conduction of Silver Halide Crystals .................... 474
Yasutada UEMURA: On the Coupled Dislocations along a Grain Boundary .................... 479
Kazuo KIMOTO: An Electron Diffraction Study on the Plastic Deformation of Aluminium Single Crystals .................... 485
Yoshikazu ISHIKAWA and Shozo SAWADA: The Study on Substances having the Ilmenite Structure I. Physical Properties of Synthesized $FeTiO_3$ and $NiTiO_3$ and $NiTiO_3$ Ceramics .................... 496
F. E. FUJITA, D. WATANABE, M. YAMAMOTO and S. OGAWA: Study of Plastic Deformation in Aluminium Crystals by Electron Diffraction and Electron Microscopy 502
Saiyu MARUYAMA and Hiroshi KIHO: Intersections of {301}, {101} Twin Bands in Tin .................... 516
Tadami TAOKA and Shoichiro AOYAGI: Electron Microscopic Study on the Structure of Mosaic Boundaries in Ni–Mn Single Crystal .................... 522
Goro HONJO, Norihisa KITAMURA, Kohji SHIMAOKA and Kazuhiro MIHAMA: Low Temperature Specimen Method for Electron Diffraction and Electron Microscopy .................... 527
Tadami TAOKA: Magnetic After-Effect in $Ni_3Mn$ Alloy .................... 537
Ryogo KUBO and Yukio OBATA: Note on the Paramagnetic Susceptibility and the Gyromagnetic Ratio in Metals .................... 547
Sōshin CHIKAZUMI: Study of Magnetic Annealing on $Ni_3Fe$ Single Crystal .................... 551
Hiroomi FUJIKAWA: The Forces Acting on Two Equal Circular Cylinders placed in a Uniform Stream at Low Values of Reynolds Number .................... 558
Mitutosi KAWAGUTI: On the Viscous Shear Flow around a Circular Cylinder II. Oseen's Approximation .................... 570
Ryuma KAWAMURA and Haruo SAITO: Reflection of Shock Waves—1 Pseudo-Stationary Case .................... 584
Sunao OGHI: On the Coarsening of Non-Sag Tungsten Lamp Filament Wires .................... 593
Itsuro KIMURA and Seiichiro KUMAGAI: Spark Ignition of Flowing Gases .................... 599

**No. 6**

Ikuro SHIMOSE: Lattice Theory of Liquid State .................... 615
Sigetosi TANISAKI: Growth Spirals on Crystals of $WO_3$ .................... 620
Terutaro NAKAMURA: On the Domain Structure of Rochelle Salt Crystal .................... 624
Toshinosuke MUTO and Hiroshi OKUNO: Electronic Structure of the Exction. I. Localized Exciton in KCl .................... 633
Sumitada ASANO and Yasuo TOMISHIMA: Calculation of the Cohesive Energy of Zincblende .................... 644
Kazuko MOTIZUKI and Takeo NAGAMIYA: Effect of Self-diffusion on the Orthopara Conversion in Oxygen Contaminated Solid Hydrogen .................... 654
Gunji SHINODA, Tatsuro SUZUKI and Susum KATO: The Soft X-ray Spectroscopy of the Solid State by the Electronic Differentiating Method: Aluminium $L_3$ .................... 657
Ichiro TSUBOKAWA: The Magnetic Properties of Chromium-Tellurium-Selenium System 662
Tokutaro HIRONE and Shu CHIBA: The Magnetic Properties of $FeSe_x$ with the NiAs Structure .................... 666
Yoshika MASUDA: Nuclear Magnetic Resonance in Molecular Chlorine Compounds .. 670
Yosiyuki TAKEISHI: Auger Ejection of Electrons from Barium Oxide by Inert Gas Ions and the Cathode Fall in the Normal Glow Discharges .................... 676
Hiroomi FUJIKAWA: The Forces acting on Two Circular Cylinders of arbitrary Radii placed in a Uniform Stream at Low Values of Reynolds Number .................... 680
Hiroshi SATO: Experimental Investigation on the Trasition of Laminar Separated Layer .................... 702
Takeo SAKURAI: The Flow past a Flat Plate accompanied with an Unsymmetric Dead Air at Mach Number 1 .................... 710

**No. 7**

Hisao YAGI: Transformations of Various Centres among Each Other in Coloured Alkali-halide Crystals ........ 723
Toshio MISAWA: A Note on the Extended Theory of the Junction Transistor........ 728
Yasuyoshi WATANABE: On the Electron Diffraction Patterns from the Oriented Silver Films........ 740
Norio KATO: Anomalous Enhancement of X-ray Reflection Intensity at the Boundary of Ground and Etched Regions on Crystal Surface ........ 748
Hachiro KOMATSU: Proton Magnetic Resonance Absorption Spectra of Long Chain Normal Primary Alcohol of Probable Carbon Number 32 ........ 755
Tutō NAKAMURA and Norikiyo URYŪ: On the Interionic Contributions to the Specific Heat of Cobalt Ammonium Tutton Salt $Co(NH_4)_2(SO_4)_2 6H_2O$ at Very Low Temperatures ........ 760
Norikiyo URYŪ: Note on the Magnetic Anisotoropy of the Cobalt Ammonium Tutton Salt $Co(NH_4)_2(SO_4)_2 \cdot H_2O$........ 770
Kiyoshi MURAKAWA: Hyperfine Structure of the Spectrum of Cu I and Test of the Hyperfine Structure Formulas ........ 774
Kiyoshi MURAKAWA: Isotope Shift in the Spectra of Ne II and W I ........ 778
Tetsuji NISHIKAWA: Fine Structure of $J=1 \leftarrow 0$ Transition due to Internal Rotation in Methyl Alcohol........ 781
Hajime NARUMI: On the Eigenvalue Problem in Terms of a Complete Set of the Casimir Operators ........ 786
Hidenori HASIMOTO: A Sphere Theorem on the Stokes Equation for Axisymmetric Viscous Flow ........ 793
Yoshio SHIBAOKA: On the Transverse Vibration of an Elliptic Plate with Clamped Edge ........ 797

**No. 8**

Masakazu MARUTAKE: A Calculation of Physical Constants of Ceramic Barium Titanate ........ 807
Masakazu MARUTAKE and Takuro IKEDA: Elastic Constants of Porous Materials, Especially of $BaTiO_3$ Ceramics ........ 814
Otohiko NOMOTO: Irreversible Production of Entropy and the Absorption of Sound .. 818
Otohiko NOMOTO: Theory of the Ultrasonic Absorption in Aqueous Solution (I). Introduction and General Theory ........ 827
Taizo IRIE: Magnetoresistance Effect of Lead Sulphide Group of Semiconductors I. Measurements on Natural Specimens of Lead Sulphide ........ 840
Shūichi IIDA: Phase Diagram of Iron-Cobalt-Oxygen System (I) Experimental Study.. 846
Yasuaki NAKAGAWA: Change of Magnetic Susceptibility of Transition Metals and Alloys at their Melting Points ........ 855
Yukito TANABE and Satoru SUGANO: On the Absorption Spectra of Complex Ions, III. The Calculation of the Crystalline Field Strength ........ 864
Michiru YASUHARA: On the Hypersonic Viscous Flow past Slender Bodies of Revolution ........ 878
Yasaku WADA and Keiji YAMAMOTO: Temperature Dependence of Velocity and Attenuation of Ultrasonic Waves in High Polymers ........ 887

**No. 9**

Akira ISOYA, Kazuo GOTO and Teruo MOMOTA: The Angular Distribution of α-particles from the Reaction $^{19}F(p\alpha)^{16}O^*(\pi)^{16}O$ ........ 899
Makoto HIRABAYASHI and Shiro OGAWA: An X-ray Study of Ordering Processes in CuAu Single Crystals........ 907
Shigenobu SHIGETOMI and Sigeyasu MORI: Electrical Properties of $Bi_2Te_3$........ 915
Hiroshi TAKETA and Tutô NAKAMURA: A Note on the Ground State of Antiferromagnetism ........ 919
Shoichiro NOMURA: Solid State Reaction between Barium Titanate and Strontium Titanate ........ 924
Atsushi OKAZAKI and Kinshiro HIRAKAWA: Structural Study of Iron Selenides $FeSe_x$. I. Ordered Arrangement of Defects of Fe Atoms ........ 930

Shoichi ANNAKA: Determination of Elastic Constants of Metals and Alloys by Temperature Diffuse Scattering of X-Rays .......... 937
Tadao KASUYA: Temperature Dependence of Anisotropy Energy of Ferromagnetics .. 944
Hidetaro ABE and Kazuo ŌNO: Paramagnetic Resonance Spectra of Some Cupric Salts (I) .......... 947
Kineo TSUKADA: Zeeman Splitting of Nuclear Quadrupole Resonance Line of Iodine .. 956
Shoji KOJIMA, Shizuko OGAWA, Shigeo HAGIWARA, Yoshihito ABE and Midori MINEMATSU: Structure of Nuclear Quadrupole Resonance Line I. Solid Iodine...... 964
Masayoshi NINOMIYA: Rotational Intensity Distribution of the OH Band .......... 970
Nobuyoshi MORITA: Optical Properties of Magnesium Fluoride Films .......... 975
Yukito TANABE: On the Expansion Formula of Atomic Orbitals in Spherical Harmonics around Another Center .......... 980
Akira SAKURAI: The Flow due to Impulsive Motion of a Wedge, II .......... 987
Joseph GILLIS: Heat Loss from a Partially Insulated Solid Body .......... 993
Yorisaburo TAKAISI: Note on the Drag on a Circular Cylinder moving with Low Speeds in a Semi-infinite Viscous Liquid bounded by a Plane Wall ..........1004
Yorisaburo TAKAISI: Note on the Drag on a Circular Cylinder moving with Low Speeds in a Viscous Liquid between Two Parallel Walls ..........1009

**No. 10**

S. HIGASHI, I. HIGASHINO, M. ODA, T. OSHIO, H. SHIBATA, K. WATANABE and Y. WATASE: On the Interaction of Cosmic Radiation with Materials at 32 m.w.e. and 200 m.w.e. Underground ..........1021
Hazime MORI: A Quantum-statistical Theory of Transport Processes ..........1029
Yukio MIDZUNO and Taro KIHARA: Non-additive Intermolecular Potential in Gases I. van der Waals Interactions ..........1045
Saburo KOBA, Shobu KANEKO and Taro KIHARA: Non-additive Intermolecular Potential in Gases. II. Cluster Integrals..........1050
Koreo KINOSITA and Jun NAKAYAMA: Spiral Cleavage of Mica ..........1055
Shin-ya MIYATANI: Point Contact of Pt and $\gamma$-Cu$_2$S ..........1059
Hazimu KAWAMURA, Eizo OTSUKA and Keiko ISHIWATARI: The Quadrupolar Effect in Alkali Halide Mixed Crystals ..........1064
Denjiro WATANABE: Electron Diffraction Study on Thin Alloy Films of Aluminium-Silver System ..........1072
Masao SHIMIZU: A Note on the Ferromagnetic Resonance in $\alpha$ Fe$_2$O$_3$ ..........1078
Tokutaro HIRONE, Seijiro MAEDA, Ichiro TSUBOKAWA: On the Magnetic Properties of the System MnSb–CrSb ..........1083
Yoshio SHIBAOKA: On the Buckling of an Elliptic Plate with Clamped Edge I ......1088
Yorisaburo TAKAISHI: The Drag on a Circular Cylinder placed in a Stream of Viscous Liquid midway between Two Parallel Planes ..........1092
Hiroshi TSUJI: Experimental Studies on the Spectrum of Isotopic Turbulence behind Two Grids ..........1096
Sadatoshi TANEDA: Experimental Investigation of the Wake behind a Sphere at Low Reynolds Numbers ..........1104
Saburo MUROGA: On the Capacity of a Discrete Channel, II. Mathematical Expression of the Capacity of a Noisy Channel which is Expressible by Corresponding Two Multi-state Diagrams ..........1109

**No. 11**

Shin-ichi KANEKO, Osamu KUSUMOTO and Shigeo MATSUMOTO: Observation of the High-Energy Proton-Proton Collision in Photographic Emulsion ..........1129
Yasumitsu SHIMOMURA, Morio KOJIMA and Shozo SAITO: Crystal Structure of Ferromagnetic Nickel Oxide ..........1136
Otohiko NOMOTO: State of Association of Water Molecules in Aqueous Solutions as deduced from Sound Velocity Data ..........1146
Hideo TAKAKI and Toshiro TSUJI: The Measurement of Magnetostriction by means of Strain Gauge ..........1153
Tadao HORIE, Takayuki NAGURA and Masamoto OTSUKA: Radiative Collisions between Electric and Molecular Beams I. Angular Momentum Distribution among OH* Radicals resulting from H$_2$O Molecules ..........1157

Hiroshi KAMIMURA: On the Magnetic Moment and $g$-Value of Complex Ions ........ 1171
J. C. COOKE: On Rayleigh's Problem for a General Cylinder ........ 1181
Yoshikazu ISHIKAWA and Shozo SAWADA: Effective Use of Radiation and Thermal Shields in a Vacuum Furnace ........ 1184
Yoshirō ŌMORI: A Device for Calibration of Anemometers for Air Flow of Low Velocities ........ 1191

**No. 12**

Kiichi KIMURA, Isao KUMABE, Kozo MIYAKE, Hiroshi OGATA: The Reaction $O^{16}(n, \alpha)C^{13}$ .. 1211
Jun-ichi HORI: On the Equivalence of Fluctuation-Dissipation Theorem and Irreversible Thermodynamics ........ 1220
Sukeaki HOSOYA, Seiya SATAKE and Satio TAKAGI: On the Polygonization of Rock Salt Crystals ........ 1228
Sukeaki HOSOYA: On the Polygonized Domain Pattern in Bent and Annealed NaCl Crystals Cisualized by Colour Centre Colloids ........ 1231
Shozo SAWADA: Thermal and Electrical Properties of Tungsten Oxide ($WO_3$) ........ 1237
Shozo SAWADA: Microscopic and X-ray Studies on Tungsten Oxide ($WO_3$) ........ 1246
Shuichiro TAKAHASHI: Internal Friction and Critical Stress of Copper Alloys ........ 1253
Eiko AIHARA and Kazuo NIIRA: The Bond Orbital Approximation for $\pi$-electron System in Benzene ........ 1261
Toshizo NAKAYA: Influence of Illumination from Outside on an Ar–Hg Discharge Tube ........ 1264
Itiro TANI and Hiroshi SATO: Boundary-Layer Transition by Roughness Element ........ 1284
Yoshio YASUOKA: On the Space Charge affected by the Magnetic Field Part II ........ 1292

## SHORT NOTES

**No. 1**

Yasuo KANAI and Riro NII: On the Impurity Conduction in Germanium ........ 83
Kazuo TORIZUKA: Pure Quadrupole Spectra of Phosphonitrile Chloride Polymers ........ 84
Yasaburo YOKOZAWA and Itaru TATSUZAKI: Sub-microwave Absorptions in Potassium Bromate ........ 85
Kuni IMAEDA and Mitsuko KAZUNO: An Analysis of Two $\tau$-Meson Decays ........ 85
Shigenori NAWATA: On the Image of Phase Microscope in Metastable Region ........ 87
Toshihiro OKADA: The Measurement of the Galvanomagnetic Tensors of Bismuth ........ 89
Shōji TANAKA, Taizō MASUMI and Sigeru IIJIMA: Change of Photocurrent of CdS Single Crystal in a Magnetic Field ........ 90
M. SHIMOJI: On the Transition Temperatures of Superlatties $Au_3Cu$ and $AuCu_3$ ........ 91

**No. 2**

Syôiti KOBAYASI: Energy Band Structure of the Carborundum SiC Crystal ........ 175
E. YAMAKA and K. SAWAMOTO: Photo-induced Hall Effect of V-center in KI ........ 176
Takayoshi OKUDA and Kenzo YAMAMOTO: Disturbance by Probe in Plasma ........ 177
KIM, Chul-Soo and Kôichi ÔSHIMA: Experimental Studies of the Interaction of a Plane Shock Wave with a Circular Cylinder ........ 178
Atsuo NISHIOKA, Kyozo SEKIKAWA and Masakazu OWAKI: Effect of $Fe_2O_3$ on the Properties of Barium Titanate Single Crystals ........ 180

**No. 3**

Tadao FUJIMURA and Yoshiharu TORIZUKA: Ferromagnetic Resonance Absorption in a Pyrrhotite Single Crystal ........ 327
Kayako TANAKA, Hidetaro ABE and Hideyo MANIWA: Variation of the Young's Modulus of the Alloy $Mg_3Cd$ with the Order-Disorder Transition ........ 328
Masige NAGAI: Graphical Solution of Linear Heat Flow with Radiation ........ 329
Isao OSHIDA and Ohi HORIGUCHI: Hydration of Ions and Coordinate Bond ........ 330
Takuzo SHINDO: A Note on the Theory of Dislocation in Germanium ........ 331
Jun KOKAME and Sukeaki YAMASHITA: Electrostatic Deflection of a Cyclotron Ion Beam ........ 332

Hiromasa **HIRAWA**, Akira **MIYAHARA** and Koichi **SHIMODA**: Microwave Spectra of Formaldehyde and Methylamine in the SHF Region ........ 334
Akira **MIYAHARA**, Hiromasa **HIRAKAWA** and Koichi **SHIMODA**: *l*-Type Doubling Spectra of HCN and DCN in the SHF Region ........ 335

**No. 4**

Y. **MIZUSHIMA**, S. **HIROTA** and H. **NOAKE**: Specimen Contamination in Electron-microscope ........ 463
Hatsujiro **HASHIMOTO**, Eiji **YODA** and Hiroshi **MAEDA**: On the Elastic Scattering of Electrons observed in Kikuchi Patterns ........ 464
Enji **UCHIDA**: Note on the Ferromagnetism of CoTe ........ 465
Morihiko **KIMATA** and Tsutomu **NOMURA**: On the Electroluminescence in ZnS phosphor.. 466
Terutaro **NAKAMURA**: On the Correlation between Screw Dislocations and Twin Structure in $WO_3$ Crystal ........ 467
Alan K. **HEAD**: The Effect of Frequency on the Fatigue of Metals ........ 468
Atsushi **OKAZAKI** and Ikuhiko **UEDA**: The Crystal Structure of Stannous Selenide SnSe ........ 470

**No. 5**

Satoshi **TANIGUCHI** and Mikio **YAMAMOTO**: On the Uniaxial Anisotropy Induced by Magnetic Annealing in Ferrites ........ 604
Chiyoe **YAMANAKA**, Hidetsugu **SAKAI** and Tokuo **SUITA**: Electron Bombardment Conductivity in Silver Bromide Single Crystall II ........ 605
Takahiko **KAMIGAICHI**, Tadamiki **HIHARA**, Hideo **TAZAKI** and Eiji **HIRAHARA**: Electrical Conductivity of Iron Sulfides Single Crystals at the Temperature Range of $\alpha$-transformation ........ 606
Miyuki **MURAKAMI** and Eiji **HIRAHARA**: On the Lithium Resonance in Lithium Sulfate Monohydrate $Li_2SO_4 \cdot H_2O$ ........ 607
Sigeharu **KOSHINO**: On the Low Temperature Conduction Phenomena in Semiconductors ........ 608
Sigehiro **KOBAYASHI**: Fermi Part $\eta_0$ of the TF Function for Free Positive Ion ...... 609
Hirosi **TUBOTA**, Hiromichi **SUZUKI** and On **MATUMURA**: The Temperature Dependence of the Optical Absorption of Zinc Selenide ........ 610
Hidenori **HASIMOTO**: Note on Rayleigh's Problem for a Circular Cylinder with Uniform Suction and Related Unsteady Flow Problem ........ 611
Teturo **INUI**, Susumu **HARASAWA** and Yukio **OBATA**: Note on the Electron Spin Resonance of the $V_1$-center ........ 612

**No. 6**

Takeo **YOKOBORI**: On the Frequency Dependence of the Fatigue of Metals ........ 715
Kimio **HASHIMOTO** and Kazuyosi **HIRAKAWA**: Electrical Properties of Stannous Telluride SnTe ........ 716
Tadanobu **KOJIMA**: Mechanism for Self-Diffusion in Metallic Lithium ........ 717
Jiro **YAMAGUCHI**: On the Inductive Reactance and Negative Resistance in the Transistor ........ 717
Sōshin **CHIKAZUMI**: On the Interpretation of Magnetic Torque Reversal ........ 718
Bogdan **SUJAK**: A Remark on the Excitement of the Electrodes when a Positive Joshi Effect Inversion is Observed under Continuous Dischange ........ 719

**No. 7**

Shoichiro **NOMURA**: On a Change of Dielectric Property of $(Ba_{0.5} \cdot Sr_{0.5})TiO_3$ Ceramics due to the Thermal Treatment ........ 803
Kiyoshi **MURAKAWA**: Nuclear Spins of Dy 163 and Dy 161 ........ 804
Shoji **KOJIMA**, Kiyoe **KATO** and Shoichi **ANNAKA**: Radio Frequency Absorption in Barium Chlorate ........ 805

**No. 8**

Y. **MIZUSHIMA** and O. **OCHI**: Recovery Process in the Evaporated Metal Films ...... 893

Wataru SASAKI and Yasuo KANAI: Galvanomagnetic Effects of a Heavily Doped Germanium Crystal ........ 894
Tadayasu MITUI: Influence of Magnetic Field on the Precipitation Process of Ferromagnetic Phase in Gu-Fe Alloy (I) ........ 895
Hidetaro ABE and Mieko OHTSUKA: Paramagnetic Resonance Absorption in Copper Hexapyridine Nitrate ........ 896
Kōji SUMINO and Mikio YAMAMOTO: Interaction of Dislocations with Atomic Order in Solid Solution ........ 897
Makoto KIKUCHI: Some Experiments on the Germanium Surface Layer ........ 898

**No. 9**

Takeshi MIYAUCHI and Harunobu KIMURA: Electrical Properties of Cd-Sb ........ 1013
Kikusaburo OSADA: The Effect of Adsorbed Water on the Phosphorescence of Sodium Acetate ........ 1014
Hazime KUSUMOTO: Proton Magnetic Resonance in Polyisoprene, Polychloroprene and Polyisobutylene ........ 1015
Muneyuki DATE: Anomalous Line Broadening of Paramagnetic Resonance Lines in $Cu(NH_3)_4SO_4H_2O$ at Liquid Helium Temperatures ........ 1016
Yasuo KANAI and Wataru SASAKI: Oscillatory Galvanomagnetic Effects in $n$-type Indium Antimonide ........ 1017
Hiroshi FUJITA: The Zero-Time Correction in Free Diffusion Experiments ........ 1018

**No. 10**

Mitsuo IDA: On the Dielectric Anomaly of $n$-Higher Alcohols in the "Waxy State" .. 1121
Ichiro NAKADA: Surface Potential and Surface Conduction of Molybdenite ........ 1122
Takahiko KAMIGAICHI, Tadamiki HIHARA, Hideo TAZAKI and Eiji HIRAHARA: Magnetic Anisotropy of the Iron Sulfide Crystal at $\alpha$-Transformation Temperature ........ 1123
Noriaki ITOH and Tokuo SUITA: Photoconduction of Silver Chloride Crystals ........ 1124
Hiroyuki MIZUNO: On the Conducting Mechanism of Oxide Coated Cathode ........ 1125
Tatsuo YAJIMA: Emitter Current Noise in Junction Transister ........ 1126
Makoto KIKUCHI and Seiichi DENDA: A Microscopy Study of Etched Germanium Surfaces ........ 1127

**No. 11**

F. Eiichi FUJITA: A Possible Mechanism for the Fracture of Metals ........ 1201
W. SASAKI and M. SHIBUYA: Experimental Evidence of the Anisotropy of Hot Electrons in $n$-type Germanium ........ 1202
Yasaku WADA: Pressure Dependence of Sound Velocity in Organic Liquids ........ 1203
Masao ATOJI: The Electron Density of the Thomas-Fermi Atom in Crystals ........ 1204
Shigeo NAGAO: Bubble Chamber Study of Electric Breakdown of Liquid ........ 1205
Susumu YOSHIDA and Yûko TSUYA: The Temperature Dependence of the Electrical Resistivity of the $\beta$-phase Titanium-Molybdenum Alloys ........ 1206
Hiromasa HIRAKAWA, Takeshi OKA and Koichi SHIMODA: Microwave Spectra of Formaldehyde-$d_1$-$d_2$ ........ 1207
Ali. A. K. IBRAHIM : On the Oscillating Cylinder Viscometer for Elastic Liquids II .. 1208
Hiromasa HIRAKAWA, Takeshi OKA and Koichi SHIMODA: $l$-type Doubling Spectra of HCN and DCN ........ 1208

**No. 12**

Syohei MIYAHARA and Haruyuki OHNISHI: Cation Arrangement and Magnetic Properties of Copper Ferrite-Chromite Series ........ 1296
Sumiaki IBUKI and Kenzō AWAZU: A Method of Growing CdS Single Crystals by Sublimation ........ 1297
Etsuro SAWAGUCHI, Takeshi MITSUMA and Zensho ISHII: Double Hysteresis Loop of $(Pb_\lambda Ca_{1-\lambda})TiO_3$ Ceramics ........ 1298
Yoshio INUISHI: On the Pulse Breakdown of Plastic Films at Higher Temperatures .. 1299
Shûichi IIDA: Note on Superexchange Interactions and Magnetic Lattices of the Rhombohedral Sesquioxides ........ 1300

Eiichi FUKADA: On the Piezoelectric Effect of Silk Fibers ..........................1301
Kiyokata MATSUURA, Yoshikazu SUGIURA and G. M. HATOYAMA: Frequency Shift in Ammonia Absorption ........................................................1301

## Erratum

Kanji HONDA and Yoshihide NAITO: On the Nature of Silent Electric Discharge...... 92
Kiyoshi MURAKAWA: Hyperfine Structure of the Spectrum of Ruthenium. Part III.. 182
Akira SAKURAI: Decrement of Blast Wave .......................................... 613
Hidenori HASIMOTO: Note on Rayleigh's Problem for a Circular Cylinder with Uniform Suction and Related Unsteady Flow Problem ................................ 721
Yukichi NOMURA and Shigetoshi KATSURA: Diffraction of Electromagnetic Waves by Circular Plate and Hole...................................................... 806
Alan K. HEAD: The Effect of Frequency on the Fatigue of Metals .................. 806
Hiroshi SATO: Experimental Investigation on the Transition of Laminar Separated Layer ..............................................................1128
S. Kojima: Structure of NQR Line I. Solid Iodine ..............................1128

# AUTHOR INDEX TO Vol. 11

ABE Hidetaro;
  J. SHIMADA, ——— and K. ŌNO: Paramagnetic Resonance Absorption in Copper Formate ........ 137
  K. TANAKA, ——— and H. MANIWA: Variation of the Young's Modulus of the Alloy $Mg_3Cd$ with the Order-Disorder Transition ........ 328
  —— and M. OHTSUKA: Paramagnetic Resonance Absorption in Copper Hexapyridine Nitrate ........ 896
  ——— and K. ŌNO: Paramagnetic Resonance Spectra of Some Cupric Salts (I) ........ 947
ABE Ryuji: On Ferroelectric Barkhausen Pulses of Rochelle Salt ........ 104
ABE Yoshihito;
  S. KOJIMA, S. OGAWA, S. HAGIWARA, ——— and M. MINEMATSU: Structure of Nuclear Quadrupole Resonance Line I. Solid Iodine ........ 964
AIHARA Eiko;
  ——— and K. NIIRA: The Bond Orbital Approximation for $\pi$-electron System in Benzene ........ 12
ANNAKA Shoichi;
  S. KOJIMA, K. KATO and ———: Radio Frequency Absorption in Barium Chlorate ........ 805
  ———: Determination of Elastic Constants of Metals and Alloys by Temperature Diffuse Scattering of X-Rays ........ 937
AOYAGI Shoichiro;
  T. TAOKA and ———: Electron Microscopic Study on the Structure of Mosaic Boundaries in Ni-Mn Single Crystal ........ 522
ASANO Sumitada;
  ——— and Y. TOMISHIMA: Calculation of the Cohesive Energy of Zincblende.. 644
ATOJI Masao: The Electron Density of the Thomas-Fermi Atom in Crystals ........1204
AWANO Mitsuru;
  J. OISHI, ——— and T. MOCHIZUKI: New Determination of the Temperature of Gold and Silver Points on the Thermodynamic Temperature Scale ...... 311
AWAZU Kenzō;
  S. IBUKI and ———: A Method of Growing CdS Single Crystals by Sublimation.1297
CHIBA Shu;
  T. HIRONE and ———: The Magnetic Properties of $FeSe_x$ with the NiAs Structure ........ 666
CHIKAZUMI Sōshin: Study of Magnetic Annealing on $Ni_3Fe$ Single Crystal ........ 551
  ———: On the Interpretation of Magnetic Torque Reversal ........ 718
COOKE J. C.: On Rayleigh's Problem for a General Cylinder ........1181
DATE Muneyuki: Anomalous Line Broadening of Paramagnetic Resonance Lines in $Cu(NH_3)_4SO_4H_2O$ at Liquid Helium Temperatures ........1016
DENDA Seiichi ;
  M. KIKUCHI and ———: A Microscopy Study of Etched Germanium Surfaces..1127
FUJIKAWA Hiroomi: The Forces Acting on Two Equal Circular Cylinders placed in a Uniform Stream at Low Values of Reynolds Number ........ 558
  ——: The Forces acting on Two Circular Cylinders of arbitrary Radii placed in a Uniform Stream at Low Values of Reynolds Number........ 690
FUJIMURA Tadao;
  ——— and Y. TORIZUKA: Ferromagnetic Resonance Absorption in a Pyrrhotite Single Crystal ........ 327
FUJITA F. Eiichi;
  —, D. WATANABE, M. YAMAMOTO and S. OGAWA: Study of Plastic Deformation in Aluminium Crystals by Electron Diffraction and Electron Microscopy ........ 502
  ———: A Possible Mechanism for the Fracture of Metals ........1201
FUJITA Hiroshi: On the Error of the Finite Difference Method in 1-dimensional Boundary Value Problems........ 160
  ———: The Zero-Time Correction in Free Diffusion Experiments........1018

FUJIWARA Hiroshi: On the Application of the Thomas-Fermi-Dirac Method to the Study of the Residual Resistance of Binary Alloys containing Foreign Atoms in small Concentrations ........ 376
FUKADA Eiichi: On the Piezoelectric Effect of Silk Fibers ........ 1301
FUKUOKA Nobuo;
    E. UCHIDA, H. KONDOH and ———: Magnetic and Electrical Properties of Manganese Telluride ........ 27
GERVAIS Henri;
    J. J. TRILLAT, N. TERAO, L. TERTIAN et ———: Application de la Methode de Decapage Ionique en Diffraction Electronique: Etude de la Structure de Dépots Thermiques d'Or sur des Supports Cristallisés ou Amorphes ........ 406
GILLIS Joseph: Heat Loss from a Partially Insulated Solid Body ........ 993
GOTO Kazuo;
    A. ISOYA, ——— and T. MOMOTA: The Angular Distribution of $\alpha$-particles from the Reaction $^{19}F(p\alpha)^{16}O^*(\pi)^{16}O$ ........ 899
HAGIWARA Shigeo;
    S. KOJIMA, S. OGAWA, ———, Y. ABE and M. MINEMATSU: Structure of Nuclear Quadrupole Resonance Line I. Solid Iodine ........ 964
HARASAWA Susumu;
    T. INUI, ——— and Y. OBATA: Note on the Electron Spin Resonance of the $V_1$-center ........ 612
HARASIMA Akira;
    ——— and Y. SHIMURA: Quantum Effects in the Theory of Surface Energy.. 14
HASHIMOTO Hatsujiro;
    ———, E. YODA and H. MAEDA: On the Elastic Scattering of Electrons observed in Kikuchi Patterns ........ 464
HASHIMOTO Kimio;
    ——— and K. HIRAKAWA: Electrical Properties of Stannous Telluride SnTe.. 716
HASIMOTO Hidenori: Note on Rayleigh's Problem for a Circular Cylinder with Uniform Suction and Related Unsteady Flow Problem ........ 611
    ———: (Errata) Note on Rayleigh's Problem for a Circular Cylinder with Uniform Suction and Related Unsteady Flow Problem ........ 721
    ———: A Sphere Theorem on the Stokes Equation for Axisymmetric Viscous Flow ........ 793
HASUNUMA Hirosi;
    ——— and J. NARA: On the Sheen Gloss ........ 69
HATOYAMA G. Mitio;
    K. MATSUURA, Y. SUGIURA and ———: Frequency Shift in Ammonia Absorption ........
HEAD Alan K.: The Effect of Frequency on the Fatigue of Metals ........ 468
    ———: (Errata) The Effect of Frequency on the Fatigue of Metals ........ 806
HIGASHI Shigeru;
    ———, I. HIGASHINO, M. ODA, T. OSHIO, H. SHIBATA, K. WATANABE and Y. WATASE: On the Interaction of Cosmic Radiation with Materials at 32 m.w.e. and 200 m.w.e. Uuderground ........ 1021
HIGASHINO Ichiro;
    S. HIGASHI, ———, M. ODA, T. OSHIO, H. SHIBATA, K. WATANABE and Y. WATASE: On the Interaction of Cosmic Radiation with Materials at 32 m.w.e. and 200 m.w.e. Underground ........ 1021
HIHARA Tadamiki;
    T. KAMIGAICHI, ———, H. TAZAKI and E. HIRAHARA: Electrical Conductivity of Iron Sulfides Single Crystals at the Temperature Range of $\alpha$-transformation.. 606
    T. KAMIGAICHI, ———, H. TAZAKI and E. HIRAHARA: Magnetic Anisotropy of the Iron Sulfide Single Crystal at $\alpha$-Transformation Temperature ........ 1123
HINOTANI Kensaku;
    S. MIYAKE, ——— and K. NUNOGAKI: A Cloud Chamber Study of the Cosmic-Ray Hard Showers ........ 76

HIRABAYASHI Makoto;

——— and S. OGAWA: An X-ray Study of Ordering Processes in CuAu Single Crystals .......... 907

HIRAHARA Eiji;

——— and M. MURAKAMI: Nuclear Magnetic Resonance Experiment on the Single Crystal of Lithium Sulfate Monohydrate, $Li_2SO_4 \cdot H_2O$ .......... 239

T. KAMIGAICHI, T. HIHARA, H. TAZAKI and ———: Electrical Conductivity of Iron Sulfides Single Crystals at the Temperature Range of α-transformation.. 606

M. MURAKAMI and ———: On the Lithium Resonance in Lithium Sulfate Monohydrate $Li_2SO_4 \cdot H_2O$ .......... 607

T. KAMIGAICHI, T. HIHARA, H. TAZAKI and ———: Magnetic Anisotropy of the Iron Sulfide Single Crystal at α-Transformation Temperature ..........1123

HIRAKAWA Hiromasa;

———, A. MIYAHARA and K. SHIMODA: Microwave Spectra of Formaldehyde and Methylamine in the SHF Region .......... 334

A. MIYAHARA, ——— and K. SHIMODA: $l$-Type Doubling Spectra of HCN and DCN in the SHF Region .......... 335

, T. OKA and K. SHIMODA: Microwave Spectra of Formaldehyde-$d_1$,-$d_2$..1207

, T. OKA and K. SHIMODA: $l$-type Doubling Spectra of HCN and DCN..1208

HIRAKAWA Kazuyosi;

K. HASHIMOTO and ———: Electrical Properties of Stannous Telluride SnTe .......... 716

HIRAKAWA Kinshiro;

A. OKAZAKI and ———: Structural Study of Iron Selenides $FeSe_x$. I. Ordered Arrangement of Defects of Fe Atoms .......... 930

HIRONE Tokutaro;

——— and S. CHIBA: The Magnetic Properties of $FeSe_x$ with the NiAs Structure .......... 666

———, S. MAEDA, I. TSUBOKAWA: On the Magnetic Properties of the System MnSb–CrSb ..........1083

HIROTA Shoji;

Y. MIZUSHIMA, ——— and H. NOAKE: Specimen Contamination in Electron-microscope .......... 463

HONDA Kanji;

——— and Y. NAITO: (Erratum) On the Nature of Silent Electric Discharge.. 92

HONJO Goro;

———, N. KITAMURA, K. SHIMAOKA and K. MIHAMA: Low Temperature Specimen Method for Electron Diffraction and Electron Microscopy .......... 527

HORI Jun-ichi: On the Equivalence of Fluctuation-Dissipation Theorem and Irreversible Thermodynamics ..........1220

HORI Tadao;

———, T. NAGURA and M. OTSUKA: Radiative Collisions between Electronic and Molecular Beams I. Angular Momentum Distribution among OH* Radicals resulting from $H_2O$ Molecules ..........1157

HORIGUCHI Ohi;

I. OSHIDA and ———: Hydration of Ions and Coordinate Bond .......... 330

HOSOYA Sukeaki;

———, S. SATAKE and S. TAKAGI: On the Polygonization of Rock Salt Crystals ..........1228

: On the Polygonized Domain Pattern in Bent and Annealed NaCl Crystals Visualized by Colour Centre Colloids ..........1231

HUZITA Humiaki;

S. NAKAGAWA, E. TAMAI, ——— and K. OKUDAIRA: On the Analysis of the Slow Particles Emitted from Cosmic-Ray Stars (I) .......... 191

IBRAHIM Ali. A. K.;

——— and Ph. D. LONDON: On the Oscillating Cylinder Viscometer for Elastic Liquids II ..........1208

IBUKI Sumiaki;
——— and K. AWAZU: A Method of Growing CdS Single Crystals by Sublimation ........1297
IDA Mitsuo: On the Dielectric Anomaly of $n$-Higher Alcohols in the " Waxy State "..1121
IIDA Shūichi: Phase Diagram of Iron-Cobalt-Oxygen System (I) Experimental Study .. 846
———: Note on Superexchange Interactions and Magnetic Lattices of the Rhombohedral Sesquioxides ........1300
IIJIMA Sigeru;
S. TANAKA T. MASUMI and ———: Change of Photocurrent of CdS Single Crystal in a Magnetic Field........ 90
IKEDA Susumu;
H. SUZUKI, ——— and S. TAKEUCHI: Deformation of Thin Copper Crystals .. 382
IKEDA Takuro;
M. MARUTAKE and ———: Elastic Constants of Porous Materials, Especially of $BaTiO_3$ Ceramics........ 814
IMAEDA Kuni;
——— and M. KAZUNO: An Analysis of Two $\tau$-Meson Decays ........ 85
INUI Teturo;
———, S. HARASAWA and Y. OBATA: Note on the Electron Spin Resonance of the $V_1$-center ........ 612
IRIE Taizo: Magnetoresistance Effect of Lead Sulphide Group of Semiconductors I. Measurements on Natural Specimens of Lead Sulphide ........ 840
ISHII Zensho;
E. SAWAGUCHI, T. MITSUMA and ———: Double Hysteresis Loop of $(Pb_{\lambda}Ca_{1-\lambda})TiO_3$ Ceramics ........1298
ISHIKAWA Yoshikazu;
——— and S. SAWADA: The Study on Substances having the Ilmenite Structure I. Physical Properties of Synthesized $FeTiO_3$ and $NiTiO_3$ Ceramics ........ 496
ISHIKAWA Yoshikazu;
——— and S. SAWADA: Effective Use of Radiation and Thermal Shields in a Vacuum Furnace ........1184
ISHIMATSU Toshiyuki;
I. NONAKA, S. MORITA, N. KAWAI, ———, S. SUEMATSU, K. TAKESHITA, Y. NAKAJIMA and Y. WAKUDA: On the Neutrons from the $N^{14}(d, n)O^{15}$ Reaction .. 1
ISHIWARI Ryutaro;
———, S. YAMASHITA, K. YUASA and K. MIYAKE: On the Ionization-energy Relation for Alpha-particles in Air ........ 337
ISHIWATARI Keiko;
H. KAWAMURA, E. OTSUKA and ———: The Quadrupolar Effect in Alkali Halide Mixed Crystals ........1064
ISOYA Akira;
———, K. GOTO and T. MOMOTA: The Angular Distribution of $\alpha$-particles from the Reaction $^{19}F(p\alpha)^{16}O^*(\pi)^{16}O$ ........ 899
ITOH Noriaki;
T. SUITA and ———: Dielectric Breakdown and Pulse Conduction of Silver Halide Crystals ........ 474
ITOH Takashi: Molecular Structure of Methylamine ........ 264
ITOH Noriaki;
——— and T. SUITA: Photoconduction of Silver Chloride Crystals ........1124
KAGEYAMA Seizaburo: The Multiple Scattering of Fast Electrons........ 348
KAMBE Kenjiro;
——— and J. F. OLLOM: Dipolar Brodening of the Central Line of a Magnetic Resonance for Half-integral Spin ........ 50
KAMIGAICHI Takahiko;
———, T. HIHARA, H. TAZAKI and E. HIRAHARA: Electrical Conductivity of Iron Sulfides Single Crystals at the Temperature Range of $\alpha$-transformation.. 606

KAMIGAICHI Takahiko;

-, T. HIHARA, H. TAZAKI and E. HIRAHARA: Magnetic Anisotropy of the Iron Sulfide Single Crystal at $\alpha$-Transformation Temperature ....1123

KAMIMURA Hiroshi: On the Magnetic Moment and $g$-Value of Complex Ions ....1171

KANAI Yasuo and R. NII: On the Impurity Conduction in Germanium .... 83

W. SASAKI and ———: Galvanomagnetic Effects of a Heavily Doped Germanium Crystal .... 894

and W. SASAKI: Oscillatory Galvanomagnetic Effects in $n$-type Indium Antimonide ....1017

KANAMORI Junjiro;

T. MORIYA, K. MOTIZUKI, — and T. NAGAMIYA: On the Magnetic Anisotropy of $FeF_2$ and $CoF_2$ .... 211

KANEKO Shin-ichi;

—, O. KUSUMOTO and S. MATSUMOTO: Observation of the High-Energy Proton-Proton Collision in Photographic Emulsion ....1129

KANEKO Shobu;

T. KIHARA, Y. MIDZUNO and ———: Virial Coefficients and Intermolecular Potential for Small Nonspherical Molecules .... 362

and T. KIHARA: Second Virial Coefficient of Helium from the Square-well Potential .... 471

S. KOBA, ——— and T. KIHARA: Non-additive Intermolecular Potential in Gases. II. Cluster Integrals ....1050

KANZAKI Hiroshi: Observation of Dislocations in Silver Halides. Part I. Annealed Crystals .... 120

: Observation of Dislocations in Silver Halides. Part II. Strained Crystals .... 126

KASUYA Tadao: Temperature Dependence of Anisotropy Energy of Ferromagnetics .. 944

KATO Kiyoe;

S. KOJIMA and — : Statistical Study of Electron Avalanches in Gaseous Discharge .... 322

S. KOJIMA, ——— and S. ANNAKA: Radio Frequency Absorption in Barium Chlorate .... 805

KATO Morio: Anomalous Enhancement of X-ray Reflection Intensity at the Boundary of Ground and Etched Regions on Crystal Surface .... 748

KATO SUSUMU;

G. SHINODA, T. SUZUKI and ———: The Soft X-ray Spectroscopy of the Solid State by the Electronic Differentiating Method: Aluminium $L_3$ .... 657

KATSURA Shigetoshi;

Y. NOMURA and ———: (Errata) Diffraction of Electromagnetic Waves by by Circular Plate and Hole .... 806

KAWAGUTI Mitutosi: On the Viscous Shear Flow around a Circular Cylinder II. Oseen's Approximation .... 570

KAWAI Nawoyuki;

I. NONAKA, S. MORITA, ———, T. ISHIMATSU, S. SUEMATSU, K. TAKESHITA, Y. NAKAJIMA and Y. WAKUDA: On the Neutrons from the $N^{14}(d, n)O^{15}$ Reaction .... 1

KAWAJI Shinji;

A. KOBAYASHI and ———: Adsorption and Surface Potential of Semi Conductors, Part. II. Surface Vacancies and its Reaction with Oxygen on ZnS .... 369

KAWAMURA Hazimu;

———, E. OTSUKA and K. ISHIWATARI: The Quadrupolar Effect in Alkali Halide Mixed Crystals ....1064

KAWAMURA Ryuma;

— and H. SAITO: Reflection of Shock Waves—1 Pseudo-Stationary Case.. 584

KAZUNO Mitsuko;

K. IMAEDA and ———: An Analysis of Two $\tau$-Meson Decays .... 85

KIHARA Taro;

, Y. MIDZUNO and S. KANEKO: Virial Coefficients and Intermolecular Potential for Small Nonspherical Molecules ................................ 362

S. TANEKO and : Second Virial Coefficient of Helium from the square-well Potential ................................................................ 471

Y. MIDZUNO and —— : Non-additive Intermolecular Potential in Gases I. van der Waals Interactions ................................................1045

S. KOBA, S. KANEKO and - - : Non-additive Intermolecular Potential in Gases. II. Cluster Integrals................................................1050

KIHO Hiroshi;

S. MARUYAMA and : Intersections of {301}, {101} Twin Bands in Tin.. 516

KIKUCHI Makoto: Some Experiments on the Germanium Surface Layer .............. 898

---- and S. DENDA: A Microscopy Study of Etched Germanium Surfaces ..1127

KIM, Chul-Soo;

and K. ÔSHIMA: Experimental Studies of the Interaction of a Plane Shock Wave with a Circular Cylinder.................................... 178

: Experimental Studies of Supersonic Flow past a Circular Cylinder .. 439

KIMATA Morihiko;

and T. NOMURA: On the Electroluminescence in ZnS phosphor ...... 466

KIMOTO Kazuo: An Electron Diffraction Study on the Plastic Deformation of Aluminium Single Crystals .................................................. 485

KIMURA Harunobu;

T. MIYAUCHI and - : Electrical Properties of Cd-Sb ....................1013

KIMURA Hiroshi: On the Plastic Deformation of $\alpha$-brass Single Crystals by Compression ........................................................................ 53

KIMURA Itsuro;

——— and S. KUMAGAI: Spark Ignition of Flowing Gases .................. 599

KIMURA Kiichi;

, I. KUMABE, K. MIYAKE, H. OGATA and K. MIYASITA: The Reaction O$^{16}(n, \alpha)$C$^{13}$ ........................................................................1211

KINOSITA Koreo;

and J. NAKAYAMA: Spiral Cleavage of Mica..........................1055

KITAMURA Norihisa;

G. HONJO, , K. SHIMAOKA and K. MIHAMA: Low Temperature Specimen Method for Electron Diffraction and Electron Microscopy .................. 527

KITANO Yoshiharu;

A. YOSHIMORI and : Theory of the Lattice Vibration of Graphite...... 352

KOBA Saburo;

, S. KANEKO and T. KIHARA: Non-additive Intermolecular Potential in Gases. II. Cluster Integrals..............................................1050

KOBAYASHI Akio;

and S. KAWAJI: Adsorption and Surface Potential of Semiconductors, Part II. Surface Vacancies and its Reaction with Oxygen on ZnS .......... 369

KOBAYASHI Shigehiro: Fermi Part $\eta_0$ of the TF Function for Free Positive Ion...... 609

KOBAYASI Syôiti: Energy Band Structure of the Carborundum SiC Crystal .......... 175

KOIDE Shoichiro: A Lattice Theory of Quantum Fluids ............................ 7

KOJIMA Morio;

Y. SHIMOMURA, and S. SAITO: Crystal Structure of Ferromagnetic Nickel Oxide ....................................................................1136

KOJIMA Shoji;

and K. KATO: Statistical Study of Electron Avalanches in Gaseous Discharge ...................................................................... 322

, K. KATO and S. ANNAKA: Radio Frequency Absoption in Barium Chlorate ........................................................................ 805

S. OGAWA, S. HAGIWARA, Y. ABE and M. MINEMATSU: Structure of Nuclear Quadrupole Resonance Line I. Solid Iodine........................ 964

: (Errata) Structure of NQR Line I. Solid Iodine ....................1128

KOJIMA Tadanobu: Mechanism for Self-Diffusion in Metallic Lithium ............... 717

KOKAME Jun;
and S. YAMASHITA: Electrostatic Deflection of a Cyclotron Ion Beam .. 332

KOMATSU Hachiro: Proton Magnetic Resonance Absorption Spectra of Long Chain Normal Primary Alcohol of Probable Carbon Number 32 ................. 755

KONDOH Hisamoto;
E. UCHIDA and ———: Magnetic Properties of Nickel Telluride ........... 21
E. UCHIDA, ——— and N. FUKUOKA: Magnetic and Electrical Properties of Manganese Telluride ............ 27

KOSHINO Shigeharu: On the Low Temperature Conduction Phenomena in Semiconductors ............ 608

KOYAMA Ryuzo;
A. NISHIOKA and ———: Apparent Molecular Weight of Polytrifluorochloroethylene ............ 139

KUBO Ryogo;
and Y. OBATA: Note on the Paramagnetic Susceptibility and the Gyromagnetic Ratio in Metals ............ 547

KUMABE Isao;
K. KIMURA, ———, K. MIYAKE, H. OGATA and K. MIYASITA: The Reaction $O^{16}(n, \alpha)C^{13}$ ............ 1211

KUMAGAI Seiichiro;
I. KIMURA and ———: Spark Ignition of Flowing Gases ............ 599

KUSUMOTO Hazime: Proton Magnetic Resonance in Polyisoprene, Polychloroprene and Polyisobutylene ............ 1015

KUSUMOTO Osamu;
S. KANEKO, ——— and S. MATSUMOTO: Observation of the High-Energy Proton-Proton Collision in Photographic Emulsion ............ 1129

MAEDA Hiroshi;
H. HASHIMOTO, E. YODA and ———: On the Elastic Scattering of Electron observed in Kikuchi Patterns ............ 464

MAEDA Seiitiro;
T. HIRONE, ———, I. TSUBOKAWA: On the Magneties of the System MnSb-CrBb ............ 1033

MANIWA Hideyo;
K. TANAKA, H. ABE and ———: Variation of the Young's Modulus of the Alloy $Mg_3Cd$ with the Order-Disorder Transition ............ 328

MARUTAKE Masakazu: A Calculation of Physical Constants of Ceramic Barium Titanate ............ 807
— and T. IKEDA: Elastic Constants of Porous Materials, Especially of $BaTiO_3$ Ceramics ............ 814

MARUYAMA Saiyu;
and H. KIHO: Intersections of {301}, {101} Twin Bands in Tin ...... 516

MASUDA Yoshika: Nuclear Magnetic Resonance in Molecular Chlorine Compounds .... 670

MASUMI Taizō;
S. TANAKA, and S. IIJIMA: Change of Photocurrent of CdS Single Crystal in a Magnetic Field ............ 90

MATSUDA Hisashi: Focusing Properties of a large Mass Spectrograph newly constructed at Osaka University ............ 183

MATSUMOTO Shigeo;
S. KANEKO, O. KUSUMOTO and ———: Observation of the High-Energy Proton-Proton Collision in Photographic Emulsion ............ 1129

MATUMURA On;
H. TUBOTA, H. SUZUKI and ———: The Temperature Dependence of the Optical Absorption of Zinc Selenide ............ 610

MATSUNOBU Yaso's: Application of Imai's Transonic Approximation Method to the Compressible Flow past a Kaplan Bump ............ 452

MATSUURA Kiyokata;

, Y. SUGIURA and G. M. HATOYAMA: Frequency Shift in Ammonia Absorption ........................................ 1301

MIDZUNO Yukio;

T. KIHARA, ——— and S. KANEKO: Virial Coefficients and Intermolecular Potential for Small Nonspherical Molecules ........................ 362

and T. KIHARA: Non-additive Intermolecular Potential in Gases I. van der Waals Interactions ........................................ 1045

MIHAMA Kazuhiro;

G. HONJO, N. KITAMURA, K. SHIMAOKA and : Low Temperature Specimen Method for Electron Diffraction and Electron Microscopy ............ 527

MINEMATSU Midori;

S. KOJIMA, S. OGAWA, S. HAGIWARA, Y. ABE and ——: Structure of Nuclear Quadrupole Resonance Line I. Solid Iodine ........................ 964

MISAWA Toshio: A Note on the Extended Theory of the Junction Transistor ........ 728

MITSUHASHI Hiroji;

—— and T. NAKAYAMA: Apparatus for the Study of Spectral Response of Photoelectric Surface ........................................ 308

MITSUMA Takeshi;

E. SAWAGUCHI, ——— and Z. ISHII: Double Hysteresis Loop of $(Pb_{\lambda}Ca_{1-\lambda})TiO_3$ Ceramics ........................................ 1298

MITUI Tadayasu: Influence of Magnetic Field on the Precipitation Process of Ferromagnetic Phase in Cu-Fe Alloy (I) ........................ 895

MIWA Hirohide: A Direct Reading Counting Rate Ratio Meter ........................ 458

MIYAHARA Akira;

H. HIRAKAWA, ——— and K. SHIMODA: Microwave Spectra of Formaldehyde and Methylamide in the SHF Region ........................ 334

, H. HIRAKAWA and K. SHIMODA: $l$-Type Doubling Spectra of HCN and DCN in the SHF Region ........................................ 335

MIYAHARA Syohei;

and H. OHNISHI: Cation Arrangement and Magnetic Properties of Copper Ferrite-Chromite Series ........................................ 1296

MIYAKE Kozo;

R. ISHIWARI, S. YAMASHITA, K. YUASA and ——: On the Ionization-energy Relation for Alpha-particles in Air ........................................ 337

K. KIMURA, I. KUMABE, ———, H, OGATA and K. MIYASITA: The Reaction $O^{16}(n,\alpha)C^{13}$ ........................................ 1211

MIYAKE Saburo;

, K. HINOTANI and K. NUNOGAKI: A Cloud Chamber Study of the Cosmic-Ray Hard Showers ........................................ 76

: A High Pressure Cloud Chamber for Cosmic Ray Observation ...... 195

MIYASITA KYOITI;

K. KIMURA, I. KUMABE, K. MIYAKE, H. OGATA and ——: The Reaction $O^{16}(n,\alpha)C^{13}$ ........................................ 1211

MIYATANI Shin-ya: Point Contact of Pt and $\gamma$-$Cu_2S$ ........................ 1059

MIYAUCHI Takeshi;

and H. KIMURA: Electrical Properties of Cd-Sb ........................ 1013

MIZUNO Hiroyuki: On the Conducting Mechanism of Oxide Coated Cathode .......... 1125

MIZUSHIMA Yoshihiko;

———, S. HIROTA and H. NOAKE: Specimen Contamination in Electron-microscope ........................................ 463

and O. OCHI: Recovery Process in the Evaporated Metal Films ...... 893

MIZUTANI Hiroshi: Determination of the End-to-End Distance of High Polymer Molecule in Solution ........................................ 245

MOCHIZUKI Takeshi;

J. OISHI. M. AWANO and ———: New Determination of the Temperature of Gold and Silver Points on the Thermodynamic Temperature Scale.......... 311

MOMOTA Teruo;
A. ISOYA, K. GOTO and ———: The Angular Distribution of α-particles from the Reaction $^{19}F(p\alpha)^{16}O^*(\pi)^{16}O$ ........ 899

MORI Hazime: A Quantum-statistical Theory of Transport Processes ........ 1029

MORI Sigeyasu;
S. SHIGETOMI and ———: Electrical Properties of $Bi_2Te_3$ ........ 915

MORITA Nobuyoshi: Optical Properties of Magnesium Fluoride Films ........ 975

MORITA Susumu;
I. NONAKA, ———, N. KAWAI, T. ISHIMATSU, S. SUEMATSU, K. TAKESHITA, Y. NAKAJIMA and Y. WAKUDA: On the Neutrons from the $N^{14}(d, n)O^{15}$ Reaction ........ 1

MOTIZUKI Kazuko;
T. MORIYA, ——— J. KANAMORI and T. NAGAMIYA: On the Magnetic Anisotropy of $FeF_2$ and $CoF_2$ ........ 211

MORIYA Tōru;
K. YOSIDA and ———: The Effects of Covalency on the Nuclear Magnetic Resonance in Ionic Crystals ........ 33

MOTIZUKI Kazuko;
——— and T. NAGAMIYA: Theory of the Ortho-Para Conversion in Solid Hydrogen ........ 93
T. MORIYA, ———, J. KANAMORI and T. NAGAMIYA: On the Magnetic Anisotropy of $FeF_2$ and $CoF_2$ ........ 211
and T. NAGAMIYA: Effect of Self-diffusion on the Ortho-para Conversion in Oxygen Contaminated Solid Hydrogen ........ 654

MURAKAMI Miyuki;
E. HIRAHARA and ———: Nuclear Magnetic Resonance Experiment on the Single Crystal of Lithium Sulfate Monohydrate, $Li_2SO_4 \cdot H_2O$ ........ 239
and E. HIRAHARA: On the Lithium Resonance in Lithium Sulfate Monohydrate $Li_2SO_4 \cdot H_2O$ ........ 607

MURAKAWA Kiyoshi: (Errata) Hyperfine Structure of the Spectrum of Ruthenium. Part III. ........ 182
———: The Quadrupole Moment of $V^{51}$ ........ 422
———: Hyperfine Structure of the Spectrum of Cu I and Test of the Hyperfine Structure Formulas ........ 774
———: Isotope Shift in the Spectra of Ne II and WI ........ 778
: Nuclear Spins Dy 163 and of Dy 161 ........ 804

MUROGA Saburo: On the Capacity of a Discrete Channel, II. Mathematical Expression of the Capacity of a Noisy Channel which is Expressible Corresponding Two Multi-state Diagrams ........ 1109

MUTO Toshinosuke;
and H. OKUNO: Electronic Structure of the Exciton. I. Localized Exciton in KCl ........ 633

NAGAI Mashige: Graphical Solution of Linear Heat Flow with Radiation ........ 329

NAGAMIYA Takeo;
K. MOTIZUKI and ———: Theory of the Ortho-Para Conversion in Solid Hydrogen ........ 93
T. MORIYA, K. MOTIZUKI, J. KANAMORI and ———: On the Magnetic Anisotropy of $FeF_2$ and $CoF_2$ ........ 211
K. MOTIZUKI and ———: Effect of Self-diffusion on the Ortho-para Conversion in Oxygen Contaminated Solid Hydrogen ........ 654

NAGAO Shigeo: Bubble Chamber Study of Electric Breakdown of Liquid ........ 1205

NAGASE Masahumi: Diffraction of Elastic Waves by a Sherical Surface ........ 279

NAGURA Takayuki;
T. HORIE, ——— and M. OTSUKA: Radiative Collisions between Electronic and Molecular Beams I. Angular Momentum Distribution among OH* Radicals resulting from $H_2O$ Molecules ........ 1157

NAITO Yoshihide;
K. HONDA and ———: (Erratum) On the Nature of Silent Electric Discharge .. 92

NAKADA Ichiro: Surface Potential and Surface Conduction of Molybdenite ..........1122

NAKAGAWA Shigeo;
———, E TAMAI, H. HUZITA and K. OKUDAIRA: On the Analysis of the Slow Particles Emitted from Cosmic-Ray Stars (I) .......... 191

NAKAGAWA Yasuaki: Change of Magnetic Susceptibility of Transition Metals and Alloys at their Melting Points .......... 855

NAKAJIMA Yutaka;
I. NONAKA, S. MORITA, N. KAWAI, T. ISHIMATSU, S. SUEMATSU, K. TAKESHITA, ——— and Y. WAKUDA: On the Neutrons from the $N^{14}(d, n)O^{15}$ Reaction .. 1

NAKAMURA Terutaro: On the Domain Structure of Rochelle Salt Crystal .......... 624
———: On the Correlation between Screw Dislocations and Twin Structure in $WO_3$ Crystal .......... 467

NAKAMURA Tutō;
——— and N. URYŪ: On the Interionic Contributions to the Specific Heat of Cobalt Ammonium Tutton Salt $Co(NH_4)_2(SO_4)_2 6H_2O$ at Very Low Temperatures .......... 760
H. TAKETA and ———: A Note on the Ground State of Antiferromagnetism .. 919

NAKAYA Toshizo: Influence of Illumination from Outside on an Ar-Hg Discharge Tube ..........1264

NAKAYAMA Jun;
K. KINOSITA and ———: Spiral Cleavage of Mica ..........1055

NAKAYAMA Tadahisa;
H. MITSUHASHI and ———: Apparatus for the Study of Spectral Response of Photoelectric Surface .......... 308

NARA Jiro;
H. HASUNUMA and ———: On the Sheen Gloss .......... 69

NARUMI Hajime: On the Eigenvalue Problem in Terms of a Complete Set of the Casimir Operators .......... 786

NAWATA Shigenori: On the Image of Phase Microscope in Metastable Region........ 87

NII Riro;
Y. KANAI and ———: On the Impurity Conduction in Germanium .......... 83

NIIRA Kazuo;
E. AIHARA and ———: The Bond Orbital Approximation for π-electron System in Benzene ..........1261

NINOMIYA Masayoshi: Rotational Intensity Distribution of the OH Band .......... 970

NISHIKAWA Tetsuji: Fine Structure of $J=1 \leftarrow 0$ Transition due to Internal Rotation in Methyl Alcohol .......... 781

NISHIOKA Atsuo;
——— and R. KOYAMA: Apparent Molecular Weight of Polytrifluorochloroethylene .......... 139
———, K. SEKIKAWA and M. OWAKI: Effect of $Fe_2O_3$ on the Properties of Barium Titanate Single Crystals .......... 180

NOAKE Haruo;
Y. MIZUSHIMA, S. HIROTA and ———: Specimen Contamination in Electronmicroscope .......... 463

NOMOTO Otohiko: Irreversible Production of Entropy and the Absorption of Sound .. 818
———: Theory of the Ultrasonic Absorption in Aqueous Solution (I). Introduction and General Theory .......... 827
———: State of Association of Water Molecules in Aqueous Solutions as deduced from Sound Velocity Data ..........1146

NOMURA Shoichiro: On a Change of Dielectric Property of $(Ba_{0.5}\cdot Sr_{0.5})TiO_3$ Ceramics due to the Thermal Treatment .......... 803
———: Solid State Reaction between Barium Titanate and Strontium Titanate 924

NOMURA Tsutomu;
M. KIMATA and ———: On the Electroluminescence in ZnS Phosphor........ 466

NOMURA Yukichi;
 ——— and S. KATSURA: (Errata) Diffraction of Electromagnetic Waves by Circular Plate and Hole...... 805

NONAKA Itaru;
 —, S. MORITA, N. KAWAI, T ISHIMATSU, S. SUEMATSU, K. TAKESHITA, Y. NAKAJIMA and Y. WAKUDA: On the Neutrons from the $N^{14}(d, n)O^{15}$ Reaction ...... 1

NUNOGAI Kan-ichi;
 S. MIYAKE, K. HINOTANI and -: A Cloud Chamber Study of the Cosmic-Ray Hard Showers ...... 76

OBATA Yukio;
 R. KUBO and ———: Note on the Paramagnetic Susceptibility and the Gyromagnetic Ratio in Metals...... 547
 T. INUI, S. HARASAWA and ———: Note on the Electron Spin Resonance of the $V_1$-center ...... 612

OCHI Osamu;
 Y. MIZUSHIMA and ———: Recovery Process in the Evaporated Metal Films.. 893

ODA Minoru;
 S. HIGASHI, I. HIGASHINO, ———, T. OSHIO, H. SHIBATA, K. WATANABE and Y. WATASE: On the Interaction of Cosmic Radiation with Materials at 32 m. w. e. and 200 m.w.e. Underground ......1021

OGATA Hiroshi;
 K. KIMURA, I. KUMABE, K. MIYAKE, ——— and K. MIYASITA: The Reaction $O^{16}(n, \alpha)C^{13}$ ......1211

OGAWA Shiro;
 D. WATANABE and ———: On the Superstructure of the Ordered Alloy $Cu_3Pd$ I. Electron Diffraction Study ...... 226
 F. E. FUJITA, D. WATANABE, M. YAMAMOTO and ———: Study of Plastic Deformation in Aluminium Crystals by Electron Diffraction and Electron Microscopy ...... 502
 M. HIRABAYASHI and ———: An X-ray Study of Ordering Processes in CuAu Single Crystals ...... 907

OGAWA Shizuko;
 S. KOJIMA, ———, S. HAGIWARA, Y. ABE and M. MINEMATSU: Structure of Nuclear Quadrupole Resonance Line I. Solid Iodine...... 964

OGHI Sunao: On the Coarsening of Non-Sag Tungsten Lamp Filament Wires ...... 593

OGUCHI Hakuro: Supersonic Jet with the Ambient Pressure corresponding to its Constant Pressure Point ...... 155

OHNISHI Haruyuki;
 S. MIYAHARA and ———: Cation Arrangement and Magnetic Properties of Copper Ferrite-Chromite Series ......1296

OHTSUKA Mieko;
 H. ABE and ———: Paramagnetic Resonance Absorption in Copper Hexapyridine Nitrate...... 896

OISHI Jiro:
 ———, M. AWANO and T. MOCHIZUKI: New Determination of the Temprature of Gold and Silver Points on the Thermodynamic Temperature Scale ...... 311

OKA Takeshi;
 H. HIRAKAWA, ——— and K. SHIMODA: Microwave Spectra of Formaldehyde-$d_1$-$d_2$ ......1207
 H. HIRAKAWA, ——— and K. SHIMODA: $l$-type Doubling Spectra of HCN and DCN ......1208

OKADA Toshihiro: The Measurement of the Galvanomagnetic Tensors of Bismuth.... 89

OKAYA Akira: A Theoretical Analysis of the Magnetic Hyperfine Structure of the Microwave Spectrum of $C_{2v}$ Molecules ...... 249
 —: The Microwave Hyperfine Spectrum of Formaldehyde ...... 258

OKAZAKI Atsushi:
———— and I. UEDA: The Crystal Structure of Stannous Selenide SnSe ...... 470
— and K. HIRAKAWA: Structural Study of Iron Selenides $FeSe_x$. I. Ordered Arrangement of Defects of Fe Atoms ........ 930

OKUDA Takayoshi;
K. YAMAMOTO and ——: On the Floating Probe Method for the Measurement of Ionized Gas ........ 57
and K. YAMAMOTO: Disturbance by Probe in Plasma ........ 177

OKUDAIRA Kiyoaki;
S. NAKAGAWA, F. TAMAI, H. HUZITA and : On the Analysis of the Slow Particles Emitted from Cosmic-Ray Stars (I) ........ 191

OKUNO Hiroshi;
T. MUTO and ———: Electronic Structure of the Exciton. I. Localized Exciton in KCl ........ 633

OLLOM John F.;
K. KAMBE and ———: Dipolar Broadening of the Central Line of a Magnetic Resonance for Half-integral Spin ........ 50

ŌMORI Yoshirō: A Device for Calibration of Anemometers for Air Flow of Low Velocities........1191

ÔNO Kazuo;
J. SHIMADA, H. ABE and ———: Paramagnetic Resonance Absorption in Copper Formate ........ 137
H. ABE and —: Paramagnetic Resonance Spectra of Some Cupric Salts (I) ........ 947

OSADA Kikusaburo: Phosphorescence of Sodium- and Potassium-Acetates ........ 425
: The Effect of Adsorbed Water on the Phosphorescence of Sodium Acetate........1014

OSHIDA Isao;
—— and O. HORIGUCHI: Hydration of Ions and Coordinate Bond ........ 330

ÔSHIMA Kôichi;
C. KIM and ———: Experiment Studies of the Interaction of a Plane Shock Wave with a Circular Cylinder ........ 178

OSHIO Takanori;
S. HIGASHI, I. HIGASHINO, M. ODA, ————, H. SHIBATA, K. WATANBE and Y. WATASE: On the Interaction of Cosmic Radiation with Materials at 32 m.w.e. and 200 m.w.e. Underground........1021

OTSUKA Eizo;
H. KAWAMURA, ———— and K. ISHIWATARI: The Quadrupolar Effect in Alkali Halide Mixed Crystals ........1064

OTSUKA Masamoto;
T. HORIE, T. NAGURA and ————: Radiative Collisions between Electronic and Molecular Beams I. Angular Momentum Distribution among OH* Radicals resulting from $H_2O$ Molecules........1157

OWAKI Masakazu;
A. NISHIOKA, K. SEKIKAWA and ————: Effect of $Fe_2O_3$ on the Properties of Barium Titanate Single Crystals ........ 180

SAITO Haruo;
R. KAWAMURA and ————: Reflection of Shock Waves—1 Pseudo-Stationary Case ........ 584

SAITO Shozo;
Y. SHIMOMURA, M. KOJIMA and -: Crystal Structure of Ferromagnetic Nickel Oxide ........1136

SAKAI Hidetsugu;
C. YAMANAKA, ——— and T. SUITA: Electron Bombardment Conductivity in Silver Bromide Single Crystall II ........ 605

SAKURAI Akira: (Errata) Decrement of Blast Wave........ 613

SAKURAI Takeo: The Flow past a Flat Plate accompanied with an Unsymetric Dead Air at Mach Number 1 ........ 710
SAKURAI Akira: The Flow due to Impulsive Motion of a Wedge, II ........ 987
SASAKI Wataru;
——— and Y. KANAI: Galvanomagnetic Effects of a Heavily Doped Germanium Crystal ........ 894
Y. KANAI and : Oscillatory Galvonomagnetic Effects in $n$-type Indium Antimonide ........1017
and M. SHIBUYA: Experimental Evidence of the Anisotropy of Hot Electrons in $n$-type Germanium ........1202
SATAKE Seiya;
S. HOSOYA, and S. TAKAGI: On the Polygonization of Rock Salt Crystals ........1228
SATO Hiroshi: Experimental Investigation on the Transition of Laminar Separated Layer ........ 702
: (Errata) Experimental Investigation on the Transition of Laminar Separated Layer ........1128
I. TANI and : Boundary-Layer Transition by Roughness Element ......1284
SAWADA Shozo:
Y. ISHIKAWA and – – : The Study on Substances having the Ilmenite Structure I. Physical Properties of Synthesized FeTiO$_3$ and NiTiO$_3$ Ceramics ........ 496
Y. ISHIKAWA and : Effective Use of Radiation and Thermal Sields in a Vacuum Furnace ........1184
: Thermal and Electrical Properties of Tungsten Oxide (WO$_3$) ........1236
: Microscopic and X-ray Studies on Tungsten Oxide (WO$_3$)........1246
SAWAGUCHI Etsuro;
, T. MITSUMA and Z. ISHII: Double Hysteresis Loop of (Pb$_\lambda$Ca$_{1-\lambda}$) TiO$_3$ Ceramics ........1298
SAWAMOTO Kenichi;
E. YAMAKA and : Photo-induced Hall Effect of V-center in KI ........ 176
SAXENA S. C.: On the Two Schemes of Approximating the Transport Coefficients (Chapman—Cowling and Kihara) ........ 367
SEKIKAWA Kyozo;
A. NISHIOKA, and M. OWAKI: Effect of Fe$_2$O$_3$ on the Properties of Barium Titanate Single-Crystals ........ 180
SHIBAOKA Yoshio: On the Transverse Vibration of an Elliptic Plate with Clamped Edge ........ 797
: On the Buckling of an Elliptic Plate with Clamped Edge I ........1088
SHIBATA Hiroyuki;
S. HIGASHI, I. HIGASHINO, M. ODA, T. OSHIO, ———, K. WATANABE and Y. WATASE: On the Interaction of Cosmic Radiation with Materials at 32 m.w.e. and 200 m.w.e. Underground ........1021
SHIBUYA Motoichi;
W. SASAKI and : Experimental Evidence of the Anisotropy of Hot Electrons in $n$-type Germanium ........1202
SHIGETA Jiro: Oriented Overgrowth of Evaporated Crystallites. Fluoride Crystallites on Cleavage Surfaces of Single Crystals........ 206
SHIGETOMI Shigenobu;
and S. MORI: Electrical Properties of Bi$_2$Te$_3$ ........ 915
SHIMADA Junji;
———, H. ABE and K. ÔNO: Paramagnetic Resonance Absorption in Copper Formate ........ 137
SHIMAOKA Kohji;
G. HONJO, N. KITAMURA, ——— and K. MIHAMA: Low Temperature Specimen Method for Electron Diffraction and Electron Microscopy ........ 527
SHIMIZU Masao: A Note on the Ferromagnetic Resonance in α Fe$_2$O$_3$ ........1078

SHIMODA Koichi;
  H. HIRAKAWA, A. MIYAHARA and - : Microwave Spectra of Formaldehyde and Methylamine in the SHF Region ........ 334
SHIMODA Koichi;
  A. MIYAHARA, H. HIRAKAWA and —- : $l$-Type Doubling Spectra of HCN and DCN in the SHF Region ........ 335
  H. HIRAKAWA, T. OKA and - : Microwave Spectra of Formaldehyde-$d_1$,-$d_2$........1207
  H. HIRAKAWA, T. OKA and ——–: $l$-type Doubling Spectra of HCN and DCN ........1208
SHIMOJI Mitsuo: On the Temperatures of Superlatties Au$_3$Cu and AuCu$_3$ ........ 91
SHIMOMURA Yasumitsu;
  , M. KOJIMA and S. SAITO: Crystal Structure of Ferromagnetic Nickel Oxide ........1136
SHIMOSE Ikuro: Statistical Theory of Phase Transition III. Application to Vapor-Liquid-Solid Equilibrium ........ 202
  : Lattice Theory of Liquid State........ 615
SHIMURA Yoshihisa;
  A. HARASIMA and - : Quantum Effects in the Theory of Surface Energy ........ 14
SHINDO Takuro: A Note on the Theory of Dislocation in Germanium........ 331
SHINNAKA Yasuhiro: On the Metastable Transition and the Crystal Structure of Ammonium Nitrate (Tetragonal Modification) ........ 393
SHINODA Gunji;
  T. SUZUKI and S. KATO: The Soft X-ray Spectroscopy of the Solid State by the Electronic Differentiating Method: Aluminium L$_3$ ........ 657
SUEMATSU Shigeru;
  I. NONAKA, S. MORITA, N. KAWAI, T. ISHIMATSU, , K. TAKESHITA, Y. NAKAJIMA and Y. WAKUDA: On the Neutrons from the N$^{14}$($d,n$)O$^{15}$ Reaction ........ 1
SUGANO Satoru;
  Y. TANABE and ———: On the Absorption Spectra of Complex Ions, III. The Calculation of the Crystalline Field Strength ........ 864
SUGAWARA Masao: The Time Lag and other Undesirable Phenomena observed in Vacuum Photo-tubes at Weak Illumination I........ 169
  : The Time Lag and Other Undersirable Phenomena Observed in Vacuum Photo-tubes at Weak Illumination II ........ 271
SUGIURA Yoshikazu;
  K. MATSUURA, - -- and G. M. HATOYAMA: Frequency Shift in Ammonia Absorption ........1301
SUITA Tokuo;
  and N. ITOH: Dielectric Breakdown and Pulse Conduction of Silver Halide Crystal ........ 474
  C. YAMANAKA, H. SAKAI and - - –: Electron Bombardment Conductivity in Silver Bromide Single Crystal II ........ 605
  N. ITOH and - : Photoconduction of Silver Chloride Crystals........1124
SUJAK Bogdan: A Remark on the Excitement of the Electrodes when a Positive Joshi Effect Inversion is Observed under Continuous Discharge ........ 719
SUMINO Kōji;
  and M. YAMAMOTO: Interaction of Dislocation with Atomic Order in Solid Solution ........ 897
SUZUKI Hideji;
  , S. IKEDA and S. TAKEUCHI: Deformation of Thin Copper Crystals ..382
SUZUKI Hiromichi;
  H. TUBOTA, – —— and O. MATUMURA: The Temperature Dependence of the Optical Absorption of Zinc Selenide........ 610

SUZUKI Tatsuro;
G. SHINODA, —— and S. KATO: The Soft X-ray Spectroscopy of the Solid State by the Electronic Differentiating Method: Aluminium $L_3$ .......... 657
TAKAGI Mieko: Electron-Diffraction Study of the Structure of Supercooled Liquid Bismuth .......... 396
TAKAGI Satio;
S. HOSOYA, S. SATAKE and ——: On the Polygonization of Rock Salt Crystals .......... 1228
TAKAHASHI Shuichiro: Internal Friction and Critical Stress of Copper Alloys .......... 1253
TAKAISHI Yorisaburo: Note on the Drang on Circular Cylinder moving with Low Speeds in a Semi-infinite Viscous Liquid bounded by a Plane Wall .......... 1004
——: Note on the Drag on a Circular Cylinder moving with Low Speeds in a Viscous Liquid between Two Parallel Walls .......... 1009
——: The Drag on a Circular Cylinder placed in a Stream of Viscous Liquid midway between Two Parallel Planes .......... 1092
TAKAKI Hideo:
—— and T. TUJI: The Measurement of Magnetostriction by means of Strain Gauge .......... 1153
TAKAMI Hideo: A Study of the Compressible Flow past a Cherry Profile .......... 145
——: A Study of the Compressible Flow past Tomotika-Tamada's Profiles .......... 446
TAKEISHI Yoshiyuki: Auger Ejections of Electrons from Barium Oxide by Inert Gas Ions and the Cathode Fall in the Normal Glow Discharges .......... 676
TAKESHITA Kenji;
I. NONAKA, S. MORITA, N. KAWAI, T. ISHIMATSU, S. SUEMATSU, ——, Y. NAKAJIMA and Y. WAKUDA: On the Neutrons from the $N^{14}(d, n)O^{15}$ Reaction .......... 1
TAMAI Eiji;
S. NAKAGAWA, ——, H. HUJITA and K. OKUDAIRA: On the Analysis of the Slow Particles Emitted from Cosmic-Ray Stars (I) .......... 191
TAKEUCHI Sakae;
H. SUZUKI, S. IKEDA and ——: Deformation of Thin Copper Crystals .......... 382
TAMAKI Fumio: A Divergent Shock Tube for Obtaining Supersonic Flows .......... 434
TANABE Yukito;
—— and S. SUGANO: On the Absorption Spectra of Complex Ions, III. The Calculation of the Crystalline Field Strength .......... 864
——: On the Expansion Formula of Atomic Orbitals in Spherical Harmonics around Another Center .......... 980
TANAKA Kayako;
——, H. ABE and H. MANIWA: Variation of the Young's Modulus of the Alloy $Mg_3Cd$ with the Order-Disorder Transition .......... 328
TANAKA Shōji;
——, T. MASUMI and S. IIJIMA: Change of Photocurrent of CdS Single Crystal in a Magnetic Field .......... 90
TANEDA Sadatoshi: Experimental Investigation of the Wakes behind Cylinders and Plates at Low Reynolds Numbers .......... 302
——: Experimental Investigation of the Wake behind a Sphere at Low Reynolds Numbers .......... 1104
TANI Itiro;
—— and H. SATO: Boundary-Layer Transition by Roughness Element .......... 1284
TANIGUCHI Satoshi;
—— and M. YAMAMOTO: On the Uniaxial Anisotropy Induced by Magnetic Annealing in Ferrites .......... 604
TAKESHITA Kenji;
I. NONAKA, S. MORITA, N. KAWAI, T. ISHIMATSU, S. SUEMATSU, ——, Y. NAKAJIMA and Y. WAKUDA: On the Neutrons from the $N^{14}(d, n)O^{15}$ Reaction .......... 1

TAKETA Hiroshi;
 and T. NAKAMURA: A Note on the Ground State of Antiferromagnetism ........ 919
TANISAKI Sigetosi: Growth Spirals on Cryslals of WO$_3$ ........ 620
TAOKA Tadami;
 and S. AOYAGI: Electron Microscopic Study on the Structure of Mosaic Boundaries in Ni–Mn Single Crystal ........ 522
 : Magnetic After-Effect in Ni$_3$Mn Alloy ........ 537
TATSUZAKI Itaru;
 Y. YOKOZAWA and : Sub-microwave Absorptions in Potassium Bromate 85
TAZAKI Hideo;
 T. KAMIGAICHI, T. HIHARA, ——— and E. HIRAHARA: Electrical Conductivity of Iron Sulfides Single Crystals at the Temperature Range of α-transformation ........ 606
 T. KAMIGAICHI, T. HIHARA, and E. HIRAHARA: Magnetic Anisotropy of the Iron Sulfide Single Crystal at α-Transformation Temperature ........1123
TERAO Nobuzo;
 J. J. TRILLAT, ——, L. TERTIAN et H. GERVAIS: Application de la Méthod de Décapage Ionique en Diffraction Electronique: Etude de la Structure de Dépôts Thermiques d'Or sur des Supports Cristallisés ou Amorphes ........ 406
TERTIAN Léa;
 J. J. TRILLAT, N. TERAO, ——— et H. GERVAIS: Application de la Méthode de Décapage Ionique en Diffraction Electronique: Etude la Structure de Dépôts Thermiques d'Or sur des Supports Cristallisés ou Amorphes ........ 406
TOMISHIMA Yasuo;
 S. ASANO and ———: Calculation of the Cohesive Energy of Zincblende .... 644
TORIZUKA Kazuo: Pure Quadrupole Spectra of Phosphonitrile Chloride Polymers .... 84
TORIZUKA Yosiharu;
 T. FUJIMURA and ———: Ferromagnetic Resonance Absorption in a Pyrrhotite Single Crystal ........ 327
TRILLAT Jean Jacques;
 —, N. TERAO, L. TERTIAN et H. GERVAIS: Application de la Méthode de Décapage Ionique en Diffraction Electronique: Etude la Structure de Dépôts Thermiques d'Or sur des Supports Cristallisés ou Amorphes........ 406
TSUBOKAWA Ichiro: The Magnetic Properties of Chromium-Tellurium-Selenium System ........ 662
 T. HIRONE, S. MAEDA, ——: On the Magnetic Properties of the System MnSb-CrSb........1083
TUBOTA Hirosi;
 ——, H. SUZUKI and O. MATUMURA: The Temperature Dependence of the Optical Absorption of Zinc Selenide........ 610
TSUJI Hiroshi: Experimental Studies on the Spectrum of Isotropic Turbulence behind Two Grids ........1096
TSUJI Toshiro;
 H. TAKAKI and ——: The Measurement of Magnetostriction by means of Strain Gauge ........1153
TSUKADA Kineo: Zeeman Splitting of Nuclear Quadrupole Resonance Line of Iodine.. 956
TSUYA Yûko;
 S. YOSHIDA and ——: The Temperature Dependence of the Electrical Resistivity of the β-phase Titanium-Molybdenum Alloys ........1206
UCHIDA Enji;
 and H. KONDOH: Magnetic Properties of Nickel Telluride........ 21
 , H. KONDOH and N. FUKUOKA: Magnetic and Electrical Properties of Manganese Telluride ........ 27
 : Note on the Ferromagnetism of CoTe ........ 465
UEDA Ikuhiko;
 A. OKAZAKI and : The Crystal Structure of Stannous Selenide SnSe .. 470
UEMURA Yasutada: On the Coupled Dislocations along a Grain Boundary ........ 479

URYŪ Norikiyo;

T. NAKAMURA and ——: On the Interionic Contributions to the Specific Heat of Cobalt Ammonium Tutton Salt $Co(NH_4)_2(SO_4)_2 6H_2O$ at Very Low Temperatures........ 760

——: Note on the Magnetic Anisotropy of the Cobalt Ammonium Tutton Salt $Co(NH_4)_2(SO_4)_2 \cdot H_2O$........ 770

WADA Yasaku;

—— and K. YAMAMOTO: Temperature Dependence of Velocity and Attenuation of Ultrasonic Waves in High Polymers........ 887

——: Pressure Dependence of Sound Velocity in Organic Liquids........1203

WAKUDA Yoshihisa;

I. NONAKA, S. MORITA, N. KAWAI, T. ISHIMATSU, S. SUEMATSU, K. TAKESHITA, Y. NAKAJIMA and ——: On the Neutrons from the $N^{14}(d, n)O^{15}$ Reaction .. 1

WATANABE Denjiro;

—— and S. OGAWA: On the Superstructure of the Ordered Alloy $Cu_3Pd$ I. Electron Diffraction Study........ 226

F. E. FUJITA, ——, M. YAMAMOTO and S. OGAWA: Study of Plastic Deformation in Aluminium Crystals by Electron Diffraction and Electron Microscopy........ 502

——: Electron Diffraction Study on Thin Alloy Films of Aluminium-Silver System........1072

WATANABE Hiroshi: Experimental Evidence for the Collective Nature of the Characteristic Energy Loss of Electrons in Solids—Studies on the Dispersion Relation of Plasma Frequency—........ 112

WATANBE Kenzi;

S. HIGASHI, I. HIGASHINO, M. ODA, T. OSHIO, H. SHIBATA, —— and Y. WATASE: On the Interaction of Cosmic Radiation with Materials at 32 m.w.e. and 200 m.w.e. Underground........1021

WATANABE Yasuyoshi: On the Electron Diffraction Patterns from the Oriented Silver Films........ 740

WATASE Yuzuru;

S. HIGASHI, I. HIGASHINO, M. ODA, T. OSHIO, H. SHIBATA, K. WATANABE and ——: On the Interaction of Cosmic Radiation with Materials at 32 m.w.e. and 200 m.w.e. Underground........1021

YAGI Hisao: On the Absorption of Light by Colour-centres in the Region between F-band and M-band........ 430

——: Transformations of Various Centres among Each Other in Coloured Alkali-halide Crystals........ 723

YAJIMA Tatsuo: Emitter Current Noise in Junction Transister........1126

YAMAGUCHI Jiro: On the Inductive Reactance and Negative Resistance in the Transistor........ 717

YAMAKA Eizo;

—— and K. SAWAMOTO: Photo-induced Hall Effect of V-center in KI...... 176

YAMAMOTO Keiji;

Y. WADA and ——: Temperature Dependence of Velocity and Attenuation of Ultrasonic Waves in High Polymers........ 887

YAMAMOTO Kenzo;

—— and T. OKUDA: On the Floating Probe Method for the Measurement of Ionized Gas........ 57

T. OKUDA and ——: Disturbance by Probe in Plasma........ 177

YAMAMOTO Mikio;

S. TANIGUCHI and ——: On the Uniaxial Anisotropy Induced by Magnetic Annealing in Ferrites........ 604

F. E. FUJITA. D. WATANABE, —— and S. OGAWA: Study of Plastic Deformation in Aluminium Crystals by Electron Diffraction and Electron Microscopy........ 502

K. SUMINO and ———: Interaction of Dislocations with Atomic Order in Solid Solution ........ 897
YAMAMOTO Misazo: The Visco-elastic Properties of Network Structure I. General Formalism ........ 413
YAMANAKA Chiyoe;
, H. SAKAI and T. SUITA: Electron Bombardment Conductivity in Silver Bromide Single Crystall II ........ 605
YAMASHITA Sukeaki;
J. KOKAME and ·: Electrostatic Deflection of a Cyclotron Ion Beam .... 332
R. ISHIWARI, ———, K. YUASA and K. MIYAKE: On the Ionization-energy Relation for Alpha-particles in Air ........ 337
YASUHARA Michiru: On the Hypersonic Viscous Flow past Slender Bodies of Revolution ........ 878
YASUOKA Yoshio: On the Space Charge affected by the Magnetic Field Part II ......1292
YODA Eiji;
H. HASHIMOTO, and H. MAEDA: On the Elastic Scattering of Electrons observed in Kikuchi Patterns ........ 464
YOKOBORI Takeo: On the Frequency Dependence of the Fatigue of Metals .......... 715
YOKOZAWA Yasaburo;
and I. TATSUZAKI: Sub-microwave Absorptions in Potassium Bromate 85
YOSHIDA Susumu: Electron Diffraction and Microscope Study of the Surface Structure of Copper Single Crystals ........ 129
– and Y. TSUYA: The Temperature Dependence of the Electrical Resistivity of the $\beta$-phase Titanium-Molybdenum Alloys ........1206
YOSHIMORI Akio;
——— and Y. KITANO: Theory of the Lattice Vibration of Graphite ........ 352
YOSHIDA Kei;
and T. MORIYA: The Effects of Covalency on the Nuclear Magnetic Resonance in Ionic Crystals ........ 33
YUASA Kazunori;
R. ISHIWARI, S. YAMASHITA, and K. MIYAKE: On the Ionization-energy Relation for Alpha-particles in Air ........ 337

DATE DUE

OVERNIGHT APR 13 '71
MAR 21 '72 OVERNIGHT
OVERNIGHT JAN 10 [illegible]
SEP 1 [illegible] '76
RES. APR 13 '77
JUN 2 [illegible]
RES. SEP [illegible] '79

PERIODICALS MUST BE RETURNED
TO PERIODICALS DESK ONLY

GAYLORD PRINTED IN U.S.A.

THE UNIVERSITY OF ILLINOIS AT CHICAGO
3 8198 314 284 124